

PROCEEDINGS

**Fourth International Conference on
Science, Engineering & Environment**



SEE-2018

12-14 November 2018

Meitetsu New Grand Hotel, Nagoya, Japan

Edited by

Zakaria Hossain

Jim Shiau

ISBN: 978-4-909106001 C3051



SEE 2018, NAGOYA, JAPAN
SCIENCE, ENGINEERING AND ENVIRONMENT

PROCEEDINGS OF FOURTH INTERNATIONAL CONFERENCE – SEE 2018
SCIENCE, ENGINEERING & ENVIRONMENT NAGOYA, JAPAN 12-14 NOVEMBER, 2018

Science, Engineering and Environment

Edited by

Prof. Zakaria Hossain

Graduate School of Bioresources

Mie University, Japan

Dr. Jim Shiau

School of Civil Engineering and Surveying

University of Southern Queensland, Australia



THE GEOMATE INTERNATIONAL SOCIETY

Copyright @ 2018 by The GEOMATE International Society

All rights reserved. In principle, no part of this publication or the information contained herein may be reproduced in any form or by any means, translated in any language, stored in any data base or retrieval system, or transmitted in any form or by any means without prior permission in writing from the publisher.

Disclaimer: The editors and the publisher have tried their best effort to ensure the integrity and the quality of this publication and information herein. However, they give no warranty of any kind, expressed or implied with regard to the material contained in this book, and will not be liable in any event for the consequences of its use.

Published by:
The GEOMATE International Society
Tsu city, Mie, Japan
E-mail: society@geomate.org
<http://www.geomate.org/>

ISBN Number: 978-4-909106018 C3051

Table of Contents

	Preface	xii
	Organization	xiii
ID	Keynote Papers	1
1k	RUNOFF CHARACTERISTICS OF DEBRIS FLOW FLOWING DOWN A TORRENT OF MILD GRADIENT Naomasa Honda	2
2k	MECHANICAL PROPERTY OF CHLOROPRENE BEARING PAD FOR BRIDGE UNDER CYCLIC TEMPERATURE CHANGE Hidenori Tanaka, Kazuki Kurosawa and Masatake Yoshino	7
	Technical Papers	13
ID	Science	14
4503	EFFECT OF OKRA AND TANGERINE RATIOS ON PRODUCTION OF MIXED JUICE WITH LYCOPENE SUPPLEMENTATION Wattana Wirivutthikorn	15
4508	OPTIMAL RAIN GAUGES NETWORK USING GEOSTATISTICS AND HYBRID PARTICLE SWARM-SIMULATED ANNEALING OPTIMIZATION Mohd Khairul Bazli Mohd Aziz, Fadhilah Yusof, Zalina Mohd Daud, Zulkifli Yusop, Mohammad Afif Kasno	20
4513	SCREENING CRUDE EXTRACTS FROM PIPER SPP. ON COLLETOTRICHUM SP. AND PHYTOPHTHORA SP. CAUSING PLANT DISEASE Pornprapa Kongtragoul, Parinya Janthong, Theerachart Leepasert, and Chalernpol Suwanphakdee	26
4519	EXPRESSION OF HYALURONAN SYNTHASE (hasA) AND PRODUCTION OF HYALURONIC ACID THROUGH BIOSYNTHESIS IN RECOMBINANT ESCHERICHIA COLI Lai Zee Wei, Aayushree Kharel and Chong Jun Yi	30
4521	THE UTILIZATION OF THE MITOCHONDRIAL COI AND THE NUCLEAR HISTONE H3 GENES FOR DNA BARCODING STUDY OF INTERTIDAL SHELLLED GASTROPODS FROM NADA COAST IN WAKAYAMA PREFECTURE, JAPAN Nagisa Nakaji, Shoma Iwamoto, Shinnosuke Teruya, Masataka Kusube, Akira Kosaka, Takenori Sasaki, Davin H. E. Setiamarga	38
4527	THE EFFECTS OF THAI MASSAGE ON LEG MUSCLE OXYGENATION AND TIME TO FATIGUE IN HEALTHY MALE SUBJECTS Wirapong Sucharit, Wichai Eungpinichpong, Uraiwan Chatchawan, and PanneePeungsuwan	46
4551	APPLICATION OF SCMR AND FLUORESCENCE FOR CHLOROPHYLL MEASUREMENT IN SUGARCANE Darika Bunphan, Naris Sinsiri and Ruchuon Wanna	53
4567	THE EFFECTS OF AGROCHEMICAL RESIDUES ON AQUATIC INVERTEBRATES IN SEMI-ORGANIC RICE FIELDS Pattira Kasamesiri and Wipavee Thaimuangphol	59
4577	THE EFFECT OF SOIL DEPTH ON GROWTH OF CLOVER FERN AND USING CLOVER FERN ON THE GERMINATION OF FERN SPORE Sawat Pimsuwan and Yaowarat Wongsrisakulkaew	64
4580	CHEMICAL COMPOSITION AND INSECTICIDAL ACTIVITY OF ESSENTIAL OIL FROM INDIAN BORAGE AGAINST MAIZE WEEVIL Ruchuon Wanna and Jiraporn Krasaetep	70

4583	ANGIOTENSIN CONVERTING ENZYME INHIBITOR ACTIVITY OF THE SOYBEAN TEMPEH PROTEIN AS FUNCTIONAL FOOD Sri Yadiyal Chalid, Sandra Hermanto Amalia Rahmawati	75
4590	THE MODIFIED DECOMPOSITION METHOD FOR SOLVING VOLTERRA INTEGRAL EQUATION OF THE SECOND KIND USING MAPLE Dalal Adnan Maturi	81
4594	STRUCTURE-BASED VIRTUAL SCREENING OF INDONESIAN NATURAL PRODUCT COMPOUNDS AS EBOLA VIRUS VP30 PROTEIN INHIBITORS Givan Andris Tio, Andrei Bernadette, Mochammad Arfin Fardiansyah Nasution, Puteri Aprilia Sitadevi, Syahrul Ridzki Pratama, and Usman Sumo Friend Tambunan	84
4629	EFFECTS OF PIPERACEAE PLANTS EXTRACTS ON INHIBITION OF <i>Aspergillus flavus</i> AND SEED GERMINATION OF MAIZE (<i>Zea mays</i>) Chua Jedton, A. and Boonkorn, P.	91
4638	FORMULATION OF THE BODY SCRUB CREAM CONTAINING MORINGA SEED POWDER (<i>MORINGA OLEIFERA</i>) AND ITS EXAMINATION DERMAL ACUTE IRRITATION Hendrawati, Annita Karunia Savitri, Nina Fitriyati, Aulia Andi Mustika	95
4645	COMPATIBLE ACTION GRAPH FOR FINITE CYCLIC GROUPS OF p -POWER ORDER Mohammed Khalid Shahoodh, Mohd Sham Mohamad, Yuhani Yusof, Sahimel Azwal Sulaiman and Nor Haniza Sarmin	101
4650	FRAGMENT-BASED DRUG DESIGN TO INHIBIT DNA METHYLTRANSFERASE 1 (DNMT1) FOR BREAST CANCER THERAPY Ade Hanna Natalia, Ahmad Husein Alkaff, Mutiara Saragih, Ina Nur Istiqomah, and Usman Sumo Friend Tambunan	107
4658	CONSTRUCTION AND ANALYSIS OF M-POINT NON-STATIONARY SUBDIVISION SCHEME Mehwish Bari, Najma Abdul Rehman and Mehboob Alam	113
4673	ECOLOGY OF RUMINAL MICROORGANISMS UNDER THE INFLUENCE OF QUERCUS CORTEX EXTRACT Galimzhan Duskaev, Il'shat Karimov, Georgy Levakhin, Baer Nurzhanov, Albert Rysaev and Hamdiya Dusaeva	118
4679	STUDY OF THE UTILIZATION OF CU(II) MODIFIED LIQUID SMOKE TO INHIBIT THE GROWTH OF FUNGI (<i>SCHIZOPHYLLUM COMMUNE</i>) Muhammad Faisal, Shara Utari, Zammera Hayvia, and Ilham Maulana	126
4688	SHORT-TERM EFFECTIVENESS OF INNOVATION PILLOW RELAX TO STRESS AND HEART RATE VARIABILITY IN THE ELDERLY Peerada Damapong and Pongmada Damapong	131
4689	EFFECTIVENESS OF HERBAL STEAM FOR REDUCING STRESS IN PATIENTS DIABETICS Pongmada Damapong and Peerada Damapong	135
4690	EFFICIENCY OF INDIAN BORAGE ESSENTIAL OIL AGAINST COWPEA BRUCHIDS Ruchuon Wana and Phanthiwa Kwang-Ngoen	139
4694	THE CAPACITY OF SOIL WATER INFILTRATION UNDER HORTICULTURAL CROPS IN THE WATERSHED UPSTREAM SUMANI Aprisal and Bambang Istijono	144
4696	DISCOVERY OF NOVEL DNMT-1 INHIBITOR BY FRAGMENT-BASED DRUG DESIGN AS A POTENTIAL BREAST CANCER TREATMENT Mutiara Saragih, Ahmad Husein Alkaff, Ade Hanna Natalia, Ina Nur Istiqomah, and Usman Sumo Friend Tambunan	149
4697	NITRIDING OF PURE TITANIUM BY HIGH DENSITY PLASMA USING H ₂ -N ₂ GAS MIXTURE AT LOW TEMPERATURE Dionysius J. D. H. Santjojo, Masruroh, Setyawan P. Sakti, Maharani S. Rajapadni	155
4698	OPTICAL EMISSION SPECTROSCOPY STUDIES DURING NITROGEN PLASMA OF POLYSTYRENE SURFACES MODIFICATION Masruroh, Dionysius J. D. H. Santjojo Heraniawati, Muhamad A. Abdillah, Tyas N Zafirah and Eka Maulana, Setyawan P. Sakti	160

4706	EFFECTS OF SOIL QUALITY ON EATING QUALITY OF 'Namwa' BANANA (Musa ABB) FRUIT Pannipa Youryon and Suriyan Supapvanich	164
4708	ASSESSMENT OF N-(3-OXOHEXOYL)-L-HOMOSERINE LACTONE AND VEGETABLE MOLECULES IN VITRO Il'shat Fayzelgayanovich Karimov, Galimzhan Kalikhanovich Duskaev	169
4709	SIMULATION SEA SURFACE TEMPERATURE OVER GULF OF THAILAND BY USING ROMS MODEL Pramet Kaewmesri, Usa Humphries and Zhu Jiang	176
4726	EFFECTS OF SEED PREPARATION, SOWING MEDIA, SEED SOWING RATE AND HARVESTING PERIOD ON THE PRODUCTION OF CHIA MICROGREENS Anjana Junpatiw, Akarapon Sangpituk	181
4728	EFFECTS OF PLANTING SUBSTRATES SUPPLEMENTED WITH VERMICOMPOST AND VERMICOMPOST FORTIFIED WITH <i>Trichoderma asperellum</i> CB-PIN-01 ON GROWTH AND PYTHIUM ROOT ROT OF LETTUCE Phraomas Charoenrak, Chiradej Chamswarn, Wanwilai Intanoo and Naowarat keawprasert	186
4738	EFFECT OF OZONE MICROBUBBLES WITH VARIOUS TEMPERATURES ON THE CHLORPYRIFOS INSECTICIDE REMOVAL IN TANGERINE CV. SAI NAM PHUENG Wirin Singtoraj, Jamnong Uthaibutra and Kanda Whangchai	192
4739	EFFECTS OF ACIDIC ELECTROLYZED WATER WITH DIFFERENT TEMPERATURES ON MICROBIAL CONTROL AND QUALITY OF FRESH-CUT BANANA LEAVES DURING STORAGE Varumporn Kuljaroensub, Kanda Wangchai and Usawadee Chanasut	197
4749	ESTIMATION OF AMMONIUM SOURCES IN ALLUVIAL GROUNDWATER USING CI- AND GIS: A CASE STUDY OF INDRAMAYU CITY, INDONESIA Anna Rusydi, Mitsuyo Saito, Seiichiro Ioka, Rizka Maria, Shin-ichi Onodera	203
4756	ESTIMATION OF SEDIMENTATION RATE AND FRESH-SALINE ENVIRONMENT IN A COASTAL ALLUVIAL PLAIN, USING BORING CORES OF ALLUVIUM IN THE CENTRAL PART AREA OF SETO INLAND SEA, JAPAN Tohru Takeuchi , Shin-ichi Onodera , Kazuhiro Yamaguchi and Koiti Kitaoka	208
4782	IMMEDIATE EFFECTIVENESS OF HERBAL STEAM ON CERVICAL RANGE OF MOTION WITH STRESS IN THE ELDERLY Chamiporn Kongmong, Peerada Damapong and Pongmada Damapong	213
4786	EFFECTS OF LOW INTENSITY EXERCISES ON BODY BALANCE AND MUSCLE STRENGTH OF COMMUNITY ELDERLY PEOPLE Worawut Chompoopan, Warangkana Chompoopan, Wichai Eungpinichpong, and Wilai Eungpinichpong	216
4792	INVESTIGATION OF CATHEPSIN B (CTSB) and CATHEPSIN L (CTSL) POLYMORPHISM FOR CARCASS AND MEAT QUALITY IN SWINE Dounnapa Promket, Kajorngiat Nabundit, and Khanitta Ruangwittayanusorn	221
4799	EFFECT OF HARVESTING STAGES ON JELLY SEED SYMPTOM OF PLANGO (<i>Bouae burmanica</i>) CV. THUNL KLAO FRUITS Pattarawan Wattanakeeboot and Usawadee Chanasut	226
4801	USING BEEF MORPHOLOGY TO PREDICT CARCASS WEIGHT WHICH CUTTING IN THAI-ISAAN STYLE Khanitta Ruangwittayanusorn, Dounnapa Promket, Songsak Champawadee, Jaturaput Muapkunton, Ornicha Sriboon, Kewlin Pukkawan	230
4813	DETERMINATION OF CAROTENOIDS AND DOBI CONTENT IN CRUDE PALM OIL BY SPECTROSCOPY TECHNIQUES: COMPARISON OF RAMAN AND FT-NIR SPECTROSCOPY Rayakorn Nokkaew, Vittaya Punsuvon, Tetsuya Inagaki and Satoru Tsuchikawa	235
4822	THE USE OF FISH AGGREGATING DEVICES (FAD'S) TO REDUCE DESTRUCTIVE FISHING IN PACITAN COASTAL INDONESIA Tuty Handayani, Cinthia, Jarot Mulyo Semedi and Sajiharjo Marto Suro	241
4849	ANTIMICROBIAL RESISTANCE IN SALMONELLA ISOLATED FROM BEEF IN UPPER NORTHEASTERN THAILAND Natthamon Tangjitwattanachai and Denpong Sakhong	246

4851	STUDY OF QUALITY AND CONSUMER TEST OF EMULSION SAUSAGE FROM BUFFALO AND TURKEY MEAT Thassawan Somchan and Suthipong Uriyapongson	251
ID	<i>Engineering</i>	254
4501	PARAMETRIC STUDY ON THE RESPONSE OF COMPOSITE SINGLE PILES TO LATERAL LOAD BY NUMERICAL SIMULATION (FDM) Alex Otieno Owino, Zakaria Hossain, Jim Shiau	255
4510	EXTRACTION OF STATIC FEEDBACK COEFFICIENT FOR SPICE MODEL OF DRAIN INDUCED BARRIER LOWERING IN JUNCTIONLESS DOUBLE GATE MOSFET Hakkee Jung	261
4514	PERFORMANCE EVALUATION OF PARTIALLY PRESTRESSED CONCRETE BEAMS UNDER LIMITED CYCLES OF REPEATEDLY APPLIED LOADING Nazar K. Oukaili and Mohammed M. Khattab	267
4516	THE EFFECT OF FGD GYPSUM AND BOTTOM ASH ADDITION IN SHOTCRETE MIXTURE Pisut Rodvinij , Pitiwat Wattanachai and Sattaya Chaiwithee	273
4523	USE OF DRY MIXING METHOD IN FLY ASH BASED GEOPOLYMER AS A STABILIZER FOR DREDGED SOIL Jonathan R. Dungca, Kimberly D. Ang, Aila Mae L. Isaac, John Joshua R. Joven and Ma. Beatrice T. Sollano	279
4524	RADIAL FLOW PERMEAMETER: A PROPOSED APPARATUS TO MEASURE HORIZONTAL HYDRAULIC GRADIENT OF FLY-ASH BASED GEOPOLYMER-SOIL MIX Jonathan R. Dungca, Winchell Dunley T. Lao, Matthew Lim, Wilson D. Lu and Juan Carlos P. Redelicia	284
4525	VERTICAL PERMEABILITY OF DREDGED SOIL STABILIZED WITH FLY-ASH BASED GEOPOLYMER FOR ROAD EMBANKMENT Jonathan R. Dungca, Winchell Dunley T. Lao, Matthew Lim, Wilson D. Lu and Juan Carlos P. Redelicia	290
4528	PERFORMANCE OF SOIL SUBGRADE IMPROVEMENT USING WASTE MATERIAL Harnedi Maizir, Reni Suryanita, Ulfa Jusi and Raihan Arditama	296
4529	EFFECT OF GRADATION OF BOTTOM ASH AS FINE AGGREGATE ON ENGINEERING PROPERTIES OF SHOTCRETE Sattaya Chaiwithee, Pitiwat Wattanachai and Pisut Rodvinij	300
4530	A STUDY OF THE QUALITY OF SOIL INFILTRATION AT THE DOWNSTREAM OF KURANJI RIVER, PADANG CITY Aprisal, Bambang Istijono, Taufika Ophiyandri and Nurhamidah	306
4537	MICROSTRUCTURE AND MECHANICAL PROPERTIES OF CONCRETE WITH TREATED RECYCLED CONCRETE AGGREGATES Richard De Jesus, Anthony Tang and Alvin Cunanan	311
4549	A COMPARATIVE STUDY ON VIBRATION SIGNALS OF A MOTORCYCLE AT VARIOUS POSITIONS Suphattharachai Chomphan	317
4550	FREQUENCY ANALYSIS OF THE ENGINE SUPPORT VIBRATION WITH HYDROGEN-DIESEL DUAL-FUELING Boonthum Wongchai, Poranat Visuwan, Sathaporn Chuepeng	322
4552	ASSESSMENT OF OUT-OF-PLANE FAILURE OF NON-ENGINEERED MASONRY WALL DUE TO TYPHOON HAIYAN-INDUCED STORM SURGES Jenes P. Borais, and Richard De Jesus	328
4555	WALKABILITY AND RAIL NODES ALONG THE TRANSEUROPEAN TRANSPORT NETWORK: THE CASE OF GENOA BRIGNOLE STATION Noriko Otsuka, Dirk Wittowsky, and Marlene Damerau	334

4564	THE COMPARISON OF DRAINED SHEAR STRENGTH BETWEEN SINGLE STAGE AND MULTISTAGE OF KHON KAEN LOESS FROM TRIAXIAL TEST S. Chatchawan , R. Nuntasarn and D. Hormdee	340
4565	BEARING CAPACITY OF KHON KAEN LOESS BY PLATE BEARING TEST P. Thaowandee, R Nuntasarn and P Punrattanasin	346
4566	DRAINED SHEAR STRENGTH PARAMETERS OF COMPACTED KHON KAEN LOESS BY DIRECT SHEAR TEST Atchariya Saengthongthip, Ratamanee Nuntasarn and Chinawat Muktabhant	352
4568	ABSORPTION OF NI, CU AND ZN ON BENTONITE CLAY MIXED WITH POZZOLANIC MATERIALS Natta Orprasert, Pongsakorn Punrattanasin and Dolrerdee Hormdee	358
4569	ADSORPTION OF ZINC ON BENTONITE CLAY MIXED WITH POZZOLANIC MATERIALS BY COLUMN LEACHING TEST Pittaya Satiman, Pongsakorn Punrattanasin and Chinawat Muktabhant	363
4570	EFFECT OF INITIAL CONCENTRATION OF HEAVY METALS ON THE ADSORPTION CAPACITY OF BENTONIRE CLAY MIXED WITH PORTLAND CEMENT Anunt Sirisombunphatthana, Pongsakorn Punrattanasin and Ratamanee Nuntasarn	369
4571	ADSORPTION CAPACITY OF HEAVY METALS ON ILLITE, KAOLINITE AND MONTMORILLONITE CLAYS FROM BATCH TEST Keatniyom Teerawattanaparpha, Pongsakorn Punrattanasin and Dolrerdee Hormdee	375
4572	ADSORPTION CAPACITIES OF HEAVY METALS TO SAND MIXED WITH SODIUM BENTONITE USING BATCH SORPTION TESTS Yuttapong Chaipanha, Pongsakorn Punrattanasin, Dolrerdee Hormdee and Chinawat Muktabhant	381
4576	OPTICAL RESPONSE ANALYSIS OF InGaAs HIGH-ELECTRONMOBILITY TRANSISTORS WITH A 1550-nm WAVELENGTH FEMTOSECOND PULSE LASER Taiki Kozakai, Itsuki Takagi, Shun Nakajima, and Hirohisa Taguchi	386
4581	VIBRATION AND SOUND SIGNAL ANALYSIS FOR A GASOLINE ENGINE WITH LPG-INSTALLATION AND FAULT SIMULATIONS Suphattharachai Chomphan, Theerathan Kingrattanasase and Saereephap Boonsit	390
4585	AN ARTIFICIAL NEURAL NETWORK MODEL FOR THE CORROSION CURRENT DENSITY OF STEEL IN MORTAR MIXED WITH SEAWATER Cheryl Lyne C. Roxas and Bernardo A. Lejano	396
4589	IMPLEMENTATION OF CONNECTION SYSTEM OF WOODEN PLATE AND WOODEN CLAMP ON JOINT MODEL OF BAMBOO TRUSS STRUCTURES Astuti Masdar, Suprpto Siswosukarto, Noviarti and Des Suryani	401
4592	EXPERIMENTAL INVESTIGATION OF SEISMIC PERFORMANCE OF REINFORCED BRICK MASONRY INFILLED REINFORCED CONCRETE FRAMES WITH A CENTRAL OPENING Maidiawati, Jafril Tanjung, Yulia Hayati and Hamdeni Medriosa	407
4596	THE ANALISIS OF RIVER RUNOFF IN THE ABUKUMA RIVER BASIN Masanobu Taniguchi and Hiroyuki Ii	413
4599	INFLUENCE OF POZZOLANIC MATERIALS IN THE ADSORPTION OF HEAVY METALS ON RED LOESS SOIL Pongsakorn Punrattanasin, Arnun Chantaduag and Chinawat Muktabhant	419
4609	EXPERIMENTAL STUDY AND MODELLING OF STRESS-STRAIN RELATIONSHIP OF RC COLUMNS STRENGTHENED BY BAMBOO REINFORCED CONCRETE JACKETS Ari Wibowo, Indradi Wijatmiko and Christin Remayanti Nainggolan	425
4615	STUDY OF MODULUS ELASTICITY OF PVC COATED WELDED MESH FIBER CONCRETE Christin Remayanti Nainggolan, Indradi Wijatmiko and Ari Wibowo	431

4617	EFFECT OF BRICK MASONRY INFILLS TO SEISMIC CAPACITY OF INDONESIA MULTI-STORY RC BUILDING Jafril Tanjung, Maidiawati and Aditya Alfajri	437
4620	STRENGTH CHARACTERISTICS OF WASTED SOFT DRINKS CAN AS FIBER REINFORCEMENT IN LIGHTWEIGHT CONCRETE Indradi Wijatmiko, Ari Wibowo and Christin Remayanti Nainggolan	443
4628	OPTIMIZED PREPARATION OF RICE HUSK ASH (RHA) AS ASUPPLEMENTARY CEMENTITIOUS MATERIAL Carmela Denise C. Isberto, Krystoffer Lloyd D. Labra, Jan Marielle B. Landicho, and Richard M. De Jesus	449
4635	INVESTIGATION OF CHANGES IN INDOOR RADON CONCENTRATIONS BEFORE AND AFTER SEISMIC ACTIVITIES IN GYEONGJU AND POHANG, KOREA Hanyoung Joo, Jae Wook Kim and Joo Hyun Moon	455
4636	FIELD PERFORMANCE OF THE CAPILLARY WICK IRRIGATION (CAPILLARIGATION) SYSTEM FOR RICE-BASED CROPS Ricardo F. Orge and Derosé A. Sawey	461
4639	INTERNATIONAL WATER MODEL UNDER PRODUCTIVITY CONDITIONS: THE CASE OF THE TIGRIS AND THE EUPHRATES Abdulmir Hussein Qasim	470
4644	UNDRAINED SHEAR STRENGTH OF SOFT CLAY REINFORCED WITH SINGLE ENCAPSULATED LIME BOTTOM ASH COLUMN Muzamir Hasan, Kwan Hui Yee, Fat-hi Muhamad and Masayuki Hyodo	475
4646	IMPROVEMENT OF ENZYMATIC CATALYSIS IN ORGANIC SOLVENTS VIA IMMOBILIZATION ON BIOCHAR Hidetaka Noritomi, Jumpei Nishigami, Nobuyuki Endo, Satoru Kato and Shinsuke Takagi	480
4651	PROPERTIES OF LIGHTWEIGHT AERATED GEOPOLYMER SYNTHESIS FROM HIGH-CALCIUM FLY ASH AND ALUMINIUM POWDER Charoenchai Ridditirud and Prinya Chindaprasirt	486
4654	FLUIDIZED BED COAL-BARK FLY ASH GEOPOLYMER WITH ADDITIVES CURED AT AMBIENT TEMPERATURE Prinya Chindaprasirt, Pornnapa Kasemsiri, Suttipong Poomsrisa and Patcharapol Posi	495
4655	EFFECT OF CUTTING PARAMETER AND FIBER PULL-OUT ON MACHINABILITY KENAF FIBER REINFORCED PLASTIC COMPOSITE MATERIALS USING DOE Azmi Harun, Che Hassan Che Haron, Jaharah A. Ghani, Yuzairi Abdul Rahim, Roshaliza Hamidon, Tan Chye Lih	501
4657	EMBEDDED INTELLIGENCE FOR QUALITY OF SERVICE-BASED VERTICAL HANDOVER MANAGEMENT IN SEAMLESS WIRELESS NETWORKS Sunisa Kunarak	508
4661	GREEN CARGO MOVEMENT, LOCALITY: MEKONG Leonard Johnstone, Vatanavongs Ratanavaraha	512
4662	EFFECT OF FLY ASH FINENESS ON COMPRESSIVE, FLEXURAL AND SHEAR STRENGTHS OF HIGH STRENGTH-HIGH VOLUME FLY ASH JOINTING MORTAR Patcharapol Posi, Pornnapa Kasemsiri, Surasit Lertnimoolchai and Prinya Chindaprasirt	520
4665	THE USE OF BOTTOM ASH TO IMPROVE THE STRENGTH OF POOR SUBBASE LATERITIC SOIL IN ROAD CONSTRUCTION Chotikan Ratchakrom	526
4668	DAMAGE LEVEL PREDICTION OF MULTI-STORY STEEL STRUCTURE IN SUMATRA USING BACKPROPAGATION NEURAL NETWORK Reni Suryanita, Harnedi Maizir, Ismeddiyanto, Vindi Trisatria and Raihan Arditama	532
4670	BRAIN TISSUE SWELLING DURING ISCHAEMIA-REPERFUSION: 2D FINITE ELEMENT ANALYSIS USING POROELASTICITY Mohamed Mokhtarudin, M. J., Shabudin, A. and Payne, S. J.	538

4672	DESIGN OF BASE ISOLATED REINFORCED CONCRETE BUILDING SUBJECTED EARTHQUAKE EXCITATION USING EC 8 Norliyati Mohd Amin, Nabihan Ayub and Anizahyati Alisibramulisi	544
4676	STRENGTH AND BEHAVIORS OF DRY-JOINT RETAINING NANO-BLOCK Poungchompu Pongsagorn, Buyarat Tanakrit, Bubpi Attaphol	550
4683	ASSESSMENT OF STRENGTH PARAMETERS OF UNREINFORCED MASONRY (URM) BLOCKS IN HERITAGE STRUCTURES IN THE PHILIPPINES Lessandro Estelito Garciano, Darlene Clarice Campado, Nitchell Andrei Castillo, Mary Grace Odiamar, and Marcelino Tongco, Jr.	557
4695	EFFECTS OF WATERSHED TOPOGRAPHY AND LAND USE ON BASE FLOW HYDROLOGY IN EQUATORIAL REGION: A CASE STUDY IN UPPER KOMERING WATERSHED SOUTH SUMATERA, INDONESIA Rosmalinda Permatasari, Arwin Sabar, Dantje Kardana Natakusumah and Hazairin Samaulah	563
4702	TENSILE CREEP BEHAVIOR CONSIDERING YOUNG'S MODULUS DEVELOPMENT OF FLY ASH CONCRETE AT EARLY AGE Yuki Watanabe, Yoichi Mimura, Vanissorn Vimonsatit, Isamu Yoshitake and Itaru Horiguchi	568
4710	DATA BASE STRUCTURE MANAGEMENT INFORMATION SYSTEM LAND ALLOCATION IN SPATIAL PLANNING Sarino, Dinar DA Putranto, Agus Lestari Yuono, and I.C. Juliana	574
4721	ANALYSIS OF TRAFFIC ENVIRONMENT AND DYNAMIC BEHAVIOR OF BRIDGE GIRDERS BASED ON IMAGE SENSING TECHNIQUES Kouichi Takeya, Koharu Ota, Shiho Takagi and Junji Yoshida	581
4722	NON-CONTACT ESTIMATION OF STRAIN PARAMETER-TRIGGERING LIQUEFACTION Erica Elice Saloma Uy, Toshihiro Noda, Kentaro Nakai and Jonathan Rivera Dungca	587
4729	INFLUENCE OF DEVELOPMENT/DIMINISHING OF ANISOTROPY ON THE MECHANICAL BEHAVIOR OF CLAYEY SPECIMEN Imran Khan, Kentaro Nakai, Toshihiro Noda and Kota Mizukami	593
4732	FACTORS IMPACTING PRECAST UTILIZATION IN CAMBODIA CONSTRUCTION Kaya Ting, Phatsaphan Charnwasununth, Vachara Peansupap and Nobuyoshi Yabuki	599
4733	DEVELOPMENT OF INTEGRATED SATELLITE-BASED DROUGHT MODEL IN THAILAND USING MULTIPLE LINEAR REGRESSION Mongkol Raksapatcharawong and Watcharee Veerakachen	605
4740	COMPARATIVE ANALYSIS AND DESIGN OF TRANSVERSE BOX GIRDER BRIDGE BETWEEN STAAD.PRO AND MIDAS CIVIL SOFTWARES Muhammad Naim Abdul Halim, Anizahyati Alisibramulisi, Mohammad Noor Abu Hassan, Ahmad Ramlan Abu Talib, Noor Rita Ismail, and Norliyati Mohd Amin	611
4746	THE SPEED LIMIT FOR MOTORCYCLE: URBAN ARTERIAL ROAD IN KHON KAEN CITY, THAILAND Jetsada Kumphong, Thaned Satiennam and Wichuda Satiennam	617
4747	MOTORCYCLE HELMET USE INTENTION WITH THE THEORY OF TRAFFIC PSYCHOLOGY FOR BEHAVIOR CHANGE IN LAO PDR Jetsada Kumphong, Thaned Satiennam, Wichuda Satiennam and Phongsavanh Inthavongsa	622
4748	PSYCHOLOGICAL MOTIVATION OF ELDERLY' INTENTION TO USE PUBLIC TRANSIT: A CASE STUDY OF LIGHT RAIL TRANSIT SYSTEM (LRT) IN KHON KAEN, THAILAND Kawin Muenrit, Wichuda Satiennam	628
4755	DEVELOPMENT OF A CRACK REPAIR METHOD USING YEAST-INDUCED CALCIUM CARBONATE PRECIPITATION AND MODELING THE PRECIPITATION OF CALCIUM CARBONATE USING GEOCHEMICAL SIMULATION Yoko Sakakihara and Shinichirou Okazaki	633
4759	ELECTRET CONDENSER MICROPHONE AS SENSOR IN ARTERIAL PULSE RECORDING DEVICE Erni Yudaningtyas, Waru Djuriatno, Achsanul Khabib and Dionysius J.D.H. Santjojo	638

4764	EXPERIMENTAL INVESTIGATION OF HOLLOW BRICK UNREINFORCED MASONRY BUILDING RETROFITTED BY FERROCEMENT LAYERS Fauzan, Abdul Hakam, Febrin Anas Ismail and Jonathan Vincensius Osman	644
4765	USING FUZZY MULTI ATTRIBUTE DECISION MAKING (FMADM) APPROACH FOR RAILWAY TRACK REHABILITATION PLANNING: A CASE STUDY IN THAILAND Thawatchai Phanyakit and Thaned Satiennam	651
4766	VEHICLE ACTUATED SIGNAL CONTROL FOR LOW CARBON SOCIETY Thanapol Promraksa and Thaned Satiennam	658
4772	EXPERIMENTAL STUDY ON THE EFFECT OF STEEL FIBER WASTE TYRE ON HIGH STRENGTH CONCRETE Fauzan, Rudy Kurniawan, Oscar Fitrah N and Claudia Lovina A. N	665
4778	AN ANALYTICAL INVESTIGATION OF EWECS COMPOSITE COLUMN WITH AND WITHOUT SHEAR STUD Fauzan, Ruddy Kurniawan and Zev Al Jauhari	671
4779	WATER RESOURCES AND STORMWATER MANAGEMENT STRATEGIES USING DUAL FUNCTION RAINWATER TANK IN LABU RIVER BASIN MALAYSIA Y.F. Huang, Effie Nyanong, K.F. Fung	678
4783	A PRICE SETTING FOR AN EXCESS-BAGGAGE SERVICE AS A FUNCTION OF FREIGHT PRICE I.A. Shaban, F.T.S. Chan, and S.H. Chung	684
4785	BOND STRENGTH PREDICTION MODEL OF CORRODED REINFORCEMENT IN CONCRETE USING NEURAL NETWORK Nolan C. Concha and Andres Winston C. Oreta	690
4800	DIFFERENTIAL SETTLEMENT OF SHORT PILED RAFT FOUNDATION SYSTEM ON PEAT DURING LOADING TEST Sajiharjo Marto Suro, Adnan Zainorabidin, Agus Sulaeman and Ismail Bakar	696
4804	SETTLEMENT BEHAVIOR OF ROAD SURFACES CAUSED BY DISSOLUTION OF SALT LAYERS Siwadol Saenseela, Pongsagorn Pongchompu and Gomin Chairatanangamdej	701
4808	PRODUCTION OF ETHYL ESTER BIODIESEL FROM USED COOKING OIL WITH ETHANOL AND ITS QUICK GLYCEROL-BIODIESEL LAYER SEPARATION USING PURE GLYCEROL Mallika Tapanwong, Vittaya Punsuvon	706
4810	AN INTEGRATED APPROACH FOR SUSTAINABILITY IN THE APPLICATION OF INDUSTRIALISED BUILDING SYSTEM (IBS) Riduan Yunus, Abdul Rahim Abdul Hamid and Siti Rahimah Mohd Noor	711
4816	PRODUCTION OF Cu MICROPARTICLES UTILIZING HIGH PURITY Cu DENDRITE CRYSTALS AND DEVELOPMENT OF CONDUCTIVE PAINTS Junya Kuroda, Risa Uda, Honoka Tanabe, Kimihiro Yamanaka and Hirohisa Taguchi	717
4817	THERMOGRAVIMETRIC ANALYSIS OF TREATED WASTE ABACA FOR FLY ASH-BASED GEOPOLYMER REINFORCEMENT Janne Pauline S. Ngo, Roy Alvin Malenab and Michael Angelo Promentilla	721
4819	INTEGRATED MAINTENANCE SCHEDULING AND STAFF SCHEDULING FOR AN AIRCRAFT HANGAR MAINTENANCE PROBLEM Yichen Qin, Felix T.S. Chan, S.H. Chung, B. NIU, T. QU	725
4825	SYNTHESIS OF ONE-PART GEOPOLYMER USING D-OPTIMAL MIXTURE DESIGN FOR SOIL STABILIZATION April Anne S. Tigue, Jonathan R. Dungca, and Michael Angelo B. Promentilla	731
4828	FLOW INVESTIGATIONS WITHIN A CONCENTRIC CYLINDERS OF GAS SENSOR MODULE FOR I.C. ENGINES Tatsuya Kawaguchi, Yoona Jeong, Takushi Saito and Isao Satoh	737

4830	APPLICATION STATIC LOAD TEST (SLT) AND PILE INTEGRITY TESTING (PIT) OF PILES IN SEA PORT "PRORVA" (WEST KAZAKHSTAN) Askar Zhussupbekov, Zhanbolat Shakhmov and Gulshat Tleulenova	742
4840	DAMAGE DETECTION OF TRUSS STRUCTURES BY APPLYING MACHINE LEARNING ALGORITHMS Koji Unno, Atsushi Mikami and Masaki Shimizu	746
4841	DAMAGE DETECTION OF TRUSS STRUCTURES BASED ON VIBRATION CHARACTERISTICS Masaki Shimizu, Atsushi Mikami and Koji Unno	752
4961	AN AGENT-BASED SUPPLY CHAIN NETWORK WITH QUALITY AGENT MEDIATORS FOR QUALITY COORDINATION C.Y. Lam	758
4863	DESIGN, ANALYSIS, FABRICATION AND ANALYSIS OF SMALL WATER TURBINE Gwo-Chung Tsai	764
4864	FLEXURAL STRENGTH OF RIGID PAVEMENT USING RECYCLED CONCRETE AGGREGATES IMPROVED BY POLYVINYL ALCOHOL Suksun Horpibulsuk, Teerasak Yaowarat, Arul Arulrajah, Mehdi Mirzababaei and Ahmad Safuan A Rashid	770
ID	<i>Environment</i>	776
4504	OPERATING CONDITIONS EFFECTS OF AN ELECTRODIALYSIS MODULE ON HYDROCHLORIC ACID AND HYDROXIDE FORMATION FROM A SODIUM CHLORIDE MODEL SOLUTION Medina Juan, Diaz Zoila and Rojas Jorge	777
4507	WOODY DEBRIS RECRUITMENT CAUSED BY DISASTERS RELATED TO TROPICAL STORM NANMADOL (2017) IN HEADWATER OF ASAKURA CITY, FUKUOKA, JAPAN Thapthai Chaithong, Daisuke Komori and Yuto Sukegawa	784
4509	REVERSIBLE JUMP MCMC METHOD FOR HIRARCHICAL BAYESIAN MODEL SELECTION IN MA MODELS WITH EXPONENTIAL NOISE Suparman	791
4532	GAP COMPETENCY ANALYSIS FOR EMPLOYEE OF ANIMAL FEED WAREHOUSE DEPARTMENT Siti Rochaeni, Siska Nurita, Eny Dwiningsih and Farahdita Soeyatno	795
4534	ENVIRONMENTAL REGENERATION AND MANAGEMENT IN PARTNERSHIP IN THE NORTHWEST OF ENGLAND Tomoko Miyagawa, Clare Olver, Noriko Otsuka, and Hirokazu Abe	801
4535	THE INCORPORATION OF LEAN SIX-SIGMA INITIATIVES TO REDUCE WATER FOOTPRINT OF A PUBLIC UNIVERSITY Karin Kandananond	807
4536	PREPARATION OF GEOPOLYMER CEMENT FROM CRUSHED STONE BY-PRODUCT USING ALKALI FUSION Kazuki Sakamoto ¹ , Takaaki Wajima ¹	811
4538	DESALINATION OF SEAWATER USING NATURAL ZEOLITE FOR AGRICULTURAL UTILIZATION Takaaki Wajima	817
4539	COMPARISON OF COD AND TSS REMOVALS FROM ARTIFICIAL RIVER WATER BY MUDBALLS MADE WITH ACTIVATED EM1 AND EM4 SOLUTIONS Fadjari Lucia Nugroho, Deni Rusmaya and Muthia Damayanti	822
4553	THE ESTIMATION OF THE LAKE COLAC WATER BALANCE USING ISOTOPIC RATIO OF WATER, AMOUNT OF PRECIPITATION AND EVAPORATION VALUES IN VICTORIA, AUSTRALIA Hiroki Kitagawa, Peter G Dahlhaus Hiroyuki Ii	828

4554	EFFECT OF α 17-METHYLTESTOSTERONE ON SEX REVERSAL OF RED TILAPIA (OREOCHROMIS NILOTICUS X OREOCHROMIS MOSSAMBICUS) IN FREE-SWIMMING STAGE Supamas Sriwongpuk	834
4558	SEASONAL VARIATION AND SOURCE ANALYSIS OF MONITORING PM10 DATA IN NORTHERN THAILAND Pantitcha Outapa and Katiya Ivanovitch	840
4575	SPATIAL ANALYSIS OF COMMUNITY'S ACCEPTANCE FOR SUDS APPLICATIONS IN NHIEU LOC – THI NGHE SUB-BASIN, HO CHI MINH CITY, VIETNAM Nguyen Hoang My Lan, Vo Le Phu and Le Van Trung	846
4578	DEVELOPING FINE PARTICLE FILTERING SYSTEM FOR MOTORCYCLE EXHAUST USING COCO FIBERS Arinto Y.P. Wardoyo, Firdy Yuana, and Selly Y. A. Elbasari	852
4579	POLYETHYLENETEREPTHALATE-BASED ACTIVATED CARBON PRODUCTION: PRELIMINARY STUDY ON KOH ACTIVATION WITH MICROWAVE ASSIST Sirasit Meesiri, Nattawut Seayang, Weeraphong Homnan, Navadol Laosiripojana, and Anusorn Boonpoke	857
4587	EFFECT OF SUSPENDING TRAFFIC ON A HIGHWAY IN A MOUNTAINOUS REGION IN CENTRAL JAPAN ON THE SUCCESSION OF SLOPE VEGETATION Teruo Arase, Akane Nishio, Tetsuo Okano and Taizo Uchida	863
4595	ISOTOPIC RATIOS AND CHEMICAL COMPOSITION OF PRECIPITATION BETWEEN FOOT OF THE BUILDING AND TOP OF THE BUILDING IN OSAKA CITY AND WAKAYAMA CITY, JAPAN Toshiki Ueda and Hiroyuki Ii	869
4597	REGENERATION FOR SOCIO ECOLOGICAL PRODUCTION LANDSCAPE IN SERIOUSLY ENVIRONMENTAL DAMAGED RURAL AREA Takato Azegami, Hirokazu Abe, Noriko Otsuka and Tomoko Miyagawa	875
4601	HOLISTIC LANDSCAPE PLANNING'S VALUE FOR NATURAL DISASTER RECONSTRUCTION: WILLINGNESS TO PAY FOR NEW RESIDENCE IN DIFFERENT RECONSTRUCTION PLANNING APPROACHES Misato Uehara	882
4603	THE ADSORPTION OF HEAVY METALS FROM INDUSTRIAL WASTEWATER USING SARGASSUM CRASSIFOLIUM Lily Surayya Eka Putri and Eka Syafiq	888
4606	MEDICAL WASTE MANAGEMENT IN PRIVATE CLINICS IN SURABAYA AND FACTORS AFFECTING IT Susi A Wilujeng, Enri Damanhuri and Mochammad Chaerul	895
4608	PUBLIC HEARING WITHIN THE ENVIRONMENTAL AND HEALTH IMPACT ASSESSMENT SYSTEM: A CASE STUDY FORM THAILAND Chutarat Chompunth	901
4619	SEMI-ARTIFICIAL SLUDGE PRODUCTION BY UTILIZING INORGANIC MATTERS OBTAINED FROM NATURAL "HEDORO" Hirosuke Hirano, Davin H. E. Setiamarga	907
4630	EFFECTIVENESS OF USING CICADA SHELL AND RIVER BRYOPHYTE AS AN INDEX OF AVAILABLE CU, ZN, PB, AS, NI AND CR CONTAMINATION Hiroyuki Ii1	914
4631	STUDY ON REMOVAL OF CONTAMINATED SOIL ON FOREST SLOPE FOCUSING ON DIFFERENCE IN DENSITY OF SUBSURFACE GROUND Keiichiro Shibata, Hidenori Yoshida, Daisuke Matsumori, Matsumoto Naomichi and Kazushi Moriki	920
4632	MAPPING STABLE ISOTOPIC RATIOS OF STREAM WATER AND CU, ZN, PB AND AS CONCENTRATIONS OF BRYOPHYTE ALONG STREAMS IN THE EAST OF OKAYAMA AND TOTTORI PREFECTURES, JAPAN Hiroyuki Ii and Masahito Yoshimura	925
4633	REDUCTION OF NUTRIENTS IN PUBLIC MARKET WASTEWATER BY PHYCOREMEDIATION Radin Maya Saphira Radin Mohamed, Alfituri Ibrahim Abdullah Abuala, Najeeha Mohd. Apandi, Adel Al-Gheethi , Aisha A. Amhimmid Alqantosh and Amir Hashim Mohd. Kassim	931
4634	AMOUNT OF PRECIPITATION ON TOPOGRAPHY FROM OSAKA PLAIN TO NARA BASIN ACROSS IKOMA MOUNTAINS, JAPAN Hiroki Nishiwaki and Hiroyuki Ii	935

4641	STUDY ON ADSORPTION PERFORMANCE OF FOOD WASTES FOR VARIOUS HEAVY METALS Keiichiro Shibata, Hidenori Yoshida, Tsumugi Inoue, Matsumoto Naomichi and Yoshihiro Suenaga	941
4656	THE ACUTE EFFECT OF TRADITIONAL THAI MASSAGE ON RECOVERY FROM FATIGUE IN BASKETBALL PLAYERS Nopparak Kaesaman and Wichai Eungpinichpong	947
4680	THE POTENTIAL OF TROPICAL MICROALGAE AS FLOCCULANT IN HARVESTING PROCESS Astri Rinanti, Ronny Purwadi	953
4681	UTILIZATION OF WATER QUALITY MODELING TO DETERMINE MAXIMUM BOD LOAD OF UPSTREAM CITARUM RIVER Yonik Meilawati Yustiani, Sri Wahyuni and Syarifah Nur Fitria Dewi	959
4682	TURBIDITY REDUCTION OF THE RAW DRINKING WATER FOR PILOT SCALE ELECTROCOAGULATION DEVELOPMENT E. Afiatun, H. Pradiko and E. Fabian	964
4684	GEOSPATIAL MODEL OF PHYSICAL AND SOCIAL VULNERABILITY FOR TSUNAMI RISK ANALYSIS Abu Bakar Sambah, F. Miura, Guntur, Sunardi, and A. F. Febriana	970
4687	HYDROLOGICAL AND NITRATE LOADING MODELING IN LAM TAKLONG WATERSHED, THAILAND Chau Ngoc Tran, Chatpet Yossapol	976
4693	WATER QUALITY ASSESSMENT BASED ON THE WATER QUALITY INDEX (WQI) APPROACH USING GEOSPATIAL ANALYSIS Rina Febrina and Abu Bakar Sambah	981
4700	THE AWARENESS OF ENVIRONMENT CONSERVATION BASED ON OPINION DATA MINING FROM SOCIAL MEDIA Kunyanuth Kularbphettong	987
4703	LIFE CYCLE IMPACT ASSESSMENT OF NEWGROUND MATERIAL AND EMBANKMENT CONSTRUCTION METHODS CONSIDERING RECYCLING Hideyuki Ito, Kento Aimonon and Takahiro Fujii	992
4712	TRACE ELEMENTS CONCENTRATIONS OF SEAWEED BESIDE MANY CLOSED COPPER MINES IN SADAMISAKI PENINSULA Erika Ueno and Hiroyuki Ii	999
4715	HEATING VALUE ENHANCEMENT BY BIOGAS PURIFICATION USING NATURAL ZEOLITE AND RICE STRAW-BASED BIOCHAR Ambar Pertiwinigrum, Margaretha Arnita Wuri, Andang Widi Harto, Rachmawan Budiarto and Misri Gozan	1005
4720	THE POTENTIAL IMPROVEMENT OF PUBLIC TRANSPORT IN MINIMIZING AIR POLLUTION Lasmini Ambarwati, and Amelia K. Indriastuti	1010
4735	PURIFICATION EXPERIMENTS ON THE PASIG RIVER, PHILIPPINES USING A CIRCULATION-TYPE PURIFICATION SYSTEM Okamoto Kyoichi, Komoriya Tomoe, Toyama Takeshi, Hirano Hirosuke	1016
4736	PERFORMANCE OF A CIRCULATION TYPE PURIFICATION SYSTEM DURING THE TREATMENT OF SLUDGE FROM MANILA BAY AND TWO PORTS IN JAPAN Komoriya Tomoe, Okamoto Kyoichi, Toyama Takeshi, Hirano Hirosuke	1021
4742	ESTIMATION OF GROUNDWATER RECHARGE AND SALINIZATION IN A COASTAL ALLUVIAL PLAIN AND OSAKA MEGACITY, JAPAN, USING $\delta^{18}\text{O}$, δD , AND Cl^- Yusuke Tomozawa, Shin-ichi Onodera, Mitsuyo Saito	1026

4751	ANALYSIS OF STATISTICAL METHODS FOR WATER-LEVEL FORECASTS OF NIGER INNER DELTA IN MALI Barry Kassambara, Homayoon Ganji and Takamitsu Kajisa	1032
4773	ENHANCEMENT OF BIOMETHANE PRODUCTION POTENTIAL FROM THE ALKALINE PRETREATED POLY (LACTIC ACID) WASTE BY THE CO-DIGESTION PROCESS Sutisa Samitthiwetcharong and Orathai Chavalparit	1039
4774	PERFORMANCE OF AIR CONDITIONING SYSTEM IN EDUCATIONAL BUILDING FOR ENERGY CONSERVATION Nantamol Limphitakphong, Nuttasate Chaikatetham, Therdthai Khaimook, and Orathai Chavalparit	1045
4780	WILLINGNESS TO PAY (WTP) BY CONTINGENT VALUATION METHOD (CASE STUDY: WASTE MANAGEMENT SERVICES) Marselina, Ria Virsa	1051
4795	BIOETHANOL PRODUCTION FROM AGRICULTURAL PRODUCTS AND FRUITS OF BANGLADESH Md. Abul Kalam Azad and Nilufa Yesmin	1056
4796	ISOLATION OF STRESS TOLERANCE YEAST STRAIN FROM PAPAYA WASTES Gemilang Lara Utama, Dwi Wahyudha Wira and Roostita L. Balia	1060
4815	MOBILE DEVICES: ITS IMPACT TO ACADEMIC PERFORMANCE Charito G. Ong, Cipriana P. Flores	1066
4821	GEOPOLYMER BEADS FROM COAL FLY ASH AND WASTE PEN SHELLS Kimmie Dela Cerna, Jose Isagani Janairo Roy Alvin Malenab and Michael Angelo Promentilla	1070
4823	DIFFUSION OF MERCURY FROM ARTISANAL SMALL-SCALE GOLD MINING (ASGM) SITES IN MYANMAR Tomonori Kawakami, Misa Konishi, Yuki Imai and Pyae Sone Soe	1075
4824	REMOVING ARSENIC AND FLUORIDE FROM HOT SPRING WATER BY ELECTROLYSIS Yuki Imai, Misa Konishi, and Tomonori Kawakami	1082
4832	A DEVELOPMENT OF WASTE MANAGEMENT MODEL: A CASE STUDY OF SI MUM MUANG MARKET IN THAILAND Anucha Jaisai and Chutarat Chompunth	1089
4834	MECHANICAL PERFORMANCE OF ABACA-GEOPOLYMER COMPOSITE EXPOSED TO ELEVATED TEMPERATURES Roy Alvin J. Malenab and Michael Angelo B. Promentilla	1094
4838	ON THE IMAGE BASED ON SMART PHONE USERS IN PUBLIC SPACE Yuki Ogimoto and Kazunari Tanaka	1100
4847	IMAGE ANALYSIS ON NIGHT SEQUENTIAL IMAGES Hiroki Komai and Kazunari Tanaka	1104
4848	ON THE SPATIAL ELEMENTS FROM A BIRD’S-EYE VIEW SCAPE Nobuaki Tanaka, Kazunari Tanaka	1107
4857	THE EFFICIENCY OF FLY ASH AND CEMENT SLAG TO DEVELOPMENT BUILDING Ranti Hidayawanti, Supriadi Legino, Iriansyah Sangadji, Rony Panca Adi Widodo	1111

4862	GEOSPATIAL PREDICTION OF SOIL EROSION USING MODIFIED BIVARIATE FREQUENCY RATIO TECHNIQUE Abdulkadir Taofeeq Sholagberu, Muhammad Raza Ul Mustafa, Khamaruzaman Wan Yusof, Ahmad Mustafa Hashim, Muhammad Waris A. Khan	1116
4642	NONLINEAR BEHAVIOR AND THERMAL DAMAGE OF THERMAL LAGGING IN CONCENTRIC LIVING TISSUES SUBJECTED TO GAUSSIAN DISTRIBUTION SOURCE Hamdy M. Youssef and Najat A. Al-Ghamdi	1122
4707	THE COMPLEX OF FIELD PILING STATIC LOADING TESTS ON AKSAI, NORTHWEST KAZAKHSTAN Askar Zhussupbekov, Iwasaki Yoshinori, Abdulla Omarov, Karlygash Borgekova and Sungat Akhazhanov	1129

Preface

On behalf of the SEE 2018 Organizing Committee, it is our great pleasure to welcome you to the Fourth International Conference on Science, Engineering & Environment, held at the Meitetsu New Grand Hotel, Nagoya, Japan organized in conjunction with Mie University Research Center for Environmental Load Reduction, The GEOMATE International Society, Useful Plant Spread Society, Glorious International, AOI Engineering, HOJUN, JCK, CosmoWinds and Beppu Construction, Japan.

The conference covers three major themes with many specific themes including:

Engineering	Science	Environment
<ul style="list-style-type: none">· Environmental Engineering· Chemical Engineering· Civil and Structural Engineering· Computer Software Web Engineering· Electrical and Electronic Engineering· Energy and Thermal Engineering· Aerospace Engineering· Agricultural Engineering· Biological Engineering and Sciences· Biological Systems Engineering· Biomedical and Genetic Engineering· Bioprocess and Food Engineering· Geotechnical Engineering· Industrial and Process Engineering· Manufacturing Engineering· Mechanical and Vehicle Engineering· Materials and Nano Engineering· Nuclear Engineering· Petroleum and Power Engineering· Forest Industry Engineering	<ul style="list-style-type: none">· Environmental Sciences· Chemistry and Chemical Sciences· Fisheries and Aquaculture Sciences· Astronomy and Space Sciences· Atmospheric Sciences· Botany and Biological Sciences· Genetics and Bacteriology· Forestry Sciences· Geological Sciences· Materials Science and Mineralogy· Statistics and Mathematics· Microbiology and Medical Sciences· Meteorology and Palaeo Ecology· Pharmacology· Physics and Physical Sciences· Plant Sciences and Systems Biology· Psychology and Systems Biology· Zoology and Veterinary Sciences	<ul style="list-style-type: none">· Environmental Technology· Recycle Solid Wastes· Environmental dynamics· Meteorology and Hydrology· Atmospheric and Geophysics· Physical oceanography· Bio-engineering· Environmental sustainability· Resource management· Modelling and decision support tools· Institutional development· Suspended and biological processes· Anaerobic and Process modelling· Modelling and numerical prediction· Interaction between pollutants· Water treatment residuals· Quality of drinking water· Distribution systems on potable water· Reuse of reclaimed waters

As expected, this year we have received many submissions from different countries all over the world. The technical papers were selected from the vast number of contributions submitted after a review of the abstracts. The final papers in the proceedings have been peer reviewed rigorously and revised as necessary by the authors. It relies on the solid cooperation of numerous people to organize a conference of this size. Hence, we appreciate everyone who support as well as participate in the joint conferences.

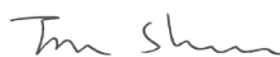
Last but not least, we would like to express our gratitude to all the authors, session chairs, reviewers, participants, institutions and companies for their contribution to SEE 2018. We hope you enjoy the conference and find this experience inspiring and helpful in your professional field. We look forward to seeing you at our upcoming conference next year.

Best regards,

Prof. Dr. Zakaria Hossain, Chairman



Dr. Jim Shiau, USQ, Australia (Assistant to Chairman)



Organization

Scientific Committees:

Honorary Chairman: Dr. Sohji Inoue, E/Prof. Mie University, Japan
Conference Chairman: Dr. Zakaria Hossain, Prof. Mie University, Japan
Assistant to Chairman Dr. Jim Shiau, University of Southern Queensland, Australia

Conference Organizing Committee:

Dr. Zakaria Hossain, Prof. Mie University, Japan (Chair)
Dr. Jim Shiau, USQ, Australia (Assistant to Chairman)
Dr. Satoshi Kaneco, Prof., Mie University, Japan (Co-Chair)
Dr. Sohji Inoue, E/Prof. Mie University, Japan (Co-Chair)
Dr. Toshinori Sakai, Prof. Mie University, Japan (Co-Chair)
Dr. Takamitsu Kajisa, Prof. Mie University, Japan (Co-Chair)
Dr. Masaaki Kondo, A/Prof. Mie University, Japan (Co-Chair)

National & International Advisory Committee:

Dr. Fumio Tatsuoka, Prof., Tokyo University of Science, Japan
Dr. Junichiro Takeuchi, Prof., Kyoto University, Japan
Dr. Kingshuk Roy, Prof., Nihon University, Japan
Dr. Nakib Dan Khan, A/Prof. Mie University, Japan
Dr. Sai Vanapalli, Prof., University of Ottawa, Canada
Dr. Musharraf Zaman, Prof. Univ. of Oklahoma, USA
Dr. Rafiqul Tarefder, Prof. University of New Mexico, USA
Dr. M. Bouassida, Prof., National Sch. of Engg. of Tunis
Dr. L.R. Austriaco, Prof., Angles Univ. Found., Philippines
Dr. A.S.M. Abdul Awal, Prof., Univ. Technology Malaysia
Dr. M. Ibn Ibrahimy, Prof., Int. Islamic Univ., Malaysia
Dr. Mohammad Shariful Islam, Prof., BUET, Bangladesh.
Dr. Bujang B.K. Huat, Prof., Univ. Putra Malaysia
Dr. Nemy Banthia, Prof., UBC, Canada
Dr. Ian Jefferson, Prof., Univ. of Birmingham, UK
Dr. John Bolander, Prof., Univ. of California, USA
Dr. Shamsul Chowdhury, Prof., Roosevelt Univ., USA
Dr. Isabel Pinto, Prof., University of Coimbra, Portugal
Dr. Mark Jaksa, Prof., University of Adelaide, Australia
Dr. Jim Shiau, A/Prof., USQ, Australia
Dr. Hj. Ramli Bin Hj. Nazir, A/Prof., UTM, Malaysia
Dr. H.M. Shahin, Prof., Islamic University of Technology, Bangladesh
Dr. Md. Ariful Islam, A/Prof. Dhaka University, Bangladesh
Dr. Md. Nurul Amin, Prof. Dhaka University, Bangladesh
Dr. D.K. Chauhan, Prof. Noida International Univ., India
Dr. Chan Chee-Ming, A/Prof. Universiti Tun Hussein Onn Malaysia
Dr. Ahmed H. A. Dabwan, A/Prof. TATI Univ. College, Malaysia

International Technical Program Committee:

Prof. Adolf Heinrich Horn, Geological Institute - Federa University of Minas Gerais, Brazil
Prof. Bang-Fuh Chen, National Sun Yat-sen University, Taiwan
Prof. Bindeshwar Singh, Kamla Nehru Institute of Technology, India
Prof. Catherine Mulligan, Concordia Institute of Water, Energy and Sustainable Systems, Canada
Prof. Chi-Min Liu Chienkuo Technology University, Taiwan
Prof. Daffalla Rabih, Kenana Sugar Company, Sudan
Prof. Essaid Bilal, Ecole Nationale Supérieure Des Mines De Saint Etienne, France
Prof. Hakan Caliskan, Usak University, Faculty of Engineering, Turkey
Prof. Ibrahim Maiyza, National Institute of Oceanography & Fisheries, Egypt
Prof. Loc Nguyen, Sunflower Soft Company, Vietnam
Prof. Marilia Hagen, Indiana University, United States
Prof. Md Najib bin Ibrahim, Universiti Teknologi MARA, Malaysia
Prof. Md. Abdul Baset Mia, BSMR Agri. Univ., Bangladesh
Prof. Mihaela Popescu, University of Craiova, Romania
Prof. Mohamed Abdou, Faculty of Education Department of Mathematics, Egypt
Prof. Mohamed Tahiri, Présidnce de l'Université Hassan II de Casablanca, Morocco
Prof. Nazar Oukaili, University of Baghdad, Iraq
Prof. Radim Cajka, Technical University Ostrava, Faculty of Civil Engineering, Czech Republic
Prof. Rajaraman Jambunathan, AMET University, India
Prof. Saad Farhan Ibrahim Alabdullah, University of Almustansiriyah, Iraq
Prof. Salem Alsanusi, Benghazi, Libya
Prof. Sudhir Kumar Das, Retired Senior Project Manager of Indian Railways, India
Prof. Zachary Senwo, Alabama A&M University, United States
Prof. Imed Jabri, University of Tunis, Tunisia
A/Prof. Bindeshwar Singh Kamla Nehru Institute of Technology, India
A/Prof. Hasi Rani Barai, Yeungnam University, South Korea
A/Prof. Jamaluddin Mahmud, Universiti Teknologi MARA, Malaysia
A/Prof. Mohamed Ramadan, University of Hail, Saudi Arabia
A/Prof. Najam Hasan, Dhofar University, Oman
A/Prof. Nosina Krishna Chaitanya, Jawaharlal Nehru Technological University, India
A/Prof. Nurbek Saparkhojayev, Almaty Management University, Kazakhstan
A/Prof. Pandian Vasant, Universiti Teknologi Petronas, Malaysia
A/Prof. Teodor Lucian Grigorie, University of Craiova, Romania
A/Prof. Zawawi Daud, Universiti Tun Hussein Onn Malaysia
A/Prof. Abdull Halim Abdul, Oil and Gas department, Malaysia
A/Prof. Baoping Cai, China University of Petroleum, China
A/Prof. Dariusz Jakóbczak, Koszalin University of Technology, Poland
A/Prof. Edgar Allan Mendoza, University of the Philippines
A/Prof. Lakhveer Singh, Universiti Malaysia Pahang (UMP) Malaysia, Malaysia
A/Prof. Lidia Sas Paszt, Research Institute of Pomology, Poland
A/Prof. Mahmood Barbooti, University of Yechology, Iraq
A/Prof. Majid Mirzaei, Universiti Tunku Abdul Rahman, Malaysia
A/Prof. Najeh Lakhoua, University of Carthage, Tunisia
A/Prof. Ryan Joseph Calinao, Lyceum of the Philippines University-Laguna
A/Prof. Sarawut Thepanondh, Mahidol University, Thailand
A/Prof. Yasir Al Hussein, Jerash University, Faculty of Engineering, Jordan
A/Prof. Grigorie Teodor Lucian, University of Craiova, Romania
A/Prof. Hêriş Golpîra, Islamic Azad University, Sanandaj, Iran
A/Prof. Muhammad Aslam, King Abdulaziz University, Saudi Arabia
A/Prof. Tomasz Plech, Medical University of Lublin, Poland
A/Prof. Fellah Mamoun, Abbes laghrour University, Algeria
A/Prof. R. S. Ajin, GeoVin Solutions Pvt. Ltd., India
A/Prof. Roman Szewczyk, Industrial Research Institute for Automation and Measurements, Poland

Dr. Abolghasem Akbari, University Malaysia Pahang, Malaysia
 Dr. Ahmad Safuan A Rashid, Universiti Teknologi Malaysia, Malaysia
 Dr. Akinola Johnson Olarewaju, Federal Polytechnic Ilaro, Ogun State, Nigeria
 Dr. Alexandre Costa, Federal University of the valleys of Jequitinhonha and Mucuri, Brazil
 Dr. Angelo Gallone, Scotland's Rural College (SRUC), United Kingdom
 Dr. Azizul Azhar Ramli, Universiti Tun Hussein Onn Malaysia
 Dr. Bashir Dar, University of kashmir Delina Baramulla J&K India, India
 Dr. Bassam Abdellatif, National Authority for Remote Sensing and Space Sciences, Egypt
 Dr. Binh Phu Nguyen, National University of Singapore, Singapore
 Dr. Cazacu Gabriela, S.C. Geotech Dobrogea, Romania
 Dr. Chengen Yang, Intel Corporation, United States
 Dr. Dayang Norulfairuz Abang Zaidel, Universiti Teknologi Malaysia
 Dr. Evgeni Starikov, KIT, Karlsruhe, Germany; Chalmers, Gothenburg Sweden, Germany
 Dr. Fatma Khanchel, University of Tunis El Manar, Tunisia
 Dr. Hamidreza Khataee, Griffith University, Australia
 Dr. Hêriş Golpîra, Islamic Azad University, Iran
 Dr. Iskhaq Iskandar, Dept. Physics, University of Sriwijaya, Indonesia
 Dr. Jingwei Zhao, University of Wollongong, Australia
 Dr. Jitendra Agrawal, Rajiv Gandhi Proudhyogiki Vishwavidyalaya, India
 Dr. Liza Patacsil, Malayan Colleges Laguna, Philippines
 Dr. Mohamed Amine, Ferrag Guelma University, Algeria
 Dr. Mohd Afendi Rojan, Universiti Malaysia Perlis, Malaysia
 Dr. Mohd Altaf, University of kashmir Delina Baramulla J&K India, India
 Dr. Mohd Hairy Ibrahim, Sultan Idris Education University, Malaysia
 Dr. Mostafa Khater, Egypt - El sharqia - Zagazig, Egypt
 Dr. Najam Hasan, Dhofar University, Oman
 Dr. Namir Alkawaaz, University of Almustansiriyah, Iraq
 Dr. Nashrul Fazli Mohd Nasir, Universiti Malaysia Perlis, Malaysia
 Dr. Naufal Mansor Kampus Uniciti Alam, Universiti Malaysia Perlis (UniMAP), Malaysia
 Dr. Obed Majeed Ali, Northern Technical University, Iraq
 Dr. Piyapong Janmaimool, King Mongkhut' University of Technology, Thailand
 Dr. Po-Sheng Chiu, National Cheng Kung University, Taiwan
 Dr. Prabu Mohandas, Adhiyamaan College of Engineering, India
 Dr. Raman Kumar, D A V Institute of Engineering and Technology, India
 Dr. Riccardo Colella, University of Salento, Italy
 Dr. Rolando Javellonar, Romblon State University, Philippines
 Dr. Shikha Agrawal, Rajeev Gandhi Technical University, India
 Dr. Stefania Tomasiello CORISA, University of Salerno, Italy
 Dr. Sumiyyah Sabar, Universiti Sains Malaysia, Malaysia
 Dr. Suphaphat Kwonpongsagoon, Mahidol University, Thailand
 Dr. Wei Hong Tan, Universiti Malaysia Perlis, Malaysia
 Dr. Yoshiro Fujii, Shin Kobe Dental Clinic, Japan
 Dr. Yuk Feng Huang, Universiti Tunku Abdul Rahman (UTAR), Malaysia
 Dr. Zongyan Zhou, Monsh University, Australia
 Dr. Purnanand Savoikar, Goa Engineering College, India
 Dr. Ahmed Toaha Mobashsher, University of Queensland, Australia
 Dr. Chupong Pakpum, Maejo University
 Dr. Emanuele Quaranta, Politecnico di Torino, Italy
 Dr. Jiangling Yin, Apple Inc., Cupertino, CA, United States
 Dr. Khor Shing Fhan, Universiti Malaysia Perlis, Malaysia
 Dr. Mario Chauca, Ricardo Palma University, Peru
 Dr. Santosh Gaikwad, Model College, Ghansawangi, India
 Dr. Tse Guan Tan, Universiti Malaysia Kelantan
 Dr. Vikas Panthi, National Institute of Technology, India
 Dr. Watoo Phrompittayarat, Naresuan University, Thailand

Dr. Hamidreza Namazi, Nanyang Technological University, Singapore
Dr. Parichat Phumkhachorn, Ubon Ratchathani University, Thailand
Dr. Subhasis Roy, University of Calcutta, India

Conference Correspondence:

Prof. Dr. Zakaria Hossain (Director)
Dept. of Environmental Science and Technology, Mie University, Japan
Mr. Md. Aminul Islam (Secretary)
Dept. of Environmental Science and Technology, Mie University, Japan
E-mail: conference@geomate.org
Tel & Fax: +81-59-231-9578

Editorial and Executive Committee:

Prof. Dr. Zakaria Hossain
Dr. Jim Shiau
Engr. Alex Otieno Owino
Engr. Mohamed Mahmoud Ahmed Eltaher

Keynote Papers

RUNOFF CHARACTERISTICS OF DEBRIS FLOW FLOWING DOWN A TORRENT OF MILD GRADIENT

Naomasa Honda¹

¹ Faculty of Regional Environment Science, Tokyo University of Agriculture, Japan

ABSTRACT

When a river bed slope is steep, the debris flow generally erodes the bed material and travels down on a large scale. When the bed slope becomes gentle at an equilibrium bed slope for a debris flow that corresponds to a sediment concentration based on volume as a boundary, the debris flow allows sediment deposits and stops soon. But when the debris flow includes such fine sand as volcanic ash, it may flow down at a smaller incline than a general stop gradient. We discuss the factors under which a debris flow moves downhill even if the bed slope is very small, based on the relationship between the bed slope and the sediment concentration. We investigated two actual debris flows in Japan: Ohkanazawa torrent of Izuohshima in Tokyo Prefecture in 2013 (caused by heavy rainfall) and Sanohdani torrent of the Aso district in Kumamoto Prefecture in 2016 (caused by two huge earthquakes). Judging from the results, when the debris flow structure consisted of a high sand-water mixture, the material of a small size particle raised the density of the pore water. A mudflow formed in the mild gradient torrent, arrived downstream, and overflowed.

Keywords: Torrent of mild gradient, Debris flow, Pore water, Fine sand concentration, Mudflow

INTRODUCTION

The characteristics of debris flow runoff strongly depend on the river bed slope as shown in Fig. 1. A debris flow is generally formed in the reach where sediments exist that might be eroded and the bed slope is 15° above. The debris flow erodes the bed material and flows down on a large scale [1]–[3].

When the bed slope becomes gentle at an equilibrium bed slope for a debris flow that corresponds to a sediment concentration by volume as a boundary, the sediment transport mode changes from debris flow into an earthflow with the bed slope's decrease [4]. Then the debris flow allows a sediment deposit and stops quickly [5], [6]. But when the debris flow includes such fine sand as volcanic ash, it may flow down at a smaller incline than a general stop gradient [7], [8].

Next we discuss the factors under which a debris flow moves downhill even if the bed slope gradient is

very small, based on the relationship between the bed slope and the debris flow's sediment concentration. We chose two actual debris flows in Japan for investigation and discussion: one caused by a heavy rainfall and another due to huge earthquakes.

METHOD AND PROCEDURE

Relationship between debris flow's bed slope and sediment concentration

The following shows the relationship between the bed slope and the sediment concentration of the debris flow [1]:

$$\tan \theta_e = \frac{(\sigma / \rho - 1)c}{(\sigma / \rho - 1)c + 1} \tan \phi \quad (1)$$

where θ_e is the equilibrium bed slope for a debris flow that corresponds to the sediment concentration by volume c , which is a bed slope that produces neither erosion nor deposition on the bed. σ is the mass density of gravel, ρ is the mass density of the pore water, and ϕ is the sediment's interparticle friction angle.

Equation (1) is updated as follows:

$$c_e = \frac{\tan \theta}{(\sigma / \rho - 1)(\tan \phi - \tan \theta)} \quad (2)$$

where c_e is the equilibrium sediment concentration by volume corresponding to a bed slope θ , which is

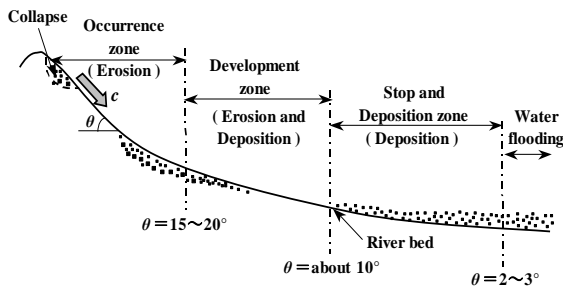


Fig. 1 Debris flow runoff process

the sediment concentration where neither erosion nor deposition is produced on the bed.

For Eq. (1), Egashira et al. [7] proposed the following formula based on the mudflow characteristics:

$$\tan \theta_e = \frac{(\sigma / \rho - 1)c}{(\sigma / \rho - 1)c + 1} \frac{h_s}{h} \tan \phi \quad (3)$$

where h is the flow depth and h_s is the thickness of the bedload layer ($h_s \leq h$).

In Eq. (3), when h_s / h equals 0.3, the flow forms a mudflow. When h_s / h equals 1.0, Eq. (3) completely agrees with Eq. (1) and the flow forms a debris flow.

The mudflow consists of water and material of small particle size. On the other hand, the debris flow consists of water and sediment of relatively large scale. Eq. (3) shows that the mudflow has higher fluidity than the debris flow.

Previous work on relationship between bed slope and debris flow runoff characteristics

Egashira et.al [8] performed a numerical analysis of the debris flow of the Gamaharazawa torrent (a tributary of the Hime river) caused by snowmelt in 1996, based on one-dimensional governing equations for the sediment-water mixture. In their simulations, they assumed that the debris flow consists of sediment and muddy water containing a large amount of fine sand (concentration assumed to range from 30 to 50 %). Based on their results, they explained the sediment runoff phenomenon as follows:

- Since the debris flow added to the fluidity due to the increase of buoyancy with muddy water, the debris flow flowed down the channel works of a small incline less than 3°.
- When the influence of the fine sand was ignored, the debris flow was deposited in the middle of the torrent and didn't arrive downstream.
- The sediment flowed down the Hime River with little sediment deposition in the channel works.

Outline of actual debris flows

Case 1: Mud flow at Ohkanazawa torrent [10]

Izuohshima is an island in Tokyo Prefecture as shown in Fig. 2. In October, 2013, typhoon No.26 caused a record-breaking heavy rainfall (824 mm/24 hours), following by a huge mud flow of Ohkanazawa torrent.

Ohkanazawa torrent was formed by the eruption of Mt. Mihara in the center of Izuohshima. As shown in Fig. 3, its downstream bed slope was loose. The surface layer of the mountain slope that constituted both sides of the torrent included volcanic



Fig. 2 Location of debris flow occurrences

ash of small particle size. The soil layer under the surface layer was aquiclude.

The mud flow, which consisted of water and volcanic ash, flowed down at a mild gradient, reached the sea, and overflowed over a wide area. By this mud flow, 39 peoples were left dead or missing and such serious damage as house collapses occurred successively.

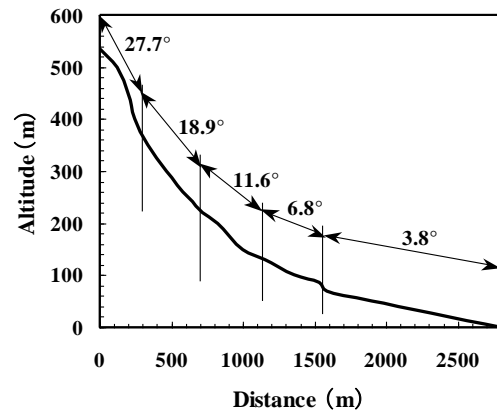


Fig. 3 Bed profile of Okanazawa torrent

Case 2: Debris flow at Sanohdani torrent [11]

Two huge earthquakes of Japanese seismic intensity scale 6 and 7 struck Kumamoto Prefecture (Fig. 2) in April 14 and 16, 2016. By these earthquakes named “the 2016 Kumamoto Earthquake” later, 50 people died over two days. Such serious damage as house collapses, road surface cave-ins, and train derailments also occurred.

Such sediment-related disaster occurrences as landslides, collapses, and debris flows were concentrated near the earthquake faults. Ten people died in two days from sediment-related disasters. In Minamiaso village, a debris flow occurred in Sanohdani torrent.

Sanohdani torrent has a watershed area of 2.34 km², a reach of about 5km and a mean bed slope of 6.9 °. It is designated as a debris flow torrent based

on Japanese law as shown in Fig. 4. The sediment,

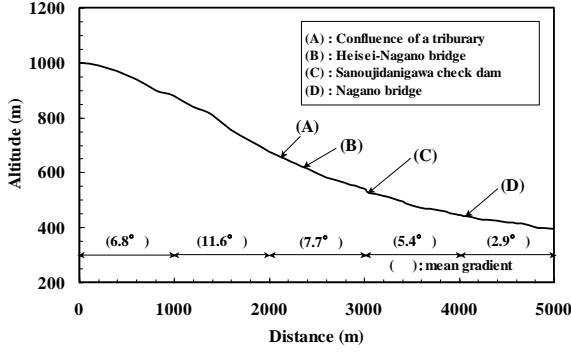


Fig. 4 Bed profile of Sanohdani torrent

which was produced by the hillside landslide due to the earthquake, formed a debris flow without a water supply, arrived downstream, and overflowed. The debris flow's soil material was mainly composed of clay and silt of a small particle size, except just after the earthquake. Its reference grain size, d_{50} , was less than 0.1mm.

Calculation Conditions

To clarify the factors under which a debris flow moves downhill even if the bed slope gradient is very small, we investigated the relationship between the bed slope and the sediment concentration of the debris flow using Eqs.(1), (2) and (3).

When the pore water includes fine sand, we cannot ignore how it influences the buoyancy [8]. Therefore, ρ is given as follows:

$$\rho = (\sigma - \rho_w)c_s + \rho_w \quad (4)$$

where ρ_w is the mass density of the fresh water and c_s is the fine sand concentration in the pore water. In this study, we used $\sigma = 2.70 \text{ g/cm}^3$ and $\rho_w = 1.00 \text{ g/cm}^3$.

RESULTS AND DISCUSSIONS

Case 1: Mud flow at Ohkanazawa torrent

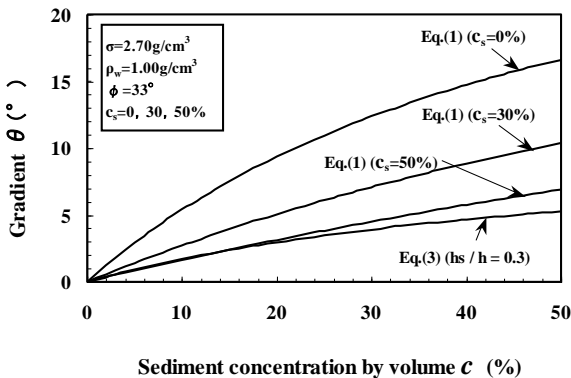


Fig. 5 Relationship between c and θ

Figure 5 shows the relationship between c and θ by Eq. (1) and Eq. (3). In Fig. 5, ϕ is set at 33° . It ranges from 33° to 39° and is frequently in the debris flow runoff analysis [8], [11]. It is also a minimum value in the range considering the debris flow's high fluidity. In Eq. (1), c_s 's values are 0, 30 and 50 %. In Eq. (3), h_s/h is set at 0.3, which shows the characteristics of the mud flow, and ρ equals ρ_w [7].

In Fig. 3, the mean gradient of the downstream that reaches Ohkanazawa torrent is 3.8° . In Fig. 5, when θ is 3.8° in Eq. (1), the flow, whose c_s is 30 %, has around 15 % of c and keeps the earthflow characteristics; the flow whose c_s is 50 %, has a little less than 30 % of c and retains the hyper concentrated debris flow characteristics. Similarly, in Fig. 5, when θ is 3.8° in Eq. (3), the mudflow may have a high sediment concentration over than 30 %.

When h_s/h equals 0.3 in Eq. (3), c_s , which is θ_e from Eqs. (1) and (3), approximately equals 55 % and almost equals the sediment concentration of the bed layer (the critical concentration at which the debris flow can entrain the sediment). In addition, the range from 30 to 50 % of c_s is in good agreement with the results of Egashira et al. [8].

Judging from the results, in Ohkanazawa torrent, the material of the small particle size, which was mainly composed of volcanic ash, raised the mass density of the pore water that constituted the debris flow and increased the fluid's buoyancy. The mudflow was formed by a sediment-muddy water mixture and flowed down a mild gradient torrent. It arrived downstream with high fluidity and overflowed.

Case 2: Debris flow at Sanohdani torrent

Figure 6 shows the relationship between ϕ and c_e by Eq. (2) when the θ values are 3° and 6° . In Eq. (2), c_s 's values are 0, 30 and 50 %. When ϕ equals to 35° (it ranges from 33° to 39° , it is frequently used for debris flow runoff analysis [7], [11] and is a middle value in the range), and c_s ranges from 30 to 50 %, c_e is as follows:

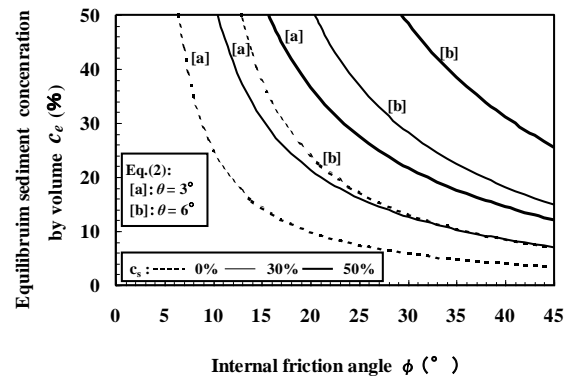
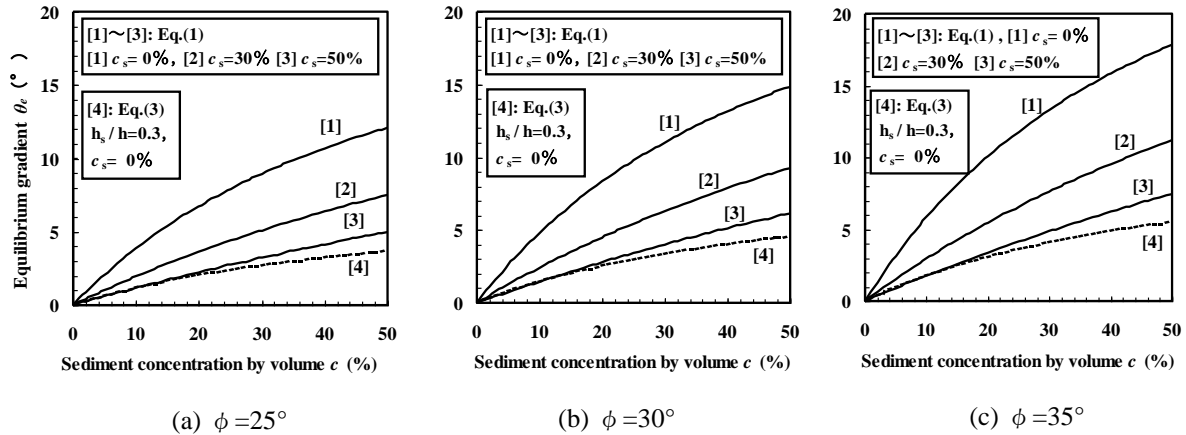


Fig. 6 Relationship between ϕ and c_e

Fig. 7 Relationship between c and θ_e

- When θ is 6° , the flow has a sediment concentration from 22 to 38 % and retains the hyper concentrated debris flow characteristics.
- When θ is 3° , the flow has a sediment concentration from 10 to 18 % and retains the earthflow characteristics even if the bed is gentle.

The reference grain size of the soil material constituting debris flow d_{50} was very small (less than 0.1 mm.) and ϕ was probably smaller than a normal value of the debris flow, which is mainly composed of relatively large-scale gravel.

Figures 7(a), (b), and (c) show the relationship between c and θ_e when ϕ is 25° , 30° and 35° in Eqs. (1) and (3). In Eq. (1), the values of c_s are 0, 30, and 50 %, h_s/h equals 0.3, and c_s is 0 % in Eq. (3).

In Fig. 7(a) ($\phi = 25^\circ$), c , where θ_e equals 3° , ranges from 16 to 28 % in Eq. (1) (c_s ranges from 30 to 50 %) and around 35 % in Eq. (2). Similarly, in Fig. 7(b) ($\phi = 30^\circ$), c , where θ_e equals 3° ranges from 13 to 22 % in Eq. (1) (c_s ranges from 30 to 50 %) and around 26 % in Eq. (2). As shown in these figures, the flow can keep the hyper-concentrated debris flow characteristics on a mild bed slope.

When h_s/h equals 0.3 in Eq. (3), c_s , which is θ_e by Eqs. (1) and (3), approximately equals 55 % and almost equals the sediment concentration of the bed layer, too. In addition, the range from 30% to 50 % of c_s is in good agreement with the results of Egashira et al. [8].

Judging from our results, in Sanohdani torrent, the material of small particle size, which is mainly composed of clay and silt, raised the mass density of the pore water that constituted the debris flow and increased the fluid's buoyancy. Such hyper concentrated flow as earthflow and mudflow was formed by a sediment-muddy water mixture and flowed down a mild gradient torrent. It arrived

downstream with high fluidity and overflowed.

CONCLUSION

With both cases (Ohkanazawa torrent and Sanohdani torrent), the material of small particle size raised the mass density of the pore water that constituted the debris flow and increased the fluid's buoyancy.

A debris flow is generally recognized as a sediment-related disaster of steep slopes. But runoff characteristics strongly depend on the materials that comprise the debris flow (sediment and the muddy water) with the bed slope. As a result, the sediment transport mode changes from a debris flow into general contact loads and the disaster form and its scale change, too. They must be examined in countermeasures against debris flow hazards.

ACKNOWLEDGEMENTS

Part of the present study was supported by Strategic Research Project from Tokyo University of Agriculture.

REFERENCES

- [1] Takahashi T., A Mechanism of Occurrence of Mud-Debris Flows and Their Characteristics in Motion. Annuals of Disaster Prevention Research Institute, Kyoto University, Vol. 20, Issue B-2, 1977, pp.405-435 (in Japanese).
- [2] Takahashi T., Study on the Deposition of Debris Flow (3) -Erosion of Debris Fan -. Annuals of Disaster Prevention Research Institute, Kyoto University, Vol. 25, Issue B-2, 1982, pp.327-348 (in Japanese).
- [3] Takahashi T. and Fu Kuang, Formation of Debris Flow on Varied Slope Bed. Annuals of Disaster Prevention Research Institute, Kyoto

- University, Vol. 29, Issue B-2, 1986, pp.343–359 (in Japanese).
- [4] Hashimoto H., Tsubaki T. and Hirano M., Sediment Gravity Flow on Relatively Gentle Slopes. Annual Journal of Hydraulic Engineering, Japan Society of Civil Engineering, Vol. 30, 1986, pp.235-240 (in Japanese).
- [5] Egashira S., Mechanism of Sediment Deposition from Debris Flow (Part 1). Journal of the Japanese Society of Erosion Engineering, Vol. 46, Issue 1, 1993, pp.45-49 (in Japanese).
- [6] Egashira S., Mechanism of Sediment Deposition from Debris Flow (Part 2). Journal of the Japanese Society of Erosion Engineering, Vol. 46, Issue 2, 1993, pp.51-56 (in Japanese).
- [7] Egashira S., Sato T. and Chishiro K., Effect of Particle Size on the Flow Structure of Sand-Water Mixture. Annuals of Disaster Prevention Research Institute, Kyoto University, Vol. 37, Issue B-2, 1994, pp.359–369 (in Japanese).
- [8] Egashira S., N Honda. and Miyamoto K., Numerical Simulation of Debris Flow at the Gamaharazawa in the Hime River Basin. Annual Journal of Hydraulic Engineering, Japan Society of Civil Engineering, Vol. 42, 1998, pp.919-924 (in Japanese).
- [9] Japan Society of Civil Engineering, the Japanese Geotechnical Society, Japan Society of Engineering Geology and the Japanese Landslide Society, Investigation Report of Heavy Rainfall Disasters caused by Typhoon No. 26 in Izuoshima in October 2013, 2014, pp. 1–90 (in Japanese).
- [10] Japan Society of Erosion Control Engineering, Urgent Investigation Report of the sediment-related disasters caused by the 2016 Kumamoto Earthquake, 2016, 81pp (in Japanese).
- [11] Egashira S., Honda N., Itoh T. and Arimura S., Experimental Study on the Entrainment of Bed Material into Debris Flow. Physics and Chemistry of the Earth, Part C, Vol. 26, Issue 9, 2001, pp.645-650.

MECHANICAL PROPERTY OF CHLOROPRENE BEARING PAD FOR BRIDGE UNDER CYCLIC TEMPERATURE CHANGE

Hiddenori Tanaka¹, Kazuki Kurosawa² and Masatake Yoshino³

¹Civil Engineering, Gunma National College of Technology, Japan; ^{2,3} Former student, Japan

ABSTRACT

Rubber materials are very indispensable to keep infrastructure safe against earthquakes. In Japan, these are normally used to support the structures (bridges, buildings). Generally speaking, They are non-compressive and hyper-elastic material so that the mechanical properties of them have not been clarified sufficiently into design codes. Based on this, we conducted simple compressive creep and thermal fatigue tests by using cylindrical specimens (the diameter is 80mm, the height is 80mm) made of chloroprene rubber as a bearing pad for bridge. We pressed the specimen to equivalent forces which are equal to the serviceability state. We have kept them and set into freeze-thaw test machine. And then, we applied cyclic temperature change (from -10 to 3 Celsius) Finally, we have compared the creep properties at normal temperature with those of cyclic temperature change for seven months. We found that the elastic damage would be occurred in proportion to cyclic numbers.

Keywords: Chloroprene, Irreparable creep, Cyclic temperature change, Fatigue, Finite displacement theory

INTRODUCTION

Seismic isolation rubber has been used for bearing pad of bridges and buildings. The isolated effect would be dependent on the horizontal deformation of rubber under earthquakes. There were many experiments to evaluate the horizontal deformation without considering axial (vertical) mechanical properties which are creep, visco-plasticity and thermal fatigue.

Rubber is usually non-compressive and non-volumetric material. So, if there is residual deformation caused by vertical inelastic behavior such as creep or visco-plasticity. The horizontal deformation is restricted. And, the isolated effect would become smaller. On the top of these, The inelastic behavior including large displacement will be occurred even though the applied loads are small.

Finally, it is very important to take into account of the isolated effect due to inelasticity of rubber.

Rubber also has a great influence on temperature change. Especially, the mechanical property caused by thermal fatigue has not been cleared sufficiently.

Therefore, we have conducted simple compressive creep and thermal fatigue test under cyclic low temperature change using chloroprene specimen [1].

In this study, we show the numerical analysis of compressive deformation by Ogden's model that is the basic theory to explain large displacement behavior in two dimensional axisymmetric problem comparing with the result of experiment [2].

COMPRESSIVE TEST

The load-displacement curve

The quasi-compressive loads were applied on the cylindrical specimen (ϕ 80mm, H=80mm) with upper and lower steel plates (refer Fig.1).

Figure 2 shows the relationship between applied loads and longitudinal displacements.

In this test, The applied loading speed was 10mm/minute.

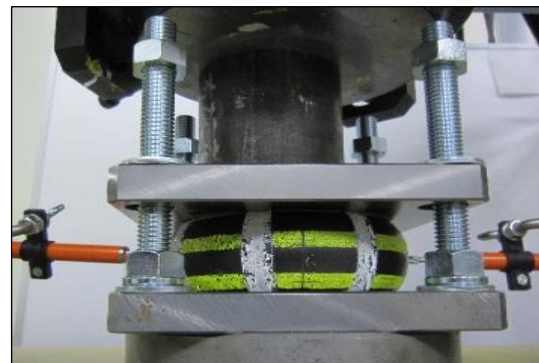


Fig 1. Deformation of rubber (compressive test)

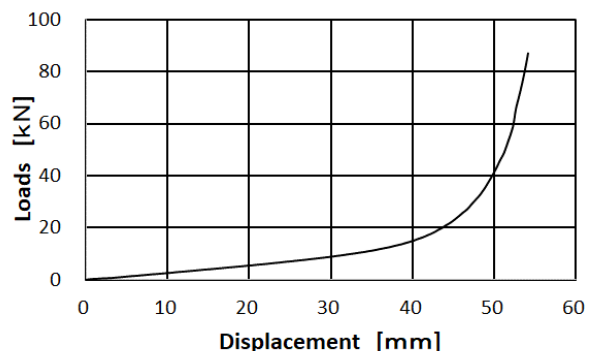


Fig.2 Loads-displacements curve

The curve was typical compressive behavior and showed the strong non-linearity after the applied loads passed 10 (kN) [3].

Compressive creep test

We conducted the Compressive creep test as follows. At first, we measured the displacements and applied loads until serviceability state which was supporting the self-weight of bridge girders. Secondly, The stresses have been holding for seven months to fix securely upper steel plate by four bolts with nuts at the corner (refer to Fig.3).

Finally, we measured the displacements again after stresses were released unfastening the bolts and nuts (refer to Fig.4). We could evaluate non-linear state that including unloading elasticity, delayed elasticity and irreparable creep to describe the deformation curve after the stresses were released.

We determined serviceability state to consider relationship between real chloroprene pad section area and girders weight.

The red point in Fig.5 was equivalent to the serviceability state (Load (P)=5.5 (kN)).

This point was approximately within linear state .

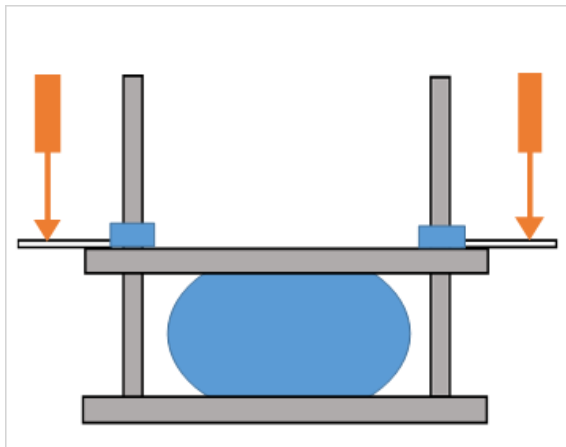


Fig.3 holding stress (serviceability state)

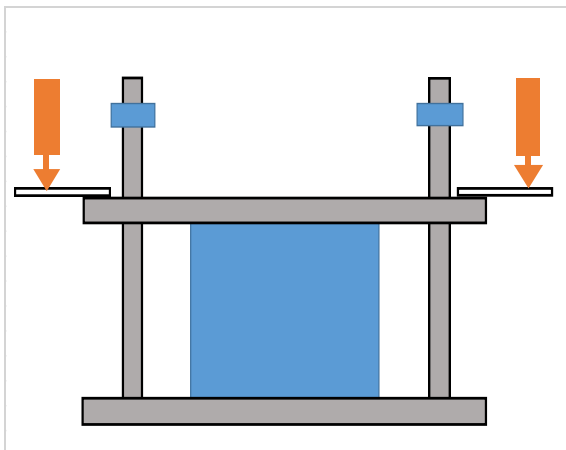


Fig.4 Releasing stress

We set the specimen into the freeze-thaw test machine to evaluate the affection by cyclic temperature change for seven months at the serviceability state .

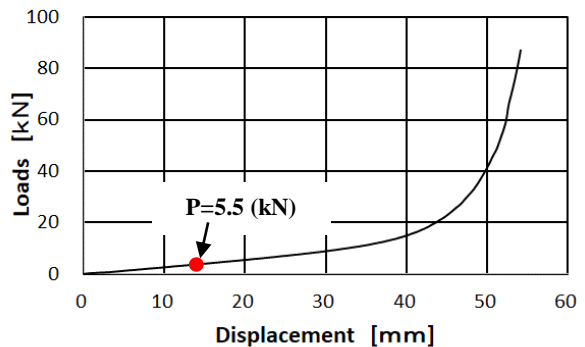


Fig.5 Serviceability state (red point)

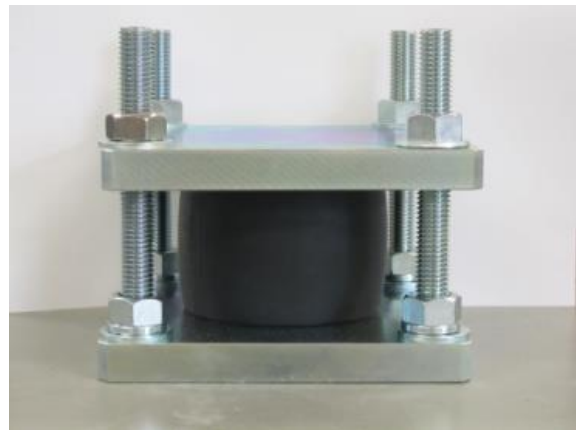


Fig.6 Specimen at serviceability state



Fig.7 Freeze and thaw test machine

The specimen was shown in Fig.6. We checked the creep properties of the specimen at normal temperature and under cyclic temperature change which indicated the mean temperature of winter in Tohoku area. We determined the change period by specified machine property as long as we could.

The freeze-thaw test machine was shown in Fig.7. The applied temperature change was shown in Fig.8. The maximum and the minimum temperature were +3 , -10 Celsius respectively.

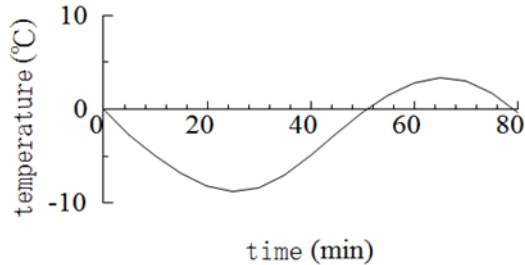


Fig.8 Temperature change

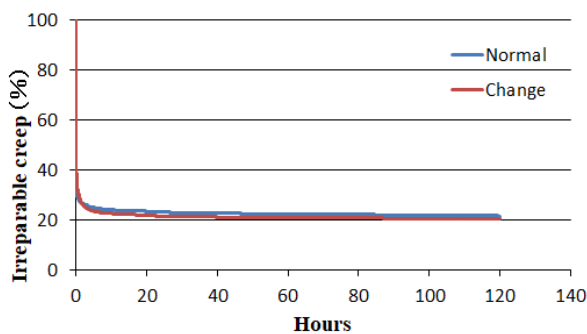


Fig.9 Irreparable creep properties

The curve after releasing stresses indicated creep characteristics (refer to Fig.9). This curve was mainly consist of three parts. The sharp descending line near 0 (hour) was unloading elasticity, by 80 (hours) it showed delayed elasticity, and after 80 (hours) it showed irreparable creep, respectively.

Even though the holding times were less than for a year , it was found that the irreparable creep reached about 20 % of total displacement. In addition, The creep would be occurred under the small load that was equal to serviceability state.

‘Normal’ showed the result at normal temperature and ‘Change’ showed the result of that the cyclic number reached 3,200 in Fig.9. It was found that there were not much difference about creep properties between two curves.

FATIGUE TEST

Hysteresis curves

The strain gauge was set the middle of specimen to evaluate the damage or deterioration caused by cyclic temperature change (refer to Fig.10).

Figure 11 showed the relationship between principal strain and temperature change . The plastic strain was increased by 500 cycles. These hysteresis

curves were similar like ellipses.

So , Each curve was approximately represented as ellipses.

Figure 12 indicated the strain energy which was equivalent to the area of ellipse responding to cyclic numbers.

The energy of 500 cycles or after has been decreasing proportional to cyclic numbers. We considered that the energy was one of the indexes to evaluate the damage caused by thermal fatigue.

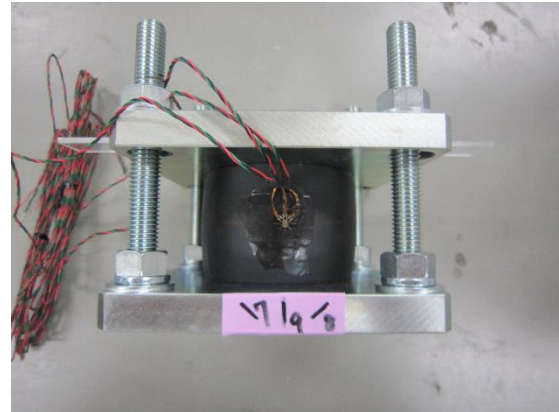


Fig.10 Set the strain gauge

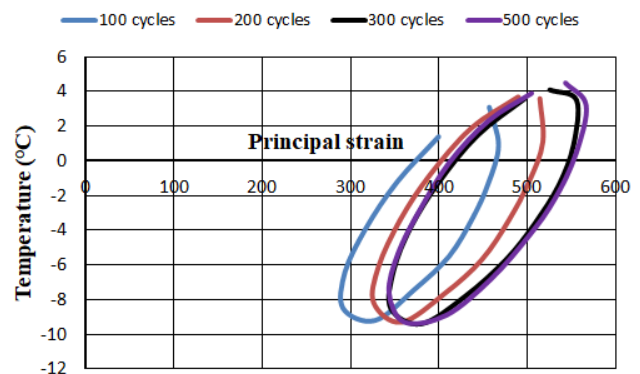


Fig.11 Hysteresis curves by 500 cycles

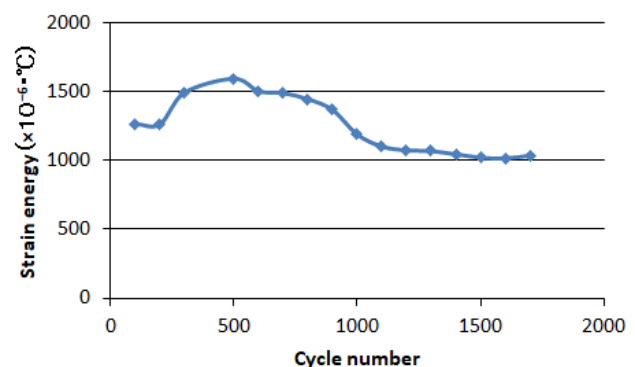


Fig.12 Relationship strain-energy and cyclic numbers

Equivalent thermal expansion coefficient change

We focused on the equivalent thermal expansion coefficient (ETEC) change derived from hysteresis curves, because the value was closely related with damage by thermal fatigue [4].

We defined ETEC as the linear gradient which shown the average gradient of ellipses (refer to Fig.13).

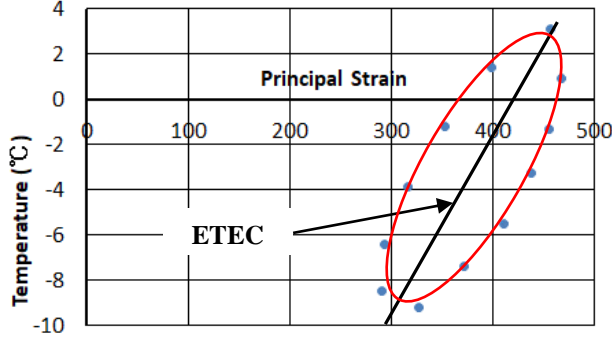


Fig.13 ETEC of hysteresis curve

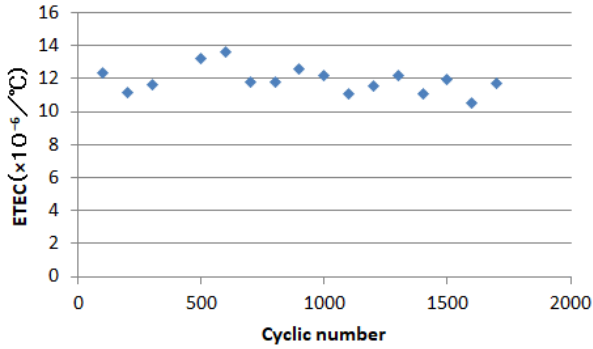


Fig.14 Relation ETEC and cyclic numbers

We showed relationship between ETEC and cyclic numbers in Fig.14.

ETEC was decreased due to cyclic numbers. So, we found that ETEC was one index to evaluate the damage by cyclic temperature change.

NUMERICAL ANALYSIS

Base of finite displacement theory

Rubber has generally large deformation under compressive loads. So, There are some limitations to apply the infinitesimal deformation theory.

The deformation gradient tensor has been used to describe the mechanical properties of rubber. For example, Cauchy stress, Green strain tensor[5]. In this paper, The deformation gradient tensor was defined as follows[6].

$$F = \frac{\partial \mathbf{x}}{\partial \mathbf{X}} \quad (1)$$

F : Deformation gradient tensor

\mathbf{x} : infinitesimal line element vector(after deformation)

\mathbf{X} : infinitesimal line element vector(before deformation)

Green-Lagrange strain tensor

The strain should be described more than second rank orders to apply this analysis. Green-Lagrange strain tensor was reasonable for variational principle [7].

$$E = \frac{1}{2} \frac{d\mathbf{x}^2 - d\mathbf{X}^2}{d\mathbf{X}^2} \\ = \frac{1}{2} \left(\frac{\partial u_i}{\partial X_j} + \frac{\partial u_j}{\partial X_i} + \frac{\partial u_k}{\partial X_i} \frac{\partial u_k}{\partial X_j} \right) \quad (2)$$

E : Green – Lagrange strain tensor

$u_{i,j,k}$: displacement

The Second Piola-Kirchhoff stress tensor

This stress tensor is the best expression corresponding to the Green-Lagrange strain tensor. And then, This form is useful formulation in analysis because of the symmetric form[5].

$$S = J F^{-1} \sigma F^{-T} \quad (3)$$

S : second Piola – Kirchhoff stress

J : det(F)

F^{-1} : Inverse tensor of F

F^T : Transpose of F

σ : Cauchy stress tensor

Ogden's model

Strain energy function has been used to analyze the large deformation of rubber under various loads. Moony-Rivlin and Neo- Hooke models are popular functions for analysis. But, these models are inadequate for nonlinearity in high strain region. So, here, we adopted Ogden's model to simulate high nonlinearity region in analysis[8].

$$W = \sum_{n=1}^N \frac{\mu_n}{\alpha_n} (\lambda_1^{\alpha_n} + \lambda_2^{\alpha_n} + \lambda_3^{\alpha_n} - 3) \quad (4)$$

W : strain energy function

α_n, μ_n : material constant

$\lambda_1, \lambda_2, \lambda_3$: principal stretch ratio

In this paper, we considered third rank (N=3). The material properties were shown in Table.1.

Table.1 Material properties

Constant value	α	μ
First rank	$\alpha_1=1.3$	$\mu_1=1.491$ (N/mm ²)
Second rank	$\alpha_2=5.0$	$\mu_2=0.003$ (N/mm ²)
Third rank	$\alpha_3=-2.0$	$\mu_3=-0.0237$ (N/mm ²)

Results of deformation analysis

We carried out two dimensional axisymmetric analysis considering the shape of specimen [2]. Therefore, The analysis area was half model.

Figure 15 showed the deformation and the equivalent stress distribution .

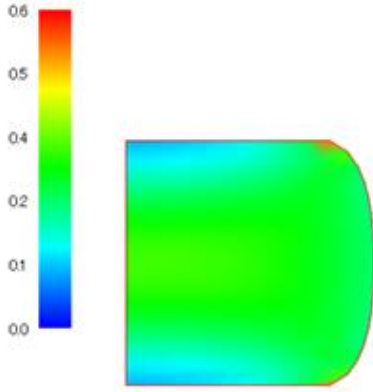


Fig.15 Deformation and equivalent stress

Equivalent stress was defined in equation (5).

$$\sigma_{eq} = \sqrt{3J_2'} \quad (5)$$

σ_{eq} : Equivalent stress(N/mm²)

J_2' : Second invariant of deviatoric stress

We adopted the displacement control method. The equivalent stress distribution was typical for compression state. The highest stress was distributed at the corner of specimen which was contacted with steel plates (upper and lower). The maximum equivalent stress was approximately 0.6 (N/mm²).

Unsteady thermal conduction analysis

The unsteady thermal analysis is simulated under cyclic temperature change (refer to Fig.8). This is preliminary step to check the evolution of viscoplastic and damageable properties of this pad under cyclic temperature change [9].

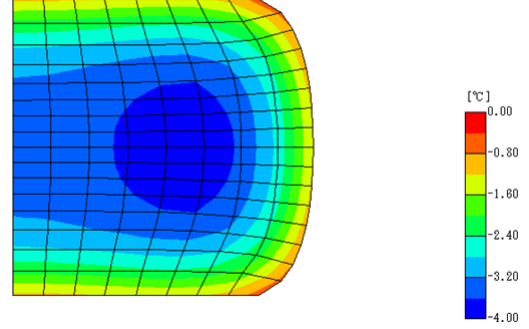


Fig.16 Thermal distributions

We have carried out the freeze and thaw test keeping the deformation of rubber at serviceability state. So, In this analysis, the compressive final deformation was the initial form .

For example, Figure 16 showed the thermal distributions when the temperature reached 0 from -10 °C. The center line was heat insulation and the others of model were heat transferable borders. The material properties were shown in Table 2.

Table 2 Thermal properties

Specific heat	1.65 (J/g · K)
Specific gravity	1.39
Heat transfer coefficient	14 (W/m ² °C)

Thermal distributions was changed in about four degrees from the surface to the center of rubber. The model was also half considering axisymmetric.

CONCLUSION

The knowledge found in this research are as below.

The irreparable creep is occurred under the serviceability state even though the elapsed time is only for seven months. And this value is about 20 % of total displacement. This means that the 20 % of total deformation energy is dissipated by creep.

About thermal fatigue, The equivalent thermal expansion coefficient as well as the strain energy provides the indication of damage caused by thermal fatigue. Because the relationship between both parameters and cyclic numbers are closely similar. Specially, The equivalent thermal expansion coefficient will be approximately linear and reduced about 15 % comparing with the initial value. This reduction shows damage quantitatively.

After the thermal fatigue test, the irreparable creep value is almost same result at normal temperature. From these results, we found that the thermal fatigue damage in this case is elastic.

From the results of simulation, we found that the maximum equivalent stress at serviceability state is distributed at the corner of specimen which is contacted with steel plates. The damage also would be distributed same parts. And then, There are only four degrees difference from surface to center by the conduction analysis. Second Piola-Kirchhoff stress and Green-Lagrange strain tensor are suitable expression for large displacement problem of rubber.

Finally, as the next stage, we have a plan to adopt F-bar method that is the popular numerical way to describe elasto-viscoplasticity of rubber. And, we would like to analyze the thermal fatigue behavior keeping serviceability state under cyclic temperature.

ACKNOWLEDGEMENTS

The author appreciates Tokyo Fabric Co.,Ltd for providing the chloroprene specimens. And, Research Center of Computational Mechanics, Inc. for supporting two dimensional unsteady thermal conduction analysis.

REFERENCES

- [1] Yoichi Yuki, Hiroki Tamai et al, "Fundamental experiment of shape and confining effect on rubber pieces' cushioning characteristics", Journal of structural engineering, Vol.61A, March,2015, pp. 313–321.
- [2] EA de Souza Neto, D Peric, DRJ Owen," Non-linear finite element method", June, 2012.
- [3] Hisanari Uruta, Kazuhiko Kawashima et al , "Evaluation of stress-strain relation for a rubber rectangular shock absorbing device under an extreme compression stress", Journal of JACE, No.661,Oct,2000,pp.71-83.
- [4] Masakazu Takagaki, Tutaka Toi," Thermal Fatigue Analysis of Toroidal Cracks by Local Approach to Fracture,2005,3C01
- [5] Takashi Kyoya,"Continuum Mechanics ",Japan Association for Non-linear CAE,Dec,2008
- [6] Shigeru Kuranishi,"Introduction to Mathematical Models of Material Characteristics", Subcommittee of Structural Mechanics Committee of Structural Engineering, J.S.C.E.,Aug.,1989
- [7] B.R.Seth, "Generalized strain measure with applications to physical problems", IUTAM Symposium on Second Order Effects in Elasticity, Plasticity and Fluid Mechanics, 1962, pp. 1-14.
- [8] R.W.Ogden,D.G.Roxburgh, "A pseudo-elastic model for the Mullins effect in filled rubber",The royal society, 1999, pp. 2861-2877.
- [9] Hidenori Tanaka, Fimiyasu Makinoshima,"The adhesive characteristic of concrete block with fiber sheets under cyclic temperature", International Conference on the Regeneration And Conservation of Concrete Structures 2015,I-17

Technical Papers

Science

EFFECT OF OKRA AND TANGERINE RATIOS ON PRODUCTION OF MIXED JUICE WITH LYCOPENE SUPPLEMENTATION

Wattana Wirivutthikorn

Faculty of Agricultural Technology, Rajamangala University of Technology Thanyaburi (RMUTT) 2

Phaholyothin 87 Soi 2 Phaholyothin Road Thanyaburi Pathumthani 12130 Thailand

ABSTRACT

Thailand has many herbal plants. The major advantage is that there are good bioactive ingredients and antioxidants that are beneficial to the body are possible when used as a drink. There are research reports related to the production of various Thai herbal drinks and fruits such as okra and tangerine were used as raw materials. The objective of this research was to study the optimum ratios of okra and tangerine with lycopene supplementation on Thai herbal beverage production. Four ratios of okra and tangerine were performed into 4 experiments; Experiment 1: (control formula) okra juice: tangerine juice 50:50 ratio; Experiment 2: okra juice: tangerine juice 60:40 ratio; Experiment 3: okra juice: tangerine juice 70:30 ratio; Experiment 4: okra juice: tangerine juice 80:20 ratio. Physical properties, i.e. L^* , a^* , b^* and turbidity showed that all experiments were significantly different except for L^* and a^* value. Chemical properties, i.e. pH, percent of total acidity and total soluble solid revealed that all experiments were statistically significant differences. ($P < 0.05$) Sensory evaluation was done by using 9-points hedonic scale. The results indicated that Experiment 1 had the highest scores of sensory acceptance. From the information obtained, the formulation of beverages produced from Thai herbal and fruit can be developed to be accepted by consumers, which has increased steadily and expanded in the large future level in beverage industry.

Keywords: Okra, Tangerine, Juice, Lycopene, Supplementation

INTRODUCTION

Nowadays, health drink products enroll a greater role in everyday life. Most of the health drinks are derived from the ingredients of plants or herbs to be processed to meet the needs. Some consumers may not consume vegetables. Some fruits or herbs due to odor, spicy or bitter taste. It is not very popular with consumers. But because of the benefits of the various types of Thai herbal that can be processed in the form of health drinks, the benefits will be different according to the properties of the raw materials [1]. Okra is a popular health food due to its high fiber, vitamin C and folate content. It is also known for being high in antioxidants have a good source of calcium and potassium and the mucilage contains soluble fiber. Some people prefer to minimize the sliminess; keeping the pods intact, and brief cooking. Some of the advantages of okra are aids in improving digestion, help to relax blood vessels and arteries and protect heart against clotting [2]. Tangerine is an orange-colored citrus fruit that is closely related to, or possibly a type of

mandarin orange. It is a good source of vitamin C, folate and β -carotene. It also contains some potassium, magnesium, vitamins B₁, B₂, and B₃ [3]. There are some researches about blended okra, gac fruit and passion fruit juice to produce Thai herbal drink. The result found that the different ratios of okra, gac fruit and passion fruit had influence on consumer acceptance [4]. For this reason, of okra and tangerine benefits, the researchers are interested in producing water-based okra and tangerine with healthy drink by studying appropriate amounts of okra and tangerine ratios with lycopene supplementation which help with the quenching of thirst and help relax or make the body. The data obtained from this research was an alternative to make okra and tangerine as raw materials for beverage production to improve the nutritional quality and good health of consumers. The purpose of this research was to study the appropriate quantities of okra and tangerine ratios with lycopene supplementation for the development of beverage products.

MATERIALS AND METHOD

The research was carried out at the Faculty of Agricultural Technology, Rajamangala University of Technology Thanyaburi. (RMUTT) Pathumthani Province Thailand. The samples used in this study were purchased from Rangsit Market Pathumthani Province Thailand.

Okra Preparation

The okra was washed and cut into small pieces and boiled in hot water for 15 minutes. Okra samples were dried by using hot air oven at 75 °C for 3 hours [5].

Tangerine preparation

The tangerine was washed with clean water and slice into thin small pieces as 2.1 and peeled theirs to juice with fruit juice extractor. The blended aliquots were placed in clean container [6].

This was performed as four experiments (two replications): 1) blended okra and tangerine juice 50:50 (the control); 2) blended okra and tangerine juice 60:40; 3) blended okra and tangerine juice 70:30 and 4) blended okra and tangerine juice 80:20. The ingredients were detailed in Table 1 [6].

Production of okra and tangerine juice with lycopene supplementation

The blended dried okra and tangerine juice were placed in a stainless steel pot (3 liters of clean water) and heated to 50°C. for 15 minutes, then, filtered through a cloth. Addition of some detailed ingredients followed as Table 1 [5], [6].

Physical Measurement

Brightness (L^*), color as red (a^*) and yellow (b^*) and the clarification value measured as percentage of transmittance (%T) were recorded as adapted from [8].

Chemical Measurement

The pH, percentage of total acidity and the total soluble solids (TSS) were measured as adapted from [9].

Sensory Evaluation

The sensory evaluation was carried out by 30 untrained panelists in Rajamangala University of

Technology Thanyaburi (RMUTT), Thailand. Panelists was asked to analyze their level of preference for each treatment using a 9-point hedonic scale test based on the attributes of color, odor, taste, sediment and overall liking. A randomized complete block design was used with analysis of variance. Analysis of the mean differences of experiments was performed using Duncan's new multiple range test [10].

RESULTS AND DISCUSSION

Physical measurement

The values of L^* , a^* and b^* and physical appearance depending on different ratios of okra and tangerine [11]. The results showed that b^* and %T value had differences ($P \leq 0.05$). For L^* value, it was found to be decreasing compared to control samples. Because of the increase in okra juice which gave dark brown color. For a^* value, they were found to be decreasing compared to control samples. Due to the reduction of tangerine juice revealed orange yellow color. For b^* value, they were found to be decreasing compared to control samples (the same as a^* value). Due to the increasing of okra juice indicated green color. For percent of transmittance, clarification value increased with comparison to control samples. The Experiment 4 gave the highest value, while the Experiment 1 gave the lowest value. Possible reasons were that the reduction of tangerine juice contained pulp could be affected on the cause of turbidity [12].

Chemical measurement

Results, pH values depending on different ratios of okra and tangerine, there was a tendency towards increased acidity and alkalinity when compared to control samples due to the reduction of tangerine juice. In tangerine juice contains of citric acid, it has an increased amount of acidity and alkalinity [13]. For total soluble solid values showed that there was

a tendency of decrease compared to the control sample due to the reduction of tangerine juice. Organic acids, i.e., citric acid naturally occurring in many foods including citrus, such as orange and lime reduces low total acidity values. [14].

Sensory evaluation

The results of the sensory analysis showed that there were differences in all experiments. ($P \leq 0.05$) When considering the average all score tests, Experiment 1 was the most acceptable in comparison to other experiments. One possible reason might be due to the proportion of okra and tangerine was equal. Tangerine juice can reduce the smell of okra, which is a smell that consumers did not like. As a result, the characteristics of color, smell, taste, sediment, and overall acceptance, received the highest scores [15].

Physical appearance

From the Fig 1, the images could be seen that the red color in all experiments were not significantly different. As a result of the ratio of okra juice and tangerine juice. When considering the appearance, it was found that all the experiments were suspended, which is the pulp of tangerine, which is derived from tangerine. When considering the color, revealed that all the samples were reddish orange as the color result of the lycopene [16]. The color is yellow, orange, red and orange - red. Okra and tangerine consist of three pigments (chlorophyll, carotenoid and lycopene) were quite distinct and different chemical compositions and structures such as carotenoid in tangerine, chlorophyll in okra and lycopene supplementation. The odor will vary with the amount of increased okra juice and the decrease amount of tangerine juice which compared to control

samples. The taste indicated that all experiments were sweet and sour. Due to the taste adjustment with same amount of sugar and citric acid [17].

Table 1 Optimum ratios of okra juice and tangerine with lycopene supplementation [17].

Ingredients (g)	Experiment no.			
	1	2	3	4
okra juice	300	360	420	480
tangerine juice	300	240	180	120
lycopene	0.1	0.1	0.1	0.1
sugar	40	40	40	40
salt	1	1	1	1
citric acid	0.3	0.3	0.3	0.3

Table 2 Physical measurement of blended okra juice and tangerine juice

Experiment	Physical value			
	L* ^{ns}	a* ^{ns}	b*	%T*
1	27.88	9.89	1.79 ^a	15.53 ^d
2	24.74	9.56	0.85 ^a	22.63 ^c
3	23.12	9.26	0.84 ^a	26.47 ^b
4	22.33	7.44	-3.35 ^b	30.67 ^a

a-d The different letters in the same column mean significant difference ($P \leq 0.05$) ns non significant difference ($P > 0.05$)

Table 3 Chemical measurement of blended okra juice and tangerine juice

Experiment	Chemical value		
	pH*	Total acidity (percent)*	Total soluble solid (°Brix)*
1	3.81 ^c	3.41 ^a	13.00 ^c
2	3.97 ^b	2.56 ^b	11.90 ^b
3	3.99 ^b	1.92 ^c	11.00 ^c
4	4.16 ^c	1.28 ^d	10.70 ^d

a-d The different letters in the same column mean significant difference ($P \leq 0.05$)

Table 4 Mean score of preference for sensory properties of okra and tangerine juice

Experiment	Scores*				
	color*	odor*	taste*	sediment*	overall liking*
1	7.37 ^a	7.40 ^a	7.50 ^a	7.17 ^{ab}	7.40 ^a
2	6.70 ^b	7.27 ^a	7.50 ^a	7.47 ^a	7.30 ^a
3	6.90 ^b	6.53 ^b	6.43 ^b	6.87 ^{bc}	6.60 ^b
4	6.73 ^b	6.47 ^b	6.20 ^b	6.63 ^c	6.33 ^b

a-d The different letters in the same column mean significant difference ($P \leq 0.05$)

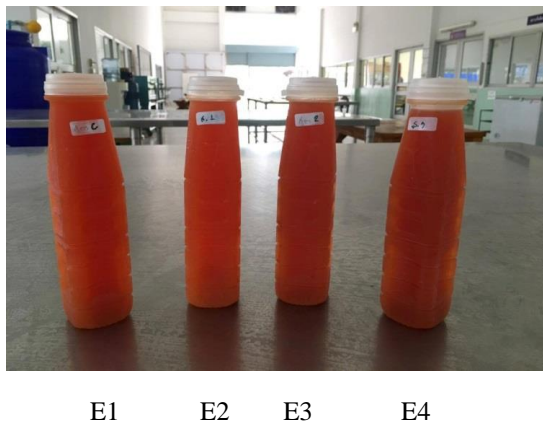


Fig. 1 Product of different ratios of okra blended with gac fruit and passion fruit.

E1: okra: tangerine juice 50:50 (control experiment)

E2: okra: tangerine juice 60 :40

E3: okra: tangerine juice 70:30

E4: okra: tangerine juice 80:20

Copyright Form

Copyright form signed by all authors is necessary for GEOMATE. It should be submitted along with the paper submission. Copyright form can be downloaded from geomate web site.

CONCLUSIONS

1. The uses of different ratios of raw material preparation had effects on color of mixed okra, tangerine and lycopene supplementation.

2. The results of the physical properties analysis showed that only b^* and percent of transmittance values were statistically significant differences. ($P \leq 0.05$)

3. The results of the chemical analysis showed that all values were significantly different. ($P \leq 0.05$)

4. Experiment 1 involved that gave the most acceptable from the panelists.

5. Based on this research, researchers will be able to launch new beverage products in the future by selecting Thai local herbs that are beneficial for antioxidants, an option for health conscious consumers

ACKNOWLEDGEMENTS

The researchers would like to thank the 4th students and personal officials of Division of Food Science and Technology, Faculty of Agricultural Technology Rajamangala University of Technology Thanyaburi (RMUTT) Pathumthani Thailand that contributed some part in the research. We would also like to thank the Faculty of Agricultural Technology for their support facilities and budgets on our research and travel expense for this conference.

REFERENCES

- [1] Nguyen, T.H. and Gizaw, A., Factors that influence consumer purchasing decisions of Private Label Food Products, School of Business, Society And Engineering Bachelor thesis in Business Administration, 2014, 92 pp.
- [2] Singh, P., et al., An overview on okra (*Abelmoschus esculentus*) and it's importance as a nutritive vegetable in the world, International Journal of Pharmacy and Biological Sciences, Vol. 4, 2014, pp.227-233.
- [3] Obasi, B.C., Whong C.M.Z. and Ameh, J.B., Nutritional and sensory qualities of commercially and laboratory prepared orange juice, African Journal of Food Science, Vol. 11, 2017, pp. 189-199.
- [4] Wirivutthikorn, W., Effect of ratio of okra gac fruit and passion fruit on color and preferences of mixed juice, International Journal of Food Engineering, Vol 4, 2018, pp. 212-215.
- [5] Mak, S. and Engwongtrakoon, A., The optimum temperature on dried okra for phenolic compound of green tea mixed with okra by tray drying, B.Sc. Senior Project, Division of Food Science and Technology Faculty of Agricultural Technology Rajamangala University of Technology Thanyaburi. Thailand, 2013, 97 pp,

- [6] Rapeesak, S., Effect of Pasteurization storage and food additive on capable of antioxidant in tangerine Juice, Faculty of Agricultural Technology, King Mongkut's Institute of Technology Ladkrabang, 2004.
- [7] Pomeranz, Y. and Meloan, C.E., Food Analysis: Theory and practice, 3rd edition. Van Nostrand Reinhold, 1994.
- [8] Lozano, J.E., Fruit manufacturing: Scientific: basis, engineering properties, and deteriorative reactions of technological importance, Springer Science & Business Media, LLC.. USA, 2006.
- [9] AOAC, Official Method of analysis. Verginia: The Association of official Analytical Chemists, 2000.
- [10] Anprung, P., Principle of food analysis by sensory evaluation, Bangkok.: Chulalongkorn University Press.
- [11] Wirivutthikorn, W. and Jenkunawatt, S., Preference colors of gac fruit blended with pineapple juice, Tien-Rein LEE (Editor –in-Chief), The 2nd Conference of Asia Color Association URBAN COLOR FOR LIFE 4-7 September 2014, Taipei, Taiwan, 2014, pp.304-307.
- [12] Wirivutthikorn, W. and Jenkunawatt, S., Study of color preferences of gac fruit blended with mixed mushroom juice, Hirohisa Yaguchi et al. (Editor) AIC 2015 Tokyo Color and Image. Midterm Meeting of the International Colour Association (AIC) 19-22 May 2015, Tokyo, Japan, 2015, pp. 820-823.
- [13] Rebecca, L.J., et al., Extraction and purification of carotenoids from vegetables, Journal of Chemical and Pharmaceutical Research, Vol. 6, 2014, pp. 594-598.
- [14] Wirivutthikorn, W. and Jenkunawatt, S., Color differences of okra blended with green tea powder on consumer acceptabilities, ACA 2016 The 3rd International Conference of Asia Color Association, 21-22 May 2016, Changshu, China, 2016, pp. 89-92.
- [15] Wirivutthikorn, W. and Jenkunawatt, S., Factors affecting on drying of okra and gac fruit in okra blended with gac fruit powdered beverage production, Research Report. Faculty of Agricultural Technology, Rajamangala University of Technology Thanyaburi, 2017, pp. 1-44.
- [16] Vuong, L.T., Franke, A.A., Custer, L.J. and Murphy, S.P., *Momordica cochinchinensis* Spreng. (gac) fruit carotenoids reevaluated, Journal of Food Composition and Analysis, Vol. 19, 2006, pp.664-668.
- [17] Wirivutthikorn, W., Effect of lemongrass and pandan leaf ratios on production of mixed juice with lycopene supplementation, International Conference of Agriculture and Natural Resources 26-28 April 2018, Proceedings ANRES 2018, Bangkok., pp. 378-381.

OPTIMAL RAIN GAUGES NETWORK USING GEOSTATISTICS AND HYBRID PARTICLE SWARM-SIMULATED ANNEALING OPTIMIZATION

Mohd Khairul Bazli Mohd Aziz¹, Fadhilah Yusof², Zalina Mohd Daud³, Zulkifli Yusop⁴, Mohammad Afif Kasno⁵

¹Faculty of Industrial Sciences & Technology, Universiti Malaysia Pahang, Malaysia,

²Department of Mathematical Sciences, Faculty of Science, Universiti Teknologi Malaysia, Malaysia,

³UTM Razak School of Engineering and Advanced Technology, Universiti Teknologi Malaysia, Malaysia,

⁴Institute of Environmental and Water Resource Management (IPASA), Faculty of Civil Engineering,

Universiti Teknologi Malaysia, Malaysia, ⁵Department of Electronic & Computer Engineering Faculty

Universiti Teknikal Malaysia, Melaka, Malaysia.

ABSTRACT

An optimal design of rain gauge network is important as it produces fast, accurate and important rainfall data which can be used to design an effective and economic hydraulic structure for flood control. In this paper, geostatistical method integrated with hybrid of particle swarm optimization-simulated annealing is proposed to determine the optimal number and location of rain gauge network. This paper considers the repositioning of the existing rain gauge into new locations to improve its effectiveness and accuracy. The analyses of daily rainfall data, latitude and longitude of the rain gauge location, elevation, humidity, wind speed, temperature and solar radiation reveal that the proposed method is successful in providing the optimum number and location of the stations. It also indicates that the repositioning of all rain gauge stations to new locations would provide better results in terms of the estimated variance value but, is not cost effective due to its expensive costs.

Keywords: Rain Gauge Network, Geostatistics, Particle Swarm Optimization, Simulated Annealing

INTRODUCTION

A reliable and optimal rain gauge network can provide accurate and precise rainfall data as rainfall data are employed in numerous water resources management tasks such as water budget analysis and assessment, flood analysis and forecasting, streamflow estimation, and design of hydraulic structures. Good rainfall data will help the researchers to minimize the hydrological and economic risk and errors involved in different water resources projects. A well-designed rain gauge network thus should contain a sufficient number of rain gauges, which reflect the spatial and temporal variability of rainfall in a catchment [3].

Thus, identification and selection of the optimal rain gauge network configuration with optimal number and locations of rain gauge stations is the main objective of the network design. Hence, the optimal rain gauge network should contain the number and locations of rain gauge stations in such a way that it can produce optimum rainfall information and data with minimum uncertainty and cost [2]-[4]. One can approach the problem either by removing redundant stations from the network to minimize the cost or by expanding the network with installation of additional stations to reduce the estimation uncertainty [5]. Some studies applied the kriging

technique in combination with other techniques such as entropy [3] and multivariate factor analysis [7] for the network design. A few studies also combined optimization method based on simulation tools (e.g. simulated annealing) with the kriging technique [2], [8],[9] to obtain the optimal rain gauge network.

A network design methodology was developed in this paper to determine optimal number and locations of the existing stations in the current rain gauge network located in the Johor state, Malaysia is based on geostatistical and hybrid of particle swarm optimization-simulated annealing (PSO-SA) as an optimization method. The basic idea of the hybrid algorithms study in this paper is simply based on running PSO algorithm first and then improving the result by employing a SA. The major contribution here is that unlike the work of [2], the developed methodology considered the hybrid of PSO-SA technique as an optimization method which capable of escaping from a local optimum with a fast convergence.

STUDY AREA AND DATA DESCRIPTION

Johor is the second largest state in the Malaysia Peninsular, with an area of 18,941 km². The catchment area contains a dense rain gauge network, 84 rain gauges covering 19,210 km² in Johor (see

Figure 1). The current overall network density for the whole of Johor state is about 194 km² per gauge, which surpasses even the ideal WMO recommendation of one gauge per 600 – 900 km² for flat areas. In fact, it also fulfills the ideal density for mountainous region of 100 – 200 km² per gauge. The data used to perform the analysis was from the daily rainfall data, latitude and longitude of the rain gauge location, elevation, humidity, wind speed, temperature and solar radiation from November until February of 1975 through 2008 from 84 rain gauge stations that are located all over Johor obtained from Department of Irrigation and Drainage (DID) Malaysia and Malaysia Meteorological Department (MMD).

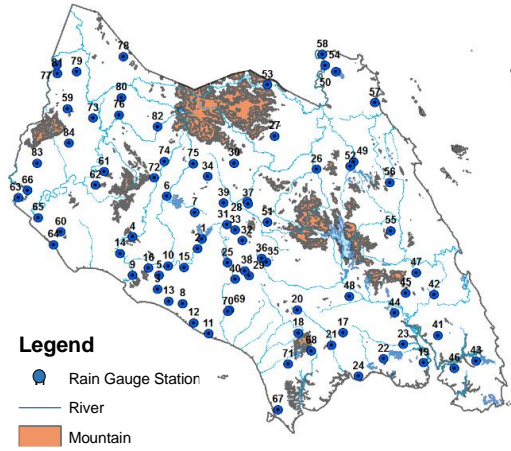


Fig.1 Rain gauge locations

METHODOLOGY

Geostatistical Method

The network design problem consists in obtaining the number N and the location of rain gauges stations that give the best estimate areal mean rainfall. The estimation variance σ^2 is a basic tool of variance reduction techniques for optimal selection of sampling locations. For the application of the variance reduction method to optimal location of sampling sites, a semivariogram must be modelled.

A semivariogram, $\gamma(h)$ is one of the significant functions to indicate spatial correlation in observations measured at sample locations. Semivariogram is represented as a graph that shows the difference in measure with distance between all pairs of sampled locations. The estimated variance depends on the semivariogram model, the number N of rain gauges and its spatial location. Therefore, choosing an appropriate semivariogram model is vital in determined the optimal estimation variance.

Let h be the lag or distance, and Z be an intrinsic random function and let $Z(x_i)$, for $i = 1, 2, \dots, N$ be

a sampling of size N . Then the following expression is an unbiased estimator for the semivariogram of the random function:

$$\gamma(h) = \frac{1}{2n(h)} \sum_{i=1}^{n(h)} [Z(x_i + h) - Z(x_i)]^2 \quad (1)$$

Equation 1 is used to compute experimental semivariogram from the data under study. By changing h , both in distance and direction, a set of the sample (or experimental) semivariograms for the data is obtained [10].

The exponential semivariogram models are selected to fit the data. The exponential semivariogram model equation is as follow:

$$\gamma(h) = C \left(1 - e^{-\frac{3h}{a}} \right) \quad (2)$$

where C is the sill and a is the range.

Once the model of the semivariogram is fixed, the estimation variance only depends on the number N and the location of the rain gauges. To calculate the estimation variance using ordinary kriging,

$$\sigma^2(x_0) = 2 \sum_{i=1}^k \lambda_i \gamma(x_i, x_0) - \sum_{i=1}^k \sum_{j=1}^k \lambda_i \lambda_j \gamma(x_i, x_j) \quad (3)$$

Where

$$\hat{Z}(x_0) = \sum_{i=1}^k \lambda_i Z(x_i) \quad (4)$$

Subject to $\sum_{i=1}^k \lambda_i = 1$.

This is an algorithm for the ordinary kriging estimation to calculate the estimation variance [13]:

1. Calculate each term in matrix G .

Let x_i 's be the sampling sites of a sample subset of size k , $i = 1, 2, \dots, k$ and let $\gamma(x_i, x_j)$'s be the experimental variogram. Then the G is the matrix

$$G = \begin{bmatrix} \gamma(x_1, x_1) & \gamma(x_2, x_1) & \cdots & \gamma(x_k, x_1) & 1 \\ \gamma(x_1, x_2) & \gamma(x_2, x_2) & \cdots & \gamma(x_k, x_2) & 1 \\ \cdots & \cdots & \cdots & \cdots & \cdots \\ \gamma(x_1, x_k) & \gamma(x_2, x_k) & \cdots & \gamma(x_k, x_k) & 1 \\ 1 & 1 & \cdots & 1 & 0 \end{bmatrix} \quad (5)$$

2. Calculate each term in matrix g .

Let x_0 be the estimation location, then the g is the matrix

$$g = [\gamma(x_0, x_1) \quad \gamma(x_0, x_2) \quad \cdots \quad \gamma(x_0, x_k) \quad 1]' \quad (6)$$

3. Solve the system of equations

$$GW = g,$$

$$W = gG^{-1},$$

$$\text{Where } W = [\lambda_1 \quad \lambda_2 \quad \cdots \quad \lambda_k \quad -\mu].$$

4. Calculate the ordinary kriging estimation variance

$$\sigma^2(x_0) = g'W = g'G^{-1}g. \quad (7)$$

Partical Swarm Optimization

PSO was developed by Kennedy and Eberhart, [12] in 1995, inspired by the social behavior of bird flocking. The movement of each swarming particle is determined by a combination of a stochastic element and a deterministic element, [1]. A population (swarm) of particles is initialized in an n -dimensional search space in which each particle $x_i = (x_{i1}, x_{i2}, \dots, x_{in})$ represents a possible solution. Each particle is aware of its current position, its own personal best position, its current velocity and the single global (or local) best position. The global best position is represented as $g_i = (g_{i1}, g_{i2}, \dots, g_{in})$ and symbolizes the best position of all particles in the population (swarm). The personal best position represents the best position found by a particle so far and is denoted as $p_i = (p_{i1}, p_{i2}, \dots, p_{in})$.

The velocity $v_i = (v_{i1}, v_{i2}, \dots, v_{in})$ gives the position change of a particle. In the original proposed PSO of Kennedy and Eberhart, the new velocity for each particle is calculated according to Eq. (8). To update the new position of each particle, Eq. (9) is used:

$$v_i = v_i + c_1 \cdot r_1 \cdot (p_i - x_i) + c_2 \cdot r_2 \cdot (g - x_i) \quad (8)$$

$$x_i = x_i + v_i \quad (9)$$

where $i = 1, 2, \dots, N$, with N as population size. c_1 and c_2 are two positive constants; r_1 and r_2 are two random numbers with range (0,1).

The original version of PSO is as follows:

1. Initialize a population (swarm) of particles with random positions and velocities on d dimensions in the problem space.
2. For each particle, evaluate the desired optimization fitness function in d variables.
3. Compare particle's fitness evaluation with particle's $pbest$. If current value is better than $pbest$, then set $pbest$ value equal to the current value and the $pbest$ location equal to the current location in d -dimensional space.
4. Generate new particles from the neighbourhood. Compare fitness evaluation with the population's overall previous best. If current value is better than $gbest$, then reset $gbest$ to the current particles array index and value.
5. Change the velocity and position of the particle according to Equations 8 and 9 respectively.

6. Loop to Step 2, until criterion is met, usually a sufficiently good fitness or a maximum number of iterations (generations).

Simulated Annealing

Annealing is a family of techniques for creating metals with desirable mechanical properties. The SA technique originates from the theory of statistical mechanics and is based upon the analogy between the annealing of solids and solving optimization problem. SA was first introduced by Kirkpatrick and Vecchi [6].

Basic SA algorithm:

1. Select an initial solution x and initial temperature T_0 , set $k = 0$. Set $x = x_0, \hat{x} = x_0$.
2. Choose a solution x' in $N(x)$ and compute $\delta = F(x') - F(x)$
3. If $(\delta \leq 0)$ or $(\delta > 0 \text{ and } e^{-(\delta/T_k)} \geq \theta \in U\{0,1\})$ then accept the new solution x' and set $x = x'$. Else keep x .
4. If $F(x') < F(\hat{x})$, then set $\hat{x} = x'$ and $\hat{T} = T_k$.
5. If some stopping criteria are satisfied, stop.
6. Update the temperature $T_{k+1} = g(T_k) \leq T_k$, set $k = k + 1$ and go to step 2.

Hybrid of Particle Swarm Optimization and Simulated Annealing

The basic idea of the hybrid algorithms study in this research is simply based on running PSO algorithm first and then improving the result by employing a simulated annealing. As we know, the most significant character of SA is the probabilistic jumping property, i.e. probability to accept a worse solution to be a new solution. Therefore, through integration of SA to PSO, the proposed algorithm is capable of escaping from a local optimum with a fast convergence. Based on the PSO and SA characteristics, the whole procedure of PSO-SA is described as follows:

1. Initialization:
 - 1a. Randomly initialize the x particles representing different combinations of N rain gauge placements.
 - 1b. Evaluate each particle in the population using the fitness function in Eq. (7) and minimum fitness function is set as $pbest$.
- 1c. Set all parameters, including c_1 and c_2 , v_{\max} , initial temperature T_0 , cooling rate α .
2. Repeat this step until the stopping criterion is satisfied:

- 2a. Evaluate velocity and position of each particle by Eq. (8) and Eq. (9).
- 2b. Calculate the fitness of each particle, x' .
- 2c. Calculate $\delta = f(x') - f(x)$ and then randomly generate a number $\theta \in (0,1)$. If $\delta < 0$, as the objective is to minimum, meaning that the new position is improved, then the new position is accepted as the new position of particle i . Otherwise, new position is accepted according to the following criterion: $\theta > e^{\frac{-\delta}{T_k}}$. Proceed to step 2d when the velocity of all particles are determined, or return to step 2a for those particles failing to be accepted. And generate new velocities using the same evaluation process.
- 2d. Renew each particle to the new velocity and position and modify g_{best} and p_{best} by simple comparison of their fitness values.
- 2e. When the evolution process has achieved a stopping criterion (or maximum iteration is reached), proceed to step 3, otherwise, modify the annealing temperature and return to step 2.

Output the best solution g_{best} and its fitness value. The output is the optimal number and location of stations with the minimum estimated variance.

Optimization Procedure

The optimization model to determine the optimal number and locations of rain gauge can be divided into two different scenarios and formulated mathematically as below.

1. The model for optimal number and locations of the rain gauges:

Minimize

$$\sigma^2(x) = 2 \sum_{i=1}^k \lambda_i \gamma(h_{i0}) - \sum_{i=1}^k \sum_{j=1}^k \lambda_i \lambda_j \gamma(h_{ij})$$

subject to

$$\sum_{i=1}^k \lambda_i = 1$$

where

$$\gamma(h) = C \left(1 - e^{-\frac{3h}{a}} \right)$$

2. The model for relocating the rain gauges:

Minimize

$$\sigma^2(x) = 2 \sum_{i=1}^k \lambda_i \gamma(h_{i0}) - \sum_{i=1}^k \sum_{j=1}^k \lambda_i \lambda_j \gamma(h_{ij})$$

subject to

$$\sum_{i=1}^k \lambda_i = 1$$

$$\sum_j x_j = p$$

where

$$\gamma(h) = C \left(1 - e^{-\frac{3h}{a}} \right)$$

$$x_j = \begin{cases} 1, & \text{if a rain gauge is placed at a point } j \\ 0, & \text{otherwise} \end{cases}$$

p = number of rain gauges relocated

RESULTS AND DISCUSSION

The variance reduction technique requires an appropriate semivariogram model that fitted the observed data. Initially, an experimental semivariogram from the experimental data is derived. Then, a functional semivariogram model is fitted to the experimental variogram. The obtained semivariogram model has essential information to be used in kriging interpolation of observed data. Fitting and selection of suitable semivariogram model can be accomplished through the variogram modelling technique. Once a proper semivariogram model is selected for the observed dataset, kriging is applied for the generation of interpolated surfaces and the estimation of the corresponding kriging error. The semivariogram model fitted to the experimental data is shown as in table below:

Table 1 Exponential semivariogram model

Nugget	Sill	Range
0.93917	1.5568	1.05449

When the semivariogram is successfully fitted to the empirical rainfall data, the PSO-SA method is applied to find the minimum objective function (equation 3) in order to get the optimum number and location of rain gauge stations. The optimization technique done based on the steps mentioned earlier. The results of the optimization process were shown in Figure 1 and Table 2.

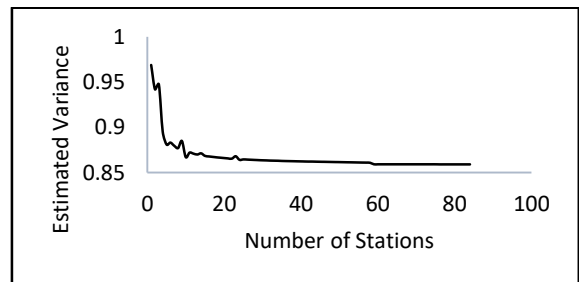


Fig. 2 Estimation variance versus number of stations

Table 2 Estimated variance value with optimal number of stations

No. of Iterations	Number of Stations Selected	Estimated Variance	Removed Stations
50	62	0.8608	22
100	61	0.8607	23
500	59	0.8604	25
1000	59	0.8604	25

The new optimal rain gauge network demonstrates that the high density of existing rain gauge in Johor has been reduced by removing several stations. Fig. 2 depicts that the estimated variance value decreased as the number of rain gauges increased. This value approach optimal value when the optimization process gives the number of optimal rain gauge stations. In Table 2, it is shown that the optimal number of rain gauge stations is 59 stations with estimated variance value 0.8604 is achieved when the iterations is more than 500. The locations of the 59 selected locations are as shown in Fig. 3 below. From Fig. 3, most of the removed stations are redundant stations that are unnecessary needed.

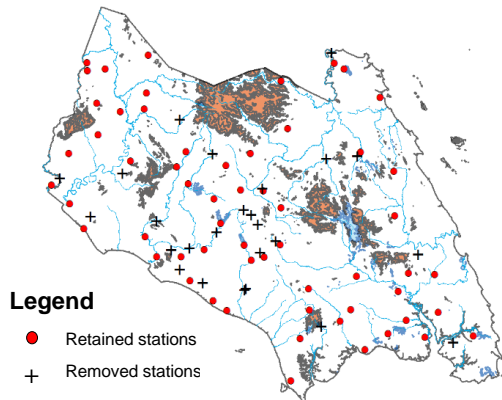


Fig. 3 Optimal locations for 59 selected rain gauge stations.

After the execution of the optimization process, two scenarios were considered for the 25 removed stations in Table 2.

- Scenario-1: Optimal positioning of 25 removed stations to find their new optimal locations.
- Scenario-2: All 84 existing stations were reset into new optimal locations

For the redesignation purpose of the network, the whole study area is discretized into 250 square grids with each unit equivalent to 100km² (Fig. 4). This is in line with the criterion set by the World Meteorological Centre [11] which stated that every rain gauge in the mountain region of temperate,

Mediterranean and tropical zone need to be in the area of 100-250km² each.

The PSO-SA algorithm is applied once again to determine the optimal rain gauge location for the scenario 1 and 2. The humidity, temperature, solar radiation, wind speed and elevation data will help the algorithm locates suitable locations for the rain gauges.

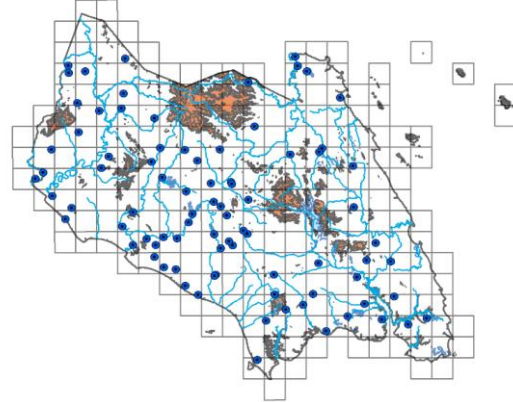


Fig. 4 Johor with grids

Table 4 shows the resulted estimated variance for both scenarios. For scenario 1, the estimated variance value reduces when the removed stations were located into new optimal locations. This shows that the removed stations were able to improve the accuracy of the network by placing it in an optimum location. For scenario 2, the estimated variance decreases lower than scenario 1 and previous estimated variance. This shows that in order to achieve an optimal network with the existing stations, all stations must be reorganized and relocated into new locations. Elevation, temperature, wind speed, solar radiation and humidity data has help in identifying the optimal locations in the discretized Johor and the new locations of the restructured rain gauge networks for both scenarios are as shown in Fig.5. The PSO-SA algorithm managed to determine a new site for each rain gauge stations.

Table 4 Estimated variance

	Scenario 1	Scenario 2
Estimated Variance	0.8473	0.7163

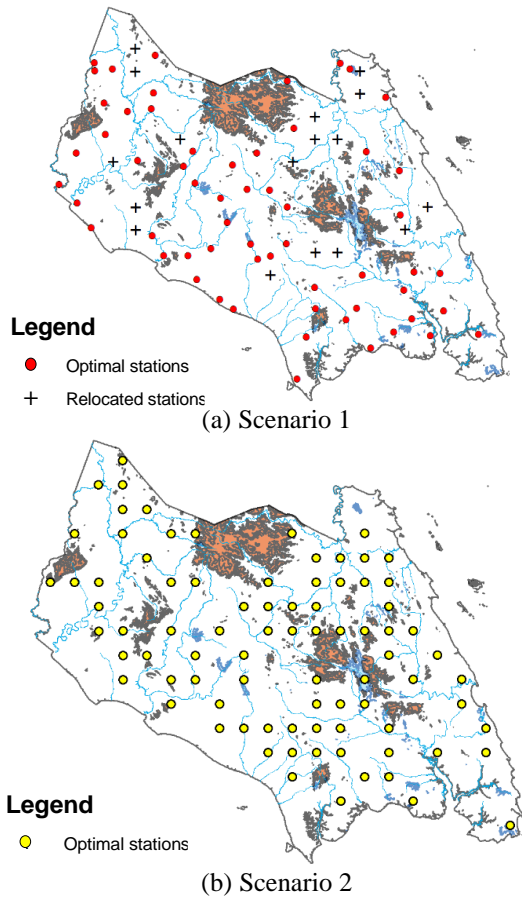


Fig. 5 New optimal locations for 84 rain gauge stations

CONCLUSIONS

Combination of geostatistics methods and PSO-SA as an algorithm of optimization can be used as a framework for rain gauge network design models as it improves the existing rainfall network by minimizing the variance of estimation value. Overall, this study has illustrated that the geostatistics method with PSO-SA annealing can be used as the optimization method to provide the solution in designing an optimal rain gauges network system. This optimal network also is essential in providing better rainfall data. This model and methodology can provide information that will help decision makers to understand the relationship between numbers and locations of rain gauge stations in order to provide a better and more accurate rainfall data. Further researches on the optimization technique are required for better results.

ACKNOWLEDGEMENTS

The authors would like to thank the Universiti Malaysia Pahang under UMP grant RDU1703196 for their financial funding and support.

REFERENCES

- [1] Yang, X. S., *Engineering optimization: An introduction with metaheuristics applications*. Wiley Publications. 2010.
- [2] Pardo-Igúzquiza, E. Optimal selection of number and location of rainfall gauges for areal rainfall estimation using geostatistics and simulated annealing. *Journal of Hydrology* 210: 206–220. DOI: 10.1016/S0022-1694(98)00188-7. 1998.
- [3] Yeh, H. C., Chen, Y.C., Wei, C., Chen, R. H., Entropy and kriging approach to rainfall network design. *Paddy and Water Environment* 9: 343–355. DOI: 10.1007/s10333-010-0247-x. 2011.
- [4] Kassim, A. H. M., Kottegoda, N.T. Rainfall network design through comparative kriging methods. *Hydrological Sciences Journal* 36: 223–240. DOI: 10.1080/02626669109492505. 1991.
- [5] Mishra, A. K., Coulibaly, P. Developments in hydrometric network design: a review. *Reviews of Geophysics* 47: RG2001. DOI: 10.1029/2007RG000243. 2009.
- [6] Kirkpatrick, S., & Vecchi, M. P. (1983). Optimization by simulated annealing. *Science*, 220(4598), 671–680.
- [7] Shaghaghian, M. R., Abedini, M. J. Rain gauge network design using coupled geostatistical and multivariate techniques. *Scientia Iranica* 20: 259–269. DOI: 10.1016/j.scient.2012.11.014. 2013.
- [8] Barca, E., Passarella, G., Uricchio, V. Optimal extension of the rain gauge monitoring network of the Apulian regional consortium for crop protection. *Environmental Monitoring and Assessment* 145: 375–386. DOI: 10.1007/s10661-007-0046-z. 2008.
- [9] Chebbi, A., Bargaoui, Z. K., Cunha, M. D. C., Optimal extension of rain gauge monitoring network for rainfall intensity and erosivity index interpolation. *Journal of Hydrologic Engineering* 16: 665–676. DOI: 10.1061/(ASCE)HE.1943-5584.0000353. 2011.
- [10] Burrough, P. A. *Principles of Geographical Information Systems for Land Resources Assessment*. Clarendon Press, Oxford, pg. 147–165. 1987.
- [11] Guide to Meteorological Instruments and Methods of Observation, (WMO-No.8, Seventh edition), WMO, Geneva, 2008.
- [12] Eberhart, R. and Kennedy, J. A new optimizer using particle swarm theory. In *Proceedings of the Sixth International Symposium on Micro Machine and Human Science (MHS '95)*, pages 39–43. IEEE Press, 1995.
- [13] Olea, R. A. *Geostatistics for Engineers and Earth Scientists*, Kluwer Academic Publishers, ISBN 0-7923-8523-3, Massachusetts, 2003.

SCREENING CRUDE EXTRACTS FROM *PIPER* SPP. ON *COLLETOTRICHUM* SP. AND *PHYTOPHTHORA* SP. CAUSING PLANT DISEASE

Pornprapa Kongtragoul¹, Parinya Janthong¹, Theerachart Leepasert², and Chalermopol Suwanphakdee²

¹King Mongkut's Institute of Technology Ladkrabang, Prince of Chumphon, THAILAND

²Faculty of Science, Kasetsart University, Bangkok, Bangkok, THAILAND

ABSTRACT

The effect of crude extracts from *Piper* spp. on *Colletotrichum* sp. and *Phytophthora* sp. causing plant diseases were studied *in vitro*. The paper disc diffusion method was applied for evaluation of mycelial growth at 0, 25,000, 50,000 and 100,000 ppm and the spore germination test was implemented for determining the inhibition of spore germination at 0, 12,500, 25,000 and 50,000 ppm. The results show that crude extracts at 100,000 ppm had the greatest activities compared to others in inhibition of the mycelia growth of *Colletotrichum* sp. at 35.50% with samples no. P18 and P39 and *Phytophthora* sp. at 50% and 53.33% with samples no. P38 and P8, respectively. Moreover, all samples with all concentrations evaluated completely prevented the germination of spores (100%).

Keywords: *Piper*, Plant extract, Plant disease, Botanical fungicides

INTRODUCTION

Plant diseases have caused severe losses to humans in several ways. They are causing economic losses of plant production and reducing the aesthetic values of landscape plants. The chemical fungicides have been used for more than a hundred years and new fungicides continue to be developed for controlling plant diseases. However, the side effects of fungicides cause risks such as serious hazards to environment and humans, including to the development of fungicide-resistance in plant pathogen. Several researchers have attempted to find alternative ways to solve these problems. Currently, the search for natural products with novel uses, particularly related to plant disease management is very active. Aromatic and medicinal plants have attracted interests in the field of plant disease control, particularly plant extracts with antimicrobial properties and contain a spectrum of secondary metabolites. The concentration of these bioactive compounds in each plant species depends on the environmental conditions.

Piper is a genus of family Piperaceae, with more than 2,000 species. These plants are distributed mainly in tropical and subtropical regions of the world. Some of these species are also found in Thailand. They have been used for many other purposes such as foods and medicines in Thai culture [1], [2]. They are reported for potential pharmaceutical or agricultural fungicide development. A total of 68 compounds isolated from 22 *Piper* species have been reported to possess significant antifungal activities. These compounds include amides, flavonoids, prenylated benzoic acid derivatives, lignans, phenylpropanoids, butenolides,

and cyclopentenones. Some of them show antifungal activity against several pathogenic fungi [3], [4]. Therefore, the objective of this study was to screen the antifungal activity of crude extracts from samples of *Piper* spp. in Thailand against *Colletotrichum* sp. and *Phytophthora* sp. causing plant disease *in vitro*.

MATERIALS AND METHODS

Plant material

The leaves of the plants used in this study were collected from wild vegetation in Thailand forests. Sixteen samples were processed for extraction. Leaves of sample plants were cut into small pieces and air dried. The small pieces of dry leaves were blended to obtain fine powder and used for crude extraction. The crude extracts were collected using ethanol extraction process, using vacuum rotary evaporator.

Test plant pathogenic fungi

Two plant pathogenic fungi: *Colletotrichum* sp., and *Phytophthora* sp. were tested for antifungal activity. They were respectively isolated from infected mango and durian fruits.

Determination of antifungal activity of crude extract

Mycelial growth test

Antifungal activity test of the crude extracts (the

original plant extracts without separation) were tested on mycelial growth by using agar disc diffusion method. Sixteen samples of crude extracts at 25,000, 50,000 and 100,000 ppm were used in this experiment. Mycelia discs (5 mm diameter) were taken from the peripheral region of 5 day old of culture, which grown on PDA plates. Each of the mycelia discs was then transferred to the center of the PDA and incubated for 2 days at room temperature. After incubation, the 20 µl of each crude extract solution was loaded on the sterile paper discs (6 mm in diameter). Sterilized distilled water were used as a control. The plates were then incubated at room temperature. Radius of each colony was measured and the percentage inhibition of mycelia growth was calculated. Each treatment was performed in four with a complete randomized design.

Spore germination test

The conidia of *Colletotrichum* sp., and sporangium of *Phytophthora* sp. were obtained from a 10 day old culture grown on PDA and V8, respectively. The spore suspension were harvested by flooding the medium surface with sterilized distilled water and adjusted to 1×10^6 spores/ml and using a hemacytometer cell counting. Each crude extract solution and spore suspension were dropped into Eppendorf tube to give a final concentration at 12,500, 25,000 and 50,000 ppm. The mixture was transferred onto water agar. 100 spores were observed for germination and recorded using a compound microscope at 24 hr.

RESULTS AND DISCUSSION

The results of this study indicate that all *Piper* species ethanol crude extracts could inhibit growth of *Colletotrichum* sp., and *Phytophthora* sp., which are the causative agents of mango and durian diseases in Thailand. However, the crude extracts of sample no. P18 and P39 at 100,000 ppm gave the highest inhibition activity to the mycelial growth of *Colletotrichum* sp. at 35.50%, followed by the sample no. P24 at 31.10%. Moreover, it was also found that, the crude extracts of sample no. P8 and P38 at 100,000 ppm showed the highest inhibition activity to mycelial growth of *Phytophthora* sp. at 53.33% and 50% respectively, followed by the sample P38 at 50,000 ppm (Table 1). This situation is similar to that *Piper* species have been reported to possess significant antifungal activities. Many researchers reported that the crude extract from *Piper* species exhibited pronounced antifungal activity against phytopathogenic fungi, such as *Aspergillus flavus*, *A. fumigatus*, *A. niger*, *Rhizopus* sp., *Microsporum canis*, *M. gypseum*, *Trichophyton mentagrophytes*, *T. rubrum*, *Epidermophyton floccosum*, *Cryptococcus neoformans*, *Candida albicans*, *C. tropicalis*,

Colletotrichum capsici, *C. acutatum*, *C. gloeosporioides*, *B. theobromae*, and *Fusarium oxysporum* f.sp. *cubense* [5]-[10].

Table 1 Effect of crude extracts from 16 samples of *Piper* spp. on the mycelial growth of *Phytophthora* sp. and *Colletotrichum* sp.

Sample code	Concentration (ppm)	Mycelial inhibition (%)	
		<i>Phytophthora</i> sp.	<i>Colletotrichum</i> sp.
control	0	0.00 V	0.00 V
mancozeb	100	7.73 R-U	6.60 P-S
P8	25,000	25.50 D-F	12.20 L-N
	50,000	36.63 BC	17.73 H-K
	100,000	53.33 A	29.97 BC
P9	25,000	5.50 TU	1.10 UV
	50,000	10.00 P-T	4.40 R-U
	100,000	15.50 K-O	11.10 M-O
P11	25,000	21.10 F-J	12.20 L-N
	50,000	24.40 D-G	19.97 G-I
	100,000	28.83 D	25.50 DE
P12	25,000	15.53 K-O	4.40 R-U
	50,000	21.10 F-J	12.20 L-N
	100,000	28.83 D	21.10 F-H
P14	25,000	7.73 R-U	2.20 T-V
	50,000	11.10 O-S	8.87 N-Q
	100,000	21.10 F-J	23.30 E-G
P15	25,000	11.10 O-S	8.87 N-Q
	50,000	19.97 G-K	14.40 K-M
	100,000	24.40 D-G	18.83 HIJ
P16	25,000	6.60 S-U	4.40 R-U
	50,000	11.10 O-S	6.60 P-S
	100,000	17.73 I-M	11.10 M-O
P17	25,000	8.87 Q-U	3.30 S-V
	50,000	13.30 M-Q	7.73 O-R
	100,000	17.73 I-M	12.20 L-N
P18	25,000	11.07 O-S	17.73 H-K
	50,000	16.63 J-N	26.63 C-E
	100,000	21.06 F-J	35.50 A
P22	25,000	15.50 K-O	11.10 M-O
	50,000	21.10 F-J	15.50 J-L
	100,000	26.63 DE	17.73 H-K
P23	25,000	7.7333 R-U	10.00 N-P
	50,000	11.10 O-S	14.40 K-M
	100,000	18.87 H-L	19.97 G-I
P24	25,000	13.30 M-Q	11.10 M-O
	50,000	21.10 F-J	16.60 I-K
	100,000	24.40 D-G	31.10 B
P26	25,000	11.10 O-S	16.60 I-K
	50,000	17.73 I-M	23.30 E-G
	100,000	25.50 D-F	28.83 B-D
P27	25,000	12.20 N-R	16.63 I-K
	50,000	12.20 N-R	18.83 H-J
	100,000	22.20 E-I	24.40 EF
P38	25,000	34.40 BC	12.20 L-N
	50,000	41.10 B	18.87 H-J
	100,000	50.00 A	25.50 DE
P39	25,000	5.50 TU	15.50 J-L
	50,000	7.73 R-U	25.50 DE
	100,000	11.10 O-S	35.50 A

Moreover, it was observed that after 24 hr. of incubation, all tested those *Piper* species with all tested concentrations could completely prevented the

germination of spores in *Phytophthora* sp. and *Colletotrichum* sp. (Table 2). This results indicated that the active compound contained in crude extract of *Piper* species possesses fungicidal activity to kill or inhibit the spores of fungi [3]-[4].

Table 2 Effect of crude extracts from 16 samples of *Piper* spp. on spore germination of *Phytophthora* sp. and *Colletotrichum* sp.

Sample code	Concentration (ppm)	Inhibition of spore germination (%)	
		<i>Phytophthora</i> sp.	<i>Colletotrichum</i> sp.
control	0	0 C	0 B
mannose	100	68 B	100 A
P8	12,500	100 A	100 A
	25,000	100 A	100 A
	50,000	100 A	100 A
	100,000	100 A	100 A
P9	12,500	100 A	100 A
	25,000	100 A	100 A
	50,000	100 A	100 A
	100,000	100 A	100 A
P11	12,500	100 A	100 A
	25,000	100 A	100 A
	50,000	100 A	100 A
	100,000	100 A	100 A
P12	12,500	100 A	100 A
	25,000	100 A	100 A
	50,000	100 A	100 A
	100,000	100 A	100 A
P14	12,500	100 A	100 A
	25,000	100 A	100 A
	50,000	100 A	100 A
	100,000	100 A	100 A
P15	12,500	100 A	100 A
	25,000	100 A	100 A
	50,000	100 A	100 A
	100,000	100 A	100 A
P16	12,500	100 A	100 A
	25,000	100 A	100 A
	50,000	100 A	100 A
	100,000	100 A	100 A
P17	12,500	100 A	100 A
	25,000	100 A	100 A
	50,000	100 A	100 A
	100,000	100 A	100 A
P18	12,500	100 A	100 A
	25,000	100 A	100 A
	50,000	100 A	100 A
	100,000	100 A	100 A
P22	12,500	100 A	100 A
	25,000	100 A	100 A
	50,000	100 A	100 A
	100,000	100 A	100 A
P23	12,500	100 A	100 A
	25,000	100 A	100 A
	50,000	100 A	100 A
	100,000	100 A	100 A
P24	12,500	100 A	100 A
	25,000	100 A	100 A
	50,000	100 A	100 A
	100,000	100 A	100 A
P26	12,500	100 A	100 A
	25,000	100 A	100 A
	50,000	100 A	100 A
	100,000	100 A	100 A
P27	12,500	100 A	100 A
	25,000	100 A	100 A
	50,000	100 A	100 A
	100,000	100 A	100 A
P38	12,500	100 A	100 A
	25,000	100 A	100 A
	50,000	100 A	100 A
	100,000	100 A	100 A
P39	12,500	100 A	100 A
	25,000	100 A	100 A
	50,000	100 A	100 A
	100,000	100 A	100 A

CONCLUSION

In conclusion, the preliminary screening in this study indicate that ethanol crude extract of *Piper* species leaves significantly inhibited the mycelial growth and spore germination of *Colletotrichum* sp., and *Phytophthora* sp. There is a great scope in studying that *Piper* are potentially to be develop as a natural and effective alternative to synthetic fungicide for using in the treatment of plant diseases management in the future. However, we will study the chemical composition of the bioactive materials in *Piper* species leaves from different location in Thailand.

ACKNOWLEDGEMENTS

The authors express the sincere appreciation to the King Mongkut's Institute of Technology Ladkrabang, Prince of Chumphon Campus and Kasetsart University for supporting the study financially.

REFERENCES

- [1] Chaveerach, A., Tanee, T., Sudmoon, R. and Mookamul, P. 2009. The genus *Piper* in Thailand. Second edition. Khon Kaen: Khon Kaen Karnpim. 163 pp. ISBN 978-616-549-005-4. (in Thai).
- [2] Chaveerach, A., Sudmoon, R., Tanee, T. and Mookamul, P. 2008. The species diversity of the genus *Piper* from Thailand. Acta Phytotaxonomica et Geobotanica, Vol. 59, No. 2, pp.105-163.
- [3] Xu, Li, Antifungal Compounds from *Piper* Species, Current Bioactive Compounds, Vol.7, No.4, 2011, pp. 262-267.
- [4] Ghosh R., Darin K., Payel N., and Deb P. An Overview of Various *Piper* Species for Their Biological Activities. International Journal of Pharma Research & Review, Vol. 3, No.1, 2014, pp. 67-75.
- [5] Nazmul M.H.M., Salmah I., Syahid A. and Mahmood AA. In-vitro screening of antifungal activity of plants in Malaysia. Biomedical Research, Vol. 22, No.1, 2011, pp. 28-30.
- [6] Marina P. D. C., Valdir C., Rosi Z. D. S., Rosendo A. Y., Susana Z., Sabina J., Rosana C. C., and Alexandre B. C., Evaluation of Antifungal Activity of *Piper solmsianum* C. DC. var. *solmsianum* (Piperaceae)., Biol. Pharm. Bull. Vol. 28, No. 8, 2005. pp. 1527-1530.
- [7] Singburadom N., Hydroxychavicol from *Piper betel* Leave is An Antifungal Activity Against Plant Pathogenic Fungi. JBiopest., Vol. 8, No. 2, 2015. pp.82-92.
- [8] Rodrigo P. M., Samuel V. P., Carlos M. G. P., Jesús H. Gil G.1, and Diego L. Durango R., Chemical Composition and Antifungal Activity of *Piper auritum* KUNTH and *Piper holtonii* C.

- DC. Against Phytopathogenic Fungi, Chilean Journal of Agricultural Research, Vol.74, No. 4, 2012, pp. 507-515.
- [9] Ounchokdee, U., Rueangrit, S. and Dethoup, T. , Antifungal Activity Profile of *Piper longum* Fruit Extract Against Plant Pathogenic Fungi, JBiopest, Vol.9, No. 2, 2016, pp. 97-103.
- [10] Jorge R., Luis C., Vladimir M., Silvio A., Omar M., Antifungal Activity of Raw Extract and Flavanons Isolated From *Piper ecuadorensis* from Ecuador, Revista Brasileira de Farmacognosia Brazilian Journal of Pharmacognosy, Vol.23, No. 2, 2013, pp. 370-373.

EXPRESSION OF HYALURONAN SYNTHASE (*hasA*) AND PRODUCTION OF HYALURONIC ACID THROUGH BIOSYNTHESIS IN RECOMBINANT *ESCHERICHIA COLI*

Lai Zee Wei¹, Aayushree Kharel¹ and Chong Jun Yi¹

¹School of Biosciences, Faculty of Health and Medical Sciences, Taylor's University, Malaysia

ABSTRACT

Hyaluronic acid (HA) is a biodegradable, high molecular weight polymer and a major component of mucoid capsule in bacteria and extracellular matrix (ECM) of vertebrate tissue. Due to its unique characteristics, HA is used extensively in medical and cosmetic field. HA was extracted from animal tissues or produced by fermentation using native producer of the biopolymer, *Streptococcus zooepidemicus*. However, due to exotoxins production from these sources, HA production by recombinant microorganisms has gained interest. A fragment of an approximate size of 1.5kb that encodes the hyaluronan synthase (*hasA*) gene from *S. zooepidemicus* ATCC 39920 was amplified by PCR using the designated primers. The *hasA* gene was ligated into the plasmid pLbADH and cloned into the expression host, *Escherichia coli* BL21 strain and further identified by miniprep and DNA sequencing. Then, genetically engineered *E. coli* strain BL21 was used for the production of HA by fermentation using different glucose concentration in shake flask culture. Varying glucose concentration (10-50 g/L) was used and carried out at 200 rpm for 7 hours in shaking incubator. Biomass concentration was determined using dry cell weight (DCW) method, whereas, colorimetric method was used to determine the amount of glucose consumption and HA concentration. Amongst varying glucose concentrations, results showed that 50 g/L glucose produced the highest HA concentration (0.074±0.001 g/L) and HA productivity (0.018 g/L.h⁻¹). The use of nutrient rich media containing nitrogen source along with 50 g/L glucose was able to produce the highest HA concentration (0.115±0.002 g/L) and HA productivity (0.028 g/L. h⁻¹).

Keywords: *hyaluronic acid, hyaluronan synthase, Streptococcus zooepidemicus, Escherichia coli*

INTRODUCTION

Hyaluronic acid (or hyaluronan or HA) is a polysaccharide that belongs to glycosaminoglycan family and consists of *D*-glucuronic acid (GlcUA) and *N*-acetylglucosamine (GlcNAc), linked alternately by β -1,3 and β -1,4 glycosidic bond [1]. HA is a high molecular weight linear polysaccharide with the molecular weight ranging from 10⁴ to 10⁷ Da [2]. HA is abundantly present in the umbilical cord, synovial fluid and vitreous humor (eye). Due to its biocompatibility, viscoelasticity and hygroscopicity, HA is extensively used for the treatment of ulcer and burn [3], in ophthalmology, rheumatology and dermatology [4]. In conjunction with the properties of HA, it is also widely used in cosmetic products, medicine and specialty foods. According to Widner et al. [5], the market value of HA was estimated to be over a billion dollars.

Previously, HA was extracted from rooster comb. According to a study conducted by Rosa et al. [6] they concluded that rooster comb was composed of about 90% HA, making it suitable for extraction. However, use of animal-derived

biochemical can be risky due to zoonosis and unpremeditated infection transfer [3]. Hence, currently, HA production from microbial fermentation is the commonly used method to meet the demands of the market. Since the 1980s, HA was produced by fermentation of group C *Streptococci* [7]. However, these microorganisms are potential human pathogens, thus making HA purification costly. Genetic engineering of microorganisms for HA synthesis has allowed HA production from non-pathogenic microorganisms [8]. HA production is commonly observed in Gram-positive bacteria, but by genetic engineering of gram negative bacteria such as *Escherichia coli*, synthesis of HA has been possible and they can be used as potential host candidate for industrial HA production [7]. Scientists have used Generally Regarded as Safe (GRAS) microorganisms for HA production, such as recombinant *Lactococcus lactis* that produced 0.65 g/L of HA [9], recombinant *Escherichia coli* that produced 0.203 g/L of HA [10].

Since the biosynthesis pathway of HA is partially similar to cell wall biosynthesis, the heterologous expression of *hasA* gene alone is

sufficient to induce production of hyaluronic acid in these organisms. The effort of using recombinant systems to produce HA started when the hyaluronan synthase gene (*hasA*) encoding for the enzyme that polymerizes UDP-GlcNAc and UDP-GlcUA into hyaluronan was isolated from *Streptococcus pyogenes* [11]. In HA fermentation, carbon source plays a vital role as the intermediates are shared for both biomass formation and HA production [2]. There is limited study on the biosynthetic capabilities of recombinant *E. coli* BL21 for the production of HA. Hence, the aim of this research study is to clone and express *hasA* gene into *E. coli* BL21 and use this recombinant *E. coli* strain BL21 as host in order to explore the biosynthetic capabilities for HA production in batch fermentation using shake flask culture.

MATERIALS AND METHODS

Bacteria Strains and Plasmid

Streptococcus equi sub sp. *zooepidemicus* (American Type Culture Collection® 39920™) was used and stored at -80°C in 50% (v/v) glycerol stock, *Escherichia coli* BL21 was used as the recombinant host cell and plasmid pLbADH was used.

Isolation of *hasA* Gene using PCR Amplification from *S. zooepidemicus*

The *hasA* gene was isolated from *S. zooepidemicus* and amplified by PCR using the designed forward (5' GGG GAA TTC ATG AGA ACA TTA AAA AAC CTC 3') and reverse (5'GCC AAG CTT ATT ATA ATA ATT TTT TAC GTG TTC CCC 3') primers, which named HasA_01F and HasA_01R, respectively. With the bacteria *S. zooepidemicus* used as the template, polymerase chain reaction (PCR) was performed with KOD Hot Start DNA polymerase in a thermal cycler using the following program: 1 cycle at 95°C for 3 minutes, 30 cycles of 95°C for 15 seconds, 60°C for 30 seconds, 72°C for 90 seconds and 1 cycle of 72°C for 5 minutes. 5µL of PCR product was taken to perform gel electrophoresis, and the remaining were stored in the freezer at -20°C until use.

Preparation of Competent *E. coli* Cell

A single *E. coli* bacteria colony from an overnight bacteria culture was transferred into a 50mL falcon tube with 50mL of LB broth. The culture was incubated in a growth incubator at 37°C for about 4 hours. The growth of the culture was monitored after 2 hours. The OD₆₀₀ of the culture was until the reading of cell OD₆₀₀ reach 0.35. The

bacteria culture was put on ice for 10 minutes to cool down to 0°C.

The *E. coli* cells were recovered by centrifugation at 4100 rpm for 10 minutes at 4°C. The medium was separated and removed completely from the cell pellets. The pellets were then resuspended in 30 mL of ice-cold MgCl₂-CaCl₂ solution by gently swirling. The cells were centrifuged again at 4100 rpm for 10 minutes at 4°C and separated it from medium. The pellet was then added with ice-cold 0.1M CaCl₂ solution and resuspended by gently swirling. The competent *E. coli* cells culture was then aliquoted into 1.5mL microcentrifuge tubes with 100 µL of culture in each tube.

Cloning of *hasA* Gene into Bacteria Expression Vector (pLbADH)

The PCR product obtained from *hasA* gene and the plasmid pLbADH were digested separately with FastDigest enzyme EcoRI and HindIII in an incubator at 37°C for 1 hour. The tubes were then put on a rack in an 80°C water bath for 20 minutes to heat inactivate the enzyme.

Both digestion products were transferred to a same 0.5mL microcentrifuge tube for ligation using T4 DNA ligase enzyme. The ligation takes place in a thermal cycler at 22°C for overnight. The ligation product was then used for transformation.

Transformation of Recombinant *E. coli* Bacteria

Five µL of the ligation product were transferred into the tube containing the competent cells. The contents of the cells were mixed by swirling gently. The tubes were rested on ice for 30 minutes before the heat shock step. The tubes were then put on a rack in a pre-heated 42°C water bath for exactly 90 seconds. The tubes were immediately transferred back to the ice for 5 minutes. 900 mL of LB broth was added into the tubes, and placed in a shaking incubator at 37°C, 200rpm for an hour.

The tubes were centrifuged at 5000 rpm for 5 minutes. 900 mL of medium was removed by pipetting. The remaining medium was resuspended with the cell pellets, and transferred onto a LB agar plate with ampicillin. Spread plate was applied and incubated in a 37°C incubator for 12 to 16 hours.

PCR Screening for Positive Transformant

All the colonies grown on the LB agar plates were collected and screened with PCR using the following program: 1 cycle at 95°C for 3 minutes, 30 cycles of 95°C for 15 seconds, 60°C for 30 seconds, 72°C for 90 seconds and 1 cycle of 72°C for 5 minutes. HasA_01F and HasA_01R were used as primer in selection of positive transformant.

PCR products were performed with gel electrophoresis and gel documentation allowed the comparison of base pairs with the original *hasA* gene to be made. PCR products that showed difference were discarded, while the colonies containing the *hasA* gene were subcultured for HA analysis.

Medium and Fermentation

The cells were grown at 37°C with 200 rev/min shaking speed for 5 h in the LB broth (as an inoculum) supplemented with 100 mg/ml of ampicillin. The fermentation medium contained two different types of components; one is LB and glucose (10-50 g/L) only; one is nutrient rich medium which consisted of (in g/L) glucose 50, tryptone 15, yeast extract 5, KH₂PO₄ 2, K₂HPO₄ 2, MgSO₄·7H₂O 0.5. The culture medium was sterilized at 121°C for 15 min. The glucose and MgSO₄·7H₂O were autoclaved separately. The ampicillin was sterilized by filtration using 0.45 µm nylon syringe membrane filter. Fermentations were carried out in duplicates and the mean value of each experiment was obtained.

To investigate the effect of glucose concentrations (10 – 50 g/L) for HA biosynthesis by the recombinant *E. coli* strain, experiments were carried out using a 500 mL Erlenmeyer flask. The flask cultures were incubated in rotary shaker at 200 rev/min with different glucose concentrations. To initiate the fermentation, 1 loop of colony culture was transferred to 50 mL of LB inoculum medium for 5 hours at pH 7, and 10 % (v/v) of inoculum was inoculated into the 500 mL shake flask containing 180 mL of the production medium and run for another 7 hours at initial pH 7, 37°C. Inducer of 0.5 mM isopropyl β-D-1-thiogalactopyranoside (IPTG) was added to induce the expression of *hasA* genes when OD₆₀₀ reached about 0.6.

Analytical Methods

All samples were withdrawn at regular time intervals for analysis of cell, HA and glucose concentration. Cell growth was observed by measuring the optical density of the culture broth at 600 nm using a spectrophotometer. Correlation between the dry cell weight (DCW) and OD was estimated from several batch experiments using the equation: DCW (g/L) = 2.2511 x OD

The supernatants were used for HA and reducing sugar determination. After the removal of the cell pellet for cell growth determination, two volumes of ethanol were added to one volume of the supernatant in a 15 ml centrifuge tube and the solution was refrigerated at 4°C for 1 h to

precipitate HA. The precipitate was re-dissolved in 1 ml of 0.15 mol/L of NaCl solution and centrifuged at 3,000 x g for 20 min; then was re-dissolved with a 2 to 3-fold volume of distilled water. The HA concentration was determined using the carbazole method [12] and the optical density was measured at 530 nm. The HA concentration was calculated using a standard curve prepared at different concentrations of HA standards (Sigma-Aldrich, Malaysia). For reducing sugar concentration, 3,5-dinitrosalicylic acid (DNS) method was used [13].

RESULTS AND DISCUSSIONS

Cloning of *hasA* gene from *S. zooepidemicus*

The *hasA* gene from *S. zooepidemicus* was successfully amplified by PCR and cloned into the plasmid pLbADH as shown in Fig. 1 with ProTAC promoter (constitutive promoter). There was several plasmid constructed along with different promoters to transformed *hasA* gene into other recombinant hosts. Jeong, Shim & Kim [14] utilized two types of plasmid, pAO815 and pGAPZB which have an inducible promoter (AOX) and a constitutive promoter (GAP), respectively. Their study use the vector with constitutive promoters to accumulate of both sugar precursors of HA in the cell, then activate the inducible promoter preceding the *hasA* gene, leading to an increased production and higher MW of HA.

Plasmid Rearrangement in Transformed Recombinant *E. coli*

PCR analysis on initial culture of recombinant *E. coli* colony showed that *hasA* gene is successfully cloned and transformed into *E. coli* BL21 (Fig. 1). Interestingly, no *hasA* gene was detected in second subculture of recombinant *E. coli*. In addition, restriction enzyme analysis carried out on the recombinant *hasA* plasmid isolated from second subculture showed multiple bands with different MW (data not shown). To confirm whether the unidentified extra bands are from contamination or due to the rearrangement of recombinant *hasA* plasmid, the miniprep products were digested separately using different combination of restriction enzymes to evaluate the plasmid size. Further restriction analysis on isolated plasmid DNA confirmed that the recombinant *hasA* plasmid was rearranged. A cloned plasmid will be more prone to be selected against by the host cell, either by deletion or rearrangement when the plasmid size is too large [15].



Fig. 1 Screening for positive transformant. Lane 1: 1kb plus DNA ladder; Lane 2: positive control of *hasA* gene; lane 3-5: Sample 1-3.

This is further supported by the evidence that further analysis with carbazole method showed the presence of HA produced by the recombinant *E. coli*, and the ability of the bacteria to propagate under selection of 100mg/mL ampicillin.

Effect of Different Glucose Concentrations on HA Production by Recombinant *E. coli* BL21

Based on the kinetic parameter values (Table 1), highest biomass concentration (X_m) and highest HA concentration (P_m) was 3.031 ± 0.004 g/L and 0.074 ± 0.001 g/L respectively, both achieved at 50 g/L glucose concentration. However, lowest X_m and P_m was 2.161 ± 0.002 g/L and 0.018 ± 0.013 g/L respectively, both achieved with control. This is in accordance to our expected results, as the bacteria requires carbon source for cell growth and HA production. In control, there was no glucose present, so there was insufficient precursor for HA production. However, as glucose concentration increased, the precursors, GlcUA and GlcNAc were made and HA concentration increased. According to a study conducted by Don & Shoparwe [1] highest HA concentration of 0.589 g/L was achieved at 50 g/L glucose concentration. However, in their experiment, when glucose concentration was increased to 60 g/L, HA concentration decreased.

Highest cell yield coefficient (Y_{XS}) was achieved at 20 g/L glucose concentration. This result suggests that highest Y_{XS} does not mean highest productivity. The result matches with an experiment conducted by Holmstrom & Ricica [16], which also proposed that highest yield of cell does not necessarily mean highest HA production. At 50 g/L, the Y_{XS} value was the least, 0.313 g cell/g substrate, suggesting that less cells were produced

per gram of glucose. It is suggested that glucose concentration above 50 g/L glucose concentration causes reduction in water activity which may lead to growth inhibition. Glucose is a monosaccharide and hence its' osmotic pressure will be higher, so microorganisms will detect the changes in osmotic pressure and alter their metabolic pathway [17]. Ding & Tan [18] also stated that high initial glucose concentration in batch fermentation method can cause low cell mass due to substrate inhibition.

At 50 g/L, product yield per substrate produced (Y_{PS}) and maximum productivity (P_r) had maximum values of 0.004 g HA/g cell and 0.018 g HA/L.h⁻¹ respectively. At 40 g/L, Y_{PS} was 0.003 g HA/g cell and at 50 g/L, Y_{PS} was 0.004 g HA/g cell suggesting that glucose was more efficiently consumed at 50 g/L. Values for product yield per biomass produced (Y_{PX}) increased with increase in glucose concentration, reaching a maximum value of 0.010 g HA/g cell at 50 g/L glucose concentration. This suggested that as the number of cells increased, the amount of HA production also increased. Hence, the results showed that HA fermentation by recombinant *E. coli* BL21 is highly growth associated as shown in Fig. 2. However, studies conducted by Huang et al. [19] suggested that HA production was delayed-growth associated which was in accordance to several other reports.

At 50 g/L, Y_{XS} was least and Y_{PS} was highest, suggesting glucose was mainly used for HA production. Precursors such as glucose-1-phosphate, UDP-glucose and UDP-N-acetylglucosamine are shared in HA synthesis and cell growth. Hence, competition between these two pathways exist to consume the same precursors. In addition, competition for carbon flux exists between HA synthesis and glycolysis [2]. Metabolites such as glucose-6-phosphate and fructose-6-phosphate are consumed by hexomonophosphate shunt and glycolysis, respectively. Hence, there is strong competition for metabolites between HA production and cell growth [20]. HA production is an energy intensive process and total of 4 mol ATP is required for production of 1 mol of repeating unit of HA disaccharide. Hence, in order to balance between biomass and HA production, maintenance of metabolic balance is important as well [21].

Izawa et al [21] suggested that use of aerobic bacteria for HA production can cause increase in viscosity of the culture broth, inhibiting the transport of nutrients and gas. However, it has been found that aeration can improve the yield of HA compared to corresponding anaerobic culture. But Mausolf et al. [22] suggested that under aerobic conditions, degradation of HA can take place due to the presence of oxygen-derived free radicals.

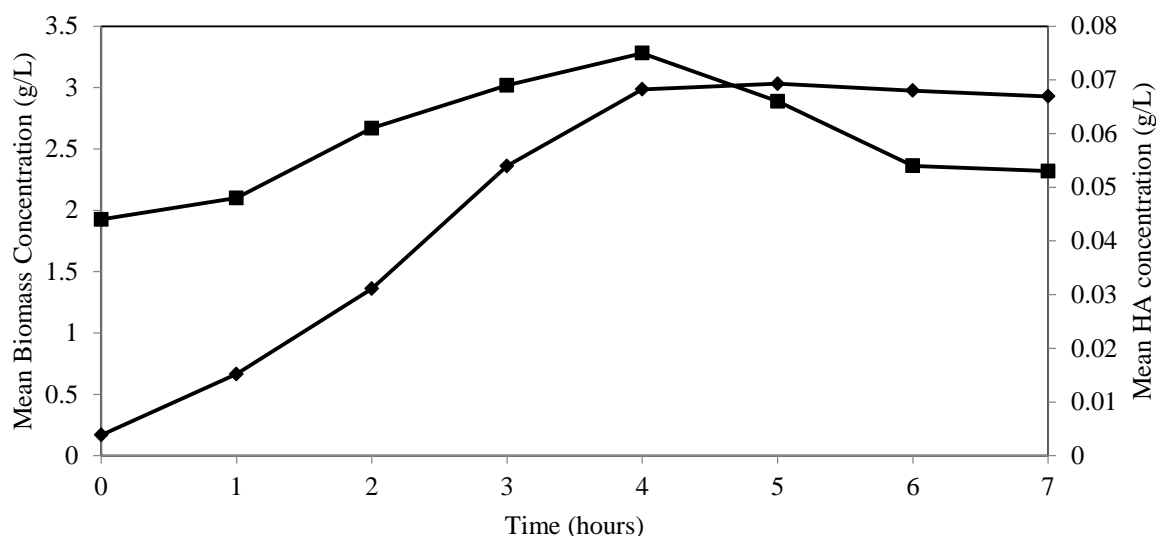


Fig. 2 Graph of mean biomass and HA concentration (g/L) by recombinant *E. coli* BL21 in shake flask culture using 50 g/L glucose. All concentrations were represented as the mean value of duplicated results from independent fermentation. (■) HA (◆) Biomass

Table 1 Kinetic parameter values of HA production by recombinant *E. coli* BL21 using different glucose concentrations

Kinetic parameters	Glucose concentration (g/L)				
	10	20	30	40	50
X_m (g cell /L)	2.501±0.010	2.602±0.011	2.656±0.002	2.879±0.004	3.031±0.004
P_m (g HA/L)	0.026 ^b ±0.001	0.029 ^c ±0.0001	0.037 ^d ±0.0001	0.057 ^e ±0.003 ^e	0.074±0.001 ^f
S (g glucose/L)	5.260	6.396	6.476	8.686	11.341
μ_m (h ⁻¹)	0.500	0.520	0.531	0.575	0.606
$Y_{X/S}$ (g cell/g substrate)	0.669	0.682	0.415	0.446	0.313
$Y_{P/S}$ (g HA/g substrate)	0.001	0.001	0.001	0.003	0.004
$Y_{P/X}$ (g HA/g cell)	0.002	0.002	0.004	0.005	0.010
P_r (g HA/L.h ⁻¹)	0.006	0.007	0.009	0.014	0.018

Legend: (X_m) maximum biomass concentration; (P_m) maximum HA concentration; (S) consumed substrate concentration; (μ_m) maximum specific growth rate; ($Y_{X/S}$) cell yield coefficient; ($Y_{P/S}$) product yield coefficient; ($Y_{P/X}$) product yield per biomass produced; (P_r) maximum productivity. All results are expressed as means ± standard deviation of means; Values are means of duplicates from two separate runs (n = 2). p-value for average HA concentration in accordance to glucose concentration was obtained using two way ANOVA statistical analysis ($\alpha=0.05$). ^{a b c d e f}: Values with different lowercase superscript are significantly different.

Effect of Nutrient Rich Media on HA fermentation by Recombinant *E. coli* BL21

The use of nutrient rich media for HA production yielded higher biomass concentration and HA concentration when compared to use of glucose

alone. As shown in Table 2, maximum biomass concentration (X_m) was 3.280±0.108 g/L when 50 g/L glucose along with nutrient rich media was used. However, when only 50 g/L glucose was used, the biomass concentration was 3.031±0.004 g/L. Studies by other researchers were conducted with constant

glucose concentration and varying yeast extract concentration (as nitrogen source). The results supported our results, suggesting that presence of organic nitrogen source improves the microorganism growth, with maximum cell growth when C: N ratio is 2:1 [23]. The increase in biomass concentration is because yeast extract is a good substrate for many microorganisms as it contains important components such as amino acid, peptide, water-soluble vitamins and carbon source which are required for growth and metabolism. With nutrient rich media, maximum HA concentration (P_m) was 0.115 ± 0.002 g HA/ L, whereas with 50 g/L glucose concentration it was only 0.074 ± 0.001 g HA/L. This might have been due to availability of amino acid and B-vitamins provided by organic nitrogen source, yeast extract and tryptone. Additionally, presence of these organic nitrogen source provides large portion of carbon for the growth and production of cells [24]. The specific growth rate (μ_m) was slightly higher at 50 g/L glucose concentration. This can be explained by the cell yield coefficient ($Y_{X/S}$) which is also higher for 50 g/L glucose concentration, which suggests that more cells are produced per substrate consumed at 50 g/L. In nutrient rich media, more of the metabolised carbon source might have been used for HA production, as a result slightly lower specific growth rate was achieved. The product yield coefficient ($Y_{P/S}$) and product yield per biomass coefficient ($Y_{P/X}$) was higher with nutrient rich media containing 50 g/L glucose. The productivity is also higher in nutrient rich media, with a value of 0.028 g HA/ L.h⁻¹ which is in accordance to results obtained by other researchers which suggests that presence of nitrogen source increases the production of HA [24].

According to Aroskar, Kamat & Kamat [25], the overall HA production is dependent on the nitrogen sources present in the fermentation media. However, there is limited information about the consequence of medium carbon-to-nitrogen (C/N) ratios which will cause an effect on the metabolic flux [23]. Studies show that presence of potassium dihydrogen phosphate (KH_2PO_4) and magnesium sulphate heptahydrate ($MgSO_4 \cdot 7H_2O$) also contribute to increase in biomass and HA productivity [25]. Hence, the presence of these substances in nutrient rich media may have also contributed to higher biomass and HA concentration.

CONCLUSION

The *hasA* gene was cloned from *S. zooepidemicus* and successfully expressed in recombinant *E.coli* BL21 cells. 50 g/L glucose concentration along with nitrogen source such as yeast and tryptone is the preferred combination to produce the highest concentration of HA through fermentation by recombinant *E. coli* BL21 using shake flask culture.

The results obtained from this study showed that amongst the range of glucose concentration used from 10-50 g/L, 50 g/L glucose produced highest concentration of HA of 0.074 ± 0.001 g/L at 4th hour of fermentation in shake flask culture. Comparison between HA production in media consisting of only glucose and nutrient rich media containing glucose showed that higher HA production was achieved in nutrient rich media with HA concentration of 0.115 ± 0.002 g/L. The findings can be used to further optimize HA production by varying other parameters such as nitrogen source, agitation rate and aeration rate before upscaling the process.

Table 2 Kinetic parameter values of HA production by recombinant *E. coli* BL21 using different media

Kinetic parameters	Glucose concentration (g/L)	
	50 without nutrient rich components	50 & Nutrient Rich Media
X_m (g cell /L)	3.031 ± 0.004	3.280 ± 0.108
P_m (g HA/L)	0.074 ± 0.001	0.115 ± 0.002
S (g glucose/L)	11.341	13.126
μ_m (h ⁻¹)	0.606	0.546
$Y_{X/S}$ (g cell/g substrate)	0.313	0.259
$Y_{P/S}$ (g HA/g substrate)	0.004	0.006
$Y_{P/X}$ (g HA/g cell)	0.010	0.0195
P_r (g HA/L.h ⁻¹)	0.018	0.0287

Legend: (X_m) maximum biomass concentration; (P_m) maximum HA concentration; (S) consumed substrate concentration; (μ_m) maximum specific growth rate; ($Y_{X/S}$) cell yield coefficient; ($Y_{P/S}$) product yield coefficient; ($Y_{P/X}$) product yield per biomass produced; (P_r) maximum productivity. All results are expressed as means \pm standard deviation of means; Values are means of duplicates from two separate runs (n = 2). p-value was obtained using two-way ANOVA statistical analysis ($\alpha=0.05$).

ACKNOWLEDGEMENTS

This work was financially supported by Emerging Research Funding Scheme funded by Taylor's University Lakeside Campus.

REFERENCES

- [1] Don, M.M., and Shoparwe, N.F., Kinetics of Hyaluronic Acid Production by *Streptococcus zooepidemicus* Considering the Effect of Glucose. Biochemical Engineering Journal, Vol. 49, Issue 1, 2010, pp. 95-103.

- [2] Liu, L., Liu, Y., Li, J., Du, G., and Chen, Microbial Production of Hyaluronic Acid: Current State, Challenges, and Perspectives. *Microbial Cell Factories*, Vol. 10, Issue 1, 2011, pp. 99.
- [3] Chong, B.F., Blank, L.M., Mclaughlin, R., and Nielsel, L.K., Microbial Hyaluronic Acid Production. *Applied Microbial Biotechnology*, Vol. 66, 2005, pp. 341-351.
- [4] Weindl, G., Schaller, M., Schafer-Korting, M., and Korting, H.C., Hyaluronic Acid in the Treatment and Prevention of Skin Diseases: Molecular Biological, Pharmaceutical and Clinical Aspects. *Skin Pharmacology and Physiology*, Vol. 17, Issue 5, 2004, pp. 207-213.
- [5] Widner, B., Behr, R., Dollen, S.V., Tang, M., Heu, T., Sloma, A., Sternberg, D., DeAngelis, P.L., Weigl, P.H., and Brown, S., Hyaluronic Acid Production in *Bacillus subtilis*. *Applied and Environmental Microbiology*, Vol. 71, Issue 7, 2005, pp. 3747-3752.
- [6] Rosa, C.S., Tovar, A.F., Mourao, P., Pereira, R., Barreto, P., and Beirao, L.H., Purification and Characterization of Hyaluronic Acid from Chicken Combs. *Ciencia Rural*, Vol. 42, Issue 9, 2012, pp. 1682-1687.
- [7] Yamada, T., and Kawasaki, T., Microbial Synthesis of Hyaluronan and Chitin. *Journal of Bioscience and Bioengineering*, Vol. 99, Issue. 6, 2005, pp. 521-528.
- [8] de Oliveira, J.D., Carvalho, L.S., Gomes, A.M.V., Queiroz, L.R., Magalhaes, M.S. and Parachin, N.S., Genetic Basis for Hyper Production of Hyaluronic Acid in Natural and Engineered Microorganisms. *Microbial Cell Factories*, Vol. 15, Issue 119. 2016.
- [9] Chien, L.J., and Lee, C.K., Hyaluronic Acid Production by Recombinant *Lactococcus lactis*. *Applied Microbial Biotechnology*, Vol. 77, Issue 2, 2007, pp. 339-346.
- [10] Yu, H., and Stephanopoulos, G., Metabolic Engineering of *Escherichia coli* for Biosynthesis of Hyaluronic Acid. *Metabolic Engineering*, Vol. 10, Issue 1, 2008, pp. 24-32.
- [11] DeAngelis, P.L., Molecular Directionality of Polysaccharide Polymerization by the *Pasteurella multocida* Hyaluronan Synthase. *The Journal of Biological Chemistry*, Vol. 274, Issue 37, 1999, pp. 26557-26562.
- [12] Bitter, T., and Muir, H.M., A Modified Uronic Acid Carbazole Reaction. *Analytica Biochemistry*, Vol. 4, Issue 4, 1962, pp. 330-334.
- [13] Miller, G.L., Use of Dinitrosalicylic Acid Reagent for Determination of Reducing Sugars. *Analytical Chemistry*, Vol. 31, 1959, pp. 426-428.
- [14] Jeong, E., Shim, W.Y., and Kim, J.H., Metabolic Engineering of *Pichia pastoris* for Production of Hyaluronic Acid with High Molecular Weight. *Journal of Biotechnology*, Vol. 185, 2014, pp.28-36.
- [15] Al-Allaf, F.A., Tolmachov, O.E., Zambetti, L.P., Tchetchelnitski, V., and Mehmet, H., Remarkable Stability of an Instability-prone Lentiviral Vector Plasmid in *Escherichia coli* Stbl3. *3 Biotech*, Vol. 3, 2013, pp. 61-67.
- [16] Holmstrom, B., and Ricica, J., Production of Hyaluronic Acid by a Streptococcal Strain in Batch Culture. *Applied Microbiology*, Vol. 15, Issue 6, 1967, pp. 1409-1413.
- [17] Don, M.M. Kinetics of Hydrogen Peroxide Formation and its Relation to Hyaluronic Acid Production by *Streptococcus zooepidemicus* Hyaluronic acid. Universiti Malaya, 2006.
- [18] Ding, S., and Tan, T. *L-Lactic acid production by Lactobacillus casei* Fermentation Using Different Fed-batch Feeding Strategies. *Process Biochemistry*, Vol. 41, Issue 6, 2006, pp. 1451-1454.
- [19] Huang, W.C., Chen, S.J., and Chen, T.L., Modelling the Microbial Production of Hyaluronic Acid. *Journal of the Chinese Institute of Chemical Engineers*, Vol. 38, 2007, pp. 355-359.
- [20] Lai, Z.W., Rahim, R.A., Ariff, A., and Mohamad, R., Comparison of Hyaluronic Acid Biosynthesis by the Recombinant *Escherichia coli* strains in Different Mode of Bioreactor Operation. *Journal of Microbiology, Biotechnology and Food Sciences*, Vol. 6, Issue 3, 2016, pp. 905-910.
- [21] Izawa, M., Serata, M., Sone, T., Omasa, T., and Ohtake, H., Hyaluronic Acid Production by Recombinant *Streptococcus thermophiles*. *Journal of Bioscience and Bioengineering*, Vol. 111, no. 6, 2011, pp. 665-670.
- [22] Mausolf, A., Jungmann, J., Robenek, H., and Prehm, P., Shedding of Hyaluronate Synthase from Streptococci. *Biochemical Journal*, Vol. 267, no. 1, 1990, pp. 191-196.
- [23] Chen, S.J., Chen, J.L., Huang, W.C., and Chen, H.L., Fermentation Process Development of Hyaluronic Acid Production by *Streptococcus zooepidemicus* ATCC 39920. *Korean Journal of Chemical Engineering*, Vol. 26, Issue 2, 2009, pp. 428-432.
- [24] Pan, N.C., Marques, R., Pereira, H.C.B., Vignoli, J.A., and Celligoi, MAPC. 'Effects of Different Nitrogen Sources on the Production of Hyaluronic Acid by *Streptococcus*. *BMC Proceedings*, Vol. 8, Issue 4, 2014, pp. 204.
- [25] Aroskar, V. J., Kamat, S.D., and Kamat, D.V., Effect of Various Physical Parameters and Statistical Medium Optimization on Production of Hyaluronic Acid Using *S. equi* subsp. *zooepidemicus* ATCC 39920. *IIOAB Letters*, Vol. 2, no. 1, 2012, pp. 7-15.

THE UTILIZATION OF THE MITOCHONDRIAL COI AND THE NUCLEAR HISTONE H3 GENES FOR DNA BARCODING STUDY OF INTERTIDAL SHELLED GASTROPODS FROM NADA COAST IN WAKAYAMA PREFECTURE, JAPAN

Nagisa Nakaji¹, Shoma Iwamoto¹, Shinnosuke Teruya², Masataka Kusube¹, Akira Kosaka⁴,
Takenori Sasaki³, Davin H. E. Setiamarga^{1,3,*}

¹ National Institute of Technology, Wakayama College, Gobo, Wakayama, Japan

² Okinawa Prefectural Deep Sea Water Research Center, Kumejima, Okinawa, Japan

³ The University Museum, The University of Tokyo, Bunkyo, -ku, Tokyo, Japan ⁴

⁴ Wakayama Prefectural Museum of Natural History, Kainan, Wakayama, Japan

[†] *Equal contributions (Co-first Authors)*

* *Corresponding Author / Senior Author* (email: davin@wakayama-nct.ac.jp)

ABSTRACT

DNA Barcoding, especially when coupled with Environmental DNA (eDNA), has been acknowledged as a powerful method for biodiversity monitoring due to its minimal invasiveness and relatively high accuracy. However, this method depends heavily on the availability of useful DNA markers and a reliable reference DNA data base. Although the coasts of Wakayama Prefecture are known to be among the most biologically diverse coastal areas of Japan and thus have a rich assemblage of shelled gastropods, very little molecular-based biodiversity studies have been conducted in the area. In this paper, we report the result of our study to provide a reliable reference DNA data of the mitochondrial gene COI and the nuclear gene Histone H3, for the shelled gastropods of the intertidal area of the Nada Coast in central Wakayama. In order to do so, we collected up to five individuals of nine species of shelled gastropods from the intertidal rocky beach. Samples were identified morphologically and then vouchered at the University Museum of the University of Tokyo. PCR and sequencings were conducted using previously reported Histone H3 and COI primers. We also found that the Histone H3 of most of our target species are not available on Genbank. Sequence comparisons and phylogenetic analyses indicated that the both genes have enough substitutions to differentiate species. Our result thus contributed to the building of a set of reference DNA sequences for future DNA-based environment and biodiversity monitoring.

Keywords: DNA Barcoding, Gastropoda, Monitoring, Intertidal

INTRODUCTION

Recent development in sequencing technology has made DNA Barcoding a powerful and practical method for taxonomic identification of samples collected from the field, due to its relatively high accuracy [1]. DNA barcoding, which can be defined as "Identification of organism samples by interrogating query samples against data base-registered DNA data of taxonomically identified samples", depends heavily on the availability of useful DNA markers and a reliable reference DNA data base.

However, the lacks of reliable databases, including those of DNA, have been a problem. For example, Troudet et al [2] has reported biases in taxon sample representatives in the Global Biodiversity Information Facility (GBIF) database. They found that while popular vertebrate taxa such as bird and mammals were over-represented, data for all major invertebrate lineages, such as gastropods and arthropods, were poorly represented.

Marine gastropods and other mollusks have

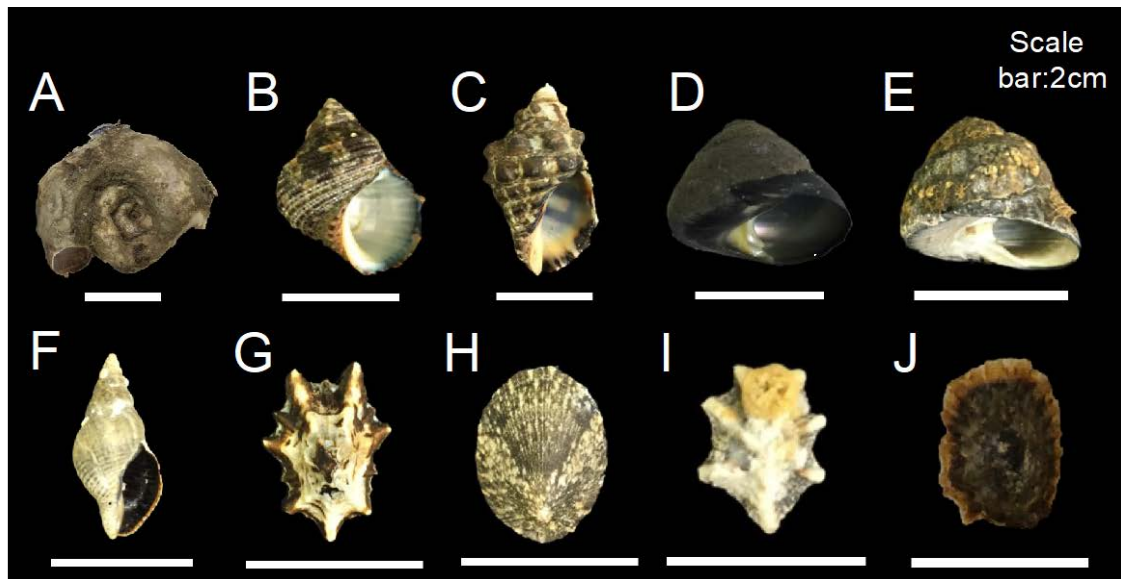


Figure1. Target species of this study. A: *Eurytrochus cognatus*, B: *Turbo stenogyrys*, C: *Reishia clavigena* D: *Chlorostoma xanthostigma*, E: *Omphalius nigerrimus*, F: *Japeuthria ferrea*, G: *Patelloida saccharina lanx*, H: *Nipponacmea fuscoviridis*, I: *Siphonaria sirius*, J: *Siphonaria japonica*.

been known to be sensitive to environmental changes [3, 4]. Meanwhile, with an estimated number of extant species to be ca. 32,000-40,000, intertidal shelled marine Gastropod is a mollusk taxon with high biodiversity. Members of this group are distributed widely around the coastal area around the world. Accordingly, this group is a useful model taxon for the assessment of the impacts of environmental changes, at both the global and local scales.

The coasts of Wakayama Prefecture, including the Nada Coast in central Wakayama, are known to be among the most biologically diverse coastal areas of Japan [5, 6], and thus have a rich assemblage of shelled gastropods. However, although many ecological and species observation studies have been reported (e.g. [7] [8]), very little molecular-based biodiversity studies have been conducted in the area.

In this study, we report the result of our DNA Barcoding study on the shelled gastropods of the intertidal area of the Nada Coast in central Wakayama, using the mitochondrial gene COI and the nuclear gene Histone H3 (H3). We aimed to test the usefulness of these two gene markers, and to provide reliable sequence data linked to vouchered museum samples, for intertidal shelled gastropods barcoding studies.

MATERIALS AND METHODS

Taxon sampling

41 individuals of shelled gastropods from nine species were collected from the rocky intertidal area of the Nada Coast in central Wakayama. (Table 1, Fig. 1). Samples were identified morphologically based on current taxonomical classification [9] and then preserved in 95% ethanol and vouchered at the University Museum of the University of Tokyo.

DNA extraction and amplification

Pieces of muscle tissue (ca. 0.25 mg) were excised from samples. DNA was extracted using standard CTAB-phenol-chloroform method. The mitochondrial cytochrome c oxidase I (COI) gene was amplified using LCO1490 and HCO2198 [10] and LCO mod_Kano2008 and HCO mod_Kano 2008 [11]. Primer pairs H3aF' and H3aR [12] were used for the nuclear Histone H3 gene. PCR reactions were then conducted at the annealing temperatures of 45° and 50°, respectively. PCR products were visualized on a 0.7% agarose gel. Sanger sequencings of successful PCR products were performed by FASMAC (Japan).

We confirmed our sequence data using BLAST on NCBI optimized for highly similar sequences setting (megablast). When we obtained no hit, we researched using the somewhat similar sequences setting (blastn).

Sequences were aligned using MAFFT version 7 [13]. we used the online version of Gblocks 0.91b to remove ambiguously aligned positions with the least stringent settings [14]. We used Mesquite version 3.40 [15] for sequence visualizations.

Table.1 Sample list

specimen ID	specimen	Voucher No.	COI	Accession No.	BLAST Hits	Length	E-value	Percent Identity	H3	Accession No.	BLAST Hits	Length	E-value	Percent Identity
M-DV-013	<i>Agavepeltia foveola</i> 1	under registration	LC383955	LC383955	<i>Agavepeltia cingulata</i>	595,630	0	90%	LC384080	<i>Nephrolepis sinuata</i>	260,276	5.0E-118	96%	
M-DV-014	<i>Agavepeltia foveola</i> 2	under registration	LC383956	LC383956	<i>Agavepeltia cingulata</i>	601,625	0	90%	LC384081	<i>Nephrolepis sinuata</i>	261,265	3.0E-119	97%	
M-DV-137	<i>Agavepeltia foveola</i> 3	under registration	LC383957	LC383957	<i>Agavepeltia cingulata</i>	457,457	7.00E-173	91%	LC384082	<i>Nephrolepis sinuata</i>	278,279	3.0E-125	96%	
M-DV-017	<i>Ruellia clavigera</i> 1	under registration	LC383965	LC383965	<i>Ruellia clavigera</i>	636,636	0	99%	LC384090	<i>Thais laticostata</i>	280,284	2.0E-141	99%	
M-DV-133	<i>Ruellia clavigera</i> 2	under registration	LC383966	LC383966	<i>Ruellia clavigera</i>	631,631	0	100%	LC384091	<i>Thais laticostata</i>	282,282	2.0E-142	99%	
M-DV-134	<i>Ruellia clavigera</i> 3	under registration	LC383967	LC383967	<i>Ruellia clavigera</i>	636,636	0	100%	LC384092	<i>Thais laticostata</i>	273,279	3.0E-140	100%	
M-DV-094	<i>Nipponosaurus fuscoviridis</i> 1	under registration	LC383961	LC383961	<i>Nipponosaurus fuscoviridis</i>	620,620	0	99%	LC384086	<i>Nipponosaurus fuscoviridis</i>	271,271	4.0E-138	100%	
M-DV-095	<i>Nipponosaurus fuscoviridis</i> 2	under registration	LC383962	LC383962	<i>Nipponosaurus fuscoviridis</i>	620,620	0	94%	LC384087	<i>Nipponosaurus fuscoviridis</i>	283,283	1.0E-144	100%	
M-DV-096	<i>Nipponosaurus fuscoviridis</i> 3	under registration	LC383963	LC383963	<i>Nipponosaurus fuscoviridis</i>	620,620	0	99%	LC384088	<i>Nipponosaurus fuscoviridis</i>	282,284	4.0E-144	100%	
M-DV-097	<i>Nipponosaurus fuscoviridis</i> 4	under registration	LC383964	LC383964	<i>Nipponosaurus fuscoviridis</i>	619,619	0	100%	LC384089	<i>Nipponosaurus fuscoviridis</i>	274,274	4.0E-133	99%	
M-DV-007	<i>Pantoloda saccharina lineis</i> 2	under registration	LC383960	LC383960	<i>Pantoloda saccharina lineis</i>	512,512	0	90%	LC384085	<i>Harpagophylla ruberrima</i>	288,290	5.0E-143	99%	
M-DV-092	<i>Pantoloda saccharina lineis</i> 3	under registration	LC383958	LC383958	<i>Pantoloda saccharina lineis</i>	630,630	0	99%	LC384083	<i>Pantoloda saccharina</i>	291,299	2.0E-147	99%	
M-DV-093	<i>Pantoloda saccharina lineis</i> 4	under registration	LC383959	LC383959	<i>Pantoloda saccharina lineis</i>	630,630	0	99%	LC384084	<i>Harpagophylla ruberrima</i>	281,296	4.0E-139	99%	
M-DV-029	<i>Siphonaria striata</i> 1	under registration	LC383968	LC383968	<i>Siphonaria sp</i>	620,620	0	99%	LC384093	<i>Siphonaria denticalata</i>	256,294	1.0E-119	98%	
M-DV-030	<i>Siphonaria striata</i> 2	under registration	LC383969	LC383969	<i>Siphonaria sp</i>	631,631	0	99%	LC384094	<i>Siphonaria denticalata</i>	273,294	5.0E-118	98%	
M-DV-067	<i>Siphonaria striata</i> 3	under registration	LC383970	LC383970	<i>Siphonaria sp</i>	641,671	0	99%	LC384095	<i>Siphonaria denticalata</i>	254,292	3.0E-120	98%	
M-DV-068	<i>Siphonaria striata</i> 4	under registration	LC383971	LC383971	<i>Siphonaria sp</i>	644,694	0	99%	LC384096	<i>Siphonaria denticalata</i>	250,290	2.0E-116	98%	
M-DV-069	<i>Siphonaria striata</i> 5	under registration	LC383972	LC383972	<i>Siphonaria sp</i>	638,675	0	100%	LC384097	<i>Siphonaria denticalata</i>	254,291	3.0E-120	98%	
M-DV-140	<i>Siphonaria japonica</i> 2	under registration	LC384442	LC384442	<i>Siphonaria sp</i>	630,639	0	99%	LC384343	<i>Siphonaria denticalata</i>	254,298	1.0E-113	96%	
M-DV-141	<i>Siphonaria japonica</i> 3	under registration	LC384443	LC384443	<i>Siphonaria japonica</i>	629,639	0	99%	LC384346	<i>Siphonaria denticalata</i>	254,297	1.0E-113	96%	
M-DV-158	<i>Siphonaria japonica</i> 4	under registration	LC384444	LC384444	<i>Siphonaria sp</i>	630,638	0	99%	LC384347	<i>Siphonaria denticalata</i>	256,301	1.0E-119	98%	
M-DV-024	<i>Omphalotus nigerrimus</i> 1	under registration	LC383976	LC383976	<i>Omphalotus nigerrimus</i>	634,634	0	98%	LC384101	<i>Tagula etnei</i>	295,295	1.0E-134	97%	
M-DV-025	<i>Omphalotus nigerrimus</i> 2	under registration	LC383977	LC383977	<i>Omphalotus nigerrimus</i>	629,639	0	97%	LC384102	<i>Tagula etnei</i>	293,293	6.0E-132	96%	
M-DV-026	<i>Omphalotus nigerrimus</i> 3	under registration	LC383978	LC383978	<i>Omphalotus nigerrimus</i>	630,630	0	98%	LC384103	<i>Tagula etnei</i>	295,295	2.0E-136	97%	
M-DV-027	<i>Omphalotus nigerrimus</i> 4	under registration	LC383979	LC383979	<i>Omphalotus nigerrimus</i>	630,630	0	98%	LC384104	<i>Tagula etnei</i>	281,281	3.0E-125	96%	
M-DV-129	<i>Eurytrochus cognatus</i> 1	under registration	LC383973	LC383973	<i>Eurytrochus cognatus</i>	627,627	0	99%	LC384098	<i>Gibbula zinnata</i>	298,298	1.0E-139	97%	
M-DV-130	<i>Eurytrochus cognatus</i> 2	under registration	LC383974	LC383974	<i>Eurytrochus cognatus</i>	626,626	0	99%	LC384099	<i>Gibbula turbinata</i>	262,262	9.0E-120	97%	
M-DV-131	<i>Eurytrochus cognatus</i> 3	under registration	LC383975	LC383975	<i>Eurytrochus cognatus</i>	626,626	0	99%	LC384100	<i>Gibbula zinnata</i>	297,297	4.0E-139	97%	
M-DV-132	<i>Eurytrochus cognatus</i> 4	under registration	LC383980	LC383980	<i>Eurytrochus cognatus</i>	627,627	0	99%	LC384105	<i>Gibbula zinnata</i>	293,293	6.0E-137	97%	
M-DV-009	<i>Chlorostoma naethoidigma</i> 1	under registration	LC383981	LC383981	<i>Chlorostoma argyrostomum</i>	634,634	0	99%	LC384106	<i>Tagula etnei</i>	286,286	4.0E-124	95%	
M-DV-135	<i>Chlorostoma naethoidigma</i> 2	under registration	LC383982	LC383982	<i>Chlorostoma argyrostomum</i>	644,644	0	99%	LC384107	<i>Tagula etnei</i>	301,301	1.0E-134	96%	
M-DV-136	<i>Chlorostoma naethoidigma</i> 3	under registration	LC383951	LC383951	<i>Chlorostoma argyrostomum</i>	642,642	0	99%	LC384076	<i>Tagula etnei</i>	300,309	4.0E-139	96%	
M-DV-032	<i>Turbo stansgrynus</i> 1	under registration	LC383952	LC383952	<i>Turbo stansgrynus</i>	593,593	0	97%	LC384077	<i>Turbo sp</i>	255,256	3.0E-124	99%	
M-DV-033	<i>Turbo stansgrynus</i> 2	under registration	LC383953	LC383953	<i>Turbo stansgrynus</i>	609,609	0	98%	LC384078	<i>Turbo sp</i>	254,258	5.0E-127	99%	
M-DV-034	<i>Turbo stansgrynus</i> 3	under registration	LC383954	LC383954	<i>Turbo stansgrynus</i>	612,612	0	98%	LC384079	<i>Turbo sp</i>	254,258	5.0E-127	99%	

Outgroup bivalves were selected based on the availability of gene sequence data. We used sequences of *Crassostrea gigas* (Genbank: AB904889) and *Pinctada fucata* [16] (Genbank: GQ355871) for COI. The out groups for H3 were *C. gigas* [17] (Genbank: HQ809488) and *P. fusca* (Genbank: HQ329300) [18].

We made five datasets for phylogenetic analyses: Dataset A: COI sequences; Dataset B: COI sequence with the 3rd codon removed; Dataset C: Histone H3 sequences, D: concatenated A and C dataset, E: concatenated B and C dataset. The outgroup sequences *C. gigas* and *P. fusca* were chimeric on D and E datasets.

Phylogenetic tree of A-E datasets were constructed by two inference methods: the Maximum Likelihood (ML) analysis using RaxmlGUI v.1.5 on the GTR-GAMMA substitution model, with 1000 bootstrap replications [19], and Neighbor-joining (NJ) analysis using MEGA 7 with the partial deletion option and the Maximum Composite Likelihood model, also with 1000 bootstrap replications [20].

RESULTS

Sequencing results and GenBank availability

Using various primers mentioned previously, we succeeded in amplifying both genes of all samples. We obtained 700 bases for COI, and 313 bases for Histone H3. After sequence editing, alignment, and removals ambiguously aligned regions, we obtained 607 positions for COI and 269 positions for Histone H3. When the 3rd codon positions were omitted on COI, 406 positions were left.

All BLAST searches of the obtained COI and H3 sequences using megablast of blastn on the nr databases, hit gastropod sequences of the same families, and, if reference sequence data were available, genera and species (Table1). In COI, reference sequences for nine species were available in Genbank database. The one species hit a congeneric sequence. Meanwhile, for the H3, only the reference sequence of one species was available. six species hit at the genus level, while three species hit only at the family level.

Phylogenetic analysis

Phylogenetic analyses on the datasets A (only COI), C (only H3), and concatenated datasets (D and E) showed well supported trees (Fig2, Fig3). All species were monophyletic in the COI trees, but *Chlorostoma xanthostigma* and *Omphalius*

nigerrimus were not monophyletic in the H3 trees.

The topologies of the COI and H3 gene trees were different (Fig. 2). At the family level, the topologies of both gene trees disagree with morphology-based systematics by Sasaki [21]. For example, *Siphonaria* (Pulmonata) was not included in Neogastropoda, in both gene trees.

On the other hand, ML and NJ analyses on the concatenated datasets resulted in trees with well resolved topologies, regardless of the inclusion of the 3rd codons of COI. Monophyly was observed at the species, genus and order levels in both inference methods. The monophylies at the family and subfamily level were observed on phylogenetic trees inferred on dataset E (COI 3rd codon excluded), but not on trees of dataset D (COI 3rd codon included). For example, Turbinidae was found to be paraphyletic to Trochidae on dataset D trees, while Turbinidae was monophyletic on dataset E trees.

DISCUSSION

Phylogenetic analyses on our concatenated data showed that removing 3rd codon data improves tree topology and the taxonomic placements of samples. Taxonomic grouping of samples also agreed with the morphology-based classification by Sasaki [21]. Mitochondrial genomes are known to have fast evolutionary rates, and thus the 3rd codons of the mitochondrial gene COI were probably saturated [22], causing homoplasies and thus incorrect phylogenetic inference caused by long branch attractions. However, the nuclear gene Histone H3 is known to have a low substitution rate, and was considered useful for phylogenetic analyses at the higher taxonomic levels. Exclusion of the 3rd codon positions of this gene might be detrimental, because of the lack of enough nucleotide variations for phylogenetic inference.

When we use only one gene, all samples were monophyletic at the species level, but at the genus level and above, many clades were taxonomically misplaced. This was remedied when both genes were concatenated and analyzed as a single dataset. However, despite the lack of resolution at the higher taxonomic level, both genes were successful in placing conspecific samples in a single monophyletic group with high bootstrap supports regardless of the inference method (NJ or ML). Therefore, we suggest that both genes are useful to differentiate species for barcoding and

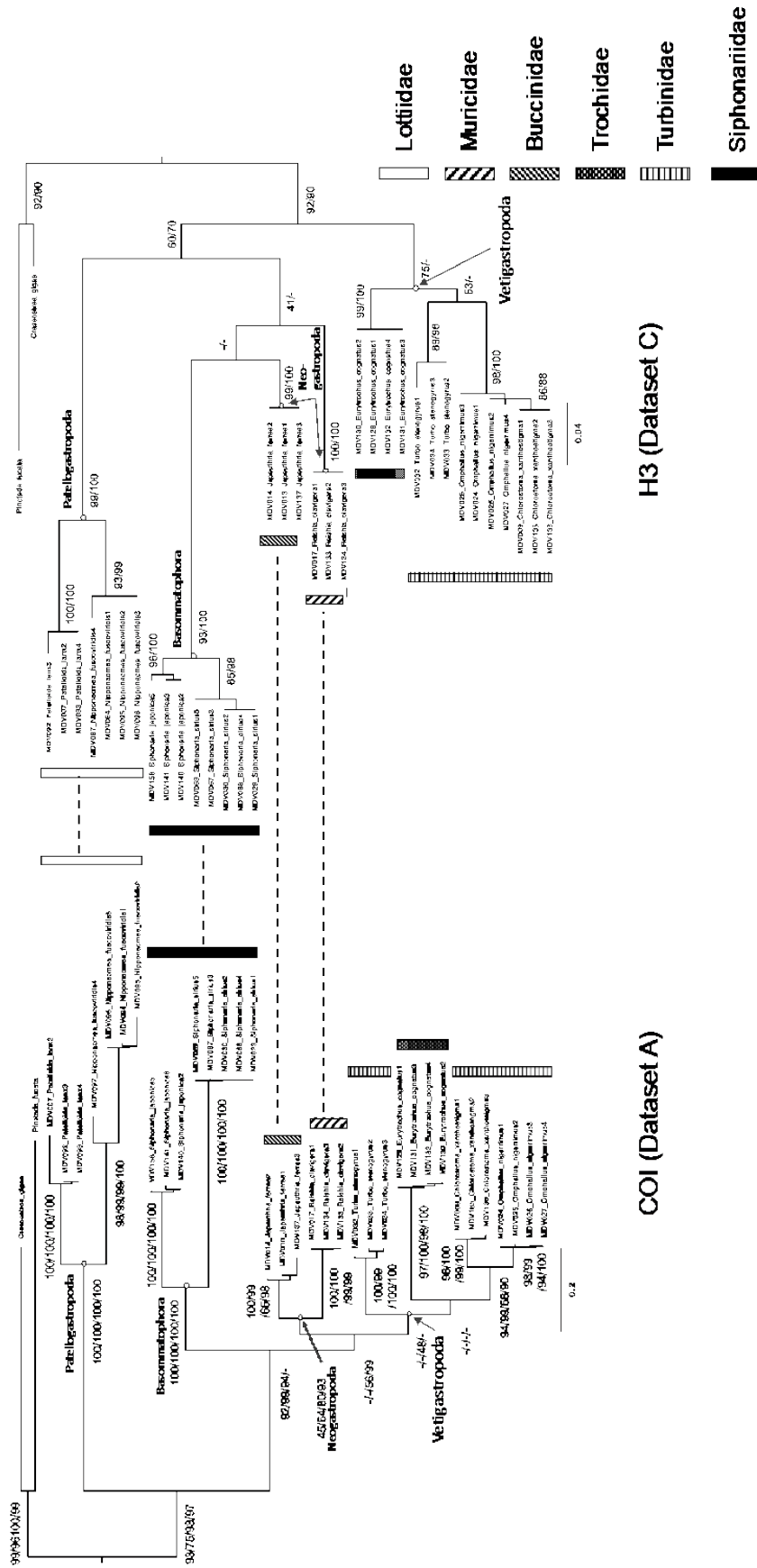


Figure2. Maximum-likelihood tree of our samples under GTR+Gamma model with support rate of Neighbor-joining(NJ) tree. The tree on the right side was analyzed using whole H3 sequence data, while the left one using whole COI sequence data. Numbers above the node represent bootstrap values (1000 replicates).

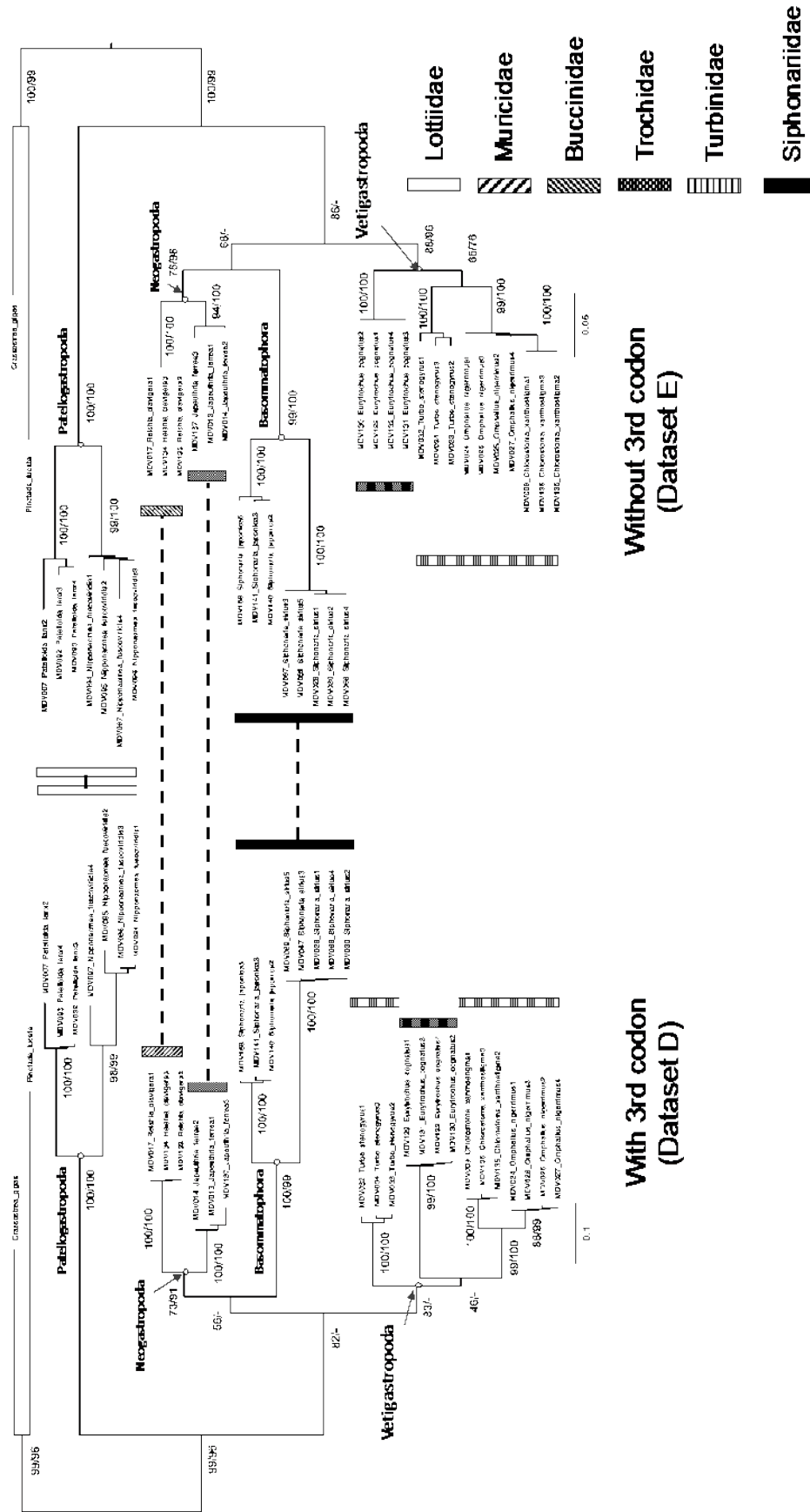


Figure 2. Maximum-likelihood tree of our samples under GTR+Gamma model with support rate of Neighbor-joining(NJ) tree. The tree on the right side was analyzed using whole edited sequence data, while the left one using sequence data of removing no-3rd codon position. The number above the node represent bootstrap analysis after 100 replicates.

identification purposes. All results considered, we thus suggest that using at least two gene markers, the mitochondrial COI and nuclear Histone H3, for barcoding purposes, will provide more reliable results. Moreover, utilizing two gene markers or more is useful as a fail-safe in DNA Barcoding and eDNA studies: one marker gene might pick sequences of organisms uncollected using another marker gene.

CONCLUSION

We were successful in providing novel sequence data for 10 intertidal shelled gastropod species collected from Nada coast in central Wakayama, especially for the Histone H3 gene. Since our samples are vouchered as museum collections (Table. 1), the sequences we provide here will be useful as references for future DNA Barcoding and eDNA studies. Moreover, the sequences could also be useful for future molecular phylogenetic studies on gastropods.

REFERENCES

- [1] Hebert P.D., Cywinska A., Ball S.L., Biological identifications through DNA barcodes, Vol. 270, Issue 1512, 2003, pp. 313–321.
- [2] Appeltan W., Ah Yong S.T., and other 111 authors, The Magnitude of Global Marine Species Diversity, Current Biology, Vol. 22 Issue 23, 2012, pp. 2189–2202.
- [3] Orr J.C., Fabry V.J., Yool A., and other 24 authors, Anthropogenic ocean acidification over the twenty-first century and its impact on calcifying organisms, Nature, Vol. 437, 2005, pp. 681–686.
- [4] Rodolfo-Metalpa R., Houlbàque F., Tambutté É., Boisson F., Gabbini C., Patti F.P., Jeffreev R., Fine M., Foggo A., Gattuso J-P., Hall-Spencer J.M., Coral and mollusk resistance to ocean acidification adversely affected by warming, Nature Climate Change, Vol. 1, 2011, pp. 308–312.
- [5] Fuse S., Nishikawa T., Abe N., Fukui Y., Yamamoto T., Yamanishi R., Reef organisms from the rocky coasts of Nada, Gobo City, Wakayama Prefecture (1). The Nanki Seibutsu, Vol. 21, Issue 1, 1979, pp. 11–17, (In Japanese),
- [6] Fuse S., Nishikawa T., Abe N., Fukui Y., Yamamoto T., Yamanishi R., Reef organisms from the rocky coasts of Nada, Gobo City, Wakayama Prefecture (2). The Nanki Seibutsu, Vol. 21, Issue 1, 1979, pp. 88–101. (In Japanese),
- [7] Teramoto S., Teruya S., Setiamarga D.H.E., Record of a living Chelyconus fulmen (Reeve, 1843) (Gastropoda: Conidae) in Nada-cyo, Gobo-shi, Wakayama Prefecture (In Japanese), The Nanki Seibutsu, Vol. 59, Issue 1, 2017, pp. 104–106.
- [8] Teruya S., Community structure and distribution of intertidal shells on the rocky and boulder shore in Mio, Mihamacho, Wakayama (In Japanese), The Nanki Seibutsu, Vol. 58., Issue 1, 2016, pp. 75–81.
- [9] Okutani T., Marine Mollusks in Japan in Japanese, The Association of Japanese University Presses, 2017.
- [10] Folmer O., Black M., Hoah W., Lutz R., Vrijenhoek R., DNA primers for amplification of mitochondrial cytochrome c oxidase subunit I from diverse metazoan invertebrates, Molecular Marine Biology and Biotechnology, Vol. 3, 1994, pp. 294–299.
- [11] Kano Y., Vetigastropod phylogeny and a new concept of Seguenzioidea: independent evolution of copulatory organs in the deep-sea habitats, Zoological Scripta, Vol. 37, 2008, pp. 1–20.
- [12] Colgan D.J., McLauchlan A., Wilison G.D.F., Livingston S.P., Edgecombe G.D., Macaranas J., Cassis G., Gray M.R., Histone H3 and U2 snRNA DNA sequences and arthropod molecular evolution, Australian journal of Zoology, Vol. 46, Issue 5, 1998, pp. 419–437.
- [13] Katoh, K., Rozewicki J., Yamada K.D., MAFFT online service: multiple sequence alignment, interactive sequence choice and visualization, Briefings in Bioinformatics, bbx108, 2017, pp. 1–7.
- [14] Castresana J., Selection of conserved blocks from multiple alignments for their use in phylogenetic analysis, Molecular Biology and Evolution, Vol. 17, Issue 4, 2002, pp. 540–552.
- [15] Maddisison W., Maddisison D., MESQUITE: a modular system for evolutionary analysis, Evolution Vol. 11, Issue 5, 2009, 824
- [16] Cunha R. L., Blanc F., Bonhomme F. and Arnaud-Haond S., Evolutionary patterns in

- pearl oysters of the genus *Pinctada* (bivalvia: Pteriidae), Vol. 13, Issue 2, 2011, pp. 181–192.
- [17] Bouilly K., Chaves R., Fernandes M. and Guedes-Pinto H., Histone H3 gene in the Pacific oyster, *Crassostrea gigas* Thunberg, 1793: molecular and cytogenetic characterizations, *Comp Cytogenet*, Vol. 4, Issue 2, 2010, pp. 111–121.
- [18] Temkin I., Molecular phylogeny of Pearl and their Relatives (Mollusca, Bivalvia, Pterioidea), *BMC Evolutionary Biology*, Vol. 10, 2010, 342.
- [19] Silvestro D., Michalak I., raxmlGUI: a graphical front-end for RaxML, Vol. 12, Issue 4, 2012, pp. 335–337.
- [20] Kumar S., Stecher G., Tamura K., MEGA7: Molecular Evolutionary Genetics Analysis Version 7.0 for Bigger Datasets, *Molecular Biology and Evolution*, Vol. 33, 2016, pp. 1870–1874.
- [21] Sasaki T., *Malacology* (in Japanese), University of Tokyo Press, 2010, pp. 57–58.
- [22] Phillips M.J., Penny D., The root of mammalian tree inferred from whole mitochondrial genomes, *Molecular Phylogenetic and Evolution*, 2003, Vol. 28, pp. 171–185.

THE EFFECTS OF THAI MASSAGE ON LEG MUSCLE OXYGENATION AND TIME TO FATIGUE IN HEALTHY MALE SUBJECTS

Wirapong Sucharit¹, Wichai Eungpinichpong², Uraiwan Chatchawan³, and PanneePeungsuvan⁴

¹Back, Neck and Other Joint Pain Research Center (BNOJP), Thailand

^{2,3,4} Faculty of Associated Medical Science, KhonKaen University, Thailand

ABSTRACT

Thai massage is a kind of the alternative medicine commonly used in Thailand for relieving of muscle fatigue and pain. Several studies reported that it can increase blood circulation. This may be due to increasing muscle oxygenation and time to fatigue. However, there is no evidence to support. A cross-over study design was employed to evaluate the effects of Thai massage on leg muscle oxygenation, time to fatigue and muscle force. Twenty-five healthy males were allocated to receive isometric exercise by performing series of 10s of sustained contraction and 5s rest until they reach peripheral fatigue point where the quadriceps torque declined to less than 60% of peak torque in the last 10 times (control period). Conversely they received a 60-minutesession of Thai massage before isometric exercise (massage period). The results showed that after massage, the muscle oxygenation was significantly increased ($79.47 \pm 9.24\%$) ($P < 0.05$) when comparing to control period ($75.04 \pm 10.68\%$). In addition, the time to fatigue and quadriceps muscle force revealed no significant differences ($P > 0.05$) although the massage period tended to have more prolonged duration (8.74 ± 2.68 min.) than the control period (7.82 ± 1.79 min), and massage period showed higher quadriceps muscle force. As a result, Thai massage is effective to increase muscle oxygenation levels. Also, it seems to be associated with increased duration of isometric muscle fatigue and higher muscle force.

Keywords: Thai massage, muscle oxygenation, time to fatigue, isometric exercise.

INTRODUCTION

Basic characteristic of Traditional Thai Massage (TTM or Nuad Thai) includes deep pressure massage along the meridian lines (SenSib) of the body using sustained pressure by thumbs, palms or elbows of a practitioner, and muscle stretching technique. Moreover, TTM is also used in many athletes or patients for increasing muscle blood circulation and time to fatigue; however, there is not any evidence to support these methods [1]. Several studies report that TTM can increase skin blood flow, skin temperature, and muscle blood volume, but the study has used Laser Doppler technique where the depth of measurement may not reach the muscle layer, so stimulation of muscle blood flow has not been verified [2].

Recently, near infrared spectroscopy (NIRS) was developed to measure clinical muscle with 17.5mm depth length of measurement. NIRS is a non-invasive technique and multiple-wave-length method based on the principle of Beer-Lambert law used for continuous measurement of muscle blood flow including intravascular hemoglobin (Hb), intra muscular myoglobin (Mb), muscle oxygenation, and tissue oxygen index [3]-[5]. Currently, NIRS has high reproducibility and agreement with gold standard techniques [6]. Previous studies show that NIRS can be used to study both athlete and clinical

assessment [7]-[10].

The sustain isometric muscles contraction increasing intramuscular pressure (IMP) linearly and ultimately reaches a critical level which compresses intramuscular blood vessel resulting in impaired circulation [11], alterations in O₂ delivery, and other substrate. These affect working muscles and lead to lower muscle oxygen saturation throughout exercise [12], which causes increased acidity of blood and muscle cells [13], [14]. Additionally, the study of Hepple [15] on localized muscle fatigue reports that hypoxic or ischemia condition of exercise is related to muscle force decreased. Therefore, oxygen is an important factor contributing to muscle fatigue [16]-[18]. However, the study of Murthy [19] determining the relationship between muscle oxygenation and twitch force demonstrates positive correlation ($r = 0.78$). Also, this study shows that ischemia and muscle hypoxemia is probably the cause of muscle fatigue. Conversely, TTM can increase local muscle microcirculation, lymph flow, and muscle flexibility but reduce muscle stiffness [1]. Thus, this study speculates that TTM may improve muscle oxygenation, time to localized muscle fatigue, and muscle force.

MATERIALS AND METHOD

Subjects

Male healthy subjects were recruited using oral requests and bulletin boards. They were screened by researcher and rechecked by internist using developed inclusion criteria; male between 18-35 years of age, no history of cardiopulmonary problems (i.e. heart arrhythmias, aortic stenosis, pulmonary embolus), no reported hypertension (i.e. uncontrolled hypertension with diastolic above 110mmHg. and systolic above 180 mmHg.) [2], [20]-[21], no present acute pain in isometric exercise [21], and values of adipose tissue thickness (ATT) less than 6.7 mm [5]. Subjects must not recently receive caffeine, nicotine, alcohol, and mixed meal or a glucose load within 30 min well as perform any extensive physical activity [20].

Twenty eight male subjects initially enrolled in this study. But, two subjects dropped out from the study due to loss of follow up in final session. Twenty six subjects (22.62±2.43 years of age; height 173.2±6.6 cm; body mass 68.8±6.9 kg; BMI 22.9±2.0; ATT 3.9±1.2 mm) completed the study. Each subject was informed about the experimental procedures and signed an informed consent statement before taking part in the study. The study was approved by the Human Research Ethics Committee of KhonKaen University (Fig.1).

Procedures

Each of twenty-six male participated in two experimental sessions conducted on separate days. The interval between each session was one week [22] in order to avoid carrying over effects. The subjects who meet the inclusion criteria were randomly assigned to the first experimental session control group or TMM group based on a computer-generated block randomization code. Then they received intervention in reverse order [23].

Before getting into TTM or control group, the subjects were allowed to wear comfortable clothes and familiarized with the testing procedure by performing isometric muscle contraction for 5 times. Later, subjects who were randomized into TTM group were asked to lie in a supine position on a treatment table for one-hour Thai massage by an experienced therapist while control group lie in the same position only. Then both groups received fatiguing protocols using a quadriceps broad connected with electronic scale. The subjects comfortably lied supine with the Rt. Knee joint flexion at 25°-30° on quadriceps broad while the opposite leg was placed in the appropriate posture, and arms were placed across the chest with each hand clasping the opposite shoulder during testing [24]-[28]. The subjects were asked to perform

maximal isometric voluntary contraction (MIVC) i.e. 10s for sustain and 5s for rest until reaching the localized muscle fatigue; the point at which the last 10 contractions decreased less than 60% of peak torque. The peak torque was defined as the highest torque obtained from the first 3 maximal isometric contractions at baseline [29] (Fig.2).

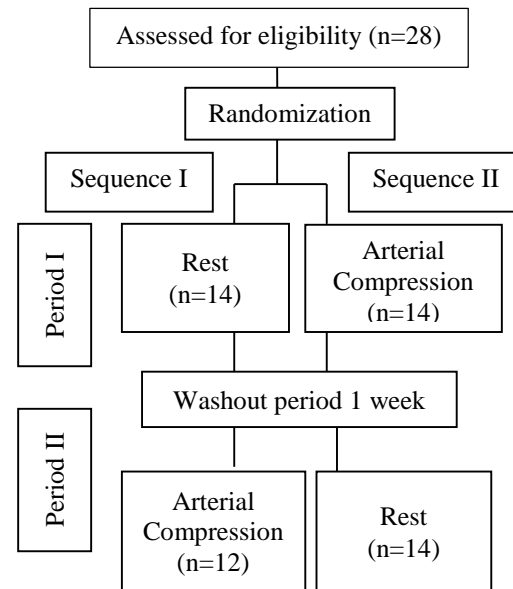


Fig. 1 Procedures of experimental study

Measurements

Muscle oxygenation was measured by NIRS (MOXY oxygen monitor; SROC: $r = 0.842-0.993$, ICC: $r = 0.773-0.992$) [30]. It is noninvasive technique which is able to continuously measure covering after received intervention, highest muscle force period, continuous MVIC to fatigue muscle force period, and recovery period to monitor the changes in muscle tissue saturation. The probe of NIRS was positioned on the belly of right vastus lateralis muscle (about 10 cm from the center of the patella and 25° laterals to the midline of the thigh) [31]. Pen-marks were made in transparent to confirm the margins of the probe to enable reproduction of the placement position in the subsequent procedure. The probe was secured with tape. Then black elastic bandages were wrapped around the leg with MOXY to protect artifacts.

Time to fatigue was recorded by video recording starting from the first MVIC to fatigue point.

The quadriceps muscle force was measured using a quadriceps broad [24] that Rt. distal leg at lateral malleolus was fixed with electronic scale (ICC=0.908) which passed calibrates. Then muscle torque and muscle force were calculated by equation of joint moment as Eq. 1, 2, and 3.

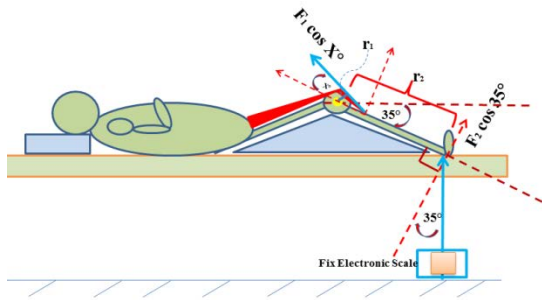


Fig. 2 Position of moment arms and joint angle

Equations

Muscle torque can be calculated based on magnitude of force multiplied by distance from the fulcrum dragged perpendicular to the force as the equations below [32]:

$$F_2 = ma$$

$$F_2 = (kg) (9.8m/s^2) \quad (1)$$

$$M_2 = F_2 \times r_2$$

$$M_2 = F_2 \cos 35^\circ \times r_2 \quad (2)$$

Quadriceps muscle force can be calculated on balance of joint moment.

$$\Sigma M = 0$$

$$M_1 + M_2 = 0$$

$$F_1 \cos X^\circ(r_1) + (-)F_2 \cos 35^\circ(r_2) = 0$$

$$F_1 = F_2 \cos 35^\circ(r_2) / \cos X^\circ(r_1) \quad (3)$$

(M =magnitude of moment or torque, F= magnitude of leg kick (kg), r=distance (m) from the fulcrum dragged perpendicular to the force)

Statistical Analysis

Subjects' baseline characteristics were presented as mean \pm standard deviation (SD). Each variable was evaluated by Shapiro–Wilk test in terms of normal distribution. The carryover effects were measured sequence, period, and treatment effects using cross analysis methods [36] and sample *t*-tests. Comparisons for the dependent variables within groups were analyzed using repeated measures ANOVA. Paired sample *t*-tests analyses were used to compare the pairs of means between groups. Data were analyzed using the SPSS (IBM SPSS, version 23.0). Statistical significance was set at $P < 0.05$.

RESULTS

Muscle Oxygenation

Muscle oxygenation represented data from twenty-six subjects. TTM revealed that muscle

oxygenation was statistically significant higher in muscle oxygenation after received TTM period than control group 4.43% ($79.47 \pm 9.24\%$, $75.04 \pm 10.68\%$; $P < 0.05$ respectively). However, when both of them received MIVC exercise, both TTM and control groups tend to be statistically significant lower in muscle oxygenation ($P < 0.05$) comparing to after received intervention period. Moreover, in recovery period after subjects received MIVC exercise protocol, they showed higher muscle oxygenation of both groups comparing to resting period. However, TTM tended to be higher in recovery muscle oxygenation than control groups without statistical significance (Tab. 1 and Fig.3).

Time to Fatigue

Time to quadriceps muscle fatigue in TTM group (8.74 ± 2.68 min.) was increased to 0.92 min comparing with control group (7.82 ± 1.79 min). However, there was not statistically significant ($P > 0.05$) between groups (Fig.4).

Quadriceps Muscle Force

The highest quadriceps muscle force tended to increase in TTM group (2727.50 ± 860.84 N.) to 156.60 N. comparing with control group (2570.90 ± 669.64 N.), but it was not statistically significant. In addition, the fatigue quadriceps muscle force was higher in TTM (1334.37 ± 449.12 N.) than control group (1218.96 ± 248.42 N.), but it was not statistically significant (Tab.1).

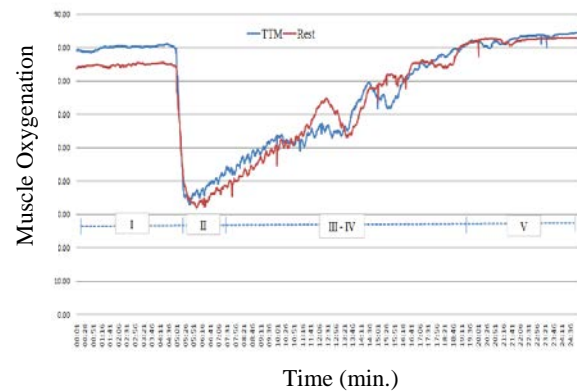


Fig. 3 The mean value of vastus lateralis muscle oxygenation levels (n=26) after received intervention (I), highest muscle force period (II), continuous MVIC to fatigue muscle force period (III-IV), and recovery period (V).

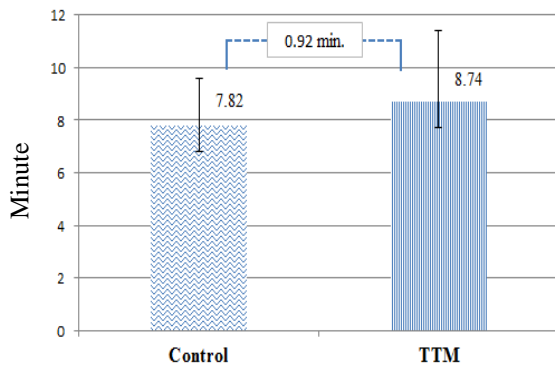


Fig. 4 Time to fatigue between TTM and control group (n=26)

DISCUSSION

TTM affects many mechanism such as mechanical pressure on tissues (increased muscle compliance, ROM, and decreased tissue adhesion) [1] and changes tissue circulation (increased skin and muscle blood flow) described by physiological effects [33]. This investigation evaluates the possible increased muscle oxygenation, time to fatigue, and muscle force.

Influence of TTM can stimulate both skin and muscle blood circulations measured by laser Doppler flow meter. However, this effect is thought to help enhance muscle oxygenation which is measured by NIRS. The present study shows significant increase of muscle oxygenation in period of after received intervention 4.43% after receiving TTM for one hour. This result is consistent with previous studies [1], [33], and it is supported by physiological mechanism. After massage, local heating increases and results in hyperaemia of skin and intramuscular temperature, so O_2 circulated with hemoglobin into myoglobin may be higher. The present study also reveals higher level of muscle oxygenation which agrees with previous studies [3], [4], [6], [9], [33]. Conversely, the study of Weerapong [33] shows that there could be several possible mechanisms such as psycho physiological, biomechanical, and neurological effects. Besides, the result shows that during MVIC exercise at highest muscle force period of both TTM and control group, muscle oxygenation is rapidly lower and gradually increases reversing with the decrease of muscle force until recovery period which tends to be higher in muscle oxygenation comparing to after received intervention period. The present study is different from the study of Murthy [19] in case of measurement method of the muscle contraction amplitude. Murthy uses electrical muscular stimulation, but compression to vascular cannot be seen, so it can lead to positive correlation between muscle oxygenation and muscle force. Nevertheless, the present study discovers negative correlation

between muscle oxygenation and muscle force. This can be described that measurement method implemented in the study has an effect on IMP increases during MVIC exercise that affects mechanical compression of local blood vessel resulting from force of contraction going up that causes an increase in the capillary perfusion. Thus, fluid from the vascular space gets into the interstitial tissue resulting in the increase of IMP [11], [12]. Moreover, MVIC leads to hypoxic condition that causes the decrease of arterial oxygen content (CaO_2). As a result, hypoxic sensor such as endothelium cells, vascular smooth muscle cells, and RBC is stimulated to produce NO and PGs, so higher blood flow and muscle oxygenation was found in recovery period. In addition, in recovery period of TTM group tends to get higher than control group because massage can stimulate the creation of NO, and it is possible to decrease IMP. Nevertheless, further study should be carried on [34], [35].

Time to localized muscle fatigue of TTM group is longer than control group for 0.92 min. that can be seen from muscular acidity. In other words, during isometric exercise, anaerobic respiration is stimulated and inorganic phosphate (P_i) including hydrogen ions (H^+) are produced influencing acidity of blood and muscle cells [14]. Moreover, this acidity slow down enzyme activity, and muscle is aggravated that can lead to nerve ending, pain, and irritation of the central nervous system [14]. On the contrary, the present study shows increased muscle oxygenation that reduces the acidity of the muscle cells. In other words, when O_2 in both blood concentration and muscle oxygenation increases, bicarbonate (HCO_3^-) also increase at the same time, so acidity is lower. This is the theory clarifying that fatigue can be delayed, and exercise can be continuously carried on. However, there is not statistical significance for time to localized muscle fatigue. Also, local muscular fatigue protocol may be inappropriate, so different metabolic demands are imposed.

Highest quadriceps muscle force increase to 156.60 N. after TTM, but there is not statistical significance. However, the increase of muscle force can be explained by physiological effect that massage can increase blood circulation and oxygen delivery to working muscle. Additionally, it can decrease metabolic waste products from anaerobic respiration [33]. On the other hand, during MVIC, metabolic waste products is produced metabolize from anaerobic respiration such as P_i , H^+ and lactic acid. This metabolize is stored within the muscle cells where the P_i is allowed to bind to Ca^{2+} and precipitate, respectively. As a result, Ca^{2+} is decreased, and cross-bridge turnover is decreased, eventually [15].

Table 1 the comparisons of muscle oxygenation, muscle force, and time to fatigue between control and TTM group.

Outcome	Seq.	Period 1 Mean \pm SD	Period 2 Mean \pm SD	Effect size	95% Conf. Interval	<i>P</i>
Mo ₂ after received INT.	1	77.66 \pm 9.95	77.46 \pm 11.19	I (-4.62)	(-8.10 to -1.14)	0.01*
	2	81.48 \pm 7.28	72.42 \pm 11.41	II (0.31)	(-3.38 to 4.00)	0.86
				III (-4.43)	(-7.91 to -1.90)	0.01*
Mo ₂ of highest force	1	25.75 \pm 23.52	24.91 \pm 20.37	I (-4.50)	(-10.12 to 9.22)	0.92
	2	32.14 \pm 26.36	32.07 \pm 26.26	II (-3.38)	(-12.04 to 5.27)	0.42
				III (0.38)	(-9.29 to 10.05)	0.94
Mo ₂ of fatigue force	1	48.83 \pm 27.42	50.33 \pm 22.82	I (-1.54)	(-7.18 to 4.10)	0.57
	2	59.07 \pm 23.62	54.50 \pm 22.49	II (-3.60)	(-12.96 to 5.76)	0.43
				III (-3.04)	(-8.68 to 2.61)	0.28
Mo ₂ of recovery	1	83.83 \pm 7.04	83.25 \pm 7.46	I (-2.26)	(-5.49 to 0.98)	0.16
	2	85.79 \pm 5.06	81.86 \pm 7.28	II (-0.14)	(-2.35 to 2.07)	0.90
				III (-1.67)	(-4.91 to 1.56)	0.30
Highest muscle force	1	2527.39 \pm 599.57	2747.95 \pm 613.80	I (63.96)	(-163.22 to 291.14)	0.57
	2	2707.06 \pm 1107.88	2614.42 \pm 739.70	II (-11.54)	(-318.32 to 295.24)	0.94
				III (-156.6)	(-383.78 to 70.58)	0.17
Fatigue muscle force	1	1222.52 \pm 230.60	1347.71 \pm 427.40	I (9.78)	(-140.18 to 159.75)	0.90
	2	1321.034 \pm 70.84	1215.40 \pm 266.23	II (8.45)	(-119.40 to 136.30)	0.90
				III (-115.41)	(-265.37 to 34.55)	0.12
Time to Fatigue	1	7.56 \pm 2.21	8.90 \pm 2.65	I (0.41)	(-0.83 to 1.65)	0.50
	2	8.59 \pm 2.70	8.08 \pm 1.37	II (-0.06)	(-0.77 to 0.66)	0.88
				III (-0.92)	(-2.16 to 0.33)	0.14

Abbreviations: INT.; Intervention, I; Period effect, II; Carryover effect and III; Treatment effect

Note: The data were presented using mean \pm SD which were analyzed by cros analysis (method of Alman DG.).

**P* < 0.05

CONCLUSION

This study evaluated the effects of TTM on muscle oxygenation, time to fatigue, and muscle force. The results show that TTM increases muscle oxygenation after received intervention period, and it seems prolong duration of time to fatigue and higher muscle force. It would be interesting to characterize the effect of TTM for boxing, tennis or endurance exercise and to analyze its possible influence on muscle oxygenation, time to fatigue, and muscle force in the subsequent performance.

ACKNOWLEDGEMENTS

Financial support for this research is granted by Back, Neck and Other Joint Pain Research Center (BNOJP), and this research work is partially supported by Thai massage room at 5th floor, Faculty of Associated Medical Science, Khon Kaen

University, Thailand.

REFERENCES

- [1] Buttagat V, Eungpinichpong W, Chatchawan U, Araya wichanon P. Therapeutic effects of traditional Thai massage on pain, muscle tension and anxiety in patients with scapula costal syndrome: A randomized single-blinded pilot study. J Body wMovTher, Vol. 16, Issue 1, 2012, pp.57-63.
- [2] Eungpinichpong W and Kongnaka T., Effects of femoral artery temporarily occlusion on skin blood flow of foot.JMed tech Ther, Vol. 14, Issue 2, 2002, pp. 151-159.
- [3] Hamaoka, T.,Muscle oxygenation monitoring using near-infrared spectroscopy. J. Phys. Fit. Sports Med., Vol. 2, 2013, pp. 203–207.
- [4] Ferrari, M., Muthalib, M., Quaresima, V., The use of near-infrared spectroscopy in

- understanding skeletal muscle physiology: recent developments. *Philos. Trans. R. Soc. Math. Phys. Eng. Sci.*, Issue 369, 2011, pp. 4577–4590
- [5] Van Beekvelt, M.C.P., Borghuis, M.S., Van Engelen, B.G.M., Wevers, R.A., Colier, W., Adipose tissue thickness affects in vivo quantitative near-IR spectroscopy in human skeletal muscle. *Clin.Sci.*, Issue 101, 2001, pp.21–28.
- [6] Jones, S., Chiesa, S.T., Chaturvedi, N., Hughes, A.D., Recent developments in near-infrared spectroscopy (NIRS) for the assessment of local skeletal muscle microvascular function and capacity to utilise oxygen. *Artery Res.*, Issue 16, 2016. pp. 25–33.
- [7] Allart, E., Olivier, N., Hovart, H., Thevenon, A., Tiffreau, V., Evaluation of muscle oxygenation by near-infrared spectroscopy in patients with Becker muscular dystrophy. *Neuromuscul.Disord*, Issue 22, 2012, pp. 720–727.
- [8] Amann, M., Calbet, J.A.L., Convective oxygen transport and fatigue. *J. Appl. Physiol.* Issue 104, 2008, pp. 861–870.
- [9] Kragelj, R., Jarm, T., Erjavec, T., Prešern-Štrukelj, M., Miklavčič, D., Parameters of Postocclusive Reactive Hyperemia Measured by Near Infrared Spectroscopy in Patients with Peripheral Vascular Disease and in Healthy Volunteers. *Ann. Biomed. Eng.*, Issue 29, 2001, pp. 311–320.
- [10] Shang, Y., Gurley, K., Symons, B., Long, D., Srikueta, R., Crofford, L.J., Peterson, C.A., Yu, G., Noninvasive optical characterization of muscle blood flow, oxygenation, and metabolism in women with fibromyalgia. *Arthritis Res.Ther.*, Issue 14, 2012, pp. 236.
- [11] Crenshaw A.G., Karlsson S., Gerdle B., Friden J. Differential responses in intramuscular pressure and EMG fatigue in dicators during low-Vs. high- level isometric contraction to fatigue. *ActaphysiolScand*, Issue 160, 1997, pp. R353–361
- [12] Chris J. McNeil, Matti D. Allen, Eric Olympico, J. Kevin Shoemaker and X Charles L. Rice. Blood flow and muscle oxygenation during low, moderate, and maximal sustained isometric contractions. *Am J PhysiolRegulIntegr Comp Physiol*, Issue 309, 2015, pp. R475–R481.
- [13] Kawahara Y, Saito Y, Kashimura K, Muraoka I., Relationship between muscle oxygenation kinetics and the rate of decline in peak torque during isokinetic knee extension in acute hypoxia and normoxia. *Int J Sports Med.*, Vol.29, Issue5, 2008, pp. 379–83.
- [14] Allen DG, Lamb GD, Westerblad H., Skeletal muscle fatigue: cellular mechanisms. *Physiol Rev.*, Vol. 88, Issue 1, 2008, pp. 287–332.
- [15] Hepple RT, Hagen JL, Krause DJ. Oxidative capacity interacts with oxygen delivery to determine maximal O₂ uptake in rat skeletal muscles in situ. *The Journal of Physiology*, Issue 541, 2002, pp. 3
- [16] Hogan, M.C., Richardson, R.S. and Kurdak, S.S (1994). Initial fall in skeletal muscle force development during ischemia is related to oxygen availability. *J. Appl. Physiol.*, Issue 77, 1994, pp. 2380–2384.
- [17] Hogan, M.C., Richardson, R.S. and Haseler, L.j. Human muscle performance and PCr hydrolysis with varied inspired oxygen fractions: A P-MRS study. *J.Appl.Physiol.*, Issue 86, 1999a, pp. 1367–1373.
- [18] Hogan, M.C., Kohin, S., Stary, C.M., and Hepple, R.T. (1999b). Rapid force recovery in contracting skeletal muscle after brief ischemia is dependent on O₂ availability. *J.Appl.Physiol.*, Issue 87, 1999b, pp. 2225–2229.
- [19] Murthy G, Alan R. Hargens, Steve Lehman, David M. Rempel. Ischemia causes muscle fatigue. *J Orthopaedic*, Vol. 19, 2001, pp. 436–440.
- [20] Staron, R.S., Hagerman, F.C., Hikida, R.S., Murray, T.F., Hostler, D.P., Crill, M.T., Ragg, K.E., Toma, K., Fiber type composition of the vastus lateralis muscle of young men and women. *J. Histochem. Cytochem.*, Issue 48, 2000, pp. 623–629.
- [21] Wu, S.C., Crews, R.T., Najafi, B., Slone-Rivera, N., Minder, J.L., Andersen, C.A., Safety and efficacy of mild compression (18–25 mm Hg) therapy in patients with diabetes and lower extremity edema. *J. Diabetes Sci. Technol.*, Issue 6, 2012, pp. 641–647.
- [22] Rathmacher EA., Fuller Jr JC., Baier SM., Abumrad NN., Angus HF. and Sharp RL .Adenosine-5'-triphosphatesupplementation improves low peak muscle torque and torque fatigue during repeated high intensity exercise sets. *Journal of the International Society of Sports Nutrition*, Issue 9, 2012, pp. 48
- [23] Mori H, Ohsawa H, Tanaka TH, Taniwaki E, Ceisman G, Nishijo K. Effect of massage on blood flow and muscle fatigue CR following isometric lumbar exercise. *Med SciMonit.*, Vol.10, Issue5, 2004, pp. CR173–178
- [24] Kim WK, MD., Kim DK., MD, Seo KM., MD, Kang SH., MD. Reliability and Validity of Isometric Knee Extensor Strength Test With Hand-Held Dynamometer Depending on Its Fixation: A Pilot Study. *Ann Rehabil Med.*, Vol. 38, Issue 1, 2014, pp. 84–93
- [25] Joshua M. Drouin Æ Tamara C. Valovich-mcLeod Sandra J. Shultz Æ Bruce M. Gansneder David H. Perrin. 2004, Reliability and validity of the Biodex system 3 pro

- isokinetic dynamometer velocity, torque and position measurements. *Eur J Appl Physiol.*, Issue 91, 2004, pp. 22–29
- [26] Jenny Toonstra and Carl G. Mattacola., Test–Retest Reliability and Validity of Isometric Knee-Flexion and -Extension Measurement Using 3 Methods of Assessing Muscle Strength. *Journal of Sport Rehabilitation*, 2013
- [27] K Takey, OA Kandil, SNA Elazm. Isokinetic quadriceps peak torque, average power and total work at different angular knee velocities. *Nat Conference of PhysTher Cairo.*, 2009
- [28] Katoh M, Hiiragi Y and Uchida M. Validity of Isometric muscle strength measurement of the lower limbs using a HHD and Belt : a comparison with an Isokinetic Dynamometer. *J.phys.Ther.Sci.*, Issue 23, 2011, pp.553-557.
- [29] Yeung, S.S., Ting, K.H., Hon, M., Fung, N.Y., Choi, M.M., Cheng, J.C., Yeung, E.W., Effects of Cold Water Immersion on Muscle Oxygenation During Repeated Bouts of Fatiguing Exercise: A Randomized Controlled Study. *Medicine (Baltimore)*, Issue 95, 2016.
- [30] Crum EM, O'Connor WJ, Van Loo L, Valckx M, Stannard SR. Validity and reliability of the Moxy oxygen monitor during incremental cycling exercise. *Eur J Sport Sci.*, Vol. 17, Issue 8, 2017, pp. 1037-1043.
- [31] Kennedy, M.D., Haykowsky, M.J., Boliek, C.A., Esch, B.T., Scott, J.M., Warburton, D.E., Regional muscle oxygenation differences in vastus lateralis during different modes of incremental exercise. *Dyn.Med.*, Issue 5, 2006, pp. 8.
- [32] Sherman M, Seth A, Delp S. How to compute muscle moment arm using generalized coordinates. Retrieved January 20, 2017, from <https://simtk-confluence.stanford.edu>.
- [33] Pornratshanee Weerapong, Patria A. Hume and Gregory S. Kolt., The Mechanisms of Massage and Effects on Performance, Muscle Recovery and Injury Prevention. *Sports Med* 2005, Vol. 35, Issue 3, 2005, pp. 235-256.
- [34] Hoffmann U, Uckay I, Fischer M, Wen F, Franzeck UK, Bollinger A. Simultaneous assessment of muscle and skin blood fluxes with the laser-Doppler technique. *Int J Microcirc*, Issue 15, 1995, pp. 53-9.
- [35] Dinunno FA. Skeletal muscle vasodilation during systemic hypoxia in humans. *Journal of Applied Physiology.*, Vol. 120, Issue 2, 2016, pp.216-225
- [36] Altman DG. (1991) *Practical Statistics for Medical Research*. Chapman and Hall, London

APPLICATION OF SCMR AND FLUORESCENCE FOR CHLOROPHYLL MEASUREMENT IN SUGARCANE

Darika Bunphan^{1*}, Naris Sinsiri¹ and Ruchuon Wanna¹

¹Department of Agricultural Technology Faculty of Technology, Mahasarakham University,
Mahasarakham 44150, Thailand

*Corresponding author: e-mail; darika.bu@msu.ac.th

ABSTRACT

Chlorophyll is necessary for photosynthesis in plant and also affecting for crop yield, chlorophyll can be directly measured however, that method is destructive leaves. In sugarcane, indirect methods were used for drought or stress condition however literature is lacking for normal condition. The objective of this research was to study on relationship between directly and indirectly chlorophyll measurement. The experiment was conducted under two locations in Mahasarakham Thailand. RCBD with 4 replications and 16 varieties were used. The chlorophyll content (CC), SPAD chlorophyll meter reading (SCMR) and chlorophyll fluorescence (CF) were measured five times and a month interval between 8-12 months after planting. The results revealed that CC and SCMR of sixteen varieties in both locations were significantly different however, CF was not significantly different. The interaction between location and varieties were found. The relationships between methods of measurement were also found. At Kut Rung, CC and SCMR was positive correlated in 8 to 12 months except 11 months (0.71**, 0.55*, 0.77** and 0.78** respectively). Another location, CC and SCMR was correlated in 8 and 9 months (0.51* and 0.73** respectively) and CF was not correlated with CC and SCMR. Combined analysis, CC was positive correlated with SCMR at 8-12 months except 11 months (0.61*, 0.55*, 0.63** and 0.50* respectively). SCMR is a useful strategy for indirectly chlorophyll measurement in sugarcane. However, CF could not apply for measurement in this case. For further research, we are looking for relationship between chlorophyll content and sugarcane yield or other desirable characteristics in sugarcane.

Keywords: Correlation, Chlorophyll content, SPAD chlorophyll, SCMR

INTRODUCTION

Sugarcane (*Saccharum officinarum* L.) is known as effective crop for sugar and biomass production according to bio-fuel production. It can produce high cane yield and high quality of juice, however seem to be greatly reduced by drought stress and others [1]. Sugarcane is one of the most important cash crop in Thailand which occupies around 1.76 million ha [2], and most of sugarcane production in Thailand is under rain-fed condition and drought is usually appearance during growth season and it affect to reduce growth and yield of sugarcane. Several previously researches studied on effect of drought to physiological characteristics such as chlorophyll content, SCMR [3]-[5], chlorophyll fluorescence [5], cane yield [6]-[7], root length, root dry weight, root/shoot ratio, stalk diameter and biomass [8]. Chlorophyll is a pigment that is important for photosynthesis in plant and also related to crop yield. Photosynthetically active radiation (PAR) is absorbed by chlorophyll and accessory pigments of chlorophyll protein complexes and related to PS I and II [9]. Analysis of chlorophyll content is important for evaluating health or detecting and quantifying plants tolerance to drought stress [10]. Chlorophyll measurement can be measured both direct and

indirect methods however direct method must be destructive leaves, expensive, laborious and time consuming. Indirect methods are the alternative methods which are more rapid and straightforward. Generally, chlorophyll measurements are usually using for drought condition for detecting drought tolerance in plant including sugarcane, however literature is lacking for normal condition and the relationship between direct and indirect methods require more study in normal condition. Therefore, the objective of this research was to study on relationship between directly and indirectly chlorophyll measurement to determine the rapid and accurate methods for chlorophyll measurement in sugarcane.

MATERIAL AND MATHEODS

Plant Material

Sixteen varieties of sugarcane namely KK06-501, KK07-478, NSUT08-22-3-13, RT2004-085, CSB06-2-15, CSB06-2-21, CSB06-4-162, CSB06-5-20, TBy27-1385, TBy28-0348, MPT02-458, MPT03-166, 91-2-527, KK3, LK92-11 and KPS01-12 were used. All of varieties were improved from government agency and private company in Thailand.

Experimental design

The experiment was conducted in 2016-2017 under rain-fed condition at two locations in Maha Sarakham province where is located in Northeast of Thailand. The first location was Kut Rang district and 16 varieties were planted in November 9 2016. Another location was Wapi Prathum district, it is and sugarcane was planted in December 18 2016. The experiment was laid out in randomized complete block design (RCBD) with 4 replications, 4 rows a plot, 50 cm between plant and 130 cm between row, plot size was $5.2 \times 5 \text{ m}^2$ (Wapi Prathum district) and $5.2 \times 6 \text{ m}^2$ (Kut Rang district). Chemical fertilizer formula 15-15-15 at rate 50 kg/rai at 4 and 6 months after planting.

Data Collection

Chlorophyll content (CC), SPAD chlorophyll meter reading (SCMR) and chlorophyll fluorescence (CF) were observed 5 times from 8 to 12 months after planting and a month interval, three parameters were measured on 2nd or 3rd expanded leaf from the top. The SCMR was measured using by SPAD-502 meter (Minolta SPAD-502 meter, Tokyo, Japan). The data points were recorded at three positions along the length of leaf blade (avoid veins and midribs) and then data points were averaged as a single value. The CC in leaves was measured by the method described by Moran [11]. Briefly the leaf was cut one small leaf disc with the area 1 cm^2 using cork border, the leaf disc was placed in a vial containing 5 ml DMF (N, N-dimethylformamide) and incubated in 4°C for 24 h in dark. The chlorophyll extract was measured at 647 and 664 nm by spectrophotometer. The equations to calculate for total chlorophyll, chlorophyll a (Chl a) and b (Chl b) were as follows: $\text{Chl a} = 12.64 A_{664} - 2.99 A_{647}$, $\text{Chl b} = -5.6 A_{664} + 23.24 A_{647}$, expressed in $\mu\text{g cm}^{-2}$. The CF was measured two positions in middle of leaf and midrib was avoided, Fv/Fm was used and averaged as single value, the CF was measured using chlorophyll fluorescence meter (PAM-2000, Heinz Walz GmbH, Germany). The measured leaf was dark-adapted for 30 min using leaf clips (FL-DC, Opti-Science) before fluorescence measurements. The chlorophyll fluorescence was determined following the procedures of Maxwell and Johnson [12].

Statistical Data Analysis

Analysis of variance (ANOVA) was conducted on the collected data using STATISTICS 9 and treatment means were separated using DMRT at 5 % probability level. Location \times treatment was analyzed and correlation among CC SCMR and CF were done.

RESULTS AND DISCUSSIONS

The results showed that SCMR and CC were significantly different in both locations however, CF was not significantly different.

For combine analyzed between location we

found interaction between location and varieties in SCMR and CC and also two parameters were significantly difference, however an interaction between CF was not found. At 8 months after planting, KKU06-501 had the highest SCMR (44.15 SPAD Unit) following CSB06-2-21 and NSUT08-22-3-13 (42.30 and 41.86 SPAD unit, respectively), however, at 9 months NSUT08-22-3-13 had the highest SCMR following KK06-501 (42.06 and 40.76 SPAD unit, respectively). Whereas 91-2-527 had the highest SCMR at 10 months following RT2004-085 and CSB06-2-15, however at 11 and 12 months KK06-501 had the highest SCMR (40.73 and 40.13 SPAD unit, respectively) following CSB06-4-162 (40.09 and 39.24 SPAD unit, respectively) (Table 1). In previous studies, SCMR was measured at 90, 100 and 110 days after transplanting (DAT), they reported that SCMR at 90 and 110 DAT compared between drought and FC was not significantly different (average SCMR at 90 and 100 DAT was 33.23 and 33.44 SPAD unit, respectively) but SCMR at 100 DAT had significant between stress and FC (27.36 and 30.06 SPAD unit, respectively) [3]. In normal condition, SCMR was observed at 60, 90, 120 and 150 days after planting (DAP), they found that increasing trend of SCMR up to 120 DAP in all promising clones and decreasing trend was noticed in some clones and SCMR of all clones was under 50 SPAD unit [6] and this value was similar to present study however, in present study SCMR was observed during 8 to 12 months after planting whereas previous study was done 4 times during 60-150 DAP. Sudhakar [4] reported that SCMR at 60 and 120 DAP of 14 genotypes under irrigated condition was significantly different and the value ranged between 35.0 to 40.5 for 60 DAP and 35.5 to 46.6 for 120 DAP, the SCMR values were slightly lower than present study. Radhamani, Kannan and Pakkiyappan [13] reported that SCMR at 3 growth stages was investigated in 15 cultivars of sugarcane and they showed significant at different stages, an average SCMR value at tillering, grand growth and maturity was 24.34, 24.04 and 22.00 respectively. SCMR value at 120 DAP of 12 cultivars was significant that ranged between 39.63 to 51.15 [14]. Moreover, SCMR was measured in other crops in normal condition i.e. sweet sorghum [15], [16], sorghum and barley. The SCMR of sweet sorghum in 50% days to flowering ranged between 36.03-48.36 that the values were not different with sugarcane and SCMR had related to biomass yield ($r=0.39^*$) [15] but this relationship did not study in our research. It would be studied in further research.

Chlorophyll content (CC) at Kut Rung was significantly different all of five times interval a month during 8-12 months. At 8 months, NSUT08-22-3-13 had highest CC whereas KK06-501 had the highest CC at 9 months, however at 10 months both variety NSUT08-22-3-13 and CSB06-5-20 had

highest CC, moreover NSUT08-22-3-13 had the highest CC at 11 months as well and CSB06-4-162 had the highest CC at 12 months (data not show). The CC at Wapi Prathum district was significantly different, KK06-501 had the highest CC at 8 months whereas CSB06-5-20 had the highest CC at 9 months.

However, at 10 months CSB06-2-15 gave the highest CC and MPT02-458 gave the highest CC at 11 months, 91-2-527 have the highest CC in 12 months (data not show).

Table 1 SCMR of 16 sugarcane varieties during 8-12 months after planting under two locations

variety	SCMR (SPAD unit)				
	8 m	9 m	10 m	11 m	12 m
KK06-501	44.15a	40.76ab	35.04abc	40.73a	40.13a
KK07-478	37.94c-g	33.18e	29.20e	33.30fgh	33.49cde
NSUT08-22-3-13	41.86abc	42.06a	34.86abc	34.66d-h	33.78cde
RT2004-85	37.90d-g	33.31e	35.63ab	36.05c-f	36.37a-d
CSB06-2-15	40.14b-f	39.28abc	35.60ab	36.40cde	39.16ab
CSB06-2-21	42.30ab	37.20bcd	31.81d	36.70cd	35.40bcd
CSB06-4-162	41.45a-d	37.94bc	33.69a-d	40.09ab	39.24ab
CSB06-5-20	37.85d-g	37.54bcd	35.01abc	33.69e-h	32.06de
TBy27-1385	41.13a-d	37.03cd	34.25a-d	32.84ghi	33.63cde
TBy28-0348	35.56g	36.08cde	32.01d	38.28abc	36.66abc
MPT02-458	37.06efg	36.50cde	35.53ab	36.60cd	36.14a-d
MPT03-166	36.50fg	34.18de	31.81d	35.45c-g	33.78cde
91-2-527	40.74a-e	36.43cde	35.86a	37.38bcd	39.09ab
KK3	38.61b-g	38.74abc	34.20a-d	32.08hi	33.80cde
LK92-11	39.04b-g	36.60cde	32.71cd	30.08i	32.41cde
KPS01-12	40.56a-e	37.48bcd	33.21bcd	34.71d-h	29.64e
F-test	**	**	**	**	**
CV (%)	10.07	9.71	7.54	8.02	12.31

** significant at $P < 0.01$,

Mean in the same column followed by the same letter(s) are not significantly different

For combined analysis, CC was significantly at 8-12 months except 11 months after planting. At 8 months, both variety KK06-501 and CSB06-4-162 gave the highest CC following NSUT08-22-3-13 (8.92, 8.68 and 7.41 $\mu\text{g cm}^{-2}$ respectively). At 9 months we found that CSB06-2-15 had the highest CC following CSB06-5-20, whereas NSUT08-22-3-13 showed the highest CC at 10 months following CSB06-5-20 and CSB06-2-15 and 12 months CSB06-4-162 had the highest CC following 91-2-527 and KK06-501 (8.84, 8.41 and 8.26 $\mu\text{g cm}^{-2}$ respectively) (Table 2). The previous researches, chlorophyll content under drought and field capacity (FC) was not significantly different at 90 and 110 except 100 DAT, it was different CC between drought and FC (3.78 and 6.64 $\mu\text{g cm}^{-2}$ respectively). The average CC of 10 cultivars ranged between 4.07 to 7.65 (90 DAT), 4.07 to 6.07 (100 DAT) and 4.89 to 9.21 $\mu\text{g cm}^{-2}$ (110 DAT) [3], in the one hand, total chlorophyll under stress was lower than non-stress condition [17], that results were slightly lower than

present study especially CC under FC condition because present research studied on non-stress condition and chlorophyll content was observed at different growth stage. Chlorophyll content was measured under non-stress condition at 3 growth stage; tillering, grand growth and maturity stage, the results showed that chlorophyll content of 15 varieties had significant and total chlorophyll content decreased with stage of plant [13]. However, present study chlorophyll content was observed 5 times and a month interval therefore the results of both study was different.

The association between SCMR, CC and CF, at Kut Rung, CC and SCMR were positive correlated in 8 to 12 months except 11 months (0.71**, 0.55*, 0.77** and 0.78** respectively) (data not show). For another location, CC and SCMR were positive correlated only in 8 and 9 months (0.51* and 0.73** respectively) (data not show) and CF was not correlated with CC and SCMR.

Table 2 Chlorophyll content (CC) of 16 sugarcane varieties during 8-12 months after planting under two locations

variety	Chlorophyll content ($\mu\text{g cm}^{-1}$)				
	8 m	9 m	10 m	11 m	12 m
KK06-501	8.92a	9.03abc	13.85a-d	5.89	8.26ab
KK07-478	5.09e	5.70g	12.56efg	4.81	4.97e
NSUT08-22-3-13	7.41b	8.40a-e	14.94a	6.29	7.07bcd
RT2004-85	5.93cde	8.24a-e	12.89d-g	6.56	5.77de
CSB06-2-15	6.73bc	9.39a	14.48ab	6.14	6.11cde
CSB06-2-21	6.14cde	7.88c-f	12.31fg	5.36	5.97cde
CSB06-4-162	8.68a	8.74a-d	14.16abc	6.04	8.84a
CSB06-5-20	6.50bcd	9.37ab	14.63ab	4.87	7.37bc
TBy27-1385	6.53bcd	7.72c-f	12.54efg	4.61	5.97cde
TBy28-0348	6.42bcd	6.69fg	12.21fg	6.54	6.74cd
MPT02-458	5.96cde	7.19ef	13.97a-d	7.24	6.65cd
MPT03-166	5.63cde	8.12a-e	12.04g	5.79	7.27bc
91-2-527	6.11cde	7.53def	13.76a-e	6.21	8.41ab
KK3	6.06cde	7.49def	12.95c-g	4.86	6.30cde
LK92-11	5.84cde	8.04b-e	13.80a-d	6.24	6.71cd
KPS01-12	5.31de	8.79a-d	13.44b-f	4.88	6.16cde
F-test	**	**	**	ns	**
CV (%)	19.55	16.95	9.23	19.94	21.05

** and ns; significant at $P < 0.01$ and not significant,

Mean in the same column followed by the same letter(s) are not significantly different

For combined analysis, the correlation coefficients between SCMR and CC were calculated from means of 16 sugarcane cultivars of two locations we found that SCMR had positive correlated with CC at 8-12 months except 11 months after planting.

At 8 months after planting, the correlation coefficient between SCMR and CC was positive and significant ($r=0.61$, $p \leq 0.05$) (Fig. 1a). At 9 months, SCMR had positive correlated with CC and significantly different ($r=0.55$, $p \leq 0.05$) (Fig. 1b) whereas at 10 months the relationship between SCMR and CC was positive and highly significant ($r=0.63$, $p \leq 0.01$) (Fig. 1c) and 12 months, the correlation coefficient between SCMR and CC was positive and significant different ($r=0.50$, $p \leq 0.05$) (Fig. 1d). For previous studies, the correlation coefficients between chlorophyll content and SCMR were calculated from means of 10 sugarcane cultivars at 90 and 100 DAT ($r=0.78^{**}$, 0.74^{**}) [3] whereas SCMR and CC were calculated from 15 cultivars and significant correlation was found ($r=0.833^{**}$) [13]. The relationship between SCMR and chlorophyll content of 24 cultivars both control and iron deficiency had positive correlated (0.900^{**}) [18], this results were slightly higher than present study. In species more closely related to sugarcane such as sweet sorghum, the relationship between SCMR and

CC was found during 40 to 100 DAP [16], wheat ($r=0.90$) [19] and also found in maize [20], moreover SCMR was positively correlated with biomass yield in sweet sorghum ($r=0.39^{**}$) [15]. However, SCMR had positive correlated with other traits i.e. stalk number and tiller number ($r=0.72^{*}$ and 0.77^{**} respectively) [7].

CONCLUSION

Chlorophyll content and SCMR of 16 varieties in both locations were significantly different however, CF was not significantly different. The interaction between location and varieties were found. The relationships between methods of measurement were also found. At Kut Rung, CC and SCMR had correlated in 8 to 12 months except 11 months (0.71^{**} , 0.55^{*} , 0.77^{**} and 0.78^{**} respectively). For another location, CC and SCMR were correlated in 8 and 9 months (0.51^{*} and 0.73^{**} respectively) and CF was not correlated with CC and SCMR both locations. Combined analysis, CC was significantly correlated with SCMR in 8 to 12 months except 11 months (0.61^{*} , 0.55^{*} , 0.63^{**} and 0.50^{*} respectively). SCMR is a useful tool for indirectly chlorophyll measurement in sugarcane. However, CF could not apply for measurement in this case. For the further study, we are looking forward using the

knowledge from present study to estimation yield or desirable traits in sugarcane. It could be alternative

methods for selection or investigation good performances of sugarcane.

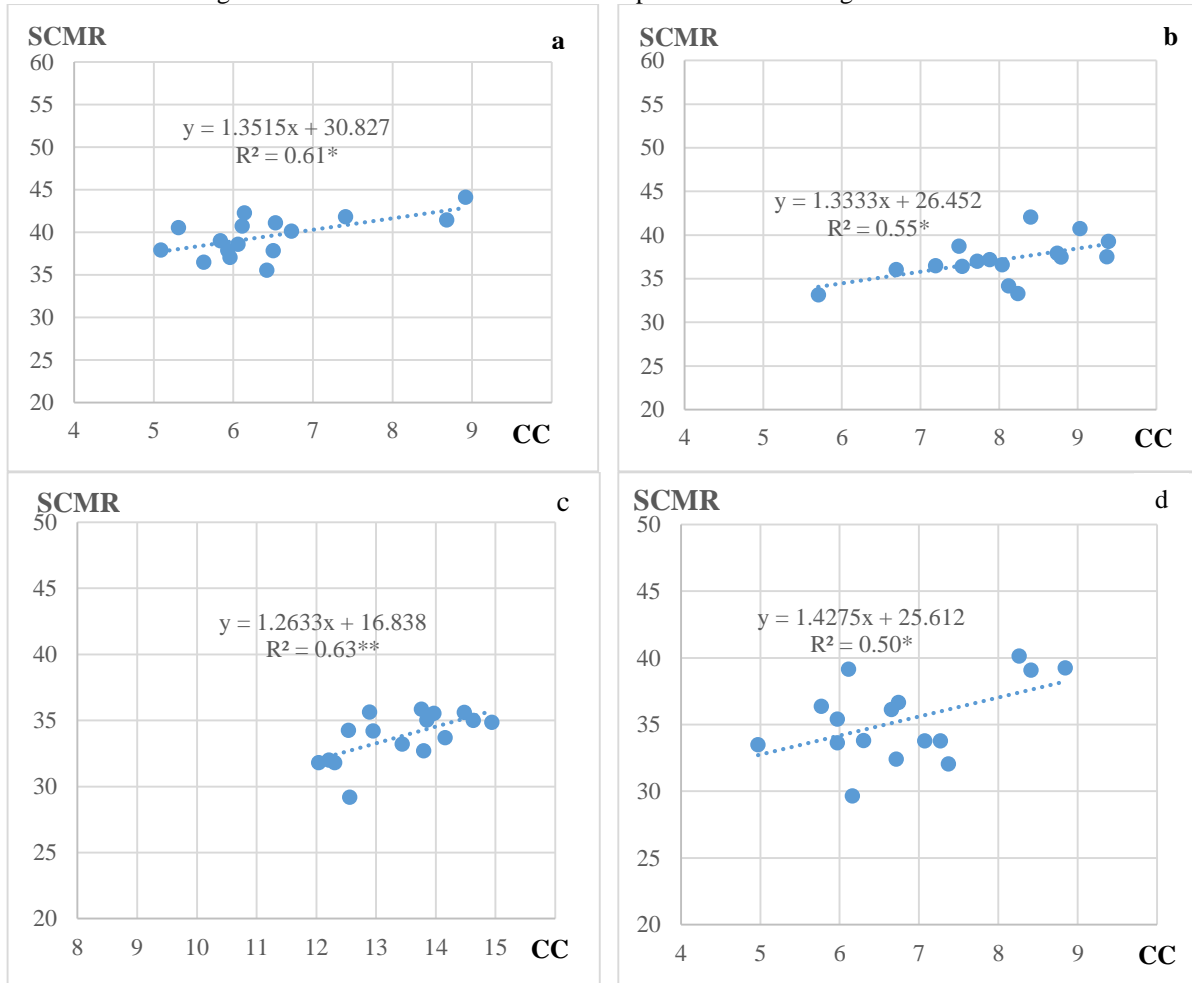


Fig. 1 Relationship between SCMR and CC of 16 sugarcane varieties at 8, 9, 10 and 12 months after planting (1a, 1b, 1c and 1d, respectively) under two locations in Maha Sarakham province.

ACKNOWLEDGEMENTS

This research was supported by grant from National Science and Technology Development Agency (NSTDA). I would like to thank you Department of Agricultural Technology, Faculty of Technology Mahasarakham University and 4th year of under graduate students of Department of Agricultural Technology Mahasarakham University.

REFERENCES

- [1] Wiedenfeld R.P., Water Stress During Different Sugarcane Growth Periods on Yield and Response to N Fertilizer. *Journal of Agriculture Water Management*, Vol.43, 2000, pp. 173-182.
- [2] Office of the Cane and Sugar Board (OCSB), Sugarcane production in Thailand report, 2017, Available source: <http://www.ocsb.go.th/upload/journal/fileupload/923-9999.pdf>.
- [3] Jangpromma N., Songsri P., Thammasirirak S. and Jaisil P., Rapid Assessment of Chlorophyll Content in Sugarcane using a SPAD Chlorophyll Meter Across Different Water Stress Conditions, *Asian Journal of Plant Sciences* Vol.9, No.6, 2010, pp. 368-374.
- [4] Sudhakar P., Latha P. and Babu A.M., Evaluation of Sugarcane Genotypes for High Water Use Efficiency and Thermostability Tolerance Under Imposed Moisture Stress at Formative Stage, *Sugar Tech* Vol.12, No.1, 2010, pp. 72-75.
- [5] Khonghintaisong J., Songsri P., Toomsan B. and Jongrunklang N., Rooting and Physiology Traits Responses to Early Drought Stress of Sugarcane Cultivars, *Sugar Tech* Vol.20, No.4, 2018, pp. 396-406.
- [6] Reddy A.N.G., Madhudi K.V.N., Rajeswari V.R. and Sudhakar P., Evaluation of Different Morpho-

- Physiological Traits of Pre-release Early Sugarcane Clones, International Journal of Applied Biology and Pharmaceutical Technology Vol.5, Issue3, 2014, pp. 233-238.
- [7] Khonghintaiong J., Songsri P., and Jongrunklang N., Growth and Physiological Patterns of Sugarcane Cultivars to Mimic Drought Conditions in Late Rainy Season System, Naresuan University Journal: Science and Technology Vol.25, No.2, 2017, pp. 102-112.
- [8] Jangpromma N., Thammasirirak S., Jaisil P. and Songsri P., Effect of Drought Recovery from Drought Stress on Above Ground and Root Growth, and Water Use Efficiency in Sugarcane (*Saccharum officinarum* L.), Australian Journal of Crop Science Vol.6, No.8, 2012, pp. 1298-1304.
- [9] Rong-hua L.I., Pei-pol G.U.O., Baumz M., Grando S., and Ceccarelli S., Evaluation of chlorophyll content and fluorescence parameters as indicators of drought tolerance in barley, Agricultural Sciences in China Vol.10, 2006, pp. 551-557.
- [10] Clark A.J., Landolt W., Bucher J.B. and Strasser R.J., Beech (*Fagus sylvatica*) response to ozone exposure assessed with a chlorophyll fluorescence performance index, Environmental Pollution Vol. 109, 2000, pp. 501-507.
- [11] Moran R., Formulae for determination of chlorophyllous pigments extracted with N, N dimethylformamide, Plant Physiology Vol.69, 1982, pp.1376-1381.
- [12] Maxwell K. and Johnson G.N., Chlorophyll fluorescence-A practical guide, Journal of Experimental Botany Vol.51, No.345, 2000, pp. 659-668.
- [13] Radhamani R., Kannan R. and Rakkiyappan P., Leaf chlorophyll meter reading as an indicator for sugarcane yield under Iron deficient Typic Haplustert, Sugar Tech Vol.18, No.1, 2016, pp.61-66.
- [14] Bhavana M., Kumar M.V., Bindu G.S.M. and Reddy D.V.V., Study on Morpho-Physiological Characters in Different Clones of Sugarcane (*Saccharum officinarum* L.), International Journal of Current Microbiology and Applied Sciences Vol.6, No.11, 2017, pp. 205-217.
- [15] Bunphan D., Jaisil P. and Sanitchon J., Genetic Variation and Correlation of Some Agronomic Traits, Biomass and Ethanol Yield in Diverse Sweet Sorghum (*Sorghum bicolor* L. Moench) Cultivars, Khon Kaen Agriculture Journal Vol.46, No.1, 2018, pp. 155-162.
- [16] Bunphan D., Jaisil P., Sanitchon J., Knoll J.E. and Anderson W.F., Association of Chlorophyll Content and Spad Chlorophyll in Diverse Sweet Sorghum Cultivars Under Different Environments, Khon Kaen Agriculture Journal Vol.42, No.4, 2014, pp. 605-616.
- [17] Medeiros D.B., da Silva E.C., Nogueira R.J.M.C., Teixeira M.M., Buckeridge M.S., Physiological limitations in Two Sugarcane Varieties Under Water Suppression and After recovering, Theoretical and Experimental Plant Physiology Vol.25, No.3, 2013, pp. 213-222.
- [18] Radhamani R. and Kannan R., Nondestructive and Rapid Estimation of Leaf Chlorophyll Content of Sugarcane using a SPAD Meter, International Journal of Science and Research Vol.5 No.4, 2013, pp.2392-2397.
- [19] Udding J., Gelang-Alfredsson J., Piikki K. and Pleijel H., Evaluating the relationship between leaf chlorophyll concentration and SPAD-502 chlorophyll meter readings, Photosynthesis Research Vol. 91, No.1, 2007, pp. 37-46.
- [20] Markwell J., Osterman J.C. and Mitchell J.L., Calibration of the Minolta SPAD-502 leaf chlorophyll meter, Photosynthesis Research Vol. 46, 1995, pp. 467-472.

THE EFFECTS OF AGROCHEMICAL RESIDUES ON AQUATIC INVERTEBRATES IN SEMI-ORGANIC RICE FIELDS

Pattira Kasamesiri¹ and Wipavee Thaimuangphol¹
¹Faculty of Technology, Mahasarakham University, Thailand

ABSTRACT

We present a case study of semi-organic rice farming in which a farmer decided to change the rice farming system from conventional to organic. This study compared the alteration of aquatic invertebrate composition and diversity between semi-organic and conventional rice farming. Aquatic invertebrates were collected in semi-organic and conventional rice fields during the flooding periods from August to October. The results showed that a total of 4 phylum 12 taxa of aquatic invertebrates. The average abundance of aquatic invertebrates in semi-organic and conventional samples were 10,676 and 5,735 individuals/m², respectively. The Shannon diversity index in conventional and semi-organic samples ranged between 0.45-0.62 and 0.35-0.59, respectively. Water quality parameter, temperature, dissolved oxygen and pH were not significantly different between two sites. The present study found signs of chemical substance contamination in semi-organic rice fields. The abundance of pollution indicator species in semi-organic paddies indicated that agrochemical residues persisted from former conventional rice farming.

Keywords: Ecotoxicology, Semi-Organic Rice Farming, Aquatic Invertebrate, Soil Ecology

INTRODUCTION

Rice is a semi-aquatic annual grass that is cultivated on almost countries of the world [1]-[2]. Rice fields are temporary wetland that are important habitats for many aquatic organisms such as earthworm, aquatic insect, water bird and fish [3]-[5]. Agrochemical induce the rice fields are contaminated from pesticides and chemical fertilizers [4]-[7]. In conventional rice cultivation, herbicides and insecticides are applied during the rice vegetative growth stage to the reproductive growth stage, this may cause a variation of benthic community [8]. Many groups of benthic invertebrate have been used as indicator of freshwater ecology [9]-[10], [21]. The Chironomidae in rice fields had statistically significant relationship with dissolved oxygen [11]. Usually, in the soil of flooded rice fields predominated by aquatic oligochaetes such as the tubificid *Branchiura sowerbyi* [12].

The rice cultivation have categories into three groups based on cultivated methods: (1) conventional rice farming, which have application mineral fertilizers and pesticides, and source of water come from irrigation water (2) semi-organic farming, has just developed to organic farming, the farmer applied organic fertilizer and bio pesticides but may have some chemical compounds remain contamination into rice field areas and may applied some inorganic fertilizers [13], (3) organic rice cultivation, completely without chemical fertilizers and pesticides and the water source is fully from spring water or rainfed paddy fields [14]. The aim of this

study to investigate the influence of rice field managements between conventional and semi-organic farming on the abundance and community of benthic animals.

MATERIALS AND METHODS

Study Sites and Sampling Methods

The study areas were located at Maha Sarakham Province, northeast of Thailand. The sampling sites cultivated rice crops by conventional and semi-organic techniques. The conventional rice cultivation technique, the farmers burned straw stubbles with fire, applied inorganic fertilizers, herbicides, insecticides and used gravity-fed irrigation water. In the semi-organic rice farming, the farmer prepared the soil by incorporated stubbles and soil with the tractor, applied inorganic and organic fertilizers, avoided herbicides or insecticides and used irrigation water. The invertebrate samples were collected from 3 paddy fields of conventional plots (16° 20' 15" N; 103° 9' 56" E) and semi-organic plots (16° 20' 9" N; 103° 10' 13" E) and 3 replicates of each paddy field by using sediment corer 12 cm diameter during flooding period from August to October 2015. The benthos were sieved through a 0.5 mm mesh net and preserved in 80% ethanol. The water quality (temperature, pH and dissolved oxygen) were investigated by using OAKTON (Eutech PCD 650).

Aquatic Invertebrates Identification

Benthos samples were sorted under the light microscope and identified taxa to the lowest possible level according taxonomic keys [20]. The benthos of each taxa were counted and recorded total number.

Data Analysis

The diversity and evenness indices [15] were calculated following Eq. (1) to (3) and dominance index [16] used Eq. (4).

$$H' = -\sum p_i \ln p_i \quad (1)$$

$$p_i = n_i / N \quad (2)$$

$$E_H = H' / \ln S \quad (3)$$

$$D = \sum p_i^2 \quad (4)$$

While H' is the Shannon's diversity index; p_i is the proportion of individuals found in a taxon i ; n_i is the number of individuals in a taxon i ; N is the total number of individuals of all taxa; E_H is the evenness index; S is the total number of taxa; D is the dominant index.

The benthos abundance, diversity, evenness and dominance indices between the conventional and semi-organic rice farming were compared by using Levene's test for equality of variances and t-test for equality of means (significant level p-values less than 0.05).

RESULT AND DISCUSSION

The Composition and Abundance of Benthos

The freshwater invertebrates were found 3 phylum 12 taxa in conventional rice fields and 4 phylum 11 taxa in semi-organic rice fields. The taxa richness showed no difference between conventional and semi-organic. Five taxa as Chironomidae, Ephemerellidae, Cyclopoida, Oligochaeta and Viviparidae were found in all plots. While 3 taxa (Odonata, Anisoptera, and Hirudinea) were only observed in conventional rice fields and 3 taxa (Nematoda, Tipulidae and Baetidae) found only semi-organic plots (Table 1).

The total numbers of benthos found in conventional and semi-organic rice fields were 1,753 and 3,266 individuals, respectively. The composition in conventional rice fields included Oligochaeta (88%), followed by Gastropoda (10%) and Insecta (2%) whereas the semi-organic rice fields composed of Oligochaeta (91%), Gastropoda (8%) and Arthropoda (1%) (Fig. 1). The Oligochaeta were dominant taxa of all sampling sites.

The average abundance of benthos in conventional and semi-organic were 5,735 and 10,676 individuals/m², respectively (Table 2). Average abundance between rice field treatments

showed no significant difference because of high variability of abundance between sampling sites.

The diversity, Evenness and Dominant Indices

The diversity index in conventional and semi-organic was ranged between 0.45-0.62 and 0.35-0.59, respectively. The benthos diversity index of both study sites lower than previous report in conventional and organic rice fields of Kalasin province, Thailand (0.88 in conventional, 1.36 in organic) [5].

Water Quality of Soil Surface Water

The water quality parameters, temperature, dissolved oxygen and pH ranged between 26.33-33.34, 2.93-8.08 and 6.11-7.50, respectively (Table 3). All parameters were no significant difference between conventional and semi-organic paddy fields ($p > 0.05$)

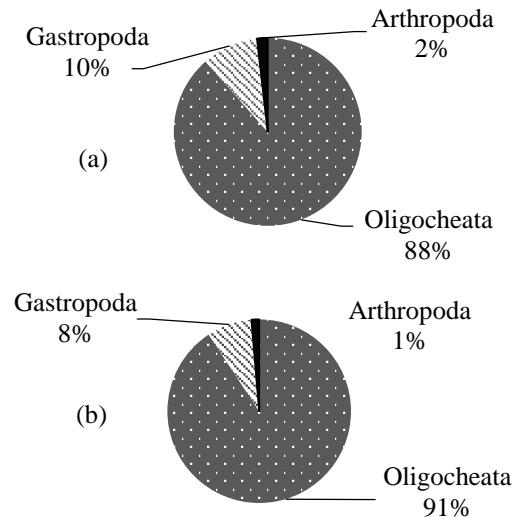


Fig. 1 The composition of benthos in (a) Conventional (b) Semi-organic rice fields.

The effects of rice field managements have not showed significant difference in taxa richness, abundance, diversity, evenness and dominant indices ($p > 0.05$). In contrast, apparent of some taxa may resulted from agrochemical used in rice field areas. Abundance of aquatic insect (Baetidae) were negatively correlated with pesticide used in conventional rice fields [4], which this taxa was present only conventional paddy fields. Cyclopoida was high abundance in semi-organic fields, it was used as indicator of non-polluted area [17]-[18]. Same as Chironomidae was applied to indicator of nutrient enrichment in water and sediment [6], found more abundance in semi-organic rice fields than conventional plot.

Table 1 Total number (individuals) of Benthos classified to taxa between conventional and semi-organic rice farming during the cycle of flooded.

Benthos Taxa	Conventional	Semi-Organic
ANNELIDA		
Oligochaeta	1550	2964
Hirudinea	1	0
NEMATODA	0	7
MOLLUSCA		
Gastropoda		
Architaenioglossa		
Hydrobiidae	9	12
Viviparidae	161	247
ARTHROPODA		
Insecta		
Odonata	1	0
Anisoptera	1	0
Zygoptera	5	0
Diptera		
Chironomidae	7	11
Tipulidae	0	1
Ephemeroptera		
Ephemerellidae	13	3
Baetidae	0	1
Copepoda		
Cyclopoida	2	16
Entognatha		
Collembola	1	0
Branchiopoda		
Cladocera	1	0
Crustacea		
Decapoda	1	3
Ostracoda	0	1
Total number	1753	3266

Table 2 Abundance (individuals/m²), diversity index, evenness index and dominant index of benthos during the flooding period

Index	Conventional			Semi-Organic		
	Aug	Sep	Oct	Aug	Sep	Oct
Abundance	1,990	8,328	6,833	2,510	21,843	7,676
Diversity	0.62	0.45	0.58	0.59	0.35	0.42
Evenness	0.65	0.26	0.39	0.71	0.23	0.28
Dominant	0.63	0.78	0.69	0.63	0.81	0.78

Table 3 Water quality in rice fields

Rice fields	Parameters	Aug	Sep	Oct
Conventional	Temperature (°C)	33.33	29.43	26.33
	DO (mg/l)	8.08	3.04	2.93
	pH	7.14	6.31	6.64
Semi-Organic	Temperature (°C)	33.43	30.33	26.83
	DO (mg/l)	6.97	4.83	4.53
	pH	7.50	6.53	6.65

However, the oligochaete was used as indicator of application herbicide and positively correlated with pH in rice fields [4], [19]. The present study, oligochaetes were found more total number in semi-organic than conventional rice fields. The represent semi-organic rice fields in this study used water from irrigation canal, this may cause of chemical substance contaminated in semi-organic paddy fields, which make similarity of benthic community between two sites. Moreover, the farmer just change rice cultivation method from conventional to semi-organic which the chemical substance may remain in soil. This cause of low diversity and more abundance of oligochaetes were found in both sites.

CONCLUSION

The present study is a case study of farmer that decided to change the rice farming system from conventional to semi-organic. However, we found a sign of the chemical substance contamination in semi-organic farming system. The abundance of polluted indicator species (Oligochaeta and Chironomidae) in semi-organic system was effect of pesticide or herbicide that contaminated from source of water or residue of agrochemical in former conventional rice farming system.

ACKNOWLEDGEMENTS

For jointed conference was supported by Mahasarakham University Development Fund. Moreover, we would like to special thanks to Ms. Thidarat Yimphung, Mr.Utai Wannagul, Ms. Natthida Thaneepoon and Ms. Duanghathai Maliloest for ensuring the success of the field operations.

REFERENCES

- [1] Muthayya S., Jonathan D.S., Montgomery S. and Maberly G.F., An Overview of Global Rice Production, Supply, Trade, and Consumption. *Annals of the New York Academy of Sciences*, Vol. 1324, 2014, pp. 7-14.
- [2] FAO, The State of Food Insecurity in the World, Italy: Food and Agriculture Organization of the United Nations, 1999.
- [3] Schoenly K.G., Justo H.D., Barrion A.T., Harris M.K. and Bottrell D.G., Analysis of Invertebrate Biodiversity in a Philippine Farmer's Irrigated Rice Field, *Community and Ecosystem Ecology*, Vol. 27, Issue 5, 1998, pp. 1125-1136.
- [4] Mesleard F., Garnerio S., Beck N. and Rosecchi E., Uselessness and Indirect Negative Effects of an Insecticide on Rice Field Invertebrates, *Comptes Rendus Biologies*, Vol. 328, 2005, pp. 955-962.
- [5] Kasamesiri P. and Thaimuangphol W., The Benthic Communities Comparison between Organic and Conventional Rice Fields, *Communications in Agricultural and Applied Biological Science*, Vol. 80, Issue 3, 2015, pp. 367-374.
- [6] Al-Shami S.A., Rawi C.S.M., Ahmad A.H., Hamid S.A. and Nor S.A.M., Influence of Agricultural, Industrial, and Anthropogenic Stresses on the Distribution and Diversity of Macroinvertebrates in Juru River Basin, Penang, Malaysia, *Ecotoxicology and Environment Safety*, Vol. 74, 2011, pp. 1195-1202.
- [7] Maeder P., Fließbach A., Dubois D., Gunst L., Fried P. and Niggli U., Soil Fertility and Biodiversity in Organic Farming, *Science*, Vol. 296, 2002, pp.1694-1697.
- [8] Miranda M.S., Fonseca M.L., Lima A., Moraes T.F. and Rodrigues F.A., Environmental Impacts of Rice Cultivation, *American Journal of Plant Science*, Vol. 6, 2015, pp. 2009-2018.
- [9] Azrina M.Z., Yap C.K., Ismail A.R., Ismail A. and Tan S.G., Anthropogenic Impacts on the Distribution and Biodiversity of Benthic Macroinvertebrates and Water Quality of the Langat River, Peninsular Malaysia, *Ecotoxicology and Environmental Safety*, Vol. 64, 2006, pp. 337-347.
- [10] Kasamesiri P. and Thaimuangphol W., Oligochaeta as Bioindicator on Ecotoxicology of Conventional and Organic Rice Fields, *Communications in Agricultural and Applied Biological Science*, Vol. 82, Issue 2, 2017, pp. 81-86.
- [11] Al-Shami S.A., Salmah M.R.C., Hassan A.A. and Azizah M.N.S., Temporal Distribution of Larval Chironomidae (Diptera) in Experimental

- Rice Fields in Penang, Malaysia, *Journal of Asia-Pacific Entomology*, Vol. 13, 2009, pp. 17-22.
- [12] Kimura M., Population, Community Composition and Biomass of Aquatic Organisms in the Floodwater of Rice Fields and Effects of Field Management, *Soil Science and Plant Nutrition*, Vol. 51, Issue 2, 2010, pp. 159-181.
- [13] Lestari Y.K., Comparative Analysis of Technical Efficiency of Semi Organic and Conventional Rice Farming in Bogor (Case in Situ Gede and Sindang Barang Villages), Bogor Agricultural University, 2013, pp. 7-8.
- [14] Sukritiyonubowo R., Wiwik H., Sofyan A., Benito H.P., and De Neve S., Change from Conventional to Organic Rice Farming System: Biophysical and Socioeconomic Reasons, *International Research Journal of Agricultural Science and Soil Science*, Vol. 1, Issue 5, 2011, pp. 172-182.
- [15] Shannon C.E. and Weaver W., *The Mathematical Theory of Communication*. University of Illinois Press, 1949, 114 p.
- [16] Simpson E.H. Measurement of Diversity, *Nature*, Vol. 163, 1949, p. 688.
- [17] Lim R.P., Abdullah M.F. and Fernando C.H., Ecological Studies of Cladocera in the Ricefields of Tanjung Karang, Malaysia, Subjected to Pesticide Treatment, *Hydrobiologia*, Vol. 113, 1984, pp. 99-103.
- [18] Adamczuk M., Mieczan T., Tarkowska-Kukuryk M. and Demetraki-Paleolog A., Rotatoria-Cladocera-Copepoda Relations in the Long-term Monitoring of Water Quality in Lakes with Trophic Variation (E. Poland), *Environmental Earth Science*, Vol. 73, 2015, pp. 8189-8196.
- [19] Ilyashuk B.P., Littoral Oligochaete (Annelida: Oligochaeta) Communities in Neutral and Acidic Lakes in the Republic of Karelia, Russia, *Boreal Environment Research*, Vol. 4, 1999, pp. 277-284.
- [20] Mekong River Commission, Identification of Freshwater Invertebrates of the Mekong River and Its Tributaries, Mekong River Commission, 2006, 274 p.
- [21] Krupnova T.G., Mashkova I.V., Kostyukova A.M. and Artyukov E.V., The Distribution and Accumulation of Chemical Elements in The Ecosystem of Lake Ilmenskoe, *International Journal of GEOMATE*, Vol. 12, Issue 34, 2017, pp. 82-88.

THE EFFECT OF SOIL DEPTH ON GROWTH OF CLOVER FERN AND USING CLOVER FERN ON THE GERMINATION OF FERN SPORE

Sawat Pimsuwan¹ and Yaowarat Wongsrisakulkaew¹

¹ Faculty of Agricultural Technology, Rajamangala University of Technology Thanyaburi, Thailand

ABSTRACT

Clover fern is water fern weed. It grows well in soft mud by most likely shallow water. Some country used it for vegetable and medicine. After this fern dies every part still has the sticky fiber. It can be used for plant material. This experiment was conducted in pots at the nursery. As follow the depths of soil: 5, 10, 15, 20 and 25 cm in the planting pots were expected to demonstrate some effects on the growth of clover fern (*Marsilea crenata* C. Presl.). The observations were made on 3 replications in a RCBD experiment. The mean comparisons were made with the Duncan's test at 0.05 significant level. It was found that the ferns on the 15 cm deep soil possessed the longest internode length of 7.43 cm, while those with the 20 cm depth possessed the longest stalk of 16.16 cm and those of the 25 cm depth showed the widest leaf diameter at 4.00 cm. However, there was no significant difference for the latter three measurements. The clover ferns on the soil with 25 cm depth demonstrated the highest fresh weight of 971.11 g and dry weight of 146.11 g ($p < 0.05$). The spores germinated on the mixed media with clover fern and peat moss, it was only observed in one chamber containing 1:2 clover fern to peat moss, and another one with 2:1 mixture but the germination rate was low. Clover fern should study for use as agricultural materials, vegetables and medicine

Keywords: Clover fern, Water fern, Planting material, weeds

INTRODUCTION

Weeds are defined as native plant species that grow in cultivating fields. Most weeds give important impact on crop yields [1]. Some of them grow along and compete with the cultivating crops [2] while some clog irrigation networks [3]. In wetland plantation such as rice field, there are also weed problems. Some water weed outbreaks have been reported "In press" [4]. Clover fern (*M. crenata* C. Presl) is one of the cause. This fern is known as aquatic, semi-aquatic fern or water fern [5], [6] which has been classified as a weed. It grows well in shallow water such as in the rice field. It is found mainly in Southeast Asia, the rainforest zone with high humidity [7]. The general characters of the clover fern are: rhizome (stem) consisting nodes and internodes, growing on soil or the mud surface, having four leaflets (frond) on the top of a petiole that grows from node of the rhizome. It has fibrous roots and sporocarps growing from the nodes [8]. The clover fern is one of edible wild plants. Some Thais take this fern as a vegetable, and it could be found in many Thai recipes. So, it is a part of Thai culture [9], [10], [11].

The clover fern can also be an ornamental plant. It is unique when it is planted in a pot and placed in a garden or a pond [12]. It can also be grown in aquarium or shallow water basin [13]. This fern has some medicinal properties as well. Its extract has

been proved for estrogen therapies [14]. The use for hepatitis and colic treatment by Thai folk healers in the south of Thailand has long been known [15].

In an environmental point of view, this fern could be used to test the soil for lead contamination. A stronger inhibition to the growth of the fern was found in relation to the increasing of lead in soil [16].

This research team has been looking for some native plants that can replace the imported peat moss. In nursery environment, it was notice that the clover fern grew well on clay, in containers with some water, especially in the rainy season. In the dry season, the ferns became disrepair and died off. They could be harvested, dried, and then used as a planting material. Some other fern species and epiphytic plants can grow on them when they have a suitable moisture content. Drying and cracking of clover fern are very similar physical properties to peat moss. Usually, peat moss is popular in use for sowing seeds and fern spores, also transplanting some fern seedlings [17]. However, potentially, the stems and petioles of clover ferns consist of aerenchymal tissues which allow good gas exchange. [18], [8]

The objectives of this study were to determine 1) the effects of the soil depths on clover fern growth and 2) the effects of clover fern in germination media for bird-nest-fern spores.

MATERIAL PREPARATION

Fern stock preparation: The clover fern tips were collected from the ferns naturally grown on rice field. The tips were then planted on clay in large plastic bowls. After two months, the ferns grew up and filled up each bowl. These ferns were used as the fern stock for this experiment. Some small clusters of the ferns were collected from the stock with their roots attached on the clay on which they were grown. Each cluster was allowed a 10 x 10 cm clay block with it (fig.1). Five clusters each were then planted in a container containing some clay. The same procedure was applied to other containers. All containers were 60 cm in diameter and 30 cm in height. After planting, some water was added up to the top of the containers. (fig.2)

Germinating media preparation: Some dried clover ferns were ground and sieved. The ground product was mixed with some peat moss at three different ratios: 1:1, 1:2 and 2:1 (table 3). The mixture was added into moisture chambers (6.5 cm in width, 8.5 cm in length and 3 cm in height) and spread evenly. It was then sprayed with some water prior to use.

METHOD

Planting experiment: Some clay was used as the as planting soil for the clover ferns in this experiment. It was added into planting containers to achieve five different depths: 5, 10, 15, 20 and 25 cm and water height was 30 cm. These depths were expected to demonstrate some effects on the growth of clover ferns. The observations were made on 3 replications in a randomized complete block design (RCBD). The internode lengths, stalk lengths, leaf diameters, fresh weights and dry weights were collected and analyzed. The mean comparisons were made with the Duncan multiple range test at 0.05 significant level.

Germinating experiment: The spores from bird-nest fern (*Asplenium nidus*) were chosen for this experiment. They were sown onto the moisten media prepared early on, at amount of 2.5 mg per chamber. The chamber were closed and observed for the presence of prothalli.

RESULTS

It was found that the clover ferns on the 15 cm deep soil possessed the longest internode length with an average of 7.43 cm. Those on the 20 cm depth demonstrated the longest stalk of 16.16 cm in average. On the other hand, the ones on the 25 cm depth showed the average width of leaves of 4.00 cm. However, there was no significant difference ($p > 0.05$). (Table 1, fig. 3-7)

In term of weights, the clover ferns which planted on 25 cm deep soil were the heaviest by fresh weight

(971.11 g in average). They also showed the highest dry weight (146.11 g) as well. These figures were significantly different ($p < 0.05$) and the details could be found (Table 2, fig. 8-9)

On the other hand, the bird-nest-fern spores could germinate in all chambers with pure peat moss but no germination was found with pure clover fern. Some spores could germinate on the mixed media but the germination rate was low. It was only observed in one chamber containing 1:2 clover fern to peat moss, and another one with 2:1 mixture (Table 3, fig. 10-14)

Tables

Table 1 The growth of Clover ferns planted on clay with different depths, at 13 weeks

Treatment ¹	Growth of Clover fern (\bar{x} /cm)		
	Internode length	Stalk length	Leaf diameter
5cm	6.97	15.00	3.79
10cm	7.26	13.39	3.94
15cm	7.43	14.84	3.91
20cm	7.24	16.16	3.87
25cm	7.16	14.09	4.00
CV%	6.83	13.38	6.18
F test	ns	ns	ns

¹ depth of clay soil

Table 2 The fresh and dry weights of clover fern at 13 weeks on clay with different depths.

Treatments ¹	Weight of Clover fern (\bar{x} /g)	
	Fresh weight/g	Dry weight/g
5cm	524.99 c	66.11 c
10cm	683.88 b	89.99 bc
15cm	798.88 b	118.88 ab
20cm	793.88 b	123.33 ab
25cm	971.11 a	146.11 a
CV%	11.52	2.60
F test	*	*

¹ depth of clay soil, * = significantly different ($p < 0.05$)

Table 3 The germination of bird-nest fern spores on dried-ground clover fern, peat moss and their mixtures

Material ratio	Box number					
	1	2	3	4	5	6
C	-	-	-	-	-	-
P	+	+	+	+	+	+
C: P=1:1	-	-	-	-	-	-
C: P=1:2	-	-	+	-	-	-
C: P=2:1	-	+	-	-	-	-

C= clover fern, P= peat moss,
presence of prothalli: + = found, - = not found

Figures

The clover ferns in the soil depth experiment are shown in figure 1-9. The bird-nest ferns spore in the germinating experiment are shown in figure 10-14.



Fig.1 Collected clover fern clusters



Fig.2 The experimental clover ferns in the nursery



Fig.3 The clover ferns on 5cm deep clay soil



Fig.4 The clover ferns on 10cm deep clay soil



Fig.5 The clover ferns on 15cm deep clay soil



Fig.6 The clover ferns on 20cm deep clay soil



Fig.7 The clover ferns on 25cm deep clay soil



Fig.8 The fresh clover ferns



Fig.9 The dried clover ferns



Fig.10 The germination of bird-nest fern spores on ground clover fern

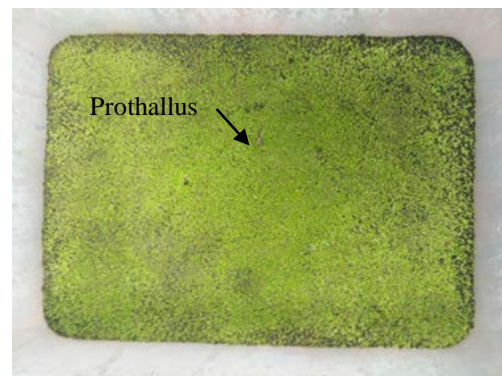


Fig.11 The germination of bird-nest fern spores on peat moss



Fig.12 The germination of bird-nest fern spores on 1:1 clover fern: peat moss mixture

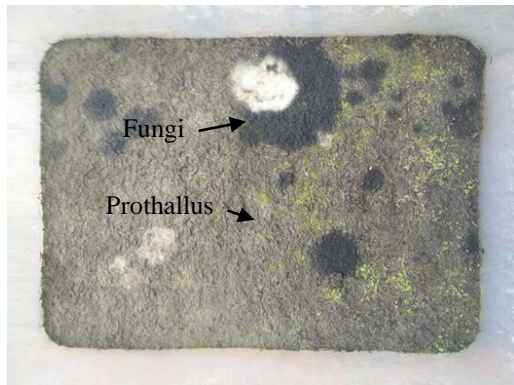


Fig.13 The germination of bird-nest fern spores on 2:1 clover fern: peat moss mixture



Fig.14 The germination of bird-nest fern spores on 1:2 clover fern: peat moss mixture

CONCLUSION

The values of many native plants have not been well studied. This study chose to test the clover fern for its production potential and its potential use as a planting material. The study was conducted in a plant nursery for 13 weeks in a rainy season. On the basis of fresh weight and dry weight, ferns appeared to grow well on 25 cm deep clay soil and 5 cm shallow water.

To be used as a germination material, the ground clover fern did not show a positive result with respect peat moss. Although some bird-nest-fern spores can germinate on 1:2 and 2:1 clover fern for mixing peat moss, germination has been delayed for a few weeks. In contrast, fern spores completed their germination in the first month.

The observation made during the experiment had noticed that the ground clover fern was looked perfectly sound, but it generated some decomposition odor. This may suggest the negative effect found in this experiment. It might be caused by some toxins generated during the decomposition process which are required some further studies. Clover fern should

be developed for use as agricultural materials because it free material from nature and also research to be vegetable commercial and medicine.

ACKNOWLEDGEMENTS

This research was partially funded by The Faculty of Agricultural Technology, Rajamangala University of Technology Thanyaburi, Thailand. And this report was edited by Dr. Satain Pogool.

REFERENCES

- [1] Yeganehpour F., Salmasia S.Z., Abedib G., Samadiyanc F. and Beyginiyad V., Effects of cover crops and weed management on corn yield. *Journal of the Saudi Society of Agricultural Sciences*. Vol.14, Issue2,2015, pp.178-181.
- [2] Gaba S., Reboud X., and Fried G., Agroecology and conservation of weed diversity in agricultural lands. *Botany Letters*, Vol.163, Issue.4,2016, pp.351-354.
- [3] Kamoshita A., Araki Y., and Nguye Y.T.B., Weed biodiversity and rice production during the irrigation rehabilitation process in Cambodia. *Agriculture, Ecosystems & Environment*, Vol.194,2014, pp.1-6.
- [4] Seng T., Sou C., Goh S., and Sahi I., Weed management issues, challenges, and opportunities in Malaysia. *Crop protection*. 2017 (In press)
- [5] Short P.S., MARSILEACEAE in Short P.S. and Cowie I. D. (eds), *Ferns and allied plants. Flora of the Darwin Region*. Vol.1,2011,pp.17-20
- [6] Pimsuwan s., Wongsrisakulkaew Y., Jumradjit N., Thumsuk P., and Mulmanee S., The effects of watering frequencies and slow released-fertilizer levels on the growth of *Platyserium coronarium* in young sporophyte phase Vol.13, Issue40, 2017, pp.24-28.
- [7] Wu T-C., and Wen-Yuan Kao W-Y., *Ecophysiological Traits of Leaves of Three Marsilea Species Distributed in Different Geographical Regions*, Taiwan,Vol.56, No.4, 2011, pp.279-286.
- [8] Agil M, Kusumawati I., and Purwitasari N., Phenotypic Variation Profile of *Marsilea crenata* Presl. Cultivated in Water and in the Soil. *Journal of Botany*. Volume 2017,2017, pp.1-6.
- [9] Cruz-Garcia G.S., Struikc P.C., and Johnson D.E., Wild harvest: distribution and diversity of wild food plants in rice ecosystems of Northeast Thailand, *Wageningen Journal of Life Sciences* Vol.78, 2016,pp.1-11.
- [10] Cruz-Garcia G.S., and Price L.L., Weeds as important vegetables for farmers. *Acta Soc Bot Pol*, Vol.81, No.4, 2012, pp.397-403
- [11] Calvert G. and Liessmann L., *Wetland Plants of the Townsville-Burdekin Flood Plain*. Lower

- Burdekin Landcare Association Inc., Ayr. 2014, pp.1-144
- [12] Yusuf U.K., Ferns of Malaysian Rain Forest a Journey through the Fern World. Serdang ;Universiti Putra Malaysia Press, 2010, pp.1-107
- [13] Zhigila D.A., Sawa F.B.J., Oladele F.A., and Muhammad S., Aesthetic Values and Significance of Ferns to Landscaping Industries – A Taxonomic Review. International Journal of Current Research in Biosciences and Plant Biology, Vol.2, No.3, 2015, pp.7-13
- [14] Titisari N., Fauzi A., Adyana A., and Trisunuwati P., The Effects of Water Clover (*Marsilea crenata*) Extract against Estrogen, Progesterone And Uterine Histology on Rat (*Ratus norvegicus*). International Journal of Pharm Tech Research, Vol.9, No.6, 2016, pp.165-171
- [15] Neamsuvan O., and Ruangrit T., A survey of herbal weeds that are used to treat gastrointestinal disorders from southern Thailand: Krabi and Songkhla provinces. Journal of Ethnopharmacology, Vol.209, 2017, pp.318–327.
- [16] Nurhayatia A.Y., Hariadia Y. C., and Lestaria P., Early detection of lead stress on *Marsilea crenata* using. bioelectricity measurement. Procedia Environmental Science, Vol.28, 2015, pp.57 – 66.
- [17] Pimsuwan S, Hongthong P, Krangpanich P., and Suwanpinta C., The Effect of Fertilizer on Growth of Staghorn Fern at Seedling Stage. International Journal of GEOMATE, Vol.11, Issue28, 2016, pp.2879-2882.
- [18] Jung J.D., Lee S.C., and Choi H.K., Anatomical patterns of aerenchyma in aquatic and wetland plants. Journal of Plant Biology, Vol. 51, Issue 6, 2008, pp.428–439.

CHEMICAL COMPOSITION AND INSECTICIDAL ACTIVITY OF ESSENTIAL OIL FROM INDIAN BORAGE AGAINST MAIZE WEEVIL

*Ruchuon Wanna¹ and Jiraporn Krasaetep¹

¹Faculty of Technology, Mahasarakham University, Thailand

ABSTRACT

Biopesticide has become more important in stored product pest management, since the use of synthetic insecticides causes adverse effects to human health and the environment. The aim of this research was to determine the chemical composition and toxicity of essential oil from Indian borage, *Plectranthus amboinicus* (Lour.), leaves against adults of maize weevil, *Sitophilus zeamais* Motschulsky. The essential oil was investigated by Gas Chromatograph-Mass Spectrometer (GC-MS) technique. The efficacy of this essential oil against *S. zeamais* using impregnated filter paper and vapor-phase tests. Experiments were performed under Completely Randomized Design (CRD) with 4 replications. Contact toxicity towards maize was investigated at 6 concentrations of essential oil 0 5,000 10,000 15,000 20,000 and 25,000 ppm and fumigant activity was performed using bioassay at 6 concentrations including 0 50 100 150 200 and 250 μ L/L air. Data were recorded as number of deaths maize weevil from 24 to 168 hours. The principal compounds in the oil were carvacrol (40.49%), caryophyllene (16.76%), ζ -terpinene (11.61%), o-Cymene (8.50%), humulene (5.88%), caryophyllene oxide (2.75), p-mentha-1,4(8)-diene (2.17%), and terpinen-4-ol (1.19%). The essential oil of *P. amboinicus* leaves showed strong contact toxicity at 120 hours and fumigant toxicity at 72 hours against adults of *S. zeamais* with 100% adult mortality of 25,000 ppm and 250 μ L/L air, respectively. The results indicated that the essential oil of *P. amboinicus* leaves showed potent for management of *S. zeamais* population.

Keywords: Chemical composition, Toxicity, Essential oil, *Plectranthus amboinicus*, *Sitophilus zeamais*

INTRODUCTION

Preservation and protection of stored grain are dietary, economic, and social requirements [1]. Damage caused by insects in stored maize, *Zea mays* L., is a serious problem worldwide. Losses are 10% in developed countries and 20% in developing countries [2]. A major insect pest of stored maize is the maize weevil, *Sitophilus zeamais* Mostchulsky (Coleoptera: Curculionidae) found in moist tropics and subtropics and temperate zones [3]. This specie is generally controlled by insecticides such as phosphine [1]. However, insecticides are toxic to humans and pollute the environment such as ozone depletion, environmental pollution, increasing costs of application, pesticide residue in food, insects develop insecticidal resistance and toxicity hazards on non-target organisms in addition to direct toxicity to users [4], [5]. These problems have highlighted the need to develop new types of selective insect-control alternatives.

Plant essential oils have traditionally been used to kill or repel insects [4] being considered as an alternative to stored grain conventional pesticides because of their low toxicity to warm-blooded mammals, their high volatility [6], [7], rapid degradation [8], and the most terpenoids and phenols found in plant essential oil have low toxicity [9], [1]. Essential oils are effective against insect pests of

stored products [10]. Some components cause larvicidal effect and oviposition deterrence in agricultural pests [11]. Phenolic compounds in essential oils react with chemical groups of enzymes through hydrogen bonds or hydrophobic interactions, inhibiting activity [12]. Essential oil from wild *L. palmeri* is a good option for controlling maize weevil. The aim of this research were determination of chemical composition of the essential oil of Indian borage, *Plectranthus amboinicus* (Lour.), from fresh leaves and evaluation of the insecticidal activities against adult stage of *S. zeamais* as a possible alternative for synthetic chemical insecticidal compounds.

MATERIALS AND METHODS

Insect Rearing

Maize weevil, *Sitophilus zeamais* Mostchulsky, from the grain store located in Kantharawichai district, Maha Sarakham Province, Thailand were used throughout this study. Fifteen pairs of adults were maintained in a plastic box (diameter 15 cm, height 30 cm). The cultures were reared on 1 kg of jasmine rice, *Oryza sativa* L. at 30 \pm 5°C and 70 \pm 5% relative humidity and 16:8 h light/dark cycle and were allowed for mating and oviposition. Adult of maize weevil used for tests were 7 days old.

Extraction of Essential Oil

Essential oil was extracted from fresh leaves of Indian borage, *Plectranthus amboinicus* (Lour.), using a Clevenger-type apparatus, (200 g of an air-dried sample, 1:3 plant/distilled water ratios) were hydrodistilled for 3 hours. Anhydrous sodium sulphate was used to remove water after the extraction. Essential oil was kept in a refrigerator at 4 °C until its use.

Analytical Essential Oil

Essential oil constituents from fresh leaves of Indian borage *P. amboinicus* were established by the gas chromatograph-mass spectrometry (GC-MS) analyses. GC-MS analyses were performed on a PerkinElmer Clarus SQ8 GC/MS system (Roster, USA) operating in EI mode (70 eV). A Rtx-5MS capillary column (with a 5% phenyl-methylpolysiloxane stationary phase, 30 m x 0.25 mm, 0.25 µm film thickness) was used. The GC settings were as follows: the initial oven temperature was kept at 60 °C for 1 min and increased to 180 °C at a rate of 10 °C/min, held for 1 min, and then increased at 3 °C/min to 246 °C for 15 min. The injector temperature was maintained at 250 °C. The samples (1 µL, dilute to 1% with acetone) were injected, with a split ratio of 1:10. The carrier gas was helium with a flow rate of 1.0 mL/min. Spectra were scanned from 50 to 550 m/z. The identification of essential oil components was undertaken firstly by comparing their mass spectra with those stored in National Institute of Standard and Technology (NIST) Mass Spectral Search Program and Chemstation Wiley Spectral Library. Essential oil components were done by comparison of their retention times with authentic samples to a series of n-alkanes under the same operating conditions.

Contact Toxicity

A series of dilutions of essential oil from Indian borage *P. amboinicus* (0 5,000 10,000 15,000 and 25,000 ppm) was prepared using 100% acetone as solvent as described. Aliquot of each dilution (100 µL) was separately applied on top surface of filter paper (whatman no.1, diameter 9 cm) with a micropipette. The solvent was allowed to evaporate for 2 min and placed into each petri-dish (diameter 9 cm). Ten active of female adults *S. zeamais* (7 days) were introduced into the each petri-dish separately. After incubation at 30±5°C and 70±5% relative humidity and 16:8 hours light/dark cycle and 24 hours exposure to 168 hours, adult mortality was recorded. The insects were considered to be dead as no leg or antennal movements were observed. A control experiment was maintained in which treatment was made with 100% acetone alone. Each

set of treatment was repeated four times and percentage adult mortality was calculated by using the Abbott formula.

Fumigant Toxicity

Whatman (no.1) filter paper strips (1.5x5 cm) were impregnated with 100 µL of 0 (100 % Acetone; control) 50 100 150 200 and 300 µL/L air dilution of essential oils as prepared earlier. After evaporating the solvent for 2 min. Filter paper strips were placed into the hanging of glass vials (diameter 2.5 cm x height 5 cm) from the center of screw cap of fumigation bottle (diameter 5.5 cm x height 10.5 cm) to avoid contact effect of insects with paper strip. Ten active of female adults *S. zeamais* (7 days) were placed inside the fumigation bottle by vapor-phase test. The cap of each bottle was screwed tightly and kept at 30±5 °C, 70±5% relative humidity, and 16:8 hours light/dark cycle. Adult mortality was observed after 24 hours exposure to 168 hours. The insects were considered to be dead as no leg or antennal movements were detected. A control experiment was maintained in which treatment was made with 100% acetone alone. Each set of treatment was repeated four times and percentage adult mortality was calculated by using the Abbott formula.

RESULTS AND DISCUSSION

Identification of Compounds

Chemical composition of essential oil from the leaves of Indian borage, *Plectranthus amboinicus*, is given in Table 1. The major components in the essential oil from *P. amboinicus* leaves were: carvacrol (40.49%); caryophyllene (16.76%); γ -terpinene (11.61%); p-cymene (8.50%); humulene (5.88%); caryophyllene oxide (2.75%); terpinolene (2.17%); α -bergamotene (1.97%); germacrene-4 (1.51%); 5,10(14)-trien-1 α -ol (1.28%); and terpinen-4-ol (1.19%).

Chemical analysis indicated clearly that carvacrol was the main component of Indian borage essential oil. Ortega et al. [13] indicated the chemical constituents varied according to genetic and environmental factors as well as harvest. Erler and Cetin [14] evaluated components and potential larvicidal effects of *Origanum onites* and *O. minutiflorum* against brown-tail moth, *Euproctis chrysorrhoea* (L.), and found carvacrol, thymol, γ -terpinene, and terpinen-4-ol, with the major component being carvacrol for both species of oregano. Toxic effects of terpenoid compounds can be attributed to reversible competitive acetylcholinesterase inhibition occupying the hydrophobic site of the enzyme active site [15].

Carvacrol has insecticidal activity against pests of stored products and is toxic to termites and to nymphs and adults of rice weevil, *S. oryzae*, *Callosobruchus chinensis*, and *Lasioderma serricorne*. Toxic effects in the current study could be attributed to constituents such as thymol,

carvacrol, and *p*-cymene. Successful insecticidal plant constituents are monoterpenes and because of volatility, fungicidal, bactericidal, and insecticidal activity might be used to control stored product insects [16].

Table 1 Chemical composition of the essential oil from leaves of Indian borage *Plectranthus amboinicus* (Lour.)

No.	Compounds	Retention time (min)	Area%
1	2-Thujene; β -Thujene	8.224	0.35
2	Orthodene	8.534	0.13
3	α -Myrcene	10.068	0.84
4	1-Hepten-3-ol	10.068	0.24
5	α -Pellandrene	11.294	0.23
6	Terpinolene	11.817	2.17
7	<i>p</i> -Cymene	12.172	8.50
8	trans-1,2-bis-(1-methylethenyl)cyclobutane	12.340	0.40
9	ζ -Terpinene	13.688	11.61
10	Terpinolene	14.979	0.13
11	Linalool	15.345	0.28
12	Terpinen-4-ol	19.120	1.19
13	α -Terpineol	19.698	0.10
14	2-isopropyl-5-methylphenol	23.802	0.10
15	Thymol	24.104	0.25
16	Carvacrol	24.775	40.49
17	Caryophyllene	30.059	16.76
18	α -Bergamotene	30.449	1.97
19	Humulene	31.420	5.88
20	α -Amorphene	33.187	0.37
21	Cadina-1(6),4-diene	34.095	0.10
22	Caryophyllene oxide	36.664	2.75
23	Humulene epoxide II	37.655	0.33
24	11,11-Dimethyl-4,8-dimethylenebicyclo[7.2.0]undecan-3-ol	38.624	0.12
25	Germacrene-4(15),5,10(14)-trien-1 α -ol	39.835	1.28
26	α -Longipinene	41.218	0.10
27	1,3-Bis-(2-cyclopropyl,2-methylcyclopropyl)-but-2-en-1-one	41.463	0.10
28	n-Hexadecanoic acid	49.275	0.10
29	Ethyltetramethylcyclopentadiene	52.818	0.10
30	3,7,11,15-Tetramethyl-2-hexadecen-1ol	54.091	0.38
Total identified			97.31

Contact Toxicity

Mortality of maize weevil (*S. zeamais*) at 120 h after treatment was highest at the concentration of 25,000 ppm of essential oil from Indian borage (*P. amboinicu*) leaves with cumulative values of 100% and there was a significant difference ($P<0.01$) in relation to the other concentrations. However, that was not different compared with 20,000 ppm (Table 2). The number of dead insects increased as the concentration of the essential oil and time of exposure increased.

Fumigant Toxicity

Mortality value exposed with 250 $\mu\text{L/L}$ air of essential oil from Indian borage (*P. amboinicu*)

leaves to adults of maize weevil (*S. zeamais*) after treatment at 72 h resulted in mortality values 100% and it caused the highest significant difference ($P<0.01$). However, it was not different compared with 100 150 and 200 $\mu\text{L/L}$ air (Table 3). All concentrations of essential oil had greater efficiency against maize weevil (*S. zeamais*) at 168 h with 100% of adult mortality when compared with 0 $\mu\text{L/L}$ air, acetone treatments and also was highly significant different. Maize weevil (*S. zeamais*) was more sensitive to oil at greater concentrations during the first 72 hours and adapted as time passed. Compared with data from this study, Indian borage oil shows greater potential as an insecticide.

Table 2 Mortality of maize weevil *S. zeamais* with contact toxicity treated Indian borage essential oil

Conc. (ppm)	Mean (\pm SE) of adult mortality (%) of maize weevil <i>S. zeamais</i>						
	24 h	48 h	72 h	96 h	120 h	144 h	168 h
0	0.0 \pm 0.0 ^d	0.0 \pm 0.0 ^c	0.0 \pm 0.0 ^e	0.0 \pm 0.0 ^e	0.0 \pm 0.0 ^e	0.0 \pm 0.0 ^d	0.0 \pm 0.0 ^c
5,000	2.5 \pm 5.0 ^d	15 \pm 12.6 ^b	17.5 \pm 5.0 ^d	30.0 \pm 8.2 ^d	40.0 \pm 8.2 ^d	50.0 \pm 8.2 ^c	92.5 \pm 9.6 ^b
10,000	12.5 \pm 5.0 ^c	20.0 \pm 8.2 ^b	30.0 \pm 8.2 ^c	47.5 \pm 5.0 ^c	60.0 \pm 8.2 ^c	77.5 \pm 5.0 ^b	100.0 \pm 0.0 ^a
15,000	32.5 \pm 9.6 ^b	55.0 \pm 5.8 ^a	65.0 \pm 5.8 ^b	67.5 \pm 5.0 ^b	72.5 \pm 9.6 ^b	95.0 \pm 5.8 ^a	100.0 \pm 0.0 ^a
20,000	47.5 \pm 12.6 ^b	80.0 \pm 8.2 ^a	87.5 \pm 5.0 ^a	92.5 \pm 9.6 ^a	92.5 \pm 9.6 ^a	100.0 \pm 0.0 ^a	100.0 \pm 0.0 ^a
25,000	70.0 \pm 8.2 ^a	77.5 \pm 9.6 ^a	85.0 \pm 5.8 ^a	95.0 \pm 5.8 ^a	100.0 \pm 0.0 ^a	100.0 \pm 0.0 ^a	100.0 \pm 0.0 ^a

Means within the same column followed by the same letter are not significantly different (DMRT: $P>0.05$)

Table 3 Mortality of maize weevil *S. zeamais* with fumigant toxicity treated Indian borage essential oil

Conc. ($\mu\text{L/L}$ air)	Mean (\pm SE) of adult mortality (%) of maize weevil <i>S. zeamais</i>						
	24 h	48 h	72 h	96 h	120 h	144 h	168 h
0	0.0 \pm 0.0 ^c	0.0 \pm 0.0 ^c	0.0 \pm 0.0 ^c	0.0 \pm 0.0 ^c	0.0 \pm 0.0 ^c	0.0 \pm 0.0 ^b	0.0 \pm 0.0 ^b
50	10.0 \pm 8.2 ^b	50.0 \pm 14.1 ^b	67.5 \pm 12.6 ^b	77.5 \pm 15.0 ^b	92.5 \pm 9.6 ^b	97.5 \pm 5.0 ^a	100.0 \pm 0.0 ^a
100	17.5 \pm 9.6 ^b	70.0 \pm 8.2 ^{ab}	87.5 \pm 12.6 ^a	95.0 \pm 5.8 ^a	95.0 \pm 5.0 ^{ab}	100.0 \pm 0.0 ^a	100.0 \pm 0.0 ^a
150	25.0 \pm 5.0 ^{ab}	85.0 \pm 5.8 ^a	87.5 \pm 5.0 ^a	97.5 \pm 5.0 ^a	100.0 \pm 0.0 ^a	100.0 \pm 0.0 ^a	100.0 \pm 0.0 ^a
200	17.5 \pm 17.1 ^b	65.0 \pm 28.9 ^{ab}	92.5 \pm 9.6 ^a	100.0 \pm 0.0 ^a	100.0 \pm 0.0 ^a	100.0 \pm 0.0 ^a	100.0 \pm 0.0 ^a
250	47.5 \pm 15.0 ^a	82.5 \pm 5.0 ^a	100.0 \pm 0.0 ^a	100.0 \pm 0.0 ^a	100.0 \pm 0.0 ^a	100.0 \pm 0.0 ^a	100.0 \pm 0.0 ^a

Means within the same column followed by the same letter are not significantly different (DMRT: $P>0.05$)

Copyright Form

Copyright form signed by all authors is necessary for GEOMATE. It should be submitted along with the paper submission. Copyright form can be downloaded from geomate web site.

CONCLUSION

Indian borage *P. amboinicu* (Lour.) essential oil could be used as a botanical insecticide postharvest since it consists of potential terpenoids such as carvacrol, p-cymene, terpinen-4-ol, and thymol complementary to conventional insecticide. Indian

borage essential oil is an alternative control method for maize weevil *S. zeamais* because it results in higher adult mortality by contact and fumigant toxicity. The effectiveness of the components of essential oils might be a viable option to control insect pests in stored maize.

ACKNOWLEDGEMENTS

This research was financially supported by Mahasarakham University. The laboratory assistance from Miss Phitchanart Kaewwichean is gratefully acknowledged.

REFERENCES

- [1] Rajendran S., and Sriranjini V., Plant Products as Fumigants for Stored Product Insect Control. *Journal of Stored Products Research*, Vol. 44, 2008, pp. 126-135.
- [2] Phillips T. W., and Throne J. E., Biorational Approaches to Managing Stored Product Insects. *Annual Review of Entomology*, Vol. 55, 2010, pp. 375-397.
- [3] García L. S., Burt A. J., Serratos J. A., Díaz P. D. M., Arnason J. T., and Bergvinson D., Defensas naturales en el grano de maíz al ataque de *Sitophilus zeamais* (Coleoptera: Curculionidae): mecanismos y bases de la resistencia. *Rev. Educ. Bioquímica*, Vol. 22, 2003, pp. 138-145.
- [4] Isman M.B., Botanical Insecticides, Deterrents and Repellents in Modern Agriculture and An Increasingly Regulated World. *Annual Review of Entomology*, Vol. 51, 2006, pp. 45-66.
- [5] Ogendo O., Kostyukovsky M., Ravid U., Matasyoh J., Deng A., and Omolo E., Bioactivity of *Ocimum gratissimum* L. and Two of Its Constituents Against Five Insect Pests Attacking Stored Food Products. *Journal of Stored Products Research*, Vol. 44, 2008, pp. 328-334.
- [6] Shaaya E., Kostjukovski M., Eilberg J., and Sukprakarn C., Plant Oils as Fumigants and Contact Insecticides for the Control of Stored Product Insects. *Journal of Stored Product Research*, Vol. 33, 1997, pp. 7-15.
- [7] Li Y.S., and Zou H.Y., Insecticidal Activity of Extracts from *Eupatorium adenophorum* Against Four Stored Grain Insects. *Entomological Knowledge*, Vol. 38, 2001, pp. 214-216.
- [8] Sha Sha C., Jin Fen H., and Zhi Long H., Composition of Essential Oil of Chinese *Chenopodium ambrosioides* and Insecticidal Activity Against Maize Weevil: *Sitophilus zeamais*. *Pest Management Science*, Vol. 67, 2010, pp. 714-718.
- [9] Isman M.B., Plant Essential Oils for Pest and Disease Management. *Crop Protection*, Vol. 19, Issue 8-10, 2000, pp. 603-608.
- [10] Usha R. P., and Devanad P., Efficiency of Different Plant Foliar Extracts on Grain Protection and Seed Germination in Maize. *Journal of Scientific Research*, Vol. 4, 2011, pp. 1-14.
- [11] Tapondjou A. L., Adlerb C., Fontemc D. A., Boudaa H., and Reichmuth C., Bioactivities of Cymol and Essential Oils of *Cupressus sempervirens* and *Eucalyptus saligna* Against *Sitophilus zeamais* Motschulsky and *Tribolium confusum* du Val. *Journal of Stored Products Research*, Vol. 41, 2005, pp. 91-102.
- [12] Ouattara B., Simard R. E., Holley R. A., Piette G. J. P., and Beign A., Antibacterial Activity of Selected Fatty Acids and Essential Oils Against Six Meat Spoilage Organisms. *International Journal of Food Microbiology*, Vol. 37, 1997, pp. 155-162.
- [13] Ortega N. M. M., Robles B. R. M., Acedo F. E., González L. A., Morales E. A., and Vázquez M. L., Chemical Composition and Antimicrobial Activity of Oregano (*Lippia palmeri* S. Wats) Essential Oil. *Revista Fitotecnica*, Vol. 34, Issue 1, 2011, pp.11-17.
- [14] Erler F., and Cetin H., Components from the Essential Oils from Two Origanum Species as Larvicides Against *Euproctis Chrysorrhoea* (Lepidoptera: Lymantriidae). *Journal of Agricultural and Urban Entomology*, Vol. 26, 2009, pp. 31-40.
- [15] Cinco-Moroyoqui F. J., Rosas-Burgos E. C., Borboa-Flores J., and Cortez-Rocha M. O., α -Amylase Activity of *Rhyzopertha dominica* (Coleoptera: Bostrichidae) Reared on Several Wheat Varieties and Its Inhibition With Kernel Extracts. *Journal of Economic Entomology*, Vol. 99, 2006, pp. 2146-2150.
- [16] Negahban M., Moharramipour S., and Sefidkon F., Insecticidal Activity of Essential Oil from *Artemisia sieberi* Beser Against Three Stored-Product Insects. *Journal of Stored Products Research*, Vol. 43, 2007, pp. 123-128.

ANGIOTENSIN CONVERTING ENZYME INHIBITOR ACTIVITY OF THE SOYBEAN TEMPEH PROTEIN AS FUNCTIONAL FOOD

* Sri Yadi Chalid¹, Sandra Hermanto² Amalia Rahmawati³

^{1,2,3} Chemistry dept. Faculty of Science and Technology, Islamic State University Syarif Hidayatullah,
Indonesia

ABSTRACT

Tempeh is an Indonesia's indigenous fermented food that is widely preferred by the community. Fermented food have functional food as an antihypertensive by angiotensin converting enzyme (ACE) inhibitor. This study was aimed to measure protein activity of tempeh as ACE inhibitor. Soybean was fermented using *Rhizopus* sp. with various fermentation times of 0, 6, 12, 18, 24, 30, 36, 42 and 48 hours. Protein extraction was performed at the isoelectric point, the degree of hydrolysis was considered as trichloroacetic-dissolved nitrogen. The best fermentation time was determined by the degree of hydrolysis (DH) and protein content. Protein extract was fractionated by using an ultra membrane with 3 kDa cut off. Proximate analysis was performed by AOAC method. The measurement of ACE inhibitor was based on the formation of hippurate acid-H-Histidyl-L-leucine (HHL). Results of this study revealed that the lipid content of tempeh was lower than that of soybean while the water content of tempeh was higher than soybean. The best fermentation time was found at 24 hours. Protein content was 236.31 ppm and DH was 36.03%. The best fraction that was able to inhibit ACE was a fraction below 3 kDa with an inhibitory capability of 67.43%. Protein of tempeh contained proline, valine, isoleucine, histidine, leucine, tyrosine, aspartic acid, lysine, glycine, arginine, alanine, phenylalanine, glutamic acid, serine and methionine. This study concludes that tempeh was able to inhibit ACE by in vitro and is potentially continued to in vivo examination, thus tempeh can be claimed as a functional food

Keywords: Tempeh, Indigenous fermented, Angiotension converting enzym, Isoelectric point

INTRODUCTION

Tempeh is a traditional Indonesian food which is made by fermentation, is widely preferred and proven to provide benefits for the health of human body. Opportunity to develop local food such as tempeh to be recognized internationally is not impossible since Indonesia has proposed to the 34th Codex Alimentarius Commission (CAC) meeting in Geneva on July 9, 2011.

Tempeh has the potential to be developed into functional foods as antihypertensive if there is scientific data obtained through in vitro and in vivo assessment. Tempeh is made by fermentation using *Rhizopus* sp. This fungus produces several antibiotics that are active against *Bacillus* species, particularly *Bacillus subtilis* [1], has anticancer and antiangiogenesis (the formation of new blood vessels) properties which are also shown by genistein compound of isoflavone derivative extracted from tempeh [2]. Ansarullah [3] states that blood pressure of hypertension sufferers decreases after consumption of soybean drink. Tempeh is useful in inhibiting the formation of blood vessels of cancer cells [2], improving bone health [4], as anti-bacterial agent [5] and active antioxidant. In addition, [6] tempeh extract is beneficial in the management and prevention of dementia and Alzheimer's disease [7].

Therefore, the functional effect of soy protein which acts as ACE inhibitor can be enhanced by fermentation [8].

Hypertension and cardiovascular disease increase along with an unhealthy lifestyle and a low facility for prevention of hypertension [9]. Currently, there are available various synthetic drugs for the treatment of hypertension. Although those are effective, synthetic drugs have many side effects such as a chronic dry cough that causes acute respiratory distress even to death [10].

Synthetic antihypertensive drugs such as Captopril® and Lisinopril® inhibit the ACE enzyme, increase bradykinin and reduce angiotensin II, but the long-term using the medicines may cause side effects. A total of 36% of patients complained about the side effects of captopril and as many as 45% complained of amlodipine [11]. Several studies indicated that hydrolyzed soy protein could lower blood pressure in vitro basis.

The objective of this study was to determine fermentation time, the degree of hydrolysis, protein fractionation and inhibitory activity assessment of angiotensin converting enzyme (ACE). The ACE inhibitor assessment was based on the release of hippurate acid from hippuryl-L-histidyl-L-leucine substrate [12], [13].

METHOD

Soybean Fermentation

The fermentation period of soybeans was varied as follows 0, 6, 12, 18, 24, 30, 36, 42 and 48 hours. A total of 1000 grams soybeans (from traditional market) were soaked in the water with ratio of 2:1 for 18 hours, it was further removed from the skin. Cleaned soybeans were steamed using the corm for 30-40 minutes (until tender) and were then cooled. 2 grams starter Raprima (from PT Aneka Fermentasi Industri (AFI) Indonesia) was inoculated by mixing the starter with steamed soybean evenly. Furthermore, it was inserted into the measuring plastic that has been given small holes. Inoculation result was incubated at 30°C until tempeh was formed.

Disposal of Lipid from Tempeh Flour

Tempeh was crushed using blender and soaked in a hexane solution at a ratio of 1: 5 (sample: hexane) for 1 hour at a room temperature while stirring. The supernatant was removed and the precipitate was repeated with the same process by adding hexane solution twice with the same ratio for removing the remaining lipid. The lipid-free flour was collected and dried to liberate hexane [14] thus resulting in lipid-free tempeh flour .

Protein Extraction of Tempeh

Protein extraction was performed by precipitation method at isoelectric point [15]. Lipid-free tempeh flour was soaked in the water a ratio of 1:10 (w/v), pH 8.5 with addition of 1N NaOH solution. Suspension was stirred using a magnetic stirrer at a room temperature for 1 hour and centrifuged (6000 x g) for 20 minutes at 4°C. Supernatant was collected and adjusted to pH 4.5 with the addition of 1.0 N HCl solution. The suspension was centrifuged at 6000xg for 20 min, a temperature of 4°C [16]. The resulting hydrolysis was lyophilized and stored in freezer with temperature of -20°C, thus protein hydrolysates would be obtained.

Protein Analysis and Degree of Hydrolysis

Hydrolysate of tempeh protein was dissolved in aquadest with a ratio of 1:10 (g/v) while stirring until dissolved evenly. The mixture was centrifuged (13000 xg, 15 min, 4°C). A total of 100 µL supernatant was piped into the test tube and added with 5 mL of Bradford solution while shaking and allowed to stand for 15 min. The absorbance was measured using a spectrophotometer at a wavelength of λ 595 nm [17].

The degree of hydrolysis was calculated using the SN-TCA method [18], a total of 2 mg of protein hydrolysate was added with 2 mL 10% (w/v) trichloroacetic acid solution. The mixture was allowed for 30 minutes to obtain the precipitate and then centrifuged (7.800 g, 4 °C, for 15 minutes). Protein levels of supernatant and precipitate were measured by using Kjeldhal method.

ACE inhibitory Examination

Enzyme activity was determined using the Hip-His-Leu (HHL) synthetic peptide as a substrate which was based on the developed method [12],[13]. A protein extract solution of 15 µl was added with 125 µl of 100 mM sodium borate buffer solution (pH 8.3) containing 7.6 mM Hip-His-Leu and 608 mM NaCl, and was preincubated for 5 min at temperature of 37 °C. The reaction begins with the addition of 50 µL ACE enzyme (rabbit lung-derived angiotensin I-converting enzyme) dissolved in the aquadest. The mixture was incubated for 30 minutes at temperature of 37 °C. As a blank, it was used 50 µL aquadest.

The reaction was discontinued with the addition of 125 µL 1N HCl. Hippurate acid released by ACE was extracted by adding 750 µL ethyl acetate to the mixture and was immediately shaken using vortex. The mixture was centrifuged at a velocity of 13.760 x g for 10 min, a total of 500 µL top layer of the supernatant was collected and dried at 90 °C for 30 min. Furthermore, hippurate acid was dissolved in 1 mL distilled water and the absorbance was measured by spectrophotometer at 228 nm wavelength.

$$\% \text{ Inhibitory Activity} = [(C-A)/(C-B)] \times 100\%$$

Description:

A= sample absorbance

B= blank absorbance

C= control absorbance (aquadest).

Amino Acid Analysis

Amino acid composition analysis determined was the result of fractionation with 3 kDa membrane. Sample was added with 5 mL 6 N HCl while stirring with stirrer, and flowed with nitrogen and hydrolyzed at temperature of 110 °C for 22 hours. Hydrolysates obtained was then cooled at room temperature, and transferred into a 50 ml measuring flask, also added with aquabidest. The solution was filtered by a filter membrane with a size of 0.45 µm. A total of 500 µl filtrate was added with 40 µL AABA (alpha amino butyric acid) and 460 µl aquabidest. A total of 10 µl solution was added with 70 µl AccQ-fluor borate and shaken using vortex. Furthermore, a total of 20 µl fluorine A reagent was added and shaken using a vortex, and allowed to stand for 1 minute. Subsequently, the solution was incubated for 10 minutes at a

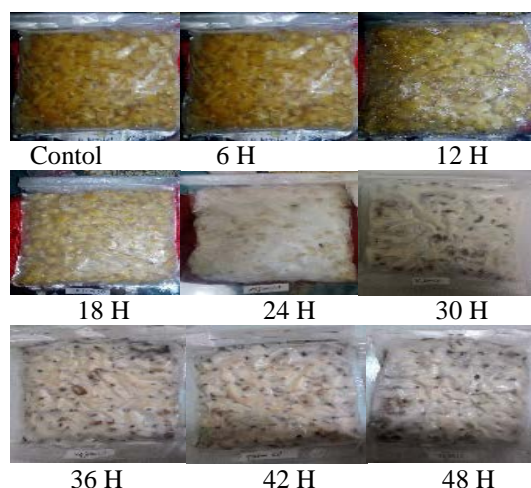
temperature of 55 °C and injected in UPLC (ultra high performance liquid chromatography) [19].

RESULTS AND DISCUSSION

Tempeh

There are four steps in the making process of tempeh, namely soaking, boiling, inoculation of *Rhizopus* and incubation at room temperature [20]. Tempeh was made using a starter containing a mixture of *Rhizopus* sp. Variety of fermentation times used were 0 hour as control 0, 6, 12, 18, 24, 30, 36, 42 and 48 hours. The best physical appearance of tempeh depends on the duration of fermentation (hour) which is based on observation of physical shape, odor and the increase of *Rhizopus mycelium* on the surface of the soybean. The physical appearance of tempeh during fermentation is shown in Fig. 1.

Fig. 1 Physical appearance of tempeh at various fermentation times (H)



The 24 hours fermentation produced tempeh with better texture and good odor in which *Rhizopus* sp. mycelium covered the surface of soybean evenly. *Rhizopus* sp. started to grow at 18th hour and continued to next hours. The best growth of *Rhizopus* sp. was obtained at 24th hour fermentation. *Rhizopus* mycelium of 30 hours fermentation showed a black color which indicates that tempeh began to rot. Types of *Rhizopus* which primarily found on tempeh starter are *Rhizopus oligosporus* dan *Rhizopus oryzae* [20].

Fermentation of soybean into tempeh that is widely done by Indonesian people lasts between 18 to 36 hours. After 36 hours, tempeh begins to decompose which can be seen from discoloration of tempeh such as blackening color and bad odor. Yet in this study, 30 hours fermentation had produced out of odor tempeh, thus we conclude that tempeh produced in this study is faster to decompose

compared with tempeh in the other studies. Good tempeh has a fresh aroma such as the scent of mycelium and free amino acids. The quality of tempeh can be known from the growth of mycelium. If the mycelium grows evenly on the surface of tempeh, it can be declared as good tempeh. Otherwise, if the mycelium is accumulated on the certain points of soybean surface, it is declared as a not good tempeh [21].

Proximate Analysis Results

Table 1 Results of proximate analysis of tempeh of 24 hours incubation

Parameter	Sample	
	Soybea	Tempeh
Water content (%)	11.81	57.42
Ash content (%)	4.95	1.64
Lipid (%)	15.28	9.86
Protein (%)	37.17	21.84
Dissolved Protein (ppm)	75.19	236.31

Based on Table 1, it is known that lipid content of fermented soybean (tempeh) was lower than that of unfermented soybean (control) with a decrease of 64.53%. Similar with [22], lipid content of soybean was 18.38%. Meanwhile, dissolved protein content for control and tempeh was 75.19 and 236.31 ppm, respectively.

Lipid on tempeh

Lipid disposal from tempeh in this study was aimed to obtain a higher protein extract. Wu [15] states that the samples with lipid disposal have a high protein content of 72.35% while samples without lipid disposal have a protein content of 55.88%. Results of this study indicate that fermentation can reduce lipid content in tempeh. Furthermore, the lowest lipid content obtained at 24 hours fermentation was 9.04%. We presume this lipid reduction activity is caused by lipase.

Degree of Hydrolysis and Protein Content

Degree of hydrolysis (DH) is defined as the proportion of peptide bonding broken down in protein hydrolysates. The DH value increased significantly at 18 hours fermentation and the highest value was obtained at 24 hours fermentation in which the mycelium has been seen to grow covering the surface of tempeh. The result of the calculation is presented in Table 2. The DH value increased rapidly over 18 hours fermentation since the mycelium is already grown.

Table 2 Value of degree of hydrolysis and amount of protein on tempeh

Fermentation	Degree of	Protein Level
--------------	-----------	---------------

Time (H)	Hydrolysis (%)	(g)
0	1.76	0.54
6	4.48	1.17
12	2.94	1.65
18	31.71	0.24
24	36.03	3.13
30	30.93	0.45

A high degree of hydrolysis indicates that the protein is easily hydrolyzed (Table 1). In accordance with this study, increased DH value and protein content are suspected as a result of protease activity produced by *Rhizopus* sp. The main function of *Rhizopus* in fermentation is the synthesis of enzymes that hydrolyze compounds in soybean [21].

The DH value increased significantly on tempeh of 18 hours fermentation, where mycelium was seen growing on the surface of soybean (Fig.1). Bioactive peptide of the food is produced during the enzymatic hydrolysis process and fermentation or in the gastrointestinal tract. The resulting peptide has antihypertensive activity [23]. "Hrckova [24] showed that the highest degree of hydrolysis was 39.5% with lipid content had been disposed from protease of commercial soy flour". The high dissolved protein content in this study was obtained in fermented soybean (tempeh) for 6 and 24 hours (data not shown).

ACE Inhibitor Activity

Bioactive peptide released from dietary protein is widely used for the management of hypertension based on the Angiotensin I-Converting Enzyme (ACE) inhibitory activity, which is an enzyme regulates the mechanism of regulation of Renin Angiotensin System (RAS), which is food peptide that interacts with RAS and the vascular system and contributes to a decrease in blood pressure [25]. Peptides with sequences of Leu-Val-Tyr, Leu-Gln-Pro and Leu-Lys-Tyr of soy flour indicate Angiotensin I-Converting Enzyme (ACE) inhibitory activity [26]. Peptides with sequences of Met-Asn-Pro, As-Pro-Pro, Pro-Pro-Lys, Ile-Thr-Thr, Thr-Thr-Asn, and Thr-Asn-Pr have ACE inhibitory activity [13]. Angiotensin I-Converting Enzyme (ACE) catalyzes the conversion of angiotensin I to angiotensin II, which is a vasoconstrictor and also inactivates the antihypertensivity of a bradykinin as a vasodilator. Peptides derived from food proteins may have ACE inhibitory activity [27].

Some fermented foods have ACE inhibitory activity such as brown rice [28], tofuyo extract [29], a traditional Japanese food like steamed soybeans fermented by *Bacillus* (natto) [30]. By in vivo, Natto is antihypertensive [31], also pigeon pea fermented using *Bacillus subtilis* [32], a pasta made from Korean soybeans is proven to act as an

antihypertensive food [33] so that the above products can be claimed as functional food.

In order to make tempeh as a functional food, it must be obtained in vitro and in vivo data from research findings. For in vitro, it was obtained a value of 67.43%, which is the result of measurement of ACE inhibitory activity of protein extract of tempeh. This value was obtained from the fraction below 3 KDa.

Amino Acid Composition of Protein Hydrolysates using 3 Kda Membrane

Amino acid analysis was performed to determine the type and level of amino acid found in soybean hydrolysate. Results of the amino acid analysis using UPLC are presented in Table 3. The result showed that tempeh contains both essential and non-essential amino acids. Predominant amino acids are glutamic acid, lysine, leucine, alanine, valine and phenylalanine, while predominant essential amino acids are Thr, Leu, Lys, Val, Met and Phe.

Table 3. Amino acid content of tempeh hydrolysate using 3 KDa membrane

No	Type of Amino Acid	Amino Acid Content (ppm)
1	L-Histidine	1106.79
2	L-Threonine	1442.295
3	L-Proline	1636.755
4	L-Tyrosine	2907.28
5	L-Leucine	4774.595
6	L- Aspartic acid	895.45
7	L-Lysine HCl	3688.065
8	Glycine	1516.235
9	L-Arginine	2276.61
10	L-Alanine	3257.36
11	L-Valine	2235.715
12	L-Isoleucine	2053.84
13	L-Phenylalanine	3905.97
14	L- Glutamic acid	6936.845
15	L-Serine	1005.745
16	L-Methionine	614.43
17	L- Cysteine	-
18	L-Tryptopane	-

"Kitts [34] revealed that bioactive peptides generally have low molecular weight consisting 2-9 amino acid residues and are resistant to digestive enzymes have hydrophobic amino acid residues from the type of proline, lysine or arginine". In this study, it was obtained hydrophobic amino acids such as alanine, valine, isoleucine, proline, phenylalanine, and methionine, thus authors presume that the functional properties of tempeh as ACE inhibitors are obtained from the above amino acids.

CONCLUSION

Fermentation for 24 hours produced tempeh with the best texture, low lipid and high protein content. Protein extract showed a high ACE inhibitory capacity with a total of 16 essential and non-essential amino acid compositions. Tempe has the potential to be developed as a functional food.

ACKNOWLEDGEMENT

Authors thank the Rector of UIN Syarif Hidayatullah Jakarta for research funding through Puslitpen LP2M 2017

REFERENCES

- [1] Kobayasi S. Y., Okazaki N., and Koseki T., Purification and characterization of an antibiotic substance produced from *Rhizopus oligosporus* IFO 8631, *Biosci. Biotechnol. Biochem.*, Vol. 56, Issue. 1, 1992, pp. 94–98.
- [2] Kiriakidis S., O. Högemeier, S., Starcke F., Dombrowski J. C. Hahne, M. Pepper, H. C. Jha, and N. Wernert, Novel tempeh (fermented soyabean) isoflavones inhibit in vivo angiogenesis in the chicken chorioallantoic membrane assay, *British Journal of Nutrition.* Vol. 93, Issue 3, 2005, pp. 317–323.
- [3] Ansarullah A., Marliyati, S. A., and Astawan., Efek intervensi minuman tempe terhadap tekanan darah penderita hipertensi dan hiperkolesterolemia. *Jurnal Gizi dan Pangan, Jurnal Gizi dan Pangan*, Vol. 12, Issue 2, 2017, pp. 101–108,
- [4] Kusumorini, N., Manalu, W., and Maheshwari, H., Supplementation of tempeh extract for improving quality of bone in premenopausal conditions using rats as animal models, in *Proceedings of The Annual International Conference, Syiah Kuala University-Life Sciences & Engineering Chapter*, 2013, Vol. 3, Issue 1.
- [5] Kuligowski, M., Jasinska-Kuligowska, I., and Nowak, J. Evaluation of bean and soy tempeh influence on intestinal bacteria and estimation of antibacterial properties of bean tempeh *Polish journal of microbiology*, 62 issue 2, 2013, pp.189-194
- [6] Hoppe, M. B., Jha, H. C., and Egge, H., Structure of an antioxidant from fermented soybeans (tempeh)., *Journal of the American Oil Chemists' Society.*, 74, issue 4,1997, pp. 477-479.
- [7] Hamad, A., Mani, V., Ramasamy, K., Lim, S. M., and Majeed, A. B. A., Memory enhancement in rats by soybean and tempeh extracts is associated with improved cholinergic and reduced neuroinflammatory activities, *Sains Malaysiana*, Vol. 45, Issue 9, 2016. pp. 1299-1310.
- [8] Gibbs, B. F., Zougman, A., Masse, R., and Mulligan, C. Production and characterization of bioactive peptides from soy hydrolysate and soy-fermented food, *Food research international*, Vol. 37, Issue 2, 2004, pp. 123-131.
- [9] Depertemen Kesehatan Republik Indonesia. Pharma Cheutical Care untuk Penyakit Hipertensi. 2016. <http://pafisumut.or.id/wp-content/uploads>.
- [10] Cheung, L. K., Aluko, R. E., Cliff, M. A., and Li-Chan, E. C., Effects of exopeptidase treatment on antihypertensive activity and taste attributes of enzymatic whey protein hydrolysates, *Journal of Functional Foods*, Vol. 13, 2015. pp. 262–275.
- [11] Kristanti P., Effectiveness and Side Effects of Antihypertensive Medication Usage in Hypertension Patients at Puskesmas Kalirungkut Surabaya. *Jurnal Ilmiah Mahasiswa Universitas Surabaya*. Vol. 4 Issue 2. pp. 1-13.
- [12] Cushman, D. W., and Cheung, H. S. Spectrophotometric assay and properties of the angiotensin-converting enzyme of rabbit lung. *Biochemical pharmacology*, Vol. 20 Issue 7, 1971. pp 1637-1648.
- [13] Arihara, K., Nakashima, Y., Mukai, T., Ishikawa, S., and Itoh, M., Peptide inhibitors for angiotensin I-converting enzyme from enzymatic hydrolysates of porcine skeletal muscle proteins. *Meat Science*, Vol. 57, Issue 3, 2001, pp. 319–324.
- [14] Liu, C., Wang, H., Cui, Z., He X., Wang X., Zeng X., and Ma H., Optimization of extraction and isolation for 11S and 7S globulins of soybean seed storage protein. *Food Chemistry*, Vol. 102, Issue 4, 2007, pp. 1310–1316.
- [15] Wu, H., Wang, Q., Ma, T., and Ren, J., Comparative studies on the functional properties of various protein concentrate preparations of peanut protein. *Food Research International*, Vol. 42, Issue. 3, 2009, pp. 343–348.
- [16] Chove, B. E., Grandison, A. S., and Lewis, M. J., Emulsifying properties of soy protein isolate fractions obtained by isoelectric precipitation. *Journal of the Science of Food and Agriculture*, Vol. 81, Issue. 8, 2001. pp. 759–763.
- [17] Bradford, Marion M., A rapid and sensitive method for the quantitation of microgram quantities of protein utilizing the principle of protein-dye binding. *Analytical*

- biochemistry, Vol. 72, 1976, pp. 248–254.
- [18] Hoyle N. T., and Merritt, J. O. H. N., Quality of fish protein hydrolysates from herring (*Clupea harengus*). *Journal of food Science*, Vol. 59, Issue. 1, 1994, pp. 76–79.
- [19] Boogers I., Plugge W., Stokkermans Y. Q., and Duchateau A. L., Ultra-performance liquid chromatographic analysis of amino acids in protein hydrolysates using an automated pre-column derivatisation method. *Journal of Chromatography A*, Vol. 1189, Issue. 1–2, 2008, pp. 406–409.
- [20] Astawan, M., Wresdiyati, T., Widowati, S., Bintari, S. H., and Ichsan, N., Physico-chemical Characteristics and Functional Properties of Tempe Made from Different Soybeans Varieties. *Jurnal Pangan*, Vol. 22, Issue. 3, 2013, pp. 241–252.
- [21] Hachmeister, K. A., and Fung, D. Y., Tempeh: A mold-modified indigenous fermented food made from soybeans and/or cereal grains. *Critical reviews in microbiology*, Vol. 19, Issue. 3, 1993, pp. 137–188.
- [22] Banaszkiwicz T, For Chapter in a Book, *Soy bean And Nutrition*, H. El-Shemy, Ed. 2011, pp. 1–20.
- [23] Hernández-Ledesma, B., del Mar Contreras, M., and Recio, I., Antihypertensive peptides: Production, bioavailability and incorporation into foods. *Advances in colloid and interface science*. Vol. 165, Issue 1, 2011, pp. 23–35.
- [24] Hrkova, M., Rusnakova, M., and Zemanovic, J. Enzymatic hydrolysis of defatted soy flour by three different proteases and their effect on the functional properties of resulting protein hydrolysates. *Czech journal of food sciences*, Vol. 20, Issue 1, 2002, pp. 1467–1471.
- [25] Udenigwe, C. C., and Mohan A., Mechanisms of food protein-derived antihypertensive peptides other than ACE inhibition. *Journal of Functional Foods*, Vol. 8, 2014, pp. 45–52.
- [26] Nakano, D., Ogura, K., Miyakoshi, M., Ishii, F., Kawanishi, H., Kurumazuka, D, Kwak, C, Ikemura, K., Takaoka M., and Moriguchi S, Antihypertensive effect of angiotensin I-converting enzyme inhibitory peptides from a sesame protein hydrolysate in spontaneously hypertensive rats. *Bioscience, biotechnology, and biochemistry*, Vol. 70, Issue. 5, 2006, pp. 1118–1126.
- [27] Nishibori, N., Kishibuchi, R., Sagara, T., Itoh, M., Horie, Y., and Shrestha S., Angiotensin I-converting enzyme inhibitory peptides derived from food proteins and their physiological and pharmacological effects. *Nutrition research*, Vol. 24, Issue 7, 2004, pp. 469–486.
- [28] Nishibori, N., Kishibuchi, R., Sagara, T., Itoh, M., Horie, Y., and Morita, K., Angiotensin-I converting enzyme (ACE) inhibitory activity of aqueous extract prepared from fermented brown rice: A potential functional food for management of hypertension, *Phytoparmacol. 2013a*, Vol. 4, pp. 237–245.
- [29] Kuba, M., Tanaka, K., Tawata, S., Takeda, Y., and Yasuda M, Angiotensin I-converting enzyme inhibitory peptides isolated from tofuyo fermented soybean food. *Bioscience, biotechnology, and biochemistry*, Vol. 67, Issue. 6, 2003, pp. 1278–1283.
- [30] Okamoto, A. H., Hanagata, Y., Kawamura, and Yanagida, F., Anti-hypertensive substances in fermented soybean, natto. *Plant foods for human nutrition*, Vol. 47, Issue. 1, 1995, pp. 39–47.
- [31] Ibe, S., Yoshida, K., Kumada, K., Tsurushiin, S., Furusho, T., and Otohe K, Antihypertensive effects of natto, a traditional Japanese fermented food, in spontaneously hypertensive rats. *Food science and technology research*, Vol. 15, Issue 2, 2009, pp. 199–202.
- [32] Lee, B. H., Lai, Y. S., and Wu, S, C Antioxidation, angiotensin converting enzyme inhibition activity, nattokinase, and antihypertension of *Bacillus subtilis* (natto)-fermented pigeon pea. *Journal of food and drug analysis*, Vol. 23, Issue. 4, 2015, pp. 750–757.
- [33] Shin, Z. I., Yu, R., Park, S. A., Chung, D. K., Ahn, C. W., Nam, H. S., and Lee H. J., His-His-Leu, an angiotensin I converting enzyme inhibitory peptide derived from Korean soybean paste, exerts antihypertensive activity in vivo. *Journal of Agricultural and Food Chemistry*, Vol. 49, Issue 6, 20011, pp. 3004–3009.
- [34] Kitts D. D., and Weiler K., Bioactive proteins and peptides from food sources. Applications of bioprocesses used in isolation and recovery. *Current pharmaceutical design*, Vol. 9, Issue. 16, 2003, pp. 1309–1323.

THE MODIFIED DECOMPOSITION METHOD FOR SOLVING VOLTERRA INTEGRAL EQUATION OF THE SECOND KIND USING MAPLE

Dalal Adnan Maturi¹

¹Departement of Mathematics, Faculty of Science, king Abdulaziz University, Saudi Arabia

ABSTRACT

In this paper, we obtain the approximate solution for Volterra integral equation of the second kind through using modified decomposition method by using Maple program, so all calculations can be easily using Maple to find that exact solution.

Keywords: Volterra integral equation of the second kind, Modified Decomposition method, Maple.

INTRODUCTION

The modified decomposition method [1]-[4] has been efficiently used to solve linear and nonlinear problems such as differential equations and integral equations.

A Modification in successive approximation method for solving nonlinear Volterra Hammerstein integral equations of the second kind by Sh. Javadi [5]. Also, Modification of Laplace Adomian Decomposition method for solving nonlinear Volterra integral and integro-differential equations based on Newton Raphson formula by Dimple Rani., and Vinod Mishra [6].

The modified decomposition needs only a slight variation from the standard decomposition method may provide the exact solution by using iterations only and sometimes without using the so-called adomain polynomials, its effectiveness is based on the assumption that the function f can be divided into two parts and the paper choice of f_1 and f_2 .

THE MODIFIED DECOMPOSITION METHOD

The standard decomposition method,

$$u_0(x) = f(x),$$

$$u_{k+1}(x) = \lambda \int_0^x K(x, t) u_k(t) dt, \quad k \geq 0, \quad (1)$$

Having determined the components $u_0(x)$, $u_1(x)$, $u_2(x)$, ..., the solution $u(x)$ in a series form defined by

$$u(x) = \sum_{n=0}^{\infty} u_n(x) \quad (2)$$

The modified decomposition method [3]. The modification is based on the assumption that the function $f(x)$ can be divided into two parts,

namely, $f_1(x)$ and $f_2(x)$. Under this assumption we set

$$f(x) = f_1(x) + f_2(x). \quad (3)$$

Accordingly, a slight variation was proposed only for the components $u_0(x)$ and $u_1(x)$. The suggestion was that only the part $f_1(x)$ will be assigned to the zeroth component $u_0(x)$, whereas the remaining part $f_2(x)$ will be combined with the other terms given into (1) to define $u_1(x)$.

Consequently, the modified recursive relation

$$u_0(x) = f_1(x),$$

$$u_1(x) = f_2(x) + \lambda \int_0^x K(x, t) u_0(t) dt,$$

$$u_{k+1}(x) = \lambda \int_0^x K(x, t) u_k(t) dt, \quad k \geq 1. \quad (4)$$

was developed. It is important to note here that there were some conclusions made in [1]. First, the slight variation in reducing the number of terms of $u_0(x)$ will result in a reduction of the computational work and will accelerate the convergence. Second, this slight variation in the definition of the components $u_0(x)$ and $u_1(x)$ may provide the solution by using two iterations only.

Third, there is no need sometimes to evaluate the so-called Adomian polynomials required for the nonlinear equations.

EXAMPLE

Example 1. Consider the Volterra integral equation of second kind

$$u(x) = 1 + 2x + \sin x + x^2 - \cos x - \int_0^x u(t) dt.$$

Applying the Modified Decomposition Method using Maple we find

Table 1 Numerical results and exact solution of Volterra integral equation for example 1

x	$u(x)$	<i>Exact</i> $= 2x + \sin x$	<i>Error</i>
0.10000	0.2998334	0.2998334	0.0000000
0.20000	0.5986693	0.5986693	0.0000000
0.30000	0.8955202	0.8955202	0.0000000
0.40000	1.1894183	1.1894184	0.0000000
0.50000	1.4794255	1.4794256	0.0000001
0.60000	1.7646425	1.7646429	0.0000004
0.70000	2.0442177	2.0442191	0.0000014
0.80000	2.3173561	2.3173603	0.0000042
0.90000	2.5833269	2.5833376	0.0000107
1.00000	2.8414710	2.8414958	0.0000248

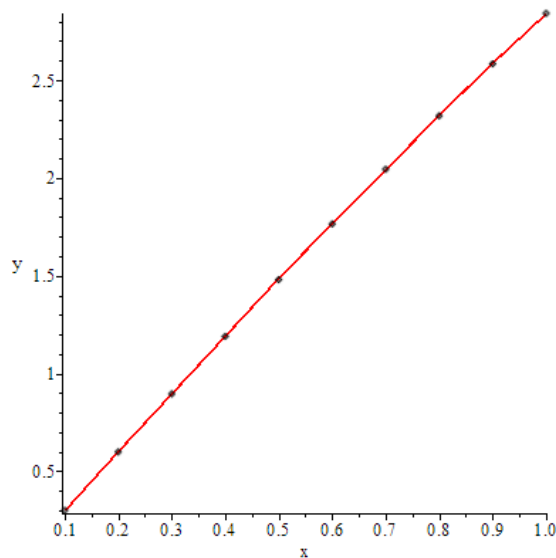


Fig.1 Plot 2D of the exact solutions result Of Volterra integral equation for example 1.

Example2. Consider the Volterra integral equation of second kind

$$u(x) = 1 + x + x^2 + \frac{1}{2}x^3 + \cosh x + x \sinh x - \int_0^x xu(t)dt.$$

Applying the Modified Decomposition Method using Maple we find

Table 2 Numerical results and exact solution of Volterra integral equation for example 2

x	$u(x)$	<i>Exact</i> $= 1 + x + \cosh x$	<i>Error</i>
0.10000	2.1050042	2.1050042	0.0000000
0.20000	2.2200668	2.2200667	0.0000000
0.30000	2.3453385	2.3453385	0.0000000

0.40000	2.4810724	2.4810723	0.0000000
0.50000	2.6276260	2.6276259	0.0000001
0.60000	2.7854652	2.7854652	0.0000000
0.70000	2.9551690	2.9551674	0.0000016
0.80000	3.1374349	3.1374288	0.0000061
0.90000	3.3330864	3.3330613	0.0000251
1.00000	3.5430806	3.5429900	0.0000900

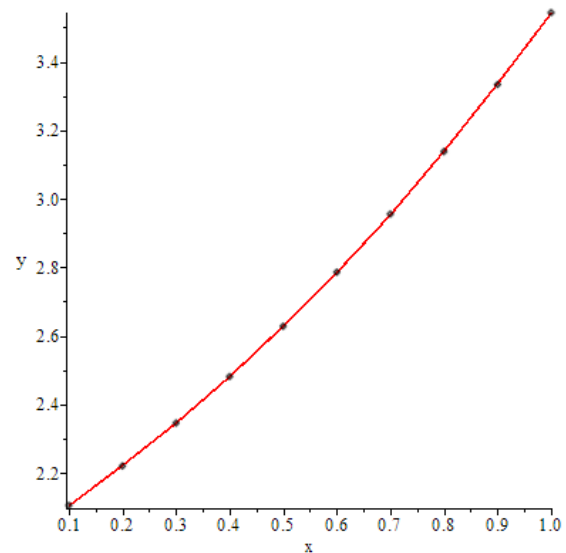


Fig. 2 Plot 2D of the exact solutions result Of Volterra integral equation for example 1.

Example 3. Consider the Fredholm integral equation of second kind

$$y(x) = e^x - xe^x + \sin x + x \cos x - \int_0^x xy(t)dt.$$

Applying the Modified Decomposition Method using Maple we find

Table 3 Numerical results and exact solution of Volterra integral equation for example 3.

x	$u(x)$	<i>Exact</i> $= e^x + \sin x$	<i>Error</i>
0.10000	1.2050043	1.2050000	0.0000043
0.20000	1.4200721	1.4200000	0.0000721
0.30000	1.6453790	1.6450000	0.0003790
0.40000	1.8812430	1.8820000	0.0007570
0.50000	2.1281468	2.1290000	0.0008532
0.60000	2.3867613	2.3890000	0.0022387
0.70000	2.6579704	2.6580000	0.0000296
0.80000	2.9428970	2.9450000	0.0021030
0.90000	3.2429300	3.2430000	0.0000700
1.00000	3.5597528	3.5610000	0.0000000

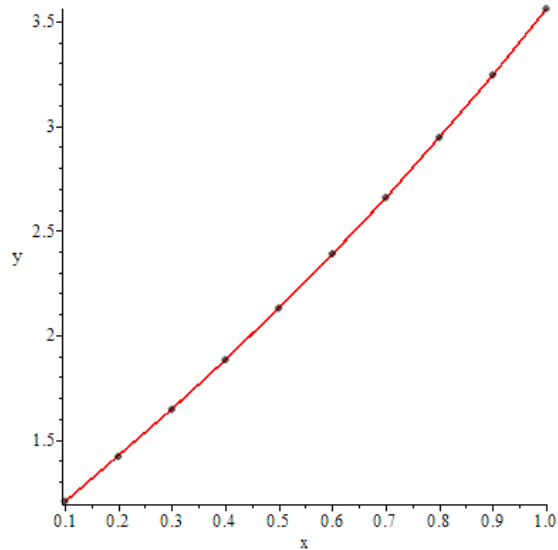


Fig. 3 Plot 2D of the exact solutions result Of Volterra integral equation for example 3.

CONCLUSION

In this paper, the Modified Decomposition Method to the solution of Volterra integral equation numerical results demonstrate that our method is an accurate and reliable numerical technique for solving Volterra integral equation. Finally, The Modified Decomposition Method using Maple can be easily extended and applied to linear or nonlinear Fredholm and Volterra integral equations of the first or second kind.

ACKNOWLEDGEMENTS

This paper was supported by the Deanship of Scientific Research (DSR), King Abdulaziz University, Jeddah..

REFERENCES

- [1] Abdul-Majid. W., A reliable Modification of Adomian Decomposition Method,. Applied Mathematics and Computation, Vol. 102, No.1, 1999, pp.77-86.
- [2] Abdul-Majid. W., and Said. A. El-S., Anew Modification of the Adomian Decomposition Method for Linear and Nonlinear Operators,. Applied Mathematics and Computation, Vol. 122, No.3, 2001 , pp.393-405.
- [3] Abdul-Majid. W., Linear and Nonlinear Integral Equations, Higher Education Press, Beijing, China, 2011.
- [4] Lie-june Xie., A New Modification of Adomian Decomposition Method for Volterra Integral Equations of the Second Kind, Volume 2013, Article ID 795015, 7pages.
- [5] Sh. Javadi., A Modification in Successive Approximation Method for Solving Nonlinear Volterra Hammerstein Integral Equations of the Second Kind, Journal of Mathematical Extension, Vol.8, No.1, 2014, 69-86.
- [6] Dimple Rani., and Vinod Mishra., Modification of Laplace Adomian Decomposition Method for Solving Nonlinear Volterra Integral and Integro-differential Equations based on Newton Raphson Formula, European Journal Of Pure And Applied Mathematics, Vol.11, No.1, 2018, 202-214.
- [7] Peter. L., Analytical and Numerical Methods for Volterra Equations, Studies in Applied Mathematics 7, SIAM, Philadelphia, 1985.
- [8] Dalal A.M, Amani..Z.B.I, Badreeh..M. G., Numerical Solution of Volterra Integral Equation of Second Kind Using Implicit Trapezoidal, Journal of Advances In Mathematics, Vol8,No.2,pp.1540-1553,2014.
- [9] Dalal .A. M., Adomian Decomposition Method of Fredholm Integral Equation of the Second Kind Using Maple, Journal of Advances In Mathematics, Vol9,No.1,pp.1868-1875,2014.
- [10] Dalal. A.M., Application of Adomian Decomposition Method for Solving of Fredholm Integral Equation of the Second Kind, European Journal of Science and Engineering, Vol9,No.2,pp.1-9,2014.
- [11] Dalal .A.M., Adomian Decomposition Method for Solving of Fredholm Integral Equation of the Second Kind Using Matlab, International Journal of GEOMATE, Dec., 2016, Vol. 11, Issue 28, pp.2830-2833.Special Issue on Science, Engineering and Environment, ISSN: 2186-2990, Japan.
- [12] Dalal A.M. and Honida M.M., Numerical Solution of System of Three Nonlinear Volterra Integral Equation Using Implicit Trapezoidal, Journal of Mathematics Research, Vol.10, No. 1, February 2018,ISSN 1916-9795 E-ISSN 1916-9809.

STRUCTURE-BASED VIRTUAL SCREENING OF INDONESIAN NATURAL PRODUCT COMPOUNDS AS EBOLA VIRUS VP30 PROTEIN INHIBITORS

Givan Andris Tio¹, Andrei Bernadette¹, Mochammad Arfin Fardiansyah Nasution¹, Puteri Aprilia Sitadevi¹,
Syahrul Ridzki Pratama¹, and Usman Sumo Friend Tambunan*

¹Department of Chemistry, Faculty of Mathematics and Natural Sciences, Universitas Indonesia, Indonesia

ABSTRACT

Indonesia is the second-highest biodiversity in the world. At least 9,600 out of 30,000 plant species exist in Indonesian tropical forests known to have medicinal properties. Hence lots of potentials still need to be explored including their abilities as an antiviral agent. Ebola virus (EBOV) continues as a major health threat worldwide with currently neither effective vaccine nor drug available. VP30 is one of the most important proteins for viral transcription activator of EBOV. Therefore, inhibiting this protein can be a viable choice for disturbing the life cycle of this virus. In this research, about 3,430 Indonesian natural product compounds had been screened through computational studies. These compounds were subjected into computational ADMET test using DataWarrior v4.7.2 while the molecular interaction and Gibbs free binding energy ($\Delta G_{\text{binding}}$) value of the selected compounds were analyzed and calculated using MOE 2014.09 software. Finally, the oral bioavailability of the selected compounds would be predicted using SwissADME software. Through this study, three compounds were selected to be potential VP30 inhibitors due to the lowest $\Delta G_{\text{binding}}$ value. They were aglamide C, IDNP-206, and scoulerine, which have $\Delta G_{\text{binding}}$ value of -9.7940 kcal/mol, -8.2686 kcal/mol, and -7.3823 kcal/mol, respectively. Moreover, the all of these compounds did not possess any toxicity properties, nor have low oral bioavailability, suggested that all three compounds may be highly absorbed in the human body through oral administration. Thus, these compounds should be liable to be selected as the drug candidate of EBOV targeting VP30 and analyzed its antiviral activities further through molecular dynamics simulation and in vitro experiment.

Keywords: Indonesian natural products, EBOV, VP30, Molecular docking, ADMET test.

INTRODUCTION

Ebola virus disease (EVD) is one of the fatal diseases around the globe, which infected no less than 28,642 people and killed 11,319 people globally [1]. Although extensive ongoing research has been performed, to date, no approved cure has been affirmed for this malignant disease. EVD can be easily characterized by severe hemorrhagic fever, focal necrosis of the liver, kidney, and spleen, bleeding diathesis and sudden shock with a mortality rate of 90% [2]. EVD caused by Ebola virus (EBOV), a lipid-enveloped negatively stranded RNA virus affecting both human and non-human primates. There are five species of the virus been identified; include Zaire, Sudan, Ivory Coast, Bundibugyo and Reston EBOV with the highest fatality attributed to the Zaire species [3].

EBOV outbreak drew much attention to the drug discovery and development for this deadly pathogen. Currently, several approaches have been undergone to effectively combat EBOV, such as the development of peptides, application of monoclonal antibodies, small molecules inhibitors, recombinant DNA vectors as well as repurposing existing drugs [4], [5]. Therapeutics target and attack the virus at different stages of its life cycle, thereby halting virus

replication and reducing destruction of the host immune system [6].

Due to the high mutable genome that resides in EBOV, the developments of EBOV drug are focused on the high-conserved regions. One of them is VP30, the transcription activator domain in EBOV. This virus had multiple functions, such as transcription activator and involved in nucleocapsid assembly. VP30 phosphorylation assumed to be a crucial regulatory factor in establishing if the protein is indeed involved in transcription or assembly of the virus. The N-terminal of EBOV VP30 presents with a Cys3-His zinc-binding domain native to M2-1 proteins of pneumoviruses and MARV VP30 [7]–[9].

Natural products have been considered as one of the potential lead compound sources because of their attractive bioactivities. Furthermore, many drugs have been sold on the market are either acquired or derived from natural sources compounds [10]. As the second-highest biodiversity country in the world, Indonesia has a high potential to produce a new drug candidate from its natural sources, either from its plants or animals [11]. Thus, this research aims to obtain new drugs from Indonesian natural products for combating Ebola disease by inhibiting in the VP30 protein through in silico drug design method.

RESEARCH METHODOLOGY

Tools and Materials

This study was conducted using both offline and online software such as Molecular Operating Environment (MOE) 2014.09 [12], DataWarrior v4.7.2 [13], SWISS-MODEL [14], and SwissADME [15]. Then, the structure of Indonesian Natural Products that used as ligands was obtained from Herbal Database (HerbalDB), which developed by the Faculty of Pharmacy, Universitas Indonesia (<http://herbaldb.farmasi.ui.ac.id/v3/index.php>) [11]. This research was conducted based on the research pipeline that has been previously performed by our research group [16]–[18].

Preparation and Optimization of Indonesian Natural Products

The molecular structures of Indonesian Natural Products were retrieved from HerbalDB in .mol file format. Followed by the computational ADME-Tox test using DataWarrior v4.7.2 software. All Indonesian natural product ligands were screened based on their druglikeness and their toxicity properties, such as mutagenic, tumorigenic, irritant, and reproductive effect. Then, the remaining ligands were prepared and optimized by using default protocol on MOE 2014.09 software.

Preparation of EBOV VP30

In this research, EBOV VP30 sequence was obtained from the National Center for Biotechnology Information (NCBI) database (<http://www.ncbi.nlm.nih.gov/>) in FASTA file format. Then, the 3D-structure of EBOV VP30 was searched by using SWISS-MODEL then downloaded from the Research Collaboratory for Structural Bioinformatics - Protein Data Bank (RSCB-PDB) (<http://rcsb.org/pdb/home/home.do>) in .pdb file format. The downloaded structure was prepared and optimized by using 'LigX' protocol on MOE 2014.09 software, which slight modification has been made compared to the default protocol.

Molecular docking simulations

The docking simulations of EBOV VP30 protein was done by using MOE 2014.09 software. Molecular docking simulations were divided into four stages. First, the prepared ligands underwent rigid docking with 30-1 retains. Then, these ligands were selected based on RMSD (Root Mean Square Deviation) and free binding energy calculations. Second, the selected ligands underwent rigid docking with 100-1 retains. Third, 100-1 retains flexible docking protocol was performed to decrease the number of selected ligands. Finally, these selected ligands underwent flexible docking with 300-3 retains.

Bioavailability and Pharmacokinetics Predictions

In this study, SwissADME online web service was utilized to predict the bioavailability and pharmacokinetic properties of the selected Indonesian natural products that have remained after the docking simulation. In the end, about three ligands that have the best properties were selected as best drug candidates for treating Ebola through the inhibition of EBOV VP30.

RESULTS AND DISCUSSIONS

Pre-docking Simulation

In this study, the Indonesian natural products molecular structures were retrieved from HerbalDB in .mol file format. The compounds itself were obtained through the literature study that mentioned any plants, fungi, or microbes that resides or can be found exclusively in Indonesia according to literature and extensive study [11]. Throughout this method, about 3,429 Indonesian natural product compounds were retrieved from this database. This step was followed up by computational ADME-Tox test to determine their drug-likeness and toxicity properties. Any toxicity properties that owned by any ligand may lower their efficiency and effectivity when used as the drug. Hence, this step was compulsory to eliminate any compounds that have a low probability as drug candidates. According to the results from this step, about 3128 Indonesian natural product compounds were omitted through this test because they possessed either toxicity properties, such as mutagenic, tumorigenic, reproductive effect, and irritant properties, or have a low possibility to be developed as a drug, according to their druglikeness score. Thus, only 301 ligands have passed this stage and can be prepared further in the ligand optimization processes.

In this study, the optimization of ligand structure was utterly achieved using MOE 2014.09 software. This step was conducted to obtain the ligand pose that resembles the molecular structure when treated in the real condition, especially in the human body. At first, the remaining 301 Indonesian natural product compounds, which saved earlier in .sdf file format, were opened and prepared according to the default protocols in the respective software, including the 'Wash', 'Partial Charge' and 'Energy Minimization' features in Database Viewer, MOE 2014.09. The prepared ligands were later saved in .mdb file format for the docking simulation processes.

The 3D structure of EBOV VP30 that used for the research was listed with PDB ID: 2I8B [19], which obtained from RSCB-PDB. The corresponding 3D structure was prepared using MOE 2014.09 software as well. First, The forcefield that used for the protein preparation was selected. In this research, Amber10:EHT with Gas Phase solvation was used. After that EBOV VP30 is prepared and optimized using 'LigX' that is featured on MOE 2014.09. The

preparation was done by removing the water molecules and tether the receptors and the optimization was done by fixing the atoms positions and hydrogen that will interact with EBOV VP30 position with the ligands. The optimized EBOV VP30 protein structure was later saved in .moe file format to retain its forcefield and structure, which can be used later on for the docking simulation.

Molecular Docking Simulation of EBOV VP30 and Indonesian Natural Products

In this study, the determination of binding sites of VP30 protein was obtained through 'Site Finder' feature in MOE 2014.09 software by searching the favorable binding sites based on several parameters, such as solvent's exposures and lipophilicity of the binding sites. The result shows that the binding sites of VP30 protein are Leu144, Arg179, Lys 180, Phe181, Ser182, Lys183, Ser184, Gln185, Leu188, His215, Leu249, Pro250, Cys251, Glu252, and Ser253. These binding sites were selected due to their resemblance to the previous research [20], [21]. Thus, the molecular docking simulation would be performed on these binding sites.

The docking simulation of EBOV VP30 protein was done by using MOE 2014.09 software. The inhibition of EBOV VP30 protein can be achieved if the ligands capable of binding to a target receptor of the VP30 binding site. In this study, 301 compounds of Indonesian natural product, which already underwent ADME-Tox test, acted as "ligands" to inhibit the EBOV VP30 protein. These ligands went into molecular docking simulation. The simulation was done to determine the free binding energy calculations and the number of molecular interactions between the complexes of ligand and protein. Free binding energy ($\Delta G_{\text{Binding}}$) is associated with the binding affinity between ligand and receptor and can be determined by the stability of ligand-protein complexes. To find a suitable candidate ligand for inhibiting the target receptor of EBOV VP30, that ligand must have a higher Gibbs free binding energy and better molecular interaction with the binding site of EBOV VP30 pocket regarding binding energy and molecular interaction. The free binding energy value of the ligands was expected to have a negative value and lower than the standard ligands. So, this ligand can be applied as a novel compound for inhibiting EBOV VP30 protein [17].

In this study, BCX4430, gossypetin, and taxifolin were selected as the standard ligands. The first ligand was chosen because it has been utilized as a drug for combating Ebola through in vitro and in vivo experiments, while the latter two ligands were chosen because they have the highest binding affinity among all tested ligand through in silico experiment that performed in the previous research [22], [23]. According to the docking results from this research,

these ligands have a $\Delta G_{\text{Binding}}$ value of -7.3054, -7.1857 and -7.8649 kcal/mol, respectively. Furthermore, the docking simulation results revealed about five ligands have better molecular interaction, and some of them have lower $\Delta G_{\text{Binding}}$ value compared to the standard ligands, as shown in Table 1. In this study, aglamide C was determined as the Indonesian natural product compounds which have the lowest $\Delta G_{\text{Binding}}$ value, sitting at -9.7940 kcal/mol. In addition, lissoclibadin 4, IDNP-206 (IUPAC Name: 3,10,11-trihydroxydibenzo[b,e]oxonine-7,13(6H,8H)-dione), epiafzelechin and scoulerine also have $\Delta G_{\text{Binding}}$ value as well, respectively at -8.7101, -8.2686, -7.8768, and -7.3823 kcal/mol. Except for scoulerine, which has lower binding affinity than taxifolin, all of these ligands possessed higher binding affinity on EBOV VP30 protein on its binding site. Thus, these compounds, regarding Gibbs free binding energy, are suitable to be progressed as Ebola drug candidates.

In addition to free binding energy, the molecular interaction between the ligands and the binding site of EBOV VP30 protein is another important aspect of determining whether the ligand can be considered as a suitable inhibitor or not.

Table 1. The docking results of EBOV VP30 and the best Indonesian natural product compounds, along with three standard ligands

No.	Ligand Code (Compound Name)	$\Delta G_{\text{binding}}$ value (RMSD (Å))
1.	IDNP-268 (Aglamide C)	-9.7940 kcal/mol (1.4500)
2.	IDNP-206 (Lissoclibadin 4)	-8.7101 kcal/mol (1.4388)
3.	IDNP-204 (3,10,11-Trihydroxydibenzo[b,e]oxonine-7,13(6H,8H)-dione)	-8.2686 kcal/mol (1.6453)
4	IDNP-70 (Epiafzelechin)	-7.8768 kcal/mol (1.0326)
5	IDNP-123 (Scoulerine)	-7.3823 kcal/mol (1.0382)
S1	Galidesivir / BCX4430	-7.3054 kcal/mol (0.9212)
S2	Gossypetin	-7.1857 kcal/mol (1.2655)
S3	Taxifolin	-7.8649 kcal/mol (0.8521)

First, the molecular interactions of standard ligands were observed. As is displayed in Fig. 1.

BCX4430 formed a molecular interaction with Lys180 via hydrogen bonds through its backbone, with other two molecular interaction with Cys251 were observed that act as sidechain donor and several other interactions within the binding pocket through van der Waals interaction. Moreover, gossypetin formed a molecular interaction with Gln185 as a sidechain acceptor, with two molecular interaction with Cys251 that act as sidechain donor. Finally, taxifolin has two molecular interaction with Cys251 as a sidechain donor.

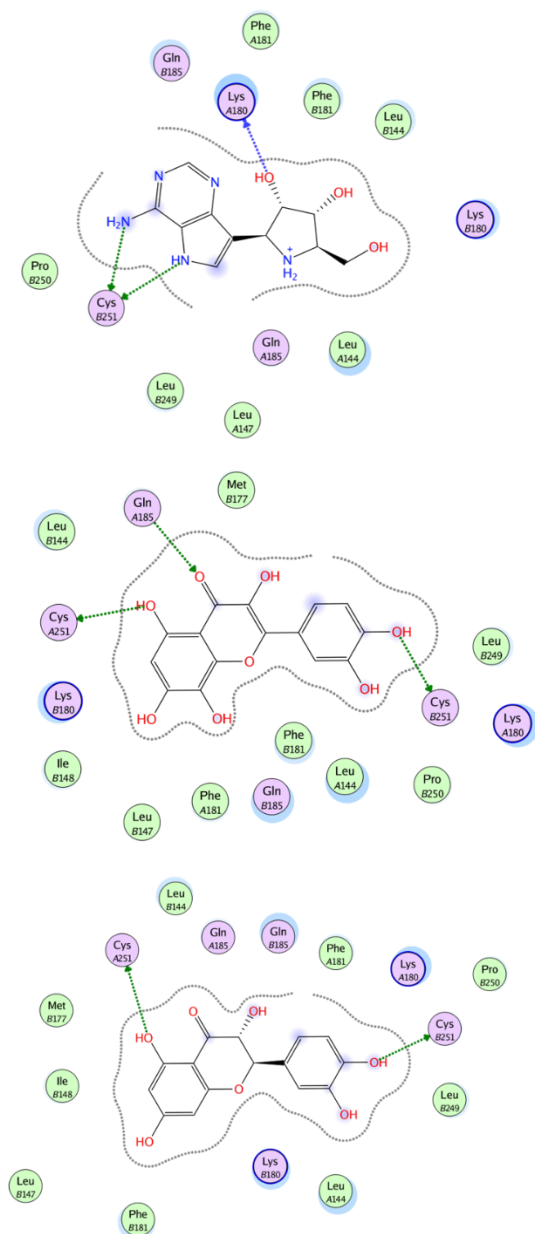


Fig. 1. The molecular interaction of BCX4430 (top), gossypetin (middle) and taxifolin (bottom) in the binding site of EBOV VP30.

In this research, the molecular interaction between the Indonesian natural product compounds and EBOV VP30 were also compared as well. Even

though scoulerine has the highest Gibbs free binding energy compared to other four ligands, but this compound has better molecular interaction within the EBOV VP30 binding pocket. Scoulerine has four interesting molecular interactions formed in EBOV VP30 binding site, such as arene-H interaction with Phe181, hydrogen bonds with the side chain of Gln185, and two hydrogen bonds interaction with the backbone of Lys180. Other Indonesian natural product ligands such as lissoclibadin 4, IDNP-206, aglamide C, and epiafzelechin only have one to two interactions within the binding pocket, which is not preferred, even though they have better Gibbs free binding energy. Thus, scoulerine has the better result in terms of molecular interaction compared to any other Indonesian natural product compounds. The molecular interactions of scoulerine in the binding site of EBOV VP30 is displayed in Fig. 2.

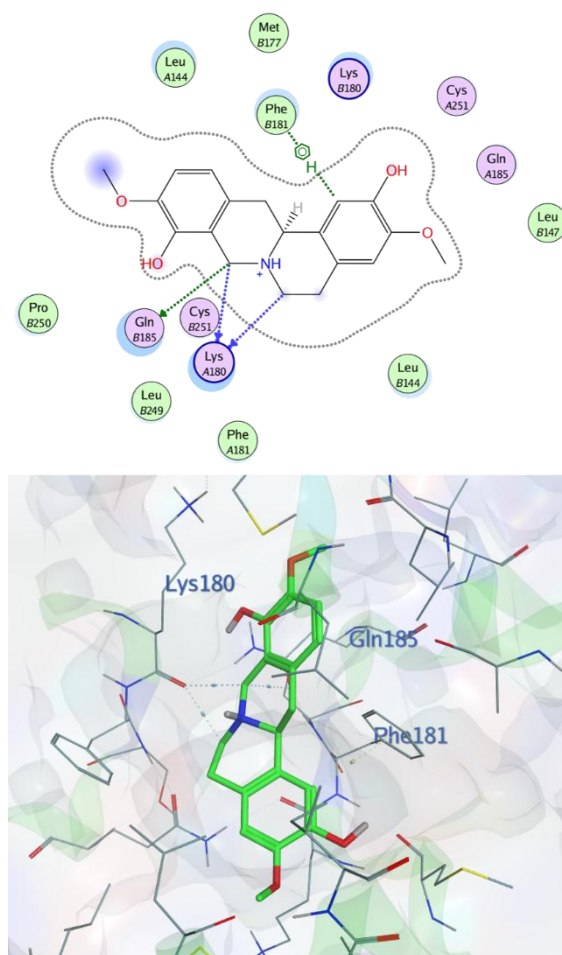


Fig. 2. The two-dimensional and three-dimensional molecular interaction of scoulerine in the binding site of EBOV VP30.

Results of Bioavailability and Pharmacokinetics Predictions

In this study, the remaining five Indonesian

natural product compounds, along with the three standard compounds, were subjected to bioavailability and pharmacokinetics prediction test. This test was done to measure the pharmacokinetic properties of the ligands, as well as the oral bioavailability of the selected ligands according to several parameters such as physicochemical properties (e.g., molecular weights, TPSA) that have been predicted through this test. This prediction was entirely made by using SwissADME online web service, which can be accessed through this website <http://www.swissadme.ch/>. Also, DataWarrior v4.7.2 software was also utilized to measure the druglikeness score and molecular properties that also determine the oral bioavailability of the compound.

Table 2 shows the results of the druglikeness and Also, the oral bioavailability prediction of

molecular properties prediction tests. From the result, all of the Indonesian natural product ligands have a molecular weight less than 500 Daltons, logP less than 5.0, hydrogen bond acceptor less than 10 and hydrogen bond donor less than 5, which obey Lipinski's Rule of Five [24]. This means that all of the Indonesian natural product ligands have likable properties to be absorbed and administrated through the oral system in the human body. However, according to the same prediction test, only two out of five Indonesian natural product compounds, namely IDNP-206 and aglamide C, that has the positive druglikeness value, which indicates these ligands have a likeness to become the drug compounds than any other ligands, based on their molecular fragments.

one on Egan's, while it did not break any Lipinski's

Table 2. The physicochemical properties of the selected Indonesian natural products and the standard ligands

Ligand	Druglikeness					Druglikeness
	MW	clogP	H-acceptor	H-donor	TPSA (Å ²)	
Lissoclibadin 4	484.70	4.32	4	4	152.52	-1.5525
3,10,11-Trihydroxydibenzo[b,e]oxonine-7,13(6H,8H)-dione	300.26	1.16	6	3	104.06	0.29065
Scoulerine	328.38	3.07	4	3	63.36	-1.4498
Aglamide C	300.40	2.86	2	1	49.41	2.9194
Epiatzelechin	274.27	1.51	5	4	90.15	0.3153
BCX4430	266.28	0.12	5	6	144.89	-0.2121
Gossypetin	318.24	1.33	8	6	151.59	-0.0083
Taxifolin	304.25	0.71	7	5	127.45	0.4448

Indonesian natural product compound was also conducted as well along with the molecular properties prediction using the same web service. The result can be seen in Table 3. According to the results, both the best Indonesian natural product compounds and the standard ligands owned the average bioavailability score; it is indicated by the low violation number of any rules that determined the oral bioavailability in any compounds. For instance, lissoclibadin 4 ligand violates two rules of Ghose's, one on Veber's, and

rule. Although the bioavailability of this compound is mediocre, the high violation number of these rules made lissoclibadin 4 has a low gastrointestinal absorption prediction. Surprisingly, other four compounds (IDNP-206, scoulerine, aglamide C and epiatzelechin) did not break any of these rules. Hence these ligands have higher gastrointestinal absorption than lissoclibadin 4, even higher than BCX4430 and gossypetin.

Table 3. The oral bioavailability prediction of the selected Indonesian natural products and the standard ligands

Ligands	GI	Lipinski's	Ghose's	Veber's	Egan's	Bioavailability Score
Lissoclibadin 4	Low	0	2	1	1	0.55
3,10,11-Trihydroxydibenzo[b,e]oxonine-7,13(6H,8H)-dione	High	0	0	0	0	0.55
Scoulerine	High	0	0	0	0	0.55
Aglamide C	High	0	0	0	0	0.55
Epiatzelechin	High	0	0	0	0	0.55
BCX4430	Low	1	1	1	1	0.55
Gossypetin	Low	1	0	1	1	0.55
Taxifolin	High	0	0	0	0	0.55

CONCLUSIONS

In this research, about 3,429 Indonesian natural product compounds were subjected into the computational ADME-Tox screening test, molecular docking simulation, and bioavailability prediction test to determine the best compounds that can be utilized as the EBOV VP30 inhibitors. In the end, after the series of docking simulations and prediction test, three Indonesian natural product compounds, namely IDNP-206, scoulerine, and aglamide C were selected as the best Indonesian natural product compounds to inhibit EBOV VP30 due to their binding affinity, in terms of Gibbs free binding energies and molecular interactions, towards the binding site of EBOV VP30, lacks of toxicity properties and high oral bioavailability through gastrointestinal system. Thus, the antiviral activities of these compounds should be determined further through molecular dynamics simulation and in vitro studies, to determine their complex stability and molecular interaction under real environment, and their antiviral activities toward EBOV VP30, respectively.

ACKNOWLEDGMENTS

This research publication has been funded entirely by Hibah Penelitian Kerjasama Luar Negeri No: 538/UN2.R3.1/HKP.05.00/2017, given by *Kementerian Riset, Teknologi dan Pendidikan Tinggi*, Republic of Indonesia through *Direktorat Riset dan Pengabdian Masyarakat*, Universitas Indonesia. Finally, no conflict of interest was declared.

6. REFERENCES

- [1] CDC, Ebola (Ebola Virus Disease), 2014.
- [2] De Clercq E., Ebola virus (EBOV) infection: Therapeutic Strategies. *Biochem. Pharmacol.*, Vol. 93, Issue 1, pp. 1–10, 2015.
- [3] Gebre Y., Gebre T., and Peters A., The Ebola Virus: A Review of Progress and Development in Research. *Asian Pac. J. Trop. Biomed.*, Vol. 4, Issue 12, 2014, pp. 928–936.
- [4] Haque A., Hober D., and Blondiaux J., Addressing Therapeutic Options for Ebola Virus Infection in Current and Future Outbreaks. *Antimicrob. Agents Chemother.*, Vol. 59, No. 10, 2015, pp. 5892–5902.
- [5] Rewar S. and Mirdha D., Transmission of Ebola Virus Disease: An Overview. *Annals of Global Health*, Vol. 80, Issue 6, 2014, pp. 444–451.
- [6] Nyakatura E. K., Frei J. C., and Lai J. R., Chemical and Structural Aspects of Ebola Virus Entry Inhibitors. *ACS Infectious Diseases*, Vol. 1, Issue 1, 2015, pp. 42–52.
- [7] Balmith M., Faya M., and Soliman M. E. S., Ebola Virus: A Gap in Drug Design and Discovery - Experimental and Computational Perspective. *Chem. Biol. Drug Des.*, Vol. 89, Issue 3, 2017, pp. 297–308.
- [8] Feldmann H. and Geisbert T. W., Ebola Haemorrhagic Fever. *Lancet*, Vol. 377, Issue 9768, 2011, pp. 849–862.
- [9] Groseth A., Charton J., E., Sauerborn M., Feldmann F., Jones S., M., Hoenen T., Feldmann H., The Ebola Virus Ribonucleoprotein Complex: A Novel VP30-L Interaction Identified. *Virus Res.*, Vol. 140, Issue 1–2, 2009, pp. 8–14.
- [10] Patrick G. L., Introduction of Medicinal Chemistry, 5th Ed. Oxford: Oxford University Press, 2013.
- [11] Yanuar A., Mun'im A., Lagho A. B. A., Syahdi R. R., Rahmat M., and Suhartanto H., Medicinal Plants Database and Three Dimensional Structure of the Chemical Compounds from Medicinal Plants in Indonesia. *Int. J. Comput. Sci.*, Vol. 8, Issue 5, 2011, pp. 180–183.
- [12] Vilar S., Cozza G., and Moro S., Medicinal Chemistry and The Molecular Operating Environment (MOE): Application of QSAR and Molecular Docking to Drug Discovery. *Curr. Top. Med. Chem.*, Vol. 8, Issue 18, 2008, pp. 1555–1572.
- [13] Sander T., Freyss J., Von Korff M., and Rufener C., DataWarrior: An Open-source Program for Chemistry Aware Data Visualization and Analysis. *J. Chem. Inf. Model.*, Vol. 55, Issue 2, 2015, pp. 460–473.
- [14] Biasini M., Bienert S., Waterhouse A., Arnold K., Studer G., Schmidt T., Kiefer F., Gallo Cassarino T., Bertoni M., Bordoli L., Schwede T., SWISS-MODEL: Modelling Protein Tertiary and Quaternary Structure Using Evolutionary Information. *Nucleic Acids Res.*, Vol. 42, 2014, pp. W252–8.
- [15] Daina A., Michielin O., and Zoete V., SwissADME: A Free Web Tool to Evaluate Pharmacokinetics, Drug-likeness and Medicinal Chemistry Friendliness of Small Molecules. *Sci. Rep.*, Vol. 7, 2017.
- [16] Tambunan U. S. F., Zahroh H., Parikesit A. A., Idrus S., and Kerami D., Screening analogs of β -OG pocket binder as fusion inhibitor of dengue virus 2. *Drug Target Insights*, Vol. 9, 2015, pp. 33–49.
- [17] Tambunan U. S. F., Parikesit A. A., Adam V. C., Nasution M. A. F., Puspitasari R. D., and Kerami D., Virtual Screening of Commercial Cyclic Peptides as β -OG Pocket Binder Inhibitor in Dengue Virus Serotype 2. *Int. J. GEOMATE*, Vol. 13, Issue 37, 2017, pp. 60–68.

- [18] Tambunan U. S. F. and Nasution M. A. F., Identification of novel Ebola virus (EBOV) VP24 inhibitor from Indonesian natural products through in silico drug design approach. AIP Conf. Proc., Vol. 030091, 2017, pp. 1–9.
- [19] Hartlieb B., Muziol T., Weissenhorn W., and Becker S., Crystal structure of the C-terminal domain of Ebola virus VP30 reveals a role in transcription and nucleocapsid association. Proc. Natl. Acad. Sci., Vol. 104, Issue 2, 2007, pp. 624–629.
- [20] Balmith M. and Soliman M. E. S., Potential Ebola drug targets – filling the gap: a critical step forward towards the design and discovery of potential drugs. Biologia (Bratisl.), Vol. 72, Issue 1, 2017, pp. 1–13.
- [21] Setlur A. S., Naik S. Y., and Skariyachan S., Herbal Lead as Ideal Bioactive Compounds Against Probable Drug Targets of Ebola Virus in Comparison with Known Chemical Analogue: A Computational Drug Discovery Perspective. Interdiscip. Sci., 2016.
- [22] Janeba Z., Development of Small-Molecule Antivirals for Ebola. Med. Res. Rev., Vol. 35, Issue 6, 2015, pp. 1175–1194.
- [23] Raj U. and Varadwaj P. K., Flavonoids as Multi-target Inhibitors for Proteins Associated with Ebola Virus: In Silico Discovery Using Virtual Screening and Molecular Docking Studies. Interdiscip. Sci. Comput. Life Sci., Vol. 8, Issue 2, 2016, pp. 132–141.
- [24] Lipinski C. A., Lombardo F., Dominy B. W., Feeney P. J., Experimental and computational approaches to estimate solubility and permeability in drug discovery and development setting. Adv. Drug Deliv. Rev., Vol. 46, Issue 1-3, 2001, pp. 3–26.

EFFECTS OF PIPERACEAE PLANTS EXTRACTS ON INHIBITION OF *Aspergillus flavus* AND SEED GERMINATION OF MAIZE (*Zea mays*)

Chua Jedton, A.¹ and Boonkorn, P.¹

¹Faculty of Science, Lampang Rajabhat University, Thailand

ABSTRACT

This study investigated the effects of Piperaceae plants extracts on inhibition of *Aspergillus flavus* and seed germination of maize (*Zea mays*). The crude extracts of four Piperaceae, namely, Betel (*Piper betle*), Wild betel (*P. sarmentosum*), Long pepper (*P. retrofractum*) and Sakhan (*P. interruptum*) were extracted with 95% ethanol and prepared in PDA agar by using poisoned food technique at several concentrations (0, 1500, 3000 and 4500 ppm). The result showed that the crude extract from Betel at 3000 and 4500 ppm completely inhibited (100%) the growth of *A. flavus* meanwhile Wild betel and Long pepper crude extract could inhibit the growth about 82.50 % and 82.20 %, respectively, after incubation for 72 hr. For seed germination of maize, the experiment was done through 7 days. It was found that the crude extract from Wild betel at 4500 and Sakhan at 3000 ppm revealed percentage of germination were 85.56 % and 82.22 %, respectively. Therefore, the antifungal activity from Piperaceae extract may control plant pathogenic fungi and had no effect on seed germination.

Keywords: antifungal activity, crude extract, Piperaceae, seed germination.

INTRODUCTION

Maize (*Zea mays*) is the most produced cereal crop and belong to Gramineae. It is the one of important cereal crop in the world. However, the maize seed faced the common problem caused by various fungi infection which have been found to causing seed-borne pathogens [1]. Maize seed and seedling are susceptible to soil and seed-borne pathogens before or after germination. It may suffer from stunted growth or die as a result of poor root system [2]. The high quality seed of maize required the application of chemicals for seed treatment with fungicide. Seed treatment also had disadvantages by increased the risk of phytotoxicity. It has been reported that some fungicide could act as suppressors or stimulators of germination [3].

Fungi of the genera *Aspergillus*, *Fusarium* and *Penicillium* are known to produce the toxic metabolites [4] and the toxic metabolites such as mycotoxins has been degrade seed quality and reduce viability [5]. Especially, *Aspergillus flavus* was contaminated maize seed during storage and seed infection [6]. Ng'ang'a [7] reported that *A. flavus* reduced the quality and economic value of products. Therefore, the fungi found to contaminate maize seeds usually controlled by chemical fungicide but these agents had effects on human health and environment [8]. Normally, the fungicide those applied during the postharvest period are Benzimidazoles and

Prochloraz. Nowadays, the research of using natural antimicrobial and antifungal substance were increasing and had much attention.

Application of control pathogenic fungi in agricultural products by direct contact with plant extracts had been reported. The controlling of Zingiberaceae family (Ginger, Turmeric and Chinese keys) were used for inhibition of *Penicillium digitatum* [9]. The studied on control of *Rhizoctonia* spp. and *Sclerotium hydrophilum* of rice found that using clove extract had the best growth inhibition [10]. Piperaceae family showed the several secondary metabolites and potential antimicrobial activity. Examples of controlling of *A. flavus* and *F. verticillides* by using Betel extracts [11]. The essential oil of Amazon Piper species showed the powerful antifungal activity with *Cladosporium cladosporioides* and *C. sphareospermum* [12] and the leaves of *Piper marginatum* contain the antifungal compounds [13]. The extract from *P. sarmentosum* stems and leaves exhibits antimicrobial activity against *Escherichia coli* and *Bacillus subtilis* ([14].

The damaging effects on maize seed and seedling disease may be minimized with proper seed handling, culture practice and seed applied, especially, good culture practice can reduce seedling disease [15]. However, the study about the effects of seed treatments with natural antifungal substances on seed germination of maize was little known, especially, seed infected

by *A. flavus*. Thus, the objective of this research was to determine the effects of Piperaceae plants extracts on inhibition of *A. flavus* and seed germination of maize.

MATERIALS AND METHODS

The plant materials and extraction

Four Piperaceae, namely, Betel (*P. betle*), Wild betel (*P. sarmentosum*), Long pepper (*P. retrofractum*) and Sakhan (*P. interruptum*) were rinsed with distilled water and dried in the air. Dried of plants were grinded into fine powder using a grinding machine. The powders were extracted with 95% ethanol (1:5 w/v ratio) at room temperature for 48 hr and then filtered through the filter paper Whatman No. 1. The filtrates were evaporated with rotary evaporator at 40°C. The crude extracts were dried with Vacuum Freeze Dryer until the weight constant.

Antifungal assay

A. flavus was obtained from Faculty of Science, Lampang Rajabhat University, Lampang, Thailand. The fungus was cultured on potato dextrose agar (PDA) slants at 30°C for 7 days. A spore suspension was harvested by pouring old cultures of *A. flavus* with sterile distilled water. Subsequently the spore suspension was transferred into 100 ml of sterile distilled water in a 250 ml in flask. Then, the suspension was shaken for 10 min on an orbital shaker at 27°C and it was filtered through two layers of sterilized muslin cloth. The cell numbers were counted with a haemocytometer and the initial concentration was adjusted with sterile distilled water to a concentration of 10^6 CFU/ml. Then, Maize seeds were soaked in *A. flavus* spore suspension (10^6 CFU/ml) and allowed to air dry after that seeds were placed onto the center of PDA containing the crude extracts of four Piperaceae by using poisoned food technique at several concentrations (0, 1500, 3000 and 4500 ppm) and incubated at room temperature ($28 \pm 1^\circ\text{C}$) for 72 hr. The antifungal effects were estimated by the following formula: Antifungal activity (%) = [(Diameter of growth in control plate – Diameter of growth in the plate containing plant extracts)/ Diameter of growth in control plate] x 100.

Standard germination test

Maize seeds were obtained from the farmer in Lampang Province, Thailand. And then seeds were coating with plant extracts {Betel (*P. betle*), Wild betel (*P. sarmentosum*), Long pepper (*P. retrofractum*) and Sakhan (*P. interruptum*)} at various concentrations (0, 1500, 3000 and 4500 ppm) and incubated at room temperature

($28 \pm 1^\circ\text{C}$) for 7 days. Then, the maize seeds were analyzed for the percentage of germination by using standard germination tests. All treatments were conducted according to the method of the International Seed Testing Association [16]. Seeds were placed on moisture germination paper at 30 seeds per paper towel. Paper towels were placed in incubator at $25 \pm 1^\circ\text{C}$. Percentage germination was determined after 7 days. Results were presented as the percentage of germination. They were calculated using the following formula: Percentage of germination = [Seed germinated/Total seed] x 100

Statistical analysis

All experiments were replicated three times and evaluated with regression procedure using SPSS version 17. Differences among treatments performed using Duncan's Multiple Range test ($P = 0.05$).

RESULTS AND DISCUSSION

Antifungal activity of crude extracts

Crude extracts from four Piperaceae, Betel (*Piper betle*), Wild betel (*P. sarmentosum*), Long pepper (*P. retrofractum*) and Sakhan (*P. interruptum*) were sticky and dark green. Antifungal activity of crude extracts was showed in Table 1. At 3000 and 4500 ppm of *P. betle* extracts exhibited the best result in growth inhibition (100%) meanwhile *P. sarmentosum* at 4500 ppm and *P. retrofractum* at 4500 ppm crude extract could inhibit the growth about 82.50 % and 82.20 %, respectively when compared to control (Fig. 1). Ounchokdee [17] reported that the crude extract with diethyl ether and ethyl acetate from *P. longum* exhibited potent antifungal activity against tested plant pathogens (*C. cladosporioides*, *C. capsici* and *F. oxysporum*) as well as the extraction of Betel leaf with 95% ethanol at 10000 ppm completely inhibited the growth of *A. flavus* and *F. verticillidices* [11]. Reigada [13] reported that the extract from leaves of *P. maginatum* contain the antifungal compounds. The result of this research also suggested that the crude extracts from Piperaceae might contain the several secondary metabolites and antifungal activity for controlling plant pathogen fungi.

The effects of crude extracts on seed germination

Seed germination was evaluated by the percentage of germination. Seed germination of maize effected by crude extracts was showed in Table 2. The control had germination of 74.44 % meanwhile the crude extract from *P. sarmentosum* at 4500 and *P. interruptum* at 3000

ppm revealed percentage of germination were 85.56 % and 82.22 %, respectively and the result showed no significantly difference (same letter showed in Table 2) In the another report, Perelló [18] reported the garlic extract promoted the growth activities on wheat seedling and percent seedling germination for wheat cultivars tested

was > 85% and was greatly increased by either fungicide or garlic juice treatments. However, the antifungal activity from Piperaceae extract had no effect on seed germination.

Table 1 Growth inhibition of *A. flavus* (%) after treated with plant extracts

Treatments	Growth inhibition of <i>A. flavus</i> (%)			
	Concentrations of plant extracts (ppm)			
	0	1500	3000	4500
<i>P. sarmentosum</i>	0.00 ^g	68.50 ^d	75.50 ^c	82.50 ^b
<i>P. betle</i>	0.00 ^g	80.50 ^b	100.00 ^a	100.00 ^a
<i>P. interruptum</i>	0.00 ^g	66.25 ^d	72.91 ^c	75.50 ^c
<i>P. retrofractum</i> (leaf)	0.00 ^g	58.33 ^f	62.58 ^e	68.75 ^d
<i>P. retrofractum</i> (fruit)	0.00 ^g	72.91 ^c	75.50 ^c	82.20 ^b

Data followed by the same letter within the column are not significantly different (*P=0.05)

Table 2 Percentage of germination of Maize seed after coating with plant extracts

Treatments	% Germination			
	Concentrations of Plant Extracts (ppm)			
	0	1500	3000	4500
<i>P. sarmentosum</i>	74.44 ^{abcde}	47.78 ^f	71.11 ^{abcde}	85.56 ^a
<i>P. betle</i>	74.44 ^{abcde}	56.67 ^{ef}	75.56 ^{abcde}	64.47 ^{bc}
<i>P. interruptum</i>	74.44 ^{abcde}	76.67 ^{abcd}	82.22 ^{ab}	60.00 ^{def}
<i>P. retrofractum</i> (leaf)	74.44 ^{abcde}	73.33 ^{abcde}	62.22 ^{cdef}	81.11 ^{abc}
<i>P. retrofractum</i> (fruit)	74.44 ^{abcde}	65.56 ^{bcdef}	58.89 ^{def}	74.47 ^{abcde}

Data followed by the same letter within the column are not significantly different (*P=0.05)

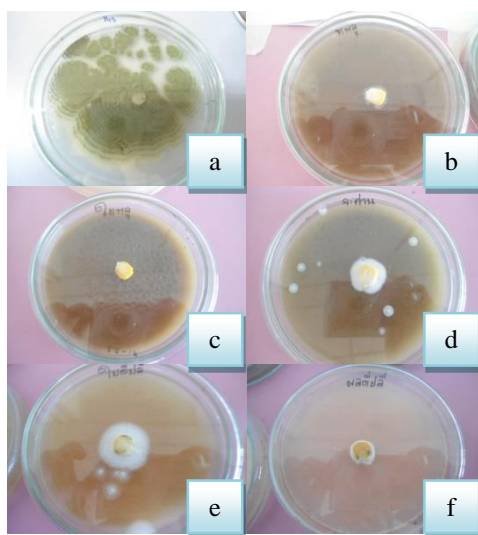


Fig. 1 Effect of plant extracts (a) Control (b) *P. sarmentosum* (c) *P. betle* (d) *P. interruptum* (e) *P. retrofractum* (leaf) (f) *P. retrofractum* (fruit) after incubated at room temperature ($28 \pm 1^\circ\text{C}$) for 72 hr

CONCLUSION

The crude extracts of four Piperaceae might contain antifungal compound for controlling plant pathogen fungi. The crude extract from Betel at 3000 and 4500 ppm completely inhibited (100%) the growth of *A. flavus*. For seed germination of maize, the crude extract from Wild betel at 4500 and Sakhan at 3000 ppm revealed percentage of germination were 85.56 % and 82.22 %, respectively. The result of this research also suggested that the antifungal activity from Piperaceae extract could control plant pathogenic fungi and had no effect on seed germination.

ACKNOWLEDGEMENTS

This work has been supported by Department of Biology, Faculty of Science, Lampang Rajabhat University.

REFERENCES

- [1] Shetty, H. S. Different Types of Damages in Seed Caused by Seed-borne Fungi. Seed Pathology. Proc CTA Seminar Copenhagen Denmark, 20th-25th June, 1998, pp. 53-62.

- [2] Vincelli, P. Seed and Seedling Disease of Corn. Plant Pathology Fact Sheet University of Kentucky- College of Agriculture PPES-AG-C-02. 2008.
- [3] Stevanovic, V., Indic, D. and Knezevic, B. The effect of fungicide for seed treatment on germination of barley. Pesticidi I Fitomedicina. Vol. 24, 2009, pp. 35-41.
- [4] Caster, L. and Frederikson, R. A. *Fusarium* head blight, occurrence of effect on sorghum yield and grain characteristics in Texas. Journal of Plant disease. Vol. 64, 1980, pp. 1017-1017.
- [5] Jalander, V. and Gachande, B. D. Effect of Fungal Metabolites of Some Rhizosphere Soil Fungi on Seed Germination and Seedling Growth of Some Pules and Cereals. Science research reporter. Vol. 2, Issue. 3, 2012, pp. 265-267.
- [6] Ellis, W. O., Smith, J. P., Simpson, B. K., Oldham, J. H. and Scott, P. M. Aflatoxins in food: occurrence, biosynthesis, effects on organism, detection, and methods of control. Crit. Rev. Food Sci. Nutr. Vol. 30, 1991, pp. 403-439.
- [7] Ng'ang'a, J., Mutungi, C., Imathiu, S. and Affognon, H. Effect of triple- layer hermetic bagging on mold infection and aflatoxin contamination of maize during multi-month on farm storage in Kenya. J. Stored Prod. Res. Vol. 69, 2016, pp. 119-128.
- [8] Vicente, A., Arques, F. A., Villabi, J. R., Centrich, F., Serrahima, E., Ilebaria, E. and Casa, C. X. Plguicides en la dieta: aportando piezas al rompecabezas. Gac. Sanit. Vol. 18, 2004, pp. 425-430.
- [9] Matvijit, S., Techavuthiporn, C., Khewkhom, N., Wongsaree, C. and Kanlayanarat, S. Effect of Zingiberaceae crude extract on inhibition of *Penicillium digitatum* Sacc. Agricultural Sci. J. Vol. 42, Issue. 3(Suppl.), 2011, pp. 303-306.
- [10] Aye S. S. and Mutsumoto M. Effect of some plant extracts on *Rhizoctonia* spp. and *Sclerotium hydrophilum*. Journal of Medicinal Plants Research., Vol. 5, Issue 5, 2011, pp. 3751-3757.
- [11] Srichana D., Phumruang A. and Chongkid B. Inhibition Effect of Betal Leaf Extract on the Growth of *Aspergillus flavus* and *Fusarium verticillioides*. Thammasat Int. J. Sc. Tech., Vol. 14, No.3, July-September 2009.
- [12] Silva, J. K. R., Pinto, L. C., Burbano, R. M. R. and Montenegro, R. C. Essential oils of Amazon Piper species and their cytotoxic, antifungal, antioxidant and anti-cholinesterase activities. Industrial Crops and Products. Vol. 58, 2014, pp. 55-60.
- [13] Reigada, J. B., Tcacenco, C. M., Andrade, L. H. and Kato, M. J. Chemical constituents from *Piper marginatum* Jacq.(Piperaceae)-antifungal activities and kinetic resolution of (RS)-marginatumol by *Candida antarctica* lipase (Novozym 435). Trtrahedron Asymmetry. Vol. 18, 2007, pp. 1054-1058.
- [14] Masuda, T., Inazumi, A., Yamada, Y., Padolina, W. G., Kikuzaki, H. and Nakatani, N. Antimicrobial phynylpropanoides from *Piper samentosum* . Phypchemstry. Vol. 30, 1991, pp. 3227-3228.
- [15] McGee, D. C. Seed pathology: its place in modern seed production. Plant Dis. Vol. 65, pp. 638-641.
- [16] International Seed Testing Association. (2007). International Rule for Seed Testing. Seed Sci. & Technol. 27 Supplement.
- [17] Ounchokdee U., Rueangrit S. and Dethoup T. Antifungal activity profile of Piper longum fruit extract against plant pathogenic fungi. JBiopest. Vol. 9, Issue 2, 2016, pp 97-103.
- [18] Perelló, A., Gruhlke, M. and Slusarenko, A. J. Effect of Garlic Extract on Seed Germination, Seedling Health, and Vigour of Pathogen Infected Wheat. Journal of Plant Protection Research. Vol.53, No. 4, 2013, pp. 317-323.

FORMULATION OF THE BODY SCRUB CREAM CONTAINING MORINGA SEED POWDER (*MORINGA OLEIFERA*) AND ITS EXAMINATION DERMAL ACUTE IRRITATION

Hendrawati¹, Annita Karunia Savitri¹, Nina Fitriyati¹, Aulia Andi Mustika²

¹Departement of Chemistry Faculty of Science and Technology State Islamic University Syarif Hidayatullah Jakarta. Jl. Ir. H Djuanda no. 95 Ciputat Tangerang Selatan Banten Indonesia

² Bogor Agricultural University IPB. Jl Raya Dramaga, Bogor 16680, West Java, Indonesia.

ABSTRACT

Moringa seeds (*Moringa oleifera*) have many substances such as antioxidants, minerals and vitamins that are useful for skin health. Moringa seed could be used as an additional material of cosmetic. One of the misscrub cream by using moringa seed as abrasive material (abrasiver). The purpose of this research are to know the optimal formulation of scrub cream moringa seed and characterization based on the requirement of quality skin moisturizers according to SNI 16-4399-1996, and the safety of its use by conducting dermal acute irritation test. The dermalacute irritation test was performed by Draize test method on white rats (*Rattus norvegicus*) male sprague-dawley strain. The results of the study show that the most optimum scrub cream products based on panelist preferences level is scrub cream with the addition of 4.5% moringa seed with a score of 5.67. Formulation scrub cream with the addition of 3.5; 4.5; and 5.5 % moringa seed qualify skin moisturizers according to SNI 16-4399-1996 with pH value of 6.88-7.31; density 1 g/mL; emulsion stability of 95.19-96.61%; and negative microbial contamination. The three formulations of moringa seed scrub cream also do not give skin irritation effect to test animals at 24 and 48 hours with primary dermal irritation index or PDII=0.

Keywords: Body scrub cream, Bioseed, Draize test, *Moringa oleifera*, Cosmetics

INTRODUCTION

Moringa seeds produce oil commercially known as the behen oil. The oil is widely used in beauty products because it has a high antioxidant content with an IC₅₀ value of 91.13 µg/mL [1] – [2]. Moringa seeds are also known to have nutrients such as vitamins and minerals that are beneficial to skin health. Compaore et al [3] states that moringa contains high enough minerals such as calcium, copper, phosphorus, zinc, magnesium, manganese, potassium and sodium. Mineral content of calcium, sulfur, magnesium, and potassium can lift dead skin cells (exfoliator) and nourish the skin so the skin feels soft and smooth [4]. Moringa seeds are rich in vitamins B1, B2, B3, C, and E [5]. Vitamin B1, B2, B3 are known to have a role in maintaining skin moisture and brightening the skin [4].

Burlando et al. [6] states that moringa seeds have potential as raw materials in cosmetic because they have a high nutrient content that is beneficial to the skin. Cosmetics has now become a necessity that is considered important for some people. Various types of cosmetic products are used for skin care in order to appear more attractive. Ojiako and Okeke [7] utilize high antioxidant content in moringa seed oil in body lotion, while Duraivel et al. [8] utilizes moringa seed oil in an anti-wrinkle cream. Cosmetic

product used for other skin care is scrub cream.

Based on the content of vitamins, minerals, and high antioxidant content in moringa seeds, researchers have an interest in using moringa seed powder as an active component of skin abrasive and also as a nutritional addition to cream scrub. The effort to add moringa seed powder in scrub cream has never been done before. Scrub cream is made by varying the concentration of moringa seed powder 3,5; 4,5; and 5.5%, followed by organoleptic test by 30 panelists and characterization test (pH analysis, emulsion stability, species weight, and total microbial contamination) in accordance with the quality standard of National Standardization Body 1996. Body scrub cream fulfill the quality requirement of Agency National Standardization 1996 followed by dermal acute irritation test.

The content of the substances used for production of scrub cream has the possibility to cause irritation to the skin, therefore to know the safety of the use of cream scrubs on the skin, then this study conducted dermal acute irritation test [9]. This test uses the white rat rats (*Rattus norvegicus*) Sprague-Dawley strain with the method Draize [10]. Draize method is done by observing the reaction of erythema and edema in the skin that occurs after cream scrub products applied to the skin of test animals for 24 hours and 48 hours.

METHOD

Time and Place of Implementation

The research was conducted in January until September 2017 in Chemical Laboratory, Central Integrated Laboratory (PLT), Syarif Hidayatullah State Islamic University Jakarta and Laboratory Animal Laboratory Unit (UPHL), Faculty of Veterinary Medicine, Bogor Agricultural University.

Tools and Materials

The tool used in this research is oven (Memmert), analytical scale (Ohaus), pH meter (Martini MI 150), incubator (Lequeux), bath (Heidolph MR 3001 K), micro tube (Eppendorf), petri dish (Pyrex), vortex mixer (Thermolyne M 16700 Maxi), micropipet (Socorex), filter paper 0.45 µm (Whatman), thermometer (Boeco), magnetic stirrer, spiritus, stopwatch, glassware, organoleptic test equipment, sterile gauze (DRC) hypoallergenic plaster (Mikropore), and hair shaver (Wahl).

The materials used in this study were Moringa oleifera samples obtained from Pamulang, Ciputat, South Tangerang, stearic acid, cetyl alcohol, triethanolamine, glycerin, methyl paraben, propyl paraben, isopropyl mericate (BratacoChemika), fragrance, aquadest, commercial cream scrubs for comparison, sterile NaCl, plate count agar, and white rat test animals (*Rattus norvegicus*) Sprague-Dawley strains of male sex with age 2-3 months and weight 200-250 grams (UPHL FKH IPB). Approval of ethical review for experimental animals (rats) in this study was obtained from Animal Ethics Committee, Faculty of Veterinary Medicine, Bogor Agricultural University, with number 076 / KEH / SKE / XI / 2017.

Procedures

Preparation of moringa seed [11]

Moringa selected fruit that is dark brown then taken the seeds. Seeds selected moringa good quality (has a round and whole shape dry) then the seeds moringa peeled skin. The contents of moringa seeds are dried with oven at 60 °C for 1 hour. The content of moringa seeds was then smoothed using a blender and sieved with a particle size filter of 595-420 µm according to Yuliati and Binarjoresearch [12].

Formula scrubs cream [13]

The preparation of a cream base is carried out according to the composition of the formula shown in Table 1. F0; F1; F2; F3 is a cream scrub formulation with the addition of moringa seed

powder respectively 0; 3.5; 4.5; and 5.5% (w / w) of the dough weight.

Table 1 The basic formula of cream

Material	Weight (gram)
Glycerin	15
Stearic acid	12
Cetyl alcohol	4
Triethanolamine	3
Isopropyl misle	2
Propylparabene	0,02
Fragnance	0,2
Distilled water, up to	100

The method of making moringa seed cream scrub is as follows stearic acid and cetyl alcohol which is the oil phase mixed and melted in porcelain cup until it reaches 70 °C above water bath, after a perfect melt the temperature is lowered to 65 °C then fed into a cup of trophies and then added propyl paraben and isopropyl impregnate into the oil phase mixture while stirring until homogeneous (Dough 1). Glycerin and water which is a water phase mixed and heated to temperature 80°C in different containers and then cooled to a temperature of 65 °C while slowly incorporating triethanolamine (Dough 2). Dough 1 and 2 are mixed while stirring until a fine cream emulsion (dough 3) is formed. Dough 3 is allowed until the temperature drops to 40 °C. Moringa flower dust and powder with concentration variation (b/b) is added while continuous stirring. A cold cream scrub is inserted into a plastic bottle.

Organoleptic test scrubs cream [14]

Organoleptic test conducted on herbal cream products include: color, aroma, consistency, texture, and overall product acceptance. Sample used include Moringa seed cream scrub and cream scrubs on the market (commercial). Panelists who conducted the organoleptic test were 30 untrained panelists. The result of organoleptic test was processed by statistical method using SPSS application with one way Anova test method.

Characterization scrubs cream

Analysis of the scrub cream produced include analysis of pH [15], the stability of the emulsion [15], the specific gravity [16] and total microbial contamination [17]. As a comparison used

commercial cream scrubs. Scrub cream characterization test results processed with statistical methods using SPSS with one way ANOVA test method.

Dermal Acute irritation scrub cream [10] – [18]

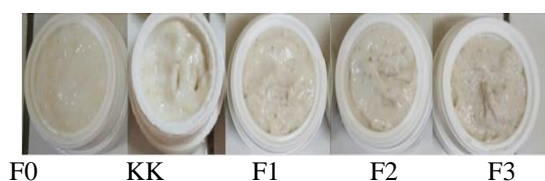
The number of rats required for each group is determined by Federer's $(n-1)(t-1) \geq 15$, where t represents the number of treatments and n is the number of replications. This research has 6 treatments to get the number of rats each treatment 4 mouse (value $n \geq 4$). Samples tested were cream base, 3 moringa cream seed scrub; 4,5; 5.5%. The normal control treatment is mice without treatment.

The acclimatized mice for 14 days had their heads shaved with an electric razor on the back with an area of 3x3 cm until cleaned up before the sample application. The shaving is done carefully so as not to injure the rats' backs. The test material is applied to the back of the mice that has been shaved hair of 0.3 grams per head, then covered with sterile gauze and glued with hypoallergic plaster. The rats were then placed and left in individual cages. The plaster and sterile gauze are opened and the test area rinsed with water after 24 hours. Observation on mouse skin was done after 40 minutes of plaster and the sterile gauze was opened and then scoring of erythema and edema formed based on Draize Method. Observations continued at 48 hours after treatment (mice smeared test material).

RESULT AND DISCUSSION

Organoleptic Test Scrubs Cream

Here is the result of organoleptic test scrub cream produced in this study.



The results of color organoleptic test showed that the highest panelist's favorite level was on the cream formula without the addition of Moringa seed powder (K0%) of 5.9. Formula cream without Moringa seed dust has a typical white cream scrub color. This indicates that the panelists prefer a creamy white scrub. Cream formula with the addition of moringa seed powder 3.5; 4.5; 5.5% (w/w) respectively decreased favor rate by 5.20; 4.50; and 4.03. This indicates that the more concentrated the color of herbal cream scrubs the panelist's favorite level decreases.

Table 2 Organoleptic test results of scrubs cream

Para-meter	Treatment					Anova results
	F0	F1	F2	F3	KK	
Color	5.90	5.20	4.00	4.03	5.12	0.000
Aroma	5.10	5.43	5.53	5.63	5.20	0.434
Viscosity	4.10	4.40	5.67	4.27	4.57	0.001
Texture	3.57	4.73	5.30	4.90	5.67	0.000
General	2.60	4.93	5.67	4.33	6.03	0.000

Noted: F0 = formulation scrub cream without addition of moringa seed scrub, F1 = formulation scrub cream with addition of 3.5% (w / w) moringa scrub, F2 = formulation scrub cream with addition of 4.5% (b / w) moringa scrub, F3 = formulation scrub cream with addition of 5.5% (w/w) Moringa scrub, KK = commercial scrub cream .

Color

Based on statistical test results using one-way Anova, there are significant differences in the color preferences level of each treatment is indicated by a probability value of 0.000 ($P < 0.05$). According to Diana and Thaman[19] color formed on the product is affected by the color of its constituent materials. Moringa seed powder that is added to the formula was instrumental in giving color to the product. Moringa seed powder has a brownish yellow color. The more moringa seed powder added then the color of cream scrubs formed will be more brown.

Aroma

The smell of cream scrub products is influenced by the ingredients. The most influential ingredients give the flavor of Moringa seed powder, so it is added fragrance to the formula to reduce the aroma from the sample of moringa. The scent produced by cream scrub depends on the concentration of the moringa seed powder. The more moringa seed powder added to the formula the stronger the aroma. Based on the organoleptic test, the highest scores were obtained in F3 cream scrub with a score of 5.63 followed by cream scrub F2; F1; KK; and F0 with a score of 5.53; 5.43; 5.20; and 5.10.

Based on statistical test results using one-way Anova, there is no significant difference in aroma preferences level of each treatment which is shown with probability value of 0.434 ($P > 0.05$). This suggests that the addition of moringa seed powder in the cream formula does not affect the panelist's preference level. This is because the panelists who conduct the assessment are panelists who are not trained so as not to be sensitive to the aroma of the products produced.

Viscosity

Based on the results of organoleptic test, the most preferred scrub cream by the panelists is the formula scrub cream with the addition of 4.5 mole seed (F2) with an average score of 5.67. The result of statistical test using one-way anova shows that there is significant (mean) difference between the viscosity favorite level of each treatment. It is shown with the probability value of 0.001 ($P < 0.05$).

Generally panelists prefer a product scrub cream that is not too thick. The more moringa seed powder added to the formula will make the more thickness of the scrub cream. Likewise, when the less the Moringa seed powder, will be shaped less scrub and look watery. This is because Moringa seeds have stearic acid content of 12.62% [20]. Stearic acid is an emulsion stabilizer and a thickening agent which is useful in forming a thickened or semi-solid (cream) [21].

Texture

Based on organoleptic tests, scrub cream F2 with a score of 5.3 is more preferable to scrub cream F3 and F1 with a score of 4.9 and 4.73. Based on statistical test results using one-way Anova, there is significant difference in texture preferences level of each treatment is indicated by probability value of 0,000 ($P < 0.05$). This suggests that the addition of moringa seed powder in the cream formula affects the panelist's preference level. This is due to the increasing percentage of scrub increase the friction power contained in the product with the skin so it is easier to remove dead skin cells and impurities in the skin. The scrub grinder also serves as a massaging effect on the body. The percentage of good scrubs ranges from 34% of the cream scrub weights because the amount is ideal for stimulating exfoliation of skin epidermis. Percentage of scrub above 5% will damage skin tissue and make skin dry [22].

Results of Scrubs Cream Characteristics

The following is the result of characteristic test of scrub cream produced in this research.

pH value

The result of pH analysis of scrub cream product each treatment has pH value which is still in the range of quality requirement according to SNI 16-4399-1996, that is with pH value range 6,88-7,45. Based on statistical test results with one-way anova showed a significant difference in the four samples. The pH value on the Moringa seed cream scrub product increased when compared with the scrub cream product without the addition of moringa

seeds. This proves that moringa seeds capable of affecting the acidity of the cream product. Cream formula with addition of 3.5; 4,5; 5.5% (b / b) of moringa seeds increased pH value compared with cream formula without moringa seed powder due to moringa seed powder is base with pH value of 7.5-5.5.

Table 3 Characteristics of scrubs cream

Parameter	Treatment					SNI
	F0	F1	F2	F3	KK	
pH	6,8 8	7,12	7,22	7,45	7,31	4,5-8
Specific gravity (g/mL)	1,0 0	1,00	1,00	1,00	1,00	0,95-1,05
Stability of emulsion (%)	95, 1	95,3	95,4	95,8	96,0	-
Total microbial contaminan (colony/ g)	Nol	Nol	Nol	Nol	Nol	Max 10 ²

Specific gravity

The test results scrub cream characteristics indicate that the value of specific gravity is still within the range of quality requirements SNI 16-4399-1996 with the average value of a specific gravity of 1 g/ mL. This means that the resulting scrub cream product has a good level of stability. The result of stastistic test with one-way Anova showed that scrub cream F0 with F1; F2; F3; and LK did not show any significant difference. This proves that with the addition of moringa seed powder does not affect the specific gravity of a cream product.

Stability of emulsion

The test results of cream scrub characteristics showed that the average emulsion stability value reached 95.19 - 96.01%. These results indicate that the sample hardly indicates a phase separation or a very small phase separation indicating that the cream product has a stable emulsion. The result of statistical test with one-way Anova showed no significant difference, probability value 0.453 ($P > 0,05$). This indicates that moringa seed powder tend not affect the stability of the emulsion on a scrub cream products.

Total microbial contamination

The result of characteristic test of total microbial contamination to cream scrub product showed that microorganisms contained in the four negative products. This is due to the addition of propyl paraben and methyl paraben formula scrub cream products. Propyl and methyl paraben is a preservative that can prevent the growth of bacteria and fungi. Moringa seed is also able to optimize the prevention of microbial contamination in cream product samples in addition. This is because Moringa seeds contain active compounds of seeds that are antimicrobial, including saponins, tannins, flavonoids, and alkaloids. Moringa seed active compounds work by inhibiting protein synthesis and destroying bacterial cell membranes so as to be antimicrobial [23].

Test Result Dermal Acute Scrub Cream

Based on the irritation test results (Table 3), no erythema and edema reaction in the skin of test animals of any formula with the value of the primary skin irritation index (PDII) was 0. If seen from the category of skin irritation index response then the PDII value goes into the range 0-0,4 so that it can be categorized as a material that does not irritate the skin. These results indicate that the scrub cream with the addition of a moringa seed scrub 3.5; 4.5; 5.5% and the base is safe to use. Test animal skin does not show an erythema reaction and edema is probably caused by the resulting moringa seed cream scrub having a pH still in the range of SNI 16-4399-1996 quality requirements so that its use does not cause irritation. According to Tranggono and Fatmah [24], pH is one of the things that can trigger the occurrence of side effects on the skin such as erythema and edema.

Table 4. Primary irritation test results of moringa seed scrub cream on Sprague-Dawley's white rats skin

Treatment	24th hours		48th Hours		PDII
	Erythema	Edema	Erythema	Edema	
F0	0	0	0	0	0
F1	0	0	0	0	0
F2	0	0	0	0	0
F3	0	0	0	0	0
KK	0	0	0	0	0
KN	0	0	0	0	0

Note: F0 = rat smeared cream formula without addition of moringa seed scrub, F1 = rat smeared cream formula with addition of 3.5% (b/ w) moringa seed scrub, F2 = rat smeared cream formula with addition of 4.5% (w / w) moringa seed scrub, F3 = rat smeared cream formula with addition of 5.5% (b/b) moringa seed scrub, KK = rat smeared cream of commercial cream, KN = untreated rat.

Some components in cosmetics can potentially irritate the skin such as preservatives (antimicrobial substances), surfactants, fragrances, and dyes [25]. Scrub cream products in this study using commercial preservatives are methyl and propyl paraben. The JECFA (Joint FAO / WHO Expert Committee on Food Additives) [26] in 1990 stated that methyl and propyl paraben had an ADI (Acceptable Daily Intake) value of 0-10 mg / kg body weight, while methyl and propyl paraben toxicity data in mice orally is 0.5-2 g / 250 grams of body weight. This study used methyl paraben as much as 0.2 gram and propyl paraben as much as 0.02 gram which is still in safe range according to JECFA guideline. The study also used cetyl alcohol, stearic acid, and triethanolamine

CONCLUSION

Based on the research that has been done can be concluded: The most optimum scrub cream formulation is scrub cream with the addition of 4.5% moringa seed which has the highest general favorite level with a score of 5.67. Characteristic of scrub cream with addition of moringa seed 3.5; 4.5; and 5.5% fulfill the standard that has been determined SNI 16-4399-1996, that is with pH value 6.88-7.31; weight of type 1 g/mL; emulsion stability of 95.19-96.61%; and negative microbial contamination.

The irritation test results showed that the scrub cream with the addition of moringa seed 3.5; 4.5; 5.5% and the base do not cause irritation effect on the skin of white rat test animals (*Rattus norvegicus*) with the value of primary skin irritation index (PDII) equal to 0 that indicates scrub cream moringa seed safe to use.

ACKNOWLEDGEMENTS

This research was supported by Centre for Research and Publication of UIN Jakarta. The authors would like to thank for helpful supports.

REFERENCES

- [1] Ogbunug H.A., Uneh. F.U., Ozumba A. N., Ezikpe O., Igwilol O., Adenekan S.O., and Onyekwelu O.A, Physico-chemical and Antioxidant Properties of *Moringa oleifera* Seed Oil, Pakistan Journal of Nutrition, Vol. 10 Issue 5, 2011, pp. 409-414.
- [2] Unigbe C., Okeri H., Erharuyi O., Oghenero E., and Obamedo D., Phytochemical and Atioxidant Evaluation of *Moringa oleifera* (Moringaceae) Leafand Seed. Journal of Pharmacy and Bioresources, Vol. 11, Issue 2, 2014, pp. 51-57.
- [3] Compaore W.R., Nikiema P.A., Bassole H. I., Savadogo A., Mouecoucou J., Hounhouigan D. J., and Traore S.A, Chemical Composition and

- Antioxidative Properties of Seed of *Moringa oleifera* and Pulps of *Parkia biglobosa* and *Adansonia digitata* Commonly used in Food Fortification in Burkina Faso. *Journal of Biological Sciences*, Vol. 3, Issue 1, 2011, pp. 64-72.
- [4] Alam M., Gladstone H., and Tun R, *Cosmetic Dermatology: Requisites in Dermatology Series*, Elsevier Health Sciences, 2009.
- [5] Gopalakrishnan L., Doriya K., dan Kumar D., *Moringa oleifera*, *Food Science and Human Wellness*, Vol. 3, Issue 3, 2016, pp. 49-56.
- [6] Burlando B., Verotta L., Cornara L., and Bottini E., *Herbal Principle in Cosmetics*, CRC Press, 2010.
- [7] Ojiako EN. And Okeke C. 2013. Determination of Antioxidant of *Moringa oleifera* Seed Oil and Its Use in the Production of a Body Lotion Cream. *Asian Journal of Plant Science and Research*, Vol. 3, Issue 3, 2013, pp. 1-4.
- [8] Duraivel S., Shaheda A., Basha R., Pasha E., and Jilani, Formulation and Evaluation of Antiwrinkle Activity of Cream and Nano Emulsion of *Moringa oleifera* Seed Oil, *Journal of Pharmacy and Biological Sciences*, Vol. 9, Issue 4, pp 58-73.
- [9] Badan Pengawas Obat dan Makanan Republik Indonesia BPOM, Nomor 7 Tahun 2014 tentang Pedoman Uji Toksisitas Nonklinis secara In Vivo, Vol. 1, 2014, pp. 65-72.
- [10] Draize T.H., Woodland, and Calvey, Methods for the Study of Irritation and Toxicity of Substances Applied Topically to the Skin and Mucous Membranes. *Journal Pharmacol*, Vol. 8, Issue 2, 1959, pp. 377-390.
- [11] Hendrawati, Rohaeti E., Effendi H., and Darusman L. K., Characterization of Physico-Chemical Properties of Nano-Sized *Moringa oleifera* Seed Powder and Its Application as Natural Coagulant in Water Purification Process, *Journal of Environment and Earth Science*, Vol. 5. Issue 21, 2015, pp 19-26.
- [12] Yuliati E. dan Binarjo A., Conference proceedings, Conf. on Prosiding Ilmiah XVIII, 2012, pp 378-382.
- [13] Sharon N., Anam S., and Yuliet. Formulasi Krim Antioksidan Ekstrak Etanol Bawang Hutan, *Journal of Natural Science*, Vol. 2, Issue 3, 2013, pp. 111-122.
- [14] Badan Standarisasi Nasional BSN, SNI 01-2346-2006 Petunjuk Pengujian Organoleptik dan atau Sensori, Vol. 1, 2006, pp 1-11.
- [15] Association of Official Analytical Chemists AOAC, *Official Methods of Analysis Chemist*, Vol. 1A, 1995, pp. 3-4.
- [16] Badan Standardisasi Nasional, SNI 16-4399-1996 Sediaan Tabir Surya, Vol. 1, 1996, pp. 2-4.
- [17] Badan Standarisasi Nasional, SNI 16-2897-1992. Cara Uji Cemar Mikroba, Vol. 1, 1992, pp. 1-6.
- [18] Kuncari E. S., Iskandarsyah, and Praptiwi, Uji Iritasi dan Aktivitas Pertumbuhan Rambut Tikus Putih: Efek Sediaan Gel Apigenin dan Perasan Herba Seledri (*Apium graveolens* L.), *Media Litbangkes*. Vol 25, Issue 1, 2015, pp. 15-22.
- [19] Diana Z. D. and Thaman A, *Cosmetic Formulation Skin Care Products*, Taylor and Francis Group, 2006.
- [20] Ijarotimi O., Oluwole A., and Oluwaseun A., Comparative Study on Nutrient Composition, Phytochemical, and Functional Characteristics of Raw, Germinated, and Fermented *Moringa oleifera* Seed Flour, *Food Science and Nutrition*, Vol. 1, Issue 6, 2013, pp. 452– 463.
- [21] Rowe R.C., Sheskey P.J., and Owen, *Handbook of Pharmaceutical Excipients*, Pharmaceutical Press and American Pharmacist Association, 2009.
- [22] Lassen C., Hansen S. F., Magnusson K., Hartmann N. B., Rehne Jensen P., Nielsen T. G., and Brinch A., *Microplastics Scubber in Cosmetic Products*, Danish Environmental Protection Agency, 2015.
- [23] Buckle K. A., Edwards R. A., Fleet G. H., and Wotton M, *Ilmu Pangan*, Universitas Indonesia Press, 2010.
- [24] Tranggono R.I. and Fatma L., *Buku Pegangan ilmu Pengetahuan Kosmetik*, PT. Gramedia Pustaka Utama, 2007
- [25] Barrel A.O., Paye M., Maibach H.I., *Handbook of Cosmetic Science and Technology*, Informa Healthcare USA, 2009, pp. 553–562.
- [26] Joint FAO/ WHO Expert Committee on Food Additives JECFA. 1990. Evaluation of certain food additives and contaminants (Thirty-fifth Report of the Joint FAO/WHO Expert Committee on Food additives). Geneva: World Health Organization.

COMPATIBLE ACTION GRAPH FOR FINITE CYCLIC GROUPS OF p -POWER ORDER

Mohammed Khalid Shahoodh¹, Mohd Sham Mohamad², Yuhani Yusof³, Sahimel Azwal Sulaiman⁴ and Nor Haniza Sarmin⁵

^{1,2,3,4} Applied & Industrial Mathematics (AIMs) Research Cluster, Faculty of Industrial Sciences & Technology, Universiti Malaysia Pahang, Lebuhraya Tun Razak, 26300 Gambang, Kuantan, Pahang Darul Makmur, Malaysia

⁵ Department of Mathematical Sciences, Faculty of Science, Universiti Teknologi Malaysia, 81310 UTM Johor Bahru, Johor, Malaysia

ABSTRACT

The compatible actions are important in determining the nonabelian tensor product of groups. In this paper, finite cyclic groups of p -power order, where p is an odd prime are considered. The purpose of the paper is to introduce a new graph called the compatible action graph for the nonabelian tensor product for the finite cyclic groups of p -power order, where p is an odd prime. Furthermore, some properties of the compatible action graph have been studied.

Keywords: Cyclic Groups, Nonabelian Tensor Product, Compatible Actions, Number Theory, Graph Theory.

INTRODUCTION

It is well-known that the compatible actions played an important role in determining the nonabelian tensor product of groups. The concept of the nonabelian tensor product has been defined for a pair of groups G and H that satisfy the compatibility conditions. Recently, much attention has been given to investigate the compatible actions and the nonabelian tensor products. Bardakov and Neshchadim [1] studied the compatible actions by providing some necessary conditions for the compatibility of the actions. They have focused on the case that for the given groups G and H such that G acts on H , whether it is possible to define an action of H on G such that this pair of the actions are compatible. Moreover, Ellis and McDermott [2] investigated the compatible actions for two different groups D_4 and Q_4 . They found that there are only 292 compatible pairs of actions between $D_4 \otimes Q_4$. Visscher [3] gave a complete conditions for the actions to be compatible for the finite cyclic groups of p -power order when one of the actions is trivial or both actions are trivial. Furthermore, Mohamad [4] used the order of the action as a condition and provide new necessary and sufficient conditions for the pair of finite cyclic groups of p -power order acts compatibly on each other. Meanwhile, Sulaiman *et al.* [5] studied the compatible pairs of actions for finite cyclic groups of 2-power order. They determined the exact number of compatible pairs of actions that can be identified between the nonabelian tensor product for two finite cyclic groups of 2-power order. In addition, Shahoodh *et al.* [6] investigated the compatible pairs of actions for the finite cyclic groups

of 3-power order and they determined the exact number of the compatible pairs of actions with the actions that have order one, order three and the highest 3-power order.

Nowadays, there are many studies have been considered the theoretical relationship between group theory and graph theory. The study of this relationship can establish graphs in different ways based on the algebraic structures of the group or the semigroup by using the properties of graph. For example, Alireza *et al.* [7] investigated some results on the power graphs of the finite groups, while Kelarev and Quinn [8] defined the directed power graph of the semigroups. Meanwhile, Mansoori, *et al.* [9] defined the non-coprime graph associated to the group G , where the vertex set is $G \setminus \{e\}$ and two distinct vertices are adjacent connected by the edge with the orders relatively the non-prime. They determined the general properties of the non-coprime graph, such as diameter, girth, connectivity, Hamiltonian, independence number and domination number. The conjugacy class graph of some finite groups with its energy have been investigated by Mahmoud *et al.* [10]. They computed the energy of the conjugacy class graphs of the dihedral groups of order $2n$, then generalized quaternion groups of order $4n$ and quasidihedral groups. Again, they introduced the general formulas for the energy of the conjugacy class graphs of those types of groups. In this paper, a new graph namely compatible action graph has been defined for the nonabelian tensor

product for the finite cyclic groups of the p -power order where p is an odd prime. Furthermore, this graph is denoted by $\Gamma_{C_{p^\alpha} \otimes C_{p^\beta}}^p$, then some properties of this graph have been studied.

This paper is organized as follows. In Section Two, some preparatory results and definitions on the compatible pairs of actions and automorphism group of such type of groups are given with some fundamental concepts of graph theory that are needed in this research. While, the main results of this paper are presented in Section 3. Lastly, the conclusions of this paper are given in Section 5.

THE PREPARATORY RESULTS

This section contains some of the definitions and previous results on the automorphism group and the compatible actions for the finite cyclic groups of the p -power order, where p is an odd prime with some fundamental concepts on the graph theory. We started with the definition of the compatible actions which is given as follows.

Definition 1 [11]

Let G and H be the groups, which act on each other and each of which acts on itself by conjugation. These mutual actions are said to be compatible if

$${}^{(s_h)}g' = {}^s({}^{(h)}g') \quad \text{and} \quad {}^{(h_g)}h' = {}^h({}^{(g)}h') \quad \text{for all } g, g' \in G \text{ and } h, h' \in H.$$

The automorphism group of the finite cyclic group of p -power order is an isomorphic with a direct product of two finite cyclic groups as stated in following theorem.

Theorem 1 [12]

Let p be an odd prime and $\alpha \in \mathbb{N}$. If G is a cyclic group of order p^α , then

$$\text{Aut}(G) \cong C_{p-1} \times C_{p^{\alpha-1}} \cong C_{(p-1)p^{\alpha-1}} \quad \text{and} \quad |\text{Aut}(G)| = \varphi(p^\alpha) = (p-1)p^{\alpha-1}.$$

The following corollary showed that when G is abelian, then the trivial action is always compatible with any other action.

Corollary 3.1 [3]

Let G and H be groups. Furthermore, let G act trivially on H . If G is abelian, then for any action of H on G , the mutual actions are compatible.

The following theorem stated the compatibility for the pair of the actions that have p -power order for the two finite cyclic groups of p -power order, where p is an odd prime.

Theorem 2[4]

Let $G = \langle g \rangle \cong C_{p^\alpha}$ and $H = \langle h \rangle \cong C_{p^\beta}$ be groups such that $\alpha, \beta \geq 3$. Furthermore, let $\sigma \in \text{Aut}(G)$ with $|\sigma| = p^k$, where $k = 1, 2, \dots, \alpha-1$ and $\sigma' \in \text{Aut}(H)$ with $|\sigma'| = p^{k'}$ where $k' = 1, 2, \dots, \beta-1$. Then (σ, σ') is a compatible pair of actions if and only if $k + k' \leq \min\{\alpha, \beta\}$.

The next theorem gives the exact number of the compatible pairs of actions that can be identified between the nonabelian tensor product of two finite cyclic groups of p -power order where p is an odd prime.

Theorem 3 [13]

Let $G \cong C_{p^\alpha}$ and $H \cong C_{p^\beta}$ be finite cyclic groups of p -power order with $\alpha, \beta \geq 3$. Then, there exist

$$(p-1)p^{\beta-1} + \sum_{k=1}^{\alpha-1} (p-1)p^{k-1} + \sum_{k=1}^{\alpha-1} (p-1)p^{k-1} \sum_{k=1}^{\alpha-1} \sum_{i=1}^r (p-1)p^{i-1}$$

compatible pairs of actions when and $k = 1, 2, \dots, \alpha-1$
 $r = \min\{\alpha, \beta\} - k.$

Next, the following proposition gives the number of the compatible pairs of actions when one of the actions is trivial.

Proposition 1[13]

Let $G \cong C_{p^\alpha}$ and $H \cong C_{p^\beta}$ be finite cyclic groups of the p -power order. Furthermore, let $\rho \in \text{Aut}(G)$ with $|\rho| = 1$ and $\alpha, \beta \geq 1$. Then, the number of the compatible pairs of actions is $(p-1)p^{\beta-1}$.

The next proposition presented the number of the compatible pairs of actions for every value of k where $k = 1, 2, \dots, \alpha-1$.

Proposition 2[13]

Let $G \cong C_{p^\alpha}$ and $H \cong C_{p^\beta}$ be finite cyclic groups of p -power order where p is an odd prime such that $\alpha, \beta \geq 3$. Furthermore, let $\rho \in \text{Aut}(G)$ with $|\rho| = p^k$

where $k = 1, 2, \dots, \alpha - 1$. Then, the number of the compatible pairs of actions is

$$(p-1)p^{k-1} + (p-1)p^{k-1} \sum_{i=1}^r (p-1)p^{i-1}$$

where $r = \min\{\alpha, \beta\} - k$ and $k = 1, 2, \dots, \alpha - 1$.

Next, some definitions and fundamental concepts of graph theory that are needed in this research are presented as follows. These fundamental concepts with the definitions can be found in [14].

A graph G is a mathematical structure consisting of two sets, the set of the vertices and the set of the edges which are denoted by $V(G)$ and $E(G)$ respectively. Then, the order of the graph G is the number of the vertices in the graph G which is denoted by $|V(G)|$. In addition, the graph G is called connected graph if there is a path between every pair of distinct vertices. Moreover, the graph G is said to be complete if each ordered pair of the vertices are adjacent to each other. Then, a simple graph G is said to be bipartite graph if its vertex set can be partitioned into two disjoint sets V_1 and V_2 such that every edge in the graph G connects vertex in V_1 and vertex in V_2 , and there is no edge in the graph G connects either two vertices in V_1 or two vertices in V_2 .

Additionally, the graph which consists of the set of vertices and the set of directed edges, is called the directed graph such that the directed edges are associated with the ordered pair (u, v) is said to start at u and end at v , where $u, v \in V$. Furthermore, in the directed graph, the degree of the vertex v has two types, the out-degree and the in-degree. The out-degree is denoted by $\deg^+(v)$ which is the number of the edges with v as their initial vertex, while the in-degree is the number of the edges with v as their terminal vertex which is denoted by $\deg^-(v)$. For the directed graph G , the path of the length n from u to v , where n is positive integer, is defined as a sequence of edges e_1, e_2, \dots, e_n of G such that e_1 is associated with (x_0, x_1) , e_2 is associated with (x_1, x_2) and so on, with e_n is associated with (x_{n-1}, x_n) , where $x_0 = u$ and $x_n = v$.

MAIN RESULTS

In this section, our main results of this paper are

presented. The compatible action graph for the nonabelian tensor product for the finite cyclic groups of the p -power order, where p is an odd prime are introduced. Furthermore, some properties of compatible action graph have been investigated. We started with the definition of compatible action graph which is given as follows.

Definition 3.1

Let G and H be two finite cyclic groups of p -power order with p an odd prime. Furthermore, let (ρ, ρ') be a pair of the compatible actions for the nonabelian tensor product of $G \otimes H$, where $\rho \in \text{Aut}(G)$ and $\rho' \in \text{Aut}(H)$. Then, $\Gamma_{C_{p^\alpha} \otimes C_{p^\beta}}^p = (V(\Gamma_{C_{p^\alpha} \otimes C_{p^\beta}}^p), (E(\Gamma_{C_{p^\alpha} \otimes C_{p^\beta}}^p)))$ is a compatible action graph with the set of vertices $V(\Gamma_{C_{p^\alpha} \otimes C_{p^\beta}}^p)$, which is the set of $\text{Aut}(G)$ and $\text{Aut}(H)$, and the set of edges, $E(\Gamma_{C_{p^\alpha} \otimes C_{p^\beta}}^p)$ that connects these vertices which is the set of all compatible pairs of actions (ρ, ρ') . Furthermore, two vertices ρ and ρ' are adjacent if they are compatible.

The order of the graph G is defined as the number of the vertices in the graph G , which is denoted by $|V(G)|$. Thus, the order of the compatible action graph has been determined and is denoted by $|V(\Gamma_{C_{p^\alpha} \otimes C_{p^\beta}}^p)|$. The order of the compatible action graph has been considered into two cases when $G \neq H$ and $G = H$. Hence, the order of the compatible action graph is presented in the following proposition.

Proposition 3.1

Let $G \cong C_{p^\alpha}$ and $H \cong C_{p^\beta}$ be the finite cyclic groups of p -power order where p is an odd prime and $\alpha, \beta \geq 3$. Then, the order of the compatible action graph is

- (i) $|V(\Gamma_{C_{p^\alpha} \otimes C_{p^\beta}}^p)| = (p-1)(p^{\alpha-1} + p^{\beta-1})$ if $G \neq H$.
- (ii) $|V(\Gamma_{C_{p^\alpha} \otimes C_{p^\beta}}^p)| = (p-1)p^{\alpha-1}$ if $G = H$.

Proof:

From the definition of the order of the graph, the order of the compatible action graph is the number of the vertices in $V(\Gamma_{C_{p^\alpha} \otimes C_{p^\beta}}^p)$. Furthermore, by Definition 3.1, $V(\Gamma_{C_{p^\alpha} \otimes C_{p^\beta}}^p)$ is the nonempty set of $\text{Aut}(G)$ and

$\text{Aut}(H)$. Thus, there are two cases needed to be considered, which are $G \neq H$ and $G = H$.

Case I: Suppose that $G \neq H$. Then,

$$\begin{aligned} \left| V(\Gamma_{C_{p^\alpha} \otimes C_{p^\beta}}^p) \right| &= |\text{Aut}(G)| + |\text{Aut}(H)| \\ &= (p-1)p^{\alpha-1} + (p-1)p^{\beta-1} \\ &= (p-1)(p^{\alpha-1} + p^{\beta-1}). \end{aligned}$$

Case II: Suppose that $G = H$. Without loss of generality, let α be the order where $\alpha = \beta$, then

$$\begin{aligned} \left| V(\Gamma_{C_{p^\alpha} \otimes C_{p^\beta}}^p) \right| &= |\text{Aut}(G)| = (p-1)p^{\alpha-1}. \quad \text{Therefore,} \\ \left| \Gamma_{C_{p^\alpha} \otimes C_{p^\beta}}^p \right| &= (p-1)(p^{\alpha-1} + p^{\beta-1}) \quad \text{when } G \neq H \text{ and} \\ \left| \Gamma_{C_{p^\alpha} \otimes C_{p^\beta}}^p \right| &= (p-1)p^{\alpha-1} \quad \text{when } G = H. \quad \square \end{aligned}$$

Since the action of the group G on the group H is the mapping $\Phi: G \rightarrow \text{Aut}(H)$, then the compatible action graph of the finite cyclic groups of the p -power order is considered as a directed graph. Thus, the cardinality of the edges of the compatible action graph for such type of groups are presented in the following proposition.

Proposition 3.2

Let $G \cong C_{p^\alpha}$ and $H \cong C_{p^\beta}$ be the finite cyclic groups of p -power order where p is an odd prime and $\alpha, \beta \geq 3$. Then,

$$\left| E(\Gamma_{C_{p^\alpha} \otimes C_{p^\beta}}^p) \right| = (p-1)p^{\beta-1} + \sum_{k=1}^{\alpha-1} (p-1)p^{k-1} \left[1 + \sum_{i=1}^r (p-1)p^{i-1} \right],$$

where $r = \min\{\alpha, \beta\} - k$ and $k = 1, 2, \dots, \alpha - 1$.

Proof:

It follows from Definition 3.1 and Theorem 3. \square

Table 1 is given as some examples for the cardinality of the edges for $\Gamma_{C_{p^\alpha} \otimes C_{p^\beta}}^p$ with the same prime p and $\alpha, \beta \in \square$.

Table 1 Cardinality of the edges for $\Gamma_{C_{p^\alpha} \otimes C_{p^\beta}}^p$.

p	α	β	$\left E(\Gamma_{C_{p^\alpha} \otimes C_{p^\beta}}^p) \right $
3	3	3	54
	3	4	90
	3	5	198
	3	6	522

5	3	7	1494
	3	8	4410
	3	9	13158
	3	3	300
	3	4	700
	3	5	2700
	3	6	12700
	3	7	62700
7	3	8	312700
	3	9	1562700
	3	3	882
	3	4	2646
	3	5	14994
	3	6	101430
	3	7	706482
	3	8	4941846
	3	9	34589394

Since the compatible action graph has been considered as a directed graph, then the compatible pairs of actions (ρ, ρ') is defined as a directed edge of the compatible action graph. Therefore, according to the definition of the directed graph, the vertex ρ is considered as an initial vertex of (ρ, ρ') and ρ' is the terminal vertex of (ρ, ρ') . Furthermore, the out-degree of the vertex v in the directed graph is denoted by $\deg^+(v)$, where it needs to be found in order to investigate the number of the edges in the graph. Thus, in the following proposition the out-degree for the given vertex ρ in the compatible action graph is presented.

Proposition 3.3

Let $G \cong C_{p^\alpha}$ and $H \cong C_{p^\beta}$ be the finite cyclic groups of the p -power order where p is an odd prime and $\alpha, \beta \geq 3$. Furthermore, let $v \in V(\Gamma_{C_{p^\alpha} \otimes C_{p^\beta}}^p)$ where $v \in \text{Aut}(G)$ and $|v| = p^k$. Then $\deg^+(v)$ is one of the following:

- (i) $(p-1)p^{\beta-1}$ if $k = 0$.
- (ii) $(p-1)p^{k-1} + (p-1)p^{k-1} \sum_{i=1}^r (p-1)p^{i-1}$,

with $r = \min\{\alpha, \beta\} - k$ if $k = 1, 2, \dots, \alpha - 1$.

Proof:

It follows from Propositions 1 and 2 \square

From Theorem 2, the actions that have the p -power order are always compatible when

$k + k' \leq \min\{\alpha, \beta\}$. Thus, we conclude in the following corollary that the out-degree and the in-degree for the compatible action graph are the same.

Corollary 3.1

Let G and H be the finite cyclic groups of the p -power order where p is an odd prime and $v \in V(\Gamma_{C_{p^\alpha} \otimes C_{p^\beta}}^p)$.

Then, $\deg^-(v) = \deg^+(v)$ for $\Gamma_{C_{p^\alpha} \otimes C_{p^\beta}}^p$.

Proof:

From Propositions 3.3, for any vertex $v \in V(\Gamma_{C_{p^\alpha} \otimes C_{p^\beta}}^p)$ where $v \in \text{Aut}(G)$ and $|v| = p^k$, we have $\deg^+(v) = (p-1)p^{\beta-1}$ if $k = 0$, and when $k = 1, 2, \dots, \alpha-1$, then

$$\deg^+(v) = (p-1)p^{k-1} + (p-1)p^{k-1} \sum_{i=1}^r (p-1)p^{i-1},$$

where $r = \min\{\alpha, \beta\} - k$. By Theorem 2, the actions are compatible when $k + k' \leq \min\{\alpha, \beta\}$, which present that the vertices are adjacent. Similarly, when $v \in \text{Aut}(H)$ and $|v| = p^{k'}$. Therefore, $\deg^-(v) = \deg^+(v)$ for $\Gamma_{C_{p^\alpha} \otimes C_{p^\beta}}^p$. \square

Next, the connectivity of the compatible action graph is studied. The next proposition presented the connectivity of the compatible action graph.

Proposition 3.4

Let $G \cong C_{p^\alpha}$ and $H \cong C_{p^\beta}$ be the finite cyclic groups of the p -power order where p is an odd prime such that $\alpha, \beta \geq 3$. Then, $\Gamma_{C_{p^\alpha} \otimes C_{p^\beta}}^p$ is a connected graph.

Proof:

Let $G \cong C_{p^\alpha}$ and $H \cong C_{p^\beta}$ be the finite cyclic groups of the p -power order where p is an odd prime such that $\alpha, \beta \geq 3$. Furthermore, let $v_1 \in V(\Gamma_{C_{p^\alpha} \otimes C_{p^\beta}}^p)$ with $v_1 \in \text{Aut}(G)$ and v_1 is trivial action. By Proposition 3.3, $\deg^+(v_1) = (p-1)p^{\beta-1}$. Similarly, if we have $v_2 \in V(\Gamma_{C_{p^\alpha} \otimes C_{p^\beta}}^p)$ such that $v_2 \in \text{Aut}(H)$ and v_2 is trivial action, then by Corollary 3.1, v_2 is compatible with every $v \in \text{Aut}(G)$. Thus, $\Gamma_{C_{p^\alpha} \otimes C_{p^\beta}}^p$ is a connected graph. \square

The next proposition shows that the compatible action graph is a bipartite graph when $G \neq H$.

Proposition 3.5

Let $G \cong C_{p^\alpha}$ and $H \cong C_{p^\beta}$ be two finite cyclic groups of p -power order where p is an odd prime such that $\alpha, \beta \geq 3$. Then, $\Gamma_{C_{p^\alpha} \otimes C_{p^\beta}}^p$ is the bipartite graph if and only if $G \neq H$.

Proof:

Let $G \cong C_{p^\alpha}$ and $H \cong C_{p^\beta}$ be two finite cyclic groups of p -power order where p is an odd prime such that $\alpha, \beta \geq 3$. First need to show that if the compatible action graph $\Gamma_{C_{p^\alpha} \otimes C_{p^\beta}}^p$ is a bipartite graph then $G \neq H$. By contradiction method, assume that $G = H$, then $\text{Aut}(G) = \text{Aut}(H)$. Thus, there exists a loop which cannot be partitioned into two disjoint sets, which contradicts on the assumption. Thus, $G \neq H$.

Next, if $G \neq H$ then any $v \in \text{Aut}(G)$ only compatible with some $v' \in \text{Aut}(H)$. Thus, clearly it can be partitioned into two disjoint sets $\text{Aut}(G)$ and $\text{Aut}(H)$ respectively. Therefore, $\Gamma_{C_{p^\alpha} \otimes C_{p^\beta}}^p$ is a bipartite graph. \square

The complete graph K_n contains exactly one edge between each pair of the vertices. As a result, the compatible action graph is not a complete graph. This result is given as follows.

Proposition 3.6

Let $G \cong C_{p^\alpha}$ and $H \cong C_{p^\beta}$ be the finite cyclic groups of the p -power order where p is an odd prime and $\alpha, \beta \geq 3$. Then, $\Gamma_{C_{p^\alpha} \otimes C_{p^\beta}}^p$ is not a complete graph.

Proof:

By Proposition 3.1, there are $(p-1)(p^{\alpha-1} + p^{\beta-1})$ number of vertex in $\Gamma_{C_{p^\alpha} \otimes C_{p^\beta}}^p$. If $\Gamma_{C_{p^\alpha} \otimes C_{p^\beta}}^p$ is a complete graph, then there exist $\left[(p-1)(p^{\alpha-1} + p^{\beta-1})\right]^2$ edges. By Proposition 3.2,

$$\left|E(\Gamma_{C_{p^\alpha} \otimes C_{p^\beta}}^p)\right| = (p-1)p^{\beta-1} + \sum_{k=1}^{\alpha-1} (p-1)p^{k-1} \left[1 + \sum_{k=1}^{\alpha-1} \sum_{i=1}^r (p-1)p^{i-1}\right] \leq \left[(p-1)(p^{\alpha-1} + p^{\beta-1})\right]^2.$$

Thus, $\Gamma_{C_{p^\alpha} \otimes C_{p^\beta}}^p$ is not a complete graph. \square

CONCLUSION

In this paper, the compatible action graph has been introduced for the nonabelian tensor product for the finite cyclic groups of p -power order, where p is an odd prime. Some properties of the compatible action graph are studied, such as the cardinality of the edge, the order of the compatible action graph, and the out-degree for the given vertex in this graph. As a result, the compatible action graph is a connected and bipartite graph but it is not a complete graph. The results can be extended by introducing the subgraph of the compatible actions graph. Then, the number of the edges and the order of the subgraph of compatible action graph can be determined.

ACKNOWLEDGEMENTS

This research is supported by UMP research grant, RDU1703265.

REFERENCES

- [1] Bardakov V. G., and Neshchadim M. V., Compatible Actions and Non-abelian Tensor Products. arXiv preprint arXiv:1709.07708, 2017.
- [2] Ellis G. and McDermott A., Tensor Products of Prime Power Groups. J. Pure Applied Algebra. Vol. 132, Issue. 2, 1998, pp.119-128.
- [3] Visscher M, On the Non-abelian Tensor Products of Groups, PhD Dissertation, State University of New York, Binghamton, NY. 1998.
- [4] Mohamad M. S., Compatibility Conditions and Non-abelian Tensor Products of Finite Cyclic Groups of p -Power Order, PhD Dissertation, Universiti Teknologi Malaysia, 2012.
- [5] Sulaiman S. A., Mohamad S. M., Yusof Y. and Shahoodh M. K., The Number of Compatible Pair of Actions for Cyclic Groups of 2-Power Order. International Journal of Simulation--Systems, Science & Technology, Vol. 18, Issue. 4, 2017.
- [6] Shahoodh M. K., Mohamad S. M., Yusof Y. and Sulaiman S. A., Number of Compatible Pair of Actions for Finite Cyclic Groups of 3-Power Order, International Journal of Simulation--Systems, Science & Technology, Vol. 18, Issue 4, 2017.
- [7] Alireza D., Ahmad E., and Abbas J., Some Results on the Power Graphs of Finite Groups. ScienceAsia, Vol. 41, 2015, pp. 73-78.
- [8] Kelarev A. V. and Quinn. S. J, Directed Graph and Combinatorial Properties of Semigroups. J. Algebra Vol. 251, 2002, pp. 16–26.
- [9] Mansoori F., Erfanian A. and Tolue B., Non-coprime Graph of a Finite Group. In AIP Conference Proceedings Vol. 1750, No. 1, 2016, pp. 050017). AIP Publishing.
- [10] Mahmoud R., Sarmin N. H. and Erfanian A., The Conjugacy Class Graph of Some Finite Groups and its Energy. Malaysian Journal of Fundamental and Applied Sciences, Vol. 13, Issue. 4, 2017, pp.659-665.
- [11] Brown R. and Loday J., Van Kampen Theorem for Diagrams of Spaces. J. of Topology, Vol. 26, Issue. 3, 1987, pp. 311-335.
- [12] Dummit D. and Foote R., Abstract Algebra. John Wiley and Sons, USA., 2004, pp. 136-137.
- [13] Shahoodh M. K., Mohamad S. M., Yusof Y. and Sulaiman S. A., Number of Compatible Pair of Actions for Finite Cyclic Groups of p -Power Order, Jurnal Teknologi (Sciences and Technology): Vol.80. 2018.
- [14] Rosen K., Discrete Mathematics and Its Applications. 7 Ed. McGraw-Hill. New York, 2012, pp. 641-735.

FRAGMENT-BASED DRUG DESIGN TO INHIBIT DNA METHYLTRANSFERASE 1 (DNMT1) FOR BREAST CANCER THERAPY

Ade Hanna Natalia¹, Ahmad Husein Alkaff¹, Mutiara Saragih¹, Ina Nur Istiqomah¹, and Usman Sumo Friend Tambunan¹

¹Faculty of Mathematics and Natural Science, Universitas Indonesia, Indonesia

ABSTRACT

Breast cancer is the biggest cancer among women in the worldwide. The uncontrollably high DNA Methyltransferase-1 (DNMT1) activity which leads to abnormal gene expression is one of the primary cause of breast cancer. Therefore, DNMT1 as an essential enzyme in epigenetic regulation is considered as a potential therapeutic target for breast cancer treatment. In this research, the inhibitors of DNMT1 were designed through fragment-based drug design. About 168,646 natural products from PubChem database were used as fragment candidates. Initial screening based on toxicity and Lipinski's Rule of Three by Osiris DataWarrior was performed to obtain 2,601 favorable fragments. Pharmacophore-based rigid and flexible molecular docking simulation was employed with DNMT1 as the target protein. The selected fragments from docking simulation underwent fragment linking modification and second toxicity screening, generating 23 ligands. Subsequently, the newly designed ligands were subjected to pharmacophore-based flexible molecular docking simulation. Two ligands, HAMI_9 and HAMI_14, with Gibbs free binding energy of -11.6095 and -11.5904 kcal/mol, respectively, are considered as a promising inhibitor of DNMT1. The pharmacological properties of the ligands were analyzed using Osiris DataWarrior, Toxtree, SwissADME, admetSAR, and Molinspiration. The ligands show not only superior affinity and molecular interaction to DNMT1 but also have advantageous pharmacological properties compared to the standards. Additional in silico as well as in vivo experiments are needed to further assess the potency of HAMI_9 and HAMI_14 as drug candidates against breast cancer.

Keywords: Breast cancer, DNA methyltransferase, natural products, fragment-based drug design, molecular docking simulation.

INTRODUCTION

Breast cancer is the biggest evidence of cancer among women and the second prominent cause of cancer mortality after lung cancer in the world [1], [2]. Breast cancer occurs due to genetic aberration such as gene deletions, point mutations, chromosomal rearrangements and epigenetic misregulation [1]. DNA methylation pattern guides epigenetic regulation. DNA methylation plays an essential role in the regulation of the gene expression and the structure of chromatin, which leads to the manifestation of diseases in humans, such as various types of cancer [3]-[6].

DNA methylation pattern managed by the DNA methyltransferase (DNMT) enzymes, which will catalyze the transfer of methyl groups from S-Adenosyl-L-Methionine (SAM) to the C5 position of cytosine residues in CpG dinucleotides. DNMT in human is classified into three families: DNMT1, DNMT2, and DNMT3 [7].

DNMT1 is an enzyme composed of 1616 amino acids in humans and is the ubiquitous methyltransferase in humans. DNMT1 maintained the methylation pattern of the DNA parent strand to the new DNA daughter strand and expressed during

the S phase [5], [8]. The misregulation of DNMT1 initiates to hypermethylation in DNA promoter gene and hypomethylation which lead to the abnormal growth of cancer cells [5]. In breast cancer, the DNMT1 is overexpressed; it has uncontrollably high activity [8]. Therefore, the inhibition of the DNMT1 enzyme, which keeping its activity under control, is a promising method of epigenetic therapy for the treatment of breast cancer [5], [6], [8].

The in silico method is one of the methods that widely used in drug discovery for various diseases. The natural products have long been used by in silico method for drugs discovery and development in various diseases, such as cancer, because of its pharmacological activity and bioavailability in living organisms [9]. The natural products can be used as fragment library for lead compound discovery through fragment-based drug design. The fragment-based drug design is a method to construct the ligands by linking, merging or growing the ligands from small fragments to improve its interaction with target protein binding site [10]. In this research, the natural products are selected as the source of fragments which then modified by fragment-based drug design to inhibit DNMT1 protein. Thus, obtaining the inhibitor of DNMT1 for breast cancer therapy.

METHODS

In silico method were used in this research to obtain the compounds that have high affinity and have advantageous pharmacological properties. The compounds through in silico method were used for drug discovery in human disease, and the compounds would be used to inhibit DNMT1 protein. In this research, the in silico method were performed through Molecular Operating Environment (MOE), Osiris DataWarrior v04.07.02, Toxtree v2.6.13, SwissADME, AdmetSAR, and Molinspiration software.

Preparation of DNMT1 Protein

The three-dimensional (3D) structures of DNMT1 protein were acquired from RCSB Protein Data Bank with PDB ID: 3AV5, 3AV6, 3SWR, 3PTA, and 4WXX. The DNMT1 proteins were acquired from RCSB as one of protein structures source for molecular docking. Afterward, the protein structures were prepared and optimized by protonation and energy minimization using the LigX function in MOE 2014.09 with R-field solvation and AMBER 10: EHT as a forcefield. Finally, the DNMT1 proteins were stored in .moe format.

Protein-Ligand Interaction Fingerprints (PLIF) and Pharmacophore Selection of DNMT1 Protein

The pharmacophore construction of DNMT1 proteins was performed through PLIF method using MOE 2014.09 software with Amber10: EHT as a forcefield, and R-field solvation. The PLIF method used to determine interaction fingerprints between ligand–protein based on surface contacts according to the residues, hydrogen bonds, and ionic interactions [11]. Afterward, the proteins were performed superpose to compare three-dimensional (3D) structure of the protein and to superimpose the protein structures that differ based on protein sequence, size or shape [12].

Afterward, the pharmacophore feature that commonly applied in drug discovery were used in this research [13]. The pharmacophore feature is used to determine interaction site between the ligands and protein target. Therefore, the molecules that potentially trigger the desired biological effect were obtained [14], [15]. The pharmacophore site was stored in .ph4 format.

Preparation of The Fragments

The natural products from PubChem database were used as fragment library and were stored in sdf format. The fragment library was screened based on toxicity prediction test (tumorigenic, mutagenic, irritant, reproductive effect predictions) and

Lipinski's Rule of Three using Osiris DataWarrior to obtain favorable fragments that can be used for molecular docking [16], [17].

Afterward, all of the fragments underwent preparation and energy minimization by MOE 2014.09 software with MMFF94x modified as a forcefield. Three ligands, namely S-Adenosyl-L-Methionine (SAM), S-Adenosyl-L-Homocysteine (SAH), and sinefungin (SFG), were selected as standard compounds for the experiment. Finally, the fragment library was stored in .mdb format.

Molecular Docking Simulation and Fragment Linking Method

The fragments underwent pharmacophore-based rigid and flexible molecular docking with DNMT1 protein using MOE 2014.09 software with AMBER 10: EHT as the forcefield and R-field solvation. The fragments were eliminated if their root-mean-square deviation (RMSD) value lower than 2.0 Å and have higher Gibbs free binding energy ($\Delta G_{\text{binding}}$) than the standards.

Afterward, the fragments were linked to developing new ligands through fragment linking method. Fragment linking is one of fragment-based drug design method, the fragment linking method applied to acquire compounds that have higher affinity to bind with the pocket [18]. The new ligands were acquired from the fragments that do not overlap and have been linked. Afterward, the new ligands were docked with DNMT1 protein by pharmacophore-based rigid and flexible molecular docking using retain 100 through MOE 2014.09 software.

Analysis of Pharmacological Properties

The pharmacological properties of the best ligands were analyzed through some software. The tumorigenic, mutagenic, and drug-likeness properties were identified by Osiris DataWarrior. The ligands mutagenicity and carcinogenicity properties were predicted by Toxtree software [19]. The physicochemical, pharmacokinetics and drug-likeness of ligands were evaluated by SwissADME (<http://www.swissadme.ch/>) [20]. The admetSAR (<http://lmmd.ecust.edu.cn/admetSar1>) used to predict absorption, distribution, metabolism, excretion, and toxicity (ADMET) properties of ligands [21]. The bioactivity properties of ligands were analyzed through Molinspiration software [22].

RESULT AND DISCUSSION

Preparation of DNMT1 Protein

The DNMT1 protein has responsibility for DNA methylation and can lead as promising target for the

treatment of breast cancer [7], [8]. The water, metal, and unnecessary molecules in DNMT1 proteins from RCSB Protein Data Bank were removed because can influence interactions between the protein and ligand. The binding site of DNMT1 protein can be determined based on site finder feature in MOE 2014.09 software.

Protein-Ligand Interaction Fingerprints (PLIF) and Pharmacophore Selection of DNMT1 Protein

The interactions between DNMT1 proteins and ligands were compared through PLIF method. Five proteins of DNMT1 (3AV5, 3AV6, 3SWR, 3PTA, 4WXX) have similarity interactions. The protein of DNMT1 with PDB ID: 4WXX were chosen because its 3D structure has an excellent resolution (2.622 Å) and it comes from a human. The pharmacophore of DNMT1 protein was analyzed and was validated using standard ligands. Finally, there are three pharmacophore site namely HydA, Don and Acc indicated in green, pink, and blue respectively (Fig. 1). The 3D structures and the pharmacophore site of the DNMT1 protein can be seen in Fig. 1.

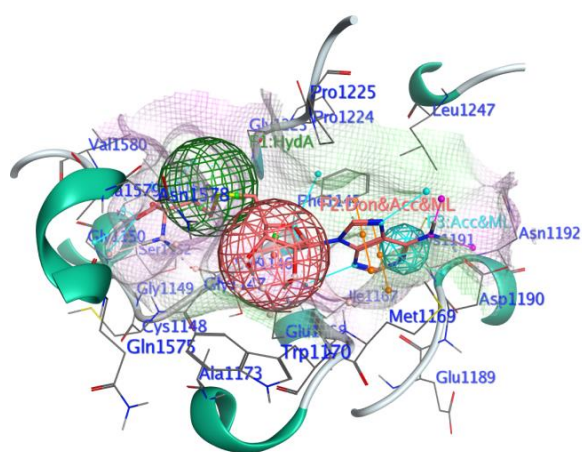


Fig. 1 The pharmacophore site and SAH in the binding pocket of DNMT1 protein (4WXX)

Preparation of The Fragments

In this research were used 168,646 natural products from PubChem database. All of the natural products were screened through Osiris Data Warrior v04.07.02 to find the potential fragment as inhibitor candidate of the DNMT1 protein. The natural products were screened based on toxicity prediction test to predict and to eliminate the compounds that have tumorigenic, mutagenic, reproductive effect and irritant characteristics. The natural products also were screened based on Lipinski's Rule of Three, which are they must fulfill three parameters: (1) mass of the molecules are less than 300Da, (2) the hydrogen donor and acceptor molecules are up to three, and (3)

the calculated clogP of molecules are three [23]. After screening by Osiris Data Warrior, there are 2,601 fragments obtained.

Molecular Docking Simulation and Fragment Linking Method

The 2,601 fragments were docked with DNMT1 protein based on Acc and HydA pharmacophore site and also based on Hyd and Don pharmacophore site. The molecular docking simulation was performed twice in rigid docking simulations using retain 30 in the first simulation and retain 100 in the second simulation with AMBER10: EHT as a forcefield. After docked using retain 100, there are 11 ligands based on Acc and HydA pharmacophore points, and also there are 76 ligands based on Hyd and Don pharmacophore site.

The linker between fragments was generated through fragment linking; there are three ligands which did not overlap and eligible to create linker. About 31 ligands were acquired from the fragments and the linkers screened by Osiris DataWarrior. Afterward, 23 linkers were obtained after screened and were docked with DNMT1 protein based on Acc, HydA and Don pharmacophore site by pharmacophore-based rigid and flexible molecular docking simulation using retain 100 with AMBER100: EHT as a forcefield. Finally, two best compounds were potential can inhibit DNMT1 refer to standard RMSD value, $\Delta G_{\text{binding}}$, and pharmacological properties.

The two of best compounds structure, namely HAMI_9 and HAMI_14, can be seen in Fig. 2.

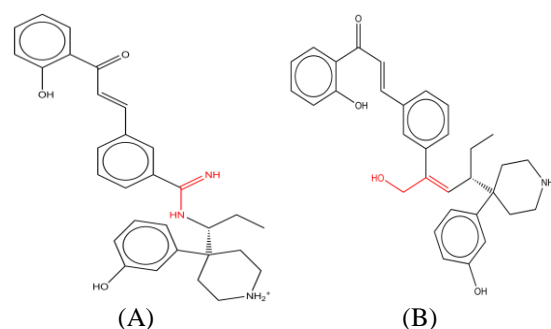


Fig. 2 The structure of (A) HAMI_9 and (B) The structure of HAMI_14

The HAMI_9 and HAMI_14 are the best drug candidate because they have RMSD value lower than 2.0 Å and have lower $\Delta G_{\text{binding}}$ energy compared to the SAM and Sinefungin as a standard, even though their $\Delta G_{\text{binding}}$ energy is not lower than SAH. The properties of the standards and all of the best ligands are appropriate with the Lipinski's Rule of Five and Veber's rule, even though the HAMI_14 has a logP value higher than five (Table 1).

Table 1 Molecular properties of the selected linked compounds and standard ligands

Ligand Name	Flexible Docking		MW	LogP	H-Don	H-Acc	TPSA	Rotatable Bond
	$\Delta G_{\text{binding}}$	RMSD						
*SAM	-11.1980	1.6134	399.451	-3.9384	4	11	187.08	7
*SFG	-10.9068	1.1838	382.400	-3.9574	5	12	214.72	7
*SAH	-11.8062	0.9106	384.416	-3.7275	4	11	212.38	7
HAMI_9	-11.6094	1.7746	484.618	3.8948	5	6	110.02	8
HAMI_14	-11.5903	1.5264	498.641	5.1464	4	5	94.37	9

Note: The meaning of * is the standard compound.

The HAMI_9 interacts with 22 amino acid residues DNMT1 protein and has four hydrogen bond interactions with Asparagine 1578, Glutamine 1223, and Cysteine 1148. On the other hand, HAMI_14 interacts with 21 amino acid residues and has two hydrogen bond interactions with Asparagine 1578, Alanine 1579 (Fig. 3 and 4).

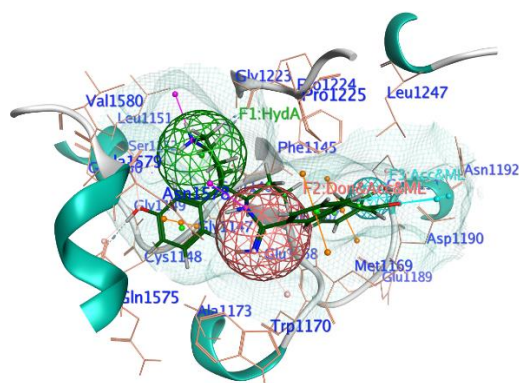


Fig. 3 The HAMI_9 molecular interactions.

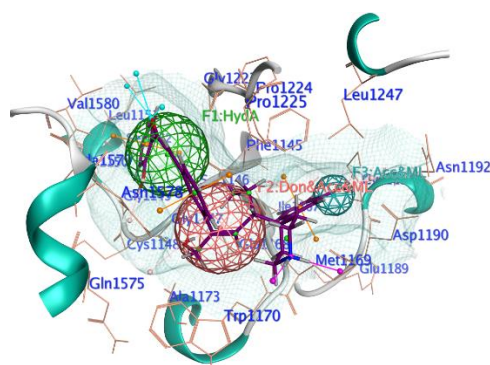


Fig. 4 The HAMI_14 molecular interactions.

Analysis of Pharmacological Properties

Both ligands have similar molecular properties. However, they show different characteristics in the pharmacological tests through SWISSADME, Molinspiration, and ADMETSAR. The results of pharmacological tests can be seen in Table 2. All of the best ligands are better than Sinefungin as the standard because they have high gastrointestinal (GI)

absorption. The HAMI_9 and HAMI_14 have subcellular localization in mitochondria.

The kinase and protease inhibitors of the ligands have a different value; the score higher than 0.00 indicates the ligand has high activity, while a score between 0.00 to -0.5 indicates that the ligand has moderate activity, and score less than -0.5 indicates the ligand does not have activity [24]. HAMI_9 is the best drug candidate based on kinase and protease inhibitor value because of its moderate activity as kinase inhibitor and high activity as a protease inhibitor. Protein kinases are essential for proliferation, metabolism, and apoptosis cells. The molecule that inhibits kinases cause a decreased cellular proliferation and increased apoptosis cells. The inhibition of protein kinase is one strategy of cancer therapy such as breast cancer therapy [25]. HAMI_9 also has high activity as protease inhibitor that can be used to against cancer. Metastases and cancer progression are highly dependent on nutrient and oxygen supply, which are affected by various proteases in the tumor and organs. The proteases are essential for cell death, cell differentiation, gene expression, cancer growth and metastases [26]. The protease inhibitors have activity as anti-cancer because they can inhibit proteolytic activity in cancer development and metastases [27]. Therefore, HAMI_9 has an activity to interfere with the development of cancer.

HAMI_9 and HAMI_14 are not organic cation transporter (SLC22A2) and CYP inhibitor. It indicates that they are able to translocate the molecules, have proper drug elimination, and does not lead unwanted effects because of the accumulation of the drug [20], [28]. The ligands are both none in carcinogens and AMES toxicity test. Therefore, the ligands are non-carcinogens and non-mutagenic [29] (Table 2).

The best ligands have good drug-likeness properties refer to Veber's and Egan's Rule. The bioavailability of the best ligands is at moderate level because their bioavailability score is 0.55. All of the best ligands are more readily synthesized than the standard because it has lower synthetic accessibility value than standard ligands [20]. All of the best ligands do not have PAINS alerts, but the HAMI_9 as the best ligand has 3 BRENK alerts (Table 3).

Table 2 ADME-Tox prediction all of the ligands using admetSAR, Molinspiration, and SwissADME software

ADME-Tox	Properties	Ligands				
		*SAM	*SFG	*SAH	HAMI_9	HAMI_14
Absorption	GI Absorption	High	Low	High	High	High
Distribution	Sub Localization	Nucleus	Nucleus	Nucleus	Mitochondria	Mitochondria
	Kinase Inhibitor	0.56	0.58	0.57	-0.04	-0.14
Metabolism	Protease Inhibitor	0.38	0.10	0.23	0.19	-0.04
	CYP Inhibitor	No	No	No	No	No
Excretion	SLC22A2	No	No	No	No	No
	AMES Toxicity	No	No	No	No	No
Toxicity	Carcinogens	No	No	No	No	No
	Biodegradation	No	No	No	No	No

Table 3 The druglikeness and medicinal chemistry properties all of the ligands using SwissADME software

Ligand Name	Druglikeness			Medicinal Chemistry		
	Veber	Egan	Bioavailability score	PAINS	Brenk	Synthetic accessibility
*SAM	Yes	No	0.55	0 alert	1 alert	4.94
*Sinefungin	Yes	No	0.55	0 alert	0 alert	4.78
*SAH	Yes	No	0.55	0 alert	0 alert	4.69
HAMI_9	Yes	Yes	0.55	0 alert	3 alert	4.31
HAMI_14	Yes	Yes	0.55	0 alert	1 alert	4.44

Note: The meaning of * is the standard compound.

CONCLUSION

The in silico method is essential in drug discovery, especially in the identification of new lead compounds as drug candidate through fragment-based drug design. The new lead compounds namely HAMI_9 and HAMI_14 derived from the natural products. The HAMI_9 and HAMI_14 can be used as a DNMT1 inhibitor for breast cancer therapy because of its excellent molecular properties, pharmacological properties to inhibit DNMT1 protein. Based on the result, the HAMI_9 is the best drug candidate to inhibit DNMT1 because HAMI_9 has the lowest Gibbs free binding energy, has the most significant molecular interaction, and has the best pharmacological properties. Therefore, the HAMI_9 is the promising drug candidates against breast cancer.

ACKNOWLEDGMENTS

The authors would like to give appreciation toward Directorate of Research and Community Engagement (DRPM) Universitas Indonesia for the facilities and financial through Hibah Publikasi Internasional Terindeks Untuk Tugas Akhir Mahasiswa (PITTA) No: 2328/UN2.R3.1/HKP.05.00/2018. The authors declare that there is no conflict of interest regarding this manuscript.

REFERENCES

- [1] Widschwendter M., and Jones P. A., DNA Methylation and Breast Carcinogenesis, *Oncogene*, Vol. 21, Issue 35, 2002, pp. 5462–5482.
- [2] Kwa M., Makris A., and Esteva F. J., Clinical Utility of Gene-Expression Signatures In Early Stage Breast Cancer, *Nature Reviews Clinical Oncology*, Vol. 14, Issue 10, 2017, pp. 595-610.
- [3] Girault I., Lidereau R., and Bie I., Expression Analysis of DNA Methyltransferases 1, 3A, and 3B in Sporadic Breast Carcinomas, *Clinical Cancer Research*, Vol. 9, Issue 12, 2003, pp. 4415–4422.
- [4] Jurkowska R. Z., Jurkowski T. P., and Jeltsch A., Structure and Function of Mammalian DNA Methyltransferases, *ChemBiochem*, Vol. 12, Issue 2, 2011, pp. 206–222, 2011.
- [5] Agrawal A., Murphy R. F., and Agrawal D. K., DNA Methylation In Breast and Colorectal Cancers, *Modern Pathology*, Vol. 20, Issue 7, 2007, pp. 711–721.
- [6] Arrowsmith C. H., Bountra C., Fish P. V., and Lee K., Epigenetic Protein Families: A New Frontier For Drug Discovery, *Nature Reviews Drug Discovery*, Vol. 11, Issue 5, 2012, pp 384-400.
- [7] Fuks F., and Brenner C., Part II. DNA Methyltransferases: Facts, Clues, Mysteries, 1st ed. Vol. 301, Springer, 2006, pp. 45–66.

- [8] Shin E., Lee Y., and Koo J. S., Differential Expression of The Epigenetic Methylation-Related Protein DNMT1 by Breast Cancer Molecular Subtype and Stromal Histology, *Journal of Translational Method*, Vol. 14, Issue 1, 2016, pp. 1–11.
- [9] Fang J., Liu C., Wang Q., Lin P., and Cheng F., In silico polypharmacology of natural products, *Briefings In Bioinformatics*, Vol. -, Issue -, 2017, pp. 1–19.
- [10] Loving K., Alberts I., and Sherman W., Computational Approaches For Fragment-Based and De Novo Design, *Current Topics In Medicinal Chemistry*, Vol. 10, Issue 1, 2009, pp. 14–32.
- [11] Da C., Kireev D., Structural Protein–Ligand Interaction Fingerprints (SPLIF) For Structure-Based Virtual Screening: Method and Benchmark Study, *Journal of Chemical Information and Modelling*, Vol. 54, Issue 9, 2015, pp. 2555–2561.
- [12] Maiti R., Van Domselaar G. H., Zhang H., and Wishart D. S., SuperPose: A Simple Server For Sophisticated Structural Superposition, *Nucleic Acids Research*, Vol. 32, Web Server Issue, 2004, pp. 590–594.
- [13] Zhou L., Griffith R., and Gaeta B., Combining Spatial and Chemical Information For Clustering Pharmacophores, *BMC Bioinformatics*, Vol. 15, Issue 16, 2014, pp. 1–12.
- [14] Yang S., Pharmacophore Modeling and Applications In Drug Discovery: Challenges and Recent Advances, *Drug Discovery Today*, Vol. 15, Issue 11–12, 2010, pp. 444–450.
- [15] Qing X., Yin Lee X., De Raeymaeker J., Tame J., Zhang K., De Maeyer M., Pharmacophore Modeling: Advances, Limitations, and Current Utility In Drug Discovery, *Journal of Receptor, Ligand and Channel Research*, Vol. 7, Issue, pp. 81–92.
- [16] Ramharack P., and Soliman M. E. S., Zika Virus NS5 Protein Potential Inhibitors: An Enhanced In Silico Approach In Drug Discovery, *Journal of Biomolecular Structure & Dynamics*, Vol. 36, Issue 5, 2017, pp. 1–16.
- [17] Mortier J., Rakers C., Frederick R., and Wolber G., Computational Tools For In Silico Fragment-Based Drug Design, *Current Topics Medicinal Chemistry*, Vol. 12, Issue 17, 2012, pp. 1935–1943.
- [18] Kumar A., Voet A., and Zhang K. Y. J., Fragment-Based Drug Design: From Experimental to Computational Approaches, *Current Medicinal Chemistry*, Vol. 19, Issue 30, 2012, pp. 5128–5147.
- [19] Guedes I. A., de Magalhães C. S., and Dardenne L. E., Receptor-Ligand Molecular Docking, *Biophysical Reviews*, Vol. 6, Issue. 1, 2014, pp. 75–87.
- [20] Daina A., Michielin O., and Zoete V., SwissADME: A Free Web Tool To Evaluate Pharmacokinetics, Drug-likeness and Medicinal Chemistry Friendliness of Small Molecules, *Scientific Reports*, Vol. 7, Issue 42717, 2017, pp. 1–13.
- [21] Cheng F., Li W., Zhou Y., Shen J., Wu Z., Liu G., Lee P. W., and Tang Y., AdmetSAR: A Comprehensive Source and Free Tool For Assessment of Chemical ADMET Properties, *Journal of Chemical Information and Modelling*, Vol. 52, Issue 11, 2012, pp. 3099–3105.
- [22] Singh A. N., Baruah M. M., and Sharma N., Structure-Based Docking Studies Towards Exploring Potential Anti-androgen Activity of Selected Phytochemicals Against Prostate Cancer, *Scientific Reports*, Vol. 7, Issue. 1, 2017, pp. 1–8.
- [23] Scott D. E., Coyne A. G., Hudson S. A., and Abell C., Fragment-Based Approaches In Drug Discovery and Chemical Biology, *Biochemistry*, Vol. 51, Issue 25, 2012, pp. 4990–5003.
- [24] Ammar O., In Silico Pharmacodynamics, Toxicity Profile and Biological Activities of The Saharan Medicinal Plant *Limoniastrum feei*, *Brazilian Journal of Pharmaceutical Sciences*, Vol. 53, Issue 3, 2015, pp. 1–10.
- [25] García-Aranda M., and Redondo M., Protein Kinase Targets In Breast Cancer, *International Journal Molecular Sciences*, Vol. 18, Issue 12, 2017, pp. 1–31.
- [26] Eatemadi A., Aiyelabegan H. T., Negahdari B., Mazlomi M. A., Daraee H., Daraee N., Eatemadi R., and Sadroddiny E., Role of Protease and Protease Inhibitors In Cancer Pathogenesis and Treatment, *Biomedicine and Pharmacotherapy*, Vol. 86, Issue, 2017, pp. 221–231.
- [27] Castro-Guillén J. L., García-Gasca T., and Blanco-Labra A., Chapter V. Protease Inhibitors as Anticancer Agents, 1st ed. Vol. -, Nova Science Publishers, 2010, pp 91–124.
- [28] Volk C., OCTs, OATs, and OCTNs: Structure and Function of The Polyspecific Organic Ion Transporters of The SLC22 Family, *Wiley Interdisciplinary Reviews: Membrane Transport and Signaling*, Vol. 3, Issue 1, 2014, pp. 1–13.
- [29] McCarren P., Springer C., and Whitehead L., An Investigation Into Pharmaceutically Relevant Mutagenicity Data and The Influence On Ames Predictive Potential, *Journal of Cheminformatics*, Vol. 3, Issue 11, 2011, pp. 1–20.

CONSTRUCTION AND ANALYSIS OF M-POINT NON-STATIONARY SUBDIVISION SCHEME

* Mehwish Bari¹, Najma Abdul Rehman² and Mehboob Alam³

^{1,3} Department of Mathematics, NCBA&E, Sub-Campus, Bahawalpur, Pakistan; ² Department of Mathematics, COMSATS, Sahiwal, Pakistan

ABSTRACT

In this article, construction of m-point non-stationary ternary interpolating subdivision schemes having tension parameter with the help of Lagrange identities have been discussed. Different limit curves can be obtained by adjusting the appropriate value of parameter in the proposed schemes. Tension or bagginess of the final (curve) depends upon the raise or drop the value of parameter. The proposed hyperbolic non-stationary schemes are as consistent as the regular curves by the control polygon as compared to the existing non-stationary schemes by trigonometric Lagrange polynomial. Few existing parametric and non-parametric stationary schemes are the counter part of proposed schemes. Asymptotically equivalence relation is used to determine the continuity or smoothness of the proposed schemes. The main demand of this article is to reproduce hyperbolic functions and the proposed schemes reproduce hyperbolic functions very well. Numerical examples show that the proposed scheme has the potential to reproduce hyperbolas and parabolas.

Keywords: Subdivision; Non-stationary; Interpolation; hyperbolas; parabolas

INTRODUCTION

Nowadays one of the important approach in geometric modeling is the subdivision approach. It deals with symbolization, interpolation, construction and hypothesis of curves and surfaces. the subdivision schemes are more appropriate because these schemes are simple, affecting, easy to understand, easy to analyze, their applications are easy and have good cordiality and best for geometric design. Deslauriers and Dubuc presented an iterative symmetric interpolation processes [1]. They showed the symmetric behavior of different subdivision schemes. Hassan et al. [2] proposed an interpolating 4-point ternary stationary subdivision scheme and they prove that the scheme has C^2 continuity. A class of binary, ternary, a-ary subdivision schemes are produced by [3]. Currently, technology and science emphasize on the applications that should allow to control the shape of the different objects and being capable of reproducing different curves widely used in Computer Graphics, Computer Aided Design and in geometric modeling, such as conics and polynomials. In the end of twentieth century stationary schemes are constructed but they do not have the competency to produce conics. The work on non-stationary schemes grows fast in twenty first century. Binary 4-point non-stationary scheme was proposed in [4] in which two rules of subdivision are used to subdivide the initial control polygon. Beccari et al. [5] proposed a 4-point scheme with a single tension parameter and it preserve the shape because of interpolating property. Ternary 4-point interpolating non-stationary scheme was proposed by Daniel and Shunmugaraj [6]. A family of 4-point non-stationary

interpolating schemes were proposed Bari and Mustafa [7]. Odd-point non-stationary interpolating subdivision schemes are also mentioned in [8]. Novara and Romani [9] gave a new direction to obtain new class of non-stationary schemes by building blocks. Siddiqi et al. [12-14] construct binary and ternary non-stationary subdivision schemes by using hyperbolic B-spline, they show that the proposed scheme has the potential to produce hyperbolic curves. To find the continuity of their schemes they used the asymptotic equivalence approach. Using the Lagrange polynomial and trigonometric identities, Bari and Mustafa [15] construct some new non-stationary subdivision scheme.

This paper consists of four sections. First, define some results which are helpful to generate a class of non-stationary schemes in section 2. Construction of non-stationary m-point ternary interpolating schemes in Section 3. Convergence of proposed interpolating schemes is presented in section 4.

PRELIMINARIES

In terms of mask $\mathbf{a}^k = \{\mathbf{a}_i^k : i \in \mathbf{Z}\}$, a ternary univariate subdivision scheme is according to the following subdivision rule:

$$f_i^{k+1} = \sum_{j \in \mathbf{Z}} \mathbf{a}_{i-3j}^k f_j^k, \quad i \in \mathbf{Z}.$$

Independence of k (level) in the mask \mathbf{a}^k shows that the subdivision scheme $\mathbf{S}_{\mathbf{a}^k}$ is called stationary and the dependence of k (level) in the mask \mathbf{a}^k shows that the subdivision scheme $\mathbf{S}_{\mathbf{a}^k}$ is called non-stationary

Definition-1: [5] Let \mathbf{S}_{a^k} and \mathbf{S}_{b^k} be two ternary subdivision schemes and $\mathbf{S}_{a^k}, \mathbf{S}_{b^k}$ are asymptotically equivalent if

$$\sum_{k=0}^{\infty} \|\mathbf{S}_{a^k} - \mathbf{S}_{b^k}\| < \infty,$$

where

$$\|\mathbf{S}_{a^k}\|_{\infty} = \max \left\{ \sum_{i \in \mathbb{Z}} |a_{3i}^k|, \sum_{i \in \mathbb{Z}} |a_{3i+1}^k|, \sum_{i \in \mathbb{Z}} |a_{3i+2}^k| \right\}.$$

Dyn and Levin [10] gave the idea behind asymptotic equivalence.

Theorem-1: [10] Let \mathbf{S}_a (stationary) and \mathbf{S}_{a^k} (non-stationary) ternary subdivision schemes having finite masks. If \mathbf{S}_a is \mathcal{C}^m and

$$\sum_{k=0}^{\infty} 3^{mk} \|\mathbf{S}_{a^k} - \mathbf{S}_a\|_{\infty} < \infty,$$

holds, then \mathbf{S}_{a^k} is also \mathcal{C}^m .

CONSTRUCTION OF M-POINT NON-STATIONARY SUBDIVISION SCHEME

Lagrange interpolation was first used by Deslauriers and Dubuc [1] to construct subdivision schemes. We are also going to use Lagrange polynomial to build a class of hyperbolic non-stationary schemes. First we define the Lagrange fundamental polynomials of degree m and $m-1$, where $m=2n$, for $n \geq 2$, corresponding to $\{t_j\}_{-(n-1)}^n$ and $\{t_j\}_{-(n-2)}^n$ respectively,

$$L_p^m(t) = \prod_{t_j=-(n-1), p \neq t_j}^n \frac{t-t_j}{p-t_j}, \quad p = -(n-1), -(n-2) \dots n \quad (1)$$

and

$$L_p^{m-1}(t) = \prod_{t_j=-(n-2), p \neq t_j}^n \frac{t-t_j}{p-t_j}, \quad p = -(n-2), -(n-3) \dots n \quad (2)$$

Applying the arithmetical processes on the Lagrange identities in Eq. (1) and Eq. (2), we get Eq. (3) and Eq. (4):

$$L_p^m(t) = \frac{(-1)^n (3n-1)!}{3^{3n-2} (1-3p)(n-1)!} \quad (3)$$

$p = -(n-1), -(n-2), \dots n$ and

$$L_p^{m-1}(t) = \frac{(-1)^n (3n-1)(3n-4)!}{3^{3n-4} (1-3p)(n-2)!} = \frac{\sigma_1}{\sigma_2}, \quad (4)$$

implies

$$L_p^{m-1}(t) = \frac{\sigma_1}{\sigma_2}, \quad \text{for } p = -(n-2), -(n-3), \dots n$$

where

$$\sigma_1 = \frac{l_1}{l_2} \quad (5)$$

The values of l_1 and l_2 are

$$l_1 = (-1)^n (3n-1)(3n-4)! \quad , \quad l_2 = 3^{3n-4} (1-3p)(n-2)!,$$

and

$$\sigma_2 = (-1)^{n-m} (n-p)! (n+p-2)!. \quad (6)$$

When $p = -n+1$ in Eq. (3), we have

$$\sigma_3 = L_{-n+1}^m \left(\frac{1}{3} \right) = \frac{(-1)^{-n+1} (3n-1)!}{3^{3n-2} (3n-2)(2n-1)(n-1)!} \quad (7)$$

Furthermore, we have to calculate

$$\sigma_4 = L_p^m \left(\frac{1}{3} \right) - L_p^{m-1} \left(\frac{1}{3} \right) = \frac{(-1)^p (3n-1)!}{3^{3n-2} (n-1)! (3n-2)(n-p)! (n+p-1)!} \quad (8)$$

where $p = -(n-2), -(n-3), \dots n$.

We refer to [11] for further details.

M-POINT TERNARY INTERPOLATING SCHEME

We are going to present general formulae to construct non-stationary m -point ternary interpolating subdivision scheme.

Let $n \geq 2$, the rules of m -point ternary interpolating scheme are

$$\begin{cases} f_{3i}^{k+1} = f_i^k, \\ f_{3i+1}^{k+1} = \sum_{p=-n}^{n-1} \mu_{-p}^{k,m} f_{i+p+1}^k, \\ f_{3i+2}^{k+1} = \sum_{p=-(n-1)}^n \mu_p^{k,m} f_{i+p}^k, \end{cases} \quad (9)$$

by introducing hyperbolic sine function, triadic subdivision $\frac{1}{3^{k+1}} = \kappa$, the parameter ω , we get the first coefficient $\mu_{-p}^{k,m}$ for $p = -n$. The other coefficients $\mu_{-p}^{k,m}$ for $p = -n+1, \dots, n-1$ are formed by the equations (5)-(8).

$$\begin{cases} \mu_{-n+1}^{k,m} = \frac{\sinh(\frac{\omega}{\kappa})}{\sinh(\frac{1}{\kappa})}, \quad \omega < 1 \\ \mu_p^{k,m} = \frac{\sinh(\frac{\sigma_1}{\kappa})}{\sinh(\frac{\sigma_2}{\kappa})} + \frac{\sinh(\frac{\sigma_4 \omega}{\kappa})}{\sinh(\frac{\sigma_3}{\kappa})}, \quad p = -n+2, \dots n. \end{cases} \quad (10)$$

Using Eq. (9) and Eq. (10), we get 4-point ternary scheme having parameter ω , so by substituting $n = 2$,

$$\begin{aligned} f_{3i}^{k+1} &= f_i^k, \\ f_{3i+1}^{k+1} &= \mu_2^{k,4} f_{i-1}^k + \mu_1^{k,4} f_i^k + \mu_0^{k,4} f_{i+1}^k + \mu_{-1}^{k,4} f_{i+2}^k, \\ f_{3i+2}^{k+1} &= \mu_{-1}^{k,4} f_{i-1}^k + \mu_0^{k,4} f_i^k + \mu_1^{k,4} f_{i+1}^k + \mu_2^{k,4} f_{i+2}^k, \end{aligned} \quad (11)$$

where

$$\begin{aligned} \mu_{-1}^{k,4} &= \frac{\sinh(\frac{\omega}{\kappa})}{\sinh(\frac{1}{\kappa})}, \\ \mu_0^{k,4} &= \frac{\sinh(\frac{10}{9\kappa})}{\sinh(\frac{2}{\kappa})} - \frac{\sinh(\frac{5\omega}{27\kappa})}{\sinh(\frac{5}{81\kappa})}, \\ \mu_1^{k,4} &= \frac{\sinh(\frac{5}{9\kappa})}{\sinh(\frac{1}{\kappa})} + \frac{\sinh(\frac{5\omega}{27\kappa})}{\sinh(\frac{5}{81\kappa})}, \end{aligned}$$

and

$$\mu_2^{k,4} = -\frac{\sinh(\frac{2}{9\kappa})}{\sinh(\frac{2}{\kappa})} - \frac{\sinh(\frac{5\omega}{81\kappa})}{\sinh(\frac{5}{81\kappa})},$$

By introducing the normalized scheme, we get

$$\begin{aligned} \mu_{-1}^{k,4} + \mu_0^{k,4} + \mu_1^{k,4} + \mu_2^{k,4} &= \frac{\sinh(\frac{\omega}{\kappa})}{\sinh(\frac{1}{\kappa})} + \frac{\sinh(\frac{10}{9\kappa})}{\sinh(\frac{2}{\kappa})} - \frac{\sinh(\frac{5\omega}{27\kappa})}{\sinh(\frac{5}{81\kappa})} + \frac{\sinh(\frac{5}{9\kappa})}{\sinh(\frac{1}{\kappa})} + \\ &\frac{\sinh(\frac{5\omega}{27\kappa})}{\sinh(\frac{5}{81\kappa})} - \frac{\sinh(\frac{2}{9\kappa})}{\sinh(\frac{2}{\kappa})} - \frac{\sinh(\frac{5\omega}{81\kappa})}{\sinh(\frac{5}{81\kappa})} = \theta^{k,4}. \end{aligned} \quad (12)$$

We can define the normalized scheme as

$$\begin{aligned} f_{3i}^{k+1} &= f_i^k, \\ f_{3i+1}^{k+1} &= \gamma_2^{k,4} f_{i-1}^k + \gamma_1^{k,4} f_i^k + \gamma_0^{k,4} f_{i+1}^k + \gamma_{-1}^{k,4} f_{i+2}^k, \\ f_{3i+2}^{k+1} &= \gamma_{-1}^{k,4} f_{i-1}^k + \gamma_0^{k,4} f_i^k + \gamma_1^{k,4} f_{i+1}^k + \gamma_2^{k,4} f_{i+2}^k, \end{aligned} \quad (13)$$

where

$$\gamma_i^{k,4} = \frac{\mu_i^{k,4}}{\theta^{k,4}}, \quad i = -1, \dots, 2. \quad (14)$$

Remark-1: Generally we can write the coefficients of the proposed schemes for $n \geq 2$ by

$$\gamma_i^{k,m} = \frac{\mu_i^{k,m}}{\theta^{k,m}}, \quad i = -n+1, \dots, n.$$

Remember that the sum of weights of proposed(normalized scheme) is 1.

SMOOTHNESS for $m=4$

Zhu [16] gave the following inequalities

$$\frac{\sinh a}{\sinh b} \leq \frac{a}{b} \text{ for } 0 < a \leq b < \infty, \text{ and } \frac{\sinh a}{a} < \frac{1}{2} (1 + \cosh a) \text{ for } 0 < a < \infty,$$

Convergence of proposed scheme can be found by using the above mentioned inequalities. Asymptotically equivalence is necessary to prove the convergence of non-stationary schemes.

Lemma-1:

For $m=4$ the proposed scheme has the following inequalities:

$$\begin{aligned} (i) \quad \omega &\leq \gamma_{-1}^{k,4} \leq \frac{\omega \cosh(\frac{5}{81\kappa})}{\cosh(\frac{1}{\kappa})} \\ (ii) \quad \frac{5}{9} - \frac{3\omega}{\cosh(\frac{5}{81\kappa})} &\leq \gamma_0^{k,4} \leq \frac{5}{9} - 3\omega \\ (iii) \quad \frac{5}{9} + 3\omega \cosh\left(\frac{5}{81\kappa}\right) &\leq \gamma_1^{k,4} \leq \frac{5}{9} + 3\omega \\ (iv) \quad -\frac{1}{9 \cosh(\frac{2}{\kappa})} - \frac{\omega}{\cosh(\frac{5}{81\kappa})} &\leq \gamma_2^{k,4} \leq -\frac{1}{9} - \omega \cosh\left(\frac{5}{81\kappa}\right) \end{aligned}$$

Proof: The proof of above inequalities can be followed by [12].

Lemma-2:

Taking $\omega = -\frac{1}{18} - \frac{1}{6}u$ or $u \in (\frac{1}{15}, \frac{1}{9})$ in the scheme

(13), we have

$$\begin{aligned} (i) \quad -\frac{1}{18} - \frac{1}{6}u &\leq \gamma_{-1}^{k,4} \leq \frac{(-\frac{1}{18} - \frac{1}{6}u) \cosh(\frac{5}{81\kappa})}{\cosh(\frac{1}{\kappa})} \\ (ii) \quad \frac{5}{9} - 3 \frac{(-\frac{1}{18} - \frac{1}{6}u)}{\cosh(\frac{5}{81\kappa})} &\leq \gamma_0^{k,4} \leq \frac{13}{18} + \frac{1}{6}u \\ (iii) \quad \frac{5}{9} + 3 \left(-\frac{1}{18} - \frac{1}{6}u\right) \cosh\left(\frac{-5}{81\kappa}\right) &\leq \gamma_1^{k,4} \leq \frac{7}{18} - \frac{1}{6}u \\ (iv) \quad -\frac{1}{9 \cosh(\frac{2}{\kappa})} - \frac{(-\frac{1}{18} - \frac{1}{6}u)}{\cosh(\frac{5}{81\kappa})} &\leq \gamma_2^{k,4} \leq \left(-\frac{1}{18} + \frac{1}{6}u\right) \cosh\left(\frac{5}{81\kappa}\right) \end{aligned}$$

Lemma-3:

Following inequalities also hold for scheme (13):

$$(i) \quad |\gamma_{-1}^{k,4} - \omega| \leq G_0 \left(\frac{1}{32k}\right)$$

$$\begin{aligned}
(ii) \quad & \left| \gamma_0^{k,4} - \left(\frac{5}{9} - \frac{3\omega}{\cosh(\frac{5}{81.k})} \right) \right| \leq G_1 \left(\frac{1}{3^{2k}} \right) \\
(iii) \quad & \left| \gamma_1^{k,4} + \left(\frac{5}{9} + 3\omega \cosh \left(\frac{5\omega}{27.k} \right) \right) \right| \leq \\
& G_2 \left(\frac{1}{3^{2k}} \right) \\
(iv) \quad & \left| \gamma_2^{k,4} - \left(-\frac{1}{9 \cosh(\frac{2}{k})} - \frac{\omega}{\cosh(\frac{5}{81.k})} \right) \right| \leq \\
& G_3 \left(\frac{1}{3^{2k}} \right)
\end{aligned}$$

G_0, G_1, G_2 and G_3 are k -independent.

Similarly we can construct another lemma by adding the value of parameter $\omega = -\frac{1}{18} - \frac{1}{6}u$ in Lemma 3 to find out the continuity of proposed scheme by asymptotic equivalence.

Remark: By making the above inequalities for the normalized scheme as done in [8] and applying the asymptotic equivalence relation on the prescribed non-stationary scheme with the stationary scheme, we get the C^2 smoothness.

Theorem 2: The proposed hyperbolic scheme with $\omega = -\frac{1}{18} - \frac{1}{6}u$ having range $u \in (0.066, 0.111)$ is C^2 .

Proof. Since

$$\sum_{k=0}^{\infty} 3^{2k} \|S_{a^k} - S_a\|_{\infty} < \infty,$$

We already define

$$\begin{aligned}
\|S_{a^k} - S_a\|_{\infty} = \max \left\{ \sum_{i \in \mathbb{Z}} |a_{i-3j}^k - a_{i-3j}| : i \right. \\
\left. \in 0, 1, 2, 3 \right\}.
\end{aligned}$$

We can write now

$$\begin{aligned}
\sum_{k=0}^{\infty} 3^{2k} \|S_{a^k} - S_a\|_{\infty} \\
= \sum_{k=0}^{\infty} 3^{2k} \left\{ \left| \gamma_{-1}^{k,4} \right. \right. \\
- \left(-\frac{1}{18} - \frac{1}{6}u \right) \left|, \left| \gamma_0^{k,4} \right. \right. \\
- \left(\frac{13}{18} + \frac{1}{2}u \right) \left|, \left| \gamma_1^{k,4} \right. \right. \\
- \left(\frac{7}{18} - \frac{1}{2}u \right) \left|, \left| \gamma_2^{k,4} \right. \right. \\
\left. \left. + \left(-\frac{1}{18} - \frac{1}{6}u \right) \right\},
\end{aligned}$$

It follows

$$\begin{aligned}
\sum_{k=0}^{\infty} 3^{2k} \left| \gamma_{-1}^{k,4} - \left(-\frac{1}{18} - \frac{1}{6}u \right) \right| \leq \\
\sum_{k=0}^{\infty} 3^{2k} G_0 \left(\frac{1}{3^{2k}} \right) < \infty
\end{aligned}$$

For $\omega = -\frac{1}{18} - \frac{1}{6}u$, scheme S_{a^k} by Eq. (13) and scheme S_a of [2] we can write as $\sum_{k=0}^{\infty} 3^{2k} \|S_{a^k} - S_a\|_{\infty} < \infty$, so the scheme in [2] is C^2 so by Theorem-2, hyperbolic non-stationary scheme (13) is C^2 .

Numerical Examples

The solid boxes (initial control points) insertion in Fig. 1 are calculated by the parametric form of hyperbola and parabola. The solid boxes in Fig 1. (a)-(b) show the initial control points of parabola and hyperbola and the limit curve formed by proposed subdivision scheme.

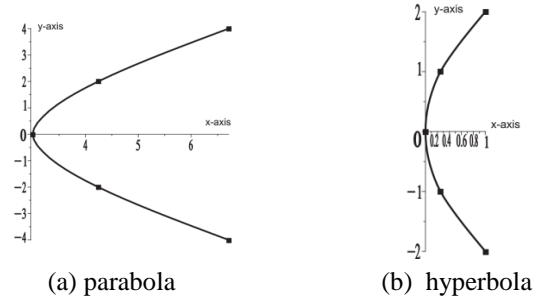


Fig. 1 Shows the parabola and hyperbola by proposed scheme.

CONCLUSION

Lagrange identities are useful to construct m-point non-stationary hyperbolic subdivision schemes to produce parabolas and hyperbolas in well-designed manner. The proposed schemes in this article are counterpart of the existing stationary schemes. The established schemes in this article has the potential to reproduce important parts in conics such as hyperbolas and parabolas. Our next target to extend this work for 3-D modeling such that to create hyperboloid and paraboloid.

ACKNOWLEDGEMENTS

This work is supported by the SRGP Project No. 1741 of Higher Education Commission (HEC) Pakistan.

REFERENCES

- [1] Deslauriers, G. and Dubuc, S. Symmetric iterative interpolation processes in Constructive approximation, ed: Springer, 1989, pp. 49-68.
- [2] Hassan, M. F., Ivriissimitzis, I. P., Dodgson, N. A., and Sabin, M. A., An interpolating 4-

- point C^2 ternary stationary subdivision scheme. *Computer Aided Geometric Design*, Vol 19, 2002, pp. 1-18.
- [3] Lian, J. A. On a-ary subdivision for curve design, I. 4-point and 6-point interpolatory schemes. *Applications and Applied Mathematics*, Vol. 3, 2008, pp. 18-29.
- [4] Jena, M., Shunmugaraj, P. and Das, P. A non-stationary subdivision scheme for curve interpolation. *Anziam Journal*, Vol. 44, 2008, pp. 216-235.
- [5] Beccari, C., Casciola, G. and Romani, L, A non-stationary uniform tension controlled interpolating 4-point scheme reproducing conics. *Computer Aided Geometric Design*, Vol. 24, 2007, pp. 1-9.
- [6] Daniel, S. and Shunmugaraj, P. Some interpolating non-stationary subdivision schemes. In *Computer Science and Society (ISCCS)*, 2011, International Symposium on, 2011, pp. 400-403.
- [7] Bari, M. and Mustafa, G. A Family of 4-Point n-Ary Interpolating Scheme Reproducing Conics. *American Journal of Computational Mathematics*, Vol. 3, 2013, pp. 217-221.
- [8] Mustafa, G. and Bari, M. A new class of odd-point ternary non-stationary schemes. *British Journal of Mathematics & Computer Science*, Vol. 4, 2014, pp. 133, 2014.
- [9] Novara, P. and Romani, L. Building blocks for designing arbitrarily smooth subdivision schemes with conic precision. *Journal of Computational and Applied Mathematics*, Vol. 279, 2015, pp. 67-79.
- [10] Dyn, N. and Levin, D. Analysis of asymptotically equivalent binary subdivision schemes. *Journal of mathematical analysis and applications*, Vol. 193, 1995, pp. 594-621.
- [11] Aslam, M., Mustafa, G. and Ghaffar, A. (2n-1)-Point Ternary Approximating and Interpolating Subdivision Schemes. *Journal of Applied Mathematics*, Vol. 2011, 2011.
- [12] Siddiqi, S.S., Salam, W.Us. and Rehan, K Binary 3-point and 4-point non-stationary subdivision scheme using hyperbolic function. *Applied Mathematics and Computation*, Vol 258, 2015, pp. 120-129.
- [13] Siddiqi, S. S., Salam, W. U. and Rehan,K., Hyperbolic forms of ternary non-stationary subdivision schemes originated from hyperbolic B-splines. *Journal of Computational and Applied Mathematics*, Vol 301, 2016, pp. 16-27.
- [14] Siddiqi, S.S., Salam, W. U. and Rehan, K., Construction of binary four and five point non-stationary subdivision schemes from hyperbolic B-splines. *Journal of Computational and Applied Mathematics*, Vol 280, 2016, pp. 30-38.
- [15] Bari, M. and Mustafa, G. A family of 2n-point Ternary Non-Stationary Interpolating Subdivision Scheme. *Mehran university research journal of engineering and technology*. Vol. 36, No 4, 2017, pp. 921-932.
- [16] Zhu, L. Inequalities for hyperbolic function and applications. *Journal of inequalities and applications*, 2010.

ECOLOGY OF RUMINAL MICROORGANISMS UNDER THE INFLUENCE OF QUERCUS CORTEX EXTRACT

Galimzhan Duskaev,¹ Il'shat Karimov^{1,2}, Georgy Levakhin¹, Baer Nurzhanov¹, Albert Rysaev¹ and Hamdiya Dusaeva²

¹Federal Research Center of Biological Systems and Agro-technologies of the Russian Academy of Sciences,
Orenburg, Russia

²Orenburg State University, Orenburg, Russia

ABSTRACT

The study was performed for assessing the elemental status and the bacterial composition of the rumen fluid microflora in cattle after incubation in vitro with Quercus cortex extract and exogenous enzymes. The mixture of alfalfa hay, Sudan grass and concentrates (60:40) was used as the substrate. The results showed that in the protozoa a decrease in such elements as P, Na, Ca ($P \leq 0.05$) was observed when substrate with enzyme was added. The level of essential elements in bacteria three hours after the incubation together with the enzyme changed similar to the protozoa, except for copper, the content of which increased two times ($P \leq 0.05$). The introduction of Quercus cortex extract into the substrate with the enzyme preparation three hours after the incubation promoted a significant increase in iron, manganese and cobalt content in the protozoa ($P \leq 0.05$). Unlike other variants, incubation of the substrate with the enzyme together with the extract increased the number of representatives of the taxa Firmicutes by 13.2%, Bacteroidetes - by 13.4% ($P \leq 0.05$) against the background of a slight decrease in Proteobacteria, Saccharibacteria and Fibrobacteres. An increase was observed in the number of microorganisms belonging to the taxa Clostridia (by 23.7%; $P \leq 0.05$) and Bacteroidia (by 13.4%; $P \leq 0.05$). The biosensor based on *B.subtilis* on samples with the extract reacted by quenching the luminescence by 60% on the 5th minutes and by 32% on the 60th minute contact. Thus, the chemical composition of oak bark extract significantly influenced the elemental profile and the bacterial composition of cattle rumen microorganisms.

Keywords: *Quercus cortex extract, elemental status, rumen microorganisms, cattle.*

INTRODUCTION

Limitations in the use of antibiotic substances for preventing diseases and increasing cattle productivity make it urgent to search for new substances with similar properties. Among these substances, there are plant extracts (essential oils, saponins, tannins, etc.) with positive effect on protein metabolism, production of volatile fatty acids and gases in the rumen of ruminants [1, 2, 3]. At the same time, a number of scientists identified in plant extracts a new class of substances capable of efficiently preventing development of infectious and inflammatory processes in human and animal organisms through the system of intercell chemical communication in bacteria ("quorum sensing") [4]. Thus, when screening 20 medicinal plants used by the Russian (Eastern European) folk medicine, the most pronounced ability to inhibit the "quorum sensing" system of wild and mutant strains of *C. violaceum* was identified in extracts of oak bark (cortex Quercus), birch buds (*Betula verucosa*) and eucalyptus leaves (*Eucalyptus viminalis*) [5]. At the same time, the need for studying the influence of these extracts directly on the microbiome, changes in its biochemical parameters may be of interest when studying intercellular chemical communication in bacteria in the rumen. The previously obtained results confirm the promising nature of these studies [6,7].

In this regard, the research aimed at studying the ability of plant extracts to inhibit microorganisms, and the influence on the elemental status of microflora of the rumen of cattle is of interest.

The aim of the research. Studying the effect of feeding Quercus cortex extract on the elemental status and the bacterial composition of cattle rumen fluid in vitro against the background of enzyme diet.

MATERIALS AND METHODS

Phytochemical analysis. Dry Quercus cortex extract was used for the research, which was dissolved in ethanol before chromatography-mass spectrometry, and injected into the analytical cell of the chromatograph using microsyringe Hamilton 1700. Chemicals in Quercus cortex extract were identified in the gas chromatograph with mass selective detector GCMS 2010 Plus (Shimadzu, Japan), in column HP-5MS. The research results were interpreted with the following software: GCMS Solutions, GCMS PostRun Analysis; compounds were identified with a set of spectra libraries CAS, NIST08, Mainlib, Wiley9 and DD2012 Lib. The quantitative presence of individual identified components was assessed by relative value (%), which correlated the area of the peak to the total area of the extract. In the extract of

oak bark 35 substances were identified (according to IUPAC): propanetriol-1,2,3*; decane*; 2-furancarboxylic acid*; 1,3,5-triazine-2,4,6-triamine*; pentadecane*; 2,3-dihydroxypropyl*; butanedioic acid*; 2,3-dihydro-3,5-dihydroxy-6-methyl-4H-pyran-4-one*; 2-amino-9-[3,4-dihydroxy-5-(hydroxymethyl) oxolan-2-yl] -3H-purine-6-one*; cyclopentane-1,2-diol*; 1,2:5,6-dianhydrogalaxytole*; 5-hydroxymethylfurfural*; acetylcysteine, -2-acetamido-3-mercaptopropionic acid*; 1-methylundecyl ether 2-propenoic acid*; 2,3-dihydro-3,5-dihydroxy-6-methyl-4H-pyran-4-one*; 1- (2-hydroxyethyl) -4-methylpiperazine*; 6- (4-hydroxy-6-methoxy-2-methyl -, tetrahydro-pyran-3-yloxy) -2-methyl-dihydro-pyran-3-one*; 1,2,3-trihydroxybenzene* (pyrogallol); 2-methyl-5-nitro-pyrimidine-4,6-diol*; 4-hydroxy-3-methoxybenzaldehyde*(vanilla); 2-amino-9- [3,4-dihydroxy-5- (hydroxymethyl) oxolan-2-yl] -3H-purine-6-one*; 1,6-anhydro- β -D-glucopyranose*; 1- (β -D-arabinofuranosyl) -4-O-trifluoromethyl uracil*; 4-hydroxy-3-methoxy benzoic acid*; 1,6-anhydro- β -D-glucofuranose*; 4-propyl-1,3-benzenediol* (propylresorcinol); 1,2,3,4,5-cyclohexanol*; 4-(hydroxymethyl)-2,6-dimethoxyphenol*; 4- (3-hydroxy-1-propenyl) -2-methoxyphenol*(coniferyl alcohol); 9 -[(2R, 3R, 4S, 5R) -3,4-dihydroxy-5- (hydroxymethyl) oxolan-2-yl]-3H-purine-2,6-dione*; 7-hydroxy-6-methoxy-2H-1-benzopyran-2-one*(coumarine); methyl- α -D-glucopyranoside*; 2H-1-benzopyran-2-one*(scopoletin); 2 ethoxy-6-(methoxymethyl) phenol*; 3,4,5-trimethoxyphenol*(antiarol) (*components identified with the probability of over 90%; ** components identified with the probability of at least 90%).

Scheme of the experiment. Reference - ruminal fluid + ethanol (0.5% of volume), variant I – ruminal fluid + exogenous enzyme + ethanol (0.5% of volume), variant II - scar liquid + phytoextract in ethanol (0.5% of total) + exogenous enzyme.

The exogenous enzyme preparation contained glucoamylase and related cellulolytic enzymes (xylanase, β -glucanase, cellulase). The preparation was dosed in the amount of 0.05% of dry ingredients.

Experimental studies were performed at the scientific equipment common use center of Federal Research Center of Biological Systems and Agrotechnologies of the Russian Academy of Sciences.

Ruminal digestion in vitro. The previously used method of studying ruminal fermentation in vitro [8] was considered to be an acceptable method for assessing the influence of phytocompounds on ruminal microflora. Two heads of cattle (males) with chronic rumen fistula were kept on a diet consisting of 60% coarse forage (alfalfa hay and Sudan grass) and 40% pellets containing barley grain, wheat bran, wastes of vegetable oil,

limestone, salt, vitamins and a premix. The chemical composition of the diet: (g/kg of dry matter) was 153 non-decomposing protein, 485 neutral detergent fiber, 47 crude fat, 85 ash and 10.00 MJ/kg exchange energy of dry matter. The fodder was supplied twice a day, and animals had free access to drinking water. The animals were used as donors of ruminal fluid.

Two hundred milligrams of dry matter in the forage consisting of hay and concentrates (pellets) in the ratio of 60:40 were used as substrate for fermentation in vitro. The incubation medium was prepared as described by Menke and Steingass [9], and 30 ml of it were anaerobically placed into a 100 ml syringe.

The mixture of substances was dissolved in ethanol; the substrate based on dry matter (9 mg) was introduced into each syringe at the concentration of 4.5% (by weight). The final concentration of ethanol in each syringe was 0.5%. The reference was substrate with 0.5% ethanol. The syringes were incubated at 39° C for 24 hours. Degradability of the dry matter, quantitative assessment of the rumen microorganisms' population, and their elemental composition were measured. The total of nine syringes were used for each research.

Assessment of the effect on luminescent bacterial biosensors. Strains of *Escherichia coli* MG1655 pXen7, *Salmonella typhimurium* LT2 pACXen and *Bacillus subtilis* EG168-1 were used as test objects. Cells were grown within 24 hours on LB agar (Sigma-Aldrich, USA) with a selectable marker, and then suspended in a 0.5% solution of sodium chloride to OD450 = 0.50 rel. units in transparent wells at a volume of 200 μ l using StatFax 303+ photometer (Awareness, USA). Two-fold dilutions from 100% to 1.56% were prepared in wells of a 96-well plate with a volume of 50 μ l from samples of ruminal fluid, then 150 μ l of biosensor cell suspension were added. The luminescence of bacteria was registered in a kinetic mode using LM-01T luminometer (Immunotech, Czech Republic) for 60 minutes [10].

Analysis of the rumen microbial population. Assessment of the microbial biodiversity included: sampling, isolation, purification, measuring DNA concentration, PCR, validation and normalization of libraries followed by sequencing at the platform of high-performance sequencer MiSeq Illumina (USA). Bioinformatical analysis of the results was made in application PEAR (Pair-End Assembler, PEAR v0.9.8, April 9, 2015) [11].

Analysis of the substrates' elemental status. The elemental composition of the extract, animalculines and bacteria (liquid samples) was determined by atomic emission and mass spectrometry (AES-ISP and MS-ISP) at the test laboratory of Autonomous Nonprofit Organization "Biotic Medicine Centre", Moscow (Registration Certificate of ISO

9001: 2000, Number 4017-5.04.06). Biological substrates were ashed using a microwave decomposition system MD-2000 (USA). Elements' content in the obtained ash was assessed using a mass spectrometer Elan 9000 (Perkin Elmer, USA) and an atomic emission spectrometer Optima 2000 V (Perkin Elmer, USA). Elemental composition of *Quercus cortex* extract, mg/g was the following: Ca - 246; P - 8.22; K - 124; Mg - 32.5; Na - 85.0; Zn - 1.75; Mn - 5.8; Cu - 0.05; Fe - 2.01; Co - 0.018; Se - 0.02; I - 0.037; Al - 0.46; Sr - 0.7; Cr - 0.11; Cd - 0.001; Pb - 0.008.

Statistical processing. Statistical processing was made in application IBM "SPSS Statistics Version 20", calculating the mean value (M), the standard deviation (σ), the standard deviation error (m). The level of significance was considered veracious with $p < 0.05$. The student's t-criterion was used for statistical processing.

RESULTS AND DISCUSSION

According to the research results, the level of essential elements in protozoa after incubation of variant I decreased, except for copper, the value of which increased 2 times, compared to the reference. Incubation of the II variant contributed to a significantly increased amount of substances; this was particularly evident for iron (21.8%),

manganese (8.8%) and cobalt (16.5 times). Similar pattern was observed in studying the composition of bacteria: for copper, the increase was 11.3 times, for zinc – 3.3 times, and for iron – 2.4 times (Table 1). Due to the fact that the topic has been poorly studied, and to the lack of direct data in the literature, one can see the need for using indirect facts in the discussion. Thus, it is necessary to consider the fact that bacteria are in some ways "food" for the animalcules, and increasing the amount of macro- and essential elements in them may be explained by ingestion, or by normal digestion process. Besides, it should be noted that microelements' concentration in plants largely depends on the environment, the climate, the age, as well as the composition of diets, and other factors [12, 13, 14, 15, 16]. It is known that metal ions are cofactors for a number of enzymes, including microorganisms and protozoa [17]; therefore, the probability of their influence on the activity of the enzyme systems of the ruminal microflora is quite high.

At the same time *Quercus cortex*, which is positioned as the source of tannins, has no adverse effect on fermentation in the rumen of cattle, positively influences energy exchange and protein utilization in the rumen [18,19], the number of protozoa [20], although this requires further research [21,22].

Table 1 The mean values of essential elements' content in protozoa and bacteria, $\mu\text{g/g}$

Diet	Zn	Mn	Cu	Fe	Co	Se	I
Protozoa							
reference	1.6 ± 0.24	1.6 ± 0.25	0.14 ± 0.028	7.5 ± 1.12	0.003 ± 0.00094	<0.0039	0.007 ± 0.00229
Protozoa (after 3 hours)							
MD+E	1.2 ± 0.18	0.7 ± 0.148	0.31 ± 0.063	4.0 ± 0.61	0.002 ± 0.00067	<0.0039	0.006 ± 0.00198
MD+E+extract	5.7 ± 0.85	6.2 ± 0.93	1.6 ± 0.24	87.4 ± 13.11	0.033 ± 0.008	0.017 ± 0.004	0.027 ± 0.007
Bacteria							
reference	1.3 ± 0.19	0.5 ± 0.108	0.2 ± 0.039	2.6 ± 0.39	0.004 ± 0.00133	<0.0039	0.005 ± 0.00158
Bacteria (after 3 hours)							
MD+E	1.2 ± 0.18	0.5 ± 0.099	0.3 ± 0.06	2.9 ± 0.44	0.004 ± 0.0013	<0.0039	0.008 ± 0.00245
MD+E+extract	3.9 ± 0.6	0.7 ± 0.148	3.4 ± 0.51	7.0 ± 1.06	0.007 ± 0.00218	<0.0039	0.012 ± 0.003

In turn, the use of enzyme-containing diet could not influence the microflora in view of the numerous data indicating their efficient use in feeding cattle [23, 24, 25]. In studying bioavailability of microelements in the gastrointestinal tract of ruminants, it is necessary to veraciously consider their bonding with the coarse fiber part of the fodder, with undigested fodder components and newly formed complexes insoluble

in acidic environment [26, 27, 28]. The results of the research show low bioavailability of selenium for both protozoa and bacteria. This is determined by the results of previous experiments that showed low digestion of selenium by these animals, and the transition of its available form into a less available one directly in the ruminal medium [29]. Some authors [30] indicate that high levels of calcium in

the diet result in low selenium absorption, which was also observed in this experiment.

The results of the research show the prevalence of iron concentration over the same value of copper in the experiment in both protozoa and bacteria, especially against the background of enzyme diet. This increase is also due to the high iron content in *Quercus cortex* extract. Several researchers in their studies indicated a decreased level of copper in the organism of ruminants with increasing the level of iron in the diet [31]. Zinc concentration in protozoa and bacteria in the reference and after the incubation virtually did not change, probably due to the relatively high absorption capacity of this

element in the rumen, and the availability of the phytase activity of the microflora [32]. Manganese is absorbed insignificantly in the rumen of ruminants [33]. This may explain its low content in the bacteria after fermentation of the fodder, but after the extract had been included into the diet, the concentration of the element in animalcules increased.

Analysis of the microbiocenosis of ruminal content showed that before incubation it had been represented by bacteria (82.1%) and microscopic fungi (17.9%) (Table 2).

Table 2 – Taxonomic diversity of the bacterial composition of the ruminal fluid

Group	Taxon			
	phylum	class	family	genus
MD	Firmicutes (32.4%)	Bacilli (17.3%)	Lactobacillaceae (13.9%)	Lactobacillus (13.9%)
		Clostridia (11.1%)	Lachnospiraceae (6.93%)	-
			Clostridiaceae (4.2%)	Faecalibacterium (4.2%)
	Proteobacteria (12.8%)	Negativicutes (3.99%)	Acidaminococcaceae (3.99%)	Succiniclasicum (3.99%)
		Gammaproteobacteria (12.8%)	Moraxellaceae (2.52%)	Acinetobacter (2.52%)
			Enterobacteriaceae (10.3%)	Escherichia (5.04%)
			Prevotellaceae (19.4%)	Prevotella (18.1%)
	Bacteroidetes (30.1%)	Bacteroidia (30.1%)	Porphyromonadaceae 3.15%)	-
			Bacteroidaceae (7.56%)	-
	Fibrobacteres (5.04%)	Fibrobacteria (5.04%)	Fibrobacteraceae (5.04%)	Fibrobacter (5.04%)
MD+Enzyme+extract	Saccharibacteria (18.7%)	-	-	-
	Other* (1%)	Other* (19.7%)	Other*(23%)	Other* (42%)
	Firmicutes (43.5%)	Clostridia (34.8%)	Ruminococcaceae (17.4%)	-
			Lachnospiraceae (13%)	-
			Clostridiaceae (4.35%)	-
	Saccharibacteria (13%)	-	-	-
MD+Enzyme	Bacteroidetes (43.5%)	Bacteroidia (43.5%)	Bacteroidaceae (17.4%)	-
			Prevotellaceae (26.1%)	Prevotella (26.1%)
	-	Other* (21.7%)	Other* (21.7%)	Other* (73.9%)
	Firmicutes (2.11%)	Clostridia (2%)	-	-
MD+Enzyme	Bacteroidetes (85%)	Bacteroidia (83.5%)	Prevotellaceae (59%)	Prevotella (58%)
	Saccharibacteria (5.32%)	-	-	-
	Other* (7.6%)	Other* (14.5%)	Other* (41%)	Other* (42%)

* This group combines the taxa, with number of each not exceeding 2% of the total

The bacteriological composition was represented by phyla such as Firmicutes (32.4%), Saccharibacteria (18.7%), Proteobacteria (12.8%), Fibrobacteres (5.04%), and others (1% from the reference), where the dominant classes were Bacilli (17.3%), Gammaproteobacteria (12.8%), Bacteroidia (30.1%), and Clostridia (11.1%). Species diversity was represented by bacteria belonging to genera such as *g. Lactobacillus* (13.9%), *g. Prevotella* (18.1%), *g. Escherichia* (5.04%), *g. Enterobacter* (5.25%), *g. Fibrobacter* (5.04% of the reference), etc. The most abundant in the samples were *Lactobacillus salivarius* (13%), and *Prevotella ruminicola* (2.94%). The use of the enzyme in the diet was accompanied by a significant decrease in the number of bacteria in the rumen, which related to the taxa Firmicutes by 30.3% ($P \leq 0.05$), Saccharibacteria - by 13.4%, and Proteobacteria - up to 2% of the total, and by an increase in the number of the phylum Bacteroidetes by 54.9% ($P \leq 0.05$) from the reference, which was reflected in the change in the percentage of representatives of classes Clostridia, Bacteroidia, and Bacilli in the microbiocenosis.

For taxa Firmicutes and Proteobacteria, a decreased number was observed for bacteria of classes Clostridia (9.1%), Bacilli (less than 2% of the total) and Gammaproteobacteria (less than 2% of the total). At the same time, an increased number of bacteria of class Bacteroidia by 53.4% ($P \leq 0.05$) was observed within the Bacteroidetes taxon, which was mainly due to the increase in representatives of *g. Prevotella* (by 39.9%; $P \leq 0.05$). On the contrary, the use of the enzyme together with the extract in the diet increased the number of representatives of taxon Firmicutes by 13.2%, and taxon Bacteroidetes by 13.4% ($P \leq 0.05$), but decreased the number of bacteria that belong to phyla Proteobacteria, Saccharibacteria, and Fibrobacteres up to 2% of the total number in the sample. The similar effect when using tannin-containing substances was observed in recent experiments by other researchers as well [34].

An increase was observed in the number of microorganisms belonging to the taxa Clostridia (by 23.7%; $P \leq 0.05$) and Bacteroidia (by 13.4%; $P \leq 0.05$). Analysis of the microbiocenosis showed an increase, compared to the reference, in the number of bacteria of *g. Prevotella* (by 8% of the reference), and a decrease in the number of bacteria of other genera that were the most numerous in the reference.

Since there is currently no accurate method for describing changes in microorganisms in a complex system such as rumen, this study has been focused on bacteria. *Quercus cortex* extract in the composition of the fodder contributed to decreasing the number of cellulolytic microorganisms

(Fibrobacteres). This result is consistent with the previous studies [35,36,37], where a similar process was also observed in sheep and rats after introducing plants (extract) containing tannins into the diet. The decreased levels of Proteobacteria and Fibrobacteres may be explained by different molecular weights of the substances in the extract, including tannins [38]; this fact was not considered in this experiment.

Assessment of acute toxicity with luminescent bacteria showed that during the first five minutes of contact with the whole ruminal fluid the luminescence in the control samples is inhibited by no more than 25% for *E. coli* pXen7 and up to 20% for *S. typhimurium* pACXen, and indicators remain at the level of control for I and II variants (Figure 1). Nevertheless, the use of samples diluted two or more times for these strains removes toxic effect and leads to an increase in luminescence, most likely associated with a change in membrane permeability and activation of proton systems due to acidification of the medium. On the other hand, the biosensor based on *B. subtilis* EG168-1 also reacted on the control samples with a drop in luminescence up to 15%, however, samples of the I and II variants led to quenching by 65% and 60%, respectively.

A similar effect was registered earlier [6], it was established that after contact of native ruminal fluid with bioluminescent *E. coli* strain, a dose-dependent inhibition of luminescence was registered on the first seconds of contact.

Assessment of luminescence on the 60th minute of contact showed that it exceeded the control by 35% for *E. coli* pXen7 in the case of samples of the second variant, indicating a restoration of luminosity and no bactericidal effect. In general, similar effects were recorded for *S. typhimurium* pACXen, - luminescence was restored in control variants, in the samples with the extract, a luminescence was observed, only variants with a vervum were characterized by a 19.5% drop. Studies are known [39] with positive effects of inhibition against *E. coli* isolated from cattle are found against the background of *Caryocar brasiliense* plant extracts. In this case, the role of tannins in the manifestation of antibacterial effects was registered. In our case, the results of studies using ruminal fluid of cattle are presented. A high inhibitory effect of *Quercus infectoria* gall extracts against *Staphylococcus aureus* was also observed in the study of antibacterial activity in vitro [40].

A different picture was developed for *B. subtilis* EG168-1, where the luminescence of the control sample exceeded the initial level 8 times, in the first variant - 1.6 times, and the II variant inhibited the luminescence by 32%. Moreover, the second variant in the case of *B. subtilis* biosensor was

characterized by the absence of a luminescence dependence on the sample concentration. The data obtained are in agreement with the studies [41], where positive results were registered when

evaluating the antibacterial activity of the oak extract against *B. subtilis*.

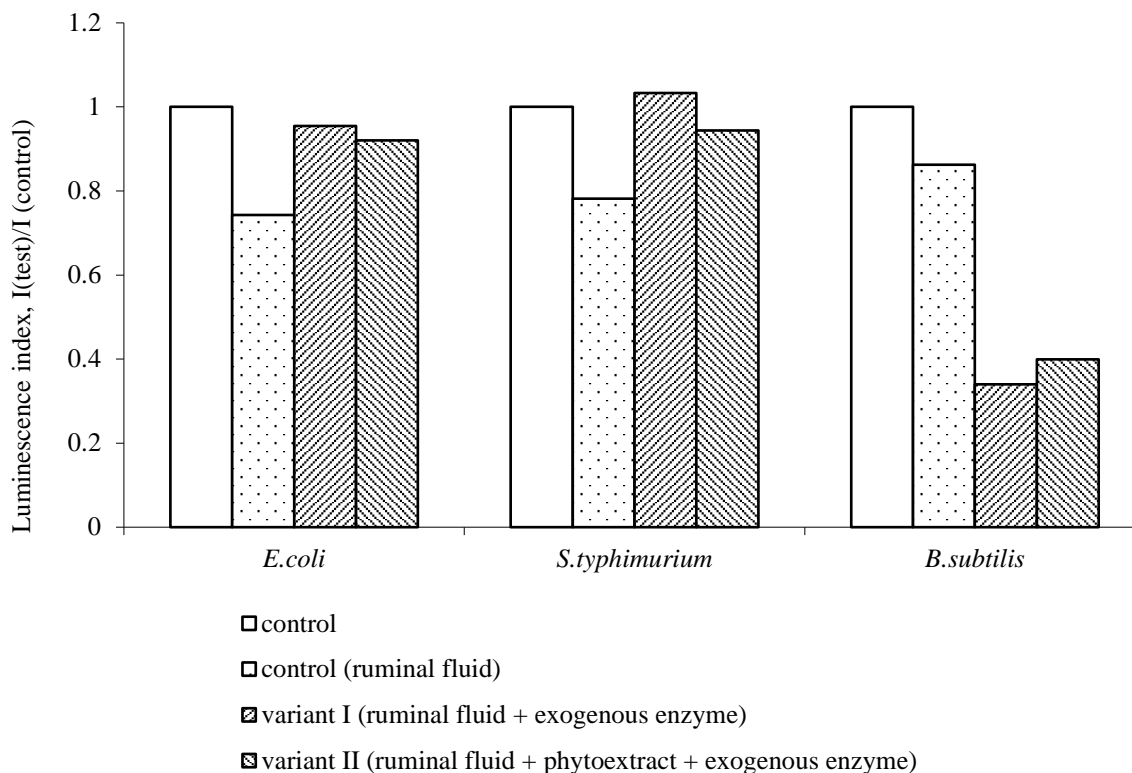


Fig. 1 Luminescence of bacterial biosensors on the fifth minute in the presence of ruminal fluid from cows with various feeding factors.

CONCLUSION

The chemical composition of *Quercus cortex* extract has a significant effect on the elemental profile of cattle rumen microorganisms. At the same time, the introduction of the extract into the diet does not change the overall bacterial structure of rumen microflora. The ratio of phyla Firmicutes and Bacteroidetes, the parameter associated with the energy accumulation function, was increased, same as the number of microorganisms that belonged to the taxon Clostridia. Further study is required for assessing the influence of plant extracts on ruminal microorganisms and changing the products of fermentation associated with the productivity of animals. The biosensor based on *B. subtilis* EG168-1 reacted more actively to the introduction of the extract into ruminal fluid. Further work is required to assess the effect of individual components of plant extracts on ruminal microorganisms and changes in fermentation products associated with animal productivity.

ACKNOWLEDGEMENTS

This research was performed with financial support from the Russian Science Foundation (project No. 16-16-10048).

REFERENCES

- [1] Patra A.K. and Saxena J. A new perspective on the use of plant secondary metabolites to inhibit methanogenesis in the rumen. *Phytochem.* 71, 2010, pp.1198–222.
- [2] Hart K.J., Yanez-Ruiz D.R., Duval S.M., McEwan N.R. and Newbold C.J. Plant extracts to manipulate rumen fermentation. *Anim Feed Sci Technol.*, 2008, 147: pp.8–35.
- [3] Cobellis G., Trabalza-Marinucci M. and Yu Z. Critical evaluation of essential oils as rumen modifiers in ruminant nutrition: A review. *Sci Total Environ.* 545. 2016. pp.556–68.
- [4] Fuqua W.C., Winans S.C. and Greenberg E.P. Quorum sensing in bacteria: the LuxR-LuxI family of cell density responsive transcriptional regulators. *J. Bacteriol.* V. 176. 1994, P. 269–275.

- [5] Tolmacheva A.A., Rogozhin E.A. and Deryabin D.G. Antibacterial and quorum sensing regulatory activities of some traditional Eastern-European medicinal plants. *Acta Pharm.* V. 64. 2014, P. 173–186.
- [6] Logachev K., Karimov I., Duskaev G., Frolov A., Tulebaev S. and Zav`yalov O. Study of Intercellular Interaction of Ruminant Microorganisms of Beef Cattle. *Asian Journal of Animal Sciences*, 9, 2015, 248-253.
- [7] Karimov I., Duskaev G., Inchagova K. and Kartabaeva M. Inhibition of bacterial quorum sensing by the ruminal fluid of cattle. *International Journal of GEOMATE*. Dec. Vol. 13, Issue 40, 2017, pp.88-92.
- [8] Makkar H. P. S. In vitro gas methods for evaluation of feeds containing phytochemicals. *Animal Feed Science and Technology*, vol. 123-124, 2005, pp. 291–302.
- [9] Menke K. H. and Steingass H. Estimation of the energetic feed value obtained from chemical analysis and in vitro gas production using rumen fluid. *Animal Research and Development*, vol. 28, 1988, pp. 7–55.
- [10] Duskaev G.K., Deryabin D.G., Karimov I., Kosyan D.B. and Notova S.V. Assessment of (in vitro) Toxicity of Quorum Sensing Inhibitor Molecules of *Quercus cortex*. *J. Pharm. Sci. & Res.* Vol. 10(1), 2018, 91-95.
- [11] Zhang J., Kobert K., Flouri T. and Stamatakis A. PEAR: a fast and accurate Illumina Paired-End reAd mergeR. *Bioinformatics*. Mar 1;30(5), 2014, pp. 614-20.
- [12] Gupta U.C., Kening W.U. and Siyuan L. Micronutrients in soils, crops, and livestock. *Earth Science Frontiers*.15(5), 2008, 110–125.
- [13] Socha M.T., Tomlinson D.T., Rapp C.J. and Johnson A.B. Effect of nutrition on claw health. *Proceedings of the Society of Dairy Cattle Veterinarians*, New Zealand Veterinary Association Conference; Palmerston North, New Zealand. Foundation for Continuing Education of the NZ Veterinary Association, Massey University; 2002, pp. 73–91.
- [14] Griffiths L.M., Loeffler S.H., Socha M.T., Tomlinson D.J. and Johnson A.B. Effects of supplementing complexed zinc, manganese, copper and cobalt on lactation and reproductive performance of intensively grazed lactating dairy cattle on the South Island of New Zealand. *Animal Feed Science and Technology*. 137(1-2), 2007, pp.69–83.
- [15] Hopkins A., Adamson A.H. and Bowling P.J. Response of permanent and reseeded grassland to fertilizer nitrogen—2. Effects on concentrations of Ca, Mg, K, Na, S, P, Mn, Zn, Cu, Co and Mo in herbage at a range of sites. *Grass and Forage Science*. 49(1), 1994, 9–20.
- [16] Patra K.A. and Saxena, J. Dietary phytochemicals as rumen modifiers: a review of the effects on microbial population. *Antonie Van Leeuwenhoek* 96, 2009, pp.363–375.
- [17] Oberlis D., Harland B. and Skalny A. Biological Role of Macroand Microelements in Humans and Animals. *Nauka, Sankt-Petersburg*, 2008, 544. (Oberlis D., Harland B. & Skalny A. (2008). *Biologicheskaja rol' makro- i mikrojelementov u cheloveka i zhivotnyh*. SPb: Nauka, 2008, 544 s. [In Russ.]).
- [18] Hassanat F. and Benchaar C. Assessment of the effect of condensed (acacia and quebracho) and hydrolysable (chestnut and valonea) tannins on rumen fermentation and methane production in vitro. *J. Sci. Food Agric.*, 93, 2013, 332–339.
- [19] Huyen N. T., Frygasas C., Uittenbogaard G., Mueller-Harvey I., Versteegen M. W. A., Henndriks W. H. and Pellikaan W. F. Structural features of condensed tannins affect in vitro ruminal methane production and fermentation characteristics. *The Journal of Agricultural Science*, 154, 08, 2016, p.1474.
- [20] Suttle N.F. *Mineral Nutrition of Livestock*. Cabi Publishing; 2010, 587 p. ISBN 9781845934729.
- [21] Li Z., Wright A.G., Hanlu Liu., Fan Z., Zhigang Zhang F.Y. and Li G. Response of the Rumen Microbiota of Sika Deer (*Cervus nippon*) Fed Different Concentrations of Tannin Rich Plants. *PLoS One.*; 10(5), 2015, e0123481.
- [22] Newbold C.J., de la Fuente G., Belanch A.E., Ramos-Morales E. and McEwan N.R. The Role of Ciliate Protozoa in the Rumen. *Front Microbiol.* 6, 2015, 1313.
- [23] Schingoethe D.J., Stegeman G.A. and Treacher J.R. Response of lactating dairy cows to a cellulase and xylanase enzyme mixture applied to forages at the time of feeding. *Journal of Dairy Science*, 82, 1999, pp.996-1003.
- [24] Beauchemin K.A., W.Z. Yang and Rode L.M. Effects of Grain Source and Enzyme Additive on Site and Extent of Nutrient Digestion in Dairy Cows. *J. Dairy Sci.* 83, 1999, pp.378-390.
- [25] Yang W.Z., Beauchemin K.A. and Rode L.M. Effects of enzyme feed additives on extent of digestion and milk production of lactating dairy cows. *J. Dairy Sci.* 82, 1999, pp.391–403.
- [26] Whitehead D. C., Goulden K. M. and Hartley R. D. The distribution of nutrient elements in cell wall and other fractions of the herbage of some grasses and legumes. *J. Sci. Food Agric.* 36, 1985, pp.311–318.
- [27] Kabaija E. and Smith O. B. Trace element kinetics in the digestive tract of sheep fed diets with graded levels of dietary fibre. *J. Anim. Physiol. Anim. Nutr. (Berl.)* 59, 1988, pp.218–224.
- [28] Waghorn G. C., Shelton I. D. and Sinclair B. R. Distribution of elements between solid and supernatant fractions of digesta in sheep given six diets. *N. Z. J. Agric. Res.* 33, 1990, pp.259–269.

- [29] Wright P. L. and Bell M. C. Comparative metabolism of selenium and tellurium in sheep and swine. *Am. J. Physiol.* 211, 1966, pp.6–10.
- [30] Harrison J. H. and Conrad H. R. Effect of dietary calcium on selenium absorption by the nonlactating dairy cow. *J. Dairy Sci.* 67, 1984, pp.1860–1864.
- [31] Prabowo A., Spears J. W. and Goode L. Effects of dietary iron on performance and mineral utilization in lambs fed a forage-based diet. *J. Anim. Sci.* 66, 1988, pp.2028–2035.
- [32] Cragle R.G. Dynamics of mineral elements in the digestive tract of ruminants. *Fed. Proc.* 32(8), 1973, pp.1910-1914.
- [33] VAN Bruwaene R., Gerber G. B., Kirchmann R., Colard J. and VAN Kerkom J. Metabolism of ⁵¹Cr, ⁵⁴Mn, ⁵⁹Fe and ⁶⁰Co in lactating dairy cows. *Health Phys.* 46, 1984, pp.1069–1082.
- [34] Carrasco J. M. D., Cabral C., Redondo L. M., Pin Viso N. D., Colombatto D., Farber M. D. and Miyakawa M. E. F. Impact of Chestnut and Quebracho Tannins on Rumen Microbiota of Bovines. *Biomed Res Int.* 2017; 2017: p.9610810.
- [35] McSweeney C. S., B. Palmer and Krause D. O. Rumen microbial ecology and physiology in sheep and goats fed a tannin-containing diet, 2000, p. 140-145. In J. D. Brooker (ed.), *Tannins in livestock and human nutrition: proceedings of an international workshop*, Adelaide, Australia. ACIAR Proceedings no. 92. Australian Centre for International Agricultural Research, Adelaide, Australia.
- [36] Smith A. H. and Mackie R. I. Effect of Condensed Tannins on Bacterial Diversity and Metabolic Activity in the Rat Gastrointestinal Tract. *Appl Environ Microbiol.* Feb; 70(2), 2004, 1104–1115.
- [37] Min B. R., Solaiman S., Terrill T., Ramsay A., and Mueller-Harvey I. The effects of tannins-containing ground pine bark diet upon nutrient digestion, nitrogen balance, and mineral retention in meat goats. *J Anim Sci Biotechnol*; 6(1), 2015, p.25.
- [38] Saminathan M., Sieo C.C., Gan H.M., Ravi S., Venkatachalam K., Abdullah N., Wong C.M., and Ho Y.W. Modulatory effects of condensed tannin fractions of different molecular weights from a *Leucaena leucocephala* hybrid on the bovine rumen bacterial community in vitro. *J Sci Food Agric.* Oct;96(13), 2016, pp.4565-74.
- [39] de O Ribeiro I.C., Mariano E.G.A., Careli R.T., Morais-Costa F., de Sant'Anna F.M., Pinto M.S., de Souza M.R. and Duarte E.R. Plants of the Cerrado with antimicrobial effects against *Staphylococcus* spp. and *Escherichia coli* from cattle. *BMC Vet Res.* 2018, Jan 30;14(1): p.32.
- [40] Wan Nor Amilah W.A., Masrah M., Hasmah A. and Noor Izani N.J. In vitro antibacterial activity of *Quercus infectoria* gall extracts against multidrug resistant bacteria. *Trop Biomed.* 2014, Dec;31(4): pp.680-8.
- [41] Qadir M. A., Shahzadi S. K., Bashir A., Munir A., and Shahzad S. Evaluation of Phenolic Compounds and Antioxidant and Antimicrobial Activities of Some Common Herbs. *Int J Anal Chem.* 2017; 2017: p.3475738.

STUDY OF THE UTILIZATION OF CU(II) MODIFIED LIQUID SMOKE TO INHIBIT THE GROWTH OF FUNGI (*SCHIZOPHYLLUM COMMUNE*)

Muhammad Faisal¹, Shara Utari², Zammera Hayvia², and Ilham Maulana²

¹Department of Chemical Engineering, Engineering Faculty, Syiah Kuala University, Banda Aceh, Indonesia; ²Department of Chemistry, Faculty of Mathematics and Natural Sciences, Syiah Kuala University, Banda Aceh, Indonesia

ABSTRACT

This study aims to examine the possibility of utilizing Cu(II) modified liquid smoke as an antifungal agent against *Schizophyllum commune* Fr. in a laboratory test. The liquid smoke was obtained through the pyrolysis of oil palm kernel shells at 300°C, 340°C, and 380°C. The analysis of liquid smoke as an antifungal agent was performed using potato dextrose agar (PDA) media and nystatin as positive controls. The white-rot fungi of *Schizophyllum commune* Fr. were isolated from fungally infected wood and regenerated for 5x24 hours. Observation of the inhibiting zone was done in 24 hours. The results showed that the presence of Cu(II) can increase the inhibiting zone of white rot fungus. The Cu(II)-modified liquid smoke was able to significantly inhibit the growth of white-rot fungi even in low liquid smoke concentrations. The highest inhibiting zone of *Schizophyllum commune* Fr. was obtained with 3% Cu(II)-modified liquid smoke (obtained from a pyrolysis temperature of 380°C).

Keywords: Liquid smoke, Wood damage, White-rot fungi, Inhibiting zone, Antifungal

INTRODUCTION

Liquid smoke is produced from the condensation of smoke resulting from the pyrolysis of wood containing acid, phenol, and carbonyl compounds [1], [2]. These compounds act as antibacterial [3], antifungal [4], [5], biopreservative [6], antioxidant [7], insecticide [8], and flavoring agents [9]-[11]. Compounds such as phenol and derivatives of carboxylate acid can produce differences in antifungal activities [12], [13]. Velmurugan et al. [14] report that their research shows that liquid smoke can inhibit the growth of *Ophiostoma polonicum*, *O. flexuosum*, *O. narcissi*, and *O. tetropii*. This means that liquid smoke has the potential to be used as an alternative for preserving wood because it can control microorganisms such as fungi and termites. The main compounds in liquid smoke are phenolic and organic acid, which can work effectively to control microbial growth and increase the wood's resistance to fungi, such as white-rot (*Schizophyllum commune* Fr.). The white-rot fungus is capable of degrading lignins and wood components [15], making the wood brittle and significantly reducing the elasticity of its fibers. Moreover, this fungus grows quickly and easily, so it requires effective handling.

Current and commonly used wood preservatives are chromated copper arsenate (CCA) [16], copper azole (CuAz), and alkaline copper quaternary (ACQ)

[17]-[19]. These compounds are made synthetically using several metal combinations. However, some of these substances have been discontinued because they are detrimental to the environment due to their dangerous metal contents, such as arsenic and chromium. Copper (Cu) has the best antimicrobial properties that do not harm the environment. A combination of organic biocides with antioxidants, such as metal, provide prospective alternatives in the development of wood-preserving materials [20]. This research is a preliminary study on the effect of Cu(II) modified liquid smoke. as an antifungal agent against *Schizophyllum commune* Fr. in-vitro, which is expected to benefit the wood preservation industry by discovering an environmentally friendly alternative to preserving wood.

METHODOLOGY

Processing the Liquid Smoke

The liquid smoke was produced based on previous research [4], [21]. Thus, 5 kg of oil palm kernel shells were processed in a pyrolysis reactor made of stainless steel with temperatures set between 300°C and 380°C. The resulting smoke was then condensed into a liquid called liquid smoke, which was then left for one day to separate from the tar content. The liquid smoke was then filtered through filtering paper to remove dirt and dust

before it was analyzed using Gas Chromatography Mass Spectrometry (GCMS-QP2010, Shimatsu, Japan).

Preparing the Cu(II)-Modified Liquid Smoke

The concentrations of liquid smoke used to test the antimicrobial effectiveness were 1%, 2%, and 3%. Each concentration was added into a CuSO_4 solution to create a Cu content of 0.2 M before it was homogenized. This Cu-modified liquid smoke was then characterized using an Fourier Transform InfraRed (FT-IR) test.

Processing the Potato Dextrose Agar (PDA) Solution

As much as 3.9 g of PDA powder was poured into an Erlenmeyer before 100 mL of distilled water was added. This solution was then heated on a hot plate with occasional stirring to mix the content well. The Erlenmeyer was then covered with cotton and paper and sterilized in an autoclave at 121°C for 15 minutes [22].

Isolating the White-Rot Fungi

The fungi were extracted from the infected wood, cleaned and isolated in the PDA for 4-7 days, then inoculated into a new PDA for another 4-7 days before it was suspended in a Potato Dextrose Broth (PDB). Afterwards, it was homogenized in a shaker for 4×24 hours. Finally, the fungi were placed under a microscope to identify their hypha.

Testing the Effectiveness of Liquid Smoke against *Schizophyllum Commune* Fr. Fungi

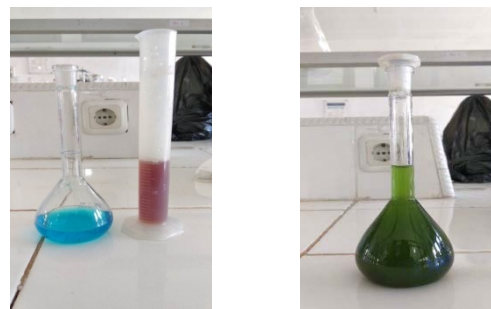
Sample testing was carried out using the diffusion disk method on paper disks with 6mm diameters. As much as 100 μL of the fungi's pure isolates were extracted and evenly dripped onto the PDA media using a triangle stir bar. Then, they were left for ± 15 minutes. Afterwards, each paper disk was dipped into the 1%, 2%, and 3% Cu(II)-modified solutions and left for ± 10 minutes to dry at room temperature. The discs were then lined up on the surface of the testing media using tweezers and incubated at room temperature for 24 hours. Afterwards, the clear-colored area that formed on each disc was analyzed [23].

RESULTS AND DISCUSSION

Characteristics of Cu(II) in Liquid Smoke Using FT-IR

When the liquid smoke reacted with the 0.2 M of Cu(II) sulphate, it resulted in the color changes

shown in Figure 1. There are two possible reactions between the copper and the organic compounds, since the liquid smoke that have the potential to become ligands, such as carbonyl derivatives of aniline, which are capable of forming complex compounds. First, these liquid smoke compounds play important roles in metal binding. Phenol can bind metal with its hydroxyl group, whereas carbonyl and acid can bind metal with their carbonyl and carboxylate groups. These organic compounds donate multiple free electron pairs (chelation). Second, copper is reduced from oxidation +2 to 0 due to the carboxylate's derivatives acting as redactors. This is shown in the color change seen when it returned to its basic, liquid smoke color after a while and from the presence of small particles that made the solution cloudy. These fine particles signify the formation of Cu(0) in very small amounts within the liquid smoke.



(a) before mixing (b) Cu-Liquid smoke
Fig. 1 The liquid smoke's changes in color.

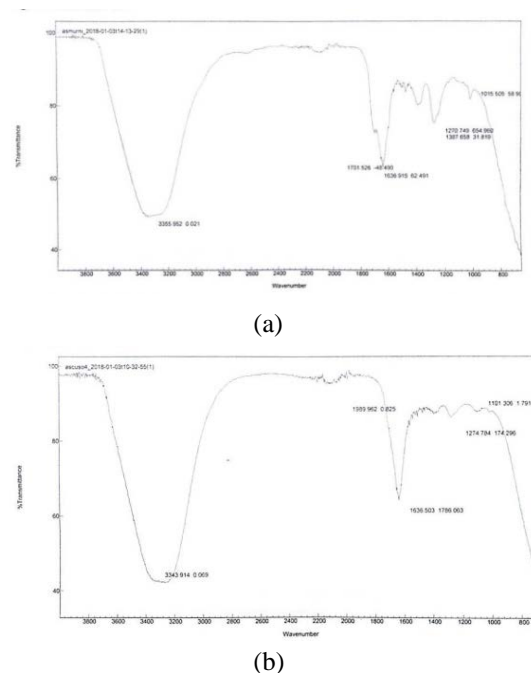


Fig. 2 FT-IR results: (a) Liquid smoke, (b) Cu (II)-modified liquid smoke

The FT-IR test results are shown in Figure 2. The bonding between the liquid smoke and the Cu (II) is indicated by the shifts and peaks recorded. In Figure 2(a), the peaks are recorded at 3355.9 cm^{-1} (signifying O-H (alcohol)), 1636.91 cm^{-1} (signifying C-C (aromatic)), 1387.66 cm^{-1} (signifying C-H (alkyl)), 1270 cm^{-1} (signifying C-O (phenol)), and 1015 cm^{-1} (signifying C-O). In Figure 2(b), the IR spectrum does not indicate meaningful changes in wave numbers, but the shifts in the peaks signify the binding of new compounds after adding Cu(II) sulphate into the liquid smoke. The shift from 1701 cm^{-1} to 1636 cm^{-1} and at 1274 cm^{-1} also signifies missing groups (-C-O). The new peak at 1989.96 cm^{-1} signifies reactions occurring. Wen et al. [26] state that the shifts indicate changes in functional groups.

Testing Liquid Smoke Against White-Rot Fungi

The diffusion disc method was used to test the Cu(II)-modified liquid smoke against the white-rot fungi. The effectiveness of the liquid smoke was shown by the formation of an inhibiting zone, which was a clean or clear area around the antifungal agent. The inhibiting zone was then compared with the diameters of the positive control, nystatin, and the negative control, distilled water.

The analysis showed that the modified liquid smoke's concentration level had a significant impacted on the resulting antifungal index: the higher the concentration, the higher the index was. This was seen from the formation of inhibiting zones on the discs in each concentration variation, wherein a stronger concentration produced a wider diameter. The liquid smoke that was formed from oil palm kernel shells had antibacterial and antifungal properties due to its alcohol, phenol, and organic acid compounds. Its antimicrobial properties were suspected to be able to disrupt the cytoplasm of fungal by destroying the membrane's surface pressure, causing a loss of active transport through the membrane and destabilizing various cell functions and structures.

The fungal growth inhibiting zones for the various concentrations of liquid smoke are shown in Tables 1-3. The copper-modified liquid smoke had significant effects on the diameters of the fungal growths. The inhibiting zones that formed using 1%, 2%, and 3% of the copper-modified liquid smoke that was formed from pyrolysis at 300°C had diameters of 21 mm, 22 mm, and 24 mm (on average), respectively. The inhibiting zones formed using the same concentrations of copper-modified liquid smoke that were formed from pyrolysis at 340°C had diameters of 22.3 mm, 23.6 mm, and 26 mm, respectively.

Table 1 Inhibition zone testing of liquid smoke (temperature pyrolysis of 300°C)

Treatment	Inhibition zone (mm)
Control (+)	23.3
Liquid smoke 1 % + CuSO ₄	21
Liquid smoke 2 % + CuSO ₄	22
Liquid smoke 3 % + CuSO ₄	24
CuSO ₄	15.3
Liquid smoke 2%	19.3
Control (-)	0

Table 2 Inhibition zone testing of liquid smoke (temperature pyrolysis of 340°C)

Treatment	Inhibition zone (mm)
Control (+)	23.3
Liquid smoke 1 % + CuSO ₄	22.3
Liquid smoke 2 % + CuSO ₄	23.6
Liquid smoke 3 % + CuSO ₄	26
CuSO ₄	15.3
Liquid smoke 2%	19.3
Control (-)	0

Table 3 Inhibition zone testing of liquid smoke (temperature pyrolysis of 380°C)

Treatment	Inhibition zone (mm)
Control (+)	23.3
Liquid smoke 1 % + CuSO ₄	24.5
Liquid smoke 2 % + CuSO ₄	26
Liquid smoke 3 % + CuSO ₄	27.3
CuSO ₄	15.3
Liquid smoke 2%	19.3
Control (-)	0

Pyrolysis at 380°C resulted in inhibiting zone diameters of 24.3 mm, 26 mm, and 27.3 mm, respectively. The inhibiting zones formed using 2%

liquid smoke and .02 M of CuSO₄ had diameters of 15.3 mm and 19.3 mm, respectively, while the positive and negative controls formed inhibiting zones of 23.3 mm and 0 mm in diameter, respectively. The antifungal property tests conducted on the Cu-modified liquid smoke showed the highest inhibiting zones at a pyrolysis temperature of 380°C. Oramahi et al. [27] stated that liquid smoke produced from oil palm trunks (pyrolysed at 350°C) can inhibit the growth of the white-rot fungus, *T. versicolor*, at concentrations of 1.5%.

CONCLUSION

Liquid smoke formed from the pyrolysis of oil palm kernel shells at various temperatures has the potential to be used as an antifungal agent against *Schizophyllum commune* Fr., as proven by the inhibiting zones that formed around the fungal growths. The copper-modified liquid smoke displayed significant effects in producing effective inhibiting zones, which are equally effective compared to the liquid smoke concentrations. This research shows that copper-modified liquid smoke can be categorized as a powerful and effective antifungal agent due to its ability to produce ≥20 mm inhibiting zones.

ACKNOWLEDGEMENTS

The authors would like to acknowledge and thank the Ministry of Research, Technology, and Higher Education of Indonesia and Syiah Kuala University for the research funding (Contract no.57/UN11.2/PP/SP3/2018).

REFERENCES

- [1] Zuraida, I. and Budijanto, S., Antibacterial Activity of Coconut Shell Liquid Smoke (CS-LS) and Its Application on Fish Ball Preservation. *International Food Research Journal*, Vol. 18, Issue 1, 2011, pp. 405-410.
- [2] Faisal M., Chamzurni T., and Daimon H., A study on the Effectiveness of Liquid Smoke Produced from Palm Kernel Shells in Inhibiting Black Pod Disease in Cacao Fruit In Vitro. *International Journal of GEOMATE*, Vol. 14 Issue 43, 2018, pp. 36-41.
- [3] Saloko, S., Darmadji, P., Setiaji, B. and Pranoto, Y., Antioxidative and Antimicrobial Activities of Liquid Smoke Nanocapsules Using Chitosan and Maltodextrin and Its Application on Tuna Fish Preservation. *Food Bioscience*, Vol.7, 2014, pp.71-79.
- [4] Faisal M, Gani A, Husni, Baihaqi A, Daimon H., Pyrolysis of Oil Palm Kernel Shell into Liquid Smoke and Its Application to Control Anthracnose Disease on Chili (*Capsicum annum* L.). *Journal of Engineering and Applied Sciences*, Vol.11, Issue. 12, 2016, pp. 2583-2587.
- [5] Ariestya, D.I., Swastawati, F. and Susanto, E., Antimicrobial Activity of Microencapsulation Liquid Smoke on Tilapia [*Oreochromis Niloticus* (Linnaeus, 1758)] Meat for Preservatives in Cold Storage (±5 C°). *Aquatic Procedia*, Vol.7, 2016, pp.19-27.
- [6] Faisal M., and Gani A. The Effectiveness of Liquid Smoke Produced from Palm Kernel Shells Pyrolysis as a Natural Preservative in Fish Ball. *International Journal of GEOMATE*, Vol. 15 Issue 47, 2018, pp. 145-150.
- [7] Faisal M., Gani A., Husni, and Daimon H., A Preliminary Study of the Utilization of Liquid Smoke from Palm Kernel Shells for Organic Mouthwash. *International Journal of GEOMATE*, Vol. 13 Issue 37, 2017, pp. 116-120.
- [8] Gani, A., Husni, H., Baihaqi, A. and Faisal, M., Potential Development of Liquid Smoke from Oil Palm Solid Waste as Biofungicides. *International Journal of Science and Engineering*, Vol.7, Issue 1, 2014, pp.65-69.
- [9] Tian, J., Zeng, X., Feng, Z., Miao, X., Peng, X. and Wang, Y., *Zanthoxylum Molle* Rehd. Essential Oil as a Potential Natural Preservative in Management of *Aspergillus flavus*. *Industrial Crops and Products*, Vol. 60, 2014, pp.151-159..
- [10] Varlet V., Serot T., and Prost C., Smoke Flavoring Technology in Seafood. In Nolle LML, Toldra F. (Eds.), *Handbook of seafood and seafood products analysis* Boca Raton, FL: CRC Press. 2010, pp. 233-254.
- [11] Guillen M.D., and Ibargoitia M.L., New Components with Potential Antioxidant and Organoleptic Properties, Detected for the First Time in Liquid Smoke Flavoring Preparations. *Journal of Agricultural and Food Chemistry*, Vol. 46, Issue 44, 1998, pp. 1276-1285
- [12] Oramahi, H.A., Diba, F. and Yoshimura, T., Optimization of Production of Lignocellulosic Biomass Bio-Oil from Oil Palm Trunk. *Procedia Environmental Sciences*, Vol. 28, 2015, pp.769-777.
- [13] Oramahi, H.A. and Yoshimura, T., Antifungal and Antitermitic Activities of Wood Vinegar from *Vitex Pubescens* Vahl. *Journal of wood science*, Vol. 59, Issue 4, 2013, pp.344-350.
- [14] Velmurugan, N., Han, S.S. and Lee, Y.S., Antifungal Activity of Neutralized Wood Vinegar with Water Extracts of *Pinus Densiflora* and *Quercus Serrata* Saw Dusts. *International Journal of Environmental Research*, Vol. 3, Issue 2, 2009, pp.167-176.
- [15] Zhang, Z., Yang, T., Mi, N., Wang, Y., Li, G., Wang, L. and Xie, Y., Antifungal activity of

- monoterpenes against wood white-rot fungi. *International Biodeterioration & Biodegradation*, Vol. 106, 2016, pp.157-160.
- [16] Ahn, S.H., Oh, S.C., Choi, I.G., Han, G.S., Jeong, H.S., Kim, K.W., Yoon, Y.H. and Yang, I., Environmentally Friendly Wood Preservatives Formulated with Enzymatic-Hydrolyzed Okara, Copper and/or Boron Salts. *Journal of hazardous materials*, Vol.178, Issue 1-3, 2010, pp.604-611.
- [17] Gerengi, H., Tascioglu, C., Akcay, C. and Kurtay, M., Impact of Copper Chrome Boron (CCB) Wood Preservative on the Corrosion of S37 Steel. *Industrial & Engineering Chemistry Research*, Vol. 53, Issue 49, 2014, pp.19192-19198.
- [18] Hingston, J.A., Collins, C.D., Murphy, R.J. and Lester, J.N., Leaching of Chromated Copper Arsenate Wood Preservatives: A Review. *Environmental Pollution*, Vol. 111, No. 1, 2001, pp.53-66.
- [19] Freeman, M.H. and McIntyre, C.R., A Comprehensive Review of Copper-Based Wood Preservatives. *Forest Products Journal*, Vol 58, Issue 11, 2008, pp. 6-27.
- [20] Schultz, T.P. and Nicholas, D.D., Development of Environmentally-Benign Wood Preservatives Based on the Combination of Organic Biocides with Antioxidants and Metal Chelators. *Phytochemistry*, Vol. 61, Issue 5, 2002, pp.555-560.
- [21] Faisal M., Gani A., and AbuBakar, Removal of Copper Ions from Aqueous Solution using Palm Shell Charcoal Activated by NaOH, *International Journal of GEOMATE*, Vol. 15 Issue 48, 2018, pp. 143-147.
- [22] Berlian, Z., Aini, F., and Lestari, W., Aktivitas Antifungi Ekstrak Daun Kemangi (*Ocimum americanum* L.) Terhadap Fungi *Fusarium oxysporum* Schlecht. (In Indonesia), *Jurnal Biota*, Vol. 2, Issue 1, 2016, pp.99-105.
- [23] Sutton, S., Determination of Inoculum for Microbial Testing. *Microbiology Topic*, Vol. 15, Issue 3, 2011, pp. 49-53.
- [24] Maga, J.A., The Flavor Chemistry of Wood Smoke. *Food Reviews International*, Vol.3, Issue 1-2, 1987, pp.139-183.
- [25] Girard, J.P., *Technology of Meat and Meat Product Smoking*, Ellis Harwood, New York, 1992, pp. 162-201.
- [26] Wen, Y., Huang, W., Wang, B., Fan, J., Gao, Z., and Yin, L. Synthesis of Cu Nanoparticles for Large-scale Preparation. *Materials Science and Engineering: B*, Vol. 177, Issue 8, 2012, pp. 619-624.
- [27] Oramahi, H.A., Yoshimura, T., Diba, F. and Setyawati, D., Antifungal and Antitermitic Activities of Wood Vinegar from Oil Palm Trunk. *Journal of Wood Science*, Vol. 64, Issue 3, 2018, pp.311-317.

SHORT-TERM EFFECTIVENESS OF INNOVATION PILLOW RELAX TO STRESS AND HEART RATE VARIABILITY IN THE ELDERLY

Peerada Damapong¹, Pongmada Damapong¹,

¹College of Allied Health Science Suan Sunandha Rajabhat University, Bangkok 10300, Thailand

ABSTRACT

This research aims to innovate a relaxing pillow for elders, and study short-term effectiveness of the aforementioned pillow innovation regarding reduction of stress and heart rate variability among elders. This research is a Quasi-Experimental Research. Volunteers comprise of elders suffering from stress, selected through a survey on stress level. There are 19 individuals whose SPST-20 is higher than 3. The relaxing pillows were provided to all volunteers to nap on for the duration of 10 minutes per day for 3 consecutive days. The assessment measures heart rate variability using Heart Rate Variability (HRV) machine both before and after the experiment. The research reveals a difference in results of Heart Rate Variability (HRV) comparatively, before and after. It appears that the SDNN value has increased significantly ($P<0.05$). From the research, it can be concluded that the relaxing pillow innovation helps increase the parasympathetic nerve pathway's function, thus reducing the volunteers' stress level. It decreases factors related to stress level and helps create positive change among stressed elders.

Keywords: Effectiveness, innovation, pillow relax, stress, heart rate variability, the elderly

INTRODUCTION

Stress is a health issue that can occur to any individuals. It is a reaction of the body, the mind, thoughts, and behavior of a person to both external and internal stimuli. The stimuli may be another individual, thoughts, circumstance or the environment. An individual would recognize a threatening and high pressure situation. If one fails to adapt, then the person would feel stress. This may impact their life balance as they live in society. In the study by World Health Organization (WHO) on a global scale of situations or pain related to the level of stress and mental health, it appears that being a witness to violent acts comprises 21.8%, being involved in interpersonal violence 18.8%, having an accident 17.7%, experiencing warfare 16.2%, and having a loved one who is a victim of trauma 12.5%.[1] Among elders, stress is an important factor affecting their health [2]. If an elder became stressed, it may lead to insomnia and depression respectively.[3] The likelihood of stress among elders is increasing continuously. Thai society is moving forward towards an 'elderly society.' Therefore, it is important to place an emphasis on stress among elders [4]. The older humans become, the more stress they are. Elders are the age of changes, both physically and mentally. This can directly induce stress. Relaxation methods are simple, and one of the most effective methods is to sleep for the body to restore itself.

Mental relaxation is also another thing to be worked on simultaneously with physical relaxation. For stress management, WHO has created Guidelines for the Management of Conditions Specifically Related to Stress to serve as a guideline and standard for stress management [5]. This is applicable to patients with stress, both through medication, alternative approach, or natural healing. There are also herbal treatment and aromatherapy as another alternative in treating patients with stress [6]

Due to this issue, the researcher is therefore interested in developing a relaxing pillow innovation to help treat stress among elders, and study the short-term effectiveness of pillow innovation in reducing stress and heart rate variability among elders. The results can be used to address stress among elder people.

MATERIALS AND METHODS

Design

This research is a Quasi – Experimental Research and took place at the Health Clinic build to honor the Late His Majesty for coming to 60 years old, in Bang Khan Tak sub-district, Meung District, Samut Songkram.

This research has been approved by the ethics committee for researches with humans, by Sirindhorn College of Public Health, Khon Khaen (number 80/2561, number HE 610661).

Participants

The sampling group comprises of elders at least 60 years old with stress. They were identified through a survey inquiring of their stress level. There are 19 individuals whose SPST-20 is higher than 3. In this research, the Inclusion criteria is as follows: Males or females, of at least 60 years old, with the stress level of at least 3. They must be able to travel on their own to participate in the program. The Exclusion criteria is as follows: those with severe contagious diseases, depression, infection, migraine, nausea, allergic to *Aromatherapy*, and those taking medicines affecting the nervous and the heart system, such as sleeping and calming

Intervention

Volunteers received a relaxing pillow innovation, and are requested to use it during the nap for 10 minutes per day for 3 consecutive days. They would use a private room, with the room temperature at 25 degrees, with no odor or noise to disturb, or impacting their nervous system, mental and physical health.

Measurement Instruments

The tools used in the research Suanprung Stress Test 20 (SPST-20), satisfactory surveys, and Heart Rhythm Scanner PE (Biocom Technologies, USA) for measurement the heart rate variability (HRV).

Procedures

The process composites of 3 phrases, as follows:

Phase 1 Development of relaxing pillow innovation

1.1 Study fundamental information with regards to pillows, properties of coconut fiber, and jasmine oil in stress treatment

1.2 Utilize the information in the development of relaxing pillow case for elders, by designing and developing a prototype

1.3 Test the prototype in a representative groups similar to the targeted sample group

1.4 Make use of the test results and feedback for further improvement. Develop the second prototype for usage with the sample group.

Phase 2 Test the relaxing pillow innovation

Researchers recruit volunteers meeting the criteria to participate in the project and provide the research details to volunteers. Volunteers were selected according to inclusion criteria, and were requested to respond surveys with regards to personal information and stress information. Once a volunteer is officially selected, the researchers would then allow the volunteer to sign in for participation.

Afterwards, volunteers would be tested prior to treatment, via Suanprung Stress Test 20 (SPST-20) and Heart rate variability (HRV) test. Once the pre- treatment assessment is completed, volunteers will receive the relaxing pillow innovation to use for 10 minutes per days for 3 consecutive days. Variables will be measured before and after the treatment. The assessment should take only 15 minutes in total.

Phase 3 Effectiveness of the relaxing pillow innovation

From the experiment in using relaxing pillow innovation, the results can be analyzed and converted to collect data on the innovation's effectiveness.

Statistical Analysis

Descriptive statistics is used to explain the characteristics of volunteers, average, the standard deviation. Analysis of the pre- and post- variables are conducted using paired t-test, setting the level of statistical significance (α) at less or equal to 0.05.

RESULTS

The study results can be divided into 3 phases.

Results in phase 1: development of relaxing pillow innovation for elders, using researches information on the appropriate coconut fiber, appropriate size of pillow, anatomical science and ergonomics. The research eventually yields a relaxing pillow case, whose design has a hold in the middle to support the neck and the head. The stuffing of the pillow is made with coconut fiber and candle-roasted jasmine, providing a calming scent. For the test, a representative groups, of 10 people, similar to the target groups was studied. Results of the test was used for the first improvement. The test reveals that the pillow was too hard. Furthermore, because of the hole, the stuffed coconut fibered is too packed, and candle-roasted jasmine was too diluted. For the new design, there is no holes and the aroma was changed to 100% jasmine oil.

Upon implementation, the results can be developed for the second time. The pillow is adjusted to have flexibility, and to have larger gap for aroma oil. It becomes the prototype. For the 3rd improvement, the functional features become even more convenient, resulting in the final relaxing pillow innovation for elders.

Phase 2 of the study: Testing relaxing pillow innovation, and Phase 3: Effectiveness of the relaxing pillow innovation.

Results of the study on participating volunteers' characteristics.

Personal information of the research reveals that the majority of the sampling group is at 64-67 years old, 26.3%; mostly are female at 63.2%, and males at 36.8%. Most of the volunteers are married at 57.9%

Test results comparing the Heart rate variability (HRV)

The research results compare the average Heart rate variability by studying Time Domain Analysis is SDNN and Frequency Domain Analysis, which are: LF, HF. By comparing the pre- and post-test result, it appears that SDNN, LF and HF increase significantly ($P < 0.05$) in Table 1.

Table 1 Compare outcome measures between before and after the treatment

Outcome	Baseline (Mean± SD) (N=19)	Short-term effectiveness (Day 3) (Mean± SD)	P-value
Heart rate variability (HRV) - SDNN (Ms)	52.93±56.48	60.33±57.36	< 0.05*
- LF (ms ²)	4.49±2.04	4.36±1.67	0.005*
- HF (ms ²)	4.34±2.01	4.26±1.67	0.010*

Note.* $P < 0.05$ is statistically significant differences as compare between before and after the treatment from baseline.

DISCUSSION

From the pre- and post-test result, upon comparison, it appears that the SDNN value has increased with statistic significance ($P < 0.05$). The result affects the parasympathetic nerve, reducing the stress according to the research by Lee YT, 2016. There was a study of the effect of lavender floral-water eye-mask aromatherapy on the autonomous nervous system, which reveals that, based on the NN data analysis, the relationship weightings of the psychological factors regarding the autonomic nervous system increased from 1.6 to 9.1 times following the eye-mask aromatherapy. Furthermore, the physical stress index decreased by 33.5% and the total degree of HRV went up by 44.5%, which showed that the lavender floral-water eye-mask aromatherapy resulted in the relief of stress. In addition, there was improvement with regard to the condition of the autonomic nervous system as can be seen by the LF/HF ratio being closer to the normal value for people in good health [7]. This is consistent with the study by Yang et al., 2015 on Comparison of the efficacy of aroma-acupressure and aromatherapy for the treatment of dementia-associated agitation. The study reveals that, in comparison to the control group, the results of the HRV test for the sympathetic nervous system showed that the LF/HF ratio was significantly higher in the aroma-acupressure group [8]. Relaxing pillow innovation helps relax muscles, and therefore reduce the stress level. There is consistency with the research by Peerada Damapong et al., 2016. The study was on Short-term effects of Court-type Traditional Thai massage on Pressure Pain Threshold and pain intensity in patients with Chronic tension-type headache [9]. It is also in consistent with the research by Peerada Damapong et al, on A Randomized Controlled Trial on the Effectiveness of Court-Type Traditional Thai

Massage versus Amitriptyline in Patients with Chronic Tension-Type Headache. A study for those with stress-induced migraine. By measuring the heart rate variability (HRV) both before and after the treatment, it appears that the treatment using Court-Type Traditional Thai Massage shows changes in the heart rate variability =, demonstrating an increased work by parasympathetic nervous system ($P < 0.05$) [10]. The result here explains why relaxing pillow innovation and jasmine aromatherapy helps increase parasympathetic nervous system, reducing elders' stress level.

CONCLUSION

Study of short-term effectiveness of relaxing pillow innovation in reducing stress and heart variability among elders, by measuring before and after the test the heart rate variability, it appears that the SDNN has increased with statistical significance. After receiving a relaxing pillow innovation, volunteers became less stress (more relaxed). It can therefore be concluded that the use of relaxing pillow case with jasmine aromatherapy helps increase the parasympathetic nervous system's function. This enables a stressed individual to become less stressed. It also decreases variables correlating to stress, and therefore creates positive changes among stressed elders.

ACKNOWLEDGEMENTS

This publication has been supported by Suan Sunandha Rajabhat University, Bangkok, Thailand.

REFERENCES

- [1]. Stein, D.J., Chiu, W.T., Hwang, I., Kessler, R.C., Sampson, N., Alonso, J., Borges, G., Bromet, E., Bruffaerts, R., de Girolamo, G., Florescu, S., Gureje, O., He, Y., Kovess-Masfety, V., Levinson, D., Matschinger, H., Mneimneh, Z., Nakamura, Y., Ormel, J., Posada-Villa, J., Sagar, R., Scott, K.M., Tomov, T., Viana, M.C., Williams, D.R., Nock, M.K. Cross-national analysis of the associations between traumatic events and suicidal behavior: findings from the WHO World Mental Health Surveys. *PLoS One*. 2010 May 13;5(5):e10574.
- [2]. Luchesi BM, Souza ÉN, Grato ACM, Gomes GADO, Inouye K, Alexandre TDS, et al. The evaluation of perceived stress and associated factors in elderly caregivers. Vol. 67, *Archives of Gerontology and Geriatrics*. 2016. p. 7–13.
- [3]. Liu Y, Li T, Guo L, Zhang R, Feng X, Liu K. The mediating role of sleep quality on the relationship between perceived stress and depression among the elderly in urban communities: a cross-sectional study. *Public Health*. 2017;149:21–7.
- [4]. Ministry of Public Health. Public health statistics A.D.2015. Strateg Plan Div [Internet].

2016;233. Available from:
http://bps.moph.go.th/new_bps/sites/default/files/health_statistic2558.pdf
[5]. World Health Organisation. Guidelines for the Management of Conditions Specifically Related to Stress. Assess Manag Cond Specifically Relat to Stress mhGAP Interv Guid Modul (version 10) [Internet]. 2013;1–273. Available from:
<http://www.ncbi.nlm.nih.gov/pubmed/24649518>
[6]. Hozumi H, Hasegawa S, Tsunenari T, Sanpei N, Arashina Y, Takahashi K, et al. Aromatherapies using *Osmanthus fragrans* oil and grapefruit oil are effective complementary treatments for anxious patients undergoing colonoscopy: A randomized controlled study. *Complement Ther Med* [Internet]. 2017;34(February):165–9. Available from:
<http://dx.doi.org/10.1016/j.ctim.2017.08.012>
[7]. Lee YT. A study of the effect of lavender floral-water eye-mask aromatherapy on the autonomous nervous system. *Eur J Integr Med* [Internet].

2016;8(5):781–8. Available from:
<http://dx.doi.org/10.1016/j.eujim.2016.05.008>
[8]. Yang MH, Lin LC, Wu SC, Chiu JH, Wang PN, Lin JG. Comparison of the efficacy of aromacupressure and aromatherapy for the treatment of dementia-associated agitation. *BMC Complement Altern Med*. 2015;15(1):1–8.
[9]. Damapong, P. Kanchanakhan, N. Eungpinichpong, W., Putthapitak, P, and Damapong P., Short-Term Effects of Court-Type Traditional Thai Massage on Pressure Pain Threshold and Pain Intensity in Patients with Chronic Tension-Type Headach. *International Journal of GEOMATE*. vol. 11, no. Dec., 2016..
[10]. Damapong P, Kanchanakhan N, Eungpinichpong W, Putthapitak P, Damapong P. A Randomized Controlled Trial on the Effectiveness of Court-Type Traditional Thai Massage versus Amitriptyline in Patients with Chronic Tension-Type Headache. *Evidence-based Complement Altern Med*. 2015;2015.

EFFECTIVENESS OF HERBAL STEAM FOR REDUCING STRESS IN PATIENTS DIABETICS

Pongmada Damapong¹ and Peerada Damapong¹

¹College of Allied Health Science Suan Sunandha Rajabhat University, Bangkok 10300, Thailand

ABSTRACT

This research aims to study the immediate effectiveness of herbal streaming in reducing stress among type 2 diabetic patients. This research is a Quasi – Experimental Research. The volunteers are type 2 diabetic patients with stress, who were selected basing on the questionnaire measuring the stress level. There were 30 people tested for SPST-20 at higher than Level 3. The volunteers received herbal stream treatment for 30 minutes. There were 2 sessions, 15 minutes each; alternating with a 5 minute rest outside. The heart rate variability will be measured with a Heart Rate Variability (HRV) Machine both before and after the experiment. Results on Heart Rate Variability (HRV) was conducted using a Time Domain Analysis, which are SDNN, RMS-SD; and a Frequency Domain Analysis, which are: LF, HF, LF/HF. A comparison before and after the experiment reveals that the values of SDNN, RMS-SD and LF/HF have increased with statistical significance ($P < 0.05$). From the study results, it can be concluded that herbal steaming helps increase the functions of parasympathetic nervous system, enabling individuals' stress to reduce. This helps ameliorate factors related to stress among Type 2 diabetic patients.

Keywords: *Effectiveness, Herbal steam, Hear Rate Variability, Reduce stress, Diabetics*

INTRODUCTION

Diabetes is high up in the priority public health issues globally, as noted by WHO. In 2014, there were approximately 422 million adults living with diabetes worldwide, a significant increase from 108 million in 1980. The global prevalence (age-standardized) of diabetes, which has increased to 8.5% from 4.7% in the adult population, is nearly two times as high as it was in 1980. These statistics indicate that the associated risk factors, such as being overweight or obese, have also risen. Throughout the previous decade, diabetes prevalence has increased more rapidly in low- and middle-income countries than in high-income countries. In 2012, diabetes resulted in 1.5 million deaths, while an additional 2.2 million deaths were caused by having excessive blood glucose levels, which increases the risks of cardiovascular disease and other serious health conditions. A total of 43% of these 3.7 million deaths occurred prior to 70 years of age. High blood glucose or diabetes is responsible for a higher percentage of deaths occurring before the age of 70 in low- and middle-income countries than those occurring in high-income countries.[1] Diabetes is a condition which may allow for dangerous complication to the body, such as an eye complication, abnormally high sugar level due to tear excretion from the lens, which disrupt the retina. A common condition found among diabetic patients is Retinopathy, a sight-related

condition. This can impact patients to the point of blinding [2]. There were studies on how the dietary intake of fish of patients with type 2 diabetes is related to diabetic retinopathy and retinal vascular caliber[3]. In Thailand, diabetic is a high priority public health issue of the country. According to national statistics during 2010-2014, the numbers of patients increase continuously [4]. The frequency rate of diabetes among males has decreased from 6.4% to 6.0%. For females, the rate increases slightly from 7.3% to 7.7% [5]. Diabetes is commonly found and is more likely to be found among elder people. The cause for diabetes may vary. One of the key cause is genetics and obesity, particularly for direct family, such as parents. Diabetes cannot be completely treated. 90% of diabetic patients suffer from the type of diabetic which does not require insulin. This is chronic and affects patients physically, mentally and socially, even their quality of life. As it was chronic and life-threatening, resulting in many inevitable changes in daily life. This causes them to lose their self-confident, resulting in stress. If the patients cannot address this stress, it would affect the quality of life and well-being of the patients. In terms of stress management WHO established Guidelines for the Management of Conditions Specifically Related to Stress to serve as a guideline and an approach in stress management [6]. For treatment of patients with stress, options include medication, alternative treatment, natural treatment, relaxing massage, the use of

Aromatherapy and herbal streaming. Apart from helping with respiratory disease, herbal streaming [7], it uses heat and the herbs is of aroma therapeutic properties, enabling relaxation for patients with stress. Due to this premise, the researcher became interested in studying the immediate effectiveness of herbal streaming for stress reduction among Type 2 diabetic patients. The study's results will be used as a guideline to treat patients suffering stress.

MATERIALS AND METHODS

Design

This research is a Quasi – Experimental Research, operated in Phakdi District, Chaiyaphum province.

This study has been approved by the Ethics Committee of Sirindhorn Public Health College of Khon Khaen (No. 81/2561, No. HE 610662).

Participants

The sampling group comprises of Type 2 diabetic patients age 35-85 with stress. They have been identified with a questionnaire on stress level. There were 30 people whose SPST-20 is at 3 or higher. Volunteers receive stress treatment, utilizing herbal streaming. The heart rate variability (HRV) is monitored by the machine, both before and after the study for result comparison. The research has an Inclusion criteria, as follows: females or males, age 35-85 years, diagnosed as Type 2 diabetic, with stress level of SPST-20 at more than 3. The exclusion criteria comprises of a fever higher than 38 degree, as there may be further contamination, severe contagious disease, conditions: kidney disease, heart disease, epilepsy, chronic asthma, severe respiratory disease, females on period who were having fever, infection from various wounds, migraine, nausea or those with history of allergies to herbs.

Intervention

Volunteers received herbal streaming for 30 minutes, allocated into two sessions; 15 minutes each. Then there is a 5 minute rest. There will be a Heart Rate Variability (HRV) assessment before and after the herbal streaming immediately. (Figures 1)

The treatment used in herbal streaming is a formulae with relaxing properties, relieving muscle pains, such as Phlai, Turmeric, Bergamot's skin, jasmine, and bullet wood etc.

Measurement Instruments

The tool used for research is one that measures the level of stress, Suanprung Stress Test 20 (SPST-20). It is a test created by Suanprung Hospital, Chiang Mai. This was complemented by the Heart Rhythm Scanner PE (Biocom Technologies, USA) for measurement the heart rate variability (HRV).

Procedures

The research team announced for volunteer recruitment, explained the research project details to

volunteers, and selected diabetic patients with stress through doctors' diagnosis. Volunteers would then respond the questionnaire with regards to personal information and stress-related information. When volunteers pass the inclusion criteria, they will be accepted for herbal streaming. Research team would then let the volunteers sign for participation in the research.

Volunteers will be assessed for certain conditions prior to the treatment, for example, their stress level using Suanprung Stress Test 20 (SPST-20), and Heart rate variability (HRV). Once the assessment prior to the treatment is completed, then volunteers will receive herbal streaming. In the experiment, doctors practiced in traditional medicine or modern medicine, with no less than 3 years of work experience, will be monitoring the herbal streaming process. The process takes 30 minutes in duration. Before the treatment, volunteers will be assessed before and after the treatment. The entire process of the assessm

Statistical Analysis

Use descriptive statistics to explain the volunteers' characteristics, the average, the standard derivation. Then analyze the results of comparative factors of the same group before and after the treatment using paired t-test.



Figure 1: The Herbal Steam.

RESULTS

Results of the research on volunteers participating in the research project demonstrates the following personal information: there are 30 volunteers, with females being the majority, at 24. 80% of the volunteers age between 49 to 61 years old, there were 16 volunteers in this range. 53.30% of the volunteers, the majority, weight between 52-69 kilograms or 63.30%. Those in the height range between 150 to 159 centimeters makes up 15 people or 50%.

The result compares Heart rate variability (HRV).

Research results demonstrates the comparative Heart rate variability, by studying Time Domain Analysis, comprises SDNN, RMS-SD; and study Frequency Domain Analysis (LF, HF, LF/HF). By comparison before and after the study, the SDNN, RMS-SD and LF/HF have a value that increases with statistic difference ($P < 0.05$) in Table 1.

Table 1 Compare outcome measures between before and after the treatment

Outcome	Baseline (Mean± SD)	Immediate Effectiveness (Mean± SD)	P-value
Heart rate variability (HRV) - SDNN (Ms)	22.71±14.89	37.76±18.74	< 0.05*
- RMS-SD (Ms)	17.92±15.02	31.60±18.26	< 0.05*
- LF (ms ²)	27.16±21.12	24.60±22.74	0.348
- HF (ms ²)	22.11±20.59	24.20±23.38	0.346
- LF/ HF (ms ²)	1.59±0.68	2.01±1.10	0.047*

Note.* $P < 0.05$ is statistically significant differences as compare between before and after the treatment from baseline.

DISCUSSION

From the study results before and after the experiment, it appears that volunteers receiving the herbal streaming will have SDNN, RMS-SD, and LF/HF of HRV which increased with statistical difference ($P < 0.05$). Result of the study affects the parasympathetic nerve. This reduces stress, in consistent with the research by Rajesh Kumar Goit et al. in 2014. The study was on Mild-to-moderate intensity exercise improves cardiac autonomic drive in type 2 diabetes. The following materials and methods were applied: assessment of heart rate variability was conducted with 20 patients with type 2 diabetes by recording the resting electrocardiogram for the heart rate variability analysis at spontaneous respiration for 5 min in the supine position prior to and following 6 months of supervised aerobic training that was conducted three times each week. The results of the study show that: in the time domain measures, the square root of the mean of the sum of the squares of differences between the adjacent R-R intervals (RMSSD; $P = 0.023$) and the percentage of consecutive RR intervals that differ by more than 50 ms (pNN50; $P = 0.025$) rose significantly following exercise. In the frequency domain measures, low frequency ($P = 0.003$) and low frequency/high

frequency ($P = 0.009$) were significantly lower, while, in contrast, high frequency ($P = 0.006$) and high frequency ($P = 0.003$) were significantly higher following exercise. Additionally, when using a Poincare plot, the standard deviation perpendicular to the line of the Poincare plot ($P = 0.027$) greatly increased following exercise [8]. There are also studies related to Antihypertensive treatment and heart rate variability in diabetic patients: role of cardiac autonomic neuropathy [9]. For this research, volunteers receive herbal streaming which helps volunteers' muscle to relax. This helps stress level to reduce. There is consistency with the study by Peerada Damapong et al, 2016. There were also studies related to Short-Term Effects of Court-Type Traditional Thai Massage on Pressure Pain Threshold and Pain Intensity in Patients with Chronic Tension-Type Headach [10]. This is also consistent with the study by Peerada Damapong et al., on A Randomized Controlled Trial on the Effectiveness of Court-Type Traditional Thai Massage versus Amitriptyline in Patients with Chronic Tension-Type Headache It studied patients with migraine induced by stress. This was measured through an assessment on Heart rate variability both before and after the treatment. The study reveals that after treating the patients with Court-Type Traditional Thai Massage, there was a change in HRV. This demonstrates the increased functions of parasympathetic nervous system ($P < 0.05$) [11]. The study's result reveals that herbal streaming helps increase the work of parasympathetic nervous system, enabling receivers of herbal streaming to have less stress; this was amongst Type 2 diabetic patients.

CONCLUSION

By studying the immediate effectiveness of herbal streaming in stress reduction for type 2 diabetic patients. Results of the Heart rate variability from before and after the treatment demonstrates that SDNN, RMS-SD and LF/HF values increased with statistical significance. After the herbal streaming, volunteers become less stress. However, it can be concluded that herbal streaming helps increase the functions of parasympathetic nervous system. This enables type 2 diabetic patients to become less stress.

ACKNOWLEDGEMENTS

The researchers are very grateful to all participants for contributing important information.

This research was supported by National Research Council of Thailand and Suan Sunandha Rajabhat University, Thailand.

REFERENCES

- [1]. World Health Organization. Global Report on Diabetes. Isbn [Internet]. 2016;978:88. Available

from:

http://www.who.int/about/licensing/%5Cnhttp://apps.who.int/iris/bitstream/10665/204871/1/9789241565257_eng.pdf

[2]. Al-Kharashiv AS. Role of oxidative stress, inflammation, hypoxia and angiogenesis in the development of diabetic retinopathy. Saudi J Ophthalmol [Internet]. 2018;1–6. Available from: <http://linkinghub.elsevier.com/retrieve/pii/S1319453418301826>

[3]. Chua J, Chia A-R, Chee ML, Man REK, Tan GSW, Lamoureux EL, et al. The relationship of dietary fish intake to diabetic retinopathy and retinal vascular caliber in patients with type 2 diabetes. Sci Rep [Internet]. 2018;8(1):730. Available from: <http://www.nature.com/articles/s41598-017-18930-6>

[4]. Ministry of Public Health. Public health statistics A.D.2015. Strateg Plan Div [Internet]. 2016;233. Available from: http://bps.moph.go.th/new_bps/sites/default/files/health_statistic2558.pdf

[5]. Ministry of Public Health. Bureau of Non Communicable Diseases. Annual Report 2015 ;13–4. Available from: <http://www.thaincd.com/document/file/download/per-manual/Annual-report-2015.pdf>

[6]. World Health Organisation. Guidelines for the Management of Conditions Specifically Related to Stress. Assess Manag Cond Specifically Relat to Stress mhGAP Interv Guid Modul (version 10) [Internet]. 2013;1–273. Available from: <http://www.ncbi.nlm.nih.gov/pubmed/24649518>

[7]. P. T, P. N, W. W. Efficacy and safety of herbal steam bath in allergic rhinitis: a randomized controlled trial. J Integr Med [Internet]. 2018;16(1):39–44. Available from:

<http://www.elsevier.com/journals/journal-of-integrative-medicine/2095-4964%0Ahttp://ovidsp.ovid.com/ovidweb.cgi?T=JS&PAGE=reference&D=emexb&NEWS=N&AN=619975684>

[8]. Goit RK, Paudel BH, Khadka R, Roy RK, Shrewastwa MK. Mild-to-moderate intensity exercise improves cardiac autonomic drive in type 2 diabetes. J Diabetes Investig. 2014;5(6):722–7.

[9]. Salo TM, Viikari JSA, Anttila KJ, Voipio-Pulkki L-M, Jalonen JO, Välimäki IAT. Antihypertensive treatment and heart rate variability in diabetic patients: role of cardiac autonomic neuropathy. J Auton Nerv Syst [Internet]. 1996;60(1–2):61–70. Available from: <http://linkinghub.elsevier.com/retrieve/pii/0165183896000367>

[10]. Damapong, P. Kanchanakhan, N. Eungpinichpong, W., Putthapitak, P, and Damapong P., Short-Term Effects of Court-Type Traditional Thai Massage on Pressure Pain Threshold and Pain Intensity in Patients with Chronic Tension-Type Headach. International Journal of GEOMATE.vol. 11, no. Dec., 2016..

[11]. Damapong P, Kanchanakhan N, Eungpinichpong W, Putthapitak P, Damapong P. A Randomized Controlled Trial on the Effectiveness of Court-Type Traditional Thai Massage versus Amitriptyline in Patients with Chronic Tension-Type Headache. Evidence-based Complement Altern Med. 2015;2015.

EFFICIENCY OF INDIAN BORAGE ESSENTIAL OIL AGAINST COWPEA BRUCHIDS

*Ruchuon Wanna¹ and Phanthiwa Kwang-Ngoen²

¹Faculty of Technology, Mahasarakham University, Thailand

²Faculty of Agriculture, Chiang Mai University, Thailand

ABSTRACT

Cowpea bruchids is a one of the most important insect pests in stored products, especially of whole grains used for breeding or consumption. Currently, synthetic insecticides cause adverse effects to human health and the environment, thus new alternative biopesticides from herb or plant are needed for cowpea bruchids control. The aim of this research was to evaluate insecticidal activities of essential oil from Indian borage, *Plectranthus amboinicus*. Efficacy of this essential oil against *C. maculatus* was investigated by impregnated filter paper and vapor-phase tests. Experiments were conducted under Completely Randomized Design (CRD) with 4 replications. Contact activity was considered on essential oil at 6 concentrations of 0 300 600 900 1,200 and 1,500 ppm and fumigant activity was performed at 6 concentrations including 0 3 6 9 12 and 15 $\mu\text{L/L}$ air. All experiments were assessed under laboratory conditions ($30\pm 2^\circ\text{C}$, 70-80%RH and 16L:8D photoperiods). Data of deaths cowpea bruchids were recorded after treated at 24 to 168 hours. Contact activity showed 1,200 ppm of *P. amboinicus* essential oil at 168 hours was the best performance in the contact toxicity on cowpea bruchids and fumigation activity presented 12 $\mu\text{L/L}$ air of *P. amboinicus* essential oil at 72 hours had the highest effectiveness in the fumigation toxicity on cowpea bruchids, with 100% adult mortality. The data pointed that *P. amboinicus* essential oil showed high potential of insecticidal activity for cowpea bruchids control. Hence, the essential oil of *P. amboinicus* might be used as an alternative for grain protection against stored product insects.

Keywords: Insecticidal activity, Essential oil, *Plectranthus amboinicus*, *Callosobruchus maculatus*

INTRODUCTION

Callosobruchus maculatus (Fabricius) (Coleoptera: Chrysomelidae: Bruchinae), the cowpea bruchids which is the most important pest of during the storage period [1], has involved the great attention because it is widely distributed throughout the tropical and sub-tropical regions. Generally the infestation starts in the field where the adults lay eggs on green or drying pods. Infestation in the field has no serious implications as the damage in the field is low. However, once infested seeds are stored, enormous damage occurs due to rapid multiplication of insects in a very short time. This specie can cause damage of legume seeds up to 100 % during storage [2], resulting in maximum damage of 2 to 5 kg seeds within 45 to 90 days in optimum temperature ($30\pm 1^\circ\text{C}$) and moisture conditions ($75\pm 3\%$). The adult female lays eggs on the seed surface and the hatching larvae bore into the seed. The neonate larvae penetrate the grains causing serious damage, such as grain weight loss, and reductions in germination and nutritional value [3], [4]. The whole development takes place inside a single seed and the adults emerge out by leaving behind holed seed [5]. More than one larva can develop within a single grain. Damaged legume seeds have thus reduced

weight, become unsuitable for human or animal consumption and have poor germinating ability [6].

Synthetic pesticides are currently the method of choice to protect stored grain from insect damage. However, continuous or excessive uses of synthetic pesticides have created serious problems arising from factors such as ozone depletion, environmental pollution, increasing costs of application, pesticide residue in food, insects develop insecticidal resistance and toxicity hazards on non-target organisms in addition to direct toxicity to users [7], [8]. Therefore, environment needs some other alternatives of chemical pesticides. These problems have highlighted the need to develop new types of selective insect-control alternatives. One alternative to synthetic insecticides is the botanical pesticides i.e. insecticidal plants or plant compound and the use of natural compounds, such as essential oils that result from secondary metabolism in plants. Currently, essential oil is in use for insect management [7].

Essential oils and their constituents in relation to contact and fumigant insecticidal actions have been well demonstrated to be a potent source of botanical pesticide against stored grain product pests [9], [10]. Especially their main compounds monoterpenoids, offer promising alternatives to classical fumigants [11] and also have some effects on the physiological,

biological and behavior of insects such as growth rate, life span, reproduction and can cause their death [12], [13]. Studies on essential oils have stimulated research on stored grain pest control, with very promising results. Mahmoudvand et al. [14] demonstrated the contact insecticidal activity of essential oils of *Lippia citrodora* Kunth., *Rosmarinus officinalis* L., *Mentha piperita* L. and *Juniperus sabina* L. presented activity against *C. maculatus* (F.). According to Raja et al. [15], the essential oil of *Mentha spicata* L. caused increased mortality, decreased oviposition and emergence of insects in cowpeas. Some chemical components of essential oils, extracted from plants of the Labiatae family, exhibit low toxicity to mammals but can interfere in specific regions of the nervous system of pest insects [16] causing the insect death. In the present investigation the essential oil of Indian borage, *Plectranthus amboinicus* (Lour.), from fresh leaves was studied for their contact and fumigant activities on the adult *C. maculatus*. The results may be used for *C. maculatus* control in storage units, providing direct and indirect benefits for small and medium cowpea producers.

MATERIALS AND METHODS

Insect rearing

Cowpea bruchids, *Callosobruchus maculatus* (Fabricius) was used for the present experiment. A small population of *C. maculatus* was obtained from the seed store located in Maha Sarakham province, Thailand. Fifteen pairs of cowpea bruchids adults were maintained in a plastic box (diameter 22 cm, height 10 cm). The cultures were reared on diet of 500 g of mungbean seeds, *Vigna radiata* (L) Wilczek. They were reared and allowed for mating and oviposition under laboratory conditions, inside a growth chamber at $30\pm5^{\circ}\text{C}$, $70\pm5\%$ relative humidity, and a photoperiod of 16 h: 8 h (L:D). Adult insects of cowpea bruchids used for tests were 3 days old.

Extraction of essential oil

Essential oil was extracted from fresh leaves of Indian borage, *Plectranthus amboinicus* (Lour.) following by using hydrodistillation in a modified Clevenger-type apparatus. In carrying out the steam distillation process, 200 g of an air-dried sample of *P. amboinicus* was weighed in to the distillation flask and 600 ml of distilled water added. The apparatus was set up using a clamp on a heating mantle and heated for a period of 3 hours. The essential oil deposited on water was then collected through the attached graduated measuring tube by opening the tap. The essential oils treated with anhydrous sodium sulphate to remove the remaining

water after the extraction. Essential oil was preserved in sealed glass containers and refrigerated in the dark at 4°C until its use. The essential oils were tested separately in a completely randomized design, consisting of six treatments (essential oils and control) with four replicates.

Contact activity

The insecticidal contact activity of essential oil of Indian borage *P. amboinicus* against adults of cowpea bruchids *C. maculatus* was evaluated by impregnated filter paper test. Essential oil prepared in acetone (1mL) at different concentrations (0 300 600 900 1,200 and 1,500 ppm) were applied on filter papers (Whatman No. 1, diameter 9 cm). The solvent was allowed to evaporate for 2 min and place at the bottom of each petri-dish (diameter 9 cm). Ten adults (unsex) of cowpea bruchids *C. maculatus* (3 day olds) were introduced into each petri dish and covered with a lid, in a room condition at $30\pm5^{\circ}\text{C}$, $70\pm5\%$ relative humidity, and a photoperiod of 16 h: 8 h (L:D). Control was maintained in which treatment was made with 1 mL of acetone alone. Adult mortality was assessed after treatment 24 hours exposure to 168 hours. The insects were considered to be dead as no leg or antennal movements were observed.

Fumigant activity

The insecticidal fumigant activity of Indian borage *P. amboinicus* was assessed by vapour phase test. In brief, each filter paper strip (Whatman No. 1, cut into 1.5x5 cm) treated with each test oils (0 3 6 9 12 and 15 $\mu\text{L/L}$ air) previously dissolved in acetone (100 μL), it was placed into the hanging of glass vials (diameter 2.5 cm x height 5 cm) from the center of screw cap of fumigation bottle (diameter 5.5 cm x height 10.5 cm) to avoid contact effect of insects with paper strip. Ten adults (unsex) of cowpea bruchids *C. maculatus* (3 day olds) were placed in fumigation bottles and covered with a lid, in condition at $30\pm5^{\circ}\text{C}$, $70\pm5\%$ relative humidity, and a photoperiod of 16 h: 8 h (L:D). Controls received 100 μL of acetone only. Adult mortality was observed after 24 hours exposure to 168 hours. The insects were considered to be dead as no leg or antennal movements were detected.

RESULTS

Contact toxicity

Mortality of cowpea bruchids *C. maculatus* at 168 hours after treatment was highest at the concentration of 1,200 ppm of essential oil from Indian borage *P. amboinicus* with cumulative values of 100% and there was a significant difference

($P < 0.01$) in relation to the other concentrations. However, it did not show any differences compared with 600 900 and 1,500 ppm (Figure 1). The number that died increased as the concentration of the essential oil and time of exposure increased for

insect. At all concentrations treated of essential oil for 120 hours caused more than 50% adult mortality of cowpea bruchids *C. maculatus* compared with the control.

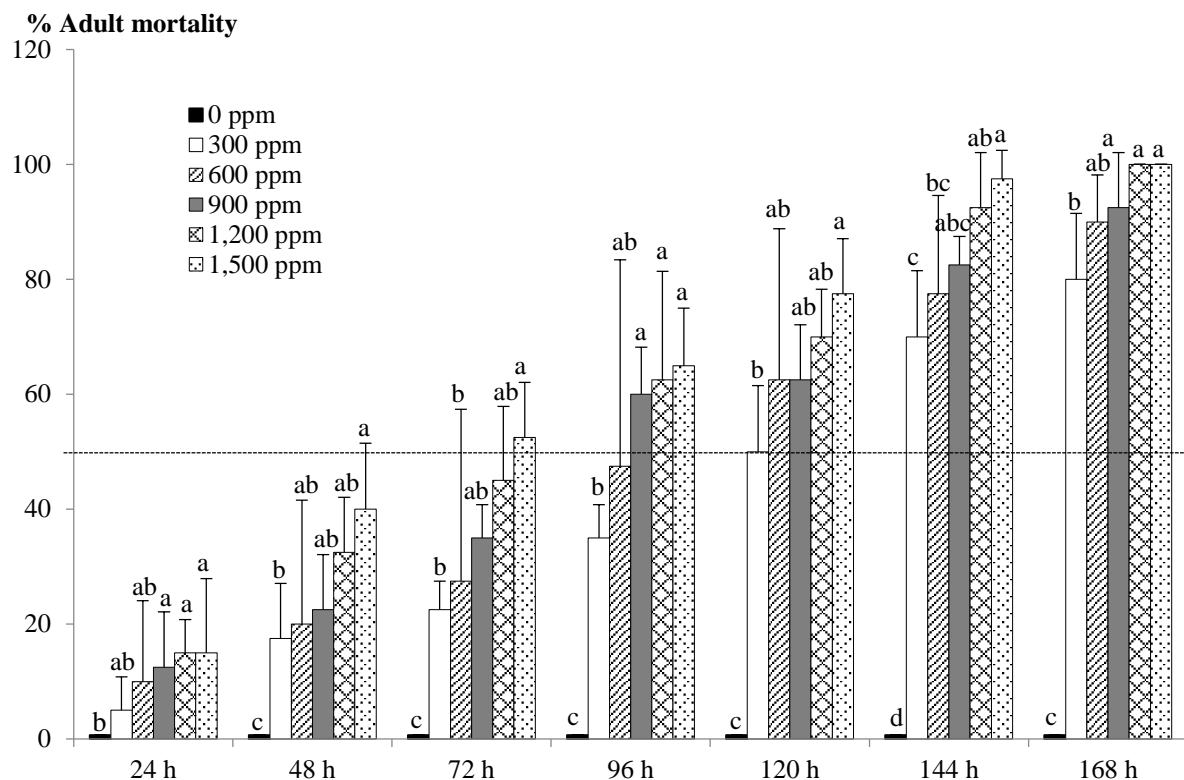


Fig. 1 Contact activity of essential oil of Indian borage *P. amboinicus* on adult mortality of cowpea bruchids *C. maculatus* within 168 hours

Fumigant toxicity

Mortality value exposed with 12 $\mu\text{L/L}$ air of essential oil from Indian borage *P. amboinicus* leaves to adults of cowpea bruchids *C. maculatus* after treatment at 72 h resulted in 100% mortality and it caused the highest significant difference ($P < 0.01$). However, it did not show differences compared with 9 and 15 $\mu\text{L/L}$ air (Figure 2). All concentrations of essential oil were significantly different efficiency against cowpea bruchids *C. maculatus* with adult mortality when comparison with 0 $\mu\text{L/L}$ air, acetone treatments and at 120 hours showed $>50\%$ adult mortality of cowpea

bruchids *C. maculatus*. Cowpea bruchids *C. maculatus* was more sensitive to essential oil of Indian borage *P. amboinicus* by insecticide fumigant than contact activities at greater mortality during the first 72 hours.

Copyright Form

Copyright form signed by all authors is necessary for GEOMATE. It should be submitted along with the paper submission. Copyright form can be downloaded from geomate web site.

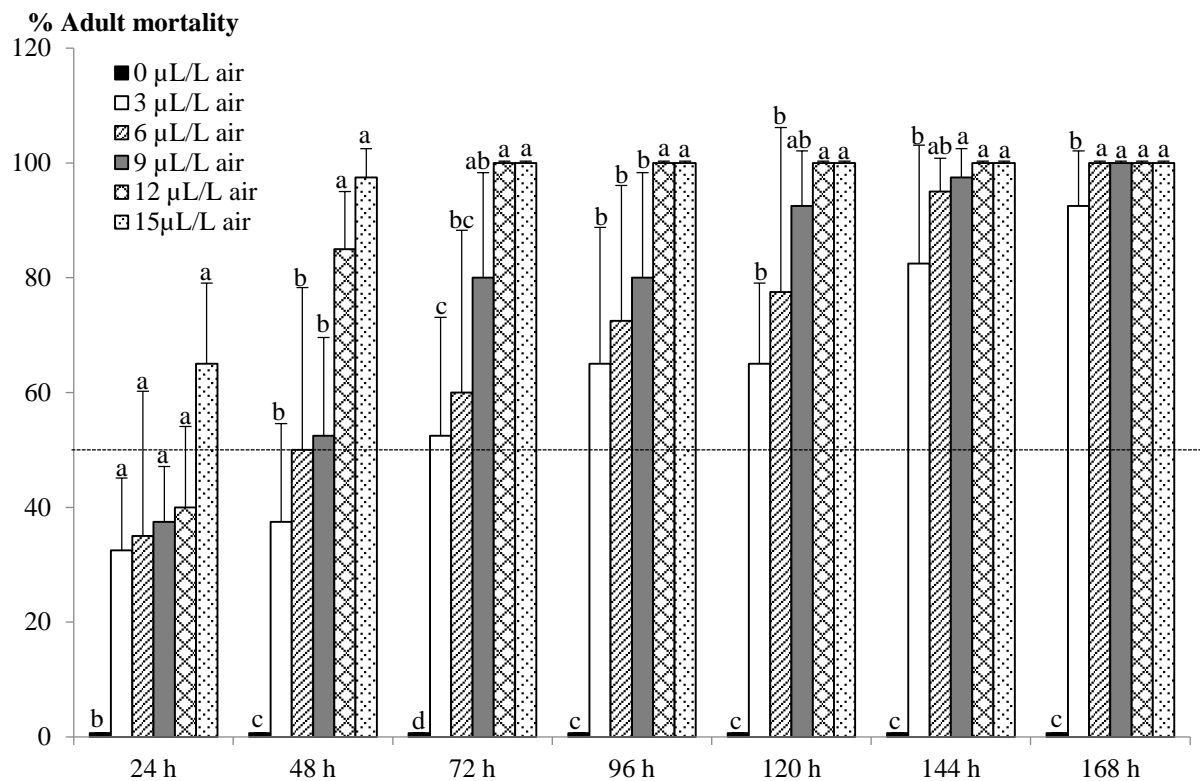


Fig. 2 Fumigant activity of essential oil of Indian borage *P. amboinicus* on adult mortality of cowpea bruchids *C. maculatus* within 168 hours

CONCLUSION AND DISCUSSION

In the current study, the essential oils obtained from leaves of Indian borage *P. amboinicus* demonstrated fumigant and contact activity to cowpea bruchids *C. maculatus*. In contact method, tested essential oil showed a significant increase of mortality ($P < 0.001$) to the test insects at higher dosage (1,200 ppm) after 120 hours of treatment with 100% adult mortality, whereas in fumigation method insecticidal properties were more rapid to test insects within 72 hours of treatment. In fumigation method, cowpea bruchids *C. maculatus* showed high susceptibility to essential oil of Indian borage *P. amboinicus* oil, even at low concentrations (12 µL/L air) after 72 hours of treatment with 100% adult mortality. The insecticidal activity of many plant essential oils might be attributed to monoterpenoids [17]. Due to the high volatility they have fumigant activity that might be of importance for controlling stored product insects. Monoterpenoids were reported earlier as fumigants and contact toxicants on various insect pests [18]. Many studies have demonstrated differential susceptibility of stored product beetle species to the essential oils. *Callosobruchus* species was more susceptible to essential oils or their components than those of other insect species [19],

[20]. The results obtained suggest good potential for the use of essential oils of Indian borage *P. amboinicus* as both fumigant and contact toxic agents against cowpea bruchids *C. maculatus*. Though the examined essential oils had contact as well as fumigant activity, the fumigant toxicity of the essential oils were much more potential in shorter period (72 hours). From this study, it is concluded that Indian borage *P. amboinicus* (Lour.) essential oil could be used as botanical insecticides postharvest or fumigant since it is a potential alternative control method for cowpea bruchids *C. maculatus*.

ACKNOWLEDGEMENTS

This research was financially supported by Mahasarakham University. The laboratory assistance from Miss Jiraporn Krasaetep and Miss Kanokorn Kotraksa are gratefully acknowledged.

REFERENCES

- [1] Deshpande V. K., Makanur B., Deshpande S. K., Adiger S., and Salimath P.M., Quantitative and Qualitative Losses Caused by *Callosobruchus maculatus* in Cowpea During

- Seed Storage, Plant Arch., Vol. 11, 2011, pp. 723-731.
- [2] Gbaye O. A., Millard J. C., and Holloway G. J., Legume Type and Temperature Effects on The Toxicity of Insecticide to The Genus *Callosobruchus* (Coleoptera: Bruchidae). Journal of Stored Products Research, Vol. 47, 2011, pp. 8-12.
 - [3] Melo R. A., Forti V. A., Cicero S. M., Novembre A. D. L. C., and Melo P. C. T., Use of Xray to Evaluate Damage Caused by Weevils in Cowpea Seeds. Horticultura Brasileira, Vol. 28, 2010, pp. 472-476.
 - [4] Oke O. A. and Akintunde E. M., Reduction of The Nutritional Values of Cowpea Infested with *Callosobruchus maculatus* (Coleoptera: bruchidae). International Journal of Agri Science, Vol. 3, 2013, pp. 30-36.
 - [5] Messina F. J. and Jones J. C., Does Rapid Adaptation to a Poor-Quality Host By *Callosobruchus maculatus* (F.) Cause Cross-Adaptation to Other Legume Hosts. Journal of Stored Products Research, Vol. 45, 2009, pp. 215-219.
 - [6] Elhag E. A., Deterrent Effects of Some Botanical Products on Oviposition of the Cowpea Bruchid *Callosobruchus maculatus* (F.) (Coleoptera: Bruchidae). International Journal of Pest Management, Vol. 46, Issue 2, 2000, pp. 109-113.
 - [7] Isman M. B., Botanical Insecticides, Deterrents and Repellents in Modern Agriculture and An Increasingly Regulated World. Annual Review of Entomology, Vol. 51, 2006, pp. 45-66.
 - [8] Ogendo O., Kostyukovsky M., Ravid U., Matasyoh J., Deng A., and Omolo E., Bioactivity of *Ocimum gratissimum* L. and Two of Its Constituents Against Five Insect Pests Attacking Stored Food Products. Journal of Stored Products Research, Vol. 44, 2008, pp. 328-334.
 - [9] Ahmed M. E. A., Fumigant Toxicity of Seven Essential Oils Against the Cowpea Weevil, *Callosobruchus maculatus* (F.) and the Rice Weevil, *Sitophilus oryzae*. Egyptian Academic Journal of Biological Sciences, Vol. 2, 2010, pp. 1-6.
 - [10] Ayvaz A., Sagdic O., Karaborklu S., and Ozturk I., Insecticidal Activity of the Essential Oils From Different Plants Against Three Stored-Product Insects. Journal of Insect Science, Vol. 10, 2010, pp.1-13.
 - [11] Papachristos D. P. and Stamopoulos D. C., Selection of *Acanthoscelides obtectus* (Say) for Resistance to Lavender Essential Oil Vapour. Journal of Stored Products Research, Vol. 39, 2003, pp. 433-441.
 - [12] Pascual-Villalobos J. M., Evaluation of the Insecticidal Activity of *Chrysanthemum coronarium* L. Plant Extracts. Boletín de Sanidad Vegetal Plagas, Vol. 22, 1996, pp. 411-420.
 - [13] Islam R., Khan R. I., Al-Reza S. M., Jeong Y. T., Song C. H., and Khalequzzaman M., Chemical Composition and Insecticidal Properties of *Cinnamomum aromaticum* (Nees) Essential Oil Against the Stored Product Beetle *Callosobruchus maculatus* (F.). Journal of the Science of Food and Agriculture, Vol.89, 2009, pp. 1241-1246.
 - [14] Mahmoudvand M., Abbasipour H., Hosseinpour M. H., Rastegar F., and Basij M., Using Some Plant Essential Oils As Natural Fumigants Against Adults of *Callosobruchus maculatus* (F.) (Coleoptera: Bruchidae). Munis Entomology and Zoology, Vol. 6, 2011, pp. 150-154.
 - [15] Raja N. S., Gnacimusthu S. I., and Dorn S., Effect of Plant Volatile Oils in Protecting Stored Cowpea *Vigna unguiculata* (L.) Walpers Against *Callosobruchus maculatus* (F.) (Coleoptera: Bruchidae) Infestation. Journal of Stored Products Research, Vol. 37, 2001, pp. 127-132.
 - [16] Kostyukovsky M., Rafaeli A., Gileadi C., Demchenkoand N., and Shaaya E., Activation of Octopaminergic Receptors By Essential Oil Constituents Isolated From Aromatic Plants: Possible Mode of Action Against Insect Pests. Pest Management Science, Vol. 58, 2002, pp. 1101-1106.
 - [17] Tong F. and Coats J. R., Effects of Monoterpenoid Insecticides on [3H]-TBOB Binding in House Fly GABA Receptor and 36 Cluptake in American Cockroach Ventral Nerve Cord. Pesticide Biochemistry and Physiology, Vol. 98, Issue 3, 2010, pp. 317-324.
 - [18] Rice P. J. and Coats J. R., Insecticidal Properties of Several Monoterpenoids to the House Fly (Diptera: Muscidae), Red Flour Beetle (Coleoptera: Tenebrionidae), and Southern Maize Rootworm (Coleoptera: Chrysomelidae). Journal of Economic Entomology, Vol. 87, 1994, 1172-1179.
 - [19] Tripathi A. K., Prajapati V., and Kumar S., Bioactivities of L-Carvone, D-Carvone, and Dihydrocarvone toward Three Stored Product Beetles. Journal of Economic Entomology, Vol. 96, 2003, pp. 1594-1601.
 - [20] Lee B. H., Annis P. C., Tumaalii F., and Lee S. E., Fumigant Toxicity of *Eucalyptus blakelyi* and *Melaleuca fulgens* Essential Oils and 1,8-Cineole Against Different Development Stages of the Rice Weevil *Sitophilus oryzae*. Phytoparasitica, Vol. 32, 2004, pp. 498-506.

THE CAPACITY OF SOIL WATER INFILTRATION UNDER HORTICULTURAL CROPS IN THE WATERSHED UPSTREAM SUMANI

Aprisal ¹ and Bambang Istijono ²

¹ Agriculture Faculty, Andalas University, Padang, Indonesia

², Engineering Faculty, Andalas University, Padang, Indonesia

ABSTRACT

Generally, the farming activities in the Sumani upstream watershed community are; cultivating horticulture or vegetables such as cabbage, onions, potatoes, carrots and flowers. The land cultivation for these purposes is made possible due to the high fertility rate of the land in this region which is suitable for horticultural crops. The soil in this area (including the order Andisol) develops from the weathering of the residue from the eruption of Mount Talang. Most farmers do not implement soil and water conservation which invariably leads to erosion and on the long run, the land will finally be degraded. A base research is very vital to assess the ability of the soil water to penetrate to the ground floor. The purpose of this research is to assess the capacity of water infiltration on some types of horticultural crops in the Sumani Upper watershed. The survey method is used to determine the sampling points and the measurement of the rate of infiltration is read using a ring infiltrometer. The soil samples were analyzed in the laboratory of the Department of Soil Science under the Faculty of Agriculture, Andalas University. While the infiltration rate of the data was processed using Horton's equation. To determine the main factor affecting the infiltration rate, the principal component analysis (PCA) was performed. The results showed that infiltration rate in three groups of farmers ranged from moderate to fast. The main factors affecting it are; bulk density, texture and depth of the root zone.

Keyword; Horticulture, infiltration capacity, soil degradation.

INTRODUCTION

Water penetrates the soil through pores to the ground this process is also called infiltration. Infiltration is very important in restoring the soil water lost due to evapotranspiration.

The characteristics of infiltration greatly depend on the soil's physical properties amongst other soil properties and is a good indicator of changes in the soil's physical and biological characteristics [1]. The availability of water in the soil greatly affects the process of plants taking up nutrients from the soil; this is because nutrients are taken up in form of ions in solution. Water infiltration greatly affects the production of crops and also, the drainage of agricultural land. [2].

Several factors influence the infiltration rate of soil, some of them include; slope, texture and soil structure, vegetation cover, management system, soil moisture content, and organic material [1]. If the factors that affect infiltration are not kept in optimal conditions, more rainwater will flow and erode the soil surface and leading to the loss of many nutrients.

Horticulture farming around the upstream of Sumani watershed is mostly practiced by farmers who do not apply soil and water conservation procedures. Allegedly, the land erodes every growing season. The soil is the main natural resource of the people living in the [3] upstream of Sumani watershed which is why they practice intensive farming to meet their life necessities. This dynamic and intensive farming causes rapid land degradation.

The issue above causes damage to the soil's biophysical properties in horticulture, such as soil pores and infiltration rate. If water absorption is

interfered with the root zone of plants, this affects the development of the plant roots in this zone and in turn will reduce the productivity of the soil. The purpose of this research is to study the infiltration capacity in horticulture farming in the upstream area of the Sumani watershed.

MATERIALS AND METHODS

Time and Location

The has been done on February 2018 to June 2018. It was conducted at several sample points on the horticultural lands in upstream of Sumani watershed, Solok Regency, West Sumatera. The soil Quality Indicator Analysis was carried out in the Laboratory of the Department of Soil Science under the Faculty of Agriculture, Andalas University.

Research Tools and Materials

The materials used were aquades, chemicals, as well as materials for the analysis of the physical properties of the laboratory. The tools used to identify the soil quality for horticultural biomass productivity in the field include GPS, loops, maps, sample rings, knives, plastics, label paper. The tools used for Laboratory analysis includes desiccators, ovens, erlenmeyers, bottles, measuring cylinders, analytical scales, eksikator, trophy glasses, wet screen, filter, mouthpiece, Kjeldhal tube, burette, distillation flask, stative, and measuring pipette.

Research Methodology

The research was conducted in the field to collect secondary and primary data. Secondary data was taken from rainfall data, interview with farmers and related institutions. (1) Primary data were land samplers from several points of land units in the three horticultural farmer's field. Soil samples were taken by means of purposive random sampling as an example of representative land from established land units.

The soil samples taken were natural soil samples for analysis of the soil's physical properties. While the altered soil samples were taken for the analyzing the chemical and biological properties of the soil. Soil samples were taken from a 20 cm depth. (2) Secondary data was required in this research, and was collected in form of the area's condition and an aspect of horticultural cultivation of the area. The technique of collecting secondary data by collecting data from several related agencies and interviews with the farmers as supporting data. Results of interviews with

farmers were be scored, and the results of these scores were used as supporting information on the horticultural productivity in the upstream of Sumani watershed, Solok. ((3) The data analysis method which is determined based on the least influential nature in determining the quality of the soil or at least the data set (MDS) using Minitab 17.0 software. Minimum Data Set obtained from the calculation of Principal Component Analysis (PCA).

RESULT AND DISCUSSION

Principal Component Analysis of Soil Physical Characteristics

The main component in determining the main properties of the soil determines the infiltration capacity of the soil. Based on the PCA, the eigenvalue is greater than one, i.e. there are four main components, i.e. PC1, PC2, PC3 and PC4 (Table 1). The selected variables from PC 1 to PC4 are taken as factors to determine the rate of infiltration capacity in horticultural farming.

Table 1. Principal component analysis results

Eigenvalue	2.9122	2.0070	1.4565	1.0767
Proportion	0.364	0.251	0.182	0.135
Cumulative	0.364	0.615	0.797	0.932
Variable	PC1	PC2	PC3	PC4
Infiltration capacity	0.404	0.285	0.314	-0.295
Bulk density	0.522	-0.214	0.018	-0.295
Total of pore space	-0.522	0.214	0.018	0.295
Organic matter	0.033	-0.456	0.496	-0.191
Soil Depth	0.053	0.460	0.516	-0.152
Sand	-0.023	0.527	0.527	0.023
Dust	0.396	-0.107	0.287	0.605
Clay	-0.360	-0.343	0.169	-0.559

The main components selected are the four variables which are highly influential in infiltration capacity, i.e. bulk density, sand-fraction texture, effective depth of soil, and dust fraction.

Infiltration Capacity

The high rate of infiltration capacity in the horticultural farming area in upstream of Sumani watershed is strongly influenced by the soil's physical nature and the dominant soil is micropore. Lands dominated by macropores will have a higher infiltration rate compared to the land dominated by

micropores. Weahatni horticultural field in the study has infiltration capacity of 6cm/h to 12cm/h with the medium to fast range. Farmer groups A and B lands have a moderate level infiltration capacity. The infiltration capacity of farmer group C land is on the quick range. The variations in infiltration capacity of the three horticultural farming groups (Figures 1, 2 and 3) are due to the differences in soil properties and planted crops as well as land management practices conducted by farmers.

Based on regression analysis seen in the equation of the line on the farmers group A is exponential with value $R^2 = 0.678$ While in group B the equation of line of exponential infiltration capacity with value $R^2 = 0.935$ In farmer group C, the equation of line of exponential infiltration capacity with value $R^2 = 0.162$

The infiltration capacity is a dynamic trait that can change significantly during certain precipitation events, in response to seasonal changes in groundwater, temperature, and plant type, as a result of annual farming activities. Increasing infiltration capacity decreases the flow of water in the soil surface. Conversely, a smaller infiltration capacity is due to a large number of clogged soil pores, the surface water flow increases [4]. Furthermore, [5] regarding hydrology, infiltration is important as it marks a shift from the surface of the earth that moves rapidly into the water in the slow-moving ground.

The infiltration capacity of soil is influenced by its physical properties and its degree of ability, water content, and permeability of the subsurface layers.

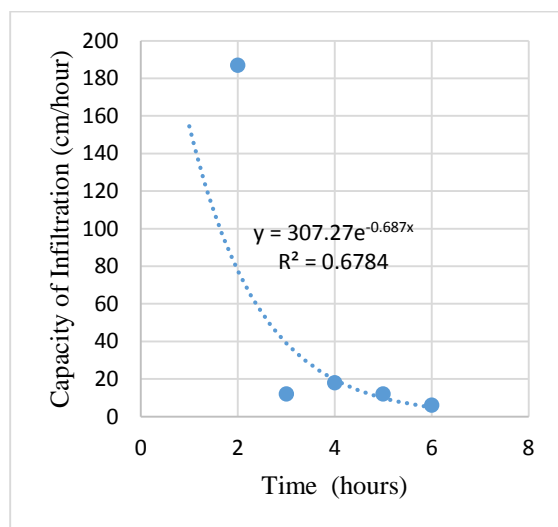


Figure 1. Infiltration capacity on farmland A

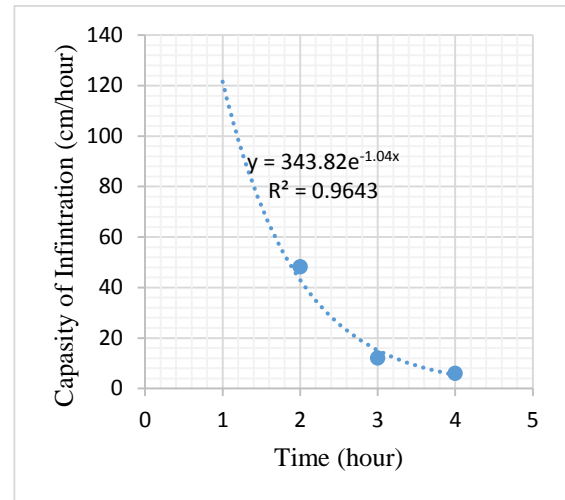


Figure 2. Infiltration capacity on farmland B

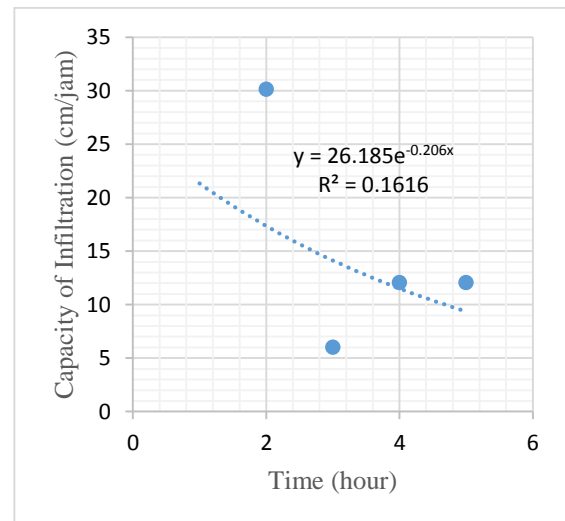


Figure 3. Infiltration capacity on farmland C

Effect of texture on infiltration capacity

Soil texture at the research location of farmer group A was clay, farmer group B was dust, and group C with the texture of fine clay. According to [6] the soils with coarse fraction, the level of the aeration is good and water conductivity is fast, but the holding power of the water is low. Because the soil is dominated by macropores, Figure 2 shows the effect of soil texture of the study sites on infiltration capacity.

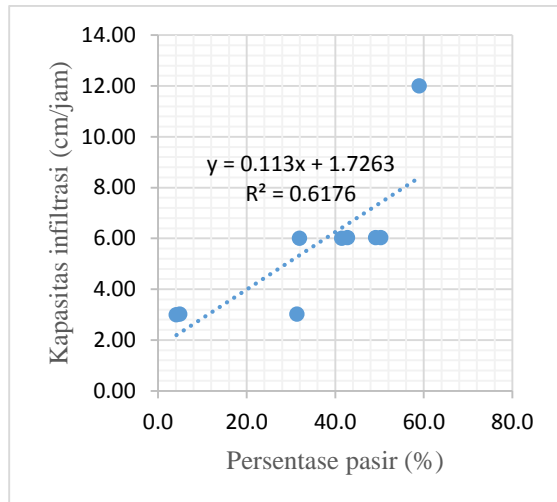


Figure 4. Sand percentage correlation with infiltration capacity

Based on simple regression analysis, the relationship between infiltration capacity and texture was quite close with R^2 value as 0.617. This meant that infiltration capacity of 61.7 percent was influenced by the soil texture of the research locations in farmer groups A, B, and C, the influence from other factors amounted to 38.3 percent. This proved that soil texture greatly influenced the infiltration rate of the soil. For the infiltration capacity of the farming land, a routine management is required to increase the soil absorption matrix by adding organic fertilizer or crop residue to the soil to retain the groundwater ensure it doesn't penetrate to the lower layers of the root zone. The addition of organic material from remaining plants acts as a cemented agent for soil grains, nutrient sources, increasing CEC and energy for soil microbes [7].

Cumulative Infiltration

Cumulative infiltration is incoming water into the soil in a specific time and duration in a certain amount of volume, depending on the total soil pore space to store and hold it.

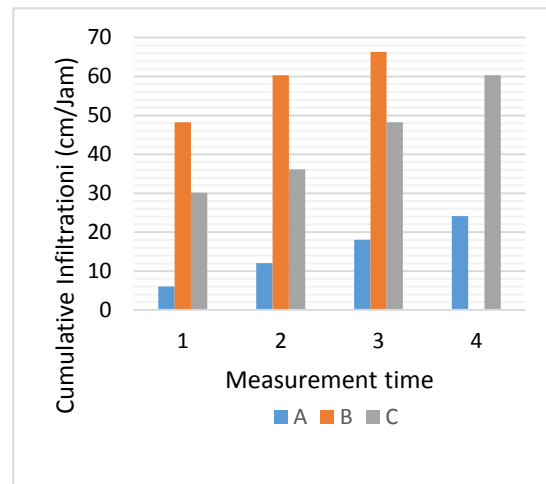


Figure 5. Cumulative infiltration rate on the three farming groups (A, B, and C)

Cumulative infiltration in the three locations of the farmland group is shown in Figure 4. Cumulative infiltration varied considerably between the three types of land farming groups based on measurement time. Higher cumulative infiltration is found in group B, followed by group C then next, group A. This was caused by soil type and crop management which troubled each of farming group. Group B farmers usually return the rest of the plant to the land to increase the ability of soil to absorb water. Good management of soil can improve soil quality such as cumulative infiltration. According to the study [8] it also showed that improving soil quality may increase cumulative infiltration up to five times. However, continuous land acquisition without proper management can reduce cumulative infiltration. According to the results of the study, [9] the improvement in infiltration capacity and cumulative infiltration is by addition of materials that can increase total pore space of soil such as ameliorant material from rice husk biochar. This is because biochar is an active charcoal capable of increasing the soil cavity and biochar is not easily decomposed by soil microbes.

CONCLUSION

Based on the research of the infiltration capacity in the upstream watershed of Sumani, it can be concluded that; the research area of soil infiltration capacity is influenced by soil physics properties, i.e. bulk density, texture, and depth of root zone. The rate of infiltration in the three farmer groups of the study sites was from the moderate to rapid range. From the equation of infiltration capacity, soil texture factor

influence is more dominant and equals about to 61.7 percent.

ACKNOWLEDGEMENT

I am grateful to the chairman of Universitas Andalas for the opportunity and assistance given to us to do the research and the transportation assistance provided. Hopefully, this would be useful to improve the performance of the research team as a lecturer of Universitas Andalas.

REFERENCES

- [1] Radke J.K. and Berry E.C. 1993. Infiltration as a tool for detecting soil changes due to cropping, tillage, and grazing livestock. *American Journal of Alternative Agriculture* 8: 164–174.
- [2] Mukhtar S., Baker J.L., Horton R. and Erbach D.C. 1985. Soil water infiltration as affected by the use of the paraplow. *Transaction of ASAE* 28: 1811–1816.
- [3] Istijono.B. 2006. Watershed Conservation and Farmers Income: Studies on Watershed Management Integration (Case Study: Sumani Watershed of Solok Regency / Solok City, West Sumatera). PPs.Unand Dissertation.
- [4] Kartasapoetra, AG. 1989. *Introduction to Soil Science, Land Formation, and Agricultural Land*. Jakarta: Rineka Cipta.
- [5] Lee, R. 1990. *Forest Hydrology*. Yogyakarta: UGM Press
- [6] Hardjowigeno S. 2003. *Soil Science*. Akademikan Pressindo. Jakarta
- [7] Gardiner, DT dan Miller RW. 2004. *Soil in Our Environment 10th Edition*. Prentice Hall. New Jersey
- [8] Bharati1. L., K. H. Lee, T.M. Isenhardt and R.C. Schultz. 2002. Soil-water infiltration under crops, pasture, and established riparian buffer in Midwestern USA. *Agroforestry Systems* 56: 249–257, 2002. 249. *Kluwer Academic Publishers. Printed in the Netherlands*
- [9] Aprisal, Adrinal dan Wulan Herman. 2018. The Influence of Rice Husk Biochar Against InfiltrationCapacity on Ultisol. *Proceedings of National Seminar of Suboptimal Land 2017, Palembang 19-20th October 2017* “Development of Agricultural Science and Technology with Local Farmers for Optimizing Suboptimal Land”

DISCOVERY OF NOVEL DNMT-1 INHIBITOR BY FRAGMENT-BASED DRUG DESIGN AS A POTENTIAL BREAST CANCER TREATMENT

Mutiara Saragih¹, Ahmad Husein Alkaff¹, Ade Hanna Natalia¹, Ina Nur Istiqomah¹, and Usman Sumo Friend Tambunan^{1*}

¹Faculty of Mathematics and Natural Science, Universitas Indonesia, Indonesia

ABSTRACT

Breast cancer is the deadliest and the most common type of cancer among women in the world. Epimutation is the leading cause of the tumorigenesis of breast cancer. DNA methyltransferase 1 (DNMT1) is the key enzyme which involved in the regulation of DNA methylation pattern. In this research, fragment-based drug design approach on natural products was performed to discover novel inhibitor of the DNMT1 as a therapeutic strategy against breast cancer. About 2,601 fragments out of 168,646 compounds were obtained from the Lipinski's Rule of Three and toxicity screening. The fragments were docked into the S-Adenosyl-L-methionine (SAM) binding site of DNMT1. The potential fragments were merged with S-Adenosyl-L-homocysteine (SAH), generating nine ligands. The ligands underwent flexible docking simulation and ADME-Tox prediction by using AdmetSAR, Toxtree, SwissADME software. Three ligands show favorable characteristics as a new drug candidate for the DNMT1 inhibitor according to the interaction of the amino acid residues, RMSD, and $\Delta G_{\text{binding}}$. MAHI1 being the best ligands in term of $\Delta G_{\text{binding}}$ -12.6300 kcal/mol, molecular interaction, and pharmacological properties.

Keywords: Breast cancer, DNA methyltransferase, natural products, molecular docking simulation, fragment-based drug design

INTRODUCTION

Cancer is a major public health problem worldwide [1]. Breast cancer is among the main causes of death in women [2]. It is also the most current cancer in women worldwide with 1.7 million diagnosed cases in 2012 [3]. The human genome consists of genetic information and epigenetic. Epigenetics regulate how and where the genetic information should be used [4]. DNA methylation is one of the essential mechanism in functional epigenetic [5]. DNA methyltransferases (DNMTs) is the leading enzyme in the epigenetic regulation of gene expression in mammalian cells [6]. DNMT1 is the most abundant DNMTs in the mammalian cells and have a role in maintaining methylation pattern [7].

DNA methylation, whether hypomethylation or hypermethylation, affects gene expression and chromosomal instabilities. Hypomethylation causes overexpression of transcription of proto-oncogenes, and reactivation of transposable elements and demethylation of xenobiotic [8]. On the other hand, hypermethylation causes suppression of tumor suppressor genes and downregulation of DNA repair genes. DNA hypermethylation also plays an essential role in silencing the tumor suppressor genes as one of the most consistent hallmarks of human cancer [7].

Aberrant DNMT1 activity leads to local hypermethylation in DNA promoter gene and global hypomethylation which pose potential causes for the abnormal growth of cancer cells [8]. Thus, the inhibition of DNMT1 activity has been established as

a possible way to reactivate gene silenced by methylation of their promoters in some disease, including breast cancer [9]

Natural products have been known as one of a candidate drug. It is a potential source of drugs due to its molecular diversity and low toxicity [9], [10]. One of the methods of lead compound discovery is fragment-based drug design (FBDD). One of the advantages of FBDD is that it results in a lower molecular weight lead, that is likely to have higher oral bioavailability [11]. Fragment merging is an elaboration of the fragment which incorporates a structural portion of overlapping molecules, usually an already known substrate or inhibitor of the target protein, into a fragment [12]. Hence, preserving the essential molecular interaction of initial substrate or inhibitor while improving the activity by the introduction of new fragment. In this research, the fragment merging approach is utilized on the potential natural product compounds and the already known product of the DNMT1 enzymatic reaction, S-Adenosyl-L-homocysteine (SAH), to generate lead compounds as an inhibitor for DNMT1 through in silico molecular docking simulation method and pharmacological test.

RESEARCH METHODOLOGY

This research has been done through an in silico method by employing Molecular Operating Environment (MOE) 2014.09, Osiris DataWarrior v04.07.02, ChemBioDraw Ultra 14.0, Toxtree v2.6.13, SwissADME (<http://www.swissadme.ch/>),

and AdmetSAR (<http://lmmd.ecust.edu.cn/1>) software. The 3D structure of DNMT1 protein was obtained from Protein Data Bank at the Research Collaboratory for Structural Bioinformatics (RCSB PDB). The database of natural products was acquired from PubChem.

Preparation of DNMT1 Protein

The 3D structure of DNMT1 with PDB ID 3AV5, 3AV6, 3PTA, 3SWR, and 4WXX were obtained from the RCSB. The chosen 3D structures were saved in PDB format. The optimization DNMT1 was done using MOE 2014.09 by removing water molecules and unnecessary metal atoms and optimizing the structure using LigX with the default setting. Last, all of the DNMT1 protein were saved in .moe format.

Protein-Ligand Interaction Fingerprints (PLIF)

PLIF was applied to summarize the interaction between ligands and protein using a fingerprinting scheme. This method has been done using MOE 2014.09 with potential setup AMBER 10EHT, forcefield, R-field solvation and superpose. Superpose generates sequence alignment, structure alignments, PDB coordinates, RMSD statistics, difference distance plots, and interactive image of the superimposed structures [13], [14]. The procedure of PLIF has been done based on standard default in MOE 2014.09.

Preparation of The Natural Product Fragments

The standard ligands SAM, SAH, and Sinefungin (SFG), as well as the natural products as candidate fragment, were obtained from PubChem database. The ligands were then optimized through MOE 2014.09. MMF94x force field with RMS gradient of 0.001 was selected as the optimization parameters. Natural products of The optimized ligands were stored in .mdb format. The prepared natural products were screened to get fragments which fulfill Lipinski's Rule of Three (RO3) [15] and Toxicity test by Osiris DataWarrior.

Molecular Docking of Natural Product Fragments and Fragment Merging

The selected fragments were on docked into the SAM-binding site of DNMT1 by using pharmacophore query through using MOE 2014.09. The fragments with favorable Gibbs binding energy, RMSD, and molecular interaction were selected to be merged with the standard molecule, SAH. This merging process of fragments and standards have been done using MOE 2014.09 and ChemBioDraw Ultra 14.0 [12].

Molecular Docking of Ligands

The molecular docking simulation for ligands and standard were conducted with rigid docking and then flexible docking protocol. All the parameters for the molecular docking simulation have been done according to MOE 2014.09 software with AMBER 10: EHT as the forcefield.

Pharmacological Properties ADMET

The potential ligands from molecular docking simulation underwent pharmacological properties prediction. Toxtree was used to screened the carcinogenicity and mutagenicity. The toxic properties of the ligands were analyzed using Osiris DataWarrior and AdmetSAR. The health effects of the ligands on human organ were predicted using SWISSADME.

RESULT AND DISCUSSIONS

Preparation and Visualization of DNMT1

DNMT1 is responsible for replicating the DNA methylation pattern during replication. DNMT1 has also been considered as an essential target for cancer therapy [16]. In this research, the 3D structures of DNMT1 were obtained from RCSB PDB. The water molecule and other unnecessary molecule were eliminated because solvation effect is not taken into account in the molecular docking simulation [17]. Hydrogen atoms were incorporated into the protein. The protein structures from RCSB PDB is generated from X-ray crystallography which commonly does not have a hydrogen atom because of the limited resolution of the instrumentation. The presence of complete atom on protein structures is essential because it will affect the molecular mechanics, dynamics, and electrostatic calculations involved in molecular docking simulation [17], [18]. The last step of protein preparation was energy minimization to generate zero gradients of all atoms; the lowest energy and the most stable condition that can be used to investigate the mechanism of a chemical or biological process [19]. PLIF method is employed to quantify and compare ligand-protein interactions. In this method, fingerprints are covered into a normalized quantitative score that expresses the similarity between the interaction profile of docking pose and that of a reference protein-ligand complex [20]. Furthermore, the pharmacophore was validated to assess its ability to distinguish active compounds that have potentially inhibit DNMT1 to the other [21]. In addition, the purpose of pharmacophore validation is to evaluate the quality of pharmacophore features that have been created. Standard ligands were utilized to perform the validation test. Visualization on the

binding site of DNMT1 was done with 'Surface Navigation and Maps' tools in MOE 2014.09 (Fig. 1).

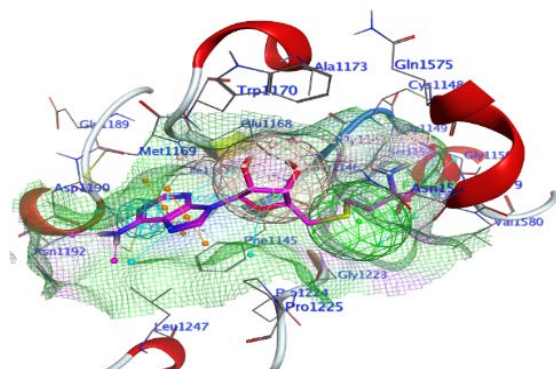


Fig. 1. Binding site visualization of DNMT1 with pharmacophore, The green color is HydA, the pink color is Don&Acc, and the blue color is Acc.

Preparation of Natural Product Fragments

About 168,646 compounds of natural products were obtained from PubChem database. It was screened by RO3 which has parameters such as, molecular weight lower than 300 Da, LogP lower than 3.0, the number of hydrogen donor less than 3, and the number of hydrogen acceptor less than 3, which suitable for the screening of small compound for fragment development [15]. The natural products also screened based on the veber rule [22], rotatable bond no more than 3 and polar surface area (TPSA) lower than 60 Å. Natural products which druglikeness lower than 0, and shows the toxicity potential such as mutagenic, tumorigenic, reproductive effective and irritant were also eliminated. From the initial screening, 2,601 compounds were saved in a .mdb format as the fragment for the next experiment.

Analysis of Molecular Docking Simulation of DNMT1 Protein and Fragments

Molecular docking simulation has become an essential tool in drug design and discovery to predict the conformation of small molecule ligands with compatible target binding site and define binding affinity of the ligand to form a stable complex structure [23], [24]. The selected fragments from the previous step were further screened molecular docking simulation. In the first molecular docking simulation, only 543 compounds bind to the pharmacophore point in the binding pocket. Then, the second molecular docking simulation produced only 282 compounds that bind to the pharmacophore point. Only 77 compounds fulfilled the RMSD lower than 2.0. The $\Delta G_{\text{binding}}$, the number of a hydrogen bond between the ligand and the protein, and the position

of the fragment in the binding site were determined to choose the best fragments (Table 1).

Preparation of Natural Product Ligands

The fragment merging was performed by deploying MOE 2014.09. The fragments were connected to the part of the lead compound (SAH) by building a bond and replace the overlap part. New ligands were generated based on Lipinski's Rule of Five (RO5) and Veber rule). Molecular weight lower than 500 Da, TPSA lower than 140, and logP between -0.5 and 5.6, number of hydrogen donor no more than 5, and number of hydrogen acceptor no more than 10 [25]. The produced ligands must undergo the ADME-TOX screening following druglikeness, and toxicity prediction test (carcinogenic, mutagenic, irritant, and reproductive effect risks). A total of 9 ligands generated from this process. The best ligands through this process were shown in Fig. 2.

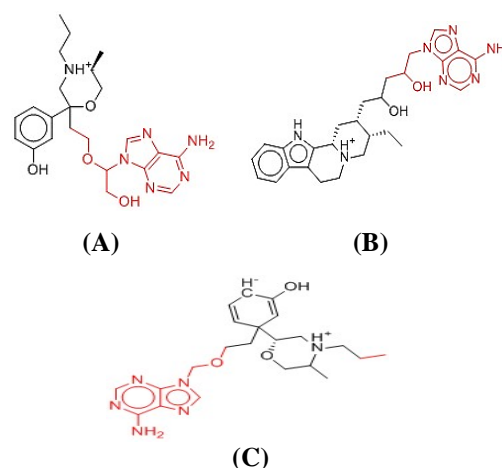


Fig. 2. The Selected Fragments and the merging position (A) MAHI1. (B) MAHI2. (C) MAHI3. The red color is the part of lead compounds, and the black color is the fragment.

Analysis of Molecular Docking Simulation of DNMT1 Protein and The Ligands

Nine ligands and standards underwent molecular docking simulation using MOE 2014.09. 'Rigid Receptor' protocol was used for first and second simulation with the retain of 1 and 30 repetitions, respectively. In the first step, only 7 ligands bind to the site and have RMSD value lower than 2.0. Only six ligands have potential properties such as $\Delta G_{\text{binding}}$ lower than standard. The six ligands were docked with 'Induced Fit' protocol, and retain the value of 100. The most potential ligands were obtained by examining the molecular interaction of the ligands with the binding pocket of DNMT1. The result of the best three ligands along with the standards from

flexible molecular docking simulation is shown in Table 2.

Table 1. List of the best natural product fragments

No	Compound Name	logP	TPSA	Weight	H-Acc	H-Don
1	2-hydroxy-1-methoxy-5,6,6a,7-tetrahydro-4H-dibenzo[de,g]guinolin-6-ium	2.69	46.07	268.34	3	2
2	2-(3-hydroxyphenyl)-4-propylmorpholin-4-um	-0.25	33.90	222.31	3	2
3	2-(3-hydroxyphenyl)-5-methyl-4-propylmorpholin-4-ium	0.08	33.90	236.33	3	2
4	(Z)-1-((1-hydroxy-2-methylbutylidene)amino)octahydropyrrolizin-4-ium	-0.47	37.03	211.33	3	2
5	1-(hydroxymethyl)octahydropyrrolizin-4-ium	1.26	40.46	299.44	3	3
6	(E)-1,3-bis(2-hydroxyphenyl)prop-2-en-1-one	2.61	57.53	240.26	3	2
7	(E)-1-(2-hydroxyphenyl)-3-phenylprop-2-en-1-one	2.96	37.30	224.26	2	1

Table 2. The $\Delta G_{\text{binding}}$, RMSD value, and molecular properties of ligands

Ligand	$\Delta G_{\text{binding}}$	RMSD	logP	TPSA	Weight	H-Acc	H-Don
MAHI1	-12.6301	0.4025	-0.49	132.98	457.55	10	4
MAHI2	-12.7872	1.6431	0.57	130.31	490.63	9	5
MAHI3	-11.6353	1.0117	-0.46	112.15	428.54	9	3
SAM*	-11.2605	1.3306	-3.94	187.08	399.45	11	4
SAH*	-11.2323	1.8644	-3.73	212.38	384.47	11	4
SFG*	-10.9262	1.6747	-3.96	214.72	382.40	12	5

Note: *Standard Ligand

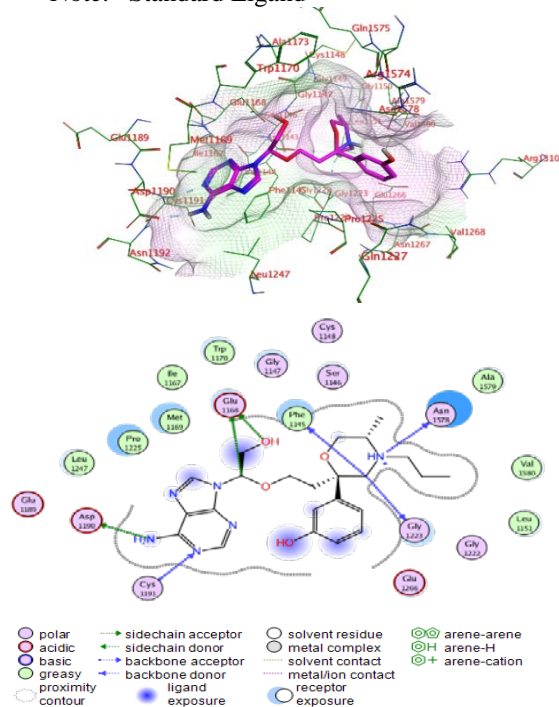


Fig. 3. Interaction of SAMI1 ligand with Amino acid residue (A) in 3D and (B) in 2D visualization

As the best ligand, MAHI1 has the lower $\Delta G_{\text{binding}}$ value than standards and have bound on the best position in the binding site. As shown in Fig. 3, MAHI1 has 20 interaction with the amino acids

residue in the binding site. Seven hydrogen bonds are binding the ligands in the pocket binding such as Asp1190, Cys1191, Gly1223, Phe1145, Asn1578, and Glu1168.

Analysis of Molecular Docking Simulation of DNMT1 Protein and The Ligands

The ADME-Tox analysis of the best ligands that have been obtained from the molecular docking simulation was performed by employing admeSAR [26], and SwissADME [27] software. Determining the pharmacological properties is essential because not all of the best ligands may be ready to prepare as drug candidates due to its toxicity and low ADME properties that may reduce the efficiency of the ligands to served as a drug in the human body. The result of the ADME-Tox analysis using admeSAR and SwissADME is shown in Table 3. The gastrointestinal (GI) absorption and Cytochrome P450 (CYP) inhibitors parameters were analyzed using SwissADME software, and the subcellular localization, organic cation transporter, AMES toxicity, carcinogens, and biodegradation parameters were checked using the admetSAR software. Two of the best ligands had subcellular localization in lysosome and one of these in the nucleus. The ADME-Tox properties should be same for all of the best ligands. Besides, standard ligands have several bad ADME-Tox properties. For example, SFG has low GI absorption compared to other ligands.

The druglikeness and the medicinal chemistry properties of the best and standard ligands were obtained by using SwissAdme software. The druglikeness based on Veber's and Egan's rule was determined, and the bioavailability value was obtained. Furthermore, the PAINS (Pan-assay interference compounds), Brenk, and synthetic accessibility value were also predicted. The result is shown in Table 4. Based on this test, all of the best ligands have good druglikeness according to both Veber's and Egan's Rule. All of ligands shown the

same bioavailability value (0.55). According to the result of analysis from SwissADME software, the bioavailability of all the best ligands was at similar level. The synthetic accessibility score of the ligands was relatively the same as well, varying such as 4.82 (MAHI1). Furthermore, MAHI1 and MAHI3 were not determined to have any Brenk fragments. However, some of the best ligands were obtained to have one molecular fragment that contains PAINS property. In addition, MAHI1 were not predicted to have PAINS property.

Table 3. ADME-Tox prediction using admetSAR and SwissADME software

Ligand	GI Absorption	Subcellular Localization	CYP Inhibitor	Organic Cation Transporter (SLC22A2)	AMES toxicity	Carcinogens	Biodegradation
MAHI1	High	Lysosome	None	Non-inhibitor	No	No	No
MAHI2	High	Lysosome	None	Non-inhibitor	No	No	No
MAHI3	High	Nucleus	None	Non-inhibitor	No	No	No
SAM*	High	Nucleus	None	Non-inhibitor	No	No	No
SAH*	High	Nucleus	None	Non-inhibitor	No	No	No
SFG*	Low	Nucleus	None	Non-inhibitor	No	No	No

Table 4. The druglikeness and medicinal chemistry properties of selected and standards compounds using SwissADME software

Ligand	Druglikeness			Medicinal Chemistry		
	Veber	Egan	Bioavailability score	PAINS	Brenk	Synthetic accessibility
MAHI1	Yes	Yes	0.55	0 alert	0 alert	4.82
MAHI2	Yes	Yes	0.55	1 alert	0 alert	5.13
MAHI3	Yes	Yes	0.55	0 alert	1 alert	5.05
SAM*	No	No	0.55	1 alert	1 alert	4.94
SAH*	No	No	0.55	0 alert	0 alert	4.69
SFG*	No	No	0.55	0 alert	0 alert	4.78

Note: *Standard Ligand

CONCLUSION

MAHI1, MAHI2, and MAHI3 have lower $\Delta G_{\text{binding}}$ energy and better interaction with DNMT1. After all process, the selected ligands MAHI1 shows the best conformation and interaction in the binding site of DNMT1 and have better ADME-Tox properties than all the ligands. The result indicates that fragment-based drug design can be an essential method to discovered in developing a new drug for inhibiting the DNMT1. Finally, our result must be examined through *in vitro* and *in vivo* methods to determine its potential in the biological condition.

ACKNOWLEDGEMENTS

This research is financially supported by the Directorate of Research and Community Engagement of Universitas Indonesia (DRPM UI) through Hibah

Publikasi Internasional Terindeks Untuk Tugas Akhir Mahasiswa (PITTA) UI No: 2328/UN2.R3.1/HKP.05.00/2018 All authors were responsible in writing of the manuscript. Herewith, the authors declare that there is no conflict of interest regarding of the manuscript.

REFERENCES

- [1] Siegel R. L., Miller K. D., Jemal A., Cáncer Statistics. Ca Cáncer J, Vol. 67, Issue. 1, 2017, pp. 7–30.
- [2] Ghoncheh M., Pournamdar Z., and Salehiniya H., Incidence and Mortality and Epidemiology of Breast Cancer in the World. Asian Pac. J. Cancer Prev, Vol. 17, Special Issue, 2016, pp. 43–46.
- [3] World cancer Research Fund., Breast cancer statistics | World Cancer Research Fund

- International.
- [4] Lyko F., The DNA methyltransferase Family: A Versatile Toolkit for Epigenetic Regulation. *Nature Reviews Genetics*, Vol. 19, Issue 2, 2018, pp. 81-92
- [5] Miletic V., Odorcic I., Nikolic P., and Svedruzic M. Z., In Silico Design of The First DNA-Independent Mechanism-based Inhibitor of Mammalian DNA methyltransferase DNMT1. *PLoS One*, Vol. 12, Issue 4, 2017, pp. 1-21.
- [6] Subramaniam D., Thombre R., Dhar A., and Anant S., DNA Methyltransferases: A Novel Target for Prevention and Therapy. *Front. Oncol.*, Vol. 4, Issue May, 2014, pp. 1-13.
- [7] Mirza S., Sharma G., Parshad R., Gupta S. D., Pandya P., and Ralhan R., Expression of DNA methyltransferases in Breast Cancer Patients and to Analyze The Effect of Natural Compounds on DNA methyltransferases and Associated Proteins. *J. Breast Cancer*, Vol. 16, Issue 1, 2013, pp. 23-31.
- [8] Agrawal A., Murphy R. F., and Agrawal D. K., DNA methylation in Breast and Colorectal Cancers. *Modern Pathology*, Vol. 20, Issue 7, 2007, pp. 711-721.
- [9] Maldonado-Rojas W., Olivero-Verbel J., and Marrero-Ponce Y., Computational Fishing of New DNA methyltransferase Inhibitors from Natural Products. *J. Mol. Graph. Model*, Vol. 60, Issue July, 2015, pp. 43-54.
- [10] Cragg G. M., Newman D. J., and Snader K. M., Natural Products in Drug Discovery and Development. *Journal of Natural Product*, Vol. 60, Issue 1, 1997, pp. 52-60.
- [11] Scoffin R., and Slater M., The Virtual Elaboration of Fragment Ideas: Growing, Merging and Linking Fragments with Realistic Chemistry. *Drug Discovery, Development & Delivery*, Vol. 7, Issue 2, 2015, pp. 2-5.
- [12] Scott D. E., Coyne A. G., Hudson S. A., and Abell C., Fragment Based Approaches in Drug Discovery and Chemical Biology. *Biochemistry*, Vol. 51, Issue 25, 2012, pp. 4990-5003.
- [13] Kelly K., Multiple Sequence and Structure Alignment in MOE. *Chemical Computing Group ULC*, 2018.
- [14] Maiti R., Domselaar G. H. V., Zhang H., and Wishart D. S., SuperPose: A Simple Server for Sophisticated Structural Superposition. *Nucleic Acids Res*, Vol. 32, Issue Web Server, 2004 pp. 590-594.
- [15] Medina-Franco J. L., and Caulfield T., Advances in The Computational Development of DNA methyltransferase Inhibitors. *Drug Discov. Today*, Vol. 16, Issue 9-10, 2011, pp. 418-425.
- [16] Tambunan U. S. F., Alkaff A. M., Nasution M. A. F., Parikesit A. A., and Kerami J., Screening of Commercial Cyclic Peptide Conjugated to HIV-1 Tat peptide as Inhibitor of N-terminal Heptad Repeat Glycoprotein Ectodomain Ebola Virus Through In Silico Analysis. *J. Mol. Graph. Model*, Vol. 74, Issue -, 2017, pp. 1-7.
- [17] Labute P., MOE Forcefield Facilities. *Chemical Computing Group Inc*, Vol. -, Issue -, 1997.
- [18] Taylor R. D., Jewsbury P. J., and Essex J. W., A Review of Protein-small Molecule Docking Methods. *J. Comput. Aided. Mol.*, Vol. 16, Issue 3, 2002, pp. 151-166.
- [19] Da C., and Kireev D., Structural Protein - Ligand Interaction Fingerprints (SPLIF) for Structure-Based Virtual Screening: Method and Benchmark Study. *Chem. Inf. Model*, Vol. 54, Issue -, 2015, pp. 2555-2561.
- [20] Krishna S., Shukla S., Lakra A. D., Meeran S. M., and Siddiqi M. I., Identification of Potent Inhibitors of DNA methyltransferase 1 (DNMT1) Through A Pharmacophore-based Virtual Screening Approach. *J. Mol. Graph. Model.*, vol. 75, 2017, pp. 174-188.
- [21] Rees C. D., Congreve M., Murray C. W., and Carr R., Fragment-Based Lead Discovery. *Nat. Drug Discov*, Vol. 3, Issue August, 2004, pp. 660-672.
- [22] Veber D. F., Johnson S. R., Cheng H. Y., Smith B. R., Ward K. W., and Kopple K. D., Molecular Properties That Influence The Oral Bioavailability of Drug Candidates. *Journal of Medicinal Chemistry*, Vol. 45, 2002, pp. 2615-2623.
- [23] Ferreira L. G., Santos R. N., Oliva G., and Andricopulo A. D., Molecular Docking and Structure-Based Drug Design Strategies. *Molecules*, Vol. 20, Issue 7, 2015, pp. 13384-13421.
- [24] Tripathi A., and Misra K., Molecular Docking: A Structure- Based Drug Designing Approach *JSM Chem*, Vol. 5, Issue 2, 2017, pp. 1042.
- [25] Lipinski C. A., Lead Profiling Lead and Drug-Like Compounds: The Rule of Five Revolution. *Drug Discov. Today Technol.*, Vol. 1, Issue 4, 2004, pp. 337-341.
- [26] Cheng F., Li W., Zhou Y., Shen J., Wu Z., Liu G., Lee P. W., and Tang Y., AdmetSAR: A Comprehensive Source and Free Tool for Assessment of Chemical ADMET properties. *J. Chem. Inf. Model*, Vol. 52, Issue 11, 2012, pp. 3099-3105.
- [27] Daina A., Michielin O., and Zoete V., SwissADME: A Free Web Tool to Evaluate Pharmacokinetics, Drug-likeness and Medicinal Chemistry Friendliness of Small Molecules. *Sci. Rep*, Vol. 7, Issue October 2016, 2017, pp. 1-13.

NITRIDING OF PURE TITANIUM BY HIGH DENSITY PLASMA USING H₂-N₂ GAS MIXTURE AT LOW TEMPERATURE

Dionysius J. D. H. Santjojo ¹, Masruroh ¹, Setyawan P. Sakti ¹, Maharani S. Rajapadni

¹Department of Physics, FMIPA, Brawijaya University, Malang, 65145, Indonesia

ABSTRACT

Most plasma nitriding of titanium was successfully carried out at the temperature higher than 500 °C. A lower temperature process is needed to save energy. The experiment was carried out by varying the substrate temperature from 350 to 450 °C. The plasma was generated in a vacuum chamber by a 2 MHz RF power supply. A gas mixture of nitrogen and hydrogen was introduced into the chamber resulted in a significantly effective nitriding of the titanium. The plasma was intensified to a higher density by utilizing a combination of DC bias technique and a hollow cathode. At the optimum mixture of 80% N₂ and 20% H₂, by the pressure of 35 Pa, a four-hour nitriding resulted in 20 µm nitrided layer. The hardness of the treated surface was varied between 550 and 1990 HV depending on the process temperature. XRD measurements showed that the nitriding leads to the formation of Ti₂N and TiN precipitates. Expansion of the original hcp-structured lattices was also noticed. The hardening was a result of a lattice straining induced by the precipitates and also a possible small percentage of nitrogen solid-solution.

Keywords: Plasma nitriding, High density plasma, Low temperature, Titanium, Hardening

INTRODUCTION

Titanium has been tremendously the interest in many fields of applications, such as aerospace [1], automobile industries [2], home appliances, and medical implants [3]. The metal is lightweight and yet performs high mechanical performances. It has high stability at high temperature and high corrosion resistance. Alloying the titanium with other metals such as aluminum, vanadium and molybdenum produces a wider range of application [4].

However, the drawback of the utilization of the titanium is due to its poor tribological properties, i.e., low surface hardness, low wear resistance and high friction coefficient. It is important to enhance the tribological properties so that even wider utilization is possible in the future. The enhancement should also consider the durability and usage life especially when frictions cannot be avoided [5].

There have been many efforts to enhance the tribological properties of pure titanium by surface modifications such as nitriding process. It is well known that the nitriding process can increase the surface hardness and hence the wear resistance of metals [6]. From the history of titanium nitriding, it has been learned that the metal can be hardened effectively by incorporating the nitrogen into the hcp structured or the α -phase. A number of methods and techniques have been proposed such as a gas nitriding by a nitrogen thermo-diffusional treatment [7] or depositing a layer of nitride by physical vapor deposition (PVD) [8].

Recently, a plasma nitriding is utilized to modify the titanium's surface. It is a common nitriding

method which has been established for metals [9]. The method has proven itself to be efficient due to its shorter process time and reduction of gas usage. In addition, it is an environmentally friendly process [10]. Other advantages of the plasma nitriding come from its flexibility for selective nitriding and high possibility to be implemented in industrial scale.

A study of the plasma nitriding for a titanium alloy Ti6Al4V, show that the process carried out at a temperature of 1000 °C for 10 hours was able to increase the hardness up to 1365 HV [11]. Another researcher successfully hardened a Ti5Al4V2Mo titanium alloy by plasma nitriding at 1173 K for 4 hours. The surface hardness was 1.7 times higher than the original hardness. The thickness of the nitrided layer was 30 µm containing nitride precipitates [12]. Researchers found that the increase of the surface hardness in the plasma nitriding was caused by the increase of nitrogen concentration in the surface and subsurface in the form of a solid solution and TiN [13]. Despite the many advantages of the plasma nitriding technique, the high temperature thermo-chemical process for titanium may cause degradation of fatigue strength and a detrimental of microstructural changes in titanium substrates [14].

Further advancements of the technique should be undertaken to reduce the holding temperature during the process which can minimize the degradation of the fatigue strength and the microstructural deterioration. The low temperature process is also desirable for reducing the usage of energy.

This work was focused on the plasma treatment of pure titanium to gain fundamental knowledge of an

alternative high density plasma utilized for surface hardening. Other researchers reported that at a relatively low holding temperature of 500 °C, the hardening was controlled by the nitrogen solid solution. On the other hand, at higher holding temperature the hardening was also affected by the formation of TiN and Ti₂N precipitates [15]. The application of the alternative high density plasma was intended to compensate the lower holding temperature. A combination of a DC bias voltage and a hollow cathode was employed to produce the high density nitrogen plasma. Other than the combination, the previous study has shown that incorporation of a small amount of hydrogen in the nitrogen plasma produced active nitrogen species in the plasma which resulted in highly effective nitriding [16]. The amount of the hydrogen inclusion was determined by means of optical emission spectroscopy (OES) and Langmuir impedance measurement. It was found that the appropriate concentration of the hydrogen to be around 17%. The ratio resulted in nitrogen plasma containing a large density of N₂^{*}, N₂⁺ and NH complexes behaving as positively charged species. The species are chemically active and are able to produce a high concentration of high energy atomic nitrogen which diffuses into the metal uniformly via complex surface reactions.

EXPERIMENTS

A high density nitrogen plasma reactor was utilized to achieve the successful low temperature nitriding. The reactor consists of a vacuum chamber, an RF generator a high voltage DC generator. The nitrogen plasma was generated by applying the RF generator on the two floating electrodes (anodes) in the chamber. The base frequency of the RF was 2 MHz. The reflected power was minimized by an electronic matching system shifting the frequency around the base. A high DC voltage was applied to a cathode to accelerate ions toward it. The application of the DC bias increased the density of the plasma in the cathode area [6]. Further enhancement of the plasma density was achieved by setting up a hollow rectangular metal tube on the cathode. Due to the electrical connection, the tube functioned as a hollow cathode. The cathode assembly was equipped with a controlled heater providing a constant temperature. The system is described in Figure 1.

Samples for this study was obtained from a 1 mm thick pure titanium (Industrial Grade I) sheet which was cut into 20 x 20 mm rectangular pieces. A cleaning procedure was applied including alkaline degreasing and ultrasonic cleaning. After a drying process, the sample was immediately loaded into the plasma reactor by placing it in the hollow cathode as seen in Figure 1.

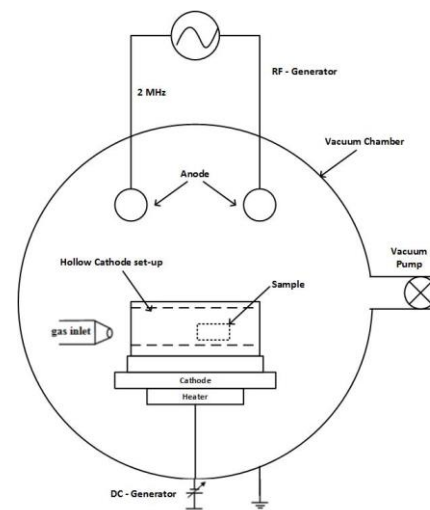


Fig. 1 A schematic representation of the hollow cathode plasma nitriding system.

After the loading procedure, the chamber was pumped down to 0.5 Pa to evacuate the air. The heater was then turned on to increase the substrate temperature to the process temperature, i.e., 350, 375, 400, 425 or 450 °C. Before the main plasma treatment process, the samples underwent a pre-treatment for 1 hour. The pre-treatment process was carried out by applying a 100% nitrogen plasma at the process temperature and at the chamber pressure of 70 Pa. The RF and DC bias voltage during the pre-treatment process was 250 and 500 volts respectively. The main plasma nitriding treatment was carried out immediately at a lower pressure of 35 Pa with a mixture of 80% N₂ and 20% H₂ for 4 hours. The RF and DC bias voltage during the main process was 250 and 600 volts respectively.

Surface hardness characterization of the specimens was carried out using a Vickers micro-hardness testing system (Akashi MVK-H1). The measurement was taken at five different points on every specimen with the applied load of 1N or 100 gfs. Cross-sectional hardness measurements were conducted to obtain a hardness depth profile characteristic of the specimens. The measurements were taken at points having the distance of 10, 20, 30, 40, 50 and 60 μm from the surface. Accompanying the depth profiling measurement, cross-sectional micrograph observations were conducted by using a scanning electron microscope (JEOL JSM-7100 F).

An X-ray diffractometer (XRD, Rigaku SmartLab) was utilized to identify the crystallographic phases of the specimens. The observation was carried out under a monochromated Cu Kα radiation with $\lambda = 1.54598 \text{ \AA}$ at a range of diffraction angle of 30 to 90 degrees with a step angle of 0.010 degrees.

RESULTS AND DISCUSSIONS

The high density nitrogen plasma treatment by the application of a combination of DC bias voltage and a hollow cathode resulted in an effective hardening of pure titanium. The original hardness of the titanium was 319.4 HV. Depending on the sample temperature during the plasma treatment, the surface hardness was increased up to 1989 HV (at 450 °C). Measurement of the hardness on the cross-sectional surface revealed the depth hardness profile due to the plasma treatment as shown in Figure 2.

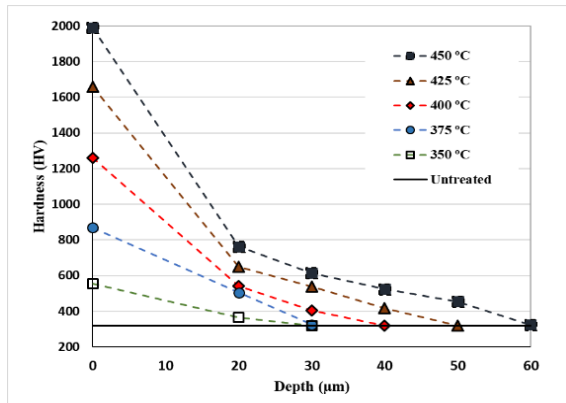


Fig. 2 Hardness depth profile of pure titanium specimens treated with the high density plasma at various temperature for 4 hours.

It can be seen from the Figure 2, the hardness profile shows preservation of a relatively high hardness to the deep and abruptly decrease at around 20 μm depth. The SEM micrographic observation confirmed that the profile is related to the nitrogen distribution in the nitriding area. Figure 3 shows a relational illustration of the SEM micrograph and the hardness depth profile measurement.

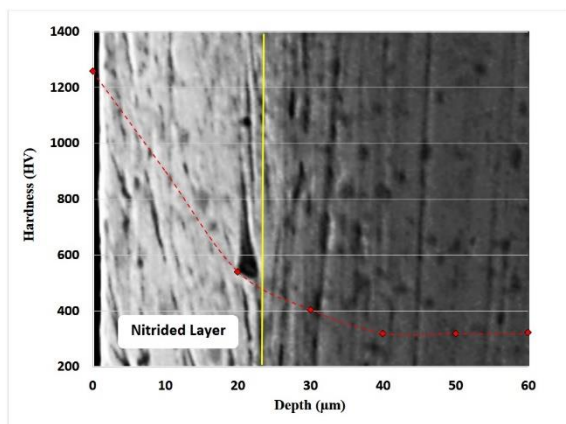


Fig. 3 SEM micrograph observation related to the hardness depth profile of pure titanium specimen treated with the high density plasma at a temperature of 400 °C for 4 hours.

The SEM image shows a whitish area indicated the existence of a nitrided layer reaching the depth of 23 μm . The thicker layer was observed on the specimen treated at higher holding temperature.

Further study was carried out by examining the change of the titanium phase before and after the treatment by means of XRD measurements as shown in Figure 4.

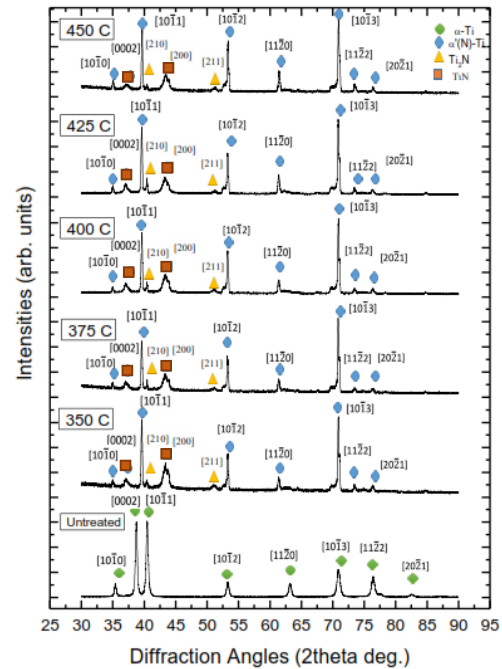


Fig. 4 X-ray diffractogram of untreated and plasma treated specimens.

Pure titanium used in this work has an ideally hexagonal close packed (hcp) structure. This untreated α -titanium can be confirmed by the peaks shown in Figure 4 which match the database for the pure titanium (α -Ti). In the plasma treated specimens, some of these line peaks are shifted to the lower angles. The shift of the peak indicates the occurrence of lattice straining of the α -Ti due to the interstitial nitrogen resulted in α' (N)-Ti. The expansion can be observed from the shift of peak at 40.5 degree toward 39.5 degree. The peak is assigned to $[10\bar{1}1]$ plane as seen in Figure 5.

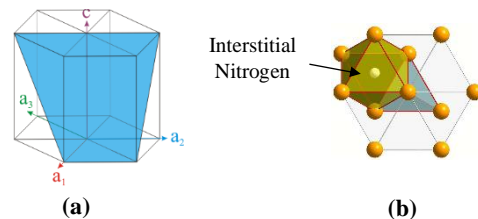


Fig. 5 Illustration of: (a) the $[10\bar{1}1]$ plane in the hcp structure; and (b) interstitial nitrogen residing at the octahedral vacancy site.

The solid solution interstitial nitrogen can reside at either octahedral or tetrahedral site in the hcp structure. However, the expansion of the $[10\bar{1}1]$ plane indicated that the interstitial nitrogen prefers the octahedral vacancy sites (Figure 5). The radius of nitrogen solute or r_N is 0.92 Å, while the size of the octahedral r_o and tetrahedral r_T vacancy sites are = 0.6 Å and 0.33 Å respectively. The relative available space size of the vacancy and the replacement solute size determine the possibility of site occupation for the solute to vacancy [17]. Generally, the wider size of octahedral vacancy site is preferable for the nitrogen solute occupation in the localization process. Since the $r_N > r_o$, the occupation of the nitrogen is accompanied with lattice expansions, especially in the c-axis.

Other than the shift, new peaks were observed in the diffractogram of the treated specimens. The peaks are related to the phase of TiN and Ti₂N. The peak at 37.15 and 43.4 degree are related to the TiN diffraction plane, while the Ti₂N phase was indicated by the peaks at 51.3 degree and 40.3 which overlap with the previous $[10\bar{1}1]$ plane reflection. The previous study suggested a possibility of the occurrence of a phase transformation from α -Ti to ω -Ti which was indicated by the peak at 37.15 degree [18]. However, the transformation should include the β -Ti which was not observed in the diffractogram. This is due to the plasma treatment process was conducted far below the α to β transformation temperature, i.e., 1156 K (883°C) [15]. The effect of the holding temperature during the plasma nitriding on the lattice straining is summarized in Table 1.

Table 1 The effect of holding temperature during plasma nitriding process on lattice straining

Nitriding Temp. (°C)	α -Ti phase			Lattice Straining (%)
	a (Å)	c (Å)	c/a	
Unprocessed	2.9421	4.6703	1.5874	-
350	2.9642	4.8669	1.6419	4.21
375	2.9658	4.8681	1.6414	4.24
400	2.9658	4.8694	1.6419	4.26
425	2.9658	4.8707	1.6423	4.29
450	2.9658	4.8719	1.6427	4.32

It can be seen from the table, the plasma nitriding treatment resulted in lattice strains. However, the expansion was anisotropic since the crystalline strains in the c-axis is larger than those in the a-axis. The straining in the a-axis was not changed at the temperature above 375 °C. On the other hand, the straining in the c-axis continues to grow with the increase of the holding temperature. The relation between the lattice straining in c-axis and the

hardening as a function of the holding temperature is shown in Figure 6.

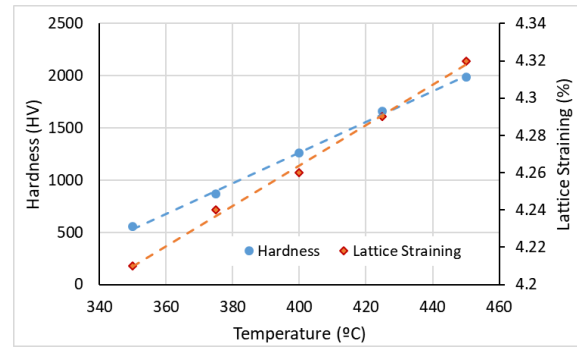


Fig. 6 Illustration of: (a) the $[10\bar{1}1]$ plane in the hcp structure; and (b) interstitial nitrogen residing at the octahedral vacancy site.

The hardening was evidently controlled by the lattice straining. In this low temperature process, the nitrogen diffuse into the α -Ti matrix forming fine precipitation of TiN and Ti₂N and also the interstitial solid solution, i.e., $\alpha'(N)$ -Ti. The combination of the three phases was varied with the change of the holding temperature. In the high temperature nitriding, the hardening was strongly controlled by both the precipitation reaction and also the α to β phase transformation [11], [14]. Closely observation on the peak at 43.4 degree for the $[200]$ plane of the TiN and 61.5 degree for the $[11\bar{2}0]$ plane of the $\alpha'(N)$ -Ti in Figure 4 reveals that the increase of the increase of the holding temperature decrease the TiN population. At the same time, the intensity of the $\alpha'(N)$ -Ti was increased. This indicates that the formation of the solid solution phase was related to nitrogen super-saturation state in the hcp structure. The hardening of the pure titanium by means of the low temperature nitriding is strongly affected by the presence of the interstitial nitrogen in the hcp structure.

CONCLUSION

The high density plasma nitriding using a mixture of 80% nitrogen and 20% has effectively hardened the pure titanium at low temperature. The nitrogen diffused deep into the α -Ti matrix forming TiN, Ti₂N and $\alpha'(N)$ -Ti phases. A nitrided layer with the thickness of 30 μ m was obtained with the holding temperature of 425 °C resulted in surface hardness of 1696 HV. The hardness of the surface reached 1989 HV after the nitriding with the temperature of 450 °C.

The nitrided layer was anisotropically strained in the c-axis. The lattice straining which was noticeably increased with the increase of the increase of the

α' (N)-Ti phases. The nitrogen solid solution resides at the octahedral vacancy sites. Although the high hardness is usually attributed to fine precipitation of Ti₂N and TiN, evidently the existence of nitrogen super-saturation in the α -Ti lattices greatly affect the hardness.

Further study of the diffusion and the formation of phases related to the high density nitrogen plasma will open new possibilities in hardening titanium and its alloy efficiently.

ACKNOWLEDGMENTS

The authors would like to express their gratitude to Prof. Tatsuhiko Aizawa of Shibaura Institute of Technology, Japan for the long-life research and development collaboration especially in the field of surface modification. This study is managed by Collaborative Research Center for Advanced System and Material Technology (Brawijaya University) and partly supported by JSPS-DGHE program on the international collaborative research in 2017.

REFERENCES

- [1] X. Zhang, Y. Chen, and J. Hu, "Recent advances in the development of aerospace materials," *Prog. Aerosp. Sci.*, vol. 97, no. August 2017, pp. 35–60, 2018.
- [2] S. Yadav, S. Gangwar, and S. Singh, "Micro/Nano Reinforced Filled Metal Alloy Composites: A Review over Current Development in Aerospace and Automobile Applications," *Mater. Today Proc.*, vol. 4, no. 4, pp. 5571–5582, 2017.
- [3] M. Kaczmarek et al., "In vitro biocompatibility of titanium after plasma surface alloying with boron," *Mater. Sci. Eng. C*, vol. 69, pp. 1240–1247, 2016.
- [4] C. Veiga, J. P. Devim, and A. J. R. Loureiro, "Properties and applications of titanium alloys: a brief review," *Rev. Adv. Mater. Sci.*, vol. 32, no. 2, pp. 133–148, 2012.
- [5] Y. Yang, C. Zhang, Y. Dai, and J. Luo, "Tribological properties of titanium alloys under lubrication of SEE oil and aqueous solutions," *Tribol. Int.*, vol. 109, no. November 2016, pp. 40–47, 2017.
- [6] D. Santjojo, T. Aizawa, S. Muraishi, and H. Morita, "Micro-Texturing of Stainless Steels Via High Density Plasma Nitriding," in *Proceedings of the 9th International Conference on MicroManufacturing*, 2014.
- [7] D. B. Lee, I. Pohrelyuk, O. Yaskiv, and J. C. Lee, "Gas nitriding and subsequent oxidation of Ti-6Al-4V alloys," *Nanoscale Res. Lett.*, vol. 7, no. 1, p. 21, 2012.
- [8] S. H. N. Lim, D. G. McCulloh, S. Russo, M. M. M. Bilek, and D. R. McKenzie, "Characterisation of titanium nitride thin films prepared using PVD and a plasma immersion ion implantation system," *Nucl. Instruments Methods Phys. Res. B*, vol. 190, pp. 723–727, 2002.
- [9] Istiroyah, I. N. G. Wardana, and D. J. Santjojo, "Comparison of AISI 316L plasma nitriding behavior in low and medium temperature," vol. 493, 2014.
- [10] L. Han, J. T. Dai, X. R. Huang, and C. Zhao, "Study on the fast nitriding process of active screen plasma nitriding," *Phys. Procedia*, vol. 50, no. October 2012, pp. 94–102, 2013.
- [11] E. Koyuncu, F. Kahraman, and Ö. Karadeniz, "Investigation of surface properties of high temperature nitrided titanium alloys," *J. Achiev. Mater. Manuf. Eng.*, vol. 37, no. 2, pp. 434–441, 2009.
- [12] Y. V. Borisyuk, N. M. Oreshnikova, M. A. Berdnikova, A. V. Tumarkin, G. V. Khodachenko, and A. A. Pisarev, "Plasma nitriding of titanium alloy Ti5Al4V2Mo," *Phys. Procedia*, vol. 71, no. February, pp. 105–109, 2015.
- [13] A. Samanta et al., "Nano- and micro-tribological behaviours of plasma nitrided Ti6Al4V alloys," *J. Mech. Behav. Biomed. Mater.*, vol. 77, no. August 2017, pp. 267–294, 2018.
- [14] H. Yilmazer, S. Yilmaz, and M. E. Acma, "Treatment of Surface Properties of Titanium with Plasma (Ion) Nitriding," *Defect Diffus. Forum*, vol. 283–286, no. March, pp. 401–405, 2009.
- [15] A. Zhecheva, W. Sha, S. Malinov, and A. Long, "Enhancing the microstructure and properties of titanium alloys through nitriding and other surface engineering methods," *Surf. Coatings Technol.*, vol. 200, no. 7, pp. 2192–2207, 2005.
- [16] D. J. Santjojo, T. Aizawa, and Istiroyah, "THE ROLE OF HYDROGEN IN HIGH RATE PLASMA NITRIDING OF MARTENSITE STAINLESS STEEL," in *4th Asian Symposium on Materials and Processing*, 2015, vol. 2, pp. 3–4.
- [17] A. Gicquel, N. Laidani, and P. Saillard, "Plasma and nitrides: application to the nitriding of titanium," *Pure Appl. Chem.*, vol. 62, no. 9, pp. 1743–1750, 1990.
- [18] J. M. Windajanti, D. J. Djoko H S, and Abdurrouf, "Low-Temperature Nitriding of Pure Titanium by using Hollow Cathode RF-DC Plasma," *IOP Conf. Ser. Mater. Sci. Eng.*, vol. 202, no. 012026, 2017.

OPTICAL EMISSION SPECTROSCOPY STUDIES DURING NITROGEN PLASMA OF POLYSTYRENE SURFACES MODIFICATION

Masruroh^{1*}, Dionysius J. D. H. Santjojo¹, Heraniawati¹, Muhamad A. Abdillah¹, Tyas N Zafirah¹ and Eka Maulana², Setyawan P. Sakti¹

¹Department of Physics, FMIPA, Brawijaya University, Malang, 65145, Indonesia

²Department of Electrical Engineering, Brawijaya University, Malang, 65145, Indonesia

*corresponding author: Masruroh, email: ruroh@ub.ac.id

ABSTRACT

Nitrogen plasma treatment was successfully performed to modify polystyrene surfaces from hydrophobic into hydrophilic. The objective of the work was to achieve better wettability of the polystyrene surfaces. Various surface characters of the polystyrene were obtained by synthesising the polystyrene layer from different molecular weight (Mw) solution using a spin coating method. The solution prepared for the coating procedure was made by dissolving monomers which have Mw of 35,000 g/mol, 192,000 g/mol, and 280,000 g/mol into toluene solvent at the concentration of 6%. The polystyrene surfaces then treated by means of the nitrogen plasma using a 2MHz plasma generator with the power of 40 watts and the gas flow of 20 ml/minutes for 2 minutes. The optical emission spectroscopy (OES) provided the measurement of plasma species and the calculated electron temperature (T_e) and electron density (n_e). The species N_2^+ ion was identified from the intensity emission of OES. The existence of the N_2^+ ion and corresponding to the condition of T_e and n_e in the plasma plays a key role in the polystyrene's surface changes as found in the polystyrene surface after plasma treatment. After plasma treatment, nitrile functional group ($C\equiv N$) was found in the polystyrene surface which is indicated by the FTIR fingerprint of the nitrile functional group at the vibration peak of 2300-2400 cm^{-1} . The existence of the $C\equiv N$ represent the surface changed from hydrophobic to hydrophilic. This result was in agreement with a lower contact angle of the polystyrene surface.

Keywords: Nitrogen Plasma, N_2^+ ion, OES, nitrile and polystyrene

INTRODUCTION

Plasma-based approach has gained considerable popularity for modifying interfacial polymers to enhance bondings with subsequent molecular immobilization layer designed to contact with specific biological responses [1]. This is because the plasma has the ability to change physical and chemical properties of surfaces without affecting bulk properties [2]. In addition, this method also requires a shorter treatment time compared to other surface modification methods. When the plasma is exposed to polymer surfaces, formation of new functional group, graft polymerization, coating, and molecular crosslink is occurred [2]. In general, modification using plasma will increase the surface energy and cause the surface of the polymer increasingly hydrophilic [3]. Modification of polymers using a plasma nitrogen can also cause the formation of polar groups such as amine, imine, amide, and nitrile on the polymer surface [4]. The presence of such functional groups is due to the chemical interactions between the plasma species (ions, electrons, neutrals, and radicals) with the polymer chains.

Optical Emission Spectroscopy (OES) in UV-vis regions is a method that can be used to diagnose plasma as non-invasive and *in situ* method. Since most of the plasma is generated in a vacuum chamber, the OES system measure the emission via an optical fiber attached to the chamber. These emissions are the result of the particle de-excitation [5]. It provides valuable information such as electron temperature, ion density, and electron density. Where the data are presented in the form of line-ratio. That is, each line spectrum shows an optical transition between two levels of quantum energy [6].

Polymeric materials are widely used in many applications due to their mechanical properties (including flexibility) of thermal conductivity, transparency, chemical inertia, etc. However, some applications require certain surface properties (wettability, adhesion, biocompatibility), which can be achieved by plasma treatment [7, 8]. Polystyrene (PS) is one of the most widely used materials for applications included in sensor development. The polystyrene can be used as itself and also combined with other materials. One of the objectives of the

polystyrene modification in the sensor world is to achieve better adsorption of biomolecules on the surface. In the present paper, OES was used to diagnose and determine the state of the nitrogen plasma i.e., plasma species, electron temperature T_e and electron density n_e during the plasma treatment process. This characterization is important to control the nitrogen plasma processing on polystyrene's surface. The relationship between the species plasma, T_e and n_e with the surface wettability and functional polar group is discussed.

EXPERIMENTAL DETAILS

Samples in this work were a layer of polystyrene thin film deposited on a QCM surface. The raw materials were polystyrene granules with various molecular weight of 35,000 g.mol⁻¹, 192,000 g.mol⁻¹, and 280,000 g.mol⁻¹. The granules of each Mw were dissolved in toluene solvent to make of 6% solution of the polymer. The polystyrene solution was deposited on the QCM surface with spin coating technique with a rotational speed of 3000 rpm and a deposition time of 60 seconds.

Modification polystyrene surface was performed using a 2 MHz plasma generator at 40 watt RF power, 40 Pa pressure, 20 ml / min gas flow rate and treatment time for 2 min. During the plasma treatment process, the plasma spectrum was characterized by Optical Emission Spectroscopy (AURORA-4000). The experimental set-up for identifying the plasma species is shown in Fig. 1. An optical sensor was fixed to the chamber window and connected to an optical spectrometer. The active plasma species then analyzed using a computer controlled system with software spectral analysis which appear the graph between wavelength (λ) vs. the intensity. The measurable wavelength detected in the spectrometer is from 200 nm to 1000 nm. Then the emission spectra was performed with NIST's Atomic Database to determine species plasma, the electron Temperature (T_e) and electron density (n_e).

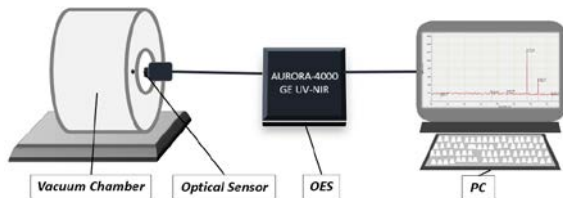


Fig. 1 Scheme of the optical emission spectroscopy for measurement of species in the plasma process

In this work, the NII was selected for the estimation of the temperature electron. Based on the experimental results the NII was found at the spectral

line at wavelength of 387.8 nm, 424.1 nm, and 467.4 nm. The relative intensity for selected spectral line of the NII was used to calculate temperature electron by using Boltzmann's equation:

$$\ln \frac{I\lambda}{gA} = \text{Const} - \frac{E_i}{kT} \quad (1)$$

I = observed emission intensity

λ = wavelength of the emission line

g = statistical weight

A = transition probability for spontaneous emission

E_i = excitation energy

K = Boltzmann constant

T = temperature

T_e is calculated from the slope of the straight line ($-\frac{1}{kT}$) fitted to a plot of the left-hand side of equation (1) against E_i .

The calculated electron density was determined by from spectral line broadening by the Stark-effect [9, 10]. This method was selected due to the appeared relative emission intensities only singly ionized species. The Stark broadening can be deduced and the FWHM of Stark broadening is related to the electron density by the following equation:

$$\Delta\lambda_{1/2} = 2\omega \left(\frac{n_e}{10^{16}} \right) \quad (2)$$

$$n_e = \left(\frac{\Delta\lambda_{1/2} 10^{16}}{2\omega} \right) \quad (3)$$

$$n_e \geq 1,6 \times 10^{16} T_{1/2} (\Delta E)^3 \quad (4)$$

n_e = electron density in m⁻³

$\Delta\lambda$ = full-width at half-maximum (FWHM) in nm

ΔE = energy of the emitting level

The contact angle was measured using the contact angle [11]. Measurement and the polar functional groups are observed with Fourier Transform Infrared (FTIR) before and after treated by nitrogen plasma.

RESULTS AND DISCUSSION

In nitrogen plasma, the active species that interact with polystyrene surfaces, electron temperature and electron density are observed with OES. Fig. 2 shows a typical emission spectrum of nitrogen plasma as function of wavelength and intensity obtained from Mw with 35,000 g/mol.

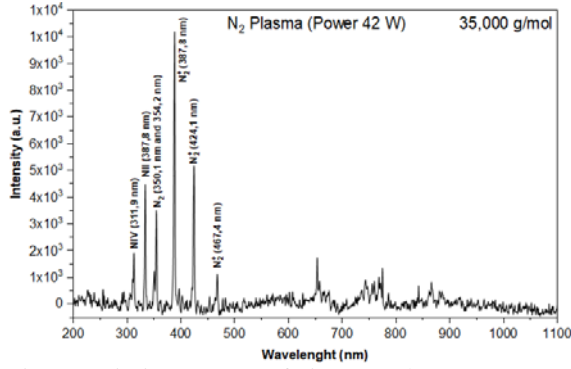
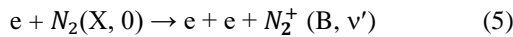


Fig. 2 Emission spectra of nitrogen plasma at Mw of 35,000 g/mol

As seen in Fig. 2, the main emitted species are observed at the wavelength of 387.810 nm, 424.123 nm and 467.7 nm. Based on the *Atomic Database NIST* spectrum, this main emission spectrum is NII which show ion N_2^+ [12]. The presence of N_2^+ species has a very important role in the polystyrene surface modification process.

The N_2^+ ionic state is essentially produced the electron impact process [13], the reaction mechanism can be seen below:



As shown in Fig 3, the intensity of emission of N_2^+ ions in a variation of Mw indicates a decreasing intensity change. This corresponds to the increasing number of N_2^+ ions reacting with the C atom to form the $C \equiv N$ group. The appearance of ion N_2^+ in the OES spectra is attributed to the observation with FTIR as shown in Fig. 4. The FTIR spectra show the new peaks at the wavelength of 2300-2400 cm^{-1} after treated by plasma nitrogen. This peaks represent to the nitrile functional group ($C \equiv N$) which is the polar group. The presence of such polar groups indicates a thin layer of polystyrene having wettability due to changes in functional groups which make the polystyrene surface properties more reactive. The presence of a polar group indicates that the surface is hydrophilic as indicated by the low angle of contact as shown in Fig. 5. The contact angle reduced with the higher molecular weights after treated by plasma treatment. The higher the molecular weight the absorbance intensity of the $C \equiv N$ increases.

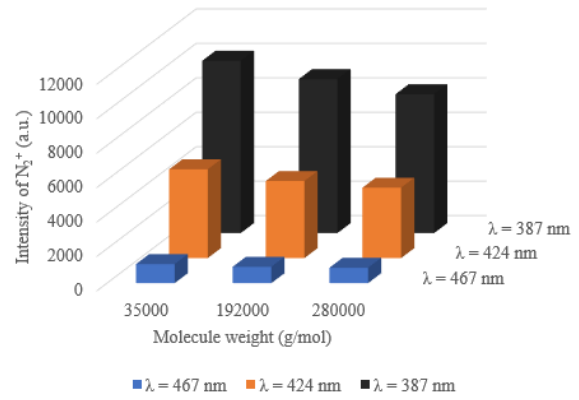


Fig. 3. The OES intensity of emission spectral ion N_2^+ in the polystyrene surfaces during plasma process with different Mw.

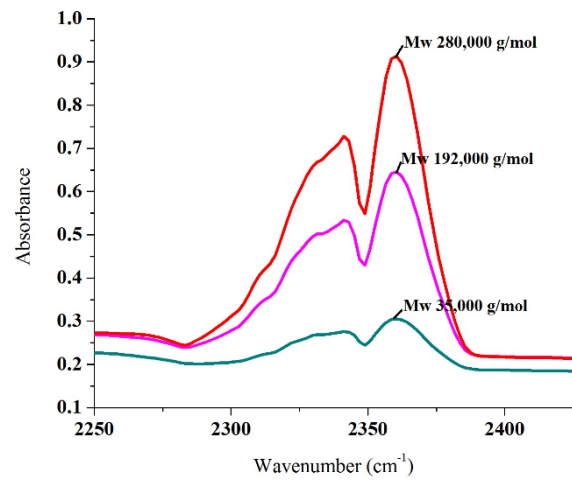


Fig. 4 The FTIR nitrile spectra of the polystyrene surface treated by nitrogen plasma with different Mw.

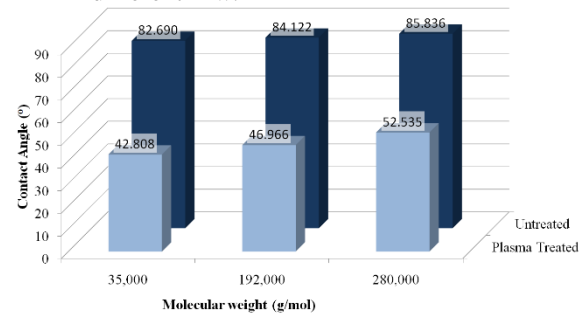


Fig. 5 Contact angle of the polystyrene surface before and after treated by nitrogen plasma varied with different Mw.

Fig. 6 shows the plotted graphic between electron temperature (T_e) and electron density (n_e) and various Mw. The electron temperature indicates the energetic electrons that initiate dissociations and ionizations. Plasmas with high electron temperatures (i.e., energies) give the ion N_2^+ bombard the surface of polystyrene and their energies are enough to break the C atom from polystyrene to form the C-N bond. The higher the T_e , the more the ion bombardment

occurred and affected by the ionization process. The higher the ionization, the stronger the bond between N and C atom. The electron temperature is increased until Mw of 192,000 g/mol then slightly decreased at 28,000 Mw. However, the FTIR absorption spectra show the increasing of the $C\equiv N$ functional group. This phenomena cannot be described clearly due to complex plasma chemistry and will be investigated in the future. On the other hand, the electron density show decrease with the increasing Mw. This phenomenon due to the more the formation of $C\equiv N$ bond results in the reduction of the species ion N_2^+ due to the N ion incorporate with C atom to form C-N bond.

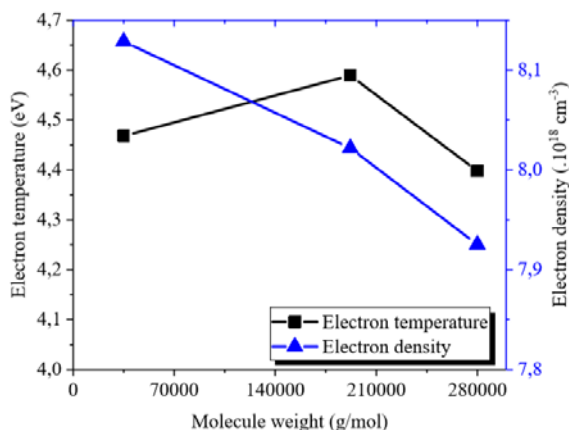


Fig. 6 The relationship between electron temperature (T_e) and electron density (n_e) for variation molecular weight.

CONCLUSION

The wettability of the polystyrene's surface changes from hydrophobic to hydrophilic after treated in nitrogen plasma using 2 MHz RF generator. The results proved that the enhanced wettability due to reaction of the $C\equiv N$ and the N_2^+ ion detected with corresponding T_e and n_e of the plasma. The intensity of the N_2^+ ion and electron density decrease with the increasing the Mw. However, the T_e was slightly increase with the Mw then decreasing. This phenomenon cannot be described clearly due to the complex plasma chemistry and will be studied in the future.

ACKNOWLEDGEMENTS

This work is supported by Ministry of Research, Technology and Higher Education of the Republic of Indonesia.

REFERENCES

[1] Kim Shyong Siow, Leanne Britcher, Sunil Kumar, Hans J. Griesser, Plasma Methods for The Generation of Chemically Reactive Surfaces

- for Biomolecule Immobilization and Cell Colonization - A Review, Plasma Process. Polym., 2006, 3, pp. 392-418
- [2] S. Yoshida, K. Hagiwara, T. Hasebe, and A. Hotta, Surface Modification of Polymers By Plasma Treatments for The Enhancement of Biocompatibility and Controlled Drug Release, Surf. Coat. Technol., vol. 233, 2013, pp. 99-107.
- [3] S. Ebnesajjad and C. F. Ebnesajjad, Surface Treatment of Materials for Adhesive Bonding, 2nd edition., Waltham, USA, Elsevier Inc, 2014.
- [4] D. Pal, S. Neogi, and S. De, Surface Modification of Polyacrylonitrile Co-Polymer Membranes Using Pulsed Direct Current Nitrogen Plasma, Thin Solid Films, vol. 597, 2015, pp. 171-182.
- [5] J. Koo et al., Design of Optical Emission Spectroscopy Based Plasma Parameter Controller for Real-Time Advanced Equipment Control, Comput. Chem. Eng., vol. 100, 2017, pp. 38-47.
- [6] K. E. Evdokimov, M. E. Konishev, V. F. Pichugin, and Z. Sun, "Study of Argon Ions Density and Electron Temperature and Density in Magnetron Plasma by Optical Emission Spectroscopy and Collisional-Radiative Model, Resour. Technol., vol. 3, no. 2, pp. 187-193, 2017.
- [7] M. D. Ionita, M. Teodorescu, T. Acsente, M. Bazavan, E.R. Ionita, G. Dinescu, Romanian Journal of Physics, 56, 2011.
- [8] M. D Ionita, M. Teodorescu, C. Stancu, E.C. Stancu, E.R. Ionita, A. Moldovan, T. Acsente, M. Bazavan, and G. Dinescu, Journal of Optoelectronics and Advanced Materials, 12, 2010, pp. 3.
- [9] Musadiq, M., Nasir Amin, Yasir Jamil, Munawar Iqbal, M. Asif Naeem, Hafiz Akif Shahzad, Measurement of Electron Number Density and Electron temperature of Laser-Induced Silver Plasma, International Journal of Engineering and Technology. Vol. 2, No. 1, 2013.
- [10] Dezhi Xiao, Yuedong Meng, Cheng Cheng, Jiangang Li, Jie Shen, Yan Lan, Paul K. Chu, Hongbing Xie, and Xingsheng Shu, Electron density measurements of atmospheric-pressure non-thermal N_2 plasma jet by Stark broadening and irradiance intensity methods, Physics of Plasma 21, 2014, 053510
- [11] Setyawan P Sakti, Rizal Y Aji, Laili Amaliyah and Masrurh, Low-Cost Contact Angle Measurement System for QCM Sensor, Telkomnika Vol. 15, 2017, pp. 560-569.
- [12] Z. Machala, M. Janda, K. Hensel, I. Jedlovsky, L. Lestinska, V. Foltin, V. Martisovits, and M. Morvova, Emission Spectroscopy of Atmospheric Pressure Plasmas for Bio-Medical and Environmental Applications, Journal of Molecular Spectroscopy 243, 2007, pp.194-201
- [13] L. M. Isola, B.J.G omez and V Guerra, Determination of The Electron Temperature and Density in The Negative Glow of a Nitrogen Pulsed Discharge Using Optical Emission Spectroscopy, J. Phys. D: Appl. Phys. 43, 2010, 015202 (10pp)

EFFECTS OF SOIL QUALITY ON EATING QUALITY OF ‘Namwa’ BANANA (*Musa ABB*) FRUIT

Pannipa Youryon¹ and Suriyan Supapvanich²

¹Department of Agricultural Technology, Prince of Chumphon Campus, King Mongkut's Institute of
Technology Ladkrabang, Chumphon Province, Thailand

² Department of Agricultural Education, Faculty of Industrial Education and Technology, King Mongkut's
Institute of Technology Ladkrabang, Bangkok, Thailand

ABSTRACT

The purpose of this research was to investigate the quality of ‘Namwa’ banana fruit grown in different soil quality places. The bananas were cultivated at Pathiu, Thasae and Muang districts, Chumphon province (Southern Thailand), where the pH and organic matter are 5.58 and 0.75%, 5.32 and 1.66%, and 6.93 and 2.45%, respectively. Physicochemical quality attributes of the ripe banana (2 days after colour break) were determined. The results show that the banana grown in Pathiu had the highest fruit weight compared to the others. No significant difference in total acidity, total soluble solids contents, texture and peel colour of all bananas were found. Pulp yellowness of the banana grown in Muang was significantly higher than the bananas grown in Pathiu and Thasae ($P < 0.05$). The banana grown in Muang and Thasae had antioxidant activity being higher than the banana grown in Pathiu district. The highest total phenolic compounds and flavonoids contents were found in the banana grown in Muang followed by the banana grown in Thasae and Pathiu, respectively. In conclusion, the soil quality such as neutral pH and high organic matter content promotes high edible quality of ‘Namwa’ banana fruit.

Keywords: ‘Namwa’ banana, soil quality, eating quality and bioactive compounds

INTRODUCTION

Banana is an important commercial tropical fruit belonging to the family Musaceae genus *Musa*. In Thailand, the most three banana cultivars grown for commercial are Hom Thong (*Musa* AAA group), ‘Kluai Khai’ (*Musa* AA group) and ‘Kluai Nam Wa’ (*Musa* ABB group) [1]. Banana is an exotic fruit which commonly recognized having high nutrients including oligosaccharides, vitamins, potassium as well as a rich source of bioactive compounds such as antioxidants, phenolic and flavonoid compounds [2, 3]. Many previous works had been reported the nutritional value of bananas which consisting of high valuable phytochemicals such as gallic acid, catechin, gallic acid and naringenin [4]. Moreover, banana has been proven having free radical scavenging activity more than guava and rose apple [5].

‘Kluai Nam Wa’ banana (*Musa* ABB group) is one of the most popular commercial bananas in Thailand. The banana is mostly produced for domestic market which 70 % of this banana has been grown around Thailand [1]. It is commonly accepted that preharvest factors such as climate, season, the level of rainfall and soil quality affecting postharvest quality of fruits including bananas. Elgar et al. [6] Lenthic et al. [7] and Streif and Saquet [8] suggest that preharvest factors especially climate of season and soil characteristics influence on eating and nutritional qualities of fruit. Recently, the most researches of banana have been focused on *Musa*

AAA or *Musa* AA which the research work of postharvest quality of *Musa* ABB is rare. Thus, we are interested to investigate the physicochemical quality of ‘Kluai Nam Wa’ banana grown in different areas in Chumphon province. The quality of ‘Kluai Nam Wa’ banana fruit grown in three districts of Chumphon province such as Muang, Thasae and Pathiu where having different soil quality were investigated.

MATERIALS AND METHODS

Raw Materials

The soil quality of banana plantations of each district was also determined and the data of soil quality was shown in Table 1.

Table 1 Soil quality of banana plantation at Pathiu, Thasae and Muang districts, Chumphon province, Southern Thailand.

Soil compositions	Banana plantation area		
	Pathiu	Thasae	Muang
pH	5.85	5.32	6.93
Organic matters (%)	0.75	1.66	2.45
P (mg kg ⁻¹)	25.21	12.56	36.89
K (mg kg ⁻¹)	35.93	62.05	33.84
Ca (mg kg ⁻¹)	5002.27	642.73	109.56
Mg (mg kg ⁻¹)	853.02	286.15	20.46

Colour Measurement

Peel and pulp colour attributes were measured using a Chroma meter CR 400 (Minolta, Japan). Lightness (L^*) and yellowness (b^*) values of banana peel were observed and L^* , b^* and whiteness index (WI) values of banana pulp were monitored.

Colour Measurement

Peel and pulp colour attributes were measured using a Chroma meter CR 400 (Minolta, Japan). Lightness (L^*) and yellowness (b^*) values of banana peel were observed and L^* , b^* and whiteness index (WI) values of banana pulp were monitored.

Texture, TSS and TA Measurements

Texture of the banana fruit pulp was determined using cutting force. The whole peeled fruit was cut using shear blade prob at the middle part of the fruit by using a TA-Plus Texture Analyser (Lloyds, England). The maximum force of the measurement was recorded and the data was presented as N.

TSS content was measured using a hand-held refractometer (ATAGO MNL-1125, Japan). The fruit pulp was squeezed using cloth sheet and the banana juice was used to determine TSS content and the data were expressed as ° Brix.

TA content was determined using the method of AOAC [9]. Five grams of banana pulp was homogenised with 10 mL of distilled water and then centrifuged at 6,000 rpm. Three mL of supernatant was titrated with 0.1 N NaOH until pH of the solution was 7.0 by using 1 % (w/v) of phenolphthaleine as the indicator. TA was defined as the percentage of malic acid content.

DPPH Free Radical Scavenging Activity and Bioactive Compounds Assays

A 3 grams of banana pulp was homogenised with 10 mL of absolute ethanol and then added the volume to 30 mL using distilled water. The mixture was vortexed for 5 min and then centrifuged at 6,000 rpm for 20 min. The supernatant was collected to determine DPPH free radical scavenging activity and bioactive compounds concentrations. DPPH free radical scavenging activity was determined following the method of Brand-William et al. [10]. The data were expressed as the percentage of DPPH free radical scavenging activity (%) per min.

Total phenols and flavonoids concentrations were assayed using the method described by Slinkard and Singleton [11], Zhishen Mengcheng and Jianming [12] and the data were presented as mg gallic acid per kilogram fresh weight (mg kg^{-1}) and mg catechin per kilogram fresh weight (mg kg^{-1}), respectively.

Statistical Analysis

The data were statistically analysed using ANOVA and the means of each treatment was compared by Duncan's New Multiple Rang Test (DMRT). The data were shown as the mean of ten replications and standard deviation.

RESULTS AND DISCUSSIONS

Colour Attributes

Table 2 show colour attributes of peel and pulp of 'Namwa' banana fruit cultivated in three places having different soil quality. The results show that no significant differences in L^* and b^* values of the banana fruit peel grown in Pathiu, Thasae and Muang districts. Interestingly, we found that cultivation area where having different soil quality had influence on pulp colour of the ripe banana fruits. The yellowness of banana pulp fruits grown in Pathiu was higher than that of the fruit grown in Thasae and Muang as the b^* value being higher than other samples. The WI of banana pulp grown in Muang seemed to be higher than other samples. However, no statistical differences in the WI values of all samples was observed. The L^* value of pulp banana fruits cultivated from the three places was similar. Regarding to Table 1, the low organic matters and high Ca and Mg contents in soil might effect on the yellowness of banana pulp which the soil sampled from banana plantation at Pathiu contained markedly high Ca and Mg contents compare to the soil from Thasae and Muang. The lowest Ca and Mg contents were observed in the soil from Muang which WI of banana pulp from Muang was higher than that from Thasae and Pathiu, respectively. However, previous work reported that high Ca content in media caused the low carotenoids content of tomato fruit [13]. Whereas, magnesium application increased carotenoids content in apple fruit [14]. Thus, the high Mg content in soil might cause the high carotenoids content in banana pulp resulting the high pulp yellowness.

Table 2 Peel and pulp colour attributes of ripe 'Namwa' banana fruit cultivated in Pathiu, Thasae and Muang Districts, Chumphon province, Southern Thailand.

Area	Peel colour		Pulp colour		WI
	<i>L</i> *	<i>b</i> *	<i>L</i> *	<i>b</i> *	
Pathiu	72.91	45.83	84.32	21.50 ^a	73.36
Thasae	69.80	49.21	83.31	18.68 ^b	74.89
Muang	72.18	49.22	84.37	17.00 ^b	76.91

Data represent mean of 10 replications. Difference letter indicates statistically difference.

Texture, TSS and TA

Texture, TSS and TA values of ripe 'Namwa' banana fruits grown in the three districts were shown in Figure 1. Shear force of the banana fruit was identified as the fruit texture. The texture of the banana fruit from Pathiu was significantly higher than that of banana fruit from Thasae and Muang ($P < 0.05$). The TSS and TA contents of banana fruits grown in the three districts did not differ. We found that the texture of the banana fruit was associated with the Ca content in soil. Soil sampled from Pathiu contained higher Ca than others which positively associated with the higher cutting force of the banana compared to other samples. The TSS content of all samples in this study was similar. This indicates that quality of soil from the three district has no influence on TSS content of the banana fruit. The TA of the fruits grown in Thasae trended to be higher than that of fruits grown in Pathiu and Muang. This might be related to the high potassium content of soil from Thasae which potassium content in soil and the acidity of the fruit are closely correlated [15, 16].

Antioxidant Activity and Bioactive Compounds

Figure 2 shows antioxidant activity and certain bioactive compounds concentration such as total phenols and flavonoids of the "Namwa" banana fruits. The results show that DPPH free radical scavenging activity of the banana fruits grown in Pathiu and Thasae was slightly higher than that of the fruit grown in Muang. The banana fruits grown in Thasae had both phenols and flavonoids concentrations being significantly lower than the banana fruits grown in Pathiu and Muang ($P < 0.05$).

The banana fruit grown in Pathiu had total phenols and flavonoids concentrations being higher than the fruit grown in Muang and Thasae, consequently. Regarding to the soil quality as shown in Table 1, the high concentrations both total phenols and flavonoids

content of banana fruit from Pathiu were related to the high Ca and Mg contents in soil. This recent work was agreed with the work of Awad and Jager [17] which suggested that Ca and Mg concentration in soil had positively correlation with the high content of flavonoids and phenolic compounds in the skin of apple fruits.

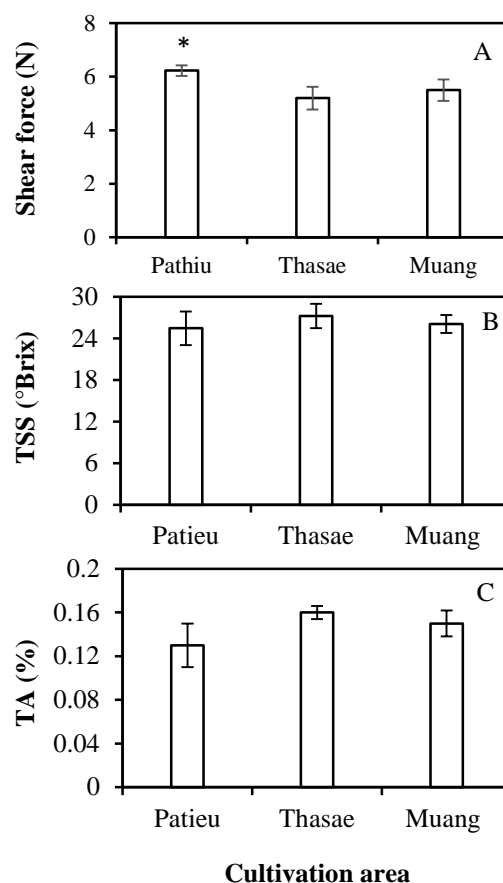


Fig. 1 Texture (A), TSS (B) and TA (C) of ripe 'Namwa' banana fruit cultivated in Pathiu, Thasae and Muang Districts, Chumphon province, Thailand. Error bar represent the mean ± standard deviation (n = 10).

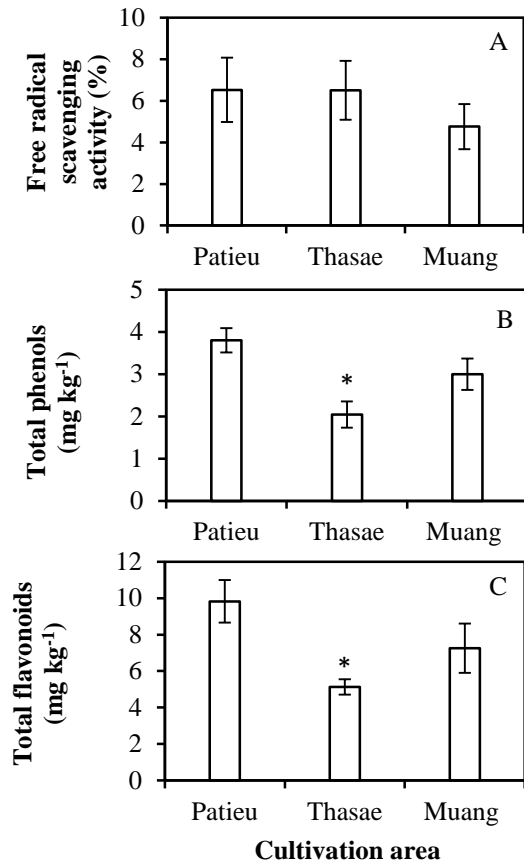


Fig. 2 Free radical scavenging activity (A), total phenols content (B) and flavonoids content (C) of ripe 'Namwa' banana fruit cultivated in Pathiu, Thasae and Muang Districts, Chumphon province, Thailand. Error bar represent the mean \pm standard deviation ($n = 10$).

CONCLUSION

Soil quality of difference plantation areas influence on eating quality of 'Namwa' banana fruits. The banana fruit grown in the soil containing high Mg (Pathiu) had higher pulp yellowness and lower WI compared to the fruit grown in soil containing low Mg, Thasae and Muang. The banana fruit grown in the soil containing high organic matter (Muang) had higher pulp WI compared to others. Ca content in soil might be positively related to the fruit texture and high acidity content in the banana might be related to the high K content in soil. High Ca and Mg contents in soil caused high total phenolic compounds and flavonoids contents of the banana fruits. These suggest that soil quality has influence on eating and nutritional qualities of 'Namwa' banana fruit.

ACKNOWLEDGEMENTS

Author would like to thank Prince of Chomphon campus, King Mongkut's Institute of Technology Ladkrabang for supporting laboratory facilities.

REFERENCES

- [1] Youryon P., and Supapvanich S., Quality and bioactive compounds of ripe 'Kluai Nam Wa' and 'Kluai Khai' bananas during storage. *International Food Research Journal*. Vol. 23, Issue 3, 2016, pp. 1027-1032.
- [2] Sulaiman S.F., Yusoff N.A.M., Eldeen I.M., Seow E.M., Sajak A.A.B., and Supriatno O.K.L.. Correlation between total phenolic and mineral contents with antioxidant activity of eight Malaysian bananas (*Musa* sp.). *Journal of Food Composition Analysis*. Vol. 24, 2011, pp. 1-10.
- [3] Ummarat N., Matsumoto T.K., Wall M.M., and Seraypheap K. Changes in antioxidants and fruit quality in hot water-treated 'Hom Thong' banana fruit during storage. *Scientia Horticulturae*. Vol. 130, 2011, pp. 801- 807.
- [4] Bennett R.N., Shiga T.M., Hassimotto N.M.A., Rosa E.A.S., Lajolo F.M., and Cordenunsi B.R. Phenolics and antioxidant properties of fruit pulp and cell wall fractions of postharvest banana (*Musa acuminata* Juss.) cultivars. *Journal of Agriculture and Food Chemistry*. Vol. 58, 2010, pp. 7991-8003.
- [5] Kondo S., Kittikorn M., and Kanlayanarat S. Preharvest antioxidant activities of tropical fruit and the effect of low temperature storage on antioxidants and jasmonates. *Postharvest Biology and Technology*. vol. 36, 2005, pp. 309-318.
- [6] Elgar H.J., Watkins C.B., and Lallu, N. Harvest date and crop load effects on a carbon dioxide related storage injury of 'Braeburn' apple. *HortScience*. Vol. 34, 1999, pp. 305-309.
- [7] Lenthéric I., Pinto E., Vendrell, M., and Larrigaudière C. Harvest date affects the antioxidative systems in pear fruits. *The Journal of Horticultural Science and Biotechnology*. Vol. 74, 1999, pp. 791-795
- [8] Streif J., and Saquet A.A. Internal flesh browning of 'Elstar' apples as influenced by pre- and postharvest factors. *Acta Horticulturae*. Vol. 599, 2003, pp. 523-527.
- [9] AOAC. Official Methods of Analysis, 16th ed. Association of Official Analytical Chemists International, 1995, Washington, DC.
- [10] Brand-Williams W., Cuvelier M. E., and Berset C., Use of Free Radical Method to Evaluate Antioxidant Activity. *LWT – Food Science and Technology*. Vol. 28: 1995, pp. 25-30.
- [11] Slinkard, K., and Singleton, V.L., Total Phenol Analysis: Automation and Comparison Manual Methods. *American journal of Enology and Viticulture*, Vol. 28, Issue 1, 1977, pp. 49-55.
- [12] Zhishen J., Mengcheng T., and Jianming W., The Determination of Flavonoid Contents in Mulberry and their Scavenging Effects on Superoxide Radical. *Food Chemistry*. Vol. 64, 1999, pp. 555-559.

- [13] Paiva E. A. S., Sampaio R. A., and Martinez H. E. P., Composition and Quality of Tomato Fruit Cultivated in Nutrient Solutions Containing Different Calcium Concentrations. *Journal of Plant Nutrition*, Vol. 21, Issue 12, 1998, pp. 2653-2661.
- [14] Reay P. F., Fletcher R. H., and Thomas V. J., Chlorophylls, Carotenoids and Anthocyanin Concentrations in the Skin of 'Gala' Apples during Maturation and the Influence of Foliar Applications of Nitrogen and Magnesium. *Journal of the Science of Food and Agriculture*, Vol. 76, 1998, pp. 63-71.
- [15] Davies J. N., and Windsor, G. W., Effect of Nitrogen, Phosphorus, Potassium, Magnesium and Liming on the Composition of Tomato Fruit. *Journal of the Science of Food and Agriculture*, Vol. 18, Issue 10, 1967, pp. 459-466.
- [16] Moor U., Põldma P., Tõnutare T., Karp K., Starast M., and Vool E., Effect of Phosphate Fertilization on Growth, Yield and Fruit Composition of Strawberries. Vol. 119, Issue 3, 2009, pp. 264-269.
- [17] Awad M. A., and Jager, A., Relationships between Fruit Nutrients and Concentrations of Flavonoids and Chlorogenic Acid in 'Elstar' Apple Skin. *Scientia Horticulturae*, Vol. 92, Issues 3-4, 2002, pp. 265-276.

ASSESSMENT OF N-(3-OXOHEXANOYL)-L-HOMOSERINE LACTONE AND VEGETABLE MOLECULES *IN VITRO*

^{1,2}Il'shat Fayzelgayanovich Karimov, ¹Galimzhan Kalikhanovich Duskaev

¹ Federal Research Centre of Biological Systems and Agro-technologies of the Russian Academy of Sciences, Russia, 460000, Orenburg, 29, 9 Yanvarya St.

² Orenburg State University, Russia, 460018, Orenburg, 13 Pobedy Pr.

SUMMARY

The ban on the use of antibiotics in the feed of farm animals has promoted an active search for new substances with similar properties. Particular attention of researchers has been devoted to the search for these substances among medicinal plants. The effect of substances of vegetable origin, such as coumarin and coniferyl alcohol which both form part of oak bark, on the activity of acyl homoserine lactone (AHL) molecules has been investigated. Reporter luminescent test systems were used to quantify the stress effects using bioluminescent analysis. It was found that the absorption spectrum of coumarin is characterised by the presence of four peaks at 205, 215, 275, 310 nm. The interaction with coniferyl alcohol was characterised by a shift in the absorption maxima (250 and 265 nm). The introduction of a molecule of AHL into the system led to the disappearance of the peak at 250 nm and a significant decrease in the absorption at 265 nm. The formation of a complex of ruminal fluid and coumarin led to a decrease in the expression efficiency of the sensory promoter luxI to a level of 476626 RLU using the same concentration of GSL (homoserine lactone). The combination of ruminal fluid and coniferyl alcohol led to a decrease in the quantum yield of the *E. coli* strain to the level of 345896 RLU following the use of GSL at a concentration of 10^{-4} M. The use of natural plant components (synthetic analogues) enhances the level of inhibition of quorum sensing (QS) system activity by the inactivation of regulatory molecules.

Keywords: *Coumarin, Coniferyl Alcohol, Quorum Sensing*

INTRODUCTION

The ban on the use of antibiotics in the feed of farm animals has promoted an active search for new substances with similar properties. Particular attention has been given to the search for these substances among medicinal plants, which were previously used in the treatment of animal diseases. Therefore, substances from natural sources targeted at certain types of molecules have been extracted and found to be useful for preventing insulin resistance [1]. Methylated quercetin derivatives, which are usually found in fruits and vegetables, and which have antioxidant and anti-inflammatory properties (block the enzymes responsible for inflammation) [2] were identified. Other investigators [3] observed the inhibition of secretory phospholipase A 2 by bioactive molecules from the extract of *Boerhaavia diffusa* L both *in vitro* and *in vivo*. The possible application of polyphenolic extracts for plant protection is considered in view of the absence of any toxicity of these compounds. The inhibition of *Pseudomonas savastanoi* by polyphenolic extracts isolated from plant residues was registered [4]. Studies on the extraction, identification and evaluation of cytotoxicity of the new terpene saponin from *Salicornia bigelovii* Torr, a potential chemotherapy drug for cancer treatment

[5], were conducted. It was noted that natural indoles inhibit the activation of T cells of the staphylococcal enterotoxin [6].

When assessing molecules of plant origin, it is necessary to take into account the species of plants. This establishes a 100-fold difference in toxicity between saponin-rich extracts of different plant species [7] and individual vegetative parts [8].

The safety of plant matter is also assessed using laboratory animals. Thus, it was established that extracts from tea flowers do not contain toxic substances, based on the assessment of mutagenicity, and acute and subchronic toxicity in rats [9]. A significant number of studies are being conducted to assess the toxicity of plant extracts and their anti-inflammatory properties, for example in *Parinari kerstingii* Engl [10], their toxicological effects [11], and the anti-tumour and cytotoxic activity of essential oils (*Haplophyllum tuberculatum* A. Juss) [12], as well as acute and subchronic studies of the toxicity of the aqueous extract of *Desmodium adscendens* (Sw) DC [13].

The subchronic toxicity, immunoregulation and anti-tumour effect of Nordamnacantal and anthraquinone, extracted from the stems of *Morinda citrifolia* L. [14], and the antifungal and cytotoxic activity of selected medicinal plants from Malaysia were detected [15].

Substances with anti-quorum activity have been isolated from plant extracts, with Zingerone (ginger substance) not only having a marked effect on the production of quorum sensing signalling molecules by *Pseudomonas aeruginosa* clinical isolates, but also showing a significant effect on the activation of reporter QS strains [16].

In our studies, we used substances with confirmed antibacterial and QS activity that had been previously isolated from the extract of *Quercus cortex* [17].

The aim of the work was to estimate the toxicity of chemically synthesised small molecules isolated from the extract of *Quercus cortex* using strains of *Escherichia coli* JLD271 pAL103 bacteria as test objects, including against the background of cattle ruminal fluid.

MATERIALS AND METHODS

The bacterial strains of *E. coli* K12, transformed by plasmids with cross-linking receptor genes (*rhIR*, *lasR* from *Pseudomonas aeruginosa* and *luxR* *Vibrio fischeri*) and luminescence genes (*luxCDABE*) of *Photobacterium luminescens*, as well as additional molecular factors such as aqueous oak extract containing coniferyl alcohol and coumarin (Fig. 1), which are part of the oak bark, were used; the ability to inhibit the production of violaceine from *Chromobacterium violaceum* was subsequently detected.

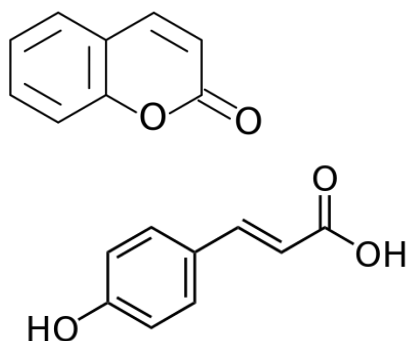


Figure 1 – Structural formulas of coumarin (left) and coniferyl alcohol (right).

Cultivation was performed on LB agar (Sigma, USA), with the addition of 10 µg/ml doxycycline for 18 hours at 37°C. Then, cells were transferred to LB broth (Sigma, USA) and incubated for 90 minutes at 37°C to reach the early exponential phase.

The reporter luminescent test systems (*E. coli* K-12 pAL103) were used as the material for the study, due to the possibility of the quantitative evaluation of stress effects using widely applied bioluminescent analysis.

As objects of research we used:

1. Autoinducers - N-(3-oxo)-hexanoyl-L-homoserine lactone (oxo-C6-GSL) in the concentration range from 10^{-8} to 10^{-4} M.

2. Bovine ruminal fluid, subjected to centrifugation at 5000 rpm for 10 minutes.

Equipment: luminometer LM-01T (Immunotech, Czech Republic), with the level of luminescence expressed in RLU (relative luminescent units); spectrophotometer Fluorat-02M "Panorama" (Lumex, Russia); multicentrifuge CM-6M.

Statistical processing was performed using the program "Statistica 10 RU", calculating the average value (M), standard deviation (σ), and standard deviation error (m). The significance level was considered reliable at $p < 0.05$.

RESULTS

At the first stage, the absorption spectra of N-(3-oxo)-hexanoyl-L-homoserine lactone and plant molecule complexes were evaluated. The change in the absorption spectra of these compounds was studied in the range from 200 to 400 nm, with the most typical and widespread AHL of gram-negative bacteria: N-(3-oxo)-hexanoyl-L-homoserine lactone. The absorption spectrum of coumarin was found to be characterised by the presence of four peaks corresponding to 205 nm ($I = 0.255$), 215 nm ($I = 0.269$), 275 nm ($I = 0.211$), and 310 nm ($I = 0.112$) (Table 1, Fig. 2).

The results of interactions with coniferyl alcohol turned out to be somewhat different and were characterised by a shift in the absorption maxima (Table 2).

It was found that the original substance has two significant approximate absorption maxima at 250 nm and 265 nm, with an intensity of 1.389 and 1.293 relative units, respectively. In addition, there are insignificant peaks at 205 nm, 220 nm and 230 nm (Fig. 3).

However, the introduction of AHL molecules into the system led to the disappearance of the peak at 250 nm and a significant decrease in the absorption at 265 nm. In this case, the peculiarity of this interaction was the formation of a pronounced maximum at 220 nm with an absorbance value of 0.853 relative units, which exceeds the initial level by 66%. As a result, the curve acquired qualitatively different characteristics compared to the original version.

In the second stage, studies were performed on ruminal tissue with natural and chemically synthesised inhibitors added, including the aqueous extract of oak and solutions of coumarin and coniferyl alcohol. In this case, N-(3-oxo)-hexanoyl-L-homoserine lactone (oxo-C6-GSL) was used as an autoinducer in the concentration range from 10^{-8} to 10^{-4} M.

Table 1. The absorption intensity of coumarin and its complex with N-(3-oxo)-hexanoyl-L-homoserine lactone (oxo-C6-HSL).

Name	Maxima of the absorption curve			
	205 nm	215 nm	275 nm	310 nm
Coumarin	0.255	0.269	0.211	0.112
Coumarin + oxo-C6-HSL	0.106	0.134	0.100	0.069
Character of change	-58%	-50%	-53%	-38%

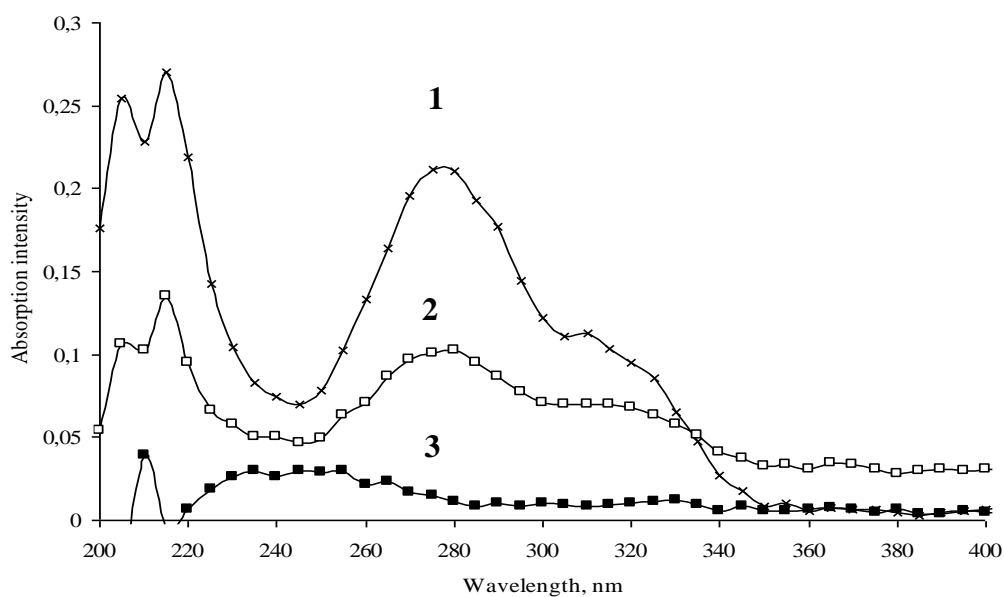


Figure 2 – Absorption spectrum of coumarin (1), N-(3-oxo)-hexanoyl-L-homoserine lactone (3) and their complex in the aqueous medium (2).

Table 2. Intensity of absorption of coniferyl alcohol and its complex with N- (3-oxo)-hexanoyl-L-homoserine lactone (oxo-C6-GSL).

Name	Maxima of the absorption curve				
	205 nm	220 nm	230 nm	250 nm	265 nm
Coniferyl alcohol	0.442	0.513	0.584	1.389	1.293
Coniferyl alcohol + oxo-C6-HSL	0.430	0.853	0.719	0.568	0.862
Decrease percentage	-3%	+66%	+23%	-59%	-33%

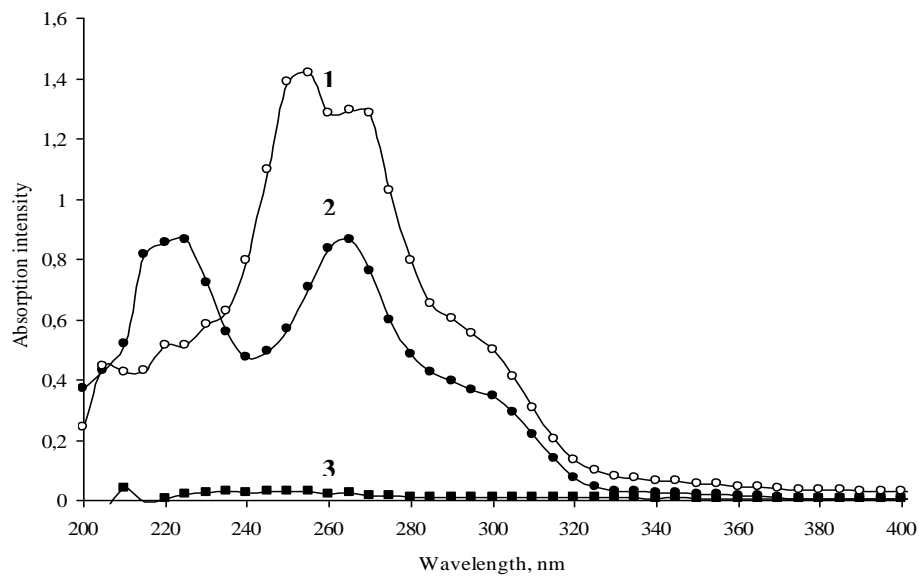


Figure 3 – Absorption of coniferyl alcohol (1), N-(3-oxo)-hexanoyl-L-homoserine lactone (3) and their complex in aqueous medium (2).

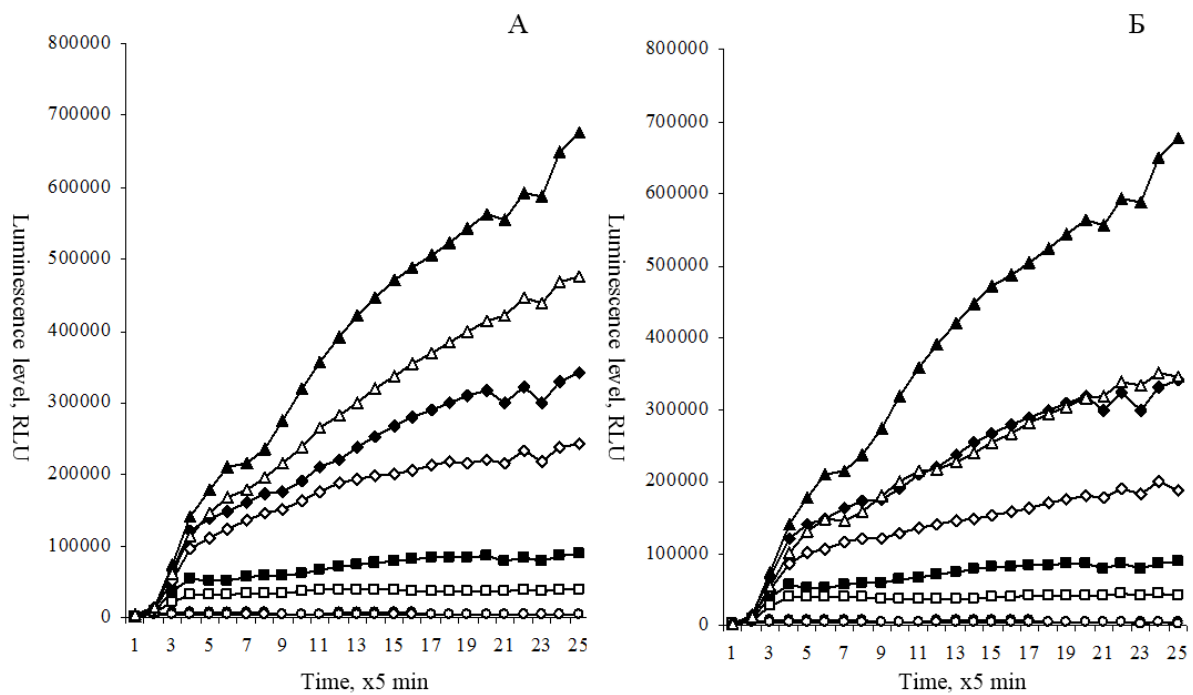


Figure 4 – Enhancement of inhibition activity of N-(3-oxo)-hexanoyl-L-homoserine lactone molecules by ruminal fluid (black figures) in combination with coumarin (A) and coniferyl alcohol (B) (white figures).

In this context, a sample of ruminal tissue diluted to 12.5% served as a control group, and the level of luminescence of *E. coli* JLD271 pAL103 was 676031 ± 10521 RLU at an autoinducer concentration of 10^{-4} M (Fig. 4).

The formation of a complex of ruminal fluid and coumarin led to a decrease in expression of the *luxI*

sensory promoter to a level of 476626 ± 13791 RLU using the same concentration of oxo-C6-GSL, indicating an additional 29% of signalling molecules. Likewise, lower concentrations reduced the luminescence level to 241603 ± 7791 RLU at 10^{-5} M and to 39960 ± 2791 RLU at 10^{-6} M, which is an

additional inhibition of 29% and 55% of the molecules, respectively (Fig. 4A).

The creation of a similar system representing the combination of ruminal tissue and coniferyl alcohol also led to a decrease in the quantum yield of the *E. coli* strain JLD271 pAL103 to a level of 345896 ± 11669 RLU using oxo-C6-GSL at a concentration of 10^{-4} M, indicating the decrease of an additional 48% of signalling molecules. Likewise, lower concentrations reduced the luminescence level to 187329 ± 5238 RLU at 10^{-5} M and to 42525 ± 1988 RLU at 10^{-6} M, which is an additional inhibition of 45% and 52% of the molecules, respectively (Fig. 4B).

On the other hand, the formation of a mixture of ruminal tissue and oak bark extract, representing a whole set of different molecules, demonstrated an even more pronounced change in anti-quorum activity (Figure 5).

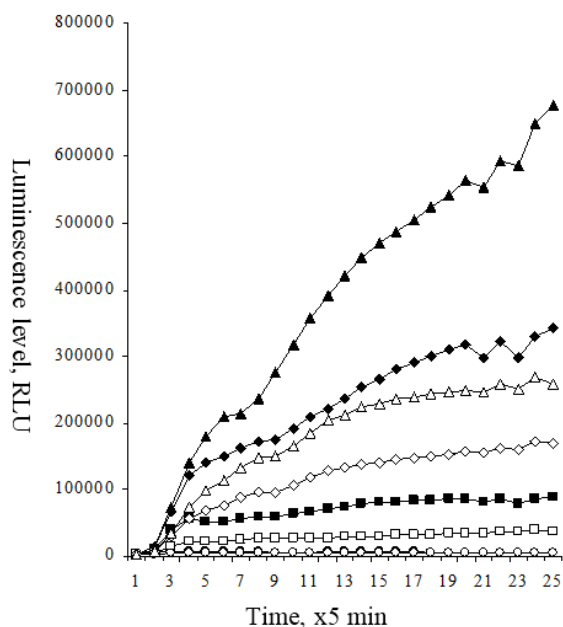


Figure 5 – Increased activity inhibition of N-(3-oxo)-hexanoyl-L-homoserine lactone with ruminal fluid (black figures) in combination with an extract of the oak bark (white figures).

Therefore, the effect of inhibition is increased by 61% in the maximum concentration of oxo-C6-HSL, corresponding to a level of 259479 ± 854 RLU, which is 57% of that at 10^{-6} M.

DISCUSSION

Because the feed substrate of cattle is formed from plant material, its composition or individual components can influence the signal molecules or receptor proteins of representatives of the microbial community. Therefore, to study the effect of plant extracts directly on ruminal tissue, it may be relevant to undertake investigations into the intercellular

communication between bacteria in the rumen. At the same time, scientists have revealed a new class of substances in plant extracts that can effectively prevent the development of infectious and inflammatory processes in animal bodies due to suppression of the system of intercellular communication in bacteria.

In the first stage, the absorption spectra of N-(3-oxo)-hexanoyl-L-homoserine lactone and plant molecule complexes were evaluated. The formation of mixtures of coumarin and AHL did not lead to qualitative changes in the absorption spectrum, but resulted in a decrease in amplitude instead. This is due to the formation of aggregates that increase the area to more than that of 340 nm and reduce the concentration of coumarin in the system by about half of the initial amount.

The results of the interaction with coniferyl alcohol turned out to be somewhat different, apparently due to covalent interactions, which leads to the formation of new types of compounds with different characteristics; in the context of our work, it potentially leads to the inactivation of mechanisms of intercellular communication using acyl derivatives of homoserine lactone.

In the second stage, studies on ruminal tissue were performed with natural and chemically synthesised inhibitors added, including the aqueous extract of oak and solutions of coumarin and coniferyl alcohol. The formation of a complex of ruminal fluid with coumarin and coniferyl alcohol resulted in a decrease in the expression of the sensory promoter and a decrease in the quantum yield of *E. coli* strain JLD271 pAL103. This can probably be explained by the dose-dependent inhibition of luminescence, as shown by the results of previous studies [18] on the assessment of toxicity degree in cattle ruminal fluid, using indicator luminescent strains designed on the basis of *E. coli*.

Inhibition can be associated with an ambiguous action of the molecules. Therefore, an earlier toxicity assessment (*in vitro*) of *Quercus cortex* inhibitory molecules showed that coumarin did not affect the luminescence kinetics of the *E. coli* strain MG1655 pXen7 [19], which is different from the results of the *E. coli* strain JLD271 pAL103. At the same time, it exerted a toxic effect on *Stylomychia mytilus*, 24 hours before the triplicate dilution (0.1-0.025).

The EC50 values for coniferyl alcohol with respect to *E. coli* strain MG1655 pXen7 were 0.54 mg/ml [19]; a similar inhibition of luminescence was confirmed in this study.

In view of the limited information on the effect of coumarin on microorganisms living in the gastrointestinal tract of animals, an analysis of its possible complex effect on the body was carried out. For example, coumarins in *Hydrangea paniculata*

caused the inhibition of caspase splitting, the infiltration of neutrophils and macrophages in the tissues of kidneys and the production of cytokines and chemokines, and could be metabolised into two biologically active compounds, umbelliferone and esculetin [20,21]. Thus, the probability of the interaction of coumarin with biologically active substances present in the composition of ruminal tissue is high, which can lead to the formation of new compounds.

It should also be taken into account that coumarin can exert a selective effect on certain microorganisms. Thus, coumarin derivatives were assessed as potential inhibitors of the production of the virulent factor of the *Pseudomonas aeruginosa* pyocyanin; the results show that coumarin derivatives suppress the growth of *P. aeruginosa* [22,23].

The presence of a quorum inhibitory effect can be considered here as a possible mechanism of action, as confirmed earlier [17]; this is from the coumarin extracted from oak bark.

This was also confirmed in recent studies comparing seven structurally related coumarins and inhibition of the quorum sensitivity of *Pseudomonas aeruginosa* and *Chromobacterium violaceum* [23,24].

As for coniferyl alcohol, its effect on gastrointestinal tract microorganisms is unknown, while at the same time there is evidence that it reduces the growth of *Nicotiana* cells at high concentrations [25]; it is also metabolised by BY-2 cells into several compounds as proposed earlier.

CONCLUSION

The data obtained made it possible to state that the use of natural plant components and their synthetic analogues increases the inhibition level of Quorum Sensing activity by inactivating regulatory molecules. In the future, this will make it possible to determine the nature of diet and the type of feed substrates used, as well as additives which act as additional factors in regulation of the activity of biochemical communication channels in the ruminal microbial community of ruminant animals.

ACKNOWLEDGEMENTS

The study was performed according to the project No.0761-2014-0010

REFERENCES

- [1] Mutlur Krishnamoorthy R., and Carani Venkatraman A. Polyphenols activate energy sensing network in insulin resistant models. *Chem Biol Interact.* Vol. 275, 2017, 95-107. doi: 10.1016/j.cbi.2017.07.016.
- [2] Novo Belchor M., Hessel Gaeta H., Fabri Bittencourt Rodrigues C., Ramos da Cruz Costa C., de Oliveira Toyama D., Domingues Passero L.F., Dalastra Laurenti M., and Hikari Toyama M. Evaluation of rhamnetin as an inhibitor of the pharmacological effect of secretory phospholipase A2. *Molecules*, Vol. 22, Issue 9, 2017, pii: E1441. doi: 10.3390/molecules22091441.
- [3] Giresha A. S., Pramod S. N., Sathisha A. D., and Dharmappa K. K. Neutralisation of inflammation by inhibiting *in vitro* and *in vivo* secretory phospholipase A2 by ethanol extract of *Boerhaavia diffusa* L. *Pharmacognosy Res.* Vol. 9, Issue 2, 2017, 174-181. doi: 10.4103/0974-8490.204650.
- [4] Biancalani C., Cerboneschi M., Tadini-Buoninsegni F., Campo M., Arianna Scardigli, Romani A., and Tegli S. Global analysis of type three secretion system and quorum sensing inhibition of *Pseudomonas savastanoi* by polyphenol extracts from vegetable residues. *PLoS One*. Vol. 11, Issue 9, 2016, e0163357. doi:10.1371/journal.pone.0163357
- [5] Guan F., Wang Q., Wang M., Shan Y., Chen Y., Yin M., Zhao Y., Feng X., Liu F., and Zhang J. Isolation, identification and cytotoxicity of a new noroleanane-type triterpene saponin from *Salicornia bigelovii* Torr. *Molecules*. Vol. 20, Issue 4, 2015, 6419-31. doi: 10.3390/molecules20046419.
- [6] Busbee P. B., Nagarkatti M., and Nagarkatti P. S. Natural indoles, indole-3-carbinol and 3,3'-diindolymethane, inhibit T cell activation by staphylococcal enterotoxin B through epigenetic regulation involving HDAC expression. *Toxicol Appl Pharmacol.* Vol. 274, Issue 1, 2014, 7-16. doi: 10.1016/j.taap.2013.10.022. Epub 2013 Nov 5.
- [7] Jiang X Hansen H. C. B., Strobel B. W., and Cedergreen N. What is the aquatic toxicity of saponin-rich plant extracts used as biopesticides? *Environ Pollut.* Vol. 236, 2018, 416-424. doi: 10.1016/j.envpol.2018.01.058.
- [8] Guo N., Tong T., Ren N., Tu Y. & Li B. Saponins from seeds of genus *camellia*: Phytochemistry and bioactivity. *Phytochemistry*. Vol. 149, 2018, 42-55. doi: 10.1016/j.phytochem.2018.02.002.
- [9] Chen Y., Zhou Y., Zeng L., Dong F., Tu Y., and Yang Z. Occurrence of functional molecules in the flowers of tea (*Camellia sinensis*) plants: Evidence for a second resource. *Molecules*. Vol. 23, Issue 4, 2018, pii: E790. doi: 10.3390/molecules23040790.
- [10] Linus L. O., Wang S. L., Shi N., Hanson C., Lu Y. T., Alolga R. N., Liu Q., Njokuocha R. C., and Qi L. W. The new plant *Parinari kerstingii* Engl.: Toxicity studies and anti-inflammatory

- properties. J Ethnopharmacol. 2018, 220:26-34: S0378-8741(17)34019-9. doi: 10.1016/j.jep.2018.03.016.
- [11] Guru-Pirasanna-Pandi G., Adak T., Gowda B., Patil N., Annamalai M., and Jena M. Toxicological effect of underutilised plant, *Cleistanthus collinus* leaf extracts against two major stored grain pests, the rice weevil, *Sitophilus oryzae* and red flour beetle, *Tribolium castaneum*. Ecotoxicol Environ Saf. Vol. 154, 2018, 92-99. doi: 10.1016/j.ecoenv.2018.02.024.
- [12] Hamdi A., Bero J., Beaufay C., Flamini G., Marzouk Z., Vander Heyden Y., and Quetin-Leclercq J. *In vitro* anti-leishmanial and cytotoxicity activities of essential oils from *Haplophyllum tuberculatum* A. Juss leaves, stems and aerial parts. BMC Complement Altern Med. Vol. 18, Issue 1, 2018, 60. doi: 10.1186/s12906-018-2128-6.
- [13] Quaye O., Cramer P., Ofosuhen M., Okine L. K. N., and Nyarko A. K. Acute and subchronic toxicity studies of aqueous extract of *Desmodium adscendens* (Sw) DC. J Evid Based Complementary Altern Med. Vol. 22, Issue 4, 2017, 753-759. doi: 10.1177/2156587217736587.
- [14] Abu N., Zambari N. R., Yeap S. K., Nordin N., Mohamad N. E., Romli M. F., Rasol N.E., Subramani T., Ismail N.H., and Alitheen N.B. Subchronic toxicity, immunoregulation and anti-breast tumour effect of Nordamnacantal, an anthraquinone extracted from the stems of *Morinda citrifolia* L. BMC Complement Altern Med. 27, Issue 1, 2018, 31. doi: 10.1186/s12906-018-2102-3.
- [15] Chan Y. S., Cheah Y. H., Chong P. Z., Khor H. L., Teh W. S., Khoo K. S., Ong H. C., and Sit N. W. Antifungal and cytotoxic activities of selected medicinal plants from Malaysia. Pak J Pharm Sci. Vol. 31, Issue 1, 2018, 119-127.
- [16] Kumar L., Chhibber S., Kumar R., Kumar M. & Harjai K. Zingerone silences quorum sensing and attenuates virulence of *Pseudomonas aeruginosa*. Fitoterapia. Vol. 102, 2015, 84-95. doi: 10.1016/j.fitote.2015.02.002.
- [17] Deryabin D. G., and Tolmacheva A. A. Antibacterial and anti-quorum sensing molecular composition derived from *Quercus cortex* (oak bark) extract. Molecules. Vol. 20, Issue 9, 2015, 17093-17108.
- [18] Logachev K., Karimov I., Duskaev G., Frolov A., Tulebaev S., and Zav`yalov O. Study of intercellular interaction of ruminal microorganisms of beef cattle. Asian J. Animal Sci., Vol. 9, 2015, 248-253. DOI: 10.3923/ajas.2015.248.253.
- [19] Duskaev G. K., Deryabin D. G., Karimov I., Kosyan D. B. & Notova S. V. Assessment of *in vitro* toxicity of quorum sensing inhibitor molecules of *Quercus cortex*. J. Pharm. Sci. & Res. Vol. 10, Issue 1, 2018, 91-95/J. Pharm. Sci. & Res. Vol. 10(1), 2018, 91-95.
- [20] Zhang S., Ma J., Sheng L., Zhang D., Chen X., Yang J., and Wang D. Total coumarins from *Hydrangea paniculata* show renal protective effects in lipopolysaccharide-induced acute kidney injury via anti-inflammatory and antioxidant activities. Front Pharmacol. Vol. 8, 2017, 872. doi: 10.3389/fphar.2017.00872.
- [21] Sen Z., Jie M., Jingzhi Y., Dongjie W., Dongming Z., and Xiaoguang C. Total coumarins from *Hydrangea paniculata* protect against cisplatin-induced acute kidney damage in mice by suppressing renal inflammation and apoptosis. Evid Based Complement Alternat Med. Vol. 2017, 2017, 5350161. doi: 10.1155/2017/5350161.
- [22] da S M Forezi L., Froes T. Q., Cardoso M. F. C., de Oliveira Maciel C. A., Nicastro G. G., Baldini R. L., Costa D. C. S., Ferreira V. F., Castilho M. S., and de C da Silva F. Synthesis and biological evaluation of the coumarin derivatives as potential inhibitors of the production of the *Pseudomonas aeruginosa* virulence factor pyocyanin. Curr Top Med Chem. 2018, 18(2):149-156. . doi: 10.2174/1568026618666180329122704.
- [23] D'Almeida R. E., Molina R. D. I., Viola C. M., Luciardi M. C., Nieto Peñalver C., Bardón A., and Arena M.E. Comparison of seven structurally related coumarins on the inhibition of quorum sensing of *Pseudomonas aeruginosa* and *Chromobacterium violaceum*. Bioorg Chem. Vol. 73, 2017, 37-42. doi: 10.1016/j.bioorg.2017.05.011
- [24] Reen F. J., Gutiérrez-Barranquero J. A., Parages M. L., & O'Gara F. Coumarin: a novel player in microbial quorum sensing and biofilm formation inhibition. Appl Microbiol Biotechnol. Vol. 102, Issue 5, 2018, 2063-2073. doi: 10.1007/s00253-018-8787-x.
- [25] Väisänen E. E., Smeds A. I., Fagerstedt K. V., Teeri T. H., Willför S. M., and Kärkönen A. Coniferyl alcohol hinders the growth of tobacco BY-2 cells and *Nicotiana benthamiana* seedlings. Planta. Vol. 242, Issue 3, 2015, 747-60. doi: 10.1007/s00425-015-2348-7.

SIMULATION SEA SURFACE TEMPERATURE OVER GULF OF THAILAND BY USING ROMS MODEL

Pramet Kaewmesri¹, Usa Humphries^{1,*} and Zhu Jiang²

¹Department of Mathematics, Faculty of Science, King Mongkut's University of Technology Thonburi (KMUTT), 126 Pracha-Uthit Road, Bang mod, Thung khru, Bangkok 10140, Thailand

²International Center for Climate and Environment Sciences (ICCES), Institute of Atmospheric Physics, Chinese Academy of Sciences

ABSTRACT

The Gulf of Thailand and neighbor area was studied using the Regional Oceanic Model System (ROMS). The horizontal resolution and vertical levels were 10 km × 10 km and 40 layers respectively. The domain situated between longitudes 95° E to 109° E and latitudes 0° N to 17° N. The initial and boundary conditions was used in this study that includes potential temperature, salinity, u-component of current, v-component of current and sea surface height relative to geoid from NCEP-CFSV2 data. The simulation dates were the end of month of May, June and July. Discussion from the literature review is found that the Sea Surface Temperature (SST) is a very important factor in the ocean and coupled atmosphere-ocean interaction. In this study used Generic Length Scale (GLS) vertical mixing method to simulate SST. The results from the model simulation are compared with spatial pattern with grids global observation data from the Optimum Interpolation Sea Surface Temperature (OISST) observation data. Overall the ROMS model can capture trend of SST pattern similarly OISST observation especially June 30 and July 31, 2018. In future work will simulate monthly mean SST from ROMS model and will compare with OISST monthly observation data in spatial pattern and statistical.

Keywords: The Gulf of Thailand, ROMS, GLS, and OISST

INTRODUCTION

The Gulf of Thailand is located in Southeast Asia immediately to the west of the South China Sea. The Gulf is a semi-enclosed sea that measures approximately 400 km by 800 km, covering an area of about 320,000 square kilometers. The Gulf of Thailand is the main factor agriculture, fishing, industrial, oil and etc. in Thailand. The location is between Latitude at 6°N to 14°N and Longitudes at 99°E to 105°E. It is surrounded by the Kingdom of Cambodia, Malaysia, the Kingdom of Thailand and the Socialist Republic of Vietnam. Over the Sunda Shelf, which is a submerged connection between Southeast Asia, Malaysia, Sumatra, Java and Borneo [1].

Since a study about SST over the Gulf of Thailand didn't receive a lot of attention studies emphasizing on oceanic model.

From [2] were used the coupled model to simulate rainfall over Thailand. The SST parameter was main to exchange between atmospheric and Oceanic in coupled model for simulating rainfall. But in this study was used ROMS ideal case simulation to simulate SST in oceanic model. So the rainfall simulation can be less accuracy SST than ROMS real time simulation. So, this study was simulated the ROMS real time over the Gulf of Thailand for

checking performance of SST from ROMS model.

Because a good simulation and forecasting SST are main factor for improving the rainfall from coupled model over Thailand. Then a good rainfall simulation that can manage and decrease the risk from natural disasters.

In this study, to use the ROMS model simulating SST pattern over The Gulf of Thailand and neighbor area. The vertical mixing scheme was used in this research that was Generic Length Scale (GLS). The dates of simulation was on May 31, June 30, and July 31, 2018. The results were basic spatial pattern comparing with gridded data from NOAA OISST observation data.

2. METHODOLOGY

2.1 MODEL DESCRIPTION

2.1.1 The Regional Oceanic Model System (ROMS)

The Regional Oceanic Model System (ROMS) is a member of a general class of three-dimensional, free-surface, terrain-following numerical models that solve the Reynolds-averaged Navier-Stokes equations using the hydrostatic and Boussinesq

assumptions. The governing equations in Cartesian coordinates can be written:

The momentum balance in the x - and y -directions are:

$$\frac{\partial u}{\partial t} + \vec{v} \cdot \nabla u - f v = -\frac{\partial \phi}{\partial x} - \frac{\partial}{\partial z} \left(\overline{u'w'} - \nu \frac{\partial u}{\partial z} \right) + F_u + D_u \quad (1)$$

$$\frac{\partial v}{\partial t} + \vec{v} \cdot \nabla v - f u = -\frac{\partial \phi}{\partial y} - \frac{\partial}{\partial z} \left(\overline{v'w'} - \nu \frac{\partial v}{\partial z} \right) + F_v + D_v \quad (2)$$

$$\frac{\partial \phi}{\partial z} = \frac{-\rho g}{\rho_0} \quad (3)$$

with the continuity equation:

$$\frac{\partial u}{\partial x} + \frac{\partial v}{\partial y} + \frac{\partial w}{\partial z} = 0 \quad (4)$$

and temperature and salinity given by:

$$\frac{\partial T}{\partial t} + \vec{v} \cdot \nabla T = -\frac{\partial}{\partial z} \left(\overline{T'w'} - \nu_\theta \frac{\partial T}{\partial z} \right) + F_T + D_T \quad (5)$$

$$\frac{\partial S}{\partial t} + \vec{v} \cdot \nabla S = -\frac{\partial}{\partial z} \left(\overline{S'w'} - \nu_\theta \frac{\partial S}{\partial z} \right) + F_S + D_S \quad (6)$$

An equation of state is also required

$$\rho = \rho(T, S, P) \quad (7)$$

The variables are shown in Table 1. An over bar represents a time average and a prime represents a fluctuation about the mean. These equations are closed by parameterizing the Reynolds stresses and turbulent tracer fluxes as:

$$\begin{aligned} \overline{u'w'} &= -K_M \frac{\partial u}{\partial z}; & \overline{v'w'} &= -K_M \frac{\partial v}{\partial z}; & \overline{T'w'} &= -K_T \frac{\partial T}{\partial z}; \\ \overline{S'w'} &= -K_S \frac{\partial S}{\partial z}; \end{aligned} \quad (8)$$

Equation (1) and (2) express the momentum balance in the x - and y -directions, respectively. In the Boussinesq approximation, density variations are neglected in the momentum equations except for their contribution to the buoyancy force in the vertical momentum equation (3). Under the hydrostatic approximation, it is further assumed that the vertical pressure gradient balances the buoyancy force. Equation (4) expresses the continuity equation for an incompressible fluid. The time evolution of temperature and salinity are governed by the advective-diffusive equation (5 and 6). For the moment, the effects of forcing and horizontal dissipation will be represented by the schematic terms F and D , respectively.

Table 1. The variables used in the description of the ocean model

Variable	Description
D_u, D_v, D_T, D_S	Diffusive terms
F_u, F_v, F_T, F_S	Forcing terms
$f(x, y)$	Coriolis parameter
g	Acceleration of gravity
$h(x, y)$	Bottom depth
ν, ν_θ	Molecular viscosity and diffusivity
K_m, K_T, K_S	Vertical eddy viscosity and diffusivity
P	Total pressure $P \approx -\rho_0 g z$
$\phi(x, y, z, t)$	Dynamic pressure $\phi = \left(\frac{P}{\rho_0} \right)$
$\rho_0 + \rho(x, y, z, t)$	Total in situ density
$S(x, y, z, t)$	Salinity
t	Time
$T(x, y, z, t)$	Potential temperature
u, v, w	The (x, y, z) components of vector velocity \vec{v}
x, y	Horizontal coordinates
z	Vertical coordinate
$\zeta(x, y, t)$	The surface elevation

2.2 Vertical Mixing Parameterizations

2.2.1 Generic Length Scale

A generic two-equation turbulence closure scheme [3] which can be tuned to be have similarly several of the traditional schemes, including that Generic Length Scale (GLS) vertical mixing scheme and was introduced to ROMS in [4]. The first of Warner et al. (2005)'s [4] equations is define $k = 0.5q^2$. Their dissipation is given by

$$\varepsilon = \left(c_\mu^0 \right)^{3+p/n} k^{3/2+m/n} \psi^{-1/n}$$

where ψ is a generic parameter that is used to establish the turbulence length scale. The equation for ψ is:

$$\frac{D\psi}{Dt} = \frac{\partial}{\partial z} \left(K_\psi \frac{\partial \psi}{\partial z} \right) + \frac{\psi}{k} (c_1 P_s + c_3 P_b - c_2 \varepsilon F_{wall})$$

Coefficients c_1 and c_2 are chosen to be consistent with observations of decaying homogeneous, isotropic turbulence. The parameter c_3 has differing values for stable (c_3^+) and unstable (c_3^-) stratification. Also

$$\psi = (c_\mu^0)^p k^m l^m, \quad l = (c_\mu^0)^3 k^{3/2} \varepsilon - 1$$

2.3 Initial condition, boundary condition and data observations

The initial condition and boundary condition were used the National Centers for Environmental Prediction Climate Forecast System Version 2 (NCEP-CFSV2). The data is 6 hourly atmospheric, oceanic and land surface reanalysis products and forecast. In this study, five parameters was included potential temperature, salinity, U-component of current, V-component of current and sea surface height relative to geoid to use initial and boundary condition in ROMS model [5].

The observation data was used the OISST version 2 AVHRR SST. This data is cover global observation data and developed by National Oceanic and Atmospheric Administration (NOAA) from United State of America. This data is an analysis constructed by combining observations from different platforms (satellites, ships, buoys) on a regular global grid [6].

2.4 Domain description and Experiments design

The domain experiment is cover on the Gulf Thailand and neighbor area. The domain situated between longitudes 95°E to 109°E and latitudes 0°N to 17°N (Fig 1). The horizontal and vertical level in this study that were 10 km ×10 km and 40 layers respectively.

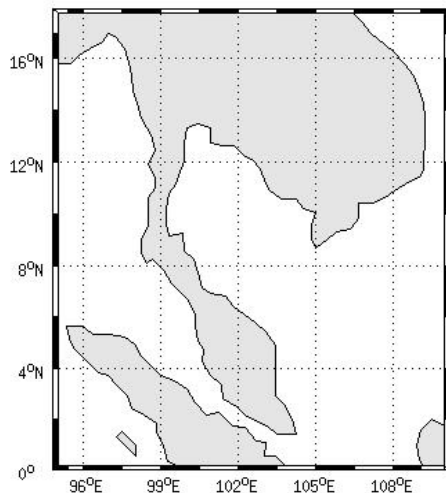


Fig. 1 The domain was used in this study.

In this study, the experiments design was included three cases simulation. The first of simulation was on May 31, 2018. The second of simulation was on June 30, 2018. The last simulation was on July 31, 2018. Table 2 was shown about summary of methodology part in this study.

Table 2. Summary method used in this study.

Parameters	Detail
Model	The Regional Oceanic Model System (ROMS)
Vertical Mixing Parameterizations	Generic Length Scale (GLS)
Initial and Boundary Condition	The National Centers for Environmental Prediction Climate Forecast System Version 2 (NCEP-CFSV2)
Observation Data	OISST version 2
Parameter from Initial and Boundary Condition	<ul style="list-style-type: none"> - Potential temperature - Salinity - U-component of Current - V-component of Current - Sea Surface Height relative to geoid
Domain	Longitudes 95° E to 109° E and Latitudes 0° N to 17° N
Horizontal Grids	10 km×10 km
Vertical Levels	40 layers
Date of Simulation	<ul style="list-style-type: none"> - May 31, 2018 - June 30, 2018 - July 31, 2018

RESULTS AND DISCUSSION

Fig 2 shows the Sea Surface Temperature from the NOAA OISST version 2 and ROMS on May 31, 2018.

The OISST observation data show the SST pattern (in the rage of 28.2 °C to 28.4 °C) almost over Andaman Ocean. But the SST pattern with high temperature (more than 29.4 °C) almost over nearly Malay Peninsula, eastern Indonesia Peninsula, Gulf of Thailand nearly Cambodia, Prachuap Khiri Khan province and lower southern Thailand, as shown in Fig 2(a).

The ROMS model show the SST pattern (in the rage of 28.2 °C to 28.4 °C) almost over Andaman Ocean similarly OISST observation data. But the SST pattern with high temperature (more than 29.4 °C) almost over nearly Malay Peninsula, western and eastern Indonesia Peninsula, Gulf of Thailand nearly Cambodia, eastern and lower southern Thailand, as shown in Fig 2(b).

Fig 3 shows the Sea Surface Temperature from the NOAA OISST version 2 and ROMS on June 30, 2018.

The OISST observation and ROMS model show similar the SST pattern (in the rage of 28.2 °C to 28.4 °C) almost over Andaman Ocean. In case temperature more than 29.4 °C OISST observation and ROMS model can capture SST pattern over Malay Peninsula and Indonesia Peninsula. Over eastern Malay Peninsula ROMS model and capture temperature over 28.8 °C similarly OISST observation.

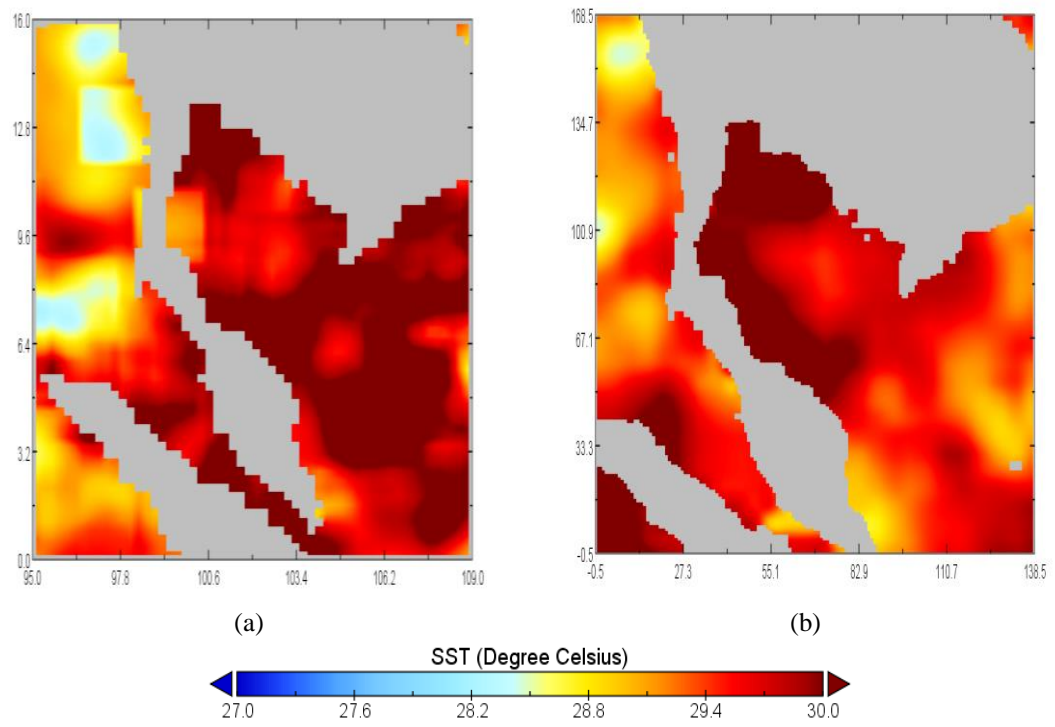


Fig. 2 Spatial SST (Degree Celsius) pattern on May 31, 2017: a) OISST observation and b) ROMS model.

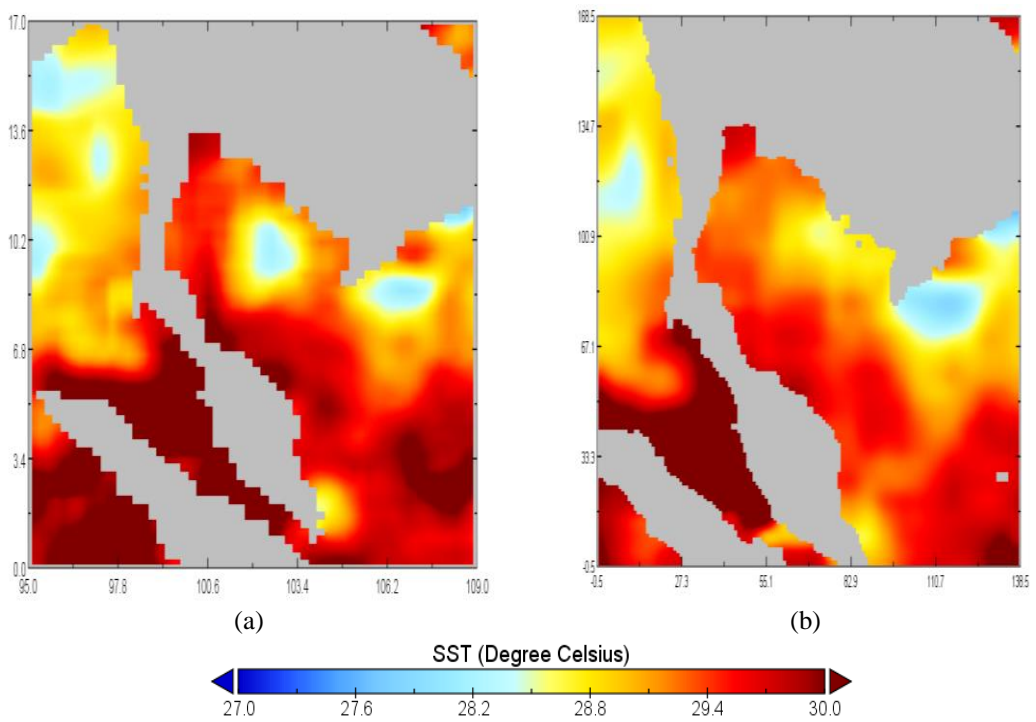


Fig. 3 Spatial SST (Degree Celsius) pattern on June 30, 2017: a) OISST observation and b) ROMS model.

Fig 4 shows the Sea Surface Temperature from the NOAA OISST version 2 and ROMS on July 31, 2018.

The OISST observation and ROMS model show similar the SST pattern (in the rage of 28.2 °C) almost

over Andaman Ocean. In case temperature more than 29.4 °C OISST observation and ROMS model can capture SST pattern over Malay Peninsula and Indonesia Peninsula.

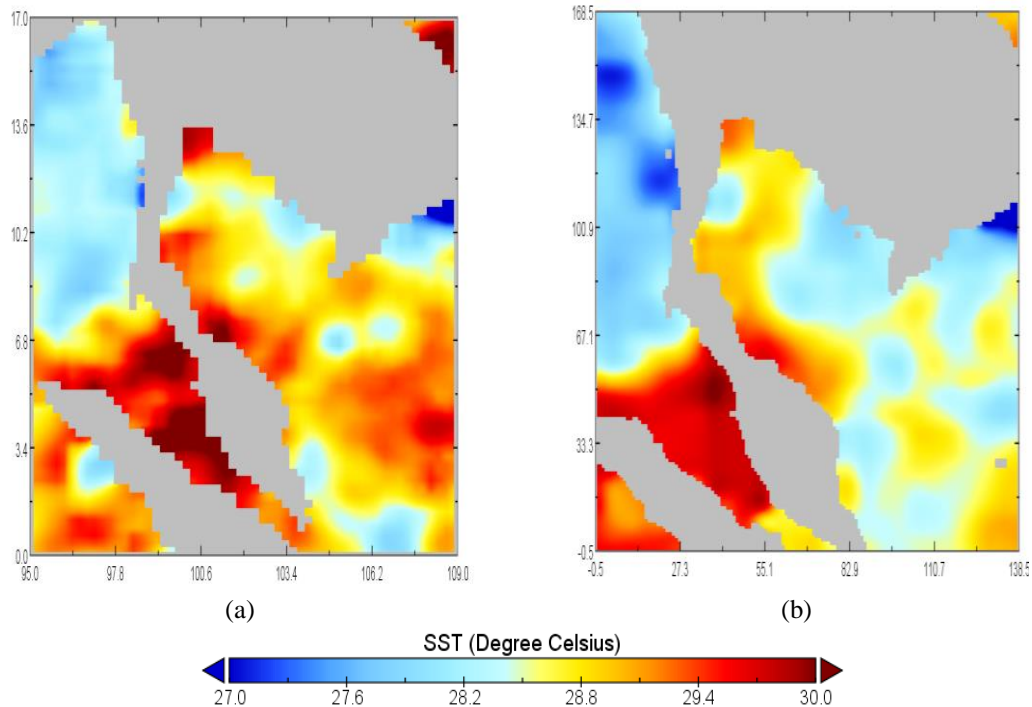


Fig. 4 Spatial SST (Degree Celsius) pattern on July 31, 2017: a) OISST observation and b) ROMS model.

CONCLUSION

In this study, to use the ROMS mode simulation performance SST on 3 cases that included May 31, June 30 and July 31, 2018 over the Gulf of Thailand and neighbor area. Overall the ROMS model can capture trend of SST pattern similarly OISST observation especially June 30 and July 31, 2018. In Future work will simulate monthly mean SST from ROMS model and will compare with OISST monthly observation data in spatial pattern and statistical.

ACKNOWLEDGEMENTS

The authors are also grateful NCEP for the CFSV2 data sets, NOAA for the gridded data sets, IMCS for the ROMS model and the Department of Mathematics, Faculty of Science, King Mongkut's University of Technology Thonburi (KMUTT). The authors acknowledge the financial support provided by National Research Council Thailand (NRCT). This research was fully supported by the International Research Net-work (IRN) (IRN5701PDW0002).

REFERENCES

- [1] Ascharyaphotha N., Wongwises P., Wongwises S., Humphries W U., and Xiaobao Y., Simlation of Seasonal Circularion and Thermohaline

Variabilities in the Gulf of Thailand. Advance in Atmospheric Science, Vol 25, No 3, 2008, pp.489-506.

- [2] Kaewmesri. P, Humphries. U, Archevarapuprok. B, and Sooktawee. S., The Performance Rainfall during Rainy Seasonal over Thailand by Using Preliminary Regional Coupled Atmospheric and Oceanic model. International Journal of GEOMATE, Vol. 14, Issue 45, 2018, pp.109-115.
- [3] Umlauf L, and Burchard H., A generic length-scale equation for geophysical turbulence models. J. Marine Res., Vol 61, 2003, pp.235–265.
- [4] Warner C J, Sherwood R C, Arango G H, and Signell P R., Performance of four turbulence closure models implemented using a generic length scale method. Ocean Modelling, Vol 8, 2005, pp.81–113.
- [5] Saha S, Suranjana M, Xingren W, Jiande W, Sudhir N, Patrick T, Davie B, Yu T H, Hui Y C, Mark I, Michael E, Rongqian Y, Malaquias M, Huug V D D, Qin Z, Wanqiu W, Mingyue C, and Emily B., The NCEP Climate Forecast System Version 2, Vol 27, 2014, pp.2185-2208.
- [6] Reynold R W, Smith M T, Liu C, Chelton B D, Casey S K, and Schlax G M., Operational processing of Satellite Sea surface temperature retrivals at the Naval Oceanographic Office, Bull. Amer. Met. Soc, Vol 79, pp 5473-5496.

EFFECTS OF SEED PREPARATION, SOWING MEDIA, SEED SOWING RATE AND HARVESTING PERIOD ON THE PRODUCTION OF CHIA MICROGREENS

Anjana Junpatiw¹, Akarapon Sangpituk¹

¹ Faculty of Agricultural, King Mongkut's Institute of Technology Ladkrabang Prince of Chumphon Campus,
Thailand

ABSTRACT

Chia (*Salvia hispanica* L.), a species of seeds with high essential fatty acid and nutraceutical content has encouraged increased crop production worldwide. Keeping value-added products into consideration, four experiments were conducted with the CRD method. In the first experiment, seed preparation was done by soaking the seeds in water, followed by being sown in the media. In the first treatment, T1, seeds were sown without soaking. In T2, seeds were sown after being soaked for 6 hours at room temperature and for 12 hours, in T3. In T4, after being soaked at 70-80°C, the seeds were allowed to cool down at room temperature for 6 hours and for 12 hours in T5, before sowing. According to the results, T4 treatment produced the highest germination percentage, microgreen height, and fresh weight. In the second experiment, seeds were sowed in 5 different seeding media for 7 days. The mix of coconut coir with sand and rice husk ash (1:1:1) produced the highest percentage of germination, microgreen height, and fresh weight. The third experiment was conducted to study the best seed sowing rate amongst 56, 93, 130, 167 and 204 g/m². The results showed that the seed sowing rate of 204 g/m² gave the highest fresh weight. The fourth experiment was to study the effect of harvesting period, by focusing on the harvesting periods of 5, 6, 7, 8 and 9 days, after sowing. The results showed that the period of 6-9 days after sowing gave the highest fresh weight.

Keywords: *Chia, Microgreens, Seed Preparation, Sowing Media, Harvesting Period*

INTRODUCTION

Today, more attention is given to a healthy nutrition to prevent certain diseases [1]. As public health awareness is increasing day by day, throughout the world, the demand for functional food with multiple health benefits is also increasing.

Microgreens are considered “functional foods” which are food products that possess particular health promoting or disease preventing properties, above their normal nutritional values [2]. These are also classified as a good source of minerals in the human diet [3].

Microgreens are a new class of edible vegetables, a very specific type which includes seedlings of edible vegetables, herbs or other plants [3]. The commonly cultivated microgreens are spinach, mustard, buckwheat, arugula, bull's blood beet, celery, cilantro, amaranth, golden pea, basil, spinach, mizuna, peppercress, popcorn shoots, red mustard, red beet, red cabbage, red orach, sorrel, red sorrel, wasabi, cabbage, broccoli, radish, lettuce. The size of these greens is between 3 and 10 cm in height which usually occurs within 7–14 days after germination, depending on the plant species. Over the past few years, microgreens have gained increasing popularity as new culinary ingredients due to their wide range of intense flavors, attractive colors, and tender texture.

Microgreens can be served in salads, soups, sandwiches and main dishes [3], [4], [5].

Chia (*Salvia hispanica* L.) is an annual plant belonging to the Lamiaceae family, native to Mexico and Guatemala [6]. Recently, chia seeds have become important for human health and nutrition because it has a high content of ω-3 fatty acids and high antioxidant properties that promote beneficial health effects [7]. It is considered as a Dietetic Nutritional Supplement by the Food and Drug Administration (FDA) [8]. Chia is now widely cultivated, its cultivation is not only limited to America but is also extended to other areas such as Australia and Southeast Asia [9].

The objectives of this work are to study the effects of seed preparation, sowing media, seed sowing rate and harvesting period of chia microgreen for use as information and guidelines for the production of Chia microgreen.

MATERIALS AND METHODS

In these experiments, we only used Chia seeds that were free from any defect and physical damage. They were obtained from a commercial microgreens seed source (Jamthong Farmshop, Thailand).

Experiment 1: To study the effect of seed preparation and soaking treatments on the production of Chia microgreens.

Chia seed preparation for germination was done by soaking the seeds, followed by them being sown in media. In the first treatment, seeds were sown without being soaked. In the second and third treatment, seeds were soaked in water at 70-80°C and then allowed to cool down at room temperature 6 hours and 12 hours, respectively, before it's sown in media. They were sown in a plastic basket (20 cm × 27 cm) containing coconut coir mixed with sand and rice husk ash (1:1:1) which was sprayed twice a day with the same amount of water.

Four replicates were used per treatment in the experiment. Chia microgreens were randomly selected from each replicate to measure the germination percentage, microgreen height and fresh weight per 100 microgreens after sowing for 7 days.

Experiment 2: To study the effect of sowing media on the growth of Chia microgreens.

Chia seeds were soaked in water at 70-80°C and then allowed to cool down at room temperature for 12 hours before it's sown in media. Seeds were sown in a plastic basket (20 cm × 27 cm) with five medias; coconut coir, rice husk ash, sand, coconut peat mixed with rice husk ash (1:1) and coconut peat mixed with sand and rice husk ash (1:1:1) which is sprayed twice a day with the same amount of water.

Four replicates per treatment were used in the experiment. Chia microgreens were randomly selected from each replicate to measure the germination percentage, microgreen height and fresh weight per 100 microgreens after sowing for 7 days.

Experiment 3: To study the effect of seed sowing rate on the growth of Chia microgreens.

Chia seeds were sown at the seeding rate of 56, 93, 130, 167 and 204 g/m². Soaked in water initially at 70-80°C and then allowed to cool down at room temperature for 12 hours, before it's sown in media. Seeds were sown in a plastic basket (20 cm×27 cm) containing coconut peat mixed with sand and rice husk ash (1:1:1) and which is sprayed twice a day with the same amount of water.

Four replicates per treatment were used in the experiment. Chia microgreens were randomly selected from each replicate to measure the germination percentage, microgreen height and fresh weight per 100 microgreens after sowing for 7 days.

Experiment 4: To study the effect of harvesting period on the production of Chia microgreens

Chia seeds were soaked in water for 12 hours at room temperature and then sown in a plastic basket (20 cm × 27 cm) containing coconut coir mixed with sand and rice husk ash (1:1:1) which was sprayed twice a day with the same amount of water. In this experiment, to study the harvesting period, by focusing on the harvesting periods at 5, 6, 7, 8 and 9 days after sowing.

Four replicates per treatment were used in the experiment. Chia microgreens were randomly selected from each replicate to measure microgreen height and fresh weight per 100 microgreens.

The experiment was completely randomized by design (CRD). All data were analyzed using the repeated measurement of the ANOVA procedure. Means were separated by Duncan's New Multiple Range Test (DMRT).

RESULTS AND DISCUSSION

Experiment 1: To study the effect of seed preparation by soaking treatments on the production of Chia microgreens.

This was to study the influence of soaking treatments on growth characteristics of Chia microgreens after it's grown for 7 days. The results showed that different soaking treatments had significantly different effects on the germination percentage, microgreen height and fresh weight of Chia seeds. The germination percentage of soaking the seeds at different water temperature and duration of soaking ranged from 96-98%. Seeds that were soaked initially at 70-80°C and then allowed to cool down at room temperature for 12 hours had the highest microgreen height (7.25 cm) and fresh weight (1.63 g/100 microgreens) (Table 1).

The germination percentage in Chia seeds that were soaked was higher than in the seeds that weren't soaked (Table 1) agreed with published results for table beet [10], carrot, snap bean, bell pepper [11], beet and chard [12]. Khan Abawi and Maguire [10] found that washing the seeds for 8 or 24 hours in running water improved table beet germination, and the subsequent osmotic priming led to further improvement.

Many species germinate easily and grow promptly while others are slow and may require pre-sowing treatments to improve, standardize and shorten the production cycle. Seed preparation used to advance the early stages of germination range from simple water soaking to physiological treatments, such as matrix priming and seed pre-germination. The substances inhibitory to germination are removed during seed washing [12], [13].

Experiment 2: To study the effect of sowing media on the growth of Chia microgreens.

The influence of seeding media on growth characteristics of Chia microgreens after grown for 7 days. The result showed that Chia seeding media were significantly different in germination percentage, microgreen height, and fresh weight. Seeds were sown in coconut coir and coconut coir mixed with sand and rice husk ash (1:1:1) provided the highest germination percentage range from 96-98%. Especially, seeds that were sown in coconut coir with sand and rice husk ash (1:1:1) provided the highest microgreen height (7.02 cm) and fresh weight (1.12 g/100 microgreens) (Table 2).

Muchjajib Muchjajib Suknikom and Butsai [14], Di Gioia De Bellis Mininni Santamaria and Serio [15] had documented the same result on a comparison of alternative media to provide maximum yield. Natural fiber-based media have also been developed and currently commercialized for microgreens. Low-cost alternatives of natural and renewable origin (e.g. cellulose pulp, cotton, jute, kenaf and sunn hemp fibers) and mixtures of materials combining desirable properties constitute potential as growing media for microgreens [15].

Experiment 3: To study the effect of seed sowing rate on the growth of Chia microgreen.

The result of the effect of seed sowing rate on the growth of Chia microgreens after grown for 7 days, presented that there was no significant difference ($P \leq 0.05$) in the microgreen height. While fresh weight showed statistically different in seed sowing rate. Chia seeds with sowing rate of 204 g/m² had the highest fresh weight (1.83 g/100 microgreens) (Table 3). On arugula and table beet, Murphy and Pill [16] and Murphy Llorca and Pill [17] observed a linear increase in fresh yield per unit area by increasing sowing rate. Increasing sowing rate to maximize yield will reflect on the cost of production, while excessive stand density may produce undesirably elongated shoots and limited air circulation, conducive to the development of fungal diseases. Optimal sowing rate is crop-specific, based on average seed weight, germinability and desired shoot population density, ranging from 1 seed/cm² in large-seeded species such as pea, chickpea, and sunflower, up to 4 seeds/cm² in small-seeded species like arugula, watercress, mustard [18].

Experiment 4: To study the effect of harvesting period on the growth of Chia microgreens.

The effect of different harvesting period on the growth of Chia microgreens at 5, 6, 7, 8 and 9 days

after sowing. Results showed significant differences in microgreen height and fresh weight.

The results showed that the seeds harvested after 9 days of sowing provided the best results of the highest microgreen height (7.5 cm) whereas the seeds harvested after 6 - 9 days of sowing gave the highest fresh weight (1.43-1.45 g/100 microgreens) (Table 4). This crop has a quick production cycle (one to three weeks) and occupies very little space in production. However, to shorten the production cycle and thus to reduce the production cost is one of the major goals of the current production [19], [20]. So, the best harvesting period of Chia microgreen is harvesting after 6 days of sowing.

This study, in agreement with the published results for lettuce [21] found that young lettuce seedlings, 7 days after germination, had the highest fresh weight and total phenolic concentration and antioxidant capacity in comparison to the older seedling. Unlike the result of Murphy Llorca and Pill [17] found that at 15 days after planting table beet gave the highest shoot fresh weight.

Microgreens are edible greens having two or more developed cotyledonary leaves. Harvesting of microgreens at the right stage is one of the most important production strategies. They are harvested at 7-14 days after germination with short crop cycle and usually with the average height of 2.5-7.6 centimeters, depending on the species [2], [3], [17].

CONCLUSION

Study of the effect of seed preparation, sowing media, seed sowing rate and harvesting period of Chia microgreen can be concluded as follows:

Chia seeds that were soaked initially at 70-80°C and then allowed to cool down at room temperature for 12 hours had the highest germination percentage (98%) microgreen height (7.25 cm) and fresh weight (1.63 g/100 microgreens).

Chia seeds sown in coconut coir with sand and rice husk ash (1:1:1) provided the best results of highest germination percentage (98%), microgreen height (7.02 cm) and fresh weight (1.12 g/100 microgreens).

Chia seeds sown at the rate of 204 g/m² provided the highest fresh weight (1.83 g/100 microgreens).

The harvest of 6 days after sowing gave highest fresh weight (1.45 g/100 microgreens).

ACKNOWLEDGMENTS

We are grateful for the financial support provided by King Mongkut's Institute of Technology Ladkrabang Prince of Chumphon Campus.

Table 1 Effect of soaking treatments on the germination percentage, microgreen height and fresh weight per 100 microgreens of Chia seeds after sowing for 7 days.

soaking treatments	germination percentage (%)	microgreen height (cm)	fresh weight per 100 microgreens (g)
without soaking	92 b	5.97 d	0.83 d
6 hours at room temperature	96 a	6.30 c	1.15 c
12 hours at room temperature	97 a	6.75 b	1.12 c
initial temperature at 70-80°C until cool down at room temperature for 6 hours	96 a	6.50 b	1.43 b
initial temperature at 70-80°C until cool down at room temperature for 12 hours	98 a	7.25 a	1.63 a
F-test	*	**	**
CV (%)	2.38	7.12	22.09

**Significantly different at $P<0.01$, *significantly different at $P<0.05$. Means within the same column with the different letters are significantly different to DMRT at $P<0.05$.

Table 2 Effect of sowing media on the germination percentage, microgreen height and fresh weight per 100 microgreens of Chia seeds after sowing for 7 days.

soaking media	germination percentage (%)	microgreen height (cm)	fresh weight per 100 microgreens (g)
coconut coir	96 ab	6.27 b	0.97 b
rice husk ash	88 c	5.67 c	0.90 c
sand	92 cb	5.70 c	0.93 c
coconut peat mixed with rice husk ash (1:1)	94 b	6.32 b	1.08 ab
coconut peat mixed with sand and rice husk ash (1:1:1)	98 a	7.02 a	1.12 a
F-test	*	**	*
CV (%)	3.36	9.13	3.33

**Significantly different at $P<0.01$, *significantly different at $P<0.05$. Means within the same column with the different letters are significantly different to DMRT at $P<0.05$.

Table 3 Effect of seed sowing rate on microgreen height and fresh weight per 100 microgreens of Chia seeds.

**Significantly different at $P<0.01$, ns = not

seed sowing rate g/m^2	microgreen height (cm)	fresh weight per 100 microgreens (g)
56	7.62	1.63 c
93	7.51	1.63 c
130	7.36	1.65 c
167	7.34	1.70 b
204	7.23	1.83 a
F-test	ns	**
CV (%)	9.89	1.98

significantly different. Means within the same column with the different letters are significantly different from DMRT at $P<0.05$.

Table 4 Effect of harvesting period on microgreen height and fresh weight per 100 microgreens of Chia seeds.

**Significantly different at $P<0.01$. Means within the

harvesting period (days after sowing)	microgreen height (cm)	fresh weight per 100 microgreens (g)
5	3.62 e	0.78 b
6	4.56 d	1.45 a
7	5.38 c	1.42 a
8	7.22 b	1.43 a
9	7.57 a	1.43 a
F-test	**	**
CV (%)	9.23	10.58

same column with the different letters are significantly different from DMRT at $P<0.05$.

REFERENCES

- [1] Marton M., Mandoki Zs., Csapo J., Evaluation of biological value of sprouts. Fat content, fatty acid Composition, Acta Univ. Sapientiae Alimentaria, Vol. 3, 2010, pp. 53-65.
- [2] Xiao Z., Lester, G. E., Luo, Y. and Wang, Q., Assessment of vitamin and carotenoid concentrations of emerging food products: Edible microgreens, Journal of Agricultural and Food Chemistry, 60(31), 2012, pp. 7644–7651.
- [3] Pinto E., Almeida, A. A., Aguiar, A. A., and Ferreira, I. M. P. L. V. O., Comparison between the mineral profile and nitrate content of microgreens and mature lettuces, J. Food Compos Anal., 2015, pp. 37: 38-43.
- [4] Sun J., Xiao Z., Lin L., Lester G.E., Wang Q., Harnly J.M., Chen P., Profiling polyphenols in five *Brassica* species microgreens by UHPLC-PDAESI/HRMS. J. Agric. Food. Chem., Vol. 61, 2013, pp. 10960-10970.
- [5] Bhatt P. and Sharma S., Microgreens: A Nutrient Rich Crop that can Diversify Food System, International Journal of Pure & Applied Bioscience, Volume 6, issue 2, 2018, pp. 182-186.
- [6] Ixtaina V.Y., Nolasco S.M. and Tomas M.C., Physical properties of chia (*Salvia hispanica* L.) seeds. Ind. Crops. Prod., 28, 2008, pp. 286–293.
- [7] Vuksan V, Jenkins A.L. and Dias A.G., Reduction in postprandial glucose excursion and prolongation of satiety, a possible explanation of the long-term effects of whole grain Salba (*Salvia hispanica* L.), Euro. J. Clin. Nutr., 64: 2010, pp. 436–438.
- [8] Pal S. and Kumar A., Effect Of Chia Seeds (*Salvia Hispanica*) Supplementation On Buckwheat Flour In The Development Of Gluten Free Bread. Int J. Nutr. Sci. & Food Tech 3:2, 2017, pp. 50-52
- [9] Jamboonsri W., Phillips T., Geneve R., Cahill J. and Hildebrand D., Extending the range of an ancient crop, *Salvia hispanica* L.—A new ω 3 source. Gen. Res. Crop. Evo., 59, 2012, pp. 171–178.
- [10] Khan A.A., Abawi G.S. and Maguire J.D., Integrating Matriconditioning and Fungicidal Treatment of Table Beet Seed to Improve Stand Establishment and Yield, Crop Science, Vol. 32 No. 1, 1992a, pp. 231-237.
- [11] Khan A.A., Maguire J.D., Abawi G.S. and Ilyas S., Matriconditioning of Vegetable Seeds to Improve Stand Establishment in Early Field Plantings, Journal of American Society of Horticultural Science, 117, 1992b, pp. 41-47.
- [12] Lee J.S., Pill, W.G., Cobb, B.B., and Olszewski, M., Seed treatments to advance greenhouse establishment of beet and chard microgreens, Journal of Horticultural Science and Biotechnology, 79(49), 2004, pp. 565-570.
- [13] Kyriacou M.C., Rouphael Y., Gioia Di F., Kyratzis A., Serio F., Renna M., Pascale De S., Santamaria P., Micro-scale vegetable production and the rise of microgreens, Trends in Food Science & Technology, Vol. 57, 2016, pp. 103-115.
- [14] Muchjajib, U., Muchjajib, S., Suknikom, S. and Butsai, J., Evaluation of organic media alternatives for the production of microgreens in Thailand. Acta Horticulturae, 1102, 2015, pp. 157-162.
- [15] Di Gioia F., De Bellis P., Mininni C., Santamaria P. and Serio F., Physicochemical, agronomical and microbiological evaluation of alternative growing media for the production of rapini (*Brassica rapa* L.) microgreens. Journal of the Science of Food and Agriculture, Volume 96, issue 4, 2017, pp. 1212-1219.
- [16] Murphy C.J. and Pill W.G., Cultural practices to speed the growth of microgreen arugula (roquette; *Eruca vesicaria* subsp. sativa). Journal of Horticultural Science and Biotechnology, 85(3), 2010, pp. 171-176.
- [17] Murphy C.J., Llort K.F., and Pill W.G., Factors affecting the growth of microgreen table beet. International Journal of Vegetable Science, 16(3), 2010, pp. 253-266.
- [18] Di Gioia F. and Santamaria P., Microgreens: Novel fresh and functional food to explore all the value of biodiversity, Italy: ECO-logica srl Bari., 2015, p. 118.
- [19] Kopsell D.A., Pantanizopoulos N.I., Sams C.E., Kopsell D.E., Shoot tissue pigment levels increase in 'Florida Broadleaf' mustard (*Brassica juncea* L.) microgreens following high light treatment. Scientia Horticulturae 140, 2012, pp. 96–99.
- [20] Viršilė A., Sirtautas R., Light irradiance level for optimal growth and nutrient contents in borage microgreens. Rural Development, 2013, pp. 272-275.
- [21] Oh M.M., Carey E.E., Rajashekar C.B. Regulated water deficits improve phytochemical concentration in lettuce, J. Am. Soc. Hortic. Sci. 2010, 135, 223–229.

EFFECTS OF PLANTING SUBSTRATES SUPPLEMENTED WITH VERMICOMPOST AND VERMICOMPOST FORTIFIED WITH *Trichoderma asperellum* CB-PIN-01 ON GROWTH AND PYTHIUM ROOT ROT OF LETTUCE

Phraomas Charoenrak¹, Chiradej Chamswarn², Wanwilai Intanoo² and Naowarat keawprasert²

¹Faculty of Agricultural Technology, Rajamangala University of Technology, Thanyaburi, Thailand

²Faculty of Agriculture at Kamphaeng Saen, Kasetsart University, Kamphaeng Saen Campus,
Nakhon Pathom, Thailand

ABSTRACT

Vermicompost products are the efficient organic fertilizers. Therefore, vermicompost fortified with a biocontrol agent may have potential to improve plant growth and also suppress plant disease. In this research, planting substrates (chopped coconut husk: coir dust; 50:30 % by volume) supplemented with vermicompost (VC) (20 % by volume) or VC fortified with *Trichoderma asperellum* CB-Pin-01 (VCT) (20 % by volume) were evaluated for the effects on lettuce growth and root rot caused by *Pythium aphanidermatum* (Pa). The 14-day-old lettuce (Butter Head) seedlings grown in sowing substrate (perlite:vermiculite; 2:1 V/V) were transplanted into the 6-inch plastic pot contained with prepared substrates. Plant nutrient solution with electrical conductivity (EC) of 1.6 mS/cm and pH 5.5-6.0 was applied weekly on substrate at 200 ml/pot. Results revealed that both VC and VCT increased plant growth after planting for 42 days as compared to a control (substrate without vermicompost). However, a substrate contained with VCT significantly increased the height, leaf number, leaf area, basal stem cutting surface area, plant fresh and dry weights when compared with the control. When the substrates were inoculated with Pa, the VCT (+Pa) treatment increased the height, leaf number, leaf area, basal stem cutting surface area, plant fresh and dry weights when compared with a *Pythium* treated control (VC(+Pa)). After lettuce harvesting, *T. asperellum* CB-Pin-01 could be completely recovered from planting substrate (100%) and lettuce root (100%), while this fungus help reduce substrate and lettuce root colonization by Pa when compared with a control (VC(+Pa)).

Keywords: *Trichoderma*, Vermicompost, Planting substrate, Root rot, Biocontrol

INTRODUCTION

Lettuce (*Lactuca sativa*) is the most important crop in the group of leafy vegetables [1]. Butter Head lettuce (*Lactuca sativa* L. var. *capitata* L.) is a heading type with soft and tender leaves, eaten raw. It is most popular in England, France, the Netherlands and other western and central European countries [2]. In recent decades many cultivars have been bred and grown in the USA [3].

Soilless culture, can increase productivity whatever the climate conditions, but also optimize the management of inputs (fertilizers or pesticides), within a given economic and environmental framework. They also aim at controlling diseases more efficiently [4]. For hydroponically and soilless substrate grown lettuce, *Pythium* spp. particularly *P. aphanidermatum* (Pa) is a major fungal pathogen causing root rot disease. Zoospores produced by Pa are asexually motile biflagellate spores which can live in water and move toward to infect the roots, causing root rot disease on various kinds of lettuce [5]. This disease causes significant reduction of lettuce growth, yield and quality, especially when

the lettuce was grown during high temperature (>35°C) season.

At present, biological control (biocontrol) is an alternative method for the control of plant diseases. The most widely used biocontrol agent (BCA) throughout the world belongs to the genus *Trichoderma* [6], [7]. *Trichoderma* has been well-known BCA which provides high efficacy to control fungal pathogens directly by antibiosis and mycoparasitism. However, abilities to induce resistance to plant disease and increase plant growth are indirect benefits [6], [7], [8].

In Thailand, Chamswarn and Intanoo [9] prepared *Trichoderma asperellum* strain CB-Pin-01 (Ta) (formerly identified as *T. harzianum*) as pure stock culture in the form of coarse powder. This semi-finished bioproduct has been used for producing a fresh culture bioproduct (fungal colonized semi-cooked rice seeds) by using the simple technique [9]. Spore suspension derived from fresh culture can be used for seed soaking, soil drenching and plant spraying for the control of fungal diseases on fruits, vegetables, cereals, ornamental crops and hydroponically grown lettuce

[10]. Incorporation of Ta-spore suspension into the mineral nutrient solutions using for growing lettuce (Green Cos) in the Nutrient Film Technique (NFT) system effectively reduced *Pythium* root rot and promoted lettuce growth [11]. Similar results were obtained by Kaensarn [12] who reported that sowing and planting Butter Head lettuce in biosubstrates supplemented with *T. asperellum* CB-Pin-01 could enhance plant growth and control root rot disease caused by *Pythium aphanidermatum*.

Vermicomposting is the non-thermophilic biodegradation of organic material through the interaction between earthworms and microorganisms as an environmentally friendly highly cost-effective conversion method of biodegradable organic wastes into valuable products. Vermicompost products have been proved to be efficient as organic fertilizers and biological control agents providing suppression on many plant disease incidences caused by soil-borne or foliar plant pathogens and pests [13], [14]. Application of compost not only suppress disease severity but also involved induced systemic resistance [15], [16]. Compost fortified with plant growth promoting microorganisms (PGPM) have shown that it increased its disease suppressiveness against fungal pathogens, plant growth and soil health [17].

Therefore, this study was conducted to evaluate the efficacy of planting substrates supplemented with vermicompost and vermicompost fortified with *T. asperellum* CB-Pin-01 (Ta) for promoting plant growth and yield of Butter Head lettuce and for reducing lettuce root and substrate colonization by Pa.

MATERIALS AND METHODS

Trichoderma Fresh Culture

For fresh culture preparation, four parts of broken milled rice were added with two parts of tap water (v/v) in automatic rice cooker. After the switch turn off, 250 g of semi-cooked rice was placed into 8x12 inch heat tolerant plastic bag. The bags with folded open-end were left for cooling down. Warm semi-cooked rice was inoculated with aliquot (0.3-0.5 g/bag) of pure Ta stock culture. All bags were sealed with stapler or plastic sealer and then each bag was punched along under the sealed line with fine needle for 20-30 holes. The Ta-inoculated bags were incubated at 25-30°C for 6-7 days (d). To prepare the spore suspension, 50 g of Ta fresh culture were added into 10L of clean water contained in a bottle. The bottle was vigorously shaken in order to remove dark greenish Ta spores from the surface of semi-cooked rice. The spore suspension was filtered through double layers of cheesecloth [18].

Pythium Inoculation

The plant pathogenic isolate of *Pythium aphanidermatum* (Pa) was isolated from rotted roots of lettuce (Green Cos). The Pa fungus was cultured on potato dextrose agar (PDA) for 48 hr at room temperature (25-30 °C). The agar contained with Pa mycelia in each plate was cut into small pieces before added with 100 ml of sterile water. To prepare mycelial suspension, agar pieces were homogenized at 9500 rpm for 15 sec [11]. For Pa inoculation, 200 ml/pot of mycelial suspension were applied onto planting substrate at 14 d after planting.

Preparation of Basal Nutrient Solution

Mineral nutrient solution stocks modified from Cooper [19] were prepared according to the methods provided by Chiemchaisri [20]. In 1 L of each concentrated nutrient solution stock comprised of 220.0 g calcium nitrate for stock A; 53.0 g potassium dihydrogen phosphate, 117.0 g potassium nitrate and 112.8 g magnesium sulfate for stock B; 10.0 g Fe DTPA, 5.0 g Fe DDHA, 2.0 g Mn EDTA, 0.1 g ammonium molybdate, 0.06 g nickle sulfate and 10.0 g Nic-Spray® (7.0% Mg, 1.8% Fe, 1.8% Mn, 1.9% Ca, 1.7% Zn, 1.7% B, 0.01% Mo) as micronutrient fertilizer for stock C. To prepared basal nutrient solution, 200 ml of concentrated stock solutions A, B and C were mixed with 100 L of water. The pH and EC in nutrient solution were adjusted at 5.5-6.5 and 1.6-1.8 mS/cm, respectively.

Lettuce Planting and Experimental Design

The formula of planting substrate was developed by Associate Prof. Dr. Chiradej Chamswarn. There are included by chopped coconut husk : coir dust; (50:30 % by volume) supplemented with vermicompost (VC) (20 % by volume) or VC fortified with *T. asperellum* CB-Pin-01 (VC+T and VCT) (20 % by volume) was used for lettuce planting. Butter head seedlings were grown in small cup (36 ml) contained with perlite : vermiculite (2:1 v/v) for 14 d using nutrient solution. The seedlings were transplanted into the 6-inch plastic pot (1,000 ml) contained with prepared substrates. Plant nutrient solution was added for 200 ml with weekly adjustments of pH (5.5-6.5) and EC (1.6-1.8 mS/cm) during plant growth.

The completely randomized design (CRD) was performed in seven treatments, four replications for each treatment, four pots per replication and one plant per pot. Treatments 1-4 comprised of using (1) substrate only (control), (2) substrate supplemented with VC (20% v/v) (VC), (3) substrate supplemented with VC (20 % v/v) and added with 200 ml/pot of Ta spore suspension prepared from Ta-fresh culture at 14 d after sowing (VC+T) and (4)

substrate supplemented with VCT (20% v/v) (VCT). All four treatments were not inoculated with Pa (-Pa). While treatments 5-7 were the same as treatments 2-4 but were inoculated with Pa (+Pa) as previously described.

Promotion of Plant Growth

After harvesting of 42-d-old lettuce (Butter Head) plants, plant growth characteristics were recorded. These included the height, width, fresh and dry weights of lettuce leaves, leaf numbers, leaf area (measured by Li-3100 Area Meter) and basal stem cutting surface area of each plant.

Fungal Colonization of Roots

Colonization of lettuce roots by Pa and Ta were detected on modified BNPR [21] and Martin's medium, respectively. The samples of roots collected from 42-d-old lettuce plants were disinfested in 0.525% sodium hypochlorite for 3 min, washed three times with sterile distilled water, blotted dry and cut into 1.0 cm pieces before placing on the selective media. Mycelial growth developed from the lettuce root samples were detected and recorded.

Substrate Colonization by *Pythium* and *Trichoderma*

Substrate samples from all treatments were collected and enumerated for surviving populations of Pa and Ta using modified BNPR and Martin's medium, respectively. All plates were incubated for 3-5 days at room temperature (25-30 °C). Colonies developed from substrate samples were observed and counted.

Statistical Analyses

All data were statistical analysis using analysis of variance (ANOVA). The significance of difference between the treatment means was determined by Least Significant Difference (LSD) using the statistical programs R [22]. The significance level was set at $P \leq 0.05$.

RESULTS

Effects of VCT and VC+T on Plant Growth Promotion

Both of treatments without Pa inoculation, VCT (-Pa) and VC+T (-Pa) significantly enhanced the heights of butter head lettuce by 22.13 and 15.07 %, respectively as compared to a control (-Pa). While treatments inoculated with Pa, VCT (+Pa) and

VC+T (+Pa) significantly increased the heights of butter head lettuce by 9.43 and 9.43 % %, respectively when compared with a control (VC (+Pa)) (substrate supplemented with vermicompost and Pa- inoculation). Similar results were obtained for the width of Butter Head lettuces, which VCT and VC+T treatments without Pa inoculation (-Pa) significantly increased the width of butter head lettuce by 12.16 and 18.56 %, respectively. While only VCT treatment with Pa inoculation (VCT (+Pa)) significantly increased the width of butter head lettuce by 6.27 % when compared with a control (VC (+Pa)) (Table 1).

Table 1 Effects of planting substrates supplemented with vermicompost (VC) and vermicompost fortified with *Trichoderma asperellum* CB-Pin-01 (VCT and VC+T) on the height and width of 42-d-old Butter Head lettuce

Treatment	Height (cm)	Width (cm)
1.Control (-Pa)	16.58 c ^{1/}	24.67 cd
2.VC (-Pa)	18.83 b (+13.57%) ^{2/}	24.75 cd (+0.32%)
3.VC+T (-Pa)	19.08 b (+15.07%)	29.25 a (+18.56%)
4.VCT (-Pa)	20.25 a (+22.13%)	27.67 b (+12.16%)
5.VC (+Pa)	16.75 c	23.92 d
6. VC+T (+Pa)	18.33 b (+9.43%) ^{3/}	24.33 cd (+1.71%)
7. VCT (+Pa)	18.33 b (+9.43%)	25.42 c (+6.27%)
C.V. (%)	1.98	1.97

^{1/} Means in each column followed by the same letter (s) are not significantly different according to the Least Significant Difference (LSD) ($P \leq 0.05$).

^{2/} Percentage of increment (+) of each treatment mean when compared with a control (-Pa) (substrate without VC, Pa-uninoculation).

^{3/} Percentage of increment (+) of each treatment mean when compared with a control (VC (+Pa)) (substrate with VC and inoculated with Pa).

Two *Trichoderma* treatments (VC+T and VCT) increased leaf number, leaf area and basal stem cutting surface area by 13.06 and 21.05 %, 8.44 and 16.97% and 10.56 and 32.54 %, respectively when compared with a control (-Pa). When treatments were inoculated with Pa (+Pa), the *Trichoderma* treatments, VC+T (+Pa) and VCT (+Pa) could also increase leaf number, leaf area and basal stem cutting surface area by 10.73 and 11.18 %, 7.19 and 20.16% and 27.62 and 39.15 %, respectively when compared with a control (VC (+Pa)) (Table 2).

Table 2 Effects of planting substrates supplemented with vermicompost (VC) and vermicompost fortified with *Trichoderma asperellum* CB-Pin-01 (VCT, VC+T) on leaf number, leaf area and basal stem cutting surface area of 42-d-old Butter Head lettuce

Treatment	Leaf number	Leaf area (cm ²)	Basal stem cutting surface area (cm ²)
1.Control (-Pa)	25.5 cd ^{1/}	64.27 ab	1.84 e
2.VC (-Pa)	26.33 c (+3.35%) ^{2/}	71.48 ab (+11.21%)	2.44 bcd (+32.54%)
3.VC+T (-Pa)	28.83 b (+13.06%)	75.57 a (+16.97%)	2.04 cd (+10.56%)
4.VCT (-Pa)	30.92 a (+21.25%)	69.70 ab (+8.44%)	3.01 a (+63.61%)
5.VC (+Pa)	24.13 d	61.02 c	1.99 de
6.VC+T (+Pa)	26.72 c (+10.73%) ^{3/}	65.41 bc (+7.19%)	2.55 bc (+27.62%)
7.VCT (+Pa)	26.83 c (+11.18%)	73.36 a (+20.16%)	2.78 ab (+39.15%)
C.V. (%)	1.97	1.96	2.10

^{1/} Means in each column followed by the same letter (s) are not significantly different according to Least Significant Difference (LSD) (P≤0.05).

^{2/} Percentage of increment (+) of each treatment mean when compared with a control (-Pa) (substrate without VC, Pa-uninoculation).

^{3/} Percentage of increment (+) of each treatment mean when compared with a control (VC (+Pa)) (substrate with VC and inoculated with Pa).

Effects of VCT and VC+T on Plant Weight

The treatments of VC+T and VCT significantly increased fresh and dry weights of 42-d-old butter head lettuce by 12.51, 28.60 and 29.11, 35.58 %, respectively when compared with a control (-Pa). The treatments inoculated with Pa, VC+T (+Pa) and VCT (+Pa) increased fresh and dry weights of Butter Head lettuce by 2.33, 9.81 and 7.36, 15.07 %, respectively. When VC treatment (substrate supplemented with only vermicompost and Pa-uninoculation) could increase butter head lettuce fresh and dry weight by 0.61 and 15.88 % when compared with a control (-Pa) (Table 3).

Table 3 Effects of planting substrates supplemented with vermicompost (VC) and vermicompost fortified with *Trichoderma asperellum* CB-Pin-01 (VCT, VC+T) on

fresh and dry weight of 42-d-old Butter Head lettuce

Treatment	Fresh weight (g)	Dry weight (g)
1.Control (-Pa)	98.83 b ^{1/}	3.40 d
2.VC (-Pa)	99.44 b (+0.61%) ^{2/}	3.94 bc (+15.88%)
3.VC+T (-Pa)	111.00 a (+12.51%)	4.39 ab (+29.11%)
4.VCT (-Pa)	127.10 a (+28.60%)	4.61 a (+35.58%)
5.VC (+Pa)	89.17 c	3.08 d
6.VC+T (+Pa)	91.25 c (+2.33%) ^{3/}	3.31 d (+7.36%)
7.VCT (+Pa)	97.92 c (+9.81%)	3.55 cd (+15.07%)
C.V. (%)	1.96	2.08

^{1/} Means in each column followed by the same letter (s) are not significantly different according to Least Significant Difference (LSD) (P≤0.05).

^{2/} Percentage of increment (+) of each treatment mean when compared with a control (-Pa) (substrate without VC, Pa-uninoculation).

^{3/} Percentage of increment (+) of each treatment mean when compared with a control (VC (+Pa)) (substrate with VC and inoculated with Pa).

Effects of VCT and VC+T on Root and Substrate Colonization by Pa and T

Lettuce roots and planting substrates from all *Trichoderma* treatments were found highly colonized by *T. asperellum* CB-Pin-01 by 30-100 and 100 %, respectively. Colonization of roots and planting substrates by Pa in treatments using VCT (+Pa) and VC+T (+Pa) were 0, 53.33 and 0, 80.00 %, respectively, whereas 100 % of colonization was found from the treatment of VC (+Pa) without T (Table 4 and 5).

Table 4 Colonization percentages of *Pythium aphanidermatum* (Pa) and *Trichoderma asperellum* (T) on 42-d-old lettuce roots planted in substrates supplemented with vermicompost (VC) and vermicompost fortified with *T. asperellum* CB-Pin-01 (VCT, VC+T)

Treatment	Root colonization (%)	
	Pa	T
1.Control (-Pa)	nd ^{1/}	nd
2.VC (-Pa)	nd	nd
3.VC+T (-Pa)	nd	100

4.VCT (-Pa)	nd	35
5.VC (+Pa)	100	nd
6.VC+T (+Pa)	53.33	100
7.VCT (+Pa)	0	30

^{1/} nd = Non determined

Table 5 Colonization percentages of *Pythium aphanidermatum* and *Trichoderma asperellum* on planting substrates supplemented with vermicompost and vermicompost fortified with *T. asperellum* CB-Pin-01 (T) at 42 d after sowing

Treatment	Planting substrates colonization (%)	
	Pa	T
1.Control (-Pa)	nd ^{1/}	nd
2.VC (-Pa)	nd	nd
3.VC+T (-Pa)	nd	100
4.VCT (-Pa)	nd	100
5.VC (+Pa)	100	nd
6.VC+T (+Pa)	80	100
7.VCT (+Pa)	0	100

^{1/} nd = Non determined

DISCUSSION

Enhancement of plant growth induced by *Trichoderma* species has been reported for a large number of different groups of plants including cereal, vegetable, ornamental and forestry crops. Various mechanisms have been proposed to explain plant growth promotion associated with *Trichoderma* species. These include synthesis of phytohormones, either by microbe or plants; production of vitamins; increased uptake and translocation of nutrient; enhanced solubilization of soil nutrient; enhanced root development and increased in the rate of carbohydrate metabolism; photosynthesis and plant defense mechanisms [6],[7]. Benitez *et al.* [23] reported that *Trichoderma* strains were able to produce plant growth hormones like cytokinin-like molecules, *e.g.* zeatin and gibberellin GA3 or GA3-related which directly affected on plant growth.

There were many researchers reported the abilities of root colonization by *T. harzianum* to increase nutrient uptake and fertilizer utilization efficiency which resulted in plant growth promotion. *T. harzianum* T22 treated maize seed showed the high efficacy to increase the nitrogen use efficacy [6], [7]. Similar to Lamool [11] who reported that the application of spore suspension of *T. asperellum* CB-Pin-01 (1 kg-fresh culture 2,000 L⁻¹) into nutrient solution of lettuce grown in the NFT hydroponic system effectively provided not only the reduction of *Pythium* root rot but also the promotion

of lettuce growth. Root colonization by *T. asperellum* CB-Pin-01 also resulted in the enhancement of phosphorus, potassium and nitrogen in lettuce leaves by 70, 18 and 6% as compared to untreated control, respectively. Similar to Kansarn [12] who reported that the transplanting of lettuce seedlings sown in sowing substrate supplemented with spore suspension of *T. harzianum* CB-Pin-01 into planting substrate with a ratio 70:20:10 (percent by volume) of *T. harzianum* CB-Pin-01 – soaked chopped coconut husks, compost and ash powder reduced the percentage of *P. aphanidermatum* infected roots and promoted growth of lettuce when compared with the *Pythium* inoculated control. Buasuwan [24] reported that the treatment used *Bacillus mycoides* FL17 bacteria bioproduct-vermicompost combination could promote plant growth by giving the highest fresh weight of butter head lettuce plant (149.19 g/plant). Chaoem [25] reported that *T. asperellum* CB-Pin-01 (Ta)-fortified vermicompost (VCT) and cow manure (CM+Ta) promoted the growth of yard-long bean by increasing plant height and root length. While these treatments also increased percentages of seed germination and survived seedlings of yard long bean grown in planting substrate inoculated with *Rhizoctonia solani*.

CONCLUSIONS

This study revealed that the planting substrate supplemented with VCT provided the highest growth promotion of lettuce by increasing the height, leaf number, leaf area, basal stem cutting surface area, plant fresh and dry weights when compared with the control (substrate without vermicompost). When the substrates were inoculated with *P. aphanidermatum* (+Pa), the treatment VCT (+Pa) completely reduced Pa-colonization on lettuce roots and planting substrates. Moreover, *T. asperellum* CB-Pin-01 could be completely recovered from planting substrates (100%) and lettuce roots (100%).

ACKNOWLEDGEMENTS

The authors are grateful to members of the Plant Disease Biocontrol Laboratory, Department of Plant Pathology, Kasetsart University, Kamphaeng Saen Campus for their warm co-operation in all experiments.

REFERENCES

- [1] Křístková, E., Doležalová, I., Lebeda, A., Vinter, V. and Novotná, A. Description of morphological characters of lettuce (*Lactuca sativa* L.) genetic resources. Hort. Sci. (Prague), Vol 35, No. 3, 2008, pp. 113–129.

- [2] Ryder E.J. Lettuce breeding. In: Bassett M. (ed.), *Breeding Vegetable Crops*. Westport, AVI Publishing Co. 1986, pp. 433–474.
- [3] MIKEL M.A. Genealogy of contemporary North American lettuce. *Hort Science*. Vol 42, 2007. pp. 489–493.
- [4] Gullino, M.L., Daughtrey, M.L., Garibaldi, A., Elmer, W.H., *Fusarium wilts of ornamental crops and their management*. *Crop Prot*. Vol 73, 2015. pp. 50–59.
- [5] Chamswarn, C. Biological control of plant disease. Department of Plant Pathology, Faculty of Agriculture at Kamphaeng Saen, Kasetsart University, Kamphaeng Saen Campus, Nakhon Pathom. 2006. 323 p. (in Thai).
- [6] Harman, G.E. Multifunctional fungal plant symbionts : new tools to enhance plant growth and productivity. *New Phytologist* Vol. 189. 2011a, pp. 647-649.
- [7] Harman, G.E. *Trichoderma*-not just for biocontrol anymore. *Phytoparasitica* Vol 39, 2011b, pp. 103-108.
- [8] Saldajeno, M.G.B., H.A. Naznin, M.M. Elsharkawy, M. Shimizu, and M. Hyakumachi. Enhanced resistance of plants to disease using *Trichoderma* spp., In V.K. Gupta, M. Schmoll, A. Herrera-Estrella, R.S. Upadhyay, I. Druzhinina and M.C. Tuohy (eds) *Biotechnology and Biology of Trichoderma*, Elsevier, Netherlands. 2014, pp 477-493
- [9] Chamswarn, C., Intanoo, W.. Production of *Trichoderma* fresh culture by simple technique for controlling damping-off of yard long bean caused by *Sclerotium rolfsii*. In: *Proceedings of 40th Kasetsart University Annual Conference (Subject: Plants)*. Bangkok, Thailand. 2002, pp. 114-122.
- [10] Chamswarn, C. *Trichoderma* species for biological control of plant diseases in Thailand. In: *Proceedings of International Symposium for Agricultural Biotechnology*, Nakhon Pathom, Thailand. 2015, p. 15.
- [11] Lamool, P. Efficacy of *Trichoderma harzianum* for the control of root rot of hydroponically grown lettuce caused by *Pythium aphanidermatum*. M.S. Thesis, Kasetsart Univ. Bangkok. 2006.
- [12] Kansarn, A. Effects of sowing and planting biosubstrates supplemented with microbial antagonists on growth of lettuce and the control of root rot caused by *Pythium aphanidermatum*. M.S. Thesis, Kasetsart Univ. Bangkok. 2014.
- [13] Simsek-Ersahin, Y. *The Use of Vermicompost Products to Control Plant Diseases and Pests Biology of Earthworms*. 2010, pp. 191-213.
- [14] Ayneband, A., Gorooei, A. and Moezzi, A.A. Vermicompost: an eco-friendly technology for crop residue management in organic agriculture. *Energy Procedia* Vol. 141, 2017 pp.667-671.
- [15] Hootink, H.A.J. and Boehm, M.J. Biological control with the context of microbial communities: A substrate-dependent phenomenon. *Annu. Rev. Phytopath.* Vol.37, 1999. pp. 427-446.
- [16] Pharand, B., Carisse and Benhamou, N. Cytological aspects of compost-mediated induced systemic resistance in bean. *Mol. Plant Microb. Interact.* Vol. 18, 2002. pp. 562-569.
- [17] Ng, L.C., Sariah, M., Sariam, O., Radziah, O. and Zainal, Abidin, M.A. Bio-efficacy of microbial-fortified rice straw compost on rice blast disease severity, growth and yield of aerobic rice. *Australas. Plant Pathol.* Vol. 41 No.5, pp. 541-549.
- [18] Charoenrak, P. and Chamswarn, C. Application of *Trichoderma asperellum* fresh culture bioproduct as potential biological control agent of fungal diseases to increase yield of rice (*Oryza sativa* L.). *J. ISSAAS* Vol. 21, 2015, pp. 67-85.
- [19] Cooper, A.J. *The ABC of NFT: Nutrient Film Technique*. Grower Books, London, UK. 1979, 170 p.
- [20] Chiemchaisri, Y., Niyomthai, W., Suboonsan, A. Nutrient solution. In *Mimeograph of the academic training for safety vegetable production in hydroponic system*. Kasetsart University, Bangkok, Thailand. (in Thai), 2016, pp. 58-65.
- [21] Chamswarn, C., Leeprasert, P., Chantanatan, S. Population assessments of soilborne plant pathogens, *Sclerotium rolfsii*, *Pythium* spp., *Phytophthora* spp. in soil and their correlation to disease incidence on intercropping system. In *Cropping Programmes KU-ACNARP*. Fact. of Agri., Kasetsart Univ., Bangkok, Thailand. ., 1985, p. 97.
- [22] R Core Team. R: A Language and Environment for Statistical Computing. R Foundation for Statistical Computing. Vienna, Austria. Retrieved on July 28, 2015 from: <https://www.r-project.org/>, 2014.
- [23] Benítez, T., A.M. Rincon, M.C. Limon and A.C. Codon. Biocontrol mechanisms of *Trichoderma* strains. *Int. Microbiol.* Vol. 7. 2004, pp. 249-260.
- [24] Buasuwan, J. Efficacy of *Bacillus* spp. bioproducts for the control of root rot caused by *Pythium aphanidermatum* on NFT-hydroponically grown lettuce. M.S. Thesis, Kasetsart Univ. Bangkok. 2013.
- [25] Chaohem, S. Efficacy of organic fertilizers fortified with *Trichoderma asperellum* CB-Pin-01 for the control of damping-off on yard long bean caused by *Rhizoctonia solani*. B.S. Thesis, Kasetsart Univ. Bangkok. 2017.

EFFECT OF OZONE MICROBUBBLES WITH VARIOUS TEMPERATURES ON THE CHLORPYRIFOS INSECTICIDE REMOVAL IN TANGERINE CV. SAI NAM PHUENG

Wirin Singtoraj^{1,4}, Jamnong Uthaibutra^{1,3,4} and Kanda Whangchai^{1,2,3,4*}

¹Department of Biology, Faculty of Science, Chiang Mai University, Chiang Mai 50200, Thailand;

²Center of Excellence in Bioresources for Agriculture, Industry and Medicine Chiang Mai University, Chiang Mai 50200, Thailand; ³Postharvest Technology Research Institute, Chiang Mai University, Chiang Mai 50200, Thailand; ⁴Postharvest Technology Innovation Center, Office of the Higher Education Commission, Bangkok 10400, Thailand

ABSTRACT

Chlorpyrifos, a type of organophosphate insecticide, is widely used to destroy pests in tangerine orchard for reduce the loss and maintain the quality of fruit. Consequently, the application of insecticides during production leads to the insecticide residues problem in tangerine that can be dangerous to human health. This study investigated the effect of ozone microbubbles (OMBs) on the removal of chlorpyrifos residues in the fruit. Tangerines were sprayed with chlorpyrifos solution at a concentration of 10 minutes. Then, they were treated with OMBs at different temperatures (15, 20 and 25 °C) for various exposing times (0, 10, 20, 30, 40, 50 and 60 minutes). Removal percentage of chlorpyrifos residues in tangerines was determined by gas chromatography-flame photometric detector (GC-FPD). The results showed that chlorpyrifos residues in tangerines was decreased at lower water temperature, especially at 15 °C resulting in the removal up to 81% after treating with OMBs for 30 minutes when compared to control (distilled water). After that, the fruits were stored at 25 °C for 7 days to determine quality changes. The percentage of weight loss, total soluble solids (TSS), titratable acidity (TA), disease incidence and ascorbic acid content in all treatments were not affected by OMBs. These results demonstrate that OMBs treatment at 15 °C is the most effective treatment for removing chlorpyrifos residues in tangerine and have no effects on the fruit quality.

Keywords: Tangerine, Chlorpyrifos, Insecticide residues, Ozone microbubbles

INTRODUCTION

Chlorpyrifos, a type of organophosphate insecticide, is widely used to destroy pests in tangerine orchard for reduce the loss and maintain the quality of fruit. Consequently, the application of insecticides during production leads to the insecticide residues problem in tangerine that can be dangerous to human health. Thai Pesticide Alert Network reported that tangerine in northern Thailand had chlorpyrifos, insecticide residues more than 1.0 mg/L and this exceeded the Maximum Residue Limits (MRLs) [1]. This leads to possible chronic or acute health risk for consumers. Therefore, there is a requirement for effective oxidation technology such as ozone microbubbles that has been applied for removing insecticide residues in tangerine.

Ozone is environmentally friendly and confirmed as a Generally Recognized As Safe (GRAS) for food contact application. Ozone is a powerful oxidant with a wide range of sanitizing application. Due to its instability with a half-life of 20-30 minutes in distilled water at 20 °C [2], it degrades quickly into oxygen and leaves no residues after application [3]. Ozone has been used as sanitizer in food surface

hygiene and to extend shelf life of many postharvest agricultural products [4]. Moreover, it was found that oxidation by ozone is an effective treatment to degrade the insecticide residues on agricultural products [5]. For example, Whangchai *et al.* [6] reported that using ozone gas for 60 minutes can reduce 45% chlorpyrifos insecticide on lychee fruits without changes in fruit quality. Kusvuran *et al.* [7] found that fumigation with 10 minutes of ozone gas for 5 minutes can reduce the tetradifon and chlorpyrifos insecticides on the surface of citrus fruits in the ratio of 100% and 98.6% respectively and Wu *et al.* [8]. stated that low level dissolved ozone (1.4 mg/L) was able to reduce diazinon, parathion and methyl parathion insecticide residues in Pak Choi (*Brassica rapa*) in 30 minutes. Nevertheless, the low water solubility and rapid degradation of ozone are problems for an attack on insecticide molecules.

Ozone microbubbles (OMBs) is a good alternative technique that can transform ozone gas into micro-size bubbles (less than 10 µm) in the water. These micro-bubbles can keep the ozone inside for a longer period and they will be slowly floated up to the water surface that increased the dissolving potential of ozone. In this process, the

surface of microbubbles will be surrounded by anionic molecules, therefore they will not be combined together to form big- bubbles. Likewise, the microbubbles enhance the oxidizing efficiency of the ozone which help to destroy the insecticide structures [9]-[11]. It has been reported that OMBs removed water pollutants (ammonia and diethyl phthalate) from wastewater in a pilot plant [12], [13]. Furthermore, Ikeura *et al.* [14] found that sanitizing with OMBs (2 mg/L) for 20 minutes could reduce the fenitrothion insecticide residues in lettuce, cherry tomatoes and strawberries with no effect on product quality. Therefore, the objective of this research is to study the effect of OMBs with various temperatures on the chlorpyrifos insecticide removal in tangerine cv. Sai Nam Phueng.

MATERIALS AND METHODS

Chemicals Preparation

Standard chlorpyrifos insecticide was purchased from Sigma-Aldrich Laborchemikalien GmbH (Stenheim, Germany) with 99% purity. Standard chlorpyrifos insecticide stock solution (1000 mg/L) for the insecticide residues analysis was prepared in acetone. The chlorpyrifos insecticide solution was diluted with distilled water to appropriate working concentrations.

Ozone Microbubbles Preparation

The OMBs used ozone generator (Ozonizer, Model SO5AE) and microbubbles water generator (Model 15KED02S, Nikuni Co., Ltd., Japan) at a flow rate of 7L/minute with an internal pressure of 0.25 MPa for distilled water. OMBs water came out from the microbubbles nozzle and circulated in the microbubbles bath.

Effect of Ozone Microbubbles on the Removal of Standard Chlorpyrifos Insecticide at Different Temperatures and Exposing Times

The optimum condition for the removal of chlorpyrifos insecticide using OMBs water was determined at various conditions at different temperatures (15, 20 and 25 °C) and various exposing times (0, 10, 20, 30, 40, 50 and 60 minutes). Standard chlorpyrifos insecticide solution were prepared in the flask. Each standard chlorpyrifos insecticide solution sample was added with 20 ml of OMBs water treatment previously mentioned and distilled water (control). The

concentration of dissolved ozone was determined by an ozone solution detector (Prominent Dulcotest DT1B photometer) and the removal percentages of each standard chlorpyrifos insecticide sample was determined by gas chromatography-flame photometric detector (GC-FPD).

Ozone Microbubbles Treatment on the Removal of Chlorpyrifos Insecticides and Postharvest Quality Changes in Tangerine

Organic tangerines (*Citrus reticulata* Blanco cv. Sai Nam Pueng) were purchased from the orchards in Mae Tang district, Chiang Mai Province, Thailand. The fruits were sorted for free of wound from harvesting and insect bites. Each fruit sample was sprayed with 10 mg/L chlorpyrifos insecticide solution and then air dried at room temperature. Then, they were sanitized in OMBs with the same conditions as the best result from above Experiment. Insecticide residues of tangerine was extracted with the Agilent Quick, Easy, Cheap, Effective, Rugged and Safe (QuEChERS) extraction kit. Then the samples were analyzed insecticide residues by GC-FPD to determine the removal percentage of chlorpyrifos insecticide.

Postharvest quality changes in tangerine

Tangerines were immersed into OMBs water in the same way as the previous experiment. Samples were stored at 25 °C and taken everyday for 7 days to determine the fruit quality. The percentage of weight loss, total soluble solids (TSS), titratable acidity (TA), disease incidence and ascorbic acid content were measured.

Statistic Analysis

All the experiments were replicated 3 times and evaluated with regression procedure using the SPSS version 17, while the differences among various treatments by Duncan's New Multiple Range test ($p < 0.05$).

RESULTS AND DISCUSSION

Effect of Ozone Microbubbles on the Removal of Standard Chlorpyrifos Insecticide at Different Temperatures and Exposing Times

The concentration of dissolved ozone in water was determined using an ozone solution detector

(Prominent Dulcotest DT1B photometer). It was found that OMBs treatments at 25 °C obtained the concentration of 0.22, 0.24, 0.29, 0.24, 0.26 and 0.29 mgO₃/L, at 20 °C obtained the concentration of 0.25, 0.30, 0.35, 0.30, 0.30 and 0.35 mgO₃/L and at 15 °C obtained the concentration of 0.49, 0.53, 0.61, 0.52, 0.48 and 0.48 mgO₃/L at 10, 20, 30, 40, 50 and 60 minute, respectively (Fig. 1). The dissolved ozone concentration of OMBs treatment were increased when exposure time 10-30 minutes and then they were stabled during experiment times. All OMBs treatment at 15 °C obtained the concentration of dissolved ozone more than at 20 and 25 °C. Due to the low temperature may increase the dissolved ozone in water, while the high temperature increase the chemical reaction between substrate and oxidant, but decrease the dissolved ozone in water [15].

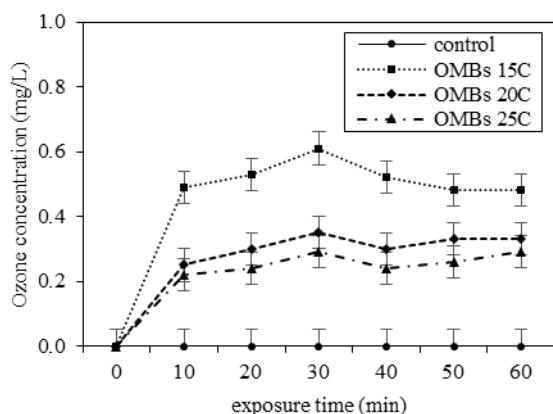


Fig. 1 Concentration of dissolved ozone after OMBs at different temperatures and exposing times.

The effect of OMBs to remove the standard chlorpyrifos insecticide solution was also examined. It was found that the removal percentage of standard chlorpyrifos insecticide was significantly induced with low temperature and prolonged OMBs exposure time for 30 minutes. Furthermore, OMBs at 15 °C for 30 minutes was the most effective treatment for removing standard chlorpyrifos insecticide residues, insecticide removal was 42%. But, the trend of standard chlorpyrifos insecticide residues removal percentage after exposure time for 40-60 minutes in all OMBs treatment was decreased. There were significant ($P < 0.05$) difference in each OMBs treatment (Fig. 2).

Ozone is a powerful oxidant, probably modified the chemical structure of chlorpyrifos insecticide by oxidizing sulfate ion in thiophosphorile bonds ($P=S$) of chlorpyrifos insecticide into phosphorile bonds ($P=O$) [16], [17]. And, decreasing of ozonated water temperature cause positive effect on the removal percentage of organophosphate insecticides [18]. Moreover, microbubbles has a high surface area,

which can maintain the ozone for a long time. In addition, the usefulness effect of low OMBs water temperature may be due to the increasing dissolved ozone in water, which enhance the oxidizing efficiency of the OMBs to collapse with insecticide structure [19].

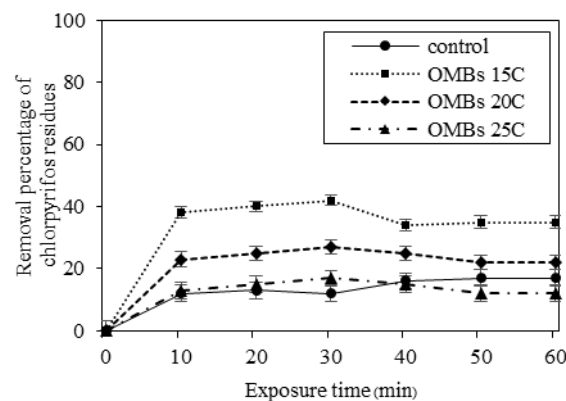


Fig. 2 Removal percentage of standard chlorpyrifos solution after OMBs treatment at different temperatures and exposing times.

Ozone Microbubbles Treatment on the Removal of Chlorpyrifos Residues and Postharvest Quality Changes in Tangerine

Tangerines were sanitized in OMBs treatment in order to remove residual chlorpyrifos insecticide. The results showed that OMBs at 15 °C for 30 minutes was the most effective to remove chlorpyrifos insecticide from tangerine that related with concentration of dissolved ozone. It was found that the chlorpyrifos residues on fresh tangerine showed the highest removal percentage of chlorpyrifos residues (81%) with significant ($P < 0.05$) different when compared with an individual treatment and the control, which was

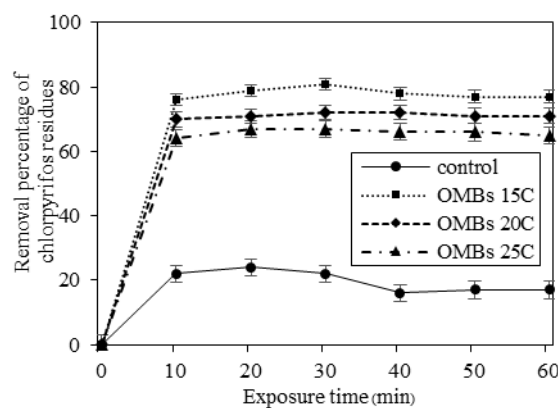


Fig. 3 Removal percentage of chlorpyrifos in fruit after OMBs at different temperatures and exposing times.

Table 1 Changes in percentage of weight loss, TSS, TA, disease incidence and ascorbic acid content of tangerine after sanitizing with ozone microbubbles at 15°C for 60 minutes, and storage at 25 °C for 7 days

treatment	Weight loss (%)	TSS (%)	TA (%)	Disease incidence (%)	Ascorbic content (mg/ml)
Control	0.92a	10.76a	0.23a	3.43ab	0.91ab
OMBs 10 minutes	0.80a	10.42a	0.28ab	3.33a	1.01a
OMBs 20 minutes	0.83a	9.60a	0.32ab	3.33a	1.09a
OMBs 30 minutes	0.82a	9.80a	0.28ab	3.33a	1.04a
OMBs 40 minutes	0.81a	9.82a	0.30ab	3.43ab	1.06a
OMBs 50 minutes	0.81a	9.75a	0.29ab	3.43ab	1.05a
OMBs 60 minutes	0.83a	9.75a	0.29ab	3.43ab	1.06a

Note: The data followed by the same letter within the column are not significantly different ($P < 0.05$)

sanitized in distilled water (Fig. 3). This trend could be explained by the reaction of OMBs with low temperature increasing dissolved ozone in water leading to high hydroxyl radical producing, which effectively distinguished chlorpyrifos residues on the tangerine surface. Similarly, Wu *et al.* [8] reported that application of the ozonated water at 14°C for insecticide removal from Pak Choi (*Brassica rapa*) was more effective than at 24 °C.

Thus, this research showed that the efficiency of OMBs on chlorpyrifos insecticide removal depended on the decreasing of the temperature of OMBs water and exposure times. Temperature of OMBs water related to the efficacy of dissolved ozone in water. Therefore, the low temperature could be increase the ability of dissolved ozone in water.

The postharvest quality changes in the tangerine after sanitizing with OMBs treatment, and then storing at 25 °C and taken everyday for 7 days were concluded and shown in Table 1. All treatments had non-significant differences as fruit quality changes during storage at 25 °C for 7 days. The percentage of weight loss, TSS, TA, disease incidence and ascorbic acid content in all treatment were not significant changes during storage in all the treatments. Similarly, treatment of vegetables such as arugula, bell pepper, cabbage, carrot, cucumber, leek, pasley and tomatoes with ozonated water at 25 °C can remove chlorpyrifos insecticide residues higher than at 35 °C without changing in antioxidant capacity, total phenolic and ascorbic acid [20].

CONCLUSION

OMBs at different temperatures had effects on the removal of chlorpyrifos insecticide. The exposure times of OMBs at 15°C for 30 minutes provide the best result on the removal of chlorpyrifos insecticide (81%) in tangerine and have no effects on the fruit quality.

ACKNOWLEDGEMENTS

This research has been supported by Postharvest Technology Innovation Center, Office of the Higher Education Commission, Bangkok, Thailand., Postharvest Technology Research Institute, Chiang Mai University, Chiang Mai, Thailand and the Graduate School Chiang Mai University, Chiang Mai, Thailand.

REFERENCES

- [1] Ousap P., Road Map of Food Safety, Report from Thai Pesticide Alert Network, 2017. <http://www.thaipan.org/node/831>.
- [2] Chelme-Ayala P., El-Din M.G., and Smith D.W., Kinetics and Mechanism of the Degradation of Two Pesticides in Aqueous Solutions by Ozonation, *Chemosphere*, Vol. 78, Issue 5, 2010, pp. 557–562.
- [3] Carletti L., Botondi R., Moschetti R., Stella E., Monarca D., Cecchini M., and Massantini, R., Use of Ozone in Sanitation and Storage of Fresh Fruits and Vegetables, *Journal of Food, Agriculture and Environment*, Vol. 11, 2013, pp. 585-589.
- [4] Coke A.L., For Chapter in a Book, *Ozone in Food Processing*, Ed. Blackwell Publishing Ltd., 2012, pp. 48-51.
- [5] Ormad M.P., Miguel N., and Claver A., Pesticides Removal in the Process of Drinking Water Production, *Journal of Antimicrobial Chemotherapy*, Vol. 71, Issue 1, 2008, pp. 97-106.
- [6] Whangchai K., Uthaibutra J., Phiyanalinmat S., Pengphol S., and Nomura N., Effect of Ozone Treatment on the Reduction of Chlorpyrifos Residues in Fresh Lychee Fruits, *Ozone: Science and Engineering*, Vol. 33, 2011, pp. 232-235.

- [7] Kusvuran E., Yildirim D., Mavruk F., and Ceyhan M., Removal of Chlorpyrifos Ethyl, Tetradifon and Chlorothalonil Pesticide Residues from Citrus by Using Ozone, *Journal of Hazardous Materials*, Vol. 2, Issue 4, 2012, pp.287-300.
- [8] Wu J.G., Luan T., Lan C.Y., Lo T.W.H., and Chan G.Y.S., Removal of Residual Pesticides on Vegetable Using Ozonated Water, *Food Control*, Vol. 18, 2007, pp. 466-472.
- [9] Sumikura M., Hidaka M., Murakami H., Nobutomo Y., and Murakami T., Ozone Microbubble Disinfection Method for Wastewater Reuse System, *Water Science and Technology*, Vol. 56, Issue 5, 2007, pp. 53-61.
- [10] Takahashi M., Chiba K., and Li P., Formation of Hydroxyl Radicals by Collapsing Ozone Microbubbles under Strong Acid Conditions, *The Journal of Physical Chemistry*, Vol. 111, 2007, pp. 11443-11446.
- [11] An T., Gao Y., Li G., Kamat P.V., Peller J., and Joyce M.V., Kinetics and Mechanism of OH Mediated Degradation of Dimethyl Phthalate in Aqueous Solution: Experimental and Theoretical Studies, *Environmental Science and Technology*, Vol. 48, Issue 1, 2014, pp. 641-648.
- [12] Khuntia S., Majumder S.K., and Gosh P., Removal of Ammonia from Water by Ozone Microbubbles, *Industrial and Engineering Chemistry Research*, Vol. 52, Issue 1, 2013, pp. 318-326.
- [13] Jabesa A., and Ghosh P., Removal of Diethyl Phthalate from Water by Ozone Microbubbles in a Pilot Plant, *Journal of Environmental Management*, Vol. 180, 2016, pp. 476-484.
- [14] Ikeura H., Hamasaki S., and Tamaki M., Effects of Ozone Microbubble Treatment on Removal of Residual Pesticides and Quality of Persimmon Leaves, *Food Chemistry*, Vol. 138, Issue 1, 2013, pp. 366-371.
- [15] Hart E.J., and Henglein A., Free Radical and Free Atom Reactions in the Sonolysis of Aqueous Iodide and Formate Solutions, *Journal of Physic Chemistry*, Vol. 89, 1985, pp. 4342-4347.
- [16] Pond A.L., Chambers H.W., and Chambers J.E., Organophosphate Detoxication Potential of Various Rat Tissues via A-esterase and Aliesterase Activities, *Toxicology Letters*, Vol. 78, Issue 3, 1995, pp. 245-252.
- [17] Wu J.G., Lan C.Y., and Chan G.Y.S., Organophosphorus Pesticide Ozonation and Formation of Oxon Intermediates, *Chemosphere*, Vol. 76, 2009, pp. 1308-1314.
- [18] Kusvuran E., Yildirim D., Mavruk F., and Ceyhan M., Removal of Chlorpyrifos Ethyl, Tetradifon and Chlorothalonil Pesticide Residues from Citrus by Using Ozone, *Journal of Hazardous Materials*, Vol. 2, Issue 4, 2012, pp. 287-300.
- [19] Guidance Manual Alternative technique and Oxidant, Information from United States Environmental Protection Agency, 2001. http://water.epa.gov/lawsregs/rulesregs/sdwa/mdbp/upload_2001_12_mdbp_alter.pdf.
- [20] Khaled A.O., Fahad B., and Abdullah A., Ozone as a Safety Post-Harvest Treatment for Chlorpyrifos Removal from Vegetables and Its Effects on Vegetable Quality, *International Journal of Food and Nutritional Science*, Vol. 3, Issue 2, 2017, pp. 1-11.

EFFECTS OF ACIDIC ELECTROLYZED WATER WITH DIFFERENT TEMPERATURES ON MICROBIAL CONTROL AND QUALITY OF FRESH-CUT BANANA LEAVES DURING STORAGE

Varumporn Kuljaroensub¹, Kanda Wangchai^{1,2} and Usawadee Chanasut^{1,2}

¹Department of Biology, Faculty of Science, Chiang Mai University, Chiang Mai 50200, Thailand;

²Postharvest Technology Institute/ Postharvest Technology Innovation Center, Chiang Mai University, Chiang Mai 50200, Thailand

ABSTRACT

The effects of acidic electrolyzed water (AEW) on microbial control and quality of fresh-cut banana leaves during storage were studied. Fresh-cut banana leaves cv. Taneer (TN) and cv. Klauay Namwa (KN) were sanitized with either 4°C or 27±2°C of 50 ppm acidic AEW for various times (10, 20 and 30 minutes). The sanitized samples were packed in polyethylene (PE) bag and storage at 5±2°C for 7 days, before transferred to 27±2°C to evaluate their shelf-life. The results showed that sanitization with 4°C and 27±2°C of AEW for 30 minutes were completely eliminated the microorganism on fresh-cut samples from both cultivars. Nevertheless, these contact time had the highest loss more than 78% after 5 days at room temperature. Sanitized samples with AEW for 20 and 30 minutes effectively delayed the microbial growth, therefore the amount of microorganism remained below EU Regulation (EC) No. 2073/2005 criteria after storage. The shelf-life of fresh-cut samples was 13 days and terminated after their visual appearance such as yellowing or browning occurred. Fresh-cut samples sanitization with both treatments had similar quality changes such as color changes and chlorophyll contents. However, sanitization with 4°C AEW had lower weight loss than those of with 27°C AEW during storage at room temperature. It also effectively reduced the microorganism on fresh-cut samples and had the lowest loss which was 22%. Therefore, sanitization with 4°C AEW for 20 minutes was an appropriate method to sanitized fresh-cut banana leaves for both cultivars.

Keywords: Sanitization, Fresh-cut, Acidic electrolyzed water, Banana leaves

INTRODUCTION

Banana leaves have been used for food wrapped and decoration since the ancient times due to their appearance and aroma made food is appetizing. Nowadays cut banana leaves are widely used for food wrapping and decoration in restaurants both in Thailand and overseas. The banana leaves exported from Thailand was frozen. The bag of banana leaves contained at least 5 kilograms of cut banana leaf sheath. However there were less than 50% can be used from each bag, and the rest became waste because of the trimming to suitable for consumer purposes.

Today's consumer is demanding for foods that require minimal process, for example, Fresh cut fruit and vegetables, initially called minimally processed or lightly processed products, are those that have been trimmed, peeled and/or cut into 100% usable product that is bagged or pre-packed and kept at refrigerated storage. These foods are in great demand because of their convenience [1]. The food service industry and restaurants are the major users of minimally processed products [2]. However, fresh-cut products deteriorate quickly and have limited shelf-life [3]. Major problems of deterioration in fresh-cut products associated with

the microbial growth in the products. Raw fresh produce could be contaminated with pathogens during harvesting through fecal material (manure, both of human and animal origin), human handling, washing procedure, processing equipment, transportation, and distribution [4].

Electrolyzed Water (EW) has been used as sanitizer in the food industry for many years [5][6]. AEW are conventionally generated by electrolysis of aqueous sodium chloride (0.5–1.0% NaCl), and an electrolyzed acidic solution is produced at the anode. Acidic Electrolyzed water (AEW) has a strong bactericidal effect on pathogenic and spoilage microorganisms [7][8]. This effect is attributed to its low pH (2.1–4.5), high oxidation–reduction potential (higher than 1000 mV), and the presence of active oxidizers such as hypochlorous acid [9][10]. Previously, Issa-Zacharia *et al.* [11] reported that Slightly AEW technology had stronger decontamination ability than other sanitizers in fresh-cut lettuce and carrot. Tomas-Callejas *et al.* [12] also reported that acidic electrolyzed water has the most effective on microbial reduction of mizuna baby leaves compared with other sanitizers.

There are numerous reports which describe the efficacy of AEW on the microbial growth on fruit and vegetables [13][14]. Therefore, this sanitizer

should effectively remove microbial contamination on the fresh-cut banana leaves too. The purpose of the current study was to evaluate the efficacy of 4°C and 27±2°C AEW at different time (10, 20 and 30 minutes) for controlling microbial growth and their effect on quality of fresh-cut banana leaves during storage at low temperature.

MATERIALS AND METHODS

Plant Materials

Banana leaves cv. Tanee (*Musa balbisiana* Colla.) and cv. Klauy namwa (*M. sapientum* Linn.) from Muang mai market (Chaing mai, Thailand) were transported to the postharvest laboratory (Chiangmai University, Thailand). The leaves were physically inspected and defective parts such as mechanical damage or yellowing pieces were removed. Selected leaves were cut into 7 inches diameter of circle for following study.

Processing and Storage Conditions

The fresh-cut samples were sanitized with either 4°C or 27°C acidic electrolyzed water (final chlorine concentration 50 ppm, pH 2-4) for 10, 20, 30 minutes. After air dried, sanitized samples were placed in PE bags. All steps were performed under sanitary conditions. Samples were stored at 5±2°C for 7 days and then transfer at room temperature (27±2°C) for 8 days. For each treatment, ten replicated were used. The microbial growth, quality changes such as, chlorophyll content, percentage of weight loss and color changes of sample were evaluated on the day 0) and after 3, 5, 7 days of storage at 5±2°C and after 9, 11, 13, 15 days at room temperature.

Microbial Content Determination

Samples were examined according to the standard methods for the microbiological analysis. Thirty nine grams of potato dextrose agar (PDA) were suspended in 1 L distilled water and sterilizing at 120 psi pressured for an hour. Spread plate technique after serial dilution in sterile distilled water was used in all tests. The first dilution was prepared by shaking 5x5 cm² of leaf samples with 5.8 ml of sterile distilled water and further dilutions were made according to the need. Ten plates were used for each treatment. Total viable plate count agar was determined after incubation at 37°C for 48 hours.

Quality Changes Determination

Weight loss

The weight loss of samples was determined by weighing each fresh-cut leaf samples on the day after each period of storage using a laboratory level weighing balance. Values are reported as percentage of weight loss per initial sample weight.

Color evaluation

The upper and lower surface color of fresh-cut banana leaves were determined using a HunterLab colourimeter (ColourFlex, Hunter Associates Laboratory, Inc., VA, USA). Color was measured using the CIE L*, a* and b* scale. The color values were expressed as L* (whiteness or brightness/darkness), a* (redness/greenness) and b* (yellowness/blueness) at any time, respectively. Each sample was scanned at three different locations to determine the average L*, a* and b* values during the measurements.

Chlorophyll content

The chlorophyll pigments were extracted from 5 g. of fresh-cut sample with 20 ml acetone for 20 minutes and then filter with filter paper No.1. Quantification was performed in a spectrophotometer (UV-1603 Shimadzu Tokyo, Japan) The total chlorophyll, chlorophyll a and chlorophyll b content was expressed as mg per 100 g of fresh weight using [15] method.

Experimental Design and Statistical Analysis

The experimental units were bags and there were ten replications per sanitizing treatment, application system and evaluation period. ANOVA tests were used depending on the homogeneity of the variances. The differences among various treatments by Tukey's range test (P<0.05) using SPSS version 14 [16].

RESULTS AND DISCUSSION

Microbial Content Determination

The initial total microorganism on the TN leaves was 313.33 and the KN leaves was 434.44 CFU/cm². Cleaning with distilled water reduced the microbial population to 48.75 (TN). and 90.93 (KN) CFU/cm² The longer contact time, the higher effective of microorganism inactivation (Fig. 1,2) for both temperatures. the sanitizing treatment.

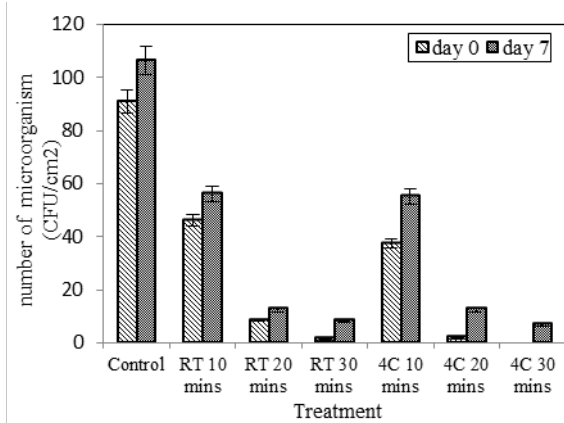


Fig. 1 The number of microorganism on TN fresh-cut banana leaves after sanitization with AEW and after storage at $5\pm 2^\circ\text{C}$ for 7 days.

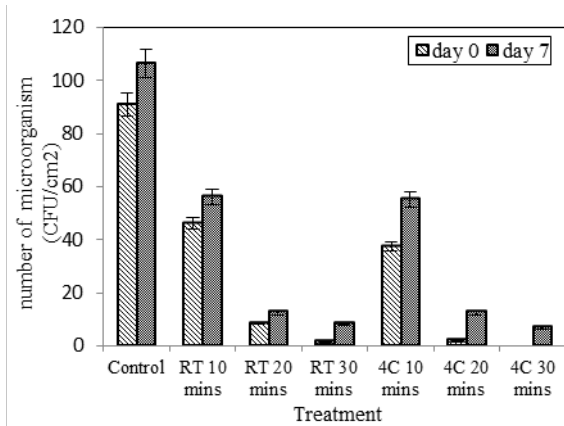


Fig. 2 The number of microorganism on KN fresh-cut banana leaves after sanitization with AEW and storage at $5\pm 2^\circ\text{C}$ for 7 days.

The maximum reduction of total microorganism on fresh-cut banana leaves was observed by AEW 4°C for 30 minutes which were completely eliminated the microorganism on fresh-cut samples from both cultivars at the day 0. The number of microorganism slightly increased to 5.00 (TN) and 6.75 (KN) CFU/cm² after 7 days storage at $5\pm 2^\circ\text{C}$. Sanitization with 4°C AEW for 20 minutes were significantly reduced the total microbial content on both cultivars to 1.5 (TN) and 1.77 (KN) CFU/cm². Although the number of microbial population in the leaves sample increased to 8.75 (TN) and 12.5 (KN) CFU/cm² after 7 days storage. [Fig 1,2], they were below the EU Regulation and acceptable for using as fresh cut. The temperature of sanitizer and washing time were factors that affected the microbial efficacy of AEW [17]. Koide *et al.* [18] also reported that when fresh-cut cabbage was wash by slightly AEW, the reduction were found in total bacteria count. The number of bacteria increased during storage. Similar results were reported by Beltran *et al* [19] and

Lopez-Galvez [20] that found the microbial growth on fresh-cut products even stored at low temperature.

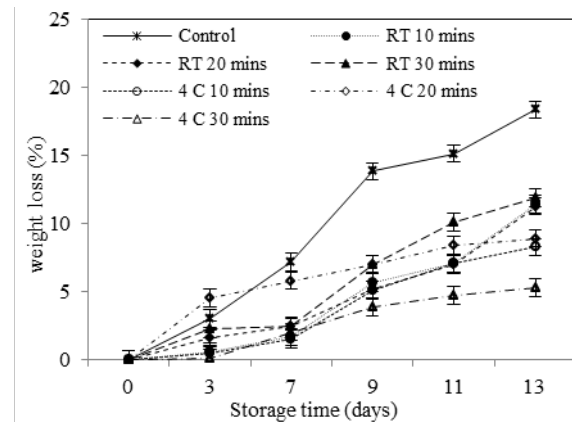


Fig. 3 Effects of AEW on % weight loss of TN fresh-cut banana leaf storage at $5\pm 2^\circ\text{C}$ for 7 days and $27\pm 2^\circ\text{C}$ for 6 days.

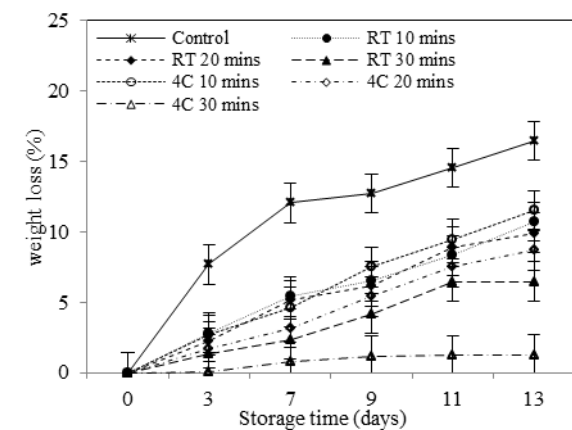


Fig. 4 Effects of AEW on % weight loss of KN fresh-cut banana leaf storage at $5\pm 2^\circ\text{C}$ for 7 days and $27\pm 2^\circ\text{C}$ for 6 days.

Quality Changes Determination

In this study, the shelf life of fresh-cut banana leaves was 13 days regardless to their visual appearances such as the occurrence of yellowing or browning. No difference in the appearance quality were observed among sanitizing agents after washing on day 0 and after 7 days of storage at $5\pm 2^\circ\text{C}$. However, the visual appearance rapidly deteriorated after transferred to $27\pm 2^\circ\text{C}$. Fresh-cut banana leaves that sanitized with 4°C AEW had lower quality loss than fresh-cut banana leaves that sanitized with 27°C AEW. The appearance of fresh-cut banana leaves sanitized with 4°C AEW for 30 minutes quickly declined and more than 78% of the sample had to be discarded. The lowest quality loss was found on fresh-cut banana leaves sanitized with 4°C AEW for 20 minutes which were 22%. Park *et*

al. [22] also report that long treatment times adversely affect the general appearance and nutritional content of the product.

The percentage of weight loss from all treatment slightly increased during storage at 5°C for 7 days

Table 1 Changes of surface color and chlorophyll content in TN fresh-cut banana leaves after sanitized with electrolyzed water and storage for 13 days.

treatment	Upper surface color			Lower surface color			Chlorophyll content		
	L*	a*	b*	L*	a*	b*	total	a	b
control	37.32a	-7.29a	24.58a	48.49a	-7.16a	26.59a	0.14 a	0.09a	0.01a
RT-AEW									
-10 mins	42.36a	-5.16a	24.65a	52.13a	-7.52a	31.53a	0.14 a	0.10a	0.02a
-20 mins	35.59a	-6.16a	24.14a	47.12a	-6.77a	25.26a	0.19 a	0.10a	0.08a
-30 mins	49.08a	-6.54a	28.23a	50.55a	-6.50a	27.53a	0.14 a	0.10a	0.04a
4°C-AEW									
-10 mins	34.13a	-7.05a	23.65a	47.51a	-7.83a	27.05a	0.15 a	0.07a	0.06a
-20 mins	35.69a	-7.16a	24.46a	47.22a	-8.07a	26.12a	0.17a	0.10a	0.06a
-30 mins	35.55a	-7.93a	23.95a	47.95a	-7.46a	26.22a	0.16a	0.10a	0.05a

Note: The data followed by the same letter within the column are not significantly different ($P < 0.05$)

Table 2 Changes of surface color and chlorophyll content in KN fresh-cut banana leaves after sanitized with electrolyzed water and storage for 13 days.

treatment	Upper surface color			Lower surface color			Chlorophyll content		
	L*	a*	b*	L*	a*	b*	total	a	b
control	43.35a	-9.28a	26.67a	54.66a	-6.54a	30.13a	0.06a	0.04a	0.02a
RT-AEW									
-10 mins	40.16a	-9.42a	27.21a	59.17a	-6.16a	31.51a	0.06a	0.05a	0.01a
-20 mins	52.12a	-8.24a	31.21a	57.84a	-5.16a	31.45a	0.07a	0.05a	0.01a
-30 mins	50.42a	-8.15a	31.30a	54.91a	-6.52a	32.55a	0.07a	0.05a	0.01a
4°C-AEW									
-10 mins	44.15a	-8.54a	27.65a	52.23a	-8.63a	32.01a	0.06a	0.04a	0.01a
-20 mins	41.20a	-9.16a	32.20a	53.13a	-6.79a	30.01a	0.06a	0.05a	0.01a
-30 mins	41.16a	-9.12a	25.22a	52.52a	-6.15a	30.45a	0.09a	0.06a	0.02a

Note: The data followed by the same letter within the column are not significantly different ($P < 0.05$)

and they rapidly increased after transferred to $27 \pm 2^\circ\text{C}$. There were no significant differences among AEW treatments during storage period from both on TN and KN fresh-cut banana leaves [Fig.3,4].

The surface color of fresh-cut banana leaves both upper and lower sides were evaluated. The L^* , a^* , and b^* value exhibited no significant differences among washing treatments after storage for 13 days. Furthermore, the chlorophyll contents of fresh-cut banana leaves from each sanitizing temperature exhibited no significant differences after storage for 13 days [table1, 2]. Therefore, the temperatures of the sanitizers had no effect on the color changes and the chlorophyll content of the fresh-cut banana leaves. This finding agreed with a previous study that no significant differences in weight loss, color and chlorophyll content were found on fresh-cut banana leaves after sanitized with sanitizers [23]. In addition, Martinez-Sanchez *et al* [24] reported that sanitized rocket leaves with sanitizers before storage did not affects the quality such as color and

chlorophyll content during storage. Similarly results were reported by Izumi [25] on mizuna baby leaves and Wang *et al.* [26] on cilantro leaves. However,

the effect of sanitization treatment on fresh-cut product quality depends on the fruit or vegetable, time of exposure, and concentration of sanitizer [27].

CONCLUSION

Sanitization with 4°C AEW for 20 minutes was an appropriate method to sanitized fresh-cut banana leaves for both cultivars. The treatment used had least effect on the appearance quality of fresh-cut banana leaves such as weight loss, surface color and chlorophyll content after washing and storage. Therefore, this method will be applied in sanitizing process of fresh-cut banana leaves for export in foreign market.

ACKNOWLEDGEMENTS

This research has been support by Postharvest

Technology Research Institute/Postharvest Technology Innovation Center, Chiang Mai University and The Graduate School Chiang Mai University, Chiang Mai, Thailand., Science Achievement Scholarship of Thailand.

REFERENCES

- [1] Tirkey B., Pal U.S., Bal L.M., Sahoo. N.R., Bakhara C.K. and Panda M.K., Evaluation of physic-chemical changes of fresh-cut unripe papaya during storage, Food packing and shelf life international, 2014, pp. 190-197.
- [2] Watada A.E., Ko N.P. and Minott, D.A., Factors affecting quality of fresh-cut horticultural products, Postharvest Biology and Technology, vol. 9, 1996, pp. 115-125.
- [3] Montero-Calderón M., Rojas-Graü M.A. and Martín-Belloso O., Effect of packaging conditions on quality and shelf-life of fresh-cut pineapple (*Ananas comosus*), Postharvest Biology and Technology, vol. 50, 2008, pp. 182-189.
- [4] Hyun J.E., Bae Y. M., Yoon J.H. and Lee S.Y., Preservative effectiveness of essential oils in vapor phase combined with modified atmosphere packaging against spoilage bacteria on fresh cabbage, Food Control, vol. 51, 2015, pp. 307-313.
- [5] Liao L.B., Chen W.M., Xiao X.M., The generation and inactivation mechanism of oxidation-reduction potential of electrolyzed oxidizing water, Journal of Food Engineering, vol. 78, 2007, pp. 1326-1332.
- [6] Rico D., Martín-Diana A., Barry-Ryan C., Frías J., Henahan G., Barat J.M., Use of neutral electrolyzed water (EW) for quality maintenance and shelf-life extension of minimally processed lettuce, Innovative Food Science and Emerging Technologies, vol. 9, 2008, pp. 37-48.
- [7] Selma M. V., Allende A., Lopez-Galvez F., Conesa M. A., and Gil M. I., Disinfection potential of ozone, ultraviolet-C and their combination in wash water for the fresh-cut vegetable industry, Food Microbiology, vol. 25, Issue 6, 2008, pp. 809-814.
- [8] Ramos B., Miller F.A., Brandão T.R.S., Teixeira P. and Silva C.L.M., fruits and vegetables—An overview on applied methodologies to improve its quality and safety, Innovative Food Science and Emerging Technologies, vol. 20, 2013, pp. 1-15.
- [9] Keskinen L.A., Burke A. and Annous B.A., Efficacy of chlorine, acidic electrolyzed water and aqueous chlorine dioxide solutions to decontaminate *Escherichia coli* O157:H7 from lettuce leaves, International Journal of Food Microbiology, vol. 132, Issue 2-3, 2009, pp. 134-140.
- [10] Rico D., Martin-Diana A.B., Barat J.M. and Barry-Ryan C., Extending and measuring the quality of fresh-cut fruit and vegetables: A review, Trends in Food Science & Technology, vol. 18, Issue 7, 2007, pp. 373-386.
- [11] Cadwell K.N., Adler B.B., Anderson G.L., Williams P.L. and Beuchat L.R., Ingestion of *Salmonella enterica* serotype Poona by a free-living nematode, *Caenorhabditis elegans*, and protection against inactivation by produce sanitizers, Applied Environmental Microbiology, vol. 69, 2003, pp. 4103-4110.
- [12] Rodgers S.L., Cash J.N., Siddiq M. and Ryser E.T., A comparison of different chemical sanitizers for inactivating *Escherichia coli* O157:H7 and *Listeria monocytogenes* in solution and on apples, lettuce, strawberries, and cantaloupe, Journal of Food Protection, vol. 67, 2004, pp. 721-731.
- [13] Issa-Zacharia A., Kamitani Y., Miwa N., Muhimbula H. and Iwasaki K., Application of slightly acidic electrolyzed water as a potential; non-thermal food sanitizer for decontamination of fresh ready-to-eat vegetables and sprouts, Food Control, vol. 22, 2011, pp. 601-607.
- [14] Tomas-Callejas A., Martinez-Hernandez G.B., Artes F., Artes-Hernandez F., Neutral and acidic electrolyzed water as emergent sanitizer for fresh-cut mizuna baby leaves, Postharvest Biology and Technology, vol. 59, 2011, pp. 298-306.
- [15] Witham F.H., Blaydes D.F. and Devlin R.M., Experiment in Plant Physiology. D. Van Nostrand Company, NY., 1971.
- [16] FDA, Food and drugs administration, Center for Food Safety and Applied Nutrition, Draft final guidance for industry: guide to minimize food safety hazards for fresh-cut fruits and vegetables, 2007, pp.11364-11368.
- [17] Ding T., Rahman S.M.E., Oh D.H., Inhibitory effects of low concentration electrolyzed water and other sanitizers against foodborne pathogen on oyster mushroom, Food Control, vol. 22, 2011, pp. 318-322.
- [18] Koide S., Takeda, J., Shi J., Shono H. and Atungulu G.G., Disinfection efficacy of slightly acidic electrolyzed water on fresh-cut cabbage, Food Control, vol. 20, 2009, pp. 294-297.
- [19] Beltran D., Selma M.V., Tudela J.A., Gil M.I., Effect of different sanitizers on microbial and sensory quality of fresh-cut potato strips stored under modified atmosphere or vacuum packaging, Postharvest Biology Technology, vol. 37, 2005, pp. 37-46.
- [20] Lopez-Galvez F., Allende A., Selma M.V. and Gil M.I., Prevention of *Escherichia coli* cross-contamination by different commercial

- sanitizers during washing of fresh-cut lettuce, *International Journal of Food Microbiology*, vol. 133, 2009, pp. 167-171.
- [21] Perish M.E., Beuchart L.R., Suslow T.V., Harris L.J., Gerret E.H., Farber J.N. and Busta F.F., Methods to reduce/eliminate pathogens from fresh and fresh-cut produce, *Comprehensive Reviews in Food Science and Food Safety*, 2003.
- [22] Park E.J., Alexander E., Taylor G.A., Costa R. and Kang D.H., Effect of electrolyzed water for reduction of foodborne pathogens on lettuce and spinach, *Journal of Food Science*, vol. 73, 2008, pp. 268-272.
- [23] Kuljarensab V., Effects of Some Sanitizers on Microbial Reduction and Quality of Fresh-cut Banana Leaf during Storage, Master of Science in Biology, Chiang Mai University, 2015.
- [24] Martinez-Sanchez A., Allende A., Bennett R.N., Frereres F., Gill M.I., Microbial, nutritional and sensory quality of rocket leaves as affected by different sanitizers, *Postharvest Biology and Technology*, vol. 42, 2006, pp. 86-97.
- [25] Izumi H.M., Electrolyzed water as a disinfectant for fresh-cut vegetables, *Journal of Food Science*, vol. 64, 1999, pp. 536-539.
- [26] Wang H., Feng H. and Luo Y., Microbial reduction and storage quality of fresh-cut cilantro washed with acidic electrolyzed water and aqueous ozone, *Food Research International*, vol. 37, 2004, pp. 949-956.
- [27] Mani-Lopez E., Palou A. and Lopez-Malo A., Effect of different sanitizers on the microbial load and selected quality parameters of “chile de arbol” pepper (*Capsicum frutescens* L.) fruit, *Postharvest Biology and Technology*, vol. 119, 2016, pp. 94-100.

ESTIMATION OF AMMONIUM SOURCES IN ALLUVIAL GROUNDWATER USING Cl^- AND GIS: A CASE STUDY OF INDRAMAYU CITY, INDONESIA

*Anna RUSYDI^{1,4}, Mitsuyo SAITO², Seiichiro IOKA³, Rizka MARIA⁴, Shin-ichi ONODERA¹

¹Graduate School of Integrated Arts and Sciences, Hiroshima University, Japan; ²Graduate School of Environmental and Life Sciences, Okayama University, Japan; ³Research Institute for Sustainable Energy, Hirosaki University, Japan; ⁴Research Center for Geotechnology, Indonesian Institute of Sciences, Indonesia

ABSTRACT

The aim of this study was to evaluate the sources of ammonium (NH_4^+) in a groundwater of coastal alluvial plain in Indonesia, using both chemical properties and geographic information. The study site was Indramayu, a developing rural area located in the northern part of West Java. The site is an ideal location for studying the impacts on groundwater during the initial stages of urbanization. In August 2017, 20 groundwater and river water samples were collected from sites representative of various types of land-use. The chloride (Cl^-) concentration in the samples ranged from 15 ppm to 12,000 ppm. These concentrations represented fresh-brackish to brackish-salt water conditions, indicating the influence of seawater on the groundwater samples. Furthermore, analysis of several nitrogen species identified high NH_4^+ concentrations in the samples. Based on the relationship between Cl^- and NH_4^+ , samples were clustered into three groups. The first and second groups exhibited linear correlations, while in the third group, no relationship between these two parameters was identified. The land-use associated with each group was then evaluated. The main NH_4^+ source in the first group was identified as organic sediment, where NH_4^+ may be released through ion exchange with sodium, facilitated by the high salinity conditions and potentially, from dissimilatory nitrate reduction to ammonium (DNRA) reactions. The source of NH_4^+ in the second group was suggested to be a combination of sediment, fertilizer, and human and animal waste. Finally, it was hypothesized that the source of NH_4^+ in the third group is mainly human waste.

Keywords: groundwater, alluvial plain, chloride, ammonium, land-use

1. INTRODUCTION

Groundwater is the largest unfrozen freshwater resource on earth, with a total volume of approximately 11 million km^3 [1]. This highly valuable resource could be used as drinking water for at least 50% of the world's population [2]. Despite this, unsustainable groundwater abstraction has led to a global groundwater depletion problem [1], [3]–[4]. Groundwater depletion can have knock-on effects, which are usually complex and dependent on the condition of the aquifer [1]. The direct effect, a decrease in the water table, can lead to serious issues, such as land subsidence and groundwater contamination. Such problems are already occurring in Indonesia. According to UNESCO [3], Indonesia is one of the top ten groundwater abstracting countries, with an abstraction rate of $14 \text{ km}^3/\text{year}$; this is predicted to increase by 1–2% annually [3].

Recently, these groundwater depletion effects have been increasingly observed in Indonesian coastal alluvial plains. An aquifer in alluvial plain has a large groundwater storage capacity, and thus forms

the main source of clean water for many developing cities. Thus, urbanization is one of the major triggers of groundwater contamination in these environments [5]–[6]. Jakarta and Semarang are examples of Indonesian coastal alluvial plain cities facing groundwater perturbation and nitrogen species contamination because of urbanization. For example, in Jakarta, extensive groundwater depletion has caused land-subsidence [7]–[8], shallow and deep groundwater mixing, seawater intrusion, and nitrogen contamination [5], [9]–[10]. Similarly, groundwater abstraction in Semarang has also resulted in land-subsidence [11], seawater intrusion, and nitrate contamination [12].

In this study, an investigation of groundwater in a coastal alluvial plain located in Indramayu, Indonesia, which can be found in the northern part of West Java (Fig. 1), was conducted. Indramayu is currently a rural area, but has a potential to become urbanized in the future. Unlike the big cities of Jakarta and Semarang, human environmental impact is not significant in Indramayu. This relatively pristine condition is ideal for studying the nature of the

groundwater environment during the early stages of urbanization.

In this study, the nitrogen concentration in the groundwater, particularly ammonium (NH_4^+), was studied. Furthermore, NH_4^+ source apportionment is attempted by evaluating the relationship between NH_4^+ and chloride (Cl^-) concentrations, in addition to an assessment of land-use.

2. METHODS

2.1 Study area

The study site was located in the eastern part of Indramayu, on the north Coast of Java (Fig. 1). The total area of Indramayu is approximately 2,100 km^2 , with a coastline length of about 147 km [13]. The topography of the area is low land to shore, with an average slope of 0-2%. The area has a tropical climate, with an average annual rainfall of 2,146 mm/year.

2.1.1 Geology

The Indramayu coast is a river delta, formed by sedimentation processes fed by the Cimanuk River [14]. Generally, Indramayu soil was formed from an alluvial plain environment, but also includes deposits from beach ridge, coastal, deltaic, and floodplain environments, along with the erosion of tuffaceous sandstone and conglomerate (Fig. 1).

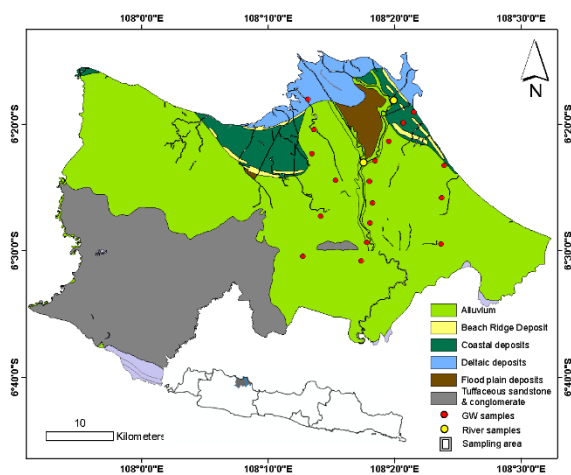


Fig. 1 Geology of Indramayu.

Alluvial plain is the dominant geologic formation in the area, with a groundwater water level of approximately 0.4 m to 3.2 m [15] and unconfined groundwater reserves of approximately 370 L/s [16]. The alluvial plain groundwater is also highly vulnerable to contamination.

2.1.2 Land-uses

Land-use in the Indramayu area is depicted in Fig. 2. The dominant land-use types are paddy fields and brackish fishponds. Settlements are concentrated on the delta formation, next to Cimanuk River. Oil and gas operations are also present, as this is the main industry located in the northeastern region of Java. This industry is owned by the Indonesian government.

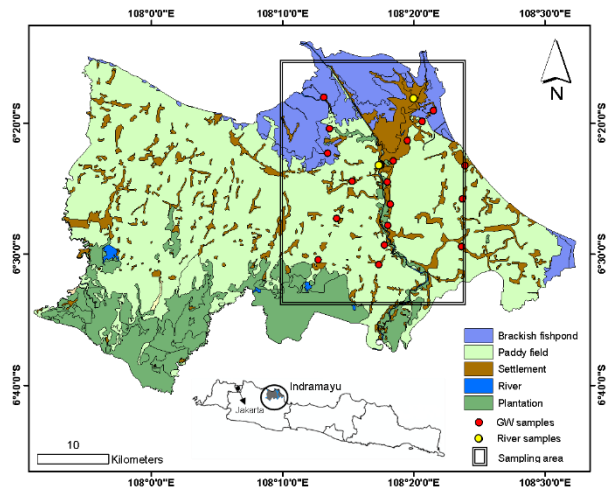


Fig. 2 Land-use types of Indramayu and sampling locations.

2.2 Sample collection

A total of 20 samples were collected from unconfined groundwater aquifers (18 samples) and the Cimanuk River (2 samples), in August 2017 (Fig. 2). Sampling locations were selected to represent the dominant land-use types in Indramayu area. The field campaign took place during the dry season with rainfall amounts between 20 – 50 mm.

2.3 Parameter and chemical analysis

This study focuses on the analysis of nitrogen species, including nitrate (NO_3^-), nitrite (NO_2^-), and ammonium (NH_4^+), in addition to chloride (Cl^-). Initially, samples were filtered through a 0.2 μm cellulose ester membrane filter and stored in a freeze condition until analysis. The concentrations of nitrogen species were determined with a continuous-flow automated nutrient analyzer and Cl^- was quantified with ion chromatography.

3. RESULTS AND DISCUSSION

3.1 Chloride and nitrogen species

3.1.1 Chloride concentration

The groundwater Cl^- concentrations varied from 15 ppm to 12,000 ppm. Using the Stuyfzand classification [17], the groundwater samples can be classified as fresh, fresh-brackish, brackish, brackish-salt, and salt water based on Cl^- concentration (Fig. 3). Freshwater was mainly identified in the settlement areas, while other classifications were identified in paddy fields and brackish fishpond areas. Samples with high Cl^- (> 150 ppm) were dominant over low Cl^- (<150 ppm).

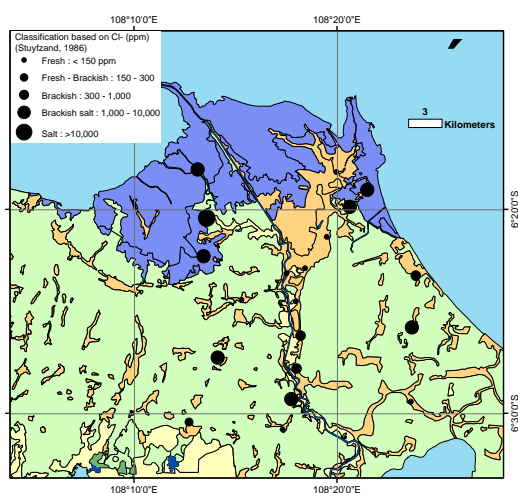


Fig. 3 Cl^- classification distribution.

Cl^- is ubiquitous in water and is relatively stable to chemical reactions. Therefore, Cl^- is usually used as a tracer to help evaluate water quality and chemical reactions occurring in aquatic environment. There are several natural sources of Cl^- in the freshwater environment, including the intrusion of saltwater from the ocean, natural weathering of bedrock or geologic deposits containing halite, unconsolidated sediments and soils, saline groundwater (brines), and volcanic activity [18]. In coastal regions, a major source of Cl^- is likely the result of saltwater intrusion from the ocean. Therefore, it was assumed the groundwater associated with a coastal area in this study, is heavily influenced by the seawater intrusions, owing to the high Cl^- concentrations observed.

3.1.2 Nitrogen species concentrations

Recent research suggests, that nitrogen contamination poses significant risks to the environment [19]–[22]. According to many previous studies [5]–[6], [23]–[24], the dominant speciation of nitrogen contamination in groundwater worldwide is

NO_3^- . In contrast, groundwater analysis of samples from Indramayu, exhibited higher NH_4^+ concentrations in comparison to NO_3^- (Fig. 4). The concentration of NH_4^+ fell between < 0.01 – 11 ppm and was detected at the majority of sites, while NO_3^- could only dominant at two sites. The presence of high NH_4^+ -N indicates the presence of human and animal wastes, and agricultural influences, such as fertilizer [23]–[25].

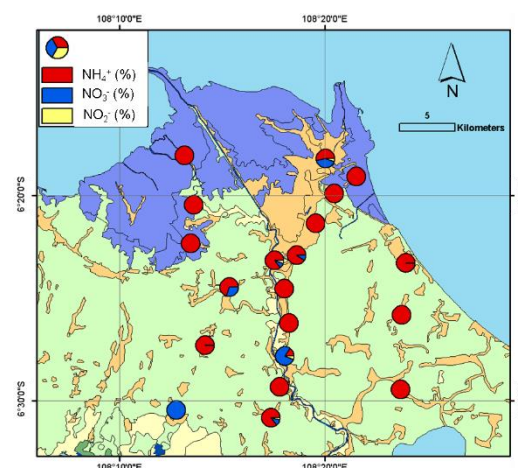


Fig. 4 Nitrogen species percentage at each sampling point.

As shown in Fig. 4, relatively high concentrations of NH_4^+ -N were not only found in the settlement and paddy field areas, but also in the brackish fishpond. Therefore, another source of NH_4^+ other than human and animal wastes and fertilizer is suspected.

3.1.3 Ammonium sources based on chloride distribution and land-uses evaluation

To evaluate the source apportionment of NH_4^+ , it was assumed that the non-reactive nature of Cl^- along with land-use type variability, could be used to trace sources of NH_4^+ other than human and animal waste. Fig. 5 depicts the correlation between observed NH_4^+ and Cl^- concentrations. Based on the correlations, underlying values can be clustered into three groups (I – III).

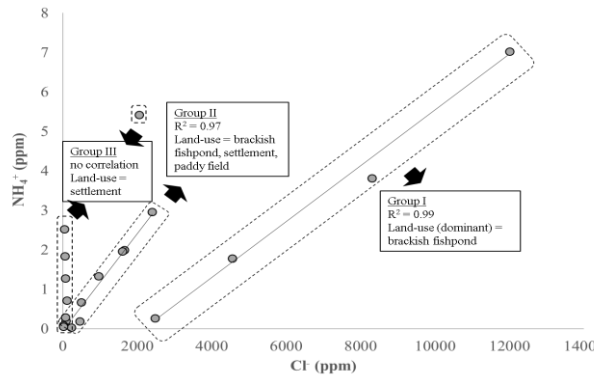


Fig. 5 Correlation between NH_4^+ and Cl^-

Groups I and II form linear correlations, while group III shows no relationship between NH_4^+ and Cl^- . Based on the groups formed, a land-use evaluation was conducted to determine the possible sources of NH_4^+ (Fig. 6).

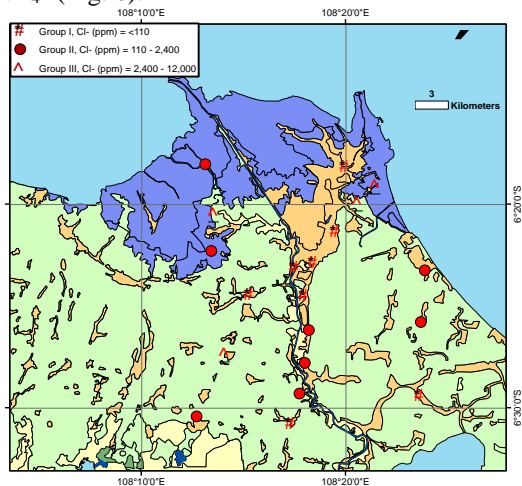


Fig. 6 Distribution of 3 groups clustered by Cl^- and NH_4^+ concentrations

Samples in group I exhibited the largest range in Cl^- concentration and also the strongest correlation with NH_4^+ concentrations ($R^2 = 0.99$). Group I samples are mainly located in the brackish fishpond, with the exception of a single point is located in a paddy field area. This point has a much higher Cl^- concentration (2,470 ppm) compared to other points located in paddy field areas. We therefore suggest that the NH_4^+ associated with group I is mainly derived from organic sediment, where NH_4^+ ion exchange with sodium (Na^+) could be facilitated under the high salinity conditions, and possibly from dissimilatory nitrate reduction to ammonium (DNRA) reactions [26].

Group II also produced a strong correlation between NH_4^+ and Cl^- concentrations ($R^2 = 0.97$). The concentration of Cl^- ranged from 1,100 and 2,400 ppm. The land-use type associated with this group is more varied than other two groups, and include brackish fishpond, paddy field, and settlement.

Therefore, the source of NH_4^+ for samples from group II is suggested to be from organic sediment, fertilizer, and human and animal wastes.

Finally, group III demonstrates no relationship between NH_4^+ and Cl^- concentrations. The samples for this group were associated with the lowest Cl^- concentrations (<110 ppm). The land-use type associated with this group is mainly settlements. It is therefore suggested, that the source of NH_4^+ for group III is mainly human waste.

4. CONCLUSION

In the early stages of urbanization of a coastal alluvial plain, groundwater resources may have high concentrations of NH_4^+ . The source of NH_4^+ is not limited to fertilizer and human and animal waste, but also from organic sediment. Organic sediment NH_4^+ can be released through ion exchange reactions with sodium (Na^+) under high salinity conditions, and possibly from the dissimilatory nitrate reduction to NH_4^+ .

5. ACKNOWLEDGMENTS

The authors acknowledge the Graduate School of Integrated Arts and Sciences, Hiroshima University and the Research Center for Geotechnology LIPI for facilitating this research. We would also like to express our gratitude for the valuable comments provided by reviewers and the editor of GEOMATE.

6. REFERENCES

- [1] Hertig W.A., and Gleeson T., Regional strategies for the accelerating global problem of groundwater depletion, *Nature Geoscience* 5, 2012, pp. 853-861.
- [2] Van der Gun, J., *Groundwater, and Global Change: Trends, Opportunities and Challenges*, UNESCO, 2012.
- [3] Gurdak J.J., Leblanc M., Aureli A., Resende T.C., Faedo G., Green T.R., Tweed S., Longuevergne L., Allen D.M., Elliot J.F., Taylor R.G., and Conti K., *Groundwater and the climate change: mitigating the global groundwater crisis and adapting to climate change*, UNESCO, 2015.
- [4] Konikow L.F., and Kendy L., *Groundwater depletion: a global problem*, *Hydrogeology Journal* 13, 2015, pp. 317-320.
- [5] Onodera S., Saito M., Sawano M., Hosono T., Taniguchi M., Shimada J., Umezawa Y., Lubis R.F., Buapeng S., and Delinom R., Effects of intensive urbanization on the intrusion of shallow groundwater into deep groundwater: Examples from Bangkok and Jakarta. *Science of the Total Environment*, Vol. 404, Issue 9, 2009, pp. 401 – 410.
- [6] Onodera S., *Subsurface pollution in Asian*

- Megacities, for Chapter in a Book: Groundwater and subsurface environments: Human impacts in Asian Coastal Cities, Springer Tokyo, 2011, pp. 159 – 184.
- [7] Abidin H.Z., Andreas H., Djaja, R., Darmawan D., and Gamal M., Land subsidence characteristics of Jakarta between 1997 and 2005, as estimated using GPS surveys, GPS Solutions, Vol. 12, Issue 1, 2008, pp. 23 - 32.
- [8] Lubis R.F., Onodera S., Onishi K., Saito M., Bakti H., Delinom R., and Shimizu Y., Interaction between river and groundwater in Jakarta megacity, coastal alluvial plain, Indonesia. IAHS-AISH Publication, Vol. 345, 2011, pp. 151 - 155.
- [9] Saito M., Onodera S., Umezawa Y., Hosono T., Shimizu Y., Delinom M., Lubis R.F., and Taniguchi M., Transport and transformation of chemical components in the groundwater flow system of Jakarta Metropolitan Area. Indonesian Journal of Geology and Mining, Vol. 21, Issue 2, 2011, pp. 1 – 6.
- [10] Delinom R.M., and Taniguchi M., Ancaman Bawah Permukaan Jakarta. LIPI Press. Jakarta, 2014.
- [11] Abidin H.Z., Andreas H., Gumilar I., Sidiq T.P., and Fukuda Y., Land subsidence in coastal city of Semarang (Indonesia): Characteristics, impacts, and causes. Geomatics, Natural Hazards and Risk, Vol. 4, Issue 3, 2013, pp. 226 – 240.
- [12] Sudaryanto M., and Wibawa Y.S., Sejarah perkembangan Kota Semarang (Jawa Tengah) di masa lalu dan dampak kehadiran polutan nitrat pada airtanah di masa kini. Indonesian Journal of Geology and Mining, Vol. 23, Issue 1, 2013, pp. 25 – 36.
- [13] Indonesian Statistic of Indramayu, Indramayu dalam angka 2017, Indonesian Statistic of Indramayu Regency, 2017.
- [14] Yuanita N., and Tingsanchali T., Development of a river delta: a case study of Cimanuk river mouth, Indonesia. Hydrological Processes, Vol. 22, Issue 18, 2008, pp. 3785 - 3801.
- [15] Rusydi A.F., Maria R., and Sudaryanto M., The distribution pattern of water type based on major ions content on shallow groundwater in Indramayu, West Java (in Bahasa Indonesia). Indonesian Journal of Geology and Mining, Vol. 27, Issue 2, 2017, pp. 201 - 211.
- [16] Saputra S.F., Perhitungan potensi air tanah di Kecamatan Gabus Wetan, Kabupaten Indramayu, Jawa Barat. J. Teknik Sipil dan Lingkungan, Vol. 1, Issue 3, 2016, pp 147 - 158.
- [17] Stuyfzand P.J., A new hydrochemical classification of water types with examples of application to The Netherlands. H2O, Issue 19, 1986, pp. 562-568.
- [18] Mullaney J.R., Lorenz D.L., and Arntson A.D., Chloride in groundwater and surface water in areas underlain by the glacial aquifer system, Northern United States, USGS, National Water-Quality Assessment Program, 2009, pp. 1 – 35.
- [19] Gruber N., and Galloway J.N., An Earth-system perspective of the global nitrogen cycle, Nature, Vol. 451, Issue 7176, 2008, p. 293.
- [20] Steffen W., Richardson K., Rockström J., Cornell S.E., Fetzer I., Bennett E.M., Biggs R., Carpenter S.R., De Vries W., de Wit C.A., and Folke C., Planetary boundaries: Guiding human development on a changing planet. Science, Vol. 347, Issue 6223, 2015, pp. 736-742.
- [21] Zhang X., Davidson E.A., Mauzerall D.L., Searchinger T.D., Dumas P., and Shen Y., Managing nitrogen for sustainable development, Nature, 528(7580), 51, 2015, pp. 51 – 59.
- [22] Hansen B., Thorling L., Schullehner J., Termansen M., and Dalgaard T., Groundwater nitrate response to sustainable nitrogen management, Scientific Reports, Vol. 7, Issue (1):8566, 2017, pp. 1 - 12.
- [23] Umezawa Y., Hosono T., Onodera S., Siringan F., Buapeng S., Delinom R., Yoshimizu C., Tayasu I., Nagata T., and Taniguchi M., Sources of nitrate and ammonium contamination in groundwater under developing Asian megacities, Science of the Total Environment, 15;404(2-3), 2008, pp. 361-76.
- [24] Briand C., Sebilo M., Louvat P., Chesnot T., Vauray V., Schneider M., and Plagnes V., Legacy of contaminant N sources to the NO_3^- signature in rivers: a combined isotopic ($\delta^{15}\text{N}$ - NO_3^- , $\delta^{18}\text{O}$ - NO_3^- , $\delta^{11}\text{B}$) and microbiological investigation, Scientific Reports, Vol. 7, Issue 41703, 2017 pp. 1 -11.
- [25] Nikolenko O., Jurado A., Borges A.V., Knöller K., and Brouyère S., Isotopic composition of nitrogen species in groundwater under agricultural areas: A review. Science of the Total Environment, Vol. 621, 2017, pp. 1415-1432.
- [26] Giblin A.E., Tobias C.R., Song B., Weston N., and Banta G.T.H., RIVERA-MONROY VI. The importance of dissimilatory nitrate reduction to ammonium (DNRA) in the nitrogen cycle of coastal ecosystems, Oceanography, Vol. 26, Issue 3, 2013, pp. 124-131.

ESTIMATION OF SEDIMENTATION RATE AND FRESH-SALINE ENVIRONMENT IN A COASTAL ALLUVIAL PLAIN, USING BORING CORES OF ALLUVIUM IN THE CENTRAL PART AREA OF SETO INLAND SEA, JAPAN.

Tohru Takeuchi¹, Shin-ichi Onodera², Kazuhiro Yamaguchi³ and Koiti Kitaoka³

¹ Fujita Geology co. Ltd., ² Hiroshima University, ³ Okayama University of Science

ABSTRACT

To estimate the sedimentary environment between the last glacial stage and the Holocene epoch of an enclosed sea in the Okayama Plain, which constitutes a portion of the Seto Inland Sea coast, we collected 4 boring cores at depths of 6 to 19 m, performed radiocarbon dating of the organic matter contained in the clay, identified the volcanic glass from the Aira Caldera eruption, and measured the electrical conductivity of the pore water. Based on these dating analyses, it was evident that the Holocene clay layer that is widely distributed throughout the Okayama Plain had already accumulated prior to 10,000 years ago. In addition, the different hardness and the presence of Aira volcanic ash in the clay layer indicated the sedimentation since Pleistocene. Because the sea level at the time was lower than this clay sedimentation level, those facts suggest freshwater lakes existed in the Okayama Plain which was dammed up by the shallower granite basement in the mouth of Kojima Bay. Based on the long clay core and date for the last 30,000 years, the sedimentation rates were estimated to be 0.18 mm/ year before 8,100 years ago and 1.19 mm/year for the last 8,100 years, respectively. In the sea water rising after 7,000 years ago, the sea level exceeded the dam and the bay became saline condition.

Keywords: Holocene clay, radiocarbon dating, volcanic-ashes analysis, Sea-level change

INTRODUCTION

Various studies have revealed that the current Seto Inland Sea, which was a land area with freshwater lakes scattered in the Last Glacial Stage, changed to a sea area after the Holocene glacial retreat[2][6]. Therefore, it can be said that the sediments of the Seto Inland Sea and its coastal areas have recorded and preserved the sedimentary environments from the period when the area was land through to when it was a sea or brackish water area. This is a valuable information source for obtaining findings about environmental changes after the Pleistocene in the southwestern region of the Japanese Archipelago as well as in the Seto Inland Sea region.

Land water brought by rainfall flows out into the Seto Inland Sea in the form of river water or groundwater and plays an important role in characterizing the water quality as a part of the water source in the closed sea area. It is clear that sedimentary strata in the coastal area with low water permeability lowers the velocity of the passage of groundwater but affects not only the quality of the river water and groundwater but also that of the water in the closed sea area [3]. The current coastal zone, where the land and the sea area are in contact, has continued to be a water passage area in the water circulation from the ancient times. So, there is a possibility that not only the transition of sedimentary

environment from the land area to the sea area (brackish water area) is recorded in the sedimentary strata but also the clay of low permeability retains some water of those days[1][4][5][9].

Based on the chronological values obtained at the time of installation of the observation wells and the age determination obtained in the previous studies, we proved that the old Lake Kojima had existed in the Okayama Plain at the end of the Pleistocene[8]. It turned out that the deposition rate could be assumed to be unique in either age of the Pleistocene and the Holocene by connecting measured chronological values at each observation point. So, we were able to estimate the time of the seawater intrusion into the Okayama Plain and the elevation of the surface of the deposition at that time.

ANALYSIS

OUTLINE OF ANALYSISs

In order for fine grain particles from rivers to be deposited as sediment, water zones with low flow velocities such as lakes and seas are necessary. Sedimentation process is different depending on whether freshwater or seawater is in the water area, and in the water area where river water encounters seawater, the particles floating until then are more likely to aggregate and precipitate. Agglomeration occurs because the thickness of the electric double layer around the particle decreases in the

concentrated solution and the particles tend to collide and coalesce and the size of the clustered particles increases. Therefore, the rate of sedimentation varies depending on whether the process is in fresh water or in sea water.

The transition from the Pleistocene to the Holocene is generally supposed to have begun with the seawater intrusion into land area due to the rise in sea level caused by global warming after the Last Glacial Stage[2].

It is presumed that the difference in the sedimentation rate before and after the seawater intrusion has been recorded and preserved in the formation.

MATERIALS FOR ANALYSIS

By means of radiocarbon dating and identification of volcanic glass, eight sets of data of chronological values were obtained from cores collected from the right bank of the Asahi river (Tabl.1)[8]. In addition, 12 sets of data were obtained from the materials of the previous studies in the Okayama Plain (Tabl.2)[7]. The points where the chronological values were obtained are shown in Fig.1.

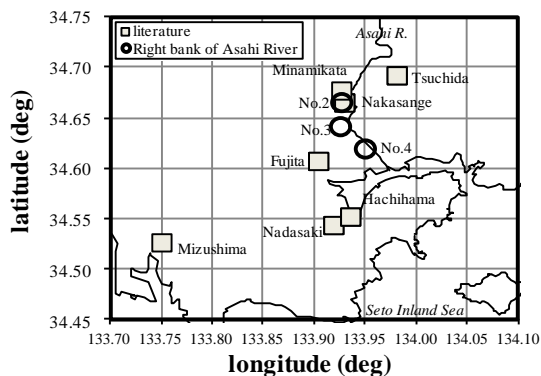


Fig.1 Position diagram of dating measurement sampling

Tabl.1 Radioactive carbon dating result of 2008 and age of volcanic ash

Number	Well No.	Depth (m)	Elevation (m)	Libby Age (yr B.P.)	Calibrated Age (cal B.P.)
IAAA-90200	No.2	6.60- 6.70	- 2.72 ~ - 2.82	6,560±40	7,510 - 7,420
IAAA-90201		8.60- 8.70	- 4.72 ~ - 4.82	9,100±40	10,300 - 10,200
IAAA-90202	No.3	5.60- 5.70	- 3.05 ~ - 3.15	5,620±40	6,480 - 6,310
IAAA-90203		8.00- 8.10	- 5.45 ~ - 5.55	7,600±40	8,460 - 8,350
IAAA-90204	No.4	5.00- 5.10	- 3.67 ~ - 3.77	2,240±30	2,270 - 2,160
IAAA-90205		13.00-13.10	-11.67 ~ -11.77	8,270±40	9,420 - 9,130
AhsType	Well No.	Depth (m)	Elevation (m)	Libby Age (yrBP)	Calibrated Age (calBP)
K-Ah	No.4	11.6	-10.27	6,300	7,300
AT		14.5	-13.17	24,000-25,000	26,000-29,000

Tabl.2 Radioactive carbon dating result by past record of Okayama plain

Number	Place	Elevation (m)	Libby Age (yrBP)	Calibrated Age (calBP)	
GaK-5784	Nadasaki	-14.5	7,920±250	8,876	8,311 - 9,441
GaK-5786		-23.4	24,900 ³⁴⁵⁰ ₃₄₅₀	28,808	22,390 - 35,225
No Data	Hachihama	-14.7	10,500±125	12,336	12,021 - 12,650
		-15.9	29,000±720	33,242	31,685 - 34,799
No Data	Fujita	-11.8	8,150±90	9,130	8,927 - 9,332
		-14.3	21,100±410	25,212	24,125 - 26,298
No Data	Tuchida	1.8	2,670±70	2,828	2,700 - 2,956
		-1.2	19,270±220	22,975	22,385 - 23,564
Beta-168007	Mizushima	-17	8,230±40	9,189	9,070 - 9,308
No Data	Nakasange	0.7	2,790±110	2,976	2,730 - 3,221
KN-89028	Nakasange	0.1	6,220±95	7,104	6,881 - 7,327
No Data	Minamigata	0	3,820±40	4,229	4,140 - 4,317

Fig. 2 shows the relationship between the elevation of the sampling points and the measured ages. As a whole, although the samples obtained at the lower elevation tend to be older, the correlation between the data does not appear to be high. The low correlation is presumed to be mainly due to the fact that the elevation of the sedimentary surfaces varies depending on the location, even if their ages are identical.

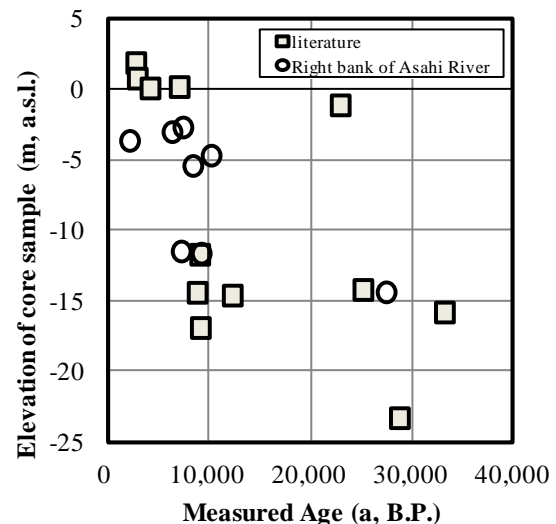


Fig. 2 Relation between age value and altitude

It is clear that not only the Holocene but the Pleistocene is also included in the sedimentary layer of the Okayama Plain, as the samples cover the range period of 2,000 to 30,000 calibrated BP. Therefore, sediments before and after the seawater intrusion are mixed in the measurement samples.

ANALYSIS METHOD

The elevation distribution of the chronological measurement is considered to include the event of seawater intrusion and the amount of fine particles in the river water can be influenced by the weather and hydrological conditions of the upstream area. However, it is presumed that no significant changes will occur in the long-term average hydrological climate of the catchment basin, so we can assume

that the amount of fine grain soil particles transported from the upstream is almost invariant. Therefore, the sedimentation rate of the lake bottom is largely dependent on whether the lake water is fresh water or brackish water. For the sake of convenience, we call the point at which seawater intrusion occurred the “transition year” and the hypotheses for analysis are set as follows.

1. The sedimentation rate is unique for either period (the Holocene and the Pleistocene) before and after the transition year.
2. The relationship between elevation and age at a sampling site can be represented by two straight lines with different inclinations before and after the transition year.
3. In order to correlate geographically widespread data, it is assumed that there was a lake vast enough to include the sampling sites.
4. The sedimentation rate was identical over the most area in the vast lake.

By making the above assumptions, mutual parallel relationships between elevations and ages are formed among points of different elevation of sedimentary level (at the lake bottom). This means that we can arrange all the data on a single straight line by shifting the elevation of the sample at each point upward or downward. By applying the least-squares method, a regression line representing the average elevation of the sedimentation surface for each point is obtained, and the sedimentation rate and the shift amount for each point can also be estimated.

When the material covers the periods both before and after the transition year, two regression lines with different inclinations are required. In that case, the intersection of the two straight lines represents the transition year and the average elevation of the sedimentation surface at that time.

First, we consider the case where all the material is from the Holocene. With the shift amount (adjustment amount) for each observation well as a parameter, we estimate the value of this parameter so that the entire line becomes a single straight line. Therefore, the regression line is set to $y=ax+b$, and the coefficients a and b are also included in the parameters and are also estimated. Here, y represents the average elevation of the sedimentary surface (at lake bottom) when set to a single straight line, while x represents the measured age of the material, and a represents the average sedimentation rate.

We will name the measured elevation of each material to which shift amount has been added the “adjusted elevation”. This method is aimed to obtain a regression line between adjusted elevation and measured age. In other words, we can obtain the

shift amount at each point and the most probable value of the coefficients of the regression line that would minimize the mean square deviation from the regression line of the adjusted elevation of each material. Once the coefficients of the regression line and the shift amount for each point are obtained, the shift amount for each point is subtracted from the regression line. Also, the elevation of the sedimentary surface at x , a certain point of time (age), can be obtained by subtracting the shift amount from y , the adjusted elevation calculated with the regression line $y=ax+b$.

In the same way, we assume that the regression line $y=cx+d$ and the shift amount at each point are also obtained in the Pleistocene stratum, too. Here, the coefficient c represents the sedimentation rate of the Pleistocene.

When applying the least-squares method, an initial value is given to the transition year, while samples from the ages later than the transition year are to be assumed as those of the Holocene layers, and older samples are to be assumed as those of Pleistocene layers. Then, we obtain the optimal parameters that would minimize the mean square deviation by giving some initial value to the elevation shift amount for each point and to the parameters of the coefficients of the two regression lines.

The x -coordinate of the intersection of the two straight lines thus obtained is called the “crossover transition year”. When the crossover transition year obtained deviates from the initial value of the transition year, the optimum value is to be recalculated with this crossover transition year as a new initial value. By repeating this process, the final optimum value can be obtained.

RESULTS AND DISCUSSION

The optimum value 8,078 calibrated BP of the crossover transition year obtained by means of regression with two straight lines of the Holocene and Pleistocene is shown (Fig. 3).

The decor relation of the data is remarkable, and the mean square deviation around the regression line, of which the range is indicated with the dotted line, is large. Estimated deviation of the transition year is $\pm 1,200$ years. This significant deviation is presumed to be due to radiocarbon dating performed in different ways.

Analyses only on the basis of the material from the right bank of the Asahi river show that the transition year was 8,100 calibrated BP, which is fairly accurate with the deviation only ± 0.003 years. The deviation of the elevation (y -coordinate) in the transition year, which is the intersection of the two straight lines, is 0.005 mm.

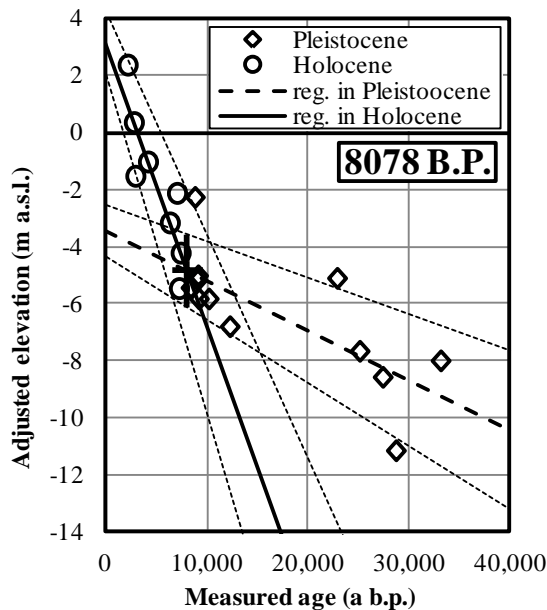


Fig.3 Relationship between adjusted altitude and measured age

It is noteworthy that the transition year $8,080 \pm 1,200$ calibrated BP obtained from wide area samples and the transition year $8,100 \pm 0.003$ calibrated BP obtained from the samples along the Asahi river have high identity in terms of the mean value. This suggests that the assumption of the unique sedimentation rate applied in this method is not so far from reality.

The sedimentation rate observed in the entire Okayama Plain is 1.0 ± 0.2 mm/y in the Holocene, and 0.18 ± 0.05 mm/y in the Pleistocene stratum, which are considered to be the average value observed in the vast area of the Okayama Plain. Thus, it appears to be clear under certain assumptions that the seawater intrusion into the Okayama Plain occurred in 8,100 calibrated BP, while the sedimentation surface at the transition year can be described as 8.89 meters below sea level.

Therefore, it is generally considered that if there are about ten chronological materials available including those of the Holocene and Pleistocene, accurate estimation of the transition year will be made possible by means of this method.

On the basis of the distribution of Jomon ruins, we can estimate that the surface of the brackish lake formed after the seawater intrusion was several meters higher than the current sea level. It is considered that the alluvial clay layer of the Okayama Plain developed in the warm weather of this Jomon Transgression.

CONCLUDING REMARKS

We found out that, given the condition that the sedimentation rate was unique either in the Holocene or Pleistocene era, the chronological data could be arranged on a single straight line by shifting the elevation of the observation points upward or downward in either of the periods. By doing so, the chronological data of sediments obtained by measurements at different locations were related to each other, and

It was possible to estimate that the sedimentation rate was almost unique over a vast area at either of the periods.

1. It was possible to estimate the average of sedimentation rate either in the Holocene or Pleistocene.
2. It was possible to estimate the time of seawater intrusion from the point of intersection of the two straight lines.
3. It was possible to estimate the elevation of the sedimentary surface when the seawater intrusion occurred at each observation well.

As a result, seawater intrusion into the Okayama Plain is considered to have occurred in 8,100 calibrated BP with the elevation of the sedimentary surface 8.89 meters below sea level. The sedimentation rate proved to have been 1.19 mm/y in the Holocene, and 0.18 mm/y in the Pleistocene.

REFERENCES

- 2 F. Larsen, L.V. Tran, H. Van. Hoang, L.T. Tran, A.V. Christiansen, N.Q. Pham.: Groundwater salinity influenced by Holocene seawater trapped in incised valleys in the Red River delta plain. *Nature Geoscience*, 10(5), 2017, pp. 376-381.
- 3 Masuda, F. Miyahara, B. Hirotsu, J. Iritsuki, T. Iwabuchi, H. Yoshikawa, S.: Marine status variation in Osaka Bay for Holocene, marine sediment cores in the offshore of Kobe, Jap. *Journal of Geology*, 106, 2000, pp. 482-488.
- 4 Masuda, H.: The future of urban water resources and groundwater. Kyoto University Academic Press, Kyoto. 2011.
- 5 Molliex, S., Siame, L., Bourlès, D., Bellier, O., Braucher, R., Clauzon G.: Quaternary evolution of a large alluvial fan in a periglacial setting (Crau Plain, SE France) constrained by terrestrial cosmogenic nuclide (^{10}Be). *Geomorphology*, 195, 2013, pp. 45-52.
- 6 Piovan, S., Mozzi, P., Zecchin, M.: The interplay between adjacent Adige and Po alluvial systems and deltas in the late Holocene (Northern Italy). *Géomorphologie: relief, processus, environnement*, 18(4), 2012, pp. 427-440.
- 7 Shimada, J.: Water beneath the sea bottom of the Seto Inland Sea. *Seto Inland Sea*

- (The Association for the Environmental Conservation of The Seto Inland Sea), 43, 2005, pp. 22-27.
- 8 Suzuki, S.: *Relative sea-level changes of Okayama Plain Area during the Holocene, Southwest Japan. Okayama University Earth Science Reports*, 11, 2004, pp. 33-37.
- 9 Takeuchi, T. Kitaoka, K. Yamaguchi, K. Onodera, S.: Formation process of the Holocene clay layer in a coastal alluvial plain of an enclosed sea: case study of the Okayama Plain. *Journal of Japanese Association of Hydrological Sciences*, 44, 2014, pp.161-177.
- 10 Wild, M., Cochrane, T., Davies, T., Hicks, D. M., Painter, D., & Palmer, G.: Recent sedimentation rates for the Rees-Dart braided river delta. *IAHS Red Books Publication*, 325. 2008, pp.312 -315.

IMMEDIATE EFFECTIVENESS OF HERBAL STEAM ON CERVICAL RANGE OF MOTION WITH STRESS IN THE ELDERLY

Chamiporn Kongmong¹, Peerada Damapong² and Pongmada Damapong³

^{1,2,3}College of Allied Health Science Suan Sunandha Rajabhat University, Bangkok 10300, Thailand

ABSTRACT

Stress is one of the common psychological problems. This study aimed to evaluate the effects of the Herbal Steam on cervical range of motion with reduce stress in the elderly. The data was compiled using the quasi-experimental research design; the populations of this research were 30 patients with stress in the elderly, the assessment was before and after receiving 30-minute of Herbal Steam. The results were assessed immediately after the intervention which consisted of the increased cervical range of motion after receiving the Herbal Steam while a significant difference was occurring ($P < 0.05$). In conclusion, the effectiveness of Herbal Steam will reduce stress in the elderly by reducing its pain and increase the cervical range of motion.

Keywords: Immediate Effectiveness, Cervical Range of Motion, Herbal Steam, Stress, The elderly

INTRODUCTION

Stress is a mental health problem that can happen to the general public. Stress is a reaction. The response of the body, mind, thoughts and behavior of the person to the inner and outer vesicles, which may be person, the feeling. Situation or environment The person will recognize that the pressure is threatening and the uncontrolled cave will make the person stress. This may result in a disproportionate loss of life. Stress is a barrier and the problem that many people in many age to meet on a daily basis. Whether it comes from work. Personal life problems And especially the money. And the older the elderly. It is very easy to face stress. Start by yourself. The body began to regress. With the disease that comes to arouse discomfort, physical and mental stress. In addition, the external environment is not good, such as the elderly away from their children. Some people are alone, it causes more stress. It also causes depression as well. The changes in the elderly population in Thai society have shown that the proliferation of chronic diseases and disability has led to an increase in the elderly is dependence and increased need for care. And care in the service [1].

The current state of problems and conditions, although the knowledge of medical science has advanced. And is widely accepted in the care. But still find that. The health care and maintenance. For the elderly there is a distinction of the traditional way of life in Thailand. Especially the rural elderly who have a culture of faith and lifestyle that is linked to the path of nature. This is different from the people in the city. Health care behaviors of rural people are characterized by social stereotypes. And that culture has been instilled and transferred knowledge to maintain their own health. In the form of local wisdom (Local wisdom)

It is still used today. Herbal Steam It is used for heat therapy. Traditional herbal steam is used in women. The new baby, which will have hot baths. Drink hot water with boiled water. And lay a fire on bamboo lined with herbs, but now has developed. Sauna Heater Thai people in traditional medicine use herbal steam over the sauna. it has herbs that help the airway. Skin care or treatment. types of Herbal Steam Herbal Steam 1) Drying is a traditional method of cooking. There are rituals that maintain morale. For mothers after birth Herbal bath and turmeric treatment to maintain inflammation in the skin and is popular after birth with fire on the litter, warm wood to the body will help stimulate the uterus contraction. 2) Wetting is one of the treatments. The beginning of the tent of the woman after birth. Using cloth to make a tent covered with boiled herbal boiling pot. Bake and smoke steam. Nowadays, this method has been developed to suit the present society by creating a modern herbal steam room [3], [4].

The composition of herbs used may vary by purpose. To treat such symptoms as refreshing the body. Skin shine Helps to sweat, relieve stress. Relaxation and tightness of the joints and pain in the current medical conditions have accepted that heat treatment can help blood circulation. The vapor of herbs will have properties according to the properties of the herb, which in most cases helps the body freshen up. [3], [4].

In consequence, the researcher is interested in the use of traditional herbal medicine. Take care of stress problems of the elderly. To reduce the stress that is the cause of other diseases followed.

MATERIALS AND METHODS

Design

This research was the quasi-experimental research design which the cervical range of motion assessment was conducted in the public health center, Phakdi Chumphon District, Chaiyaphum Province, Thailand. This study was approved by Ethics Review Committee Sirindhorn College of Public Health Khon kaen (HE NO.610660)

Subjects

The sample used in this study is Elderly people over 60 years old 30 people with stress. the elderly have moderate stress.

Assessment

This research was the cervical range of motion assessment, the questionnaires and Perceived Stress Scale.

Measurement Instruments

In this research, The instruments used in the experiment were 2 parts: A screening test to screen elderly people with stress. Three levels of stress, low, moderate and high, Recorded results are moderate. Additionally, the Cervical Range Of Motion (CROM) was used to assess the cervical range of motion; cervical flexion, cervical extension, cervical left lateral flexion, cervical right lateral flexion, will measure before healing herbs. And after measure herbal immediately. and the results were recorded as degree.

Intervention

The samples were treated by getting 15-minute of Herbal steam.

Statistical Analysis

In this research, descriptive statistics were used to describe the characteristics of the sample. mean and standard deviation It also uses a pair t-test to analyze the variables negatively by analyzing the immediate effect of the evaluation.

RESULTS

The findings of the general information of 30 sample revealed that; most of them were female (80.00%), most of the marital status was married (80.00%) and most of have a farming career (40.00%).

The assessment of the cervical range of motion; cervical flexion, cervical extension, cervical left lateral flexion, cervical right lateral flexion before and after the Herbal steam immediately revealed that the immediate cervical range of motion was increased with 0.95 level of significance ($P < 0.05$) (Table 1).

Table 1 Comparison of the outcome measures between baseline (pre-test) and post-test assessments in Cervical range of motion (degree) (paired t-tests).

Outcome	Baseline	Immediate (Mean \pm SD)	P- value
Cervical flexion	± 53.50 9.39	± 58.83 8.57	<0.05
Cervical extension (%); mean \pm SD	± 54.50 10.28	± 60.33 9.99	<0.05
Cervical left lateral flexion	± 38.66 8.29	± 44.33 7.84	<0.05
Cervical right lateral flexion; mean \pm SD	± 34.33 7.27	± 42.66 9.07	<0.05

Note:

DISCUSSION

This research was aimed to evaluate the effects of Herbal Steam on cervical range of motion with reduce stress in the elderly. The findings of the immediate cervical range of motion assessment were different in each motion with 0.95 level of significance ($P < 0.05$). In consequence, it was different in the clinical significance that the sample were treated Herbal Steam.

The findings were consistent with the study of “Kitkra [2] shows 58.3% of the respondents used the herbal steam service twice a week, 68.0% of them drank 2-5 times, 33.5% of them tried to keep their body healthy. 88.0% found that herbal steam helped to work more. 86.3% helped to sleep well 84.7% help to lighten the mobility 81.3% help to breathe fluently 80.0% help relieve pain. Maps For those with knee pain, knee pain, muscle aches and back pain, waist circumference 90.5 percent 82.2 .

CONCLUSION

Thai herbal steam results in a neck movement. The effect of neck movement increased in all directions from the corm measurements, which were different before and after herbal steam. It can be concluded that the herbal baking herbs have properties that make the muscles in all parts of the body more flexible. Heat causes circulatory system to work effectively. As a result, stress is reduced.

ACKNOWLEDGEMENTS

This study was supported by Suan Sunandha Rajabhat University, Bangkok, Thailand.

REFERENCES

- [1] BodhiSita, C. Science and Arts of Qualitative Research (4th ed.). Bangkok: Amarin Printing, 2009.
- [2] Kitkra, J. Buddharak, S. Wattanachai, A. Vadisai, N. Wattanapichakul, A. Herbal Steam: Health Care Options for People. Journal of Pharmacy; 9 (1): 28, 2013.
- [3] Subcharoen, P. Herbal Steam for Health. And to treat the disease. Prachinburi: Office of Public Health Prachinburi Ministry of Public Health, 1995.
- [4] Thai Traditional Herbs and Herbs Promotion Group Thai Traditional Medicine Institute. Traditional Thai Medicine Practice in Public Health Facilities. 4th edition. Nonthaburi: Department of Alternative Medicine and Alternative Medicine. Ministry of Public Health, 2011.

EFFECTS OF LOW INTENSITY EXERCISES ON BODY BALANCE AND MUSCLE STRENGTH OF COMMUNITY ELDERLY PEOPLE

Worawut Chompoopan^{1,3}, Warangkana Chompoopan^{1,3}, Wichai Eungpinichpong^{2,3}, and
Wilai Eungpinichpong¹

¹Sirindhorn College of Public Health, Khon Kaen, Thailand

²Faculty of Associated Medical Sciences, Khon Kaen University, Khon Kaen, Thailand

³Research Center in Back, Neck, Other Joint Pain and Human Performance, Khon Kaen University, Thailand

ABSTRACT

The purpose of this experimental study was to determine the effects of low-intensity group exercise on muscle strength and balance of elderly people in the communities. Seventy-two healthy elderly people from two communities participated in this study. Thirty-six elderly people were randomly selected and allocated into an experimental group and control group. The experimental group performed a supervised group exercise program in every work day's evening for three months. The exercise program began with warming up for five minutes, followed with low-intensity exercise program, and cooling down for another five minutes. The data were collected before and after three months of performing the exercise program. The outcome measures included muscle strength, body balance, and fear of falling. The data were analyzed by using ANCOVA to compare between the experimental group and the control group. After performing the exercise program for three months, the experimental group had developed better health status than before participating the program and it was significantly different from the control group. The experimental participants' muscle strength was increased by 1.79 points. Their dynamic balance periods were shorter than before receiving the exercise program by 1.32 seconds. Moreover, it was revealed that the experimental participants' fear of falling was decreased by 17.74 points. After three months of involving in the low-intensity exercise program, their health status remained better and healthier while the participants' health status of the control group remained the same as the starting period. The results revealed that the low-intensity group exercise program could improve muscle strength, body balance, and fear of falling among elderly people.

Keywords: Exercise, Balance, Muscle strength, Elderly

INTRODUCTION

The world has been becoming an aging society. Each country where has senior citizen accounting for over 10% of the total population can be classified as an aging society [1]. For example, by the year 2004, the proportion of elderly people in Japan was the highest percentage (31%), followed by Italy and Germany (27% and 26% respectively) [2]. In 2007, in the Southeast Asia region, the proportion of elderly people in Singapore was almost equal to Thailand of which Singapore was 11.9 while Thailand was 10.7 [3].

Not only the proportion of elderly people has been increasing, but the seniors have also encountered an increase in age-related diseases. Around 34.6 percent of people over 80 years through self-assessment were found having poor health status [3]. Naturally, people tend to get chronic health conditions when they are getting older. For example, high blood pressure was commonly found in the seniors at 31.7%, meanwhile, the prevalence of diabetes was 13.3%. Other chronic health conditions prevalence like heart disease, paralysis, coronary artery disease, and cancer prevalence were 7.0, 2.5, 1.6 and 0.5 percent, respectively [3]. These common

health conditions in the ageing people including injuries from falls indicate degenerative health status among the older adults [4].

Falling is one of the common and major health problems occurring in the old-age people. In 2007, a study on falls in the ageing people found that, within six months, the percentage of the falls in the seniors was up to 10.3. As far as gender is concerned, the proportion of falls among female elderly people was 12.6 percent while in the same-age male proportion was 7.4 percent. In addition, age also plays a part. The very senior citizens had the highest proportion of falls at 12.7% whereas the proportion of falls in the middle or early age group was 11.7% and 9.2%, respectively [4]. The major physical cause associated with falls in the elder people is a decline in muscle mass which could result a decrease in physical activities. The decline in muscle mass has always been replaced by free fat, collagen, and fibrous tissue [5]. This includes the deterioration of the neuro-musculoskeletal system, especially in lower extremities which could also cause muscle weakness and fall in the old-age people [6].

Therefore, an exercise program to improve muscular strength and body balance for elderly people is crucial to prevent their health problems. A low intensity exercise has been recommended for maintaining and improving health status in elderly people because it has low risk and yet could gradually let the elderly participants adapt to physiological as well as psychological effects resulting from the exercise training program. To accomplish and maintain these effects, the exercise program should be regularly performed, enjoyable, and relevant to local culture of physical activities. The main purpose of this study was to develop an appropriate exercise program to improve both muscular strength and body balance of elderly people living in a community.

METHODS

Design and setting

A parallel two-arm, randomized control trial (RCT) was applied. The settings for intervention and data collection were at two districts in Khon Kaen, Thailand.

Participants

The participants were healthy elderly people aged 60 years and over recruited from the communities. The inclusion criteria were healthy elderly people and have been living in the community over one year. Participants with disability, body balance problem, contra-indications to exercise were excluded. Seventy-two participants who met the criteria were randomly allocated either in the experimental or control arms by using a block randomized method (Block of 4).

Intervention

The exercise program was designed based on the criteria which included low intensity, simple, enjoyable, relevant to local culture, and group participation. The components of exercise consisted of the following supervised group exercises.

Squats exercise

The instructor commanded with demonstration to the group of participants as follows. "Stand as tall as you can with your feet apart about shoulder-width. Lower your body as far as you can by pushing your hips back and bending your knees. Push yourself back to the starting position while squeezing your glutes. Repeat the movement 10 times, performing 2 sets. For each repetition, count to 3 on the way up and on the way down to ensure you are not going too fast. Then rest 30 seconds in between sets."

Calf exercise

The participants stood on the feet while the hands grasp the chair back to balance the body. Then they raised their heels up, and put the body weight on the toes, and old in this position for 5 seconds. Then returned to the starting position and repeated 10 times. They performed 2 sets and rested 30 seconds in between.

Sideways walking

The participants stood with their feet together, and knees slightly bent. Then, they stepped sideways in a slow and controlled manner by moving one foot to the side, then they moved the other to join it. Repeat 10 steps each way or step from one side of the room to the other. They repeated the movements 10 sets.

Heel to toe walk

They stood upright. Then, they placed the right heel on the floor directly in front of the left foot. Then they did the same with the left heel. They were instructed to keep looking forward at all times. If necessary, they were allowed to put their fingers against the wall for stability. Repeated 10 steps and performed 5 sets

Participants in the control group were suggested to maintain their routine daily life activities although they didn't participate in the exercise program.

Procedure

The objectives and the study design were described to all the participants for both the experimental and control groups. The consent form was read and signed at the Local Health Promoting Hospital. The appointment was arranged right after screening accordingly to the criteria in order to participate in the study and signed the informed consent. Every participant was provided with a recording-book to sign every time he/she participated in the exercise. The exercise program was performed at the community meeting center in the village where most of the elderly people regularly came for chatting.

Outcome measures including dynamic body balance (timed up-and-go test), muscle strength (thirty-second chair stand test), and fear of falling (Falls Efficacy Scale) were recorded before and 3 months after participating the study. Village health volunteers supervised the daily group exercise whereas Health Promoting Hospital officers followed up to ensure the exercise program had been

regularly performed. All the participants were encouraged to regularly participate accordingly to the study design. The researcher and research assistants regularly visited and interviewed the participants.

Measurement Equipments

The timed up-and-go test (TUG) was used to measure the dynamic body balance purposely to assess the balance, walking ability, and fall risk of elderly people. The participants were suggested to wear their regular footwear while they were performing the test. The procedure of TUG measurement began with the advice for each of the participants to sit on a chair. When the researcher gave a signal, he/she got up and walked along the three-meter line, then went back to the seat. The duration of this performance was timed and recorded.

A thirty-second chair stand was tested (30CST). This test aimed to measure leg strength and endurance of elderly people. Each participant sat at the middle of the chair. Place their hand on the opposite shoulder while keeping the feet flat on the floor, back straight, and arms against the chest. After receiving the signal "Go" he/she stood up straight, then sat down again. This was repeated for 30 seconds. The researcher counted the number of completed rounds.

A Falls Efficacy Scale (FES) was a test aimed to assess perception of balance and stability during activities of daily living and fear of falls among the elderly population. The Falls Efficacy Scale was a 10-item questionnaire designed to assess confidence of their ability to perform 10 daily tasks without falling as an indicator of how one's fear of falling impacts physical performance. Each item was rated from 1 ("very confident") to 10 ("not confident at all"), and the per item ratings were added to generate a summary total score. Total scores could be ranged from 10 (best possible) to 100 (worst possible). Thus, lower scores indicated more confidence and higher scores indicated lack of confidence and greater fear of falling.

STATISTICAL ANALYSES

Data were analyzed by using SPSS for Windows Version 19 (IBM Corp. Released 2010, IBM SPSS Statistics for Windows, Version 19.0. Armonk, NY: IBM Corp.) under licensed of Khon Kaen University.

Shapiro-Wilk test was used to verify the normal distribution of continuous variables. An intention-to-treat analysis was used for avoiding misleading data. The data were analyzed by using Independent t-test for comparing between the experimental and control groups before the experiment. After experiment data were analyzed by using analysis of covariance (ANCOVA) for between-group comparison. Paired t-test was used for within-group comparison. Differences were considered statistically significant at $p < 0.05$.

RESULTS

The demographic variables based on gender, age, income, and occupation were stratified between the experimental and the control groups (EX and CON). Thirty-six participants were allocated in each group. Most of them were female (52.78% in EX group, and 72.22% in CON group). The average age was 70.89(5.38), and 70.58(7.03) years and their average income were 2,500(3,600), and 1,000(3,025) Baht/Month for the EX and CON respectively. Most of the participants worked as farmers. (Table 1)

Table 1 This is the example of table formatting

Characteristics	EX n(%)	CON n(%)
<i>Gender</i>		
Male	17(47.22)	10(27.78)
Female	19(52.78)	26(72.22)
<i>Age</i>		
60-69	17(47.22)	18(50.00)
70-79	15(41.67)	15(41.67)
≥80	4(11.11)	3(8.33)
($\bar{X} \pm S.D.$)	70.89±5.38	70.58±7.03
(MIN, MAX)	(63, 86)	(60, 83)
<i>Income (Baht)</i>		
500-1000	19(52.78)	26(72.22)
1001-1500	12(33.33)	7(19.44)
Over 1500	5(13.89)	3(8.33)
($\bar{X} \pm S.D.$)	2500±3600	1000±3025
(MIN-MAX)	600-20000	600-10000
<i>Occupation</i>		
Farmer	27(75.00)	26(72.22)
Homework	4(11.11)	6(16.72)
Retire	5(13.89)	4(11.11)

Baseline data before the intervention were compared between the two groups and found no significant difference in terms of body balance, muscle strength, and fear of falling (Table 2).

Table 2 Baseline data before the intervention of both groups.

Variables	EX Group $\bar{X} \pm S.D.$	CON Group $\bar{X} \pm S.D.$	<i>p</i>
Balance	11.91 \pm 2.07	12.89 \pm 4.34	0.231
Muscle strength	12.42 \pm 2.85	12.44 \pm 3.48	0.971
Fear of falling	22.50 \pm 36.20	17.42 \pm 27.36	0.504

Note: T-test

After 3 months of participating in the intervention, the experimental group had significantly improved in their body balance, muscle strength, and fear of falling when compared to the control group (Table 3).

Table 3 Comparison between the two groups after 3 months of intervention.

Variables	EX Group $\bar{X} \pm S.D.$	CON Group $\bar{X} \pm S.D.$	<i>p</i>
Balance	11.28 \pm 2.01	12.60 \pm 4.43	0.002
Muscle strength	13.94 \pm 2.80	12.15 \pm 4.64	0.006
Fear of falling	15.91 \pm 22.51	33.65 \pm 36.09	0.001

Note: ANCOVA, adjusted mean using baseline as covariate

Within-group analysis of the experimental group revealed that after 3 months of participating in the exercise program, the participants had significantly increased their body balance and muscle strength, whereas the fear of falling was not significantly improved (Table 4).

Table 4 Within-group analysis of the experimental group

Variables	Baseline $\bar{X} \pm S.D.$	After 3 m. $\bar{X} \pm S.D.$	<i>p</i>
Balance	11.91(2.07)	10.97(2.02)	0.004
Muscle strength	12.42(2.85)	14.14(2.80)	0.001
Fear of falling	22.50(36.20)	10.33(22.51)	0.089

Note: Paired t-test

Within-group analysis of the control group revealed that after 3 months without any intervention, the participants had no significantly changed in their body balance and muscle strength, but the fear of falling was significantly increased from the baseline (Table 5).

Table 5 After the experiment in CON group

Variables	Baseline $\bar{X} \pm S.D.$	After 3 m. $\bar{X} \pm S.D.$	<i>p</i>
Balance	12.87(4.34)	12.96(4.44)	0.784
Muscle strength	12.44(3.48)	11.94(4.64)	0.318
Fear of falling	17.42(27.36)	36.97(36.09)	0.010

Note: Paired t-test

The results showed that participating in the 3 months of low-intensity exercise could significantly improve both body balance and muscle strength. None of the participants had shown any serious adverse effect. These findings were in the line with those of the previous study that employed the three-month home based low intensity exercise for elderly people in different settings and cultures [7]-[9]. In the current study, the participants' fear of falling after 3 months of the intervention had significantly decreased in the experimental group compared to the control group. This could be due to the increase in muscle strength of the lower extremities and body balance of the experimental group as a result of participating in the low intensity exercise program [10].

According to the study design, this study employed a randomized controlled trial of which has been known as the gold standard for intervention study. This could provide the high quality of the study. However, this study had some limitations because the blind assessment was not possible due to the nature of the community trial. In addition, it might be possible that group contamination might occur since the participants in the control group could easily access in the exercise group. Fortunately, this group contamination did not occur since the participation to this exercise program was strictly controlled by the community's health volunteers and the research assistants.

CONCLUSION

Based on the results of this study, participation on regular (low intensity) exercise, 5 times a week and lasted for 3 months, may increase muscle strength, improve the dynamic body balance and reduce fear of falling in elderly people. This kind of activity could contribute a lot to the communities where there are a lot of elderly people in terms of health promotion, opportunities for social gathering, having fun, more importantly low cost. Any elderly people with any social status can perform this exercise program. Beneficially, older people could use their leisure time worthwhile for the rest of their lives.

ACKNOWLEDGEMENTS

This study would not have been possible without the generous cooperation of the 72 elderly participants, research grants from the Research Center in Back, Neck, Other Joint Pain and Human Performance (BNOJPH), Khon Kaen University, Thailand.

REFERENCES

- [1] David A. Swanson. The Methods and Materials of Demography, Second Edition, Academic Press 2004, pp. 159.
- [2] John, B., Simon, B., David, B., Linda, F., Paul, H., Alexandre, K., & Jay, O. Global Population Ageing: Peril or Promise?, World Economic Forum. 2000, pp. 6.
- [3] Bureau of Socio-Economic and Opinion 1, National Statistical Office Thailand, Report on the 2007 survey of the older persons in Thailand, 2008, pp. 35-48.
- [4] Chuenta Witchawut, Review and Synthesis of Thai Elderly Knowledge. Foundation of Thai Gerontology Research and Development Institute (TGRI), 2009, pp. 41-43.
- [5] Payton, O. D., & Poland, J. L., Aging Process: Implications for Clinical Practice. Phys Ther, Vol. 63, Issue 1, 1983, pp. 41-48.
- [6] Moreland, J. D., Richardson, J. A., Goldsmith, C. H., & Clase, C. M., Muscle weakness and falls in older adults: a systematic review and meta - analysis. J Am Geriatr Soc, Vol. 52, Issue 7, 2004, pp. 1121-1129.
- [7] Arai, T., Obuchi, S., Inaba, Y., Shiba, Y., & Satake, K. (2009). The relationship between physical condition and change in balance functions on exercise intervention and 12-month follow-up in Japanese community-dwelling older people. Arch Gerontol Geriatr, Vol. 48, Issue 1, 2009, pp. 61-66.
- [8] Karabulut, M., Abe, T., Sato, Y., & Bembem, M. G., The effects of low-intensity resistance training with vascular restriction on leg muscle strength in older men. Eur J Appl Physiol, Vol. 108, Issue 1, 2010, pp. 147-155.
- [9] Arai, T., Obuchi, S., Inaba, Y., Shiba, Y., & Satake, K. (2009). The relationship between physical condition and change in balance functions on exercise intervention and 12-month follow-up in Japanese community-dwelling older people. Arch Gerontol Geriatr, Vol. 48, Issue 1, 2009, pp. 61-66.
- [10] Gusi, N., Carmelo Adsuar, J., Corzo, H., Del Pozo-Cruz, B., Olivares, P. R., & Parraca, J. A. (2012). Balance training reduces fear of falling and improves dynamic balance and isometric strength in institutionalised older people: a randomised trial. [Randomized Controlled Trial Research Support, Non-U.S. Gov't]. J Physiother, Vol. 58, Issue 2, 2012, pp. 97-104.

INVESTIGATION OF CATHEPSIN B (*CTSB*) and CATHEPSIN L (*CTSL*) POLYMORPHISM FOR CARCASS AND MEAT QUALITY IN SWINE

Doungnapa Promket^{1*}, Kajorngiat Nabundit², and Khanitta Ruangwittayanusorn¹

¹Lecture of Animal science, Department of Agricultural Technology, Faculty of Technology, Mahasarakham University, Thailand

²Graduate student of Animal science, Department of Agricultural Technology, Faculty of Technology, Mahasarakham University, Thailand

ABSTRACT

The objectives of the research were to evaluate genotype frequencies and to investigate polymorphism in the cathepsin B gene (*CTSB*) and cathepsin L gene (*CTSL*) with carcass and meat quality in 288 crossbreeds (large white x landrace x duroc). Pigs whose weights ranged from 78-134 kg were assigned to slaughter. PCR-RFLP protocols were used to identify polymorphisms of both genes. The frequencies of AA, AC and CC genotypes of *CTSB* were 0.340, 0.615, and 0.045, respectively. The frequencies of A and C alleles of *CTSB* were 0.648 and 0.352, respectively. Regarding *CTSL*, the frequencies of CC, CT and TT genotypes were 0.625, 0.354, and 0.021, respectively. The frequencies of C and T alleles of *CTSL* were 0.802 and 0.198, respectively. The significant effects of *CTSB* polymorphism were detected on body length (BL), scan of loin eye area (U_LAE), loin eye area (LAE), and weight loss (WL) ($P < 0.05$). The pigs carrying the AC genotype had higher level of BL, U_LAE and LAE than the ones carrying the homozygous genotype (AA or CC). The pigs with the CC genotype of *CTSB* had lower WL (1.86 kg) than the ones carrying the AA or the AC genotype (2.19 and 1.97 kg). The *CTSL* variants represented statistically significant effects on BL trait ($P < 0.05$). The CC genotype (77.92 cm) had higher BL value compared to the CT (76.14 cm) and the TT genotypes (76.92 cm). The *CTSB* and *CTSL* were high polymorphism and their alleles could be as the potential genetic markers for swine selection.

Keywords: Cathepsin B, Cathepsin L, Swine, Polymorphism

INTRODUCTION

The selection of pig has focused on increase of carcass and meat quality. The carcass and meat characteristics, especially the back fat thickness and ham weight, are economically important for the pig industry [1]. However, making genetic progress by traditional breeding is challenging because meat and carcass qualities are low to moderately heritable [2], [3]. The meat and carcass quality are of complex nature, influenced by several genes with high impact of environmental effect [4].

Ultrasound technique has been used to predict carcass and meat traits of live animals for several years. Deza [1] has found that the R^2 model between hams weight and slaughter live weight and ultrasound fat thickness was 0.82. Moreover, the correlation between 10th rib back fat measurement by real – time ultrasound and 10th rib back fat was 0.84 [5]. Newcom [6] has used real-time ultrasound technique to predict intramuscular fat percentage in live swine and found that the product moment correlation and rank correlation coefficients between predict loin intramuscular fat percentage and carcass loin intramuscular fat percentage of Duroc population were 0.60 and 0.56, respectively. Results show that real-time ultrasound image analysis can be used to predict intramuscular fat percentage in live

swine. The prediction meat and carcass quality of measurement carried out in live pigs before slaughter and interesting aspect for producer and for the industry.

Marker assisted selection (MAS) is one of the possibilities related to breeding program. Several studies have identified gene marker associated with the genetic variation process through MAS that has an increased possibility for implementation [7]. The cathepsin genes belong to the enzyme family (*CTSL*, *CTSB*, *CTSD*, *CTSH*, *CTSF* and *CTSZ*), which are a group of genes that produce lysosomal proteinases and are important for the degradation of proteins. Their main role is in the *post-mortem* proteolysis of meat. These genes or their mutations may profoundly affect the qualitative properties of meat [8], [9]. Recent studies have shown that the polymorphism in the cathepsinB (*CTSB*) and cathepsinL (*CTSL*) gene is associated with carcass and meat quality traits in swine. Vera [8] has found a trend of allele T increased fatness and the effect of allele C on lean meat in swine. The significant results of *CTSB* mutation was observed for higher carcass yield and weight of ham [9]. Moreover, Russo [10] also found the marker identified at the *CTSB* loci involved in meat quality traits. *CTSL* marker shows a tendency towards back fat thickness and weight of lean cuts [11], [12]. In the present

study, we predicted the carcass and meat quality by real – time ultrasound that might improve the efficiency of measure methods for evaluating meat quality on a routine basis. Thus, the objectives of this research are to investigate genotype of *CTSB* and *CTSL* polymorphism and confirm the association between the polymorphisms and carcass and meat quality in Thai crossbred swine. The results from this study might improve the efficiency of selection swine.

MATERIALS AND METHODS

Animals

Two hundred and eighty eight cross breeds pig (Large White × Landrace × Duroc Jersey) were purchased from commercial farm with an initial live weight of 78 to 134 kg and no any phenotypic criteria.

Ultrasound Image Collection

All pigs were weighed body weight (BW), body length (BL) and were scaled of loin eye area (U_LAE), back fat thickness (U_BF) obtained 2 h were scanned before slaughter by real – time ultrasound (Honda electronic Inc., a 3.5 MHz, 10 cm long probe and a 1.5 - 2 MHz, 13 cm long). Images were recorded and then linear and area measurements were taken by means of the between 10th rib. The pigs were slaughtered at commercial slaughter house after electrical stunning.

Carcass and Meat Data Collection

At the slaughterhouse, within 10 min of *post-mortem*, hot carcass weight (Hot_C, kg), pH0 at 0 h Post – mortem (pH0) and carcass length (CL) were collected. pH at 45 min post – mortem (pH45) were determined using pH meter. After chilling, carcass weight after chilling (Chill_C), pH 22 h (pH22), back fat thickness (BF), loin weight (LW), ham weight (HW), fillet weight (FW) and shoulder weight (SW) were determined.

Tissue Collection and DNA Extraction

Approximately 20-30 mg of tissue was collected from the carcass of each pig into tube containing 99% of ethanol. Genomic DNA was isolated from tissue using Puregene (Gentra Inc., Minneapolis, MN) according to the supplied protocol. Briefly, tissues were separately minced were washed twice with 0.9% NaCl sample were centrifuged for 5 min at 3,000 rpm at room temperature. Cell lysis buffer and protein precipitation buffer were added to the pellet. Cell lysate was then centrifuged for 5 min at 10,000 rpm at 4°C. The supernatant was then transferred to 1.5 ml tube, and absolute isopropanol

was added. The DNA was precipitated at 10,000 rpm for 5 min at 4°C. The supernatant was discarded, and DNA pellet was washed 2 to 3 times with 75% ethanol. The DNA pellet was air-dried at room temperature and dissolved in DNA hydration buffer. Deoxyribonucleic acid quality and concentration were determined by UV spectroscopy. The DNA was diluted to 50 ng/μL as a working solution and stored at –20°C before use.

PCR –Restriction fragment length polymorphism analysis (PCR-RFLP)

The reactions of PCR were carried out in a total volume of 10 μL containing: 1 μL of diluted DNA template (50 ng/μL); 1X PCR buffer (1 μL of 10XPCR buffer), 4 mM MgCl₂ (0.8 μL of 50 mM MgCl₂), 0.1 mM dNTP (1 μL of 1 mM dNTP), 0.5 μM of each primer (1 μL of 5 μM of each primer), and add 0.1 μL of *Taq* DNA polymerase (Promega, San Diego, CA). PCR amplification was carried out in a PCR thermal cycle (COBETT RESEARCH, Australia 2003, iCycler thermal cycler, BioLad, U.S.A) using the following amplifying program: preheating at 95°C for 5 min followed by 35 cycles at denature 95°C, 30 s; annealing temperature (Table 1), 40 s; and extension 72°C, 30 s. Final extension was carried out at 72°C for 5 minutes and the amplified products were hold at 4°C until needed. At the end of PCR cycle, amplified products were analyzed by 0.8% agarose gel with 1X loading dye. After electrophoresis at 100 V for 35 min, gel was stained with GELSTARTM (Gelstar Inc, NY) for 10 min. DNA fragments were visualized by gel documentation.

Table 1 Sequences of primer and Ta (annealing temperatures) for PCR amplification

Genes	Primer sequence	Ta (°C)
CTSB ^{1/}	Forward:5'GTGGCCGGGT	55
	GGTTTTA 3'	
CTSL ^{2/}	Reverse:5'TCCTCTGGTG	64
	CTGCTAATTCTGAC 3'	
CTSL ^{2/}	Forward:5'TCACTGCCGT	64
	GAAGAATCAG 3'	
CTSL ^{2/}	Reverse:5'GCAGAGCTGT	64
	AATGGCAAGA 3'	

Note: ^{1/} [16], [12]

^{2/} [12], [8]

Restriction of PCR Products

Polymerase chain reaction (PCR) products from each pig were digested separately with 1 restriction endonucleases, *MspI* for *CTSB* and *TaqI* for *CTSL*. Each digestion reaction contained 2 μL of PCR products, 1 μL of cut smart, and 0.2 μL of enzyme, add water 4.8 μL in a total volume of 10 μL. Subsequently, each reaction was incubated at 37°C for *MspI* and 65°C for *TaqI* for at least 6 h.

Genotyping of *CTSB* deoxyribonucleic acid fragments were detected on a vertical electrophoresis (Mini-Protein III, Bio-Rad Laboratories, Richmond, CA) using a 12% denaturing polyacrylamide gel (Sigma Inc., St. Louis, MO) with 1X polyacrylamide dry 5 μ L. After electrophoresis at 150 V for 120 min, gels were stained with GelStar (Gelstar Inc., Patchogue, NY) for 10 min. Deoxyribonucleic acid fragments were visualized by UV transillumination and photographed with the Syngene gel documentary system (Syngene Inc., Cambridge, IL). For *CTSL*, detected on a horizontally electrophoresis unit (Mini-Protein III, Bio-Rad Laboratories, Richmond, CA) using a 2% agarose gel.

Statistical analysis

The means of ultrasound, carcass and meat quality traits were analyzed by PROC MEANS. [13]

Associations between the genotypes of the candidate genes (*CTSB* and *CTSL*) on carcass and meat quality were assessed by the procedure MIXED in SAS version 8.02 (SAS Institute Inc. Cary, NC, USA), with a model that included sire as a random effect and the fixed effects sex and genotype of the analyzed DNA markers.

Results and discussion

Phenotypic analysis

The means (Means), standard deviation (Std.), minimum (Min.) and maximum (Max.) of carcass and meat quality traits in the pigs are showed in Table 2. Means of BW and Hot_C weight were 105.62 kg and 78.96 kg, respectively. Data from ultrasound showed that, U_LEA and U_BF were 38.30 cm² and 17.09 mm, respectively. The previous study of Schwab [2] reported that ultrasound 10th rib loin muscle areas were 41.05 cm² and showed larger than this study. Ayuso [14] found the means of 10th rib by ultrasound were 38.12 mm and carcass measurements were 43.11 mm. Moeller [15] reported loin eye area of swine was 35.2 cm².

Table 2 Means, standard deviations (Std.), minimum (min) and maximum (max) values for carcass and meat quality parameters

Variable	Means	Std.	Min.	Max.
BW, kg	105.62	9.63	80.00	126
BL, cm	73.28	6.41	58.80	90.00
U_LAE, cm ²	38.30	4.61	20.29	50.25
U_BF, mm	17.09	3.45	8.80	25.60
CL, cm	76.64	3.14	69.00	84.00
Hot_C, kg	78.96	8.04	57.10	95.90
Chill_C, kg	77.04	7.94	55.60	93.80
%carcass, %	74.79	4.23	61.69	95.77
Weight loss, kg	2.43	0.42	0.24	3.81
LAE, cm ²	40.20	5.14	39.00	56.00
BF, mm	31.98	8.19	14.00	51
pH ₀	6.40	0.16	5.98	6.79
pH ₄₅	6.22	0.15	5.82	6.66
pH ₂₂	6.00	0.21	5.32	6.78
FW, kg	0.80	0.13	0.54	1.32
LW, kg	4.94	0.83	3.06	7.49
HW, kg	9.87	1.02	7.25	12.08
SW, kg	7.04	0.81	5.32	9.58

PCR-RFLP analysis and genotype frequency

The expression of *CTSB* and *CTSL* genes was analyzed by PCR-RFLP. The length of PCR products were 139 bp (*CTSB*) and 380 bp (*CTBL*) (Fig.1). The frequencies of three investigated genotypes in the *CTSB* (AA, AC and CC) and *CTSL* (CC, CT and TT) gene are presented in Table 3. Of 177 investigated pigs, 0.61 were heterozygous AC genotype, 0.34 were homozygous AA genotype, and 0.05 were homozygous CC genotype in *CTSB*. The frequencies of A and C alleles of *CTSB* were 0.65 and 0.35, respectively. Russo [16] showed that alleles frequency A was higher than alleles C. Regarding *CTSL*, the frequencies of CC, CT and TT genotypes were 0.625, 0.354, and 0.021, respectively. The frequencies of C alleles (0.80) were higher than T alleles (0.20) (Table 3). The high frequency of CC genotype of *CTSL* is in accordance with previous reports [8]. However, Fontanesi [12] reported the highest frequency of TC genotype, which is not in accordance with results of this study.

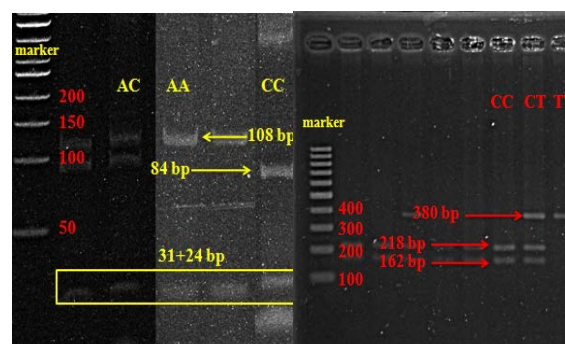


Figure 1 The genotype of *CTSB* gene: AA (108, 31+24 bp), AC (108, 84, 31+24 bp) and CC (84, 31+24); *CTSL* gene: CC (218, 162 bp), CT (380, 218, 162 bp) and TT (380 bp) digested with *MspI* and *TaqI*, respectively

Table 3 Genotype and allele frequency of *CTSB* and *CTSL* in crossbreed swine

Genes	Genotype frequency			Total	Allele Frequency		Total
	AA	AC	CC		A	C	
<i>CTSB</i>	0.34	0.61	0.05	1	0.65	0.35	1
N	98	177	13	288			
	CC	CT	TT		C	T	
<i>CTSL</i>	0.63	0.35	0.02	1	0.80	0.20	1
N	180	102	6	288			

Association of *CTSB* and *CTSL* polymorphism on carcass and meat quality

The significant effects of *CTSB* polymorphism were detected on body length (BL), ultrasound scan of loin eye area (U_LAE), weight loss (WL) and loin eye area (LAE) ($P < 0.05$, $P < 0.01$). The pigs carrying the AC genotype had higher level of BL, U_LAE and LEA than the ones carrying the homozygous genotype (AA or CC). The pigs with the CC genotype of *CTSB* had lower WL (1.86 %) than the ones carrying the AA or the AC genotype (2.19 % and 1.97 %). The *CTSL* variants represented statistically significant effects on BL trait ($P < 0.05$). The CC genotype (77.92 cm) had higher BL value compared to the CT (76.14 cm) and the TT genotypes (76.92 cm). The *CTSB* and *CTSL* were high polymorphism and their alleles could be potential genetic markers for swine selection (Table 4). Previous studies have shown that the significant associations were observed between *CTSB* and back-fat thickness [10]. In addition, Piorkowska [9] found that AC genotype characterized higher carcass yield and loin than in AA pig.

CTSL is a gene that produce lysosomal proteinases and is important for the degradation of proteins. Its main role is in the post-mortem proteolysis of meat [8]. Fontanesi [12] have claimed that *CTSL* marker showed a tendency towards association with back fat thickness and weight of lean cuts. On the other hand, Vera [8], no statistically significant differences were detected in qualitative traits. However, we identified a trend of allele T on increased fatness and the effect of allele C on lean meat.

Table 4 Association of *CTSB* and *CTSL* on carcass and meat quality in crossbreed swine

Genes	traits	Genotypes		P-

		AA	AC	CC	value
<i>CTSB</i>	BW	102.54	101.93	100.90	0.83
	BL	75.38	77.81	77.79	*
	U_LEA	36.52	39.43	36.56	**
	U_BF	16.34	15.68	15.71	0.23
	CL	76.16	76.93	75.71	0.17
	Hot_C	78.72	79.05	77.71	0.88
	Chill_C	76.52	77.07	75.84	0.85
	%Carcass	73.38	74.21	73.85	0.23
	Weight loss	2.19	1.97	1.86	*
	LEA	39.79	41.32	38.70	**
	BF	31.55	30.78	30.78	0.68
	pH0	6.42	6.49	6.49	0.09
	pH45	6.25	6.33	6.31	0.15
	pH22	6.01	6.03	6.10	0.37
	FW	0.75	0.83	0.77	0.37
	LW	4.92	5.13	4.80	0.13
	HW	9.88	9.86	10.01	0.88
	SW	7.12	7.16	7.20	0.96
<i>CTSL</i>		CC	CT	TT	
	BW	103.30	103.75	98.29	0.73
	BL	77.92	76.14	76.92	*
	U_LEA	37.61	37.32	36.94	0.57
	U_BF	15.74	15.92	14.97	0.68
	CL	76.12	76.44	78.99	0.45
	Hot_C	78.64	78.33	75.69	0.71
	Chill_C	76.65	76.28	73.17	0.71
	% Carcass	74.19	73.51	74.57	0.18
	Weight loss	1.99	2.05	2.52	0.50
	LEA	40.35	40.16	39.43	0.75
	BF	30.13	31.96	29.83	0.06
	pH0	6.47	6.47	6.50	0.96
	pH45	6.31	6.27	6.36	0.26
	pH22	6.07	6.05	6.26	0.58
	FW	0.80	0.76	0.78	0.41
	LW	4.92	4.98	5.00	0.61
	HW	10.00	9.85	9.73	0.28
	SW	7.18	7.12	6.60	0.60

Note: * $P < 0.05$; ** $P < 0.01$

CONCLUSION

CTSB and *CTSL* were analyzed using the PCR-RFLP technique for detection of genotypes. Three alleles were found on *CTSB* gene (AA, AC and CC) and *CTSL* gene (CC, CT and TT) with frequency ranging from 0.20 to 0.80. The results obtained from the present study indicated that the investigated *CTSB* and *CTSL* gene markers were associated with carcass and meat quality traits in Thai cross breeds pig (Large White \times Landrace \times Duroc Jersey). The means of Hot_C and Chill_C were 78.78 and 76.71 kg, respectively. LEA was 40.20 cm². For the *CTSB* polymorphism was significant with BL, U_LEA,

WL and LEA. The pigs carrying the AC genotype had higher level of BL, U_LEA and LEA than homozygous genotype (AA or CC). CC genotype of *CTSB* had lower WL (1.86 kg) than AA or the AC genotype (2.19 and 1.97 kg). *CTSL* was related to BL traits. The CC genotype (77.92 cm) had higher BL than CT (76.14 cm) and TT genotypes (76.92 cm). Therefore, this polymorphism of *CTSB* and *CTSL* could be of interest in marker assisted selection programs.

ACKNOWLEDGEMENTS

We would like to thank Mahasarakham University, Mahasarakham, Thailand, for financial support and Betagro Company Limited, Thailand, for tissue supply and the data, which were the main information of this research.

REFERENCES

- [1] Daza A., Mateos A., Lopez C. C., Rey A., Ovejero I., Lopez-Bote C. J., Effect of feeding system on the growth and carcass characteristics of Iberian pigs, and the use of ultrasound to estimate yields of joints. *Journal of Meat Science*, Vol. 72, 2006, pp. 1–8.
- [2] Schwab, C. R., Baas T. J., Stalder K. J., Results from six generations of selection for intramuscular fat in Duroc swine using real – time ultrasound. *Journal of Animal Science*, Vol. 88, 2010, pp. 69-79.
- [3] Miar Y., Plastow G. S., Moore S. S., Manafiazar G., Charagu P., Kemp R. A., Van Haandel B., Huisman A. E., Zhang C. Y., McKay R. M., Bruce H. L., Wang Z., Genetic and phenotypic parameters for carcass and meat quality traits in commercial crossbred pigs. *Journal of Animal Science*, Vol. 92, 2014, pp. 2869-2884.
- [4] Zhang, Q., Boichard D., Hoeschele I., Ernst C., Eggen A., Murkve B., Pfister-Genskow M., Witte L.A., Grignola F.E., Uimari P., Thaller G., Bishop M.D., Mapping quantitative trait loci for milk production and health of dairy cattle in a large outbred pedigree. *Journal of Genetics*, Vol. 149, 1998, pp. 1959–1973.
- [5] Ragland K. D., Christian L. L., Baas T. J., Evaluation of real-time ultrasound and carcass characteristics for assessing carcass composition in swine. *Journal of Zootech*, Vol. 41, 2004, pp. 2463-2466.
- [6] Newcom D. W., Baas T. J., Lampe J. F., Prediction of intramuscular fat percentage in live swine using real-time ultrasound. *Journal of Animal Science*, Vol. 80, 2014, pp. 3046–3052.
- [7] Dekkers, J. C. M., Commercial application of marker- and gene-assisted selection in livestock: Strategies and lessons. *Journal of Animal Science*, Vol. 82, 2004, pp. 313-328.
- [8] Vera, D., Roman S., Michal S., Jaroslav C., Monika O., Eva K., Lubos B., The effect of gene *CTSL* on the quantitative and qualitative production traits of pork meat. *Journal of Maso international brno*, Vol. 1, 2011, pp. 47-50.
- [9] Piorkowska, K., Ropka-Molik K., Eckert R., Tyra M., Zukowski K., Analysis of polymorphisms of cathepsin B and cystatin B impact on economically important traits in pigs raised in Poland. *Journal of Livestock Science*, Vol. 146, 2012, pp. 99-104.
- [10] Russo V., Fontanesi L., Davoli R., Nanni Costa L., Cagnazzo M., Buttazzoni L., Virgili R., Yerle M., Investigation of candidate genes for meat quality in dry-cured ham production: the porcine cathepsin B (*CTSB*) and cystatin B (*CSTB*) genes. *Journal of Animal Genetics*, Vol. 33, 2002, pp. 123-131.
- [11] Fontanesi, L., Speroni C., Buttazzoni L., Scotti E., Nannicosta L., Davoli R., Russo V., Association between cathepsin L (*CTSL*) and cathepsin S (*CTSS*) polymorphisms and meat production and carcass traits in Italian Large White pigs. *Journal of Meat Science*, Vol. 85, 2010, pp. 331-338.
- [12] Fontanesi, L., Speroni C., Buttazzoni L., Scotti E., Dallolio S., Davoli R., Russo V., Association between polymorphisms in cathepsin and cystatin genes with meat production and carcass traits in Italian Duroc pigs: confirmation of the effects of a cathepsin L (*CTSL*) gene marker. *Journal of Molecular Biology*, Vol. 39, 2012, pp. 109-115.
- [13] SAS. User's Guide: Statistics, V.6.12, 1998, SAS Institute Inc., Cary, NC.
- [14] Ayuso D., Gonzalez A., Hernandez F., Corral J. M., Izquierdo M., Prediction of carcass composition, ham and foreleg weights, and lean meat yields of Iberian pigs using ultrasound measurements in live animals. *Journal of Animal Science*, Vol. 91, 2014, pp. 1884-1892.
- [15] Moeller S. J., Evolution and use of ultrasonic technology in the swine industry. *Journal of Animal Science*, Vol. 80(E. Suppl. 2), 2002, pp. E19–E27.
- [16] Russo, V., Fontanesi L., Scotti E., Beretti F., Davoli R., Nannicosta L., Virgili R., Buttazzoni L., Single nucleotide polymorphisms in several porcine cathepsin genes are associated with growth, carcass, and production traits in Italian Large White pigs. *Journal of Animal Science*, Vol. 86, 2008, pp. 3300-33

EFFECT OF HARVESTING STAGES ON JELLY SEED SYMPTOM OF PLANGO (*Bouae burmanica*) CV. THUNL KLAO FRUITS

¹Pattarawan Wattanakeeboot and ²Usawadee Chanasut

¹Postharvest Technology Research Center, Faculty of Agriculture, Chiang Mai University, Chiang Mai 50200

²Department of Biology, Faculty of Science, Chiang Mai University, Chiang Mai 50200

ABSTRACT

Plango or Marian plum (*Bouae burmanica*) has a short harvesting period and usually harvested at ripe fruit stage. Therefore, the jelly-seed often occurred inside the fruit. The jelly-seed is a physiological disorder and causes fruit softening and wilting. This symptom will affect the storage period and shelf-life of the fruit. Jelly-seed also found after harvesting. This study was determined the activities of two important cell wall degradation enzymes which were PG and PME from 3 harvesting stages of plango fruits at 75, 85 and 95 days after full bloom (DAFB). Fruits were storage at 10 and 25°C. It was found that the jelly-seed symptom only occurred in the 95 DAFB fruits after harvest and storage at 25°C. This fruits also had the highest activity of PG and increased with the ripen stages and storage period. The activity of PG and PME were delayed when storage at 10°C compared with the activity of PG and PME from the fruit kept at 25°C

Keywords: cell wall degradation, polygalacturonase, pectin methyl esterase

INTRODUCTION

Plango (*Bouea burmanica*) in Thai is called Ma-yong-chid. It names from plum mix mango then new commercial name “Plango”. Plango are same Marian plum but it is big fruit, oblong and not sweetest or irritate in oesophagus. We are Thai people call the Marian plum is Ma-prang, small and sour taste somebody eaten are feel irritate. Marian plum (*Bouea burmanica* Griff) is tropical fruit, tree belonging to Anacardiaceae family and it is native Southeast Asia and commercially grown in the ASEAN region in Malaysia, Thailand and Indonesia [17]. Other popular names of this fruit are Mayun called in Myanmar, Ramania ugandaria in Indonesia and Kundang rembung and setar called in Malaysia. It is flowering occurs during the cool season on January and fruits are mature on March. Color of maturity stages; green, orange and dark orange. Ripe fruit is orange pulp and stone is purple color. Plango belong to same family as mango but the taste is not really the same. It is tastes of flesh a bit like mango, texture rind of fruit a bit like plum.

Plango has a short harvesting period and ripening stage of plango when harvested, it's most important influencing for textural properties when harvested over ripe, the textural are like jelly around seed. The major textural changes are resulting in softening of fruits, due to enzyme mediated alteration of the compositions and structure of cell wall polysaccharides such as pectic polysaccharides and cellulose, which leads to their partial solubilisation [18]. Enzymes are about softening, pectin methyl esterase (PME), polygalacturonase (PG) and cellulase are among enzymes generally

recognised as having a crucial effect on fruit texture during ripening [4] such as disorder in plums, they are very sensitive to low temperature and benefits of cold storage maybe limited by development of various physiological disorders for example flesh translucency (gel breakdown), internal browning, reddening or bleeding, loss of flavor and delayed softening or retarded ripening after prolonged cold storage [11]. Flesh translucency is one of the most frequently observed chilling injury symptoms, it showed as translucent gelatinous breakdown in mesocarp and related to the presence of water soluble pectin [2] besides disorder in plum it showed also mango. Mango fruit qualities are respected to taste, flavor, color, aroma, weight, size and shape [9], quality performance of mangoes depend on maturity stage at harvest. Generally, physical, physiological and chemical parameters are used to define the maturity stage. Therefore, fruit has to be harvested at suitable stage of maturity for develop the optimum sensory quality attributes and extended postharvest life [19]. Fruit harvested at over maturity stage is highly susceptible to mechanical damage such as bruising, decay and water loss and showed defects like jelly seeds or jelly pulp after harvest [19]. ‘Amrapali’ mango fruit is a physiological disorder of unknown aetiology called jelly seed (JS) which adversely affects the eating quality of mature ripe pulp [13]. Therefore, the present study was plango quality and to effect of harvesting stages caused jelly seed symptom.

MATERIALS AND METHODS

Fruits harvest and storage

'Thul Klao' plango (*Bouea burmanica*) were harvested on 75 (Immature ripe), 85 (Mature ripe) and 95 (Over ripe) day after full bloom of March 2017, from Dussanee orchard located in Mae Thang district, Chiang Mai province, Thailand. Plango were picked by hand and sorted according to uniformity of shape, color and size. Fruits were stored at 10 and 25°C.

Color of plango

Fruits were measured Lightness (L) and b* by colorimeter, Color Quote XE.

Measurements of fruit firmness, total soluble solid (TSS)

Measurements of plango fruit firmness were measured using Texture analyzer TA.XT plus, plunger set to pierce 8 mm depth. Firmness was expressed as the maximum force (N). The juice from plango were measured using a digital refractometer (Agro Pocket refractometer PAL-1) the results expressed in °Brix. Titratable acidity (TA) was measured from three grams of plango pulp with 100 ml of deionized water. It used automatic titrator, Schott Titroline easy M2-230V.

Quantification of enzymatic activity

The enzymatic activity of PG and PME were measured on fresh plango.

Polygalacturonase (PG) activity was quantified according to the method by [7]. Plango mesocarp tissues were sliced into around seed 1 cm wide segment was frozen immediately in liquid Nitrogen. An enzymatic extract was 3 g of pulp plango with 0.1 M sodium phosphate buffer (pH 6.4) and adding 1 mM EDTA. They were centrifuged at 8,000 rpm for 30 min at 4 °C [5]. Supernatants were used as enzyme extracts for assaying PG activity measured enzymatic activities. The reaction mixture containing 0.1 ml of 200 mM Sodium chloride, 0.5% polygalacturonic acid, 0.1 ml of crude enzyme. It was incubated at 37 °C for 1 hr. followed by addition of 3,5 dinitrosalicylate (DNS) reagent. The absorbance was measured at wavelength 540 nm in UV-VIS spectrophotometer, Analytik Jena AG, SPECORD 40. PG activity was expressed as Units/mg protein.

PME activity was measured follow [12]. Enzyme extract was adjusted 7.5 with 0.01 M NaOH. Each 5 ml assay mixture contain 2 ml of 1% pectin solution (w/v), 0.2 ml of NaCl, 0.15 ml of 0.01% (w/v) bromothymolblue, 0.45 ml of distilled water and 0.2 enzyme extract and was mixed. The

absorbance at 620 nm. PME activity was expressed in Units/ mg protein/min.

Statistical analysis

Data were analyzed by SPSS 18.0, Significant difference were considered at the level of $p < 0.05$.

RESULTS

Firmness

The softening of plango all harvesting stages was delayed during storage at 10°C. The firmness of fruits declined during storage at 25°C. Plango, 75 day after full bloom at 10°C were decreased slowly and beginning of softening after 6 day (Fig. 1). The firmness of plango storage at 25°C in 95 day after full bloom were declined during storage.

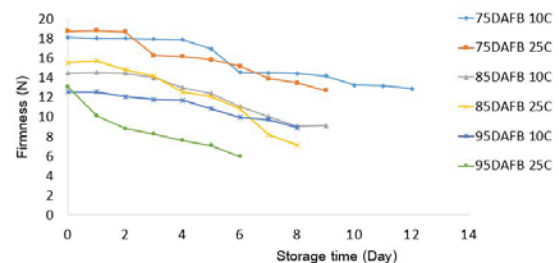


Fig. 1. Firmness in plango fruit on 75, 85 and 95 harvesting stages storage at 10 and 25 °C

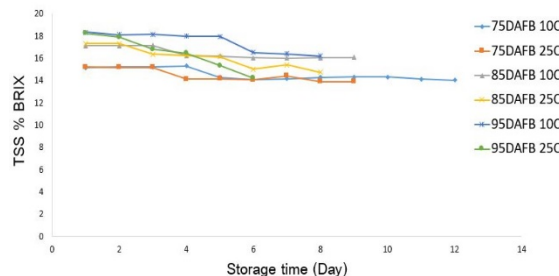


Fig. 2. Total soluble solid (TSS %Brix) of plango on 75, 85 and 95 harvesting stages storage at 10 and 25 °C

Plango were found highest total soluble solid (TSS) in mature ripe (85 DAFB). Immature ripe (75 DAFB) were found that TSS decreased slowly. Mature ripe (85 DAFB) and Over ripe (95DAFB) were decreased during storage (Fig. 2)

Enzyme activity

PG activity was increased with harvesting stage and during storage and found low level in immature ripe (75 DAFB) and fruit was storage at 10°C for 12 day. PG are 7.99 Unit/mg protein. Mature ripe (85 DAFB) were 15.91 Unit/ mg protein

in fruit storage 10°C for 9 day and found highest PG activity in the over ripe (95 DAFB) at 25°C 33.68 Unit/ mg protein on 6 day at storage time. (Fig.3).

PME activity was increased slowly on all harvesting stage and during storage. Fruits were storage at 10 °C, immature ripe, mature ripe and over ripe found that 3.34, 3.20 and 3.69 Unit/ mg protein respectively (Fig.4).

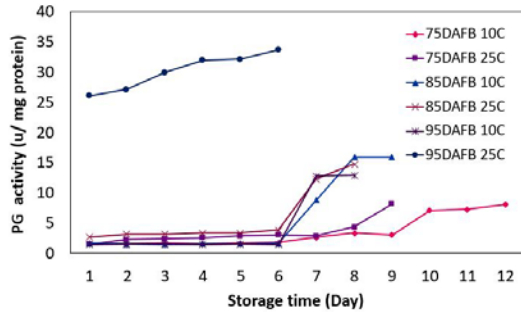


Fig. 3. Changes in activity of PG in plango on 75, 85 and 95 harvesting stages storage at 10 and 25 °C

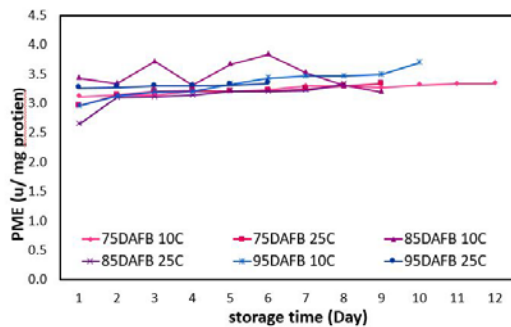


Fig. 4. Changes in activity of PME in plango on 75, 85 and 95 harvesting stages storage at 10 and 25 °C

Lightness (L) was decreased with harvesting stages, immature ripe, mature and over ripe. Lightness value were found that high value, 66.94 in immature ripe (75 DAFB). Color changes occurred in pulp are dark yellow and show jelly texture on fruits storage at 10 °C found beginning of color changes on 8, 7 and 7 storage time (day), (immature ripe, mature ripe and over ripe respectively) (Fig. 5). Plango were showed jelly severe around seed storage at 25 °C then showed on 9, 8 and 6 storage time (Day); immature ripe, mature ripe and over ripe respectively (Fig. 5). Yellow color (b*) were increased with harvesting stages, Over ripe (95 DAFB) are high b* value on 6 storage time (Day), 49.1 conform with PG activity and firmness due to jelly texture in pulp (Fig. 6).

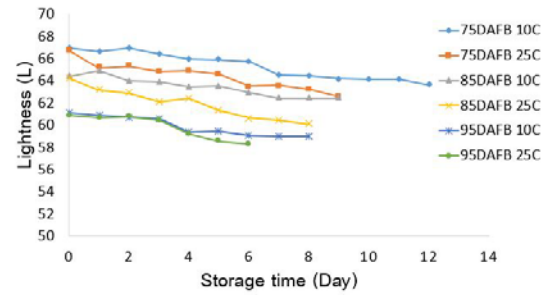


Fig. 5. Changes in lightness of plango fruit on 75, 85 and 95 harvesting stages storage at 10 and 25 °C

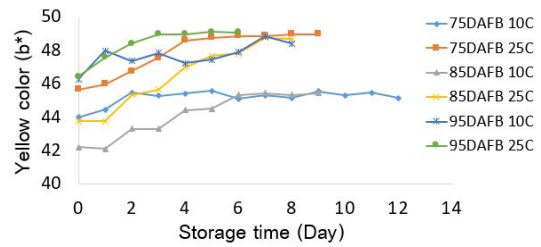


Fig. 6. Changes in yellow color (b*) in pulp of plango on 75, 85 and 95 harvesting stages storage at 10 and 25 °C

DISCUSSION

The plango are short harvesting period, harvesting stages are important for quality. The fruit harvested at the suitable stage of maturity in order to develop the optimum sensory quality attribute and extend postharvest life [19]. Plango was three harvesting stages, immature ripe (75 DAFB), mature ripe (85 DAFB) and over ripe (95 DAFB), mature level at harvest is crucial factor for the development of acceptable flavor quality during ripening [8]. It is optimum harvesting, mature ripe. According to [6], during fruit maturation, Total soluble solid tend to increase while titratable acidity (TA) decrease. Three harvesting stages of jelly seed during storage were 25 °C on over ripe, pulp of fruits were showed jelly and dark yellow color. According to [10] flesh translucency manifests itself as a translucent gelatinous breakdown of the mesocarp of stone fruits and related to presence of WSP in the tissues. In this study, fruits are showed jelly seed, high polygalacturonase based on an increase during storage. Resulting in severe texture change and softening, the increase of polygalacturonase and cellulose activities during ripening should contribute to the loss of texture through action on cell wall pectic polysaccharide and cellulose, changing their structure and solubilizing cell wall component [1] [14] therefore softening is a developmentally programmed ripening process in many fruits, providing difference texture with various fruits including juiciness, crispness and stiffness [14].

Pectin methyl esterase are increase slowly all harvesting stages. According to [13], jelly seed had higher polygalacturonase (PG) and increase pectin methyl esterase activities (PME). Pectin methyl esterase (PME) catalyses the removal of methy ester groups from pectin chains making them more susceptible to PG-mediated degradation. Subsequently, the rapid increase in PG activity depolymerised cell wall polygalaturonides to produce galacturonic acid [3]. According to [15] and [16], PME activity had little effect on fruit firmness or ripening characteristics but resulted in significant favorable changes is soluble solids content of raw juice.

CONCLUSION

This study 3 harvesting stage of plango fruits at 75, 85 and 95 days after full bloom (DAFB). Fruits were storage at 10 and 25°C. It was found that the jelly-seed symptom only occurred in the 95 DAFB fruits after harvest and storage at 25°C. This fruits also had the highest activity of PG and increased with the ripen stages and storage period. The activity of PG and PME were delayed when storage at 10°C compared with the activity of PG and PME from the fruit kept at 25°C.

ACKNOWLEDGEMENT

We would like to thank the Postharvest Technology Research Center, Faculty of Agriculture, Chiang Mai University, Department of Biology, Faculty of Science, Chiang Mai University, Chiang Mai, Thailand and The Graduate School Chiang Mai University, Chiang Mai, Thailand.

REFERENCES

- [1] Ali, Z. M., Chin, L.-H., & Lazan, H. (2004). A comparative study on wall degrading enzymes, pectin modifications and softening during ripening of selected tropical fruits. *Plant Science*, 167(2), 317-327.
- [2] Candan, A. P., Graell, J., Larrigudiere, C. 2011. Postharvest quality and Chilling injury of plums: benefits of 1-methylcyclopropene. *Span. J. Agric. Res.* 9, 554-564.
- [3] Carpita, N. C., & Gibeaut, D. M. (1993). Structural models of primary cell walls in flowering plants: Consistency of molecular structure with the physical properties of the wall during growth. *The Plant Journal*, 3, 1-30.
- [4] Claudia, N., Conceicao, S., Gloria, P., Sonia, S., Jose, A., and Lopes-da, V. (2009). Effect of ripening on microstructure and texture of 'Ameixa d'Elvas' candied plums. *Food Chemistry*, 115, 1094-1101.
- [5] Denes, J. M., Baron, A., & Drilleau, J F. (2000). Purification, properties and heat inactivation of pectin methylesterase from apple (cv Golden Delicious). *Journal of the Science of food and Agricultural*, 80(10), 1503-1509.
- [6] Dharini, S., Yuming, J., & Elhadi, M. Y. (2011). Maintaining mango (*Mangifera indica* L.) fruit quality during the export chain. *Food research International*, 44, 1254-1263.
- [7] Gross, K. C. (1982). A rapid and sensitive spectrophotometric method for assaying poligalacturonase using 2 -cyanoacetamide. *HortScience*, 17, 933-934.
- [8] Kader, A., & Mitcham, B. (2008). Optimum produres for ripening mangoes. Fruit Ripening and Ethylene Management. *Postharvest thechnology*, 47-48.
- [9] Kader, A. A. (2002). Quality and safety factors: Definition and evaluation for fresh horticultural crops. *Postharvest technology of horticultural crops*, 279-285.
- [10] Manganaris, G. A., Vicente, A. R., Crisosto, C. H., & Labavitch, J. M. (2008b). Effect of delayed storage and continuous ethylene exposure on flesh reddening of 'Royal Diamond' plums. *J. Sci. Food Agric.* 88, 2108-2185.
- [11] Minas, I. S., Crisosto, G. M., Holcroft, D., Vasilakakis, M., Crisosto, C. H., (2013). Postharvest handling of plums (*Prunus salicina* Lindl.) at 10 °C to save energy and preserve fruit quality using and innovative application system of 1-MCP. *Postharvest Biol. Thechnol.* 76, 1-9.
- [12] Nunes, C. S., Castro, S. M., Saraiva, J. A., Coimbra, M. A., Hendrickx, M. E., & Van Loey, A. M. (2006). Thermal and high-pressure stability of purified pectin methylesterase from plums (*Prunus domestica*). *Journal of food Biochemistry*, 30(2), 138-154.
- [13] Seshadri, S., Manoharan, S., & Hari, S. S. (2016). Premature seed germination induced by very-long-chain fatty acids causes jelly seed disorder in the mango (*Mangifera indica* L.) cultivar 'Amrapali' in India. *Horticultural Science and Biotechnology*, 91:2, 138-147.
- [14] Seymour, G. B., Manning, K., Eriksson, E. M., Popovich, A. H., & King, G. J. (2002). Genetic identification and genomic organization of factors affect fruit texture. *J. Exp. Bot.* 53, 2065-2071.
- [15] Tieman, D. M., Harriman, R. W., Ramamohan, G. & Handa, A. K. (1992)/ An antisense pectin methylesterase gene alters pectin chemistry and soluble solid in tomato fruit. *The plant Cell* 4: 667-679.
- [16] Thakur, B. R., Singh, R. K., & Handa, A. K. (1996). Effect of an antisense pectin methylesterase gene on the chemistry of pectin in tomato (*Lycopersicon esculentum*) juice. *J. Agric. Food chem.* 44: 628-630.
- [17] Vusie, L. M., & Yapwattanapun, C. (2001). Effect of environmental conditions on flower induction of marian plum (*Bouea burmanica* Griff). *Agricultural and natural resources*, 51, 243-246.
- [18] Waldron, K. W., Smith, A. C., Parr, A. J., Ng, A., & Parker, M. L. (1997). New approaches to understanding and controlling cell separation to fruit and vegetable texture. *Trends in Food Science and Thechnology*, 8(7), 213-221.
- [19] Yahia, E. M. (1998a). Modified and controlled atmospheres for tropical fruits. *Horticultural Reviews.*, 22, 123-183.

USING BEEF MORPHOLOGY TO PREDICT CARCASS WEIGHT WHICH CUTTING IN THAI-ISAAN STYLE

Khanitta Ruangwittayanusorn^{1*}, Doungnapa Promket¹, Songsak Champawadee¹,
Jaturaput Muapkunton¹, Ornicha Sriboon¹, Kewlin Pukkawan¹

Division of Animal Science, Department of Agriculture Technology, Faculty of Technology, Mahasarakham
University, Thailand

ABSTRACT

The trading of beef cattle market in Thailand is based on price satisfaction agreement between sellers and buyers. The rancher, the middlemen and the butcher shop will estimate the return from carcass composition by beef characteristic. The forecast of return from carcass composition depends on personal skill. The highest price of carcass cutting in Thai-Isaan style compost with all meat, liver, spleen, kidney, heart, tongue and gastric. The objective of the study was to determine the best-fitted regression model for predicting the carcass composition using different linear body measurements. Data on carcass composition cutting in Thai-Isaan style and linear body measurements recorded from 100 crossbred male beefs in Isaan region were used for this study. The simple and multiple regression models were fitted with carcass composition as dependent variable and heart girth, body height, body length, hip width and hip length as independent variables. The correlation coefficients between carcass composition and body measurements were strongly and significantly ($P < 0.01$). Body length was best fit to simple regression model for predict carcass composition weight ($R^2 = 0.712$). Stepwise method was used to select factor effect in multiple regression models. Multiple regression for predict carcass composition had highest R^2 when all body measurements were included ($R^2 = 0.816$), however the recommend model was the 3 factors model (heart girth, body length and hip length) with $R^2 = 0.810$. The study concludes that linear body measurements can predict carcass composition weight and their return. The rancher, the middlemen and the butcher shop can use this equation to forecast the return and setting the beef price for trading.

Keywords: Carcass, Estimate the return, Total trimmed meat, Morphology, cattle

INTRODUCTION

Number of beef cattle in Thailand in year 2017 was around 4,876,000. Forty-seven percent of all were in Isaan region [1]. With extensive areas and Isaan people prefer to consume meat from beef and they have a culture about consumption beef, so there are a lot of beef cattle in Isaan.

The butcher shops in Isaan region mostly trimming meats that were killed in the municipal slaughterhouse. They buy live cattle from the middlemen or some from local beef cattle market. The trading of beef cattle market is based on price satisfaction agreement between sellers and buyers. The rancher, the middlemen and the butcher shop will estimate the return from carcass composition by beef characteristic. Estimate of the carcass to be derived from the appearance of cattle is a unique skill expertise and the wisdom of beef buyer.

Weight of carcasses directly depends on body weight [2]. Forecasting the carcass weight of cattle must have information on live weight. Nevertheless, the trading in the countryside, no scale is used to weight. As a reason, the linear type trait of live animal is applied to estimate the live weight and the carcass weight and inference to the return.

Estimation from sight, there will be a lot of error if not expert. Body measurements taken on live animals have been used expansively for a variety of reasons both in experiments and in selection purpose [3]. The accuracy of prediction carcass weight from live weight is a financial contribution to livestock enterprise. The producers and buyers can estimate revenue from the sale of live cattle and access value-based trading systems.

The purpose of this study was to predict the carcass weight from body measurement using simple and multiple linear regression.

Slaughter and cutting Thai-Isaan style Thailand.

Several percent of beef cattle in Thailand are cutting in standard way but for Isaan, they cutting to suitable for the local cooking. The people in Isaan eat almost every part of the cattle carcass except for skin, bone, horn. Parts of carcass are grouped by the value, each group sale in the same price, although they are different types of tissues.

The slaughter method starts with stunning cattle by a hammer at the front of the skull, X crossing line between horn and eye. After cattle fall down use a sharp knife to pierce the jugular vein to bleed until the blood flow is negligible. Hang 4 legs

separately and clean body outside. Cut the skin along the middle line to the tail. Skin for 4 legs should be removed accepts under knee to hoof. The horns are removed and the head is skinned. The head is detached by cutting through the neck muscles and the occipital joint. Cut along middle line to open a flum and removed internal organs such as stomach intestine liver heart, etc. Front legs, from scapula to hoof, hind legs from femur to hoof (round bottom) were separated out for hanging show in a butcher shop. All red meat remaining in frame is trimmed out of the bone. Each part is weight before sent to butcher shop. Hot carcass weight cannot done because of the slaughterhouse does not have the instrument to pull the body up and that trait is less important for local trading.

MATERIAL AND METHODS

Crossbred Brahman were bought from many provinces around Isaan region to municipality slaughterhouse in Kalasin province, Thailand. About 8-10 heads per week of beef were slaughtered, totally 100 beefs were used in this study. Before slaughter process, beef were taken in to restraint box for body measurement. The parameters compost with heart girth (HG): the body circumference posterior to the front legs, body length (BL): the distance between the point of shoulder to the outer and central tuberosity of left humerus to left tuber ischii, body height (BH): the vertical distance from ground to scapular of the withers, hip width (HW): the widest point at the center of the stifles, hip length (HL): the distance between pin bone to the stifle.

Several beef were slaughter in a day, one by one for tracking and recording each part of body. Beef carcasses were trimmed in the style of Isaan. Carcass compositions were group by price. The first price group (W1) was a high value group composted with total trimmed meat such as shanks, chuck, sirloin, rump, round, loin, brisket, etc. Internal organ high value group (W1_1) composted with tongue, heart, liver, spleen and kidney. Second price group was intermediate price (W2) composted with rib, meat scraps, fat, and intestine. Third price group was the lowest price (W3) compost with lung, trachea, bladder, cartilage, rumen, reticulum, omasum abomasum and their ligament. Each group was weighed after trimmed and recorded. Whole legs with bone-in were weighed before sold and weighed only bone again after meat sold out to calculate meat.

Simple correlation coefficients between body measurements and weight of each carcass group were calculated and test for significant. To predict carcass weight, the stepwise procedure was used to select the variable of body measurements for fitting

prediction equations. R-square assessed the accuracy of the equations.

RESULTS AND DISCUSSION

Mean and ranges of body measurement and carcass weight were showed in Table 1. All observations were normally distributed. The high correlation between body measurements were found for hip width and hip length (0.926), Hip width and heart girth (0.824). The balance and relationships of animal body part is stable when they rise in nearly management. [4]. Correlation between all body measurements and carcass group weight were significant correlated (Table 2). Body length was reported to have the highest correlation with W1 and heart grid was the highest correlation with W1_1.

Table 1 Descriptive value of body measurement and carcass weight groups

Variable	N	Mean	Std Dev	Mini mum	Maxi mum
Body measurement					
Heart grid (cm)	100	177.08	11.461	155	220
Body height (cm)	100	131.60	11.347	112	170
Body length (cm)	100	133.20	13.505	102	165
Hip width (cm)	100	45.08	6.552	30	59
Hip length (cm)	100	52.21	6.392	37	67
Weight of carcass group					
W1 (kg)	100	170.00	23.680	118	230
W1_1 (kg)	100	17.82	1.493	15	24
W2 (kg)	100	25.25	3.955	17	39
W3 (kg)	100	25.06	3.348	17	36
W1 = weight of first price group composted with total trimmed meat.					
W1_1 = weight of internal organ high value group composted tongue, heart, liver, spleen and kidney.					
W2 = weight of second price group composted with rib, meat scraps, fat, colon, and intestine.					
W3 = weight of third price group composted with lung, trachea, bladder, cartilage, rumen, reticulum, omasum abomasum and their ligament.					

Table 2 Correlation between body measurements and carcass weight

parameters	W1	W1_1	W2	W3
Heart grid	0.8054 ***	0.4727 ***	0.4066 ***	0.6037 ***
Body height	0.7196 ***	0.4540 ***	0.4742 ***	0.5762 ***
Body length	0.8453 ***	0.3316 ***	0.2359 ***	0.5115 ***
Hip width	0.7966 ***	0.3773 ***	0.3692 ***	0.6298 ***
Hip length	0.7403 ***	0.3987 ***	0.4546 ***	0.6357 ***
W1 = weight of first price group composted with total trimmed meat.				
W1_1 = weight of internal organ high value group composted tongue, heart, liver, spleen and kidney.				
W2 = weight of second price group composted with rib, meat scraps, fat, colon, and intestine.				

W3 = weight of third price group composted with lung, trachea, bladder, cartilage, rumen, reticulum, omasum abomasum and their ligament.

*** p<0.01

Prediction equation for carcass weight group

Simple linear regression for prediction 4 price group weights were calculated from their highest correlation with body measurement (Table 3). Highest correlation between W1, W1_1, W2 and W3 were body length, heart girth, body height and hip length, respectively. Body length explained 71.5% of the variation in W1. It was observed that one cm change in HG resulted in approximately 1.482 kg change in weight of first price group.

Table 3 Simple linear regression equations for estimation of weight of first price group, weight of second price group and weight of third price group

Dependent variables	Equations	R ²
W1	= -27.500+1.482BL	0.715
W1_1	= 6.872+0.06HG	0.223
W2	= 3.491+0.165BH	0.225
W3	= 7.676+0.333HL	0.404

W1	= weight of first price group composted with total trimmed meat.
W1_1	= weight of internal organ high value group composted tongue, heart, liver, spleen and kidney.
W2	= weight of second price group composted with rib, meat scraps, fat, colon, and intestine.
W3	= weight of third price group composted with lung, trachea, bladder, cartilage, rumen, reticulum, omasum abomasum and their ligament.

The main return for the butcher from beef carcass was the W1, it made around 80.00%, of all income from whole carcass, as a reason the prediction equations were focus on this trait.

In prediction of W1, when only one parameter of body measurement included the model, the R² was highest for body length (Table 4). For making the equation easier, non-intercept model were also calculated. In many studies, heart girth is the best body measurement for prediction body weight in buffalo [5], in Brahman crossbred [6], in Bali cattle [7] but for the carcass weight, body length was better.

Table 4 Simple linear regression equations for estimation of weight of first price group from body measurements

Regression equations	R ²	P-Value
W1 = -125.86+1.66(HG)	0.6486	0.0001
W1 = -27.74+1.50(BH)	0.5178	0.0001
W1 = -27.49+1.48(BL)	0.7144	0.0001
W1 = 40.15+2.87(HW)	0.6345	0.0001
W1 = 26.76+2.74(HL)	0.5479	0.0001

W1= 0.959(HG)	0.9912	0.0001
W1= 1.129((BH)	0.9906	0.0001
W1= 1.278(BL)	0.9943	0.0001
W1= 3.752(HW)	0.9919	0.0001
W1= 3.248(HL)	0.9910	0.0001

W1 = weight of first price group composted with total trimmed meat.

For prediction equation using all body measurements in the model, the R² was highest (0.8157) according to many prediction study [8, 9]. The model was W1= -106.30 +0.525(HG) +0.201(BH) +0.922(BL) -0.657(HW) +1.212(HL). However, when all parameter were in the model, it was not practical to use. Stepwise was used to select the appropriate parameter in the model. There were 3 parameters, BL, HG, HL with p-value better than 0.15 were remain in the equation with R²=0.8101 (Table 5).

Table 5 Variable left in the multiple linear regression for estimation of first price group

Variable	Parameter Estimate	C(p)	Partial R ²	Model R ²	p-value
INTERCEP	-89.782				
Heart girth	0.547	49.633	0.715	0.7145	0.0001
Body length	0.898	13.585	0.075	0.7891	0.0001
Hip length	0.820	4.864	0.021	0.8101	0.0015

Carcass weight is an important trait in animal husbandry, due to economic profit. Carcass weight might be depended on many effects such as gender, age, breed, feeding condition etc. [10]. In this study, we used only male cattle and age approximately 18-36 months. Dressing percentage was not affected by during this age [11]. Beef cattle in the Isaan market were usually Native-Brahman and raised in small farming system. Management in small farming system was not quite different, cattle grazing in the pasture and sometime supplemented with concentrated food.

In previous studies, body measurement in beef cattle were focused on live weight such as in Brown Swiss [12] in Kamphaengsaen beef [13], in Sahiwal cattle [9] and in Brahman crossbred [14] for rural livestock enterprises or for selection purpose because of the measure of body measurement were easier from a live animal and can determine body weight approximately lacking of a scale. The use of linear measurements to predict carcass composition in cattle was rear; there were some studies in sheep [15], [16] and goat [17]. In this study, we calculated the predictive equation to estimate the total trimmed meat from the live appearance. It is very useful for predicting carcass weight without expensive

instruments such as ultrasound. Although the use of ultrasound could improve accuracy in predicting carcass weight [18] and could reduce the cost of collection estimates of carcass composition in live seedstock [19], conversely it is not suitable for use in the rural situation. In a report from Afolayan [20] they suggest to predict meat weight by live weight, stifle width, body height and hip width with higher R^2 (0.87) than this study, however, they used more parameter.

The butcher in Isaan gets income of carcass mostly from W1. The average incomes from each group were 79.77%, 8.38%, 7.63%, and 4.22% for W1, W1_1, W2 and W3, respectively. Economic weighting price of W1 W2 and W3 varied according to the quality of the carcass and the likelihood of consumption. Price per kilogram of W1 and W1_1 were 3.0 times of W3 and W2 was 1.8 times of W3, it fluctuated in a narrow range depended on demand and supply.

The one composition measurement could predict total trimmed meat was the body length. A prediction chart for determining total trimmed meat weight from various body lengths have been prepared and shown in figure 1.

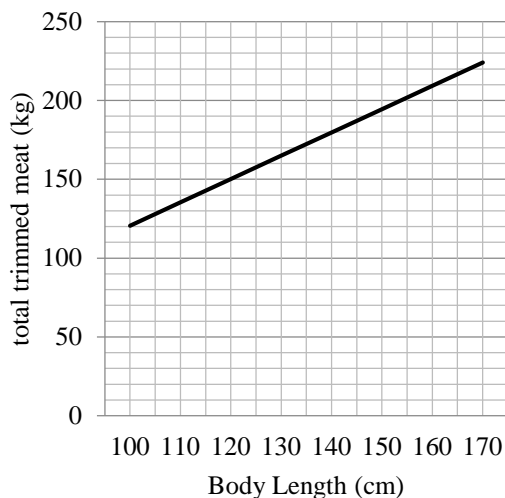


Fig. 1 Prediction chart for determining total trimmed meat weight from body length in male crossbred Brahman.

CONCLUSION

Linear body measurements in crossbred Brahman can predict carcass composition weight and their return. The practical application of the result in those situations that weight measurements might not be feasible to setting the price such as in small farmers or in a cattle market where do not have access to a weighbridge. Linear body measurements will help the rancher, the middlemen,

and the butcher shop to forecast the return and setting the beef price for trading. This study is significant for the prediction of carcass weight, so, the buyers can estimate revenue from the sale of live cattle and access value-based trading system. For fitting equation, The fitting equation to predict the total trimmed meat using three parameters was $W1 = -89.782 + 0.547(HG) + 0.898(BL) + 0.820(HL)$.

REFERENCES

- [1] OIC, Office of the Official Information Commission. Available on June 2018. <http://www.oic.go.th/web2017/en/main.html>
- [2] Greiner S. P., Rouse G. H., Wilson D. E., Cundiff L. V., and Wheeler T. L. Prediction of Retail Product Weight and Percentage Using Ultrasound and Carcass Measurements in Beef Cattle. *J. Anim. Sci.* Vol. 81, 2003, pp.1736–1742.
- [3] Bene S., Nagy B., Nagy L., Kiss B., Péter Polgár J. And Szabó F. Comparison of Body Measurements of Beef Cows of Different Breeds. *Arch. Tierz.*, Vol. 50, Issue 4, 2007. pp. 363-373.
- [4] Afolayan R.A., Adeyinka I.A. and Lakpini C.A.M.. The Estimation of Live Weight from Body Measurements in Yankasa sheep. *Czech J. Anim. Sci.* Vol. 51, 2006, pp. 343-348.
- [5] Nikorn K., Wattanachan C. and Towburan W. Estimation Buffalo Body Weigh from Heard Girth Body High and Hip High. *KKU. Vet. J.* Vol. No. 1. 1994.
- [6] Rashid Md. M., Hoque Md. A., Huque K. S., Talukder Md. A. I. and Bhuiyan A. K. F. H. Morphometric Characterization of Brahman Crossbred Cattle and Prediction of Live Weight Using Linear Body Measurements. *Asian J. Med. Biol. Res.* Vol. 1, Issue 3, 2015, pp. 569-577; doi: 10.3329/ajmbr.v1i3.26480
- [7] Gunawan A., and Jakaria. Application of Linear Body Measurements for Predicting Weaning and Yearling Weight of Bali Cattle. *Animal Production*, Vol. 12 Issue 3, 2010, pp. 163-168.
- [8] Bozkurt Y. Prediction of Body Weight from Body Measurements in Brown Swiss Feedlot Cattle Fed under Small-Scale Farming Conditions. *J. app. Anim. Res.* Vol 29, 2006, pp 29-32.
- [9] Siddiqui M. U., Lateef M, Bashir M. K., Bilal M.Q., Muhammad G., Mustafa M. I. and Rehman S. Estimation of Live Weight Using Different Body Measurements in Sahiwal Cattle. Available from: https://www.researchgate.net/publication/281980408_Estimation_of_live_weight_using_different

- body measurements in Sahiwal cattle
[accessed Jun 10 2018].
- [10] Albertí P., Panea P. B., Sañudo C., Olleta J.L., Ripoll G., Ertbjerg P., Christensen M., Gigli S., Failla S., Concetti S., Hocquette J.F., Jailler R., Rudel S., Renand G., Nute G.R., Richardson R.I., and Williams J.L. Live Weight, Body Size and Carcass Characteristics of Young Bulls of Fifteen European Breeds. *Livestock Science*. Vol. 114, 2008, pp. 19-30.
- [11] Plessis I. du and Hoffman L.C. Effect of Slaughter Age and Breed on the Carcass Traits and Meat Quality of Beef Steers Finished on Natural Pastures in the Arid Subtropics of South Africa. *South African J. of Anim. Sci.* Vol. 37 Issue 3, 2007, pp 143- 153.
- [12] Ozkaya S and Bozkurt Y. The Accuracy of Prediction of Body Weight from Body Measurements in Beef Cattle. *Archiv Tierzucht* Vol. 52, Issue 4, 2009, pp. 371-377.
- [13] Sawanon S., Boonsaen P., Innuruk P. Body Measurements of Male Kamphaengsaen Beef Cattle as Parameters for Estimation of Live Weight. *Kasetsart J. (National Science)*, Vol. 45, 2011, pp. 428-434.
- [14] Rashid Md. M., Hoque Md. A., Huque K. S., Talukder Md. A. I., and Bhuiyan A. K. F. Hu. Morphometric Characterization of Brahman Crossbred Cattle and Prediction of Live Weight Using Linear Body Measurements. *Asian J. Med. Biol. Res.* Vol. 1, Issue 3, 2015, pp. 569-577.
- [15] Agamy R., Abdel-Moneim A.Y., Abd-Alla M.S., Aboel-Mageed I.I. and Ashmawi G.M. Using Linear Body Measurements to Predict Body Weight and Carcass Characteristics of Three Egyptian Fat Tailed Sheep Breed. *Asian J. of Anim. Vet. Adv.* Vol. 10, Issue 7, 2015, pp. 335-344.
- [16] Cam M.A., Olfax M. and Soydan E. Body Measurements Reflect Body Weights and Carcass Yields in Karayaka Sheep. *Asian J. of Anim. Vet. Adv.* 2010, pp.1-8.
- [17] Rahman MD. F. Prediction of Carcass Weight From the Body Characteristics of Black Bengal Goats. *Int. J. Agri. Biol.*, Vol. 9. Issue 3, 2007, pp. 431-434.
- [18] Silva S. da L., Tarouco J. U., Ferraz J. B. S., Gomes R. da C., Leme P. R., Navajas E. A. Prediction of Retail Beef Yield, Trim Fat and Proportion of High-Valued Cuts in Nellore Cattle Using Ultrasound Live Measurements. *R. Braz. Zootec.* Vol. 41, Issue 9, 2012, pp. 2015-2031.
- [19] Bergen R., Miller S. P., Mandell I. B., and Robertson W. M. Use of Live Ultrasound, Weight and Linear Measurements to Predict Carcass Composition of Young Beef Bulls. *Canadian Journal of Animal Science.* Vol. 85, Issue 1, 2005, pp. 23-35.
- [20] Afolayan R.A., Deland M.P.B., Rutley D.L., Bottema C.D.K., Ewers A.L., Ponzoni R.W. and Pitchford W.S. Prediction of Carcass Meat, Fat and Bone Yield across Diverse Cattle Genotypes Using Live-Animal Measurements. *Anim. Prod. Aust.* Vol. 24, 2002, pp. 13-16.

DETERMINATION OF CAROTENOIDS AND DOBI CONTENT IN CRUDE PALM OIL BY SPECTROSCOPY TECHNIQUES: COMPARISON OF RAMAN AND FT-NIR SPECTROSCOPY

Rayakorn Nokkaew¹, Vittaya Punsuvon^{1,2}, Tetsuya Inagaki³, Satoru Tsuchikawa³

¹Center of Excellence-Oil Palm, Kasetsart University, Bangkok, 10900 Thailand

²Department of Chemistry, Faculty of Science, Kasetsart University, Bangkok, 10900 Thailand

³Graduate School of Bioagricultural Sciences, Nagoya University, 4648601 Japan

ABSTRACT

Crude palm oil (CPO) is a rich source of carotenoids which are a precursor of vitamin A as an important antioxidant. Carotenoids and Deterioration Of Bleachability Index (DOBI) are important factors to indicated quality of CPO. The conventional method for DOBI and carotenoids determination use UV-Vis spectrophotometry and HPLC, respectively which methods use solvents and spend time for analysis. This research interests Raman and FT-NIR spectroscopy for carotenoids and DOBI determination due to those techniques are alternative technique for rapid measurement, non-destruction of material, and environmental suitability. The results indicated that Raman is better for determination than FT-NIR spectrometry. In Raman analysis, multiplicative scatter correction (MSC) and standard normal variate (SNV) treated methods were the best models for carotenoids and DOBI, respectively. The bands of carotenoids were at 1,100 and 1,500 cm^{-1} wavenumber. Validation on carotenoids produced 0.94 of correlation coefficient (R), 0.88 of coefficient of determination (R^2), 40.65 ppm of root mean square error of prediction (RMSEP), and 3.25 of ratio of standard error of prediction to standard deviation (RPD). The validation of DOBI produced 0.76 of R, 0.57 of R^2 , 0.31 of RMSEP, 1.92 of RPD of 1.92. The limitation of carotenoids and DOBI determination using FT-NIR is having sufficient concentration of carotenoids for analysis. In addition, data for various samples regarding location, season, and oil palm species are important to build models for precise prediction.

Keywords: DOBI, Carotenoids, Crude palm oil, Rapid analysis, Raman, FT-NIR

INTRODUCTION

Thailand is an agricultural country where the major crops include rice, para rubber, cassava, oil palm, sugarcane, and corn as top exports [1]. However several years ago, oil palm became important as an economic crop because it has many advantages for consumption (such as in food, cosmetics, pharmaceuticals, etc.) and alternative energy (such as lubrication oil, biodiesel, biofuel, etc.). Furthermore, the Thai government has promoted oil palm plantations to farmers by launching several policies to facilitate and create stakeholder activity. Consequently, oil palm cultivation and the crude palm oil (CPO) yield have increased every year.

At present, commercial palm oil is a highly competitive commodity with importance placed on CPO properties such as free fatty acid, iodine value, peroxide value, oil content and Deterioration Of Bleachability Index (DOBI). The CPO quality is a trade barrier and the DOBI value is of interest because it is an important factor for CPO classification of crude palm mills Thailand and the carotenoids content is depended on the DOBI value. The price of

the CPO in the commercial is decided by the CPO quality. There are a premium quality (The $\text{DOBI} \geq 3$), a good quality (grade A; $2.3 < \text{DOBI} < 3$) and a poor quality (grade B; $\text{DOBI} < 2.3$). The high quality gives the high price for purchase. The DOBI is an index for determining the bleachability of palm oil [2] and carotenoids in CPO. However, mills cannot detect it themselves because they lack the knowhow, laboratory skills, and instruments for analysis. Good CPO quality requires not only high carotene but also should contain low secondary oxidation products (peroxide, aldehyde, ketone, acid, etc.) [3], [4]. Other characteristics of the DOBI could indicate the ripeness of palm fruits, the amounts of carotenoids, and the freshness of palm fruits.

The conventional methods for DOBI and carotenoids determination involve UV-Vis spectrophotometry or high performance liquid chromatography [2], [3], [5]. However, the sample preparation uses chemical solvent (introducing a waste chemical problem) and the analysis is time consuming. Many researchers have studied spectroscopy techniques for carotenoids analysis in various vegetables and fruits. Spectroscopy offers a

powerful, nondestructive, and intensively applied method for rapid analysis such as; (1) Fourier Transform Raman (FT-Raman) and Fourier Transform Near Infrared (FT-NIR) techniques were applied to determine carotenoid in tomato fruits. The concentration range of carotenoids was 28.5-631.83 ppm and the major component of carotenoids was lutein. The results indicated that FT-Raman produced better analysis than FT-NIR with the coefficient of determination (R^2) and standard error of cross-validation (SECV) using FT-Raman and FT-NIR being 0.91, 74.31 and 0.85, 91.19, respectively [6]. (2) FTIR spectroscopy was determine the commercial β -carotene in refined-bleached and deodorized (RBD) palm olein. The commercial carotene was spiked into RBD at 200-2,000 ppm. A partial least squares (PLS) calibration model indicated this was a good method that was efficient and accurate for quality control analysis [7]. (3) Raman was used to determine carotenoids in various vegetables and fruits (such as apricot, carrot, saffron, Broccoli, chamomile, nautilus, periwinkle, etc.). They found two strong bands in the 1,100-1,200 cm^{-1} and 1,400-1,600 cm^{-1} region, of the Raman spectrum. These bands are due to C-C stretching vibrations of the polyene chain, C=C stretching of conjugate carotenoids, with the shift of bands depending on the length of the chain and the number of double bonds of carotenoids [8]. (4) The application of NIR for carotenoids determination in CPO, a calibration curve range from 200 to 800 ppm was prepared by spiking a known concentration of carotenoid into a normal CPO. PLS calibration was developed from 18,315-12,210 cm^{-1} of the spectral region. The R^2 and standard error calibration (SEP) values were 0.95 and 23.6, respectively, while validation produced an R^2 of 0.98 and an SEP of 19.96 [9]. (5) Using NIR spectroscopy to study the chemical properties of oils (a mixture of soybean, rapeseed and palm oil) such as the iodine value, moisture content, acid value, etc. [10]. Although many researchers have studied carotenoids determination using spectroscopy techniques, there has been no report on the study of the DOBI or carotenoids content in extracted CPO from under-ripe palm fruits, with the reported work involving extracted CPO from ripe-palm fruits, whereas the palm oil mills extract CPO from under-ripe and ripe palm fruits. The under-ripe palm fruits (inner section of the spikelet from the oil palm bunch) have a very low carotenoids content which may affect measurement using spectrometry.

This research investigated the application of Raman and FT-NIR for rapid and direct measurement of carotenoids and DOBI in extracted CPO from ripe and under-ripe palm fruits. The results were compared and the best calibration model was determined using the Unscrambler program to confirm possible implementation in a palm oil mill. The Raman and the NIR techniques are the novelty of

determination of the DOBI and carotene content in the crude palm oil. They are destructure of crude palm oil which the conventional method has to sample preparation with n-hexane solvent and the both techniques can reduce the operated time of analysis from 5 mins to less than 1 min. One advantage of the both technique is friendly environment. The one objective of my research was determination the DOBI and carotene from unripe-palm fruit which is not found in any research.

MATERIAL AND METHOD

Sample preparation

This research focused on the *Tenera* species of oil palm obtained from the Oil Palm Technology Development for Local Commercial Biodiesel Industry in Newly Planted Area Project, in the Faculty of Agriculture, Kasetsart University, Thailand. For sample preparation, the fresh palm bunches (FPBs) were divided into three zones (apical, equatorial and basal zones). Each zone was divided into two categories of palm fruit sample—ripe and under-ripe palm fruit. The ripe palm fruits were the outer section of the spikelet having dark-orange or dark-red palm fruits while the under-ripe palm fruits were from the inner section of the spikelet and were light-yellow to light-orange whole fruit. For each sample the CPO was obtained using solvent extraction with hexane solvent and solvent evaporation in a vacuum evaporator. Oil palm fruit samples were collect every day for a week, resulting in 126 CPO samples.

Measurement using spectroscopy techniques

Raman spectra measurement

The all samples were warmed at 60°C using a hot-air oven before measurement of Raman. Then, Raman spectra were recorded using a Serstech Indicator Kit (model Serstech 100 Indicator; Serstech Chemical Intelligence Solutions, Sweden). Spectra data of CPO were accumulated at 20.50 seconds of scan time in the range 400-2,300 cm^{-1} with a laser power of 300 mW. For each sample, two spectra were collected and subsequently averaged.

NIR spectra measurement

The all samples were analyzed using a Bruker spectrometer (model MPA, Bruker, GmbH, Ettlingen, Germany). This FT-NIR spectrometer is designed for transmittance analysis of a liquid sample. The oil sample was dropped in a quartz with 1mm path length (S10-SQ-1; GLSciences Inc. Japan) and all samples were warmed in a dry thermo bath (model MG-2000, Eyela thermo bath, Germany) at 60°C before analysis

for homogeneous CPO samples. NIR spectra were measured directly on the sample and acquired between 4,000 to 12,500 cm^{-1} , setting the resolution to 8 cm^{-1} at 60°C, and 64 scans of the average reading. For each sample, two spectra were collected and subsequently averaged.

DOBI and carotenoids content analysis (reference analysis)

DOBI was determined according to the Palm Oil Research Institute of Malaysia (PORIM) test method which was developed by Swoboda (1982) and the carotenoids content was determined according to the PORIM test method (1995). About 0.1 g of CPO was weighed and dissolved in 25 ml of hexane solvent. The solution sample was placed in a 1 cm wide of cuvette and absorbance measured at 446 nm (measurement of carotenoids) and at 269 nm using a spectrophotometer (T70+UV/VIS spectrometer, PG Instruments, USA). The DOBI and carotenoids content were calculated using eq. 1 and eq. 2, respectively.

$$\text{DOBI} = \frac{A_{446}}{A_{269}} \quad (1)$$

$$\text{Carotenoids (ppm)} = \frac{383 \times A_{446} \times V}{W \times 100} \quad (2)$$

where: A_{446} = absorbance at 446 nm, A_{269} = absorbance at 269 nm, 383 = diffusion coefficient, V = value of hexane (ml) and W = weight of CPO sample (g).

Calibration parameters and prediction model

PLS regressions were fitted to describe the relationship between dependent variables (DOBI and carotenoids in CPO samples) and Raman or NIR spectra using a multivariate statistic program (the Unscrambler 9.7 version). The calibration models were developed from the 126 spectra of all CPO samples. PLS calibrations were fitted using the PLS-1 method. Model validation was performed using the full cross validation method. The number of latent variables (factor) adopted for each model was suggested by the statistical program.

The statistical results of PLS models built using original and pretreated spectra were compared using MSC (multiplicative correction), SNV (standard normal variate), 1D (first derivative), and 2D (second derivative).

The criteria for selection of the prediction model included: factor-number of latent variables; correlation coefficient of calibration (R_c); coefficient of determination of calibration (R_c^2); root mean square error of calibration (RMSEC); correlation coefficient of calibration (R_c); coefficient of

determination of validation (R_v^2); root mean square error of prediction (RMSEP); and the ratio of standard error of prediction to standard deviation (RPD), being the ratio of the standard deviation of data (SD) to RMSEC. Models with a high R , R^2 , and RPD and a low RMSEC and RMSEP are considered to be optimum.

RESULTS AND DISCUSSION

The DOBI and carotenoids content of the extracted CPO from ripe palm fruits were greater than in the extracted CPO from under-ripe palm fruits. With increased palm fruit ripening (observed from the color change from light yellow to dark red), the carotenoids content in the CPO increased but the DOBI only increased to a maximum value at 3 days of storage time and after that the DOBI decreased due to the autoxidation reaction of oil over longer storage. The fatty acid or triglyceride was in radical forms. The hydrogen atom from the fatty acid or triglyceride in oils is removed and lipid alkyl radicals are converted into lipid peroxide for which oxygen, UV, and heat are the catalysts for autoxidation. The lipid peroxide decomposed to alkoxy radicals and then formed aldehydes, ketones, acids, esters, alcohols, and short-chain hydrocarbons (secondary products of oxidation). Table 1 shows the distribution of the DOBI and carotenoids content in all samples. The maximum carotenoids content was 539.79 ppm in CPO extracted from ripe palm fruit while the minimum carotenoids content was 2.79 ppm in CPO extracted from under-ripe palm fruit. In general, commercial CPO has a carotenoids content between 400 and 700 ppm [3] – [6] but the current experiment resulted in a low carotenoids content because of the drought in Thailand at the time the samples were collected and this affected the production of oil palm products (less weight of oil palm bunch, less palm oil yield, slow growth of oil palm, slow ripeness of oil palm bunch, etc.).

Table 1 Distribution of DOBI and carotenoids content in crude palm oil samples

Parameters	Min.	Max.	X	SD
DOBI	0.07	2.09	0.87	0.50
Carotenoids	2.79	539.79	191.02	121.96

Spectra analysis

Carotenoids are a group of tetraterpenoids consisting of isoprenoid units. Double bonds in carotenoids are conjugated forms and usually are all trans forms. CPO is a source of carotenoids, having 60% β -carotene and 40% α -carotene [6]. Fig. 1 and Fig. 2 show Raman spectra and NIR spectra for the DOBI and carotenoids content determination, respectively.

Raman spectra

Figure 1 (a) compares spectra between the extracted CPO from ripe and under-ripe oil palm fruits. The spectra show the C=C stretching vibration of carotenoids with a dominant signal observed in the range 1,500-1,550 cm^{-1} ; the position of this band depends on the ripeness of the oil palm fruit. At 1,168 cm^{-1} the C-C group with the C-CH₃ of carotenoids is presented. The two wavenumber positions of the carotenoids are characteristic of the spectrum of the β -carotene standard (Fig. 1 (b)). In the spectrum of the β -carotene standard, the characteristic bands have three main peaks which are located at 1,512, 1,154, and 1,004 cm^{-1} . These wavenumber positions are correlated with the wavenumbers of the polyene chain (C=C), C-C coupled with C-CH₃, and C-C stretching of carotenoids, respectively [9] – [14]. At other positions in the CPO, 1,442 and 1,656 cm^{-1} are correlated with the wavenumbers of CH₂ or CH₃ deformation of fatty acid or triglyceride, and C=C stretching of unsaturated fatty acid or triglyceride, respectively.

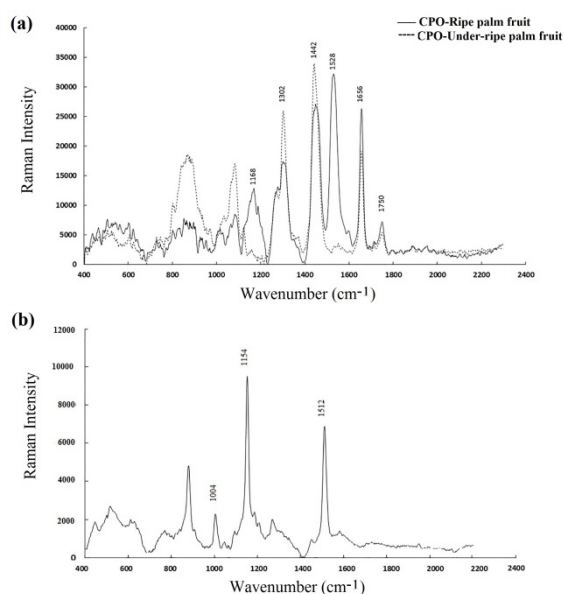


Fig. 1 Comparison between Raman spectra of CPO from ripe and under-ripe palm fruit (a), and β -carotene spectrum (b).

NIR spectra

The NIR region was more difficult to explain mainly because of the extensive band overlapping due to overtones and combinations of fundamental vibrations involving hydrogen stretching modes. However, it was possible to predict the DOBI and carotenoids content in CPO. Fig. 2 (a) shows the comparison of NIR spectra between the extracted CPO from ripe and under-ripe palm fruits. The results indicated that the spectra had the same patterns, with the bands at around 5,789 and 5,681 cm^{-1} due to the

combination of bands and the first overtone of the C-H of methylene of the aliphatic group of oil and the second overtone being observed at 8,211 cm^{-1} [15]. The bands at around 4,655 and 4,535 cm^{-1} may be attributed to combination bands of C-C and C-H stretching vibrations of cis-unsaturated fatty acids, and at 7,058 and 7,139 cm^{-1} are attributed to a C-H combination band of methylene [11]. Quantitative analysis of carotenoids by FT-Raman was based on the trans-CH=CH-functional group but this characteristic band did not exist in the NIR region [9]. In the current research, the best conditions for NIR spectra pretreatment were in the wavenumber range between 5,500 and 4,600 cm^{-1} (Fig. 2 (b)) where there were strong correlations.

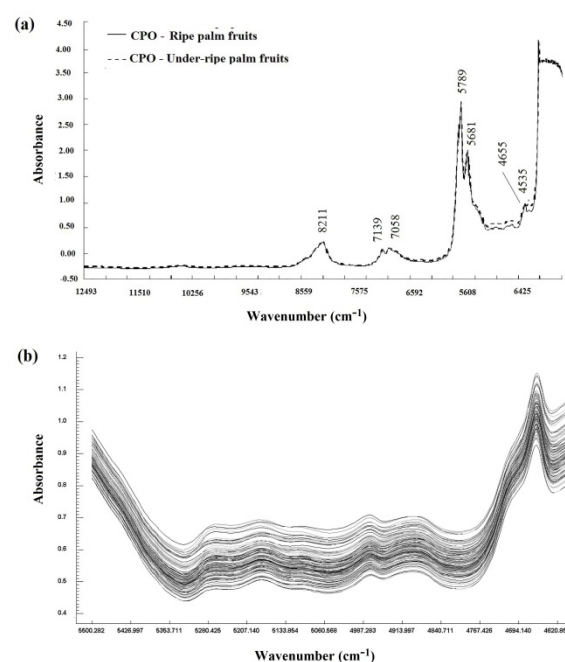


Fig. 2 Comparison between NIR spectra of CPO from ripe and under-ripe palm fruits, 12,500-4,000 cm^{-1} wavenumber (a), and 5,500-4,600 cm^{-1} wavenumber (b).

Calibration and cross-validation results

Raman analysis

The precision calibration models can be checked using the cross-validation method. The model was calibrated using different mathematical treatments of spectra, selected by the variable uncertainty test used for the validation method. The criteria for best model selection were the highest R^2 and RPD, and the lowest RMSEP. MSC pretreatment was the best method for all spectral improvement and this model can predict the carotenoids content in CPO. The statistical results of the prediction model were 0.94 for R_v , 0.88 for R_v^2 , 40.65 ppm for RMSEC, and 3.25 for RPD. RPD is calculated from the ratio of the standard deviation of

the data to RMSEC thus providing a ratio of the performance to the deviation. Hence, the highest RPD value indicates the best method too. In the DOBI prediction model, the SNV pretreatment was the best. The statistical results of the prediction model were 0.76 for Rv, 0.57 for Rv², 0.31 for RMSEP, and 1.92 for RPD using the cross-validation method.

Figure 3 (a) and Fig. 3 (b) show the MSC-Raman spectra for carotenoids and the SNV-Raman spectra for DOBI, respectively. In the 400-2,300 cm⁻¹ wavelength range of the Raman spectra, the results showed broad bands around 1,100 and 1,500 cm⁻¹ due to the C-C group with C-CH₃ and C=C stretching of carotenoids [7] – [9], [12] – [13], [15]. Both wavenumbers were significant for carotenoids determination and they were clearly confirmed with the regression coefficients in Fig. 5 (a). The other positions, around 1,400 and 1,600-1,700 cm⁻¹ have been assigned to the fatty acid or triglyceride.

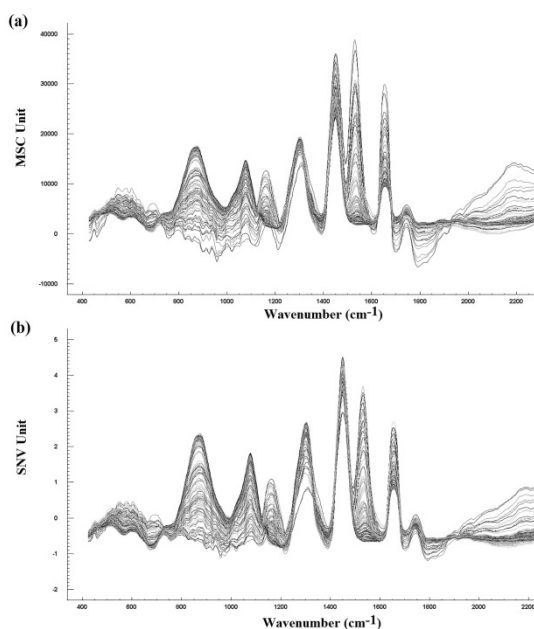


Fig. 3 Raman spectra pretreatment of crude palm oil on carotenoids and DOBI, carotenoids- MSC (a), and DOBI-SNV (b).

FT-NIR analysis

The calibration models using cross validation for carotenoids and DOBI determination in CPO where all samples were measured using FT-NIR. The 1D pretreatment using the Gap-Segment method was the best method for improvement of CPO spectral base for carotenoids and DOBI. The statistical results for carotenoids were 0.71 for Rv, 0.50 for Rv², 86.70 ppm for RMSEP, and 1.63 for RPD. In the DOBI prediction, the 1D pretreatment by the Gap-Segment method was the best method. The statistical results were 0.80 for Rv, 0.64 for Rv², 0.29 for RMSEP, and 1.72 for RPD.

Figure 4 shows the NIR spectra in the 5,500-4,600

cm⁻¹ range for spectral samples pretreatment. The results indicated that the PLS model built using the 1D method was the best model for carotenoids and DOBI determination. The data on the carotenoids content and DOBI following analysis using the Unscramble program showed very low contents (2.79-537.79 ppm for carotenoids and 0.07-2.09 for DOBI) and the regression of carotenoids showed a wavelength of 5,276 cm⁻¹ (Fig. 5 (b)) which is near the 5,263 cm⁻¹ of H-O-H stretching and bending vibrations of water [13]. Therefore, the amount of carotenoids, the DOBI, and the amount of water affected measurement using FT-NIR.

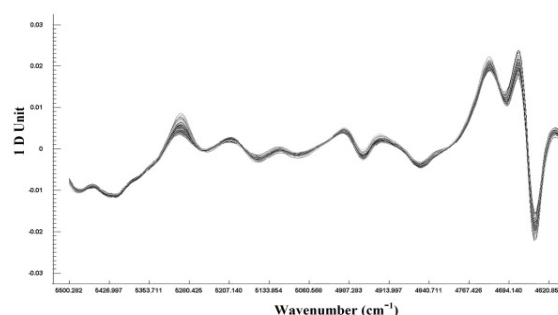


Fig. 4 1D NIR spectra pretreatment of crude palm oil on DOBI and carotenoids.

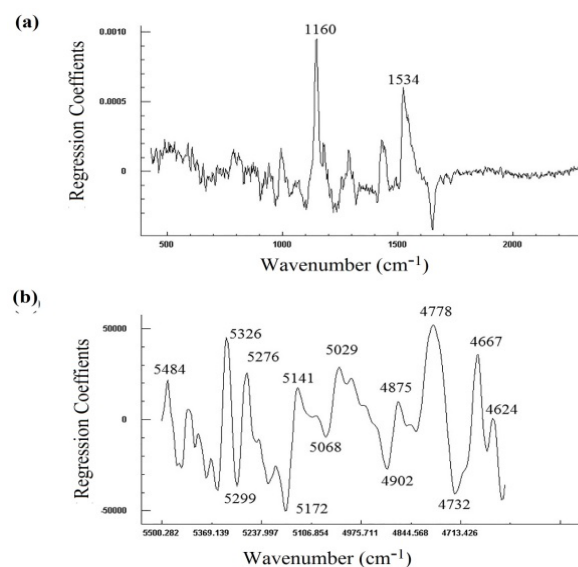


Fig. 5 Regression coefficients of the MSC-pretreated PLS model measured using Raman (a) and the 1D-pretreated PLS model measured using FT-NIR (b) on carotenoids content in the extracted crude palm oil from palm fruits

CONCLUSION

Raman and FT-NIR techniques are environmentally friendly, use no solvent, and provide rapid measurement which is required for industrial

application. The results showed that Raman spectrometry was better than the conventional method and FT-NIR spectrometry. Raman provided good DOBI and carotenoids determination in CPO and provided clear carotenoids determination at around 1,100 and 1,500 cm^{-1} in CPO. Raman was better at measuring both parameters than FT-NIR, although the concentration of carotenoids was very low. In addition, model development has to be extended with calibrations using more samples of palm fruits obtained from many locations, in different seasons, and for different species to ensure maximum accuracy of analysis.

ACKNOWLEDGEMENTS

We would like to thank the Oil Palm Technology Development for Local Commercial Biodiesel Industry in Newly Planted Area Project in the Faculty of Agriculture of Kasetsart University, Thailand for raw material support. We also would like to thank the Graduate School of Bioagricultural Sciences, Nagoya University, Japan, the Bruker Company, Japan, and the Center of Excellence Oil Palm, Kasetsart University, Thailand for partial support of this research.

REFERENCES

- [1] Office of Agricultural Economics (OAE), Main Agricultural Exports and Imports, 2011.
- [2] Swoboda P.A.T., Bleachability and the DOBI, PORIM Bulletin. 1982. 5: 28-38.
- [3] Bonnie T.Y.P. and Choo Y.M., Valuable Minor Constituents of Commercial Red Palm Olein: Carotenoids, Vitamin E, Ubiquinone and Sterols, J. Oil Palm Res., Vol. 12, 2000, pp. 14-24.
- [4] Choe E. and Min D.B., Mechanisms and Factors for Edible Oil Oxidation, Compr. Rev. Food Sci. Food Safe, Vol. 5, 2006, pp. 169-186.
- [5] Jacobsberg B., Palm Oil Characteristics and Quality, Conference proceeding, in Proc. 1st Malaysian Agricultural Research and Development Institute Workshop on Oil Palm Technology, 1974, pp. 48-68.
- [6] Ammawath W. and Man Y.C., A Rapid Method for Determination of Commercial β -carotene in RBD Palm Olein by Fourier Transform Infrared Spectroscopy, Asian J. Food Agro-Ind., Vol. 3, Issue 4, pp. 443-452.
- [7] Baranska M., Schultze W. and Schulz H., Determination of Lycopene and α -carotene Content in Tomato Fruits and Related Products: Comparison of FT-Raman, ATR-IR, and NIR spectroscopy, Anal. Chem, Vol. 78, 2006, pp. 8456-8461.
- [8] Withnall R., Chowdhry B.Z., Silver J., Edwards H.G.M. and Oliveira L.F.C., Raman Spectra of Carotenoids in Natural Products, Spectrochim. Acta Part A. Vol. 59, 2003, pp. 2207-2212.
- [9] Moh M.H., Man Y.B.C., Badlishad B.S., Jinap S., Saad M.S. and Abdullah W.J.W., Quantitative Analysis of Palm Carotene Using Fourier Transform Infrared and Near Infrared Spectroscopy, JOCS. Vol. 76, 1999, pp. 249-252.
- [10] Baptista P., Felizado P., Menezes J.C. and Correia M.J.N., Monitoring the Quality of Oils for Biodiesel Production Using Multivariate Near Infrared Spectroscopy Models, J. Near. Infraes. Spectrosc, Vol. 16, 2008, pp. 445.
- [11] Kasemsumran S., Thanapase W., Punsuvon V. and Ozaki Y., A Feasibility Study on Non-destructive Determination of Oil Content in Palm Fruits by Visible-near Infrared Spectroscopy, J. Near Infrared. Spectrosc, Vol. 20, 2012, pp. 687-694.
- [12] Ozaki Y., Cho R., Ikagawa K., Muraishi S. and Kawaochi K., Potential of Near Infrared Fourier Transform Raman Spectroscopy in Food Analysis, Appl. Spectrosc, Vol. 46, 1992, pp. 1503-1507.
- [13] Tarantilis P.A., Beljebbar A., Manfait M. and Polissiou M., FT-IR, FT-Raman Spectroscopy Study of Carotenoids from Saffron (*Crocus sativus* L.) and Some Derivatives, Spectrochim. Acta Part A, Vol. 54, 1998, pp. 651-657.
- [14] Kushwaha K., Saxena J., Tripathi B.K. and Agawal M.K., Detection of Carotenoids in Psychotrophic Bacteria by Spectroscopic Approach, J. BioSci. Biotech, Vol. 3, Issue 3, 2014, pp. 253-260.
- [15] Osborne B.G., Fearn T.F. and Hindle P.H., Practical NIR Spectroscopy with Application in Food and Beverage Analysis, Longman Scientific & Technical, Harlow, USA. 1993.
- [16] Kawano H., Abe H. and Iwamoto M., Development of a Calibration Equation with Temperature Compensation Compensation for Determining the Brix Value in Intact Peaches, J. Near Infrared Spectrosc., Vol. 3, 1995, pp. 211.

THE USE OF FISH AGGREGATING DEVICES (FAD'S) TO REDUCE DESTRUCTIVE FISHING IN PACITAN COASTAL INDONESIA

Tuty Handayani¹, Cinthia¹, Jarot Mulyo Semedi¹ and Sajiharjo Marto Suro²

¹Universitas Indonesia, Indonesia; ² STT-PLN, Indonesia

ABSTRACT

Pacitan regency is located on the south coast of East Java Province, Indonesia. The Pacitan coastal regions consist of a bay and open sea. The number of the populations who work as fishermen as many as 7228 people. Mostly they catch fish in Pacitan Bay. Initially, there were some fishermen who carry out fishing by destructive methods such as using bombs and poisons. Fish Aggregating Devices (FADs) are tools that helps fishermen to increase their catch in a definite location. The purpose of this study was to determine how big the use of FADs so as to reduce destructive fishing and the possibility of FADs placement area development in Pacitan coastal. The research method was done by using interview technique to fishermen for fishery production with and without FADs. While for observing the development of FADs, GIS Techniques and Remote Sensing were used. To obtain the suitability of FAD's location, NOAA and Landsat 8 Images were used, with parameters such as sea surface temperature, salinity, current, brightness and chlorophyll-a. The depth was obtained from the bathymetry map. The results showed that FAD's greatly increased production up to 200%, accompanied by an increment in the quality of fish. However, due to the location of FADs in the open sea. needed a modern fishing equipment, so that only about 20% of fishermen take advantage of FADs. Nevertheless the arresting destructively method has decreased. The development of FADs can be done at suitable area, about 70% of Pacitan coastal about 12 miles from the coast line.

Key word : Fish Aggregating Devices (FADs), Destructive fishing, Suitable area

INTRODUCTION

The exploration of fish resources in the waters of Pacitan by local fishermen mostly located around the coast and using traditional fishing facilities of various shapes and types. Fishing activities in Pacitan Regency until 2004 were dominated by boats without engines and boats under 10 GT in sizes with outboard motors. The ships are equipped with fishing gear, gill net, and fishing line that only operate in coastal waters up to 3 miles from the coast. The fishermen's catch usually only small pelagic fishes with low economic value such as mackarel tuna, scads, beltfish, and anchovies [1].

Although the production of fisheries is not much, but from year to year the number of fishing fleets is increasing, especially boats with engines. To increase the production, there are fishermen that use catching methods that tend to damage the environment, such as the use of potassium and explosives, or placing nets and anchors carelessly. That causes environmental damage is inevitable.

According [2] Pacitan off-shore sea is rich in resources of large pelagic fish such as skipjack and tuna. The utilization rate of pelagic fish resources in these waters is still below the maximum potential of its sustainability. The value of maximum sustainability yield (MSY) of pelagic fish in the South of East Java in 2009- 2013 was 219,189,453

tons / year with average fish utilization rate of 49.48%. The condition of fish utilization in the area is still below the allowable catch amount of 80% [2]. MSY values for tuna species (yellow fin tuna and large eye tuna) in the southern waters of East Java are estimated to be around 2,568 tons / year with a utilization rate of about 78.81% .

The Pacitan Regency Government [1] through the Office of Marine and Fisheries introduced the use of Fish Aggregating Devices (FADs) to fishermen in early 2005, as well as bringing ships measuring above 30 GT with a seine fishing gear. Fads installed by fishermen Pacitan is a type of fixed rumpon (CTF 2014) installed in waters with a depth of 1,500-5,500 meters, so it is classified as deep sea rumpon.

The use of FADs as a tool for collecting fish in fishing activities has proven able to increase production and productivity of catch in Pacitan Regency. Production of catches in this district prior to the use of FADs is only 500 tons. The use of FADs increased production to 1,560 tons in 2005 and continued to increase in the following years to reach 7.823 tons in 2013.

This encourages fishermen to install new Fads so that the number of fishing FADs installed by more and more. By 2015 Pacitan fishermen have begun to complain that as more FADs are installed in the waters, their catch is declining. The size of the fish

is also smaller, so the selling price is low. For that we need to find the location of something for the expansion of FADs. So that the new installation does not decrease production.

RESEARCH OBJECTIVES

1. Search for a suitable location for expansion of FADs
2. Knowing the readiness of traditional fishermen using FADs to reduce destructive fishing.

METHOD

Pacitan regency is located on the south coast of East Java. Overlooking the Indian Ocean, lies on 1100 55' - 1110 25' east and 070 55' - 080 17' LS. The Pacitan coastal region consists of bays and open seas. On the coast of Pacitan residents who work as fishermen as many as 7228 people[1].

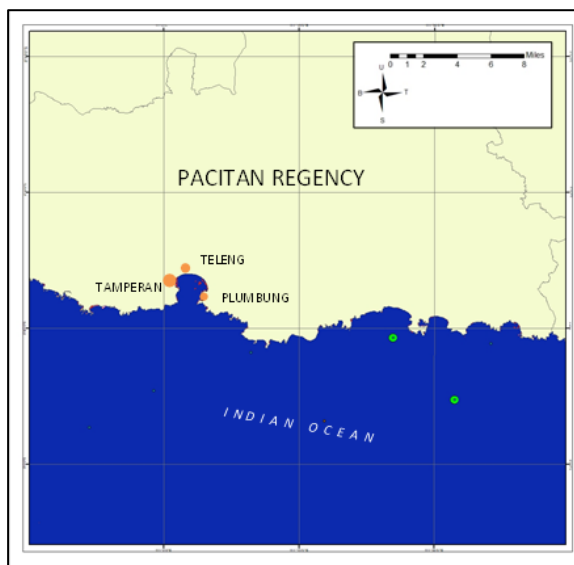


Fig.1. Resarch Site

This research was conducted along the Pacitan seaport. Includes Pacitan bay. In Pacitan Bay there are no Fads, but on the bay there is Fishery Port of Tamperan Beach, Fish Landing Base accompanied by Fish Auction Place, Teleng and traditional Plumbung fish landing. Plumbung is one of 17 traditional fish landing sites.[4] The Tamperan Fisheries Port, a modern port, is very important because it is a landing and fish trade place that comes from Fads.

Research Framework

There are two types of fishermen catch in Pacitan local residents who generally do the traditional and modern way, utilizing Fads. Fishermen of Fads are not only local Pacitan titles but also from outside Pacitan

Traditional fishermen with small incomes and activities that often disturb the environment, are expected to be larger incomes and leave the way of looking for a tie that tend to be distraktif. For that need to find new locations to be used as a place to put Fads. Remote Sensing Techniques can help find the location.

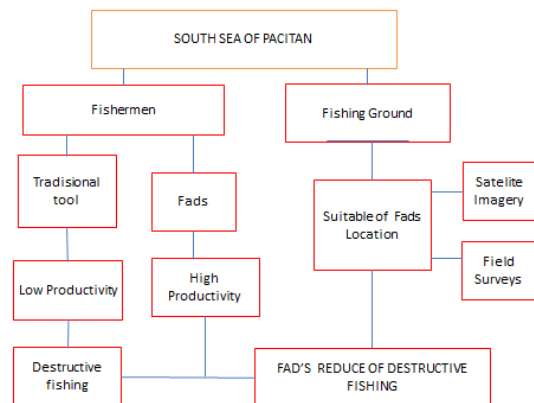


Figure 2. Research framework

Method of Collection and Data Analysis To describe the data to find a suitable location for Fads development site, two ways are done with Landsat 8 and NOAA Image. [5] Various oseagrafi variables such as temperature, salinity, current velocity, turbidity and depth using Landsat image 8. As for chlorophyl using NOAA image, with wider coverage. To find out the pH is done by taking water samples around the Fads location. By using GPS, the sampling location is marked.

To find out the readiness of local fishermen to move from traditional fishing gear to Fads, interviews were conducted. The sampling frame consists of the traditional fishermen born in Pacitan, the head of the household, may be the owner of the ship or just as a worker. The selection of respondents was done by technical random sampling for 30 traditional fishermen.[4]

To obtain the conformity region, data analysis uses overlay techniques. As for knowing the preparedness of traditional fishermen using Fads as a tool to find fish, conducted by descriptive analysis.

In the overlay technique of each layer the resulting map is given scores as follows in table 1.

Parameter	Very Suitable	Suitable	Not Suitable
Velocity of current	0.01- 0.1	0.1-0.5	>0.5
Depth	100-500	100 - >30	<30
Turbidity	<5	5 – 15	>15
Temperate	14.35-20.35	8.35-14.35	<8.35
Salinity	30-34	7.95-8.2	>34
pH	7.95-8.2		<7.95

Source : Modification from [6]

RESULT AND DISCUSSION

Expansion Area of Fads

Suitability of Oceanographic parameters with landsat 8.

The suitability of oceanographic parameters in Pacitan Bay indicates that most of the bay area is less suitable for Fads.[5] Although chlorophyll concentrations are quite high, the production is low. This is because Pacitan bay is also used for 30 GT-sized vessel traffic carrying catches from Fads to Tamperan Fish Port and there are tourist sites in Teleng. Fishermen who used the ships with a GT motor. Fish landing used besides TPI Teleng also PPI Lumbung.[3]

Suitability with NOAA Satellite Imagery

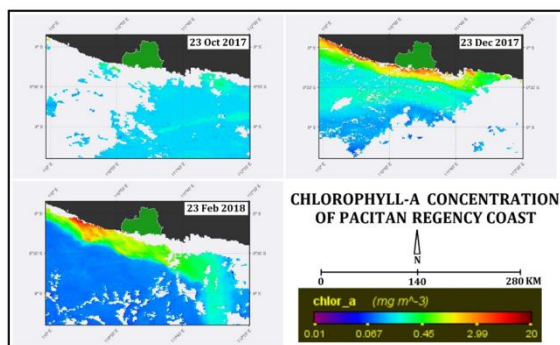


Fig. 3. Chlorophyll-A concentration of Pacitan Regency coast during west monsoon season (source: Ocean color data, NASA OB.DAAC)

NOAA Satellite Applications and Research, NOAA STAR) which is part of NOAA's Satellite and Information Service (NESDIS) are managing

the ocean color product satellite sensors including the Sea-viewing Wide Field-of-view Sensor (SeaWiFS), the Moderate Resolution Imaging Spectroradiometer (MODIS), and the Visible Infrared Imaging Radiometer Suite (VIIRS) on the Suomi National Polar-orbiting Partnership (SNPP) and the Joint Polar Satellite System (JPSS), as well as various satellite sensors from other countries (<https://www.star.nesdis.noaa.gov/sod/mecb/color/>). Figure 1 shows the spatial temporal pattern of chlorophyll-a concentration of Pacitan Regency Coast during the west monsoon season (October – April).

The image from NASA ocean color data were selected based on the lowest cloud cover during west monsoon season.[5] The spatial pattern of the chlorophyll-a concentration shows that by time the high concentration are moving more closer to the coastline. This phenomena also explained why fisherman cannot sail to the open seas, it is because of the chlorophyll-a concentration are very low towards the ocean. The west monsoon also called by a rainy season where the ocean waves are high and will give a high risk for fisherman to sail.

The suitability of the Landsat data.

From Image Processing results downloaded from <https://www.usgs.gov/> and sampling pH at sea Pacitan show, in terms of Salinity, turbidity, current velocity and pH of almost entire sea in Pacitan suitable for Fads. Based on the edge depth is not suitable for deep sea fads. However, the chorofil abundance at the high edges, making it suitable for simple shallow sea fads. The temperature parameter indicates that there is a less suitable area. The statements of the overlay analysts show like fig. 4, below:

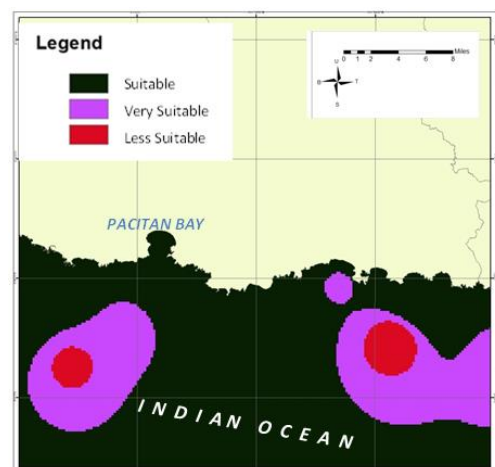


Fig.4. The suitability of the location for the expansion of Fads

At this time at sea off Pacitan, deep Sea Fads are installed at locations between latitudes 8°LS to 10°LS. Each Ships and Tonda Fishing Line install 3-5 Fads at each point. Until 2013 it is estimated that there are 250 units of Fads installed by fishermen, mostly fishermen, who are based in VAT tamperan [1]

The advantages of using FADs

Fishing vessels / boat in Pacitan based on used machine is divided into boat without motor (PTM), outboard motor boat (PMT), and motor boat (KM). Boat without motor is only 6%.[8] PMT dominates the number of fishing vessels in Pacitan Regency as much as 1 240 units or 84 percent. While the motor boat size 30 GT or more as much as 10%. Tradiisonal fishermen use boats under 10 GT, as they only fish up to 4 miles. Motorboats are mostly owned by fishermen from outside Pacitan. The engine power used illustrates the range of fishing operations. [7]explains that fishing gear used by small-scale fishermen is generally passive, selective, and used and adapted to specific seasons.

Traditional fishing boats and fishing gear using vessels cost 4000 USD [8] 70%, using vessels costing 18,000 USD as much as 20%, and only 10% using vessels cost 36,000 USD. With a daily charge per trip averages 25 USD ranges from 25 USD - 40 USD. As for fishermen who use FADs, the vessels owned worth more than 100,000 USD with the expenditure of 1 trip, for 10 days about 7000 USD - 85 USD. Using the Productivity tool approach is calculated by the Setyorini equation in [2] namely:

$$Average = \frac{\sum Production}{\sum Capture effort}$$

The results shown that the average productivity increased 10 to 12 times when using Fads.

Benefits of FADs on local fishermen

From the results of spatial analysis of the expansion area of Fads, shows most of the Pacitan waters are very suitable. But the fact is there are many local fishermen who do not utilize Fads technology. The reasons are mostly due to large capital, expensive operational costs, long distances that must be at sea up to 10 days and some people feel they can not follow the technology. The results can be seen as Figure below

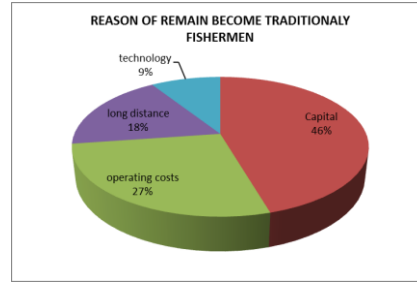


Fig.5. The reason remains a traditional fisherman

The narrower the fishing ground and the increasing number of fishing boats, the destructive fishing is still happening. Although **the current** destructive fishing form is no longer the case with Blast. They are already aware that the blast is damaging the environment. But what can not be avoided is in the operation of fishing gear is often negligent. Both from how to throw anchors, crashing reefs, or using the eyes of a wide net. It is done because it has to compete to get adequate production. The hope that if you have a simple Fads, then the negligence that is destructif fishing is declining.

CONCLUSION

1. The results show that using FADs greatly increases the production up to almost 10-fold, accompanied by an increase in the quality of fish that is the number of large pelagic fish that catch.
2. Pacitan fishermen only about 20% utilize Fads in pairs in the deep sea. However, the destructive arrest has been greatly reduced. Fishing ground Pacitan bay which is in shallow sea utilized by fisherman with traditional boat. Fads Fumps location development can be done in about 70% of Coastal Pacitan. On a shallow coast 4 miles away, simple Fads can be installed at low cost for traditional fishermen

ACKNOWLEDGEMENTS

The research work reported in this paper was funded by PITTA Grant No. 2326/UN2.R3.1 /HKP.05.00/2018 Universitas Indonesia (UI).

Thank to directorate Research and Community Service Universitas Indonesia also my sudents in Hibah Pitta group

REFERENCE

- [1].Laporan Statistik Perikanan Kabupaten Pacitan Tahun 2014. DKP Dinas Kelautan dan Perikanan Kabupaten Pacitan DKP 2015.
- [2] Muhamad RE. Prayitno1, Domu Simbolon, Roza Yusfiandayani, Budy Wiryawan Produktivitas Alat Tangkap yang dioperasikan di Sekitar Rumpon Laut Dalam. **Marine Fisheries** Vol. 8, No. 1, Mei 2017 Hal: 101-112
- [3] Mohammad Rizal Kurniawan, Daduk Setyohadi, Gatut Bintoro Pengaruh Pemasangan Rumpon Pada musim Barat Terhadap Hasil Tangkapan. Alat Tangkap Payang. PSPK Student Journal, VOL. I NO. Universitas Brawijaya pp 16-20 =15 May 2013
- [4]Yusuf Fathanah. Analisis Karakteristik Perikanan Tangkap Skala Kecil di Kabupaten Pacitan. IPB Bogor. .2014 p 8-8
- [5] Martin. Seelye. An Introduction to Ocean Remote Sensing. 2014 TJ International Ltd. Padstow. Cornwall. UK
- [6] Pradipta Gede Yatha. Sistem Pengambilan Keputusan Penempatan Rumpon Laut. Institut Teknologi Bandung, 2014 p16-18
- [7] Kurien J. Overcapacity, overfishing and subsidies: how do they relate to smallscale fisheries? In: Presented at the 8th Pacific Rim Fisheries Conference 2006., Hanoi, 22–24 March.
- [8] Rully Indra Taruna . Konstruksi Kapal Perikanan dan Ukuran utama Dalam Penentuan Konstruksi Kapal. Universitas Pajajaran. 2012. P 45-51
- [9] Handayani, Tuty. Youth Education in Self-Preparing as Marine Ecotourism Guide in Kepulauan Seribu. 1st International conference o Geography Education. Malang Indonesia. No. 29.10.3/UN32.7/DL/2016. P 3-2

ANTIMICROBIAL RESISTANCE IN *SALMONELLA* ISOLATED FROM BEEF IN UPPER NORTHEASTERN THAILAND

Natthamon Tangjitwattanachai¹ and Denpong Sakhong²

¹Division of Animal Science, Faculty of Technology, Mahasarakham University, Thailand

²Veterinary Research and Development Centre (upper northeastern region), Department of Livestock Development, Thailand

ABSTRACT

This study investigates the distribution of *Salmonella* serotypes, antimicrobial susceptibility and patterns of multidrug resistance of *Salmonella* spp. isolated from beef, received from different slaughterhouses and butcher shops in Upper Northeastern Thailand. Amongst the beef samples, one hundred and forty-five isolates were detected. There are three serogroups of salmonella which can be classified into eight serovars; five serovars belonging in three serogroups were contaminated on meat from slaughterhouses, likewise, seven serovars which included two serogroups were detected from butcher shops; by which, 12.50 % (32/145) of the salmonella strains was resistant to antimicrobial agents and almost 6.89 % (10/145) were multidrug resistant. The most multiresistant serotype was *Salmonella* Derby, with a pattern of multi-resistance to six antibiotics, followed by *S. Rissen*, *S. Anatum*, and *S. Muenchen*, respectively. Moreover, the most of salmonella strains were resistant to ampicillin, oxytetracycline and sulfamethoxazole/trimethoprim, whilst, colistin, gentamicin, kanamycin, nalidixic acid, and norfloxacin are considered highly susceptible drugs. In summary, beef from the local slaughterhouses and retail butcher shops in Upper Northeastern Thailand, was found to be contaminated with *Salmonella* spp., notably, from the serogroups B, C and E, which are multidrug resistant. For this reason, veterinarian and all relevant authorities need to strictly regulate the use of antibiotics in animal production, whether for use as therapy, prophylaxis, or growth promotion.

Keywords: Antibiotics, Contamination, Drug-resistance, *Salmonella* spp.

INTRODUCTION

Antimicrobial resistance is a public health problem throughout the world, and causes increased morbidity and mortality among humans and animals. If not strictly regulated, the application of antibiotics delivered to animals for therapy, prophylaxis, or growth promotion/feed efficiency in domestic livestock, can potentially lead to widespread dissemination of antimicrobial-resistant bacteria. The antibiotics resident in animal products may be harmful or provide an antibiotic-resistant bacteria from animals to the consumer, and lead to increase a pathogenic resistance to antibiotics, becoming a reservoir of resistance genes for pathogenic transmission in and between microorganisms and spread into humans through various routes [1, 2].

Salmonella as a foodborne pathogen in animal products, is a major cause of human salmonellosis and food poisoning. They are common inhabitants on the intestinal tract of humans and mammals, which can be distributed in the environment and contaminate the food chain in the process of food production. Normally, humans are infected by eating or touching an infected animal or their faeces, in particular, during the processing of meat production

[3]. The processes during the pre-slaughter, slaughter and the storage period after slaughter are suitable for contamination of pathogenic salmonella, which can cause serious diseases in humans and animals. Thus, the purpose of this study was to investigate the distribution of *Salmonella* serotypes, and *Salmonella* spp. that are resistant to antibiotics, which has contaminated beef from difference slaughterhouses and which available for purchase in a retail butcher shops in Upper Northeastern Thailand.

MATERIALS AND METHODS

A total of 145 beef samples were taken from local slaughterhouses and a retail butcher shops within 12 provinces of the Northeastern Region of Thailand, for analysis of *Salmonella* spp. contamination and resistance to antimicrobial drugs.

Isolation and Identification

Salmonella were isolated from beef samples by standard methods [4]. Briefly, a beef sample was minced, then 225 ml sterile Buffered peptone water (BPW) was added into 25 g minced sample, this was incubated at 37±1°C overnight. After that, the pre-

enriched cultures were transferred to two enrichment media; Rappaport Vassiliadis (RV) was incubated at $41.5 \pm 1^\circ\text{C}$ for 24 ± 3 h and Muller-Kauffmann tetrathionate novobiocin broth (MKTTn) was incubated at $37 \pm 1^\circ\text{C}$ for 24 ± 3 h. Subsequently, the enriched cultures from RVS and MKTTn were transferred to Xylose lysine desoxycholate agar (XLD) and Brilliant green agar modified (BGM) were incubated at $37 \pm 1^\circ\text{C}$ for 24 ± 3 h. Then, pick a pink colony with or without black centres with sterile inoculating loop are selected and inoculated to the Nutrient agar (NA) then incubated at $37 \pm 1^\circ\text{C}$ for 24 ± 3 h. Subsequently, the samples were biochemically tested on Triple sugar iron agar (TSI), L-lysine decarboxylation medium (LIM), Urea agar, VP medium incubated at $37 \pm 1^\circ\text{C}$, 24 ± 3 h, and ONPG disc incubated at $35 \pm 1^\circ\text{C}$, observed every 1 h for 6 h to identify the species of salmonella resin as serotypes. The slide agglutination test was carried out by slurry agglutination test somatic-antiserum specific for O-antigen on slides, read reaction results, sedimentation and serotyping by culture on swarm agar. The flagella-antiserum is specific for H-antigen on slides and reads the precipitation reaction. The results of the tests were compared with antigenic formulas of the salmonella serovars according to Kauffmann-White Scheme [5, 6].

Antimicrobial susceptibility testing

Salmonella isolates were tested for antimicrobial susceptibility by disk diffusion method and interpreted according to standards established by the Clinical and Laboratory Standards Institute (CLSI, 2008), *E. coli* ATCC 25922 were used as a quality control strain. The following antimicrobial were tested: amoxicillin/clavulanic acid (AMC) 20/10 µg/mL, ampicillin (AMP) 10 µg/mL, cephalothin (KF) 30 µg/mL, chloramphenicol (C) 30 µg/mL, ciprofloxacin (CIP) 5 µg/mL, colistin (CT) 10 µg/mL, enrofloxacin (ENR) 5 µg/mL, gentamicin (CN) 10 µg/mL, kanamycin (K) 30 µg/mL, nalidixic acid (NA) 30 µg/mL, neomycin (N) 30 µg/mL, norfloxacin (NOR) 10 µg/mL, oxytetracyclin (OT) 30 µg/mL, streptomycin (S) 10 µg/mL, sulfamethoxazole/trimethoprim (SXT) 1.25/23.75 µg/mL and tetracycline (TE) 30 µg/mL. The diameter zone of growth inhibition surrounding the paper disk is measured and compared to the standard inhibition diameter [7].

RESULTS AND DISCUSSION

Salmonella contamination in meat from slaughterhouses and butcher shops.

One hundred and forty-five samples that originated from beef carcasses at sixty four slaughterhouses and eighty one butcher shops, in the

Upper Northeastern region of Thailand were included for determination of *Salmonella* spp. prevalence.

The results as shown in Table 1, indicated that, a total of sixteen samples (11.03 %) detected *Salmonella* spp., nine samples (14.06 %) were from slaughterhouses and the other seven samples (8.64 %) were from butcher shops. There were five serovars from three serogroups in contaminated meat from slaughterhouses and seven serovars, which included two serogroups, were detected from butcher shops. Notably, only *S. Derby* was found in beef from a slaughterhouse in Roi-Et province. In addition, *S. Kouka* and *S. Okefoko* were detected in beef from a butcher shop in Sakon Nakhon province only. The serovar *S. Lexington* was found in beef from the butcher shop in Nakhon Phanom only. Furthermore, the most prevalent serovars was *S. Weltevreden* (4.68 %), followed by *S. Rissen* (2.07 %), *S. Anatum* (2.07 %) and *S. Muenchen* (1.38 %), which is same serotypes as [8]. The presence of *Salmonella* spp. in beef suggests poor hygiene management. *Salmonella* is commonly found in the animal gastrointestinal tract, therefore food contamination with this pathogen could happen throughout the food chain. This study was found *Salmonella* spp. contamination in beef carcasses (11.03 %) much less than in previous reported [8] which found a prevalence of 52 % (28/54) in beef samples and included Thai self-service style restaurants in Khon Kaen municipality, Thailand.

When comparing the rate of *Salmonella* spp contamination in beef between a slaughterhouse and retail butcher shop, there are no statistically significant differences. This shows that the transportation from the local slaughterhouse to the butcher shop, including the preservation and deliver to the butchers shop, are carried out hygienically. The production of Thai beef is in the process of developing into a standard, where most slaughtering is carried out in a local, municipal slaughterhouses or private slaughterhouses that are certified by the Department of Livestock Development. Most slaughterhouses now operate to a good standard of practice.

However, some local slaughterhouses still operate with poor hygiene and meat is usually delivered in open buckets in a cars. Typically, meat in butcher shops are sold at ambient temperatures, this indicates the application of strict hygiene practices is therefore essential. The regulatory authorities should control policy for a good manufacturing practice for cattle abattoir' together with stringent sanitation in fresh meat production.

Table 1 Prevalent of *Salmonella* serotypes obtained from beef carcasses in slaughterhouse and butcher shop

<i>Salmonella</i> spp.	Number of positive samples (%)			Provinces*
	Slaughterhouse (n=64)	Butcher shop (n=81)	Total (n=145)	
Group B	1 (1.56)	0 (0.00)	1 (0.69)	
<i>S. Derby</i>	1 (1.56)	0 (0.00)	1 (0.69)	Roi Et(Sh:1)
Group C	3 (4.69)	2 (2.47)	5 (3.45)	
<i>S. Muenchen</i>	1 (1.56)	1 (1.23)	2 (1.38)	Roi Et(Bs:1), Sakon Nakhon(Sh:1)
<i>S. Rissen</i>	2 (3.13)	1 (1.23)	3 (2.07)	Roi Et(Sh:1), Sakon Nakhon(Bs:1), Khon Kaen(Sh:1)
Group E	5 (7.81)	5 (6.17)	10 (6.90)	
<i>S. Anatum</i>	2 (3.13)	1 (1.23)	3 (2.07)	Kalasin(Sh:1), Maha Sarakham(Bs:1), Roi Et(Sh:1)
<i>S. Kouka</i>	0 (0.00)	1 (1.23)	1 (0.69)	Sakon Nakhon(Bs:1)
<i>S. Lexington</i>	0 (0.00)	1 (1.23)	1 (0.69)	Maha Sarakham(Bs:1)
<i>S. Okefoko</i>	0 (0.00)	1 (1.23)	1 (0.69)	Sakon Nakhon(Bs:1)
<i>S. Weltevreden</i>	3 (4.68)	1 (1.23)	4 (2.76)	Kalasin(Sh:1), Maha Sarakham(Bs:1), Sakon Nakhon(Sh:2)
Total	9 (14.06)	7 (8.64)	16 (11.03)	Kalasin, Khon Kaen, Maha Sarakham, Sakon Nakhon, Roi Et

* Sh=Slaughterhouse; Bs=Butcher shop

Antimicrobial susceptibility testing results were isolated from beef showed that 12.50 % of isolates were resistant to at least one antimicrobial agents and 25.00 % were multi-drug resistant. Resistance rate to amoxicillin/clavulanic acid, ampicillin, cephalothin, chloramphenicol, ciprofloxacin, oxytetracycline, streptomycin, sulfamethoxazole/trimethoprim and tetracycline were 6.25 %, 43.75 %, 6.25 %, 6.25 %, 6.25 %, 43.75 %, 12.50 %, 43.75 % and 31.25 %, respectively. (Table 2).

These antibiotics residues in meat are present in farmed animals being treated under veterinary control. The presence of these antibiotic residues in meat may be due to the short withdrawal period before slaughtering or prolonged courses of antibiotics. The misuse of antibiotics may lead to the development of drug-resistant salmonella. Besides this, resistant salmonella present in meat, may be transmitted to consumers and be the cause of poor response of treatment with human medicines. Likewise, a recent report [9]. found amoxicillin/clavulanic acid, ampicillin, cephalothin, chloramphenicol, ciprofloxacin, oxytetracycline, streptomycin, sulfamethoxazole/trimethoprim and tetracycline are used in human medicine too [10].

It is astonishing to observe the isolates resistant to chloramphenicol, in spite of the fact that the drug has been forbidden use in food-producing animals. It was suggested that this phenomenon may be generated by other antibiotics on co-selection or cross-resistance. [11]. This suggests that the removal of certain antimicrobial selections may not completely eliminate AMR and be a transfer of resistance to other important human pathogens.

As shown in Table 3, nine salmonella isolates were classified with six antimicrobial resistance patterns, which were resistant to three, four and six antimicrobial agents. The most common resistance patterns were AMP-OT-S-TE and AMP-OT-TE-SXT, whereas the highest number antimicrobial resistance pattern is AMP-C-CIP-OT-SXT-TE. Similar results have been reported recently too [12]. The previous survey showed that the resistance pattern of isolated salmonella contaminated with pork, identified as multidrug resistant and the most resistance pattern was AMP-TE-SXT. Whereas chloramphenicol is the one antibiotic agent found in the resistance pattern, like in accordance with those of this study. For this reason, veterinarian and relevant authorities need to regulate the use of antibiotics in animal production strictly, whether for disease treatment, prevention, or growth promotion.

Table 2 Antimicrobial susceptibility of *Salmonella* spp. isolated from beef by disk diffusion methods

Antimicrobial disk	Number of antimicrobial susceptibility*									Total (%)		
	Group B (n=1)			Group C (n=5)			Group E (n=10)			(n=16)		
	S	I	R	S	I	R	S	I	R	S	I	R
AMC (20/10 µg)	1	0	0	3	1	1	10	0	0	14 (87.50)	1 (6.25)	1 (6.25)
AMP (10 µg)	0	0	1	1	0	4	8	0	2	9 (56.25)	0 (0.00)	7 (43.75)
KF (30 µg)	1	0	0	3	1	1	10	0	0	14 (87.50)	1 (6.25)	1 (6.25)
C (30 µg)	0	0	1	5	0	0	10	0	0	15 (93.75)	0 (0.00)	1 (6.25)
CIP (5 µg)	0	0	1	5	0	0	10	0	0	15 (93.75)	0 (0.00)	1 (6.25)
CT (10 µg)	1	0	0	5	0	0	10	0	0	16 (100.00)	0 (0.00)	0 (0.00)
ENR (5 µg)	0	1	0	5	0	0	10	0	0	15 (93.75)	1 (6.25)	0 (0.00)
CN (10 µg)	1	0	0	5	0	0	10	0	0	16 (100.00)	0 (0.00)	0 (0.00)
K (30 µg)	1	0	0	5	0	0	10	0	0	16 (100.00)	0 (0.00)	0 (0.00)
NA (30 µg)	1	0	0	5	0	0	10	0	0	16 (100.00)	0 (0.00)	0 (0.00)
N (30 µg)	0	1	0	2	3	0	7	3	0	9 (56.25)	7 (43.75)	0 (0.00)
NOR (10 µg)	1	0	0	5	0	0	10	0	0	16 (100.00)	0 (0.00)	0 (0.00)
OT (30 µg)	0	0	1	2	0	3	7	0	3	9 (56.25)	0 (0.00)	7 (43.75)
S (10 µg)	0	1	0	2	1	2	8	2	0	10 (62.50)	4 (25.00)	2 (12.50)
SXT (1.25/23.75)	0	0	1	2	0	3	7	0	3	9 (56.25)	0 (0.00)	7 (43.75)
TE (30 µg)	0	0	1	4	0	1	7	0	3	11 (68.75)	0 (0.00)	5 (31.25)
Total	7	3	6	59	6	15	144	5	11	210 (82.03)	14 (35.84)	32 (12.50)

* S = sensitive, I = intermediate, R = resistant

Table 3 Patterns of multidrug resistance of *Salmonella* spp. isolated from beef receiving difference slaughterhouse and butcher shop

Number of multidrug resistance	The pattern of <i>Salmonella</i> isolate showed multidrug resistance (n)			
	Group B	Group C		Group E
	<i>S. Derby</i>	<i>S. Muenchen</i>	<i>S. Rissen</i>	<i>S. Anatum</i>
3	-	AMC-AMP-C (1)	-	OT-TE-SXT (1)
4	-	-	AMP-OT-S-TE (2) AMP-OT-TE-SXT (1)	AMP-OT-TE-SXT (2)
6	AMP-C-CIP-OT-SXT-TE (1)	-	-	-

In conclusion, the results demonstrate the low contamination rate of MDR *Salmonella* spp. in beef carcasses in local slaughterhouses and retail butcher shops of Northeastern Thailand. Evidently, antimicrobial use in beef production is controlled more strictly and under supervision by veterinarians. This confirms that slaughterhouses and butcher shops in Thailand generally have a good manufacturing practice and are developing to international standards.

ACKNOWLEDGEMENTS

The authors would like to thank the Northeastern veterinary research and development centre (upper part) which facilitating on the laboratory for isolation and identification of *Salmonella* spp. in this study. In addition, thank Mr. Andrew Michael Chilcott for assistance with the English language presentation of the manuscript.

REFERENCES

- [1] Yang B., Qiao L., Zhang X., Cui Y., Xia X., Cui S., Wang X., Meng X., Ge W., Shi X., Wang D., Meng J. Serotyping, antimicrobial susceptibility, pulse field gel electrophoresis analysis of *Salmonella* isolates from retail foods in Henan Province, China. Food Control Volume 32, Issue 1, 2013, pp. 228-235.
- [2] Sanchez-Maldonado A.F., Aslam M., Service C., Narváez-Bravo C., Avery B.P., Johnson R., Jones T.H. Prevalence and antimicrobial resistance of *Salmonella* isolated from two pork processing plants in Alberta, Canada. International Journal of Food Microbiology Volume 241, 2017, pp. 49-59.
- [3] Bailey, J. S. and Maurer J.J. *Salmonella* Species. In: Food Microbiology: Fundamentals and Frontiers, 2nd ed., Doyle, M. P., Beuchat L. R., and Montville T. J., ASM Press, Washington D.C., 2001, pp. 141–178.
- [4] ISO. Microbiology of food and animal feeding stuff - Horizontal method for the detection of *Salmonella* spp. ISO 6579:2002(E) 4th ed. International Organization of Standardization, Geneva, Switzerland, 2002, pp.1-27.
- [5] Popoff M., Bockemühl J., Brenner F.W., Gheesling L.L. Supplement 2000 (no. 44) to the Kauffmann-White scheme. Res. Microbiol. Volume 152, 2001, pp. 907–909.
- [6] Grimont, P.A.D., Weill, F.X. Antigenic Formulae of the *Salmonella* Serovars, (9th ed.) Paris: WHO Collaborating Centre for Reference and Research on *Salmonella*, Institute Pasteur. 2007. Available at: http://www.pasteur.fr/sante/clre/cadrechr/salmoms/WKLM_En.pdf.
- [7] Clinical and Laboratory Standards Institute. Performance standards for antimicrobial susceptibility disk and dilution susceptibility tests bacteria isolated from animals; Approved Standard 3rd ed. Vol. 28 No. 8. Pennsylvania, USA, 2008, pp. 1-75.
- [8] Angkititrakul S., Polpakdee A., and Chuanchuen R. Prevalence of *Salmonella enterica*, *Escherichia coli* and *Staphylococcus aureus* in raw meat in Thai self-service style restaurants in Khon Kaen Municipality. Thai J Vet Med. Vol. 43, Issue 2, 2013, pp.265-268.
- [9] Hao H., Cheng G., Iqbal Z. et al. Benefits and risks of antimicrobial use in food-producing animals. Frontiers in microbiology. Vol. 5, Issue 288, 2014, pp. 1-11.
- [10] Marshall B.M. and Levy S.B. Food animals and antimicrobials: Impacts on human health. Clinical microbiology reviews. Vol. 24, Issue 4, 2011, pp. 718-733.
- [11] Bischoff K.M., White D.G., Hume M.E., Poole T.L., and Nisbet D.J. The chloramphenicol resistance gene *cmlA* is disseminated on transferable plasmids that confer multiple-drug resistance in swine *Escherichia coli*. FEMS Microbiol Lett. Vol. 243, 2005, pp. 285-291.
- [12] Pulsrikarn C., Chaichana P., Pornruangwong S., Morita Y., Yamamoto S., and Boonmar S. Serotype, antimicrobial susceptibility, and genotype of *Salmonella* isolated from swine and pork. Thai J Vet Med. Vol. 42, Issue 1, 2012, pp.21-27.

STUDY OF QUALITY AND CONSUMER TEST OF EMULSION SAUSAGE FROM BUFFALO AND TURKEY MEAT

Thassawan Somchan¹ and Suthipong Uriyapongson²

¹ Graduate Student, ² Associate Professor, ^{1,2} Department of Animal Science,
Faculty of Agriculture, Khon Kaen University Thailand

ABSTRACT

The objective of this research were to study of quality and consumer test of emulsion sausage from buffalo and turkey meat. The experiment was assigned in the completely randomized block design(RCBD). Sausage from buffalo and turkey meat were produced in 5 treatments include turkey meat 100 % (T1), buffalo meat 100% (T2), turkey meat 75 % : buffalo meat 25% (T3), turkey meat 50% : buffalo meat 50% (T4) and turkey meat 25% : buffalo meat 75% (T5). Sausages were stored in refrigerator (4°C) for 24 hours before determined for pH, color (L^* a^* b^*). Lipid oxidation (TBA) of sausage were determined after stored in refrigerator for 0,7,14 and 21 days. The results showed that pH of sausages were approximately 5-5.9. Color of T1 sausages had the highest L^* (27.54) and b^* (19.39) but had the lowest a^* (6.38) value ($p<0.05$), T5 sausages had the highest a^* (7.58) . The TBA of T1 sausage after stored for 1,7, 14 and 21 day were higher ($p<0.05$) than in other groups. Consumer acceptance score of T1 and T3 sausages received the highest score and 6.9 5.8 (score of the 9 level). It could be concluded that buffalo meat reduced lightness, yellowness score and improved redness score in sausage. Higher buffalo meat reduced lipid oxidation in the turkey sausage.

Keywords: Emulsion sausages, Turkey meat, Buffalo meat

INTRODUCTION

In Thailand, turkey farming is getting popular. Government agencies are promoting new livestock. Turkey meat was high calcium but lower chicken and saturated than other meats [1]. It also had higher protein and essentials amino acids. However, turkey meat was a white meat [2] and meat products were white and pale. Buffalo meat consumption is related to its nutritional advantages compared to beef. It is richer in iron, contains a higher amount of high biological value protein and essential fatty acids, along with lower quantities of fat and cholesterol [3]. Buffalo meat had dark red color and also had high water holding capacity [4]. The main ingredients of the sausage are chicken, pork, beef and lamb meat. At present, emulsion such as Vienna and Frankfurter sausage are the popular meat products around the world. Turkey and Buffalo meat are interesting on raw material of emulsion sausage in Thailand. Therefore, buffalo meat mixes to turkey meat by in emulsion sausage may improve color and texture sausage. The objectives of this research are to study on quality (pH, color and lipid oxidation) and consumer test of emulsion sausage from turkey meat with difference level of buffalo meat.

MATERIALS AND METHOD

Fresh meat from turkey and buffalo were purchased and chill overnight at 4°C. Emulsion

sausage of turkey were produced with the ingredients as showed in table 1. Buffalo meat was added to substitute for turkey meat at 25, 50, 75 and 100 % respectively.



a. Buffalo meat



b. Turkey meat

Fig. 1 Fresh meat



a. Turkey sausages



b. Buffalo sausages

Fig. 2 Emulsion sausages (Vienna sausages)

Sausage products were stored overnight at 4°C (24 hour) before determined pH valued used portable pH-meter (Hanna Instrument, Eibar, Spain). Color of sausage samples were evaluated using by Konica Minolta CR-410 and reported as

L*(lightness), a*(redness) and b*(yellowness). Lipid oxidation was evaluated by measure thiobabaturic acid (TBA) after stored in refrigerator (4°C) for 1,7,14 and 21 days according to the methods suggested by Turk Standards Institute 2409 [5]. Consumer test was performed using of 1 to 9 in the Hedonic scale [6] [7].

Table 1 Ingredients for emulsion sausage

Ingredients	Ratio 100 (%)
Meat	46.87
Leaf fat	24
Ice	24
Soy protein isolate	2
NaCl	1
Vienna Powder	0.48
Sodium tri-polyphosphate	0.28
Sodium Erythorbate	0.28
Smoke powder	0.28
Monosodium glutamate	0.2
Sugar	0.2
Pepper powder	0.2
Coriander seeds	0.2
Sodium nitrite	0.01

Source: [8]

The experimental design was Randomized completely block design (RCBD) experiment with 5 treatments and 3 replications as follow:

Treatment 1 Turkey meat 100% (T1)

Treatment 2 Buffalo meat 100% (T2)

Treatment 3 Turkey meat 75% : Buffalo meat 25% (T3)

Treatment 4 Turkey meat 50% : Buffalo meat 50% (T4)

Treatment 5 Turkey meat 25% : Buffalo meat 75% (T5)

Statistical analysis were performed using SAS [9]. Mean of all values were analyzed of variance (ANOVA) and compared using Duncan New Multiple Rang Test (DMRT)

Results

The effects of variation in the ratio of the raw

material components include turkey and buffalo on the quality characteristics of the sausages showed in the Table 2. The pH values of turkey sausages were found range pH 5.0-5.9. In the pH, lightness and yellowness values of the treatment T1 (100% turkey) exhibited the highest value than the others ($p<0.05$). Also, all of treatments show significant difference in the lightening values. The redness values of the treatment T1 indicated the lowest value was 6.38. The redness value of the T2, T3, T4 and T5 (7.53, 7.5, 17.29 and 7.58 respectively) did not significantly differ but had higher value than T1 ($p<0.05$). Added buffalo meat reduced pH but increased redness value of emulsion sausage.

Table 2 pH and color of emulsion sausage

	pH	L*	a*	b*
T1	5.94 ^a	27.54 ^a	6.38 ^b	19.39 ^a
T2	5.73 ^{ab}	23.87 ^b	7.53 ^a	14.30 ^d
T3	5.35 ^b	19.63 ^c	7.51 ^a	17.17 ^b
T4	5.36 ^b	16.57 ^d	7.29 ^a	15.17 ^c
T5	5.61 ^{ab}	14.16 ^e	7.58 ^a	14.66 ^{cd}
SE	0.11	0.34	0.11	0.26

^{a,b,c,d} Means with different letters within the same column were significantly different ($p<0.05$).

SE = Standard error

T1 = Turkey meat 100%

T2 = Buffalo meat 100%

T3 = Turkey meat 75% : Buffalo meat 25%

T4 = Turkey meat 50% : Buffalo meat 50%

T5 = Turkey meat 25% : Buffalo meat 75%

Lipid oxidation analysis

Table 3 Thiobabaturic acid (TBA) of emulsion sausage at different storage time.

	Storage time (day)			
	1	7	14	21
T1	0.88 ^a	1.03 ^a	0.99 ^a	0.97 ^a
T2	0.43 ^c	0.41 ^c	0.51 ^c	0.43 ^c
T3	0.77 ^{ab}	0.80 ^b	0.78 ^{ab}	0.72 ^b
T4	0.64 ^{bc}	0.70 ^b	0.69 ^{bc}	0.68 ^b
T5	0.53 ^c	0.50 ^c	0.57 ^{bc}	0.56 ^{bc}
SE	0.07	0.05	0.07	0.07

^{a,b,c,d} Means with different letters within the same column were significantly different ($p<0.05$).

SE = Standard error

TBA = $\mu\text{g MA/g}$.

T1 = Turkey meat 100%

T2 = Buffalo meat 100%

T3 = Turkey meat 75% : Buffalo meat 25%

T4 = Turkey meat 50% : Buffalo meat 50%

T5 = Turkey meat 25% : Buffalo meat 75%

The sausages were stored at 1,7,14 and 21 days. The T1 showed the highest TBA value (1.03 µg MA/g.) at 7 day of storage. The TBA of T1 sausage was higher ($p < 0.05$) compared to in other groups. However, TBA values of T2 and T5 sausages were lower than other groups.

Consumer test

Table 4 showed consumer acceptance score of emulsion sausage. The T1 and T3 sausages had the highest score of color, odor, flavor, juiciness, tenderness and overall acceptability while T2 and T5 sausages received the lowest score.

Table 4 Consumer acceptant test on Hedonic scale of emulsion sausage.

	Col	Od	flav	Juic	Tend	Over
T1	6.74 ^a	6.30 ^a	6.87 ^a	6.91 ^a	6.97 ^a	6.86 ^a
T2	3.99 ^c	3.80 ^b	4.21 ^b	3.54 ^c	3.87 ^d	3.95 ^c
T3	6.40 ^a	5.85 ^a	6.51 ^a	6.39 ^a	6.32 ^{ab}	6.47 ^a
T4	5.45 ^b	4.80 ^b	5.30 ^b	5.31 ^b	5.31 ^{bc}	5.44 ^b
T5	4.41 ^c	4.36 ^b	4.83 ^b	4.38 ^{bc}	4.57 ^{cd}	4.90 ^{bc}
SE	0.29	0.32	0.34	0.31	0.33	0.31

^{a,b,c,d} Means with different letters within the same column were significantly different ($p < 0.05$).

SE = Standard error

Col = Color

Od = Odor

flav = Flavor

Juic = Juiciness

Tend = Tenderness

Over = Overall acceptability

T1 = Turkey meat 100%

T2 = Buffalo meat 100%

T3 = Turkey meat 75% : Buffalo meat 25%

T4 = Turkey meat 50% : Buffalo meat 50%

T5 = Turkey meat 25% : Buffalo meat 75%

DISCUSSION

Redness (a^*) score of T2, T4 and T5 sausage were higher with the mixture of buffalo meat due to the darker color of buffalo meat. The T1 and T3 sausage had the highest lightness and yellowness value. Sausages with more buffalo meat had less TBA because of less unsaturated fatty acids [10] compared to turkey meat. Consumer acceptant of sausages with buffalo meat had low accepted value. Because of odor and hard of texture from buffalo meat.

CONCLUSION

Study of quality and consumer test of turkey emulsion sausage with difference level of buffalo

meat found that: pH values were similar among treatments. Added buffalo meat reduced pH but increased redness value of emulsion sausage. Sausages with more buffalo meat had lower rancidity during storage time. Consumer acceptance score showed that more buffalo meat sausages received lower acceptant score. There should be a study on odor reduction in buffalo meat sausages.

ACKNOWLEDGEMENTS

Thanks for the teacher development fund. Mahasarakham University. Animal Science Laboratory, Department of Animal Science, Faculty of Technology, Mahasarakham University. Meat Laboratory, Department of Animal Science Khonkaen University.

REFERENCES

- [1] Kerd Sang P., Turkey. <http://www.eto.ku.ac.th/>
- [2] Kantapanit C., Meat Science. Thai Wattana Panich Publishing Bangkok, 1986, pp.1-260.
- [3] Voloski F.L.S., Tonello L., Ramires T., Reta G.G., Dewes C., Iglesias M., Mondadori R.G., Gandra E.A., da Silva W.P., and Duval E.H., Influence of cutting and deboning operations on the microbiological quality and shelf life of buffalo meat Journal of Meat Science 116, 2016, pp. 207–212.
- [4] Uriyapongson S., Buffalo and Buffalo Meat in Thailand, World Buffalo Congress and the 7th Asian Buffalo Congress, Buffalo Bulletin (Special Issue 1), Vol.32, 2013, pp.329-332.
- [5] Available from Department of Livestock Development. 2003.
- [6] Turkish Standart Instiýtute .Chicken carcass meat. Chemical properties. Ankara, Turkey.2007.
- [7] Anprung P., Principles analysis of food with Sensory Chulalongkorn University Publishing, 2008, pp. 1-360.
- [8] Peryam D.R., & Pilgrim, F.J. Hedonic scale method of measuring food preferences. Food Technology, 11(9), 1957, pp. 9–14.
- [9] Steel R. G. D. and Torrie J. H., Principle and procedures of statistics: A Biomaterial Approach 2nd. McGraw Hill Book Co, New York.1980.
- [10] Mariutti L., Influence of salt on lipid oxidation in meat and seafood product: A review. Food Research International, 2017, pp. 90-100.

Engineering

PARAMETRIC STUDY ON THE RESPONSE OF COMPOSITE SINGLE PILES TO LATERAL LOAD BY NUMERICAL SIMULATION (FDM)

¹Alex Otieno Owino, ¹Zakaria Hossain, ²Jim Shiau

¹Dept. of Environmental Science Graduate School of Bioresources, Mie University, Japan

²School of Civil Engineering and Surveying, University of Southern Queensland, Queensland, Australia

ABSTRACT

This paper entails a detailed numerical and parametric study on the lateral behaviour of piles in foundation designs. Single-piles are one of the major components of a foundation as they act as the primary component in the transmission of the weights above the structure into the ground for stability to be attained. For this reason, a detailed study on the influence generated on the p-y curves is mandatory to create a numerically valid model for use in the process of foundation design without much ado. Modelling procedure under consideration employs the use of the finite difference method (FMD) embedded in FLAC2D. FDM is used to implement a solution to the coded input for example soil and pile element parameters. The model validation process done in this paper involves the variation of some of the critical parameters such as the variation on the type of soil in the area under consideration. Next, modification of the elastic modulus of the given soil as a check on the cohesiveness, change on the loading velocity at the top of the pile, a variation of the pile material stiffness and the difference of the pile eccentricity. The results obtained from the p-y curves generated from the parameters undergo sifting through for any effects on the ultimate loading capacity of the pile to the allowed design loading limits upon full structural installation. This variation is necessary for the approval of the validity of the model in engineering design. The parametric study from this study shows that the structure is of functional strength and a tolerable factor of safety.

Keywords: Lateral load, p-y curve, Soil-pile interaction, Finite difference method, FLAC2D

INTRODUCTION

The response of laterally loaded piles is a function that is dictated by many related parameters that act upon the pile foundation during loading. At any considerable time of loading, the effects of each parameter input can cause a substantial influence on the reaction of the pile foundation and the adjacent soil components. Engineers always propose pile foundation for the transfer of loads of overlying structures as it offers adequate bearing capacity for lateral loads and also gravity loads. In the past studies on pile foundations, several approaches have been carried out to analyze this response from loads. These approaches include force method, beam on elastic foundation method, soil plasticity, and elasticity continuum method. But most recently the practice of finite element method FEM [1], finite difference method FDM [2] is being put in to use. FEM and FDM are flexible and can be manipulated to give a variety of responses and an in-depth analysis of the pile and the soil interface.

The analysis of laterally loaded piles in most cases is expressed mostly by using the load-displacement curve methods also referred to as the p-y curve method. Using the p-y curves, the response of the soil during loading is shown by a series of springs that produce the resistance offered by the load when acting upon them. The curvilinear load-displacement p-y characteristics of the springs are given as input to

the analysis, and numerical methods are used to obtain the pile load-displacement response [3]. From the p-y curve obtained, the pile foundations, in this case, the single pile foundation should be able to withstand the imposed load with a reasonable factor of safety, the pile head displacement should not exceed the tolerable movements for the structure it supports, for example, the solar panels in this study and lastly the intermediate soil should not receive excessive stresses that may make it achieve the ultimate load carrying capacity upon full construction and operation [4]. A closer consideration is given on the response of the soil to the short piles as this provides a clear understanding of the pile element because at this depth the displacement is entirely reliant on the resistance of the soil as illustrated by [5].

To obtain a clear picture of the pile responses in this study, the parametric research is necessary to investigate the sensitivity towards fluctuating some of the typical inputs to the program. Klepikov [6], conducted a study to examine the influence generated by the modulus of subgrade reaction at the ground surface as the primary parameter influencing the pile structure response to the soil grid. The subgrade reaction has also enabled the engineer to develop models that can withstand seismic activities without the fear of structural failure as stipulated by [7], who predicted the foundation response to seismic and dynamic loads. As a step to simplify and ease the analysis of pile foundations, 2D and 3D modelling

have become handy as it allows for the closer analysis and input of flexible functions that can be executed by any given geotechnical software like FLAC2D using finite difference method. Numerical models have been developed to help comprehend the pile and soil structures [8], to perceive the effect of the parameters to the pile setup when subjected to various modes of loading. This study, therefore, employs the use of FLAC2D in the development of a model to represent the soil and pile interaction and the resultant displacements used to investigate the various parameters discussed in the analysis section.

FLAC2D FINITE DIFFERENCE MODELLING PROCEDURE

The model was made using FLAC2D which is a sufficient way to solve such complex matters as it gives a clear picture of the performance of the structure for the applied load. By finite difference analysis, a mesh was generated to represent the ground/soil conditions which had fixed grids points with pinned boundary conditions (B) applied along the bottom of the model and roller boundaries (X) on both sides. The final model has been chosen so that the overall velocity field is distributed within the domain and no boundary effect is presented. In general, the model size has to be greater than 2 times the pile length (i.e. 2.8 m radius from pile element axis by 2.8 m depth) as shown in Fig. 1.

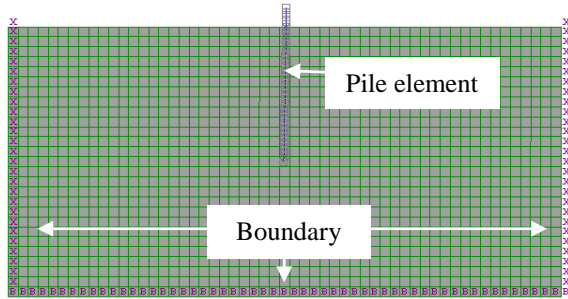


Fig. 1 Mesh, boundary condition, and pile displacement pattern

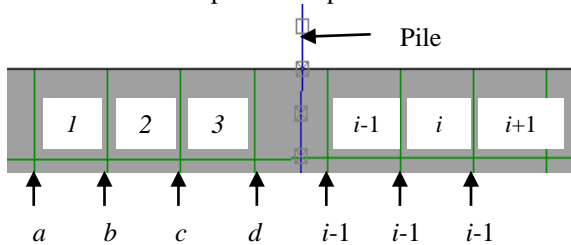


Fig. 2 Schematic representation of the grid points and the zones

Figure 2 is a representative of an extended view of the top of the model with 1, 2 and 3 indicating the zones and inscribed within the zones ($i-1$, i , and $i+1$),

shows the stresses involved during stress and strain development process. On the other hand, a , b and c indicated the grid points upon which the velocities are applied to produce deformations that lead to the grid displacement.

Finite-difference method (FDM) is numerical methods for solving differential equations by approximating them with difference equations, in which finite differences approximate the derivatives. FDMs [9] are thus discretization methods and are the dominant approach to numerical solutions of partial differential equations. FLAC2D applies the FDM to implement a solution to the coded input, for example, the analysis of the pile foundation. FLAC2D therefore, allow for the vector quantities for example forces, velocities and displacements storage in the finite difference grid generated while all scalar quantities, for example, stresses, pressure, and material properties stored in the zone locations. To ensure stability in the numerical scheme, FLAC2D includes the dynamic equations of motion (equilibrium equation) in the formulation. The balance thus provides there is no sudden failure or collapse to the structural component during the lateral loading procedures [10]. The primary explicit calculation cycle is as shown in Fig. 3.

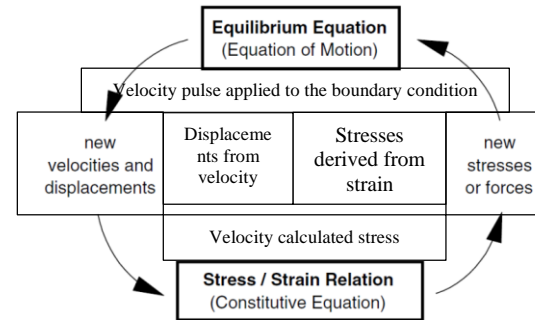


Fig. 3 Basic explicit calculation cycle

The response of a pile element during loading is similar to the elastic model in FLAC2D. Regarding Fig. 2, three main equations that dictate the response of the pile element include Stress-Strain Constitutive Law (Hooke's Law), Equation of Motion for Dynamic Equilibrium (wave equation) and FDM formulation using central finite difference equation as shown in Eqn. (1), (2) and (3) respectively.

$$\sigma_{xx} = E \frac{\partial u_x}{\partial x} \quad (1)$$

$$\rho \frac{\partial u_i}{\partial t} = \frac{\partial \sigma_{ij}}{\partial x_j} + \rho g_i \quad (2)$$

$$\tilde{\sigma}_{xx}^i(t) = E \frac{u_x^{i+1}(t) - u_x^i(t)}{\Delta x} \quad (3)$$

Where ρ is the mass density, u_x is the velocity component, E is the elastic modulus, t is the time, x_i is the component of the coordinate vector, g_i is the

component of gravitational acceleration and σ is the component of the stress tensor. Equation 2 illustrates the dynamic force equilibrium which indeed shows the relationship between gravitational forces and the changes in stress in the model grid. As reflected earlier in this paper, FLAC2D consists of mainly useful formulations where the variations in velocity are quickly solved. Consequently, the rate at which strain is experienced in the model grid can be related to the velocity [11]. The finite difference equation for the equation of motion using central finite difference Eqn. 3, can further be simplified and classified into two sections, with the left side of the equation showing the changes in velocity while the right side represents the changes in the stresses involved during the model code execution as shown in Eqn. 4.

$$\frac{\rho}{\Delta t} \left\{ \dot{u}_x^i(t + \frac{\Delta t}{2}) - \dot{u}_x^i(t - \frac{\Delta t}{2}) \right\} = \frac{1}{\Delta x} \left\{ \sigma_{xx}^i(t) - \sigma_{xx}^{i-1}(t) \right\} \quad (4)$$

$$\dot{u}_x^i(t + \frac{\Delta t}{2}) = \dot{u}_x^i(t - \frac{\Delta t}{2}) + \frac{\Delta t}{\rho \Delta x} \left\{ \sigma_{xx}^i(t) - \sigma_{xx}^{i-1}(t) \right\} \quad (5)$$

$$u_x^i(t + \Delta t) = u_x^i(t) + \dot{u}_x^i(t + \frac{\Delta t}{2}) \Delta t \quad (6)$$

This paper, therefore, presents a numerical parametric study that investigates the effects of several parameters such as pile head displacement variations for two types of soil (silty soil and clayey soil), soil elastic modulus, loading velocity, stiffness of the standard coupling spring represented by the pile element and the pile eccentricity on the p-y curves. The p-y curves will help in the determination of the pile bearing capacity, the factor of safety as well as a step towards the model validation for engineering use in structural design for solar panel foundations.

RESULTS AND DISCUSSION

Effects different soils: silty soil and clay soils

The type of soil is one of the main parameters to be put into consideration for any construction procedure to be practiced. The cohesive nature of different soils dictates the bearing capacity of the foundation. In addition to bearing capacity, the soil type also dictates the modulus of subgrade reaction, K_s which is a ratio of contact pressure intensity, P and the soil settlement, y . Due to the fact that clayey soil has a higher modulus of subgrade reaction, 80,000 kN/m³, it attains a higher ultimate load of 15 kN at lower pile head displacement of 4mm as compare to the silty soils ($K_s=48,000$ kN/m³) that achieves the final pressure at more massive movements of 10mm as shown in Fig. 4.

A closer examination of the pile element and the soil displacement patterns depicts the more vertical movement of the ground in the clay soil than in the silty soil. This high-intensity soil movement depends

on the standard pressure induced by the pressing nature of the pile element as well as the modulus of subgrade reaction, K_s and the displacement, y produced at the pile head as shown in Eqn. 7. The soil movements of FLAC2D output are as shown in Fig. 5 and Fig. 6.

$$\text{High-pressure side: } P = P^* + K_h y \quad (7)$$

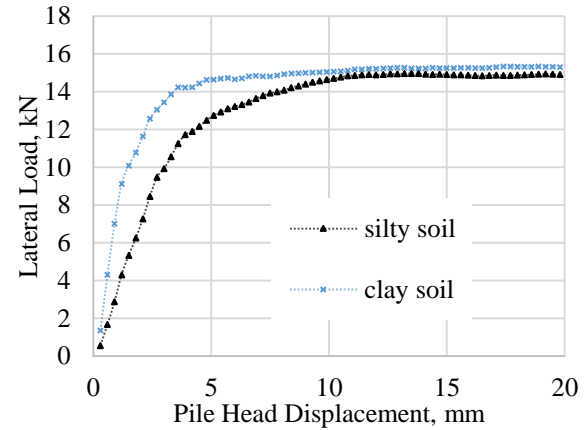


Fig. 4 Effects of different soils: Silty soil and clay soils

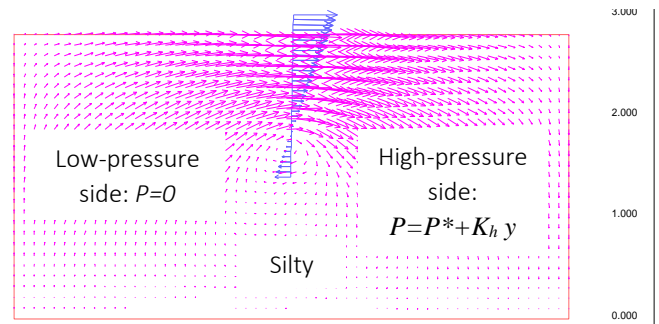


Fig. 5 Soil-pile displacement patterns for silty soil

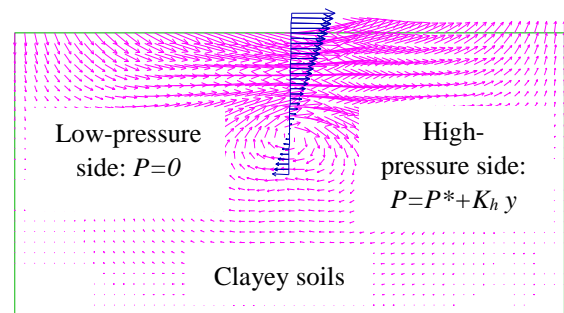


Fig. 6 Soil-pile displacement patterns for clayey soil

Effects of soil elastic modulus

In this case, it's the elastic modulus of the soil that is studied. The value for the elastic modulus is ranged from 11e6 to 31e6 kPa for silty soils and 40e6 to 60e6 kPa for the clayey soils. The other conditions are held constant as per the design parameters (Pile length= 1.4m, pile diameter=0.13m, the rate of loading force constant). The p-y curves generated from FLAC2D at

the design depth shows that the elastic modulus, E , has minimal effects in the silty soils whereas in the clay soils deviations in the ultimate load are noticed at displacements of 5 mm as shown in Fig. 7 and 8. This E variation is a clear indication that the cohesiveness of the soils should be highly considered in the clayey soils if the design bearing capacity is to be achieved.

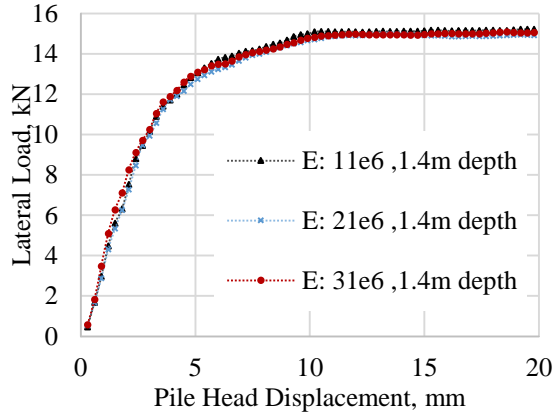


Fig. 7 Effects of elastic modulus for silty soil

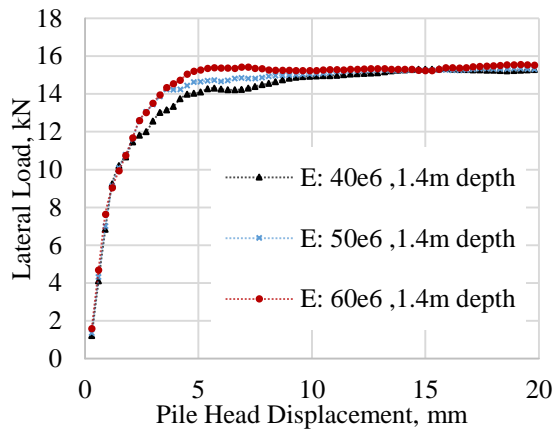


Fig. 8 Effects of elastic modulus for clayey soil

Effects of loading velocity with depth on ultimate load

Velocity is a time-dependent parameter when incorporated into FLAC2D. It ensures that the deformations on the grid follow the stress/strain law. To achieve the ultimate bearing capacity, the correct loading velocity should be determined as it plays a significant role in the damping of the equations of motion to provide static or quasi-static also known as non-inertial solutions. The non-inertial solutions help in achieving the equilibrium state in a numerically stable way with minimal computation effort in FLAC2D. In this study, the velocity was varied from $1.0e7$ to $2.5e7$ for the single pile foundation depths of 0.7m, 1.4m, and 2.8m. Based on the results, it is evident that increasing the velocity at 0.7m and 1.4m depth increases the ultimate loading capacity in the silty soil, but in the clayey soil, the ultimate loading

capacity reduces once the ultimate load is attained at $2.0e7$. At the pile depth of 2.8m, increasing the velocity have detrimental effects on the ultimate loading capacity as in both cases (silty and clay soils) there is significant decrease in the ultimate loads as shown in Fig. 9.

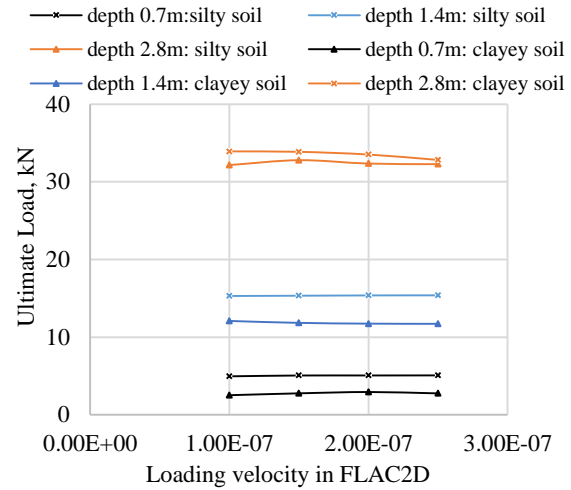


Fig. 9 Effects of Loading velocity with depth on ultimate load

Effects of pile stiffness: stiffness of normal coupling spring

In FLAC2D, the coupling springs are a representative of the interaction between the soil and the pile element under consideration. The normal coupling spring is the medium in which the lateral forces applied at the given velocity transmission, occur to the grid at the prescribed location along the pile element nodes. To obtain a desirable ultimate loading capacity of the pile, then the choice of the pile material should also be put on a check. A numerical description of the action of the normal coupling spring stiffness and the displacements produced during loading is as shown in equation 8

$$\frac{F_n}{L} = cs_{stiff} (u_p^n - u_m^n) \quad (8)$$

Where F_n represents the normal force that develops in the normal coupling spring, cs_{stiff} is the normal coupling spring stiffness, u_p^n is the displacement of the pile in the axial direction, u_m^n is the displacement of the grid(soil) normal to the axial direction of the pile, and L is the pile element length.

In this study, the stiffness of the normal coupling springs was varied from $1.3e7$ kN/m² to $1.3e11$ kN/m² with all other parameters held constant (Pile length= 1.4m, pile diameter=0.13m, the rate of loading force constant) for the two types of soils (silty and clayey soils). Based on the output, it's seen that an increase in the stiffness of the coupling spring increases the ultimate loading capacity of the pile. Clayey soils depict high ultimate loads up to 16 kN at $1.3e11$ kN/m²

at minimum displacements 7mm as compared to silty soils at 15kN. Figure 10 and Fig. 11 shows a plot of the stiffness parameter influence in ultimate loading capacity for silty and clayey soils respectively.

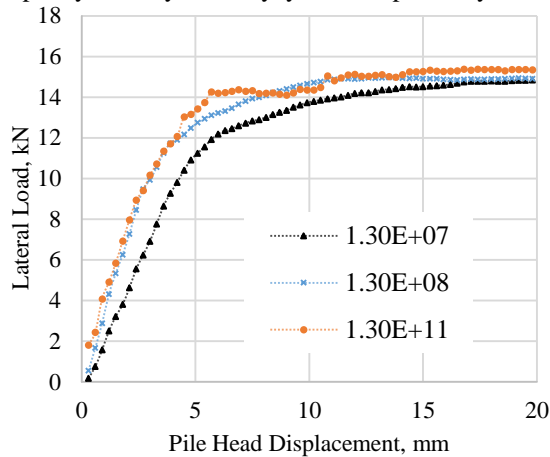


Fig. 10 Effects of pile stiffness silty soil

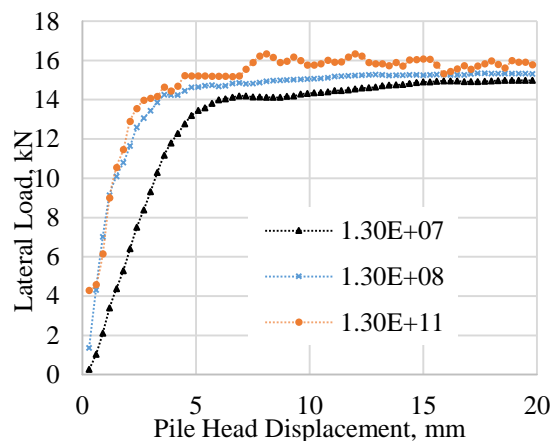


Fig. 11 Effects of pile stiffness clayey soil

Effects of eccentricity, e

The height of the pile above the ground is an excellent determinant on the moments above the ground level. The moment equilibrium equation is the product of the lateral force and the eccentricity. When the bending moments tend to increase then the ultimate load that the pile element can withstand reduces considerably. This reduction is due to the rotational effect produced by the lateral pressure above the ground level. When this rotational effect cannot be transmitted to the grid, then the pile tends to fail closer to the ground level at minimal lateral loads. In this study, the eccentricity effect is evaluated at 0.2m, 0.4m, 0.6m and 0.8m for both types of soil and the corresponding ultimate load plotted as shown in Fig. 12 and Fig. 13 for silty soil and clayey soil respectively. Based on the results, the eccentricity of 0.2m produced the highest ultimate loading capacity of 15kN in silty soil and 15.8kN in clayey soils. An eccentricity of 0.8m recorded the minimum value of

8.4kN hence this shows that the point of the load applied to a pile is also a strong determinant of the ultimate strength concerning bearing capacity.

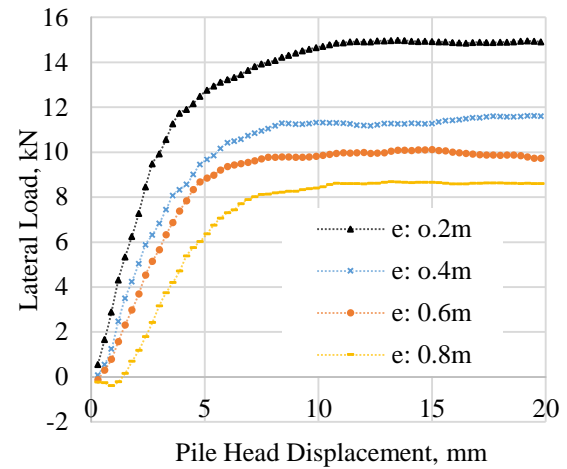


Fig. 12 Effects of pile eccentricity in silty soil

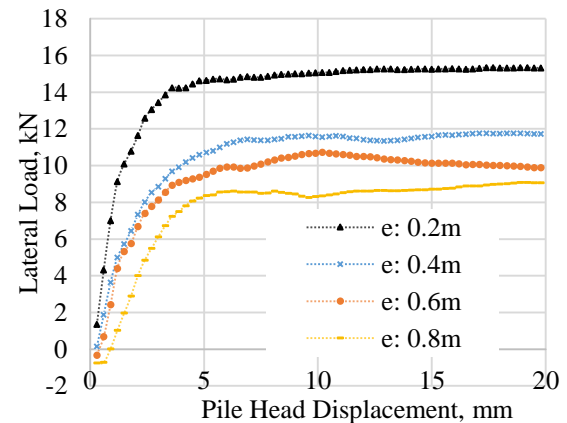


Fig. 13 Effects of pile eccentricity in clayey soil

CONCLUSION

The primary objective of this study was to evaluate the response of the load transfer curve and the displacements produced. This response shows the influence factor of the lateral load under different circumstances depending on the parameter under study. The parametric study, therefore, acts as a model validation process as it shows clearly the influence produced by a given setting concerning the design value at hand. From this study, it is evident that the integration of the stresses in the grid element around the pile element is an obvious way of understanding the p-y curve characteristics in the soil. Additionally, the variation of the parameters such as pile stiffness, loading velocity, and eccentricity have shown that clayey soils have the highest ultimate load bearing capacities of between 15.5kN to 15.8kN at minimal pile displacements of below 5mm.

It is also valid that FLAC2D as a numerical technique in the modelling field is a vital tool for investigating the realistic soil behaviour under different conditions

and is helpful in simulating all construction sequences concerning the provided design parameters.

ACKNOWLEDGEMENTS

Thanks are also to Japan International Cooperation Agency (JICA) for giving the postgraduate scholarship to the first author

REFERENCES

- [1] Poulos, HG 1971, The behaviour of laterally loaded piles: I- single piles. *Journal of Solid Mechanics, Foundation Division, ASCE*, 97, 711-731.
- [2] Brown, DA, Shie, C & Kumar, M 1989, P-y curves for laterally loaded piles derived from three-dimensional finite element model, *Numerical Models in Geomechanics, NUMOG III*, 683-690 Elsevier Applied Science.
- [3] Cox, W & Reese, L 1978, Pullout Tests of Grouted Piles in Stiff Clay. *Journal of Petroleum Technology*, 30(03), pp.349-356.
- [4] Duncan, JM, Jr. Evans, LT & P. S. K.Ooi 1994, Lateral Load Analysis of Single Piles and Drilled Shafts, *Journal of Geotechnical Engineering ASCE*, Vol. 120, No. 5, pp.1018- 33.
- [5] Broms, B 1964 The lateral resistance of piles in cohesionless soils. *J Soil Mech Found Div, ASCE* 90(SM3):123-156
- [6] Klepikov, S 1965, Calculation of beams on an elastic foundation with a variable modulus of subgrade reaction. *Soil Mechanics and Foundation Engineering*, 2(5), pp.296-299.
- [7] Caseiro, C 1986, Behavior of Elastomeric Materials Under Dynamic Loads -- IV. *The Shock and Vibration Digest*, 18(1), pp.3-6.
- [8] O'Neill, MW, Blaney, GG & Muster, GL 1982, Behavior of Single Pile and Pile Group in Overconsolidated Clay Under Relatively Low-Frequency Loading, *Fugro-Gulf, Inc., and Univ. of Houston-University Park*.
- [9] Cundall, PA 1976, Explicit Finite Difference Methods in Geomechanics, in *Numerical Methods in Engineering, Proceedings of the EF Conference on Numerical Methods in Geomechanics, Blacksburg, Virginia, Vol. 1*, pp. 132-150.
- [10] Britto, AM, & Gunn, MJ 1987, *Critical State Soil Mechanics via Finite Elements*. Chichester U.K.: Ellis Horwood Ltd.
- [11] Banerjee, PK, and Davis, TG 1978. The behaviour of axially and laterally loaded single piles embedded in non-homogeneous soils, *Geotechnique*, 28, No. 3, 309-326.
- [12] Trochanis, AM, Bielak, J & Christiano, P 1991, Three-dimensional nonlinear study of piles. *Journal of Geotechnical Engineering, ASCE*, 117, 429-447.

EXTRACTION OF STATIC FEEDBACK COEFFICIENT FOR SPICE MODEL OF DRAIN INDUCED BARRIER LOWERING IN JUNCTIONLESS DOUBLE GATE MOSFET

Hakkee Jung¹

¹Department of Electronic Engineering, Kunsan National University, South Korea

ABSTRACT

A SPICE model of Drain Induced Barrier Lowering (DIBL) has been proposed for a Junctionless Double Gate (JLDG) MOSFET. For this purpose, the potential distribution in the channel is obtained using the Poisson equation, and the threshold voltage is determined by the third derivative (TD) method. The DIBL should be expressed as a function of silicon thickness as well as channel length and oxide thickness due to the effect of silicon thickness on carrier transport in a nanostructure JLDG MOSFET, even though it is only defined by channel length and oxide thickness in SPICE model of conventional MOSFET. As a result, it is found that the DIBL is proportional to the power of -3 for the channel length, 2 for the silicon thickness, and 1 for the oxide thickness, where the proportional constant is 22.0. It is observed that the SPICE parameter, the static feedback coefficient, is reasonably between 0.2 and 0.9. The DIBLs obtained by using the threshold voltage model published in other papers show a good agreement with those of this model regardless of the channel length at 20 nm or more, but the DIBLs of the other models are different at the sub-20 nm channel lengths from one another. The DIBL model proposed in this paper is consistent with results of other models in all range of channel length.

Keywords: Junctionless cylindrical surrounding, Threshold voltage, DIBL, Static feedback coefficient

INTRODUCTION

The conventional MOSFET structure is no longer usable due to the short channel effect in the structure below 20 nm. In particular, it is necessary to improve the ON/OFF current ratio due to the increase of the power consumption by the increase of the parasitic current, and it is required to improve the control ability of the carriers in the channel by the gate voltage. In addition, the variation of the doping concentration between the source/drain region and the channel shows the limit of the conventional MOSFET process while the channel length is decreased [1]. To solve this problem, the transistor structure of a Junctionless Double Gate (JLDG) MOSFET is developed. The JLDG MOSFET has advantages of simplifying the process because it has no junctions between source/drain and channel, and it can use the existing MOSFET process as well as reducing the process cost. Therefore, transport model and process development for a JLDG MOSFET as well as junctionless structure FET such as Junctionless Cylindrical Surrounding Gate (JLCSG) MOSFET are under study [2]-[4]. Especially, it is necessary to develop a model for SPICE simulation because it has reached the stage of analyzing characteristics in circuit configuration using a JLDG MOSFET [5]. Therefore, in this paper, we propose SPICE-used model of Drain Induced Barrier Lowering (DIBL) σ_D , induced by threshold voltage in JLDG MOSFET, as known as the short channel

effect. The threshold voltage will be derived from the transfer characteristics between the drain current and the gate voltage by the third derivative (TD) method that has already been verified [6].

The SPICE model σ_D of the DIBL for a Junction Based Double Gate (JBDG) MOSFET has been proposed [7]. In the case of JLDG MOSFETs, the channel shows a fully depleted state in the subthreshold voltage, and is partially depleted at the threshold voltage, indicating the on-state characteristic as the current flows into the partially formed neutral region [8]. When the voltage further increases to reach a flat voltage, the entire channel becomes a neutral state and enters the accumulation state. In the conventional MOSFET, the current amount is determined by the amount of charge formed in the inversion layer. The inversion layer thickness has more influence on the current amount than the silicon thickness in the case of the conventional MOSFET, but the amount of current for the JLDG MOSFET will be determined, depending on the oxide film thickness and silicon thickness as well as channel length. Therefore, in this paper, σ_D will be expressed mathematically after observing the change of DIBL according to channel length, silicon thickness, and oxide thickness. The model will be set so that the static feedback coefficient, which is a SPICE parameter of σ_D , has a reasonable value. Raksharam et al. described the change in the threshold voltage for a JLDG MOSFET with a channel length of 22 nm as an analytical model [9].

Jiang et al. defined the threshold voltage using the potential distribution of the series form and expressed analytically the change of threshold voltage due to drain voltage [10]. In addition, Lin et al. obtained the potential distribution by solving the one-dimensional Poisson equation and the two-dimensional Laplace equation, and calculated the threshold voltages for JLDG MOSFETs with channel lengths of 20 nm or more [11]. We will verify the validity of the proposed model by comparing the DIBL values derived from the threshold voltage model obtained from other papers with those procured from the model presented in this paper.

In Section 2, we will explain the DIBL derivation process using the analytical potential distribution and current-voltage characteristics of JLDG MOSFETs. In Section 3, we will present the SPICE-used model by analyzing the obtained DIBL according to the channel structure. Conclusions are given in Section 4.

DIBL OF JLDG MOSFET

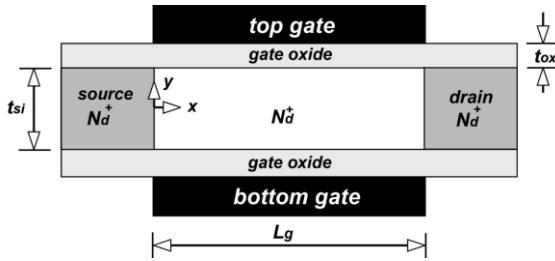


Fig. 1 Schematic cross sectional diagram of Junctionless Double Gate (JLDG) MOSFET

Figure 1 shows the cross sectional view of JLDG MOSFET. As shown in Fig. 1, the JLDG MOSFET is a junctionless structure with the same doping type and concentration for source/drain and channel. In this study, $N_D = 10^{19}/\text{cm}^3$ is used. Most of the carriers in the symmetrical structure will be transmitted through the center of the channel, and the potential distribution is obtained using the following Poisson equation when the channel length changes from 10 nm to 50 nm, the silicon thickness from 5 nm to 10 nm, and the oxide thickness from 1 nm to 4 nm.

$$\frac{\partial^2 \phi}{\partial x^2} + \frac{\partial^2 \phi}{\partial y^2} = -\frac{qN_d}{\epsilon_{si}} \quad (1)$$

In the case of JLDG MOSFET, as shown in Jiang et al.'s method, the potential distribution can be obtained as follows [10].

$$\phi(x, y) = V_{ref} + \frac{V_{ds}}{L_g} x + \sqrt{\frac{2}{L_g}} \sum_{n=1}^{\infty} \left[2C_n \cosh(k_n y) - \frac{f_n}{k_n^2} \right] \sin\left(\frac{n\pi}{L_g} x\right) \quad (2)$$

$$C_n = \frac{1}{2\alpha_n} \left[\frac{f_n}{k_n^2} + \sqrt{\frac{2}{L_g}} \frac{(-1)^{-n}}{k_n} (V_{ds} + V_{FB} - V_{gs}) - \sqrt{\frac{2}{L_g}} \frac{1}{k_n} (V_{FB} - V_{gs}) \right]$$

$$f_n = -\frac{qN_d}{\epsilon_{si}k_n} \sqrt{\frac{2}{L_g}} [1 - (-1)^n], \quad k_n = \frac{n\pi}{L_g}$$

$$\alpha_n = t_{ox} \frac{\epsilon_{si}}{\epsilon_{ox}} k_n \sinh\left(\frac{t_{si}k_n}{2}\right) + \cosh\left(\frac{t_{si}k_n}{2}\right)$$

where V_{ref} is the reference potential, V_{ds} is the drain voltage, and ϵ_{si} is the dielectric constant of silicon. In this study, we used the results calculated up to $n = 30$. The relationship between the drain current and the gate voltage is derived using the potential distribution in Eq. (2) and the following diffusion-drift current equation.

$$I_d = \frac{qn_i\mu_n W kT \{1 - \exp(-\frac{qV_{ds}}{kT})\}}{\int_0^{L_g} \frac{1}{\int_{-\frac{t_{si}}{2}}^{\frac{t_{si}}{2}} \exp(\frac{q\phi(x,y)}{kT}) dy} dx} \quad (3)$$

where W is the channel width, n_i is the intrinsic semiconductor concentration of silicon, μ_n is the mobility, k is the Boltzmann constant and T is the absolute temperature. Since the validity of Eq. (3) is described in the previous paper [12], the relationship between drain current and gate voltage obtained using Eq. (3) is used to obtain the threshold voltages. Figure 2(a) shows the relationship between drain current and gate voltage obtained in this study. We used the TD method proposed by Wong et al. [6] to extract the threshold voltage. As shown in Fig. 2(b), the

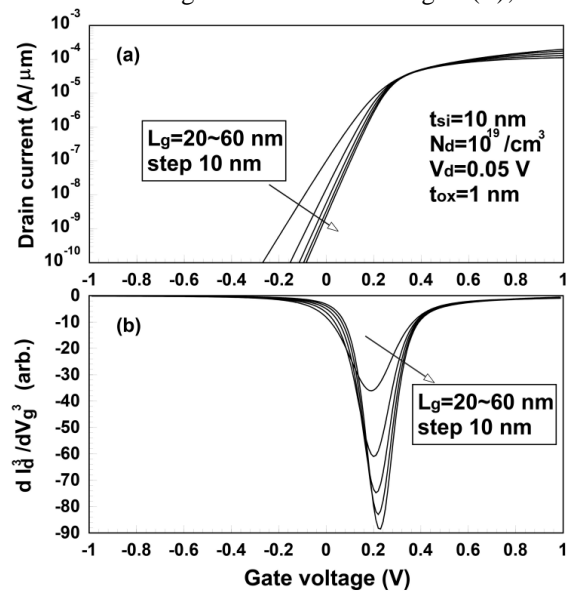


Fig. 2. (a) Transfer characteristics for drain current vs. gate voltage with channel length as a parameter, and (b) the threshold voltage extraction method by third

derivatives for transfer characteristics of (a). threshold voltage is extracted as the minimum of the third-order differential coefficient obtained by using the current-voltage relationship in Fig. 2(a) because the TD method can be used efficiently in determining the threshold voltage including the physical meaning.

As shown in Fig. 2(b), the gate voltage corresponding to the inflection point of the curve is defined as the threshold voltage, and the DIBL is obtained using the following Eq. (4).

$$\sigma_D = \frac{[V_{th}(V_{ds}=0.05\text{ V}) - V_{th}(V_{ds}=0.55\text{ V})]}{0.5} \quad (4)$$

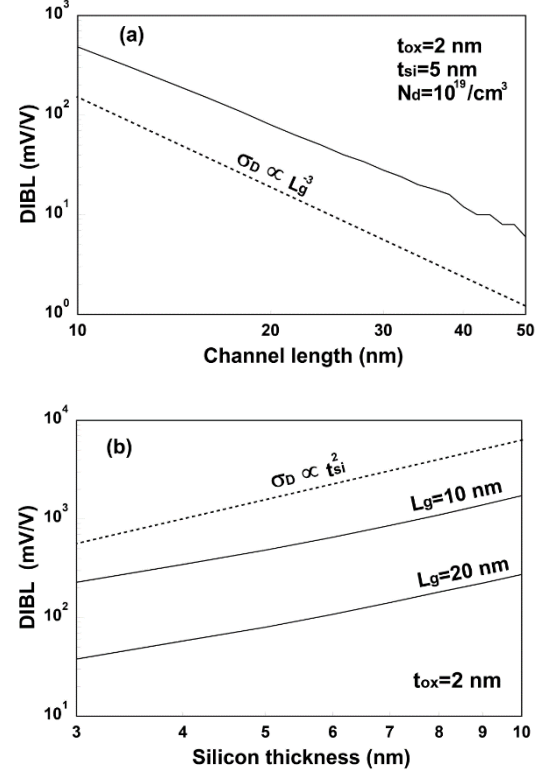
In general, DIBL is varied according to the channel size and oxide thickness, and DIBL model σ_D in SPICE is expressed using these variables and the static feedback coefficient β as a parameter. In the conventional MOSFET, the static feedback coefficient β is generally 0.7 [13]. In this paper, we propose SPICE model of DIBL which depends on channel size and oxide thickness with reasonable static feedback coefficient β for JLDG MOSFET. In the nanostructure JLDG MOSFET, unlike the conventional MOSFET, the size of the channel must be involved in obtaining DIBLs because the entire channel affects current flow when JLDG MOSFET changes from a fully depleted state to a partially depleted state. That is, not only the channel length but also the silicon thickness will affect the carrier transmission. It is known that the σ_D is proportional to L_g^{-3} for the channel length in the conventional MOSFET [13]. In addition, the σ_D is proportional to the square of silicon thickness for a nanostructure junction-based double gate MOSFET [7]. Therefore, in this paper we will derive the σ_D of JLDG MOSFET including all of the above mentioned variables.

SPICE DIBL MODEL FOR JLDG MOSFET

In this paper, we use Eq. (4) to find the DIBL from threshold voltage at the drain voltage of 0.05 V and 0.55 V, and present the SPICE-used DIBL model by observing the change of DIBL, with respect to channel length, silicon thickness and oxide thickness.

Figures 3(a), 3(b), and 3(c) show the variation of DIBLs with respect to channel length, silicon thickness, and oxide thickness, respectively. As shown in Fig. 3(a), the relation of $\sigma_D \propto L_g^{-3}$ is indicated by a dotted line to observe whether DIBL is proportional to L_g^{-3} . Figures 3(a) and (b) use a logarithm-logarithmic graphs. In these graph, it is easy to grasp the multiplier by using the slope of the straight line since the relationship appears as a straight line. As shown in Fig. 3(a), the σ_D for the channel length is proportional to the power of -3 as in

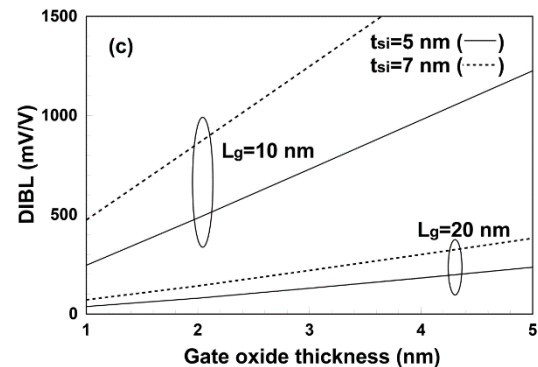
the conventional MOSFET. Figure 3(b) shows the



change in DIBL with respect to the silicon thickness,

Fig. 3 (a) DIBLs for channel length of JLDG MOSFET. Dotted line denotes proportional line for power of -3 for channel length, (b) DIBLs for silicon thickness of JLDG MOSFET with channel length as a parameter. The dotted line denotes proportional line for power of 2 for silicon thickness, and (c) DIBLs for gate oxide thickness of JLDG MOSFET with channel length as a parameter for silicon thickness of 5 and 7 nm. We know DIBLs are proportional for power of 1 for gate oxide thickness.

with the relation of $\sigma_D \propto t_{si}^2$ denoted as a dotted line, and the σ_D shows good agreement with the proportional relation to the power of 2 for silicon thickness. As shown in Fig. 3 (b), the inclination is the same when the channel length is 10 nm and 20 nm. Finally, in order to observe the relationship between oxide thickness and DIBL, the relationship between DIBL and oxide thickness is shown in Fig. 3



(c) when the silicon thickness is 5 nm and 7 nm with the channel length as a parameter. Note that the linear scale for x and y axis is used in Fig. 3 (c), unlike Figs. 3(a) and (b). As shown in Fig. 3(c), the relations between DIBL and oxide film thickness are linear regardless of channel length and silicon thickness although the slope is different. It will be inversely proportional to the gate oxide capacitance since it is linear to the oxide thickness. That is, the influence of the gate voltage on the carrier transmission in the channel will be further blocked when gate oxide capacitance increases; as a result, the carrier transmission control ability of the gate voltage will be weakened. The threshold voltage will be less affected and the DIBL will also decrease as the oxide film thickness decreases. Therefore, it is reasonable to assume that the σ_D representing DIBL in Eq. (4) is linearly proportional to t_{ox} . As a result, the σ_D can be expressed as a function of the following channel size and oxide thickness.

$$\sigma_D = A\eta L_g^{-3} t_{si}^2 t_{ox} \quad (5)$$

In the case of the JLDG MOSFET of Eq. (5), the SPICE-used DIBL model, which can be expressed by only the channel size and the oxide thickness, is derived by setting the A value to have the static feedback coefficient η of between 0 and 1 that is SPICE parameter of σ_D . First, the value of $A\eta$ in Eq. (5) is obtained in the range of $10 \text{ nm} \leq L_g \leq 50 \text{ nm}$, $5 \text{ nm} \leq t_{si} \leq 10 \text{ nm}$, $1 \text{ nm} \leq t_{ox} \leq 4 \text{ nm}$, and the maximum value of $A\eta$ is set as A to sustain the static feedback coefficient η between 0 and 1. The value of A thus obtained is 22.0. Therefore, the SPICE-used DIBL model of the JLDG MOSFET can be obtained as follows.

$$\sigma_D = 22.0\eta L_g^{-3} t_{si}^2 t_{ox}. \quad (6)$$

Figure 4 shows the static feedback coefficient η obtained using Eq. (6) from the range of the channel size and the oxide thickness as mentioned in the previous paragraph. As can be seen in Fig. 4, the values of η is ranged from 0.2 to 1.0. As the channel length increases, the variation rate of η increases. Especially, the variation of the static feedback coefficient η increases as the oxide thickness and silicon thickness increases. Note that it is small enough that the η varies between 0.4 and 0.8 as known in the results in Fig. 4 (a) with oxide film thicknesses down to 1 nm. From the above results, it can be concluded that Eq. (6) is a SPICE-used DIBL model which can fully express the DIBL phenomenon of JLDG MOSFET.

In order to verify the validity of Eq. (6) presented in this paper, the results of the comparison with the DIBL values obtained using the threshold voltage

model presented in other papers are shown in Fig. 5. Since the potential model used in this paper basically uses the model proposed by Jiang et al., it can be seen that the results are in good agreement with the results

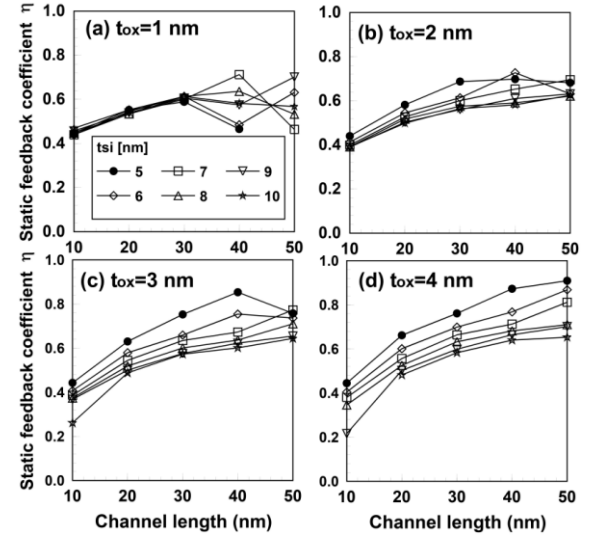


Fig. 4. Static feedback coefficients for JLDG MOSFET in the range of $10 \text{ nm} \leq L_g \leq 50 \text{ nm}$, $5 \text{ nm} \leq t_{si} \leq 10 \text{ nm}$, and (a) $t_{ox} = 1 \text{ nm}$, (b) $t_{ox} = 2 \text{ nm}$, (c) $t_{ox} = 3 \text{ nm}$, and (d) $t_{ox} = 4 \text{ nm}$.

of Jiang et al. except for the case of Fig. 5 (c) with the silicon thickness of 3 nm. The smaller the silicon thickness, the greater the difference between Jiang's model and this model. The reason for this is that Jiang et al. calculated the potential distribution using the series form and defined the threshold voltage model using only the first term. That is, the smaller the silicon thickness becomes, the larger the error increases as the channel length increases as shown in Fig. 5 (c). To clarify this point, Fig. 6 shows the variation of $1/\alpha_n$ which is used to calculate the threshold voltage in the model of Jiang et al.

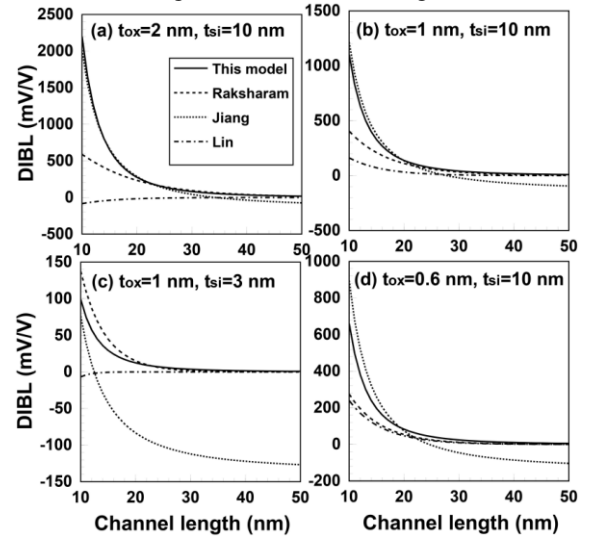


Fig. 5. Comparisons this model with various models for DIBL of JLDG MOSFET in the range of

$10 \text{ nm} \leq L_g \leq 50 \text{ nm}$, and (a) $t_{ox} = 2 \text{ nm}$, $t_{si} = 10 \text{ nm}$, (b) $t_{ox} = 1 \text{ nm}$, $t_{si} = 10 \text{ nm}$ (c) $t_{ox} = 1 \text{ nm}$, $t_{si} = 3 \text{ nm}$ and (d) $t_{ox} = 0.6 \text{ nm}$, $t_{si} = 10 \text{ nm}$.

As shown in Fig. 6, when n increases, the value of $1/\alpha_n$ sharply decreases, and the value of $1/\alpha_n$ decreases more sharply with increasing silicon thickness and smaller channel length. If the silicon thickness is small and the channel length is large, it can be seen that the approximation of $n = 1$ in Eq. (2) is not valid.

It is clear that Jiang's model shows a big difference from other models as the channel length increases in Fig. 5 (c) due to this reason. Compared with Lin's model, results of Lin's model show good agreement with those of other models only when the oxide thickness is very small (0.6 nm). In addition, Lin et al. calculated for the channel length over 20 nm and found that results agree well with other models in this range. There is a large difference from other models when the thickness of the oxide film is increased at a channel length of 20 nm or less. Even though Raksharam's model uses a different potential distribution model than the one proposed in this study, it is observed that their results are in good agreement to these results when the silicon thickness and the oxide thickness are small as shown in Fig. 5 (c). The results are well matched regardless of the model in the range of the channel length of 20 nm or more, but note the differences of DIBL models are more significant in case that the channel length is 20 nm or less.

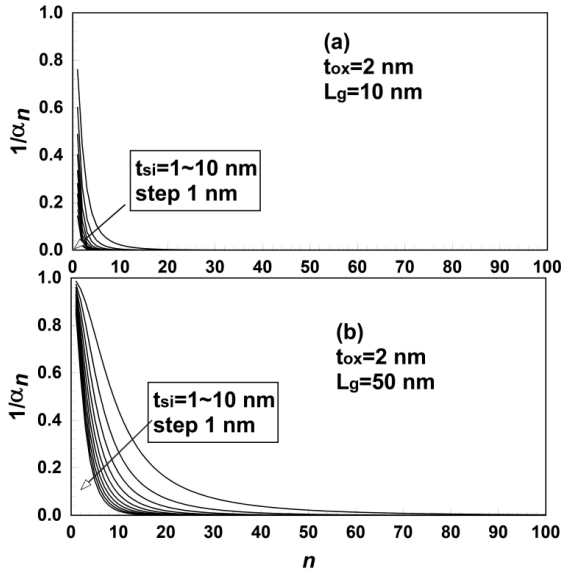


Fig. 6. Deviations of $1/\alpha_n$ for higher order terms in Jiang et al.'s potential model in the range of (a) $t_{ox} = 2 \text{ nm}$, $L_g = 10 \text{ nm}$, and (b) $t_{ox} = 2 \text{ nm}$, $L_g = 50 \text{ nm}$.

CONCLUSION

In this paper, a SPICE-used DIBL model for a JLDG MOSFET has been presented. Since the parameters of the SPICE-used DIBL model are static feedback coefficients, the model equations are constructed to represent the reasonable range in the SPICE simulation. For this purpose, the threshold voltage was derived by the TD method in the relation between drain current and gate voltage to obtain using the potential distribution of the series form derived from the Poisson equation. The validity of the DIBL obtained using this threshold voltage was verified by comparing it with other papers. As a result, it was found that the σ_D representing DIBL is proportional to the channel length by the power of -3, the silicon thickness by 2, and the oxide thickness by 1 where the proportional constant A is 22.0. In this case, the static feedback coefficient η , SPICE parameter, is found in the range of $10 \text{ nm} \leq L_g \leq 50 \text{ nm}$, $5 \text{ nm} \leq t_{si} \leq 10 \text{ nm}$, and $1 \text{ nm} \leq t_{ox} \leq 4 \text{ nm}$, and is in the range of $0.2 \leq \eta \leq 0.9$. The variation of the static feedback coefficient η decreased with decrease in the oxide and silicon thickness. Especially, the static feedback coefficient η was nearly constant regardless of the silicon thickness when the oxide thickness was 1 nm and the channel length was below 30 nm. These results will be useful for circuit simulation using JLDG MOSFET.

REFERENCES

- [1] Chen Z., Xiao Y., Tang M., Xiong Y., Huang J., Li J., Gu X., and Zhou Y., Surface-Potential-Based Drain Current Model for Long-Channel Junctionless Double-Gate MOSFETs, IEEE Trans. on Electron Devices, Vol. 59, Issue 12, 2012, pp.3292-3298.
- [2] Pradhan K. P., Kumar M. R., Mohapatra S. K., and P. K. Sahu, Analytical modeling of threshold voltage for Cylindrical Gate All Around (CGAA) MOSFET using center potential, Ain Shams Engineering Journal, Vol. 6, Issue 4, 2015, pp. 1171-1177.
- [3] Hu G., Xiang P., Ding Z., Liu R., Wang L., and Tang T. A., Analytical Models for Electrical Potential, Threshold Voltage, and Subthreshold Swing of Junctionless Surrounding-Gate Transistors, IEEE Trans. on Electron Devices, Vol. 61, Issue 3, 2014, pp.688-695.
- [4] Trivedi N., Kumar M., Halder S., Deswal S., Gupta M., and Gupta R. S., Analytical modeling of Junctionless Accumulation Mode Cylindrical Surrounding Gate MOSFET (JAM-CSG), International Journal of Numerical Modeling, Vol.29, Issue 6, 2016, pp. 1036-1043.
- [5] Baidya A., Lenka T. R., and Baishya S., Mixed-mode simulation and analysis of 3D double gate junctionless nanowire transistor for CMOS circuit applications, Superlattices and Microstructures,

- Vol. 100, 2016, pp.14-23.
- [6] Wong J. S., Ma J. G., Yeo K. S., and Do M. A., A New Approach for the Extraction of Threshold Voltage for MOSFET's, Technical Proceedings of the 2001 International Conference on Modeling and Simulation of Microsystems, (North Carolina, NC, 2001) p. 534-537.
 - [7] Jung H. K., Drain Induced Barrier Lowering(DIBL) SPICE Model for Sub-10 nm Low Doped Double Gate MOSFET, Journal of the Korea Institute of Information and Communication Engineering, Vol. 21, Issue 8, 2017, pp. 1465-1473.
 - [8] Colinge J. P., Kranti A., Yan R., Lee C. W., Ferain I., Yu R., Akhavan N. D., and Razavi P., Junctionless Nanowire Transistor (JNT): Properties and design guidelines, Solid-State Electronics, Vol. 65-66, 2011, pp. 33-37.
 - [9] Raksharam, and Dutta A. K., A unified analytical drain current model for Double-Gate junctionless Field-Effect Transistors including short channel effects, Solid-State Electronics, Vol. 130, 2017, pp. 33-40.
 - [10] Jiang C., Liang R., Wang J., and Xu J., A two-dimensional analytical model for short channel junctionless double-gate MOSFETs, AIP ADVANCES, Vol. 5, Issue 5, 2015, pp.057122-1-13.
 - [11] Lin Z., Lin H., Liu K., and Huang T., Analytical Model of Subthreshold Current and Threshold Voltage for Fully Depleted Double-Gated Junctionless Transistor, Japanese Journal of Applied Physics, Vol. 51, Issue 2S, 2012, pp. 02BC14-1-7.
 - [12] Jin X., Liu X., Wu M., Chuai R., Lee J., and Lee J., Modelling of the nanoscale channel length effect on the subthreshold characteristics of junctionless field-effect transistors with a symmetric double-gate structure, J. Phys. D: Appl. Phys., Vol. 45, Issue 37, 2012, pp. 375102-1-5.
 - [13] Dimitrijević S., Principles of Semiconductor Devices, 2nd ed. New York, NY: Oxford University Press, 2012, p.453.

PERFORMANCE EVALUATION OF PARTIALLY PRESTRESSED CONCRETE BEAMS UNDER LIMITED CYCLES OF REPEATEDLY APPLIED LOADING

Nazar K. Oukaili¹ and Mohammed M. Khattab²

¹Professor, University of Baghdad, Iraq; ²Ph.D. Candidate, University of Baghdad, Iraq

ABSTRACT

This paper involves results of the study undertaken on the partially prestressed concrete beams with bonded prestressing steel subjected to limited cycles of repeated loading. The flexural behavior of partially prestressed concrete beams has been investigated through an experimental program involving testing six full-scale simply supported beams with a clear span of (3000) mm. The goal of this study was to investigate the effect of limited repeated loading cycles on strength and serviceability (cracking and deformability) of partially prestressed concrete beams. Accordingly, these beams were divided into two identical sets. The first set consisted of three beams, one of tension-controlled, the second of transition-controlled, and the last one is compression-controlled. These beams are tested under static loading and considered as controlled beams. They were subjected to four-point bending by using two symmetrical concentrated static loads up to destruction. The loads were applied at the middle third of the clear span length. The second set consisted of exactly the same three beams as in set one but they were subjected to ten cycles of repeated load. The range of repeated load was between "0.4 to 0.6" of ultimate load produced from the static test. After the ten cycles, the load was released and then the beams were subjected to monotonic static test until failure. Readings were made for strains in nonprestressed and prestressed steel, midspan deflections, crack widths and crack spacing at different loading increments. Findings show that partially prestressed compression-controlled beams were less sensitive to the repeated loading.

Keywords: Partial Prestressing, Bonded, Flexure, Deflection, Cracking, Repeated Load, Concrete Beams.

INTRODUCTION

Civil engineering structures may be exposed to different types of loads and among these loads is the repeated loading. The nature of loads that are exposed to bridges, offshore and multistory car parking are in fact repeated loading. Extensive theoretical and experimental studies of prestressed concrete beams over so many years have led to very well established methods for strength and serviceability design under static loads. However, the influence of repeated loading on deformability and cracking of prestressed concrete beams are still limited and rarely understood. Moreover, having clear understanding and reasonable interpretation of the basics of deformability and cracking of concrete beams under different types of loading will improve the serviceability design and help handling any difficult situation, particularly if not addressed by available codes and standards. For that research on serviceability of concrete structures under repeated loading has become more essential in the last years. Concrete structures subjected to repeated loading experience higher deflection comparing to those exposed to static loading. These deflections were including significant permanent sets. With the increasing of the number of load cycles, the permanent deflections are also increased. This phenomenon has been observed by several

researchers [1] – [5], however, suitable experimental information is still poor. The objective of the current research is to examine the influence of limited number of repeated load cycles on the flexural characteristics of partially prestressed concrete beams with bonded strands.

EXPERIMENTAL PROGRAM

The experimental program involves testing six full-scale simply supported beams with overall dimensions of (200x300x3300) mm, which were divided into two groups. The first group consisted of three beams, PP-B-TC-S, PP-B-TRC-S, and PP-B-CC-S. According to ACI code [6], these specimens were tension-controlled, transition-controlled and compression-controlled, respectively. Beams of the first group (I) were tested under monotonic static loading to collapse and regarded as controlled beams. The static loading was applied with increments ranged approximately between 2.5% to 5% of the predicted ultimate load. The deflection readings at midspan section were monitored by mechanical dial gauge at the end of each increment. The time consuming for testing one beam under static loading on average is between four to six hours depending on the load capacity of tested beam.

The second group (II) is consisted of three beams, also, which identical to the beams of the first group

but they were subjected to repeat loading as follows:

- Stage one: the minimum and maximum cyclic loads P_{min} and P_{max} were taken, respectively, as 40% and 60% of the ultimate load of the accompanying beams of group (I). The repeated static load was applied by increments each equals to 5% of static ultimate load until reaching P_{max} and then unloaded to P_{min} by the same increments. Ten cycles of loading and unloading were implemented. The deflections, crack widths, crack spacing, crack numbers, and strand slip were recorded for each loading increment.
- Stage two: after ten cycles of loading, the load was released to zero. The residual deflections, crack width and strand slip were investigated.
- Stage three: in this stage, the beams were subjected to monotonic static loading until failure with increment equal to approximately 5% of the ultimate load of the accompanying beams of group (I). During the third stage, the same measurements (deflections, crack width, number of cracks, distance between cracks and strand slip) were taken for each load increments. The whole repeated load test took on average between 10 to 14 hours.

For the six rectangular pretensioned beams, the reference concrete mix was designed to achieve the target compressive strength of 40 MPa at 28 days for (150x300) mm cylinder specimen. Concrete proportions by weight, cement: sand: gravel, were 1: 1.5: 2 with a maximum aggregate size of 9.5 mm and water cement ratio by weight of 0.40. The beams were designed in such a way that the expected failure should occur due to flexure rather than shear; therefore, steel stirrups of $\emptyset 10$ mm @ 100 mm c/c were used in shear spans. The steel stirrups were tied to two longitudinal bars of (10 mm) diameter at the top and to different number of bars at the bottom depending on whether the beam is tension-controlled, transition or compression-controlled. In all prestressed concrete beams, two low-relaxation seven wires strands were used with target initial prestress f_{pi} of 70% of the steel ultimate strength f_{pu} . Yield stress of the longitudinal and the transverse mild steel bars was (570 MPa) and the characteristics strength of prestressed low-relaxation strand was (1862 MPa). Table 1 illustrates the PPR value and the nonprestressing tensile steel of each tested beams. Figure 1 shows the reinforcement details of each tested beam.

Two variables were investigated in this study, they are:

- Type of test (monotonic static and repeated loading)
- Partial Prestressing Ratio (PPR) which defined as the ratio of ultimate resisting moment due to prestressing steel to the ultimate resisting moment due to the total tensile steel [7].

All beams were loaded in four-point bending using two symmetrical concentrated static loads applied at the middle-third of span length. All the measurements, such as midspan beam deflection, crack width and strand slip was recorded twice, immediately after the application of the load and 10 minutes later.

Deflection was measured at midspan of the beam using dial gauge of (0.01) mm accuracy. The cracks along the beams, the maximum crack width, average crack spacing and number of cracks were measured during loading, sequentially. Strain in both types of steel (prestressed and nonprestressed) was recorded starting from stress transfer passing through load test until failure by using two electrical strain gauges fixed on each reinforcing bar.

Table 1 Details of experimental beams

First group	PP-B-TC-S	PP-B-TRC-S	PP-B-CC-S
Second group	PP-B-TC-R	PP-B-TRC-R	PP-B-CC-R
PPR	0.771	0.529	0.358
Mild steel in tension zone	2- $\emptyset 10$	2- $\emptyset 10$ + 2- $\emptyset 12$	6- $\emptyset 12$

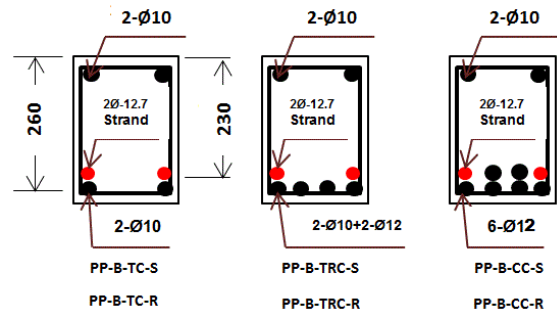


Fig. 1 Reinforcement details of experimental beams.

EXPERIMENTAL RESULTS

All beams in this study showed no fracture of steel or bond slip between concrete and any type of reinforcement (prestressed and nonprestressed). The failure was due to yielding of steel followed by crushing of concrete at compression zone for tension-controlled beams or by crushing of concrete for compression-controlled beams.

Load - Deflection Response

The load deflection curves for the tested beams are shown in (Fig. 2). Each two curves for identical beams were depicted together (one for the specimen under monotonic static loading and the other for the

specimen which exposed to ten cycles of repeated loading) to simplify comparison process. Also, the ten load cycles behavior was magnified for more clarity.

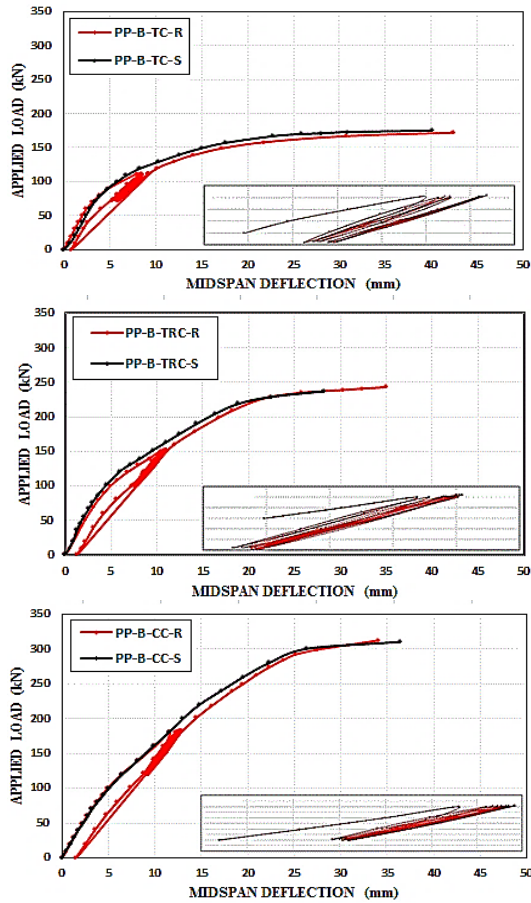


Fig. 2 Load-deflection curves for the tested beams.

Inspecting these diagrams, the following observations may be recorded:

- In monotonic static test, tension-controlled and transition-controlled concrete beams, three distinctive points could be observed. These points are characterized by cracking, yielding and ultimate loads. Compression-controlled concrete beams are characterized by two points only which are the cracking and ultimate loads. Thus, clear yielding point cannot be distinguished.
- Prior to cracking all beams deformed elastically. After cracking, beams with low (PPR) developed approximately a linear load-deflection response.
- All beams experienced decreasing of stiffness after cracking, depending on the level of (PPR). Increasing the area of tension reinforcement produced stiffer beam which led to low rate of deflection progress versus the applied load.
- For tension-controlled and transition-controlled beams, almost nonprestressed steel in tension zone yielded prior to prestressed steel due to the far

geometrical location of this steel relative to the member neutral axis.

- Beams with low amount of nonprestressed steel (high level of PPR) exhibited more ductile behavior by their flatter and longer load deflection curve.
- After ten cycles of repeated loading, when the load is decreased gradually to zero, all the beams suffered from permanent deflection. For specimen PP-B-TC-R which has high PPR, the permanent deflection was minimum (0.85 mm) and this may attributed to the fact that, the high ratio of prestressing moment to the total nominal moment has considerable effect to decrease the permanent deflection to minimum value. Otherwise beam PP-B-CC-R which has high nonprestressing steel (low PPR), the permanent deflection after load release was the higher and it was 1.55 mm. It seems that the small ratio of prestressing moment to the total nominal moment has no ability to restrain the deformability of that beam.

Table 2 illustrates the load carrying capacities for both beam's groups.

It can be seen that the difference in load carrying capacity for the identical beams are very small in both tests. The maximum difference was about 5% only. It can be seen also that both values of ultimate load in both tests are very close to the theoretical value [8].

Table 2 Theoretical and experimental load carrying capacities

Beam's labeling	$P_{theor,S}$ (kN)	$P_{exp,S}$ (kN)	$P_{exp,R}$ (kN)	$\frac{P_{exp,S}}{P_{exp,R}}$
PP-B-TC-S,R	172	182	177	1.03
PP-B-TRC-S,R	213	230	243	0.95
PP-B-CC-S,R	209	310	312	0.99

Note: $P_{theo,S}$ = theoretical ultimate load due to monotonic static loading [8]; $P_{exp,S}$ = ultimate load produced from monotonic static test; $P_{exp,R}$ = ultimate load produced from repeated static test.

Figure 3 characterizes midspan deflection at maximum service load stage ($0.6 P_u$) versus number of load cycles for the three tested beams under repeated loading.

The diagram shows that the variation of deflection with respect to load cycles can be represented by the following regression logarithmic expression:

$$\Delta = \Delta_{st} + \alpha \ln(N) \quad (1)$$

where

Δ = midspan deflection due to repeated static

loading;

Δ_{st} = midspan deflection due to monotonic static loading immediately before the application of the repeated loading;

α = parameter depends on PPR value; and

N = number of cycles of repeated static loading.

The above mentioned expression can be regarded as a general equation because the number of beams which were tested under repeated loading in this study is not sufficient to get a satisfied value of α . It is required to test further beams with different PPR value to find a reliable value of the parameter α .

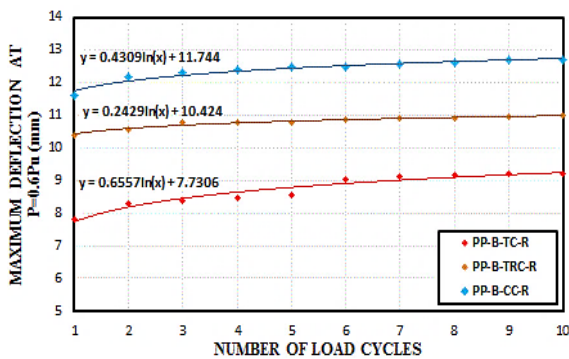


Fig. 3 Midspan deflection at the maximum load range ($0.6 P_u$) for each loading cycle.

Strain in Steel Reinforcement

The strain in both types of steel has been documented starting from the moment of initial prestressing passing through stress transfer, testing until failure. Two strain gauges were fixed at each strand as well as nonprestressing tensile steel. Table 3 shows prestressed and nonprestressed steel strain at different stages for the tested beam under repeated loading.

Analyzing Table 3, the following findings may be noticed:

- The difference in strain between the first and the tenth loading cycles was very small in prestressed steel. It was between 1% and 2.8%. While, the change was significant in nonprestressed steel, it was between 20% and 29%.
- The residual strain after ten cycles of repeated loading and load release to zero was very little in both types of steel. Actually, this strain is due to plastic deformation of concrete because neither prestressed steel nor nonprestressed steel reach yielding when they subjected to these cycles.
- At failure, all strands in the three tested beams under repeated loading reached yielding (the stress was beyond 90% of ultimate strength of prestressed steel).

Table 3 Progress of steel micro-strains during

loading

Beam's labeling	PP-B-TC-R	PP-B-TRC-R	PP-B-CCR
ε_{pe}	+6032	+6091	+5741
$\varepsilon_{ps(1)}$	+7014	+7272	+6677
$\varepsilon_{ps(10)}$	+7211	+7350	+6794
$\varepsilon_{ps(release)}$	+6189	+6209	+5897
ε_{ps}	+11299	+11128	+8783
f_{ps} , (MPa)	1786	1786	1683
ε_{se}	-786	-393	-236
$\varepsilon_{s(1)}$	+480	+624	+1412
$\varepsilon_{s(10)}$	+848	+746	+1735
$\varepsilon_{s(residual)}$	-327	-218	+227
ε_s	+3021	+3211	+2652
f_s , (MPa)	570	570	530

where: ε_{pe} =effective prestrain; $\varepsilon_{ps(1)}$, $\varepsilon_{ps(10)}$ = total strain in prestressed steel strain at the first and the tenth loading cycles, respectively; $\varepsilon_{ps(release)}$ = strain in prestressed steel at load release; ε_{ps} , f_{ps} prestressed steel total strain and stress at failure, respectively; ε_{se} = strain in nonprestressed steel at the beginning of test; $\varepsilon_{s(1)}$, $\varepsilon_{s(10)}$ = nonprestressed steel strain at the first and the tenth loading cycles, respectively; $\varepsilon_{s(residual)}$ = residual nonprestressed steel strain at load release; and ε_s , f_s nonprestressed steel total strain and stress at failure, respectively.

Crack Spacing and Crack Width

The evaluation of flexural crack width and distances between cracks and how to control their development becomes very essential. Studies in this area are very limited due to the various parameters affecting crack width. Primary cracks initiated when the applied load reaches the cracking load. As the applied loading increased, additional cracks will appear. The number of cracks will be stabilized if the stress in concrete does not exceed the tensile strength irrespective of loading increase. This condition produces the absolute minimum crack spacing which happens at high stress in steel. This is called "stabilized minimum crack spacing". The maximum crack spacing is twice the minimum and is called "stabilized maximum crack spacing". The stabilized mean crack is the mean value of the above two extremes [9].

Number of expressions was developed by researchers to expect stabilized mean crack spacing but the most reliable equation was anticipated by Nawy [9] which is as follows:

$$a_{cs} = k A_t / \sum o \quad (2)$$

where

a_{cs} = stabilized mean crack spacing;

$k = 1.2$ for pretensioned beams and 1.54 for posttensioned beams;

A_t = area of concrete surrounding the tensile reinforcement bars; and

$\sum o$ = sum of the reinforcement element's circumferences.

Recent studies on crack width control are supported on experimental studies. Based on these studies, some concluding points can be considered, mainly, using of deformed bars is minimizing the crack widths, the maximum crack width is proportional to reinforcement stress, the distribution of reinforcement over the concrete tension zone will minimize the flexural crack widths, and the crack width at the extreme tensile concrete fiber is proportional to the concrete cover.

Gergely and Lutz [10] suggested the following equation to determine crack width:

$$w_{cr} = 1.10276 \times 10^{-5} R_i \Delta f_s \sqrt[3]{d_c A_b} \quad (3)$$

where

R_i = ratio of distances from tension face and steel centroid to neutral axis;

Δf_s = net tensile stress in reinforcing steel;

d_c = thickness of concrete cover measured from center of bar closest to the concrete face to the tension concrete face; and

A_b = concrete area surrounding one bar, equal to total effective tension area of concrete surrounding reinforcement and having same centroid divided by number of bars.

Most cracks in all tested beams were propagated at the location of the middle third perpendicular to the longitudinal axis of the beam and extended to the tensile reinforcement. Mean crack spacing, crack width and number of cracks were monitored and measured throughout the test.

Figure 4 illustrates number of cracks versus load cycles at the maximum service load range of ($0.6 P_u$) for the beams tested under repeated loading.

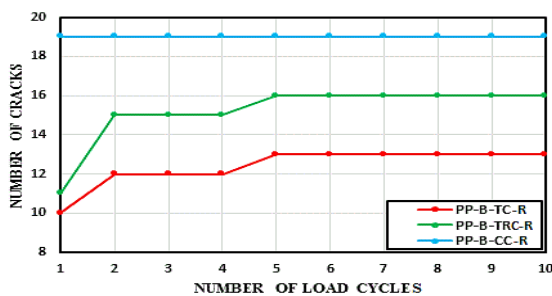


Fig. 4 Number of cracks versus number of load cycles at load level of ($0.6 P_u$).

These diagrams indicate that the number of

cracks is stabilized from the first load cycle for compression-controlled beam (PP-B-CC-R) while for the other beams; it is stabilized at the fifth loading cycle.

Table 4 illustrates experimental mean crack spacing for beams under monotonic static test and the value determined using Nawy's expression (Eq. (2)). Table 4 shows also mean crack spacing for beams subjected to repeated test at service load stage ($0.6 P_u$) for the first and the tenth loading cycles.

Since the number of cracks is increased for beams PP-B-TC-R and PP-B-TRC-R between the first and the tenth loading cycles, therefore, the mean crack spacing due to that is decreased as shown in Table 4. The crack spacing is decreased for beam PP-B-TRC-R but with a small difference in comparison to specimen PP-B-TC-R. Except for beam PP-B-TC-R, Nawy's equation gave a comparable crack spacing results with respect to the experimental results of static test.

Table 4 Mean crack spacing for tested beams

Beam's labeling	Monotonic static loading		Repeated static loading	
	Theor. a_{cs} , (mm)	Exp. a_{cs} , (mm)	Exp. a_{cs} , (mm)	
			at 1 st cycle	at 10 th cycle
PP-B-TC-S,R	185	110	140	115
PP-B-TRC-S,R	115	100	125	120
PP-B-CC-S,R	85	100	115	115

Table 5 shows crack width of the beams tested under static loading and the counterpart beams that were exposed to repeated loading. As in Table 4, the results are at service load stage ($0.6 P_u$) and for repeated test, the table shows crack width at the first and tenth loading cycles.

Table 5 Crack width at loading stage of ($0.6 P_u$)

Beam's labeling	Monotonic static loading		Repeated static loading	
	Theor. w_{cr} , (mm)	Exp. w_{cr} , (mm)	Exp. w_{cr} , (mm)	
			at 1 st cycle	at 10 th cycle
PP-B-TC-S,R	0.05	0.03	0.10	0.15
PP-B-TRC-S,R	0.10	0.17	0.15	0.15
PP-B-CC-S,R	0.15	0.12	0.10	0.10

From Table 5, the following observations may be reported:

- Crack width calculated using Gergely and Lutz expression, for specimens under monotonic static

loading, gave good agreements of results comparing to the experimental results.

- Only for beam PP-B-TC-R, the crack width is influenced by repeated loading. It is increased by about 50% during the ten loading cycles.

Figure 5 shows all the tested beams at failure. It can be observed that, the limited repeated loading has no significant effect on the number of cracks, cracks propagation and crack alignment. The figure shows also that, in compression-controlled beams the cracks were of flexural and flexural-shear types. On the other hand, in tension-controlled beams, the cracks were only of flexural type and they were approximately located at the pure bending moment zone (the middle third).

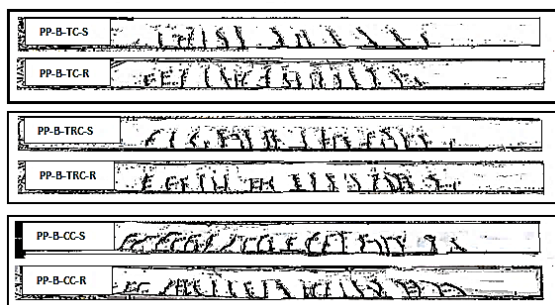


Figure 5 Crack propagation of tested beams.

CONCLUSIONS

The following conclusions can be drawn:

1. The ultimate load carrying capacities of partially prestressed concrete beams exposed to limited cycles of repeated loading was approximately the same as the capacities of accompanying beams under monotonic static loading.
2. The response of load-deflection curve under repeated loading can be represented by the envelope curve of monotonic static loading.
3. The increasing rate of deflection, crack width, and crack spacing was significant in the first five load cycles especially for tension-controlled beam.
4. All beams in this study showed no bond slip between concrete and any type of reinforcement. The failure was due to steel yielding followed by crushing of concrete at compression zone for tension-controlled beams or by crushing of concrete for compression-controlled beams.
5. Partially prestressed concrete beams with large area of nonprestressing tension reinforcement, (i.e., low level of PPR), were less sensitive to repeated loading.
6. Increasing the amount of nonprestressing steel enhanced the flexural characteristics and the ability of partially prestressed concrete beams to resist the effect of repeated loading.
7. The residual deflection depends on the value of PPR, as PPR increased the residual deflection

decreased. Accordingly, in beams with high nonprestressing steel (i.e., low level of PPR) the prestressing force has no ability to restrain the deformability of the beam in small range.

8. All strands in all the beams, attained yielding strength.

REFERENCES

- [1] Kulkarni, G., & Ng, S., Behavior of limited prestressed concrete beams under repeated loads, Canadian Journal of Civil Engineering, Vol. 6, Issue 4, 1979, pp. 544-556.
- [2] Naaman, A., Fatigue in partially prestressed beams, Fatigue of Concrete Structures, SP-75, American Concrete Institute, 1982, Farmington Hills, Michigan, pp. 25-46.
- [3] Wong, Y., the Deflection of Reinforced and Partially Prestressed Concrete Box Beams under Repeated Loading, Ph.D. Thesis, University of Wollongong, 1984.
- [4] Harajli, M., & Namman, A., Cracking in partially prestressed beams under static and cyclic fatigue loading, Cracking in Prestressed Concrete Structures, SP-113, American Concrete Institute, 1989, Farmington Hills, Michigan, pp. 29-54.
- [5] Harajli, M., Strengthening of concrete beams by external prestressing, PCI Journal, Vol. 38, Issue 6, 1993, pp. 76-88.
- [6] ACI 318M-2014, Building code requirements for structural concrete (ACI 318M-14) and commentary, ACI Committee 318, 2014, Farmington Hills, Michigan.
- [7] Harajli, M.H. and Naaman, A. E., Deformation and Cracking of Partially Prestressed Concrete Beams Under Static and Cycles Fatigue Loading, Report No. UMEE 84R1 Department of Civil Engineering, the University of Michigan, College of Engineering, 1984, pp. 21.
- [8] Oukaili, N. K. and Khattab, M. M., Cracking and Deformability of Bonded and Unbonded Prestressed Concrete Beams under Monotonic Static Loading, Third International Conference on Science, Engineering & Environment (SEE), USQ, Brisbane, Australia, Nov.13-16, 2017, ISBN: 978-4-9905958-9-0 C3051
- [9] Nawy, E. G., Prestressed Concrete: A Fundamental Approach, Prentice Hall, 5th Edition, 2009, pp. 198 - 20.
- [10] Gergely, P., and Lutz, L., Maximum Crack Width in Reinforced Concrete Flexural Members, Cracks, Mechanism, and Control of Cracking in Concrete, ACI Publication SP-20, pp.87-11, 1966.

THE EFFECT OF FGD GYPSUM AND BOTTOM ASH ADDITION IN SHOTCRETE MIXTURE

Pisut Rodvinij¹, Pitiwat Wattanachai¹ and Sattaya Chaiwithee¹

¹Faculty of Engineering, Chiang Mai University, Thailand

ABSTRACT

The slope in Mae Moh mine has been eroded when it is exposed to weather changes. Therefore, shotcrete was used for temporary protection of slope surfaces. In order to improve the efficiency and reduced cost of shotcrete, by-product materials from Mae Moh power plant is a good alternative to use in the mixture. This study focused on the influence of flue gas desulphurization (FGD) gypsum on the properties of shotcrete used bottom ash as fine aggregate. The mixture of mortar mixed with by-product materials was a combination of Portland cement type 1 and bottom ash is a ratio of 1:3. FGD gypsum added in the mixture 0-12% by weight of cement. Water to cement ratio for a mortar is 0.6. The results demonstrated the slump flow of mortar decreases with FGD gypsum increment. However, the initial setting time and final setting time of the shotcrete were longer with gypsum increment. The compressive strength of the samples contains FGD gypsum 4% can be developed the strength of approximately 8-20% of the samples without FGD gypsum. Moreover, the compressive strength and durability of mortar which contains gypsum at 4% could be able to give the highest strength. Nevertheless, the compressive strength and durability of mortar tend to decrease when the samples containing FGD gypsum exceed 4%. In conclusion, the development of the properties of shotcrete was the most efficient when adding 4% of FGD gypsum in the mixture.

Keywords: Shotcrete, FGD gypsum, Bottom ash, Compressive strength, Durability

INTRODUCTION

Mae Moh mine is the largest surface mine in Southeast Asia. Its annual production is approximately 15 million tons [1]. The overburden consists of claystone layer. Beneath claystone layer was lignite layer. To excavate lignite for generated the electricity, claystone must be mined out. Therefore, the surface of claystone slopes or claystone backfill might be exposed to weather change. The deterioration and erosion can occur on the surface of the slope and induced the reduction of the slope stability.

Pisut and Pitiwat [2] suggested that claystone deteriorated when it has been exposed to weather change. This can lead to slope stability problems. The failure of claystone slope can be induced many problems with mining activities. However, the protection of claystone from weather change can maintain the physical characteristics of claystone and the strength of claystone [2].

Therefore, shotcrete becomes the suitable stabilization method to stabilize the stability of slopes in Mae Moh mine. Shotcrete is often used for temporary protection of exposed rock surfaces that will deteriorate when exposed to the air. Moreover, shotcrete also used to permanently cover slopes or cut that may erode in time or otherwise deteriorate [3]. Application of shotcrete to the surface of landfills and other waste area is beneficial to prevent

surface water infiltration [4]. Shotcrete offers high work performance in larger areas. However, a lot of shotcretes might spray on the face of the slope. This induced a high cost for the slope stabilization.

Therefore, by-product materials from Mae Moh power plant is a good alternative to be used in the mixture of shotcrete to reduce the cost. By-product materials consist of fly ash, bottom ash, and FGD gypsum. Literature review demonstrated by-product materials from Mae Moh power plant is pozzolanic materials. The pozzolanic reaction can increase the strength of mortar in a long term. Moreover, by-product materials can be increased the efficiency of the fresh mortar [5].

This study focused on bottom ash used as fine aggregate and FGD gypsum used as an admixture in the mixture of shotcrete. The bottom ash particles were relatively large and very irregular, showing agglomeration of some spherical particles and other fragments with observable pores [6]. The replacement of sand by bottom ash in the mixture mortar can be reduced the unit weight approximately 20% due to the unit weight of bottom ash particles is less than sand [7], [8]. However, bottom ash used as fine aggregates in mortar can only reach 60%-70% the compressive strength of natural fine aggregates mortar [9].

SO₂ is one of the major environmental contaminations generated from coal-burning power stations. It is very important to develop flue gas

desulphurization (FGD) technologies to remove SO_2 for FGD clean coal combustion. Although FGD technology is successful in reducing SO_2 discharge, it generates a large quantity of FGD gypsum at the same time. Normally, FGD gypsum contains in mix proportion of mortar can be increased the flexural strength and compressive strength was higher than the mixture without FGD gypsum. Although the setting time was prolonged for the composition of FGD gypsum [10]. Moreover, FGD gypsum can be increased the durability of concrete from the sulfate attack [11]. However, the suitable amount of FGD gypsum contains in the mixture should be determined. This is due to the excessive amount of FGD gypsum in the mixture can decrease workability and the strength of mortar.

Therefore, the influence of FGD gypsum on the properties of shotcrete used bottom ash as a fine aggregate is an important determinant. The properties of shotcrete containing FGD gypsum should be passed the requirement of the properties of shotcrete for the slope stabilization. Thus, the test results can suggest the optimum content of FGD gypsum contain in the shotcrete mixture. The optimum FGD gypsum content is the most efficient to develop the properties of shotcrete.

MATERIALS PREPARATION AND MIX PROPORTION OF SHOTCRETE

This study focused on the wet mix shotcrete. Wet mix shotcrete is predominantly used because of its homogeneity in quality and high work efficiency [12]. The normal mixture proportion of shotcrete consists of sand used as fine aggregate, cement, and water. For the shotcrete mixed with by-product materials, the mixture proportion consists of bottom ash used as fine aggregate, cement, water and FGD gypsum used as an admixture. However, the fine aggregate should comply with the quality requirements of ASTM C 33 [4]. Particle size distribution of fine aggregate in this experiment was, according to Fig. 1. Ordinary Portland cement type 1 is used throughout the experiments. Bottom ash and FGD gypsum obtained from a Mae Moh power plant in Lampang province of Thailand.

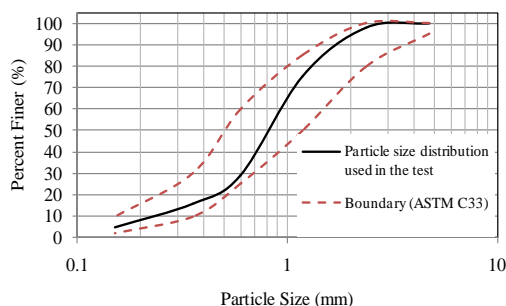


Fig. 1 Particle size distribution of fine aggregate.

The mixture of a normal mortar was a combination of Portland cement type 1 and natural sand is in a ratio of 1:3 by weight. However, the mixture of a mortar mixed with by-product materials was a combination of Portland cement type 1 and bottom ash is in a ratio of 1:3 by weight. FGD gypsum adds in the mixture 0-12% by weight of cement. Water to cement ratio for a normal mortar and a mortar mixed with by-product materials is 0.6. The mix proportion of shotcrete used in the experimental shown in Table 1.

Table 1 Mix proportion of shotcrete mortar

Mixture code	Cement	Sand	Bottom Ash	Water	FGD Gypsum (%)
M01	1	3	-	0.6	-
MB01	1	-	3	0.6	-
MB01G4	1	-	3	0.6	4
MB01G8	1	-	3	0.6	8
MB01G12	1	-	3	0.6	12

Note: The amount of FGD gypsum in the mixture is the percent by weight of cement.

THE EXPERIMENTAL PROGRAM

Shotcrete mortar mixed according to Table 1 were used in the test. Fresh properties and hardened properties of mortar were conducted on each experiment to measure the influence of FGD gypsum on the properties of shotcrete.

The fresh properties evaluation consists of the slump flow and setting time. The slump flow test is intended to be used to determine the flows of mortar, according to ASTM C1437 [13]. The setting time is intended to be used to determine the initial setting time of mortar according to ASTM C191 [14]. The hardened properties evaluation consists of the compressive strength and durability. The compressive strength test is intended to be used to determine the compressive strength of mortar according to ASTM C109 [15]. The specimen for each proportion cast in the mold of mortar at 5×5×5 cm cube. The specimens were cured in the water for 3, 7, 14, 28 and 56 days.

Shotcrete will be used as the surface protection of claystone slopes from weather change. Therefore, the durability of shotcrete is an important property has been considered. The durability test was conducted on the cube samples at 5×5×5 cm after curing in the water for 28 days. The wet-dry process was used to accelerate a deterioration of the samples. The samples were immersed in the water for 24 hr and heating in an oven at 100±5 °C for 24 hr. This represents one cycle [16]. The experimental investigated the durability of mortar in six cycles. The unconfined compression test was conducted on

the samples which throughout the wet-dry process for each cycle to determine the compressive strength of deteriorated samples. The results can be represented by the alteration of the compressive strength of shotcrete mortar during the wet-dry process.

The results obtained from the experiment can be demonstrated the influence of FGD gypsum on the properties of shotcrete. Moreover, the properties of the samples in each mixture have compared with the required target properties of shotcrete in Table 2. In order to determine the optimum content of FGD gypsum in the mixture of shotcrete for stabilizing the slope in Mae Moh mine.

Table 2 The requirement for the properties of shotcrete

Test	Target	Standard of testing
Initial setting time (min)	≥ 180	ASTM C191
Slump flow (mm)	203-248	ASTM C1437
Compressive strength (ksc)	>100	ASTM C109
28 days		
Durability (ksc)	> 100	-
6 cycles		

FRESH PROPERTIES OF SHOTCRETE

Slump flow tests and setting time tests were conducted on the fresh mortar to determine the fresh properties of shotcrete. The trial mixes according to Table 1 were used in the test.

Slump Flow

The requirement of flowability of mortar should be between 203-248 mm. The results of slump flow for each mix shown in Fig. 2.

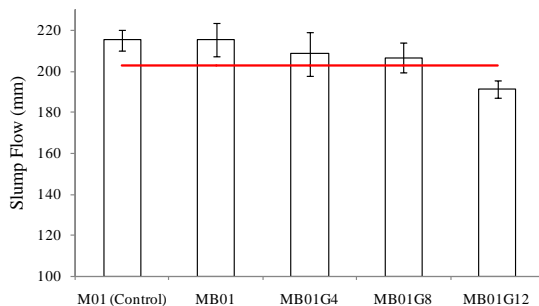


Fig. 2 The flowability of shotcrete mortar.

The results demonstrated that the slump flow of shotcrete mortar used sand as fine aggregate and shotcrete mortar used bottom ash as a fine aggregate

was similar. The flow of mortar which is not contained FGD gypsum in the mixture was approximately 215 mm. The slump flow was in the range of the recommendation between 203-248 mm.

However, the flow of mortar tends to decrease with an increase in the amount of FGD gypsum contain in the mixture. The flow of the samples which contains FGD gypsum 4%, 8%, and 12% was 209 mm, 207 mm and 191 mm, respectively. The mixture which contains FGD gypsum more than 8% demonstrated the slump flow was lower than the minimum required. Therefore, the optimum amount of FGD gypsum adds in the shotcrete mixture should not exceed 8% by the weight of cement.

Setting Time

The requirement for the initial setting time of the shotcrete mortar should be longer than 180 minutes. The setting time for each mix of mortar as shown in Fig. 3.

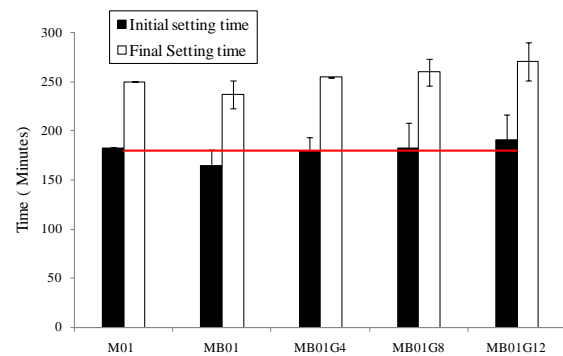


Fig. 3 The setting time of shotcrete mortar for each mixture.

The results demonstrated that the initial setting time and the final setting time of the mortar used bottom ash as a fine aggregate was shorter than the mortar used sand as a fine aggregate. The initial and final setting times of M01 were 18 minutes and 13 minutes longer than MB01. The initial and final setting time of M01 was 183 minutes and 250 minutes respectively. However, the requirement for the initial setting time, it should be longer than 180 minutes. Thus, the initial setting time of mortar used bottom ash as a fine aggregate was 165 minutes that less than the minimum requirement.

Although, the initial setting time of MB01 less than the minimum requirement but FGD gypsum add in the mixture can be increased the setting times of mortar. This phenomenon caused by the absorbability of FGD gypsum. The soluble gypsum provides a range of available sulfate ions during cement hydration. When gypsum exists, the sulfates react with tricalcium aluminates to form ettringite

immediately. It is assumed that ettringite forms initially on the reacting C_3A surface, a more or less impermeable coating that impedes diffusion of the ion needed to form hydrates that cause setting. Consequently, the solubility of gypsum becomes lower than ever and therefore cannot form ettringite to retard setting time until gypsum is released [10].

The results demonstrated the initial and final setting time tend to increase with an increase in the amount of FGD gypsum contains in the mixture. The initial setting time of MB01G4, MB01G8, and MB01G12 was 180 minutes, 183 minutes and 191 minutes, respectively. The final setting time of MB01G4, MB01G8, and MB01G12 was 255 minutes, 260 minutes and 271 minutes, respectively. Thus, the mixture which contains FGD gypsum exceeds 4% can be increased the initial setting time of mortar was longer than the requirement. Moreover, MB01G4 demonstrated the initial setting time and the final setting time was near M01.

HARDENED PROPERTIES OF SHOTCRETE

Compressive strength tests and durability tests were conducted on the mortar samples to determine the hardened properties of shotcrete.

Compressive Strength

The trial mixes according to Table 2 and curing in the water in 0-56 days were conducted on the compression machine to determine the compressive strength of mortar. The minimum requirement for the compressive strength of shotcrete is 100 ksc at the curing time 28 days. The results of the compressive strength of each mix as shown in Fig. 4.

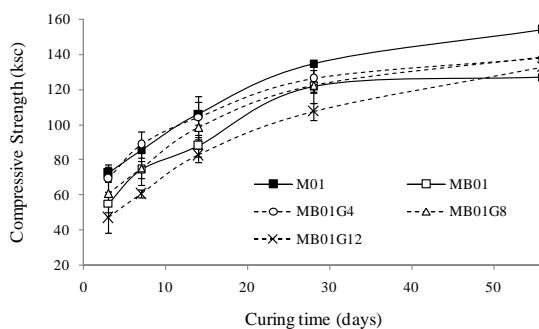


Fig. 4 The compressive strength of the shotcrete mortar of each mix.

The results show the compressive strength of the normal shotcrete mortar was higher than the shotcrete mortar used bottom ash as fine aggregate. This is because the particle strength of bottom ash was less than the particle strength of sand. The bottom ash particles were with the much pores cause of a low strength of the particles [6]. Fig. 5 shows

the failure plane of the mortar samples which used bottom ash as fine aggregate. The samples demonstrated the failure plane occur on the bottom ash particles.

Bottom ash fine aggregates mortar can only reach 75-85% of the compressive strength of the normal shotcrete mortar. However, the pores in the particle of bottom ash can be reduced the unit weight of shotcrete mortar. The unit weight of the bottom ash aggregate mortar was approximately 1.8 T/m^3 which is lower than sand aggregates mortar approximately to $0.2\text{-}0.3 \text{ T/m}^3$. Therefore, the reduction of the unit weight of MB01 was approximately 10-15% of M01.



Fig. 5 The failure plane of shotcrete mortar used bottom ash as fine aggregate.

However, the compressive strength of bottom ash aggregates mortar was increased when the mixture containing FGD gypsum. The results demonstrated the mixture which containing FGD gypsum 4% by weight of cement can be increased the compressive strength nearly the normal mortar in 3-14 days. However, MB01G4 can only reach 90% the compressive strength of the normal mortar at 28 and 56 days. The influence of FGD gypsum on the compressive strength of shotcrete used bottom ash as fine aggregate represented in Fig. 6. The relationship between the amount of FGD gypsum in the mixture and compressive strength was shown.

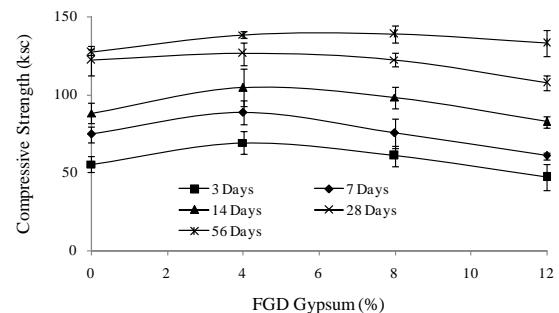


Fig. 6 The influence of FGD gypsum on the compressive strength of shotcrete mortar.

The result demonstrated FGD gypsum 4% contain in the mixture was the most efficient to increase the compressive strength. The compressive strength was higher than the samples without

gypsum approximately 8-20%. This is because FGD gypsum obtained from Mae Moh power plant consist of SO_3 approximately 49.54%. Therefore, the strength increased when the content ratio of SO_3 was the optimum percentage [10]. SO_3 seems to be responsible for the higher early compressive strength [17].

The early strength of the samples contains gypsum exceed 4% tend to decrease with an increase in the amount of gypsum. The compressive strength of MB01G8 and MB01G12 can be reached 90% and 70% of the compressive strength of MB01G4 in 3-14 days. However, the compressive strength of MB01G8 and MB01G12 was near the samples contain gypsum 4% at 56 days. This is due to the later age strength of the mixture is controlled mainly by calcium silicate hydrate [17]. Consideration of the minimum required strength at 28 days was 100 ksc, the strength of MB01, MB01G4, MB01G8 and MB01G12 passed the requirement.

The Durability of Shotcrete Mortar

The investigation on the durability of shotcrete mortar which through the wet-dry process for each cycle shown in Fig. 7. The results demonstrated the compressive strength of shotcrete mortar decreased due to the deterioration. The compressive strength of mortar tends to decrease with an increase in the number of wet-dry cycles. This is because the deterioration occurs in the shotcrete mortar when it has been exposed to the wet-dry conditions.

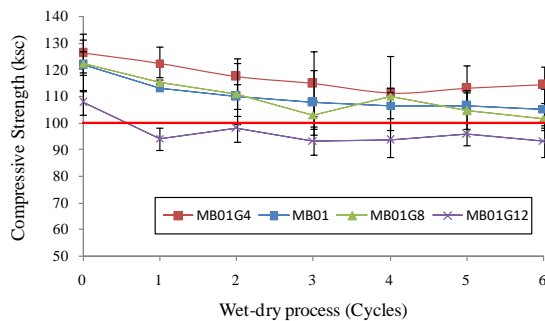


Fig. 7 The compressive strength of the samples for each cycle.

MB01G4 demonstrated the highest compressive strength in six cycles. The compressive strength of MB01G4 for each cycle was higher than MB01 and MB01G8 approximately 4-10%. Moreover, the strength of MB01G4 for each cycle was higher than MB01G12 approximately 15% - 23%. In cycle six, the compressive strength of MB01G4 reduced approximately 9% of the strength at the curing age 28 days. The remaining compressive strength in the sixth cycle was 115 ksc.

The results demonstrated that the deterioration

severely affects decreased the compressive strength of MB01G12. The reduction of the compressive strength was approximate to 12% in the first cycle followed by slight decreased. However, MB01G8 and MB01 demonstrated the compressive strength was similar in cycles 0-6. The compressive strength of MB01 and MB01G8 decreased approximately 15% in six cycles.

The requirement for the compressive strength of the shotcrete mortar which through the wet-dry process in six cycles should be more than 100 ksc. However, the remaining compressive strength of MB01, MB01G4, MB01G8 MB01G12 in cycle six was 105 ksc, 115 ksc, 102 ksc and 93 ksc respectively. Therefore, the compressive strength of the samples with gypsum 12% was lower than the requirement.

The influence of FGD gypsum on the compressive strength of deteriorated samples shown in Fig. 8. The highest strength was demonstrated in the samples with 4% FGD gypsum. The compressive strength of the samples containing gypsum 8% and 12% were less than MB01G4 in every cycle. Moreover, the results show the reduction of the compressive strength occurs in cycles 1-2. However, the compressive strength tends to similar in cycles 3-6. The compressive strength of MB01G8 and MB01G12 was less than MB01G4 approximately 10% and 17% respectively in cycle 3-6. Thus, the deceleration of deterioration occurs in the samples which through the wet-dry process more than three cycles. This result demonstrated the most deterioration of shotcrete mortar due to wet-dry conditions.

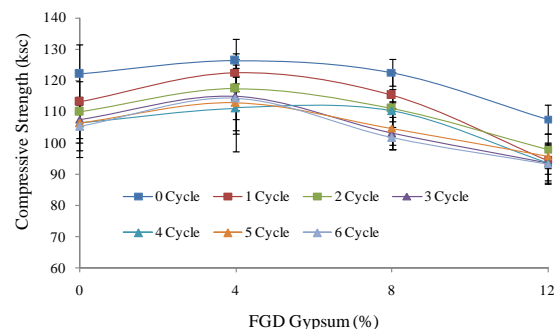


Fig. 8 The influence of FGD gypsum on the compressive strength of deteriorated samples.

CONCLUSION

In order to investigate the effect of FGD gypsum on the properties of shotcrete used bottom ash as fine aggregate. This study investigated the fresh properties and hardened properties of the shotcrete samples. The fresh properties were carried out by setting time tests and slump flow tests. The hardened

properties were carried out by the compressive strength tests and durability tests.

Based on the experimental test obtained in this study, the following conclusion was made:

1. The slump flow of shotcrete mortar used bottom ash as fine aggregate decreased with an increase in the amount of FGD gypsum. However, the initial setting time and final setting time of shotcrete were longer with an increase in the amount of gypsum.

2. The compressive strength of the samples contains FGD gypsum 4% can be developed the strength 8-20% of the samples without gypsum. However, the compressive strength tends to decrease when the amount of FGD gypsum in the mixture exceeds 4%.

3. The samples with 4% FGD gypsum demonstrated the highest compressive strength when the samples through the wet-dry process in six cycles. The remaining compressive strength in the sixth cycle was 115 ksc. Therefore, the mixture of shotcrete containing FGD gypsum 4% was the most efficient to develop the durability of mortar.

4. Bottom ash aggregate mortar can be reduced the cost approximately 40% of the normal mortar.

ACKNOWLEDGMENTS

The research work was done during the study at Chiang Mai University. The authors would like to express their appreciation to the Graduate School, Chiang Mai University, for the financial support.

REFERENCES

- [1] Leelasuksaree C, Mavong N, Khosravi MH, Pipatpongsa T, "Physical and numerical models of undercut slope lying on steeply inclined bedding plane", in 17th National Convention on Civil Engineering, 2012, pp.GTE045-1-GTE045-10.
- [2] Rodvinij P, Wattanachai, P, "Influence of claystone deterioration on shear strength of backfill", International Journal of GEOMATE, Vol. 13, 2017, pp. 54-59.
- [3] Abramson LW, Lee TS, Shama S, Boyce GM, Slope Stability and Stabilization Methods, Second Edition, New Jersey: John Wiley & Sons, 1996.
- [4] US Army Corps of Engineering, "Engineering and Design Standard Practice for Shotcrete", 1993, pp. 2-1 -4-7.
- [5] Chindaprasirt P, Jaturapitakkul C, Chalee W, Rattanasak U, "Comparative study on the characteristics of fly ash and bottom ash geopolymers", Waste Management, 29, 2008, pp.539-543.
- [6] Sathonsawaphak A, Chindaprasirt P, Pimraksa K, "Workability and strength of lignite bottom ash geopolymer mortar", Journal of Hazardous Materials, 168, 2009, pp. 44-50.
- [7] Jaturapitakkul C, Cheerarot R, "Development of bottom ash as pozzolanic material", Journal of Materials in Civil Engineering, volume 15, Issue 1, 2003.
- [8] Kim HK, Lee HK, "Use of power plant bottom ash as fine and coarse aggregates in high-strength concrete", Construction and Building Materials, Vol. 25, 2010, pp. 1115-1122.
- [9] Yang MJ, Wang HY, Liang CF, "Effects on Strengths of Cement Mortar When Using Incinerator Bottom Ash as Fine Aggregate, World Journal of Engineering and Technology, 2, 2014, pp.42-47.
- [10] Guo XL, Shi HS, "Thermal treatment and utilization of flue gas desulphurization gypsum as an admixture in cement and concrete", Construction and Building Materials, Vol. 22, 2008, pp. 1471-1476.
- [11] Guo XL, Shi HS, Liu HY, "Effects of a combined admixture of slag powder and thermally treated flue gas desulphurization (FGD) gypsum on the compressive strength and durability of concrete", Materials and Structures, Vol. 42, 2009, pp. 263-270.
- [12] Samaru Y, Sugiyama K, " Slope Stabilization Using the Shotcrete Grid Beam System in Japan", Shotcrete Spring, 2005, pp. 36-40.
- [13] ASTM C1437, Standard Test Method for Flow of Hydraulic Cement Mortar, 2007.
- [14] ASTM C191, Standard Test Method for Time of Setting of Hydraulic Cement by Vicat Needle, 2007.
- [15] ASTM C109, Standard Test Method for Compressive Strength of Hydraulic Cement Mortars Cube Specimens, 2007.
- [16] Sadisun IA, Shimada H, Ichinose M, Matsui K, "Study on the physical disintegration characteristics of Subang claystone subjected to modified slaking index test", Geotechnical and Geological Engineers, pp. 199-218.
- [17] Agahabaglou AM, Boyaci OC, Hosseinneshad H, Felekoglu B, Ramyar K, "Effect of gypsum type on properties of cementitious materials containing high range water reducing admixture", Cement and Concrete Composites, Vol 68, 2016, pp. 15-26.

USE OF DRY MIXING METHOD IN FLY ASH BASED GEOPOLYMER AS A STABILIZER FOR DREDGED SOIL

Jonathan R. Dungca¹, Kimberly D. Ang², Aila Mae L. Isaac², John Joshua R. Joven² and Ma. Beatrice T. Sollano²

¹Faculty, De La Salle University, Philippines; ²Graduate, De La Salle University, Philippines

ABSTRACT

This study aims to improve the properties of dredged soil obtained from a river in the Philippines. Different percentages of fly-ash based geopolymer, namely 10%, 20%, 30% were used using dry mixing method to determine the optimum mix. The procedures based on the ASTM standards were conducted to determine the index properties namely Grain Size Distribution Curve (ASTM D422), Specific Gravity (ASTM D854), Atterberg's Limits (D4318), and CBR Test (ASTM D1833) and UCS test (ASTM D2166) of untreated soil. While only the California Bearing Ratio Test and UCS test were conducted on the treated soil. The experimental results showed that the fly-ash based geopolymer improved both the CBR index and the Unconfined Compression Strength of the dredged soil. The optimum mix for the soil-geopolymer mix was 30% because it displayed the largest increase in the CBR index (50.23%) and Unconfined Compressive Strength (912.88 Kpa).

Keywords: fly ash, geopolymer, soil stabilization, california bearing ratio, unconfined compressive strength

INTRODUCTION

Soil stabilization is an engineering process which is used to modify and improve the properties of the natural soil. The main objective of soil stabilization is to increase its soil strength and stability. Other soil properties like its durability, permeability and bearing capacity must also be considered in order to achieve the required soil specifications for construction applications. This process can be applied to the construction of roads, pavements, embankments and other uses. Two processes of soil stabilization include mechanical stabilization and chemical stabilization. Chemical stabilization is subjected to chemical reactions of the stabilizer and the minerals of the soil. Based on previous studies, cement, lime, bitumen and fly ash are the commonly used stabilizing agents that utilize the industrial wastes and natural resources [1]. The use of dredged material as a resource has broad social, environmental, and financial benefits, thus, contributes to global sustainability. Its two broad categories of uses are engineering uses and environmental uses and the utilization of the dredged soil for beneficial uses may be considered as an environmental friendly and economical option. In order to achieve this goal, chemical admixtures are to be added to the dredged material so that its properties are modified. Past studies have been attempted to modify dredged material as the fill materials, for instance, the use of blast furnace slag cement and quicklime as additives to modify the dredged material as the embankment fill [2].

Geopolymer is synthesized through a mixture of aluminosilicate raw material from industrial wastes

such as blast furnace slag, silica fume, fly ash or bottom ash and an alkali activator. Through this synthesis, a structured polymer is created forming series of silicate monomers that has similar properties to cement. Fly-ash based geopolymers have already been studied as an alternative for cement that have showed an increase in compressive strength, resistance to acid and low shrinkage. With the reduction of carbon dioxide in the production of a cementitious material through geopolymer, the study aims to create an effective geopolymer mix that will stabilize the dredged soil. Thus for this study, a geopolymer based on fly ash will be used to modify and improve the geotechnical properties of dredged soil that will be obtained from a river beside a coal fired power plant in Mindanao. Numerous studies have shown that coal combustion by-products, or more commonly known as CCPs, have been found to be a good choice because it is very abundant in the country and has a problem in disposal [3-10]. The tests that will be conducted in the study are the Standard Proctor test, CBR and Unconfined Compression Test [11-13].

The primary objective of the study is to investigate the effects of using dry mixing method of fly ash based geopolymer as stabilizer to improve on the geotechnical properties of dredged soil. Moreover, the study aims to incorporate the soil stabilization process by performing tests on the untreated soil and at the same time evaluate the increase on the shear strength and load bearing capacity. Lastly is to determine the application of the various mixture proportions of dredged soil and geopolymer.

METHODOLOGY

Tests in accordance to the ASTM standards are utilized on the dredged soil sample to determine the effect of using dry-mixing method in fly ash based geopolymer as a stabilizing agent on the untreated soil.

In this study, the soil that was dredged from a heavily silted river beside the coal fired power plant in Mindanao was used as the soil specimen. The properties and characterizations of the dredged material were obtained by conducting several test procedures. The determination of its water content and its optimum moisture content are its prime importance.

Dry alkaline activators which are the sodium silicate and sodium hydroxide were utilized in this study. Sodium silicate is a common name for sodium metasilicate and its term is also known as a water glass solution. This can be both in solid and in liquid form, thus, it is constant in both neutral and alkaline solution. Sodium silicate alone is not advisable to be used as an alkaline activator, since it does not possess enough potential to initiate pozzolanic reaction independently. Thus, it is commonly mixed with Sodium hydroxide as an assisting agent to improve the overall strength of specimen. Sodium hydroxide, NaOH, is an organic compound and is also known as caustic soda. It is described as a white solid with a highly caustic metallic base and alkali salt. It can be in powdered form or any granular or flakey material. It is a commonly used activator for geopolymerization and it can be combined with sodium silicate for the production of geopolymer paste.

The study involved experimental procedures in the laboratory including its soil characterization tests, design mix, soil-geopolymer mix, soil-cement mix, curing of specimen, testing of the strength of the soil stabilized with geopolymer and analysis of results.

Before the specimens were prepared, the geopolymer paste was prepared first prior to mixing with the dredged soil. The formulation of the geopolymer mix was already determined. Sodium Hydroxide and Sodium Silicate were mixed in the mixer, then fly-ash were placed with the mixture after the activators were thoroughly mixed. Water was then added and mixed for 10 minutes, to which produced the geopolymer paste. The mix of dry and wet ingredients varies on the percentage of geopolymer to soil.

RESULTS AND DISCUSSIONS

Compressive Strength of Pure Geopolymer Paste

A compressive strength test was conducted on the pure geopolymer paste using the two different fly ash that was given by the power plant. The difference with the two types of fly ash was that, Fly Ash 1 (FA1) did not undergo desulfurization in the production of power, however Fly Ash 2 (FA2) undergone desulfurization in its production of power. The geopolymer paste was consisted of of 0% soil and 100% geopolymer using the dry mix method. Table 1 shows that it garnered an average compressive strength of 10.46MPa, while at Table 2 shows that it only reached a strength of 2.2MPa.

Table 1. Compressive Strength of FA1 (Without Desulfurization)

Area (mm ²)	F (N)	Strength (MPa)
2,451.28	31,100	12.69
2,450.91	31,600	8.81
2,429.08	34,000	9.88
Average		10.46

Table 2. Compressive Strength of FA2 (With Desulfurization)

Area (mm ²)	F (N)	Strength (MPa)
2,409.70	5,400	2.24
2,437.65	4,800	1.98
2,353.70	4,300	1.83
Average		2.20

Characterization of Geotechnical Properties of Dredged Material

The basic physical characterization of the pure dredged soil such as the specific gravity, particle size analysis, atterberg limits and standard proctor test were examined to obtain its geotechnical properties. More so, based on the Unified Soil Classification System (USCS) and AASHTO, the dredged soil was classified as Poorly Graded Sand (SP) and Fine Sand (A-3) respectively. The untreated soil was oven-dried prior to testing to attain consistent results, following the ASTM procedures and thus, Table 3 shows the garnered results from the three trials that were conducted per test.

Table 3. Geotechnical Properties of Dredged Soil

Description	Value
Specific Gravity, G _s	2.66
Liquid Limit, LL	None
Plasticity Index, PI	NP
Optimum Moisture Content (OMC, %)	17.59
Max Dry Unit Weight (KN/m ³)	17.23
Unsoaked CBR (%)	1.19

Strength Tests

It can be observed that there was a significant increase in the CBR strength when the geopolymers were introduced to the dredged soil. It was shown that for a 10% geopolymer concentration, a minimum value of 8.57 was generated and a general rating of fair for subbase was obtained. A general rating of good for base and subbase course resulted for the 20% replacement while a general rating of excellent for base course was obtained for the replacement of 30% geopolymer on the dredged soil.

The increase in the CBR Index follows a polynomial trend. The polynomial correlation was chosen to demonstrate the relationship between the percentages and the CBR Index since it resulted to greatest regression value.

It shows that a pure dredged soil is not capable of performing unconfined compressive strength test alone, but blending geopolymer with the soil allowed to produce a confinement as little as 10%, following a series of 20% and 30%. When soil was mixed with a geopolymer concentration of 10%, the value of the gained strength of 100.94 kPa belonged to typical strength of stiff soil (100-200 KPa). As the geopolymer concentration increased to 20%, the gained strength value of 157 kPa still belonged to the typical strength of stiff soil (100-200 KPa). A significant increase can be observed when the soil was mixed with a geopolymer concentration of 30% since the gained strength of about 912.88 KPa belonged to the typical strength of hard soil (>400 KPa).

The statistical analysis of the Unconfined Compression Strength test results indicated that an exponential relationship can be developed between the varying geopolymer concentration and its average UCS values. It can be seen that as the percentage of geopolymer increases, the UCS values also tend to increase and vice versa. This relationship was chosen as the best measure since the regression value (R^2) resulted close to 1.

Morphological Analysis

Since most of soils properties such as unit weight and strength are attributed to its microstructure. Scanning Electron Microscope (SEM) was conducted on soil-geopolymer mix to clearly visualize the particle angularity, assemblage and surface texture. Figures show the SEM microphotographs of the 10% 20% and 30% geopolymer mix, shown on Figure 1. It was found that the spherical particles, which represents fly ash gradually decrease as more geopolymer percentage was added on the soil.

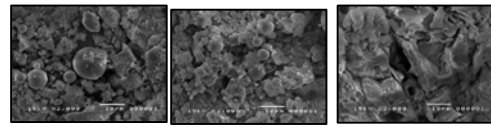


Figure 1. SEM photomicrographs of 10%(right), 20%(middle) and 30%(left) geopolymer mix at 2000x

There were no more spherical objects and more of the white particles had appeared even forming crystalline like structures. This indicates that the geopolymer had fully formed. As the percent of the geopolymer was increased the presence of the geopolymer had become more evident. This would explain why the 30 % geopolymer mix had the largest increase in strength. Since the formation of the geopolymer was more extensive compared to the other mixes.

CONCLUSIONS

The load bearing capacity of the dredged soil stabilized with geopolymer through dry mixing method showed that there is an increase in the strength behavior of the sample. The dry mixing method was able to improve the geotechnical properties of the dredged soil, but at the same time it is practical to use on site. The strength of the geopolymer improved with time because of its cementitious reaction. However, excess alkali activator resulted as there in an increase of geopolymer to the sample, still, results showed an exponential increase. The replacement of 30% geopolymer on the dredged soil resulted to be best used for Base course with a general rating of excellent, according to the DPWH Standard. The 20% replacement of geopolymer to the dredged soil resulted to a general rating of fair for Base and Subbase course and the 10% replacement of geopolymer to the dredged soil was only rated good as a subbase course.

The dredged soil ran through series of geotechnical tests, and it was classified as a poorly graded sand. The dredged soil moisture-density relationship resulted to values of (OMC) and max dry density (MDD) within the range of Poorly Graded Sand which was (12% - 21%) and (15.71 KN/m³-18.85 KN/m³). Additionally, the unconfined compressive strength test on the dredged soil produced an invalid strength, due to its dry and crumbly characteristics that was not suitable for the strength test.

The CBR value of 1.19 resulted for the dredged soil alone. However, with the variation of mixes of 10%, 20% and 30%, it was found that CBR index values increased with the further increase of

geopolymer added to the dredged soil. The maximum CBR value was obtained at 30% geopolymer replacement on the soil, at a CBR value of 51.33%. The minimum CBR value was obtained at 10%, with a CBR value of 8.57. The improvement of the dredged soil when replaced with geopolymer it increased by 3.21 – 19.22 times the base CBR value of the dredged soil alone.

More so through the unconfined compressive strength of the stabilized dredged soil had an increasing trend as the mixed ratio of geopolymer increased. The 10% replaced geopolymer gained a strength value that is classified as strength of medium soil at 100.94kPa. The 20% and 30% replaced geopolymer gained a strength value that is classified as strength of stiff at 157.0kPa and strength of hard soil at 912.88kPa, respectively. It is evident that the unstabilized dredged soil, on the other hand, showed a significant improvement, due to the fact that sample was too loose to stand by itself to begin with; it had no coherent value.

Previous studies have not performed the California Bearing Ratio test for soils that is to be stabilized with geopolymer; although, statistical analyses are provided. Comparing the results of the CBR test with the results of the UCS test, it was observed that the behaviour of the increase in CBR value of the three geopolymer concentrations is similar with the behaviour of the increase in strength for the unconfined compression strength test results.

RECOMMENDATIONS

Due to time constraint and limited resources, both the fly ash and dredged soil come from only one coal-fired power plant source was used. However, it is recommended to use samples from other power plants and dredged soil across the country for verification of the results in order to avoid geographic limitation on its widespread use. Moreover, only the CBR (ASTM D1822) [14] and unconfined compression test (ASTM D2166) [15] were conducted on the treated soil. Furthermore, other tests such as particle size analysis (ASTM D422) [16], specific gravity (ASTM D854) [17], Atterberg's limit (ASTM D4318) [18], standard proctor test (ASTM D698) [19] to be conducted to on the treated soil to determine its effect on the geotechnical other properties.

Moreover, from that additional test for different curing period such as 7 days, 14 days and 28 days for both the CBR and UCS test this is to observe the behavior of the increase in strength of the soil and geopolymer mix. It is also highly recommended to wear protective gloves in mixing geopolymer to avoid

skin infection.

Lastly, aside from strength, other factors such as draining should be considered when dealing with road embankments. That is why the researchers would also recommend conducting permeability test (ASTM D2434) to determine the hydraulic conductivity of both the untreated and treated soil. This would determine its suitability to be used in road embankments.

REFERENCES

- [1] Zaliha, S., Mustafa AL Bakri, A.M., Kamarudin, H., & Fauziah, A. (2015). Characterization of Soils as Potential Raw Materials for Soil Stabilization Application Using Geopolymerization Method. *Trans Tech Publications*, 8(03), pp. 135-143.
- [2] Huang, Y., Zhu, W., Zhang, C., Wang, S. Zhang, N. (2010). Experimental Study on Dredged Material Improvement for Highway Subgrade soil. *Pavement Materials and Pavement Analysis*. 335-340.
- [3] Roy, D.M. (1999). Alkali-activated cements opportunities and challenges. *Cement & Concrete Research*, vol. 29, no.2 pp.249-254.
- [4] Dungca, J.R., Jao, J.A.L. (2017). Strength and permeability characteristics of road base materials blended with fly ash and bottom ash. *International Journal of GEOMATE*, 12 (31), pp. 9-15.
- [5] Dungca, J., Galupino, J., Sy, C., Chiu, A.S.F. (2018). Linear optimization of soil mixes in the design of vertical cut-off walls. *International Journal of GEOMATE*, 14 (44), pp. 159-165.
- [6] Dungca, J.R., Galupino, J.G., Alday, J.C., Barretto, M.A.F., Bauzon, M.K.G., Tolentino, A.N. (2018). Hydraulic conductivity characteristics of road base materials blended with fly ash and bottom ash. *International Journal of GEOMATE*, 14 (44), pp. 121-127.
- [7] Dungca, J.R., Galupino, J.G. (2017). Artificial neural network permeability modeling of soil blended with fly ash. *International Journal of GEOMATE*, 12 (31), pp. 76-83.
- [8] Dungca, J.R., Galupino, J.G. (2016). Modelling of permeability characteristics of soil-fly ash-bentonite cut-off wall using response surface method. *International Journal of GEOMATE*, 10 (4), pp. 2018-2024.
- [9] Galupino, J.G., Dungca, J.R. (2015). Permeability characteristics of soil-fly ash mix. *ARN Journal of Engineering and Applied Sciences*, 10 (15), pp. 6440-6447.
- [10] Dungca, J.R., Codilla, E.E.T., II. (2018). Fly-ash-based geopolymer as stabilizer for silty sand embankment materials. *International Journal of*

- GEOMATE, 14 (46), pp. 143-149.
- [11] Davidovits, J. (1991). Geopolymers: Inorganic Polymeric New Materials. *Journal of Thermal Analysis*, 1633-1656.
 - [12] Davidovits, J., PROPERTIES, O. G. C. (1994). Alkaline cements and concretes. *Kiev State Technical University, Ukraine*, 131.
 - [13] Duxson, P., Fernandez - Jimenez, A., Proveis, J.L., Lukey, G.C., Palomo, A. (2007) Geopolymer technology: the current state of art. *Journals of Material Science*, 42(9), 2917-2933.
 - [14] American Society for Testing and Materials. (2017). Standard Test Methods for California Bearing Ratio. ASTM D1822.
 - [15] American Society for Testing and Materials. (2017). Unconfined OCMpression Test. ASTM D2166.
 - [16] American Society for Testing and Materials. (2017). Standard Test Method for Particle-Size Analysis of Soils. ASTM D422.
 - [17] American Society for Testing and Materials. (2017). Standard Test Methods for Specific Gravity of Soil Solids by Water Pycnometer. ASTM D854.
 - [18] American Society for Testing and Materials.(n.d.). Standard Test Methods for Liquid Limit, Plastic Limit, and Plasticity Index of Soils. ASTM D4318.
 - [19] American Society for Testing and Materials. (2017). Standard Proctor Test. ASTM 698.

RADIAL FLOW PERMEAMETER: A PROPOSED APPARATUS TO MEASURE HORIZONTAL HYDRAULIC GRADIENT OF FLY-ASH BASED GEOPOLYMER-SOIL MIX

Jonathan R. Dungca¹, Winchell Dunley T. Lao², Matthew Lim², Wilson D. Lu² and Juan Carlos P. Redelicia²

¹Faculty, De La Salle University, Philippines; ²Graduate, De La Salle University, Philippines

ABSTRACT

Fly-ash based geopolymer has been proven by many scholars as a viable material to replace cement. Due to its high compressive strength and abundance in industrial areas, it was advocated to partially replace the conventional material in constructing infrastructure, especially in road embankment. Merely consider the load capacity or strength of the materials in designing a road embankment may overlook the durability of the infrastructure. One vital parameter that leads to deterioration and failure of the road is the permeability of the materials. Flow of water in the road structure comes in different direction but commonly runs in horizontal way or longitudinal along the road. Neither ASTM nor AASHTO have established a standard procedure in determination of the horizontal hydraulic gradient of the soil. Hence, a proposed radial flow permeameter was adopted to determine the permeability of the fly-ash based geopolymer-soil mix. The mixes included dredged soil with 10% (G10), 20% (G20), and 30% (G30) replaced by geopolymer in mass. The interpretation of the test is quantified using theoretical model and verified using graphical and statistical analysis. The computation was then further verified through anisotropy factor ratio of k_h/k_v with the data that provided in a literature with similar geopolymer-soil blend mix. The outcome of the model displayed the degree of the permeability of G10, G20, and G30 was $\times 10^{-4}$, $\times 10^{-6}$, and $\times 10^{-7}$ in cm/s, respectively. Lastly, the proposed permeameter was found out to be permissive in determining the horizontal permeability of specimen with low permeability having degree of 10^{-4} or lower.

Keywords: Horizontal Coefficient of the Permeability, Radial Flow Permeameter, geopolymer, flyash

INTRODUCTION

Engineers often overlook the drainage capacity of road embankments, which can lead floods in some areas in the Philippines. The Philippines often experiences floods because it is in the typhoon belt. The soil's drainage property is important because with low performance of drainage can cause floods when an insufficient surface drainage is provided. For engineers, considering a good drainage is one of the fundamental design considerations for a road to minimize road maintenance costs and maximize the service life-time of the road during operation [1].

In analyzing the permeability of road embankments, both direction, vertical and horizontal, should be considered because the water will flow not only downward but also horizontally. To have a good drainage, horizontal permeability should be considered because the water entering the road embankment should have an exit through the sides. Most of the tests for the permeability are for vertical permeability since it is easier to conduct compared to the horizontal permeability because in getting the horizontal permeability the flow of water should be horizontal only. Most of the set up that are being used in getting the horizontal permeability are rectangular [2-6], which is not common to some of the

manufacturers. In some studies, the set up for the horizontal permeability test are custom made, which is difficult to do. Another problem is that in this study, geopolymer will be used as soil stabilizers which will result to a low permeability soil. Most of the set up for the horizontal permeability test are for high permeability soils so it would be difficult for the researchers to use the set ups proposed given the limited time.

The objective of this study is to be able to identify the horizontal permeability of the stabilized soil with fly ash based geopolymer. It also aims to propose a new set up for getting the horizontal permeability that will give credible results.

METHODOLOGY

Neither ASTM nor AASHTO have established a standard apparatus and standard way in measuring the horizontal permeability. Hence, a proposed new permeameter set-up based from a well-concept (confined aquifer) incorporating with Darcy's Law, see Eq. 1, was used to measure the horizontal permeameter.

$$Q = k_i A \quad (1)$$

The sample will be a hollow cylinder which is shown in Figure 1:

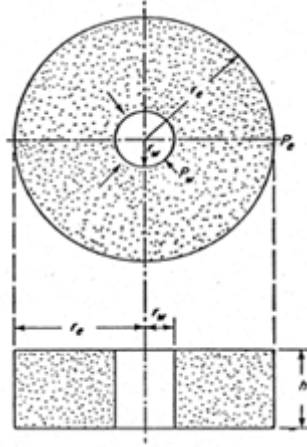


Fig. 1. Model for radial flow of fluids to the well bore [7]

As shown in Figure 1, an external boundary pressure, P_e , is located at the outer radius and an internal pressure, P_w , is located at the inner radius. The two pressures will give the general equation of Darcy's Law two boundary conditions. Given that there is a constant change in pressure, the change in pressure head along the horizontal direction can be expressed as,

$$i = dP/dr \quad (2)$$

The area that will be considered in the formula is the area of the external radius which is expressed as,

$$A = 2\pi r h \quad (3)$$

Substituting the area and hydraulic gradient into Darcy's Law will give,

$$Q = 2\pi r h K \frac{dP}{dr} \quad (4)$$

Integrating the equation with the boundary condition,

$$Q \int_{r_e}^{r_w} \frac{dr}{r} = 2\pi h K \int_{P_e}^{P_w} dP \quad (5)$$

Which gives

$$Q \ln(r_e/r_w) = 2\pi h k (P_e - P_w) \quad (6)$$

Rearranging the equation, the coefficient of permeability can be solved by using the equation,

$$k = \frac{Q \ln(\frac{r_e}{r_w})}{2\pi h (P_e - P_w)} \quad (7)$$

Where:

k = coefficient of permeability(cm/s)

Q = flowrate (cm^3/s)

r_e = interior radius of the cell or boundary radius (cm)

r_w = interior radius of the wellbore (cm)

h = height of the medium (cm)

P_e = pressure head at the boundary radius (cm)

P_w = pressure head at the wellbore radius (cm);

use atmospheric pressure, $P_w = 0$

In figure 2, the graphical model of the new horizontal permeameter was designed with the specimen having a height of 65mm and a diameter of 60 mm in total including the PVC pipe. The new set-up will also be using the same acrylic glass used in vertical permeability test with a wooden base at the bottom that will keep the sample in place when being poured and tamped. A space between the specimen and acrylic glass was provided to allow the water to flow into the side and permeate horizontally. The topmost part of the specimen was covered with sealant ensure that the water will enter the space at the side and will pass horizontally through the sample. The permeameter was constructed with PVC pipe on the center having a diameter of 20mm. The PVC pipe was subjected to 4 holes within the height of the specimen having a diameter of 8mm. The holes were made at every quarter of the PVC pipe. On top of the PVC pipe, the hole was wrap with sealant and left to dry and solidify to prevent the water going into the holes. It was then glued to the base having a 10mm thickness and 65mm diameter. The actual model of the proposed and actual set-up is seen figure is presented in Fig. 3. The design was made with the help of Dr. Alfaro [8].

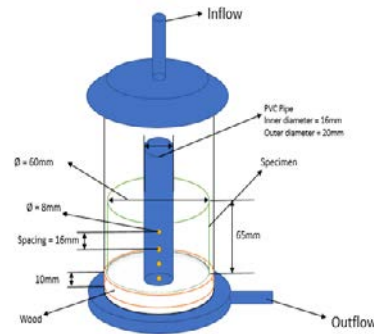


Fig. 2. Graphical Model of the New Horizontal Permeameter

For the preparation of the stabilized soil with fly ash based geopolymer, in order to provide a standard

uniformity between samples, the dredged soil and fly ash was obtained only from a thermal power plant in Mindanao. The dredged soils were sieved to have up to the required maximum sizes, particularly sieve number 4 or a nominal opening of 4.76mm followed by the removal of its moisture content thru oven-drying. The fly ash obtained was classified as Class F.

The index properties of the dredged soil was determined by conforming to the ASTM procedures.

- Specific Gravity of Soils (ASTM D854) [9]
- Particle Size Analysis (ASTM D422) [10]
- Standard Proctor Test (ASTM D698) [11]

Conventional materials and blended samples were individually subjected to microscopic testing in order to evaluate the void spaces present using the Scanning Electron Microscopy (SEM) [12-14].

The geopolymer based fly ash mix used was based on the mix design formulated by Ang, et al. (2016) [15] which were used for the preparation of samples for the testing of strength and permeability tests of each blends. The geopolymer mix design is presented in Table 1:

Table 1. Geopolymer Mix [15]

Geopolymer Concentration (%)	Alkaline Activator/ Fly Ash	Sodium Silicate/ Sodium Hydroxide	NaOH Concentration
10, 20, 30	0.4	2	14 M

The blended samples varies from 10%, 20% and 30% of partial replacement of geopolymer to the total weight of dredged soil. The blended samples are obtained by providing first the dredged soil to attain its maximum dry unit weight based from optimal moisture content (OMC) that was determined through the Standard Proctor Test.

Constant Head Permeability Test were conducted to evaluate the drainage characteristics of all the blends considering a relative compaction of 100%. However, a relative compaction of 100% is somehow unattainable due to tamping constraints, each samples were just subjected to a constant of 25 blows per 3 layers using hand tamping.

There are some advantages in using the proposed new set-up in getting the horizontal permeability. According to the study of Dungca and Galupino (2015) [6], the horizontal permeability is expected to have higher value because of the pressure that was induced in their sample, but they were not able to take into account the layers. In the new set-up, the layers caused by the tampering was considered. Another set-up that the researchers compared is the set-up made by Baretto et. al. (2015) [3]. Their set-up was a rectangular permeameter, unfortunately the researchers did not used their set-up due to the fact that their sample has properties similar to concrete like shrinkage. The researcher designed their set-up

by making sure that side wall leakage will not affect the results. One limitation of the set-up is that it can only be used to low permeability samples such as geopolymers. The set-up takes up less time compared to the others because the passage way of the water is much shorter compared to the other proposed set-ups.

RESULTS AND DISCUSSIONS

Scanning Electron Microscopy (SEM) Results

In graphical analysis, scanning electron microscopy (SEM) was used to evaluate the morphology of the specimen. It provided a high-resolution image of the spaces formed between the particles inside the specimen. Two levels of magnification, x500 (see Figure 3) and x5000 (see Figure 3), were used in the analysis to fully understand the bonds between the particles of the sample.

Figure 3 showed the microstructure of the three blends under magnification of x500. As shown in the Figure 3, the voids present in Figure 3 (a) were more visible compared to the voids seen on Figures 3(b), and 3(c). This meant that G10 could be more permeable as compared to the G20 and G30 because the presence of spaces between the particles were the path for the water to easily pass through. Furthermore, it was observed that the void spaces presented in G20 and G30 were exiguous, making the microstructure of the both blends indistinguishable under x500 magnification.

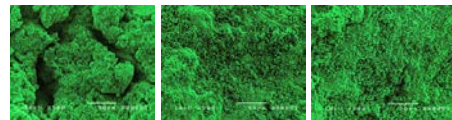


Figure 3. a) 10% b) 20% c) 30 % replacements with magnification level of x500

To clearly distinguish the difference between G20 and G30 in terms of the void spaces, an increased magnification level of x5000 was conducted. As can be seen from the SEM photo (x5000) presented in Figure 3, voids spaces were still present in both blends that allowed water to pass through. Under magnification of 5000, G20 was observed to have more void spaces as compared to the G30; thus, the G20 replacement was more permeable than the G30. In addition, there was great difference in the bonding formations of the particles between G20 and G30. Under G20, there still some particles of fly ash that could be seen in the SEM photo. They were the spherical particles easily seen in Figure 2(a). Those particles implied that the fly-ash did not completely react with the alkaline activator. Unlike in G30, the sand and fly-ash particles in G30 were completely reacted. The geopolymer in 30% replacement could coat the sands particles and provided greater bonding

with the other sand particles, blocking the passageway for the water.

From the microstructure of each blends, it could forecast that as the percentage replacement increase the permeability of that blend would decrease. This observation would be later on proven through experimental result.

Horizontal Permeability

As stated, a proposed radial flow permeameter was used in determining the horizontal permeability of the dredged soil stabilized with fly-ash based geopolymer under 10, 20, and 30 percent replacement in mass. Shown in Table 2, were the ranges of permeability value gathered from the proposed constant head radial flow permeameter test. G10 produced an average of $2.72\text{E-}04$ cm/s. G20 had an average of $5.25\text{E-}06$ cm/s. G30 produced an average of $7.86\text{E-}07$ cm/s. The lower the degree in the value implied a slower flow of water through the voids of the specimen.

Table 2. Ranges of Horizontal Permeability

Soil Mixture	Minimum Kh, cm/s	Maximum Kh, cm/s	Average Kh, cm/s
G10	$1.66\text{E-}04$	$3.62\text{E-}04$	$2.72\text{E-}04$
G20	$4.89\text{E-}06$	$5.52\text{E-}06$	$5.25\text{E-}06$
G30	$6.35\text{E-}07$	$9.27\text{E-}07$	$7.86\text{E-}07$

To determine the effect of the amount of geopolymer replaced in the soil, a box and whisker plot was delineated, as shown in Figure 4. Box and whisker plot provided the midspread values of each replacement. Using an IQR of 1.5, the obtained coefficient of permeability was fall in the ranges; therefore, there is no outlier.

As expected from the SEM photo, it was observed from Figure 4 that the permeability decreases as the percentage replacement of geopolymer mixed to the sample increases. Due to the increased geopolymerization took place in the blends, the void spaces between the soil particles was coated and bonded with the geopolymer, hence, blocking the passage of the water. Dungca & Jao (2016) [1] and Galupino (2015) [6] also result with a decrease of permeability as fly ash increased in fly-ash-soil mix.

Classifying the blend with drainage characteristics defined by Casagrande and Fadum (1940) [16], G10 fall in poor drainage, meanwhile, G20 and G30 fall under practically impervious. With the classification, engineers must design with enough drainage system in road embankment to prevent water ingress in the road pavement.

Anisotropy ratio, kh/kv

To further validate the results of the horizontal

permeability tests, anisotropy ratio must be within the given range of Das (2008) [17]. The collected usual ratio of horizontal and vertical permeability of soils by Das (2008) [17] is with the range of 1.2-3.3, thus, the data gathered must be within the range.

Vertical permeability of the soil-geopolymer mix investigated [18] was utilized and tabulated in Table 4. From the value of the permeability, it shown that horizontal permeability was slightly higher than the vertical permeability.

Table 4. Ranges of Vertical Permeability [18]

Soil Mixture	Minimum Kv, cm/s	Maximum Kv, cm/s	Average Kv, cm/s
G10	$1.14\text{E-}04$	$2.42\text{E-}04$	$1.60\text{E-}04$
G20	$3.90\text{E-}06$	$4.98\text{E-}06$	$4.32\text{E-}06$
G30	$4.62\text{E-}07$	$7.55\text{E-}07$	$5.97\text{E-}07$

Computing the anisotropy ratio tabulate in Table 5, the ratio for all the blends ranges between 1.2-1.7, thus, ratios are within Das' desired range. The proposed permeability was viable to obtain the horizontal permeability of the soil.

Table 5. Anisotropy ratio of kh/kv

Soil Mixture	Average Kh, cm/s	Average Kv, cm/s	Average Kh/Kv
G10	$2.72\text{E-}04$	$1.60\text{E-}04$	1.70
G20	$5.25\text{E-}06$	$4.32\text{E-}06$	1.21
G30	$7.86\text{E-}07$	$5.97\text{E-}07$	1.32

CONCLUSIONS

The study investigated the effect of the geopolymer on the soil, particularly on the drainage characteristics. SEM analysis was conducted to provide a better understanding on the formulation and construction of pores spaces on the mix. The SEM showed a graphical progression of the effect of the amount of geopolymer on the soil. With the increasing percentage replacement, the pore spaces are being covered up. Consequently, the water will have limited passageway to flow through, resulting to a lower permeability.

A proposed radial flow permeameter was used to determine the horizontal coefficient permeability of the mix. The experiment obtained the degree of the permeability of G10, G20, and G30, the values were $\times 10^{-4}$, $\times 10^{-6}$, and $\times 10^{-7}$ in cm/s, respectively. As expected from the SEM, the permeability decreases along with the increase of geopolymer.

With the given set of data, the soil-geopolymer mixes were classified with their respective drainage characteristics. With the criteria provided by Casagrande and Fadum (1940), G10 fall in poor drainage, meanwhile, G20 and G30 fall under practically impervious. Based from the evaluation, the soil mixtures were concluded to be poor in drainage. However, it still can be used as an embankment material, given that the engineers must design properly the drainage system to prevent deterioration and failure of the road caused by the ingress of water.

To validate the horizontal permeability, anisotropy ratio of k_h/k_v must be fall in within Das' desired range (1.2 to 3.3). The computed ratios of all mixtures were ranged from 1.2 to 1.7, hence, the obtained horizontal permeability was acceptable. In addition, it was observed that horizontal permeability is much higher than the vertical permeability which means the flow of water in the horizontal direction is much faster compare to the vertical direction.

Lastly, with all the validation made, the proposed permeameter is viable in determining the horizontal permeability. However, the apparatus is only limited to permeability having a degree of 10^{-4} or lower.

ACKNOWLEDGEMENTS

They would like to thank their professors Dr. Mary Ann Q. Adajar, Engr. Joenel G. Galupino, Engr. Erica S. Uy, and Engr. Maria Emilia S. Miguel for imparting to them their knowledge and helping them complete their study. They would also like to thank Dr. Marolo C. Alfaro for sharing and imparting his idea and knowledge for the formation of the new horizontal permeameter set-up. They are also very thankful to Mr. Manny Leuterio and Ms. Ghaye Alegrio for providing them the dredged soil and fly ash samples for their experiments. Their experiments could not have been completed without the accommodation of their patient laboratory technician, Mr. Antonio Kalaw.

REFERENCES

- [1] Dungca, J.R., Jao, J.A.L. (2017). Strength and permeability characteristics of road base materials blended with fly ash and bottom ash. *International Journal of GEOMATE*, 12 (31), pp. 9-15.
- [2] Dungca, J., Galupino, J., Sy, C., Chiu, A.S.F. (2018). Linear optimization of soil mixes in the design of vertical cut-off walls. *International Journal of GEOMATE*, 14 (44), pp. 159-165.
- [3] Dungca, J.R., Galupino, J.G., Alday, J.C., Barretto, M.A.F., Bauzon, M.K.G., Tolentino, A.N. (2018). Hydraulic conductivity characteristics of road base materials blended with fly ash and bottom ash. *International Journal of GEOMATE*, 14 (44), pp. 121-127.
- [4] Dungca, J.R., Galupino, J.G. (2017). Artificial neural network permeability modeling of soil blended with fly ash. *International Journal of GEOMATE*, 12 (31), pp. 76-83.
- [5] Dungca, J.R., Galupino, J.G. (2016). Modelling of permeability characteristics of soil-fly ash-bentonite cut-off wall using response surface method. *International Journal of GEOMATE*, 10 (4), pp. 2018-2024.
- [6] Galupino, J.G., Dungca, J.R. (2015). Permeability characteristics of soil-fly ash mix. *ARPN Journal of Engineering and Applied Sciences*, 10 (15), pp. 6440-6447.
- [7] Engler, T. W. (2010). Fluid flow in porous media. Retrieved from <http://infohost.nmt.edu/~petro/faculty/Engler524>
- [8] De Guzman, E., Stafford, D., Alfaro, M., Dore, G., & Arenson, L. (2016). Large-Scale Direct Shear Testing of Laboratory-Compacted Frozen Soil Under Freezing and Thawing Conditions.
- [9] American Society for Testing and Materials. (2017). Standard Test Methods for Specific Gravity of Soil Solids by Water Pycnometer. ASTM D854.
- [10] American Society for Testing and Materials. (2017). Standard Test Method for Particle-Size Analysis of Soils. ASTM D422.
- [11] American Society for Testing and Materials. (2017). Standard Proctor Test. ASTM 698.
- [12] Dungca, J.R., Codilla, E.E.T., II. (2018). Fly-ash-based geopolymer as stabilizer for silty sand embankment materials. *International Journal of GEOMATE*, 14 (46), pp. 143-149.
- [13] Tigue, A.A.S., Dungca, J.R., Hinode, H., Kurniawan, W., Promentilla, M.A.B. (2018). Synthesis of a one-part geopolymer system for soil stabilizer using fly ash and volcanic ash. *MATEC Web of Conferences*, 156, art. no. 05017, .
- [14] Dungca, J. R., & Dychangco, L. F. T. (2016). Strength properties of road base materials blended with waste limestones. *International Journal of GEOMATE*, 11(3), 2493-2498.
- [15] Ang, Isaac, Joven, & Sollano. (2016). Use of dry mixing method in fly ash based geopolymer as a stabilizer for dredged soil (Unpublished undergraduate thesis). De La Salle University.
- [16] Casagrande, A. and R.E. Fadum (1940). "Notes on soil testing for engineering purposes," Harvard Univ. Grad. School of Engineering Publ.

268, 74 pp.

[17]Das B. M. (2008). Advanced soil mechanics.
New York: Taylor & Francis.

[18]Dungca J., Lao W., Lim M., Lu W., and
Redelicia J. C. (2017). Permeability

characteristics of dredged soil stabilized with fly-
ash based geopolymer for road embankment . De
La Salle University.

VERTICAL PERMEABILITY OF DREDGED SOIL STABILIZED WITH FLY-ASH BASED GEOPOLYMER FOR ROAD EMBANKMENT

Jonathan R. Dungca¹, Winchell Dunley T. Lao², Matthew Lim², Wilson D. Lu² and Juan Carlos P. Redelicia²

¹Faculty, De La Salle University, Philippines; ²Graduate, De La Salle University, Philippines

ABSTRACT

This study presents the vertical permeability and strength relationship of dredged soil stabilized with fly-ash based geopolymer which is to be used for constructing road embankments. The fly-ash used for this study was a low-calcium (Class F) fly-ash. The varying effects on both properties due to the different partial replacements of geopolymer were studied. 10%, 20%, and 30% of the soil sample's mass were used as partial replacement. The samples were prepared using the dry-mix method and subjected to 28 days of air-dried curing. Tests like the unconfined compressive strength test and the falling head permeability test were conducted. The morphological features of the samples were investigated using the scanning electron microscopy (SEM). The test results showed that as the percentage replacement of geopolymer increases, the samples become less permeable. SEM analyses confirmed the results, showing that the geopolymer tend to cover up the pore spaces of the soil, causing the water to have less passageways.

Keywords: Fly-ash, Geopolymer, Dredged soil, Permeability, Unconfined Compressive Strength

INTRODUCTION

Road infrastructure is very essential to developing countries like the Philippines. These facilitate the trade, communication, and travelling purposes. The advancement of the economy is heavily reliant on these. Having bad and poorly maintained roads causes inconvenience like road damages and flooding, which cause severe traffic and leads to slow progression of the economy.

Permeability is a very important parameter to consider when designing road embankments. There should be a compromise between the strength and the permeability. Numerous studies have shown that an increase in the strength of the soil leads to a decrease in its permeability. In a country like the Philippines wherein heavy rains are very frequent, it becomes a must for roads to exhibit good drainage. When there is low permeability, water tends to accumulate very fast and exert pore water pressure, causing ponding and the deterioration of the embankment.

The construction of roads embankments requires different materials like aggregates, lime, and cement. Unfortunately, the production of cement may impose some harm to the environment, as it generates greenhouse gases due to the emission of carbon dioxide. The can constitute to the rising state of global warming [1]. Numerous studies have shown that coal combustion by-products, or more commonly known as CCPs, have been found to be a good choice because it is very abundant in the country and has a problem in disposal [2]-[8]. Furthermore, the use of these CCP's can bring economic and environmental benefits.

One of the most common examples of CCP's is fly-ash. It is a by-product of the coal-fired power plant and is posing a great threat to the environment. When discharged by the power plants, it is immediately considered as wastes. Only around half of it are used for recycling. The rest are thrown out into lands and bodies of water [2]. Some studies have been made to utilize these ashes in different fields. Some are used as embankment fill, cement alternative and as soil stabilizer for road embankments.

Since dredged soil possess weak strength, there is a need to stabilize it, for it to be usable for construction purposes. The soil for this study will be stabilized using geopolymer mixed with class F fly-ash. Geopolymer is synthesized through a natural reactive property of aluminosilicate material when mixed with an alkali-activator. It is an inorganic polymer made up of covalently bonded molecules. It undergoes polymerization which involves a chemical reaction on Si-Al minerals under alkaline condition forming series of sialate monomers like cement properties [9].

The aim of this study is to analyze the relationship between the strength and permeability of the blends and give recommendations based on the results generated.

METHODOLOGY

To provide a standard uniformity between samples, the dredged soil and fly ash was obtained only from a thermal power plant in Mindanao. The dredged soils were sieved to have up to the required

maximum sizes, particularly sieve number 4 or a nominal opening of 4.76mm followed by the removal of its moisture content thru oven-drying. The fly ash obtained was classified as Class F.

The index properties of the dredged soil were determined by conforming to the ASTM procedures.

- a. Specific Gravity of Soils (ASTM D854) [10]
- b. Particle Size Analysis (ASTM D422) [11]
- c. Standard Proctor Test (ASTM D698) [12]

Conventional materials and blended samples were individually subjected to microscopic testing to evaluate the void spaces present using the Scanning Electron Microscopy (SEM).

The geopolymer based fly ash mix used was based on the mix design formulated by Ang, et al. (2016) [9] which were used for the preparation of samples for the testing of strength and permeability tests of each blends. The geopolymer mix design is presented in Table 1.

Table 1. Geopolymer Mix

Geopolymer Concentration (%)	Alkaline Activator/ Fly Ash	Sodium Silicate/ Sodium Hydroxide	NaOH Concentration
10, 20, 30	0.4	2	14 M

The blended samples vary from 10%, 20% and 30% of partial replacement of geopolymer to the total weight of dredged soil. The blended samples are obtained by providing first the dredged soil to attain its maximum dry unit weight based from optimal moisture content (OMC) that was determined through the Standard Proctor Test.

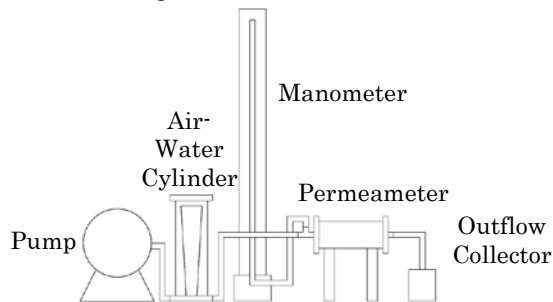


Figure 1. Experimental Set-up for Vertical Permeability [3-7]

Falling Head Permeability Test (ASTM D5084) [13] were conducted to evaluate the drainage characteristics of all the blends considering a relative compaction of 100%. However, a relative compaction of 100% is somehow unattainable due to tamping constraints, each sample were just subjected to a constant of 25 blows per 3 layers using hand tamping. The acquired set-up for the permeability test is shown on Figure 1.

RESULTS AND DISCUSSIONS

Scanning Electron Microscopy (SEM) Results

The scanning electron microscopy (SEM) is commonly used for getting a high-resolution image of the spaces between particles in the surface. Two levels of magnification, x500 and x5000, were used in the analysis to fully understand the bonds between the particles of the sample.

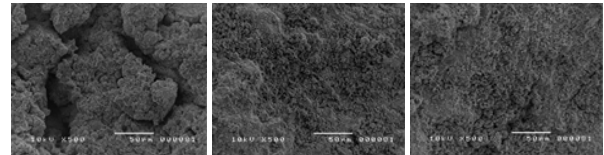


Figure 2. a) 10% b) 20% c) 30 % replacements with magnification level of x500

Comparing the voids seen on the SEM of each blend as shown in figure 2, figures 2(b), and 2(c) are observed to have almost no voids while figure 2(a) clearly shows the presence of spaces between the particles where the water can easily pass through. This means that the sample with 10% replacement of geopolymer could be more permeable, as compared to the 20% and 30% replacements. Furthermore, the researchers have observed that there is only a small difference between the void spaces between 20% and 30% replacement.

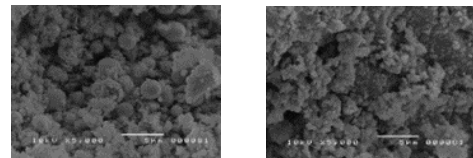


Figure 3. a) 20% b) 30% replacements with magnification level of x5000

An increased magnification level by x5000 was conducted to clearly distinguish the difference between the 20% and 30% replacement in terms of the void spaces present. As can be seen from the SEM photo (x5000) presented in Figure 3, voids spaces are still present that allows water to pass through. The 20% replacement is observed to have more void spaces as compared to the 30% replacement; thus, the 20% replacement is more permeable than the 30%, as expected by the group. Also, the particles in 30% replacements are completely covered, as shown in figure 3(b). The case is different with the 20% replacement, wherein there can still be found some particles of fly ash that did not react with the reactors which represented by the spheres seen in figure 3(a). The geopolymer in 30% replacement was able to coat the sands and provided greater bonding with the other sand particles, blocking the passageway for the water.

Gradation

The variation of particle size of the dredged soil can be measured based on the parameters, coefficient of uniformity and curvature, as shown in Table 2. These coefficients define the grade of soil which is based on ASTM D2487. As observed, the coefficient of uniformity (Cu) of the dredged soil was found to be having values less than 6. This indicates that the soil contains particles having uniform size. Moreover, the grain size distribution curve (GSDC) of the 3 trials was observed to have steep slopes which are almost vertical. Thus, this verifies that the variation of particles sizes is within a narrow limit.

The coefficient of curvature (Cc) of the dredged soil was found to be having an average of 2.97, which is within the range 1-3. This signifies a well-graded soil. Thus, the dredged soil could cover almost all grain sizes. Also, observed from the GSDC, there were no sudden changes of slope which would signify the absence of certain grain sizes. The dredged soil was found to be falling under the classification of poorly graded soil since the Cu was less than 6 (Cu>6, well-graded soil for sand) but the Cc was between the range 1-3 (1-3, well-graded soil) though it was already at the limit's boundary.

Table 2. Uniformity and Curvature of Dredged Soil

Trial	Coefficient of Uniformity (Cu)	Coefficient of Curvature (Cc)
1	4.06	3.01
2	4.35	2.96
3	4.26	2.93
Average	4.22	2.97

Unconfined Compressive Strength

A dredged soil is mostly made up of sandy particles which allows it to exhibit the property of the sand and not being able to provide confinement. Thus, it is incapable of maintaining a firm stand and form a cylindrical shape even though there has been no load being applied. Also, the dredged soil obtained has been identified to manifest poor geotechnical properties. As a result, geopolymers would be added to enhance the geotechnical properties of the dredged soil. Consequently, for that reason, the researchers are incapable to produce soil samples made up of only pure dredged soil for the unconfined compression test (UCT). The unconfined compression strength test is commonly used for

determining the improvement of stabilized soils [14].

Given that the UCT cannot be done for pure dredged soil, blending of geopolymer mix of different percentage was incorporated, specifically 10%, 20% and 30%. By observation, the addition of geopolymer mix with an inclusion of curing for twenty-eight days showed that it was able to bind the soil particles allowing the soil to stand firmly and form a cylindrical shape without confining pressure. Based from observation, the geopolymer acts as the binder for the soil in the form of stabilization. In addition, the geopolymer mix exhibits cement-like properties that similarities on its physical properties are noticeable.

Table 3 presents the progression of the stabilized soil as more of the geopolymer is being added. It is anticipated that the unconfined compressive strength of the mixture increases with the continual addition of the geopolymer. As observed, the incremental increase of strength is exponentially related to the percent replacement of geopolymer.

Table 3. Unconfined Compressive Strength of Mix

28 days Curing	Geopolymer Mix		
	10%	20%	30%
Unconfined Compressive Strength (MPa)			
Trial 1	0.198	0.3217	1.309
Trial 2	0.2228	0.2868	1.550
Trial 3	0.1789	0.3265	1.432
Average	0.1999	0.3117	1.4306

A 10% partial replacement produced an average unconfined compressive strength of 199.9kPa. This was classified as a stiff soil, based on the classification set by Liu and Evett, 2009 [15]. The classification is shown below in Table 4. When the percentage replacement was increased to 20%, on the other hand, it resulted to an average unconfined compressive strength of 311.7kPa. This was classified as a very stiff soil. Lastly, 30% partial replacement resulted to an average unconfined compressive strength of 1430.6kPa. This was classified as a hard soil.

The strength behavior brought about by the geopolymer to the soil is because the geopolymer possesses cementitious materials. These undergo polymeric reactions, resulting in the formation of aluminosilicate three-dimensional networks whose

strength can be even higher to that of conventional concrete [16].

The stress-strain diagram of each blends, specifically 10%, 20% and 30%, with 3 different trials were conducted. The illustrations presented are the behavior of the soil mixture at different percentages when subjected to loading. By analyzing the graphs, the increase in the concentration of geopolymer had caused the mixture to become brittle with the increase in strength. It exhibits the same property with concrete wherein high compressive strength concrete produces low strain and suddenly fails.

Table 4. Standard Relationship of Consistency and Unconfined Compressive Strength of Soil [15]

Classification	Unconfined Compressive Strength (KPa)
Very Soft Soil	25
Soft Soil	25-50
Firm Soil	50-100
Stiff Soil	100-200
Very Stiff Soil	200-400
Hard Soil	>400

Vertical Permeability

Permeability is an important factor to consider when increasing the strength of the soil. The effect of the polymerization is presented in Table 5, wherein it shows the change in permeability between dredged soils with and without geopolymer present. The dredged soil alone was found to have an average hydraulic conductivity of $1.04\text{E-}02$ cm/s. A 10% geopolymer replacement produced an average of $1.60\text{E-}04$ cm/s. A 20% geopolymer replacement had an average of $4.32\text{E-}06$ cm/s. And the 30% replacement produced an average of $5.97\text{E-}07$ cm/s.

The results were classified in accordance to the criteria set by Casagrande and Fadum (1940) [17].

A 10% geopolymer replacement resulted in poor permeability. The 20% and 30% replacements were considered as practically impervious.

The trend shows that the additional replacement of the geopolymer further decreases the permeability. According to Ma, Hu, and Ye (2012) [18], the pore size distribution and connectivity, including the shape and volume of the pore spaces

are very important factors in the investigation of the permeability. Much of this is governed by the amount of geopolymer applied to the sample. During the process of increasing the strength of the soil through stabilization, the sample undergoes through geopolymerization. The pozzolanic reaction causes the particles to bind together. This then closes the pore spaces to increase the strength. Therefore, it becomes more difficult for the water to flow through the sample.

Table 5. Coefficient of Permeability in the Vertical Direction for Varying Replacement of Geopolymer-Soil Mix (cm/s)

Trial No.	Pure	10%	20%	30%
1	9.85E-03	2.42E-04	3.90E-06	4.77E-07
2	9.51E-03	1.27E-04	4.98E-06	7.55E-07
3	1.01E-02	1.18E-04	3.94E-06	4.62E-07
4	1.16E-02	1.99E-04	4.45E-06	7.16E-07
5	1.06E-02	1.14E-04	4.34E-06	5.73E-07
Ave.	1.04E-02	1.60E-04	4.32E-06	5.97E-07

Box and whisker plot provided the midspread values of each replacement. Using an IQR of 1.5, the obtained coefficient of permeability was fall in the range between 25th and 75th percentile; therefore, there is no outlier.

As discussed, there was a significant behaviour that relates permeability with strength. It could be observed that the permeability is inversely related to strength. A related study conducted by Olivia and Nikraz (2011) [19], also noticed and stated that there is an inverse relationship between the strength and permeability of the geopolymer mix. As the strength increases, the permeability starts to decrease. They compared their trend to the results of Cheena, et. al (2009) [20] where both researchers got similar trend for the permeability and unconfined strength. The researchers observed that their samples had the same trend as Olivia and Nikraz'. The same trend can also be found in the study of Wongpa et. al (2010) [21], stating that the permeability is indeed dependent on the strength of the geopolymer mix. The reason behind the trend is that as the percentage replacement of geopolymer increases, the void spaces decrease as seen from the SEM images which resulted to the increase of strength and consequently, the decrease of its permeability.

The difference between each mix's void spaces affected the permeability since more void spaces means that water can easily flow and pass through the samples. Another observation that was made from the SEM analysis was the small difference of void spaces between 20% and 30% replacement. It can be seen from the graph that there is also a small difference between the permeability of 20% and 30% compared to the 10%. The void spaces from the 10% mix can be clearly seen by the naked eyes

while the void spaces of 20% and 30% mix can only be seen through SEM.

By Regression Analysis, an empirical formula was formulated to obtain the coefficient of permeability with respect to percent replacement. The coefficient of permeability can be obtained from the formula:

$$k = e^{(-5.08 - 0.329G)} \quad (1)$$

Where:

k = coefficient of permeability (cm/s)

G = percent replacement of fly-ash based geopolymer

The regression was able to obtain a coefficient of correlation equal to 0.9744 which is almost equal to 1, thus, makes the empirical formula acceptable. The model or formula formulated allows engineer to have the desired permeability characteristics for its embankment based on the geopolymer replacement. Also, it could allow engineers to approximate permeability characteristics in order to design the appropriate drainage needed for the embankment with respect to the replacement desired for the project. However, the model provided is only limited in providing the estimated hydraulic conductivity value up to 30% replacement, thus, further study must be conducted if greater geopolymer mix is needed. Also, this study is only applicable for a single compaction which was based from the Proctor Test achieving a theoretical 100% relative compaction.

Recommendation on the Results

When using stabilized materials for constructing road pavements, there will always be a compromise between the strength and the permeability, The American Concrete Pavement Association (1994) [22]. Even though the material possesses good permeability, it may be still possible to become insufficient in supporting construction operations and carrying loads, since the strength is not that high. When stabilized materials are used, a sacrifice in its permeability comes along with the increase in strength.

This study was able to confirm that fly-ash based geopolymers are indeed capable of enhancing the strength of soil at a significant amount. Unfortunately, it has also resulted in a drastic decrease in its permeability, as discussed earlier. This raises a big concern especially that this material is to be used as road embankments in countries which experience frequent heavy rain like the Philippines. Another challenge arises on how to efficiently utilize such a material with good strength but poor permeability for the construction of road embankments.

Since the stabilized soil possess poor permeability, Lovering and Cedergren (1962) [23] suggested that there should be sufficient drainage outlets, for the embankments to be effective in draining. They strongly recommended that these drainage outlets should also be maintained regularly so that they do not become clogged and create a “bathtub” effect in the drainage layer. Past studies have come to conclusions that the drainage layer alone cannot guarantee an improved permeability performance. The entire drainage system must have enough capacity and must also be working efficiently. Thus, it is important to have the drainage layer, outlet drains, and outlet pipes to be efficient for the expected water infiltration during rainfall. Regular maintenance must also be conducted. This is to ensure that water infiltrated can be drained out as quickly as possible before they get into the embankment [24].

CONCLUSIONS

A pure dredged soil, in its nature is capable of draining water at a good rate. However, it is very weak and cannot be purely used for road embankment purposes. Soil types such as this needed to be stabilized. A fly-ash based geopolymer was found to be a very good stabilizer in enhancing the strength of the soil mixture. A 10% partial replacement by mass of the geopolymer resulted in an average unconfined compressive strength of 0.1999 MPa, and has been classified as a stiff soil. A 20% replacement produced an average unconfined compressive strength of 0.3117 MPa, and was classified as a very stiff soil. The researchers also noticed that the 30% replacement has vastly improved the strength of the soil. Its unconfined compressive strength reached an average of 1.432 MPa. This was classified under the hard soil category. It is very evident that the strength increases along with the additional amount of geopolymer being added. The soil mixtures were observed to have almost the same properties with those of concrete.

The vertical permeability of the samples was also investigated. As expected, there was an inverse relationship between the strength and the permeability of the samples. The permeability decreases as the strength increases. Pure dredge soil has an average hydraulic conductivity of 1.04E-02 cm/s. A 10% partial replacement results in an average hydraulic conductivity of 1.60E-04 cm/s. A 20% partial replacement, on the other hand, results in an average hydraulic conductivity of 4.32E-06 cm/s. Last, a 30% partial replacement results in an average hydraulic conductivity of 5.97E-07 cm/s. The 10% replacement was classified to have poor permeability, and both the 20% and 30% were considered practically impervious.

The use of this material can be very helpful in constructing road embankments. However, engineers must take precautions in using this since the permeability is not that good. They must find a way to be able to compromise both the strength and the permeability in order to maximize the use of this material. It is important to always remember that the drainage of roads must not be relied solely on the road embankments. There should always be proper surface drainage systems installed. They must also be working efficiently and frequently maintained.

REFERENCES

- [1] Roy, D.M., Alkali-activated cements opportunities and challenges. *Cement & Concrete Research*, Vol. 29, No.2, 1999, pp.249-254.
- [2] Dungca, J.R., Jao, J.A.L. Strength and permeability characteristics of road base materials blended with fly ash and bottom ash. *International Journal of GEOMATE*, 12 (31), 2017, pp. 9-15.
- [3] Dungca, J., Galupino, J., Sy, C., Chiu, A.S.F. Linear optimization of soil mixes in the design of vertical cut-off walls. *International Journal of GEOMATE*, 14 (44), 2018, pp. 159-165.
- [4] Dungca, J.R., Galupino, J.G., Alday, J.C., Barretto, M.A.F., Bauzon, M.K.G., Tolentino, A.N. Hydraulic conductivity characteristics of road base materials blended with fly ash and bottom ash. *International Journal of GEOMATE*, 14 (44), 2018, pp. 121-127.
- [5] Dungca, J.R., Galupino, J.G. Artificial neural network permeability modeling of soil blended with fly ash. *International Journal of GEOMATE*, 12 (31), 2017, pp. 76-83.
- [6] Dungca, J.R., Galupino, J.G. Modelling of permeability characteristics of soil-fly ash-bentonite cut-off wall using response surface method. *International Journal of GEOMATE*, 10 (4), 2016, pp. 2018-2024.
- [7] Galupino, J.G., Dungca, J.R. Permeability characteristics of soil-fly ash mix. *ARPJ Journal of Engineering and Applied Sciences*, 10 (15), 2015, pp. 6440-6447.
- [8] Dungca, J.R., Codilla, E.E.T., II. Fly-ash-based geopolymer as stabilizer for silty sand embankment materials. *International Journal of GEOMATE*, 14 (46), 2018, pp. 143-149.
- [9] Ang, Isaac, Joven, & Sollano. Use of dry mixing method in fly ash based geopolymer as a stabilizer for dredged soil (Unpublished undergraduate thesis). De La Salle University, 2016.
- [10] American Society for Testing and Materials. Standard Test Methods for Specific Gravity of Soil Solids by Water Pycnometer. ASTM D854, 2017.
- [11] American Society for Testing and Materials. Standard Test Method for Particle-Size Analysis of Soils. ASTM D422, 2017.
- [12] American Society for Testing and Materials. Standard Proctor Test. ASTM 698, 2017.
- [13] American Society for Testing and Materials. Falling Head Permeability Test. ASTM D5084, 2017.
- [14] Wong, L., Hashim, R., & Ali, F. Improved strength and reduced permeability of stabilized peat: Focus on application of kaolin as a pozzolanic additive. *Construction and Building Materials* 40, 2012, pp. 783-792.
- [15] Liu, C., & Evett, J.. SOIL PROPERTIES: Testing, Measurement, and Evaluation (6th ed.), 2009.
- [16] Mehta, A. and Siddique, R. Strength, permeability, and micro-structural characteristics of low-calcium fly ash based geopolymers. *Construction and Building Materials* 141 (2017), 2017, pp. 325-334.
- [17] Casagrande, A. and R.E. Fadum. Notes on soil testing for engineering purposes, Harvard Univ. Grad. School of Engineering Publ. 268, 1940, 74 pp.
- [18] Ma. Y., Hu. J., & Ye, G. (2012). The pore structure and permeability of alkali-activated fly ash. *Fuel* 104 (2013), 2012, pp. 771-780.
- [19] Olivia, M., & Nikraz, H. R. (2011). Strength and water penetrability of fly ash geopolymer concrete . *ARPJ Journal of Engineering and Applied Sciences*, Vol. 6 No. 7, 2011, pp. 70-78.
- [20] Cheena D.S., Llyod N.A., and Rangan B.V. Durability of geopolymer concrete box culverts- a green alternative. In: 34th conference on Our World in Concrete and Structures. CiPremier, Singapore, 2009.
- [21] Wongpa, J., Kiattikomol K., Jaturapitakkul, C., Chindaprasirt C. Compressive strength, modulus of elasticity, and water permeability of inorganic polymer concrete. *Materials and Design*, 31, 2010, pp. 4748-4754.
- [22] American Concrete Pavement Association. Cement-treated permeable base for heavy-traffic concrete pavements. *Concrete Information*, 1994.
- [23] Lovering, W. & Cedergren, H. Structural section drainage. *Proceedings, International Conference on the Structural Design of Asphalt Pavements*, University of Michigan, Ann Harbor, Mich., August 20-24, 1962, pp. 773-784.
- [24] Harvey, J., Tsai, B., Long, F., & Hung, D. CAL/APT Program - Asphalt treated permeable base. *Laboratory Testing, Performance, Predictions, and Evaluation of the Experience of Caltrans and other Agencies*, 1999.

PERFORMANCE OF SOIL SUBGRADE IMPROVEMENT USING WASTE MATERIAL

Harnedi Maizir¹, Reni Suryanita², Ulfa Jusi³ and Raihan Arditama⁴

^{1,3}Faculty of Civil Engineering, Sekolah Tinggi Teknologi Pekanbaru, Indonesia;

² Faculty of Engineering, University of Riau, Pekanbaru, Indonesia

⁴ Faculty of Engineering, University of Andalas, Padang, Indonesia

ABSTRACT

The last decades, many researchers present the paper regarding to the potential of using fly ash and bottom ash as a waste material in order to improve the soil subgrade layer in road project. The fly ash and bottom ash used in this study from one of power plant in pulp paper industry in Riau. The aim and objective of this study is to determine the California Bearing Ratio (CBR) value for soil road subgrade mixed with some percentage of waste material, especially from fly ash. The second objective is to determine the optimum of percentage using fly ash mixed with the soil. The laboratory testing of the soil mixed with the fly ash on the CBR value for soaked and un-soaked condition. The stabilized of the soil subgrade mixed with the waste material were compared to the control sample of the road subgrade criteria accordingly to Indonesia Public Work Department (PUPR) from Standard Specification for Road Works. According to the laboratory testing result shows, the improvement of CBR value from two type of mixed of soil and fly ash, first is soil : fly ash = 60%:40% and the second is 50%:50%. The optimum percentage of fly ash used is the second mixed. The use of second mixed in order to improve the soil subgrade of CBR value for soaked and un-soaked condition. However, the result of CBR value for both condition were fulfil the requirement for road subgrade criteria from PUPR Indonesia for Standard Specification for Road Works. These study shows, waste material like bottom ash could be used as an alternative solution to mix with the soil to improve the CBR value.

Keywords: Waste material, Fly ash, California bearing ratio, Road subgrade

INTRODUCTION

The last decades, most of researcher from other countries focus to the coal as a fuel alternative for power generation. Indonesia was introduced coal as raw material for power generation since 1986. Nowadays, there are two coal power plants in Riau province namely, Riau Andalan Pulp and Paper (RAPP), Indah Kiat Pulp and Paper (IKPP). Increasing in electricity consumption demand has led to increase the coal consumption required and thus more produced, more waste products. Coal ash mostly consists of fly ash and bottom ash. Wahab (2006) mentioned that, about 2500 ton/months of fly ash was produced by RAPP as waste material. The problems become worse to disposal of ash are limited availability of land and this has a significant problem to the environmental.

The previous studies showed that the engineering properties of waste materials, such as fly ash and bottom ash were more effective to improve the performance of subgrade layer of the pavement than those common pavement material. (Norazalan et al., 2011) and (Ferreira et al., 2003).

This study focuses on the alternatives for using waste material from coal power plants, especially from fly ash and the potential as additives to the road subgrade layer of pavement. This study was

determined the California Bearing Ratio(CBR) value for soaked and unsoaked condition to the use of fly ash mixed to the soil subgrade layer of pavement.

MATERIALS AND METHODS

Waste Material (Fly ash)

The waste material used in this study considered were collected from RAPP Plant in Pangkalan Kerinci – Riau Province. The waste materials are waste product produced from combustion of coal for electric power generation. A detail physical properties of waste material from plants was shown in Table 1.

Table 1 Physical properties of RAPP waste material

Properties	Values
Spesific gravity	2,05
Particle size distribution:	
Gravel (%)	0
Sand (%)	22,92
Fine/Silt (%)	77,08

The result for chemical properties of the waste material test is shown in Table 2.

Table 2. Chemical properties of RAPP Fly ash (FA)

Chemical properties	Chemical values (%)
Silicaon Dioxide	48,2
Aluminium Trioxide	13,2
Fero Oxide	4,3
Calcium Oxide	18,6
Magnesium Oxide	0,9
Loss on Ignition	8,4

Based on the result of physical properties test, it shows that the RAPP fly ash (FA) classified as light materials due to the specific gravity is about 2,05. According to (Muhardi et al., 2010), the lower specific gravity of fly ash due to the lower fero oxide content since the specific gravity related to the chemical composition. Based on Table 2 shows that the RAPP fly ash (FA) classified as class C fly ash accordance to ASTM C618. RAPP fly ash (FA) consists of total combination composition of silicon dioxide, aluminium dioxide and fero oxide more than 50%.

Soil Road sub-grade.

The properties of soil using in this study are given in Table 3. As per Unified Soil Classification System (USCS), the soil is a MH soil.

Table 3. Soil properties

Description parameter	value
Specific Gravity	2,56
Atterberg Limits	
LL	61,67
PL	44,10
IP	17,60
Compaction Factor	
γ (gr/cc)	1,27
w (%)	38,25
Particle size distribution	
Passing #200 (%)	97,33
Passing #4 (%)	100,00

Laboratory Testing

The are some testing carried out in this study to determine the index and engineering properties of the soil sub-grade. The testing method based on ASTM standard for each test.(ASTM & D1883, 2014)

Preparation of sample

The testing used in this study is the California Bearing Ratio (CBR) test. Two sets of sample were prepared to determine the CBR value of this samples. First sample is mixed with the soil 60% and waste material 40%. The second sample is mixed with the soil 50% and waste material 50%. There are two number of sample for each test to be prepared.

California Bearing Ratio (CBR) Test

The California Bearing Ratio(CBR) tests were carried out to determine the CBR index value and the test carried out based on standard procedure given in ASTM D1883. CBR test method is used to evaluate the potential strength of the subgrade material. CBR defined as the ratio of the load sustained by the specimen at 2,5 or 5,0 mm penetration to the load sustained by standard load aggregate at corresponding penetration level.

The entire tests to determine CBR value were performed in soaked and unsoaked condition. The samples were prepared with its optimum moisture content and were compacted at their maximum dry density.

RESULTS AND DISCUSSIONS

The Laboratory result for CBR value for soaked and unsoaked condition

Figure 1 and Figure 2 shows the laboratories result for CBR value of soil subgrade (50%) mixed with waste material (50%) for soaked and unsoaked condition.

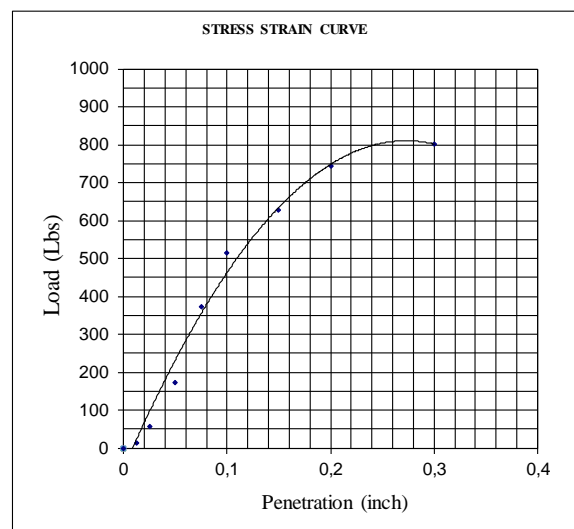


Fig. 1 The laboratory result for CBR value soaked 50%-50%

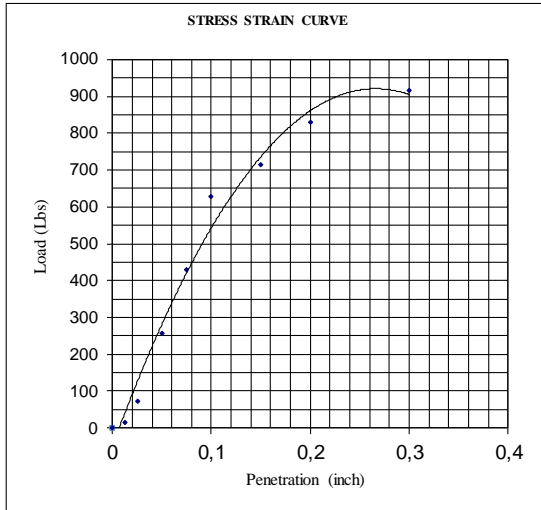


Fig. 2 The laboratory result for CBR value unsoaked 50%-50%

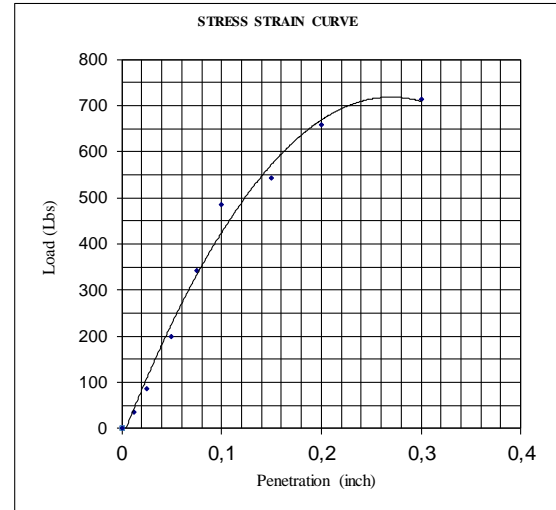


Fig 4 The laboratory result for CBR value unsoaked 60%-40%

Figure 3 and Figure 4 shows the laboratories result for CBR value of soil subgrade (60%) mixed with waste material (60%) for soaked and unsoaked condition.

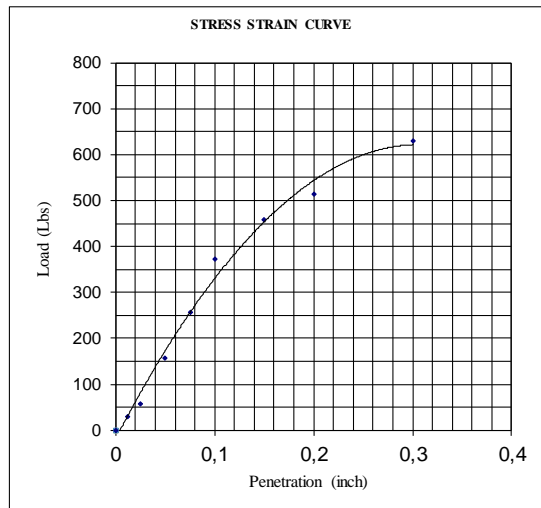


Fig 3 The laboratory result for CBR value soaked 60%-40%

The California Bearing Ratio (CBR) mixed with waste material

Table 4 shows the CBR value versus percentage of waste material from RAPP mixed with soil subgrade for soaked and unsoaked condition. Its shows that the CBR value for soaked condition relatively lower than CBR value for unsoaked condition. Its cause of saturated of soil for soaked condition. It shows the CBR values increase 24,3% for 60%-40% soil mixed for soaked and unsoaked condition. For the 50%-50% mixed with the soil and waste material, the CBR value increase 17,9% for soaked and unsoaked condition

Table 4 The CBR value for soaked and unsoaked condition at every percentage of waste material

Sample	Soil:Waste of material (%:%)	CBR soaked %	CBR unsoaked %
1	60 : 40	11,9	14,8
2	50 : 50	16,2	19,1

CONCLUSION

According to this study, waste material from RAPP coal power plant (fly ash and bottom ash) are suitable material to be used as additive for soil subgrade. It was proved by laboratory experimental result. By using the waste material (fly ash and bottom ash) as an additive material to the soil mixed was improved the CBR value strength. The percentage is suitable for soaked and unsoaked condition accordingly to the CBR value index

ACKNOWLEDGEMENTS

The authors would like to thank STT-Pekanbaru for using the soil mechanic laboratory and Kemenristekdikti-Indonesia for funding this research year 2018.

REFERENCES

- [1] ASTM, & D1883. (2014). Standard test method for California bearing ratio (CBR) of laboratory-compacted soils: ASTM International West Conshohocken, PA.
- [2] Ferreira, C., Ribeiro, A., & Ottosen, L. (2003). Possible applications for municipal solid waste fly ash. *Journal of hazardous materials*, 96(2-3), 201-216.
- [3] Muhandi, A., Khairul, A., Wei, L., & Lim, Y. (2010). Engineering Characteristics of Tanjung.
- [4] Norazalan, Norbaya, & Fadzil, M. (2011). *The Potential of using Bottom Ash (BA) Additives in Road Base*. Paper presented at the International Building and Infrastructure Technology Penang, Malaysia.

EFFECT OF GRADATION OF BOTTOM ASH AS FINE AGGREGATE ON ENGINEERING PROPERTIES OF SHOTCRETE

Sattaya Chaiwithee¹, Pitiwat Wattanachai¹ and Pisut Rodvinij¹

¹Faculty of Engineering, Chiang Mai University, Thailand

ABSTRACT

This study focused on the effect of grain size distribution of bottom ash on the engineering properties of shotcrete. Bottom ash was used as fine aggregate replaced fine sand in the mixture of shotcrete. Size distribution of aggregate that used in the test consists of upper boundary and lower boundary of gradation No.1 references from ASTM C33 and aggregates passed sieve No.4. The mixture of mortar was a combination of Portland cement and fine aggregate is the ratio of 1:3. Water to cement ratio for a mortar is 0.6. The physical characteristics of the bottom ash particles showed high porosity, very irregular and brittle. Therefore, the compressive strength of bottom ash aggregate mortar was less than sand aggregate mortar approximately 45%. The compressive strength of the samples mixed with bottom ash passed sieve No.4 gave the highest strength. The compressive strength of the samples contains the maximum, minimum size distribution and aggregate passed sieve No.4 were 7.7, 10.6 and 12.6 MPa respectively. The results of slump flow tests demonstrated the flow of mortar tends to increase with the reduction in the particle size of aggregate. Nevertheless, the setting time tends to decrease with the reduction in the particle size of aggregate. In conclusion, bottom ash passed sieve No. 4 was the most suitable to use as fine aggregate in the mixture of shotcrete.

Keywords: Bottom ash, Shotcrete, particle size and light weight

INTRODUCTION

Area 4.1 located on the northeast side of the pit wall in Mae Moh mine as shown in Fig. 1. According to the mine plan, K and Q seams (green layer and red layer in Fig.1) of lignite must be excavated [1]. The cut and fill method become a suitable method was used to excavate lignite in this area. The area will be mined and partially undercut. After completion of mining, backfilling will begin to support the slope face and maintaining adequate room for mining activities. The mining- backfilling cycle is iterative until all the lignite in area 4.1 is completely mined out. It is necessary to fill the current pit and cut the neighboring slope in a subsequent procedure [1], [2].

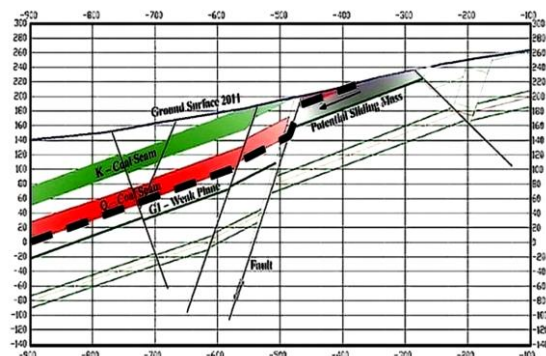


Fig. 1 Cross section plot of area 4.1 [1].

Claystone has been used as a backfill material to counterweight and supported the potential mass. However, claystone deteriorated when it has been exposed to weather change was a cause of decreased in a stability of backfill [3].

The literature review demonstrated claystone protected from a weather change can maintain physical properties of claystone and shear strength of backfill [3]. Thus, shotcrete becomes the suitable stabilization method to maintain the stability of claystone backfill slopes. Due to shotcrete is often used for temporary protection of exposed rock surfaces that will deteriorate when exposed to air and also used to permanently cover slopes or cut that may erode in time or otherwise deteriorate [4].

Normally, the proportion of the shotcrete mixture consists of cement, sand, and water and the unit weight of normal shotcrete was approximately 2.2 T/m³ [5]. The external load that increases on a backfill due to the unit weight of shotcrete can lead to reducing the stability of slopes. Thus, the lightweight shotcrete became a good choice to stabilize the stability of backfill slope better than a normal shotcrete.

Therefore, this study focused on the lightweight shotcrete by using bottom ash, which is by-product materials from Mae-Moh power plant as fine aggregate in the mixture of shotcrete.

However, Aggregate of shotcrete mortar should comply with the quality requirements of ASTM C 33. Table 1 shows acceptable grading limits. Grading No. 1 should be used if a mortar mixture

desired [4]. However, grading No.1 shown the lower and upper limit of the aggregate. The different size distribution of aggregate in the mixture of mortar can be altered the properties of shotcrete mortar. Thus, the investigation on the influence of the different size distribution of fine aggregate in the mixture can suggest a lower and upper limit properties of shotcrete.

Table 1 Grading Limits for Aggregate [4]

Sieve Size	Percent by Mass Passing Individual Sieves		
	Grading No.1	Grading No.2	Grading No.3
¾ inch			100
½ inch		100	80-95
3/8 inch	100	90-100	70-90
0.19inch(No.4)	95-100	70-85	50-70
0.093inch(No.8)	85-100	50-70	35-55
0.046inch(No.16)	50-85	35-55	20-40
0.024inch(No.30)	25-60	20-35	10-30
0.012inch(No.50)	10-30	8-20	5-17
0.006inch(No.100)	2-10	2-10	2-10

BOTTOM ASH

Bottom ash (BA) is a solid waste from the combustion of coal. The annual output of lignite bottom ash in the Mae Moh power plant in the north of Thailand is around 0.8 million tons and is disposed of a landfill near the power plant. Several types of research on the utilization of coal bottom ash for use as a cementitious material have been conducted. The bottom ash has to be ground to increase the pozzolanic activity and used to partially replace Portland cement. The utilization of bottom ash as a cementitious replacement material has not yet been well received as it needs grading and only a partial replacement of cement is possible. Moreover, the bottom ash itself is porous and increase the water requirement of the mix. On the other hand, the grinding of coal bottom ash results in a prolonged setting time and causes a reduction in the workability of the paste.

The as-received bottom ash particles were relatively large and very irregular, showing agglomeration of some spherical particles and other fragments with observable pores. The chemical composition of BA was 39.3 % SiO₂, 21.3% Al₂O₃, 13.5% Fe₂O₃, 2.1% K₂O, 16.5% CaO, 1.0% Na₂O and 1.4% loss of ignition [5].

Typically, the bottom ash contains assorted size closer to the sand. The gradation 50-90 percent passing sieve No.4, 10-60 percent passing sieve No. 40 and 0-10 percent passing sieve no.200. The maximum particle size about 19.0-38.1 mm.

However, the particle size of bottom ash depends on the source [6]. The density of mortar which replacement of sand with bottom ash can be reduced approximately 0.4 T/m³ due to a particle of bottom ash has a high porosity [7].

Bottom ash fine aggregate has prepared by heating in an oven at 100 °C for 24 hours. Then, bottom ash mixing with the water at moisture absorption and curing them for 24 hours. Bottom ash, which passed this process has been used as fine aggregate in shotcrete mortar.

MATERIALS PREPARATION AND MIX PROPORTION OF SHOTCRETE

Wet mix shotcrete is predominantly used because of its homogeneity in quality and high work efficiency [8]. The normal mixture proportion of shotcrete consists of sand as fine aggregate, cement, and water. However, the mixture proportion of lightweight shotcrete consists of bottom ash as fine aggregate, cement, and water.

Ordinary Portland cement type 1 is used throughout the experiments. Sand which passed sieve No.4 is coming from the natural river sand. Bottom ash obtained from a Mae Moh power plant in Lampang province of Thailand. Bottom ash, which used in this experiment should be passed sieve opening No.4 to replaced as sand in mortar mixture. Size distribution of sand was shown in Fig.2. Size distribution of bottom ash was shown in Fig.3. The three different size distribution of aggregate consists of lower boundary, an upper boundary, and middle grade was used in this test. Middle gradation of sand and bottom ash is the aggregate passed sieve No. 4.

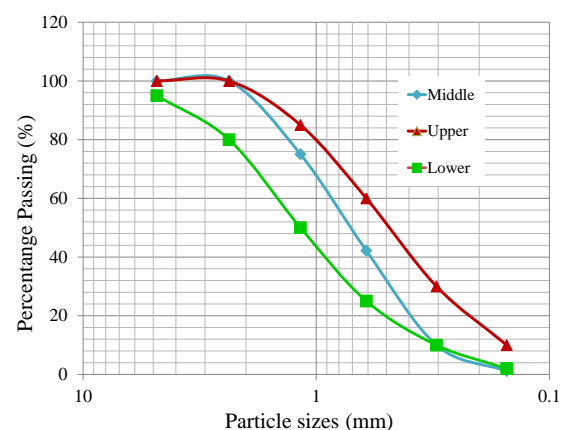


Fig. 2 Size distribution of sand used as fine aggregate.

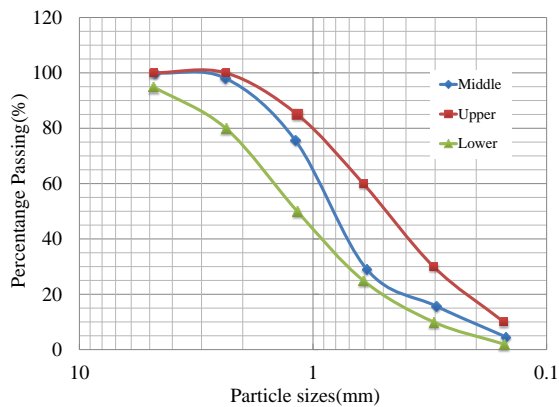


Fig. 3 Size distribution of bottom ash used as fine aggregate.

The mix design of shotcrete mortar in this study consist of a mixture used sand as fine aggregate and a mixture used bottom ash as fine aggregate. The three difference size distribution of fine aggregate, according to Fig 3 and Fig 4 were used in the mixture. The mixture of mortars was a combination of Portland cement Type 1 and fine aggregate is in a ratio of 1:3 by weight of cement. Water to cement ratio for a mixture of mortar is 0.6. The six mix proportion of shotcrete mortar as shown in Table 2.

Table 2 Mix proportion of shotcrete mortar

Mixture code	W/C	S/C,BA/C	Sand (%)	Bottom Ash(%)
SU	0.6	3:1	100	0
SM	0.6	3:1	100	0
SL	0.6	3:1	100	0
BU	0.6	3:1	0	100
BM	0.6	3:1	0	100
BL	0.6	3:1	0	100

EXPERIMENTAL PROGRAM

Shotcrete mortar mixed according to Table 2 were conducted to determine fresh properties and hardened properties. Fresh properties evaluation consists of slump flow test, setting time and sagging and build-up thickness. Hardened properties evaluation consists of compressive strength.

Slump flow test

This test method is intended to be used to determine the flow of mortars, according to ASTM C 1437. Workability of mortar is its ease of use measured by the flow of the mortar. The flow table and flow mold were used to determine slump flow. The mortar sample if placed on a flow table and dropped 25 times within 15 seconds. As the mortar

is dropped, it spreads out on the flow table. Measured the diameter of the mortar along the four lines. The flow is the average of the diameter of mortar on the table.

Setting time

This test method is intended to be used to determine the initial setting time of mortar according to ASTM C191. Vicat initial time of setting is calculated as the time elapsed between the initial contact of cement and water and the time when the penetration is at 25 mm. The Vicat final time of setting is calculated as the time elapsed between initial contact of cement and water and the time when the needle does not sink visibly into a paste.

Sagging and Build up thickness

This test method is intended to be used to determine the build thickness of shotcrete mortar. The build-up test consists of substrates with a build thickness of framework at 300 mm. The surface of substrates was claystone backfill. The trial mixes will be plastered into an incline 300 x 300 mm by hand application to measure the build-up thickness of mortar as shown in Fig 4. The inclination angle that used in this test was 30, 45 and 60 degrees at the thickness of the samples 5, 8 and 10 cm. The sagging of mortar can be investigated by the increasing thickness of mortar.



Fig. 4 Sagging and Build-up thickness of mortar.

Compressive strength

This test method is intended to be used to determine the compressive strength of mortar according to ASTM C109. The specimen each mix proportion cast in the mold of mortar at 50x50x50 mm cube specimens. Make three specimens of mortar for each period of test or test age. The specimens were cured in the water after the mortar hardened. Test the specimens immediately after their removal from storage water after 3, 7, 14, 28 and 56 days. The Universal testing machine was used to determine compressive strength.

FRESH PROPERTIES OF SHOTCRETE

The fresh properties of shotcrete mortar consist of slump flow test, setting time and sagging and build up thickness conducted on the samples mixed according to Table 1.

The results of slump flow test

The slump flow of all mix proportions should be $225 \pm 10\%$ mm. [8].

Table 3 and Fig.5 shown the test results of slump flow on a fresh mortar. The flow of mortar mixed with sand aggregate was approximately 20 cm -21 cm. However, The flow of mortar mixed with bottom ash aggregate was approximately 19.2 cm -20.6 cm. The results demonstrated the flow of mortar tends to increase with the reduction in the particle size of aggregate. This is due to a large particle of bottom ash has a high porosity and high water absorption[6].

Table 3 Results of flow ability

Mixture code	Slump Flow (cm)
SU	21
SM	20.5
SL	20.0
BU	20.6
BM	20.4
BL	19.2

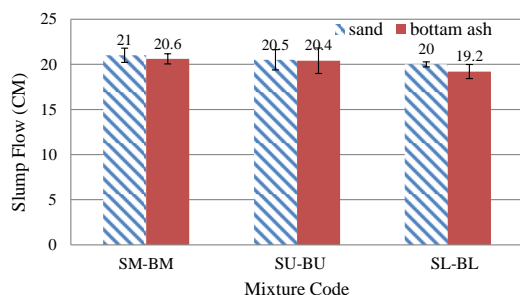


Fig. 5 Slump flow of a various shotcrete mixture.

The results of setting time

The setting time of shotcrete mortar with a various size distribution of sand aggregate and bottom ash aggregate was presented in Table 4 and Fig 6. The result showed an initial setting time of the mortar mixed with sand aggregate increased with the increase in the size distribution of aggregate. Therefore, the initial setting time of SL was higher than SM and SU approximately 10 and 20 minutes

respectively. A final setting time of SU and SM tend to similar but a final setting time of SL was higher than SU and SM approximately 45 minute.

Like, the initial setting time of mortar mixed with bottom ash increased with the increase in the size distribution of aggregate. Therefore, the initial setting time of BL was higher than BM and BU approximately 5 and 15 minutes respectively. Moreover, a final setting time of BL was higher than BU and BM approximately 60 minute and 45 minutes respectively.

Table 4 Setting time of shotcrete mortar

Mixture code	Initial setting time (minutes)	Final setting time (minutes)
SU	142	225
SM	150	225
SL	162	270
BU	140	210
BM	151	225
BL	156	270

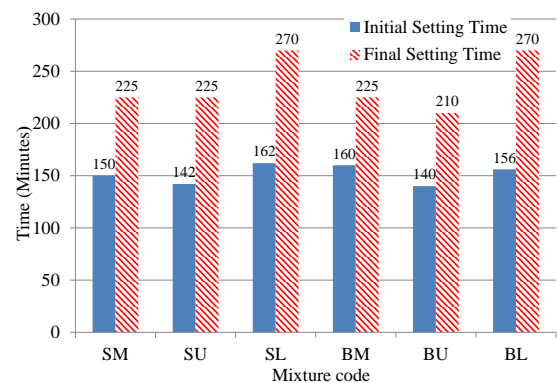


Fig. 6 Setting time of a various shotcrete mixture.

The results of sagging built-up thickness

The sagging and built-up thickness was conducted on SM and BM samples. The trial mixes plastered on the surface of backfill which paste in the incline box by hand application. The inclination angle was 30, 45 and 60 degrees at the thickness 5, 8 and 10 cm. The results of sagging built-up thickness of shotcrete with different thickness and inclination angle presented in Fig 7.

Sagging of SM was higher than BM at the same thickness and inclination angle. This is due to the unit weight of SM was more than BM. The unit weight of SM was 2.15 g/cm^3 and the unit weight of BM was 1.70 g/cm^3 . The maximum sagging of mortar occurs with SM samples at a thickness 10 cm and inclination angle of 60 degrees. The maximum sagging of SM was approximately 10 cm. However,

BM was not sagging at the inclination angle of 45 degrees and a thickness 8 cm but SM was sagging 3 cm. Thus, the result shown the lower unit weight of the mortar can be reduced sagging and increase the thickness of mortar.

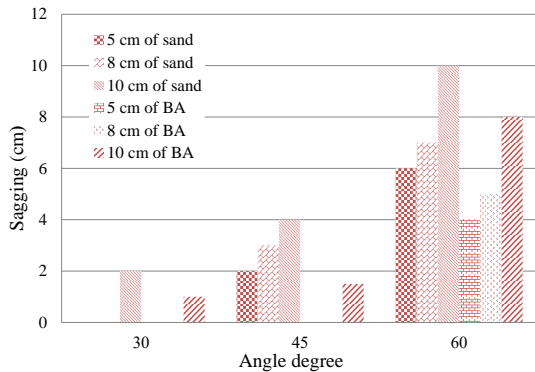


Fig. 7 Sagging and Built up thickness of each shotcrete mixture.

HARDENED PROPERTIES OF SHOTCRETE

This section presented the hardened properties of shotcrete by a compressive strength test. All tests are done in accordance with the American of Testing and Materials standard (ASTM).

The results of compressive strength

The compressive strength of all mixtures in this study was presented in Fig.8. It obtained from a compressive strength test of shotcrete cubes in 3, 7, 14, 28, 56 days. Each reported value is the average of three cube specimens.

The result shown the compressive strength of SU, SM and SL were slightly different at 7 days. The compressive strength of SL was the highest in 56 days. However, SU demonstrated the lowest compressive strength in a shotcrete mixed with sand aggregate. In 56 days, the compressive strength of SL was higher than SU and SM approximately 12 and 21 MPa, respectively.

The compressive strength of a shotcrete mixed with bottom ash aggregate was slightly different between BU, BM, and BL. However, the compressive strength of BU was higher than BM and BL, respectively in 56 days. This is due to a large particle size of bottom ash is weak and it has a high porosity [6].

The comparison between the compressive of shotcrete mixed with bottom ash and shotcrete mixed with sand was shown the compressive strength of BM was lower than SM approximately 26 MPa. This is because a particle strength of bottom ash was weaker than sand.

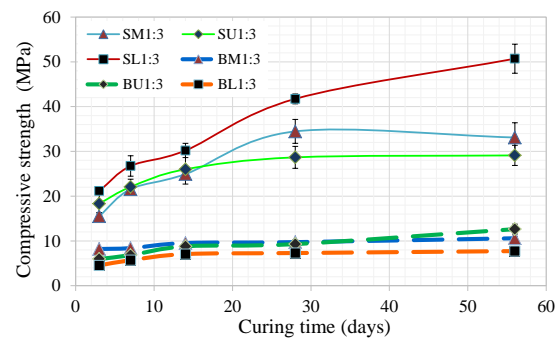


Fig. 8 The compressive strength of a various shotcrete mixture.

CONCLUSION

Based on the results which obtained from an experimental study, it can be concluded that

The used bottom ash as an aggregate in the mixture of shotcrete was reduced flowability because a particle of bottom ash has a high porosity and high water absorption. However, a slump flow of shotcrete mixed with the upper boundary and middle gradation of bottom ash was in the requirement of slump flow of shotcrete.

Sagging of shotcrete mortar mixed with sand aggregate was higher than shotcrete mortar mixed with bottom ash aggregate at the same thickness and an inclination angle. This is because the unit weight of shotcrete mixed with sand aggregate was more than shotcrete mixed with the bottom ash aggregate.

The compressive strength of a shotcrete mixed with bottom aggregate was less than shotcrete mixed with sand aggregate. Due to the particle of bottom ash was weaker than sand particles and bottom ash have a high porosity. The maximum strength of shotcrete mixed with bottom ash was 13 MPa at a curing time 56 days. However, the compressive strength of shotcrete mixed with bottom ash was possible to use for protecting a backfill from deterioration. Thus, the all result shown the possibility to use bottom ash as fine aggregate in shotcrete mortar.

ACKNOWLEDGEMENTS

The research work is done during the study at Chiang Mai University, and also express an appreciation to the Graduate School, Chiang Mai University for the financial support.

REFERENCES

- [1] Leelasuksaree C, Mavong N, Khosravi M H, Pipatpongsa T, "Physical and Numerical Models of Undercut Slope Lying on Steeply Inclined Bedding Plane", 17th National Convention on Civil Engineering, 2012, pp. GTE045-1 -GTE045-10.
- [2] Mavong N, Tunkeaw S, Mungpayabal N, Boonsritun N, "Mining Plan and Progressive Excavation in Lowwall Area 4.1 of Mae Moh Mine", International Symposium on Earthquake Hazard Potential and Preparedness for Safety in Coal Mining, 2011.
- [3] Rodvinij P, and Wattanachai P, "Influence of Claystone Deterioration on Shear Strength of Backfill", International Journal of GEOMATE, July 2017, Vol. 13, Issue 35, 54-59.
- [4] US Army Corps of Engineers, Engineering and Design Standard Practice for Shotcrete, 1993, pp. 2-1 - 4-7.
- [5] Sathonsaowaphak A, Chindaprasirt P, and Pimraksa k, "Workability and strength of lignite bottom ash geopolymer mortar," Journal of Hazardous Materials 168, 2009, pp. 44-50.
- [6] Moulton, "Properties of Pozzolan", Chiang Mai University, 1973
- [7] Torkittikul P, and Nochaiya T, "Compressive Strength, Density and Thermal Conductivity of Mortar containing fly ash and Bottom ash," Proceeding the 7th National Science Research Conference, 2015, pp. PY-O-029.
- [8] Samaru Y, and Sugiyama K, "Slope Stabilization Using the Shotcrete Grid Beam System in Japan," Shotcrete Spring, 2005, pp. 36-40.
- [9] American Society for Testing and Materials, "Standard Test Method for Compressive Strength of Hydraulic Cement Mortars(Using 2-in. or [50-mm] Cube Specimen)", ASTM C109M-16a,2011
- [10] American Society for Testing and Materials, "Standard Test Method for Time of Setting of Hydraulic Cement by Vicat Needle", ASTM C191,2007
- [11] American Society for Testing and Materials, "Standard Test Method for Flow of Hydraulic Cement Mortar", ASTM C1437,2007

A STUDY OF THE QUALITY OF SOIL INFILTRATION AT THE DOWNSTREAM OF KURANJI RIVER, PADANG CITY

Aprisal, Bambang Istijono*, Taufika Ophiyandri and Nurhamidah
Andalas University, Padang, Indonesia
*Email: bistijono@eng.unand.ac.id; bistijono@gmail.com

ABSTRACT

The watershed at the downstream of Kuranji river often experience flooding. This is due the rainfall runoff and the flat condition of the downstream area. Other factor might be due to low soil infiltration rate. The objective of this research was to analyze the quality of soil infiltration at the downstream of Kuranji River's watershed. Research methodology that had been choosed was field survey. Soil infiltration rate was measured using double ring infiltrometer. Location of soil sample was selected by purposive random sampling and was analyzed at the Department of Soil Science Andalas University. The data was analyzed using Horton formula to identify the capacity and the cumulative soil infiltration rate. The result showed that the area which often inundated and has high soil watertable had low infiltration rate. The results showed that the bulk density factor, clay fraction and dust significantly affect the capacity of soil infiltration. Moreover, bulk density, clay fraction, and dust influence soil infiltration capacity. Areas that have high infiltration capacity are Gunung Sariiek, Aie Pacah, Ampang, Kurao Pagang, and Dadok Tunggul Hitam. Other sampling locations have low infiltration rate due to high soil watertable.

Keywords: Infiltration capacity, Runoff, Watershed, Watertable

INTRODUCTION

Water infiltrates the soil through the soil surface. In the ground, water flows in the lateral direction as the flow between (interflow) to springs, lakes and rivers; or vertically, known as percolation to the ground water. The motion of water in the soil is affected by the force of gravity and the capillary force [1].

A technical report on Infiltration Characteristics of Soils Under Forestry and Agriculture in the Upper Waikato Catchment has been done due to increasing pressure for conversion of forest to agricultural land within the upper Waikato catchment. The study found that the conversion of forest to agricultural land within the upper catchment area to increase the accurance of flooding, both of peak and intensity of the flood, and also increase erosion and sedimentation. [2]

The special work for advanced study in the assessment of the maximum water storage capacity of soils under different land-use and land-management situations in a real river catchment has been done [3]. The study is done by field measurements of infiltration under several land-use and land-management situations. Then, a development of modelling approach to estimate the maximum potential water storage capacity also proposed. The study found that due to the change in land-use and land-management could reduce the storage infiltration capacity by 17 %.

The rainwater absorption in the downstream

Kuranji river basin is often impaired due to rapidly saturated soils. As a result, the city of Padang is often flooded and inundated causing houses to be flooded (Fig. 1). Factors causing the soil is saturated rapidly due to high groundwater level, soil texture is very smooth and layered consequently inhibit the entry of water into the soil. According to Asdak [4] when the rain falls on the surface of the ground some of the water will be retained by the depressed part of the soil, some of it into the soil and some into the runoff. The rainwater that enters the soil fills the pores of the empty soil until the water reaches the field capacity. Furthermore, the water will move more deeply due to the force of gravity into percolation of water to reach the saturated region. Water in saturated regions can also move horizontally due to plant root uptake and capillary forces. Radke and Berry [5] stated that the vertical entry of water into the soil is closely related to the structure or physical and biological characteristics of the soil. Further, other factors that affect water infiltration is slope, soil texture, land use, land processing, soil water content and soil organic chart. The state of the soil surface and the number of soil pores will determine the volume of water that can enter into the soil [6]. Soil pores that are numerous and interlocked into the deeper soil will increase the rate of infiltration. Includes pore holes made by roots and soil fauna.



Fig. 1 Area Flooded at Gunung Pangilun, Downstream of Kuranji Watershed.

The rate of infiltration decreases because of the changing of soil porosity which blocked by fine particles. The fine particles may come from spatter or from mud brought by flood. Dense soil surface becomes water resist [4, 7]. This study aims to examine the quality of soil absorption in the downstream Kuranji river basin.

RESEARCH METHODOLOGY

Location and Time of Research

This research was conducted from March to April 2018 at the downstream Kuranji watershed in Padang City, West Sumatra, Indonesia. Based on the geographical position of the study sites are at 00047'21" "to 00055'57" LS and 100020'31" "to 100033'54" BT, with a height of 0 up to 1859 above sea level. Research location are at Aie Pacah 1, Kurao Pagang, Dadok Tunggul Hitam, Aie Pacah 2, Gunung Sariiek, Ampang, Gunung Pangilun, and Korong Gadang (1-8 locations).

Tools and Materials

The tool used in this study is a set of computers with ArcView / ArcGIS program, Microsoft Excel, Global Positioning System (GPS), infiltrometer. Materials used in this study are Digital Elevation Model (DEM) data in the form of Triangulated Irregular Network (TIN), map of Kuranji watershed administration, land use map, soil type map, and monthly rainfall data.

Data Collection

The data collected were 1) soil parameters (texture, soil structure, soil permeability, and soil effectiveness), 2) infiltration capacity measured directly in the field using double ring infiltrometer. Soil sampling is done purposively (purposive sampling), which is based on the consideration of spatial distribution and areas that often get flooded during the rain at 8 locations. The examples of soil taken are examples of intact soils and disturbed soil samples. The soil samples were used for the analysis

of soil physical characteristics (BD / bulk density, TRP/total pore space, organic C, permeability, texture, etc.), and soil samples were disturbed for soil organic C-analysis. Infiltration measurements were performed at each location of the soil sampling point.

Data Calculation and Analysis

1. The soil texture parameters were analyzed by using triangle texture to determine the soil texture class.
2. Hydraulic conductivity set by using the Deboodt method using Darcy's legal principle.
3. Establish infiltration capacity using double ring infiltrometer, and data are analyzed using Horton formula ie $F = f_c + (f_o - f_c) e^{-kt}$.
4. Analyze the result of soil physics characteristics from laboratory in statistical analysis with correlation analysis and Principal Component Analysis (PCA) or main component analysis with Minitab 17 software. So it can be selected main factor most determine infiltration capacity at Kuranji downstream basin.

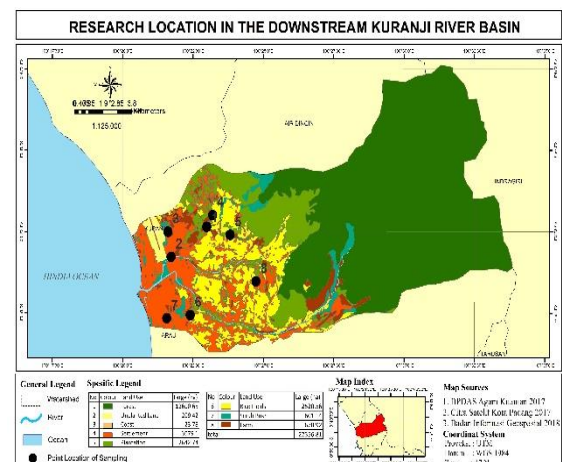


Fig. 2 Research Location in the Downstream Kuranji Watershed.

RESULT AND DISCUSSION

The main factors of soil physical characteristics that affect the infiltration capacity

The results of principal of component analysis (PCA) [8] on soil physical characteristics, showed that eigenvalue is greater than one ie PC1 (principal component1) and PC2 (principal component2). On the PC most variable values affect the infiltration capacity is greater value on PC1 is bulk density (BD) 0.417, clay fraction 0.416. While on PC2 is 0.445 dust fraction. Based on this selected variable hence can be made graph relation between variable and infiltration capacity.

Table 1 This is the example for table formatting

Eigenvalue	3.9644	1.2777
Proportion	0.566	0.183
Cumulative	0.566	0.749
Variabel	PC1	PC2
BD	0.417	-0.370
TRP	-0.417	0.370
C Organik	0.056	-0.648
Permeability	-0.349	-0.238
Sand	-0.462	-0.227
Dust	0.374	0.445
Clay	0.416	-0.023

Based on PCA result analysis, asimple regression relationship between infiltration capacity with soil physical characteristics variable and sampling point location was made.

The correlation of infiltration capacity to the location of flood affected areas

The infiltration capacity with some flood-affected sites has an exponential relationship (Figure 2). The closeness of the relationship between the infiltration capacity and the location of the flood is quite strong with the value of R^2 equal to 0.9297. It means that flood affected locations affect infiltration capacity by 93 percent. This is because the locations affected by the flood caused a change in the characteristics of soil physical characteristic that affect the maximum ability of the soil in the water. Floods generally carry a lot of sediment loads of very fine sand fractions, dust and clay. The results of Huria [9] show that the Batang Kuranji river carries the sediment 194,08 mg / l. The sediment material comes from forest exploitation, mixed gardens, shrubs, and settlements. The sediment material carried to the floodplain will affect the physical characteristics of the soil, especially the composition of the fraction and the pores of the soil in the soil layer.

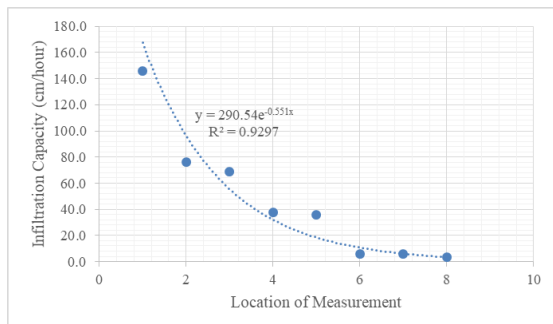


Fig. 3 Correlation of infiltration capacity with research location in downstream Kuranji watershed of Padang.

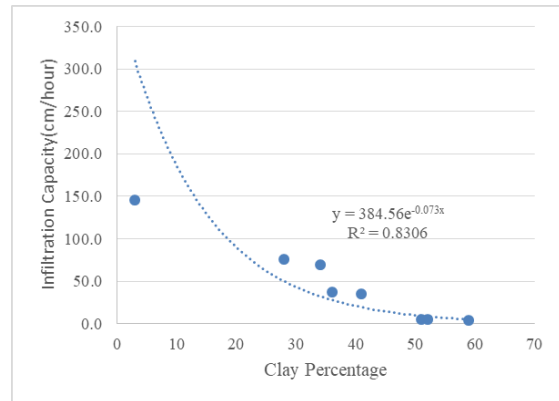


Fig. 4 Correlation of infiltration capacity with percentage of clay content in downstream Kuranji watershed in Padang.

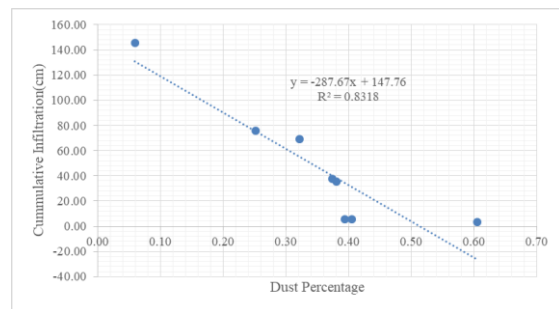


Fig. 5 Correlation of infiltration capacity with percentage of dust in downstream Kuranji watershed in Padang.

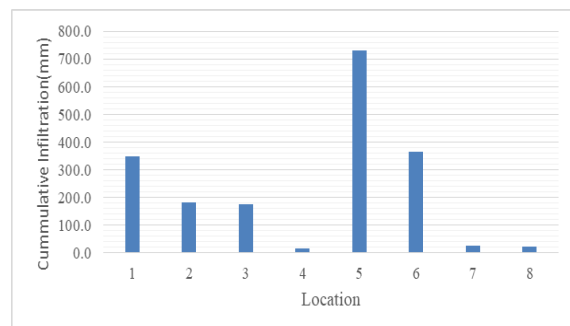


Fig. 6 Correlation of cumulative infiltration with the research location in the downstream watershed in Padang.

The correlation of infiltration capacity with clay fraction

The highest percentage of clay fraction is found in Aie Pacah area, Gunung Sariiek and Korong Gadang. The clay content of the soil will increase the soil micro pore from the micro pores. The percentage of this pore affects the movement that enters the soil. Based on the results of major component analysis (PCA) clay fraction is one of the variables that determine the infiltration capacity in the lower Kuranji river basin. Based on simple

regression analysis of clay correlation with infiltration capacity very closely with value $R^2 = 0,8306$ (Figure 4). This means that 83 percent infiltration capacity is influenced by clay fraction. It is also stated by Foth [10] that clay-textured soils will be dominated by micro pores and unlike sandy terraces will be dominated by micro pores. The infiltration capacity is not determined by the micro pores but is the macro pore. In macro pore the infiltration capacity will be greater than slow-moving micro pores. Soil fraction or soil texture, also called soil grain, is one of the most important properties of the soil. This is because soil fractions are closely related to the movement of water and solutes, air, heat movement, weight of soil volume, specific surface area, compressibility, etc. [11].

Correlation of infiltration capacity with dust fraction

The correlation between the fraction of dust and the infiltration capacity was strongly correlated, with the R^2 value of 0.8318 (figure 5). This means that 83% of the infiltration capacity is affected by dust fraction. When compared to the size of the dust with clay, then illite is smoother than dust so there is a difference in relationship between infiltration capacity between dust and clay.

According to Hardjowigeno [12], soil texture shows the comparison of grains of sand (2mm-50 μ), dust (50-2 μ) and clay (< 2 μ) in the soil. The soil texture class is divided into 12 classes, namely: sand, sand, sandy clay, clay, dusty clay, dust, clay, sandy clay clay, dusty clay clay, sandy clay, dusty clay, clay. Based on its size, the soil solid material is classified into three particles of sand, dust, and clay. Sandy soils are sand > 70%, low porosity (< 40%), most of the pore space is large, resulting in good aeration of rapid water conductivity, but the ability to hold water and low nutrients. The soil is called textured clay if the clay content is > 35%, the porosity is relatively high (60%), but most of it is small pore, water conductivity is very slow and air circulation is substandard [13]. In the sand soil texture, the percolation rate will be very fast, in the clay soil texture the percolation rate is moderate to fast and in the clay texture the rate of percolation will be slow [14].

Cumulative infiltration in frequently flooded area

Cumulative infiltration at various sampling sites showed that the largest cumulative infiltration was located at location 1, 5, and 6 (Fig. 6). It means that these locations have more ability to absorb water than other locations. Areas that have larger cumulative infiltration can be used as surface water

absorption areas.

The difference in infiltration capacity between the sample sites is due to the differences of soil physical properties of the soil. Based on the analysis of PCA has sort out the variable of soil physics properties that are very influential are BV, clay fraction and dust fraction. The different of soil properties on sampling locations caused by the influence of the material cumulative floods (fine fractions). This means that the location is often inundated gradually so the nature of the soil will experience changes, especially the bulk density nature of the increasing tendon and reduce the movement of water into the soil. According to research results Mukhtar et al. [9] and Aprisal et al. [15], finds the infiltration rate which tends to fall due to the surface which always hit the raindrops causing the soil to become slippery and smooth.

CONCLUSIONS

Based on the research, it can be concluded, that;

1. The main factors affecting the capacity of infiltration capacity in flooded areas are bulk density, clay fraction, and dust.
2. The magnitude of infiltration capacity is influenced by soil physical properties having the first high correlation with clay fraction ($R^2 = 0,83$) and dust has negative correlation ($R^2 = - 0,83$).
3. Areas that have high water absorption or cumulative rate of infiltration capacity are Gunung Sariek, Aie Pacah, Ampang, Kurao Pagang, and Dadok Tunggul Hitam.

ACKNOWLEDGEMENTS

This research was funded by Andalas University under Research Grant No 43/UN.16.17/ PP.RGB /LPPM/ 2018 dated April 23, 2018.

REFERENCES

- [1] Bambang Triadmodjo 2008. Applied Hydrology. Beta Offset Yogyakarta. 380 pages.
- [2] Taylor M., Mulholland M. and Thornburrow D., Infiltration Characteristics of Soils Under Forestry and Agriculture in the Upper Waikato Catchment, Environment Waikato Technical Report 2009
- [3] Desoky M S., Dissertation: Impact of land-use and land-management on the water infiltration capacity of soils on a catchment scale, Fakultät Architektur, Bauingenieurwesen und Umweltwissenschaftender Technischen Universität Carolo-Wilhelmina, March 2011

- [4] Asdak 1995. Hydrology and Watershed Management. Revised Edition. Third Edition. Gadjah Mada University Presss. Yogyakarta.
- [5] Radke J.K. and Berry E.C. 1993. Infiltration as a tool for detecting soil changes due to cropping, tillage, and grazing livestock. American Journal of Alternative Agriculture 8: 164–174.
- [6] Mukhtar S., Baker J.L., Horton R. and Erbach D.C. 1985. Soil water infiltration as affected by the use of the paraplow. Transaction of ASAE 28: 1811–1816.
- [7] Istijono.B. 2006. Watershed Conservation and Farmers Income: Studies on Watershed Management Integration (Case Study: Sumani Basin of Solok Regency / Solok City, West Sumatera). PPs.Unand Dissertation.
- [8] Jolliffe I.T. Principal Component Analysis, Series: Springer Series in Statistics, 2nd ed., Springer, NY, 2002
- [9] Huria Teguh 2014. Prediction of erosion and sedimentation in Upper Kuranji Watershed. Unand Graduate Tesis.
- [10] Foth, H. D. and L. M. Turk. 1988. Fundamentals of Soil Science. Fifth Edition. Wiley international Edition. John Wiley and Sons, Inc. 454p
- [11] Purkait, B. 2010. The Use of Grain Size Distribution Patterns to Elucidate Aeolian Processes on a Transverse Dune of Thar Desert, India. Earth Surface Processes Landforms. 35 : 525-530.
- [12] Hardjowigeno. 2008. Geology. PT. Mediatama Sarana Perkasa. Jakarta. 286 Pages
- [13] Utomo 2008. Sustainable Dry Land Raw Material Management. University of Lampung. Bandar Lampung. 25 pages.
- [14] Sarief 2008. Physics-Chemistry Agricultural Land. Publisher Pustaka Buana. Bandung. 220 pages.
- [15] Aprisal, Adrinal dan Wulan Herman. 2017. The Influence of Rice Husk Biochar Against Infiltration Capacity on Ultisol. Proceeding of National Seminar of Land of Suboptimal 2017, Palembang 19-20 October 2017 “Development of Agricultural Science and Technology with Local Farmers for Optimizing Suboptimal Land”

MICROSTRUCTURE AND MECHANICAL PROPERTIES OF CONCRETE WITH TREATED RECYCLED CONCRETE AGGREGATES

Richard De Jesus¹, Anthony Tang² and Alvin Cunanan²

¹Assistant Professor, De La Salle University (Manila)

² Civil Engineering Undergraduate Students, De La Salle University (Manila), Philippines

ABSTRACT

Recycled concrete aggregates (RCA) are sourced from construction demolitions. Weaker concrete, however, often resulted when using RCA as partial or full replacement of coarse aggregates due to the presence of adhered (old) mortar. Several treatment methods for RCA target this old mortar to completely remove it, or enhance its properties, to make RCA suitable for construction use. Three treatment methods were employed in this study: (1) sulfuric acid (SA), (2) silica fume impregnation (SF), and (3) the combination of both (SASF). Experimental results showed improvement in the physical properties of RCA compared to untreated RCA, however, statistical tests showed that these improvements are not significant. SA treatment was found to have a detrimental effect on the surface of RCA, which developed a weaker layer of adhered mortar on the RCA surface resulting to a reduction in the mechanical strength of the concrete thus, its strength is lower compared to SF-treated RCA concrete. SF treatment resulted in improved compressive strength in comparison to untreated RCA concrete, SA-treated RCA concrete, and SASF-treated RCA concrete. It was also observed that 50% RCA replacement in all concrete mixes with treated RCA resulted to highest obtained compressive strength.

Keywords: Recycled concrete aggregates, RCA treatment, Sulfuric acid, Silica fume, RCA concrete

INTRODUCTION

Raw materials used in producing concrete are not renewable. Consumption of these raw materials, (e.g. sand, gravel, and crushed rock) is at the rate of 10 to 11 billion tons per year [1]. Disposing of construction and demolition wastes brings another environmental issue as its disposal requires a lot of space. The total amount of waste generated by construction and demolition activities in the European Union in 2012 was 821 million tons, and is expected to increase annually [2]. According to [3], 530 million tons of construction and demolition debris were generated in the United States in 2013. Since construction and demolition debris have no reusable components other than steel reinforcement, they are often hauled and shipped to landfill.

Over the years, many studies were conducted on the use of demolition and construction debris for various purposes. Several studies have proposed the idea of recycled aggregate concrete (RAC) where construction debris and demolition wastes are used as full or partial replacement of coarse aggregates in concrete. However, the use of RCA in concrete often results to a weaker concrete due to high water absorption, lower concrete workability, and higher drying shrinkage [4]. The strength of RAC with 100% RCA results in a 20% to 25% reduction in strength compared to normal concrete and requires more cement to reach comparable strength [5]. Moreover,

they showed that cement has to be increased by 6% of cement mass for 50% RCA replacement, and 8.3% increase for 100% RCA replacement to reach similar compressive strength compared to normal concrete. Also, the use of RCA brings about workability issue. Salesa [6] showed that the workability of RCA concrete is reduced due to adhered mortar and higher absorption capacity of RCA.

The use of acid pre-soaking method has been aimed toward removing adhered mortars. The study [7] used three kinds of acid solution (i.e. hydrochloric acid, sulfuric acid and phosphoric acid) to treat RCA. Results showed that the properties of RCA improved in terms of water absorption, compression, and flexural strength. The rate of disintegration of adhered mortars depend on the concentration and molarity of the acid solution. Based on [8] & [9], the change in molarities of acid solution enhanced the density, water absorption, and mechanical strength of RCA. Akbarnezhad [7], employed various treatment methods for RCA like mechanical, heating, microwave, and acid-soaking treatment and showed that the quality of RCA depends on the quantity of the adhered mortars on its surface. Additionally, they showed that acid-soaking treatment method removed more adhered mortars than other treatment approaches. Furthermore, [7] showed that for RCA treated with weaker acid reduces water absorption significantly and improved mechanical properties. Kim [10] combined sulfuric (weak) acid treatment

with abrasion in treating RCA and demonstrated improved qualities.

Concrete is prone to acid attack, and aggregates react negatively to silica, thus, researchers devised an alternative to treat RCA through silica impregnation. Katz [11] investigated the use of impregnation of silica fume by soaking RCA for 24 hours in silica fume solution. Results showed that silica fume treatment resulted in an increase of 23 to 33%, and 15%, in the compressive strength at ages 7 and 28 days, respectively. Cakir [12] showed that water absorption of concrete with RCA treated with silica fume decreased significantly especially at latter ages. This effect is more significant in concrete with RCA using higher amount of silica fume. However, compressive strength decreased with an increase in the silica fume content in RCA treatment. Huoth [13] used 100% RCA replacement treated with varying silica fume content of 5%, 10% and 15% and showed comparable compressive strength results of RAC to conventional concrete.

This study explored three treatment methods for RCA, namely; weak acid (sulfuric acid) treatment, condensed silica fume impregnation, and the combination of both. Moreover, the study investigated the influence of these methods to physical properties, in terms of water absorption, bulk density, and abrasion resistance, and microstructure of RCA. Scanning electron microscopy (SEM) was employed to explore the microstructure. Additionally, the investigation was further extended to compressive strength of concrete with untreated and treated RCA, and varying amounts of treated RCA.

MATERIALS AND METHODS

Sourcing and Preparation of RCA

RCA used in this study was obtained from demolished concrete pavements, which was mainly composed of cement mortar and aggregates. Demolished concrete pavement was then crushed to a maximum nominal size of 50 mm. The crushed recycled concrete was then graded using sieve in accordance to ASTM C136 [14]. Natural coarse and fine aggregates were used for the control concrete mix, while parts of coarse aggregates were replaced by RCA, by volume, in non-control concrete mixes.

Treatment of RCA

RCA were treated prior to testing of its physical and, strength properties after it has been incorporated in concrete. In this study, the three methods of treatment used were weak acid treatment using sulfuric acid (SA-treatment), condensed silica fume impregnation treatment (SF-treatment), and the

combination of these two treatments (SA-SF treatment).

Weak Acid Treatment using Sulfuric Acid (SA-treatment)

This method of acid treatment was adapted from [7]. The recycled concrete aggregates were soaked in 0.5 molarity of sulfuric acid solution for 24 hours. The RCA in the acid bath was shaken occasionally to ensure efficient removal of bond between adhered mortar and aggregate. After soaking, RCA was washed to remove acidic solvents. A final soaking in water for 24 hours was done to ensure that no residue from acid solvents remains on the aggregates.

Condensed Silica Fume Impregnation Treatment (SF-treatment)

This method was adapted from [11], with little modification, as condensed silica fume was used instead of raw silica fume. To create a silica fume solution, 1 kg of condensed silica was mixed with 10 liters of water. RCA was then soaked in this solution for 24 hours for silica fume impregnation to occur. After soaking, the treated RCA was air-dried.

Combined Treatment Method (SA-SF treatment)

Combined treatment involved repetition of procedure for acid-soaking sulfuric acid treatment followed by repetition of silica fume impregnation method.

Physical and Microstructure Characterization of RCA

Several tests were conducted enable to compare the physical properties and microstructure of treated and untreated RCA. These tests are relative density (specific gravity) and water absorption as per ASTM C127 [15], abrasion loss as per ASTM C131 [16], bulk density as per ASTM C29 [17], and surface microstructure using Scanning Electron Microscope as per ASTM C295 [18].

Concrete Mix Design and Proportions

Mix design proportions are shown in Table 1. Due to scarcity of Portland cement locally, this study used Type 1P cement for all concrete samples. The proportions used in the design mix was based on ACI 211.1 design mix procedure adopting a water to cement (w/c) ratio of 0.45 for all mixes. Concrete samples were made with 100%, 75%, 50% and 25% replacement of RCA by volume of coarse aggregates.

Compression Tests of Concrete with RCA

All concrete specimens were made in accordance with ASTM C192 [19]. Concrete cylinder sample of size 100mm x 200mm was used. For each mix type, 8 samples were prepared, and cured in water for 7 and 28 days. Compressive strength tests were conducted as per ASTM C39 [20].

RESULTS AND DISCUSSIONS

Physical Properties of Untreated and Treated RCA

Bulk Density, Specific Gravity, Water Absorption and Abrasion Loss

Table 2 summarizes the average values both untreated and treated RCA. Bulk density and specific gravity increased for all treated RCA. Water absorption and abrasion loss decreased for treated RCA. Combined treatment (SASF), however, exhibited an increase in water absorption compared to untreated RCAs. Except for bulk density, statistical t-tests showed that changes in physical properties of treated RCA compared to untreated RCA were not significant.

Surface Microstructure of RCA

Scanning electron microscope (SEM) of untreated RCA (Fig. 2a) showed noticeable porous surface and covered with different impurities and loose crumbs of cement paste. This impurities and loose crumbs of cement paste can be observed better with higher magnification (x7500) in Figure 3a. These observations were consistent with the study of [8] & [7]. SEM of SA-treated RCA shown in Figure 2b exhibited smaller pores and less jagged surface, represented by dark spots and craggy formations. Both SF-treated RCA and SASF treated RCA (Figures 2c and 2d) exhibited smoother, less porous and jagged surface.

The surface of the SF-treated, and SASF-treated RCAs are shown in Figures 2c, and 2d, respectively. Images showed that the porosity of RCA was reduced significantly compared to untreated RCA and SA-treated RCA. The surface of SF-treated RCA compared to SASF-treated RCA appeared with much larger irregular crags. Contrary to the effects of sulfuric acid, which alters the surface topography of RCA, silica fume coats the surface resulting to smoother and less craggy surface.

SEM of treated and untreated RCAs with 7500x magnification are shown in Figure 3. Untreated RCA (Fig. 3a) displayed a rougher surface compared to that of SA-treated RCA (Fig. 3b) with smoother crystalline-like structure. However, the surface structure of the SA-treated RCA appeared more disconnected, with broken strand formations and particles around the sample. In Figures 3c and 3d, it

can be observed that small particles were present which were not observed in Fig 3a and 3b. This can be attributed to the presence of micro silica that clings to micro-surfaces around the RCA, thus filling voids along the surface of the RCA.

Figure 1 shows a cross-sectional image of SA-treated RCA. It can be inferred from this image that acid treatment created a layer of weakened mortar on the RCA, implying that farther exposure to acid may result to complete removal of this layer. Incomplete removal, on the other hand, resulted to a weaker aggregate mortar interface which leads to weaker mechanical strength.

Compressive Strength of Concrete with RCA

Except for concrete with 100% of coarse aggregates replaced by treated RCA, all other RCA replacement have higher compressive strength than that of concrete with untreated RCA. This was observed in both 7-day and 28-day, as seen in Fig. 4 and 5.

Comparison between concrete with RCA under different treatment method

For 7-day compressive strength, concrete samples with SA-treated RCA and SF-treated gained the higher strength for coarse aggregate replacement of 25% and 50% compared to concrete with SASF-treated RCA. Coarse aggregate replacement higher than 50% (i.e. 75% and 100%) showed varying results but samples with SF-treated RCA consistently got the highest or next to highest compressive strength.

Concrete with SF-treated RCA also gained the highest for 28-day compressive strength consistently for all. Concrete with SASF-treated RCA had the lowest strength except for mix with 75% RCA replacement.

Comparison between concrete with SA-treated RCA and with SF-treated RCA revealed that SF-treated RCA concrete had higher mechanical strength for both 7-day and 28-day strength. SASA-treated RCA concrete performed better than SA-treated RCA concrete in 7-day strength but not in 28-day strength.

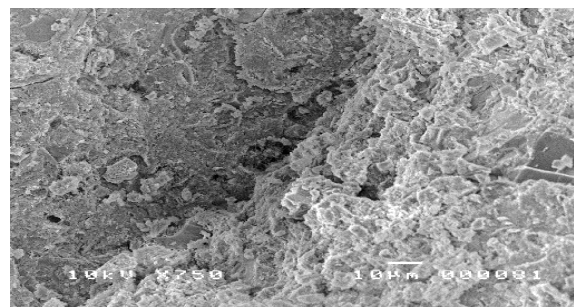


Fig. 1 Cross-sectional surface microstructure of SA-treated RCA

Table 1. Mix Design for 1m³ concrete volume

Type of Mix	Cement (kg)	Fine Aggregates (kg)	Water (kg)	Coarse aggregates (kg)	RCA (kg)
U-RCA	376	948	169	0	948
25SF	376	870	169	1167	258
50SF	376	870	169	779	515
75SF	376	870	169	389	773
100SF	376	870	169	0	1030
25SA	376	880	169	1168	255
50SA	376	880	169	779	510
75SA	376	880	169	389	765
100SA	376	880	169	0	1020
25SASF	376	877	169	1171	256
50SASF	376	877	169	781	512
75SASF	376	877	169	390	767
100SASF	376	877	169	0	1023

Table 2. Average physical properties of untreated and treated RCAs

RCA Physical Properties	Untreated	SF-treated	SA-treated	SASF-treated
Bulk density (kg/m ³)	1142	1223	1229	1234
Specific gravity (SSD)	2.31	2.41	2.37	2.33
Water absorption (%)	7.7	6.6	7.0	9.6
Abrasion loss (%)	29	27	27	27

Effects of varying amounts of RCA replacement

For 7-day compressive strength, an increase was observed for SA-treated RCA concrete for 25% and 50% replacement while SF-treated RCA concrete did not exhibit any strength increase until replacement reached 75%. Concrete with SASF-treated RCA exhibited rising strength pattern from 25% to 75% RCA replacement then drop at 100% replacement. SA-treated RCA concrete and SF-treated RCA concrete exhibited a decrease in strength for more than 50% RCA replacement.

Compressive strength for 28-day showed more consistency with respect to trend in strength gain and loss (Fig. 4 & 5) than 7-day. SA-treated RCA concrete, and SF-treated RCA concrete, both showed increasing strength from 25% to 50% RCA replacement then followed by decrease in strength for 75% up to 100% RCA replacement. For SASF-treated concrete, however, the strength increase was observed up to 75% RCA replacement then decrease thereafter. This observation was similar to that of SASF-treated concrete for 7-day strength.

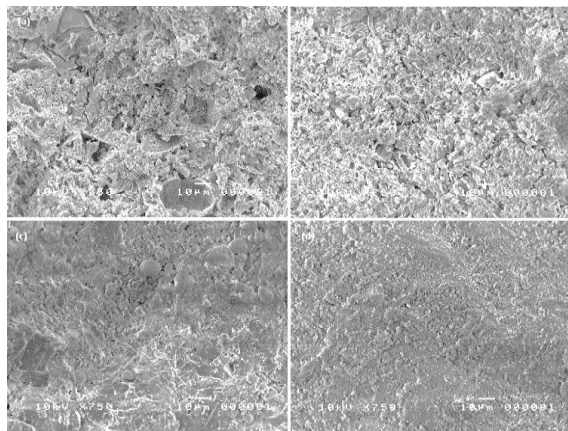


Fig. 2 Surface microstructure of treated and untreated RCA at 750x magnification (a: Untreated RCA, b: SA-treated, c: SF-treated, d: SASF treated)

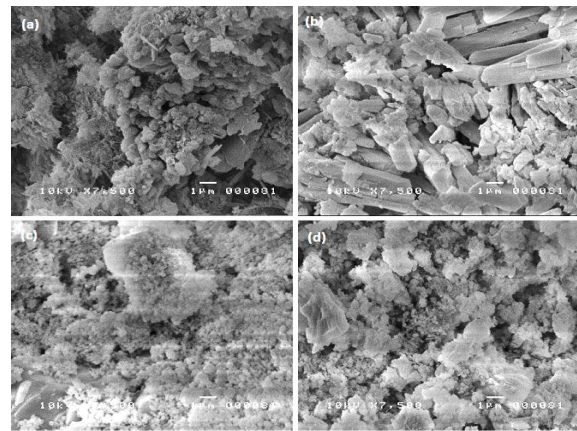


Fig. 3 Surface microstructure of treated and untreated RCA at 7500x magnification (a: Untreated RCA, b: SA-treated, c: SF-treated, d: SASF treated)

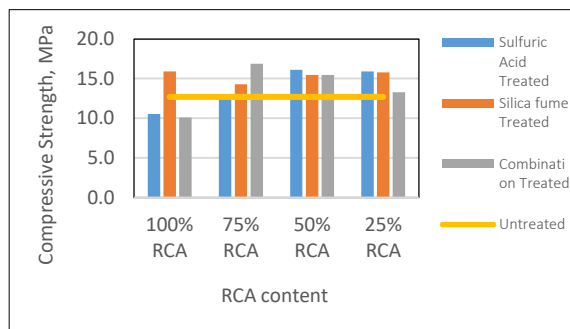


Fig. 4. 7-day compressive strength of concrete with treated and untreated RCA

CONCLUSIONS

There is a slight improvement on the physical properties, such as bulk density, water absorption, abrasion loss and specific gravity, of RCA treated by sulfuric acid (SA), silica fume impregnation (SF), and the combination of both (SASF). However, statistical t-test showed that these improvements were not significant.

The microstructure surface of SA-treated RCA was cleaner and free from loose particles compared to the untreated RCA. However, the remaining adhered mortar on RCA that the sulfuric acid failed to penetrate became weak and affected the mechanical strength of concrete with SA-treated RCA. Thus, compared to SF-treated RCA concrete, SA-treated RCA concrete had lower mechanical strength.

The microstructure surface of the SF-RCA tends to be smoother than the untreated RCA and SA-treated RCA validating the claim that silica fume particles occupy void spaces of RCA resulting to smoothening of the rough microstructure surface of RCA.

Treated RCA produced concrete with higher compressive strength compared to concrete with untreated RCA. Combination of SA and SF treatments do not result in better strength compared to concrete with RCA employing separate treatment.

While increase in percentage replacement decreases compressive strength of RCA concrete, it was observed that with treated RCA, the decrease in strength occurred at replacements higher than 50%. Based on results, SF-treatment is the more effective method of treating RCA.

REFERENCES

[1] Mehta, P., Reducing the Environmental Impact of Concrete, 2011, Retrieved October 08, 2016, <http://maquinamole.net/EcoSmartconcrete.com/docs/trmehta01.pdf>.

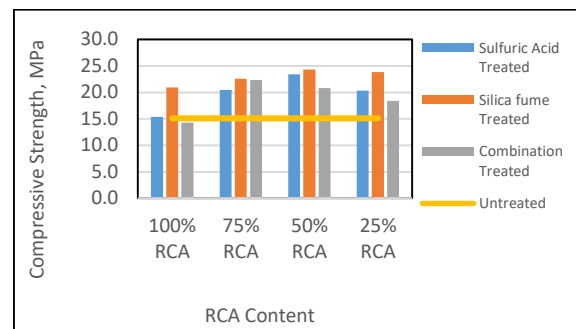


Fig 5. 28-day compressive strength of concrete with treated and untreated RCA

- [2] EU Waste statistics, 2015, Retrieved October 08, 2016, http://ec.europa.eu/eurostat/statisticsexplained/index.php/Waste_statistics#Total_waste_generation.
- [3] Advancing Sustainable Materials Management: Facts and Figures Report, 2013, Retrieved October 08, 2016, <https://www.epa.gov/smm/advancing-sustainable-materials-management-facts-and-figures-report>.
- [4] Sagoe-Crentsel, K., Brown, T., and Taylor, A., Performance of concrete made with commercially produced coarse recycled concrete aggregate, *Cement and Concrete Research*, Vol. 31, Issue 5, 2001, pp. 707-712.
- [5] Etxeberria, M., Vasquez, E., Mari, A., and Barra, M., Influence of amount of recycled coarse aggregates and production process on properties of recycled aggregate concrete, *Cement and Concrete Research*, Vol. 37, Issue 5, 2007, pp. 735-742.
- [6] Salesa, A., Perez-Denedicto, J. A., Colorado-Aranguren, D., Lopez-Julian, P. L., Esteban, L. M., Sanz-Balduz, and L. J. Olivares, D., Physico-mechanical properties of multi-recycled concrete from precast concrete industry, *Journal of Cleaner Production*, 2016, pp. 248-255.
- [7] Akbarnezhad, A., Ong, K. C., Zhang, M. H., and Tam, C. T., Acid Treatment Technique for Determining the Mortar Content of Recycled Concrete Aggregates, *Journal of Testing and Evaluation*, Vol. 41, Issue 3, 2013, pp. 441-450, doi:10.1520/jte20120026.
- [8] Ismail, S., and Ramli, M., Engineering properties of treated recycled concrete aggregate (RCA) for structural applications, *Construction and Building Materials*, Vol. 44, 2013, pp. 464-476, doi:10.1016/j.conbuildmat.2013.03.014.
- [9] Ismail, S., and Ramli, M., Mechanical strength and drying shrinkage properties of concrete containing treated coarse recycled concrete aggregates, *Construction and Building Materials*, 68, 2014, pp. 726-739, doi:10.1016/j.conbuildmat.2014.06.058.

- [10] Kim, H., Park, S., and Kim, H., The Optimum Production Method for Quality Improvement of Recycled Aggregates Using Sulfuric Acid and the Abrasion Method, *International Journal of Environmental Research and Public Health IJERPH*, Vol. 13, Issue 8, 2016, 769, doi:10.3390/ijerph13080769.
- [11] Katz, A., Treatments for the Improvement of Recycled Aggregate, *Journal of Materials in Civil Engineering*, Vol. 16, Issue 6, 2004, pp. 597-603., doi:10.1061/(asce)0899-1561(2004)16:6 (597).
- [12] Cakir, O. and Sofyanli, O., Influence of silica fume on mechanical and physical properties of recycled aggregate concrete, *HBRC Journal*, Vol. 11, Issue 2, 2015, pp. 157-166.
- [13] Huoth, P., Suntharavadivel, T.G., and Duan, K., Effect of silica fume on recycled aggregate concrete, *Australasian Conference on the Mechanics of Structures and Materials (ACMSM23)*, Vol. I, 2014, pp. 249-254, ISBN: 9780994152008.
- [14] ASTM C136, Standard Test Method for Sieve Analysis of Fine and Coarse Aggregates and Grading, ASTM International, Conshohocken, PA, 2016, www.astm.org.
- [15] ASTM 27, Standard Test Method for Relative Density and Absorption of Coarse Aggregates, ASTM International, Conshohocken, PA, 2016, www.astm.org.
- [16] ASTM C131, Standard Test Method for Resistance to Degradation of small-size Coarse Aggregate by Abrasion and Impact in the Los Angeles Machine, ASTM International, Conshohocken, PA, 2016, www.astm.org.
- [17] ASTM 29, Standard Test Method for Bulk Density and Voids in Aggregates, ASTM International, Conshohocken, PA, 2016, www.astm.org.
- [18] ASTM 295, Standard Guide for Petrographic Examination of Aggregates for Concrete, ASTM International, Conshohocken, PA, 2016, www.astm.org.
- [19] ASTM C192, Standard Practice for Making and Curing of Concrete Test Specimens in the Laboratory, ASTM International, Conshohocken PA, 2016, www.astm.org.
- [20] ASTM C39, Standard Testing Method for Compressive Strength of Cylindrical Concrete Specimens, ASTM International, Conshohocken PA, 2016, www.astm.org.

A COMPARATIVE STUDY ON VIBRATION SIGNALS OF A MOTORCYCLE AT VARIOUS POSITIONS

Suphattharachai Chomphan
Faculty of Engineering at Sriracha, Kasetsart University, Thailand

ABSTRACT

The motorcycle is becoming popular in the present days because of their swiftness and conveniences in the crowded cities. It is considered the most popular choice in various aspects of transportation in the urban area. When starting and accelerating the engine, it has been found that there was a vibration throughout all parts of the motorcycle. If the driver perceives more vibration, he will feel more uncomfortable. Consequently, the researcher conducted a study of the vibration signal sent through four core points which are the contacts between driver or rider and the motorcycle body including motorcycle left hand, seat, left front footrest, and left rear footrest. The specimen motorcycle in this research is Honda Wave 100s model. The comparison results have been performed by using two parameters of averaged peak and averaged energy of the vibrational signal. The results reveal that the left front footrest has the highest vibration level in both parameters, while the seat has the lowest vibration level. All in all, it can be concluded that the mechanical structure of the motorcycle must be developed by considering the engine's vibration sent through all parts especially the position of front footrest which has the highest impact in order to increase the driver's comfort.

Keywords: Engine vibration, Vibration signal, Averaged peak of vibration signal, Averaged energy of vibration signal

INTRODUCTION

Nowadays, motorcycles play an important role in the transportation in the modern and crowded towns especially in the capital cities. Their swiftness and economical cost make a number of people turn to use them more and more. One of the reasons to choose a motorcycle of motorcyclist and stackers is its convenience. The feelings of users to the motorcycle seat, hands, and footrests are significant factors that cannot be ignored. These interface positions are affected from the vibrations of its engine and adjacent environments [1, 2].

Motorcycle vibration mainly occurs when the engine starts. The acceleration of the engine reinforces the additional vibration to the motorcycle body. The analysis of the vibration signal has been developed for years in many fields of studies. Distinguishing signal components and its major attributions can be accurately accomplished. Therefore, the concept of signal analysis technique is applied to analyze the vibration of motorcycle at various positions in this paper [3, 4].

In the experiments, the HONDA WAVE 100s is selected as an instance because of its popularity in Thailand. The positions of left hand, seat cushion, left front footrest, and left rear footrest are the four targets

to measure the vibration transmitted from its engine. The engine is set to run at five different speeds of 2,000 rpm, 2,500 rpm, 3,000 rpm, 3,500 rpm and 4,000 rpm. The measurement of vibration signals has been using an accelerometer passing through its corresponding base station. Subsequently, the measured signals are analyzed using some selected signal processing techniques. Two main parameters of averaged peak and averaged energy of the vibrational signal are calculated and discussed afterward.

BACKGROUND

This section introduces some basic related information of engine vibration, and corresponding parameters used to indicate the condition of the machine.

Engine Vibration

Vibration is the phenomenon of moving back and forth of an object under force. The engine vibrations are an integral sum of every mechanically moving component on the motorcycle body [5-7]. These vibrations in motorcycle engines are a result of periodic and aperiodic oscillations caused about an

equilibrium point. These things are not wanted; however, it cannot be avoided. Therefore, the appropriate thing to do is to limit the size of these vibrations. The core amplitudes and frequencies of the vibration signals should be adequately and properly analyzed.

Averaged Power of Vibration Signal

The power of signal is defined as the amount of energy consumed per unit time. The signal attribute is very meaningful to present the energy of the signal in a period of time. The energy of the engine-running vibration signal often goes to infinity; in other words, it can be assumed to be not-squarely-summable as long as the engine does not stop running. The calculation of power of signal is defined by using the sum of square of the signal samples [8, 9]. Mathematically, the averaged power of an aperiodic sequence $x[n]$ is defined as the following equation.

$$Px = \lim_{K \rightarrow \infty} \frac{1}{2K+1} \sum_{n=-K}^K |x[n]|^2, \quad (1)$$

where K is the sequence half length which extends its limit of number of samples to infinity.

Averaged Peak of Vibration Signal

In addition to the power of engine vibration signal is described in the previous section. The averaged peak of signal is defined as the averaging amount calculated from a number of peak values of periodic or semi-periodic signals existing in a unit of time. Since the engine vibration is characterized as semi-periodic signal as depicted in Fig.1, the averaged peak of signal is selected in this study. This attribute is calculated to compare with power of engine vibration signal for all experimental conditions.

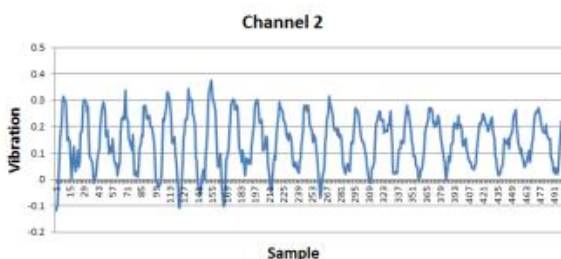


Fig. 1 An example of motorcycle engine vibration signal with semi-periodic waveform.

EXPERIMENTAL PROCEDURE

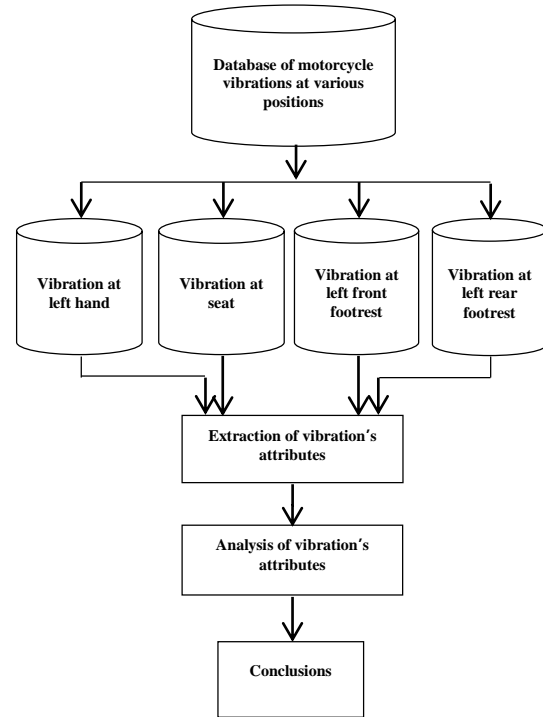


Fig. 2 Experimental Procedure.

The experimental procedure has been conducted as depicted in Fig.2. The database of motorcycle vibrations at various positions are implemented. Subsequently, the distinction of motorcycle vibrations at all four points is conducted. Thereafter, the extraction of vibration's attributes of averaged power of vibration signal and averaged peak of vibration signal as mentioned in the previous section has been performed. An analysis of these vibration's attributes has been done comparatively. Finally the conclusions has been summarized.



Fig. 3 Experimental allocation of accelerometers over the specimen motorcycle; (1) left hand, (2) seat, (3) left front footrest, and (4) left rear footrest.

The specimen motorcycle in the experiment is

Honda Wave 100s model. The accelerometers are attached at four core points which are the contact points between driver or rider and the motorcycle body including motorcycle left hand, seat, left front footrest, and left rear footrest as depicted in Fig.3. These engine vibration signals are measured in the form of acceleration by these accelerometers and recorded by the G-link microstrain serial base station through a host computer. The vibration signal is in the form of an approximate periodic sequence which is assumed to be a power signal with a finite average power [9-11]. Therefore, this equation has been adapted with a specific length recorded in 10 iteration samples for all five various levels of engine speeds of 2,000, 2,500, 3,000, 3,500, and 4,000 rpm, respectively. The duration of each sample lasts 10 seconds at the sampling rate of 2,048 Hz.

From the measured values of vibration signals, the root sum square of the accelerations of all three directions is calculated. The equally-divided sections of the root sum square values are therefore provided for all experiments. Subsequently, the extraction of vibration's attributes of averaged power of vibration signal and averaged peak of vibration signal as mentioned earlier has been performed.

EXPERIMENTAL RESULTS

In the preliminary stage, the experimental results of the values of vibration signals is obtained from the accelerometer measurement. A number of portions of motorcycle engine vibration signals at its left hand with the engine speed of 2,000 rpm are presented in Fig.4. All experimental graphs insist the semi-periodicity which reflects from the working periodic cycle of ignition inside the engine and the corresponding effects of surrounding environments.

From these values of vibration signals, the vibration's attributes of averaged power of vibration signal and averaged peak of vibration signal are extracted and plotted in comparative way with different engine speeds as depicted in Figs. 5 and 6.

It can be seen from Figs. 5 and 6 that when the engine speed is increased, the averaged power of vibration signal and averaged peak of vibration signal are in upward trends for nearly most of the positions of the accelerometers. When comparing among the positions, both of the vibration's attributes of the seat are mostly lowest, meanwhile those of the left front footrest are at the highest levels. Moreover, at the high engine speeds from 3000-4000 rpm, the second highest is of that of left rear footrest, subsequently, the third highest is of that of left hand.

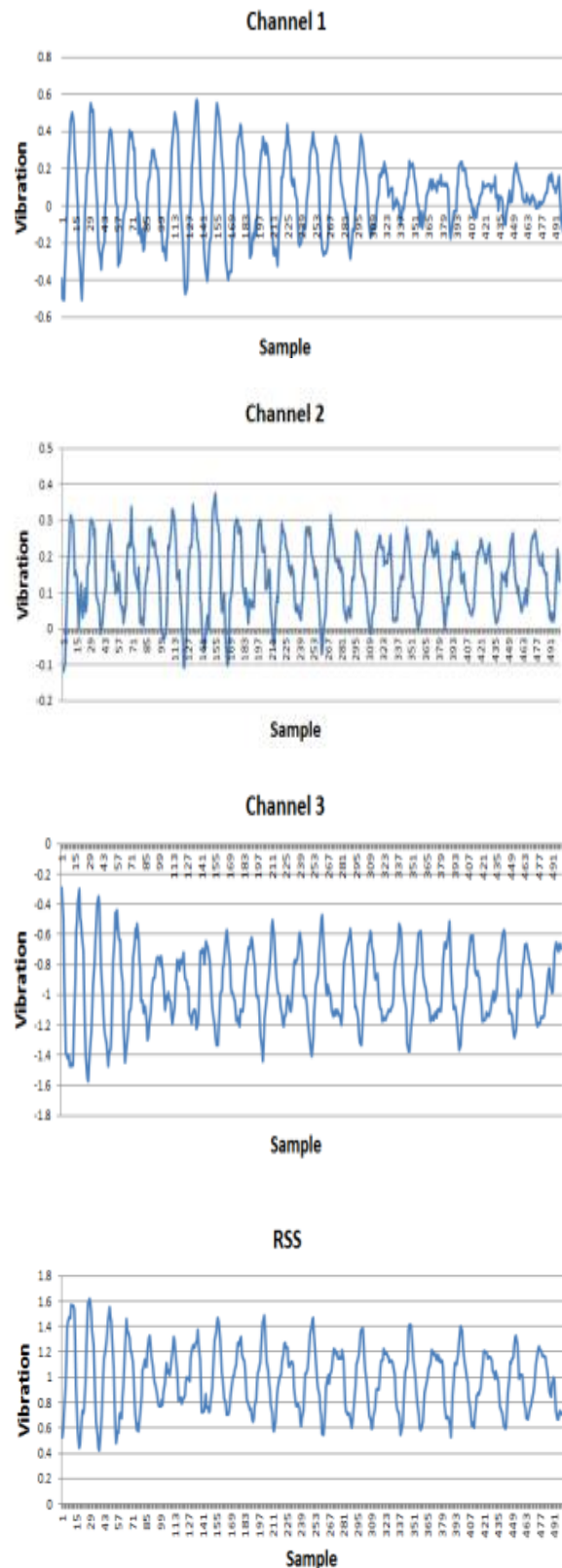


Fig. 4 Some examples of motorcycle engine vibration signals at left hand with the engine speed of 2,000 rpm.

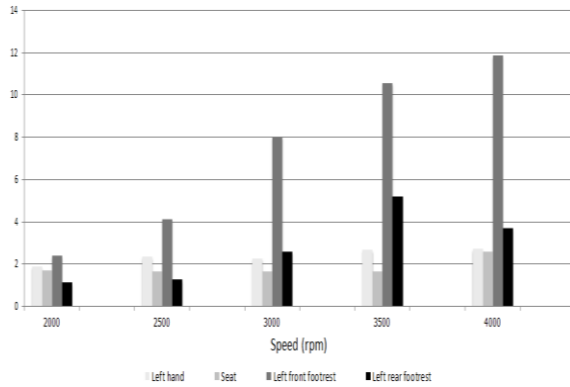


Fig. 5 Comparison of averaged peak of vibration signal for four core contacting points including motorcycle left hand, seat, left front footrest, and left rear footrest at five different engine speeds from 2000-4000 rpm.

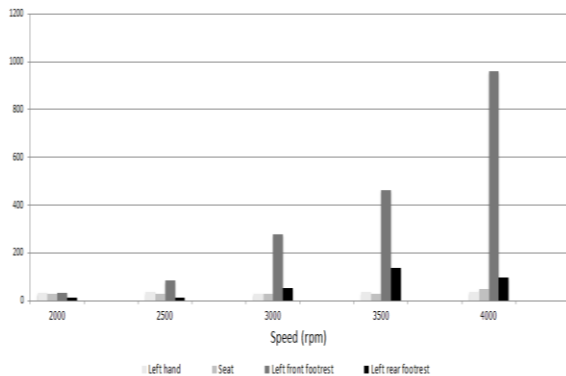


Fig. 6 Comparison of averaged power of vibration signal for four core contacting points including motorcycle left hand, seat, left front footrest, and left rear footrest at five different engine speeds from 2000-4000 rpm.

As for at the lower engine speeds from 2000-2500 rpm, the lowest is of that of left rear footrest, then the second lowest is of that of seat. It was obviously observed that both of the attributes of left front foot are at the highest levels. The core reason is that this position is closest to the motorcycle engine. The vibration is sent directly through the body structure of motorcycle with the shortest distance. On the other hand, the attributes of the seat position are mostly minimal. A concrete reason is that it is in furthest distance from the engine. Moreover, a supporting reason is that the sponge stuffed within the seat serves as a vibration absorber.

CONCLUSIONS

This paper has studied the vibration of a motorcycle at four different parts where the driver or rider exposes to the motorcycle. This vibration has been transferred from the working engine and all surrounding environments. In this experiment, a study of the vibration signal sent through four core points has been performed. These points are the contacts between driver or rider and the body of the specimen motorcycle body including motorcycle left hand, seat, left front footrest, and left rear footrest. The selected motorcycle which is used in this experiment is Honda Wave 100s model. Calculation of two parameters of averaged peak and averaged energy of the vibrational signal has been conducted in a comparison way. The experimental results showed that when the engine speed is increased, the averaged power of vibration signal and averaged peak of vibration signal are in upward trends for nearly most of the positions of the accelerometers. By comparing among all positions, both of the attributes of the seat are mostly in the lowest levels, meanwhile those of the left front footrest are at the highest levels. In conclusion, it is obviously summarized that the mechanical structure of the motorcycle should be developed by considering the engine's vibration sent through all parts in order to improve the comfort for the driver and rider.

ACKNOWLEDGEMENTS

The research was partly sponsored by the Faculty of Engineering at Sriracha's Fund. In addition, the author would like to express the gratitude to Mr. Thapakorn Pankaew for some related experimental data.

REFERENCES

- [1] Yujun L., Peter W. T., Xin Y., Jianguo Y., EMD-based fault diagnosis for abnormal clearance between contacting components in a diesel engine, *Mechanical Systems and Signal Processing*, Vol. 24, Issue 1, 2010, pp.193–210.
- [2] Xia W., Changwen L., Fengrong B., Xiaoyang B., Kang S., Fault diagnosis of diesel engine based on adaptive wavelet packets and EEMD-fractal dimension. *Mechanical Systems and Signal Processing*, Vol. 41, Issue 1-2, 2013, pp. 581–597.
- [3] Binqiang C., Zhousuo Z., Chuang S., Bing L., Yanyang Z., Zhengjia H., Fault feature extraction of gearbox by using over complete rational dilation discrete wavelet transform on signals measured from vibration sensors. *Mechanical Systems and Signal Processing*, Vol. 33, Issue 11, 2012, pp. 275–298.

- [4] Ahmad T. A., Barat G., Teymour T. H., Seyed S.M., Vibration analysis of a diesel engine using biodiesel and petro diesel fuel blends, *Fuel*, Vol. 102, Issue 12, 2012, pp. 414–422.
- [5] Zunmin G, Jin C., Barry H., Analysis of engine vibration and design of an applicable diagnosing approach. *International Journal of Mechanical Sciences*, Vol. 45, Issue 8, 2003, pp. 1391–1410.
- [6] Xianhua L., Randall R. B., Jerome A., Blind separation of internal combustion engine vibration signals by a deflation method. *Mechanical Systems and Signal Processing*, Vol. 22, Issue 5, 2008, pp.1082–1091.
- [7] Xianhua L., Randall R. B., Blind source separation of internal combustion engine piston slap from other measured vibration signals. *Mechanical Systems and Signal Processing*, Vol. 19, Issue 6, 2005, pp. 1196–1208.
- [8] Liang B., Iwnicki S. D., Zhao Y., Application of power spectrum, cepstrum, higher order spectrum and neural network analyses for induction motor fault diagnosis. *Mechanical Systems and Signal Processing*, Vol. 39, Issue 1-2, 2013, pp. 342–360.
- [9] Akhand R., Upadhyay S. H., A review on signal processing techniques utilized in the fault diagnosis of rolling element bearings, *Tribology International*, Vol. 96, Issue 4, 2016, pp. 289-306.
- [10] Chomphan S., Chaimanatsakun A., Sakornsir R., Khumneungratavongsa S., Rattanasat K., A Comparative Study of LPG-modified Engine and Normal Oil-usage Engine. in *Proc. Int. Conf. On Engineering and Applied Sciences*, 2016, pp. 219-225.
- [11] Carlucci A. P., Chiara F. F., Laforgia D., Analysis of the relation between injection parameter variation and block vibration of an internal combustion diesel engine. *Journal of Sound and Vibration*, Vol. 295, Issues 1–2, 2006, pp. 141–164

FREQUENCY ANALYSIS OF THE ENGINE SUPPORT VIBRATION WITH HYDROGEN-DIESEL DUAL-FUELING

Boonthum Wongchai, Poranat Visuwan, Sathaporn Chuepeng
Department of Mechanical Engineering, Faculty of Engineering at Sriracha,
Kasetsart University, 199, Sukhumvit Rd., Thungsukhla, Sriracha, Chonburi, 20230, Thailand

ABSTRACT

In the present days, diesel engines are mainly used in the transportation and the logistic systems. Hydrogen is used as an alternative energy in diesel engine called hydrogen-diesel dual fuel for saving diesel fuel and protecting environment. Hydrogen adding affects diesel engine vibration and car seat vibration. This article presents the effect of hydrogen flow rate on the spectrum of the vibration of the engine support. The four stroke single cylinder diesel engine is tested with hydrogen-diesel dual fuel by varying hydrogen flow rate. The vibration of the engine support is measured at two constant speeds with three different loads. The fast Fourier transform of the engine support vibration are calculated to analyze the vibration signals at the resonance frequency of the car seat vibration. The fast Fourier transform spectrums in the experimental results show that the average peak acceleration of the first three engine frequencies around 0 to 70 Hz tend to decrease by adding the hydrogen flow rate. The engine support vibration and the car seat vibration at this frequency range can be reduced by adding the hydrogen flowrate.

Keywords: *Hydrogen-diesel dual fuel, Fast Fourier transform, Frequency analysis, Vibration*

INTRODUCTION

Diesel engines are nowadays widely used in vehicles and stationary applications. Many researchers study effect of hydrogen addition on diesel engine performance and pollution [1-5]. Hydrogen is sustainable, renewable, and carbon free and can be produced from various procedures such as water electrolysis, steam reforming, and dehydrogenation of organic chemical hydrides. Carbon and hydrocarbon emission can be reduced by adding hydrogen in a diesel engine. For the thermal efficiency, hydrogen-diesel dual fuel operation shows higher thermal efficiency than a conventional diesel operation at condition of relatively high engine load [6]. Adding of hydrogen affects cylinder pressure, noise, and also vibration of a diesel engine. Nguyen and Mikami [7] studied the effect of hydrogen addition to intake air on combustion noise. The results showed that the combustion noise at late diesel fuel injection greatly decreased by hydrogen addition of 10 vol% while the mean effective pressure was almost the same with or without hydrogen addition. Uludamar et al. [8] reported that the Hydroxyl (the mixture of hydrogen and oxygen gases) addition with diesel-biodiesel blends decrease the engine vibration.

Engine block vibration is produced by the cylinder pressure. Pressure force pushes a piston and transmits through connecting rod, crankshaft, engine support and other components. For four stroke diesel engine, diesel oil is injected and fires one time per two revolutions of the crankshaft. The first main harmonic frequency of an engine with i cylinders can be

computed from

$$N = 120f / i, \quad (1)$$

where N is the engine speed in RPM and f is the first main harmonic frequency in Hz [9]. Frequency analysis are mainly used to analyze an engine vibration and acoustic emission such as root mean square value (RMS), fast Fourier transform (FFT), power spectrum density (PSD), and short-time Fourier transform (STFT) [10-13]. The FFT shows an amplitude of an engine vibration at any frequencies and PSD is the power of FFT. The STFT is used to analyze transient vibration signals such as valve impact, injector-pulses, and prompt initial knock detection. Taghizadeh-Alisaraei et al. [14-16] used FFT and STFT to analyze the vibration of the compression ignition engine (CI) with biodiesel-diesel fuel blends and ethanol-diesel fuel blends. For biodiesel-diesel fuel blends, the results showed that D100 and B80 had lowest vibration and STFT can be used for the real-time knock detection and injection control. In addition, the FFT, and STFT are used in engine noise and vibration analysis [17-19].

Engine support vibration can be separated into the responses of excitation force and torque. The force at the engine support has two components in longitudinal and lateral direction of the piston travel. The vibration at an engine support transmits throughout the other car components and finally reach to car seats. The vertical and horizontal vibration of the car seats causes of driver and passengers discomfort with low resonance frequencies [20-21].

Qiu and Griffin [22] reported that the resonance frequencies of the fore-aft vibration of the seat pan and the backrest are below 50 Hz.

In this study, the engine support vibration of the hydrogen-diesel dual fuel engine with the variation of hydrogen flow rate injected into the engine intake port are investigated and discussed at two constant speeds with three different loads. The FFT is used to analyze the vibration signals. The obtained results will be beneficial for vibration diagnostics of hydrogen-diesel dual fuel engines.

MATERIALS AND METHOD

Test engine and vibration measurement

The horizontal single cylinder Kubota RT100 Plus direct injection diesel engine as shown in Fig.1 is used in this study. The piston moves along x direction with the connecting rod and the crankshaft move on x-z plane. The engine is supported by four springs. The specifications of the engine are listed in Table 1.

Table 1 Engine specification

Model	Kubota RT100 plus
Number of cylinder	1
Bore × stroke	88 mm × 90 mm
Cycle	4-stroke, water cooled
Compression ratio	18:1
Maximum power	7.4 kW at 2,400 rpm
Maximum torque	33.4 Nm at 1,600 rpm
Injection timing	Variable; 20 to 45 degrees BTDC

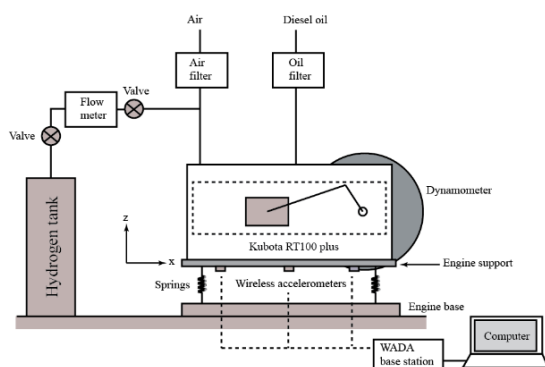


Fig. 1 Test engine and accelerometer installations at engine support (front view).

Five G-Link wireless triaxial accelerometers are installed at the bottom of the engine support using hot glue as shown in Figs. 1 and 2.

The engine support acceleration data are stored in on-board flash memory of G-Link accelerometer with sampling rate of 2,048 samples per second and are transferred to computer after the tests are completed. G-Link accelerometers are controlled by Node Commander software through WADA base station. The accelerometer specification are listed in Table 2.

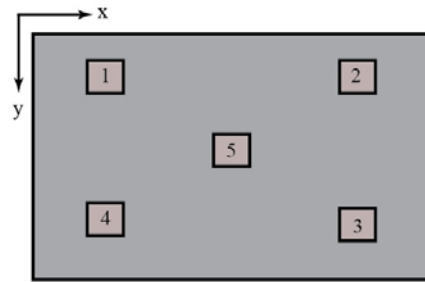


Fig. 2 Accelerometer installations at engine support (bottom view).

Table 2 Accelerometer specification

Instrumentation	Characteristics
G-Link	Sample rate: 2,048 samples per channel per second Measuring acceleration: X, Y and Z axes Range: ± 2 g or ± 10 g On-board flash memory: 2 MB
WADA base station	Power: USB Frequency: 2.405 GHz to 2.480 GHz

Experimental test program

The hydrogen-diesel dual fuel is use in this study. Hydrogen is injected through the flow meter and mixes with air at the manifold with pressure at 1 bar. Hydrogen-air mixture flow into the cylinder during the intake stroke and the main diesel fuel is injected before the piston reaching to TDC during the compression stroke. The hydrogen volume flow rate is varied at five levels of 0, 5, 10, 15 and 20 lpm with the engine speed (N) and the engine load (T) are shown in Table 3. The controlled engine loads are in percentages of the maximum engine torque as described in Table 1. The engine has been set to reach a steady state prior to collecting all data. The engine base accelerations are acquired 100,000 data with sampling rate 2,048 samples per second.

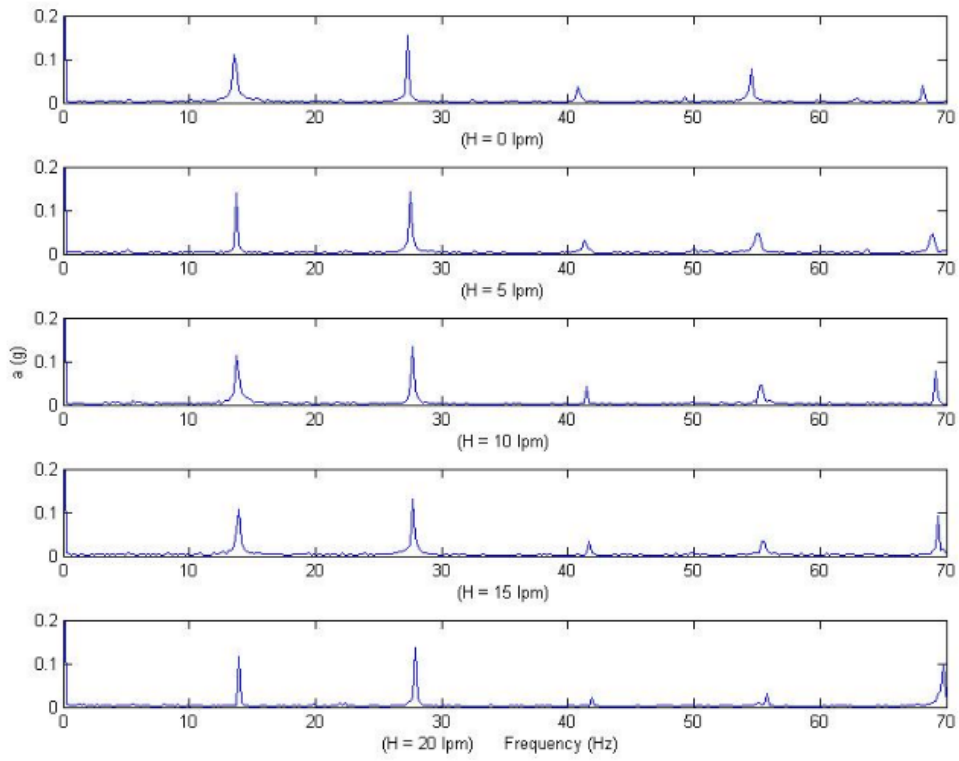


Fig. 3 0 to 70 Hz spectrum of the total acceleration at position 5; $N = 1,600$ rpm, $T = 25\%$.

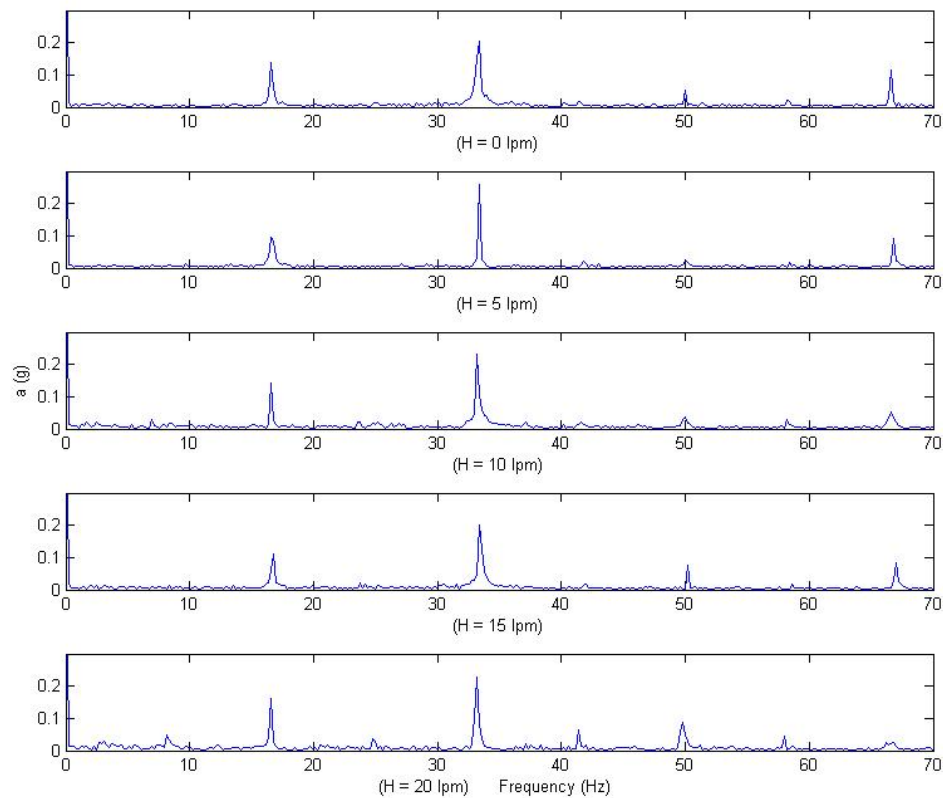


Fig. 4 0 to 70 Hz spectrum of the total acceleration at position 5; $N = 2,000$ rpm, $T = 25\%$.

Table 3 Engine parameter

Test program	N (rpm)	T (%)
1	1,600	15
2	1,600	25
3	2,000	25
4	2,000	50

All data are saved in cvs file format. After using FFT, the vibration signals in frequency domain can be analyzed in the frequency range from 0 to 1,024 Hz. However, for the engine support vibration, this frequency range can be used.

RESULT AND DISCUSSION

For four stroke single piston diesel engine, the engine vibration is generated by the combustion of the mixture vapor one time per two revolutions. The engine frequency f in Hz can be calculated from $f = N / (120)$ and the harmonic frequencies are $n \times f$ where n are 1, 2, 3, 4, etc. The four stroke engine with speed of 1600 rpm has the engine frequencies of 13.33, 26.67, 53.33 Hz, etc. For the engine speed of 2,000 rpm, the engine frequencies are 16.67, 33.33, 66.67 Hz, etc.

Frequency analysis is used to analyze the vibration data from the accelerometers. Figures 3 to 4 show the FFT of the total acceleration of the engine support at position 5 with the engine speed of 1,600 and 2,000 rpm at 25% engine load. The total acceleration can be computed from

$$a = \sqrt{a_x^2 + a_y^2 + a_z^2}, \quad (2)$$

where a_x , a_y , and a_z are the acceleration in x, y, and z axes.

The first three dominant engine frequencies around 0 to 70 Hz affect resonance frequencies of the car seat and cause discomfort of driver and passengers. The average amplitude of the first three engine frequencies around 0 to 70 Hz is define as the average peak acceleration (APA) and can be computed from

$$APA = (APA_{f1} + APA_{f2} + APA_{f3})/3, \quad (3)$$

where APA_{f1} , APA_{f2} , and APA_{f3} are the amplitudes at the first, the second, and the third harmonic frequency of the engine vibration.

Figs. 5 and 6 show that the APA tend to reduce by increasing the hydrogen flow rate. In addition, there are other frequencies generated by other components occur around 0 to 70 Hz. However, the present study interests to discuss only the effect of added hydrogen on the vibration amplitude at the engine frequencies

because the engine is the vibration source and added hydrogen directly affects the engine vibration. For the APA at positions 1 to 4, the results similar to the APA at position 5.

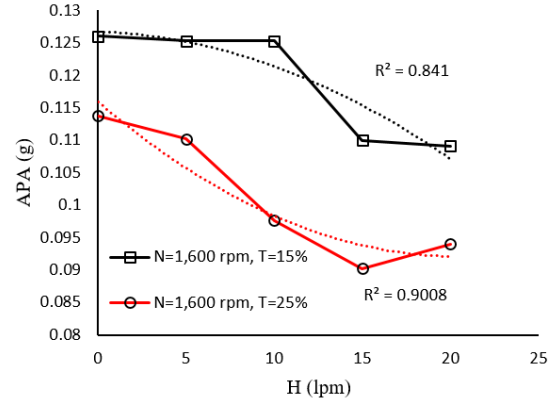


Fig. 5 Average peak of the total acceleration of the first three engine frequencies; N = 1,600 rpm.

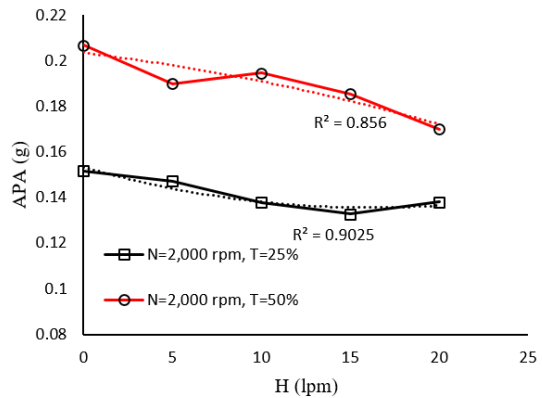


Fig. 6 Average peak of the total acceleration of the first three engine frequencies; N = 2,000 rpm.

CONCLUSION

This paper present a frequency analysis of engine support vibration, the hydrogen-diesel dual fuel engine is tested by varying hydrogen flow rate. The vibration of the engine support is measured at two different speeds and three different loads.

The FFT is used to analyze the signals of the engine support vibration at the resonance frequencies of the car seat vibration. From the FFT spectrum, the added hydrogen flow rate reduces the average peak acceleration of the first three engine frequency around 0 to 70 Hz. For this frequency range, the engine support vibration and the car seat vibration can be reduced by increasing the hydrogen flow rate.

ACKNOWLEDGMENTS

The study was conducted at Kasetsart University Sritacha Campus. The authors would like to thank the

Kasetsart University Research and Development Institute (KURDI) for the provision of the research grant to this project under the contract number V-T(D)173.53. The Kasetsart University Center for Advanced Studies in Industrial Technology under the National Research University (NRU) project is also acknowledged for the support to this study.

REFERENCES

- [1] Shekar R. D., and Purushothama H. R., Hydrogen Induction to Diesel Engine Working on Bio Diesel: A Review. *Procedia Earth and Planetary Science*, Vol. 11, 2015, pp. 385-392.
- [2] Wu H.W., Hsu T.T., He J.Y., and Fan C.M., Optimal performance and emissions of diesel/hydrogen-rich gas engine varying intake air temperature and EGR ratio, *Applied Thermal Engineering*, Vol. 124, 2017, 381–392.
- [3] Aldhaidhawi M., Chiriac R., Bădescu V., Descombes G., and Podevin P., Investigation on the mixture formation, combustion characteristics and performance of a Diesel engine fueled with Diesel, Biodiesel B20 and hydrogen addition, *International Journal of Hydrogen Energy*, Vol. 42, Issue 26, 2017, pp. 16793-16807.
- [4] Taghavifar H., Anvari S., and Parvishi A., Benchmarking of water injection in a hydrogen-fueled diesel engine to reduce emissions, *International Journal of Hydrogen Energy*, Vol. 42, Issue 26, 2017, pp. 11962-11975.
- [5] Hoseinia S. S., Najafia G., Ghobadian B., Mamatb R., Sidikc N. A. C., and Azmib W.H., The effect of combustion management on diesel engine emissions fueled with biodiesel-diesel blends, *Renewable and Sustainable Energy Reviews*, Vol. 73, 2017, pp. 307–331.
- [6] Tsujimura T., and Suzuki Y., The utilization of hydrogen in hydrogen/diesel dual fuel engine, *International journal of Hydrogen Energy*, Vol. 42, Issue 19, 2017, pp. 14019-14029.
- [7] Nguyen T. A., and Mikami M., Effect of hydrogen addition to intake air on combustion noise from a diesel engine, *International Journal of Hydrogen Energy*, Vol. 38, Issue 10, 2013, pp. 4153-4162.
- [8] Uludamar E., Tosun E., Tüccar G., Yıldızhan S., Çalık A., Yıldırım S., Serin H., and Özcanlı M., Evaluation of vibration characteristics of a hydroxyl (HHO) gas generator installed diesel engine fuelled with different diesel-biodiesel blends, *International Journal of Hydrogen Energy*, 42, Issue 36, 2017, pp. 23352-23360
- [9] Lin H., and Ding K., A new method for measuring engine rotational speed based on the vibration and discrete spectrum correction technique, *Measurement*, Vol. 46, Issue 7, 2013, pp. 2056–2064.
- [10] Yao J., Xiang Y., Qian S., Li S., and Wu S., Noise source separation of diesel engine by combining binaural sound localization method and blind source separation method, *Mechanical Systems and Signal Processing*, Vol. 96, 2017, pp. 303–320.
- [11] Moosavian A., Najafi G., Ghobadian B., and Mirsalim M., The effect of piston scratching fault on the vibration behavior of an IC engine, *Applied Acoustics*, Vol. 126, 2017, pp 91–100.
- [12] Barelli L., Bidini G., Bonucci F., and Moretti E., The radiation factor computation of energy systems by means of vibration and noise measurements: The case study of a cogenerative internal combustion engine, *Applied Energy*, Vol. 100, 2012, pp. 258–266.
- [13] Giancarlo C., Ornella C., Fulvio P., and Andrea P., Diagnostic methodology for internal combustion diesel engines via noise radiation, *Energy Conversion and Management*, Vol. 89, 2015, pp. 34–42.
- [14] Taghizadeh-Alisaraei A., Ghobadian B., Tavakoli-Hashjin T., and Mohtasebi S. S., Vibration analysis of a diesel engine using biodiesel and petrodiesel fuel blends, *Fuel*, Vol. 102, 2012, pp. 414-422.
- [15] Taghizadeh-Alisaraei A., Ghobadian B., Tavakoli-Hashjin T., Mohtasebi S. S., Rezaei-asl A., and Azadbakht M., Characterization of engine's combustion-vibration using diesel and biodiesel fuel blends by time-frequency methods: A case study, *Renewable Energy*, Vol. 95, 2016, pp. 422-432.
- [16] Taghizadeh-Alisaraei A., and Rezaei-Asl A., The effect of added ethanol to diesel fuel on performance, vibration, combustion and knocking of a CI engine, *Fuel*, Vol. 185, 2016, pp. 718–733.
- [17] Uludamar E., Tosun E., and Aydın K., Experimental and regression analysis of noise and vibration of a compression ignition engine fuelled with various biodiesels, *Fuel*, Vol. 177, 2016, pp. 326-333.
- [18] Çelebi K., Uludamar E., Tosun E., Yıldızhan S., K., and Özcanlı M., Experimental and Aydın artificial neural network approach of noise and vibration characteristic of an unmodified diesel

- Toward M. G.R., and Griffin M. J., The transmission of vertical vibration through seats: Influence of the characteristics of the human body, *Journal of Sound and Vibration*, Vol. 330, Issue 26, 2011, pp. 6526–6543.
- [19] Qiu Y., and Griffin M.J., Transmission of fore-aft vibration to a car seat using field tests and laboratory simulation, *Journal of Sound and Vibration*, Vol. 264, Issue 1, 2003, pp. 135–155.
- [20] engine fuelled with conventional diesel, and biodiesel blends with natural gas addition, *Fuel*, Vol. 197, 2017, pp. 159-173.
- [21] Patel C., Agarwal A. K., Tiwari N., Lee S., Lee C. S., and Park S., Combustion, noise, vibrations and spray characterization for Karanja biodiesel fuelled engine, *Applied Thermal Engineering*, Vol. 106, 2016, pp. 506–517.
- [22] Zhang X., Qiu Y., and Griffin M. J., Transmission of vertical vibration through a seat: Effect of thickness of foam cushions at the seat pan and the backrest, *International Journal of Industrial Ergonomics*, Vol. 48, 2015, pp. 36-45.

ASSESSMENT OF OUT-OF-PLANE FAILURE OF NON-ENGINEERED MASONRY WALL DUE TO TYPHOON HAIYAN-INDUCED STORM SURGES

Jenes P. Borais¹, and Richard De Jesus²

¹Graduate Student, De La Salle University, Philippines;

²Assistant Professor, De La Salle University, Philippines

ABSTRACT

Typhoon Haiyan, in 2013, caused massive destruction central Visayan region in the Philippines. Failure (collapsed) of non-engineered masonry walls were the most common failure experienced by residential structures in the area. This exposed the high vulnerability of non-engineered masonry walls of residential structures in rural areas, against extreme events. Existing building codes for large reinforced concrete frame structures had performed well, however, the masonry walls of low-rise structures along coastal areas have high vulnerability to out-of-plane failures due to poor construction methodology and insufficient design considerations. On-site survey along the coastal barangays of Tacloban City was conducted to determine the method of construction and design consideration for masonry walls. The structural investigation utilized finite element modelling (elastic) and yield line method (plastic). The estimated maximum pressure capacity using yield line method for the non-engineered masonry walls and National Structural Code of the Philippines (NSCP 2015)/ACI 530-02 compliant design was found to be inadequate. Thus, improved design was proposed and assessed against similar loads with consideration about the cost and suitability for the local worker's skills and techniques. Improvements in design includes modification in spacing and size of steel reinforcements, increased in concrete hollow block thickness, and modification on masonry wall dimensions. Based on the analytical results, it is concluded that the maximum pressure capacity of the improved masonry design increased significantly by 2 to 3 times compared to the current non-engineered masonry design. The new standard design could be used for new construction with potential disaster risk reduction against out-of-plane collapse.

Keywords Storm surge, typhoon Haiyan, out-of-plane failure, masonry walls

INTRODUCTION

Super Typhoon Haiyan made landfall on the 7th day of November, 2013 with estimated wind speeds up to 314km/hr. in the Philippines and then five other areas, including southern China and Vietnam. However, the Philippines was one of the worst affected. The typhoon caused excessive rainfall, landslides and flash floods throughout the region that caused casualties. The main cause of death is due to drowning, mainly caused by extreme storm surge. Storm surge is caused by irregular rise of ocean water caused by tropical cyclones. Rise in sea water level is caused by high winds that push on the ocean's surface and the low pressure at the center of a storm system [1].

The aftermath of the typhoon has recorded more than 6,300 deaths, 28,688 injured and 1,062 are still missing. [2]. Based on NDRRMC records, it is ranked No.1 among the top 10 worst typhoons in terms of damage to properties amounting to Php 93B (infrastructure, production, social and cross-sectoral) [2]. Several structures had been severely damaged in the path of Typhoon Haiyan more particularly to the

non-engineered structures in coastal areas in Tacloban City, Leyte. Structures had collapsed due to strong winds, and extreme storm surge resulting to injuries and casualties. Most of this structures are not designed to resist lateral forces caused by storm surges. Non-engineered masonry walls are vulnerable to out-of-plane failure since they are not designed to carry lateral pressure. This type of structural failure can lead to major injuries and even death to the occupants. This natural catastrophic event motivated the researcher to investigate the safety of the masonry walls. An on-site survey was conducted to identified the current construction method of the masonry walls of low-rise residential/commercial structures along the coastal barangays. Tacloban City was chosen for several reasons. First, it has the most number of damaged houses and number of casualties after the typhoon. Second, there was a lack of measures for risk reduction for coastal structures in Tacloban City. Third, the strength of Typhoon Haiyan exceeded the scale of estimations of storm surge and hazard zones and left tremendous devastation behind.

The survey objectives were to identify the method of construction, material used, and the design process

of the non-engineered masonry walls in order to understand the coastal damage condition and future risk assessments. Structural investigation was performed using finite element modelling and yield line method. A standard design for masonry walls was established.

INTERVIEW SURVEY

Based on the damage assessment of Tacloban City after the Typhoon Haiyan, barangays along the coastal areas were identified. On-site interview survey was conducted on these areas to determine the necessary information needed to assess the OOP failure of masonry walls.

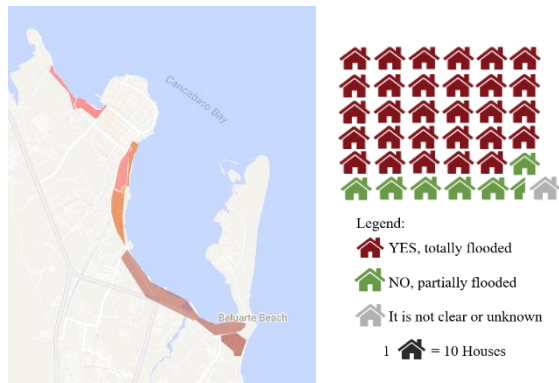


Figure 1: (a) On-site survey areas in coastal barangays in Tacloban City, (b) Percentage of totally/partially damaged houses.

A total of 380 low-rise residential/commercial houses were interviewed. These houses are located mostly at Brgy. 36, 37, 66, 67, 68, 69 and 70 in Anibong, at Brgy. 30, 48-B, 52, 54, 58 and 60-A along Esperas Avenue and Real St., at Brgy. 83 and 85 at San Jose (see Fig. 1).

Almost 84% of the 380 houses were built without the proper supervision of a licensed civil engineer or professional architect (see Fig. 2). Since coastal areas are the most vulnerable to high storm surges, around 79% of the houses surveyed were categorized as totally damaged after Typhoon Haiyan (see Fig. 2). The number of houses that were considered as totally damaged is directly proportional to the number of houses that are totally flooded (see Fig. 1).

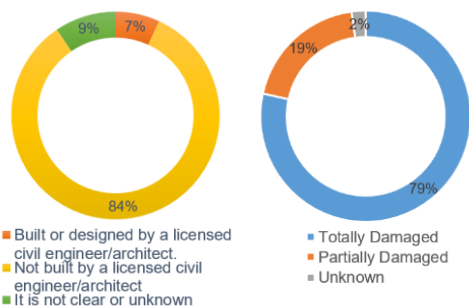


Figure 2: (a) Percentage of houses per designer, (b) Percentage of totally/partially damaged houses after Typhoon Haiyan (2013).

Around 58% out of the 380 houses surveyed are within the 40meter No Build Zone implemented by the local government of Tacloban City. Almost 69% of the houses within the No Build Zone areas are single storey houses and the remaining 31% has the capabilities to move on higher grounds since their houses were two storey structures. On the other hand, 65% of the total houses within 40-100meter from shoreline are considered as single storey structures and the remaining 35% are two storey structures.

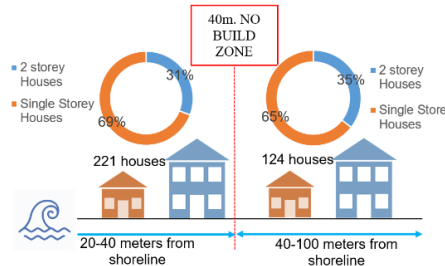


Figure 3: Number of houses within/beyond the No Build Zone in the coastal areas of Tacloban City. (survey conducted March, 2018)

CURRENT CONSTRUCTION METHOD AND STRUCTURAL DETAILS

Based on the survey of the housing structures in the coastal area, a typical house, named House E shown in Fig. 4, is selected for investigating the current construction method and structural details of masonry walls. House E is a 2 stories non-engineered RC framed with masonry wall structure and is constructed 2 years ago. The non-engineered design for masonry walls was 10cm thick CHB, 10mmØ (horizontal) every 4th CHB layer, 10mmØ (vertical) every 80cm OC and partially grouted. These design was based on the on-site survey conducted.



Figure 4: Actual photos of House E in Tacloban City.

ESTIMATION OF STORM SURGE PRESSURE

To estimate the pressure load imposed by the storm surge during Typhoon Haiyan, different flood loads were calculated. Different flood loads include hydrostatic load, breaking wave load, hydrodynamic load and debris impact load. A typical time series of the complex combination of storm surge pressure loads is illustrated in Fig. 5. In this figure, a dashed line represents the actual capacity of the structure. There is a decrease in capacity that can be attributed

to the buoyancy force reducing the resistance of the structure to global failure. In this research, it was difficult to calculate the exact pressure load on the masonry walls as a function of time, thus, the researcher determined the estimated pressure ranges or the possible minimum and maximum values of pressure load.

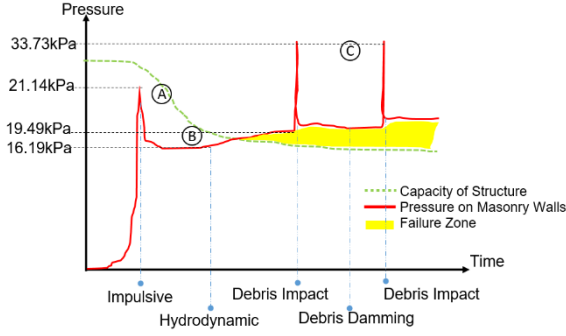


Figure 5: Typical time series of the complex combination of storm surge pressure loads.

The hydrostatic pressure is a force under static condition. Lateral hydrostatic loads are given by Eq. (1). Note that f_{static} is equivalent to the area of the pressure triangle and acts at a point equal to $2/3 d_s$ below the water surface.

$$P_{static} = \gamma_w d_s \quad (1)$$

where γ_w is the specific weight of floodwater, d_s is the floodwater depth. Considering a flood depth ranges from 2 to 3 meters high, the estimated hydrostatic pressure on masonry wall was 9.81 to 14.72 kPa.

The impulsive force is caused by the impingement of a leading edge of initial surging floodwater onto the structure. The impulsive force acts only on the front side of the structure. Presently, there is no established and rational method available to predict the force. Based on laboratory studies, the upper limit of the impulsive force is approximately 150% of the subsequent maximum hydrodynamic force in a quasi-steady flow, see Eq. (2).

$$F_{imp} = 1.5 F_{dyn} \quad (2)$$

The hydrodynamic pressure exists when the floodwater under dynamic conditions. In the Coastal Construction Manual of FEMA [3], the velocity of floodwater is assumed to be constant or steady-state flow. Hydrodynamic loads can be calculated using Eq. (3).

$$F_{dyn} = \frac{1}{2} C_d \rho V^2 A \quad (3)$$

where C_d is the drag coefficient, ρ is mass density of floodwater, V is velocity of floodwater, and A is the

surface area of obstruction normal to flow. Based on the observed maximum velocity of floodwater in Tacloban City, flow velocity ranges from 0.60 to 0.80 m/s [4]. When the floodwater is in motion around the structure, the hydrostatic condition no longer exists. However, the deviation caused by the initial flow of floodwaters is mainly small in comparison with the hydrostatic state. Considering the range of observed flow velocity, the estimated hydrodynamic pressure ranges from 16.19 to 19.49 kPa.

Theoretically, debris impact forces can be evaluated with impulse-momentum principle. The impact force when waterborne debris can be a cause of building damage. This can be estimated using Eq. (4).

$$F_i = 1.3 u_{max} \sqrt{k m_d (1 + c)} \quad (4)$$

where F_i is the impact force, 1.3 is the importance coefficient for Risk Category IV structures that is specified by ASCE 7 Chapter 5 for debris impact, u_{max} is the maximum flow velocity carrying the debris at the site (the debris is conservatively assumed to be moving at the same speed as the flow), c is the hydrodynamic mass coefficient which represents the effect of fluid in motion with the debris, k is the effective net combined stiffness of the impacting debris and the impacted structural elements deformed by the impact, m_d is the mass of the debris. Based on the local condition of Tacloban City, debris may include woods, garbage, stone, etc.

The debris damming forces are due to the jamming effect of debris on a structure, which increases the hydrodynamic forces by increasing the surface area exposed to the flow. This force follows after the initial impact force of the debris. This can be calculated by replacing the width of the structure with the width of the jammed debris, thus increasing the force. The damming forces can be estimated using Eq. 5.

$$F_{dm} = \frac{1}{2} \rho_s C_d B_d (h u^2)_{max} \quad (5)$$

where ρ_s is the fluid density including sediments, C_d is the drag coefficient, B_d is the breadth of the debris dam, h is the flow depth, and u is the flow velocity at the location of the structure. It is recommended that the drag coefficient be taken as $C_d = 2.0$

ESTIMATION OF LATERAL PRESSURE CAPACITY OF MASONRY WALL

Masonry walls subject to lateral forces can suffer from instability and collapse laterally. For walls which carry light gravity loads, out-of-plane loading typically induces a stability failure where a wall bursts outward or topples over.

The OOP behavior of masonry walls has not been studied as well as the corresponding in-plane

behavior, however, some research has been carried out on the OOP behavior. For example, Rivera, Rivera, Macias, Baqueirro, & Moreno [5] constructed six full scaled masonry walls tested against OOP loading. Crack patterns are similar to those predicted by the yield line theory adapted from that for reinforced concrete slabs. Steel reinforcements are the main component that resist the tensile stresses in masonry walls.

Yield line method is a well-established and a highly effective method used in determining the load bearing capacity of concrete slabs and plates. Yield line method is considered as economical, simple and versatile design method. It is economical because it considers features at the ultimate limit state [6]. The similarity of the failure pattern in masonry walls and reinforced concrete slabs has been driven to apply Johansen's yield line method to laterally loaded masonry walls. Yield line method requires the technical knowledge on how the masonry panels will fail. Several crack patterns have been observed based on experimental studies conducted and based on historical records for masonry failures. With these, all possible failure mechanisms for any masonry wall must be investigated to confirm the correct solution that will give the lowest failure load [7]. Some of the most common yield patterns was shown in Fig. 6.

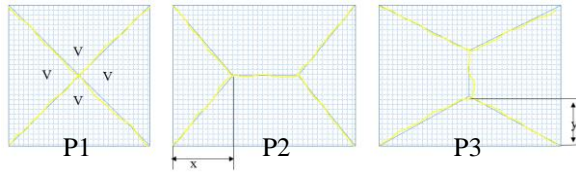


Figure 6: Most common yield line pattern for masonry OOP failure (Wang, Salmon, & Pincheira, 2007.)

$$P1 \quad \frac{M_{nx}}{M_{ny}} = \frac{a^2}{b^2} \quad \frac{w_u}{\phi} = 12 \left(\frac{M_{nx}}{a^2} + \frac{M_{ny}}{b^2} \right) \quad (7a)$$

$$P2 \quad \frac{M_{nx}}{M_{ny}} < \frac{a^2}{b^2} \quad \frac{w_u}{\phi} = \frac{24a(M_{nx} + M_{ny})}{2b^2x + 3b^2(a - 2x)} \quad (7b)$$

$$P3 \quad \frac{M_{nx}}{M_{ny}} > \frac{a^2}{b^2} \quad \frac{w_u}{\phi} = \frac{24b(M_{nx} + M_{ny})}{2a^2y + 3a^2(b - 2y)} \quad (7c)$$

The analysis using virtual work method can be used to determine the relationship between the applied loads and the resisting moments. Moments and loads are in equilibrium when the yield line pattern has formed, an infinitesimal increase in load will cause the structure to deflect further. The external work done by the loads to cause a small arbitrary virtual deflection must equal the internal work done as the masonry wall rotates at the yield lines to accommodate this deflection. The maximum pressure for the most common yield pattern can be estimated using Eq. 7a, 7b, and 7c [8] where w_u is the maximum pressure capacity, ϕ is reduction factor, M_{nx} and M_{ny} are the nominal moment strength in x

and y direction respectively, a and b are the width and height of the masonry walls. Nominal moment capacity of the masonry walls, M_{nx} and M_{ny} was calculated in accordance with the design procedure stated in the Building Code Requirements for Masonry Structures [9]. The design strength for out-of-plane wall loading was calculated in accordance with Eq. (8).

$$M_n = (A_s f_y + P_u) \left(d - \frac{a}{2} \right) \quad (8)$$

where A_s is the area of steel reinforcement, f_y is the specified yield strength of steel reinforcement, P_u is the factored axial load, d is the distance from extreme compression fiber to centroid of tension reinforcement, a is the depth of an equivalent compression zone at nominal strength, f'_m is the specified compressive strength of masonry, and b is the width of section. The width of section, b in Eq. (9) is the least value of the following: (1) center to center bar spacing, (2) six times the wall thickness, and (3) 72 inches or 1829mm.

$$a = \frac{(A_s f_y + P_u)}{0.80 f'_m b} \quad (9)$$

In order to organize the difference between each masonry wall design. Design specifications were categorized as: S-Category, C-Category, B-Category, and D-Category as shown in the Table 1.

Table 1: Category per design of masonry wall.

Spacing of Rebar S- Category	CHB Thickness C- Category	Rebar Diameter B- Category	Wall Dimension D-Category
S1(80cm)	C1(10cm)	B1(8mm)	D1(3x3m)
S2(60cm)	C2(15cm)	B2(10mm)	D2(3x4m)
S3(40cm)	C3(20cm)	B3(12mm)	D3(3x2.5m)

Based on the survey, most of the non-engineered masonry walls are under S1 Category. This are masonry walls whose horizontal reinforcement are spaced every 4th CHB layer and whose vertical reinforcements are spaced at 80cm O.C. It is also worth-mentioning that some masonry walls do not have steel reinforcements mainly because of financial incapability of the occupants. Some houses also used 40 x 20x 10cm thick CHB even if the desired designed CHB thickness for exterior walls are 40 x 20 x 15cm CHB. This has been verified during the survey since around 65% of the 380 houses confirmed that their house is not made of 6" CHB (40 x 20 x 15cm). According to some construction hardware,

majority of the locals purchased/used 10mmØ for the construction of their houses. Based on House E, the distance of the lateral supports or columns ranges from 2.5m to 4m apart. In this research, non-engineered masonry walls are categorized as S1-C1-B2. Using yield line analysis, the maximum pressure capacity for S1-C1-B2 was 10.32 kPa, 7.97 kPa, and 12.53 kPa for wall dimensions of 3 x 3m (pattern 1), 3 x 4m (pattern 2), and 2.5 x 3m (pattern 3) respectively. For S1-C2-B2, the maximum pressure capacity was 11.80 kPa, 9.12 kPa, and 14.34 kPa for wall dimensions of 3 x 3m (pattern 1), 3 x 4m (pattern 2), and 2.5 x 3m (pattern 3) respectively. Maximum pressure capacity of different masonry wall design consideration is graphically represented as shown in the Fig. 7.

DEVELOPMENT OF IMPROVEMENT

Considering the estimated maximum pressure capacity of the non-engineered masonry walls, it is evident that the current non-engineered masonry wall design has experienced difficulty in sustaining lateral pressure due to floodwater induced by storm surges.

The researcher conducted several attempts to improve the lateral pressure capacity of the masonry walls by: (1) Minimizing the on-center distance of the steel reinforcements, (2) Increasing the CHB wall thickness from 4" to 6" and 8" thick, (3) Providing a larger steel rebar diameter.

The lateral pressure capacity of the different masonry walls with steel reinforcements under S2 and S3 category and CHB thickness under C2 and C3 category are also included in Fig. 7. Comparing all the estimated lateral pressure capacity of each masonry wall design, the recommended design is S2-C2-B3. The S2-C2-B3 is masonry design whose vertical and horizontal reinforcements are 12mmØ spaced @ 40cm, CHB thickness of 150mm or 6" and the column distance is from 2.5 to 3meters. The S2-C2-B3 has the estimated lateral pressure capacity that is sufficient enough to resist impulsive forces. The S3-C2-B3 can be upgraded to C3 category to improve resistance to severe debris impact. The concept of improvement is to reinforce the strength of the masonry walls with minimum cost increase. The proposed improvements are listed in Table 2.

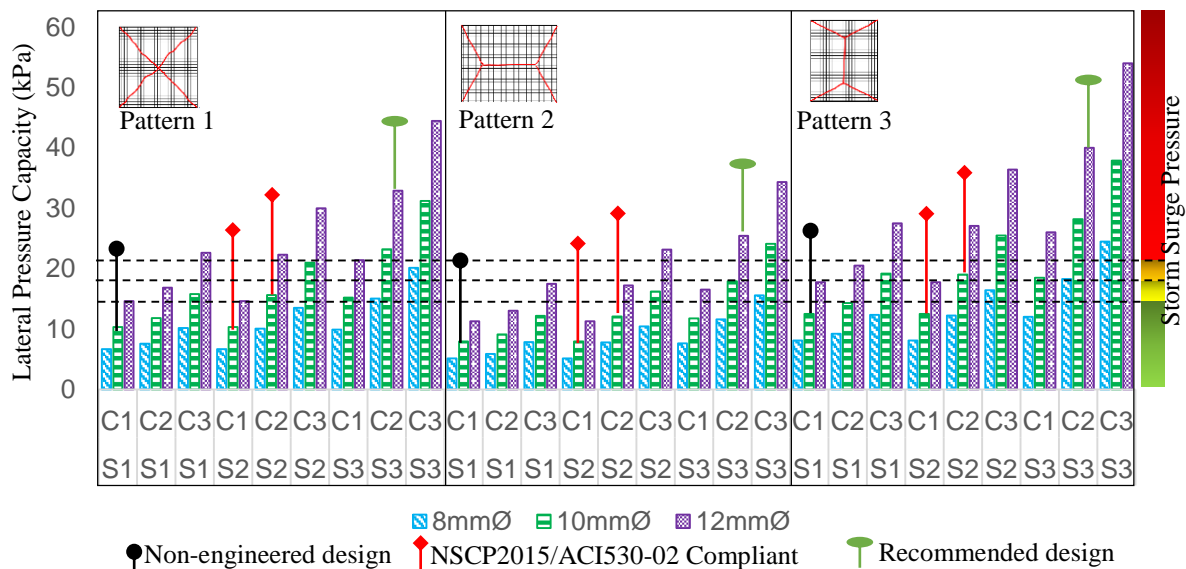


Figure 7: Estimated lateral pressure capacity of different masonry walls per pattern using yield line analysis

Table 2: List of Improvements

Part	Non-engineered design	NSCP 2015	ACI 530-02	Recommended design
Horizontal Reinforcement	80cm O.C	Max. of 1.2meter	Max. of 1.2meter	40cm O.C.
Vert. Reinforcement	80cm O.C.	Max. of 1.2meter	Max. of 1.2meter	40cm O.C.
Thickness of CHB	10 cm	10 cm Thick CHB (Table 411.3.1.1)	Minimum of 6" or 152mm (Sec. 5.6.2)	15 cm-20cm
Bar Size	Max. of 10mmØ	Min. of 10mmØ	Min. of 10mmØ	Min. of 12mmØ
Spacing of Support (Column)	Min of 3 m.	l/t or h/t is 18 to 20 or 2.7 to 3meters	l/t or h/t is 18 to 20 or 2.7 to 3meters	2.5 to 3 meters

To estimate the cracking pressure and of masonry walls, finite element analysis using Staad Pro V8. Four models of 3 x 3m masonry walls were developed, one for each design considerations as shown in Fig. 8. The masonry walls were modelled as isotropic linear elastic using a structures mesh with square shell elements of 4 nodes and 6 degrees of freedom per node, corresponding CHB thickness per design consideration. Modulus of elasticity of masonry wall was $550f'_m$, where f'_m was 6.89Mpa based on the minimum compressive strength of masonry required. Modulus of elasticity and yield strength of steel reinforcement was 200 GPa and 275 Mpa, respectively. Poisson's ratio was assumed equal to 0.20. Hinge supports were located along the confining elements to simulate the presence of columns and ring beams. The endpoints of the reinforcements were considered fixed to consider the effects of embedment to the supports, increasing uniform lateral pressure was applied perpendicular to the face of the masonry walls and the corresponding maximum lateral displacement was determined (see Fig. 8).

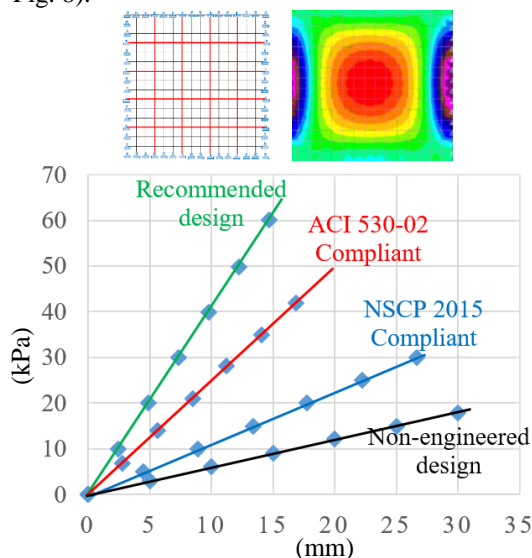


Figure 8: Pressure-displacement curves for different masonry wall design.

The results were graphically represented in Fig. 8. Increasing the CHB wall thickness and reducing the spacing of reinforcement significantly improves the lateral pressure capacity and reduce the lateral displacement of the masonry walls. The recommended design can sustain lateral pressure 2 to 3 times of the non-engineered masonry walls considering a 10mm lateral displacement.

CONCLUSION

Based on the field surveys and the corresponding analytical results, the following conclusions and recommendations are presented. Existing codes for large RC frame structures had performed well during

Typhoon Haiyan, however, the current construction method for masonry walls for coastal structures was high vulnerability to OOP failures due to poor construction methodology and used of poor quality materials. No Build Zone Policy along coastal barangays was not totally implemented due to economic and social considerations. A standard design for masonry walls was established. Additional improvements must be considered for structures with high exposure to heavy debris.

RECOMMENDATION

To achieve a much lower fatality count, there is a need to strengthen the structures against natural hazards. Building codes and hazard zoning may be enough for large structures, however additional safety measures must be implemented at the barangay level and develop a culture of preparedness. Although this is already embodied in our laws, its actual implementation leaves must be desired.

REFERENCES

- [1] National Geographic. (2017, March 24). National Geographic. Retrieved from <http://www.nationalgeographic.org/encyclopedia/storm-surge/>
- [2] NDRRMC. (2013). Final report of effects of Typhoon "Yolanda" Haiyan. Quezon City: National Disaster Risk Reduction and Management Council.
- [3] FEMA. (2012). Guidelines for Design of Structures for Vertical Evacuations from Tsunamis. National Oceanic and Atmospheric Administration.
- [4] Takagi, H., Li, S., de Leon, M., Esteban, M., Mikami, T., & Matsumaru, R. (2015). Storm surge and evacuation in urban areas during peak of a storm. *Coastal Engineering*.
- [5] Rivera, J. V., Macias, D. N., Baqueirro, L. F., & Moreno, E. I. (2011). Out-of-plane behavior of confined masonry walls. *Engineering Structures*, *Engineering Structures* 33 (2011) 1734-1741.
- [6] Kennedy, G., & Goodchild, C. H. (2004). *Practical Yield Line Design*. Camberley: The Concrete Centre.
- [7] Nilson, A. H., Darwin, D., & Dolan, C. W. (2003). *Design of concrete structures*. Singapore: McGraw-Hill.
- [8] Wang, C.-K., Salmon, C. G., & Pincheira, J. A. (2007). *Reinforced concrete design* 7th Ed. United States of America: John Wiley & Sons, Inc.
- [9] Masonry Standards Joint Committee (MSJC). (2005). *Building Code Requirements for Masonry Structures*. American Concrete Institute (ACI).

WALKABILITY AND RAIL NODES ALONG THE TRANS- EUROPEAN TRANSPORT NETWORK: THE CASE OF GENOA BRIGNOLE STATION

Noriko Otsuka¹, Dirk Wittowsky¹, and Marlene Damerau¹
ILS – Research Institute for Regional and Urban Development, Germany

ABSTRACT

This paper discusses the walkability around railway stations along the Rhine-Alpine Corridor, which is one of the nine Core Network Corridors under the Trans-European Transport Network (TEN-T) Regulations. Research draws upon an EU funded project, RAISE-IT (Rhine-Alpine Interregional Seamless and Integrated Travel Chain) which consists of nine partners from the Netherlands, Germany and Italy. The project explores seamless rail networks and intermodal connections at stations, and aims to improve passengers' experience at six urban nodes along the Rhine-Alpine Corridor connecting Rotterdam and Genoa through six European countries. The accessibility of a rail node (i.e. station) has been examined at three levels of spatial contexts: 1) accessibility within a node; 2) walkability of a node and its surrounding area within a radius of 800m from the node; and 3) accessibility to and from a node at urban scale within the boundaries of the city. Research reported in this paper focuses on the second spatial level: the walkability around stations. With reference to existing benchmark indicators and urban design parameters to assess the walkability (e.g. urban structure, design of the street, obstacles and traffic safety, and personal impression), a tailor made methodology has been developed including field observation and map analysis. Results from Genoa Brignole Station, one of the six case studies, have revealed the fact that the walkability has been influenced by various factors, not only the quality of physical infrastructure, but also other subjective aspects such as fear of crime and traffic safety, which are caused by structural constraints of the streets and the maintenance and quality of public spaces.

Keywords: walkability, Tran-European Transport Network (TEN-T), accessibility, urban node

INTRODUCTION

Background: RAISE-IT project

Railway stations have increasingly been expected to play multifunctional roles beyond their traditional transportation functions. Their roles have extended ranging from facilitating interchanges for multimodal transport networks, to the creation of public space since various amenities (e.g. cafes, restaurants, and shops, etc.) are accommodated within the station premise. Interchanges represent places where public transport modes, and private or alternative forms of travelling (e.g. walking, cycling, private car use, car sharing, and carpooling) all come together [1]. Furthermore, in the post-industrial era the role of railway has been rediscovered in providing a better pedestrian access to the city centre and in acting as a catalyst for 'urban renaissance'. The regeneration of station and its surrounding area has been intensively carried out in Europe that has contributed to the shift from car-dependent lifestyle and the change of image in urban centres [2].

This paper presents preliminary results of an EU project, RAISE-IT (Rhine-Alpine Integrated and

Seamless Travel Chain), which is funded by the Connecting Europe Facility (CEF) programme. This project focuses on the assessment of railway node accessibility along the Rhine-Alpine Corridor that is one of the nine Core Network Corridors (CNCs) under the TEN-T Regulations [3]. This project involved nine partners from the Netherlands, Germany and Italy, and the consortium consists of regional and local authorities within Interregional Alliance for the Rhine-Alpine Corridor European Grouping of Territorial Corporation (EGTC), and also three research institutions. To optimise access and travel time within and to/from a railway station, it is necessary to address a range of infrastructure and operational aspects such as station facilities, wayfinding for transferring passengers and information provision. Furthermore, the design and management of station should be analysed in terms of the integration of all the urban travel modes, including walking, cycling, private car and public transport as well as the spatial relationship with its surrounding areas. In order to facilitate complex intermodal connections, the urban node accessibility should be discussed in a holistic way with reference to different urban scales.

Objectives of this paper

Within the framework of the RAISE-IT project, a new methodology for assessing the urban node accessibility has been developed with reference to six railway stations along the Rhine-Alpine Corridor (Arnhem, Nijmegen, Düsseldorf, Frankfurt am Main, Karlsruhe and Genoa). For this project, the term ‘urban node’ refers to an ‘urban area’ where the railway station is located, while ‘node’ means railway station. ‘Urban area’ is concerned with area within the municipality’s boundary of the studied city. The following three levels of spatial contexts are examined during the analysis: 1) accessibility within a node; 2) walkability of a node and its surrounding area within a radius of 800m from the node; and 3) accessibility to and from a node at urban scale within the boundaries of the city. In this paper, the second spatial level (walkability) is focused. The rest of the paper explains the methodology for the walkability study and results from Genoa since it has illustrated useful findings such as the importance of pedestrian friendly streets and subjective aspects related to the street structure and environment.

METHODOLOGY

Target area and indicators for walkability study

The target area of the walkability study is concerned with a node and its surrounding area, and therefore we started with defining physical proximity meant by ‘surrounding area’. The concept of Transit Oriented Development (TOD) is used as a basis of our definition since it refers to station area development in terms of ‘a mixed use place, with a certain urban density and high-quality walking environment located within half-mile (800 m), i.e. 10 minutes’ walk of a transit stop [4]’. Previous research has acknowledged the prominent role of TOD in integrating mixed land use planning with multimodal accessibility around a transit node which leads the creation of pedestrian oriented urban environment [4][5][6]. This concept stemmed from the ‘node-place model’ which emphasises the strong link between the transportation node and its urban surroundings by considering the node as the place of human activities [7]. This project considers an area within a radius of 800 m of a station (i.e. 10 minutes’ walk) as a basis of assessing physical proximity for pedestrians in the walkability study (Fig 1).

In general, the walkability is examined in terms of the objective capacity and subjective quality of the built environment characteristics to support walking for different purposes. In particular, the access to the train and the public transport system is regarded as the central component. A wealth of previous literature introduced numerous indicators for the walkability study. For example, Geurs and van Wee maintained

that accessibility should be based on a structure of effects whose components consist of land use, the transport system, the time resources and the individual resources of a particular person [8]. Recent work published by ITDP (2018), *Pedestrians First*, discussed the framework for measuring the walkability ranging from the most basic requirements for walking to be possible (e.g. passable, accessible and safe), to factors adding extra benefits for pleasant walking (e.g. convenient, comfortable and enjoyable) [9].

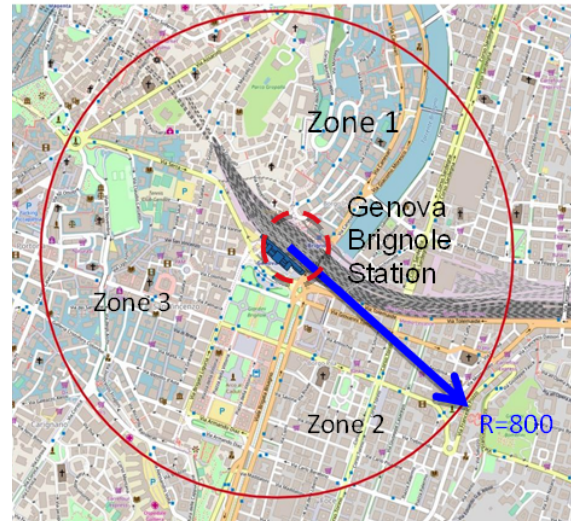


Fig. 1: Target area of the walkability study in Genoa, Source: Map by Commune di Genova (2017) and other added information by Otsuka

Methodology for the RAISE-IT walkability study

The walkability study in the present research has addressed both the objective environmental characteristics and subjective aspects, which are grouped into four key criteria: urban structure; design of the street; obstacles and traffic safety; and personal impression, together with some background information. A walkability checklist has been developed using 21 indicators (Table 1).

A Likert scale (1 to 5) was used to assess each indicator under the four criteria using the checklist. Annotations were made on an OpenStreetMap (OSM), and photographs have been taken for collecting visual evidence. Within the target area of a radius 800 m around a railway station two or three zones were generally defined in collaboration with local project partners of each node (Fig 1). Subsequently, the respective local partner suggested two or three major walking routes per zone which are most frequently used when people are walking to and from the station. The authors and local partners walked all the selected routes between the ending point of the 800 m's circle line and the information centre of train operator normally located in the middle of station building.

Firstly, the walking was carried out starting from

the information centre towards the ending point of the 800 m circle, while filling in the checklist and taking photographs. Then we walked straight back from the ending point towards the information centre while time required for walking was measured.

Table 1. Selected indicators for the walkability study, Source: ILS, 2017.

Criteria	Indicators
BACKGROUND	Condition of observation (date/time/ weather)
	Name of streets along each route
	Distance to travel (Measuring time for walking the route)
	Key characteristics of the street
URBAN STRUCTURE	Land use
	Building type
DESIGN OF STREET	Pedestrian walkway
	Width of the streets
	Streetscape
	Street furniture
	Tree and vegetation
	Shelter
	Pavement material
	Arts
OBSTACLE AND TRAFFIC SAFETY	Barrier free
	Safe crossing roads and streets
	Speed of cars and traffic calming
	Waiting time for traffic light
	Street parking
	Street connectivity
	Access for bikes
PERSONAL IMPRESSION	Comfortable in walking
	Fear of crime
	Cleanliness of streets
	Pedestrian flow

The following sections explain results from the Genoa node including background information of the city and the walkability analysis.

CASE STUDY ON GENOA

General Information of the city of Genoa

The city of Genoa is situated in the region of Liguria on the Mediterranean coast. It is the sixth largest city in terms of the population of Italy (583.601) with an area of ca. 240 square kilometer [10]. The node of Genoa is located at the south end of the Rhine-Alpine Corridor (Fig. 2) and plays a key role in transferring from/to land and to/from the sea.

The Genoa node is served by two main stations: Piazza Principe and Brignole. The both station buildings were constructed during the second half of the 19th century and the two transport hubs are located between the historic centre and the 18th century part of the city centre. Due to Genova's geographical characteristics constrained by hills and the Mediterranean Sea, it is difficult to apply major infrastructure redevelopment in the city centre. Furthermore, the protection of historic station buildings takes a priority and thus only small-scale

interventions are possible when upgrading the stations for meeting modern standard of interchange and multifunctional facilities. The two stations have gone through major refurbishment works over the last 15 years which have improved the both internal and external parts of the building and intermodal connections. More than 60,000 passengers use each of these stations per day.

The modal split of Genoa for daily trips (Fig.3) indicates that there is a similar distribution in terms of the use of sustainable modes of transport: 25% by walking and 27% by public transport, while bicycle is not used due to the difficult in cycling on steep hills. Private means of transport represent 37% for car drivers and 11% for others which consists of 9% for motorbikes and 2% for other vehicles such as light duty vehicles. The share of private car is the highest among the different transport modes (37%).

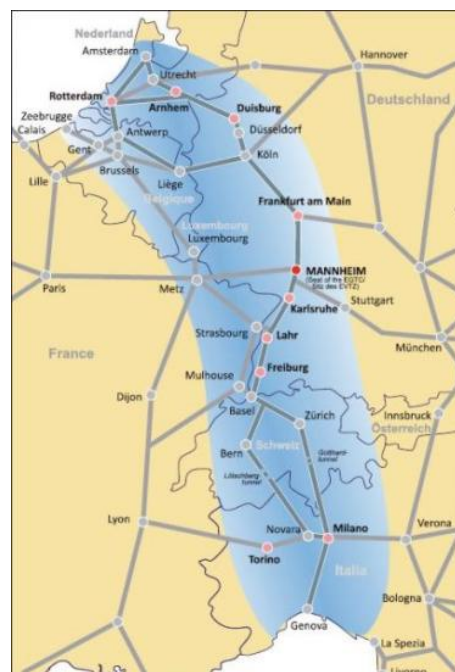


Fig. 2: The location of Genoa on Rhine-Alpine Corridor, Source: <http://blog.interreg.de> [3]

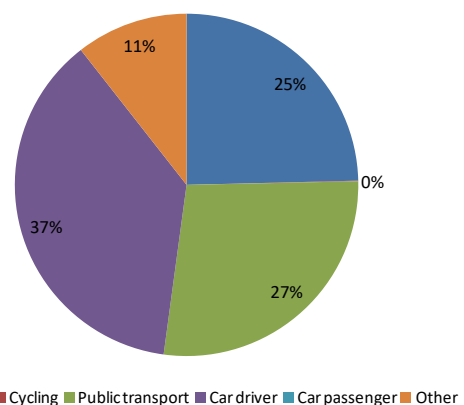


Fig. 3: Genoa Modal Split (2016), Source: CDG - Città di Genoa.

Results from the Walkability study

The local partners in Genoa: the municipality of Genoa (CDG) and a local research institution (IIC), have decided to conduct the walkability analysis in the Brignole station since more people are walking around there because of its central location in the heart of business and retail districts. Three zones have been identified within the 800 m circle (Fig 1), and two or three walking routes have been selected per zone. The fieldwork was conducted on the 25th of October 2017 and the weather was sunny and dry. The study results were presented in walkability maps which include a variety of quantitative and qualitative data: walking routes, measured time per route, position of public transport stops and traffic lights, the number of car sharing and bike sharing, points of interests such as public squares and museums, spatial and social problems due to empty buildings, graffiti and steep stairs (Fig.4).

Generally speaking, more people were walking in the southern area of Brignole, and thus walking routes appeared to be more visible being informed by the constant flow of pedestrians (Zone 2 and 3), compared to the area in the north (Zone 1). In this paper the walkability map of Zone 3 (San Vincenzo and Carignano) is presented since it has revealed a

striking difference in the environmental quality between three studied streets (Fig.4).

Two of the three routes in Zone 3 go through major shopping districts of the Genoa node, and offer comfortable pedestrianised streets (Fig. 5 and Fig. 6) with a variety of shops, cafes and restaurants. In particular, Via San Vincenzo was still lively even during the lunchtime (around 14:00 in Italy where many people go home for lunch) when the study was conducted (Fig. 6). Via Galata also offers a pedestrian friendly and further wider street which allows the placement of much street furniture such as benches and plant boxes as well as tables and chairs by cafes and restaurants (Fig.5). However, the end of the 800 m circle on Via Galata (hospital, Mura delle Capuccine) is situated at much higher level from the city centre, and it is inevitable for pedestrians to walk up and down many stairs if they choose this short cut to the city centre.

A striking difference from the two routes was a poor environmental quality found in Via Serra. Despite the fact that this route recorded the shortest walking time, narrow pedestrian walkway continues along lengthy stone made walls without windows on a long downhill (Fig.7). Furthermore, closer to the Brignole station, it was not pleasant to walk next to concrete wall of multi-storey car parking.

Walkability_Zone 3_San Vincenzo - Carignano

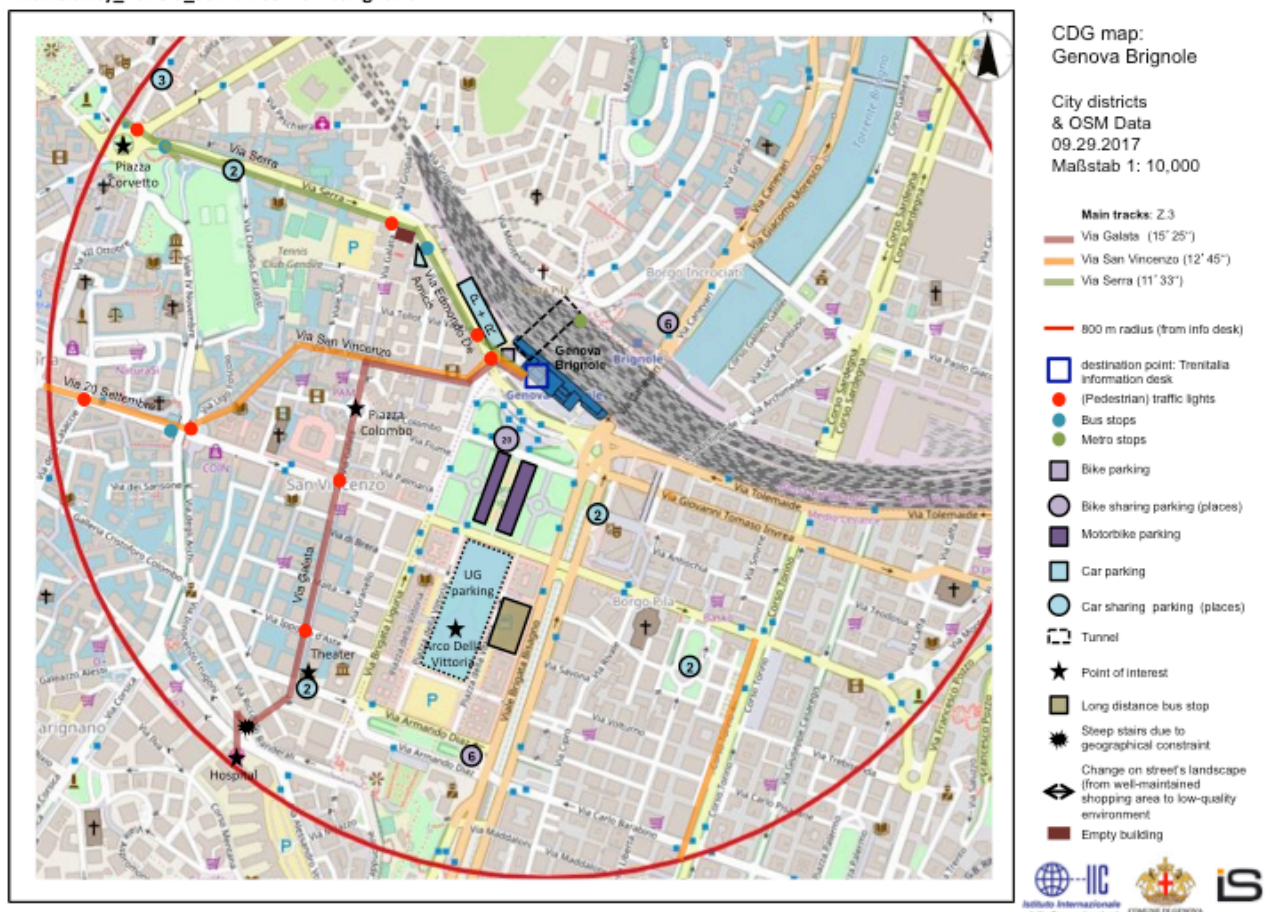


Fig. 4: Walkability map, Zone 3: San Vincenzo and Carignano, Source: CDG and ILS, 2017

Using Likert scale scored by the researcher and the local partners, radar graphs of the studied routes have been created in respect of the four walkability criteria (Fig. 5-7). Results from the radar graphs have echoed to remarks from the walkability map analysis. Via Galata and Via San Vincenzo presents the higher scores owing to pedestrianised streets and mixed land

use along the main shopping streets. Only drawback is many steep stairs because of the difference in the land level on the Via Galata route, which resulted in the low score of 'obstacles and traffic safety' (Fig. 5). This is a typical example caused by geographical constraint of Genoa.

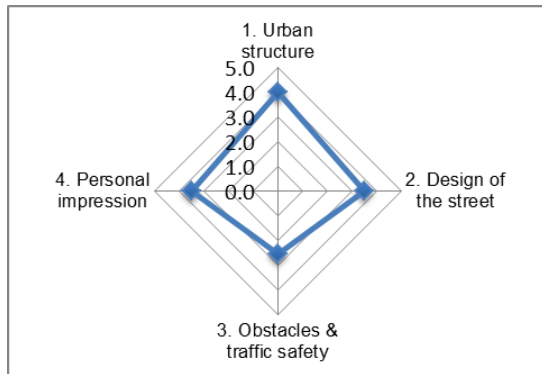


Fig. 5: Zone 3 Walkability results on Via Galata and pedestrianised street, Source: Otsuka, ILS, 2017

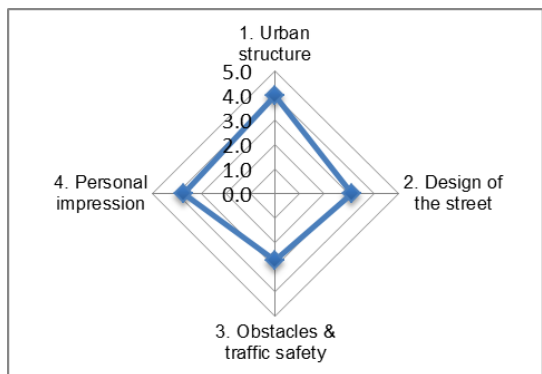


Fig. 6: Zone 3 Walkability results on Via San Vincenzo and pedestrianised shopping street, Source: Otsuka, ILS, 2017

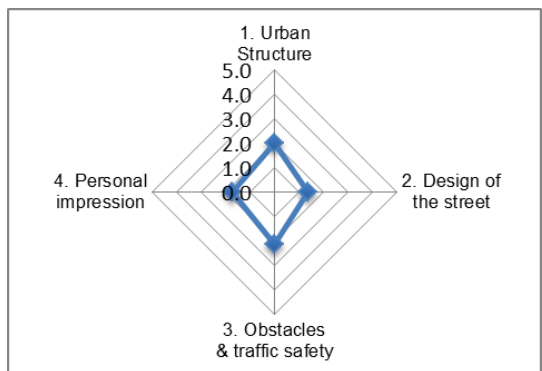


Fig. 7: Zone 3 Walkability results on Via Serra and narrow downhill pedestrian walkway, Source: Otsuka, ILS, 2017

Via Serra has got the poorest scores due to narrow pedestrian walkways along the long stone made walls and the multi-storey car parking (Fig. 7). The score of 'design of the street' is the worst among the seven streets selected for the Genoa case study. Since Via Serra has always been considered by the Genoese as a service road from Corvetto to Brignole, the design of the streets is rather road traffic oriented, while pedestrians' needs seem to be set aside. Although

there are a few historic palaces located along Via Serra, their internal courtyards are not visible from the street and the massive stone walls and narrow sidewalk are main physical obstacles when considering the future improvement of the walking route to and from the station.

In Zone 3 'traffic safety' has scored relatively low in all the three routes (Fig. 7) since the access to and from the station square has to go through two traffic

lights crossing the busy main access road to the station. Although there is an official multi-storey car parking right next to the station, people tend to use an unofficial space for short-term parking and Kiss & Ride, and the entrance to that space clashes with the pedestrian flow.

Finally, there is a tunnel walkway connecting two sides of the city between Zone 1 and Zone 3 (Fig. 4), which was covered with a full of graffiti at the time of the fieldwork. Local people know it is safe to walk through the tunnel, however, untidy graffiti and less maintained floor pavement tend to generate a negative image and make visitors feel uncomfortable and even a fear of crime.

CONCLUSIONS

This paper presented the methodology for assessing the walkability around railway stations with reference to the six urban nodes along the Rhine-Alpine Corridor. Results from the Genoa node highlighted that the walkability has been affected by both the objective environmental characteristics and subjective aspects (e.g. traffic safety and fear of crime). These are caused by structural constraints of the streets and the maintenance and quality of public spaces.

Data collection of the walkability study is based on the field observation using a tailor made checklist, and results can be influenced by subjective views of the researchers and local partners. To overcome this issue, findings from the fieldwork and the analysis of the walkability maps and radar graphs have been crosschecked by information gained through semi-structured interview with the station manager and a series of discussions with respective local partners. The idea of methodological triangulation [11] has been carefully integrated when the methodology was designed.

Findings from each urban node have been used for a roundtable discussion by various stakeholders (e.g. station manager, local authority planning officers, transport operations, user groups, etc.) who play a key role in developing, managing and using the station in the respective case study location. The walkability study aims to develop a tool for capturing and visualising the current state of pedestrian accessibility from and to the station building in order to present tangible evidence to practitioners. The next step is to explore the transferability of the methodologies to other urban nodes along CNCs beyond the Rhine-Alpine Corridor.

ACKNOWLEDGEMENTS

RAISE-IT is co-financed by the European Union's Connecting Europe Facility [Grant number: 130E]. The authors would like to thank Paola Debandi of Commue di Genova (CDG) and Sara Canevello

of Istituto Internazionale delle Comunicazioni (IIC) for their contributions to conducting the walkability study in Genoa.

REFERENCES

- [1] Van der Hoeven F, van Nes A, van der Spek S, Albecoa J, Skonieczki P, Berends H, Venema A, van Hagen M, and Cré I, State of the Art (Deliverable 2.1 - Final). EU project: NODES, 2013.
- [2] Peters D, and Novy J, "Rail Station Mega-Projects: Overlooked Centrepieces in the Complex Puzzle of Urban Restructuring in Europe", *Built Environment*, Vol. 38(1), 2012, pp. 5-12.
- [3] European Union, TEN-T Regulation. REGULATION (EU) No 1315/2013 OF THE EUROPEAN PARLIAMENT AND OF THE COUNCIL of 11 December 2013, 2013.
- [4] Vale D.S, "Transit-oriented development, integration of land use and transport, and pedestrian accessibility: Combining node-place model with pedestrian shed ratio to evaluate and classify station areas in Lisbon", *Journal of Transport Geography*, Vol. 45, 2015, pp.70-80.
- [5] Papa E, and Bertolini L, "Accessibility and Transit-Oriented Development in European metropolitan areas", *Journal of Transport Geography*, Vol. 47, 2015, pp. 70-83.
- [6] Bertolini L, Curtis C, and Renne J, "Station Area Projects in Europe and Beyond: Towards Transit Oriented Development", *Built Environment*, Vol. 38(1), 2012, pp.31-50.
- [7] Bertolini L, "Nodes and places: complexities of railway station redevelopment", *European Planning Studies*, Vol. 4(3), 1996, pp. 331-345.
- [8] Geurs KT, and Van Wee B, "Accessibility Evaluation of Land-Use and Transport Strategies: Review and Research Directions", *Journal of Transport Geography*, Vol.12, 2004, pp. 127-140.
- [9] ITDP (Institute for Transportation and Development Policy), *Pedestrians First, Tool for Walkability City*, First Edition, New York: ITDP, 2018
- [10] ISTAT - Italian National Institute of Statistics, 31/12/2016.
- [11] Denscomb, M, *The Good Research Guide: For Small-Scale Social Research Projects*, 6th Edition. Maidenhead: Open University Press, 2017

THE COMPARISON OF DRAINED SHEAR STRENGTH BETWEEN SINGLE STAGE AND MULTISTAGE OF KHON KAEN LOESS FROM TRIAXIAL TEST

S. Chatchawan¹, R. Nuntasarn² and D. Hormdee³
^{1,2,3} Faculty of Engineering, Khon Kaen University, Thailand

ABSTRACT

This study was conducted to compare the drained shear strength of compacted Khon Kaen loess between the single stage method and the multistage method by a consolidated drained triaxial test. The single stage method is a conventional method of triaxial and direct shear test. At least three samples are used to determine the shear strength of soil. Meanwhile, only one sample is used to determine the shear strength of soil for a multistage method. Therefore the multistage is a safe time for testing than the single method. The investigation of this two method of this study will be checked the accuracy of the multistage method. A result of this study will help to make a decision to choose between the single stage method and the multistage method for the studied of the drained shear strength of compacted Khon Kaen loess. The result from the consolidated drained triaxial test by the multistage method showed a quite well compared to single stage test results.

Keywords: single stage, multistage, drained shear strength, Khon Kaen Loess, Compacted soil

INTRODUCTION

There are many reports of devastated buildings at Khon Kaen University. The foundation of these building is a shallow foundation, which seats on Khon Kaen loess. The structure of Khon Kaen loess is honeycomb which is instability. When the soil moisture content is increased, the shear strength of Khon Kaen loess is decreased and then suddenly subsidence. Udomchoke [1] found that Khon Kaen Loess is collapsible soil with a very server degree. Moreover, [1] found that the shear strength parameters (c and ϕ) are decreased with increasing of soil moisture content as shown in Figure 1 and 2.

The objective of this project is to determine the effect of matric suction on the shear strength parameters. However, the conventional method of triaxial test consumes the time for testing. Therefore, this project is carried out using a multistage method to reduce the time of testing. However, the test results between the single stage and multistage have to compare prior to the study. The scope of this paper is to compare the test result from the consolidated drained triaxial test of saturated and compacted soil.

For the multistage method, one specimen is subjected to several confining pressures. Each pressure, the specimen is not tested reach to the shear failure. The shear strength of Khon Kaen loess by the direct shear tests was carried out using the multistage technique and the results are quite well compared to those of traditional shear tests [2].

METHODOLOGY

Preparation of Specimens

In this study, the size of soil specimen for consolidation drained triaxial test is 50 mm in diameter 100 mm in height. The specimen was statically compacted to achieve 90% wet side of maximum dry density by modified compaction. Three confining pressure of 100, 250 and 450 kPa were used for a single method. Moreover, three confining pressure of 60, 210 and 510 kPa were used for the multistage.

Single Stage Testing

The shear strength testing of saturated soil by the consolidated drained triaxial test can be divided into 3 steps.

Step 1: Saturation, the specimen compacted then set up a soil specimen into triaxial compression apparatus and apply water pressure into specimen until soil specimen saturated with a B value of 95% by an equation for B value shown in Eq. (1).

$$B = \frac{\Delta u}{\Delta \sigma_3} \quad (1)$$

Where;

Δu = pore pressure change in the chamber
pressure when drainage valves closed
 $\Delta \sigma_3$ = isotropic change in the chamber
Pressure

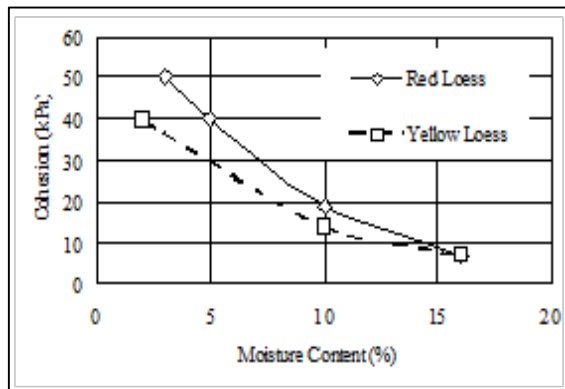


Fig. 1 Variation of the cohesion of Khon Kaen loess with moisture content (Udomchoke 1991)

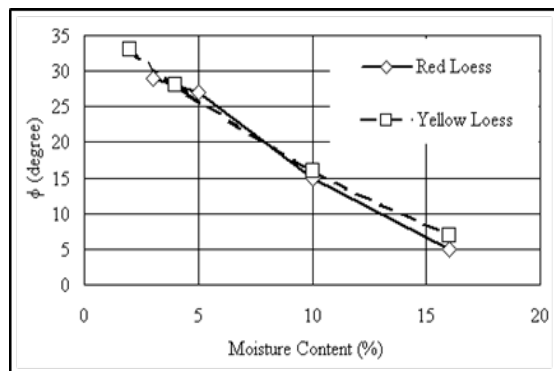


Fig. 2 Variation of the friction angle of Khon Kaen loess with moisture content (Udomchoke 1991)

Step 2: Consolidation, consolidation by increasing the confining pressure, according defined in this study and let the soil specimen drain until it was equilibrium.

Step 3: Shearing, the shear rate or strain rate was derived from the relationship of the graph between volume change and square root time by using Eq. (2) as present in Table 1. The shear rate from Eq (2) was used to shear the specimen until it reaches the failure. Repeat step 1 to step 3 at least 3 specimens to find out shear strength parameter from Mohr-Coulomb shown in Eq. (3), (4).

$$\varepsilon = \frac{4\%}{16t_{90}} \quad (2)$$

Where;

t_{90} = square root time derived from x-intercept in the relationship of graph between volume change and square root time

$$\tau = c + \sigma \tan \phi \quad (3)$$

$$\tau = c' + \sigma' \tan \phi' \quad (4)$$

Where;

τ = shear stress

σ = total compressive stress

c = apparent cohesion

ϕ = angle of internal friction

$\sigma' = \text{effective stress} = \sigma - u_w$

$c' = \text{effective cohesion intercept}$

$\phi' = \text{effective internal friction angle}$

Table 1. Shear rate of single stage method

Sample No.	σ_c (kPa)	t_{90} (min)	ε (mm/min)
1	100	0.036	0.069
2	250	0.058	0.043
3	450	0.160	0.015

Table 2. Shear rate of multistage method

Sample No.	σ_c (kPa)	t_{90} (min)	ε (mm/min)
1	60	0.040	0.062
2	210	0.073	0.034
3	510	0.160	0.016

Multistage Testing

The multistage method is used only one specimen to subject several confining pressures. The specimen is not tested to reach the shear failure.

The steps are as follows: first, the specimen is saturated identical a single stage method when the soil is saturated at B value of 95%. Second, the specimen is consolidated at confining pressures as determined (100 kPa). Third, the shearing stage, the specimen is sheared at the shear rate as determining from Eq (2) as shown in Table 2. The deviator stress is applied until reaching a yield value and then release load back to zero. Afterward, the second confining pressure of 210 kPa was applied to consolidate and then shear (repeat step 2 and 3). The third confining pressure of 510 kPa is repeated step2 and 3. However, this confining pressure the specimen had to shear until the specimen was failed and can found strength parameter from Mohr-Coulomb shown in (3), (4).

A multistage method can found strength parameter from one specimen which different from single stage method that to use at least 3 specimens. So, a multistage method it is a test the shear strength of soil rapid than single stage method. However, [3] found multistage method testing affect structure of soil specimen and causing the loose shear strength during the testing.

RESULTS AND DISCUSSION

Khon Kaen loess sample was collected as a disturbed sample at a depth of 2 m. The index properties and compaction characteristics are shown in Table.3.

Table 3 Properties of soil

Properties	
Liquid limit (LL), %	16.5
Plastic limit (PL), %	NP
Plasticity index (PI), %	-
Specific gravity	2.65
Optimum moisture content (OMC), %	9
Maximum dry density (ρ_d), t/m ³	2.0
Sand (%)	55
Silt (%)	30
Clay (%)	15
USCS classification	SM

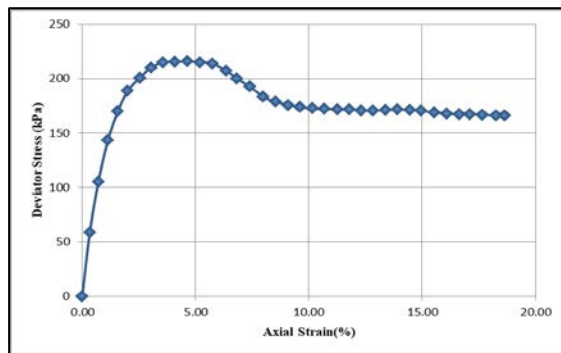


Fig.3 The testing results in single stage CD test at confining pressure of 100 kPa.

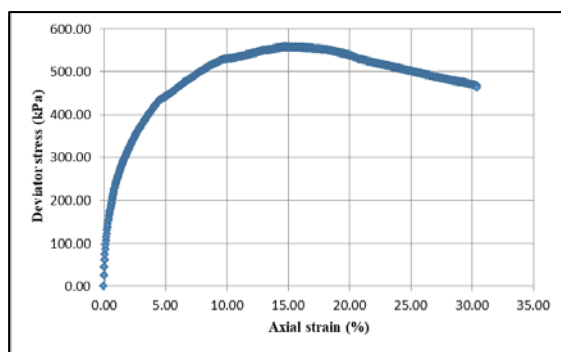


Fig.4 The testing results in single stage CD test at confining pressure of 250 kPa.

Compacted and saturated Khon Kaen loess was tested for consolidated drained triaxial. Three confining pressures of 100, 250 and 450 kPa was used for single stage testing and pore water of 20 kPa was applied to samples. The testing results of the relationship between deviator stress and the axial strain were shown in Figures 3, 4 and 5. The

relationship indicated that the maximum deviator stress from the single stage was 215, 556 and 970 kPa, respectively. Moreover, the relationship between deviator stress and axial strain from the single stage testing showed a strain hardening behavior, which is the behavior of dense sand. The relationship between the volumetric strain and axial strain showed the dilation behavior of three specimens as illustrated in Figures 6, 7 and 8, respectively. The dilation behavior is also the characteristic of dense soil.

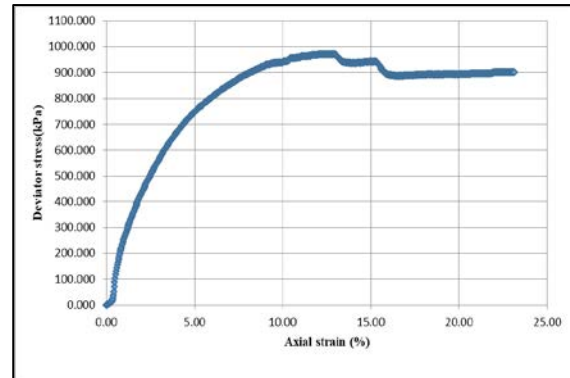


Fig.5 The testing result in single stage CD test at confining pressure of 450 kPa.

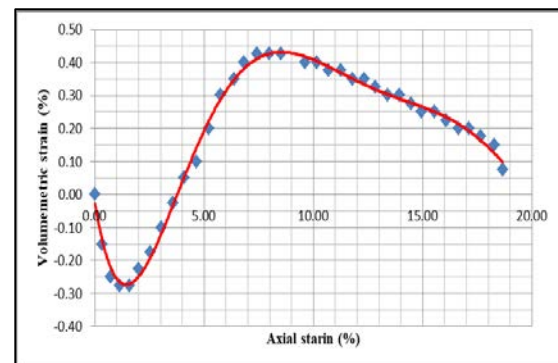


Fig.6 The relationship between volumetric strain and axial strain in single stage testing at confining pressure of 100 kPa

The multistage testing results at confining pressure of 60, 210 and 510 kPa and a pore water of 20 kPa were applied to the specimen. The testing results showed the relationship between deviator stress and axial strain as shown in Figures 9, 10 and 11. The relationship indicated that the maximum deviator stress from the multistage were 115, 389 and 1,037 kPa, respectively. In addition, the relationship between deviator stress and axial strain from the multistage testing also showed a strain hardening behavior at confining pressure of 60 and 510 kPa. However, the relationship between deviator stress and axial strain at confining pressure of 210 kPa showed a strain softening behavior. The stress-

strain curve was derived from various ensembles in multistage testing shown in Figure 12.

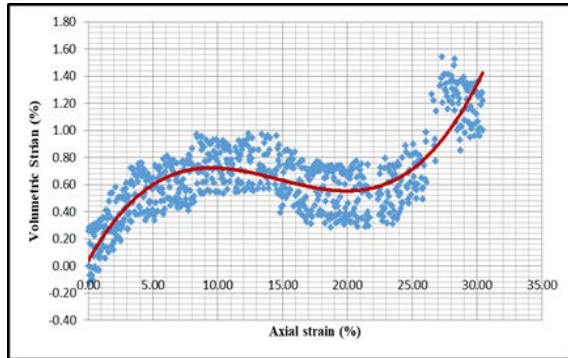


Fig.7 The relationship between volumetric strain and axial strain in single stage testing at confining pressure of 250 kPa

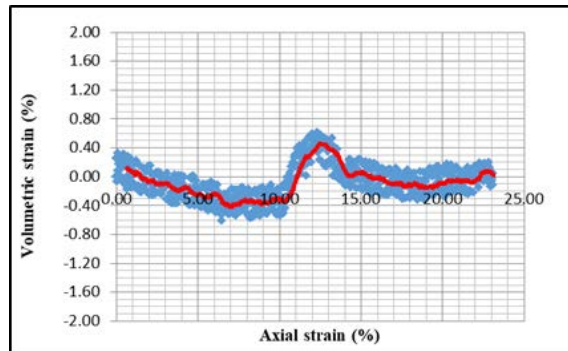


Fig.8 The relationship between volumetric strain and axial strain in single stage testing at confining pressure of 450 kPa

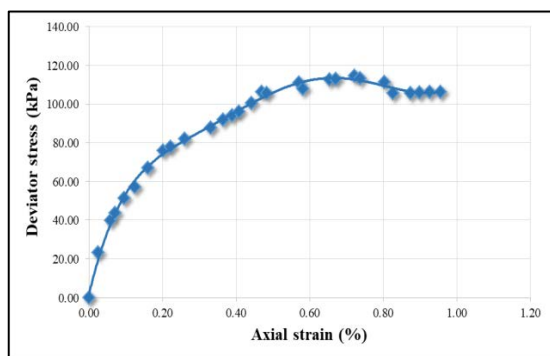


Fig.9 Testing results in multistage CD test at confining pressure of 60 kPa

The maximum stress value derived from the relationship between deviator stress and the axial strain was drawn to the Mohr circle. The Mohr circle of total stress showed that $\phi = 31^\circ$ and $c = 0$ kPa in a single stage method and $\phi = 29.7^\circ$ and $c = 0$ kPa in a

multistage method as shown in Figures 13 and 14, respectively. Table 4 showed the comparison of total strength parameter between a single stage and multi-stage. The Mohr circle of effective stress showed that $\phi' = 31^\circ$ and $c' = 25$ kPa in a single stage method and $\phi' = 29.7^\circ$ and $c' = 20$ kPa in a multistage method as shown in Figures 15 and 16, respectively. Table 5 showed the comparison of effective strength parameter between a single stage and multi-stage.

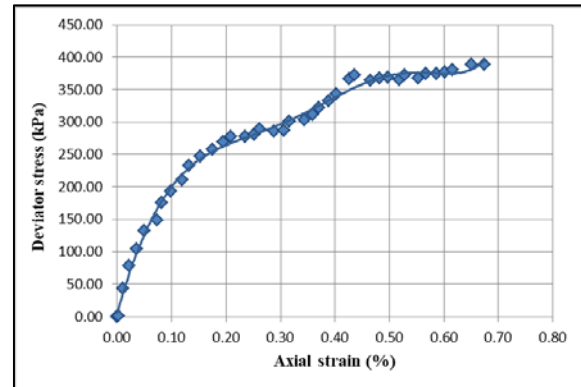


Fig.10 Testing results in multistage CD test at confining pressure of 210 kPa

Table 4. The comparison of total shear strength parameters between a single stage and a multistage

	c (kPa)	ϕ (Degree)
Single stage	0	31
Multistage	0	27.9
Differential	0%	4.2%

CONCLUSION

The stress-strain behavior of saturated and compacted Khon Kaen loess showed a strain hardening except to multistage testing at confining pressure of 210 kPa, which showed a strain softening. The relationship between the volumetric strain and axial strain from single stage testing results showed the dilation behavior. The comparison of shear strength parameters between a single stage and a multistage as shown in Table 4 and 5 indicated a small change. So, Khon Kaen loess can be found shear strength by multistage method. The multistage method is more simple and rapid than single stage. The results showed that the strength parameter of the test consolidated drained triaxial test of Khon Kaen loess by multistage less valuable than single stage. Therefore, the shear strength parameters from the multistage test result

are appropriate for conservative designs in geotechnical engineer.

Table 5 The comparison of effective shear strength parameters between a single stage and a multistage

	c' (kPa)	ϕ' (Degree)
Single stage	25	31
Multistage	20	27.9
Differential	20%	4.2%

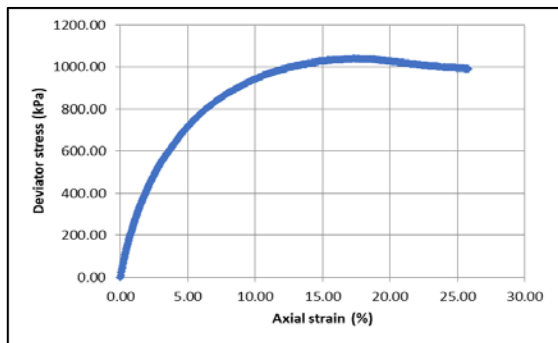


Fig.11 Testing results in multistage CD test at confining pressure of 510 kPa

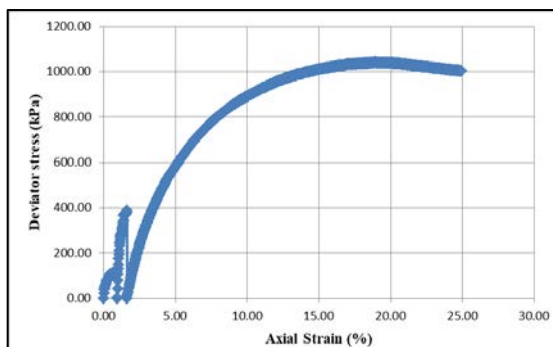


Fig.12 The stress– strain curve derived from various ensemble in multistage testing

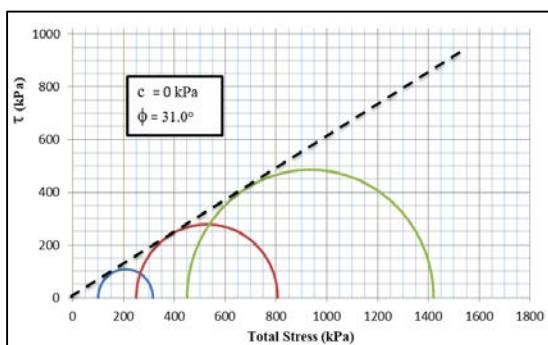


Fig.13 The Mohr circle of total stress from a single stage method

ACKNOWLEDGEMENTS

Acknowledgement is given to Faculty of Engineering, Khon Kaen University for the support of this research. Grateful to Advisor Asst. Prof. Ratamane Nuntasarn for the suggestions and solutions to the problems in this research. Thanks other students at Department of Civil Engineering, Khon Kaen University in preparing the soil samples for the testing.

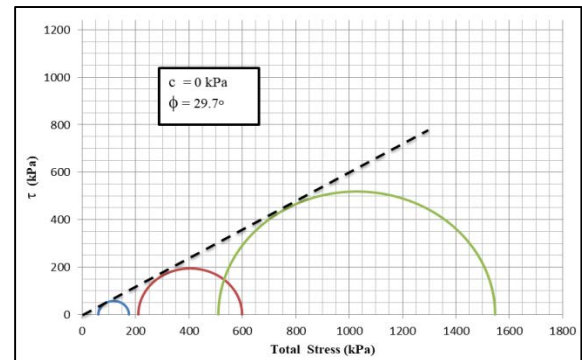


Fig.14 The Mohr circle of total stress from a multistage method

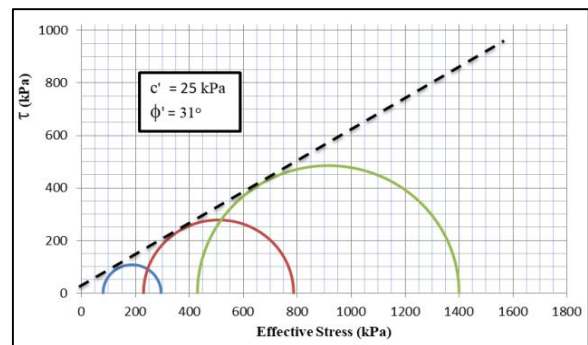


Fig.15 The Mohr circle of effective stress from a single stage method

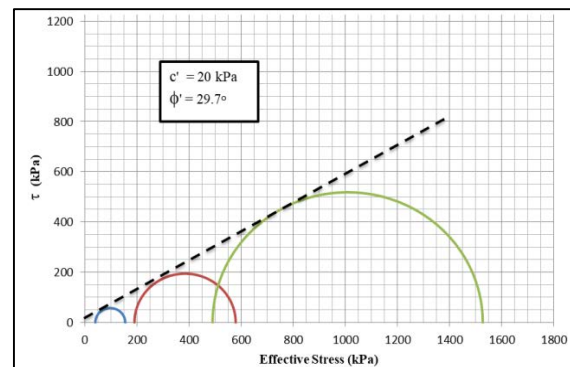


Fig.16 The Mohr circle of effective stress from a multistage method

REFERENCES

- [1] Udomchoke, V. (1991). Origin and Engineering Characteristics of the Problem Soil a in the Khorat Basin, Northeastern Thailand. Ph.D. dissertation Asian Institute of Technology Bangkok Thailand.
- [2] Hormdee D., Kaikeerati N., and Angsuwotai P. "Evaluation on the Results of Multistage Shear Test" , Int. J. of GEOMATE, 2012, pp. 140-143 Behaviour of Concrete Containing Waste Carpet Fiber, International Journal of GEOMATE, Vol. 9, Issue 17, 2015, pp. 1441-1446.
- [3] Ho, D. and Fredlund, D., "A Multistage Triaxial Test for Unsaturated Soils," Geotechnical Testing Journal, 1988 , pp. 132-138. Author H., A Book New York Publisher, Year, pp.1-200.
- [4] Wykeham Farrance. 2007. Triaxial test: Double wall cell. http://www.wfi.co.uk/pdf/wf_catalogue_double_wall_triaxial_cell.pdf. 23 september 2007.
- [5] Gan, J.K., Fredlund, D.G. and Rahardjo, H., "Multistage direct shear testing of Unsaturated Soil", Geotechnical Testing Journal, GTJODJ, Vol. 111, No. 2, June 1988, pp.132-138.
- [6] Runtasarn and W. Wannakul," Drained Shear Strength Of Compacted Khon Kaen Loess", International Journal of GEOMATE, 2017, pp.28- 33.
- [7] Terzaghi, Karl, Ralph B. Peck, and Gholamreza Mesri. Soil mechanics in engineering practice. John Wiley & Sons, 1996.

BEARING CAPACITY OF KHON KAEN LOESS BY PLATE BEARING TEST

P. Thaowandee¹, R Nuntasarn² and P Punrattanasin³
^{1,2,3}Faculty of Engineering, Khon Kaen University, Thailand

ABSTRACT

The purpose of this study is to determine bearing capacity and settlement of Khon Kaen loess by plate bearing test. Khon Kaen loess is classified as a collapsible soil, which is an unstable structure. According to USCS, Khon Kaen loess is classified as silty sand (SM). The structure of Khon Kaen loess is a honeycomb structure, which consists of fine sand and silt. Moreover, clay particles and iron oxide is the binder. If the soil is wetting, the binder will be washing. Therefore, the volume of soil decrease suddenly and the shear strength also decreases. In this study, the bearing capacity and the settlement of Khon Kaen loess will be compared between wet and dry condition. The plate size 0.3x0.3 m will be seated at a depth of 0.4 m from the ground surface. The ultimate bearing capacity of Khon Kaen loess at the moisture content of 9.76% is 12 t/m². Moreover, the ultimate bearing of Khon Kaen loess after soaked for 4 days (moisture content of 30%) is 8 t/m².

Keywords: Khon Kaen loess, settlement, plate bearing,

INTRODUCTION

Collapsible soil behavior is typical in Khon Kaen province, in deposits of yellow or red Aeolian (wind-blown) silty sand (according to the Unified Soil Classification System or USCS). The structure of Khon Kaen loess is a honeycomb structure, which is an unstable structure. The majority of Khon Kaen loess consists of fine sand and silt. Whereas, clay particles and iron oxide is the binder. If the soil is wetting, the binder will be washing. Therefore, the volume of soil decrease suddenly and the shear strength also decreases. The decreasing strength of undisturbed Khon Kaen collapsing loess with increasing moisture content was investigated by unconsolidated undrained (UU) triaxial testing as shown in Figures 1 and 2 [1]. The apparent friction angle decreased linearly with increasing moisture content, but the dropping of apparent cohesion with increasing moisture content was not linear. Moreover, the collapse index of Khon Kaen loess showed the severe degree [1].

In the past, the engineering designed the spread footings, which seat on loess, for the building in Khon Kaen University. Due to the strength of Khon Kaen loess is high on the dry season. Therefore, the structure of these old buildings severe suffered damage when the leaking of water to the foundation. To determine the bearing capacity of spread footing in the filed, therefore a plate bearing test was used to study in this project.

Plate bearing test was used to studied the behavior of collapsible many projects. For example collapsible soil at the United Arab Emirates was studied to develop a laboratory method of simulating

the loaded behavior of collapsible soils and to measure its deformation at constant surcharge and ground water infiltration rates [2]. Moreover, the plate bearing tests was used to studied the stabilized collapsing soil by sand blended with coarse aggregate of various sizes and proportions [3], compacted, partial replacement by compacted sand/crushed stone layers over the collapsible soil [4].

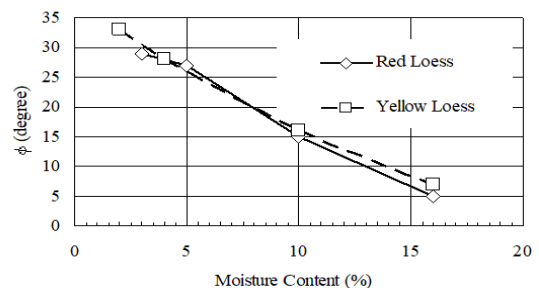


Fig. 1 Variation of the undrained friction angle of Khon Kaen loess with moisture content [1]

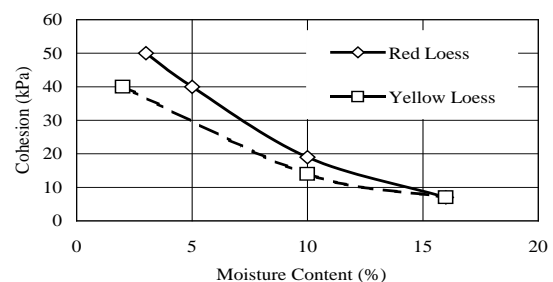


Fig. 2 Variation of the undrained cohesion of Khon Kaen loess with moisture content [1]

However this project was also study the bearing capacity of Khon Kaen loess in filed by plate bearing and then compare with the calculation from the standard penetration test (N-value) and the unconfine compression test.

SCOPE

The soil profile of investigated site showed that Khon Kaen loess is 0 to 1.5 m depth from the ground surface and seat on the laterite. So that the plate size of 0.3x0.3 m was seated at a depth of 0.4 m from the ground surface. The maximum pressure was computed from the load column of CB building, which is nearby the investigated site. The maximum pressure of this project is 36 t/m². Therefore the interval load for the dry condition was 2 t/m². The test was determinate after the settlement rate of more than 0.2 mm/min or total settlement of more than 25 mm [5]. After testing at the dry condition, the maximum pressure of wet condition was estimated at 50% of the maximum pressure at the dry condition. Therefore the interval load for the wet condition was 0.5 t/m².

The testing pit between wet and dry condition was farther of 5 times of plate size, which was 1.5 m [5]. Both sites were measured the matric suction and moisture content during the testing.

METHOD

Plate Bearing

According to the design pressure of 36 ton/m² and plate size of 0.3x0.3 m, hence the allowable load was 4 tons. However, the factor of safety of 2 was applying therefor the ultimate load was 8 ton. Therefore a nine piles was used as a dead load for this project. The capacity of hydraulic jack was 50 tons with 10 ton of proving ring. Four dial gauges were used to measure the settlement at the corner of the plate by attached with the reference beam. The installation of apparatus was present in Fig 3.

The dry condition, the matric suction was measure via KU-tensiometer as shown in Fig. 4 before installation. The load was applied after the installation was completed.

Water was applied in the testing pit for four days as shown in Fig.4 for the wet condition. Then a water was drained out from the testing pit before the apparatus was installed as shown in Fig. 6. The moisture content of wet pit was 31%, which was measured after testing. Both conditions wet and dry, were tested during the weather 25 to 35°C.

As a design load of 36 t/m², therefore the increment of loading was 2 t/m² for the dry condition.

A design load for wet testing was a half of the maximum load of dry testing. The maximum load of dry testing was 12 t/m². Therefore, the design load of wet testing was 6 t/m². Moreover, the increment of loading was 0.5 t/m² for the wet condition.

After loading, the settlement was recorded at 1, 2, 4, 8, 15, 30 and 60 min. The failure was defined as the total settlement of 25 mm, or the rate of settlement was over 0.2 mm/min.



Fig. 3 The installation of plate bearing test in a dry pit



Fig. 4 Measurement matric suction by using KU tensiometer



Fig. 5 Wetting pit (soaking for 4 days)



Fig. 6 The installation of plate bearing test in the wet pit

Unconfined Compressive Strength

The undisturbed soil sample was taken as a block sample from the open pit as shown in Fig. 7. Then the block sample was frozen before trim as shown in Fig. 8. The size of the sample was 50 mm diameter and 100 mm height as shown in Fig. 9. The proving ring of 3 kN and dial gauge was set up for testing. Three

samples were used to determine the unconfined compressive strength. The shearing rate was 1 mm/min.



Fig. 7 Sampling block sample

Soil Water Characteristic Curve

The drying soil water characteristics curve (SWCC) for the compacted Khon Kaen loess was determined by pressure plate. According to [6], the pressure plate method was used to establish SWCC for a suction values between 1 to 1,500 kPa.

TEST RESULT

The properties of soil sample were shown in Table 1. Soil sample consisted of 60% sand and 40% silt-clay with PI of 0.92%. Therefore the soil sample of this study was classified as silty sand (SM) according to [7].



Fig. 8 Frozen undisturbed sample

Plate Bearing

The relationship between settlement and pressure of dry and wet condition as shown in Fig. 10 and 11, respectively found that the ultimate pressure of dry and wet condition was 12 and 8 t/m², respectively. The yield point of dry and wet condition was 4 and

1.5 t/m², respectively. Moreover, the young modulus of a dry condition is higher than the wet condition about 12 times. The young modulus of dry and wet condition was 20,000 and 1,730 kPa, respectively. Fig. 10, 11 and 12 also presented the failure mode of local shear failure, which is the characteristic of medium dense sand. All test result represented in Table 2.

The differential settlement between wet and dry condition was shown in Fig 13. The different settlement at the applied pressure of 8 t/m² showed a severe collapsing about 20% (Loess thickness of 1.1 m).



Fig. 9 Specimen after trimming

Table 1 Basic Properties of Khon Kaen loess

Properties	
Liquid limit (LL), %	14.3
Plastic limit (PL), %	13.21
Plasticity index (PI), %	0.92
Specific gravity	2.65
Natural moisture content, %	10
Dry density (ρ_d), t/m ³	1.6
Sand (%)	60
Silt – Clay (%)	40
USCS classification	SM

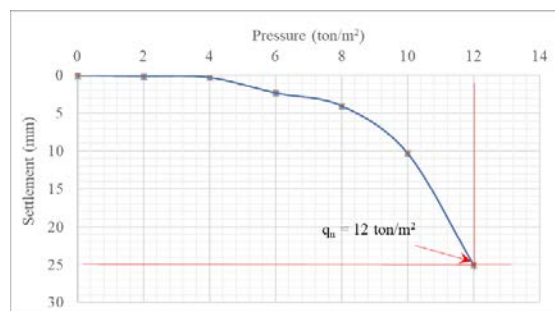


Fig. 10 The relationship between pressure and settlement of dry condition

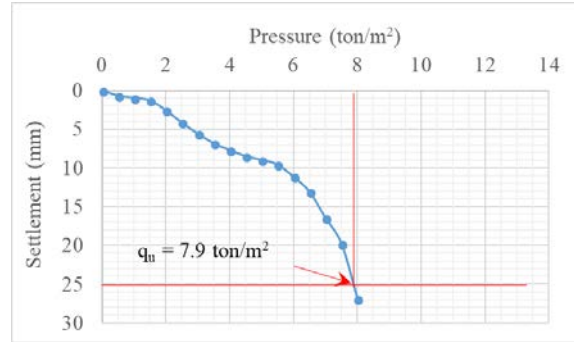


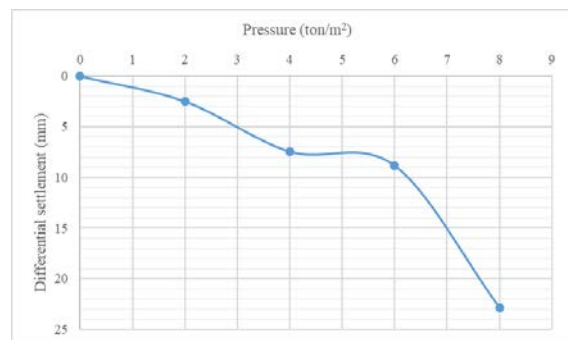
Fig. 11 The relationship between pressure and settlement of wet condition



Fig. 12 Failure surface at field

Table 2 Plate bearing results

	Wet	Dry
Yield Point (kPa)	1.5	4
Young Modulus (kPa)	1,730	20,000
Ultimate pressure (kPa)	8	12



Moreover, the standard penetration test presented the N-value of 2, which is also classified as very loose sand. However, the dry density is 1.6 t/m³. The tensiometer showed the matric suction was 28 kPa for the dry condition, which is on the residual regime according to SWCC as illustrated in Fig. 14.

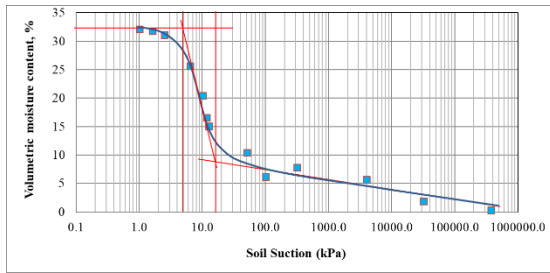


Fig. 14 Soil water characteristic curve of undisturbed Khon Kaen loess

Unconfined Compressive Strength

Three sample was studied. The initial moisture content and the dry density was 7% and 1.6 t/m², respectively. The relationship between axial strain and deviator stress was present in Fig. 15. The average unconfined compressive strength is 2.5 t/m².

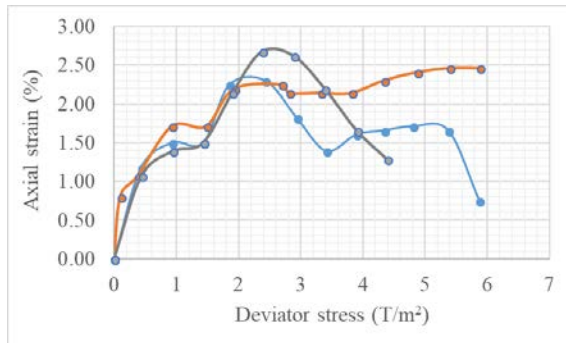


Fig. 14 The stress-strain relationship of unconfined compression test

DISCUSSION

The test result showed that the bearing capacity of dry condition was 1.5 times higher than the wet condition. However, the young modulus of Khon Kaen loess at dry condition is much higher than a wet condition. The failure mode of bearing capacity was a local shear failure, which is the characteristic of medium dense soil. According to the matric suction of dry condition, Khon Kaen loess was in the residual regime.

According to Terzaghi's equation for local shear failure mode of square foundation as present in Eq. (1). Also, the unconfined compressive strength of undisturbed Khon Kaen loess of 2.5 t/m² or the undrained shear strength of 1.25 t/m² at a dry condition. The ultimate bearing capacity of Khon Kaen loess at a dry condition was 7 t/m², which was underestimated almost 2 times.

According to SPT result, the friction angle was 26 deg [8]. The ultimate bearing capacity was 5.32

t/m², which was also underestimated.

$$q_u = 0.867c'N'_c + qN'_q + 0.4\gamma BN'_\gamma \quad (1)$$

Where

q_u	= ultimate bearing capacity
c'	= cohesion
N'_c, N'_q, N'_γ	= codified bearing capacity factor
q	= $\gamma \cdot D_f$
D_f	= depth of foundation
B	= width of foundation

CONCLUSION

The bearing capacity of Khon Kaen loess of a wet condition was a slightly lower than a dry condition. However Khon Kaen loess showed at a severe collapsing at pressure of 8 t/m². Moreover, unconfined compressive strength and N-value from SPT give a lower the ultimate bearing capacity, which was derived from Terzaghi's equation for local shear failure, from plate bearing test.

ACKNOWLEDGEMENTS

Acknowledgement is given to Faculty of Engineering, Khon Kaen University for the support of this research. Grateful to Advisor Asst. Prof. Ratamane Nuntasarn for the suggestions and solutions to the problems in this research. Thanks other students at Department of Civil Engineering, Khon Kaen University in preparing the soil samples for the testing.

REFERENCES

- [1] Udomchoke, V. (1991), 'Origin and Engineering Characteristics of the Problem Soil a in the Khorat Basin, Northeastern Thailand', Ph.D. dissertation, Asian Institute of Technology, Bangkok, Thailand.
- [2] Laboratory Simulation of Irrigation-Induced Settlement of Collapsible Desert Soils Under Constant Surcharge, Ramesh Vandanapu . Joshua R. Omer . Mousa F. Attom Geotech Geol Eng (2017) 35:2827–2840
- [3] Kesharwani R.S., Sahu A. K. and Khan N.U., 2015, LOAD SETTLEMENT BEHAVIOUR OF SANDY SOIL BLENDED WITH COARSE AGGREGATE, Journal of Asian Scientific Research, 5(11): 499-512
- [4] Ali A. Naema, (2015), Performance of partially replaced collapsible soil – Field study,

- Alexandria Engineering Journal 54, 527–532
- [5] ASTM - American Society for Testing Material. 2000. Standard Practice for Bearing Capacity of Soil for Static Load and Spread Footings (ASTM D 1194-94). West Conshohocken. Pennsylvania
- [6] ASTM - American Society for Testing Material. Standard Test Method for Capillary-Moisture Relationships for Coarse- And Medium-Textured Soils By Porous-Plate Apparatus (ASTM D2325-98). Ann Arbor. Michigan. 1998
- [7] ASTM - American Society for Testing Material. 2000. Standard Practice for Classification of Soils for Engineering Purposes (Unified Soil Classification System) (ASTM D 2487-00). West Conshohocken. Pennsylvania.
- [8] HATANAKA, M., and UCHIDA, A. (1996). “Empirical Correlation between Penetration Resistance and Internal Friction Angle of Sandy Soils,” *Soils and Foundations*, Vol. 36, No. 4, pp. 1–10.

DRAINED SHEAR STRENGTH PARAMETERS OF COMPACTED KHON KAEN LOESS BY DIRECT SHEAR TEST

Atchariya Saengthongthip¹, Ratamanee Nuntasarn² and Chinawat Muktabhant³
^{1,2} Faculty of Engineering, Khon Kaen University, Thailand

ABSTRACT

This study aims to determine the relationship between drained shear strength and matric suction of compacted Khon Kaen loess soil. This soil samples were investigated shear strength parameters of compacted Khon Kaen loess from CD method. A direct shear test determined these shear strength parameters. The initial dry density of CD samples was 1.95 t/m³, which was 90% of maximum dry density by a modified method. The shear rates of CD method was determined by consolidation. However, soil samples were tested for CD method under saturated and unsaturated conditions. Unsaturated soil samples had been divided into three states by dry soil samples in the air. 30, 60 and 90 minutes are times of dry soil samples in the air. The shear rate was 0.005 mm/min. The results of a saturated consolidated drained direct shear test (CD Test) presented that a friction angle (ϕ') and a cohesion (c) was 32.6 degree and 4 kPa, respectively. Moreover, the relationship between drained shear strength and matric suction is linear. However, the slope of the graph or the ϕ^b value is not constant. It is varied with the vertical stress. The friction angle is constant with matric suction, but the cohesion increased with matric suction.

Keywords: Direct Shear, Saturated, Unsaturated, Consolidated Drained, Khon Kaen Loess, Compacted soil

INTRODUCTION

In the present, there are many constructions in Khon Kaen province. Moreover, Khon Kaen soil was used as construction material for landfill. Therefore the engineering should know the shear strength parameters for design the foundation. The shear strength parameters can be evaluated by consolidated drained method (CD). This method can test by triaxial and direct shear test. This study used a direct shear test to determine shear strength parameters of this method as mention previously.

In this study, Khon Kaen loess had been investigated at compacted and saturated condition. Soil samples for CD method were compacted at 90% of maximum dry density by a modified method. The unsaturated soil has three phases which are solid, liquid and air. Therefore, the Terzaghi's effective stress law for saturated soil is not appropriate for unsaturated soil. Fredlund and Rahardjo [1] formulated the shear strength equation for an unsaturated soil as given in Eq (1).

$$\tau_{ff} = c' + (\sigma_n - u_a) \tan \phi' + (u_a - u_w) \tan \phi^b \quad (1)$$

Where τ_{ff} is a shear stress at failure. c' is an effective apparent cohesion, which is the shear strength intercept when the effective stress is equal to zero. σ_f is total normal stress at failure. u_{af} is pore-air pressure at failure. u_{wf} is pore-water pressure at failure. ϕ' is an effective angle of internal friction.

And ϕ^b is an angle indicating the rate of increase in shear strength relative to the soil suction at failure.

BASIC PROPERTIES

Khon Kaen loess, which was used in this study, was classified as silty sand (SM) according to [2]. The results of sieve and hydrometer analysis showed that Khon Kaen loess consists of 55% sand, 30% silt, and 15% clay [2]. The majority of Khon Kaen sand size was a fine grain as illustrated in Fig. 1. The natural density of Khon Kaen loess was 1.65 t/m³, which is the loosed sand. Atterberg's limit results also presented a liquid limit was 16.5% and a non-plastic limit. The specific gravity was 2.65. The basic properties of Khon Kaen loess were present in Table 1.

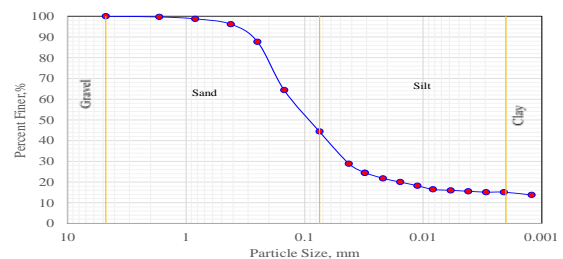


Fig. 1 Grain Size Distribution

Also, the modified compaction was decided to use in this project because Khon Kaen loess was used in pavement construction rather than another

construction. The maximum dry density was 2 t/m³, and the optimum moisture content was 9%.

Table 1 Basic Properties of Khon Kaen loess

Properties	
Liquid limit (LL), %	16.5
Plastic limit (PL), %	NP
Plasticity index (PI), %	-
Specific gravity	2.65
Optimum moisture content (OMC), %	9
Maximum dry density (ρ_d), t/m ³	2.0
Sand (%)	55
Silt (%)	30
Clay (%)	15
USCS classification	SM
Pre-consolidation pressure (P_c)	56

DIRECT SHEAR

Soil samples were compacted at 90% of maximum dry density at the wet side (moisture content of 11.85%) by a modified method. Soil samples were trimmed by cutting ring and taken into direct shear apparatus as shown in Fig 2 and 3, respectively.



Fig.2 Preparation specimen

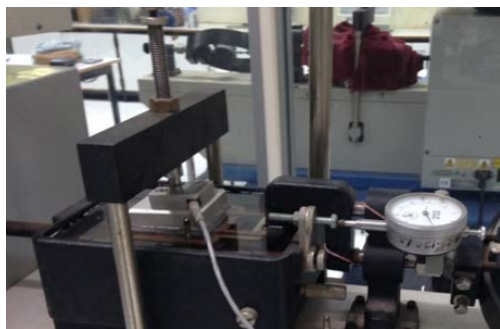


Fig. 3 Direct shear setup
Consolidated Drained Method

The saturated specimen had to be soaked for 24

hours before being consolidated for 24 hours. But the unsaturated specimen was air dry before consolidating. Three series of air dry sample, which are 30, 60 and 90 minutes, was studied in this project.

The shear rate of this method has to determine from consolidation stage as shown in Table 2. Three vertical stress of 200, 400 and 800 kPa was used to study. The failure time of 200, 400, 800 kPa vertical load as shown in Table 2, 3, 4, 5, respectively. However, the consolidation results found that that pre-consolidation pressure (P_c) was 56 kPa and OCR was 1.74, which was less than 2. Therefore the failure time has to determine t_{50} or t_{90} as shown in Eq. [2] and 3, respectively. The shear rate was calculated from the maximum value of the failure time as shown in Eq. [3]. The failure time, which was derived from t_{50} was higher than t_{90} . The shear rate of this study equaled to 0.005 mm/min.

$$t_f = 50t_{50} \quad (2)$$

$$t_{50} = 11.6t_{90} \quad (3)$$

$$R_d = \frac{d_f}{t_f} \quad (4)$$

Where d_f equal to 0.2 inches according [3] because Khon Kaen loess was coarse grain soil. Moreover, t_f is a failure time, which equaled to 60 min.

Table 2 Failure time of CD saturated

Vertical Stress (kPa)	$t_{50}(\text{min})$	t_f (min)	$t_{90}(\text{min})$	t_f (min)
200	7.5	375	5.9	68.44
400	7.8	390	6.9	80.04
800	8	400	4.6	53.36

Table 3 Failure time of CD Unsaturated of air dry for 30 minutes

Vertical Stress (kPa)	$t_{50}(\text{min})$	t_f (min)	$t_{90}(\text{min})$	t_f (min)
200	1.5	75	5.8	67.28
400	6.5	325	3.3	38.28
800	0.45	22.5	16	185.6

Table 4 Failure time of CD Unsaturated dry 60 minutes

Vertical Stress (kPa)	$t_{50}(\text{min})$	t_f (min)	$t_{90}(\text{min})$	t_f (min)
200	1.357	67.5	3.5	40.6
400	0.857	42.85	8.5	98.6
800	0.55	27.5	9	104.4

Table 5 Failure time of CD Unsaturated dry 90 minutes

Vertical Stress (kPa)	$t_{50}(\text{min})$	t_f (min)	$t_{90}(\text{min})$	t_f (min)
200	1.07	83.5	3.5	40.6
400	0.85	42.5	2.5	29
800	1.71	85.5	8.6	99.76

TEST RESULT

The test result was shown in Figure 4 to 7 for saturated, air dry for 30, 60 and 90, respectively. The summary test result present in Table 6.

The effective friction angle and cohesion of saturated soil was 32.6 degree and 4 kPa, respectively, as shown in Fig. 4.

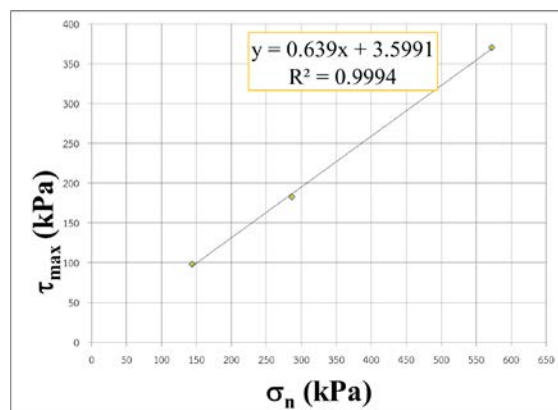


Fig. 4 Drained shear strength of saturated soil sample

Table 6. The summaries of test result

Sample	ϕ'	c'
Saturated	32.6	3.6
Air dry for 30 min	34.8	13.3
Air dry for 60 min	35.2	22.9
Air dry for 90 min	34.7	25.62

The effective friction angle of saturated condition was 2 degrees lower than an unsaturated condition. The effective cohesion of unsaturated is 35 degree. However, the cohesion was increased with decreasing of soil moisture dramatically.

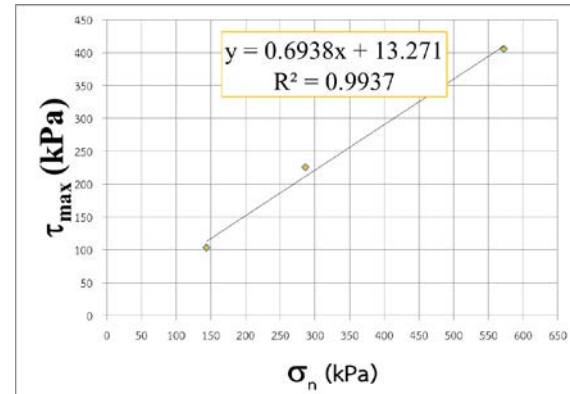


Fig. 5 Drained shear strength of unsaturated sample for 30 mins air dry

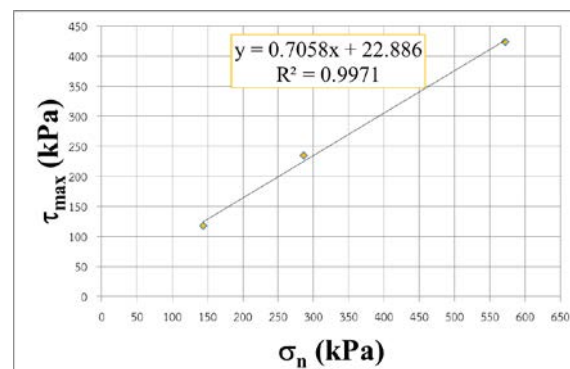


Fig. 6 Drained shear strength of unsaturated sample for 60 mins air dry

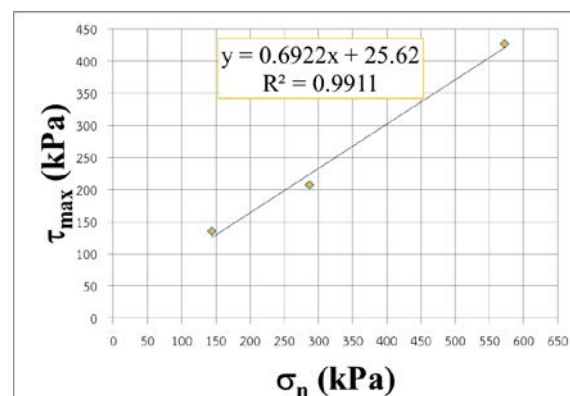


Fig. 7 Drained shear strength of unsaturated sample for 90 mins air dry

The relationship between horizontal displacement and shear stress of saturated sample and unsaturated sample for 30 and 60 mins air dry showed the strain hardening as shown in Fig. 8, 9 and 10, respectively. But the relationship between horizontal displacement

and shear stress of unsaturated sample for 90 min air dry showed the strain softening as shown in Fig. 11.

Besides, the relationship between vertical displacement and horizontal displacement of both conditions as present in Fig. 12 to 15 showed a compression behavior.

DISCUSSION

The relationship between matric suction and shear stress at initial state showed a quite linear relationship. However, the slope of the graph or the ϕ^b angles were not constant, but the ϕ^b angles were linearly decreased with a vertical pressured from 200 to 800 kPa, as shown in Fig.16 and Table 7.

The relationship between matric suction and shear stress at a failure state as shown in Fig.16 showed a linear relationship with R^2 of 0.87. Moreover, the slope of the graph or the ϕ^b angles were not also constant same as the initial state, but the ϕ^b angles were linearly increased with a vertical pressured as shown in Fig.17 and Table 7.

Finally, the relationship between matric suction and shear stress at residual state showed that ϕ^b angles were constant at a lower vertical pressured. Nevertheless, that showed a quite linear at highest vertical pressured, as shown in Fig.18 and Table 9.

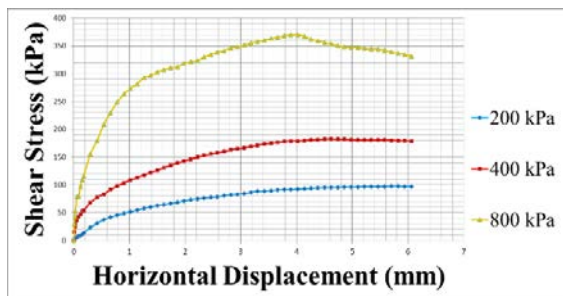


Fig. 8 The relationship between horizontal displacement and shear stress of saturated sample

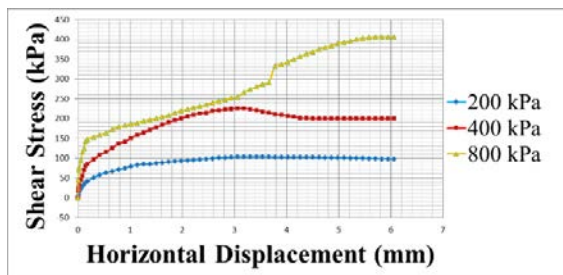


Fig. 9 The relationship between horizontal displacement and shear stress of unsaturated sample for 30 mins air dry

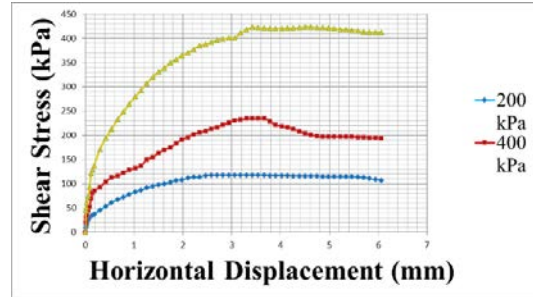


Fig. 10 The relationship between horizontal displacement and shear stress of unsaturated sample for 60 mins air dry

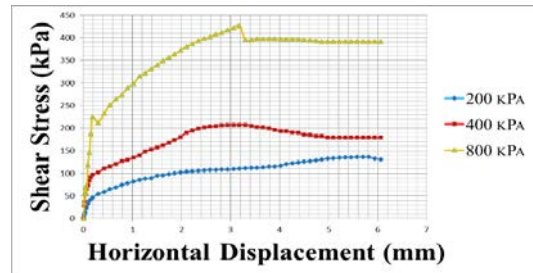


Fig. 11 The relationship between horizontal displacement and shear stress of unsaturated sample for 90 mins air dry

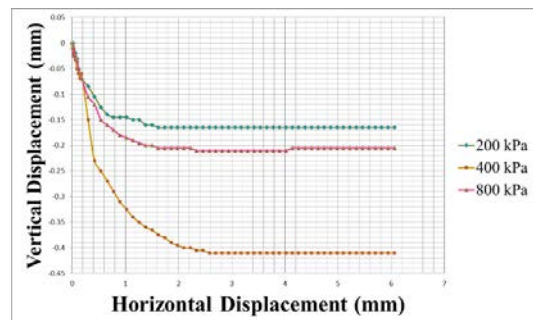


Fig. 12 The relationship between vertical displacement and horizontal displacement of saturated sample

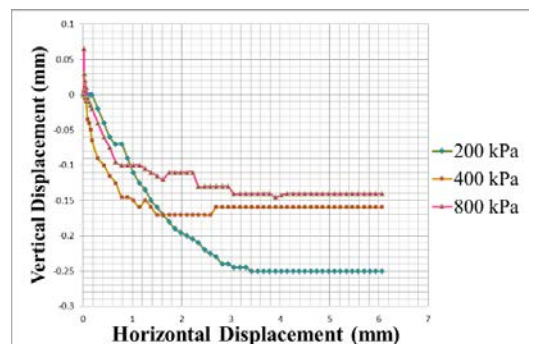


Fig. 13 The relationship between vertical displacement and horizontal displacement of unsaturated sample for 30 mins air dry

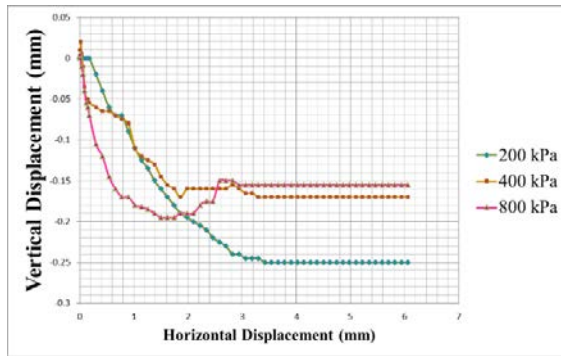


Fig. 14 The relationship between vertical displacement and horizontal displacement of unsaturated sample for 60 mins air dry

Table 7. The ϕ^b angle at initial state

Vertical load kPa	Shear stress kPa	matric suction kPa	y-intercept	ϕ^b (deg)
200	98.00	0.55	2.99	71.5
	103.83	14.75		
	118.03	16.83		
	135.92	19.72		
400	182.78	0.55	2.04	63.9
	225.75	14.75		
	234.50	16.83		
	207.67	19.72		
800	370.42	0.55	1.58	57.7
	405.61	14.75		
	423.50	16.83		
	427.00	19.72		

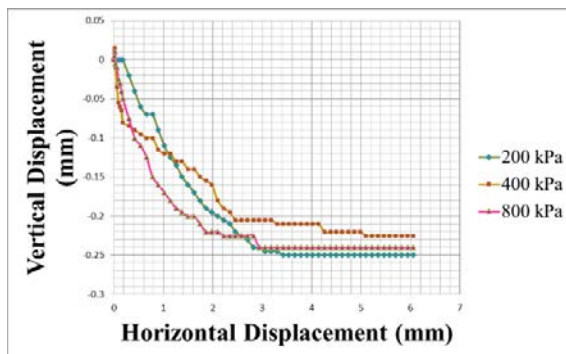


Fig. 15 The relationship between vertical displacement and horizontal displacement of unsaturated sample for 90 mins air dry

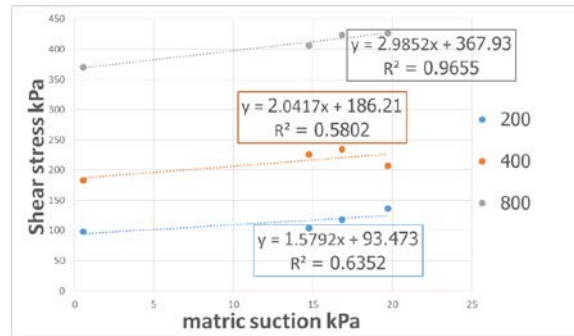


Fig. 16 the relationship between matric suction and shear stress of direct shear at initial state

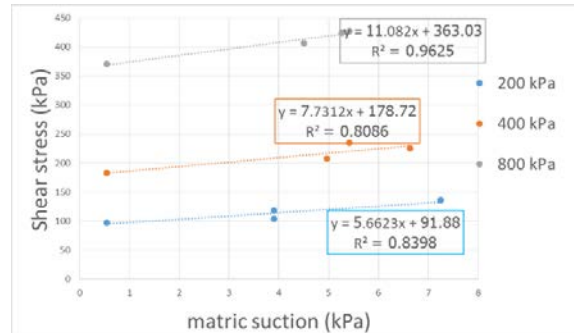


Fig. 17 the relationship between matric suction and shear stress of direct shear at failure state

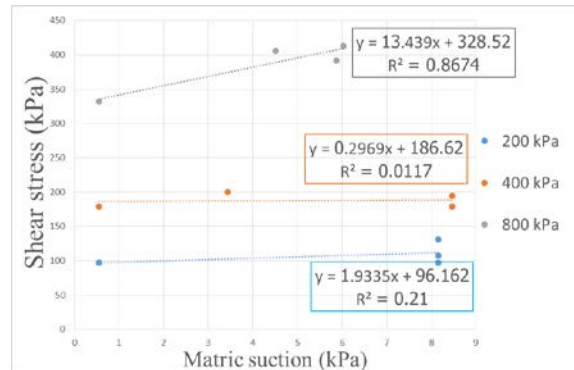


Fig. 18 the relationship between matric suction and shear stress of direct shear at residual state

Table 8. The ϕ^b angle at failure state

Vertical load kPa	Shear stress kPa	matric suction kPa	y-intercept	ϕ^b (deg)
200	98.00	0.55	5.66	80.0
	103.83	3.89		
	118.03	3.89		
	135.92	7.25		
400	182.78	0.55	7.73	82.6
	225.75	6.63		
	234.50	5.42		
	207.67	4.96		
800	370.42	0.55	11.08	84.8
	405.61	4.51		
	423.50	5.27		
	427.00	5.42		

Table 9. The ϕ^b angle at residual state

Vertical load kPa	Shear stress kPa	matric suction kPa	y-intercept	ϕ^b (deg)
200	97.22	0.55	1.93	62.7
	97.22	8.16		
	107.33	8.16		
	131.25	8.16		
400	178.89	0.55	0.29	16.5
	200.08	3.44		
	194.44	8.46		
	179.28	8.46		
800	331.72	0.55	13.44	85.7
	405.61	4.51		
	412.61	6.03		
	392.00	5.88		

CONCLUSION

All test results were present in Table 6. The different of the effective friction angle between saturated and unsaturated are slight. However, the cohesion was increased dramatically with matric suction. Moreover, the direct shear test showed a linear relationship between drained shear strength and matric suction. However, the ϕ^b is not constant with the vertical stress.

ACKNOWLEDGEMENTS

Acknowledgement is given to Faculty of Engineering, Khon Kaen University for the support of this research.

REFERENCES

- [1] Fredlund, D.G. and Rahardjo, H. Soil Mechanics for Unsaturated Soils. Wiley. New York. 1993
- [2] ASTM - American Society for Testing Material. 2000. Standard Practice for Classification of Soils for Engineering Purposes (Unified Soil Classification System) (ASTM D 2487-00). West Conshohocken. Pennsylvania.
- [3] ASTM - American Society for Testing Material. 2011. Standard Test Method For Direct Shear Test of Soils Under Consolidated Drained (ASTM D3080/D3080M). West Conshohocken. Pennsylvania.

ABSORPTION OF NI, CU AND ZN ON BENTONITE CLAY MIXED WITH POZZOLANIC MATERIALS

¹Natta Orprasert, ²Pongsakorn Punrattanasin and ³Dolrerdee
Hormdee ^{1,2,3}Faculty of Engineering, Khon Kean University,
Thailand

ABSTRACT

Clay is the main material used to absorb contaminants and heavy metals in treated ponds. It has a very large specific surface area and its negative charge in the surface structure can bond well with heavy metals. Bentonite mainly consists of montmorillonite, which is a type of clay mineral. This laboratory-based study experimented with using sodium bentonite to adsorb Ni, Cu, and Zn. Bentonite was used and mixed with various pozzolanic materials, including (1) cement, (2) bottom ash, and (3) fly ash. Batch sorption tests were selected as the method to evaluate sorption capacity. Factors controlled in this study were mixing time, temperature, and pH. The findings from this experiment can be the capacity to describe adsorption potential and to find the best ratio of adsorbent to be used in construction sites. In this study, sodium bentonite showed a very high Cu adsorption performance. Mixing bentonite with cement resulted in a more effective performance relative to using pure bentonite.

Keywords: Adsorption, Bentonite clay, Pozzolanic materials, Batch adsorption test, Cement, Isotherm

INTRODUCTION

Thailand State of Pollution Report 2016 discovered that various water sources have contaminated with heavy metals [1]. The main causes were the waste water discharged from factories and densely industrial estates [2]. Heavy metals cannot be decomposed in natural processes and then accumulated in soil, water and organism [3]. In the remove of heavy metals from waste water, it can be done by various methods such as ion exchange, foam flotation, coagulation and chemical coagulation etc. In these methods, adsorption with soil is an effective and inexpensive solution. Therefore, the objective of this study mainly focuses on the adsorption of heavy metals including Ni, Cu and Zn on bentonite clay mixed with cement, bottom ash and fly ash by batch sorption test. The findings from this experiment can be used to describe adsorption potential and to find the best ratio of adsorbent to be used in construction site.

MATERIALS USED

The adsorbent in this study is bentonite clay (Fig.1) [4]. The Pozzolanic materials used to mix with the bentonite for improve the adsorption capacity consist of (1) cement (Fig.2), (2) bottom ash (Fig.3) and (3) fly ash (Fig.4). All of the Pozzolanic materials were dry and were then sieved through sieve No. 16. Most of Pozzolanic materials are by products and easy to find. The composition of the mineralogical and chemical of bentonite clay, bottom ash, fly ash and cement determined by X-Ray Fluorescence

(XRF) are tabulated in Tables 1 to 2 [5]. Figures. 5 to 8 display the SEM photographs of samples with expansion rate of 500 times.

Table 1 Chemical analysis of bentonite clay, bottom ash and fly ash by XRF

	Bentonite Clay	Bottom Ash	Fly Ash
Constituent	Wt. %	Wt. %	Wt. %
SiO ₂	56.80	47.45	41.16
Al ₂ O ₃	15.10	20.32	22.30
Fe ₂ O ₃	9.79	10.92	11.51
MgO	4.61	2.60	2.70
Na ₂ O	2.01	1.03	1.66
CaO	2.81	13.16	15.27
SO ₃	-	1.16	1.43
K ₂ O	-	-	2.93
LOI	-	-	0.20

Table 2 Chemical analysis of cement by XRF

Constituent	Wt. %
SiO ₂	20
Al ₂ O ₃	5
Fe ₂ O ₃	3
MgO	1.1
CaO	60

SO₃

2.4



Fig. 1 Bentonite clay

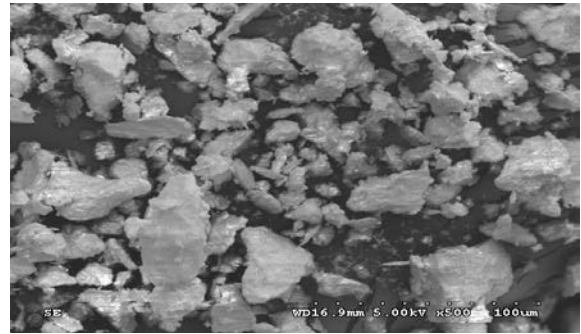


Fig. 5 SEM photograph of bentonite clay



Fig. 2 Cement

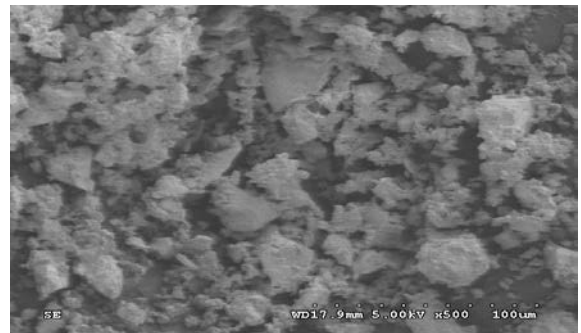


Fig. 6 SEM photograph of cement



Fig. 3 Bottom ash

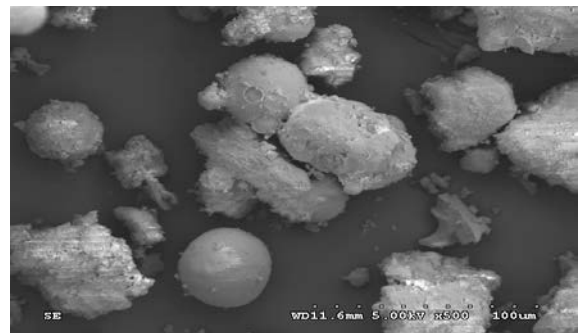


Fig. 7 SEM photograph of bottom ash



Fig. 4 Fly ash

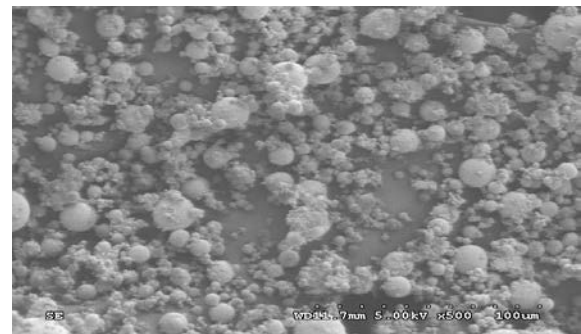


Fig. 8 SEM photograph of fly ash

Copper (Cu), nickel (Ni), and zinc (Zn) were selected to represent the range of the common heavy metals and prepared in the form of the solution to be the adsorbates. The stock solutions of Cu (NO₃)₂, Ni (NO₃)₂, and Zn (NO₃)₂ were dissolved in the deionized water to obtain the preferred initial concentration of solution [6]. The chosen initial concentration of the heavy metal solutions was 10,000 mg/L. The properties of heavy metal solutions are presented in Table 3.

Table 3 Properties of heavy materials solution

Property	Nickel (II) Nitrate	Copper (II) Nitrate	Zinc (II) Nitrate
Formula	Ni(NO ₃) ₂	Cu(NO ₃) ₂	Zn(NO ₃) ₂
Molecular (g/mol)	290.80	241.60	297.50
Density (g/cm ³)	2.05	2.32	2.06
Solubility (g/100cm ³)	94.20	137.80	184.30

EXPERIMENTAL WORK

The bentonite clay was replaced with the bottom ash, fly ash and cement at the amount of 0, 10, 20, 30, 40 and 50% by weight. In this study, batch adsorption test was carried out to investigate the heavy metal adsorption. The test processes can be performed by mixing a 2.5 g of sample with the Cu, Ni and Zn solutions [6]. The initial concentration of Ni(NO₃)₂, Cu(NO₃)₂, and Zn(NO₃)₂ was 10,000 mg/L and put it in 120 mL plastic bottle. Then the mixture was shaken by the horizontal shaker with a speed of 150 cycles per minute for 1, 3, 6, 12, 24, 36, 48, 72, 96 and 120 hours [7]. After reaching equilibrium time, the soil was separated from the heavy metal solution by using a 0.45µm filter and diluted it into the solution [6]. Finally, concentration of the residual solution was analyzed by using Atomic Adsorption Spectrometer (Fig.9) which repeat three samples in one experiment set in order to find an average value [8]. Finally, the results can then be evaluated the adsorption capacity, equilibrium times and adsorption isotherm. Factors controlled in this study were mixing time, temperature, and pH.

RESULT AND DISCUSSION

Equilibrium Time Determination

The equilibrium time is time from start adsorption until being to equilibrium state. Samples were determining equilibrium time by batch test at

1, 3, 6, 12, 24, 36, 48, 72, 96 and 120 hours. The bentonite clay replaced with the bottom ash, fly ash and cement at the amount of only 10% by weight was selected to find the equilibrium time. The amount adsorbed of Ni, Cu and Zn at any time (q_t) was illustrated in Figs. 10 to 12 for bentonite mixed with cement, bottom ash and fly ash, respectively. It can be seen in Fig.9 that the adsorption took place rapidly at the beginning of the reaction which the concentration rapidly decreased at the period of 48 hours. Thereafter, the amount adsorbed was almost constant for all Ni, Cu and Zn. This was due to the adsorption sites which interacted with the metal decreased. Thus, the adsorption of Ni Cu and Zn by bentonite mixed with cement reached to equilibrium within 48 hours. Unlike the others soils, the equilibrium occurs approximately only within 3 hours. The same trend of results was also found when performing the tests with bottom ash and fly ash.



Fig.9 Atomic Adsorption Spectrometer (AAS)

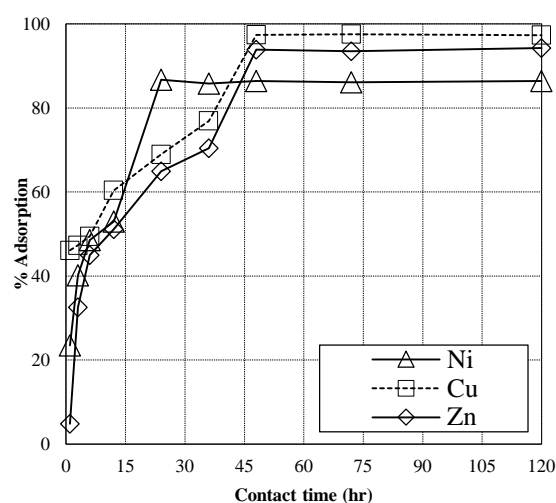


Fig. 10 Effect of contact time of Ni, Cu and Zn adsorption on bentonite clay mixed with cement at 10% by weight.

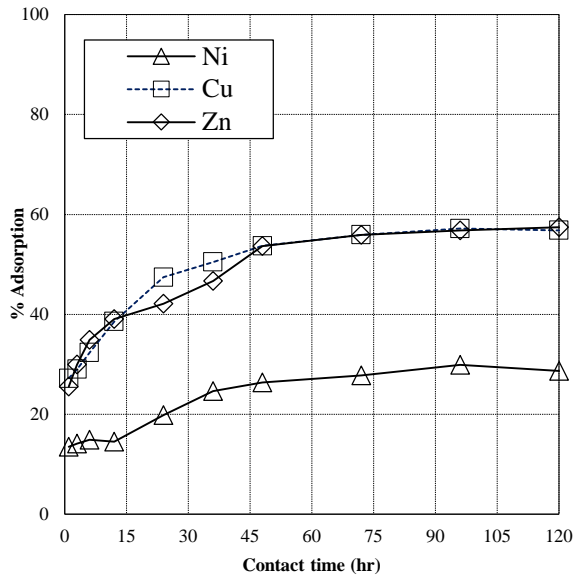


Fig. 11 Effect of contact time of Ni, Cu and Zn adsorption on bentonite clay mixed with bottom ash at 10% by weight.

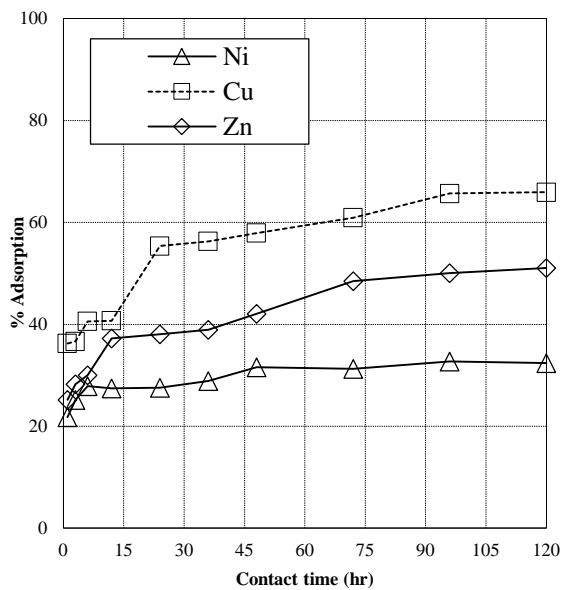


Fig. 12 Effect of contact time of Ni, Cu and Zn adsorption on bentonite clay mixed with fly ash at 10% by weight.

The Best Ratio of Adsorbent Determination

Because the bentonite has very high adsorption capacity, this soil was chosen as a representative of all soils to find the method of improvement of the adsorption capacity. The bentonite clay was replaced with the cement, bottom ash and fly ash at the amount

of 0, 10, 20, 30, 40 and 50% by weight. The effects of the three additional Pozzolanic materials on the adsorption capacity of Cu, Ni and Zn are presented in Figs.13 to 15. As presented in Figs.13 to 15, additional material especially cement can dramatically improve the adsorption capacity of heavy metals. The adsorption capacity increased with increasing amount of cement content. While using 20% of cement in the replacement, the results showed the maximum adsorption capacity of Ni, Cu and Zn. It was possible to conclude that the proper amount of cement which should be used to replace the bentonite clay was 20% for increasing the adsorption capacity of Ni, Cu and Zn. In Fig.15, the results show that the adsorption capacity of Ni and Cu increased linearly with amount of fly ash. No change in adsorption capacity was found in the case of Zn. Unlike cement and bottom ash, the results of bottom ash was shown in Fig. 14. Increasing the amount of bottom ash can reduce the sorption capacity for all Ni, Cu and Zn. It can be concluded that bottom ash is not recommended to replace in the bentonite.

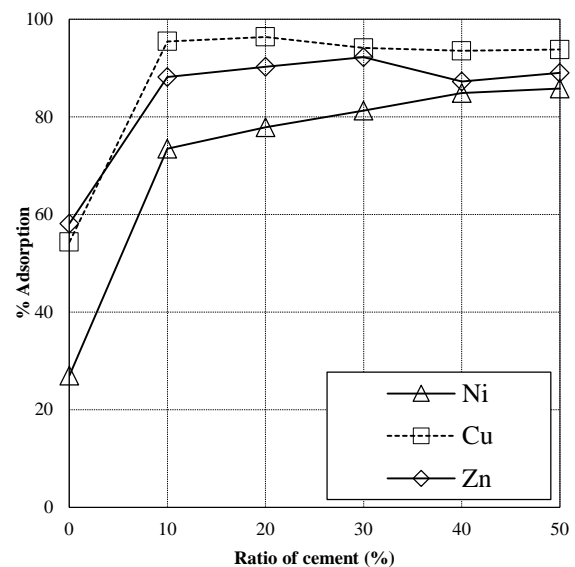


Fig. 13 Effect of ratio between bentonite with cement

The material surface characteristic is an important factor affecting on the adsorption capacity. Figures. 5 to 8 display the SEM photographs of material samples with expansion rate of 500 times. It can be seen that bentonite clay and cement show high roughness of their surfaces, while Bottom ash and fly ash show the lower roughness. High surface of roughness results in high surface area, and vice versa. Thus, adsorption capacity of bentonite with cement were higher than that of bottom ash and fly ash. The

bentonite with bottom ash provided the lowest adsorption capacity because the specific surface area and roughness were the important factors which affected on the adsorption.

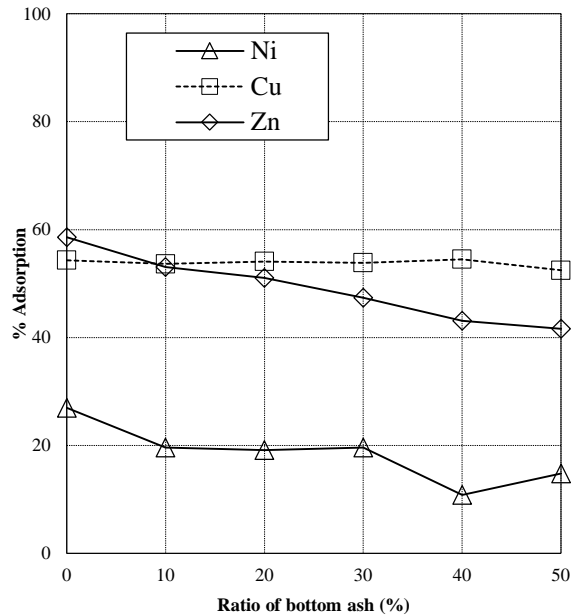


Fig. 14 Effect of ratio between bentonite with bottom ash

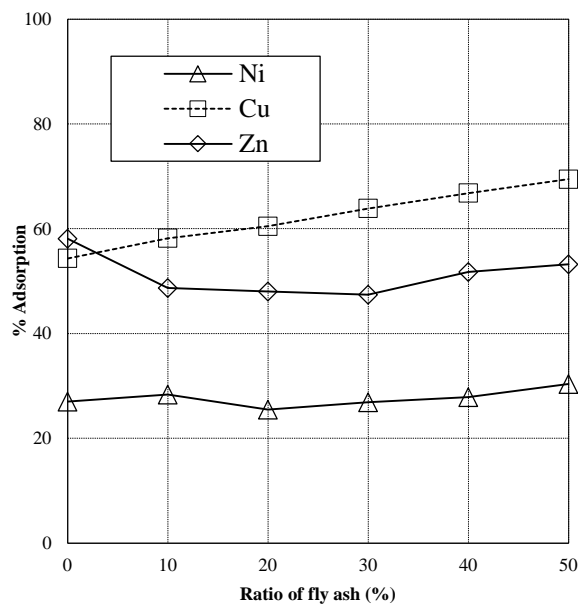


Fig. 15 Effect of ratio between bentonite with fly ash

CONCLUSIONS

In this study, the adsorption capacities of Cu, Ni and Zn by bentonite clay was investigated. Further, the new method was introduced to improve the adsorption capacity of the bentonite clay by mixing the soil with cement, bottom ash and fly ash. The results indicated that the adsorptions of these materials reach the equilibrium time within approximately 48 hours and higher than that of normal soils. The adsorption capacity of samples was in the order of cement > fly ash > bottom ash. The bentonite with bottom ash provided the lowest adsorption capacity because the specific surface area and roughness were the important factors which affected on the adsorption. From the improvement of the adsorption capacity only cement and fly ash can increase the adsorption capacity of the bentonite clay. Cement showed the highest performance for improvement of Cu, Zn and Ni adsorption. The recommended contents of cement was 20% by weight of bentonite clay.

ACKNOWLEDGEMENTS

This research was supported by Department of Civil Engineering, Faculty of Engineering, Khon Kean University.

REFERENCES

- [1] Pollution Control Department, Ministry of Natural Resources and Environment, Thailand State of Pollution Report, 2016.
- [2] Saad A. Aljlil and Fares D. Alsewaleim, Adsorption of Cu & Ni on Bentonite Clay from Waste Water, Athens Journal of Natural & Formal Sciences., Vol. 1, No. 1, 2014.
- [3] A.Dube, R. Zbytniewski, T. Kawalkowski, E. Cukrowska, and B. Buszewski, Adsorption and Migration of Heavy Metals in Soil, Polish Journal of Environment Studies, Vol. 10, No. 1, 2001, pp. 1-10.
- [4] Mohammad Kashif Uddin., A review on the adsorption of heavy metals by clay minerals, with special focus on the past decade., Chemical Engineering Journal., Vol 308, 2017, pp 438-462.
- [5] Arnun Chantaduang, Influence of Pozzolanic Materials in The Adsorption of Heavy Metals on soils, 2017, pp. 14-47.
- [6] Noppadol Sangiumsak and Pongsakorn Punrattanasin, Adsorption Behavior of Heavy Metals on Various Soils, Polish Journal of Environment Studies, Vol. 23, No. 3, 2014, pp. 853-865.
- [7] Pongsakorn Punrattanasin and Noppadol Sangiumsak, The Effect of Clay, Lime and Rice Husk Ash Contents on the Sorption Capacity of Cu, Ni and Zn by Soils, Conference proceedings, in Proc. 1st Int. Conf. on GEOMATE, 2011, pp. 263-267.
- [8] Arwut Yimtae, Pongsakorn Punrattanasin and Noppadol Sangiumsak., The Sorption Capacity of Cu by SC-Soil from Batch and Column Tests, Conference proceedings, in Proc. 1st Int. Conf. on GEOMATE, 2011, pp. 203-207.

ADSORPTION OF ZINC ON BENTONITE CLAY MIXED WITH POZZOLANIC MATERIALS BY COLUMN LEACHING TEST

¹Pittaya Satiman, ²Pongsakorn Punrattanasin and ³Chinawat
^{1,2,3}Muktabhant Faculty of Engineering, Khon Kaen University,
Thailand

ABSTRACT

This research mainly focuses on the adsorption of zinc on bentonite clay when mixing with various Pozzolanic materials by column leaching test. The Pozzolanic materials in this study consist of 1) fly ash, 2) bottom ash, 3) rice husk ash, 4) blast furnace slag, 5) silica fume, 6) metakaolin, and 7) cement. Only zinc was selected as an important heavy metal that was found around the vicinity area of industry. Cycles of loop in column leaching test were systematically done. The main cycles consist of releasing heavy metal solution to the example model and then releasing distilled water to the model with continuous flow. This two steps can simulate the actual condition of the discharge of zinc in waste water into the soil and washed it by rain. Cycle 3 was then carried out to verify the adsorption capability after the desorption process. The adsorption behavior in this study can be illustrated in the breakthrough curves. The breakthrough curve is a relationship between the rates of absorption versus service time. In this study, bentonite mixed with cement shows the highest zinc adsorption performance.

Keywords: Bentonite clay, Adsorption, Column leaching test, Pozzolanic materials, Breakthrough curve

INTRODUCTION

Rapid growth of industries has led to increase the environmental problem. Every years, large amount of waste water has been discharged into river without treatment. The waste water often contaminated with heavy metals. These heavy metals may cause damage to mankind and animals. There are many methods for remove the heavy metals from the waste water such as a reduction process, magnetic ferrites treatment, ion exchange, reverse osmosis, chemical oxidation, membrane separation, coagulation, flotation, filtration, adsorption and evaporation [1], [2], [3]. Adsorption is one of the most common methods for heavy metal removal. It offers benefits in terms of availability, simplicity of operation. Soils, especially clay, have been widely used as the adsorbents for the wastewater treatment. Because high efficiency and inexpensive, it motivates many researchers to do research with soils in the adsorption study [4], [5]. Several soils were previously selected as the adsorbent of batch and column adsorption tests. The adsorption capacity of bentonite, one type of clay, were primarily studied by the batch technique. In batch sorption test, the results show the beneficial evidence on adsorption capacity of the heavy metals on the bentonite. To understand details of contaminate flow, column leaching test could provide the most practical way and can simulate closer to the circumstances than the batch adsorption experiment. The objective of this study is to investigate the adsorption capability of bentonite clay mixed with various Pozzolanic materials by the small-scale column test. The purpose of adding the Pozzolanic materials into the bentonite is to relatively evaluate the enhancement of sorption capacity.

MATERIALS USED

Bentonite clay was selected as an adsorbent in this study. The Pozzolanic materials used to mix with the bentonite consist of 1) bottom ash (BA), 2) rice husk ash (RHA), 3) blast furnace slag (BFS), 4) silica fume (SF), 5) metakaolin (MK), 6) cement (CE) and 7) fly ash (FA). The bentonite was replaced with the Pozzolanic materials at the only amount of 50% by weight. The chemical contents of the bentonite clay and the Pozzolanic materials were verified by X-ray fluorescence (XRF) and then summarized in Table 1. Figures 1 to 8 display the SEM photographs of all samples with a magnification rate of 3,000 times. Heavy metals chosen as adsorbate in this research was zinc (Zn). The properties of Zn solutions are shown in Table 2. The chosen initial concentration of the zinc was 10,000 mg/L and this concentration is higher than that of the use in other soils before due to its high sorption capacity of the bentonite.

Table 1 Chemical analysis of bentonite clay and the Pozzolanic materials by XRF

Constituent	% by weight						
	1	2	3	4	5	6	7
SiO ₂	56.8	20	48	37	92	90	55
Al ₂ O ₃	15.1	5	26	11	0.7	0.5	40
Fe ₂ O ₃	9.8	3	10	0.3	1.2	2	0.5
CaO	2.8	60	5	40	0.5	0.5	-
MgO	4.6	1.1	2	7	0.2	0.2	-
SO ₃	-	2.4	0.7	0.3	-	1.5	-
Lol.	-	2	3	-	-	4.7	-

Where: 1 = Bentonite, 2 = Cement, 3 = Fly and bottom ash, 4 = Blast furnace slag, 5 = Silica fume, 6 = Rice husk ash, 7 = Metakaolin.

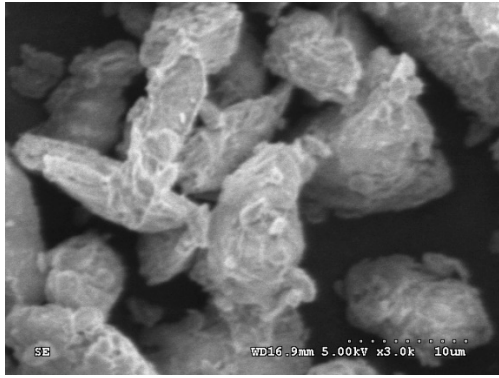


Fig.1 SEM photograph of bentonite



Fig.5 SEM photograph of silica fume

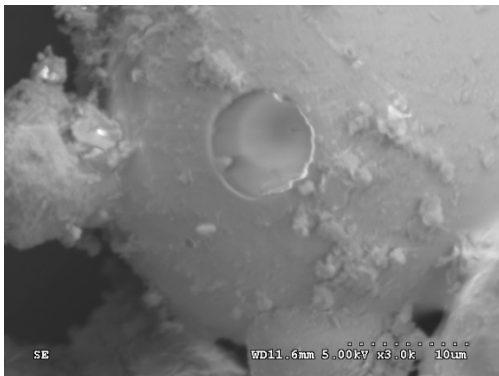


Fig.2 SEM photograph of bottom ash

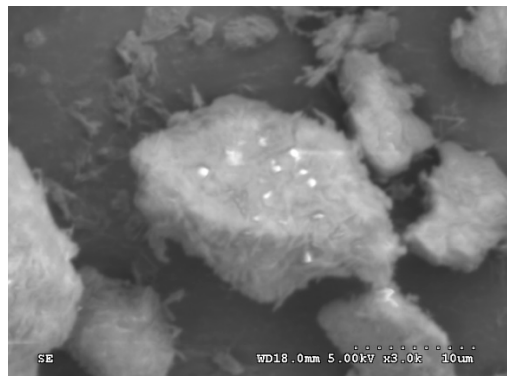


Fig.6 SEM photograph of metakaolin

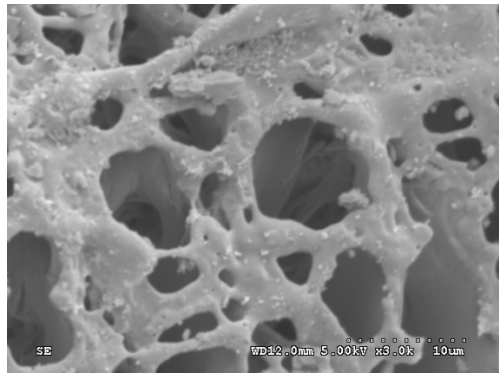


Fig.3 SEM photograph of rice husk ash

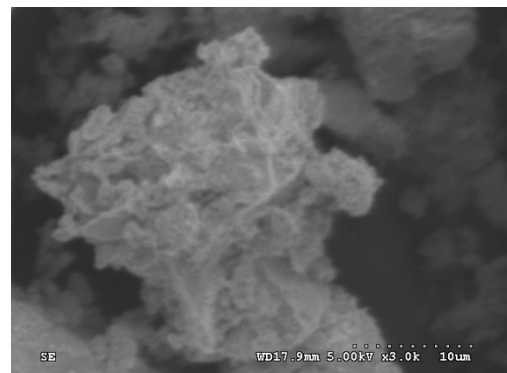


Fig.7 SEM photograph of cement

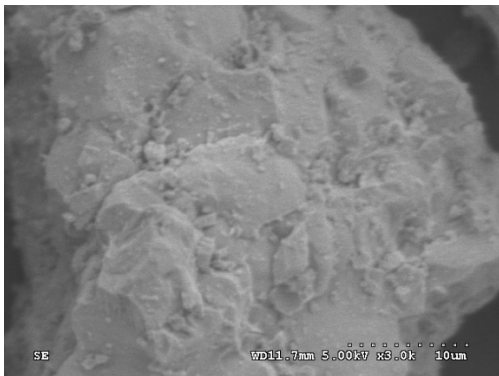


Fig.4 SEM photograph of blast furnace slag

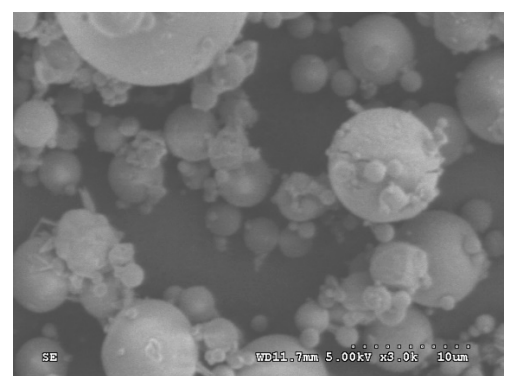


Fig.8 SEM photograph of fly ash

Table 2 Properties of zinc solution

Property	Zinc (II) Nitrate
Formula	$\text{Zn}(\text{NO}_3)_2$
Molecular (g/mol)	297.50
Density (g/cm ³)	2.06
Solubility (g/100cm ³)	184.30

EXPERIMENTAL WORK

The components of the column adsorption apparatus are schematically shown in Fig. 9. PVC tube with an internal diameter and height of 2.54 cm was used as a fixed-bed column. The adsorbent with the mass of 20g were compacted in the column before conducting the flowing process. Three cycles of loop in column leaching test were systematically done. Cycles 1 and 2 consist of releasing heavy metal solution to the example model and then releasing distilled water to the model with continuous flow. This two steps can simulate the actual condition of the discharge of zinc in waste water into the soil and washed it by rain. The main purpose of cycle 2 was to evaluate the desorption behavior. Cycle 3 was then carried out to verify the adsorption capability after the desorption process. The procedure of the column adsorption is described in Fig.10.

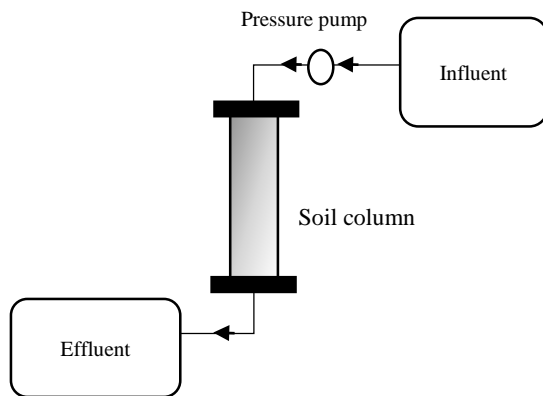


Fig. 9 Schematic drawing of column leaching test

The flowing processes of each cycle were at least finalized until the exhaustion period of the adsorbent. The flow rate of the influent was designated to be equal to 1.0 mL/min. The pressure pump was used to drive the pressure into the PVC tube and to set at a constant flow rate. A chronometer was employed to measure the service time (t) at different collections of effluent. The effluent was diluted with 1% of nitric acid (HNO_3). Atomic Absorption Spectrometer was used to measure the concentration of the effluent. The concentration of the effluents (C_e) could finally be identified.

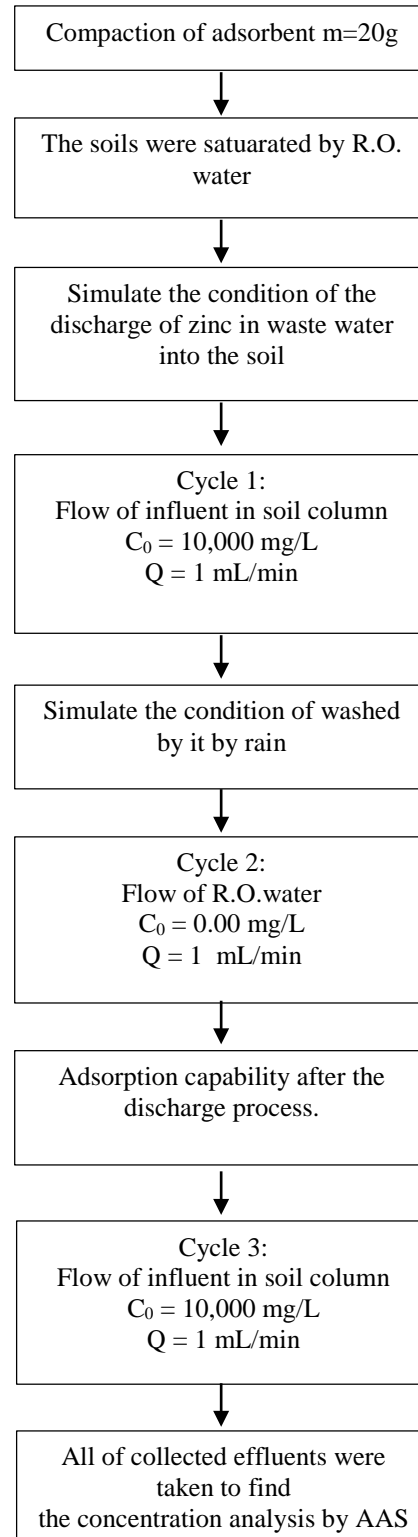


Fig. 10 Procedure of column adsorption test

RESULTS AND DISCUSSIONS

The breakthrough time and the shape of the breakthrough curve were significant features to define the operation response of an adsorption column [1], [3]. The typical breakthrough curve is

represented by plotting between the service time (t) and the ratio of $C_{effluent}$ to $C_{influent}$ (C/C_0). The breakthrough point and the point of the exhaustion of column of the breakthrough curve was correspondingly selected to be the point at which $C/C_0 = 5\%$ and the point at which $C/C_0 = 95\%$, respectively. Figures 11 to 17 demonstrate the s-curves ($t - C/C_0$) representing the adsorption process of zinc on bentonite (B) when mixing with bottom ash (BA), rice husk ash (RHA), blast furnace slag (BFS), silica fume (SF), metakaolin (MK), cement (CE) and fly ash (FA), respectively. Three consecutive cycles of adsorption, desorption, and adsorption were continuously illustrated.

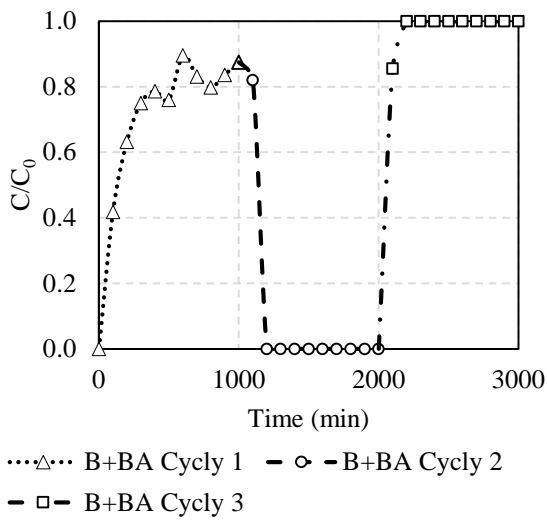


Fig. 11 Breakthrough curve of Zn on B+BA

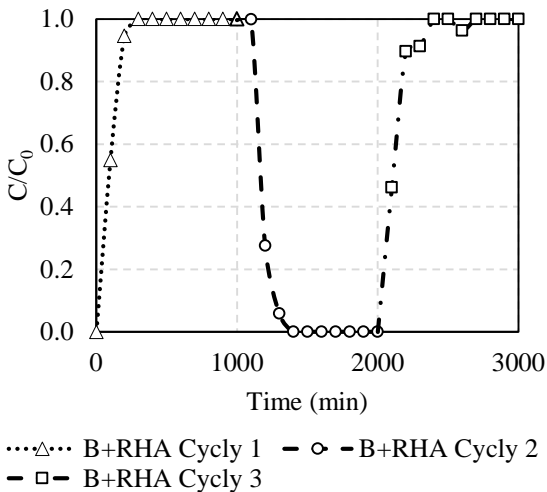


Fig. 12 Breakthrough curve of Zn on B+RHA

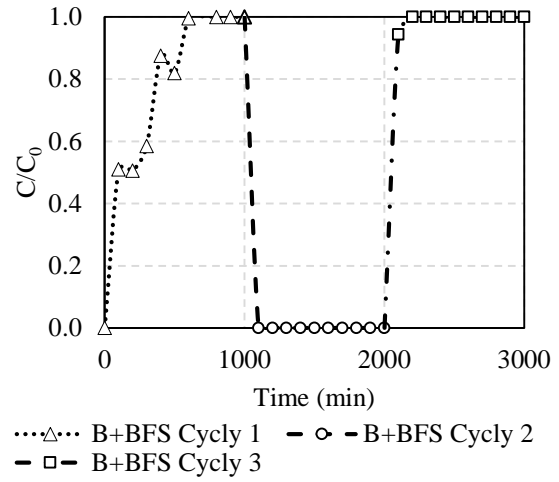


Fig. 13 Breakthrough curve of Zn on B+BFS

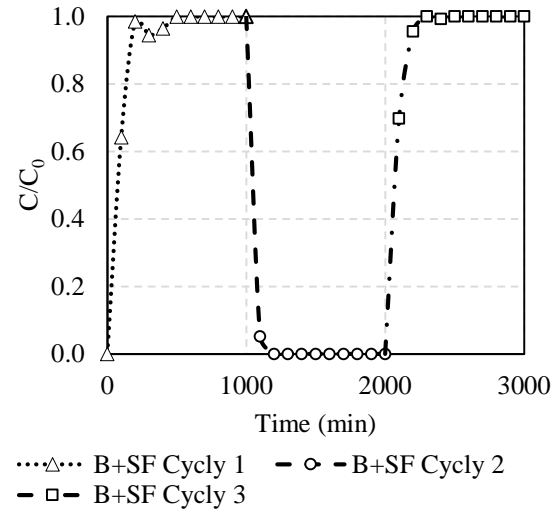


Fig. 14 Breakthrough curve of Zn on B+SF

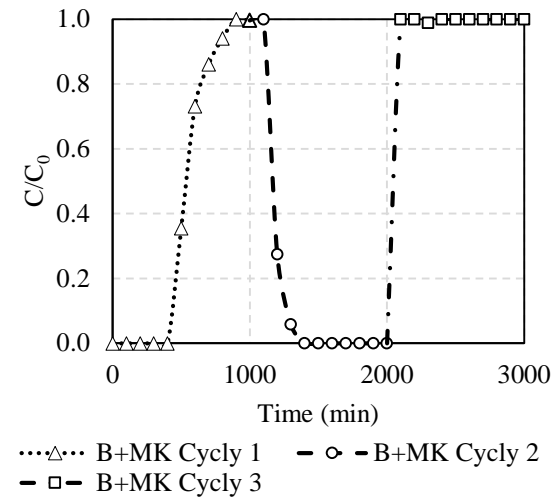


Fig. 15 Breakthrough curve of Zn on B+MK

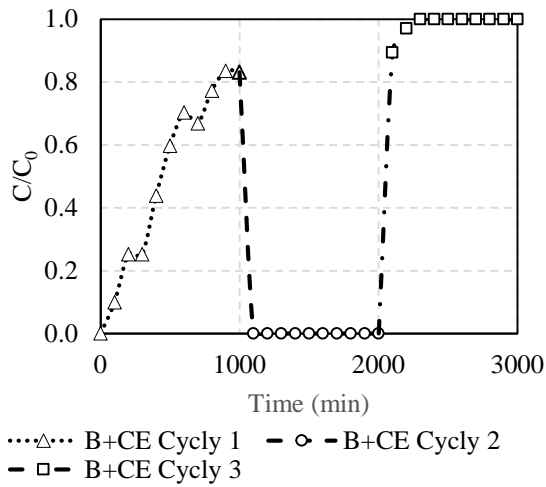


Fig. 16 Breakthrough curve of Zn on B+CE

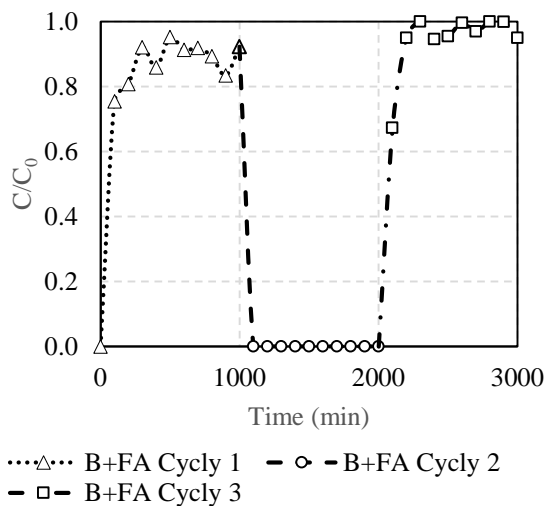


Fig. 17 Breakthrough curve of Zn on B+FA

The breakthrough curves were found in the cycle I for all samples. The results showed that the concentration of the effluent in cycle I of rice husk ash, silica fume and fly ash increased sharply after the starting point and then reached the point of the exhaustion of column or it implies that bentonite mixed with these three materials reached the saturated point of adsorption or its highest sorption capacity. The adsorption occurred with high volume in the Cycle 1. For other cases, especially cement, the adsorption continues to increase with service times but not reached the saturated point of adsorption. It was observed that the S-shaped curves of adsorption by using bottom ash and cement show the beneficial effect of adding them into the bentonite. This two curves demonstrate that the bottom ash and cement

have a higher volume of adsorption than that of other Pozzolanic materials.

The concentration of the effluent samples in cycle II at the beginning of the flowing period was found positive. The zinc solutions were observed in the effluents in the cases of bottom ash, rich husk ash and metakaolin. It means that zinc ions were removed by water in cycle 2. This could be due to the reversible process or desorption process of the ions on the adsorbent surface during the flow of the water. Comparing the results of materials than can sustain the leaching by water, it can be ranked as follows: rice husk ash < silica fume < bottom ash < fly ash < metakaolin < blast furnace slag. For cement, no detection of zinc is in the effluent. The progression of the concentrations of the effluents in cycle III was similar to the cycle I. In cycle 3 of fig. 16, the value of concentration of zinc shows the continuous in sorption of zinc. Mixing bentonite with cement resulted in a more effective performance relative to using other materials.

CONCLUSIONS

The results in this research study show the adsorption capability of bentonite clay mixed with seven Pozzolanic materials by using a small-scale column leaching apparatus. The purpose of adding the Pozzolanic materials into the bentonite is to enhance the capacity of the bentonite. The results from column test can be illustrated by the breakthrough curves. High adsorption occurred in the beginning of Cycle 1 was observed for some samples. Thereafter, the adsorption decreased until it reached to the saturated point. The leaching of zinc by water occurred with a fractional volume. The breakthrough curves representing the adsorption process ultimately identified the adsorption behaviors. The desorption process in cycle II could not fully remove the zinc ions from the surface of the adsorption. Cement depicted great adsorption capacity comparing to other Pozzolanic materials.

ACKNOWLEDGEMENTS

This research was support by Department of Civil Engineering, Faculty of Engineering, Khon Kean University.

REFERENCES

- [1] Punrattanasin P., Sariem P., Adsorption of Copper, Zinc, and Nickel using Loess as Adsorbent by Column Studies, Pol. J. Environ. Stud. 24, (3) 2015, pp.1267-1275.
- [2] Martins T, Leitão TE, Carvalho MR. 2017. Assessment of Wastewater Contaminants Retention for a Soil-aquifer Treatment System

- Using Soil-column Experiments. *Procedia Earth and Planetary Science*. 17(15), pp. 332–335.
- [3] E.D. de Freitas 614 et al. 2018. Continuous adsorption of silver and copper by Verde-lodo bentonite in a fixed bed flow-through column *Journal of Cleaner Production*. 171, pp. 613-621.
- [4] JV Smart, Bentonite, Mineral Information Leatlet No. 1, Department of Mines and Energy, 1999.
- [5] Tsiridis V, Petala M, Samaras P, Sakellariopoulos GP. 2015. Evaluation of interactions between soil and coal fly ash leachates using column percolation tests. *Waste Manag.* 43, pp. 255–263.

EFFECT OF INITIAL CONCENTRATION OF HEAVY METALS ON THE ADSORPTION CAPACITY OF BENTONITE CLAY MIXED WITH PORTLAND CEMENT

¹Anunt Sirisombunphatthana, ²Pongsakorn Punrattanasin and ³Ratamanee
^{1,2,3}Nuntasarn Faculty of Engineering, Khon Kean University, Thailand

ABSTRACT

This research study examined the influence of initial concentration of heavy metals that affect the adsorption capacity of nickel (Ni), copper (Cu) and zinc (Zn) on bentonite clay. The bentonite clay was widely used as a waterproofing material in hazardous waste landfill. An idea of mixing between bentonite clay and Portland cement can increase the adsorption capacity was adopted in this study. The laboratory results can be clearly proofed from a series of batch sorption test. A varieties of initial concentration of Ni, Cu and Zn were prepared in the study. The results showed that increasing in the initial concentration of heavy metals can reduce the adsorption efficiency of the soil. The Langmuir Isotherm model was able to efficiently explain the adsorption behavior of the bentonite clay. Adsorption capacities were ranked as follows: Cu > Ni > Zn.

Keywords: Heavy metals, Adsorption, Isotherm, Bentonite clay, Cement, Batch test

INTRODUCTION

Rapid growth of industries during many decades has led to increase the environmental problems. It was found that a large amount of waste waters, especially heavy metals, has been directly discharged from industrial factories into river without carefully treatment. There are various methods for remove the heavy metals from the waste water [1, 2, 3]. Adsorption is one of the most common methods for heavy metal removal. It was proven that adsorption by soils is an effective and economical technique [4]. The objective of this study is to investigate the effect of initial concentration of heavy metals on the adsorption capacity of bentonite clay mixed with Portland Cement Type1. Cement used is easy to find and cheap. An idea of mixing between bentonite clay and cement can increase the adsorption capacity was also adopted in this study. The adsorptions were done at very high initial concentrations ranging from 7,000 to 10,000 ppm.

MATERIALS USED

Because clay has the highest adsorption capacity relative to other soils, bentonite clay was then chosen and used as an absorbent in this study. To increase the adsorption capability, Portland cement type I was added into the bentonite clay with the amount of 5% by weight. Chemical analysis of the bentonite clay and cement by XRF was shown in Table1. Figures 1 and 2 graphically show the SEM photographs with magnification rates of 50, 500, 1,000 and 3,000 times of bentonite clay and cement, respectively. Three heavy metals chosen as the adsorbed materials in this study were copper (Cu), nickel (Ni) and zinc (Zn). They were prepared by dissolving Copper Nitrate

(Cu(NO₃)₂), Nickel Nitrate (Ni(NO₃)₂) and Zinc Nitrate (Zn(NO₃)₂) in distilled water. The solutions were varied with initial concentrations. Table 2 summarized properties of Cu, Ni and Zn. Selection were based on heavy metals that commonly found in industrial wastes.

Table 1 Chemical analysis of the bentonite clay and Portland cement by XRF technique

Constituent	Bentonite Clay	Cement
	Wt%	Wt%
SiO ₂	56.8	20
Al ₂ O ₃	15.1	5
Fe ₂ O ₃	9.79	3
MgO	4.61	60
Na ₂ O	2.01	1.1
CaO	2.81	2.4

Table 2 Properties of heavy metal solutions

Property	Copper (II) Nitrate	Nickel (II) Nitrate	Zinc (II) Nitrate
Formula	Cu(NO ₃) ₂	Ni(NO ₃) ₂	Zn(NO ₃) ₂
Molecular (g/mol)	241.60	290.80	297.50
Density (g/cm ³)	2.32	2.05	2.06
Solubility (g/100 cm ³)	137.8	94.20	184.30

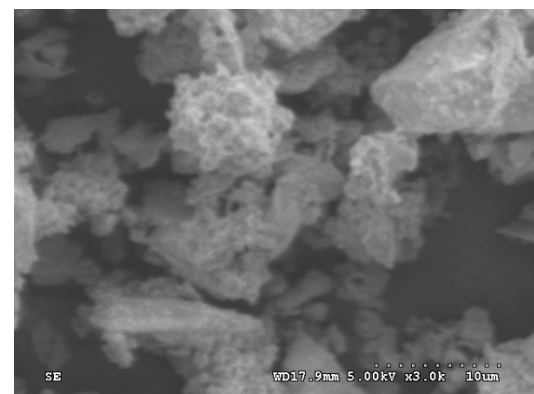
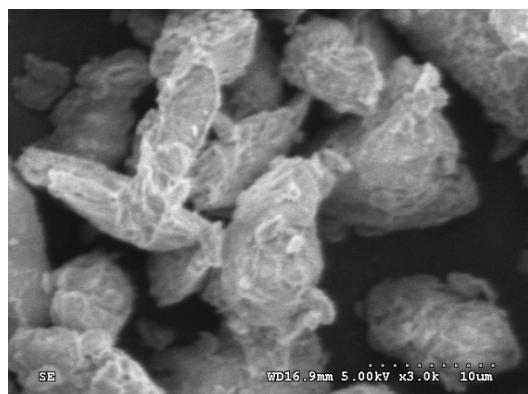
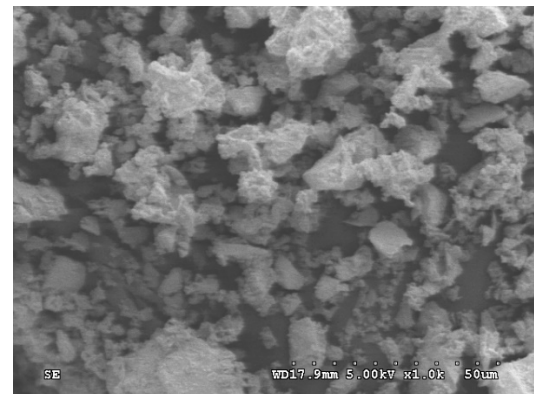
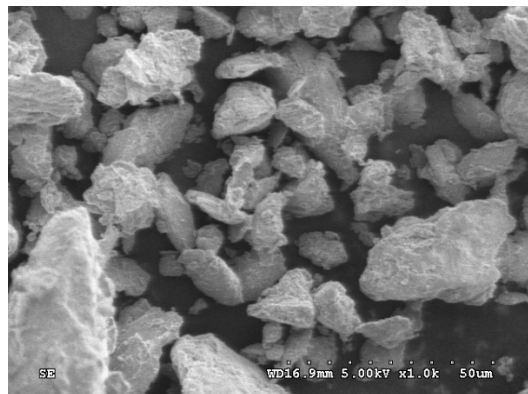
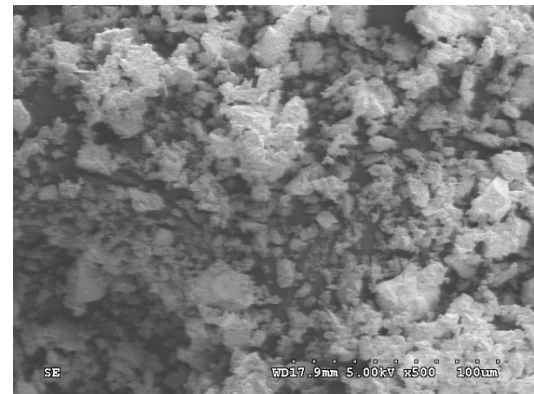
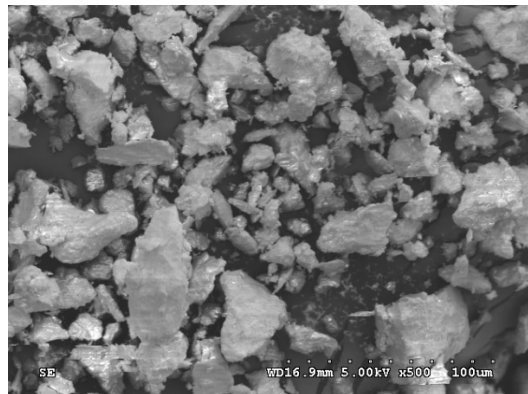
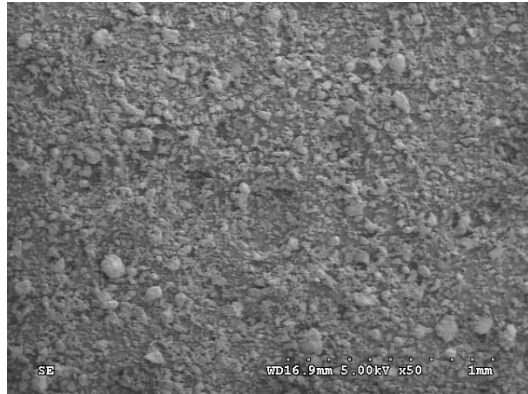


Fig.1 SEM photograph of bentonite

Fig.2 SEM photograph of cement

EXPERIMENTAL WORK

Batch Sorption Test

In this study, batch tests were carried out to evaluate the adsorption capacity of three heavy metals. The batch test processes can be performed by mixing the bentonite clay with heavy metals. The initial concentrations used in the pilot test were ranged from 500 to 6,000 ppm and put it in 120 mL plastic bottle. Then the mixture was shaken by the horizontal shaker with a speed of 150 cycles per minute for 48 hours. After a particular period of the time, the soil was separated from the heavy metal solution by using a 0.45 μ m filter and diluted it into the solution. Finally, concentration of the residual solution was analyzed by using Atomic Adsorption Spectrometer (Fig.3). From the step above, it can be measured the percentage of adsorption. The suitable initial concentration of heavy metals for main test can be evaluated.

To find an appropriate initial concentration to use with bentonite mixed with cement, the next series of batch sorption test was then carried out. The bentonite weight of 2.375g is mixed with 0.125g of cement. After that, a 50ml of heavy metal solution was then added to the soil sample. The samples were diluted with nitric acid after shaking. The initial concentrations of heavy metals chosen were 7,000, 8,000, 9,000 and 10,000 ppm.



Fig.3 Atomic Absorption Spectrometer

Equilibrium Time Determination

The equilibrium time is the time adsorption takes to reach an equilibrium state. To determine the equilibrium time, the batch method was performed at various lengths of time, i.e. 0.5, 1, 3, 6, 12, 24, 36, 48, and 72 hours, with a concentration of heavy metal solutions at 7,000 ppm. By employing this method, the concentrations of solutions at any time were known, and so the adsorption equilibrium time could be established.

Adsorption Isotherm Determination

The adsorption isotherm is the relationship between the concentrations of heavy metal solutions, at equilibrium C_{eq} , and the amounts of heavy metals adsorbed by the soil (q). The value of q can be calculated as follows:

$$q = \frac{(C_0 - C_{eq})V_{sol}}{M_s} \quad (1)$$

Where: q is the amount of adsorption of heavy metals per unit weight within soil (mg/g), C_0 is the initial concentration of heavy metal solution (mg/l), C_{eq} is the equilibrium concentration of the solutions (mg/l), V_{sol} is the volume of solution (cm^3) and M_s is the mass of soil (g).

Percentage of adsorption can be calculated by this equation.

$$\% \text{ adsorption} = \frac{(C_0 - C_{eq})}{C_{eq}} \times 100 \quad (2)$$

The adsorption isotherm is relationship between concentration of heavy metal solution (C_{eq}) and the amount of heavy metals adsorbed by adsorbent (q). Langmuir's adsorption isotherm (eq.3).

$$q = \frac{\alpha\beta C_{eq}}{1 + \alpha C_{eq}} \quad (3)$$

Where: q is the amount of adsorbent absorbed at 1 g (mg/g), C_{eq} is the concentration of the adsorbent in liquid at equilibrium (mg/g), β is the maximum amount of metal solution adsorbed on the amount of adsorbable soil. (mg/g) and α is the adsorption constant of Langmuir (l/mg). Figure 4 shows the relationship between all Langmuir adsorption isotherm parameters.

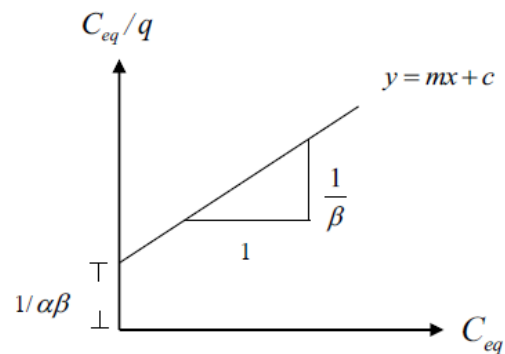


Fig.4 Langmuir isotherm parameters

RESULTS AND DISCUSSIONS

Suitable initial concentration

The results of percentage of adsorption of Cu, Ni and Zn at a concentration of 500 ppm on sand, clay and bentonite clay were illustrated in Fig.5. It was

shown that bentonite has the highest capacity compared to sand and clay. The 100% of adsorption demonstrates that an initial concentration of 500 ppm of heavy metals is not enough to use. The next series of pilot test was then carried out with various initial concentrations ranging from 500 to 6,000 ppm. This series only pure bentonite was selected to identify the suitable initial concentrations. It was shown in Fig. 6 that pure bentonite can adsorb 100% of Cu up to an initial concentration of 3,500 ppm. The suggestion from these results is that for bentonite mixed with cement, the suitable initial concentration higher than 6,000 ppm is recommended.

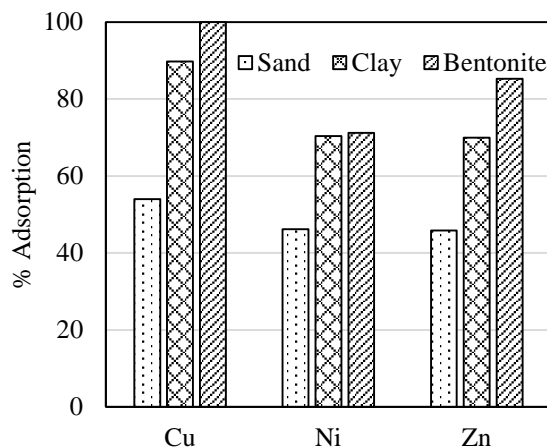


Fig.5 The comparison on performance of sand, clay and bentonite in the adsorption capability at 500 ppm of heavy metals

Equilibrium time for bentonite mixed with cement

To find the effects of contact times, the adsorptions in bentonite mixed with cement samples were investigated at different times. Figure 7 shows the remaining concentrations, C_t of Cu, Ni, and Zn solutions at any elapsed time. It can be seen that the concentrations of solutions decrease rapidly, especially during the first periods of 0-3 hours. After that, they decline slowly, until they reach a constant within 48-120 hours. After that, the samples were saturated, as a result of the accumulation of the metals on the bentonite and cement surface. It can be concluded that the equilibrium times of Cu, Ni, and Zn adsorption, by all their samples, occurred within 48-120 hours.

Effect of initial concentrations and adsorption isotherm

The results of adsorption capacity with different initial concentrations of heavy metals were plotted and shown in Fig.8. The sorption capacities of Cu by bentonite mixed with cement were found that the percentage of adsorption starting from 91.0 and reduce

to 85.7% at the initial concentrations of 7,000 and 10,000 ppm, respectively. The same tends of results were found in cases of zinc and nickel. It means that increasing the initial concentration of heavy metals can reduce the adsorption efficiency of the bentonite mixed with clay. Adsorption capacities were ranked as follows: Cu > Ni > Zn.

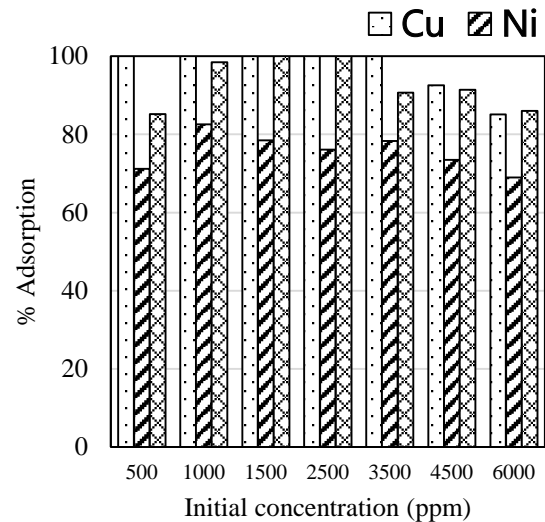


Fig.6 Percentage of adsorption with different initial concentration of pure bentonite

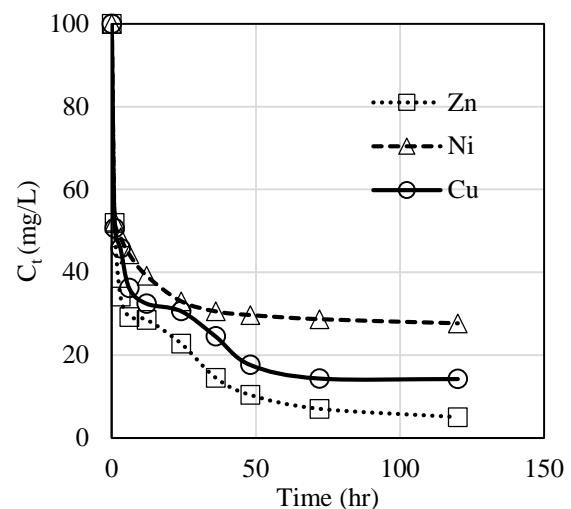


Fig.7 Effect of contact time on Cu, Ni and Zn adsorption by bentonite mixed with cement

Figure 9 shows the adsorption isotherm of Cu, Ni and Zn. As shown in 9, the amount of adsorption (q) increased linearly with increasing equilibrium concentration (C_{eq}). The adsorption isotherm can be represented by Langmuir adsorption isotherm as shown in Figs 10 and 12. The Langmuir isotherm parameters can be calculated from the relationship between concentration at equilibrium (C_{eq}) and the ratio of C_{eq}/q by referring Fig.4. The consistency of the isotherm describes well that the surface of

samples was covered with monolayer of the heavy metal particles. Langmuir parameters (β and α) and the coefficient of correlation (R^2) were then calculated and summarized in Table 3. Very high coefficient of correlation (R^2) from this model indicated that the adsorption of Cu, Ni and Zn by bentonite-cement sample favorable fit to Langmuir adsorption isotherm. The maximum value of the adsorbed metal solution on the amount of absorbable soil is represented by β -value. This value indicates the maximum amount of bentonite mixed with cement can absorb heavy metals. $\beta=181.8$ means that 1g of bentonite mixed with cement (19: 1 ratio) can absorb copper as much as 181.8 mg. Comparing β -values in Table 3, it can be concluded that adsorption capacities of bentonite clay when mixing with cement were ranked as follows: Cu > Ni > Zn.

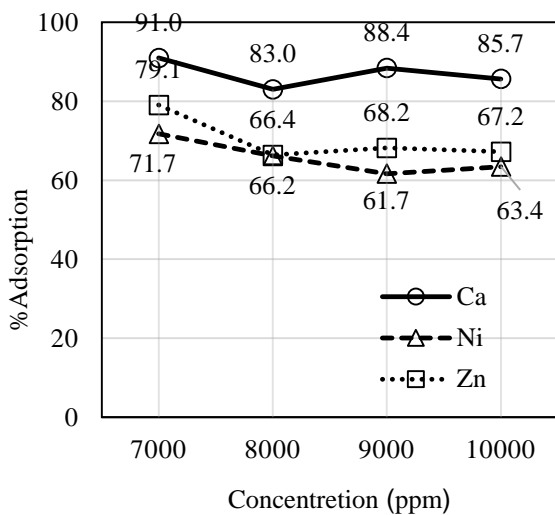


Fig.8 The effect of initial concentration on the adsorption capacity

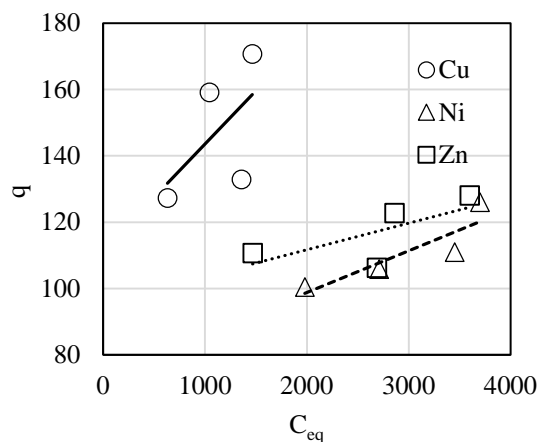


Fig.9 Adsorption isotherm of Cu, Ni and Zn

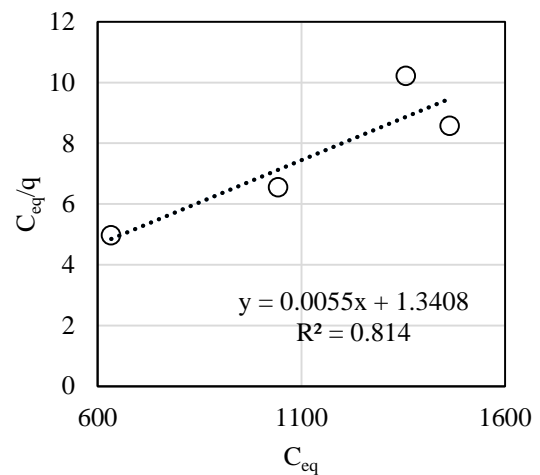


Fig.10 Langmuir's adsorption isotherm of Cu

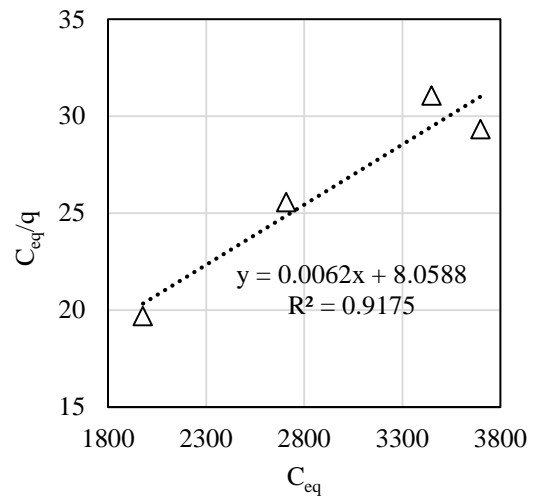


Fig.11 Langmuir's adsorption isotherm of Ni

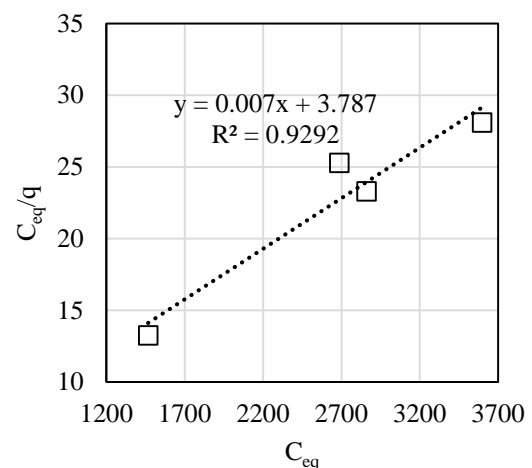


Fig.12 Langmuir's adsorption isotherm of Zn

Table 3 Parameters of Langmuir adsorption isotherm

	α	β	R ²
Copper	0.0041	181.80	0.8140
Nickel	0.0007	162.29	0.9175
Zinc	0.0018	142.86	0.9292

CONCLUSIONS

In this study, the adsorption capacity of Cu, Ni and Zn on bentonite clay mixed with cement was investigated by performing batch sorption test. The results from batch test indicated that the equilibrium times of Cu, Ni, and Zn adsorption occurred within 48-120 hours. The suitable initial concentration higher than 6,000 ppm is recommended in the batch test for bentonite-clay sample. The adsorption capacity slightly decreased with increasing initial concentration of heavy metals. Langmuir isotherm model can favorable and well describe the adsorption of this sample. It can be concluded from β -values that adsorption capacities of bentonite clay when mixing with cement were ranked as follows: Cu > Ni > Zn.

ACKNOWLEDGEMENTS

This research was support by Department of Civil Engineering, Faculty of Engineering, Khon Kean University.

REFERENCES

- [1] Aar M., Mclaughlin M.J., Kirby J.K., Stacey S.P. Adsorption and desorption of copper and zinc in tropical peat soils of Sarawak, Malaysia. *Geoderma*. 175, 59, 2012.
- [2] Ijagbemi C.O., Baek M.H., Kim D.S. Montmorillonite surface properties and sorption characteristics for heavy metal removal from aqueous solutions. *J. Hazard. Mater.* 166, 538, 2009.
- [3] Bulut Y., Tez Z. Removal of heavy metals from aqueous solution by sawdust adsorption. *J. Environ. Sci.* 19, 160, 2007.
- [4] Meena A.K., Kadirvelu K., Mishra G.K., Rajagopal C., Nagar P.N. Adsorption removal of heavy metals from aqueous solution by treated sawdust (*Acacia Arabica*). *J. Hazard. Mater.* 150, 604, 2008.

ADSORPTION CAPACITY OF HEAVY METALS ON ILLITE, KAOLINITE AND MONTMORILLONITE CLAYS FROM BATCH TEST

¹Keatniyom Teerawattanaparpha, ²Pongsakorn Punrattanasin and ³Dolrerdee
^{1,2,3}Hormdee Faculty of Engineering, Khon Kaen University, Thailand

ABSTRACT

This study investigated and compared the adsorption efficiency of the various types of clay by adsorb heavy metals. Three types of adsorbents were used are kaolinite clay, illite clay and montmorillonite clay. The heavy metals used are adsorbed is copper (Cu). The equilibrium times of Cu by montmorillonite clay is occurred within 70 hours. The method that used to test the adsorption efficiency is batch sorption test. The initial concentrations of copper solution used were 500, 1,000, 2,000, 4,000 and 6,000 ppm. The results of this study demonstrate that montmorillonite clay have the best adsorption efficiency, followed by illite clay and kaolinite clay. Langmuir and Freundlich isotherm models can favourable describe the adsorption behaviour of clays. The montmorillonite provided the highest adsorption capacity because of large specific surface area and roughness which affected on the adsorption.

Keywords: Illite clay, Kaolinite clay, Montmorillonite clay, Batch test, Copper, Adsorption efficiency

INTRODUCTION

Nowadays, industrial factories are expanding. As a result, the amount of pollution generated from the production process is increasing. Most of the pollution from the factory is usually heavy metals. The factory have to treat those wastes by putting in the wastewater treatment pond before releasing to environment. The all ponds have to construct with materials that have adsorption efficiency such as clay to prevent contamination of environment. This research mainly focuses on investigate the adsorption capacity of copper on clays. Copper (Cu) will greatly affect the organism [1] whether it is human beings, animals or plant. Direct impact, such as human contact with copper directly, it can get into the body and get sick or maybe to death. Indirect impacts such as human consumption of fish containing copper residue may make sick or maybe to death. This research investigated the adsorption efficiency of the various types of clay which have different clay mineral compositions. Three types of adsorbents are kaolinite, illite and montmorillonite clays [2][3]. The heavy metal used in this study is only copper. The batch sorption technique was used as a method to evaluate the adsorption capacity.

MATERIALS USED

Three types of adsorbents are kaolinite (Fig.1), illite (Fig.2) and montmorillonite (Fig.3) clays. Table 1 summarizes the chemical analysis of these clays by XRF technique. Kaolin clay consists of layers of silica arranged alternately with layers of alumina. The chemical composition is $\text{Al}_2\text{Si}_2\text{O}_5(\text{OH})_4$. The specific gravity is 2.42 and the chemical analysis is given in Table 1. Illite clay

consists of a two layers of silica floor with alumina layer and in each unit there is an ion of potassium inserted. The chemical composition is $(\text{KH}_3\text{O})(\text{AlMgFe})_2(\text{SiAl})_4\text{O}_{10}[(\text{OH})_2(\text{H}_2\text{O})]$. The specific gravity is 2.60. Montmorillonite clay, its structure like an illite group, but in the structural layer there is a water molecule inserted. Most of the cations are found to be calcium, magnesium, iron and sodium. This clay has the ability to swell in water well [4]. Figures. 4 to 6 display the SEM photographs of clays with expansion rate of 1,000 times. The chemical composition is $(\text{Na,Ca})(\text{Al,Mg})_6(\text{Si}_4\text{O}_{10})_3(\text{OH})_6 \cdot n\text{H}_2\text{O}$. The specific gravity is 2.0. In this research, copper (Cu) was selected to represent the range of the common heavy metal and prepared in the form of the solution to be the adsorbates. The stock solutions of $\text{Cu}(\text{NO}_3)_2$ were dissolved in the deionized water to obtain the preferred initial concentration of solution. The chosen initial concentrations of the heavy metal solutions were 500, 1,000, 2,000, 4,000 and 6,000 ppm. The properties of the solutions are presented in Table 2.

Table 1 Chemical Analysis by XRF Technique

Type	Kaolinite	Illite	Montmorillonite
SiO ₂	58.0	79.5	56.80
Al ₂ O ₃	31.0	14.5	15.10
TiO ₂	<0.10	<0.10	-
Fe ₂ O ₃	<0.5	0.6	9.79
Na ₂ O	2.0	0.65	2.01
K ₂ O	0.5	5.0	-
CaO	0.3	0.1	2.81
MgO	0.5	<0.02	4.61
LOI	11.0	3.5	-

Table 2 Properties of copper solution

Property	Copper (II) Nitrate
Formula	$\text{Cu}(\text{NO}_3)_2$
Molecular (g/mol)	241.60
Density (g/cm ³)	2.32
Solubility (g/100cm ³)	137.80



Fig. 1 Illite clay.



Fig. 2 Kaolinite clay.



Fig. 3 Montmorillonite clay.

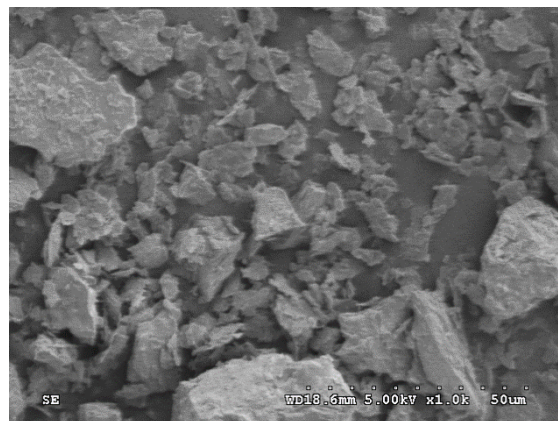


Fig. 4 SEM photograph of illite clay.

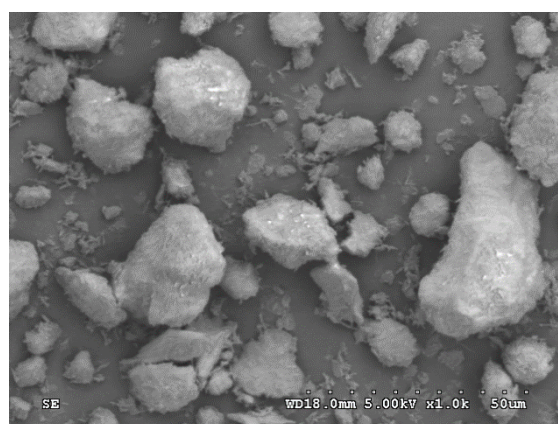


Fig. 5 SEM photograph of kaolinite clay.

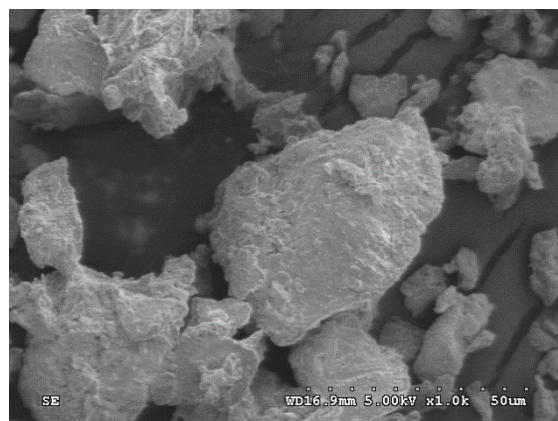


Fig. 6 SEM photograph of montmorillonite clay.

EXPERIMENTAL WORK

Batch Sorption Test

The procedures of the batch testing begin by mixing 2.5g of each clay with 50cm³ of copper solution in bottles. Next, the mixtures were shaken at a velocity rate of 130 cycles per minute using a

horizontal shaker. After a defined time, soils were percolated from the copper solution using a 0.45µm filter. The solutions were then diluted by mixing them with 1% nitric acid. These steps were performed at a room temperature of 30°C. The diluted solution concentrations were finally determined using an Atomic Absorption Spectrometer (Fig.7). Batch tests were repeated three times in each experiment for high accuracy of the results. The purposes of doing batch test are to identify an equilibrium time and to evaluate the adsorption isotherm.

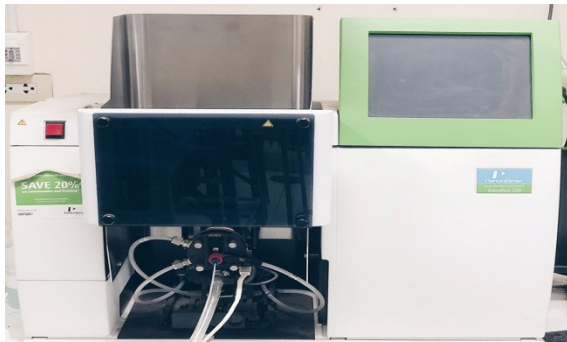


Fig 7. Atomic Adsorption Spectrometer.

Determine the Adsorption Equilibrium Time

The equilibrium time is the time adsorption takes to reach an equilibrium state. To determine the equilibrium time, the batch method was performed with only montmorillonite clay various lengths of time, i.e. 3, 6, 12, 24, 48, 72 and 120 hours, with a concentrations of copper solution at 6,000 ppm. By employing this method, the concentrations of solutions at any time were known, and so the adsorption equilibrium time could be established.

Adsorption Capacity

The percentage of adsorption was calculated by using equation (1).

$$\%adsorption = \frac{(C_0 - C_{eq})}{C_{eq}} \times 100 \quad (1)$$

Where: C_0 and C_{eq} are the equilibrium concentration of adsorbate in copper solution before and after adsorption. The amount of copper solution that adsorbed by the adsorbent was calculated by equation (2).

$$q = \frac{(C_0 - C_{eq})V}{M} \quad (2)$$

Where: q is amount of copper solution that adsorbed by the adsorbent, C_0 and C_{eq} are the equilibrium concentration of adsorbate in copper solution before and after adsorption, V is the volume of copper solution and M is the volume of clay.

Adsorption Isotherm

When the data between C_{eq} and q are plotted, one can obtain what is called the adsorption isotherm. The most commonly used models are the Langmuir and Freundlich isotherms. The Langmuir adsorption isotherm has been widely applied to many adsorption processes, specifically those assuming monolayer adsorption on the adsorption surface. The Langmuir isotherm is defined as:

$$q = \frac{\alpha\beta C_{eq}}{1 + \alpha C_{eq}} \quad (3)$$

Where: α is the Langmuir constant, related to the bonding energy between the adsorbed ion and the adsorbent (L/mg) and β is the maximum adsorption capacity (mg/g). Figure 8 shows the relationship between C_{eq} and C_{eq}/q values of the Langmuir isotherm.

The Freundlich isotherm is the most common isotherm model, used to describe physical adsorption in a solid-liquids system and is defined as follows:

$$q_e = K(C_{eq})^{1/n} \quad (4)$$

Where: q_e is the amount of adsorbed heavy metal per unit weight of soil at equilibrium (mg/g), K is Freundlich constant (mg/g) and $1/n$ is the adsorption intensity (dimensionless). Figure 9 shows the relationship between Log C_{eq} and Log q values.

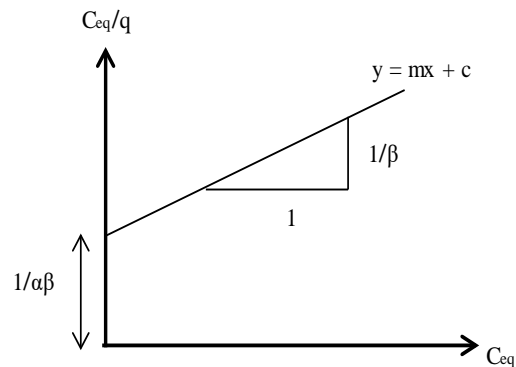


Fig 8. The relationship between C_{eq} and C_{eq}/q values of the Langmuir isotherm.

RESULTS AND DISCUSSIONS

Equilibrium Time

To find the effect of contact times, the copper adsorptions in montmorillonite clay were investigated at different times. Figure 10 shows the percentage of the adsorption of Cu solutions at any elapsed time. It can be seen that the percentage of adsorption increases rapidly, especially during the first periods of 20 hours. After that, it increases

slowly, until reaching a constant within 70 hours. After that, the montmorillonite clay were saturated, as a result of the accumulation of the copper on the surface. It can be concluded that the equilibrium times of Cu by montmorillonite clay, occurred at 70 hours.

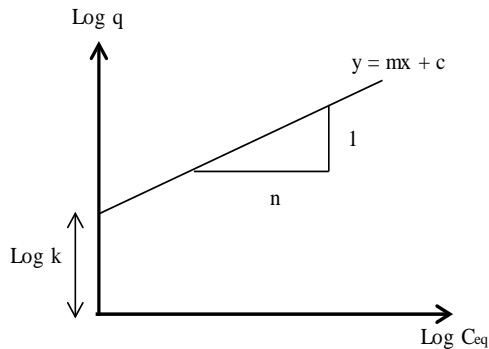


Fig 9. The relationship between Log Ceq and Log q values of Freundlich isotherm.

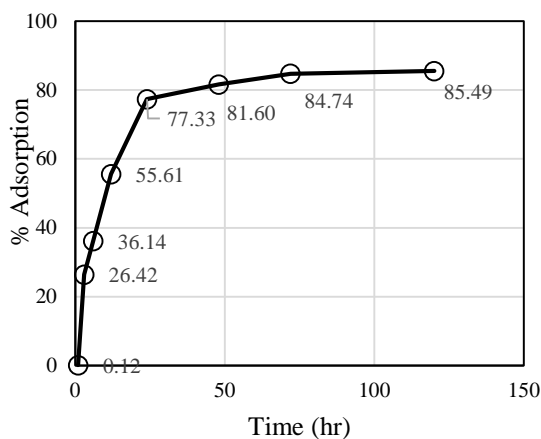


Fig 10. Adsorption of copper solution with montmorillonite clay at various times.

Adsorption Capacity

The batch sorption test with illite, kaolinite and montmorillonite clays were performed at various initial concentrations of 500, 1,000, 2,000, 2,000, 4,000 and 6,000 ppm. The relationship between percentage of adsorption and initial concentrations of are presented in Figs.11 and 12. Montmorillonite clay shows the beneficial trend in the adsorption capacity of heavy. At a particular initial concentration, the adsorption capacity of montmorillonite is higher than illite and kaolinite approximately 10 and 15 time, respectively. The adsorption capacity of clays was in the order of montmorillonite > illite > kaolinite.

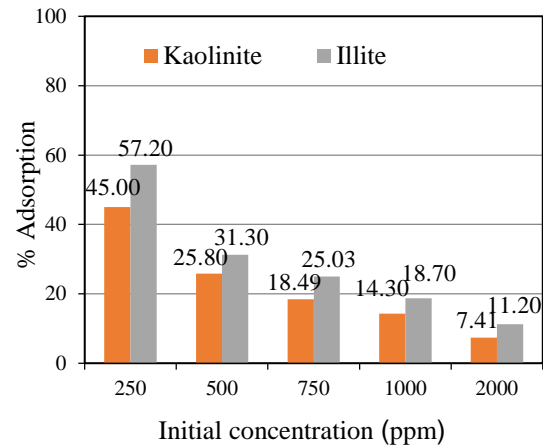


Fig 11. Adsorption of copper solution with kaolinite and illite clays.

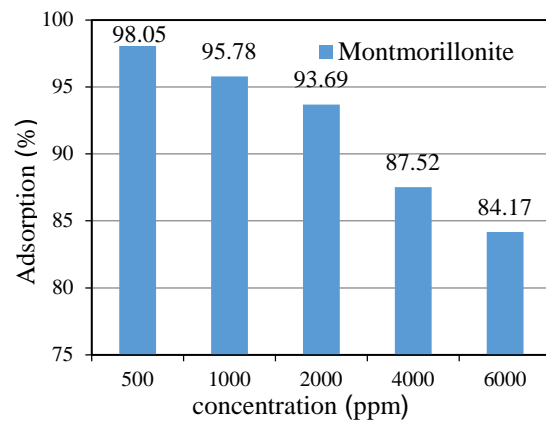


Fig 12. Adsorption of copper solution with montmorillonite clay.

Adsorption Isotherm

The amounts of adsorbed copper, q and the equilibrium concentrations, C_{eq} are plotted in Figs. 13 and 14. These called the adsorption isotherm. It can be seen that the amount of adsorption increased with equilibrium concentrations. The increasing rate of the amount adsorbed tends to gradually decrease, and converge to the maximum value. The Langmuir and Freundlich adsorption isotherms were adopted to describe the isotherm. Figures 15 to 17 show the Langmuir isotherm and figs. 18 to 20 show the Freundlich isotherm of all clays. Adapted from Figs. 8 and 9, the important parameters of both models can be calculated. Tables 3 and 4 show the parameters of the Langmuir and Freundlich isotherms. Higher values of R^2 (almost all higher than 0.95) indicate that both models can accurately describe the adsorption isotherm. The β -parameters of the Langmuir isotherm represent the maximum adsorption capacity of clays. It can clearly be seen in Table 3 that the montmorillonite displayed the highest

adsorption capacity, while kaolinite provided the lowest adsorption capacity. The important factor affecting the value of β was specific surface area of illite, kaolinite and montmorillonite, which can be evaluated using SEM picture. Figures 4 to 6 display photographs of samples using SEM at 1,000x magnification. As shown in Fig. 6, the surfaces of the montmorillonite are rougher and larger than illite and kaolinite.

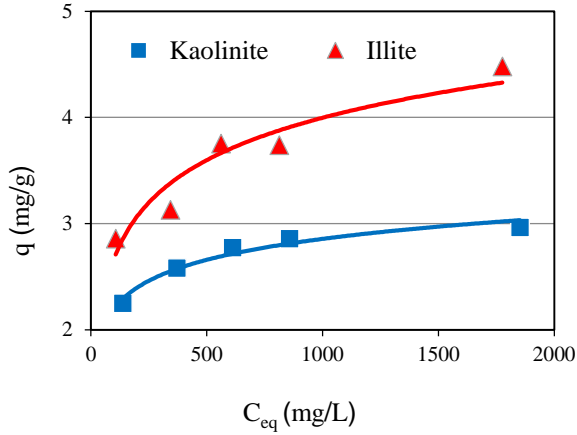


Fig 13. Isotherm graph of kaolinite and illite clays.

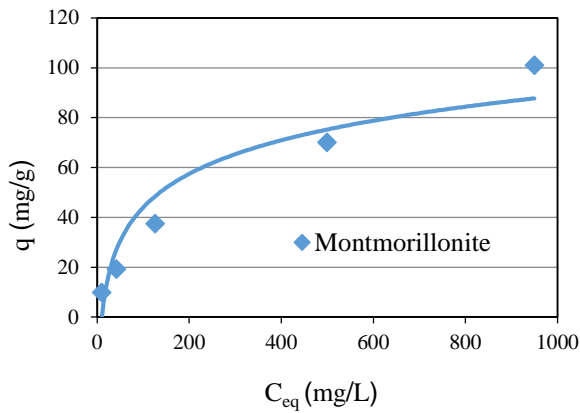


Fig 14. Isotherm graph of montmorillonite clay.

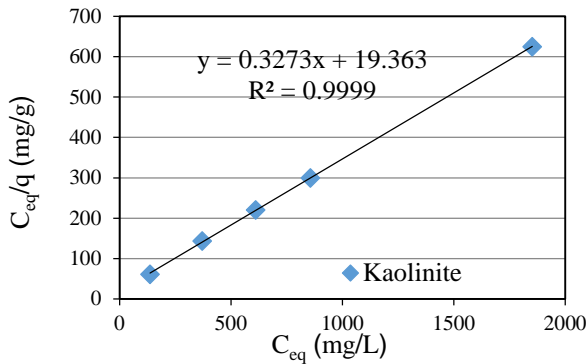


Fig 15. Langmuir isotherm of kaolinite clay.

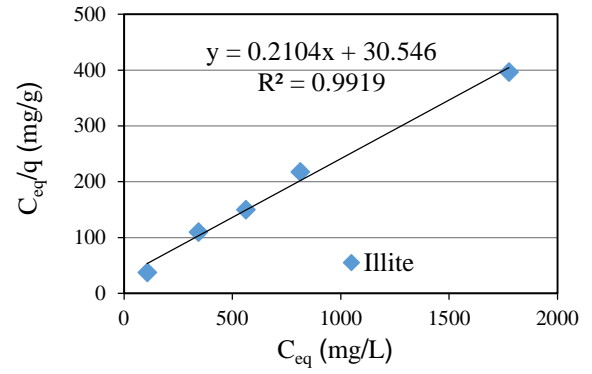


Fig 16. Langmuir isotherm of illite clay.

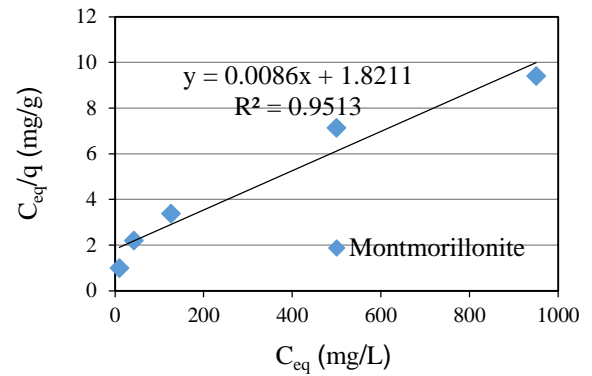


Fig 17. Langmuir isotherm of montmorillonite clay.

Table 3 Parameters of Langmuir adsorption isotherm

Clay	α	β	R^2
Kaolinite	1.69×10^{-2}	3.06	0.999
Illite	0.69×10^{-2}	4.75	0.992
Montmorillonite	0.47×10^{-2}	116.28	0.951

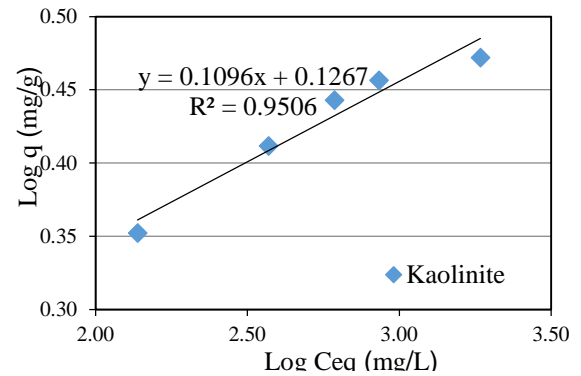


Fig 18. Freundlich isotherm of kaolinite clay.

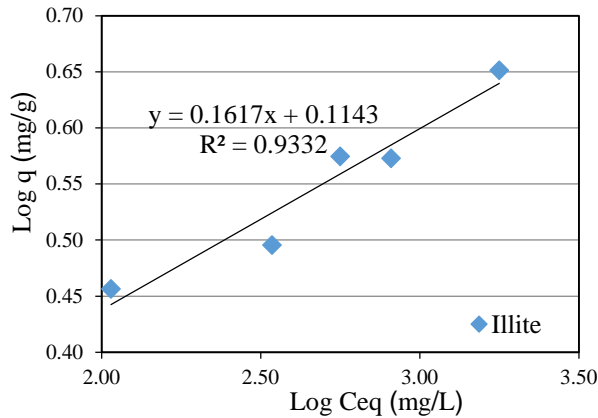


Fig 19. Freundlich isotherm of illite clay.

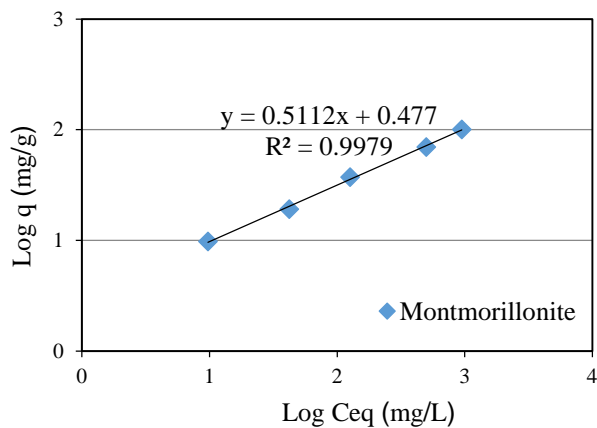


Fig 20. Freundlich isotherm of montmorillonite clay.

Table 4 Parameters of Freundlich adsorption isotherm

Clay	k	1/n	R ²
Kaolinite	1.32	0.11	0.951
Illite	1.30	0.16	0.933
Montmorillonite	2.99	0.51	0.998

CONCLUSIONS

In this study, the adsorption capacity of Cu on three types of clay were investigated. Three types of adsorbent were used are kaolinite clay, illite clay and montmorillonite clay. The results indicated that the adsorption reaches the equilibrium time within 70 hours. The adsorption capacity increased with increasing equilibrium concentration. Langmuir and Freundlich isotherm models can favorable describe the adsorption. Montmorillonite clays have the best adsorption efficiency, followed by illite clay and kaolinite clay, respectively. The kaolinite provided the lowest adsorption capacity because the specific surface area and roughness

were the important factors which affected on the adsorption. Montmorillonite clay can adsorb all of copper solution at 500, 1,000 and 2,000 ppm. But it can adsorb 94.96% and 84.17% at 4,000 and 6,000 ppm.

ACKNOWLEDGEMENTS

This research was support by Department of Civil Engineering, Faculty of Engineering, Khon Kean University.

REFERENCES

- [1] Zhiqiang W., Chen H., Yi X., Kang W., Yifei L., Lihui F., and Silu M., Spatial distribution and sources of heavy metals in natural pasture soil around copper-molybdenum mine in Northeast China., *Ecotoxicology and Environmental Safety.*, Vol 154., 2018, pp 329-336.
- [2] Di L., Mansour E., and Luke B., Investigating the settling behaviour of saline tailing suspensions using kaolinite, bentonite, and illite clay minerals., *Powder Technology.*, Vol 326., 2018, pp 228-236.
- [3] Joanna M., Marta K., AnnaBialk B., Wojciech M., Jolanta K., Piotr S., Richard P., Oliver K., and Ute K., Column and batch tests of sulfonamide leaching from different types of soil., *Journal of Hazardous Materials.*, Vol 260, 2013, pp 468-474.
- [4] Tetsuo Y., YukariImotoa K., Masayuki S., Kazuo H., Ute K., and Hirofumi S., Effects of colloidal particles on the results and reproducibility of batch leaching tests for heavy metal contaminated soil ., Vol 57., Issue 5, 2017, pp 861-871.

ADSORPTION CAPACITIES OF HEAVY METALS TO SAND MIXED WITH SODIUM BENTONITE USING BATCH SORPTION TESTS

¹Yuttapong Chaipanha, ²Pongsakorn Punrattanasin, ³Dolrerdee Hormdee and ⁴Chinawat
^{1,2,3,4}Muktabhant Faculty of Engineering, Khon Kaen University, Thailand.

ABSTRACT

Heavy metals are some of the most dangerous materials. A method to reduce the occurrence of heavy metals involves the adsorption of materials by using absorbents. This research focused on the adsorption of copper, nickel, and zinc to sand when mixed with different ratios of sodium bentonite. Batch sorption tests were performed to investigate adsorption behavior. The purpose of using batch tests was to find the adsorption capacities of the sand mixed with bentonite. The test results show that the adsorption of heavy metals to sand increases with the amount of sodium bentonite. Sand benefited from the bentonite. Adsorption capacities were ranked as follows: copper > nickel > zinc.

Keywords: Heavy metals, Sodium bentonite, Batch sorption test

INTRODUCTION

Today's society is competitive and progressive in many sides, both technology and economic growth. As a result, the expansion and establishment of industrial plants are increased. The establishment of more factories. These plants are the main cause of pollution in various forms such as air, water, and soil, especially waste water. When someone consumes a contaminated water source, a heavy metal solution consequently centers into the body that may cause a health problem. Therefore, the plant needs to protect these heavy metals [1, 2]. One method to reduce the occurrence of heavy metals is to use septic pond. In the septic pond construction, absorbent materials are needed to absorb heavy metals in the bottom of the pond. One needs to prevent the toxins moving out from the wastewater into the groundwater below. There are many recent research works [4] on the adsorption capacity of heavy metals by various soils. It was shown that clay was the most efficient adsorption material. In this research, sodium bentonite, one type of clay, is then selected and used to mix with sand with various mixing ratios. The main objective of this study is to evaluate the beneficial effect of bentonite in the improvement of the adsorption capacity to the sand.

MATERIALS USED

Adsorbent

The material used as an adsorbent was local sand collected from Khon Kaen Province that is located in the upper part of Northeastern region of Thailand. It was excavated at a depth of 50 cm from the soil surface. The sand was dried at a temperature

of 110° C for 48 hours and were sieved through sieve No.16. It can be classified by the Unified Soil Classification System (USCS) as Clayey Sand (SC). Basic and engineering properties of the sand sample are tabulated and shown in Table 1.

Additional Materials

Because clay has the highest adsorption of heavy metals, the additional material used to mix with the sand for improve the adsorption capacity in this study was sodium bentonite, a one kind of clay. The sodium bentonite was replaced with the sand at the amount of 0, 10, 20, 30 and 40% by weight. The composition of the mineralogical and chemical of sand and sodium bentonite determined by X-Ray Fluorescence (XRF) are tabulated in Table 2. Figures. 1 and 2 display the SEM photographs of sand and the bentonite with expansion rate of 500 times, respectively.

Table 1 Properties of sand

Properties	Sand
Soil classification (USCS)	SC
Specific gravity	2.62
Natural dry unit weight (kN/m ³)	16.30
Natural water content (%)	5-12
Optimum moisture content (%)	10.0
Maximum dry unit weight (kN/m ³)	19.1
Coefficient of Permeability (cm/s)	1.46 x 10 ⁻⁵
Specific surface area (S _{BET}), m ² /g	54
Micropore volume (V _{DR}), cm ³ /g	0.021
Total pore volume (V _T), cm ³ /g	0.11
Average pore diameter (D _P), nm	8

Table 2 Compound composition (% by weight)

Items	Sand	Bentonite
Silica	99.80	56.80
Magnesia	0.10	4.61
Alumina	0.04	15.10
Iron Oxide	0.02	9.79
Lime	0.02	2.81
Sodium	-	2.01

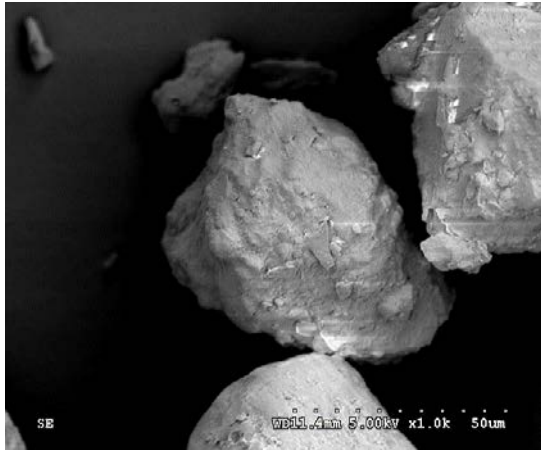


Fig. 1 SEM photograph of sand

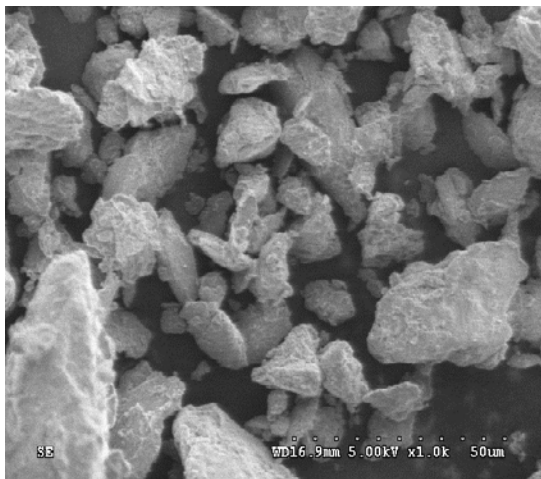


Fig. 2 SEM photograph of bentonite

Heavy metal solutions

Heavy metals chosen as the adsorbed materials in this study were Cu, Ni and Zn. Selection of heavy metals was based on its low toxicity, easily found in all areas and commonly discharged from various industries. They were prepared by dissolving Copper Nitrate ($\text{Cu}(\text{NO}_3)_2$), Nickel Nitrate ($\text{Ni}(\text{NO}_3)_2$) and Zinc Nitrate ($\text{Zn}(\text{NO}_3)_2$) in distilled water. In pilot tests, the solutions were varied with concentrations of 500, 1,000, 1,500, 2,500, 3,500, 4,500 and 6,000

ppm. The purpose of varying the initial concentrations is to obtain a suitable concentration for sand and bentonite in the next series. Finally, the chosen initial concentration of the heavy metal solutions in this study was 6,000 ppm. Table 3 summarized properties of heavy metals.

Table 3 Properties of heavy metal solutions

Property	Nickel (II) Nitrate	Copper (II) Nitrate	Zinc (II) Nitrate
Formula	$\text{Ni}(\text{NO}_3)_2$	$\text{Cu}(\text{NO}_3)_2$	$\text{Zn}(\text{NO}_3)_2$
Molecular (g/mol)	290.80	241.60	297.50
Density (g/cm ³)	2.05	2.32	2.06
Solubility (g/100cm ³)	94.20	137.80	184.30

EXPERIMENTAL PROCEDURE

Batch sorption test

The procedures of the batch sorption testing began by mixing 2.5 g of mixed sample with 50 cm³ of heavy metal solutions in bottles. Next, the mixtures were shaken at a velocity rate of 150 cycles per minute using a horizontal shaker (Fig.3). After a defined time, solid particles were percolated from the heavy metal solutions by using a 0.45 μm filter. Then the solutions were diluted by mixing them with 1% nitric acid (HNO_3). These steps were performed at a room temperature of 25 °C. Finally, the diluted solution concentrations were determined using an Atomic Absorption Spectrometer (AAS) with the flame method. Figure 4 shows the AAS machine.

Equilibrium time of adsorption determination

The equilibrium time of adsorption is the time adsorption takes to reach an equilibrium state. To determine the equilibrium time, the batch sorption method was performed at various lengths of time, i.e. 1, 3, 5, 12, 24, 48, 72, and 120 hours, with concentrations of heavy metal solutions at 6,000 ppm. By employing this method, the concentrations of solutions at any time were known, and then the adsorption equilibrium time could be established.

Volume adsorption determination.

Determination of adsorption capacity of heavy metals is based on the amount of heavy metals remaining in the solution. The remaining concentration is then used to convert the percentage of adsorption by using eq.(1).

$$\% \text{ adsorption} = \frac{(C_0 - C_r)}{C_0} \times 100 \quad (1)$$

Where: C_0 is an initial concentration and C_r is the remaining concentration in the solution.



Fig. 3 shaker

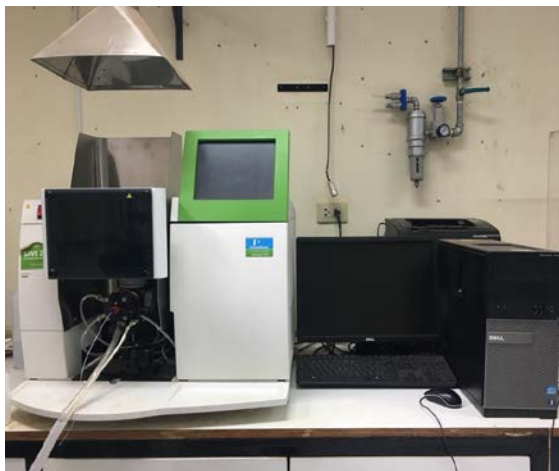


Fig. 4 Atomic Absorption Spectrophotometer (AAS)

Effect of bentonite content on the adsorption capacity of sand

The sodium bentonite was mixed with sand with different contents. The bentonite contents were starting from 10% up to 40% by weight. Heavy metals used in the experiment were the same as in the previous section. A constant mass of oven soil powder of 2.5g, percentage of bentonite by weight of sand and 50 mg/L of metal solution were added into a set of 120 ml plastic bottles. The soil solution ratios

were then shaken at 130 rpm for 48 hours by using a horizontal shaking machine. After that, the experiment was the same as batch adsorption test.

RESULT AND DISCUSSION

Suitable initial concentration of heavy metals

Varieties of initial concentration of heavy metal solutions were well prepared in laboratory. The chosen initial concentrations of 500, 1,000, 1,500, 2,500, 3,500, 4,500 and 6,000 ppm were then tested. The percentage of adsorption for all Cu, Ni and Zn are summarized and shown in Table 4 and Fig.5. The results show that the initial concentrations up to 3,500 ppm, Cu can completely adsorb by mixed sample. An initial concentration of 6,000 ppm was then chosen for the next series of batch sorption test.

Table 4 the adsorption capacity at different initial concentrations

Initial Concentration (ppm)	% Adsorption		
	Cu	Ni	Zn
500	100.00	71.17	85.23
1,000	100.00	82.55	98.45
1,500	100.00	78.49	100.00
2,500	100.00	76.09	100.00
3,500	100.00	78.33	90.66
4,500	92.53	73.44	91.38
6,000	85.10	68.95	86.03

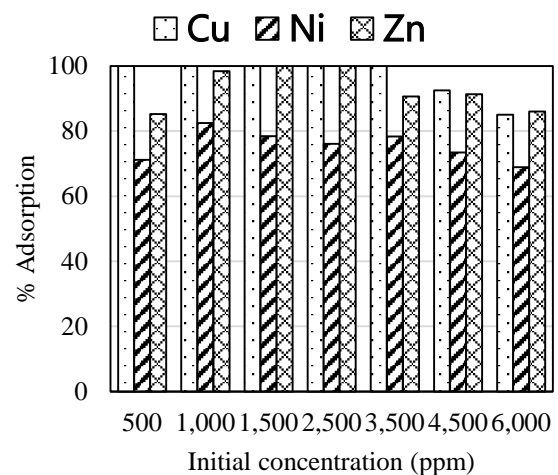


Fig. 5 The comparison of adsorption capacity for heavy metals at different initial concentrations

Equilibrium time of adsorption

To find equilibrium time of adsorption, a series of batch adsorption test in sand with sodium bentonite were investigated at different times.

Figures 6 to 8 show the volume adsorption of Cu, Ni, and Zn solutions at any elapsed time. It can be seen that the volume adsorption increase rapidly, especially during the first periods of time (0-5 hours). After that, they increase slowly. The adsorption of Cu, Ni and Zn by sand mixed with bentonite finally reached to equilibrium at about 48 hours. Unlike the others soils, the equilibrium occurs approximately only within 3 hours [4].

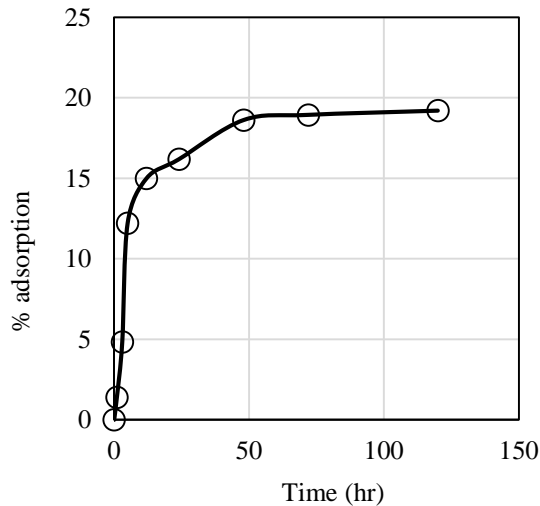


Fig. 6 the equilibrium time for Cu.

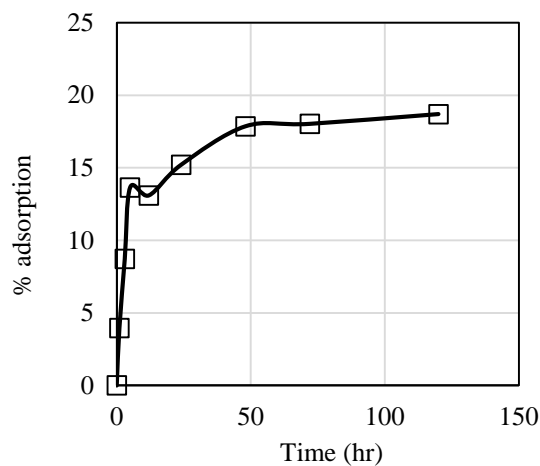


Fig. 7 the equilibrium time for Ni.

Effect of bentonite content on the adsorption capacity

The effect of the bentonite content on the adsorption capacity of Cu, Ni and Zn are presented in Figs. 9 to 11, respectively. As presented in Figs. 9 to 11, bentonite can dramatically improve the adsorption capacity of sand. The adsorption capacity increased linearly with increasing amount of bentonite content. While using 10% of sodium

bentonite in the replacement, the results in Table 5 showed that the adsorption capacity of Cu, Ni and Zn are 16%, 19% and 17%, respectively. In case of Cu, the adsorption capacity of sand reached 46% of adsorption when 40% of bentonite was used in the replacement. The same tends of results were also found with Ni and Zn. Table 6 summarizes the calculated percentage of adsorption improvement when adding the sodium bentonite to sand. It can be seen that all the heavy metals especially Zn and Cu the adsorption capacity can improve up to 700% compared to pure sand by only adding 40% of bentonite to the sand. From Table 6 it can be concluded that the percentage of adsorption improvement when adding the bentonite to sand were ranked as follows: zinc > copper > nickel.

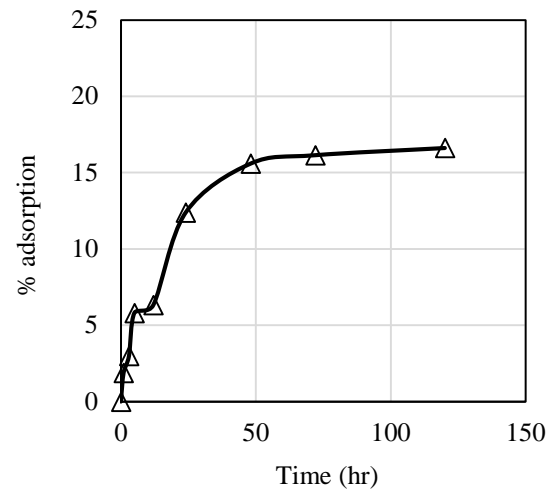


Fig. 8 the equilibrium time for Zn.

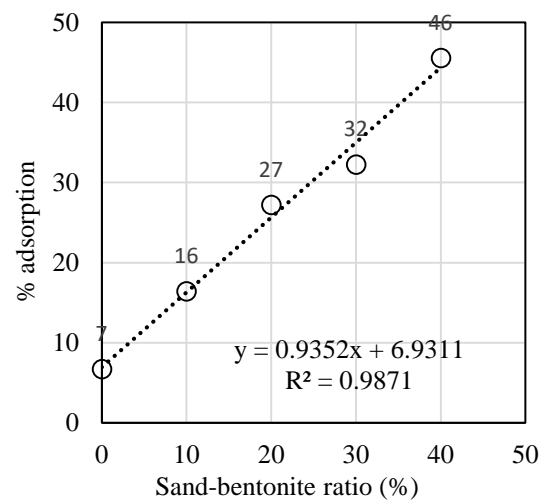


Fig. 9 Percentage of adsorption for Cu.

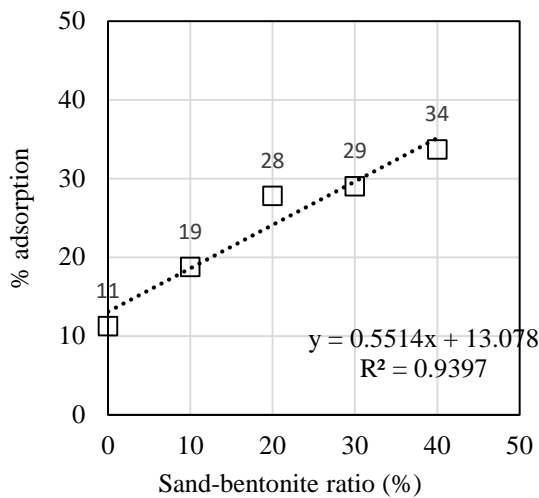


Fig. 10 Percentage of adsorption for Ni.

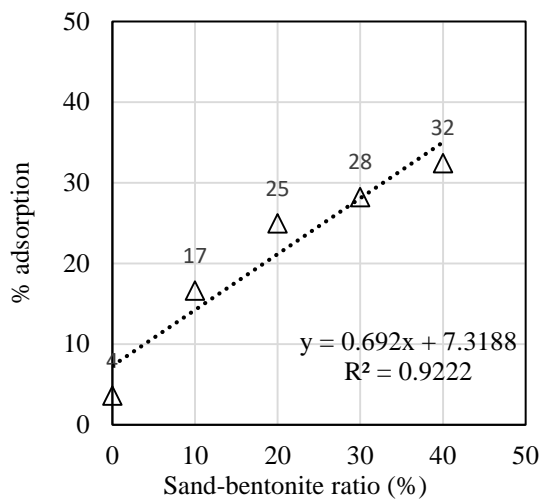


Fig. 11 Percentage of adsorption for Zn.

CONCLUSIONS

This research presents the adsorption capacity of heavy metals on sand which can be found in common everywhere. A possible method of improving the adsorption to sand is proposed by adding and mixing the sodium bentonite content into the original sand. From batch sorption test, it was found that the adsorption reaches the equilibrium time at about 48 hours for the initial concentration of Cu, Ni and Zn of 6,000 ppm. Unlike the others soils, the equilibrium occurs approximately only within 3 hours. The adsorption capacity increased linearly with increasing bentonite content. The adsorption capacity of sand reached 46%, 34% and 32% of adsorption when 40% of bentonite was used in the

replacement in cases of Cu, Ni and Zn, respectively. Adsorption capacities were ranked as follows: copper > nickel > zinc but the percentage of adsorption improvement when adding the bentonite to sand were ranked as follows: zinc > copper > nickel.

Table 5 Percentage of adsorption for Cu, Ni and Zn

Sand-bentonite ratio	% Adsorption		
	Cu	Ni	Zn
0	7	11	4
10	16	19	17
20	27	28	25
30	32	29	28
40	46	34	32

Table 6 The percentage of adsorption improvement when adding the bentonite to sand

Sand-bentonite ratio	Percentage of improvement		
	Cu	Ni	Zn
10	128.57	72.27	325.00
20	285.71	154.54	325.00
30	357.14	163.63	525.00
40	557.14	209.09	700.00

ACKNOWLEDGMENT

This research was funded by Department of Civil Engineering, Faculty of Engineering, Khon Kaen University.

REFERENCES

- [1] Eveliina Repo, Jolanta K. Warchol, Amit Bhatnagar, and Mika Sillanpää, Heavy metals adsorption by novel EDTA-modified chitosan-silica hybrid materials, *Journal of Colloid and Interface Science* 358, 2011, pp. 261-267.
- [2] Sariem Panha and Punrattanasin Pongsakorn. Adsorption of Copper, Zinc, and Nickel Using Loess as Adsorbents. *Polish Journal of Environmental Studies* No. 24, 2015, pp. 319-326.
- [3] Shengtao Xing, Meiqing Zhao, and Zichuan Ma, Removal of heavy metal ions from aqueous solution using red loess as an adsorbent, *Journal of Environmental Sciences* 23(9), 2011, pp. 1497-1502
- [4] Sangiumsak Noppadol and Punrattanasin Pongsakorn. Adsorption Behavior of Heavy Metals on Various Soils. *Polish Journal of Environmental Studies* No. 23, 2014, pp. 853-865.

OPTICAL RESPONSE ANALYSIS OF InGaAs HIGH-ELECTRON-MOBILITY TRANSISTORS WITH A 1550-nm WAVELENGTH FEMTOSECOND PULSE LASER

¹Taiki Kozakai, ²Itsuki Takagi, ³Shun Nakajima, and ⁴Hirohisa Taguchi

^{1,2,3,4}Department of Electrical and Electronic Engineering, School of Engineering, Chukyo University, 101-2
Yagoto Honmachi, Shouwa-Ku, Nagoya City, Aichi, Japan

ABSTRACT

InGaAs is known as a material system with high electron mobility derived from InAs and can be formed by metal organic chemical vapor deposition. The base material substrate is InP and is formed by controlling the composition ratio of In and Ga to lattice match with this InP. The bandgap energy E_g of InGaAs is 0.87 eV, and photoelectric conversion of 1550-nm light, which is a communication wavelength band, can be executed. Therefore, it is now used as a detector material in optical communication technology. In this study, we investigated the photoresponsive properties of InGaAs high-electron-mobility transistors (HEMTs) with simultaneous utilization of photoresponse characteristics and high-frequency response characteristics of this InGaAs crystal. A 1550-nm wavelength femtosecond pulse laser (with a pulse width of 100 fs and a period of 50 MHz) was coupled with DC light with a wavelength of 1480 nm and irradiated from the InGaAs HEMT metal electrode surface. Laser light transmitted through the side of the gate metal electrode into the device structure generates electron-hole pairs via the photoelectric effect in the InGaAs layer, and it was confirmed that the maximum drain current of 0.4 mA was reduced. A current response is detected inside the semiconductor by transporting electrons to the drain electrode side and holes to the source electrode side. Because the laser used is pulsed light, the process of generation and disappearance of electron-hole pairs was confirmed as photoresponsive properties. These results suggest that InGaAs HEMTs may function not only as electronic response devices but also as photoresponsive devices.

Keywords: InGaAs HEMT, Photoresponsive property, Photoelectric effect, Hole accumulation effect

INTRODUCTION

GaAs is an indispensable material in our current advanced information society [1]. It is used as a base material of key devices for transmitting and receiving packet communications in mobile terminals. Because GaAs is used for transmitting and receiving devices, the operating frequency has been dramatically expanded [2]. However, because of the demand for increasing amounts of information, further increases in transmission and reception speeds are required, and situations where it is difficult to use GaAs are approaching [3]. It is essential to develop new material systems. InGaAs, a ternary material, has been a subject of focus for a long time [4]. InGaAs is known as a material system with high electron mobility derived from InAs and can be formed by metal organic chemical vapor deposition [5]. The base material substrate is InP and is formed by controlling the composition ratio of In and Ga to lattice match with this InP. The bandgap energy E_g of InGaAs is 0.87 eV, and photoelectric conversion of 1550 nm light, which is a communication wavelength band, can be executed [6]. Therefore, it is now used as a detector material in optical communication technology [7].

In this study, we investigated the photoresponsive properties of InGaAs high-electron-mobility

transistors (HEMTs) with simultaneous utilization of photoresponse characteristics and high-frequency response characteristics of this InGaAs crystal. A 1550-nm wavelength femtosecond pulse laser (with a pulse width of 100 fs and a period of 50 MHz) was coupled with a DC light with a wavelength of 1480 nm and irradiated from the InGaAs HEMT metal electrode surface. Laser light transmitted through the side of the gate metal electrode into the device structure generates electron-hole pairs by the photoelectric effect in the InGaAs layer. The significance of this research is the possibility of HEMT which is an active device to be passive device.

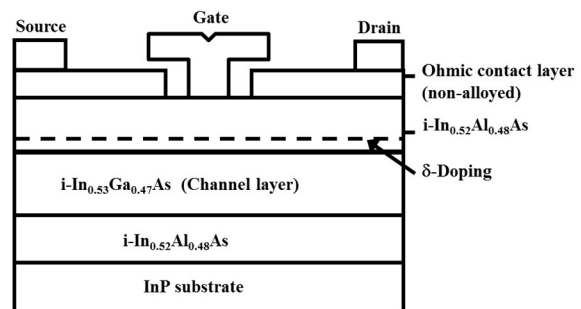


Fig. 1 Schematic cross section of a HEMT.

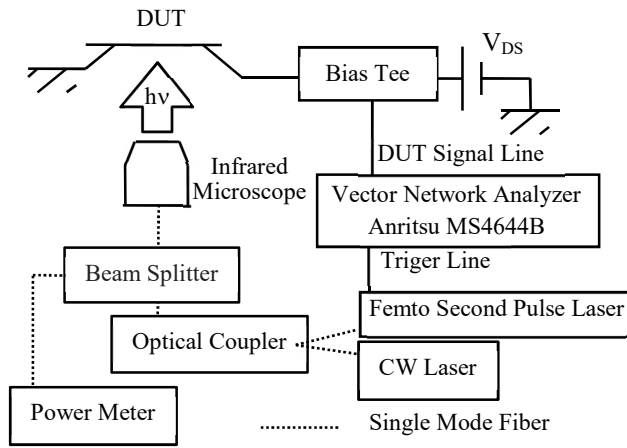


Fig. 2 Measurement block diagram.

A current response is detected inside the semiconductor by transporting electrons to the drain electrode side and holes to the source electrode side. Because the laser used is pulsed light, the process of generation and disappearance of electron-hole pairs was confirmed as photoresponsive properties. These results suggest that InGaAs HEMTs may function not only as electronic response devices but also as photoresponsive devices.

EXPERIMENTAL METHOD

Figure 1 shows the crystal structure cross section of the InGaAs-based HEMT used in this study. The current frequency band of InGaAs is at the 12-GHz level, and it is intended for satellite communication. Therefore, the mounting line was a micro split line with a coplanar structure. Figure 2 shows the measurement block diagram. An AF4B125 laser (Anritsu Corporation) was used as a direct current laser. The femtosecond pulse laser (Karma Corporation) had a pulse width of 100 fs, a period of 50 MHz, and an average output of 20 mW. These two

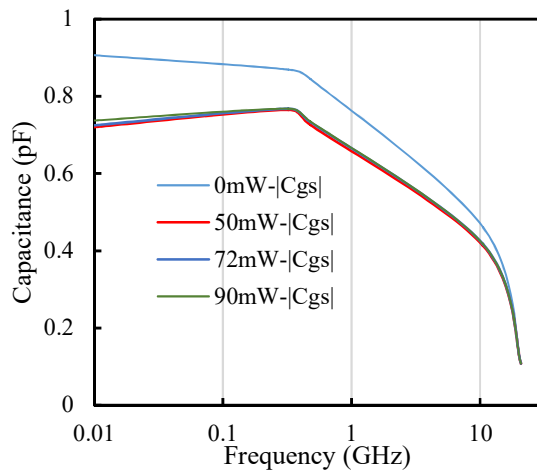
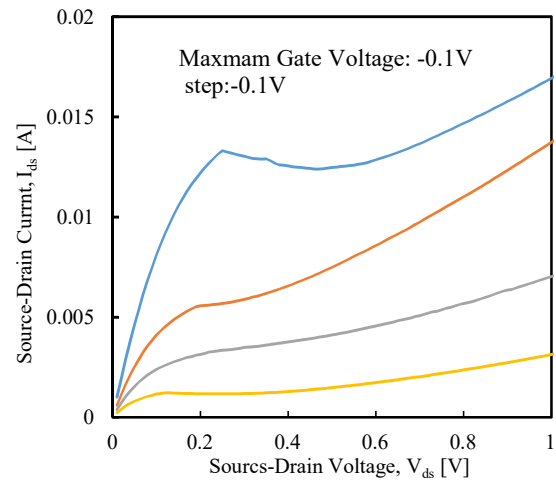
Fig. 4 Frequency dependence characteristics of the source-gate capacitance C_{GS} (left) and the gate-drain capacitance C_{DG} (right).

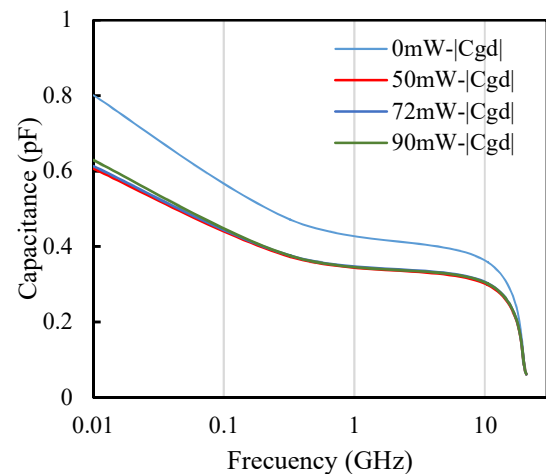
Fig. 3 DC characteristic of an InGaAs HEMT

lasers were polymerized with an optical coupler, and the light intensity was controlled by the direct light intensity. The multiplexed light was split by the optical splitter into an output of 10:90. The 10% output was monitored with a light intensity meter and the remaining 90% was converted to a parallel-plate beam via a drum lens. The incident light output was changed by CW laser. The top of the InGaAs HEMT electrode was irradiated via an aerial transition process and the photoresponsive characteristics were confirmed. For the measurement, a network analyzer at the 40-GHz level (Anritsu MS4664B) was used. Single-mode fiber was used for the light transmission path. For the high-frequency-response measurement, a 40-GHz-level adaptation system was used.

RESULTS AND DISCUSSION

DC Characteristics of InGaAs HEMTs

Figure 3 shows the DC current-voltage characteristics (IV characteristics) of the InGaAs HEMT used this time. As is clear from the IV characteristics, the HEMT used in this study is of



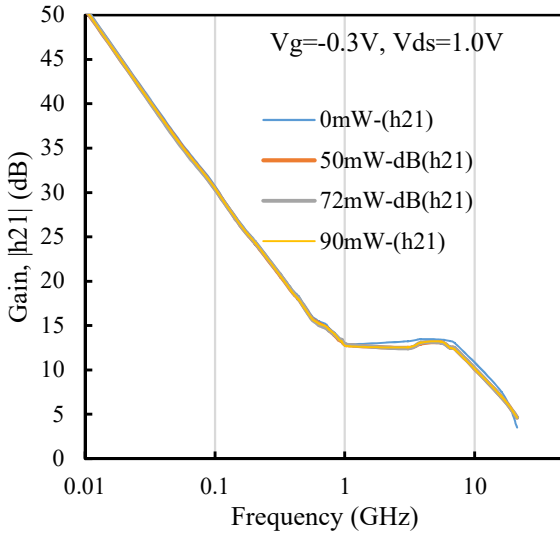


Fig. 5 Frequency dependence of the current gain before and after light irradiation.

depletion type. Although a relatively good drain current rise is seen in the linear region, the current does not exhibit a complete saturation state in the saturated region but rather a slightly rising upward characteristic. For this reason, the drain conductance G_d has a certain value or more, but the transconductance G_m has a good value of 100 S.

Confirmation and Analysis of Photoresponse Characteristics

Clear optical response characteristics were confirmed in the IV characteristics of Fig. 3. At the stage when the coupling light entered the HEMT, the drain current value was reduced by 0.4 mA at the maximum. To clarify that this lowering phenomenon is a photoresponsive characteristic, the S parameter was measured by a vector network analyzer (Anritsu MS4644B) and a parameter analysis was conducted.

Figure 4 shows the frequency dependence characteristics of the source–gate capacitance C_{GS} and the gate–drain capacitance C_{DG} . The light output was controlled by CW laser output. The output intensity was 50 mW, 72 mW, 90 mW. This is the incident light output on the top of InGaAs-HEMT. In Fig. 4, the blue line shows the frequency dependence before light irradiation and other lines show the frequency dependency during light irradiation. Slight decreases in both C_{GS} and C_{GD} induced by light irradiation can be seen. Electron–hole pairs should have been generated in the InGaAs layer by light irradiation. Photogenerated electrons are transported to the drain side together with a two-dimensional electron gas (2DEG). Figure 5 shows the frequency dependence of the current gain before and after light irradiation. There is almost no difference before and after. It is thought that the gain current was as weak as 0.4 mA at the maximum and was not reflected in

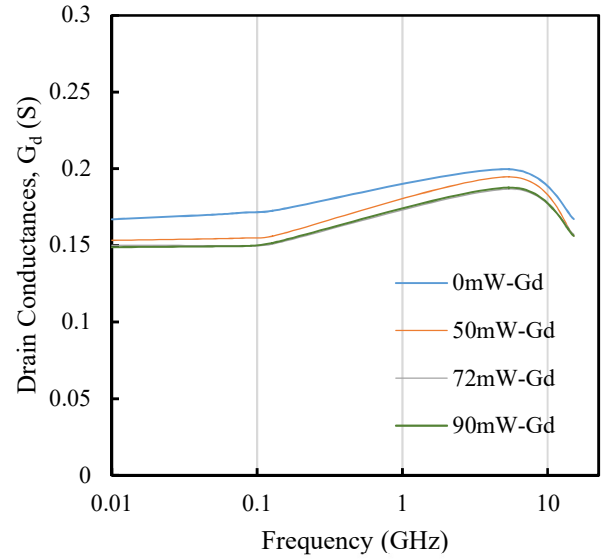


Fig. 6 Frequency dependence characteristic of the drain conductance G_d .

the h_{21} parameter.

Figure 6 shows the frequency dependence characteristic of the drain conductance G_d . A clear difference was confirmed for G_d depending on the presence or absence of light irradiation. It was confirmed that the drain conductance was lowered by light irradiation. The reason for this will be discussed below. It is known that the InGaAs layer originally has a hole accumulation effect [8]. At this time, holes are accumulated in the InGaAs between the gate and the source. The accumulated holes are recombined with a 2DEG, attenuating the amount of transferred electrons, and this attenuation is a frequency dispersion phenomenon of G_d . [9], [10]. Now, the light incident to the InGaAs layer has almost the same energy as the bandgap energy of this crystal. Electron–hole pairs are generated as photogenerated carriers within the InGaAs layer by light irradiation. At this time, electrons are transported together with a 2DEG toward the drain electrode, but holes are transported toward the source electrode and accumulate in the source–gate region. As a result, the hole surface density for recombination with the 2DEG increases and the frequency dispersion effect of G_d increases, which is considered to be confirmed by the high-frequency measurement.

CONCLUSIONS

A 1550-nm wavelength femtosecond pulse laser (with a pulse width of 100 fs and a period of 50 MHz) and DC light with a wavelength of 1480 nm were coupled to an InGaAs HEMT and irradiated from the device metal electrode surface. Semiconductor laser light penetrating into the device structure from the side surface of the gate metal electrode generated electron–hole pairs by the photoelectric effect in the

InGaAs layer, and it was confirmed that the maximum drain current of 0.4 mA was reduced. In electron-hole pairs generated by incident light, holes accumulated in the source region. It is clear from the S parameter analysis that the hole accumulation effect is due to noticeable frequency dispersion of the drain conductance. These results suggest that InGaAs HEMTs may function not only as electronic response devices but also as photoresponsive devices. From now on, we will investigate system-on-chip of photoresponsive element and signal processing element on InGaAs crystal.

ACKNOWLEDGMENTS

The authors are grateful to the Chukyo University Research Found for financial assistance with this research.

REFERENCES

- [1] M.S. Shur, Low Ballistic Mobility in Submicron HEMTs, *IEEE Electron Device Letters*, Vol. 23, Issue 9, 2002, pp. 511–513.
- [2] J.T. Aberle, S.-H. Oh, D.T. Auckland, and S.D. Rogers, Reconfigurable antennas for wireless devices, *IEEE Antennas and Propagation Magazine*, Vol. 45, Issue, 6, 2003, pp. 148–154.
- [3] Y. Yuan, Y. Fan, Z. Chen, L. Li, and Z. Yang, Ku Band 2 Watt TR Chip for Phased Array Based on GaAs Technology, *IEICE Electronics Express*, Vol. 13, Issue 7, 2016, pp. 1–6.
- [4] H. Taguchi, H. Murakami, M. Oura, T. Iida, and Y. Takanashi, Analysis of Deviation of Threshold Voltage from Hole Accumulation Model, *Japanese Journal of Applied Physics*, Vol. 45, No. 11, 2006, pp. 8549–8555.
- [5] K. Otsuki, Y. Kainuma, R. Miyashita, K. Yamanaka, and H. Taguchi, DC and RF Characteristics Fluctuation of InAlAs/InGaAs HEMTs, *International Journal of GEOMATE*, Vol. 12, Issue 34, 2017, pp. 28–31.
- [6] T. Kawasaki, K. Sugawara, A. Dobroiu, H. Wako, T. Watanabe, T. Suemitsu, V. Ryzhii, K. Iwatsuki, S. Kuwano, J. Kani, J. Terada, and T. Otsuji, InGaAs Channel HEMTs for Photonic Frequency Double Mixing Conversion over the Sub-THz Band, *Proceedings of 2015 IEEE MTT-S International Microwave Symposium (IMS)*.
- [7] J. Zhang, M.A. Itzler, H. Zbinden, and J.-W. Pan, Advances in InGaAs/InP Single-photon Detector Systems for Quantum Communication, *Light: Science & Applications*, Vol. 4, e286, 2015, pp. 1–15.
- [8] H. Taguchi, M. Kawaguchi, M. Hayakawa, Y. Nakamura, T. Iida, and Y. Takanashi, Frequency Dependence of Drain Conductance due to Hole Accumulation in InAlAs/InGaAs High Electron Mobility Transistors, *Japanese Journal of Applied Physics*, Vol. 45, Part 1, Number 6A, 2006, pp. 4960–4967.
- [9] H. Taguchi, T. Sato, M. Oura, T. Iida, and Y. Takanashi, Dependence of Carrier Lifetime of InAlAs/InGaAs High Electron Mobility Transistors on Gate-to-Source Voltage, *Japanese Journal of Applied Physics*, Vol. 47, No. 4, 2008, pp. 2858–2861.
- [10] S. Nakano and H. Taguchi, Analysis of Intrinsic Delay Time in InAlAs/InGaAs High-Electron-Mobility Transistors at Cryogenic Temperature, *Proceedings of IEEE TENCON2017*, pp. 1685–1689.

VIBRATION AND SOUND SIGNAL ANALYSIS FOR A GASOLINE ENGINE WITH LPG-INSTALLATION AND FAULT SIMULATIONS

¹Suphattharachai Chomphan, ²Theerathan Kingrattanase and ³Saereephap
^{1,2,3}Boonsit Faculty of Engineering at Sriracha, Kasetsart University, Thailand

ABSTRACT

Presently, number of vehicles and cost of gasoline have been tremendously risen, liquefied petroleum (LPG) is a prominent alternative choice of fuel because of its popularity and economical cost. However, the LPG-installation may cause some degradations of the engine efficiency. The important perceptions of the driver are the engine vibration and sound. Therefore, an analysis of vibration signals and sound signals to distinguish between LPG-modified and normal oil-usage 2,200-cc engine is essentially inevitable. It has been reviewed in the first stage of this paper. The power of signal is applied for both engines at five different engine speeds. A ten-second sample of signal has been measured with the sampling rate of 2,048 Hz. The experimental results of the analysis of vibration signals show that the power of signals of the LPG-modified engine are mostly above those of the normal oil-usage engine. As for the analysis of sound signals, the LPG-modified engine has higher power than that of normal oil-usage engine at low engine speed. Meanwhile, the normal oil-usage engine cause higher power of signals when comparing with the LPG engine at the engine speed over 1,300 rpm. In the second stage, a study of fault simulations has been reviewed. The fault simulations of butterfly valve and sparking plug have been studied. The experimental results show that the vibration of engine is directly proportional to the engine speed. Moreover, the engine faults cause significant engine vibration at the speed above 1,500 rpm for both normal gasoline and LPG modified engines. In conclusions, LPG-installation and engine faults cause degradations in engine efficiency which can be concretely evidenced by using the proposed signal processing technique.

Keywords: Engine vibration, Sound signal, Liquefied petroleum, Power of signal, Fault simulation

INTRODUCTION

Alternative sources of energy are primary importance to drive the current business and the ongoing industrial sector. Supply preparation of energy in accordance with user's need must be vitally considered. Moreover, quality of energy such as gasohol and biodiesel are very important for engine in transportation system. Furthermore, renewable energy are alternative way for the automotive industrial. However the factors of economics and the decrease of petroleum resources reinforce the current research and development of energy made from natural gas considerably.

In general, natural energy can be divided into two types. Compressed Natural Gas (CNG) which is known as the Natural Gas for Vehicle (NGV) and Liquefied Petroleum Gas (LPG) are both made from hydrocarbons. Almost all demands in Thailand, the LPG is however much more popular because its installation cost is more economical [1-3]. The number of service stations is also greater than that of NGV. Therefore, the LPG-installation engine is an interesting issue to be chosen to study in this paper.

By investigating the reviews on detection and diagnosis the faults in rotating machinery, the vibration-based techniques have been tremendously and efficiently developed. These techniques are seldom applied to gasoline or diesel engines. The application of vibration-based techniques to these engines are very burdensome due to the transient and non-stationary nature [1]. The exploitation of vibration signals of engines give much dynamic information of mechanical system condition. Many useful techniques of signal analysis have been applied as the useful methods for fault diagnosis of the engines [2]. The power spectrum, cepstrum, higher order spectrum and neural network analyses were applied in the specified induction motor fault diagnosis [4]. Power of signal has been successfully used in the previous work to compare the engine sound of LPG-modified engine [5]. As for the fault diagnosis, the discrete wavelet transform were efficiently exploited with the vibration signal of the diesel engine and the gearbox [2, 3]. The power of signal analysis; one of the powerful techniques, has been chosen to adaptively applied in the paper thanks to its low complexity and minimal time consumption

[5, 6].

Modification of the engine and also the different temperature of the combustion make the working condition of the engine changed. The problems of LPG-installation cause the engine vibration and sound both direct and indirect effects [7-10]. The vibration and sound signals are therefore investigated and analyzed to differentiate between the LPG-modified engine and the normal oil-usage engine [11, 12], because they are ones of important measurable attributes to indicate the causes or evidences of irregular conditions of engines.

In the conventional engine diagnosis, the expertise of the mechanic is used to find the cause of the engine faults. To improve the conventional approach, this research aims at discovering a suitable technique to compare the signal power of vibration and sound of the LPG-modified engine and the normal oil-usage engine. At the first stage of this study, two cases of basic normal engine and LPG-modified engine are focused. The study is limited at the personal car with gasoline engine. We basically apply the power of sound signal of speech analysis to extract the power of engine vibration and sound. We expected that these techniques are applicable that of the engine vibration and sound.

In the second stage of this study, the simulation of engine faults for both normal gasoline engine and LPG modified engine has been performed to study the characteristics of them in all conditions. Finally, the conclusions of this study has been conducted.

MATERIAL AND METHODS

In the first stage of the study, the comparison between two cases of basic normal engine and LPG-modified engine are introduced. The gasoline engine with 2,200 cc piston has been used in the study. The installation of alternative LPG system has been conducted. There were two modes of fuel supply including normal gasoline supply mode and LPG supply mode. At the beginning of these modes, the engine has been started and waited until reaching the stable period of working engine. Five various levels of engine speeds have been set at 900, 1,100, 1,300,



Fig. 1 Sensor allocation design : the first stage

1,500 and 1,700 rpm. To measure the vibration and sound signals, a number of accelerometers and microphones have been installed. The positions of these sensors are partly allocated in Fig. 1. A wireless receiver which perceives the measured vibration and sound signals has been attached to a computer notebook. The corresponding data are then recorded in a specified file format.

Power of signal calculated for engine vibration or sound is mainly applied in this paper due to its simplicity and fast calculation. The signal power is an amount of energy consumed per unit of time. This quantity is very useful to described the signal which its energy goes to infinity where this engine vibration and sound signal can be assumed to be not-squarely-summable as long as the engine does not stop running. The calculation is developed by using the sum of square of the signal samples [6, 10]. The average power of an aperiodic sequence $x[n]$ is mathematically defined as in Eq. (1).

$$P_x = \lim_{K \rightarrow \infty} \frac{1}{2K+1} \sum_{n=-K}^K |x[n]|^2, \quad (1)$$

where K is the sequence half length which extends its limit of number of samples to infinity.

The engine vibration and sound has been measured by a number of accelerometers and microphones and recorded by the G-link microstrain serial base station and a number of softwares through a host computer notebook. These infinite energy signals (called power signal) in this research have been measured and recorded with some approximately periodic sequences. Therefore this equation has been adapted with a specific length which reflects the whole vibration and sound sequences for both normal oil-usage and LPG-modified engines. Therefore this equation has been adapted with a specific length recorded in a number of iteration samples for all five various levels of engine speeds as explained earlier in previous section.

In the latter stage of the study, the simulation of engine faults for both normal gasoline engine and LPG modified engine has been conducted. In this experiment, the 1,500 cc gasoline engine has been chosen as a specimen. The LPG installation has been



Fig. 2 Sensor allocation design : the second stage

implemented by using the European standard. The LPG with injection system has been installed by experienced mechanics. To simulate [9] two faults of working conditions, the engine has been set up by the mechanics [10] as follows. Type I, the engine with butterfly valve fault has been conducted by releasing the corresponding valve out. Type II, the engine with sparking plug fault has been done by pulling the plug off. These fault simulations have been performed with both regular gasoline engine and LPG modified engine. To measure the vibration from the engine, a couple of accelerometers [1] are attached with the engine piston surface as allocated in Fig. 2.

EXPERIMENTAL DESIGNS

The experiments in this paper have been organized as two stages including the comparison of normal gasoline engine and LPG-modified engine and the simulation of engine faults. At the first stage, the study focused on the comparison between the normal gasoline engine and the LPG-modified engine by considering the extracted parameters of engine vibration and sound signals; averaged power, as described in the previous section. Thereafter, the latter study concentrated on two major engine faults (type I and type II) simulated by the experienced mechanics. The averaged power of engine vibration at various engine speeds has been investigated to differentiate all conditions of faults.

Comparison of Normal Gasoline Engine and LPG-Modified Engine

The experimental procedure for the first stage of study has been implemented as depicted in Fig. 3 [5, 13]. The accelerometers are attached at the pistons of the engine. Meanwhile, the microphone with a recording software is applied to implement the database of engine sound. The vibration and sound signals are recorded in the form of connected samples to attain the database of LPG modified engine's vibration and sound signals. The database consists of the vibration and sound signals of both conditions including normal engine and LPG-modified engine. A number of repetitions of signals were measured at the engine speeds of 900, 1,100, 1,300, 1,500, and 1,700 rpm for both engine conditions. The duration of each sample lasts 10 seconds at the sampling rate of 2,048 Hz. Subsequently, the calculation of signal's power has been conducted as described in the previous section. The signal powers, thereafter, were analyzed using comparative approach. The analysis and discussion are presented in the next section. In the final process, the conclusions have been performed. In this study, five couples of linear plots of the vibration and sound signals at different samples have been presented. The overall presentation of the averaged powers of vibration and sound signals at

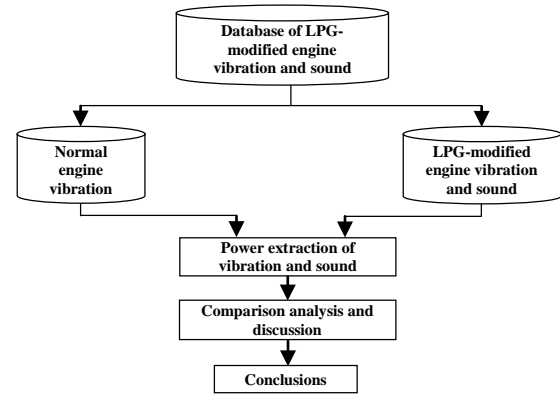


Fig. 3 Experimental procedure : the first stage

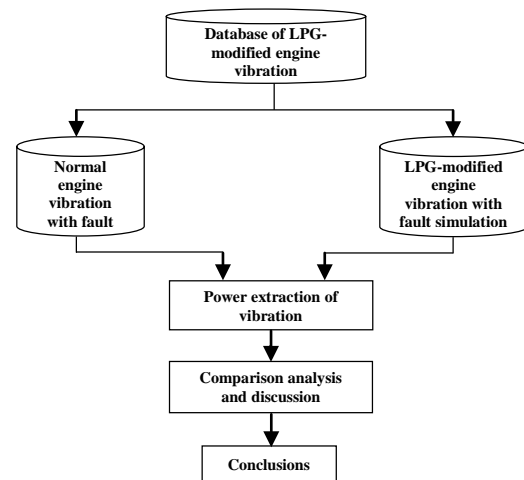


Fig. 4 Experimental procedure : the second stage

various engine speeds is also summarized.

Simulation of Engine Faults

The experimental procedure for the second stage of study has been implemented as depicted in Fig. 4 [14]. The accelerometers are attached at the pistons of the engine. The vibration signal is recorded in the form of acceleration to attain the database of LPG modified engine's vibration signal [7]. The database consists of the vibration signals of two conditions including normal gasoline engine and LPG-modified engine. A number of repetitions of vibration signals were measured at the engine speeds at 700, 900, 1,100, 1,300, 1,500, 1,700, 1,900, and 2,100 rpm for six engine conditions. The duration of each sample lasts 10 seconds at the sampling rate of 2,048 Hz. Subsequently, the calculation of signal power has been performed. The signal powers, thereafter, were analyzed using discrete signal formulation in Eq. (1) [8, 12]. Subsequently, the comparison analysis and discussion is presented. The overall presentation of the averaged powers of vibration signal at different engine speeds is finally concluded.

EXPERIMENTAL RESULTS

The experimental results consisted of two stages including the comparison of normal gasoline engine and LPG-modified engine and the simulation of engine faults.

Comparison Results of Normal Gasoline Engine and LPG-Modified Engine

In the first stage of the study, the comparisons between the normal gasoline engine and the LPG-modified engine are comprised of the comparison by using engine vibration and the comparison by using engine sound. Both of the comparisons utilize the averaged power of the corresponding signals. The experimental results are then explained, respectively.

Comparison by Using Engine Vibration

The engine vibration is investigated in this section. The normalized averaged powers of vibration signal for both engine conditions including normal oil-usage engine and LPG-modified engine are calculated and thereafter comparatively plotted in different engine speeds. All in all, figure 5 summarily presents the averaged power of vibration signal at different engine speeds. It can be noticeably concluded that the normalized averaged power of vibration signals of the LPG-modified engine are mostly above those of the normal engine with oil supply except for the engine speeds of 1,100 and 1,300 rpm.

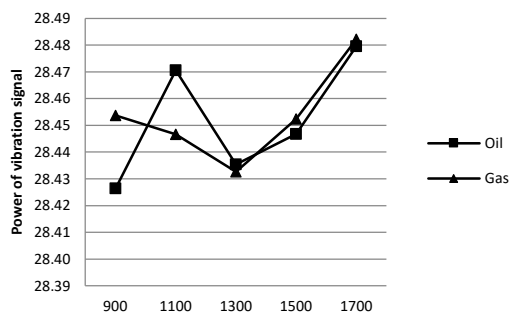


Fig. 5 Normalized averaged power of vibration signal at different engine speeds (rpm)

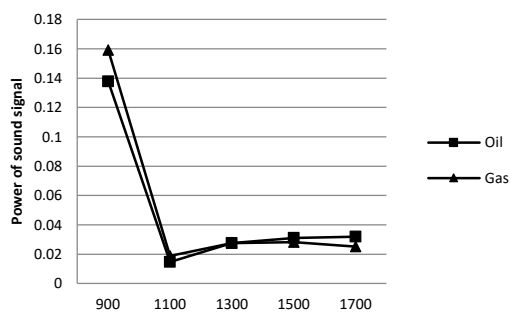


Fig. 6 Normalized averaged power of sound signal at different engine speeds (rpm)

Comparison by Using Engine Sound

After measuring the sound signals through the provided microphones, the normalized averaged power of sound signals are calculated. A comparison in power of sound signal of all engine's conditions including normal oil-usage engine and LPG-modified engine is shown. Figure 6 summarily illustrates the conclusion of these experimental results. It can be obviously observed that at the engine speeds of 900 and 1,100 rpm, LPG-modified engine has power of sound signal more than that of normal engine with oil supply. When the engine speed is increased above 1,300 rpm, the LPG-modified engine has power of engine sound signal lower than that of normal engine with oil supply.

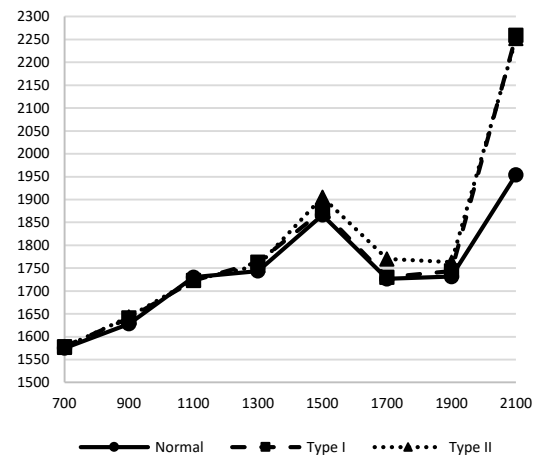


Fig. 7 Absolute averaged power of vibration signal for normal gasoline engine at different engine speeds with 3 conditions (power of vibration signal vs engine speeds)

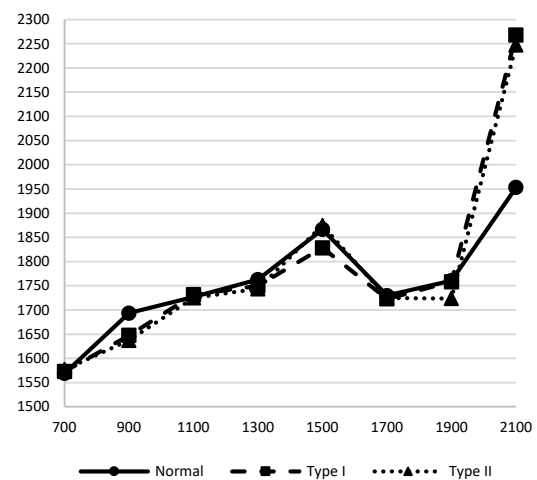


Fig. 8 Absolute averaged power of vibration signal for LPG modified engine at different engine speeds with 3 conditions (power of vibration signal vs engine speeds)

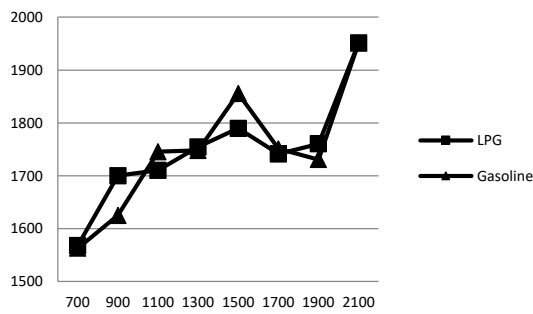


Fig. 9 Absolute averaged power of vibration signal for normal gasoline engine vs LPG modified engine at different engine speeds with normal condition (power of vibration signal vs engine speeds)

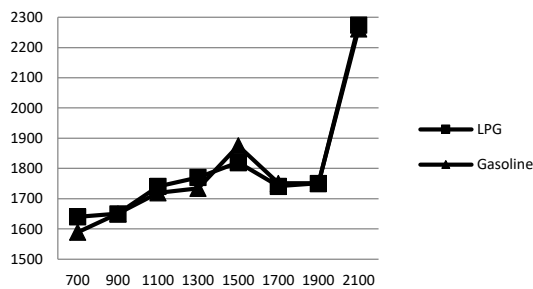


Fig. 10 Absolute averaged power of vibration signal for normal gasoline engine vs LPG modified engine at different engine speeds with type I fault condition (power of vibration signal vs engine speeds)

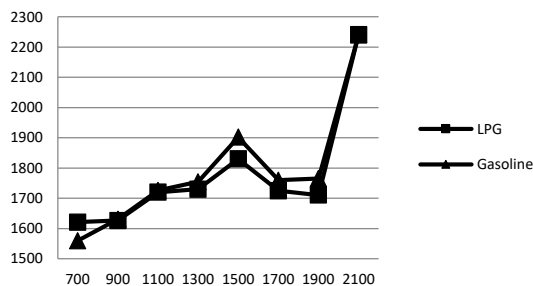


Fig. 11 Absolute averaged power of vibration signal for normal gasoline engine vs LPG modified engine at different engine speeds with type II fault condition (power of vibration signal vs engine speeds)

Simulation Results of Engine Faults

In the second stage of the study, the main focus is how the simulated engine faults affect the vibration of the engine at different engine speeds. From the first stage, it can be noticed that both vibration and sound give quite corresponding results. The vibration has been therefore selected as the main signal to study for the fault simulation in the second stage. The range of engine speeds has been consequently broadened for investigating the vibration in deep. The averaged

powers of vibration signal for these engine conditions including normal oil-usage engine and LPG-modified engine are calculated and comparatively plotted in different engine speeds. Figures 7-8 demonstrate the absolute averaged power of vibration signal at different samples at the engine speeds of 700 - 2,100 rpm.

From Fig. 7, the absolute averaged power of vibration signal for normal gasoline engine in three engine's conditions have been compared in those different engine speeds. When noticing at low engine speeds, the powers of vibration signal of all conditions are closed to each other. When the engine speed is increased above 1,500 rpm, the powers of engine vibration signal with faults type I and type II become significantly lying above than that of the normal engine without faults.

From Fig. 8, the absolute averaged power of vibration signal for LPG modified engine in three engine's conditions have been displayed in those different engine speeds. The experimental results are corresponding to those of the normal gasoline engine as demonstrated in Fig. 7. Last but not least, it can be noticeably seen from both figures that almost all of the absolute averaged powers of vibration signal are increasing from lower engine speeds to higher engine speeds. Therefore it can be concluded that the averaged power of the vibration signal are directly proportional to the speed of the engine.

From Figs. 9-11, the absolute averaged power of vibration signal for LPG modified engine in three engine's conditions have been displayed and compared to those of normal gasoline engine in different engine speeds. These absolute averaged powers of vibration signal are directly proportional to the engine speeds. All of them have the similar behaviors, the absolute averaged powers of vibration signal at 1700 rpm and 1900 rpm fall slightly compared to those of the previous engine speed of 1500 rpm.

CONCLUSIONS

This paper presents a study of vibration and sound signal analysis for a gasoline engine with LPG-installation and fault simulations. The paper is organized as two stages including the comparison of normal gasoline engine and LPG-modified engine and the simulation of engine faults. In the first stage, the study focused on the comparison between the normal gasoline engine and the LPG-modified engine by considering the averaged power extracted from the engine vibration and sound signals. From the experimental results, it can be seen from the vibration analysis that the power of vibration signals of the LPG-modified engine are mostly above those of the normal engine with oil supply except for the engine speeds of 1,100 and 1,300 rpm. Moreover, it has been concluded from the sound analysis that at engine

speed at 900 and 1,100 rpm, LPG-modified engine has lower power of sound signal more than that of normal engine with oil supply. At the engine speed of 1,500 and 1,700 rpm, LPG-modified engine has the power of sound signal lower than that of normal engine with oil supply. In the second stage, the study concentrated on two major engine faults. The absolute averaged power of engine vibration at various engine speeds has been investigated to differentiate all conditions of faults. From the experimental results, it can be summarized that the vibration of engine are directly proportional to the speed of engine. Moreover, the engine faults cause significant engine vibration at the speed above 1,500 rpm for both normal gasoline and LPG modified engines. In conclusions, LPG-installation and engine faults cause degradations in engine efficiency which can be concretely evidenced by using the proposed signal processing technique. The expanded simulated faults can be further studied, moreover the other types of engines should be experimentally conducted in the future.

ACKNOWLEDGEMENTS

The research was partly sponsored by Kasetsart University, Faculty of Engineering at Sriracha's Fund.

REFERENCES

- [1] Yujun L., Peter W. T., Xin Y., Jianguo Y., EMD-based fault diagnosis for abnormal clearance between contacting components in a diesel engine, *Mechanical Systems and Signal Processing*, Vol. 24, Issue 1, 2010, pp.193–210.
- [2] Xia W., Changwen L., Fengrong B., Xiaoyang B., Kang S., Fault diagnosis of diesel engine based on adaptive wavelet packets and EEMD-fractal dimension. *Mechanical Systems and Signal Processing*, Vol. 41, Issue 1-2, 2013, pp. 581–597.
- [3] Binqiang C., Zhousuo Z., Chuang S., Bing L., Yanyang Z., Zhengjia H., Fault feature extraction of gearbox by using over complete rational dilation discrete wavelet transform on signals measured from vibration sensors. *Mechanical Systems and Signal Processing*, Vol. 33, Issue 11, 2012, pp. 275–298.
- [4] Liang B., Iwnicki S. D., Zhao Y., Application of power spectrum, cepstrum, higher order spectrum and neural network analyses for induction motor fault diagnosis. *Mechanical Systems and Signal Processing*, Vol. 39, Issue 1-2, 2013, pp. 342–360.
- [5] Chomphan S., Chaimanatsakun A., Sakornsin R., Khumneungratavongsa S., Rattanasat K., A Comparative Study of LPG-modified Engine and Normal Oil-usage Engine. in *Proc. Int. Conf. On Engineering and Applied Sciences*, 2016, pp. 219-225.
- [6] Akhand R., Upadhyay S. H., A review on signal processing techniques utilized in the fault diagnosis of rolling element bearings, *Tribology International*, Vol. 96, Issue 4, 2016, pp. 289-306.
- [7] Ahmad T. A., Barat G., Teymour T. H., Seyed S.M., Vibration analysis of a diesel engine using biodiesel and petro diesel fuel blends, *Fuel*, Vol. 102, Issue 12, 2012, pp. 414–422.
- [8] Zunmin G, Jin C., Barry H., Analysis of engine vibration and design of an applicable diagnosing approach. *International Journal of Mechanical Sciences*, Vol. 45, Issue 8, 2003, pp. 1391–1410.
- [9] Xianhua L., Randall R. B., Jerome A., Blind separation of internal combustion engine vibration signals by a deflation method. *Mechanical Systems and Signal Processing*, Vol. 22, Issue 5, 2008, pp.1082–1091.
- [10] Xianhua L., Randall R. B., Blind source separation of internal combustion engine piston slap from other measured vibration signals. *Mechanical Systems and Signal Processing*, Vol. 19, Issue 6, 2005, pp. 1196–1208.
- [11] Zbigniew S., Jan W., Application of vibration signals in the diagnosis of combustion engines – exploitation practices. *Journal of KONES Powertrain and Transport*, Vol. 18, Issue 3, 2011, pp. 405-412.
- [12] Carlucci A. P., Chiara F. F., Laforgia D., Analysis of the relation between injection parameter variation and block vibration of an internal combustion diesel engine. *Journal of Sound and Vibration*, Vol. 295, Issues 1–2, 2006, pp. 141–164
- [13] Kingrattanasat T., Chomphan S., Vibration Signal Analysis for LPG-modified Engine and Normal Oil-usage Engine with Different Engine Speeds. in *Proc. Global Conference on Engineering and Applied Science*, 2016, pp. 312-317.
- [14] Boonsit S., Chomphan S., Vibration Signal Analysis for LPG-modified Engine and Normal Oil-usage Engine with Different Engine Speeds and Faults. in *Proc. International Congress on Engineering and Information*, 2017, pp. 102-107.

AN ARTIFICIAL NEURAL NETWORK MODEL FOR THE CORROSION CURRENT DENSITY OF STEEL IN MORTAR MIXED WITH SEAWATER

Cheryl Lyne C. Roxas¹ and Bernardo A. Lejano²
^{1,2}Faculty, De La Salle University - Manila, Philippines

ABSTRACT

Corrosion is a very complicated phenomenon in the field of science and engineering. Over the years, several numerical models have been developed to predict the damage caused by the corrosion process. The use of artificial neural network in modelling corrosion has gained popularity in the recent years. Many of the factors affecting corrosion are difficult to control. Thus, artificial neural network may be a better technique to consider due to its ability to tolerate relatively imprecise, noisy or incomplete data, less vulnerability to outliers, filtering capacity and adaptability. This study aims to generate a corrosion current density prediction model using the artificial neural network approach. Microcell corrosion current density is defined as the rate of corrosion expressed in electric current per unit area of cross section. Several variables were considered as input variables namely: age, water to cement ratio, cement content, compressive strength, type of mixing water, corrosion potential, solution resistance and polarization resistance. These variables were entered into the neural network architecture and simulated in MATLAB. The feedforward backpropagation technique was used to generate the best model for the corrosion current density. The best neural network architecture consists of 8 input variable, 8 neurons in the hidden layer and one output variable. The resulting neural network model satisfactorily predicted the corrosion current density with coefficient of correlation values of 0.96536, 0.80817, and 0.7662 for training, validation and testing phases, respectively,

Keywords: Neural network, Corrosion current density, Seawater, Mortar

INTRODUCTION

Concrete is probably the most-widely used building material in the world. It is a composite material made of cement, aggregates, water and some admixtures. The durability of concrete may be compromised through processes like alkali-aggregate reaction, sulfate attacks, freeze-thaw cycles and corrosion, among others. Among all these, corrosion of the reinforcing steel in concrete has become a great concern as this may result to sudden failure of structures. Thus, developments in the design, construction and maintenance of concrete structures are encouraged to mitigate huge economic, social, health, safety and environmental impacts.

Corrosion of steel is one of the main causes of failure in concrete structures. Theoretical and empirical models help determine its behavior over time and therefore engineers can decide on maintenance and repairs needed to prolong the service life of a structure. Moreover, it is a very complicated phenomenon in the field of science and engineering. Over the years, several numerical models have been developed to predict the damage caused by the corrosion process. Numerical methods can be classified as deterministic and probabilistic. Deterministic models helped understand the mechanisms of localized corrosion but were not really practical for actual prediction [1]. On the other

hand, probabilistic (stochastic) approaches presented high-level statistics and other mathematical methods in processing field data and were found to predict local corrosion phenomena successfully [1]. Examples of modelling techniques are the multiple linear regression, finite element method (FEM), Bayesian updating and artificial neural network (ANN).

FEM has been applied in previous studies [2], [3] [4], [5] and [6]; while a Bayesian updating approach of an existing steel loss model based on monitored data was proposed in [7].

The use of ANN in modelling corrosion has gained popularity in the recent years. The technique can be applied to complex problems and is independent of the physical processes involved but rather the relationships present in a set of data [8]. Many of the factors affecting corrosion are difficult to control. Thus, ANN may be a better technique to consider due to its ability to tolerate relatively imprecise, noisy or incomplete data, less vulnerability to outliers, filtering capacity and adaptability.

Therefore, a model that can predict such corrosion behavior of steel reinforcement will help design engineers in developing better design practices for corrosion management, i.e., repair and rehabilitation procedures, thus extending the service life of structures and saving costs. Modeling is a

useful tool in the quantitative understanding of key elements in concrete and their interactions. This can be accomplished by considering time-dependency of transport properties of concrete, repair or replacement of concrete cover, corrosion propagation, chloride penetration mechanisms other than diffusion, structure geometry, environmental humidity and temperature fluctuations and decay of structures under combined physical, chemical and mechanical deterioration processes as summarized by [9]. Therefore, improvements on existing models can be made to better simulate the corrosion behavior of reinforced concrete structures, especially those mixed with non-conventional materials like seawater and fly ash. Additionally, their performance on chloride-laden environment through time can be assessed.

This study aims to generate a corrosion current density prediction model using the ANN approach. Corrosion current density is defined as the rate of corrosion expressed in electric current per unit area of cross section. Several variables were considered as input variables namely: age, water to cement ratio, cement content, compressive strength, type of mixing water, corrosion potential, solution resistance and polarization resistance.

This paper is organized as follows: The introduction is followed by some literature on ANN modelling of corrosion; followed by the methodology highlighting the data collection, identification of the input and output variables, and building the ANN models; and then results and discussion; finally, conclusions of the research are presented.

ANN MODELING FOR CORROSION

With the development of new technology and computer softwares, mathematical modelling and computation became easier and faster. In this proposed study, regression and artificial neural network (ANN) modelling are the initial modelling techniques being considered.

ANNs mimic the learning process of the human brain. They generalize mathematical models by processing information at elements called neurons. Signals are passed between neurons over connections links. A weight is assigned on each link which multiplies the signal transmitted. The output is obtained by applying an activation function to the net input. A neural network is characterized by its architecture, training or learning algorithm and activation function. A network architecture is the arrangement of neurons into layers and the connection patterns within and between layers. Neural networks are further classified as single or multilayer, and are therefore feedforward networks.

Training is the method for setting the values of the weights. An activation function is applied to the sum of the weighted input signal. Typical activation functions are unit step, linear, sigmoid and hyperbolic tangent. Neural networks are used to find the solutions to constrained optimization problems and can be applied for storing, recalling classifying and mapping data or patterns [10].

Some ANN models related to measuring steel corrosion in concrete are found in [8], [11], [12], [13], [14] and [15].

METHODOLOGY

Data Collection and Identification of Input Variables

Input data were obtained from the experimental quantities and equipment test results in [16]. Rectangular mortar prism specimens (40 mm x 40 mm x 160 mm) with steel reinforcements of 10 mm in diameter and 100 mm length were cast. Ordinary Portland cement (OPC) was the main binder used and replaced with fly ash. The fly ash content in the specimens was varied from 0% to 50% at 10% interval, while the water to cement (w/c) ratios were held at 0.35, 0.40, 0.45, 0.55, 0.65.

A 5 mm cover was applied from the top surface of the prism specimen. Insulated copper wires were soldered at both ends of the steel and then covered with epoxy. These wires were necessary for the corrosion monitoring equipment (CT-7) in measuring the potential and polarization resistance.

In this study, several input variables as used in previous literature were considered in determining the best ANN model. A total of eight (8) input variables were entered namely: age (days), w/c, cement content (%), compressive strength (MPa), type of mixing water (freshwater or seawater), corrosion potential (mV), solution resistance (Ω) and polarization resistance (Ω). The corrosion potential, solution resistance and polarization resistance were measured from the corrosion monitoring equipment. On the other hand, the output variable is the microcell corrosion current density defined as the rate of corrosion expressed in electric current per unit area of cross section.

Structuring the ANN Models

The Neural Network Toolbox in MATLAB R2018a was used in constructing the ANN corrosion current density model estimation. Data were divided into three sets: 60% for training the neural network, 20% for validation and 20% for testing. These sets were randomly selected in MATLAB. The feedforward backpropagation technique was used to generate the best model. This algorithm gradually

reduces the error between the model output and the target output by minimizing the mean square error (MSE) over a set of training set [17]. The MSE is a good overall measure of the success of the training process [18], [19]. The weights and bias value, on the other hand, were updated according to the Levenberg-Marquardt network training function. This is often the fastest backpropagation algorithm and highly recommended, though it requires more memory than other algorithms [20]. A two-layer feed-forward network with sigmoid hidden neurons and linear output neurons was used. This can fit multi-dimensional mapping problems arbitrarily well, given consistent data and enough neurons in its hidden layer [20].

Trial ANN Model Architectures

The best ANN model to estimate the microcell corrosion current density was determined by defining the number of neurons (nodes) in the input and output layers, number of hidden layers and the number of neurons in each hidden layer. The model generated utilized the 8 input variables. There is no specific rule in determining the number of hidden layers and the number of neurons in each hidden layer [21]. In this study, one hidden layer was used and the following rules were employed to determine the optimum number of neurons: (a) a network with n -input and m -output units requires a hidden layer with at most $2n+1$ units, (b) should be between the average and the sum of nodes on the input and output layers; (c) seventy-five percent (75%) of the input nodes [22]. Thus, simulation was done in the range of 5-17 neurons in the hidden layer.

RESULTS AND DISCUSSION

After several simulations, ANN Structure 8-8-1 (8-input variables, 8-nodes in the hidden layer, 1-output) was found to be the best model to estimate the microcell corrosion current density. Figure 1 shows the ANN Structure 8-8-1. ANN Structure 8-8-8 obtained a satisfactorily acceptable correlation coefficient, R , values of 0.96536, 0.80817, and 0.7662 for training, validation and testing phases, respectively. A correlation coefficient of 0.85983 was achieved considering all data points. Figure 2 presents the regression line while Fig. 3 shows the training performance for ANN Structure 8-8-1. The resulting MSEs for each phase are seen in Table 1.

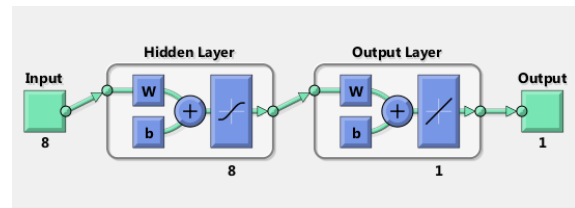


Fig. 1 ANN structure 8-8-1

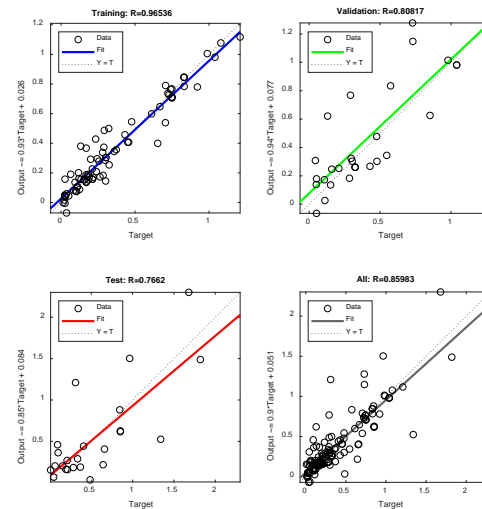


Fig. 2 Regression lines for ANN structure 8-8-1

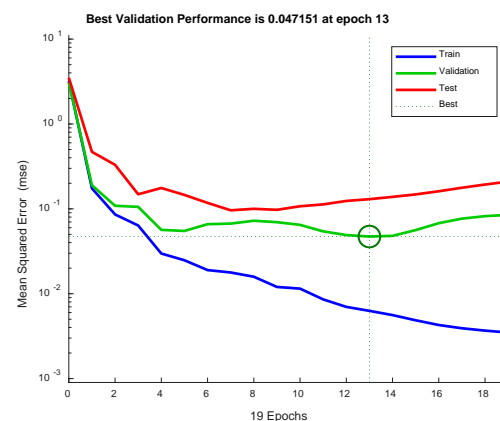


Fig. 3 Training performance of ANN structure 8-8-1

Table 1 MSE for different training phases

Phase	Samples	MSE
Training	85	0.0062789
Validation	28	0.0471508
Testing	28	0.1299260

CONCLUSION

This paper presents an artificial neural network model for estimating the microcell current density of steel in mortar mixed with seawater. This value is necessary in computing the corrosion rate of steel, which is one of the main causes of failure in structures. Several input variables were considered in constructing the ANN model namely: age, water to cement ratio, cement content, compressive strength, type of mixing water, corrosion potential, solution resistance and polarization resistance.

From several trials, ANN Structure 8-8-1 was chosen as the best architecture having the highest correlation coefficient values of 0.96536, 0.80817, and 0.7662 for training, validation and testing phases, respectively, in a range of 5-17 neurons in the hidden layer. The resulting MSE in the training phase is 0.0062789. The best validation performance is 0.047151 and occurred at epoch 13. The test set and validation set errors have relatively similar characteristics.

Finally, it can be concluded that the neural network technique provided good predicting ability despite the non-uniform distribution and incompleteness of the data set. Expanded data set may improve the results. Sensitivity analysis and relative importance of the input variables can be conducted to enhance the reliability and validity of the results.

ACKNOWLEDGMENTS

The authors would like to thank their colleagues, staff, technicians and former students of the Civil Engineering Department, De La Salle University – Manila, especially Engr. Edrick Dan Lim.

REFERENCES

- [1] Fujimoto, S., Numerical Modeling for Corrosion, 2014, The Electrochemical Society Interface Winter 2014, p. 45.
- [2] Pan, T., & Wang, L., Finite-Element Analysis of Chemical Transport and Reinforcement Corrosion-Induced Cracking in Variably Saturated Heterogeneous Concrete, *Journal of Engineering Mechanics*, 2011, pp. 334-345.
- [3] Dao, L. T., Dao, V. T., Kim, S.-H., & Ann, K. Y., Modeling Steel Corrosion in Concrete Structures - Part 2: A Unified Adaptive Finite Element Model for Simulation of Steel Corrosion, *International Journal of Electrochemical Science*, 2010, Vol. 5, pp. 314-326.
- [4] Lin, G., Liu, Y., & Xiang, Z., Numerical modeling for predicting service life of reinforced concrete structures exposed to chloride environments. *Cement & Concrete Composites*, 2010, Vol. 32, pp. 571-579.
- [5] Shekarchi, M., Ghods, P., Alizadeh, R., Chini, M., & Hoseini, M., DuraPGulf, A Local Service Life Model for the Durability of Concrete Structures in the Couth of Iran. *The Arabian Journal for Science and Engineering*, 2008, 33(1B), pp. 77-88.
- [6] Song, H.-W., Kim, H.-J., Saraswathy, V., & Kim, T.-H., A Micro-mechanics Based Corrosion Model for Predicting the Service Life of Reinforced Concrete Structures. *International Journal of Electrochemical Science*, 2007, 2, pp. 341-354.
- [7] Faroz, S. A., Pujari, N. N., & Ghosh, S., Reliability of a corroded RC beam based on Bayesian updating of the corrosion model. *Engineering Structures*, 2016, 126, pp. 457-468.
- [8] Ukrainczyk, N., & Ukrainczyk, V., A neural network method for analyzing concrete durability. *Magazine of Concrete Research*, 2008, 60(7), pp. 475-486.
- [9] Shi, X., Xie, N., Fortune, K., & Gong, J., Durability of steel reinforced concrete in chloride environments: An overview. *Construction and Building Materials*, 2012, 30, pp. 125-138.
- [10] Fausett, L., *Fundamentals of Neural Networks: Architectures, Algorithms, and Applications*, 1994.
- [11] Parthiban, T., Ravi, R., Parthiban, G., Srinivasan, S., Ramakrishnan, K., & Raghavan, M., Neural network analysis for corrosion of steel in concrete. *Corrosion Science*, 2005, 47, pp.1625-1642. doi:10.1016/j.corsci.2004.08.011
- [12] Shi, X., Tuan Anh Nguyen, P. K., & Liu, Y., A phenomenological model for the chloride threshold of pitting corrosion of steel in simulated concrete pore solutions. *Anti-Corrosion Methods and Materials*, 2011, pp. 179-189. doi:10.1108/00035591111148894
- [13] Sadowski, L., & Nikoo, M., Corrosion current density prediction in reinforced concrete by imperialist competitive algorithm. *Neural Computing and Applications*, 2014, 25, pp. 1627-1638. doi:10.1007/s00521-014-1645-6
- [14] Hodhod, O., & Ahmed, H., Modeling the corrosion initiation time of slag concrete using the artificial neural network. *HBRC Journal*, 2014, 10, pp. 231-234.

- [15]Guo-dong, L., Corrosion Evaluation Model of Reinforcement in Concrete Based on ANN. 8th International Conference on Intelligent Computation Technology and Automation, 2015, pp. 341-344. Nanchang, China : IEEE. doi:10.1109/ICICTA.2015.92
- [16]Lim, E.D.P., Influence of Seawater on Reinforced Mortars with Varying Fly Ash Replacement Ratio, Water-Binder Ratio, Curing Conditions and Type of Steel Bars, Thesis, De La Salle University – Manila, Philippines, 2012.
- [17]Gunaydin, H. and Dogan, S., A neural network approach for early cost estimation of structural systems of building, International Journal of Project Management, 2004, Volume. 22, pp. 595 - 602.
- [18]Al - Tabtabai, H., et.al., Preliminary cost estimation of highway construction using neural networks, Construction Engineering, 1999, Vol. 41, pp.19 - 24.
- [19]Turochy, et.al., Highway project cost estimating methods used in the planning stage of project development, Technical Assistance Report, Virginia Transportation Research Council, 2001.
- [20]MATLAB R2018a, Neural network toolbox.
- [21]Shtub, A. and Versanob, R., Estimating the cost of steel pipe bending, a comparison between neural networks and regression analysis”, International Journal for Production Economics, 1999, Vol. 62, Issue 3, pp. 201 – 207.
- [22]Oreta, A. Artificial neural networks: Multi - layer feedforward networks using back propagation, CIV578D Lecture Notes, 2012, De La Salle University Manila.

IMPLEMENTATION OF CONNECTION SYSTEM OF WOODEN PLATE AND WOODEN CLAMP ON JOINT MODEL OF BAMBOO TRUSS STRUCTURES

*Astuti Masdar¹, Suprpto Siswosukarto² Noviarti³ and Des Suryani⁴

^{1,3}Department of Civil Engineering, Sekolah Tinggi Teknologi Payakumbuh, Indonesia

², Department of Civil and Environmental Engineering, Faculty of Engineering, Gadjah Mada University, Indonesia

⁴Department of Informatics, Faculty of Engineering, Universitas Islam Riau, Pekanbaru, Indonesia

ABSTRACT

The study of wooden plate bamboo connection system with the addition of wooden clamp was carried out taking into account the variety the angle of the stems at the joint. The loading was preceded through the application of compressive force at the joint's member under studied up to reaching the maximum load and the connection was collapsed. It is known that the strength of bamboo not parallel to the direction of fiber is lower than those parallel to fiber. Therefore, the strength of connection must be determined considering the strength of bamboo not parallel to the fiber direction. The experiment was carried out under static loading on the bamboo truss connections model with various angle of connection stems of 0°, 30° and 45° toward bamboo fiber direction. From the test result, it was found that there is a decrease in the connection strength at stem angle of 30° and 45° for about 16,80% and 12,21%, respectively, compared to the strength of the stem angle of 0°. The test results also resulted the value of average elastic stiffness (S_e) of the connection also indicates a decrease in the of elastic stiffness value (S_e) of the connection for the stem's angle 30° and 45° for about 42,62% and 82,95%, respectively, compared to stem angle of 0°. It can be concluded that there is a decrease in the strength and stiffness of the joints along with the increase in stem's angle of the bamboo truss connection system using wooden plate and clamp.

Keywords: Bamboo, Connection system, Wooden plate, Wooden clamp, Truss

INTRODUCTION

Bamboo plants has been known as the plant of "source of livelihood". As a source of life, bamboo plants can produce a lot of oxygen. The roots of plants can store water and strengthen the soil to prevent erosion, especially in the slope of a steep cliff. For human life, the bamboo plant can be used to basic human needs such as the need for food, clothing and housing.

Bamboo is highly an environmentally friendly construction material that suitable to support green building program as part of program to combat global warming. Bamboo is very fast growth of which can reach a maximum height of 15-18 cm in 4-6 weeks, while wood take year [1]. As a construction material, compared to wood, bamboo is a renewable material because of its rapid growth and fast growth as well as short period of planting of about 3 - 5 years, can used as a construction material [2].

Owing to its relatively high strength, stiffness and lightweight characteristics, bamboo is a potential substitute for wood. It is also easily worked

using simple tools when employed in construction practices. Bamboo culms is available in variety of length and has high strength-weight ratio that make it suitable to be used as structural material. As a structural material, bamboo can be used in a variety of building components such as beams, columns, partitions, floors or as a truss structure. In truss structures, bamboo is commonly applied as structural members in roof construction and bridge structures.

High strength bamboo material cannot be fully utilized due to the constraints of the connection system. Researches to obtain a strong connection system to overcome the problem of the weakness of a connection have been widely done. Examples include the connection system with connecting bolts and filling cement mortar in internode of culm of bamboo [3], the connection system with gusset plate of steel and devices connecting bolts [4], the connection system with gusset plate of plywood materials and devices connecting bolts [5] and the connection system with gusset plate of plywood materials or hard wooden planks and devices connecting nails [6]. A connection system without filler material on bamboo culms with wooden gusset

plate and wooden clamps used to increase the contribution to the shear at the connection has been proposed by Masdar [7].

Need of the Study

In the development of connection system on bamboo truss structure, the behavior aspects must be considered, including the connections between components of connection system. Furthermore, in joint model of bamboo truss structure, behavior the connection system for joint with variations of angle between culm of bamboo need to know.

The Objective of the Study

This paper addresses this subject, with the objective of the study of: (i) knowing influence of variations of angle between culm of bamboo on joint model against strength and stiffness of bamboo truss structure and (ii) experimentally, assessing their structural behaviour and performance under static loading.

DESCRIPTION OF CONNECTION SYSTEM

A connections systems that use of steel for gusset plates and relatively heavy infill material has made this connection system to be less desirable of the significant increase of structure weight and construction costs that make it uneconomical. A bamboo connection system that possesses lightweight nature but higher strength and lower cost while keeping the form of the bamboo being connected remains natural has been developed by Masdar [7], [8], [9].

The proposed bamboo connection system consists of bolts, wooden gusset plates and special wooden clamps that have been adjusted with the shape and dimension of the bamboos being connected as shown in Fig. 1. The wooden clamps were placed between the bamboo and wooden gusset plates make contact area that capable of mobilizing its friction capacity to transfer the applied load for stronger and reliable connection as shown in Fig. 2.

The wooden clamp with ring angle of 90° was determined to be optimal and thus recommended to be applied to connections of bamboo truss structure [7]. Based on the results of previous research conducted by Masdar [7], [8], [9] can be known that the strength of this bamboo connection system is influenced by several factors such as material characteristics in the connection system, the angle of wood clamps to the bamboo circumference and bolt tightening force.

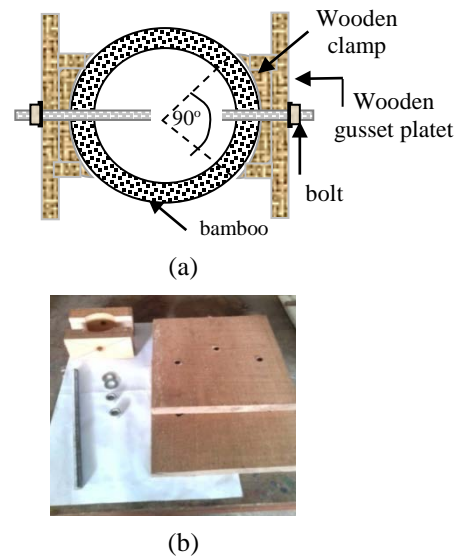


Fig. 1 The proposed bamboo connection system [8], [9] (a) connection system on bamboo truss structure (b) component of connection system.

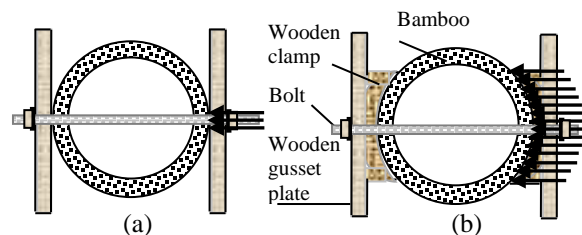


Fig. 2 Distribution of force on the bolt and wooden gusset plate to a bamboo culm (a) direct force into a bamboo culm (b) force through to a wooden clamps

EKSPERIMENTAL INVESTIGATION

The study was conducted experimentally in two phases of testing. In the early stage of the research preliminary testing on basic properties of the materials used have been conducted. The second phase of the research involved designing and fabricating several types of joint model of bamboo truss structure with full scale sizes and tested experimentally in the laboratory. The experiment was carried out under static loading on the bamboo truss connections model with various angle of connection stems of 0° , 30° and 45° toward bamboo fiber direction

Test Set-up and material

Test Set-up

Tests on joint model of bamboo truss structure are carried out in static loading. Static loading is carried out until it reaches ultimate load and

observation on deflection that occurs. In this test the load-displacement relationship is measured with load instrument in the form of load cell capacity 10 Ton and displacement with LVDT capacity of 50 mm.

The testing method of basic material properties was based on ISO N22157-2 [10] for bamboo and ASTM D 143 for wood [11]. The testing method of bearing strength of bamboo was adopted from ASTM D 5764 standard test method for evaluating dowel bearing strength of wood and wood based products [12]. Bearing strength test has been carried out on bamboo and wood with deformed bolt diameter of 12.2 mm.

The test set-up for joint models is shown in Fig. 3. The experiment was carried out under static loading on joint model of bamboo truss structure with various angle of connection stems toward bamboo fiber direction is shown in Fig. 4. The test is performed by giving compression test on bamboo culm with three of varied of angle between bamboo culm.

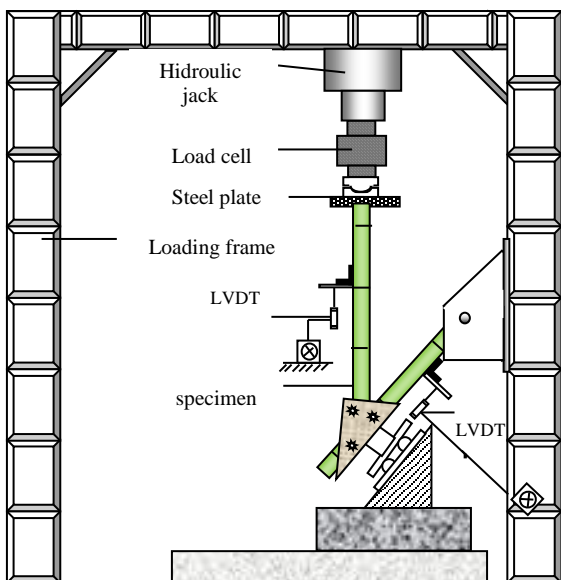


Fig. 3 Test set-up for compression tests of the specimen.

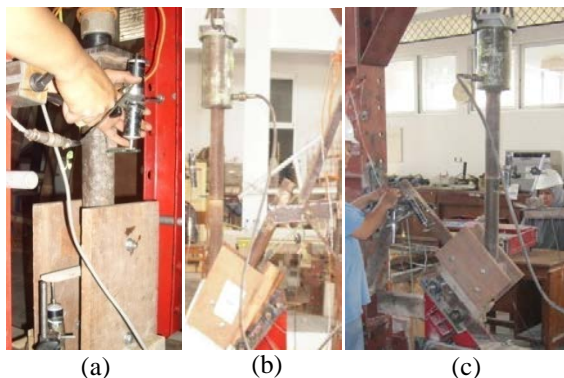


Fig. 4 Specimen of compression test (a) bamboo stem angle 0° (b) bamboo stem angle 30° (c) bamboo stem angle 45°

The connection system with three variation of joint model on bamboo truss structure which are distinguished by angle between bamboo culm, i.e. 0°, 30° and 45°, respectively. The result obtained with compression test on joint model of bamboo truss structure is the strength, stiffness and behavior of the connection by observing the amount of load and deflection that occurred.

Material

The material used on the joint model of bamboo truss structure is a natural material and a bolt made of steel with a diameter of 12,2 mm. The type of bamboo used as the main structural material in this study was *Gigantochloa atroviolacea*. The gusset platesware made of Keruing wood (*Dipterocarpaceae*), while Mahoni wood (*Swietenia Mahagoni*) was used for the clamps. The material properties used on the joint model of bamboo truss structure are shown in Tables 1, 2 and 3.

Table 1 Physical properties of material

Material	Density gram/cm ³	Moisture Content %
Bamboo	0,62	12
Wooden clamp	0,56	12
Wooden gusset plate	0,75	12

Table 2 Mechanical properties of bamboo

Testing	Stress (MPa)	
	range	average
Compressive strength (σ_c)	51 – 56	54
Shear strength (τ)	7 – 8	7,8
Bearing strength (f_e)	33 – 41	37
Tensile strength (σ_t)	150 – 263	217
Bending strength (σ_b)	55 – 79	58
Tensile MOE (E_t)	11219 – 18984	15450
Bending MOE (E_b)	12544 – 20620	16051

Table 3 Mechanical properties of wood

Material	Grain direction	Stress (MPa)		
		bearing (σ)	shear (τ)	Tensile (σ)
Wooden clamp	Parallel	46	6,2	
	Perpendicular	22		5,8
Wooden gusset plate	Parallel	62	8,4	
	Perpendicular	26		4,1

Result and discussion

The strength and stiffness of the joints model

The relationship between load and displacement obtained from the tests is shown in Fig. 5.

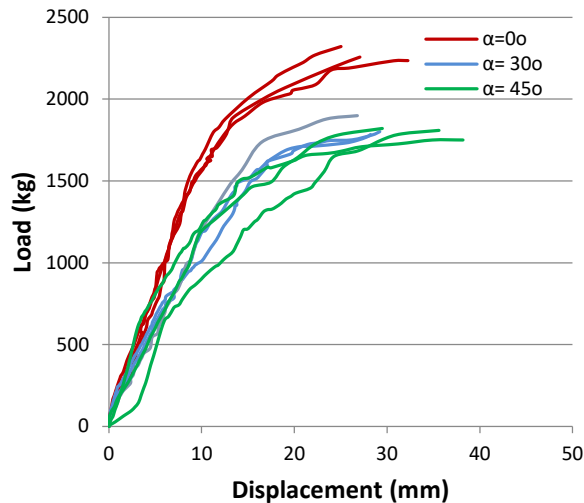


Fig. 5 The relationship between load and displacement on joint model of bamboo truss structure

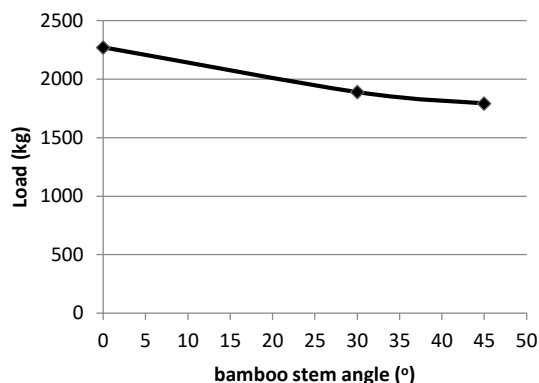


Fig. 6 Graph of the relationship between the maximum force average and bamboo stem angle variation

There are nine joint specimens with three variations of bamboo stem angle were tested under compression as shown in Fig. 5. The result of testing the connection model with the direction of force 0° toward the direction of bamboo fiber on each specimen shows the maximum load ranged from 2236 kg up to 2322 kg with displacement respectively is 32,24 mm and 25,05 mm. The result of testing the connection model with the direction of force 30° toward the direction of bamboo fiber on each specimen shows the maximum load ranged from 1802 kg up to 1967 kg with displacement respectively is 29,2 mm and 30,2 mm. The result of testing the connection model with the direction of

force 45° toward the direction of bamboo fiber on each specimen shows the maximum load ranged from 1751 kg up to 1820 kg with displacement respectively is 38,2 mm and 29,58 mm.

Table 4 The average maximum strength of the connection on the compression test against the bamboo stem angle on joint model of bamboo truss structure

No.	Specimen	average maximum strength (kN)	Average elastic stiffness (S_e) N/mm
1.	MS ($\alpha=0^\circ$)	22,71	2051,52
2.	MS ($\alpha=30^\circ$)	18,89	1176,93
3.	MS ($\alpha=45^\circ$)	17,93	1121,33

The compression test results shown that the maximum strength on joint model of bamboo truss structure is affected by the angle of a bamboo joint. The greater the angle to the direction of bamboo fiber on joint model of bamboo truss structure, the strength and stiffness of the joints are smaller as shown in Fig. 6 and listed in Table 4.

Fig. 6 shown the relationship between the maximum force average with various angle of connection stems of 0° , 30° and 45° toward bamboo fiber direction, where the strength of the connection decreases as the angle of force increases in the connection system. The average maximum strength on joint model of bamboo truss structure with bamboo stem angle of 0° , 30° and 45° obtained from these compression tests were 22.71 kN, 18.89 kN and 17.93 kN, respectively. From the test result, it was found that there is a decrease in the connection strength at stem angle of 30° and 45° for about 16,80% and 12,21%, respectively, compared to the strength of the stem angle of 0° .

Similarly, the test results also resulted the value of average elastic stiffness (S_e) of the connection also indicates a decrease in the of elastic stiffness value (S_e) of the connection for the stem's angle 30° and 45° for about 42,62% and 82,95%, respectively, compared to stem angle of 0° .

The maximum loads and the loads that correspond to the yielding of the connections were different among variation of bamboo stem angle. Based on the compression test results of the connections depicted in Fig. 6 and listed in Table 4, it can be concluded that the greater bamboo stem angle, α , the lower the strength and stiffness of the connection would be. It can be concluded that there is a decrease in the strength and stiffness of the joints along with the increase in stem's angle of the bamboo truss connection system using wooden plate and clamp.

Failure modes of the joints model

Failure modes of various angle of connection stems are presented in Fig. 7.

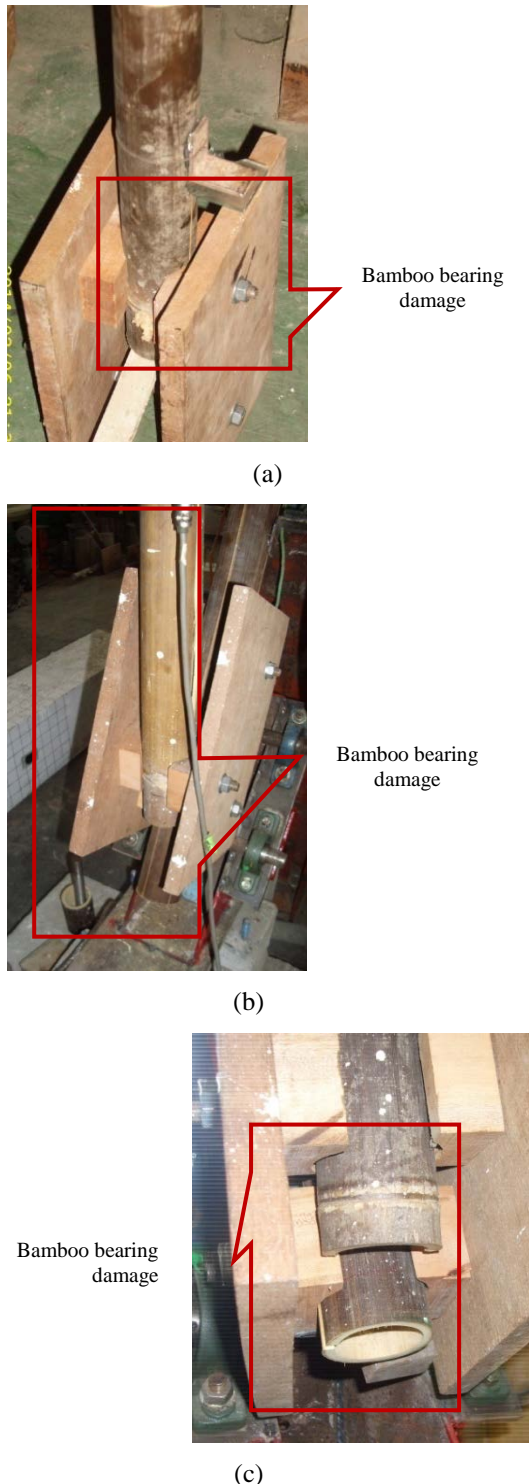


Fig. 7 Failure modes of the specimen (a) bamboo stem angle 0° (b) bamboo stem angle 30° (c) bamboo stem angle 45°

In Fig. 7 can be seen the damage occurred on the bamboo is marked with a red line. In the specimen with stems angle of 0°, 30° and 45°, the most damage occurs in bamboo, while the other connection system components damage is not so big or just a small damage.

The mechanical behavior of the components of the connection system of bamboo, wooden clamp, wooden gusset plate and bolt connectors greatly affect the strength of connection system on the bamboo truss structure. The mechanical behavior of material on connection system related to the strength of the connection components need to be considered to determine the strength of the connection. In this research, analytical method considering failure mode and the strength of bamboo connection will be verified with result from experimental work. The strength of connection of bamboo and the failure mode can be estimated from the formula which was introduced by Masdar [7], [8]. In Fig. 7, it appears that the damage occurred is in the middle of the connection system (bamboo). Failure mode I occurs in the specimens. Failure mode I occurs when the bamboo bearing is reached. It can be concluded, The component of the connection system determines the strength of bamboo connections.

CONCLUSION

This paper presented a study about implementation of connection system of wooden plate and wooden clamp on joint model of bamboo truss structure. The proposed connections system were implemented considering that information and references about joint model of bamboo truss structure are very important. The following main conclusions may be drawn from this study:

1. There is a decrease in the connection strength at stem angle of 30° and 45° for about 16,80% and 12,21%, respectively, compared to the strength of the stem angle of 0°.
2. elastic stiffness (S_e) of the connection also indicates a decrease in the of elastic stiffness value (S_e) of the connection for the stem's angle 30° and 45° for about 42,62% and 82,95%, respectively, compared to stem angle of 0°.
3. There is a decrease in the strength and stiffness of the joints along with the increase in stem's angle of the bamboo truss connection system using wooden plate and clamp.
4. The mechanical properties of the basic material influenced the overall connection behavior, namely the bearing strength, shear strength and tensile strength perpendicular of grain, where in the proposed connection system failure generally occurs in bamboo.

ACKNOWLEDGEMENTS

This study was conducted by using the research funding of Hibah Berbasis Kompetensi. It is funded by DRPM DIKTI, Ministry of Research, Tecnology and Higher Education of Indonesia, Ref. No. 065/K10/KONTRAK-PENELITIAN/2018 (DIPA Kopertis Wil X). The authors warmly thank all the sponsors and collaborators, especially all the bamboo lovers.

REFERENCES

- [1] Akinlabi E. T., Fenin K.A., and Akwada D.R., Bamboo The Multi Purpose Plant, Spinger International Publishing, 2017, pp. 1-3.
- [2] Morisco, Rekayasa Bambu, Nafiri Offset, 2000, pp. 1-87.
- [3] Trujillo, D.J.A. Axially Loaded Connection in Guadua Bamboo, Proceedings of the 11th International Conference on Non-conventional Materials and Technologies, 2009, pp 1-8
- [4] Morisco, Sambungan dengan Celah Pengisi. Jurnal Forum Teknik, Vol. 24 No.1, 2000, pp. 99-109.
- [5] Davies C., Bamboo Connections. The Department of Architecture and Civil Engineering. Bath: The University of Bath, 2009, pp. 46-47.
- [6] Misra, H. N. Know How of Bamboo House Contruction, Proceedings of International Bambo Workshop, 1988. pp. 242-246.
- [7] Masdar A., Suhendro B., Siswosukarto S. and Sulistyo J., The Study of Wooden Clamp for Strengthening of Connection on Bamboo Truss Structure. Jurnal Teknologi (Sciences Engineering), Vol. 72, Issue 5, 2015, pp. 97-103.
- [8] Masdar A., Suhendro B., Siswosukarto S. and Sulistyo J., Development of Connection System Bamboo Truss Structure, Proceedings of 4th International Confrence on Sustainable Future fo Human Security, 2013, pp. 78-86.
- [9] Masdar A., Suhendro B., Siswosukarto S. and Sulistyo J., Influenced of bolt of tighening's force to The Strength of Connection System of Bamboo Truss Structure With Wooden Clamp, Procedia Engineering, 2017. Vol. 171. pp. 1370-1376.
- [10] ISO N22157-2. Bamboo-Determination of Physical and Mechanical Properties, Part 2, Laboratory Manual, 2004.
- [11] American Society for Testing and Materials. 2008. Annual Book of ASTM Standards 2008–Section 4 Volume 04.10 Wood. American Society for Testing and Materials.
- [12] American Society of Mechanical Engineer, ASTM D5764: Standard Test Method for Evaluating Dowel-bearing Strength of Wood and Wood-based Products. Annual Book of ASTM Standard, 2002. Vol. 04.10., West Conshohocken, PA, USA.

EXPERIMENTAL INVESTIGATION OF SEISMIC PERFORMANCE OF REINFORCED BRICK MASONRY INFILLED REINFORCED CONCRETE FRAMES WITH A CENTRAL OPENING

Maidiawati¹, Jafril Tanjung², Yulia Hayati³ and Hamdeni Medriosa¹

¹Civil Engineering and Planning Faculty, Padang Institute of Technology, Indonesia;

²Engineering Faculty, Andalas University, Indonesia

³Engineering Faculty, Syiah Kuala University, Indonesia

ABSTRACT

This paper discusses the experimental results of reinforced concrete (RC) frame with brick infills with a central opening with and without rebar reinforcements on the opening interface to the masonry. 1/4 scale-down of single-story single-bay RC frame specimens were constructed. These specimens included one RC frame without infill, one unreinforced brick masonry infilled frame, two unreinforced brick masonry infilled frames with a central opening and two brick masonry infilled frames with a central opening with 206 steel reinforcements embedded in infill above and below openings. The opening size to the panel area ratios were 25% and 40%. All the specimens were subjected to in-plane reversed cyclic lateral loading. Consequently, the experimental results show that the existence of the opening reduces the stiffness, the lateral strength, and energy dissipation of the RC infilled frame system. However, the infilled frames with 25% and 40% openings showed better performance compare to bare frame specimen. Although the strengthening by using embedded rebars does not significantly increase the performance of the RC frame system, the brick infill with horizontal reinforcements installed above and below the opening was verified to resist large deformation of masonry infill in out of plane direction.

Keywords: Brick wall with opening, Lateral strength, Reinforced concrete frame, Reinforced masonry infill, Stiffness.

INTRODUCTION

Contributions of brick masonry infills have been ignored for seismic design of buildings in many countries. It seems because of deficiency of understanding on seismic performance of brick infills under seismic loads. Several studies have been performed by researchers for evaluating the effects of masonry infill on the seismic performance of RC frame buildings [1]-[5].

The first author has also conducted a series of past studies related to RC frame structure with brick masonry infills [4]-[6]. The first author investigated the earthquake-damage buildings after the 2007 Sumatra earthquake in Padang city and nearby as reported in [4]. It was found that brick infill contributed to resist the seismic load in the RC building, and it made the building can survive during the earthquake. Further, the author performed a series of experimental test on RC frames without and with brick infill under reversed cyclic lateral loading. The test results revealed that brick infill increases the lateral strength and stiffness of the whole structure however it decreases ductility of structure [5]. Moreover, an analytical method was proposed to calculate the lateral strength of infill in elastic range based on a diagonal compression strut

concept. Consequently, the lateral force of infill can be derived as a function of strut width [6]. The proposed analytical model has been verified through experimental results of brick infilled frames.

All the past studies mentioned above are focused only on the performance of RC frames with solid brick infills and neglected the presence of infills with openings assuming no contribution from infills with openings on seismic performance of RC frame [7]. However, a lot of studies reported that masonry infills with opening affect to reduce the lateral strength and stiffness of infilled frame structure in which it depends on area and location of the opening in panel wall [8]-[10]. This circumstance revealed that the seismic behavior of the infilled frame with opening still was not known well. Maidiawati [8] carried out an experimental study on brick infilled frames with openings through monotonic lateral load tests. The results disclosed that the openings in brick-masonry infill control the failure mechanism, the lateral strength and the stiffness of the overall structure. Failure of infill occurred at the corners of openings as the weakest part of the panel [8]. In the current study, the behavior of RC frames with brick infills with a central opening with steel reinforcements placed above and below openings was investigated through cyclic lateral load tests.

EXPERIMENTAL PROGRAM

Test Model

Six of 1/4-scaled single bay and single story RC frame specimens were constructed. The parameters studied in this experimental evaluation were influence of ratio of opening size to panel wall area, α , of 25% and 40% and effects of 2Ø6 reinforcement horizontally embedded at the below and above the opening. No shear connectors were used between columns and infill. The elements of RC frame of all specimens were constructed with identical

dimensions and detailing structure which represented the first story of typical Indonesian low-rise RC buildings. The cross-sectional and reinforcement arrangement of frame elements are shown in Fig. 1(a). The figures 1(b) to 1(f) show the specimens of IF_{SW}, IF_{O-1}, IF_{O-2}, IF_{OR-1}, and IF_{OR-2}, respectively. Table 1 summarized the specimens and their variance. Brick units of 1/4 scale clay bricks of dimensions of 60 mm in length, 30 mm in width and 13 mm in height and mortar beds with the composition of cement: water = 1: 0.5 were used to construct the infills. The wall surfaces were plastered with mortar of 5.0 mm in thickness.

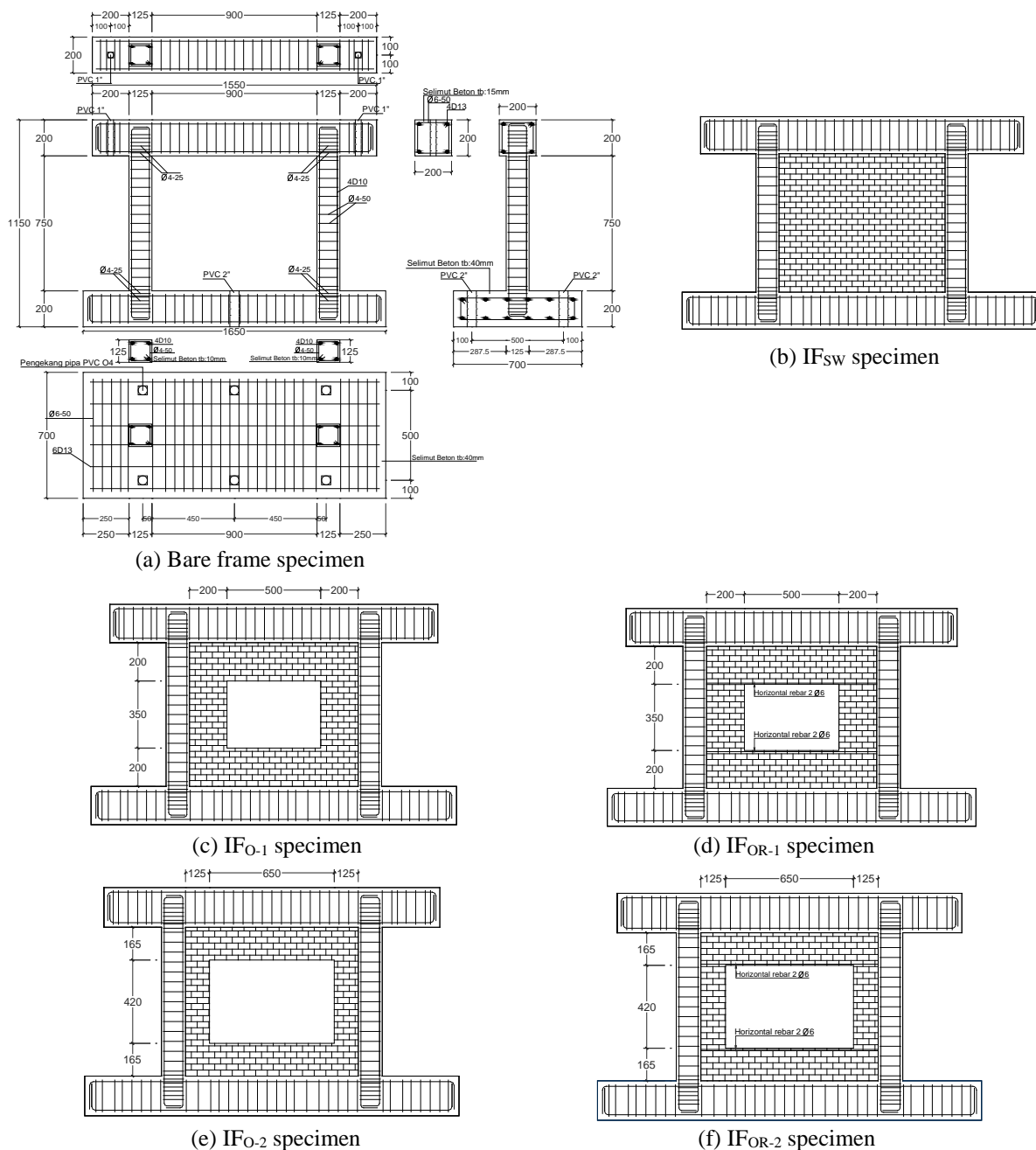


Fig. 1 Detailed drawing of specimens.

Table 1. Experimental parameters of the specimens

Specimens	Column	Brick infill	
		α (%)	Reinforcement
BF	cross-section:	0	-
IF _{SW}	125x125	0	-
IF _{O-1}	main bar:	25	-
IF _{OS-1}	4D10	25	2Ø6
IF _{O-2}	hoop: 2-	40	-
IF _{OS-2}	Ø4-50	40	2Ø6

Material Properties

The mechanical properties were the same for all specimens which were obtained through material samples tests. The compressive strengths of concrete and brick masonry prism were 49.9 N/mm² and 13.0 N/mm², respectively. The yield strengths of reinforcements were 390.2 N/mm², 346.8 N/mm², 462.0 N/mm², and 421.1 N/mm² for rebars of Ø4, Ø6, D10, and D13, respectively. The tensile strengths of reinforcements were 598.3 N/mm², 448.6 N/mm², 619.7 N/mm² and 582.4 N/mm² for rebars of Ø4, Ø6, D10, and D13, respectively. The average compressive strength of brick was 10.9 N/mm².

Loading Method and Measurement

The experimental tests were conducted at the Structural and Construction Material Lab. of Civil Engineering Dept., Syiah Kuala University. The specimens were subjected only by reversed cyclic lateral loads as shown in the schematic of the test setup and loading system in Fig. 2.

The horizontal and vertical displacements of the specimens were measured with transducers positioned on specimens. The applied loads, as well as displacements, were monitored throughout the tests. To identify the failure process and mechanisms of specimens, initiated cracks and crack propagation were marked on the specimens at the peak and

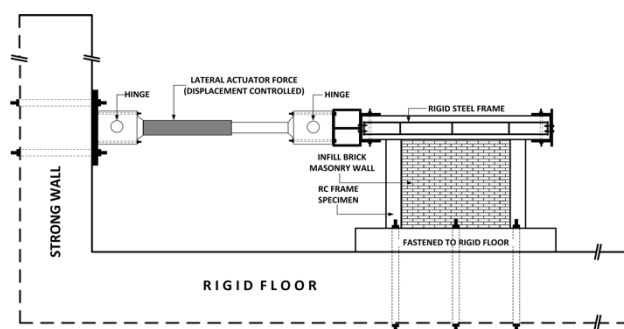


Fig. 2 Schematic view of test setup

residual drifts in each loading cycle.

Figure 3 shows the loading history of cyclic loading referred to [11]. The drift angle R used to control the incremental lateral load applied on specimens was an initial cycle to $R=1/800$ and then followed by two cycles to $R=1/400$, $1/200$, $1/100$, $1/50$, $1/25$, $1/12.5$ and $1/10$. If the specimens failed before the final cycles, the loading was stopped.

TEST RESULTS AND DISCUSSION

Failure Process and Mechanism

Failure process and mechanism for all specimens were investigated during experimental works. The following compares the failure process of specimens.

BF specimen

The initial flexural crack was detected during the cycle of $1/400$ at the top of the tensile column at the lateral displacement of 1.2 mm and initial shear crack was during the cyclic $1/200$ at 3.8 mm lateral displacement at the bottom of the compressive column. The cracks developed during the next cycle loading. During the cycle of $1/12.5$, the compressive column failed in shear at 58.8 mm lateral displacement. Soon after the shear failure of both columns, the lateral strength significantly degraded. Fig 4(a) shows the condition of BF specimen under the cyclic loading to drift angle $1/50$ rad.

IF_{SW} specimen

A separation crack was discovered between column and wall at loading cycle of $1/800$. Initial flexural and shear cracks were found out at tensile column during the cycle of $1/400$ at the lateral displacements of 1.3 mm and 1.6 mm, respectively. An initial diagonal shear crack was observed during cycle $1/200$ at 3.4 mm displacement at the center of the panel wall. Shear failure of brick wall occurred during the cycle $1/50$, and then the lateral strength degraded significantly. After the failure of the brick wall in out of plane direction, the boundary column failed in shear at the cycle of $1/12.5$. Fig. 4(b) shows the condition of the IF_{SW} specimen by cycles to $1/50$ rad.

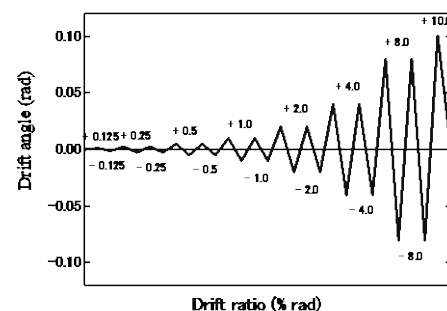


Fig. 3 Loading history.

IF_{O-1} specimen

Initial shear cracks in infill existed at the top left corner of opening and the bottom right corner of opening at a displacement of 0.45 mm during the cycle 1/800. Initial flexural crack at the tensile column happened at 1.9 mm displacement during the cycle 1/400. Initial shear crack appeared at the tensile column at 3.5 mm displacement during the cycle 1/200. Infill wall failed in shear at the corner of opening at the cycle 1/25 and column failed in shear at the cycle 1/12.5. Fig. 4(c) shows the condition of IF_{O-1} specimen by cycles to 1/50 rad.

IF_{O-2} specimen

During the cycle 1/800, it was found out the initial flexural crack at the tensile column at 0.4 mm displacement and the initial shear crack in infill at the left top corner of opening at the displacement of 0.8 mm. During the cycle 1/200, initial shear crack at the top of the tensile column was explored at 2.4 mm displacement. Shear failure of the bottom compressive column occurred during the cycle 1/12.5 followed by failure of the wall in out of direction. Fig. 4(d) shows the condition of IF_{O-2} specimen by cycles to 1/50 rad.

IF_{OR-1} specimen

Initial shear crack at the left corner of the opening and initial flexural crack above the opening of infill was observed at 0.75 mm displacement during the cycle 1/800. Initial flexural crack took place at the tensile column at the displacement of 1.7 mm during the cycle 1/400. An initial shear crack appeared at the tensile column at the displacement of 3.8 mm during the cycle 1/200. During the subsequent cycles, flexural cracks at along height of

both columns and shear cracks at the bottom of the compressive column were developed. Shear cracks propagated in infill at the left and right sides of the opening and below the opening. Shear failure of tensile column occurred at the cycle 1/12.5. Infill failed in out of plane direction at the cycle 1/10. Fig. 4(e) shows the condition of IF_{OR-1} specimen by cycles to 1/50 rad.

IF_{OR-2} specimen

During the cycle 1/800, initial flexural and shear cracks in infill were detected at the top left corner of the opening at 1.4 mm displacement. Initial flexural crack at the top of the tensile column was observed at the displacement of 1.1 mm during the cycle 1/400. The initial shear crack appeared at the top of the tensile column at the displacement of 2.9 mm. At the subsequent cycles, propagation of flexural and shears cracks in both columns and development of shear cracks at the left side was noticed. The top of the tensile column failed in shear during the cycle 1/12.5. Moreover, brick infill failed in out of plane direction at the cycle 1/10. Fig. 4(f) shows the condition of IF_{OR-2} specimen by cycles to 1/50 rad.

Comparison of Seismic Performance

Figure 5 shows the relationship between lateral force and lateral displacement in hysteresis loops and envelop curves to indicate the seismic performance of specimens. The bare frame (BF) and solid infilled frame (IF_{SW}) specimens achieved the maximum lateral strength of 51.3 kN and 127.7 kN at the 57.8 mm and 7 mm displacements, respectively.

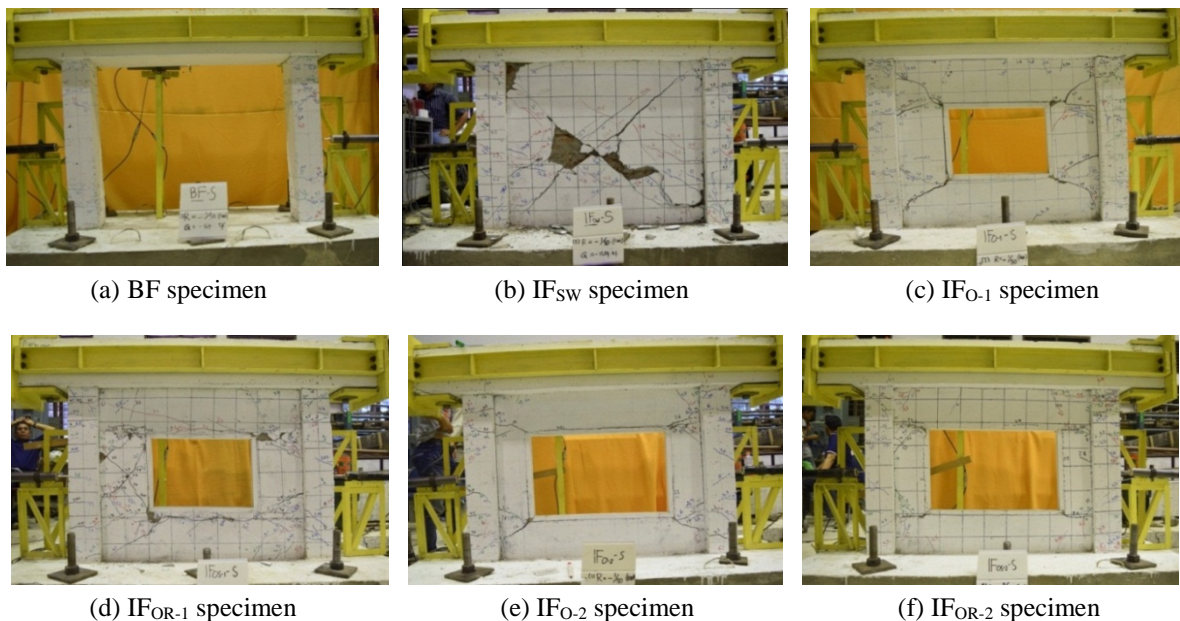


Fig. 4 Specimen at drift angle, $R=1/50$.

In the cases of infilled frames with opening specimens, the maximum lateral strength of 74.1 kN, 76.1 kN, 61.5 and 60.4 kN at 14.0 mm, 14.8 mm, 14.9 and 13.9 mm lateral displacements for IF_{O-1}, IF_{OR-1}, IF_{O-2}, and IF_{OR-2}, respectively. It revealed that the presence of a center opening reduces the lateral strength and stiffness of the overall infilled frame structure. The solid brick infill increased the lateral strength of RC frame by about 2.5 times compared to the bare frame. The opening of 25% and 40% in infill decreased the lateral strength of solid brick infilled frame to 0.59 times and 0.48 times, respectively. However, the lateral strengths of infills with openings of 25% and 40% were higher 1.4 times and 1.2 times than that of the bare frame, respectively. Based on the Fig. 5, it seems that the

horizontal reinforcements installed at the bottom and above opening were ineffective to increase the lateral strength of the overall structure, but they contributed to preventing the failure of infill in out of plane direction, and they effectively controlled the growth of the shear cracks at the corners of the opening. The deformation capacities of structure were a deformation as the lateral force degraded to 80% after the maximum of the force that was reached at displacements of 63.0 mm for BF, 27.7 mm for IF_{SW}, 57.7 mm for IF_{O-1}, 59.5 mm for IF_{OR-1}, 69.6 mm for IF_{O-2} and IF_{OR-2} specimens. It indicates that the infilled frames with a central opening more ductile than the solid infilled frame. The reinforced opening infills were not more ductile than unreinforced opening infills.

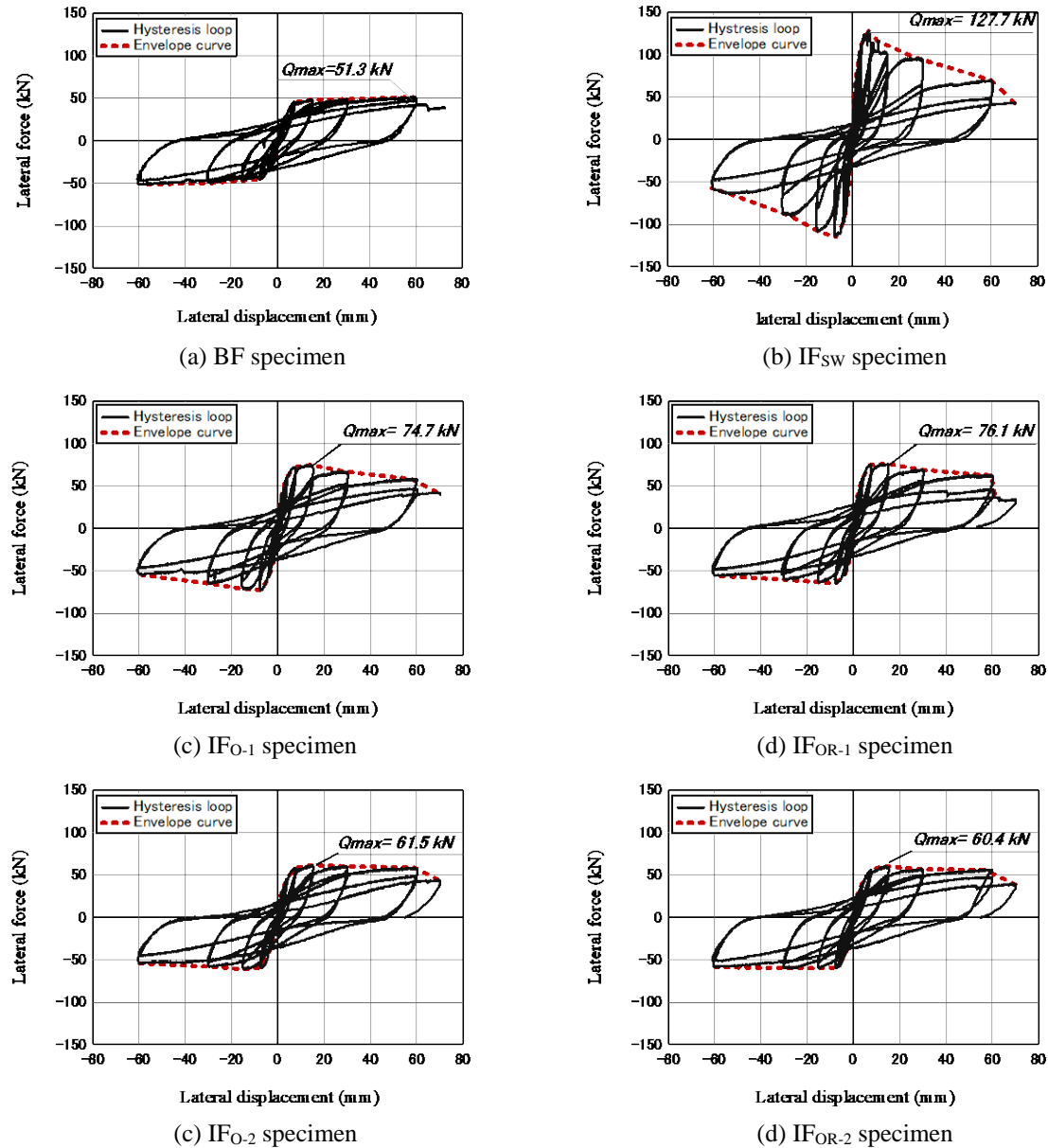


Fig. 5 Lateral strength-displacement relationship.

Energy Dissipated

Energy on frame structure due to the seismic force can be dissipated by response of hysteresis loop without a significant reduction in strength of structure [12]. Therefore, the area enclosed by hysteresis loops indicated in Fig. 5 can be evaluated to represent the energy dissipated of specimens. The comparisons of cumulative energy dissipation of specimens are presented in Fig. 6. The figure exhibits that the dissipated energy of the infilled frame decreased as opening existed in infill. The energy dissipation of the infilled frame with opening of 40% is the same with that of the bare frame. In the case of infilled frames with embedded rebar reinforcements, their energy dissipations were relatively the same with that of unreinforced ones.

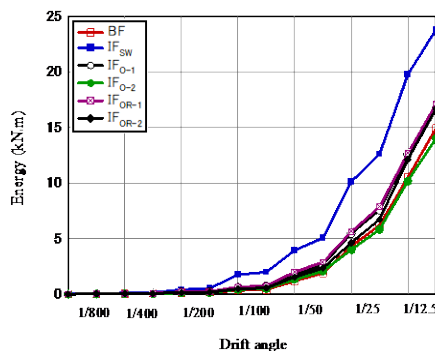


Fig. 6 Cumulative energy dissipated of specimens.

CONCLUSION

Experimental tests on brick infilled RC frame with a central opening and with/without reinforcements in infills were carried out under cyclic lateral loading to assess their seismic performance. As the results, a central opening reduced the lateral strength and energy dissipation of solid infilled frame. Horizontal reinforcements embedded in infill above and below the opening were ineffective to increase the lateral strength and energy dissipation, however, it verified to resist large deformation of masonry infill in out of plane direction.

ACKNOWLEDGEMENT

This paper reports the results of research developed under financially supported by the Ministry of Research, Technology, (DIKTI) Indonesia, with the reference 529/27.O10.4.2/PN/2017.

REFERENCES

[1] Dautaj A.D., Kadiri Q., and Kabashi N, Experimental Study on the Contribution of

- Masonry Infill in the Behavior of RC Frame under Seismic Loading, *Journal of Engineering Structures*, Vol. 165, 2018, pp. 599-621.
- [2] Mynarz M. and Mynarzova L., Non-Linear Approaches to the Response of Brick Masonry Wall to Lateral Loading, *International Journal of GEOMATE*, Vol. 14, Issue 42, 2018, pp. 76-82.
- [3] Perrone D., Leone M., and Aiello M.A., Evaluation of the Infill Influence on the Elastic Period of Existing RC Frames, *Journal of Engineering Structures*, Vol. 123, 2016, pp. 419-433.
- [4] Maidiawati, Sanada Y., Investigation and Analysis of Buildings Damaged during the September 2007 Sumatra, Indonesia Earthquakes, *Journal of Asian Architecture and Building Engineering* Vol.7, No.2, 2008, pp. 371-378.
- [5] Maidiawati, Sanada Y., Sanada, Konishi D., and Tanjung J., Seismic Performance of Nonstructural Brick Walls Used in Indonesian R/C Buildings, *Journal of Asian Architecture and Building Engineering*, Vol.10, No.1, , 2011, pp.203-210.
- [6] Maidiawati and Sanada Y., R/C Frame-Infill Interaction Model and Its Application to Indonesian Buildings, *Earthquake Engineering and Structural Dynamics*, Vol.46, Issue 2, 2017, pp. 221-241.
- [7] Choi H., Nakano Y., and Sanada Y., Seismic Performance and Crack Pattern of Concrete Block Infilled Frames, In *Bulletin of ERS*, No.38, 2005.
- [8] Maidiawati, Tanjung J., and Medriosa H., Conference proceedings, in *AIP Conf. Proc.1892 of IGNITE-AICCE'17*, 2017, pp. 020013-1-020013-8
- [9] Mondal G., and Jain, S., K., Lateral Stiffness of Masonry Infilled Reinforced Concrete (RC) Frames with Central Opening, *Earthquake Spectr.*, *Earthquake Engineering Research Institute (EERI)*, Vol.24, No.3, 2008, pp. 701-723.
- [10] Mohammadi M., and Nikfar F., Strength and Stiffness of Masonry-Infilled Frames with Central Openings Based on Experimental Results. *Journal of Structural Engineering*, Vol.139, 2013, pp.974-984.
- [11] Interim Testing Protocols for Determining the Seismic Performance Characteristic of Structural and Nonstructural Component," *FEMA 461*, pp. 21-25, 2007.
- [12] Rodrigues H., Varum H., Arede A., and Costa A., A Comparative Analysis of Energy Dissipation and Equivalent Viscous Damping of RC Columns Subjected to Uniaxial and Biaxial Loading, *Journal of Engineering Structures*, Vol.35, 2012, pp.149-164.

THE ANALYSIS OF RIVER RUNOFF IN THE ABUKUMA RIVER BASIN

Masanobu Taniguchi¹, Hiroyuki Ii²

¹Faculty of system engineering, Wakayama University, Japan ¹.

ABSTRACT

The characteristic of the river runoff in the Abukuma River Basin has been not to clarify. The area of the Abukuma River basin is 5,400 km². The flow path extension of the Abukuma River is 239km. There is the hydrophobic pass from the Inawashiro Lake. The water is used by some cities, so the water pass is complex, therefore the analysis of river runoff is difficult. It is important that the river runoff in the each little basin for floods estimation. The river cross section was surveyed, and the river flow rate is calculated. In the flood caused by the typhoon in August 1985 which recorded the largest flood after the war, it suffered a tremendous damage. The research objective is clarify the ratio of river runoff of each little basin. The analysis will be basic information for the analysis of pollutant load and movement of cesium.

Keywords: runoff, river flow, Abukuma River,

INTRODUCTION

The gradient of Abukuma River is gentle, so the cities in the basin was damaged from floods often in past. So it is important to know the flow rate for floods countermeasure, the river basin has lots of data since 1930 in some observing station. The Typhoon gave big damage often in 1938, 1941, 1943, 1947, 1948, 1950, 1958, 1966, 1971, 1981, 1982, 1986, 1991, 1998, and 2002. In other hand, the drought damage has also occurred in other years in the Abukuma River Basin in 1967, 1973. 1978, 1987, 1997. The Abukuma Basin River history was old, the observing station was constructed in early period in 1900's. The first Dam, Shinobu Dam in the Abukuma River Basin was constructed in 1939. The Basin has problem of waterless in long period. The agriculture water was send from the Inawashiro Lake by the Asakasosui water pass in 1890 in first, the water pass was connected to the larger rice field region in 1900's.

The basin is researched in past about water quality and floods.[1][2]

Therefore, in the Abukuma River Basin, the water moving was changing from 1938 to 2017, it is important to clear the relation between water runoff and precipitation. The research will be clarify the relation between the rain runoff and river runoff of before and after the construction of dams and land use changes.

RESEARCH METHOD

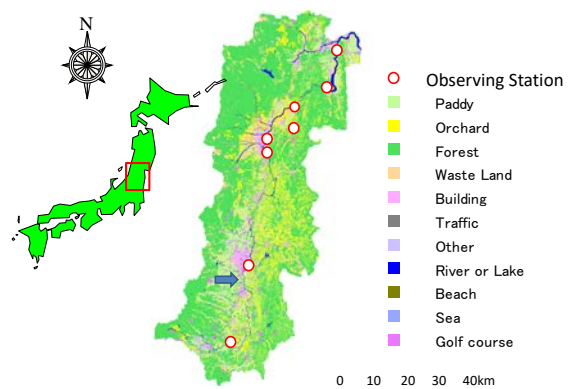
The water runoff analyze system is developed. The system has database on the river structure made by GIS data. Therefore, the system is able to automatically calculated upper area, compared with

precipitation quickly. [3]

The precipitation data was imported from downloaded at government original data not converted. The used data is Meteorological Agency and Ministry of Land, Infrastructure and Transport (MLIT).[4] Moreover, the water level and flow rate data is imported from government data, MLIT. The analysis system can handle big data, and the datas linked GIS data, the system can execute several runoff analysis. The flow rate data was not measured in few year, so the flow rate was estimated by the water level data.

The river cross section was measured the distance from the bridge to riverbed between 5m length each. In addition, river velocity is observed, velocity decided the by average of three times measured. The missing data of flow rate can be estimated used by relation between water level and river cross section.

OVERVIEW OF RESEARCH AREA



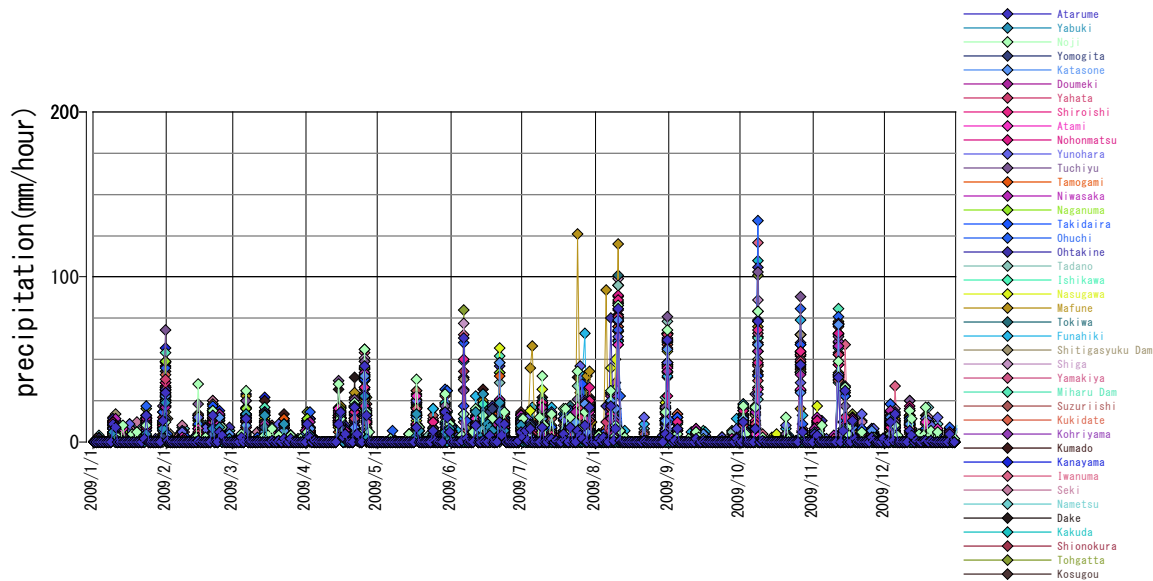


Fig.1 shows overview of Abukuma River Basin. The area in Abukuma River basin is 5,400 km². The flow path extension of the Abukuma River is 239km.[5] The length is 2nd long in Tohoku Area in Japan. The population is about 1.78 million people in the Basin. The Abukuma River has 17 cities in Fukushima Prefecture, has five cities in Miyagi Prefecture. The Abukuma River is originated at Asahidake in South - East of Fukushima. The land use of 56% in whole basin is forest, 16% is paddy, 14% is orchard, and 6% is building. The water of the Inawashiro lake inflows in the upper stream of Abukuma River Basin shown in arrow in figure. The sending water is mainly used for paddy. So it was estimated that the sending water increases the amount of river basin water. However, in other side, Dams control the river water, it is considered that the amount of water in the Basin does not necessarily increase.

THE TIME SERIES OF PRECIPITATION

Fig.2 shows time series of daily precipitation in 2009. There are 40 observing station of precipitation around the Abukuma Basin. Some observing station did not have precipitation, and the distance between stations is different. Since the basin area is too big, the max of precipitation is different place each event. Therefore, it was necessary to calculate rain runoff with each little basin. The precipitation in one event is different with each places, so the sum of rain runoff in the Abukuma River Basin needs to be calculated by sum of multiply the precipitation and basin area.

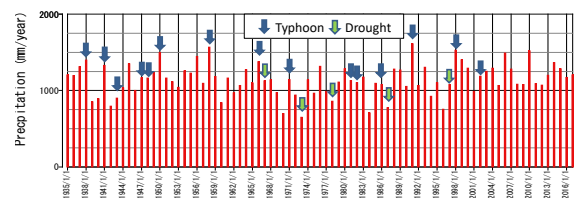


Fig.3 Time series of annual precipitation from 1935 to 2017 at Fukushima.

Fig.3 shows time series of annual precipitation from 1935 to 2017 at Fukushima. The annual precipitation is constantly not changed and the average is 1143 mm/year. The max value is 1613 mm/year in 1991, and minimum is 652 mm/year in 1973.

RELATION BETWEEN WATER LEVEL AND FLOW RATE

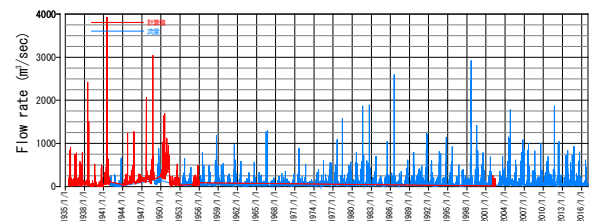


Fig.4 The time series of the flow rate from 1935 to 2016 at Hongu

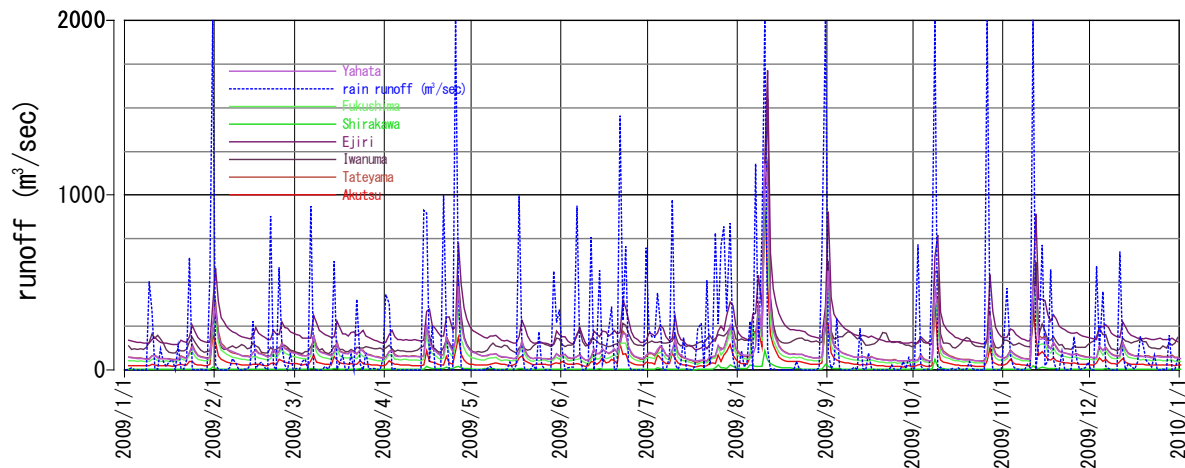


Fig.6 The time series of flow rate and rain runoff in 2009

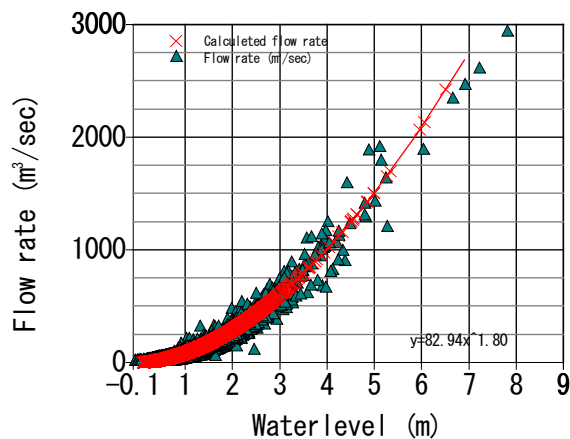


Fig.5 The relation between the water level and the flow rate from 1935 to 2016.

Fig.4 shows the time series of the flow rate from 1935 to 2016 at Hongu, middle stream of observing station in the Abukuma River Basin. Fig.5 shows the relation between the water level and the flow rate from 1935 to 2016. The flow rate was measured from 1942, so generally the flow rate is not measured directly, thus the flow rate is calculated from water level, and the calculated flow rate was compared with survey data sometimes measured. The dot line shows calculated from the water level data. The calculated flow rate data is fitting from the relation between the water level and the flow rate statistically. [6][7]

The fit line function is shown in formula (1).

$$f(x) = 82.94x^{1.80} \quad (1)$$

$f(x)$:flow rate (m³/sec) x :water level (m)

Compare with the flow rate before 1960, the peak of flow rate was small after 1960. From 1967 to 1998, drought occurred shown in Fig.3, moreover the period was the High Growth Period in Japan, so the

amount of using water increased. Many water is used, and the Basin has not enough Dams. Six Dam built in the period, and two dams built in 2000's. First Dam built in 1938, so if it is considered the influence of dam, it is need to estimate the flow data from the water level for the comparing before 1938. Therefore, as the flow rate has related to the water level, the flow rate was calculated from relation with the water level.

COMPARING WITH THE FLOW RATE AT EACH OBSERVING STATION

The flood flowing is not constant, so the velocity cannot be measured easily. Therefore, the flow rate in flood time was not sometimes measured. So, the flow rate was calculated by the water level, the fit line formula of constant was calculated. Table 1 shows the list of the fit line formula of constant at each observing station.

Table.1 The calculated constant parameter

Observing station	constant a	constant b
Akutsu	190.500	1.2
Tateyama	4.277.E-13	12
Iwanuma	581.486	1.05
Ejiri	0.016	5
Kuroiwa	59.947	2.15
Shirakawa	-	-
Fukushima	117.007	2.15
Yahata	345.145	1.26

$$f(x) = ax^b$$

THE COMPARING OF THE FLOW RATE

Fig.6 shows the time series of flow rate and rain runoff in 2009. Fig.7 shows the time series of rate of

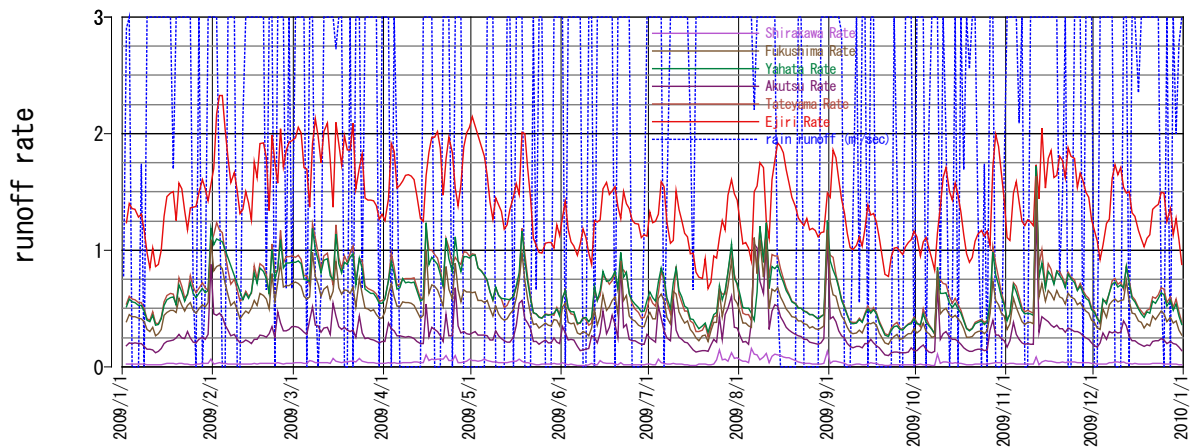


Fig.7 The time series of runoff rate against the flow rate at Iwanuma in 2009

runoff against the flow rate at the lowest station of the Abukuma Basin, Iwanuma in 2009. The change of flow rate tend to same change at each observing station. The rate of each flow rate of observing station against the lowest point was calculated. It is need to know the rate of water runoff in the river basins, so the flow rate at the main stream was compared. The observing station is lowest observing station of Iwanuma, next Ejiri, Tateyama, Yahata, Fukushima, Shirakawa. Generally, the flow rate at lowest station is biggest, however comparing with the flow rate at Iwanuma and at Ejiri, the flow rate is sometimes reversed in two station. There is another river basin flow into at upper Iwanuma, however the flow rate do not increased. So the riverbed is sand, it is estimated that the infiltration is occurred. Fig.7 shows the time series of runoff rate against the flow rate at Iwanuma in 2009. The runoff rate was calculated by next formula.

$$\text{runoff rate} = \frac{\text{each Station flow rate}}{\text{flow rate at Iwanuma}} \quad (2)$$

If the runoff rate shows one, it shows that the flow rate was not changed. In addition, if the value is bigger than one, it shows that the flow rate decreased. The runoff rate at Ejiri shows almost more than one, the rate increased in rain time shown by blue dot line in Fig.7, and decreased in fine days. The runoff rate at another observing station shows almost less than one. The runoff rate average at Yahata is 0.64, the value at Tateyama is 0.65, the value at Fukushima is 0.50 the value at Akutsu is 0.28, and the value at Shirakawa is 0.04. The upper basin area at Yahata is 4128km², Fukushima is 3304km², and Akutsu is 1940km². The runoff rate was calculated less about 10% than basin area rate against the whole basin.

In rain time, the flow rate is increased all observing station, and the flow rate is seemed near value at each stations in Fig. 6. The rate of flow rate against the lowest station was compared. In middle January, the runoff rate is constant in fine days, and

the runoff rate tend in middle July is same in fine days. However, in rain time, the runoff rate is changeable, and the runoff rate increased to about one at some observing station. It was estimated that there is rainfall in mainly upper area, and so some basin has no rain, it is necessary to calculate the amount of rainwater by sum of the rainfall in whole basin.

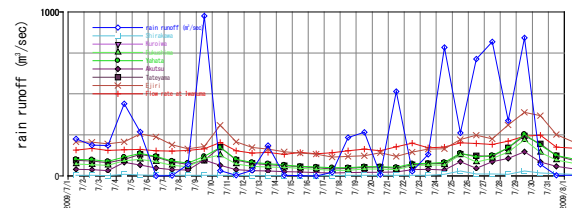


Fig.8 The time series of the water runoff in July 2009

Fig.8 shows the time series of the water runoff in July 2009. The peak of flow rate tend to be late than 1 day of the peak of rain runoff. The flow rate tends to be higher in 5 days after precipitation. Therefore, if the water runoff of analysis was carried out, it is necessary to calculate the 5 days of data at least. The Abukuma River Basin has some dams, minimum flow rate is promised. The rain runoff is 200m³/sec from 1 July to 3 July, and the flow rate is same value in the period. The flow rate and rain runoff is balanced, the values is constant. The rain runoff is less from 11 July to 20 July, the flow rate change little. The minimum flow rate is 115m³/sec, if the rain runoff is higher than the flow rate, it is estimated that the flow rate increase.

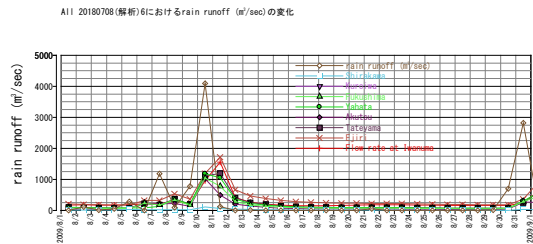


Fig.9 The time series of the water runoff in August 2009

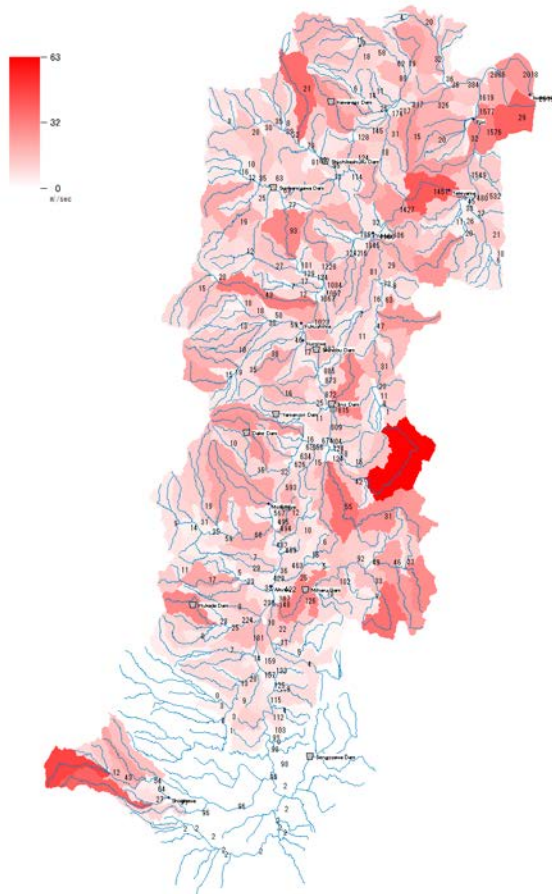


Fig.10 The distribution of integrated rain runoff from upper stream at August 10, 2009

Fig.9 shows the time series of the water runoff in August 2009. In August 10, the rain runoff is 4000m³/sec. It is estimated that the peak of the rain runoff is caused by the typhoon 9. West Japan is big damaged by the typhoon 9. Compare with the peak of rain runoff and the peak of flow rate, the peak of flow rate is tend delay one day except the Shirakawa observing station. The Shirakawa observing station is the most upstream observing station. The rain runoff at Shirakawa observing station did not increased compare with the other stations. It was estimated that the Shirakawa observing station had no rain or a little. Fig.10 shows the distribution of integrated rain runoff from upper stream at August 10, 2009. The rain

runoff was calculated by 50% of amount of the rain runoff at each basin. The reason is that the all of the precipitation do not flow out directly. The rain runoff was adjusted to the flow rate value. The rain runoff at Shirakawa observing station was 96 m³/sec, Akutsu was 492m³/sec, Fukushima was 1023m³/sec, Ejiri was 1577m³/sec and Iwanuma was 2018m³/sec.

Table. 2 The list of flow rate and rain runoff at the typhoon 9 in August 2009

年月日 (m ³ /sec)	Iwanuma	Ejiri	Tateyama	Yahata	Fukushima	Akutsu	Shirakawa	rain runoff
2009/8/9	214	365	201	191	165	134	18	777
2009/8/10	956	1192	1108	1182	1045	1021	109	4095
2009/8/11	1553	1714	1188	1046	776	496	57	122

Table. 2 shows the list of flow rate and rain runoff at the typhoon 9 in August 2009. The flow rate data shows observed data. The Shaded data was compared with the rain runoff. As the flow path extension of the Abukuma River is 239 km, if the flow velocity is 2m/sec between 200 km distance, the reach time is calculated about 1 day. The calculation is very rough, however the result shows important information. The Shirakawa observing station has directly rain and the other stations is far from rain place.

Therefore, the rain runoff was compared with the next day of flow rate, except the Shirakawa observing station. The flow rate is same to 50% of amount of the rain runoff at each basin, it is estimated that the runoff rate is average 50%. The flow velocity was estimated about 2m/sec at the typhoon time.

CONCLUSION

The research will be clarify the relation between the rain runoff and river runoff of before and after the construction of dams and land use changes. The water runoff analyze system is developed. The system has database on the river structure made by GIS data. Therefore, the system is able to automatically calculated upper area, compared with precipitation quickly. The long-term flow rate is compared, it was estimated that the flow rate is not effect from dams, the cause of less flow rate is little precipitation in 1990's, and the max of flow rate did not decreased dams construction before and after. The typhoon influence was analyzed by the distribution of rain runoff, the flood reach time was about 1day, and the flow velocity was estimated to 2m/sec.

REFERENCES

- [1] Tokuo KISHII, On the Flood Disaster in the Abukuma River Basin at the End of August 1998, Natural Disaster Research Report of the National Research Institute for Earth Science and Disaster Resilience 37, pp. 91-105, 2001.
- [2] Tsuyoshi KINOCHI and Katumi MUSIAKE, Water quality and nutrient loads in the abukuma

- watershed under normal flow condition, Water Engineering paper, vol. 51, February 2007(in Japanese)
- [3] Ralia, <https://www.wakayama-u.ac.jp/~masa/profile/soft/index.html>, 2018.
- [4] Ministry of Land, Infrastructure and Transport, Japan, Water information system, <http://www1.river.go.jp/>
- [5] Digital national land information, <http://nlftp.mlit.go.jp/ksj/>
Japan Meteorological Agency, <http://www.jma.go.jp/jma/index.html>
- [6] Kazuyuki Mizumura, Hydrosphere hydrology, 1998.
- [7] Isamu Kayane, Hydrology, Daimeido 1980.

INFLUENCE OF POZZOLANIC MATERIALS IN THE ADSORPTION OF HEAVY METALS ON RED LOESS SOIL

¹Pongsakorn Punrattanasin, ²Arnun Chantaduang and ³Chinawat
^{1,2,3}Muktabhant Faculty of Engineering, Khon Kean University, Thailand

ABSTRACT

This study presents the results from laboratory in the adsorption of heavy metals on red loess when mixing with Pozzolanic materials. The Pozzolanic materials consist of fly ash, bottom ash, rice husk ash, blast furnace slag, silica fume, metakaolin, and Portland cement. Most of Pozzolanic materials are byproducts and easy to find. Copper, nickel and zinc were selected as heavy metals and batch sorption test was selected as a method to evaluate the sorption capacity. It was also found that the potential of Pozzolanic materials were ranged from Portland cement, fly ash, bottom ash, blast furnace slag, rice husk ash, silica fume and metakaolin, respectively. The results from this experiment can be by identifying the adsorption isotherm model. The isotherm can describe and analyze the adsorption potential. The Langmuir and Freundlich isotherm models were able to efficiently explain the adsorption behavior of the loess.

Keywords: Adsorption, Loess, Pozzolanic materials, Batch sorption test, Cement, Isotherm

INTRODUCTION

The Northeastern part of Thailand covers an area of 170,000 km². Approximately one-third of Thailand's populations live in this region. The general physiography is mainly undulated by high plateau. The top most soil layer found in these areas is loess layer or wind-deposited soil (Fig.1). Loess can be defined as a terrestrial clastic sediment, which composed predominantly of silt-size particles essentially formed by the accumulation of wind-blown dust [1]. This research aims as one method to investigate and study the effect of industrial companies to the environmental issue of neighboring community. Ground contamination due to a variety of inorganic compounds can surely be occurred as a result of leaks of hazardous chemicals. The sorption value of contaminations such as heavy metals on loess soil is investigated and a possible method of improving the sorption capacity of contaminated flow into this red loess is also proposed in this study by adding variety of Pozzolanic materials.

MATERIALS USED

Red loess (R) in the Northeastern part of Thailand were designated as the adsorbent of this study. The samples were collected and dug at the depth of 50 cm from its surfaces and were dried in the oven at 110 °C for 24 hours for bulk water elimination purpose. The basic and engineering properties of the adsorbent are shown in Table 1. From the results of the sieve analysis, and Atterberg limits test, the soil sample can be classified as silty sand (SM) by using

the Unified Soil Classification System (USCS). The Pozzolanic materials used to mix with the loess for improve the adsorption capacity in this study (Fig.2) consist of (1) fly ash (Fa), (2) bottom ash (Ba), (3) rice husk ash (Ra), (4) blast furnace slag (Bs), (5) silica fume (Sf), (6) metakaolin (Mk), and (7) Portland cement (Ce). All of the materials were dry and were then sieved through sieve No. 16. Most of Pozzolanic materials are byproducts and easy to find. The chemical analysis by X-ray fluorescence (XRF) technique and the specific surface area of the materials are summarized in Tables 2 and 3. In this study, a 5% of Pozzolanic materials was mixed with the 95% of loess by weight. This suggested ratio is from the previous study [2]. Copper (Cu), nickel (Ni), and zinc (Zn) were selected to represent the range of the common heavy metals and prepared in the form of the solution to be the adsorbates. The stock solutions of Cu (NO₃)₂, Ni (NO₃)₂, and Zn (NO₃)₂ were dissolved in the deionized water to obtain the preferred initial concentration of solution. The chosen initial concentration of the heavy metal solutions were 250, 500, 750 and 1000 mg/L. The properties of heavy metal solutions are presented in Table 4.

Table 1 Properties of Red Loess

Properties	Red Loess
% Passing # 200 sieve	11.71
% Passing # 4 sieve	96.45
Liquid Limit, LL (%)	18.03
Plasticity Index, PI (%)	5.03
Permeability, k (cm/s)	4.0 x 10 ⁻⁶

Table 2 Chemical analysis by XRF

Chemical analysis (%)	SiO ₂	Al ₂ O ₃	Fe ₂ O ₃	CaO	MgO
Red Loess	64.5	14	2.7	0.2	-
Cement	20	5	3	60	1.1
Fly ash	35	26	10	15	2
Bottom ash	48	20	11	13	2
Blast furnace	40	11	0.3	32	7
Rice husk ash	92	0.7	-	0.5	0.2
Silica fume	79.5	0.5	1	0.5	0.5
Metakaolin	55	40	-	-	-

Table 4 Properties of Heavy Metal Solutions

Properties	Copper Nitrate	Zinc Nitrate	Nickel Nitrate
Formula	Cu(NO ₃) ₂	Ni(NO ₃) ₂	Zn(NO ₃) ₂
Molecular weight (g/mol)	241.60	290.80	297.50
Density (g/cm ³)	2.32	2.05	2.06
Solubility (g/100ml)	137.80	94.20	184.30

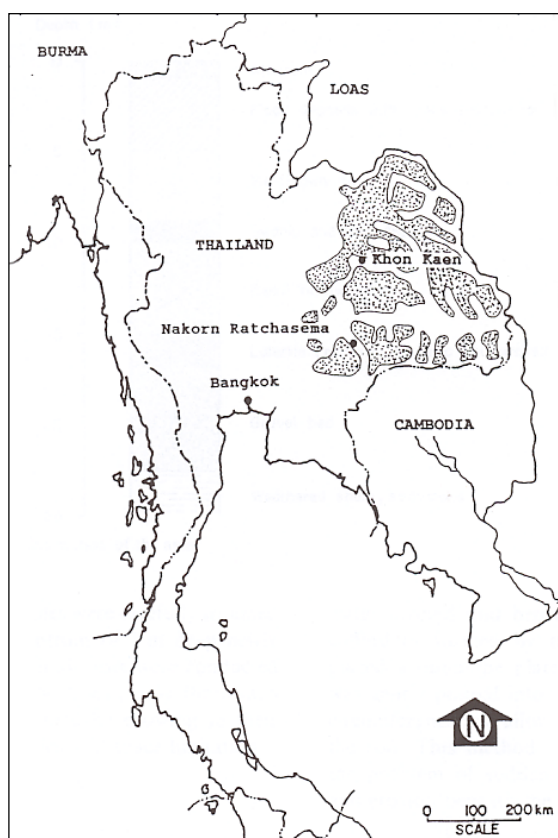


Fig. 1 Areas of loess deposits (stippled area) in Thailand (after Phien-wej et al. 1992).



(a) Portland cement



(b) Fly ash



(b) Bottom ash

Fig. 2 The Pozzolanic materials

Table 3 Specific surface area of materials

Sample	Specific surface area (m ² /g)
Red Loess	7.68
Cement	0.21
Fly ash	0.15
Bottom ash	3.88
Blast furnace	2.32
Rice husk ash	43.94
Silica fume	20.32
Metakaolin	14.47



(d) Blast furnace



(e) Rice husk ash



(f) Silica fume



(g) Metakaolin

Fig. 2 The Pozzolanic materials

EXPERIMENTAL WORK

A series of batch sorption test was performed to examine the adsorption behavior of Cu, Zn and Ni. Adsorption is the process in which atoms or molecules of a substance in one phase become bonded to the surface of a second substance in a different phase [3]. The procedures of the batch test can be done by mixing 2.5 g of soil sample with 50 cm³ of the heavy metal solution in the bottle. Then shaking the mixture with a velocity of 130 cycles per minute by the horizontal shaker until the desired time is reached. Next, the soils were separated from the heavy metal solution by using a 0.45 μm filter. After that, the solutions were diluted by mixing them with 1% Nitric Acid (HNO₃) before taking to measure the concentrations by the Atomic Adsorption Spectrometer (AAS). The effect of the initial concentration of heavy metal solution can be studied by running the batch test with 250 to 1000 mg/L of the heavy metal solutions. The concentrations of solutions at equilibrium were determined. Then, calculating the adsorption percentage at each initial concentration by using Eq. 1.

$$\% \text{adsorption} = \frac{(C_0 - C_{eq})}{C_{in}} \times 100 \quad (1)$$

Where: C_0 and C_{eq} are the initial and equilibrium concentrations of heavy metal solution (mg/L), respectively. There are many mathematical models used to represent the adsorption isotherm, although the two most commonly used models are the Langmuir and Freundlich isotherms. The Langmuir adsorption isotherm has been widely applied to many adsorption processes, specifically those assuming monolayer adsorption on the adsorption surface. The Langmuir isotherm is defined as:

$$q = \frac{\alpha\beta C_{eq}}{1 + \alpha C_{eq}} \quad (2)$$

Where: q is the amount of adsorption of heavy metals per unit weight within soil (mg/g), α is the Langmuir constant, related to the bonding energy between the adsorbed ion and the adsorbent (L/mg) and β is the maximum adsorption capacity (mg/g). The Freundlich isotherm is the most common isotherm model, used to describe physical adsorption in a solid-liquids system, and is defined as follows:

$$q_e = K(C_{eq})^{1/n} \quad (3)$$

Where: q_e is the amount of adsorbed heavy metal per unit weight of soil at equilibrium (mg/g), K is Freundlich constant (mg/g) and $1/n$ is the adsorption intensity (dimensionless) [4].

RESULT AND DISCUSSION

By using the concentration of 250, 500, 750 and 1000 mg/L, the adsorption percentage at each

concentration can be shown in Figs. 1 to 3. It can be seen that the adsorption percentage decreased with the increasing initial concentration. This can be explained by a reason of saturation on the soil surface where the adsorption took place [5].

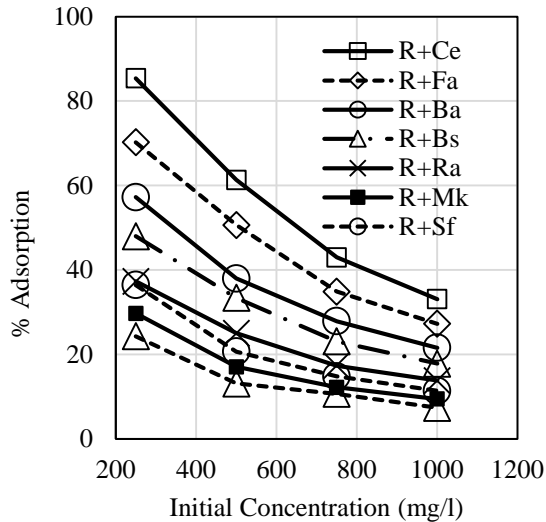


Fig. 1 Effect of initial concentration on Cu

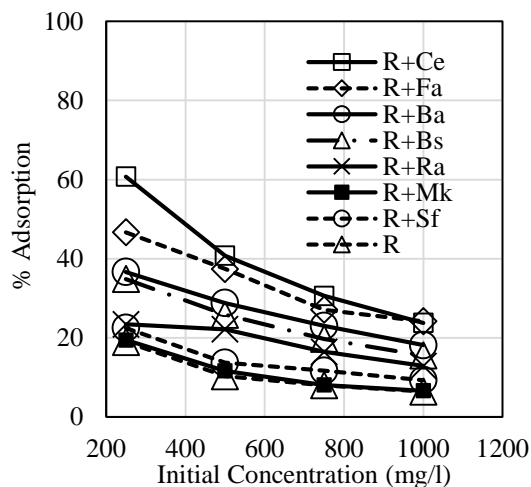


Fig.2 Effect of initial concentration on Ni

The adsorption isotherm obtained from the tests are shown in Figs. 4 to 6. It can be seen that the amount adsorbed increased with the equilibrium concentration. This was due to the driving force of the metals toward active sites increased when the concentration increased. Figures 7 and 8 show examples of how to convert and calculate the data from Fig. 4 to 6 into the parameters for Langmuir and Freundlich adsorption isotherms in the case of Cu for red loess mixed with cement. The adsorption isotherm parameters of Langmuir and Freundlich models were summarized in Tables 5 and 6, respectively. High values of R^2 reveal that the adsorption isotherm was well fitted to both models.

From Langmuir model, the β -parameters summarized in Table 5 is the maximum adsorption capacity of the samples. It can be seen that loess mixed with cement (R+Ce) show the highest adsorption capacity, while loess mixed with metakaolin (R+Mk) provided the lowest capacity. It was also found in Table 5 that the potential of Pozzolanic materials were ranged from Portland cement, fly ash, bottom ash, blast furnace slag, rice husk ash, silica fume and metakaolin, respectively. The adsorption capacity of Cu was higher than the capacity of Ni and Zn for all samples. Figure 9 shows the comparison of the maximum adsorption capacity (β -parameter) of the loess mixed with seven Pozzolanic materials.

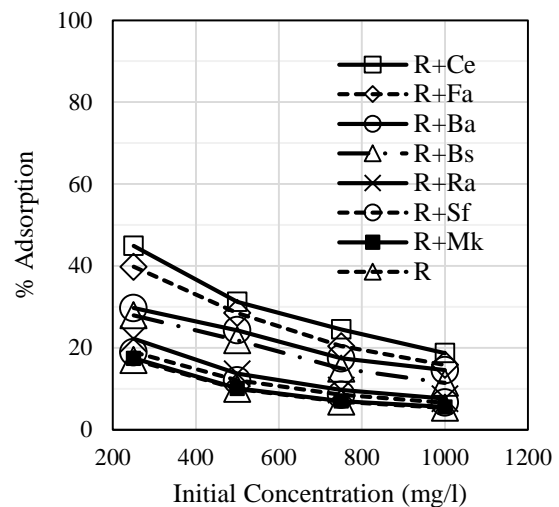


Fig.3 Effect of initial concentration on Zn

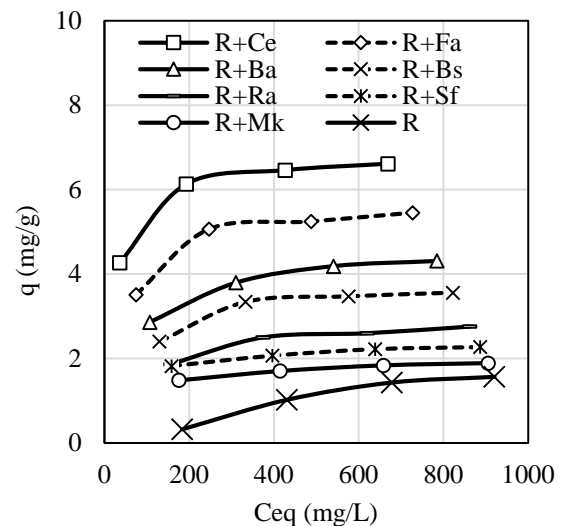


Fig. 4 Adsorption isotherm of Cu

Table 7 summarizes the calculated percentage of adsorption improvement when adding the Pozzolanic materials to the loess. It can be seen that all the materials especially cement and fly ash can

dramatically improve the adsorption capacity of Cu, Ni and Zn. The adsorption capacity can improve up to 350% compared to pure loess by adding only 5% of cement to the loess.

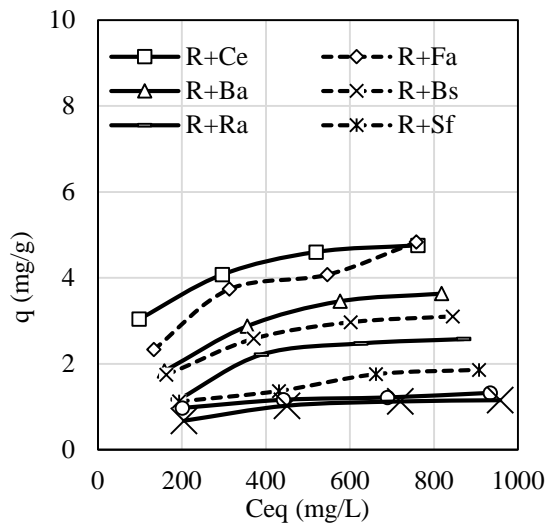


Fig. 5 Adsorption isotherm of Ni

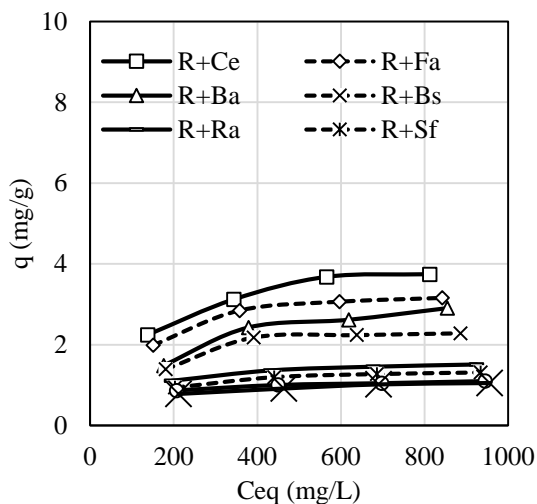


Fig. 6 Adsorption isotherm of Zn

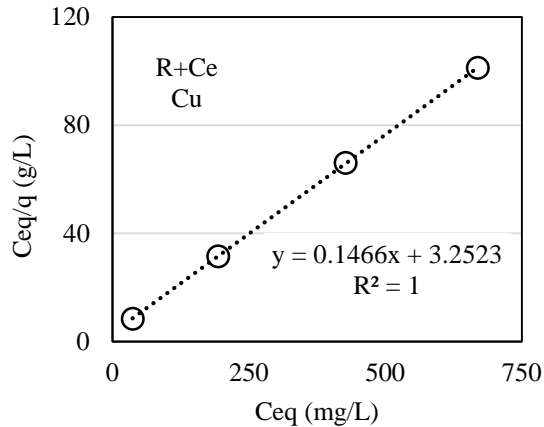


Fig.7 Langmuir adsorption isotherm of Cu for R+Ce

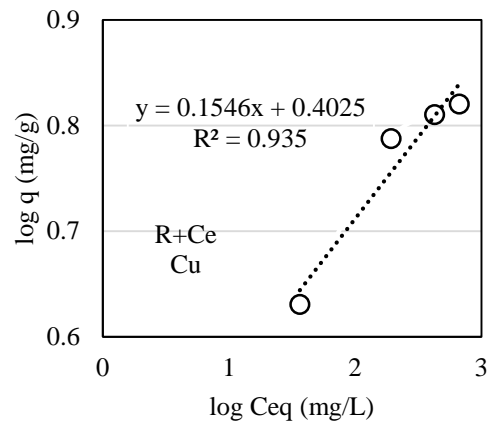


Fig.8 Freundlich adsorption isotherm of Cu for R+Ce

Table 5 Parameters of Langmuir adsorption isotherm

Sample	Heavy metals	β (mg/g)	α (L/mg)	R^2
R+Ce	Cu	6.8213	0.0451	1.0000
	Ni	5.2247	0.0134	0.9995
	Zn	4.3956	0.0076	0.9975
R+Fa	Cu	5.7670	0.0231	0.9995
	Ni	6.0241	0.0047	0.9846
	Zn	3.6010	0.0091	0.9982
R+Ba	Cu	4.7015	0.0142	0.9999
	Ni	4.7801	0.0041	0.9962
	Zn	3.7411	0.0041	0.9905
R+Bs	Cu	3.8790	0.0145	0.9986
	Ni	3.8168	0.0054	0.9985
	Zn	2.6724	0.0076	0.9881
R+Ra	Cu	3.0497	0.0105	0.9987
	Ni	3.7439	0.0029	0.9468
	Zn	1.6722	0.0102	1.0000
R+Sf	Cu	2.4125	0.0175	0.9996
	Ni	2.3474	0.0041	0.9801
	Zn	1.4747	0.0093	0.9996
R+Mk	Cu	2.0288	0.0142	0.9996
	Ni	1.4499	0.0093	0.9966
	Zn	1.1889	0.0125	0.9994
R	Cu	1.6508	0.0102	0.9845
	Ni	1.1684	0.0041	0.9625
	Zn	0.9823	0.0021	0.9747

Table 6 Parameters of Freundlich adsorption isotherm

Sample	Heavy metals	k (mg/g)	1/n	R^2
R+Ce	Cu	2.5264	0.1546	0.9350
	Ni	1.0957	0.2260	0.9797
	Zn	0.5159	0.3032	0.9663
R+Fa	Cu	1.5915	0.1935	0.9028
	Ni	0.3393	0.4018	0.9591
	Zn	0.5257	0.2738	0.9199
R+Ba	Cu	1.0832	0.2122	0.9702
	Ni	0.2158	0.4302	0.9625
	Zn	0.1817	0.4174	0.9304
R+Bs	Cu	0.8738	0.2162	0.8892

Sample	Heavy metals	k (mg/g)	1/n	R ²
R+Ra	Ni	0.2897	0.3595	0.9592
	Zn	0.2990	0.3105	0.8291
	Cu	0.6094	0.2272	0.9346
	Ni	0.0819	0.5248	0.8779
	Zn	0.3911	0.2010	0.9709
R+Sf	Cu	0.9348	0.1322	0.9919
	Ni	0.1825	0.3417	0.9641
	Zn	0.2996	0.2209	0.9483
R+Mk	Cu	0.6866	0.1500	0.9936
	Ni	0.3543	0.1917	0.9822
	Zn	0.3852	0.1544	0.9868
R	Cu	0.5847	0.1745	0.9125
	Ni	0.2431	0.26540	0.8974
	Zn	0.2955	0.1342	0.9254

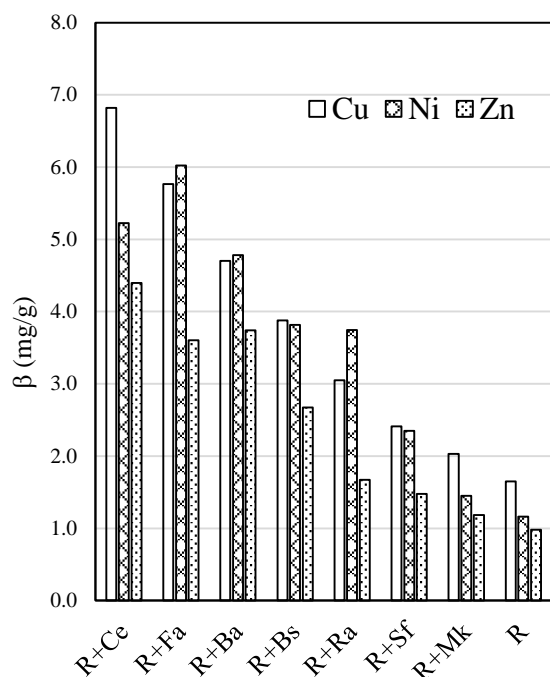


Fig. 9 Maximum adsorption capacity of samples

Table 7 The percentage of adsorption improvement when adding the materials to the loess

Sample	Percentage of Improvement		
	Cu	Ni	Zn
R+Ce	313.41	350.41	348.53
R+Fa	249.52	419.32	267.45
R+Ba	184.94	312.08	281.74
R+Bs	135.09	229.03	172.69
R+Ra	84.83	222.75	70.63
R+Sf	46.21	102.36	50.48
R+Mk	22.96	24.99	20.60

CONCLUSIONS

This research studied the behaviors of adsorption of loess on seven kinds of Pozzolan materials i.e., fly ash, bottom ash, rice husk ash, blast furnace slag, silica fume, metakaolin, and Portland cement. The adsorption capability and the adsorption isotherm were investigated by the batch method. The concentrations of the solution used in the batch test were 250, 500, 750 and 1000 mg/L. The adsorption capability decreased when the initial concentration increased. The Langmuir and Freundlich isotherm models were able to efficiently explain the adsorption behavior of the loess mixed with all seven Pozzolan materials. Mixing red loess with cement or fly ash resulted in a more effective performance relative to using pure loess. Adsorption capacities were ranked as follows: Portland cement > fly ash > bottom ash > blast furnace slag > rice husk ash > silica fume > metakaolin.

ACKNOWLEDGEMENTS

This research was support by Department of Civil Engineering, Faculty of Engineering, Khon Kean University.

REFERENCES

- [1] Phien-wej N., Pientong T., and Balasubramaniam, A.S., Collapse and strength characteristics of loess in Thailand. *Engineering Geology*, Vol.32, 1992, pp.59-72.
- [2] Tongew N. and Punrattanasin P., Influence of alternative materials in the adsorption of heavy metals on loesses. in *Proc. of the 21th National Conference on Civil Engineering*, 2016, pp. 1198-1203.
- [3] Dube A., Zbytniewski R., Kowalkowski T., Cukrowska E., and Buszewski B., Adsorption and migration of heavy metals in soil. *Pol. J. Environ. Stud.* Vol.101, 2001, pp.1-10.
- [4] Mohammad Kashif Uddin., A review on the adsorption of heavy metals by clay minerals, with special focus on the past decade, *Chemical Engineering Journal*., Vol 308, 2017, pp 438-462.
- [5] S. Veli, B. Alyuz, Adsorption of copper and zinc from aqueous solutions by using natural clay, *J. Hazard. Mater.* 149 (2007) 226-233.

EXPERIMENTAL STUDY AND MODELLING OF STRESS-STRAIN RELATIONSHIP OF RC COLUMNS STRENGTHENED BY BAMBOO REINFORCED CONCRETE JACKETS

Ari Wibowo¹, Indradi Wijatmiko¹ and Christin Remayanti Nainggolan¹

¹Faculty of Engineering, Brawijaya University, Malang, Indonesia, 65145

ABSTRACT

Bamboo bars as replacement of steel reinforcement for structural concrete columns have gained increasing interest due to the consideration of sustainability and green construction issues. Its application on concrete jacketing method is being studied in this paper. In order to comprehensively understand the strength capacity and behavior of such columns, the stress-strain relationship needs to be investigated. However, most available stress-strain model were developed for steel reinforced concrete columns as found in many papers and codes; but not for bamboo reinforced concrete columns. Therefore, experimental tests on axial load-deformation and the related stress-strain curve of damaged concrete columns retrofitted with bamboo concrete jacket has been undertaken. The parameters investigated in the test were longitudinal and transverse reinforcement ratios, spacing of the stirrups, and the longitudinal bar configuration. The stress-strain model bamboo was then developed and in a reasonable agreement with the experimental data.

Keywords: Stress-strain formula, Bamboo reinforcement, Concrete column, Axial load test

INTRODUCTION

Concrete jacketing techniques are well known for improving the performance of structural elements. In this research study, the focus was aimed on the rehabilitation of damaged elements instead of strengthening weak structures. Weak elements are normally caused by improper design or poor construction method, whereas damaged elements are resulted from the excessive load beyond the limit strength capacity due to natural phenomenon such as earthquake, soil settlement, flood, etc. Main difference is the condition of the elements when the retrofitting is applied i.e. under serviceability limit for weak elements or experiencing failure stage close to the collapse limit; which lead to different approximation on strength analysis.

Concrete jacketing method has been comprehensively investigated [1-6] covering various mechanism (axial, flexural, and shear behaviour) and various elements (beams and columns). However, those research projects mainly focused on the use of regular reinforced concrete which depends largely on the steel application. As the green material and sustainability issues are more prominent, it is necessary to obtain alternative material to replace steel. The common material to be used as reinforcement is bamboo which also has been studied thoroughly [7-16]. Interestingly, very few of those studies studied about its application on retrofitting. And therefore, this study aimed on the application of bamboo as steel replacement on concrete jacket method in retrofitting damaged concrete columns.

EXPERIMENTAL TEST SET-UP

Three parameters varies were longitudinal reinforcement ratio, configuration of main bars, and stirrups spacing which were aimed at investigating the effectiveness of confinement of concrete jacket to the damaged columns.

Four groups of specimen in the form of short columns were axially loaded in two stages (original and retrofitted columns). The dimension of original columns were 12x12x30 cm, and were reinforced with four $\phi 6$ mm steel bars (longitudinal reinforcement ratio of 1.23%) as shown in Fig. 1.

A transverse reinforcement ratio of 0.81% was used using $\phi 6$ stirrups spaced at 140mm. The specified concrete compressive strength was 20 MPa, whilst the yield strength for main rebars and stirrups were 270 MPa and 170 MPa respectively.

The rehabilitation of damaged column after the first axial load test were conducted using concrete jacketing reinforced with bamboo bars as longitudinal and transverse reinforcement (refer Table 1 and Fig. 2) as follows:

- Two longitudinal reinforcement ratios used were 1.23% and 2.47%, where each ratio was represented by 4 and 8 square/rectangle bars configuration, i.e., 4 bars 10x10 mm and 8 bars 10x5 mm (for the same $\rho_v = 1.23\%$), and 4 bars 20x10 mm and 8 bars 10x10mm (for the same $\rho_v = 2.47\%$). Petung bamboo (*Dendrocalamus asper*) applied for longitudinal reinforcement had yield strength of 190 MPa.

- For the transverse reinforcement, square bar 10x5 mm bamboo stirrups were set at about 7.5cm, 10 cm and 15 cm spacing corresponding to transverse reinforcement ratios of 0.8%, 1.2% and 1.6% respectively. Apus Bamboo (*Gigantochloa apus*) with yield strength of 120 MPa was used for stirrups fabrication since it was less stiffer compared to the Petung Bamboo and hence relatively easier to be bent.

Table 1 Column set-up configuration

Columns	Longitudinal Reinforcement		Transverse Reinforcement	
	Dimension	Ratio (%)	Spacing	Ratio (%)
Original	4 ϕ 8	1.40	ϕ 6 - 140	0.81
A1R	4 bamboo bars	1.23	10x5 - 100	1.21
A2R			10x5 - 150	0.81
A5R			10x5 - 75	1.61
B1R	8 bamboo bars	1.23	10x5 - 100	1.21
B2R			10x5 - 150	0.81
B5R			10x5 - 75	1.61
C1R	4 bamboo bars	2.47	10x5 - 100	1.21
C2R			10x5 - 150	0.81
C5R			10x5 - 75	1.61
D1R	8 bamboo bars	2.47	10x5 - 100	1.21
D2R			10x5 - 150	0.81
D5R			10x5 - 75	1.61

Axial compression tests were conducted on original columns until reaching 50% reduction of peak load. Then, the damaged columns were retrofitted and further subjected to the second axial load test until reaching failure. The axial load and deformation were continuously measured using compression testing machine and dial gauge as shown in Fig. 2.

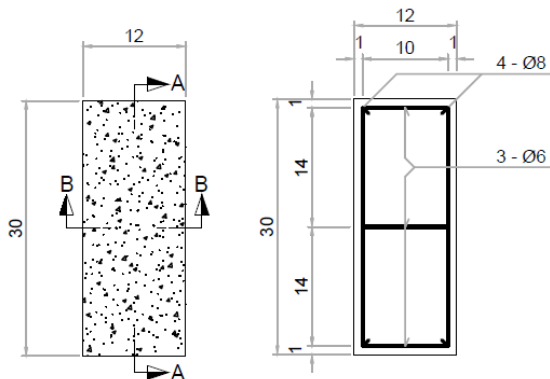
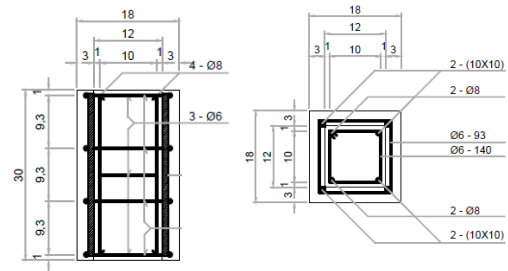
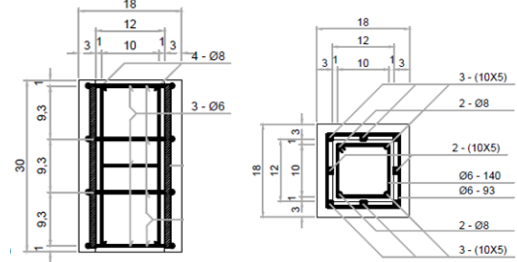


Fig. 1 Typical original columns



a. Set-up for columns with four bamboo main bars



b. Set-up for columns with eight bamboo main bars

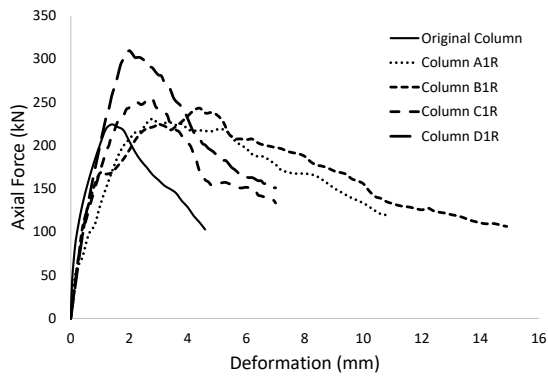
Fig. 2 Typical retrofitting of damaged columns

EXPERIMENTAL TEST RESULTS

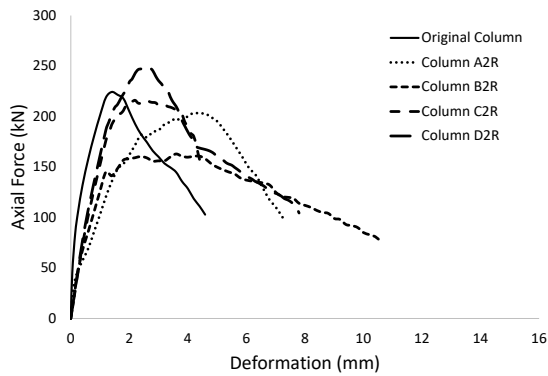
The recorded axial loads and deformations for all columns are shown in Fig. 3-4 and Table 2 which showed interesting outcomes as follows:

- The average peak axial strength and displacement ductility ratio of original column specimens were about 212 kN and 3.29 respectively.
- Generally there were improvement of ductility on all configuration of retrofitting compared to the damaged columns as shown in Fig. 2. The results also showed that the closer the stirrups spacing, the higher the ductility ratio of retrofitted columns.
- At the same longitudinal reinforcement ratio, the use of 8 smaller bar configuration exhibited ductility ratio of about 30% higher than those of columns with 4 larger bars. And hence it is preferable to distribute the bars uniformly over the column perimeter to obtain higher confinement effectivity.
- The increase rate of ductility when reducing the stirrups spacing from 150mm, 100mm to 75mm was found higher on configuration of 4 main bars longitudinal reinforcement rather than 8 bars configurations. It is understandable since the application of 8 bars configuration has provided greater ductility ratio at similar stirrups spacing.
- The use of stirrups with spacing closer than that of original columns seemed to increase the peak

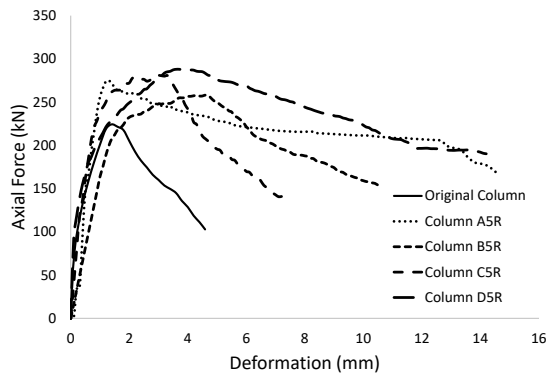
load capacity of retrofitted columns; and vice versa for the wider stirrups spacing.



a. Columns with stirrups spacing of 100mm

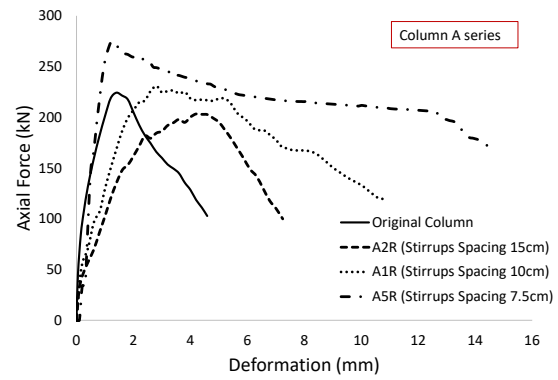


b. Columns with stirrups spacing of 150mm

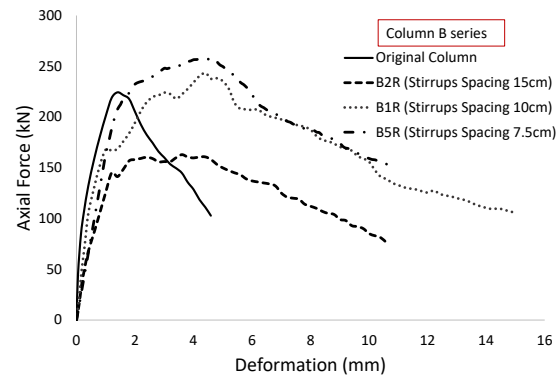


c. Columns with stirrups spacing of 75mm

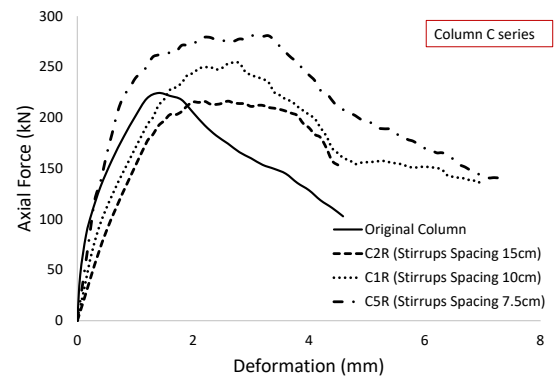
Fig. 3 Comparison of longitudinal reinforcement ratio effect



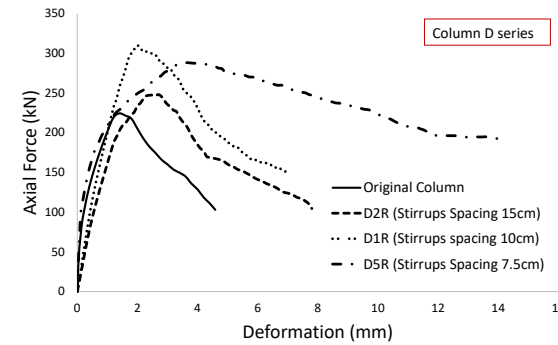
a. Columns with $\rho_h=1.23\%$ (4 main bars 10x10 mm)



b. Columns with $\rho_h=1.23\%$ (8 main bars 10x5 mm)



c. Columns with $\rho_h=2.47\%$ (4 main bars 20x10 mm)



d. Columns with $\rho_h=2.47\%$ (8 main bars 10x10 mm)

Fig. 4 Comparison of the confinement effect due to various stirrups spacing.

Table 2 Column set-up configuration

Col.	P _{peak} (kN)	P ₅₀ (kN)	Δ _y (mm)	Δ _{peak} (mm)	Δ ₅₀ (mm)	μ
Original	229	104	1.60	2.40	5.25	3.28
A1R	231	118	2.00	2.81	10.88	5.44
A2R	204	100	2.00	4.20	7.24	3.62
A5R	278	173	1.60	1.30	14.40	9.00
B1R	243	106	2.20	4.40	14.90	6.77
B2R	163	76	1.80	3.60	10.60	5.89
B5R	257	156	1.80	4.40	14.20	7.89
C1R	253	133	1.60	3.00	7.00	4.38
C2R	216	120	1.50	2.20	4.80	3.20
C5R	280	140	1.00	2.30	7.30	7.30
D1R	305	151	1.70	2.00	7.00	4.12
D2R	250	124	1.60	2.60	6.90	4.31
D5R	288	190	1.70	3.80	14.20	8.35

STRESS-STRAIN MODEL

The simple stress-strain formula for damaged concrete confined with bamboo reinforced concrete jacket was developed based on Modified Kent-Park model [17]. Since the bamboo stirrups had lower yield strength and modulus of elasticity, the effectiveness of confinement will be lower than that provided by steel stirrups; and hence, it was reasonably assumed that the peak strength occurs at 0.004 concrete strain instead of 0.002 as the case of steel confinement. The model for predicting the stress-strain curve can be elaborated as follows (refer Fig. 5):

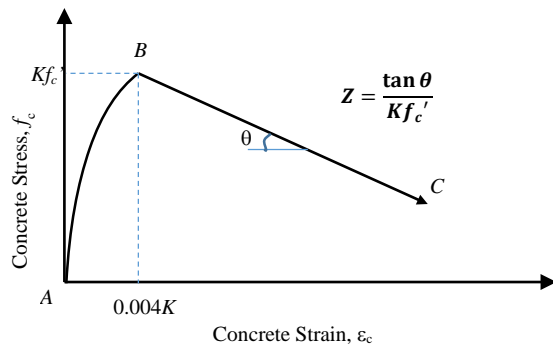


Fig. 5 Stress-strain model for bamboo reinforced confinement on concrete jacket.

- Region AB ($\varepsilon_c < 0.004K$)

$$f_c = Kf'_c \left[\frac{2\varepsilon_c}{0.004K} + \left(\frac{\varepsilon_c}{0.004K} \right)^2 \right]$$

- Region BC ($\varepsilon_c > 0.004K$)

$$f_c = Kf'_c [1 - Z(\varepsilon_c - 0.004K)]$$

but not less than $0.2Kf'_c$

where:

$$K = 1 + \rho_h \frac{f_{yh}}{f'_c}$$

$$Z = \frac{0.5}{\frac{3+f'_c}{250f'_c-1000} + \frac{3}{4}\rho_h \sqrt{\frac{h_s}{s_h}} - 0.004K}$$

f'_c = concrete strength

f_{yh} = bamboo rupture strength

ρ_h = volumetric transverse reinforcement ratio

s_h = spacing of stirrups

b_s = width of concrete core measured to outside of stirrups.

The comparison of typical concrete stress-strain curve of unconfined, steel confinement and bamboo reinforced concrete jacket for concrete strength f'_c of 15 MPa and similar reinforcement configuration is presented in Fig. 6. The application of the proposed model to the axial load-deformation prediction of the tested columns are shown in Fig. 7-9. The predicted axial load-deformations took a more conservative approach compared to the experimental results which is suitable for preliminary design or nominal capacity checking purposes.

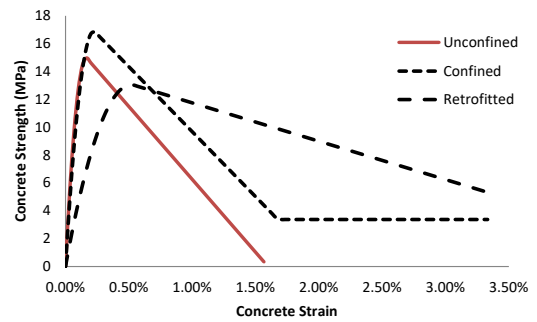


Fig. 6 Stress-strain curve comparison for 3 cases (unconfined, confined with steel, and confined with bamboo).

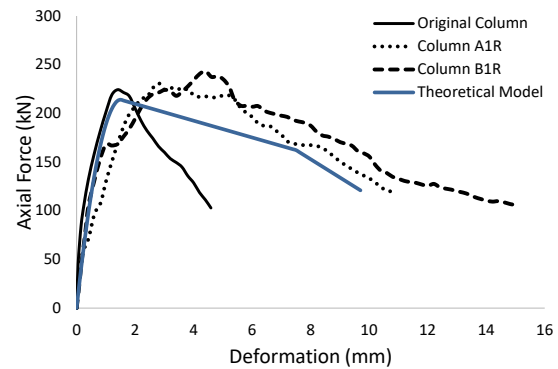


Fig. 7 Comparison of the proposed model and the experimental results

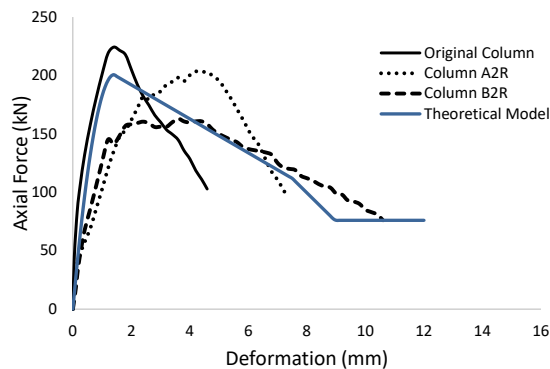


Fig. 8 Comparison of the proposed model and the experimental results

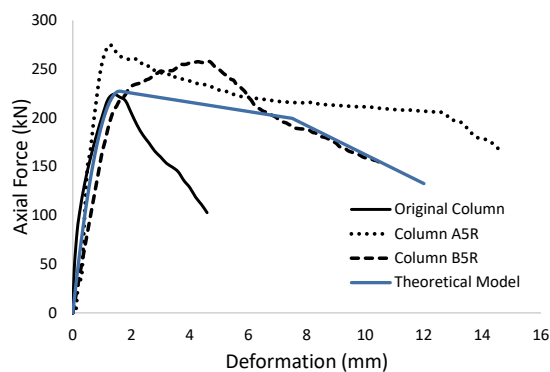


Fig. 9 Comparison of the proposed model and the experimental results

CONCLUSION

Experimental test on four groups of short columns retrofitted by bamboo reinforced concrete jacket has been undertaken, with interesting outcomes as follows:

- Retrofitting using bamboo reinforced concrete jacket were generally able to improve the ductility ratio of damaged columns.
- However, for reaching the similar nominal strength of original columns, the stirrups spacing needs to be set closer than that of damaged columns.
- It is preferable to distribute the bars uniformly over the column perimeter to obtain higher effectiveness of confinement.

Further, the simple model for predicting stress-strain of damaged columns retrofitted using bamboo reinforced concrete jacket has been developed. The analytical predictions showed a reasonable agreement with the experimental test results with a more conservative approach which is suitable for simple checking or preliminary design purposes.

ACKNOWLEDGEMENTS

We acknowledge the support of Higher Education Excellent Research Grant from Ministry of Research, Technology and Higher Education of the Republic of Indonesia.

REFERENCES

- [1] Georgia E. Thermoua, Vassilis K. Papanikolaou, Andreas J. Kappos, Flexural behaviour of reinforced concrete jacketed columns under reversed cyclic loading, *Engineering Structures* Vol. 76, 2014, pp. 270–282.
- [2] Giovanni Minafò, A practical approach for the strength evaluation of RC columns reinforced with RC jackets, *Engineering Structures*, Vol. 85, 2015, pp. 162–169.
- [3] Giovanni Minafò, Fabio Di Trapani, Giuseppina Amato, Strength and ductility of RC jacketed columns: A simplified analytical method, *Engineering Structures*, Vol. 122, 2016, pp. 184–195.
- [4] Bertha Alejandra Olmos Navarrete, José Manuel Jara Guerrero, María de la Consolación Trinidad Juana Gómez Soberón, Manuel Jara Díaz, Influence of RC jacketing on the seismic vulnerability of RC bridges, *Engineering Structures*, Vol. 123, 2016, pp. 236–246
- [5] Giovanni Minafò, Maurizio Papia, Concrete softening effects on the axial capacity of RC jacketed circular columns, *Engineering Structures*, Vol. 128, 2016, pp. 215–224.
- [6] M. Monir A. Alhadid, Maged A. Youssef, Analysis of reinforced concrete beams strengthened using concrete jackets, *Engineering Structures*, Vol. 132, 2017, pp. 172–187.
- [7] Bhavna Sharma, Ana Gatóo, Maximilian Bock, Michael Ramage, Engineered bamboo for structural applications, *Construction and Building Materials*, Vol. 81, 2015, pp. 66–73.
- [8] Qingfeng Xu, Kent Harries, Xiangmin Li, Qiong Liu, Jennifer Gottron, Mechanical properties of structural bamboo following immersion in water, *Engineering Structures*, Vol. 81, 2014, pp. 230–239.
- [9] J.G. Moroz, S.L. Lissel, M.D. Hagel, Performance of bamboo reinforced concrete masonry shear walls, *Construction and Building Materials*, Vol. 61, pp. 2014, pp. 125–137.
- [10] Atul Agarwal, Bharadwaj Nanda, Damodar Maity, Experimental investigation on chemically treated bamboo reinforced concrete beams and columns, *Construction and Building Materials*, Vol. 71, 2014, pp. 610–617.

- [11] Bhavna Sharma, Ana Gat6o, Michael H. Ramage, Effect of processing methods on the mechanical properties of engineered bamboo, *Construction and Building Materials*, Vol. 83, 2015, pp. 95–101.
- [12] Alireza Javadiana, Mateusz Wielopolski, Ian F.C. Smith, Dirk E. Hebel, Bond-behavior study of newly developed bamboo-composite reinforcement in concrete, *Construction and Building Materials*, Vol. 122, 2016, pp. 110–117.
- [13] Masakazu Terai, Koichi Minami, Fracture Behavior and Mechanical Properties of Bamboo Reinforced Concrete Members, *Procedia Engineering*, Vol. 10, 2011, pp. 2967–2972.
- [14] Abhijeet Dey, Nayanmoni Chetia, Experimental study of Bamboo Reinforced Concrete beams having various frictional properties, *Materials Today: Proceedings*, Vol. 5, 2018, pp. 436–444.
- [15] Ari Wibowo, Indradi Wijatmiko, Christin Remayanti Nainggolan, Bamboo reinforced concrete slab with styrofoam lamina filler as solution of lightweight concrete application, *MATEC Web of Conferences*, Vol. 101, 2017, Article number 05012.
- [16] Ari Wibowo, Indradi Wijatmiko, Christin Remayanti Nainggolan, Structural behavior of lightweight bamboo reinforced concrete slab with EPS infill panel, *AIP Conference Proceedings*, Vol. 1887, 2017, Article number 020024.
- [17] Robert Park, M. J. Negel Priestley, Wayne D. Gill, Ductility of Square-Confined Concrete Columns, *Journal of the Structural Division*, Vol. 108, Issue 4, pp. 929-950.

STUDY OF MODULUS ELASTICITY OF PVC COATED WELDED MESH FIBER CONCRETE

Christin Remayanti Nainggolan¹, Indradi Wijatmiko¹ and Ari Wibowo¹
¹Faculty of Engineering, Brawijaya University, Malang, Indonesia, 65145

ABSTRACT

Modulus elasticity is an important parameter that show the ability of concrete to deform elastically. Data analysis to obtain that value of modulus elasticity can be done with several empirical models. To compare some of these empirical models and to study the effect of fiber to the modulus elasticity of concrete, an experiment on the addition of PVC coated welded wire mesh fiber to the concrete mixture has been conducted. The specimen in this experiment was a cylindrical specimen with a diameter 150 mm and height 300 mm. There are 3 variations in this experiment : (1) variations in fraction of percentage of wire fiber; (2) fiber's length variation and (3) length interlocking variation. Extensometer was installed onto the specimen to measure stress strain of concrete while the compressive strength were conducted. The result of analysis showed that 1.5% of fiber fraction, 24mm of fiber length and 0.6 mm of fiber interlocking length generated higher modulus elasticity compare to other variations. However, PVC coated welded mesh fiber concrete has a less value of modulus elasticity when it compared with normal concrete due to slip effect between fiber and concrete. Furthermore, there are some empirical models with a good agreement and some in different results depends on the country code and the parameters in the models.

Keywords: Fiber concrete, Modulus elasticity, Stress-strain, PVC coated welded wire mesh

INTRODUCTION

Fibers concrete is concrete made of cements, aggregates, water and discrete fibers (steel fibers, glass fibers, synthetic fibers, etc.). According to ACI Comitee 544.1R-96 [1], the length and diameter of the fibers used for fibers concrete should not exceed 76 mm and 1 mm respectively. The addition of fiber to the concrete has a purpose to fix the weakness of the concrete that has a low tensile strength.

There are a variety of fibers used for fibers concrete. Iwan R. [2] used fibers made from waste cans with variation fraction and water cement ratio 0.45. The width, length and thickness of the fibers are 3 mm, 50 mm and 0.2 mm respectively. The result of the research is that the addition of fiber with fraction 0.6% increased the compressive strength of 30.65% and the tensile strength of 49.69%. Another research done by Kampa R. [3] use coca-cola can waste as fiber, the width and length of the waste tin fibers are 2 mm and 20 mm respectively. The fibers manually twisted by 180° to improve bondage between cement, aggregates and fibers. The addition of waste tin fibers shown insignificant change in compression and tensile strength. Waste carpet fibers with the length of the fibers is 20 mm and the variation of fraction are between 0 – 1.25% were used by Hossein M, Jamaludin M. Y., Abdul R. M. S. And A. S. M. Abdul Awal [4] as a fibers concrete. In addition to used waste carpet fibers, Hossein also added palms oil fuel ash (POFA). The interaction between carpet fibers and POFA subsequently led to the lower drying

shrinkage of the concrete. Ankur C. B. and Narendra K. A. [5], used metalized plastic waste fibers were shredded into 5 mm, 10 mm and 20 mm long fibers. The fraction variation is from 0% to 2% of mix design volume. The results of his research is that metalized plastic waste fibers did not significantly affect the compressive strength and flexural strength but it increased tensile strength and ductility. From these studies, the results obtained that the addition of fiber can increased tensile strength where the magnitude of the increase is influenced by the type of the fibers. Swamy and Al-Noori (in Haryanto Y. W. and Recky S. G., pp.3 [6]) state that the shape of fibers affects the bonding and the properties of the concrete. Concrete using fibers with interlocking will increase its bonding and structural properties rather than the fibers without interlocking.

The addition of fibers can increase tensile strength wherein concrete generally has a low tensile strength and has a brittle nature. Determining the tensile strength is important to determine the crack load where the crack is a form of tensile failure. To have a better understanding about fibers concrete and its influence to tensile strength, it is necessary to know the modulus elasticity of fibers concrete.

Modulus elasticity is one of the strength parameter of a material, in which is to measure the resistance of an elastic deformation when the material under the load. It can be said that modulus elasticity is a measure of the stiffness of a material so that it can affect the strength of a material. There are several approaches used to obtain modulus elasticity of

concrete. Emi M. [7] calculated modulus elasticity of concrete used the equation of Wang and Salmon. Wang and Salmon predict the modulus elasticity based on stress-strain of concrete. H. Z. Cui, Tommy Y. L., Shazim A. M., F. Xing and X. Shi [8] used empirical model from ACI and institute of structural to predicted the modulus elasticity of lightweight concrete, which is influenced by compressive strength and weight of concrete. Turhan B. [9] used several empirical models such as Euro Code 2, TS500, Norwegian Code, etc. , and used composite material models such as Voigt model, Reuss model, Popovics Model, etc. to predicted modulus elasticity of high quality concrete.

Based on previous studies, this research used PVC coated welded wire mesh fibers and investigated it influence to modulus elasticity of fiber concrete. This research also studied and compared the modulus elasticity from several empirical models.

EXPERIMENTAL INVESTIGATION

PVC coated wire is a modified type of wire bend. It is also known as *PVC coated welded wire mesh*, is a high quality stainless steel wire with stainless resistance much better than ordinary iron wire. This wire consists galvanized wire (diameter 0.8 mm) coated by PVC (thickness 0.2 mm). The advantages of this wire are high rust resistance, easy to get, great savings in time, effort and money.

The specimen in this research is a cylinder with a diameter 150 mm and height 300 mm with 3 variations :

- (1) Variation of fraction (0.5 %, 1 %, 1.5% of cylinder volume) with fiber length 36 mm and interlocking length 12 mm (Fig. 3.b)
- (2) Variation of fiber's length (12 mm, 24 mm, 36 mm) with fraction 1% and interlocking length 12 mm (Fig. 4)
- (3) Variation of fiber's interlocking length (6 mm, 12 mm, 18 mm) with fraction 1% and fiber length 36 mm (Fig. 5)

The specimen was tested with compressive test machine and an extensometer to measure concrete strain. (Fig.1)



Fig. 1. Test model with compressive test machine

To prepare the materials, it is necessary to know the density of wire mesh. After 3 experiments, the density of PVC coated welded wire mesh as shown at Table 1.

Table 1. PVC coated welded wire mesh density

	Density (gr/cm ³)
Experiment A	0.373
Experiment B	0.351
Experiment C	0.388
Average	0.371

After knowing the density, then calculate the need for each fraction. For example the calculation for one cylinder with fraction 1%.

$$\begin{aligned}
 W_{\text{wire mesh}} &= \% \text{fraction} \times V_{\text{cylinder}} \times \text{density}_{\text{wire mesh}} \\
 &= 1\% \times 5298.75 \text{ cm}^3 \times 0.371 \text{ gr/cm}^3 \\
 &= 19.658 \text{ gr}
 \end{aligned}$$

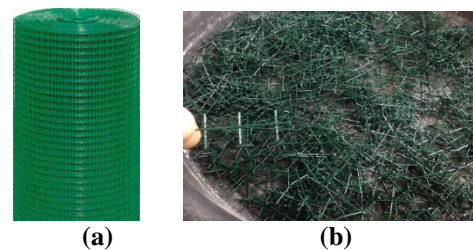


Fig. 2. (a) PVC coated welded wire mesh, (b) PVC coated welded mesh fiber

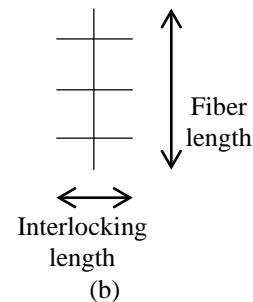
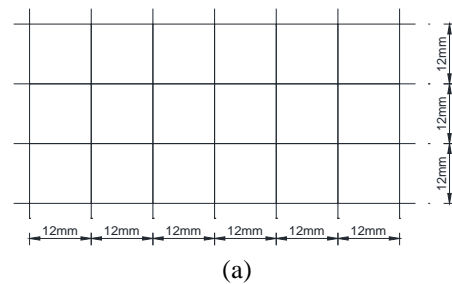


Fig. 3. (a) PVC coated welded wire mesh before cutted , (b) PVC coated welded wire mesh after cutted

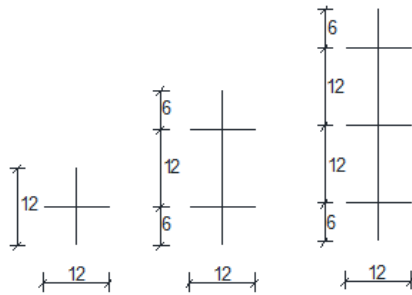


Fig. 4. Variation of fiber's length

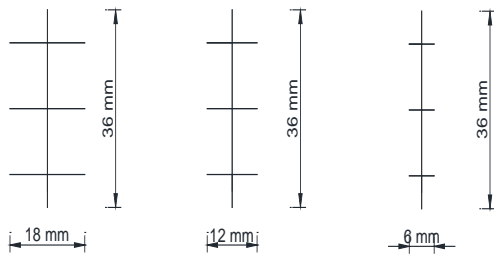


Fig. 5. Variation of fiber's interlocking length

Mix design in this research refers to SNI 03-2834-2000 [10]. From the calculation obtained ratio of actual proportion (in kg).

Table 2. Ratio of mix design

Cement	Water	Fine aggregate	Coarse aggregate
1.00	0.5	1.18	2.02

MODELING APPROACH

Modulus elasticity is the ratio of the stress and strain of the material as seen in the Eq.1.

$$E = \frac{\sigma}{\varepsilon} = \frac{P \times L}{A \times \Delta L} \dots\dots\dots(1)$$

According to Wang and Salmon [11], modulus elasticity depends on the age of the concrete, materials properties, the loading rate, the type and size of the specimen. The empirical model used in this research can be seen at Table 3. According to theory of elasticity, the slope of the curve in the early stage illustrates the modulus elasticity of concrete (Fig.6).

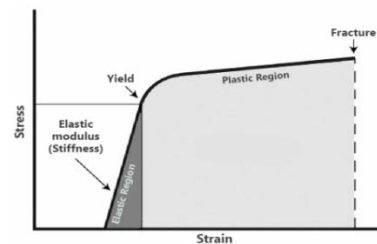


Fig. 6. Stress-strain curve [12]

Elastic proportional limits (ASTM C 469 and Eurocode 2 - 1992) in predicting modulus are important because the nature of the concrete is a elasto plastic, where as a result of a fixed loading, the material exhibits the elastic ability of the material and also exhibits permanent deformation. The modulus elasticity based on the material resistance to the compressive strength test (deformation) is called modulus elasticity static. In addition there is also empirical model of elastic modulus containing concrete compressive strength factor (SNI 03-2847-2002 and TS 500).

Table 3. Summary of empirical model to estimate the modulus elasticity

Empirical model	Parameters	Ref. source
$E = \frac{0.4 f'c}{\varepsilon(0.4 f'c)} \dots\dots\dots(2)$	E is the modulus elasticity static (MPa), $f'c$ is compressive strength (MPa), ε is axial strain	Eurocode 2 - 1992
$E = \frac{\sigma_2 - \sigma_1}{\varepsilon_2 - \varepsilon_1} \dots\dots\dots(3)$	E is the modulus elasticity static (MPa), σ_1 is tegangan saat regangan 0.00005, σ_2 is tegangan saat 40% $f'c$, $\varepsilon_1 = 0.00005$, ε_2 is regangan saat σ_2	ASTM C 469
$E = 0.043 \times W_c^{1.5} \times f_c^{0.5} \dots\dots\dots(4)$ ($1500 \leq W_c \leq 2500 \text{ kg/m}^3$)	E is the modulus elasticity (MPa), W_c is unit weight (kg/m^3), $f'c$ is compressive strength (MPa)	SNI 03-2847-2002 (Indonesian Standart)
$E = 4700 f_c^{0.5} \dots\dots\dots(5)$ ($W_c \pm 2300 \text{ kg/m}^3$)	E is the modulus elasticity (MPa), W_c is unit weight (kg/m^3), $f'c$ is compressive strength (MPa)	SNI 03-2847-2002 (Indonesian Standart)
$E = (3250 \times \sqrt{f'c}) + 14000 \dots\dots\dots(6)$	E is the modulus elasticity (MPa), $f'c$ is compressive strength (MPa)	TS 500 (Turkey Standart)

RESULT AND DISCUSSION

In Table 4, 5 and 6 are shown the results of modulus elasticity calculations using the empirical model contained in Table 3. It can also be seen the percentage values of the difference for each calculation method of modulus elasticity. Eurocode 2 - 1992 (eq.2) and ASTM C 469 (eq.3) are similar to each other and the value of modulus elasticity also close to each other, they have the smallest percentage of the difference between

empiric formulas (2.3% - 2.6%), this is because both formulas consider the value of strain stress that occurs in the concrete. If Eurocode 2 - 1992 (eq.2) is compared with TS 500 (eq.6) and ASTM C 469 (3) compared with SNI 2002 (eq.4), where as TS 500 and SNI 2002 related to compressive strength as the parameter of elastic modulus, then the percentage difference is quite large (average more than 50%).

Table 4. Modulus elasticity of PVC coated welded mesh fiber concrete with variation of fiber's fraction

No.	Specimen code	f _c (MPa)	Modulus elasticity (MPa)					difference between empiric formulas (%)				
			2 Eurocode 2 - 1992	3 ASTM C 469	4 SNI 2002 (1500 ≤ W _c ≤ 2500 kg/m ³)	5 SNI 2002 (W _c ± 2300 kg/m ³)	6 TS 500	(2) & (3)	(3) & (4)	(4) & (5)	(2) & (6)	(4) & (6)
1	N.A1	32.75	38158.5	37391	28326.8	26897.6	32599.4	2.1	32	5.3	14.6	15.1
2	N.A2	33.03	62778	58705	28448.8	27013.5	32679.5	6.9	106	5.3	47.9	14.9
3	F.0.5.A1	19.40	10924.5	10757	21672.3	20702.4	28315.5	1.6	50	4.7	159.2	30.7
4	F.0.5.A2	17.99	41827.4	42121	20493	19933.7	27783.9	0.7	106	2.8	33.6	35.6
5	F.1.A1	30.32	16970	16970	27581	25879.5	31895.4	0.0	38	6.6	88	15.6
6	F.1.A2	32.41	41957.6	42121	26843.2	26757.9	32502.8	0.4	57	0.3	22.5	21.1
7	F.1.5.A1	31.68	40600.7	38788	27360.2	26452.6	32291.7	4.7	42	3.4	20.5	18
Average % difference between empiric model								2.3	61.6	4.1	55.2	21.6

Table 5. Modulus elasticity of PVC coated welded mesh fiber concrete with variation of fiber's length

No.	Specimen code	f _c (MPa)	Modulus elasticity (MPa)					difference between empiric formulas (%)				
			2 Eurocode 2 - 1992	3 ASTM C 469	4 SNI 2002 (1500 ≤ W _c ≤ 2500 kg/m ³)	5 SNI 2002 (W _c ± 2300 kg/m ³)	6 TS 500	(2) & (3)	(3) & (4)	(4) & (5)	(2) & (6)	(4) & (6)
1	N.A1	32.75	38158.5	37391.0	28326.8	26897.6	32599.4	2.0	24.2	5.0	14.6	15.1
2	N.A2	33.03	62778	58705.0	28448.8	27013.5	32679.5	6.5	51.5	5.0	47.9	14.9
3	L.1.2.A1	28.91	13319.7	13346	26452.6	25268.8	31473.11	0.2	98.2	4.5	136.3	19.0
4	L.1.2.A2	30.60	56253.8	58645	27545.3	25987.7	31978.71	4.3	53.0	5.7	43.2	16.1
5	L.2.4.A1	22.91	18840.1	18683	23832.8	22495.8	29555.62	0.8	27.6	5.6	56.9	24.0
6	L.2.4.A2	23.42	67726.1	63636	24096.2	22744.4	29727.51	6.0	62.1	5.6	56.1	23.4
7	L.3.6.A1	30.32	16970	16970	27581	25879.6	31895.37	0.0	62.5	6.2	88.0	15.6
8	L.3.6.A2	32.41	41957.6	42121	26843.2	26757.9	32503.04	0.4	36.3	0.3	22.5	21.1
Average % difference between empiric model								2.5	51.9	4.7	58.2	18.6

Table 6. Modulus elasticity of PVC coated welded mesh fiber concrete with variation of fiber's length interlocking

No.	Specimen code	f _c (MPa)	Modulus elasticity (MPa)					difference between empiric formulas (%)				
			2 Eurocode 2 - 1992	3 ASTM C 469	4 SNI 2002 (1500 ≤ W _c ≤ 2500 kg/m ³)	5 SNI 2002 (W _c ± 2300 kg/m ³)	6 TS 500	(2) & (3)	(3) & (4)	(4) & (5)	(2) & (6)	(4) & (6)
1	N.A1	32.75	38158.5	37391.9	28326.8	26897.6	32599.4	2.0	24.2	5.0	14.6	15.1
2	N.A2	33.03	62778.0	58705.9	28448.8	27013.5	32679.5	6.5	51.5	5.0	47.9	14.9
3	I.0.6.A1	22.80	27402.6	26428	23632.5	22440.2	29517.2	3.6	10.6	5.0	7.7	24.9
4	I.0.6.A2	22.00	44146.46	43217	23357.3	22047	29245.3	2.1	46	5.6	33.8	25.2
5	I.1.2.A1	30.32	16970.6	16970	27581	25879.6	31895.4	0.0	62.5	6.2	88.0	15.6
6	I.1.2.A2	32.41	41957.6	42121	26843.2	26757.9	32502.78	0.4	36.3	0.3	22.5	21.1
7	I.1.8.A1	30.21	18537.2	17755	27366.5	25831.2	31862	4.2	54.1	5.6	71.9	16.4
8	I.1.8.A2	32.07	23258.1	22810	27603.4	26617.4	32405.7	1.9	21	3.6	39.3	17.4
Average % difference between empiric model								2.6	38.3	4.6	40.7	18.8

Value of modulus elasticity from SNI 2002 formula for concrete weight $\pm 2300 \text{ kg / cm}^3$ (eq.5) and for concrete weight between $1500 \text{ s.d } 2500 \text{ kg / cm}^3$ (eq.4) has not too much different (4.1% - 4.6%). This is because the normal concrete and fiber concrete has a specific gravity and compressive strength for each variation that not too much different.

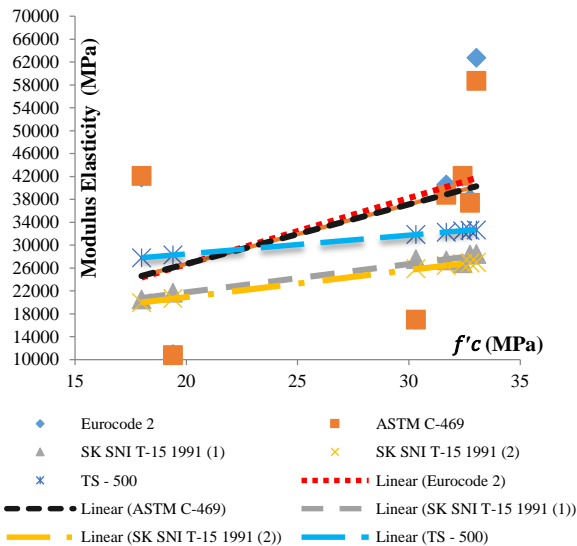


Fig. 7. Regression of modulus elasticity of PVC coated welded mesh fiber concrete with variation of fiber's fraction

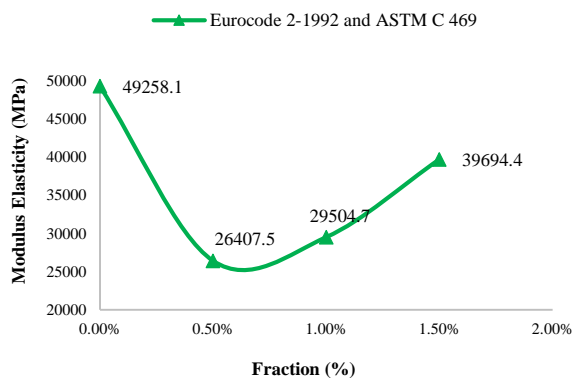


Fig. 8. Summary of modulus elasticity of PVC coated welded mesh fiber concrete with variation of fiber's fraction

Figure 7 presented that the data regression of Eurocode 2-1992 and ASTM C-469 are coincide. Both methods of SK SNI 2002 also produce linear lines that are mutually coincide. Although with different models and parameters, it can be seen that compressive strength increased followed by the increased of modulus of elasticity. This

statement is similar with the theory of modulus elasticity in Eq. 1.

In this paper, the effect of PVC coated welded mesh fiber as a fiber in concrete will be analyzed based on Eurocode 2-1992 and ASTM C-469. Experimental result (Fig.8) showed that the higher the fiber's fraction added to the concrete mixture, the greater the modulus elasticity resulted. However, PVC coated welded mesh fiber concrete has a less value of modulus elasticity when it compared with normal concrete. The addition of PVC coated welded mesh fiber did not give a positive effect to the compressive strength or it can be said the compressive strength was decreased (decreased by 19.4%).

Based on previous research, fiber increase tensile strength although it has little effect on compressive strength. However in this study it can be seen that the addition of PVC coated welded mesh fiber did not give positive effect to modulus elasticity of concrete. The wire coated by PVC and give slip effect, so that bonding between concrete and fiber did not work well. The addition of fibers are supposed to improve the tensile strength, but the slip effect causes the fiber did not give a good effect to tensile strength. However, modulus elasticity of PVC coated welded mesh fiber concrete increased as fiber's volume fraction increased, even though modulus elasticity of fiber concrete less than normal concrete.

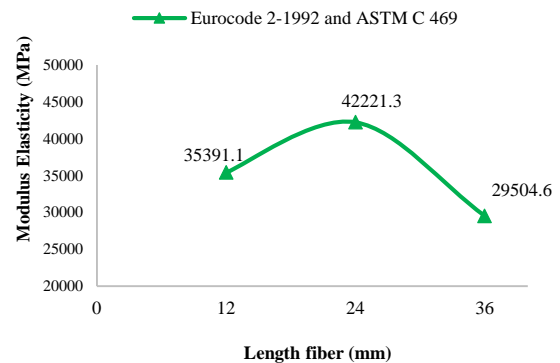


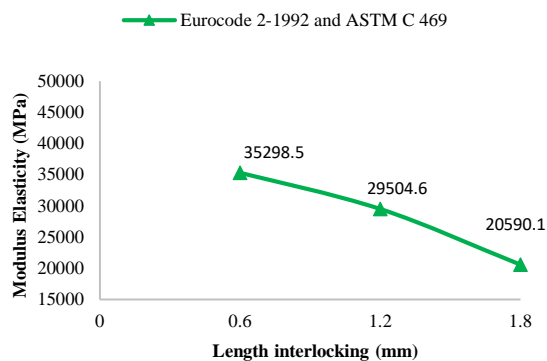
Fig. 9. Summary of modulus elasticity of PVC coated welded mesh fiber concrete with variation of fiber's length

Figure 10. Summary of modulus elasticity of PVC coated welded mesh fiber concrete with variation of fiber's length interlocking

Figure 9 showed that PVC coated welded mesh fiber concrete with variation of fiber's length 24 mm had the highest value of modulus elasticity. However it decreased 14.29% from normal concrete.

The effect of PVC coated welded mesh fiber concrete with variation of fiber's length showed in Fig. 10. The addition of fiber's length interlocking produced a decreasing effect on the modulus elasticity. Compared with normal concrete, modulus

elasticity of PVC coated welded mesh fiber concrete decreased by 24%.



SUMMARY

1. Modulus elasticity calculated by Eurocode 2 - 1992 and ASTM C 469 are similar to each other because both of the empirical models related to stress-strain relationship of fiber concrete. The other empirical model such as SNI 2002 and TS-500 also similar to each other and related to compressive strength.
2. Although each of empiric models have a different paramaters, however have the same pattern that is an increase in compressive strength followed by an increase in modulus elasticity
3. Based on variation of fraction, PVC coated welded mesh fiber fraction of 1.5% produced the highest modulus elasticity. However, compared to normal non-fiber concrete, modulus elasticity decreased by 19.4%.
4. Based on variation of fiber's length, the modulus elasticity produced the highest value on variation of fiber's length 24 mm. However, compared to normal non-fiber concrete, the elasticity modulus value decreased by 14.29%.
5. Based on variation of fiber's interlocking length, fiber's length interlocking of 0.6 mm produced the highest modulus elasticity. However, compared to normal non-fiber concrete, the elasticity modulus value decreased by 24%.
6. Less bonding between fibers with concrete may cause the use of PVC coated welded mesh fiber as

a fiber material is not effective in increasing the modulus elasticity of concrete.

REFERENCES

- [1] ACI 544.1R-96. State of The Art Report on Fiber Reinforced Concrete
- [2] Iwan R. Utilization of Waste Can As Fibers To Improve Concrete Characteristic. Teodolita, Vol.14, No.2, 2013, pp.56-70. (in Indonesian)
- [3] Kampa R. Strength Characteristics of Coca-Cola Tin Waste As Fibres in Concrete. IJARF, Vol.3, Issue 2, 2016, pp.9-12.
- [4] Hossein M., Jamaludin M. Y., Abdul R. M. S, A. S. M. Abdul Awal. Journal of Cleaner Production, 144, 2017, pp.448 – 458.
- [5] Ankur C. B, Narendra K. A. Construction and Building Materials, 146, 2017, pp.455 – 463.
- [6] Haryanto Y. W., Recky S. G. Effect of Wire Fibers To Square Column Capacity. Jurnal Teknik Sipil, Vol. 7, No. 1, 2006, pp.1 – 13. (in Indonesian)
- [7] Emi M. Review of Compressive Strength and Modulus Elasticity For Diatomaceous As Additives. Teras Jurnal, Vol. 6, No. 2, 2016, pp. 81 – 90. (in Indonesian)
- [8] H. Z. Cui, Tommy Y. L., Shazim A. M., F. Xing, X. Shi. Analitical Model for Compressive Strength, Elastic Modulus and Peak Strain of Structural Lightweight Aggregate Concrete. Construction and Building Materials, 36, 2012, pp.1036 – 1043.
- [9] Turhan B. Investigation of Performance of Some Empirical and Composite Models for Predicting The Modulus of Elasticity of High Strength Concretes Incorporating Ground Pumice and Silica Fume. Construction and Building Materials, 127, 2016, pp.850 – 860.
- [10] SNI 03-2834-2000. Indonesian National Standard. Procedures Mix Design For Normal Concrete. (in Indonesian)
- [11] Chu-Kia Wang, Charles G. Salmon. Design of Reinforced Concrete. Vol.1, Fourth Edition. Jakarta: Erlangga. 1994 (in Indonesian)
- [12] <https://www.transtutors.com/homework-help/civil-engineering/modulus-of-elasticity.aspx>

EFFECT OF BRICK MASONRY INFILLS TO SEISMIC CAPACITY OF INDONESIA MULTI-STORY RC BUILDING

Jafril Tanjung¹, Maidiawati² and Aditya Alfajri²

¹Engineering Faculty, Andalas University, INDONESIA; ²Padang Institute of Technology, INDONESIA

ABSTRACT

This paper discusses an analytical study on the effect of brick masonry infills to seismic capacity of the multi-story reinforced concrete (RC) structures by using the finite element computer codes called STructural Earthquake Response Analysis 3D (STERA 3D). A survived three-story RC building after the 2007 Sumatra earthquake was considered as an analytical model. The building was located in Padang city, West Sumatera, Indonesia. The model was analyzed for pushover and time history analyses. The pushover analysis was conducted followed UBC code and the recorded ground acceleration of 2009 West Sumatra earthquake was applied as input motion in time history analysis. The structural detail and material properties used in the analysis were collected from site investigated building after 2007 Sumatra earthquake. Two analytical RC building models were analyzed and compared in this study, i.e. bare RC frame model and brick masonry infilled RC frame model. The results of the analytical study were compared to the resume of the field observation after the earthquake for the considered building. The analytical results are clearly shown that the brick masonry infills may significantly improve the seismic capacity of the RC building. The RC building could be survived to large ground motion even the building was designed by applying the old Indonesia building code.

Keywords: RC building, Brick masonry, Seismic capacity, STERA 3D, Sumatra earthquake

INTRODUCTION

The successive M8.5 and M7.9 earthquakes have struck the south of Sumatra Island on September 12, 2007 (6:10 PM local time in Western Indonesia) and September 13, 2007 (6:49 AM local time in Western Indonesia) [1]. The epicenters of these earthquakes are marked in yellow and red stars in Fig.1. A location of the epicenter of the first event was approximately 30 kilometers off the coast southwest of Bengkulu city at the depth of about 30 kilometers. The second event was located about 225 kilometers off the northwest of the first event at the depth of 10 kilometers. These ground motions caused massive damaged of thousand houses and hundreds of RC building along the coastline in Bengkulu and West Sumatra provinces and Mentawai Islands [2]. One of the most affected city by the earthquakes was Padang city, West-Sumatera province, located approximately 180 kilometers from the epicenter of the second event.

Post-earthquake investigation of the damaged RC buildings caused by this 2007 Sumatra earthquake in Padang city, has been conducted and well-reported by Maidiawati and Sanada [3]. Their investigation has shown the interesting results about the effects of the brick masonry infills to the seismic capacity of the RC multi-story building. They found that two adjacent comparable tree-story RC buildings have differently behaved due to ground motion of the 2007 Sumatra earthquake. These RC buildings were Suka Fajar and Sutan Kasim buildings. The locations of these RC

buildings are shown as two red-boxes in Fig. 2. These buildings were built in 1980. There was no detail information about the structural design of these RC building. However, it has been believed that the structure of these RC buildings was not designed to resist the strong ground motion such as 2007 Sumatra earthquake. The Suka Fajar building was used as a car's showroom, while the Sutan Kasim building as a company's office and car's tire dealer. Since Suka Fajar was occupied as the car shown room, most of the infills used tempered-glass. Contrast to Suka Fajar building, Sutan Kasim building used brick masonry as infills.

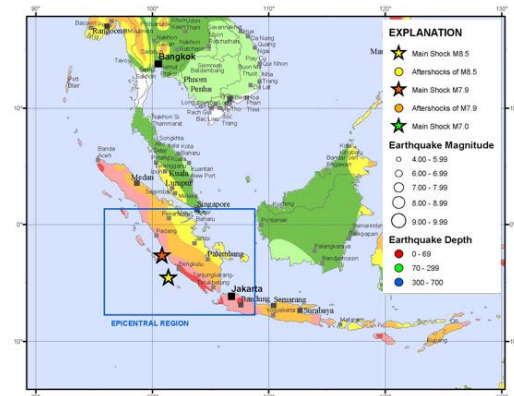


Fig. 1 Epicenters of the 2007 Sumatra Earthquake.

Due to the 2007 Sumatra earthquake, the Sutan

Kasim building had survived, while the Suka Fajar building collapsed. Maidiawati and Sanada [3] have also evaluated the seismic capacity of these RC buildings by using the Nakano's method [4] and the Japanese standard [5]. They concluded that the brick masonry infills has significantly contributed improve the seismic capacity of Sutan Kasim RC building. In their study, the seismic capacity was only considered the first-story of the buildings. The presence of the brick masonry infills in Sutan Kasim RC frame structure helped the building survive during the earthquake. More detail of this field observation and evaluation works has been clearly summarized in [3].



Fig. 2 Location of Evaluated RC Buildings.



(a) Suka Fajar Building (b) Sutan Kasim Building

Fig. 3 Photos of Evaluated RC Buildings.

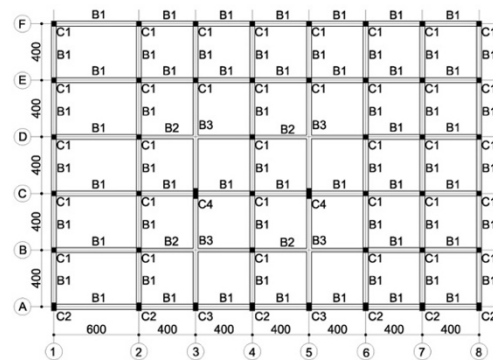
Obviously, several researchers have been focused on the investigation of effects and behaviors of the masonry infills to seismic performance, including the seismic capacity, of the RC structure. For instances, Tanjung and Maidiawati [6,7]; Maidiawati et.al. [8]; and Maidiawati and Sanada [9] have studied these effects through experimental works by testing the single-bay and single-story of RC frame structures subjected to lateral static loads. Their works have concluded that the masonry infill increases the lateral strength and stiffness of the RC frame structures, but reduce the structure's ductility. The comprehensive discussion of this topic has also been explained by Asteris [9], Barnaure and Stoica [10] in their research articles. They have discussed the failure modes and the mathematical model for the masonry infills in related to the seismic performance of the RC frame structure.

In this paper, an analytical study for defining the effects of brick masonry infills to the seismic capacity of the multi-story RC building is presented. For this

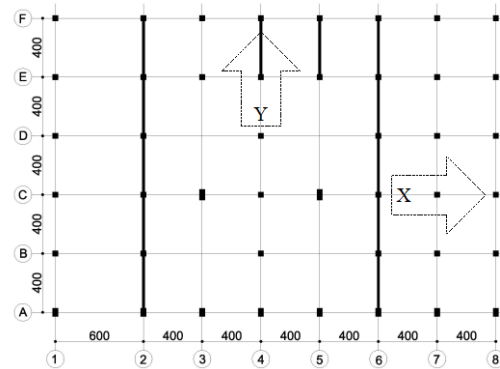
analytical purpose, a survived Sutan Kasim building has been considered. The computer codes called SStructural Earthquake Response Analysis 3D (STERA 3D) was used as an analytical tool [11,12]. These codes were developed by Professor Taiki Saito from Toyohashi University of Technology, Japan.

THE MATERIAL AND METHODS

Figure 4. shows the typical floor plan for all floors of the Sutan Kasim building according to detail site measurement. The notation C and B which is shown in Fig. 4a denotes the column and beam of the RC structure, respectively. The detail reinforcements arrangements for these columns and beams are given in Table 1 and Table 2, respectively. The location of the masonry infill walls is notated by the bold line in Fig.4b.



(a) Typical Floor Plan



(b) The Location of Brick Masonry Infill

Fig. 4 Floor Plan Used in the Analytical Model.

The compressive strength of the existing concrete used in the considered structure was about 26.7 MPa [9]. Its compressive strength was obtained by conducting the non-destructive Schmidt Hammer test and the uniaxial compressive test on the cylinder concrete specimens taken by the core drill machine. All RC structures installed plain rebar with nominal yield tensile stress about 307 MPa for the longitudinal flexure and 240 MPa for shear reinforcements,

respectively [3,9]. The compressive strength of the brick masonry is 4 MPa.

Table 1 Reinforced Arrangements of Columns

n	Column	C1	C2	C3	C4
	B x D	350x350	350x550	350x700	
1	Main rebar	4 ϕ 22 4 ϕ 16	8 ϕ 22	10 ϕ 22	18 ϕ 22
	Hoop		2 ϕ 6@200		
	B x D	350x350	350x550	350x700	
2	Main rebar	4 ϕ 22 4 ϕ 16		4 ϕ 22 6 ϕ 16	4 ϕ 22 14 ϕ 16
	Hoop		2 ϕ 6@200		
	B x D	350x350	350x550	350x700	
3	Main rebar		8 ϕ 16		18 ϕ 16
	Hoop		2 ϕ 6@200		
	B x D	350x350	350x550	350x700	

Unit: mm; n: story number

Table 2 Reinforced Arrangements of Beams

N	Beam	B1	B2	B3
	B x D	350 x 550	250 x 420	350 x 720
2	Main rebar	4 ϕ 16 4 ϕ 12	10 ϕ 16 2 ϕ 12	10 ϕ 12
	Stirrup	2 ϕ 6@100 (middle: 2 ϕ 6@150)		
	B x D	300 x 450	250 x 420	350 x 720
3	Main rebar	4 ϕ 16 4 ϕ 12	10 ϕ 16 2 ϕ 12	6 ϕ 22
	Stirrup	2 ϕ 6@100 (middle: 2 ϕ 6@150)		
	B x D	300 x 450	250 x 420	300 x 550
R	Main rebar		4 ϕ 16 4 ϕ 12	4 ϕ 22 4 ϕ 12
	Stirrup	2 ϕ 6@100 (middle: 2 ϕ 6@150)		
	B x D	300 x 450	250 x 420	300 x 550

Unit: mm; n: story number

The STERA 3D computer codes were used to create the analytical models for the given floor plan shown in Fig 4. The STERA 3D is the computer codes based on the nonlinear finite element method which can be used to evaluate the seismic performance of the RC and Steel buildings. The STERA 3D computer codes have the capabilities to performs the elastic modal analysis, the nonlinear lateral static pushover and the nonlinear lateral static cyclic analysis and the nonlinear earthquake responses analyses. STERA 3D comes with the graphic user interface to create and to analyze the building model and then also to show the analysis results. To make the analysis more reliable, the beam is modeled as a line element with nonlinear bending and shear springs. The column is also modeled as a line element, however, considering the nonlinear interaction between axial force and bending moment. The interaction is furthermore expressed by the nonlinear axial springs for concrete and nonlinear multi springs for the reinforcements. The masonry infill is defined as a line element with nonlinear shear spring and vertical spring in the middle of the brick wall [11]. The final images of the analytical models for the bare frame and the bare frame with brick masonry infills models, respectively, are shown in Fig

5. As it mentioned above, two types of analysis were performed on the models, i.e. the pushover and the time history analyses. The pushover analysis was conducted for maximum drift ratio 1/100 in X and Y directions, respectively. For the time history analysis, the input ground motions with a maximum acceleration of about 320 gals for 60 seconds' excitation was applied. The maximum acceleration of 320 gals was applied in according to the reported peak ground motion on the coastline of Padang city caused by the 2007 Sumatra earthquake [1]. These input ground motions were generated from the recorded ground motion of 2009 West Sumatra earthquake which was recorded by seismograph installed at Singkarak Hydro Electric Power Plant [13]. The works of the analytical study described in this paper thus following an analytical matrix as is tabulated in Table 3.

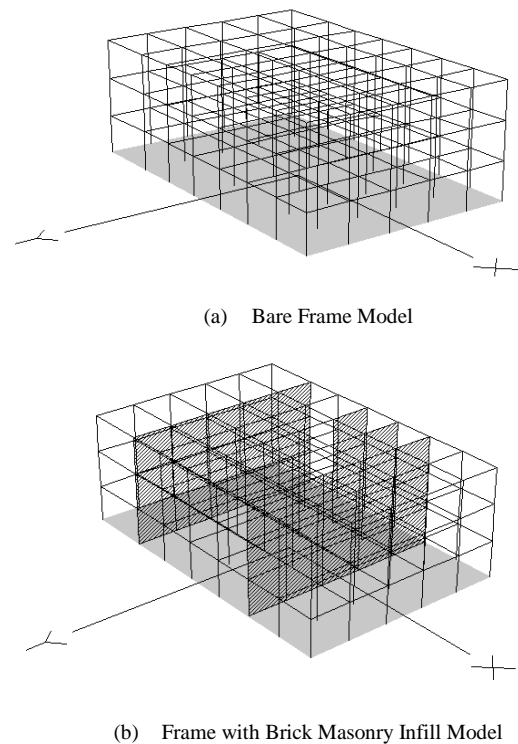


Fig. 5 3D Analytical Models.

Table 3 Matrix of the Analytical Study

Analytical Works	Codes
Bare Frame Model	
Pushover X-direction	PO-X-WO
Pushover Y-direction	PO-Y-WO
Time History Analysis	EQ-WO
Bare Frame with Infills Model	
Pushover X-direction	PO-X-MW
Pushover Y-direction	PO-Y-MW
Time History Analysis	EQ-MW

NUMERICAL RESULTS AND DISCUSSION

Figure 7. shows the comparison of the post-images of the analytical models between the RC frame structure and RC frame structure with brick masonry infills. In STERA 3D, the damages on the structural components of the RC building is defined by the ductility of its structural components. When the ductility in a range of one to five denotes its structural components experience light to moderate damage, while for ductility great than five denotes severe damage. The comparison of these damage structural components is tabulated in Table 4. The presence of the brick masonry infill can reduce the damage of the columns up to 17% and beam almost 50%. As we have been presumed, the analytical results show the presence of the brick masonry infill can reduce the number of the damaged structural components.

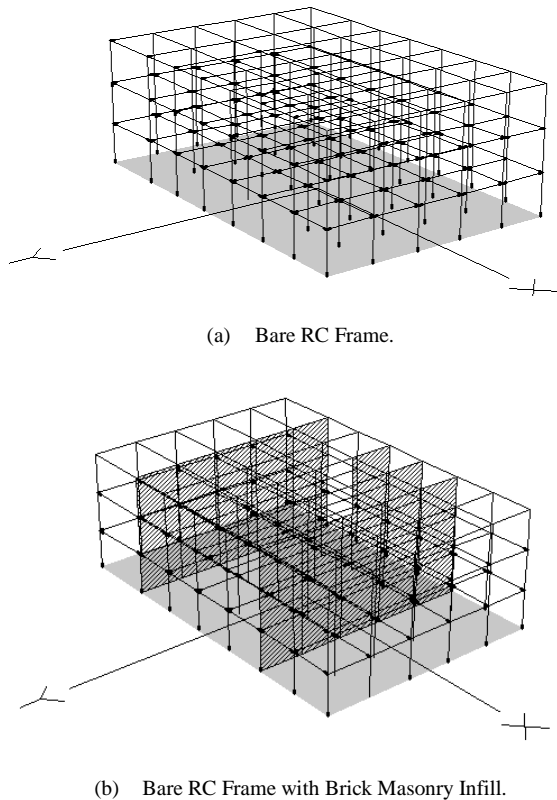
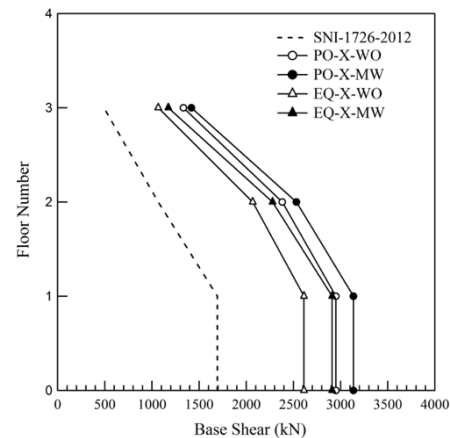


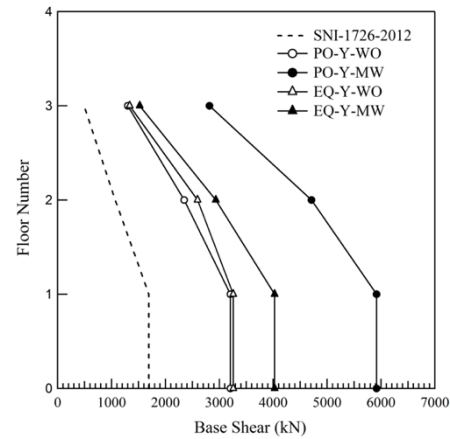
Fig. 7 Post-images of the Analytical Models.

Table 4 The Damage of Structural Components

Components	Percentage of Damage	
	Moderate	Severe
<i>Bare RC Frame</i>		
Column	67%	0%
Beam	56%	18%
<i>Bare RC Frame with Brick Masonry Infill</i>		
Column	40%	0%
Beam	8%	0%



(a) X-direction

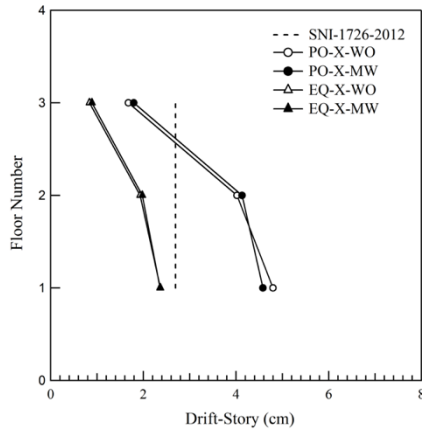


(b) Y-direction

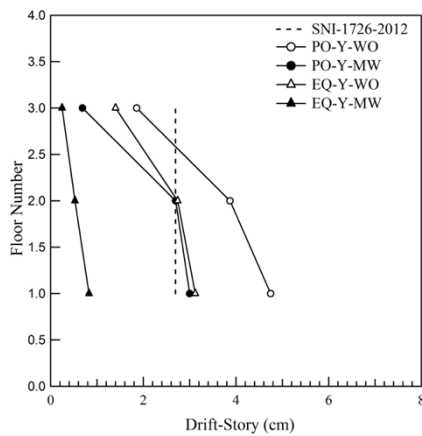
Fig. 8 Comparison of the Base Shear.

The comparison of analytical results in the term of base shear of the models, including the comparison with the requirement base shear design following Indonesia RC building code SNI-1726-2012 [14], is shown in Fig. 8. Noting that for the time history analysis, the North-South and East-West directions coincide with X and Y directions of the building, respectively. The minimum requirement of the base shear design was evaluated based on seismic site parameters where the building was constructed. These parameters are the soil specification is the medium soil; the maximum spectral response acceleration at short periods S_s is 1,35; the maximum spectral acceleration at a period of 1 second S_1 is 0,599; the acceleration-based site coefficient F_a is 1,0; the velocity-based site coefficient F_v is 1,3; the maximum spectral acceleration at short periods adjusted for site class S_{MS} is 1,35; the maximum spectral acceleration at a 1 second period adjusted for site class S_{M1} is 0,779; the design spectral response acceleration at short periods S_{DS} is 0,9; and the design spectral response acceleration at a period of 1 second

S_{DI} is 0,519. The above seismic site parameters were defined by Indonesia Seismic Design Map [15]. The importance factor I is 1,0, and response modification coefficient R is 8. These analytical results show that the presence of the brick masonry infills seems to have given a significant contribution for increasing the base shear, especially in Y-direction. Obviously, all base shears of the analytical models greater than minimum requirement by Indonesia code SNI-1726-2012 [14].



(a) X- direction



(b) Y-direction

Fig. 9 Comparison of the Inter-Story Drift.

The analytical results of the inter-story drift for the analytical models are given in Fig. 9. Refer to SNI-1726-2012 [14], in the case of RC frame structure, with or without brick masonry infills, the inter-story drift is limited to 1% of the inter-floor height and then divided by 1,3. All results of the pushover analysis passed the limitation of the inter-story drift of the current Indonesia code, while the results of the time history analysis still adequate the code. Again, the brick masonry infill shows it superior to increase the seismic performance of the RC structure by reducing the inter-story drifts of

structures; see the comparison results for Y-direction in Fig. 9b.

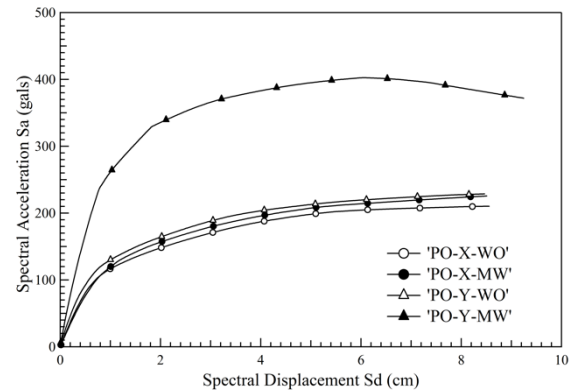
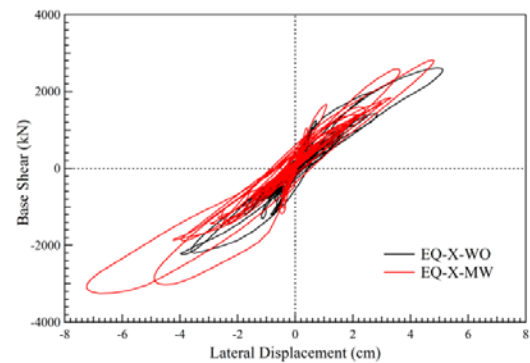
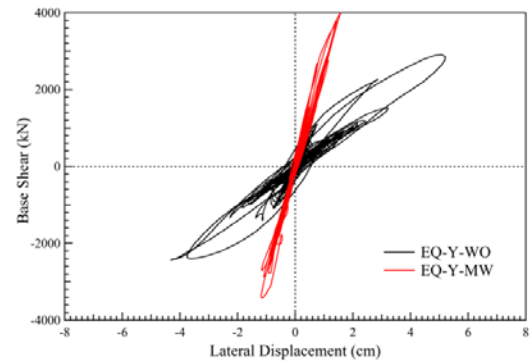


Fig. 10 Comparison of the Seismic Capacity.



(a) X-direction



Y-direction

Fig. 11 Seismic Response of the Structure.

Comparison of seismic capacity which is plotted based on the results of the pushover analyses of the analytical models is shown in Fig. 10. These graphs also clearly show the effect of the presence of the brick masonry infills on the seismic capacity of the RC frame building, i.e. have significantly increased the frame's seismic capacity. In this case, since the location of the brick masonry infills is parallel to the Y-direction, the increased of the seismic capacity is

more observable in this direction.

A similar tendency regarding the effect of the brick masonry to the seismic capacity of the RC building is also shown by the graphs of the relation between base shear and the lateral displacement of the RC building as is shown in Fig 11. The lateral displacements in it figure were picked-up on the top of the building. The result of it comparison, again especially in Y-direction, confirms the effect of brick masonry infills can significantly improve the seismic capacity of the RC building. The stiffness of the RC frame is significantly raised due to the existence of the brick masonry infill, especially in Y-direction.

CONCLUSION

The analytical study to define the effects of brick masonry infill on the seismic capacity of the multi-story RC building by using computer code STERA 3D has been presented in this paper. The survived tree-story RC building during the 2007 Sumatra earthquake was evaluated as an analytical model. The structural detail and the material properties used in the analysis were collected after the earthquake from the building site. To the analytical model, the pushover and time history analyses were applied. The pushover analysis followed the UBC method while for the time history analysis, the input motion generated from the 2009 West Sumatra earthquake was used. From the analytical results are clearly shown that the brick masonry infills may significantly improve the seismic capacity of the RC building. The evaluated RC building could be survived to large ground motion even though the building was designed by applying the old Indonesia building code.

ACKNOWLEDGMENTS

The authors sincerely acknowledge to Andalas University for partially financial supporting to this research works.

REFERENCES

- [1] https://earthquake.usgs.gov/earthquakes/eventpage/official20070912111026830_34#executive
- [2] EERI, Observations on the Southern Sumatra Earthquakes of September 12-13, 2007, EERI Special Earthquake Report — November 2007.
- [3] Maidiawati and Sanada Y., Investigation and Analysis of Buildings Damaged during the September 2007 Sumatra, Indonesia Earthquakes, *Journal of Asian Architecture and Building Engineering (JAABE)*, Vol.7 No.2, 2008, pp. 371-378.
- [4] Nakano Y., Maeda M. and Kuramoto H., *Guideline for Post-Earthquake Damage Evaluation and Rehabilitation of RC Buildings in Japan*. 13th World Conference on Earthquake Engineering, 2004.
- [5] The Japan Building Disaster Prevention Association, English Version, 1st, *Standard for Seismic Evaluation of Existing Reinforced Concrete Buildings*, 2001, 2005.
- [6] Tanjung J. and Maidiawati, Studi Eksperimental tentang Pengaruh Dinding Bata Merah Terhadap Ketahanan Lateral Struktur Beton Bertulang, *Jurnal Teknik Sipil ITB*, Vol. 23 No. 2, 2016, pp. 99-106.
- [7] Tanjung J. and Maidiawati, The Experimental Investigation on Beneficial Effects of the Local Brick Masonry Infills to Seismic Performance of R/C Frame Structures in West Sumatera, *International Journal of Civil Engineering and Technology (IJCIET)*, Volume 8, Issue 10, 2017, pp. 687-697.
- [8] Maidiawati, Sanada Y., Konishi D. and Tanjung J., Seismic Performance of Nonstructural Brick Walls Used in Indonesian R/C Buildings, *Journal of Asian Architecture and Building Engineering (JAABE)*, Vol.10 No.1, 2011, pp. 203-210.
- [9] Maidiawati and Sanada Y., R/C frame-infill interaction model and its application to Indonesia buildings, *Earthquake Engng Struct. Dyn.* 46, 2017, pp. 221-24.
- [10] Asteris P.G., Kakaletsis D.J., Chrysostomou C.Z. and Smyrou E.E., Failure Modes of In-filled Frames, *Electronic Journal of Structural Engineering* 11(1), 2011, pp. 11-20.
- [11] Saito T., *STructural Earthquake Response Analysis 3D*, Technical Manual Version 5.8, Toyohashi University of Technology, 2017.
- [12] Saito T., *STructural Earthquake Response Analysis 3D*, User Manual Ver. 5.6, Toyohashi University of Technology, 2017.
- [13] Mangkoesobroto S.P., *Seminar dan Pameran HAKI Perkembangan dan Kemajuan Konstruksi Indonesia*, 2010.
- [14] SNI-1726-2012, *Tata Cara Perencanaan Ketahanan Gempa Untuk Struktur Bangunan Gedung dan Non Gedung*, BSN, 2012.
- [15] http://puskim.pu.go.id/Aplikasi/desain_spektra_indonesia_2011/

STRENGTH CHARACTERISTICS OF WASTED SOFT DRINKS CAN AS FIBER REINFORCEMENT IN LIGHTWEIGHT CONCRETE

Indradi Wijatmiko¹, Ari Wibowo¹ and Christin Remayanti Nainggolan¹

¹Faculty of Engineering, Brawijaya University, Indonesia 65145

ABSTRACT

Nowadays the problems of lightweight concrete flexural strength have been approached by adding fiber to the mixture. Meanwhile waste materials are continuously produced as a result of modern industry. This paper aims to increase the strength characteristic of both compressive and flexural lightweight concrete by introducing wasted soft-drink cans as fiber reinforcement. Comprehensive study has been conducted to investigate the optimal amount of fiber fractions and the effect of fiber shape to the concrete mechanical strength. This study cleared the effect of various fractions (10%, 15% and 20% by volume of concrete), followed by two types of fiber shape (hooked and clipped) to the lightweight concrete compressive and split tensile strength. The experimental results of cylindrical lightweight concrete were compared to the normal lightweight concrete. The result showed that the introduction of 10% of fiber performed in higher tensile strength with the increase of 23%, while the hooked shape of fiber increased the compressive strength by more than 40%. It can be concluded that the introduction of waste recycle tin increased the mechanical properties of normal lightweight concrete, however further study can be performed to effectively increase the strength characteristics.

Keywords: lightweight concrete, fiber reinforcement, waste materials, compressive strength, tensile strength

INTRODUCTION

Performance and durability become main purposes in upgrading construction method and material. One of the methods is by reducing the weight of dead load through applying lightweight concrete materials. However, the common problem related with lightweight concrete is the low mechanical properties. Meanwhile fiber reinforced concrete (FRC) is a composite material, which aims to increase mechanical properties (i.e. compressive and tensile strength), increase the toughness and improve the energy absorption of concrete [1]. Various type of fiber has been researched, such as glass, steel, synthetic and un-synthetic fiber [2]. Adding fibers into concrete create mixtures that are more cohesive and less prone against segregation, thus the interlock and entanglement around aggregate particle tended to reduce the workability.

Inclusion of short fibers in a small fraction improve mechanical performance of FRC by reducing size and amount of defect in concrete. One of the benefit of FRC is providing resistance against crack propagation, which may lead to pulled out and rupture. FRC has been known could reduce the bleeding of water that lead to plastic and drying shrinkage cracking. However, each type of FRC has different properties, advantages and limitations.

Steel fibers has been a common applied material due to its significant improvement. However, producing steel fibers cost more than its benefit. Therefore, an alternative material based on recycle or

wasted is needed.

It has been known that 3R's program (Reduce, Reuse and Recycle) helps to preserve conserve environment for sustainability purposes. However, one of the environmental issue is the difficulty to recycling and bio-grade of steel waste material. In the other hand, steel waste material may provide higher tensile characteristic increase the compressive and tensile strength in the concrete, especially lightweight concrete[3][4][5].

Therefore, some study on the use of recycle or waste material has been conducted to understand the behavior of concrete strength. G.C. Behera concluded that the use of soft drink bottle caps as a fiber with the fraction of 0.25%, 0.5% and 1.0% of the total weight increased the compressive strength, split tensile and flexural strength especially in the case of 1.0% with 10-15% increment [6][7]. G. Murali et al studied that introducing crumpled steel fiber concrete with a portion of 0.8% volume of concrete resulting to higher compressive strength, split tensile and flexural strength compare to normal concrete [8]. The used of polyethylene terephthalate (PET) bottles fiber was investigated as reinforcement of specimens [9][10]. The result showed a significant increase to indicate the adherence between PET and concrete for structural reinforcement [11].

This research study on the optimum fraction of wasted soft drink can as fiber to improve compressive and tensile strength, also to study the effectiveness of interlocking in the wasted soft drink can to reinforce the lightweight concrete. Further, two types of

interlocking are introduced to get clearer understanding the mechanical properties of fiber reinforce concrete.

MATERIALS

Thirty sixth cylindrical specimens were casted in order to have deep understanding on the use of soft drink can as fiber reinforce in lightweight concrete. The component materials are described below.

Cement

All specimens used locally manufactured Pozzoland Portland Cement (PPC) type 1, which is correspondent with ASTM type 1.

Aggregates

Fine aggregates were obtained from river around Lumajang residency, coarse aggregates were obtained from Pasuruan city. Both places are known as fine production of aggregates materials in East Java provinces (Indonesia). In order to produce lightweight concrete, pumice aggregates were ordered from Bali (Indonesia). Some of the part were required to be washed to improve the quality, while the rest were in the good quality. A group of grain pumice aggregates 8-16 mm were dipping into a polymer liquid in order to prevent excessive water absorption, which would disturb water-cement ratio [12]. The coated pumice then dried 24 hours at the room with the temperature of $25 \pm 2^\circ\text{C}$. The properties of aggregates can be seen in Table 1.

Table 1 Properties of aggregates

Aggregates	Specific	Bulk density (kg/m ³)		Water absorption 24hr (%)
	gravity	ASTM		
	Ovendry	Shoveled	Rodded	
		Ovendry	Ovendry	
Coarse Aggregates				
GA	2.67	2696	2589	3.20
PA	1.85	-	-	14
CPA	1.79	-	-	10
Fine Aggregates				
River sand	2.60	2530	2693	3.22

Note: GA (Gravel Aggregates), PA (Pumice Aggregates), CPA (Coated Pumice Aggregates)

As seen in Table 1, coated pumice has lower specific gravity and water absorption ability compares to uncoated ones.

Fibers

Fibers were constructed from metallic waste of soft drink can as shown in Fig.1. After removing the

top and bottom of can, the rectangular shapes of body were washed thoroughly and dried. Body of can then was cut into several sizes depend on the interlocking length and the type of interlocking (i.e. type A and type B) as can be seen in in Fig. 2.



Fig. 1 Wasted soft drink can as fiber reinforcement



Fig. 2 Sample of fiber with width of 2mm and length 40mm without interlocking shape.

Water

Local tap water of the city of Malang, Indonesia were used and measured for water-cement ratio and also being used for the curing process of the lightweight concrete.

METHODOLOGY

In this research, the concrete mix design was aimed for 17MPa at 28 days. Referring to Indonesia code (SNI 03-2834-2000), the concrete mix proportion can be seen in Table 2 with the ratio of water-cement was 0.5.

In this research 36 cylindrical specimens were casted with the height of 300mm and the diameter of 150mm. For the purposes of investigating the optimum fraction of fiber, 24 cylindrical specimens were casted with four different fraction of fiber's i.e. 0%, 10%, 15% and 20% of volume, with 6 casted specimens for each scenarios.

Table 2 Mix Design proportion

Materials	Bulk density (kg/m ³)	Unit weight (kg)	Volume (m ³)	Ratio
Cement	1350	363	0.268	1
Fine Aggregates	1400	743	0.530	2
Coarse Aggregates	1300	1069	0.822	3
Water	1000	225	0.225	1

Fiber was made from aluminum soft drink can with the dimension of 40mm length and 2mm width without any particular interlocking shape. Coding of specimens and the attribute data are described in Table 3.

Table 3 Lightweight specimens properties

Specimens code	Amount (specimens)	Fiber's fraction (% vol)	Interlocking type
Norm	6	0	No
Fr1	6	10	No
Fr2	6	15	No
Fr3	6	20	No
II1	6	10	A
II2	6	10	B

Further, in order to investigate the effectiveness of interlocking, this study introduced two types of interlocking as can be seen in Fig. 3(a) and Fig. 3(b).

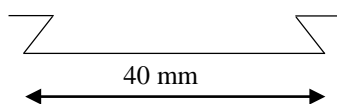


Fig. 3(a) Fiber interlocking type A.

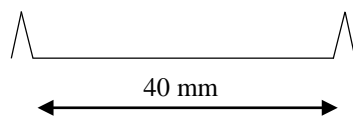


Fig. 3(b) Fiber interlocking type B.

All types of specimens were subjected to compressive tests (3 specimens) and tensile test (3 specimens). Therefore, in total there were 18 specimens under the compressive tests and another 18 specimens under the tensile tests. An extensometer and stress-strain gauges were used during the compressive tests to measure the stress strain abilities and elastic modulus.

RESULT AND DISCUSSIONS

All specimens were subjected to compressive and tensile test at the day of 28, with the result that can be described in term of the density and workability, compressive strength and tensile strength.

Density and Workability

The purposes of coated pumice was to prevent the water absorption, which has been indicated from the reduction of fiber pumice reinforce concrete density compare to normal ones.

Table 4 Density and slump of specimens

Specimens code	Density (kg/cm ³)	Slump (cm)
Norm	2250.45	14.5
Fr1	2226.42	14.5
Fr2	2183.33	12
Fr3	2215.30	8
II1	2213.84	9
II2	2232.71	14.5

Workability of mixture can be associated with the slump measurement. Table 4 shows the density and slump of specimens, which indicated that the inclusion of fiber have lower slump value. It has been confirmed by many scholar and in ACI 213R-87 that the coated pumice and fiber inclusion produced lower slump value due to the low weight as a consequence of water absorption reduction. In order to avert the segregation and to maintain the cohesive, a higher slump value is demanded with the additional effort to preserve the ideal surface of specimens. In this study the slump value can be keep between 7.5-15cm, however the addition of waste soft drink can as fiber caused reduction of slump value and resulting to minor porous on the surfaces as can be seen in Fig. 4.



Fig. 4 Identified porous on the concrete surfaces.

Compressive Strength

Compressive strength tests were performed on three cylindrical specimens for each fraction and interlocking type. The dots on Fig. 5 shows the compressive strength on various fractions (0%, 10%, 15% and 20% respectively), while the continuous line is used to connect the average value of each type. Further, Fig. 5 indicated that though substitution of strong gravel aggregate by relatively weak pumice aggregates might reduce the compressive strength, however the inclusion of wasted soft drink can as fiber tended to increase the compressive strength compare to normal ones.

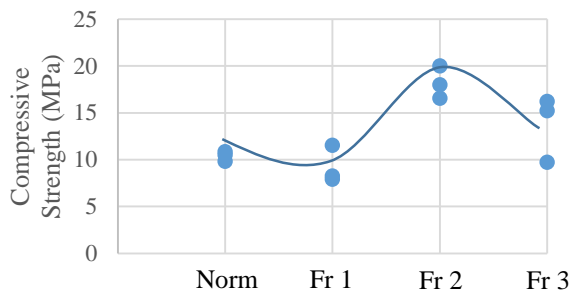


Fig. 5 Compressive strength of FRC with various fiber fractions.

The coated pumice commonly reduce the compressive strength due to the lack of clinker (C_3S), which may resulting on slow hydration and decrease the heat development. However, the inclusion of thin aluminum can help to distribute the heat quicker and the ongoing pozzolanic reactions lead to the continuous hydration phase. Though the FRC tended to have higher compressive strength, the optimum value can be taken from adding 15% volume of fiber. An excessive fiber higher than 15% of volume lead to the lack of workability and resulting to porous and multiple fragmented parts.

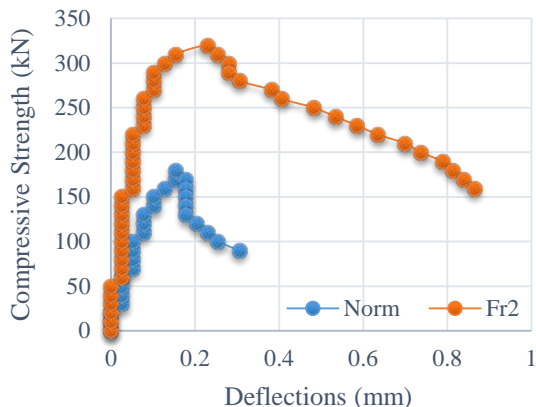


Fig. 6 Compressive strength vs deflection of normal and 15% volume of fiber fractions.

Figure 6 shows the comparison of compressive strength and deflection between normal concrete and concrete with 15% of fiber inclusions, which can also indicated the stiffness of specimens. The addition of fiber not only increase the compressive strength, but it tended to increase the stiffness as well. The stiffness of specimens with 15% fiber's volume were increased 14% compare to the normal ones.

The compressive strength of all various interlocking system generated much stronger compressive ability compare to the normal ones, which can be seen in Fig. 7. Although the average of interlocking type B was the highest, interlocking type A most likely produce higher compressive strength for each specimen.

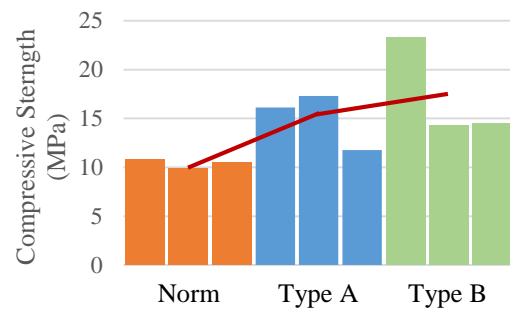


Fig. 7 Compressive strength of FRC with various fiber interlocking.

Tensile Strength

Tensile tests were conducted on three specimens for each type at the age of 28 days, as can be seen in Fig. 8.



Fig. 8 Tensile strength of FRC with various fiber interlocking

Figure 9 shows the tensile strength of various fiber fraction. As can be seen, the inclusion of waste soft drink can increase tensile strength compare to normal ones. Further, the optimum result obtained from the fiber with 10% volume fraction. However, the smooth and slippery surface of soft drink can failed the homogenous mix between concrete and fiber, therefore the increasing of tensile strength was considered mild (23% from the normal ones).

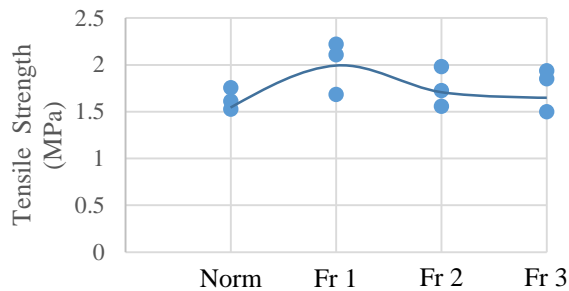


Fig. 9 Tensile strength of FRC with various fiber fractions.

The effectiveness of fiber on increasing tensile strength can be observed visually on the failure mechanism. In the case of normal concrete, the failure mechanism occurred all of sudden followed by strong sound indicate the failure phase achieved. Meanwhile, the FRC based on the waste soft drink can begun the failure mechanism with several cracks on the concrete surface, especially at the section where load applied. The failure of specimen occurred without strong sound, when the crack elongate from the upper section into the bottom ones as can be seen in Fig. 8. At the same time the load dial stopped, and started showing the reverse number.

Figure 10 shows the sticking out of fiber at the concrete surfaces in full-length size. This evidence indicated the slip mechanism during tensile strength due to the smooth and slippery surface of fiber can.



Fig. 10 Fiber sticking out of concrete surfaces.

Figure 11 shows the tensile strength result of various interlocking. Despite the smooth and slippery surface of fiber, the result indicate that interlocking increase tensile strength. Interlocking created stronger bound between fibers, which were effective against tensile and strain effect.

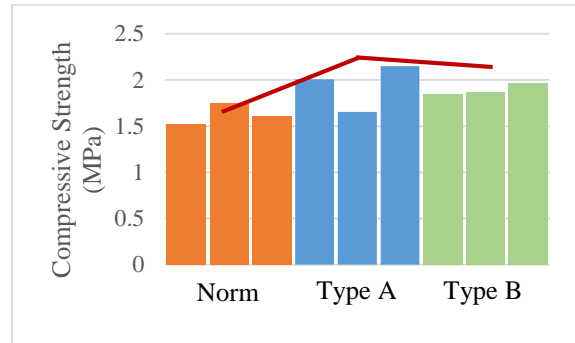


Fig. 11 Tensile strength of FRC with various fiber interlocking

The tensile strength of fiber with interlocking tended to increased as shown in Fig. 11. The interlocking type A has higher tensile due to the shape of interlocking effectively bond each other during the load. However, the distribution of fiber also give significant impact as shown by specimen with type A interlocking code I11.2 that had lower tensile strength due to uneven distribution of fiber. Crack was generated at the location without fiber, as it becomes the weakest part against the tensile stress.

This research also give significant founding to the issue related to the fiber reinforce concrete by pumice. It has been known that the low density of pumice keep it difficult to distribute equally during the casting due to floating pumice. However, the inclusion of fiber with interlocking effectively keep pumice from floating and as a result pumice can be distributed equally all around specimen.

Figure 12 shows the equal distribution of pumice due to the existence of fiber.



Fig. 12 Pumice distributions on the concrete with high fiber inclusions.

CONCLUSION

Thirty sixth lightweight fiber reinforce concrete were investigated to have clear understanding the effect of waste soft drink can as fiber and its interlocking to the concrete mechanical properties. Several outcomes can be observed as follows:

1. Waste soft drink can increase the compressive strength of lightweight concrete with the optimum volume fraction of fiber is 15%. Further, the interlocking type generate higher compressive strength, which is shown by interlocking type B. The inclusion of fiber also increase the stiffness of specimens as well as its deflection under the axial load.
2. The addition of waste soft drink can give advantage on the tensile abilities of concrete specimens, as it increase 5-23% from the normal ones. The introduction of two type of interlocking fiber slightly increase the tensile strength with the highest increasing was in the interlocking type A.
3. The inclusion of fiber, especially with interlocking, give additional advantages as it help keeps pumice from floating to the surfaces and hold pumice at the evenly distributed places.

ACKNOWLEDGEMENTS

We acknowledge the support of Higher Education Excellent Research Grant (*Penelitian Unggulan Perguruan Tinggi-PUPT*) from Ministry of Research, Technology and Higher Education of the Republic of Indonesia.

REFERENCES

- [1] Blaszczyński, T., and Przybylska-Falek, M., Steel fiber reinforced concrete as a structural material, *Procedia Engineering* Vol. 122, 2015, pp. 282-289.
- [2] Noaman, A.T., Abu Bakar, B.H., and MD. Akils, H., Investigation on the Mechanical Properties of Rubberized Steel Fiber Concrete, *Engineering Structures and Technologies*, Vol. 9, Issue 2, 2017, pp. 79-92.
- [3] Ismail, Z.Z., and Al-Hashmi, E.A., Validation of Using Mixed Iron and Plastic Wastes in Concrete, *Second International Conference on Sustainable Construction Materials and technologies*, 2011, ISBN 978-1-4507-1490-7.
- [4] RajPrasad, J., Anuradha, V., and Gridharan, P., Experimental Investigation on Fibre Reinforced Concrete using Waste Materials, *International Journal of Engineering Trends and Technology (IJETT)*, Vol. 34, Number 3, 2016, pp.100-105.
- [5] Balaguru, P., and Foden, A., Properties of fiber reinforced structural lightweight concrete. *ACI Structural Journal* Vol. 93, issue 1, 1996, pp. 62-78.
- [6] Behera, G.C. and Behera, R.K., Increase in Strength of Concrete by Using Bottle Caps, *International Research Journal of Engineering and Technology (IRJET)*, Vol. 02, Issue 03, 2015, pp. 1937-1942.
- [7] Behera, D., Ahmed, A.E., and Chala, N., Innovative and Sustainable Application of Soft Drink Bottle Caps as Fiber in Concrete Structures, Vol. 5, Issue 2, 2018, pp. 556-564
- [8] Murali, G., Vardhan, C. M. V., Sruthee, P., and Charmily, P., Influence of Steel Fibre on Concrete, *Journal of Engineering Research and Applications (IJERA)*, Vol. 2, Issue 3, 2012, pp. 075-078.
- [9] Christian, S., Patel, K., Vasava, M., Vasava, P., and Purohit, S., Evaluating Strength of Concrete Using Bottle Caps and PET, *International Journal of Advance Engineering and Research Development*, Vol. 04, Issue 3, 2017.
- [10] Darshan N., Rajani V.A., and Sharath B.P., Experimental Study on the Hardened Properties of Concrete by Using Soft Drink Bottle Caps as Partial Replacement for Coarse Aggregates, *International Journal of Emerging Trends in Science and Technology*, Vol. 1, Issues 08, 2014, pp. 1335-1341.
- [11] Akhund, M.A., Sannd, A., Memon, U., and Oad, S.J., Utilization of Soft Drink Tins as Fiber Reinforcement in Concrete, *Engineering Science and Technology International Research Journal*, Vol. 1, No. 2, 2017, pp. 47-52.
- [12] Wijatmiko, I., Wibowo, A., Nainggolan, C.R., The effect of polymer-coated pumice to the stiffness and flexural strength of reinforce concrete beam. *MATEC Web Conf., SICEST 2016*, 2017.

OPTIMIZED PREPARATION OF RICE HUSK ASH (RHA) AS A SUPPLEMENTARY CEMENTITIOUS MATERIAL

*Carmela Denise C. Isberto¹, Krystoffer Lloyd D. Labra¹, Jan Marielle B. Landicho¹, and
Richard M. De Jesus²

¹Undergraduate Student of Civil Engineering in De La Salle University (Manila), Philippines

²Faculty of Civil Engineering in De La Salle University (Manila), Philippines

*Corresponding Author

ABSTRACT

In the last decade, supplementary cementitious materials (SCM) has been extensively used as an integral component in the production of concrete. This practice has been motivated by the aspect of sustainability and reduced environmental impact by cutting down substantial amounts of greenhouse gas emission. Correspondingly, the researchers intend to develop an appropriate method for the use of rice husk ash (RHA), a by-product of rice husk (RH) which exists in ubiquitous amount in the Philippines, as a partial replacement to ordinary Portland cement (OPC). Different studies have suggested optimal percentage replacement values of RHA, from 10% to 20%, which demonstrated vast improvement in strength of the resulting blended concrete. These optimal values, however, immensely depends on the burning preparation of RHA which adversely affects the amorphous silica components, and therefore the pozzolanic activities of RHA in concrete. In this research, a potential approach to convert RH into optimized and highly reactive RHA by controlled burning and grinding is provided. The effect of RHA on concrete is investigated through the various proportions of 5, 10, 15, and 20% RHA by weight replacement of cement. Some of the findings are: (i) controlled combustion of RH with temperature ranging from 400 to 600 °C and a slow method of cooling for 6 to 8 hours are some of the critical factors needed to produce high silica content, (ii) concrete containing up to 10% RHA replacement is optimal in maximizing the strength of concrete, and (iii) the incorporation of RHA in concrete by 15% and 20% replacement by weight indicates a lower workability of the concrete.

Keywords: Rice husk ash, Cementitious material, Incineration, High silica content, Optimized RHA

INTRODUCTION

Clearly today, rapid urbanization and the massive leap in industrialization create ever-increasing demands for concrete. Concrete production has then been castigated as it involves consumption of massive amounts of natural resources and persistently constitutes to several issues on carbon dioxide (CO₂) emissions which pose huge threat on both the society and environment. Waste management is another interrelated issue that is constantly being addressed by environmentalists and many researchers. It is established that one of the solutions to lessen the adverse effects of CO₂ emissions brought about by the production of concrete is to build sustainable and environmentally sound cities. Most recent studies [1,2,3] leaned towards green technology and sustainability distinctly acknowledge utilization of SCMs in concrete.

In evaluating SCMs, chemical analysis using any appropriate methods as standardized by ASTM C114, C311, and D4326 should be carried out [4]. One notable characteristic of SCMs is its ability to

improve the mechanical properties of concrete, due to its highly reactive silica content, which relatively makes it a good pozzolanic material [5]. Commonly and successfully established known SCMs in the concrete industry include silica fume, fly ash, blast furnace slag cement, etc. These SCMs indeed essentially contribute to durability and strength properties of concrete and generally help reduce CO₂ emissions.

Countless significant researches have been carried out and various explorations were done in search for a material that can pass as a cementitious material. A popular candidate is RHA.

RH is one of the most common agricultural wastes in the Philippines which serves as an outer covering of the rice grain during its growth. According to [6], once the RH is detached from the grain during the rice milling process, it usually ends up being dumped in an open space making it worthless thus inducing deterioration to land and environmental problems [7]. On the other hand, RH has its compelling usage; it has been broadly employed as a fuel for boiler feed to produce electricity for the power generation of rice

mill. With this, voluminous amount of RHA is being produced.

RHA is a natural carbon by-product obtained from RH that is converted to ash during ignition process [6]. The potential of RHA as a SCM has very well been regarded since it contains high content of silica.

Several researches have been made concerning the factors that affect the mechanical strength of the concrete incorporated with RHA such as time of incineration, temperature, time required for cooling process and fineness of the substance [8]. Nanoscale analysis is being performed to verify the physical and chemical properties of RHA through different test methods namely SEM, XRD, XRF-EDX [6,8,9]. Based on the analysis stated in the study of [7], results show that RHA possesses amorphous SiO_2 when gathered from a low temperature of 600°C [9]. Many studies validated that generating RHA by controlled burning of RH between 550°C and 600°C temperature converts the silica content into amorphous phase [8,9,10]; and partially substituting cement with 10% RHA by weight tends to improve the compressive strength of Portland cement concrete [9].

In this study, an attempt to transform locally available RH into high quality RHA that will exhibit heightened pozzolanic activity to be suitable as a cement replacement is done. To ascertain its quality, chemical composition, physical properties and characterization of the produced RHA will be carried out using X-Ray Fluorescence spectrometry (XRF), X-Ray Diffraction spectrometry (XRD), and Scanning Electron Microscopy (SEM). Also, further investigation is carried out to determine the optimum level of replacement of cement by the produced optimized and highly reactive RHA.

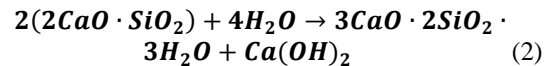
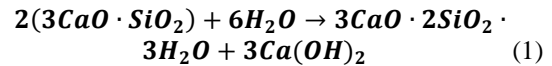
THEORETICAL BACKGROUND

Hydration of Portland Cement

The hydration of cement is the result of mixing between anhydrous cement with water involving a series of exothermic reactions taking place both simultaneously and successively. The main compounds in cement are as follows: alite (Ca_3SiO_5 , C_3S), belite (Ca_3SiO_4 , C_2S), aluminate ($\text{Ca}_3\text{Al}_2\text{O}_6$, C_3A), and ferrite ($\text{Ca}_4\text{Al}_2\text{Fe}_2\text{O}_{10}$, C_4AF). A set controlling agent, such as gypsum, is usually added to prevent rapid setting brought about by the high reaction rate of aluminate. However, this paper only examines the chemical reactions involving tri-calcium silicate, C_3S , and di-calcium silicate, C_2S , since only these silicates produce the calcium hydroxide ($\text{Ca}(\text{OH})_2$) needed for further reaction with RHA.

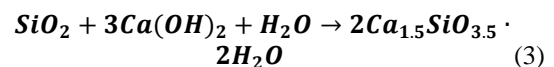
The product of reaction of cement with water is commonly referred to as Calcium-Silicate-Hydrated

(C-S-H) gel (previously referred to as tobermorite gel) which is the primary agent that binds the cement and aggregate particles together in concrete. The approximate hydration reactions of C_2S and C_3S are illustrated using the following chemical equations:



Chemical Contribution of RHA

High quality RHA which exhibits high pozzolanic activity can be produced under controlled conditions. From the study of [11], it was found that burning RH at 600°C yields the highly pozzolanic RHA consisting of amorphous silica. From Eq. (1) and (2), aside from the C-S-H gel produced, the hydration reaction also yields a certain amount of $\text{Ca}(\text{OH})_2$. This $\text{Ca}(\text{OH})_2$ will further react with the amorphous silica (SiO_2) found in high quality RHA to form a secondary type of C-S-H gel. In a research by [12], a comprehensive study was conducted on the pozzolanic effect of RHA on a cementitious system and provides the following chemical reaction:



Physical Contribution of RHA

Grinding of RHA is usually done to reduce particle size and improve surface area. Also, it is established that an inverse relationship exists between particle size and pozzolanic activity of RHA. However, this parameter does not significantly change beyond $5.6\mu\text{m}$. Habeeb & Mahmud (2010) reported that concretes incorporated with finer RHA resulted in denser concrete mix wherein the finer particles acted as micro fillers to enhance the cement paste pore structure contributing to the overall strength development of the concrete.

METHODOLOGY

Preparation of RHA

A custom-built muffle furnace, with chimney and air inlet, was used to burn the RH. The interior dimensions of the furnace are 1m wide, 1m height and 1m deep. The RHs were laid flat, measuring about 2-3cm in thickness, on 28 ceramic hearth plates. The plates were stacked in multiple layers inside the furnace using ceramic tubes as columns. About 12kgs of RH could be loaded in the oven each burning and

only about 20% of which remains as high quality RHA.

The muffle furnace utilizes burners (4pcs, 1 in each corner) and is semi-controlled, that is, the fuel is supplied from a propane tank and the main mode of control is through its pressure valve. When in operation, the control of the temperature inside the oven is not absolute but fluctuates within a small manageable range. The temperature is monitored using a Benetech GM700 infrared thermometer through the 4 holes (1 on each side and 2 in front) of the furnace, temperature was strictly limited within the range of 400-600°C. Since the temperature only ranged below the exact optimal temperature of burning (600°C), the burning duration was prolonged to 10 hours to make up for this temperature deficiency. During burning, fresh air continuously flows into the furnace through the 4 holes, this condition was defined as free air supply.

After the burning process, RHA is cooled to room temperature by leaving the furnace door ajar. This step usually takes 6-8 hours before RHA can be safely recovered from the furnace.

Grinding of RHA was done using a Los Angeles machine. About 2.4kgs of RHA is placed into the LA machine for each batch; 12 pieces of 2" steel balls were used for grinding. The machine had a rate of 36rpm and was operated for 2hrs in each grinding. To avoid unwanted absorption of moisture, the RHA is stored in an airtight container every after burning and grinding

Table 1 Mix Proportion of Mortar Specimens

Material	0%	5%	10%	15%	20%
(g)	0	05	10	15	20
	RHA	RHA	RHA	RHA	RHA
Cement	500	475	450	425	400
RHA	0	25	50	75	100
Sand	1375	1375	1375	1375	1375
Water	242	242	242	242	242

Physical and Chemical Analysis of OPC and RHA

Chemical composition of OPC and RHA used in the present investigation were determined using an Olympus Delta Professional Handheld XRF. Mineralogical analysis of RHA was done by X-ray diffraction analysis using Shimadzu Maxima X 7000. A JEOL 5300 scanning electron microscope (SEM) with the aid of a Gold Coater was used to obtain electron micrographs of the RHA sample and powdered RHA blended mortars.

Mix Proportion and Compressive Strength of Cement Mortars with RHA

Ordinary Portland Cement type I was used for this study [13]. Ottawa sand passing through 1.18mm sieve was used as fine aggregate [14].

RHA blended cement mortars were prepared by replacing OPC with varying amounts of RHA (5%, 10%, 15%, and 20% by weight of cement). The cement mixes were designated as 05RHA-20RHA, and 0RHA for the control mix. The mix proportions are presented in Table 1.

The mortars were mixed using a planetary 4.8 liter-capacity mixer. Each RHA proportion was produced in batches of 6 mortars and were mixed for a total of 2.5 min with a total of 1.75min rest in between. Preparation and mixing of materials were done in the following sequence: (i) water in mixer bowl (ii) cement poured into bowl and then mixed (30s slow speed) (iii) sand slowly added while mixing (30s slow speed) (iv) further mixing (30s medium speed) (v) resting cement mix (15s scraping + 90s) and (vi) final mixing (60s medium speed) [15]. Flow tests were done following each mixing, after which another 15s of mixing were done before casting cement mix into a mortar mold [16]. Compressive strength of RHA blended cement mortars cubes of 5.08cm size were determined after 7 and 28 days of moisture curing, as prescribed by ASTM C 109: Standard test method for compressive strength of cement mortars hydraulics [17].

Table 2 Chemical Properties of OPC and RHA

Oxide Composition (%)	OPC	RHA
Silicon dioxide (SiO_2)	19.6	93.47
Aluminum oxide (Al_2O_3)	5.20	0.92
Ferric oxide (Fe_2O_3)	3.20	1.08
Calcium oxide (CaO)	64.8	0.87
Magnesium oxide (MgO)	1.40	3.18
Sodium oxide (Na_2O)	0.40	-
Titanium oxide (TiO_2)	-	0.04

DATA, RESULTS AND ANALYSIS

Effects of Burning Conditions

Obtaining high quality RHA largely depends on burning techniques which include (but are not limited to) the duration, and temperature of burning, type of incinerator, method of combustion and others. The process of layering the RH on each slab plate level inside the furnace notably shows an effect on the color characteristic of RHA. As observed, laying the RH thinly flat (less than 2 inches thick) on ceramic hearth plates (Fig. 1a) resulted to a faint pink colored

RHA after the incineration process (Fig. 2a). At same duration, RH placed on the slabs in a triangular prism manner (Fig. 1b), which was done in attempt to maximize the area of the slabs and mass produce RHA, appeared blackish in color (Fig. 2b). According to [1], RHA exhibits a dark color due to its high carbon content resulting from partial combustion while a gray or pink-ish-white colored RHA indicates lower carbon content which is due to complete combustion. Since complete combustion implies better activity of the produced ash [18], the latter color appearance is more favourable. Furthermore, it is reckoned that attaining such color of RHA is vital as it substantially ascertains the degree to which RHA can be suitable for use in concrete.



Fig. 1 Layering of RH on slab plates in two manners: (a) thinly flat (b) triangular prism

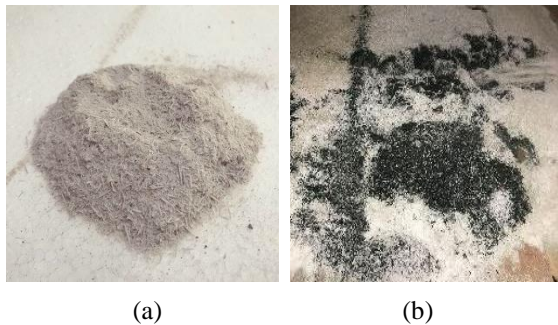


Fig. 2 Distinguished color of resulting RHA (a) faint pink (b) blackish

Experimentally, it was found out that incinerating RH kept at a semi-controlled temperature ranging from 400°C-600°C yields a predominantly optimized pinkish-white RHA by-product. This indicates that RH was burned to ash completely. Since the burning process involves large amounts of RHA, slow cooling method was done which, in turn, affected the chemical compositions of RHA.

Properties of RHA

The microstructure of RHA and ground RHA were observed through a scanning electron microscope as shown in Fig. 4 (a-d). As these figures show, grinding RHA have broken down its cellular structure; its microporous and multilayered particles have become fine and uniformly sized particles. The

significantly smaller RHA particles is anticipated to improve its pozzolanic activity.

XRD analysis was performed to identify the mineralogical phase (amorphous or crystalline) of the RHA produced. Figure 3 displays the XRD pattern of the produced RHA. The broad band on 2θ around 22° represents the RHA as mainly amorphous in form. Table 2 presents the chemical analysis of both OPC and the produced RHA using XRF analysis. This particular RHA consists of 93.47% silica. The aforementioned results confirm that the burning process was carried out properly and that the RHA produced may be used as a SCM due to its potential high pozzolanic activity.

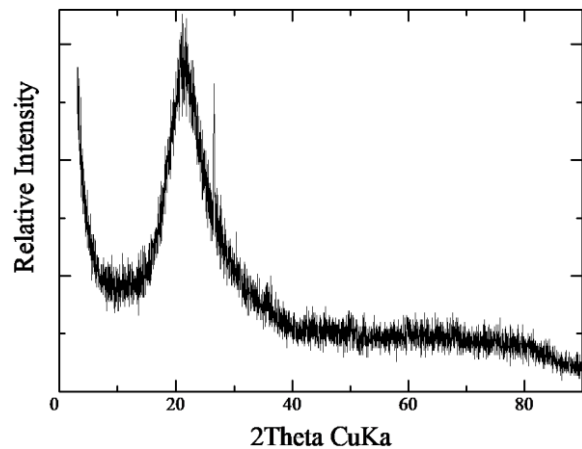


Fig. 3 The XRD Analysis of RHA

Fresh Concrete Properties

Workability is a property of fresh concrete mixture used to assess the ease of mixing, placing, compacting and finishing of concrete. Flow tests were performed on each proportion of RHA blended cement mortars using a flow table to quantitatively evaluate the effects of RHA on the property of workability.

Table 3 Flow Test Results

% of RHA	Flow (mm)
0RHA	175.30
5RHA	161.20
10RHA	141.33
15RHA	133.33
20RHA	-

The result of the flow table test indicates that the incorporation of RHA in concrete leads to a decrease in flow value, which is inversely proportional to the RHA content as shown in Table 3. As listed in the table, the 20RHA mix was so vicious that it had no flow reading. The large surface area of RHA particles

attracts more water molecules to its surface, causing the absorption of water by the RHA particles and consequently reducing the flow value of a concrete mix. Hence, the amount of water intended for the hydration of cement and fluidity of the mixture is decreased so it is imperative that incorporation of RHA increases the water demand of concrete.

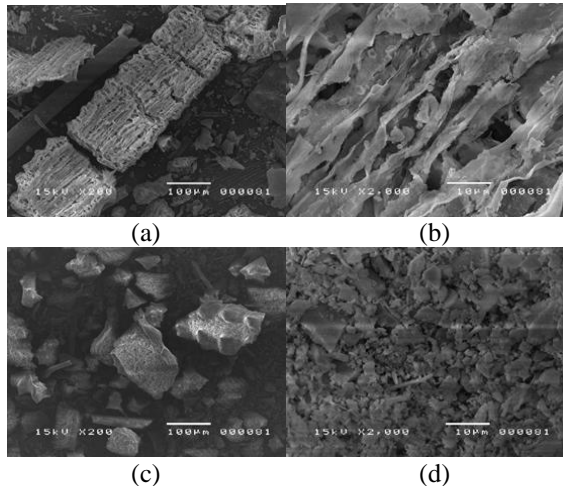


Fig. 4 SEM Photographs (a) RHA (x200) (b) RHA (x2000) (c) ground RHA (x200) (d) ground RHA (x2000)

Compressive Strength

Figure 5 demonstrates the development of compressive strength of cement concrete mortars with varying mixture proportions of RHA. Because of the hydration process that took place during the curing of the concrete mortars, result shows that the compressive strength values at 28 days were higher compared to 7 days except for concrete containing 20%RHA by weight. As presented in Fig. 5, the compressive strength of the concrete comprising 10% RHA at the age of 7 and 28 days were 33.972 MPa and 52.768 MPa, respectively. The results clearly showed that the 10% incorporation of RHA to OPC mix has significantly outweighed the compressive strengths of other mix proportions as well as those of the control OPC mix for 7 and 28 days which were 32.808 MPa and 40.228 MPa, respectively. Thus, it is deduced that replacement level of 10% is the optimal mixture proportion in maximizing the strength of RHA blended concrete. This obtained strength can be due to the high reactivity of the pozzolanic material burned under controlled conditions [6, 8, 9, 10]. The resulting high silica content of RHA validates the statement reported by [6] in which RHA can be considered as a SCM in manufacturing concrete.

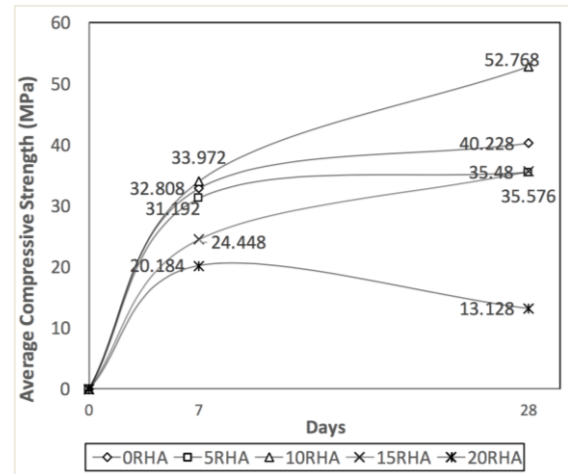


Fig. 5 Comparison of compressive strengths obtained for 7 and 28 days of RHA blended cement concrete mortars.

However, a substantial decrease in strength of concrete was observed for concrete mortars containing up to 15% and 20% of RHA. The decline in strength indicates that there is too much silica content in RHA blended concrete specimens wherein the produced C-S-H during the hydration process could not react anymore with the amount of silica available in chemical reaction. Thus, an increase in the replacement level of optimized and highly siliceous RHA in supplementary mortar concrete mixes would less likely enhance the strength properties of concrete.

CONCLUSIONS AND RECOMMENDATION

Presently around the world, extensive and continuous researches are being initiated to alleviate some of the most pressing issues of the environment, among which is CO₂ emissions brought about by concrete production. Widespread use of SCMs has long been recognized and firmly supported by many significant studies as a result of a growing environmental and sustainability awareness. As shown in this study, RHA, an agro-waste byproduct, was used as a partial replacement of cement. The effects of RHA preparation and burning techniques on enhancing its composition and pozzolanic properties were discussed. Some of the substantial conclusions drawn are as follows:

1. There are critical factors that need to be considered in attaining an optimized and highly reactive RHA which includes correct and proper burning conditions, controlled incineration temperature, method of cooling, grinding, and the type of incinerator or furnace used.
2. High quality RHA are produced by burning RH at a semi-controlled temperature of 400°C-600°C

and by slowly cooling the resulting RHA for 6-8 hours.

3. A pinkish-white RHA indicates complete combustion while a blackish colored one results from partial combustion. Hence, the former has better reactivity.
4. As a result of subjecting RH under the specified burning temperature, the silica content obtained for RHA is 93.47% which makes it highly siliceous and most likely qualified as SCM.
5. Incorporation of RHA in concrete by 15 to 20% leads to a significant low flow value making it less workable concrete.
6. 10% is the optimal replacement level in maximizing the strength of concrete. Mortar strength results show that incorporating 10%RHA into the mix greatly enhances the compressive strength of concrete as compared to OPC and other mix proportions.

It is highly recommended for future researchers that different duration, burning temperature, and nominal particle sizes of RHA be explored.

REFERENCES

- [1] Yang, W., Xue, Y., Wu, S., Xiao, Y. & Zhou, M. (2016). Performance investigation and environmental application of basic oxygen furnace slag – Rice husk ash based composite cementitious materials. *Construction and Building Materials*, 123, 1-2.
- [2] Thomas, B. (2017). Green concrete partially comprised of rice husk ash as a supplementary cementitious material – A comprehensive review. *Renewable and Sustainability Energy Reviews*, 82, 1-2.
- [3] Ahsan, M., & Hossain, Z. (2018). Supplemental use of rice husk ash (RHA) as a cementitious material in concrete industry. *Construction and Building Materials*, 178, 1-2.
- [4] American Society for Testing and Materials. (n.d.). Standard Guide for Evaluation of Alternative Supplementary Cementitious Materials (ASCM) for Use in Concrete. ASTM C1709-11.
- [5] Saad, S., Nuruddin, M., Shafiq, N. & Maisarah, A. (2016). The Effect of Incineration Temperature to the Chemical and Physical Properties of Ultrafine Treated Rice Husk Ash (UFTRHA) as Supplementary Cementing Material (SCM). 4TH International Conference on Process Engineering and Advanced Materials, Kuala Lumpur, Malaysia, August 15-17, 2016. Elsevier.
- [6] Aprianti, E., Bahri, S., Farahani, J., & Shafigh, P. (2015). Supplementary cementitious materials origin from agricultural wastes – A review. *Construction and Building Materials*, 74, 176-187.
- [7] Bakar, R., Gan, S., & Yahya, R. (2016). Production of high purity amorphous silica from rice husk. *Procedia Chemistry*, 19, 189-195.
- [8] Alex, J., Ambedkar, B., & Dhanalakshmi, J. (2016). Experimental investigation on rice husk ash as cement replacement on concrete production. *Construction and Building Materials*, 127, 353-362.
- [9] Bie, R., Chen, P., Ji, X., Liu, Q., & Song, X. (2015). Studies on effects of burning conditions and rice husk ash (RHA) blending amount on the mechanical behavior of cement. *Cement & Concrete Composites*, 55, 162-168.
- [10] Ganesan, T., Rajagopal, K., & Thangavel, K. (2007). Rice husk ash blended cement: Assessment of optimal level of replacement for strength and permeability properties of concrete.
- [11] Bie, R.X., Song, X.F., Liu, Q.Q., Ji, X.Y., Chen, P. (2015). Studies on effects of burning conditions and rice husk ash (RHA) blending amount on the mechanical behavior of cement. *Cement and Concrete Composites*, 55, 162-168.
- [12] Jamil, M., Kasih, A.B.M.A., Raman, S.N., Zain, M.F.M. (2013). Pozzolanic contribution of rice husk ash in cementitious system. *Construction and Building Materials*, 47, 588-593.
- [13] ASTM C 150 (2018), Specification for Portland Cement, ASTM International, PA, USA.
- [14] ASTM C 778 (2017), Specification for Standard Sand, ASTM International, PA, USA.
- [15] ASTM C 305 (2014), Practice for Mechanical Mixing of Hydraulic Cement Pastes and Mortars of Plastic Consistency, ASTM International, PA, USA.
- [16] ASTM C 1437 (2015), Test Method for Flow of Hydraulic Cement Mortar, ASTM International, PA, USA.
- [17] ASTM C 109 (2016), Standard Test Method for Compressive Strength of Hydraulic Cement Mortars (Using 2-in. or [50-mm] Cube Specimens), ASTM International, PA, USA.
- [18] Geetha, D., Ananthiand, A., & Ramesh, P.S. (2016). Preparation and characterization of silica material from rice husk ash –an economically viable method. *Research & Reviews: Journal of Pure and Applied Physics*, 4, 3.

INVESTIGATION OF CHANGES IN INDOOR RADON CONCENTRATIONS BEFORE AND AFTER SEISMIC ACTIVITIES IN GYEONGJU AND POHANG, KOREA

Hanyoung Joo¹, Jae Wook Kim¹ and Joo Hyun Moon¹

¹Department of Nuclear Energy System engineering, Dongguk University, Gyeongju; Republic of Korea

ABSTRACT

This paper made continuous measurement of the indoor radon concentrations at university building in Gyeongju, Rep. of Korea, to check if there is any notable pattern between the indoor radon concentrations and seismic activities. On September 12, 2016, earthquakes with magnitude of 5.1 and 5.8 consecutively occurred in Gyeongju. 14 months later, earthquake with magnitude of 5.5 occurred in Pohang, about 30 km away from Gyeongju, on November 15, 2017. This study investigated the change in the indoor radon concentrations before and after earthquakes to identify if there is any pattern between them, and found an interesting pattern. Prior to earthquakes, radon anomalies, which are radon concentration deviating by more than $\pm 2\sigma$ from the seasonal average, was usually identified. When 5.0 or greater magnitude earthquakes occurred, the indoor radon concentrations decreased sharply a few days before them, and then continuously increased until the occurrence of the earthquake.

Keywords: Earthquake, Gyeongju, Pohang, Indoor radon concentration, Radon abnormality

INTRODUCTION

Radon is a radioactive gas produced by uranium and radium decaying naturally in soil, rock and water. About 90% of indoor radon comes from cracks on floor and wall, and the rest comes from building material such as gypsum board, monazite, and cement [1].

It is known that an elevated concentration of radon in soil or groundwater could be a precursor of earthquake. Several studies have investigated the relationship between the radon concentration and earthquake. Sac et al monitored the radon concentration at an active tectonic zone in western Turkey and, found that there was a linear correlation between the radon emission rate and the seismic activities in the area under investigation [2]. Argha et al monitored soil radon concentration and analyzed correlation earthquake precursor in india [3]. Wakita et al observed precursory changes in the radon concentration of groundwater prior to Izu-Oshima-kinkai earthquake of 7.0 magnitude 14 January 1978 [4]. Also Kuo et al observed anomalous decrease in groundwater radon concentration before earthquake of magnitude 6.4 in Taiwan[5]. Omori et al observed anomalous emanation of radon preceding large earthquakes and considered it to be linked to pre-seismic electromagnetic phenomena such as great changes of atmospheric electric field and ionospheric disturbance [6]. Kim et al observed considerable variations of radon concentrations before the

occurrence of the earthquake [7]. Kumar et al studied the correlation that the between tectonic activities and abnormal measurements of radon concentrations in the North-West Himalayan [8]. Kim et al studied prediction earthquake occurrence by detecting radon radioactivity change[9]. Iovine et al have conducted and analyzed the 3 area, where occurred earthquake, radon concentration which before/after through continuous long-term monitoring [10].

In contrast with the previous studies focusing on the outdoor radon concentration, we have measured and analyzed the indoor radon concentrations at a university building in Gyeongju, which is located 10 km away from the epicenter of the 5.1- and 5.8-magnitude earthquakes in Gyeongju on September 12 2016, and 22 km away from the epicenter of the 5.5 magnitude earthquake in Pohang in November 15, 2017. Gyeongju and Pohang are known to be on the same Yangsan Fault and share the geology characteristic [11]. This study checked if there is any notable pattern between the indoor radon concentrations and earthquakes, and if the notable pattern, if any, is repeated during the Gyeongju and the Pohang earthquakes.

MATERIAALS AND METHODS

Radon measurement device and procedure

As shown in Fig. 1, a RAD7 detector was used to measure the indoor radon concentration. The RAD7

can detect radon concentration in the range of 0.1 pCi/L to 20,000 pCi/L with the relative uncertainty of $\pm 5\%$ [12].

The RAD7 is able to make continuous measurement. The measurements were made on the basis of the U.S Environmental Protection Agency (U.S. EPA) protocols [13]. Before measurement, Rad 7 was purged more than 10 minutes to evacuate the remaining radon gas including thorium inside the RAD7. After purging, the air inlet nozzle of the RAD7 was positioned 1.5 m above the floor, considering the breathing zone of a standard man. The indoor radon concentration was continuously measured every 30 minutes for each measurement. The measurements were made at the corridor neighboring the main entrance of the first floor in the Energy Engineering Hall of Dongguk University in Gyeongju. In the corridor, there was no forced air-conditioning except natural ventilation through the entrance door opened and closed by visitors. The measurement data were recorded and analyzed by using the program embedded in RAD7.

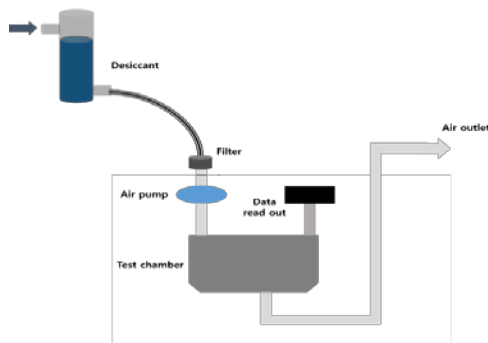


Fig. 1 Structure of RAD7 detector

Data analysis method

Gyeongju is located in the southeastern area of the Korean peninsula, approximately 360 km away from Seoul. Pohang is located 22 km away from Gyeongju. In Pohang on November 15, 2017, the 5.5-magnitude earthquake occurred. Gyeongju and Pohang are on the same Yangsan Fault [14].

The measurement point was 22 km and 10 km away from the epicenter of 5.5-magnitude Pohang earthquake and 5.1, 5.8-magnitude Gyeongju earthquake as the crow flies, respectively, as shown Fig. 2 and Fig. 3.

Table 1 Monthly and seasonal indoor radon concentrations

Season	Month (measurement period)	Monthly average indoor radon concentration [Bq/m ³]	Average air inlet temperature [°C]	Seasonal average indoor radon concentration [Bq/m ³]
Winter	2017.02	18.4	11.0	18.4 \pm 1.2
Spring	2017.03	15.5	13.5	12.4 \pm 0.9

Radon concentration could be affected by the ambient temperature and humidity. Hence, the inlet air temperature was measured by RAD7 upon each measurement.

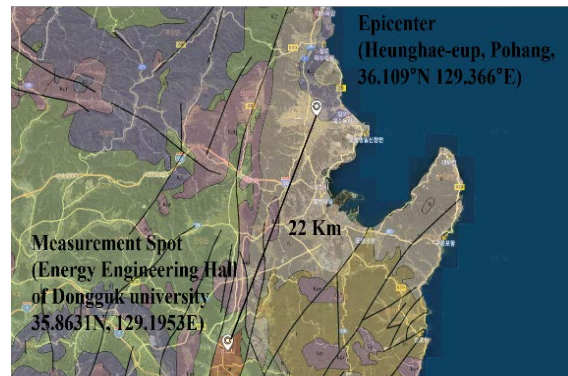


Fig. 2 Pohang earthquake epicenter and measurement spot.

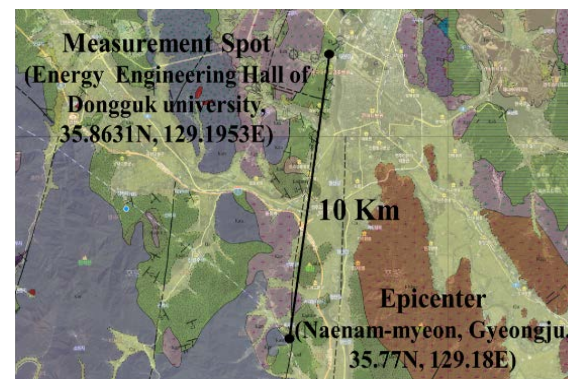


Fig. 3 Gyeongju earthquake epicenter and measurement spot

RESULTS AND CONCLUSION

Measurement results

Indoor radon concentration variation over time

Fig. 4 and Table 1 show the monthly average indoor radon concentrations from February 2017 to February 2018, except for December 2017 when the measurement was not made because of maintenance of the RAD7.

	2017.04	10.5	18.7	
	2017.05	10.6	22.3	
Summer	2017.06	10.0	24.4	
	2017.07	10.6	28.4	9.9 ± 0.7
	2017.08	9.0	27.9	
	2017.09	12.2	23.9	
Autumn	2017.10	11.4	20.4	15.3 ± 0.9
	2017.11	15.3	14.3	
	2018.01	19.8	10.8	
Winter	2018.02	18.8	9.9	19.4 ± 1.2

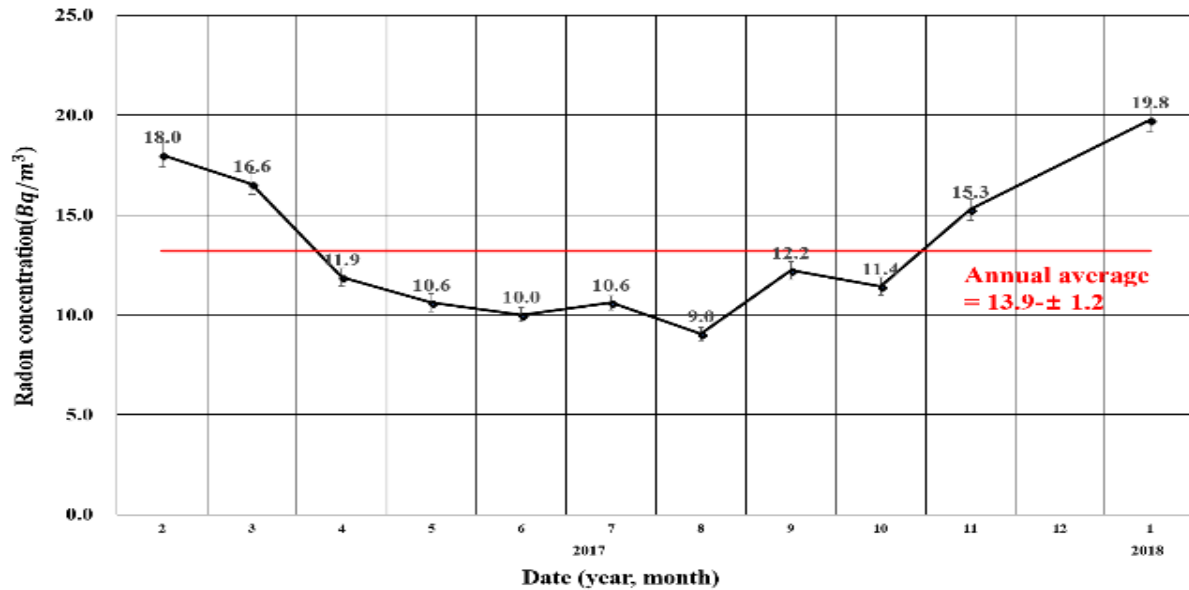


Fig. 4 Monthly average indoor radon concentrations

The curve of the monthly average indoor radon concentrations is shaped like V-letter. While temperatures in spring and summer are higher than those in fall and winter, the indoor radon concentrations are vice versa. As shown in Fig. 4, the annual average indoor radon concentration was 13.9 ± 1.2 Bq/m³. Table 1 shows the seasonal average indoor radon concentrations in autumn and winter period in 2017, 15.3 ± 0.9 and 19.4 ± 1.2 Bq/m³, respectively.

Previous studies showed that the radon concentration could be impacted by temperature, pressure, humidity, rainfall, and wind. Using the rainfall data obtained from the Korea Meteorological Administration, we examined the rainfall's effect on the indoor radon concentration but did not find its regular pattern between the two variables in our measurements, as shown in Fig. 5 that shows radon concentrations and rainfall data over the duration from July 10 to Nov 20, 2017. Because our measurements were made inside building, wind had virtually no impact on it.

We focused on temperature and humidity. The temperature effects were analyzed by comparing the

radon concentrations during the periods with the similar temperatures. Table 2 summarizes inlet temperature, humidity, and the average radon concentrations.

Examination of Table 2 and Fig. 5 let us find two interesting facts. During the duration from July 10 to November 2, 2017, the average radon concentration was 11.9 ± 0.9 Bq/m³, as shown in Fig. 5. The indoor radon concentrations for the duration from October 2 to October 16 were mostly less than the average. After October 16, the indoor radon concentration was much more than the average.

If the radon concentration deviates by more than $\pm 2\sigma$ from the related seasonal value, it is possible to say that radon anomalies are possibly caused by earthquake events and not by meteorological parameters [15]. We took closer look at the period of September 25 to November 21 2017. During that period, the average radon concentration was 14.80 ± 1.0 Bq/m³ and 2σ value was 20.01 Bq/m³. Over the duration of November 2 to 17, 2017, the indoor radon concentrations exceeded the average $+ 2\sigma$, 34.8 Bq/m³ every day.

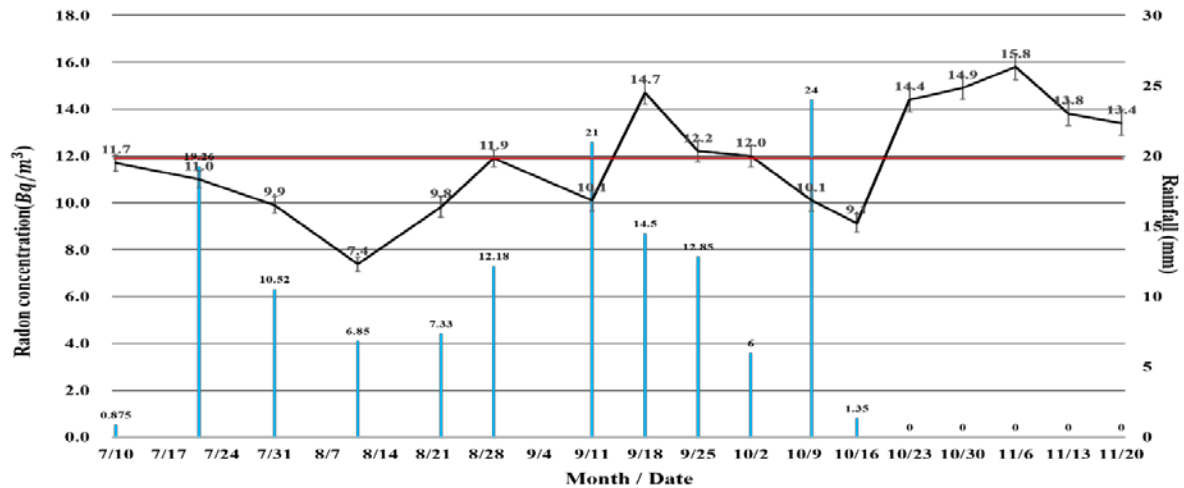


Fig. 5 Radon and rainfall during July 10 to Nov 20

Table 2 Comparison of average radon concentration under similar temperature

Year	Date	Inlet air temperature [°C]	Humidity [%]	Average radon concentration [Bq/m³]
2017	08/29 ~ 09/11	25.1	30.30	11.9
	05/10 ~ 05/15	21.4	3.03	9.2
	09/11 ~ 09/18	24.1	5.61	10.1
	05/15 ~ 05/21	22.2	10.00	9.3
	09/18 ~ 09/25	23.8	4.10	14.7
	05/21 ~ 05/31	23.4	7.61	12.9
	09/25 ~ 10/02	22.4	3.86	12.2
Average		23.9	22.3	11.0
2017	10/02 ~ 10/10	21.6	4.25	12.0
	04/17 ~ 04/25	18.2	3.38	9.8
	10/10 ~ 10/16	21.1	3.95	10.1
	04/25 ~ 05/01	19.9	15.40	10.9
	10/16 ~ 10/23	20.1	3.61	9.1
	05/01 ~ 05/10	20.8	3.02	11.0
	10/23 ~ 10/30	18.6	3.08	14.4
Average		20.4	20.5	3.7
2017	10/30 ~ 11/06	16.3	2.88	14.9
	03/14 ~ 03/21	13.2	2.00	16.9
	11/06 ~ 11/13	15.7	2.72	15.8
	03/21 ~ 03/27	13.8	2.13	13.8
	11/13 ~ 11/20	13.5	2.18	13.8
	03/27 ~ 04/06	15.2	2.15	16.0
	11/20 ~ 11/27	13.2	17.30	13.4
Average		14.7	15.1	6.3

Fig.6 showed the indoor radon concentrations before and after the earthquake. On November 16, the

indoor radon concentration did not exceed the average + 2σ , but on November 17, exceeded average + 2σ again. Since 3.5- and 3.6-magnitude earthquakes on November 19/20, respectively, the concentration did not decrease but increases again.

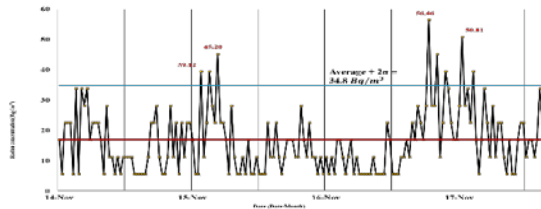


Fig. 6 Radon concentration between Nov 14 to 17

Comparison with the Gyeongju Earthquake

Gyeongju earthquake occurred on September 12 2016. On August 10 2016, about 1 month earlier than the earthquake, the peak indoor radon concentration was 117.6 Bq/m^3 , and the average

over August of 2017 was $26.6 \pm 24.69 \text{ Bq/m}^3$ [15]. One year later, August 10 to 16, 2017, the average and peak indoor radon concentrations were $10.2 \pm 0.9 \text{ Bq/m}^3$ and 45.21 Bq/m^3 .

We examined the changes in the indoor radon concentrations due to Pohang earthquake. The average and peak radon concentrations over November 2017 were $17.0 \pm 1.1 \text{ Bq/m}^3$ and 79.05 Bq/m^3 , respectively. Over November 2016, the average and peak concentrations were $14.4 \pm 1.0 \text{ Bq/m}^3$ and 76.8 Bq/m^3 , respectively. Table 3 summarized the indoor radon concentrations in 2016 and those in 2017.

The peak indoor radon concentration over November 2017 was not much different that over November 2016. It was thought that because the distance between the Pohang epicenter and the measurement spot is two times longer than that between the Gyeongju epicenter and the measurement spot, the seismic activities had less impact.

Table 3 Comparison between the indoor radon concentrations in 2016 and those in 2017

Measurement period	Average indoor radon concentration [Bq/m^3]	Maximum radon concentration [Bq/m^3]	Measurement period	Average indoor radon concentration [Bq/m^3]	Maximum radon concentration [Bq/m^3]
Gyeongju earthquake (2016. 09.12)					
2016.06.21 ~ 2016.06.23	8.4		2017.06.21 ~ 2017.06.23	14.3	
2016.07.11 ~ 2016.07.31	11.0	117.6	2017.07.11 ~ 2017.07.31	14.5	62.16
2016.08.10 ~ 2016.08.18	26.6		2017.08.10 ~ 2017.08.18	10.2	
Pohang earthquake (2017. 11. 15)					
2016. 10.19 ~ 2016.10.26	9.8		2017. 10.19 ~ 2017.10.26	15.0	
2016.11.01 ~ 2016.11.30	14.4	67.8	2017.11.01 ~ 2017.11.30	17.0	79.05

Concussion

To check if there are any notable changes in the indoor radon concentration before and after the earthquake, we measured and analyzed the indoor radon concentrations at one university building near the epicenter of Gyeongju and Pohang.

As shown in Table 3, we compared the indoor radon concentrations at the same periods in the year of 2016 and 2017, to identify if the radon concentration is influenced by any environmental factor except for earthquake. No significant factor, except for earthquake, was found, which had significantly influenced on the indoor radon concentration.

For earthquakes with magnitudes of 5.0 or greater, radon anomalies, that is, the indoor radon concentrations exceeding 2σ above the seasonal average, were observed even month earlier than the earthquakes. In some cases, there were noticeable patterns between earthquakes and indoor radon concentrations.

We hope that our study will be helpful in identifying a clearer relationship between earthquakes and indoor radon concentrations.

REFERENCES

- [1] M.K. Timothy, Geological Hazards: A Sourcebook, Greenwood Press, 2003.

- [2] M. M. Sac., C. Harmansh., B. Camgoz., H. Sozbilir., Radon Monitoring as the Earthquake. *Ekoloji*, Issue 79, 2011, pp.93-98
- [3] A. Deb., M. Gazi., J. Ghosh., S. Chowdhury., and C. Barman, *Journal of Environmental Radioactivity*, Vol. 184-185, 2018, pp.63-70.
- [4] H. Wakita., Y. Nakamura., H. Notsu., M. Noguchi., and T. Asada., Radon Anomaly: A Possible Precursor of the 1978 Izu-Oshima-Kinkai Earthquake. *Science*, Vol 207, Issue 4433, 1980, pp. 882-883.
- [5] T. Kuo., W. Chen., and C. Ho: Anomalous decrease in groundwater radon before 2016 M 6.4 Meinong earthquake and its application in Taiwan, Vol. 136, 2018, pp.68-72.
- [6] Y. Omori., Y. Yasuoka., and H. Nagahama., et al., Anomalous radon emanation linked to preseismic electromagnetic phenomena, *Natural hazards and earth system science*, Vol 7, Issue 5, 2007, pp. 629-635.
- [7] Y.S. Kim., C.M. Lee., T. Lida., and K. Yoshioka., A study of the prediction of earthquake occurrence by detecting radon radioactivity, *Journal Environmental Science*, Vol. 12, Issue 6, 2003, pp.677-688.
- [8] A. Kumar., S. Singh., S. Mahajan., B. S. Bajwa., R. Kalia., and S. Dhar., Earthquake precursory studies in Kangra valley of North West Himalayas, India, with special emphasis on radon emission, *Applied Radiation and Isotope*, Vol. 67, Issue 10, 2009, pp. 1904-1911.
- [9] J. S. Kim., M. J. Kim., S. W. Kim., and H. M. Lee., An Analysis of anomalous radon variation caused by M 5.8 Gyeonog-ju earthquake, *The Korean Society of Economic and Environmental Geology*, Vol. 51, Issue 1, 2018, pp. 1-13.
- [10] G. Iovine., I. Guagliardi., C. Bruno., R. Greco., A. Tallarico., G. Falcone., F. Luca., and G. Buttafuoco: Soil-gas radon anomalies in three study areas of Central-Northern Calabria(Southern Italy), *Natural Hazards*, Vol. 91, 2018, pp. 193-219.
- [11] K. H. Kim., T.S. Kang, Rhie. J., et al., The 12 September 2016 Gyeongju earthquakes: 2. Temporary seismic network for monitoring aftershocks, *Geosciences Journal*, Vol. 20, Issue 6, 2016, pp. 753-757.
- [12] DurrIDGE Company Inc, RAD7, Electronic Radon Detector User Manual, 2009.
- [13] U.S. Environmental Protection Agency (U.S. EPA), Indoor Radon and Radon Decay Product Measurement Device Protocols, Office of Air and Radiation, U.S. EPA Publication, 1992, 402-R-92-004.
- [14] A. Gregoric., B. Zmazek., S. Dzeroski., D. Torkar., J. Vaupotic., Radon as an Earthquake Precursor – Methods for Detecting Anomalies, *Earthquake Research and Analysis Statistical Studies, Observations and Planning*, 2012.
- [15] J. W. Kim., H.Y. Joo., R. Kim., J.H. Moon., Investigation of the relationship between earthquakes and indoor radon concentrations at a building in Gyeongju, Korea, *Nuclear Engineering and Technology*, Vol. 50, Issue 3, 2018, pp. 512-518.

FIELD PERFORMANCE OF THE CAPILLARY WICK IRRIGATION (CAPILLARIGATION) SYSTEM FOR RICE-BASED CROPS

*Ricardo F. Orge¹ and Derosé A. Sawey²

¹Scientist I and ²Science Research Specialist I, Philippine Rice Research Institute, Philippines

ABSTRACT

The Philippines is suffering from the devastating effect of climate change. During extreme drought periods when it is already too risky to plant rice, farmers are advised to plant vegetables and other short duration crops so as to maximize the use of limited water supply and have alternate source of income. This study evaluated the field performance of a locally developed irrigation system designed to be as efficient as possible so as to maximize the use of limited supply of water during such conditions and as low cost as possible so that smallholder farmers could afford to use it. The resulting prototype is a do-it-yourself type irrigation system which is almost similar in layout as that of the drip irrigation system, except that, among other things, it makes use of capillary wicks as drippers (hence called as *capillarigation* system) and maximizes the use of local and recycled materials. Results of field tests consistently showed that the *capillarigation* system outperformed the existing farmers' irrigation practices (drip and hose) in terms of water productivity. In a field planted with green pepper (*Capsicum annuum* L.), the system yielded a higher water productivity of 36.6 g/L as compared to the drip irrigation system (9.9 g/L). The same trend was observed when tested in another field planted with eggplants (*Solanum melongena esculentum*). Being able to work with unfiltered water, with very low operating pressure (15-20cm) and discharge rate (20-30mL/h), the *capillarigation* system offers some advantages when compared with other existing irrigation methods. It however still needs more field tests so as to further evaluate its performance under various crop, field, soil, and water conditions.

Keywords: *Capillarigation, Capillary wick irrigation, Climate change, Drip irrigation, Drought*

INTRODUCTION

The Philippines is suffering from the devastating effect of climate change. Droughts, for instance, have become more intense and frequent, causing significant losses in crop production. These extreme drought events are associated with El Niño which, as reported by Roberts et al. [1] is affecting the country's rice production both in irrigated and in rainfed areas. The 1998-1999 El Niño in particular, resulted to a significant reduction in the paddy rice production, leaving most small holder rice farmers in debt. Another strong El Niño hit the country in 2015-2016 which, according to the damaged report of the Philippine Department of Agriculture as cited by the Food and Agriculture Organization [2], 'affected 16 of the country's 18 regions and of which the impact was strongest in Mindanao where 27 provinces were affected'. The occurrence of these extreme drought events is expected to continue in the future not only in the Philippines but also in other Southeast Asian countries, basing from the results of the study by the World Resources Institute [3].

To help enhance farmers' resilience to climate change, the Philippine Rice Research Institute (PhilRice) is encouraging the farmers to diversify

their farming activities through the *Palayamanan*, a highly diversified and integrated rice-based farming system wherein farmers not only plant rice but also other crops (vegetables, fruit trees, etc.) as well as engage in other farming activities like mushroom production (utilizing the rice straws generated from rice production as by-products), poultry, livestock, and fresh water fish production, among others, so as to maximize the use of farm inputs and agricultural wastes, and provide farmers additional sources of income [4]. During extreme drought conditions, vegetables and other upland crops are usually planted by *Palayamanan* farmers so as to maximize the use of limited supply of water.

While the commercially available drip irrigation system (DIS) is proven efficient [5, 6], its cost of acquisition is high and beyond the financial capability of these small holder farmers. Thus, PhilRice developed an irrigation system which was designed to be as low cost and highly efficient as possible. To lower down the cost and make it affordable to small holder farmers, one of the basic criteria in the design and development of the system is to make the components easy to fabricate and install by the farmers themselves, maximizing the use of recycled materials or those that can easily be sourced out within their locality. This led to the

idea of using capillary wicks as means of dispensing water. The use of capillary wicks in irrigating plants was proven to efficiently work in nurseries, saving water, time and labor in irrigation [7]. However, no advancements had been done yet in making use of the capillary wicks in field crop production [8].

Our initial work proved that the use of capillary wicks can feasibly be used in an irrigation system that is laid out in almost similar manner as that of the drip irrigation system. In this system, called as *capillarigation* system (CS), capillary wicks serve as substitute of the drippers following a setup shown in Figure 1. From the tank (made of 200L steel drum), water flows out of the float valve into a container wherein its depth sets the system's operating depth, typically not more than 15 cm. Because water seeks its own level, this level sets the limit in all 'risers' where capillary wicks are placed. Details on the design and construction of the whole system, including the results of the laboratory studies conducted to identify appropriate wick materials and design parameters, was described in our previous publication [9]. This paper presents the results of our follow up studies conducted to evaluate the performance of the CS under actual field conditions, together with the existing irrigation methods/systems.

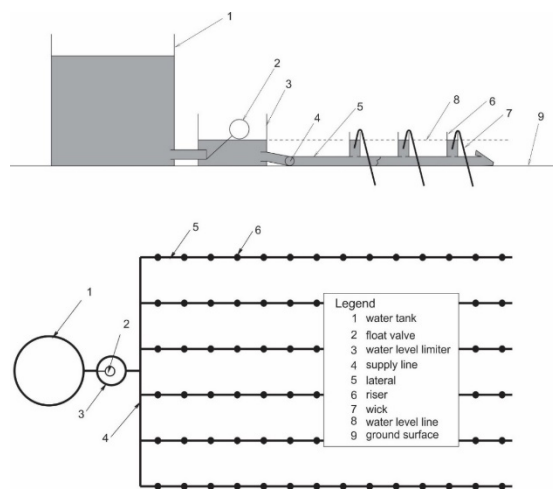


Fig.1 Schematic diagram of the *capillarigation* system showing the various parts [9].

MATERIALS AND METHODS

This study was conducted at the Central Experiment Station of the Philippine Rice Research Institute (PhilRice-CES) in Muñoz Science City, Nueva Ecija, Philippines (15.6712° N, 120.8908° E) during the dry season of 2015 and of 2016. The soil at PhilRice-CES, as reported by Javier et. al [10], was classified as Maligaya clay soil, which is typically fine and has a bulk density of 1.33 g cm⁻³. In the PhilRice Soil Series Information System, this

soil is described as 'heavy clay having poor drainage characteristics, high shrink and swell capacity upon wetting and drying, producing wide cracks in the soil, hard when dry, and has very slow permeability'.

Field trials of the prototype CS were established together with two existing irrigation methods: the hose irrigation (HI) which is commonly practiced by small holder and resource-challenged farmers when growing short duration crops, and the DIS which is used mostly by advanced and financially stable farmers. The experimental sites were within 500m radius from the PhilRice's Agrometeorology station. In all of the field test trials conducted, the objective was to compare the performance of the CS with the existing irrigation practices in terms of the test crop's performance (yield and agronomic parameters) and the water productivity. Monitoring of the soil moisture content (MC) was done at different growth stages of the crop, details of which are described in each of the following test setup.

Capillarigation vs. hose irrigation (2015 dry season)

A 6m x 6.5m field, divided into six parallel 80 cm x 650 cm plots spaced 20cm apart, was prepared for testing the performance of the CS side by side with the farmers' practice of HI using green pepper (*Capsicum annuum* L.) as the test crop. Using garden tools, each plot was tilled up to 15-20 cm depth, pulverized, and applied with rice hull biochar as soil amendment at 5 kg m⁻² prior to final leveling. In the setting up of the irrigation treatments, each plot served as one replication. No randomization was done on the assignment of the plots in order to simplify the setting up of the CS. Thus, the first three adjacent plots were used in the CS while the remaining three plots were used in the HI. In the CS, lateral pipes made from commercially available 25mm diameter flexible black Polyvinyl Chloride (PVC) plastic hose were laid out in the middle of each of the three plots. Risers were installed at every 50cm length of the lateral. Each riser was made from the same material (PVC hose) cut to 15cm lengths and provided with a rubber seal at the bottom and a means for water from the lateral to flow into it. Final trimming of the risers was done to maintain a freeboard of 2-3 cm. Two capillary wicks were installed at each riser, providing a means for dispensing water into the soil. Each capillary wick was made from 5mm (average diameter) x 20cm long cotton strands extracted from mop heads normally sold in local groceries or supermarkets. To minimize mold accumulation as well as water loss due to evaporation, plastic drinking straw (6mm dia x 30mm length) were used to cover each individual wick. Once the whole CS was laid out, 2-week old green pepper seedlings

were transplanted in two rows for each plot, 60cm apart and 60cm between hills, with the system's lateral pipe in between each pair of row (Fig. 2). Wicks were then directed to each row, maintaining a distance of 10cm from its tip to the nearest plant. The tip of the wick was also positioned 5cm below the ground surface. In the HI plot, the plants were watered twice a day, one in the morning (8-9 AM) and one in the afternoon (4-5 PM), at an application rate of 0.5 liter per plant using a 20mm garden hose, simulating a backyard gardening practice. Following the recommended nutrient management practice [11], a commercially available complete fertilizer (14-14-14) was applied in the second week after transplanting (WAT) at 5g/hill followed by Urea (46-0-0) and Muriate of Potash (0-0-60) each at 4g/hill in the 4th and 6th WAT.

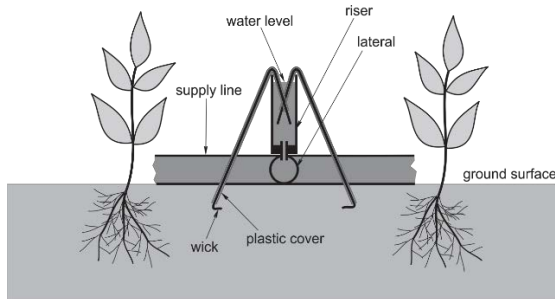


Fig. 2 A typical setup of a *capillarigation* system showing the placement of the lateral and the wicks serving two rows of plants.

To determine the influence of each of the two irrigation methods on the moisture of the soil within the plants' root zone, soil samples were taken using a soil auger at 10 cm distance from the nearest plant and, in the case of the CS, not more than 10cm from the nearest wick. The time of getting of soil samples was referenced from the time water was applied in the HI plot. The first sampling was done one hour before (B) and the second one was six hours after (A) irrigation water was applied in the morning. For the HI plot, the second sampling time (A) was done prior to the application of water in the afternoon. Each set of soil samples were taken at 0, 10, 20, 30, and 40cm depth and were oven-dried following the standard laboratory procedures for soil MC determination. For the whole crop growth duration, three sets of the soil samples were taken, one at vegetative stage, another at flowering and at fruiting stages of the crop.

To determine if the irrigation treatments have some influence on weed population, occasional weeding was done in all plots to keep them weed-free and the total air-dried weight of all of the removed weeds were determined.

To check the consistency of the wicks to deliver water as time passed by, the water flow rate at the

point where the float valve was installed (which represents the sum of all the wicks' flow rates) was monitored weekly.

Capillarigation vs. drip irrigation (2016 dry season)

The components for the drip irrigation system (DIS) used in the study were locally purchased, comprising of 25mm flexible plastic pipe with built-in emitters (1.2 L h^{-1} discharge rate) spaced at 30cm, cut-off valves, pipe connectors and water filters. A 1m^3 plastic container was used as water tank which was provided with a platform made from iron angle bars to elevate it 1m from the ground.

Water application using the DIS was done by opening the valve for a period of two hours daily in the morning (8-9 AM) until harvest, simulating the typical practice of the local users of the technology. In the CS, the lateral which was made of flexible PVC pipe in the previous setup, was replaced with tarpaulin sheet that had been cut to 30cm width, folded longitudinally to form a U-shaped cross-section and then folded at the ends so that it resembled a small channel to hold water (Fig. 3). Bamboo sticks anchored on the ground were used as stiffeners so that the sides of the tarpaulin would stay vertical and be able to hold water. With this modification, the installation of individual risers along the length of the lateral was no longer needed, further reducing the cost of the system. Like in the previous setup, the same freeboard of 2-3 cm was maintained.

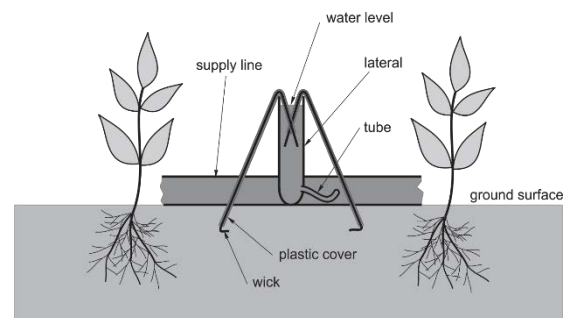


Fig. 3 The improved CS setup which made use of the tarpaulin sheet for the lateral.

Two field setups were established to compare the performance of the CS with that of the DIS. In the first setup, eight $1\text{m} \times 15\text{m}$ parallel plots were made and planted with the same test crop (green pepper) and management practices as in the 2015 setup (CS vs HI). The first 4 plots were devoted to the CS and the remaining four plots were for the DIS. Soil samples were also collected in similar manner as in the 2015 setup except for the depth which was only up to 30cm. To measure the total volume of water applied in each irrigation treatment

(CS and DIS) throughout the whole period of crop growth, a calibrated mechanical-type flow meter with a resolution of 0.001 m³ was installed at the main line of each irrigation system.

In the second setup, the test crop used was eggplant (*Solanum melongena esculentum*), transplanted at 14 days old and spaced at 60cm between rows and hills. Urea (46-0-0) solution of 10g per 5L water was applied at a rate of 170 mL hill⁻¹ at 3, 5, and 9 WAT. On the other hand, Muriate of Potash (0-0-60) solution (10g per 5L water) was applied at 7 WAT at 170 mL hill⁻¹ following Inque and Agres (2017) recommendation.

Monitoring of soil MCs at different root zone depths and crop stages were done only in the first setup in the same manner as in the 2015 (CS vs HI) setup. The time of getting of soil samples was referenced from the time water was applied in the DIS, i.e. one hour before drip irrigation was done. Each set of soil samples were taken at 0, 10, 20 and 30cm depth and were oven-dried following standard laboratory procedures for MC determination. For the whole crop growth duration, three sets were taken, one at vegetative stage, another at flowering and fruiting stages of the crop.

Data gathered

Unless otherwise specified, the following data were gathered in all of the field setups established under this study:

Soil MC profile

This was derived from the MC of the set of soil samples taken during the three stages of the test crop's growth (vegetative, flowering, and fruiting). Standard procedure for oven dry method was followed and the MC was expressed in gravimetric dry weight basis.

Average soil MC maintained (*aMC*)

This parameter was used to evaluate the performance of the irrigation method in terms of supplying water and maintaining soil MC conducive for crop growth. The following formula was used:

$$aMC = \frac{(dMC)+(sMC)}{nd+ns} \quad (1)$$

Where *dMC* = the sum of the MCs taken from the represented soil depths, *sMC* = sum of the MCs taken from the represented crop growth stages, *nd* = number of soil depths represented, and *ns* = number of crop stages represented

Volume of water applied (*V*)

This was expressed in per plant and in per unit area basis, using the formula,

$$V = \frac{Vt}{n} \quad (2)$$

Where *Vt* = total accumulated volume of water applied throughout the whole duration of crop growth and *n* = number of plants

Yield

Yield data were taken from five randomly selected inner plants in a selected row of an inner plot. An average was taken to represent the average plant yield in each irrigation treatment.

Water productivity (*E_{wu}*)

This was computed following the standard formula:

$$E_{wu} = \frac{Vt}{Y} \quad (3)$$

Where *Vt* = total accumulated volume of water applied throughout the whole duration of crop growth and *Y* = total crop yield in the area covered

Labor requirement

This refers to the labor needed in the setting up and in the operation of each of the irrigation method.

Cost of irrigation

The cost of irrigation of each irrigation method was computed by taking note of the cost of establishing the irrigation system (materials and labor) and the cost of operation.

Statistical analysis

Whenever applicable, an analysis of variance (ANOVA) was done on the gathered data by considering the irrigation methods as treatments following a Completely Randomized Design.

RESULTS AND DISCUSSION

Capillarigation vs. hose irrigation

Effect on soil moisture content

Comparing the soil MCs at the two sampling times during the vegetative stage of the crop, it can be observed from Figure 4 that there was an increase in soil MCs from the first soil sampling time (B) to the second sampling time (A) in the hose irrigation method. The difference is more prominent at the ground surface than those beneath. On the other hand, in the CS where water was applied all the time in small amounts, a reverse trend was observed - the soil MC was higher in B than in A, in all depths considered, with the largest difference observed at the ground surface. This could be explained by the fact that the second sampling time occurred in the afternoon (2-3 PM) and the decrease observed in the CS could be due to water evaporation. For the hose irrigation, higher soil MC was observed at the second sampling time (A) since it occurred in the afternoon, just six hours away from its most recent application of water (8-9 AM, same day) while in the first sampling time (B), it occurred 23 hours away from its most recent application of water. At 25 DAT and 35 DAT, there was no remarkable difference observed in the soil MC taken at the ground surface for the two irrigation treatments. One of the reasons is because the ground surface had already been covered by the crop's canopy during this time and water loss due to surface evaporation was therefore minimized. As shown also in Figure 4, the highest soil MC for the CS was observed at 10cm depths particularly during the sampling period of 15 and 25 DAT. This is because the tip of the wicks were buried close to this depth.

As shown in Figure 5, the CS maintains a higher soil MC than the HI in all depths covered. Except for the 10cm depth which is close to where the tip of the wick was buried (5cm), the soil MC in all other points are almost the same (~20%). In the HI, on the other hand, the lowest MC was at the surface which doubles at 10cm and then gradually increased and stabilized at 20 up to 40cm depths. The marked difference in the MC at the first 10cm depth between the CS and the HI can be attributed to the fact that, in the CS, water in very small amount is constantly delivered into the soil throughout the whole duration of crop growth whereas in the HI, soil dryness happened in between each application of water which was twice a day (morning and afternoon).

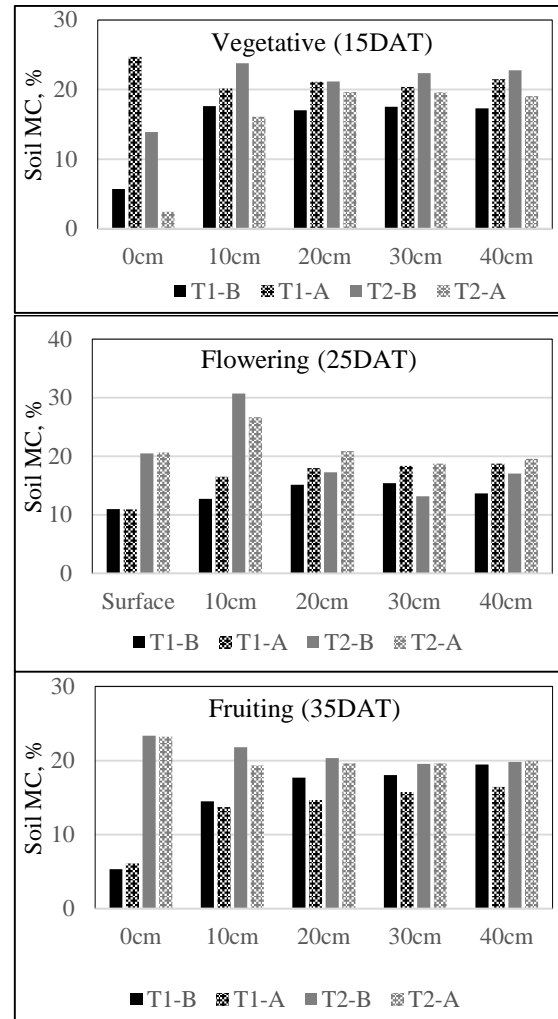


Fig. 4 A comparison of the soil MCs at different soil depths between the hose irrigation (T1) and the capillarigation system (T2) taken at two sampling times (B=1h before and A= 6h after water was applied in T1), during three stages of green pepper growth.

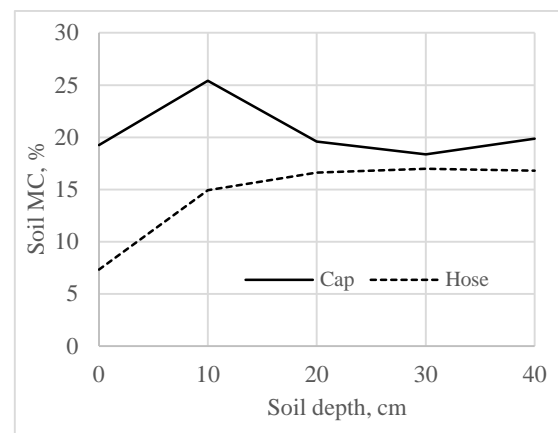


Fig. 5 Soil moisture content profiles of the capillarigation and the hose irrigation.

Effect on crop performance and water use

As presented in Table 1, the CS maintained a significantly higher average soil MC (20.49%) than the HI (14.54%) throughout the whole duration of crop (green pepper) growth. Although their yields did not vary statistically, the yield difference is remarkable which may merit a deeper analysis. One possible reason could be the assigning of the plots which was not randomized, resulting in a high coefficient of variance. Another could be the fact that in the CS-irrigated plants, the soil MC was always maintained at field capacity while in the HI, the soil underwent alternate drying and rewetting which may have some beneficial effects. In spite of this however, the CS utilized water more efficiently than the HI.

Table 1 A comparison of the average soil moisture maintained, total amount of water applied and water use efficiency of the two irrigation treatments.

Treatment	Average soil MC maintained*	Yield per plant (g)	Water applied (L plant ⁻¹)	Water productivity (g/L)
Capillari-gation	20.49	68.67	29.07	1.61
Hose Irrigation	14.54	86.00	51.00	1.25
ANOVA	*	ns	s	s
CV	8.51	41.87	2.69	7.8

Capillarigation vs. drip irrigation

Figure 6 shows the field setup of the CS and the DIS wherein in the CS, tarpaulin sheets were used as laterals, replacing the PVC hose. With this modification, the labor requirement in the installation of the laterals and the wicks had been reduced as compared to that in the previous setup which made use of the PVC hose as laterals and risers.

Effect on soil moisture content

As shown in Figure 7, the CS maintained a significantly higher soil MC than the DIS especially in the first 10cm of the root depth, in all stages of the test crop's growth. The reason for the low soil MC in the DIS especially at the soil surface is because sampling was done prior to the application of water, or 23 h from the most recent application of water. Thus, prior to sampling, the soil surface had been exposed to the hottest period of the day. In the CS, on the other hand, water was applied continuously in small amounts throughout the whole period of crop growth.



Fig. 6 The field setup of the *capillarigation* system making use of tarpaulin sheets as laterals.

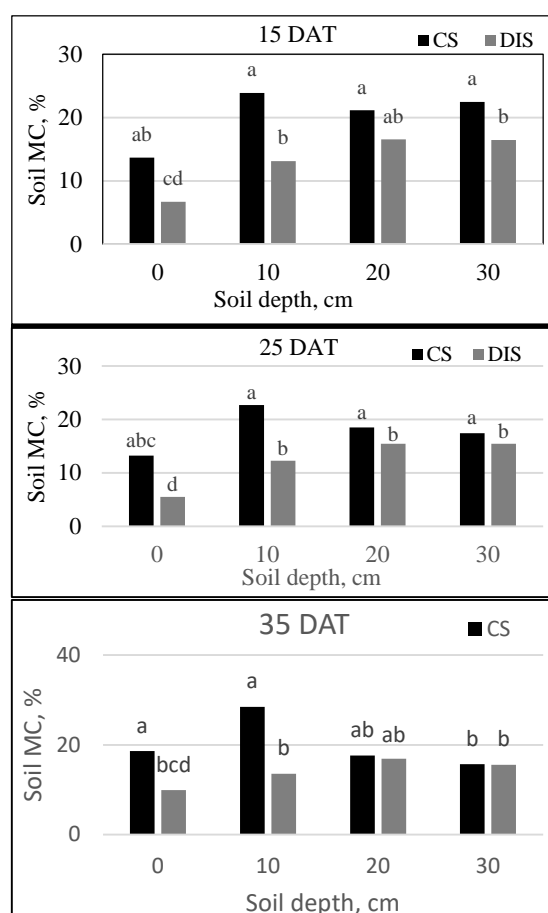


Fig. 7 Moisture content (%) profile of the soil taken during three stages of crop (green pepper) growth and 24h after water was applied in the drip-irrigated plants. Means with the same letter do not vary significantly

On the average, combining all the soil samples taken at different crop stages, the soil MC in CS followed the same trend as that in the previous trial (CS vs HI) where the highest soil MC was at 10 cm depth and slightly decreased at 30-40cm depths. On the other hand, the soil MC in the DIS was lowest at the ground surface and increases at increasing soil depths and stabilizes at 20-30cm (Fig. 8).

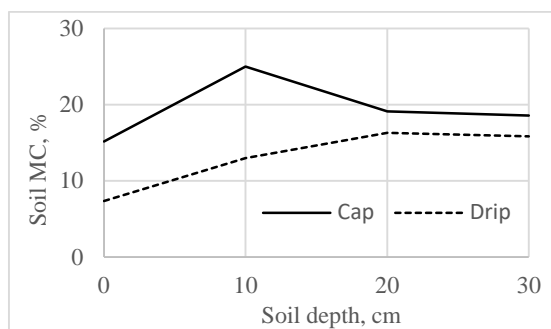


Figure 8. Soil moisture content profiles under the two irrigation methods, the capillarigation and the drip irrigation system.

Effect on crop performance and water use

There was no significant difference between the two irrigation methods in terms of the number of days from transplanting to flowering (22 DAT) and fruiting (30 DAT). In terms of yield, however, plots irrigated with the DIS yielded a significantly higher harvest than that in the CS (Table 2). However, like in the previous trials, the CS outperformed the DIS in terms of water productivity.

Table 2 Performance of the CS as compared to the DIS (2016 trial).

	Capillary	Drip	ANOVA	CV
Setup No. 1 (green pepper, 60m ²)				
Yield (g plant ⁻¹)	433.1	599.8	ns	15.8
Water consumption (L plant ⁻¹)	11.8	60.6	s	10.7
Water productivity (g L ⁻¹)	36.6	9.9	s	29.6
Weed density (g m ⁻²)	29.2	32.2	ns	28.8
Setup No. 2 (eggplant, 100 m ²)				
Yield (g/plant)	330.0	352.0	ns	4.5
Water consumption (L/plant)	104.8	237.9	s	11.7
Water productivity (g/L)	3.1	1.5	s	8.48

Labor requirement

The CS requires labor in setting up its various components which is significantly higher than that of the DIS (Table 3). In the DIS, all the parts are already available hence only the labor of setting up was required. For the CS, on the other hand, around 70% of the labor is spent in the preparation (fabrication) of its various components. However, once the CS had been established, no effort is no longer needed with regards to applying water to the crops while in the DIS, there are cut-off valves to open and close so as to ensure that the water is applied just at the right amount. With regards to the hose irrigation, 100% of the labor needed were in the application of water to the plants for the whole duration (68 days) totaled to 22 labor-h for the 19.5 m² area or an average of 1.13 labor-h per m².

Table 3 Labor requirement in the setting up establishment of the two irrigation systems.

Irrigation system	Labor required in the establishment (labor-h)		Average labor requirement (labor-h m ⁻²)
	60 m ²	100 m ²	
Capillarigation	9	15.5	0.153
Drip irrigation	1.5	2	0.022

Material cost

As shown in Table 4, the cost of materials needed in establishing the CS is computed at Php 14.58 m⁻² while that of the DIS is Php 74.03 m⁻², a reduction of 80.31%. Among the reasons that contributed to the reduced cost of materials in the CS is its operating pressure that is much lower than that of the DIS such that an elevated tank is no longer needed in the CS. Another reason is the fact that in the CS, a water filter is no longer necessary since water is discharged through the capillary wicks which does not necessarily require clean or filtered water.

Table 4 Comparison between the materials used for, and cost of components of, the two irrigation systems for a 100m² irrigated area.

Major Component	Material Used		Cost of Component (Php)*	
	Drip	Capillarigation	Drip	Capillarigation
Water supply tank	1 m ³ plastic tank	200L steel drum	4,000	900
Water tank stand	Structure made from a 4mm thick x 38mm x 38mm steel angle bar holding the tank 1m above the ground	no stand needed; the steel drum was directly placed on the ground	1,500	-
Water filter and other accessories prior to delivery of water	Superflow screen filter, 3m ³ /hour, 3/4" diameter, 1 pc @ Php 475/pc	No filter needed	475	-
Supply line	3/4" dia flexible PVC hose, 6m @ Php 8/m	1 pc plastic pail (10L) 1 pc plastic faucet	48	20 8
Lateral and components for dispensing water	3/4" dia flexible PVC hose, 6m @ Php 8/m	Flexible PVC hose, 12.5mm dia, 25m at Php 13/m	48	54
	Dripline, 11.8mm ID, 12.3mm OD with emitters (1.2 Lh ⁻¹ discharge) spaced 30 cm apart, 160m long at Php7/m	Cotton twine (from mop heads), 5mm dia x 100mm, 42 pcs at Php2.33/pc	1,120	325
		Plastic drinking straw, 60 pcs at Php 0.13/pc	-	97.86
Fittings	Quick start fitting, 48mm x 20mm, 8pcs @ Php15/pc	PVC elbow, 1/2 x 3/4", 2 pcs at Php 15/pc	-	7.8
	PVC tee, 3/4", 1 pc @Php30/pc	PVC tee 3/4" x 1/2" x 3/4", 1 pc at Php 15/pc	120	30
	poly reducing tee, 16mm x 12mm x 16mm, 4 pcs at Php15/pc	-	30	15
	Tee, 16mm x 16mm x 16mm, 1 pc at Php20/pc	-	60	-
	Elbow, 12mm x 16mm, 2 pcs at Php15/pc	-	20	-
		-	30	-
Total cost			7,403	1,458
Cost per m ²			74.03	14.58
% Reduction				80.31

SUMMARY AND CONCLUSION

With the advent of climate change, drought has become more frequent and intense. Hence, it is important to consider how water is applied to the plants especially during the time when its supply is very scarce. Drip irrigation systems which are already commercially available had been proven to be efficient however, for small holder farmers especially in developing countries like the Philippines, it is not widely used simply because of its high cost of acquisition. This study presented the field test results of the developed *capillarigation* system which is a low cost variant of the drip irrigation system that makes use of

capillary wicks instead of the conventional drippers. From the results of the study, the following conclusions are drawn:

- The use of capillary wicks is not only applicable in nurseries but also in field crops following a setup that is patterned from the drip irrigation system. In this system (*capillarigation* system), the capillary wicks replace the emitters in drip irrigation systems as means for dispensing water to the plants and some parts had been added to lower down the system's operating pressure and provide some means to put up the individual wicks;
- In all the field trials conducted, the *capillarigation* system yielded the highest

water productivity when compared to the other irrigation systems/practices tested;

- c. The material cost of the capillarigation system is lower by up to 80% as compared to the drip irrigation system.

More field tests however are still to be done to verify these results and to further evaluate the performance of the system in wider areas and various field and crop conditions. In particular, there is a need to further investigate the reason why, in some trials, the yield of the wick-irrigated crops are lower than those in the drip-irrigated crops.

ACKNOWLEDGEMENTS

The authors acknowledge the assistance of Engr. Lolita Leal, Science Research Analyst of the Rice Engineering and Mechanization Division, PhilRice, during the conduct of the study.

REFERENCES

- [1] Roberts, M.G., Dawe, D., Falcon, W.P., and Naylor, R. L. El Nino–Southern Oscillation Impacts on Rice Production in Luzon, the Philippines. *Journal of Applied Meteorology and Climatology*, Volume 48, 2009, pp.1718-1724.
- [2] Food and Agriculture Organization of the United Nations. El Nino and La Nina in the Philippines. 2017. Retrieved from <http://www.fao.org/3/a-i6775e.pdf>
- [3] Luo, T., Young, R., & Reig, P. Aqueduct projected water stress country rankings. World Resources Institute. 2015. Retrieved from <http://www.wri.org/sites/default/files/aqueduct-water-stress-country-rankings-technical-note.pdf>.
- [4] Corales, R. G., Juliano, L. M., Capistrano, A. O. V., Tobias, H. S., Dasalla, N. V., Cañete, S. D., Casimero, M. C. & Sebastian, L.S. Palayamanan: a rice-based farming systems model for small-scale farmers, *Philippine Journal of Crop Science*, Volume 29, Issue 1, 2004, pp. 21-27.
- [5] Goodwin, P.B., Murphy, M., Melville, P., & Yiasoumi, W. Efficiency of water and nutrient use in containerized plants irrigated by overhead, drip or capillary irrigation, *Aust. J. Exp. Agric.*, Volume 43, Issue 2, 2003, pp. 189–194.
- [6] Weatherspoon, D.M., & Harrell, C.C. Evaluation of drip irrigation for container production of woody landscape plants. *HortScience*, Volume 15, Issue 4, 1980, pp. 488–489.
- [7] Nalliah, V. and Ranjan, R. Sri. Evaluation of a capillary-irrigation system for better yield and quality of hot pepper (*Capsicum annum*). *Appl. Eng. Agric.*, Volume 26, Issue 5, 2010, pp.807-816
- [8] Million, J., Yeager, T., & Larsen, C. Water use and fertilizer response of *Asalea* using several no-leach irrigation methods. *Hortechonology*, Volume 17, Issue 1, 2007, pp. 21-25.
- [9] Orge, R.F. and Sawey, D.A. Coping with water scarcity in rice-based farms: development of a capillary irrigation system for small holder farmers in the Philippines, *Agricultural Research Updates*, Volume 16, Gorawala, P. and Mandhatri, S., Eds., Nova Science Publishers, New York, 2017, pp. 191-207.
- [10]Javier, E.F., Marquez, J.M., Grospe, F.S., Mamucod, H.F., & Rodante E Tabien, R.E. Three-year effect of organic fertilizer use on paddy rice. *Philippine Journal of Crop Science*, Volume 27, Issue, 2002, pp.11-15.
- [11]Inque, K. and Agres, E.P. Training guide for Palayamanan vegetable production. Philippine Rice Research Institute, 2007.

INTERNATIONAL WATER MODEL UNDER PRODUCTIVITY CONDITIONS: THE CASE OF THE TIGRIS AND THE EUPHRATES

¹Abdulmir Hussein Qasim

¹Faculty of Engineering, Department of Civil Engineering, Kirkuk University, Iraq

ABSTRACT

Allocation of international water resources needs to play a vital role in the shared river basins. An environmental and reliable framework involves not only the competing parties divided by geography and national boundaries but also spatially - variable environmental parameters such as water productivity in agriculture. In international rivers, the inflow of turbid materials from the drainage basins of the upstream definitely affects water quality at the downstream. Consequently, emerging global challenges, such as climate change, water scarcity, and population growth have to meet rising demand over time. The Tigris and Euphrates (as a case study) give us a good example of the water system in a region politically unstable. Although a number of studies on water resources allocation modeling, such as ITETRB and WATER-Model, have analyzed the geographic nature of basins, success in achieving sustainable development calls for an optimal water allocation model. Based on water productivity conditions, and to achieve stable, long-term cooperation among riparian countries and sustainable use of the water resources, international Water Model Under Productivity Conditions (WMUPC) gives us an optimal solution. In order to show the impacts of water quality changes on downstream users, these results are presented via histogram. The significant finding, under previous conditions, is the water quantity available in downstream will be less than the quantity required.

Keywords: International Water Resources, Spatial Equilibrium Analysis, The Tigris and the Euphrates

1. INTRODUCTION

Freshwater is an indispensable resource for human life. It is used for different purposes: irrigation, industry, energy production etc., but the intensity of its use varies according to climatic conditions, economic development, urbanization, etc. More than 286 international watercourses cross the boundaries of two or more countries [1]. The Tigris and the Euphrates are the largest two rivers in the Middle East. Their basins span notably three countries, Iraq, Turkey, and Syria, including more than 126 million people, which cover 1.4 million km² and produce around 70 km³ of river discharges each year [2].

By water resource allocation, international rivers developments, including their basins within various riparian, can obtain extremes of cooperation or dispute. It is generally accepted that conflicting demands over the Tigris and the Euphrates will intensify. Yet, although the importance of recent water allocation models, such as ITETRB and WATER-Model, the literature on international water resources allocation an modeling is still far from an encompassing complex environment common factors. Therefore, most of the rivers basins, in politically unstable regions, are not able to establish a long-term cooperative agreement between the riparian.

2. NEEDS FOR NEW WATER MODEL

The appearance of international water disputes, especially in unstable politically and economically regions, raises concerns for the future. The disputes clearly stem from the mismatch between demand and supply of water. The climate challenge currently carries very serious issues which call for a strategic focus on water resources management. Due to low precipitation, Iraq depends exclusively on the Tigris and the Euphrates waters [2]. If climate change has played, and still, a role in reducing the water flow of these two rivers, the dams which control the rivers flow in the upstream riparian also have negative impacts, not only on the volume of the rivers' waters but also on their quality levels.

Inferior water quality will have a serious impact on land and water productivity. The decline of water quality needs to be addressed and to be included in any allocation model. Due to environmental concerns and the rising complexity of water demands, realize a water model under productivity conditions needs to explain the basin's real water availability and to confront population growth and development.

3. WATER MODEL DESIGN

The linear water model WMUPC illustrates the

international Water Model Under Productivity Conditions. In contrast to the other two preceding water models, WMUPC model can be used to analyze the reduction of water quantity as a reason for quality fall. This model facilitates efficient analysis of integrated water management among the different riparian not only for the present but also for the future. Its actual scope covers the Tigris and the Euphrates basins. Moreover, WMUPC has the ability to be developed to cover not only other international watercourse but also to add any other environment parameters on specific regions and countries.

3.1 Boundary conditions

For the international basins, the optimal model of water will depend on a mix of factors, including hydrologic characteristics, quality of water entering the basins, the water volume that will travel down towards the downstream riparian and by taking into consideration the constant riparian water rights. It is important to recognize that the upstream country, Turkey in the case of the Tigris and the Euphrates, will always have a different agenda for the river that it shares with other countries, Iraq and Syria. Thus Turkey will have easy access to better quality water sources.

The Tigris and the Euphrates take their sources in Turkey, pass through Syria and enter Iraq from the north and north-west. The characteristics of these two rivers vary from upstream to downstream according to the zones crossed by them. The variability of climatic conditions in each riparian country, such as temperature and precipitation, has played an important role in modifying water resources qualitatively and quantitatively. Therefore, changes in water properties by adding the agricultural drainage water, particularly near the northern border of Iraq, will seriously affect the water stress in this country.

For agriculture country, good quality of water for irrigation is a prime requisite. There is a continuous debate on whether the riparian have to respect water quality in an international watercourse or just use any quantity of water without taking into consideration the water demands of downstream water users. Nevertheless, as long as the water of good purity helpfully affects the productivity of the land, the poor quality of the water negatively affects the productivity of the land. This change can be expressed mathematically by in the WMUPC water model.

3.2 Structure of WMUPC

The WMUPC is inspired from the Inter-Temporal Euphrates and Tigris River Basin Model

ITETRB, and from Water Allocation of the Tigris and Euphrates Rivershed WATER-Model, which developed by [3] and [4] respectively. Without consideration of water quality requirements, these models aim to allocate water resources in the international rivers among Turkey-Syria-Iraq through a network of supply and demand nodes. However, due to water quality changes, ignoring these changes will increase certainty the conflicts, and significantly reduces the chance of successful negotiations along the international rivers. In an optimistic manner, the WMUPC allocates all nodes of water demand and supply by comprising water quality indicators.

A hydraulic network of supply and demand nodes was established and illustrated, as an example of the case study, among Iraq, Syria, and Turkey. All of the variables pertaining to water volume in various regions and sub-regions of the Tigris and the Euphrates, such as the volume of inflow, outflow, and water consumption for agriculture, municipal and industrial, were determined during a certain period of time. The relationships between the unknown variables and the given variables were expressed by a number of functions of the given variables.

The mathematical details of the WMUPC are based on quantitative outcome variables as follows:

$$D = \varepsilon (\sum TTW_i + \sum Q_i + \sum TRW_i) - Ev_j - \sum TAMIW_j - GF_j \quad \forall i, j \in n \quad (1)$$

Subject to:

$$\sigma = \sum SW - \sum TAMIW / \sum SW \quad (2)$$

$$\varepsilon = k - \sigma \quad (3)$$

where D is the quantity of water Demand; TTW refers to the Total Tributary Water; Q is the Quantity of water inflow; TRW indicates to Total Return Water; Ev expresses the loss of Evaporation; TAMIW is the Total Agricultural, Municipal and Industrial Water withdrawal; GF assigns the Groundwater Feeding; i, is the demand and j is the supply nodes of the total nodes n; σ refers to the adjustability ratio of water resource; SW is the Storage Water quantity; and ε ascribes water's adeptness and its productivity, which depends on a constant factor $k=1$ in this paper.

The water productivity term is used in a variety of ways and there is no single definition that suits all situations [5]. Therefore, the concept of water productivity has been used sometimes as a measure of the ability of agricultural systems to convert water into food, and sometimes used to evaluate the function of irrigation systems as the amount of crop per drop [6]. Consequently, the

water's adeptness quantitative symbol ε is developed here to simulate the impacts of irrigation on the water resources system, such as the side effects of increasing the Total Dissolved Solid TDS, the impact of biological oxygen demand BOD, dissolved oxygen DO etc. of the rivers.

The problem of estimating water productivity could become more complex for large areas. The discrepancy of the meaning of water productivity between different users, especially in international river basins, will complicate the model considerably. To simplify this, the water productivity can be assessed by subtracting the value of water adjustability, which is demonstrated here by the symbol ε . This step will help us to illustrate the reduction of productivity of the water resource.

3.3 Model network applications

The WMUPC contains 63 demand and 45 supply nodes similar to the first version of the figure, which is developed by [1]. The typical allocations of these nodes are illustrated schematically in Fig.1.

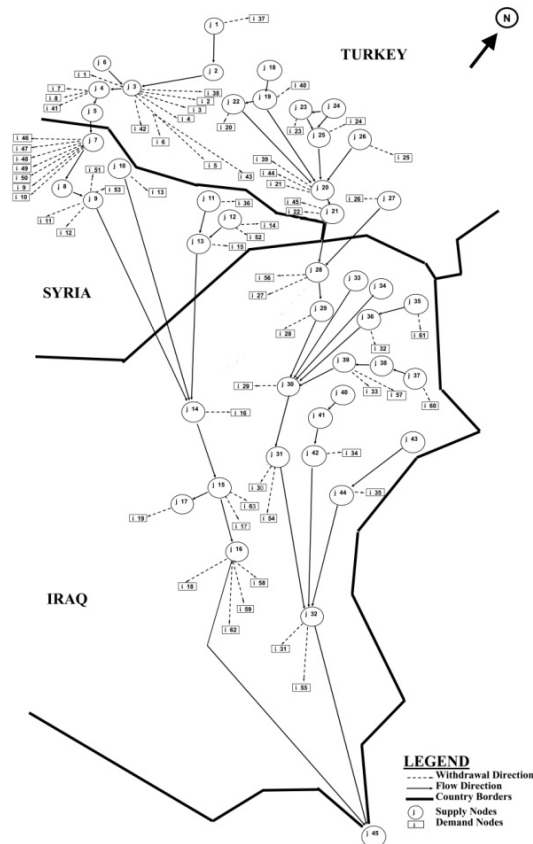


Fig.1 Network structure of the international Water Model Under Productivity Conditions WMUPC of the Euphrates and Tigris Rivers which is modified from [1] with kind permission from the authors.

In order to be more confident of WMUPC outcomes, the model should be calibrated and verified to a satisfactory accuracy. Thus, the model details are improved and amended significantly in accordance with the actual water nodes distribution the main riparian countries in the Tigris and the Euphrates basins.

The WMUPC model measures the relations between the proposed demand and supply nodes of two periods, both lasting for about six months. Rainy period is ongoing from January till June, while nearly no rainfall can be seen in the dry season from July to December. The storage option in the reservoirs enables the model to simulate water amount for the included periods which could satisfy the minimal demands. Water inflows depend on tributary inflows in addition to backflow water coming from upstream nodes. While water outflows depend on evaporation losses as well as agricultural, domestic and industrial water withdrawal which are illustrated by a number of supply nodes.

To indicate water productivity and quality effectiveness at downstream nodes, at this stage of research, there is a need for highlight water use in various productive and consumptive activities. Consequently, to find out the true figure of how water quality is affecting its productivity at each node, further research needs to be conducted to assess that in more detail. It is clear, however, the highest level of water use efficiency, reasonably achievable by the upstream countries, Turkey and Syria in this case. While water use efficiency in the downstream countries, like Iraq, will be the lowest level. To summarize and simplify the results, the indication of water productivity, across different sections of the rivers, could hypothetically be equivalent to ε in the WMUPC model.

4. RESULTS AND DISCUSSION

In the simulation of WMUPC model, the sensitive parameters listed in this water model were selected for the Tigris and the Euphrates rivers among the riparian countries, in addition to water use for domestic, agricultural and industrial purposes, including water quality indicator facing water productivity.

The domestic and industrial sectors in Iraq, Syria, and Turkey offer a large return rate of water for irrigation purposes. So, in case of low water flows in an arid zone as Iraq, only the minimum agricultural water demands are met. Therefore, the country is suffering from a critical lack of water as shown in Fig.2.

In Iraq, the clear indication of the impact of changes in water quality on land, although a pretty good amount of water, is the significant decrease

in land productivity, for example, the number of date trees decreased from 33 to 13 million between 1950 and 2010; the number of sandstorm between 1951 and 1990 was about 24 days/year, while the Ministry of the Environment in Iraq records 122 sandstorms and more than 280 dusty days from 2000 to 2010 in addition to the prolonged drought and desertification [2].

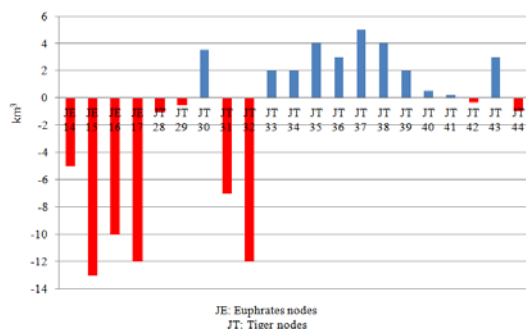


Fig.2 Water lack and abundance in Iraq.

While in the case of high water flows in a humid zone as Turkey, the minimum agricultural water demands almost are satisfied and will easily meet the requirements of the irrigation. Thanks to dam construction in the Euphrates and Tigris in the upstream, however, increases the water welfare and could thus foster water abstraction in that region as shown in Fig.3 and 4.

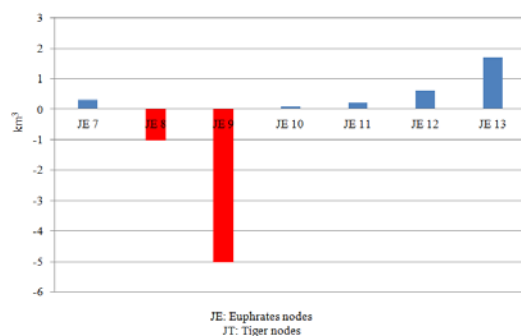


Fig.3 Water lack and abundance in Syria.

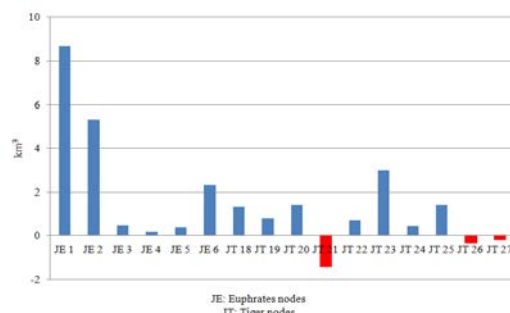


Fig.4 Water lack and abundance in Turkey.

Thus, the outcomes of the WMUPC show that

the water productivity is responsible for water welfare, even though if this issue has a small interest in all riparian countries so far. Highlighting the importance of these results and the importance of water productivity, as mentioned above, isn't in the sense that the water quantity is less important quality. The WMUPC is established here to increase focus attention on both water quality and quantity.

5. CONCLUSION

The asymmetries driven by population growth, climate change, economic competition and agriculture evolution, over the last century, highlight the importance of water efficiency evaluation. The quantification of the lack or the abundance of international waters, due to changes in water quality, is applicable by the modeling of water under productivity conditions WMUPC. So, the calculations show the ability to reflect water quality changes along any river to a valuable amount of water quality.

A shortcoming of this model is that the water productivity values do not cover the actual value of the nodes in this case study. However, the impact of different water uses and effects of water quality changes has recently become more observable in downstream countries. Therefore, a comprehensive database needs to be established in order to evaluate and analyze variations of water productivity. Furthermore, if the objective is finding an effective international water allocation tool, the WMUPC enables to represent an alternative mechanism for fulfilling the dispute of water sharing among any riparian.

6. REFERENCES

- [1] L. De Stefano, Jacob D. Petersen-Perlman, Eric A. Sproles, Jim Eynard, Aaron T. Wolf. Assessment of transboundary river basins for potential hydro-political tensions, Global Environmental Change, No. 45, April 2017, pp. 35-46.
- [2] Abdulamir H. Qasim. Impacts du changement climatique sur les ressources en eau (quantité et qualité) dans les bassins du Tigre et de l'Euphrate en Irak. Ph.D. Thesis, University of Poitiers, France, 2017.
- [3] Kucukmehmetoglu M., Sen Z., Özger M. Coalition possibility of riparian countries via game theory and fuzzy logic models, 2010, Water Resour Res., Vol. 46, W12528, pp.1-20.
- [4] Oei, P., Siehlow, M. WATER-Model: An Optimal Allocation of Water Resources in Turkey, Syria and Iraq, DIW Berlin Discussion Paper No. 1381, Germany, 2014.

- [5] Randolph Barker, David Dawe, Arlene Inocencio. Economics of Water Productivity in Managing Water for Agriculture. In: Kijne, J. W. II. Barker, Randolph. III. Molden, D. J. (Eds) 2003. Water productivity in agriculture: limits and opportunities for improvement. CABI international. Wallingford, Oxon, UK.
- [6] Gichuki, F., H. Turrall and S. Cook. Water Productivity Assessment: Measuring and Mapping Methodologies, 2007, Basin Focal Project Working Paper No. 2. Colombo, Sri Lanka, CGIAR Challenge Programme on Water and Food.

UNDRAINED SHEAR STRENGTH OF SOFT CLAY REINFORCED WITH SINGLE ENCAPSULATED LIME BOTTOM ASH COLUMN

Muzamir Hasan^{1,2,3} and Kwan Hui Yee² and Fat-hi Muhamad^{1,2} and Masayuki Hyodo⁴

¹ Centre for Earth Resources Research & Management, University Malaysia Pahang, Lebuhraya Tun Razak
26300 Gambang Kuantan Pahang Malaysia

² Faculty of Civil Engineering & Earth Resources, University Malaysia Pahang, Lebuhraya Tun Razak
26300 Gambang Kuantan Pahang Malaysia

³ Earth Resources & Sustainability Centre, University Malaysia Pahang, Lebuhraya Tun Razak 26300
Gambang Kuantan Pahang Malaysia

⁴ Department of Civil and Environmental Engineering, Faculty of Engineering, Yamaguchi University, 2-16-
1 Tokiwadai, Ube-shi, Yamaguchi 755-8611, Japan

ABSTRACT

Soft clay soils are type of problematic soil that causes bearing capacity failure and excessive settlement, leading to severe damage to buildings and foundation. In this study, bottom ash is used to replace the natural aggregate while quicklime is used to increase the bonding between bottom ash particles. This research is aimed to investigate the role of single encapsulated lime bottom ash column (LBAC) in improving the shear strength by using laboratory scale model. Kaolin is being used as soil sample while lime bottom ash as the reinforced column and the column is encapsulated with non-woven geotextile. Laboratory tests are conducted to determine the physical properties of bottom ash, kaolin clay, and quicklime sample. Unconfined Compression Test (UCT) also used to test the shear strength of the reinforced kaolin samples. There are 21 kaolin samples being tested in this study and the dimension of the specimen used is 50mm in diameter and 100mm in height. However, there are two different types of diameter of single lime bottom ash column being used which are 10mm and 16mm. The heights of the column are 60mm, 80mm and 100mm. The improvement of shear strength of single encapsulated lime bottom ash column with area replacement ratio of 4.00% (10mm column diameter) and 10.24% (16 mm column diameter) are 43.58%, 50.00%, 49.17% and 38.08%, 42.67%, 32.75% at sample penetration ratio, H_c/H_s of 0.6, 0.8 and 1.0 respectively. It can be concluded that the shear strength of soft clay could be improved by installation of single encapsulated lime bottom ash column.

Keywords: sand column, sustainable construction, single encapsulated lime bottom ash column

INTRODUCTION

Soft clay soils are type of soil that composed of very fine particles and can impedes the flow of water. Clay soils are commonly stiff in dry state but heavy and sticky when saturated with water. The reduction in strength and stiffness of soft clays causes bearing capacity failure and excessive settlement, leading to severe damage to buildings and foundation [1]. Therefore, deep mixing method is used to improve the permeability, strength and deformation properties of the soil. This method mainly depends on increasing the stiffness of natural soil by adding a strengthening admixture material such as lime.

Granular columns are widely used to improve the performance of weak deposits in order to reduce foundation settlement and to increase load-bearing capacity [2]. The performance of granular columns depends entirely on the characteristics of the surrounding material.

The use of stone columns as a ground improvement technique in soft cohesive soils is increasingly being extended to sites with poorer conditions [3]. This is being achieved with the use of geosynthetic reinforcement which acts to provide additional lateral support to columns, preventing excessive bulging and column failure. Although the use of geotextile encasement has been investigated and implemented on numerous projects, research into complex reinforced behavior is ongoing. In addition, the concept of using other geosynthetic materials such as geogrid for columns, small-scale laboratory testing of model sand columns was undertaken. In conjunction with this, a numerical modelling study was undertaken to further understand the interaction between the geogrid, column material and surrounding soil. Particular emphasis was placed on comparing the behavior of partially encased columns to fully encased columns. To simply modelling, the side wall friction in the cell was considered negligible

and no resistance was applied to the model boundary.

The critical column length is the shortest column which can carry the ultimate load regardless of settlement [4]. [5] found from their model study that the load carrying capacity of the column increases up to $L/D = 4.1$, beyond which there is no increase in column capacity. [6] suggested a minimum L/D ratio of 4.5, which is required to develop the full limiting axial stress on the stone column. [7], [8] reported from their experimental study that L/D ratio of minimum 6 is required to develop the full limiting axial stress on the column. [9] found out from their model study that the critical length to be 4–5 D for example beyond this length of stone column, no significant increase in its capacity has been observed. [10] supports the hypothesis of a critical column length corresponding to about six column diameters.

Columns longer than critical length did not show further increase in load-carrying capacity, however, longer columns may be needed to control the settlements. Accordingly, rational decisions can be taken to tailor design of stone column installations to achieve maximum performance at optimum cost.

In this study, bottom ash not only used to improve the soft soil strength as it also can reduce the need to quarry rock, since bottom ash is used as a substitute for natural crushed rock. In addition, it can reduce the need to dispose the product to landfill storage. Hence, using this material is more sustainable and environmentally friendly and avoids the use of natural resources such as sand and gravel. However, lime is used as a binder to increase the bonding between the bottom ash which able to enhance the shear strength of the soft soil. Lastly, the undrained shear strength of soft clay reinforced with single encapsulated lime bottom ash column is determined in order to prove the feasibility to implement lime bottom ash column in real construction. Thus, varies type of laboratory tests need to be conduct based on British Standard (BS) or the American Society of Testing Material (ASTM). The purpose of this study is to investigate the undrained strength of soft clay reinforced with single encapsulated lime bottom ash column.

METHODOLOGY

Few tests are conducted toward a small-scale model of the bottom ash as granular column and kaolin as the soft clay by adding some lime as binder. Laboratory tests are conducted to determine the characteristics of lime, kaolin and bottom ash based on British Standard and American Society of Testing Material (ASTM). The model is 50mm in diameter and 100mm in height. All the experiments are carried out at Soil and Geotechnical Laboratory of Universiti

Malaysia Pahang. Table 1 shows a list of tests and standard used

Installation of Single Lime Bottom Ash Column

In preparing for the installation of Lime Bottom Ash Column (LBAC) for the reinforced specimens, the holes for the installation of LBAC were drilled using drill bit of respective diameter with the specimens still inside the mould to prevent it from expanding. The lime and bottom ash are installing in the holes to achieve relative density of 13.31%.

To maintain a uniform density in each LBAC and maintain the lime at 6%, the mass of bottom ash and lime used to fill the pre-drilled hole had been based on the volume of pre-drilled hole. By referring to this method, the same density of $8.15 \times 10^{-4} \text{g/mm}^3$ had been produced for every specimen in this study

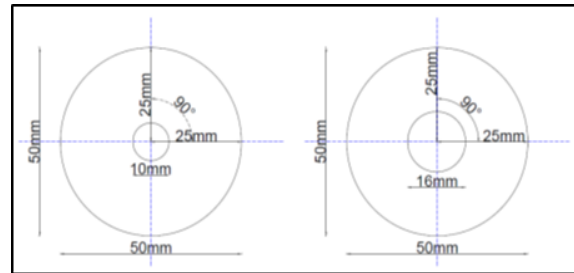


Figure 1. Arrangement of installed column in clay specimen

Table 1. A list of tests and standard used

Materials	Tests	Standards
Kaolin	Hydrometer	BS 1377: Part 2 1990: 9.6
	Standard	BS 1377: Part 4
	Compaction	1990: 3.3
	Falling Head	ASTM D 2434
	Permeability	BS 1377: Part 2:
	Specific Gravity	1990: 8.3
Lime	Atterberg Limit	BS 1377: Part 2:
	Liquid Limit	1990: 4.3
	Plastic Limit	BS 1377: Part 2:
		1990: 5.3
Lime	Hydrometer	BS 1377: Part 2 1990: 9.6

Bottom Ash	Specific Gravity	BS 1377: Part 2: 1990: 8.3	
	Atterberg Limit	BS 1377: Part 2: 1990: 4.3	
	Liquid Limit	BS 1377: Part 2: 1990: 5.3	
	Plastic Limit	BS 1377: Part 2: 1990: 9.3	
	Dry Sieve	BS 1377: Part 2: 1990: 9.3	
	Specific Gravity	BS 1377: Part 2: 1990: 8.3	
	Standard	BS 1377: Part 4: 1990: 3.3	
	Compaction	ASTM D 2434	
	Constant Head Permeability	ASTM D 2434	
	Standard	BS 1377: Part 4 1990: 3.3	
Bottom Ash with Lime	Compaction	BS 1377: Part 4 1990: 3.3	
Soft Kaolin Clay			
Reinforced with Single Encapsulated Lime Bottom Ash Column	Unconfined Compression Test (UCT)	ASTM D 2166	

RESULTS AND DISCUSSIONS

Physical and Mechanical Characteristics of Kaolin, Quicklime, and Bottom Ash

The physical properties of kaolin clay, quicklime, and bottom ash have been summarized in Table 2. The characteristic of kaolin is nearly same as soft clay while bottom ash is almost similar to the natural aggregate like sand and fine gravel. In this study, quicklime able to increase the bonding between bottom ash particles based on its fine particle properties

Table 2. Physical and mechanical properties of kaolin, quicklime, and bottom ash

Test	Parameter	Kaolin	Lime	Bottom Ash
	AASHTO	A-6	A-7-5	A-1-a (0)
Soil Classification	USCS (Plasticity Chart)	MI	MV	-
Atterberg Limit	Plastic Limit, w_p (%)	26	72	-
	Liquid Limit, w_L (%)	36	61	-

Standard Compaction	Plastic Index, I_p (%)	10	11	-
	Optimum Moisture Content, w_{opt} (%)	20.91	43.00	23.60
	Maximum Dry Density, $\rho_{d(max)}$ (Mg/m ³)	1.53	1.11	1.313
Small Pycnometer	Specific Gravity, G_s	2.62	2.26	2.33
Falling Head Permeability	Coefficient of Permeability, k (m/sec)	8.96 $\times 10^{-12}$	-	-
Constant Head Permeability	Coefficient of Permeability, k (m/sec)	-	-	5.03 $\times 10^{-3}$

Effect of Single Lime Bottom Ash Column on Shear Strength

The shear strength of all the reinforced specimens are proved to be higher than the control sample. Meanwhile, the shear strength able to be improve after installed the single encapsulate lime bottom ash column. Table 3 shows the shear strength results and its improvement.

Figure 2 and Figure 3 show the correlation line for sample shear strength and improvement shear strength of single encapsulated lime bottom ash column. From Figure 2 the value of correlation cohesion, R^2 for diameter 10mm and 16mm are 0.9124 and 0.7443 respectively. Whereas, From Figure 3 the value of correlation cohesion, R^2 for diameter 10mm and 16mm were 0.9255 and 0.6767 respectively. If the value of correlation cohesion, R^2 nearer to 1, thus means the result is more accurate.

Table 3. Shear strength results and its improvement

Height Penetration Ratio, H_c/H_s	Shear Strength, S_u (kPa)			Average Shear Strength, S_u (kPa)	Improvement of Shear Strength, ΔS_u (%)
	1	2	3		
Controlled Sample					
0	11.59	12.43	11.98	12.00	-
Single Encapsulated Lime Bottom Ash Column (10mm)					
0.6	17.33	16.28	18.07	17.23	43.58
0.8	18.27	17.08	18.66	18.00	50.00
1.0	17.93	17.10	18.66	17.90	49.17

Single Encapsulated Lime Bottom Ash Column (16mm)

0.6	17.4 2	16.7 4	15.5 4	16.57	38.08
0.8	17.0 8	17.5 4	16.7 4	17.12	42.67
1.0	16.3 5	15.9 4	15.5 0	15.93	32.75

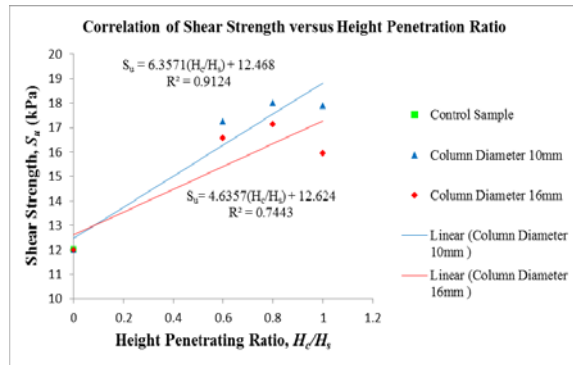


Figure 2. Correlation graph of shear strength with height penetration ratio for single lime bottom ash column with diameter 10mm and 16mm

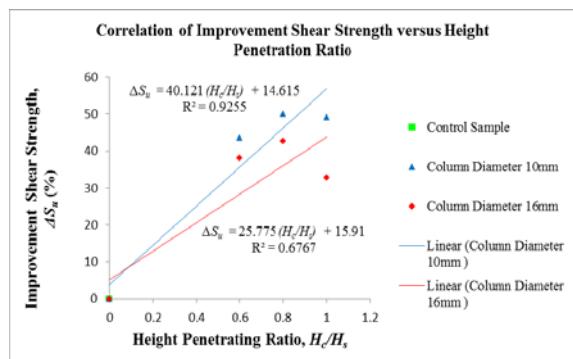


Figure 3. Correlation graph of improvement shear strength with height penetration ratio for single lime bottom ash column with diameter 10mm and 16mm

Morphological Properties

From the Scanning Electron Microscope (SEM), the particles of the lime bottom ash were greyish, spherical and had rough, gritty surface textures. Some of the particles were spherical whereas there are also popcorn type particles. The surfaces of the particles are observed to have pores and dusty. The appearance of the bottom ash particles is porous, angular and irregular in shape and possesses a rough texture by using microscope. Figure 4 And Figure 5 show Morphology images of lime bottom ash by SEM at 10μm and 100 μm magnification. Based on the figures, quicklime can enhance the bonding between bottom ash particles

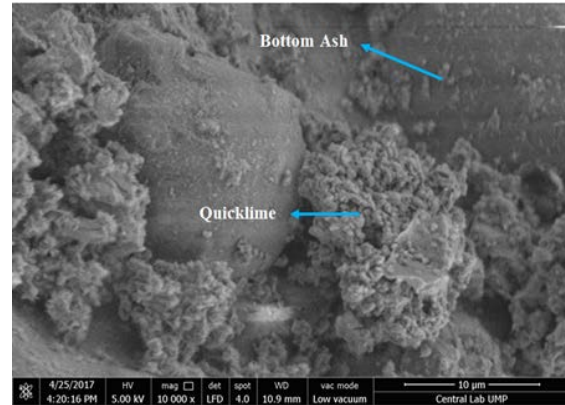


Figure 4. Morphology images of lime bottom ash by SEM at 10μm magnification

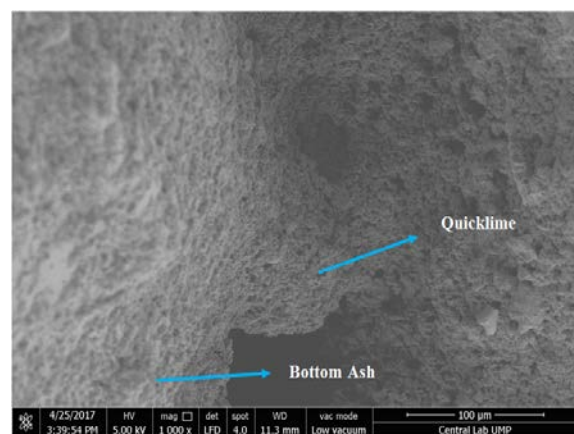


Figure 5. Morphology images of lime bottom ash by SEM at 100μm magnification

CONCLUSIONS

The major focus of this study is to check out whether there is any improvement on undrained shear strength of soft kaolin soil after reinforced with single encapsulated lime bottom ash column with two different column diameters and different length of penetration. Based on laboratory test results analysis, the following conclusions can be made:

1. Kaolin characterized as MI by referred to Unified Soil Classification System (USCS) which indicates that it was medium plasticity silts based on its liquid limit (36%) and plasticity index (10%). The specific gravity of kaolin is 2.62 and it also classified as clayey soil, A-6, based on AASHTO classification system. This is because kaolin clay is well graded and its grain size is in the range between clay to fine silt. From the compaction test, the result show that maximum dry density, $\rho_d(\max)$ for kaolin is 1.53Mg/m³ with the optimum moisture content of 20.91%. Other than that, the permeability coefficient of kaolin is 8.96×10^{-12} m/s.

- 2 Tanjung Bin bottom ash that used in this study was categorized as A-1-a group which consisting predominantly of stone fragments or gravel, either with or without a well-graded binder of fine material. The maximum dry density of bottom ash is 1.313Mg/m³ while its optimum moisture content is 23.60% based on the result of the compaction test. Its specific gravity is 2.33. However, the permeability coefficient of bottom ash is 5.03×10^{-3} m/s which mean it has a good drainage characteristic that able to discharge water.
- 3 For quicklime, it characterized as by referred to the Unified Soil Classification System (USCS). From the result, it shows that its liquid limit is 71% while its plasticity index is 10% thus considered as low plasticity silt. Besides that, the specific gravity of quicklime is 2.26. According to the AASHTO classification system, this kaolin to be classified as clayey soil, A-7-5 which proved that it has moderate plasticity indexes in relation to liquid limit and may be highly elastic as well as subject to considerable volume change. Moreover, the maximum dry density for quicklime is 1.11Mg/m³ with optimum moisture content 43.00%.
4. Installation of single encapsulated lime bottom ash column into kaolin soil can enhance the shear strength of the soft soil. For the result, it shows that with the installation of single encapsulated lime bottom ash column of diameter 10mm with penetration ratio H_c/H_s of 0.6, 0.8 and 1.0, it can increase the shear strength from 12kPa up to 17.23kPa, 18.00kPa and 17.90kPa respectively. However, for the single encapsulated lime bottom ash column of diameter 16mm with penetration ratio H_c/H_s of 0.6, 0.8 and 1.0, the shear strength increase from 12kPa up to 16.57kPa, 17.12kPa and 15.93kPa respectively.
5. In this study, the installation of single encapsulated lime bottom ash column proved that it able to improve the shear strength of kaolin soil. Based on the test conducted, the installation of 10mm diameter of single encapsulated lime bottom ash column with area replacement ratio of 4% can improve the shear strength of kaolin up to 43.58%, 50.00% and 49.17% at sample penetration ratio, H_c/H_s of 0.6, 0.8 and 1.0 respectively. However, for the 16mm diameter of single encapsulated lime bottom ash column with

area replacement ratio of 10.24%, it can improve the shear strength up to 38.08%, 42.67% and 32.75% at sample penetration ratio, H_c/H_s of 0.6, 0.8 and 1.0 respectively. This shows that the improvement of shear strength does not fully rely on the column penetration ratio.

REFERENCES

- [1] Sakr et al, 2009. Utilization of Lime for Stabilizing Soft Clay Soil of high organic content. Curtin University of Technology: Civil Engineering, pp.2.
- [2] Sivakumar, V., Boyd, J. L., Black, J. A., McNeill, J. A., Serridge, C. J., Slocombe, B. C., & Bell, A. L. (2012). Discussion: Effects of granular columns in compacted fills. *Geotechnical Engineering - Proceedings of the ICE*, 165(4), 267–270. <https://doi.org/10.1680/geng.11.00065>
- [3] M. LEONI, M. KARSTUNEN and P. A. VERMEER (2008), *Géotechnique* 58, No. 3, 215–226.
- [4] Hughes, J. M. O. and Withers, N. J. (1974). Reinforcing of Soft Cohesive Soils with Stone Columns. *Ground Engineering*, 7, No. 3, 42–49.
- [5] Hughes, J. M. O., Withers, N. J., and Greenwood, D. A. (1975). A Field Trial of The Reinforcing Effect of a Stone Column in Soil. *Geotechnique*, Vol. 25(1), 31–44.
- [6] Mitra S, Chattopadhyay BC (1999) Stone columns and design limitations. In: *Proceedings, Indian geotechnical conference, Calcutta, India*, pp 201–205
- [7] McKelvey, D., Sivakumar, V., Bell, A., & Graham, J. (2004). Modelling Vibrated Stone Columns In Soft Clay. *Geotechnical Engineering*, Vol. 157, 137 -149.
- [8] Black, J., Sivakumar, V., and McKinley, J. D. (2007). Performance of Clay Samples Reinforced with Vertical Granular Columns. *Canadian Geotechnics Journal*, Vol.44, 89-95.
- [9] Samadhiya NK, Maheswari P, Basu P, Kumar MB (2008) Load-settlement characteristics of granular piles with randomly mixed fibres. *Indian Geotech J* 38(3):345–354
- [10] Najjar, S. S., Sadek, S. and Makaroun, T. (2010). Effect of Sand Columns on the Undrained Load Response of Soft Clays. *Journal of Geotechnical and Geoenvironmental Engineering*, Vol. 136, No. 9, September 1, 2010. ASCE, 1263–1277.

IMPROVEMENT OF ENZYMATIC CATALYSIS IN ORGANIC SOLVENTS VIA IMMOBILIZATION ON BIOCHAR

Hidetaka Noritomi¹, Jumpei Nishigami¹, Nobuyuki Endo², Satoru Kato¹ and Shinsuke Takagi¹

¹Department of Applied Chemistry for Environment, Tokyo Metropolitan University, Japan; ²EEN Co., Ltd., Japan

ABSTRACT

We have found that the adsorption immobilization of the serine protease α -chymotrypsin (α -CT) onto bamboo charcoal powder (BCP), which is a kind of biochar, improves the transesterification rate of *N*-acetyl-L-tyrosine ethyl ester (*N*-Ac-Tyr-OEt) with *n*-butanol (BuOH) in 9 organic solvents. Organic solvents strongly affected the catalysis of BCP-adsorbed α -CT. The transesterification rate of BCP-adsorbed α -CT was much superior to that of free α -CT in every organic solvent. Especially, the transesterification rate of BCP-adsorbed α -CT was about 760 times higher than that of free α -CT in *n*-butyl acetate.

Keywords: Biochar, Adsorption, Enzymatic catalysis, Solvent effect

INTRODUCTION

An enormous amount of greenhouse gas such as CO₂ has recently been emitted from industries, and thereby has caused serious global warming problems [1], [2]. Accordingly, the application of biomass materials, which are carbon neutral, to energies and functional materials is crucial to reduce greenhouse gas emissions [3], [4]. However, most of biomass materials such as forestry residues have hardly been utilized in the field of functional materials. Accordingly, the development in the high value-added application of biomass materials has been desired to provide the multiple effective utilization system of biomass materials.

Enzymes are biocatalysts, which exhibit their outstanding biological activity under mild conditions, and have widely been used in pharmacy, biotechnology, and chemical industry [5]-[7]. Typical applications of enzymes are biotransformation, biosensor, biofuel cell, and so on. Enzymes are generally stable in a cell. However, they are gradually denatured and inactivated under various physical and chemical stresses such as heat, organic solvents, and so on [8]. In order to enhance the stability of enzymes used in vitro, enzyme immobilization, where enzyme molecules are attached to solid carriers, has widely been used [9]-[11]. The main required features of enzyme carriers are chemical stability, thermal stability, insolubility under reaction conditions, high affinity to enzymes, biocompatibility, presence of reactive functional groups, availability, price, regeneration, reusability, and so on. When enzymes are immobilized onto carriers through adsorption, the catalytic activity, specificity, and stability of enzymes are influenced by the nature of carriers. Accordingly, the performance of enzymes can be enhanced by selecting an appropriate carrier.

In order to apply biomass materials to enzyme carriers, we have so far examined the adsorption of enzymes onto biochar, which is derived from biomass materials such as forestry residues. We have found that enzymes are effectively adsorbed onto biochar [12], [13], and biochar-adsorbed enzymes exhibit the high thermal stability in water [14]-[17]. Moreover, we have reported that the adsorption of enzymes onto biochar sufficiently improve the enzyme activity in acetonitrile [18], [19].

In our present work, we have assessed how the nature of organic solvents affects the catalysis of enzymes adsorbed onto biochar in organic solvents. We have used bovine pancreas α -chymotrypsin (α -CT) as a model protein since it is well investigated regarding its structure, functions, and properties [20].

MATERIALS AND METHODS

Materials

α -Chymotrypsin (EC 3.4.21.1 from bovine pancreas) (type II, 52 units/mg solid) (α -CT) was purchased from Sigma-Aldrich Co. (St. Louis, USA). *N*-Acetyl-L-tyrosine ethyl ester (*N*-Ac-Tyr-OEt) and *N*-acetyl-L-tyrosine (*N*-Ac-Tyr-OH) were also from Sigma-Aldrich Co. (St. Louis, USA). Organic solvents used in the present work were of guaranteed grade, and were obtained from Kanto Chemical Co. (Tokyo, Japan). All organic solvents were dried by storing them over dry 0.3 nm molecular sieves (Wako Chemical Co.) for at least 24 h prior to use.

Preparation of Bamboo Charcoal Powder

To prepare bamboo charcoal as a biochar, under nitrogen atmosphere, bamboo waste was dried at 180 °C for 2 h, was pyrolyzed at 450 °C for 2 h, was

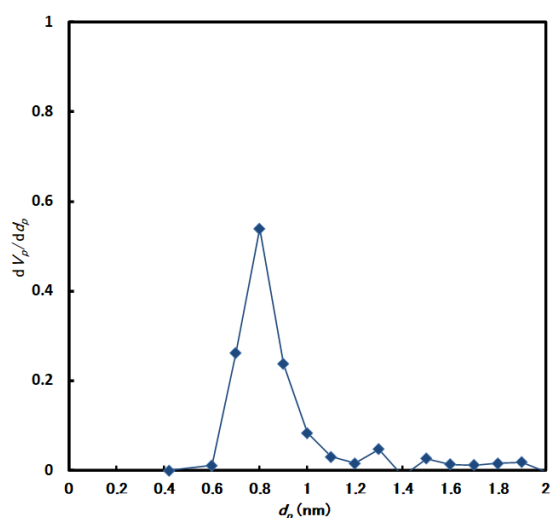


Fig. 1 Pore size distribution of bamboo charcoal powder (BCP).

carbonized at 350 °C for 3 h, and then was cooled at 100 °C for 1 h by pyrolyzer (EE21 Pyrolyzer, EEN Co. Ltd., Japan) [19]. Bamboo charcoal powder (BCP) was obtained by grinding the resultant bamboo charcoal with jet mill (100AS, Fuji Sangyo Co. Ltd., Japan).

Characterization of Bamboo Charcoal Powder

The SEM micrograph was obtained using a scanning electron microscope (JSM-7500FA, JEOL, Japan) operating at 15 kV. The sample for SEM was prepared on a carbon tape without vapor deposition.

All samples were outgassed at 300°C for 8 h prior to the nitrogen adsorption measurements. The specific surface area of BCP was obtained using a micropore system (BELSORP-mini II, BEL JAPAN, INC.), and the pore size distribution was calculated with the use of the micropore analysis method (MP method).

The surface of BCP was analyzed by X-ray photoelectron spectroscopy (XPS) (Quantum-2000, ULVAC-PHI Co. Ltd.) operating at an x-ray beam size of 100 μ m.

Adsorption of α -Chymotrypsin onto Bamboo Charcoal Powder

As a typical procedure, 5 mL of 0.01 M phosphate buffer solution at pH 7 containing 300 μ M α -CT and 3 g/L BCP was placed in a 10-mL test tube with a screw cup, and was incubated at 25 °C and 120 rpm for 24 h. After adsorption, the mixture was filtrated with a membrane filter (pore size: 0.1 μ m, Millipore Co. Ltd.). The amount of α -CT adsorbed onto BCP was calculated by subtracting the amount of α -CT included in the supernatant liquid after

adsorption from the amount of α -CT in the aqueous solution before adsorption. The amount of α -CT was measured at 280 nm by UV/vis spectrophotometer (UV-1800, Shimadzu Co. Ltd.).

Measurement of Catalytic Activity of α - Chymotrypsin

The standard reaction for transesterification was carried out as follows: Three milliliter of an organic solvent containing 0.2%(v/v) water, 10 mM *N*-Ac-Tyr-OEt, 1000 mM *n*-butanol, 1 mM acetanilide, and free α -CT or BCP-adsorbed α -CT (30 μ M) was placed in a 4 mL screw-cap vial, and was incubated at 120 rpm and 25 °C. The amounts of the reaction components were periodically determined with HPLC (Shimadzu LC-10A) (Shimadzu Co., Kyoto, Japan) using a TSK-GEL ODS-80TM column (Tosoh Co., Tokyo, Japan) eluted with water-acetonitrile (6:4 by volume) at 0.5 mL/min with detection at 270 nm. Acetanilide was used as an internal standard.

Measurement of Fourier Transform Infrared (FTIR) Spectroscopy

FTIR measurements of free α -CT and BCP-adsorbed α -CT were carried out using a Jasco FT/IR spectrometer model FT/IR-4100. A KBr pellet containing 0.5 mg of free α -CT or BCP-adsorbed α -CT powder per 100 mg of KBr was prepared, and the measurements were performed using 512 scans under 4.0 cm^{-1} resolution.

RESULTS AND DISCUSSION

Characterization of Bamboo Charcoal Powder

Bamboo charcoal has been prepared by pyrolyzing bamboo waste at low temperatures under nitrogen atmosphere to produce functional groups, which were used as a binding site for the adsorption of enzymes. The resultant bamboo charcoal was grinded by jet mill to obtain the fine bamboo charcoal powder (BCP), whose diameter was about 7 μ m.

The surface area of BCP was 294 m^2/g , and was similar to that of a conventional wood charcoal. Figure 1 shows the pore size distribution of BCP. The range of pore diameter was mainly from 0.6 nm to 1.2 nm, and was much smaller than the size of α -CT since the size of α -CT is 5.1 x 4.0 x 4.0 nm [20]. This result indicates that most of enzymes is adsorbed onto the surface of BCP in direct contact with bulk organic solvents during the enzymatic reaction in organic solvents.

Figure 2 shows the scanning electron micrograph of BCP. The surface of BCP looked like smooth. As mentioned above, since the pore size of BCP was the order of micropores, the pores on the

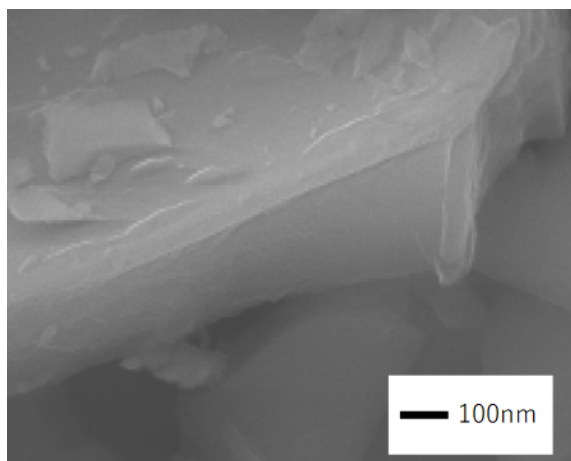


Fig. 2 SEM image of bamboo charcoal powder (BCP).

Table 1 Waveform separation of C_1 peaks.

Peak number	Band	Binding energy (eV)	Atomic percentage (%)
1	C-C, C-H	284.78	63.87
2	C-O	286.12	10.93
3	O-C-O	287.1	3.29
4	C=O	288.48	2.57
5	COOH	289.48	0.03

Table 2 Ratio of the absorbance at 1650 cm^{-1} to the absorbance at 1630 cm^{-1} (ABS_{1650}/ABS_{1630}) of free α -CT and BCP-adsorbed α -CT provided by the FTIR measurement after the solvent immersion.

Solvent	ABS_{1650}/ABS_{1630} (-)	
	Free α -CT	BCP-adsorbed α -CT
None	1.14	1.47
Acetonitrile	1.15	1.51
<i>n</i> -Octane	1.20	1.53

surface of BCP might not be observed under the magnification measured in the present work.

The chemical property of the surface of BCP has been measured by X-ray photoelectron spectroscopy (XPS). The elemental composition and binding state from the surface to 3~5 nm depth can be detected by XPS. As shown in Table 1, aromatics, aliphatics, single C-O bond (alcohol, ether, phenol, C-OH of an enol-keto group), double bonded carbon oxygen groups, carbonyl, quinone, and carboxyl groups were mainly detected by waveform separation of C_1 peaks of narrow scan spectrum.

The amount of α -CT adsorbed onto BCP was 9.8 $\mu\text{mol/g}$. The charge of α -CT was positive in the buffer solution at pH 7 since the isoelectric point of α -CT is 9.1 [20]. On the other hand, the ζ -potential of BCP was negative at pH 7 in the buffer solution at pH 7 [12]. These indicate that the electrostatic force between the positively-charged α -CT molecules and the negatively-charged surface of BCP mainly contributes to the adsorption of α -CT onto BCP.

Solvent Dependence of Conformation of BCP-Adsorbed α -CT

There have been some reports that the native conformation of enzymes may be altered when enzymes are immersed in organic solvents [21], [22].

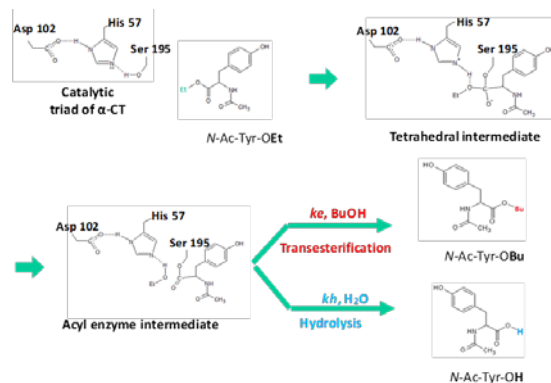


Fig. 3 Reaction scheme of α -CT-catalyzed transesterification of *N*-acetyl-L-tyrosine ethyl ester (*N*-Ac-Tyr-OEt) with *n*-butanol (BuOH) to *N*-acetyl-L-tyrosine butyl ester (*N*-Ac-Tyr-OBu) and competing hydrolysis (*N*-Ac-Tyr-OH).

Table 2 shows the ratio of the absorbance at 1650 cm^{-1} to the absorbance at 1630 cm^{-1} (ABS_{1650}/ABS_{1630}) of free α -CT and BCP-adsorbed α -CT after they were immersed in organic solvents for 24 hr. The bands at ca. 1650 and 1630 cm^{-1} are respectively assignable to α -helix and intramolecular β -sheet, which are secondary structures of enzymes [23]. Before the solvent immersion, the absorbance ratio (ABS_{1650}/ABS_{1630}) of BCP-adsorbed α -CT was greater than that of free α -CT. The absorbance ratio (ABS_{1650}/ABS_{1630}) of BCP-adsorbed α -CT after the solvent immersion was different from that before the solvent immersion. Likewise, the absorbance ratio (ABS_{1650}/ABS_{1630}) of free α -CT was altered by the solvent immersion. Moreover, the absorbance ratio (ABS_{1650}/ABS_{1630}) of BCP-adsorbed α -CT after acetonitrile immersion was almost similar to that after *n*-octane immersion, while the absorbance ratio (ABS_{1650}/ABS_{1630}) of free α -CT after acetonitrile immersion was smaller than that after *n*-octane immersion. The α -helical structure of α -CT molecule is more changeable than β -sheet, since the β -sheet structure is the main backbone of α -CT molecule [20]. Consequently, the higher absorbance ratio corresponds to the higher secondary structure. Those results indicate that the conformation of BCP-adsorbed α -CT is hardly influenced by the nature of solvents, compared to the case of free α -CT.

Solvent Dependence of Catalysis of BCP-Adsorbed α -CT

Figure 3 shows the α -CT -catalyzed reaction scheme [24], [25]. When *N*-acetyl-L-tyrosine ethyl ester (*N*-Ac-Tyr-OEt) is used as a substrate, the enzymatic reaction proceeds by the formation of enzyme intermediates between the active site of enzymes and the substrate. In water α -CT catalyzes the hydrolysis reaction of *N*-acetyl-L-tyrosine ethyl

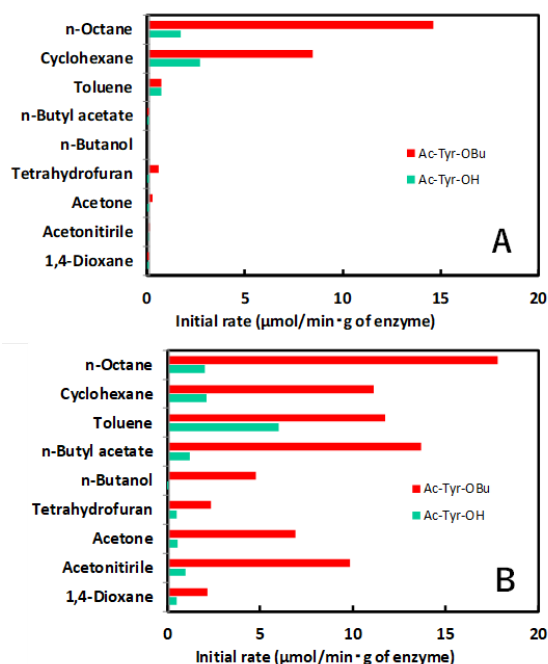


Fig. 4 Solvent dependence of transesterification catalyzed by free α -CT (A) and BCP-adsorbed α -CT (B). Free or BCP-adsorbed α -CT was placed in the organic solvent containing 0.2% (v/v) water, 10 mM *N*-Ac-Tyr-OEt, 1000 mM BuOH, and 1 mM acetanilide, and the resulting mixture was shaken at 120 rpm and 25 °C.

ester (*N*-Ac-Tyr-OEt) with water to give *N*-acetyl-L-tyrosine (*N*-Ac-Tyr-OH). On the other hand, in organic solvents α -CT mainly catalyzes the transesterification reaction of *N*-acetyl-L-tyrosine ethyl ester (*N*-Ac-Tyr-OEt) with another substrate, *n*-butanol (BuOH) to produce *N*-acetyl-L-tyrosine butyl ester (*N*-Ac-Tyr-OBu). Thus α -CT, which is hydrolase, can beneficially catalyze the synthetic reaction in organic solvents, although expensive energy substances such as adenosine triphosphate (ATP) are needed to take place conventional synthetic reactions by enzymes in water [24].

The catalysis of free α -CT and BCP-adsorbed α -CT was markedly dependent upon the nature of organic solvents as shown in Fig. 4. The catalytic activity of BCP-adsorbed α -CT was much superior to that of free α -CT in organic solvents. The transesterification rate of free α -CT in *n*-octane exhibited 813-fold, compared to that in *n*-butyl acetate, while the transesterification rate of BCP-adsorbed α -CT in *n*-octane was 1.3 times greater than that in *n*-butyl acetate.

Figure 5 shows the relation between the catalytic activity and the hydrophobicity defined as log *P* where *P* is a partition coefficient for a given solvent between *n*-octanol and water [26]. The transesterification rate of free α -CT and BCP-adsorbed α -CT increased with an increase in the

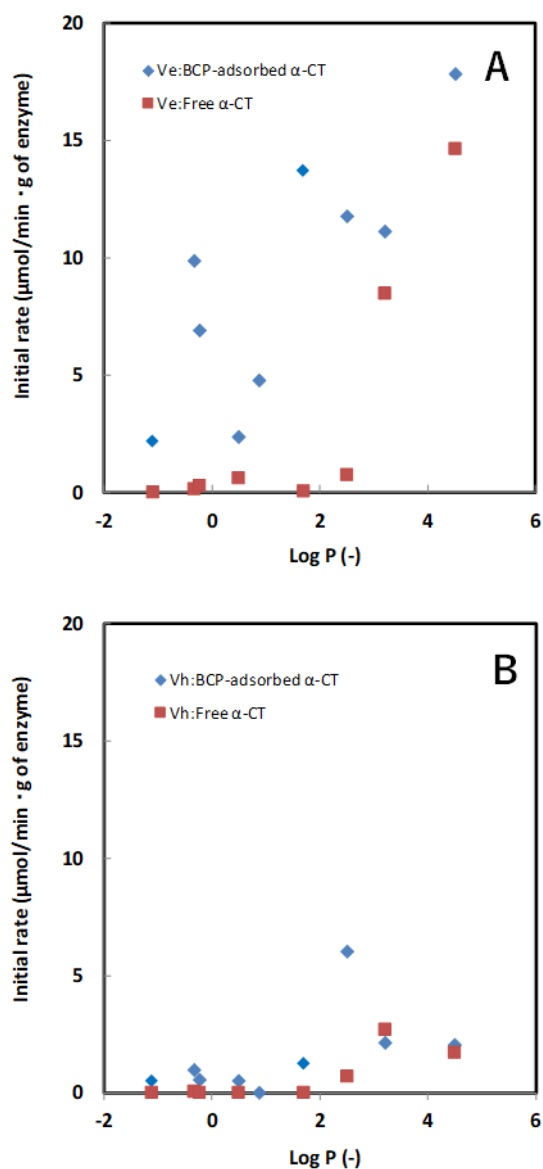


Fig. 5 Relationship of log *P* of organic solvents with transesterification rate (A) or hydrolysis rate (B) of free α -CT and BCP-adsorbed α -CT.

hydrophobicity of organic solvents. Likewise, the hydrolysis rate of free α -CT and BCP-adsorbed α -CT tended to increase with increasing the hydrophobicity of organic solvents. The hydrophobicity contributes to the partition of water between enzyme molecules and the bulk organic phase in reaction systems [27], [28]. When a certain amount of water is added into organic solvents, the amount of water associated with enzyme molecules increases in an increase in the hydrophobicity of organic solvents. Thereby, the flexibility of enzyme molecules, which is essential for catalytic activity, is enhanced by the hydration of enzyme molecules, and then the catalytic activity increases. On the other hand, hydrolysis reaction is promoted by water molecules around enzymes. As

shown in Fig.5, the transesterification rate of BCP-adsorbed α -CT was much superior to that of free α -CT at the low hydrophobicity. For instance, the transesterification rate of BCP-adsorbed α -CT was about 760 times higher than that of free α -CT in *n*-butyl acetate ($\log P = 1.7$). Moreover, BCP-adsorbed α -CT depicted the high transesterification rate in acetone and acetonitrile, compared to the case of free α -CT. An enzymatic reaction in hydrophilic solvents has the advantage of the solubility of a variety of substrates including drug derivatives, which are poorly soluble in hydrophobic solvents [29]. As discussed above, since the native conformation of BCP-adsorbed α -CT was maintained in hydrophilic organic solvents, BCP-adsorbed α -CT could exhibit the high catalytic activity, compared to the case of free α -CT. On the other hand, no correlation between the catalytic activity and the other parameter (e.g. dielectric constant, hydrogen bonding parameter, solubility parameter, and viscosity) was shown.

CONCLUSION

We have demonstrated that the nature of organic solvents affects the catalysis of free α -CT and BCP-adsorbed α -CT. BCP-adsorbed α -CT exhibited the high catalytic activity, compared to the case of free α -CT in organic solvents. Especially, the transesterification rate of BCP-adsorbed α -CT was much superior to that of free α -CT in hydrophilic organic solvents. The native conformation of BCP-adsorbed α -CT did not change with the nature of organic solvents, while that of free α -CT changed to some extent.

REFERENCES

- [1] Olivier JGJ, Muntean M, Peters JAHW, Trends in Global CO₂ Emissions: 2017 Report, 2017.
- [2] IPCC, Climate Change 2014: Synthesis Report, Intergovernmental Panel on Climate Change (IPCC), Geneva, Switzerland, 2014.
- [3] Ho YC, Show KY, "A perspective in renewable energy production from biomass pyrolysis-challenges and prospects", *Current Organic Chem.*, Vol. 19, 2015, pp. 423-436.
- [4] Straathof AJJ, "Transformation of biomass into commodity chemicals using enzymes or cells", *Chem. Rev.*, Vol. 114, 2014, pp. 1871-1908.
- [5] Buchholz K, Kasche V, Bornscheuer UT, *Biocatalyst and Enzyme Technology* 2nd ed., Wiley-Blackwell, 2012.
- [6] Silwana B, Horst CVD, Iwuoha E, "Aerometric determination of cadmium, lead, and mercury metal ions using a novel polymer immobilized horseradish peroxidase biosensor system", *J. Environmental Sci. Health Part A*, Vol. 49, 2014, pp.1501-1511.
- [7] Leech D, Kavanagh P, Schuhmann W, "Enzymatic fuel cells: Recent progress", *Electrochimica Acta*, Vol. 84, 2012, pp. 223-234.
- [8] Bailey JE, Ollis DF, *Biochemical Engineering Fundamentals* 2nd ed., McGraw-Hill, 1986.
- [9] Zdata J, Meyer AS, Jesionowski T, Pinelo M, "A general overview of support materials for enzyme immobilization: characteristics, properties, practical utility", *Catalysts*, Vol. 8, 2018, pp. 92-118.
- [10] Mateo C, Palomo JM, Fernandez-Lorente G, Guisan JM, Fernandez-Lorente R, "Improvement of enzyme activity, stability and selectivity via immobilization techniques", *Enzyme Microbial Technol.*, Vol. 40, 2007, pp. 1451-1463.
- [11] Elnashar MMM, "Review article: immobilized molecules using biomaterials and nanobiotechnology," *J. Biomaterials Nanobiotechnol.*, Vol. 1, 2010, pp. 61-77.
- [12] Noritomi H, Iwai D, Kai R, Tanaka M, Kato S, "Adsorption of lysozyme on biomass charcoal powder prepared from plant biomass wastes", *J. Chem. Eng. Jpn.*, Vol. 46, 2013, pp. 196-200.
- [13] Noritomi H, Hishinuma K, Kurihara S, Nishigami J, Takemoto T, Endo N, Kato S, "Adsorption of α -chymotrypsin on plant biomass charcoal", *J. Surface Eng. Materials Adv. Technol.*, Vol. 3, 2013, pp. 269-274.
- [14] Noritomi H, Kai R, Iwai D, Tanaka H, Kamila R, Tanaka M, Muneki K, Kato S, "Increase in thermal stability of proteins adsorbed on biomass charcoal powder prepared from plant biomass wastes", *J. Biomedical Sci. Eng.*, Vol. 4, 2011, pp. 692-698.
- [15] Noritomi H, Ishiyama R, Kai R, Iwai D, Tanaka M, Kato S, "Immobilization of lysozyme on biomass charcoal powder derived from plant biomass wastes", *J. Biomaterials Nanobiotechnol.*, Vol. 3, 2012, pp. 446-451.
- [16] Noritomi H, Kurihara S, Endo N, Kato S, "Heat-resistant properties of α -chymotrypsin adsorbed onto biomass charcoal powder", *J. Biomaterials Nanobiotechnol.*, Vol. 5, 2014, pp. 179-185.
- [17] Noritomi H, Kurihara S, Endo N, Kato S, Uchiyama K, "Effect of adsorption condition on thermal stability of proteins adsorbed onto biomass charcoal powder", *International J. GEOMATE*, Vol. 11, 2016, pp. 2123-2128.
- [18] Noritomi H, Nishigami J, Endo N, Kato S, Uchiyama K, "Organic solvent-resistant properties of proteins adsorbed onto biomass charcoal powder", *International J. GEOMATE*, Vol. 12, 2017, pp. 140-145.
- [19] Noritomi H, Nishigami J, Endo N, Kato S, Uchiyama K, "Influence of water activity on protease adsorbed on biochar in organic solvents", *J. Materials Sci. Research*, Vol. 6, 2017, pp. 96-102.

- [20] Kumar A, Venkatesu P, "Overview of the stability of α -chymotrypsin in different solvent media", *Chemical Reviews*, Vol. 112, 2012, pp. 4283-4307.
- [21] Mozhaev VV, Khmelnitsky YL, Sergeeva MV, Belova AB, Klyachko NL, Levashov AV, Martinek K, "Catalytic activity and denaturation of enzymes in water/organic cosolvent mixtures. α -Chymotrypsin and laccase in mixed water/alcohol, water/glycol and water/formamide solvents", *Eur. J. Biochem.*, Vol. 184, 1989, pp. 597-602.
- [22] Ryu K, Dordick JS, "How do organic solvents affect peroxidase structure and function?", *Biochemistry*, Vol. 31, 1992, pp. 2588-2598.
- [23] Surewicz WK, Mantsch HH, "New insight into protein secondary structure from resolution-enhanced infrared spectra", *Biochim. Biophys. Acta*, Vol. 952, 1988, pp. 115-130.
- [24] Leninger AL, Nelson DL, Cox MM, *Principles of Biochemistry* 2nd ed., Worth Publishers, 1993.
- [25] Wescott CR, Noritomi H, Klibanov AM, "Rational control of enzymatic enantioselectivity through solvation thermodynamics", *J. Am. Chem. Soc.*, Vol. 118, 1996, pp. 10365-10370.
- [26] Laane C, Boeren S, Vos K, Veeger C, "Rules for optimization of biocatalysis in organic solvents", *Biotechnol. Bioeng.*, Vol. 30, 1987, pp. 81-87.
- [27] A.M. Klibanov, Improving enzymes by using them in organic solvents, *Nature* 409 (2001) 241-246.
- [28] A. Zaks, A.M. Klibanov, Enzymatic catalysis in nonaqueous solvents, *J. Biol. Chem.* 263 (1988) 3194-3201.
- [29] Kise H, Hayakawa H, Noritomi H, "Protease-catalyzed synthetic reactions and immobilization-activation of the enzymes in hydrophilic organic solvents", *J. Biotechnol.*, Vol. 14, 1990, pp. 239-254.

PROPERTIES OF LIGHTWEIGHT AERATED GEOPOLYMER SYNTHESIS FROM HIGH-CALCIUM FLY ASH AND ALUMINIUM POWDER

Charoenchai Ridtirud¹ and Prinya Chindaprasirt²

¹Dept. of Civil Engineering, Faculty of Engineering, Rajamangala University of Technology Isan Khon Kaen Campus, Khon Kaen, 40000, Thailand; ² Sustainable Infrastructure Research and Development Center, Dept. of Civil Engineering, Faculty of Engineering, Khon Kaen University, Khon Kaen 40002, Thailand

ABSTRACT

In the present work, efforts to decrease unit weights of the geopolymer mortar around 2,400 kilograms per cubic meter to be lightweight aerated geopolymer which density lower than 1,800 kilograms per cubic meter and study the properties of lightweight aerated geopolymer based on binders composed of high calcium fly ash, and aluminium powder was studied. Compressive strengths and densities of lightweight geopolymers with aluminium powder contents of 0-0.20%wt, NaOH concentrations of 7.5-12.5 molar, liquid to fly ash ratios of 0.45-0.65, Na₂SiO₃ to NaOH ratios of 0.33-1.5, sand to fly ash ratio of 0.6-1.4, curing temperatures of 25-100 degree Celsius, and curing period of 1-24 hours. were tested. In addition, SEM and ultrasonic pulse velocity of lightweight aerated geopolymer were determined. Results showed that the lightweight aerated geopolymer high calcium fly ash and aluminium powder with the 28-day compressive strength of 1.2-12.6 MPa and densities of 770-1,560 kilogram per cubic meter, with satisfactory strength could be made.

Keywords Geopolymer, High Calcium fly ash, Aluminium powder, Lightweight aerated Geopolymer, Curing.

INTRODUCTION

The unit weight of normal concrete is 2,300 - 2,500 kg/m³ which contributes a large dead load on the building design. Lightweight concrete as shown in Table 1 has thus been invented to reduce the unit weight and in effect reduce the dead weight of the structure. Lightweight concrete with unit weight less than 1,800 kg/m³ [1] but still maintains the required compressive strength for various tasks. For example, lightweight structural concrete is defined as concrete with compressive strength more than 17.0 MPa and a 28- day air-dried unit weight not exceeding 1,850 kg/m³ [2]. Special structural lightweight concrete with a density of 1,725 kg/m³ and maximum compressive strength of 60.0 MPa has been reported [3]. Lightweight concrete can be used in roof decks and floors or lightweight concrete masonry block.

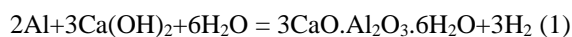
Table 1 Classification of concrete in accordance with unit weight [1]

Classification	Unit Weight (kg/m ³)
Ultra-lightweight concrete	<1200
Lightweight concrete	1200 < UW < 1800

Normal-weight concrete	~2400
Heavyweight concrete	>3200

Lightweight can be divided into three categories. The first type is no-fine concrete (NFC) consisting of cement, coarse aggregate, and water with no sand. The cement paste is coated around the coarse aggregate and provide point-to-point contact to leave interstitial voids. The second type is lightweight aggregate consisting of both coarse and fine lightweight aggregate for producing lesser unit weight concrete. Lightweight aggregates were drawn from 2 sources viz., natural materials such as pumice stone and burnt clay, and synthetic materials such as foam and plastic. The last type is aerated and foamed concrete with voids in the hardened cement paste or mortar matrix causing low-density. This type of concrete can be divided into two main types; foam concrete and aerated concrete. Foam concrete is obtained by mixing cement paste or mortar with stabilized foam. After hardening, the foam cells form concrete of a cellular structure [4]. Foam filling is divided into two processes; the first drawing foam from foam machine and injecting into concrete for mixing and second filling foaming agent into mortar

admixture then mixing by the high shear mixer. Aerated concrete mostly related with this study since aerated or gas concrete can be mixed with or without aggregates which fizz within concrete by a chemical reaction between hydrate calcium oxide and aluminium following equation (1).



However to obtain good quality aerated concrete, the products need autoclaving at a temperature of 175°C and a pressure of 8 atm [4]. The manufacturing thus requires high energy and also involves high budget in the assembly line.

However, the essential material for autoclaved aerated concrete is Portland cement which constitutes the cost and environmental considerations. The production of Portland cement in 2014 was around 4.3 billion tons [5]. The production of 1 ton of cement produces nearly 1 ton of CO₂ emission [6]. Geopolymer is an alternative binder with lower carbon dioxide emission than Portland cement with many similar or better qualities such as heat-resistant, high performance and chemical-resistant [6]. Besides good quality, a number of recycled waste materials can be used for producing geopolymer [7] [8] [9] with the implication that it is liable to be significant cementing material in the future. It is synthesized using starting material rich in silica and alumina and activated with a high alkali solution at normal room temperature or higher temperatures of 40-80 °C [10] [11].

In the alkaline environment of geopolymer, aluminium powder can react and form hydrogen [12] [13]. The reaction between NaOH and aluminium is used to produce lightweight aerated geopolymer [14] [15] [16]. The present paper aims to produce lightweight aerated high calcium fly ash-based geopolymer mortars using aluminium powders. The density, compressive strength, microstructure and spatial distribution of void were studied. With the different amount of aluminium powder, NaOH concentration, liquid/fly ash ratio, Na₂SiO₃/NaOH ratio, sand/fly ash ratio, various curing temperatures and curing periods.

EXPERIMENTAL PROGRAM

Materials

The fly ash from Mae Moh power station in the north of Thailand was used as a starting material with basic qualities as shown in Table 2 and the chemical composition analyzed by X-ray fluorescence (XRF) technique as shown in Table 3. The chemical

composition of 64.3% of SiO₂+Al₂O₃+Fe₂O₃ and 23% CaO indicate that it is a high calcium fly ash according to ASTM C 618 [18]. From the XRD analysis, it consists mainly of amorphous phase with some peaks of crystalline phases of magnetite, magnesioferrite, dachiardite, and calcium aluminum oxide as shown in Fig. 1. This lot of fly ash was rather fine with the Blaine fineness of 5,100 cm²/g. The fly ash particles are spherical with a smooth surface as shown in Fig. 2. The aluminium powder with the minimum assay of 93.0 % is irregular in shape as shown in Fig.3. River sand passed sieve #50 (300 um) and retained on sieve #100 (150um), with basic properties as shown in Table 2 was used. The 7.5, 10, and 12.5 molar (M) NaOH solutions and sodium silicate (Na₂SiO₃) solution with 15.32% Na₂O, 32.87% SiO₂, and 51.8% water were used as alkali activators.

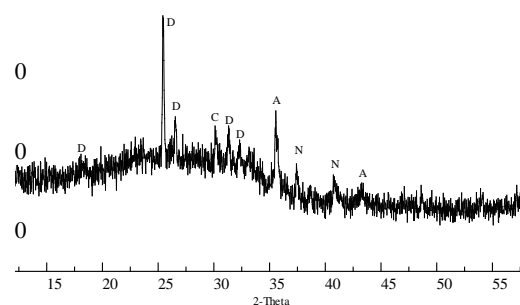


Fig. 1 XRD patterns of fly ash. A-Magnetite: Fe₃O₄; C-Magnesioferrite: Fe₂MgO₄; D-Dachiardite: Na_{1.1}K_{0.7}Ca_{1.7}Al_{5.2}Si_{18.8}O₄₈(H₂O)_{12.7}; N-Calcium Aluminum Oxide: CaAl₂O₄.

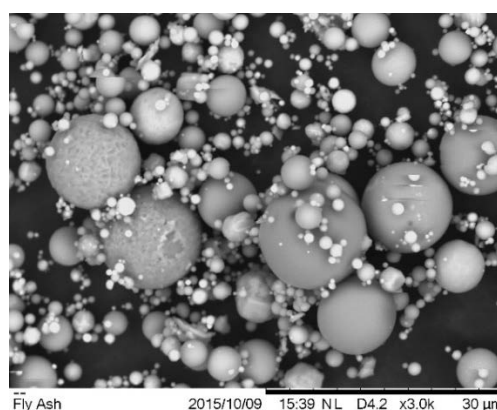


Fig. 2 SEM micrograph of fly ash powder

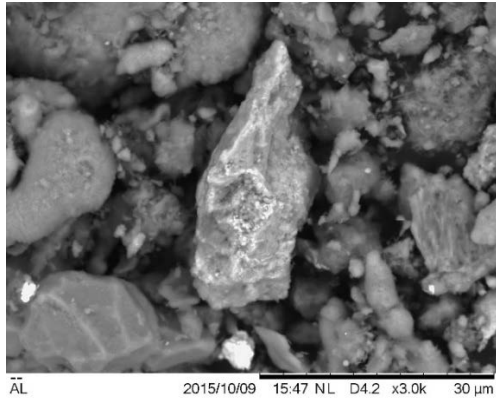


Fig. 3 SEM micrograph of aluminium metal fine powder

Table 2 Physical properties of materials

Materials	Fly ash	Sand
Specific gravity	2.49	-
Fineness by Blaine air permeability (cm ² /g)	5,166.00	-
Fineness modulus	-	1.00
Density (kg/m ³)	-	2.60
Water absorption (%)	-	3.63

Table 3 Chemical composition of Fly Ash (by weight)

Chemical composition	Content (wt. %)
SiO ₂	30.58
CaO	22.81
Al ₂ O ₃	17.10
Fe ₂ O ₃	16.60
SO ₃	5.64
MgO	2.24
K ₂ O	2.21
Na ₂ O	1.47
TiO ₂	0.53
P ₂ O ₅	0.21
BaO	0.15
SrO	0.14
MnO	0.12
L.O.I.	0.20

Mix proportion

Mix compositions

From the preliminary test, a mix with NaOH concentration 10 molar, liquid to ash ratio (L/A) of 0.55, sodium silicate/ sodium hydroxy ratio (NS/NH) of 1.5, sand/ash ratio (S/A) of 1, curing temperature of 40 °C, curing period of 24 hr. and test age of 28 days was used as the standard mix. Eight series of mixes

were summarized in Table 4.

Table 4 Weight ratios of geopolymer lightweight mixes

Series	Variant	Unit
AL	0.0(A),0.05(B),0.1(F),0.15(J),0.2(K)	%
NH	7.5(E),10(F),12.5(G)	M
LA	0.45, 0.55(F),0.65	-
SH	3/2,3/3,2/3(F),1/3	-
SA	0.6(H),0.8,1.0(F),1.2,1.4(D)	-
CT	25(I),40(F),60,80,100(C)	°C
TC	1,3,6,12,24(F)	hr.
DA	3,7,14,28	Day

Note:

AL: Percent of Aluminium powder by weight of fly ash, NH: NaOH concentration, LA: Liquid alkaline/ash ratio, SH: Sodium silicate/NaOH ratio, SA: Sand/ash ratio, CT: Curing temperature, CP: curing period, DA: Age of sample

Details of mixing

The mixing process began with mixing fly ash and sodium hydroxide solution for three minutes. After that, sand was added, and mixing was continued for minutes. Sodium silicate and aluminium powder were then added and mixed for another 3 minutes. The fresh mortar was placed into 50 mm cube molds. The samples were left to expand for 30 minutes and leveled off the excess. The samples were left in a controlled 25 °C room for 24 hr. Finally, the specimens were demolded and wrapped with plastic sheet and stored in a 25°C and 50% RH controlled room.

Details of test

The unit weight of aerated geopolymers was determined as described in ASTM C 138/C138M-14 [17]. The compressive strength was tested after the unit weight determination in accordance with ASTM C109/C109M-13 [18]. The report results are the average of three samples. The test of ultrasonic pulse velocity (UPV) was done in accordance with ASTM C597 [19]. The microstructure of sample was studied with SEM.

RESULTS AND DISCUSSIONS

Fig.4 showed that Physical description of lightweight geopolymer when sample gets a hard status that clearly when add more aluminium powder there was more pore on the sample surface.

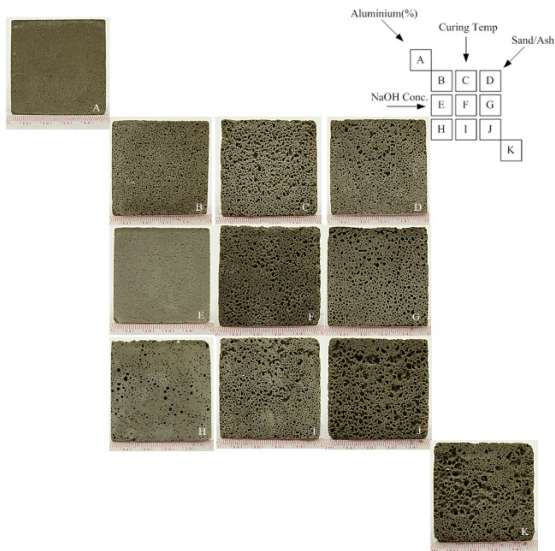


Fig. 4 Physical description of lightweight geopolymer

Aluminium powder contents (Series AL)

The results of density and compressive strength of lightweight aerated geopolymers with various aluminium powder contents are shown in Fig. 5. The density and compressive strength decreased with the increasing aluminium powder contents as expected. The density of geopolymer was in the range of 750-1,950 kg/m³ with the corresponding strength range of 1.20-3.70 MPa. The 28-day compressive strength of samples with aluminium powder contents of 0, 0.05, 0.10, 0.15, and 2.0 % were 3.71, 2.84, 2.35, 1.73, and 1.22 MPa, respectively. The increase in aluminium powder contents increases the air bubbles [15] and thus reduce the strength of the sample which accord with SEM analysis in Fig.6. Shows structure deteriorated when more bubbles were added.

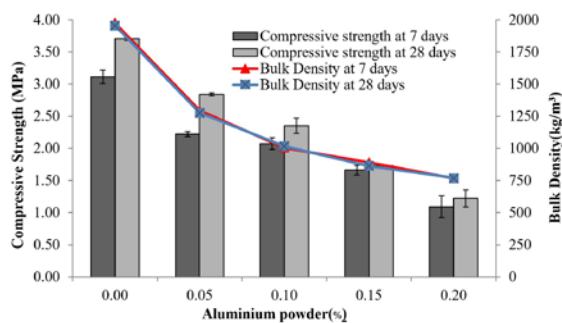


Fig. 5 Compressive strength and density at 7 and 28 days of lightweight geopolymer at various aluminium powder contents (Series AL)

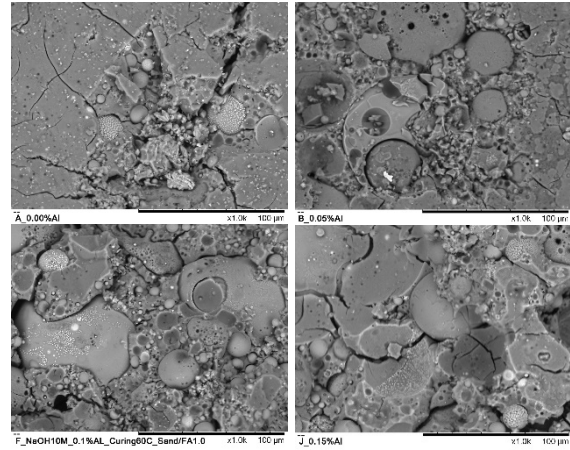


Fig.6 SEM of sample A, B, F and J Order from left to right and top to bottom, respectively.

NaOH Concentration (Series NH)

The results of the effects of NaOH solution concentrations on density and compressive strengths of lightweight aerated geopolymer are shown in Fig. 7. The increase in NaOH concentration resulted in the reduction in density and compressive strength. For normal high calcium fly ash geopolymer, the increase in NaOH concentration enhanced the dissolution of fly ash [20], but the very high NaOH concentration resulted in the increased viscosity of the mix and the polycondensation was hindered [21]. The NaOH concentration for optimum strength is around 10 M. For the system with aluminium powder; the low 7.5 M NaOH resulted in high density and high strength mixture. The relatively high density was a result of the formation of a low amount of bubble. At low NaOH concentration, the setting time of geopolymer was rather fast due to the high calcium ion content. The fast setting characteristic resulted in the stiffening of the matrix and thus hindered the formation of a bubble. For the mix with high NaOH concentrations of 10 and 12.5 M, the leaching out of calcium ions was suppressed and the setting time was lengthened. The matrix was thus less stiff than that with low 7.5 M NaOH mix and the formation of the bubble could continue resulting in the lower density geopolymer and lower strength as well. After considered SEM Fig.8 found that the texture of sample E had most density but in sample G, the surface of fly ash able to react but not much in density like sample E and F

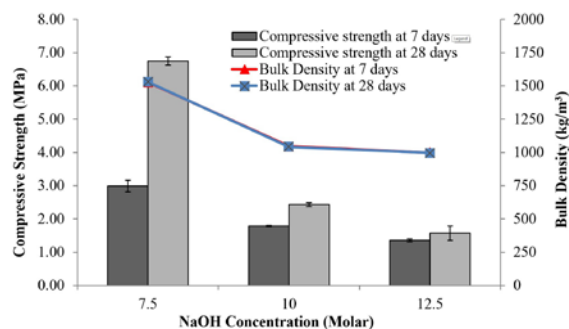


Fig. 7 Compressive strength and density at 7 and 28 days of lightweight geopolymer at various NaOH Concentration (Series NH)

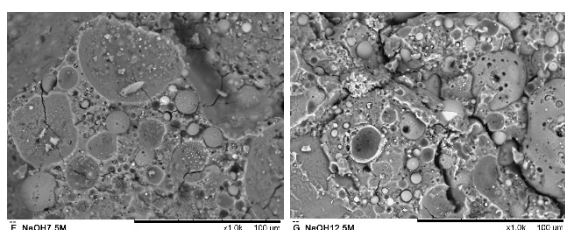


Fig.8 SEM of sample E and G Order from left to right and top to bottom, respectively.

Liquid alkaline to fly ash ratio (Series LA)

The results of density and compressive strength of lightweight aerated geopolymer with various liquid alkaline to fly ash ratios are shown in Fig. 9. The mix with L/A ratio of 0.55 had the lowest density of 1,100 kg/m³ and lowest compressive strength of 4.6 MPa. At low L/A ratio of 0.45, the workability of the mixture was low due to the low liquid in the mix. The formation of the bubble was hindered in this case as the paste was too stiff resulting in high density and slightly high strength geopolymer. Increase in the liquid portion to L/A ratio of 0.55 resulted in a mixture with adequate workability which allowed the bubble to form and resulted in the geopolymer with required low density. Further increase in the liquid portion to L/A ratio of 0.65 resulted in a high workability mix with low ability to retain the formed gas resulted in a high-density geopolymer. It is thus very important to use the proper amount of liquid to ash ratio to obtain an optimum mix with required low density with adequate strength.

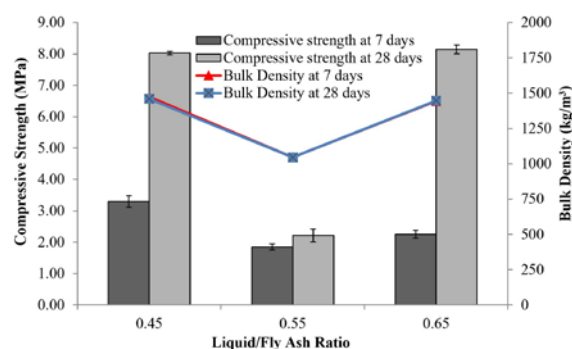


Fig. 9 Compressive strength and density at 7 and 28 days of lightweight geopolymer at various Liquid to Fly Ash Ratio (Series LA)

Na₂SiO₃ to NaOH (Series SH)

The result found that Na₂SiO₃ to NaOH plentifully affected to compressive strength and density. Even though 28-day optimum compressive strength that had 45 MPa was obtained with Na₂SiO₃ to NaOH ratios of 1.00 but density rate was over than 1,800kg/m³ and not regarded as lightweight aerated concrete. If consider in density, we might realize that Na₂SiO₃ to NaOH ratios reducing will cause lower viscosity since sodium silicate was more viscous than sodium hydroxide. Therefore, Na₂SiO₃ can keep more air bubbles [10] when Na₂SiO₃ to NaOH ratios decreased which showed in Fig.10, Na₂SiO₃ to NaOH ratios of 1/3, found that compressive strength was reduced since the decreasing in strength in this range of Na₂SiO₃ to NaOH ratios was due to the silica content of mixture reducing [22]. Moreover, high NaOH did not cause higher SiO₂ and Al₂O₃ leaching [20] since SiO₂ and Al₂O₃ in Fly ash are limited but NaOH solution exceed will reduce compressive strength rate. A similar trend of the result was reported for the normal weight high calcium fly ash based- geopolymer mortars. The compressive strengths of mortars with high Na₂SiO₃ to NaOH ratios of 1.5 and 3.0 were reduced compared to that with Na₂SiO₃ to NaOH ratios of 1.0 [11] over OH filling will fizz a large number of air bubbles and reduce density rate [13].

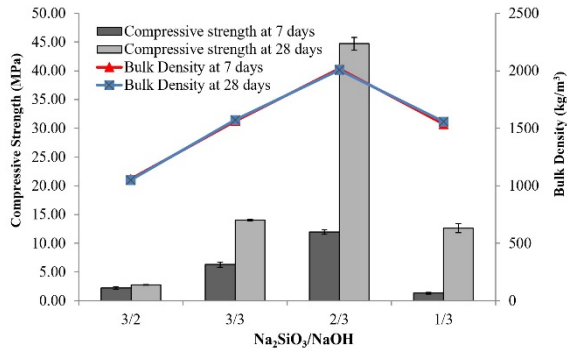


Fig. 10 Compressive strength and density at 7 and 28 days of lightweight geopolymer at various Na_2SiO_3 to NaOH (Series SH)

Sand to Fly ash ratio (Series SA)

The results of the effects of sand to fly ash ratio on compressive strength and density of lightweight aerated geopolymer are shown in Fig. 11. Sand to Fly ash ratio had an influence on the strength of geopolymer but the influence was rather small. The result showed that after filled sand into the compressive composition strength and density of lightweight aerated geopolymer rate will increase because of sand replacing air bubbles. After considering the results, sand to fly ash ratio more than 1 will not be beneficial to compressive strength and increase the sample density rate. From SEM Fig.12, found that texture paste of the sample H had highest homogeneous since air bubbles not kept within the sample. If we only applied the result from SEM, we might not explain the result of the low compressive strength of sample H, but after explained by SEM displays, the results that accorded with compressive strength were clearly showed. The sample that had low rate of sand to fly ash ratio could not keep air bubbles like sample H since most of the large bubbles will rise up because sand is the factor that increases sticky rate for fresh lightweight aerated geopolymer and compresses the bubbles in order to stop their floating as showed in Fig.6 and 12 (D, F, and H).

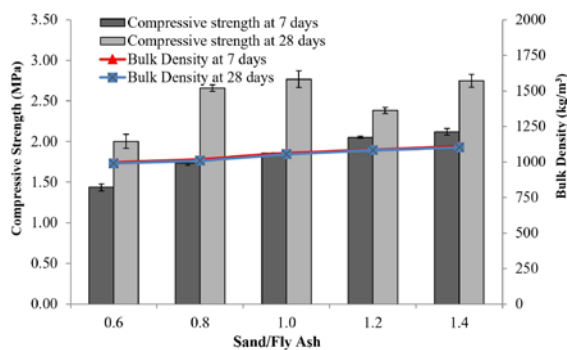


Fig. 11 Compressive strength and density at 7 and 28 days of lightweight geopolymer at various Sand to Fly ash ratio (Series SA)

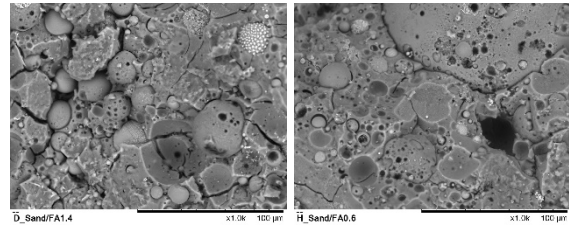


Fig.12 SEM of sample D and H Order from left to right, respectively.

Curing temperature (Series CT)

The results of compressive strength and density of lightweight aerated geopolymer with various curing temperatures are shown in Fig.13. The optimum curing temperatures was 60 °C and the strength of 3.3 MPa. An increase in curing temperatures from 25 °C to 60 °C resulted to develop on compressive strength accorded with several research works that studied about an increase in temperature of curing to 60 °C enhanced the geopolymerization and increased the compressive strength [11], [23], [24], [25]. Even though temperature curing increasing is the factor that support geopolymerization method but when the temperature reaches over 80 °C, the solution will rapidly evaporate, the reaction will not extremely occur, the sample will be dry, shrink and become to micro crack sample. In term of SEM analysis that showed in Fig.14, the compressive strength was plentifully reduced from temperature curing at 60 °C was 3.3 MPa to 1.8MPa at 80 °C decreasing as 45 % in order that temperature curing increasing will reduce compressive strength as well. Moreover, the temperature that higher than 80 °C restrained the development of compressive strength and the sample's compressive strength tends to be reduced based on the further ages. However, an increasing of curing temperatures reduced density rate but not much effective since the high-temperature curing caused watered solution lost their moistness more than curing at a low temperature, so the sample weight was decreased as well [11], [26]. An interesting aspect of lightweight aerated geopolymer production is; autoclave treatment is not important for producing, on the other hand, OPC concrete production still needs autoclave [27], [28] that will reduce the process, energy and production cost.

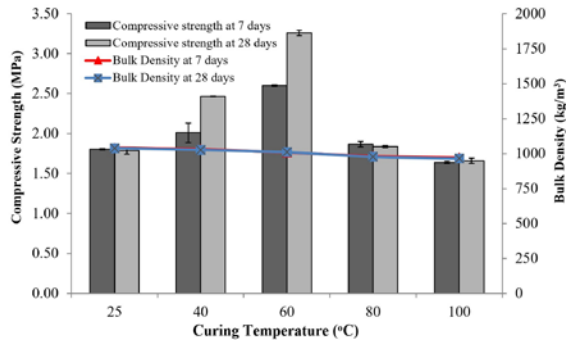


Fig. 13 Compressive strength and density at 7 and 28 days of lightweight geopolymer at various curing temperature (Series CT)

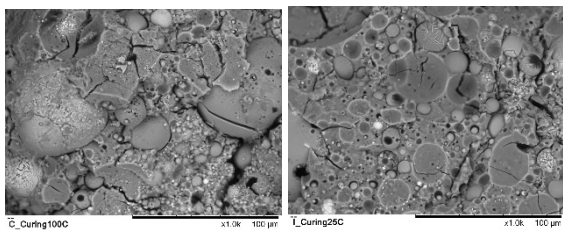


Fig.14 SEM of sample C and I Order from left to right, respectively.

Curing period (Series CP) and Age of the sample (Series DA)

The results of compressive strength and density of lightweight aerated geopolymer with various curing period are shown in Fig.15. Density had changed without significance with 1,055 Kg/m³ as its rate signified that the curing period could not affect to air bubbles fizzing or the sample evaporation when cured with 40 °C. However, an increasing curing period will increase compressive strength rate. The results accorded with Görhan 2014 research which described, when curing temperature of 65°C and increasing curing period from 2, 5 and 24 hours geopolymer that compounded with NaOH 9 M's compressive strength will increase to 13, 16 and 21 MPa, respectively. [29].

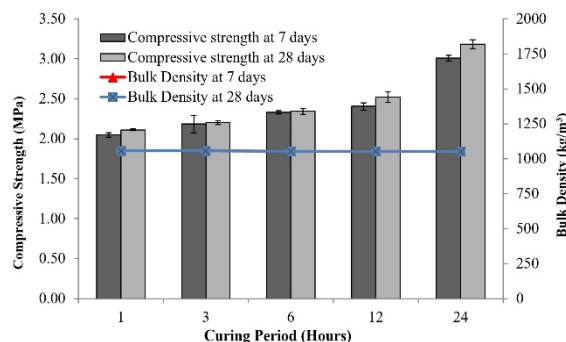


Fig. 15 Compressive strength and density at 7 and 28 days of lightweight geopolymer at various

curing period (Series CP)

Fig.16 showed that when the sample aged compressive strength will continuously develop and density rate of the sample had a little change with average density rate as 1,058 kg/m³. However, in this test the sample was cured with 40 °C and the result accorded with Fernández-Jiménez 1999 research that studied about curing temperature of 45 °C [33] but cannot find out that lightweight aerated geopolymer will develop their compressive strength further aged in any cases. Since the relation of lightweight aerated geopolymer compressive strength development has to consider the main factor like curing temperature. According to the research, curing in high temperature will be beneficial to early compressive strength but it will reduce along with its ages [30] Moreover, if curing with relative humidity > 90%, the sample's compressive strength will continuously develop [31].

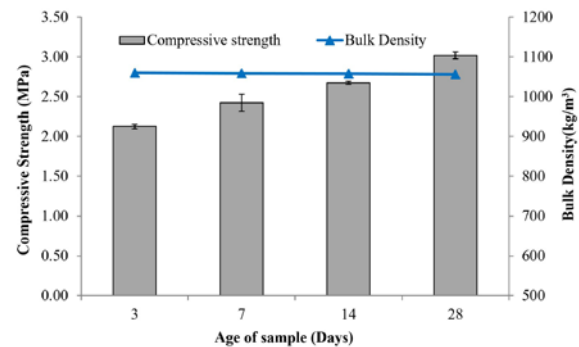


Fig. 16 Compressive strength and density of lightweight geopolymer age (DA)

CONCLUSION

Based on the obtained data, the following conclusions can be drawn.

1. Suitable Liquid to Fly Ash Ratio for lightweight aerated geopolymer production, lowest density should be 0.55.

2. An aluminium powder increasing increased H₂ bubbles and reduced sample's density and when the numbers of void increased compressive strength and its development will be reduced.

3. An increasing of NaOH Concentration make rapid and aggressive H₂ bubbles on the other hand high increasing NaOH Concentration generate large air bubbles but density not much reduced.

4. Na₂SiO₃ to NaOH have a major effect on the viscous of fresh specimens If there are high quantities the specimens will give a highly viscous, and also affect the setting time, therefore, air bubbles

maintaining has to relate with setting time if setting time is late, the bubbles will rise up to the surface and density rate will increase.

5. Sand to Fly ash ratio not much affect to density rate and found that the suitable Sand to Fly ash ratio is 1.0

6. Curing temperature and curing period gave a little effect to density rate but in compressive strength, an increasing of curing temperature during 25-60 °C will increase compressive strength on the other hand if curing with over 60 °C will harm to compressive strength and its development tends to be reduced.

7. The results showed that the lightweight aerated geopolymer High- Ca fly ash and aluminium powder with 28-day compressive strength of 1.2- 12.6 MPa and densities of 770-1,560 kg/m³ could be made.

ACKNOWLEDGEMENTS

This research was supported by fund budget revenue form Faculty of Engineering Rajamangala University of Technology Isan Khon Kaen Campus. We thank our colleagues Associate professor Petcharakorn Hanpanich from Department of radiology, Faculty of medicine, Khon Kaen University who provided insight and expertise that greatly assisted the research.

REFERENCES

- [1] P. K. Mehta and P. J. M. Monteiro, *Concrete microstructure, properties, and materials* vol. Third Edition. United States of America, 2006.
- [2] A. C. Institute, "Guide for Structural Lightweight Aggregate Concrete," in *ACI Committee 213R-03*, ed. Detroit, 2003, pp. 213R-1 to 213R-38.
- [3] Y.-s. Guo, K. Kaolu, M. W. Li, J. t. Ding, and M. j. Huang, "Properties of high performance lightweight aggregate concrete.," in *Second International Symposium on Structural Lightweight Aggregate Concrete*, Kristiansand Norway, 2000, pp. 548-561.
- [4] S. K. Duggal, *BUILDING MATERIALS: NEW AGE INTERNATIONAL (P) LIMITED*, 2008.
- [5] CEMBUREAU, 2014. Activity Report, pp. 44.
- [6] J. Davidovits, *Geopolymer Chemistry and Applications*. France: Institut Géopolymère, 2008.
- [7] S. Onutai, S. Jiemsirilers, P. Thavorniti, and T. Kobayashi, "Aluminium hydroxide waste based geopolymer composed of fly ash for sustainable cement materials," *Construction and Building Materials*, vol. 101, Part 1, pp. 298-308, 2015.
- [8] A. I. Badanoiu, T. H. A. Al Saadi, S. Stoleriu, and G. Voicu, "Preparation and characterization of foamed geopolymers from waste glass and red mud," *Construction and Building Materials*, vol. 84, pp. 284-293, 2015.
- [9] A. Nazari and J. G. Sanjayan, "Synthesis of geopolymer from industrial wastes," *Journal of Cleaner Production*, vol. 99, pp. 297-304, 2015.
- [10] A. Sathonsaowaphak, P. Chindaprasirt, and K. Pimraksa, "Workability and strength of lignite bottom ash geopolymer mortar," *Journal of Hazardous Materials*, vol. 168, pp. 44-50, 2009.
- [11] P. Chindaprasirt, T. Chareerat, and V. Sirivivatnanon, "Workability and strength of coarse high calcium fly ash geopolymer," *Cement and Concrete Composites*, vol. 29, pp. 224-229, 2007/03/01/ 2007.
- [12] C. B. Porciúncula, N. R. Marcilio, I. C. Tessaro, and M. Gerchmann, "Production of hydrogen in the reaction between aluminum and water in the presence of NaOH and KOH," *Brazilian Journal of Chemical Engineering*, vol. 29, pp. 337-348, 2012.
- [13] C. Vargel, "Chapter E.4 - Inorganic Bases," in *Corrosion of Aluminium*, C. Vargel, Ed., ed Amsterdam: Elsevier, 2004, pp. 385-393.
- [14] J. G. Sanjayan, A. Nazari, L. Chen, and G. H. Nguyen, "Physical and mechanical properties of lightweight aerated geopolymer," *Construction and Building Materials*, vol. 79, pp. 236-244, 2015.
- [15] R. Arellano Aguilar, O. Burciaga Díaz, and J. I. Escalante García, "Lightweight concretes of activated metakaolin-fly ash binders, with blast furnace slag aggregates," *Construction and Building Materials*, vol. 24, pp. 1166-1175, 2010.
- [16] R. Brooks, M. Bahadory, F. Tovia, and H. Rostami, "Properties of alkali-activated fly ash: high performance to lightweight," *International Journal of Sustainable Engineering*, vol. 3, pp. 211-218, 2010/09/01 2010.

- [17] ASTM C138/C138M-14. Standard test of method for unit weight of mortar. Annual Book of ASTM Standard. 2014;Vol.04.01.
- [18] ASTM C109/C109M-13. Standard Test Method of Compressive Strength of Hydraulic Cement Mortars (using 2-in. or [50 mm] cube specimens). Annual Book of ASTM Standard. 2013; Vol.04.01.
- [19] ASTM C597-09. Standard Test Method for Pulse Velocity Through Concrete, . Annual Book of ASTM Standard, 2002;Vol.04.02.
- [20] Z. Zuhua, Y. Xiao, Z. Huajun, and C. Yue, "Role of water in the synthesis of calcined kaolin-based geopolymer," *Applied Clay Science*, vol. 43, pp. 218-223, 2009.
- [21] P. Posi, C. Ridditirud, C. Ekvong, D. Chammanee, K. Janthowong, and P. Chindaprasirt, "Properties of lightweight high calcium fly ash geopolymer concretes containing recycled packaging foam," *Construction and Building Materials*, vol. 94, pp. 408-413, 2015.
- [22] U. Rattanasak and P. Chindaprasirt, "Influence of NaOH solution on the synthesis of fly ash geopolymer," *Minerals Engineering*, vol. 22, pp. 1073-1078, 2009.
- [23] C. Ridditirud, "Comparison of Compressive Strength and Drying Shrinkage by Various Portland Cement Type and Geopolymer," presented at the International Conference on Advances in Civil Engineering for Sustainable Development, Suranaree University of Technology, 2014.
- [24] P. Rovnaník, "Effect of curing temperature on the development of hard structure of metakaolin-based geopolymer," *Construction and Building Materials*, vol. 24, pp. 1176-1183, 2010.
- [25] A. S. de Vargas, D. C. C. Dal Molin, A. C. F. Vilela, F. J. d. Silva, B. Pavão, and H. Veit, "The effects of Na₂O/SiO₂ molar ratio, curing temperature and age on compressive strength, morphology and microstructure of alkali-activated fly ash-based geopolymers," *Cement and Concrete Composites*, vol. 33, pp. 653-660, 2011.
- [26] G. Görhan and G. Kürklü, "The influence of the NaOH solution on the properties of the fly ash-based geopolymer mortar cured at different temperatures," *Composites: Part B*, vol. 58, pp. 371-377, 2014.
- [27] P. Walczak, P. Szymański, and A. Różycka, "Autoclaved Aerated Concrete based on Fly Ash in Density 350kg/m³ as an Environmentally Friendly Material for Energy - Efficient Constructions," *Procedia Engineering*, vol. 122, pp. 39-46, 2015.
- [28] X.-y. Huang, W. Ni, W.-h. Cui, Z.-j. Wang, and L.-p. Zhu, "Preparation of autoclaved aerated concrete using copper tailings and blast furnace slag," *Construction and Building Materials*, vol. 27, pp. 1-5, 2012.
- [29] G. Görhan and G. Kürklü, "The influence of the NaOH solution on the properties of the fly ash-based geopolymer mortar cured at different temperatures," *Composites Part B: Engineering*, vol. 58, pp. 371-377, 2014.
- [30] E. Altan and S. T. Erdoğan, "Alkali activation of a slag at ambient and elevated temperatures," *Cement and Concrete Composites*, vol. 34, pp. 131-139, 2012.
- [31] M. Criado, A. Fernández-Jiménez, and A. Palomo, "Alkali activation of fly ash. Part III: Effect of curing conditions on reaction and its graphical description," *Fuel*, vol. 89, pp. 3185-3192, 2010.

FLUIDIZED BED COAL-BARK FLY ASH GEOPOLYMER WITH ADDITIVES CURED AT AMBIENT TEMPERATURE

Prinya Chindaprasit¹, Pornnapa Kasemsiri², Suttipong Poomsrisa³ and Patcharapol Posi^{4*}

¹ Sustainable Infrastructure Research and Development Center, Department of Civil Engineering, Faculty of Engineering, Khon Kaen University, Khon Kaen 40002, Thailand, and Academy of Science, The Royal Society of Thailand, Dusit, Bangkok, Thailand 10300

² Sustainable Infrastructure Research and Development Center, Department of Chemical Engineering, Faculty of Engineering, Khon Kaen University, Khon Kaen 40002, Thailand

³ Thai Paper Co., Ltd. 1 Siam Cement Rd., Bangsue, Bangkok 10800, Thailand

⁴ Department of Civil Engineering, Faculty of Engineering, Rajamangala University of Technology Isan KhonKaen Campus, KhonKaen, 40000, Thailand

ABSTRACT

In this research, the properties of fluidized bed coal-bark fly ash geopolymer mortar containing additives viz., ordinary Portland Cement (OPC) and micro silica (MS) were studied. The fluidized bed coal-bark fly ash was a waste from a power plant boiler in Khon Kaen, Thailand. The geopolymer mortar was made from fluidized bed coal-bark fly ash, sand, sodium silicate solution, NaOH solution, and additives. The additives were used to replace the fluidized bed coal-bark fly ash at the level of 0 - 15 % by weight. The mortars with liquid alkaline/ash ratios of 0.9-1.4, sodium silicate/NaOH ratios of 0.33-3.00, NaOH concentrations of 5-15 molars, OPC and micro silica contents of 0 - 15 % by weight of fly ash, and curing at ambient temperature were tested. The geopolymer mortars with 28-day compressive strengths between 5.5 and 27.0 MPa and densities between 1970 and 2175 kg/m³ were obtained. The addition of OPC and micro silica enhanced the strength development of geopolymer mortar with the optimum OPC content of 10 % and micro silica content of 15 %. It is shown here that the fluidized bed coal-bark fly ash geopolymer mortar containing OPC and micro silica as additives with ambient temperature curing possesses sufficient strength. The use of this product can reduce the energy consumption in cement production and increases the sustainability of construction industry.

Keywords: Coal-bark fly ash, Fluidized bed, OPC, Micro silica, Geopolymer

INTRODUCTION

Cement is the main material in construction. In the cement production process, a large amount of limestone is obtained from the limestone mountain. It is processed through washing, grinding, baking and other processes and huge energy is thus used. The temperature up to 1,400 degrees Celsius is needed and a large amount of carbon dioxide (CO₂) is released into the atmosphere. Every 1 ton of Portland cement comes out of the furnace, about 1 ton of CO₂ is produced [1]. This results in an increase in the greenhouse effect.

For this reason, the researches have been conducted to develop alternative materials to substitute cement to reduce the above-mentioned problems. The potential binder to substitute Portland cement is geopolymer materials. Geopolymer is an environmentally friendly binder with binding capacity based on aluminosilicate [2, 3]. It provides high strength in a short time when modulate heat is applied. The temperature used is not very high around 40-80 degrees Celsius [4]. The geopolymer can be

used for the production of precast concrete such as pillars, beams, walls and finished flooring which are suitable for work requiring high compressive strength in a short time.

Today, the precast concrete is in high demand in the market because it is convenient and fast to work. However, heat curing also increase the cost of the product. Curing at room temperature causes the geopolymer to develop the strength slowly [4]. The additive materials such as silica fume or micro silica are used to help develop strengths. It helps to improve the compressive strength of the geopolymer cured at room temperature.

In addition, the production of geopolymer can utilize the waste from the manufacturing process in the industrial sector. This includes agricultural products such as rice husk ash, bagasse ash, and other biomass ash; the garbage industry, including waste ash, and the electricity industry, including fly ash and bottom ash.

In this research, fly ash was selected to use. The fly ash was a waste from a power plant boiler in Khon Kaen, Thailand. It used the wood scraps, which are

the waste materials from the paper production process. The factory has burned these wood scraps to produce electricity together with the use of sub-bituminous coal in the Fluidized Bed Combustion (FBC).

The fluidized bed combustion uses small scale pulverized coal mixed with limestone, and sprays into the furnace with the hot air. The coal and limestone, which are sprayed into the furnace, are suspended in the hot air. It looks like a boiling liquid while the coal burns, the limestone acts as a sponge trapping sulfur dioxide. This process can reduce the amount of sulfur that is released by combustion by as much as 90% [5]. In addition, the combustion at temperatures below 1,000 °C reduces the amount of pollution caused by nitrogen in the combustion system. However, the fly ash obtained from this system is irregular in shape with high crystallinity because the burnt temperature is not very high. This fly ash can be used as a pozzolanic material but it is not as good as the fly ash obtained from the pulverized burning system. Also, it has high calcium and sulfur content [6] to be used in the work of geopolymer materials. The properties and effects of ash will have to be investigated. The co-burning of coal and biomass is now also practiced in the other country [7, 8]. This co-burning of coal and biomass has recently been applied and thus there is no statistical report on this. In addition, the use of fluidized bed coal-bark fly ash as a binder source is not yet financially supported by the Thai government. The support would promote the use of waste materials and is an essence tool for future use of waste.

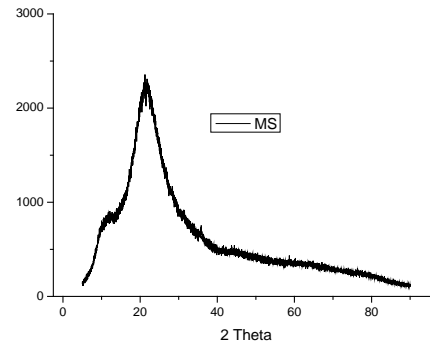
Therefore, this research has studied the properties of geopolymer with fluidized bed furnace system ash from burning sub-bituminous coal with wood derived from the paper production at burning temperature below 1,000 °C. It has high calcium and sulfur contents. The purpose is to recycle the waste from the industry for maximum benefit. This is the development of materials for use in the construction which is environmental friendly and sustainable.

EXPERIMENTAL PROGRAM

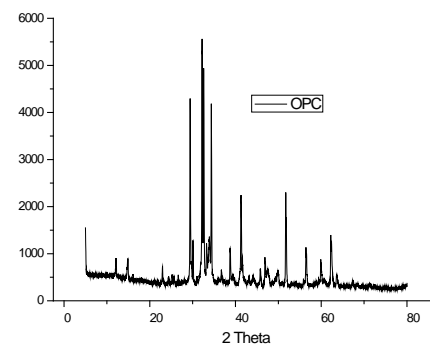
Materials

In this study, materials consisted of fluidized bed coal-bark fly ash (FCB-FA) was a waste from a power plant boiler in Khon Kaen, Thailand, ordinary Portland cement (OPC) and micro silica (MS) of 0, 5, 10, and 15 % by weight of fly ash, sodium hydroxide (NaOH) of 5, 10, and 15 M, sodium silicate with 15.32% Na₂O, 32.87% SiO₂, and 51.8% water, and river sand. the physical properties of materials are shown in Table 1. The specific gravity of FCB-FA was 2.86 with median particle size of 23.9 µm. The FCB-FA consisted of a high content of 21.14% SiO₂, 8.02% Al₂O₃, 10.98% Fe₂O₃, and 35.8% CaO with the loss on ignition (LOI) of 0.28% as shown in Table 2. It was, therefore, a class C in accordance which ASTM C618 [9]. The XRD of MS and OPC as shown

in Fig. 1 and the morphology of FCB-FA by SEM as shown in Fig. 2 indicated that the shape of FCB-FA was irregular with some additional small pores.



a. MS



b. OPC

Figure 1. The XRD of MS and OPC

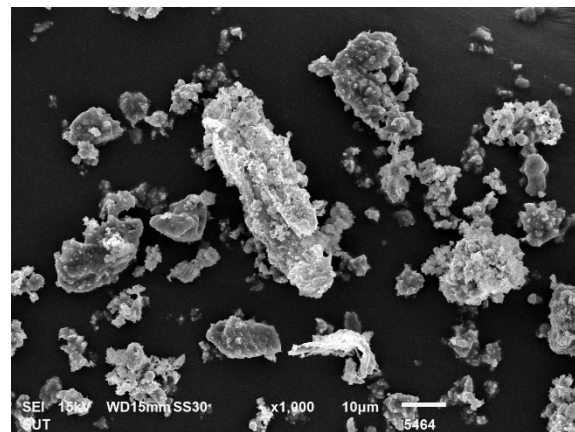


Figure 2. The morphology of FCB-FA by SEM

Mix proportion

OPC and MS content

To study the effect of OPC and MS content, the OPC and MS contents of 0, 5, 10, and 15 % by weight of fly ash were used in one series. The compressive strength and density of fluidized bed coal-bark fly ash geopolymer were determined.

Table 1. The physical properties of materials

Materials	MS	OPC	FCB-FA	Sand
Specific gravity	2.16	3.15	2.86	2.61
Median particle size (μm)	13.8	18.7	23.9	-
Fineness modulus	-	-	-	2.65
Unit weight (kg/m^3)	460	1440	875	1360
Water absorption (%)	-	-	-	1.17

Table 2. Chemical composition of materials (by weight)

Chemical compositions (%)	FCB-FA	MS	OPC
SiO ₂	21.14	92.4	20.8
Al ₂ O ₃	8.02	-	4.7
Fe ₂ O ₃	10.98	0.33	3.4
CaO	35.8	2.52	65.3
K ₂ O	5.36	3.13	0.4
Na ₂ O	0.33	-	0.1
SO ₃	11.56	0.96	2.7
LOI	0.28	0.21	0.9

Mix compositions

In order to obtain adequate data, a number of series of mixes were tested as follows.

Series OPC: To study the effect of OPC content, all mixtures used constant NaOH of 10 M, NS/NaOH ratios of 1.00, aggregate (A)/FA of 2.75 cured at ambient temperature. L/FA of 0.9, 1.0, 1.1, 1.2, and 1.3 and OPC content of 0, 5, 10, and 15 % by weight were tested.

Series MS: To study the effect of MS content, all mixtures used constant NaOH of 10 M, NS/NaOH ratios of 1.00, A/FA of 2.75 cured at ambient temperature. And varies L/FA of 0.9, 1.0, 1.1, 1.2, and 1.3 and MS content of 0, 5, 10, and 15 % by weight were tested.

Series NS/NaOH: This series was used to study the effect of sodium silicate/NaOH ratios. All mixtures used constant NaOH of 10 M, OPC and MS content of 10 % by weight, A/FA of 2.75 cured at ambient temperature, and NS/NaOH ratios of 0.33, 0.67, 1.0, 1.5 and 3.0.

Series [NaOH]: All mixtures used constant OPC and MS content of 10 % by weight, NS/NaOH ratios of 1.00, A/FA of 2.75 cured at ambient temperature. Three NaOH concentrations viz., 5, 10 and 15 molars were used to study the effect of NaOH concentration.

Series A/FA: This series was used to study the effect of aggregate/fly ash ratio. all mixture used constant OPC and MS content of 10 % by weight, NS/NaOH ratios of 1.00, NaOH of 10 M with cured at ambient temperature. The A/FA of 2.50, 2.75, and 3.00 were tested.

Details of Mixing

All mixtures were made and cured at ambient temperature. OPC and MS content of 0, 5, 10, and 15 % by weight of FCB-FA, concentration of NaOH of 10, 12.5, and 15 molars, sodium silicate/NaOH ratios (NS/NaOH) of 0.67, 1.00, and 3.00, aggregate/ash ratios of 2.50, 2.75, and 3.00. The mixing was done in a pan mixer with following step:

- FCB-FA, OPC and MS were mixed for 5 min.
- NaOH was added and mixed for 5 min.
- Sand was added and mixed for 5 min.
- Sodium silicate was added and mixed for 5 min.

The fresh fluidized bed coal-bark fly ash geopolymers were placed into 50 x 50 x 50 mm cubes molds according to ASTM C109/C109M-16a [10]. The specimens were wrapped with plastic sheet and placed in a 25 °C controlled room for 24 hours. Finally, the specimens were demolded and stored in a 25 °C controlled room. The textures of fluidized bed coal-bark fly ash geopolymer mortar containing additives are shown in Fig. 3.

**Figure 3.** The sample of fluidized bed coal-bark fly ash geopolymer mortar containing additives

Details of test

Compressive strength and density

The 50 x 50 x 50 mm cube specimens were tested for density and compressive strength. The density was determined at 28 days using the compressive strength specimens as described in ASTM C 138/C138M-14 [11]. The compressive strength was measured after the density determination. The cube specimens were tested to determine the compressive strength in accordance with ASTM C109/C109M-16a [10]. The reported unit weight and compressive strengths were the average of three samples.

RESULTS AND DISCUSSIONS

Compressive strength and density

Series OPC

The results of compressive strength of fluidized bed coal-bark fly ash geopolymer with various L/FA and OPC content are shown in Fig. 4. The compressive strength of fluidized bed coal-bark fly ash geopolymer with additives depended on both L/FA and OPC contents. For the OPC content, the compressive strength increased with increasing OPC content from 0 to 10 % by weight of fluidized bed coal-bark fly ash. This was due to the increased

amount of calcium from Portland cement. As a result, the reaction form additional hydration products of C-S-H and C-A-S-H which coexisted with normal geopolymer products and improved compression [12, 13]. For the high OPC replacement level of 15 %, the increase in compressive strength started to cease and in some cases significant decreases were observed. The high OPC content of 15 % resulted in some strength reduction due mainly to the modifications of microstructure of hydration products and the amount of cement is too high to make the mixture dry [14, 15]. For example, the compressive strengths at 28 days of mixes with L/FA of 0.9 with volume of OPC of 0, 5, 10, and 15 % by weight were 9.2, 16.8, 22.9, and 22.0 MPa, respectively.

With regards to L/FA, the compressive strength decreased with increasing L/FA. Due to the ratio of liquid to fly ash is too high, the result was bleeding and thus resulted in the reduction in compressive strength [16, 17]. For example, the compressive strengths at 28 days of 15 % OPC with L/FA of 0.9, 1.0, 1.1, 1.2, and 1.3 were 22.0, 20.4, 19.6, 18.4, and 16.4 MPa, respectively.

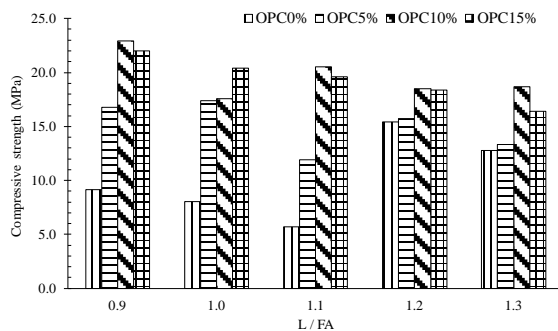


Figure 4. Compressive strength of series OPC at 28 days

Series MS

The results of compressive strength of fluidized bed coal-bark fly ash geopolymer with various L/FA and MS contents are shown in Fig. 5. For the MS content, the compressive strength increased with increasing MS content from 0 to 15 % by weight of fluidized bed coal-bark fly ash. The particles of silica fume were very small and highly amorphous phase could react quite quickly [18]. For example, the compressive strengths at 28 days of mixes with L/FA of 0.9 with volume of MS of 0, 5, 10, and 15 % by weight were 9.8, 18.6, 24.5, and 34.5 MPa, respectively.

With regards to L/FA, the compressive strength of fluidized bed coal-bark fly ash geopolymer tended to decrease with increasing L/FA. For the example, the compressive strengths at 28 days of 15 % OPC with L/FA of 0.9, 1.0, 1.1, 1.2, and 1.3 were 34.5, 25.0, 30.5, 20.5, and 4.2 MPa, respectively.

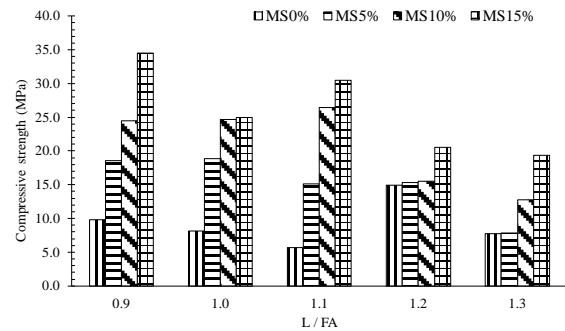


Figure 5. Compressive strength of series MS at 28 days

Series NS/NaOH

The results of compressive strength of fluidized bed coal-bark fly ash geopolymer with various sodium silicate/NaOH ratios and OPC, MS content of 10 % by weight are shown in Fig. 6. It was found that the optimum compressive strength was with sodium silicate/NaOH ratios of 1.00. The increased in silicate/NaOH ratios affect to the pH value and increased the compressive strength [19]. In contrast, for the silicate/NaOH ratios above 1.00, the increase in sodium silicate content also increased the viscosity of mixture and this resulted in the difficulties in casting and adversely affect the compressive strength [20]. For example, the compressive strengths at 28 days of mixes with control and NS/NH of 0.67, 1.00, and 3.00 were 6.7, 15.5, and 11.1 MPa, respectively.

When considering MS and OPC contents; the 10 % MS gave mix with compressive strength higher than 10 % OPC due to MS or micro silica is a very reactive pozzolanic material because of its extreme fineness and very high amorphous silicon dioxide content [21]. For example, the compressive strengths at 28 days of mixes with NS/NH of 0.67 of control, 10 % OPC and 10 % MS were 6.7, 9.3, and 15.4 MPa, respectively.

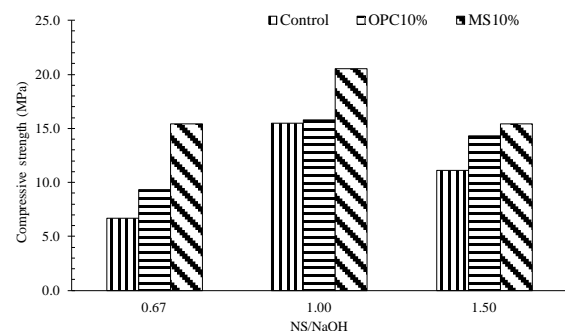


Figure 6. Compressive strength of series NS/NaOH at 28 days

Series [NaOH]

The results of the compressive strength of fluidized bed coal-bark fly ash geopolymer with various [NaOH] and OPC, MS content of 10 % by weight are shown in Fig. 7.

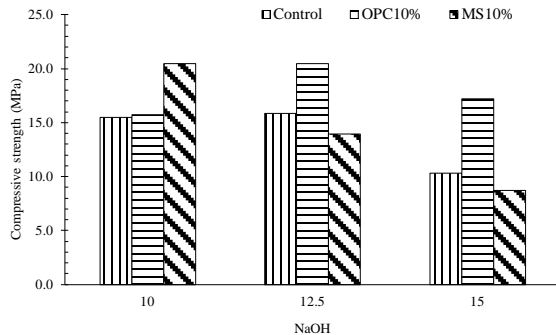


Figure 7. Compressive strength of series [NaOH] at 28 days

The increased in NaOH from 10 M to 12.5 M resulted in the increasing compressive strength. For example, the compressive strengths at 28 days with the volume of control with NaOH of 10, 12.5, and 15 M were 15.5, 15.8, and 10.3 MPa, respectively. The low compressive strength with low NaOH due to setting time of paste was short with low NaOH [22, 23]. The NaOH influence the setting time of the geopolymer. At low NaOH, the leaching out of silica and alumina was low but high in Ca^{2+} and the amount of calcium was sufficient for the precipitation and reacted to form calcium aluminate hydrate and calcium silicate hydrate. Thus, the setting time of geopolymer was related to the amount of available calcium [24, 25]. In contrast, an increased NaOH from 12.5 to 15 M resulted in a decrease in the compressive strength. At high concentration of NaOH, the compressive strength decreased due to the excessive hydroxide ions causing aluminosilicate gel precipitation at the very early stages and resulting in low compressive strength [13, 26, 27].

Series A/FA

The results of compressive strength of fluidized bed coal-bark fly ash geopolymer with various aggregate/fly ash ratio (A/FA) and OPC, MS contents of 10 % by weight are shown in Fig. 8. The increase in aggregate/fly ash ratio resulted in a slightly decrease in compressive strength due to the volume of cementitious materials decreased.

When considering MS and OPC contents; at the same Series NS/NaOH, the compressive strength of 10 % MS was higher than that of 10 % OPC due to MS is a very reactive pozzolanic material.

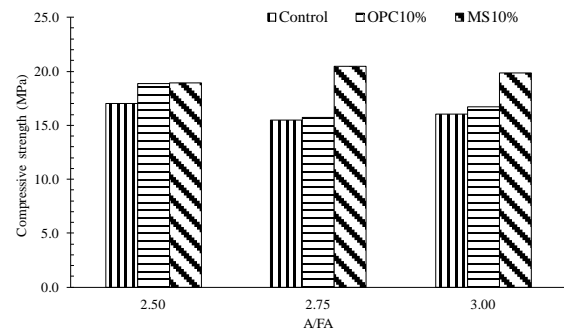


Figure 8. Compressive strength of series A/FA at 28 days

CONCLUSIONS

Based on the obtained data, the following conclusions can be drawn:

1. When considering varies L/FA with OPC and MS contents; the compressive strength increased with the increasing volume of OPC from 0 to 10 % by weight. In contrast, when the OPC increased from 10 to 15 % by weight, the compressive strength decreased. For the volume of MS, the compressive strength increased with the increasing of the volume of MS from 0 to 15 % by weight.

2. For series NS/NaOH; the NS/NaOH of 1 gave the highest compressive strength and apart from this, the strength of geopolymer started to drop. The 10 % MS gave compressive strength higher than 10 % OPC due to MS is a very reactive pozzolanic material.

3. For the control and 10 % OPC samples of series [NaOH], the increase in NaOH from 10 M to 12.5 M resulted in the increasing compressive strength. In contrast, an increase in NaOH from 12.5 to 15 M resulted in a decrease in the compressive strength. At 10 % MS, the increase in NaOH from 10 M to 15 M resulted in the decreasing compressive strength

4. For series A/FA; the increase in A/FA resulted in a slight decrease in compressive strength and the compressive strength of 10 % MS was higher than that of 10 % OPC.

5. The results showed that the 28-day compressive strengths between 5.5 and 27.0 MPa and densities between 1970 and 2175 kg/m^3 were obtained. The addition of OPC and MS enhanced the strength development of geopolymer mortars with the optimum OPC content of 10 % and MS content of 15 %. The use of this product can reduce the energy consumption in cement production and increases the sustainability of construction industry.

ACKNOWLEDGEMENT

This work was financially supported by the Phoenix Pulp & Paper Public Company Limited, Khon Kaen, Thailand. The support of the Faculty of

Engineering, Rajamangala University of Technology Isan Khon Kaen Campus, and the Thailand Research Fund (TRF) under the TRF Distinguished Research Professor Grant No. DPG6180002 is gratefully acknowledged here.

REFERENCES

- [1] Malhotra VM. Introduction: Sustainable Development and Concrete Technology. *ACI Concrete International*, Vol. 24, Issue 7, 2002, pp. 7-22.
- [2] Chindapasirt P, Rattanasak U. Characterization of the high-calcium fly ash geopolymer mortar with hot-weather curing systems for sustainable application. *Advanced Powder Technology*, Vol. 28, Issue 9, 2017, pp. 2317-24.
- [3] Wongkvanklom A, Sata, V., Sanjayan, J., & Chindapasirt, P. Setting time, compressive strength and sulfuric acid resistance of a high calcium fly ash geopolymer containing borax. *Engineering and Applied Science Research*, Vol. 45, Issue 2, 2018, pp. 89-94.
- [4] Chindapasirt P, Rattanasak U. Improvement of durability of cement pipe with high calcium fly ash geopolymer covering. *Construction and Building Materials*, (Supplement C), 2016, pp. 956-61.
- [5] Chindapasirt P, Rattanasak U. Utilization of blended fluidized bed combustion (FBC) ash and pulverized coal combustion (PCC) fly ash in geopolymer. *Waste Management*, Vol. 30, Issue 4, 2010, pp. 667-72.
- [6] Chindapasirt P, Rattanasak U, Jaturapitakkul C. Utilization of fly ash blends from pulverized coal and fluidized bed combustions in geopolymeric materials. *Cement and Concrete Composites*, Vol. 33, Issue 1, 2011, pp. 55-60.
- [7] Kubacki ML, Ross AB, Jones JM, Williams A. Small-scale co-utilisation of coal and biomass. *Fuel*, Vol. 101, 2012, pp. 84-9.
- [8] Ross AB, Jones JM, Chaiklangmuang S, Pourkashanian M, Williams A, Kubica K, et al. Measurement and prediction of the emission of pollutants from the combustion of coal and biomass in a fixed bed furnace. *Fuel*. Vol. 81, Issue 5, 2002, pp. 571-82.
- [9] ASTM C 618. Standard Specification for Coal Fly Ash and Raw or Calcined Natural Pozzolan for Use in Concrete. *Annual Book of ASTM Standard*. 2012;Vol.04.01.
- [10] ASTM C109/C109M-13. Standard Test Method of Compressive Strength of Hydraulic Cement Mortars (using 2-in. or [50 mm] cube specimens). *Annual Book of ASTM Standard*. 2013; Vol.04.01.
- [11] ASTM C138/C138M-14. Standard test of method for unit weight of mortar. *Annual Book of ASTM Standard*. 2014;Vol.04.01.
- [12] Yip CK, Van Deventer JSJ. Microanalysis of calcium silicate hydrate gel formed within a geopolymeric binder. *Journal of Materials Science*, Vol. 38, Issue 18, 2003, pp. 3851-60.
- [13] Somna K, Jaturapitakkul C, Kajitvichyanukul P, Chindapasirt P. NaOH-activated ground fly ash geopolymer cured at ambient temperature. *Fuel*, Vol. 90, Issue 6, 2018, pp. 2118-24.
- [14] Temuujin J, van Riessen A, Williams R. Influence of calcium compounds on the mechanical properties of fly ash geopolymer pastes. *Journal of Hazardous Materials*, Vol. 167, Issue 1-3, 2009, pp. 82-8.
- [15] Pangdaeng S, Phoo-ngernkham T, Sata V, Chindapasirt P. Influence of curing conditions on properties of high calcium fly ash geopolymer containing Portland cement as additive. *Materials & Design*, Vol. 53, 2014, pp. 269-74.
- [16] Wongpa J, Kiattikomol K, Jaturapitakkul C, Chindapasirt P. Compressive strength, modulus of elasticity, and water permeability of inorganic polymer concrete. *Materials & Design*, Vol. 31, Issue 10, 2010, pp. 4748-54.
- [17] Kharita MH, Yousef S, AlNassar M. The effect of the initial water to cement ratio on shielding properties of ordinary concrete. *Progress in Nuclear Energy*, Vol. 52, Issue 5, 2010, pp. 491-3.
- [18] Grabiec AM, Zawal D, Szulc J. Influence of type and maximum aggregate size on some properties of high-strength concrete made of pozzolana cement in respect of binder and carbon dioxide intensity indexes. *Construction and Building Materials*, Vol. 98, 2015, pp. 17-24.
- [19] Chindapasirt P, Chareerat T, Sirivivatnanon V. Workability and strength of coarse high calcium fly ash geopolymer. *Cement and Concrete Composites*, Vol. 29, Issue 3, 2007, pp. 224-90.
- [20] Sathonsaowaphak A, Chindapasirt P, Pimraksa K. Workability and strength of lignite bottom ash geopolymer mortar. *Journal of Hazardous Materials*, Vol. 168, Issue 1, 2009, pp. 44-50.
- [21] Siddique R. Utilization of silica fume in concrete: Review of hardened properties. *Resources, Conservation and Recycling*, Vol. 55, Issue 11, 2011, pp. 923-32.
- [22] Alonso S, Palomo A. Calorimetric study of alkaline activation of calcium hydroxide–metakaolin solid mixtures. *Cement and Concrete Research*, Vol. 31, Issue 1, 2001, pp. 25-30.
- [23] Hanjitsuwan S, Hunpratub S, Thongbai P, Maensiri S, Sata V, Chindapasirt P. Effects of NaOH concentrations on physical and electrical properties of high calcium fly ash geopolymer paste. *Cement and Concrete Composites*, Vol. 45, 2014, pp. 9-14.
- [24] Rattanasak U, Chindapasirt P. Influence of NaOH solution on the synthesis of fly ash geopolymer. *Minerals Engineering*, Vol. 12, 2009, pp. 1073-8.
- [25] Rattanasak U, Pankhet K, Chindapasirt P. Effect of chemical admixtures on properties of high-calcium fly ash geopolymer. *International Journal of Minerals, Metallurgy, and Materials*, Vol. 18, Issue 3, 2011, pp. 364-9.
- [26] Lee WKW, Van Deventer JSJ. The effects of inorganic salt contamination on the strength and durability of geopolymers. *Colloids and Surfaces A: Physicochemical and Engineering Aspects*, Vol. 211, Issue 2-3, 2002, pp. 115-26.
- [27] Pimraksa K, Chindapasirt P, Rungchet A, Sagoe-Crentsil K, Sato T. Lightweight geopolymer made of highly porous siliceous materials with various Na₂O/Al₂O₃ and SiO₂/Al₂O₃ ratios. *Materials Science and Engineering: A*, Vol. 528, Issue 21, 2011, pp. 6616-23.

EFFECT OF CUTTING PARAMETER AND FIBER PULL-OUT ON MACHINABILITY KENAF FIBER REINFORCED PLASTIC COMPOSITE MATERIALS USING DOE

Azmi Harun¹, Che Hassan Che Haron², Jaharah A. Ghani², Yuzairi Abdul Rahim¹, Roshaliza Hamidon¹, Tan Chye Lih¹

¹School of Manufacturing Engineering, Universiti Malaysia Perlis, Malaysia,

²Department of Mechanical and Materials Engineering, Faculty Engineering and Built Environment,
Universiti Kebangsaan Malaysia, Malaysia

ABSTRACT

Milling surface quality normally depends on the value of surface roughness and delamination factor. The milling parameters, which are cutting tool geometry and fiber pull-out, are the major factors affecting the value of surface roughness and delamination factor in milling kenaf fiber reinforced plastic composite. The objectives of this research are to study the effects of milling parameters, to evaluate the fiber behavior, and to determine the optimum conditions for a range of milling parameters in order to minimize surface roughness (Ra) and delamination factor (Fd) using response surface methodology (RSM). RSM with central composite design (CCD) approach was used to conduct a non-sequential experiment and analyzed the data from the measurements of surface roughness and delamination factor. This study focused on the investigation of relationship between the milling parameters and their effects on kenaf reinforced plastic composite materials during cutting process. Kenaf composite panels were fabricated using vacuum assisted resin transfer molding (VARTM) method that was pressurized below 15 psi using a vacuum pressure. The results showed that the optimum parameters for better surface roughness and delamination factor were cutting speed of 500 rpm, feed rate of 200 mm/min, and depth of cut of 2.0 mm. The feed rate and cutting speed are expected to be the biggest contributors to surface roughness and delamination factor. Finally, different cutting tool geometries also influenced the fiber pull-out that affect surface roughness and delamination factor in milling kenaf fiber reinforce plastic composite materials.

Keywords: Kenaf fiber, Surface roughness, Delamination factor, Response surface methodology

INTRODUCTION

Natural fiber is a hairy-like raw material that comes from natural resources such as animal, mineral, and plant fibers. Also, natural fiber is sustainable as well as eco-efficient; therefore, it has been used to replace glass fiber and other synthetic polymer fibers that have various kinds of applications in engineering [1]. Natural fiber is famous for its flexibility for processing because it is less delicate to health hazards and damage in machine tools during manufacturing. Furthermore, natural fiber has a lot of beneficial characteristics, for example considerably high tensile strength, satisfying aspect ratio of fiber, and low density, but due to the nature of the composite, machining of composite materials becomes a major cause of concern in the industry [1]. Natural fiber is a renewable source; hence, its cost is very low compared to man-made fibers. In addition, natural

fiber is a biodegradable material. In other words, it is an environmentally friendly fiber that is not harmful to the environment. Therefore, it can be used to substitute non-biodegradable materials in product development.

Kenaf Fiber Composite

The main constituents of kenaf are cellulose (45–57 wt.%), hemicelluloses (21.5 wt.%), lignin (8–13 wt.%), and pectin (3–5 wt.%) [2]. Wambua et al. claimed that poor mechanical properties could be the result of lack of firmness between the polymers (hydrophobic) and the natural fiber (hydrophilic) [3]. Kenaf fiber offers better interfacial adhesion to matrix polymer than other natural fibers [4]. Matrix polymer can support the fibers, transfer the stresses to fibers to bear most of the load, prevent direct

physical damage to fibers, and improve ductility and toughness of the whole composite [5]. Epoxy produces no toxic gases and offers high temperature resistance that enables it to be used at high temperature [6]. Hafizah et al. studied the tensile behavior of kenaf fiber reinforced with several polymer composites and concluded that kenaf reinforced epoxy composite had the highest ultimate tensile strength and the Young's modulus [7]. Various research has been conducted and it has been proven that machining parameters possess significant effects on the performance and quality of natural fiber composite [8], [9].

Milling Kenaf Fiber Composite

Erkan et al. claimed that increased spindle speed worsened the damage factor and increased the plastic deformation rate on an end-milled fiber reinforced plastic composite [10]. Davim et al. claimed that feed rate was expected to affect delamination rather than cutting speed for the machining of fiber reinforced plastic [11]. Ramulu et al. studied the machining of polymer composite and stated that better surface finish could be obtained with higher cutting speed [12]. The impact of depth of cut is not as important as cutting speed and feed rate in composite machining; however, it still gives a significant effect on machining process [13]. Besides, the milled surface is getting smoother as the flute of the cutting tool increases [10]. The end-mill cutter can be made of either a high-speed steel or a carbide insert and usually has a straight shank or a tapered shank. Normally, the cutter rotates on a workpiece in a perpendicular axis but it can still be tilted in order to match the need of producing a machine-tapered or curved surface. However, milled composites always tend to have surface roughness and delamination problem that depends much on cutting parameters and the composite's characteristic [14]. Thus, an optimum setting of these parameters is needed to find out in order to control the quality of a workpiece. The advantages of a high-speed steel (HSS) cutting tool over a carbide cutting tool are higher strength to withstand cutting forces and lower cost. However, a carbide insert cutting tool is better than an HSS tool in metal cutting due to its great abrasion resistance and high temperature resistance, which allows it to be used in machining process at high speed without the need to consider overheating situation. For machining of natural fiber composites, an HSS cutting tool is sufficient to meet this research's purpose.

Delamination Factor

Delamination of a natural fiber composite can be described as the loss of adhesion between the layers that can lead to critical damage of the reinforcement layers (separation). Hocheng et al. believed that delamination can be worsened by increasing the feed rate of milling parameters [15]. The damage of the composite is greater if the operation is conducted with high cutting speed and high feed rate [14]. Furthermore, Hocheng et al. stated that delamination can be worsened by increasing the feed rate and tool life can be shortened by increasing the cutting speed that causes higher torque [15]. Davim et al. studied the effects of cutting speed and feed rate on delamination of glass fiber reinforced plastic during machining with two different matrices [16]. The damage of the composite is greater if operated with high cutting speed and high feed rate [14].

METHODOLOGY

Materials Preparation

Kenaf reinforced epoxy composite materials were prepared using vacuum-assisted resin transfer molding (VARTM) method. The method was used to transfer resin to natural fiber in a vacuum condition for molding with the assistance of a vacuum pump. The kenaf fiber in mat form was cut into the dimensions of 300 mm × 300 mm × 5 mm (thickness). Two layers of kenaf fiber mat were used and mixed with epoxy resin. The resin was prepared in the ratio of 4 (800 g epoxy) to 1 (200 g hardener). The VARTM manufacturer recommended this ratio for fabricating kenaf fiber reinforced plastic composite materials. The VARTM method is gaining the interest of manufacturers due to its ease of handling and low preparation cost. Figure 2 shows the actual setup of VARTM. The composite panels were then cut into small workpiece with the approximate dimensions of 75 mm × 30 mm × (8–10 mm) for milling process.

Milling Parameter

The milling parameters of this research were based on the work by Babu et al. since they studied the machining of natural fiber composite. The parameter setting in this research was based on the previous parameters used in the work by Babu et al. [8]. Table 1 shows the parameters used in this research in which all the units were converted to suit the use of a computer numerical control (CNC) milling machine. The three parameters used in this research were spindle speed (rpm), feed rate (mm/min), and depth of cut (mm), with low and high

levels for each parameter. A two-level factorial design of experiment was selected with eight experiment runs designed using Design Expert 7.0 software. Four center points were added to seek for the significance of the curvature and error testing. If the curvature of the results is insignificant, a linear modeling equation is sufficient to express the optimization. If the curvature is significant, there is a chance for applying RSM. In RSM, the CCD approach was used to obtain a quadratic modeling equation for parameter optimization. RSM was used to develop a second-order modeling equation that has better accuracy in expressing the optimization.

Table 1 Parameter setting for milling process.

Milling parameters	Low	Hig h	Center point
Spindle speed (rpm)	500	1000	700
Feed rate (mm/min)	200	1200	750
Depth of cut (mm)	1	3	2

Measurement of Delamination factor

The results of delamination factor were obtained after milling processes. The delamination factor (F_d) can be determined using (1).

$$F_d = W_{\max} / W \quad (1)$$

Where,

F_d = Factor of delamination

W_{\max} = maximum width of the delamination area

W = width of original cut

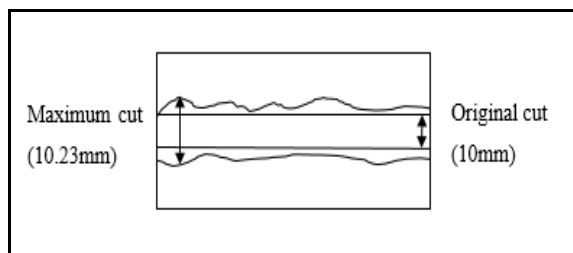


Fig. 1 Example measurement of delamination factor (F_d)

RESULTS AND DISCUSSION

Table 2 Result for delamination factor (F_d) using screening parameter setting.

Run	Spindle speed (rpm)	Feed rate (mm/min)	Depth of cut (mm)	F_d
1	1000	1200	1	1.113
2	500	200	1	1.039
3	500	1200	1	1.077
4	750	700	2	1.042
5	750	700	2	1.067
6	1000	1200	3	1.016
7	750	700	2	1.062
8	1000	200	3	1.134
9	1000	200	1	1.124
10	750	700	2	1.034
11	500	1200	3	1.075
12	500	200	3	1.035

ANOVA analysis for screening process of delamination factor (F_d)

The curvature is significant (see Table 3) and it indicates that there is a chance for developing a quadratic modeling equation using RSM with CCD approach. From the analysis of variance (ANOVA) test for delamination factor (F_d), spindle speed was the most significant factor (p value = 0.0068) affecting delamination. The depth of cut was the second significant factor (p value = 0.0292) whereas the feed rate was the least factor (p value = 0.2237). In order to apply RSM, CCD (see Table 4) was added to further investigate the parameters for delamination by constructing a second-order modeling equation.

Results of delamination factor (F_d) using Central Composite Design (CCD)

Table 4 Result for delamination factor (F_d) using Central Composite Design.

Run	Spindle Speed (rpm)	Feed rate (mm/min)	Depth of Cut (mm)	F_d
1	1000.00	1200.00	1.00	1.075
2	1000.00	200.00	1.00	1.134
3	500.00	1200.00	3.00	1.077
4	750.00	700.00	2.00	1.062
5	1000.00	200.00	3.00	1.113

6	500.00	200.00	1.00	1.035
7	750.00	700.00	2.00	1.034
8	500.00	1200.00	1.00	1.124
9	1000.00	1200.00	3.00	1.067
10	750.00	700.00	2.00	1.042
11	750.00	700.00	2.00	1.039
12	500.00	200.00	3.00	1.016
13	1170.45	700.00	2.00	1.083
14	750.00	-140.90	2.00	1.012
15	329.55	700.00	2.00	1.021
16	750.00	700.00	2.00	1.059
17	750.00	700.00	2.00	1.038
18	750.00	1540.90	2.00	1.087
19	750.00	700.00	0.32	1.054
20	750.00	700.00	3.68	1.046

of lack of fit of the quadratic modeling equation as shown in Table 5. From Table 5, the main factors significant to F_d were spindle speed with F value of 9.67 (0.72%), feed rate with F value of 4.86 (4.4%) and the AB interaction with F value of 18.43 (0.06%). The AB interaction (spindle speed and feed rate) had the largest effect on kenaf composite to laminate, followed by A (spindle speed) and B (feed rate). The graphs of F_d versus A, B, and AB interaction are plotted in Figure 2, Figure 3, and Figure 4, respectively.

Table 3 ANOVA result of delamination factor (F_d) using 2FI Design

Source	Sum of squares	Degree of freedom	Mean square	F-value	p-value Prob>F
Model	0.012	4	2.957E-003	20.75	0.0012
A-spindle speed	2.319E-003	1	2.319E-003	16.27	significant 0.0068
B-feed rate	2.622E-004	1	2.622E-004	1.84	0.2237
C-depth of cut	1.157E-003	1	1.157E-003	8.12	0.0292
AB	8.090E-003	1	8.090E-003	56.78	0.0003
Curvature	3.456E-003	1	3.456E-003	24.26	0.0026 significant
Residual	8.549E-004	6	1.425E-004	-	-
Lack of Fit	4.073E-004	3	1.358E-004	0.91	0.5300
Pure Error	4.476E-004	3	1.492E-004	-	Not significant -

ANOVA analysis using Central Composite Design of delamination factor (F_d)

Table 5 ANOVA result of delamination factor (F_d) using Central Composite Design

Source	Sum of squares	Degree of freedom	Mean square	F-value	p-value Prob>F
Model	0.0145	3	0.0048	10.99	0.0005
A-Spindle speed	0.0043	1	0.0043	9.67	significant 0.0072
B-Feed rate	0.0021	1	0.0021	4.86	0.0435
AB	0.0081	1	0.0081	18.43	0.0006
Residual	0.0066	15	0.0004	-	-
Lack of fit	0.0059	11	0.0005	3.21	0.1357
Pure of error	0.0007	4	0.0002	-	Not significant -
Cor Total	0.0227	19	-	-	-

After obtaining the experimental result using CCD, ANOVA test was conducted again to determine the significance of the three factors and the significance

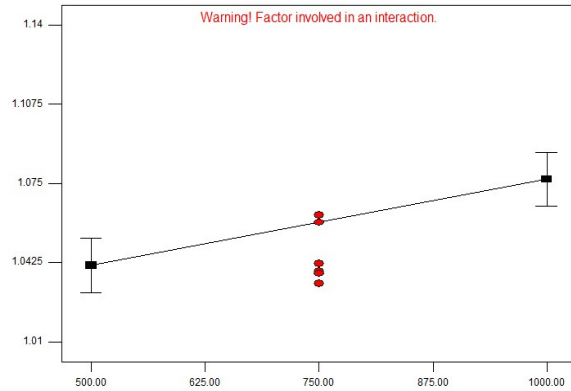


Fig. 2 Effect of A (Spindle speed) for delamination factor (F_d)

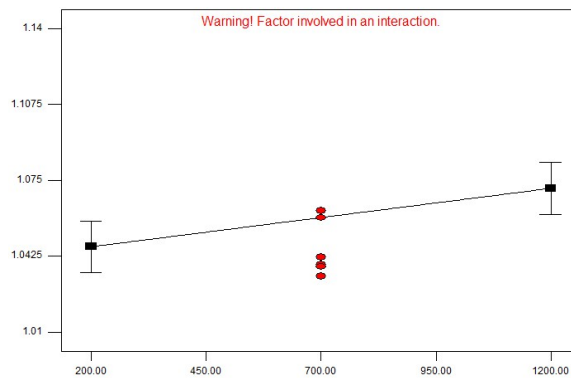


Fig. 3 Effect of B (Feed rate) for delamination factor (F_d)

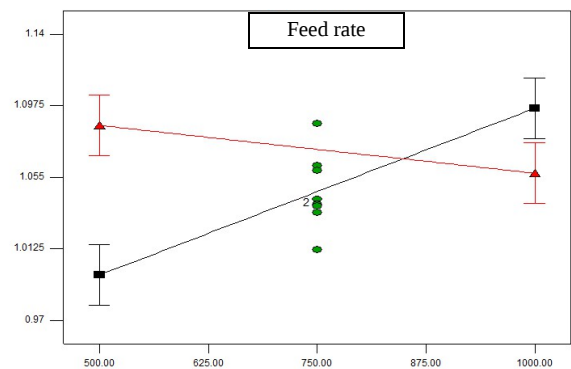


Fig. 4 Effect of AB (Spindle speed and Feed rate) interaction for delamination factor (F_d)

Figure 2 shows the effect of spindle speed on F_d , where F_d increased slightly with the increase of spindle speed at feed rate of 700 mm/min

and depth of cut of 2 mm. F_d decreased for lower spindle speed. This phenomenon is caused by the vibration of the cutting tool with high spindle speed during milling process. With large vibration, high F_d is produced on top of the ductile composite materials laminated. Besides, high feed rate (Figure 3) produced high F_d . Spindle speed and depth of cut remained in the middle range.

In Figure 4, the depth of cut maintained at 2 mm, where the red line indicates the high level of feed rate (1200 mm/min) and the black line indicates the low level of feed rate (200 mm/min). It can be clearly observed that low feed rate (200 mm/min) with high spindle speed will produce the worst delamination factor. A good F_d will be produced using lower feed rate (200 mm/min) with lower spindle speed. Davim et al. shared the same viewpoint that high cutting (spindle) speed caused great damage on glass fiber reinforced plastic composites during machining [19]. The non-linear relationship between the feed rate and F_d might be caused by opposite milling to the orientation of kenaf fiber. The results obtained might be less accurate if all the specimens are not milled in the direction of orientation of fiber. In addition, previous researchers concluded that low feed rate causes small damage on composites [8], [15].

Optimum parameter and modeling equation for optimization of delamination factor

The second order modeling equation for optimization of milling parameters on minimizing delamination factor (F_d) is shown in (1).

$$F_d = 0.85466 + 2.492 \times 10^{-4} A + 2.163 \times 10^{-4} B - 2.55 \times 10^{-7} AB \quad (1)$$

Where

A= spindle speed (rpm)

B= feed rate (mm/min)

C= depth of cut (mm) in terms of actual value.

Table 6 Optimum parameter and conformation test for delamination factor (F_d)

Spindle speed (rpm)	Feed rate (mm/min)	Depth of cut (mm)	Calculated F_d	Measured F_d	Percentage error (%)
530	310	2	1.012	1.032	1.93

Table 6 shows the percentage error between calculated (F_d) using the equation (1) and the measured F_d . The measured (F_d) was located at the prediction range (0.96 - 0.06) and the percentage error was only 1.93% which proved the modeling equation and the suggested optimum parameters can be accepted.

CONCLUSION

The suggested optimum milling parameters in this research for the minimization of F_d were 530 rpm of spindle speed, 310 mm/min of feed rate, and 2 mm of depth of cut. For the optimization of delamination, the curvature shown in ANOVA after the 2^3 factorial design of experiment was significant. This enabled the utilization of RSM with CCD approach that requires more experimental runs to collect data for constructing a second-order modeling equation. CCD approach was selected and eight additional experimental runs were added. Low spindle speed and low feed rate caused less delamination on milled kenaf composites. In addition, with deeper depth of cut, the possibility of delamination can be reduced.

ACKNOWLEDGMENTS

Machine shop, laboratory facilities and their staff at the Faculty of Engineering and Built Environment of Universiti Kebangsaan Malaysia are gratefully acknowledged. Thanks to the Ministry of Higher Education Malaysia for supporting this project under the grant LRGS/TD/2012/USM-UKM/PT/05.

REFERENCES

- [1] Ho, M., J.H. Lee, C. Ho, K. Lau, J. Leng, D. Hui and H. Wang, 2012. "Critical factors on manufacturing processes of natural fiber composite," *Compos. Part B*, 3549–3562.
- [2] R. M. Rowell, "A new generation of composite materials from agro-based fiber," in *Proceedings of the 3rd International Conference on frontiers of polymers and advanced materials*, 1995, pp. 659–665.
- [3] P. Wambua, J. Ivens, and I. Verpoest, "Natural fibres : can they replace glass in fibre reinforced plastics?," *Compos. Sci. Technol.*, vol. 63, pp. 1259–1264, 2003.
- [4] B. F. Yousif, A. Shalwan, C. W. Chin, and K. C. Ming, "Flexural properties of treated and untreated kenaf / epoxy composites," vol. 40, pp. 378–385, 2012.
- [5] S. R. Schmid and S. Kalpakjian, *Manufacturing Engineering and Technology*, 6th ed. New Jersey: Prentice Hall, 2009, pp. 172, 216–226, 662, 662–668.
- [6] K. K. Chawla, *Composite Materials*. New York, NY: Springer New York, 2012, pp. 81–83.
- [7] N. A. K. Hafizah, M. W. Hussin, M. Y. Jamaludin, M. A. R. Bhutta, M. Ismail, and M. Azman, "Tensile behaviour of kenaf fiber reinforced polymer composites," *J. Teknol.*, vol. 3, pp. 11–15, 2014.
- [8] G. D. Babu, K. S. Babu, and B. U. M. Gowd, "Effect of machining parameters on milled natural fiber-reinforced plastic composites," *J. Adv. Mech. Eng.*, pp. 1–12, 2013.
- [9] N. Abilash and M. Sivapragash, "Optimizing the delamination failure in bamboo fiber reinforced polyester composite," 2013.
- [10] Ö. Erkan, I. Birhan, A. Çiçek, and F. Kara, "Prediction of Damage Factor in end Milling of Glass Fibre Reinforced Plastic Composites Using Artificial Neural Network," 2012.
- [11] J. Davim, J. Rubio, and A. M. Abrao, "A novel approach based on digital image analysis to evaluate the delamination factor after drilling composite laminates," *Compos. Sci. Technol.*, vol. 67, no. 9, pp. 1939–1945, Jul. 2007.
- [12] M. Ramulu, D. Arola, and K. Colligan, "Preliminary investigation on the surface Integrity of fiber reinforced plastics," *Am. Soc. Mech. Eng. Pet. Div.*, vol. 64, no. 2, pp. 93–101, 1994.
- [13] K. Palanikumar, "Modeling and analysis for surface roughness in machining glass fibre reinforced plastics using response surface methodology," *Mater. Des.*, vol. 28, no. 10, pp. 2611–2618, Jan. 2007.
- [14] J. P. Davim, P. Reis, and C. Conceição António, "A study on milling of glass fiber reinforced plastics manufactured by hand-lay up using statistical analysis (ANOVA)," *Compos. Struct.*, vol. 64, pp. 493–500, 2004.

- [15] H. Hocheng, H. Y. Puw, and K. C. Yao, "Experimental aspects of drilling of some fiber-reinforced plastics," in *Proceedings of the Machining of Composites Materials Symposium*, 1992, pp. 127–138.
- [16] J. Davim, J. Rubio, and A.M. Abrao, "A novel approach based on digital image analysis to evaluate the delamination factor after drilling composite laminates," *Compos. Sci. Technol.*, vol. 67, no. 9, pp. 1939–1945, Jul. 2007.

EMBEDDED INTELLIGENCE FOR QUALITY OF SERVICE-BASED VERTICAL HANDOVER MANAGEMENT IN SEAMLESS WIRELESS NETWORKS

Sunisa Kunarak

Department of Electrical Engineering, Srinakharinwirot University, Nakhonnayok, Thailand 26120

Email: sunisaku@g.swu.ac.th

ABSTRACT

This paper presents the development and hardware implementation of the hybrid artificial neural networks that is included learning vector quantization (LVQ) and radial basis function (RBF) for the vertical handover decision algorithm in order to keep the always best connected (ABC) ubiquitous wireless networks. The LVQ is unsupervised learning and also the RBF is appropriate the non-linear data decision. The proposed approach is based on the merit function as the received signal strength indicator, bandwidth requirement, mobile speed and monetary cost of service to consider using field programmable gate arrays (FPGAs) logical architecture design. Additional, the hybrid architecture describes in VLSI hardware description language (VHDL). WCDMA, Advanced LTE and WLAN are cooperated topology in the experimental. The experimental results are depicted a high correlation with the hybrid artificial neural networks that is simulated by MATLAB and can increase the computation speed compared with the standard personal computer (PC) thus FPGA is suitable in the real world situations as the non-real time and real time applications for the future wireless communication system.

Keywords: Embedded, Field Programmable Gate Array, Quality of Service, Vertical Handover, Wireless Networks

INTRODUCTION

Artificial neural networks (ANNs) have been studied widely over many years. One of the most popular with ANNs is the radial basis function neural network (RBFNN) [1] that is suitable the non-linear data but this algorithm does have to use the large information. Additionally, the artificial neural networks are the mathematical model that is inspired the functioning of the human brain. It can be utilized in classification, clustering, prediction, control system, recognition problems and so on [2]-[5]. In this paper, the hybrid artificial neural networks includes the learning vector quantization (LVQ) and radial basis function (RBF) that is used for the vertical handover decision since this algorithm is appropriate the small to medium information and can support the non-linear data that is proper the non-real time and real time applications for the fifth generation (5G) wireless networks as the future communications.

Nowadays the wireless mobile devices such as smartphones or tablets need to access the internet at anywhere and anytime. When the mobile terminals can connect the same network is also known the horizontal handover (HH) procedure; on the other hand, the mobile terminals can connect the different networks or technologies as the vertical handover (VH) procedure. The VH procedure is supported the increasing complexing of the wireless networks in heterogeneous scenarios furthermore the quality of

service (QoS) parameters are the indicator of the effective heterogeneous networks (HetNets), respectively.

The remainder of this paper is structured as follow. Section II, the hybrid artificial neural networks approach based on FPGA for vertical handover decision is depicted. Finally, the experimentation results and conclusion are discussed in Section III and IV, respectively.

HYBRID ARTIFICIAL NEURAL NETWORKS APPROACH BASED ON FPGA FOR VERTICAL HANDOVER DECISION

The hybrid artificial neural networks (Hybrid ANNs) consist of the learning vector quantization (LVQ) that is based on the competitive layer and the radial basis function (RBF) layer i.e. the Gaussian distribution function neural networks as shown in Fig. 1. The Kohonen presents the LVQ owing to the classification method the same way as the competitive layer of cluster with Self-Organizing Map (SOM) also known as unsupervised learning while the RBF is the technique of training by descent gradient algorithm with updated the weights and centers of learning. Firstly, the competitive layer is the distance learning as follow [6]-[8]. The distance learning is based on the Euclidean distance that is measured to adaptive during the training data sets i.e. received signal strength indicator (RSSI), bandwidth

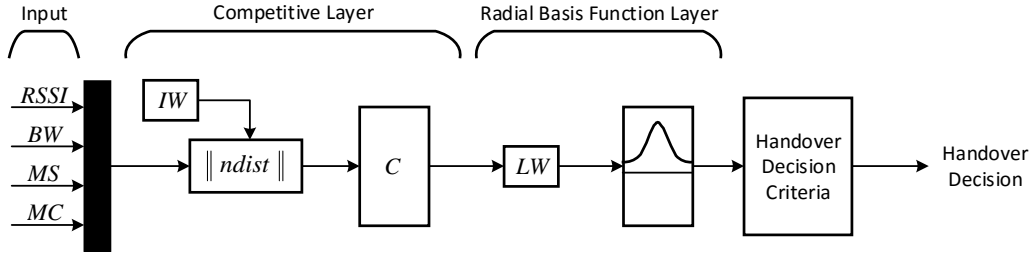


Fig. 1 Hybrid artificial neural networks for vertical handover decision.

(BW), mobile speed (MS) and monetary cost (C) metrics as Eq. (1)

$$d^{\Lambda}(\mathbf{w}, \mathbf{x}) = (\mathbf{x} - \mathbf{w})^T \Lambda (\mathbf{x} - \mathbf{w}) \quad (1)$$

where $\mathbf{x} = (x_1, \dots, x_D) \in \mathcal{R}^D$ is the input samples with D dimensional. Also, the $y_i \in \{1, \dots, C\}$; $i = 1, \dots, N$ is the sample labels, and C is the number of classes. The Λ is a full $D \times D$ matrix size and must be the positive definite and the \mathbf{w}_i is defined as the receptive field of training patterns as

$$R_{\Lambda}^i = \{\mathbf{x} \in \mathbf{X} | \forall \mathbf{w}_j (j \neq i) \rightarrow d^{\Lambda}(\mathbf{w}_i, \mathbf{x}) \leq d^{\Lambda}(\mathbf{w}_j, \mathbf{x})\} \quad (2)$$

The arbitrary Euclidean distance in Eq. (1) is reduced to Eq. (3) when the Λ is ignored to being diagonal matrix and use instead with the Gaussian distribution function learning in the radial basis function neural networks layer

$$d^{\lambda}(\mathbf{w}, \mathbf{x}) = \sum_{j=1}^D e^{-\frac{(x_j - w_j)^2}{2\lambda_j^2}} \quad (3)$$

Hybrid Artificial Neural Networks for Vertical Handover Decision

The hybrid ANN has been programmed in VLSI hardware description language with the objective of allowing its portability to any processing environment for mobile device. In this case, it has been successfully tested on an embedded processor based on a small and low power FPGA device. Additionally, the hybrid ANN is operated procedure that is depicted in Table 1.

Hardware Evaluation of Hybrid Artificial Neural Networks

Field programmable gate arrays (FPGAs) have been promoted in many applications such as wireless

Table 1 Pseudo-code of proposed algorithm

Hybrid Artificial Neural Networks Approach

- 1: Collect the handover metrics: RSSI, BW, MS, C
- 2: Generates the initial hybrid artificial neural networks-
- 3: in order that the handover occurs or not?
- 4: **if** handover factor > 0.6 then
- 5: Handover initiation process ++
- 6: **else**
- 7: Dropped call ++
- 8: **end if**
- 9: Obtain the number of handover
- 10: Obtain the number of dropped call

communications, data processing, and etc [9]-[10]. The FPGAs consist of the three fundamental components as the logic blocks, interconnection resources and I/O cells in order to achieve configurability. In this paper, the cmod A7-35T breadboardable artix-7 FPGA module is used because it is the same look like a mobile device. In addition, there is a small and the breadboard friendly has 48-pin DIP form factor board built around a Xilinx Artix-7 FPGA. The board also includes a USB-JTAG programming circuit, USB-UART bridge, clock source, Pmod host connector, SRAM, Quad-SPI Flash, and basic I/O devices. These components make it a formidable, albeit compact, platform for digital logic circuits and MicroBlaze embedded soft-core processor designs using Xilinx's development software as Vivado as shown in Fig. 2.



Fig. 2 Platform of cmod A7-35T breadboardable artix-7 FPGA module.

EXPERIMENTAL RESULTS

In the experimentation, the handover decision is performed by a mobile terminal (MT) that is adopt the mobile-controlled handover (MCHO) strategy.

Moreover, this section is divided into 3 sub-sections as experimental structure, experimental parameters and performance analysis, respectively.

Experimental Structure

The heterogeneous wireless networks cooperate with Wide-band Code Division Multiple Access (WCDMA), Long Term Evolution (LTE) and Wireless Local Area Network (WLAN) as illustrated in Fig. 3. The coverage areas of WCDMA, LTE and WLANs are equal to 2,500 meters, 1,000 meters and 35 meters, respectively. The tightly and loosely coupled are interworked in the seamless wireless topology. WLAN and LTE are connected to WCDMA core network via radio access network in tightly coupled type. In the other hand, the WLAN and LTE can access the IP network without connecting to WCDMA. Thus, the loosely coupled type is introduced in the proposed algorithm since its coupling provides a flexible and an independent environment due that this scheme is based on mobile IP (MIP) [11].

The user preferences and network characteristics are different therefore the handover decision criteria in the proposed approach is different together. Such as, the real time applications (e.g. video conference), handover should be performed as rapid as possible in order to minimize the delay. On the contrary, the amount of data transmission is more important than the delay so that the handover criteria for non-real time service is to attempt to connect WLAN/LTE as long as possible due to higher data rate.

Experimental Parameters

The correspondent node (CN) generates the constant bit rate (CBR) multimedia traffic using a 64-byte packet size is sent every 0.1 second and user datagram protocol (UDP) is the transport protocol applied between the networks that includes the detection of the new networks and the allocation of new IP address. The experimental parameters of WCDMA, LTE and WLAN are utilize as depicted in Table 2.

Performance Analysis

The experimental, the average arrival rate of new calls is fixed at 10 calls/sec and average call holding time is equal to 180 sec. The user's speed is a uniform distribution as equal to 1-30 m/s and user movement is modeled as the random waypoint mobility in 6,000 x 6,000 sq.m topology size for each speed. The hybrid ANN can decrease the number of handover since this proposed method brings the benefit of self-organizing map and radial basis function that is suitable the non-linear data communication namely the Gaussian

distribution as demonstrated in Fig. 4. Also, the number of dropped call refers to the unsuccessful handover call causes the mobile node to be disconnected and is the fewest by using hybrid ANN as illustrated in Fig. 5.

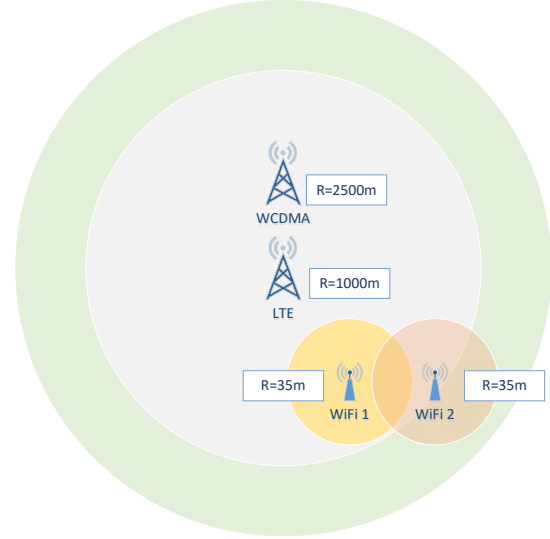


Fig. 3 Heterogeneous wireless networks structure.

Table 2 Summary of the experimental parameters

Parameters	WCDMA	LTE	WLAN
Frequency (GHz)	2.1	2.6	2.4
Coverage area (m)	5000	1000	100
Transmission power (w)	1.0	0.5	0.1
Bit rate (Mbps)	0.384	35	54
Latency (ms)	35	25	3
Mobile speed (m/s)	80	130	5
Bit error rate (per 10 ⁸)	50	100	200
Monetary cost rate	0.8	0.7	0.4

In another experimental, the execution time displays the time needed by the FPGA and PC implementation as shown in Fig. 6. Figure 6 indicates the algorithm is nearly executed with the constant number of neurons when compares with the PC although increases almost linearly as the number of neurons in the approach increases.

CONCLUSION

The hybrid artificial neural networks are used the received signal strength indicator, bandwidth requirements, mobile speed and monetary cost as the multi-criteria factors in order to the vertical handover decision. The experimental results indicate the proposed approach that outperforms another

algorithm as reducing the unnecessary handover and dropping call, respectively. Correspondingly, the execution time is independently the number of neurons.

ACKNOWLEDGEMENTS

This research was supported by the research grant (No. 582/2559) from Srinakharinwirot University revenue 2559, for the 2559 fiscal year.

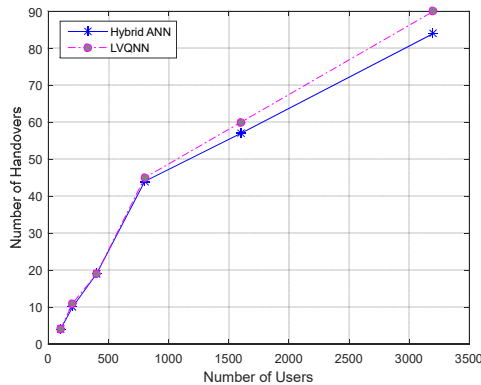


Fig. 4 Number of users and number of handovers.

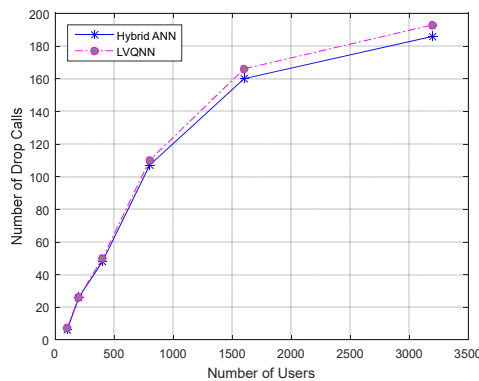


Fig. 5 Number of users and number of drop calls.

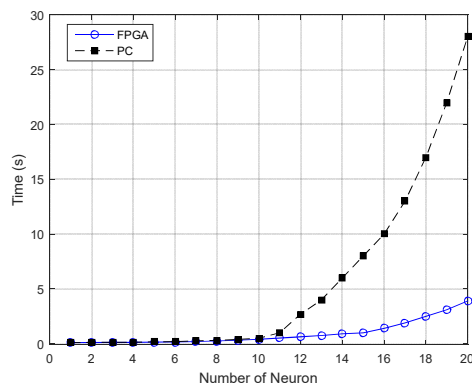


Fig. 6 Number of neuron and execution time.

REFERENCES

- [1] Renteria-Cedano J. A., Aguilar-Lobo L. M., Loo-Yau J. R. and Ortega-Cisneros S., Implementation of a NARX Neural Network in a FPGA for Modeling the Inverse Characteristics of Power Amplifiers, IEEE 57th International Midwest Symposium on Circuits and Systems, 2014, pp. 209-212.
- [2] Zamorano F. O., Jerez J. M., and Franco L., FPGA Implementation of the C-Mantec Neural Network Constructive Algorithm, IEEE Transactions on Industrial Informatics, Vol. 24, No. 2, 2014, pp. 1154-1161.
- [3] Gómez I., Franco, L. and Jerez J., Neural Network Architecture Selection: Can Function Complexity Help?, Neural Process. Letters, Vol. 30, Issue 2, 2009, pp. 71-87.
- [4] Hunter D., Hao Y., Pukish, Kolbusz J. and Wilamowski B., Selection of Proper Neural Network Sizes and Architectures—A Comparative Study, IEEE Transactions on Industrial Informatics, Vol. 8, No. 2, 2012, pp. 228-240.
- [5] Lakshmi K. and Subadra M., A Survey on FPGA based MLP Realization for On-Chip Learning, International Journal of Scientific & Engineering Research, Vol. 4, Issue 1, 2013, pp. 1-9.
- [6] Nova D. and Estévez P. A., A Review of Learning Vector Quantization Classifiers, Neural Computing and Applications, Vol. 25, 2014, pp. 511-524.
- [7] Yang W. A., Monitoring and Diagnosing of Mean Shifts in Multivariate Manufacturing Processes Using Two-Level Selective Ensemble of Learning Vector Quantization Neural Networks, Journal of Intelligent Manufacturing, Vol. 26, Issue 4, 2015, pp. 769-783.
- [8] Ortiz-Bayliss J. C., Terashima-Marin H. and Conant-Pablos S. E., Learning Vector Quantization for Variable Ordering in Constraint Satisfaction Problems, Pattern Recognition Letters, Vol. 34, Issue 4, 2013, pp. 423-432.
- [9] Liu Q., Gao M. and Zhang Q., Knowledge-Based Neural Network Model for FPGA Logical Architecture Development, IEEE Transaction on Very Large Scale Integration (VLSI) System, Vol. 24, No. 2, 2016, pp. 664-677.
- [10] Tisan A. and Chin J., An End-User Platform for FPGA-Based Design and Rapid Prototyping of Feedforward Artificial Neural Networks with On-Chip Backpropagation Learning, IEEE Transaction on Industrial Informatics, Vol. 12, No. 3, 2016, pp. 1124-1133.
- [11] Nithyanandan L. and Parthiban I., Seamless Vertical Handoff in Heterogeneous Networks Using IMS Technology, IEEE International Conference on Communications and Signal Processing, 2012, pp. 32-35.

GREEN CARGO MOVEMENT, LOCALITY: MEKONG

Leonard Johnstone¹, Vatanavongs Ratanavaraha²

^{1,2}Suranaree University of Technology, 111 University Avenue, Suranaree Sub-district, Muang District,
NakhonRatchasima 30000, Thailand

Email for correspondence: vatanavongs@g.sut.ac.th

ABSTRACT

There is an issue in the identification of commonality across several localities associated with the problem of cargo movement via modes of transport other than road. The approach in this paper considers movement from the locality of the multi jurisdiction of the Mekong Region, an agglomeration of Myanmar, Thailand, Laos, Vietnam, Cambodia and southern China. A mathematical approach was developed to analyze the impact of cargo movement away from the road transport sector to greener alternative rail mode. The analytical appreciation is considered from the review of large scale cargo movement across the region. Results from the data analysis are indicative of an environmentally friendly or a green freight alternative. The mathematical model described in this paper is used to consider freight modal shifts under various infrastructure development scenarios. The outcome from the analysis results is the input into ongoing research to identify common mathematical functions across other jurisdictions. The conclusion is that there is a likelihood that common mathematical procedures are applicable in several localities.

Keywords: Mekong, GDP, Cargo, Mode

INTRODUCTION

The Mekong region in this context is defined to include seven localities namely the nation states of Myanmar, Thailand, Lao People's Democratic Republic (PDR), Cambodia, Vietnam and the two southern provinces of Guangxi and Yunnan within the People's Republic of China (PRC). The extent of the major infrastructure network is presented in Fig 1. The focus of this paper is the modal analysis of cargo or freight movement throughout the Mekong.

Within the any region, the transport mode of cargo transport by road is an essential factor in economic activity and has historically played a strong role in the development for many areas across the globe. In many regions and countries with a single jurisdiction, there is growing trend to develop strategies that move away from the dominance of cargo transport by road toward alternative environmental friendlier modes.

In a broader world context, almost all cargo movements are dependent on road transport. In for example, even in the European Union as reported in an earlier report [1], cargo movement in 2009 was dominated by the road sector. The road modal share for any of the major country members did not fall below sixty percent. This was true even in the case of Germany where twelve percent of cargo moves via the mode of inland water.

In France, the cargo modal share is eighty percent increasing to eighty five percent in the United Kingdom. Whilst the modal share in Italy is just over ninety percent. Thus, even in the context of the developed European Union cargo movement, road transport is the most significant mode. This dominance of the road sector makes it difficult to realize the objective of the European Union to reduce the dependence on road transport.

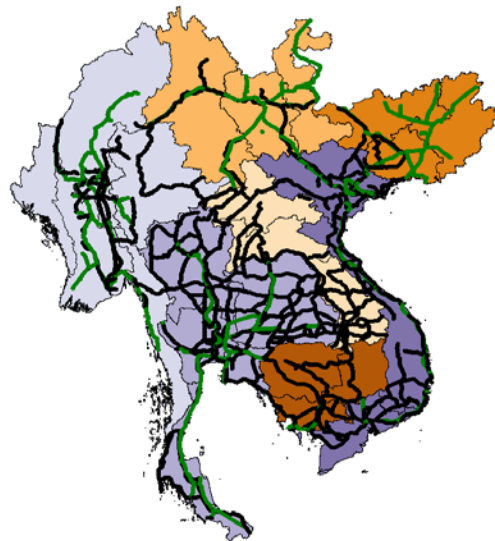


Fig. 1 The Mekong Region.

The Agenda 2020 of the European Union calls for member countries to reduce greenhouse gas emissions. There is implicit in this agenda within the Union the desirability of taxing fuels on road based transport, [2] thus encouraging by financial incentives a modal shift away from the dominant road sector. The Union is providing incentives towards a greener movement of freight with consequently fewer greenhouse emissions which in essence is to reduce the road component of cargo movement following the Paris Agreement on Climate Change [3] and [4]. This of course leads to the need of improving the alternatives to cargo movements by road.

THE REGIONAL SITUATION

There are two parts in the understanding of regional cargo movement namely the movement infrastructure, the transport supply and the actual amount and nature of cargo movement on the network, the demand side.

Within the framework of the regional transport network for the Mekong assembled as part of this research in the development of an analytical transport modelling tool, the primary regional road network identified as depicted in the earlier Fig. 1 is some 37,000 kilometers in length. The identified rail network is of some 17,000 kilometers in length. The length of the rail network is thus some 34% of the major transport corridor by comparison in length. There is a significant regional rail network although there are some missing connections between the earlier defined seven localities within the Mekong.

In addition to the land transport network, there is a further 10,000 kilometers each of Inland Waterway Transport(IWT) and Coastal Shipping or Sea Mode included in the transport network. For the movement of people an extensive air transport network is incorporated into the overall network framework.

The cargo road mode of transport is often driven by the lack of high quality alternatives. In the understanding of the cargo transport demand today and that of the future, the key inputs are the macro economic indicators. These indicators reflect the overall development of each of the seven locality and the propensity for cargo movement.

Historical Activity Levels

Between 1998 and 2014, the Gross Domestic Product (GDP), as measured in constant US dollars in the base year of 2010 at market prices has grown at an overall of 8.6% per annum. The regional population has grown at 0.8% per annum. As depicted in Table 1, there is differential growth by locality with Myanmar registering the highest growth in GDP closely following by the two Chinese provinces. Thailand which is starting at a higher level of GDP also registers significant economic growth over this

period.

Population growth is seen as the higher in the two larger population localities of Cambodia and Vietnam. The Lao PDR has the highest historical population growth albeit from a lower base.

The noted differential growth rates in the future are likely to lead to changes in the distribution of GDP Use at most three levels of headings that correspond to chapters, sections and subsections.

Table 1 Locality growth per annum 1998 - 2014

Locality	GDP	Population
Cambodia	10.1%	1.4%
Guangxi, PRC	12.4%	0.1%
Yunnan, PRC	11.3%	0.9%
Lao PDR	9.7%	2.1%
Myanmar	13.4%	0.8%
Thailand	6.3%	0.7%
Viet Nam	8.6%	1.1%

Associated environmental concerns

The continued movement of cargo via the road mode especially over long distances will also lead to a continued increase in emission gases. This is not in alignment with the overall Paris environmental agreement. Whilst to some degree, such emissions from within cities for personal mobility have been contained. This is not the case for the movement of cargo especially over long distances. Within the context of another large jurisdiction namely Egypt [5], the use of the road-based transport mode has increased exponentially in the last few years.

Whilst this phenomenon has fulfilled a variety of economic goals and expectations, unfettered growth is increasingly contributing to various negative environmental impacts. This high level of usage in Egypt is a historic consequence of pricing policies (such as the fuel subsidy), and "road focused" capital works programs. There is a beginning of an understanding of the notion that a more balanced approach to providing cargo mobility is desirable especially in respect to the transportation of cargo within the borders of Egypt.

For example, in another large country jurisdiction such as Australia, over the period 1990 to 2006, overall transport emissions grew by 27.4 per cent, however emissions from the movement of freight grew by 40 per cent. Freight transport emissions now contribute around four per cent of the national emissions total throughout the country and are forecast to more than treble to thirteen per cent by 2020 as reported in a recent freight transport review paper [6].

METHODOLOGY

The most commonly used tool for understanding the movement of people or cargo throughout a defined geographical space is a transport model, [7] and [8]. A classic four step transport model is developed as the analytical tool for the examination of cargo movement through the region. The structure for understanding movement within the Mekong is built initially from the understanding the existing regional movement.

Of course, cargo movement does not happen in isolation. The four-step procedure is followed both for the movement of cargo and people as depicted in Fig. 2. In the final step, the network assignment combines all movement across all transport network infrastructure. In fact, the performance of the road network is defined by both the movement of people and cargo.

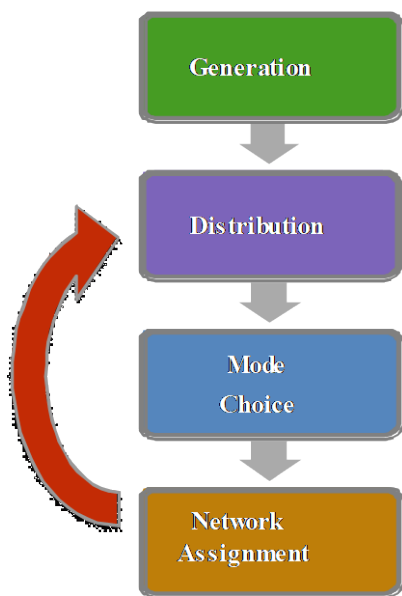


Fig. 2 The regional model structure.

Data Preparation

The base input data are a collation of databases available by locality held by the various responsible agencies throughout the region. The master transport network includes all known transport projects at present, both existing and proposed, that are incorporated into a master network with the potential opening year of any new project provided as a network parameter. At the same time the economic and population datasets are prepared for the base time horizon of 2015 and a future time horizon of 2050.

The data is prepared in detail at the level of traffic analytical zone that correspond to administrative boundaries with the amalgamation of smaller administrative areas into a single traffic zone.

The zone system adopted for model is the same as that for the earlier 2006 GMS Transport Sector

Strategy Study[9]. Within the two provinces of China there are 30 zones. In Myanmar, there are 40 zones whilst Thailand has a total of 56 zones. There are 17 zones and 24 zones in Lao PDR and Cambodia respectively. Finally, Viet Nam has 49 zones. Thus, the model has a total of 216 internal zones. The total number of zones is 254 including 38 external zones of which 30 of the externals represent seaports.

The Key Inputs – the Drivers of Future Demand

The two planning inputs, drivers of future cargo movements are the regional GDP and the population. The future economic and population projections are based on trend data except for Thailand[10], Myanmar[11] and Vietnam[12]. In these three localities, the economic and population projections were derived from the national transport databases.

Regional GDP distribution

The Mekong wide GDP is projected to increase at 6.2% per annum until the year 2025 and estimated to grow at 5% per annum thereafter until 2050. These overall projected growth rates are in line with earlier detailed historical growth rates[13] as well as those available from national transport databases. The key important change in the future is the forecast distribution balance of GDP. As earlier noted, the differential locality growth rates predict a change in regional economic distribution.

In 2015, as depicted in Fig 3., Thailand has nearly 40% of regional GDP. This is projected to decrease to under 20% by 2050. This share of GDP is transferred to the two Chinese provinces and Myanmar by 2050. By 2050, the two Chinese provinces are projected to increase their share of overall GDP by 15% from an initial 39% to 54% whereas Myanmar will increase its share of regional GDP from 7% to 10%. The remaining localities of Lao People's Democratic Republic (PDR), Cambodia, Vietnam are expected to maintain approximately their existing share of GDP.

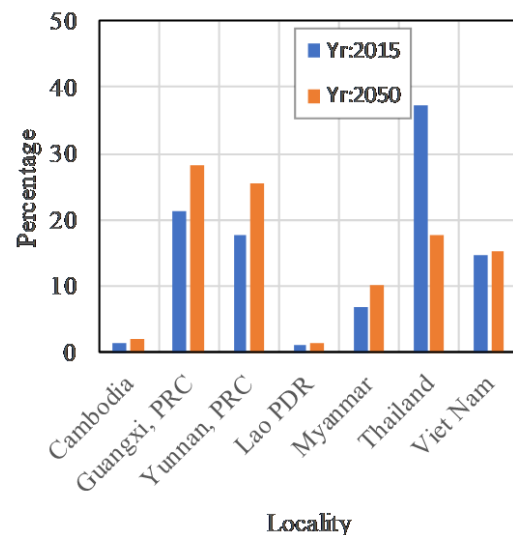


Fig. 3 Distribution of GDP by locality.

Regional population Distribution

The regional population is projected to increase at 0.8% over the overall time horizon between 2015 and 2050. Between 2015 and 2050, the regional population is anticipated to grow from 340 million to some 453 million people thus forming a potentially significant trading block. The regional population distribution is depicted in Fig 4.

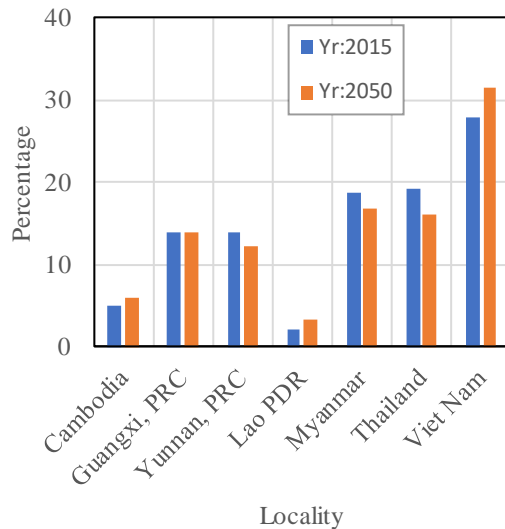


Fig. 4 Distribution of Population by locality.

Unlike GDP, the population distribution is unlikely to change significantly. The regional population share of Viet Nam increases from 28% to 32%. The regional population share of Thailand decreases by approximately three percent. The change in distribution in all other localities is less than 2%.

Impact of Distribution Change

The change in distribution between localities is important because such change will impact the likely future pattern exchange of cargo movement between the localities.

The Structure of Cargo Movement

For the analysis of cargo movements, the key modes represented within the model are road, rail, inland waterways transport and coastal shipping. The model developed is known as the Mekong Regional Transport Model henceforth referred to simply as the MRTM.

Cargo movement is divided into 5 commodity classifications. The MRTM was developed to produce forecasts of passenger and 5 categories of cargo movement by mode for the time horizons of the base year of 2015 and two future horizons of 2025 and 2050.

The parameters in the equations vary by locality and commodity group. The five commodity groups were summarized based on the international Harmonized System codes also referred to as simply the HS codes. These codes are an internationally standardized system of names and numbers to identify an individual product. The code is an 8-digit number but broad classifications are developed using the first two digits of the code.

Broadly the five commodity categories in numerical order one through to five are agriculture, processed food, wood products, chemicals and miscellaneous goods. The link of the five commodity categories to the Harmonized System of coding is presented in Table 2 which tabulates the first two-digits of the HS code against the commodity category.

Table 2 Cargo commodity category

Category	Description	HS Code	
		Start	End
1	Agricultural	1	15
2	Processed Food	16	24
3	Chemical/Mineral	25	40
4	Wood/Skins	41	49
3	Chemical/Mineral	50	63
4	Wood/Skins	64	67
5	Miscellaneous	68	97

THE ANALYSIS

The focus of this research as stated earlier is on the modal allocation and the key input parameters namely the population and GDP. However, prior to the modal allocation step, there are the two earlier steps associated with trip generation and distribution of cargo movement. Cargo movement generations are estimated by traffic zone via a relationship linking population and GDP per capita in a series of linear regression equations derived for each locality separately.

Cargo trip distribution used the Fratar growth factor distribution method [14] that takes as a base an existing distribution patterns sourced from an earlier Mekong study [9]. The trip distribution is across all localities so that there are not separate trip distribution procedures via locality.

For the mode split step, the commodity movement cost and travel times are the key inputs into the freight mode split model. The mode split structure for freight is a hierarchical three-level mode split logit model as depicted in Fig 5. The total cargo trips were distributed across four modes. At the first level, coastal trips are separated while at the second level, inland water transport trips are separated, with the final level being the allocation of movement between road and rail. In many cases, the mode choices were limited to road and rail since there was

no logical route via other modes.

The MRTM's master transport network includes all known transport projects at present, both existing and proposed, that are incorporated into a master network with the potential opening year of any new project provided as a network parameter. In this manner, there is an inbuilt flexibility as it is actual possible to develop the network other than for the two future time horizons of 2025 and 2050.

The structure of the binary logit equations is shown in Eq. 1.

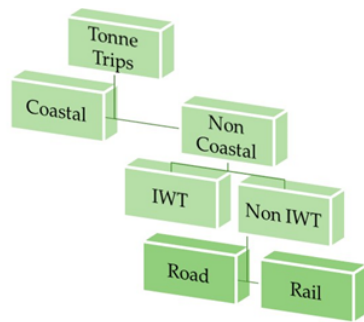


Fig. 5 Modal Allocation Structure

The cost of travel on alternative modes is referred to as the generalized cost of travel and is a function of time and cost.

$$P_1 = \frac{\exp^{V_1}}{\exp^{V_1} + \exp^{V_2}} \quad (1)$$

Equation (1) defines the probability of using mode 1 as opposed to mode 2 whereas V_1 and V_2 are the generalized travel costs associated with modes 1 and 2 respectively.

The variables in the determination of generalized travel cost namely travel time and the cost are weighted by scale factors. These scale factors are presented in Table 4 by commodity category for each level of the modal analysis. The cost of travel by the various modes of travel was determined by locality.

The final step was the assignment or the allocation of the flow of people and freight to air, road, rail, inland waterway and coastal shipping networks. The final network travel times across the road network were estimated following a capacity restrained assignment.

In the case of the road network, the movement of persons by car and bus were converted into equivalent passenger car units together with the cargo-carrying trucks on the network. The impact of person and cargo trips were combined in consideration of the impact on the shared road network.

It was necessary to convert cargo movements allocated to road network into vehicles via load factors. The remaining freight trips do not use the

road network except for access to the non-road network (e.g. truck to rail).

In the case of truck trips there was also an implied back loading factor to allow for trucks returning from their destination without any load. The non-road trips are then assigned to their respective networks such as rail. This results in a final network that represent travel across all modes.

Table 4 Scale factors by commodity category

Category	Equation Level	Time	Cost
1	1	-0.2244	-0.0001
2	1	-0.0004	-0.0004
3	1	-0.0858	-0.0004
4	1	-0.0355	-0.0004
5	1	-0.0355	-0.0004
1	2	-0.0194	-0.0001
2	2	-0.0387	-0.0004
3	2	-0.0732	-0.0006
4	2	-0.0169	-0.0004
5	2	-0.0173	-0.0001
1	3	-0.3892	-0.0008
2	3	-0.2078	-0.0003
3	3	-0.176	-0.0008
4	3	-0.5941	-0.0034
5	3	-0.5891	-0.0006

Passenger vehicles and trucks share the road networks. For the traffic movements assigned to the road network, there is a feedback loop to adjust the road traffic speed until there is equilibrium across the network (i.e. that assumed input speeds match the actual output speeds after the traffic assignment). The travel time on the road network impacts the mode split of both person and cargo movement. All the assigned trips across all networks are combined into a single output network following the equilibrium procedure.

One potential bottleneck for the movement of cargo between the different localities is both the formality and physical barriers at international border crossing points. This is currently being addressed by various cross regional organizations such as The Greater Mekong Rail Association. In the distant future scenario, these are resolved to facilitate economic prosperity.

The Model Validation

The validation of the model was undertaken from data sources not currently used as input data in the model development. Two such comparisons are discussed here. The base output from combined road vehicle movement in 2015 was validated against

screen line traffic counts in Thailand in the north-west and south-east where such traffic has the potential to be travelling to locality crossing points. The screenline comparison of vehicle traffic was within 10%.

A Big Data comparison was made between the model estimation of the overall trade between Thailand and the two localities of Yunnan and Guangxi in China via a comparison of the two custom databases. The estimation of trade between the two Chinese localities and Thailand is 1,409 tonnes on average per day in 2015 compared to an observed volume of 1,400 tonnes per day. The comparison is good.

RESULTS AND CONCLUSIONS

In the current situation incorporating all infrastructure proposals, there is a small modal shift in terms of tonne-kilometres of travel. However, this implies that significant more effort is required to ensure modal shift away from the road sector.

The Future Result

Cargo movement as measured in terms of tonne-kilometres of travel is estimated to grow at 4.9 % per annum between 2015 and 2025. However, as a result of the changing interaction between the economic parameters, the differential distribution of cargo across localities changes as depicted in Fig 6.

In 2015, Thailand has nearly 50% of regional cargo movements. This is projected to decrease to under 40% by 2050. This share of cargo is transferred across all localities by 2050. By 2050, the two Chinese provinces are projected to increase their share of overall cargo movements by 40% from an initial 14% to 20% whereas Myanmar will decrease its share of regional movement from 12% to 9%. The localities of Lao People's Democratic Republic (PDR) and Vietnam are expected to increase approximately their share of cargo movement.

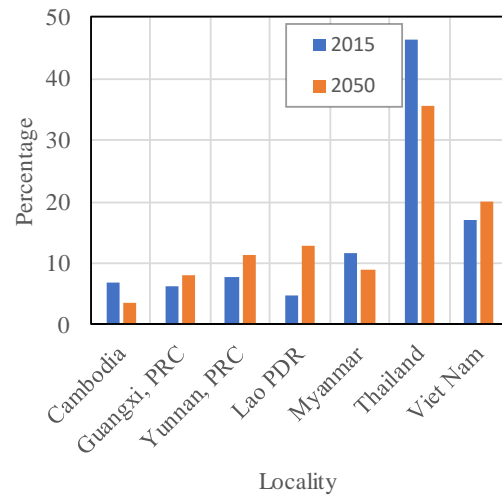


Fig. 6 Distribution of cargo travel by locality

In the current proposal incorporating all new rail infrastructure proposals of the seven localities, there is a small modal shift in the movement of cargo as reported in Table 5. Truck remains the dominant mode of transport across the region.

The modal share of the alternative non-road modes in combination increases nearly four times. The modal share increases of rail alone increases by nearly 150%. There is in this case also an estimated shift to IWT as a direct result of increased road congestion.

Table 5 Modal shift between 2015 and 2050

Mode	2015	2050
Truck	98.43%	96.29%
Rail	0.78%	1.30%
IWT	0.18%	0.24%
Sea	0.62%	2.17%

Another issue that arises from the continual maintenance of the high cargo modal split towards road movement is that by 2050, there is an estimated significant change in the distribution of road traffic across the region. As depicted in Fig. 7, by 2050, that there is a dramatic shift in the sharing of regional road space in terms of road movement as measured in terms of passenger car units.

Today, trucks account 23% of all movements across the regional road network, the model developed in this research suggests that this will rise to 45% in a future scenario. This is a significant change and is likely to have an impact on traffic accidents.

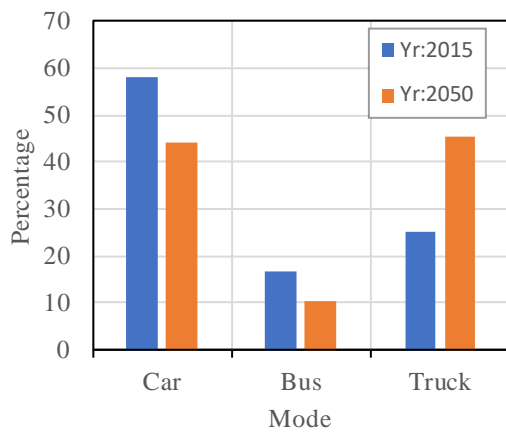


Fig. 7 Road Usage (pcu-km of travel)

The Future Result-Ultimate Scenario

In the case of an ultimate rail scenario such as the double tracking of the complete existing region rail together with improved border crossings, there is in this case an ultimate shift in cargo movement. Truck remains the dominant mode of transport across the region. The modal share of the alternative modes in combination increases nearly seven times.

The modal share increase in rail alone is of the order of five times higher as depicted in Table 6. The transport model prepared as part of this research is an analytical tool that is an initial starting point for researchers to understand the mobility of cargo throughout the Mekong.

Table 6 Modal comparison – increase infrastructure

Mode	2015	2050
Truck	98.43%	92.62%
Rail	0.78%	5.09%
IWT	0.18%	0.46%
Sea	0.62%	1.83%

If the localities of the Mekong are to consider modal shift away from the road there will likely need to be a change in the pricing structure of the movement of cargo by road and rail. Such a change in cost is reported in a test case in Table 7.

Table 7 Modal comparison – cost differential

Mode	2015	2050
Truck	98.43%	89.48%
Rail	0.78%	7.90%
IWT	0.18%	0.45%
Sea	0.62%	2.15%

In this test case, the cost differential is changed with an increase in the cost of cargo movement by truck whilst at the same decreasing the cost of cargo movement by rail. This suggests that there is a potential for the truck modal share of the movement of cargo across the Mekong to fall below the 90% level.

Feasibility of Green Cargo Shift

When considering the development of new infrastructure in the Mekong Region to assist in the transfer to Green freight movement, the desired modal split should be pursued in a realistic manner taking the growth trend in road cargo into account. Large increases in the sector capability of the non-road sector are implementable but difficult from a practical and economic point of view.

The long-term forecast for the region demographically in accordance with the various locality economic forecasts demonstrates via infrastructure development that it is possible to halt the fact that the road sector for cargo movements was continuing to approach the one hundred percent mark. Of course such movement away from the road sector is not achievable overnight so that the mathematical model considers a thirty five year time frame for intermodal shift[15].

The dilemma is the establishment of Green Cargo Movement and the shifting of cargo movements from the dominant road mode to alternative modes. The development of the mathematical model for cargo movement has enabled the transport planner practitioner to advance the understanding of cargo movements and provide a numerical framework for the understanding the impact of a green cargo modal

ACKNOWLEDGEMENTS

The authors acknowledge the support by the government agencies within the Mekong and the Asian Development Bank in the preparation of existing datasets and the development of the analytical tools.

All ideas and views expressed in this paper are those of the authors. They do not necessarily reflect any of the sponsoring authorities of projects discussed in this paper or any organizations associated with the respective authors.

REFERENCES

- [1] Colliers International, European Internal Demand Shifts, in European Logistics Report 2016.
- [2] Bartocci, A. and M. Pisani, "Green" fuel tax on private transportation services and subsidies to electric energy. A model-based assessment for

- the main European countries. *Energy Economics*, 2013. 40: p. S32-S57.
- [3] Klein, D.R., et al., *The Paris agreement on climate change : analysis and commentary*. 2017, Oxford, United Kingdom: Oxford University Press. xxxii, 435 pages.
 - [4] Hossain, M., R. Hales, and T. Sarker, *Pathways to a sustainable economy : bridging the gap between Paris climate change commitments and net zero emissions*. xviii, 225 pages.
 - [5] Johnstone, L. and V. Ratanavaraha, *Green Freight Movement: The Dilemma of the Shifting of Road Freight to Alternatives*. *Transportation Research Procedia*, 2017. 21: p. 154-168.
 - [6] Eren, C., *Freight Transport and Climate Change*. Total Environmental Centre Inc, 2008.
 - [7] Johnstone, L.C. and N. Chanchaoen Workshop & Lectures on Sustainable Multimodal Transport & Urban Development: with Evaluation of Transport Projects, Land Use Mix and Supply Controls., 2010, Griffith University, Australia.
 - [8] Johnstone L. 2015. *Transport Demand Modeling Methods Training*., Asian Development Bank.
 - [9] Asian Development Bank., *Greater Mekong Subregion Transport Sector Study*. 2006
 - [10] Office of Transport and Traffic Policy and Planning.,2014., *Transport Data and Model Integrated with Multimodal and Logistics (TDL2)*. 2014.
 - [11] JICA,2014., *The Survey Program for the National Transport Development Plan in the Republic of the Union of Myanmar(2014)*., prepared by Japan International Cooperation Agency(JICA).
 - [12] JICA, 2009., *The Comprehensive Study on the Sustainable Development of Transport System in Vietnam (VITRANSS 2)*., prepared by Japan International Cooperation Agency(JICA).
 - [13] Asian Development Bank., *Greater Mekong Subregion Statistics on Growth, Infrastructure, and Trade*, 2nd. Edition, Editor. 2016. p. 5-25.
 - [14] Horowitz, A., J., *Origin Destination Disaggregation Using Bipropotional Least Squares Estimation for Truck Forecasting*. University of Wisconsin-Milwaukee, 2009. 09(1).
 - [15] Li, L., R.R. Negenborn, and B. De Schutter, *Intermodal freight transport planning – A receding horizon control approach*. *Transportation Research Part C: Emerging Technologies*, 2015. 60: p. 77-95.

EFFECT OF FLY ASH FINENESS ON COMPRESSIVE, FLEXURAL AND SHEAR STRENGTHS OF HIGH STRENGTH-HIGH VOLUME FLY ASH JOINTING MORTAR

Patcharapol Posi¹, Pornnapa Kasemsiri², Surasit Lertnimoolchai³ and Prinya Chindaprasirt^{4*}

¹Department of Civil Engineering, Faculty of Engineering, Rajamangala University of Technology Isan Khon Kaen Campus, Khon Kaen, 40000, Thailand

²Sustainable Infrastructure Research and Development Center Department of Chemical Engineering, Faculty of Engineering, Khon Kaen University, Khon Kaen, 40002, Thailand.

³Managing Director, Concrete Precision Unique, Udonrthani 41000, Thailand

⁴Sustainable Infrastructure Research and Development Center Department of Civil Engineering, Faculty of Engineering, Khon Kaen University, Khon Kaen, 40002, Thailand, and Academy of Science, the Royal Society of Thailand, Dusit, Bangkok, Thailand 10300

ABSTRACT

In this research, the compressive, flexural, and shear bond strengths of high strength-high volume fly ash mortar containing high calcium fly ash (HCFA) of various finenesses were studied. The mortars were made from ordinary Portland cement (OPC), HCFA, sand, water, and Type D admixture. The HCFA was from Mae Moh power station in the north of Thailand. Three types of HCFA fineness viz., as-received coarse fly ash (CF), medium fineness fly ash (MF, passed sieve No. 100), and fine fly ash (FF, passed sieve No. 200) were used to replace OPC at the levels of 0-70 % by weight of binder. The results showed that the high strength-high volume fly ash mortars with satisfactory 28-day compressive strengths between 70.0 and 114.0 MPa, shear bond strengths between 7.2 and 18.0 MPa, and flexural strengths between 15.9 and 27.6 MPa were obtained. Test results also indicated that the use of FF gave significantly higher strengths than the use of CF and MF. Specifically, the compressive strength of mortar containing 50%FF was very high at 110.0 MPa. The FF could thus be used to improve the strengths of high volume fly ash mortar for uses in various architectural and structural works requiring high strength products.

Keywords: High calcium fly ash, Fly ash fineness, High volume fly ash, High strength mortar, Shear bond strength

INTRODUCTION

Currently, the construction of wall in building mainly uses ready-made concrete materials in the form of concrete blocks. In the past, the concrete blocks for wall possesses low strength and thus the use is relatively limited. For diverse usage, the strength development is substantially improved such that it can be used in structural work as well [1].

One of the important use of the block is the preformed wall for the housing units. The ready-made preformed wall can be fabricated at the concrete plant and transport to the construction site. This drastically reduces the time required for the construction of building or housing complex. This results in rapid construction using concrete block panels as shown in Fig. 1. The joining of the blocks in making preformed wall required a high strength mortar such that the wall can be transported to the site without damage.

To develop a sufficiently high strength mortar, it is necessary to use a high cement content and this results in high cost. In addition, the production of cement is an energy intensive process. Coupled with

the burning of calcareous material, the production of cement thus produces a large amount of carbon dioxide. For every ton of Portland cement coming out of the furnace, almost 1 ton of carbon dioxide (CO₂) was released into the atmosphere [2].



Figure 1. The rapid construction of wall using preformed concrete blocks

It is therefore important to reduce this greenhouse gas emissions into the atmosphere by using the environmental friendly cementitious material products [3] or alternatively use less cement with the use of high volume pozzolanic material to replace Portland cement. The available fly ash in large quantity is the high calcium fly ash from Mae Moh Power station in the north of Thailand which has been shown to be a good pozzolan. This amount of calcium is rather high and increases with the increasing depth of coal mining [4]. The use of this fly ash in concrete increases the porosity, but the average pore size is reduced [5, 6] and the interfacial zone between aggregate and matrix is improved [7].

In order to utilize the fly ashes effectively, the coarse portions of fly ashes have to be processed. Grinding and classification can be used to increase the fineness of the fly ash. It has been demonstrated that the compressive strength of concrete with fly ash can be improved by using finer fly ashes [8-13]. In addition, the use of fine fly ash with spherical particle and smooth surface result in some better mechanical properties i.e. to increase the strength and improve the durability of mortar and concrete compared to the coarse fly ash [8-10]. The shrinkage is also in reduced compared to the control but slightly increased compared to the use of coarser fly ash [14].

Therefore, in this study, the use of high calcium fly ash with different finesses to improve the strength of high volume fly ash jointing mortar is studied. The as-received fly ash, the medium fineness fly ash passed sieve No. 100 and the fine fly ash passed sieve No. 200 were used to produce high strength mortar. The results will enable the use of fly ash more effectively through the classification and high volume usage with ensured high strength.

EXPERIMENTAL PROGRAM

Materials

Materials used in this research consisted of ordinary Portland cement (OPC), river sand, water and high calcium fly ash (HCFA). The HCFA was the by-products from Mae Moh power station in Lampang province, northern Thailand. It was classified to three lots of HCFA fineness viz., as-received coarse fly ash (CF), medium fineness fly ash passed sieve No. 100 (MF), and fine fly ash passed sieve No. 200 (FF). The physical properties of materials are shown in Table 1.

The morphology of HCFA by SEM as shown in Fig. 2 indicated that the shape of HCFA was spherical with smooth surface. The chemical compositions of HCFA are shown in Table 2. The specific gravity of HCFA was 2.66 with median particle size of 18.6 μm . The HCFA consisted of a high content of 36.20% SiO_2 , 15.52% Al_2O_3 , 14.25% Fe_2O_3 , and 22.57% CaO with the loss on ignition (LOI) of 0.88%. The XRD of HCFA as shown in Fig. 3 indicated the high

amorphous content with relatively large hump around $22-38^\circ 2\theta$.

Table 1. The physical properties of materials

Materials	Sand	OPC	HCFA
Specific gravity	2.61	3.15	2.66
Median particle size (μm)	-	14.6	18.6
Fineness modulus	2.65	-	-
Unit weight (kg/m^3)	1360	1440	-
Water absorption (%)	1.17	-	-

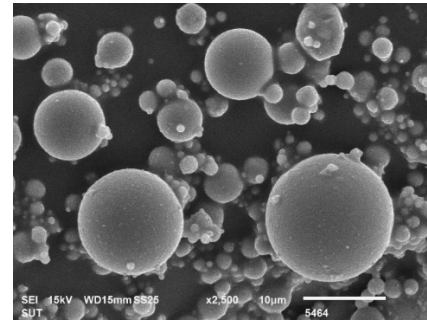


Figure 2. The morphology of HCFA by SEM

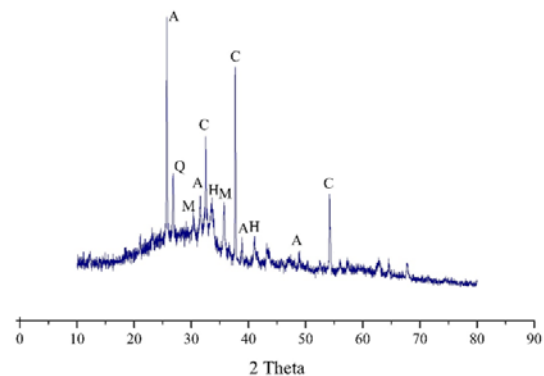


Figure 3. The XRD of HCFA. M-Maghemite: Fe_2O_3 ; Fe_3O_4 ; H-Hematite; A-Anhydrite; C-Calcium Oxide; Q-Quartz.

Table 2. Chemical composition of materials (by weight)

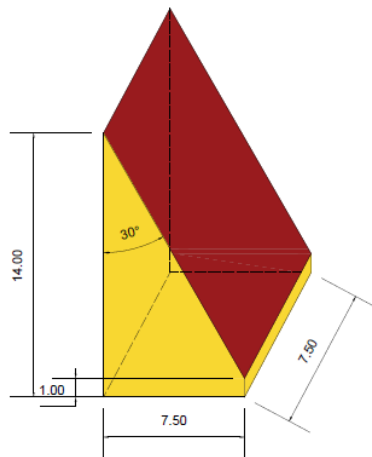
Chemical compositions (%)	HCFA	OPC
SiO_2	36.20	20.8
Al_2O_3	15.52	4.7
Fe_2O_3	14.25	3.4
CaO	22.57	65.3
K_2O	1.63	0.4
Na_2O	0.33	0.1
SO_3	8.9	2.7
LOI	0.88	0.9

Mix proportion

The HCFA contents

To study the effect of HCFA fineness, as-received coarse fly ash (CF), medium fineness fly ash passed sieve No. 100 (MF), and fine fly ash passed sieve No. 200 (FF) were used to replace OPC at the levels of 0-70 % by weight for the manufacturing of high strength jointing mortars.

The compressive strength, flexural and shear bond strengths of high volume fly ash-high strength mortar were determined.



a. Dummy Bottom Section



b. testing of shear bond strength

Figure 4. The shear bond strength test of high volume fly ash-high strength mortar

Details of Mixing

All mixtures were made with binder to sand ratio of 1:0.33, superplasticizer (SP) of 0.50 % of binder and water to binder ratio of 0.24. For mixing, OPC and HCFA were firstly mixed together until the mixture was homogenous. Next, sand was added and mixed for 5 min. Finally, water and SP were added

and mixed for 3 minutes to obtain a homogenous mixture.

The fresh high strength mortar was placed into 50x50x50 mm cube molds, 75x75x150 mm and 75x75x300 mm prism molds. The specimens were demolded at 1 day and stored in water.

Details of test

Compressive strength and density

The cube specimens size 50x50x50 mm were tested to determine the compressive strength in accordance with ASTM C109/C109M-16a [15]. The reported compressive strengths were the average of three samples.

Shear bond strength

The prism specimens size 75x75x150 mm were tested to determine the shear bond strength in accordance with ASTM C882/C822M [16]. The reported shear bond strength was the average of three samples. The sample bond strength of high volume fly ash-high strength mortar with concrete by slant shear are shown in Fig. 4. The 28 day-strength of dummy concrete was 70.0 MPa. The contact surface of the dummy concrete was cut surface by diamond saw.

Flexural strength

The prism specimens size 75x75x300 mm were tested to determine the flexural strength in accordance with ASTM C293-02 [17]. The reported flexural strength was the average of three samples.

RESULTS AND DISCUSSIONS

Compressive strength

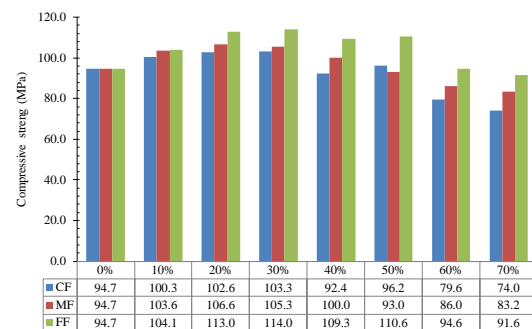


Figure 5. Compressive strength of high volume fly ash-high strength mortar at 28 days

The results of compressive strength of high volume fly ash-high strength mortar are shown in Fig. 5. The compressive strength increased with increasing HCFA content from 0 to 30 % by weight. The compressive strength development from all fly ash was quite good, especially the fine fly ash. At low replacement level, the compressive strengths of fly ash mortar were higher than mortar without fly ash

due to the pozzolanic reaction of fly ash and the filling effect [10]. In contrast, for the high volume HCFA replacement, the strength started to decrease with more than 30 % replacement. With more than 50% replacement the compressive strengths were less than that of the control. For example, the compressive strengths at 28 days of mixes with CF with volume of HCFA of 0, 10, 20, 30, 40, 50, 60, and 70 % by weight were 94.7, 100.3, 102.6, 103.3, 92.4, 96.2, 79.6, and 74.0 MPa, respectively.

With regards to types of HCFA fineness, the compressive strength increased with increasing HCFA fineness. The filling effect of fly ash contribute to the relatively good compressive strength development of the concrete containing HCFA. The used of finer fly ash resulted in further enhancement of the compressive of concrete [8-10]. For example, the compressive strengths at 28 days of 30 % fly ash with HCFA fineness of CF, MF, and FF were 103.3, 105.3, and 114.0 MPa, respectively.

Shear bond strength

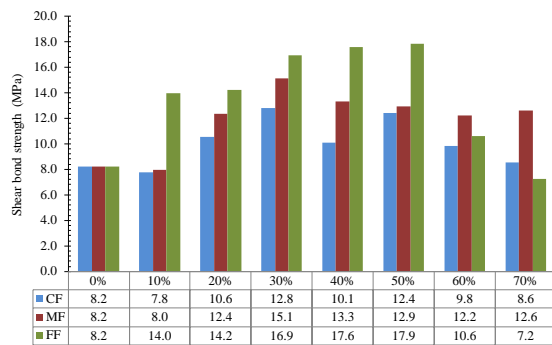


Figure 6. Shear bond strength of high volume fly ash-high strength mortar at 28 days

The results of 30° slant shear bond strength test of high volume fly ash-high strength mortar are shown in Fig. 6. For the mixes with CF and MF, the shear bond strength increased with the increasing volume of HCFA from 0-30 % fly ash. For example, the shear bond strength at 28 days of mixes with MF with volume of HCFA of 0, 10, 20, 30, 40, 50, 60, and 70 % by weight were 8.2, 7.8, 10.6, 12.8, 10.2, 12.4, 9.8, and 8.6 MPa, respectively. The increase in the replacement levels resulted in a drop in the strength of the samples. However, the results also indicated that the strength of the 70% fly ash mortar was still comparable to that of the control. For the fine fly ash, the shear bond strength of FF increased with the increasing volume of HCFA from 0-50 % replacement levels. The increased shear bond strength was due to increased compressive strength with the increase in pozzolanic reaction of fly ash and the filling effect of the fine fly ash particles [9].

With regards to types of HCFA fineness, the shear bond strength increased with increasing HCFA fineness. For example, the shear bond strength at 28 days of 30 % fly ash with HCFA fineness of CF, MF, and FF were 12.8, 15.1, and 16.9 MPa, respectively. This is because the high fineness HCFA has high surface area resulting in the high internal bond strength of the cement paste [18] and thus resulted in the high shear bond strength between high strength mortar and old concrete substrate.

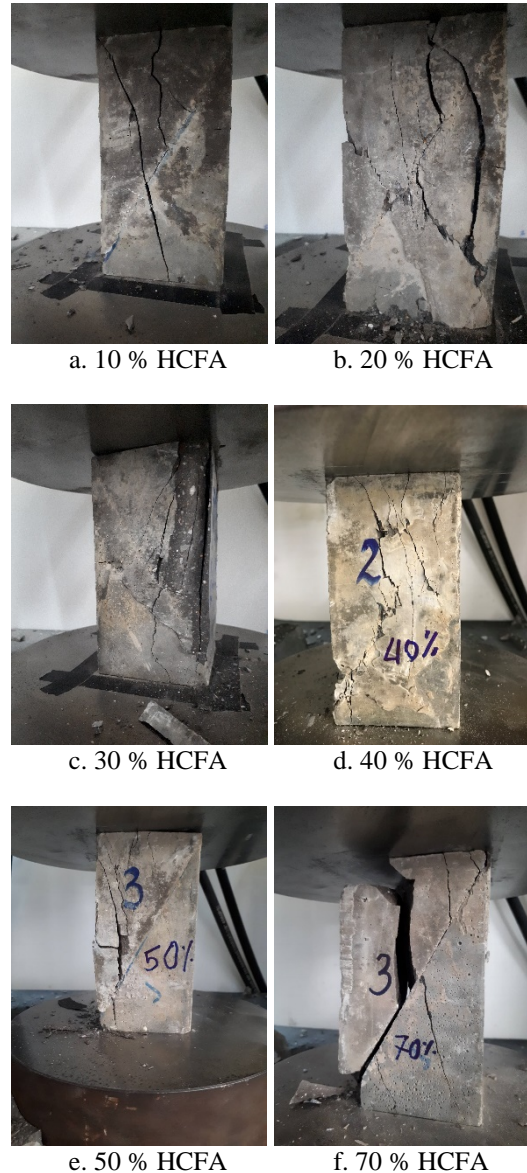


Figure 7. The failure of shear bond strength

In addition, the fracture characteristics of slant shear prisms are shown in Fig. 7. The slant shear bond prisms failed in the monolithic mode where cracks were formed in both section of high strength mortar and old concrete substrate [19] which indicated the relative high resistance to damage of high strength mortar and high bonding between the two surfaces.

Flexural strengths

The results of flexural strength of high volume fly ash-high strength mortar are shown in Fig. 8. For the mixes with CF and MF, the flexural strengths increased with the incorporation of the fly ash. For example, the flexural strength at 28 days of mixes with MF with volume of HCFA of 0, 10, 20, 30, 40, 50, 60, and 70 % by weight were 15.9, 21.1, 18.3, 18.9, 18.8, 18.4, 19.4, and 19.0 MPa, respectively. Moreover, the flexural strength of FF were further increased with the incorporation of FF especially at the 10 – 30 % replacement levels. Normally, the trend of flexural strengths was similar to those of compressive strengths [20]. In this case, with the incorporation of fly ash, the flexural strengths were improved slightly better than those of compressive strengths.

With regards to types of HCFA fineness, the flexural strength of base line was 15.9 MPa and the flexural strength increased with increasing of HCFA fineness. For example, the flexural strength at 28 days of 10 % fly ash with HCFA fineness of CF, MF, and FF were 17.5, 21.1, and 26.6 MPa, respectively and representing an average improvement of 67 % from base line. The increasing of flexural strength was due to the increase in the reaction products from increased reaction of fine HCFA. This was associated with the improvement of compressive strength and shear bond strength of high strength mortar which led to overall improvement in the flexural strength [19].

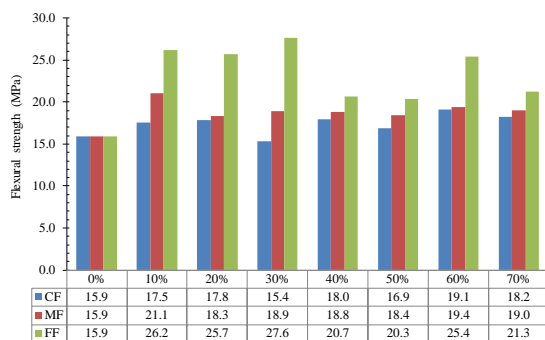


Figure 8. Flexural strengths of high volume fly ash-high strength mortar at 28 days

CONCLUSIONS

Based on the obtained data, the following conclusions can be drawn:

1. The increasing in HCFA fineness resulted in the improvement of the compressive, shear bond and flexural strengths of mortar.

2. For compressive strength, the optimum volume of HCFA was 30 % with substantial increase in compressive strength.

3. For shear bond strength, the behavior was similar to that of compressive strength. However, the

optimum replacement level of fine FF was increased to 50 % suggesting that a larger amount fly ash could be incorporated providing that its particle was fine.

4. For the flexural strength, the trend of results was similar to the improvements in compressive and shear bond strengths. The improvement with the incorporation of FF was more evident in the flexural strength. The improvement represented an average of 67 % from base line for the 10 % replacement level.

5. The results showed that high strength-high volume fly ash mortars with satisfactory 28-day compressive strengths of between 70 and 114 MPa, shear bond strength between 7.2 and 18.0 MPa, and flexural strength between 15.9 and 27.6 MPa were obtained. Moreover, test results indicated that the use of FF gave significantly higher strengths than the use of CF and MF. The FF could thus be used to improve the strengths of OPC mortar and used as an alternative mortar for various architectural and structural works requiring high strength products.

ACKNOWLEDGEMENT

This work was financially supported by the Concrete Precision Unique, Udonthani, Thailand. The support of the Faculty of Engineering, Rajamangala University of Technology Isan Khon Kaen Campus, and the Thailand Research Fund (TRF) under the TRF Distinguished Research Professor Grant No. DPG6180002 is gratefully acknowledged here.

REFERENCES

- [1] Wongkvanklom A, Posi P, Khotsopha B, Ketmala C, Pluemsud N, Lertnimoolchai S, et al., Structural lightweight concrete containing recycled lightweight concrete aggregate. KSCE Journal of Civil Engineering, Vol., 2017, pp.
- [2] Malhotra VM. Introduction: sustainable development and concrete technology. Concrete International, Vol. 24, Issue, 2002, pp. 22.
- [3] Wongkvanklom A, Sata, V., Sanjayan, J., & Chindaprasirt, P., Setting time, compressive strength and sulfuric acid resistance of a high calcium fly ash geopolymer containing borax. Engineering and Applied Science Research, Vol. 45, Issue 2, 2018, pp. 89-94.
- [4] Chindaprasirt P, Rattanasak U., Characterization of the high-calcium fly ash geopolymer mortar with hot-weather curing systems for sustainable application. Advanced Powder Technology, Vol. 28, Issue 9, 2017, pp. 2317-24.
- [5] Poon CS, Wong YL, Lam L., The influence of different curing conditions on the pore structure and related properties of fly-ash cement pastes and mortars. Construction and Building Materials, Vol. 11, Issue 7, 1997, pp. 383-93.

- [6] Chindaprasirt P, Jaturapitakkul C, Sinsiri T., Effect of fly ash fineness on compressive strength and pore size of blended cement paste. *Cement and Concrete Composites*, Vol. 27, Issue 4, 2005, pp. 425-8.
- [7] Kuroda M, Watanabe T, Terashi N. Increase of bond strength at interfacial transition zone by the use of fly ash., *Cement and Concrete Research*, Vol. 30, Issue 2, 2000, pp. 253-8.
- [8] Erdoğan K, Türker P. Effects of fly ash particle size on strength of portland cement fly ash mortars. *Cement and Concrete Research*, Vol. 28, Issue 9, 1998, pp. 1217-22.
- [9] Chindaprasirt P, Homwuttiwong S, Sirivivatnanon V., Influence of fly ash fineness on strength, drying shrinkage and sulfate resistance of blended cement mortar. *Cement and Concrete Research*, Vol. 34, Issue 7, 2004, pp. 1087-92.
- [10] Chindaprasirt P, Chotithanorm C, Cao HT, Sirivivatnanon V., Influence of fly ash fineness on the chloride penetration of concrete. *Construction and Building Materials*, Vol. 21, Issue 2, 2007, pp. 356-61.
- [11] Payá J, Monzó J, Borrachero MV, Peris E, González-López E., Mechanical treatments of fly ashes. Part III: Studies on strength development of ground fly ashes (GFA) — Cement mortars. *Cement and Concrete Research*, Vol. 27, Issue 9, 1997, pp. 1365-77.
- [12] Kiattikomol K, Jaturapitakkul C, Songpiriyakij S, Chutubtim S., A study of ground coarse fly ashes with different finenesses from various sources as pozzolanic materials. *Cement and Concrete Composites*, Vol. 23, Issue 4, 2001, pp. 335-43.
- [13] Payá J, Monzó J, Borrachero MV, Peris-Mora E, Amahjour F., Mechanical treatment of fly ashes: Part IV. Strength development of ground fly ash-cement mortars cured at different temperatures. *Cement and Concrete Research*, Vol. 30, Issue 4, 2000, pp. 543-51.
- [14] Vimonsatit V, Chindaprasirt P, Ruangsiriyakul S, Sata V., Influence of fly ash fineness on water requirement and shrinkage of blended cement mortars 2015.
- [15] ASTM C109/C109M-16a. Standard Test Method of Compressive Strength of Hydraulic Cement Mortars (using 2-in. or [50 mm] cube specimens). *Annual Book of ASTM Standard*, Vol. Vol.04.01, Issue, 2016, pp.
- [16] ASTM C882/C882M. Standard Test Method for Bond Strength of Epoxy-Resin System Used with Concrete by Slant Shear. *Annual Book of ASTM Standard*, Vol. vol. 04.02, Issue, 2005, pp.
- [17] ASTM C293-02. Standard Test Method for Flexural Strength of Concrete (Using Simple Beam with Center-Point Loading). *Annual Book of ASTM Standard*, Vol. vol.04.02, Issue, 2002, pp.
- [18] Husem M., The effects of bond strengths between lightweight and ordinary aggregate-mortar, aggregate-cement paste on the mechanical properties of concrete. *Materials Science and Engineering: A*, Vol. 363, Issue 1–2, 2003, pp. 152-8.
- [19] Phoo-ngernkham T, Sata V, Hanjitsuwan S, Ridditirud C, Hatanaka S, Chindaprasirt P., High calcium fly ash geopolymer mortar containing Portland cement for use as repair material. *Construction and Building Materials*, Vol. 98, Issue, 2015, pp. 482-8.
- [20] Arif E, Clark MW, Lake N., Sugar cane bagasse ash from a high efficiency co-generation boiler: Applications in cement and mortar production. *Construction and Building Materials*, Vol. 128, Issue, 2016, pp. 287-97.

THE USE OF BOTTOM ASH TO IMPROVE THE STRENGTH OF POOR SUBBASE LATERITIC SOIL IN ROAD CONSTRUCTION

Chotikan Ratchakrom¹

¹Faculty of Civil Engineering Technology, Valaya Alongkorn Rajabhat University under the Royal Patronage, Thailand

ABSTRACT

This research investigates the use of bottom ash to improve the unconfined compressive strength of poor subbase. Lateritic soil that used in test represented weak subbase soil in road construction. This research performed on lateritic soil mixed with cement 1-1.5%, kaolin 0.5-1% and the different percentages of bottom ash was between 2-8% by weight of soil. The unconfined compressive strength of the soil improvement tends to increase with an increase in the amount of bottom ash. However, the unconfined compressive strength of the samples slightly increased when the amount of bottom ash was exceeded 6%. The results demonstrated bottom ash can develop the early strength of soil. As shown in the results of soil mixed with cement 1.5%, kaolin 1%, and bottom ash 6-8% can be developed the strength near the soil mixed with cement 3% in 7 days. Moreover, the addition 6% of bottom ash and 0.5% of kaolin in the soil samples mixed with cement 1.5% can be increased the compressive strength 87% of the samples without bottom ash and kaolin. The required strength of subbase improvement should more than 689 kPa at the curing time 7 days. The results demonstrated the strength of soil mixed with 1.5% cement, 0.5% kaolin and 4-8% bottom ash was higher than the required strength. Therefore, bottom ash can develop the strength of poor subbase and reduced the utilized amount of cement to improve the strength of soil.

Keywords: Lateritic soil, Bottom ash, Compressive strength, Kaolin, Subbase

INTRODUCTION

The lateritic soil has been used in road construction of Thailand and developing in the rural area. The subbase of road constructions was constructed by lateritic soil. However, it's become the real problem of lateritic soil. This is because the poor lateritic soil is low compressive strength and poor durability. Therefore, the bearing capacity of poor subbase was lower than the minimum strength requirement for road construction. Subsequently, the rain infiltration or the water inundates the subbase can be causing the road damage. [1], [2]. This problem represents to emphasis for improvement in engineering properties of lateritic soil such as compressive strength, durability, and permeability [2].

The most commonly used additive for soil stabilization is ordinary Portland cement. To build a subbase with cement stabilized ash alone is not yet common, but this is one of the high volume ash application being promoted by ash producers [3]. The use of ash or the pozzolanic materials combined with cement to improve the strength of soil can be reduced the cost of the soil stabilization. Therefore, this study investigated on the use of bottom ash, which is the by-product from Mae Moh power plant to improve the strength of poor subbase.

Ash removed from the base of the furnace is termed bottom ash [3]. Bottom ash (BA) is a solid waste available in Mae Moh power plant in the north of Thailand is about 0.8 million tons and is disposed of a landfill near the power plant [4]. It is coarser than fly ash, ranging in size from fine sand to gravel [3]. Bottom ash is larger in size and very irregular, containing pores and cavities [5]. Ground to a proper fineness, bottom ash can be used as a pozzolan that produces relative strength [6]. The chemical compositions of bottom ash were 39.3% SiO₂, 21.3% Al₂O₃, Fe₂O₃, 2.1% K₂O, 16.5% CaO, 1.0% Na₂O and 1.4% loss on ignition. The bottom ash has increased pozzolanic activity and used to partially replace Portland cement. The utilization of bottom ash as a cementitious a partial replacement of cement is possible [4].

Bottom ash serves well as structural fill and construction [3]. A variety of research on the mobilization of coal bottom ash for use as the cementitious material has been utilized. The bottom ash has increased the pozzolanic activity [7], [8]. Therefore, many types of research have been used the bottom ash as fine aggregate in concrete [9], asphaltic [10]. On the other hand, the bottom ash can involve clay minerals and increases the value of supporting capacity of the clay and increasing the compressive strength value [11].

This paper investigated the use of bottom ash

combined with cement which a partial replacement by kaolin to improve the strength of the poor quality of soils. There are many of additive that has been tested the effect to develop the engineering properties of lateritic soil. In order to reduce costs by replacing some cementations stabilizers with non-cementations additives [12, 13, 14]. Kaolin soil is a mineral of soil, which some of these noncement additives. In chemical terms, kaolin has many cementing materials consists of SiO_2 , Al_2O_3 , and Fe_2O_3 . These elements can improvement bonding, durability and stabilization of soil. [15].

The objective of this paper is investigating the use of bottom ash to improve the strength of poor subbase. In order to increase the strength of subbase higher than the required strength which suggested by the Thailand Department of highways. The unconfined compressive strength of the soil improvement should be more than 689 kPa.

MATERIALS AND METHODS

The lateritic soil which has poor quality was used in the experiment. The strength of the soil samples was less than the required strength which suggested by the Thailand department of highways. The soil samples were conducted on Atterberg limits and sieve analysis test to determine the properties and classification of the samples. Portland cement type 1, kaolin and bottom ash were mixed in the soil samples to improve the strength. Kaolin obtained from Lampang province of Thailand. Bottom ash obtained from Mae Moh power plant in Lampang province of Thailand as shown in Fig. 1.

The maximum size of bottom ash mixed with the soil samples was 4.75 mm. All admixture stored in plastic bags to maintain their dry condition. The soil samples were mixed with cement, kaolin and bottom ash in the ratio accordance with Table 1. The mixture code in group A represented the soil samples mixed with cement 1.5-3% by weight of the soil samples. The mixture code in group B represented the soil samples mixed with cement 1%, kaolin 1% and the different percentages of bottom ash 2-8% by weight of soil. The mixture code in group C represented the soil samples mixed with cement 1.5%, kaolin 0.5% and the different percentages of bottom ash 2-8% by weight of soil.

The difference between the mixture in group B and C is the percentage of Portland cement and kaolin. The combination of cement and kaolin in the mixture of B and C samples was 2% by weight of the soil samples. However, the amount of cement in the mixture group B was less than group C 0.5%.



Fig.1 Bottom ash obtained from Mae Moh power plant.

The soil samples mixed with cement, kaolin and bottom ash, according to Table 1 were conducted in modified compaction tests and unconfined compression tests.

Table 1. The mixture ratio of admixture mixed with the soil samples.

Mixture Code	Cement (%)	Kaolin (%)	Bottom Ash (%)
A1	1.5	-	-
A2	2	-	-
A3	3	-	-
B1	1	1	2
B2	1	1	4
B3	1	1	6
B4	1	1	8
C1	1.5	0.5	2
C2	1.5	0.5	4
C3	1.5	0.5	6
C4	1.5	0.5	8

Note: The amount of cement, kaolin and bottom ash mixed with soil is percent by weight of soil.

The modified Proctor compaction tests on the samples in each mixture were conducted in accordance with AASHTO T180. This test is intended to be used to determine the maximum dry density and optimum moisture content in each mixture of the samples. The samples were manually compacted in five equal layers using the modified compaction effort.

Unconfined compression tests are intended to be used to determine the compressive strength of the samples. Unconfined compression tests were conducted in accordance with AASHTO T 208. The soil samples mixed with cement, kaolin and bottom ash in the ratio according to Table 1 were used in this test. The samples mixed with water at the optimum moisture content (OMC) for each mixture which obtained the values from the modified compaction tests. The samples were compacted in five equal layers using modified compaction effort. After completing the compaction process, each

sample was extruded from the compaction mold and was then cured in the plastic bag until tested. The specimens were cured in the plastic bag for 3, 7 and 14 days. Following the curing process, the samples were soaked in water for 2 hours and then compressed the samples by the compression machine. The results represented by the influence of bottom ash on the strength of soil improvement. However, the Thailand Department of highways suggested that the unconfined compressive strength of subbase improvement should be more than 689 kPa at the curing time 7 days. Therefore, the optimum bottom ash content to improve the strength of soil can be defined by the test results.

RESULTS AND DISCUSSIONS

The Engineering Properties of Lateritic Soil

The soil samples were conducted on Atterberg limits, sieve analysis test, and modified compaction tests to determine the engineering properties of the soil samples. Liquid limit, plastic limit, and plasticity index of the soil samples were 27%, 17%, and 10% respectively. Fig. 2 shows the particle size distribution of the soil samples in this study. However, according to the AASHTO classification system, the soil samples were in A-2-4. The gradation of soil samples is excellent to good for subgrade materials when considered on the general subgrade rating of AASHTO. Moreover, the results of modified compaction tests demonstrated the maximum dry density of the soil samples was approximately 1940 kg/m³ and optimum moisture content was 9.9%.

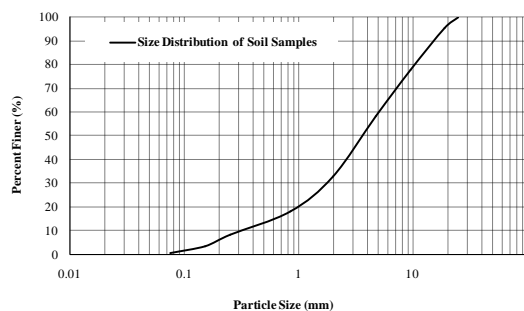


Fig. 2 Particle size distribution of the soil samples used in the test.

Maximum Dry Density and Optimum Moisture Content

The modified compaction tests were conducted on soil samples mixed with cement, kaolin and bottom ash in a ratio accordance with Table 1. The results of compacted soil samples mixed with cement 1.5%-3% as shown in Fig. 3. The results showed the dry density of the samples mixed with

cement was slightly different from the samples without cement. The maximum dry density of the samples A1, A2 and A3 was 1957 kg/m³, 1959 kg/m³, and 1946 kg/m³ respectively. The optimum moisture content of the samples A1, A2 and A3 were 9.7%, 9.8%, and 10.2% respectively.

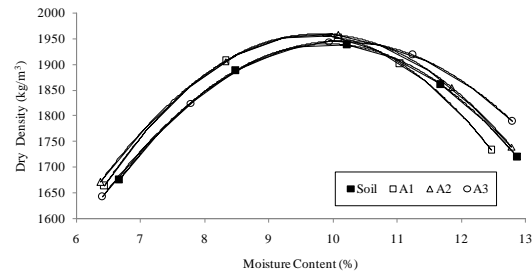


Fig. 3 Dry density and moisture content relationship of the soil improvement by cement.

The results of soil samples mixed with cement, kaolin and bottom ash shown in Fig. 4 and Fig. 5. The results in Fig. 4 illustrates dry density and moisture content of the samples in group B. The maximum dry density of the samples B1, B2, B3 and B4 was 1945 kg/m³, 1961 kg/m³, 1954 kg/m³ and 1966 kg/m³ respectively. The optimum moisture content of the samples B1, B2, B3, and B4 was 9.8%, 9.9%, 9.9% and 11.1% respectively.

Dry density and moisture content of the samples in group C illustrated in Fig. 5. The maximum dry density of the samples C1, C2, C3 and C4 was 1960 kg/m³, 1942 kg/m³, 1938 kg/m³ and 1940 kg/m³ respectively. The optimum moisture content of the samples C1, C2, C3, and C4 was 9.8%, 10.4%, 10.0% and 10.0% respectively. The results demonstrated a slight difference of maximum dry density and optimum moisture content of the samples for each mixture. The maximum dry density of the samples in each mixture was between 1940-1960 kg/m³. Therefore, bottom ash adding in the soil samples is less effect on the maximum dry density of soil.

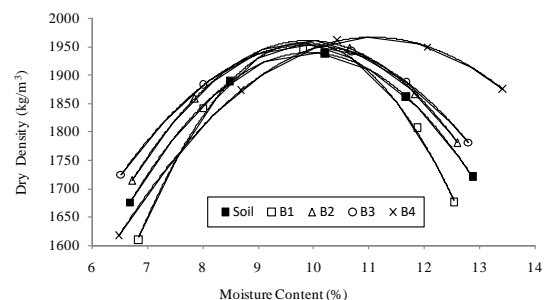


Fig. 4 Dry density and moisture content relationship of the soil improvement in group B.

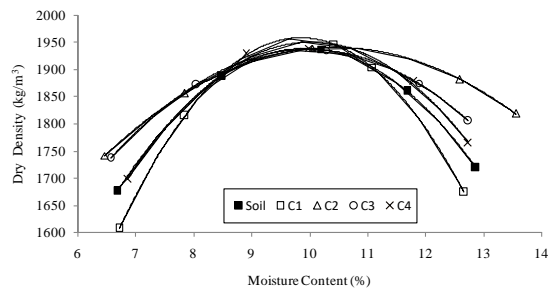


Fig. 5 Dry density and moisture content relationship of the soil improvement in group C.

Unconfined Compressive Strength

The average unconfined compressive strength values of the soil improvement for each mixture are as plotted in Fig. 6.

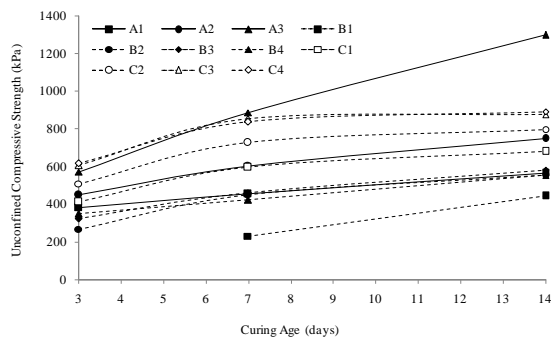


Fig. 6 Unconfined compressive strength of the soil improvement for each mixture.

The results demonstrated the soil samples mixed with 3% of cement gave the highest strength in 14 days. The strength of A3 samples was 1302 kPa in curing time 14 days. The strength of C3 and C4 samples in the curing 14 days was lower than A3 approximately 415 kPa. However, the early strength of C3 and C4 samples was near A3 in the curing time 3 and 7 days. Although, C3 and C4 samples contain Portland cement only 50% of A3. The results can be suggested that bottom ash mixed with soil developed the early compressive strength of soil. This is due to the composition of bottom ash obtained from Mae Moh power plant were 21.3% Al_2O_3 and 13.5% Fe_2O_3 [4] which Al_2O_3 and Fe_2O_3 in the bottom ash can be developed the early strength of the samples. However, the strength of A3 is more than C3 and C4 in the curing time 14 days. This is because the cement content in A3 samples was higher than C3 and C4 and the later strength is controlled mainly by calcium silicate hydrate.

Consideration on A1 samples and the samples in group C which contain the same amount of cement in the samples at 1.5% by weight of soil. The results

demonstrated the strength of the samples in group C which contained kaolin 0.5% and bottom ash 2%-8% was higher than A1 samples. Moreover, the strength of the samples tends to increase with an increase in the amount of bottom ash. The compressive strength of C3 and C4 samples was near in the curing time 3-14 days. The compressive strength of the samples C3 and C4 increased approximately 87% and 84% respectively of A1 samples in curing time 7 days. However, the strength of C3 and C4 samples in curing time 14 days was higher than A1 samples approximately 55%. Moreover, B2, B3, and B4 samples represented the unconfined compressive strength near A1 samples. Although, the samples in group B contain the amount of cement was less than the A1 samples 0.5% by weight of soil. Therefore, this result demonstrated that bottom ash can be reduced the utilized amount of cement to improve the strength of soil. The influence of bottom ash on the compressive strength of soil shown in Fig. 7 and Fig. 8.

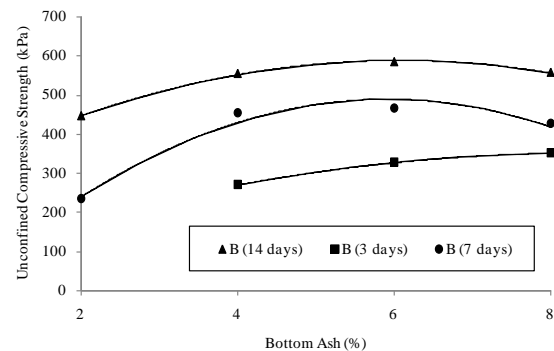


Fig. 7 The influence of bottom ash on the compressive strength of soil mixed with the admixture in group B.

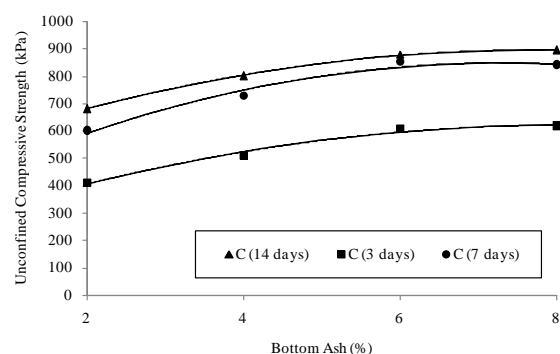


Fig. 8 The influence of bottom ash on the compressive strength of soil mixed with the admixture in group C.

The results demonstrated the strength of soil improvement tends to increase with an increase in

the amount of bottom ash. The unconfined compressive strength was rapidly increasing when bottom ash contains in the samples 2 to 6%. However, the samples which contain bottom ash 6% and 8% shown the similar value of the unconfined compressive strength. Therefore, this result can suggest the optimum content of bottom ash used to improve the strength of soil.

Nevertheless, the soil samples mixed with cement 1%, kaolin 1% and bottom ash 2% in curing time 3 days represented breakdown of the samples after soaked in the water for 2 hours. This is because the amount of cementitious materials is not enough to react. However, the increased amount of cement or bottom ash in the samples can increase the strength of soil and durability of the samples.

The required unconfined compressive strength of subbase improvement which suggested by the Thailand Department of highways should be more than 689 kPa at the curing time 7 days. Fig.9 demonstrated the unconfined compressive strength of soil mixed with an admixture of each mixture at the curing time 7 days. The samples which passed the minimum strength requirement consisted of the samples A3, C2, C3, and C4. The unconfined compressive strength value of the samples A3, C2, C3, and C4 was 889 kPa, 729 kPa, 854 kPa and 838 kPa respectively. Therefore, the samples mixed with cement at 1.5%, kaolin 0.5%, and bottom 4-8% can develop the strength of poor subbase higher than the minimum required strength. However, the soil samples mixed with admixture in group B cannot develop the strength higher than the minimum strength requirement. This is because the amount of cement in the mixture is not enough to increase the strength of soil.



Fig. 9 Unconfined compressive strength of soil mixed with an admixture for each mixture in 7 days curing time

Although the A1 samples have the amount of cement same as C2, C3, and C4, the A1 samples cannot develop the strength of soil higher than the minimum required. However, C2, C3, and C4 samples can be developed the strength was higher than the minimum requirement. This result can be demonstrated that bottom ash can develop the

strength of soil from the samples without bottom ash. Therefore, bottom ash mixed with the soil samples can be reduced the utilized amount of cement to improve the strength of soil.

CONCLUSION

Based on the experimental test obtained in this study, the following conclusion was made:

1. Bottom ash can increase the unconfined compressive strength of poor subbase. The optimum bottom ash content mixed in soil is 6% by weight of soil.

2. Bottom ash can develop the early strength of soil. The strength of the samples which contain bottom ash was higher than the samples without bottom ash approximately 84% in curing time 7 days.

3. The strength requirement which suggested by the Thailand Department of highways is 689 kPa in curing time 7 days. The soil samples mixed with cement 1.5%, kaolin 0.5%, and bottom ash 4 to 8% can be developed the unconfined compressive strength more than the strength required.

4. The strength of soil mixed with cement 1.5%, kaolin 0.5% and bottom ash 6 to 8% is equivalent to the soil mixed with cement 3% in curing time 7 days. The unconfined compressive strength was approximately 850 kPa. Therefore, bottom ash mixed in the soil samples can be reduced the utilized amount of cement to improve the strength of soil.

REFERENCES

- [1] Kavitha S., Geetha D., Ramesh P.S., Synthesis and characterizations of silver colloid nanoparticles stabilized by dextran, *J. Environ. Nanotechnol.* 4 (1), 2015, pp. 50–55.
- [2] Onyelowe K.C., Duc B.V., Durability of nanostructured biomasses ash (NBA) stabilized expansive soils for pavement foundation, *Int. J. Geotech. Eng.*, 2018, <https://doi.org/10.1080/19386362.2017.1422909>. [Online].
- [3] Hausmann M.R., Modification by admixture, *Engineering Principles of Ground Modification*, International Edition, McGraw-Hill Publishing Company, 1990, pp. 302-324.
- [4] Sathonsawaphak A., Chindaprasirt P., Pimraksa K., "Workability and Strength of lignite bottom ash geopolymer mortar", *Journal of Hazardous Materials*, 168, 2009, pp.44-50.
- [5] Chindaprasirt P., Jaturapitakkul C., Chalee W., Rattanasak U, "Comparative study on the characteristics of fly ash and bottom ash geopolymers", *Waste Management*, 29, 2008, pp.539-543.

- [6] Juturapitakkul C, Cheerarot R, "Development of bottom ash as pozzolanic material", *Journal of Materials in Civil Engineering*, volume 15, Issue 1, 2003.
- [7] Cheerarot R., "Development of disposed fly ashes and bottom ashes as pozzolanic material, Master of Eng.
- [8] Cheriaf M., Rocha J.C., P'era J., "Pozzolanic properties of pulverized coal combustion bottom ash, *Cem.Concr.Res.* 22, 1999, pp 1387-1391.
- [9] Ghafoori N., and J. Bucholc., "Investigation of lignite-based bottom ash for structural concrete." *J. Mater. Civ. Eng.* 8(3), 1996, pp.295-301.
- [10] Chorchill E. V., and Amirkhanian S.N, "Coal ash utilization in asphalt concrete mixtures." *J.Mater.Civ.Eng.*, 11(4), 1999, pp.128-13.
- [11] Hastuty P. I., Roesyanto, and B. S. Jeriko., "A study of the effectiveness of the use of cement and bottom ash toward the stability of clay in term of UCT value". *Procedia Engineering* 171, 2017, pp. 484-491
- [12] K.C. Onyelowe, B.V. Duc, Durability of nanostructured biomasses ash (NBA) stabilized expansive soils for pavement foundation, *Int. J. Geotech. Eng.* (2018), <https://doi.org/10.1080/19386362.2017.1422909> [Online]
- [13] K.J. Osinubi, V. Bafyau, A.O. Eberemu, Bagasse Ash Stabilization of Lateritic Soil, Springer Link Sciences and Business Media, 2009, pp. 271–280.
- [14] K.C. Onyelowe, Nanosized palm bunch ash stabilization of lateritic soils for construction purposes, *Int. J. Geotech. Eng.* (2017), <https://doi.org/10.1080/19386362.2017.1322797>[Online].
- [15] American Standard for Testing and Materials ASTM C618, Standard Specification for Pozzolan, ASTM, West Conshohocken, 2014,

DAMAGE LEVEL PREDICTION OF MULTI-STORY STEEL STRUCTURE IN SUMATRA USING BACKPROPAGATION NEURAL NETWORK

Reni Suryanita¹, Harnedi Maizir², Ismeddiyanto³, Vindi Trisatria⁴ and Raihan Arditama⁵

^{1,3,4}Faculty of Engineering, Universitas Riau, Pekanbaru, Indonesia; ²Sekolah Tinggi Teknologi Pekanbaru, Indonesia; ⁵Faculty of Engineering, Universitas Andalas, Padang, Indonesia.

ABSTRACT

Sumatra is one of the Indonesia islands that is prone to earthquakes both tectonic and volcanic. The research aims to predict the damage level of a multi-story steel structure due to the earthquake in Sumatra Island using the Backpropagation Neural Network (BPNN). The study used the steel structure building that received earthquake loads from ten capital cities of the province on Sumatra Island. The structure analysis used the finite element software while the BPNN method used the MATLAB Programming. The input data were the responses of the structure such as displacement, velocity, and acceleration while the output was damage level of the steel structure model. The model of BPNN has the potential accuracy to predict the damage level of steel structural more than 95%. According to the simulation result, 98,5% data could be predicted correctly by the BPNN method, and the best Mean Squared Error (MSE) is 0.028. These results have shown that BPNN can predict the damage level of multi-story steel structure in all the capital cities of the province on Sumatra Island.

Keywords: Backpropagation Neural Networks, Damage Level, Earthquake Load, Mean Squared Error, Response of Structure.

INTRODUCTION

All the coastal areas of Sumatra are in the Pacific Ring of Fire. Sumatra is one of the Indonesia islands that is prone to earthquakes both tectonic and volcanic. The characteristic of strong Indonesian quakes as occurred in Aceh on December 26, 2004 (measured 9.3 on the Richter Scale) and in Padang City on September 30, 2009 (with 7.9 on the Richter Scale) is very dangerous to the structure of buildings on these areas [1]-[2]. The collapse due to the sudden release of energy from within that creates a seismic wave. Earthquakes often occur in the location areas that are close to volcanoes and also in the regions that are surrounded by vast oceans. When this wave reaches the surface of the earth, its vibrations can be damaging or independent of source power and focal distance, besides the quality of the building and the quality of the soil in which it stands. Ordinary earthquakes are caused by the movement of the earth's crust (the earth's plates). Base on [3] the scales are used to measure the strength and magnitude of earthquakes is the Richter Scale and MMI (Modified Mercalli Intensity). However, in designing a structure, the necessary earthquake record data is in the form of Peak Ground Acceleration (PGA) units (g). The PGA is accelerogram, that is, a graph of surface acceleration comparison with time or duration during an earthquake. This accelerogram data will be an input quake parameter for a design or structural analysis.

The construction of high rise buildings is currently overgrowing. When the building goes higher, it tends to have a lower rigidity so that deformation of the structure is higher if the earthquake load is active. This excessive deformation can damage structural components. Steel structure building is a construction made from the arrangement of steel rods. Each part of the steel is connected using a joint such as bolts, nail or weld. Steel frame structure has advantages compared to concrete structures and wooden structures. Therefore, the higher tensile strength of steel, the lighter steel and more flexible when compared with concrete structures.

Therefore, the design of a building structure must meet the requirements written in the Design Codes and Standards and be well planned to minimize the occurrence of errors. In the Indonesian National Standards on Earthquake Resilience Procedures for Building Constructions, the construction of a building structure can be well designed and take into consideration earthquake loads that may occur. The requirement of quantity is outlined in [4] which the number of the mode of modal shall be sufficient to obtain the modal participating mass ratio at least 90% of the actual mass in each mode. Through the non-linear time history analysis, behavior and response of steel structure due to dynamic loading can be known in detail [5]-[6]. However, this method takes a relatively long time to process the finite element analysis compared with the static non-linear method. It is necessary to develop a smart

learning process in predicting the damage level of steel structures in different quake locations rapidly. For this reason, the study aims to identify damage level the steel structure due to earthquake load quickly based on the time history of an earthquake using Backpropagation Neural Network (BPNN).

According to FEMA 356 [7], the performance level of a building structure for primary members (P) and secondary members (S) must be at six levels of structural performance as shown in Fig.1, which are:

1. *Immediate Occupancy (IO)*, that is, there is no significant damage to the structure so that its strength and stiffness are almost the same as before the earthquake.
2. *Damage Control*, in these circumstances the structure is at the safety level (safe limit) of the structure.
3. *Life Safety (LS)*, in this situation there is damage to the structural components. The stiffness of the structure is reduced but has not experienced structural collapse. Structures that are in this state can still be used when the repair has been done.
4. *Limited Safety*, in this case, the structure is defined as being in the condition between the occupant's safety structure and the prevention of collapse. In this situation, there is "much structural damage," because it is no longer safe to be inhabited due to limited structural strength.
5. *Collapse Prevention (CP)*, defined as a state of post-collapse damage. Damage occurs in structural and nonstructural components.
6. *Structural Performance not Considered*, buildings that have been damaged in their nonstructural parts are classified at this level of performance.

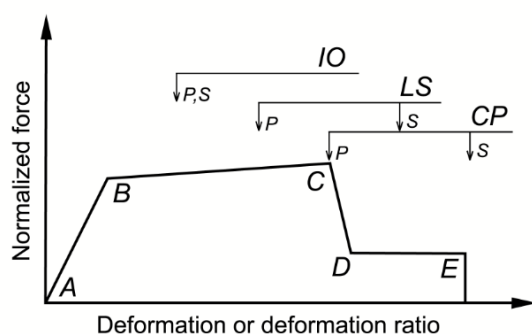


Fig.1. Acceptance criteria of component deformation

Currently, most of the earthquake-resistant buildings are planned with procedures written in the building codes. In this study, building structure was analyzed using a non-linear time history method to find out the structure behavior due to earthquake load. This time history analysis is a structural analysis method that reviews the structure response

over time to earthquake vibrations. In general, analysis using the time history of earthquake requires a relatively long time duration. One solution of rapid prediction is using the Backpropagation Neural Network (BPNN). Based on previous research, the BPNN method has been successfully used in various fields of Civil Engineering for making predictions such as [8], [9] and [10]. The previous study has resulted in the BPNN accuracy reaches 96% to 98% to predict the damage level of drift story of concrete building [11] and bridge structure [12]. The study suggests that BPNN deserves to be applied as a tool for predicting in the Civil Engineering world. However, the number of research that discusses the estimation of damage to structures of multi-story steel buildings is still relatively small. Therefore, this study aims to predict the extent of damage to building structures that occur due to earthquakes. Consequently, the matters discussed in this study include the level of damage to the multi-story steel portal that happens in a building model that has a height variation.

BACKPROPAGATION NEURAL NETWORKS

Knowledge of biological neuron cells in the brain has inspired the development of a computing system called Artificial Neural Network (ANN). The artificial neural network is a system that has a working system like the human brain. This system can model a complicated thing between input and output to determine a particular pattern. The architecture and operation of ANN can be described in the form of mathematical and computational models for data classification, clusters, and non-parametric regression or as simulations of biological neural models.

Backpropagation Neural Network (BPNN) is one of the training methods on ANN, where the characteristics of this method are to minimize the error on the output produced by the network. The BPNN training is conducted to develop the ability of memorization and generalization in weights. The strength of BPNN to memorize is the way to remember and take the learned pattern incorrectly. What is meant by generalization capability is the ability of BPNN to provide an acceptable response from similar data and input patterns to a model previously studied by the previous system. Most of the training for feedforward networks use gradients from the activation function to determine how to manage the weights in minimizing performance. The gradient is estimated by using a technique called backpropagation. The advantage of using this BPNN method is that it is possible to obtain information from a complex set of data and solve problems that are unstructured and difficult to define. The standard backpropagation training algorithm will drive the weights with the negative gradient direction. The

fundamental principle of the backpropagation algorithm is to fix network weights by making the activation function go down quickly.

Backpropagation could be estimated errors with gradient descent on each network located on the architecture of the Artificial Neural Network. BPNN consists of three layers; input, hidden and an output layer. Each neuron in the hidden layer it will receive information from the input layer neuron multiplied by the weight of the tissue entering the neuron and summed.

RESEARCH METHODOLOGY

The models of the structure are three multi-story steel building. The structure models refer to the requirements by SNI 1729-2015 Indonesian specification for structural steel building [13]. The dimensions of structural elements used are as follows:

1. Modulus of Elasticity : 200.000 MPa
2. Shear Modulus : 80.000 MPa
3. Poisson's ratio : 0.3
4. Steel density : 7.850 Kg/m³
5. Yield strength : A36 - 240 MPa

Table 1 Properties of Steel Structure Model

Story of Model	Beam	Column	Height (m)
5	WF 300x150	H 350x350	18
10	WF 300x150	H 350x350	35.5
15	WF 300x150	H 350x350	53

The structure of the building under observation is a steel portal which has the same floorplan starting from the ground floor (base) to the roof (rooftop), as shown in Fig 2. Elevation between floors is 4 meters for the ground floor and 3.5 meters for the next level. The regular building shape with X and Y direction is not symmetrical as shown in Fig 3.

The earthquake load used is in the form of time history response record. Adjustment of the scale used is determined based on the planning standards of seismic resistance of Indonesia SNI 1726-2012 [4] with medium soil conditions. The earthquake data in all provincial capitals on the island of Sumatra in Table 2.

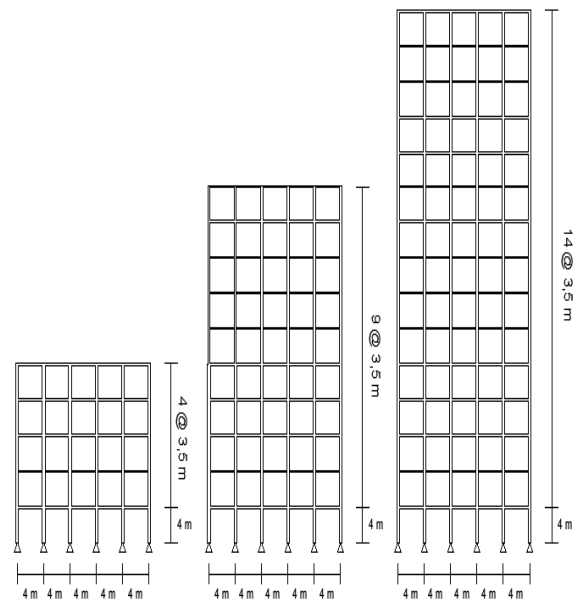


Fig 2. The steel structure model with various height.

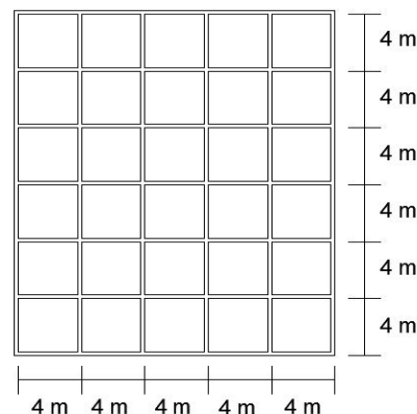


Fig 3. The layout of the steel structure building

Table 2 PGA value of Capital City of Province in Sumatra Island

No.	Capital City of Province	PGA
1	Banda Aceh	0,621g
2	Medan	0,231g
3	Padang	0,515g
4	Pekanbaru	0,214g
5	Tanjung Pinang	0,023g
6	Jambi	0,105g
7	Bengkulu	0,519g
8	Palembang	0,146g
9	Pangkal Pinang	0,026g
10	Lampung	0,356g

The time history analysis of earthquake is done by modeling the steel structure by the data that will be used into the finite element software. Following is the flowchart of the analysis steps with the finite element software, as shown in Fig 4. Meanwhile, the BPNN architecture model for this study is shown in Fig. 5.

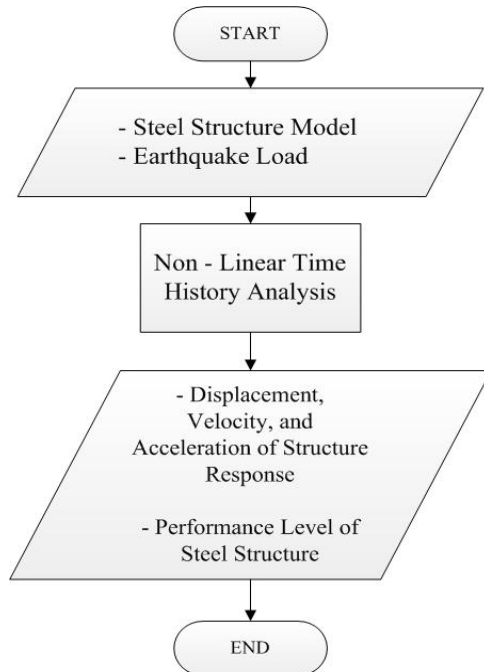


Fig 4. Flowchart of finite element method for the study

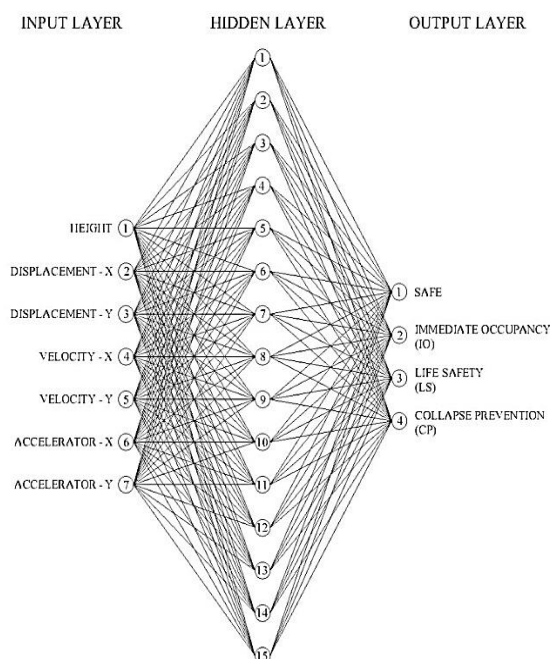


Fig 5. The BPNN architecture model

Input layer consists of the height of the steel structure building, displacement, velocity and acceleration of structural response in X and Y direction. The output layer includes the building condition after received earthquake load; Safe as index 1, Immediate Occupancy as index 2, Life Safety as index 3 and Collapse Prevention as index 4. The procedure of the study used the BPNN method as shown in Fig 6.

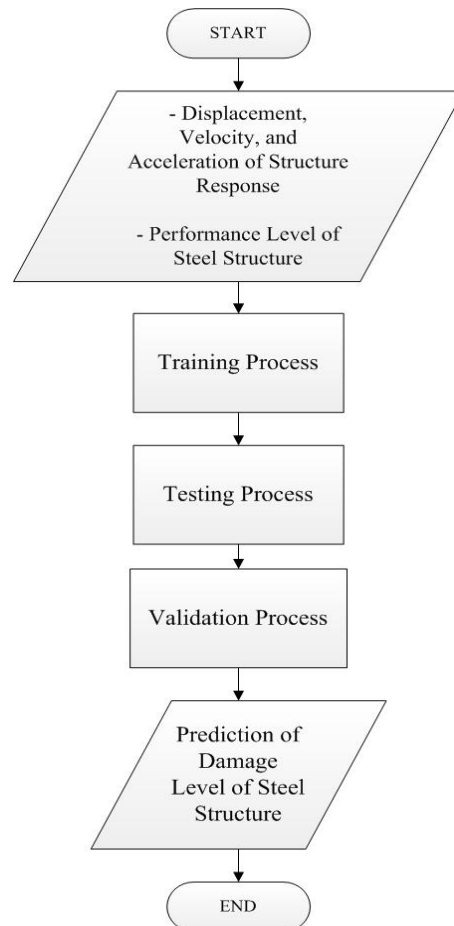


Fig 6. The BPNN method for the study

RESULTS AND DISCUSSION

Finite element analysis resulted in the time history of displacement, velocity, and acceleration at the top of the steel structure. The most considerable displacement value occurred in Banda Aceh City was 0.102 meters in X-direction. Meanwhile, the displacement value of Y-direction was 0.112 meters. The smallest displacement value happened in Tanjung Pinang City was 0.006 m for the X direction and 0.007 m for Y-direction.

The most considerable velocity value occurred in Banda Aceh City was 0.957 m/s for the X-direction and 0.926 m/s for Y-direction. The smallest velocity value happened in Tanjung Pinang

City was 0.057 m/s for the X-direction and 0.055 m/s for Y-direction.

The most considerable acceleration value occurred in Banda Aceh City was 13.832 m/s² for X-direction and 9.555 m/s² for Y-direction. The smallest acceleration value in Tanjung Pinang City was 0.820 m/s² for X-direction and 0.583 m/s² for Y-direction.

Backpropagation Neural Network (BPNN) method was used with the following input parameters: displacement, velocity, and acceleration in X and Y-direction. Whereas the predicted output parameters are Safe as 1, Immediate Occupancy as 2, Life Safety as 3 and Collapse Prevention as 4 for the label. The training process on the system was done as a whole to facilitate the learning process. The learning process was delivered repeatedly and gradually with 21 hidden layers. After the completion of the training process, the total iteration (epoch) obtained was as much as 7675 epoch by using Tan Sigmoid method. The best validation performance of Mean Squared Error (MSE) is 0.028227 as shown in Fig 7.

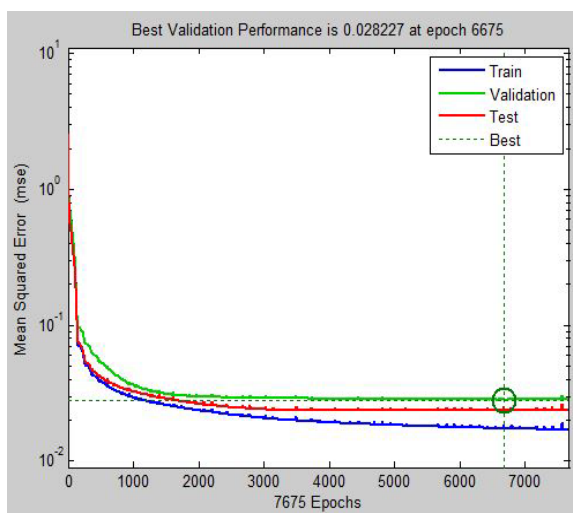


Fig 7. The best performance of MSE (MSE)

Based on the above results, the trained BPNN method has been able to predict the extent of structural damage very well. The result indicated how closely located the distribution of the target points and the prediction to the diagonal line of Regression (R) that is 0.98499. In other words, the predicted results are close to 100 percent of the actual state as shown in Fig 8.

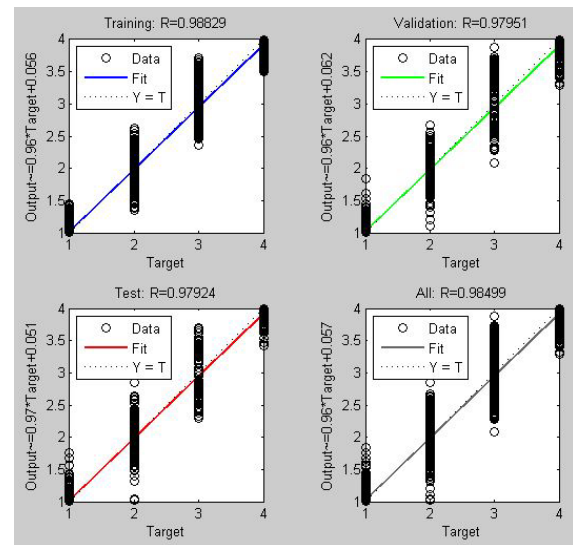


Fig 8. The best performance of Regression (R)

CONCLUSION

The displacement of a structure will increase the height of the structure due to the earthquake. The same is true for the velocity and acceleration which will also increase with the height of the building structure. Out of the ten provinces on the island of Sumatra, Banda Aceh City shows the most significant damage level due to the scaled earthquake and has the most substantial displacement is 0.102 m for the X-direction and 0.112 m for Y-directions in comparison to the other provinces. The smallest displacement values occurred in the city of Tanjung Pinang with 0.006 m for the X-direction and 0.007 m for the Y-direction. Based on the average of Regression which is 0.95573, it can be concluded that the designed ANN has a high correlation and accuracy.

ACKNOWLEDGMENTS

The authors are grateful to The Indonesian Government through the Ministry of Research, Technology and Higher Education of Indonesia with Contract No. 086/SP2H/LT/ DRPM/2017 for funding this research.

REFERENCES

- [1] T. Lay, H. Kanamori, C. J. Ammon, M. Nettles, S. N. Ward, R. C. Aster, S. L. Beck, S. L. Bilek, M. R. Brudzinski, and R. Butler, "The Great Sumatra-Andaman Earthquake of 26 December 2004," *Science* (80-.), vol.

- 308, no. 5725, pp. 1127–1133, 2005.
- [2] C. Yang, “Study on Indonesian Seismic Code SNI 03-1726-2002 and Seismic Impact to High-rise Buildings in Jakarta, Indonesia,” in *Proceedings of World Academy of Science: Engineering and Technology*, 2009, p. 50.
- [3] Y.-X. Hu, S.-C. Liu, and W. Dong, *Earthquake Engineering*. CRC Press, 2014.
- [4] SNI-1726, *The Seismic Resistance Design Standard for Buildings (Indonesian National Standard)*. 2012.
- [5] Y. Ding, X. Song, and H.-T. Zhu, “Probabilistic Progressive Collapse Analysis of Steel-Concrete Composite Floor Systems,” *J. Constr. Steel Res.*, vol. 129, pp. 129–140, 2017.
- [6] J. Setiawan and S. Nakazawa, “Study on Comparison of Special Moment Frame Steel Structure (SMF) and Base Isolation Special Moment Frame Steel Structure (BI-SMF) in Indonesia,” in *AIP Conference Proceedings*, 2017, vol. 1892, no. 1, p. 20026.
- [7] FEMA356, “Prestandard and Commentary for The Seismic Rehabilitation of Buildings,” vol. FEMA 356. Federal Emergency Management Agency, Washington, DC, 2000.
- [8] J. Gu, M. Gul, and X. Wu, “Damage Detection under Varying Temperature using Artificial Neural Networks,” *Struct. Control Heal. Monit.*, vol. 24, no. 11, p. e1998, 2017.
- [9] S. Gholizadeh, “Performance-based Optimum Seismic Design of Steel Structures by a Modified Firefly Algorithm and a New Neural Network,” *Adv. Eng. Softw.*, vol. 81, pp. 50–65, 2015.
- [10] M. Betti, L. Facchini, and P. Biagini, “Damage Detection on a Three-Storey Steel Frame using Artificial Neural Networks and Genetic Algorithms,” *Meccanica*, vol. 50, no. 3, pp. 875–886, 2015.
- [11] R. Suryanita and H. Jingga, “Application of Backpropagation Neural Networks in Predicting Story Drift of Building,” in *Lecture Notes in Engineering and Computer Science*, 2017, vol. 2227.
- [12] R. Suryanita, Mardiyono, and A. Adnan, “Intelligent bridge seismic monitoring system based on Neuro Genetic hybrid,” *Telkomnika (Telecommunication Comput. Electron. Control.)*, vol. 15, no. 4, 2017.
- [13] SNI-1729, “The Specification for Structural Steel Building (Indonesian National Standard),” 2015.

BRAIN TISSUE SWELLING DURING ISCHAEMIA-REPERFUSION: 2D FINITE ELEMENT ANALYSIS USING POROELASTICITY

Mohamed Mokhtarudin, M. J.¹, Shabudin, A.² and Payne, S. J.³

^{1,2} Faculty of Mechanical Engineering, Universiti Malaysia Pahang, 26600 Pekan, Pahang

³ Institute of Biomedical Engineering, Department of Engineering Science, Old Road Campus Research Building, University of Oxford, Headington, Oxford OX3 7DQ, UK

ABSTRACT

Brain vasogenic oedema is an injury that occurs after reperfusion treatment of ischaemic stroke patient. It can lead to brain tissue swelling consequently causing brain herniation that may affect brain functionality. In this paper, a mathematical model describing this injury are developed using capillary filtration and poroelastic theory to represent oedema formation and brain tissue swelling, respectively. An ideal 2D representation of human brain is developed and the mathematical model of ischaemia-reperfusion injury is solved using finite element method. The size and location of the ischaemic stroke infarct are varied and the movement of the midline that divides the cerebrals is observed. The midline movement represents the level of herniation. Results show that herniation level increases especially for large infarct size and for infarct located nearer to the brain ventricle. Further validation of the model using MRI data and patient-specific representation is needed to estimate brain tissue swelling subsequently predict the effectiveness of ischaemic stroke treatment.

Keywords: Poroelasticity, Finite Element Analysis, Cerebral Tissue Swelling, Ischaemia-Reperfusion Injury, Vasogenic Oedema

INTRODUCTION

Brain oedema formation due to cerebral ischaemia-reperfusion can be observed using medical imaging modalities such as CT and MRI scans by the movement of brain midline structures (also known as brain herniation) or by brain tissue swelling. Herniation usually results in the compression of brain ventricle and cerebral microvessels, which further results in the occurrence of secondary ischaemia [1]. The presence of herniation may indicate the rise in the intracranial pressure (ICP) and it may cause permanent neurological problems and even fatality [2]. Several treatments are available for brain oedema such as decompressive surgery and osmotherapy. However, the effectiveness of these treatments remains questionable due to the complicated nature of brain oedema formation.

A mathematical model has been developed to further understand the formation of brain tissue swelling due to BBB breakdown using poroelastic theory. Poroelasticity was initially used to study soil mechanics [3] and has been extensively used to study the mechanics of the pathological brain [4-6]. In this theory, the brain tissue is assumed to be homogeneous, has linear elastic property, and contain both water and blood, permeable in a solid porous matrix structure. A comprehensive mathematical framework of this theory can be found in [7].

In this paper, a mathematical model of brain tissue swelling after a cerebral ischaemia-reperfusion treatment is investigated using an ideal 2D brain geometry and solved using finite element scheme of poroelastic model. The objective here is to observe the effect of infarct size and location towards the formation and severity of brain herniation. This will be a preliminary study before a more complete validation using MRI data of ischaemic stroke patient can be done.

METHODOLOGY

Theoretical Background

During ischaemic stroke, the lack of oxygen and nutrient to the affected region creates a series of biochemical reactions that destroys the endothelial cells surrounding the cerebral microvessels leading to the blood-brain barrier (BBB) breakdown, which increases the BBB permeability [8]. When blood flow is restored after reperfusion treatment, ions and some protein plasma can filtrate through the damaged BBB creating osmotic pressure difference between the capillary and interstitial space. This can cause the flux of water from the capillary and accumulate in the tissue space and causes the formation of vasogenic oedema, eventually leading to the formation of cerebral tissue swelling. Figure 1 illustrates the process of water accumulation into the interstitial space after BBB breakdown.

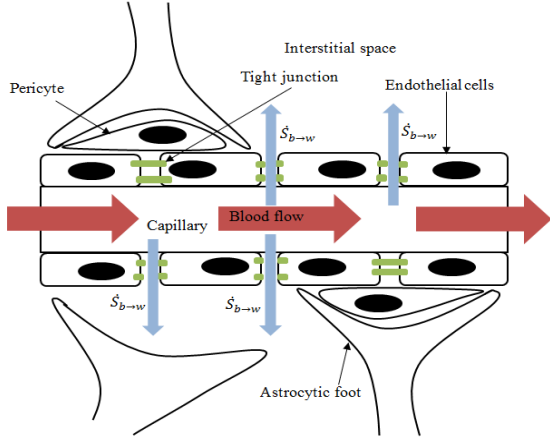


Fig. 1. Flux of water after BBB breakdown. $\dot{S}_{b \rightarrow w}$ represents the water movement from the cerebral blood flow into the tissues via capillary filtration.

POROELASTICITY MODEL

Mathematical Formulation

The formation of cerebral tissue swelling due to capillary filtration has been modelled by [7] using capillary filtration model and poroelastic theory. The governing equations are given as:

$$\sigma_{ij} - \alpha_w \nabla P_w = 0 \quad (1)$$

$$\frac{1}{Q_w} \frac{\partial P_w}{\partial t} - k_w \nabla^2 P_w - \dot{S}_{b \rightarrow w} = 0 \quad (2)$$

where σ_{ij} is the total stress of the tissue, P_w is the interstitial water pressure, α_w is the Biot parameter for water, Q_w is the relative compressibility of water, k_w is the permeability of water, t is time.

The term $\dot{S}_{b \rightarrow w}$ represents the water transfer from the capillary space into the cerebral interstitial space via capillary filtration, which occurs when BBB broke down. This term can be described by [7]:

$$\dot{S}_{b \rightarrow w} = 2\bar{n}_b \frac{L_p}{R_c} f[(P_b - P_w) - \sigma \Pi_b] \quad (3)$$

where \bar{n}_b is the baseline volume fraction of the blood, L_p is the hydraulic permeability of the capillary, R_c is the baseline value of capillary radius, σ is the reflection coefficient, Π_b is the osmotic pressure in the capillary and P_b is the blood

pressure, which has been assumed constant. Lastly, the term f represents the fraction of vessels that remain open after the reperfusion and swelling process at each point in space and time, and this can be modelled using a Heaviside function.

The total stress, σ_{ij} , is linearly related to the strain, ε_{ij} , using typical linear elasticity relation:

$$\sigma_{ij} = 2G\varepsilon_{ij} + \frac{2G\nu}{1-2\nu}\varepsilon_{ii} \quad (4)$$

where G , and ν are the shear modulus and Poisson's ratio of the brain tissue, respectively.

Numerical Procedure

Brain Geometry and Meshing

The brain geometry was drawn according to the realistic brain geometry as proposed by [9]. The brain is modelled as a circle that consists of a circular core in the middle that represents the brain ventricle. The brain radius is about 65 to 67 mm [10], hence the outer radius is taken here to be approximately as 80 mm. The circular core that represent the ventricle has the radius of 24 mm, taken to be about 30% of the brain radius [11]. The brain tissue is assumed to be homogeneous, thus there is no difference between the white and grey matter. The inner and outer boundaries of the brain geometry are named as the ventricular layer and the subarachnoid layer, respectively.

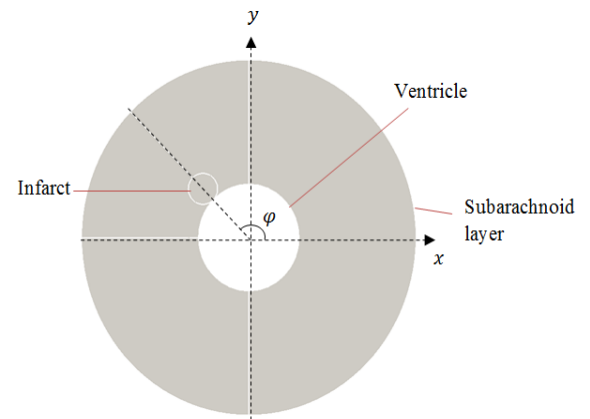


Fig. 2. Idealized 2D brain geometry with an infarct of radius 7 mm located at $\phi = 135^\circ$.

To model the effects of ischaemia, a small infarcted region is drawn within the geometry. The infarct size is varied in the range 7 mm to 28 mm radius to study the effect of size on cerebral swelling. The infarct is drawn as a circle which is located

along the line that makes an angle $\varphi = 135^\circ$, where φ is the angle measured counterclockwise from the x -axis, as shown in Fig. 2.

The infarcted region and region near it are discretised using a finer mesh than the rest of the part of the geometry. The number of elements varies depending on the sizes of the infarct of about 2000 to 5000 10-nodes tetradhedral elements. The meshing is done using Gmsh.

Boundary conditions

The boundary condition at the skull, R_s is set as stationary and pressure at baseline ICP, \bar{P} . The tissue is assumed to initially static and the fluid pressure is at the baseline ICP.

Meanwhile, we consider two types of boundary conditions at the ventricle, R_v , which are: (1) the ventricle is assumed fix and the pressure is at the baseline ICP; and (2) the ventricle is free to move during tissue swelling:

$$\sigma_{ij}(R_v, t) \cdot \mathbf{n} = -\bar{P}\mathbf{n} \quad (5)$$

The simulations are solved using open-source finite element analysis software ELMER and are analysed using ParaView.

Model Parameters

Table 1 below shows the parameters involved in this model and their respective value. Details regarding the parameters can be found in [7].

Table 1. List of parameters and their baseline value for the proposed model.

Parameter	Value
ν	0.35
G	216.3 Pa
α_w	1
Q_w	3244 Pa
Π_b	2445 Pa
σ	0.93
P_b	4389 Pa
\bar{n}_b	0.03
L_p	3.0×10^{-11} m/s.Pa
R_c	5×10^{-6} m
\bar{P}	1330 Pa

RESULTS & DISCUSSION

Fix Ventricle Boundary Condition

The brain tissue swelling during capillary filtration was simulated for simulation time until 1 hour. Figure 3 shows the cerebral interstitial pressure P_w and tissue displacement u for various infarct sizes for the case of fix ventricle boundary condition. The tissue displacement starts to develop at the outermost radius of the infarct before slowly spreading to the inside and outside of the infarct. Meanwhile, the pressure starts to rise within the centre of the core and then spreads in the direction of

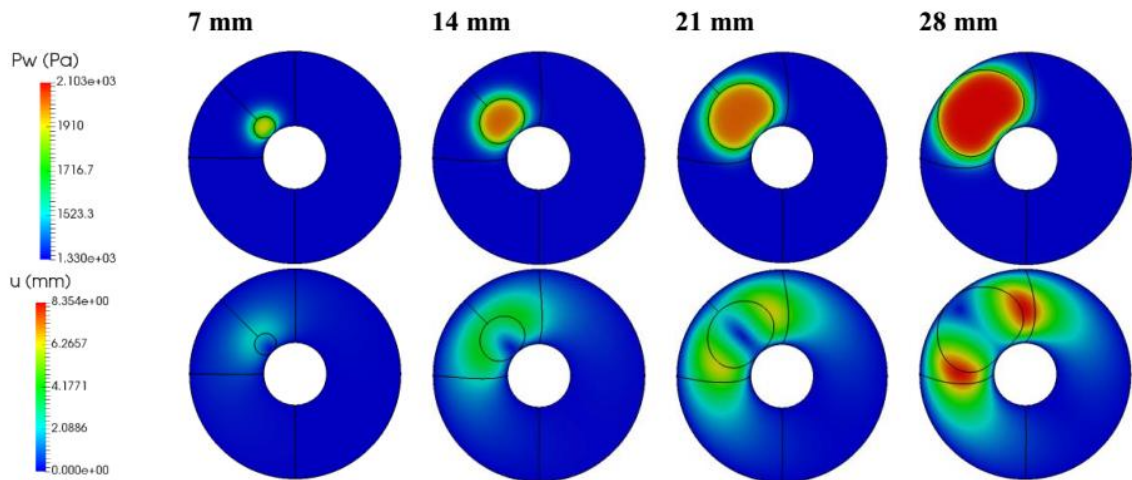


Fig. 3. 2D simulation results for various infarct sizes. (Top) Interstitial pressure. (Bottom) Tissue displacement.

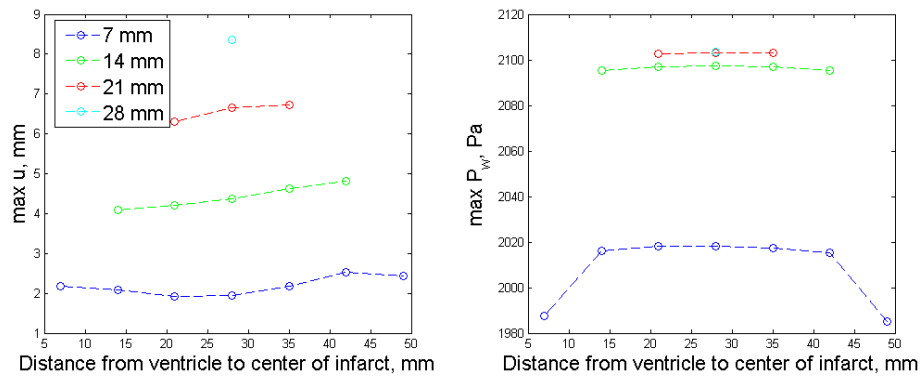


Fig. 4. Variation of the maximum brain tissue displacement and interstitial pressure with the infarct size and distance from the ventricle.

the infarct radius.

However, due to the boundary conditions imposed at the subarachnoid and ventricular layers, the displacement and pressure gradually decrease near these layers. The tissue displacement pushes the other side of the cerebral tissue as indicated by the deformation of the middle line to the right side. The deformation of this line increases as the size of the infarct becomes larger.

The changes in maximum displacement and maximum pressure when the infarct distance from the ventricle is varied are shown in Fig. 4. The maximum displacement increases when the distance from the ventricle increases except for the case of the infarct radius at 7 mm. For this infarct size, there is a slight drop in the maximum displacement for the infarct distance from 7 mm to 21 mm and the infarct distance from 42 mm to 49 mm. Meanwhile, for the maximum pressure, there is no substantial difference when the distance is varied with the exception of the case for a 7 mm infarct radius, although the difference for this case is only about 25 Pa from the other case.

This difference is due to the ‘edge effect’, in which the infarct is located near the subarachnoid and ventricle layer that have been fixed in terms of displacement and pressure values. In reality, the ventricle does not have a fixed shape and position but it may move and be compressed during brain tissue swelling. The compression of the ventricle is also a good indicator of cerebral swelling in CT images [12]. It is known that the existence of AQP4 at the interface of the ventricle and the cerebral space can help in the clearance of oedematous fluid [13]. Thus, a further improvement to the model could be made by incorporating a pressure gradient [14] and stress-free boundary conditions [15] at the ventricle to see how the presence of this fluid cavity affects the progression of cerebral swelling and fluid pressure development. However, for the sake of model simplification, this assumption is applied here.

Moving Ventricle Boundary Condition

For moving ventricle cases, we only consider two different sizes of stroke infarct – 7 mm and 14 mm radii. Then, we measure the displacement of two points on the ventricle, namely point x1 and x2 as illustrated in Fig. 5.

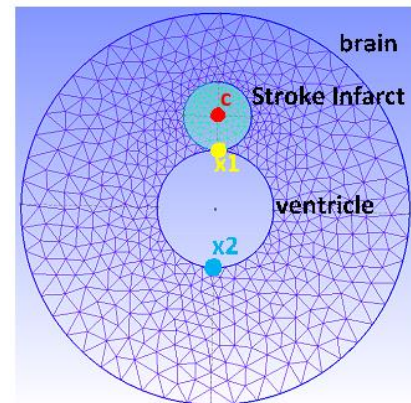


Fig. 5. Location of x1 and x2 for ventricle displacement measurement.

Figure 6 shows the displacement of point x1 for stroke infarct of radius 7 mm and 14 mm at 7 and 5 different locations, respectively. The 0 mm and 42 mm lines referred to the stroke located nearest and farthest from the ventricle, respectively.

It can be seen in Fig. 6 that the displacement of point x1 increases as the simulation time increases for all locations of the stroke. Stroke that is located nearer to the ventricle results in larger displacement of point x1, whereas stroke located further shows smaller displacement. The changes in displacement for both 7 mm and 14 mm stroke shows similar characteristic, where the displacement increase

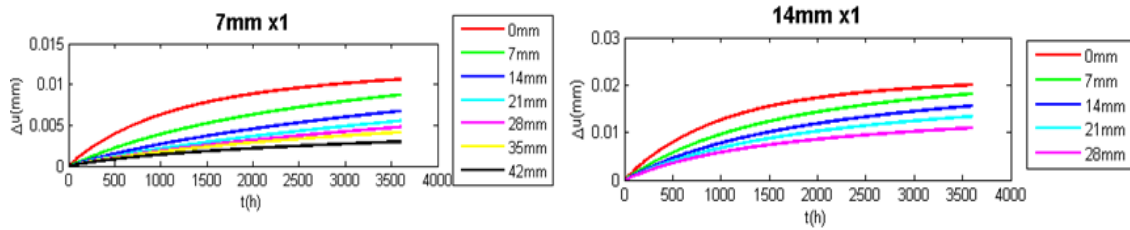


Fig. 6. Displacement of point x1 for infarct radius of 7 mm and 14 mm.

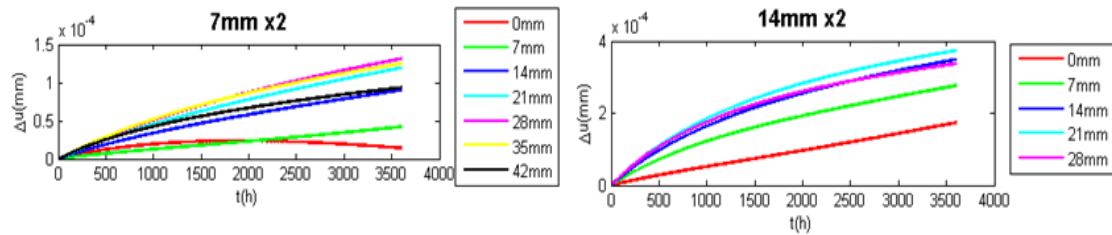


Fig. 7. Displacement of point x2 for infarct radius of 7 mm and 14 mm.

rapidly from time 0 to 2000 s. After time 2000 s, the displacement becomes almost constant. However, the displacement of point x1 is bigger for 14 mm compared to 7 mm.

Meanwhile, Fig. 7 shows the displacement of point x2 for infarct radius of 7 mm and 14 mm. It can be seen here that the displacement of point x2 increases with time for all infarct locations, with exception for the case of infarct located 0 mm and 26 mm from the ventricle, for infarct radius of 7 mm and 14 mm, respectively. It should be noted that the displacements of point x2 are much smaller compared to point x1 because point x2 is relatively farther from the stroke location than point x1.

It is important to measure the displacement of the ventricle because brain swelling after stroke can be observed by looking at the movement of ventricle in MRI images. For example, ventricle enlargement has been used as an objective measure of mild cognitive impairment in Alzheimer's disease [16]. To further accurately measure ventricle movement will require the integration of the finite element model with brain images through image-model registration procedure, as has been done, for example, by [17].

FUTURE WORKS

It has been assumed in this study that the cerebral tissue property is homogeneous throughout the geometry. In reality, the cerebral tissue material properties are different for those located in the white and grey matter of the cerebral space. Oedema is less likely to develop in the grey matter area due to its twisted structure and it has a low tissue compliance as compared to white matter [18]. The study done by Smillie [11] also assumed that the mechanical properties of white and grey matter are the same due to the lack of data available. However, they use different fluid permeability values within these two

cerebral structures. Meanwhile, the model developed by Nagashima [19] used two different cerebral tissue hydraulic conductivity values to account for their different properties. Therefore, incorporating the different mechanical properties of the brain tissues in the model could improve the brain tissue swelling prediction.

Another aspect worth studying is the vasogenic oedema resolution. The oedematous fluid will move out into the ventricles and subarachnoid spaces via glia limitans, into the capillary endothelium via the astrocytic foot or by metabolic degradation [20, 21]. The presence of aquaporin-4 (AQP4) channels in the glia limitans and astrocytic foot [21] facilitate the removal of the oedematous fluid. However, AQP4 also plays a role in the formation of cytotoxic oedema that causes intracellular swelling, which does not result in an increase in ICP and brain tissue swelling [22]. The function of AQP4 has been demonstrated by using a mathematical model [23]. Modification of the current model through the inclusion of the role of AQP4 might provide new insight towards the occurrence of reperfusion injury.

CONCLUSION

From this study, it was found that the size and location of cerebral ischaemic infarct can affect the degree of brain herniation. This is shown by the deflection of the midline that divides the two cerebrals. In addition, the maximum brain tissue displacement and interstitial pressure are increase as the infarct sizes increase. These findings indicate that ischaemic infarct size plays an important role in determining the severity of brain tissue swelling.

The results obtained here provide further useful information such as: (1) the importance of making the ventricle structure movable for better quantification of the brain tissue swelling; and (2)

confirms the occurrence of herniation during brain tissue swelling. This information is useful before the models can be applied to the actual patient data for validation purposes.

ACKNOWLEDGEMENTS

This study was supported by Universiti Malaysia Pahang (UMP) Research Grant (RDU1703310) and Tabung Persidangan Luar Negara UMP (TPLN).

REFERENCES

1. Abbott, N.J., Patabendige, A.A., Dolman, D.E., Yusof, S.R., and Begley, D.J., *Structure and function of the blood-brain barrier*. Neurobiol Dis, 2010. 37(1): p. 13-25.
2. Donkin, J.J. and Vink, R., *Mechanisms of cerebral edema in traumatic brain injury: therapeutic developments*. Curr Opin Neurol, 2010. 23(3): p. 293-9.
3. Biot, M.A., *General theory of three-dimensional consolidation*. J. Appl. Phys., 1941. 12(2): p. 155-164.
4. Taylor, Z. and Miller, K., *Reassessment of brain elasticity for analysis of biomechanisms of hydrocephalus*. Journal of Biomechanics, 2004. 37(8): p. 1263-1269.
5. Tully, B. and Ventikos, Y., *Cerebral water transport using multiple-network poroelastic theory: application to normal pressure hydrocephalus*. J. Fluid. Mech., 2011. 667: p. 188-215.
6. Vardakis, J.C., Tully, B.J., and Ventikos, Y., *Exploring the Efficacy of Endoscopic Ventriculostomy for Hydrocephalus Treatment via a Multicompartmental Poroelastic Model of CSF Transport: A Computational Perspective*. Plos One, 2013. 8(12).
7. Mohamed Mokhtarudin, M.J. and Payne, S.J., *Mathematical model of the effect of ischemia-reperfusion on brain capillary collapse and tissue swelling*. Math. Biosci., 2015. 263: p. 111-120.
8. Yang, Y. and Rosenberg, G.A., *Blood-brain barrier breakdown in acute and chronic cerebrovascular disease*. Stroke, 2011. 42(11): p. 3323-8.
9. Hakim, S., Venegas, J.G., and Burton, J., *The physics of the cranial cavity, hydrocephalus, and normal pressure hydrocephalus: Mechanical interpretation and mathematical model*. Surg. Neurol., 1976. 5: p. 187-210.
10. Cosgrove, K.P., Mazure, C.M., and Staley, J.K., *Evolving knowledge of sex differences in brain structure, function and chemistry*. Biol. Psychiat., 2007. 62(8): p. 847-855.
11. Smillie, A., Sobey, I., and Molnar, Z., *A hydroelastic model of hydrocephalus*. J. Fluid Mech., 2005. 539: p. 417-443.
12. Zimmerman, R.A., Bilaniuk, L.T., Bruce, D., Dolinskas, C., Obrisi, W., et al., *Computed tomography of pediatric head trauma: Acute general cerebral swelling*. Radiology, 1978. 126: p. 403-408.
13. Papadopoulos, M.C. and Verkman, A.S., *Aquaporin water channels in the nervous system*. Nat. Neurosci., 2013. 14: p. 265-277.
14. Taylor, Z. and Miller, K., *Reassessment of brain elasticity for analysis of biomechanisms of hydrocephalus*. J. Biomech., 2004. 37: p. 1263-1269.
15. Liu, F., Lollis, S.S., Ji, S., Paulsen, K.D., Hartov, A., et al., *Model-based estimation of ventricular deformation in the cat brain*. Med. Image. Comput. Comput. Assist. Interv., 2009. 12(Pt 2): p. 308-315.
16. Nestor, S.M., Rupsingh, R., Borrie, M., Smith, M., Accomazzi, V., et al., *Ventricular enlargement as a possible measure of Alzheimer's disease progression validated using the Alzheimer's disease neuroimaging initiative database*. Brain, 2008. 131: p. 2443-2454.
17. Kyriacou, S.K., Davatzikos, C., Zinreich, S.J., and Bryan, R.N., *Nonlinear elastic registration of brain images with tumor pathology using a biomechanical model*. IEEE Trans Med. Imag., 1999. 18(7): p. 580-592.
18. Kimelberg, H.K., Nestor, N.B., and Feustel, P.J., *Inhibition of release of taurine and excitatory amino acids in ischemia and neuroprotection*. Neurochem Res, 2004. 29(1): p. 267-74.
19. Nagashima, T., Shirakuni, T., and Rapoport, S.I., *A two-dimensional, finite element analysis of vasogenic brain edema*. Neurol. Med. Chir., 1990. 30: p. 1-9.
20. Tourdias, T., Mori, N., Dragonu, I., Cassagno, N., Boiziau, C., et al., *Differential aquaporin 4 expression during edema build-up and resolution phases of brain inflammation*. J. Neuroinflamm., 2011. 8: p. 143-160.
21. Papadopoulos, M.C., Manley, G.T., Krishna, S., and Verkman, A.S., *Aquaporin-4 facilitates reabsorption of excess fluid in vasogenic brain edema*. FASEB J., 2004. 18: p. 1291-1293.
22. Donkin, J.J. and Vink, R., *Mechanisms of cerebral edema in traumatic brain injury: Therapeutic developments*. Curr. Opin. Neurol., 2010. 23: p. 293-299.
23. Mokhtarudin, M.J. and Payne, S.J., *The study of the function of AQP4 in cerebral ischaemia-reperfusion injury using poroelastic theory*. Int J Numer Method Biomed Eng, 2017. 33(1).

DESIGN OF BASE ISOLATED REINFORCED CONCRETE BUILDING SUBJECTED EARTHQUAKE EXCITATION USING EC 8

Norliyati Mohd Amin¹, Nabihan Ayub¹ and Anizahyati Alisibramulisi¹

¹Faculty of Civil Engineering, University Teknologi MARA, Selangor, Malaysia

ABSTRACT

From past earthquakes, it is proved that many of reinforced concrete (RC) structure are totally or partially damaged due to seismic load. However, new structures will soon have the capacity for better resistance to earthquakes with a design code for buildings to raise safety standards of structures. In this study, the RC structure was modeled as bare frame of 10 storey building including ground floor using BS8110. The parameters used in this research were taken based on the data provided by case study in the past literatures. The modeling was then designed with Eurocode seismic design guidelines. A study on RC structures behaviour with and without base isolation was studied to observe the interstorey drift, lateral displacement and its base shear effect using response spectrum analysis in STAADPRO software. Spring was defined to act as base isolation system for the reinforced concrete structure. Based on the results, it was expected that the application of base isolation system significantly contributes to reduction of storey drifts, lateral displacements and base shear as well as improvement of structure behaviour as discussed throughout in this report.

Keywords: *base isolation system, response spectrum, drift, displacement, base shear*

INTRODUCTION

The major challenge in the reinforced structure designs process in which considering the seismic action is to improve the poor seismic load resistance. British Standard BS8110, do not consider seismic loading and detailing such as at the beam-column joint, bracing, bearing as base isolators or dampers. As consequences, the current structure designs were not capable to resist and withstand under field and long distant seismic. Therefore, design reinforced concrete structures using earthquake design standard should be considered so that the effect of earthquake damage in our neighboring countries can be minimized. This study concentrated on the utilization of spring base isolation system of a structure. Base isolation is becoming alternative to the current practice with regards to safety measures for earthquake design. The uncoupling of structure from the ground is accomplished by the use of specially designed devices, set at the base of the structure, that simultaneously provide an increased capacity to dissipate the energy input by the earthquakes and confer an additional flexibility and a consequent frequency shifting which usually causes a decrease in the seismic forces.

This study concerns on analysis of reinforced concrete frame only. The modeling of the whole building is carried out using the computer program STAADPRO. This study involves a theoretical 10 storey building including ground floor with normal floor loading and no infill walls. This structure modeling is conducted based on research made by

Hassaballa et al. (2013) in which focusing in Central Khartoum, Sudan. Therefore, the parameters used in this research were taken based on the data provided by the researchers themselves as well as the references used by them. Firstly, for the verification purpose a comparison of drift displacement by story were made. The design structure compliance with BS8110:1985 / 1997 as constant structure. The most important parameters governing the analysis of this frame were both gravity loads which are (dead load and live load) and seismic loads. Next, the modeling was designed using Eurocode 2 with and improvement of the structures were made with seismic design using Eurocode 8 principle which using base isolator as seismic resistant. Soil spring foundation is defined as the base isolation system. Response spectrum analysis was used to analyse the structure behaviour. This study only focuses on the result of storey drift, lateral displacement, and base shear after subjected to earthquake excitation of the building with and without base isolation system.

HISTORY OF SEISMIC ANALYSIS OF BASED ISOLATED RC BUILDINGS

Hassaballa et al. (2013) conducted a study on seismic analysis of a multi-story reinforced concrete frame in Central Khartoum, Sudan and it was analyzed under moderate earthquake loads as an application of seismic hazard and in accordance with the seismic provisions proposed for Sudan to investigate the performance of existing buildings if

exposed to seismic loads. The results of the analysis indicated that the frame suffered a maximum horizontal displacement of 28.39 cm at its top level. This represents about 0.94% of the frame total height. These nodal displacements caused drifts in excess of the allowable drifts. The result shown that the drift reached up to 35 mm in some levels while the allowable drift in this frame should not be greater than 0.004 times the story height (12 mm). In other words, the calculated drifts of the frame were about 2 to 3 times the allowable drifts.

Kamble et al. (2017) studied on 9 storey building symmetric and asymmetric having fixed base and isolation of high damping rubber bearing (HDRB). The results from the study shown that the time period 65% increases when building is isolated with HDRB compared to fixed base, time period 67% increases when building was isolated with LDRB compared to fixed base. Besides that, 40% reduction in base shear when building was isolated with HDRB compared to fixed base. The results of frequency decreased by 67.70% when building was isolated with LDRB compared to fixed base. Frequency 65.98% decreases when building is isolated with HDRB compared to fixed base and there were 43% reduction in base shear when building was isolated with LDRB compared to fixed base.

Santhosh et al. (2013) conducted a dynamic analysis structural of six storey building under both fixed supported and seismically isolated boundary conditions was studied to demonstrate the effectiveness of seismic isolation. The isolation reduces the fundamental frequency of the structure from its fixed base frequency and thus shifts the position of the structure in the spectrum from the peak-plateau region to the lower regions. Also, it brings additional damping due to the increased damping introduced at the base level, and thus further reduction in the spectral acceleration is achieved as shown in Fig. 1.

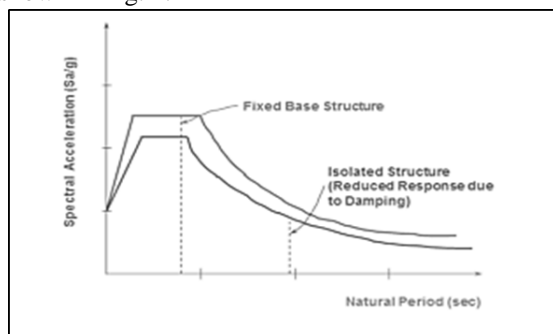


Fig.1 A graph of spectral acceleration against natural period

PROBABILISTIC SEISMIC HAZARD ASSESSMENT OF SUDAN

This section is focusing on response spectrum parameters in Central Khartoum, Sudan as according to Hassaballa et al. (2013), Mohamedzein et al. (2004) and Abdalla et al. (2001), and further analysis used for this research study.

Identification of Ground Type

The soil at Central Khartoum can be reasonably represented by curves for soils E and D. Thus, the value peak ground acceleration (PGH) of 0.214g which in ductility class moderate (DCM) with type D soil were considered.

Spectrum Type

Table 1 and Table 2 summarize the seismic source region of Sudan and its vicinity and summary of peak ground acceleration (PGA) occurs up 50, 100, 200 and 250 years span in Central Sudan.

As according to Hassaballa et al. (2013), the seismic analysis used horizontal input motion of earthquake with moderate in which ranging of peak ground acceleration (PGAH) between 0.2-0.39. Also, they referred the design ground acceleration of Central Khartoum, Sudan according to the research conducted by Mohamedzein et al. (2004). The maximum acceleration at the ground surface in Sudan varies over small range from 0.19 to 0.243g. And it was stated by Mohamedzein et al. (2004) and Abdalla et al. (2011) that for practical purposes an average value of 0.214g can be adopted for Central Khartoum. The recommended choice is the use of two types of spectra: Type 1 is recommended to be adopted since the earthquakes that contribute most to the seismic hazard defined for the site for the purpose of probabilistic hazard assessment have a surface-wave magnitude, M_s , greater than 5.5 (6.4) as according to Table 1.

Table 1 Seismic source region of Sudan and its vicinity (Abdalla et al. (2001))

Source Region No.	Source Name	Source Boundaries Coordinates (Latitude, Longitude)	Maximum Instrumental Earthquake
I	Northern Sudan	(20.1E,19.3N), (36.2E,16.0N) (30.7E,23.5N), (36.2E,20.4N)	5.8
II	Central Sudan	(29.6E,13.0N), (33.9E,10.7N) (32.0E,17.0N), (36.1E,15.0N)	6.4
III	Southwestern Sudan	(26.3E,09.4N), (32.7E,06.6N) (27.2E,10.9N), (10.7E,08.9N)	6.8
IV	Southern Sudan	(30.9E,03.6N), (33.5E,03.6N) (31.7E,06.5N), (34.4E,06.5N)	7.2
V	Equatorial Uganda	(28.8E,00.0N), (33.5E,00.0N) (08.9E,03.1N), (33.5E,03.1N)	7.5
VI	Central Ethiopia	(34.0E,02.0N), (36.5E,00.0N) (38.0E,13.3N), (40.7E,10.7N)	7.7
VII	Afar and Gulf of Aden	(36.2E,16.0N), (42.5E,09.0N) (40.7E,18.7N), (44.9E,13.8N)	7.5
VIII	Red Sea	(37.4E,18.7N), (40.0E,18.7N) (37.4E,22.4N), (40.0E,20.0N)	7.2

Table 2 PGA (in g) with 10% probability of being exceeded in time span (Abdalla et al. (2001))

Regions	Source Name	50 Years	100Years	200Years	250Years
I	Northern Sudan	0.108	0.142	0.182	0.198
II	Central Sudan	0.117	0.153	0.198	0.215
III	Southwestern Sudan	0.115	0.149	0.192	0.208
IV	Southern Sudan	0.339	0.437	0.562	0.608
V	Equatorial Uganda	0.299	0.386	0.499	0.541
VI	Central Ethiopia	0.259	0.336	0.435	0.472
VII	Afar Region & Gulf of Aden	0.329	0.425	0.547	0.592
VIII	Red Sea	0.347	0.446	0.572	0.619

MODELLING

The objective of this study is to perform analysis and design of RC structure building as well as improvement by using base isolation.

Dimension of RC Frame Structure

Table 3 shows the dimensions of cross section details of 10 storey RC frame structure prepared in STAADPRO.

Table 3 Cross-section details for RC structure model

Floor level	G-5 th	6 th to 7 th	8 th to Roof
Columns (mm)	500 × 300	400 × 300	300 × 300
Typical beams (mm)	400 × 300		
Slab thickness (mm)	130		
Support system	Fixed / Spring base support system		

The beam and column sizes are kept same for both fixed and isolated RC structure. Plan view and side view on RC structure frame are as shown in Fig. 2 and Fig. 3.

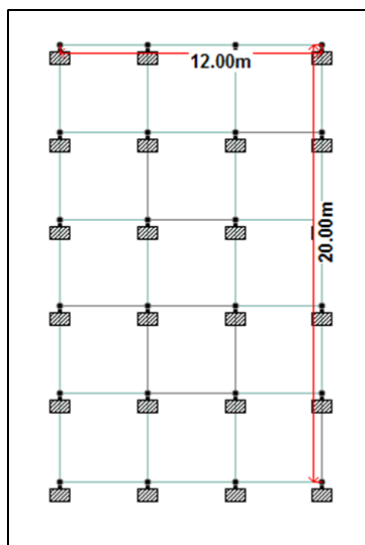


Fig. 2 Plan view of foundation

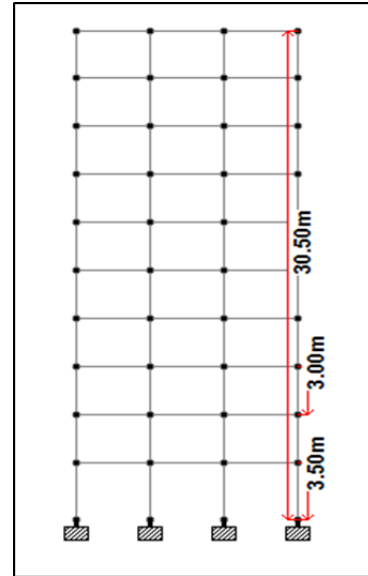


Fig. 3 Side elevation

The seismic isolators in the system are defined as spring placed between the fixed base and the columns. The parameters selected to define the utilized isolators in STAADPRO is soil spring with stiffness, $K=16000\text{kN/m}$. As dynamic analysis normally 5% damped response spectra are considered, so the 5% damped response spectrum and the effective damping ratio of the isolation system, as defined in Eurocode 8, does not exceed 30%. Thus, for spring base isolation system the damping ratio was assumed as 20%. The RC models are analyzed using Response Spectrum in STAADPRO using Eurocode 8.

RESULTS AND DISCUSSION

Inter-Storey Drift

Table 4 shows comparative study of inter-storey drift. The results that has been observed using response spectrum analysis that the story drift in spring base isolated building is higher at the ground storey than fixed base building and decreasing as the story getting higher. It was expected that the drift of the base isolated building would be less than that of the fixed-base building.

In case of fixed base structure, storey drift is comparatively lower than spring base apart from ground floor which is 0.196% while spring base isolation system is 0.312%. However, although the spring based isolated structures shown drastic increased in story drift at the ground storey and reduced significantly up to roof level.

Table 4: Comparative study of storey drift (mm) in X direction

Storey	Storey Drift (mm)	
	Fixed Support System	Spring Based Isolation System
Roof	15.265	12.444
8	25.574	16.034
7	24.281	15.401
6	29.686	17.182
5	39.740	20.585
4	45.273	22.410
3	50.064	24.156
2	54.026	26.251
1	56.952	31.826
Ground	60.254	95.254

Lateral Displacement

Table 5 shows comparative study of percentage drift without base isolators (fixed) and with base isolators system (spring) while Figure 4 shows storey against lateral displacement ratio between fixed support and spring based support system.

Table 5 Comparative study of percentage drift in X direction

Storey	Fixed Support System	Spring Based Isolation System
Roof	1.315%	0.923%
8	1.265%	0.882%
7	1.181%	0.829%
6	1.102%	0.779%
5	1.004%	0.723%
4	0.874%	0.655%
3	0.726%	0.582%
2	0.561%	0.502%
1	0.384%	0.417%
Ground	0.197%	0.312%

The percentage of lateral displacement ratio at ground storey to first storey of the reinforced concrete structure in fixed based system is lower compared to spring based isolation system. At ground floor, the ratio gives the smaller value of 0.139% for fixed support system and 0.312% for spring based isolation system. However, the lateral displacement ratio has been decreased at the spring base isolation system compared to fixed base systems as the storey getting higher. The percentage of lateral displacement ratio of roof or top storey obtained in fixed support system is 1.315% and spring based isolation system is 0.923%.

The lateral displacement of spring based isolation system building is expected to be less than that of the fixed-base building. Spring base isolated structures are likely to have larger displacement at lower level, as they are separated from the ground. In other words, base isolation lets the buildings to move over the ground so that they have less frequency.

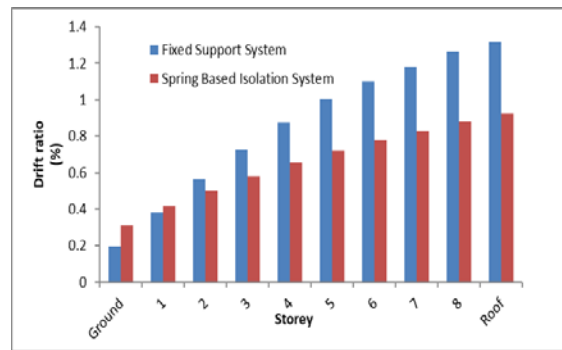


Fig. 4 Storey against lateral displacement ratio in x direction between fixed support and spring based support system

Base Shear

Table 6 shows the comparative study of base shear without base isolators and with base isolation support system while Figure 4 illustrates the base shear against the direction of earthquake

Table 6 Comparative study of base shear (kN)

Study case	Base Shear (kN)	
	X direction	Z direction
Fixed Support System	5572.36	6400.91
Spring Based Isolation System	2197.29	3384.36

The base shear value for fixed support system is 5572.36kN and the base shear for spring base isolation system is 2197.29kN for x direction earthquake whereas 6400.91kN for fixed support system and 3384.36kN for spring base isolation support system in z direction earthquake. It has been observed that the base shear for base isolated building is reduced to average range of in x direction 60.57% and 47.13% in z direction from the fixed base building. Comparison is shown in Fig. 5.

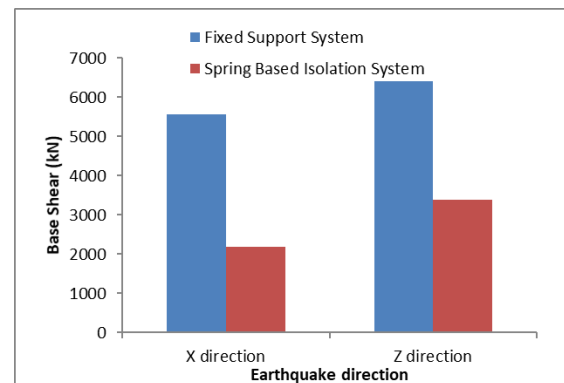


Fig. 5 Base shear against the direction of earthquake

Mode Shapes, Period and Frequency

Table 7 and Table 8 show the value of time period and frequency for their respective modes that are obtained by analysis of structure using response spectrum method for building with fixed base and spring based isolation system building.

Table 7 Comparative study of period in seconds

Mode	Period (second)		Percentage different (%)
	Fixed Support System	Spring Based Isolation System	
1	1.78184	2.51416	41.10
2	1.51689	1.93852	27.80
3	1.46657	1.89474	29.20
4	0.59524	0.75258	26.43
5	0.54349	0.64193	18.11
6	0.52399	0.61449	17.27
7	0.35886	0.39802	10.91
8	0.31198	0.39494	26.59
9	0.30711	0.36704	19.514
10	0.24816	0.34852	40.44
11	0.21963	0.34007	54.84
12	0.21522	0.33538	55.831
13	0.20689	0.31177	50.69
14	0.19432	0.29632	52.49
15	0.18627	0.26714	43.41

Table 8 Comparative study of frequency in cycle per second

Mode	Frequency (cycle/second)		Percentage different (%)
	Fixed Support System	Spring Based Isolation System	
1	0.561	0.398	29.06
2	0.659	0.516	21.70
3	0.682	0.528	22.58
4	1.680	1.329	20.9
5	1.840	1.558	15.32
6	1.908	1.627	14.73
7	2.787	2.512	9.87
8	3.205	2.532	21.00
9	3.256	2.752	15.48
10	4.030	2.869	28.8
11	4.553	2.941	35.41
12	4.646	2.982	35.82
13	4.834	3.207	33.66
14	5.146	3.375	34.41
15	5.369	3.743	30.28

Period for both support system cases decreasing from first mode shape to fifteenth mode shape. However, spring base isolation support system has higher period compared to fixed base support system. By referring with the frequency equation of the spring based isolation system has smaller frequency from first mode shape to fifteenth mode shape compared to fixed support system.

Spring based isolation system has lower frequency compared to fixed support system. The period needs to be increased to reduce the frequency in order for the structure to survive under the earthquake excitation. In this study, the base isolation

model was intentionally designed to limit the earthquake force transmitted to the structures. Considerably, higher target period of isolation is obtained using spring which can lead to a better performance. Mode shapes of buildings depend on overall geometry of building, geometric and material properties of structural members, and connections between the structural members and the ground at the base of the building. The data was presented in graph of period against mode as in Figure 6 and Figure 7 for frequency against mode.

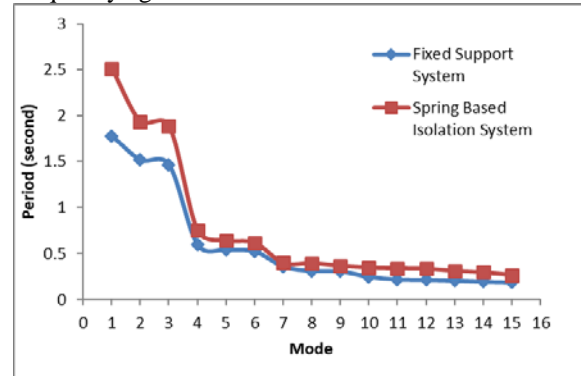


Fig. 6 A graph of period against mode

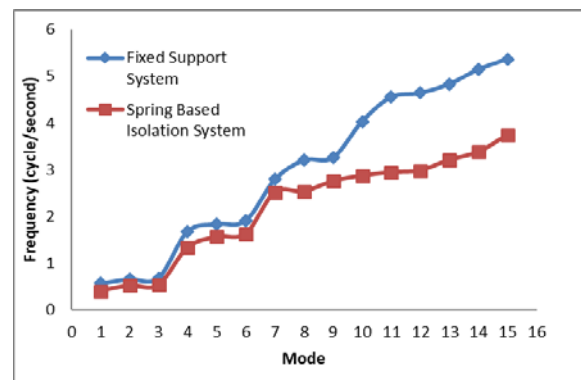


Fig. 7 A graph of frequency against mode

Elastic Spectral Acceleration

Figure 8 shows graph of elastic spectrum acceleration against period. The elastic spectral acceleration for spring based isolation system is smaller compared to fixed support system. The base isolation system reduces the frequency of the structure from its fixed base frequency thus reduces the structure in the higher spectrum to lower regions.

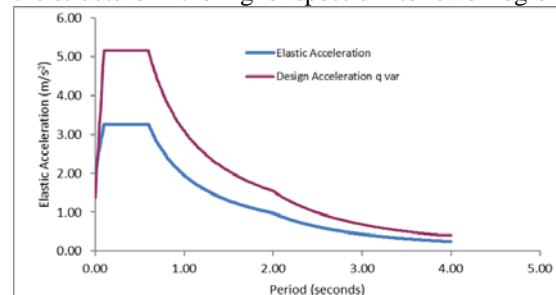


Fig. 8 Elastic spectral acceleration against period

Spring base isolation system brought to large reduction in the range of short periods and high frequencies compared to fixed based system. The damping causes high frequencies by increase in transmissibility at short period. Since the damping of the isolated building (20%) is 4 times that of the fixed base building (5%), the damping coefficient contributes positive effect to the behaviour of the structure flexibility. The spring based isolation system structure reduces the response of the first fixed base mode of the upper structure. A base isolation system must be sufficiently flexible to cause the fixed base excitation period (frequency) of the isolated structure to be significantly longer than first fixed base system excitation period.

CONCLUSIONS

The story drift for base isolated building with spring from response analysis was more compared to fixed based building at ground level and reduced as the height increases. The displacement of spring based isolation system building was smaller compared to the fixed base building due to provided flexibility controlled by the base isolators. From the analysis data, it can be summarize that base isolated building has more favorable behaviour compared to fixed base building. The base isolation system substantially increases the time period of the building and reduces the base shear. A base isolation system must also carry sufficient damping to suppress possible large displacement of the upper structure cause by seismic excitation. Thus, the period needs to increase to reduce the frequency in order for the structure to survive under seismic load.

According to the analytical study following conclusion were drawn:

1. Base isolated structures shown drastic increased in story drift at the ground storey and reduced significantly up to roof level.
2. In case of fixed based structure displacement was lesser only at lower storey of a structure but increased significantly when the storey height increases compared to spring base isolation system height in which it has higher at ground level but lesser at top storey.
3. The base shear for fixed base from response spectrum analysis was 60% times of base isolated structure. Therefore, the base shear value of base isolated structure was smaller compared to fixed base structure
4. The base isolated structure substantially increases the time period of the building and hence correspondingly reduces the frequency.
5. The elastic spectral acceleration for spring based isolation system is smaller compared to fixed support system. The base isolation system reduces the frequency of the structure from its fixed base frequency thus reduces the structure in the higher

spectrum to lower regions. Besides that, it brings additional damping due to the increased damping from 5% to 20% introduction at base level, and thus further reduction in the spectral acceleration is achieved.

REFERENCES

- [1] A. E. Hassaballa, Fathelrahman M. Adam., M. A. I. Seismic Analysis of High-Rise Building by Response Spectrum Method. *International Journal of Computational Engineering Research*, 3(3), 2013, 272–279.
- [2] Abdalla, J. A., Mohamedzein, Y. E., & Abdel Wahab, A.. Probabilistic Seismic Hazard Assessment of Sudan and Its Vicinity.pdf. *Earthquake Spectra*, 17(3), 2001, 399–415.
- [3] BS 8110-1:1997.. Structural use of concrete, (December), 2002, 160.
- [4] Efiloglu, M. . Understanding the Concept of Base Isolation, 1(July 2013).
- [5] Eurocode 2: Design of concrete structures - Part 1-1 : General rules and rules for buildings. British Standards Institution, 1(2004), 230.
- [6] Eurocode 8 : Design of structures for earthquake resistance —. (2011). Buildings, 3.
- [7] Kamble, A. R., Khot, M. S., Kagale, H. K., & Magdum, S. S. Seismic Analysis Of Symmetric Building With Base Isolation Technique. *International Journal of Recent Innovation in Engineering and Research*, 2 (3 March – 2017 (I J R I E R)), 2017, 80–84.
- [8] Mohamedzein, Y. E., Abdalla, J. A., & Abdelwahab, A. B. 13 th World Conference on Earthquake Engineering Development of Design Response Spectral For Central, 2004, 1508.
- [9] Mohamedzein, Y. E., Abdalla, J. A., & Abdelwahab, A. B. Development of Design Response Spectral for Central Khartoum, Sudan. 13th World Conference on Earthquake Engineering, 2004, 1508.
- [10] Mohamedzein, Y. E., Abdalla, J. A., Elsharief, A. M., Abdelwahab, A. B., & Ahmed, E. O. (2001). Seismic Microzonation of Central Khartoum , Seismic Microzonation of Central Khartoum , Sudan. Fourth International Conference on Recent Advance Geotechnical Earthquake Engineering and Soil Dynamics, (June 2016).
- [11] Santhosh, H. P., Manjunath, K. S., & Kumar, K. S. Seismic Analysis of Low To Medium Rise Building for Base Isolation, 2013, 1–5.

STRENGTH AND BEHAVIORS OF DRY-JOINT RETAINING NANO-BLOCK

Pongchompu Pongsagorn^{1*}, Buyarat Tanakrit¹, Bubpi Attaphol¹

¹Rajamangala University of Technology Khonkaen Campus, Thailand

ABSTRACT

This research studied the strength and behaviors of dry-joint retaining walls built with nano blocks, a new product made from wet-cast concrete of the size 20×40×18cm, with the weight of 15kg/block, and the compressive strength of 94kg/cm². Construction of retaining walls with these dry-joint nano blocks—both for permanent and temporary walls—is simple, convenient and fast without having to rely on skillful workers. The research started from producing a prototype scale model of 1:12.5 for determining appropriate experimentation. The structure of the retaining wall using 2.00×1.65×0.20meters dry-joint nano blocks allowed distribution of lateral earth pressure through the sand in a semicircular-cut cylindrical mold of 15cm radius and 1.60 meters height. Pressure was applied step by step all through the test. Gauging of both horizontal and vertical displacements was performed using a dial gauge. The testing program for the nano-block retaining wall comprised 5 patterns of walls: half-block, half-block with 1.38kg-m steel reinforcement, half-block with 2.77 kg-m steel reinforcement, half-block with 4.15kg-m steel reinforcement, and anchored half-block with 1.38kg-m steel reinforcement. Horizontal displacement was checked stepwise. Comparison of the efficiency of the 5 patterns showed that the half-block nono-block retaining wall demonstrated the highest horizontal displacement. The retaining wall yielding the highest efficiency was the anchored half-block with 1.38kg-m steel reinforcement, with the least horizontal displacement of 2.90mm. It can be concluded that steel reinforcement and structural anchoring increases stability of nano-block retaining walls in terms of lateral compressive strength.

Keywords: Retaining wall, Nano blocks, steel reinforcement, Anchored

INTRODUCTION

The present construction operations need to take into account the cost, ease, and convenience of work as well as short project period. Nevertheless, for some types of construction, soil retaining walls have to be built before the main structure. In engineering construction, retaining walls are usually designed with reinforcement for structural strength. The researchers are interested in nanoblock concrete, which is an alternative and promising material for constructing retention walls. Nanoblocks are made from wet-cast concrete that offers better engineering properties than dry cast or compression. Wet concrete is strong, durable, and locally available. Construction can rely on local labor and can be done without the use of bulky machinery. Nanoblocks, as an innovative material, do not require a high cost of transportation and are easy to remove without skilled workers. [1, 2, 3].

There is to date little research on retaining wall models due to the complicated preparation of the simulation models themselves. Therefore, information related to the movement behaviors of retaining wall is not available. However, some researchers are still interested to study retaining

wall models because they will be useful for those wanting to investigate further related topics [4, 5, and 6].

The lateral pressure of soil exerting on retaining wall can be categorized into 3 types:

- At-rest condition or no movement
- Active condition or movement away from earth filling
- Passive condition or movement toward earth filling

Retaining wall failures are caused by two major factors:

- Internal instability, structural failures occur because of the design strength which is not sufficient to accommodate moment or shear force.
- External instability, retaining wall has external stability when they do not slide, settle, or collapse due to load on soil bearing under the foundation [7].

Combined structure means a structure that is composed of two or more materials adjoined tightly until they function as one material. The objective of a combined structure is to increase strength to the structure by adding a high-strength material to a low-strength material.

A combined structure behaves in such a way that slides at the contact surface will not happen

since shear force is sufficiently transferred horizontally to the two materials. In a non-combined structure, the contact surfaces between the structures slide, resulting in each individual structure receiving moment separately [9].

MATERIALS AND METHODS

This research began from studying and producing a small-scale prototype model (Fig.1), compiling information, understanding all relevant components including approaches, patterns, and the possibility of the project before appropriately planning work on material selection, designing the study format, planning experiments and variables control. The retaining wall test cases installation details as following

- Testing retaining wall with half- nano block Combined structure:
 - Exerting force of 10 pounds (1.38 kg-m)
 - Exerting force of 20 pounds (2.77 kg-m)
 - Exerting force of 30 pounds (4.15 kg-m)
- Testing retaining wall with half-bricks interlocking bricks, reinforced bars and anchorage (1.50m*2.0m)
 - Exerting force at 10 pounds

Materials and Equipment used in the Tests

- nano block as shown in Fig.2 measures 20*40*18cm (width*length*height) and weighs roughly 15kg per block, compressive strength of about 94 ksc per block.

-Sand

The sand used for filling here was Puttaisonsong sand. The weight was 1,495 kg/m³. Sand was selected as a tested material for filling, which was quite close to a research study by Liyan Wang[10]

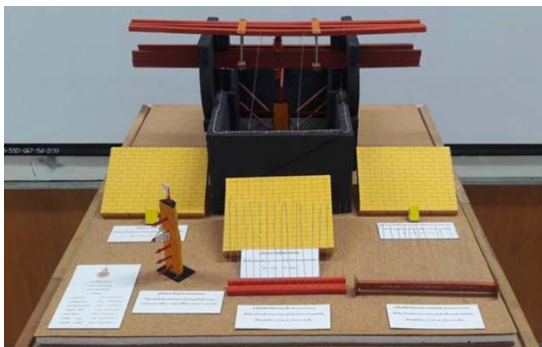


Fig.1 small-scale prototype model



Fig.2 Nano blocks

<http://www.thainanohouse.com>

-Rubber Sheet

The rubber sheets were used in the study to prevent sand flowing from the mold. The 10cm wide and 2.0mm thick sheets were freshly made and attached to the mold edges that contact two retaining wall. The height was equal to the retaining wall.

-Vertical reinforcing steel

Sixteen 12 mm threaded steel studs were used to reinforce the retaining wall structure. The studs' tensile strength was tested based on the standard. These studs were as long as the retaining wall and were 1.6m high. Both ends were bolted and the force used for the bolt was set.

-Pound wrench

The pound wrench had the highest acceleration of 90 pounds. It was used to tighten the reinforcing steel stud inserted into the retaining wall structure so that the tightening force was consistent.

-Test pond

The test pond measured 1.90x2.00x5.00m. It consisted of a restraining bar set on top

- Semi-circular iron mold

This is a cylindrical iron mold cut vertically in halves with a radius of 1.5m, height of 1.60m and 8.0mm thickness. Its strength was increased by iron fins at every 0.50m distance. The iron molds are simply used for dissipating lateral soil pressure.

-Iron plate

Iron plates that dissipate force have a radius of 0.15m and are 8.0mm thick. They have been designed to fit the iron mold. These iron plates dissipate the pressure from hydraulic jacks to filling sand.

-Hydraulic jacks

The hydraulic jacks under this study gave external vertical pressure. This simulated an external force exerting on filling sand and soil in the model. The hydraulic jacks used were 30 tons.

- Dial gauge

Dial gauges with 0.01 fineness were used to control vertical settlement of sand and gauge horizontal movements of the retaining wall.

-Sling wires

Two sling wires were used between the 3 upper reaction beams and the anchor set to increase their work efficiency by behaving together.

- Reinforced bars and restraining beam

Reinforced bars functioned like an iron anchor enhancing stability to our retaining wall with interlocking bricks. The 16 reinforcing steel studs used had 12 mm threads all through their length and each was 1.60m long. One end of each stud was joined at the upper end of the retaining wall and the other was locked with steel plate and nut to the C-shaped restraining beam so as to prevent movement while being tested.

Retaining wall test set up

The retaining wall test installation details as following (Fig.3, Fig.4, and Fig.5)

Number1 A back supporting set to stop movement of mold during the test

Number2 Two sling wires transferring force to the test set below.

Number3 Iron mold 1.50m high, 8mm thick with a radius of 15cm

Number4 One 30-ton hydraulic jack with a raising capacity of 10cm

Number5 6 dial Gauges with 0.01mm gradation, 2 installed at the tops of the test piles and 2 each at the two-sided test anchorages

Number6 Three 4x4in cross-section, 6m long steel rods

Number7 Test anchorages made from reinforced concrete on the left and right sides of the test piles

Number8 I-Beam 0.50m long strengthened with 6mm steel plate welded at the center and wings of I-Beam to prevent deformation during the test

Number9 A 10-ton hydraulic jack with a raising capacity of 10cm to transfer force from

Lower beam to upper beam and prevent deformation of lower beam during the test

Number10 9mm RB used to support lower beam to remain at its level while other equipment was installed

Number11 Threaded bolts to hold upper and lower beams so that they behaved similarly when moving during the test

Number12 Retaining wall 1.50m high, 2m wide made of interlocking bricks, with the brick size of 12.50x25x10cm

Number13 Steel plate with a radius of 15cm and thickness of 8mm

Number14 6 reaction beams or I-Beams 6m long of the size $H \times B = 150 \times 75$, $t_1 = 5$, $t_2 = 7$, $r = 8$, and cross-sectional area of 17.85 cm^2

Number15 Slings to tie between 3 upper reaction beams and anchors to increase work efficiency from co-behavior

Number16 6 square anchorage piles of the size $0.18 \times 0.18 \times 4.00 \text{ m}$, 3 on each side bolted onto the foundation of the pile test set

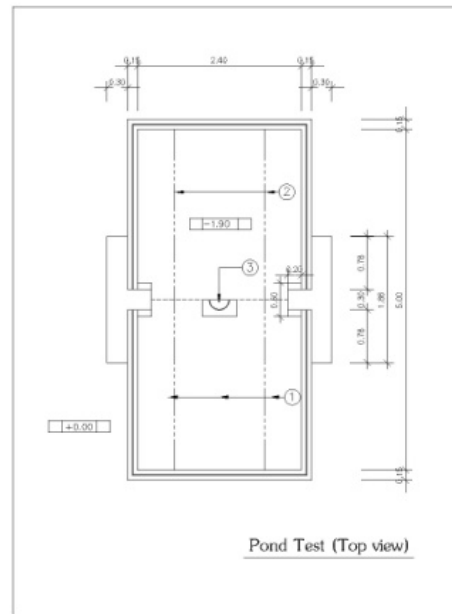


Fig.3 Pond Test (Top view)

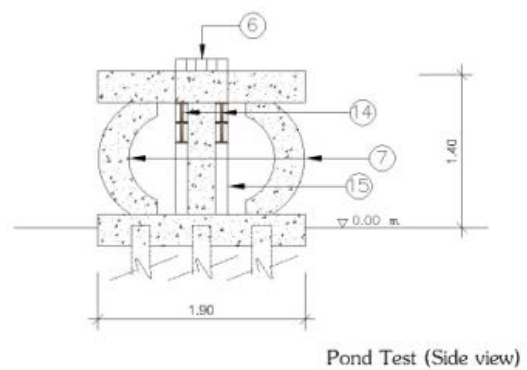


Fig.4 Pond Test (Side view)

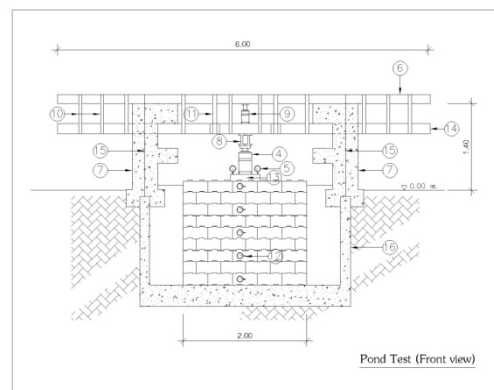


Fig.5 Test set up (Front view)

The retaining wall test procedure detail as following

2.3.1 Testing movements of retaining wall laid with half-nano block, reinforced bars and anchorages (Fig.6 and Fig.7)

-Prepare the reinforced barest set with sixteen 1.60m high, 12mm threaded studs, turn tightly with pound wrench for accelerating internal force of interlocking bricks

-Weigh the sand and fill the unit weight was 1,495 kg/m³ until the last layer

- Install steel studs and the anchorage set with the vertical studs

- Add 10-pound force to vertical studs and horizontal studs, tighten the nut so that they adjoin the restraining beams

-Install hydraulic jacks and 2 dial gauges to measure sand vertical settlement

-Install dial gauges to measure horizontal movements of 7 retaining wall at 0.05,0.25,0.45,0.65,0.85,1.05 and 1.25m, with the top position of retaining wall being 0.00m

-Add load layer by layer, each at 1.00mm settlement of filling sand and record results of horizontal movements of retaining wall

-Perform the testing until the settlement of filling sand reached 25mm; record the results of horizontal movements of retaining wall

-Repeat the tests in triplicate to obtain accurate information of movement trends

TEST RESULT AND DISCUSSIONS

When we were confident of the results from the study of the small-scale model, the large-scale model was constructed to study the behaviors of each type of retaining wall' lateral pressure resistance as shown in Fig.8. The five types of retaining wall studied were: retaining wall laid with half nano block (Fig.9); retaining wall laid with half nano block and reinforced bars given force of 10lb, 20lb and 30lb(Fig.10); retaining wall laid with half nano block, reinforced bars given force of 10lb and anchorage (Fig.11); Tests were done in triplicate to observe their tendency to deform. The results obtained were used to build graphs for comparing the data.

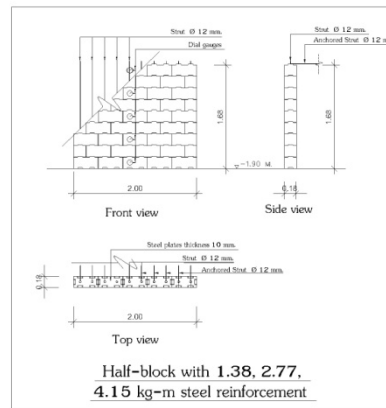


Fig.6 Half nao block with reinforced bar and anchorage test set up (Front view)



Fig.7 Half nano block with reinforced bar and anchorage test set up (Back view)

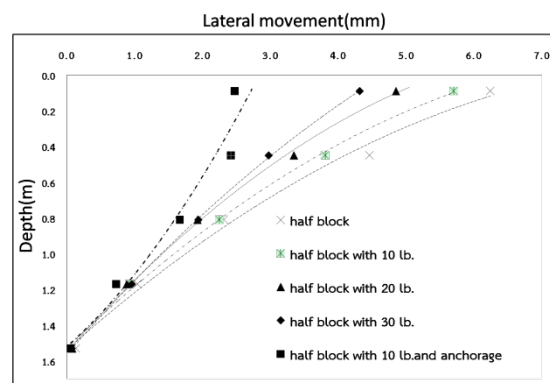


Fig.8 Test results

-The results of the five tests to compare the efficiency of horizontal movement of the retaining wall showed that the control over filling sand was at 25.00mm, which was the highest settlement parameter. The greatest horizontal movement of the retaining wall was studied; the most efficient retaining wall should move the least, which was found to be the retaining wall laid in one layer with 10lb reinforced bars with anchorage.

In order to find elastic modulus of the wall (Fig.12), strength or weakness of a combined structure is its stiffness value which depends on the elastic modulus (E_{total}) and inertia moment (I) of the cross-section. The walls laid with half nano block with no reinforced bars showed uncombined failure. Retaining wall strength depends merely on weight over it and friction of material surface. This differs from a retaining wall with half nanoblock and reinforced bars where failure will be partially uncombined. Here, inertia moment values are equal showing that the strength of a retaining wall with half nano block and reinforced bars depends on elastic modulus (Table 1)

Table 1 Composites elastic modulus

Cases	Lateral load (P) kg.	Length of retaining wall (L) cm.	Moment of inertia (I) cm^4	Lateral movement (Δ_{max}) cm.	Elastic modulus (E_{wall}) ksc.
10 ปูนซีเมนต์	174	1,620	10,860	0.7	32,437
20 ปูนซีเมนต์	290	1,620	10,860	0.7	54,062
30 ปูนซีเมนต์	335	1,620	10,860	0.7	62,451



Fig.9 Half nano block test set up (Front view)



Fig.10 Half nano block test with reinforced bar (Front view)



Fig.11 Half nano block test with reinforced bar anchorage (Front view)



Fig.12 Composites elastic modulus test set up (Front view)

The analysis under this study was conducted by comparing the costs of the construction material against the maximum horizontal movement of the 5 types of retaining walls, namely: 1) half-nanoblock retaining wall, 2) half-nanoblock retaining wall cast with a 1.38kg-m reinforced sheet, 3) half-nanoblock retaining wall cast with a 2.77kg-m reinforced bar, 4) half-nanoblock retaining wall cast with a 4.15kg-m reinforced bar, and 5) half-nanoblock anchored retaining wall cast with a 1.38kg-m reinforced bar. When considering horizontal movement of these structures, the half-nanoblock anchored retaining wall cast with a 1.38kg-m reinforced bar showed the greatest strength because of its lowest movement value. However, the cost of the half-nanoblock anchored retaining wall cast with a 1.38kg-m reinforced bar was the highest. The most appropriate structure, considered by comparing the cost and horizontal movement, was the half-nanoblock retaining wall cast with a 4.15kg-m reinforced bar. Its cost was 1,062THB/m² and its horizontal movement was 4.30mm.

The researchers investigated the behaviors of the retaining wall built with nanoblocks and anchorage. The test was compared with the result of a relevant study by Pongsagorn et al. (2018). The comparison was performed between the 3 patterns of horizontal movement, the elastic modulus values,

the cost per square meter, and the highest horizontal slides of each retaining wall.

The horizontal slide of half-block interlocking-brick retaining wall under control of fill sand settlement at 25 mm reached the maximum movement at 8.48 mm in a curvilinear pattern.

The maximum horizontal movement of the nanoblock retaining wall was less than the interlocking-brick retaining wall with less curvilinear movement tendency.

Half-nanoblock retaining wall cast with a 4.15kg-m reinforced bar. The maximum horizontal movement of the half-nanoblock retaining wall cast with a 4.15kg-m reinforced bar was 4.40 mm in an approximately linear pattern. The maximum horizontal movement of the nanoblock retaining wall was lower, but also in a linear pattern.

Half-nanoblock and anchored retaining wall cast with a 1.38kg-m reinforced bar. The maximum horizontal movement of the half-nanoblock anchored retaining wall cast with a 1.38kg-m reinforced sheet was 3.06 mm in an approximately curvilinear pattern since the anchor at the very end of the wall decreased the horizontal movement. The comparison showed that the maximum horizontal movement of the nanoblock retaining wall was much lower than the interlocking brick wall and was in a concave pattern, indicating the efficiency of the nanoblock retaining wall.

Comparison of the elastic modulus of retaining walls. The elastic modulus of the nanoblock retaining wall was higher than that of the interlocking brick retaining wall, proving its greater stability.

Comparison of reinforcement steel adhering tools. The interlocking brick retaining wall was constructed by placing a washer before steel reinforcing. The nanoblock retaining wall was constructed by using a steel plate to position the reinforcing steel. The plate was cut into a shape equal to the nanoblock so that there was no movement of reinforcing steel during the test.

Comparison of cost per square meter with the maximum horizontal slides of retaining walls. The cost of the interlocking brick retaining wall was 1,020 per m². The cost of the nanobrick retaining wall was slightly higher than the interlocking brick retaining wall. Therefore, nanoblock is an alternative material for constructing a retaining wall. The findings provide the information useful for those interested in building a retaining wall with this material.

The half-nanoblock retaining wall cast with reinforcing steel at 20-30 pound reinforcement range was found to be the most appropriate

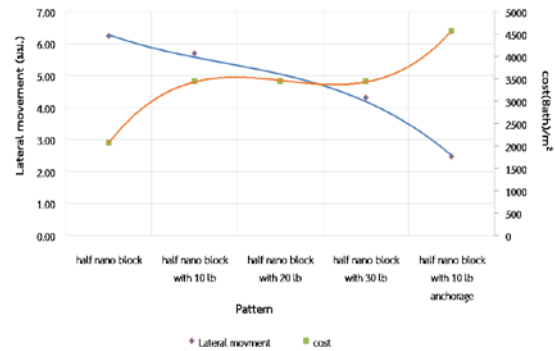


Fig.13 Comparison efficiency

CONCLUSION

Based on bricks retaining wall model test results, the following conclusions can be drawn:

The behavior of dry-retaining wall nanoblock without reinforced bars shown uncombined failure and can support low pressure. With reinforced bar and anchor showed partially uncombined.

The addition of reinforced bar to a significant reduction of lateral deformation

The results of the four tests to compare the efficiency of horizontal movement of the retaining wall showed that the control over filling sand was at 25.00mm, which was the highest settlement parameter. The greatest horizontal movement of the retaining wall was studied; the most efficient retaining wall should move the least, which was found to be the retaining wall laid in one layer with 10lb reinforced bars achorage.

ACKNOWLEDGEMENTS

The authors are grateful to the Khon Kaen Campus of the Rajamangala University of Technology Isan for supporting the research.

REFERENCES

- [1] Villemus B., Morel J.C, Boutin C Experimental assessment of dry stone retaining wall stability on a rigid foundation. Engineering Structures, Elsevier, 2007, 29 (9), pp.2124-2132; 2006
- [2] Anne-Sophie Colas, Denis Garnier, Jean-Claude Morel, Yield design modeling of dry joint retaining structures. Construction and Building Materials, Elsevier, 2013, 41, pp 912-917; 2013
- [3] Morel J.C. Experimental assessment of dry stone retaining wall stability on a rigid foundation. available from: www.elsevier.com/locate/engstruct. 25 August 2016.
- [4] Morel J.C. Building houses with local materials: Means to drastically reduce the environmental impact of construction. Building

- and Environment, 2001
- [5] Morel J.C. Full-scale field trials to assess dry-stone retaining wall stability. EngStruct, 2010.
- [6] Pongchompu P., S. Hayashi, D. Suetsugu., and Y. J. Du (2008), "Investigation into performance of Raft & Pile supported embankment on soft ground". Geotechnical Engineering Journal. Vol.39, No.4, pp.185-190.
- [7] Bowles, J.W. (1988). Foundation Analysis and Design. New York: McGraw Hill. pp. 589-693.
- [8] Principle of foundation engineering handbook. 5th. Tomson brooks/Cole Publishing, USA, pp. 293-385.
- [9] Pongchompu P., S. Hayashi, "Investigation on Raft composites for construction", The 4th KKU International Engineering Conference 2012 (KKU-IENC 2012) "Driving together towards ASEAN Economic Community" Faculty of Engineering, Khon Kaen University, Thailand, May 10-12, 2012.
- [10] Liyan Wang, Experimental study on seismic response of geogrid reinforced rigid retaining walls with saturated backfill sand. available from www.elsevier.com/locate/geotextmem. 25 August 2016.

ASSESSMENT OF STRENGTH PARAMETERS OF UNREINFORCED MASONRY (URM) BLOCKS IN HERITAGE STRUCTURES IN THE PHILIPPINES

Lessandro Estelito Garciano¹, Darlene Clarice Campado², Nitchell Andrei Castillo³, Mary Grace Odiamar⁴,
and Marcelino Tongco⁵, Jr.

¹Faculty of Civil Engineering, De La Salle University, Philippines; ^{2,3,4,5} De La Salle University, Philippines

ABSTRACT

Unreinforced masonry (URM) heritage structures, because of their rudimentary building techniques, are vulnerable during extreme environmental events, particularly earthquake. Limited literature involving these structures provide added challenge for establishing sound engineering solutions in their preservation, considering their significance in a country's history. Additional studies on the mechanical properties of masonry blocks – compressive, shear, flexural strengths, modulus of elasticity, etc., could provide an insight on the behavior of structural components subjected to excessive loading conditions, and establish parameters which can be used for seismic vulnerability assessments.

The blocks considered in this study are adobe, coralline limestone, and sandstone units. These samples are acquired from selected heritage structures and subjected to lead tests. Customized setups for shear and flexure tests were fabricated by the authors for the lack of standard test methods. Results show that response of earth masonry to various loading setups was characterized by monolithic behavior, distinct lack of elasticity, and intense deformability. Furthermore, strength values obtained from local samples of adobe and coralline limestone dictate that they are best suitable only for single-story unreinforced structures, defined to be less than 13 m or wall area not exceeding 12 m². Sandstone, while stronger in performance, posed a very drastic failure mode in the form of sudden shear and chipping off the member. Nevertheless, the masonry fabric proves to require further strengthening measures in resisting forces, as shown by their strength parameters.

Furthermore, stress-strain properties of each sample show that sandstone, the type with the greatest material strength, exhibited the smallest plastic deformation and abrupt failure, while adobe, with the least average strength, exhibited the longest plastic deformation and gradual failure. Finally, a map is presented to show the spatial diversifications of URM fabric as used on heritage structures per region in the Philippines, the most common of which are coralline in Visayas and adobe and clay bricks in Luzon.

Keywords: Unreinforced masonry, Heritage structure assessment, Modulus of elasticity, Compressive strength masonry, Shear strength masonry

INTRODUCTION

Heritage structures in the Philippines are, at best, representative of the country's rich cultural diversity and lineage, as exemplified by the many churches, chapels, convents, watch towers, bell towers, etc. scattered throughout the archipelago. These structures are also indicative of the state-of-the-art materials and construction methods at the time they were erected, circa 15th to 19th century, utilizing mostly unreinforced masonry (URM), timber, and other indigenous construction materials [1]. Over time, the in-situ condition of the URM fabric deteriorated, increasing the failure probability during extreme environmental events. This failure variability can be determined through analyzing the strength parameters – compressive, shear, flexural strengths, and modulus of elasticity, of individual blocks used to create said fabric.

The shear strength of a masonry block, for one, is

a strength parameter not commonly researched upon unlike its compressive and flexural strength, but it is a factor that should not be neglected especially when seismic forces are taken into consideration. A study was conducted [2] wherein a masonry wall, when loaded about the vertical axis, caused a splitting cycle which generated vertical cracks in the upper part of the wall. Furthermore, such kinds of shear failure are commonly observed at vertical corner angles, or near the corners of the wall [3].

Accounting for these detrimental effects, and with the recent 2013 Bohol Earthquake, a multi-hazard vulnerability assessment of heritage structures in the Philippines was conducted using FAMIVE [4]. The procedure consisted of setting up a reliable inventory profile defining the exposure of heritage structures in the region of interest. Identification of relevant building features that affect the structural performance was also considered, leading to a selection of specific case studies with performance-

based assessment framework introduced. From then, a quantitative approach for earthquake and typhoon assessment and safety conservation frameworks were considered in said study. The absence of data for the mechanical properties of URM was compensated by said research through assumptions of values utilizing other studies from foreign literature.

The lack of local references for strength parameters of commonly used URM blocks in the country became the main objective of this paper: to further provide assessment of mechanical properties of in-situ URM fabric used in selected heritage structures and determine by experimentation the range of in-situ values of the most available and ubiquitous URM materials locally – adobe, coralline limestone, and sandstone, whose results can be used for more in-depth assessment on vulnerability and mitigation measures in the country.

MATERIALS AND METHODOLOGY

The URM blocks used in the study were gathered from specific regions in Luzon and Visayas where heritage structures of distinct types of masonry are of abundance – coralline limestone in Samar, Southern Philippines; adobe in Intramuros, Manila, and sandstone in Pangasinan, north of Luzon. Five samples for each block were allotted for compression testing; 3 samples for each block type were allotted for shear, and another set of 3 samples each for flexure testing. The acquisition of more samples was constrained by the availability of debris that were from the heritage structures themselves.

The block samples for compression and shear test block have a minimum length-to-width ratio of 2, as prescribed by section 14.7.4.11 of the 2015 New Mexico Earthen Building Materials Code used for masonry blocks in general testing [5] and the Technical Standards in masonry specifications [6]. Using a diamond-brushed saw, the samples were partitioned and cut into 4'' x 4'' x 8'' blocks for compression and shear tests, and 1.5'' x 4'' x 8'' for flexure tests. To ensure even load distribution on the block surface, rough surfaces were smoothened with plaster.

Shear, Compressive, And Flexural Test Methods

For shear test, a customized shear setup was fabricated to induce shear failure for each block. One end of the block was constrained and the other half, its free end, was subjected to an area load on the top surface as shown in Fig. 1. Two fasteners held the fixed end on each side to prevent rotation. A steel cube on top of the block transformed the concentrated UTM load into an area load. Loads, including failure load, were recorded at various stages, and stored for post-processing. The average shear stress was then calculated by the general shear formula of applied

shear force over the shear area.

As for compressive testing, uniaxial compressive force was applied perpendicular to the bed surface to simulate compression loads experienced by the masonry block in-situ. The results that come from the compressive strength test were also used for the determination of Modulus of Elasticity, computed as the stress over strain or the slope of the linear graph, the graph up to the yield point of the stress-strain diagram for each masonry type. In this regard, a distance-amplifying instrument or a dial indicator was installed on the UTM to measure the displacement of the top fiber during loading until failure.

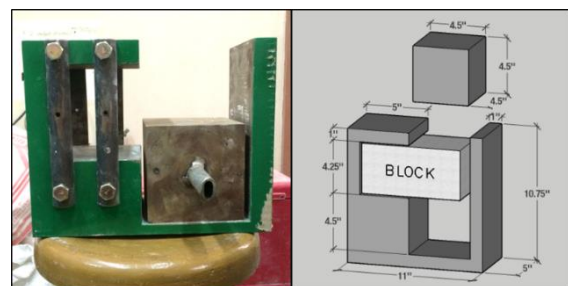


Fig. 1 Loading and instrument setup for shear test

The flexural strength of the blocks, on the other hand, was obtained as the product of maximum moment and distance of outermost fiber from the neutral axis experiencing the maximum stress, all over the moment of inertia computed from the transverse cross-section of the block. The load rate applied in the testing was at 0.01 MPa/s, with consideration on the block dimensions and the rigidity of the blocks. To obtain this parameter, a customized flexure setup was fabricated as available setups were either too large or too small for the samples. A detailed flexure setup and 3D model with the loading direction can be seen in Fig. 2.

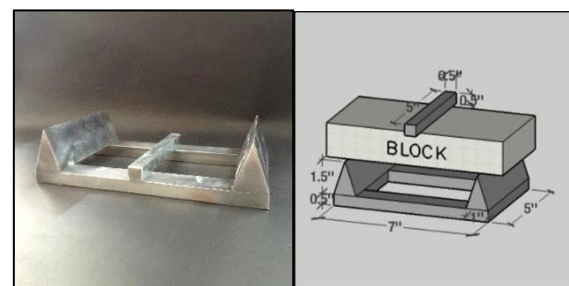


Fig. 2 Loading and instrument setup for flexure

To simulate flexural failure, blocks were made thin enough (1.5'' x 4'' x 8'') to avoid compression strut, an occurrence in which a block loaded on one face develops compression along a diagonal from the support to the applied load, as observed on deep beams defined in 2010 National Structural Code of

the Philippines provision 410.8.1 [7].

RESULTS AND DISCUSSION

Prior to shearing test, a shear preload was already introduced in the masonry block, based on the weight of the steel block (0.11625 kN) placed to initiate distributed load on the unconfined half portion of the masonry block and added to the maximum load indicated by the testing machine.

For the shear results shown in Fig. 3, adobe and coralline limestone types from Manila and Visayas, respectively, yielded almost the same strength, resisting almost the same amount of forces throughout the six tested specimens.

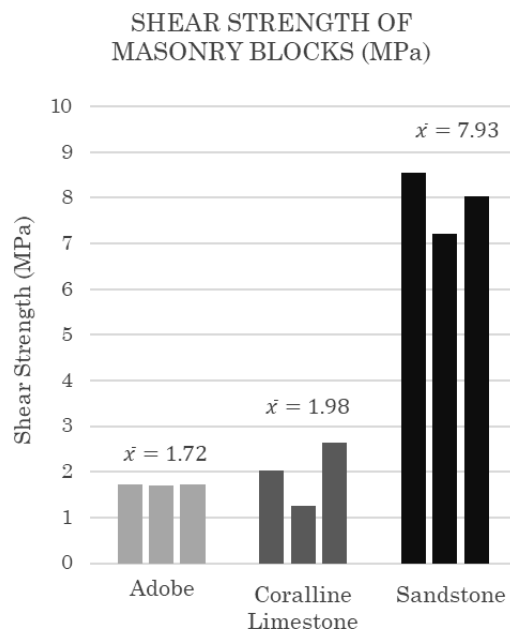


Fig. 3 Summarized shear strengths of masonry samples

These values though, were inferior to the strength of sandstone, yielding mean shear strength of 7.93 MPa or a little more than twice the combined mean shear strengths of the first two masonry types. The mean maximum load carried by the sandstone samples was 64.716 kN. Theoretically, the shear strength of a single block of sandstone surpasses even the combined material strengths of both adobe and coralline. To fail an adobe brick, it would require almost the same loading and effort as failing a coralline limestone block, but sandstone would require more than three times of the same loading to attain the same failure as that of the previous two types.

These values mean that each individual block has shear strength properties that make them suitable as

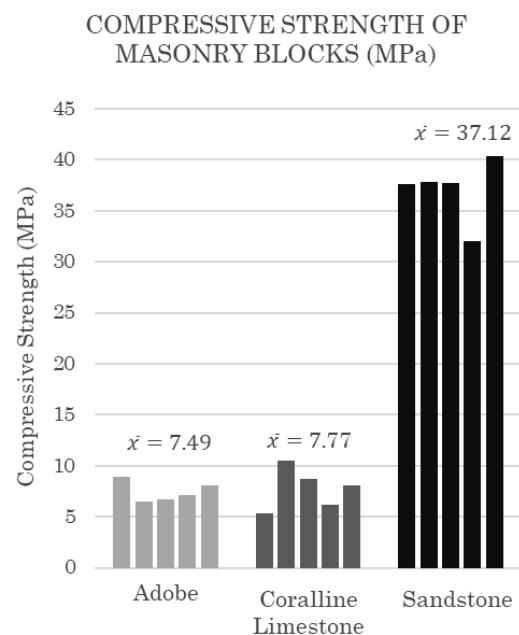
structural material for low-rise construction, based on the assessment by the World Federation of Engineering Organizations (WFEO) in 2011 [8], although their durability still depends on various factors such as the manner of placement in wall construction and strength of interface between adjacent blocks.

From Fig. 4, some adobe, coralline, and sandstone, were seen to take the shear failure and its internal distribution along the midspan, although more than one shear plane was observed in other adobe and coralline samples. This failure can be most likely attributed to the composition and density, as the two types had almost equal amount of denseness. Sandstone, being the densest type among the three, yielded to the expected failure plane.



Fig. 4 Failure of masonry blocks due to shear

As for compressive strengths, adobe yielded the lowest mean of 7.488 MPa, the summary of which can be seen in Fig. 5, with recorded values ranging from 6.49 MPa to 8.95 MPa. The mean compressive strength of coralline was not far off, with average of 7.77 MPa.



The obtained compressive strength range of adobe, coralline, and sandstone limits them to be used only for single-story structures if they are to remain unreinforced, as these blocks are inadequate alone in sustaining greater degree of loads especially as structural members or walls [8].

This data was in line with the specifications from the same assessment by WFEO, stating that in unreinforced brick walls for single-story structure for Asia [8], the compressive strength of brick must be at least 30 kg/cm² or 2.94 MPa, and wall area that the bricks would cover must not exceed 12 m².

Furthermore, for earthquake-prone countries, particularly in Japan, it requires that masonry units should be applied only for walls not exceeding 10.8m, with slenderness ratio between length and thickness more than 1/12. Each masonry unit must have allowable compressive strength of 1/3 of the sustained forces and 2/3 of the temporary forces specified by their Code.

The flexural strengths of the masonry samples, meanwhile, are summarized in Fig. 6.

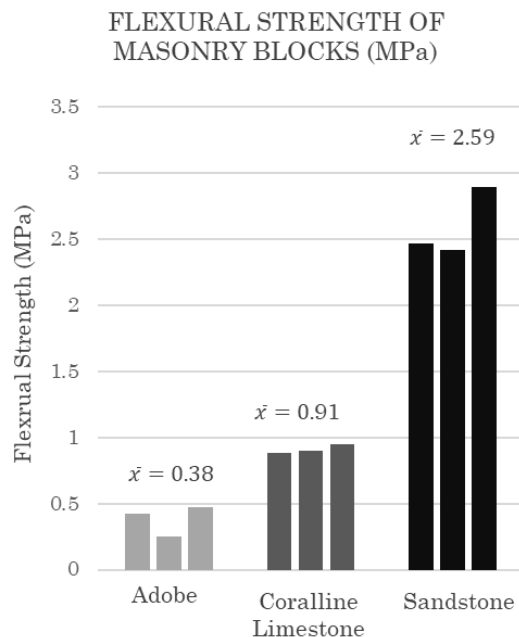


Fig. 6 Summarized flexural strengths of samples

Average flexural strengths of 0.3808 and 0.9116 MPa were observed for adobe and coralline limestone samples, respectively, while sandstone still exhibited the most resistance of 2.5946 MPa. Adobe samples were weakest in shear, compression, and flexure, while coralline limestone remained to be an average material for flexure.

From actual observations, specimens did not take

long to fail in flexure, where an abrupt collapse after reaching peak load was observed in all specimens, coinciding with the expected output and in contrast to the gradual failure induced by compression.

Experiment-wise, a single crack propagating from the bottom fiber of the specimens was generally observed for all samples. These failures verify the homogeneity as observed from similar studies [9]. The cracking patterns were generally the same for almost all specimens, as shown in Fig. 7.



Fig. 7 Failure of masonry blocks due to flexure

Concerning the stress-strain curve, a long, continued shortening after the elastic limit was observed for adobe specimens in Fig. 8a, indicating the less brittle property compared to other samples. The elastic region and the elastic limit were identified through the sudden plunge in the curve that signifies the start of plastic deformation. The respective equations on the elastic region take a general linear form.

Values for slopes of the graphs ranged from 721.27 MPa to 1058.9 MPa for adobe blocks. Mean Modulus of Elasticity was then taken to be 869.78 MPa or 0.87 GPa. A low gradient of the straight line at the elastic region means that at a low compressive stress, a considerable amount of deformation was apparent.

Sandstone samples, meanwhile, exhibited smallest plastic deformation with stress-strain diagrams propagating to rapid failure, as shown in Fig. 8b. The slopes from the graphs of the elastic regions were relatively higher compared to those of adobe and coralline limestone, while the elastic modulus yielded a mean of 5083.86 MPa or 5.83 GPa, from the range of 3.3-7.0 GPa. A higher elastic modulus indicates that its stiffness is greatest among the three types, especially when compared to coralline limestone.

For the latter, a plunge was observed after the samples have reached elastic limit as shown in Fig. 8c. At this point, the material could no longer resist loads without permanent deformations. Elastic modulus for coralline limestone yielded a mean of 816.33 MPa or 0.82 GPa from the range of 0.6-1.0 GPa.

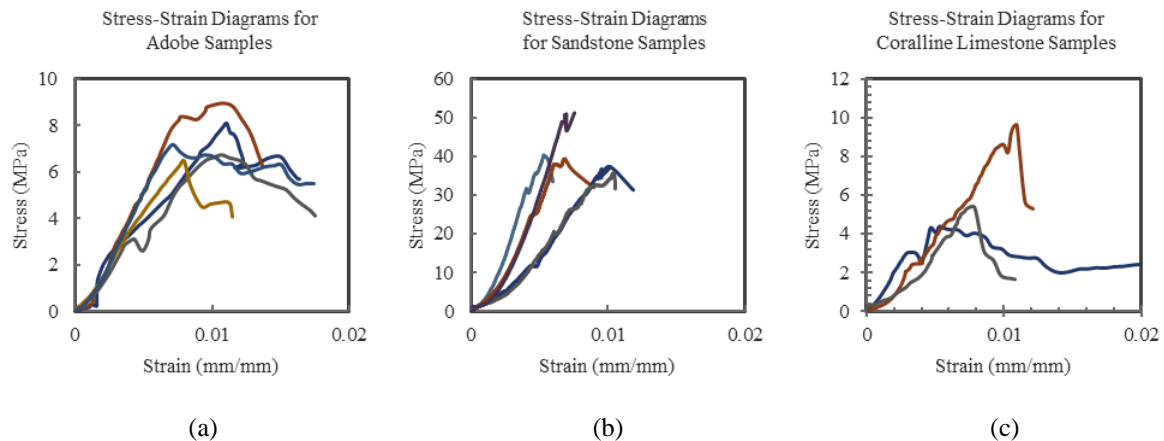


Fig. 8 Stress-strain curve for (a) adobe, (b) sandstone, and (c) coralline limestone masonry blocks

Distribution of URM Heritage Structures in the Philippines

To further complement the study, the distribution of masonry was illustrated using Quantum GIS in a Philippine Map containing points that indicate the typology and prevailing material per region of interest. Based on the available data gathered, it was found out that the most common material was coralline limestone found in Visayas, in some regions in Luzon, and in northern Mindanao. Abundance of said material was also confirmed by the Philippine Statistics Authority, where limestone accounted for 39% non-metallic resources of the country, as shown in Fig. 9. Coralline limestone is also used for cladding to rubble cores, most notable structures of which are: Bolioon Church and Carcar Church in Cebu; Loboc Church, Loon Church, and Punta Cruz Church in Bohol.

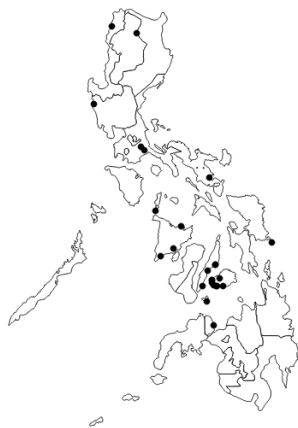


Fig. 9 Locations of coralline limestone masonry heritage structures

Clay brick, on the other hand, was the next common masonry material found in all major island groups of the Philippines, next to adobe which is

abundant in Luzon and has been commonly used in construction since the Spanish era [10], [11], as shown in Fig. 10 and Fig. 11, respectively.

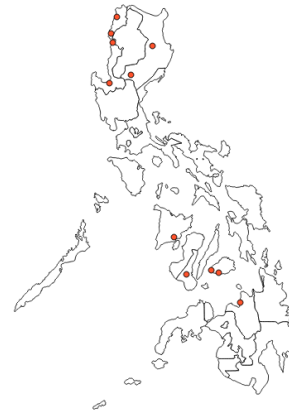


Fig. 10 Locations of clay brick masonry heritage structures

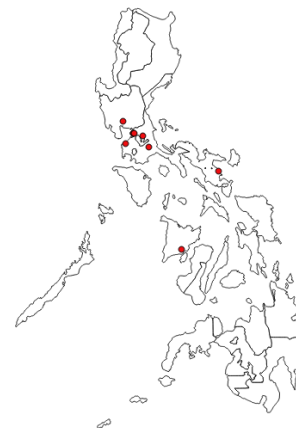


Fig. 11 Locations of adobe masonry heritage structures

Other types of masonry in abundance include riverstone and sandstone, commonly found in Iloilo,

where notable churches made of such are Sta. Barbara Church and Sto. Tomas de Villanueva Church.

CONCLUSION

From the experiments, a summary of results is provided in Table 1.

Table 1 Material properties based from experiment

Strength (MPa)	Type		
	Adobe	Limestone	Sandstone
Shear	1.71- 1.73	1.25-1.65	7.21-8.55
Compressive	5.32- 10.56	6.15- 10.56	32.06- 40.33
Flexure	0.249- 0.471	0.883- 0.954	2.42-2.89
Elastic Modulus (GPa)	0.72- 1.06	0.64- 0.989	3.33-7.01
Density (kN/m ³)	12.5- 14.52	12.11- 14.71	24-25.07

In the pilot study made, indications for the strengths of the most commonly used masonry materials for heritage structures are highlighted. The study has shown that in terms of strength, as compared from various literature [6], [8], and [12], the masonry fabric may further be improved against various risks of natural forces such as earthquake, extreme wind, or fire. Strengthening measures may be brought out towards heritage structures which, though aesthetically preserved, may have a rather deteriorating structure and pose potential risk in the long run for both multiple lives and the cultural significance of said structures.

Typology mapping, on the other hand, addresses the need for additional systematic assessment on infrastructures and provides initial clustering which can be further improved and then used for a cost-saving, efficient, and objective prioritization for risk mitigation of structures both modern and of antiquity.

ACKNOWLEDGMENTS

The researchers would like to thank Engr. Jainab Altillero from the National Museum, and National Historical Commission of the Philippines for their guidance, support, and recommendations in this research. Gratitude as well be to the DLSU Civil Engineering Faculty for the accommodations in

queries and concerns related to the study.

REFERENCES

- [1] Klassen W., *Architecture in the Philippines: Filipino Building in a Cross-Cultural Context*, University of San Carlos Press, 1986, pp.173-175.
- [2] Varum H., Tarque N., Silveira D., Camata G., Lobo B., Blondet M., Figueiredo A., Rafi M. M., Oliveira C., and Costa A., *Structural Behavior and Retrofitting of Adobe Masonry Buildings, Structural Rehabilitation of Old Buildings, Vol.2*, Springer-Verlag Berlin Heidelberg, 2014, pp. 37-75.
- [3] Aguilar R., Montesinos M., and Uceda S., *Mechanical Characterization of the Structural Components of pre-Columbian Earthen Monuments: Analysis of Bricks and Mortar from Huaca de la Luna in Peru. Case Studies in Construction Materials*, Vol. 6, 2016, pp.16-28.
- [4] D'Ayala D., Barucco P., Zerrudo E., Galasso C., Jose R., Manalo M., Oreta A., Garciano L. E., Yu K., Fadriguela C., Fanciullaci V., Bronzino C., and Putrino V., *Multi-Hazard Vulnerability Assessment Manual of Philippines Built Heritage*, in Proc. 1st Int. Conf. on Natural Hazards and Infrastructure, 2016, Chania, Greece.
- [5] *New Mexico Administrative Code, Chapter 7: Building Codes General, New Mexico Earthen Building Materials Code*, 2015, New Mexico, USA.
- [6] *National Building Standards, Technical Building Standard NTE E. 080, SENCICO*, 2000, Lima, Peru.
- [7] *Association of Structural Engineers of the Philippines, Chapter 4: Structural Concrete, National Structural Code of the Philippines*, 6th ed. Vol. 1, ASEP Inc., 2010, pp. 61-66.
- [8] *World Federation of Engineering Organizations Disaster Risk Management Committee, Current Situation of Low-Rise Wall Type Structures Part I*, 2011, Retrieved from http://www.wfeo.org/wp-content/uploads/stc-disaster_risk/WFEO-Wall_Type_Structure-1.pdf
- [9] Illampas R., Ioannou I., and Charmpis D.C., *A study on the mechanical behavior of adobe masonry*, WIT Transactions on the Built Environment, Vol. 118, 2011, pp. 485-496.
- [10] Alarcon N., *Philippine Architecture During the Pre-Spanish and Spanish Period*, UST Publishing House, 1991, pp. 64-78.
- [11] Valera-Turalba M.C., *Philippine Heritage Architecture before 1521 to the 1970s*, Anvil Publishing Inc., 2005, pp. 43-55.
- [12] Silveira D., Varum H., Costa A., Martins T., Pereira H., and Almeida J., *Mechanical Properties of Adobe Bricks in Ancient Constructions*, *Construction and Building Materials*, Vol. 28, pp. 36-44.

EFFECTS OF WATERSHED TOPOGRAPHY AND LAND USE ON BASE FLOW HYDROLOGY IN EQUATORIAL REGION: A CASE STUDY IN UPPER KOMERING WATERSHED SOUTH SUMATERA, INDONESIA

Rosmalinda Permatasari¹, Arwin Sabar², Dantje Kardana Natakusumah³, Hazairin Samaulah⁴

¹Faculty of Engineering, Palembang Tridianti University, Indonesia; ^{2,3}Bandung Institute of Technology, Indonesia; ⁴ Palembang Tridianti University, Indonesia

ABSTRACT

The characteristic hydrology of watershed is playing major role in ensuring water resource availability. Rainfall and runoff responses in catchment area are part of the hydrology cycles. There are several factors to determine the characteristic of hydrology at watershed, i.e. geological, region, soil and land cover. The existence of water resources is very substantial for surroundings. The rapid development in various sectors lead to water demands increase. Optimum utilization of water resources is needed in the sustainability of water resources or the need for integrated water resources management. The consequence of development is land use change, resulting in changes inflow characteristics, flood during wet season and drought or discharge decrease in the dry season. Adaptation and mitigation efforts are required to anticipate changes in the flow characteristics. Base flow depends on portion of stream flow and its sustained between precipitation and pathway watershed. The factors are key controls on base flow through their influence on infiltration, catchment and subsurface storage properties. This review underscores the need for more research that multiple aspects of the watershed system in explaining base flow. The result of average base flow and total flow ratio during 40 years (1971-2010) is 0.296 and the class of the hydrologic function as a BF / TF ratio value which indicated very poorly hydrology function of Komering watershed, although in certain hydrologic function was still in good category.

Keywords: Hydrology, base flow, catchment, watershed, climate, equatorial region

INTRODUCTION

Change in land cover and land use influences the runoff characteristics of a drainage basin to a large extent, which in turn, affects the surface and groundwater availability of the area [1]-[2]-[3]-[4]. Water availability in an area depends very much on how rainfall over the area is divided into various components such as surface runoff, interflow, groundwater recharge etc [5]-[6]-[7]. Stream flow can be divided into quick flow and base flow. Quick flow is normally from surface runoff, while base flow is from shallow and deep groundwater. In equatorial region, such as Upper Komering, South Sumatera, base flow becomes an important water source to support ecosystem and economic development in the region. Typically, base flow is not very sensitive to rainfall but more associated with the discharge from groundwater [8].

Degradation of hydrological function is caused by exploitation of water and land resources exceeding their bearing capacity. It is often associated with the disaster in water resources, such as floods, landslides, droughts and forest fires. A hydrologic function of watersheds is the role of the region in responding to rainfall and its flow to surface. A watershed has proper hydrologic function if its role in reducing runoff surge fluctuations caused by rainfall can

further stabilize availability of flow during the dry season. Hydrological functions of an area is determined by several factors such as geological factor, regional, soil type and land cover. The flow and surface water quality produced can only be effectively measured in a stream at the regional watershed boundary [9]-[10].

Understanding of the groundwater to stream flows is very important in planning of water resources management. The direct flow is primely the direct response of a rainfall event and includes the overland flow (runoff) and the lateral flow in the soil profile also known as interflow. The base flow is a component of the stream flow which is discharge from the natural storage of aquifers [11].

MATERIALS AND METHODS

Study Area

The study was conducted in the upstream Komering watershed, South Sumatera Province, Indonesia. Water discharge data analyzed were measured at The Perjaya (Martapura) headwork by the Department of Central River Region VIII. The upstream Komering watershed an area of about 4260 km². The temperate humid climate 28.40 – 32.20 C, humidity 80% and ratio sunshine 29%. An average

annual rainfall 2602.08 mm, wet season during October-May and dry season during June-September [12]-[13]. The study of base flow variability required data on the general condition of the upstream Komering watershed. General conditions of data was collected which associated to variability of base flow, including land use, geology, water resources infrastructure and watershed meteorological conditions. The area's climate is equatorial region and it's present at Figure 1.

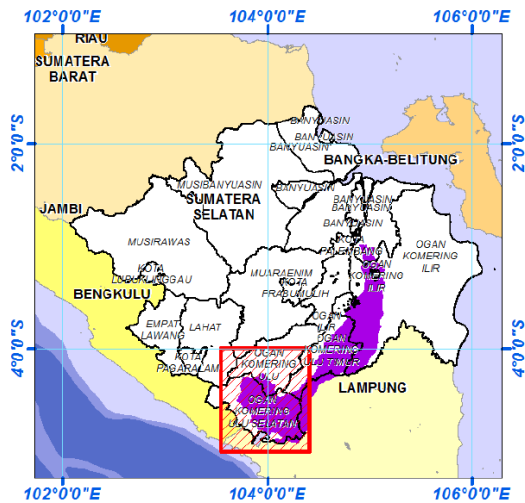


Fig. 1 The location of study area

Data Processing

Variability of base flow values were calculated from discharge rational model equation, as follow [14]:

$$Q = c (PA) + b \quad (1)$$

where Q is discharge in m³/sec, c is runoff coefficient, P is rainfall, A is area in Ha and b is base flow.

Frequency-duration analysis, known as flow duration curve, was another method used to analyse the characteristics of a stream flow. The flow duration curve is constructed from flow data and is computed as follow [11]-[15]-[16]-[17]-[18]:

$$P(Xm) = \frac{m}{N+1} \quad (2)$$

where,

P = the probability of a given flow that will be equalled

m = the rank number when daily or monthly flows are arranged in decending order

n = the total of number of observations

A stream discharge values at P = 50% (Q₅₀) is taken as the median stream flow. Stream flows greater than

Q₅₀ are taken as low flow rates [11]-[15]-[16]-[17]-[18].

Range value of base flow and total (BF/TF) ratio as well as analysis of the physical condition of Komering watershed can be used as a reference for classification of hydrological functions. The base flow index respectively, as follows [10]-[19]-[20]-[21]:

$$BFI = \frac{BF}{TF} \quad (3)$$

where,

BFI = Base flow index

BF = Base flow values

TF = Total flow values

RESULTS AND DISCUSSIONS

Study area falls under equatorial rain climate region with the average rainfall 2,728.50 mm / year, and the lowest rainfall occurred in July. Water resources at upstream watershed are original from Muara Dua, the confluence of the Saka and Selabung Rivers, with each catchment areas of 1,070 km² and 1,230 km². Selabung River upstream of Ranau Lake has a catchment area of 508 km² while at its downstream there is Perjaya headwork. The total catchment area of the upstream watershed is 5,169.74 Km². Komering watershed is dominated by swamp land systems, making it vulnerable to flooding [13].

River flow pattern is influenced by rock type and topography of Komering watershed. Limestone and shale rocks are typical at the basin. The basin has two different forms of flow patterns, moderate and moderate-fine rectangular dendritics. The flow pattern affects the efficiency of the drainage system and hydrographic characteristics. Land use changes are the factors that affect changes in the hydrologic function [22]. Table 1 and Figure 2 are present land use of study area.

Table 1 Land use in upstream Komering (2005)

No.	Land use	Area (Ha)
1	Reeds	-
2	Thicket	166,824.858
3	Shrub	-
4	Lake	12,440.171
5	Denude forest	82,030.817
6	Village/settlement	18,065.790
7	Mixed farms	23,763.092
8	Smallholder plantations	223,714.106
9	Swamp	147,420.221
10	Paddy field	167,594.918
11	Moor	81,859.053
Total		923,713.026

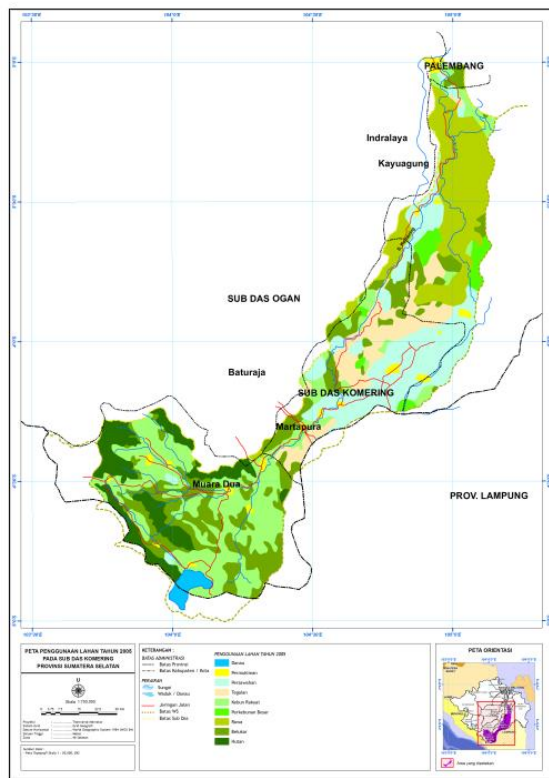


Fig. 2 The landuse of study area

Land use particularly for agricultural. In upstream basin at Belitang area is one of the largest agricultural production in South Sumatera. In order to assist the provincial government therefore irrigation project development supported by the existences of Ranau Lake Regulacy and Perjaya headwork was carried out.

Ratio of base flow and total flow (BF/TF) is as one indicator of the hydrologic functions of a watershed which is the role of the catch area responding to falling rainfall and surface runoff. The watershed category includes a good classification when it can reduce the surge in surface runoff fluctuations due to rain fall, stabilize the flow rate and ensure the sustainability of water availability [5]-[9]-[10]. Table 2 is present base flow and total flow ratio in upstream Komering.

Table 2 Base flow and total flow (BF/TF) ratio in study location during 1971-2010

Years	BFI	Years	BFI
1971	0.160	1991	0.456
1972	0.089	1992	0.315
1973	0.399	1993	0.447
1974	0.651	1994	0.182
1975	0.301	1995	0.483
1976	0.205	1996	0.386
1977	0.318	1997	0.159
1978	0.274	1998	0.158
1979	0.244	1999	0.306

1980	0.033	2000	0.733
1981	0.585	2001	0.528
1982	0.489	2002	0.014
1983	0.329	2003	0.519
1984	0.565	2004	0.014
1985	0.385	2005	0.008
1986	0.343	2006	0.020
1987	0.025	2007	0.042
1988	0.528	2008	0.240
1989	0.336	2009	0.094
1990	0.456	2010	0.004

Range value of BF / TF ratio as well as analysis of the physical condition of Komering watershed can be used as a reference for classification of hydrological functions. The criteria explained the bearing capacity of Komering watershed as a water reservoir and also as a reference to evaluate degradation level or accomplishment of watershed reservation. According Table 2 the result of average base flow and total flow ratio during 40 years (1971-2010) is 0.296. Table 3 described the class of the hydrologic function as a BF / TF ratio value which indicated very poorly hydrology function of Komering watershed, although in certain hydrologic function was still in good category.

Table 3 Hydrology function classification [23], [24]

Hydrology function classification	BF/TF
Very good	>0,9
Good	0,7-0,9
Moderate	0,5-0,7
Poor	0,5-0,3
Very poorly	<0,3

Furthermore, the determination of the classification needs further analysis by reviewing the carrying capacity of watersheds in water availability and level of watershed damage. Land use change and watershed management affect the occurrence of erosion, sedimentation and ultimately affect water quality. In general, the occurrence of erosion is determined by climate factors, especially rain intensity, topography, soil and rock characteristics, vegetation cover and land use and on the system of relationship between rain and surface flow is considered the only factor change and other factors can be as fixed variable [1]-[2]-[3]-[4]-[25]-[26].

Land cover is a fixed factor that is easily disturbed by human activities. The occurrence of erosion occurs due to changes in land use that lead to degradation of watershed quality. The distribution and classification of erosion levels in the Komering DAS are presented in Table 4 and Figure 3.

Table 4. Erosion classification

Erosion classification	Area (Ha)	(%)	Legend
Very slightly	78.008,7	8,487	Light yellow
Slight	194.559,7	21,166	Yellow
Moderate	209.321,7	22,772	Gold
Serious	292.690,4	31,842	Light brown
Very seriously	144.623,0	15,734	Brown
Total	919.203,536	100	

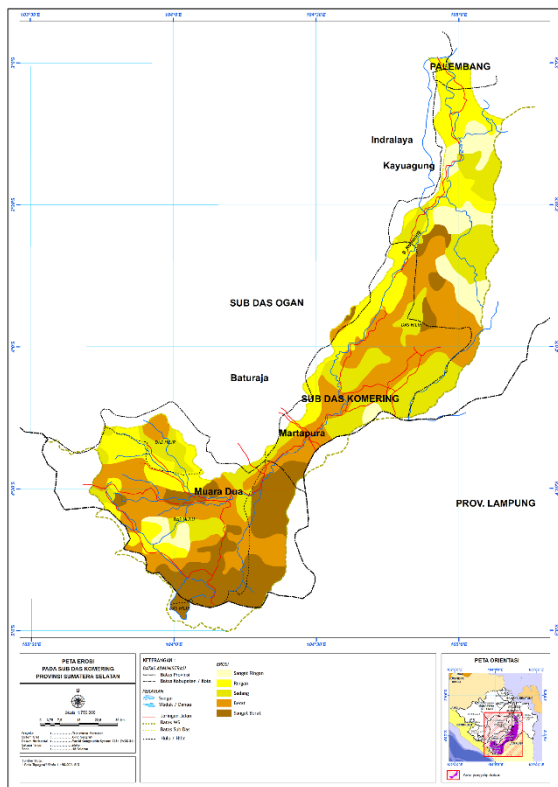


Fig. 3 Erosion classification in upstream Komering

The result of the distribution of erosion base on Figure 3 the upstream Komering has been dominated serious erosion classification. If associated with the results of data processing increased runoff with an increase in the value of runoff coefficient, the decline in base flow value and the occurrence of discharge extremity, it can be concluded there has been a change of hydrological regime. Figure 4 is presented trend of runoff coefficient (C) and base flow upstream Komering Watershed.

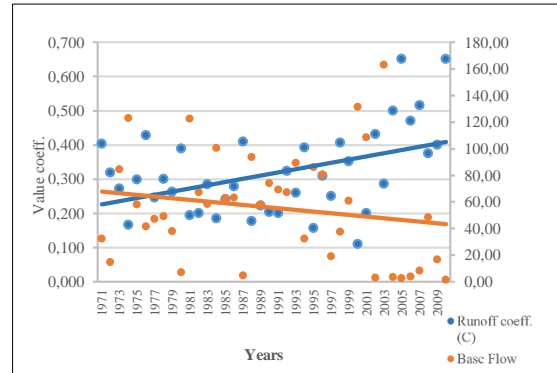


Fig. 4 Trend of runoff coeff. (C) and base flow Upstream Komering Watershed

Land use has an effect on hydrological function of watershed especially affect on runoff and base flow value. Base on Figure 2 land use due to human activities such as agricultural land (rice fields) and plantations contribute to large runoff.

CONCLUSIONS

Understanding land use and climate change will affect base flow quantity, in the context of watershed geomorphology, will aid watershed managers and stream in the protection of adequate water supply for human need and habitat availability in stream. The responses of runoff and base flow to climatic factors are different. Precipitation has a great impact on runoff, whereas temperature has a great impact on base flow. Land use changes has an impact on reducing the absorption capacity, especially in view of the proportion of changes in agricultural area in the Upper Komering Watershed and increasing the rate of surface runoff.

ACKNOWLEDGEMENTS

This research is supported by Ministry of Research, Technology and Higher Education, Indonesia. We appreciate comments provided and encouragement made by the reviewers, the editor and the associate editor.

REFERENCES

- [1] N. Sajikumar, R.S. Remya. (2014). Impact of land cover and land use change on runoff characteristics. *Journal of Environmental Management, Elsevier*, 1-9.
- [2] Gustard A and Wesselink AJ. (1993). Impact of land-use change on water-resources – Balquhidder catchments. *Journal of Hydrology* 145(3-4), 389-401.
- [3] Githui, F., Mutua, F., Bauwens, W. (2009). Estimating the impacts of land-cover change on runoff using the soil and water assessment tool

- (SWAT): case study of Nzoia catchment, Kenya. *Hydrol. Sci. J.* 54 (5), 899-908.
- [4] Alibuyog, N.R., Ella, V.B., Reyes, M.R., Srinivasan, R., Heatwole, C., Dillaha, T. (2009). Predicting the effects of land use change on runoff and sediment yield in Manupali river subwatersheds using the SWAT model. *Int. Agric. Eng. J.* 18, 15-25.
- [5] Raneesh, K.Y., Thampi, S.G. (2011). A study on the impact of climate change on streamflow at the watershed scale in the humid tropics. *Hydrol. Sci. J.* 56 (6), 946-965.
- [6] Chen, Y.N., Xu, C.C., Yang, Y.H., et al. (2009). Hydrology and water resources variation and its responses to regional climate change in Xinjiang. *Acta Geogr. Sinica* 64, 1331-1341.
- [7] Arnold JG, Muttiah RS, Srinivasan R, Allen PM. (2000). Regional estimation of base flow and groundwater recharge in the upper Mississippi river basin. *Journal of Hydrology* , 227:21-40.
- [8] Yuting Fan, Yaning Chen, Yongbo Liu, Weihong Li. (2013). Variation of baseflows in the headstreams of the Tarim River Basin during 1960-2007. *Journal of Hydrology, Elsevier*, 98-108.
- [9] Katie Price. (2011). Effects of watershed topography, soils, land use, and climate on baseflow hydrology in humid regions: A review. *Sage, Publications, DOI:10.1177/0309133311402714*.
- [10] Chapman, T. (1999). A comparison of algorithms for stream flow recession and base flow separation. *Hydrological Process*, 13:701-714.
- [11] W.A. Wolderufael and Y.E. Woyessa. (2010). Stream Flow Analysis an Comparison of Base Flow Separation Methodes, Case Study of The Modde River Basin in Central South Africa. *European Water Publications*, 31:3-12,2010.
- [12] Rusman, A. (2004). *Simulasi Alokasi Air pada Daerah Aliran Sungai Komerling Bagian Hulu dalam Pemenuhan Kebutuhan Air Tahun 2020*. Bandung: FTSL-ITB.
- [19] Pertiwi, N.S., Sudradjat, A. (2009). Analysis of Base Flow Variability at Nanjung Streamflow-Gauging Station on the Upper Part of Citarum Watershed. *FTSP-ITB*.
- [20] Eckhardt, K. (2008). A comparison of baseflow indices, which were calculated with seven different baseflow separation methods. *Journal of Hydrology* 352(1-2), 168-173.
- [21] Tallaksen, L. (1995). A review of baseflow recession analysis. *Journal of Hydrology* 165(1-4):, 349-370.
- [22] Musi Watershed Center, (2009). *Laporan Kegiatan Identifikasi dan Inventarisasi Karakteristik Sub DAS Komerling*.
- [23] Djuwansah, M. (2006). Aliran Rendah Sebagai Indikator Fungsi Hidrologi DAS. *LIPI*, 11-21.
- [24] Suherman, Dadan, Djuwansa, dkk., (2006). *Unjuk Kerja Fungsi Hidrologi*. Pusat Penelitian Geoteknologi LIPI.
- [25] Asdak, C. (2002). *Hidrologi dan Pengolahan Daerah Aliran Sungai (DAS)*. Yogyakarta: Gadjah Mada University Press.
- [26] Chow, V. (1964). *Handbook of Applied Hydrology*. New York: McGraw-Hill, NY, USA.
- [13] Balai Besar Sungai VIII (2010). *Laporan Hidrologi*. Palembang
- [14] Arwin. (2009). *Perubahan Iklim, Konversi Lahan dan Ancaman Banjir dan Kekeringan*. Bandung: FTSL, ITB.
- [15] Hughes DA, Hannart P, Watkins D. (2008). Continuous base flow separation from time series of daily and monthly data. *Water SA* 29(1), 43-48.
- [16] Hadisusanto, N. (2011). *Aplikasi Hidrologi*. Yogyakarta: Media Utama.
- [17] Indarto. (2010). *Dasar Teori dan Contoh Aplikasi Model Hidrologi*. Jakarta: Bumi
- [18] Limantara, L. (2010). *Hidrologi Praktis*. Bandung: Lubuk Agung.

TENSILE CREEP BEHAVIOR CONSIDERING YOUNG'S MODULUS DEVELOPMENT OF FLY ASH CONCRETE AT EARLY AGE

Yuki Watanabe¹, Yoichi Mimura², Vanissorn Vimonsatit³, Isamu Yoshitake⁴ and Itaru Horiguchi⁵

¹ Advanced Course, Project Design Engineering, National Institute of Technology, Kure College, Japan;

^{2,5} Department of Civil Environmental Engineering, National Institute of Technology, Kure College, Japan;

³ Department of Civil Engineering, Curtin University, Australia;

⁴ Department of Civil and Environmental Engineering, Yamaguchi University, Japan;

ABSTRACT

Thermal cracks caused by volume changes due to hydration heat of cement affect the long-term durability of concrete structures. Fly ash (FA), which is coal ash discharged from coal-fired power plants, when used to partially replace cement can reduce thermal stresses in concrete. Numerical analysis (FEM) is commonly used to predict thermal stresses. The tensile creep characteristic of concrete at early age is one of the important input data for FEM. The elastic strain for evaluation of creep behavior is generally assumed as constant. However, the Young's modulus development is remarkable at early age of concrete, therefore, it must be taken into consideration when evaluating the elastic strain. In this study, two sets of tests were conducted. The first set of tests is direct tension tests of dog-bone-shaped concrete specimens, which were conducted at the age of 3 days, and the loading stress 30% of the splitting tensile strength was sustained for 14 days. The other set of tests is splitting tensile strength tests and compression tests which were conducted to obtain the mechanical properties development such as the splitting tensile strength and the Young's modulus. The test results indicate that mixing of FA has less effect on the tensile creep behavior than considering the decrease of elastic strain at the early age.

Keywords: Early age concrete, Fly ash, Tensile creep, Young's modulus, Elastic strain

INTRODUCTION

Many concrete structures were constructed during the period of high economic growth in Japan, and thermal cracks, one of the initial cracks, became a problem [1]. Thermal cracks are caused by volume change due to hydration reaction of cement. Thermal cracks occur in approximately one or two weeks after casting and affect durability of concrete structures. Therefore, it is important to accurately predict thermal cracks and take measures.

Measures against thermal cracks are roughly classified into a method of suppressing volume change, a method of reducing constraint degree and a method of controlling crack width. One of methods for suppressing volume change of concrete is using of fly ash (FA). FA is fine particles of coal ash from coal-fired power plant. By replacing FA with cement, it can reduce the hydration heat that causes thermal cracks.

Controlling thermal cracking requires an accurate prediction of actual thermal stresses. Thermal stress analysis is normally performed by FEM which needs mechanical properties and volume change of concrete at early age, such as strength, Young's modulus and creep for the analysis. This study focuses on determining the tensile creep behavior of concrete for predicting accurate tensile thermal stress. Thermal stress is usually sustained in concrete for a long

period of time, so relaxation due to inelastic strain such as creep strain occurs. Thus, if stress estimation is made without considering the creep, thermal stresses predicted by FEM may be excessively greater than an actual stress.

To obtain the tensile creep behavior, it is important to improve the accuracy of the initial crack prediction. There are a few research reports on the tensile creep properties of FA concrete. Michimoto et al. [2] conducted direct creep tests under the loading condition of stress-strength ratio of 30% for 14 days in water. As a result, it is reported that the strain rate of FA concrete tended to be higher than that of ordinary concrete. However, in the previous report [2], the influence of Young's modulus development in early age was not considered. It is known that mechanical properties of concrete at early age (specifically the first two weeks after casting), significantly develop. Therefore, it is considered necessary to incorporate the development of Young's modulus when evaluating concrete strains, because the creep behavior evaluated by assuming constant elastic strain may not be appropriate [3].

Creep strain evaluation method is shown in Fig. 1. In evaluation of general creep strain, elastic strain is treated as constant. However, the Young's modulus is remarkably developing at early age, so elastic strain under constant stress is considered to gradually decrease.

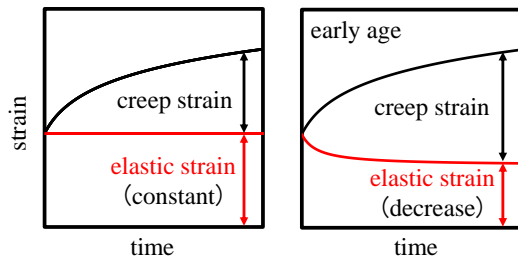


Fig. 1 Evaluation of creep strain

In this study, creep behaviors of FA concrete and ordinary concrete with a consideration of the development of Young's modulus were investigated and compared. In particular, it was aimed to determine the influence of Young's modulus development on concrete creep behaviors.

MATERIALS AND TEST PROGRAM

Materials and Mixture Proportions

Table 1 shows the materials used for concrete and mix proportion in this study. The mix IDs N and FA represent ordinary concrete mixes and FA concrete mixes, respectively, as shown in the table. The targeted slump of each mix of ordinary concrete and FA concrete is 8 ± 2.5 cm, and the targeted air content is $4.5 \pm 1.5\%$. Because FA contains unburned carbon, it reduces the effect of air-entraining and water-reducing admixture. Therefore, an air-entraining agent for suppressing the influence of unburned carbon was used in FA concrete mixes.

Specimen

In this study, direct tensile creep tests, splitting tensile strength tests (conform to Japan Industrial

Standards A 1113), and compression tests for obtaining Young's modulus were carried out. The dog-bone shaped specimen used for the direct tensile creep test is shown in Fig. 2. A small mold strain gauge having a temperature measurement function and a length of 50 mm was embedded in the center of the cross section of the dog-bone shaped specimen. In splitting tensile tests and compression tests, a standard 100 mm diameter, 200 mm long cylindrical specimen was used. For the strain measurement in compression tests, a strain gauge of length of 60 mm was attached at the center of both side faces of each specimen.

After casting, the specimens were carried into a curing room to be cured at a room temperature of 20 ± 1 °C for 24 hours before demolding. After that the specimens were cured underwater in a water tank (16 ± 1 °C) installed in the curing room until load tests were to be carried out at the age of 3 days.

Method of Tensile Creep Test

Figure 3 shows the loading apparatus used in the direct tensile creep test in this study. Tensile creep was loaded underwater, as shown in Fig. 3. The loading apparatus was installed in the water tank in the curing room with the temperature remained at 20 ± 1 °C and the temperature in the water tank remained at 16 ± 1 °C. In this test, loading was carried out in water to eliminate the effect of drying shrinkage. Therefore, tensile creep in this study is targeted for basic creep without moisture transfer.

The unloaded specimen was installed in the same environment as the loaded specimen, and the strain of the unloaded specimen was measured. By subtracting the strain of the unloaded specimen from the strain of the loaded specimen, strain caused by factors other than the loading, such as autogenous shrinkage and wet swelling, was eliminated. In this test, two loading apparatuses and two water tanks and four dog-bone

Table 1 Materials and mix proportion

Property	Materials	Proportion		Density
		Ordinary concrete	FA concrete	
Mix ID	---	N	FA	---
Water-binder ratio ^a	---	55%	55%	---
FA replacement ratio	---	0%	20%	---
Water (W)	Tap water	165 kg/m ³	165 kg/m ³	1.00 g/cm ³
Cement (C)	Ordinal Portland Cement	300 kg/m ³	240 kg/m ³	3.16 g/cm ³
Fly ash (FA)	Class II	0 kg/m ³	60 kg/m ³	2.24 g/cm ³
Fine aggregate (S)	Crushed rock sand	844 kg/m ³	833 kg/m ³	2.62 g/cm ³
Coarse aggregate (G1)	Crushed rock (20-15 mm)	499 kg/m ³	493 kg/m ³	2.67 g/cm ³
Coarse aggregate (G2)	Crushed rock (15-5 mm)	499 kg/m ³	493 kg/m ³	2.67 g/cm ³
Admixture (Ad1)	Air-entraining and water-reducing agent	3.00 kg/m ³	2.40 kg/m ³	1.07 g/cm ³
Admixture (Ad2) ^b	Air entraining agent for FA	0 kg/m ³	16.8 kg/m ³	1.04 g/cm ³

^a binder = C + FA, ^b diluted solution (diluted 100 times with water)

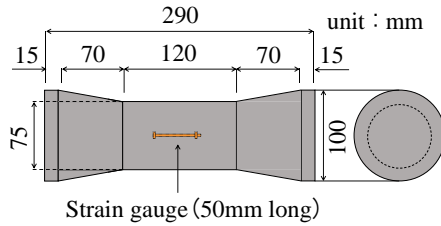


Fig. 2 Dog-bone shaped specimen

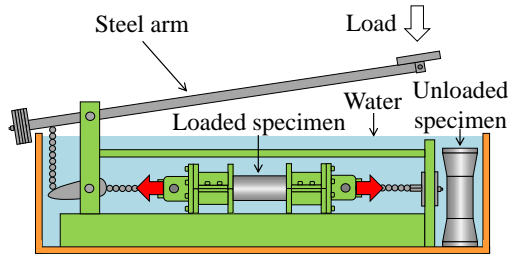


Fig. 3 Loading apparatus

shaped specimens were prepared. Therefore, one or two of each of loading specimens and unloaded specimens were used in one direct tensile creep test.

In the direct tensile creep test, the strain and the temperature of loaded specimens and unloaded specimens and the water temperature of each water tank were measured at one-hour intervals by using a data logger. The loading was started at the age of three days, and it was sustained for 14 days. The loading at the age of three days was derived from the age of changing the temperature stress from compression to tension. In addition, the loading period of 14 days was determined from the occurrence of the initial cracks at approximately two weeks after casting.

According to Davis-Granville's law, the creep strain is roughly proportional to the loading stress if the stress is less than the one-third of the concrete strength. Therefore, the loading stress in this study was set to 30% of the splitting tensile strength at the loading-start age (3 days).

Experiment Method of Young's Modulus

Compression tests were conducted to obtain the Young's modulus of concrete. In the compression test, unloading was conducted at every increase of strain of 10×10^{-6} . The strain and the load were recorded by using a data logger during the loading and the unloading. In order to eliminate the influence of inelastic strain in the evaluated Young's modulus as much as possible, strain and load were recorded until the load reached the splitting tensile strength. The relationship between strain and stress was linearly regressed. The gradient of the regression line was taken as Young's modulus. The compression test was conducted at the age of 3, 5, 7, 10 and 17 days or 3, 7,

10, 14 and 17 days. In this test, three cylindrical specimens were tested for each age.

RESULTS AND DISCUSSION

Table 2 shows the splitting tensile strength of the specimens tested at the age of three days and the loading stress for tensile creep tests. Mix IDs No. 1 to No.6 given in Table 2 are the specimens casted on different dates due to a limitation in the casting molds. Hence, the variation of the tensile strength results could be due to the casting conditions at each day. However, this difference does not affect the purpose of this study as the applied loading stress is specific for each specimen.

The relationship between Young's modulus and splitting tensile strength is shown in Fig. 4. In addition, the regression results using Eq. (1) are shown in Fig. 4. Equation (1) is obtained by changing the parameter of the equation shown in Guidelines for Control of Cracking of Mass Concrete 2016 [1] from compressive strength to splitting tensile strength. In this study, coefficients were evaluated by the using least-squares method.

$$E(t) = C_1 \times f_t(t)^{C_2} \quad (1)$$

where $E(t)$ is the Young's modulus (GPa), $f_t(t)$ is splitting tensile strength (MPa) and C_1 and C_2 are

Table 2 Splitting tensile strength and loading stress of age three days

Mix ID	Splitting tensile Strength (MPa)	Loading stress (MPa)
FA	No.1	1.32
	No.2	1.51
	No.3	1.53
N	No.4	1.22
	No.5	2.09
	No.6	2.38

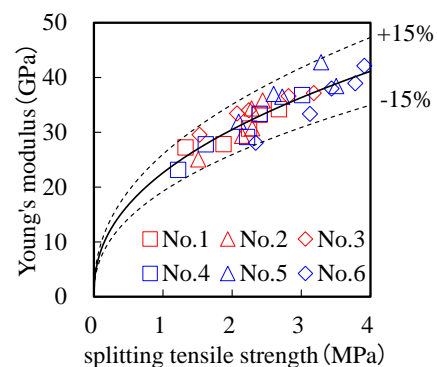


Fig. 4 Young's modulus – splitting tensile strength relationship

coefficients.

C_1 and C_2 evaluated in this study was 23000 and 0.43, respectively. Kimura et al. [4] reported that the compressive strength and Young's modulus showed a fixed relationship regardless of FA replacement ratio and age, and that mixing FA in concrete does not affect the Young's modulus. In the present study, the relationship between the Young's modulus and the splitting tensile strength shows a similar tendency in both ordinary and FA mixes, as seen in Fig. 4. Therefore, these results indicate that FA might not affect the evaluation of the Young's modulus as in the case of the previous report [4].

Figure 5 shows the time course of splitting tensile strength. In addition, the regression results using Eq. (2) are shown in Fig. 5. Equation (2) is obtained by changing the parameter of the equation shown in Guidelines for Control of Cracking of Mass Concrete 2016 [1] from compressive strength to splitting tensile strength. In this study, coefficients were evaluated by using the least-squares method.

$$f_t(t) = \frac{t}{A+Bt} f_t(28) \quad (2)$$

where $f_t(t)$ is splitting tensile strength (MPa), $f_t(28)$ is splitting tensile strength at the age of 28 days (MPa), t is age (day) and A and B are coefficients.

The coefficients used for Eq. (2) in FA concrete, A and B were 3.47 and 0.899, respectively. In ordinary concrete, A was 4.14 and B was 0.871. The splitting tensile strength of FA concrete at the age of 28 days was 3.08 MPa, and that of ordinary concrete

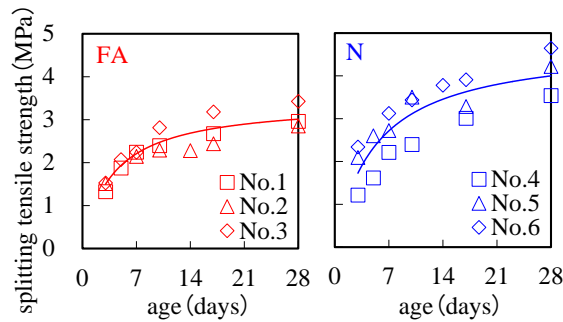


Fig. 5 Splitting tensile strength

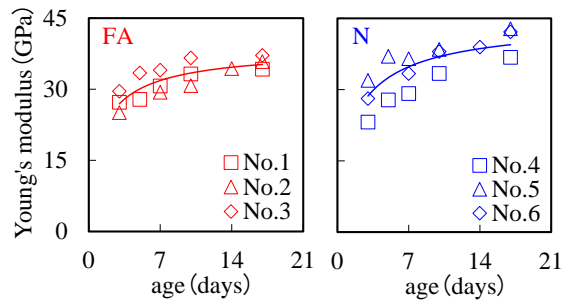


Fig. 6 Young's modulus

Was 4.14 MPa. The splitting tensile strength development of FA concrete was more gradual than that of the ordinary concrete, as shown in Fig. 5. This is probably because pozzolanic reaction of FA is slow and does not contribute to splitting tensile strength development yet.

Time course of the Young's modulus is shown in Fig. 6. In addition, the regression results are shown in Fig. 6. The curves of FA mixes and the curves of N mixes demonstrated in Fig. 6 were obtained from Eq. (1) and Eq. (2). The development of the Young's modulus was similar to that of the splitting tensile strength, which shows that the Young's modulus development of FA concrete is slower than that of the ordinary concrete.

The strain measured by the direct tensile creep tests is shown in Fig. 7. The creep strain is obtained by subtracting the elastic strain and the strain of unloaded specimen from the strain of the loaded specimen. The creep strain was evaluated by using constant elastic strain. In addition, the elastic strain in consideration of the Young's modulus development at early age was also used for evaluating the creep behavior. In other words, the elastic strain which decreases when loading concrete at older ages was evaluated. Using the regression result of the Young's modulus shown in Fig. 6, the elastic strain can be estimated by Eq. (3).

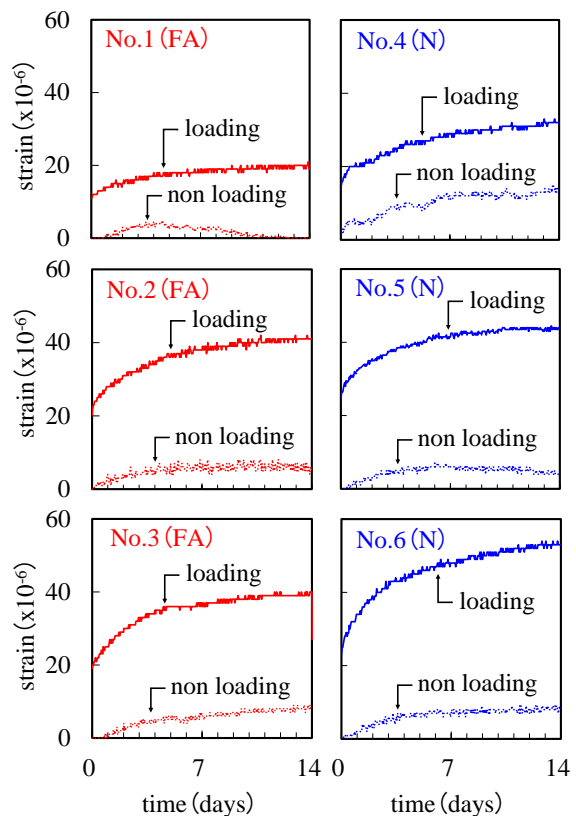


Fig. 7 Measured strain

$$\varepsilon_e(t) = \frac{E(t_0)}{E(t)} \varepsilon_e(t_0) \quad (3)$$

where $\varepsilon_e(t)$ is the elastic strain at elapsed time t , $\varepsilon_e(t_0)$ is strain of the loaded specimen at the start of loading, $E(t)$ is Young's modulus at elapsed time t (GPa) and $E(t_0)$ is Young's modulus at the start of loading (GPa).

Reduction of elastic strain is shown in Fig. 8. Elastic strain in FA concrete decreased by approximately 24%. Elastic strain in ordinary concrete decreased by approximately 28%. FA concrete demonstrates a slow development of the Young's modulus; the increase in the creep strain due to the decrease in the elastic strain was approximately 4% smaller, as shown in Fig. 8. As mentioned earlier, creep strain is roughly proportional to loading stress, so specific creep, which is the creep strain divided by the loading stress, was evaluated. The increase in the specific creep due to the decrease in the elastic strain is shown in Fig. 9. The results shown in Fig. 9 are obtained from using the decreased elastic strain (as seen in Fig. 8) divided by each loading stress. An increase of the specific creep due to a decrease of the elastic strain of FA concrete was approximately 8% smaller than ordinary concrete, as shown in Fig. 9.

The specific creep behaviors of FA concrete and ordinary concrete are shown in Fig. 10. These graphs are obtained from taking the average of the specific creep of FA concrete No. 1 to No. 3 and the average

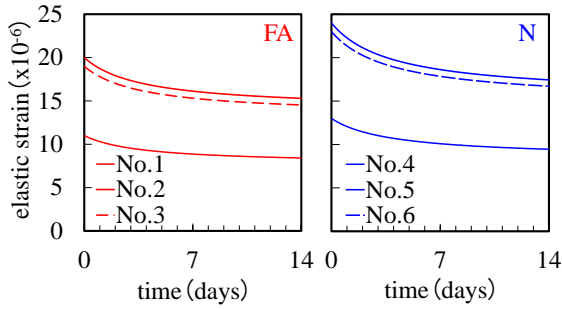


Fig. 8 Reduction of elastic strain

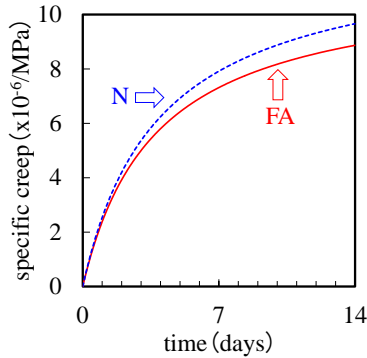


Fig. 9 Increase in specific creep by decrease in elastic strain

of specific creep of No. 4 to No. 6 ordinary concrete. Figure 10(a) shows the graphs with constant elastic strain, while 10(b) shows the graphs with decreased elastic strain due to the development of the Young's modulus. Yoshitake et al. [6] predicted the tensile creep behavior of early age concrete using the viscoelastic rheological model and Eq. (4). It is reported that the regression accuracy of Eq. (4) is high. The regression curves obtained by using Eq. (4) are included in Fig. 10. In this study, the coefficients, a , b , c and d , were evaluated by using the least-squares method.

$$J(t) = a\sqrt{t} + b[1 - \exp(-ct^d)] \quad (4)$$

where $J(t)$ is specific creep ($\times 10^{-6}/\text{MPa}$), t is elapsed time (day), a , b , c and d are coefficients.

The coefficients of Eq. (4) are shown in Table 3. Regardless of the consideration of the Young's modulus, the specific creep of FA concrete became larger than that of the ordinary concrete, as shown in Fig. 10.

The thermal stress depends on the specific creep rate rather than its magnitude. The specific creep rate was estimated by differentiating Eq. (4) with respect to time, and using coefficients given in Table 3 in order to compare the behaviors of the specific creep. The obtained specific creep rates are as shown in Fig. 11. It can be seen that the specific creep rates decrease monotonously in all cases.

Figure 12(a) shows the ratio of the specific creep rate of FA concrete to that of ordinary concrete. As shown in Fig. 12(a), the ratio of the specific creep

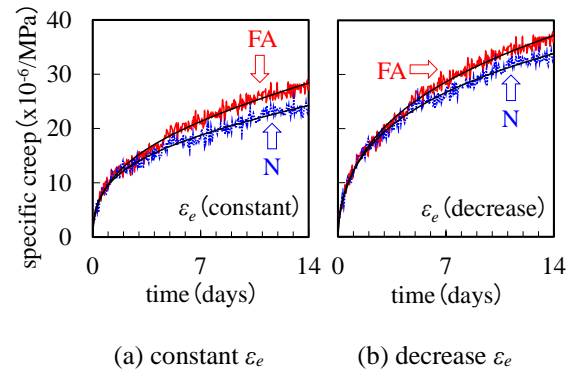


Fig. 10 Specific creep (comparison of N and FA)

Table 3 Specific creep regression result

coefficient	ε_e (constant)		ε_e (decrease)	
	FA	N	FA	N
a	0.694	0.536	0.674	0.405
b	21.2	19.0	31.5	34.6
c	0.552	0.642	0.450	0.414
d	0.516	0.457	0.592	0.533

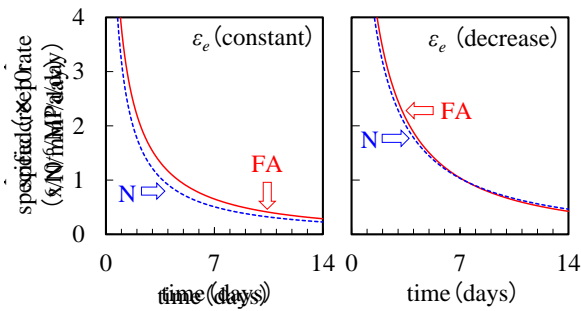


Fig. 11 Specific creep rates

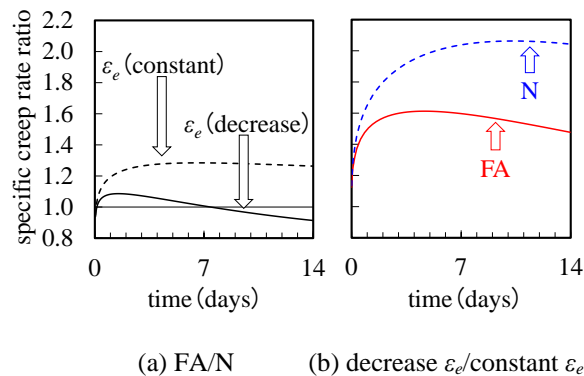


Fig. 12 Ratio of specific creep rates (FA/N)

rates in the case of constant elastic strain is more than 1.0 except for immediately after loading. This result indicates that the specific creep rate of FA concrete is greater than that of ordinary concrete. The ratio at loading period exceeded approximately one day is almost constant at 1.2. However, the specific creep speed rate in the case of the decreased elastic strain is within the range of $\pm 10\%$ during the loading period. Considering the decreased elastic strain (with the development of Young's modulus), the specific creep rate of FA concrete is not always greater than that of ordinary concrete.

Figure 12(b) shows the ratio of the specific creep rates with decreased elastic strain to that with constant elastic strain. In ordinary concrete, the specific creep rate with decreased elastic strain is 1.13 to 2.06 times that with constant elastic strain. In FA concrete, the maximum ratio is 1.61. As shown in Fig. 12(a) and Fig. 12(b), the consideration of the decrease in the elastic strain at early age affected the specific creep rate more than the FA mixing.

CONCLUSIONS

This paper presents an investigation of the tensile creep behavior of FA concrete with a consideration of the Young's modulus development in early ages of concrete. Direct tensile creep tests using dog-bone shaped specimens were conducted to obtain tensile

creep. Compression tests were performed using common cylindrical specimens to obtain the Young's modulus. Based on the test results in this study, it can be concluded as follows:

- (1) An increase of specific creep due to a decrease in elastic strain of FA concrete is about 8% smaller than that of ordinary concrete.
- (2) In ordinary concrete, the ratio of the specific creep rate with decreased elastic strain to that with constant elastic strain ranges from 1.13 to 2.06. While in FA concrete, the range of this ratio is smaller; the maximum ratio is 1.61.
- (3) If the elastic strain is assumed constant, FA concrete has greater specific creep rate than ordinary concrete. In the case of consideration of Young's modulus development during the creep test, the specific creep rate of FA concrete is almost equivalent to that of ordinary concrete.
- (4) Decreasing the elastic strain at early age has more effect on the specific creep rate than the mixing of FA.

ACKNOWLEDGEMENTS

The authors would like to thank Mr. Michimoto (a former advanced course student of National Institute of Technology, Kure College), members of Horiguchi laboratory and the Chugoku Electric Power Co. Ltd.

REFERENCES

- [1] Japan Concrete Institute, 2016, Guidelines for Control of Cracking of Mass Concrete 2016 (in Japanese).
- [2] Michimoto S., Mimura Y., Horiguchi I. and Yamada K., A Study on Stress Relaxation by Creep of Fly Ash Concrete, Japan Society of Civil Engineers 2017 Annual Meeting, V-413, pp.825-826, 2017 (in Japanese).
- [3] A. M. Neville., Properties of Concrete (5th edition), Prentice Hall, 1963.
- [4] Kimura M., Aikou Y., Ichinose T. and Yoshida T., On the Characteristic of the Concrete Using the Fly Ash, Proceedings of the Japan Concrete Institute, Vol.23, No.1, pp.301-306, 2001 (in Japanese).
- [5] Yoshitake I., Nakamura H., Nagai S. and Hamada S., A Study on the Tension Creep Equation During Hydration in the Early Age, Journal of Materials, Concrete Structures and Pavements, No.634/V-45, pp.43-53, 1999.11 (in Japanese).

DATA BASE STRUCTURE MANAGEMENT INFORMATION SYSTEM LAND ALLOCATION IN SPATIAL PLANNING

Sarino¹, Dinar DA Putranto², Agus Lestari Yuono³, and I.C. Juliana⁴

^{1,2,3,4}Faculty of Engineering, University of Sriwijaya, Km.32, Palembang-Inderalaya, Ogan Ilir District, South
Sumatera, Indonesia

ABSTRACT

Comprehensive data management systems are essential for watershed management. A large amount of spatial data of the study area has been collected for the management study of the Palembang River Basin of Indonesia. In this research will introduce database development to support the study of surface flow management in spatial planning of city area and region. This database links the geographic information system (GIS) with relational database management system (RDBMS) to facilitate the use of data in surface flow management. The method used in this research is to develop an integrated GIS-RDBMS database using the following steps: (1) to establish a database system that is easily accessible to all users; (2) developing database format and structure; (3) establish a formula for data management procedures, including input, update, conversion, QA / QC, and backup; and (4) the application of data queries and decision-making techniques for users to search, display, print, or collect information. This study aims to develop the stages of database compilation on the Jakabaring-based sub-watershed GIS-RDBMS. The process focuses on the study of surface flow management of the Jakabaring Watershed, This research introduces a concept in modeling the fuzzy geographic features in a watershed management system.

Keywords: GIS-RDBMS, run-off, fuzzy logic, DAS management

INTRODUCTION

The Jakabaring watershed is one of the sub watersheds in the area across from the ulu, Palembang City which was originally a flood plain, and some of its territory is a swamp and not widely used for activities until 1995. To develop the area across from Ulu, the government of South Sumatra Province together with the government The city of Palembang has reclaimed the swamp area and utilized for the implementation of Sports activities such as the Asian Games 2018 in Indonesia, with all facilities including residential areas, trade, offices and other supporting facilities. The process of development of the area of Seberang Ulu is done by hoarding the swamp area using the soil material derived from the dredging of the Musi River and the soil material taken from other areas.

The process of accumulating flood plains and swamps, of course, requires a water system in accordance with the conditions of the sub watershed Jakabaring that form the initial ecology of the area opposite Ulu. In its development, some areas in the area after the land conversion occurred, floods that flooded some areas such as residential areas, even runoff flooded the surrounding residential areas. This is one of the mistakes caused by the mismatch between land use allocation in spatial arrangement and the management of surface flow in a watershed. Understanding of surface flow management with

changes in urban and regional land use, will help urban planners and hydrologists in spatial planning. The Land Allocation Management System^[1] is a watershed analysis system (DAS) that will be developed by utilizing GIS techniques using land use change parameters, morphometrics and hydrometric watersheds. By using hydrodynamic analysis and spatial analysis (1D / 2D), water level in river and drainage channel, so it can get information about the change of water level distribution in sub watershed, due to land use change done when determination of land allocation. Puddle management involves the diagnosis of problems within the watershed with emphasis on the causes of rainwater runoff and tidal rivers causing flooding and puddles, and optimizing land allocation to increase water absorption into the soil to reduce surface or puddle flow.

METHODE

Land allocation management to reduce flood risk can be divided into two parts: Flood risk analysis and assessment on the one hand and risk mitigation on the other. Broadly speaking, the purpose of land allocation management is the assessment of flood risk to establish where the risk is very high, ie where mitigation measures will be required. Risk mitigation means proposing, evaluating, and providing alternative solutions to mitigate risks in the area. To map the risks and effects of flood risk

reduction due to land allocation, the utilization of Geographic Information System (GIS) with its ability to present spatial data is an appropriate tool for processing spatial data in surface runoff analysis. The approach presented in this paper is combining MCAs with GIS.

The amount of runoff surface runoff in a watershed is the relationship between topographic condition of the area, land use, soil type, drainage channel condition and the amount of rainfall. The smaller the area of infiltration, the greater runoff occurs, if rainfall and channel capacity are reduced [2]. On that basis, it can be used to translate the level of detail in the decomposition of the object class into a derived class (specialization) of the required database.

The Land Allocation Management System as defined by Sharifi (2003) is a Geospatial

Information System classification, consisting of data / information (spatial and non spatial), models, and visualization tools, especially developed to support planning and decision-making processes. In connection with the understanding as mentioned above, the method that will be developed in the manufacture of Spatial Spatial Allocation Management Information System will be focused on the planning phase, namely the preparation of database structure related to Basic Geospatial Information (IGD), such as topographic area, channel profile (river and drainage), the width and shape of the watershed, land use, and rainfall distribution. The overall architecture of the planning support system to be constructed is presented in Figure 1.

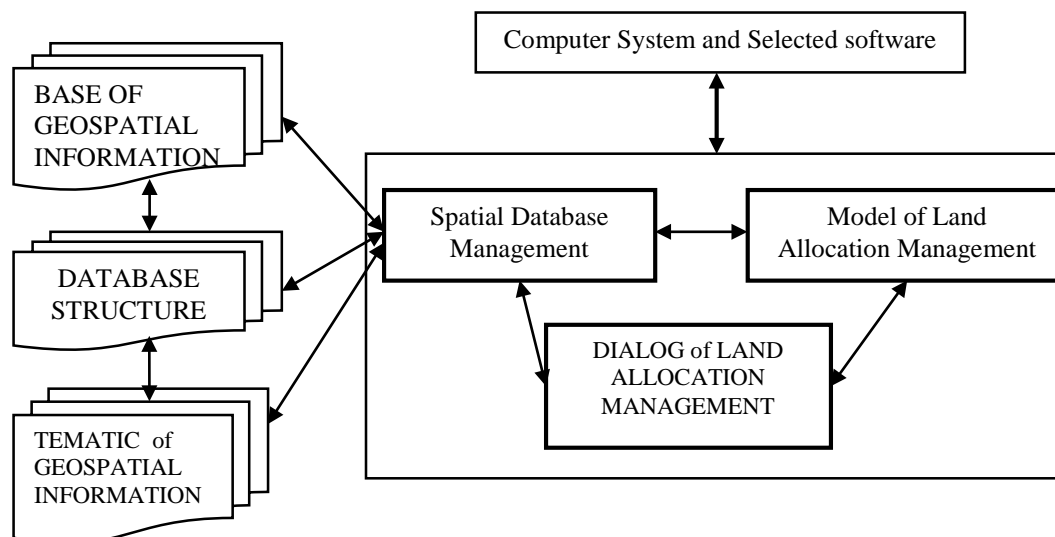


Fig. 1 Architecture Planning Decision Support System (DSS) in Land Allocation Management

The main components to be built in the Planning Support System are as follows:

- (1) A database management system. This system includes the preparation of database structure which includes the design of conceptual data model, identification of physical data collection + Meta Data, E-R Diagram designed to accommodate and organize spatial database and Geospatial Thematic information, and able to provide facilities to analyze and manipulate data
- (2) A Database Management System Model. The system includes both quantitative and qualitative models that support surface flow analysis, namely the assessment of potential surface flows and spatial capacity at different levels of land allocation management

The hydrological response of the watershed leads to the formation of surface runoff governed by

interactions with topology, land use and soil physical properties. Therefore, the use of Geographic Information Systems (GIS) will be better than traditional techniques in the quantification of appropriate surface runoff by storing and analyzing the underlying factors affecting runoff. The estimation process becomes more efficient, interactive and less complicated when Geographic Information System (GIS) is used to store, interpret and display the data required in surface runoff overlay techniques.

DATA BASE DESIGN

The design of the database in the Geographic Information System (GIS) always starts from the analysis of the appearance of geographic objects from real-fact data sources adapted to the utilization needs to be made (Raper, 1992).

Study Area and Data Acquisition

Jakabaring sub-watershed with geographic position 104° 44' 56" - 104° 47' 45" BT and 02° 07' 10" - 02° 03' 50" is one of the 19 sub-watersheds

that make up the watershed area of Palembang City, part of the Musi River Basin, within the administrative territory of South Sumatra Island, Indonesia.

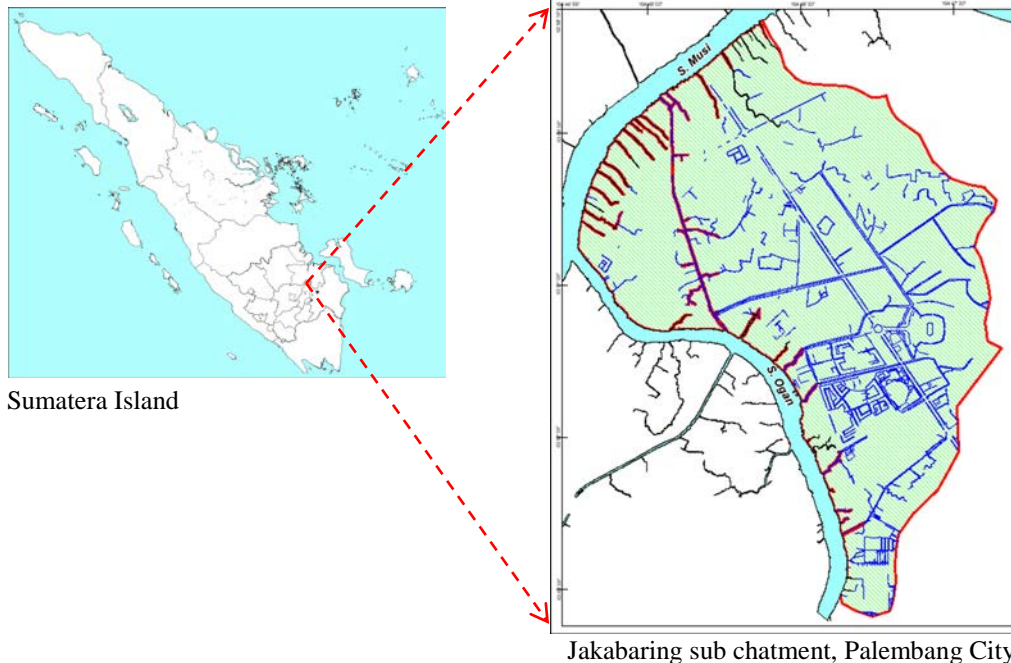


Fig. 2 Research Sites of Jakabaring Sub-watershed, Palembang City, Musi Watershed Area, Sumatera Island, Indonesia

Object Description

The introduction of objects based on the appearance of land use objects is classified according to the materials needed in river basin management. Understanding land use here, is an object that uses or requires space or land. To that end, the objects of roads, rivers and waterways (swamps, lakes, canals) are also objects that use space. Thus the sub class of road and river objects, can be incorporated into one class, called sub class of space utilization or land use. Each space utilization will be within the watershed area. For that object space utilization can be incorporated in a sub class of objects called sub class space utilization and watershed boundaries

A set of methods for calculating objects having similar characteristics and shapes can be incorporated together with their attributes and called class definitions. The class hierarchy used is, the first class is called the base class, while the second class or sub-class, commonly called the derived class. {LIMITS BOARD; LIMIT SUB; BATAS SUB RIVER SYSTEM}, is a member of the watershed sub-class sub-class. The space utilization sub class is a form of "generalization" of the subclass {P_LAHAN; LHN_HIDRO}. Sub Class PURAHAN, is a generalization of sub Class

{RESERVATION; OFFICE; INDUSTRY; EDUCATION; PUBLIC FACILITIES; TRADING; SOCIAL FACILITIES; HEALTH}. LHN_TBK Subclass Class, is a generalization of the subclass of {SPECIAL FORESTS; GREEN OPEN SPACE; WALKING ROAD; RIVER RIVER}. The HIDRO Subclass, is a generalization of the sub class {RIVER; SWAMP; CHANNEL}. The sub-class of roads, consisting of DAMIJA objects (Road Owned Areas) having spatial structures of areas (polygons) can be incorporated with PURAHAN sub-classes, into LHN_TBGN Subclasses. The merger (association) is because between the sub-class of watershed boundaries and the space utilization sub-class has many similarities in attributes and methods, such as names, spatial and non spatial relationships, widespread calculations and so on.

Figure 3. below shows a nail diagram illustrating the hierarchy between the subspace class sub-district visibility, for the watershed boundary subclass.

Identification of the data unit of the object that composed the structure of the DAS Territorial Layout for each subclass, can be fully detailed as follows:

- (1) watershed area units used as observation limits for flood or puddle analysis are used within watershed boundaries. To that end the subclasses of the watershed area contain the sub-watershed,

including the sub-sub-basins with the object identification (primary key) in this class is the OID.

- (2) spatial use specified by location and area of land for each watershed boundary, identified as land utilization sub class. The relationship (subdivision) between the land utilization class and the level of detail will be indicated by the level of numbering in the OID. Geometric shape

and geometric spatial structure is represented by geometric shape of polygon (area), consisting of geometric shape of boundary of utilization (ring) and the area of exposure (closure) and point coordinates that indicate location and relationship between geometric object based on topology (face) written in the form of non-geometric attributes

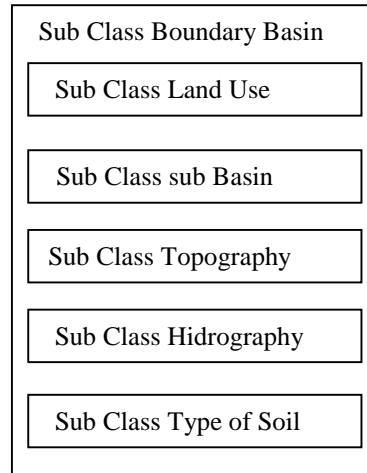
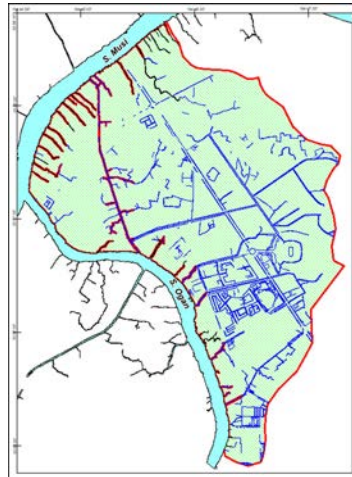


Fig. 3 Examples of specialization of DAS Basin class, Land Use sub-class and DAS sub-classes

Attribute Data

Each object must have an attribute that describes the property (property) of the object. Determination / selection of relevant attributes for an object is important in making the data model. Attribute data is compiled based on the need of GIS utilization object for watershed management. The attribute will describe the contents of the geometric object numerically (numbers) as well as spatially related to other geometric objects, which will produce the derived attributes. The subclass will inherit attributes that are similar in character to the superclass attribute. Thus, there is no need to attribute that has been defined in the "base class", redefined in the sub class, because it will only cause waste of storage in the computer.

Connectivity among Object Class

Based on the relationship between spatial objects that have been discussed earlier, then finally can be arranged a relationship diagram that explains interconnection (relation) between sub class of spatial objects that make up the Spatial Area DAS. Using the logic of relationships, such as specialization, aggregation, generalization and association, each class is linked by describing it in a spatial object linkage model diagram. Seen in FIG. 4, the logic of the relationship as illustrated in the

diagram of Figure 3, is arranged in the form of a spatially connected object diagram generalized by subclass, with the following explanation: soil, topography, and hydrographic elements are unplanned Spatial Planning and is a watershed area planning area. The watershed area, divided into observation boundaries, is called the sub-basin boundary. Within the watershed area boundary which is an observation area, based on the planned land allocation within each watershed boundary, it is known that the run-off will occur in each watershed. Thus, within each watershed boundary, there is space utilization necessary to carry out activities that are applied in space utilization zones, such as settlement, education, trade, and so forth.

Any change of land use allocated within the watershed limits will determine the value of C (catchment coefficient) for each sub class of land use object in the area, but will also determine the amount of runoff to be produced by each sub class of land use object, which will determine needs of drainage systems and retention ponds. The allocation of existing land use distribution to each sub watershed, will ultimately determine the need of drainage network system in the area. Thus there is a spatial relationship between the variables of land use change within the watershed area with the amount of runoff to be generated. The amount of land use allocation to be able to serve the population allocated to each sub-basin, will determine the

amount of distribution needs of network system Drainage (sub class utility object). Thus there is a relationship between the variables of land needs in each sub-basin with the needs of the distribution of drainage system.

The attributes for each of these spatial use objects are stored in tabular data, broken down by

land use type, sub-class of land use, within each sub-watershed. To obtain the amount of land utilization in each sub-basin, simply add up the utilization of land for each sub-basin boundary, and the utilization of each sub-basin is summed up to obtain land use throughout the basin. Connection diagram (E-R Diagram) for data storage, can be seen in Figure 5.

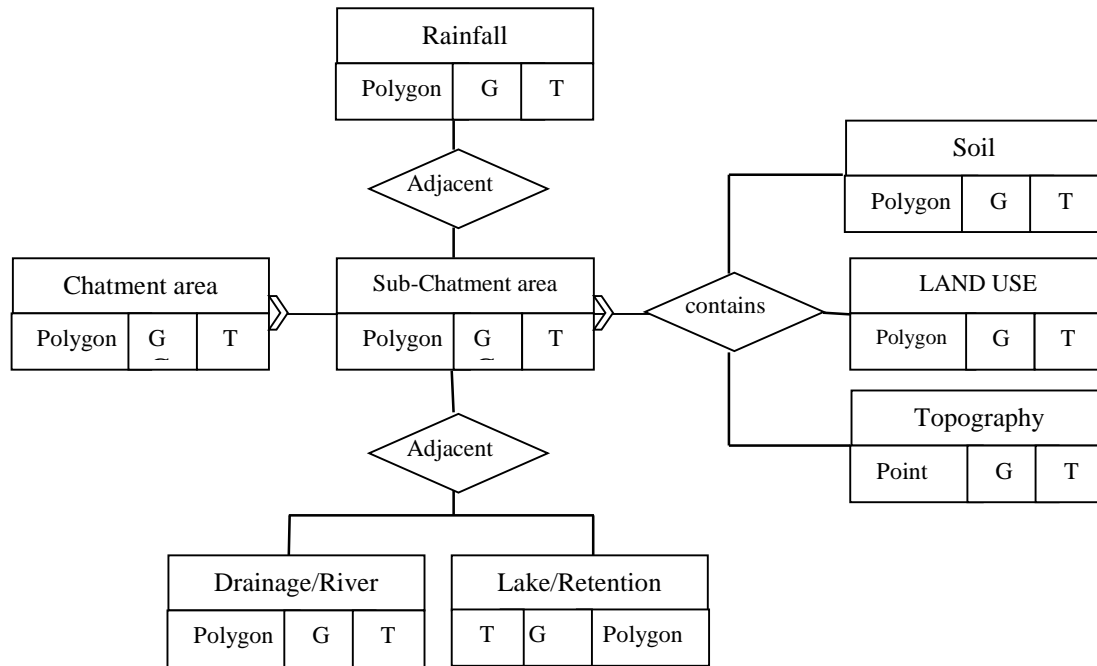


Fig. 5 Entity-Relationship Diagram for Run-off management at Chatment Area

Data Structure

Each object will have at least one data attribute, which must be defined by the type of identifier (OID), the constructor type of each data column (integer, decimal, character, etc) and the value of each data column contained in the data attribute, - the column that will be used to load the attribute value.

The object set as the base class will be specified as the key identifier, which will be represented as the primary key (Primary Key). From the primary key, then each object that belongs to the class, will have an OID that follows the hierarchy of the primary key of the class above it.

The method or commonly called function, is used to write commands to perform mathematical calculations based on the analysis model used. In determining the allocation of any required land use and placed within each sub-basin boundary, a Run-off model is used. The mathematical function used to calculate the probability of land use is directly defined in the sub-class definition of sub-basin boundaries. Thus, to know the value of the total infiltration coefficient that exists within the sub-sub class of sub-watershed or sub-basin, it is the sum of the infiltration coefficient values present in each

sub-watersheds. The principle is commonly referred to as inheritance (inheritance), polymorphism (Polymorphism) and encapsulation (encapsulated). The design of the data structures for each object classification used in the management of the Spatial Planning can be seen in Table 1 below.

Table 1 Structure Basis Data at Chatment Area

Object : <i>Chatment Area</i>		
Atribut	Data Type	Width
Qcode	Integer	(10)
N_CA	Character	(25)
NS_CA	Character	(25)
Area_Ha	Decimal	(15,3)
Perimeter	Decimal	(15,3)
Center_L	Decimal	(10,3)
Object : <i>Land Use</i>		
Atribut	Data Type	Width
OID	Integer	(10)
L_Use	Character	(30)
Class	Character	(30)
Area_Ha	Decimal	(15,3)
N_C	Decimal	(5,3)
RD	Decimal	(5,3)

ET_ETO	Decimal	(5,3)
A%	Decimal	(5,3)
P	Decimal	(5,3)

Object : <i>Topography</i>		
Atribut	Data Type	Width
OID	Interger	(10)
S_Height	Character	(10)
Z (m)	Decimal	(10,3)

Object : <i>Hydrometry</i>		
Atribut	Data Type	Width
OID	Interger	(10)
I_Countur	Character	(10)
O_Name	Character	(15)
Z	Decimal	(10,3)

Object : <i>Soil</i>		
Atribut	Data Type	Width
OID	Interger	(10)
Type_Soil	Character	(25)
Area (Ha)	Decimal	(10,2)
Z_Organic	Decimal	(5,2)
OM_Value	Decimal	(5,2)
Moisture_Sc	Decimal	(5,2)
BD	Decimal	(5,2)
pH	Decimal	(5,2)
K_Value	Decimal	(5,2)

The watershed class sub-class and space utilization shall consist of sub-basin boundary tables, which contain sub-basin objects and their attributes containing {OID; N_CA; Area_Ha; Perimeter; L_CA}, and chatment object with the same attribute, but the attribute value is the sum of all attribute values of the sub-watershed that are its members.

Land utilization subclass will contain Tables with attribute {OID; L_Use; Area_Ha; Koef_C; Root_Depht}, which is connected to the sub-basin boundary based on the typical identifier number (OID), thus forming the sub-basin table relation {OID; Land Use}.

ANALYSIS MODEL INTER OBJECT DATA

One method for analyzing flood peaks as a result of land use change in a watershed is by analyzing runoff. One important empirical formula for determining the peak rate of runoff is the Rational Formula. This formula is mostly used for designing drainage facilities for small urban and rural watersheds. It is characterized by (1) consideration of the entire drainage area as a single unit, (2) estimation of flow at the most downstream point, and (3) the assumption that rainfall is uniformly distributed over the drainage area.

Determination Peak Runoff Rate Using The Modified Rational Formula

The rational method is described by the formula 1 (Brouwer, 2012)

$$Q_p = 0.28 * C * I * A \quad [1]$$

where,

Q_p = Peak runoff rate [m³/sec].

C = Runoff coefficient.

I = Rainfall intensity [mm/hr].

A = Drainage area [km²].

In the modified version of the rational formula, a storage coefficient, C_s , is included to account for a recession time > the time the hydrograph takes to rise. In the original formula the recession time was assumed to be equal to the time of rise.

The modified rational method is then described by the formula 2.

$$Q_p = 0.28 * C_s * C * I * A \quad [2]$$

The rational method follows the assumptions that

- (1) the predicted peak discharge has the same probability of occurrence (return period) as the used rainfall intensity and
- (2) the runoff coefficient is constant during the rain storm.

A rainfall with a steady uniform intensity applied to the catchment will cause runoff that will reach its maximum rate when all parts of the watershed are contributing to the outflow. This will happen after the elapsed time t_c , the time of concentration. At this time the runoff rate equals the excess rainfall rate.

There are a few well defined criteria for selection of formulas or methods for determining the time of concentration. A number of formulas and methods for determining t_c exist. Only one of them will be presented here:

Kirpich (Ramser) time of concentration equation.
Formula 3

$$t = 0.0195 * L^{0.77} * S^{-0.385} \text{ (Kirpich/Ramser)} \quad [3]$$

where,

t_c = Time of concentration [min].

L = Length of main river [m].

S = Distance weighted channel slope [m/m].

CONCLUSION

- (1) There are 8 identifiable data objects with 7 relationships
- (2) The relationship between data objects is formulated by utilizing the SQL Select model by linking Tables and columns based on rational formulas

ACKNOWLEDGEMENTS

Acknowledgments are submitted to the Research Institute of Sriwijaya University, which has provided a Competitive research fund for this activity.

REFERENCES

- [1] He C. Integration of geographic information systems and simulation model for watershed management. *Environ Model Softw*, 2003) 18 (8–9):809–813
- [2] Mokarram, M., Hoyati, M., Using ordered weight averaging (OWA) aggregation for multi-criteria soil fertility evaluation by GIS (case study: southeast Iran), *Computers and Electronics in Agriculture*, vol. 132 (2017) pp. 1–13 Published by Elsevier B.V.
- [3] Dinar DA Putranto, Sarino, Yuono, AL., Sistem Manajemen Alokasi Lahan (SIMAL) Sebagai Dasar Dalam Melakukan Alokasi Ruang, *Prosiding, FIT-ISI dan CGISE* (2015)
- [4] Malczewski J, GIS- based multicriteria decision analysis :a survey of the literature. *Int J Geogr Inf Sci* 20 (7), 2007, :703–726
- [5] Malczewski J, Chapman T, Flegel C, Walters D, Shrubsole D, Healy MA, GIS multicriteria evaluation with ordered weight edaveraging (OWA) :case study of developing watershed management strategies. *Environ Plan A* 35 (10), (2003): 1769–1784
- [6] Olivera F, Valenzuela M, Watershed and srteam delineation tool interface. <http://cprofs.tamu.edu/folivera/GISTools/wsd/ home.htm>. Cited 26 June 2006
- [7] Sarangi A, Bhattacharya AK, Small watershed runoff generation model. *J Soil Water Conserv* 43 (3&4), (1999) :176–188
- [8] Sumi Amarina Hamim, Model Pengendalian Lingkungan sub Sistem Sungai Dalam Manajemen Sistem Drainase Kota Palembang, *Disertasi, Program Doktor Ilmu Lingkungan, Program Pascasarjana, UNSRI* (2009)
- [9] Sarangi A, Bhattacharya AK, Comparison of artificial neural network and regression models for sediment loss prediction from Banha watershed in India. *Agric Water Manag*, (2009), 78:195–208
- [10] Sarangi A, Madramootoo CA, Singh DK, Development of ArcGIS assisted user interfaces for estimation of watershed morphologic parameters. *J Soil Water Conserv*, {2004} 3(, 4):139–149
- [11] Sarangi A, Madramootoo CA, Enright P, Prasher SO, Patel RM (2005a) Performance evaluation of ANN and geomorphology-based models for runoff and sediment yield prediction for a Canadian watershed. *CurrSci*, (2005) (12):2022–2033
- [12] Sarangi A, Bhattacharya AK, Singh AK, Sambaiha A (2005b) Performance of Geomorphologic Instantaneous Unit Hydrograph (GIUH) model for estimation of surface runoff. In: *International conference on recent advances in water resources development and management*, 23rd to 25th Nov 2005, IIT, Roorkee, Uttaranchal, India, pp 569–581
- [13] SCS (1956) *Hydrology, national engineering handbook, supplement A, Section–4 Chapter 10*, Soil Conservation Service, USDA, Washington, DC
- [14] Shrestha MN (2003) Spatially distributed hydrological modelling considering land-use changes using remote sensing and GIS, *Water Resources, Map Asia Conference 2003*, Map Asia 2003. <http://www.gisdevelopment.net>
- [15] Singh AK, Bhattacharya AK (2006) *Water management and crop production, Handbook of Agriculture*, Directorate of information and publication of agriculture. ICAR, New Delhi, pp 300–348
- [16] Socher M, Sieber HU, Mu"ller G, Wundrak P (2006) Verfahren zur Priorisierung von Hochwasserschutzmaßnahmen in Sachsen. *Hydrologie und Wasserbewirtschaftung* 50(3)
- [17] Zade M, Ray SS, Dutta S, Panigrahy S (2005) Analysis of runoff pattern for all major basins of India derived using remote sensing data. *Curr Sci* 88(8):1301–1305
- [18] Sadiki, A., Faleh, A., Navas, A., Bouhlassa, S., 2007. Assessing soil erosion and control factors by the radiometric technique in the Boussouab catchment, Eastern Rif, Morocco. *CATENA* 71, 13–20.
- [19] Tyagi, J., Mishra, S., Singh, R., Singh, V., 2008. Cscn based timedistributed sediment yield model. *Journal of Hydrology* 352, 388–403.
- [20] Zeynab Karimzadeh Motlagh, Mohammad Husein Sayadi (2016). Siting MSW landfills using MCE methodology in GIS environment (Case study: Birjand plain, Iran). *Journal Waste Management, Elsevier*. Volume 46, Desember 2016, pages 322–377.
- [21] Dinar DA Putranto, Sarino, Yuono, AL, 2015, Model Medan Digital Untuk Analisis Rainfall-Runoff Sub DAS Musi Bagian Hulu-Hilir DAS Musi, *Laporan Penelitian, Hibah Strategis Nasional*.
- [22] Dinar DA Putranto, Sarino, Yuono, AL, 2009, Model 1D/2D Dalam Analisis Pemodelan Banjir Kota Palembang, *Laporan Penelitian, Hibah Strategis Nasional*.

ANALYSIS OF TRAFFIC ENVIRONMENT AND DYNAMIC BEHAVIOR OF BRIDGE GIRDERS BASED ON IMAGE SENSING TECHNIQUES

Kouichi Takeya¹, Koharu Ota², Shiho Takagi³ and Junji Yoshida⁴

^{1,4} Faculty of Engineering, Graduate School, University of Yamanashi, Japan;

^{2,3} Faculty of Engineering, University of Yamanashi, Japan.

ABSTRACT

In this study, image sensing techniques are focused to grasp the traffic environment and the dynamic behavior of bridges simultaneously. The dynamic deflection of bridge girders and the traffic environment, such as speed type of vehicles and weight, can be analyzed using the combination of the sampling moire method and optical flow process. In this research, we attempted to construct a measuring method of traffic environment and dynamic behavior of bridge girders based on these image sensing techniques.

As results of this fundamental study using a model bridge, first, a displacement measuring method was examined and constructed based on the sampling moire method. The results were compared with measured displacement by laser displacement sensors in the model experiments. It was demonstrated that the dynamic deflection of the bridge girder can be calculated with high accuracy. Second, an analysis method of traffic environment was constructed based on the optical flow process. It was demonstrated that the velocity and size of moving objects can be detected and monitored automatically.

Finally, by combining these two methods, an analysis system of the traffic weight using dynamic behavior of bridges (known as Bridge Weigh-in-Motion or B-WIM) was proposed. Since these two measuring methods use the same images taken by one camera, the proposed system can grasp the traffic environment and the dynamic behavior of the model bridge simultaneously.

Keywords: Bridge deflection, Sampling moire method, Optical flow process, Traffic environment, B-WIM.

INTRODUCTION

Aged deterioration of bridges is progressing due to traffic vehicles, weather conditions, etc. Among them, heavy vehicles including overloaded vehicles have a large influence on the deterioration of bridges. Therefore, investigation of traffic environment on bridges is highly required.

As a method to grasp the traffic environment of heavy vehicles on bridges and estimate the deterioration, Bridge Weigh-in-Motion (B-WIM) has been focused for last several decades [1]. B-WIM is a method to estimate the traffic weight by sensing the dynamic deflection or strain of the bridge members. The influence line is mainly calculated based on the dynamic strain measurement to estimate the traffic weight.

To measure deflection of bridge members, such as girders, direct measurements with contact or noncontact displacement sensors exist. However, these are difficult to install, and the applicable bridge is limited. On the other hand, a laser Doppler velocimetry or accelerometers are other candidate. However, there is a problem with integration accuracy [2].

In this research, we focused on monitoring the traffic environment using the camera and

simultaneously grasping the dynamic behavior. The dynamic deflection of bridge girders, when vehicles are passing through, is aimed at analyzing the sampling moire method by photographing target grids attached on bridges [3]-[5]. In this research, we attempted to construct an analysis system to grasp the advanced traffic environment such as the variable velocity of the traffic, the vehicle type and weight by using model experiments as a fundamental study.

DYNAMIC DISPLACEMENT MEASUREMENT

Model Bridge for Experiment

Fig. 1 shows an image of the model bridge experiment. The model bridge is made of ABS resin, the span of the girder between two rubber supports is 800 mm, the width is 50 mm and the thickness is 4 mm. Two rails are attached on the girder; four iron balls roll on the rails separately. The weights of the steel balls are 16 g, 32 g, 64 g, and 126 g. Five targets are attached on the both end and each quarter points of the girder. Three laser displacement meters (Keyence, LK-500) are also installed to evaluate the vertical displacement at the quarter points. A digital camera (Canon, EOS 60D) was used for high-speed consecutive shooting of JPEG images. The

specification of the equipment and targets are shown on the Table 1 and Table 2, respectively.

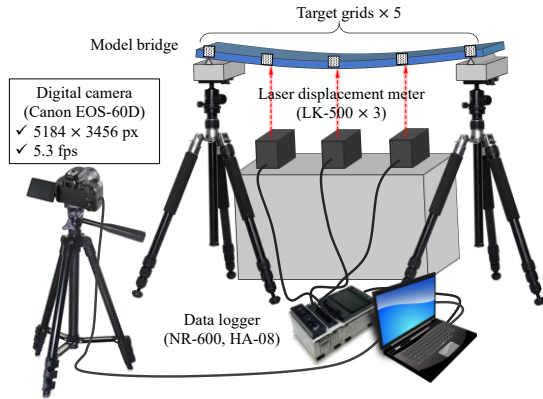


Fig. 1 The model bridge and measurement equipment of experiments

Table 1 Specification of the equipment

Camera	Canon EOS 60D	5184×3456px	5.3fps
Lens	Tamron, 28-78mm, F2.8		
Sensors	Keyence LK-500	10μm (accuracy)	analog
Logger	Keyence NR-600 HA-08	±20mm 14bit	100Hz

Table 2 Target size and pitch length of grids

	Size	Pitch length
Millimeter	25×25 mm	2.031 mm
Pixels	(V)180×(H)180 px	18 px

Sampling Moire Method

There are a lot of analysis methods of dynamic displacement using images, such as image correlation methods using the boundary or edge detection [6], [7], the sampling moire method [3]–[5]. Although bridges are large-sized structures, their deflection is on the order of a few millimeters, then the high resolution is required. Therefore, it is considered that the sampling moire method is applicable for measuring the deflection of bridge girders.

To calculate the vertical displacement or deflection of the bridge girders, the procedure by the sampling moire method is as follows.

- 1) Image preprocessing (contrast adjustment, noise cancelling, correcting image size and inclination)
- 2) Sampling every N pixel, shifting the sampling points and the linear interpolation using neighboring pixels (Creating phase-shifted sampling moire images)
- 3) Phase distribution calculated by the discrete

Fourier transform (DFT)

- 4) Conversion of the phase difference to the displacement

First, the target position is selected manually and the unnecessary images are cropped in each video frame. The parameters to correct the inclination of the image and the contrast are automatically determined from the default image. Next, grid images are divided in the vertical and horizontal directions and analyzed separately. In this study, only the vertical direction was focused. The blank columns (or rows) are interpolated linearly and stripe pattern are created as shown in Fig. 3(A). Next, the image is sampled every N pixel (N is named the sampling number) in vertical direction and the blank pixels are interpolated linearly using the neighboring pixels. Through this sampling process, N number of phase-shifted sampling moire images are obtained (Fig. 3(B)).

As the sampling number N approaches the pixel number of the pitch length in pixels, the phase period of the phase distribution becomes longer. Therefore, the resolution of the phase difference and displacement becomes higher. However, when the phase period is longer than half of the image length, the phase difference cannot be calculated correctly and error cases occur. Therefore, the largest sampling number N is determined when the phase period is less than half of the image length, and it is iteratively calculated and obtained automatically. Specifically, for the vertical direction pixel v , the phase distribution $\bar{\varphi}(N, v)$ [rad] averaged in the horizontal direction pixel h is as follows.

$$\bar{\varphi}(N, v) = \frac{1}{H} \sum_h \varphi(N, v, h) \quad (1)$$

Where, $v = 1, 2, \dots, V$ [pixel] and $h = 1, 2, \dots, H$ [pixel]. The normalized autocorrelation function $\bar{R}_{\varphi\varphi}(N, v)$ of the phase distribution are obtained with the sampling number N , where v is in the range between $-V$ and $+V$ [pixel]. The maximum sampling number N is determined when peaks of the normalized autocorrelation function $P_k(N)$ are three ($k = 1, 2, 3$). In this study, the condition of the peaks was set to 0.5 or more.

$$\bar{R}_{\varphi\varphi}(N, v) = \frac{\sum_v \bar{\varphi}(N, v) \bar{\varphi}(N, v + v)}{\sum_v \bar{\varphi}(N, v)^2} \quad (2)$$

$$P_k(N) |_{k=1,2,3} \geq 0.5 \quad (3)$$

The phase analysis by the discrete Fourier transform (DFT) is carried out and one phase distribution image is obtained (Fig. 3(C)). The phase distribution image is calculated in each video frame (Fig. 3(D)). Fig. 4 shows an example of the phase distribution with the optimized sampling number $N =$

13.

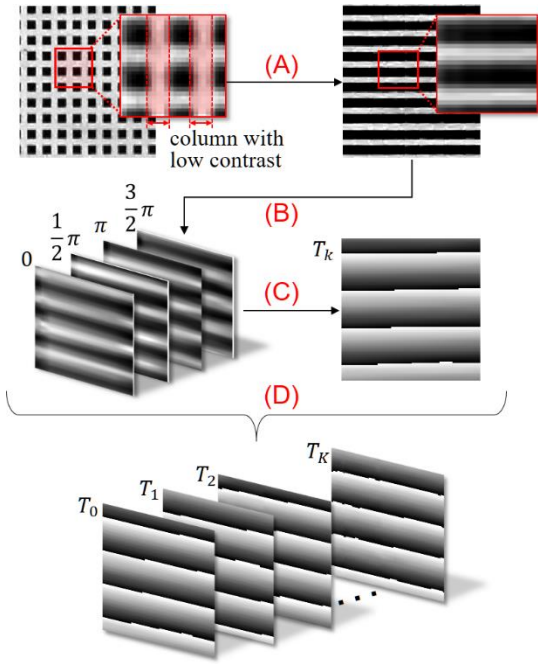


Fig. 3 Phase analysis for two-dimensional grid
 (A) 2-D grid image to 1-D stripe pattern
 (B) Phase-shifted sampling moire images
 (C) Phase distribution analyzed by DFT
 (D) Iteration for each video frame

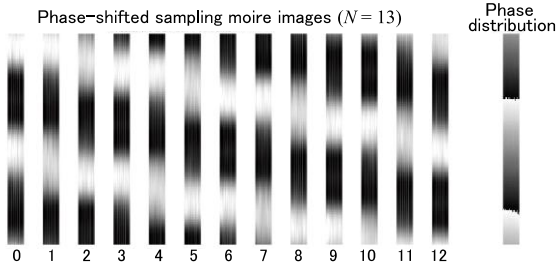


Fig. 4 Phase-shifted sampling moire images and phase distribution image with optimized sampling number ($N=13$)

As shown in Fig. 5(E), the phase difference $\Delta\phi(t, h)$ [rad] in each column ($h = 1, 2, \dots, H$) is calculated between each moved phase distribution image at $t = T_k$ ($k = 1, 2, \dots, K$) [sec] and the default phase distribution image at $t = T_0$. The average phase difference $\Delta\bar{\phi}(t)$ [rad] is calculated as follows (Fig. 5(F)).

$$\Delta\bar{\phi}(t) = \frac{1}{H} \sum_h \Delta\phi(t, h) \quad (4)$$

The average phase difference, between the moved position image and the default position image, is corrected in angles by adding multiples of $\pm 2\pi$ when

absolute jumps between consecutive elements of $\Delta\bar{\phi}(t)$ are greater than π radians. The vertical displacement $y(t)$ [mm] is finally calculated using the following relationship.

$$y(t) = dy \times \frac{\Delta\bar{\phi}(t)}{2\pi} \quad (5)$$

Where dy is the pitch length of the vertical grid [mm].

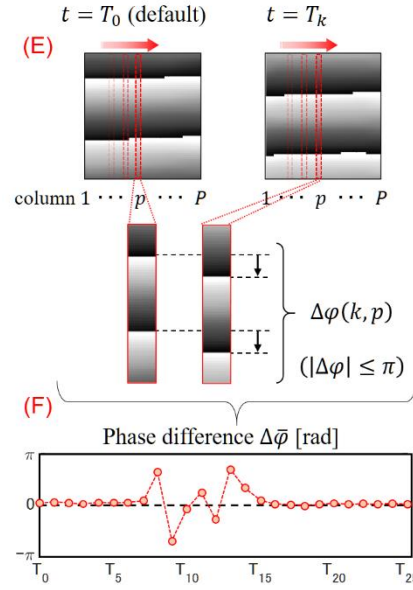


Fig. 5 Displacement analysis using phase analysis
 (E) Average phase difference in horizontal direction
 (F) Average phase difference in time domain

In Fig. 6, red dotted line shows the calculated deflection by the sampling moire method when the iron ball passes through the model bridge. The blue line shows the actual value of displacement measured by the laser displacement sensor (Keyence, LK-500). The calculated deflection by sampling moire method is matched with high precision with the actual values.

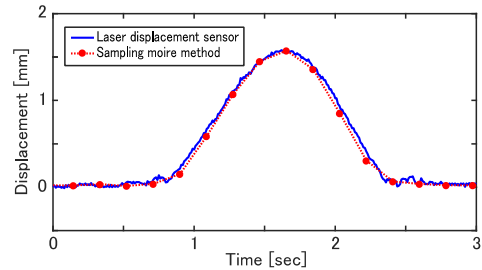


Fig. 6 Vertical deflection of the center point of the model bridge

Next, four iron balls were traveled on the model bridge around one hundred times in total. The peak displacements calculated by the sampling moire method and the actual values (the peak displacements

measured with the laser displacement sensor) are plotted in Fig 7. The closer the plots are to the solid black line, the higher the accuracy is. The black dashed line shows the range of the ± 0.2 mm from the actual displacement, which can be considered as the required accuracy for practical use of displacement measurement at bridges.

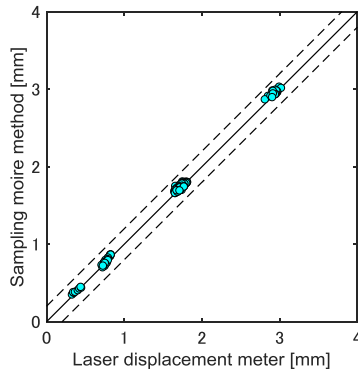


Fig. 7 Distribution of the peak values of displacement measured by sampling moire method and the laser displacement sensor

ESTIMATION OF TRAFFIC INFORMATION

Optical flow process

Considering and referring the many previous studies [8]-[11], the optical flow process to analyze the traffic on the bridges was constructed. The brief process is shown as follows;

- 1) the foreground mask using the Gaussian mixture model
- 2) the noise cancelling filters (mask processing, image erosion, morphological image processing)
- 3) the blob analysis (calculation of the size and the velocity of traffic).

MATLAB 2016b was used for these analysis. The figure was resized by 20 % (1037×692 pixels) to reduce the computational load.

First, to determine whether individual pixels are part of the background or the foreground, the foreground mask using the Gaussian mixture model compared a grayscale video frame to a background model. In this mixture model, the number of Gaussian modes was three, and the number of initial video frame for training the background was five.

Next, four noise cancelling filters were used; a mask processing, an image erosion, morphological image closing and opening. The mask processing was used for focusing only on the traffic (Fig. 8). The image erosion and the morphological image processing were used for eliminating the vertical movement of the bridge girder. The parameters of these noise cancelling filters were tuned by try and error (Table 3).

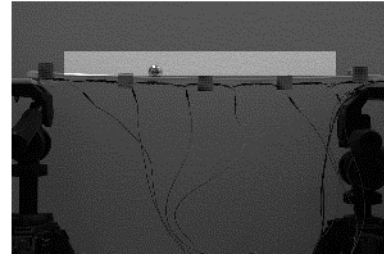


Fig. 8 An example of the mask processing

Table 3 Parameters of the noise cancelling filters

Process	Image erosion	Morphological closing	opening
Structuring elements	Line-shaped	Disk-shaped	Disk-shaped
pixels	15px (vertical)	100px (radius)	10px (radius)

Finally, the blob analysis was carried out to calculate the size and velocity of the traffic. The velocity of the traffic was calculated from the center position of the blob in each video frame. An example of the analysis is shown in Fig. 9.

Fig. 10 shows the histogram of the velocity of the traffic which pass through the model bridge. The velocity of the traffic is not constant, therefore, the shown values in the histogram are the velocities when the traffic pass through the center part of the bridge.

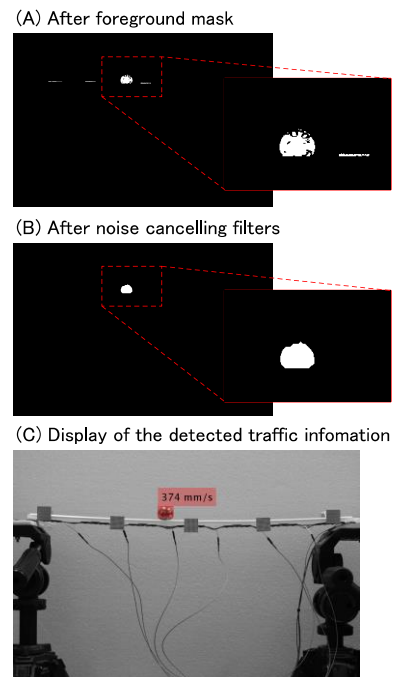


Fig. 9 An example of the noise cancelling process and the detected velocity of the traffic

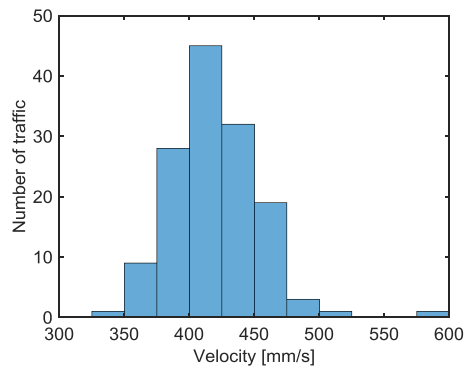


Fig. 10 Histogram of the velocity of the traffic

Deflection Based Bridge Weigh-In-Motion

The traffic load is one of the most important information of traffic environment. The method to estimate the traffic load using the dynamic structural response of bridges is called Bridge Weigh-in-Motion (or B-WIM). Various B-WIM methods have been studied and proposed in the last decades, utilizing strain, acceleration, and deflection. In this fundamental study, a new analysis system of traffic load was proposed by using the maximum deflection of the bridge girder measured by the sampling moire method. This method can be applied only when the single traffic passes through bridges. Therefore, the optical flow process functions as a trigger for distinguishing the single traffic condition, then the single traffic load is analyzed. In addition, to reduce the calculation, the sampling moire method is carried out only when the traffic is detected. The flow of the proposed method is shown in Fig. 11.

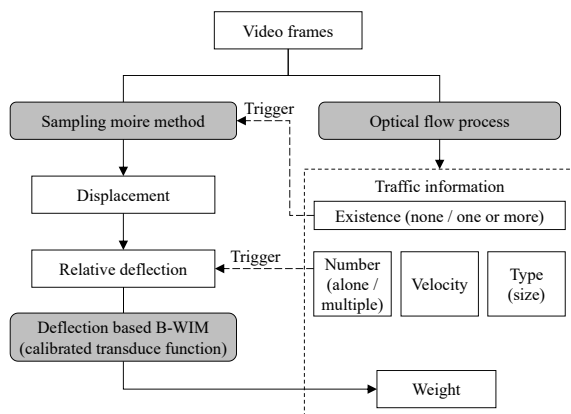


Fig. 11 Proposed image processing flow chart

In actual bridges, the static vertical position changes mainly due to the temperature and deterioration. Even in the model bridge of this study, the initial position was not zero, it fluctuated slightly during the measurement period (Fig. 12). Therefore, instead of using the peak displacement (red circle),

the relative deflection (black dotted line) from the initial position was used.

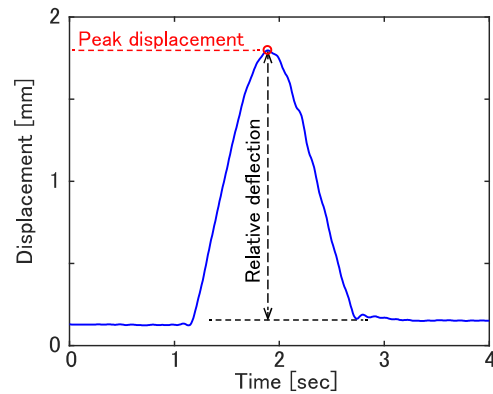


Fig. 12 Vertical displacement of the target

Fig. 13 shows the relationship between the traffic load passing through the model bridge and the relative deflection. An approximate line passing through the zero was determined by the least squared method. As shown from the coefficient of determination R^2 , the traffic load and the relative deflection are linearly related. By using the obtained linear equation (named the calibration function), it is possible to estimate the traffic load from relative deflection. The black dotted lines in Fig. 13 shows the range of traffic load $\pm 10\%$, which is the practically required accuracy of B-WIM. Although there is a tendency to underestimate when the traffic load is small, it is not an important problem because it is only heavy vehicles which influence the deterioration of bridges.

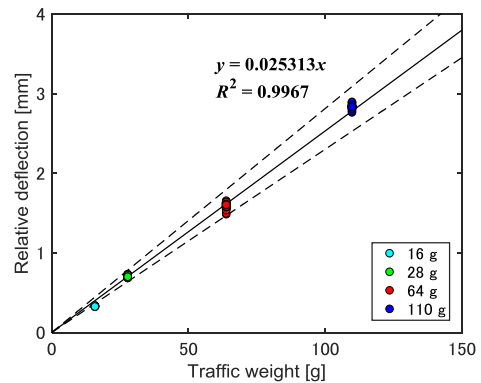


Fig. 13 Vertical displacement of the target

CONCLUSION

In this study, we proposed the analysis system to grasp the traffic environment and dynamic behavior of bridges. The following knowledge was obtained.

- 1) the displacement measuring method based on the sampling moire method was constructed. The analysis results were compared with the

laser displacement sensor, and it was shown that the displacement can be calculated with high accuracy.

- 2) To analyze the traffic environment, the optical flow process based on the foreground detection processing was constructed. Parameters of noise cancelling filters were examined by try and error, and it demonstrated that the velocity and size of moving objects can be obtained automatically in the model experiments.
- 3) Combining displacement calculation by the sampling moire method and the optical flow process, the analysis system to estimate the traffic load was proposed by focusing on the relative peak deflection.

It is possible to realize the advanced analysis, such as estimation of the multiple traffic load, by utilizing other information obtained in the image processing or combining data from other sensors. In this fundamental study, the noise cancelling process was determined by trial and error, however, machine learning techniques would be applied for practical use of the system.

ACKNOWLEDGEMENTS

I would like to thank T. Ono and T. Ohata for assistance with the model experiments.

REFERENCES

- [1] Lydon M., Taylor S. E., Robinson D., Mufti A., and Brien E. J. O., Recent developments in bridge weigh in motion (B-WIM), *Journal of Civil Structural Health Monitoring*, Vol. 6, Issue 1, 2016, pp. 69-81.
- [2] Sekiya H., Yokozeki K., Kimura K., Konishi T., and Miki C., Calculation method of bridge displacement from acceleration record, *Journal Society of Civil Engineers (JSCE) A1*, Vol. 72, No. 1, 2016, pp 61-74.
- [3] Morimoto Y., Fujigaki M., and Masaya A., Displacement and Strain Distribution Measurement by Sampling Moire Method, *Journal of the Vacuum Society of Japan*, Vol.54, 2011, pp. 32-38.
- [4] Ri S., Muramatsu T., Saka M., Nanba K., and Kobayashi D., Accuracy of the Sampling Moiré Method and its Application to Deflection Measurements of Large-Scale Structures, *Experimental Mechanics*, Vol. 52, Issue 4, 2012, pp. 331-340.
- [5] Zhang Q., Xie H., Liu Z., and Shi W., Sampling moiré method and its application to determine modulus of thermal barrier coatings under scanning electron microscope, *Optics and Lasers in Engineering*, Vol. 107, 2018, pp. 315-324.
- [6] Freitas J. D., Myers N. E., and Nobre A. C., Tracking the changing feature of a moving object, *Journal of Vision*, Vol. 16, Issue 3, No. 22, 2016, pp. 1-21.
- [7] Shiya K., Uchimura K., Izumida K., Sugita N., and Terada S., Moving Objects Detection based on Presumption of the Amount of Edge Displacement, *Electric Engineering in Japan*, Vol. 125, No. 9, 2005, pp. 1455-1463.
- [8] Stauffer, C. and W.E.L. Grimson. Adaptive Background Mixture Models for Real-Time Tracking, *Computer Vision and Pattern Recognition, IEEE Computer Society Conference on*, Vol. 2, 1999, pp. 246-252.
- [9] Wang L., and Yung N. H. C., Extraction of moving objects from their background based on multiple adaptive thresholds and boundary evaluation, *IEEE Transactions on Intelligent Transportation Systems*, Vol. 11, No. 1, 2010, pp. 40-51.
- [10] Sobral A., and Vacavant A., A comprehensive review of background subtraction algorithms evaluated with synthetic and real videos, *Computer Vision and Image Understanding*, Vol. 122, 2013, pp. 4-21.
- [11] Bouwmans T., Baf, F. E., and Vachon B., Background Modeling using Mixture of Gaussians for Foreground Detection - A Survey, *Recent Patents on Computer Science*, Bentham Science Publishers, 2008, Vol. 1, No. 3, 2008, pp. 219-237.

NON-CONTACT ESTIMATION OF STRAIN PARAMETER- TRIGGERING LIQUEFACTION

Erica Elice Saloma Uy¹, Toshihiro Noda², Kentaro Nakai³ and Jonathan Rivera Dungca⁴

¹Graduate Student, De La Salle University, Philippines; ^{2,3} Nagoya University, Japan; ⁴De La Salle University, Philippines

ABSTRACT

The strain parameter-triggering liquefaction is usually determined by implementing cyclic strain approach with a corresponding laboratory experiment. These parameters are threshold shear strain, cyclic shear strain and cyclic shear strain that would trigger liquefaction. In this study, non-contact measurement technique was implemented to estimate and monitor the development of the mentioned parameters. In this technique, a mirrorless camera and Lucas and Kanade pyramidal optical flow algorithm were utilized to track the movement of the particles. The camera was first calibrated to eliminate the errors from the lens and the scene as well. Furthermore, curvature correction was applied because the sample tested has a curved profile. The comparison was made with the loose and medium dense conditions. The samples were tested under a consolidated undrained cyclic triaxial test at 2.4, 1.6 and 0.8 mm strain amplitudes. The confining pressures used were 50, 100 and 200 kPa. Based on the results, non-contact measurement technique can estimate the parameters. A range of values was established due to the non-homogeneous movement of the soil.

Keywords: Cyclic Loading, Non-Contact Measurement, Strain Parameter-Triggering Liquefaction, Curvature Correction

INTRODUCTION

Liquefaction assessment is performed to determine the vulnerability of the soil to liquefy [1]. Assessment can be performed by cyclic stress approach or cyclic strain approach. In these approaches, parameters needed are obtained from in-situ testing techniques or laboratory testing [2]-[3]. The cyclic stress approach considers the build-up of pore water pressure related to the cyclic shear stress (τ_c). Several studies pointed out that the results of this approach are dependent on the overconsolidation ratio (OCR), preshaking effect, lateral earth pressure coefficient (K_0), relative density and method of sample preparation [2]-[3]. Due to this, researchers are focused on utilizing the cyclic strain approach. In this approach, the cyclic shear strain is being correlated to the excess pore water pressure. Since it can characterize particle rearrangement. The cyclic shear strain is associated with the deformation of the particles which is a result of ground shaking [4]. This can produce excess pore water pressure which can result in liquefaction. Strain parameter-triggering liquefaction is used in the assessment. The parameters are threshold shear strain (γ_{tv}), cyclic shear strain (γ_c) and cyclic shear strain that would trigger liquefaction (γ_{cl}). The γ_{tv} is the indicator of the initiation of development of pore water pressure in a cyclic test. This parameter is approximately $1 \times 10^{-2}\%$ existing for clean sand as seen in Fig. 1 [2]-[3]. The γ_{cl} is the parameter compared to γ_c on the triggering

of liquefaction. When γ_c exceeds the value of γ_{cl} this implies that triggering of liquefaction had occurred. Its typical value ranges from 0.4 to 3% [3]. The minimum value of this parameter can also be seen in Fig. 1. At this point, the pore water pressure ratio is almost 0.95. The strain parameter-triggering liquefaction is normally obtained from field tests or laboratory tests such as cyclic simple shear test and dynamic triaxial test. In these tests, Linear Variable Displacement Transducer (LVDT) is used to determine these parameters. Kaddouri (1991) installed the LVDT inside the triaxial cell in order to address the non-homogeneous deformations measured by Dobry et al. (1981-1982) and Youd (1972) [5]. This set-up can cause disturbances to the sample especially on how it is attached. It is also susceptible to the tilting of the sample which can lead to errors in measurement. Furthermore, this set-up cannot monitor the development of the strain parameter-triggering liquefaction. A method that can be implemented is non-contact measurement technique. It utilizes cameras to estimate the deformation of an object without causing any disturbances [6]. Deformations are estimated through image processing algorithms such as digital image correlation (DIC), particle image velocimetry (PIV) and optical flow [6]-[8]. The technique can provide local deformation, monitor the material's behavior during the experiment and assess the actual test boundary condition. The technique was applied in a cyclic triaxial test. Based on the results, the technique has the capacity to measure the

development of deformation [7]-[8]. In this study, non-contact measurement technique was used to estimate and monitor the strain parameter-triggering liquefaction. Two-dimensional image processing was implemented. Lucas and Kanade pyramidal optical flow algorithm was used to track the deformation. A mirrorless camera was used because it is more economical compared to a single lens reflex (SLR) camera or a high speed camera. Strain-controlled consolidated undrained test was performed for a loose and medium dense condition.

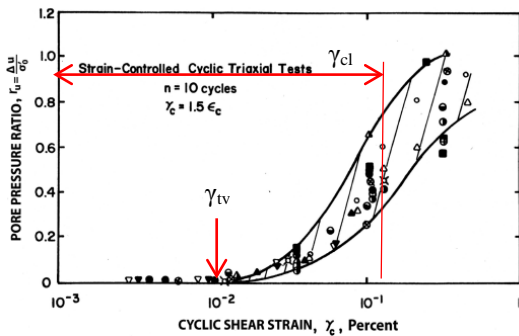


Fig.1 Pore water pressure ratio plotted against γ_c [3]

NON-CONTACT MEASUREMENT

Calibration

The non-contact measurement was carried out by using a mirrorless camera and optical flow algorithm. The camera was initially calibrated and it is divided into two phases. In the first phase, a calibration grid, as seen in Fig. 2a, with uniform dimension and spacing, was used as a target to extract the internal and external camera parameters. These parameters were used to determine the position of the points with respect to the camera coordinate system. This was followed by applying the polynomial distortion model to correct the distortion from the lens. In the second phase, a magnification factor was determined. This was to eliminate the magnification from the triaxial cell and water. Measurements were made using a straight edge block, Fig. 2b. It was carried out by placing the straight edge block in the triaxial cell and it was submerged with water. It can be seen that rectangular targets were also placed on the block. Different sizes were used to determine the amount of magnification encountered. The dimension of the block is 10.0 cm x 7.0 cm. The dimensions of the targets are tabulated in Table 1. A straight edged block and rectangular targets were also used in order to have an easy detection of the dimensions. Edge detection was the image processing method used to determine their dimensions. In order to determine the magnification factor, the actual dimension was plotted against the measurement from image processing. The slope of the plot is the magnification

factor. The values obtained were 0.7036 and 0.8579 for the x and y-directions, respectively. During this phase, the camera settings and exact location of the camera were determined. In order to ensure that the position of the camera was fixed, it was placed at the back of the equipment. It was placed 42 cm from the equipment. In this location, the camera will not be disturbed during the duration of the experiment. Lighting was also controlled in order to avoid noise from uneven lighting. The area where uneven light penetrated was covered with black paper. Furthermore, a spot light was placed to improve the distribution of light.

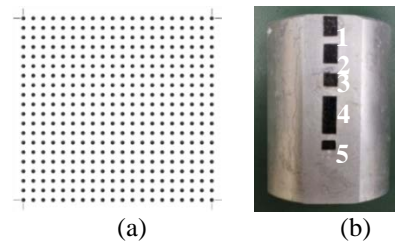


Fig.2 Calibration tools (a) calibration grid (b) straight edge block

Table 1 Dimension of the targets

Target	Dimension (LxH) (cm)
1	0.7x1.0
2	0.7x1.0
3	0.7x0.7
4	0.7x2.0
5	0.7x0.5

Curvature Correction

The samples tested were in a cylindrical shape. Since only 2D image processing was implemented in the study the curvature effect needs to be corrected. The images of the sample were corrected using the polynomial model. This model is usually applied in a geometric correction since it can correct more complicated types of distortion such as curved surfaces [9]. The model is also known as nonlinear transformation equation and it has the following expression:

$$x' = a_0 + a_1x + a_2y + a_3x^2 + a_4xy + a_5y^2 \quad (1)$$

$$y' = b_0 + b_1x + b_2y + b_3x^2 + b_4xy + b_5y^2 \quad (2)$$

where x' and y' = corrected real-world coordinates in x- and y-axis; x and y = original real-world coordinates in x- and y-axis; a_0 to a_5 and b_0 to b_5 = polynomial correction parameters. The parameters were obtained by least square error method for each experiment.

In order to validate the model applied, corrected deformation readings were compared to the LVDT. The target points chosen are shown in Fig. 3. These points were chosen since it is independent of the soil movement. The displacement of the soil based on

the results can be smaller or larger than the LVDT. The typical results are shown in Figs. 4-5. It is noticeable that the rightmost side experienced more curvature than the leftmost side. It can be seen on the extension loading of the rightmost side of the displacements from image processing (IP) were smaller. Applying the curvature correction lessened the errors from IP. The errors at the left target lessened from 0.14 - 34.32% to 0.10 - 29.81%. For the right target, it lessened from 0.133 - 37.671% to 0.031 - 29.236%. Based on these results, the polynomial model was adopted to correct the curvature present in the sample. In addition to the calibration previously discussed, curvature correction was always implemented prior to determining the deformation and strain parameter-triggering liquefaction. A correction was done with respect to the height of the sample, location, and section being monitored.

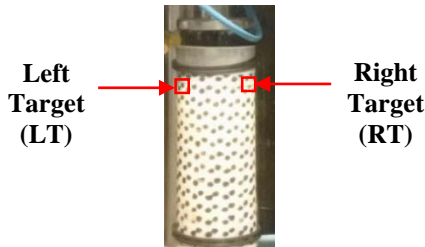


Fig.3 Monitored targets for curvature correction

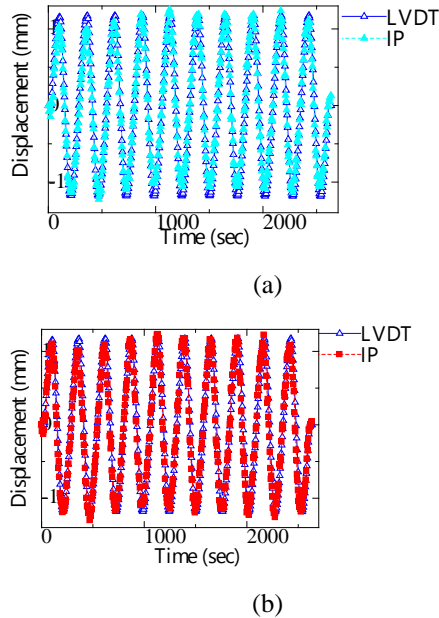


Fig.4 Monitored LT (a) not corrected (b) corrected

Optical Flow

Lucas and Kanade pyramidal optical flow algorithm were implemented to estimate monitor the movement of the soil under cyclic loading. The algorithm determines the image displacement (\vec{d}) of the point of interest by tracking it in succeeding

grayscale images. It is a type of feature based approach where it assumes that brightness is constant variable in the successive images. The algorithm uses image patches together with windowing methods. Least squares technique is implemented to extract the changes in position [11]. The residual function ε is minimized to extract the \vec{d} [10].

$$\varepsilon(\vec{d}) = \varepsilon(d_x, d_y) = \sum_{x=u_x-\omega_x}^{u_x+\omega_x} \sum_{y=u_y-\omega_y}^{u_y+\omega_y} [I(x, y) - J(x + dx, y + dy)]^2 \quad (3)$$

where $I(x, y)$ = First image with (x, y) pixel location; $J(x, y)$ = Second image with (x, y) pixel location; dx, dy = image displacement and ω_x, ω_y = are arbitrary numbers that ranges from 1, 2, 3 or more pixels.

CYCLIC TRIAXIAL TEST

Sample Preparation

Mikawa number 6 sand was used in the study. It is an artificially produced shaved sample which has high concentrations of silica. It can be considered as silica sand and can be classified as a coarse material. This makes it susceptible to liquefaction. Samples were prepared by air pluviation as specified in the Japanese Geotechnical Society (JGS) standard for sample preparation of coarse granular materials for the triaxial test (JGS 0530-2009) [12]. Loose condition (S1) and medium dense (S2) were prepared to have 30% and 50% as the target relative density, respectively.

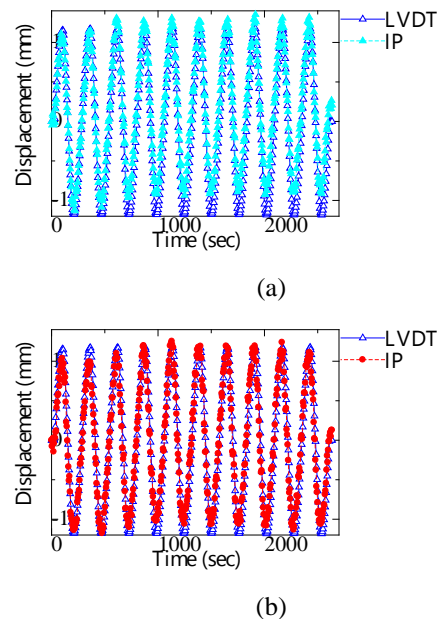


Fig.5 Monitored RT (a) not corrected (b) corrected

Cyclic Triaxial Test

The strain-controlled consolidated undrained test

was performed as specified in the JGS 0541-2009 [12]. The confining pressure applied was 50, 100 and 200 kPa. The samples were cyclically loaded with 2.4, 1.6 and 0.8 mm strain amplitudes (SA) for 10 cycles. In order to properly estimate the strain parameter-triggering liquefaction, a slow frequency was adopted. Furthermore, images were taken every 5 seconds.

STRAIN PARAMETER-TRIGGERING LIQUEFACTION

The strain parameter-triggering liquefaction was estimated using the general engineering shear strain. Equation 4 was used in the computation [13]. The γ_c was first computed. The γ_{tv} and γ_{cl} were determined in correlation with the pore water pressure ratio. This is the ratio of the excess pore water pressure with the confining pressure. The γ_{tv} has a pore water pressure ratio close to zero or less than 0.1. At this point, there is no development of pore water pressure. The γ_{cl} on the other hand has a value close to 0.95. At this point, triggering of liquefaction is about to occur. In order to apply Eqn 4, a 5 x 5-pixel rectangular grid was used in the estimation.

$$\gamma = \frac{1}{2} \left(\frac{\partial v}{\partial x} + \frac{\partial u}{\partial y} \right) \quad (4)$$

where $\frac{\partial v}{\partial x}, \frac{\partial u}{\partial y}$ = displacement gradient.

The cyclic shear strain that would trigger liquefaction was monitored at in three locations namely, left (L), center (C) and right (R) location. These locations are further subdivided into the top (T), middle (M) and bottom (B) section as seen in Fig. 6. The parameter was monitored at different locations and sections in order to investigate the occurrence of non-homogeneous deformation. The results estimated from IP were compared to the LVDT. Shear strain from LVDT was computed based on the following equation [14]:

$$\gamma = \varepsilon_a(1+\nu) \quad (5)$$

where ε_a = axial strain; ν = Poisson's ratio. The Poisson's ratio for saturated sand can be assumed to be 0.5.

RESULTS AND DISCUSSION

In order to verify the strain parameter-triggering liquefaction from the mirrorless camera, its measurements were compared with the LVDT. The LVDT used in the experiment had a rated capacity of 20 mm, a sensitivity of 5 mV/V \pm 0.1 % and measurement uncertainty of within \pm 0.1 % of its rated capacity. The comparison was made by choosing a target on the cyclic triaxial equipment. The target used was the top cap. Based on the results as seen in Fig. 7, there was a good agreement

between the LVDT and IP. For the internal measurements, the monitored sections are similar to Fig. 6. It can be observed in Fig. 8 that there is an increasing amount of deformation as the monitored section is closer to the top cap or where there is a direct contact with the applied load. Once liquefaction occurred it was observed that larger deformation was seen at the top section. The measurement from IP shows that deformation trend at different locations of the sample was not similar. This implies that non-homogeneous deformation exists during cyclic loading. The results of the strain parameter-triggering liquefaction are tabulated in Tables 2-5. Based on the results, a range of values was estimated due to the non-homogeneous movement observed from the locations and sections monitored. The estimated γ_{tv} was observed to have no consistent trend. It was observed that the minimum values estimated for both conditions are in the vicinity of $10^{-2}\%$. The results were compared to the typical values. It is consistent with the findings of Dobry and Abdoun (2011) that γ_{tv} in sands are in the order of $10^{-2}\%$ or it is approximately $1 \times 10^{-2}\%$ [2]-[3]. The maximum values, on the other hand, had larger results. This can be caused by the honeycombs present in the sample.

Table 2 γ_{tv} for S1 (%) estimated from IP

S	L	Cell Pressure (kPa)		
		50	100	200
2.4	A			
	T	0.0144-0.2948	0.0076-0.4225	0.0555-0.2619
	M	0.0265-0.3052	0.0020-1.0482	0.0066-0.6288
1.6	B	0.0037-0.5131	0.0014-1.6852	0.0102-0.4843
	T	0.0053-0.7529	0.0072-0.4165	0.0005-0.2751
	M	0.0008-0.8727	0.0324-0.6011	0.0001-0.2716
0.8	B	0.0005-0.4789	0.0172-0.6765	0.0001-0.2045
	T	0.0033-0.6206	0.0011-0.4505	0.0110-0.6521
	M	0.0014-0.8610	0.0015-0.5076	0.0077-0.5745
	B	0.0349-0.8843	0.0004-0.3942	0.0053-0.3090

A similar trend was observed when the IP results were compared with the LVDT results. The LVDT results are tabulated in Table 6. For the γ_{cl} , the effect of varying the relative density, strain amplitude and confining pressure was investigated. For the relative density, S1 had larger results compared to S2 since it has more voids present. Particle movement was more evident for S1. For the effect of strain amplitude, γ_{cl} had larger values for 2.4 mm SA. On the other hand, γ_{cl} decreased as the applied SA was smaller. The variation in the results was due to the difference in the applied amount of cyclic deformation. For the effect of increasing the confining pressure, the values for S1 and S2 for all sections and locations decreased as the confining pressure was increased. As a whole, the estimated γ_{cl} from IP was observed to be affected by the relative density, strain amplitude and confining pressure.

Table 3 γ_{cl} for S1 (%) estimated from IP

S	A	L o c	Cell Pressure (kPa)		
			50	100	200
2.4	T	M	1.6099-2.8610	1.3085-2.9153	0.6401-1.6863
			0.6910-4.5103	0.5722-2.8932	0.0047-0.9335
			0.0039-1.8144	0.0178-1.8413	0.0114-0.6625
1.6	T	M	0.2668-2.4369	0.6478-2.3364	0.6681-1.7113
			0.0567-1.8868	0.3210-1.8244	0.1803-1.4358
			0.0064-3.7311	0.0150-0.7113	0.0054-0.4504
0.8	T	M	0.5851-1.9680	0.2442-0.9192	0.1156-1.2943
			0.1452-1.6467	0.0163-3.0629	0.0187-0.6751
			0.0493-3.2151	0.0011-0.6123	0.0096-0.4909

Table 4 γ_{tv} for S2 (%) estimated from IP

SA	L o c	Cell Pressure (kPa)		
		50	100	200
2.4	T	0.0049-0.4747	0.0282-0.9028	0.0197-0.3953
	M	0.0147-0.8319	0.0216-0.8536	0.0072-0.7722
	B	0.0310-0.7378	0.0522-0.9129	0.0076-0.3258
1.6	T	0.0019-0.6675	0.0087-1.1841	0.0057-0.5601
	M	0.0042-1.6312	0.0011-1.0174	0.0045-0.4838
	B	0.0038-0.9827	0.0019-0.5110	0.0083-0.5805
0.8	T	0.0011-0.3402	0.0034-0.5605	0.0030-0.5794
	M	0.0023-0.8549	0.0019-1.5386	0.0008-0.5303
	B	0.0019-0.5144	0.0008-0.9354	0.0045-0.4112

Table 5 γ_{cl} for S1 (%) estimated from IP

SA	L o c	Cell Pressure (kPa)		
		50	100	200
2.4	T	0.2804-1.7204	0.0134-0.8547	0.1739-3.4617
	M	0.0646-1.1497	0.0061-1.8240	0.2332-1.4612
	B	0.0121-0.6603	0.0022-2.0432	0.0015-0.6380
1.6	T	0.0265-1.2563	0.0393-1.4275	0.0620-1.6479
	M	0.0238-1.6607	0.0151-1.2854	0.0261-0.9577
	B	0.0060-0.7540	0.0030-1.0280	0.0057-1.0473
0.8	T	0.02419-0.8761	0.0450-1.0730	0.0178-0.8338
	M	0.00794-1.9839	0.0094-1.3992	0.0094-0.5083
	B	0.00831-0.4566	0.0159-1.3005	0.0140-0.8141

Table 6 γ_{tv} and γ_{cl} for S1 (%) from LVDT

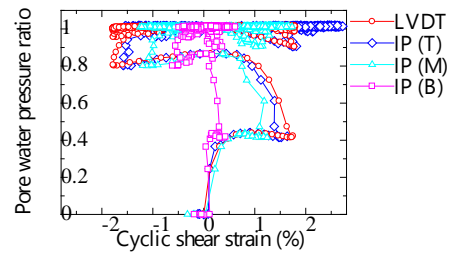
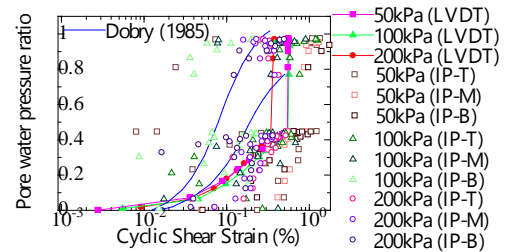
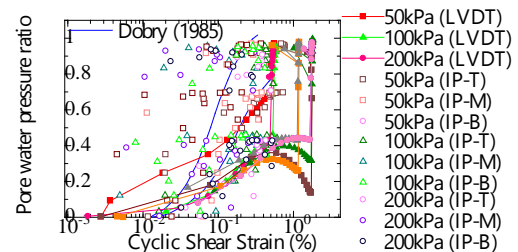
SA	γ_{tv}			γ_{cl}		
	Cell Pressure (kPa)			Cell Pressure (kPa)		
	50	100	200	50	100	200
2.4	0.0009	0.0542	0.0828	1.7180	1.7070	1.5062
1.6	0.0386	0.0359	0.0407	1.0876	1.1078	1.0769
0.8	0.0360	0.0451	0.0372	0.4868	0.3800	0.0439

Table 7 γ_{tv} and γ_{cl} for S2 (%) from LVDT

SA	γ_{tv}			γ_{cl}		
	Cell Pressure (kPa)			Cell Pressure (kPa)		
	50	100	200	50	100	200
2.4	0.0792	0.0892	0.054	1.5288	1.0169	1.3872
1.6	0.0046	0.0394	0.0659	0.5182	0.7583	0.9959
0.8	0.0184	0.0202	0.0315	0.4737	0.4855	0.9959

In order to verify the results from IP, the typical value of γ_{cl} was compared. The typical value ranges from 0.4-3% [8]. The minimum values for all conditions are within the range. On the other hand,

the maximum values are larger. The LVDT results, as seen in Table 7, were also compared and a similar trend was observed. The results were also compared with the range of pore water pressure responses for sands with different relative densities proposed by Dobry (1985). The proposed range had an upper bound and lower bound curve as seen in Fig. 1. These were overlayed to the results of IP to investigate the validity of its results. Typical results are shown in Figs. 9-10. It can be seen that for S1 γ_c exceeds the boundary but for estimations prior to liquefaction. Once liquefaction had occurred the estimations are within the boundaries. For S2, more estimation can be seen within the boundary. More movements were present for S1 since it has more voids compared to S2. A difference can also be seen for the results of LVDT when it was compared with the proposed boundary. A smaller SA was used for the proposed boundary. The SA used had a maximum value of approximately 0.675% while a maximum value of 2.4% was used for the study.

Fig.8 Comparison of the γ_c from LVDT and IP considering the sections monitoredFig.9 Comparison of the γ_c from LVDT and IP (S1)Fig.10 Comparison of the γ_c from LVDT and IP (S2)

CONCLUSION

Strain parameter-triggering liquefaction was estimated using non-contact measurement technique. Before applying the technique, calibration was

performed to eliminate the distortion from the lens and the scene. In addition to that, curvature correction was implemented with respect to the height of the sample, location, and section being monitored. The curved profile of the soil surface was corrected since it caused an error in the measurement of the deformation. Curvature correction can improve the monitoring of the mirrorless camera. The capacity of the mirrorless camera to estimate the cyclic shear strain was also investigated. The top cap was used as the target and it was compared with the LVDT. A good agreement was observed. For the internal measurement, a non-homogeneous deformation was observed. The values increased from the bottom to the top location. For the estimated γ_{tv} , no consistent trend was observed. Minimum values are within the typical values of $10^{-2}\%$ or approximately $1 \times 10^{-2}\%$. Maximum values, on the other hand, are larger. For the estimated γ_{cl} , the relative density, strain amplitude and confining pressure. When the results are compared with the proposed boundary of Dobry (1985) it was also observed that the results were greatly affected by the value of SA used. The non-contact measurement technique implemented can still be extended to three-dimensional monitoring. This can be beneficial to understating the whole behavior of the soil as it experiences liquefaction.

ACKNOWLEDGMENTS

The researcher would like to express her gratitude to the Engineering Research and Development for Technology, Civil Engineering Department of De La Salle University and the Graduate School of Civil and Environmental Engineering of Nagoya University Geotechnical Engineering Division for their support.

REFERENCES

- [1] Dungca, J.R., Kuwano, J., Takahashi, A., Saruwatari, T., Izawa, J., Suzuki, H. and Tokimatsu, K. Shaking table tests on the lateral response of a pile buried in liquid sand. *Soil Dynamics and Earthquake Engineering*, 2006, Vol. 26, Issue 2-4, pp. 287-295
- [2] Dobry R. and Abdoun, T., Recent Findings on Liquefaction Triggering in Clean and Silty Sands during Earthquakes. *Journal of Geotechnical and Geoenvironmental Engineering*, Vol. 143, Issue 10, 2017, pp. 04017077-1-19.
- [3] Dobry R. and Abdoun T., Cyclic Shear Strain Needed for Liquefaction Triggering and Assessment of Overburden Pressure Factor K_σ . *ASCE Journal of Geotechnical and Geoenvironmental Engineering*, 2015, pp. 1-18.
- [4] Derakhshandi, M. et al. (2008). The effect of plastic fines on the pore pressure generation characteristics of saturated sands. *Soil Dynamics and Earthquake Engineering*, 28, 376–386.
- [5] Kaddouri, A., Mechanical characterization of the threshold strain in sand liquefaction. *Proceedings: Second International Conference on Recent Advances In Geotechnical Earthquake Engineering and Soil Dynamics*. 1991, pp.2011-2014.
- [6] Uy E.E.S. and Boonyatee T., Image Processing for Geotechnical Laboratory Measurements. *International Journal of GEOMATE*, Vol. 10, Issue 22, 2016, pp. 1964-1970.
- [7] Longtan S., Song Y., Yong S., Chuan, H. and Xiaoxia, G., Application of Digital Image Processing Technology in Dynamic Triaxial Test of Soil Mechanics. *Journal of Theoretical and Applied Information Technology*, Vol. 48, Issue 3, 2013, pp.1358-1365.
- [8] Koseki J., Hoshino R., Miyashita Y. and Sato T., Direct and Indirect Observations of Local Properties of Saturated Sand Specimens in Undrained Cyclic Triaxial Tests. *The 6th Japan-Korea Geotechnical Workshop*, Vol. 4, Issue 1, 2016.
- [9] Wahyudi S., Miyashita Y. and Koseki, J. Shear Banding Characteristics of Sand in Torsional Shear Test Evaluated By Means of Image Analysis Technique, *Bulletin of ERS*, No.45, 2012, pp.1-8
- [10] Fernando W.S.P., Udawatta L. and Pathirana P., Identification of Moving Obstacles with Pyramidal Lucas and Kanade Optical Flow and K Means Clustering. *Proceedings on the Third International Conference on Information and Automation for Sustainability*, 2007.
- [11] Thota S.D., Vemulapalli K.S., Chintalapati K. and Srinivas, P.S., Comparison Between the Optical Flow Computational Techniques. *International Journal of Engineering Trends and Technology*, Vol. 4, Issue 10, 2013.
- [12] The Japanese Geotechnical Society, Japanese Geotechnical Society Standards: Laboratory Testing Standards of Geomaterial. Issue 1, 2008.
- [13] Sutton M.A., Orteu J.J. and Schreier H.W., Image Correlation for Shape, Motion and Deformation Measurements: Basic Concepts, Theory and Applications: Springer, 2009. Vol.25, No.3, 2011, pp.1460-1465.
- [14] Dobry R. and Abdoun T., An Investigation into Why Liquefaction Charts Work: A Necessary Step Toward Integrating the States of Art and Practice. *Proceedings of the Fifth International Conference on Earthquake Geotechnical Engineering*, 2011, pp.13-45.

INFLUENCE OF DEVELOPMENT/DIMINISHING OF ANISOTROPY ON THE MECHANICAL BEHAVIOR OF CLAYEY SPECIMEN.

Imran Khan¹, Kentaro Nakai², Toshihiro Noda³ and Kota Mizukami⁴

^{1,2,4}Department of Civil Engineering, Nagoya University, Japan

³Disaster Mitigation Research Center, Nagoya University, Japan

ABSTRACT

Anisotropy refers to the directional dependence of material properties. In order to know the true behavior of naturally deposited soil, the knowledge of development/diminishing of anisotropy are very important. The anisotropy of clays and silty clay intimately connected with their structure, which depends on the environmental conditions during which the soil is deposited as well as the stress changes subsequent to deposition. In this paper, triaxial tests were carried out using the vertical and the horizontal extraction specimen of the reconstituted clay and silty clay, for accumulating experimental facts of development of anisotropy during the preliminary consolidation process and the influence of the anisotropy on the shear behavior. Pre-consolidation pressure of 200kPa applied to induced initial anisotropy. Undrained shear triaxial test was performed with different isotropic stresses on clay and silty clay, isotopically consolidated for 24 hours and undrained shearing was carried out under constant axial strain rate of 0.0056(mm/min). Vertical sample shows larger peak strength as compared to horizontal, because of the development of anisotropy on the compression side. As the confining pressure increases, the difference between peak strength of vertical and horizontal becomes smaller and smaller which indicate that the anisotropy diminished and intensity ratio decreases. By comparing clay and silty clay, silty clay materials lose their anisotropy at lower confining pressure as compared to clay materials. Therefore, the grain sizes have significant effect on the developing and diminishing of anisotropy. Another important fact observed was critical state index is decreasing and become constant as confining pressure increases.

Keywords: Anisotropy, Clay, Silty Clay, Undrained shear test and Critical state index.

INTRODUCTION

Anisotropy refers to the directional dependence of material properties. The anisotropy of clays and silty clay intimately connected with their structure, which depends on the environmental conditions during which the soil is deposited as well as the stress changes subsequent to deposition. Neglecting the anisotropy of soil behavior may lead to highly inaccurate predictions of soil response under loading. In order to know the true behavior of naturally deposited soil, the knowledge of development/diminishing of anisotropy are very important.

Hoque et al. investigated the anisotropy in elastic deformation of granular materials by measuring local strains in both vertical and horizontal direction with static cyclic loading. He found that vertical young modulus is greater than horizontal young modulus at isotropic stress level [1]. Islam et al. investigated the strength anisotropy in both vertical and horizontal directions by trimming the specimens at different angles so as to obtain the test samples of different orientations, compared to the depositional direction and then subjected to UC and DS tests for both the horizontal and vertical planes from undisturbed clay masses. He concluded that the clay samples collected from different places and different

depths showed different coefficients of anisotropy in different laboratory tests [2]. There have been some similar studies related to this research [3]-[5] and numerous experimental studies on the effects of anisotropy have been conducted focusing on the shear strength, however, there is not much to explain how the anisotropy develops or disappears with ongoing plastic deformation.

In this paper, triaxial compression tests were carried out using the vertical and the horizontal extraction specimen of the reconstituted clay and silty clay sample, for accumulating experimental facts of development of anisotropy during the preliminary consolidation process and the influence of the anisotropy on the shear behavior. Also the comparison of clayey and silty clay and how the grain size affects the development/diminishing of anisotropy were discussed.

EXPERIMENTAL WORK

Physical properties and grain size distribution of the clay and silty clay used in the experiment are shown in Table 1 and Figure 1 respectively. After thorough stirring and degassing at a water content of 1.5 times the liquid limit, we applied pre-consolidation pressure of 200kPa for one week for clay and two days for silty clay.

The method of extracting the sample from the preliminary consolidation tank is the following; specimen pulled out so that the axis was in the vertical direction is vertical specimen and the specimen extracted so that the axis is in the horizontal direction is horizontal specimen, shown below in schematic figure 2.

By extracting the reconstituted sample from different directions, samples with different initial anisotropy were prepared. Five (5) types of isotropic stresses of 50, 100, 300, 600, 1800 kPa were applied on clay and (3) three isotropic stressed of 50,300 and 600kPa were applied on silty clay. Both clay and silty clay were isotopically consolidated for 24hours. The saturation values (B) of each sample were confirmed to be 0.96 or higher. After isotropic consolidation, undrained shearing was carried out under constant axial strain rate of 0.0056(mm/min) for clay and 0.0112(mm/min) for silty clay. These axial strain rate were considered to be slow enough to maintain element behavior (the distribution of excess pore water pressure inside the specimen is uniform) during shearing.

Table 1 Physical properties of Soil.

Description	Clay	Silty-Clay
Liquid Limit w_L (%)	81.4	45.82
Plastic Limit w_p (%)	43.7	25.37
Plasticity index I_p	37.7	20.44
G_s (g/cm ³)	2.65	2.65

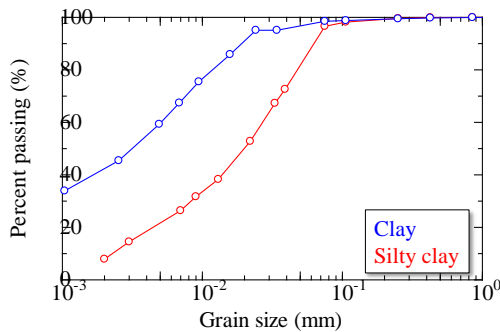


Fig.1 Grain size distributions

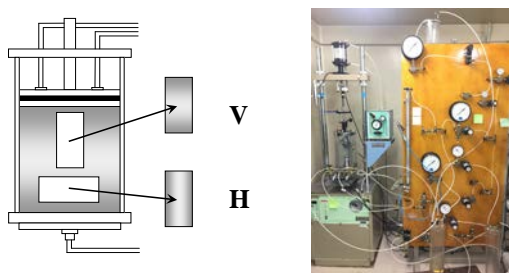


Fig.2 Extracting Vertical & Horizontal Specimen

Development/Diminishing of Anisotropy in Clay

Figures 3 to 7 shows the stress-strain relationship and effective stress path of vertical and horizontal specimen with different confining pressures of clay, 50 to 1800kPa respectively. Fig 8 summarizes the difference of shear strength in vertical and horizontal direction at the time of axial strain was 5% and 10% (almost critical state). By comparing the shear/peak strength of samples of clay, it was observed that vertical sample shows larger peak strength as compared to horizontal because of the development of anisotropy on the compression side. As the confining pressure increases, the difference becomes smaller and smaller which indicate that the anisotropy disappears/diminished and intensity ratio decreases. However, even at 300, 600, and 1800kPa, the same degree of strength difference remains. So it was found that even if we have applied high isotropic consolidation pressure, anisotropy was not completely diminished

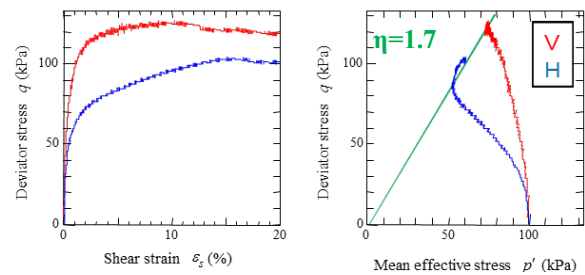


Fig.3 Confining pressure (Clay) 50kPa

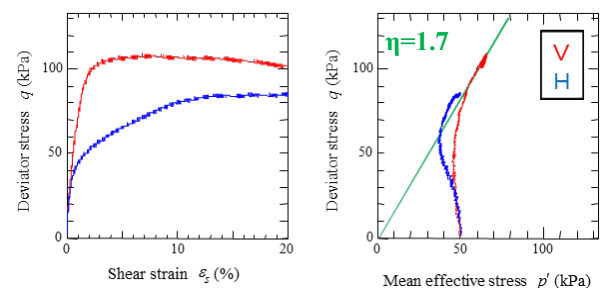


Fig.4 Confining pressure (Clay) 100kPa

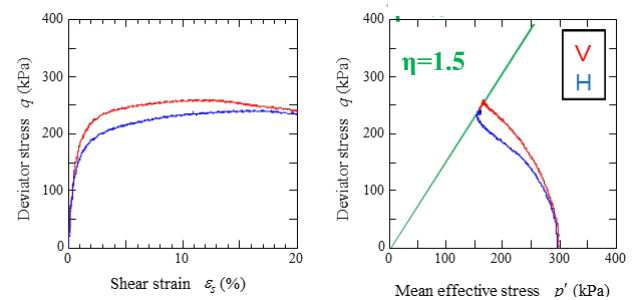


Fig.5 Confining pressure (Clay) 300kPa

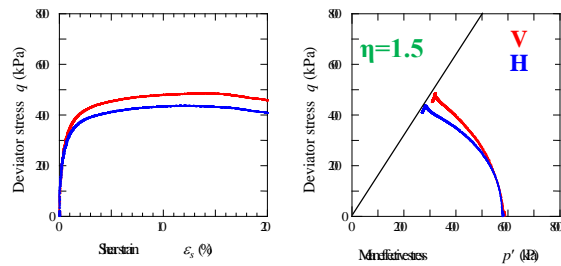


Fig.6 Confining pressure (Clay) 600kPa

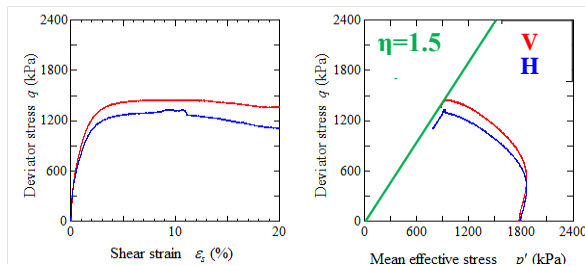


Fig.7 Confining pressure (Clay) 1800kPa

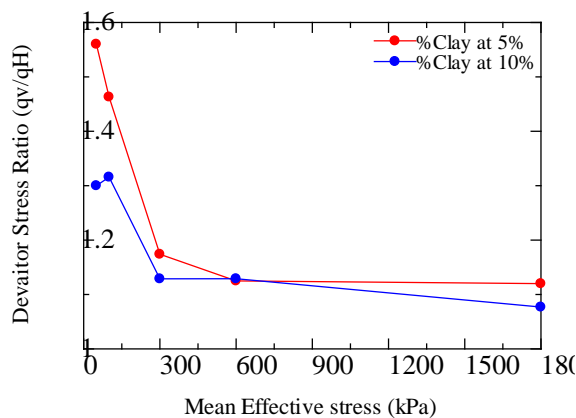


Fig.8 Difference in vertical and horizontal shear strength of Clay

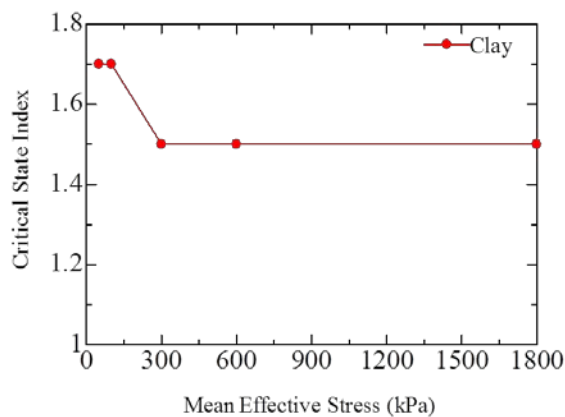


Fig.9 Difference in critical state index of clay

Figure 9 summarizes the clayey samples that the critical state index (slope of critical state line) is changing with increasing confining pressure. Also it was observed that, critical state index is decreasing and become constant as confining pressure increases.

Development/Diminishing of Anisotropy in Silty Clay

Figures 10 to 12 shows the stress-strain relationship and effective stress path of vertical and horizontal specimen with different confining pressures of silty clay at 50 to 600 kPa respectively. Fig 13 summarizes the difference of shear strength in vertical and horizontal direction at the time of axial strain was 5% and 10%. By comparing the shear/peak strength of samples of clay, it was observed that vertical sample shows larger peak strength as compared to horizontal because of the development of anisotropy on the compression side. As the confining pressure increases, the difference becomes smaller and smaller which indicate that the anisotropy disappears/diminished and intensity ratio decreases. Moreover, the anisotropy almost diminished at confining pressure of 600kPa. Figure 14 summarizes the silty clay samples that the critical state index is changing with increasing confining pressure same as in clayey specimen.

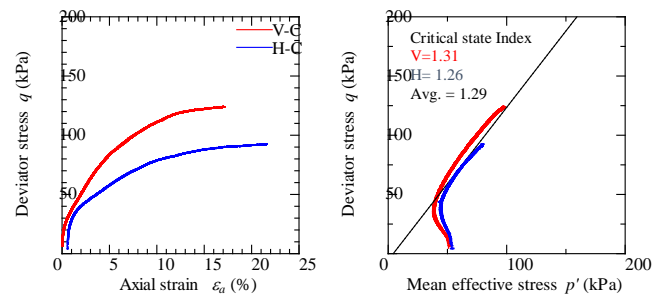


Fig.10 Confining pressure (Silty Clay) 50kPa

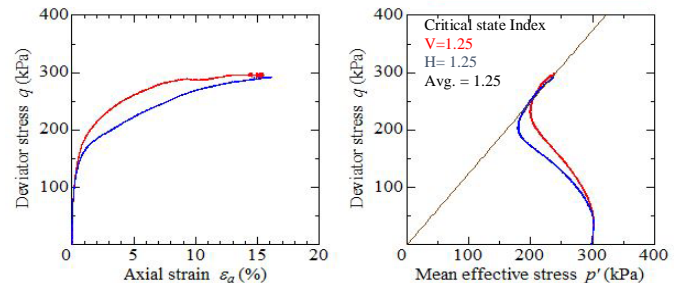


Fig.11 Confining pressure (Silty Clay) 300kPa

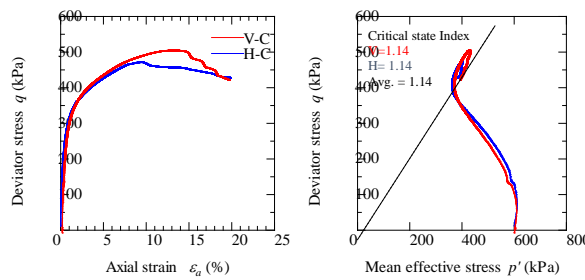


Fig.12 Confining pressure (Silty Clay) 600kPa

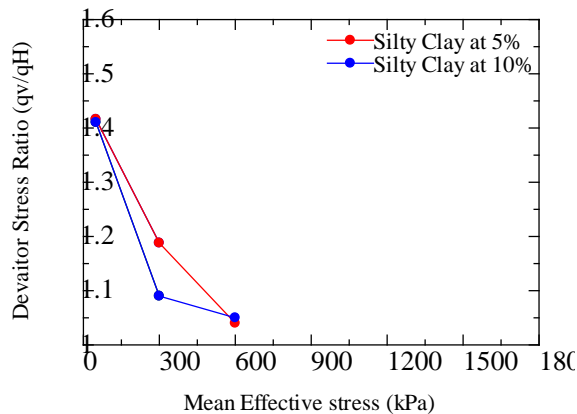


Fig.13 Difference in vertical and horizontal shear strength of Silty Clay

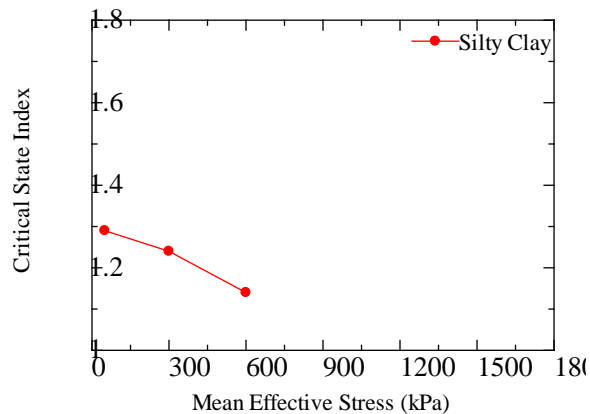


Fig.14 Difference in Critical state Index of Silty Clay

Comparison of Clay and Silty Clay

Fig 15 summarizes the clay and silty clay samples, difference in vertical and horizontal shear strength at 5%. Values were taken at 5% because, in case of silty clay sample, localized failure (sudden decrease and discontinuous curve in stress-strain relationship) can be observed after 5% especially within high confining pressure and therefore, it is difficult to recognize as element behavior furthermore. As indicated above, both vertical

samples shows larger peak strength as compared to horizontal because of the development of anisotropy on the compression side. As the confining pressure increases, the difference becomes smaller and smaller which indicate that the anisotropy disappears/diminished and intensity ratio decreases. It was found that even if we have applied high isotropic consolidation pressure, anisotropy was not completely diminished specially in case of clay soil but in case of silty clay they lose their anisotropy at rapid rate as compared to clayey materials, at confining pressure of 600kPa. So, it is concluded that the grain size has significant effect on the diminishing of anisotropy, and silty material shows rapid change in anisotropy compared with clay material.

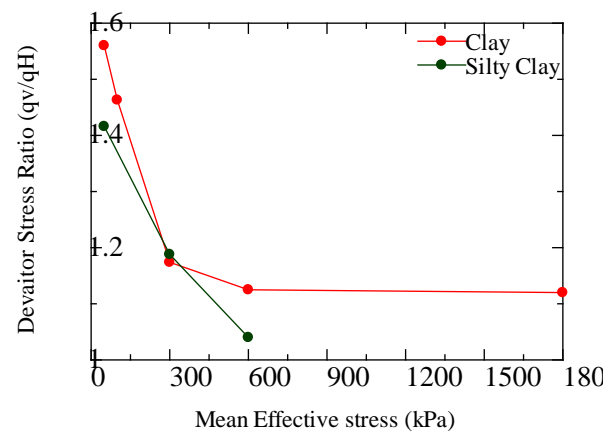


Fig.15 Difference in vertical and horizontal shear strength

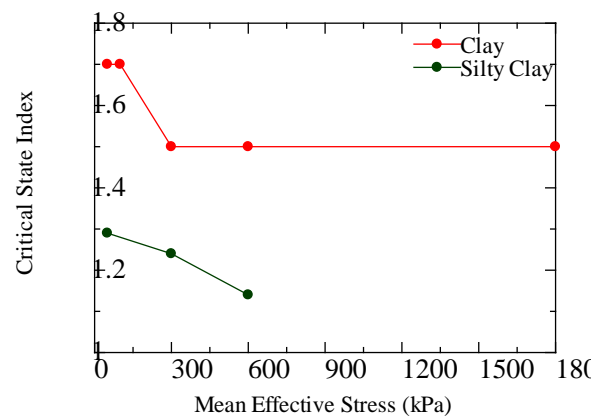


Fig.16 Difference in Critical state Index

Figure 16 summarizes the clay and silty clay samples changing of critical state index with increasing confining pressure. Comparing clay and silty clay, critical state index is larger for clay material. Another important fact observed that, critical state index is changing with different confining pressure. To describe the effect of

anisotropy, rotational hardening concept was often used. However, when introducing the rotational hardening concept directly to the original Cam clay model that is so called as Sekiguchi-Ota model, critical state index did not change even if the anisotropy develops and disappears. On the other hand, when introducing the rotational hardening concept to modified Cam clay model, critical state index changes according to the plastic deformation. Figure 17 and 18 shows the schematic diagram of an ordinary/ Sekiguchi-Ohta model and modified Cam clay model with rotational hardening, respectively. From this viewpoint, modified Cam clay model is more suitable to use as compared to the original Cam clay model.

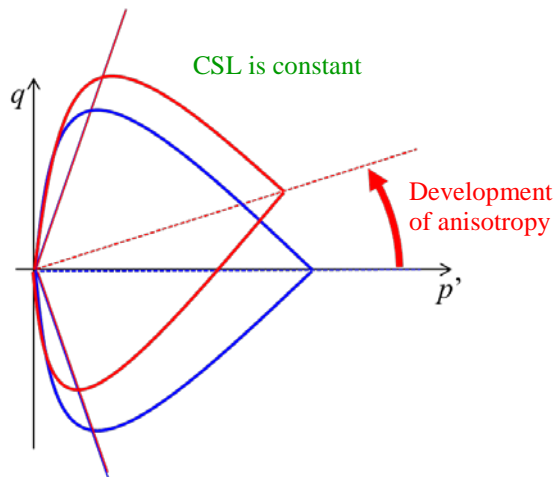


Fig.17 Sekiguchi-Ohta model

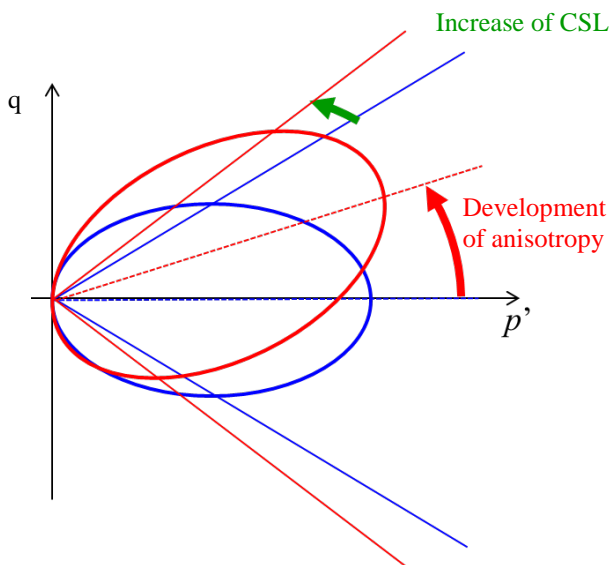


Fig.18 Modified Cam-clay model with rotational hardening

CONCLUSION

From a series of experimental results, it is concluded that anisotropy developed in the preliminary consolidation process, and anisotropy disappears due to isotropic consolidation. Nevertheless, it does not completely disappear even under high confining pressure especially in case of clay. However, if we compare clay and silty clay soil, silty clay materials lose their anisotropy at lower confining pressure as compared to clay materials. Therefore, the grain sizes have significant effect on the developing and diminishing of anisotropy.

Another important fact observed was that critical state index (slope of critical state line) is decreasing and become constant as confining pressure increases, however, when introducing the rotational hardening concept directly to the original Cam clay model that is so called as Sekiguchi-Ota model, critical state index did not change even if the anisotropy develops and disappears. On the other hand, when introducing the rotational hardening concept to modified Cam clay model, critical state index changes according to the plastic deformation. From this viewpoint, modified Cam clay model is more suitable to use as compared to the original Cam clay model.

Further experiment will be performed to observe the effect of cyclic shear test to evaluate the development/diminishing of anisotropy. In order to check the effect of an intermediate principle stress extension test will be performed.

Moreover, based on experimental facts, numerical simulation will be performed in future to validate the experimental results and the constitutive model and add some improvement if necessary.

ACKNOWLEDGEMENTS

This research work was supported by Ministry of Education, Culture, Sports, Science and Technology (Japan).

REFERENCES

- [1] Islam, M. S., and E. Haque., Strength Anisotropy in Undisturbed Dhaka Clay. *Journal of Geotechnical Engineering* 1.1 2011, pp. 7-15.
- [2] Hoque, E., and Tatsuoka, F., Anisotropy in elastic deformation of granular materials. *Soils and Foundations*, 1998, 38(1), pp. 163-179.
- [3] Sekiguchi, H. and Ohta H., Induced anisotropy and time dependency in clays, *Constitutive Equations of Soils (Proc. 9th Int. Conf. Soil Mech. Found. Eng., Spec. Session 9)*, Tokyo, 1977, pp.229-238.
- [4] Hashiguchi, K. and Chen, Z.-P., Elastoplastic

- constitutive equations of soils with the subloading surface and the rotational hardening, *Int. J. Numer. Anal. Meth. Geomech.*, 22, 1998, pp.197-227.
- [5] Asaoka, A. Noda, T., Yamada, E. Kaneda, K. and Nakano, M., An elasto-plastic description of two distinct volume change mechanisms of soils, *Soils and Foundations*, 42(5), 2002, pp.47-57.
- [6] Karstunen, Minna, and Mirva Koskinen., Plastic anisotropy of soft reconstituted clays. *Canadian Geotechnical Journal* 45.3, 2008, pp 314-328.
- [7] Liu, W., Shi, M., Miao, L., Xu, L., & Zhang, D., Constitutive modeling of the destructuration and anisotropy of natural soft clay. *Computers and Geotechnics*, 51, 2013, pp 24-41.
- [8] Duncan, J. M. and Seed, H. B., Anisotropy and stress reorientation in clay. *Journal of Soil Mechanics & Foundations Div., ASCE*, Vol. No. SM 6, 1966, pp. 81-103.
- [9] Atkinson, J. H., Anisotropic elastic deformations in laboratory tests on undisturbed London Clay. *Geotechnique* 25.2 1975, pp 357-374.
- [10] Hashiguchi, K., and Z - P. Chen. Elastoplastic constitutive equation of soils with the subloading surface and the rotational hardening. *International journal for numerical and analytical methods in geomechanics* 22.3 1998, pp 197-227.
- [11] Graham, J., and G. T. Houlsby. Anisotropic elasticity of natural clay. *Géotechnique* 33.2, 1983, pp 165-180.

FACTORS IMPACTING PRECAST UTILIZATION IN CAMBODIA CONSTRUCTION

Kaya Ting¹, Phatsaphan Charnwasununth^{2*}, Vachara Peansupap³ and Nobuyoshi Yabuki⁴

¹Faculty of Engineering, Khon Kaen University, Thailand; ^{2*}Faculty of Engineering, Khon Kaen University, Thailand; ³Faculty of Engineering, Chulalongkorn University, Thailand; ⁴Graduate School of Engineering, Osaka University, Japan

ABSTRACT

Precast construction has caught up the attention of construction practitioners since the end of World War II and has been widely implemented in both developed and developing countries all around the world. However, it has been noted that Cambodia has not enjoyed the benefit much from the use of precast method in construction since it is still nascent. Hence, this research paper aims to identify the attributes having an influential impact on precast industry and to investigate effects resulted from the demographic characteristics of precast users. Four major processes are studied ranging from Design to Production, Transportation, and Installation. A closed-ended questionnaire integrated with a Likert measurement scale was employed for the data collection after having passed the reliability and validity test. The research finished with 47 respondents participated. Analytically, the research adopted Relative Importance Index and Analysis of Variance for data analysis based on the study's objectives. Consequently, top five factors in each process are found to have an influential impact on Cambodia precast industry and three demographic characteristics are analyzed to have a significant effect on precast users in Cambodia construction. Finally, a discussion is provided together with a suggestion for further researches.

Keywords: Cambodia construction, Demographic effects, Influential impacts, Precast implementation

INTRODUCTION

Cambodia, one of the developing countries in Southeast Asia, has been seeing a perpetual growth in economy with an exceeded 7 percent over the last 20 years and is transforming itself to be a lower middle-income country. This improvement has been brought mainly by the contribution of several sectors including agriculture, garment and footwear, tourism, and construction [1].

Looking at Cambodia construction sector, there have been many construction projects undergoing recently that the investment in the construction has reached beyond the country's budget plan, totaling at 36.4 percent of the total GDP by 2016 [1–3]. In addition, the sector has seen an investment increase of 22.32 percent amounting for 6.42 billion USD with 3,052 approved construction projects on 10.74 million square meters and has contributed more than 92 million USD to the national revenue of Cambodia by the end of 2017 [4].

However, with this surging investment trend into construction, increasing concerns have been raised upon how well the sector is prepared to take up the challenges. As having been reported, it is facing the lagging of residential units' supply, the cost and schedule overrun of projects, the large inter-provincial development gap, the lack of technology integration, the failure to lift up the income status of the country, the failure to develop the human

capacity, the lack of sustainability approach, the lack of trained and skilled workers, the deprivation of educational and technical course, the lack of labor supply, the low productivity rate of local workforce, and the low workforce wage [1,5–7].

Throughout an intensive review of literatures, precast construction method has been suggested to close problematic gaps presenting in Cambodia construction industry. However, the use of this method is still nascent, and many challenges are to be faced upfront by the construction practitioners as a whole. Thus, this paper aims to close the knowledge gap by identifying the attributes having an influential impact on precast industry and investigating effects resulted from the demographic characteristics of precast users.

LITERATURE REVIEWS

By definition, precast method is a contemporary construction procedure where building structural and architectural components are casted inside high-quality and environmental-controlled manufacturing facility and transported to the construction site for installation [8,9]. Globally, it has attracted the attention of construction practitioners due to its benefits for all parties within the construction [10,11]. However, it also places drawbacks to the construction projects if it is not done in a proper manner [12,13]. Following section lists the positive

and negative reasons of using precast.

Precast Method's Positive and Negative Reasons

Beneficially, precast construction has gained its popularity over the last 50 years owing to its advantages such as (F1) improving the productivity and efficiency of the construction, (F2) saving the construction time, (F3) providing a high buildability, (F4) providing a high-quality control and assurance, (F5) saving the overall cost, (F6) promoting affordability, (F7) embedding sustainability, (F8) minimizing waste, (F9) reducing carbon emissions, (F10) providing a clean construction site, (F11) coping with labor shortage, (F12) reducing the dependency on labor, and (F13) improving the construction safety and health condition [8,11,13–21].

However, these benefits also come along with the challenges. Previous findings have mentioned 26 factors in which practitioners in different countries have faced when precast is implemented such as (F14) design incapability, (F15) lack of government promotion and incentives, (F16) lack of local policy support and regulation, (F17) lack of manufacturing capability, (F18) product quality problems, (F19) lack of standardization system, (F20) lack of skilled labor, (F21) insufficient training and upskilling, (F22) incompetency of technology and equipment, (F23) lack of sufficient supply chain, (F24) monopoly dominance, (F25) poor coordination and collaboration, (F26) higher initial cost, (F27) lack of economy-of-scale production, (F28) economic risk, (F29) lack of uniform standards, guidelines, and codes, (F30) resistance from customers and professionals, (F31) lack of expertise, (F32) lack of management, (F33) resistance to changes, (F34) long lead-in time, (F35) lack of monotone considerations, (F36) lack of standard components manufacturer, (F37) lack of research and development, support service, and technology, (F38) lack of on-site cast yard and access, and (F39) transportation inefficiency [9,11–13,15,16,18,19,21–24].

Adoption Approaches

Eventually, several countries have different reasons for taking up this technology via various approaches. For example, Malaysia brought in this technology to solve the growing needs for affordable housing and housing shortage, deal with issues related with foreign labor, and improve quality, image and productivity of the construction industry while China promoted this method so as to improve the quality and productivity and to meet the urgent demand for rapid and economically viable mass-produced housing [13,25]. Looking at Hong Kong, precast was adopted in order to reduce the amount of

waste generated from construction activities and improve buildability while Thailand shifted to this method owing to the shortage of construction labor in the industry [15,26]. In Eastern and Western Europe, this technology caught on popularity after World War II when there was a pressing and increasing needs for immediate housing and during the slum clearance in 1960s [8,13].

METHODOLOGY

Research methodology terminologically refers to how the research is carried out in a systematic and scientific way in order to meet the objectives and to solve the problem of the research [27–29]. Thus, this research was designed using quantitative approach since the objective was to evaluate numerically the level of influential impact on decision-making and to investigate the demographic characteristics which play a role in altering the method selection's consideration.

Data Collection Tools

In regards with the research's data collection tool, a closed-ended questionnaire using F1-F39 scientific-reviewed factors was distributed via an online web survey mode, and the Likert 5-scale measurement was adopted [27,29]. Initially, the questionnaire went through two critical tests which were validity and reliability tests. For the validity test, 12 experienced precast practitioners with at least 5-year working experience in Cambodia precast industry were invited to rate the level of relevance of the questionnaire items based on Cambodia construction context. Analyzed using Items of Objective Congruence (IOC) index, a list of questions was eliminated from the questionnaire as it was rated as irrelevant with the IOC value of less than 0.5 [30,31]. Then, the questionnaire was revised and went through the pilot test to check the reliability of the result. With this test, 30 respondents were invited to answer the questions, and upon finishing data analysis via SPSS Computer Program, it was found out that the questionnaire passed the test with the overall Cronbach's Alpha value of 0.861 which is over 0.70 as an acceptable value [7,32]. Thus, the questionnaire was treated as appropriate for the mass data collection.

Sample Size and Sampling Method

Since precast industry was at an early stage of introduction to Cambodia construction industry, there was no accurate information regarding the sampling frame or how many engineers were working for precast projects in Cambodia [29,32]. In

addition, the unit of analysis for this research was at an engineer level due to the reason that the goal was to study the industry prospect of precast construction in Cambodia. Hence, the key informants were from design, production, transportation, and installation teams.

Due to the absence of the sampling frame, this research study adopted non-random probability sampling methods which were purposive and snowball sampling methods. For the first one, the goal was to select only the participants who had experiences in precast works, but since precast industry in Cambodia was still at an early stage, it was needed to allow other engineers who had precast knowledge to participate in this research since their perspectives would also have an impact on their decision. For the second one, the participants were asked for the networks so that the researcher could enlarge the sample size selectively [29].

Analysis Tools

The data analysis tools of this research were Relative Importance Index (RII) and Analysis of Variance (ANOVA). For the first one, RII was employed to evaluate the impact of each factor by ranking it in ascending order [7,29,32,33]. For the second one, ANOVA was adopted in order to indicate the differences of participants in terms of the responses so as to find out if the demographic characteristics played a role in altering the decisions making process of the practitioners in regards with precast adoption in Cambodia construction industry [27,29,32].

RESULTS AND DISCUSSION

By the end of the data collection, a total of 47 respondents participated in the research questionnaire. This section will show the results of the research with an explanatory discussion of each study's objective.

Influential Impacting Attributes

Using Relative Importance Index (RII) to evaluate the influential impact of each factor which affects the decision of the practitioners when using precast, a total of 20 factors are presented in Table 1.

Table 1 Influential Impacting Attributes

Group	Factors	RII	Rank
Design	F4	77.50%	1
	F11	76.25%	2
	F2	73.75%	3

Production	F31	72.50%	4
	F29	71.25%	5
	F5	90.00%	1
	F2	88.33%	2
	F10	86.67%	3
	F15	85.83%	4
Transportation	F18	85.56%	5
	F32	85.71%	1
	F39	82.86%	2
	F35	77.14%	3
	F23	74.29%	4
	F28	60.00%	5
Installation	F18	83.33%	1
	F2	82.78%	2
	F30	81.11%	3
	F4	80.00%	4
	F1	79.44%	5

Based on the data shown in Table 1, 4 precast processes are affected by a number of factors. To begin with, top five factors were analyzed to have an influential impact on the practitioners in Design process. Firstly, the benefit that precast method can provide a high-quality control and assurance drives the practitioners to consider using precast for construction projects with an influential impact of 77.50 percent. Secondly, the fact that precast can cope with the shortage of labor has been found to be the second reason why Cambodia engineers choose precast over the conventional method with an influential impact of 76.25%. Thirdly, a number of construction methods can help the practitioners to finish the projects fast, and it is 73.75% confident that precast method will be adopted. However, the lack of expertise has been rated as 72.50% preventing the designers in Cambodia from considering precast method while the lack of uniform standards, guidelines, and codes has 71.25% affected the decision makers not to use precast method for the projects.

Looking at the data of Production process, top five factors were notified to influence the consideration of going for precast method. To start with, the respondents agreed that precast can save the overall cost and time of construction projects with an impact of 90% and 88.33% respectively. In addition, precast method is effective in providing a clean construction site which 86.67% influences the practitioners to consider this method for usage. On the contrary, the lack of government promotion and incentive and the production quality problems have hesitated Cambodia engineers from proposing precast for projects with an influential impact of 85.83% and 85.56% each.

For the Transportation process, top five factors have been analyzed to be influence the engineers negatively in terms of precast adoption. That is, the

lack of management has placed itself as the first ranked factor which 85.71% places difficulty to the precast engineers in terms of transporting the components thus dissatisfying the practitioners. In addition, the inefficiency of transportation in Cambodia has been considered as a barrier for precast engineers from utilizing precast with an influential impact of 82.86% while the lack of monotone consideration makes it difficult to transport the components as the panels cannot be optimally stacked in which the impact is 77.14%. Furthermore, the lack of sufficient supply chain does not give the practitioners many options in terms of delivery assistive tools and thus 74.29% prevents the successful transportation of precast components. Moreover, the economic risk resulted from the instability of precast usage in Cambodia has made most practitioners to reconsider whenever precast method is proposed with an influential impact of 60%.

Last but not least, three driving and two preventing factors have been founded in Installation process. That is, the product quality problems have been consistently founded to happen while erecting the components while most professionals and customers would be dissatisfied whenever precast method is adopted as ranked first and third respectively. However, the fact that precast method can save the construction time has been affirmed by installers with 82.78% confidence, and it is confirmed that precast can provide a better-quality construction as compared to the conventional method with 80% positive response. Finally, it has been agreed that precast can improve the productivity and efficiency of construction site with 79.44% influence.

Demographic Characteristics

Using Analysis of Variance (ANOVA) to investigate the demographic characteristics which cause the different responses from one respondent to another, Table 2 lists each characteristic.

Table 2 Affective Demographic Characteristics

Group	Type	Factor
Academic Background	Design	F5
		F12
		F14
		F16
	Production	F19
		F30
		F25
		F26
		F33
		F34

Years of Experiences	Transportation	F32
		F39
		F39
		F32
		F25
		F14
		F22
		F23
		F36
	Installation	F4
		F8
		F10
		F12
		F17
	Design	F18
		F27
Production		
Transportation		
Installation		
F2		
F14		
F25		
F29		
F17		
Building Heights	Production	F30
		F33
		F5
		F13
		-
		F12
		F1
		F5
		F2
	Installation	F4
		F8
		F13
		F7
		F16
		F21
		F29
Design	F32	
	F14	
	F17	
	F25	
	F31	
	F33	
	F35	

Based on the result illustrated in Table 2, there are three demographic characteristics which affect the response of each participant to be different. First of all, the academic background of each respondent determines the choice of responses. Originally, four academic choices were provided in the questionnaire such as Higher Diploma, Bachelor Degree, Master Degree, and Philosophical Doctoral Degree. As a result, it was founded that 3 factors in Design process, 9 factors in Production process, 7 factors in Transportation process, and 6 factors in Installation process were significantly influenced by the

different academic background of the respondents who have graduated with Bachelor and Master degree with the confidence interval of $p < 0.005$.

Second of all, the number of years of working experience was also confirmed to have an effect of the respondents' decision towards the adoption of precast, mainly those who have the experiences from less than 3 years to 12 years. That is, 1 factor in Design process and 7 factors in Installation process were founded to be significantly different in terms of participants' perception with the confidence interval of $p < 0.005$ while there was no significant difference of responses in Production and Transportation process.

Thirdly, the type of building as categorized by the height also affects the respondents' decision. The questionnaire provided two choices in terms of the type of building which were low-rise and high-rise building. As a result, 1 factor in Design process, 1 factor in Production process, and 18 factors in Installation process were founded to result differently depending on the experience of the respondents in regards with the building type with the confidence interval of $p < 0.005$.

CONCLUSION

Cambodia is a developing country and has been struggling over the last 30 years to build its economy. By 2017, it has seen quite a robust economic growth and has maintained at the rate of exceeded 7% for 20 years. Construction sector is one of the main role players in contributing to this growth, but it has been reported as ineffective and inefficient. Thus, precast method is suggested to solve the shortcomings in Cambodia construction sector. However, the adoption of precast has never been high since it is at an early stage of introduction, and many challenges are to face upfront. Upon distributing the closed-ended questionnaire to a number of respondents, two results have been found such the factors which give influential impacts to the decision making of the practitioners, and the characteristics of the practitioners themselves that prevent them from using precast for construction projects. In addition, each process is studied to have been affected by a number of factors. Further studies should limit out the boundary of this research by integrating infrastructure study in Cambodia in terms of precast usage and an actionable strategy should be formulized in order for the practitioners to follow if precast needs to be successful in Cambodia construction industry.

ACKNOWLEDGEMENTS

The author would like dedicate special thanks to Graduate School and Faculty of Engineering, Khon

Kaen University for providing the grants to support this research. In addition, the author would like sincerely thank the Environmental Design and Information Technology Laboratory (Yabuki Laboratory), Division of Sustainable Energy and Environmental Engineering, Graduate School of Engineering, Osaka University, Japan for admitting the researcher to be a special research student for strengthening the research quality.

REFERENCES

- [1] Royal Government of Cambodia. National Strategic Development Plan 2014-2018. 2013.
- [2] The National Bank of Cambodia (NBC). Annual Report 2016. 2017.
- [3] WB Group. Cambodia Economic Update-Staying competitive through improving productivity 2017:1-48.
- [4] Manet S. Construction investment up 22 percent. Khmer Times 2017.
- [5] Asian Development Bank. ADB Country Partnership Strategy, 2014-2018. 2014.
- [6] Durdyev S, Zavadskas E, Thurnell D, Banaitis A, Ihtiyar A. Sustainable construction industry in cambodia: Awareness, drivers and barriers. Sustainability 2018;10:392.
- [7] Durdyev S, Omarov M, Ismail S. Causes of delay in residential construction projects in Cambodia. Cogent Eng 2017;4:1-12.
- [8] Jaillon L, Poon CS, Chiang YH. Quantifying the waste reduction potential of using prefabrication in building construction in Hong Kong. Waste Manag 2009;29:309-20.
- [9] Li Z, Shen GQ, Xue X. Critical review of the research on the management of prefabricated construction. Habitat Int 2014;43:240-9.
- [10] Mohamad MI, Nekooie MA, Taherkhani R, Saleh AL, Mansur SA. Exploring the potential of using industrialized building system for floating urbanization by SWOT analysis. J Appl Sci 2012;12:486-91.
- [11] Tam VWY, Tam CM, Zeng SX, Ng WCY. Towards adoption of prefabrication in construction. Build Environ 2007;42:3642-54.
- [12] Luo L-Z, Mao C, Shen L-Y, Li Z-D. Risk factors affecting practitioners' attitudes toward the implementation of an industrialized building system a case study from China. Eng Constr Archit Manag 2015;22:622-43.
- [13] Zhang X, Skytmore M. Industrialized housing in China: a coin with two sides. Int J Strateg Prop Manag 2012;16:143-57.
- [14] Benros D, Duarte JP. An integrated system

- for providing mass customized housing. *Autom Constr* 2009;18:310–20.
- [15] Chiang YH, Hon-Wan Chan E, Ka-Leung Lok L. Prefabrication and barriers to entry-a case study of public housing and institutional buildings in Hong Kong. *Habitat Int* 2006;30:482–99.
- [16] Dave M, Watson B, Prasad D. Performance and perception in prefab housing: An exploratory industry survey on sustainability and affordability. *Procedia Eng* 2017;180:676–86.
- [17] Jaillon L, Poon CS. Life cycle design and prefabrication in buildings: A review and case studies in Hong Kong. *Autom Constr* 2014;39:195–202.
- [18] Jiang R, Mao C, Hou L, Wu C, Tan J. A SWOT analysis for promoting off-site construction under the backdrop of China's new urbanisation. *J Clean Prod* 2017;1–10.
- [19] Pour F, Goulding J, Akintoye A, Kolo S. Review of motivations, success factors, and barriers to the adoption of offsite manufacturing in Nigeria. *Procedia Eng* 2017;0:19–22.
- [20] Steinhardt DA, Manley K. Adoption of prefabricated housing-the role of country context. *Sustain Cities Soc* 2016;22:126–35.
- [21] Yunus R, Yang J. Sustainability criteria for Industrialised Building Systems (IBS) in Malaysia. *Procedia Eng* 2011;14:1590–8.
- [22] Chen Y, Okudan GE, Riley DR. Decision support for construction method selection in concrete buildings: Prefabrication adoption and optimization. *Autom Constr* 2010;19:665–75.
- [23] Mohammad MF, Baharin AS, Musa MF, Yusof MR. The potential application of IBS modular system in the construction of housing scheme in Malaysia. *Procedia - Soc Behav Sci* 2016;222:75–82.
- [24] Teng Y, Mao C, Liu G, Wang X. Analysis of stakeholder relationships in the industry chain of industrialized building in China. *J Clean Prod* 2017;152:387–98.
- [25] Azman MNA, Ahamad MSS, Majid TA, Shah MNSA. A study of precast concrete in Malaysia. *Concrete* 2012;46:50–2.
- [26] Waroonkun T, Koojaroenpaisan R. Modelling of factors impacting adoption of precast concrete systems. *Manag Innov a Sustain Built Environ* 2011.
- [27] Kothari C, Kumar R, Uusitalo O. *Research Methodology: A step-by-step guide for beginners*. 3rd ed. SAGE Publications Ltd; 2014.
- [28] Kothari CR. *Research Methodology: Methods & Techniques*. 1st ed. SAGE Publications Ltd; 2004.
- [29] Lawrence Neuman W. *Social Research Methods - Quantitative and Qualitative Approaches*. 7th Editio. Pearson Education Limited 2014; 2014.
- [30] Turner RC, Carlson L. Indexes of item-objective congruence for multidimensional items. *Int J Test* 2003;3:163–71.
- [31] Turner RC, Mulvenon SW, Thomas SP, Developments PP, Balkin RS. Computing indices of item congruence for test development validity assessments. *Stat Data Anal* 1977:1–5.
- [32] Field A. *Discovering statistics using SPSS*. 3rd Editio. SAGE Publications Ltd; 2009.
- [33] Muhwezi L, Acai J, Otim G. An assessment of the factors causing delays on building construction projects in Uganda. *Constr Eng Manag* 2014;3:13–23.

DEVELOPMENT OF INTEGRATED SATELLITE-BASED DROUGHT MODEL IN THAILAND USING MULTIPLE LINEAR REGRESSION

¹Mongkol Raksapatcharawong and ²Watcharee Veerakachen

^{1,2}Chulabhorn Satellite Receiving Station, Faculty of Engineering, Kasetsart University,
Thailand

ABSTRACT

Drought, due to climate change, has recently become more severe. Capability to monitor drought condition and to assess drought risk is essential to a development of effective drought adaptation plan, especially for an agricultural country like Thailand. Current drought monitoring is provided by separate indices such as Standardized Precipitation Index (SPI), Soil Moisture Index (SMI) and Moisture Available Index (MAI), calculated from weather station datasets which are not easily comprehensible to users. This research develops a countrywide integrated satellite-based drought model consisting of three parameters: accumulated estimate rainfall product from FY-2E satellite data, difference Land Surface Temperature (LST) and Normalized Difference Vegetation Index (NDVI) products from MODIS. A simple drought hazard is introduced as multiple linear regression model ($R^2=0.795$) of these satellite products, calibrated with daily soil moisture measurement in 2015. Consequently, drought conditions are represented by Drought Hazard Index (DHI) by assigning integer values, from -3 (extremely drought) to +3 (extremely wet), according to the defined thresholds (presently at 0.05, 0.15, 0.30, 0.70, 0.80, and 0.95) of the cumulative distribution function (CDF) of drought hazard values. The model is validated with 426 countrywide drought situations announced by the Department of Disaster Prevention and Mitigation (DDPM), during drought season 2016, yielding 0.96 probability of detection.

Since the model outputs are in georeferenced raster format, they can be processed with other relevant GIS data such as land use and irrigation to generate advanced thematic mapping called drought risk map. This map can benefit not only policy makers but also farmers themselves.

Keywords: Drought Model, FY-2E, GIS, MODIS, Multiple Linear Regression

INTRODUCTION

Drought is a major recurring natural disaster that poses a concern in water and food security [1], environmental problems as well as economic risks, especially for agricultural sector. Based on its impact, droughts are classified into four types and usually occur in a particular order which is meteorological drought, agricultural drought, hydrological drought and socioeconomic drought. Meteorological drought caused by deficit in precipitation which subsequently impacts on soil water content leading to agricultural drought that resulting in plant water stress and reducing biomass and yield. Due to low recharge from the soil to water features, hydrological drought occurs when streamflow, reservoir storage and groundwater level are in shortage. Eventually, socioeconomic drought will take place if the phenomena prolongs until water demand increased and water stress intensified by human activities [2], [3], [4].

Drought monitoring and early warning are crucial components for mitigation and adaptation plans [4]. Drought management typically responses to crisis after impacts have occurred. Moreover, drought relief providing to those affected decreases socioeconomic capabilities in adaptation to drought disaster [5].

Therefore, practical drought monitoring and risk assessment are essential to developing an effective drought early warning and adaptation plan in which potential victims are able to get involved leading to a proactive and effective drought management which can actually reduce damaging impacts.

Traditional drought monitoring uses several indices such as Standardized Precipitation Index (SPI), Soil Moisture Index (SMI) and Moisture Available Index (MAI) each represents various aspects of drought and has been widely used. The SPI presents a rainfall anomaly as a normalized variable by probabilistically comparing accumulated rainfall over a time period with historical rainfall period. The SMI indicates soil water content and the MAI determines the influence of water adequacy on yields. However, the indices calculated from meteorological observations are point-based and insufficient to monitor drought at regional scale [6]. Consequently, remote sensed satellite data has become a valuable tool and taken significant role in drought monitoring due to its grid-based feature providing spatial information on drought even at global scale. Satellite-based data also has advantage comparing to ground-based observation in that consistent data records and products can be utilized in developing advanced drought monitoring with multiple data sources.

Various satellite based drought indices have been developed to monitor drought and can be categorized into three perspectives. The first one provides precipitation information which SPI is the most widely used. The computation requires satellite data retrieval from Infrared (IR) sensors of Geostationary (GEO) satellite offering higher temporal resolution and passive microwave (PWM) sensors of Low Earth Orbit (LEO) satellite technically providing more accurate rainfall estimate. Several satellite-based precipitation products are now available including Precipitation Estimation from Remotely Sensed Information using Artificial Neural Networks (PERSIANN) [7], Tropical Rainfall Measuring Mission (TRMM) [8], CPC Morphing Technique (CMORPH) [9] and Global Satellite Mapping of Precipitation (GSMaP) [10]. However, these products have relative short length of record which imposes a limitation in SPI calculation.

Another category of satellite-based indices are based on Land Surface Temperature (LST) which relate to soil water content, such as Temperature Condition Index (TCI) and Normalized Difference Temperature Index (NDTI) [11],[12]. The Last category assess drought based on observed changes in vegetation condition with indices typically derived from the Normalized Difference Vegetation Index (NDVI) such as the Transformed Vegetation Index (TVI), the Standardized Vegetation Index (SVI), and the Vegetation Condition Index (VCI) [13], [14], [15]. The combination of LST and NDVI has been investigated in several works to provide more robust characterization of drought phenomenon [16]. LST-NDVI based indices, such as Temperature Vegetation Dryness Index (TVDI) and Vegetation Temperature Condition Index, (VTCI) have been applied over different landscapes with varying degrees of success [6], [17], [18].

This work introduces a simple satellite-based drought hazard index that combining all drought related aspects including rainfall, soil moisture and vegetation health. The model inputs are derived from satellite products. Drought hazard values obtained from the model were collected to generate a probabilistic function. The function was defined to indicate levels of drought hazard index that can be shown on a map for easy interpretation.

METHODOLOGY

Satellite-based drought hazard model consists of three dekadal (10 days) satellite data products which are accumulated rain estimate, difference LST, and NDVI values. The relationship between these input parameters and the drought hazard was investigated using multi-linear regression approach. Ground based and reference datasets were collected to be used for model calibration and comparison analysis.

The Study Region

Thailand is located in Southeast Asia on a latitude of 5° N to 21° N and a longitude of 97° E to 106° E. Climatologically, the country is classified as tropical monsoon and tropical savanna with 18-34° C average temperature and over 1,500 mm. average rainfall. Drought season is ranging from November to January (winter) and February to April (summer). The study region covers whole area of the country.

Satellite Datasets

Satellite images were received from Chulabhorn Satellite Receiving Station (CSRS). The FY-2E data is hourly received through DVB-S system while the Terra/Aqua MODIS data is received from MODIS direct broadcast receiving station at CSRS. There are totally 100*1600 pixels for each image, covering Thailand territory, at 1 km/pixel spatial resolution.

FY-2E Dekadal rain estimate

Satellite data received through DVB-S system is in a .VSR file format. Upon received, these data is automatically transformed, using Equal-Lat-Long projection, to numerical data (16-bit PNG). Only data point within the country region is retrieved and stored as a zip file every hour. Hourly satellite rain estimate is calculated from IR1 data using Infrared Threshold Rainfall with Probability Matching (ITRPM) model [19]. The model was adjusted to provide dekadal rainfall by calibrating the satellite rain estimates accumulated in 10 days with co-located rain gauges accumulated rainfall from <http://www.thaiwater.net/> using dataset in 2016. Figure 1 shows an example of the dekadal rain estimate based on ITRPM model.

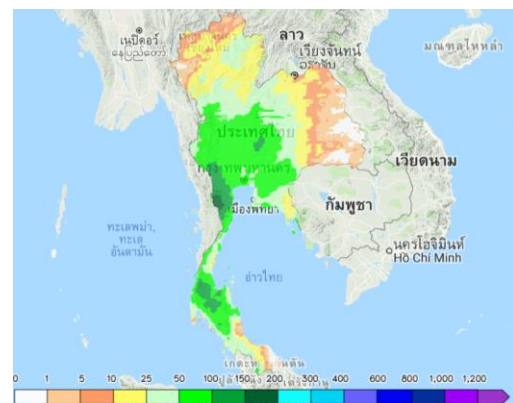


Fig. 1 Example of FY-2E dekadal rain estimate.

MODIS different Land Surface Temperature

Land Surface Temperature (LST), MODIS level-2 product with 1 km spatial resolution, is retrieve twice a day at day- and night-time. The difference

between day and night LST values relates to water content in the soil and therefore can indicate drought condition. Figure 2 (left) shows an example of MODIS LST product. Both day and night LST data are filtered by cloud mask product. Every 10 days, the maximum values of day and night LST are selected. This method is adopted from Maximum Value Composite (MVC) technique which widely accepted to improve analysis and reduce error resulting from environment and atmosphere [20], [21]. The difference between LST day and night called deltaT is then computed every 10 days becoming a dekadal deltaT to be used as input parameter of drought hazard model.

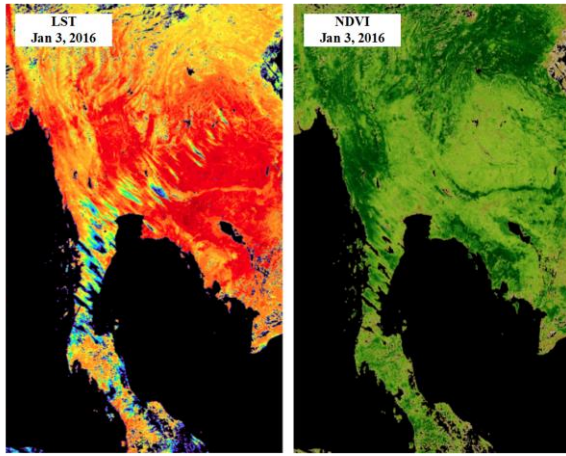


Fig. 2 Example of MODIS products (left) LST (right) NDVI.

MODIS Normalized Difference Vegetation Index

Normalized Difference Vegetation Index (NDVI) is also a level-2 MODIS product representing the wellness of vegetation. Figure 2 (right) shows an example of MODIS NDVI product. The NDVI is also processed by cloud masking and MVC technique, as shown in Fig. 3, to compute dekadal NDVI to be used as the last input parameter of drought hazard model.

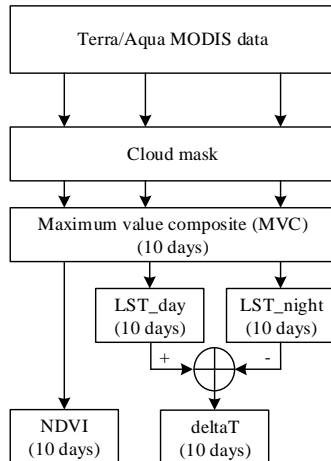


Fig. 3 Processing of dekadal NDVI and deltaT.

Drought Hazard Model

In this work, drought hazard is defined as a composite drought assessment capturing three indicators that are not fully correlated with each other including dekadal rain estimate from FY-2E satellite, deltaT and NDVI from MODIS sensors. These dataset were used as input parameters of drought hazard model. Daily soil moisture in-situ measurements collected throughout 2016 were obtained from the University of Phayao experimental site. Ten days-averaged soil moisture was used as target for drought hazard model development by means of multiple linear regression approach yielding $R^2 = 0.795$. Figure 4 shows the structure of drought hazard model development. The drought hazard model becomes

$$DH = 11.643 + 0.356 * R - 0.297 * \text{deltaT} + 6.868 * \text{NDVI} \quad (1)$$

where R is the FY-2E dekadal rain estimate, deltaT is the decadal difference LST and NDVI is the dekadal NDVI, both from MODIS. The lower the DH implies worse drought condition. This model works well during dry season. However, in rainy season, MODIS satellite data may not be available due to thick clouds. In this case, the drought hazard model is simplified as

$$DH = 12.445 + 0.135 * R \quad (2)$$

Since this model using only dekadal estimated rainfall, the output of multiple linear regression yields $R^2 = 0.371$.

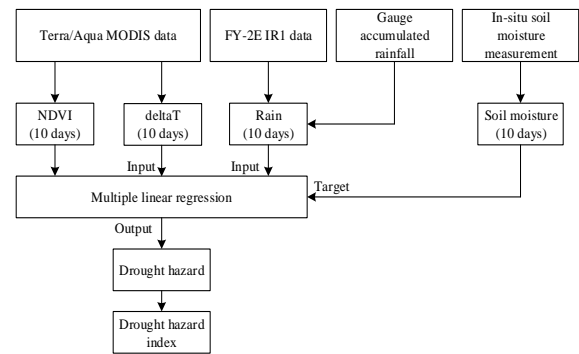


Fig. 4 Development of drought hazard model.

Drought Hazard Index

The cumulative distribution function (CDF) of drought hazard is generated using sample values computed from satellite datasets obtained in 2016. The CDF is grouped into seven threshold levels (presently at 0.05, 0.15, 0.30, 0.70, 0.80, and 0.95) to define the drought hazard index (DHI) which is represented by integer values ranging from -3

(extremely drought) to +3 (extremely wet). The thresholds corresponding to each DHI values are shown in Table 1. Drought hazard values are mapped to each DHI, representing severity of drought condition, based on the drought hazard CDF as shown in Fig. 5.

Table 1 Thresholds for Drought Hazard Index

Drought Hazard	Percentile	Drought Hazard index	
Less than 9.083156732	0 – 5	-3	Extreme drought
[9.083156732 , 12.23415100)	5 – 15	-2	Severe drought
[12.23415100 , 12.97706809)	15 – 30	-1	Moderate drought
[12.97706809 , 19.66813821)	30 – 70	0	Near Normal
[19.66813821 , 23.56635047)	70 – 85	1	Moderate wet
[23.56635047 , 29.14464206)	85 – 95	2	Severe wet
More than 29.14464206	95 – 100	3	Extreme wet

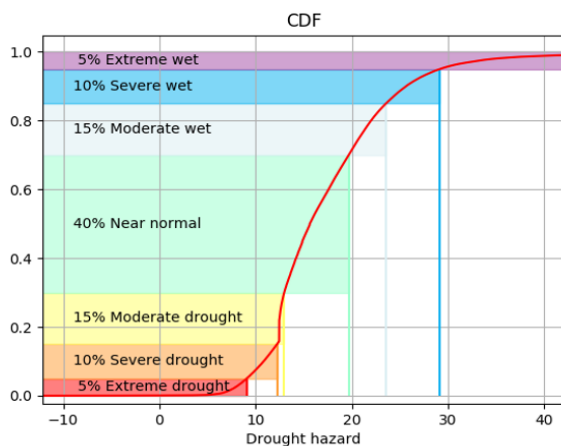


Fig. 5 Mapping between Drought Hazard CDF thresholds and DHI.

RESULTS AND DISCUSSIONS

To generate drought hazard map every 10 days, DHI for each pixel is calculated from drought hazard model mapping with the CDF threshold. The drought hazard map is in georeferenced raster format and can be displayed in geographic information system (GIS) at 1 km spatial resolution. The results are qualitatively validated by the news about drought events and by agrometeorological reports from TMD (accumulated rainfall, MAI, and SMI). Quantitative validation of the model is performed based on the probability of detection (POD) for drought events that are officially

announced by the Department of Disaster Prevention and Mitigation, Ministry of Interior.

Comparison with Agrometeorological reports

Result validation was qualitatively performed by comparison the drought hazard map with the TMD agrometeorological reports in accordance to drought event news. All TMD reports are calculated from gauge station measurements and displayed in portable document format (pdf) on TMD website. A severe drought event was posted in the news at the beginning of January 2016 when there was drought crisis, with extremely low water level, at the Bhumibol and Chaophraya dams located in the central part of Thailand. This event is clearly seen in the drought hazard map, Fig. 6 (a), showing severe to extreme drought in central part of Thailand. This is confirmed by the accumulated rainfall, Fig. 6 (b), which exhibits light rainfall in the area.

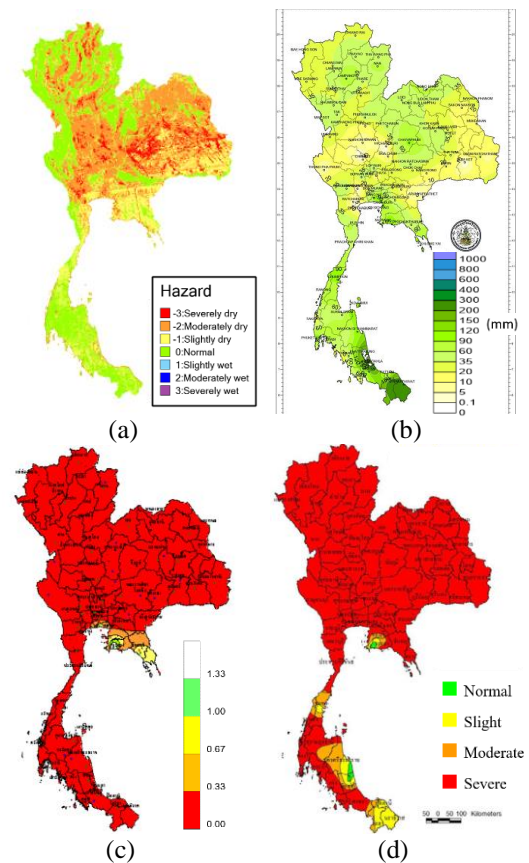


Fig. 6 Comparison of (a) drought hazard map, (b) accumulated rainfall, (c) moisture available index (MAI), and (d) soil moisture index (SMI) maps, during January 1–10, 2016.

Note that there are inconsistencies among TMD indices. For example, MAI map in Fig. 6 (c) indicates extreme drought almost throughout Thailand whereas accumulated rainfall map shows fair amount of

rainfall in the Southern part. However, the drought hazard map shows near normal to moderate drought conditions in that area which is consistent with both accumulated rainfall and SMI maps, in Fig. 6 (a) and (d). Another example is the report for the Eastern part that shows slightly less than normal rainfall with moderate drought in the MAI map but severe drought in the SMI map. All this information was correctly accounted in the drought hazard map with normal to moderate drought in the Eastern area. Evidently, the drought hazard map is useful in monitoring drought condition coping with all three aspects including rainfall, vegetation and soil condition. More importantly, it is much easier to interpret and be understandable to people in the area prone to drought risk, thus effectively supporting the proactive drought management.

Probability of Detection (POD) Analysis

During the dry season (January to April) of 2016, the Department of Disaster Prevention and Mitigation (DDPM) had announced 426 drought situations countrywide. Based on this information, the probability of detection (POD) of drought hazard for drought event is calculated. Since the drought situation announcement is at the district level, the DHI values (with 1-km resolution) at the time of announcement were averaged over the district area. For each announcement, a hit event occurs if the average DHI is less than -0.5 . The probability of detection is computed by

$$POD = \frac{\text{total number of hit events}}{\text{total number of drought announcement}} \quad (3)$$

The result was compared with the POD computed from the TMD report on MAI and SMI. The threshold for declaring drought by the MAI and SMI is 2.5. Based on the level of MAI (0 – 4) and SMI (0 – 3), the average value over the district area was computed. If this value is less than 2.5, the hit event occurs. The results are shown in Table 2. The POD of DHI is 0.96 which is higher than the POD of MAI (0.91) but less than that of SMI (1.00).

Table 2 The probability of detection for drought hazard index (DHI), Moisture available index (MAI), and Soil moisture index (SMI).

Drought hit Thresholds	Number of hit events	POD
DHI < -0.5	411	0.96
MAI < 2.5	388	0.91
SMI < 2.5	426	1.00

CONCLUSIONS

A new drought hazard index, integrating FY-2E and Terra/Aqua satellite data, is proposed for drought monitoring. Multiple linear regression is applied to develop drought hazard model with input parameters including accumulated rainfall estimate from FY-2E GEO-satellite retrieval and different LST and NDVI derived from Terra/Aqua MODIS data. The model input parameters represents precipitation information, soil water content and vegetation health respectively. Drought hazard can be calculated every 10 days at 1 km spatial resolution. The CDF of drought hazard was then generated and used to assign drought hazard index (DHI) by thresholding method. The results were qualitatively validated with drought crisis news. In comparison with the TMD agrometeorological reports, it is shown that drought hazard index is a useful tool for drought monitoring in that it integrates all three drought aspects into one easy-to-understand index with consistent interpretation. Quantitatively, the results were validated against DDPM drought situation announcement with POD equals to 0.96, higher than that of MAI. The drought hazard map is automatically generated, published, distributed, and updated in GIS format, every 10 days, at website <http://csrs.ku.ac.th/wegis/Product/KURDI>. This is beneficial to both government and farmer leading to proactive drought management.

ACKNOWLEDGEMENTS

This work is supported by Kasetsart University Research and Development Institute (KURDI) under the project “A Development of Drought Risk Analysis Platform using Multiple Satellite Sensors” and by Japan International Cooperation Agency (JICA) under the project “Advancing Co-Design of Integrated Strategies with Adaptation to Climate Change in Thailand (ADAP-T)”.

REFERENCES

- [1] AghaKouchak A., Farahmand A., Melton F., Teixeira J., Anderson M., Wardlow B., and Hain C., Remote sensing of drought: Progress, challenges and opportunities. NASA Publications, Nebraska-Lincoln, 2015.
- [2] Zargar A., Sadig R., Naser B., and Khan F. I., A review of drought indices. Environmental Reviews, pp. 333-349, 2011.
- [3] Sadegh M., Love C., Farahmand A., Mehran A., Tourian M.J., and AghaKouchak A., Multi-Sensor Remote Sensing of Drought from Space. Remote Sensing of Hydrological Extreme, Springer International Publishing Switzerland, 2017, pp. 219-236.
- [4] Senay G. B., Velpuri N. M., Bohms S., Gudde M. Y. C., Rowland J., and Verdin J. P., Drought

- Monitoring and Assessment: Remote Sensing and Modeling Approaches for the Famine Early Warning Systems Network. Hydro-Meteorological Hazards, Risks, and Disasters, Nebraska-Lincoln, USGS Staff--Published Research, 2015, pp. 233-262.
- [5] Carrao H., Naumann G., and Barbosa P., Mapping global patterns of drought risk: An empirical framework based on sub-national estimates of hazard, exposure and vulnerability. *Global Environmental Change*, vol. 39, pp. 108-124, 2016.
 - [6] Li X., Wang Y., Tang S., and Shen S., NDVI-LST Feature Space Based Drought Monitoring using MERSI Data in Hunan Province of China. International Conference on Geoinformatics (GEOINFORMATICS), Hong Kong, China, 2012.
 - [7] Sorooshian S., Hsu K., Gao X., Gupta H., Imam B., and Braithwaite D., Evaluation of the PERSIANN system satellite-based estimates of tropical rainfall. *Bulletin of the American Meteorological Society*, vol. 81, no. 9, p. 2035–2046, 2000.
 - [8] Huffman G. J., Bolvin D. T., Nelkin E. J., and Wolff D. B., The TRMM Multisatellite Precipitation Analysis (TMPA): Quasi-Global, Multiyear, Combined-Sensor Precipitation Estimates at Fine Scales. *American Meteorological Society*, vol. 8, pp. 38-55, 2007.
 - [9] Joyce R. J., Janowiak J.E., Arkin P.A., and Xie P., CMORPH: A Method that Produces Global Precipitation Estimates from Passive. *JOURNAL OF HYDROMETEOROLOGY*, vol. 5, pp. 487-503, 2004.
 - [10] Kubota T., Shige S., Hashizume H., Aonashi K., Takahashi N., Seto S., Hirose M., Takayabu Y. N., Nakagawa K., Iwanami K., Ushio T., Kachi M., and Okamoto K., Global Precipitation Map using Satelliteborne Microwave Radiometers by the GSMaP Project : Production and Validation. *IEEE Transactions on Geoscience and Remote Sensing*, vol. 45, no. 7, pp. 2259-2275, 2007.
 - [11] Kogan F., Application of vegetation index and brightness temperature for drought detection. *Advances in Space Research*, vol. 15, no. 11, pp. 91-100, 1995.
 - [12] Mc Vicar P.N. and Bierwirth R., Rapidly assessing the 1997 drought in Papua New Guinea using composite AVHRR imagery. *International Journal of Remote Sensing*, vol. 22, pp. 2109-2128, 2001.
 - [13] Tucker C., Red and photographic infrared linear combinations for monitoring vegetation. *remote sensing of environment*, vol. 8, no. 2, pp. 127-150, 1979.
 - [14] Park J.S., Kim, K.T. and Choi, Y.S., Application of vegetation condition index and standardized vegetation index for assessment of spring drought in South Korea. *Geoscience and Remote Sensing Symposium*, Boston, Mass, 2008.
 - [15] Kogan F. and Sullivan J., Development of global drought-watch system using NOAA/AVHRR data. *Advances in Space Research*, vol. 13, no. 5, pp. 219-222, 1993.
 - [16] Karnieli A., Agam N., Pinker T. R., Anderson M., Imhoff M.L., Gutman G.G., Panov N. and Goldberg A., Use of NDVI and land surface temperature for drought assessment: Merits and Limitations. *Journal of Climate*, vol. 23, pp. 618-633, 2010.
 - [17] Senay G B., Velpuri N M., Bohms S., Gudde M., Young C., Rowland J., and Verdin J. P., A Simple Interpretation of the Surface Temperature/vegetation Index Space for Assessment of Surface Moisture Status. *Remote Sensing of Environment*, vol. 79, no. 2-3, pp. 213-224, 2002.
 - [18] Wang P.X., Wan Z.M., and Gong J.Y., Advances In Drought Monitoring by Using Remotely Sensed Normalized Difference Vegetation Index and Land Surface Temperature Products. *Advance In earth Sciences*, vol. 18, no. 4, pp. 527-533, 2003.
 - [19] Veerakachen W. and Raksapatcharawong M., Rainfall estimation for real time flood monitoring using geostationary meteorological satellite data," *Advances in Space Research*, vol. 56, no. 6, pp. 1139-1145, 2015.
 - [20] Holben B., Characteristics of maximum-value composite images from temporal AVHRR data. *International Journal of Remote Sensing*, vol. 7, pp. 1417-1434, 1986.
 - [21] Liu H., Zhang A., Jiang T., Lu H., Liu X., and Wang H., The Spatiotemporal Variation of Drought in the Beijing-Tianjin-Hebei Metropolitan Region (TTHMR) Based on the Modified TVDI. *Sustainability*, vol. 8, pp. 1-15, 2016.

COMPARATIVE ANALYSIS AND DESIGN OF TRANSVERSE BOX GIRDER BRIDGE BETWEEN STAAD.PRO AND MIDAS CIVIL SOFTWARES

Muhammad Naim Abdul Halim^{1,2}, Anizahyati Alisibramulisi^{1,3}, Mohammad Noor Abu Hassan⁴, Ahmad Ramlan Abu Talib⁴, Noor Rita Ismail², and Norliyati Mohd Amin¹

¹Faculty of Civil Engineering, Universiti Teknologi MARA (UiTM), 40450, Selangor, Malaysia

²Khairi Consult Sdn Bhd, 68100, Selangor, Malaysia

³Institute for Infrastructure Engineering and Sustainable Management (IIESM), UiTM, 40450, Selangor, Malaysia

⁴Perunding ZAR Sdn Bhd, Civil & Structural Consulting Engineers, 40675, Selangor, Malaysia

ABSTRACT

In Malaysia, STAAD.Pro and MIDAS Civil software are commonly used by bridge engineer for the analysis and design of bridge structure. MIDAS software which has an auto modeling generator is preferable by the users as compared to STAAD.Pro software. However, STAAD.Pro software is much more user friendly. Therefore, in this paper, a comparison study was carried out by modeling box girder bridge using STAAD.Pro and MIDAS. The similarities, differences and limitations from these two software were investigated. Comparison of the STAAD.Pro and MIDAS software showed that the result of analysis from this two software have significant differences in live load cases as compared to permanent load cases. Whereas, for the design results, the reinforcement used was similar for cantilever part of the slab but different for other parts of the box girder segment in which MIDAS Civil requires more reinforcement. The deviation of results between STAAD.Pro and MIDAS software were most probably due to the fact that, both software have different configuration of wheel load on the bridge deck. Nevertheless, both software are recommended to be used in the analysis and design of box girder bridge, as both software have proven to be effective as Computer Aided tools. Thus, any choices of software depend on the needs and what to be solved. It is also evident from the results that there is a lack of established guidelines for modelling and verification. Such guidelines would simplify the work for engineers and set the foundation for common working procedures within the industry.

Keywords: Transverse analysis, Transverse design, Box girder bridge, STAAD.Pro software, MIDAS Civil software

INTRODUCTION

In the modern bridge construction, Box Girder Bridge is a significant type of bridge which has capability of longer span and spiral or curved road alignment. A safe bridge design requires a satisfied input by engineers during site investigation, planning, analysis and design. Besides that, an economic design is also desired for designing any structure without neglecting the worst case of loading effect. The worst case of loading effect was encouraged to be designed for higher factor of safety value to avoid the failure of structure to occur. Therefore, box girder bridge which has complex structural behaviour is needed to be modelled accordingly in the software to give appropriate result in both analysis and design.

Due to the rapid development of computational methods, different program and analysis methods are being used nowadays. To name a few; STAAD.Pro, MIDAS Civil, SAP2000 and LUSAS are the common software used in Malaysia for bridge analysis and design. However, MIDAS Civil is much preferred among bridge engineers for analysing box girder bridge as compared to STAAD.Pro, even though it is not fully utilized. Every software has its own limitations in modelling and analysing the structures. Hence, for any project, the result of analysis and design using different software may not be consistent. In order to determine the most appropriate software which

could analyse and design according to the requirement of code of practice, it is necessary to do an analysis of result comparison for the different software.

In this paper, the main objective is to compare the analysis and design of box girder bridge using STAAD.Pro and MIDAS Civil software. This study focuses only on the single component of Box Girder Bridge which is the top slab where the analysis and design is only on transverse element. Furthermore, one typical section has been used for the design stage. The bridge configurations consisted of three (3) span lengths of 95m, 160m and 95m respectively. The same bridge configuration was modelled in different software for analysis and design. British Standard [1] and Design Manual for Roads and Bridges [2] were used as a code of practice in this study together with Design Verification of Balanced Cantilever Bridge as per BS Code [3]. Whereas, STAAD.Pro Reference Manual [4] and MIDAS Reference Manual [5] were used as guidance for the modelling part. The results of maximum moment and shear force obtained were compared between the two software and the analysed results were further used in the design stage.

METHODOLOGY

Before the element was modelled using finite element program, the element geometry must be identified. For this study, the transverse model was

performed for one segment only which is located at the mid-span of the bridge. The geometry of the segment is shown in Fig. 1.

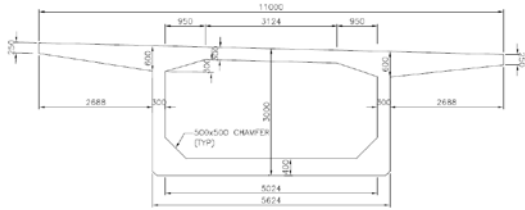


Fig. 1: Geometry of the Box Girder Segment

Structural Modelling and Analysis

General procedure to model the box girder bridge is the same for both STAAD.Pro and MIDAS Civil software. Both modeling started with assigning working environment, defining section and material properties, creating geometry of the model, assigning section and material properties, defining and assigning loading, and finally performing the analysis.

Working Environment

To perform structural modeling, the unit system are set as kilo Newton (kN) and meter (m) for basic unit of force and length respectively.

Material and Section Properties

The concrete properties adopted in the analysis and design of the segment are tabulated in Table 1. The values in the Table are based on BS 5400-4:1990.

Table 1: Concrete Properties

Cube Strength of Concrete	60 N/mm ²
Modulus of Elasticity of Concrete	36 kN/mm ²
Poisson's Ratio	0.2
Coefficient of Thermal Expansion	12 x 10 ⁻⁶ / °C
Density	25 kN/m ³

For the reinforcement properties, high yield deformed type with yield strength value of 500 N/mm² was used. As stated in BS 5400-4:1990, nominal cover requirement and crack width limit for precast superstructure external and internal faces of 30 mm and 0.25 mm shall be used respectively.

The section properties of each beam are defined manually as Tapered Section in STAAD.Pro. While in MIDAS Civil, FCM Bridge Wizard was used for defining the section. However, in order to use this wizard, the section at both mid-span and support need to be defined.

Figure 2 and Figure 3 illustrate the section properties defined in STAAD.Pro and MIDAS Civil respectively.

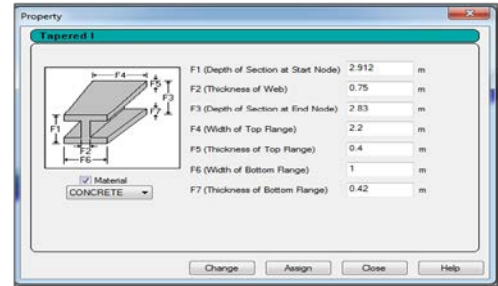


Fig. 2: Section dialog box in STAAD.Pro

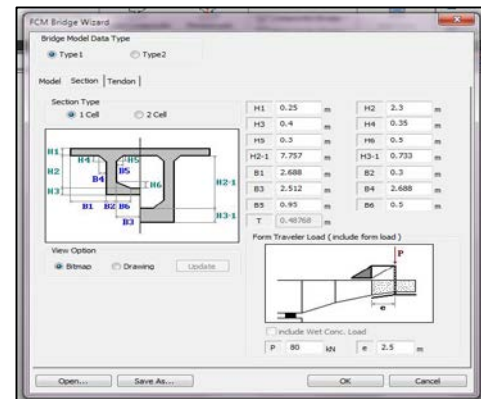


Fig. 3: Section dialog box in MIDAS Civil

Creating Geometry Model

Geometry modelling comprises combination of nodes, beams, and plates element. For STAADPro, first node was assigned as coordinate (0,0,0) in X, Y, and Z direction respectively. The nodes assignment are based on the conceptual idea of elements. To complete the structural element, nodes need to be connected by using beam assignment. The geometric arching from haunches was considered in this model as recommended by Abdullah Zaid [6]. Then, the materials and section properties are assigned accordingly to their respective members. The completed STAADPro's geometry model is shown in Fig. 4.

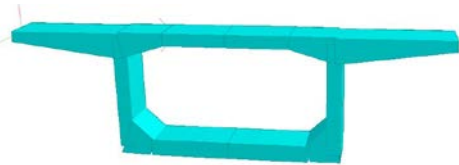


Fig. 4: 3D view of the model in STAAD.Pro

In MIDAS, the geometry of model was defined using Bridge Wizard Modelling. Firstly, the longitudinal model must be defined in order for the Bridge Wizard to automatically generate the transverse model. The material properties and geometry were specified in the model tab of Bridge Wizard, see Fig. 5. After completing longitudinal model, the transverse model was generated using transverse model wizard by defining the element's number at the mid-span as shown in Fig. 6. The completed MIDAS's geometry model is shown in Fig. 7.

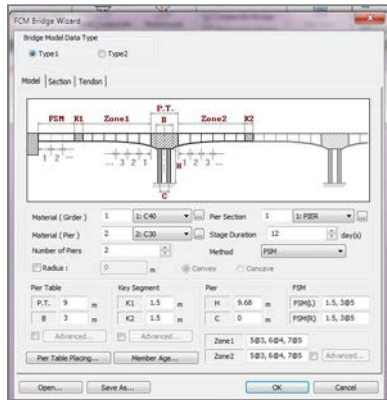


Fig. 5: Model tab of Bridge Wizard in Midas

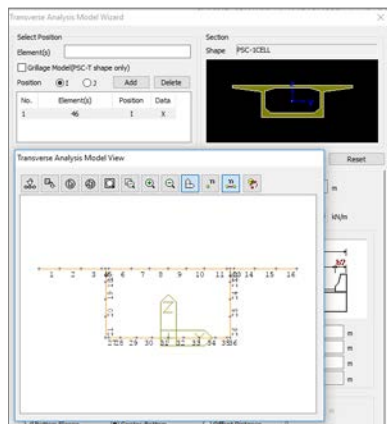


Fig. 6: Transverse model input in Midas

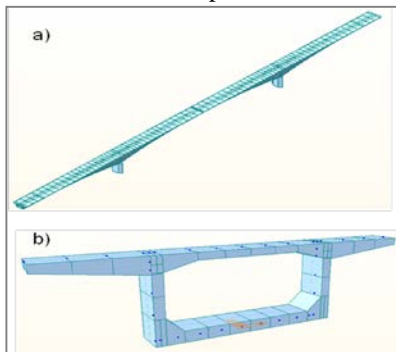


Fig. 7: 3D view of (a) Longitudinal model
Transverse model

Design Loadings

For this study, the transverse model was loaded with normal permanent load as uniformly distributed load to represent all self weight and superimposed dead load which represent 100 mm thick Asphaltic Concrete Wearing Course with 22 kN/m^3 density. For live traffic load, single axle of 45 unit of HB was applied on the slab from edge of parapet to another as inline moving load of four (4) wheel load of 112.5 kN each.

In STAAD.Pro, the run load generator was used to generate traffic loads. Vehicle load of HB45 with 1m wheels spacing was defined as shown in Fig. 8.

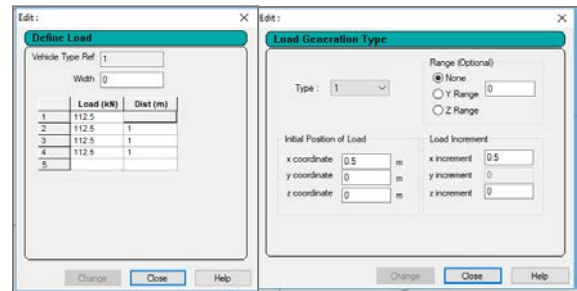


Fig. 8: Input dialog for generating traffic loads in STAAD.Pro

In MIDAS, Moving Load Analysis feature was used in generating traffic load on the bridge deck. It is automatically done in finding the maximum and minimum cases by applying a unit load along the defined traffic lanes. Figure 9 shows the input dialog for defining the traffic load in MIDAS Civil.

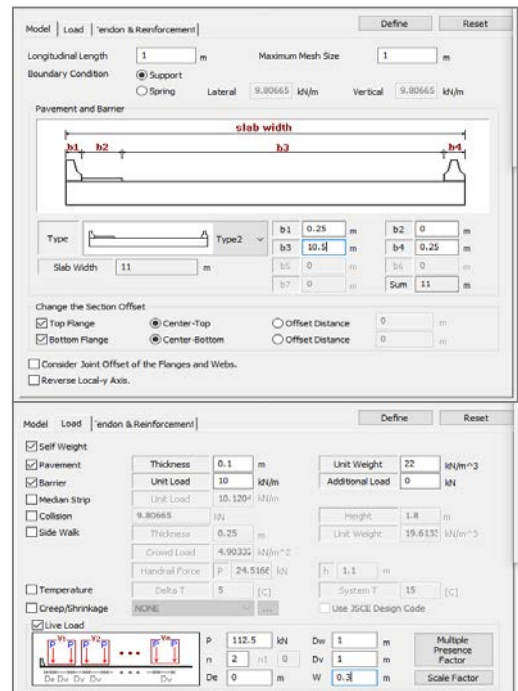


Fig. 9: Input dialog for generating traffic loads in MIDAS Civil

According to Design Manual for Roads and Bridges, BD 37/01, the analysis and design for deck component of bridge shall satisfy the Serviceability Limit State (SLS) and Ultimate Limit State (ULS) under the following load combination: Partial load factor under SLS γ_{fl} for Dead Load, SIDL and 45 HB are 1.00, 1.20 and 1.00 respectively, whereas Partial load factor under ULS γ_{fl} for Dead Load, SIDL and 45 HB are 1.20, 1.75 and 1.30 respectively. Note that, all partial load factor under ULS γ_{fl} to be multiplied by γ_f 1.10.

Perform Analysis

According to Theryo [7], stresses at five (5) points on bridge deck should be checked. However, in this study, bending moment and shear force from the model are extracted at three (3) specific points on the deck section as shown in Fig. 10.

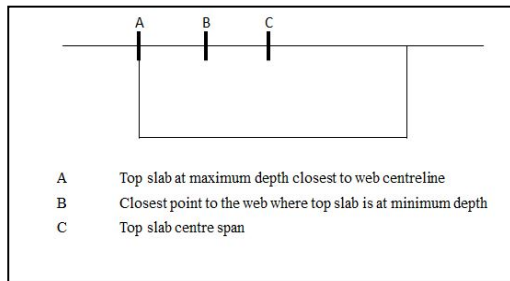


Fig. 10: Three (3) specific analysis point on the bridge deck

Deck Slab Design

From the transverse model, the worst case of transverse bending moment and shear force values obtained from each load type being applied to the deck were summarised and then adopted in the design. In general, the design of reinforced concrete member is controlled by the ultimate limit state, whereas the limitation on crack width is controlled by the serviceability limit state.

According to BS5400 Part 4, for the slab section which is without compression reinforcement, the ultimate moment resistance shall be taken as the lesser of the values obtained from Eqn. 1 and Eqn. 2.

$$M_u = (0.87 f_y) A_s z \quad (1)$$

$$M_u = 0.15 f_{cu} b d \quad (2)$$

Where

M_u is the ultimate resistance moment;

A_s is the area of tension reinforcement;

b is the width of section;

d is the effective depth to the tension reinforcement;

f_y is the characteristic strength of the reinforcement;

z is the lever arm $\left(1 - \frac{1.1 f_y A_s}{f_{cu} b d}\right) d$;

f_{cu} is the characteristic strength of the concrete.

According to BS5400 Part 4, shear stress, v at any cross section in solid slab is calculated from Eqn. 3

$$v = \frac{V}{b d} \quad (3)$$

Where

V is the shear force due to ultimate loads;

b is the width of slab under consideration;

d is the effective depth to tension reinforcement.

No shear reinforcement is required when the stress, v , is less than $\xi_s v_c \times 2d/a_v$, but should not exceed $0.75(f_{cu})^{0.5}$ or 4.75 N/mm^2 , whichever is lesser.

$$\xi_s = (500/d)^{1/4} \quad (4)$$

The crack model for load effects to BS 5400 is an empirical model and it considers the effect of cover, reinforcement diameter, spacing and stress of the reinforcement. To ensure the structure remains in the elastic phase under loading, BS 5400 set the maximum limits for stresses in the reinforcement and concrete. The maximum surface crack width, w , for flexural is calculated in BS 5400 using the following formula:

$$w = \frac{3 a_{cr} \varepsilon_m}{1 + 2 \left(\frac{a_{cr} - c_{min}}{h - x} \right)} \quad (5)$$

The maximum crack width for tension is calculated from the following expression:

$$w = 3 a_{cr} \varepsilon_m \quad (6)$$

where

a_{cr} is the distance from point (crack) considered to the surface of the nearest bar which controls the crack width;

c_{min} is the required nominal cover to the outermost reinforcement given;

x is the depth of the concrete in compression (if $x = 0$ the crack width should be calculated using Eqn. 6)

h is the overall depth of the section;

ε_m is the calculated strain at the level where cracking is being considered, allowing for the stiffening effect of the concrete in the tension zone; a negative value of ε_m should be obtained from equation:

$$\varepsilon_m = \varepsilon_1 - \left[\frac{3.8 b_t h (a' - x)}{\varepsilon_s A_s (h - x)} \right] \left[\left(1 - \frac{M_q}{M_g} \right) 10^{-9} \right] \quad (7)$$

But not greater than ε_l

RESULTS AND DISCUSSION

Transverse Analysis

The transverse analysis results obtained from both STAAD.Pro and MIDAS software were summarized in Table 2 and Table 3 and illustrated in Fig. 11.

Table 2: STAAD.Pro summary of beam end force

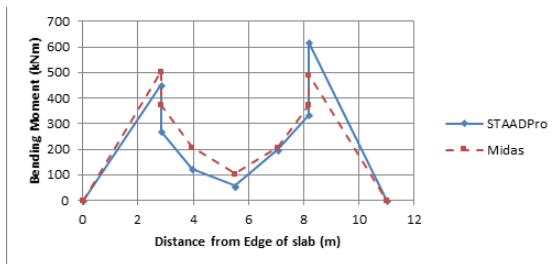
Structural Element	Cut Section	Cases	ULS Envelope	SLS	
				Permanent	Live Load
Cantilever	A	Max. Moment	985.835	74.226	681.029
		Min. Moment	-184.384	41.720	-185.904
		Max. Shear	545.650	-	-
Top Slab	B	Max. Moment	306.210	15.386	219.574
		Min. Moment	-100.581	15.385	-93.341
		Max. Shear	343.822	-	-
	C	Max. Moment	85.571	3.015	63.117
		Min. Moment	-201.613	3.015	-157.794
		Max. Shear	134.854	-	-

*Moment (kNm) and Shear (kN)

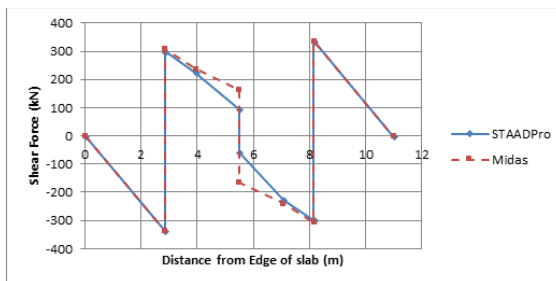
Table 3: MIDAS Civil summary of beam end force

Structural Element	Cut Section	Cases	ULS Envelope	SLS	
				Permanent	Live Load
Cantilever	A	Max. Moment	822.270	74.790	554.653
		Min. Moment	-133.790	41.690	-147.004
		Max. Shear	545.500	-	-
Top Slab	B	Max. Moment	320.040	17.480	228.030
		Min. Moment	-156.600	17.480	-128.436
		Max. Shear	362.920	-	-
	C	Max. Moment	172.600	6.630	114.257
		Min. Moment	-198.580	6.630	-159.203
		Max. Shear	297.400	-	-

*Moment (kNm) and Shear (kN)



(a)



(b)

Fig. 11: (a)Maximum bending moment diagram and (b) Maximum shear force diagram for envelope live load case from STAAD.Pro and MIDAS Civil software

Based on the summarized results in Table 3 and Table 4, the values of bending moments for cut section A of its permanent load cases and shear force values show only small differences between the two software as compared to live load cases. But not for cut section B and C, in which the value of shear force at section C result from MIDAS Civil software is more than double of STAAD.Pro software. For the maximum case of bending moments, STAAD.Pro analysis shows 26% higher than MIDAS model at the center of web while at the center of slab, MIDAS analysis shows 95.5% higher than STAAD.Pro analysis. For the minimum bending moment diagram, at center of web, STAAD.Pro shows 26.5% higher than MIDAS Civil which is same as case of maximum bending moment. At cutting section B, Midas shows 129.6% higher compared to STAAD.Pro. However, there is no significant difference value at the mid span of slab presented between this two software. The deviation of results between STAAD.Pro and MIDAS software were most probably due to the fact that, both software has different configuration of wheel load on the bridge deck. Figure 12 and Figure 13 shows the location of wheels on the deck for maximum effect at section A and B from STAAD.Pro and MIDAS Civil software respectively.

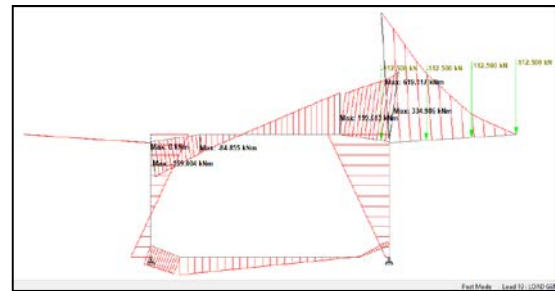


Fig. 12: Location of wheels load on the deck generated by STAAD.Pro software



Fig. 13: Location of wheels load on the deck generated by MIDAS Civil software

As shown in Fig. 12 and Fig.13, the wheels location of STAAD.Pro are able to run until the edge of slab while in MIDAS Civil, it was restricted from running until the edge of the slab. In the actual condition, the parapet was positioned at the edge of the parapet whereby the wheel was restricted to run across it. This is due to the limitation of STAAD.Pro where in the run load generator input, only the starting point and

increment of distance were defined. While in MIDAS Civil, the influence line of wheels load was determined by the location of carriageway in which it was defined during the input of barrier and pavement parameter.

Transverse Design

The design results of transverse reinforcements (ULS) and crack width (SLS) were tabulated in Table 4 and Table 5.

Table 4: Area of reinforcement required based on analysis from STAADPro software

Structural Element	Cut Section	Cases	Area Reinforcement Required for Moment Resistance, mm ²	Area Reinforcement Required for Shear Resistance, mm ²	Crack Width, mm
Cantilever	A	Top	4260	6545	0.209
		Bottom	797	2805	0.211
Top Slab	B	Top	2850	6545	0.182
		Bottom	936	6545	0.085
	C	Top	796	1964	0.217
		Bottom	1876	3927	0.219

Table 5: Area of reinforcement required based on analysis from MIDAS software

Structural Element	Cut Section	Cases	Area Reinforcement Required for Moment Resistance, mm ²	Area Reinforcement Required for Shear Resistance, mm ²	Crack Width, mm
Cantilever	A	Top	3553	6545	0.174
		Bottom	578	2454	0.215
Top Slab	B	Top	2979	8042	0.189
		Bottom	1457	8042	0.113
	C	Top	1606	4021	0.205
		Bottom	1848	4021	0.239

Top reinforcement required for cantilever part of bridge deck is similar for both envelope cases from STAAD.Pro and MIDAS software. However, the bottom reinforcement for that structural element required by MIDAS Civil is lesser. This is due to moment of live loads cases from MIDAS is smaller and thus, affect the crack width design. For both reinforcement design at section B and C, shows that analysis from MIDAS Civil requires more reinforcement as compared to STAAD.Pro. This is due to shear resistance and serviceability check where the forces developed by MIDAS Civil software are higher compared to STAAD.Pro.

CONCLUSION

Comparison between STAAD.Pro and the MIDAS software showed that the analysis result of the box girder bridge from this two software have significant difference in the live load cases as compared to permanent load cases. Whereas, for the design results, the reinforcement used is similar for cantilever part of the slab but different for other parts of the box girder segment, in which, the MIDAS Civil requires more reinforcement. This shows that MIDAS Civil software

developed more worst load case for live load in transverse analysis between the two software. The deviation of results between STAAD.Pro and MIDAS software were most probably due to the fact that, both software have different configuration of wheel load on the bridge deck. Nevertheless, both software are recommended to be used in the analysis and design of box girder bridge, as both software have proven to be effective as Computer Aided tools. Thus, it can be concluded that, the choices of software depend on the needs and what to be solved. As long as no errors in the evaluation of the response, other parameters are more important than the accuracy in the model, namely; user friendliness, verification and interpretation of results. It is also evident from the results, that there is a lack of established guidelines for modelling and verification. Such guidelines would simplify the work for engineers when establishing structural analysis models and set the foundation for common working procedures within the bridge engineering industry.

ACKNOWLEDGMENT

The authors would like to acknowledge the financial support for this work from Universiti Teknologi MARA (UiTM) as well as the industrial supports from Khairi Consult Sdn Bhd and Perunding ZAR Sdn Bhd. The provided facilities, discussion and assistance during the modelling were gratefully appreciated.

REFERENCES

- [1] British Standard, BS 5400-4:1990 Steel, concrete and composite bridges. Part 4: Code of practice for design of concrete bridges.
- [2] BD37/01, Design Manual for Roads and Bridges, Vol. 1, Highway Structures: General Design, Loads for Highway Bridges, 2001.
- [3] Jihoon Kang, Design Verification of Balanced Cantilever Bridges as per BS Code, Midas IT, 2017.
- [4] STAAD.Pro V8i, Technical Reference Manual, Bentley System Incorporated, 2012.
- [5] MIDAS Technical Reference Manual, 2011.
- [6] Abdullah Zaid, D. C., Transverse Assessment of a Concrete Box Girder Bridge. Proceeding of the Institution of Civil Engineers, 2016.
- [7] Theryo T.S., Segmental Concrete Bridges, Edited by Wai-Fah Chen and Lian Duan, Bridge Engineering Handbook 2nd Edition, Superstructure Design, Boca Raton: Taylor & Francis Group, 2014, pp 91-169.

THE SPEED LIMIT FOR MOTORCYCLE: URBAN ARTERIAL ROAD IN KHON KAEN CITY, THAILAND

Jetsada Kumphong¹, Thaned Satiennam¹ and Wichuda Satiennam¹

¹Department of Civil Engineering, Faculty of Engineering, Khon Kaen University, Thailand.

ABSTRACT

Road traffic injuries tend to be more serious all over the world, as well as the number of road fatalities, serious injuries and disabilities is also increasing. Since speeding is one of the top causes of death and injury, the speed of motorcycle vehicles should be investigated in order to analyze the speed limit. The speed of motorcycle were observed at risk points on urban arterial road in Khon Kaen City. Then, the speed values were applied to determine the speed limit of motorcycle. As the results, the road in the study area should stipulate the speed limit of motorcycle at 60-70 km/h. At present, Thai law has limited the speed in urban areas at 80 km/h. This information will be valuable for the urban and transportation engineers and planners so as to forecast the speed limit of motorcycle vehicles in Khon Kaen city when a new road will be is designed in the future.

Keywords: Speed, Motorcycle, Safety, Traffic injuries

INTRODUCTION

Traffic injuries tend to be increasingly serious all over the world, as well as the number of road fatalities and disabilities that is becoming a problem. According to Global Road Safety statistics of 2010, approximately 1.27 million deaths worldwide were caused by road accidents (3,479 people per day). If old defensive measures were still used, within 20 years, road accidents could be the leading cause of deaths globally, and road safety problems are predicted to expand dramatically. By 2030, the road fatalities may rise up to 2.4 million deaths, inclusive with a possible increase from injury rates. As a result, road accidents will become the major cause of deaths, together with disabilities, and its rank will also changed from the 9th (in 1990) to the 3rd.[1]

Thailand has the highest rate of traffic accident fatalities, also highest rate of motorized 2-or 3-wheelers deaths. [2-8] Speeding is one of the most common causes of road accident in Thailand. [9] Prior to the speed study in Thailand, Bunjaweht and Sutiwipakorn (2006) stated that traffic accidents cause a mass of casualties and damage to citizens' properties each year and can be considered as the underlying causes of deaths. Among many factors of traffic accidents was the speed of vehicles. Higher speeds of vehicles increase the risks of accidents. What is more? Fast speed intensifies the injuries and damage. In a pedestrian versus car accident, if a pedestrian is hit by a car at 64 kilometers per hour, the likelihood of his/her death is 90%, while a hitting car at 32 causes only a five-percent chance of the death. As can be seen, the decrease of the vehicular speed by 1 can decrease the likelihood of deaths by 5%. The study conducted by U-rod and Udomsri (2006)

disclosed that the means peak-hour speed of vehicles was 33.5 kilometers per hour, while the speed in Amphur Muang or inner ring roads was lower at 19.7. Based on the data of land use, the study also found that most of the areas were educational institutions.

Khon Kaen City is a province with huge areas consisting also of government sectors and educational institutions. With its mass number of educational establishments, department stores and residences, there is the daily extensive use of private transportation with the drivers' use alcohol and use of high speed frequently causing accidents. [12-13] Although, There will be traffic measures (speed camera, red-light running camera etc.). Therefore, this study of motorcycle speed (before/after) with effects of traffic measures on Mittraphap Road at Khon Kaen Urban to develop guidelines of speed limit for motorcycle in Khon Kaen City.

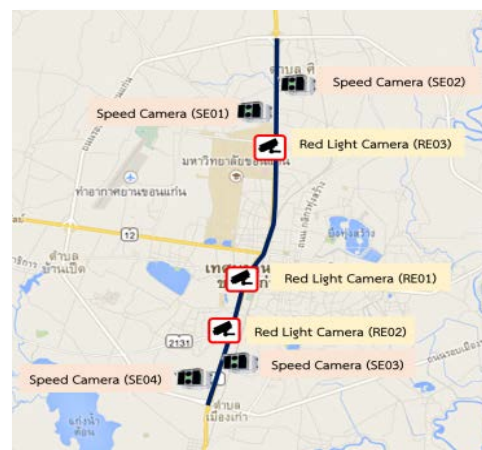


Fig. 1 Traffic measures in Khon Kaen City

METHODOLOGY

Data Collection by Observation

In this study, there are 2 types of data sets. The secondary data included the spot speed of motorcycle riding on Mittraphap Road in Khon Kaen City in 2016 [14-16] (28 points), whereas the primary data was collected from 1,555 motorcycle samples from the 28 points (S01-S28) in 2017 along the Mittraphap Road (about 16 kilometers) in Khon Kaen city (as shown in Fig. 2 and Fig. 3). The free flow speeds of vehicles between 06.00 a.m. to 07.00 a.m. were collected by using a radar gun as shown in Fig. 4.

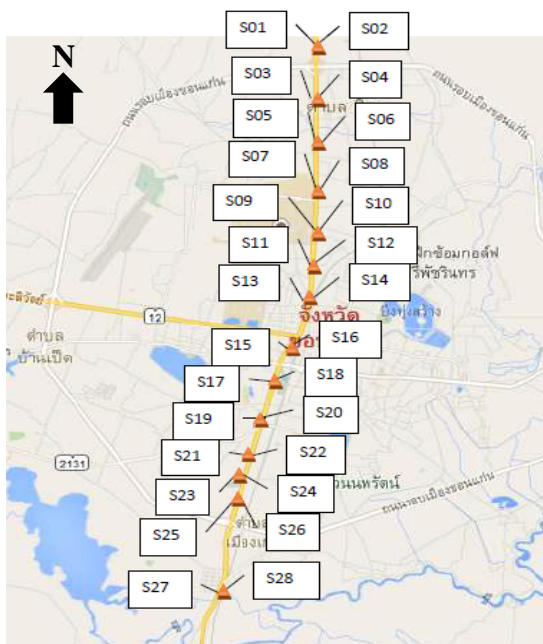


Fig. 2 Study area

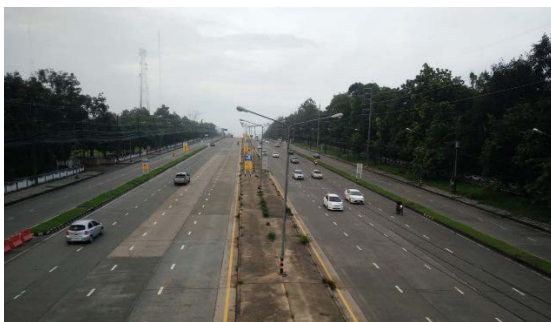


Fig. 3 Example of a cross-sectional study area of Mittraphap Road in Khon Kaen City, Thailand



Fig. 4 Observation by using a radar gun

Sample description

The spot speeds of motorcycle data in years 2016 – 2017 are calculated into the means speed and 85th percentile speed (MC85th: 85th percentile speed of motorcycle (Km/h), MCm: means speed of motorcycle (Km/h)). In addition, comparisons were performed between the averages and the 85th percentile of private cars in 2016 (PC85th: 85th percentile speed of private cars (Km/h), PCm: means speed of private cars (Km/h)) as shown in Tables 1, 2. Table 3 shows the physical characteristics of Mittraphap Road in Khon Kaen City. If the road's cross-sectional area is wider, the speed of vehicles tends to increase. [15]

Statistical Analysis

Besides the descriptive statistics (means, 85th percentile), t-test was conducted to find the difference of data at 95% confidence level [17] by SPSS program.

RESULTS AND DISCUSSION

From the speed study of motorcycles at 28 spots in Khon Kaen City, Thailand from 2016 to 2017, the results showed that in 2016, the speed of 7.1% of motorcyclists was over 59 Km/h whereas in 2017 no motorcycle was found using speed of over 59 Km/h. The majority of riders (92.90%) used a speed range of 50 – 59 Km/h (as shown in Table 4 and Fig. 5), which is the speed range difference found in the studies in Vientiane, Lao PDR. and Phnom Penh, Cambodia where the means speed was 36 Km/h and 35 Km/h, respectively. [14-15]

Table 1 Motorcycle and private car speed data in year 2016

No.	MC85th (Km/h)	MCm (Km/h)	PC85th (Km/h)	PCm (Km/h)
1	101	64	84	50
2	93	67	82	54
3	101	69	93	61
4	100	69	95	58
5	95	67	84	55
6	95	60	84	51
7	72	60	65	52
8	80	63	71	55
9	87	69	69	51
10	85	71	74	58
11	98	68	89	58
12	98	69	90	59
13	86	71	74	57
14	91	67	75	51
15	76	63	68	52
16	101	66	90	58
17	92	63	77	50
18	71	68	59	53
19	75	73	64	57
20	71	68	59	53
21	95	59	78	51
22	81	69	69	56
23	85	60	70	47
24	84	65	69	49
25	92	70	79	57
26	99	72	83	55
27	86	58	74	50
28	103	79	88	60

Note: Motorcycle speed data by Jetsada Kumphong in 2016

From Table 5, the comparison between motorcycle speeds in 2016-2017 shows the difference of the motorcycle speeds at 85 percentile at a significant level ($p < 0.05$). However, the means speeds of motorcycles of the 2 years were not different. In addition, the speed comparison between vehicles and motorcycles indicates that the vehicle speed was different from motorcycle speed at a significant level ($p < 0.001$), as shown in Table 6, the study of speed differences between private car and motorcycle. The difference of speed means of private car and motorcycles in Vientiane, Lao PDR was 9 Km/h and in Phnom Penh, Cambodia it was 4 Km/h [14-15]. If there is speed difference between vehicles, it is likely that severe injuries from accidents may lead to death. [14, 16]

Table 2 Motorcycle speed data in year 2017

No.	MC85th (Km/h)	MCm (Km/h)
1	64	52
2	69	54
3	64	50
4	68	53
5	67	52
6	64	53
7	63	53
8	65	54
9	64	52
10	63	52
11	66	54
12	66	54
13	65	54
14	65	54
15	65	55
16	65	54
17	61	52
18	65	53
19	60	51
20	60	49
21	58	49
22	60	51
23	65	53
24	66	54
25	66	56
26	68	54
27	62	54
28	66	56

Table 3 Descriptive Statistics of physical characteristics of Mittraphap Road in Khon Kaen City

Independent Variables	Mean
Left safety strip width (m)	1.1
Number of lanes	3.3
Lane width (m)	3.8
Roadway width (m)	13
Conflict point (per 1000 m)	3.5
Right safety strip width (m)	0.9

Table 4 Speeds of motorcycle in 2017 (N=1,555)

Speeds of motorcycle	Km/h
MC 85 th	53
MC m.	65

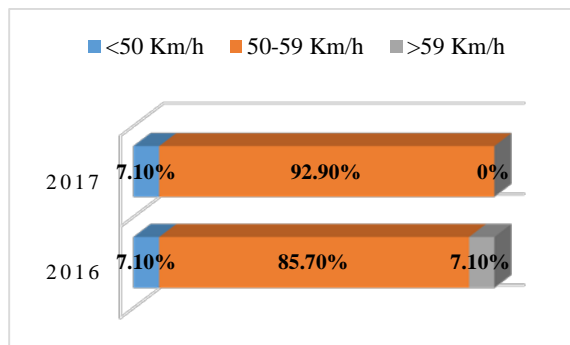


Fig. 5 The result of motorcycle speed study in 2016-2017

Table 5 Comparison between speeds of motorcycle in 2016-2017

	Difference		t
	Mean	S.D.	
2016MC85th	2.4	4.8	2.6**
- 2017MC85th			
2016MCm	1.1	3.9	1.7
- 2017MCm			

Note: *Significant at 90% confidence level,
 **Significant at 95% confidence level,
 ***Significant at 99% confidence level.

Table 6 Speed differences between private car and motorcycles

	Difference		t
	Mean	S.D.	
2016PC85th	22.4	10.2	11.6***
- 2016MC85th			
2016PCm	22.8	8.8	13.7***
- 2016MCm			
2016PC85th	24.8	9.2	14.2***
- 2017MC85th			
2016PCm	36.1	9.8	19.5***
- 2017MCm			

Note: *Significant at 90% confidence level,
 **Significant at 95% confidence level,
 ***Significant at 99% confidence level.

Fig. 6 and Fig.7 illustrates the result of speed survey at 85 percentile and vehicle speed means in 2017. Based on the road line in the study area, the speed of vehicle all through the route (S1-S28) is nearly similar; at 85 percentile the speed range was 60-70 Km/h (accept at S21 spot) and the speed was 50-60 Km/h (accept at S20-S21 spot). If adhered to engineering principle and speed limit of vehicle at 85 percentile [18-19], the road in the study area should stipulate the speed limit of motorcycle at 60-70 Km/h. At present, Thai law has limited the speed in urban areas at 80 Km/h, which is applied to motorcycles and private cars.

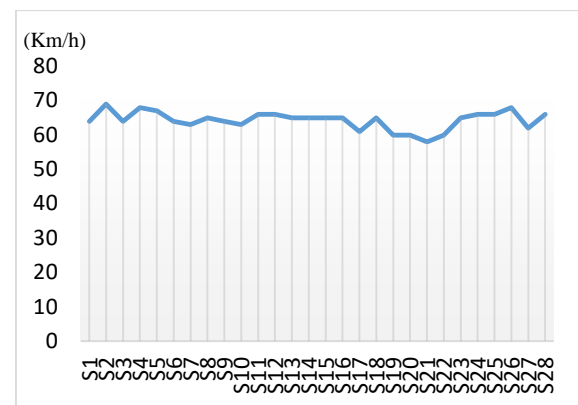


Fig. 6 The result of motorcycle speed survey at 85 percentile in 2017

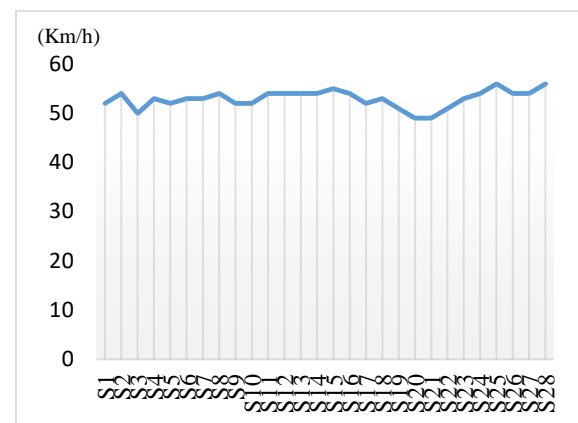


Fig. 7 The result of motorcycle speed survey at means in 2017

CONCLUSIONS

The statistical analysis in this study showed statistically significant difference between the speed of cars and motorcycles at the confidence level of 0.95. The speed limit should be lowered to less than 80 Km/h, which is the current setting. The difference between the speed and mass of the two vehicles in the collision may lead to fatality of motorcyclists.

Additionally, the study of the motorcycles speed in 2016-2017, conducted during the implementation of traffic control measures (RLR camera, speed camera etc.) indicated no statistical difference between the two years. This study indicated the motorcycle speed limit at 85th percentile, which is based on traffic engineering principle. This research therefore proposes the use of a limit of 60 - 70 Km/h, so that the private car's speed is reduced to approach the motorcycle speed. It should be noted that the speed limit for both motorcycles and private cars in Thailand is similar. The results of this study will be presented to those involved in this area for road traffic planning and prevention.

RECOMMENDATION

The law of Thailand that governs urban speed limits of cars and a motorcycle [20] is the same. As a result, fatality among motorcyclists is more likely than among motorists. In this regard, further studies should be conducted to determine the appropriate speed limit of each vehicle type for the relevant organizations to take into account in developing future policy or speed law enforcement.

ACKNOWLEDGEMENTS

This research received a Research Fund for Supporting Lecturer to Admit High Potential Student to Study and Research on his Expert Program Year 2016, Graduate School, Khon Kaen University, Khon Kaen, Thailand. Thanks are also extended to Khon Kaen University Language Institute for editing the report.

REFERENCES

- [1] Tanaboriboon Y., Satiennam T., Traffic accidents in Thailand. IATSS RESEARCH, Vol. 29, No. 1, 2005, pp. 88-100.
- [2] World Health Organization. Helmets : A road safety manual for decision-makers and practitioners. Geneva, Switzerland, 2006.
- [3] World Health Organization Global Status Report on Road Safety 2009. Geneva, Switzerland, 2009.
- [4] World Health Organization. Global Status Report on Road Safety 2013. Geneva, Switzerland, 2013.
- [5] World Health Organization. Global Status Report on Road Safety 2015. Geneva, Switzerland, 2015.
- [6] F.A.O. Fernandes R.J., Alves D.S., Motorcycle helmets-A state of the art review. Accident Analysis and Prevention 2013, Vol. 56, pp. 1-21.
- [7] Kumphong J., Satiennam T., Satiennam W., A correlation of traffic accident fatalities, speed enforcement and the gross national income of Thailand and its cross-border countries. International Journal of Technology, Vol. 7, 2016, pp. 1141-1146.
- [8] Kumphong J., Satiennam T., Satiennam W., A Study of Social Norms and Motorcycle Helmet Use Intentions among Student Riders in University: A comparison of the Theory of Reasoned Action and the Theory of Planned Behavior. Conference proceedings, in Proc. 12th Int. Conf. on the Eastern Asia Society for Transportation Studies, Vol. 11, 2017, pp. 1-14.
- [9] Royal Thai Police. Injuries and Deaths Report 2006-2013. Thailand; 2013. (In Thai)
- [10] Bunjaweht P., Sutiwipakorn V., A study of the use of traffic calming strategy in Thailand. Conference proceedings, in Proc. 3rd the Nine National Transport Conference Research (NTC3), Thailand, 2006. (In Thai)
- [11] U-rod S., Udomsri R., The Application of Handheld GPS in Speed and Travel Time Surveys. Conference proceedings, in Proc. 3rd the Nine National Transport Conference Research (NTC3), Thailand, 2006. (In Thai)
- [12] Ichikawa M., Chadbunchachai W., Marui E., Effect of the helmet act for motorcyclists in Thailand. Accident Analysis and Prevention, Vol. 35, 2003, pp. 183-189.
- [13] Nakahara S., Chadbunchachai W., Ichikawa M., Tipsuntornsak N., Wakai S., Temporal distribution of motorcyclist injuries and risk of fatalities in relation to age, helmet use, and riding while intoxicated in Khon Kaen, Thailand. Accident Analysis and Prevention, Vol. 37, 2005, pp. 833-842.
- [14] Kumphong J., A study of relations between speed of vehicles with road characteristics and accident severity. Master thesis in Department of Civil Engineering, Faculty of Engineering, Khon Kaen University, 2016. (In Thai)
- [15] Kumphong J., Satiennam T., Study of vehicle's speed of cities in Greater Mekong Subregion. Conference proceedings, in Proc. 8th Asian Transportation Research Society (ATRANS) Symposium: Young Researcher's Forum, 2015. (In Thai)
- [16] Kumphong J., Satiennam T., Satiennam W., A study of the relation between the speed of vehicles and traffic accident and road Characteristics. Conference proceedings, in Proc. 20th National Convention on Civil Engineering (NCCE20), 2015. (In Thai)
- [17] Park H M., Comparing Group Means: The T-test and One-way ANOVA Using STATA, SAS, and SPSS. The Trustees of Indiana University, 2005. (http://stat.smmu.edu.cn/DOWNLOAD/ebook/statistics_course.pdf)
- [18] Abbas S K S., Adnan M A., Endut I R., Exploration of 85th Percentile Operating Speed Model on Horizontal Curve: A Case Study for Two-Lane Rural Highways. Conference proceedings, in Proc. 6th International Symposium on Highway Capacity and Quality of Service, Stockholm, Sweden June 28 – July 1, 2011, pp.352-363.
- [19] Federal Highway Administration & MUTCD. Setting speed limits – The 85th percentile speed. (<https://lincoln.ne.gov/city/pworks/engine/traffic/pdf/regulatory-speed-limits.pdf>)
- [20] Mummuntree R., Klungboonkrong P., Determination of the speed limits in Thailand. Conference proceedings, in Proc. 19th National Convention on Civil Engineering (NCCE19), 2014. (In Thai)

MOTORCYCLE HELMET USE INTENTION WITH THE THEORY OF TRAFFIC PSYCHOLOGY FOR BEHAVIOR CHANGE IN LAO PDR

Jetsada Kumphong¹, Thaned Satiennam¹, Wichuda Satiennam¹ and Phongsavanh Inthavongsa²

¹Department of Civil Engineering, Faculty of Engineering, Khon Kaen University, Thailand.

²Department of Road-Bridge and Transport Engineering, Faculty of Engineering,
National University of Laos, Lao PDR.

ABSTRACT

Recently, there has been growing interest in motorcycle safety in ASEAN countries. Laos has a high death of motorcycle riders and helmet wearing rates remain big problem. The aim of the present study was to reduce the severity of road accidents among student riders by studying the relationship between Lao students' helmet use intention and other psychological factors based on the Theory of Planned Behavior (TPB) and to study the relationship between stages of change and processes of change among Lao students' helmet use based on Transtheoretical Model and Stages of Change (TTM) which is a traffic psychology module including. Data was collected from 219 motorcyclists and analyzed using the Structural Equation Model (SEM), Theory of Planned Behavior (TPB), which is a traffic psychology module including attitude (ATT), subjective norm (SN) and perceived behavioral control (PBC). Also, Transtheoretical Model and Stages of Change (TTM) to analyze by Pearson Correlation. The results indicated that the TPB model and TTM, the actual behavior would be adapted by changing their intentions. The TPB model showed that PBC were significant. The outcome of this study will be presented to authority for planning road safety in Lao PDR.

Keywords: Helmet, Motorcycle, Safety, Traffic injuries

INTRODUCTION

Motorcycles are used for transportation and sport activities in ASEAN countries. The correlation between high fatality rates, among motorcyclist, and low helmet use illustrate the problem. [1-6]

Japan has been successful in helmet law enforcement with a high helmet wearing rate. Unlike Japan, Laos has a high death rate from traffic accidents per 100,000 population with low helmet wearing rate and insufficient helmet law enforcement, also highest rate of motorized 2-or 3-wheelers deaths as shown in Fig. 1 and Fig. 2. [6]

Vientiane City is a big city consisting of many educational establishments, hospitals, department stores, and residences; there is thus an extensive use of motorcycle transportation on city. The average number injury on the road is 1,734/year, the average number severe injury on the road is 209/year, the average number breaths on the road is 161/year. [7] However, many riders do not wear helmets while driving (the helmet wearing rate is 60% [5]).

Vientiane City has been promoted that helmet use campaign and distributing 1,000 helmets to student rider on August 31, 2016. [8] The tow-wave panel design was applied on city, with a 1-year interval between waves. The first set of data were collected in 2016 (before- helmet use campaign). The second phase of data collection was done in 2017, under the campaign for motorcyclists to wear helmets and for

road users to conform to traffic rules. This research investigated how to reduce the severity of road accidents among student riders by studying the relationship between students' helmet use intention and other psychological factors based on the Theory of Planned Behavior (TPB), Transtheoretical Model and Stages of Change (TTM).

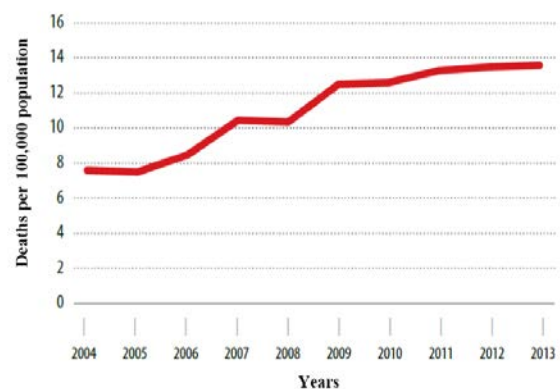


Fig. 1 Trends in reported road traffic deaths in Lao PDR. [6]

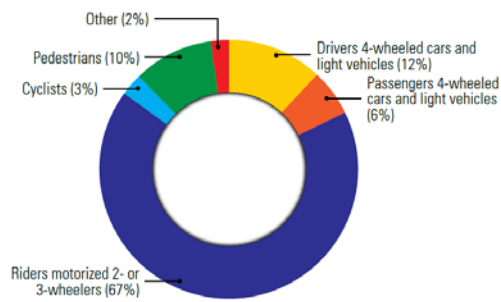


Fig. 2 Deaths by road user category in Lao PDR. [6]

METHODOLOGY

Data Collection by Observation

The questionnaire survey (as show in Fig. 3) which examined direct measurements followed the principles of TPB (Table 1.) [9-13], while TTM was used for investigating states of chances (Fig.4; Table 2, 3 and 4). [14-15]



Fig. 3 Observation by questionnaire

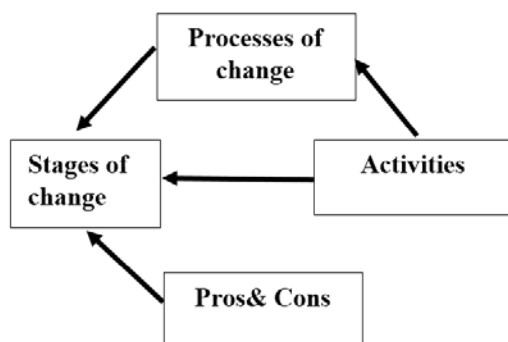


Fig. 4 Proposed study framework by TTM

Therefore, we employed the TPB to explain intention of helmet use. Accordingly, we proposed the following hypotheses:

H₁: Attitude (ATT) variable is positively related to the intention of helmet use.

H₂: Subjective norm (SN) variable is positively related to the intention of helmet use.

H₃: Perceived behavioral control (PBC) variable is positively related to the intention of helmet use.

H₄: Intention (IN) variable is positively related to the helmet use behavioral variable.

H₅: Perceived behavioral control (PBC) variable is positively related to the helmet use behavioral variable.

Based on the aforementioned literature review, following are our study models and hypotheses (Fig. 5).

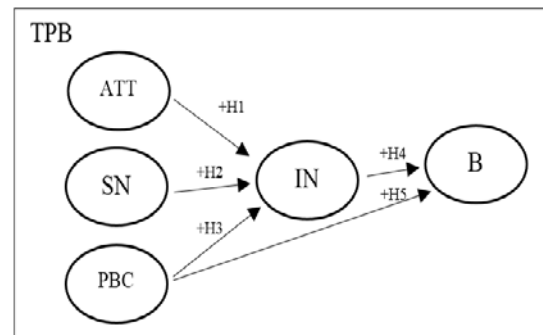


Fig. 5 Proposed study framework by TPB

Statistical Analysis

The analysis of the results was divided into three parts adapted from Kumphong J. et al. (2017). Overall, the model fit was evaluated against the number of recommended fit statistics and fit indices based on Hair et al. (2010). The first analysis was a factor analysis on latent variables (attitude (ATT), subjective (SN), perceived behavior control (PBC) and intention (IN)) from the questionnaire. Reliability of the latent variables was analyzed by Cronbach's alpha. All variables were analyzed based on TPB by confirmatory factor analysis (CFA). The second part used the Structural Equation Modeling (SEM) to analyze all variables. Respondent's factors (ATT, SN and PBC) were positively related to the behavioral intention of helmet use on campus. The final part was the analysis of the results by TTM using Pearson Correlation at 95% confidence level.

Table 1 TPB concepts and scales

Item	Scoring	M	SD
Attitude (ATT)			
ATT1 Wearing a helmet, it would be	1 = Bad : 5 = Good	4.71	0.73
ATT2 Wearing a helmet, it would be	1 = Unsafe: 5 = Safe	4.72	0.73
ATT3 Wearing a helmet, it would be	1 = Harmful : 5 = Beneficial	4.62	0.81
ATT4 Wearing a helmet, it would be	1 = Unlikely : 5 = likely	4.68	0.78
Subject norm (SN)			
SN1 Most of my friends wear a helmet when driving...	1 = disagree : 5 = agree	4.18	1.05
SN2 Most of peoples wear a helmet when driving...	1 = disagree : 5 = agree	4.12	1.02
Perceived Behavioral Control (PBC)			
PBC1 I believe I have the ability to wear a helmet.	1 = disagree : 5 = agree	4.65	0.66
PBC2 I can wear a helmet even if the other do not.	1 = disagree : 5 = agree	4.50	0.84
PBC3 I can wear a helmet even if there is no police on the street.	1 = disagree : 5 = agree	4.48	0.90
PBC4 I am confident that I could wear a helmet.	1 = disagree : 5 = agree	4.52	0.74
Intention (IN)			
IN1 Next 3 months, I will wear a helmet when driving.....	1 = disagree : 5 = agree	4.46	1.05
IN2 Next 3 months, I want wear a helmet when driving...	1 = disagree : 5 = agree	4.56	0.86
IN3 Next 3 months, I intent wear a helmet when driving.....	1 = disagree : 5 = agree	4.39	1.03
Self-report behavioral (B)			
B How often you wear a helmet when riding...	1 = Never : 5 = Always	4.39	0.82

Table 2 Stages of change concepts

Stages of change	Wearing helmet
Precontemplation stage	Wearing helmet is not an important behavior
Contemplation stage	Wearing helmet is an important behavior
Preparation stage	Wearing helmet is a behavior that I should do
Action stage	I often wore helmet
Maintenance stage	I have been wearing helmet more than a year

average age was 21 years old. 51% had a driver's license, and the average riding experience was 7 years. The interesting point founds were: the average of 1 time of a crash of participants, 27% had not experienced any accident, only 7% experienced property loss and damage, and 56% were involved in minor injuries whereas only 10% had severe injuries.

Table 3 Processes of change concepts and scales

Processes of change concepts	Item	M	SD
Experiential process			
PC1-The activities let me know and learn importance of wearing	1 = disagree : 4 = agree	3.50	0.54
PC2- The activities make me feel that not wearing helmet is a risk	1 = disagree : 4 = agree	3.21	0.86
PC3- The activities make me realize that wearing helmet is an important thing for me	1 = disagree : 4 = agree	3.60	0.60
PC4- The activities make me realize that wearing helmet is an important thing to do in the society	1 = disagree : 4 = agree	3.54	0.56
PC5- The activities make me realize that social norm is supporting wearing helmet	1 = disagree : 4 = agree	3.47	0.57
Behavioral process			
PC6- The activities make me interested to wear helmet	1 = disagree : 4 = agree	3.37	0.62
PC7- The activities make me remembrance of wearing helmet when riding motorcycle	1 = disagree : 4 = agree	3.51	0.57
PC8-The activities let me meeting those who always wear helmet	1 = disagree : 4 = agree	3.17	0.65
PC9-The activities support me to wear helmet	1 = disagree : 4 = agree	3.43	0.61
PC10-The activities make me feel that wearing helmet is useful	1 = disagree : 4 = agree	3.58	0.61

RESULTS AND DISCUSSION

Demographic Data of the Sample

The study of helmet wearing behavior change was done by the questionnaire survey from 219 student motorcyclists (80% male and 20% female), whose

Validity of measurement TPB model

The results of reliability and validation estimation were presented in Table 5. They show that all values of reliability and validation followed a good rule of internal consistency and rule of thumb, suggesting

adequate convergence. In other words, Cronbach's α , refers to consistent answers from identical group questions (e.g., Items for SN measure) of the respondents. The values threshold of 0.7 is acceptable. As a result, these values indicate latent variables of TPB model, which are good reliable representative values to explain the model. Table 6 shows that all latent variables (ATT SN and PBC) correlated with the IN variable at 0.1% level of significance.

Table 4 Decisional balance concepts and scales

Decisional balance concepts	Item	M	SD
Pros			
P1-Increase safety	1 = disagree : 5 = agree	4.73	0.59
P2-Reducing accident injury	1 = disagree : 5 = agree	4.68	0.64
P3-Sun/ dust/ insect protection	1 = disagree : 5 = agree	4.69	0.61
P4-Police enforcement	1 = disagree : 5 = agree	4.69	0.63
Cons			
C1-Reduce visibility	1 = disagree : 5 = agree	3.56	1.06
C2-Prevent hearing	1 = disagree : 5 = agree	3.60	1.04
C3-Hot and uncomfortable	1 = disagree : 5 = agree	3.06	1.34

Table 5 Exploratory factor analyses of model

TPB items		Factors			
		1	2	3	4
	α	0.914	0.675	0.767	0.756
1. ATT	ATT1	0.863			
	ATT2	0.901			
	ATT3	0.864			
	ATT4	0.869			
2. SN	SN1		0.861		
	SN2		0.824		
3. PBC	PBC1			0.715	
	PBC2			0.745	
	PBC3			0.782	
	PBC4			0.700	
4. IN	IN1				0.799
	IN2				0.812
	IN3				0.801

- Not relevant; Factor loadings > 0.7; (KMO = 0.806, $p < 0.001$)

Table 6 Reliability scales and correlation matrix TPB model

Factors	No. of items	1	2	3	4
1.ATT	4	1			
2. SN	3	0.234*	1		
3. PBC	3	0.457**	0.476**	1	
4. IN	3	0.257**	0.196*	0.465**	1

- Not relevant; ** Significant at 0.1% level; * Significant at 5% level

Test of a structural TPB model

We present the indexes in Structural Equation Model and factors influencing the indexes with standardized path coefficients. The most often indicated number of recommended statistics and indices in Tables 7 and 8 are fitted for the SEM based on Hair Jr et al. (2010). Therefore, the model fits between the theoretical constructs and observation constructs. We carried out SEM for independent TPB and extended TPB models.

Fig. 6 shows the result of structural models with standardized path coefficients for TPB model. The TPB model fit could pass a number of recommended fit indices. TPB model could explain 22% of variance for helmet use intentions and 26% of variance for helmet use behavior. From the TPB model, PBC were found to positively and significantly correlate with the helmet use intention (IN). PBC was the most significant and highly influential factor; it is the ability to regulate behavior intention. In addition, the TPB model indicated that PBC positively and significantly correlated with the helmet use behavior.

Table 7 Explanatory power and fit index of models. (N=219)

Model fit	Recommended value	Model
χ^2/df	< 3.0	1.97
GFI	> 0.90	0.917
CFI	> 0.90	0.945
RMSEA	< 0.08	0.067

Table 8 SEM results of model. (N=219)

Paths	Coefficients (β)	p-value	Hypothesis Supported
ATT \rightarrow IN (+)	0.005	0.953	No
SN \rightarrow IN (+)	-0.037	0.715	No
PBC \rightarrow IN (+)	0.488**	<0.001	Yes
IN \rightarrow B (+)	0.528	0.201	No
PBC \rightarrow B (+)	0.555**	<0.001	Yes

- Not relevant; ** Significant at 0.1% level; * Significant at 5% level

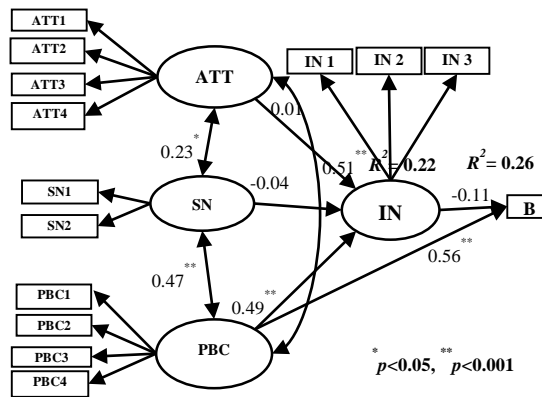


Fig. 6 Structure of TPB model of motorcyclists' helmet use on city

Test of a TTM structural

Fig. 7 shows the percentages of helmet wearing changes during the time measures were taken such as helmet wearing campaign. The proportion of riders' helmet use was found to increase. Use of campaign for support affected the rate of helmet wearing intention more than other measures.

Table 9 shows that all processes of change variables (PC1-PC10) correlated with the stages of change variable at 0.1%, 5% level of significance. In addition, the result indicated that PC7 and PC8 positively and significantly correlated with the stages of change. On the other hand, the result found that pros and cons factors non-significant with the stages of change variable.

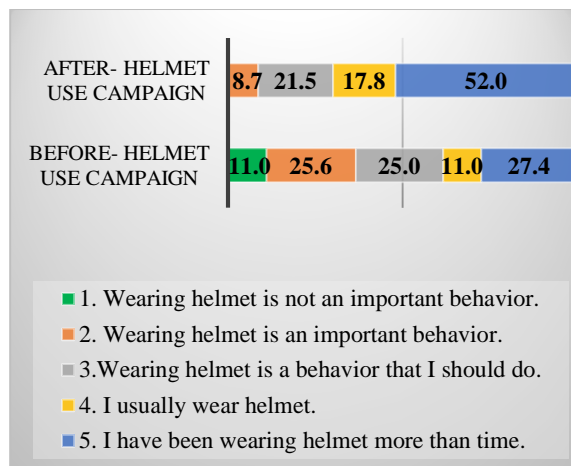


Fig. 7 Percentages changes in helmet wearing intentions

The results of this study agree with the previous studies of helmet wearing behaviors among students in Khon Kaen, Thailand and students in Ho Chi Minh,

Vietnam. SN and PBC influenced the intention to wear helmet since SN occurred from social pressure while PBC occurred from oneself or one's own decision [9-10]. In our study, the attitude factor affected helmet use intention at a statistically significant level. This differs from previous research. When considering TTM for investigated to helmet wearing intentions, it was possible that measures taken to encourage helmet use could increase motorcyclists' intention to wear helmet.

Table 9 Correlation between the stages of change and processes of change

Factors	Pearson Correlation	Sig.
PC1	0.070	0.304
PC2	-0.051	0.450
PC3	0.027	0.695
PC4	0.128	0.059
PC5	0.002	0.979
PC6	0.108	0.109
PC7	0.158*	0.019
PC8	0.169*	0.012
PC9	0.046	0.494
PC10	0.122	0.071

- Not relevant; ** Significant at 0.1% level; * Significant at 5% level

CONCLUSIONS

According to the TPB and TTM, the actual behavior would be adapted by changing their intentions. The result showed that PBC were significant factors for TPB, TTM. The traffic psychological factors are consistent with intention to wear helmet among student riders. Behavior change could occur after helmet use campaign. The results of this study will be presented to those involved in this area for road traffic planning and prevention.

Motorcycle riders are required to follow the instructions shown below, for suggest some concrete transport measures based on this research output.

- 1) Implement city road safety action plan (Helmet use 100%).
- 2) Set up the safe motorcycle riders in city areas.
- 3) Helmet law enforcement by CCTV camera 24 hr. [17-18]

ACKNOWLEDGEMENTS

This research received a Research Fund for Supporting Lecturer to Admit High Potential Student to Study and Research on his Expert Program Year 2016, Graduate School, Khon Kaen University, Khon Kaen, Thailand. Thanks are also extended to Khon Kaen University Language Institute for editing the report.

REFERENCES

- [1] Kumphong, J., Satiennam, T., & Satiennam, W., Correlations among motorcycle-related deaths, helmet law enforcement and helmet usage for ASEAN countries. *International Journal of GEOMATE*, Sept., 2018, Vol.15, Issue 49, pp. 72 -77.
- [2] Kumphong J., Satiennam T., Satiennam W., A correlation of traffic accident fatalities, speed enforcement and the gross national income of Thailand and its cross-border countries. *International Journal of Technology*, Vol. 7, 2016, pp. 1141-1146.
- [3] World Health Organization., Helmets : A road safety manual for decision- makers and practitioners. Geneva, Switzerland, 2006.
- [4] World Health Organization, Global Status Report on Road Safety 2009. Geneva, Switzerland, 2009.
- [5] World Health Organization, Global Status Report on Road Safety 2013. Geneva, Switzerland, 2013.
- [6] World Health Organization, Global Status Report on Road Safety 2015. Geneva, Switzerland, 2015.
- [7] Traffic Police, Injuries and Deaths Report 2000-2013 . Laos; 2013. (In Laos)
- [8] ThaiHealth Promotion Foundation, <http://www.thaihealth.or.th/Content/32660-รณรงค์เยาวชนลาวใส่หมวกกันน็อค.html> (In Thai)
- [9] Kumphong, J., Satiennam, T., and Satiennam, W., Psychological models for development of motorcycle helmet use among students in Vietnam, *IOP Conference Series: Earth and Environmental Science*, Vol.143, 2018.
- [10] Kumphong J., Satiennam T., Satiennam W., A Study of Social Norms and Motorcycle Helmet Use Intentions among Student Riders in University: A comparison of the Theory of Reasoned Action and the Theory of Planned Behavior. Conference proceedings, in Proc. 12th Int. Conf. on the Eastern Asia Society for Transportation Studies, Vol. 11, 2017, pp. 1-14.
- [11] Ajzen, I., Fishbein, M., *Understanding Attitudes and Predicting Social Behaviour*. Prentice-Hall, Inc., Englewood Cliffs, New Jersey, 1980.
- [12] Ajzen, I., *Attitudes, Personality and behavior*. New York, USA, 2005.
- [13] Fishbein, M., Ajzen, I., *Predicting and changing behavior: the reasoned action approach*. New York, 2010.
- [14] *Driving under the Influence of Drugs, Alcohol and Medicines, Good Practice: In-Depth Analysis on Recidivism Reasons & Analysis of Change Process and Components in Driver Rehabilitation Courses Report*, 2008.
- [15] James O. Prochaska, Colleen A. Redding, and Kerry E. Evers, *HEALTH BEHAVIOR AND HEALTH EDUCATION Theory, Research and Practice; Chapter 5 THE TRANSTHEORETICAL MODEL AND STAGES OF CHANGE*, pp. 97-117, 2008.
- [16] Hair, J.F., Black, W.C., Babin, B.J., and Anderson, R.E., *Multivariate Data Analysis a global perspective 7th ed.*, New Jersey, 2010.
- [17] Jantosut P, Kumphong J, Wonghabut P, Satiennam W, Satiennam T, Ung-arunyawee R., The Evaluation of CCTV camera enforcement to reduction of red-light running and increase of a helmet use. 13th Thailand road safety seminar: Invest for sustainable road safety 2017: 73–74. (In Thai)
- [18] Wonghabut, P., Kumphong, J., Satiennam, T., Ung-arunyawee, R. & Leelapatra, W., Automatic helmet-wearing detection for law enforcement using CCTV cameras. *IOP Conference Series: Earth and Environmental Science*, Vol.143, 2018.

PSYCHOLOGICAL MOTIVATION OF ELDERLY' INTENTION TO USE PUBLIC TRANSIT: A CASE STUDY OF LIGHT RAIL TRANSIT SYSTEM (LRT) IN KHON KAEN, THAILAND

Kawin Muenrit¹, Wichuda Satiennam²

^{1,2}Department of Civil Engineering, Faculty of Engineering, Khon Kaen University, Thailand^{1,2}

ABSTRACT

Elderly mobility is a challenging problem for the aging society in the developing countries and psychological factors play a major role to understand their mode choice behavior. This paper proposes an integrated model combining psychological factors according to the Theory of Planned Behavior (TPB) and Technology Acceptance Model (TAM) to explain the elderly' intention of using the planned Light Rail Transit system (LRT) in Khon Kaen city, Thailand. A sample of 340 participants was administered a questionnaire survey that measured a series of a construct based on TPB and TAM. Structural equation models (SEM) technique is used to test causal structure of the models. The results showed that attitude and subjective norm were all positively significant effect on elderly' intention, an especially subjective norm. The recognition that the system is easy to use and beneficial to travelers are important motivational factors behind. The implications of outcomes of this study help to understand elderly mobility and some effective ways can trigger traveler' intention to use LRT are discussed. in developing countries are discussed.

Keywords: Light Rail Transit system, Theory of Planned Behavior, Technology Acceptance Model, Elderly, Ageing society.

INTRODUCTION

Thailand is currently experiencing a rapid increase in the aging population. In 2014, Thailand had a high proportion of the elderly population, accounting for 14.9% of the total population [13]. According to a survey in 1994, the proportion of the elderly was 6.8% and increased to 9.4%. 10.7 and 12.2 percent in 2002, 2007 and 2011, respectively, due to the trend of population change. The elderly population is an important group and needs to pay attention and provide daily life support facilities.

The role of the elderly in the family today. Show that most elderly also want to help their children or family in various activities. As can be done especially in families with few members. these things play a role in every family. In addition to playing a role in the mission - responsible for family housework and also plays a role in earning money. And a career as well. Although they are very aged. The needs of the elderly in depth is "I do not want to burden myself with my family".

Some elderly people rely on themselves for using public transit for daily activities. Older people are experiencing difficulties in using public transit services that are not able to meet the needs of the elderly and obstructing the elderly in accessing services. Due to there are no policies that focus on the provision of public transit for the elderly. Therefore, the purpose of this paper aims to study the concept/factor of the elderly' intention to use public transit.

The way to encourage public transit still based policy goals of transportation management system. To achieve this goal, one important step is to understand mode choice behavior of traveler. The choice of transportation mode (private vehicle, public transit) is an individual tendency that is considered important in policy-making decisions. The recent work in choice models has emphasized the importance of the explicit treatment of psychological factors affecting decision-making for example [4], [11]. A guiding philosophy in these developments is that the incorporation of psychological factors leads to a more behaviorally realistic representation of the choice process, and consequently, better explanatory power [3]. Many researchers have used various techniques to explicitly capture psychological factors in choice models. Psychological behavior theories in modal choice are the Theory of Planned Behavior; TPB, as in [1] and the Technology Acceptance Model; TAM, as in [8]

The theory of planned behavior (TPB) is a well-researched model which is a social psychological model that has been successfully used to predict a wide range of human intentions [1]. An individual's behavior can be predicted by the behavioral intention. The constructs of theoretical include attitude toward the behavior, based on perceptions of a favorable or unfavorable evaluation on the consequences of action, subjective norm, the belief about perceived social approval for the action, and perceived behavioral control, people's perceptions of the ability to perform a given behavior [1], [2]

The TAM introduced by [8] is "one of the most referred theoretical frameworks to predict the acceptance and use of new format of technology" [16]. A TAM construct includes, Perceived ease of use is defined as the degree that using a specific technology will be free from effort and Perceived usefulness defined as the perceived degree to which an individual believes that is using a specific service or system will improve his or her task performance. Additionally, perceived ease of use has an indirect effect through perceived usefulness and attitude on intention, Perceived usefulness directly influences intention to use technology.

Both of TPB and TAM have been found to provide consistently superior explanations and predictions of human behavior [5], [6], [15], [16]. Besides, the combination of TPB and TAM can adequately define an individual's behavior with regard to use new technology. For example, the combined TAM and TPB model has been empirically applied to examine switching intentions toward public transit [5] and to examine factors affecting the adoption of Internet banking in Tunisia [16].

This paper, therefore, proposes an integrated model combining psychological factors according to the Theory of Planned Behavior (TPB) and Technology Acceptance Model (TAM) to examine the effects of psychological factors to explain the elderly' intention of using the planned Light Rail Transit system (LRT) in Khon Kaen city, Thailand. It is a high expectation that understanding the factors influencing traveler mode choice intentions will be useful in designing effective strategies to promote the use of LRT in the study area.

METHODOLOGY

Conceptual Framework

This study proposes an integrated model combining TPB and TAM as shown in Figure 1. This hypothesized model is based on theory and/or previous analytic research.

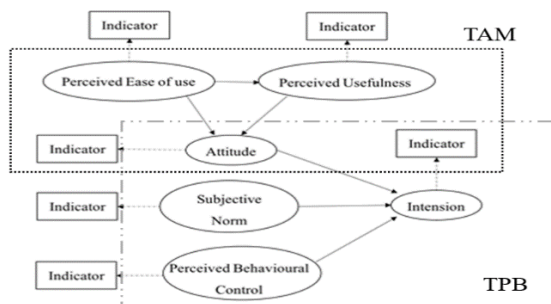


Fig. 1 This is a theoretical framework of this study.

Study Area

Reducing private vehicle use and encouraging public

transit use are an issue of immense concern for most cities around the world. In Khon Kaen city, Thailand, the LRT is planned to operate to solve traffic problems in the city. The LRT is a new public transit system which has specific lanes, uses electric energy that will provide environmental friendly, convenient and standard service. According to the plan, there are five LRT routes covering the urban area of the city. In figure 2, the red line is the main transit route and has 16 stations along the north-south of the main highway running through the city [14].

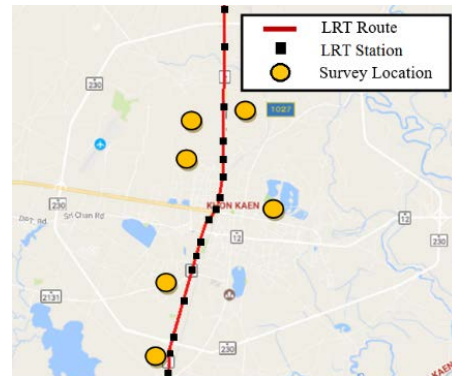


Fig. 2 Light Rail Transit system planning location in Khon Kaen City.

Participants, Procedure and Measures

Participants are the people who travel and live in communities near Mittraparb road-the main highway. The target of study is to explore the opinion of traveler about the LRT Project on the main route-the Red Line. The introduction and presentation about the planned LRT system are carried out before asking the participants to complete the questionnaires. Finally, a total of 340 participants were completed. Participants in the study were composed of 51% male and 49% female. Majority of the respondents was between 51 and over years old, which was 62.5% of the total respondents as shown in Table 1.

Table 1 This is sample demographics

		Frequency	Percentage (%)
Gender	Male	173	51.0
	Female	167	49.0
Age	Under 40	33	10.0
	41-50	93	27.5
	51-60	139	41.0
	61 and over	73	21.5
	career	45	13.0
	Housewife	108	32.0
	Entrepreneur	95	28.0
	Unemployed	92	27.0

The questionnaire contains two sections. The first part of the questionnaire asks the socioeconomic and demographic characteristics were measured in terms of gender, age, income, and existing mode. The second part consists of items for psychological measures according to TPB and TAM. All the items are measured by using a five-point Likert scales ranging from 1 (strongly disagree) to 5 (strongly agree) that were used to examine participants responded. The questionnaire with all the measures under investigation was designed based on an extensive review of the literature. The initial version of the questionnaire was then refined through with a focus group. Based on group members' suggestions on any confusing items in the questionnaire, some items were moderately re-worded. The questionnaire examined the variables according to TPB and TAM as shown in Table 2. Descriptive statistics and Cronbach alpha coefficients were calculated for all measures in a model. Table 2. reports the number of items, means, and standard deviations. All Cronbach alpha values are greater than 0.7 - suggested minimum acceptable level of Cronbach alpha, as in [9] indicating that internal consistency is acceptable.

Table 2 This is psychological constructs and their indicators

Constructs	No. of Item	Mean	SD	Cronbach's alpha
Intention	3	4.30	0.71	0.87
Attitude	4	4.51	0.56	0.82
Subjective Norm	3	4.30	0.72	0.86
Perceived Behavioral Control	3	4.34	0.58	0.70
Perceived Usefulness	3	4.46	0.60	0.77
Perceived Ease of use	3	4.33	0.66	0.77

As show in Table 3 illustrated intercorrelations for all variables.

Table 3 This is a correlation among constructs

	INT	ATT	SN	PBC	PU	PE
INT	1					
ATT	.64**	1				
SN	.65**	.66**	1			
PBC	.51**	.58**	.63**	1		
PU	.37**	.53**	.57**	.59**	1	
PE	.47**	.53**	.56**	.63**	.52**	1

Note: ** Is correlation is significantly at the 0.01 level (2-tailed)

Data Analysis

According to the frameworks of this study, as shown in Figure 1, a measurement model is first estimated using Confirmatory Factor Analysis (CFA) to test whether the data fit a hypothesized measurement model. The Structural Equation Modeling (SEM) technique is then utilized to examine the model fit and test causal structure of the proposed model. This study uses AMOS 22.0 to evaluate model fit and the significance of the hypothesized paths. The fit of the conceptual models to the empirical data is assessed with the Chi-square (χ^2) statistics, Degree of freedom (df), The root means square residual (RMR), Standardized Root Mean Square Residual (SRMR) and the root mean square of approximation (RMSEA).

RESULTS AND DISCUSSION

Measurement Model

According to the goodness-of-fit indices from the CFA results, the measurement model was parsimonious. The Chi-square statistic ($\chi^2 = 109.72$, $df = 74$) was significant. The GFI (0.95) was greater than the recommended value of 0.9. The root-mean-square error of approximation (RMSEA) was 0.043, which is less than 0.08 (Hair et al., 2006).

Structural Equation Models

There are two SEM models developed in this study to reveal traveler intention to use LRT. The first SEM model is guided by TPB (Model 1) and the second models combine TPB and TAM (Model 2) as shown in Figure 3 and 4, respectively. The fit measures indicate that the proposed model moderate to well fits the observed data. The two models accounted for 61-63 % of the variance of intention. The combining model as shown in model 2 has a slightly increased variance of mode choice intention from model 1. And Notes that * $p < 0.05$, ** $p < 0.01$, *** $p < 0.001$

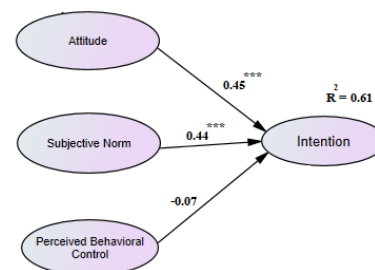


Fig. 3 This is an estimated model 1.

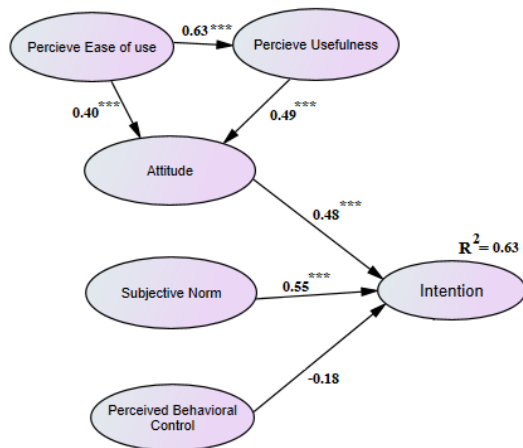


Fig. 4 This is an estimated model 2.

Figure 3. and 4. shows the estimated model in this research. In model 1, the estimated value of the standardized coefficients in model shows that attitude and subjective norm have a positive influence on Intention, but perceived behavioral control show the opposite effect. Attitude (0.45) appears to be the most influential factor of Intention followed by subjective norm (0.44) and perceived behavioral control (-0.07). The regression weight for PBC in the prediction of intention is, however, not significantly different from zero at the 0.05 level (two-tailed).

In model 2 the estimate's value of the standardized coefficients in model shows that most variables from TPB and TAM are positive and significant. The results have changed from Model 1. According to their strength, subjective norm (0.55) appears to be the most influential factor of Intention followed by attitude (0.48) and perceived behavioral control (-0.18) and the regression weight for PBC also not significantly. A perceived ease of use is found to be significantly and positively associated with perceived usefulness (0.63) and attitude toward LRT (0.40).

The results reveal that traveler intention is mainly influenced by SN and ATT - especially subjective norm. The positive relationship implies that the more the traveler has a positive attitude toward LRT and the more they perceived social pressure to use a system, they are more likely intend to use LRT. The result is confirmed with the studies by [5], [10] show the subjective norm is the most influential factor on traveler' intention to uses public transit. It is noticed that in Asian countries, an age of traveler is involved in intention. however, samples are mostly elderly, and they focus on people who are important to them greater than Self-determination. This result shows that also consistent with the nature of Thai culture as socialism elderly society.

Besides, this study also found that perceived ease of use and perceived usefulness appeared to have a significant effect on attitude. In other words, belief

underlying attitude has come from the perceived ease of use and usefulness. For example, if the accessibility to LRT station (walkway, Parking) is easy, the information board/Station name is easy to understand and clear vision, using the function of ticket system (ticket machine, ticket seller) is easy, the traveler will have positive attitude to the system and more likely intend to use the system. A plausible explanation is that perceived ease of use and usefulness might often indicate its influence on the intention through the mediator of attitude. Therefore, the LRT planner should take this information to raise intention by focused on the subjective norm coupled with attitude accounted when planning the LRT system for elderly.

CONCLUSIONS AND RECOMMENDATIONS

This study has proposed an integrated mode choice model consisting of the theory of planned behavior and a technology acceptance model, to examine elderly' intentions toward public transit in the context of the introduction of a new transit system in a study area. The results showed that the models accounted for a significant part of the variance in the intention to use LRT. Combining TPB and TAM model has a slightly increased variance of mode choice intention from only TPB model. Subjective norm and attitude are influential factors to LRT choice intention. The perceived ease of use is the motivation component underlying favorable attitude.

Since TAM is an important motivational factor behind attitude and behavioral intention, some effective ways can trigger traveler' intention to taking LRT are suggested. For example, a suitable electronic ticket system - easy to use, easy to understand. Apart from that is service of staff, LRT schedule (service frequency) and accessibility physical location of the station (universal design) should focus on safety as well.

The results from the LRT intention model of the elderly showed that in addition to the strategic planning from the conceptual framework, in addition to the focus on social strategy planning from psychological factors have come out. Another issue that should be considered is the provision of public transit for the elderly. If we consider the real current situation, it is found that elderly people have problems in using public transit services such as accessibility, Security issues, Lack of facilities, not on time, a frequency of service, a problem of system information, routes are not covered and not linked to other public transit systems [12].

However, the relevant government agencies do not give priority to the policy of allocating public transit to the elderly. The main reason is that Thailand is paying attention to other issues. The organization responsible for managing public transit services

lacked understanding about the elderly. It is difficult to push the elderly policy into concretely.

REFERENCES

- [1] Ajzen, I. (1991). A theory of planned behavior. *Organizational Behaviour and Human Decision Processes*, 50, pp. 179–211.
- [2] Bamberg, S., & Schmidt, P. (2003). Incentives, morality or habit? Predicting students' car use for university routes with the models of Ajzen, Schwartz and Triandis. *Environment and Behavior*, 35, pp. 264–285.
- [3] Ben-Akiva, Walker and Bernardino. (1997) *Integration of Choice and Latent Variable Model*, USA: MIT Press.
- [4] Ben-Akiva, M. and B. Boccara (1987). *Integrated Framework for Travel Behavior Analysis*. IATBR Conference, Aix-en-Provence, France.
- [5] Ching-Fu Chen and Wei-Hsiang Chao. (2011) Using the theory of planned behavior, technology acceptance model and habit to examine switching intentions toward public transit. *Transportation Research Part F*; (14), pp. 128–137.
- [6] Chun-Der Chen, J., Yi-wen Fan., Cheng-Kiang Farn. (2007) Predicting electronic toll collection service adoption An integration of the technology acceptance model and the theory of planned behavior. *Transportation Research Part C*, 15(2007), pp. 300-311.
- [7] Chun-Hua Hsiao and Chyan Yang. (2010) Predicting the travel intention to take High-Speed Rail among college students. *Transportation Research Part C*; (13), pp. 227-287.
- [8] Davis, F.D., 1989. Perceived usefulness, perceived ease of use and user acceptance of information technology. *MIS Quarterly* 13 (3), pp. 319–340.
- [9] Hair JF, Black WC, Babin BJ, Anderson RE, Tatham RL. *Multivariate data analysis*. 6th ed. Upper Saddle River, New Jersey: Pearson Prentice Hall; 2006.
- [10] Kaewklueklom, R., Satiennam, W., Jaensirisak, S. and Satiennam, T. Influence of psychological factors on mode choice behaviors: Case study of BRT in Khon Kaen City, Thailand, Preparing to submit in *Proceedings of the 14th World Conference on Transport Research in TRPRO*, Shanghai, China; July 10-15, 2016.
- [11] Koppelman, F. and J. Hauser (1979). Destination Choice for Non-Grocery-Shopping Trips. *Transportation Research Record* 673: pp. 157-165.
- [12] Kulachai W. (2015) *Public Transportation System for Aging People Is It a Neglected Policy*. Academic Resources, Prince of Songkla University. Thailand.
- [13] National Statistical Office. (2015). Preliminary results of the elderly population survey in Thailand 2014.
- [14] Sustainable Infrastructure Research and Development Center (SIRDC) (2016) *The study detailed design and impact on the environment of public transport in Khon Kaen city*. Khon Kaen University, Thailand.
- [15] Venkatesh, V., Morris, M.G., Davis, G.B., Davis, F.D., 2003. User acceptance of information technology: toward a unified view. *MIS Quarterly* 27 (3), pp. 425–478.
- [16] Wadie, Nasri., Lanouar Charfeddine. (2012) Factors affecting the adoption of Internet banking in Tunisia: An integration theory of acceptance model and theory of planned

DEVELOPMENT OF A CRACK REPAIR METHOD USING YEAST-INDUCED CALCIUM CARBONATE PRECIPITATION AND MODELING THE PRECIPITATION OF CALCIUM CARBONATE USING GEOCHEMICAL SIMULATION

Yoko Sakakihara¹, Shinichirou Okazaki²

¹Graduate school of engineering, Kagawa University, Japan;

²Faculty of engineering and design, Kagawa University, Japan;

ABSTRACT

Many confirmed cases of water leakage occur from the gap between the high column and the floor slab of a bridge. Although the gap is not classified as deterioration, some restoration for the gap is required. If the water circulation from the leakage in the crack is insufficient, deterioration of the reinforced concrete becomes faster than expected. Even though this is not an urgent issue, an affordable countermeasure is needed. In this study, the applicability of bio-grout using microbial metabolism for crack repairs was investigated. Bio-grout is a repair material using microbial metabolism, mainly based on water. Therefore, bio-grout is expected to penetrate cracks more easily due to a capillary tension that is quite different from conventional inorganic or organic grout. Therefore, it is unnecessary to press fit the grout into cracks, and this grout is environmentally friendly. This study examined the mixture proportion of the bio-grout used to produce a significant amount of calcium carbonate. Further, the precipitation amount of calcium carbonate was investigated via sedimentation analysis using a geochemical code. The simulation model based on the geochemical code successfully reproduced, the precipitation amount of calcium carbonate with reasonable precision.

Keywords: Grout, Calcium carbonate, Calcite, Microbial metabolism

INTRODUCTION

In Japan, post-war reconstructed bridges are currently in a state of deterioration, and restoration is required. However, the municipalities in Japan are in severe financial straits; hence, allocating a sufficient budget for repair expenses is difficult and thus, sufficient repair measures for all bridges are unattainable.

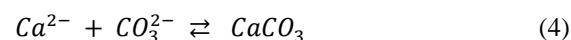
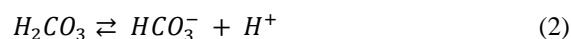
Although not classified as deterioration, many reported cases of water leakage occur from the gap between the high column and the floor slab of a bridge; it is not a pressing matter, but restoration plans and action are required. Due to inadequate water circulation in the crack, the deterioration of the reinforced concrete progresses faster than expected. Therefore, some low-cost countermeasures are required.

A conventional crack-repairing method is to fill the crack with epoxy resin via press fitting, which is laborious and expensive, mainly due to the material cost. It may also cause a leakage of the grout and produce a pervasive smell. Therefore, a method of repairing gaps and cracks using naturally derived bio-grout is proposed herein. In previous studies, calcium carbonate was precipitated from bio-grout, but that was not enough to repair the gaps. [1]-[9]

The purpose of this research is to design a repair model using a geochemical code to develop a more optimal blending condition. [10]

MATERIALS AND METHOD

Bio-grout formation comprises two reactions: biological and chemical. The former involves microorganisms consuming nutrients and releasing carbon dioxide, whereas the latter involves producing calcium carbonate from the generated carbon dioxide reacting with a calcium source. The chemical reactions can be simulated using PHREEQC, and they are outlined as follows:



In producing bio-grout, we referred to the reaction condition as shown in Table 1. [1]

The buffer is added here because of the

precipitation of calcium carbonate is a reversible reaction, and as the pH decreases, calcium carbonate dissolves, as shown in Eq. (4). Therefore, to maintain the production of calcium carbonate, Tris(hydroxymethyl) aminomethane (THAM) is added to capture the released protons to induce more carbonate ion (refer to Eq. (2) and (3)).

Table 1 Formulation of bio-grout as reference.

	Materials	Con.
Microbe	Saccharomyces Cerevisiae	9.0 g/L
Nutrient	D-glucose	0.10 M
Calcium	Calcium acetate	0.05 M
Buffer	Tris(hydroxymethyl) aminomethane	0.5 M

Note: The pH was set to 9.0 and the experimental temperature was 20°C.

Experiments with Bio-grout

In this study, the type of microbe and nutrient used were fixed. The calcium source, buffer concentration, pH adjuster of the buffer, and reaction temperature were varied.

Table 2 shows the condition of the bio-grout. Table 3 lists the conditions of the experiments.

Table 2 Proposed formulation of bio-grout.

	Materials	Con.
Microbe	Saccharomyces cerevisiae	6.0 g/L
Nutrient	D-glucose	0.4 M
Calcium	Calcium lactate	0.2 M
Buffer	Tris(hydroxymethyl)-aminomethane	Varied

Table 3 Different experimental conditions using the components from Table 2.

	Con. of THAM	Temp.
Case 1	-	25°C
Case 2	-	40°C
Case 3	0.3 M THAM	25°C
Case 4	0.3 M THAM	40°C
Case 5	0.75 M THAM	25°C
Case 6	0.75 M THAM	40°C

The experiment began by adding the pH adjuster into the buffer solution to set a specific pH. 40 mL of the buffer solution was taken into a conical tube, to which D-glucose and calcium source were added. Next, baker's yeast (*S. cerevisiae*) was added.

Following this, the mixture was kept at a constant temperature. Finally, the pH and the amount of calcium carbonate thus produced were measured.

pH change and crystal appearance confirmed the precipitation of calcium carbonate, and the precipitation amount was measured. Further analysis of the obtained crystals was done via X-ray diffraction (XRD) to examine the crystal structure.

RESULTS AND DISCUSSION

Experimental Results

From Fig. 1 and Fig. 2, the pH remarkably decreased over time in Cases 1, 2, and 4.

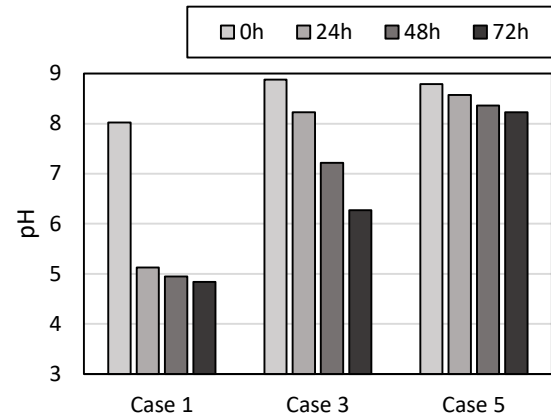


Fig. 1 pH change trends for different experimental cases when the reaction was maintained at 25°C.

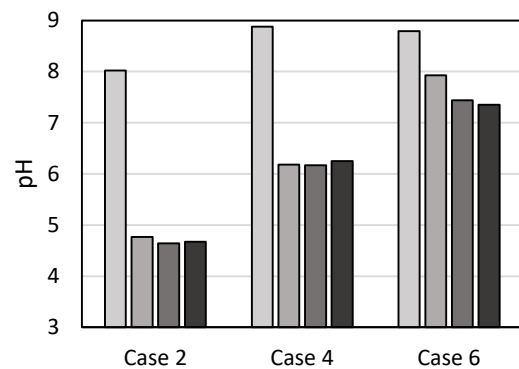


Fig. 2 pH change trends for different experimental cases when the reaction was maintained at 40°C.

Adding THAM resulted in a gentler pH change. Figures 1 and 2 show that the higher the concentration, the slower the pH change. For example, when the temperature was 40°C, the concentration of carbon dioxide increased and many

protons were generated because the microbes breathed more actively thereby producing more carbon dioxide. Figure 2 shows that using only 0.3M THAM resulted in a thin concentration and insufficient effect. However, 0.75M THAM was effective.

In Cases 1 and 2 where the buffer was not introduced, calcite and aragonite, which are crystals of calcium carbonate, did not precipitate (Figs. 3 and 4).

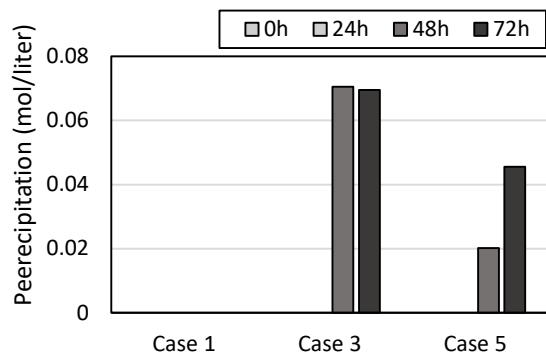


Fig. 3 Precipitation trend of calcium carbonate at 25°C

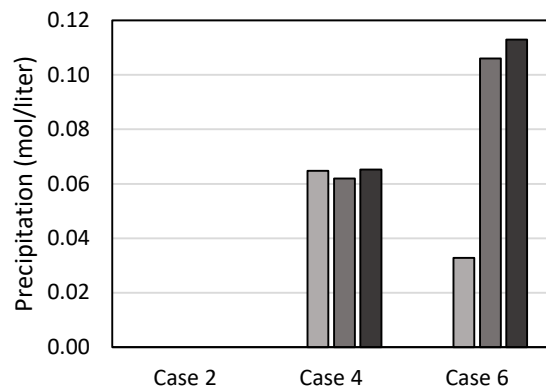


Fig. 4 Precipitation trend of calcium carbonate at 40°C

Further analysis of the precipitates via XRD revealed that only calcite is a crystal of the produced calcium carbonate.

Geochemical Code: PHREEQC

PHREEQC [11] is a computer program written in the C and C++ programming languages that is designed to perform various aqueous geochemical calculations.

PHREEQC is capable of speciation and saturation-index calculations; batch-reaction and one-dimensional (1D) transport calculations with reversible and irreversible reactions, including

aqueous, mineral, gas, solid-solution, surface-complexation, and ion-exchange equilibria; specified mole transfers of reactants; kinetically controlled reactions; mixing of solutions; pressure and temperature changes; inverse modeling.

Simulation Results Obtained via PHREEQC

In the simulation, besides the calcium ion concentration, the pH value and the temperature obtained from the experiment were used. THAM was not found in the database of PHREEQC; hence, an assumed compound as a pseudo buffer was set and used.

Similar to the experiment, precipitation of calcite and aragonite was not observed in Cases 1 and 2 (without buffer), and the change in pH was remarkable (Fig. 5).

However, the addition of a pseudo buffer resulted in a gentler pH drop, as depicted in Fig. 6, and the precipitation amount of calcite, a crystal of calcium carbonate, is shown in Fig. 7. Furthermore, no precipitation of aragonite was observed in any of the cases.

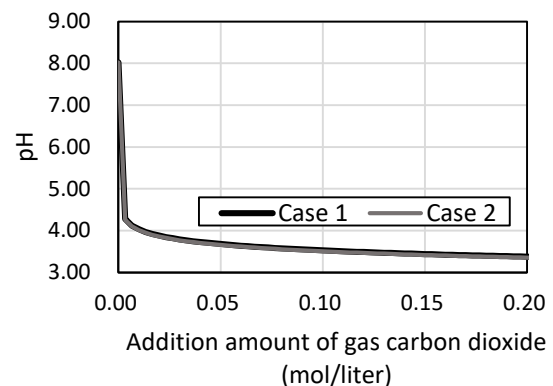


Fig. 5 pH change in Cases 1 and 2

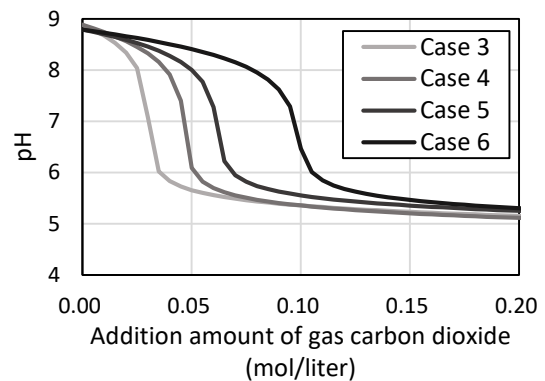


Fig. 6 pH change in Cases 3-6

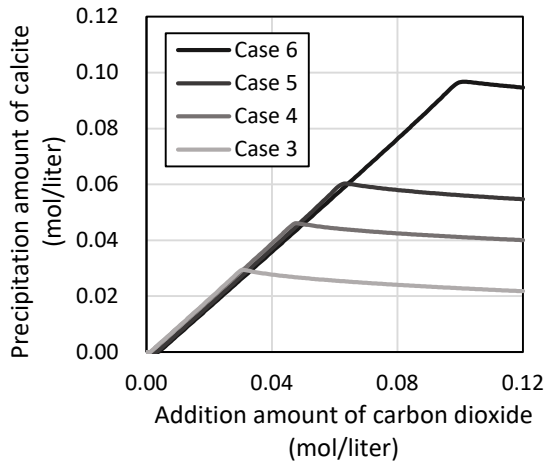


Fig. 7 Precipitation amount of calcite in Cases 3-6

Comparison Between Experimental and Simulation Results

Comparing the experimental values with the simulation values, where x -axis denotes pH and y -axis denotes the precipitation of calcite (Fig. 8), it can be observed that the simulation values accurately followed the experimental values.

Based on these results, the amount of precipitation produced from the bio-grout could be predicted to some extent from the simulation. In addition, Fig. 8 shows that maximum amount of precipitation was obtained between pH 6 and 7; however, when the pH decreased to 6 or less, the calcite dissolved, and the amount of precipitation decreased.

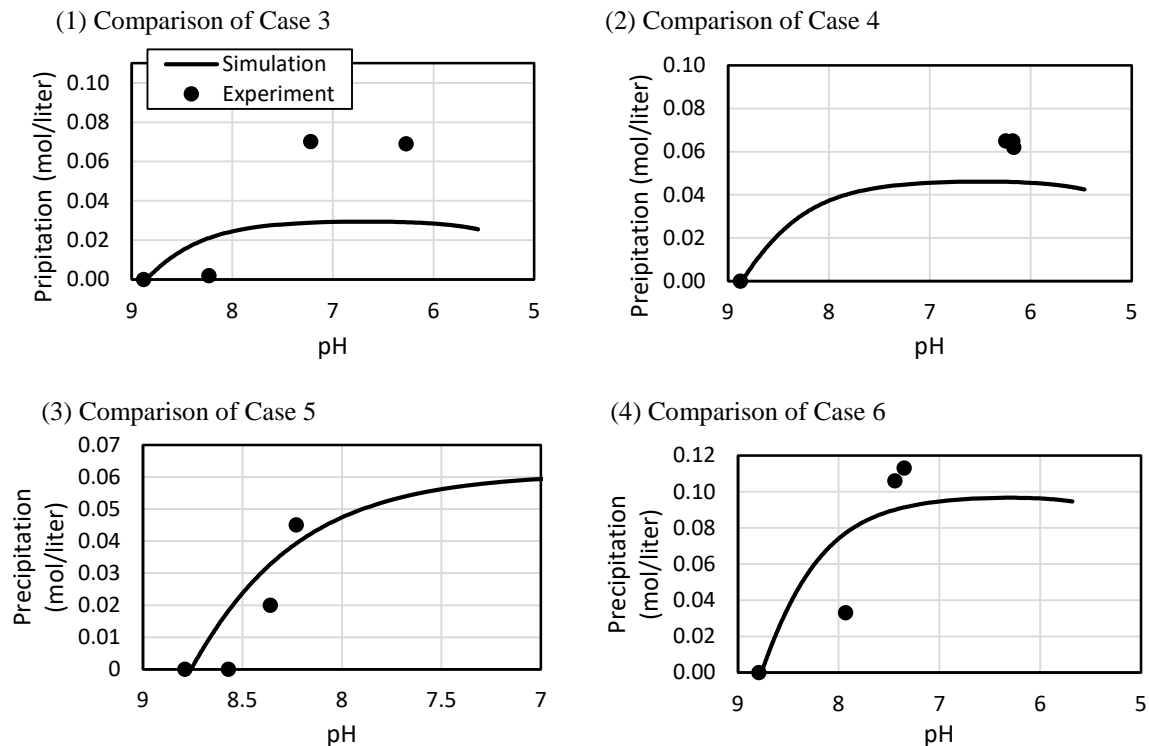


Fig. 8 Comparison of the precipitation amount between experimental and simulation results as a function of pH

CONCLUSIONS

The results show that the simulation model followed the same trend as the experimental outcome. In conclusion, the simulation model could be used to predict the amount of precipitation from the bio-grout to some extent.

The simulation also revealed that increasing the precipitation amount of calcium carbonate by setting a higher temperature and preventing the pH from decreasing is possible.

A further study has been planned to test the crack repair in concrete using the new bio-grout.

ACKNOWLEDGMENT

We would like to appreciate the great support for this research provided by the JSPS Grant-In-Aid for Scientific Research (B) task number 15h04025.

REFERENCES

- [1] Putri P. Y., Kawai K., Ujike I., and Yamamoto S., Effect of temperature on precipitation rate of calcium carbonate produced through microbial metabolic process of bio materials, *Civil Engineering Dimension*, 18(2), 2016, pp. 103-108
- [2] Bang S. S., Galinat J. K., and Ramakrishnan V., Calcite precipitation induced by polyurethane-immobilized *bacillus pasteurii*, *Enzyme and Microbial Technology*, Vol. 28, 2001, pp. 404-409
- [3] Kawaai K., Ujike I., Putri P.Y., and Yamamoto S., Some considerations on precipitation rate of calcium carbonate in bio-based materials used for concrete repair, *Concrete Solutions 2016: Proceeding of 6th International Conference on Concrete Repair*, Aristotle University of Thessaloniki, Greece, June 20-22, 2016, pp. 580-587
- [4] Kawasaki S., Muaro A., Hiroyoshi N., Taunekawa M., and Kaneko K., Fundamental study on novel grout cementing due to microbial metabolism, *Journal of Japan Society of Engineering Geology*, 47(1), 2006, pp. 2-12
- [5] Kubo K., Okazaki S., and Ujike I., Development of microbial metabolic processes to repair concrete joint leakage, *Advanced Material Research*, 845, 2013, pp. 158-162
- [6] Ujike I., Kubo F., Kawai K., and Okazaki S., Influencing factors affecting microbial metabolic processes of bio materials used for leakage repairs, *Concrete Solutions*, 2014, pp. 127-133
- [7] Wiktor V. and Jonkers, H.M., Quantification of crack healing concrete, *Cement & Concrete Composites*, 33(7), 2010, pp. 763-770
- [8] Wiktor V. and Jonkers, H.M., Field performance of Bacteria-based repair system; Pilot study in a parking garage, *Case Studies in Construction Materials*, 2, 2015, pp. 11-17
- [9] Wiktor V. and Jonkers H.M., Assessment of the functionality of bacteria-based repair system for concrete through ESEM analysis, *15th Euro Seminar of Microscopy Applied to Building Materials*, 2015, pp. 165-169
- [10] Akiyama M. and Kawasaki S., Application of numerical simulation of microbial reaction to biogrout with ureolytic bacteria, *Japanese Geotechnical Journal*, 12(3), 2017, pp. 337-349
- [11] Tokoro Chiharu, Introduction to reaction analysis by PHREEQC for beginners, Tokyo, R & D support center, pp. 1-133

ELECTRET CONDENSER MICROPHONE AS SENSOR IN ARTERIAL PULSE RECORDING DEVICE

Erni Yudaningtias¹, Waru Djuriatno¹, Achsanul Khabib² and Dionysius J.D.H. Santjojo³

¹Department of Electrical Engineering, University of Brawijaya, Jl. M. T. Haryono 167, Malang, Indonesia

²Department of Electrical Engineering, State Polytechnic of Malang, Jl. Soekarno - Hatta 9, Malang-Indonesia

³Department of Physics, University of Brawijaya, Jl. Veteran, Malang-Indonesia

ABSTRACT

An Electret condenser microphone (ECM) was designed to pick up the signal from the human radial arterial pulse. The ECM pick up system was equipped with an instrumental amplifier and a signal processing system. The characteristic of the ECM was analyzed using a sixth order polynomial equation. The equation was used to reconstruct the signal which flattened the frequency response at the range of 0.5-4.5 Hz. The signal processing consists of an FFT, a peak detection and a sixth order an anti-polynomial computational unit which are implemented in the computer. The gain was one with the frequency response closed to 0 dB for the designated frequency range. The error reached the minimum of 0.21 % at 1.5 Hz. It is maximum at the lowest frequency of 0.5 Hz.

Keywords: Sensor, ECM, an Arterial pulse signal, Frequency response

INTRODUCTION

Pulses present in several parts of the body, one of them is located in the radial artery. The pulse signal is a mechanical signal that has a frequency range of 0.5-4.5 Hz. A sensor is required to capture mechanical signal is Electret Condenser Microphone (ECM). The ECM has a relatively flat frequency response within the audio frequency range within the frequency range of 50-20,000 Hz.

ECM has been long used as part of an instrumentation. A study, compared the frequency response of ECM which has different diameters, i.e., ½ inch and ¼ inch. The results show that the ½ inch ECM has a sensitivity of ± 0.2 dB in range of 10Hz - 17kHz. On the other hand, the ¼ inch ECM showed the sensitivity within ± 0.3 dB from 100 Hz - 30 kHz. [1]. It can be inferred that large dimensions can capture a good signal.

Other factors which have to be considered are the effects due to the acoustic and the air gap between the diaphragm and the back plate. A novel design of the ECM provides a number of the acoustic holes in the diaphragm. The number of the holes, their distribution and the air gap determine the optimal performance of the microphone. The sensitivity of the optimized structure was -41.6dB with a pull-in voltage of 12V, and the frequency response was flat at 20Hz-20.6kHz [2].

In a preliminary study, the ECM has been used to record the pulse in human radial arterial. The results showed an expected pulse signal recording similar to that of Shusaka Nomura [3]. Fig. 1 shows the results of recording arterial pulse signals.



Fig. 1 ECM test arterial pulse of the human test.

At present, some researchers have proposed a pulse signal measurement system using the ECM. Eliminating noises and interferences is critical in the utilization of the ECM. One of the studies, use a soundproof sponge that is placed in a cylinder tube as an intermediate medium to isolate the captured pulse signals [4][5]. The model has advantages in terms of low cost and simple. However, the design has a large dimension because it should provide enough air passage between the soundproof to transfer the acoustic wave. A smaller design can be by using a Micro Electro Mechanical System Electret Condenser Microphone (MEMS-ECM) as a sensor to detect the arterial pulse. The MEMS-ECM is a type of microphone that has a small dimension that is 1.250 x 4720 x 3760 mm and has a frequency response at about -35 dB [3].

In the pulse measurement system, the ECM should have a frequency response at the range of 0.5-4.5 Hz to capture the mechanical signal accurately. Further study was carried out to test the ECM for its frequency response in the range of 0.5-4.5 Hz. Other researcher, tested the performance of

the ECM in the extremely low-frequency region using a computerized system. In this case, the ECM captured signals at frequencies ranging from 0.5 to 20 Hz. Reasonably good frequency response was achieved by removing the plastic cover and dust filter of ECM [6]. However, the technique has disadvantages, because the it reduced the signal to noise ratio.

In this presents study, a new arterial pulse sensor processing was added into the sensor design, where the output flattened the amplitude of the ECM in the range frequency of 0.5-4.5 Hz.

METHODOLOGY

The ECM used in this study was KUC4023 from HOSIDEN with the specification shown in Table 1 [7]. The sensitivity of the ECM over the design frequency which is from 50 Hz to 20 KHz is shown in Fig 2. A reduction of sensitivity is noticed in the band range of 5000-20000 Hz.

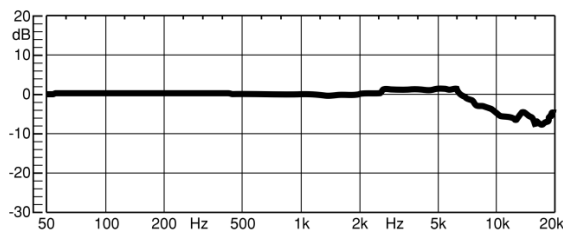


Fig. 2 ECM Frequency response Fabrication [7].

However, for the pulse reading system, the response of the ECM at the range of 0.5-4.5 Hz has to be determined. A testing system consisting of a signal generator, a low-frequency amplifier, a low-frequency speaker as the mechanical vibration source, an instrumental amplifier, and an oscilloscope. The system is shown in Fig. 3.

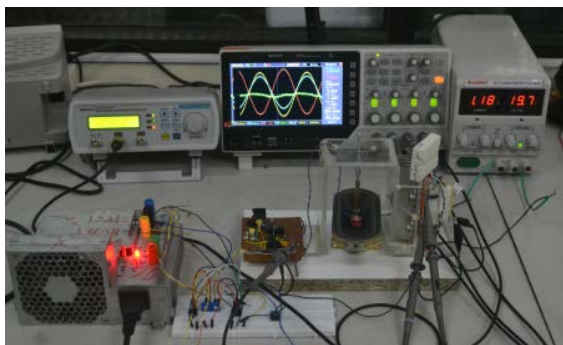


Fig. 3 Photograph of the setup of the ECM testing

The signal was amplified by a low-frequency amplifier which drives the low frequency speaker. The vibration from this speaker is sensed by the ECM through a soft silicon rubber. The soft silicon rubber functioned as a wave medium between the low-frequency speaker and the ECM. The Silicon

rubber has an acoustic impedance of 1.4 MRayl allowing the wave travels at the speed of 0.94 km/s[8]. Fig. 4 shows the placement of the soft silicone rubber as the medium between the low-frequency speakers and the ECM. The holder serves as a support to keep the ECM in place.

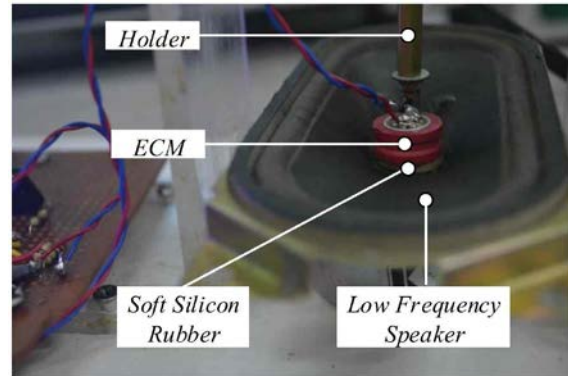


Fig. 4 Photograph of low-frequency Speaker and ECM

The signal from the ECM at the low frequency was quite small, so we designed an instrumental amplifier to amplify the small signal. Figure 5 shows the schematic wiring of signal instrumental amplifier that consists of 2 OP Amp. The function of this circuit is to eliminate low noise frequency and reducing the noise interference from the power supply

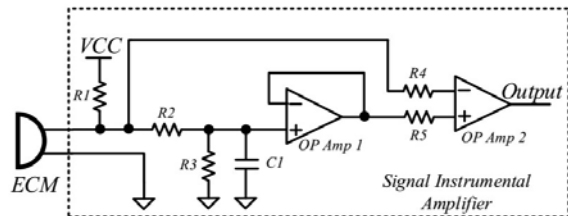


Fig. 5 Schematic wiring of the signal instrumental amplifier

To obtain an accurate signal response, we select a high input impedance OP Amp which has a typical slew rate to match the high impedance output of the ECM. The selected OP Amp was TL 062 from Texas Instrument with the specification: typical supply current: 200 μA (pre-amplifier), High Input Impedance: JFET-Input Stage and high slew rate: 3.5 V/ μs Typical. Some passive components required such as R_1 is 50 K Ω , R_2 is 1 K Ω , R_3 is 200 K Ω , R_4 is 500 Ω , R_5 is 500 Ω , and C_1 is 1 μF .

Second setup of the study was connecting the amplified signal to a computer for digital signal processing shown in Fig. 6.

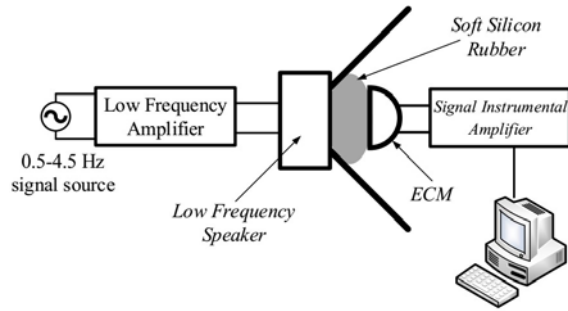


Fig. 6 Experimental setups of ECM test

Table 1 shows the test condition of the experimental setup. The test condition consists of specifications of silicone rubber, laptop specification, ECM specification and Digital storage oscilloscope.

Table 1 Test condition of the experimental setup

Items	Specification
Signal Generator	K-Moon DDS Signal Generator/Counter (Dual Channel)
Computer specifications	Intel core i5 CPU 2.30 GHz, 4 GB RAM
ECM	sensitivity: -45 dB, impedance: 1.0 K Ω PSU: 4.5 VDC Current : 0.8 mA
Oscilloscope	Digital Storage Oscilloscope Hantek MSO5074F 4 Channel 70 MHz, 1 GSa/s

Measurement of the ECM Signal

In Fig. 3, the output signal of the ECM was measured by means of an oscilloscope. The amplitude at different frequencies are displayed in Fig. 7. The character of the ECM is critical for the design of a signal processing.

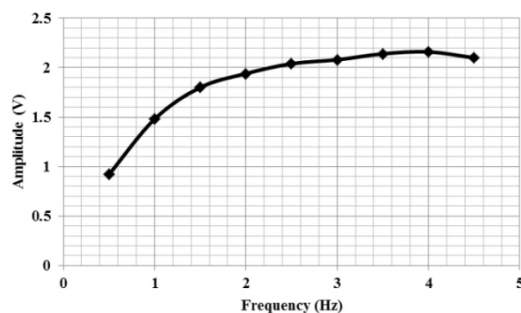


Fig. 7 Characteristic graph ECM at a frequency range of 0.5-4.5 Hz

Based on Fig. 7, the characteristic of ECM can

be interpreted in the polynomial equation. The amplitude of the ECM decreased when the frequency decreased. The smallest amplitude of the ECM characteristic is 0.92 V_{pp} (peak to peak) and the upper point amplitude 2.16 V_{pp}.

Mathematical Equation of ECM Characteristic

Based on Fig. 7, we can approach the character of the ECM into a polynomial equation. The equation consists of sixth order polynomial equation as given by the following equation:

$$y = 0.0093x^6 - 0.3226x^5 + 3.0306x^4 + 2.9419x^3 - 192.06x^2 + 1081.7x + 24.444 \quad (1)$$

Signal Reconstruction

From Eq. (1), we reconstruct signal by the using an anti-polynomial equation. The aim of the signal reconstruction was obtaining consistency of frequency response at the range frequency range of 0.5-4.5 Hz. Another goal of the anti-polynomial equation is to convert the signal to digital mode, so that it is suitable for the digital processing. The anti-polynomial equation is formulated as follow:

$$y = 0.0001x^6 - 0.0041x^5 + 0.0576x^4 - 0.04274x^3 + 1.7692x^2 - 3.9478x + 4.9001 \quad (2)$$

Based on Eq. 2, we can construct the anti polynomial graph as follows:

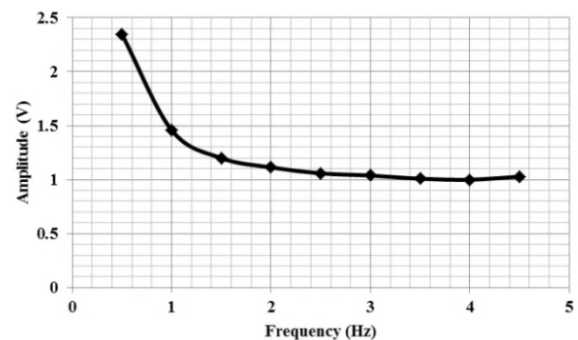


Fig. 8 Anti polynomial graph at a frequency range of 0.5-4.5 Hz

Based on Eq. 1 and Eq. 2, we can design the signal processing system. The general principle of the system is using a Fast Fourier Transform (FFT) and an inverse Fast Fourier Transform (IFFT). The FFT is a numerical computation which converts the time domain periodic signals into frequency domains data [9]. The FFT is performed for

application purpose in signal processing and data manipulation embedded in a Digital Signal Processing (DSP) or a microcontroller [10]. On the other hand, the IFFT is the inverse processing of the FFT into the time domain. The implementation of the IFFT on a DSP or microcontroller is carried out using a convolution and a correlation [10], respectively. The FFT function is represent by equation $y(k)$ where $x(k-i)$ is the input of the filter is the unit pulse response of the filter. Then, $x(k+i)$ is the input signal and the pattern to be found in the signal is represented by $h(i)$.

$$y(k) = \sum_{i=0}^{M-1} x(k-i) * h(i) \quad (3)$$

$$y(k) = \sum_{i=0}^{M-1} x(k+i) * h(i) \quad (4)$$

Figure 9 describes the steps for the implementation of equations 3 and 4.

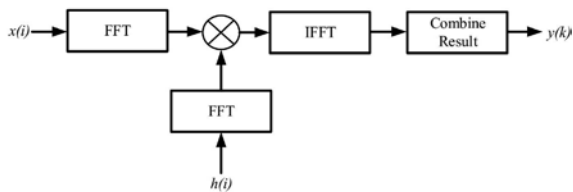


Fig. 9 Block diagram of General frequency domain processing in DSP [10].

This processing system has a high efficiency because it has the advantage of reducing signal processing computing, increase signal processing speed and reduce power consumption on DSP [11]. To get a flat response, the FFT must be multiplied by the sixth order anti polynomial equation and converted to the time domain using IFFT. The system of signal processing is shown in Fig. 9.

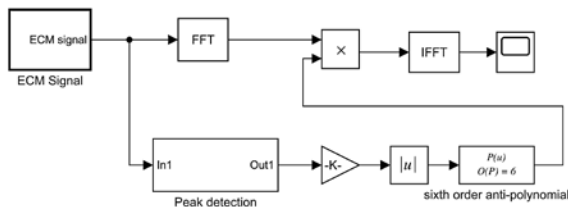


Fig. 9 System of signal processing

The Reconstructed Signal

The reconstructed signal of the system is shown and compare with the signal before processing in the result and discussion below.

RESULT AND DISCUSSION

The amplitude of ECM before and after processing are tested and analyzed. The results show that the proposed system has a good response as given in Table 1. From the Table 1, we can define that the amplitude before processing is decreased when the frequency is reduced. On the other hand, the amplitude after processing is relatively constant at a range of 2 Volt.

Table 1 The amplitude of ECM before and after processing

Frequency (Hz)	Amplitude before processing (V)	Amplitude after processing (V)
0.5	0.92	2.000
1	1.48	2.057
1.5	1.8	2.080
2	1.94	2.093
2.5	2.04	2.100
3	2.08	2.102
3.5	2.14	2.108
4	2.16	2.117
4.5	2.1	2.102

From Table 1, we can calculate the gain value of ECM amplitude. The Voltage gain is determining in A_v , where V_o is the output voltage and V_i is the input voltage. We can obtain the A_v by using the upper of the amplitude of ECM as V_i . In this case, the upper of amplitude is 2.16 Volt. To determining the Voltage gain, we can calculate the value of V_o and V_i by using the following equations:

$$A_v = \frac{V_o}{V_i} \quad (3)$$

Based on Eq. (3), the gain of the system can be shown at Fig. 10. The gain of the system after processing is relatively flat in the range of 1.

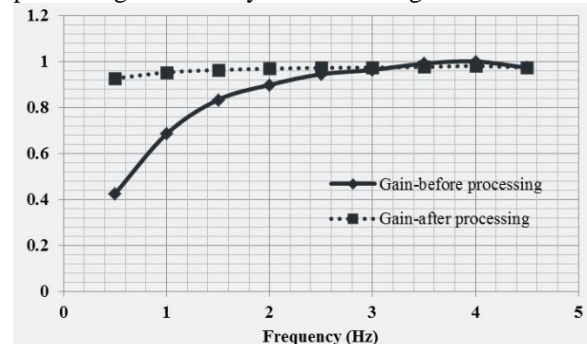


Fig. 10 Gain of before and after processing

The magnitude of the ECM frequency response in decibel (dB) or ECM (dB) can be determined by

using Eq. 4, where V_o is the output voltage and V_i is the input voltage.

$$ECM(dB) = 20 \log_{10} \frac{V_o}{V_i} \quad (4)$$

Frequency response ECM (dB) at a frequency range of 0.5-4.5 Hz is shown in Fig. 11. The frequency response before processing was decreased. However, after processing frequency response of ECM (dB) is relatively flat at the range around 0 dB.

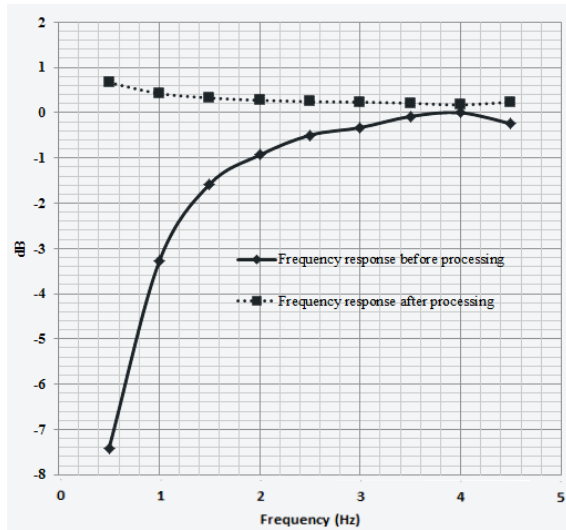


Fig. 11 Freq response of before and after processing

Based on Eq. (4), The output Voltage after processing is shown in Fig. 12. The output Voltage before processing is compared to output voltage after processing. In this figure, the Voltage before processing is decreased. However, the output Voltage after processing is relatively flat in the range of 2.1 Volt.

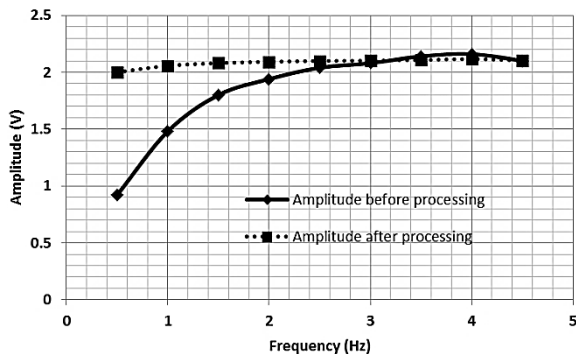


Fig. 12 The output amplitude before and after processing.

Base on Figure 12, the output voltage and input voltage are compared to get an absolute error value.

The error value is determined in Eq. (5) as follows:

$$Error = \left| \frac{V_{after} - V_{average(after)}}{V_{average(after)}} \right| \times 100\% \quad (5)$$

Figure 13 is absolute error value from the experiment. The error value from the system is about 0.21-4.05%. The error is caused by the input character of the ECM and its sixth-order polynomial representation. Furthermore, it also affected by the signal manipulation process which is the multiplication of the sixth-order anti-polynomial and the FFT output. The sixth order polynomial representation is the approach to the original signal. The error can be reduced by applying a higher order polynomial. In previous research [12] Yang Mei applied an eighth-order polynomial implemented in DSP TMS320C67x using 'C67x library functions generates over 60% and up to 70.2% of total TI library function cycles. So it can be concluded that sixth order polynomial orders are capable of being implemented in the DSP processor.

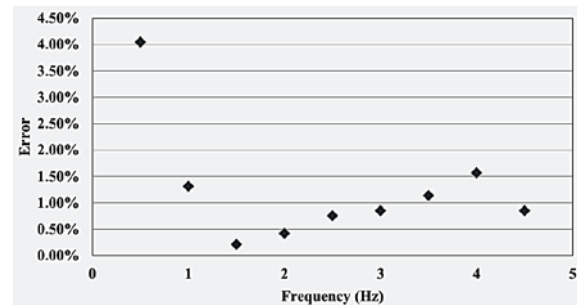


Fig. 13 The error of signal processing

CONCLUSION

In this study, ECM has been used as a sensor to record the signal of the human radial arterial pulse. To improve the output voltage amplitude, a signal reconstruction is required to obtain consistency of frequency response at the range frequency range of 0.5-4.5 Hz. The output amplitude of the system is flat around 2.1 Volt in the range frequency of 0.5-4.5 Hz, the frequency response ECM is flat at 0 dB and the system has error value is ranging from 0.21-4.05%

This device is able to provide a better choice for arterial pulse sensor because of several advantages, such as simple, cheap, compact, portable and easy to use.

ACKNOWLEDGMENTS

The research project was supported by Department of Electrical Engineering, University of Brawijaya Malang.

REFERENCES

- [1] A. Ohyagi, D. Adachi, H. Kodama, and Y. Yasuno, "Electret Condenser Microphones for Measurement Instruments," p. 185.
- [2] D. Zhang, Q. Fang, and X. He, "6 imulation and Optimization of a Micro-machined Silicon Condenser Microphone Using a Perforated Diaphragm," pp. 1682–1687, 2014.
- [3] S. Nomura, Y. Hanasaka, and H. Ogawa, "Multiple pulse wave measurement toward estimating condition of human arteries," *Proc. IADIS Int. Conf. e-Health 2013, EH 2013, Part IADIS Multi Conf. Comput. Sci. Inf. Syst. 2013, MCCSIS 2013*, vol. 11, no. 3, pp. 29–36, 2013.
- [4] Y. Y. Chen and R. S. Chang, "A study of new pulse auscultation system," *Sensors (Switzerland)*, vol. 15, no. 4, pp. 8712–8731, 2015.
- [5] W.-M. Lue, Jiann-Hwa; Chang, Rong Seng; Ko, Tai-Chuan; Su, Yu-Sheng; Cherng, Shen; Cheng, "Simple Two-Channel Sound Detectors Applying to Pulse Measurement," vol. 11, no. 4, pp. 3–5, 2014.
- [6] Y. N. Jeng, T. M. Yang, and S. Y. Lee, "Response identification in the extremely low frequency region of an electret condenser microphone," *Sensors*, vol. 11, no. 1, pp. 623–637, 2011.
- [7] E. C. Microphone, "Guide for Electret Condenser Microphones," *Current*.
- [8] N. S. Inc, *Acoustic Properties of CommonMaterials. 2013. [Online]. Available: <http://www.ndtssystems.com/Ref.>*
- [9] E. Yudaningtyas, D. H. Santjojo, W. Djuriatno, I. Siradjuddin, and M. R. Hidayatullah, "Identification of Pulse Frequency Spectrum of Chronic Kidney Disease Patients Measured at TCM Points Using FFT Processing," pp. 169–172, 2017.
- [10] W. W. S. and J. M. Smith, *Handbook of Real-Time Fast Fourier Transforms: Algorithms to Product Testing*. Wiley-IEEE Press, 1995.
- [11] A. Fertner, "Computationally Efficient Methods for Analysis and Synthesis of Real Signals Using FFT and IFFT," vol. 47, no. 4, pp. 1061–1064, 1999.
- [12] M. Yang, J. Wang, Y. Wang, and S. Q. Zheng, "Optimized Parallel Implementation of Polynomial Approximation Math Functions on a DSP Processor I-," pp. 344–347, 2001.

EXPERIMENTAL INVESTIGATION OF HOLLOW BRICK UNREINFORCED MASONRY BUILDING RETROFITTED BY FERROCEMENT LAYERS

Fauzan¹, Abdul Hakam², Febrin Anas Ismail³ and Jonathan Vincensius Osman⁴
^{1,2,3,4} Engineering Faculty, University of Andalas, Indonesia.

ABSTRACT

A retrofitting method to hollow brick unreinforced Masonry (URM) building has been developed using ferrocement layers. In this method, the ferrocement layers were applied to the URM building with the bandage system. An experimental study on hollow brick URM houses with and without ferrocement layers was conducted. Two specimens of a quarter scale hollow brick house models consisted of four walls with size 104cm x 110cm were constructed. The first model (B1) is the original hollow brick unreinforced masonry house without mortar plaster, and the second model (B2) is the same masonry house retrofitted by providing bandage ferrocement layers on both sides of the walls which are acting as sandwich structures. Both specimens were tested by using a shaking table (304x190) cm² with input motions from 0.3g to 0.6g. The test results show that the hollow brick URM house strengthened by using bandage ferrocement layers have excellent performance without any damage up to input motion 0.6g. For the original URM house model, meanwhile, the damage was initially found near the door opening at input motion 0.3g and the applied additional uniform load of 200 kg on the top of the specimen. Then, the cracks were developed and spread to the east side of the wall with the increase of the uniform load and finally, the house model collapsed at input motion 0.6g. This results indicated that the ferrocement layer significantly enhancement in ductility of hollow brick URM house model and effective in preventing the collapse of the hollow brick masonry walls when the earthquakes occur.

Keywords: *Unreinforced Masonry (URM) Building, Hollow Brick, Earthquake, Retrofit, Ferrocement Layers, Bandage System.*

INTRODUCTION

Unreinforced masonry (URM) is among the most commonly used building materials in many other developing countries including Indonesia. Most URM buildings are built with little or no consideration for seismic loading, and these are not capable of resisting the expected seismic actions. The major share of the loss of human lives and property during past earthquakes has been attributed to poorly constructed URM buildings. [1]

Earthquakes that often occur in West Sumatra province of Indonesia, cause a lot of damage to buildings, especially simple houses, ranging from minor damage to heavy damage or uninhabitable. In general, community houses are built with brick URM masonry building, as shown in Fig. 1 [2].



Fig. 1 Hollow Brick Simple House [2]

The hollow brick house without reinforcement as shown in Fig. 1, is not strong against earthquake load, because the house has no structural elements such as beams and columns. The house only has nonstructural components such as walls, roof, and ceiling. The non-structural component of a simple building is not part of the main load working on a structure, but this component can be the main cause of the earthquake losses.

Hollow brick has a very heavy material because it is made of mortar. The behavior of the hollow brick material is brittle and has almost no ductility, so the simple building of this brick wall has no resistance to horizontal load or earthquake load that occurs. Therefore, when an earthquake occurs, this building can collapse unexpectedly (Fig. 2) [3].



Fig. 2 Collapse of a hollow brick building [3]

A common method of seismic strengthening of URM buildings is the use of horizontal and vertical strips (known as bandages and splints, respectively) of ferrocement on both sides of walls. The horizontal 'bandages' are applied continuously on all the walls at lintel, sill, floor, and roof levels, whereas the vertical 'splints' are applied at corners and junctions of walls and along the jambs of the openings [1], [4]. Fig. 3 shows the typical arrangement of splints and bandages in a retrofitted URM building. The ferrocement strips consisting of welded wire mesh (WWM) reinforcement embedded in cement-sand mortar or micro-concrete have a composite action with the URM resulting in significantly enhanced strength and ductility in shear, rocking and out-of-plane bending. The bandages provide the support to the walls in out-of-plane action, whereas the splints enhance the shear and rocking behaviour of the piers.

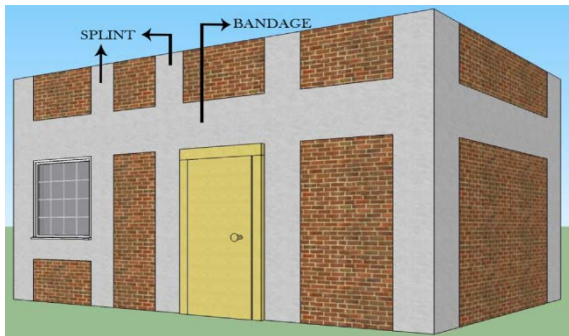


Fig. 3. Retrofitting of a masonry building using Ferro-cement splints and bandage [1]

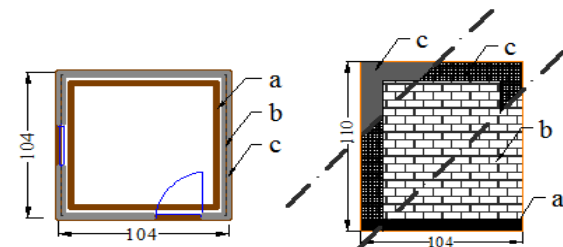
In the selection action for home improvement, it is certainly influenced by economic aspects. For the sake of the realization of a habitable home, some of the people who choose to build a simple house were destroyed first and then rebuilt, but such a solution will cost a lot. Another solution is that a simple house made of hollow brick is reinforced in the form of woven wire mesh. Such a solution is very efficient and effective because the price of wireless is relatively cheap and the work can be done by a local handyman. In addition, the reinforcement using wire mesh or commonly called ferrocement layer can be done also on houses that have been built without reinforcement.

Ferrocement is a plastering layer (mortar) woven with a wire mesh, so the ferrocement layer has a tensile strength. This ferrocement layer is placed in the position of the beam and column as a substitute for the structural element or called the bandage system. Boen introduced a retrofitting method for non-engineering building using ferrocement with wire mesh as strengthening layers and used sandwich construction analogy [5]-[6]. The ferrocement layers consist of mortar and wire mesh, in which the wire mesh was encased in the mortar. This retrofitting method uses ferrocement skin layers on walls as bandaging or jacketing.

In previous studies, strengthening of clay brick URM houses using ferrocement layers has been conducted. Imai (2014) found that the significant effect of retrofitting on the clay brick URM buildings by using ferrocement overlay as bandaging with galvanized was successfully demonstrated by the shaking table test [7]. Strengthening a clay URM house using full ferrocement layers on both sides of the walls also has been conducted with the result show that the ferrocement layers can significantly improve the performance of the clay brick URM building [8].

In this study, the behavior of two mortar hollow brick URM houses with and without bandage ferrocement layers on both sides of the walls under shaking table test was investigated.

TEST SPECIMENS



- a : U Plate (7.5 x 14) cm
- b : Masonry Hollow Brick (10 x 5 x 2.5) cm
- c : Ferrocement layers, wiremesh $\phi 1/4"$, mortar 1 : 4 (cement : sand)

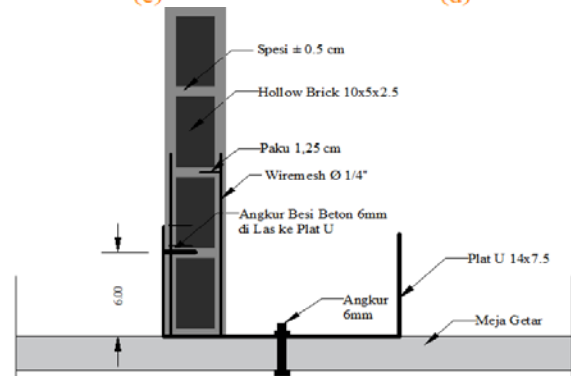
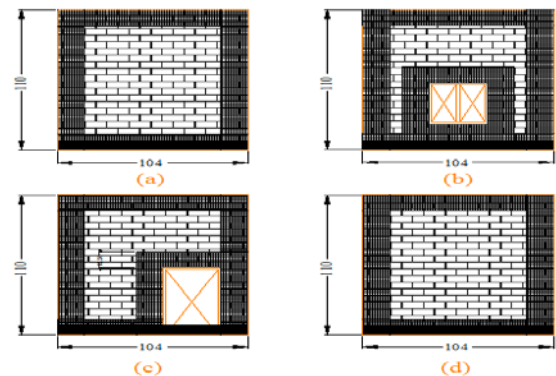


Fig. 4 Schematic drawings of the test specimen for model B2, (a) back side wall, (b) left side wall, (c) front side wall, (d) right side wall and (e) detail section of mortar brick wall with ferrocement layers

There are two URM house models that built on the shaking table in soil mechanical laboratory of Andalas University. Both models have a 1:4 scale of the actual building due to the limitation of the shaking table area. The first model (B1) is the original of an unreinforced masonry building, and the second (B2) is the same masonry structure strengthened by providing bandage ferrocement layers on both walls which are acting as sandwich structures.

Each model consisted of four walls with size 1.04m x 1.1m. Fig. 4 shows the schematic drawing of masonry walls for model B2. The masonry walls were made of hollow brick (100x50x25) mm, with the ratio cement and sand was 1/5 by volume and bonded by using mortar joints with the ratio cement and sand was 1/4 by volume. The thickness of the mortar joints is 5 mm. The width of the ferrocement bandage layer is 125 mm. The wire mesh was covered by mortar plaster with the thickness of 5 mm. The compressive strength of the hollow brick was approximately 2.5 MPa and the compressive strength of mortar to construct the Hollow Brick wall and ferrocement layer was 9.9 MPa. Fig. 5 shows the construction process of test specimens.



Fig. 5 Construction Process of the Specimens B1 and B2

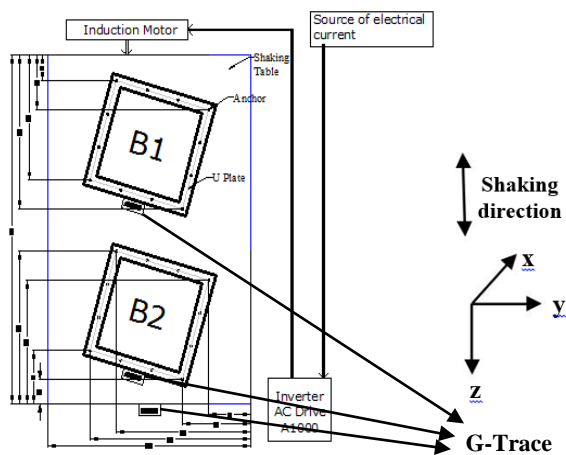


Fig. 6 Set-up of specimens on shaking table

According to the National Standardization Agency of Indonesia for Design Method of Earthquake Resistance for Buildings and Other Structures (SNI 1729–2012), clause 7.5.3, the load was applied separately in all two orthogonal directions. The most critical load effect due to the direction of earthquake forces application to the structure is considered to be fulfilled if the components and foundations are designed to carry the following set load combinations: 100 percent force for one direction plus 30 percent force for perpendicular directions [10]. Therefore, the slope of the specimens was set up on 16° in the direction of the positive x-axis, as shown in Fig. 6

TEST PROCEDURE

In this study, both specimens were tested by using a horizontal uniaxial movement type of shaking table in Soil Mechanic Laboratory of Andalas University [9]. Table 1 show, the input motions with varying the frequency of earthquake, such as the Medium earthquake (ME), and Strong earthquake (SE), were used as input motions for this test. The Input motion 0.6g is Peak Ground Acceleration (PGA) of Padang City based on Indonesia Earthquake Map 2017.

The excitation given to the specimens $a = 2.94 \text{ m/s}^2$, and 5.88 m/s^2 .

Table 1 Variation of the motions

Type of Input Motion	$a \text{ m/s}^2$
ME (0.3 g)	2.94
SE (0.6 g)	5.88

The specimens were tested in five stages. The first stage (P1), both specimens were tested with ME (input motion 0.3g). For the second until forth stages (P2-P4), the specimens were tested with an additional uniform load using sacks filled with sand on the top of specimens (Fig. 7), that is 200kg, 400kg, and 500 kg, respectively. All specimens on P1 to P4 were tested with ME (input motion 0.3g). In the last stage (P5), the specimens were tested with 500 kg additional load and input motion 0.6g until the specimen collapsed.

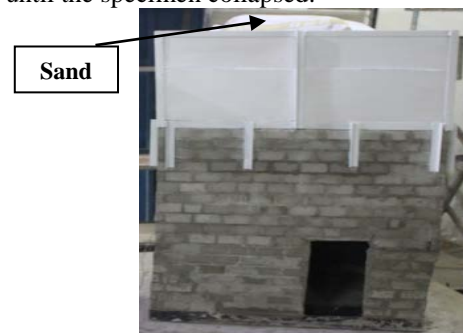


Fig. 7 Specimen with additional uniform load using sacks filled with sand (sandbags)

RESULT & DISCUSSION

The experimental results are presented in this section include the observed failure development and accelerations response of the shaking table that cause the crack on the specimens.

Test Specimens without Additional Uniform Load (P1)

The result of the first stage test with input motion 0.3g shows that there is no crack was appeared on both specimens, as shown in Fig. 8. From the analysis, the input motion is not strong enough to damage the specimen.



Fig. 8 The specimens without additional uniform loads (P1) after testing

Test Specimens with 200 kg Additional Uniform Load (P2)

In this test, both specimens were applied additional uniform load of 200 kg on the top of the specimens and tested with input motion 0.3g. The result shows that cracks started to appear in the door openings at front walls on specimen B1 (red marker), while, Specimen B2 with bandage ferrocement layers still survived without any damage, as shown in Figs. 9 and 10.

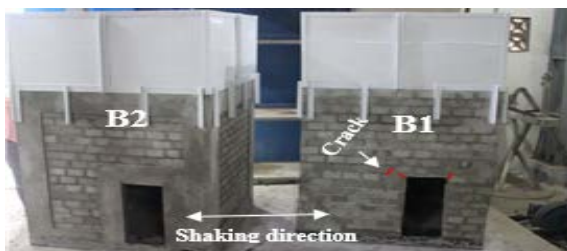


Fig. 9 The specimens with 200 kg additional uniform loads (P2) at front side after testing



Fig. 10 The specimens with 200 kg additional uniform loads (P2) at east side after testing

Test Specimens with 400 kg Additional Uniform Load (P3)

In this stage, the applied additional uniform load was increased by 400 kg in both specimens while the applied input motion was the the same those with the P1 and P2 Test (0.3g). As can be seen in Figs. 11 and 12, the cracks on Specimen B1 was developed near the door opening and spread on the east side of the wall (blue marker). Meanwhile, there is no cracks was observed on Specimen B2.

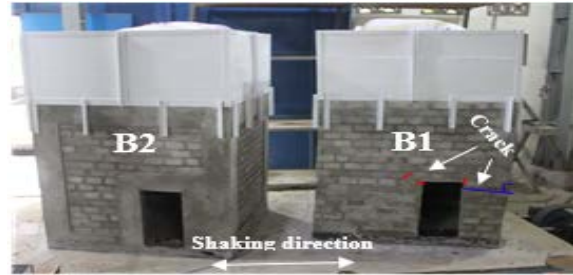


Fig. 11 The specimens with 400 kg additional uniform loads (P3) at front side after testing

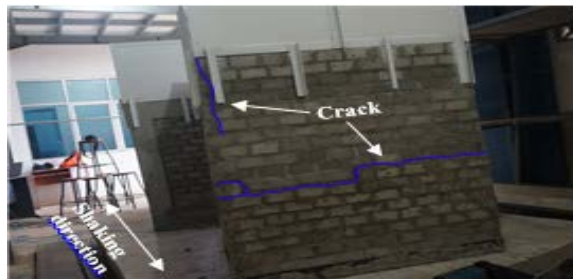


Fig. 12 The specimens with 400 kg additional uniform loads (P3) at east side after testing

Test Specimens with 500 kg Additional Uniform Load (P4)

In this test, both specimens were applied 500 kg uniform load with input motion 0.3g. In this phase, the cracks on Specimen B1 was developed on the same location with the P3 test and other cracks was observed in the walls of the building, especially on front and east sides walls (black marker). For Specimen B2, on the other hand, it still survived without any damage on the specimen, as shown in Figs. 13 and 14.

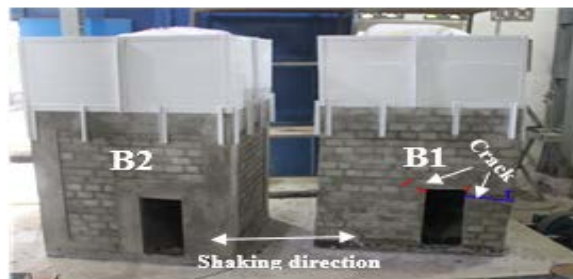


Fig. 13 The specimens with 500 kg additional uniform loads (P4) at front side after testing

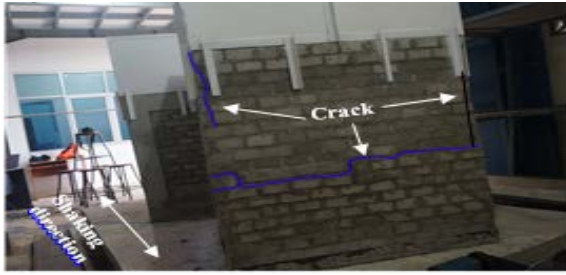


Fig. 14 The specimens with 500 kg additional uniform loads (P4) at east side after testing

Test Specimens with 500 kg Additional Uniform Load and 0.6g input motions (P5)

In order to observe the failure mode of the specimens, the applied input motion was increased by 0.6g while the additional uniform load was the same those in P4 test (500 kg). In this stage, the collapse of Specimen B1 was observed (4.5 seconds shaking), while on no cracks or damage was found on Specimen B2, as shown in Figs. 15 and 16. This indicates that the ferrocement layers enhance the seismic behavior (ductility) of the URM house and prevent the collapse of the hollow brick URM building even at a big shakings.



Fig. 15 The specimens with 500 kg additional uniform loads and 0.6g input motions (P5) at front side after testing.



Fig. 16 The specimens with 500 kg additional uniform loads and 0.6g input motions (P5) at east side after testing.

Acceleration Responses

The acceleration response is obtained from the G-trace in the form of an acceleration graph versus time. Figs. 17a–e show the acceleration response of both specimens on P1–P5 test. In these graphs, the blue lines represent the acceleration response on the

shaking table, while the red and green lines represent the acceleration response of Specimen B1 and B2, respectively.

In the P1 test (without additional load), both specimens (B1 and B2) have almost the same behavior of the acceleration responses, as shown in Fig. 17a. This might be due to the both specimens still in elastic range without any crack.

The acceleration response on the P2 test show that at $t=10$ s, the initial crack occurs on specimen B1 near the door openings with a max = $-1.2g$, as shown in Fig. 17b. In this stage, the max value of acceleration (a) on the specimen B2 was 0.9g.

For P3 test, the response of Specimen B1 is a little bit different with those in Specimen B2 due to development of cracks and additional new cracks in Specimen B1 that occurs on 2.5 seconds after shaking. The specimen B1 has the maximum value of $a = -0.7g$, while the maximum value of a for Specimen B2 is 0.85g, as shown in Fig. 17c.

Almost similar behavior with P3 test was observed on P4 test, as shown in Fig. 17d. At the P4 test, the crack appears on 25s after shaking. The specimen B1 has the maximum value of $a = 0.8g$, while in Specimen B2, the a maximum is 0.82g.

The increase of input motion from 0.3 g to 0.6 g causes the failure of Specimen B1 at $t = 4.5$ s with a maximum of $-1.75g$ (Fig. 17e). Meanwhile, for Specimen B2, with a maximum = $1.8g$, there is no crack was observed. From Fig. 17e, the collapse of the specimen B1 can be seen at suddenly breaks of the response at the beginning of the test.

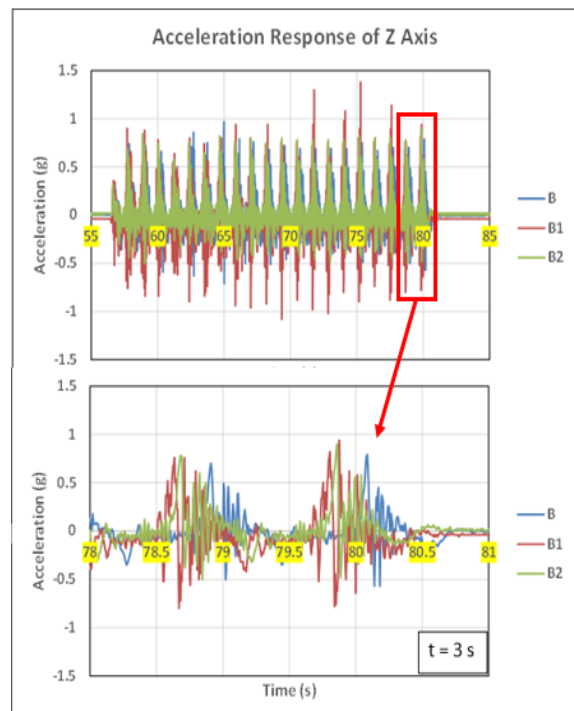


Fig. 17a Acceleration response graph for Base plat, Specimens B1 and B2 without additional uniform loads (P1 Test)

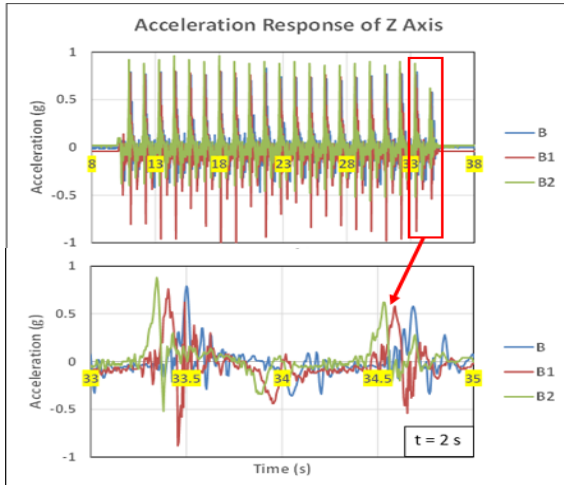


Fig. 17b Acceleration response graph for shaking table plat (B), Specimens B1 and B2 with 200 kg additional uniform loads (P2 Test)

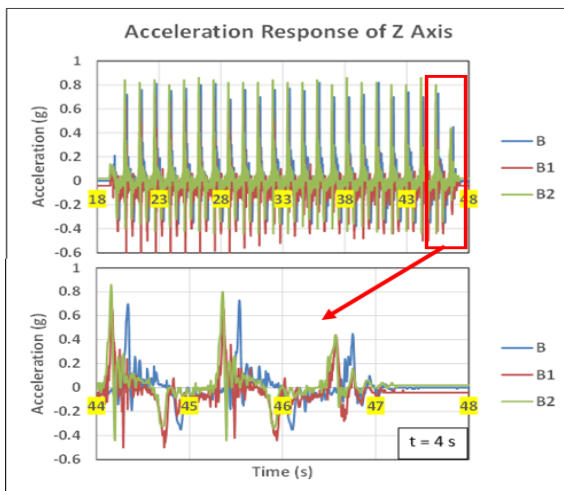


Fig. 17c Acceleration response graph for shaking table plat (B), Specimens B1 and B2 with 400 kg additional uniform loads (P3 Test)

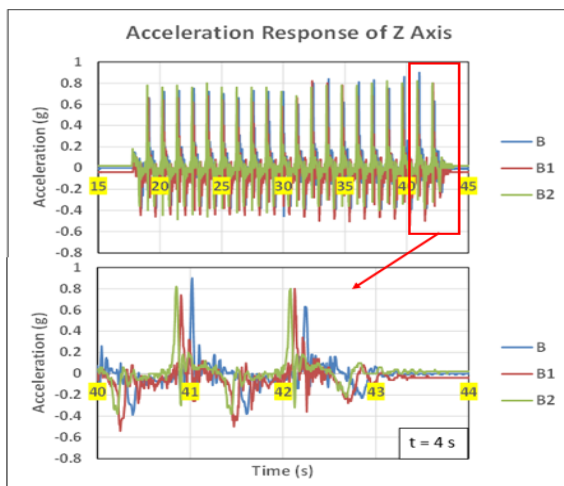


Fig. 17d Acceleration response graph for shaking table plat (B), Specimens B1 and B2 with 500 kg additional uniform loads (P4 Test)

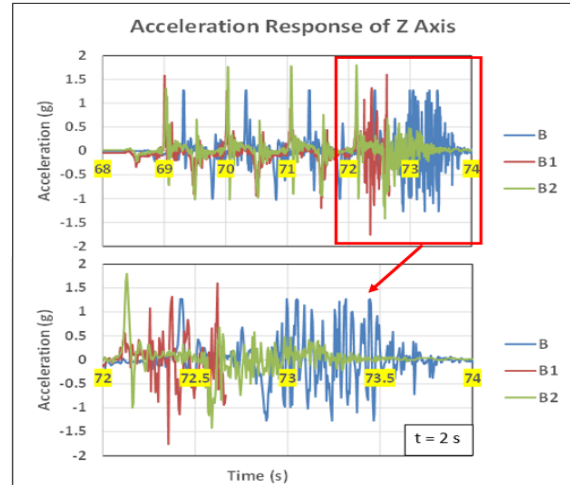


Fig. 17e Acceleration response graph for shaking table plat (B), Specimens B1 and B2 with 500 kg additional uniform loads and 0.6g input motions (P5 Test, collapsed)

CONCLUSION

Based on the experimental result, it can be concluded that:

1. There is no damage was observed for both specimens on P1 tests because the input motion is not strong enough to cause the crack of the specimen.
2. In the second stage (P2 test), cracks begin to appear in the door openings and front walls on specimen B1, while no crack was appeared on Specimen B1
3. The crack was developed near opening and spread on the east side of the wall on P3 and P4 tests.
4. Specimen B1 collapsed with input motions 0.6g and 500 kg additional uniform load, while no damage was observed on specimen B2 at this stage.
5. The results of this study indicated that the ferrocement layer significantly improve the seismic behavior of hollow brick URM house model and effective in preventing the collapse of the hollow brick URM walls when the earthquakes occur.

ACKNOWLEDGEMENTS

The authors would like to acknowledge the funding support provided by the Institute for Research and Community Service (LPPM), Andalas University, Padang, Indonesia.

REFERENCES

- [1] Kadam S.B, Singh Y, and Li B, Strengthening of unreinforced masonry using welded wire mesh and micro-concrete – Behaviour under in-

- plane action, *Construction and Building Materials*, 2014, 54, 247-257
- [2] Boen T., *Earthquake Resistant Design of Non-Engineered Buildings In Indonesia*. Kamakura, 2001.
 - [3] TEMPO., Using red brick, is more resistant to earthquakes. <https://batamerahputih.wordpress.com/category/rahasia-batu-bata-merah/>. Retrieved 10 May 2017.
 - [4] Boen T, et al., *Retrofitting Simples Buildings Damaged by Earthquake*, 2nd ed., Jakarta, Indonesia: WSSI, 2010.
 - [5] Boen T., *Challenges and Potentials of Retrofitting Masonry Non-Engineered Construction in Indonesia*, The University of Kyoto, Ph.D. thesis, 2014.
 - [6] Boen T., Arya A. S., and Ishiyama Y., *Guidelines For Repair, Restoration And Seismic Retrofitting Of Masonry Buildings*, JICA, 2012.
 - [7] Imai H., *A Study of Disaster Mitigation for Non-Engineered Construction in Developing Countries: Bridging the Gap between Experiment and Practice*, Doctoral Dissertation, 2014.
 - [8] Fauzan, Ismail F. A., Hakam A, Zaidir, and Amalia S. H., *Experimental Study on Masonry Building Strengthened with Ferrocement Layers*, *International Journal of GEOMATE*, May., 2018, Vol. 14, Issue 45, pp. 84-90
 - [9] Hakam A, Ismail F. A., and Fauzan, *Liquefaction Potential Assessment Based on Laboratory Test*, *International Journal of GEOMATE*, Oct., 2016, Vol. 11, Issue 26, pp. 2553-2557
 - [10] National Standardization Agency, *Earthquake Resistance Planning Procedures for Building Structure and Non-Building Structure (SNI 1726-2012)*, 2012, Jakarta.

USING FUZZY MULTI ATTRIBUTE DECISION MAKING (FMADM) APPROACH FOR RAILWAY TRACK REHABILITATION PLANNING: A CASE STUDY IN THAILAND

Thawatchai Phanyakit ¹ and Thaned Satiennam ^{2*}

¹Department of civil engineering, Faculty of engineering, Khon Kaen University, Khon Kaen, 40002, Thailand

²Department of civil engineering, Faculty of engineering, Khon Kaen University, Khon Kaen, 40002, Thailand

ABSTRACT

Rail transportation service from the past to present has been found that freight demand is higher than carrying capacity. Thus, this is a great chance for rail transportation to be highly promoted. Previously, the State Railway of Thailand (SRT) was not able to expand the rail transportation service to meet market growth because of limitation of network and degradation of infrastructure. Therefore, it led to the degradation of infrastructure which had an effect on service quality; in other words, rail freight transportation rate was considerably low i.e. only 2% [1]. As a result, railway track degradation has become a very interesting research topic for several organizations to conduct seriously for the purposes of safety and high level of reliability in infrastructure. Degradation factor was the main point of this study, so Fuzzy Multi Attribute Decision Making Method (FMADM) was used to analyze railway track defect and degradation to select a rehabilitation plan on schedule. Related research and literature were reviewed, and questionnaire was designed for asking opinions of the experts working for the State Railway of Thailand (SRT) including related party in selecting the rehabilitation plan. The findings have revealed that defect and degradation can lead to a high risk of derailment influenced by usability aspect. Defect code can be classified into 4 types according to the International Union of Railways (UIC) using the pairwise comparison method. Each type is different in the starting point and extension direction of railway track crack with contingency index below 0.01. The experts have specified that the severity of transverse break defect without apparent origin level of severity is the highest with relative weight of 0.396 followed by star-cracking of fish bolt holes with relative weight of 0.275, and the least severity is horizontal cracking at web-head with relative weight of 0.142. The analysis result based on FMADM has indicated that railway track structure replacement plan, considered by the experts, was better than railway track rehabilitation plan with importance weight of 0.620 and 0.380, respectively.

Keywords :Rehabilitation, Fuzzy multi attribute decision making approach (FMADM)

INTRODUCTION

Comparing the quality level of service between Thailand and foreign countries, International Institution for Management (IMD) World Competitiveness Yearbook 2014 reported that rail transportation development in Thailand was ranked at 43rd place out of 60 countries including having 0.009 kilometer/square kilometer of track network density. Also, service quality and safety were not satisfying, and train operation was not punctual as well as train speed was low i.e. 54 km/hr. and 26 km/hr. for passenger train and freight train, respectively [2]. Moreover, track network in Thailand is more than 30 years old according to a report on infrastructure quality by World Economic Forum 2013-2014[3], so infrastructure quality of track in Thailand was ranked at 72nd place which was worse than Singapore and Malaysia i.e. 10th and 18th place as shown in Table 1.

Table 1 Assessment Result of Infrastructure Quality [3]

Country	Place of Infrastructure Quality Assessment				
	Ove rall	Road	Train	Air port	Port
Singapore	5	7	10	1	2
Malaysia	25	23	18	21	24
Thailand	61	52	72	34	56

Source: World Economic Forum [3]

Rail transportation of northeastern line of Thailand from Thanon Chira junction to Nong Khai station has single-track and ballasted-track characteristic. Statistics of train and weight through track according to the report of warehouse department, State Railway of Thailand 2007-2016[4] can be seen in Fig. 1

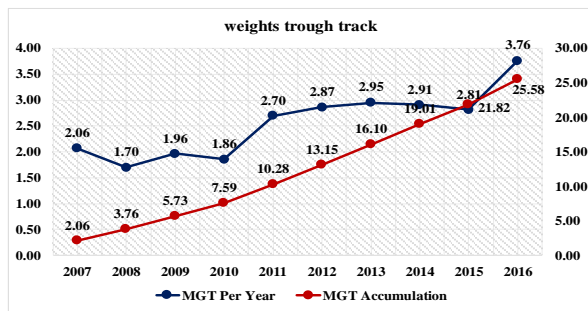


Fig.1 Weight through Track of NE Line [4]

Railway Track System

Railway track is generally divided into two main parts: superstructure and substructure. The superstructure consists of rails, fastening system, rail pads, and sleepers. The substructure consists of ballast, sub-ballast, and subgrade. Figure 2 and 3 illustrate a design of ballasted railway track [5].

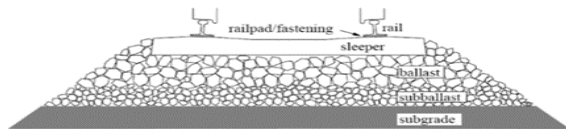


Fig.2 Track Design of Ballasted Track [5]

Ballasted track is well known that it is constructed to transport both freight and passengers with high cost of approximately 70-200 million baht. Its structure has at least 50 years of design service life cycle. Considering the cost of track maintenance and management, budget request for track construction is not a difficult task compared to track maintenance. The cost of track maintenance can vary based on usability, so it is important to keep the track in good condition or prevent from degradation. [5].

General Concept of Degradation

Track degradation process is complex, and its mechanism is related to several variables such as axle load, traffic speed, weather, rail quality, and geography as shown in Figure 3.

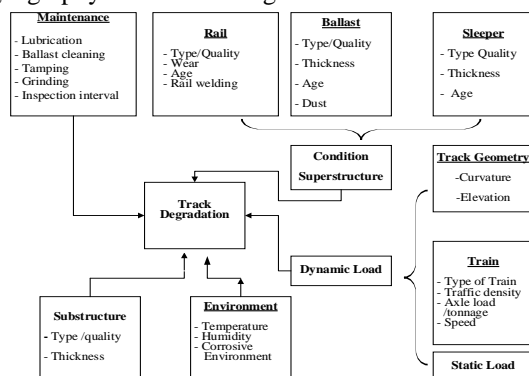


Fig.3 Influencing Parameters Track Degradation [5]

This research specifically focuses on factors

influencing track degradation as well as risk prioritization of cracked or broken track based on the standard of International Union of Railway (UIC) as shown in Fig. 7 And Fig. 8 shows track rehabilitation planning.

Area of Study

Northeast line of Thailand from Thanon Chira junction to Nong Khai station is the area of this study. Related secondary data were gathered up by collecting statistical data on defects of the Northeastern line from km.303+000 – km.623+900 between Thanon Chira junction and Nong Khai station with 320.900 km comprising 35 stations as shown in Fig.4.



Fig.4 Northeastern Line of Thailand Map

METHODOLOGY

This article aims at studying and analyzing factors influencing track defects and degradation in Thailand by applying FMADM to determine major and minor factors for analyzing and making a decision on a plan of track maintenance and renewal. The experts were interviewed to obtain knowledge about importance weight of each factor by applying analytical hierarchy process (AHP) as well as related secondary data were collected. Criteria for considering the score of each factor were low, moderate, and high levels. Also, fuzzy data were changed into the score by using fuzzy scoring method (FSM). Then total score was calculated by using simple additive weighting (SAW). The analysis results of importance weight and score as mentioned above resulted in assessment of major factors influencing track defect and degradation to develop decision making on

rehabilitation plan. Research methodology is shown in Fig.5. In this research, the experts had 15-35 years of track maintenance and rehabilitation experience in Thailand.

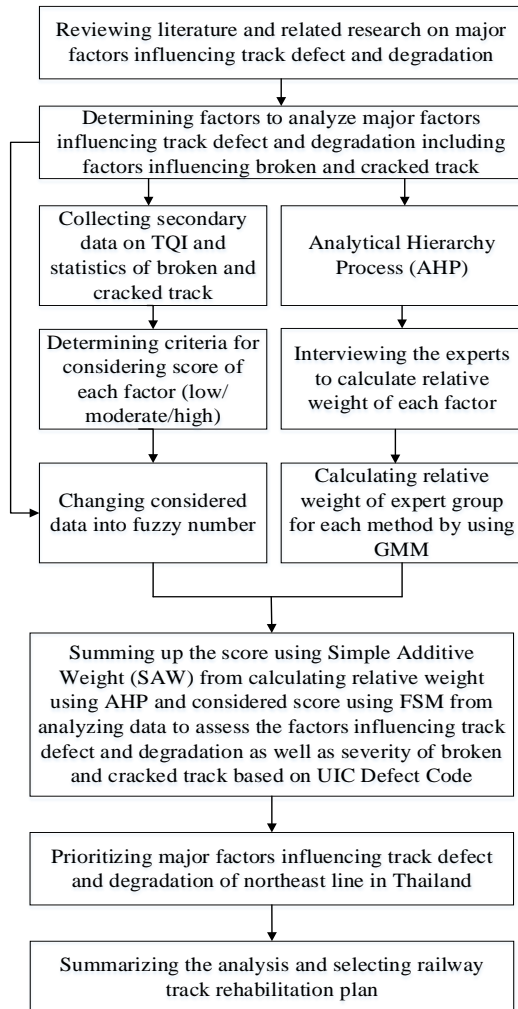


Fig. 5 Methodology Plan

Analytical hierarchy process (AHP) developed by Saaty (1988) is multi criteria decision making theory which is widely used and highly accurate. AHP is the process simplifying decision on complicated problems because it imitates natural decision making of human being. The procedure of AHP is presented in Fig. 6.

Decomposition

Decision elements used in hierarchy structure determined by a decision maker is important for demonstrating the consistency of entire decision elements from the highest hierarchy to the lowest one as presented in Fig.7-8.

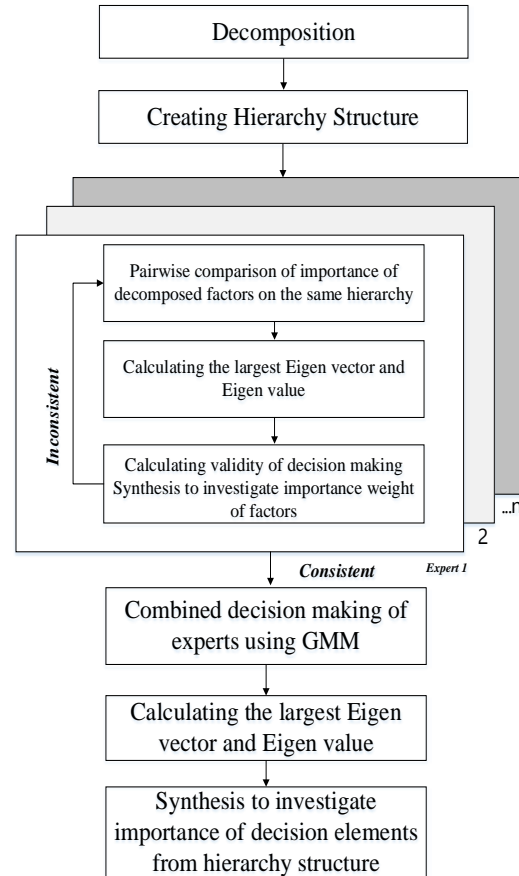


Fig. 6 Procedure of AHP [8]

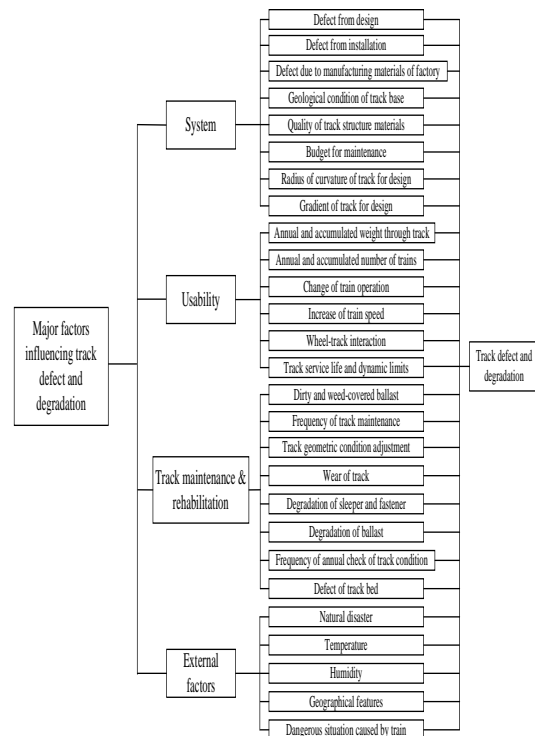


Fig. 7 Hierarchy structure for prioritizing factors influencing track defect and degradation

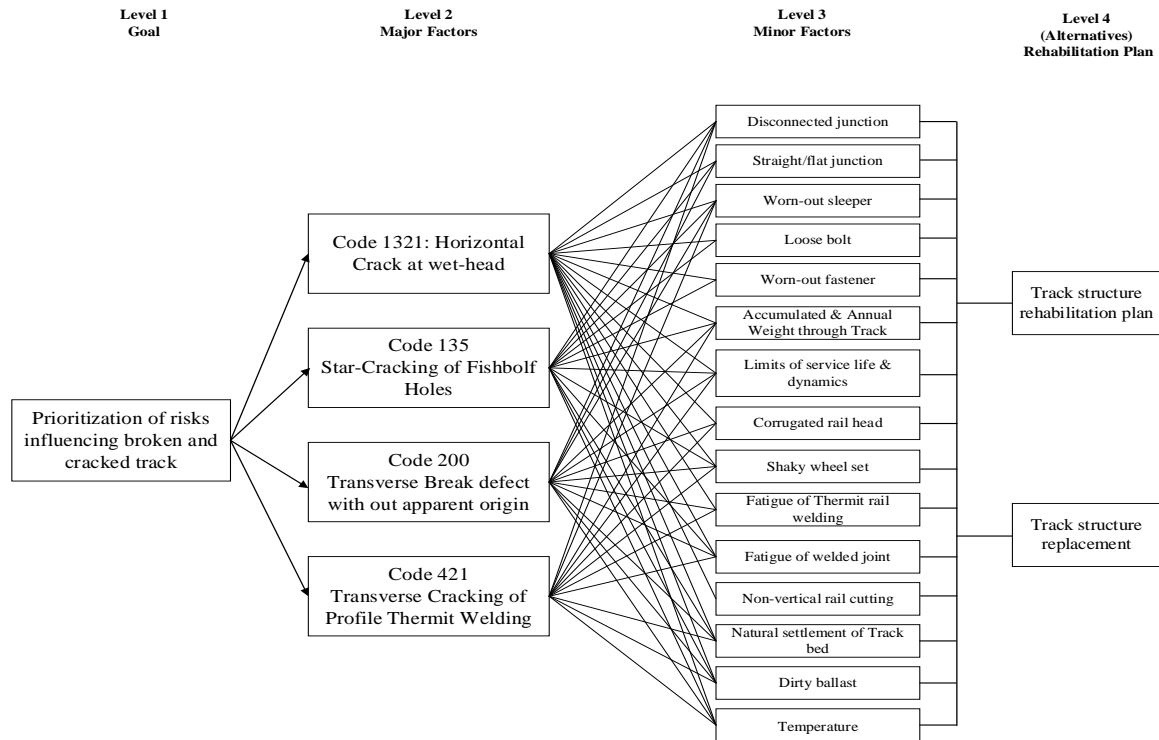


Fig. 8 Prioritization of Risks Influencing Break or Crack of Track

Table 2 Measuring Base Value Used for Decision Making in Pairwise Comparison [8]

Comparative Importance Score	Definition	Explanation
1	Equally Important	Both factors show equal result.
3	moderately more Important	One factor is moderately more important than the other.
5	Strongly more important	One factor is strongly more important than the other.
7	Very strongly More important	One factor is very strongly more important than the other.
9	Extremely more important	There is an evidence supporting satisfaction with one factor that is extremely more important than the other.

2,4,6,8

Intermediate judgment value

This is for narrowing gap in comparison judgment and being not able to explain with appropriate words.

Prioritization

Scores from 1 to 9 are used for pairwise comparison where 1 indicates that both factors have equal relative weight while 9 indicates that one factor has extremely more relative weight than the other.

Using pairwise comparison for the decision factors that are on the same hierarchy structure can be used for calculating the relative weights of decision elements of each factor. Required data are obtained from interviewing the experts. Measuring base value used for decision making in pairwise comparison is presented in Table 2.

Matrix of decision making obtained from pairwise comparison is a pair of decision factor at the same hierarchy which corresponds to other factors on the next upper hierarchy. Matrix is square value as shown in equation (1) where w_i and w_j represent relative weight of factor i and j respectively.

$$AW = \begin{pmatrix} 1 & W_1/W_2 & \cdots & W_1/W_n \\ W_2/W_1 & 1 & \cdots & W_2/W_n \\ \vdots & \vdots & \ddots & \vdots \\ W_n/W_1 & W_n/W_2 & \cdots & 1 \end{pmatrix} \begin{pmatrix} W_1 \\ W_2 \\ \vdots \\ W_n \end{pmatrix} = n \begin{pmatrix} W_1 \\ W_2 \\ \vdots \\ W_n \end{pmatrix} = nW \quad (1)$$

According to the theory of square matrix A, its consistency can be found when all elements of comparison are in the form of $a_{ik} = a_{ij} \times a_{jk}$ and $k = 1, 2, \dots, n$. Principle right eigenvector for A is equal to n (matrix sequence A). Therefore, it is very difficult for matrix A to be completely consistent as equation (1). Eigenvalue for A is not equal to n. Normally, right eigenvector (W) is represented by largest right eigenvalue (λ_{\max}) of matrix A as shown in equation (2).

$$AW = \lambda_{\max} W \quad (2)$$

Value of λ_{\max} is greater than or equal to n when λ_{\max} is similar to n. Considered matrix A is consistent and reliable, so this is why λ_{\max} is used as an indicator to express the validity of judging matrix A as presented in equation (3). Consistency index (CI) is developed from random square matrix test (500 samples) known as random consistency index (RCI) presented in Table 3[7]. Ratio between CI and RCI is called consistency ratio (CR). CR will be allowable when it is under 0.10, the value indicating the consistency of decision making judgment as shown in equation (4).

$$C.I. = \frac{(\lambda_{\max} - n)}{n-1} \quad (3)$$

$$CR = \frac{CI}{RCI} \quad (4)$$

Table 3 Sample Consistency Index [7]

Number of factors	1	2	3	4	5	6	7	8	9
RCI	0.00	0.00	0.52	0.90	1.12	1.24	1.32	2.41	1.45

There are so many ways used in calculating principle right eigenvector (W) and largest eigenvalue (λ_{\max}) for square A. This research used for normalization of the geometric mean of the row (NGM) [8] as indicated in equation (5) and (6) to estimate principle right eigenvector (W) because it is easy to calculate and understand largest eigenvalue (λ_{\max}) of square matrix A.

$$w_i = \left(\prod_{j=1}^n a_{ij} \right)^{1/n} / \sum_{k=1}^n \left(\prod_{j=1}^n a_{kj} \right)^{1/n} \quad (5)$$

$$\lambda_{\max} = \sum_{i=1}^n \left(\sum_{j=1}^n a_{ij} \times w_i \right) \quad (6)$$

Synthesis

After obtaining the importance weight of each factor on each hierarchy structure, decision making process using AHP is generally applied to “Principle of hierarchy composition” [7]. Calculated from the importance weight of each factor value, global relative importance that can be used for selecting an optimal alternative is on the lowest position of the hierarchy structure chart as equation (7)

$$C[1, k] = \prod_{i=2}^k B_i \quad (7)$$

where $C[1, k]$ = global importance of elements for decision making on hierarchy K which is consistent with decision making on upper hierarchy.

$B_i = n_i - 1$ Matrix of n_i Matrix of row that is contained for calculation.

n_i = numbers of factors used for decision making on hierarchy structure i.

Fuzzy Multi Attribute Decision Making (FMADM)

FMADM was developed based on basic concept of fuzzy set theory together with Multi Attribute Decision Making (MADM). Chen and Hwang (1992) hypothesizes that FMADM probably consists of fuzzy data (words) and numeric data. Fuzzy data can be represented by fuzzy number.

Basic Concept of FMADM

In the criteria of alternative analysis for the basic concept of FMADM, most of the decision-making problems are composed of crisp fuzzy and numeric data. Fuzzy data can be demonstrated in the form of words such as low, moderate, high, etc. or fuzzy numbers.

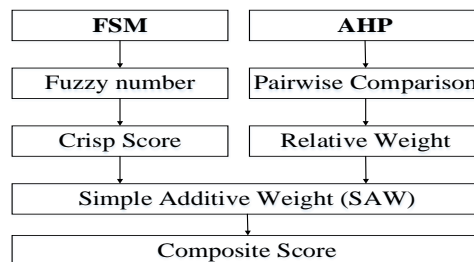


Fig.9 Procedure of FMADM [8]

RESULT AND DISCUSSION

According to analysis of factors influencing track quality particularly track degradation, rail is considered as the most significant element of track structure because it gains the highest stress compared to other elements; in other words, it directly connects with wheels. From interviewing the experts, the northeast line encounters the problem of broken and cracked track caused by degradation which exposes to high risk of derailment influenced by usability factor. Data collected from the report on broken and cracked track during 2007-2016 reveal that track

defects influencing break and crack can be divided based on the International of Railway (UIC) using the pairwise comparison method. Each type is different in the starting point and extension direction of railway track crack with contingency index below 0.01. The experts specified the severity of code 200: transverse break defect without apparent origin level of severity is the highest with relative weight of 0.396 followed by code 135: star-cracking of fish bolt holes with relative weight of 0.276, and the least severity is code 1321: horizontal cracking at web-head with relative weight of 0.142 as presented in Table 4.

Table 4 Risk causing defects

Defect Code		Severity	Prob.	Impact	Factors of cause	Risk Scoring	%	Prioritize Impact
Code 1321	Horizontal Cracking	0.244	0.145 0.035	0.142	Disconnected junction	0.110	11.00%	4
Code 135	Star Cracking	0.259	0.265 0.069	0.276	Straight/flat junction	0.120	12.00%	3
Code 200	Transverse Break	0.244	0.405 0.099	0.396	Worn-out sleeper	0.150	15.00 %	2
Code 421	Transverse Cracking of Profile Thermit Welding	0.252	0.185 0.047	0.187	Loose bolt	0.045	4.50%	10
					Worn-out fastener	0.033	3.30%	11
					Accumulated & Annual Weight through Track	0.052	5.20%	9
					Limits on service life & dynamics of Rail	0.200	20.00%	1
					Corrugated rail head	0.056	5.60%	8
					Shaky wheel set	0.083	8.30%	5
					Fatigue of Thermit rail welding	0.075	7.50%	6
					Fatigue of welded joint	0.066	6.60%	7
					Non-vertical rail cutting	0.004	0.40%	12
					Natural settlement of Track bed	0.002	0.20%	14
					Dirty ballast	0.001	0.10%	15
					Temperature	0.003	0.30%	13
					Total	1.000	100 %	

According to analytic hierarchy process (AHP), the result shows that track structure replacement plan gets the highest score (0.575) while track structure renewal plan gets lower score (0.425). As a result, track structure replacement should be selected for conducting railway track rehabilitation because it is optimal and highest consistent with all criteria. The result indicates that track quality aspect is the most important which has importance weight of 0.434 followed by return on investment aspect which has importance weight of 0.303, and risk reduction of defect aspect which has the lowest importance weight of 0.263. The result from analyzing track rehabilitation plan compared between track structure rehabilitation plan and track structure replacement plan in each criterion exhibits that each plan is different in importance weight as presented in Table 5.

Table 5 Weight of criteria for decision making plan

Criterion	Track Structure Rehabilitation	Track Structure Replacement	Weight
Quality	0.38	0.62	0.434
Risk Reduction	0.32	0.68	0.263
Return on Investment	0.58	0.42	0.303
	0.425	0.575	

To further increase the competitiveness of railway transport via quantity and quality of delivered service, improvements of track rehabilitation process are required. This research has addressed vital aspects of

track defects influencing break and crack that can be divided based on the International of Railway (UIC) for the selection of rehabilitation plan. As a result, track structure replacement should be selected for conducting railway track rehabilitation because it is optimal and most consisting with all criteria.

ACKNOWLEDGEMENTS

The researcher team would like to take this opportunity to thank the Department of Civil Engineering, Faculty of engineering, Khon Kaen University as well as the experts from the State Railway of Thailand (SRT) for giving useful data and opinions that contribute to the success of this research.

REFERENCES

- [1] Project of analytic study on factors and effects for modal shift appropriate with road travel and transportation toward rail and water transportation, The Office of Transport and Traffic Policy and Planning (2009).
- [2] Cited from journal of economy and society, vol. 52, No.2, April-June 2015, office of the national economic and social development board.
- [3] Report on infrastructure status in Thailand B.E. 2554, Office of the National Economics and Social Development Board, 2011.
- [4] Freight service department state railway of Thailand report on weight and train through the railway 2006-2016, SRT 2017.
- [5] Lake M. Farreiera L., and Murray M., 2000, Minimizing costs in scheduling railway track maintenance, International Conference on Computers in Railway No7, Bologna, Italy.
- [6] Dahlberg, T. Railway track settlements – a literature review, “Report for the EU project SUPERTRACK”, Division of Solid Mechanics, IKP, Linköping University, 2003.
- [7] Saaty TL., The analytical hierarchy process, Priority setting, resource allocation, McGraw-hill international book company, 1980.
- [8] Klungboonkrong P. and Faiboun N., Selection of a suitable area for multimodal construction of Nong Khai bus terminal using fuzzy multi attribute decision making method (FMADM), The 20th National Convention on Civil Engineering (NCCE20), 8-10 July 2015, Chonburi, Thailand.

VEHICLE ACTUATED SIGNAL CONTROL FOR LOW CARBON SOCIETY

¹Thanapol Promraksa and ²Thaned Satiennam
Faculty of Engineering, Khon Kaen University, Thailand

ABSTRACT

The purpose of this study is to propose and evaluate the vehicle actuated signal control for coordinated intersections to achieve the low carbon society. The study area is a group of 3 signalized intersections locating along the national Highway No. 2 in Phol district of Khon Kean province, Thailand. This study proposed and evaluated the several signal control strategies to increase the effectiveness of these intersections. The proposed strategies consist of i) fixed time control, ii) coordinated control, iii) semi actuated control, and iv) fully actuated control. This study applied the traffic microsimulation to evaluate the proposed strategies. The developed traffic microsimulation model was calibrated by using the traffic data surveyed during morning peak. The study found that the fully vehicle actuated signal control was the best strategy to improve the level of service of intersections and to reduce CO₂ emission. The average max queue length, average travel time, delay, stop time delay, and CO₂ emission of total systems decreased by 35%, 28%, 41%, 52% and 6%, when compared with existing fixed time control. The fully vehicle actuate signal control could promote the low carbon society.

Keywords: Vehicle Actuated Signal Control, Traffic Simulation, Low Carbon Society, CO₂ Emission

INTRODUCTION

Recently the global climate has become worse because of Global Warming. This affects the average temperature of the Earth's atmosphere and oceans. CO₂ has increased by about 36% from 1973 to 2009 [1]. Among human activities, the transport sector emits a large proportion of CO₂ emissions. The amount of CO₂ emissions has increased rapidly due to the high level of motorization caused by economic growth, particularly in developing Asian countries. The international community has recognized the need to reduce greenhouse gas (GHG) emissions by 50% by 2050 in order to keep global mean temperature change within 2 degrees Centigrade compared to preindustrial times [2]. To achieve this target, it is very important to develop Low Carbon Societies (LCS) in Asia. This is due to developing Asian countries accounting for more than half the global population and GHG emissions. The CO₂ emissions from the transport sector will significantly increase due to rapid economic growth and urban sprawl in the developing countries of Asia.

To reduce emissions from the transport sector, the World Conference on Transport Research Society [3] proposed the CUTE matrix, introducing three strategies, including AVOID, SHIFT and IMPROVE. Many researchers have proposed measures according to this matrix, including AVOID [4], SHIFT (e.g., shift to public transport [5]) and IMPROVE (e.g., changing motorcycles to electric motorcycles [6]), for Asian developing countries.

Therefore, the purpose of this study is to propose

and evaluate the vehicle actuated signal control for coordinated intersections to achieve the low carbon society.

The study area is a group of 3 signalized intersections, controlled by fixed time, along the national Highway No. 2 in Phol district of Khon Kean province as displayed in Fig. 1. It is the four lane divided highway. There is high number of traffic volumes, 41,656 pcu/day, along main highway [7]. The roadside land use is the commercial and residential areas which generated local traffic along minor roads as well.

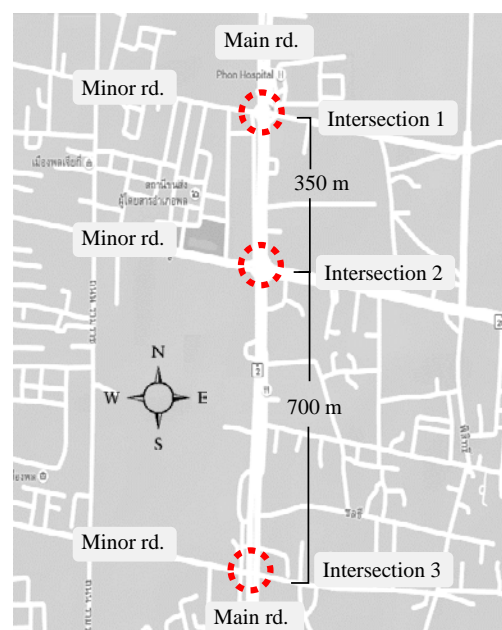


Fig. 1 A group of 3 signalized intersections

RESEARCH METHODOLOGY

The research methodology is classified into four steps: a proposal of signal control strategy, a survey of road geometry and traffic data, the development of a traffic microsimulation model and the evaluation of the signal control strategies. Each approach in the model development and application section will be described in the following sub-sections.

Proposal of Signal Control Strategy

This study proposed four types of signal control strategy, including a fixed time control, a coordinated traffic control, semi-actuated control and fully-actuated control, to achieve the low carbon society. Their definitions and application were explained as follows.

Fixed time control

The fixed time control is the pre-timed control which its phasing and timing designed by the pre-counted traffic volume. Some fixed-time systems use different preset time intervals for morning rush hour, evening rush hour, and other busy times. But it cannot compensate for unplanned fluctuations in traffic flows. They give the most green time to the heaviest traffic movement based on maximum information, regardless of changes in traffic volumes. It is ideally suited to closely spaced intersections where traffic volumes and patterns are consistent on a daily or day-of-week basis. Such conditions are often found in downtown areas [8, 9].

Coordinated traffic control

The Coordinated traffic controls is to provide smooth flow of traffic along streets and highways in order to reduce travel times, stops and delay. A well-timed, coordinated system permits continuous movement along an arterial. It is used in the case of very light side-street traffic [8, 9].

Semi-actuated control

The Semi-actuated control is used where a small side street intersects with a major arterial or collector. The detectors are placed only on the side street. The green time is on the major street at all times unless a "call" on the side street is noted. It is used in the case of very light side-street traffic, it reduces the delay incurred by the major road through movements. On the other hand, major road receives the green time based on maximum traffic flow, regardless of changes in traffic volumes [8, 9].

Fully-actuated control

The fully-actuated control refers to intersections for which all phases are actuated and hence, it requires detection for all traffic demands and patterns vary widely during the course of the day. There are several advantages of fully-actuated control. First, it reduces delay relative to pre-timed control by being highly responsive to traffic demand and to changes in traffic pattern. In addition, detection information allows the cycle time to be efficiently allocated on a cycle-by-cycle basis. Finally, it allows phases to be skipped if there is no call for service, thereby allowing the controller to reallocate the unused time to a subsequent phase [8, 9].

Survey of Road Geometry and Traffic data

The road geometry and traffic data were collected for the development of a traffic simulation model. The four vehicle types considered in this study were motorcycles (MC), passenger cars (PC), pickup trucks and vans (LT) and trucks and buses (HT). The turning count data by vehicle type was collected during morning peak hours (7:00 – 8:00 am.) for a development of OD matrices.

Development of Traffic Microsimulation Model

This study selected the VISSIM software to develop the traffic microsimulation model because the VISSIM currently is only one of traffic simulation software that has a function enabling to model lateral behaviour of motorcycle when the motorcycle taking over the slower or stopping other vehicles at signalized intersection. Moreover, the VISSIM can measure the speed-time profile of individual vehicle while it travels passing the signalized intersection. The speed-time profile of individual vehicle, i.e. instant speed and acceleration by every second, was necessary information as an input data for the CO₂ emission models.

These OD matrices were input into VISSIM through the function of turning movements by vehicle type. The approaching, turning and crossing speeds at intersections by vehicle type were surveyed using the spot speed method.

The study followed the guidelines proposed by FHWA [10] for application in the traffic microsimulation software. Before application of the traffic microsimulation model, it was necessary to calibrate the developed traffic microsimulation to be as close to the real-world traffic conditions as possible by adjusting the driving behavior parameters [11]. In the calibration process, this study simulated the OD matrix on the developed network. The criteria for traffic measures resulting from the simulation, including traffic flow and the maximum queue length, were compared with the field. The differences and GEH statistics were compared with acceptance

targets proposed by the Wisconsin Department of Transport [12] and Ahmed [13]. The driving behavior parameters were adjusted until the criteria for traffic measures passed the acceptance targets.

Evaluation of Signal Control Strategies

This study planned to propose the vehicle actuated signal control strategy for coordinated intersections to achieve the low carbon society. The conditions after implementation of several proposed signal control strategies were compared with the existing fixed time control condition. The traffic microsimulation model was applied to simulate the before and after traffic conditions. The traffic Measure Of Effectiveness (MOEs) and CO₂ emissions were considered as evaluation criteria. The traffic MOEs consist of the average travel time, average delay and average queue length of the total system. The CO₂ emission of the total system was also evaluated.

Calculation of CO₂ Emission

This study applied the methodology and the developed CO₂ emission model of motorcycle for the traffic microsimulation model, from the previous study [14], to calculate CO₂ emission of all vehicles. This study also applied the emission data measured in the Automotive Emissions Laboratory of the Pollutant Control Department [15] to develop CO₂ emission models according to fuel type, including gasoline and diesel. The results from the traffic microsimulation model, including the instantaneous speed and acceleration of each individual vehicle, were applied with the CO₂ emission models to calculate the CO₂ emission.

CO₂ emission rates (g/s) according to a motorcycle, a gasoline vehicle and a diesel vehicle were calculated by follow Eq. (1), (2) and (3):

$$LN (ER_{MC}) = 0.269 + 0.005u - 0.548a \quad (1)$$

$$LN (ER_{Gasoline}) = -1.003 + 0.02u + 0.51a \quad (2)$$

$$LN (ER_{Diesel}) = -0.239 + 0.028u + 0.193a \quad (3)$$

where ER is the emission rate (g/s), u is the instant speed (kph) and a is the instant acceleration (m/s²)

For each vehicle, its total emission was calculated from a summary of instantaneous values at each second. Finally, the total emission of all vehicles was calculated using Eq. (4).

$$\text{Total CO}_2\text{Emission} = \sum_k \sum_j \sum_i \text{Instant Emission of a Vehicle} \quad (4)$$

where

i= 1, 2, 3, ..., n (Number of time steps in second)

j= 1, 2, 3, ..., m (Number of vehicles)

k= 1= motorcycle, 2=passenger car, 3=pickup truck and van, and 4=truck and bus

RESULTS AND DISCUSSION

This section presents the results of the development of the traffic microsimulation model and the evaluation results of proposed signal control strategies for Low Carbon Society.

Results of the Model Calibration

The result of the model calibration for traffic flow is presented in Table 1. The difference between the observed and modeled traffic flow and GEH of all links passed the acceptance target, proposed by the Wisconsin Department of Transport [12]. This result means that simulated traffic volume is close to traffic volume in the field. The result of the model calibration for a maximum queue length is presented in Table 2. The difference between the observed and modeled maximum queue length passed the acceptance target, proposed by Ahmed [13]. This result means that maximum queue length of simulated traffic flow is close to maximum queue length in the field. In addition, the result of the model calibration for traffic time is presented in Table 3. The difference between the observed and modeled travel time of all vehicles passed the acceptance target, proposed by the Wisconsin Department of Transport [12]. These results imply that the developed traffic microsimulation model could closely simulate traffic condition compared with real world conditions.

Evaluation Results of Signal Control Strategies

The evaluation results of the traffic flow measures of effectiveness as well as the emissions and fuel consumption are presented in Table 4. As expected, all proposed signal control strategies could improve max queue length, travel times, delays, stop time delays and reduce CO₂ emission in the selected study intersections.

The updated fixed time control decreased the average delays, the average stopped delays, the average travel times, the maximum queue length, and CO₂ emissions for the total systems by 9.1%, 12.1%, 7.6%, 2.1% and 0.4%, respectively. This result was caused by the signal timing updated according to the current traffic volume.

The coordinated control decreased the average delays, the average stopped delays, the average travel times, the maximum queue length, and CO₂ emissions for the total systems by 19.7%, 21.1%, 9.2%, 11.2% and 1.2%, respectively. This result was caused by the traffic along the major route could cross the intersections with less stop for the traffic signal.

Table 1 Results of model calibration of traffic flow

Link	Modeled (veh/hr)	Observed (veh/hr)	Diff. (veh/hr)	GEH	Acceptance target Diff.*	GEH**	Pass/fail
<i>Intersection 1</i>							
SB-L	51	46	-5.0	0.72	Within 100	<5	Pass
SB-T	355	355	0.0	0.00	Within 100	<5	Pass
SB-R	100	108	8.0	0.78	Within 100	<5	Pass
NB-L	68	58	-10.0	1.26	Within 100	<5	Pass
NB-T	374	380	6.0	0.31	Within 100	<5	Pass
NB-R	63	67	4.0	0.50	Within 100	<5	Pass
WB-L	57	53	-4.0	0.54	Within 100	<5	Pass
WB-T	258	238	-20.0	1.27	Within 100	<5	Pass
WB-R	79	67	-12.0	1.40	Within 100	<5	Pass
EB-L	36	42	6.0	0.96	Within 100	<5	Pass
EB-T	217	206	-11.0	0.76	Within 100	<5	Pass
EB-R	252	233	-19.0	0.16	Within 100	<5	Pass
<i>Intersection 2</i>							
SB-L	52	54	2.0	0.27	Within 100	<5	Pass
SB-T	361	345	-16.0	0.85	Within 100	<5	Pass
SB-R	39	52	13.0	1.93	Within 100	<5	Pass
NB-L	185	205	20.0	1.43	Within 100	<5	Pass
NB-T	476	478	2.0	4.94	Within 100	<5	Pass
NB-R	86	107	21.0	2.14	Within 100	<5	Pass
WB-L	30	35	5.0	0.88	Within 100	<5	Pass
WB-T	252	250	-2.0	0.13	Within 100	<5	Pass
WB-R	30	36	6.0	1.04	Within 100	<5	Pass
EB-L	95	80	-15.0	1.60	Within 100	<5	Pass
EB-T	304	291	-13.0	0.75	Within 100	<5	Pass
EB-R	120	136	16.0	1.41	Within 100	<5	Pass
<i>Intersection 3</i>							
SB-L	12	22	10.0	2.43	Within 100	<5	Pass
SB-T	459	448	-11.0	4.43	Within 100	<5	Pass
SB-R	143	203	60.0	4.56	Within 100	<5	Pass
NB-L	217	215	-2.0	0.14	Within 100	<5	Pass
NB-T	525	539	14.0	0.61	Within 100	<5	Pass
NB-R	104	95	-9.0	0.90	Within 100	<5	Pass
WB-L	24	29	5.0	0.97	Within 100	<5	Pass
WB-T	85	81	-4.0	0.44	Within 100	<5	Pass
WB-R	33	21	-12.0	2.31	Within 100	<5	Pass
EB-L	85	102	17.0	1.76	Within 100	<5	Pass
EB-T	67	80	13.0	1.52	Within 100	<5	Pass
EB-R	252	233	-19.0	1.22	Within 100	<5	Pass

*Diff., hourly link flow of modeled versus observed within 100 veh/h, for flow < 700 veh/h, within 15% for 700veh/h < flow < 2,700 veh/h;

**GEH statistics < 5; $GEH = \sqrt{(V - C)^2 / ((V + C)/2)}$, where GEH is GEH statistic; V is simulated traffic flow; C is surveyed traffic flow; [12].

Table 2 Results of the model calibration of the maximum queue length

Link	Modeled (m)	Observed (m)	Diff. (%)	Acceptance target (Diff.*)	Pass/fail
<i>Intersection 1</i>					
SB	52	54	3%	Within 20%	Pass
WB	59	72	18%	Within 20%	Pass
NB	102	126	19%	Within 20%	Pass
EB	50	48	-5%	Within 20%	Pass
<i>Intersection 2</i>					
SB	96	96	0%	Within 20%	Pass
WB	63	66	4%	Within 20%	Pass
NB	112	96	-17%	Within 20%	Pass
EB	77	72	-7%	Within 20%	Pass
<i>Intersection 3</i>					
SB	158	162	3%	Within 20%	Pass
WB	21	18	-17%	Within 20%	Pass
NB	129	126	-2%	Within 20%	Pass
EB	64	72	11%	Within 20%	Pass

*Diff., maximum queue length of modeled versus observed within 20% [13].

Table 3 Results of the model calibration of the travel time

Link	Modeled (s)	Observed (s)	Diff. (%)	Acceptance target (Diff. *)	Pass/fail
NB	296	265	-12%	Within 15	Pass
SB	304	302	-1%	Within 15	Pass

*Diff, travel time of modeled versus observed within 15% [12].

Table 4 Results of the effectiveness of traffic flow measures and CO₂ emission reduction among scenarios

Parameters	Existing	Fixed time	Coordinated	Semi-actuated	Fully-actuated
Delay (s/veh)	123	111 (-9.1%)	98 (-19.7%)	105 (-14.6%)	68 (-44.3%)
Stopped delay (s/veh)	96	84 (-12.1%)	76 (-21.1%)	79 (-17.8%)	43 (-55.1%)
Travel time (s/veh)	1,141	1,075 (-7.6%)	1,060 (-9.2%)	1,059 (-6.3%)	876 (-28.1%)
Max queue length (m)	1,203	1,037 (-2.1%)	740 (-11.2%)	832 (-4.1%)	808 (-29.2%)
CO ₂ emission (kg/hr)	2,151	2,142 (-0.4%)	2,126 (-1.2%)	2,138 (-0.6%)	1,963 (-8.7%)

The semi-actuated control decreased the average delays, the average stopped delays, the average travel times, the maximum queue length, and CO₂ emissions for the total systems by 14.6%, 17.8%, 6.3%, 4.1% and 0.6%, respectively. This result was caused by a facilitation of the traffic along minor routes

The fully-actuated control decreased the average delays, the average stopped delays, the average travel times, the maximum queue length, and CO₂ emissions for the total systems by 44.3%, 55.1%, 28.1%, 29.2% and 8.7%, respectively. It caused that traffic along major and minor routes could pass the intersections with less stop.

Consequently, the fully vehicle actuated signal control is the most efficient strategy among the proposed strategies.

CONCLUSIONS AND RECOMMENDATIONS

This study proposed and evaluated the several signal control strategies to increase the level of service of the intersections and decrease CO₂ emission of total systems. The developed traffic microsimulation model was applied to evaluate the proposed strategies. The study found that the fully vehicle actuated signal control was the best strategy to improve the level of service of intersections and to reduce CO₂ emission. It should be promoted to achieve the low carbon society.

As recommendations for further studies, the study on providing advanced information regarding signal phases and timing to vehicles travelling on a signalized corridor, extending from cars [16, 17] to motorcycles with the vehicle actuated signal control for developing countries, should be evaluated on its increasing intersection's level of service and reduction on CO₂ emission.

ACKNOWLEDGEMENTS

The authors would like to express their appreciation to the Farm Engineering and Automatic Control Technology Research Group (FEAT) at Khon Kean University for a financial support on this research.

REFERENCES

- [1] Intergovernmental Panel on Climate Change (IPCC). IPCC Guidelines for National Greenhouse Gas Inventory, Volume 1, Revised, Reporting Instructions, 2006.
- [2] National Institute for Environmental Studies (NIES). Asian Low Carbon Society Research Project. Report. National Institute for Environmental Studies. Japan, 2011.
- [3] World Conference on Transport Research Society (WCTRS), Putting Transport into

Climate Policy Agenda - Recommendations from WCTRS to COP18, Report, 2012.

- [4] Klungboonkrong, P., Jaensirisak, S., Satiennam, T., Potential performance of urban land use and transport strategies in reducing greenhouse gas emissions: Khon Kaen case study, Thailand, International Journal of Sustainable Transportation, Vol.11, No.1, 2017, pp.36-48.
- [5] Satiennam, T., Jaensirisak, S., Natevongin, N. and Kowtanapanich, W., Public Transport Planning for a Motorcycle Dominated Community, Journal of the Eastern Asia Society for Transportation Studies, Vol.9, 2011, pp.970-985.
- [6] Satiennam, T., Satiennam, W., Tankasem, P., Jantosut, P., Thengnamlee, J., & Khunpumphat, W., A Study of Potential Electric Motorcycle Use to Support a Low Carbon Society: Case of a Developing Asian City, Advanced Materials Res., Vol. 931-932, 2014, pp. 541-545.
- [7] Department Of Highway (DOH), 2015, Traffic Volumes along Main National Highways in 2014 <<http://bhs.doh.go.th/download/traffic>>.
- [8] Roess P, Prassas S and McShance S. Traffic Engineering Four Edition. [n.p.]: Transportation and System Engineering, 2010.
- [9] Federal Highway Administration., Traffic Signal Timing Manual chapter5, from <http://ops.fhwa.dot.gov/publications/fhwahop08024/chapter5.htm>, 2015.
- [10] Dowling R, Skabardonis A, and Alexiadis V., Traffic Analysis Toolbox Volume III: Guidelines for Applying Traffic Microsimulation Software, Report No. FHWA-HRT-04-040, Contract or Grant No. DTFH61-01-C-00181, FHWA, 2004.
- [11] Dowling R, Skabardonis A, Halkias J, McHale G and Zammit G., Guidelines for Calibration of Microsimulation Models Framework and Applications, In Transportation Research Record: Journal of the Transportation Research Board, No. 1876, TRB, National Research Council, Washington D.C, 2004, pp. 1–9.
- [12] Freeway System Operational Assessment, Paramics Calibration & Validation Guidelines, Technical Report I-33 (Draft), Milwaukee, Wis, USA, Wisconsin Department of Transportation, 2002.
- [13] S. Ahmed, Calibration of Vissim to the Traffic Conditions of Khobar and Dammam, Saudi Arabia [Master, Thesis], King Fahd University of Petroleum and Minerals, Saudi Arabia, 2016.

- [14] Satiennam, T., Seedam, A., Radpukdee, T., Satiennam, W., Pasangtiyo, W, and Hashino, Y., Development of On-Road Exhaust Emission and Fuel Consumption Models for Motorcycles and Application through Traffic Microsimulation, *Journal of Advanced Transportation*, Vol. 2017, 2017.
- [15] Office of Transport and Traffic Policy and Planning (OTP), The Study to Develop Master Plan for Sustainable Transport System and Mitigation of Climate Change Impacts, Final Report, Office of Transport and Traffic Policy and Planning, Thailand, 2013.
- [16] Barth, M., Mandava, S., Boriboonsomsin K., and Xia H., Dynamic ECO-driving for arterial corridors, in *Proceedings of the IEEE Forum on Integrated and Sustainable Transportation Systems (FISTS '11)*, pp. 182–188, Vienna, Austria, June-July 2011.
- [17] Xia, H., Boriboonsomsin, K., and Barth, M., Indirect networkwide energy/emissions benefits from dynamic eco-driving on signalized corridors, in *Proceedings of the 14th IEEE International Intelligent Transportation Systems Conference (ITSC'11)*, pp. 329–334, IEEE, Washington, DC, USA, October 2011.

EXPERIMENTAL STUDY ON THE EFFECT OF STEEL FIBER WASTE TYRE ON HIGH STRENGTH CONCRETE

Fauzan¹, Rudy Kurniawan², Oscar Fitrah N³, Claudia Lovina A. N⁴,
^{1,2,3,4}Engineering Faculty, Andalas University, Padang, West Sumatera, Indonesia

ABSTRACT

High strength concrete (HSC) is defined as concrete with a specified compressive strength of 40 MPa or greater. Concrete with high strength is basically a brittle material, with low tensile strength. Another problem to note is the incidence of cracks in HSC due to the tensile stress. One way to improve the brittle and weak concrete properties towards tensile strength is by utilizing fiber. The utilization of steel fiber from waste tires (SFWT) in high strength concrete can be used as an alternative to improve the mechanical properties of the concrete and also has benefit to reduce the waste of used tires that are increasing every year. This research was conducted to determine the effect of the addition of steel fiber waste tire on high strength concrete (HSC) and high strength concrete containing silica fume (HSCSF). Steel fiber waste tyre is obtained from the extracting of used tires that are cut into 4 cm long. The specimen used is a cylinder with a diameter 15 cm, height 30 cm and beam with dimension 10x10x50 cm. The content of silica fume on high strength concrete is 10% by replacing of the cement weight. The addition of steel fiber waste tire in both HSC and HSCSF are 0%, 0.5%, 1.0%, 1.5%, and 2%. Mechanical properties of concrete such as compressive strength, tensile strength and flexural strength are tested at 28 days age. The results show that the addition of SFWT increases the compressive strength, tensile strength and flexural strength of HSC and HSCSF. The increase of SFWT content results in the higher mechanical properties of the high strength concrete. In addition, the presence of SFWT in the high strength concrete delays the crack width of the concrete and prevents the brittle collapse.

Keywords: High strength concrete, Steel fiber waste tire, Silica fume, Concrete properties

INTRODUCTION

Concrete is the oldest and the most widely used material in the history of human development. In general, the strength and performance of concrete before the 20th century is still low and then, it is developed to the high strength concrete (HSC). The high strength concrete is concrete with compressive strength implies 40 MPa or greater. The higher compressive strength of concrete results reduction in the size of structural elements such as columns and beams [1].

HSC can be produced by reducing the water-cement ratio of the concrete. The reduction of the water-cement ratio results in a decrease in porosity and refinement of capillary pores in the matrix so the mechanical properties will increase. However, it will affect the concrete workability. An alternative to make HSC is by using pozzolanic admixtures such as silica fume. Silica fume is a by product of producing silicon metal or ferrosilicon alloys that is very reactive pozzolan. It has been proved that the addition of silica fume on HSC increase the compressive strength, flexural strength and durability, in which the highest increase was found with the replacement of 10% and 15% silica fume by cement weight [2].

High strength concrete is inherently a brittle material, with low tensile strength and limited ductility.

Also, the cracks of HSC will easily occur due to the tensile stress. One way to improve the brittle and weak concrete tensile strength is by utilizing fiber. Fibers help to improve the post-peak ductility performance, pre-crack tensile strength, impact strength, fatigue strength, and eliminate temperature and shrinkage cracks [3]. Several studies have proved that the addition of fiber in high strength concrete can improve the mechanical properties of its concrete [4]-[8].

The utilization of special steel fiber from the used tire (steel fiber waste tire) on high strength concrete can be an alternative to produce HSC with high tensile strength. The large number of waste tires production is potential to be used to the improve the mechanical properties of HSC. This research focused on the investigation on the effect of steel fiber waste tire addition on HSC and high strength concrete containing silica fume (HSCSF).

MATERIALS AND METHODS

Materials Used

Cement

The cement that used in this research is Ordinary Portland Cement (OPC) produced by Padang Cement Factory, Indonesia.

Fine Aggregate

Locally available fine aggregate, with a maximum size of 4.75 mm is used in this study. The properties of the fine aggregate such as specific gravity, absorption, fineness modulus, and water content of fine aggregate can be seen in Table. 1

Table 1 Properties of fine aggregate

No	Property	Value
1	Specific gravity	2,44
2	Absorption	3,6 %
3	Fine Modulus(FM)	3,4
4	Water content	0,94 %

Coarse Aggregate

The locally coarse aggregate is used with the size of 5-10 mm. The properties of the coarse aggregate such as specific gravity, absorption, fineness modulus, and water content can be seen in Table. 2

Table 2 Properties of coarse aggregate

No	Property	Value
1	Specific gravity	2,51
2	Absorption	2,8 %
3	Fine Modulus (FM)	4,97 %
4	Water content	1,06 %

Water

Potable tap water which is free form acid and organic substance is used in mix preparation and curing concrete.

Steel Fiber Waste Tyre

In this study, the steel fibers taken out from waste tyres (Fig. 1) are used in the concrete mix to form a composite fibrous material. Steel fibers waste tyres (SFWT) are extracted from chips of waste tyres by the manual cutting process (Figs. 2 and 3) and cut to 4 cm length (Fig. 4), and an average diameter of the fiber is 028 mm keeping aspect ratio 80. The steel fibers are uniformly and randomly distributed in different proportions from 0-2% with an increment of 0,5% by the volume of concrete to prepare the different concrete matrix. The geometric characteristics of SFWT can be seen in Table 3.

Silica Fume

Silica fume that used in this research is Sika Fume produced by Sika Factory. The added silica fume material used meets the technical requirements in accordance with ASTM C 1240-00.

Superplasticizer

Superplasticizer used is Viscocrete-1003 manufactured by Sika Factory. The viscocrete-1003 additive material meets the technical requirements in accordance with ASTM C 494-92 Type F.



Fig. 1 Waste tyres



Fig. 2 Steel fibers extracted from waste tyres



Fig. 3 The 4cm length of steel fiber extracted from waste tyre

Table 3 Properties of steel fiber waste tyre

Characteristics of Steel fiber	Description
Form	Irregular, Sharp
Surface Texture	Invisible
Size	Diameter 0.5 mm and length 40 mm
Aspect Ratio	80
Density	7850 Kg/m ³
Tensile strength	500-2000 N/mm ²

EXPERIMENTAL PROGRAM

Mix Proportions of High Strength Concrete

A high strength concrete mix design is calculated according to the ACI (American Concrete Institute) method 211.4R-93. There are two variations of high strength concrete namely, high strength concrete and high strength concrete containing silica fume. The rate of addition of silica fume in the concrete mixture is 10% of the cement weight, in which the silica fume serves as a cement replacement material. The amount of steel fibers added in the concrete mixture is based on the total volume of the commonly referred concrete volume fraction. The mix proportions of high strength concrete (HSC) and high strength concrete containing silica fume (HSCSF) with the percentage of steel fiber waste tyre can be seen in Tables 4 and 5.

Table 4. Mix proportions of HSC

Material (Kg/m ³)	SF 0	SF 0.5	SF 1.0	SF 1.5	SF 2.0
Cement (Kg/m ³)	561.5	561.5	561.5	561.5	561.5
Sand (Kg/m ³)	638.7	638.7	638.7	638.7	638.7
Split 5/10 (Kg/m ³)	902.6	902.6	902.6	902.6	902.6
Water (Kg/m ³)	214.8	214.8	214.8	214.8	214.8
Steel Fiber (%)	0.0	0.5	1.0	1.5	2.0
Viscocrete 1003 (%)	0.69	0.69	0.69	0.69	0.69

* SF : Steel Fiber

Table 5. Mix proportions of HSCSF

Material (Kg/m ³)	SF 0	SF 0.5	SF 1.0	SF 1.5	SF 2.0
Cement (Kg/m ³)	505.3	505.3	505.3	505.3	505.3
Sand (Kg/m ³)	638.7	638.7	638.7	638.7	638.7
Split 5/10 (Kg/m ³)	902.6	902.6	902.6	902.6	902.6
Water (Kg/m ³)	214.8	214.8	214.8	214.8	214.8
Steel Fiber (%)	0.0	0.5	1.0	1.5	2.0
Silica Fume (Kg/m ³)	56.1	56.1	56.1	56.1	56.1
Viscocrete 1003 (%)	1.00	1.00	1.00	1.00	1.00

* SF : Steel Fiber

Casting of Specimens

There are 80 specimens were cast, consist of 60 cylinders specimens for compressive and splitting tensile strength tests and 20 specimens for the flexural strength test. The number of test specimens can be seen in Table 6.

Table 6. Number of test specimens

Type of concrete	Number of Concrete specimens		
	compressive	Tensile	Flexural
High strength concrete	15	15	10
High strength concrete with Silica Fume 10%	15	15	10
Total	30	30	20

Cylindrical moulds of 150 mm diameter and 300 mm length are used for casting the specimen for compressive and splitting tensile strength tests, respectively. For flexural strength test, beam specimen with the size of 100 x 100 x 500 mm is cast. The specimens are cast with 0%,0.5%,1%,1.5% and 2% content of SFWT on concrete with and without silica fume. All specimens were cured for 28 days.

Testing of Specimens

Testing of compressive strength and tensile strength is carried out on cylindrical test specimens by using a

compressive test apparatus at the Concrete Laboratory of Semen Padang Factory (Figs. 4 and 5). Flexural testing is carried out on beam specimens using a flexural testing machine in the concrete Laboratory of Semen Padang Factory (Fig. 6). Compressive, splitting tensile and flexural strengths of each specimen was determined using SNI 03-1972-2011, SNI 2491: 2014, and SNI 4154: 2014, respectively.



Fig. 4 Compressive test on cylindrical specimen



Fig. 5 Splitting tensile test on cylindrical specimen



Fig. 6 Flexural test on beam specimen

RESULTS AND DISCUSSION

Compressive Strength

The results of the compressive tests performed on HSC and HSCSF with different percentage of steel fibers tested on the 28th day is shown in Table 7 and Fig. 7.

Table 7 Test result of compressive strength

No.	SFWT (%)	Compressive Strength		Percentage of Increase	
		HSC (MPa)	HSCSF (MPa)	HSC (%)	HSCSF (%)
1	0	58.91	69.87	-	-
2	0.50	59.15	73.41	0.42	5.08
3	1.00	60.44	74.36	2.59	6.43
4	1.50	72.38	77.00	22.86	10.21
5	2.00	73.38	78.54	24.56	12.42

As seen in Table 7, the compressive strength of HSC and HSCSF containing SFWT increases with the increase of SFWT content. In HSC, the percentage increases in the compressive strength for the cylinder with 0.5%, 1%, 1.5% and 2% SFWT addition are 0.42%; 2.59%; 22.86%; and 24.56%, respectively. The highest value of compressive strength of 73,38 MPa was observed on HSC with 2% SFWT addition.

For HSCSF, meanwhile, the highest value of compressive strength occurred in the addition of SFWT by 2% that is 78.54 MPa, which is 12.4% increase in compressive strength compared to those without SFWT. Percentage increase of compressive strength with 0.5%; 1.0%; 1.5%; and 2% SFWT addition are 5.08%; 6.43%; 10.21%; and 12.24%, respectively.

The comparison of compressive strength between HSC and HSCSF with variation SFWT content is shown in Fig. 7.

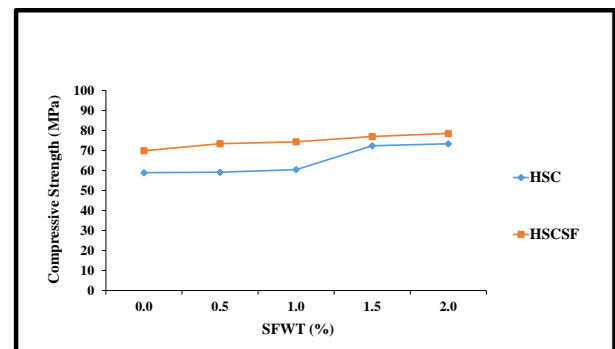


Fig. 7 Comparison of compressive strength between HSC and HSCSF with different SFWT content

As can be seen in Fig. 7, the increase in compressive strength between HSC and HSCSF has the different tendency. However, the compressive

strength of HSCSF was higher than those of HSC in each SFWT content. This indicates that the presence of Silica fume results in the higher concrete compressive strength.

Tensile Strength

Tensile strength test results on HSC and HSCSF with different content of SFWT is shown in Table 8 and Fig. 8.

Table 8 Test result of splitting tensile strength

No.	SFWT (%)	Tensile Strength		Percentage of Increase	
		HSC (MPa)	HSCSF (MPa)	HSC (%)	HSCSF (%)
1	0	3.85	5.61	-	-
2	0.50	4.77	5.65	23.87	0.76
3	1.00	4.87	6.10	26.32	8.83
4	1.50	7.61	7.75	97.55	38.27
5	2.00	8.27	9.14	114.69	62.99

The test results indicate that the tensile splitting strength increases as the increase the SFWT content on both HSC and HSCSF from 0% to 0.5%, 1%, 1.5%, and 2%. This might be in consequence of the strong mechanical interlocking force in the concrete due to the present SFWT.

For HSC, it is found that the maximum splitting tensile strength by adding 2% SFWT is 8.27 MPa, which is 114.69% increase as compared to HSC without SFWT. In HSCSF, on the other hand, the maximum percentage increase of the tensile strength at 2% SFWT content is less than those in HSC, that is 62.99% (9.14 MPa).

Fig. 8 shows the comparison of tensile strength between HSC and HSCSF with variation SFWT content.

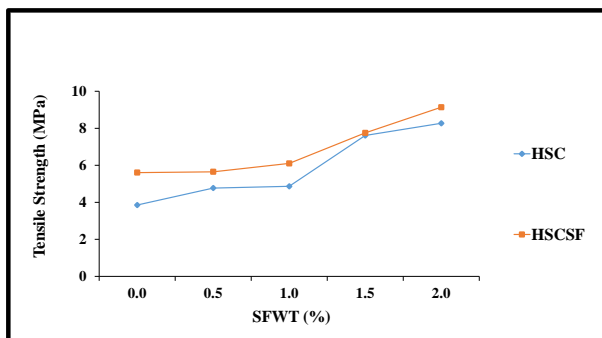


Fig. 8 Comparison of Tensile Strength between HSC and HSCSF with different SFWT content

Compare to HSCSF, the increase of tensile strength is more significant at each SFWT content. However, both HSC and HSCSF show almost similar increment

on tensile strength from 0.5% to 1% SFWT content. In general, the tensile strength of HSCSF is higher than those of HSC at each SFWT content.

Flexural Strength

The results of the flexural strength tests performed on HSC and HSCSF at different percentage of SFWT content is shown in Table 9 and Fig. 9.

Table 9 Test results of flexural strength

No.	SFWT (%)	Flexural Strength		Percentage of Increase	
		HSC (MPa)	HSCSF (MPa)	HSC (%)	HSCSF (%)
1	0	6.23	7.18	-	-
2	0.50	6.89	8.10	10.47	12.85
3	1.00	7.27	8.57	16.61	19.44
4	1.50	8.33	9.18	33.57	27.90
5	2.00	10.73	11.68	72.20	62.70

From Table 9, it can be seen that in general, there is an increase in flexural strength from the addition of 0.5%, 1%, 1.5% and 2% SFWT to both HSC and HSCSF. Steel fiber in the concrete increases the flexural strength. The highest content of fibers gives the maximum increase of the strength. The highest percentage of increase in flexural strength was observed with the addition of 2% SFWT content that is 72.2% and 62.7% for HSC and HSCSF, respectively. The maximum flexural strength on HSC and HSCSF are 10.73 MPa and 11.68 MPa, respectively.

The tendency of increase in flexural strength is almost similar for both HSC and HSCSF at each SFWT content, as shown in Fig. 9.

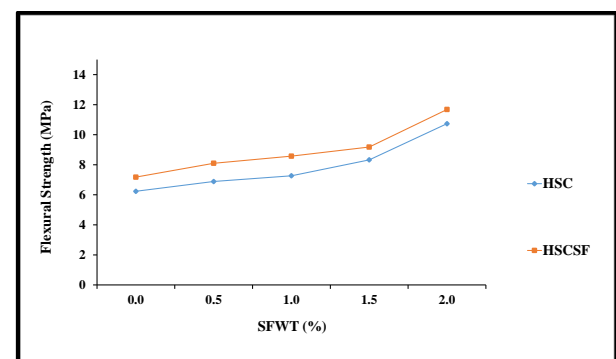


Fig. 9 Comparison of Flexural Strength between HSC and HSCSF with different SFWT content

The increases of the flexural strength with the addition of steel fiber waste tire due to the influence of high strength concrete bonds with added materials in the form of SFWT. The fiber bonds on high strength concrete can be seen in Figs. 10 and 11. The presence of SFWT increases resistance to cracking. It is clearly

seen from Fig. 11 that the steel fiber from waste tyre bridges across the cracked matrix, which will provide the higher bonding on the HSC.

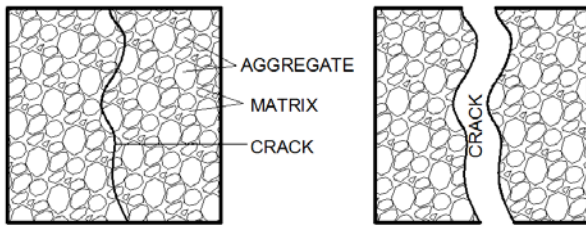


Fig. 10 Illustration of cracks in high strength concrete without SFWT

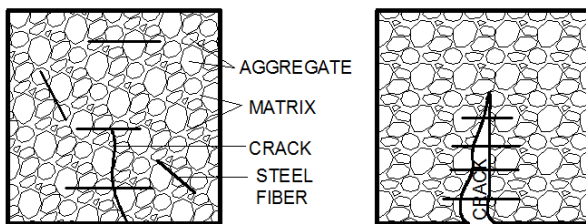


Fig. 11 Illustration of cracks in high strength concrete with the addition of SFWT

In Figs. 10 and 11, cracks in high strength concrete can pass through aggregates and matrix. This is because the mechanical properties of aggregates and matrix in high strength concrete are very similar (equally strong).

High strength concrete bonds with steel fiber waste tire can prevent the spreading of irregular small cracks in the concrete caused by the added load when the concrete is tested. So with the increase of steel fiber waste tire on the concrete, the less likely the occurrence of cracks (collapse) and test objects can receive a greater load again. In addition, steel fiber waste tire can also increase ductility, where steel fiber is still able to bind cracks in the cracks, so it can prevent the brittle collapse.

CONCLUSION

1. The addition of SFWT from 0.5% to 2% in HSC and HSCSF increases the compressive strength, tensile strength and bending strength. This is due to the contribution of the fiber to bond the concrete, reduce the cracks and prevent a brittle collapse.
2. In HSC, there is no significant increase of compressive strength with 2.0% SFWT addition, that is 24.56%, while, the significant increases of tensile and flexural strength are observed on HSCSF that are 114.7% and 72.2%, respectively.
3. For HSCSF, the replacement of 10% cement weight by silica fume results in higher of the concrete strength compared with HSC at each SFWT content. The maximum percentage increase of the compressive, tensile and flexural strength was observed on 2% SFWT addition that are 12.4%; 73.0%; and 62.7%, respectively.

ACKNOWLEDGEMENTS

The authors acknowledge the staffs of the Laboratory of Material and Structure in Andalas University and Concrete Laboratories of Padang Cement Factory Padang, Indonesia for their support.

REFERENCES

- [1] Rashid, Mohammad Abdur, and Mohammad Abul Mansur, "Considerations in producing high strength concrete", *Journal of Civil Engineering (IEB)*, 37(1) (2009) 53-63
- [2] Amarkhail, Nasratullah., "Effects of Silica Fume on Properties of High-Strength Concrete", *International Journal of Technical Research and Applications* e-ISSN: 2320-8163
- [3] Mhaske, Vijay M, Rahul D. Pandit and A. P. Wadekar, "Study on Behavior on High Strength Crimped Steel Fibre Reinforced Concrete for Grade M90", *IJRET: International Journal of Research in Engineering and Technology* eISSN: 2319-1163, ISSN: 2321-7308
- [4] Zhao, Qingxin., et. al., "Effect of Fiber Types on Creep Behavior of Concrete", *Construction and Building Materials* 105 (2016) 416-422
- [5] V, Raikar R., Karjinni V.V, and Gundakalle V. D, "Study on Strength Parameters of Steel Fiber Reinforced High Strength Concrete", *Int. Journal of Applied Sciences and Engineering Research*, Vol. 1, Issue 4, 2012, ISSN 2277 – 9442
- [6] Velayutham, G., and C. B. Cheah, "The Effects of Steel Fibre on the Mechanical Strength and Durability of Steel Fibre Reinforced High Strength Concrete (SFRHSC) Subjected to Normal and Hygrothermal Curing", *MATEC Web of Conferences* 10, 02004 (2014)
- [7] Ashwani., "To Study the Effect of Steel Fibers on Strength of Concrete with Partially Replaced Marble Dust", *International Journal of Science and Research (IJSR)*, ISSN (Online): 2319-7064
- [8] Aydin, Serdar, "Effects of Fiber Strength on Fracture Characteristics of Normal and High Strength Concrete", *Rperiodica polytechnic, Civil Engineering*, Department of Civil Engineering, DokuzEylül University, Buca 35160, Izmir, Turkey.

AN ANALYTICAL INVESTIGATION OF EWECS COMPOSITE COLUMN WITH AND WITHOUT SHEAR STUD

Fauzan¹, Ruddy Kurniawan² and Zev Al Jauhari³

^{1,2}Civil Engineering Department, Andalas University, Indonesia; ³Bengkalis State Polytechnic, Indonesia

ABSTRACT

This paper explains about numerical analysis of EWECS (Engineering Wood Encased Concrete-Steel) column accompanied with shear stud connection under constant axial and lateral cyclic loads based on the previous experiment. This is the new structure system contains concrete encased steel (CES) core with an exterior wood panel. The experiment was performed in a variation of wood panel connection to the concrete. In this study, the non-linear finite element (FE) analysis is performed by modeling the column with 3D solid element and the friction devices of shear stud with two-node-link element. The hysteresis characteristics comparison between experiment and numerical results show that the peak forces in the every last loops (story drift) and hysteresis curves shape have similarity as well as on the main stiffness, ductility, and energy dissipation. The presence of shear studs on EWECS columns improved the ductility of the column and reduced the damage of wood panel, but there was no much influence on maximum flexural strength of the column. With shear studs, the wood panel contributed to flexural capacity until maximum story drift, R of 5%, although cracks appeared at the column faces after R of 4%. Generally, the analytical method can be used to predict accurately the ultimate strength and behavior of EWECS columns.

Keywords: EWECS column, shear stud, cyclic load, numerical analysis

INTRODUCTION

To solve a problem on the story number limitation for wood structures (unfireproof material) that limited to not more than three stories based on the Building Standard Law of Japan [1], the type of hybrid structural system that called as EWECS (engineering wood encased concrete-steel) structural system has been developed by one of the authors in Japan. The proposed structural system consists of EWECS columns and engineering wood encased steel (EWES) beams, as shown in Figure 1. For the first stage of the research program, composite EWECS columns were investigated. The EWECS column consists of an exterior wood panel with concrete encased steel (CES) core (Figure 1).

In our previous studies [2], the seismic performance of EWECS column using double H-section steel had been tested to apply to columns subjected to bending moments and shear forces in two directions, such as those in the structure of frame. The results show that the column had a stable spindle-shaped hysteresis curve without degradation of load-carrying capacity until large story drift, R of 5%. It was also found that the wood panel presence on the EWECS column contributed to flexural capacity by around 12% in peak of every loop. Furthermore, EWECS columns using single H-section steel, are being developed to apply to columns of one way moment frame connected with shear wall in the orthogonal directions [3].

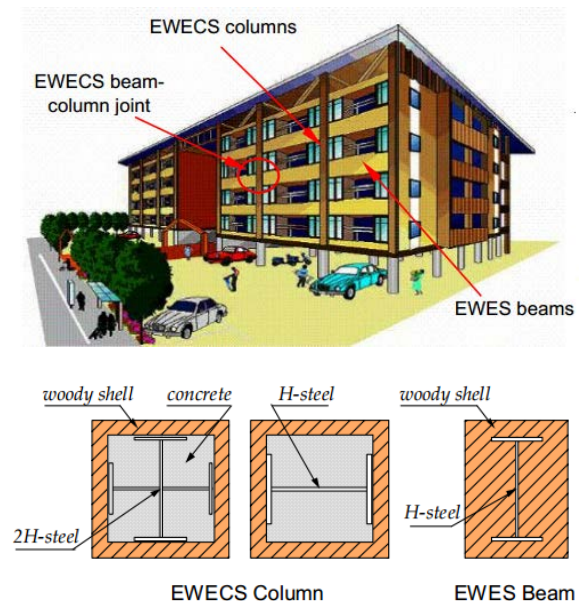


Fig. 1 Schematic view of EWECS structural system [2].

Composite action enhances structural efficiency by combining the structural elements to create a single composite section. The term “full shear connection” relates to the case in which the connection between the components is able to fully resist the forces applied [4]. The component that assures the shear transfer between the wood panel

and the concrete encased steel core in the composite construction is the shear stud. The shear studs made from steel bolts were attached from the wood panel to CES core along the column height for the column, as shown in Figure 2. The purpose of the shear studs is to enhance the bond between the CES core and the wood panel, thereby increasing the composite action of the column. The effect of shear studs on the behavior of WECS columns can be examined by comparing Models WC1 (without shear stud) and WC1-S (with shear stud). Both specimens have the same column dimensions and configurations, and the main difference is only the presence of the studs.

The objective of this research is to develop a finite element model (FEM) using ANSYS APDL 14.0 [5] to predict the response and behavior of WECS composite column subjected to lateral cyclic loads. The developed model takes into consideration the nonlinear behavior of concrete and contact between surfaces. The results of the FE model were validated with experimental test results that were conducted at Japan [2].

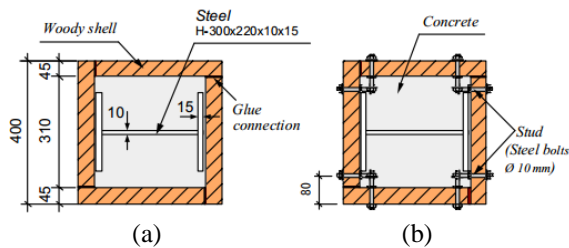


Fig. 2 The dimension and cross section of (a) WC1 and (b) WC1-S specimens [3].

ANALYTICAL WORK

Finite element analysis is a numerical method of deconstructing a complex system into very small pieces called elements. The software implements equations that govern the behaviour of these elements and solve them all, creating a comprehensive explanation of how the system act as a whole. These results then can be presented in tabulated, or graphical forms.

The 3D Models Detail

All the model of column had 1600 mm height and 400 x 400 mm² cross-section. A composite section is modelled with a single H-section steel of 300 x 220 x 10 x 15 mm and the thickness of the wood panel was 45 mm. The model of the column composite is shown in Figure 3. FEM is the outlines of the elements used to model the object of interest. An important aspect of FE modeling that affects the analysis is the aspect ratio of plane elements. The aspect ratio describes the shape of the element in the assemblage. The optimal aspect ratio at any location

within the grid depends largely on the rate of change of displacement in different directions. The total number of elements used is 7810 elements which is an adequate refinement for the constructed 3D FE model.

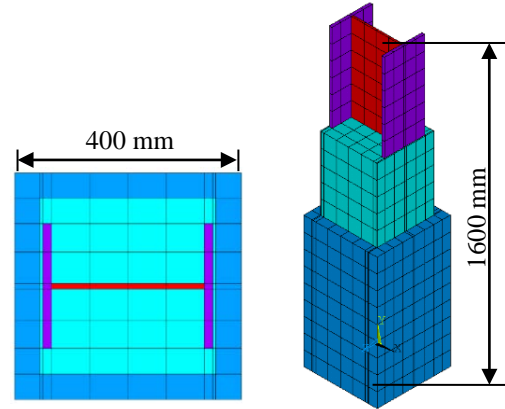


Fig. 3 The 3D FE model of WECS column.

Material Properties

The characteristics of the WECS column model and the real properties of materials are presented in Table 1. The materials properties of the section are incorporated to observe the realistic behavior.

Table 1 Material properties of WECS column

Material	Property	Value
Concrete	Compressive strength f_c' (MPa)	35
	Tensile strength f_t (MPa)	3.1
	Young's modulus E_c (MPa)	27800
	Poisson's ratio ν	0.2
	Ultimate comp. strain	0.0025
Steel (Web)	Yield stress f_{sy} (MPa)	313.3
	Poisson ratio ν	0.3
	Young's modulus E_s (MPa)	156700
Steel (Flange)	Yield stress f_{sy} (MPa)	293.6
	Poisson ratio ν	0.3
	Young's modulus E_s (MPa)	146800
Wood	*Compressive strength f_{cw}' (MPa)	45
	Tensile strength f_{tw} (MPa)	5
	Young's modulus E_c (MPa)	11500
	Poisson's ratio ν	0.34
	Ultimate comp. strain	0.0025

Note: * the direction is parallel to axis of grain.

Element Types Adopted

For representation of concrete, an eight node solid element SOLID 65 was used. The solid

element has eight nodes with three degree of freedom at each node with translations in the nodal x, y and z directions, as seen in Figure 4. The element is capable of plastic deformations, cracking in three orthogonal directions, and crushing. The most important aspect of this element is the treatment of non-linear properties.

The SOLID185 element is a 3D hexahedral element defined by eight nodes as shown in Figure 5. The element has three translational degrees of freedom at each node in the nodal x, y, and z directions. The element has capability of plastic deformation, hyperelasticity, stress stiffening, creep, large deflection, and large strain.

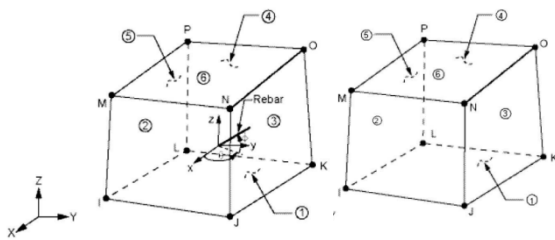


Fig. 4 ANSYS Solid65 and Solid185 elements [5].

Two element types (CONTA174 and TARGE170) are used for the contact and target surfaces since the contact is between two different surfaces. Surfaces with finer mesh were designated as contact surface while surfaces with coarser meshes were considered target surfaces. The contact element has eight nodes as shown in Figure 5. Accordingly, FE analysis sets the normal pressure to zero if separation occurs between the surfaces in contact [6].

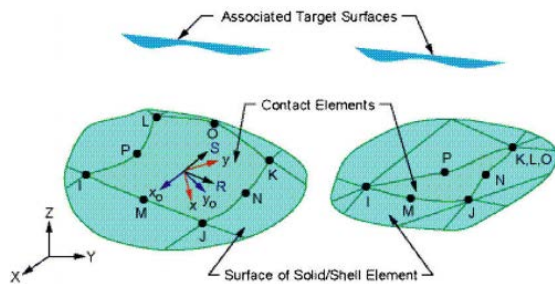


Fig. 5 ANSYS Conta174 element [5].

Constitutive Model of Material

Concrete

Concrete is a quasi-brittle material and has different behavior in tension and compression. In compression, the stress - strain curve for concrete is linearly elastic up to 30 % of the maximum compressive strength. The concrete constitutive material model used here to define the failure of

concrete is based on William and Warnke formulation [9].

An isotropic multi-linear compressive stress-strain curve for concrete is used to define the plastic behavior of concrete. The stress-strain relationship in the rising region was designed on the model developed by Saenz [7], which was built in the program, as seen in Figure 6. To account for shear stiffness reduction by shear crack deformation, shear transfer model developed by Al-Mahaidi was included in the analysis, with the use of modified shear transfer coefficient, β , of 0.75 [8].

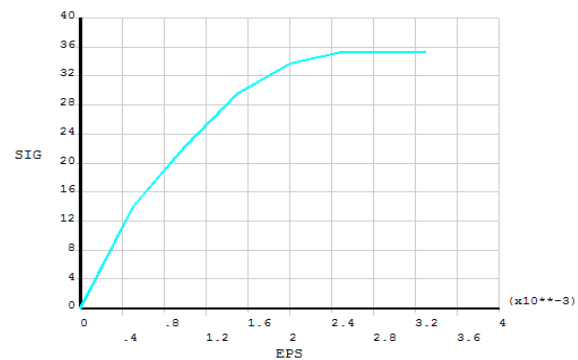


Fig. 6 Compressive stress-strain relationship for concrete.

Steel

The steel element used in ANSYS was considered to be perfectly elastic material and identical in tension and compression. The constitutive model of the steel encased inputed is shown in Figure 7.

Wood Panel

The constitutive model of wood in the paper is shown in Figure 8. Owing to the design to allow the force to be applied in the direction parallel to the annual growth ring of the wood, some existing concrete models built in the program by many researchers might be used in the analysis with some modifications. Stress-strain relationship in the rising region was modeled with the linearly increasing (perfectly elastic - plastic criterion) model, and slightly reduced by 5% for the wood without shear stud.

The fracture criterion of wood was adopted following the rule of the five parameter model of William-Warnke [9] for concrete with the input of wood material characteristic. To account for shear stiffness reduction by shear crack deformation, the shear transfer model for concrete developed by Al-Mahaidi was included with the use of modified shear transfer coefficient β of 0.35 for wood [8].

In this study, the material interface of the FE model between steel and concrete is considered

perfectly-bonded [11], while the material interface between concrete and wood for WC1 is unbonded performed by slightly reducing the stress-strain relationship of wood. The material interface between concrete and wood for WC1-S is assumed perfectly bond [12].

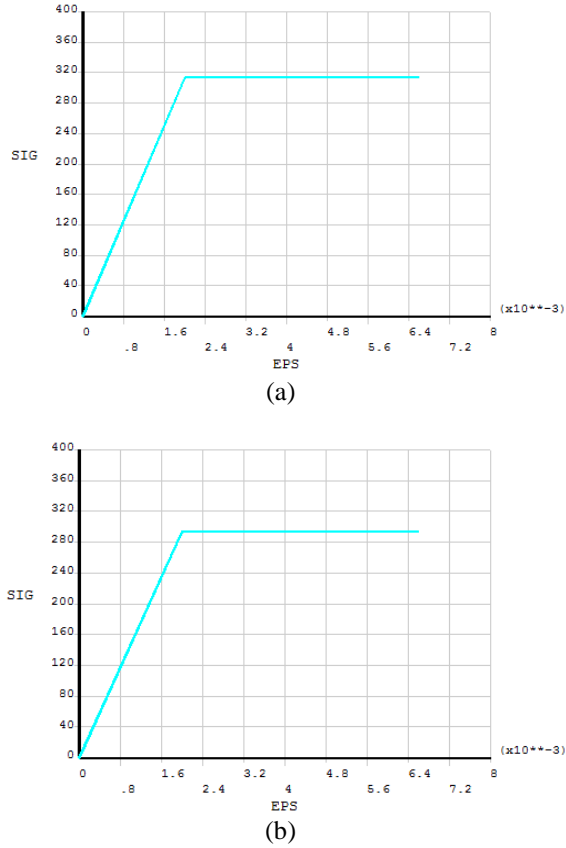


Fig. 7 Tensile stress-strain relationship for (a) web and (b) flange encased steel.

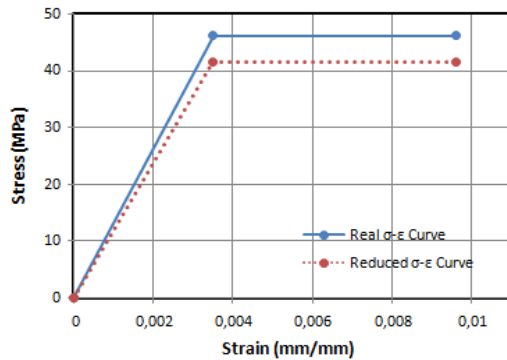


Fig. 8 Compressive stress-strain relationship for wood.

Boundary Conditions

The experimental work has been done to test the axial and lateral loads carrying capacity of EWECS column were performed by fixing the bottom end

against every possible movement, while applying the load was at the upper end. To duplicate such a procedure, the bottom end (anchor plate/ stub 700.700.400 mm) of the simulated specimens was fixed against all the degrees of freedom, as seen in Figure 9. The load application was performed by applying displacement to the upper end and the load-bearing capacity of the column was measured using a reference point at the lower end [13].

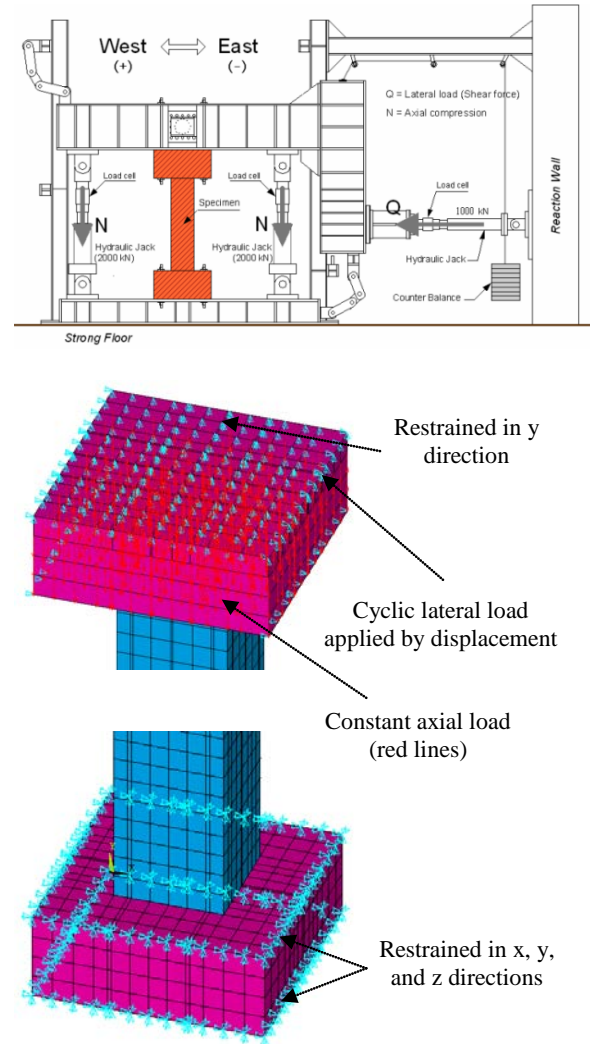


Fig. 9 Boundary conditions of FE model

Loads

The loads are made to consider the experimental test setup. The top-most columns were subjected to a constant axial load of 1031 kN represented by applying a point pressure of 1.4 kN on the stub elements with a total nodal of 717 in the FE model. The horizontal displacements were provided to simulate the cyclic load condition at the end of the column. The lateral load cycles for the column were controlled by story drift, R (the ratio between horizontal to the column height) which is δ/h . The

lateral load sequence consisted of one cycles to each R of 0.5, 1, 1.5, 2, 3, and 4%, followed by a half cycle to R of 5%. Figure 10 shows the lateral cyclic load represented in the FE model.

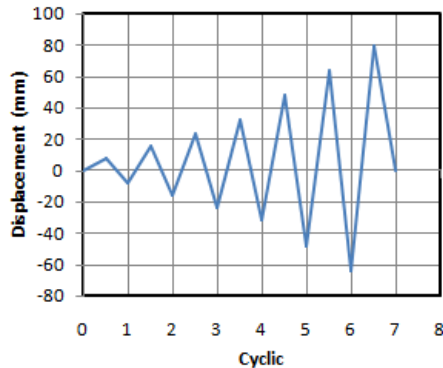


Fig. 10 Lateral cyclic load (displacement)

RESULTS AND DISCUSSION

Hysteresis Characteristics

The load carrying capacity and stress distribution are nearly same with minimum percentage of error. The experimental hysteresis loops (shear force versus story drift) for the WC1 and WC1-S are compared with those obtained from the FE analysis for the entire loading history, as shown in Figure 11. The analytical results for hysteresis curve of the FE models show a good agreement with the test results. Both the specimens and models show ductile and stable spindle-shaped hysteresis loops. Table 2 lists the measured strength both EWECs columns at first yield and at the maximum capacity.

From the FE model, the maximum lateral shear force for WC1 column is 732 kN obtained at last story drift 5%. This is approximately 3.1% higher than the results obtained from the experimental (709 kN). It is clear from Figure 12 (a) that the FE and experimental results are almost the same behavior in each stage of cyclic loading. The average of different percentage of lateral shear force in each stage of loading cycles between the FE analysis and the experimental results is around 8.7%.

The maximum shear force for WC1-S is 804 kN at R 5% from the FE analysis, which is 9.8% higher than the experimentally obtained data (725 kN) at R 5%. The FE model behaved higher dissipated energy in the each stage of loading cycles than the experimental data, as seen in Figure 12 (b). The average of different percentage of lateral shear force in each stage of loading cycles between the FE analysis and the experimental results is around 21%. From the FE models, the presence of shear studs

gives contribution to flexural capacity by around 17% in maximum.

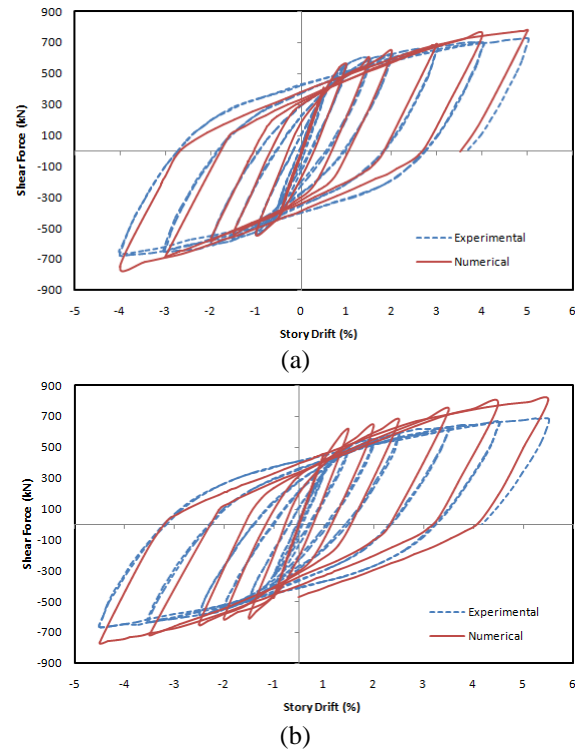


Fig. 11 Comparison of hysteresis loops between experimental and numerical results of (a) WC1 and (b) WC1-S.

Table 2 Measured strength

Model	Study	at Yielding		at the Max. Capacity	
		Q _y	R _y	Q _m	R _m
WC1	Exp.	367	0.55	709	5
	Num.	373	0.50	732	5
WC1-S	Exp.	427	0.70	725	5
	Num.	419	0.74	804	5

Note: Q (kN); and R (%).

The difference between the FE and experimental results at different stages of loading can be attributed to mesh refinement, idealized boundary conditions in the FE model, material nonlinearity, and the specified coefficient of friction between contact surfaces at the material interface of the columns.

Failure Mode and Principal Stress Distribution

The stress and strain in each of material element is also analyzed to validate the FE models. A 0.002 principal strain is respectively reached in the encased steel of WC1 and WC1-S columns models at story drift 0.51% and 1.1%, as indicated

that the steel has first yield in oval shape in the Figure 12. These results are almost similar with the test data that the first yield in the corner region both of top and bottom of the steel during experimental are respectively at R 0.91% and 1.2%. In WC1 column model, the first crack in the concrete occurs at R 0.4% in the strut zone of FE model, indicated by maximum principal stresses (tensile) is greater than the tensile strength of concrete (3.1 MPa), as shown inside the oval shape in Figure 13 (a). The cracks occur spread on the strut area and propagate along the horizontal direction.

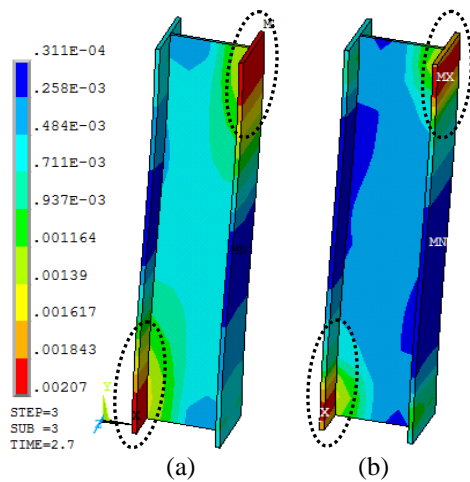


Fig. 12 The principal strain at first yielding of the (a) WC1 and (b) WC1-S models.

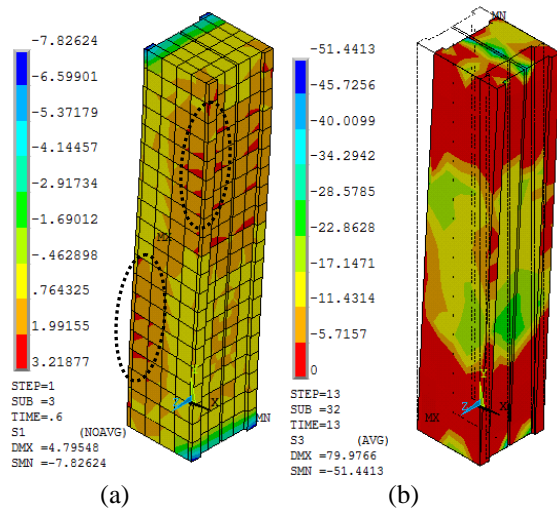


Fig. 13 The principal stress at first crack and crush in concrete core of the WC1 model.

Figure 13 (b) shows the minimum principal stress (compressive) of concrete at last story drift, where the value has exceeded the compressive strength of concrete (49 MPa) that resulting in crush on the top and bottom of the concrete.

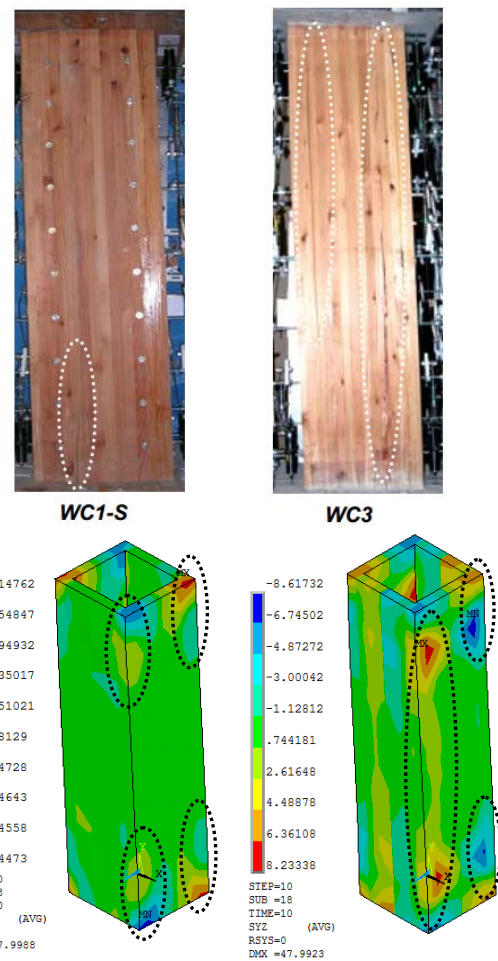


Fig. 14 Comparison of failure mode of wood panel at (a) WC1-S and (b) WC-1 between experimental and FE results.

The principal shear stress in the wood panel is shown inside the oval shape in Figure 14. The figure shows that the crack occurred in the wood panels assembled together by using wood glue at a shear stress of approximately 7.24 MPa and 8.2 MPa (maximum principal shear stress) for WC1-S and WC1, respectively. This corresponds to tangential shear strength of normal wood at averaged 7.44 MPa as suggested by Calderoni [14]. The crack occurs in this location due to the weak shear strength of the connection using wood glue during construction of the specimen test. The cracks pattern are also formed at the opposite side. They propagate along a height of the column.

Figure 15 shows the 1st principal normal stress on wood. The stress is concentrated on the edge bottom and top of the wood, where sink (due to compression) and uplift (due to tensile) occur. These good comparative results confirmed the ability of the proposed FE analysis to predict the maximum strength and behavior of EWCS column under constant axial and lateral loads reversals with acceptable accuracy.

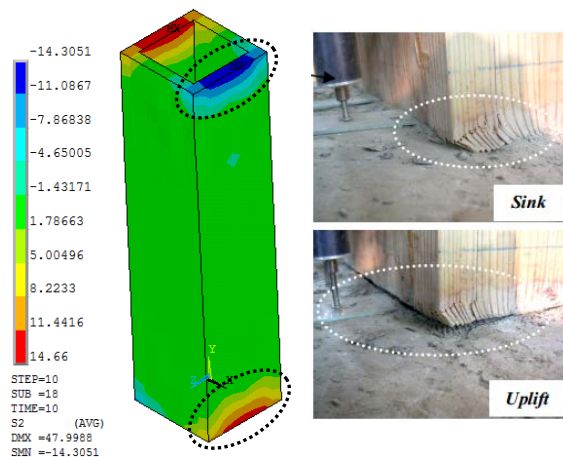


Fig. 15 Comparison of failure mode of wood panel in terms of sink and uplift of WC1 between experimental and FE results.

CONCLUSION

Based on the analytical and experimental studies presented here, the following conclusions can be drawn:

- (1) EWECS columns using single H-section steel had excellent structural performance without severe damage, even at large story drift, R of 4%.
- (2) The presence of shear studs on EWECS columns improved the ductility of the column and reduced the damage of wood panel, but there was no much influence on maximum flexural strength of the column.
- (3) To modeling the slip behavior between concrete and wood, it needs to reduce the strength of wood about 5%. With shear studs, the woody panel contributed to flexural capacity until large story drift, R of 5%, although cracks appeared at the column faces after R of 0.4 %.
- (4) The calculated hysteresis loops using finite element analysis showed a good agreement with the experimental results, indicating that the analytical method can be used to predict the ultimate strength and behavior of EWECS columns.

REFERENCES

- [1] Ministry of Construction, *Stipulation of criteria with respect to structural calculations performed to confirm the safety from the point of view of structural capacity of wooden columns*. Building Standard Law of Japan Notification No. 1349, May 23, 2000.
- [2] Fauzan, H. Kuramoto, and K.H. Kim, "Seismic performance of composite EWECS columns using single H-steel", *Proceeding of JCI* 27(2), 2005, pp. 307-312.
- [3] H. Kuramoto, and Fauzan, "Feasibility study on engineering wood encased concrete-steel composite columns", *Proceeding 11th Int. Colloquium on Structural and Geotechnical Engineering (11th ICSGE)*, Ain Shams University, Cairo, Egypt, 2005.
- [4] M. M. A. Kadhim, "Nonlinear FE analysis of reinforced H.S. concrete continuous beam strengthened with CFRP sheet", *Proceeding of the ICASEIT*, 2011, pp. 597 – 601.
- [5] ANSYS Version 14. 2010. User's and theory reference manual.
- [6] M. K. Hassan, M. F. M. Zain, and M. Jamil, "Finite element analysis of the effect of crack depth and crack opening on the girder", *Proceeding of the International Conference on Advanced Science, Engineering and Information Technology*, 2011, pp. 646 – 651.
- [7] L. P. Saenz, "Discussion of equation for the stress-strain curve for concrete" *Journal American Concrete Institute*, vol. 61(9), pp. 1229-1235, 1964.
- [8] R. S. H. Al-Mahaidi, "Nonlinear finite element analysis of reinforced concrete deep members", *Rep. No. 79(1)*, Department of Structural Engineering, Cornell University, Ithaca, New York. 1979.
- [9] K. L. Willam, and E. P. Warnke, "Constitutive model for the triaxial behavior of concrete", *Proc. International Association for Bridge and Structural Engineering (IABSE)*, vol. 19, Zurich, Switzerland, 1975.
- [10] H. Kuramoto, B. Li, K. Meas, and Fauzan, "Experimental and analytical performance evaluation of engineering wood encased concrete-steel beam-column joints", *Journal of Structural Engineering ASCE*, pp. 822-833, 2011.
- [11] A. Leskes, and S. Grambicka, "Theoretical and experimental studies on composite steel-concrete columns", *Proc. Eng. Science direct*, vol. 65, 2013, pp. 405-410.
- [12] Fauzan, and H. Kuramoto, "Seismic performance of EWECS composite columns in new hybrid structural system", *Composite Construction in Steel and Concrete*, vol. 6, pp. 263-275, 2011.
- [13] R. A. Hawileh, A. Rahman, and H. Tabatabai, "Nonlinear finite element analysis and modelling of a precast hybrid beam-column connection subjected to cyclic loads", *Journal Applied Mathematical Modelling*, vol. 34, pp. 2562-2583, 2010.
- [14] C. Calderoni, G. D. Matteis, C. Giubileo, and F. M. Mazolani, "Flexural and shear behavior of ancient wood beams: experimental and theoretical evaluation", *Journal Structural Engineering*, vol. 28(5), pp. 729-744, 2006.

WATER RESOURCES AND STORMWATER MANAGEMENT STRATEGIES USING DUAL FUNCTION RAINWATER TANK IN LABU RIVER BASIN MALAYSIA

Y.F. Huang¹, Effie Nyanong¹, K.F. Fung¹

¹Lee Kong Chian Faculty of Engineering and Science, Universiti Tunku Abdul Rahman, Malaysia

ABSTRACT

Rainwater harvesting is a water collection method that has gained more awareness, especially now that there have been increasing water issues and flood problems around the world. A hydrologic-hydraulic model was developed to evaluate the potential and effectiveness of rainwater tanks for flood reduction in the Labu River Basin. The feasibility of implementing rainwater tanks towards water supplement was then evaluated before the optimum size of dual function rainwater tanks was determined by analyzing the effectiveness of rainwater tanks in flood reduction, water supplement and also through economic analysis. The most appropriate tank size for both flood mitigation and water supplement portions was 2m³. The 2m³ tank was found to be capable of reducing the peak flow and maximum water level up to 14.29% and 1.57% respectively. Besides that, it also reduced the runoff volume and flood period up to 100% while at the same time increased the time of concentration up to 66.04%. The reliability ratios of the 2m³ tank when being simulated under the water usage of 250L and 750L for each house per day was 82.5% and 45.3%, respectively.

Keywords: rainwater harvesting system, flood mitigation, water resources, Tangki NAHRIM

INTRODUCTION

Malaysia is blessed with sunshine and rain all year round with rain being one of the main sources of water. However, it was not until a drought that occurred in 1998 during El Nino that created a surge of interest in rainwater harvesting by the Ministry of Housing and Local Government because the drought had brought unpleasant water supply disruptions for the Klang Valley residents at the time. As of now, six states have gazetted the amendments to the Uniform Building By-Laws 1984 to implement the Rainwater Harvesting and Utilisation System (SPAH) at buildings and the states are Perak, Selangor, Johor, Melaka, Kelantan and Perlis. SPAH had become very important because some states were forced to carry out water rationing when the water levels in the dams dropped following a drought. Besides drought issues, there is also a growing water demand due to the population growth and economic development. Malaysia is faced with flood issues as well, in which flooding is the most significant natural hazard in the country in terms of its effects to the population, frequency, area extent, flood duration and social economic damage.

In flood modelling, flood events are simulated to provide a better visualisation of flood events and understanding of flood risks. It usually involves both hydrologic and hydraulic modelling. Hydrologic modelling involves the characterization of real hydrologic features [3], [14] and some important parameters that can affect flow in hydrologic modelling are inclusive of precipitation, hydrological loss estimation and runoff estimation [4]. XPSWMM is a comprehensive software set for designing, modeling

and administering sustainable drainage systems, plus it is also applicable for the analysis, design and simulation of storm and wastewater systems and to model flows in natural systems [19], [5], [10], [12]. By incorporating a decentralized rainwater harvesting system, it is possible to reduce 20% of the peak discharge [8], reduce the number of flooded areas within a river catchment [15] and increase the time of concentration [20], [15]. Tangki NAHRIM software on the other hand is developed to ascertain the optimal size of a rainwater storage tank system, the volume of rainfall and rainwater distribution and also its reliability and efficiency [27], [6], [11]. It can also be used to obtain rainfall data such as average monthly precipitations, average annual precipitations and also the number of dry days [2]. In this paper, a dual-function rainwater tank is proposed to be comprised of retention storage for water supplement and detention storage for flood reduction. The following section covers the study of how the performance of each storage in water supplement and flood reduction respectively, can determine the optimum size of the dual-function rainwater tank which would minimize space and maintain the best performance, at reasonable cost.

METHODOLOGY

Study Area

The Labu River Basin was chosen mainly due to its rapid population growth and availability of its river cross-section data. It is one of the basins within the

Langat River Basin and Labu River, the main river within the basin, is the smallest tributary in Langat River Basin. The location of Labu River Basin is as shown in Figure-1.

Due to its location, Labu River Basin has an equatorial climate with annual average temperatures between 20.5°C and 36°C [9]. The rainfall patterns are of moderately dry and moist and receive the lowest yearly rainfall for Peninsular Malaysia [16], while the mean monthly relative humidity range is from 80.6% to 85.6% [18]. The types of soil within the study area are mainly (i) weathered Kenny Hill formation and (ii) quaternary alluvium that consists of unconsolidated to semi-consolidated peat, clay, silt, sand and gravel [1]. There are a number of main land uses within the area which include agricultural land, settlements, highways, industry, forests, development projects, water bodies and post landfill practices, in addition to having river banks that are wide and flat [9]. Furthermore, Labu River is the main water source for the Salak Tinggi treatment plant that caters for both Salak Tinggi and Sepang areas [7].

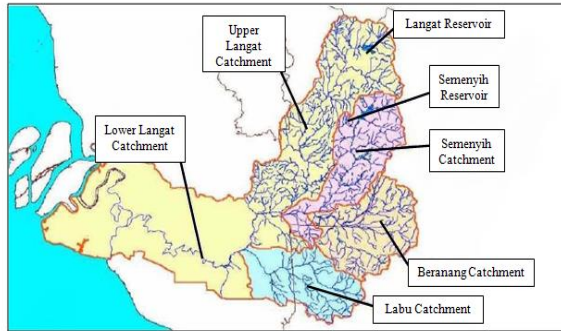


Figure 1 Location of Labu River Basin in Langat River Basin [21].

Flood Simulation

Design rainfall was used as the rainfall data for the flood simulation process and the calculations were done based on the guidelines of the Urban Storm Water Management [13] provided by Department of Irrigation and Drainage Malaysia (DID). The formulas used are as follow:

For overland flow,

$$t_o = \frac{107n^* L^{1/3}}{S^{1/5}} \quad (1)$$

t_o = Overland sheet flow travel time

L = Overland sheet flow path length

n^* = Horton's roughness value for the surface

S = Slope of overland surface

For drain flow,

$$t_d = \frac{nL}{60R^{2/3}S^{1/2}} \quad (2)$$

t_d = Travel time in the drain

L = Length of reach

n = Manning's roughness coefficient

S = Friction slope

R = Hydraulic radius

Time of concentration,

$$t_c = t_o + t_d \quad (3)$$

Storm duration,

$$d = t_c / 60 \quad (4)$$

Average rainfall intensity,

$$i = \frac{\lambda T^\kappa}{(d + \theta)^\eta} \quad (5)$$

T = Average recurrence interval (ARI)

d = Storm duration

$\lambda, \theta, \eta, \kappa$ = Fitting constants

The storm duration obtained was used to determine a set of temporal patterns from MSMA. These temporal patterns were then utilized together with the rainfall intensities to generate hyetographs in the XPSWMM software which consequently fulfilled the rainfall data requirement of the model.

For calibration and validation, the model was simulated under the base scenario, a scenario in which no rainwater tanks were installed at each house. However, before simulations were done, the database that was developed in ArcGIS had to be imported into the XPSWMM software first. The drainage system in Labu River Basin was drawn using the nodes and links provided in the software.

After the base scenario was set up with all the necessary information at both nodes and links in the Runoff mode and Hydraulics mode, the model was calibrated and validated. After that, another scenario was added to the model, which was the rainwater tank (RWT) scenario. The only difference between this scenario and the base scenario was the presence of rainwater tank in the former scenario. The Runoff mode played a major part in this scenario, thus the adjustment was mostly in the nodes of the Runoff mode. The concept of the rainwater tank used for this research is as shown in Figure-2. It is a dual tank that consists of a detention pond and also a retention pond. When rainwater goes into the tank via the inlet, it will start to fill up the tank (assuming at the beginning the tank is empty). If the rain is heavy enough such that the discharge at the inlet, Q_{in} is the same as the discharge at the first outlet, Q_{out_1} when the rainwater reaches the first outlet, it will discharge through the first outlet and into the drain. In an extreme case such as long hours of raining, the rainwater will surpass the retention pond and proceed towards the detention pond instead of discharging through the first outlet because $Q_{in} > Q_{out_1}$. Consequently, the rainwater will continue to rise until it reaches the full capacity of the tank and excessive rainwater will discharge through the second outlet.

After all the selected nodes were installed with rainwater tanks, the model was ready to be solved with both base scenario and RWT scenarios being simulated simultaneously. Three baseflows ($1/4$, $1/2$ and $3/4$), three Average Recurrence Intervals or ARIs (5, 10 and 50 ARIs) and three tank sizes ($2m^3$, $4m^3$ and $6m^3$) were

considered in the simulations and the results were recorded and analyzed.

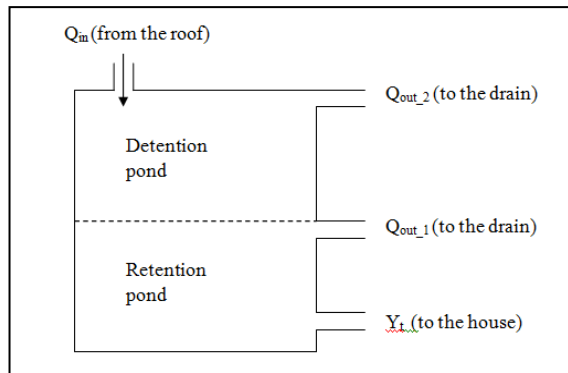


Figure 2 Rainwater tank concept used.

Water Supplement Simulation

The second main part of the methodology, the water supplement simulation part, was executed to fulfill the second objective of the research; to evaluate the feasibility of implementing rainwater tanks towards water supplement and the software used was the Tangki NAHRIM software. Before the simulations were done, there were several inputs that had to be inserted into the software first which include the rainfall station that will supply rainfall data for the simulation, the roof characteristics, the daily water usage and the size of the tank.

RESULTS AND DISCUSSION

Seven links were selected based on the percentage of houses in their respective sub catchment for the purposes of results compilation and discussion. An additional link, Link 8, which was a representative of the whole Labu catchment, was also included. The percentage of roof area covered by all 8 links were tabulated in Table-1 and it was observed that Link 5 had the biggest roof area coverage with 30.29%, followed by Link 4 (17.3%), Link 3 (15.47%), Link 6 (8.9%), Link 2 (8.81%), Link 1 (7.04%), Link 7 (1.99%) and Link 8 (0.5%).

Table 1 Links and their respective percentage of roof area coverage.

Link	Catchment area (ha)	Roof area (ha)	Percentage of roof area coverage (%)
1	278.87	19.62	7.04%
2	87.32	7.69	8.81%
3	41.04	6.35	15.47%
4	77.85	13.47	17.30%
5	20.14	6.1	30.29%
6	25.50	2.27	8.90%
7	1252.73	24.96	1.99%
8	16669.46	83.38	0.50%

Overall, the results could be divided into two categories; significant and less significant, based on the significance of peak flow, time of concentration and maximum water level improvement from the base scenario to RWT scenario. Links 2, 3, 4, 5 and 6 had significant improvement while Links 1, 7 and 8 had less significant improvement. By taking Link 3 under 50 ARI as an example, its hydrographs comprising all tank sizes (2m^3 , 4m^3 and 6m^3) and baseflows ($\frac{1}{4}$, $\frac{1}{2}$ and $\frac{3}{4}$) were presented in Figure-3 to Figure-11. For baseflow $\frac{1}{4}$, in Figures 3, 4 and 5, it was observed that the value of peak flow reduced from the base scenario to RWT scenario in each hydrograph. The peak flow values in the base scenario were discerned to be constant which was $2.718\text{m}^3/\text{s}$. Meanwhile the values in RWT scenario decreased, as tank size increased; from $2.652\text{m}^3/\text{s}$ (2m^3 tanks) to $2.645\text{m}^3/\text{s}$ (4m^3 tanks), and further decreased to $2.635\text{m}^3/\text{s}$ (6m^3 tanks). Thus the percentage of peak flow reduction for 2m^3 , 4m^3 and 6m^3 tanks scenarios were 2.43%, 2.69% and 3.05% respectively, which increased as tank size increased.

As for time of concentration, it could be seen from Figures 3, 4 and 5 that the values of time of concentration increased from base scenario to RWT scenario in each hydrograph. The time of concentration values in Figures 3, 4 and 5 were also constant in the base scenario, which was 3.433 hours. On the other hand, the values in the RWT scenario increased as tank size increased; from 5.65 hours (2m^3 tanks) to 5.717 hours (4m^3 tanks), and further increased to 5.85 hours (6m^3 tanks). Hence the percentage of time of concentration increment for 2m^3 , 4m^3 and 6m^3 tanks scenarios were 64.58%, 66.53% and 70.4% respectively, which increased as tank size increased.

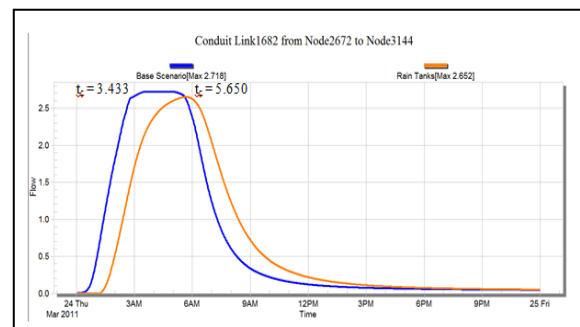


Figure 3 Flow hydrograph at Link 3 for 2m^3 tank, 50 ARI and $\frac{1}{4}$ baseflow.

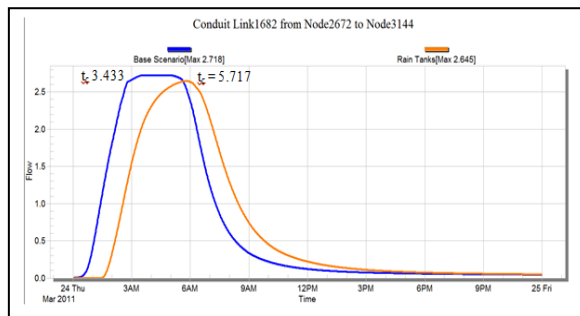


Figure 4 Flow hydrograph at Link 3 for 4m^3 tank, 50 ARI and $\frac{1}{4}$ baseflow.

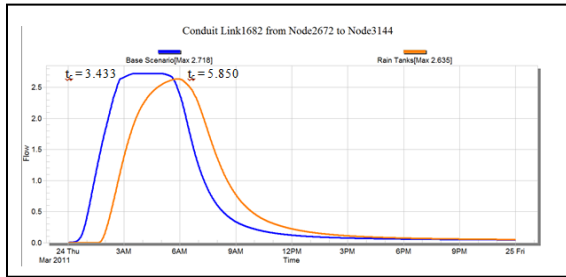


Figure 5 Flow hydrograph at Link 3 for 6m³ tank, 50 ARI and ¼ baseflow.

For the case of Link 3 under 50 ARI and ½ baseflow, it could be seen that the value of peak flow reduced from the base scenario to RWT scenario in each hydrograph. The peak flow values in the base scenario were observed to be constant which was 2.427m³/s. Meanwhile the values in RWT scenario decreased, as tank size increased; from 2.306m³/s (2m³ tanks) to 2.289m³/s (4m³ tanks), and further decreased to 2.269m³/s (6m³ tanks). Thus the percentage of peak flow reduction for 2m³, 4m³ and 6m³ tanks scenarios were 4.99%, 5.69% and 6.51% respectively, which increased as tank size increased.

For the case of Link 3 under 50 ARI and ¾ baseflow, it could be seen that the value of peak flow reduced from the base scenario to RWT scenario in each hydrograph. The peak flow values in the base scenario were observed to be constant which was 2.255m³/s. Meanwhile the values in RWT scenario decreased, as tank size increased; from 2.105m³/s (2m³ tanks) to 2.083m³/s (4m³ tanks), and further decreased to 2.063m³/s (6m³ tanks). Thus the percentage of peak flow reduction for 2m³, 4m³ and 6m³ tanks scenarios were 6.65%, 7.63% and 8.51% respectively, which increased as tank size increased.

Overall, Link 3 under 50 ARI at all tank sizes (2m³, 4m³ and 6m³) and baseflows (¼, ½ and ¾) showed positive improvement for both peak flow and time of concentration because as tank size increases, more water can be stored into the tank, thus increases peak flow reduction and time of concentration increment. Consequently, the percentage of maximum water level reduction for Link 3 under 50 ARI also increased when the tank size was increased, whereby the ranges were 0.01%-0.5%, 0.02%-0.51% and 0.03%-0.55% for 2m³, 4m³ and 6m³ respectively. Similar results were also observed for the rest of the scenarios under link 3 as well as other links in the significant improvement group.

During the simulations, there was flooding at several locations in the model, thus those were considered as flood events. The number of flood events decreased with the installation of rainwater tanks in the rainwater tank scenario as shown in Figures 6, 7 and 8. When the tank size increased on the other hand, the number of flood events reduced was not significant because the percentage of roof area coverage relative to the catchment area was only 0.5%. However, when

reduction in terms of other parameters were analysed at the flood locations specifically instead, such as runoff volume, flood period and maximum flood level, those parameters were observed to have more significant results in comparison.

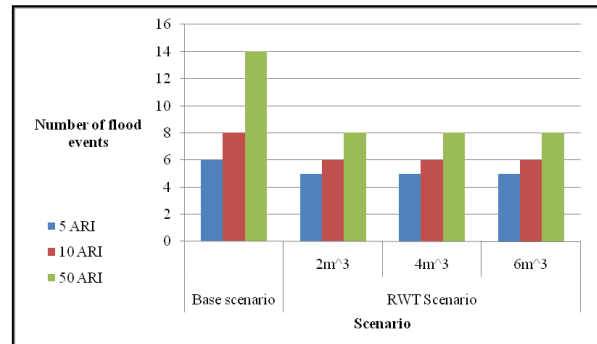


Figure 6 Number of flood events under different scenarios and ARIs for the case of baseflow ¼.

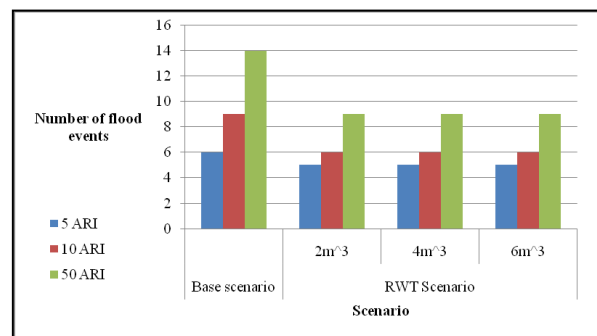


Figure 7 Number of flood events under different scenarios and ARIs for the case of baseflow ½.

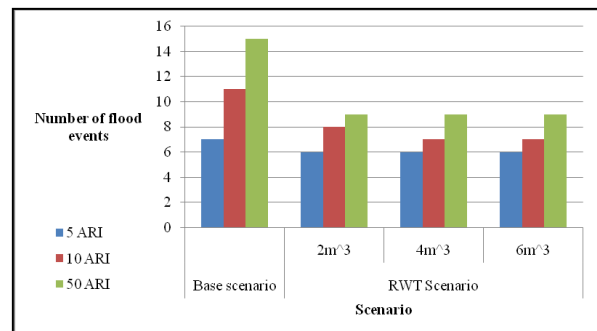


Figure 8 Number of flood events under different scenarios and ARIs for the case of baseflow ¾.

Overall, the results for volume runoff, flood period and maximum flood water level could be divided into two categories based on the significance of improvement from base scenario to RWT scenario; significant and less significant. Nodes E, H, J, K, L, M, N and O were categorized as significant, while Nodes A, B, C, D, F, G and I were categorized as less significant. By taking node E as an example, the percentage of volume runoff reduction and the percentage of flood period reduction were both 100%, under all tank sizes, baseflows and ARIs.

Consequently, the percentage of reduction of maximum flood water level increased when the tank size increased, whereby the ranges were 0.02%-0.18%, 0.18%- 0.92%, 0.56%-2.14% for 2m³, 4m³ and 6m³, respectively. Similar results were also observed for the rest of the nodes in the significant improvement group.

The results of water supplement simulation using Tangki NAHRIM software were tabulated in Table-2 and Table-3 according to the daily household water usage per house designated as 250L and 750L respectively. It was observed from both tables that the reliability ratio increased as tank size increased. However, for the same tank size, the 250L water usage showed much higher reliability than the 750L water usage. Thus it could be deduced that the higher the water usage, the lower the reliability of the tanks.

Table 2 Simulation results for water usage of 250L in each house per day

Tank size (m ³)	Rainwater captured (m ³)	Total rain volume delivered (m ³)	Average per day (m ³)	Reliability ratio (%)
1	3939.54	1239.7	0.17	67.93
2	3939.54	1505.67	0.21	82.5
3	3939.54	1621.47	0.22	88.85
4	3939.54	1678.49	0.23	91.97
5	3939.54	1719.14	0.24	94.2
6	3939.54	1744.99	0.24	95.62
7	3939.54	1764.49	0.24	96.68
8	3939.54	1777.32	0.24	97.39
9	3939.54	1785.68	0.24	97.85
10	3939.54	1789.68	0.24	98.06

Table 3 Simulation results for water usage of 750L in each house per day

Tank size (m ³)	Rainwater captured (m ³)	Total rain volume delivered (m ³)	Average per day (m ³)	Reliability ratio (%)
1	3939.54	2093.99	0.29	38.25
2	3939.54	2480.89	0.34	45.31
3	3939.54	2746.91	0.38	50.17
4	3939.54	2969.85	0.41	54.24
5	3939.54	3100	0.42	56.62
6	3939.54	3199.63	0.44	58.44
7	3939.54	3286.09	0.45	60.02
8	3939.54	3350.91	0.46	61.2
9	3939.54	3403.83	0.47	62.17
10	3939.54	3455.79	0.47	63.12

The subsequent reliability ratio graphs based on the two tables were plotted as shown in Figure-9 and it could be seen that with each 1m³ increment, the reliability ratio difference was reduced insignificantly

especially from 2m³ onwards, for both water usage cases.

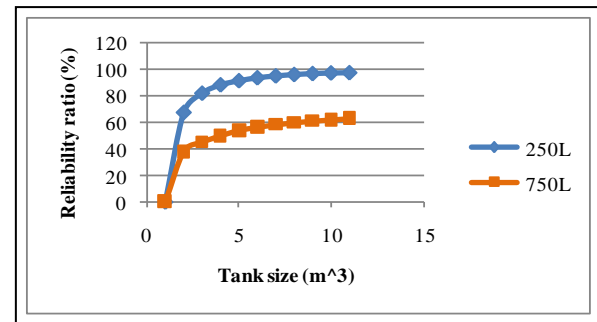


Figure 9 Reliability ratio graphs for water usage of 250L and 750L

CONCLUSION

The incorporation of rainwater harvesting systems in a catchment has the potential to reduce peak flow, maximum water level, runoff volume, maximum flood water level and number of flood events, while simultaneously increase the time of concentration in which all these will subsequently assist in flood mitigation works that would be very beneficial for the country in the future.

The 2m³ tank is the most suitable option among all the tank sizes considered for water supplement purposes (1m³, 2m³ and 3m³) and its setting up cost is RM2038.18, which is the second highest of the three. Despite not having the lowest setting up cost, its reliability ratio is higher than the 1m³ tank that has the cheapest setting up cost (RM1703.90). When the 2m³ tank was simulated under the water usage of 250L per day for each house, its reliability ratio was 82.5% as compared to the reliability ratio of the 1m³ tank which was 67.9%. Even when the water usage was increased to 750L, the reliability ratio of the 2m³ tank remained higher than the 1m³ tank, whereby the former was 45.3% as compared to the latter which was only 38.3%. The reliability of a tank is a crucial factor in determining the best tank size for any purpose but it is also essential for the tank to have a moderate pricing, thus the 2m³ tank fulfils these criteria. The 3m³ tank has the highest reliability ratio among the three (88.9% and 50.2% under water usage of 250L and 750L respectively) but consequently, its setting up cost is also the most expensive (RM2611.50). Thus, 2m³ is an adequate tank size to fit the water supplement purposes based on these reasons. Subsequently, between the three tank sizes considered for the flood mitigation portion (2m³, 4m³ and 6m³), 2m³ is the most suitable tank size considering that the consumption of either 4m³ or 6m³ tank will result in a rather unnecessarily huge tank in total when it is added on to the water supplement portion. All three tanks showed insignificant difference when it comes to number of flood events reduced at the Labu River Basin (between one to six flood events), thus a selection of any tank larger than 2m³ for the flood reduction portion is rather

redundant. Furthermore, the 2m³ tank had shown an adequate overall reduction in the following parameters; peak flow (reduction up to 14.29%), maximum water level (reduction up to 1.57%), runoff volume (reduction up to 100%) and flood period (reduction up to 100%). Besides that, the increment of the time of concentration by the 2m³ tank was satisfactory in general as well (increment up to 66.04%). Therefore, by taking all these into account, it should be sufficient to deduce that 2m³ is also an appropriate tank size for the flood mitigation purposes.

ACKNOWLEDGEMENT

The authors wish to express their sincere gratitude to The Ministry of Science, Technology and Innovation (MOSTI), Malaysia, for the financial support.

REFERENCES

- [1] Adnan, S. N. S. M., Yusoff, S. and Yan, P. C. 2013. Soil chemistry and pollution study of a closed landfill site at Ampar Tenang, Selangor, Malaysia. *Waste Management & Research*. 31: 599-612.
- [2] Alkaff, S. A., Fadhel, M. I. and Abdi M. 2013. Study of harvesting rainwater system for Multimedia University (MMU). *International Journal of Chemical and Environmental Engineering*. 4: 4.
- [3] Allaby, A., & Allaby, M. 1999. *A Dictionary Of Earth Sciences*, 2nd ed. Great Clarendon Street, Oxford: Oxford University Press.
- [4] Anees, M. T. *et al.*, 2016. Numerical modeling techniques for flood analysis. *Journal of African Earth Sciences*. 124: 478-486.
- [5] Basyanaka, A. P., & Sarukkalige, R. 2011. Comparing hydrology and hydraulics surface routing approaches in modeling and urban catchment. *Proceedings of the 2nd International Conference on Environmental Engineering and Applications*. 17. IPCBEE.
- [6] Hashim, H., Hudzori, A., Yusop, Z. and Ho, W. S. 2013. Simulation based programming for optimization of large-scale rainwaterharvesting system: Malaysia case study. *Resources, Conservation and Recycling*. 80: 1-9.
- [7] Hoo, L. S., Samat, A. and Othman, M. R. 2005. Effects of wet deposition on levels of selected heavy metals in Labu River: A snapshot study of a sub-urban Lotic Ecosystem. *Sains Malaysia*. 34: 129-133.
- [8] Huang, Y. F., & Shaaban, A. J. 2009. Potential and Effectiveness of Rainwater Harvesting Systems in Flash Flood Reduction at Taman Wangsa Melawati, Kuala Lumpur. *Proceedings of the 8th International Conference on Urban Drainage Modelling*, Japan.
- [9] Jahesh, A. S., Rahim, S. A. and Idris, W. M. R. 2016. The content of heavy metal in the Labu riverbed sediments: an assessment of the level of pollution applying sediment quality guidelines and geoaccumulation index. *American Journal of Environmental Sciences*. 12 (4): 271-281.
- [10] Kamarudin, M. K. *et al.*, 2013. The hydrodynamic of Dong River, Hutan Lipur Lata Jarum, Pahang, Malaysia. *Prudence Journal of Environmental Science Research*. 1(2): 5-11.
- [11] Man, S. *et al.*, 2014. The reliability of rainwater harvesting system as an alternative source of water supply in Malaysia: A preliminary study. *Malaysian Journal of Society and Space*. 10 (6): 97-10.
- [12] Mazlan, M. *et al.*, 2014. Hydrodynamic modelling and flood mapping of Sembrong catchment area. *Proceedings of the 13th International Conference on Urban Drainage*, Kuching.
- [13] MSMA. 2010. *Manual Saliran Mesra Alam Malaysia*. Department of Irrigation and Drainage Malaysia.
- [14] Ramana, G.V. 2014. Regression analysis of rainfall and runoff process of a typical watershed. *WARSE International Journal of Science and Applied Information Technology*. 3(1): 16-26.
- [15] Shaaban, A. J., Kardi, J. and Huang, Y. F. 2011. Potential of Catchment Wide Rainwater Harvesting System for Flash Flood Reduction in the Damansara River Catchment, Selangor, Malaysia. *Proceedings of the 15th International Rainwater Catchment Systems Conference*, Taiwan.
- [16] Shaharuddin, A., & Noorazuan, H. 2006. Analyzing rain patterns and trends in Negeri Sembilan using the GIS Polygon Thiessen and Isohyet Contours methods. *Geografia Online*. 2: 105-113.
- [17] Shanahan, P., & Doyle, K. 2010. The impact of first flush removal o rainwater quality and rainwater harvesting systems' reliability in rural Rwanda. *Proceedings of the World Environmental and Water Resources Congress*. ASCE.
- [18] Sheriza, M. R., Ainuddin, N. A., Hazandy, A. H. and Zulhaidi, M. S. H. 2011. Annual rainfall estimation based on two different methods. *Journal of Environmental Hydrology*. 19: 1-9.
- [19] Toriman, M. E. *et al.*, 2009. Integration of 1-d hydrodynamic model and GIS approach in flood management study in Malaysia. *Research Journal of Earth Sciences*, 1 (1): 22-27.
- [20] Wilkinson, M. E., Quinn, P. F. and Welton, P. 2010. Runoff management during the September 2008 floods in the Belford catchment, Northumberland. *Journal of Flood Risk Management*. 3 (4): 285-295.
- [21] Zakaria, S. 2008. Management instruments for Langat River Basin. *Proceedings of the IWRM-IHP Conference 2008 and 2nd Africa Regional Meeting of the National Committees Of UNESCO's IHP*, Cape Town ICC.

A PRICE SETTING FOR AN EXCESS-BAGGAGE SERVICE AS A FUNCTION OF FREIGHT PRICE

I.A. Shaban¹, F.T.S. Chan*, and S.H. Chung
¹Faculty, University, Country; Company, Country

ABSTRACT

According to IATA (International Air Transport Associate) reports in 2017, the uplift of passengers' demand leads to the wide use of wide-bodied aircraft, in addition to the marked drop in the sea shipping rates caused a clear decline in the air freight demand and overcapacity in the aircraft belly-hold. In this regard, we discuss the aircraft overcapacity problem to fill the unused spaces in the belly-hold. Moreover, we confer price setting for the new service with the reference to the freight price. For the sake of achieving this objective, we adopted the multi-item newsvendor-based pricing model to derive a price formula for the excess-baggage service as a function of freight price. Stochastic-Deterministic environment of excess-baggage and freight was modeled, respectively. The results showed that the optimal excess-baggage price can be determined as a function of freight price in terms of base price plus the premium price. Finally, the model can be generalized to any two products share common features and serve in the same market.

Keywords: Newsvendor model, Air freight, Combination airlines, Pricing.

INTRODUCTION

The air transportation is one of the most profitable markets beside the sea and rail freight shipping. According to IATA [1], the air freight shares over third of the world trade by value. Also, Passengers is the second sector of the air transportation business. Passenger sector is expected to grow twice by 2035 [2]. The growth of passengers leads to the wide use of the wide-bodied aircraft. This trend causes an overcapacity problem in the aircraft belly-hold. However, the freight forecasts refer to an increase, the unused space still larger[3].

In this research, we investigate the underutilized aircraft belly-hold space. In this regard, we propose an excess baggage pricing scheme to contribute in attract more demand from the passenger's excess baggage. This excess baggage demand occupies more space to fill the underutilized belly-hold space. This research is motivated by the statistics of the current excess baggage. For instance, the annual charges which collected from British travelers for the excess and overweighted bags exceeds £3.5 billion [4]. Also, the sum of profits of the American airlines for the passengers' excess baggage are more than US\$4 [5]. However, the numerical example gives a sufficient proof that the excess baggage is large enough, the passengers crooked method to avoid paying more charges for their excess bags and weights [6].

A large segment of passengers might need for excess baggage to carry the last-minute souvenir purchases. For instance, the African, Gulf country,

Southeast Asia, the Middle east and Latin America travelers are the major beneficiaries of the excess baggage services, particularly they are the largest users of wrapping services in the Southern Europe airports[7]. Moreover, the free trade agreements between the countries encourages the small merchants to purchase products from the products' country of origin [8] such as, the Hongkongers travels to South Korea to bring the original cosmetics. In this case, the larger the product amounts they buy from Korea, the higher the profit they gain, and the heavier the luggage they carry to the airport. Another significant example is the people who lives temporarily for long periods as foreigners, such as the post graduate students. The minimum study period for PhD. is three years. Most of these students during the study period buy many properties but by the end of this period they need to get them to their home countries. The expected number of international PhD. students around the world is 6.9 million by 2030[9]. therefore, they are targeted to be excess-baggage customers.

Related Work

Recently, the capacity allocation problem has taken a different direction than the last decades. In the earlier years, the problem was treated such that the capacity less than the demand. Hellermann [10] designed an option contract between the single airline and single forwarder. He induced that premium price policy is the best way to conduct the deal instead of spot price reservations. The same

capacity options contract was updated to include multiple forwarders using a Stackelberg game[11].

Usually the freight forwarder books the capacity in certain flight in advance. For the reason that the forwarder does not incur any penalties if they cancelled part of their reserved capacity, the airline sells the full capacity plus a buffer to avoid the capacity shortage. Thus, Hellermann [12], added the overbooking calculations to the option contracts.

Recently, the airlines have much space but they do not have enough demand. This situation did not occur suddenly, where the airlines update their fleet in long while. So, the overcapacity takes place in some routes and some others stay overbooked which make imbalance between these routes [13].

In this research, we believe that the unused space in the aircraft belly-hold can be filled by simplifying and relaxing the excess baggage pricing schemes. Considering two factors, the passengers' regular baggage limits which optimized by Wong [14], and using the freight prices as a reference to calculate the excess baggage new prices.

For the sake of formulating the excess baggage price as a reference of freight price, the multi-item newsvendor model was adopted.

STOCHASTIC - DETERMINISTIC MODEL

Consider an airline carries both passengers and freights. let the freight service f is sold at p_f for each freight unit, and the new excess baggage g price changes with the change of the freight price, suppose the new excess baggage price is p_g per each excess baggage unit. The airline need to determine the optimal excess baggage price and quantity which maximizes its overall expected profit. To formulate, we adopt the multi-item newsvendor with price dependent demand function for both excess baggage, and freight services.

As the freight is a stable industry and there are many demand forecasting models, we believe that freight demand can be modeled in a deterministic form. Therefore, the demand can be represented by $D(p_f) = y(p_f)$, where $y(p_f) = r_1 - t_1 p_f$, as discussed in [15], and r_1, t_1 are the additive demand function coefficients.

On the other hand, the excess baggage, according to the new price scheme, is not easy to predict. Thus, it is better to be defined in a stochastic form. The excess baggage may have a great variety because the its price must be controlled to keep the freight demand stable specially in season. Hence, its demand should be formulated in the iso-elastic form which was discussed by Kocabiyikoglu [16]. So, the excess baggage demand function is $D(p_g) = y(p_g)\delta$, and $y(p_g) = r_2 p_g^{t_2} \delta$, where r_2, t_2 are the demand function coefficients of the the iso-elastic

excess baggage demand function, and δ is the random variable of the demand function. The demand variable is defined in range $[A, B]$.

Consider a single leg flight, where the aircraft belly-hold is occupied by the passengers' regular bags and excess baggage, and freights. Wong [8] designed the limits for the passengers' regular bags limits. Therefore, theoretically, the regular bags occupy fixed space and they have the priority to allocation in the aircraft belly-hold. The rest of space is occupied by the combination of freight and the excess baggage. The airline incurs operational costs C for the combination of excess baggage and freight, see Eq. (1):

$$C = c_g x_g + c_f x_f \quad (1)$$

Where x_g, x_f are the number of excess baggage, and freight units; c_g, c_f are the unit their unit costs.

Through the newsvendor setup the flight profit π can be represented by Eq. (2)

$$\pi(p_g, p_f, x_g, x_f) = \begin{cases} p_g D(p_g) + p_f y(p_f) - C - O, & \text{if } D(p_g) + y(p_f) \leq x_g + x_f \\ p_g x_g + p_f x_f - C - S, & \text{if } D(p_g) + y(p_f) > x_g + x_f \end{cases} \quad (2)$$

where, O is the overbooking costs when the airline offers spaces for excess baggage and freight more than the expected market demand, and S is the shortage costs when the offered space is less than the forecasted market demand. Eq. 3 and Eq. 4,

$$O = o_g(x_g - D(p_g)) + o_f(x_f - y(p_f)) \quad (3)$$

$$S = s_g(D(p_g) - x_g) + s_f(y(p_f) - x_f) \quad (4)$$

To make a linear relationship between the air freight and the excess baggage, we assumed that the combination of excess baggage and freight demands equals to the aircraft belly-hold capacity G , and the proper form of the demand is $D(p_g) = r_2 p_g^{t_2} \delta$, and $D(p_f) = G - y(p_g)\delta$, define the w value for the both services by $w_g = x_g/y(p_g)$, and $w_f = x_f/(G - y(p_g)\delta)$. Thus, the excepted profit can be expressed as in Eq. 5

$$\begin{aligned} E[\pi(p_g, p_f, w_g, w_f)] &= (p_g - c_g - p_g + c_f w_f) y(p_f) \mu + (p_f - c_f w_f) G - \\ & (c_g + o_g) y(p_g) \int_A^{w_g} (w_g - \delta) f(\delta) d\delta - o_c G (w_f - 1) \int_A^{w_g} f(\delta) d\delta + o_f (w_f - 1) y(p_g) \int_A^{w_g} \delta f(\delta) d\delta - (p_g + s_g - c_g) y(p_g) \int_{w_g}^B (\delta - w_g) f(\delta) d\delta - \\ & (p_f + s_f) (1 - w_f) \int_{w_g}^B f(\delta) d\delta + (p_f - s_f) (1 - w_f) y(p_g) \int_{w_g}^B \delta f(\delta) d\delta. \end{aligned} \quad (5)$$

Define $\int_A^{w_g} (w_g - \delta) f(\delta) d\delta$, $\int_{w_g}^B (\delta - w_g) f(\delta) d\delta$, $\int_A^{w_g} f(\delta) d\delta$, and $\int_{w_g}^B \delta f(\delta) d\delta$ by $\Lambda(w_g)$, $\Theta(w_g)$, $\varpi(w_g)$, $\xi(w_g)$, respectively. Hence, the expected profit can be written in terms of the riskless profit and the expected losses as in Eq. (6)

$$E[\Pi(q_g, p_f)] = \psi(p_g, p_f) - L(q_g, q_f, p_g, p_f) \quad (6)$$

Where

$$\psi(p_g, p_f) = (p_g - c_g - p_f + c_f q_f) y(p_g) \mu + (p_f - c_f q_f) G. \quad (7)$$

, and

$$\begin{aligned} L(w_g, w_f, p_g, p_f) = & (c_g + h_g) y(p_g) \Lambda(q_g) + \\ & h_f G (q_f - 1) \int_A^{w_g} f(\delta) d\delta - h_f (w_f - 1) y(p_g) \varpi(w_g) + \\ & (p_g + s_g - c_g) y(p_g) \Theta(w_g) + (p_f + s_f) (1 - w_f) \int_{w_g}^B f(\delta) d\delta - \\ & (p_f - s_f) (1 - w_f) y(p_g) \xi(w_g). \end{aligned} \quad (8)$$

Mills [15] defined the interpretation of the riskless profit function, in equation (7), as a deterministic profit value when replacing the uncertainty value of the product value δ by the mean value μ . In this model, the profit function holds excess-baggage and freight and thus, the profit is a function of the two items prices. Also, Equation (8) is the loss function according to Silver Edward and Peterson [17] definition, which evaluates the leftover cost $(c_g + o_g)$ for each value of $\Lambda(w_g) y(p_g)$ of excess-baggage, and the expected leftover when too large value of is selected; in addition to $(o_f G)$ for each likelihood of the leftover in excess-baggage minus the mean value of o_f in the range $[A, w_g]$; moreover, if the value of w_f is chosen more than one, and the shortage costs for excess baggage is $(p_g + s_g + c_g)$ for each $\Theta(w_g) y(p_g)$ expected shortages when too small value of w_g is selected. The shortage costs of the freight service are $(p_f + s_f)$ for the likelihood of excess-baggage quantity minus $(p_f - s_f)$ for expected excess-baggage quantity; if the value of w_f is chosen less than one. The expected profit is depicted in (6), and the riskless profit occurs in certain selected demands with no uncertainty, and the uncertainty factor in the model is added to the expected penalties.

The objective of the model is to maximize the expected profit in Eq. (7):

$$\text{Maximize}_{w_g, p_g} E[(\Pi(w_g, p_g))] \quad (9)$$

The first and the second partial derivatives of $E[(\Pi(w_g, p_g))]$ are taken with respect to w_g and p_g

$$\frac{\partial E[(\Pi(w_g, p_g))]}{\partial w_g} = \quad (10)$$

$$-(c_g + h_g) y(p_g) F(w_g) + (p_g + s_g - c_g) y(p_g) [1 - F(w_g)].$$

, the maxima can be obtained if the second derivative is less than zero,

$$\frac{\partial^2 E[(\Pi(w_g, p_g))]}{\partial w_g^2} = -[(c_g + o_g) + (p_g + s_g - c_g) y(p_g) f(w_g)]. \quad (11)$$

Equations (10) and (11) prove that the expected profit function is concave in product g quantity when equation (10) is equal to zero. Similarly, the overall expected profit is concave in both excess-baggage g and freight f , Eq. (12).

$$\frac{\partial E[(\Pi(w_g, p_g))]}{\partial p^*} = 0 \quad (12)$$

Theory For fixed excess-baggage and freight quantities, the optimal price of excess-baggage g is determined uniquely as a function of the freight service f and the integrated quantities of the two services:

$$p_g^* = \frac{\mu p_g^0}{\mu - \Theta(w_g)} + \frac{b[(c_g + o_g) \Lambda(w_g) - o_f (w_f - 1) \varpi(w_g)]}{(b-1)(\mu - \Theta(w_g))} + \frac{b[(s_g - c_g) \Theta(w_g) - (p_f - s_f)(1 - q_f) \xi(w_g)]}{(b-1)(\mu - \Theta(w_g))}. \quad (13)$$

$$\text{where } p_g^0 = \frac{b(c_g + p_f - c_f q_f)}{b-1}$$

Proof. for the multiplicative demand of excess-baggage, p_g^0 is the optimal riskless price, which maximizes the riskless profit $\psi(p_g, p_f) = (p_g - c_g - p_f + c_f q_f) y(p_g) \mu + (p_f - c_f q_f) G$, where $y(p_g) = a p_g^{-b}$, by definition. The maximum value of the riskless profit function can be obtained when equating the first derivative w.r.t p_g to zero, Thus, letting:

$$\frac{\partial \psi(p_g, p_f)}{\partial p_g} = (p_g - c_g - p_f + c_f q_f) y'(p_g) \mu + y(p_g) \mu;$$

$$a \mu p_g^{-b-1} [b(c_g + p_f - c_f q_f) - (b-1) p_g^0] = 0.$$

therefore, the maximum value of $\psi(p_g, p_f)$ is at

$$p_g^0 = \frac{b(c_g + p_f - c_f q_f)}{b-1},$$

Next, regarding the overall expected profit function in equation (6), determine the optimal price of excess-baggage as a function of the air freight, and maximize the expected profit. We need to

equate the first differentiation of the (6) w.r.t p_g to zero;

$$\frac{\partial E[\Pi(w_g, p_g)]}{\partial p_g} = (p_g - c_g - p_f + c_f w_f) y'(p_g) \mu + y(p_g) \mu - (c_g + o_g) y'(p_g) \Lambda(w_g) + o_f (w_f - 1) y'(p_g) \varpi(w_g) - (p_g + s_g - c_g) y'(p_g) \Theta(w_g) - y(p_g) \Theta(q_g) + (p_f + s_f) (1 - q_f) y'(p_g) \xi(w_g).$$

hence;

$$-ab p_g^{-b-1} (p_g^* - c_g - p_f + c_f q_f) \mu + a p_g^{-b} \mu + ab p_g^{-b-1} (c_g + o_g) \Lambda(w_g) - ab p_g^{-b-1} o_f (w_f - 1) \varpi(w_g) + ab p_g^{-b-1} (p_g^* + s_g - c_g) \Theta(w_g) - a p_g^{-b-1} \Theta(w_g) - p_g^* \Theta(q_g) - ab p_g^{-b-1} (p_f + s_f) (1 - w_f) \xi(w_g) = 0.$$

Thus,

$$p_i^* = \frac{\mu p_g^0}{\mu - \Theta(w_g)} + \frac{b[(c_g + o_g) \Lambda(w_g) - o_f (w_f - 1) \varpi(w_g)]}{(b-1)(\mu - \Theta(w_g))} + \frac{b[(s_g - c_g) \Theta(w_g) - (p_f - s_f) (1 - w_f) \xi(w_g)]}{(b-1)(\mu - \Theta(w_g))}.$$

The riskless price p_g^0 is concave in the freight price, where the excess-baggage riskless price increases with the increase of freight price until it reaches a turn down point then the excess-baggage riskless price decreases. The airline can forecast short-term market demand, and is most likely a combination of the Gamma and normal distributions as mentioned by Swan [18]. Thus, the random variable is normally distributed in the application of numerical analysis with $\mu = 0.6$, and $\sigma_g = 0.2$. See Figure 1.

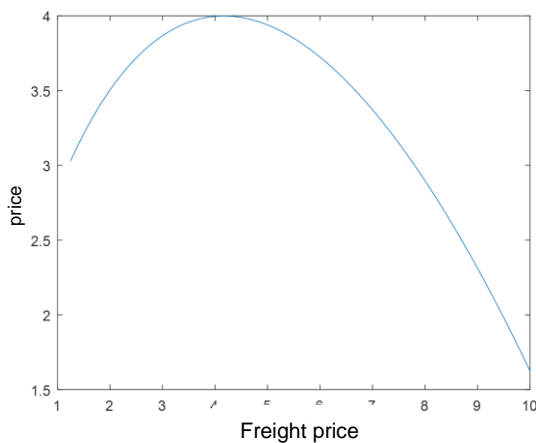


Fig. 1 A plot of excess- baggage riskless price p_g^0 as a function of freight price p_g ranging from 0.5 to 10 in increment 0.025, the freight quantity is assumed as 16000, $a_1=20000$, $b_1=1.5$, and $b_2=1.25$.

The excess-baggage price elasticity b sets the maxima of the excess-baggage riskless price, as shown in Figure 2, where the riskless price of the excess-baggage decreases exponentially with increase of the excess-baggage price elasticity.

The Theory captures the optimal price of the excess-baggage as a function of the freight price and mixed quantities of both services. The price equation contains three terms; each term expresses an important concern in order to set the price for excess-baggage with reference to the freight price. The theorem explains the main theme of the pricing scheme which can be followed to set the price of the excess-baggage with the aid of the freight price. This model is inspired from Petruzzi and Dada [19] who's model considers the use of single period newsvendor model to set the price of a single product.

The authors defined the optimal price of the product as the sum of the base price and the premium amount in the multiplicative demand function, whereas our model uses product price information to set a different product price. Theorem 1, defines the base as price equaling the riskless price of the excess-baggage multiplied by a safety factor and the premium value which is a function of the overall expected shortage and the overall expected leftover amount, and the expected sales of the excess-baggage. Hence, the excess-baggage optimal price can be expressed by equation (13),

$$p_g^* = p_{B_g} + \frac{b[E[\text{leftover}(w_g, p_g)] + (s_g - c_g)E[\text{shortage}(w_g, p_g)]]}{(b-1)E[\text{sales}(w_g, p_g)]} - \frac{b[o_f[\text{average of } w_f] + (p_f - s_f)E[\text{shortage of } w_f]]}{(b-1)E[\text{sales}(w_g, p_g)]}. \quad (13)$$

Therefore, the interpretation of the base and premium prices may be described next; the base price is obtainable from estimating the total costs of the excess-baggage service multiplied by the safety factor "SF" which ensures that the riskless price is not underestimated by dividing the mean demand over the expected sales, where $SF \geq 1$. The base price is also concave in the freight price, see Figure 3.

The base price concavity is flatter in the actual range of freight prices, so we assumed a larger range of excess-baggage at freight prices to show the curve behavior. The airline can manage the safety factor

by studying the demand average and the expected shortage.

Moreover, the premium value in selling price for the excess-baggage is based on the formula which considers the overall expected leftover of the excess-baggage,

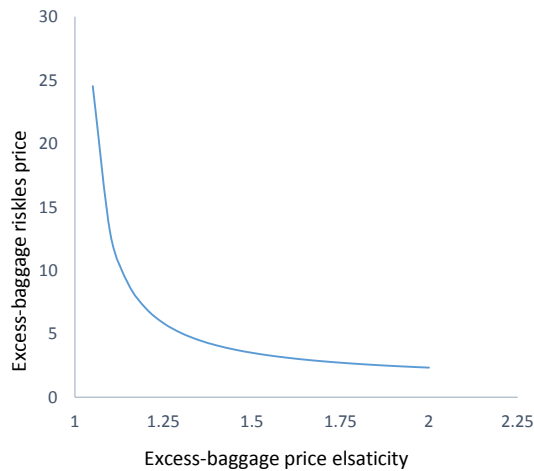


Fig. 2 A plot of excess-baggage riskless price as a function of price elasticities, (a) Freight price elasticity and, (b) Excess-baggage price elasticity.

, in addition to the overall expected shortage costs of the same service.

The result agrees with Petruzzi's results, but this model holds a defined service, freight service, which is the airline's main service, so the freight service affects the price of the new excess-baggage service.

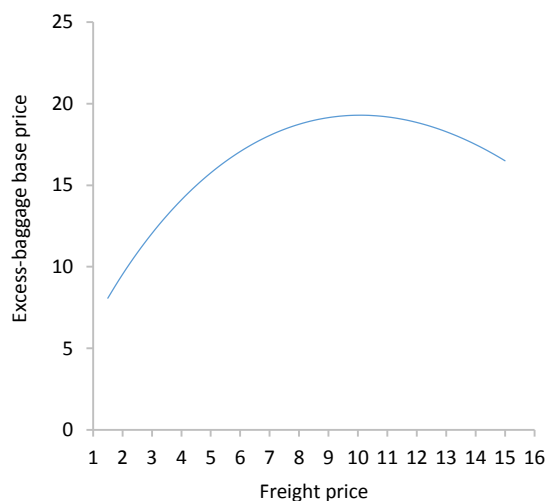


Fig. 3 A plot of excess-baggage base price as a function of freight prices.

This is because of the demand uncertainty in the excess-baggage, thus the sum of the expected penalties of the f freight service is subtracted from the expected penalties of the g excess-baggage and divided on the overall expected excess-baggage sales.

CONCLUSION

In this paper, a new excess baggage and the overweight scheme are identified and discussed as a service combined with the freight in a combination airline. The excess-baggage pricing scheme is proposed as a solution for overcapacity resulting from the extensive use of wide-bodied aircraft and the reduction in the sea shipping rates. The excess-baggage is treated as a special freight service, and we show that the excess-baggage can be considered as a freight if the passenger acts as a shipper and sends luggage to a freight forwarder. The freight forwarder in turn forwards them to the airline which assign these luggage to the aircraft belly-hold, in addition to permitted baggage.

The extra-baggage price can be set with reference to the cargo prices, in terms of base price, and premium value. The extra-baggage price is the sum of the base price and the estimated premium value. The premium value is the expected penalties over the expected sold capacity and can be either positive or negative.

ACKNOWLEDGEMENTS

The work described in this paper was supported by a grant from the Research Grants Council of the Hong Kong Special Administrative Region, China (Project No. PolyU 15201414); a grant from The Natural Science Foundation of China (Grant No. 71471158); and a grant from the Research Committee of The Hong Kong Polytechnic University under student account code RUMZ.

REFERENCES

- [1] IATA. "Enabling global trade," 23 October, 2017; <http://www.iata.org/whatwedo/cargo/pages/index.aspx>.
- [2] IATA, IATA Forecasts Passenger Demand to Double Over 20 Years, Press Release, vol. 59, 2016.
- [3] The Economist. "Too little freight, too much space; Air cargo.(demand for air-cargo businesses)," 21, February 2018;

- <https://www.economist.com/news/business/21695013-overcapacity-hits-another-part-transport-industry-too-little-freight-too-much-space>.
- [4] DailyMail. "Revealed: Brits pay out nearly £400million in excess baggage charges each year - because of baffling rules," Feb, 20, 2018; http://www.dailymail.co.uk/travel/travel_news/article-4530100/Brits-pay-395million-excess-baggage-charges.html.
- [5] Bureau of Transportation Statistics. "Baggage Fees by Airline 2016," Feb,19, 2018; https://www.rita.dot.gov/bts/sites/rita.dot.gov.bts/files/subject_areas/airline_information/baggage_fees/html/2016.html.
- [6] Helen Coffey. "Most Outrageous Ways Passengers Have Tried to Avoid Paying Airport Excess Baggage Charges," May, 3rd, 2018; <https://www.independent.co.uk/travel/news-and-advice/passengers-avoid-airport-excess-baggage-charges-flight-extra-clothing-most-outrageous-easyjet-a8161586.html>.
- [7] Airports International. "Bagging Extra Revenue " May 04, 2018, 2018; <http://www.airportsinternational.com/2012/12/bagging-extra-revenue/13027>.
- [8] Trade and Industry Department, "Hong Kong - Korea Trade Relations," 2017.
- [9] University World News. "Global Universities Unprepared for Sea Change Ahead," Jan. 26, 2018; <http://www.universityworldnews.com/article.php?story=20180126131034717>.
- [10] R. Hellermann, "Capacity options for revenue management : theory and applications in the air cargo industry," Theory and applications in the air cargo industry, Thesis (doctoral)--WHU, Otto Beisheim School of Management., Berlin, 2006.
- [11] Y. Tao, E.P. Chew, L.H. Lee, and L. Wang, "A capacity pricing and reservation problem under option contract in the air cargo freight industry," Computers & Industrial Engineering, Vol. 110, Supplement C. Supplement C, 2017/08/01/, 2017, pp. 560-572.
- [12] R. Hellermann, A. Huchzermeier, and S. Spinler, "Options Contracts with Overbooking in the Air Cargo Industry," Decision Sciences, Vol. 44, 2. 2, 2013, pp. 297-327.
- [13] B. Feng, Y. Li, and H. Shen, "Tying mechanism for airlines' air cargo capacity allocation," European Journal of Operational Research, Vol. 244, 1. 1, 2015/07/01/, 2015, pp. 322-330.
- [14] W. Wong, A. Zhang, Y. Hui, and L. Leung, "Optimal Baggage-Limit Policy: Airline Passenger and Cargo Allocation," Transportation Science, Vol. 43, 3. 3, 2009, pp. 355-369.
- [15] E.S. Mills, "Uncertainty and Price Theory," The Quarterly Journal of Economics, Vol. 73, 1. 1, 1959, pp. 116-130.
- [16] A. Kocabiyıkoğlu, I. Popescu, and C. Stefanescu, "Pricing and Revenue Management: The Value of Coordination," Management Science, Vol. 60, 3. 3, 2014/03/01, 2013, pp. 730-752.
- [17] A. Silver Edward, and R. Peterson, Decision systems for inventory management and production planning, 2nd ed., New York: Wiley. 1985.
- [18] W.M. Swan, "Airline demand distributions: passenger revenue management and spill," Transportation Research Part E: Logistics and Transportation Review, Vol. 38, 3. 3, 2002/05/01/, 2002, pp. 253-263.
- [19] N.C. Petruzzi, and M. Dada, "Pricing and the Newsvendor Problem: A Review with Extensions," Operations Research, Vol. 47, 2. 2, 1999/04/01, 1999, pp. 183-194.

BOND STRENGTH PREDICTION MODEL OF CORRODED REINFORCEMENT IN CONCRETE USING NEURAL NETWORK

Nolan C. Concha^{1,2} and Andres Winston C. Oreta³

¹PhD Student, De La Salle University, Philippines; ²Faculty, FEU-Institute of Tech., Philippines

³Faculty, De La Salle University, Philippines

ABSTRACT

The expansion of corrosion products in steel-concrete interface offers radial tensile stress resulting to development of cracks in reinforced concrete structures. This corrosion induced cracks promotes bond reduction which involves intricate non-linear interactions. To deeply understand the underlying mechanisms involved in the bond strength of corroded rebars in concrete, a novel bond prediction model using artificial neural network (ANN) was developed. Accelerated corrosion was performed to 108 cube samples using 500 $\mu\text{A}/\text{cm}^2$ current density. Steel bond strength after 35 and 70 days impressed corrosion exposure of concrete cube samples was measured using single pull out test. The compressive strength, tensile strength, rebar diameter, embedment length, concrete cover, ultrasonic pulse velocity (UPV), crack severity, and corrosion level were the predictors in the ANN bond model. Among all the bond strength models considered in this study, the proposed neural network model provided the most desirable bond estimates in good agreement with experimental results. The ANN model further showed superior prediction performance against the derived regression model.

Keywords: Bond strength, Corrosion, Crack severity, Impressed current

INTRODUCTION

Corrosion of steel reinforcements due to chloride ingress is regarded as one vital structural health concerns in concrete structures. Embedded bars at this rusting stage expand and develop radial stresses in concrete resulting to cracking, bulging, and spalling of concrete. Corrosion also results to the buckling, snapping, and ineffective bond characteristics of reinforcements due to continued reduction in the effective bar size. When subjected to reinforcement corrosion, concrete structures experience delamination in which the oxidized metal requires greater space causing a wedge-like stress. Surface and internal cracks tend to develop in concrete and promote exposure of reinforcements to corrosion. This in turn imparts excessive reduction in the bond strength characterized by the adhesion and slippage resistance between steel and the enveloping concrete. Ultimately the serviceability and durability of reinforced concrete are significantly reduced and potentially results to structural collapse. Because of this, studies in developing bond strength and corrosion resistance of reinforcing bars has remained a popular research interest [1].

In the development of corrosion models particularly in the numerical and analytical modelling, several ideal assumptions were considered. The study of El Maaddawy and Soudki [2] assumed that the thickness of corrosion around the bar was uniformly distributed and exerts a constant radial pressure in the

enveloping concrete. The actual underlying bond behavior of steel bars in concrete might not be adequately describe by these assumptions. In fact, there has been an observed contradicting results obtained between analytical and empirical equations due to the uniform thick-walled cylinder analogy adopted in the development of the models [3]–[4]. The formation of corrosion and its corresponding effect on the bond between concrete and steel involves complex interactions. One potential method to model the dominant and complicated interrelationships among the variables of corrosion and bond is artificial neural networks (ANNs). Recent researchers have found the power of ANN to model complex interactions and provide superior prediction performance [5]–[6]. Through the set of input-output data from a battery of tests conducted, ANN develops a network of neurons that can be tuned up to synthesize information and eventually learn.

A novel prediction model of bond behavior of reinforcing steel bars in reinforced concrete due to corrosion using artificial neural network will be developed in this paper. Bond strength model using multiple regression will be derived as well for further comparison. Larger number of variables will be considered in the modeling including crack and continuity of concrete. The model will allow early detection of the level of bond degradation between concrete and steel in a simple and fast approach. This in turn leads to timely repair that can improve the safety and prolong the service life of the structure.

BOND STRENGTH MODELS OF CORRODED STEEL BARS IN REINFORCED CONCRETE

Impressed corrosion method was used by most researchers in the development of bond-corrosion model. The effects of corrosion level in bond strength loss and cracking of concrete using impressed method were investigated by previous studies [7]–[9]. Monotonic pull out test was conducted on concrete samples to develop bond strength models. Derived models showed reasonable agreement between the measured experimental results and empirically estimated values of bond strength. Unlike any other studies that focus on bond strength, the study of Yaciner [1] model an equation for the ultimate bond strength (τ_{bu}) using multiple linear regression. The bond equation is dependent on concrete compressive strength (f'_c), cover (c) to bar diameter (D) ratio and corrosion level (C_L). Results showed that increase in concrete compressive strength and concrete cover improved the measured bond strength. Moreover, it was found out that an increase in the compressive strength with constant concrete protective cover resulted to higher bond strength than a constant compressive strength with increasing concrete protective cover. Using ultra-high toughness cementitious composite, Hou et al. [10] developed a model to estimate the bond strength (τ_u) of a corroded rebar as a function of rebar diameter (d), bond length l_b , and corrosion ratio (ρ_c). The bond decreased up to 15% corrosion ratio but is almost the same with non-corroded samples. The prediction equation was able to give acceptable results as compared with experimental values recorded in the conduct of pull out tests of cylindrical samples. Table 1 shows the summary of bond prediction models from various literatures.

Table 1 Bond strength models of rebars in concrete

Cabrera	$f_{bo} = 23.478 - 1.313C$
Lee and Weyers	$\tau_{max} = 0.34\sigma_b - 1.93$ if $\Delta_w < \Delta_{wc}$ $\tau_{max} = 5.21e^{-0.0561\Delta_w}$ if $\Delta_w \geq \Delta_{wc}$
Chung et al.	$u_b = 16.87$ for $C_o \leq 2.0$ $u_b = 24.7C_o^{-0.55}$ for $C_o > 2.0$
Yalciner et al.	$\tau_{bu} = 0.40551f'_c - 0.25306\left(\frac{c}{D}\right) + 0.97926C_L$ ($R^2 = 0.98$)
Hou et al.	$\tau_u = 0.335\left[-0.124\rho_c^2 + 1.183\rho_c + 93.504\right]\left(\frac{d}{l_b}\right)^{0.379}$

EXPERIMENTAL PROGRAM

Materials and Specimens

The experiment in this study used 108 concrete cube samples in total with sidelength 200 mm. Bar diameters, concrete cover (cc) and embedment lengths (L_d) were varied in the concrete cube samples. Three deformed reinforcing bars of 16mm, 20mm, and 25mm in diameters with corresponding concrete

cover of 60mm, 70mm, and 80mm were used. Embedment lengths of 50mm, 75mm, and 100mm were used to achieve an even bond stress distribution within the entire embedment length of the rebar. The properties of the materials were tested in compliance with ASTM standards. The density and water absorption of coarse aggregates were measured and found to be 1572.028 kg/m³ and 0.402% respectively. Similarly, for fine aggregates, the recorded values of 1533.801 kg/m³, 3.2 %, and 2.673 for density, water absorption, and fineness were respectively observed. These results were used to proportion three design mixes having target compressive strengths of 21 MPa, 28 MPa, and 35 MPa. Table 2 shows the material proportions and average strengths corresponding to each mixture using 0.68, 0.57, and 0.47 preliminary ratios of water-cement, slump values from 25mm to 100mm, and 2% entrapped air.

Table 2 Concrete design proportions and strengths

Design Mix	W kg/m ³	C kg/m ³	CA kg/m ³	FA kg/m ³	f'_c (MPa)	f_t (MPa)
1	189	301	1018	866	22	2.08
2	189	359	1018	806	29	2.61
3	190	436	1018	726	36	3.14

Testing of Specimens

After curing for 28 days to gain strength, the samples were immediately immersed in a 5% brine solution as shown in fig. 1. A current density (i) of 500 $\mu\text{A}/\text{cm}^2$ from a constant power source was allowed to pass through the reinforcements embedded in the concrete prism to accelerate the corrosion. A total of 108 samples were subjected to accelerated corrosion for 35 days and 70 days to generate sufficient corrosion products that will develop internal radial stress enough to cause internal and external cracks in the concrete.



Fig. 1 Concrete cubes under accelerated corrosion

Likewise, the crack severity (CS) expressed as the product of the crack length (L) and the representative crack width (W) was determined. In order to measure the opening of crack in each of the samples, several polycarbonate reference points were attached to the surface of the concrete. The development of the

distance between the reference points were measured using an electronic caliper. Using the measured values in every crack line, the product of the length and width was taken and the sum of all the results in each specimen was used to represent the crack severity of the sample. After which ultrasonic pulse velocity test was performed to assess the quality of concrete samples after 35 days and 70 days impressed current. The transducer and receiver of the UPV apparatus was positioned in direct set up. The results of the test were used as input variable in the bond model representing the homogeneity and compactness of concrete.

The bond strength of the rebar in concrete after accelerated corrosion was measured using pull out test in compliance with ASTM C234-91a. The pull-out strength was determined by measuring the maximum force required to pull the rebar from the concrete sample. The bond strength (μ) was calculated by taking the ratio of the maximum applied force (P) and the surface area of the reinforcing steel rebar in contact with concrete. Figure 2 shows the fractured concrete sample after performing single pull out test using the universal testing machine.

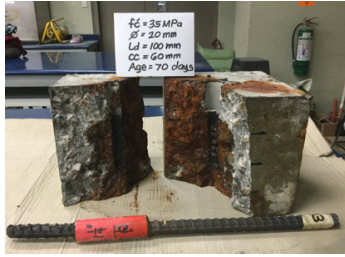


Fig. 2 Concrete cube sample after pull out test

Prior to the casting of concrete in the mold, deformed bars were weighed to determine the initial mass (M_o) before accelerated corrosion. After performing the accelerated corrosion process and pull out testing of the samples, all pulled off bars were cleaned from corrosion products at the surface of the rebar and weighed to record the final mass (M_f). The actual percentage of mass loss or corrosion level (C_L) of each bar was calculated using eq. (1).

$$C_L = \frac{M_o - M_f}{M_o} \times 100\% \quad (1)$$

EXPERIMENTAL RESULTS

Experimental Data Statistics

Among the 108 cube samples subjected to impressed current method of accelerated corrosion, 74 of which or 69% were able to exhibit crack formations due to the level of corrosion in the reinforcement. There were observed significant

changes in the recorded values between uncracked and cracked groups. Sudden drop in the UPV and bond strengths were obtained from almost all the samples in the group. The average UPV of 4081 km/s and average bond strength of 6.591 MPa for cracked samples were substantially lower than the mean values from the uncracked samples. These reductions were attributed to excessive amount of corrosion in the reinforcement resulting to the development of internal and surface cracks in the samples. Moreover, corrosion level was even higher for samples in the cracked group with an average and maximum values of 1.015% and 3.254% respectively. Samples having high corrosion levels in general correspond to high crack severity. The maximum observed crack severity was 215.492 mm² and the average value in all the samples was 77.791 mm². The dominant compressive strength in the cracked group was 29 MPa while the diameter of the rebar was 25mm. Based on the standard deviation and COV, higher variability was observed for UPV, corrosion level, crack severity, and bond strength of the samples.

Bond Strength Regression Model of Corroded Reinforcement

The bond strength as a function of concrete compressive strength, tensile strength, embedment length, diameter, concrete cover, UPV, crack severity, and mass loss was developed using multiple linear regression. The derived polynomial regression equation with adjusted R square of 0.899 and standard error of 3.262 is given in eq. (2). The embedment length, rebar diameter, the root of the product of compressive strength and tensile strength of concrete, and the crack severity offered reduction in bond strength as described by the negative coefficients in the model. For the other variables however, a direct correlation with the bond strength were observed. Among the variables considered in the model having P values less than 0.05, the embedment length, rebar diameter, UPV, and crack severity offered significant effect on the bond strength. The observation was reasonable since these parameters were interrelated and dominated the behavior of bond. Substantial change was observed in the experimental bond values particularly on the vast number of samples in the cracked group attributed to the variation of these parameters.

$$\tau = -0.106l_d - 0.236d + 0.009cc - 0.064\sqrt{f'c*ft} + 0.006UPV - 0.040C_s + 0.840C_L \quad (2)$$

The performance of the regression model in predicting bond resistance of concrete is shown in fig. 3. Vast majority of points lied closely to the 45° line indicating satisfactory prediction performance of the model. The Pearson correlation coefficient of the

scatter plot was 0.831 showing good agreement between experimental and predicted bond values. The average prediction error was 31.81% with minimum error of 0.61%. In all the predicted bond strengths, roughly 45% lied within $\pm 20\%$ error while 19% of the predictions provided more than $\pm 50\%$ error. Considering the fuzziness of the experimental bond strengths, the bond regression model was able to provide satisfactory prediction of the bond strength of concrete.

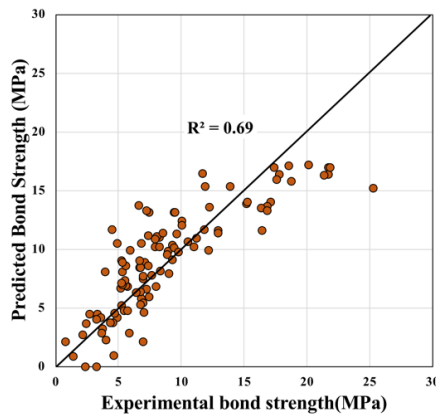


Fig. 3 Bond strength regression model predictions

NEURAL NETWORK MODELLING

Framework of the Neural Network Model

The input layer of the neural network model was composed of eight individual distinct nodes. Each node represents the predictors in the model which includes the compressive strength (f'_c), tensile strength (f_t), embedment length (l_d), rebar diameter (ϕ), concrete cover (cc), ultrasonic pulse velocity (UPV), corrosion level (C_L), and crack severity of concrete (C_s). One hidden layer was used in the model and the number of hidden nodes was varied between 5 to 8. The output layer was composed of one node representing the bond strength output of the model. Neural network model structure having 8 input nodes, 4 hidden layer neurons, and single node in the output layer was denoted as N 8-4-1. In the development of the model, the learning algorithm used was feedforward backpropagation algorithm. The hyperbolic tangent sigmoid function $f(n)=2/(1+e^{-2n})^{-1}$ was employed as neural activation function which return values between -1 to 1 in the output layer. An error tolerance of 0.001 and maximum cycles of 100000 were used as threshold criteria to cease the simulation process. Early stopping, validation phase in the development of the model, and few number of hidden nodes were considered to minimize the chance of overfitting and enhance the generalization of the ANN model.

ANN Model Experimental Data and Simulations

The bond strength results obtained from short term pull out test of 100 samples was used in the development of the model. Seventy percent of the data pairs was used in the training phase of the model and the other 30 percent was used in the testing phase. Carpenter and Barthelemy [11] suggested a minimum number of training data pairs not greater than the number of weights and biases to achieve distinct approximation. Further, an over determined data of 20-50% will yield satisfactory performance of the ANN model [12]. Considering the neural network architecture N 8-7-1 having seven nodes in the hidden layer and using 20% overdetermined network, the required minimum number of input-output data pairs must be between 76 to 96. With this constraint, the data used in the simulation was found sufficient to achieve the desired performance of the various ANN models. In selecting the best performing ANN architecture among the variations considered, mean squared error (MSE) and correlation coefficient (R) were used as performance metrics. The model having the least MSE and closest R value to 1.0 will emerge as the best ANN model. The result of simulations of four ANN models with their corresponding MSE and R are shown in table 3. Apparently, the neural network model having 7 nodes in the hidden layer provided the most desirable performance indicators. N 8-7-1 model exhibited the least bond strength prediction errors in good agreement with experimental values. The model was able to achieve learning considering multiple predictors and fuzziness in the introduced data pairs. The MSE and R of the derived model were 2.678 and 0.957 respectively. In contrast, N 8-5-1 model having 5 neurons was the least performing model.

Table 3 Variation of ANN models

Model	Number of hidden nodes	Performance criteria	
		MSE	R
N 8-5-1	5	3.623	0.941
N 8-6-1	6	3.478	0.943
N 8-7-1	7	2.678	0.957
N 8-8-1	8	3.148	0.952

Connection Weights and Biases of N 8-7-1 Model

Table 4 shows the weights and biases of the proposed neural network model. Each seven nodes in the hidden layer was associated with connection weights in the input and output layers. The relative importance of each predictor in the model using the causal inference procedure developed by Garson [13] was also reflected in the table. The ultrasonic pulse velocity was found to be the most significant predictor in the bond strength with a relative importance of 20.11%. Associated to this variable

were the crack severity and corrosion level having relative importance of 13.01% and 15.63% respectively. The results were reasonable since higher corrosion levels offer immense radial tensile stress in the samples resulting to excessive crack formations and sudden fall in the UPV values. Measured bond strengths in the pull-out test were significantly affected by the change in values of these three

independent variables. The concrete compressive strength was found to be the least significant predictor having 8.08% relative importance. The strength of concrete barely offered substantial effect on the measured bond strength of the samples. Majority of the samples achieved internal and external crack formations.

Table 4 Connection weights and biases of N 8-7-1 model

Hidden Nodes	Input Layer								Output Layer
	f'_c	f_t	L_d	ϕ	cc	UPV	Cs	C_L	
1	1.7118	1.1845	-0.6978	-0.0326	-1.0295	5.3538	-0.2653	-2.4959	0.2793
2	0.4372	0.5614	-1.4098	0.2691	-3.4692	-0.2920	2.4862	0.7990	0.0155
3	-0.4544	1.1419	1.3558	0.3752	0.2338	2.9630	-3.0908	3.2125	2.8476
4	2.4621	1.0616	3.1235	4.2368	0.5334	-1.7865	1.3760	1.3494	-0.2731
5	-0.1467	1.5563	0.8980	0.7151	0.5034	1.8726	0.3141	-0.4767	0.9385
6	0.0887	0.8101	1.4231	0.3394	0.2469	2.5854	-2.4950	2.5881	-3.0964
7	-2.2206	-1.6088	1.4915	-3.1291	-1.3239	1.0983	0.3039	2.1818	0.3688
Biases	-5.1069	-0.6449	2.8476	-0.1126	3.8667	-0.0931	-3.8237		-0.7184
Rel. Impt. (%)	8.09	10.618	12.66	10.03	9.85	20.11	13.01	15.63	

Prediction Performance of N 6-6-1 Model

About 76% and 84% from training and test data sets respectively were within the $\pm 10\%$ error. Though there were few misfits of roughly 15% providing more than 25% prediction errors, the model was able to perform well in training and testing phases of the simulation. The experimental and predicted values of the model for both phases were plotted as shown in fig. 4. The model was able to perform better in the testing phase giving an R value of 0.983 and average error of 16.27%. The R value and average error in the training phase of the model were 0.954 and 19.69% respectively. Vast majority of samples with overall R equal to 0.957 exhibited a close fit from the 45° line showing desirable agreement between predicted and experimental results. The average ratio of experimental to predicted values of 1.03 further demonstrate robust performance of N 8-7-1 model in the prediction of bond strength.

Comparison Between N 8-7-1 Model and Other Bond Strength Models

Various bond prediction models available in the literature were considered and compared to the performance of the proposed N 8-7-1 model. Eight bond strength values from experimental data were not used in the calibration. This data set was used to test

the bond performance of the proposed ANN model against the developed models of Yalciner et al. [1], Cabrera [10], Lee and Weyers [11], Chung et al. [12], Hou et al. [13], and the developed regression equation. The experimental and predicted results of the enumerated models were plotted in fig. 5. The scatter plot diagram was so dispersed demonstrating large deviations of the points from the 45° line. The models developed by Cabrera [10], Chung et al. [12], and Hou et al. [13] gave overestimated values of the bond strength due to the limitations of the variables considered. Most of the proposed models provided significant errors in the prediction results. This can be attributed to the inability of the models to capture significant bond reduction in the presence of internal and surface cracks in the concrete. The proposed N 8-7-1 model on the other hand was able to exhibit robustness in predicting the bond strength of the samples. A close fit can be seen from the graph with R value of 0.971. The limitation of the hidden nodes and the early stopping adopted in the development of the model worked so well to improve the generalization. The average observed error in the prediction results was 19.53% with maximum and minimum errors of 45.48% and 3.68% respectively. The superiority of the proposed model was credited to equally important variables such as UPV and crack severity which were not considered in other models.

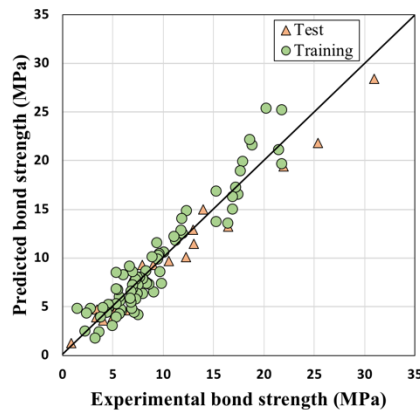


Fig. 4 Bond strength regression model predictions

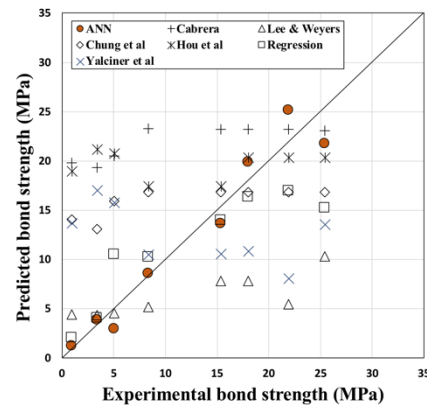


Fig. 5 Bond predictions using different models

CONCLUSIONS

In the simulation of several neural network architectures having eight input predictors and one response variable, the N 8-7-1 model with seven nodes in the hidden layer emerged as the best performing model. The proposed model provided mean squared error and Pearson correlation coefficient of 2.678 and 0.957 respectively indicating robustness in estimating the pull-out resistance of corroded reinforcements in concrete. The model further demonstrated superior prediction performance and generalization among the bond models considered in this study. Crack severity and ultrasonic pulse velocity predictors of the model in relation to the formation of corrosion products in rebars offered significant effects in the bond behavior. The emergence of these two predictors were in agreement with the results of causal inference procedure providing respective high relative importance of 20.11% and 13.01%. With all the desirable attributes of the model, the proposed N 8-7-1 can be used to conveniently estimated the bond resistance of corroded steel in reinforced concrete.

REFERENCES

- [1] Yalciner, H., Eren, O., and Sensoy, S., An experimental study on the bond strength between reinforcement bars and concrete as a function of concrete cover, strength and corrosion level, *Cement and Concrete Research*, 2012, 42(5), 643-655.
- [2] El Maaddawy, T., and Soudki, K., A model for prediction of time from corrosion initiation to corrosion cracking, *Cement and concrete composites*, 2007, 29(3), 168-175.
- [3] Rodríguez, J., Ortega, L., Casal, J. and Diez, J., Corrosion reinforcement and service life of concrete structures, *Durab. Build. Mater. Compon.*, 1996, 7 (1), pp. 117-126.
- [4] Alonso, C., Andrade, C., Rodriguez, J. and Diez, J. M., Factors controlling cracking of concrete affected by reinforcement corrosion, *Materials and Structures*, 31, August- Sept 1998, pp. 435-441
- [5] Yan, F., and Lin, Z., New strategy for anchorage reliability assessment of GFRP bars to concrete using hybrid artificial neural network with genetic algorithm, *Composites Part B: Engineering*, 2016, 92, 420-433.
- [6] Rinchon, J. P. M., Concha, N. C., and Calilung, M. G. V., Reinforced concrete ultimate bond strength model using hybrid neural network-genetic algorithm, 2017 IEEE 9th HNICEM (pp. 1-6). IEEE.
- [7] Cabrera, J. G., Deterioration of concrete due to reinforcement steel corrosion, *Cement and concrete composites*, 1996, 18(1), 47-59.
- [8] Lee, H. S., Noguchi, T., and Tomosawa, F., Evaluation of the bond properties between concrete and reinforcement as a function of the degree of reinforcement corrosion, *Cement and Concrete research*, 2002, 32(8), 1313-1318.
- [9] Chung, L., Kim, J. H. J., and Yi, S. T., Bond strength prediction for reinforced concrete members with highly corroded reinforcing bars, *Cement and concrete composites*, 2008, 30(7), 603-611.
- [10] Hou, L., Liu, H., Xu, S., Zhuang, N., and Chen, D., Effect of corrosion on bond behaviors of rebar embedded in ultra-high toughness cementitious composite, *Construction and Building Materials*, 2017, 138, 141-150.
- [11] Carpenter, W. C., and Barthelemy, J., Common misconceptions about neural networks as approximators, *J. Comput. Civ. Eng.*, 1994, 83 , 345 – 358.
- [12] Carpenter, W. C., and Hoffman, M. E., Training backprop neural networks, *AI Expert*, March 1995, 30–33.
- [13] Garson, G. D., Interpreting neural-network connection weights, *AI expert*, 1991, 6(4), 46-51.

DIFFERENTIAL SETTLEMENT OF SHORT PILED RAFT FOUNDATION SYSTEM ON PEAT DURING LOADING TEST

Sajiharjo Marto Suro¹, Adnan Zainorabidin², Agus Sulaeman³ and Ismail Bakar²

¹STT-PLN, Indonesia; ² UTHM, Malaysia; ³ ST-INTEN, Indonesia

ABSTRACT

This research observed the behavior of 3.0 m x 3.0 m large scale model of Short Piled Raft foundation system on peat during loading test. The sequence of loading test consisted of loading - unloading - reloading - remain - unloading, from 0 kN - 100 kN (100% design load) - 0 kN - 160 kN (160% design load) - remain for 24 hours - 0 kN, with increment or decrement of 20 kN, and had no failed. Five locations were observed, one at the centre and the other four at each corner. After conducting the test, it was seemed that the maximum of total settlement $S_{T(max)}$ was 7.80 mm, 29.90 mm and 36.20 mm, occurred at the center [CR], while the maximum of difference in total settlement between any two points $\Delta S_{T(max)}$ was 1.95 mm ([SW] – [NE]), 10.30 mm ([SW] – [SE]) and 9.65 mm ([SW] – [SE]), under the load of 100 kN, 160 kN and remain of 160 kN for 24 hours respectively. The $S_{T(max)}$ occurred at the centre was easily understood, because the load was acting on it. Differential settlement might occur, because peat underneath the foundation was not homogeneous, thus, response of piles to contribute supporting load might also be different, and finally produced differential settlement. It was also seemed that the piles could function as stiffener of concrete slab effectively. The tolerable settlement is $S_{T(max)} \leq 50$ mm and $\Delta S_{T(max)} \leq 20$ mm, therefore it could be concluded that $S_{T(max)}$ and $\Delta S_{T(max)}$ which occurred were tolerable.

Keywords: Differential settlement, Total settlement, Loading test, Short piled raft

INTRODUCTION

With increasing in urbanization in last three decades all over the world, and due to limited land available, many construction projects have penetrated into the problematic soil area, with some of the problems faced [1]. Completion of construction by using a conventional foundation system such as pile foundation system is still considered to be quite expensive [2]. To overcome these problems, several foundation systems have been developed, among others, is a piled raft foundation, which the concept of this system has received considerable attention in recent years [3] and even proves to be more effective on such conditions, increasingly recognized as a foundation more economical and effective on problematic soil [4].

At the peat area, the construction method on peat is different for the different depth of peat [5]. For peat with depth less than 3 m, the removal and replacement method are usually used. For the depth 3 m to 10 m, engineers normally used sand drain, lightweight fills and stone column. While for the depth more than 10 m, the suitable method is deep stabilization techniques such as pile and dynamic compaction [6].

In this study, a Short Piled Raft foundation system was introduced, built on peat which is known as problematic soil. Short Piled Raft foundation system is a modified piled raft foundation system, which is a combination between pile foundation and raft

foundation, with the pile length relatively shorter, and considered as a reinforced concrete slab resting on a number of piles. The piling activity during construction as shown in Fig. 1.



Fig. 1 Adjusting pile verticality during piling

The basic concept of Short Piled Raft foundation system considers passive soil pressure creating a stiff condition of slab-pile system. This means that the thin concrete slab floats on the supporting soil while the piles serve as stiffeners slab concrete and also to improve stability performance by reducing settlement of the foundation [7]. Figure 2 shows a phase of construction before casting concrete slab.



Fig. 2 Reinforcement of concrete slab before casting concrete slab

SCOPE, LIMITATION AND OBJECTIVE

The scope of this study was to observe the stability performance of a large scale model of Short Piled Raft foundation system on peat during loading test. The static load acted on the center of the concrete slab, as simulation of transmission line tower.

The limitation of this study was that the size of the model to be 3.0 m x 3.0 m, with 0.15 m thickness of concrete slab, piled by 9 short piles of 3.0 m length, outer diameter was 0.32 m and thickness of wall was 0.003 m. The pile was closed end galvanized steel pipe, with the pile spacing of 1.00 m, as optimum spacing [8] and constructed on peat with the layer thickness of 3.5 m.

While the objective of the study was to evaluate the differential settlement occurred at 5 points observed on concrete slab during loading test, based on the Recommendation of European Committee for Standardization on Differential Settlement Parameters.

METHODOLOGY

Loading test was conducted follows ASTM Standard D 1143 - 81: Standard Test Method for Piles under Static Axial Compressive Load. This test method covers procedures for testing vertical or batter piles individually or groups of vertical piles to determine response of pile or pile group to a static compressive load applied axially to the pile or piles within the group, regardless of their method of installation. There are three methods of applying load as follows. Considering that peat is very soft soil, the most suitable was the method of Load Applied to Pile or Pile Group by Hydraulic Jack Acting against a Weighted Box or Platform, although still needed to be modified as shown in Fig. 3.

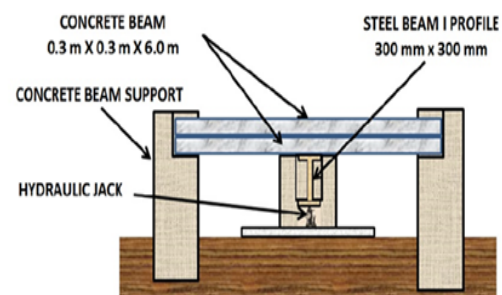


Fig. 3 Modified method of applying load for Loading Test

For conducting loading test, 16 concrete beams of 0.40 m x 0.40 m x 6.0 m were provided and laid on an I profile steel beam. Figure 4 shows arranging of concrete beam for loading test.



Fig. 4 The last concrete beam would be laid as load

Loading was carried out by jacking the steel beam at the center point of concrete slab. Location of point load and points observed shown in Fig. 5.

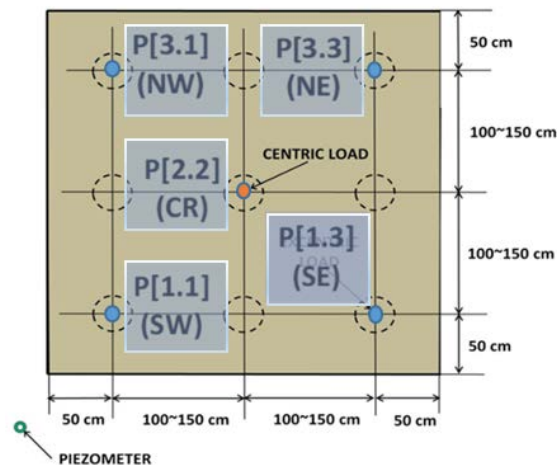


Fig. 5 Location of Point Load and Point Observed

Loading Procedure

Unless failure occurs first, load the pile up to at least 160% of the group design the pile until the settlement equals 15% of the pile diameter. Due to the magnitude of the decline could not be precisely predicted, therefor constant time interval loading was suitable procedure to be applied. Applying load increments of 20% of the design load with 1 hour between load increments and unload with 1 hour between load decrements.

Procedure of Measuring Movements

For measuring movements, a leveling instrument (Sprinter) was used to measure some staff gauges that installed at several certain observed points, as shown in Fig. 6.



Fig. 6 Leveling instrument, (a) Sprinter and (b) staff gauge.

Before testing, no-load reading should be taken for all instruments, including staff gauge, and ground water level meter. Taking the reading of time, load and movement, and record them before and after the application of each load increment or the removal of each load decrement.

The phase of loading test and its sequence as shown in Table 1.

Table 1 Sequence of Reading during Loading and Unloading Test

PHASE	Duration Cumul. (hr)	Interval (minute)	Loading/Unloading (kN)
Initial	-	-	0
Loading From 0 kN until 160 kN with increment of 20 kN	0.5	5	20
	1.0	10	40
	1.5	5	60
	2.0	10	80
	2.5	5	100
	3.0	10	120
	3.5	5	140
	4.0	10	160
	4.5	5	
	5.0	10	
	5.5	5	
	6.0	10	
Remain 160 kN	6.5	5	
	7.0	10	
	7.5	5	
Unloading From 140 kN until 0 kN with decrement of 20 kN	8.0	10	160
	10.0	20	140
	20.0	60	120
	32.0	120	100
	33.0	20	80
	34.0	20	60
	35.0	20	40
	36.0	20	20
	37.0	20	0
	38.0	20	
	39.0	20	
	40.0	20	
Final Rebound	52.0	720	0

During loading, provided that the test pile group has not failed, additional readings should be taken and recorded them at intervals 5 minutes during the first ½ hour for each load increment. After the total load has been applied, provided that the test pile group has not failed, readings and record should be taken at the interval of 20 minutes during the first 2 hours and 1 hour for the next 10 hours, and 2 hours for the next 12 hours. If pile failure occurred, the readings should be taken immediately before removing the first load decrement. During unloading, readings and record should be taken at intervals of 20 minutes. A final rebound reading has been taken 12 hours after all load has been removed.

RESULTS AND DISCUSSIONS

Loading test was conducted until 160 kN or equal to 160% of design load (100 kN) and the foundation had no failed.

The data of settlement reading at the end of every stage of loading, unloading, preloading and remain were tabulated in Table 2.

Table 2 Relationship between load and settlement

Phase	Load [kN]	Settlement [mm]				
		SW	SE	CR	NW	NE
LOADING	0.00	0.00	0.00	0.00	0.00	0.00
	20.00	0.50	0.30	0.90	0.30	0.70
	40.00	1.50	1.40	2.10	1.10	1.80
	60.00	2.35	2.20	2.90	2.00	2.30
	80.00	4.35	3.70	5.20	3.70	4.00
	100.00	6.75	6.00	7.80	5.90	5.70
UNLOADING	80.00	6.70	5.90	7.60	6.00	5.90
	60.00	6.35	6.10	7.00	5.90	5.50
	40.00	5.40	4.80	6.20	4.80	4.90
	20.00	3.90	3.70	4.40	3.60	3.50
	0.00	1.50	1.90	1.50	1.70	1.70
RE-LOADING	0.00	1.50	1.90	1.30	1.70	1.70
	20.00	2.65	2.80	2.90	2.60	2.80
	40.00	4.30	4.00	4.90	3.90	4.40
	60.00	4.95	4.80	5.60	4.50	5.10
	80.00	6.15	6.30	7.00	5.50	7.00
	100.00	9.80	9.10	10.90	8.90	10.00
	120.00	13.15	12.60	14.80	11.70	12.60
	140.00	19.05	14.50	21.30	17.00	16.50
REMAIN	160.00	26.10	16.50	30.60	22.80	19.90
	160.00	26.60	17.20	31.90	24.10	21.00
	160.00	27.90	17.10	33.00	25.00	21.60
	160.00	28.90	19.40	35.20	27.20	24.20
	160.00	31.10	23.40	36.20	28.30	24.50
UNLOADING	160.00	31.10	23.40	36.20	28.30	24.50
	140.00	32.25	23.40	36.30	28.40	24.40
	120.00	32.15	23.40	36.20	28.30	24.60
	100.00	31.70	22.70	35.60	28.00	24.50
	80.00	31.40	22.60	35.40	27.60	24.40
	60.00	30.10	21.40	33.80	26.60	23.70
	40.00	27.85	19.50	30.90	25.00	22.80
	20.00	25.10	17.30	27.50	22.90	21.10
FINAL BOUND	0.00	22.30	15.10	24.10	20.70	18.50

The data could also be presented graphically, as an example, point at the center of concrete slab (CR) was taken as typical of settlement pattern, as shown in Fig. 7.

It can be seen that the patterns of relationship between loading up to 100 kN and settlement were similar to relationship between loading up to 160 kN and settlement. The maximum of total settlement $S_{T(max)}$ occurred at the center (CR) of 7.80 mm under the load of 100 kN, 29.90 mm under the load of 160 kN and 36.20 mm under the remain load of 160 kN for 24 hours, less than 50 mm [9].

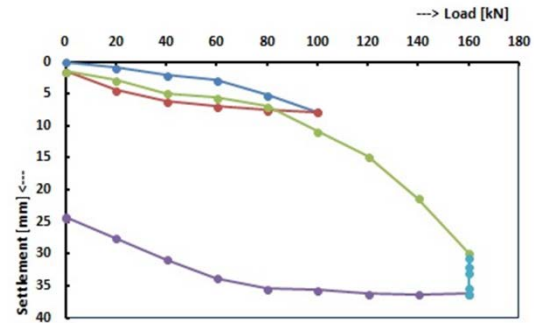


Fig. 7 Relationship between load and settlement at the center of concrete slab (CR)

From the data reading, settlement under the load of 100 kN at each point observed were not significantly different, as shown in Fig. 8.

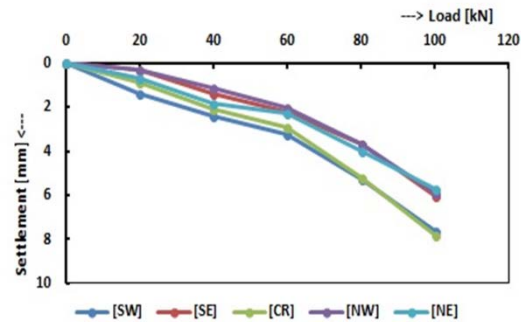


Fig. 8 Relationship between loading up to 100 kN and settlement at each point observed.

There were similar patterns of relationship between load and settlement at every observed point, it meant that the concrete slab moved down simultaneously, indicated that the pile functioned as stiffener of concrete slab effectively [7].

While at the SW point was 7.65 mm was relatively larger than at the three point at another corners, because under this part, the original soil was disturbed due to for lifting remain big tree and filled back again without any compaction. It means that heterogeneity of peat may influence immediate settlement of Short Piled Raft foundation system.

The settlement under the load of 160 kN at each point observed were presented graphically, as shown in Fig. 9.

There was a little bit strange data for curve line of settlement pattern of SE point from the load of 120 kN to 140 kN, that shown less settlement. But after reached 160 kN, the curve back to similar condition. Heterogeneity of peat might cause this phenomenon.

While the maximum of difference in total settlement between any two points $\Delta S_{T(max)}$ was 1.95 mm ([SW] – [NE]), 10.30 mm ([SW] – [SE]) and 9.65 mm ([SW] – [SE]), under the load of 100 kN, 160 kN and remain of 160 kN for 24 hours respectively, less than 20 mm [9].

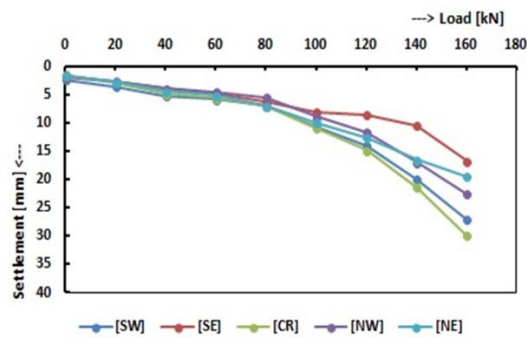


Fig. 9 Relationship between loading up to 160 kN and settlement at each point observed.

CONCLUSION

Based on the discussion, it can be concluded as follows.

1. The loading test of Short Piled Raft foundation system up to 160 kN or 160% of design load shown that settlements at each point simultaneously moved down with small differences. It means that beside as supporting the load, piles were also well functioning as stiffener of concrete slab.
2. The maximum of total settlement $S_{T(max)}$ occurred less than 50 mm and the maximum of difference in total settlement between any two points $\Delta S_{T(max)}$ less than 20 mm.

ACKNOWLEDGEMENTS

The research work reported in this paper was funded by Contract Research Grant U260 ORICC, Universiti Tun Hussein Onn Malaysia (UTHM).

The authors wish to express their gratitude to RECESS - UTHM and Geomatic Engineering Laboratory, FKAAS - UTHM in providing the equipments during carrying out this research.

REFERENCES

- [1] Patil, J. D., Vasanvala, S. A., Solanki, C. H., A Study on Piled Raft Foundation: State of Art, International Journal of Engineering Research & Technology (IJERT), 2013, pp.1464-1470.

- [2] Effendi, S., Cakar Ayam Soft Foundation System Revisited. Soft Soil Engineering International Conference 2013, Kuching, Sarawak, Malaysia, 2013.
- [3] Prakoso, W. A. and Kulway, F. H., Contribution To Piled Raft Foundation Design. Journal of Geotechnical and Geoenvironmental Engineering, 2001, pp.17-24.
- [4] Srilakshmi, G. and Moudgalya, D., Analysis of Piled Raft Foundation Using Finite Element Method. International Journal of Engineering Research and Science & Technology, Vol. 2, No. 3, 2013, pp.89-96.
- [5] Bakar, I., Challenges in Peat Soil Research - Malaysian Experiences. South East Asia Conference on Soft Soils Engineering and Ground Improvement, Bandung, 2014.
- [6] Huat, B. B. K., Prasad, A., Asadi, A. and Kazemian, S., Geotechnics of Organic Soils and Peat. CRC Press/Balkema, 2014.
- [7] Hardiyatmo, H. C., Analisis dan Perancangan Fondasi II, Gadjah Mada University Press, Edisi Ketiga, 2015, pp. 487-515.
- [8] Suro, S. M., Bakar, I. and Sulaeman, A., Pile Spacing Optimization of Short Piled Raft Foundation System for Obtaining Minimum Settlement on Peat, IOP Conference Series: Materials Science and Engineering, Volume 136, Conference 1, 2016.
- [9] Das, B. M., Principles of Foundation Engineering, Seventh Edition, Cengage Learning, 2011.
- [10] ASTM, Standard Test Method for Piles Under Static Axial Compressive LOAD, Designation D 1143 – 81 (Reapproved 1994).

SETTLEMENT BEHAVIOR OF ROAD SURFACES CAUSED BY DISSOLUTION OF SALT LAYERS

Siwadol Saenseela¹, Pongsagorn Pongchompu^{2*}, Gomin³
Chairatanangamdej Rajamangala University of Technology Khonkaen
*Corresponding author; Email: pongsagorn.pongchompu@gmail.com

ABSTRACT

This research was aimed at studying the settlement behavior of road surfaces caused by dissolution of salt layers that in turn create cavities. The dissolution can happen naturally or occur from salt mining. The proposed project's site was Highway 2229 from km4 +066 to km 4+275, Kud Ruakham Sub-district, Ban Muang District, Sakonnakhon Province. The 2015 soil layer drilling survey revealed layers of hard clay and compact soil or shale with low plasticity. Cavities were found at the depth of 42 meters over sand stone layers. The analysis of road surface settlement was based on the Empirical Method and theories of Peck(1969), O'Reilly and New(1982), and Rankin(1969) to determine the i and V_s parameters based on S_{msx} from the surveys of road surface settlement from 2013 to 2018. Using the survey results, the analysis by the theory of O'Reilly and New (1982) showed i at 21 m and V_s ranging from 95 % to 102% of V_s . The analysis based on the survey data and Rankin's theory (1969) showed i equal to 19.16m and V_s between 87% and 93 % of V_s . The analysis of the surveyed data showed end of surface settlement in 2016, which was consistent with the drilling survey in 2017 from which no cavities were found on the sand stone layers.

Keywords: Settlement, Salt layer, Cavities, Empirical Method

INTRODUCTION

The Northeast of Thailand is principally composed of mountains and glades. The two major glades are Korat Glade and Sakonnakhon Glade; the soil underneath of each contains layers of Mahasarakham rock group as shown in Figure 1, with alternate layers of halite and clay[1].

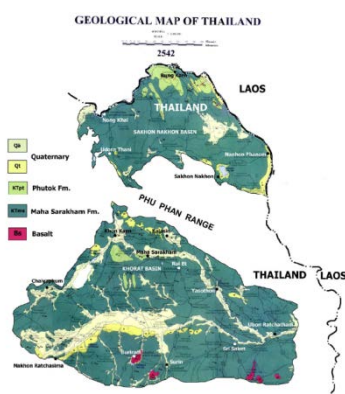


Fig. 1 1999 Geological map of Korat high plain in the Northeast containing Phu Tok and Mahasarakham rock groups - scale 1:1,000,000[2]

The Mahasarakham rock group is mainly composed of halite, which, in a great amount and in thick layers, naturally and physically becomes plastic, that is, deformable, flowable, and

unbreakable. Salt is able to flow from the edge of a glade towards the center or from top to bottom under pressure. Movement of salt is termed 'salt tectonic' (Figure 2)[2]. The geological study of the Mahasarakham rock group hierarchy as discovered from the general drilled pits indicates 4 characteristics of the rock are as following.

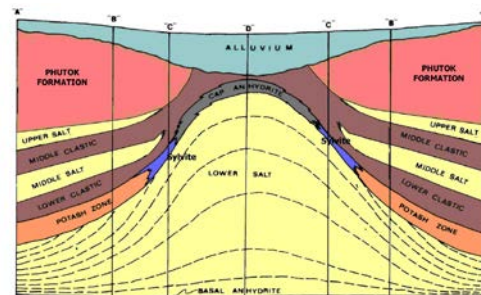


Fig.2 Structures of halite and potash classified under Mahasarakham rock group [2]

- Three salt bed
- Two salt bed
- Potash-bearing one salt bed
- Potash-barren one salt bed

Halite can be destroyed by water. When halite under soil surface has continuously been destroyed by the water retained in the same layer, a cavity is formed. This cavity, if wide and if the soil-rock layers above fail to bear the load, will collapse into a

sinkhole. The majority of sinkholes in Korat and Sakonnanhkhon Glades have been found in areas where saline water was pumped up for rock salt mining purpose and also in areas adjacent to the rock salt fields. Sinkholes in salt fields are usually not disclosed. However, if they are in the areas nearby, especially near communities or residential areas, the sinkholes will be reported on the news. Sinkholes threaten lives and assets of people living in the vicinity]3[.

Singh (1992) explained that such collapse takes place as a result of interference from external stress. Changes of stress affect the forms and movement of rock and soil layers. The extent of settlement depends on the degree of stress and the size of cavity or pit hole which lead to instability. Therefore, soil surface collapse or settlement is the function of soil tectonic activity arising from a collapse of a cavity underneath. Soil surface settlement in general results in vertical as well as lateral slides. Soil surface settlement is caused by 3 factors, namely: 1) cracks, splits, or different degrees of cracks, 2) sinkholes or holes, 3) water puddles or soil depressions]4[.

Elashiry et al. (2008) conducted a study of surface soil settlement of a phosphate mine by comparing the efficiency of the settlement equations proposed by Bal, Peng, Knothe, and Peck. In so doing, they compared the true measurement parameters against the steepness, curve, and plasticity. The method proposed by Peck yielded the parameters closest to the reality, with the coefficient accuracy over 0.9]5[.

This study was conducted on the settlement of road surface using the Empirical Method for the analysis. The survey data of road surface settlement from 2015 until 2018 were analyzed along with the data from soil survey by drilling in 2015 and 2017 comprising both vertical and horizontal soil movement (Figure 3 and Figure 4).



Fig.3 Field investigations (2017)



Fig. 4 Horizontal movement (2017)

METHODOLOGY

The study site was Highway No. 2229 from km 4+066 to km 4+275 I Kud Rua Kham Sub-District, Wanonnawat District, Sakonnanhkhon Province. The information retrieved showed that the highway was constructed before 1975 and the settlements were detected in 2012. The aerial survey showed saline water pumping from underground for a rock salt mining purpose(Figure 5).

Chaiyan Hinthong and Adul Charoenprawat (1990) indicated that they found sinkholes in the area of Ban Jampadong School in Khu Sakham Sub-District, Wanonnawat District, Sakonnanhkhon Province. There were detected sinkholes at Dinso Brook and along the brook's line. Sinkholes of 2-3 m size were also found at the school's fence. Based on the Nares Sattayarak's tectonic movement information, it is believed that the saline layer lies within the 70 m level]6[.

The drilling survey of soil layers in 2015 (Figure 6) shows that the depth of 0-2 m is the road's fill soil layer. The depth of 2-10 m is a soft to rigid clay layer, the depth of 10-11.50 m contains clay and transformed wood, the depth of 10.50-39.50 m is hard to very hard soil, the depth of 39.50-39.85 consists of cavities, and the depth of 39.85-42.00 m consists of fine sand, assumed to result from collapse of the cavity walls above. The cavity height was estimated at 2.50 m before the collapse.

Settlement data collection, the road surface settlement data was obtained from the profile leveling method done along the centerline of the road, and the inflexion parameters were recorded as per Figure 7, which were the data collected from 2015-2018. The extent of settlements began from km 4+115 to km 4+245. The greatest settlement was detected at km 4+180. All through the 4 years, the data showed: $S_{max} = 1.24$ m, 1.61 m, 1.75 m, and 1.75 m, respectively. The road surface settlement had a tendency to decrease and the settlement ceased in 2017, which is consistent with the drilling survey of soil layer in 2017 when no cavity over sandy rock layer was found (Table 1).

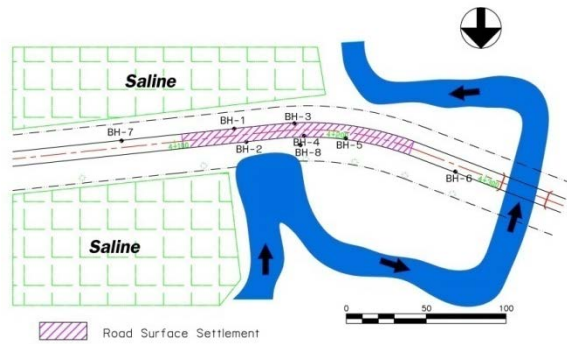


Fig. 5 Position of road surface settlement

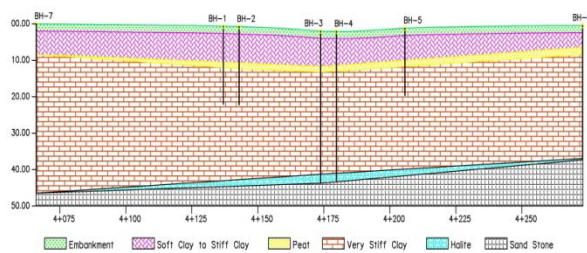


Fig. 6 soil profile (2015)

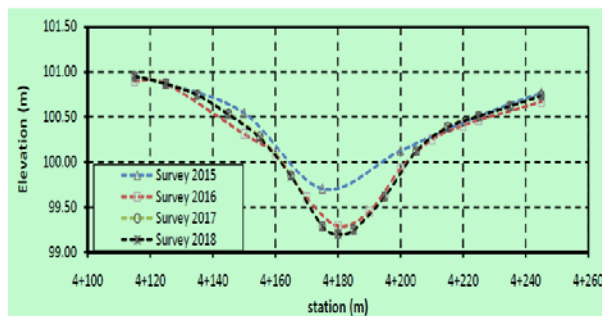


Fig. 7 road centreline elevations

Table 1 soil properties

Soil type	Thickness (m)	$\gamma_t (t/m^3)$	$w_p (%)$	LL (%)	PL (%)	$S_u (t/m^2)$
Silty sand (SM)	0.00 – 2.00	1.84	9	-	-	-
Stiff clay (CL)	2.00 – 7.50	1.88	28	44	22	9.33
Very stiff clay (CL)	7.50 – 42.00	1.92	26	47	22	31.42
Sand stone (RQD=0%)	42.00 – 43.00	-	-	-	-	-

RESULT

The Result of the road surface settlement estimation based on the Empirical Method A comparison between the road surface settlement and the scope of settlement was based on the Empirical Method of Peck's, the equation that compares the field parameters using the maximum settlement -

S_{max} , and the depth measured from the soil surface to the center of the cavity – Z_0 . From the field survey, the distance from the center of the cavity to the point where the curve i changed could be calculated in the case of clayey soil using the method of O'Reilly and New and Rankin (Table 2).

From the data Table 2, it was possible to calculate the settlement value according to Peck's theory and compare with the field data of 2015 to 2018. The results showed settlement of the surface according to Peck's, which was consistent with the real parameters obtained in the fields at the beginning of the route at km 4+115 – km 4+200. At the end of the route at km 4+200 – km 4+445, the real parameter measured was lower than the surface settlement based on Peck's theory. This was due to the non-equilibrium of the cavity which in turn, was caused by the slope of halite layers or by the fact that the settlement data was obtained from the profile leveling approach, and the curve at km 4+200 – km 4+445 led to discrepancies of the horizontal cross-section distance from the center of Cavity x . (Figure 8, Figure 9, Figure 10 and Figure 11)

A comparison was done between calculation of the road surface settlement parameter by the Empirical ($V_{S_{Empirical}}$) as per Equation 7 and the road surface settlement parameter measured in the field. The results showed that the settlement in 2015 differed from other years because the distance of 25 m between each data collection point was too long leading to the amount of field data related to soil settlement being low. Therefore, we deleted the 2015 parameters and were able to conclude the amount of soil settled per one meter unit using the distance from the cavity center to the inflexion. In the case of clayey soil, the method of O'Reilly and New showed $V_{S_{Empirical}}$ at 83.25 – 85.14% of $V_{S_{Survey}}$. The method of Rankin showed $V_{S_{Empirical}}$ at 91.23 – 93.58% of $V_{S_{Survey}}$. (Table 3 and Figure 12).

When considering the determination coefficient for more efficient method – with the value being closer to 1 – to find the surface settlement using the width of settlement hole i in the case of clayey soil between the methods of O'Reilly and New and Rankin; the results showed $R^2 = 0.96$ from O'Reilly and New method and $R^2 = 0.97$ from Rankin method, which agreed with Flashily.

The analysis of horizontal slide based on the Empirical Method by O'Reilly and New Theory (Figure 13), showed the horizontal surface slide. It was assumed that the soil slid towards the center of the cavity. As seen in the Figure, the slide began at km 4+115 and increased until the maximum at km 4+160 before it decreased again to zero at km 4+180, where the settlement point was the peak. Then horizontal slide increased again to the maximum at km.4+200 until it became 0 at km

4+445. Figure 14 depicts horizontal slides that resulted in cross-sectional cracks on the road surface. There were slides that coincided at the maximum settlement point, which resulted in swelling.

Table 2 inflexion (i)

Year	Survey		i (m)	
	Z (m)	S max	O'Reilly and New 1982	Rankin 1969
2015	42	1.24	19.16	21
2016	42	1.61	19.16	21
2017	42	1.75	19.16	21
2018	42	1.75	19.16	21

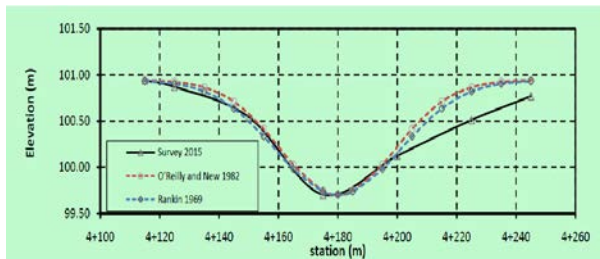


Fig. 8 road surface settlement (2015)

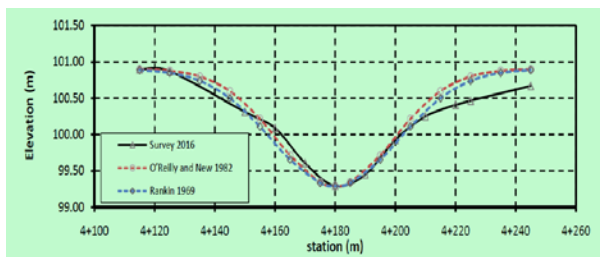


Fig. 9 road surface settlement (2016)

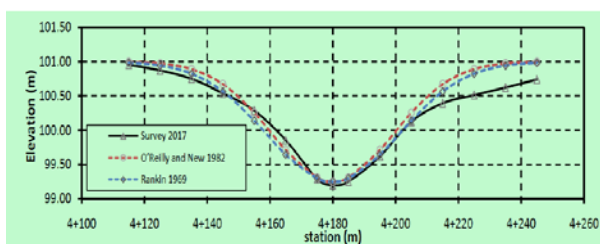


Fig. 10 road surface settlement (2017)

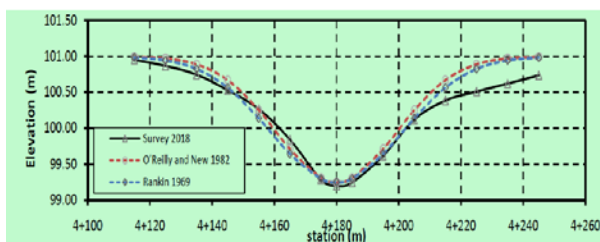


Fig. 11 road surface settlement (2018)

Table3 road surface settlement

year	V_{Survey}	$V_{Empirical}$		$V_{Empirical}/V_{Survey}(\%)$	
		O'Reilly and New 1982	Rankin 1969	O'Reilly and New 1982	Rankin 1969
2015	57.99	59.40	65.10	102.42	112.26
2016	92.65	77.12	84.53	83.24	91.23
2017	98.18	83.83	91.88	85.38	93.58
2018	98.45	83.83	91.88	85.14	93.32



Fig. 12 volume of road surface settlement

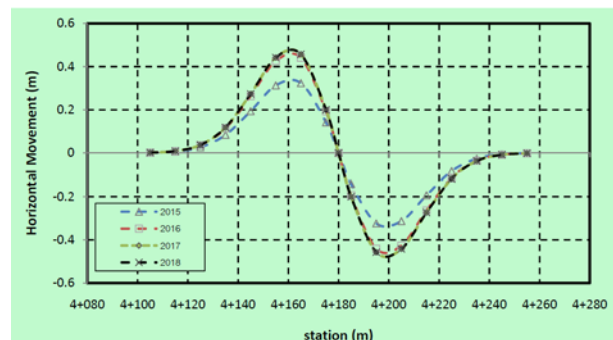


Fig.13 horizontal movement



Fig. 14 crack due to horizontal movement

CONCLUSIONS

1. The settlement of road surface was caused by solution of rock salt by water, which resulted in cavities at the depth of 42 m from the surface to the cavity center Z_0 .
2. The Empirical Method and Peck's theory gave the consistent road surface settlement value with the value measured in the field and coefficient of determination R^2 higher than 0.96.
3. The distance from cavity center to the inflexion in the case of clayey soil measured by Rankin method was 21 m. This means that the road surface settlement according to Peck's theory agreed with the real value measured in the field more than the method of O'Reilly and New. This was determined from the coefficient of determination of Rankin being $R^2 = 0.97$, which was higher than that of O'Reilly and New, where $R^2 = 0.96$.
4. The amount of the road surface settlement by the Empirical Method using the distance from the cavity center to the inflexion i by O'Reilly and New method was 83.25 – 85.14% of V_{Survey} , whereas Rankin's calculation showed 91.23 – 93.58% of V_{Survey} .
5. The horizontal slide at the road surface led to tension between km 1+115 – km 1+160 and km 4+200 – km 4+245, which in turn caused cross-section cracks on the road surface. From km 1+160 to km 1+200, compression occurred from horizontal slides, causing swelling on the surface.

ACKNOWLEDGEMENT

The researchers are grateful to Buengkan Highway Department and the Bridge Repair and Construction Center 2 (Khon Kaen), Department of Highway, for the information of the road surface settlement at the study site, site history, soil layer survey, and the assistance in the course of this research study.

REFERENCES

- [1] Peangta Satarugsa, Boundary and Evolution of Rock Salt in the Maha Sarakham Formation in the Mortheast, Thailand KKU Res. J. 2005; 10(1):(65-78)
- [2] Parkorn Suwanich1, Geological Map of Phutok Formation Improvement explored from Potash and Rock Salt drilled holes, topography and outcrops on the Khorat Plateau KKU Res. J. 2012; 17(1):(58-70)
- [3] Peangta Satarugsa and Sakorn Sangchumpoo, Comparison of Rates for Expansion of Surface and Subsurface Sinkholes: a Case Study at Ban Bo Deang Amphoe Ban Muang Changwat Sakon Nakhon KKU Res J. 2011; 16(8): 993-1002
- [4] Chaiyan Hinthong and Adul Charoenprawat, Report of Geological Study on Soil Settlement at Ban Jampadong School in Khu Sakham Sub-District, Wanonniwat District, Sakonnakhon Province. Division of Geology, Department of Geological Resources. American Railway Engineering and Maintenance-of-Way Association. Manual of Railway Engineering Volume 1 Track. AREMA, 2010.
- [5] Singh, M.M., Mine subsidence, SME Mining Engineering Handbook. Hartman, H.L. (ed). Society for Mining Metallurgy and Exploration. Inc. Littleton, Colorado, pp. 938–971, 1992
- [6] Elashiry, A.A., Gomma, W.A. and Imbaby, S.S. Surface subsidence prediction over working longwall panel at abu-tartur phosphate mines. Journal of Engineering Sciences. 36(3): 749-758, 2008
- [7] Fuenkajorn, K. and Archeeploha, S. Prediction of cavern configurations from subsidence data. Engineering Geology. 110: 21-29, 2009
- [8] Thongprapha, T., Fuenkajorn, K., and Daemen, J.J.K.. Study of surface subsidence above an underground opening using a trap door apparatus. Tunnelling and Underground Space Technology. 46: 94–103, 2015
- [9] Peck, R.B., Deep excavations and tunneling in soft ground, In: Proceedings of the 7th international conference on soil mechanics and foundation engineering, State of the art volume, ociedad exicana de ec nica de uelos, Mexico, pp. 225–290, 1969.
- [10] O'Reilly MP, New BM ,Settlements above tunnels in the UK-their magnitude and prediction. Tunneling 82:173–181, 1982
- [11] Rankin, W., Ground movements resulting from urban tunneling, In: Prediction and effects, proceedings of 23rd conference of the engineering group of the geological society, London Geological Society, pp. 79–92, 1988.

PRODUCTION OF ETHYL ESTER BIODIESEL FROM USED COOKING OIL WITH ETHANOL AND ITS QUICK GLYCEROL-BIODIESEL LAYER SEPARATION USING PURE GLYCEROL

Mallika Tapanwong¹, Vittaya Punsuvon^{1,2}

¹Center of Excellence-Oil Palm Kasetsart University, Bangkok, 10900 Thailand

²Department of Chemistry, Faculty of Science, Kasetsart University, Bangkok, 10900 Thailand

ABSTRACT

In this study, used cooking oil, ethanol and sodium hydroxide (NaOH) were used as raw material and catalyst to produce biodiesel through transesterification reaction. The occurring emulsion from ethanol acts as a surfactant in the reaction mixture make the separation of biodiesel from glycerol layer more difficult. This problem solving was done by adding pure glycerol into the reaction mixture after complete reaction to make quick layer separation between glycerol and biodiesel. The characterization of the produced biodiesel was performed by proton nuclear magnetic resonance (¹H-NMR) and gas chromatography (GC). The result showed that the optimum condition for ethyl ester biodiesel production were 8:1 of ethanol to oil molar ratio, 0.75% w/w of NaOH amount, 45 min of reaction time and 40 °C of reaction temperature. This condition gave 100% of fatty acid ethyl ester conversion that determined by ¹H-NMR. The result on the optimum condition for layer separation showed that the adding of 2.44% v/v of pure glycerol relation to the total volume of the reaction mixture took 14.38 min for glycerol-biodiesel layer separation. In addition, ethyl ester biodiesel was further analyzed its fuel properties followed ASTM biodiesel standard. The results showed the produced biodiesel met well with the standard.

Keywords: Biodiesel, Glycerol, Surfactant, Transesterification

INTRODUCTION

The limited fossil fuel resource along with the need to reduce greenhouse gas emission were a major impulse to the development of alternative fuels. As one result, increased attention has been given to biofuel, such as biodiesel, that can be used as alternative fuel to replace diesel fuel. Its production from renewable resource, such as vegetable oil and animal fat, makes it biodegradable and non-toxic substance. In addition, biodiesel contributes to the reduction of CO₂ emission because it comprises a closed carbon cycle [1]. The choice of vegetable oil as feedstock for making biodiesel rely upon the cost of production, reliability of supply and high yield. Used cooking oil (UCO) was waste that obtained from households, cafeteria and restaurants collection. The UCO offers significant potential source as a low cost raw material for biodiesel production. UCO contained low free fatty acid content, thus it is suitable for making biodiesel via transesterification reaction without any problem caused by soap formation. Furthermore from the waste management viewpoint, using UCO in biodiesel production helps to provide a cleaner way for disposing these wastes [2].

The most common way to produce biodiesel is transesterification reaction that triglycerides react with alcohol to form esters and glycerol as by-product. Transesterification consists of a sequence of

three consecutive reversible reaction. The first step is the conversion of triglycerides into diglycerides and further into monoglycerides in the second step. The final step, monoglycerides converts into ester and glycerol molecule.

Short chain alcohol such as methanol and ethanol are the most frequency employed. Methanol is highly reaction and generates satisfactory yields at lower temperatures and reaction time compared with other alcohol [3]. However, methanol presents the disadvantage of higher toxicity compared with ethanol. In our work, ethanol is selected because ethanol can be produced from agricultural renewable resource such as sugarcane that result in total independence from importing petroleum-based alcohol like methanol [4]. However, as the synthesis progresses through the transesterification reaction, ethanol promotes a more stable dispersion between the ethyl ester biodiesel and glycerol, impeding the layer separation and thus increasing the time required for the production process and lowering the quality of the obtained biodiesel [5]. Pure glycerol is usually used to disperse the layer of ethyl ester biodiesel and glycerol but the amount of adding and the waiting time for separation is not known, so this is the first time to study.

The objective of this work is to determine the optimum condition for the transesterification reaction between used cooking oil with ethanol using NaOH as alkali catalyst and pure glycerol as dispersing

compound for biodiesel-glycerol layer separation. The optimum condition in adding the amount of pure glycerol on the separation of biodiesel-glycerol layer is also determined. Moreover, the purification ethyl ester biodiesel is further characterized its fuel properties compared with the methyl ester biodiesel standard.

MATERIALS AND METHODS

Material

UCO in this research was obtained from household collection. The fatty acid composition determined by gas chromatograph (GC) consisted of 0.857%w myristic acid, 36.030%w palmitic acid, 4.383%w stearic acid, 43.372%w oleic acid, 13.606%w linoleic acid. The calculated average molecular weight of UCO was 852 g/mol and its free fatty acid content was 0.18%w. Analytical grade ethanol was purchased from Merck (Germany). Methyl heptadecanoate (C₁₇) was obtained from Fluka (Switzerland) and deuterated chloroform was obtained from QReC (New Zealand).

Transesterification Reaction

The transesterification reaction was carried out in a laboratory scale setup using a three-necked 100 ml flask equipped with a reflux condenser, a thermometer and a magnetic stirrer. The reaction was conducted with UCO that stirred constantly at 750 rpm with ethanol and NaOH catalyst. The reaction were performed at different amount of NaOH catalyst (0.25-1.25%w), different molar ratio of oil to ethanol (4:1-12:1 mole) and different reaction time (15-120 min) with keeping the constant temperature at 40 °C. After the reaction was completed, the mixture was transferred into separation funnel and 2.44%v/v of pure glycerol was added into the mixture to separate into two layers that the top layer was biodiesel and the bottom layer was glycerol. The biodiesel was further purified with warm water and dried in an oven. The obtained purified biodiesel was investigated for fatty acid ethyl ester (%FAEE) conversion by ¹H-NMR (varian, inova 400 mhz, usa).

Determination of FAEE

The ¹H-NMR spectra of UCO ethyl ester biodiesel from the ¹H-NMR analysis were obtained for monitoring the transesterification reaction in the form of percentage fatty acid ethyl ester (%FAEE) conversion. The %FAEE conversion was analyzed follow [6]. Briefly, the chemical shift at 4.15 ppm represented the ethyl ester protons and at 3.30 ppm represented the methylene proton (α-CH₂). An equation to calculate the %FAEE conversion is shown in Eq. (1).

$$C = \frac{A_{EE}/2}{A_{\alpha-CH_2}/2} \times 100 \quad (1)$$

Where, C is the percentage of FAEE conversion, A_{EE} is the integration value of the protons of the ethyl ester and A_{α-CH₂} is the integration value of the methylene protons. The 2 factor, which divides both integration value s, is the normalization factor

RESULT

Characterization of UCO

The fatty acid composition of UCO that determined by GC was revealed in Table 1.

Table 1 Fatty acid composition of UCO

Fatty acid	Molecular formular	Molecular weight	% Area
Octanoic acid	C ₈ H ₁₆ O ₂	144	0.037
Decanoic acid	C ₁₀ H ₂₀ O ₂	172	0.019
Lauric acid	C ₁₂ H ₂₄ O ₂	200	0.320
Myristic acid	C ₁₄ H ₂₈ O ₂	256	0.857
Palmitic acid	C ₁₆ H ₃₂ O ₂	256	36.030
Palmitoleic acid	C ₁₆ H ₃₀ O ₂	254	0.305
Stearic acid	C ₁₈ H ₃₆ O ₂	284	4.383
Oleic acid	C ₁₈ H ₃₄ O ₂	282	43.372
Linoleic acid	C ₁₈ H ₃₂ O ₂	280	13.606
Linolenic acid	C ₁₈ H ₃₀ O ₂	278	0.522
Arachidic acid	C ₂₀ H ₄₀ O ₂	312	0.365
Behenic acid	C ₂₂ H ₄₄ O ₂	340	0.105

The fatty acid composition showed that oleic acid (43.372%) and palmitic acid (36.030%) are the two major fatty acids, followed by linoleic acid (13.606%), stearic acid (4.383%). The minor fatty acid are octanoic acid (0.037%), decanoic acid (0.019%), lauric acid (0.320%), myristic acid (0.857%), palmitoleic acid (0.305%), linolenic acid (0.522%), arachidic acid (0.365%) and behenic acid (0.105%). The average molecular weight of UCO calculated from the fatty acid composition is 852 g/mol. The UCO also contained 0.18%w/w of free fatty acid.

¹H-NMR spectrum of ethyl ester biodiesel for %FAEE conversion calculation

The ¹H-NMR spectrum of the UCO ethyl ester biodiesel obtained after washing and drying is present

in Fig. 1.

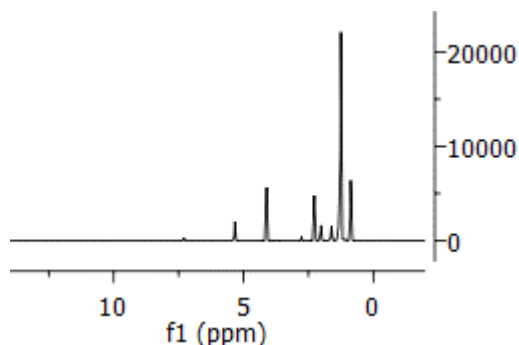


Fig. 1 ^1H -NMR spectra of UCO ethyl ester biodiesel.

The conversion of the triglyceride to monoalkyl ester is clearly observed in the ^1H -spectra by the appearance of the quartet at 4.15 ppm which related to the ethyl ester CH_2 group. From the chemical shift at 4.15 ppm and at 2.30 ppm of the CH_2 group adjacent to the carbonyl group, both chemical shifts were used to calculate the percentage conversion of fatty acid ethyl ester (%FAEE) followed Equation 2.

Optimum Condition in Biodiesel Production by Transesterification

Influence of the amount of catalyst on the percentage of fatty acid ethyl ester conversion (%FAEE)

The influence of the NaOH amount of catalyst on the %FAEE conversion is examined in Figure 2. The amount of NaOH catalyst varies from 0.25% w/w to 1.25% w/w. The %FAEE conversion using NaOH catalyst increases rapidly from 0.25% w/w to 0.50 % w/w after that the %FAEE increases gradually from 0.50% w/w to 0.75% w/w. The %FAEE conversion reaches a maximum of 100% at 0.75% w/w. Further increase in the amount of NaOH catalyst up to 1.25% w/w cannot promote the conversion. So, the selected optimum amount of NaOH catalyst was 0.75% w/w.

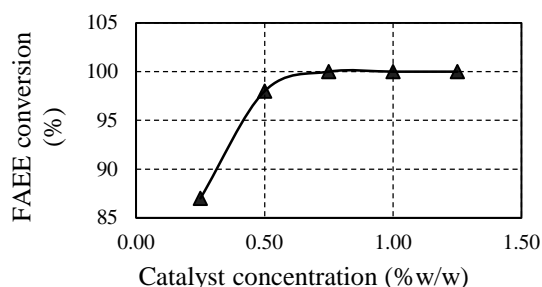


Fig. 2 Influence of the amount of NaOH catalyst on %FAEE conversion. Transesterification condition: reaction temperature = 40 °C, molar ratio of ethanol to UCO = 10:1, reaction time = 90 min at 750 rpm of constant stirring.

Influence of molar ratio of ethanol to UCO on the percentage of ethyl ester conversion (%FAEE)

The molar ratio of ethanol to UCO is one of the most important parameters affecting the transesterification conversion. Although the stoichiometric ratio requires three moles of ethanol for each mole of UCO, in practice, the mole ratio should higher to shift the equilibrium towards the direction of the ethyl ester formation. Figure 3 describes the influence of mole ratio of ethanol to UCO on the %FAEE conversion.

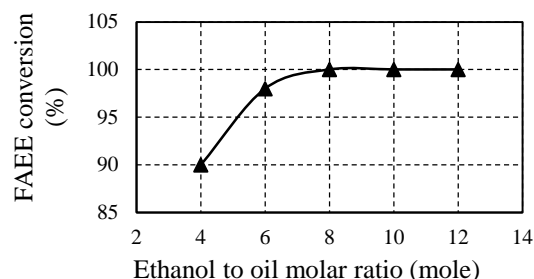


Fig. 3 Influence of molar ratio of ethanol to UCO on %FAEE conversion. Transesterification condition: reaction temperature = 40 °C, amount of NaOH catalyst = 0.75%, reaction time = 90 min at 750 rpm of constant stirring.

It can be found that the %FAEE conversion increases rapidly from 4:1 to 6:1 of molar ratio after that the %FAEE increases gradually from 6:1 to 8:1 of molar ratio. The maximum of 100% FAEE conversion obtained at 8:1 of molar ratio and further increase in the molar ratio from 8:1 to 12:1 gave the same %FAEE conversion.

Influence of reaction time on the percentage of ethyl ester conversion (%FAEE)

The influence of reaction time on the %FAEE conversion is studied and depicted in Figure 4.

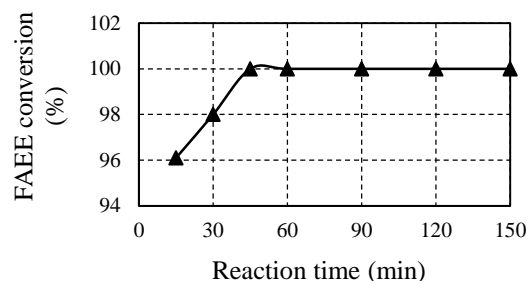


Fig. 4 Influence of reaction time on %FAEE conversion. Transesterification condition: reaction temperature = 40 °C, amount of NaOH catalyst = 0.75%, molar ratio of ethanol to UCO = 8:1 at 750 rpm of constant stirring.

It can be seen that %FAEE increased rapidly from 15 min to 45 min after that the %FAEE became almost constant. The optimum time obtained from the study was 45 min that gave 100% of FAEE conversion.

Influence of adding pure glycerol on the waiting time for layer separation

The influence of pure glycerol addition percentage on the waiting time for layer separation of biodiesel and glycerol is shown in Figure 5. Pure glycerol addition percentage varies from 2.44%, 4.76%, 6.98%, 9.09% and 11.11% v/v related to the total volume of the biodiesel and glycerol mixture.

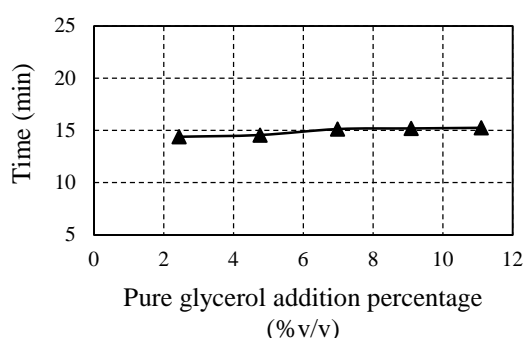


Fig. 5 Influence of adding pure glycerol on the waiting time for layer separation. Transesterification condition: reaction temperature = 40 °C, molar ratio of ethanol to UCO = 8:1, reaction time = 45 min at 750 rpm of constant stirring.

The result indicated that more pure glycerol addition percentage from 2.44% to 11.11% v/v gave the constant waiting time at 14.38 min for layer separation. Therefore, the selected optimum amount of adding pure glycerol was considered 2.44% v/v. The reason for adding a low quantity of pure glycerol provokes a rapid separation of the two layer can be understood by the formation of hydrogen bonds between ethanol and pure glycerol that are stronger than the van der Waals forces between ethanol and biodiesel.

Physico-chemical properties of ethyl ester biodiesel

The physico-chemical properties of ethyl ester biodiesel were compared with the methyl ester biodiesel standard that followed the USA (ASTM standard). The results were exhibited in Table 2.

The result revealed that all physico-chemical properties of the produced ethyl ester biodiesel meet well with methyl ester biodiesel standard. In addition, this result implied that ethyl alcohol can be replace methyl alcohol for biodiesel production.

Table 2 Physico-chemical properties of ethyl ester biodiesel

Physico-chemical properties	Test method	Ethyl ester biodiesel	Methyl ester biodiesel (ASTM)
Density at 15 °C (kg/m ³)	ASTM D1298	863	860-900
Kinematic viscosity at 40 °C (cSt)	ASTM D445	4.94	1.9-6.0
Acid Value (mg KOH/g)	ASTM D664	0.36	0.50 max
Flash point (°C)	ASTM D93	216	120 min

CONCLUSION

In this study, the transesterification of UCO with ethanol in the presence of NaOH catalyst shows a favorable reaction. A high FAEE conversion (100%) was achieved by optimizing variable effects. The optimum conditions on %FAEE determined by ¹H-NMR during transesterification was 0.75% w/w of NaOH catalyst, 8:1 of molar ratio of UCO to ethanol, 45 min of reaction time, 40 °C of reaction temperature, 750 rpm of stirring. The separation of glycerol and biodiesel layer is optimized by adding different amount of pure glycerol into the mixture of glycerol and biodiesel product. The result showed that 2.44% v/v of adding pure glycerol can accelerates the waiting time for layer separation. It took 14.38 min for optimum time for separation. Additionally, the physico-chemical properties of the ethyl ester biodiesel met well with the ASTM methyl ester biodiesel standard.

ACKNOWLEDGEMENT

This work was supported by Center of Excellence-Oil Palm, Kesetsart University and Department of chemistry, Faculty of science, Kasetsart University.

REFERENCE

- [1] Anastopoulos G., Zannikou Y., Stournas S., and Kalligeros S., Transesterification of Vegetable Oils with Ethanol and Characterization of the Key Fuel Properties of Ethyl Esters. *Energies*, Vol. 2, Issue 2, 2009, pp.362-376.
- [2] Diya'uddeen B.H., Abdul Aziz A.R., Daud W.M., and Chakrabarti M.H., Performance Evaluation of Biodiesel from Used Domestic Waste Oils: A Review. *Process Saf. Environ. Prot.*, Vol. 90, 2012, pp.164-179.
- [3] Firdaus M., Yusoff M., Xu X., and Guo Z., Comparison of Fatty Acid Methyl and Ethyl

- Esters as Biodiesel Base Stock: A Review on Processing and Production Requirement. J Am Oil Chem Soc, Vol. 91, Issue 4, 2014, pp. 525-531.
- [4] Namwong S., Punsuvon V., and Arirob W., Process Optimization of Ethyl Ester Biodiesel Production from Used Vegetable Oil under Sodium Methoxide Catalyst and its Purification by Ion Exchange Resin. Applied Mechanics and Material, Vol. 873, 2017, pp.90-94.
- [5] Silva W., Souza P., Shimato G.G., and Tubino M., Separation of The Glycerol –Biodiesel Phase in An Ethyl Transesterification Synthetic Route Using Water, J. Braz. Chem. Soc., Vol. 26, Issue 9, 2015, pp.1745-1750.

AN INTEGRATED APPROACH FOR SUSTAINABILITY IN THE APPLICATION OF INDUSTRIALISED BUILDING SYSTEM (IBS)

Riduan Yunus¹, Abdul Rahim Abdul Hamid² and Siti Rahimah Mohd Noor¹

¹Faculty of Civil & Environmental Engineering, Universiti Tun Hussein Onn Malaysia (UTHM), Malaysia;

²Faculty of Civil Engineering, Universiti Teknologi Malaysia (UTM), Malaysia

ABSTRACT

Malaysia is committed to improve deliverables of construction industry especially in meeting the sustainable objectives. Lack of systematic tools and poor collaboration between key stakeholders have been identified as the main barriers to meet the objectives. The purpose of this paper is to present an integrated approach that can be able to assist designers, who are at the forefront in decision making, to select the best strategies that have been shown to be effective in promoting sustainability for IBS application. Questionnaire survey and interviews of the local practitioners were conducted to identify critical factors and provide recommendations on how to enhance sustainability by holistically addressing the identified issues during IBS design. SWOT (Strengths, Weaknesses, Opportunities and Threats) analysis framework was used to help decision-makers maximise the opportunities by using available strengths, avoid weaknesses, and diagnose possible threats in the examined issues. From the statistical analysis, eighteen critical factors relevant to IBS sustainability have been ranked. The guidelines were formulated based on the results from interviews to local practitioners and may be used as part of the project briefing documents for IBS designers. Holistic design strategies expand “Triple Bottom Lines” considerations in achieving sustainability. This study fills a current gap by responding to IBS project scenarios in developing countries. It also provides a balanced view for designers to better understand sustainability potential and prioritize attentions to manage sustainability issues in IBS applications.

Keywords: Sustainability, Prefabrication, Guidelines, SWOT Analysis, Designers

INTRODUCTION

Construction projects are become larger and more complex. With systematic and innovative solutions, the industry players will be able to meet new and emerging challenges such as improving construction efficiencies, integrating stakeholders' management and reducing environmental impacts. Industrialised Building System (IBS) or prefabrication is recognised as alternative methods to replace conventional construction to enhance sustainable deliverables. Building production in a controlled environment offers many advantages such as reducing construction waste, minimising resources consumption, increasing the quality of buildings and improving the occupational safety and health [1-2]. In contrast, conventional on-site methods have long been criticised for being labour intensive, poor workmanship quality, overwhelming management control and excessive construction waste generation [3].

Understanding IBS benefits and its potentials, the Malaysian Government steering the local construction industry to shift from traditional practices to IBS based production. The Construction Industry Transformation Programme (CITP) 2016-2020 is specifically highlight government strategies

in ensuring faster and higher adoption of IBS application in the local industry. Despite acknowledging its benefits and the top-level advocacy, the local construction industry is still not rapidly embracing IBS [2-4]. Arditi, Ergin and Gunhan [5] highlighted that most of stakeholders do not realize of the significant cost savings in the IBS application through speedy erection and long term investment. In addition, most of the developing countries are depending on technology from industrialised countries [6]. It was highlighted that the effective communication and higher financial capital are required to accelerate technology transfer.

Currently, the implementation of IBS was lack of communication and cooperation among the key stakeholders [4-8]. Manufacturers and contractors can only become involved after the design stage. The separate functional discipline in the implementation process is akin to the ‘over the wall’ syndrome [9].

This study aims to formulate sustainable guidelines from the perspective of the designer by critically examining the relationship between sustainability and IBS. Though other researchers have developed decision tools in IBS application, no previous studies in this field have considered the potential threats and weaknesses of pursuing sustainability. This study explored perceptions

among the key stakeholders regarding both contexts and provides easy-to-understand guidelines for practitioners in developing countries such as Malaysia. This study also presents unified views from key stakeholders instead of single professions, the consideration of negatives instead of all “positives”, and the justification to enforce a sustainability focus in developing economies still grappling with finding suitable solutions in local contexts.

LITERATURE REVIEW

There are many factors that are internal and external to building projects that enhance the sustainable deliverables. Some commonly identified factors include: energy use, transport, water efficiency, ecology, land use, materials and resources, indoor environmental quality, health and well-being, sustainable site and management, and innovation [10-11]. A study of sustainable constructions aspects of using IBS in Hong Kong added to this body of literature by identifying factors that improve sustainable deliverables. Jailoon and Poon [12] found that IBS will be able to improved quality control, improved environmental performance (reduction of waste, dust and noise), improved site safety, the reduction of labour demand and construction time. In their case studies, on average, a reduction of 65% of construction waste, 16% of labour requirement on-site, 15% of construction time and 63% lower than the industry figure for the accident rate. In a similar study, Lam, Chan, Poon, Chau and Chun [13] identify principal factors leading to the success of preparing green specifications in construction projects and identified the following as the four major influencing factors: (1) green technology and techniques, (2) reliability and quality of specification, (3) leadership and responsibility, (4) stakeholder involvement, and (5) guide and benchmarking systems.

Pitt, Tucker, Riley and Longden [14] divided three key areas towards sustainable construction: (1) environmental responsibility, (2) social awareness, and (3) economic profitability. They research highlighted that financial incentives and building regulations were the two most important drivers that will be able to drive demand for sustainability buildings. An effective working environment will be able to reduce absenteeism and supports staff retention and recruitment. IBS promotes stable working conditions and organised working procedures. The local labourers have the opportunity to develop their skills and knowledge and reduce the possibility of being transferred to another region or location. Currently, IBS is seen as more expensive, especially as it involves high initial capital outlay, and higher design, crantage and transport costs compared to conventional construction [15]. Although the critical investment in the initial process is very high, once the break-even point is reached, the benefits

from IBS will increase with the number of units produced [3-16]. By implementing IBS, Malaysia is on the right track for moving forward to develop the country.

Chan, Qian and Lam [17] found that the economic force and government interventions are the strong forces to arouse interests in pursuing sustainability. Their study highlighted that “rising energy costs” will present such an economic reality that people will have to take part in sustainable development for their own interest. The other economic attraction for all stakeholders in construction industry to be involved in achieving sustainability is “lower life-cycle”. Any impact of the decisions for the long term, specifically for the demolition and deconstruction should need taken into account in making effective decision. They also stated that, it is important for a government to create mandatory regulation or building code to ensure stakeholders are taking part in sustainable efforts.

There have been several studies that integrate factors that influence the sustainability for IBS projects. Researchers have developed assessment tools to help stakeholders overcome project challenges and use opportunities available in IBS implementation [18-21]. The researchers argued that the measurement should also consider indirect attributes, such as reducing the environmental impact. While the proposed tools provide some assistance in the selection of IBS, few are capable of providing action plans on how to embed sustainability deliverables in the selected options. Most of the tools are focused solely on strategic level analysis and fails to consider sustainable factors objectively with specifics project requirement.

Current literature provides an understanding of potentials of IBS in improving sustainability. Despite this awareness, academic research has not established holistic criteria in IBS selection. It is vital to consider sustainability characteristics in improving IBS implementation, specifically to developing countries, such as Malaysia. The numbers of integral approach that takes into account all of the environmental, economic and social aspects is very small compare to approach that focus on individual aspects [22-23]. Most of the stakeholders, such as contractors and manufacturers are struggling to integrate sustainability in IBS implementation. This is due to unclear decision guidelines and the shortage of tools regarding sustainability criteria selection. Local and regional characteristics and physical environment plays a major role in measuring the level of sustainability [24]. With the flexibility for adaption, issues studied in developed countries are unlikely to be applicable or even relevant to developing countries [25]. Ofori and Kien [26] suggested that the stakeholders in the construction industry should initiate a strategy selecting the best solutions in their design and building construction. The importance of

specific actions assigned to particular stakeholders in evaluate their decisions, including the selection of raw materials to be used, energy consumed and the pollution and waste produced throughout the building life cycle was highlighted. Therefore, the study presented in this paper focuses on the holistic approach in integrating potential factors to improve sustainability at the early stage of construction.

RESEARCH METHODS

The quantitative data were collected and analysed to identify the level of significance of each potential factor in improving sustainability for IBS application. The critical factors were identified by using statistical test. Then, the qualitative interviews were conducted to further explain the details of each critical factor and to formulate the action plans. Accordingly, the guidelines were developed based on in-depth investigation on each issue using semi-structure interviews. In responding to the negative and positive contexts, the strategies on improving sustainability were properly investigated.

The questionnaire survey involved seven sample groups categorised by their organisation type, namely 1) designer/consultant companies, 2) manufacturer companies, 3) user or facility management companies, 4) developers, 5) research/academic institutions, and 7) authority/government agencies. The respondents were selected from professional databases of the Construction and Industry Development Board, Industrialised Building System Centre, and Green Building Index Malaysia. The questionnaires were distributed by post, online survey and face-to-face consultation. From 300 copies of questionnaire, 115 questionnaires were returned and can be used in the analysis. Therefore, the response rate is 38 per cent.

Consequently, the factors were explored through semi-structured interviews to extract best practices of how these factors can be dealt with. A semi-structured interview form was used because it was flexible and it gave additional scope for the interviewees to provide detailed information based on their experience and capability. It also allowed the researchers to maintain focus on the research objectives. Twenty respondents participated in the interviews. They all have different backgrounds and vast experience in construction industry. This helps researchers identify the perception of each type of organisation in pursuing sustainability. As a result, the interviewees were able to provide more in-depth and detailed answers and suggestions in their responses to the questions. SWOT (strengths, weaknesses, opportunities, and threats) analysis was used to formulate a decision-making guideline.

In summary, the design of the proposed study is including a literature review, survey, semi-structured interview, and data analysis techniques (Figure 1). With both quantitative and qualitative methods, the

results covering perceptions of key stakeholders in a sustainable IBS shall underpin the basis for establishing the decision making process models for enhancing the feature of this innovative system. Ultimately, as the final outcome of the study, the guidelines will help promote more integrated approaches to decision making about the implementation of sustainability strategies in the designing stage.

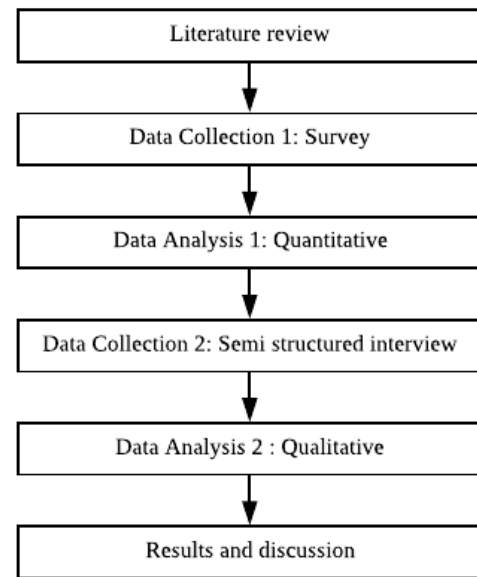


Fig. 1: Research design

QUANTITATIVE ANALYSIS

The ranking of the sustainability factors was carried out based on their mean values. In selecting the critical factors, the cut-off mean value is 4.00 which represents “significant”. Out of the 62 factors identified in the literature review, only 37 factors were rated by the respondents as “significant” and “very significant” (mean ≥ 4.00). The standard deviations in this analysis show uniformity with most below 1, thus representing good data accuracy in this study. Accordingly, a t-test was used to identify the most significant factors among the 37 factors. This method was previously proven by several researchers such as Ekanayake and Ofori [27] and Wong and Li [28] in related studies. In this study, the null hypothesis (factors were neutral, insignificant, and very insignificant) is accepted if the t-value is smaller than 1.6583 (the critical t-value). As a result, there were left with 18 critical factors, namely: “construction time”, “production”, “waste generation”, “constructability”, “knowledge and skills”, “defects and damages”, “labour cost”, “waste disposal”, “procurement system”, “durability”, “working conditions”, “standardisation”, “usage

efficiency”, “labour availability”, “material consumption”, “legislation”, “project control guidelines” and “maintenance and operation costs”.

Kendall’s coefficient of concordance measures the agreement of respondents on ranked factors. From the analysis, the coefficient value for critical factors is 0.104, which statistically shows that the respondents have different preferences and even conflicts in determining the most important factors. To improve the common understanding of key stakeholders in IBS construction, each group is to be assessed and analysed before the critical factors can be finalised. It is important to note that Kendall’s coefficient of concordance can identify the agreement levels but it cannot investigate whether there are significant differences in the stakeholders’ rankings of the significance levels. To address this issue, Kruskal-Wallis one-way ANOVA was used.

The Kruskal-Wallis one-way ANOVA test revealed that there was no significant difference between various stakeholder organisations for 13 sustainable factors. They have a consensus regarding the perceptions and expectations in achieving sustainability. On the other hand, five factors have slight differences across the key stakeholders. They are: (1) constructability, (2) defects and damages, (3) labour cost, (4) material consumption, and (5) legislation. It is interesting to note that although “constructability” is among the top five critical factors, the seven groups ranked it at different significance levels.

Among these five factors, manufacturers and users have a different agreement to other groups in determining the significance level of “defects and damages”, “labour cost”, and “material consumption”. A possible reason may be that manufacturers and users are only involved with the end product, which is contrary to other groups which play their roles in the briefing, design, and construction stages. Most of the decision-makers consider available options or potential factors based on their familiarity and personal preferences [30].

The Mann-Whitney test explores the differences between two independent groups on a continuous measure. The score on the continuous variable for the two comparable groups is converted to ranks in order to evaluate whether the ranks differ significantly. It is notable that the designer/consultant group has a different focus in improving IBS sustainability in regard to four factors, namely: 1) “constructability”, 2) “defects and damages”, 3) “labour cost” and 4) “material consumption”. The designer/consultant group was found to have a different perception on the significance level of “defects and damages” and “labour cost” compared to the contractor, manufacturer and user groups. For “legislation”, differences were identified between the contractor group and three other organisation groups (manufacturer, user and client). It is believed that

from the institutional perspective, these organisations are more focused on the details in the legal documentation and regulations. On the contrary, the contractor group normally has a low level of concern about these issues because they are more focused on the physical activities.

The results showed that all the 18 factors can be statistically considered as the most significant and relevant in improving IBS sustainability. The respondents and their organisations represent different backgrounds and experiences which can either affect or be affected in IBS projects. As key stakeholders, their opinions and views are very important to stimulate sustainability deliverables in IBS construction. Therefore, the factors selected and ranked as critical will provide a sound basis upon which decision-making guidelines for IBS implementation can be based.

QUALITATIVE ANALYSIS

Knowing the critical factors is important. But knowing how to deal with them requires appropriate and effective strategies. Based on the results from quantitative analysis, the logic and structure for processing critical factors was established. The critical factors were grouped into 5 categories: ecological performance; economic value; social equity and culture; technical quality; and implementation and enforcement.

The semi-structured interviews elicited insights and points of view from the respondents that are useful for the formulation of efficient decision-making guidelines. The remarks provided from the respondents for each critical sustainability factors were produced from the reduction and transformation process. This is important to ensure the information is readily accessible, understandable, and to draw out various themes and patterns [30]. Their remarks were analysed and grouped to form the action plans in improving sustainability. The SWOT analysis was adopted to evaluate simultaneously the internal and external factors by collecting all the possibilities and opportunities. It is important to note that the designers require lots of information to guide them in making appropriate decisions, especially when integrating sustainability efforts [31-32]. Previous research has proven that SWOT analysis can be used to evaluate risks, to gain insight into the internationalisation of construction companies in the global market and to measure the performance of construction firms in developing countries [33-35]. SWOT analysis is ideal for analysing the situation each investigated factor presents. The interrelated criteria also help to develop potential strategies. Through such analysis, decision-makers can exploit new opportunities by utilising available strengths, avoiding weaknesses and diagnosing any possible threats in the examined issues.

Accordingly, the final guidelines were approved by the respondents. It is agreed that the guidelines will be able to provide a systematic decision support tool for the stakeholders in encapsulating sustainability. The importance of the stakeholders' participation and their full understanding of this approach were highlighted. These will increase the key stakeholders' interest in using the SWOT analysis which provided in the guidelines.

DISCUSSION

The promotion of IBS usage in Malaysian construction industry is constantly faced with a number of challenges to improve, meet market demand, and overcome skills shortages. Literature studies suggest the general lack of research efforts to assess the full sustainability potential in IBS applications. The few relevant research projects attempted to deal with one aspect in Triple Bottom Line (TBL) alone - such as economic or social dimensions. A holistic approach that encompasses all important issues of the TBL and beyond is not yet available. In Malaysia to date, IBS applications tend to be linked with government projects primarily. As such political scenarios and government support are very important aspect. The quantitative methodology adopted in this study has identified the 18 critical factors and interrelationships between these factors. This study probes into the environmental, economical and social aspects the IBS potential and extends them to include 'technical quality' and 'implementation and enforcement' aspects of the sustainability assessment. Implementation and enforcement are the factors that ensure that any planning will be carried out accordingly. An effort from the authorities was identified as a starting-point to integrate sustainability for IBS applications in Malaysia. The technical issues provide physically measurable attributes of IBS construction and an opportunity to maximize the IBS benefits in improving sustainability. These considerations present a new level of thinking and knowledge paradigm in dealing with the IBS method.

Research findings noted that the adoption of SWOT analysis will be able to provide the necessary framework to understand the internal and external conditions of each critical factor.

CONCLUSION

Considerations of both the positive and negative aspects of pursuing sustainability can help "complete the scenarios" when making the best selection. Such a decision-making framework also includes action plans to present information on what and how to improve the sustainability of each critical factor. Ideally, this would form part of the project briefing documents against which sustainability solutions can be considered and implemented by the designers.

Moreover, the clear responsibility of IBS participants in regard to the sustainability deliverables can be documented and potentially embedded in contracts. Developers and designers alike will have a tool to assess the potential of IBS and to enhance sustainability.

While research findings are considered to be "representative", as respondents covered a wide range of the construction industry stakeholders such as contractors, consultants and manufacturers, the delivered decision support guides are intended for the designers. These tools will be used in the design stage and early construction stage. Further research can extend the findings to include appropriate decision mechanism and preferences for other stakeholders.

ACKNOWLEDGEMENTS

The authors would like to thank Universiti of Tun Hussein Onn, Malaysia and the Ministry of Higher Education, Malaysia (FRGS vot. 1578) for their generous sponsorship of this research.

REFERENCES

- [1] Jaillon, L, Poon, C S and Chiang, Y H (2009) Quantifying the waste reduction potential of using prefabrication in building construction in Hong Kong. *Waste Management*, 29(1), 309-20.
- [2] Kamar, K A M and Hamid, Z A (2011) Supply chain strategy for contractor in adopting industrialised building system (IBS). *Australian Journal of Basic and Applied Science*, 5(12), 2552-7.
- [3] Tam, V W Y, Tam, C M and Ng, W C Y (2007) On prefabrication implementation for different project types and procurement methods in Hong Kong. *Journal of Engineering, Design and Technology*, 5(1), 68-80.
- [4] Nawi, M N M, Lee, A and Nor, K M (2011) Barriers to implementation of the Industrialised Building System (IBS) in Malaysia. *The Built & Human Environment Review*, Volume 4, 22-35.
- [5] Arditi, D, Ergin, U and Gunhan, S (2000) Factors affecting the use of precast concrete systems. *Journal of Architectural Engineering*, 6(3), 79-86.
- [6] Polat, G (2010) Precast concrete systems in developing vs. Industrialized countries. *Journal of civil engineering and management*, 16(1), 85 - 94.
- [7] Hamid, Z A and Kamar, K A M (2011) Editorial: Aspects of off-site manufacturing application towards sustainable construction in malaysia. *Construction Innovation: Information, Process, Management*, 12(1).
- [8] Nadim, W and Goulding, J S (2011) Offsite production: A model for building down barriers - A european construction industry perspective. *Engineering, Construction and Architectural Management*, 18(1), 82-101.

- [9] Evbuomwan, N F O and Anumba, C J (1998) An integrated framework for concurrent life-cycle design and construction. *Advances in Engineering Software*, 29(7-9), 587-97.
- [10] Lee, W L and Burnett, J (2008) Benchmarking energy use assessment of HK-beam, BREEAM and LEED. *Building and Environment*, 43(11), 1882-91.
- [11] Mitchell, L (2009) Green star and nabers: Learning from the Australian experience with green building rating tools. In, 5th Urban Research Symposium – Cities and Climate Change, 29 June Marseille, France.
- [12] Jaillon, L and Poon, C S (2008) Sustainable construction aspects of using prefabrication in dense urban environment: A Hong Kong case study. *Construction Management and Economics*, 26(9), 953 - 66.
- [13] Lam, P T I, Chan, E H W, Poon, C S, Chau, C K and Chun, K P (2010) Factors affecting the implementation of green specifications in construction. *Journal of Environmental Management*, 91(3), 654-61.
- [14] Pitt, M, Tucker, M, Riley, M and Longden, J (2009) Towards sustainable construction: Promotion and best practices. *Construction Innovation: Information, Process, Management*, 9(2), 201-24.
- [15] Blismas, N and Wakefield, R (2009) Drivers, constraints and the future of offsite manufacture in australia. *Construction Innovation*, 9(1), 72-83.
- [16] Chen, Y, Okudan, G E and Riley, D R (2010b) Sustainable performance criteria for construction method selection in concrete buildings. *Automation in Construction*, 19(2), 235-44.
- [17] Chan, E H W, Qian, Q K and Lam, P T I (2009) The market for green building in developed Asian cities—the perspectives of building designers. *Energy Policy*, 37(8), 3061-70.
- [18] Song, J, Fagerlund, W R, Haas, C T, Tatum, C B and Vanegas, J A (2005) Considering prework on industrial projects. *Journal of Construction Engineering and Management*, 131(6), 723-33.
- [19] Blismas, N, Pasquire, C and Gibb, A (2006) Benefit evaluation for off-site production in construction. *Construction Management and Economics*, 24(2), 121 - 30.
- [20] Luo, Y, Riley, R, Horman, M J and Kremer, G O (2008) Decision support methodology for prefabrication decisions on green building projects. In: Mcdermott, P and Khalfan, M M A (Eds.), *Symposium on Sustainability and Value Through Construction Procurement*, 29 November – 2 December 2006, University of Salford. University of Salford.
- [21] Chen, Y, Okudan, G E and Riley, D R (2010a) Decision support for construction method selection in concrete buildings: Prefabrication adoption and optimization. *Automation in Construction*, 19(6), 665-75.
- [22] Yigitcanlar, T and Dur, F (2010) Developing a sustainability assessment model: The sustainable infrastructure, land-use, environment and transport model. *Sustainability*, 2(1), 321-40.
- [23] Singh, R K, Murty, H R, Gupta, S K and Dikshit, A K (2012) An overview of sustainability assessment methodologies. *Ecological Indicators*, 15(1), 281-99.
- [24] Gomes, V and da Silva, M G (2005) Exploring sustainable construction: Implications from Latin America. *Building Research & Information*, 33(5), 428-40.
- [25] Cohen, B (2006) Urbanization in developing countries: Current trends, future projections, and key challenges for sustainability. *Technology in Society*, 28(1-2), 63-80.
- [26] Ofori, G and Kien, H L (2004) Translating Singapore architects' environmental awareness into decision making. *Building Research & Information*, 32(1), 27-37.
- [27] Ekanayake, L L and Ofori, G (2004) Building waste assessment score: design-based tool. *Building and Environment*, 39 (7), 851-861.
- [28] Wong, J and Li, H (2006) Development of a conceptual model f
- [29] or the selection of intelligent building systems. *Building and Environment*, 41 (8), 1106-1123.
- [30] Idrus, A B and Newman, J B (2002) Construction related factors influencing the choice of concrete floor systems. *Construction Management and Economics*, 20(1), 13 - 9.
- [31] Berg, B L (2001) *Qualitative research methods for the social sciences*. 4th ed. United States of America: A Pearson Education Company.
- [32] Solla, M, Ismail, L and Yunus, R (2016) Investigation on the potential of integrating BIM into green building assessment tools. *ARP Journal of Engineering and Applied Sciences*, 11(4), p.p. 2412-2418.
- [33] Masrom, M A N, Rahim, M H I A, Mohamed, S, Chen, GK, and Yunus, R (2015) Successful criteria for large infrastructure projects in Malaysia. *Procedia Engineering*. 125, p.p. 143-149.
- [34] Luu, T V, Kim, S Y, Cao, H L and Park, Y M (2008) Performance measurement of construction firms in developing countries. *Construction Management and Economics*, 26(4), 373-86.
- [35] Lu, W, Li, H, Shen, L and Huang, T (2009) Strengths, weaknesses, opportunities, and threats analysis of chinese construction companies in the global market. *Journal of Management in Engineering*, 25(4), 166-76.
- [36] Milosevic, I N (2010) Practical application of SWOT analysis in the management of a construction project. *Leadership and Management in Engineering*, 10(2), 78-86.

PRODUCTION OF Cu MICROPARTICLES UTILIZING HIGH PURITY Cu DENDRITE CRYSTALS AND DEVELOPMENT OF CONDUCTIVE PAINTS

Junya Kuroda¹, Risa Uda¹, Honoka Tanabe¹, Kimihiro Yamanaka¹ and Hirohisa Taguchi¹

¹ Department of Electrical and Electronic Engineering, School of Engineering, Chukyo University
101-2 Yagoto Honmachi, Shouwa-Ku, Nagoya City, Aichi, JAPAN,

ABSTRACT

In recent years, metal microparticles made of Au or Ag have attracted attention as intermetallic bonding materials and low resistance materials of fine interconnects. It is also known that the electron cloud localized on the fine surface of the fine particles has a catalytic effect, and researches on chemical reaction accelerators are being advanced. However, Au and Ag have high material cost, not economical materials. Furthermore, Ag is extremely easily oxidized, and there is a problem in durability of the catalytic effect in the solution. In this research, we considered Cu microparticle formation by Cu three - dimensional tree structure (Cu dendrite). Cu has high electrical conductivity and less oxidizable than Ag. It has an extremely high economic advantage compared with Au. We have succeeded in making high purity Cu dendrites by our previous studies. This Cu dendrite was broken in an aqueous solution using ultrasonic waves. As a result, Cu fine particles having a diameter of about 1 to 10 μm were successfully formed. We also reported that this fine particle was impregnated into a water-soluble paint and succeeded in forming a printer ink with electrical conductivity.

Keywords: microparticles, Cu dendrite crystal Conductive printer ink, electrical conductivity

INTRODUCTION

In recent years, metal microparticles made of Au or Ag have attracted attention as intermetallic bonding materials and low resistance materials of fine interconnects [1]. It is also known that the electron cloud localized on the fine surface of the fine particles has a catalytic effect, and researches on chemical reaction accelerators are being advanced [2]. The mainstream of these metal fine particle production methods is a chemical reduction method [3]. A metal salt or a complex is synthesized, and a metal element is precipitated using a reducing action. Finally, it is a technique to obtain nano sized aggregates by clustering. Using this method, commercial metal nanoparticles are already present. The disadvantage of the chemical reduction method is the precipitation of metallic elements [3]. The precipitated metal element needs to be clustered. The particle diameter formed in this way is the limit of about 1 μm . It fulfills the purpose in utilizing the special surface catalytic effect of metal nanoparticles [4]. However, considering the development of conductive paste and paint, the yield of nanoparticles is important [5]. Chemical reduction forms a reliable metal nanoparticles, but the yield is not high [6]. Another method of forming fine metal particles is a physical generation method from bulk metal. This is called a pulverization method, and it is simply a method of grinding a metal bulk to obtain fine particles. In this method, it is considered difficult to reduce the particle

diameter and unify the particle shape [7]. Also, since noble metals such as Au, Ag, Cu have extensibility, physical fracture simultaneously promotes foil formation.

In this study, physical grinding method of high purity Cu dendrite crystal was investigated in order to form Cu fine particles with high industrial utilization value in high yield and low cost. High purity Cu dendrite crystals were formed by using copper sulfate solution by the application of plating method. By the method shown in this research, it was possible to form a purity of 99% or more for Cu dendrites, which was a structure containing much impurities so far. Cu dendrite crystals having a tree structure can be obtained. The Cu dendrite crystals can be easily peeled off from the plated substrate. After peeling, Cu dendrite crystals were subjected to ultrasonic vibration in ethanol. As a result, it was physically pulverized to form fine particles with a particle size of 1 to 10 μm . Then we investigated the formation of conductive ink by impregnating the fine particles into the printer ink.

EXPERIMENTAL METHOD

High purity Cu dendrite crystal formation method
Figure 1 shows the experimental system schematic used in this study. Basically, Cu plating method is used. In our previous study, it is known that Cu plating on Zn/Al alloy in concentrated copper sulfate

solution forms Cu dendrite structure including Cu/Zn alloy due to poor plating formation [8,9]. In this method, an oxygen free copper plate placed above the part where Cu dendrite was formed. A gap of 0.4 mm in thickness was formed in order to arrange an oxygen-free copper plate. Since the concentrated copper sulfate solution can penetrate into the gap of 0.4 mm, it is possible to form Cu dendrite by the inter-electrode voltage.

Cu fine particle formation method

High purity Cu dendrite crystals formed by the method is a structure entangled two-dimensional growth surface and the three-dimensional growth portion. Dynamically, it has strength enough to pick up a face with tweezers, but this is caused by entanglement of two-dimensional structure and three-dimensional structure. Further, since the ZnO crystal is present as a fragile structure on the surface of the growth substrate, it is possible to peel the Cu dendrite crystal face from the substrate simultaneously and during cleaning in the purified water. The peeled Cu dendrite thin film was held in ethanol, and physical pulverization was carried out using ultrasonic waves of a frequency of 50 kHz and an output of 150 W. After grinding, the water surface of the solution was placed in a dropper, and separation of Cu particles and ethanol was carried out with a centrifuge at 20,000 rpm for 15 minutes. The separated Cu fine particles were transferred to a petri dish, kept in a nitrogen furnace at 80 °C. for 20 minutes to evaporate the ethanol, and particle shape observation was carried out by SEM.

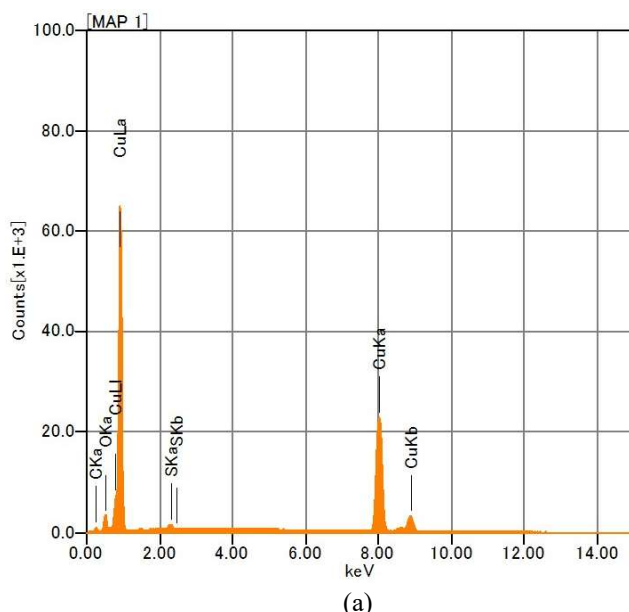


Figure 3. The surface atomic distribution image and XDS spectrum.

(a) XRD spectrum (b) SEM image (c) Carbon surface distribution (d) Carbon surface distribution (e) Oxygen surface distribution (f) Copper surface distribution

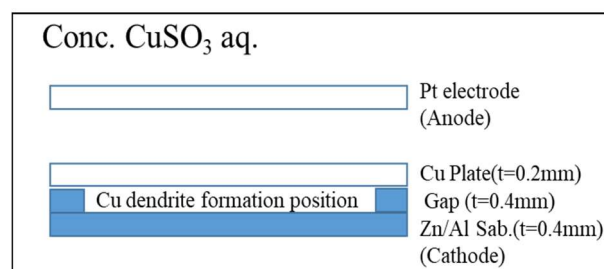


Figure 1. Schematic diagram of high purity Cu dendrite crystal formation experiment system based on Cu plating method.

Example of two-dimensional branch lobular crystals

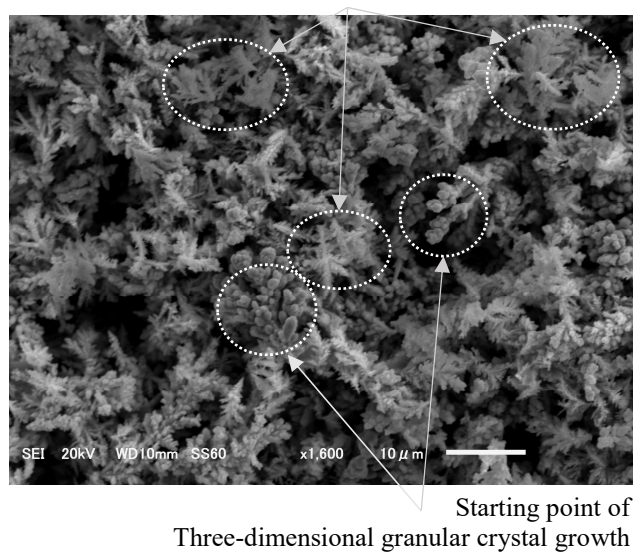
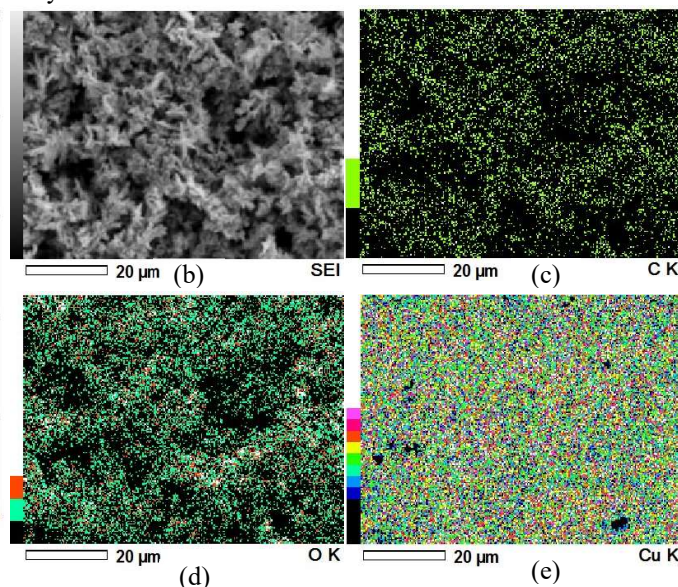


Figure 2. The SEM image showing simultaneous growth state of two-dimensional crystal and three-dimensional crystal in Cu dendrite.



Conductive printer ink formation

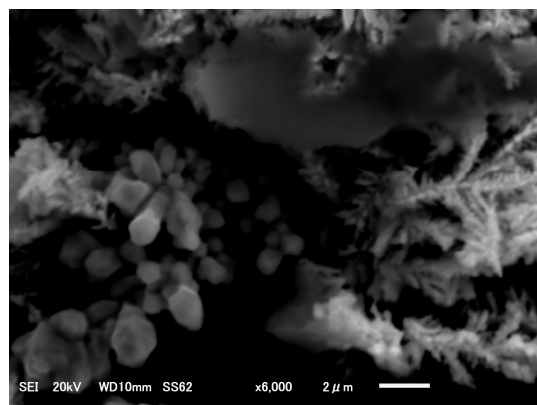
It was investigated to develop a conductive ink as practical application of Cu particles obtained in this study. Commercially available non-conductive printer ink was impregnated with the Cu fine particles indicated by the above method and dried on the insulating sheet with this ink.

RESULTS AND DISCUSSION

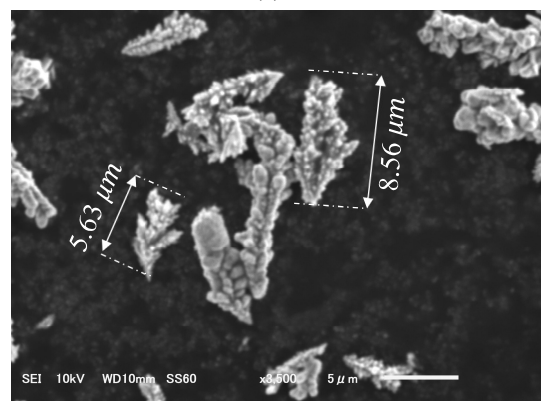
High purity Cu dendrite crystal

It was placed oxygen-free copper plate directly above the growth surface by Cu dendrite formation process. This effect will be described below. The field effect of the free electron group in the oxygen-free copper plate inhibited peeling of Zn fragments and upward movement of Zn fragments occurring simultaneously with Cu plating growth. The electric field effect of this oxygen free copper plate also affected Cu dendrite structure formation. In the previous method, it was three dimensional growth from the beginning. In the early stage of Cu dendrite crystal growth by this method, two dimensional planar growth was carried out, and a structure in which branches and leaves extended laterally was formed. However, Cu plating is stably formed at the Al site at the lower part of the plane growth surface, and longitudinal growth is performed. The Cu dendrite structure shown in figure 2 was constructed according to the experimental chart shown in figure 1. The experimental system shown in figure 1 was constructed in the supersaturated copper sulfate solution. At the beginning, it was left for 5 minutes in the electroless state. It is an object of the supersaturated copper sulfate solution be sufficiently impregnated in the gap of 0.4 mm. After that, Cu dendrite was constructed by fixing the inter-electrode current at 40 mA and holding for 10 minutes. After construction, it was washed with ultrapure water to remove sulfate ions. And dried at 80 °C. for 20 minutes in a heating furnace in an N₂ atmosphere.

In figure 2, it shows an SEM image in which the two-dimensional growth and the three-dimensional growth surface are simultaneously grown. Although lateral growth of Cu dendrite crystals is confirmed on almost the entire surface, longitudinal growth of granular crystals is confirmed in the part. In the Cu dendrite obtained by the above method, since the longitudinal transport of Zn was inhibited, the Cu concentration reached 99% level. Figure 3 shows the surface atomic distribution image and XDS spectrum. The Cu dendrite surface on which the XDS analysis shown in figure. 3 was performed is the same as that shown in figure 2. In the surface atomic distribution, Cu or C is mainly observed. Since C and O were a carbon tape for SEM observation, it means that most of the observed substance was Cu. Both the XRD spectrum and the Cu - α line lay Cu - α ray as the main and there were no other atoms other than C observed. As a result, it can be said that the formation of high purity Cu dendrite crystals was successful.



(a)



(b)

Figure 4. The Cu fine particles obtained by SEM observation

(a) Granular crystals and branched lobular crystals

(b) SEM image of branch lobe grains

Formation of fine Cu particles

The Cu fine particles obtained by SEM observation are shown in figure 4. The particle shapes are different, and the particle diameter also varies from 1 to 10 μm , but it was found that the particle formation at μm level was successful. It was found that the shape of the fine particles differs from the granular shape or the plate shape. Basically, because it is a method derived from the pulverization method, it was confirmed that control of both particle size and particle shape is difficult with this method [10]. However, in this method, since all of the obtained Cu dendrite crystals are subjected to a pulverization method, it is possible to atomize all of the Cu dendrite crystals formed.

Conductive printer ink formation

In order to study the industrial application of Cu fine particles prepared in this study, formation of conductive ink was carried out. Printer ink impregnated with fine Cu particles was measured by a four-terminal method to obtain electric resistivity. Multiple samples were formed to obtain resistivity $4.22 \times 10^{-5} \Omega\cdot\text{m}$. However, it was confirmed that the resistivity is about 10 times in some samples. This

indicates that there is dispersion in Cu fine particles that realizes conductivity. It is necessary to study in the future to have good dispersion.

CONCLUSIONS

In this research, we got the following conclusion. When placing an oxygen-free copper plate above the Cu dendritic growth portion, upward movement of Zn fragments derived from the Zn / Al substrate was inhibited, and as a result it was found that high purity Cu dendrite crystals could be formed. Next, by executing ultrasonic pulverization of this Cu dendrite crystal in ethanol, it is possible to convert all of the produced high purity Cu dendrite crystal into fine particles having a particle size of about 1 to 10 μm . Finally, by imprinting fine particles formed by this method into printer ink and executing printing, succeeded in forming printed matter with conductivity although there was a deviation between samples.

ACKNOWLEDGMENTS

The authors are grateful to the Chukyo University Research Found for financial assistance with this research.

REFERENCES

- [1] Carmen C. Garcia, Ayrat Murtazin, a Sebastian Groh, a Vlasta Horvatica and Kay Niemax, Characterization of single Au and SiO₂ nano- and microparticles by ICP-OES using monodisperse droplets of standard solutions for calibration, *Journal of Analytical Atomic Spectrometry*, NO. 25, 2010, pp.645-653.
- [2] T. Kikuta, T. Uchino, N. Akao, Y. Akahoshi, T. Koura, *Procedia Engineering*, No. 103, 2015, pp. 279-286
- [3] J. Giro-Paloma, M. Martínez, L. F. Cabeza, A. Inés Fernández, Types, methods, techniques, and applications for microencapsulated phase change materials (MPCM): A review, *Renewable and Sustainable Energy Reviews*, Volume 53, 2016, pp.1059-1075
- [4] Muhaimin, and R. Bodmeierb. Effect of solvent type on preparation of ethylcellulose microparticles by solvent evaporation method with double emulsion system using focused beam reflectance measurement, *Polymer International*, Vol. 66, Iss. 11, 2017, pp.1448–1455
- [5] M. Inoue, Y. Itabashi, Y. Tada, Development of bimodal electrically conductive pastes with Ag micro- and nano-fillers for printing stretchable E-textile systems, *Proc. of European Micro-electronics Packaging Conference*, 2015
- [6] A. B. Diciara, J. Yuan, S. Yao, A. Sylvestre, L. Zimmer, and J. Bai, Effective synergistic effect of Al₂O₃ and SiC microparticles on the growth of carbon nanotubes and their application in high dielectric permittivity polymer composites, *Journal of Materials Chemistry A*, No. 2, 2014, pp.7980-7987
- [7] J. G. Lee D. Y. Kim, T. G. Kim, J. H. Lee, S. S. A. Deyab, H. W. Lee, J. S. Kim, D. H. Yang, A. L. Yarin, S. S. Yoon, Supersonically Sprayed Copper-Nickel Microparticles as Flexible and Printable Thin - Film High - Temperature Heaters, *Advance Materials Interfaces*, No. 4, 2017, pp.1700075(1-8).
- [8] Yong Xiao, Mingyu Li, Ling Wang, Shangyu Huang, Xueming Du, Zhiquan Liu, Interfacial reaction behavior and mechanical properties of ultrasonically brazed Cu/Zn-Al/Cu joints, *Materials and Design*, NO. 74, 2015, pp. 42-49.
- [9] Zhicheng Wu, Stefanie Sandlöbes, Liang Wu, Weiping Hu, Günter Gottstein, Sandra Korte-Kerzel, Mechanical behaviour of Zn-Al-Cu-Mg alloys: Deformation mechanisms of as-cast microstructures, *Materials Science and Engineering A*, Volume 651, No.10, 2016, pp. 675-687
- [10] S. Richard, J. Selwin Rajadurai, V. Manikandan, Influence of particle size and particle loading on mechanical and dielectric properties of biochar particulate-reinforced polymer nanocomposites, *International Journal of Polymer Analysis and Characterization*, Vol. 21, No. 6, 2016, pp.462–477.

THERMOGRAVIMETRIC ANALYSIS OF TREATED WASTE ABACA FOR FLY ASH-BASED GEOPOLYMER REINFORCEMENT

Janne Pauline S. Ngo¹, Roy Alvin Malenab¹ and Michael Angelo Promentilla¹

¹Chemical Engineering, De La Salle University, Philippines

ABSTRACT

Natural fiber's use in composites is gaining more attention for its eco-friendly advantage, low cost, low density, good mechanical properties and other attractive features. In this study, enhancement of abaca fiber-geopolymer matrix interaction by chemical treatments was investigated. The study assessed the effects of subjecting waste abaca fibers to (1)NaOH pretreatment and (2) aluminum sulfate treatment, in order to modify the fiber surface. Fibers' tensile strengths were measured and were characterized using XRD and thermogravimetric analyses (TGA) to analyze changes in composition and thermal stability. Untreated and treated fibers were reinforced in geopolymer composites and withdrawn for thermogravimetric analysis to observe changes in fiber-matrix interaction. The results show that the alkali treatment removes low strength, components in the fiber, which resulted to lower fiber tensile strength. TGA results showed that treated fibers pulled out from geopolymer composites were significantly more stable (43.3% by mass decomposition) than untreated fibers (76.0%).

Keywords: natural fiber, reinforcement, geopolymer, thermogravimetric analysis

INTRODUCTION

The Philippines is a leading producer of abaca. Abaca is known for its high-strength fibers, which is increasingly being used in advanced materials, and it is broadening in application. The Philippines' annual output of abaca was reported as of 2015 is 70,400 metric tons (Philippine Statistics Authority, 2016). The large volume of abaca produced in turn generates a considerable amount of agricultural waste since only its high grade fibers are valued and as much as 75% of the plant is discarded or left in the plantation to rot (Araral, 2004). Abaca production has seen continual growth, with export demands increasing year after year. Meanwhile, researchers' interest in the utilization of raw abaca, and other natural plant fibers, has also become widespread due to its low cost and abundance. This fiber has become essential in industrial composite materials, such as in automotive applications and in composite materials.

Combination of matrix and dispersed phase/s and their proportions are the essential considerations in developing composite materials with the desired properties (Balasubramanian, 2014). For fiber-reinforced composites, the matrix is reinforced by fibers for load transfer, which enhances the overall composite strength. The interfacial bonding or interaction that develops between the fiber and the composite matrix is crucial for the material's strength, which may often be poor for plant fiber-reinforced composites. This is mainly because of the hydrophilic tendency of plant fibers. Plant-based fibers such as cotton, flax, jute, sisal, bagasse and hemp have been adapted as reinforcing components in polymers and cement materials (Yan et al., 2016; Jabbar et al.,

2016).

Treatments and surface modification techniques have been explored in studies in order to improve natural fibers' suitability for geopolymer reinforcement. One of the most studied chemical treatments is alkali treatment which involves delignification and extraction of cellulose. Lignin, hemicellulose and pectin which are hydrophilic, amorphous and forms poor bonds with the matrix, are reduced in the fiber composition. In previous studies, alkali treatment was observed to result in formation of corrugations or cause roughening of the fiber surface, enhancing the fiber-matrix adhesions. Natural fibers also have the disadvantage of being biodegradable, having the tendency to decay in alkali matrices and high temperature conditions, as observed in previous study when used in concrete (Lima, 2007). In this study, aluminum sulfate treatment was performed to deposit aluminum hydroxide precipitates on the fiber surface, providing sites for geopolymer bond and growth. This in turn could allow protection of the fiber by geopolymer's high thermal stability and fire-resistant properties.

The thermogravimetric analysis (TGA) involves measurement of sample's mass loss with respect to a gradual temperature increase. TGA is typically done to analyze fiber treatments because the thermal degradation of plant fibers is dependent on its compositional lignin, cellulose, hemicellulose, pectin and other trace components (Alvarez & Vazquez, 2003; Izani, et al., 2013). Using TGA, the degradation of hemicellulose and lignin can be observed in the specimen by observing the temperature ranges at which fractions of its mass degrade. This analysis is done in reference to the standard decomposition

stages of natural fibers, as presented in Table 1. TGA is used to determine the thermal stability of cellulosic material. Another test was performed on free treated fibers and treated fibers that were used as geopolymer reinforcement. The thermal decompositions observed from these samples were used to assess if the series of treatments have aided in developing an interaction between the geopolymer and the fiber surface, and if geopolymer's interaction with the fiber could improve the fiber's resistance to degradation.

Table 1 Decomposition Temperatures of Natural Fibers' Components (Zhang et al., 2014)

Components	Decomposition Temp, °C	T _{max} , °C
Moisture	30 – 100	80
Hemicellulose	160 – 350	245 - 298
Cellulose	240 – 365	335
Lignin	300 – 500	337

MATERIALS & METHODOLOGY.

Preparation and Treatment of Abaca

Waste abaca fibers were gathered from Dumaguete City, Philippines. Abaca fibers were extracted from the plant source by hand stripping then segregated into various grades. Residual grade fibers were collected and measured to have an average of 16 microns diameter. Sodium hydroxide micropearls (99 wt%) and aluminum sulfate powders (99 wt%) were obtained locally and were used as received.

Alkali Treatment

The fibers were segregated to one hundred strands per sample and soaked in 6 wt% NaOH solution for 48 hours in a 500 mL beaker with constant agitation at room temperature. Previous studies [11,12] show that alkali treatment dissolve impurities and weak components of the fiber resulting to a rougher fiber surface. The fibers are drawn from the solution and washed with distilled water several times. Alkali treated fibers were then air dried for 24 h, as shown in Figure 1b.

Aluminum Sulfate Treatment

Ten percent by weight (10wt%) $\text{Al}_2(\text{SO}_4)_3$ solution (pH = 3.5) was used for the aluminum sulfate treatment. Alkali-treated fibers were soaked in the solution for 6.25 hours to allow the penetration of ions into the fiber. Gradual addition of 2 M NaOH solution into the treatment resulted to increase in pH and formation of white, aluminum hydroxide $[\text{Al}(\text{OH})_3]$ precipitates. This was done until pH was adjusted to 6. The fibers were allowed to soak for 24 hours to allow further precipitation and deposition on the fiber surface. Samples were then drawn from the

mixture, washed with distilled water and air-dried for 24 hours before being stored in a desiccator. The resulting treated fiber is shown in Figure 1c.



Figure 1 (a) raw abaca fiber, (b) alkali pretreated abaca fiber and (c) alkali- $\text{Al}_2(\text{SO}_4)_3$ treated abaca fiber

Tensile Strength

Average tensile strengths of the abaca fibers (untreated and treated) were determined by taking five strands from each bundle of 100 strands randomly. Then each strand was cut to 5 cm and mounted to cardboard frames to be held by the universal testing machine (Instron model 3324) with gauge length of 3 cm. The universal testing machine (UTM) as shown in Figure 3 applies tensile load on the fiber strand equivalent to an extension rate of 5 mm per minute and recording the stress until it breaks. Prior to fracture, each strand was placed under an optical microscope (Amscope microscope) linked to a computer to measure each of their diameters. Fiber strands were assumed to have approximately circular cross-sectional areas and were computed accordingly. Tensile strength of the fiber is defined as the maximum stress it can withstand and is computed by dividing the load at failure by the original cross-sectional area per fiber. The five readings were averaged to obtain the final value recorded.

X-ray Diffraction

Using XRD analysis, the surface modification resulting from alkali treatment of waste abaca fibers was evaluated. Crystallinity index (CI) calculated using XRD deconvolution method. XRD patterns were collected on a Maxima XRD-7000 apparatus (Shimadzu, Tokyo, Japan) using $\text{Cu K}\alpha$ radiation source (40 kV; 30 mA) with wavelength of 1.54 Å to scan the surface of fibers laid on the sample holder from 2θ of 3.00° to 70.00° . The amount of fibers was enough to cover the sample holder. The resolution was set at 0.020, with scan speed maintained at $2^\circ/\text{minute}$.

Thermogravimetric Analysis

TGA was performed using a thermogravimetric analyzer (TA Instruments TGA Q50, New Castle, DE, USA). Samples were cut into small pieces (around 5 mm) of 20–25 mg and were placed on a platinum pan, then heated from 30 to 900 °C at a rate of 10 °C per min under Argon gas at 40 mL per min purge flow. Calculations of percentage mass loss and derivative plots were done using the TA Universal Analysis software.

RESULTS & DISCUSSION

Tensile Strength

The average ultimate tensile strengths measured from the treatments are summarized in Table 2. No significant change in tensile strength was observed from fibers treated with aluminum sulfate only. A significant decline in tensile strength of was observed when fibers were treated with alkali solution prior to aluminum sulfate solution. The decrease in strength could be due to the delignification as caused by the alkali solution.

Table 2 Average tensile strength of fibers under different treatments

Treatment	Tensile Strength (MPa)
Raw Abaca	432±141
Al ₂ SO ₄ -treated	420±144
Alkali-treated and Al ₂ SO ₄ -treated	296±82

X-ray Diffraction of Raw and Alkali-treated Fibers

The crystallinity indices measured for untreated and alkali-treated fibers were 61.0% and 78.8%, respectively. The observed increase in fiber crystallinity after alkali pretreatment is due to the extraction or removal of its soluble amorphous components including hemicelluloses, lignin and other non-cellulosic components. This process allows the cellulosic fibers to adopt a more crystalline structure. This also explains the decreased tensile strength observed for alkali-treated fibers.

Thermogravimetric Analyses (TGA) of Untreated and Treated Fibers

Thermal stability of the fibers was studied in terms of percent weight losses under argon atmosphere with respect to a temperature ramp (100/min) from 300 C to 9000 C. The value of Tmax represents the temperature at which the maximum decomposition rate was observed based from the differential thermogravimetry (DTG) data. The effect of alkali treatment on the rate of decomposition under thermal stress was analyzed.

Table 3. Decomposition of Untreated Abaca and Alkali-treated Abaca Fibers (Malenab et al., 2017)

	Stage 1		Stage 2		Total % mass lossp 900 °C
	Tmax (°C)	% mass loss	Tmax (°C)	% mass loss	
Un-treated	62	8.9	345	78.2	87.1
Alkali-treated	53	7.8	350	71.2	79.0

Decomposition stage 1 which primarily involves moisture loss was observed to be less significant for the alkali-treated fiber. This indicates reduction in hydrophilic components. Decomposition in stage 2 was also observed to be lower for alkali-treated fibers, indicating removal of components. Overall, alkali-treated fibers were **observed to decompose 79.0% of its total mass, whereas the untreated fibers lost 87.1%, possibly indicating improved stability.**

Untreated fibers and fully-treated fibers reinforced in geopolymer were tested in TGA and compared to confirm if geopolymer provides a protective layer over the **treated fiber surface through the deposited inorganic precipitates. Since geopolymers are known for its fire-resistance and high thermal resistance, its formation and interaction with the fiber could form a protective layer. This was performed to evaluate the hypothesized effect of the aluminum sulfate treatment. Fully-treated abaca fibers that were reinforced in geopolymer composites were removed and subjected to TGA. The results were compared to that of untreated fibers withdrawn from a geopolymer composite. The results, summarized in Table 4, show significant improvement in thermal stability observed in **treated fibers, which lost only 43.3% of its mass as opposed to untreated fibers which lost a total of 76.0%. This entails that the Al(OH)₃ deposits may have effectively served as sites for geopolymer bond and growth, forming a highly thermal resistant layer on the fiber surface.****

Table 4 Decomposition of Untreated and Fully-treated Fiber Pulled out of Geopolymer (Malenab, et al., 2017)

Parameter	Untreated	Fully-Treated
Tmax (°C)	320	287
Total % mass loss	76.0%	43.3%
Max rate of decomposition (%/°C)	1.2	0.2%

CONCLUSION

Lower tensile strength was observed for fibers treated both with alkali and aluminum sulfate solution as opposed to fibers treated exclusively with aluminum sulfate solution, whose tensile strength did not deviate significantly from untreated samples. The decrease in tensile strength caused by the alkali treatment was expected since it involves dissolution of the fiber components that hinder effective interaction and bonding with the geopolymer matrix. This was confirmed by the XRD results.

TGA was performed to analyze (1) the effect of alkali treatment alone on the thermal stability of the fiber and (2) the effect of the series of treatments on the fiber-geopolymer interaction. Results indicate that alkali-treated fibers lost a smaller fraction of its mass under thermal stress. This may signify reduction of weak fibers components after alkali treatment. TGA results of untreated and treated pulled out of geopolymer composites show that treated fibers were significantly more thermally resistant. This signified that the inorganic deposits on the fiber surface as a result of treatment have aided in formation of bond with geopolymer particles, thereby enhancing the fiber's interaction with the geopolymer and acquiring protection from it. Treated fibers that were pulled out of contact with geopolymer lost a total of 43.3% of its mass whereas treated fibers that were not contacted with geopolymer lost 76.0% of its mass in all.

ACKNOWLEDGEMENT

This research was financially supported by the National Research Council of the Philippines (NRCP), Philippine Council for Industry, Energy and Emerging Technology Research and Development (PCIEERD), Advanced Device and Materials Testing Laboratory (ADMATEL) and Electronics Product Development Center (EPDC).

REFERENCES

- [1] Alvarez, V., and Vázquez, A. Thermal Degradation of Cellulose Derivatives/Starch Blends and Sisal Fibre Biocomposites. *Polymer Degradation and Stability*, Vol. 84, Issue, 2004, pp.13-21.
- [2] Araral, R. Turning Abaca Wastes Into Export Grade Handicraft, 2004. Retrieved May 13, 2018, http://sntpost.stii.dost.gov.ph/frames/OctToDec04/pg41_exportGradehandicraft.htm
- [3] Balasubramanian, M. Composite materials and processing.; CRC Press Taylor & Francis Group: Boca Raton, FL, USA, 2014, pp. 2-4.
- [4] Izani, M., Paridah, M., Anwar, U., Nor, M., and H'Ng, P. Effects of Fiber Treatment on Morphology, Tensile and Thermogravimetric Analysis of Oil Palm Empty Fruit Bunches Fibers. *Composites part B: Engineering*, Vol. 45, Issue 1, 2013, pp. 1251-1257.
- [5] Jabbar, A., Militky, J., Wiener, J., Javid, M.U., Rwawiire, S. Tensile, Surface and Thermal Characterization of Jute Fibres After Novel Treatments. *Indian Journal Fibre & Textile Research*, Vol. 41, 2016, pp.249-254.
- [6] Lima, H.C., Willrich, F.L., Barbosa, N.P., Rosa, A.R., and Cunha, B.S. Durability Analysis of Bamboo as Concrete Reinforcement. *Materials & Structure*. Vol. 41, Issue 5, 2007, pp. 981-989.
- [7] Malenab, R.J., Ngo, J.S., and Promentilla, M.B. Chemical Treatment of Waste Abaca for Natural Fiber-Reinforced Geopolymer Composite." *Materials*, Vol. 10, no. 6, 2017, p. 579.
- [8] Philippine Statistics Authority. Selected Statistics on Agriculture Vol. 27, 2016, pp.13-18. Retrieved May 6, 2017, <https://psa.gov.ph/sites/default/files/Selected%20Statistics%20o%20Agriculture%202016.pdf>
- [9] Yan, L. Kasal, B., and Huang, L. A Review of Recent Research on the Use of Cellulosic Fibres, Their Fibre Fabric Reinforced Cementitious, Geo-olymer and Polymer Composites in Civil Engineering. *Composites Part B*. Vol. 92, 2007, pp.94-132.
- [10] Zhang, J., Feng, L., Wang, D., Zhang, R., Liu, G. and Cheng, G. Thermogravimetric analysis of lignocellulosic biomass with ionic liquid pretreatment. *Bioresource Technology*. 153, 2014, pp.379-382.

INTEGRATED MAINTENANCE SCHEDULING AND STAFF SCHEDULING FOR AN AIRCRAFT HANGAR MAINTENANCE PROBLEM

Yichen QIN¹, Felix T.S. CHAN^{2*}, S.H. CHUNG³, B. NIU⁴, T. QU⁵

¹School of Electrical and Information Engineering, Jinan University (Zhuhai Campus), Zhuhai 519070, China

²Department of Industrial and Systems Engineering, The Hong Kong Polytechnic University, Hung Hum, Hong Kong

³College of Management, Shenzhen University, Shenzhen, China

ABSTRACT

In this paper, an integrated aircraft parking layout planning and staff scheduling problem is studied. This integrated problem is motivated by the heavy maintenance activities conducted in the aircraft hangar operated by maintenance service providers, which consists of determining a maintenance schedule to meet the aircraft maintenance requests from clients, a series of hangar parking plans and a staff schedule covering the entire planning period. Instead of relying on inefficient manual handling, the concept of a mathematical model integrating the interactions among the maintenance planning, aircraft parking arrangement and staff scheduling is discussed to solve the maintenance problem. The development of geometric constraints is focused, as the number of aircraft can be placed in the hangar varies according to the incoming maintenance requests to be maintained from time to time, and the blocking of aircraft during the rolling in and out path. Moreover, the maintenance scheduling and staffing problem are further discussed in the development of mathematical models. This work is innovative in dealing with such integrated maintenance problems for aircraft maintenance company providing hangar maintenance service.

Keywords: staffing, scheduling, aircraft hangar maintenance, mixed-integer linear programming

INTRODUCTION

Aircraft maintenance ensures safety in aviation, and different types of aircraft Maintenance, Repair and Overhaul (MRO) activities should be conducted upon specific flying hours. The expenditure on aircraft maintenance activities consists around 9 percent of the overall cost within airlines annually [1]. Specifically, the maintenance cost can be classified as line maintenance and hangar maintenance, according to the place where the maintenance activities are conducted[2]. Usually, heavy maintenance activities are referred as hangar maintenance, since these maintenance checks require more inputs (equipment, licensed technicians, space and maintenance time) and the maintenance activities are undergone in aircraft hangar. Nowadays, the high maintenance costs and relevant capital input together with the fluctuations of passenger demand become the motivation to let airlines to switch their maintenance practice, ensuring satisfying the operations safety regulation and achieving a low maintenance cost and good appropriate maintenance quality [3, 4]. In this

connection, one feasible option is to outsource airlines' own heavy MRO operations to aircraft maintenance service provider, as the airlines company save its input in fixed assets related to heavy maintenance. According to the estimation by Marcontell [5], outsource of aircraft maintenance activities has risen 45 percent in the past over 20 years. Many airlines have decided to distribute their maintenance activities to the maintenance company, and therefore the airline company is able to focus on their core business, such as flight planning, marketing and so on.

For aircraft maintenance companies, meeting the increasing maintenance requests from different airlines in a timely manner becomes challenging due to different limit of resource, such as hangar space and licensed technician. In practice, many MRO tasks for different incoming aircraft need to be undergone at the same time under one hangar, and a maintenance plan, including aircraft maintenance schedule, personnel schedule and a series of hangar layout plan for the planning period, has to be carried out by the planner. The objective of the planning is to minimize

the penalty cost related to delay in fulfilling the order, as well as the labor cost. Given the situation that the aircraft to be maintained are received from different airlines or customers, the hangar planner has to arrange these aircraft in different configuration with their own maintenance request. In addition, safety regulation need to be observed while making the hangar layout plan for aircraft parking to reduce the risk of collision. In addition, labor is also a large cost for an aircraft maintenance service provider, and therefore an economic and proper scheduling of the workforce is rather significant and an appropriate personnel schedule should cover all flight with the available workers and their respective skill with minimal labor cost[6].

This paper mainly focuses on the aircraft heavy maintenance activities taking place at the maintenance hangar operated by aircraft maintenance company, and the contents of this paper discusses the concept of an integrated model assisting the maintenance scheduling problem, aircraft parking position planning problem for the aircraft under this problem background. Blocking between aircraft and improper arrangement of staff are two main causes delays in maintenance activities. As different aircraft have their own features and the specific problem needs a particular skill, only licensed workers can be assigned to maintain a specific aircraft in the hangar [6]. There are many papers studying personnel scheduling problems from the perspective of line [6-9] while the research focusing on heavy maintenance is limited [10]. This work is innovative in incorporating the geometric shape of aircraft in the MILP model, together with personnel scheduling problem, for the hangar maintenance problem. In literature, the number of aircraft can be parked in the maintenance hangar is predetermined in the problem setting of the mathematical model as a parameter, and this assumption is appropriate under the case if the maintenance hangar is operated by a single airline company given the situation that the parking position of each aircraft have been predetermined while designing the maintenance hangar since the number of aircraft type operated by a single airline is limited. However, such problem setting is inappropriate for the independent aircraft hangar maintenance company as the combination of the incoming aircraft and their size vary from day to day, making predetermining the parking stand unchanged impractical under such context.

PROBLEM DESCRIPTION

The maintenance problem with the background of aircraft heavy maintenance company is considered. The maintenance planner come up with an aircraft maintenance schedule, a personnel schedule, aligning with a set of hangar layout for aircraft parking stand arrangement across the planning period. As mentioned above, the parking stands do not fix, and the aircraft can be parked flexibly in the hangar. Furthermore, workers have different skills and the specific maintenance task for the aircraft can only be conducted by the technician with license on that particular task. Therefore, such maintenance problem is incorporated with a multi-skill personnel scheduling problem. The mathematical model has the following assumption: 1) each aircraft's parking position cannot be changed along the maintenance period once the aircraft's parking position is determined while rolling in; 2) aircraft cannot be moved out before completing the maintenance tasks; 3) if blockage happen during the moving in or moving out operations, the movement operation has to suspend until the movement pathway is clear, or reconsider the other parking positions; 4) the path of movement of any aircraft has to be a straight line and any turning movement should be avoided during moving in and out operation due to the safety consideration; and 5) only licensed technician can conduct the designated maintenance task and the maintenance equipment is assumed to be sufficient in the mathematical model.

Given a set of maintenance requests to be fulfilled by the hangar maintenance company, the maintenance planner need to come up with a maintenance schedule and personnel schedule that align with a series hangar layout for aircraft parking in the hangar with minimize tardiness cost and labor cost. In particular, each maintenance request initiated by the clients includes the aircraft type, required maintenance checks, estimated time of arrival (ETA) to the hangar and estimated time of departure (ETD) from the hangar. For the maintenance task of each incoming aircraft, only licensed technician for a particular maintenance task can conduct the corresponding jobs. Generally, each technician has multiple skill to conduct different maintenance tasks for several types of aircraft model. In addition, the legal constraints regarding the personnel scheduling should be imposed. For example, the number of working hours each week must less than a prescribed hour.

CONCEPT OF THE MATHEMATICAL MODEL

The structure of the integrated maintenance problem is illustrated in Fig. 1, which consists of the aircraft parking and movement planning problem (Part A) and the personnel scheduling problem (Part

Integrated aircraft maintenance scheduling, parking stand assignment, and personnel scheduling model with the objective of profit maximization

A. Modelling of aircraft parking stand assignment and scheduling problem

- Variance of hangar capacity and aircraft parking assignment over planning period
- Blockage between pair of aircraft during movements
- Optimizing the maintenance schedule and series of hangar layout plan for aircraft parking

B. Modelling of integrated aircraft maintenance scheduling and personnel scheduling problems

- Integrating multi-skill licensed technicians scheduling in maintenance scheduling problem
- Resource constraints

Fig. 1 Structure of the mathematical model

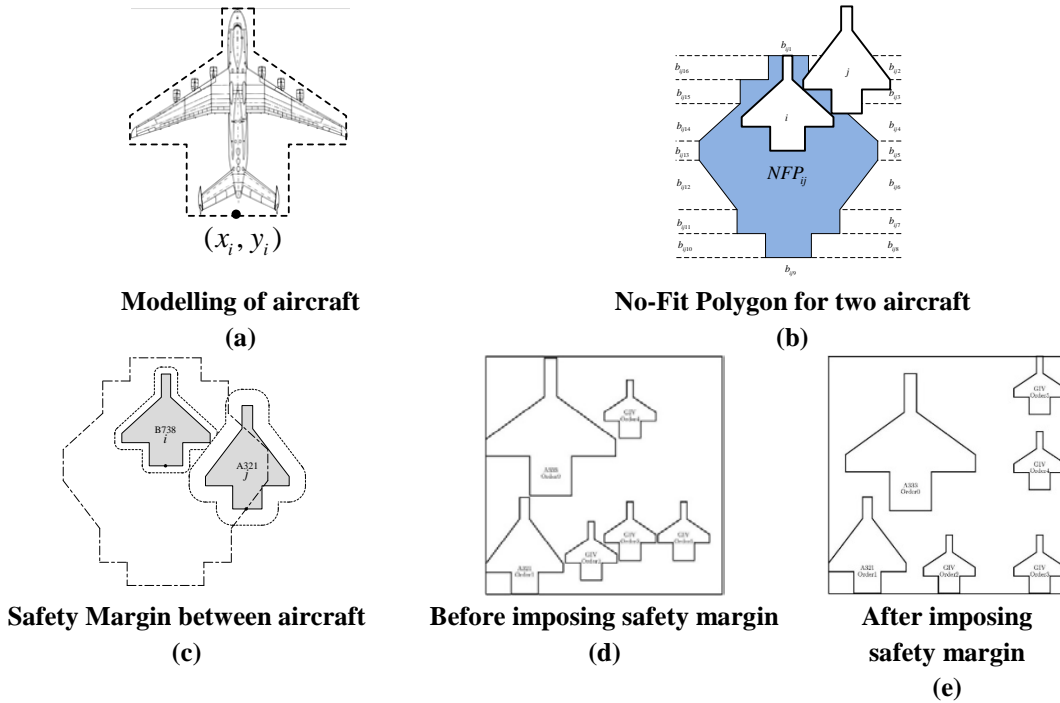


Fig. 2 Aircraft parking stand assignment problem

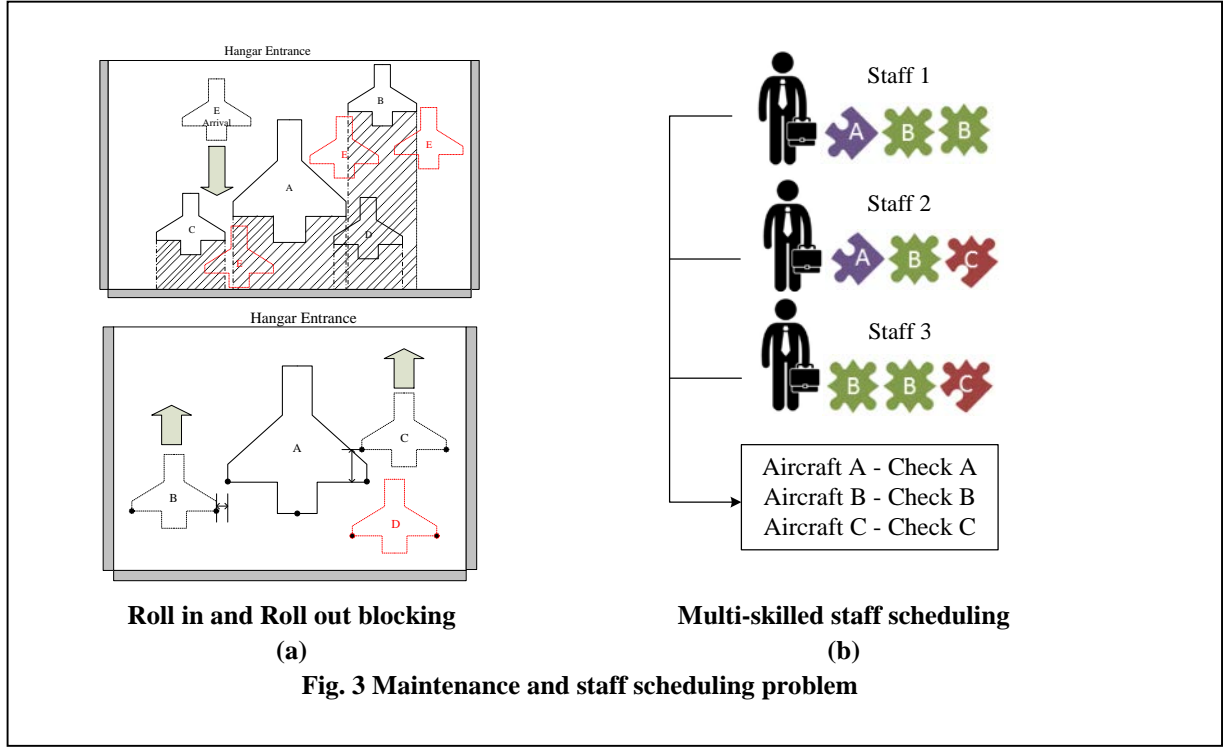
B). The following subsections describe the component to be integrated in the mathematical model.

COMPONENTS IN MATHEMATICAL MODEL

Geometric constraints

Aircraft's irregular in mathematical model can be regarded as a polygon as shown in Fig. 2(a). Let the reference point determining the position of each aircraft be the middle point of the bottom of the polygon, and the coordinates (x_i, y_i) find the position

of aircraft p_i in two-dimensional space. No-Fit Polygon (NFP) is adopted to prevent a pair of aircraft from overlapping in the mathematical model [11, 12]. In particular, for two of aircraft p_i and p_j , the NFP_{ij} refers to area where aircraft p_j would collide with aircraft p_i if the coordinate of aircraft p_j is located on the boundary or in the NFP_{ij} (Fig. 2(b)). The proper region for parking aircraft p_j preventing overlaps with p_i refers to the region outside NFP_{ij} . The NFP_{ij} is obtained by recoding the pathway of the coordinates of p_j while p_j sliding around the



boundary of p_i keep two polygons contact with each other without overlapping. There have been a few integer programming formulations that have adopted the *NFP* concept. According to Alvarez-Valdes et al. [13], each horizontal slice is defined by drawing one or two horizontal line(s) outward from each vertex of the *NFP* and they are then characterized by one or two horizontal edge(s) as well as the part of boundary of *NFP* as shown in Fig. 2(b). A set of variables b_{ijk} is associated with each horizontal slice and the coordinates of p_j is located in the slice k if $b_{ijk} = 1$. Therefore, geometric constraint preventing overlaps can be expressed as

$$\alpha_{ij}^{kf} (x_j - x_i) + \beta_{ij}^{kf} (y_j - y_i) \leq q_{ijk} + M \cdot (1 - b_{ijk}),$$

$$\forall i, j \in P, i \neq j, k = 1, 2, \dots, m_{ij}$$

where $\alpha_{ij}^{kf} (x_j - x_i) + \beta_{ij}^{kf} (y_j - y_i) = q_{ijk}$ is the expression of the line of the f th edge of the k th slice in NFP_{ij} and m_{ij} is the number of slices outside the NFP_{ij} . To further incorporate the safety distance between pair of aircraft, the original *NFP* is expanded (Fig. 2(c)) so as to separate two aircraft with a prescribed value. A comparison between before and after imposing safety margins between each pair of aircraft is presented in Fig. 2(d) and Fig. 2(e), showing that the empty space in the hangar has been fully utilized.

Blockage of movement operations

Arranging the parking position for aircraft is an important section in the maintenance problem as the movement operations can be delayed by the improper parking position arrangement, which may induce a series of delay if the parking position is arranged badly at the beginning of the planning period. In addition, insufficient hangar space and overwhelming maintenance requests during peak time can also cause delay and blocking (Fig. 3(a)) as mentioned earlier in [14]. For instance, the aircraft just arrive outside the maintenance hangar waiting for maintenance cannot be moved into the hangar timely due to insufficient space, or the aircraft finishing maintenance task is delayed from moving out from the hangar before its estimated time of departure, which are all due to improper parking during the initial parking position arrangement and the other aircraft undergoing maintenance task blocks its movement way.

Blockage of moving out from hangar

If the aircraft finishing its maintenance task is scheduled to moved out from the hangar, but blocked by the other aircraft undergoing maintenance activities in the hangar, the departing aircraft's move out operation at current time is delayed until its movement path is free with obstacles, i.e. wait for the aircraft that blocks its way to finish its maintenance task and move out from the hangar together. As a result, the maintenance schedule has to be adjusted due to the impact of such the parking layout

Blockage of moving into hangar

If the newly arrival aircraft received by the maintenance company is scheduled to move in to its designated parking position while the way of movement to the designated parking stand is blocked by the other aircraft undergoing maintenance task, then the newly arrival aircraft cannot be moved in at the scheduled time until its way of movement is cleared, i.e. wait for the aircraft blocking the pathway to finish its maintenance task and move out, or rearrange the parking position (Fig. 3(a)). Therefore, if it is the case, the newly arrival aircraft's moving in operation is delayed at the current time to the designated parking stand, and hangar planner need reschedule the maintenance plan that aligns with the hangar layout (if the designated stand for the newly arrival aircraft remain unchanged), or rearrange a new parking stand for the newly arrival aircraft in order to move in the aircraft in a timely manner if the buffer time for such maintenance request is tight.

Integrating maintenance scheduling and personnel scheduling problem

After developing the aircraft maintenance scheduling model incorporating the parking stand assignment problem with blocking consideration in physical space, other resource constraints, i.e. multi-skill workforce, shall be taken into consideration to complete the model (Fig. 3(b)). Different maintenance checks on aircraft are performed by licensed technicians with specific equipment in the aircraft hangar. Generally, each licensed technician can perform different checks according to the license they obtained, and the maintenance requests received by the service company. Therefore, the multi-skilled workforce scheduling problem with technical equipment constraint is to be integrated with the scheduling problem. In this connection, the scheduling is confined by (1) hangar capacity; (2) multi-skilled workforce, which reflects the complexity in carrying out the aircraft maintenance schedule. From the perspective of employee scheduling, personnel wages consist a large part of aircraft service company's operational costs and therefore the objective is to maximize the utilization of total contracted hours so as to minimize overtime assignment while satisfying the feasibility and legality rules prescribed by government authorities. The connection between the maintenance scheduling and personnel scheduling is established by the maintenance requirements of a particular aircraft, maintenance schedule and personnel schedule. As the maintenance scheduling and personnel scheduling are carried out simultaneously, maintenance schedule and workforce schedule might be adjusted recursively to meet a series of feasibility constraints under the occasions that the available workforce at specific time is not able to meet the maintenance requirements; the

aircraft to be maintained has not arrived or not able to roll into hangar due to insufficient space or blocking. The approach that reduces the domain time-related decision variables is further enhanced by considering the impact of personnel scheduling on the maintenance scheduling problem.

CONCLUSION

The concept of integrated maintenance scheduling, hangar layout planning for aircraft parking and staff scheduling problem for aircraft maintenance service company is discussed. Several mathematical components to be incorporated in Mixed-Integer Linear Programming (MILP) formulation are proposed. It is believed that the propose concept is able to assist aircraft maintenance companies to fully utilize their limited resource, including hangar space and personnel, so as to achieve overall maximal profit. The irregular geometric shape of aircraft has not been incorporated in maintenance scheduling problem in literature, together with multi-skill staff scheduling problem. The model considers the variation of the number of aircraft that maintenance hangar can accommodate over the planning horizon to meet the real situation, which aligns with the maintenance and staff scheduling problems. The realization of such mathematical model and efficient algorithms to tackle the realistic large-size instance are our future research direction. The mathematical model is expected to have a larger number of binary variables deciding the relative position between each pair of aircraft in the model, and therefore it is a feasible way to decompose the original mathematical problem into several subsections, then combine the sub-solution as a complete one to tackle the complexity of the original model while solving large-scale instances.

ACKNOWLEDGEMENTS

The work described in this paper was supported by grants from The Natural Science Foundation of China (Grant Nos. 71471158, 71571120, 71271140); The Research Committee of Hong Kong Polytechnic University (Project Number G-UA4F); and The Hong Kong Polytechnic University under student account code RUF1.

REFERENCES

- [1] ITAT. Airline Maintenance Cost Executive Commentary. 2015.
- [2] Van den Bergh J, De Bruecker P, Belien J, Peeters J. Aircraft maintenance operations: state of the art. FEB@Brussel research paper. 2013.

- [3] Eriksson S, Steenhuis H. The Global Commercial Aviation Industry. New York: Taylor & Francis; 2014.
- [4] Knotts RMH. Civil aircraft maintenance and support fault diagnosis from a business perspective. *Journal of Quality in Maintenance Engineering*. 1999;5(4):335-48.
- [5] Marcontell D. MRO's offshore edge shrinking. *Aviation Week & Space Technology*. 2013;175(22):56.
- [6] De Bruecker P, Belien J, Van den Bergh J, Demeulemeester E. A three-stage mixed integer programming approach for optimizing the skill mix and training schedules for aircraft maintenance. *European Journal of Operational Research*. 2018;267(2):439-52.
- [7] Belien J, Cardoen B, Demeulemeester E. Improving Workforce Scheduling of Aircraft Line Maintenance at Sabena Technics. *Interfaces*. 2012;42(4):352-64.
- [8] De Bruecker P, Van den Bergh J, Belien J, Demeulemeester E. A model enhancement heuristic for building robust aircraft maintenance personnel rosters with stochastic constraints. *European Journal of Operational Research*. 2015;246(2):661-73.
- [9] Belien J, Demeulemeester E, De Bruecker P, Van den Bergh J, Cardoen B. Integrated staffing and scheduling for an aircraft line maintenance problem. *Computers & Operations Research*. 2013;40(4):1023-33.
- [10] Chen G, He W, Leung LC, Lan T, Han Y. Assigning licenced technicians to maintenance tasks at aircraft maintenance base: a bi-objective approach and a Chinese airline application. *International Journal of Production Research*. 2017;1-14.
- [11] Burke EK, Hellier RSR, Kendall G, Whitwell G. Complete and robust no-fit polygon generation for the irregular stock cutting problem. *European Journal of Operational Research*. 2007;179(1):27-49.
- [12] Bennell JA, Dowsland KA, Dowsland WB. The irregular cutting-stock problem - a new procedure for deriving the no-fit polygon. *Computers & Operations Research*. 2001;28(3):271-87.
- [13] Alvarez-Valdes R, Martinez A, Tamarit JM. A branch & bound algorithm for cutting and packing irregularly shaped pieces. *International Journal of Production Economics*. 2013;145(2):463-77.
- [14] Qin Y, Chan FTS, Chung SH, Qu T. Development of MILP model for integrated aircraft maintenance scheduling and multi-period parking layout planning problems. 2017 4th International Conference on Industrial Engineering and Applications, ICIEA 2017. Nagoya, Japan: Institute of Electrical and Electronics Engineers Inc.; 2017. p. 197-203.

SYNTHESIS OF ONE-PART GEOPOLYMER USING D-OPTIMAL MIXTURE DESIGN FOR SOIL STABILIZATION

April Anne S. Tigue¹, Jonathan R. Dungca², and Michael Angelo B. Promentilla¹

¹Chemical Engineering Department, De La Salle University, Manila 1004, Philippines

²Civil Engineering Department, De La Salle University, Manila 1004, Philippines

ABSTRACT

Soil stabilization is a technique used to alter the natural properties of soil. Enhancing the strength and increasing the stability of in-situ soil can either be done mechanically or chemically using conventional materials which are usually extracted through mining and quarrying and have been known to pose serious environmental impacts. In addition, the production of these conventional materials, specifically cement, have a significant contribution to the global carbon dioxide emissions. Hence, waste materials such as coal fly ash and volcanic ash as substitute were utilized in this study by employing the concept of geopolymer. Pertinent experimentations have already been undertaken with the hopes of promoting geopolymer as construction material. However, less attention has been given to its application as geopolymer soil stabilizer. One reason could be attributed to the applicability of the traditional geopolymer synthesis in soil stabilization. Thus, a novel approach one-part geopolymer or 'just add water' similar to ordinary Portland cement was employed and solid alkali activators such as sodium silicate, sodium hydroxide, and sodium aluminate were explored. Characterization technique such as X-ray fluorescence was performed to examine the elemental composition of the raw materials. The effect of amount of soil, coal fly ash, volcanic ash, and alkali activators on the unconfined compressive strength response after acid immersion were investigated using D-Optimal mixture design.

Keywords: Geopolymer, Soil, Stabilizer, D-optimal, Mixture

INTRODUCTION

Soil Stabilization is a technique used to alter the natural properties of soil. Most often, it is necessary to enhance the strength and increase the stability of in-situ soil to meet a requirement prior its intended use. Other reason for using this technique is to improve the stability by increasing the load bearing capacity of the subgrade or subbase to support pavements and structure. Commonly, stabilized soil is used in structural fill, foundation, road embankment, land reclamation, in constructing low volume roadways, commercial sites, streets, and the likes. Improving and enhancing the soil properties may be performed by either mechanical or chemical means. Mechanical soil stabilization alters the physical properties of soil by blending materials to improve the gradation of particle size to obtain a material meeting the required specification. Conversely, chemical soil stabilization alters the chemical properties of soil by using an admixture. Conventional materials utilized in chemical soil stabilization are lime and cement through pozzolanic hydration process. These materials are usually extracted through mining and quarrying which have been known to pose serious environmental impacts. In fact, the production of cement has a contribution of about 5-8% to global anthropogenic carbon dioxide emissions, which makes it a vital sector to be part of

CO₂-emission mitigation strategies [1]. With a cement demand amounting to 24.4 million tons in 2015 and considering the 20% public construction growth rate, the forecast for cement may continue to increase for the coming years [2]. Thus, several approaches have been proposed to reduce the cement consumption in the construction industry by using pozzolanic materials such as coal fly ash and volcanic ash.

Alternatively, the geotechnical and engineering properties of soil may be improved with the process called geopolymerization. With the presence of an alkali activator, the precursor rich in alumina and silica will react to form into aluminosilicate ions and will turn into a hardened 3D molecule network upon polycondensation [3]. Geopolymer precursor can be any pozzolanic compound or source of silica and alumina that is readily dissolved in alkaline solution [4]. Industrial wastes such as fly ash, bottom ash, slag, etc. have been utilized as a solid geopolymer precursor for the application in making building materials such as cement, concrete, bricks, foam, composite [5-7].

In this study, the potential utilization of waste materials such as fly ash and volcanic ash that are locally available in the Philippines as geopolymer-based soil stabilizer were explored. The mix proportions and effect of amount of soil, precursors (fly ash and volcanic ash), and alkali activator on the

unconfined compressive strength (UCS) response after subjecting in acidic environment were investigated using D-Optimal mixture design.

MATERIALS AND METHODS

Sources of Raw Materials

The soil samples were obtained from a construction area situated at the southern part of Manila, Philippines. Volcanic ash (VA) samples were gathered from central region of Luzon. Soil and volcanic ash samples were immediately sieved using Mesh No. 4. On the other hand, fly ash (FA) samples, collected from a thermal power plant located at the central region of Luzon, were used as received. Analytical grade of sodium silicate (SS) with composition 44% SiO_2 , sodium hydroxide (SH) micropearls with 99% purity, sodium aluminate (SA) with 50-56% Al_2O_3 / 40-45% Na_2O as alkali activators and sulfuric acid with 95% were purchased locally.

Raw Material Characterization

Characterization such as chemical analysis, particle size analysis, specific gravity, Atterberg limit, and Unified Soil Classification System (USCS) were taken into consideration. Chemical analysis of fly ash, volcanic ash, and soil were conducted using X-ray fluorescence dispersive (XRF). Particle size analysis was performed in accordance with ASTM D-422 using sieves to determine the particle size distribution of soil and volcanic ash. For particle size analysis of fly ash, dynamic light scattering was considered. Specific gravity and Atterberg limit, which includes plastic limit and liquid limit, were performed in accordance with ASTM D-854 and ASTM D-431. The soil type was determined based on unified soil classification system.

D-Optimal Mix Design

D-optimal mix design methodology is a type of computer generated design for optimizing mixture with low and high-level constraints. The presence of upper and lower bound constraints often leads to oddly shaped region also known as a q-dimensional convex polytope making the mixture design non-orthogonal compared to typical designs [8]. In evaluating this kind of design, the forward selection in Design Expert software is utilized. This design generates points that are spread through the design region of the given parameter range. For this study, d-optimal design generated the best 21 design points that will be used in the experiment. An additional 4 replicates were added to capture the error. A total of 25 runs were employed in this experiment. The response variable considered in this experiment is the strength response of stabilized soil to sulfuric acid

resistance measured in terms of unconfined compressive strength (UCS). The factors considered in the mixture design are categorized into two mixtures. Mixture 1 consists of fly ash, volcanic ash and soil while mixture 2 consists of the alkali activators such as sodium silicate, sodium hydroxide and sodium aluminate. Dry mixing of materials (mixture of fly ash, volcanic ash, and alkali activator) using 30% (w/w) alkaline activator were performed according to the runs generated by the D-optimal mixture design with parameter range as summarized in Table 1 [9-11]. Water was added on the dry formula followed by mixing for at least 5 minutes. The geopolymer paste binder, a mixture of dry formula and water, was completely mixed with soil. After stabilization, geopolymer stabilized soil was compacted in a cylindrical mold 50 mm diameter by 100 mm height for 3 layers of about 25 tamps per layer. The molded specimen was sealed and cured for 28 days at ambient temperature.

Table 1 Experimental factors and parameter range (%w/w)

Factor	Unit	Parameter Range		
			L	H
Mix 1	FA	% of Total Ash	50%	100%
	VA	% of Total Ash	0%	50%
	Soil	% of Mixture 1	75%	95%
Mix 2	SS	Ratio	1	2.5
	SH	Ratio	1	1
	SA	Ratio	0	1.5

Acid Immersion Test

After curing for 28 days, the samples were immersed in 5% (w/w) sulfuric acid solution [11],[12]. The unconfined compressive strength (UCS) was measured after 28 days of immersion for each run.

RESULTS

Raw Material Characterization

The type of soil in this study is classified as SM-brown silty sand based on unified soil classification system and has a specific gravity of 2.54. The Atterberg limit showed that the fines are non-plastic. The particle size distribution is shown in Fig. 1. This illustrates that the median diameter (D_{50}) is 0.70 mm. The elemental analysis of soil in oxides form is shown in Table 2. It is primarily composed of SiO_2 , Fe_2O_3 , Al_2O_3 , and CaO . Fly ash utilized in this work is primarily composed of SiO_2 , Fe_2O_3 , CaO , and Al_2O_3 and has a specific gravity of 2.85. The median particle size of fly ash as shown in Fig. 1 is 1.92 microns. The result of the Atterberg limit showed that it has a liquid limit of 12 and a plasticity index of 1. On the other

hand, volcanic ash which also comprises SiO_2 , CaO , Al_2O_3 , and Fe_2O_3 has a specific gravity of 2.80. Based on the particle size analysis, 50% of the particles has diameter of 0.33 mm. The Atterberg limit showed that it comprises non-plastic particles.

Table 2 Chemical composition of raw materials

Chemical Compound	Soil (Mass %)	Fly Ash (Mass %)	Volcanic Ash (Mass %)
SiO_2	38.87	24.65	56.75
Fe_2O_3	34.06	44.63	13.00
Al_2O_3	12.53	8.55	11.34
CaO	6.82	16.04	10.93
TiO_2	3.09	1.32	1.35
K_2O	1.87	1.18	5.01
SO_3	-	1.63	-
Others	2.76	2.00	1.62

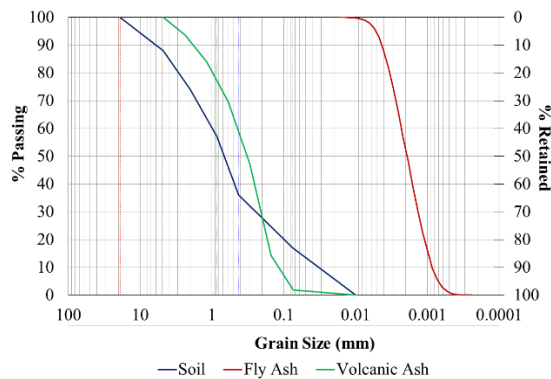


Fig. 1 Particle size distribution of raw materials.

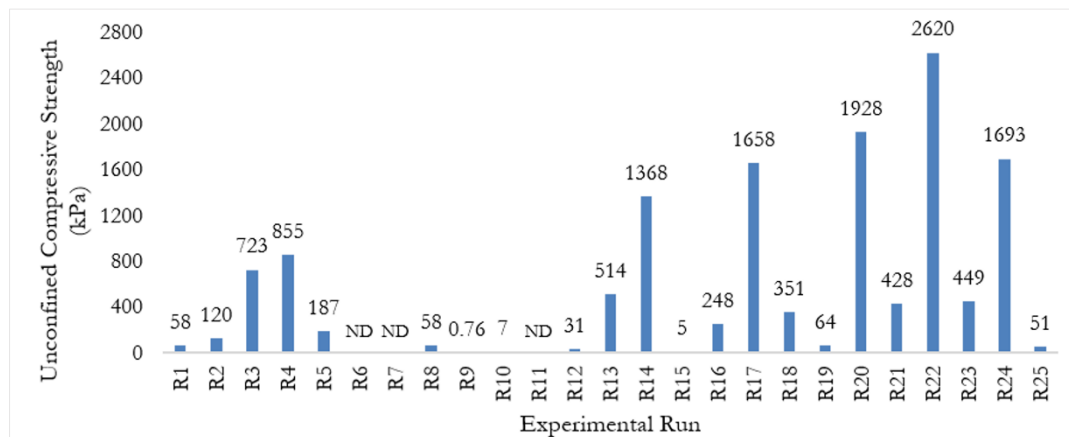


Fig. 2 Unconfined compressive strength at different mix proportions.

D-Optimal Mix Design Model

To statistically measure the effect of geopolymer mix at different mix proportions, experimental data were analyzed by fitting a model (linear or quadratic) for the unconfined compressive strength response which is dependent on different mix proportions of soil and precursors (FA and VA), and alkali activator

Unconfined Compressive Strength

Figure 2 presents the measured unconfined compressive strength after immersion in 5% sulfuric acid for 28 days of the geopolymer stabilized soil at different mix proportions of raw materials and alkali activator. The recorded unconfined compressive strength ranges from 0.76 kPa to 2620 kPa. The stabilized soil R22 (25% FA /75% soil and alkali activator 50% SH/50% SS) has the highest value of unconfined compressive strength making it the best mix sample among other runs. The samples with ND label, R6 (5% precursor/95% soil), R7(12.5% precursor/87.5% soil), and R11 (5% precursor/95% soil), were not able to withstand the acidic environment resulting to breakage of sample prior measurement of UCS. This may be due to the low amount of geopolymer precursors (fly ash and volcanic ash) and high amount of soil to be stabilized in the mixture. The mix proportion with a compressive strength of at least 75 kPa can be recommended for structural fill application. This is in accordance with the requirement of National Structural Code of the Philippines [13]. The stabilized soil developed in this study has a compressive strength comparable to soil stabilized with lime and/or cement despite its exposure in aggressive condition. Numerous studies have revealed that soil treated with lime has a range of unconfined compressive strength of 14.2 kPa-3000 kPa [14-17]. Conversely, cement stabilized soil can range to unconfined compressive strength value of 100-900 kPa [18-20].

(SS, SH and SA). The final model of the combined mixture was chosen based on the highest order polynomial where the addition of terms is significant (p -value<0.05), model lack of fit is not significant (p >0.05) and the model is not aliased. Table 3 shows the ANOVA of crossed mixture design. A p -value of 0.1595 for lack of fit indicates that it is not significant implying that the quadratic mixture crossed with

linear mixture model is fit. Quadratic mixture of soil and precursors crossed with linear mixture alkali activator was chosen having a p-value of 0.0002 and 0.0001 for mixture 1 and 2, respectively. The contour plot of the model as presented in Fig. 3 shows the effect and behavior of the various factors on the

measured unconfined compressive strength response. The intensity of unconfined compressive strength can be represented by red color which demonstrates high value of unconfined compressive strength to blue having low value of unconfined compressive strength.

Table 3 ANOVA of chosen crossed mixture design model (A= Fly ash; B= Volcanic ash; C= Soil; D=Sodium Silicate; E= Sodium Hydroxide; F= Sodium Aluminate)

Source	Sum of Squares	df	Mean Square	F Value	p-value (Prob > F)	
Model	4902.30	13	377.10	98.57	< 0.0001	significant
Linear x Linear Mixture	4008.46	8	501.06	130.97	< 0.0001	
ABF	220.23	1	220.23	57.57	< 0.0001	
ACE	222.98	1	222.98	58.28	< 0.0001	
ACF	45.02	1	45.02	11.77	0.0056	
BCD	281.19	1	281.19	73.50	< 0.0001	
BCE	51.86	1	51.86	13.56	0.0036	
Residual	42.08	11	3.83			
Lack of Fit	35.17	7	5.02	2.91	0.1595	not significant
Pure Error	6.91	4	1.73			
Cor Total	4944.38	24				

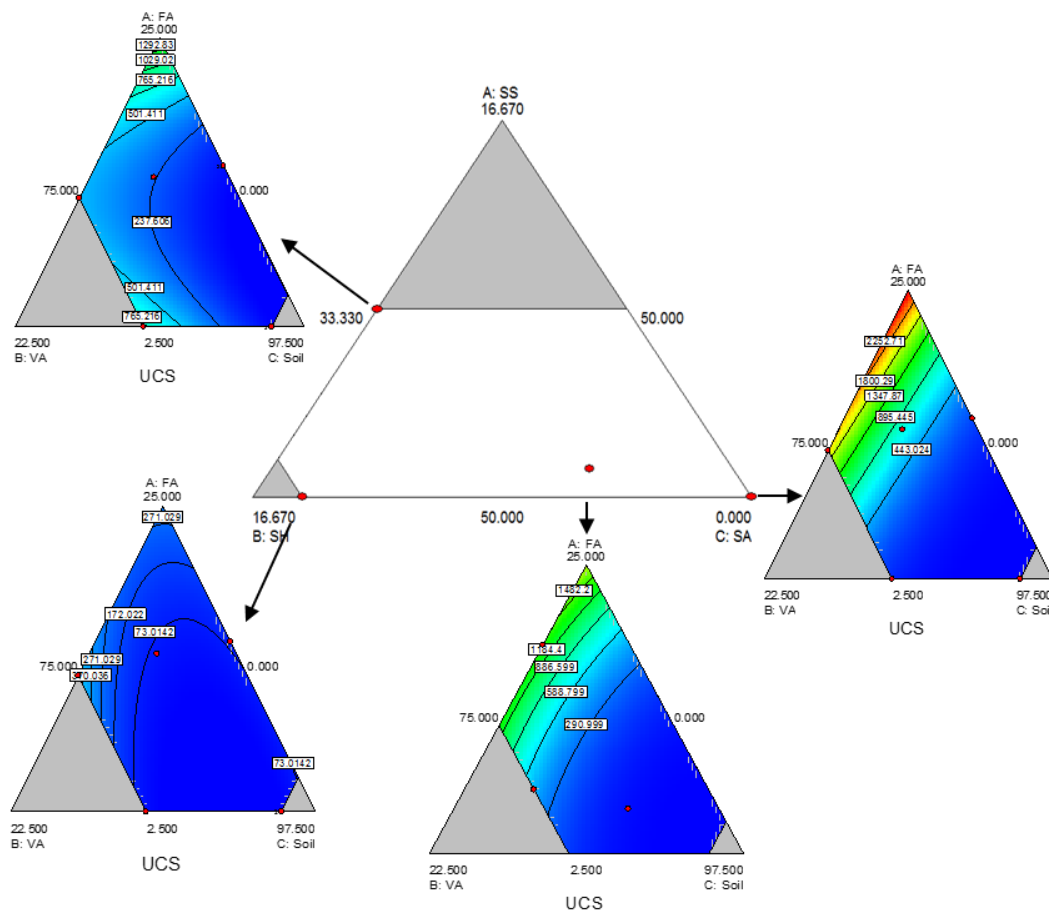


Fig. 3 Contour plot for unconfined compressive response prediction model of mixture 1 (soil and precursor) evaluated at each point of mixture 2 (alkali activator) design.

In terms of geopolymer precursor, it can be observed that high strength geopolymer stabilized soil can be produced as its nearing the apex of fly ash component, which means that high amount of fly ash could actually produce high strength geopolymer as compared with volcanic ash. Conversely, as the mixture nearing the apex of volcanic ash the strength decreases. This could mean that greater proportion of volcanic ash in the precursor relative to fly ash could produce a low strength geopolymer stabilized soil. This behavior may be attributed to the reactive nature of the precursor in terms of participation in geopolymerization process. This also implies that not all the alumina and silica content of the precursor can participate in geopolymerization [21]. The available amorphous alumina and silica content of the precursor are the only alumina and silica content participating in geopolymerization process. It is believed that the amorphous content of alumina and silica can easily be dissolved in the alkali activator thereby producing gel networks of inorganic geopolymer. The more available amorphous content of alumina and silica in the raw material, the better the mechanical strength of geopolymer stabilized soil [22].

The increase in compressive strength of the stabilized soil geopolymer have been remarkably noticed in alkali activator containing 50%SS:50%SH, 47.5% SS:40.42% SH:12.08% SA and 33% SS:33% SA:33% SA as the amount of soil decreases. It has been observed that as the component reaches the apex of SA (less SA in the mixture) as illustrated in Fig. 3, the strength increases. Presence of SS in greater proportion in alkaline activator with consideration that SH is also present in greater proportion, produces a high strength geopolymer stabilized soil. The presence of greater proportion of SH to produce high strength geopolymer stabilized soil may be explained by the initial step of geopolymerization. During this process, dissolution of material rich in aluminosilica occurs in the presence of an alkali activator such as sodium hydroxide. This activator is responsible for increasing the reactivity of the alumina silica material by attacking the Si-O-Si/Si-O-Al bond of the starting material with its OH⁻. This results in breaking down of Si-O-Si/ Si-O-Al bond thereby forming reactive aluminates and silicates [23],[24]. High amount of SH in the mixture could mean higher dissolution rate. A higher dissolution rate may mean more material can be broken down into its reactive form, hence more reactive aluminosilica source that could participate in geopolymerization. The production of low strength stabilized soil could be attributed to a lower dissolution rate, less leaching of alumina and silica ions from the precursor and lower value of unconfined compressive strength [10].

CONCLUSION

This study has explored one part-geopolymer

synthesis using precursors such as fly and volcanic ash and solid alkali activators such as sodium silicate, sodium hydroxide, and sodium aluminate with D-optimal mixture design. The unconfined compressive strength (UCS) was evaluated after exposing to a 5% (w/w) sulfuric acid solution. The final model of the combined mixture was quadratic mixture of soil and precursors crossed with linear mixture alkali activator. The mix proportion that yielded high value of unconfined compressive strength was found to be the proportion mix having 25% fly ash/75% soil with an alkali activator ratio of 50% sodium silicate/50% sodium hydroxide having a strength of 2620 kPa. The mix proportions having unconfined compressive strength of at least 75 kPa can be recommended for structural fill application. The geopolymer stabilized soil developed in this study showed promising result as potential acid-resistant material.

ACKNOWLEDGEMENTS

The authors would like to acknowledge the Engineering Research and Development for Technology (ERDT), and URCO Research Project (IR 1TAY15-3TAY16) for the financial support. The authors would also like to thank Geotechnical Laboratory and Mechanical Engineering Laboratory of De La Salle University for allowing them to use their facilities.

REFERENCES

- [1] Worrell, E. , Price, L. , Martin, N. , Hendriks, C. , and Ozawa, M. L. Carbon Dioxide Emissions from the Global Cement Industry. Annual Review of Energy and the Environment Vol. 26, Issue 1, 2001, pp. 303–329.
- [2] Cement Manufacturers' Association of the Philippines Inc. (CeMAP) 2015 Annual Cement Industry Report. (2015).
- [3] Xie, J. and Kayali, O. Effect of Initial Water Content and Curing Moisture Conditions on the Development of Fly Ash-Based Geopolymers in Heat and Ambient Temperature. Construction and Building Materials Vol. 67, Part A, 2014, pp. 20–28.
- [4] Jaarsveld, J. G. S. Van and Deventer, J. S. J. Van The Potential Use of Geopolymeric Materials to Immobilise Toxic Metals Part I. Theory And Applications Best Student Research Paper Award for Geopolymer Research , in Australia Amazing World of Science. Vol. 10, Issue 7, 1997, pp. 1–10.
- [5] Promentilla, M. A. , Thang, N. , Trung Kien, P. , Hinode, H. , Bacani, F. , and Gallardo, S. Optimizing Ternary-Blended Geopolymers with Multi-Response Surface Analysis. Waste and Biomass Valorization Vol. 7, 2016
- [6] Kalaw, M. , Culaba, A. , Hinode, H. , Kurniawan,

- W. , Gallardo, S. , and Promentilla, M. Optimizing and Characterizing Geopolymers from Ternary Blend of Philippine Coal Fly Ash, Coal Bottom Ash and Rice Hull Ash. *Materials* Vol. 9, Issue 7, 2016, pp. 580.
- [7] Malenab, R. A. J. , Ngo, J. P. S. , and Promentilla, M. A. B. Chemical Treatment of Waste Abaca for Natural Fiber-Reinforced Geopolymer Composite. *Materials* Vol. 10, Issue 6, 2017, pp. 579.
- [8] Carlson, R. Design of Experiments, Principles and Applications, L. Eriksson, E. Johansson, N. Kettaneh- Wold, C. Wikström and S. Wold, Umetrics AB, Umeå Learnways AB, Stockholm, 2000, ISBN 91-973730-0-1, Xii + 329 Pp. *Journal of Chemometrics* Vol. 15, Issue 5, 2001, pp. 495–496.
- [9] Pavithra, P. , Reddy, M. S. , Dinakar, P. , Rao, B. H. , Satpathy, B. K. , and Mohanty, A. N. A Mix Design Procedure for Geopolymer Concrete with Fly Ash. *Journal of Cleaner Production* Vol. 133, 2016, pp. 117–125.
- [10] Phetchuay, C. , Horpibulsuk, S. , Arulrajah, A. , Suksiripattanapong, C. , and Udomchai, A. Strength Development in Soft Marine Clay Stabilized by Fly Ash and Calcium Carbide Residue Based Geopolymer. *Applied Clay Science* Vol. 127–128, 2016, pp. 134–142.
- [11] Djobo, J. N. Y. , Elimbi, A. , Tchakouté, H. K. , and Kumar, S. Mechanical Properties and Durability of Volcanic Ash Based Geopolymer Mortars. *Construction and Building Materials* Vol. 124, 2016, pp. 606–614.
- [12] Jin, M. , Zheng, Z. , Sun, Y. , Chen, L. , and Jin, Z. Resistance of Metakaolin-MSWI Fly Ash Based Geopolymer to Acid and Alkaline Environments. *Journal of Non-Crystalline Solids* Vol. 450, 2016, pp. 116–122.
- [13] of Structural Engineers of the Philippines, A. National Structural Code of the Philippines 2010: Buildings, towers and other vertical structures. Association of Structural Engineers of the Philippines: 2010.
- [14] Dash, S. and Hussain, M. Lime Stabilization of Soils: Reappraisal. *Journal of Materials in Civil Engineering* Vol. 24, 2012, pp. 707–714.
- [15] Al-Mukhtar, M. , Khattab, S. , and Alcover, J.-F. Microstructure and Geotechnical Properties of Lime-Treated Expansive Clayey Soil. *Engineering Geology* Vol. 139, Issue Supplement C, 2012, pp. 17–27.
- [16] Ghobadi, M. H. , Abdilor, Y. , and Babazadeh, R. Stabilization of Clay Soils Using Lime and Effect of PH Variations on Shear Strength Parameters. *Bulletin of Engineering Geology and the Environment* Vol. 73, Issue 2, 2014, pp. 611–619.
- [17] Dungca, J. R. and Dychangco, L. F. T. Strength Properties of Road Base Materials Blended with Waste Limestones. Vol. 11, 2016
- [18] Correia, A. A. S. and Rasteiro, M. G. Nanotechnology Applied to Chemical Soil Stabilization. *Procedia Engineering* Vol. 143, Issue Supplement C, 2016, pp. 1252–1259.
- [19] Ojuri, O. O. , Adavi, A. A. , and Oluwatuyi, O. E. Geotechnical and Environmental Evaluation of Lime–cement Stabilized Soil–mine Tailing Mixtures for Highway Construction. *Transportation Geotechnics* Vol. 10, Issue Supplement C, 2017, pp. 1–12.
- [20] Choobbasti, A. J. and Kutanaei, S. S. Microstructure Characteristics of Cement-Stabilized Sandy Soil Using Nanosilica. *Journal of Rock Mechanics and Geotechnical Engineering* 2017
- [21] Tennakoon, C. , Silva, P. De , Sagoe-Crentsil, K. , and Sanjayan, J. G. Influence and Role of Feedstock Si and Al Content in Geopolymer Synthesis. *Journal of Sustainable Cement-Based Materials* Vol. 4, Issue 2, 2015, pp. 129–139.
- [22] Jaarsveld, J. G. S. van , Deventer, J. S. J. van , and Lukey, G. C. The Characterisation of Source Materials in Fly Ash-Based Geopolymers. *Materials Letters* Vol. 57, Issue 7, 2003, pp. 1272–1280.
- [23] Provis, J. L. 4 - Activating solution chemistry for geopolymers. *In Geopolymers*; Provis, J. L., Deventer, J. S. J. van, Eds.; Woodhead Publishing, 2009; pp. 50–71.
- [24] Davidovits, J. Geopolymers. *Journal of thermal analysis* Vol. 37, Issue 8, 1991, pp. 1633–1656.

FLOW INVESTIGATIONS WITHIN A CONCENTRIC CYLINDERS OF GAS SENSOR MODULE FOR I.C. ENGINES

¹Tatsuya Kawaguchi, ²Yoona Jeong, ³Takushi Saito and ⁴Isao
^{1,2,3,4}Satoh Tokyo institute of technology, Japan.

ABSTRACT

The study deal with the experimental investigation of the flow field around the inorganic sensors with concentric double protectors with apertures such as the commercial gas sensor modules for passenger vehicles. Transparent acrylic model was used in conjunction with the particle image velocimetry. The experimental result demonstrated that the magnitude of velocity in the vicinity of the sensor rod is significantly lower than that of the external main flow. The velocity fluctuation through the opening apertures enhances the mass transfer between the inside and outside of the protectors and contributes to the better response of the sensing module.

Keywords: Flow visualization, Gas sensor, Internal flow, Mixing process, Particle image velocimetry

INTRODUCTION

Regulation specifications of greenhouse gas emission and fuel economy standards for passenger vehicles or trucks were significantly progressed more than a decade. Drastic reductions of the oxidizing gases and the small particles in the exhaust gas from the I.C. engine have been required. Although only a few country had introduced mandatory greenhouse gas emission and/or fuel economy standards, many countries including European Union were announced their intention to introduce the greenhouse gas emission standards. Further improvement of gas emission sensing, monitoring and controlling for the internal combustion engine of automobiles, marine engines and power plants have been desired. Not only the reduction of the particulate matter but also the control of such emission gas as CO₂, NO₂ and SO₂ were required that enable to improve total efficiency of the thermal systems. In the recent engine system, multiple inorganic gas sensor modules are equipped to obtain the various kinds of gas concentration [1-3]. For example, precise measurement of O₂ concentration difference between catalysts was used for engine management system [4,5].

Figure 1 is the photograph of the actual engine compartment of the passenger vehicle. The head section of the exhaust gas sensor module for commercial vehicles consists of the cylindrical rod of Zirconium dioxide as a sensor core with heater and dual stainless cylindrical shrouds with multiple openings or apertures. The shrouds prevent the sensor core from the direct exposure to the high temperature exhaust gas. Since the operation temperature of the sensor rod is significantly high, the penetration of the particulate objects and liquids to the sensor core must be avoided. Therefore, the most of all commercial sensor module employ the apertures with off-axis

alignment of both concentric shrouds. Although the concentration fluctuation of the exhaust gas must be detected by the sensor, which is protected by the concentric shrouds, the primary delay or time lag occurs due to the off-axis alignment of the opening apertures. Moreover, the frequency response of the sensor module decreased due to the aforementioned delay effects. In order to understand the characteristics of the sensor and to improve the overall performance of the gas sensor, the detailed behavior of the fluid flow around the sensor core as well as the flow between protectors must be clarified. Especially, the airflow convection through the multiple opening apertures is the significant factor for the evaluation of the mass transportation between sensor core and external flow of protector.

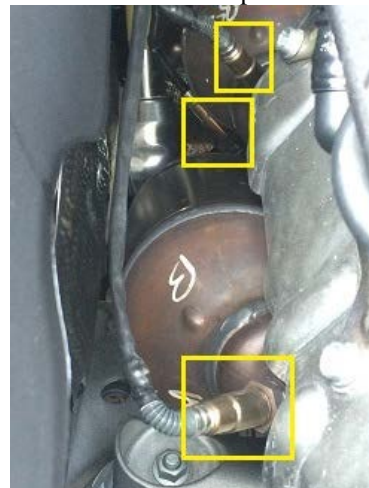


Fig 1 Gas sensors attached to the exhaust system for a passenger vehicle. Three rectangular indicate the sensor module. As the head of the module is plugged into a pipe, neither sensor element nor protecting shroud are visible.

QUANTITATIVE FLOW VISUALIZATION

For the industrial applications, gas or liquid flow around the cylinder or rectangular obstacles is one of the most important flow field. Especially the flow analysis around a finite cylinder is the important external flow; therefore, numerous experimental and numerical investigations were reported that deal with the detailed behavior of the flow around the rectangular or cylindrical objects [6-10]. However, not so many investigations of the flow structure by using the hollow cylinder or cylindrical object with by-pass channels was reported [11,12]. In the present study, we focused on the fluid flow visualization within the gas sensor module for the automobile applications.

Target model

A transparent acrylic model was designed and manufactured by noting the Reynolds number of the actual flow field. Figure 2 shows the photograph of the concentric cylinders used in the experiments. The model was divided into triple concentric cylinders, which consisted of outer protector, inner protector and sensor core rod. In this experiment, the sensor is replaced by the plastic solid cylinder instead of the Zirconium sensor rod with a heater. External diameter of the outer protector, inner protector and the core were 100 mm, 70 mm and 40 mm respectively. As shown in the figure, eight circular apertures were prepared by 45 deg for the inner cylindrical protectors. On the inner protector surface, in-line eight opening aperture were aligned. External protector has dual-line eight apertures as well. On the center-top of the cylinders, the other aperture was prepared. The diameter of each opening aperture was 20 mm.

Flow field measurement by particle image velocimetry

Figure 3 illustrated the experimental set up for the optical flow visualization used in the following experiments. Particle image velocimetry (PIV) [13] was used as a measurement method. PIV is one of the optical flow measurement technique that can measure the two dimensional two component velocity vectors in the fluid flow by means of the thin laser sheet in conjunction with the digital camera. The local velocity vector is determined with the local particle image's displacement between two or more consecutive images of tracer particles in fluid flow. In this study, normalized cross correlation function was employed for the evaluation of the local particle image similarity.

In this study, detailed airflow behavior in the concentric protectors was investigated under the steady flow. The model was installed in a rectangular

transparent channel with honeycomb and electrical fans. Both width and height of the channel were 240 mm, length of the channel was 910 mm. In the present experiments, velocity distribution at the channel entrance was assumed to be homogeneous, mean velocity of the airflow was 0.15 m/s. Continuous-wave Nd:YAG laser was used in conjunction with the high-speed CMOS camera. Output power and wavelength of the laser light source was 2 W and 532 nm respectively. Maximum frame rate of the camera was 800 fps, pixel dimension was 1920x1080 that affected the resultant frame rate due to the bandwidth of the digital connection between camera head and the computer. For the velocity vector map determination, standard recursive cross correlation calculation with the sub-pixel fitting estimation was employed.

Figure 4 is a captured image of the model and tracer particles illuminated with the monochromatic light source. As tracer particles, smoke from an incense stick was used that has the good traceability to the airflow. Mean diameter of the tracer particle was a few μm ,

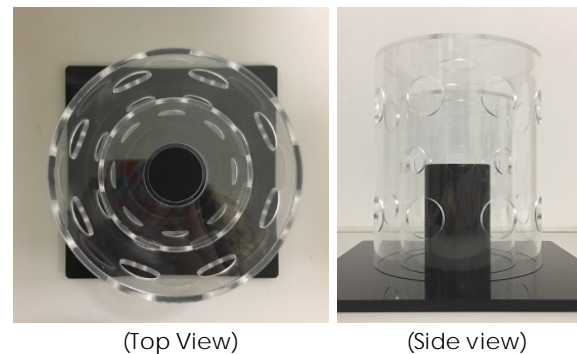


Fig 2 Transparent acrylic model for the flow visualization consisted of outer and inner hollow cylinder (protectors) and inner solid cylinder (sensor rod). Diameters of cylinders were 100, 70 and 40 mm, heights were 123, 98, and 61 mm, respectively. Both protectors have multiple opening apertures.

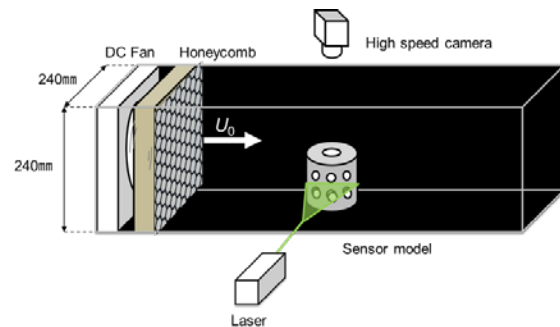


Fig 3 Experimental rig for the flow visualization by means of the particle image velocimetry.

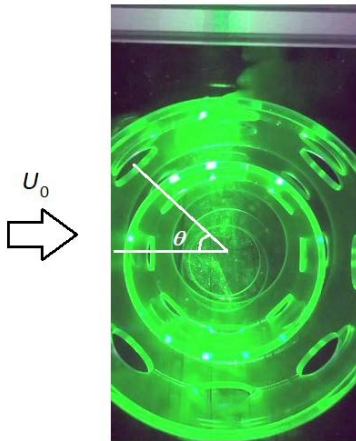


Fig. 4 Snapshot of the captured image. Tracer particles were illuminated with continuous green laser sheet.

RESULTS AND DISCUSSION

Figure 5 shows the calculated instantaneous velocity vector map. From the visualization results of the velocity vector map around the sensor core rod, the magnitude of the velocity around the sensor core was drastically decreased due to the complicated structure in the cavity and the multiple apertures. Figure 5 also shows the comparison of the velocity vector map in the vicinity of the opening aperture at the different instance. Although the external flow was steady and velocity was constant, the fluid behavior within the protector is not steady and the orientation as well as the magnitude of velocities were significantly fluctuated. To clarify the effects of the aperture positions, the location of the opening apertures and the orientation of each protector were varied as a parameter.

The parameter, θ , represents the angle from the direction of upstream, i.e. the main flow is coming from the direction of $\theta = 0$. The angular offset of both outer and inner protectors were varied from (0, 0) deg, (0, 22.5) deg, (22.5, 0) deg and (22.5, 22.5) deg

respectively. By the comparison of the aperture phase differences, the effects of the offset angle of the opening apertures was evaluated. Figure 6 compares the spatially averaged velocity transition through the opening apertures with the angles of (0, 0) deg. Velocity transition under the other three alignment were obtained with the same flow configuration. The negative sign of the normal velocity component was defined as the incoming flux to the sensor core. The positive velocity, in contrast, indicates the outgoing flow to the external main flow. At the upwind aperture, which was located at $\theta = 0$ deg, the flow through the aperture was stable and the magnitude of the cross-sectional mean velocity was -2.0 mm/s approximately. Since the opening aperture is present at the upward stagnation point at $\theta = 0$ deg in which the relative pressure is higher than that of the other apertures, mean inbound flow through the corresponding aperture was observed. In contrast, the fluid velocity through the side aperture at $\theta = 90$ deg was significantly fluctuated. The mean velocity through the side aperture was -6.7 mm/s, therefore the volume flux through the side aperture was 2.1 cm³/s of incoming direction. Comparison of the velocity fluctuations at the different alignment of the protectors of (22.5, 22.5) deg resulted that both mean velocities during the period were 2.5 mm/s and 6.3 mm/s, volume fluxes were 0.79 cm³/s and 2.0 cm³/s respectively. The comparison of the angular alignment of protectors demonstrated that the outgoing flow is occurred even at the upstream aperture.

In order to clarify the aforementioned flow pattern, angular distribution of mean velocity and velocity fluctuation of each aperture position in terms of the offset angles of the protectors were summarized. The comparison of the mean velocity through the apertures demonstrated that the incoming and outgoing flow were appeared at the downward and upward apertures respectively. The velocity distribution indicated that the overall flow direction within the inner protector was inverted to the external

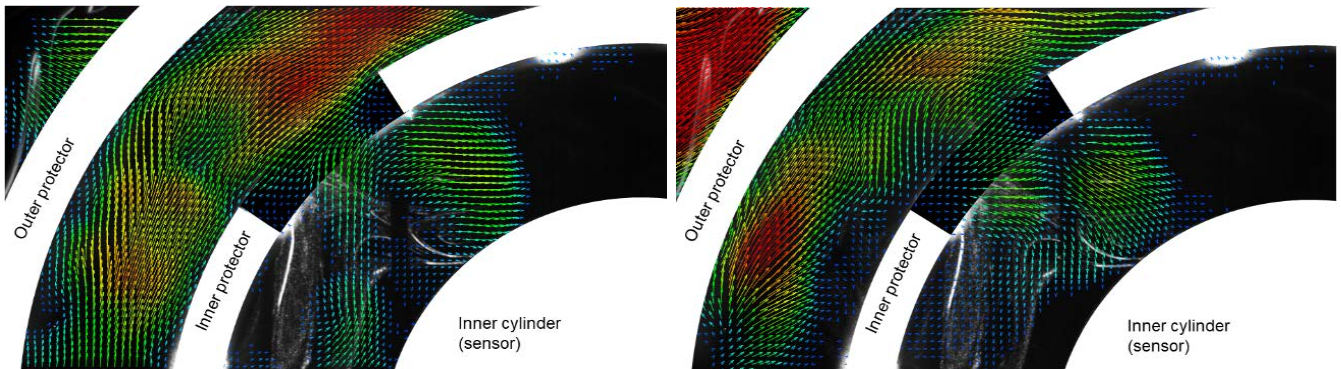


Fig. 5 Examples of the instantaneous velocity vector map near the opening aperture of the inner protector by means of the particle image velocimetry. The color of the arrows corresponds velocity magnitude, i.e., red arrow is the faster velocity magnitude. Both vector maps were obtained under the identical

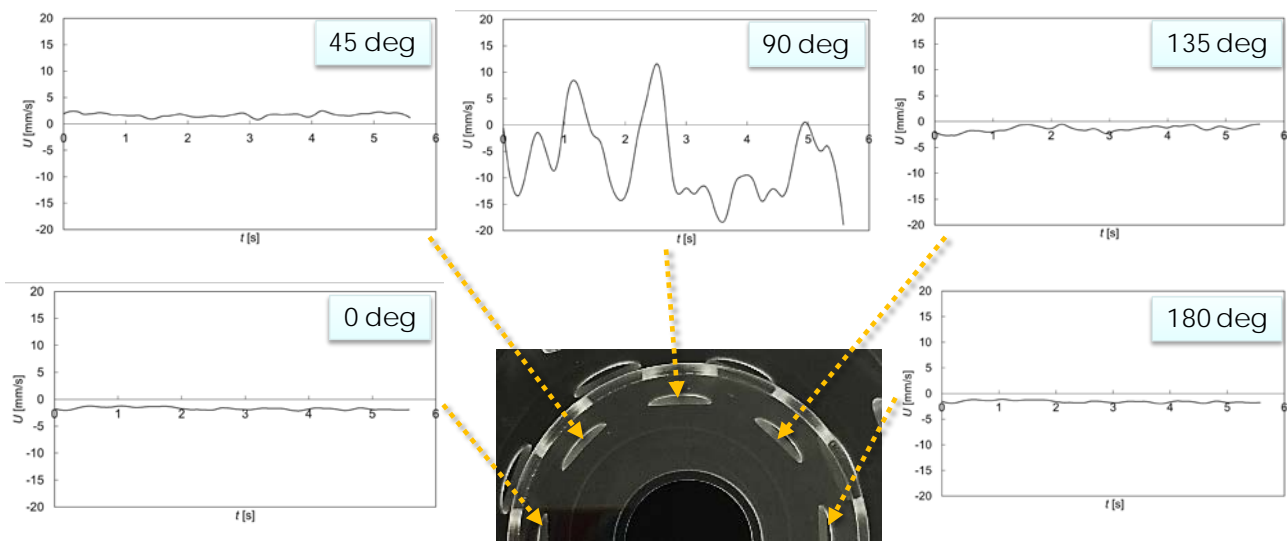


Fig. 6 Mean velocity through the opening apertures in terms of the angle. Each angle value in the figure represents the angular position of the opening apertures under (0, 0) degree alignment of dual protector.

main flow. Consequently, the direction of volume flux through the sensor core is opposed to the external main stream. In contrast to the lower and stable mean velocity distribution around the core rod, the significant velocity fluctuations were observed in the vicinity of the aperture located on the side of the inner protector that enhanced the convective mass transfer.

CONCLUSION

The flow field in the concentric triple cylinders was investigated by means of a particle image velocimetry. The transparent model was designed and used for the optical visualization. The geometrical shape was determined by considering the Re number matching with the actual gas sensor for a passenger vehicle. The quantitative visualization resulted that the flow direction within the inner protector was inverted to the external main flow. The velocity magnitude of the internal flow is significantly lower than that of the main flow. The throughput of the concentration modulation around the sensor could be enhanced by the velocity fluctuation around the side apertures that contribute to the quick response of the entire sensor module.

REFERENCES

- [1] Szabo N, Lee C, Trimboli J, Figueroa O, Ramamoorthy R, Midlam-Mohler S, Soliman A, Verweij H, Dutta P and Akbar S, Ceramic-based chemical sensors, probes and field-tests in automobile engines, *J. Materials Sci.*, Vol. 38, 21, pp. 4239-4245, 2003
- [2] Twigg M V, Progress and future challenges in controlling automotive exhaust gas emissions, *Applied Catalysis B: Environmental*, Vol. 70, pp. 2-15, 2007
- [3] Moos R, Izu N, Rettig F, Reiß S, Shin W and Matsubara I, Resistive Oxygen Gas Sensors for Harsh Environments, *Sensors(Basel)*, Vol. 11, No. 4, pp. 3439-3465, 2011
- [4] Riegel J, Neumann H, Wiedenmann H M. Exhaust gas sensors for automotive emission control, *Solid State Ionics*. Vol.152-153, pp. 783-800, 2002
- [5] Salehi R, Alasti A, Vossoughi G and Boroushaki M, Nonlinear Oxygen Sensor Output Voltage Estimation in a Gasoline Engine Using NARX Model, *The Journal of Engine Research*, Vol. 22, pp.13-20, 2011
- [6] Wang H F and Zhou Y, The finite-length square cylinder near wake, *J. Fld. Mech.*, Vol. 638, pp. 453-490, 2009.
- [7] Pattenden R J, Turnock S R and Zhang X, Measurements of the flow over a low-aspect-ratio cylinder mounted on a ground plane, *Exp. Fld.*, Vol. 39, pp. 10-21, 2005
- [8] Rostamy N, Sumner D, Bergstrom D J and Bugg, J D, Local flow field of a surface-mounted finite circular cylinder, *J. Fld and Structures*, Vol. 34, pp. 105-122, 2012
- [9] Igbalajobi A, McClean J F, Sumner D and Bergstrom D J, The effect of a wake-mounted splitter plate on the flow around a surface-mounted finite-height circular cylinder, *J. Fld.*

- Structures*, 37, pp. 185-200, 2013
- [10] Sumner D, Flow above the free end of a surface-mounted finite-height circular cylinder: A review, *J. Fld. Structures*, 43, pp. 41-63, 2013
- [11] Rinoshika H, Rinoshika A and Fujimoto S, Passive control on flow structure around a wall-mounted low aspect ratio circular cylinder by using an inclined hole, *J. Fld. Sci. and Technol.*, Vol., 12, No. 1, JFST0006, 2017
- [12] Rinoshika H, Rinoshika A and Fujimoto S, Visualization of a finite wall-mounted cylinder wake controlled by a horizontal or inclined hole, *J Visualization*. <https://doi.org/10.1007/s12650-018-0482-6>, 2018
- [13] Adrian R J, Particle-Imaging Techniques for Experimental Fluid Mechanics, *Annu. Rev. Fld Mech.*, Vol. 23, pp. 261-304, 1991

APPLICATION STATIC LOAD TEST (SLT) AND PILE INTEGRITY TESTING (PIT) OF PILES IN SEA PORT “PRORVA” (WEST KAZAKHSTAN)

Askar Zhussupbekov¹, Zhanbolat Shakhmov² and Gulshat Tleulenova³

^{1,2,3}Department of Civil Engineering, L.N. Gumilyov Eurasian National University, Astana, Kazakhstan

ABSTRACT

This working plan has been developed for the production of driving operations of precast concrete piles with section 400x400 mm on the project "Cargo Transportation Route for Facilities of The North-Eastern part of the Caspian Sea. North Caspian Marine Channel with Berthing Facilities". This scope of work provides work on the geodesic broken pile field, leader of drilling and precast reinforced concrete piles with 400x400mm section, 23.0m of length, 25.5m and 27.5m. Total amount of precast concrete piles 1100 pieces (23m of pile length - 714 pieces, 25.5m of length -368 pieces and with 27.5m length in the amount of 18 pieces). Precast concrete piles are composed of two segments: the bottom segment with length of 16.0m and upper segment length: 7.0m, 9.5m and 11.5m. The following documents have been referenced for this method statement: Standard Test Method for Low Strain Impact Integrity Testing of Deep Foundations use ASTM D 5882, Standard Test Methods for Deep Foundations Under Static Axial Compressive Load use ASTM D 1143 in seasonally freezing soil ground. In paper analyze bearing capacity of concrete pile foundations b/5, k/3. In SCLT testing, the test load on the pile is for hold on 2 cycles. Loading and unloading was carried out in the following sequence: 0, 30, 60, 90, 125, 90, 60, 30, 0, 170, 210, 250, 210, 170, 125, 80, 40 and 0% of design. In the first cycle, the experimental pile was loaded to 100% of the design value. In this paper presented results of piles of PIT methods in seasonally freezing soil grounds.

Keywords: pile, load, settlement, standard

INTRODUCTION

Most of the territory of Kazakhstan is characterized by long winter periods. The thickness of frozen soils was determined from the temperature regimes. The temperature regime depends on climate. The depth of freezing of soils varies within 0.5-2.5 meters.

Question the increasing the stability, reliability and durability of structures studied by many researches, both domestic and foreign. Most experiences in these works are considered scientific from USA, Russia, South Korea.

Nevertheless, the problem seasonally freezing soils such as change the mechanical and physical properties of frozen soils are dependent on temperature, a moisture content of a soils and etc., is quite complex and poorly understood, and the present.

The issue of strength, stability and reliability of the designed structures in seasonally freezing soil are not fully described in the standard [3]-[4].

In the problem under consideration to the usual problems of designed pile foundation in seasonally freezing soil (the study of the geotechnical properties, moisture content of soils, temperatures, etc..) authors study the problem of stability, reliability pile foundations in seasonally freezing

soil conditions.

The object of study are research bearing capacity of pile foundation in seasonally freezing soil ground..

The project "Cargo Transportation Route (CaTRo) for Facilities of The North-Eastern part of the Caspian Sea. North Caspian Marine Channel with Berthing Facilities" Seaport “Prorva” is one of important Megaproject for Atyrau region West Kazakhstan [27].

The construction Seaport “Prorva” presented by reinforced concrete structures. Totally construction area is 154980 m². The design life of this project is assigned in accordance with SNiP RK 3.04-01-2008 is 50 years.

SEAPORT “PRORVA” DESCRIPTION

The construction site is dimensions of 205 x 756 m. The site in plan has a rectangular configuration. The site used deep foundations.

This scope of work provides work on the geodesic broken pile field, leader of drilling and precast reinforced concrete piles with 400x400mm section, 23.0m of length, 25.5m and 27.5m. Total slaughter of precast concrete piles 1100 pieces (23m of pile length - 714 pieces, 25.5m of length -368 pieces and with 27.5m length in the amount of 18 pieces). Precast concrete piles are composed of two

segments: the bottom segment with length of 16.0m and upper segment length: 7.0m, 9.5m and 11.5m [5]-[21]. Geotechnical characteristics of soil ground on site “Prorva” [4]-[19].

Table 1 Engineering-geological elements

Soil type	φ	C	E_{oed}	$\gamma_{natural}$	S_u
	deg	kPa	kPa	kN/m ³	kPa
EGE-1 Fill sand	29,4	0.7	2,8	19.4	25
(EGE-2) Silt	29,4	0.7	2,75	19.3	15
(EGE-3) Sand	31,5	2.7	30	19	-
(EGE-7) Clay	24,7	20.8	2	19.1	80
(EGE-8) Sand	31,8	2.4	40	20	-
(EGE-9) Clay	23,8	22.7	4	20.6	150
(EGE-10) Clay	24,7	25	2	20.2	150

E_{oed} – Elastic unloading/reloading [kPa];

S_u – undrained shear strength [kPa].

Table 1 illustrated physical and mechanical properties of soil ground in construction site “Prorva” [4]-[26].

METHODS OF PILE FIELD TESTS

The following documents have been referenced for this method statement: Standard Test Method for Low Strain Impact Integrity Testing of Deep Foundations use ASTM D 5882, Standard Test Methods for Deep Foundations Under Static Axial Compressive Load use ASTM D 1143 in seasonally freezing soil ground [1]-[20].

Method pile integrity testing (PIT)

At the construction site Seaport “Prorva” was carried out the integrity test (PIT) precast concrete pile foundations from January to May 2017.

The purpose of the test is to check pile integrity. Following works had been done:

- Complex of low – strain dynamic testing of the piles;
- Proceeding and analyze results.

Integrity tests were performed by Pile Integrity Tester (PIT) with Serial Number - SN #3557C.

Totally 161 precast concrete pile were tested at this construction site.

Precast concrete pile with square cross section 400 x 400 mm were driving by piling rigs: Junttan PM25HD with hydraulic hammer HHK7/9A and Junttan PM25 HD with hydraulic hammer HHK9A [5]-[25].

Each test pile consist of two pile sections with length: first section – 16 m and second section 11.5 m. Due to the fact that concrete pile is composed of two sections which are connected with metal joint, conduction integrity tests possible only for the second (top) section. Heads of piles were cleaned from soil and suitable for testing. Three graph reflectograms from three blows for each pile were accepted for further processing [2]-[24].

Fig. 1 presented procedure PIT of pile foundations in construction site “Prorva”.

The acceleration signal is converted into velocity and is represented on screen by the time function. All results are easily saved into the computer to be used in the processing. The time span between the stroke and rebound is characteristic of the location and its mechanical parameters: $T = 2L/C$ (T - stroke-return time, L – pile length, C - wave propagation velocity ($c = \sqrt{E\rho}$), E – the Jung modulus of concrete, ρ – density of concrete) [2]-[25].



Fig.1 Procedure pile foundations of PIT on construction site “Prorva”.

The average velocity of wave distribution in the concrete class B20÷25 – 3800 m/s.

The accuracy of determining the length of the pile depends on the accuracy of the stress wave velocity. When the pile length is known, the wave propagation velocity can be matched to the known length.

Pile: D2 – number of pile;

WS: 3900 m/c – velocity of wave distribution in the concrete;

LE = 11,50 m – tested length of pile.

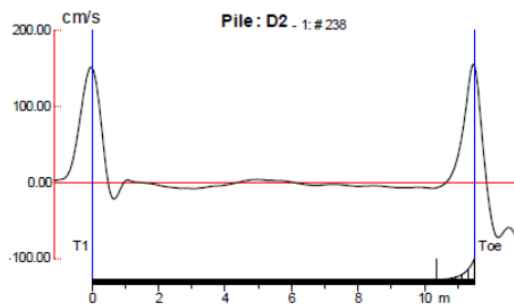


Fig. 2 Graph of velocity and length of D/2 pile.

Fig. 2 presented graphs of PIT on construction site “Prorva”.

RESULTS AND DISCUSSION

Results of Static Load Test (SLT)

The vertical load test shall be carry out to the GOST 5686-94 “Soils. Field test methods by piles” and with WBC134-3.SP.001.009 “Specification with precast concrete piles”[1]-[25].

Static vertical loading test should be carry out below sequences:

- Pile testing begin not earlier than 6 day after pile driving;
- The vertical load creating with hydraulic jack DG500G250 capacity 500 tons (for preliminary pile) and with hydraulic jack CLRG-2506 capacity 250 tons (Proof pile);
- Load increment carried out proportional stages (steps).
- In SCLT testing, the test load on the pile is for hold on 2 cycles. Loading and unloading was carried out in the following sequence: 0, 30, 60, 90, 125, 90, 60, 30, 0, 170, 210, 250, 210, 170, 125, 80, 40 and 0% of design.

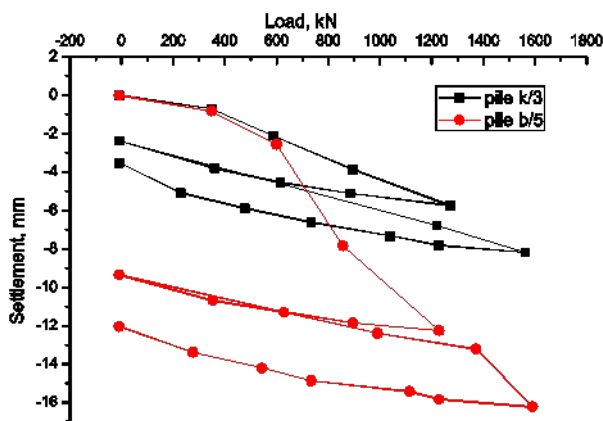


Fig. 3 Load-settlement diagrams k/3, b/5 piles.

– In the first cycle, the experimental pile was loaded to 100% of the design value. Following each application of an increment of load shall be held for not less than the period or until the rate of settlement is less than 0.25 mm/h and slowing down. The rate of settlement shall be calculated from the slope of the curve obtained by plotting values of settlement versus time and drawing a smooth curve through the points [1]-[27].

Fig. 3 presented results graph of load-settlement diagrams of piles k/3, b/5.

In Kazakhstan, a safety factor of SLT is 1.2.

According to SLT result of piles k/3, b/5 the load-settlement diagrams were illustrated in Fig. 3.

Bearing capacity of pile foundations k/3, b/5 is 1639 kN.

CONCLUSION

According to the result of the SLT tests it can be concluded.

Based on results of pile integrity testing (PIT) is included at least 3 blows for each pile and proceeding on special program of PIT-W.

Totally 161 precast concrete pile were tested on construction site seaport “Prorva”. All of the tested piles do not have defects of integrity during seasonally freezing soil ground.

Cracks and deformation in body of pile foundation D/2 are not unascertained (Fig. 2).

According to the graphs (Fig. 3), analyze to the results of SLT of driving concrete piles (40×40 cm length 27.5 m) the bearing capacity of the pile b/5 is 1639 kN, max settlement 16 cm.

REFERENCES

- [1] Standard Test Methods for Deep Foundations Under Static Axial Compressive Load D 1143-07, ASTM, 2007.
- [2] Standard Test Method for Low Strain Impact Integrity Testing of Deep Foundations use ASTM D 5882. ASTM, 2007.
- [3] MSP 5/10-101-2003-Design and installation of pile foundation, 2003, pp. 2-5.
- [4] GOST 5686-94 Soils. Field test methods by piles. M. Standard Publishing House, pp. 10-17.
- [5] WBC134-3.SP.001.009 “Specification with precast concrete piles”, Aktau.
- [6] Zhussupbekov A., Omarov A., Moldazhanova A., Tulebekova A., Borgekova K. and Tleulenova G., Investigations of the interaction of joint piles with problematical soil ground in Kazakhstan. Proc. of 7th Int. Conf. on GEOMATE, 2017, pp. 383-388.
- [7] Das Braja M., Principles of Foundation Engineering. 2nd PWS Publishing Company, 1984, pp. 360-380.
- [8] Das Braja M., Soil Mechanics Laboratory

- Manual, 2nd Ed., Department of Civil Engineering. The University of Texas at El Paso. Engineering Press, pp. 41-59.
- [9] Geotechnical Interpretation Report, WBCAS 134-3.TN.028.F01, Cargo Aktau, 2014.
- [10] GOST 5686-94. Methods for field testing by piles. Gersevanov Research Institute of Bases and Underground Structures (NIIOSP), Const. Build., 1994, pp. 25-47.
- [11] GOST 19912-2001. Soils. Field test methods by static and dynamic sounding. Gersevanov Research Institute of Bases and Underground Structures (NIIOSP), Const. Build., 2001, pp. 17-25.
- [12] GOST 25358-2012. Soils. Field temperature determination method, Const. Build., 2013, pp. 3-10.
- [13] Karlov V.D., Soil-based and Foundations on season freezing and swelling soil ground, Const. Build., 2007, pp. 135-170.
- [14] Nevzorov A.L., Foundations on seasonally frozen ground, Const. Build., 2000, pp. 30-46.
- [15] Phukan Arvind, 1991, Foundations in cold regions. Van Nostrand Reinhold, Const. Build., pp. 735-749.
- [16] Shakhmov Zh., Influence of the freezing to soil ground of foundation, PhD Thesis, 2013, pp. 114-127.
- [17] Shakhmov Zh., Assessment of the degree frost heaving soil ground by different methods, Int. Scient. Conf. of Young Scientists, 2014, pp. 4436-4443.
- [18] SNiP RK 5.01-01-2002, "Soil basement and foundations", Const. Build., 2002, pp. 15-32.
- [19] SNiP RK 5.01-03-2002. Pile foundations, Committee for Construction of the Ministry of Industry and Trade of RK, 2002, pp. 25-84.
- [20] Tsytoovich N., Mechanics of Frozen soil ground, Const. Build., 1973, pp. 125-148.
- [21] Zhussupbekov A. Zh., Omarov A., Yergen A., Borgekova K. and Tleuenova G., Piling Designing, Installation and Testing on Problematical Soil Ground of Kazakhstan. Proc. of the 50th Anniv. Symp. of the Southeast Asian Geotech. Society, 2017, pp. 77-80.
- [22] Zhussupbekov A., Shakhmov Zh. and Tleulenova G., Geotechnical problems on freezing ground soil and experimental investigations in Kazakhstan. Science in cold and arid regions. Vol. 9, Issue 3, 2017, pp. 331-334.
- [23] Zhussupbekov A., Shakhmov Zh., Lukpanov R., Tleulenova G. and Kudryavtsev S. Frost depth monitoring of pavement and evaluation of frost susceptibility at soil ground of Kazakhstan. ICSMGE 2017-19th Int. Conf. on Soil Mech. and Geo. Eng., 2017, pp. 1455-1458.
- [24] Zhussupbekov A., Shin E. Ch., Shakhmov Zh., Tleulenova G., Estimation of the bearing capacity of pile foundations in seasonally freezing soil ground. Proc. of the 2nd Geo-Institute-Kazakhstan Geotechnical. Society Joint Workshop, Const. Build., 2018, pp. 65-68.
- [25] Shin E., Zhussupbekov A., Tleulenova G., Shakhmov Zh. Application of Static Load Tests of Model Piles in Seasonally Freezing Soils in Kazakhstan. The 7th Techn. Conf. in Eastern Asia on Geo-Natural Disasters, 2018, pp. 53-54.
- [26] Zhussupbekov A., Shin E., Shakhmov Zh., Tleulenova G., Estimation of bearing capacity of model pile foundations in seasonally freezing soil ground. Soil of Mechanics in Geotechnics. Proc. of Int. Conf., 2018, pp. 83-94.
- [27] Report PIT on construction site Seaport "Prorva", 2017, pp. 2-20.

DAMAGE DETECTION OF TRUSS STRUCTURES BY APPLYING MACHINE LEARNING ALGORITHMS

Koji Unno¹, Atsushi Mikami² and Masaki Shimizu³

^{1,3}Graduate Student, Tokai University, Japan; ²Professor, Tokai University

ABSTRACT

For the damage detection of truss structures, this study assumes to utilize vibration signals obtained from sensors installed into the bridges. By preparing damaged and non-damaged bridge structures, large quantities of response data are generated. AR (Auto Regressive) model is then applied to the time signals to extract structure's soundness characteristics. Here, AR coefficients are values in which damaged structural characteristics are reflected. Then, machine learning technique is applied to the AR coefficients to classify the structures into damaged and non-damaged ones. Results showed that the machine learning method successfully detected the damage of truss members. This kind of SHM (Structural Health Monitoring) technology is expected to contribute to early damage detection and preventive maintenance of bridges.

Keywords: Damage detection, Machine learning, AR model, Decision tree

INTRODUCTION

In Japan, infrastructures including bridges constructed in the period of high economic growth are getting older. Ministry of Land, Infrastructure and Transport and Tourism (MLIT) requires bridge administrators to make short range visual observation of bridges more than once in every 5 years. Aged bridges tend to need more maintenance which requires costs and human labors. However, maintenance engineers are insufficient in number compared with the numbers of bridges. One solution to resolve the problem is to use sensors and signal processing techniques to detect damaged members and their damage level of the structures.

Our research group is tackling the damage detection problem of aged structures on the assumption of using sensor data.

Shimizu [1] conducted eigenvalue analysis to fully utilize the sensor data, aiming to find optimum sensor arrangement.

This study assumes to utilize vibration signals obtained from sensors installed into the bridges. Machine learning algorithm is applied to the sensor data to detect damage. By preparing damaged and non-damaged bridge structure models, large quantities of response data are generated giving random input motion at the base. AR model is then applied to the time signals to extract structure's characteristics. Here, AR coefficients are values in which damaged structural characteristics are reflected. Then, the decision tree technique is applied to the AR coefficients to classify those structures into damaged and non-damaged ones. This kind of SHM (Structural Health Monitoring) technology is expected to contribute to early damage detection and preventive maintenance of bridges [2].

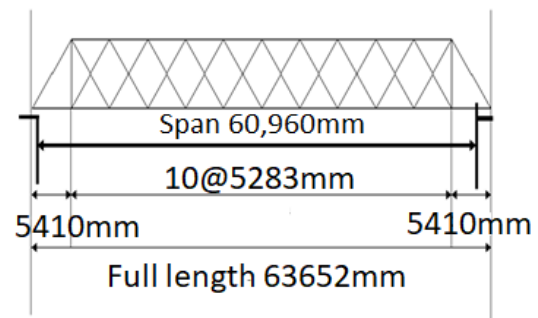


Fig. 1 Hayakawa Bridge (Hakone Tozan Railway)

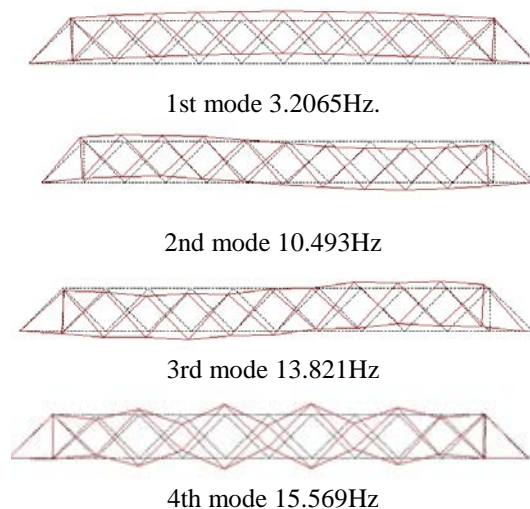
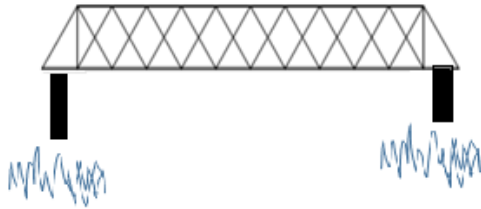


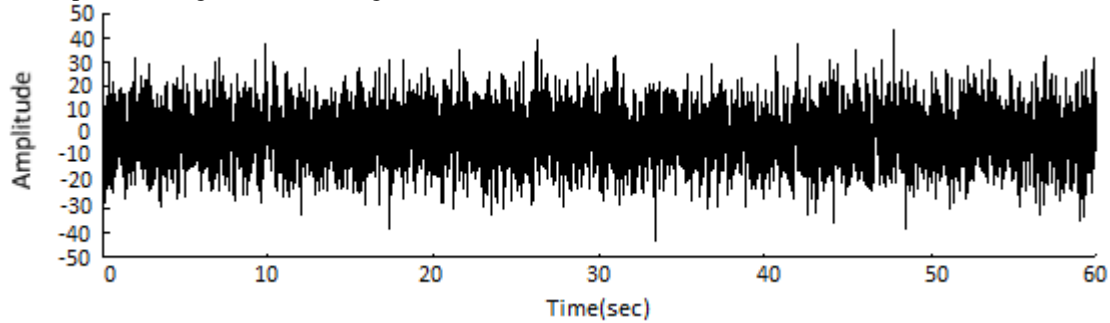
Fig. 2 The 1st to 4th mode of natural vibration [1]

Table 1 Parameters prescribing the Hayakawa Bridge truss members

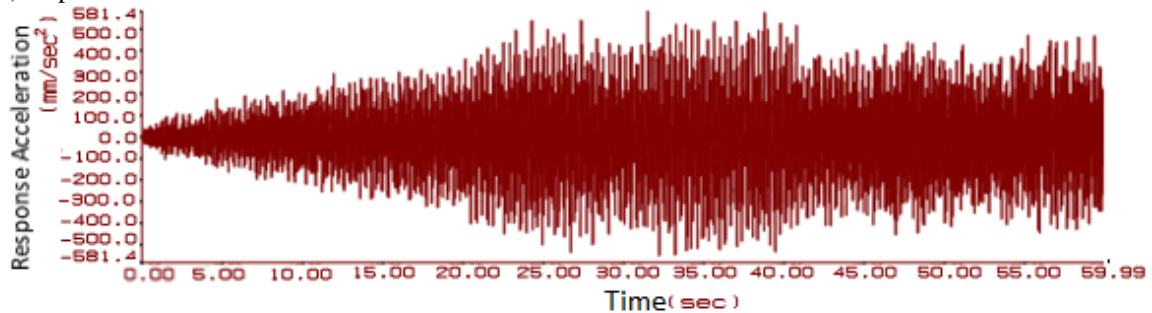
Parameter	Breadth	Height	Sectional area	Poisson's ratio	Elastic modulus
Unit	400mm	500mm	20000mm ²	0.3	206GPa



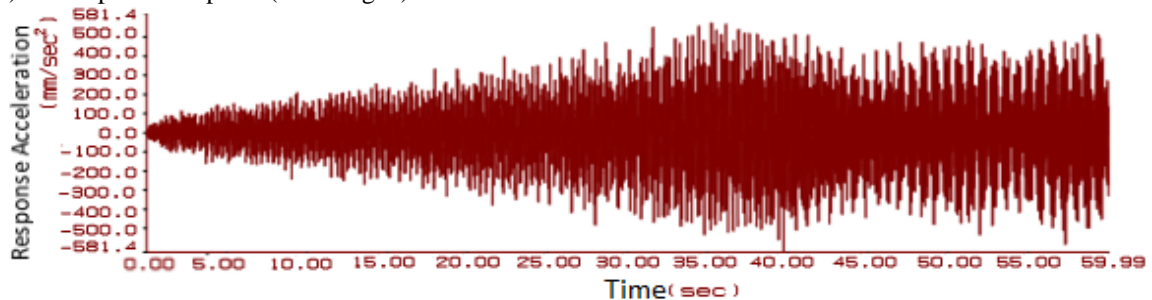
(a) Input motion given to the bridge



(b) Input motion



(c) Example of Response(undamaged)



(d) Example of Response(damaged)

Fig. 3 Input motion and Response

TRUSS BRIDGE TO BE ANALYZED

The bridge structure we picked up in this study is Hayakawa bridge administrated by Hakone Tozan Railway Co. Ltd. shown in Fig.1. It is a double Warren truss bridge which length is approximately 63

meters, constructed in 1888. The truss bridge is typical aged railway bridge in Japan. Wrought iron was used for the material [3].

MODELING AND ANALYSIS

To model the structure, finite element method is

used. The model was analyzed by two-dimensional finite element method using the software, TDAPIII [4]. For the damage detection of structures, this study assumes to utilize vibration signals obtained from sensors installed into the bridges. By preparing damaged and non-damaged truss bridges, large quantities of response data are generated. Machine learning algorithms is then applied. This study referred MATLAB Web seminar for the application of machine learning algorithms [5], [6].

DYNAMIC ANALYSIS OF THE TRUSS STRUCTURE

Parameters that prescribe the Hayakawa bridge model are shown in Table 1. Fig.2 shows 1st to 4th mode of the truss structure. 1st mode frequency is 3.2065Hz. 2nd mode frequency is 10.493Hz. 3rd mode frequency is 13.82Hz. 4th mode frequency is 15.569Hz. Stationary random input motion is given to the base of the prepared structures as shown in Fig.3 (a), (b). The duration time is 60 second and time increment is 0.01 second, hence the input motion is consisting of 6000 data. Acceleration responses from bottom chord member were calculated and accumulated in the database. Both damaged and non-damaged structures were prepared, ranging the damage level from 10% to 90% of the reduction of elastic modulus. Examples of the responses for damaged and non-damaged structures are shown in Fig.3(c), (d), respectively.

AUTOREGRESSIVE MODEL

Autoregressive model (AR model) is then applied to the accumulated signals in this study. As shown in Eq (1), the model, depending on its own previous values, regresses a value from the time signals. The order of the AR model was set as 10th.

$$X_n = a_0 + \sum_{i=1}^N a_i X_{n-i} + \varepsilon_t \quad (1)$$

a_0 is constant term. a_i is parameter of model. ε_t is white noise. The responses include both from damaged and non-damaged truss structures. AR coefficients were then calculated for both damaged and non-damaged structures, then the coefficients were saved for the machine learning process.

PREPARATION OF DATA FOR THE MACHINE LEARNING

As an input wave, the portions regarded as stationary were extracted and used. As shown in Fig.4, a total of 4000 data points out of 6000 data points were extracted, and they are divided into 40 sections. Aforementioned AR model was then applied to the data that includes both damaged and non-damaged cases. Then, AR coefficients were

determined.

Fig.5 shows the AR coefficients by taking the order of the coefficients (up to 10th mode) on the horizontal axis. It seems that we may be able to find the difference between damaged and non-damaged cases by taking the AR coefficients as feature quantities. Fig.6 shows the contributions of each mode of AR coefficients. As the order of the modes becomes higher, the contributions drastically decrease. Hence, this study focused on the only the first and the second mode. Those determined AR coefficients include non-significant coefficients, hence, dimension reduction technique (PCA: Principal Component Analysis) is utilized here.

Fig.7 represents the results of principal component analysis (PCA) by looking at the first and the second components. Clearly, we can divide the data plots into two groups, therefore, the method is capable of discriminating damaged cases from non-damaged ones. It is of importance for the efficient computation to conduct data compression as machine learning tend to use enormous data. The dimension of the data was reduced from 10 to 2 by PCA in this study as shown in Fig.8. The total data is classified

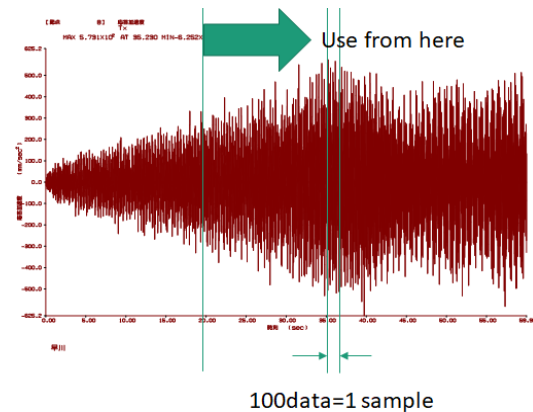


Fig. 4 Example of inputs for an Autoregressive Model

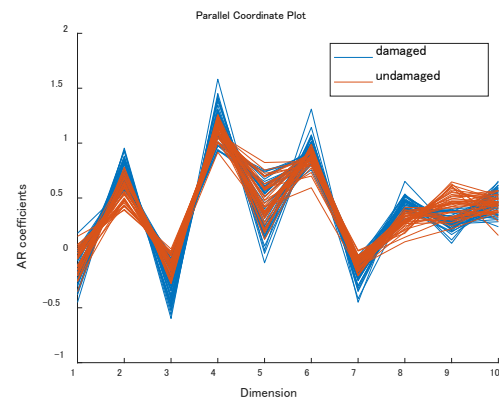


Fig. 5 Parallel coordinate plot

into two groups: data to be studied by the machine learning algorithms and data to test the performance of the machine learning algorithm.

MACHINE LEARNING

To discriminate damaged structures from non-damaged cases, machine learning algorithm is utilized. As a simple method to achieve the purpose, the decision tree method is applied to the data shown in Fig.8.

The series of analytical procedure including AR, PCA, etc., leading to the machine learning is commonly used procedures (e.g., [7]).

RESULTS

Detection of damage considering only damage to one member

Shimizu [1] paid attention to the variation of natural frequency of the entire structure due to the deterioration of a member. However, natural frequencies are not always sensitive to the damage considered [1], [8]. Hence, this study attempts to perform a different method, i.e., machine learning. Fig.9 shows an example of result by the decision tree method. The numbers are threshold determined by

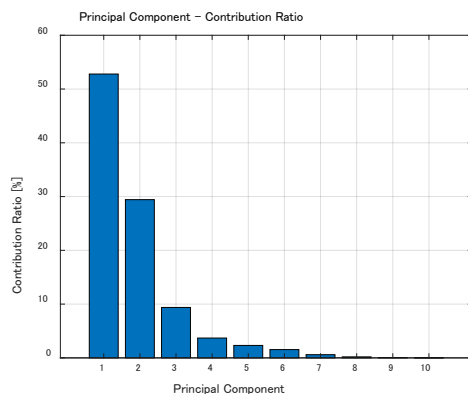


Fig. 6 Contribution rate

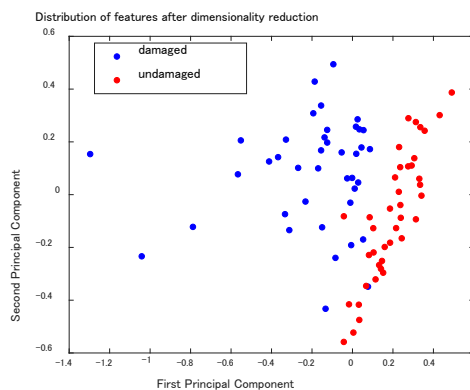


Fig. 7 Dimensionality Reduction

the algorithm. Based on the threshold number, calculated responses are classified into damaged and non-damaged structures.

Table 2-4 shows results obtained by applying the decision tree for upper chord, diagonal and bottom chord members, respectively. Here, Table 3 is the result corresponding to Fig.9. Fig.10 (a)-(c) shows the results of the relation between the first and the second principle components for upper chord, diagonal and bottom members, respectively. Blue dots stand for damaged cases and red dots non-damaged cases. It seems that we can distinguish the damaged structures from non-damaged structures from these figures by setting threshold values properly. The applied decision tree method automatically determines the threshold values.

	1 Features	2 State	3 Cond
1	0.2827	0.2021	1
2	0.3845	-0.0648	1
3	0.4075	0.0420	1
4	0.2861	0.5420	1
5	0.3635	0.1362	1

	1 Features	2 State	3 Cond
71	0.0487	-0.1822	8
72	0.0730	-0.1624	8
73	-0.1588	0.0171	8
74	-0.1823	0.1712	8
75	-0.2459	0.0806	8
76	-0.2923	0.0784	8
77	-0.1227	0.1224	8
78	-0.4356	0.1485	8
79	-0.0638	0.3259	8
80	-0.1890	0.2231	8
81			

Fig. 8 An example of calculated AR coefficients

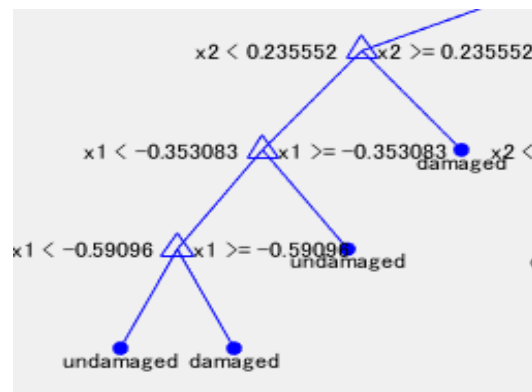
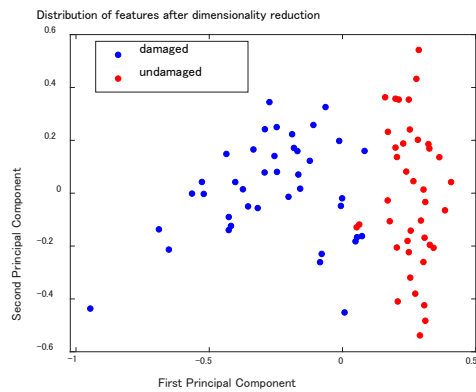
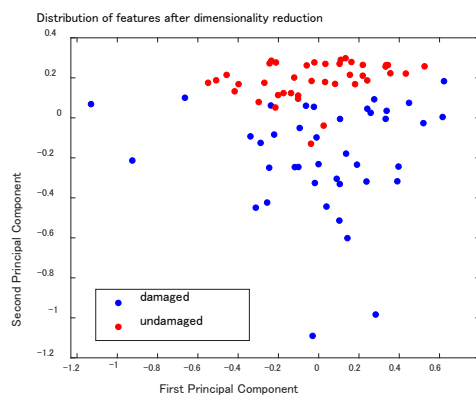


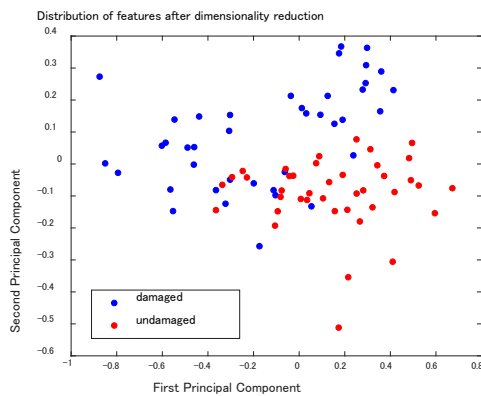
Fig. 9 Decision Tree



(a) Upper chord member



(b) Diagonal member



(c) Bottom chord member

Fig. 10 Result of Detection of damage considering only damage to one member

Table.2 Upper chord member

Items	Estimate_ damaged	Estimate_ undamaged
damaged	19	0
undamaged	0	21

Table.3 Diagonal member

Items	Estimate_ damaged	Estimate_ undamaged
damaged	20	2
undamaged	2	16

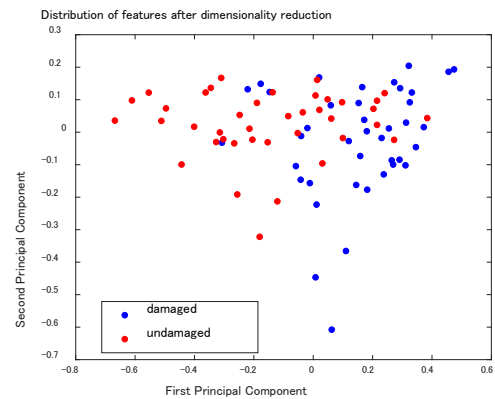
Table.4 Bottom chord member

Items	Estimate_ damaged	Estimate_ undamaged
damaged	20	2
undamaged	2	16

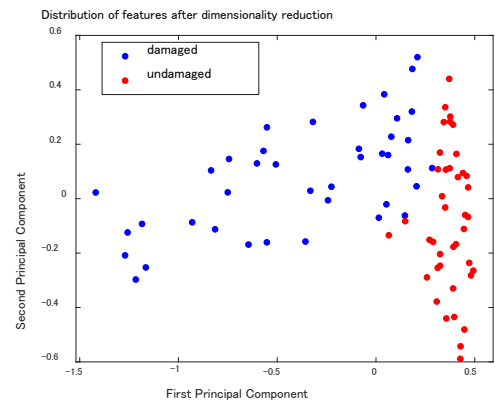
Principal component analysis of degree of damage when specified on an upper chord member

Fig.11(a)-(c) show the results of principal component analysis when degree of damage for an upper chord member changed. Based on these damage, results were obtained as shown in Table 5-7.

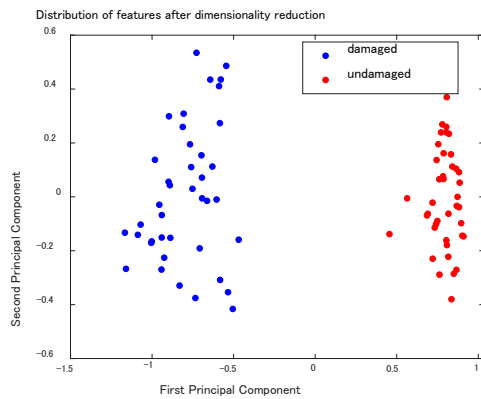
Damage classification becomes difficult when damage level decreases.



(a) 10% damage



(b) 50% damage



(c) 90% damage

Fig. 11 Principal component analysis of degree of damage when specified on an upper chord member

Table.5 10% damage

Items	Estimate_ damaged	Estimate_ undamaged
Damaged	16	4
Undamaged	8	12

Table.6 50% damage

Items	Estimate_ damaged	Estimate_ undamaged
Damaged	21	0
Undamaged	0	19

Table.7 90% damage

Items	Estimate_ damaged	Estimate_ undamaged
damaged	24	0
undamaged	0	16

CONCLUSIONS

For the damage detection of truss structures, this study assumed to utilize vibration signals obtained from sensors installed into the bridges. By preparing damaged and non-damaged bridge structures, large quantities of response data were generated. AR model was then applied to the time signals to extract structure's soundness characteristics. Here, AR coefficients are values in which damaged structural characteristics are reflected. Then, as a machine

learning technique, decision tree method was applied to the AR coefficients to classify the structures into damaged and non-damaged ones. Results showed that the decision tree method successfully detected the damage of truss members. This method is expected to contribute to automatically find deterioration of a member for aged truss structures with less costs and labors. To increase the accuracy of the damage detection is a future task.

ACKNOWLEDGMENTS

This study used TDAPIII developed by Ark Information System.

REFERENCES

- [1] Shimizu, M., Mikami, A. and Unno, K., Damage Detection of Truss Structures Based on Vibration Characteristics, 4th International Conference on Science, Engineering and Environment (SEE), 2018, (under review).
- [2] MLIT, White Paper on Land Infrastructure, Transport and Tourism in Japan, 2014.
- [3] Sekino, M., Hakone Tozan Line Hayakawa Bridge, Bridge and Foundation Engineering, Truss Bridge Feature, Kensetsutosho, Vol. 27, No. 8, 1993, p. 167 (in Japanese).
- [4] Ark Information Systems, INC., Users' Manual, 2017 (in Japanese).
- [5] MathWorks, Sensor data analysis and machine learning - Error detection from vibration data - web seminar, 2015 (in Japanese), <https://jp.mathworks.com/videos/sensor-data-analysis-and-machine-learning-anomaly-detection-using-vibration-data-100241.html> (accessed on 2018-05-20).
- [6] Figueiredo, E., Park, G., Figueiras, J., Farrar, C. and Worden, K., Structural Health Monitoring Algorithm Comparisons Using Standard Data Sets, Los Alamos National Laboratory Report: LA-14393, 2009.
- [7] Goi, Y. and Kim, C-W., Damage Detection of a Truss Bridge Utilizing a Damage Indicator from Multivariate Autoregressive Model, Journal of Civil Structural Health Monitoring, 7(12), 2017, doi:10.1007/s13349-017-0222-y.
- [8] Yoshioka, T., Harada, M., Yamaguchi, H. and Itou, S., A Study on the Vibration Characteristics Change of the Steel Truss Bridge by the Real Damage of Diagonal Member, Journal of Structural Engineering, Vol.54A, 2008, pp. 199-208 (in Japanese).

DAMAGE DETECTION OF TRUSS STRUCTURES BASED ON VIBRATION CHARACTERISTICS

Masaki Shimizu¹, Atsushi Mikami² and Koji Unno³

^{1,3}Graduate Students, Tokai University Japan, ²Professor, Tokai University

ABSTRACT

This study assumes to utilize vibration signals for the damage detection of the bridges. In the vibration-based method, one key factor is natural frequency characteristics (natural frequency and natural vibration mode) of the structure. Hence, representing the deterioration of the structural member by the reduction of the elastic modulus, eigenvalue analysis is conducted to find out the basic idea that which member among many members is more sensitive to its natural frequency and natural vibration mode of the truss structures. Results show that structural damage of upper and lower chord near the center of the structure is more influential for the first mode natural frequency while damage to members near the vibration nodes are insensitive to natural frequencies for higher modes. The knowledge obtained from this study is expected to contribute to the damage detection of structures using sensor data, i.e., to determine sensor locations.

Keywords: Damage detection, Truss bridge, Natural frequency, Vibration mode

INTRODUCTION

In Japan, infrastructures including bridges constructed in the period of high economic growth are getting older. Ministry of Land, Infrastructure and Transport and Tourism (MLIT) requires bridge administrators to make short range visual observation of bridges more than once in 5 years. Although aged bridges need maintenance, which requires costs and human labors, the problem of lack of engineers may prevent aged bridges from sufficient maintenance [1].

One solution is to utilize sensors to identify the location and degree of damage. Referring some researches related to vibration monitoring, deterioration in rigidity due to damage may lead to changes in the natural frequency of the truss. For example, Yoshioka [2] studied how the vibration characteristics of the steel truss bridge changed by the damage to the member and showed that the modal characteristics for in-plane direction was changed by the partial damage to the diagonal member.

This study assumes to utilize vibration signals for the damage detection of the truss bridges. In the vibration-based method, one key factor is natural vibration characteristics (natural frequency and natural vibration mode) of the structure. Hence, representing the damage of the structure by the reduction of the elastic modulus, eigenvalue analysis is conducted to find out the idea that which member is more sensitive to its natural frequency and natural vibration mode of the truss structures that comprise many members. The knowledge obtained from this study is expected to contribute to the damage detection of structures using sensor data, i.e., to determine optimum sensor locations

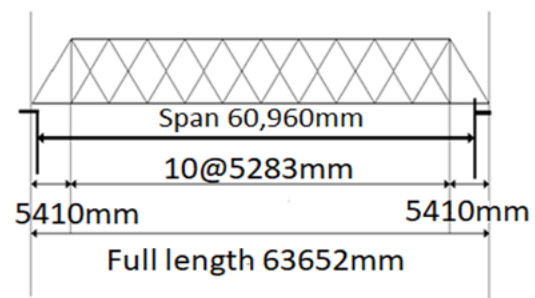


Fig. 1 Hayakawa bridge side view

TRUSS BRIDGE TO BE ANALYZED

The structure to be studied is named Hayakawa bridge of Hakone Tozan Railway. Fig.1 is Hayakawa bridge side view [3]. It is a double Warren truss bridge, which is approximately 63 meters in length, was constructed in 1888. The reason why this bridge was picked up is that this truss structure is a typical aged railway bridge in Japan. Wrought iron was used for the material.

MODELING AND EIGENVALUE ANALYSIS

This study paid attention to the change in the vibration characteristics when a member of the truss structure is assumed to be damaged.

A structural analysis software TDAPIII [4] was used in this study. Based on the Hayakawa bridge, truss model was created by two dimensional finite

Table 1 Parameter used for the analysis

Parameter	Breadth	Height	Sectional area	Poisson's ratio	Elastic modulus	Mass density
Unit	500mm	500mm	20000mm ²	0.3	206GPa	7.8×10^{-3}

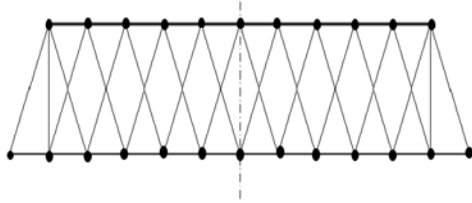


Fig. 2 Finite element model of Hayakawa bridge

elements. The finite element model of Hayakawa bridge is shown in Fig.2. The parameters used for the analysis are shown Table 1. Truss members are treated as 46 truss element and 24 nodes. Eigenvalue analysis was carried out considering up to 4th vibration mode.

RESULTS

Fundamental Vibration Characteristics

Natural vibration modes along with natural vibration frequencies of the truss bridge are shown for first to fourth mode in Fig.3. In the second and third order modes, nodes of vibration are seen near the center of the truss. In general, as higher modes are susceptible to noise, this study focuses on the first vibration mode.

Effect of the Damage to one Member on the Natural Frequency

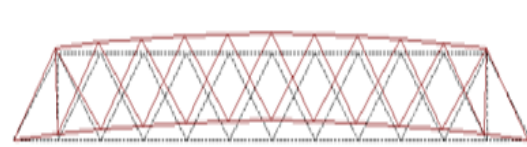
Eigenvalue analysis is performed when the elastic modulus of a member from upper chord/ diagonal/ lower chord is assumed to be changed. The degree of reduction of the elastic modulus is assumed to be 50%.

Upper chord

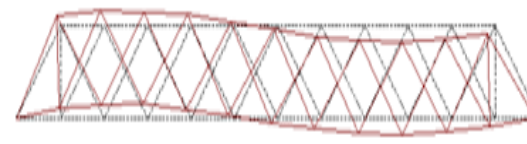
Fig.4 shows the decrease rate of the natural frequency depending on the member location. The vertical axis shows the ratio of reduction of natural frequency to its natural frequency of non-damaged structure. It seems that the central member has the biggest effect on the decrease of the natural frequency.

Diagonal member

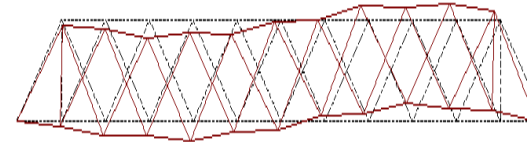
Fig.5 shows the decrease rate of the natural frequency of the truss bridge. The end member has the most significant effect on the decrease of the natural frequency while other members have similar minor effect. Near the center of the diagonal



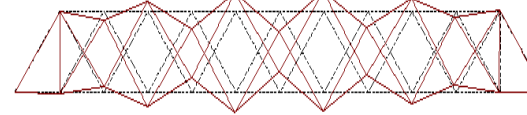
First mode 3.2065Hz.



Second mode 10.493Hz



Third mode 13.821Hz



Fourth mode 15.569Hz

Fig. 3 The first to fourth natural vibration modes

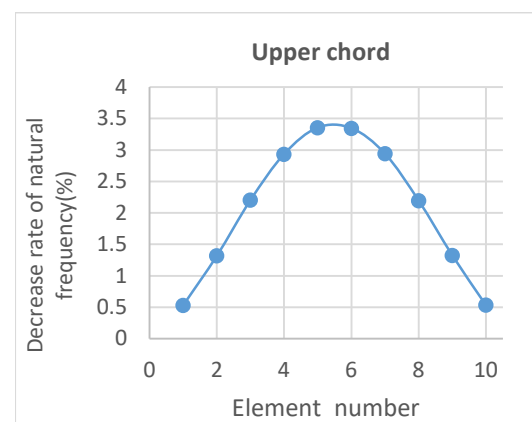


Fig. 4 Member position and decrease rate of natural frequency

members, the effect becomes almost zero, which means that damage to the central member does not affect the natural frequency.

Lower chord

Fig.6 shows the decrease rate of the natural frequency. As similar to the upper chord case, the central member has the most significant effect on the natural frequency.

From these results, the position of the truss member that is the most influential is shown red in Fig.7.

Analogy by Static Loading

The deformation shape of the 1st mode of the truss structure is analogous to the static deflection when lower chord is subjected to vertical loadings as shown in Fig.8. Hence, axial member forces are calculated when lower chord is subjected to vertical loadings.

The obtained deformation shape is shown in Fig.9. We can confirm that this shape is similar to the 1st vibration mode shape.

Axial forces were shown in shown in Fig.10 for upper and lower chord members, and Fig.11 for diagonal members. It was found that the induced axial forces became most severe at the members same as those were most influential to the natural frequency

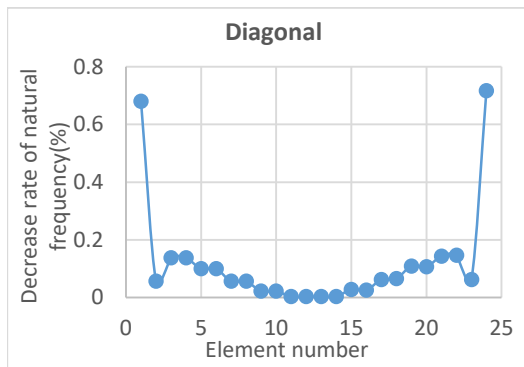


Fig. 5 Member position and decrease of natural frequency

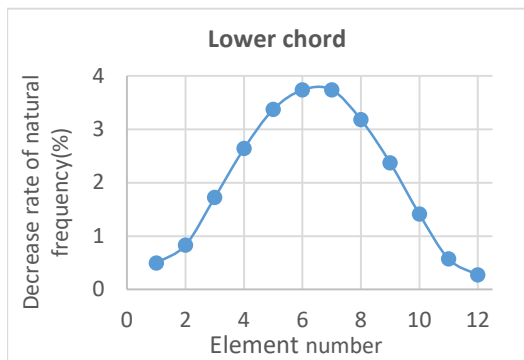


Fig. 6 Member position and decrease of natural frequency

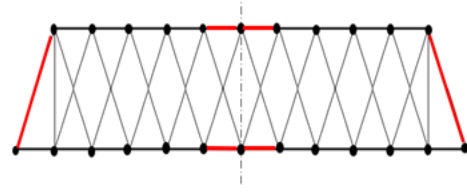


Fig. 7 The members most influential to the natural frequency of the structure

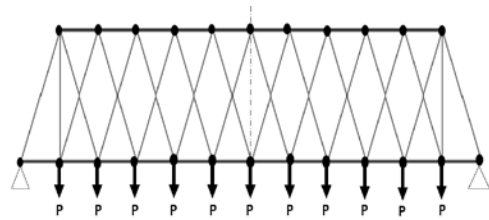


Fig. 8 The deformation shape of the truss when subjected to vertical loads

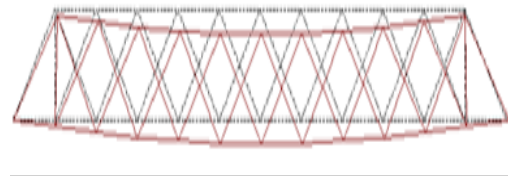


Fig.9 The deformation shape of the truss when subjected to vertical loads

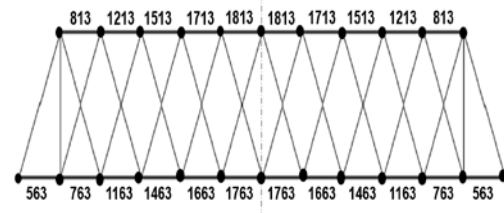


Fig. 10 Induced axial forces of upper chord and lower chord members

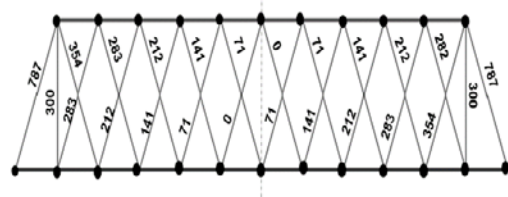


Fig. 11 Induced axial forces of diagonal members

of the truss structure as shown in Fig.10 for upper and lower chord members, and Fig.11 for diagonal members.

Effect of Damage Degree of the Most Influential Member on the Natural Frequency

Next, eigenvalue analysis was performed by lowering the stiffness ratios of the most influential member (shown in red in Fig.7) by 20%, 50%, and 80%. Fig.12 to Fig.14 show the results when the rigidity ratio of the upper chord, diagonal member, lower chord has changed, respectively. The decrease rate of the natural frequency is gradually increased by

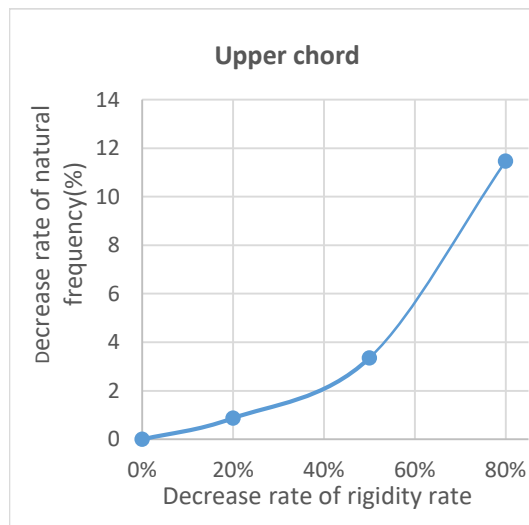


Fig. 12 Decrease rate of the natural frequency when the stiffness ratio of the upper chord material in Fig.7 is reduced by 0% to 80%

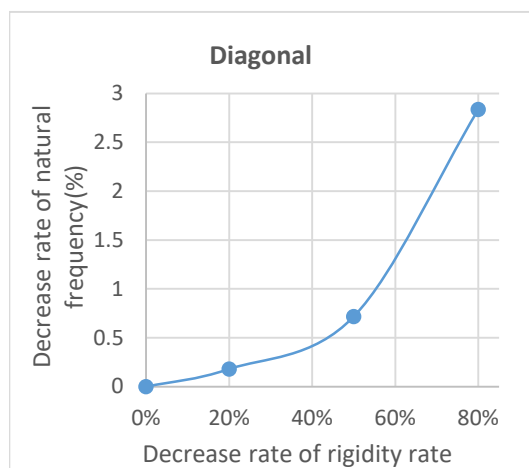


Fig. 13 Decrease rate of the natural frequency when the stiffness ratio by the upper chord material in Fig.7 is reduced by 0% to 80%

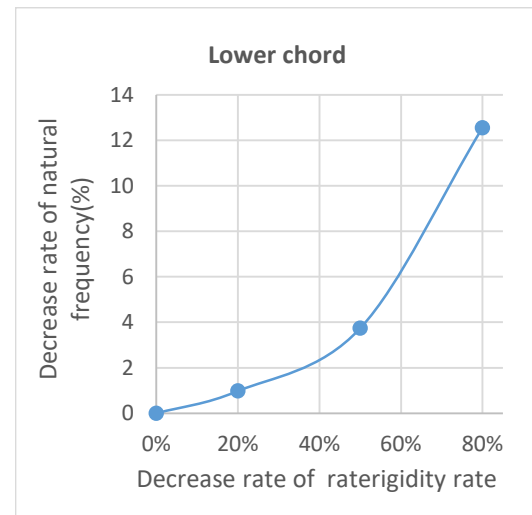


Fig. 14 Decrease rate of the natural frequency when the stiffness ratio by the upper chord material in Fig.7 is reduced by 0% to 80%

decreasing rigidity of the member. They seem to be drastically changed at around 50% reduction of original rigidity.

Changes in Natural Frequencies Accompanying the Rigidity Ratio for Higher Modes

Up to here, we consider only the fundamental vibration mode. However, the sensors installed on the bridge would observe signals that consist of vibration modes including higher modes. Hence, the effect of higher modes is investigated next.

Upper chord member

Figs.15 to 17 shows the rate of change in natural frequency for the second mode to the 4th mode when the rigidity ratio of one of the members from upper chord is reduced to 50%. Looking at the second mode, the member 4 has almost zero effect while the member 8 is the most influential. Regarding 3rd mode, members 7 and 8 seems to have the most little influence. 4th mode shows very complicated mode shape.

From the observations of the second and third mode, it seems that when the damaged members locate on the vibration node of each mode, decrease rates of the natural frequencies are insensitive to the damage. Hence, sensors should not install adjacent to the nodes if the system depends on higher mode information.

Diagonal member

Figs.18 to 20 are rate of change from the second mode to the 4th mode. Different from the upper chord member, relation between locations of node and the damaged member is not clear.

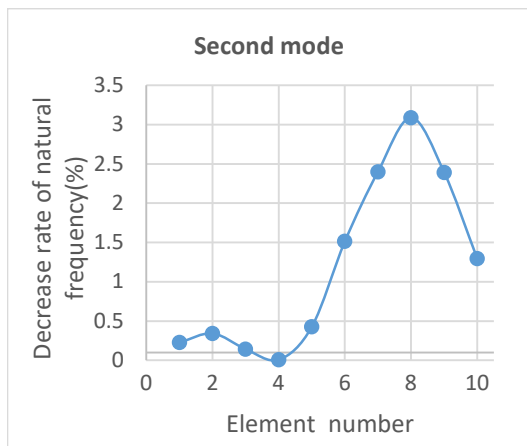


Fig. 15 Upper chord member position and decrease of natural frequency

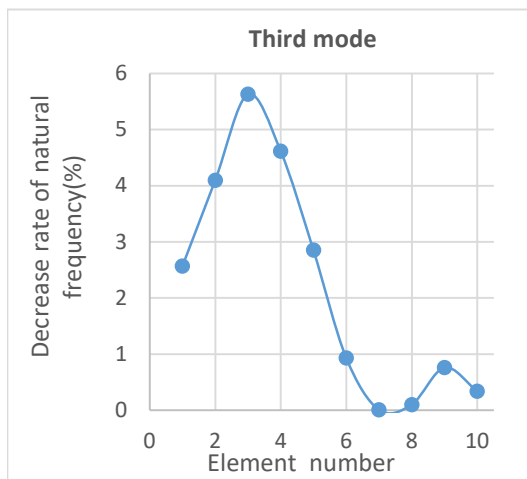


Fig. 16 Upper chord member position and decrease of natural frequency

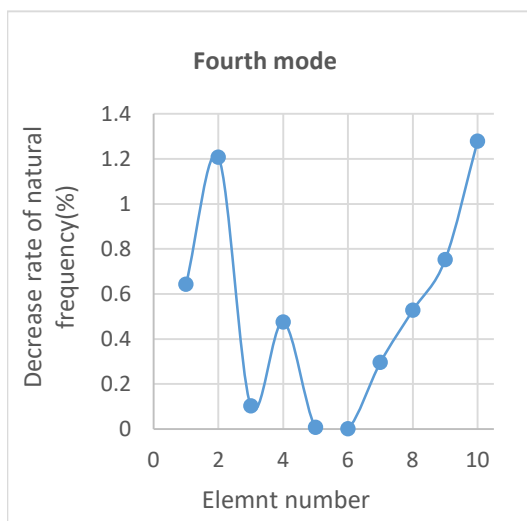


Fig. 17 Upper chord member position and decrease of natural frequency

Lower chord member

Figs.21 to 23 are rate of change of natural frequency for the second mode to the fourth mode. Looking at the second mode, if the location of the damaged member is close to the vibration node (i.e. member 7), natural frequency is insensitive to the damage. For the third mode, when member 4 or 5 is the damaged member, natural frequency is also insensitive to the damage. However, the location of the member is different from the position of vibration node.

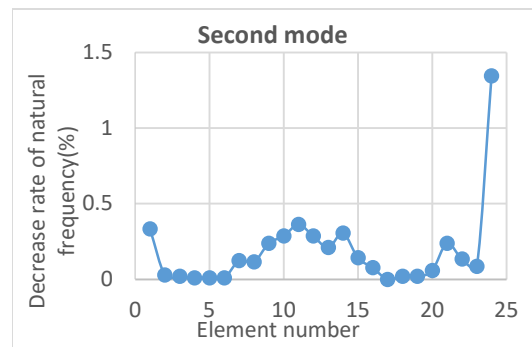


Fig. 18 Diagonal member position and decrease rate of natural frequency

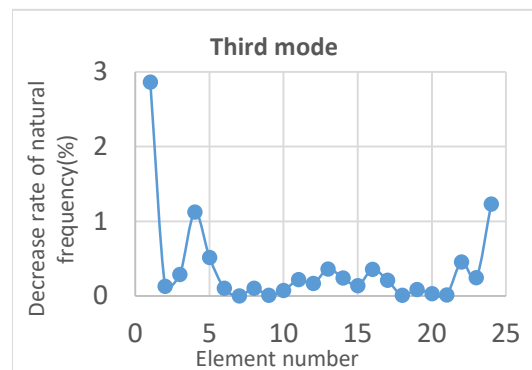


Fig. 19 Diagonal member position and decrease rate of natural frequency

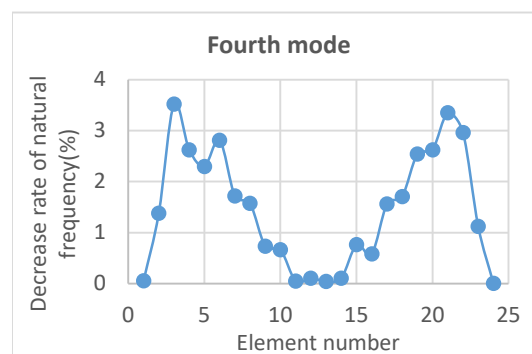


Fig. 20 Diagonal member position and decrease rate of natural frequency

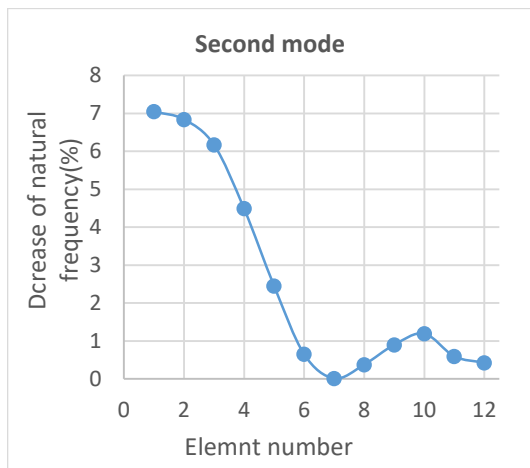


Fig. 21 Lower chord member position and decrease rate of natural frequency

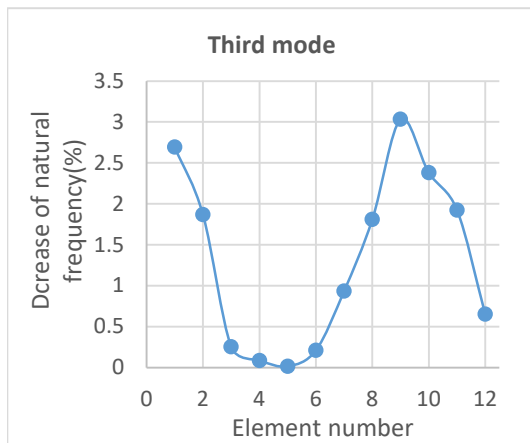


Fig. 22 Lower chord member position and decrease rate of natural frequency

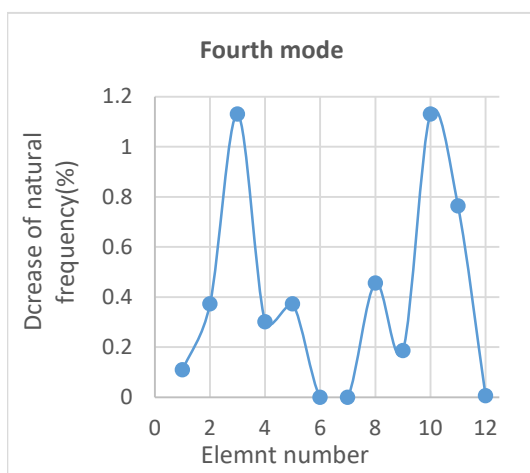


Fig. 23 Lower chord member position and decrease rate of natural frequency

CONCLUSIONS

For the damage detection of aged truss structure based on their vibration characteristics, this study conducted eigenvalue analysis, assuming to utilize sensor data (vibration signals). Deterioration of the structural member was represented by the reduction of its elastic modulus. Results show that structural damage of upper and lower chord near the center of the structure are the most influential members for the first mode natural frequency while damage to members near the vibration nodes is insensitive to natural frequencies for higher modes. These results indicate that the effect of damage to a truss member on the natural frequencies depends on vibration modes. Hence, consideration of sensor locations according to the focusing vibration mode may lead to better detection of damage to the truss member that is sensitive to the corresponding vibration mode. In this way, the knowledge obtained from this study is expected to contribute to the damage detection of structures using sensor data.

ACKNOWLEDGMENTS

This study used the software developed TDAPIII by Ark Information System.

REFERENCES

- [1] Ministry of Land, Infrastructure and Transport and Tourism, Current situation of bridge aging, issues of measures against aging of bridges (in Japanese). <http://www.mlit.go.jp/road/sisaku/yobohozen/to-rikumi.pdf>.
- [2] Yoshioka, T., Harada, M., Yamaguchi, H. and Itou, S., A Study on the Vibration Characteristics Change of the Steel Truss Bridge by the Real Damage of Diagonal Member, Journal of Structural Engineering, Vol.54A, 2008, pp. 199-208 (in Japanese).
- [3] Sekino, M., Hakone Tozan line Hayakawa bridge, Bridge and Foundation Engineering, Truss bridge feature, Kensetsutosyo, Vol. 27, No. 8, 1993, p. 167 (in Japanese).
- [4] Ark Information System, TDAP III Manual, 2017 (in Japanese).

AN AGENT-BASED SUPPLY CHAIN NETWORK WITH QUALITY AGENT MEDIATORS FOR QUALITY COORDINATION

C.Y. LAM

Graduate School of Engineering, Hiroshima University, Japan

ABSTRACT

A good quality coordination framework is necessary for a supply chain network if it is to achieve a competitive advantage in terms of customer satisfaction. It can also help to ensure quality and prevent devastating quality problems with the products or services that are delivered by the supply chain network. In this paper, an agent-based modeling approach is proposed for the development of a supply chain network, in which quality agents are used as mediators who monitor and control the input and output quality information that is generated from entities. Hence, appropriate and suitable corrective actions can then be carried out to adjust any deviations in quality. Agents need to address problems of autonomy and complexity that cause changes and disruptions with their intelligence, so under the proposed agent-based modeling approach, a supply chain network with higher visibility and better quality coordination can be constructed for the entities, and high quality can be assured in the supply chain network. An agent-based modeling approach with three types of quality agents as mediators for the supply chain network is proposed here.

Keywords: Agent Modeling, Multi-agent system, Quality coordination, Supply chain management, Supply Chain Network

INTRODUCTION

Supply chain management is the necessary cornerstone of competitive strategy, increased market share, and shareholder value, for most organizations. Many organizations have directed significant attention toward working more closely with supply chain partners, including not only customers but also various types of logistics entities in the supply chain network, such as manufacturers, distributors, and retailers. The development of more meaningful “relationships” through the supply chain network can achieve better coordination and integration among the participating entities, so the value of the delivered products or services from the supply chain network can be maintained or increased [1]-[5].

According to the literature, many researchers have studied the dynamic network relationship of the supply chain network, and have characterized the contemporary business situations and the internal functional structure of the supply chain network [6]-[10]. The importance of network relationships for the value of the delivered products or services can also be found in the literature [11]-[16].

In modeling the network relationships in the supply chain network, most research papers solely represent the supply chain network as a process flow so as to capture the paths and tasks directly. However, a supply chain network is a complex adaptive system [17]-[20] that involves a certain degree of autonomy among the entities that take part in it. Therefore, in modeling the supply chain network, researchers

have increasingly turned to the frameworks that are derived from agent-based systems [21]-[26].

The Agent-based system is a distinctive modeling technique that emerged from a number of research disciplines including artificial intelligence, system design and analysis using object-oriented methodology and human interfaces [21], [27]-[32]. Throughout these research disciplines, the agent-based system has been defined as a useful computational model for studying the coordination issues arising from the interaction of the individual behaviors of a collection of entities. The agents work through autonomous rule based reasoning in response to their internal and external environment, they also organize themselves to provide solutions by determining the structures, heterogeneity and hierarchy of the problems or environments in which they are participating. Therefore, an agent-based system represents and models agents as reasoning autonomously, interacting with other agents, adapting to environmental changes. They also pursue advantages in a rational manner [33][34]. Moreover, agents autonomously operate without the direct intervention of other humans. In full control of their actions and objectives, agents possess problem-solving capabilities; they send and receive messages concerning their current situations to agents in other related or in the same-environment, and display “evolutionary” behaviors in response to changes [21] [25] [27] [28] [32] [34].

In the research into supply chain networks, the framework of agent-based systems ranges in size and

complexity from simple diagrams of decision making to complex entities' behaviors and interactions. An agent-based system captures the interaction of independent and distributed entities as well as their behaviors. Most researchers use the agent-based system framework to represent the interactive processes within supply chain networks, and some researchers have extended the agent-based system framework to address coordination problems at the enterprise level of supply chains. Moreover, some researchers coordinate the behavior of the business functions with agents' decision making policy and processes [32]. These researchers develop agent-based systems for utilizing information into complex architectures supporting multi-objective decision making, rationalizing system design, and for reducing uncertainty. All this research shows that the autonomy of the agent-based system is potentially valuable in helping, realistically to capture and simulate the dynamics of the complexity inherent in the supply chain network.

Despite the recent growth of research interest in using agent-based systems for modeling the supply chain network, it is clear that research has yet been unable to fully exploit the potential of the agent-based system. This may due to the difficulties of fitting the agent-based system to practical disciplines, and many practitioners have turned to modeling only for single entity applications. In addition, there is relatively little direct research that addresses the usage of agent-based modeling for quality coordination in the supply chain network, and there is also relatively little research that stresses the importance of mediating agents in assisting supply chain coordination activities.

In this paper, an agent-based modeling approach is proposed for the development of a supply chain network, in which mediating agents are proposed and used as mediators to monitor and control the quality of information from entities, and appropriate and suitable actions will then be carried out to adjust the quality deviation, so a higher visibility and better quality coordination can be achieved from the supply chain network.

AGENT-BASED MODELING IN A SUPPLY CHAIN NETWORK

Agents need to address problems of autonomy and complexity that cause changes and disrupt their intelligence. Using the proposed agent-based modeling approach, a supply chain network with higher visibility and better quality coordination can be constructed among the entities. The major feature of the proposed modeling approach is the use of quality agents as mediators to monitor and control the input and output quality information from entities. The quality information including the information from the entities of manufacturers, distributors,

retailers, etc., and the quality information can be considered as the quality performance of the products or services. This information is essential for a supply chain network to produce and maintain high quality products or services for customers.

Structure of Quality Agents in the Supply Chain Network ENVIRONMENT (SCN-ENV)

A supply chain network is a network that composes a parallel flow of products, materials, services, and information from the suppliers through various intermediate entities to the customers, where all the entities are interrelated and connected together for the efficient and effective flow of information concerning the quality of the products or services in the network. In the proposed agent-based modeling approach, the quality agents respond and react to all the series or parallel events performed by the entities within the supply chain network, and these events can be denoted as a set of events E , i.e.

$$E = \{e_0, e_1, e_2, \dots, e_\infty\} \quad (1)$$

where e is the element of events E , and the events in the supply chain network can be distributed or continuous. For each recorded event in the supply chain network, there should be a related distinctive action responding to the event. These actions can be denoted as a set of actions ACT , i.e.

$$ACT = \{\alpha_0, \alpha_1, \alpha_2, \dots, \alpha_\infty\} \quad (2)$$

where α is the element of the actions ACT , and the number of actions ACT are limited to the number of events E in the supply chain network, i.e. $ACT \in E$. Each α in the set of actions α carries a series of items of quality information from the previous event as an input action for the next event; meanwhile each α in the set of actions ACT also carries a series of items of quality information after each event is completed, as an output action. Since agents are used to monitor and control the actions in the supply chain, the actions α are then adaptive to the changes that occur in the events e .

In the proposed agent-based modeling approach, the supply chain network starts from an event e_0 of an entity. Next, the quality agent will decide on a set of actions α for the event e_1 that leads to the next event of the supply chain network. Quality agents will decide on many appropriate actions for an event, but only one suitable action will be executed. This will lead to the start of the next event. The agent will continually decide the appropriate actions for each event in the supply chain network until the last event is reached.

The quality agents all possess quality information of different kinds. They will process this quality information to decide on what action is appropriate for the next event in the supply chain network. Due to

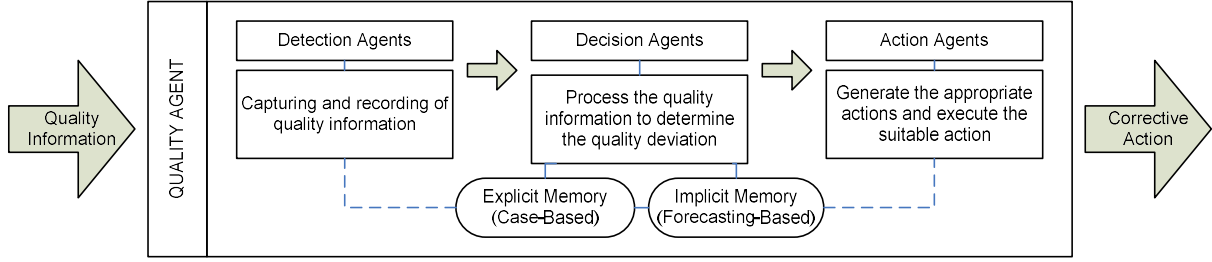


Fig. 1. The relationships and framework between the three types of intelligence quality agents.

the dynamic variables in the supply chain network, the amount of quality information input for an event may be different from the output quality information from previous events. The agent is responsible for monitoring and controlling these variations.

If the output quality information from an event is better than its input quality information, it means the performance of this particular event was good, and quality problems may not exist in this particular event. With this good quality information, the quality agent will then decide on what action is appropriate for the next event. In this way quality can be maintained within the supply chain network.

On the other hand, if the initial input quality information to an event is better than the output information from it, it means quality problems may exist in this particular event, and investigation or corrective actions will be initiated by the quality agent on this particular event or the quality agent will decide what action is appropriate for the next event so as to maintain the quality in the supply chain network. Variation between the input and output quality information can be determined by the following algorithm:

$$Q(e_{i+1}) = \tau \cdot Q(e_i) \frac{\sum x_i(e_i)}{\sum y_i(e_i)} \quad (3)$$

where $Q(e_{i+1})$ is the status of the quality information for the event e_{i+1} , $Q(e_i)$ is the status of the quality information of event prior to it e_i . $\sum x_i(e_i)$ and $\sum y_i(e_i)$ are the input and output quality information of the event e_i respectively. τ is an agent coefficient that represents the investigation or corrective actions of a quality agent in order to maintain the status of the quality information of an event.

For a supply chain network to be completed, a set of event-action routings R is involved. The set of routings R for the quality agent in the supply chain network is induced by the interchanging sequence of the events and the executed actions, and a general routing can be illustrated as:

$$r: e_0 \xrightarrow{\alpha_0} e_1 \xrightarrow{\alpha_1} e_2 \xrightarrow{\alpha_2} \dots \xrightarrow{\alpha_{x-1}} e_\infty \quad (4)$$

where r is the element of routings R , i.e. $R = \{r_0, r_1, r_2, \dots, r_\infty\}$, and R can be considered as all the possible routings for each event and the appropriate actions based on reliable quality information.

Since agents have to address problems of

autonomy and complexity that lead to changes and disruptions with their intelligence, an agent coefficient for the quality agent action is then also added to each action to represent the agent action that deviates from the normal action, as well as the routing adjustment. The set of agent-heuristic routings can further be illustrated as:

$$R^{AG} = \{r_0^{AG}, r_1^{AG}, r_2^{AG}, \dots, r_\infty^{AG}\} \quad (5)$$

where R^{AG} is the agent-heuristic routing, and $r^{AG}: e_0 \xrightarrow{\tau\alpha_0} e_1 \xrightarrow{\tau\alpha_1} e_2 \xrightarrow{\tau\alpha_2} \dots \xrightarrow{\tau\alpha_{x-1}} e_\infty$. With the set of events E , action ACT , agent-heuristic routing R^{AG} and agent coefficient τ , the Supply Chain Network ENVironment $SCN-ENV$ for the agent can then be defined as:

$$SCN-ENV = \langle E, ACT, R^{AG} : \tau \rangle \quad (6)$$

Therefore the quality agents that are involved in the supply chain network environment $SCN-ENV$, inherit the $SCN-ENV$ properties but can make their own action decisions.

Types of Quality Agents in the Supply Chain Network

In the proposed agent-based modeling approach in the supply chain, three types of intelligence quality agents are proposed, i.e. detection agent, decision agent, and action agent. All these agents are subject to the properties of the supply chain network environment, i.e.

AGENT def $\langle DETECTION_AGENT, DECISION_AGENT, ACTION_AGENT \rangle$

$$s.t. SCN-ENV = \langle E, ACT, R^{AG} : \tau \rangle \quad (7)$$

The detection agent is the intelligence agent that is responsible for the capturing and recording of the status of all the quality information within the supply chain network. Therefore, to obtain the quality information $Q(e_i)$ from an event e_i , the detection agent will capture and record the status of it as a set of quality information in the supply chain network environment $SCN-ENV$, i.e.

$$Q(e_i) \rightarrow DETECTION_AGENT: Q(e_i) = \{q_0, q_1, q_2, \dots, q_\infty\} \quad (8)$$

After the quality information is captured and recorded, the quality information will be processed by the decision agent. The decision agent possess a certain level of skill and is knowledgeable about how to process the designated quality information and has considerable skill in handling scientific algorithms

and computations so as to determine any changes needed in the quality information, i.e.

$$\begin{aligned} & DETECTION_AGENT: Q(e_i) = \{q_0, q_1, q_2, \dots, q_\infty\} \\ & \rightarrow DECISION_AGENT: Q^*(e_i) \end{aligned} \quad (9)$$

where $Q^*(e_i)$ is the designated quality information with 3 situations, i.e. $Q^*(e_i) = 1$: the output quality information is better than the input quality information; $Q^*(e_i) = 0$: the output quality information is the same as the input quality information; and $Q^*(e_i) = -1$: the output quality information is worse than the input quality information

If changes occur in the quality information and have been detected by the decision agent, a set of appropriate actions will then be generated by the action agent. Action agents are adaptable and can generate and store the appropriate actions for every events, and will select one suitable action for the event to execute, i.e.

$$\begin{aligned} & DECISION_AGENT: Q^*(e_i) = \{1; 0; -1\} \rightarrow ACTION_AGENT: ACT^AG = \{\alpha_0^{AG}, \alpha_1^{AG}, \alpha_2^{AG}, \dots, \alpha_\infty^{AG}\} \end{aligned} \quad (10)$$

where ACT^AG is the set of appropriate actions for an event, but only one suitable action α_{i+1}^{AG} will be executed by the action agent for the next event, i.e.

$$ACTION_AGENT: ACT^AG = \{\alpha_{i+1}^{AG}\} \rightarrow Q(e_{i+1}) \quad (11)$$

where α_{i+1}^{AG} is the most suitable action for the next event, in which appropriate corrective action is carried out to maintain the quality of the information $Q(e_{i+1})$ for the next event in the supply chain network. The relationships and framework between the three types of intelligence quality agents in the supply chain network are illustrated in Fig. 1.

Agent Adaptation and Learning in a Supply Chain Network

Two adaptation and learning memory mechanisms are adopted by the quality agents to enhance the monitoring and controlling of the quality information so as to determine the appropriate actions for the events. The two memory mechanisms are “explicit memory” and “implicit memory”. “Explicit memory” allows the quality agent to learn from historical agents’ actions so they can react quickly and similarly to any significant changes in the quality information, while “implicit memory” allows the quality agents to propagate the agents’ action in response to changes of the quality information.

The “explicit memory” mechanism is based on the distributed case-based learning approach that was developed from the former agents’ action and behavioral patterns on quality information, and is stored in its knowledge base. Such knowledge is then reused for future cases which possess similar quality information. This knowledge is retrieved through an extended case-based reasoning mechanism.

The main purpose of the “implicit memory”

mechanism is to modify deviation in the promissory quality information. The forecasting-based learning approach simulates the agents’ action and behavioral patterns regarding unforeseen perturbations and changes in the quality information from the events of the entities. By revealing these unpredictable behaviors, the quality agents are then able to generate appropriate agents’ action to correct any deviation in the quality information.

Communication between Agents

In the proposed agent-based modeling approach, agents communicate and interact to maximize internal utility functions and maintain stability in the supply chain network environment *SCN-ENV*. There are two main kinds of communication information between the agents, i.e. information about quality and information about action. Fig. 2 illustrates the communication cycle of a quality agent for an event in the supply chain network.

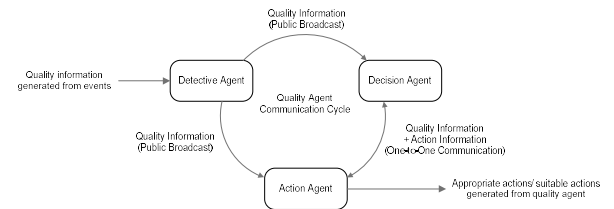


Fig. 2. The communication cycle of the quality agent for an event in the supply chain network.

In agent communication, there are two rule-based communication methods for transmitting communication signals, i.e. through public broadcasting or one-to-one communication. In communication through public broadcasting, all agents in the supply chain network environment *SCN-ENV* can receive communication signals despite the position of the event or of the entity in the supply chain network, and then the target agents can respond to the signals. In one-to-one communication, the communication signal is sent to the target agents only.

A SIMULATION STUDY

For illustrating the proposed agent-based modeling approach in the *SCN-ENV* with agents’ action and flow of quality information, a simulation study on a supply chain network is conducted. The simulation involves 3 manufacturers, 4 distributors, and 7 retailers that are targeting 10 markets.

Since there are 3 manufacturers $M = \{1, 2, 3\}$, 4 distributors $D = \{1, 2, 3, 4\}$, 7 retailers $R = \{1, 2, \dots, 7\}$, and 10 markets $M = \{1, 2, \dots, 10\}$, there are totally 840 possible agent-heuristic routings with a minimum of 2520 agents, coefficient and corrective action for each product. In this simulation, the data for the optimization of the *SCN-ENV* are quantified by the

synthetic analytical methods so as the quantified data can be used as the quality performance data. The product demand, the quantified quality standard for each entity, and the quantified quality information from entity to entity are predefined in the agent environment. For the quantified quality standard, there are upper and lower limits for the data so that flexibility can be induced for the agent coefficient τ , so for any deviation that occurs between the quality information and quality standard, quality agents will carry out the corrective action α . The agent coefficient τ and the corrective actions α are agent-heuristics that are determined by the quality agents in the simulation. For this repeated monitoring and controlling of the quality information and the agents' actions, the optimizations of the proposed agent-based modeling approach in the *SCN-ENV*, with maximum quality information in terms of the best agent-heuristic routings with corrective actions, can be simulated. The best agent-heuristic routings with case-based and forecasting-based set of $\tau\alpha_{mdp}^1(e_i)$, $\tau\alpha_{drp}^2(e_i)$, and $\tau\alpha_{rnp}^3(e_i)$ are thus defined as $M_1 \rightarrow D_1 \rightarrow R_1 \rightarrow N_5$, $M_1 \rightarrow D_2 \rightarrow R_4 \rightarrow N_3$, ..., $M_9 \rightarrow D_{10} \rightarrow R_8 \rightarrow N_{10}$. The quality information and performance within the supply chain network environment *SCN-ENV* can also be maximized: $Q_{mdp}^{1*} = 490$, $Q_{drp}^{2*} = 114$, and $Q_{rnp}^{3*} = 124$). In addition, using the agent-based modeling approach, quality agents can also identify the worst quality routings as well as the entities with relatively poor quality performance, i.e. the entities of Manufacturer M_2 , Distributor D_3 , and Retailers R_3 , R_6 , R_7 in the case study, therefore, the quality agents do not organize any agent-heuristic routing through these entities, and direct the agent-heuristic routings to other entities within their ability. Therefore, by maximizing the quality information in the supply chain network environment *SCN-ENV* with agents' action, the entities can closely interact with each others and achieve higher visibility and better quality coordination.

CONCLUSION

In this paper, an agent-based modeling approach is proposed for the development of a supply chain network, in which quality agents are proposed as mediators to monitor and control the input and output quality information that is generated by the entities. The major feature of this approach is that the model adopts the features of agent for quality coordination. Thus the proposed quality agents can autonomously and adaptively act as mediators to generate appropriate and suitable corrective actions for adjusting any deviation in quality. In this way quality performance can be assured in the supply chain network. Moreover, in optimizing the agent-based modeling approach, and by maximizing the quality information in *SCN-ENV* with agents' action, the

entities can closely interact with each other and achieve higher visibility and better quality coordination; therefore, a higher customer satisfaction can be achieved in the supply chain network.

The modeling approach proposed in this paper can be further improved in several ways. In the *SCN-ENV*, sub-agents can be used to assist with quality coordination within the events of the entities so as to enhance the autonomy and adaptively of the supply chain network. Moreover, for the quality agent, the definition of quality information can further be elaborated and equipped with other elements, such as the cost of taking corrective actions. To further elaborate these elements, the agent-based modeling approach can balance the objectives between the quality information and the operational cost of the supply chain network. Therefore, if any quality problem arises in the supply chain network, the corrective action taken by the quality agents can maximize the quality performance as well as minimize the cost of the whole operation. In turn, customers can be satisfied by the quality of the delivered products or services, the profit from the supply chain network can be maintained and the loss from taking corrective action can be controlled.

REFERENCES

- [1] Gavirneni, S., Kapuscinski, R. and Tayur, S., Value of information in capacitated supply chains. *Management Science*, Vol. 45, Issue 1, 1999, pp.16-24.
- [2] Lee, H. L., So, K. and Tang, C., The value of information sharing in a two-level supply chain. *Management Science*, Vol. 46, Issue 5, 2000, pp.626-643.
- [3] Zhao, X. D., Xie, J. X. and Leung, J., The impact of forecasting model selection on the value information sharing in a supply chain. *European Journal of Operational Research*, Vol. 142, Issue 2, 2002, pp.321-344.
- [4] Elofson, G. and Robinson, W., Collective customer collaboration impacts on supply-chain performance. *International Journal of Production Research*, Vol. 45, Issue 11, 2007, pp.2567-2594.
- [5] Javad, S., Tarokh, M. J. and Shemshadi, A., Initiating a state of the art system for real-time supply chain coordination. *European Journal of Operational Research*, Vol. 196, Issue 2, 2009, pp.635-650.
- [6] Sternman, J.D., *Business dynamics: systems thinking for a complex world*, Irwin/ McGraw-Hill, 2000.
- [7] Min, H. and Zhou, G., Supply chain modeling: past, present and future. *Computers and Industrial Engineering*, Vol. 43, 2002, pp.231-249.
- [8] Surana, A., Kumara, S., Greaves, M. and Raghavan, U. N., *Supply-chain networks: A*

- complex adaptive systems perspective. *International Journal of Production Research*, Vol. 43, 2005, pp.4235-4265.
- [9] Bae, H. and Seo, Y., BPM-based integration of supply chain process modeling, executing and monitoring. *International Journal of Production Research*, Vol. 45, Issue 11, 2007, pp.2545–2566.
- [10] Lam, C. Y., Ip, W. H. and Lau, C. W., A business process activity model and performance measurement using a time series ARIMA intervention analysis. *Experts Systems with Applications*, Vol. 36, 2009, pp.6986-6994.
- [11] Hariharan, R. and Zipkin, P., Customer-order information, leadtimes, and inventories. *Management Science*, Vol. 41, Issue 10, 1995, pp.1599-1607.
- [12] Chen, F., Echelon reorder points, installation reorder points, and the value of centralized demand information. *Management Science*, Vol. 44, Issue 12, 1998, pp.221-234.
- [13] Romano, P. and Vineli, A., Quality management in a supply chain perspective: strategic and operative choices in a textile-apparel network. *International Journal of Operations and Production Management*, Vol. 21, 2001, Issue 4, pp.446-460.
- [14] Moyaux, T., Chaibdraa, B. and D'Amours, S., Multi-agent coordination based on tokens: reduction of the bullwhip effect in a forest supply chain. *AAMAS*, Melbourne, Australia, 2003.
- [15] Hwang, H. B. and Xie, N., Understanding supply chain dynamics: a chaos perspective. *European Journal of Operational Research*, Vol. 184, Issue 3, 2008, pp.1163-1178.
- [16] Lam, C. Y., Chan, S. L., Ip, W. H. and Lau, C. W., Collaborative supply chain network using embedded genetic algorithms. *Industrial Management and Data Systems*, Vol. 108, Issue 8, 2008, pp.1101-1110.
- [17] Silva, C. A., Sousa, J. M. C., Runkler, T. A., Sá da Costa, J. M. G, Distributed supply chain management using ant colony optimization. *European Journal of Operational Research*, Vol. 199, Issue 2, 2009, pp.349-358.
- [18] Holmberg, S., A system perspective on supply chain measurements. *International Journal of Physical Distribution and Logistics Management*, Vol. 30, Issue 10, 2000, pp.847-868.
- [19] Morash, E. A., Supply chain strategies, capabilities and performance. *Transportation Journal*, Vol. 41, Issue 1, 2001, pp.37-54.
- [20] Tan, K. C., Lyman, S. B. and Wisner, J. D., Supply chain management: a strategic perspective. *International Journal of Operations and Production Management*, Vol. 22, Issue 6, 2002, pp.614-631.
- [21] Jennings, N.R., Sycara, K. and Woodridge, M., A roadmap of agent research and development. *Autonomous Agents and Multi-Agent Systems*, Vol. 1, 1998, pp.7-38.
- [22] Oliveira, E., Fisher, K. and Stepankova, O., Multi-agent systems: which research for which applications. *Robotics and Autonomous Systems*, Vol. 27, 1999, pp.91–106.
- [23] Shen, W. and Norrie, D. H., An Agent-Based Approach for Manufacturing Enterprise Integration and Supply Chain Management. Division of Manufacturing Engineering. The University of Calgary, Calgary, Canada, 1998.
- [24] Ren, Z. and Anumba, C.J., Multi-agent systems in construction-state of the art and prospects. *Automation In Construction*, Vol. 13, 2004, pp.421–434.
- [25] Allwood, J. M. and Lee, J. H., The design of an agent for modelling supply chain network dynamics. *International Journal of Production Research*, Vol. 43, 2005, pp.4875-4898.
- [26] Cerrada, M., Cardillo, J., Aguilar, J. and Faneite, F., Agent-based design for fault management systems in industrial processes. *Computers In Industry*, Vol. 58, 2007, pp.313-328
- [27] Ferber, J., Multi-agent systems: an introduction to distributed artificial intelligence, Harlow: Addison-Wesley, New York, 1999.
- [28] Krothapalli, N. K. and Deshmukh, A. V., Design of negotiation protocols for multi-agent manufacturing systems. *International Journal of Production Research*, Vol. 37, Issue 7, 1999, pp.1601-1624.
- [29] Weiss, G., Multi-agent systems: a modern approach to distributed artificial intelligence, MIT Press, USA, 1999.
- [30] Shen, W., Kremer, R., Ulieru, M. A. and Norrie D., A collaborative agent-based infrastructure for Internet-enabled collaborative enterprises. *International Journal of Production Research*, Vol. 41, Issue 8, 2003, pp.1621-1638.
- [31] Horling, B and Lesser, V. R., A survey of multi-agent organizational paradigms. *The Knowledge Engineering Review*, Vol. 19, 2004, pp.281-316.
- [32] Chau, K. Y., Liu, S. B. and Lam, C. Y., Multi-agent modeling in managing six sigma projects. *International Journal of Engineering Business Management*, Vol. 1, Issue 1, 2009, pp.9-14.
- [33] Parunak, H. V. Autonomous Agent Architectures: A Non Technical Introduction, Industrial Technology Institute (1994)
- [34] Lee, J. H. and Kim, C. O., Multi-agent systems applications in manufacturing systems and supply chain management: a review paper. *International Journal of Production Research*, Vol. 46, Issue 1, 2008, pp.233–265.

DESIGN, ANALYSIS, FABRICATION AND ANALYSIS OF SMALL WATER TURBINE

Gwo-Chung Tsai

Department of Mechanical and Electro-Mechanical Engineering National
Ilan University, I-Lan, Taiwan

ABSTRACT

This study designed different blades to make the small-impact water turbines. ANSYS / Fluent hydrodynamic software is used to calculate the torque and power for different blade shapes. From which to find the most effective of blade shape, and in accordance with its blade design, the use of anti-corrosion glass fiber and resin is to manufacture the composite blades. The amount of electricity produced by the turbine made of anti-corrosion composite blades is compared with another group of unexplored wood blade turbines. As a result, the turbine blades made of anti-corrosion composite blades can get a large amount of power.

Keywords: Turbine, ANSYS / Fluent, Anti-corrosion composite blade, Torque

INTRODUCTION

In recent years hydropower is quite popular green energy [1]. Small hydroelectric power system its advantages include the construction of small areas can be integrated into the natural environment and power generation area restrictions less ... and so on, but to develop small hydropower system to consider the main points include 1. In response to different head height, 2 different water flow options, 3. Initial investment and follow-up maintenance should not be too high. To sum up the conditions for the study is the water turbine design should pay attention to the problem [2 ~ 3]. From the literature [4 ~ 5] pointed out that the impact of water turbine blades are particularly suitable for high head low flow conditions. Nakanishi [6] also carried out the impact of water turbine blade simulation analysis and experimental data were compared, the results show that the values are similar between the two. Therefore, it is proved that the simulation analysis can effectively predict the various types of impact water turbine blades. So this study carried out the impact of the design of the form of water turbine blades, and then designed to complete the water turbine blades. And then use computational fluid dynamics (CFD) for analysis and simulation to obtain the optimum water turbine blades.

In order to increase the turbine power generation efficiency, this paper uses ANSYS / Fluent analysis to find the same boundary conditions, the maximum power blade. In accordance with its blade design, the use of glass fiber and resin is to produce the anti-corrosion composite blades. The

amount of electricity produced by the turbine made of anti-corrosion composite blades is compared with another group of unexplored wood blade turbines.

RESEARCH METHODOLOGY

THEORETICAL BACKGROUND

Turbine theory based on computational fluid dynamics theory that is a calculation method for ANSYS / Fluent software. In the case of finite volume analysis, the flow field is divided into many fine grids, using the momentum equation under the microscopic condition, the mass conservation and the mass conservation equation, and the fluid flow and the heat transfer coefficient are integrated to perform the numerical analysis. That is, using a finite grid to calculate the algebraic equations between field variables to solve the approximation between the equations of the variables [7,8]. Fluent has been used in all aspects of the application [9-11]. Many papers had proposed the small scale hydropower works[12-13]. The relevant hydrodynamic formula is as follows: (microscopic Renault transmission equation):

$$\text{Mass conservation equation: } \nabla \cdot \rho \vec{v} + \frac{\partial \rho}{\partial t} = 0 \quad (1)$$

$$\nabla: \text{grad} = \vec{i} \frac{\partial}{\partial x} + \vec{j} \frac{\partial}{\partial y} + \vec{k} \frac{\partial}{\partial z}, \quad \rho: \text{density}$$

t:time, \vec{V} :velocity

Momentum equation: Newtonian Fluid:

Navier-Stokes Equations:

X-direction:

$$\rho \left(\frac{\partial u}{\partial t} + u \frac{\partial u}{\partial x} + v \frac{\partial u}{\partial y} + w \frac{\partial u}{\partial z} \right) = \rho g_x - \mu \left(u \frac{\partial^2 u}{\partial x^2} + v \frac{\partial^2 u}{\partial y^2} + w \frac{\partial^2 u}{\partial z^2} \right) \quad (2)$$

Y-direction:

$$\rho \left(\frac{\partial v}{\partial t} + u \frac{\partial v}{\partial x} + v \frac{\partial v}{\partial y} + w \frac{\partial v}{\partial z} \right) = \rho g_y - \mu \left(u \frac{\partial^2 v}{\partial x^2} + v \frac{\partial^2 v}{\partial y^2} + w \frac{\partial^2 v}{\partial z^2} \right) \quad (3)$$

Z-direction:

$$\rho \left(\frac{\partial w}{\partial t} + u \frac{\partial w}{\partial x} + v \frac{\partial w}{\partial y} + w \frac{\partial w}{\partial z} \right) = \rho g_z - \mu \left(u \frac{\partial^2 w}{\partial x^2} + v \frac{\partial^2 w}{\partial y^2} + w \frac{\partial^2 w}{\partial z^2} \right) \quad (4)$$

ρ :density, t:time, \vec{V} = **velocity**, u:velocity

component in x-direction, v=velocity component in

y-direction, w=velocity component in z-direction,

g_x : gravitational acceleration in X direction, g_y : gravitational acceleration

μ :Viscosity coefficient.

ANALYTICAL PROCEDURES

After confirming that the tank size is 550 mm * 550 mm * 200 mm, with its size reference, the drawing software is used to plot the blades and water tank, and then ANSYS / Fluent is performed to do analysis to find the maximum power turbine for production.

The flow field and rotor were represented by many small grid, the flow field and rotor material is assigned to be the mixture to perform a steady-state analysis. The viscosity coefficient is realizable, and the inlet flow rate for the pumping motor specifications is 0.645kg / s, rotor speed is set to be 130rpm. Velocity distribution is shown in Figure 1, the pressure distribution is shown in Figure 2. And torque can be found to calculate the output power.

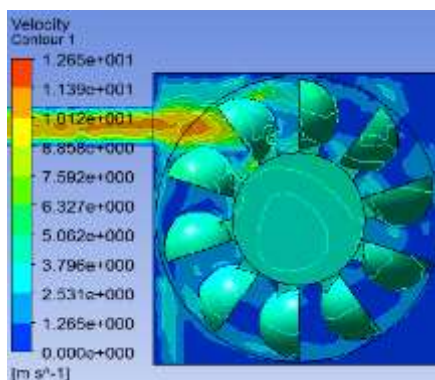


Fig. 1. Water velocity distribution

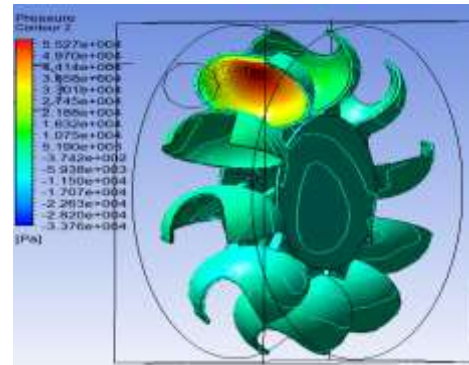


Fig. 2. Pressure distribution on blade

BLADE DESIGN

Figure 3 is the geometry of seven kinds of blades. Table 1 is the calculated torque and power for these blades. From the analysis results we can see that the blade design 7 pressure distribution is more concentrated. The pressure is also larger, as shown in Figure 4a-b, and the larger the number and the size of the blade that can produce more power. The blade design 7 uses the nozzle design 1 to produce maximum power in these blade designs. Blade design reference Bellton type is a turbine blade similar to the spoon-style blade that can absorb the impact of water. Drainage design in the blade will successfully remove the impact of water that will not be retained in the blades.

Manufacture of anti-corrosion composite blades

The reason why the glass fiber composite is selected to make the blades that with high strength, light weight, corrosion resistance and wear resistance and other characteristics. Their tensile strength of the standard state is 6.3 ~ 6.9 g / d. Its tensile strength is strong, and has the large elongation within the elastic limit of the material. So It has the capability to absorb the large impact energy, and has good water resistance, it is very suitable for the

Table 1 the calculated torque and power

Blade number	Torque(Nm)	Power(W)
Blade 1	1.02	13.9
Blade 2	1.69	22.97
Blade 3	2.22	30.22
Blade 4	8.39	114.19

Blade 5	10.98	149.53
Blade 6	8.68	118.11
Blade 7	23.03	313.55

uses a glass fiber cut blanket, shown in Figure 5, 12 μm monofilament fiber diameter yarn stocks, evenly distributed in the plane but no direction. Monofilament diameter is thick, the product surface will be rough, but there has better hardness.

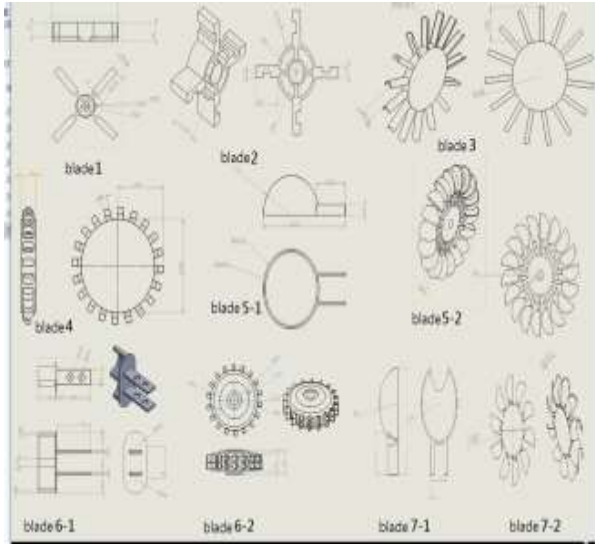


Fig. 3 The geometry of seven kinds of blades

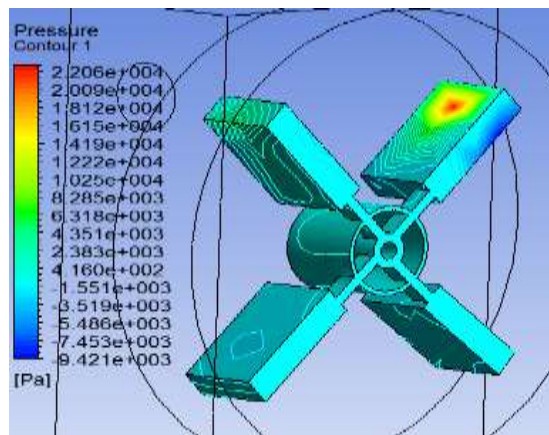


Fig. 4a. Pressure distribution for blade design 1

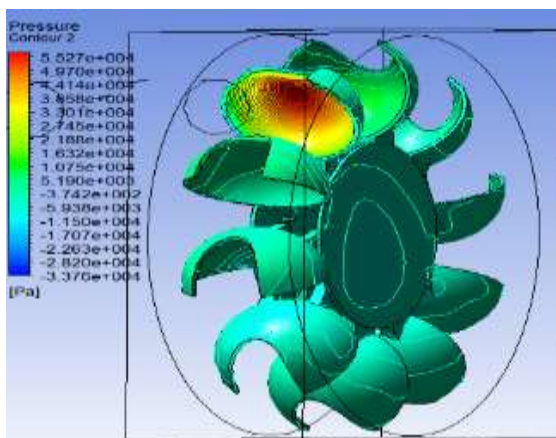


Fig. 4b. Pressure distribution for blade design 7

production of impact turbine blades [3]. This study



Fig. 5. Glass fiber cutting blanket



Fig. 6a The upper mold



Fig. 6b The upper mold

In order to understand the impact of production methods, two ways are used to make blades: closed mold making blades and open mold making blades. The use of 3D printing machine and the material is: Pla Plate 3.0mm. Print out of the upper mold and the lower mold are shown in Figure. 6a-b.

CLOSED MOLD MAKING BLADES

The resin is mixed with the hardener in proportion. Cut kraft paper, the size can be spread throughout the mold. Use double-sided adhesive, paste the kraft paper bag to the mold to help demoulding. Kraft paper bag coated with wax oil or release agent, and then put the glass fiber. At the same time a layer of resin is painted once shown in Figure 7, a total of three layers of glass fiber is put. After the resin is painted, cover the upper mold and the lock frame is used to fix the upper and lower molds. Then it is put into the oven that heated to 100 $^{\circ}\text{C}$ and time for 55 minutes as shown in Figure 8. After the work piece is

hardened, it will get the glass/epoxy blade after demold and trim as shown in Figure 9-10.

OPEN MOLD MAKING BLADES

Using the original lower mold to make open mold, add the bevels at the grooves of the two tripods, as shown in Figure 11 that will be easily open the demolding. The same method uses 3D printing machine to print out the mold, as shown in Figure 12. The production process is roughly the same as that of the closed mold. After several tests and improvements, the following best production methods are obtained: The resin is mixed with the hardener in a ratio of 2: 1 to produce a group of blades using about half can of the resin. In order to prevent the kraft paper rupture, leading to resin into the mold surface, we put two layers of kraft paper on the mold, and two layers of kraft paper with aluminum foil stickers together. The release agent was changed to be butter. The shape of the glass fiber can be cut into blades. Painted with resin, covered with glass fiber, waiting for resin impregnated glass fiber, and then painted with a layer of resin, a total of 3 layers of glass fiber are put. The mold put in the furnace and set the heating temperature of 60 °C, time is 40 minutes, wait two hours after cooling, then put it in room temperature over one night, and demolition the next day.



Fig.7. Painting the resin



Fig.8 The mold after heating

The shape of the glass fiber can be cut into blades. Painted with resin, covered with glass fiber, waiting for resin impregnated glass fiber, and then painted with a layer of resin, a total of 3 layers of glass fiber are put. The mold put in the furnace and set the

heating temperature of 60 °C, time is 40 minutes, wait two hours after cooling, then put it in room temperature over one night and demolition the next day.



Fig. 9 Demold



Fig.10 Glass/epoxy blade

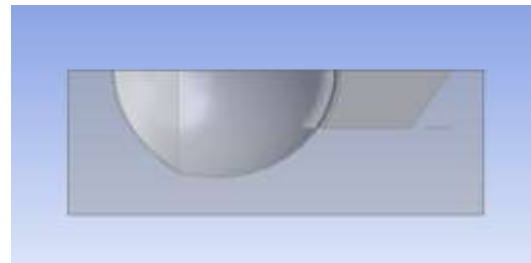


Fig. 11 Oblique angle diagram

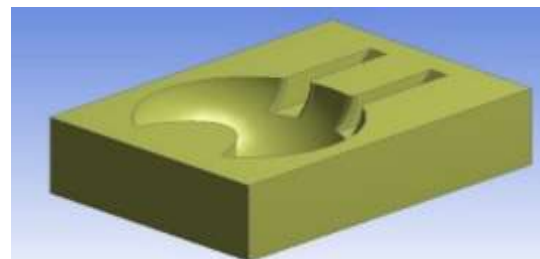


Fig. 12 Open mold for blade

Repeat to make the eight blades and use the same process to make circular axles, and drill the axle, the use of screw nut to lock the blade, that is, complete

the turbine blades shown in Figure 13.

THE OVERALL STRUCTURE OF THE TURBINE AND EXPERIMENTAL TEST

The turbine will be locked into the tank, the output of the axle will be accelerated with the speed increaser that speed ratio of 1: 2 as shown in Figure 14. Using the shrinkage jet to speed up the output water, water pipe diameter is 25mm and nozzle diameter will reduce to 15mm as shown in Figure 15. The overall structure of the turbine after the overall combination is shown in Figure 16. The generator is in series with a 3w bulb, and connect the multimeters. The use of pumping motor and long pipeline flushes the water from ground, 2,3,4 floor into the water turbine to rotate the turbine that makes the generator to generate electricity. Record voltage and current are recorded, and the tachometer is also used to measure the rotating speed that will be used in the hydraulic analysis to calculate the output power.



Fig. 13 Turbine blade after assembly



Fig. 14 speed increaser



Fig. 15 water nozzle

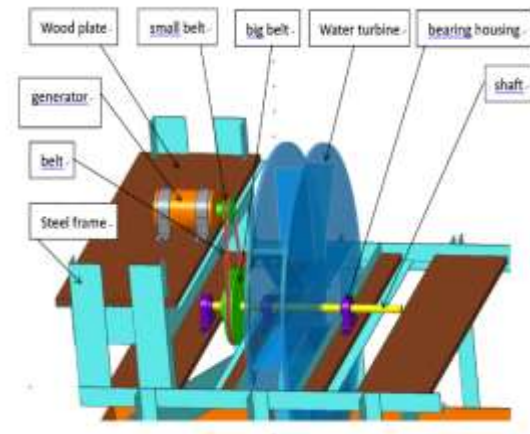


Fig. 16 The overall structure of the turbine

RESULTS

DISCUSSIONS

The power produced from the turbine with the anti-corrosion composite blade and compared with that from the turbine with the undesigned wood blade shown in Figure 17. It is shown in Figure 18 that the designed blades have a higher power generation compared to the wood blades. On the structure, we use the speed increaser to make the generator to have a larger speed and output more torque to drive the generator.

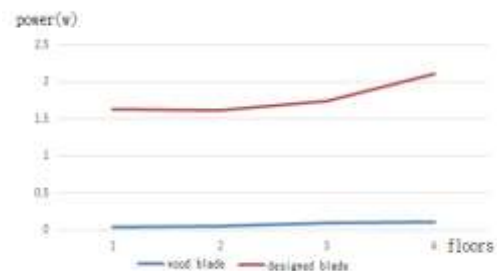


Fig. 17 Power get from two blades

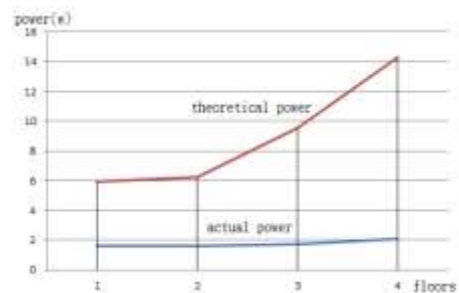


Fig. 18 Comparison between analysis results and tests

It can be seen from Figure 18 that the higher the floor, the lower the power generation efficiency. It is also found that the test results are lower than that of the theoretical data. Possible causes of this phenomenon are the following: First, the phenomenon of water pipe contraction, when the water washed down through the hose under the floor, the high-speed flow of liquid low pressure caused by water pipe contraction, so that the flow rate decreased, so the higher flow the impact. The hose is soft, the next test may change the material of hose. The second, the theoretical power calculation using gravity equation to calculate the flow rate, ignoring the water viscosity and pipeline friction, coupled with the liquid as a continuum, the gravity equation to calculate the flow rate will produce errors. Third, the blade surface is not smooth and may cause the turbulent in the water tank that will affect the overall turbine speed. Fourth, the blade weight is not even resulting in rotation when shaking, affecting the efficiency of the turbine. In order to increase the efficiency, we can try to tighten the water pipe to reduce the contraction of the pipeline, the clay is used to smooth the uneven blade surface. The weight ring is also used to adjust the center of gravity to the axle center.

CONCLUSIONS

The use of engineering software for geometric shape design and the use of computational fluid dynamic software to calculate the geometrics shape of a blade with a higher torque can reduce the wrong design. The results also show that the power get from the design of the blade will be higher than that of the unqualified design. Because the energy from the injection water completely become the output power in CFD calculation, but it is impossible in the real design equipment. Therefore more reliable analytical method must be considered.

In terms of the blade, the glass fiber hardness is good, the user can make the blades thinner and lighter. Glass fiber is more plastic than wood, it can design a wide range of contact area with the water, and within the elastic limit of the material, it has higher elongation and higher tensile strength. The design of the spoon shape is more able to absorb the impact energy of the water, plus the notch design will drain the flow water that will not water in the tank, and can reduce the generation of turbulence that will result in sufficient drive torque.

REFERENCES

[1]Wang, J. H., Energy Industry Seminar-Hydropower,2015.
[2]Yamato, N. M., and Yamaichi, T. M., *Hill hut hydraulic power generation*, Machinery, Vol.30,

No. 3, 2002.
[3]Židonis, A., Benzon, D. S., Aggidis, G.A(2015)., *Development of hydro impulse turbines and new opportunities*, Renewable and Sustainable Energy Reviews, 51, 1624-1635.
[4]Nakanishi, Y., Ito, S., Takahashi, Y., Kato(2009). A., *Development of a Simple Impulse Turbine for Nano Hydropower*, Journal of Fluid Science and Technology, 4(3), 567-577.
[5]Chen T., Fang Z., Tsai G. C.(2016). *Analysis of Fluid –Structure Coupling Calculation and Failure Analysis of Composite Materials Blades*, Master 's Thesis, National Yilan University, Yilan, Taiwan.
[6]Lai W.(2014). *Vertical Shaft Wind Pumps Vane Flow Field Analysis*, Master 's Thesis, National University of Yilan, Department of Mechanical and Electrical Engineering,..
[7]Chen Y.J.(2015). *Research on Mechanical Behavior of Glass Fiber Reinforced Polymer Composites Type I Beam - Plate System*,” Institute of Civil and Disaster Prevention, Taipei University of Science and Technology.
[8]Tsai, G.C.(2015). *Static Analysis of Artery Expansion by the Balloon*, International Journal of Engineering and Innovative Technology (IJEIT), Volume 4, Issue 12, pp. 149-153.
[9]Tsai, G.C.(2015). *”The Starting Behavior Analysis of a Micro Horizontal Axis Wind Turbine,”* Advanced Materials Research, Vols. 1079-1080, pp. 543-546.
[10]Tsai, G.C.(2015). *”Two-way Fluid-Structure Interaction Simulation of a Micro Horizontal Axis Wind Turbine,”* International Journal of Engineering and Technology Innovation, Vol. 5, No. 1, pp. 33-44.
[11]Tsai, G.C.(2014). *”The Flow Field Design and Analysis of a 2MW Offshore Wind Turbine Using Variable Wind Speed,”* Thermal Energy and Power Engineering, Volume 3, Issue 3, pp. 250-257.
[12]Caxaria, G.A., Sousa, D.M., Ramos, H., *”Small Scale Hydropower: Generator Analysis and Optimization for Water Supply System,”* World Renewable Energy Congress 2011, May, 2011, Sweden.
[13]Ramos, H., Almeida, A.B., *”Parametric analysis of waterhammer effects in small hydropower schemes,”* 2001, Journal of Hydraulic Research, IAHR, Vol. 39 (4), pp. 429-436, ISSN-0022-1686.
[14]Smith, N., *”Motors as generators for micro-hydro power,”* 2nd Edition, Practical Action Publishing, 2008.

FLEXURAL STRENGTH OF RIGID PAVEMENT USING RECYCLED CONCRETE AGGREGATES IMPROVED BY POLYVINYL ALCOHOL

Suksun Horpibulsuk¹; Teerasak Yaowarat²; Arul Arulrajah³; Mehdi Mirzababaei⁴;
and Ahmad Safuan A Rashid⁵

¹Center of Excellence in Innovation for Sustainable Infrastructure Development, Suranaree Univ. of Technology, Thailand.

²Suranaree Univ. of Technology, Thailand.

³Swinburne Univ. of Technology, Australia.

⁴Central Queensland Univ., Australia.

⁵Centre of Tropical Geoengineering (GEOTROPIK), Universiti Teknologi Malaysia, Malaysia.

ABSTRACT

Research on the utilization of recycled concrete aggregate (RCA) in civil engineering applications is gaining popularity worldwide due to the increased efforts to promote the preservation of the environment and sustainable development. Recycled concrete aggregate is, however, presently still limited to nonstructural applications. Recycled concrete aggregate can still be considered as a rigid pavement material when its flexural strength is improved adequately to sustain future traffic loads. In this study, polyvinyl alcohol (PVA), a water-soluble polymer, was used to improve the flexural strength of RCA concrete. Polyvinyl alcohol was found to retard the hydration process, resulting in the delay in initial and final setting times of cement-PVA paste, therefore reducing the compressive strength of RCA-PVA concrete. For all the w/c ratios tested, the flexural strength increased with increasing p/c ratios up to an optimum p/c ratio that provided the highest flexural strength, followed by a subsequent decrease beyond this peak value. The optimum p/c ratio tended to increase with an increase in w/c ratio, being 0.5, 0.5, 1.0, and 1.5 for w/c ratios of 0.3, 0.4, 0.5, and 0.6, respectively. Based on the requirements of the Department of Highways, Thailand, the $p/c \leq 1$ at $w/c \leq 0.5$ was found to be suitable for developing RCA-PVA concrete for rigid pavements.

Keywords: Polyvinyl alcohol, Recycled concrete aggregate, Flexural strength, Compressive strength, Pavement.

INTRODUCTION

The utilization of waste materials and research on new recycling techniques have been encouraged world widely to promote sustainable practices to reduce the impact of civil engineering construction activities on the environment. Recycled concrete aggregate (RCA) is obtained from the demolition of aged concrete buildings and essentially consists of constituents such as binding materials, water, aggregates and admixtures. The major component is the aggregates, which typically comprises 60–75% of the total concrete volume [1]. Previous researches have shown that RCA could be used sustainably as unbound or stabilized pavement base/subbase materials [2]-[3].

RCA can furthermore be used as coarse aggregates in the production of concrete, which would reduce waste concrete stockpiles at landfills and would limit the need for natural aggregate sources [4]. Reuse of waste materials from demolition activities has numerous environmental and economic benefits. However, the variable properties of RCA remain the predominant barrier in using RCA for concrete production. Several studies [5]-[8] reported that RCA concrete often exhibited low compressive strength, wide variability in quality, high drying

shrinkage, large creep and low elastic modulus. Nogchi [9] and Olorunsogo [10] indicated that the compressive strength and durability against chloride resistance of RCA concrete gradually decreased as the amount of RCA increased. Silva et al (2014) suggested that RCA concrete should only be used in non-structural applications such as rigid pavement and canal [4].

Several researchers have proposed methods to improve the strength and durability of RCA concrete, such as by using the double mixing or two-stage mixing (TSMA) approaches [8], [11].

Earlier studies on RCA concrete have focused on the compressive strength properties, while research on the essential flexural strength properties of RCA concrete is limited to date. The flexural strength plays a vital role in the stability of rigid pavement due to its low tensile strength characteristics.

The flexural strength of concrete can be improved by fiber reinforcement [12]. Water-soluble polymers have been also reported to enhance the flexural strength as well as the durability of concrete [10]-[15]. Adding PVA into cement paste improves its chemical resistance properties, such as preservation of compressive strength after exposure to chemical attacks [14]. The flexural strength of concrete specimens increases with increasing PVA-to-cement

(by weight), p/c ratio due to the significant reduction of both total permeable pore volume and water absorption of the specimens. PVA effectively packs the concrete solid ingredients and results in a dense matrix material [15].

To the authors' knowledge, there has been no research undertaken to date on the application of PVA for improving the flexural strength of RCA concrete, which is the prime focus of this research. The RCA concrete specimens were prepared by the TSMA method in this study. The role of the water to cement (w/c) ratio and PVA/cement (p/c) ratio on the compressive and flexural strengths of the RCA-PVA concrete is also investigated in this study. The flexural strength improvement of RCA-PVA concrete specimens that meets the compressive strength requirements of the Thailand national road authorities is also reported in this study.

MATERIALS AND METHODS

Materials

Natural river sand with a fineness modulus of 3.74 was used as the fine aggregate for preparing the RCA concrete. The river sand had a specific gravity in the saturated surface dry state, water absorption, and percent of voids of 2.58, 3.34%, and 42.5%, respectively. The dry-rodded unit weight of the river sand was 14.7 kN/m³. Particle size distribution of the river sand is shown in Fig. 1.

Recycled concrete aggregate (RCA) specimen had particles with sizes ranging between 4.75 mm and 19 mm. The grain size distribution curve of RCA is shown in Fig. 1. RCA had a fineness modulus and a specific gravity in saturated surface dry state of 1.34 and 2.67, respectively. Its dry-rodded unit weight was 12.1 kN/m³. The water absorption, percent of voids and Los Angeles abrasion loss were, 5.5%, 54% and 41%, respectively. Since the RCA was not scalped to remove the attached mortar. Consequently, the RCA was weaker than the natural aggregate [16].

Ordinary Portland cement (OPC) was used to make the RCA concrete specimens in this study. OPC had a specific gravity and an average particle size of 3.15 and 14.7 μ m, respectively. Chemical compositions of OPC are shown in Table 1.

Polyvinyl alcohol (PVA) was purchased from Chemipan Corporation Co., Ltd, Thailand. It is a synthetic polymer that is achromatic, odorless and soluble water (temperatures of 95~95 are generally required for complete solution). PVA had a specific gravity, hydrolyzed, and molecular weight of 1.27-1.31, 87.83%, and 22,000, respectively.

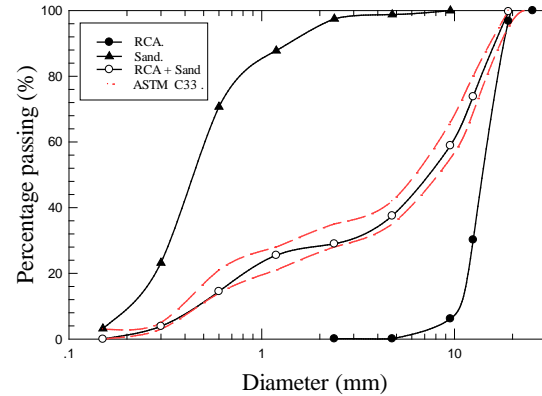


Fig. 1 Particle size distributions of sand, RCA and RCA+Sand.

Specimen Preparation

RCA-PVA concrete specimens were prepared by varying both w/c and p/c ratios. The PVA solution was prepared in five different percentages with respect to the cement weight, viz. 0, 0.5, 1, 1.5, 2.0, representing low to high values for improving workability and water retention abilities of the concrete [17]. Four different w/c ratios including 0.3, 0.4, 0.5 and 0.6 were studied. The PVA solutions were prepared by adding PVA powder at a target p/c ratio into 2 liters of boiled water until the PVA was entirely dissolved. The mixture was kept overnight in an open-air atmosphere for allowing to cool down to room temperature before mixing it with cement slurry [14]. The 2 liters of water were removed for producing normal concrete and replaced by 2 liters of PVA solution.

Table 1 Chemical compositions of ordinary OPC (percentage by weight of cement, wt%).

SiO ₂	SO ₃	Fe ₂ O ₃	Al ₂ O ₃	CaO	MgO	LOI
20.9	2.7	3.32	4.7	65.4	2.54	0.9

The mixing proportions of the RCA concrete specimens are summarized in Table 2. The RCA was used to fully replace the natural coarse aggregate in the mix proportion. The ratio of fine to coarse aggregates was fixed at 45:55 by volume. The gradation of aggregate (mixture of fine and coarse aggregates) is shown in Fig. 1 and compared with upper and lower boundaries suggested by ASTM C33 [18]. It is noted that the gradation of tested aggregates is within the suggested boundary. The slump of the fresh RCA-PVA concrete was controlled in the ranges of 10-30, 20-50, 30-70 and 50-100 mm for w/c ratios of 0.3, 0.4, 0.5 and 0.6,

Table 2 Mix proportions of concretes.

Mix	Mix Proportion (kg/m ³)						Slump (mm)
	Cement	PVA weight.	RCA ^a	Sand	SP ^b	w/c	
W3PVA0	417.4	-	1193	890	-	0.3	10
W3PVA0.5	417.4	2.087	1189	873	3.26	0.3	15
W3PVA1	417.4	4.174	1191	874	4.35	0.3	10
W3PVA1.5	417.4	6.261	1182	867	5.43	0.3	15
W3PVA2	417.4	8.348	1179	864	6.52	0.3	20
W4PVA0	417.4	-	1189	873	-	0.4	30
W4PVA0.5	417.4	2.087	1194	877	2.72	0.4	30
W4PVA1	417.4	4.174	1186	870	3.26	0.4	35
W4PVA1.5	417.4	6.261	1173	860	3.8	0.4	35
W4PVA2	417.4	8.348	1164	852	4.35	0.4	40
W5PVA0	417.4	-	1174	860	-	0.5	45
W5PVA0.5	417.4	2.087	1187	871	2.17	0.5	50
W5PVA1	417.4	4.174	1190	873	2.39	0.5	45
W5PVA1.5	417.4	6.261	1176	862	2.6	0.5	50
W5PVA2	417.4	8.348	1185	869	2.82	0.5	55
W6PVA0	417.4	-	1168	855	-	0.6	85
W6PVA0.5	417.4	2.087	1195	878	1.08	0.6	80
W6PVA1	417.4	4.174	1181	866	1.3	0.6	85
W6PVA1.5	417.4	6.261	1166	854	1.52	0.6	85
W6PVA2	417.4	8.348	1172	859	1.73	0.6	80

^a Recycled coarse aggregate in the saturated surface dry (SSD) state.

^b Superplasticizer was assumed that it had water 50% by weight.

respectively, by varying the amount of type F superplasticizer.

In this study, the TSMA method [11] was chosen to prepare the RCA-PVA concretes as this method has been proved to reduce the porosity of RCA.

Initial and Final setting times

The initial and final setting times were investigated for all specimens to explain the effect of PVA content on the hydration process of RCA-PVA concrete specimens by using the Method A-Manual Vicat Needle Apparatus in accordance with the ASTM C191 [19]. The initial setting time is reached when the penetration is 25 mm or less. Setting time ended when the tip of the needle penetrated only 0.5 mm into the cement paste.

Compressive and Flexural strengths

Based on ASTM C192 [20], all of the fresh concrete mixtures were prepared using a rotary drum mixer. For each concrete mix, Ø100×200 mm cylinders and 100×100×500 mm prismatic specimens were cast. The Ø100×200 mm cylinders were used to determine the compressive strength according to the ASTM C39 [21]. The 100×100×500 mm prismatic specimens were prepared for the flexural strength test with a center-point loading in accordance with the ASTM C293 [22]. The flexural strength of the

specimens was determined in accordance with ASTM C 293 using the following equation:

$$\text{Flexural strength} = \frac{3PL}{2bd^2} \quad (1)$$

where P is the maximum applied load, L is the span length, b and d are the average width and depth of the specimens respectively.

All the specimens were cast in steel molds and compacted by a vibrating table. The cylindrical and prismatic concrete specimens were demolded after 24 hours of curing at a room temperature, and then cured in a water-curing tank at 27 ± 2 °C for the designed curing age. The compressive and flexural strengths of RCA concrete were investigated for the curing ages of 7 and 28 days.

RESULTS

Initial and Final Setting Times

Figure 2 shows the initial and final setting times of PVA-cement pastes at various w/c and p/c ratios. The setting time was measured using Vicat apparatus on two representative specimens for each set 15 minutes after preparation time. The PVA influences the hydration process by delaying both initial and final setting times, as compared to the pure cement paste (without PVA) at the same w/c ratios. For

instance, at a p/c ratio of 2 and w/c ratios of 0.3, 0.4, 0.5 and 0.6, the initial setting times were delayed by about 44, 54, 43 and 53 minutes, respectively when compared with those of the pure cement pastes. The final setting times were 62, 51, 38 and 44 minutes, respectively longer than those of the pure cement plates, which is similar to the results reported by previous researchers [13], [15]. It is noted that for the same w/c ratio, the initial and final setting times are longer for higher p/c ratios. For example, at w/c = 0.5, the initial setting times are 215, 225, 229, 235 and 242 minutes for p/c = 0, 0.5, 1.0, 1.5 and 2.0, respectively and the final setting times are 343, 349, 355, 362 and 364 minutes for p/c = 0, 0.5, 1.0, 1.5 and 2.0, respectively.

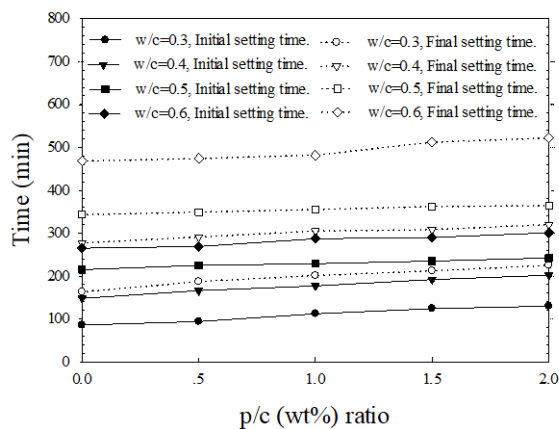


Fig. 2 Initial and final setting times of PVA-cement paste.

Compressive Strength of RCA-PVA Concrete

The compressive strength of RCA-PVA concrete specimens at 7 and 28 curing days and different w/c ratios of 0.3, 0.4, 0.5 and 0.6 are shown in Fig. 3. The highest 7-day compressive strength (Fig. 3a) was found at p/c ratio = 0 where the maximum compressive strengths are 29.5, 27.1, 24.7 and 21.2 MPa for w/c ratios of 0.3, 0.4, 0.5 and 0.6, respectively while the minimum 7-day compressive strengths were found at p/c = 2, including 20.6, 15.6, 14.1 and 12.3 MPa for w/c ratios of 0.3, 0.4, 0.5 and 0.6, respectively. This result indicates that the compressive strength reduces with increasing of w/c and p/c ratios. The additional water content (increasing of w/c ratio) leads to coarse pore distribution in a concrete specimen and increases its porosity and permeability, hence reduces its compressive strength [23].

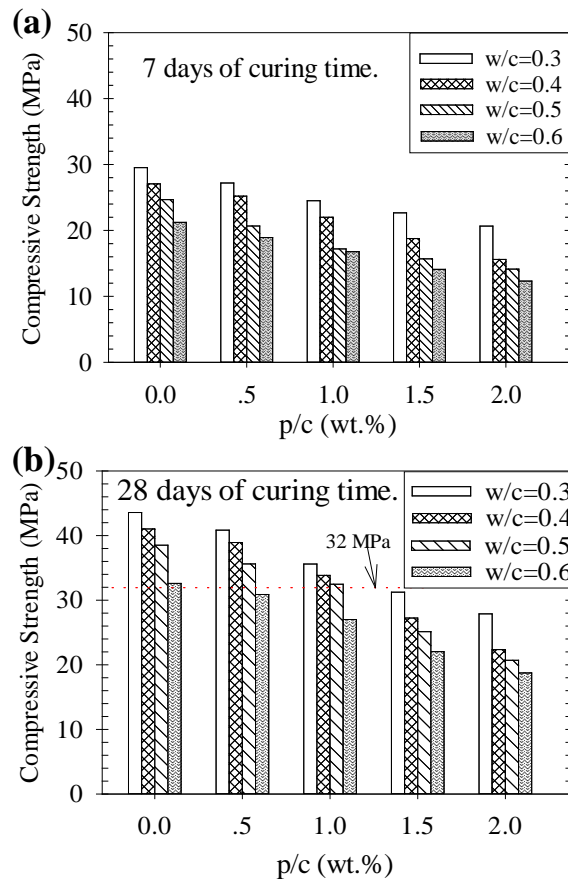


Fig. 3 Compressive Strength of RCA-PVA concrete at (a) 7 days and (b) 28 days.

Similarly, the maximum 28-day compressive strengths were also found at p/c ratio = 0 and w/c = 0.3. At p/c = 0, the 28-day compressive strength were 43.6, 41.1, 38.5 and 32.59 MPa for w/c ratios of 0.3, 0.4, 0.5 and 0.6, respectively (Fig. 3b).

It is evident from the test results that the addition of PVA to the concrete mix not only reduces the compressive strength of the specimen at a particular curing time but also the strength development with time. This is in agreement with the test results of setting times in that the initial and final setting times are longer with increasing of p/c ratio. For instance at w/c = 0.3, 7-day and 28-day compressive strengths are 29.5 and 43.5 MPa, respectively for p/c = 0; are 24.5 and 35.6 MPa, respectively for p/c = 1.0 and are 20.6 and 27.4 MPa, respectively for p/c = 2.0.

Flexural Strength of RCA-PVA Concrete

Figure 4 shows the flexural strength of the specimen at various w/c ratios, p/c ratios, and curing times. For low w/c ratios of 0.3 and 0.4, the maximum flexural strength was found at approximately the same p/c ratio of 0.5% at all curing times. The maximum flexural strengths at w/c ratios of 0.3 and 0.4 at 28 days of curing were found to be 6.7 and 5.8 MPa, respectively with an increase of 133% and

139% when compared to RCA concrete specimens at the same w/c ratios. However, the addition of PVA beyond p/c of 0.5% caused a reduction in the flexural strength.

The change in the flexural strength with p/c ratio for higher w/c ratios of 0.5 and 0.6 is also similar to that for w/c = 0.3 and 0.4, where the flexural strength increases to the maximum value at the optimum p/c and then decreases as p/c increases. However, the optimum p/c ratios providing the highest flexural strength are different from those of w/c = 0.3 and 0.4. The optimum p/c ratios were found to be 1.0 and 1.5 for w/c = 0.5 and 0.6, respectively. In other words, the optimum p/c increases with increasing of w/c ratio. At the optimum p/c ratio, the 28-day flexural strengths were 5.35 MPa and 4.93 MPa for w/c = 0.5 and 0.6, respectively. The flexural strength increased by 132% and 129% than those of RCA concrete at the same w/c ratios of 0.5 and 0.6, respectively. Compared with the strength requirement for the rigid pavement by Department of Highways [24] (the 28-day compressive strength > 32 MPa (see Fig. 3b), the RCA concrete (without PVA) meets the requirement for all w/c ratios tested. With PVA, the RCA-PVA concretes meet the requirement when $w/c \leq 0.5$ and $p/c \leq 1$.

CONCLUSIONS

This research investigates the feasibility of using polyvinyl alcohol (PVA) to improve the flexural strength of recycled concrete aggregate (RCA) concrete to be a sustainable rigid pavement material. The following conclusions can be drawn from this research study:

PVA prevents the water absorption for cement hydration process. Hence, the higher the p/c ratio results in the longer initial and final setting times of RCA-cement paste and the lower the compressive strength.

Even though PVA retards hydration, it contributes to improving the tensile strength of the cement matrix and hence results in an increased flexural strength. The flexural strength of RCA-PVA concrete is contributed from cementation bond and PVA film strength. Due to the reduction in cementation bond strength and the increase in tensile strength with increasing of p/c ratio, the flexural strength increases with increasing of p/c ratio up to the maximum value at the optimum p/c ratio and then decreases with increasing of p/c ratio.

The optimum p/c ratio is dependent upon w/c ratio. The higher w/c ratio results in the higher p/c ratio. The optimum p/c ratio was found to be 0.5, 0.5, 1.0 and 1.5 for w/c = 0.3, 0.4, 0.5 and 0.6,

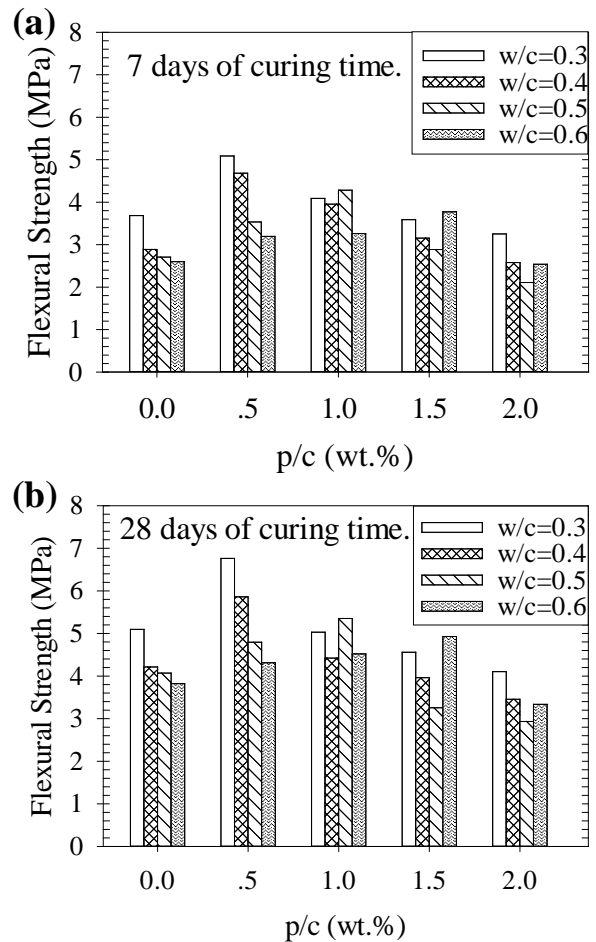


Fig. 4 Flexural Strength of RCA-PVA concrete at (a) 7 days and (b) 28 days.

respectively. Based on the national road authority (demanding a minimum 28-day compressive strength of 32 MPa), the $w/c \leq 0.5$ and $p/c \leq 1$ was found to be applicable for road construction. At the optimum p/c ratio, the flexural strength of RCA-PVA was approximately 130% higher than that of the RCA concrete.

The outcome of this research confirms the viability of using PVA to improve the flexural strength of RCA concrete to be used as an alternative sustainable rigid pavement.

ACKNOWLEDGEMENTS

This work is financially supported from the Thailand Research Fund under the TRF Senior Research Scholar program Grant No. RTA5680002 and the Ph.D. Royal Jubilee program Grant No.0143/2557, Suranaree University of Technology. The first author is grateful to the Thailand Research Fund for Ph.D. study financial support under the Ph.D. Royal Jubilee program.

REFERENCES

- [1] S.H. Kosmatka, W.C. Panarese, B. Kerkhoff, Design and control of concrete mixtures, Portland Cement Association. 5420 (2002) 60077-1083.
- [2] M.M. Disfani, A. Arulrajah, H. Haghihi, A. Mohammadinia, S. Horpibulsuk, Flexural beam fatigue strength evaluation of crushed brick as a supplementary material in cement stabilized recycled concrete aggregates, *Construction and Building Materials*. 68 (2014) 667-676.
- [3] A. Arulrajah, M.M. Disfani, H. Haghihi, A. Mohammadinia, S. Horpibulsuk, Modulus of rupture evaluation of cement stabilized recycled glass/recycled concrete aggregate blends, *Construction and Building Materials*. 84 (2015) 146-155.
- [4] R.V. Silva, J. de Brito, R.K. Dhir, Properties and composition of recycled aggregates from construction and demolition waste suitable for concrete production, *Construction and Building Materials*. 2014. 65: p. 201-217.
- [5] M. Behera, S.K. Bhattacharyya, A.K. Minocha, R. Deoliya, S. Maiti, Recycled aggregate from C&D waste & its use in concrete – A breakthrough towards sustainability in construction sector: A review, *Construction and Building Materials*. 68 (2014) 501-516.
- [6] H. Dilbas, M. Şimşek, Ö. Çakır, An investigation on mechanical and physical properties of recycled aggregate concrete (RAC) with and without silica fume, *Construction and Building Materials*. 61 (2014) 50-59.
- [7] S. Omary, E. Ghorbel, G. Wardeh, Relationships between recycled concrete aggregates characteristics and recycled aggregates concretes properties, *Construction and Building Materials*. 108 (2016) 163-174.
- [8] M.S. Otsuki, W. Yodsudjai, Influence of recycled aggregate on interfacial transition zone, strength chloride penetration and carbonation of concrete, *Journal of Materials in Civil Engineering*. 15(5) (2003) 443-51.
- [9] M.T. Nogchi, Concrete design towards complete recycling, *Structural Concrete* 2. 3(2001) 155 – 167.
- [10] FT. Olorunsogo, N. Padayachee, Performance of recycled aggregate concrete monitored by durability indexes, *Cement and Concrete Research*. (2002) 179-85.
- [11] V.W.Y. Tam, X.F. Gao, C.M. Tam, Microstructural analysis of recycled aggregate concrete produced from two-stage mixing approach, *Cement and Concrete Research*. 35(6) (2005) 1195-1203.
- [12] P. Sukontasukkul, Tensile Behaviour of Hybrid Fibre Reinforced Concrete, *Advances in Cement Research*. 16(3) (2004) 115-122.
- [13] P. Viswanath, E.T. Thachil, Properties of polyvinyl alcohol cement pastes, *Materials and Structures*. 41(1) (2008) 123-130.
- [14] A. Allahverdi, K. Kianpur, M. Moghbeli, Effect of polyvinyl alcohol on flexural strength and some important physical properties of Portland cement paste, *Iranian Journal of Materials Science & Engineering*. 7(1) (2010)
- [15] Jaroslav Topica, Zdenek Proëka, Katerina Indrová, V. Tomáš Plachá, Lubomír Kopecký, Pavel Tesárek, EFFECT OF PVA MODIFICATION ON THE PROPERTIES OF CEMENT COMPOSITES, *Acta Polytechnica*. 55(1) (2015) 64-75.
- [16] H.-J. Chen, T. Yen, K.-H. Chen, Use of building rubbles as recycled aggregates, *Cement and Concrete Research*. 33(1) (2003) 125-132.
- [17] J.H. Kim, R.E. Robertson, Effects of Polyvinyl Alcohol on Aggregate-Paste Bond Strength and the Interfacial Transition Zone, *Advanced Cement Based Materials*. 8(2) (1998) 66-76.
- [18] ASTM C33, Standard Specification for Concrete Aggregates, ASTM International, 2016.
- [19] ASTM C191, Standard Test Methods for Time of Setting of Hydraulic Cement by Vicat Needle, ASTM International, 2013.
- [20] ASTM C192, Standard Practice for Making and Curing Concrete Test Specimens in the Laboratory, ASTM International, 2016.
- [21] ASTM C39, Standard Test Method for Compressive Strength of Cylindrical Concrete Specimens, ASTM International, 2016.
- [22] ASTM C293, Standard Test Method for Flexural Strength of Concrete (Using Simple Beam With Center-Point Loading), ASTM International, 2016.
- [23] H. Ait-Aider, N.E. Hannachi, M. Mouret, Importance of W/C ratio on compressive strength of concrete in hot climate conditions, *Building and Environment*. 42(6) (2007) 2461-2465.
- [24] Thailand Department of Highways. (1996). "Standards for highway construction." DH-S309/2544, Bangkok, Thailand.

Environment

OPERATING CONDITIONS EFFECTS OF AN ELECTRODIALYSIS MODULE ON HYDROCHLORIC ACID AND HYDROXIDE FORMATION FROM A SODIUM CHLORIDE MODEL SOLUTION

Medina Juan¹, Diaz Zoila² y Rojas Jorge³
Facultad Ingeniería Química, Universidad Nacional del Callao, Perú

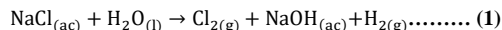
ABSTRACT

The operating conditions effect on the formation of hydrochloric acid and sodium hydroxide from the sodium chloride model solution has been studied using an electrodialysis module built at laboratory scale. In order to experiment with the electrodialysis module, a laboratory scale discontinuous equipment was used, this equipment contained two selective membranes, one cationic and one anionic (5 and 20 V) for a treatment time of 210 minutes. Both the acid solution and the basic solution reached a 0,22 N and 0,25N concentration, respectively. To reach the best operating condition a 15V tension was applied. Both the acid solution and the basic solution concentration was 0,05N and the model solution concentration 50g/L; the energy consumption of NaOH was 14,9 kWh / Kg, and and the current efficiency 53.5%.

Keywords: electrodialysis, bipolar electrodialysis, electromembrane, hydrochloric acid, sodium hydroxide.

INTRODUCTION

Inorganic products such as hydrochloric acid, sulfuric acid, phosphoric acid, nitric acid and sodium hydroxide are indispensable in many industrial processes, such as fertilizers, pickling, electroplating, steelmaking, water treatment etc. As the population and the development of the industry increase, the consumption of these chemicals must increase in the future. The chlorine alkali industry produces chlorine, sodium hydroxide and hydrogen by electrolysis of NaCl aqueous solutions as indicated in the following chemical equation



At present, the chlor-alkali process is mainly represented by three technologies; mercury cell, diaphragm and membrane cell. The main difference between these technologies is cell configuration and use of different materials. According to Fig. N° 1, a general scheme of the chlor-alkali process is shown.

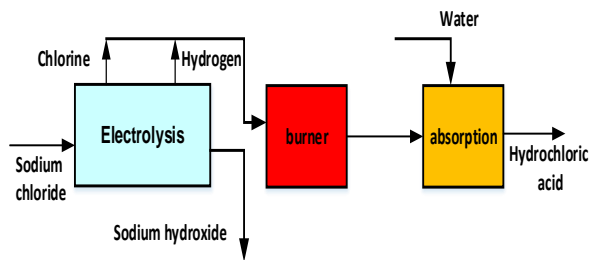


Fig. N° 1 NaOH and HCl production

According to the diagram, sodium hydroxide is produced at the electrolysis stage, however, to produce hydrochloric acid other traditional operations are needed, such as a combustion furnace and absorption column. In these traditional processes, mercury and asbestos emissions occur. This has led to the search for new alternatives to eliminate these stages of the traditional process.

Electrodialysis is a process of separation of ionic species from aqueous solutions, based on the selective migration of ions through ion exchange membranes under the influence of a direct current electric field. These processes generally contain two types of ion exchange membranes; anionic membranes (MA) selectively permeable to anions and cationic membranes (MC) which are selective to cations, placed alternately and separated by expansion joints between two electrodes.

When an electric potential is applied to the electrodes, the migration of ions to the electrodes with opposite charge begins. The cations penetrate the cationic membranes, but these are blocked by the anionic membrane. Similarly, the anions penetrate the anionic membranes but the atonic membranes block the anions. The process at the end results in increasing the concentration in one of the compartments and dilution in another compartment. Inorganic and organic sales found in effluents, such as sodium chloride, sodium sulfate, sodium nitrate, sodium acetate, etc., can

become its parameters and bases due to bipolar electro dialysis.

The ion exchange membranes can take different possible configurations forming cells of two or more compartments, each of these configurations can have various possible applications, such as desalination of brackish water, demineralization of wine, formation of hydrochloric acid and sodium hydroxide, etc. The purpose of this investigation is, first, to obtain NaOH and HCl by electro dialysis instead of NaOH, Cl₂, H₂ and second, to carry out a study of the influence of the operation variables such as initial acid concentration, base concentration of sodium chloride and electric potential on the final acid concentration and base concentration, in addition to the process efficiency and energy consumption, the latter is fundamental to understand the process economy and scalability.

MATERIALS AND METHODS

Materials

Both analytical grade reagents such as Na₂SO₄, NaCl, NaOH y HCl and deionized water produced by EDI equipment were used throughout the experience. The acid and base solutions were generated using feed solutions consisting of 0.01, 0.025 and 0.05 N of hydrochloric acid and sodium hydroxide, 5.20 and 50 g / L NaCl and applied voltage of 5-15. Volts maintaining a constant concentration of 0.05 M H₂SO₄.

Membranes

Two commercial membrane clases were selected in this work, from the company FuMA-Tech GumbH, Germany.

Table 1 Membrane characteristics

Membrane Characteristics	Cationic Membrane (FTCM-E)	Anionic Membrane (FTAM-E)
- Electric resistance (Ω/cm ²)	2,5- 3,5	2,5- 3,5
-Exchange capacity (meq/g)	1,5 - 1,8	1,4 - 1,7
-Thickness (mm)	0,17 - 0,19	0,16 - 0,18

Membrane Configuration

Figure N°2 shows the configuration of the membranes, one anionic and two cation exchange membranes placed between the cathode and the anode

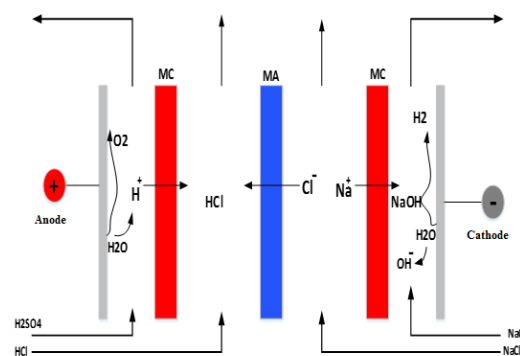


Fig. 2 Membrane Configuration

Electrolysis equipment

The cell built was a press filter type laboratory scale with four compartments, It was built with acrylic material on which three membranes were assembled with their respective turbulence promoters, and secured with 8 transverse bars with nuts to prevent any type of leakage, mixed or spilled liquid. Two acrylic plates with two inlets and two outlets at the end, disposed for the flow of salt and hydrochloric acid solutions. Two 1.5 cm thick acrylic frames, where two electrodes (of 100 cm² effective area) are inserted, made of steel and platinum titanium, each acrylic plate contains an inlet and outlet through which passes the sodium hydroxide solution and the diluted solution of sulfuric acid. The dimension of each membrane is 10 cm × 9 cm. All experiments were performed in a batch mode at room temperature. The acid, base and salt solutions were recirculated by pumps independently, he flow rate was regulated by a step valve. The initial volume of solutions in each compartment was 500 mL. The voltage and current were recorded directly from the electrical source. the time used for each experiment was 210 min.

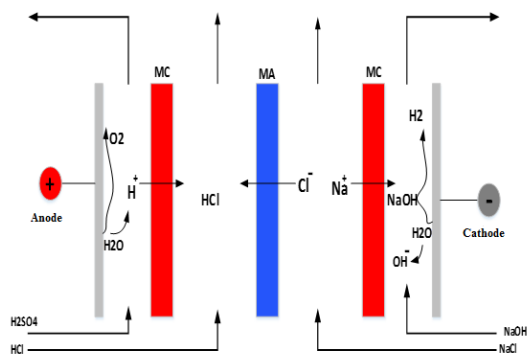


Fig. 3 Experimental equipment

Analytical methods

The concentrations of NaOH and HCl formed were determined by titration with a standard concentration of 0.01 mol / L of hydrochloric acid and sodium hydroxide. The chloride ions by titration of 0.01N silver nitrate. the conductivity was measured using an ADWA AD 330 Conductimeter and the pH in the acid and base compartment was measured by a ADWA Switzerland pH meter.

Process indicators and electro dialysis

Separation percentage

The separation percentage is evaluated by equation (1). The concentration or conductivity is measured at the beginning and then at a certain time.

$$S = \left(\frac{C_{t=0} - C_{t=t}}{C_{t=0}} \right) \times 100\% \dots \dots \dots (2)$$

Base acid concentration

Changes in the concentration of hydrochloric acid and sodium hydroxide were determined by titration using phenolphthalein as an indicator. The concentration is calculated using the following equations (4)

$$C_{HCl} = \frac{C_{NaOH} \times V_{NaOH}}{V_{HCl}} \dots \dots \dots (3)$$

$$C_{NaOH} = \frac{C_{HCl} \times V_{HCl}}{V_{NaOH}} \dots \dots \dots (4)$$

HCl, NaOH mol/L; V_{HCl} , V_{NaOH} (liters).

Efficiency electric current

The current efficiency (η) for a specific product is an important critical parameter to assess the viability of ED since it determines the applied current fraction that is effectively converted.

$$\eta = \frac{zF(C_f - C_i)V_t}{N \int_0^t i dt} \times 100\% \dots \dots \dots (5)$$

η : current efficiency: Faraday constant (96500A.s/mol), C_f , C_i - initial and final concentration of HCl solution (mol/m³); i , electric current intensity (A) and N , number of cell pairs. V_t volume of recirculated HCl solution

Energy consumption

The energy consumption was determined by the equation (3)

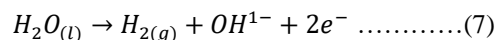
$$E = \frac{V \int i dt}{C_t V_t P.F} \dots \dots \dots (6)$$

Where: E (Kwh/kg) is the required energy consumption to form the acid and base, i (t) electric current, V is the cell potential difference t : time V_t : volume (m³) as a function of time, HCl solution final concentration mol/m³.

RESULTS ANALYSIS

pH evolution in the acid and base compartment

Figures 4 and 5 show the pH changes in the compartments of both sodium hydroxide formation and hydrochloric acid, the graphs tendency is explained in terms of the chemical reactions. In the base compartment, water is decomposed by electric current producing hydroxyl ions and hydrogen gas as indicated in the following equation.



The sodium ions of the sodium chloride compartment are permeable to the cathode through the cation exchange membrane forming sodium hydroxide

together with the oxydryl ions as indicated the equation.



The pH in this compartment increases over time due to the formation of oxydryl ions, sodium ions and sodium hydroxide concentration formed as a function of time. The figure 4 shows the pH increases more quickly when a voltage of 15 volts is applied. regardless of the initial concentration of NaOH in the range of 0.01 and 0.05 N.

In the acid compartment, the hydronium ions produced at the anode are permeable by the cationic membrane and combined with the chloride ions which are permeable by the anionic membrane forming hydrochloric acid according to the following reaction.

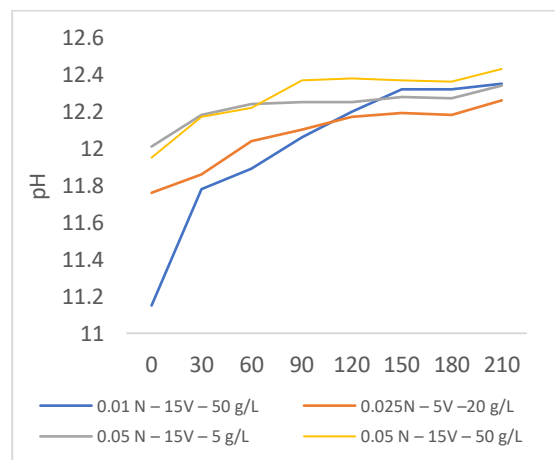
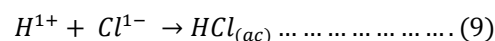


Fig.4 pH dependence in the base compartment

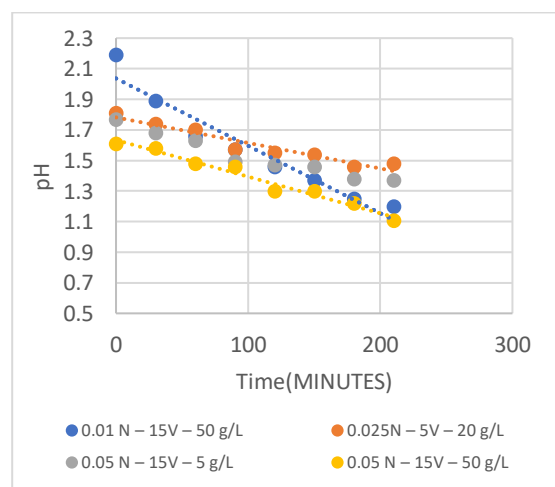


Fig.5 pH dependence in the acid compartment

Figure N°5 shows that pH decreases rapidly when a voltage of 15 volts is applied

Evolution of the acid and sodium hydroxide concentration

Figure 6 and 7 show the increase in the acid and base concentration is more significant when a voltage of 15 V is applied and it is more significant for the acid when the initial concentration is 0.05 N. The hydrochloric acid concentration reached is 0.22 N and sodium hydroxide 0.25 N for initial contractions of 0.05 N at 15 volts.

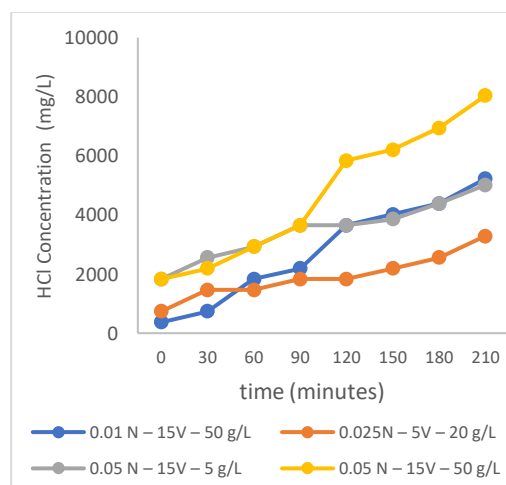


Fig.6 Changes of HCl (mg / L) concentration

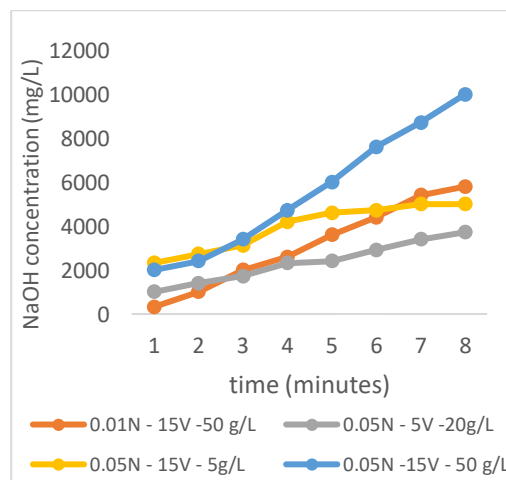


Fig.7 Changes of NaOH (mg / L) concentration

Change in conductivity of base acid

Figures 8 and 9 show that the conductivity trend grows over time for both the acid and the base, the acid conductivity grows faster than the base reaching 63.5 ms / cm, with a voltage of 15 volts for the base of 35.2 mS/cm

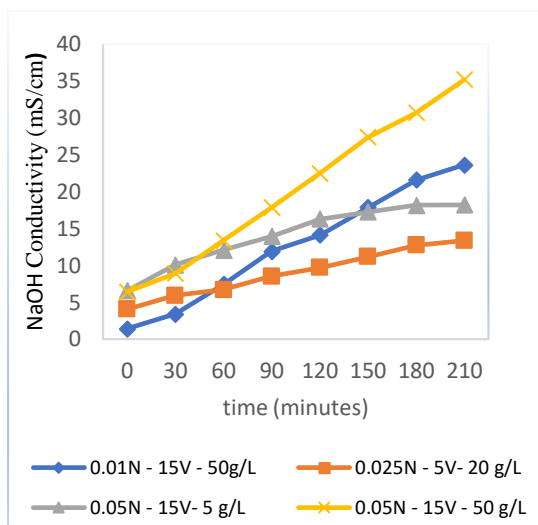


Fig.8 Change of NaOH Conductivity

Figure 10 shows that the conductivity of sodium chloride decreases, and at equation (2) the separation percentages have been evaluated at an applied voltage of 15 volts, obtaining 19.3% when the concentration of sodium chloride is 50g / L and 95.28% when the concentration of sodium chloride is 5g / L.

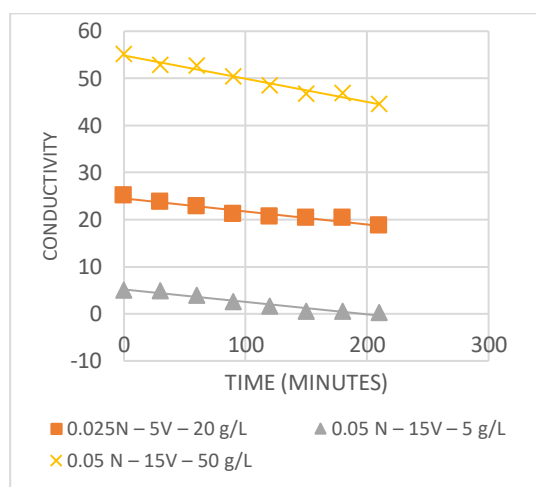


Fig.10 Changes of NaCl Conductivity (mS/cm)

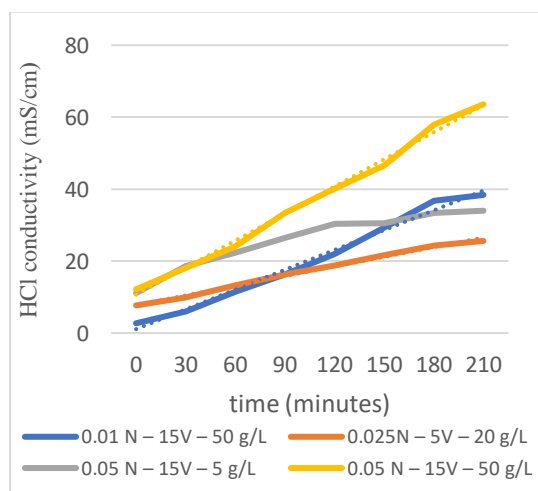


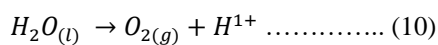
Fig.9 Change of HCl Conductivity

Variation of conductivity of NaCl

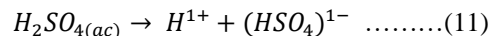
In the sodium chloride compartment, a gradual decrease in conductivity is observed as a function of time, which is the result of the diffusion of sodium ions by the cationic membrane and the chloride ions that are permeable through the anionic membrane.

Conductivity evolution of sulfuric acid

In this compartment, water decomposes into hydronium ions and oxygen ions due to the action of electric current as indicated the equation



In the first ionization stage, the sulfuric acid in aqueous solution produces hydronium ions



Simultaneously hydronium ions are permeable by the cationic membrane to the acid compartment. As expected, the conductivity and contraction of sulfuric acid in this compartment varied slightly throughout the experiment, as indicated in figure 11, due to the formation and disappearance of hydronium ions, independently of the applied electrical voltage.

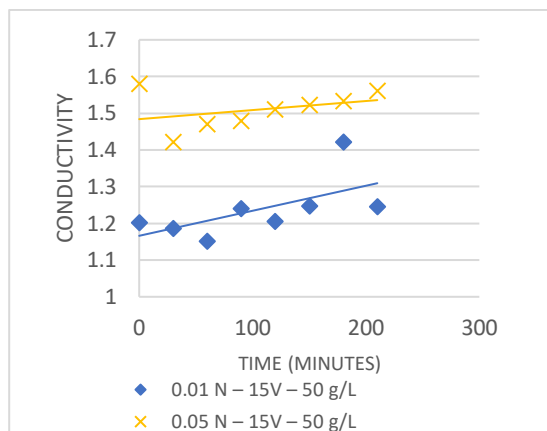


Fig. 11 Changes of sulfuric acid (mS/cm) Conductivity

Effect of initial concentration of hydrochloric acid and sodium hydroxide

To determine the evolution of initial concentrations of HCl and NaOH it was necessary to work with two initial concentrations of NaCl (20g/L and 50g/L) and two different electrical voltages (10v and 15v). The acid and base initial concentrations were 0,01N, 0,02N and 0,05N.

Considering 50g/L of NaCl as initial concentration, figure 12 shows the best result to 0,05N initial concentration of acid when a voltage of 10v is applied reached 0,14N and 0,22N when a voltage of 15v is applied. At the same figure, NaOH initial concentration is 0,05N and reached a final concentration of 0,22N when a voltage of 10v is applied, and 0,25N when a voltage of 15v is applied.

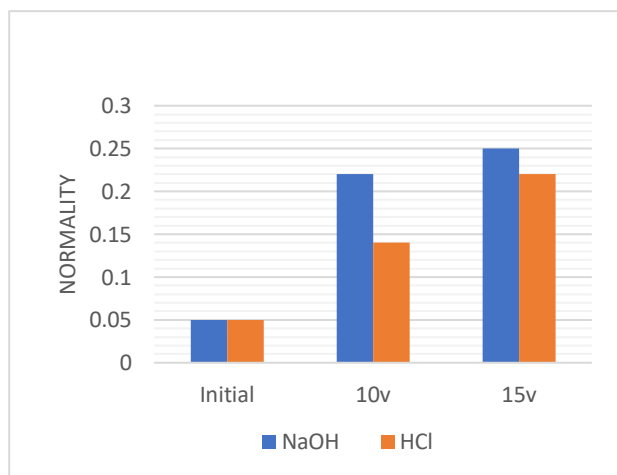


Fig.12 Evolution of normal concentration of HCl and NaOH

Effect of applied electrical voltage

Figure 6 and figure 7 show that, when the module worked with a voltage of 15 volts, it was possible to obtain the highest concentration of acid (8030mg/L - 0.22 N) and base (10000mg/L - 0.25 N) at initial concentrations of HCl (1825 mg/L- 0,05 N) and NaOH (2 000 mg/L -0,050 N) using 50 g / L of NaCl.

Equations 5 and 6 have evaluated the specific energy consumption, obtaining 14.9 kWh / Kg of NaOH, and the current efficiency was 53.5% at the most adequate operating conditions of the electrodialysis equipment.

CONCLUSIONS

Electrodialysis (ED) represents a method of separating chloride anions, sodium cations from a sodium chloride model solution and simultaneously obtaining aqueous solutions of hydrochloric acid and sodium hydroxide in different compartments.

ED with ionic membranes offers a clean technology, compared to traditional processes for the production of acid and base. In this study, it was shown that according to the sodium chloride feed concentration, the applied voltage and the initial concentration of the acid and base, the results show that when the applied voltage is 15 volts, the initial concentration of the acid and base is 0.05N and 50 g/L of NaCl an acid concentration 0.22N and 0.25N of sodium hydroxide is reached.

ACKNOWLEDGEMENTS

We thank National University of Callao for the financial support that made possible the development of this investigation.

REFERENCES

- [1] R. Ibáñez, A. Pérez-González, P. Gómez, A.M. Urtiaga, I. Ortiz, Acid and base recovery from softened reverse osmosis (RO) brines. Experimental assessment using model concentrates, *Desalination* 309 (2013) 165–170.
- [2] S. Koter, A. Warszawski Electromembrane Processes in Environment Protection Polish Journal of Environmental Studies Vol. 9, No. 1 (2000), 45-56
- [3] Jiangnan Shen, Zhendong Hou, Congjie Gao Using bipolar membrane electrodialysis to synthesize di-quaternary ammonium hydroxide and optimization design by response surface methodology
- [4] F. Schaffner a, P.-Y. Pontaher , V, Sanchez b, F. Lutin ° Comparison of diester waste treatment by conventional and bipolar electrodialysis *Desalination* 170 (2004) 113-121
- [5] Ochoa Gomez, J. (1996). “Electrosíntesis y Electrodiálisis” (Fundamentos, aplicaciones tecnológicas y tendencias) (2a ed), Cap.7; Mc Graw - Hill, Madrid, España, 199-237.
- [6] Shaposhinik, V.A., Zubets, N.N and Mill, B.E. (2001). Demineralization of wáter by electrodialysis with ion-exchange membranes, grains and nets, *Desalination*, 133, 211-214.
- [7] Mohammadi, T. and Kaviani, A. (2003). Water shortage and seawater desalination by electrodialysis, *Desalination*, 158, 267-270.
- [8] Mohammadi, T. and Kaviani, A. (2005). Modeling of metal ion removal from wastewater by electrodyalisis, *Sep Purif. Technol*, 41, 73-82.
- [9] Mohammadi, T. and Kaviani, A. (2007). Separation of Different Ions from Wastewater at Various Operating Conditions Using Electrodialysis, *Sep Purif. Technol*, 54, 147-156.
- [10] Montalvo, A., Rodríguez Torres, L.G., Govea Hernández, I., M., & Delgadillo Gómez, J.A (2002). Estudio de la densidad de corriente límite en una celda de electrodiálisis en función de la concentración y la velocidad. Facultad de Ingeniería – Instituto de Metalurgia Universidad Autónoma de San Luis Potosí.
- [11] Cowan, D.A., Brown, H.J. (1959). Efecto de la turbulencia en la corriente límite en las celdas de electrodiálisis, *Int Engng. Chem*, 51, 1445.
- [12] Lee, H. J., Strathmann, H. and Moon, S.H. (2006). *Desalination*, 190, 43.
- [13] Banasiak, L.J., and Kruttschnitt, T.W. (2007). Desalination using electrodialysis as a function of voltaje and salt concentration, *Desalination*, 205, 38-46.
- [14] Sadrazadeh, M. and Mohammadi, T. (2008). Sea water desalination using electrodialysis, *Desalination*, 221, 440–447.

WOODY DEBRIS RECRUITMENT CAUSED BY DISASTERS RELATED TO TROPICAL STORM NANMADOL (2017) IN HEADWATER OF ASAKURA CITY, FUKUOKA, JAPAN

Thapthai Chaithong¹, Daisuke Komori² and Yuto Sukegawa³

¹Graduate School of Environmental Studies, Tohoku University, Japan; ^{2,3} Graduate School of Engineering,
Tohoku University, Japan

ABSTRACT

Woody debris is a natural component of the ecosystem. It is caused by trees that have fallen and been entrained by natural disasters related to storms, such as shallow landslides, debris flow or floods, into streams or storage on the hillslope. On 4 July 2017, Tropical Storm Nanmadol made landfall on the island of Kyushu, south of the Japanese mainland. It brought heavy rainfall, floods and shallow landslides to many cities on the island of Kyushu, particularly the city of Asakura in Fukuoka Prefecture. The maximum hourly rainfall measured by the Japan Meteorological Agency at the Asakura station was 106 mm on 5 July 2017 at 6:00 p.m., and the cumulative rainfall between 4 and 6 July 2017 was approximately 590 mm. In this study, the post-disaster areas in the town of Asakura were examined after the passage of Tropical Storm Nanmadol. From these observations, we found that a significant cause of woody debris recruitment is shallow landslides, which cause the collapse of trees. The debris flow process acts as a conveyor that channels woody debris from the hillslope or origin of the landslide downward. Floods or fluvial processes in the river entrain the woody debris downstream. The volume of woody debris recruitment during this particular event was approximately 257,000 m³.

Keywords: Woody debris, Natural dam, Tropical storm, Disasters, Landslide, Flood, Debris flow

INTRODUCTION

Woody debris can be defined as logs, branches, root wads and other wooden material. Such materials play multiple roles in the ecosystem and human life. On the positive side, they have an important role in the carbon budget and nutrient cycle in forests, including forming the river habitats of fishes and other aquatic organisms [1,2]. On the negative side, they may increase the tendency of natural disasters to destroy infrastructure and housing in the event of flash floods, landslides and debris flow. Numerous studies have reported that a lot of woody debris was generated and set loose after the tropical storm made landfall. Heavy rainfall caused by extreme storms can lead to an increase in the pore water pressure or groundwater table in the soil slope and may increase the river discharge. These processes are the cause of landslides, debris flows and flash floods, as well as stream bank erosion. In 2005, an extreme flood in Switzerland entrained a volume of woody debris in excess of 69,000 m³. In August 2009, approximately 603 m³ of woody debris flowed into the downstream area of the Qijiawan catchment in Taiwan after Typhoon Morakot [3].

An examination of the historical cases of woody debris linked to heavy rainfall in Japan reveals several past cases. For instance, when Typhoon Etou hit the island of Hokkaido in 2003, approximately 50,000 m³ of woody debris was entrained by the flood into the

Nibutani Dam [4]. Moreover, enormous amounts of woody debris were generated by landslides, bank erosion and debris flows related to Typhoon Lionrock in 2016 [5]. Hence, precipitation plays a significant role in the recruitment process of woody debris. In 2017, the Pacific typhoon season produced a total of 27 named storms. Tropical Storm Nanmadol is the third name of tropical cyclone that it was Typhoon No. 1703. It hit the Island of Kyushu, to the south of the Japanese mainland, between 4 and 7 July 2017. Enormous quantities of woody debris were subsequently found in the city of Asakura in Fukuoka Prefecture. A further 2,033 m³ of woody and other debris was removed from the Ariake Sea by the Fukuoka Ariake Fishery Association, the Saga Ariake Fishery Association and the Japanese Ministry of Land, Infrastructure, Transport and Tourism [6].

The aims of this study are as follows: (1) to present the results of the post-disaster investigation related to woody debris recruitment in Asakura city and 2) to examine the characteristics of woody debris dam formation and woody debris transport processes.

TROPICAL STORM NANMADOL (2017) AND AFTERMATH

In Japan, Typhoon season runs from July to October [7]. Tropical Storm Nanmadol made landfall on Kyushu on 4 July 2017 with a wind speed of

approximately 74 km/h (40 knots). At its peak, the storm reached a wind speed of 101 km/h (55 knots) and a minimum atmospheric pressure of 985 hPa. The average wind speed was 81 km/h (44 knots). Figure 1 shows the path of the storm and the distribution of cumulative rainfall on the island of Kyushu between 4 and 6 July 2017. The storm brought more than 140 mm of rainfall in 72 hours in Saga, Fukuoka, Oita, Kumamoto and Nagasaki Prefectures. The maximum rainfall in a single 24-hour period, 514 mm, was recorded at Asakura station in the city of Asakura. This figure constitutes more than a quarter of the site's average annual rainfall of 1,918 mm (as measured from 1976 to 2017). The storm was characterised by the delivery of a high volume of intense rainfall in a short period of time; in addition,

the pattern of rainfall was similar to an advanced rainfall pattern.

The Kyushu Regional Development Bureau, which forms part of the Ministry of Land, Infrastructure, Transport and Tourism (MLIT) [6], reported that 266 houses were completely destroyed. A further 850 sustained extensive damage, with 360 suffering substantial flooding above the floor, while 1,341 experienced less substantial immersion. A total of 26 lives were lost and 14 people were injured during the storm. A further five persons were declared missing. Figure 2 shows the damage done to houses in the city of Asakura by Tropical Storm Nanmadol. Figure 3 shows the river bank damage caused by the storm.

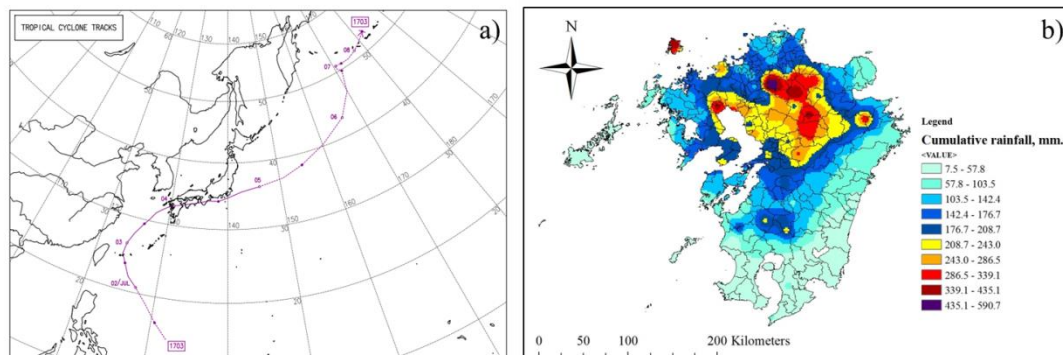


Fig. 1 (a) Path of Tropical Storm Nanmadol 2017 [8] and (b) cumulative rainfall from 4 to 6 July 2017.



Fig. 2 House damage caused by Tropical Storm Nanmadol.



Fig. 3 River bank damage caused by Tropical Storm Nanmadol.

DESCRIPTION OF STUDY AREA, FIELD SURVEY AND CHARACTERISTICS OF SHALLOW LANDSLIDES

Study area and field survey

The study area is the city of Asakura in Fukuoka Prefecture, on the island of Kyushu, Japan. Asakura suffered serious damage as a result of flooding, woody debris and landslides related to Tropical Storm

Nanmadol. Eight sites in the city of Asakura were investigated by our team after the passage of the storm. The sites examined by our team are located at the small headwaters in the city. Sugi, or Japanese cedar (*Cryptomeria japonica*), hinoki cypress (*Chamaecyparis obtusa*) and bamboo are the plants most prevalent at the investigated sites. Our team also used aerial photographs to investigate the location of woody debris deposition in the river channel. In addition, the woody debris that had flowed to the

Terauchi and Egawa Dams was also measured. Figure 4 shows the location of the city of Asakura.

For the field survey, the diameter and age of trees were measured for individual pieces of wood found in the Terauchi and Egawa Dams. The team measured the dimensions, such as the length, height, and width,

as well as the latitude and longitude of the debris. Moreover, the height and the diameter at breast height (BHD) were measured at the investigated sites. A laser measuring device and measuring tape were the main instruments used to measure the dimensions.

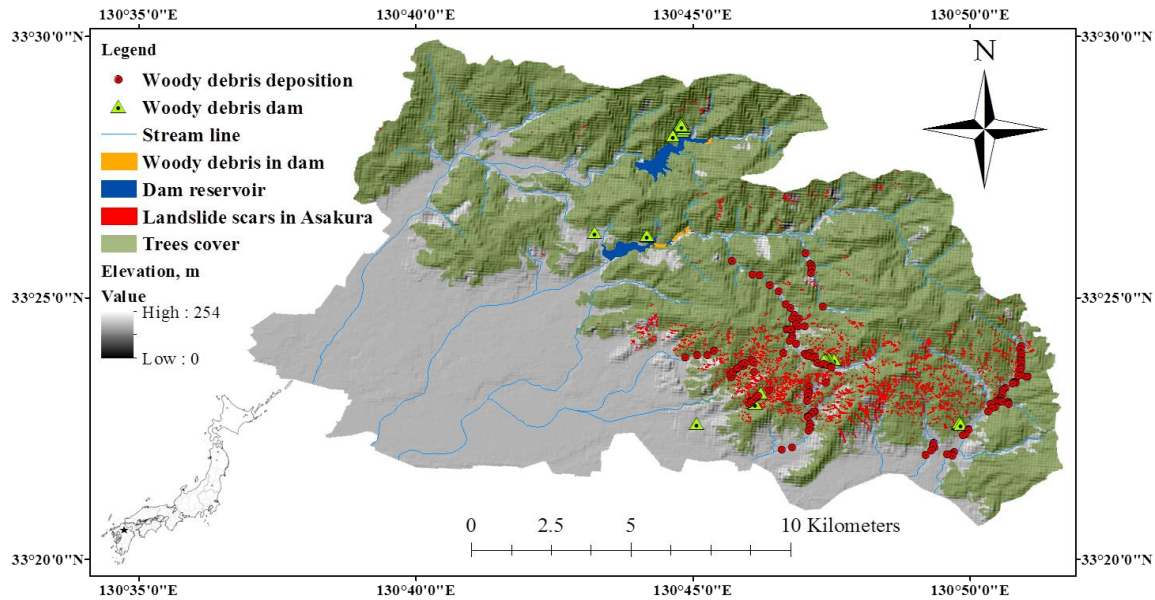


Fig. 4 Location of woody debris, landslides and dams in city of Asakura, Fukuoka, Japan.

Characteristic of shallow landslides

Figure 5 plots the number of shallow landslides, landslide ratio and slope angle. A slope angle map was extracted from a digital elevation model (DEM) to determine the relationship between shallow landslides and slope angles. Most landslide scars were found on slopes ranging in angle from 20 to 30 degrees. These accounted for approximately 27% of the total landslide scars. The landslide ratio is the ratio between the landslide area and the total area of the city of Asakura. The maximum landslide ratio occurred in slopes with angles ranging from 20 to 50 degrees. A review of the landslide areas reveals that approximately 90 per cent of landslides occurred in areas covered by trees. As a result, the landslides produced a vast quantity of woody debris.

CONCEPT OF WOODY DEBRIS BUDGETS

Woody debris budgets are mass budgets of woody debris in streams that were developed with the aim of explaining the recruitment, storage, transport and decay of woody debris for the purposes of quantitative analysis and prediction. Equation (1) is the volumetric mass balance of woody debris in a unit length of stream and is calculated based on the differences in input, output and decay [9].

$$\Delta S_c = [L_i - L_o + Q_i / \Delta x - Q_o / \Delta x - D] \Delta t \quad (1)$$

where ΔS_c is a change in storage with a unit length of stream Δx over time interval Δt . L_i is lateral woody material recruitment. L_o is the loss of woody material caused by lateral deposition. Q_i is the input of woody segment caused by fluvial transport. Q_o is the output of woody segment caused by fluvial transport. D is the in-situ decay of woody material.

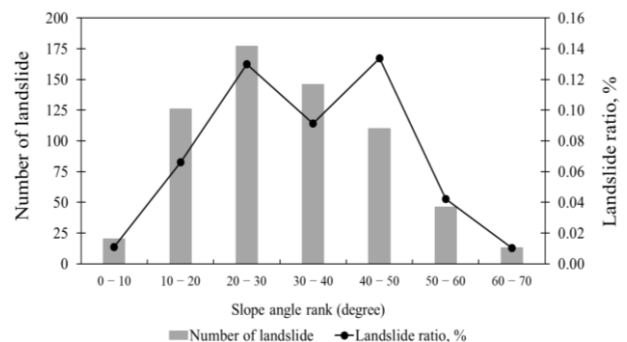


Fig. 5 Landslide area and ratio of each slope in city of Asakura, Fukuoka, Japan.

In this study, Eq. (1) is modified to a watershed system so that the modified woody debris budgets concerned both natural processes and human activity.

Equation (2) is the volumetric mass balance of woody debris in a watershed system and is a consequence of differences in input, output and decay.

$$\Delta S = [R_i + Q_i + Q_o - D] \Delta t \quad (2)$$

where ΔS is a change in the woody material storage in the watershed over time interval Δt . R_i is the woody material recruitment from the resources caused by natural processes and human activities. Q_i is the input of woody material into the watershed system from other watershed systems, whereas Q_o is the loss of woody material out of the watershed system caused by natural processes and human activities. D is the in-situ decay of woody material. Figure 6 provides an overview of the woody debris budget in the watershed system.

In relation to woody debris storage in the watershed, we draw a distinction between two main locations: within the active stream channel and outside of the active stream channel. The active stream channel is the zone that is influenced by the flood or debris flow.

$$\Delta S = \Delta S_c + \Delta S_h \quad (3)$$

where ΔS_c is the woody debris storage in the active stream channel and ΔS_h is the woody debris storage outside of the active stream channel, such as on the hillslope.

Woody debris recruitment to the watershed system represents several types of supply. In a simplified calculation, woody debris recruitment is divided into two principal sources: natural processes and human activities.

$$R_i = R_n + R_m \quad (4)$$

where R_n is woody material recruitment by natural processes such as landslides, debris flow, windstorms, snow avalanches and fires and R_m is woody material recruitment by human activities such as tree-felling.

In relation to the parameter R_n , we found that landslides play a significant role in the recruitment process. Hence, we can calculate the woody debris recruitment caused by landslide events using the areas of landslides and the properties of the forest, such as tree density in the forest and the volume of individual trees.

$$R_{n,l} = A_l \times V_t \times D_t \quad (5)$$

where $R_{n,l}$ is the woody debris recruitment by landslide, A_l is the area of the landslide, D_t is the tree density in the forest and V_t is the volume of an individual tree. In our case, the volume of an individual tree is calculated based on Huber's

equation [10]. The piece length is replaced by the tree height and the cross-sectional area at the longitudinal midpoint is replaced by the cross-sectional area of the tree at breast height.

$$V_t = H_t \times A_{BHD} \quad (6)$$

where H_t is the height of the tree and A_{BHD} is the cross-sectional area of the tree at breast-height. The decay of woody debris can be divided into five decay classes, as shown in Table 1.

Table 1 Decay classes of woody debris [11]

Decay class	Appearance of decaying fallen logs
1	No decay, Fine twigs remaining, Bark completely remaining, No moss Wood is clear, slightly stained.
2	Slightly decayed, No fine twigs, Most bark present
3	Moderately decayed, but fallen log could support itself, Branch stubs remaining, Some bark present, Sapwood and heartwood show strong signs of decay
4	Fallen log could no longer support itself, All bark often absent, Sapwood often absent and deep red-brown heartwood could be crumbled manually
5	Wood resembles red powder with a disassembled structure, The bark is completely absent, The cross section of the bole is no longer round, but elliptical

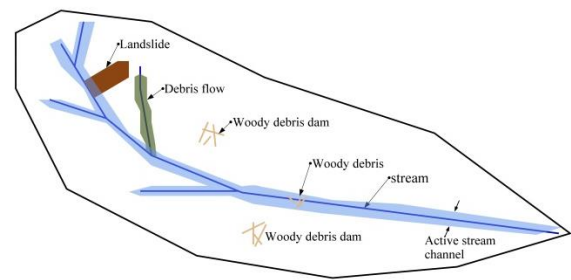


Fig. 6 Woody debris activities in the watershed.

RESULTS AND DISCUSSION

Woody debris dam in the headwaters

The site survey found the mean diameter of a piece of woody debris to be 24.9 ± 8.1 cm, whereas the maximum diameter was 48.6 m. The mean age of a piece of woody debris was 41.1 ± 16.3 years, with a maximum age of 69 years and a minimum age of 16

years. The mean length of a piece of woody debris was 12.5 ± 7.2 m. Figure 7 plots the diameter and age of pieces of woody debris. In terms of decay classes, it was observed that approximately 87 per cent of the pieces of woody debris belonged to decay class 1, with the vast majority of the remainder belonging to decay classes 2 and 3. Considering the relationship between precipitation in the southern region of Japan and woody debris, stored pieces of woody debris could be removed by typhoons and torrential rain, since tropical cyclones frequently pass over southern and central Japan. Hence, most woody debris recruited to streams falls into decay class 1 [12].

Using Eq. (5) and Eq. (6), we can estimate the potential recruitment of woody debris. The total area of landslide scars was extracted from aerial photographs taken by the Geospatial Information Authority of Japan after Tropical Storm Nanmadol passed over the city of Asakura. The total area of the landslide scars (A_l) in the city of Asakura, as shown in Figure 1, is approximately 2.82 km^2 . Tree density was measured at nine sites in the city of Asakura during the field survey, giving a mean tree density (D_l) of $0.15 \pm 0.1 \text{ trees/m}^2$. The volume of woody debris per piece was approximately 0.6 m^3 . Hence, the potential woody debris recruitment ($R_{n,l}$) caused by Tropical Storm Nanmadol is approximately $257,000 \text{ m}^3$.

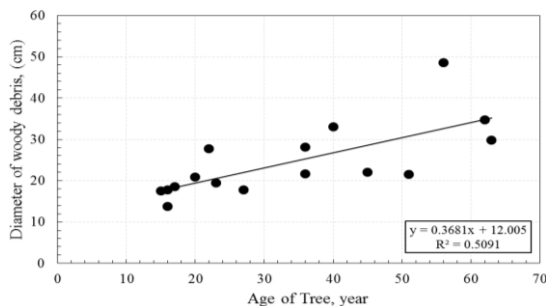


Fig. 7 Relationship between diameter and age of woody debris pieces.

In addition, an estimation of the woody debris that flowed to the Egawa and Terauchi Dams revealed that the area of woody debris recruited to the Terauchi Dam was $68,742 \text{ m}^2$, with the Egawa Dam receiving $13,583 \text{ m}^2$. By assuming that the depth of the woody debris that flowed to the two dams was equal to the mean diameter of the woody debris pieces, namely approximately 0.25 m , we estimated the volume of woody debris recruitment to Terauchi Dam at approximately $17,180 \text{ m}^3$ and to Egawa Dam at approximately $3,395 \text{ m}^3$. The woody debris in the Terauchi and Egawa Dams is outlined in yellow in Figure 1. Figure 8 shows the driftwood above the Terauchi Dam, while Figure 9 shows the driftwood above the Egawa Dam. As mentioned in the introduction, the Fukuoka Ariake Fishery Association,

the Saga Ariake Fishery Association and the Japanese Ministry of Land, Infrastructure, Transport and Tourism removed approximately $2,000 \text{ m}^3$ of woody debris from the Ariake Sea, which is located downstream from Asakura. Hence, the minimum amount of woody debris that flowed out of the city of Asakura is $22,575 \text{ m}^3$.



Fig. 8 Driftwood flows to Terauchi Dam [13].



Fig. 9 Driftwood flows to Egawa Dam [13].

In regard to the deposition of woody debris in the river channel, we found 131 points at which woody debris was deposited in the river channel in the city of Asakura. Moreover, there were two main locations of woody debris deposition: in the main river channel and on the floodplain. Figure 10 shows the location of woody debris deposition in the river.

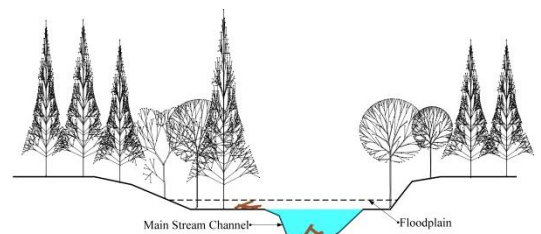


Fig. 10 Location of woody debris deposits in the river.

Woody debris dams in the headwaters

In this study, we investigated eight sites in the city of Asakura. All eight sites share steep gradient channels, small stream channels, and first- or second-order streams. Figure 11 plots the volume of the woody debris dams for these eight sites. We discovered a total of 31 woody debris dams at these eight locations. The largest such dam was 953 m³ in size and was found at station 1. When reviewing the origin of the woody debris, we found that landslides and stream bank failures were the main sources of the woody debris in the headwaters. Landslides can occur in two locations: either above the stream channel or near the stream channel. When the landslides occurred and were mobilized down the slope connected to the stream channel, the woody debris was entrained by mass movement and deposited in the stream valley. The woody debris thus deposited created a dam in the stream channel. In contrast, in the case of stream bank failure, this is the consequence of erosion; here, the erosion process may alter the soil mass of the stream bank, thereby leading to the instability of the bank slope. Figure 12 shows the landslides and stream bank failure to generate woody debris. Moreover, these sabo dams play an important role in breaking the flow of woody debris in the headwater streams; hence, we found that additional woody debris was deposited on the sabo dams, as shown in Figure 13.

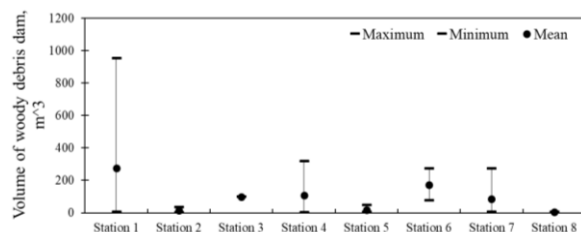


Fig. 11 Volume of woody debris dam for eight sites.



Fig. 13 Woody debris trapped at the sabo dam.



Fig. 12 a) Stream bank failure; b) landslide occurrence close to stream channel; and c) landslide occurrence above stream channel.

For five stations, the woody debris was classified as decay class 1. For two stations, the decay was classified as decay class 4. At the final station, the woody debris was classified as decay class 3. Figure 14 shows the state of decay of the woody debris dams observed at each station.

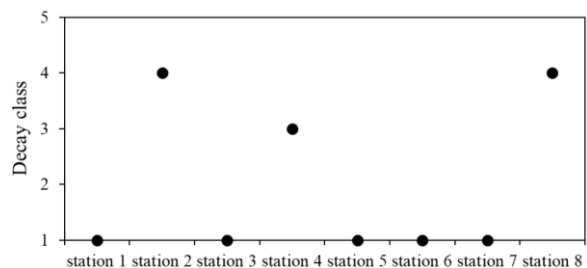


Fig. 14 State of decay of woody debris dam.

CONCLUSION

The estimated amount of woody debris generated by landslides related to Tropical Storm Nanmadol (2017) is approximately 257,000 m³. The majority of the woody debris found in the city of Asakura was fresh woody debris recruited by the landslides, debris flow and stream bank failures caused by Tropical Storm Nanmadol. We uncovered woody debris dams (decay class 1) that are thought to have been newly formed by the storm. Moreover, old woody debris dams were also found at some stations, which are believed to have formed before Tropical Storm Nanmadol. Based on the concept of the woody debris budget, woody debris storage is a common process in nature. In headwater streams, landslides and stream bank failures are the main sources of woody debris recruitment. Woody debris was entrained downstream by debris flows in the headwater stream and floods in the large stream channel.

ACKNOWLEDGEMENTS

This study was supported by the Japan Society of Civil Engineers, the Society for the Promotion of Construction Engineering, and the Social Implementation Program on Climate Change Adaptation Technology (SI-CAT). The authors are grateful to the Japan Meteorological Agency for rainfall data and the Geospatial Information Authority of Japan for the aerial photographs of landslides.

REFERENCES

- [1] Prescott C.E. and Laiho R., The Nutritional Significant of Coarse Woody Debris in Three Rocky Mountain Coniferous Forests, USDA Forest Service Gen. Tech. Rep. PSW-GTR-181, 2002, pp. 381-392.
- [2] Yan E., Wang X., and Huang j., Concept and Classification of Coarse Woody Debris in Forest Ecosystems, *Front. Biol. China*, Vol. 1, 2006, pp.76-84.
- [3] Chen S.C., Chao Y.C., and Chan H.C., Typhoon-dominated Influence on Wood Debris Distribution and Transportation in a High Gradient Headwater Catchment, *J. Mt. Sci*, Vol 10, Issue 4, 2013, pp. 509-521.
- [4] Murakami Y., Shimizu O., Sato H., and Yamada T., Sediment-related Disaster Caused by Typhoon 0310 (Etau) in Hidaka Region of Hokkaido, Japan. *International Journal of Erosion Control Engineering*, Vol. 1, 2008, pp. 30-37.
- [5] Chaithong T., Komori D., Sukegawa Y., Touge Y., Mitobe Y., Anzai S., Landslides and Precipitation Characteristics during the Typhoon Lionrock in Iwate Prefecture, Japan. *International Journal of GEOMATE*, Vol. 14, Issue 44, pp. 109-114.
- [6] Website:
http://www.qsr.mlit.go.jp/bousai_joho/H29hokubugouu.html
- [7] Abe K. and Ziemer R.R., Effect of Tree Roots on Shallow-Seated Landslides, USDA Forest Service Gen. Tech. Rep. PSW-GTR-130.1991, 1991, pp. 11-20.
- [8] Website: http://www.jma.go.jp/jma/jma-eng/jma-center/rsmc-hp-pub-eg/bstve_2017_m.html
- [9] Benda L.E., and Sias J.C., A Quantitative Framework for Evaluating the Mass Balance of In-stream Organic Debris, *Forest Ecology and Management*, Vol. 172, 2013, pp. 1-16.
- [10] Fraver S., Ringvall A., and Jonsson B.G., Refining Volume Estimates of Down Woody Debris, *Can. J. For. Res*, Vol. 37, 2007, pp. 627-633.
- [11] Sakai Y., Ugawa S., Ishizuka S., Takahashi M., and Takenaka C., Wood Density and Carbon and Nitrogen Concentrations in Deadwood of *Chamaecyparis obtuse* and *Cryptomeria japonica*, *Soil Science and Plant Nutrition*, Vol. 58, 2012, pp. 526-537.
- [12] Seo J.I., Nakamura F., Nakano D., Ichiyanagi H., and Chun K.W., Factors Controlling the Fluvial Export of Large Woody Debris, and its Contribution to Organic Carbon Budgets at Watershed Scales, *WATER RESOURCES RESEARCH*, Vol. 44, 2008, pp. 1-13.
- [13] Website:
http://www.gsi.go.jp/BOUSAI/H29hukuoka_oota-heavyrain.html

REVERSIBLE JUMP MCMC METHOD FOR HIRARCHICAL BAYESIAN MODEL SELECTION IN MA MODELS WITH EXPONENTIAL NOISE

¹Suparman

¹Faculty of Teacher Training and Education, Ahmad Dahlan University, Indonesia

ABSTRACT

The noise in the moving average (MA) model is often assumed to be normally distributed. In applications it is often found that the noise is exponentially distributed. MA model parameters include order, coefficient and noise variance. This paper proposes a procedure to estimate MA model parameters containing exponential noise. The estimation of MA model parameters is done in a hierarchical Bayesian framework. But the posterior distribution has a complex shape, the Bayes estimator cannot be determined exactly. The reversible jump Monte Carlo Markov Chain (MCMC) method is proposed to determine the Bayes estimator of the MA model parameters. The simulation result shows that this proposed method estimates MA model parameters well. As an application, MA model with exponential noise is used to model an environmental data.

Keywords: Bayesian, Moving Average, Exponential Noise, Reversible Jump MCMC

INTRODUCTION

The Autoregressive Model (AR) is a time series model used to model data in different areas of life. AR models with normal distributed errors have been extensively studied by various researchers. The AR model with exponential error has been investigated by various researchers. Shi [1] used a genetic algorithm to estimate the exponential AR model of AR. Sad [2] studied the AR model (1) whose error is exponential distributed. Larbi [3] used the Bayesian robust method to obtain the optimal bayes estimator for AR models whose errors are exponentially distributed. In the above studies, the order of the AR model is assumed to be known. Suparman [4] examined the AR model whose error is exponential distributed but the model order is unknown. The AR model was evaluated using MCMC reversible jump algorithm.

Moving Average (MA) Model is a time series model that is similar to AR model. The MA model is also used to model data in different areas of life. Rossum [5] used the MA model as a continuous quality control analysis for routine chemical tests. The MA procedure is optimized using the MA bias detection simulation procedure. Kordestani [6] used an MA filter to accelerate the acceleration signal and determine the location of the damaged steel beam. Although there are similarities between the AR model and the MA model, the MA model estimation is more difficult than the AR model estimation, especially if the order of the order MA model is unknown. In various studies, the MA model often assumes that the error is normally distributed with mean 0 and the variance unknown. However, in the

application it is often encountered that the data does not meet the assumption of normality. The estimation of MA models whose errors are exponential distributions and whose order are not known has not been investigated by researchers.

Reversible jump MCMC [7] has been applied in many areas including in signal processing and in time series data analysis. The MCMC reversible jump algorithm is used for model selection. Punsakaya [8] used the MCMC reversible jump algorithm to select a piecewise AR model that has a normal distributed error. Grummer [9] used a reversible jump for species selection. Pourhabib [10] used the MCMC reversible jump for the selection of the number and locations of the pseudo points. Fox [11] used a reversible jump MCMC to select the instrument calibration model. Newcombe [12] and Karakus [13] used a reversible jump MCMC for the selection of variables in regression. Steward [14] used a reversible jump MCMC to select non-linear models in the volterra system.

This study proposes the reversible jump MCMC method to estimate MA model parameters whose error is exponential distributed where the order is unknown. MA model parameters include order, parameter coefficients, and error variance.

METHOD

The parameter estimation is done in a bayesian framework. Bayesian estimation requires a prior distribution and likelihood function. The prior distribution and likelihood function are combined to obtain a posterior distribution. Under the quadratic loss function, the bayes estimator is obtained by

calculating the mean of the posterior distribution. Because the posterior distribution has a complex shape, the bayes estimator cannot be determined analytically. MCMC is used to determine the bayes estimator by creating a markov chain whose limit distribution is close to the posterior distribution. This markov chain is used to determine the bayes estimator. In this study, the order of the MA model is also a parameter that is estimated based on the data. This makes the dimensions of the markov chain a combination of several different dimensioned spaces. So MCMC cannot be used directly. Therefore the Reversible Jump MCMC is used to solve the problem.

The estimation procedure is as follows: First, the determination of the likelihood function, second the selection of prior distribution, third the determination of posterior distribution and the fourth determination of the bayes estimator uses reversible jump MCMC [7].

RESULTS AND DISCUSSION

The Bayesian method is used to estimate the parameters. Bayesian estimation requires a priority possibility and distribution function.

Likelihood Function

Let x_1, \dots, x_n be n data following the following MA (q) model:

$$x_t = \sum_{j=1}^q \theta_j z_{t-j} + z_t \quad (t = 1, 2, \dots, n)$$

Where $\theta^{(q)} = (\theta_1, \dots, \theta_q)$ is the coefficient vector.

Random variable z_t is the independent variable and the exponential distribution with parameter λ . The probability function z_t is

$$f(z_t | \lambda) = \lambda \exp - \lambda z_t$$

The variable transformation is used to transform from variable z to variable x . So

$$z_t = x_t - \sum_{j=1}^q \theta_j z_{t-j} \text{ and } \frac{dz_t}{dx_t} = 1.$$

Therefore, the probability density function of x_t is

$$f(x_t | \lambda) = \lambda \exp - \lambda (x_t - \sum_{j=1}^q \theta_j z_{t-j})$$

Suppose $x = (x_{q+1}, \dots, x_n)$. By taking $x_1 = \dots = x_q = 0$, the likelihood function of

x_1, \dots, x_n can be approximated by:

$$\begin{aligned} L(x | q, \theta^{(q)}, \lambda) \\ &= \prod_{t=q+1}^n f(x_t | \lambda) \\ &= \lambda^{n-q} \exp - \lambda \sum_{t=q+1}^n (x_t - \sum_{j=1}^q \theta_j z_{t-j}) \end{aligned}$$

Let I_q be the inversibility region and $\rho^{(q)} = (\rho_1, \dots, \rho_q)$ is the sample inverse partial autocorrelation vector. By using transformation

$$G : \theta^{(q)} \in I_q \rightarrow \rho^{(q)} \in]-1, 1[^q$$

Then MA(q) model is inversible if and only if $\rho^{(q)} \in]-1, 1[^q$. Finally, the approximate likelihood function of x can be written by:

$$L(x | q, \rho^{(q)}, \lambda) = \lambda^{n-q} \exp - \lambda \sum_{t=q+1}^n [x_t - \sum_{j=1}^q G^{-1}(\rho_j) z_{t-j}]$$

G^{-1} is the inverse transformation of the transformation G .

Bayesian

Before obtaining a posterior distribution, the prior distribution is selected.

Prior Distribution

The prior distribution is taken as follows. The binomial distribution is chosen as the distribution for the order q ($q = 1, 2, \dots, q_{\max}$)

$$\pi(q | \mu) = C_q^{q_{\max}} \mu^q (1 - \mu)^{1-q}$$

Where q_{\max} is the maximum for q and μ ($0 < \mu < 1$) is a hyperparameter. The uniform distribution is chosen as the distribution for the vector coefficient $\rho^{(q)}$

$$\pi(\rho^{(q)} | q) = U(-1, 1)^q$$

Also, the Jeffrey distribution is selected as the distribution for parameter λ

$$\pi(\lambda) \propto \frac{1}{\lambda}$$

Then, the hyperprior distribution for μ selected uniform distribution at interval (0,1).

Let $\pi(q, \theta^{(q)}, \lambda, \mu)$ be the prior distribution for $(q, \theta^{(q)}, \lambda, \mu)$. Since the conditional distribution of the parameter $(q, \theta^{(q)}, \lambda)$ is given the hyper

parameter μ is $\pi(q, \theta^{(q)}, \lambda | \mu) = \frac{\pi(q, \theta^{(q)}, \lambda, \mu)}{\pi(\mu)}$, the

prior distribution for $(q, \theta^{(q)}, \lambda, \mu)$ can be written as:

$$\pi(q, \theta^{(q)}, \lambda, \mu) = \pi(q, \theta^{(q)}, \lambda | \mu) \pi(\mu)$$

Posterior Distribution

Let $\pi(q, \theta^{(q)}, \lambda, \mu | x)$ be the posterior distribution for $(q, \theta^{(q)}, \lambda, \mu)$. According to Bayes teorema, the posterior distribution for $(q, \theta^{(q)}, \lambda, \mu)$ is given as follows

$$\pi(q, \theta^{(q)}, \lambda, \mu | x)$$

$$\propto L(x | q, \rho^{(r)}, \lambda) \pi(q, \theta^{(q)}, \lambda, \mu)$$

$$\propto L(x | q, \rho^{(r)}, \lambda) \pi(q, \theta^{(q)}, \lambda | \mu) \pi(\mu)$$

However, the Bayes estimator cannot be determined analytically because the posterior distribution of the θ parameter has a complex form. To solve this problem, the reversible jump MCMC algorithm [7] is used.

REVERSIBLE JUMP MCMC

Suppose $M = (q, \theta^{(q)}, \lambda, \mu)$. The MCMC method for simulating the distribution $\pi(q, \theta^{(q)}, \lambda, \mu | x)$ is a method that produces ergodic Markov chain M_1, \dots, M_m which has a stationary distribution $\pi(q, \theta^{(q)}, \lambda, \mu | x)$. The Markov chain M_1, \dots, M_m can be considered as a random variable having a distribution $\pi(q, \theta^{(q)}, \lambda, \mu | x)$. Furthermore, Markov chain M_1, \dots, M_m is used to estimate the parameter M . To realize this, the Gibbs algorithm is adopted. The simulation of distribution $\pi(q, \theta^{(q)}, \lambda, \mu | x)$ consists of 3 steps : First, simulate

$$\mu \sim B(q+1, q_{\max} - q + 1)$$

Second, simulate $\lambda \sim G(\alpha, \beta)$ where $\alpha = n - q + 1$ and

$$\beta = \frac{1}{\sum_{t=q+1}^n [x_t - \sum_{j=1}^q G^{-1}(\rho_j) z_{t-j}]}$$

Third, simulate $\pi(q, \rho^{(q)} | x)$

The distribution $\pi(q, \rho^{(q)} | x)$ has a complex form so that simulation of the distribution of $\pi(q, \rho^{(q)} | x)$ cannot be done exactly. Since the value of q is unknown, the MCMC algorithm cannot be used to simulate the distribution $\pi(q, \rho^{(q)} | x)$. Here, the MCMC reversible jump algorithm (Green, 1995) was adopted.

Let $\xi = (q, \rho^{(q)})$ be the actual point of the Markov chain. There are 3 types of transformation used: order birth, order death and order change. Next, let N_q be the probability of transformation from q to $q+1$, let D_q be the probability of transformation from $q+1$ to q , and let C_q be the probability of the transformation from q to q .

Birth/Death of Order

The transformation of the birth of order will change the MA model coefficient, from q to $q+1$.

Let $\xi = (q, \rho^{(q)})$ be the actual point and $\xi^* = (q+1, \rho^{(q^*)})$ is the new point. The birth of order from $\xi = (q, \rho^{(q)})$ to $\xi^* = (q+1, \rho^{(q^*)})$ is defined in the following way. Express $q^* = q+1$ and select random point $v \sim U(-1, 1)$. Then, create a new point $\xi^* = (q+1, \rho^{(q^*)})$ with

$$\rho^{(q^*)} = \{\rho_1^* = \rho_1, \dots, \rho_{q^*}^* = \rho_q, \rho_{q^*+1}^* = v\}$$

Conversely, the transformation of the death of order will change the MA coefficient, from $q+1$ to q . Let $\xi = (q+1, \rho^{(q+1)})$ be the actual point and $\xi^* = (q, \rho^{(q)})$ is the new point. The death of order from $\xi = (q+1, \rho^{(q+1)})$ to $\xi^* = (q, \rho^{(q)})$ is defined in the following way. Express $q^* = q$ and create a new point $\xi^* = (q, \rho^{(q)})$ with

$$\rho^{(q^*)} = \{\rho_1^* = \rho_1, \dots, \rho_{q^*}^* = \rho_q\}$$

Suppose that $\eta_n(\xi, \xi^*)$ and $\eta_d(\xi, \xi^*)$ are respective the acceptance probability for the birth of order and the acceptance probability for the death of order. The acceptance probability for the birth of order is as follows:

$$\eta_n(\xi, \xi^*) = \min\left\{1, \frac{(\beta^*)^{n-q}}{\beta^{n-q+1}} \frac{1}{n-q} \frac{q+1}{q_{\max} - q}\right\}$$

The acceptance probability for the death of order is as follows:

$$\eta_d(\xi, \xi^*) = \min\left\{1, \frac{(\beta^*)^{n-q+1}}{\beta^{n-q}} (n-q) \frac{q_{\max} - q}{q+1}\right\}$$

Change of Coefficient

Transformation of the change of coefficient will not change the order. This transformation only will change the MA coefficient. Let $\xi = (q, \rho^{(q)})$ be the actual point and $\xi^* = (q^*, \rho^{(p^*)})$ is the new point. The change of coefficient from $\xi = (q, \rho^{(q)})$ to $\xi^* = (q^*, \rho^{(p^*)})$ is defined in the following way. Express $q^* = q$, select an index randomly $j \in \{1, \dots, q\}$, and select a point randomly $u \sim U(-1, 1)$. Then a new point $\xi^* = (q^*, \rho^{(p^*)})$ is created with

$$\rho^{(q^*)} = \{\rho_1^* = \rho_1, \dots, \rho_{j-1}^* = \rho_{j-1}, \rho_j^* = u, \rho_{j+1}^* = \rho_{j+1}, \dots, \rho_{q^*}^* = \rho_q\}$$

Let $\eta_c(\xi, \xi^*)$ be the acceptance probability for the change of coefficient. The acceptance probability for the change of coefficient is as follows:

$$\eta_c(\xi, \xi^*) = \min \left\{ 1, \left(\frac{\beta^*}{\beta} \right)^\alpha \right\}$$

CONCLUSION

This study proposes an estimation of MA model parameters whose error is exponential distribution and the order is unknown. Parameters could not be estimated using the MCMC algorithm because the order of the MA model is unknown.

The MCMC reversible jump algorithm was a method that can be used to estimate the parameters of the MA model even though the order is unknown. The advantages of this method are both the order and the MA model coefficient that can be estimated simultaneously. In addition, the resulting MA model is an MA model that satisfies an invertible condition.

ACKNOWLEDGEMENTS

The authors would like to thank Ahmad Dahlan University in Yogyakarta Indonesia for the awarded research grant. Acknowledgments are also given to the Ministry of Research, Technology and Higher Education of the Republic of Indonesia which has provided grants to attend seminar in Japan.

REFERENCES

- [1] Shi, Z. and Aoyama, H. (1997). Estimation of the Exponential Autoregressive time series model by using the genetic algorithm, *Journal of Sound and Vibration*, Vol. 205(3), p. 309-321.
- [2] Sad, N. (1999). On Exponential Autoregressive Time Series Models, *J. Math*, Vol. 29(1), p. 97-101.
- [3] Larbi, L. and Fellag, H. (2016). Robust Bayesian Analysis of an Autoregressive Model with Exponential Innovations, *Afr. Stat.*, Vol. 11(1), p. 955-964.
- [4] Suparman. (2017) New Estimation in AR Models with Exponential White Noise by Using Reversible Jump MCMC Algorithm, *Proceeding of the Third International Conference on Science, Engineering, and Environment*, p. 103-106, Brisbane Australia.
- [5] Rossum, H.H.V., Kemperman, H. (2017) Implementation and Application of Moving Average as Continuous Analytical Quality Control Instrument Demonstrated for 24 Routine Chemistry Assays, *Clinical Chemistry & Laboratory Medicine*, Vol. 55, Issue. 8, p. 1142-1151.
- [6] Kordestani, H., Xiang, Y-Q, Ye, X-W. (2018) Output-Only Damage Detection of Steel Beam Using Moving Average Filter. *Shock & Vibration*, Vol. 28, No. 1, p. 1-13.
- [7] Green, P.J. (1995). Reversible Jump MCMC Computation and Bayesian Model Determination. *Biometrika*, Vol. 82, p. 711-732.
- [8] Punsakaya, E., Andrieu, C., Doucet, A., Fitzgerald, W.J. (2002). Bayesian Curve Fitting Using MCMC with Applications to Signal Segmentation, *IEEE Transactions on Signal Processing*, Vol. 50, No. 3, p. 747-758.
- [9] Grummer, J.A., Bryson JR, R.W., Reeder, T.W. (2014) Species Delimitation Using Bayes Factors : Simulations and Application to the *Sceloporus Scalaris* Species Group (Squamata: Phrynosomatidae). *Syst. Biol.*, Vol. 63, No. 2, p. 119-133.
- [10] Pourhabib, A., Liang, F., Ding, Y. (2014) Bayesian Site Selection for Fast Gaussian Process Regression. *IIE Transactions*, Vol. 46, p. 543-555.
- [11] Fox, M., Ickert, R.B. (2015) Model Selection During Sample-Standard-Bracketing Using Reversible Jump Markov Chain Monte Carlo, *Journal of Analytical Atomic Spectrometry*, Vol. 30, Issue 10, p. 2208-2213.
- [12] Newcombe, P.J., Ali, R.H., Blows, F.M., Provenzano, E., Pharoah, P.D., Caldas, C., Richardson, S. (2017) Weibull Regression with Bayesian Variable Selection to Identify Prognostic Tumour Markers of Breast Cancer Survival, *Statistical Methods in Medical Research*, Vol. 26, Issue. 1, p. 414-436.
- [13] Steward, R.M., Rigdon, S.E. (2017) Risk-Adjusted Monitoring of Healthcare Quality : Model Selection and Change-Point Estimation. *Quality & Reliability Engineering International*, Vol. 33, Issue 5, p. 979-992.
- [14] Karakus, O., Altinkaya, M.A., Kuruoglu, E.E. (2017) Bayesian Volterra System Identification Using Reversible Jump MCMC Algorithm, *Signal Processing*, Vol. 141, p. 125-136.

GAP COMPETENCY ANALYSIS FOR EMPLOYEE OF ANIMAL FEED WAREHOUSE DEPARTMENT

Siti Rochaeni¹, Siska Nurita², Eny Dwiningsih³ and Farahdita Soeyatno⁴
^{1,2,3,4}Faculty of Science and Technology, Syarif Hidayatullah State Islamic University Jakarta, Indonesia

ABSTRACT

PT Japfa Comfeed Indonesia Tbk is second with 24% market share. In order for Japfa to seize market share in the first position, the management realize the need for competent human resources. By knowing the employee competency gaps in the Livestock Warehouse Department, the company can design a program to improve the quality of human resources for the achievement of better quality objectives. The purpose of this research is to analyze the gap competency, find alternative solutions, and give the recommendation to upgrade competency of the employee. The data collected used Likert Scale, processed test data validation using Product Moment Pearson correlation technique formula and analyze by gap analysis and importance performance analysis (IPA) matrix. The value of competency gap is obtained by fulfilling importance level and capability level. Opinions used are opinions by managers and employees. The highest negative importance gap for core competence is the ability to anticipate, identify and solve the problem, while for field competence is mastering the way computer operate. The highest negative capability gap value for core competence is the ability to reach the target for permanent employees and ability to work with high spirits for outsourced employees, while for field competence is mastering how to operate computer permanent employees and master the system of implementation of the seal of vehicle loading in accordance with work instructions for employees outsourcing.

Keywords: Core competency, Field competency, Gap, Importance, Capability

INTRODUCTION

The poultry feed market is dominated by four players: PT Charoen Pokphand Indonesia Tbk, PT Japfa Comfeed Indonesia Tbk, PT Malindo Feedmill Tbk, and PT Wonokoyo Jaya Corporindo which has a combined market share of about 80%. PT Charoen Pokphand Tbk is a poultry feed company which controls the market in the first rank with a market share of 34%. PT Japfa Comfeed Indonesia Tbk is second with 24% market share. In order for Japfa to seize market share in the first position, the management realize the need for competent human resources. To improve the competence of human resources, companies need to consider the competency gap or employee competency gap at this time by looking at the extent to which employees have the competence expected by the company, especially employees of the Department of Animal Feed Warehouse who handle the finished product and directly related to product damage that occurred. The extent to which employees in this department master the necessary skills and the extent to which employees consider competence to be important in their work. By knowing the employee competency gaps in the Livestock Warehouse Department, the company can design a program to improve the quality of human resources for the achievement of better quality objectives.

METHODS

This research was conducted at PT Japfa Comfeed Indonesia Tbk Tangerang Unit. for 3 (three) months from July to September 2017. The selection of research sites was conducted purposively (deliberately) with the consideration that PT Japfa Comfeed Indonesia Tbk needs improvement in the quality of its human resources, especially the Animal Warehouse Section. Primary data was obtained directly using questionnaire. Secondary data is obtained from documents and reports of PT Japfa Comfeed Indonesia Tbk Tangerang Unit. Data collection was obtained by direct interview using questionnaire.

Respondents in this research are employees of PT Japfa Comfeed Indonesia Tbk Unit Tangerang Department of Animal Feed Warehouse which amounts to 60 people consisting of 20 employees who work in five work units namely (1) administrators; (2) production handover; (3) implementing loading and unloading; (4) forklift operators; (5) cleaners, and 40 outsourcing employees who assist in the process of over sacking and loading and unloading of feed.

The data collected consisted of data on importance and data about the ability to use Likert

Scale with range 1 to 5. Data of importance ranging very unimportant to very important. data capabilities ranging from very inadequate to very capable. Before the data is processed test data validation using Product Moment Pearson correlation technique formula as follows:

$$r = \frac{n(\Sigma xy) - (\Sigma x \Sigma y)}{\sqrt{[(n \Sigma x^2) - (\Sigma x)^2][(n \Sigma y^2) - (\Sigma y)^2]}} \quad (1)$$

Where:

r = Coefficient of validity sought
n = Number of respondents
x = Scores of each statement x
y = Score of each statement y

Test reliability using Cronbach Alpha technique with formula as follows:

$$r_{11} = \left[\frac{k}{k-1} \right] \left[1 - \frac{\Sigma \sigma b^2}{\sigma t^2} \right] \quad (2)$$

Where :

r₁₁ = Instrument reliability
k = Many points of the statement
 σt^2 = Total variance
 $\Sigma \sigma b^2$ = The number of variance items

The formula to find the value of the variety is:

$$\sigma^2 = \frac{\Sigma x^2 - \frac{(\Sigma x)^2}{n}}{n} \quad (3)$$

Where :

$\Sigma \sigma^2$ = Variety
x = Value of the selected score
n = Number of instances

The tabulation form used for this study can be seen in table 1 below.

Table 1 Tabulation of Competency Gap Analysis

Com- peten- ce	Importance					Capability					Gap	
Full- time/ out- sour- cing	1	2	3	4	5	Nki	1	2	3	4	5	Npi = Nki- Npi
1.												
2.												
3.												
4. etc												

Competency Gap Analysis

The value of importance for each competency required is as follows Setiarso (2009) in Chandra (2011: 27) :

$$Nki = \frac{(K1 \times 1) + (K2 \times 2) + (K3 \times 3) + (K4 \times 4) + (K5 \times 5)}{R} \quad (4)$$

Where :

Nki = Value of importance to competence i
K1 = Number of respondents with answer 1
K2 = Number of respondents with answer 2
K3 = Number of respondents with answer 3
K4 = Number of respondents with answer 4
K5 = Number of respondents with answer 5

The formula for calculating the value of capability for the knowledge required as follows:

$$Npi = \frac{(P1 \times 1) + (P2 \times 2) + (P3 \times 3) + (P4 \times 4) + (P5 \times 5)}{R} \quad (5)$$

Where :

NPi = Values of competence i
P1 = Number of respondents with answer 1
P2 = Number of respondents with answer 2
P3 = Number of respondents with answer 3
P4 = Number of respondents with answer 4
P5 = Number of respondents with answer 5

Importance Performance Analysis (IPA)

According to Tjiptono (2011), this technique was first proposed by Martilla and James in 1977 in their article entitled "Importance-Performance Analysis" (Oscar & Pambudi, 2014: 5. The IPA Matrix (Importance-Performance Analysis) is clearly and detail presented in Fig. 1.

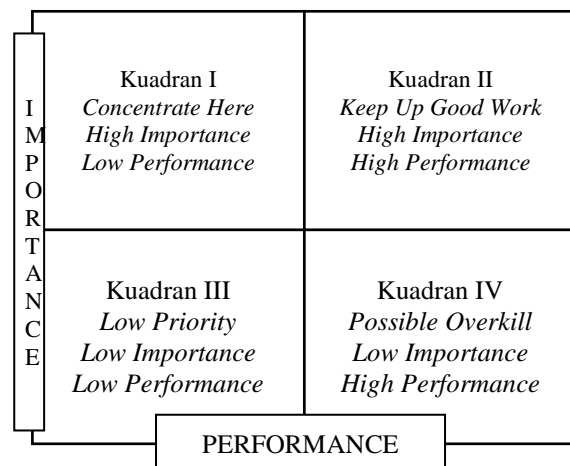


Fig. 2 Matrix IPA.

RESULTS

The value of competency gap is obtained by fulfilling importance level and capability level. Opinions used are opinions by managers and employees. The value of competency gap is obtained by calculating the difference between the average value importance level and capability level of the employees with the value given by the manager.

Importance Level

The assessed competencies are core competencies belonging to the Result Orientation, Team Focus and Global View categories that break down into 18 core competencies. In addition, there are 10 field competencies required by the Department of Animal Feed Warehouse. Assessment using five Likert scales.

Permanent Employees

Six core competencies have an average value ≥ 4.00 that is the ability to work together; the ability to complete tasks in teams effectively; ability to respect colleagues; the ability to think ahead; ability to work with high spirits and ability to anticipate challenges. The core competency that has the highest average importance level is the ability to work together, with an average value of 4.50. The core competencies that have the lowest average importance level compared to other core competencies are the ability to make changes and the ability to express opinions well, with an average importance level of 3.50. The core competency that has the largest positive importance gap is the ability to work with 0.50. While the other 14 core competencies have a negative gap value.

Seven field competencies have an average importance level ≥ 4.00 , while the other competencies have an average importance level <4.00 . Competence field that has the highest average value of interest is mastering the system of feeding identity in the warehouse in accordance with work instructions and mastering the way of loading and unloading the feed in the warehouse in accordance with work instructions with a value of 4.56. Competence field that has the lowest average importance level is mastered how to operate the computer, that is with the importance of 3.67. The competence of the field that has the biggest negative gap value is mastering how to operate the computer, that is with a negative value of 1.33.

Outsourcing Employees

The core competency that has the highest average value of interest is the ability to think creatively, with an average value of 4.03. For core competencies that have the lowest average interest compared to other core competencies is the ability to make changes with an average rating of 3.53. The core competencies that have a positive gap value are creative thinking ability with a gap value of 0.03. While other competencies have negative importance gaps. The core competencies that have the biggest negative gap value is the ability to anticipate, identify and solve the problem with the negative gap of 1.41.

There is no field competency that has an average value of interest ≥ 4.00 . The importance of the competence of the field of outsourcing employees all has a negative gap value. Competency field that has the value of the biggest negative interest gap is the way to operate the computer with negative value 1.41.

Capability Level

The assessed competencies are core competencies belonging to the Result Orientation, Team Focus and Global View categories. In addition, there are 10 field competencies required by the Department of Animal Feed Warehouse. Assessment using five Likert scales.

Permanent Employees

There is one core competency that has an average capability value of ≥ 4.00 . The core competency that has the highest average value of capability is the ability to respect colleagues, with an average value of mastery of 4.22. The core competencies that have the lowest level of mastery are the ability to take advantage of opportunities, the ability to think creatively and the ability to adjust to change, with the average value of mastery of 3.39. There are two core competencies that have more than one gap value. Core competencies that have a negative gap value with a value of more than one that is the ability to achieve targets and the ability to work with high spirits, effectively and definitely.

There is one competency field that has an average value of capability of ≥ 4.00 . While the competence of other fields has an average value of capability value between 3.00 - 3.99. There is one competency that has a value of less than one capability gap. Competency field that has the biggest negative gap value is mastering the way to operate the computer, that is a negative gap of 1.67.

Outsourcing Employees

The core competencies that have the highest average value of capability are the ability to anticipate the challenge; have the nature of want to learn, always try, add knowledge and new science; ability to see problems in micro or macro with value 3.88. While the competence that has the lowest average value of capability is the ability to think creatively with an average value of mastery of 3.50. Competence which has the biggest negative gap value is the ability to work with a high spirit that is with negative gap value 1.31.

Field competency that mainly mastered by outsourcing employees is mastering the system of handling of food damaged/leaked in accordance with work instructions that is with the average value of mastery of 4.00. For the field competencies that have the lowest average value of capability is to master the system of seal implementation vehicle fit in accordance with work instructions that is with an average value of 3.53. Field competency that has the value of the biggest negative capability gap is mastering the system of the implementation of the seal of the vehicle loaded in accordance with work instructions, that is with the negative gap 1.47.

Conformity Level

The results of the assessment of importance level and capability level will result in a calculation of the level of conformity between importance level and capability level of core competence and field competence. The level of conformity is the result of comparison of the total score of capability with the number of importance scores. The results show how far the employees capable the competence in accordance with the importance of these competencies to be mastered in their work.

Permanent Employees

The average overall competence of core competence is 93.83%. The core competencies that have the highest level of conformity are the ability to share and appreciate the contribution of work and the ability to make changes with the value of 103%. There are four competencies that have a percentage of less than 90%, there are ability to reach the target; creative thinking ability; ability to work together and able to adjust to change. The smallest level of conformity is owned by the core competence of achieving the target value of 83%. The overall value shows there are two core competencies corresponding to the importance (conformity level \geq 100%). While the other 16 core competencies have not been in accordance with the importance (level of conformity \leq 100%).

The overall conformity for field competencies is 90%. The field competency that has the highest level of conformity is mastering how to drive a forklift in accordance with work instructions with a value of 103%. The smallest level of conformity is owned by mastering the knowledge of the type of product stored in the warehouse with an 80% conformity value.

Outsourcing Employees

The overall conformity for core competencies is 99.22%. The core competency that has the highest level of conformity that is the nature of want to learn, always trying to increase knowledge and new science, that is with the value of 108%. The smallest degree of conformity is shared by the core competency of creative thinking ability with an 87% conformity score.

The overall conformity for field competencies is 99.00%. The field competency that has the highest level of conformity is mastering the handling system of damaged/leaked feed in accordance with work instructions, with a value of 111%. The smallest degree of conformity is owned by the competence of the field to control the system of the seal of the loaded vehicle in accordance with the work instructions with 93% suitability value.

DISCUSSIONS

The ratings of importance level, capability level, and conformity level are used to determine coordinate points. The coordinate points used for drawing a cartesius diagram. There is four placement in the cartesius diagram, which separated by two perpendicular lines. The first quadrant (I) is located to the upper left, the second quadrant (II) is on the upper right, the third quadrant (III) is on the lower left, and the fourth quadrant (IV) is on the lower right. The position of each core competency in the four quadrants can be used as a tool in providing alternative strategies to improve the level of competence of employees.

Quadrant I shows competencies that are considered important by permanent employees but have not demonstrated good mastery or performance, so companies need to improve the competence controls included in this quadrant. These competencies are a top priority for improvement. Quadrant II shows competencies that are considered important by permanent employees and have been mastered well. The competencies in this quadrant should be maintained by the company. Quadrant III shows competencies that are considered less important and less controlled by permanent employees so that companies do not need to prioritize or give more attention to these

competencies. Quadrant IV indicates that competence is considered less important but the employees master it well so that companies better allocate resources to increase the competence to other competencies that have a higher priority level.

Core competencies

The core competencies of permanent employees in quadrant I is the ability to reach the target. The competencies contained in quadrant II are the ability to work in high spirits, the ability to effectively complete the tasks of the team, the ability to work together, the ability to respect colleagues, the ability to anticipate challenges, and the ability to think ahead. The competencies in quadrant III are the ability to take advantage of opportunities, the ability to think creatively, the ability to make changes, the ability to convey a good opinion, the nature of the desire to learn, always trying to increase knowledge and new knowledge, the ability to adjust to change, the ability to see problems from the scope of micro and macro, and ability not limited to knowledge and skills in the field of work alone but be open to other fields. The competencies in quadrant IV are the ability to anticipate, identify and solve problems, ability to share and appreciate work contribution, and competence of innovative thinking.

The core competencies of outsourced employees in quadrant I are the ability to work with high spirits, the ability to take advantage of opportunities, the ability to think creatively, the ability to work together, the ability to think innovatively, and the ability not to limit themselves to knowledge and skills in the field of work but is open to the field others. The competencies contained in quadrant II are the ability to achieve the target, the ability to respect the co-workers, the ability to think ahead, and the ability to see the problems of micro and macro. The competencies in the quadrant III are the ability to share and appreciate the contribution of work and the ability to make changes, the ability to express opinions well. The competencies in the quadrant IV are the ability to anticipate, identify and solve problems, the ability to effectively complete the tasks of the team, the ability to anticipate challenges, the ability to recognize and solve problems outside the scope of work, have the nature of learning, always trying to increase knowledge and new knowledge, and ability to adjust to change.

Field Competencies

The field competencies of permanent employees in quadrant I is to master the knowledge of the types

of products stored in the warehouse. Competence contained in quadrant II is mastering the lotting system feed in the warehouse in accordance with work instructions, mastering the system of feeding identity in the warehouse in accordance with work instructions, master the knowledge of the flow of feed in the warehouse in accordance with work instructions, mastering knowledge of the groove of feed warehouse in accordance with work instructions, and master the way of loading and unloading the feed in the warehouse in accordance with work instructions. Competence which is in quadrant III is mastering system implementation of vehicle seal in accordance with work instructions and mastered how to operate a computer. Competencies that are in quadrant IV is Mastering the handling system broken or leaking feed in accordance with work instructions and Mastering how to drive a forklift in accordance with work instructions.

The field competencies of the outsourced employees in quadrant I is to master the food lotting system in the warehouse in accordance with work instructions and master the knowledge about the type of product stored in the warehouse. The field competencies in quadrant II is to master the knowledge of the groove of feed in the warehouse in accordance with the work instructions, to master the system of feeding identity in the warehouse in accordance with the work instructions, to master the loading and unloading of the warehouse in accordance with the work instructions, feed from the warehouse in accordance with work instructions, master the way to ride the forklift in accordance with work instructions. The field competencies that is in quadrant III is to control the implementation of the seal of the loaded vehicle in accordance with the work instructions. The field competencies in quadrant IV is to master the handling system of damaged or leaked feed in accordance with the work instructions and master the way to operate the computer.

CONCLUSION

The conclusions that can be drawn from this research are:

1. The highest negative importance gap for core competence is the ability to anticipate, identify and solve the problem, while for field competence is mastering the way computer operate.
2. The highest negative capability gap value for core competence is the ability to reach the target for permanent employees and ability to work with high spirits for outsourced

employees, while for field competence is mastering how to operate computer permanent employees and master the system of implementation of the seal of vehicle loading in accordance with work instructions for employees outsourcing.

RECOMMENDATION

Recommendations that can be given based on this research for the company are:

1. Efforts that can be made in order to improve the core competence of employees is to involve employees in targeting, compensation improvement, and carry out training and development of human resources capabilities.
2. Efforts that can be done in order to improve the field competencies of employees are training methods of self-study.

REFERENCES

- [1] CPIN Company Presentation dalam Ben Santoso. Indonesia's Growing Appetite for Animal Protein An Overview of Business Models, Opportunities and Strategies. 2016. DBS Asian Insights Sector Briefing 21.
- [2] Chandra, Leily Purnama. Analisis Kesenjangan Pengetahuan (Knowledge Gap) Karyawan PT Aneka Tambang Tbk Unit Geomin [Skripsi]. Bogor: Institut Pertanian Bogor, Fakultas Ekonomi dan Manajemen; 2011.
- [3] ICRA Indonesian Research. "Overview of the Indonesian Animal Feed Industry 2012". Desember 2012. Artikel diakses pada 19 Januari 2016 dari www.icraindonesia.com.
- [4] Oscar O & Pambudi J. Analisis Kepuasan Pelanggan dengan Important Performance Analysis di SBU Laboratory Cibitung PT Sucofindo. J@TI Undip, 2014;IX: 1.
- [5] Ramadhan, MR, Yoanita Yniati & Sugih Arijanto. Analisis Beban Kerja dan Pengukuran Gap Kompetensi Teknisi Laboratorium Umum dan Faklta Z PTS XYZ. Reka Integra: Jurnal Online Institut Teknologi Nasional, 2014; 02: 384.
- [6] Setiarso, B dkk. 2009. Penerapan Knowledge Management pada Organisasi. (Yogyakarta: Graha Ilmu, 2004).
- [7] Spencer, Lyle dan Signe Spencer. Competence at Work : Models for Superior Performance. (Canada: Wiley, 1993)
- [8] Suroto, Adi. "Gap Analysis (Analisa Kesenjangan)". 28 Juli 2015. Artikel diakses pada 2 Januari 2017 pukul 22.00 WIB dari <http://sis.binus.ac.id/2015/07/28/gap-analysis-analisa-kesenjangan/>

ENVIRONMENTAL REGENERATION AND MANAGEMENT IN PARTNERSHIP IN THE NORTHWEST OF ENGLAND

Tomoko Miyagawa¹, Clare Olver², Noriko Otsuka³, and Hirokazu Abe⁴

¹Faculty of Systems Engineering, Wakayama University, Japan; ²The Mersey Forest, the UK;

³ILS Institut für Landes- und Stadtentwicklungsforschung gGmbH, Germany;

⁴Cyber Media Centre, Osaka University, Japan

ABSTRACT

Built environment and cultural heritage are important aspects to improve the quality of life in environmental regeneration and management. This paper aims to compare two case studies to examine partnership for environmental regeneration and management in post-industrial landscapes in the northwest of England: conservation and interpretation of the salt heritage at Northwich Woodlands, and landscaping former coalfields with artworks at Bold Forest Park, St. Helens. Study methods used are literature reviews and face-to-face interviews with representatives from partnership organisations, e.g. Mersey Forest, local authority officers, and Friends of Anderton and Marbury. From the results, characteristics of the two projects became apparent with distinctive focuses: industrial heritage in Northwich Woodlands; and creating a focal point using collaborative artworks in St. Helens. Similarities are also found in outcomes of environmental regeneration to create wildlife areas with some statutory designations, and partnership patterns integrating sectors from public, private, and the community. For both case studies, the overriding issue is being able to develop the resources and partnerships to enable the sites to be managed and thus cherished by their communities in the long term.

Keywords: Post-industrial landscapes; Industrial Heritage; Art Projects; Community Participation

INTRODUCTION

Participative Environmental Regeneration in Creation of Post-industrial Landscapes in the UK

Post-industrial landscapes are brought by 'radical transformation by the industrial era', i.e., mining, in European landscape, one of the first to be faced with 'the need to restore and give new purposes to damaged industrial landscapes' [1]. However, in such damaged post-industrial landscapes, there are unused or underused lands, i.e., brownfields with unique flora and fauna, and industrial heritage in some cases [2]. In addition, in recent years, post-industrial landscapes are considered to be potential sites for creating Green Infrastructure (GI) to improve 'the health and quality of life' for the community by an 'interconnected network' with ecological process [3], [4] of blue (water) and green (open spaces) systems [5].

In the UK, processes of environmental regeneration in post-industrial landscapes are recognised in parallel to community participation in partnership with volunteer sectors and often with the community, owing to the British Urban Policies to support physical regeneration with socio-economic regeneration [1]. Because some of these sites are not always recognised by the local community due to a lack of infrastructure or its location they can be

difficult to be noticed [5]. In this way, landscape improvements can be undertaken with approval of the community and can empower the community to become engaged in long-term landscape management [1]. Therefore, creating links between the landscape and the people is inevitable for sustainability of the community and the environment [6]. Furthermore, the process can create opportunities to enhance community empowerment through local enthusiasm [7]. Partnership for community scale GI has been classified into distinctive typology patterns by characteristic, governance, and activity focuses which enables to analyse creation and management of GI from local level to city-scale [8]. In terms of the partnership capacity of the community, continuous public sector support is also necessary in long-term management in green space [9]. Therefore, environmental regeneration and management in partnership is becoming more recognised.

As a way of engaging with the community, art in the landscape is found in many cases. Artworks have been discussed to increase attractiveness for visitors and being a touristic destination, as well as to have an impact on regionally and nationally by attracting the media and the wider community which can support with increasing revenue and future funding opportunities [1].

Aims of the study and study methods

This paper aims to compare two case studies to examine the role of partnership for environmental regeneration and management in post-industrial landscapes as follows. It will focus on the improvement of the built environment and cultural heritage perspectives; conservation of industrial heritage as a result of salt production at Northwich Woodlands, and landscaping former coalfields with an iconic artwork called 'Dream' at Bold Forest Park, St. Helens. There has been little discussion about the enhancement of local distinctiveness and the quality of life in brownfield land regeneration [6]. Study methods used are literature reviews regarding on environmental regeneration and cultural heritage and interviews with four representatives of The Mersey Forest, two local authority officers from St. Helens Council, one officer from Cheshire West and Chester Council, and one representative from the Community Forest Trust, and two representatives from the Friends of Anderton and Marbury.

Both projects consist of multiple land-uses and landowners in the urban fringe in the Northwest of England. Northwich Woodlands are located next to the town centre of Northwich in Cheshire, and Bold

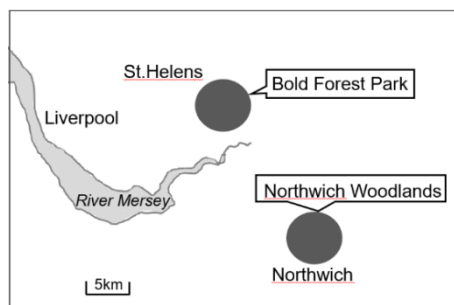


Fig.1 A map of case study areas by referencing [10] with some amendments



Fig. 2 A map of the Northwich Woodlands [11]

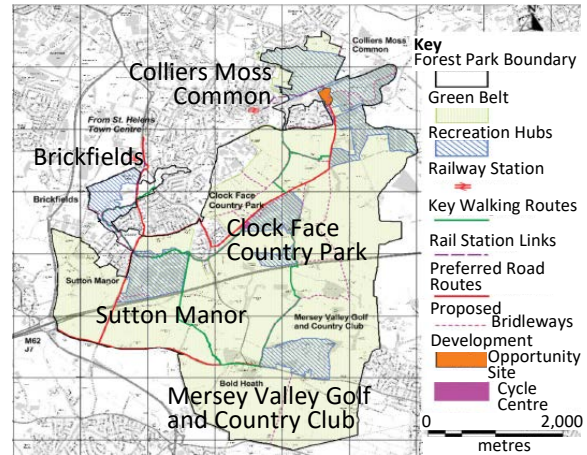


Fig 3. A map of the Bold Forest Park [12] with some amendments

Forest Park is in the south of St. Helens in Merseyside, within the Liverpool City Region (Fig 1-3). Interestingly, these projects are also connected by Sankey and St. Helens canals in St. Helens and the River Weaver in Northwich navigating to the River Mersey for transporting salt and coal. These are key projects of The Mersey Forest, one of two Community Forests in the Northwest of England since 1991.

The Mersey Forest has been leading a partnership with landowners and partners to manage long-term landscape management for over twenty years, and has 'evolved from a governmental inspired organisation to a community empowered organisation' [5]. It has supported the community to set up friends groups for anyone to join to manage and undertaking range of activities and events on green spaces since 1998 [13].

CASE STUDIES OF PARTNERSHIPS ON ENVIRONMENTAL REGENERATION AND MANAGEMENT

Outlines of case studies

Both case studies are good practice examples of post-industrial environmental regeneration which have supported the change in landscape that have improved the quality of the environment. Northwich Woodlands have undergone ground condition improvements to remediate past activities of salt-mining, through brine extraction and subsequent deposits of lime wastes (Table 1). Due to the excessive mining and extraction in the past, sudden historic subsidence has created several pools (known locally as "flashes") and altered the flow of water courses. As a result, there are a variety of waterways and wetland areas visited by people for bird watching and recreation.

Northwich Woodlands is comprised of a variety

of green spaces, including Marbury Country Park, a former country estate with a formal landscape; grazing land at Ashton's Flash; and community woodlands owned by the Forestry Commission at Uplands and Hopyards Woodland. Northwich Woodlands are located along the Trent and Mersey Canal with the size of 315 hectares, the total sum of green spaces with some private lands (Fig. 2).

Lion Salt Works, recently completed conservation works and opened as a museum in 2015 to disseminate local history and industry of salt-making, and Anderton Boat Lift, constructed in 1875 for lifting about 15 meters high to connect the Trent and Mersey Canal to the River Weaver which had a conservation work in 2002, along with the development of marinas to travel by waterways [2]. These conservation projects were mainly funded by Northwest Regional Development Agency, a government organisation which promoted regional development (abolished in 2012), and Heritage Lottery Fund supported by the proceeds of National

Lottery. It is managed by the ranger service from the Cheshire West and Chester Council and supported by the community and local Friends Group FoAM, it has also received the Green Flag Award. This is the benchmark national standard, which recognises and rewards the best green spaces in the country. For protection for wildlife and green space, a Site of Special Scientific Interest (Carey Park) [14], seven Local Wildlife Sites [14], and a Green Belt [14]-[16] for conserving undeveloped green fields by British planning system have been designated. Fig.6 illustrates Ashton's Flashes, in fragile foundation by subsidence [14] to limit accesses by fences around the site. It is now used for grazing in dry seasons and becoming a marshland in wet seasons [2].

Table 1 Outline of the Northwich Woodlands

Project name (size of sites)	The Northwich Woodlands (315ha)
Past industrial activities	Salt-mining, brine extraction, and deposits of lime wastes
Landscapes changes	Subsidence to form pools and creation of watercourses for salt-mining and industrial activities
Environmental regeneration and types of green space	Pools and watercourses, undulating landforms, and woodlands by environmental improvements and landscaping
Places of interests of green space	Bird watching places and to visit industrial heritage (Lion Salt Works; Anderton Boat Lift), travelling waterways
Characteristics of the projects and statutory designations	Conservation of industrial heritage; Green Flag Award, Site of Special Scientific Interest (Witton Mill Meadow)[14], 7 Sites of Biological Importance[14], Green Belt[15], [16]
Fundings (main funders)	Northwest Regional Development Agency, Heritage Lottery Fund
Local partnerships and their roles	Mersey Forest, Cheshire West and Chester Council, local industries and businesses, landowners, residents, and community and local groups
Community groups	Friends of Anderton and Marbury
Other local groups	Saltscape Community Forum; Northwich Business Improvement Districts; Lion Salt Works Trust; Cheshire Wildlife Trust; Canal and River Trust; Groundwork Cheshire, Lancashire, Merseyside; Cheshire West Archives; Northwest Geological Society
Events and Activities on sites	Events by community and local groups, Exhibition about Wildlife of the Northwich Woodlands
Management and responsible organisations	Areawide management by rangers with volunteers from community and local groups
Long term management plans	Securing the budget for the rangers



Fig. 4 Lion Salt Works



Fig.5 Anderton Boat Lift



Fig. 6 Ashton's flash

Bold Forest Park was formerly a moss land with diverse wildlife and nature. After coal-mining and quarrying activities during the 1950s to the 1980s, a programme of environmental regeneration was undertaken in the 1990s to create green spaces through the reclamation of spoil heaps into community woodland (Table 2). Bold Forest Park also includes privately owned agricultural land, designated as a Green Belt [12], [17], [18] (Fig.3), as well as protected areas for wildlife. This includes a Local Nature Reserve (Colliers Moss Common North) [12], and 11 Local Wildlife Sites [12] in the project. The undulating landscapes created by spoil heaps resulting from coal-mining activities (Fig.7) and soil generated by housing development are now

becoming new landmarks with great views, such as Sutton Manor.

Bold Forest Park consists of five green spaces, 320 hectares in total, such as Colliers Moss Common with a variety of wildlife areas, as well as woodlands and grassland owned by the Forestry Commission. There is a private owned golf course, an area of 51.5 hectares, included in the Bold Forest Park Area Action Plan and called to be 'recreation hubs' with green spaces [12]. Farmlands are located around green spaces with 63 percent of an area size of 1159 hectares of the park, also designated as Green Belt (Fig. 3) [12].

The woodlands and marshlands of Colliers Moss Common (North and South) are connected by a pedestrian bridge over the railway line between Manchester and Liverpool. Community Art has been used on the site to engage with the local community, such as "pit wheels" used for coal mining are featured in the design of a pedestrian bridge which has become a focal point of the Common (Fig.8).

Table 2 Outline of the Bold Forest Park

Project name (size of sites)	The Bold Forest Park (320ha of green spaces; 1808ha)
Past industrial activities	Coal-mining
Landscapes changes	Spoil heaps created from coal-mining activities and a hill created by soil constructed by a housing development
Environmental regeneration and types of green space	Reclamation of spoil heaps to form hilly landscapes and tree planting; environmental improvements and landscaping surrounded by agricultural lands
Places of interests of green space	Big Art Project called the Dream, Viewpoints to the surroundings, and green spaces created by environmental regeneration
Characteristics of the projects and statutory designations	Artworks with Big Art Project, environmental regeneration; Local Nature Reserves (Colliers Moss Common North)[12], 11 Local Wildlife Sites[12], Green Belt[12], [17], [18]
Fundings (main funders)	Northwest Regional Development Agency, EU
Local partnerships and their roles	Mersey Forest, St. Helens Council, local industries and businesses, landowners, residents, and a community group
Community groups	Friends of Colliers Moss
Other local groups	—
Events and Activities on sites	Events and management with the community
Management and responsible organisations	Site based management by St. Helens Council, Mersey Forest, Forestry Commission, and private landowners
Long term management plans	Bold Forest Park Area Action Plan (2017)
Project name (size of sites)	The Bold Forest Park (320ha of green spaces; 1808ha)

There is also a Big Art Project called 'Dream' mainly funded by Northwest Regional Development Agency and European Regional Development Fund [19]. The sculpture is the key output of collaborative work of the artist and the member of the community who worked in the coalmines, reflecting the community's wish to have something new and looking to the future. The process of the collaborative work was documented on a Channel 4 TV programme and the project is widely known. It is located on the highest point of Bold Forest Park, on the former coalfield, Sutton Manor (Fig.9) and is an important local focal point.



Fig.7 Landscaping at Sutton Manor



Fig.8 A bridge at Colliers Moss Common



Fig. 9 A sculpture at Sutton Manor

Partnerships of case studies

Partnership of Northwich Woodlands

The Northwich Woodlands partnership includes Cheshire West and Chester Council, the Mersey Forest, Forestry Commission, Canal and River Trust, local industries, businesses and community groups. The well-established Friends of Anderton and Marbury (FoAM) and other local groups in the area (Table 1) to undertake a programme of events. FoAM was founded in 1999 and now has a membership of over 240; it continues to play an active role to manage the sites. Area-wide management is undertaken by Cheshire West and Chester Council and Forestry Commission rangers, supported by volunteers from community and local businesses.

Important tasks for the future are to secure the budget to be able to continue to manage the habitats created.

Partnership of Bold Forest Park

Partnership of Bold Forest Park includes St. Helens Council, the Mersey Forest, Forestry Commission, local industries and businesses, landowners, residents, and a community group called Friends of Colliers Moss. The Friends of Colliers Moss was founded in 2016 to undertake events and management on sites.

Table 3 A timeline of the Northwich Woodlands

1970's	1975 Environmental improvements at Marbury Country Park
1980's	1987 Environmental Regeneration at Furey Wood
	1989 Cheshire West and Chester Land Regeneration Unit to start environmental regeneration(-2005)
1990's	—
2000's	2006 Vale Royal Borough Local Plan (-2015) (Northwich Woodlands identified)
	2007 Supplementary Planning Document 5, Landscape Character, Vale Royal Borough Council
2010's	2012 Saltscape Landscape Partnership (-2017)
	2015 Local Plan (Part One, adopted), Cheshire West and Chester Council
	2016 Northwich Business Improvement District Green Infrastructure Plan, Mersey Forest (Northwich Woodlands identified)

Table 4 A timelines of the Bold Forest Park[20]

1970's	—
1980's	1986 Economic Strategy
	1987 Ravenhead Renaissance established
	1989 Wasteland to Woodland (-1998)
1990's	1998 St. Helens Unitary Development Plan 1998 (-2013)
2000's	2003 The First City Growth Strategy (Public-private partnership)
	2005 Forestry Commission District Valuer's Report
	2006 St. Helens Town in the Forest Strategic Vision Document (Forest Park identified)
	2008 City Growth Strategy (-2018) (Forest Park identified)
2010's	2012 St. Helens Core strategy (Bold Forest Park identified)
	2016 St. Helens Local Plan (2018-2033), Scoping Consultation Document (Bold Forest Park identified)
	2017 Bold Forest park Area Action Plan

Planning timelines of case studies

A planning timeline of Northwich Woodlands can be described as project based, starting from environmental improvements at Marbury Country Park in 1975, then Cheshire County Council Land Regeneration Unit to take over environmental regeneration during 1989 to 2005 [14], and more recently through the Saltscape Landscape Partnership

(2012-2017) supported by the Heritage Lottery Fund [21] (Table 3). The importance of good access and connections to Northwich town centre have been discussed by developing Green Infrastructure in Northwich Business Improvement District Green Infrastructure Plan by Mersey Forest, since Northwich Woodlands are closely located to the town centre [22].

Northwich Woodlands has been identified in Vale Royal Borough (reorganised into Cheshire West and Chester Council) Local Plan (2006; saved policies until 2015) [15]. However, a recently published Local Plan (2015) by Cheshire West and Chester Council mentions only selected sites but not entire Northwich Woodlands [16].

A planning timeline of Bold Forest Park has been led by planning system, starting from strategies in the 1980s and a development plan in the 1990s (Table 4). Forest Park has been identified in the 2000s, and it appeared in documents such as St. Helens Town in the Forest Strategic Vision Document (2006) [23], and City Growth Strategy (2008) [24]. In the 2010s, Bold Forest Park has been identified in statutory documents as follows; St. Helens Core strategy (2012) [25], and St. Helens Local Plan (2016) [18], and the Bold Forest Park Area Action Plan (2017) [12]. St. Helens Local Plan (2016) is discussing about a release of Green Belt [18], which may also have effects to the future development in the area, such as a development opportunity site identified in the Fig. 3.

CONCLUSIONS

From the results, the two case studies present good examples of environmental regeneration and management creating community green spaces in post-industrial landscapes. There are similarities in outcomes of environmental regeneration creating wildlife areas with some statutory designations, and partnership with the public, private and community.

Moving forward there will be distinctive focuses: most likely around industrial heritage in Northwich Woodlands, and active recreation and collaborative artwork in St. Helens. In both Northwich Woodlands and Bold Forest Park the community and local groups are actively participating in running events and exhibitions, as well as assisting to manage their green spaces.

For both case studies, the overriding issue is being able to develop the resources and partnerships to enable the sites to be managed and cherished by their communities in the long term. The recently published UK's government's '25 Year Plan for the Environment' acknowledges that there needs to be long-term direction with flexibility to adapt to new evidence and circumstances: *'the right mix of public and private funding and financing for projects that protect and enhance natural assets will be crucial.'*

Increasing pressures on local authority budgets has meant the need to consider innovative funding and land holding mechanisms in order to realise the natural capital benefits the two case studies provide.

ACKNOWLEDGEMENTS

The authors would like to express our gratitude for the financial support provided by the Japan Society for the Promotion of Science (no.17K06705).

REFERENCES

- [1] Davies C, "Old culture and damaged landscapes: The new cultural landscapes of post-industrial sites in Britain", in *New cultural landscapes*, Roe and Taylor, Ed., Abingdon: Routledge, 2014, pp.41-58.
- [2] Miyagawa T, Olver C, Otsuka N, Kurose T, and Abe H, "The landuse changes and formation of partnerships through the environmental regeneration in Cheshire, the UK", *J. of the Japanese Institute of Landscape Architecture*, Vol.79(5), 2016, pp.555-558 (in Japanese).
- [3] Williamson, K.S., "Growing with Green Infrastructure", *Heritage Conservancy*, 2003, pp.1-20.
- [4] Handley, J, Pauleit, S and Gill, S, "Landscape, sustainability and the city", in *Landscape and Sustainability*, Benson and Roe, Ed., Abingdon: Routledge, 2007, pp.167-195.
- [5] Miyagawa T, Olver C, Otsuka N, Kurose T, and Abe H, "Lessons and achievements from the Mersey Forest by networking partnership for twenty years", *Proc. 7th Int. Conf. on GEOMATE*, 2017, pp.564-570.
- [6] Ling C, Handley J, and Rodwell J, "Restructuring the Post-industrial Landscape: A Multifunctional Approach", *Landscape Research*, Vol. 32(3), 2007, pp.285-309.
- [7] Roe M, "Exploring future cultural landscapes, in *New cultural landscapes*", Roe and Taylor, Ed., Abingdon: Routledge, 2014, pp.241-269.
- [8] Jerome G, Mell C, Shaw D, "Re-defining the characteristics of environmental volunteering: Creating a typology of community-scale green infrastructure", *Environmental Research*, vol.158, 2017, pp.399-408.
- [9] Mathers, A, Dempsey, N and Molin JF, "Place-keeping in action: Evaluating the capacity of green space partnerships in England", *Landscape and Urban Planning*, vol.139, 2015, pp.126-136.
- [10] Ordnance Survey Map, <<http://www.osmaps.ordnancesurvey.co.uk/>>, 2107, [Accessed 2017.8.22.].
- [11] Northwich Woodlands, Map of the Park, <<http://www.northwichwoodlands.org.uk/visit/index.shtml>>, undated, [Accessed 2017.8.22.].
- [12] St.Helens Council, "Bold Forest Park Area Action Plan", 2017.
- [13] Mersey Forest, "More from trees, The Mersey Forest Plan", 2014.
- [14] Cheshire West and Chester Council, "Local Plan, Planning Policy Mapping 2015", <<http://maps.cheshire.gov.uk/cwac/localplan/>>, undated, [Accessed 2017.8.22.].
- [15] Vale Royal Borough Council, "Vale Royal Borough Local Plan - Policies saved after 29 Jan 2015", <http://consult.cheshirewestandchester.gov.uk/events/24925/2535161_accessible.pdf#search=%27Vale+Royal+Borough+Local+Plan%27>, 2006, [Accessed 2017.8.22.].
- [16] Cheshire West and Chester Council, "Local Plan (Part One) Strategic Policies", <http://consult.cheshirewestandchester.gov.uk/portal/cwc_ldf/adopted_cwac_lp/lp_1_adopted?tab=files>, 2015, [Accessed 2017.8.22.].
- [17] St. Helens Council, "St. Helens Unitary Development Plan", <<https://www.sthelens.gov.uk/media/3391/sthelens-unitary-development-plan-saved-policies-2013-addendum.pdf>>, 1998, [Accessed 2017.8.22.].
- [18] St. Helens Council, "St. Helens Local Plan Scoping Consultation Document", <<https://www.sthelens.gov.uk/localplan>>, 2016, [Accessed 2017.8.22.].
- [19] St. Helens Council, "St. Helens, the heart of the Northwest", <<http://www.dreamsthelens.com/dream-facts-figures/>>, undated, [Accessed 2017.8.22.].
- [20] The Mersey Forest, provided materials, undated.
- [21] Heritage Lottery Fund, "Saltscape secures Heritage Lottery Fund investment", <<https://www.hlf.org.uk/about-us/media-centre/press-releases/saltscape-secures-heritage-lottery-fund-investment>>, 2014.8.22, [Accessed 2017.9.4.].
- [22] The Mersey Forest, "Northwich Business Improvement District Green Infrastructure Plan", 2016.
- [23] St.Helens Council, "St. Helens Town in the Forest Strategic Vision Document", Gillespies, 2006.
- [24] St.Helens Council, "City Growth Strategy", 2008.
- [25] St.Helens Council, "St. Helens Core strategy", 2012.

THE INCORPORATION OF LEAN SIX-SIGMA INITIATIVES TO REDUCE WATER FOOTPRINT OF A PUBLIC UNIVERSITY

Karin Kandananond

Faculty of Industrial Technology, Valaya Alongkorn Rajabhat University, Thailand

ABSTRACT

Water footprint is the amount of water use related to human activities. Currently, the water scarcity and untreated water are the main problems many organizations have confronted with. In this study, the water consumption activities of a public University are studied and assessed within the context of the three types of water footprints. First of all, the water consumption of an organization in the form of the blue and green water footprints are assessed and calculated. Secondly, the polluted water or gray water footprint is also included in the study. Finally, the total water footprint of the organization is evaluated in term of liter per campus community member. The second phase of the study focuses on the application of the lean six-sigma initiatives on the water consumption activities of the University. The application will point out the most critical activity with the highest priority to implement the water saving solution. This consequence will result in the significant reduction of the water footprint of the organization. Therefore, this incorporation will lead to the expedition of the environmental sustainability in the University.

Keywords: Lean six sigma, Public University, Water footprint.

INTRODUCTION

Water is the important resource for every aspects of human's life. However, the emerging problem is the scarcity of water in many areas of the world and the water conservation is the key to solve this problem. Although most people realize the importance of the water saving, the crucial problem is that they do not take it seriously. The study shows that most people might not get the whole picture of how much water is spent on each process. As a result, if water consumption of each product or process is calculated and is attached to like a price tag. They will know exactly the impact of their activities on the environment. According to the study, since the amount of water usage in the public sector is high, it is important to implement the efficient method to reduce the water consumption. Public University is a part of the public organizations. Therefore, if the appropriate intervention technique is applied to the current activities of the University, it will result to the significant saving of the water consumption in the organization.

REVIEW

For the success story in the industry, Sadraoui, Afef, and Fayza [1] utilized six sigma technique to reduce and optimize the water consumption at Coca Cola Company. Moreover, Kaushik, and Khanduja [2] reported that the water consumption in the thermal power plant was significantly reduced after the implementation of six sigma method. Franchetti,

Bedal, Ulloa, and Grodek [3] show that the technique of lean six sigma and green is a potential tool to increase the water efficiency in the industry. Parveen, Kumar, and Rao [4] also applied the integrated method of lean and green supply chain in the manufacturing firms to reduce the water usage. The study of the impact of lean and agile method on the reduction of water footprint in the construction industry was conducted by Sertyesilisik [5].

SCENARIO

A public University in Thailand, Valaya Alongkorn Rajabhat University, is selected to be a case. Valaya Alongkorn Rajabhat University is a public University established under the Rajabhat University Act, B.E. 2547 (A.D. 2004), and the main campus is located in Prathumthani province, Thailand as shown in Fig. 1.



Fig. 1 University campus.

The University offers both undergraduate and graduate degrees to part-time and full-time students and it is operated daily from Monday to Sunday except the national holidays. It is the medium-sized University. There are about 10,000 students and 700 University personnel. There are many activities in the organization that are related to water consumption. This includes the transportation for official use, electricity use, and direct water consumption.

RESEARCH PROCEDURES

The main research procedures are divided into two sections. The first is to assess the amount of water consumption regarding two major processes in the organization, transportation and electricity use. The second is the application of six sigma methodology to reduce the water consumption.

The pathway to the reduction of water footprint is differentiated into five steps, i.e., define, measure, analyze, improve and control (DMAIC).

-Define

Since the main concept of problem defining is “vital few, trivial many”, the Pareto diagram was used to identify the problem which contributed to the highest amount of water consumption. According to the Pareto chart in Fig. 2, the main source of water footprint is the fuel consumption for the transportation which holds the highest percentage of water consumption (88 percent) followed by electricity, daily use water, and etc..

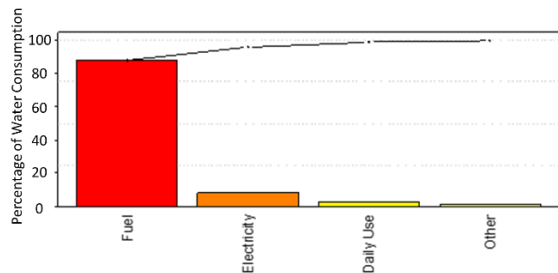


Fig. 2 Pareto chart.

Therefore, it is interesting to note that the first priority to reduce the water consumption should focus on the reduction on the fuel use for the combustion in the University car fleet.

-Measure

The water footprint are calculated by focusing on the activities of the organization which lead to the water consumption. The consumption is based on two main activities, electricity use and fuel consumption on the transportation.

The electricity use was measured from January to April 2018 and the water footprint is calculated. The measurement is done through the meter reading at each building in the University. The total number is

20 buildings. The unit of electricity measurement is kWh (kilowatt-hour) and the life cycle analysis of water consumption on the electricity generation is 0.26 liter/MWh. As a result, the total amount of water consumption according to the electricity use is shown in Table 1.

Table 1 Water consumption of the electricity use

Building	kWh	Liter
Office of Learning Promotion and Provision Academic Services	66,116	17.19016
Language and Computer Center	65,392	17.00192
Demonstration School 1	65,920	17.1392
Demonstration School 2	635	0.1651
Demonstration School 3	97,675	25.3955
Green House	32,200	8.372
Plant Genetics Preservation	2,182	0.56732
Student Affairs Division	1,596	0.41496
Faculty of Science and Technology (Office and lecture hall/rooms)	3,200	0.832
Faculty of Science and Technology (Home economics lecture rooms/laboratory)	66,440	17.2744
Faculty of Humanities and Social Science (Office and lecture hall/rooms)	6,600	1.716
Faculty of Humanities and Social Science (Student government office)	59,697	15.52122
Faculty of Industrial Technology	39,200	10.192
Faculty of Agriculture Technology (Office and lecture rooms)	30,560	7.9456
Faculty of Agriculture Technology (Laboratories)	63,909	16.61634
Faculty of Education 1	9,680	2.5168
Faculty of Education 2	261,280	67.9328
Faculty of Management Science 1	19,200	4.992
Faculty of Management Science 2	14,960	3.8896
Faculty of Management Science 3	7,680	1.9968
Total	1,015,022	263.9057

On the hand, the fuel consumption due to the transportation activities is put into the account

Table 2 Water consumption of the fuel use

Fuel	Density (kg/liter)	Fuel used (liter)	Fuel used (kg)	(Liter/kg)	Water footprint (Liter)
Gasoline	0.77	24307	18716	857	16,039,612
Diesel	0.832	2640	2196	690	1,515,240
					17,554,852

It is interesting to note that the major water consumption is from the fuel consumption for the transportation. Moreover, the detailed study shows that gasoline use contributes to the highest water consumption (16,039,612 liter). Therefore, the best pathway leading to the water reduction is to decrease the use of gasoline.

-Analyze

The major gasoline consumption is from the

University vehicle fleet which is for official use. Therefore, the only solution is to reduce the consumption. As a result, the cause and effect or Ishikawa diagram is utilized to analyze the causes of the effect, i.e., gasoline use reduction. Different experts are interviewed and brainstormed, a potential list of the causes is depicted in the form of cause and effect diagram as shown in the following Fig. 3.

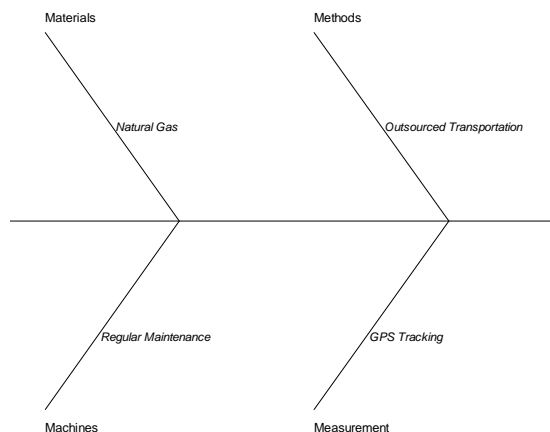


Fig. 3. Cause and effect diagram

According to Fig. 3, different categories of causes are listed based on four main genres, i.e., materials, methods, machines, and measurements.

-Materials

For materials, the commonly used fuel in the vehicle fleet is gasoline. As a result, different type of fuel with less consumption of water, e.g., natural gas, should be used instead of gasoline.

However, the engine system needs an upgrade so the economic analysis must be assessed. Moreover, since the vehicle engine is originally designed for the gasoline used, the natural gas might affect the tribology of the engine. The engine might need more frequent service in the long run.

-Machines

In this case, machine is the engine itself. To increase the fuel saving rate, the regular maintenance might help to increase the engine performance. Therefore, this will lead to the significant saving of the fuel.

-Measurements

Since Bangkok is the capital of Thailand and her traffic is among the worst in the world, the fuel consumption is contributed to the traffic. Moreover, it also has the complex road network so it is easy to get lost. As a result, the solution to this problem relies on the technology. Currently, the GPS tracking system mostly come up with smart phones and Google map is the powerful software which will help to find the fastest route to the destination. As a result, if all drivers use the GPS and its software, it will

reduce the time spent in the traffic significantly.

-Methods

To reduce the official use of the fleet, the alternative solution turns to the outsourced service. Although the transportation activities will switch from the University's vehicle fleet.

-Identify

After all the options is identified, the experts have brainstormed together and score the potential option to practice. The results show that the utilization of GPS might be the best option to practice. Because of the advanced technology, GPS and its navigation software is equipped in most smartphones. Therefore, most drivers have access to the efficient and robust navigation system. The sample of the navigation through Google map is shown in Fig. 4.

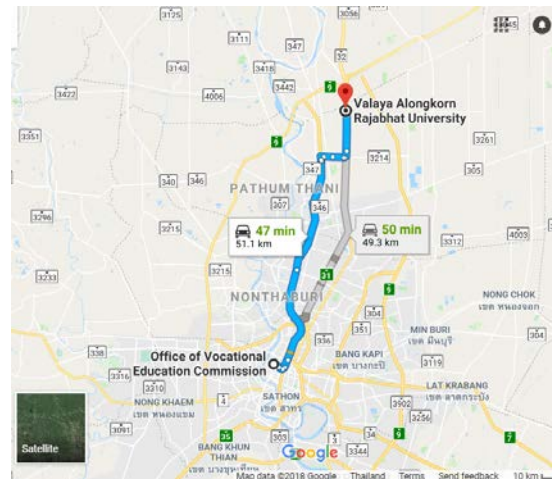


Fig. 4. Navigation system

-Control

The solution to the problem is practice to ensure that the cause of the problem is solved. The measurement has been done in order to validate the results.

RESULTS

After the efficient navigation system is introduced and used in the University vehicle fleet for one month, the result indicate that the average fuel saving is approximately 5 percent for each trip (in the first month after the implementation). Therefore, the total amount of gasoline saving per month is about 300 liter/month or 197,967 liter of water consumption.

CONCLUSIONS AND DISCUSSIONS

The fuel used for the transportation in the organization is the main concern which will lead to the major saving of the water consumption. The lean six sigma method has been applied to reduce the water use in the organization. The tool points out that

the navigation system should be fully used in the University vehicle fleet and this results in the significant saving in both the fuel and water consumption. Besides the use of DMAIC, other methods, e.g., 5S and Kaizen, might be used in addition to the proposed method in order to reduce the water usage.

REFERENCES

- [1] Sadraoui T., Afef A., and Fayza J., Six Sigma: A New Practice for Reducing Water Consumption with Coca Cola Industry. *International Journal of Six Sigma and Competitive Advantage*, Vol. 9, Issue 2, 2012, pp. 217-244.
- [2] Kaushik P. and Khanduja D., Application of Six Sigma DMAIC Methodology in Thermal Power Plants: A Case Study. *Total Quality Management & Business Excellence*, Vol. 20, 2009, pp. 197-207.
- [3] Franchtti M., Bedal K., Ulloa J., and Grodek S., Lean and Green: Industrial Engineering Methods Are Natural Stepping Stones to Green Engineering, *Industrial Engineer*, 2009, pp. 24-34.
- [4] Parveen C. M., Kumar A. R. P., and Rao T. V. V. L. N., Integration of Lean and Green Supply Chain - Impact on Manufacturing Firms in Improving Environmental Efficiencies. *International Conference on Green Technology and Environmental Conservation (GTEC 2011)*.
- [5] Sertyesilisik B., Lean and Agile Construction Project Management: As a Way of Reducing Environmental Footprint of the Construction Industry. *Optimization and Control Methods in Industrial Engineering and Construction*, Vol. 72, 2014, pp. 179-196.

PREPARATION OF GEOPOLYMER CEMENT FROM CRUSHED STONE BY-PRODUCT USING ALKALI FUSION

Kazuki Sakamoto¹, Takaaki Wajima¹

¹Department of Urban Environment Systems, Chiba University, Japan

ABSTRACT

In the crushed stone production process, crushed stone fines, such as dust and slurry cake, are generated as by-products, and most of them are landfilled. Recently, it is becoming difficult to secure landfill sites, and effective utilization of by-products is desired. On the other hand, geopolymer cement has attracted attention due to the higher acid resistance than that of ordinary portland cement.

In this study, we attempted to prepare geopolymer cement from crushed stone by-products using alkali fusion. In the experiment, crushed stone dust, discharged from one of the quarries in Japan, the fused dust, which prepared from the dust by heating at 500 °C with NaOH addition (weight ratio of addition is 1:1.6) for 0.5 h using rotary kiln, tap water and coal fly ash were used as raw materials. Crushed stone dust, fused dust, and tap water is mixed on various mixed ratio, with or without addition of coal fly ash, heat at 30 °C or 80 °C for 24 h, and then stand at room temperature, in air or distilled water to prepare geopolymer cement. Acid resistances for the obtained product and ordinary portland cement was also investigated. As a result, 7 g of mixture of crushed stone dust, water and fused dust (mix ratio is 1: 1: 2) with 3 g of coal fly ash, heated at 80 °C, and cured in water to obtain the geopolymer cement with hard structure, and the obtained geopolymer cement indicates higher acid resistance than ordinary portland cement.

Keywords: Crushed stone, Slurry cake, Coal fly ash, Alkali fusion, Geopolymer cement

INTRODUCTION

In the crushed stone industry, crushed stone dust / cake is generated as a by-product in large quantities from crushing, cutting, polishing and cleaning processes in the stone production process. Currently, most of them are landfilled, but in recent years it is becoming difficult to secure landfill sites, and further development of effective utilization of by-products, such as crushed stone dust and cakes, is desired by laws in Japan [1].

Crushed stone dust is mainly composed of SiO₂ and Al₂O₃, and the particle is fine and uniform. It is also characterized as sparingly soluble. In previous studies, we succeeded to convert sparingly soluble crushed dust into highly soluble dust by alkali fusion treatment to synthesize zeolitic materials [2] - [9].

Geopolymer cement is a cement produced from mixing sodium silicate, sodium hydroxide, water and some industrial by-products, such as coal fly ash, blast furnace slag and so on [10] - [12]. Geopolymer cement has attracted attention because it has less CO₂ emissions in the manufacturing process than ordinary Portland cement and has high acid resistance [10] [13] - [17].

Ordinary Portland cement is mainly solidified by the formation of needle-like calcium silicate hydrate (C-S-H), while geopolymer cement is mainly solidified by the polymerization of silicate ions

sparked by metal ions, such as Al³⁺, Fe²⁺ and so on, which is similar to the reaction of zeolite synthesis [18] [19]. Therefore, there is a possibility to make geopolymer cement using fused dust.

In this study, we attempted to prepare geopolymer cement from crushed stone by-product using the dust fused with alkali. The conditions, such as mixing ratio and curing methods, to prepare the geopolymer product with hard structure were investigated and the acid resistance of the prepared geopolymer cement was evaluated.

EXPERIMENT

Samples

Crushed stone dust generated from one of the domestic crushed stone companies in Japan was used for the experiment. Coal fly ash used in this study was commercially available fly ash type IV. The fused dust was prepared by mixing crushed stone dust with sodium hydroxide at a weight ratio of 1: 1.6 and heating at 500 °C for 0.5 h using a rotary kiln [2].

Preparation of Geopolymer Cement from Dust

Crushed stone dust, tap water and the fused dust were mixed so that total weight of the mixture is 7 g. In addition, the mixture with or without coal fly ash

was prepared to clarify the effect of coal fly ash addition. The mixing ratio of the mixture is shown in Table 1. The mixture was cured at room temperature for 1 day and 7 days, and 7 days passed and heated at 50 °C for 24 hours. The hardness of the product was judged with a bamboo needle to insert into the product.

Table 1 The mixing ratio of the mixture.

The mixing ratio	
Dsut : Water	1 : 1
	1 : 2
	2 : 1
Fused dust : Water	1 : 1
	1 : 2
	2 : 1
Dsut : Water : Fused dust	1 : 1 : 1
	2 : 1 : 1
	1 : 1 : 2
	1 : 2 : 1
	1 : 2 : 2
	2 : 2 : 1
	2 : 1 : 2
	3 : 1 : 1
	1 : 1 : 3
	1 : 3 : 1
	3 : 1 : 2
	2 : 1 : 3

Next, 1 - 7 g of coal fly ash was added to 7 g of the mixture (the mixed ratio of dust : water : fused dust is 1 : 1 : 2). The mixture was kneaded, and the condition of the mixture was observed to obtain the product precursor with high workability.

The raw materials and the products were observed with a scanning electron microscope (SEM, JSM-6510A, manufactured by JEOL).

Curing Experiment

The curing experiment was conducted to increase the strength of the product.

The mixture (7 g) of dust, water and fused dust (the ratio is 1 : 1 : 2) with 3 g of coal fly ash was used for curing experiment. The mixture was filled and formed in a ring with a formwork of ϕ 25 mm \times 5 mm. The ring stands for 24 h in a drying oven at 30 °C and 80 °C, and the product after 24 h was removed from the ring to observe the condition. In addition, the ring with the mixture was heated at 80 °C for 24 h, removed from the ring and then stand at room temperature in air or in 200 mL of distilled water for 96 h. After 96 h, the product was picked up from the beaker and the state was observed. For curing in water, the elution amounts of Si, Al, Na and Ca to water

were examined using atomic absorption spectrometer (AAnalyst 200, Perkin Elmer).

Acid resistance Test

Acid resistance test was conducted for the product in comparison with Portland cement. The sample was prepared with a mold of ϕ 25 mm \times 5 mm. The product was formed by heating at 80 °C and standing in water for 24 hours. The Portland cement (Ordinary Porto Portland Cement, N.C.C. Ltd.) was mixed at 50 % of water to cement ratio, poured into a mold, and stand at room temperature for 24 h. Each sample was immersed in a 5% sulfuric acid solution (200 mL) for 10 days, and the pH of the sulfuric acid solution and the mass of the samples were measured every 24 h.

3. RESULTS AND DISCUSSION

Formation of Geopolymer

The ternary diagrams of mixing condition for formation of hardened body (a) without coal fly ash and (b) with coal fly ash are shown in Fig. 1. The plots indicate the condition when hardened body was confirmed.

For the product without coal ash (Fig. 1(a)), hardening could not be confirmed when the amount of water was large (above 40 %) and those of crushed stone dust and fused dust were small. With decreasing the amount of water and increasing the amounts of crushed stone dust and fused dust, the number of days used for hardening the product became shorter.

For the product with coal fly ash (Fig. 1), hardening could not be also confirmed when the amount of water was large and those of crushed stone dust and fused dust were small. In comparison with the product without coal fly ash, the conditions for no hardening decrease, and the product becomes a powder when the amount of water is small and that of the crushed stone dust is large. In addition, under the same mixing condition, the time for hardening becomes shorter. It is considered that the addition of coal fly ash accelerate the formation of geopolymer. It is noted that the product added with coal fly ash was harder than the product without coal fly ash added.

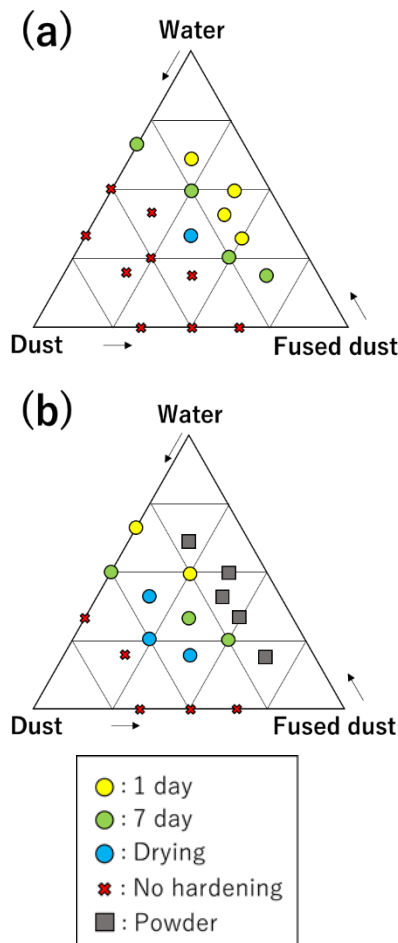


Fig. 1 Ternary diagrams of mixing condition for formation of hardened body (a) without coal fly ash and (b) with coal fly ash.

Figure 2 shows the condition after kneading the mixture with varying amount of coal ash added. The ratio of crushed stone dust, water, and fused dust is 1: 1: 2. The mixture after kneading was in liquid form when the amount of coal ash added was 1 - 3 g, while the mixtures with 5 g and 7 g of coal fly ash added were semisolid and powder, respectively. The viscosity increases as the amount of coal ash added increases. Therefore, it is considered that the mixture with 3 g of coal fly ash addition has a good workability to obtain the geopolymer cement product.

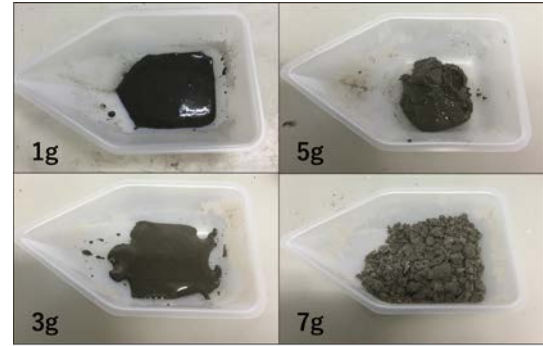


Fig. 2 Observation of the mixture with various amount of coal fly ash.

The XRD patterns of the raw materials and the product are shown in Fig. 3. The product was obtained by adding 3 g of coal fly ash to the mixture (the mixed ratio is 1: 1: 2 of crushed stone dust, water and fused dust). Crushed stone dust contains SiO_2 and CaCO_3 (Fig. 3(a)), and the fused dust consists of alkali salts, such as Na_2SiO_3 and Na_4SiO_4 (Fig. 3(b)). On the other hand, coal fly ash consists of SiO_2 , $\text{Si}_2\text{Al}_6\text{O}_{13}$ and amorphous glass (Fig. 3(c)). Peaks of SiO_2 , CaCO_3 and $\text{Si}_2\text{Al}_6\text{O}_{13}$ remained, and Na_2SiO_3 and Na_4SiO_4 disappeared in the product formed by mixing these raw materials (Fig. 3(d)). In addition, hydrated sodalite ($\text{Na}_6\text{Al}_6\text{Si}_6\text{O}_{24} \cdot 8\text{H}_2\text{O}$) was produced in the product.

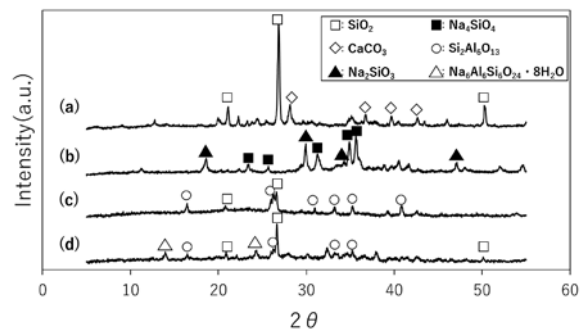


Fig. 3 XRD patterns of (a) crushed stone dust, (b) alkali fused dust, (c) coal fly ash and (d) product.

Raw materials were observed with SEM, as shown in Fig. 4. Crushed stone dust has aggregates particle of thin flake-like sticks with about 20 μm diameter (Fig. 4(a)). The fused dust is the particles with some small particles, alkaline salts, on the surface (Fig. 3(b)). Coal fly ash was a spherical particle with a smooth surface having a particle diameter of 5 to 10 μm .

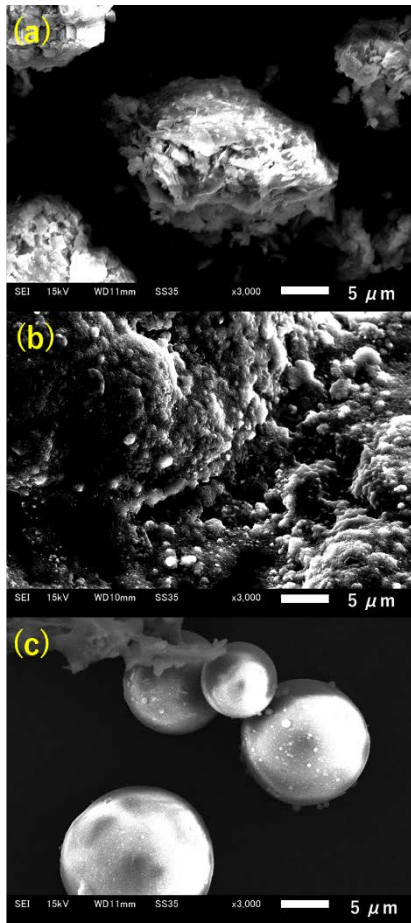


Fig. 4 SEM image, (a) dust, (b) fused dust and (c) coal fly ash.

The product prepared with or without coal fly ash was observed with SEM, as shown in Fig. 5. The product was prepared from the mixture with a ratio of crushed dust, water and fused dust of 1: 1 : 2 with or without addition of coal fly ash. For the product without coal fly ash, particles of crushed stone dust were covered and solidified by gel-like materials. For the product with coal fly ash, the product composed of many ball-like shapes, which would be coal fly ash covered with some gel-like materials and sodalite-like crystals and crushed stone dust like particles covered with gel-like materials. For the XRD pattern of the product with coal fly ash, there was no change in the crystal structure of the crushed stone dust and coal fly ash. It is considered that crushed stone dusts and coal fly ash were covered with the gels formed from fused dust and water, and coal fly ash were more impregnated in the product to be hardened.

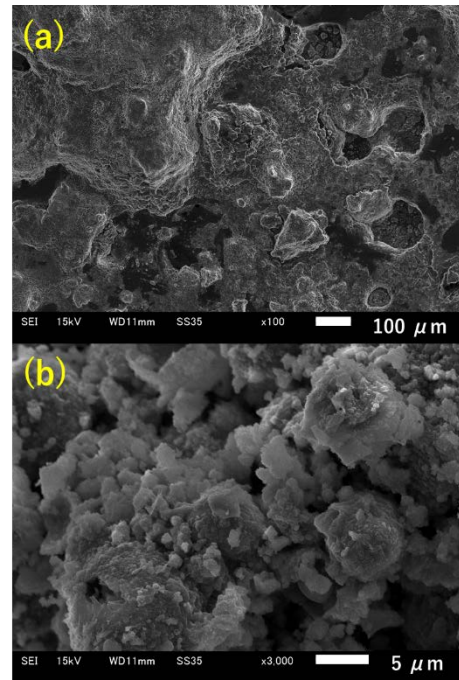


Fig. 5 SEM image, (a) the product without coal fly ash and (b) the product with coal fly ash.

Figure 6 shows the state of the sample after 24 h standing at 30 °C and 80 °C. Although the sample at 30 °C is wet and brittle because chipping occurred at demolding, the sample at 80 °C is hardened and no chipping occurred at demolding.

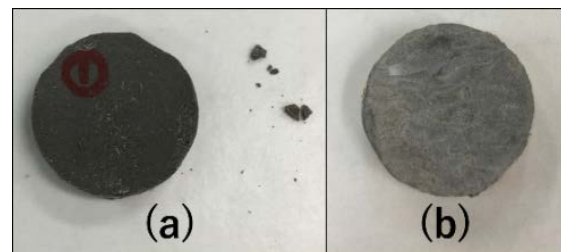


Fig. 6 Sample state after standing at (a) 30 °C and (b) 80 °C for 24 h.

Figure 7 shows the state of the product after 72 h in air and water. For the product prepared in air, some precipitates were observed on the surface. It is noted that the product became fragile and cracked by washing the precipitates on the surface with distilled water. For the product prepared in water, no component was precipitated on the surface, and the hard structure of the product was kept.

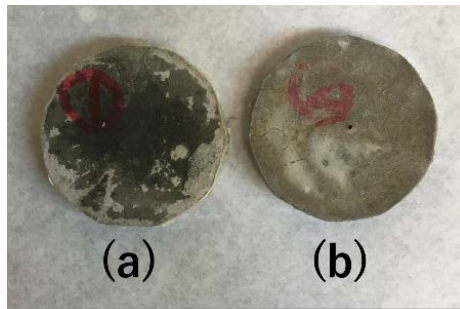


Fig. 7 Observation of the product after 72 h in (a) air and (b) water.

Figure 8 shows the elution amounts of Si, Al, Ca and Na into water. While Al and Ca were hardly eluted, elution of Si and Na was confirmed. Elution of Si and Na into water increased to 46 mg/g and 85 mg/g, and be constant after 48 h. The percentages of Na and Si eluted from the product into water are about 60% and 25%, respectively. Therefore, the precipitate on the surface of the product prepared in air is caused from excess amounts of Na and Si in the product, and the product prepared in water has no precipitate on the surface and hardened due to the removal of excess Si and Na during the curing in water.

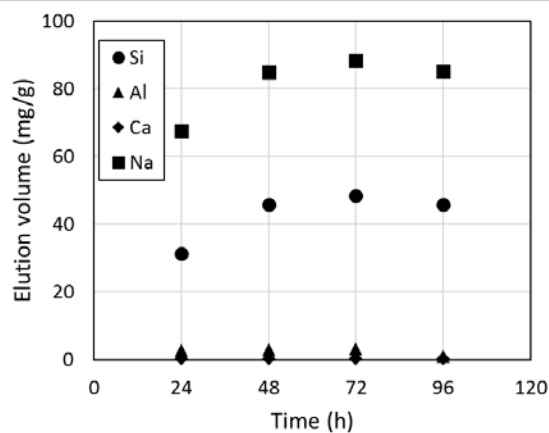


Fig. 8 Elution amounts of Si, Al, Ca and Na into water.

Figure 9 shows the state of the sample before and after acid resistance test. The shape and color of Portland cement change to be small and the color become white after the test, while the shape of the product did not change after the test.

Figure 10 shows the mass changes of the product and Portland cement in sulfuric solution. It is noted that the pH of the sulfuric acid solution was stable at below pH 1 during the immersion period. The mass of portland cement decreases for 10 days, while that of the product decreases in 2 days and be almost constant after 2 days. After 10 days, the mass of the

product is 90 % of the product before the test, while that of Portland cement is 20 % of the portland cement before the test. It was found that the obtained product has acid resistance of geopolymer cement.

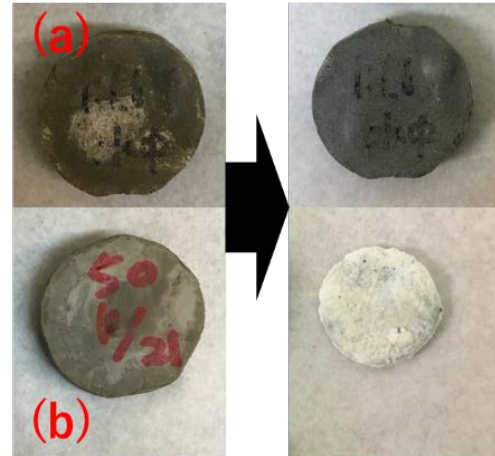


Fig. 9 Observation of (a) product and (b) Portland cement before and after immersion in sulfuric solution.

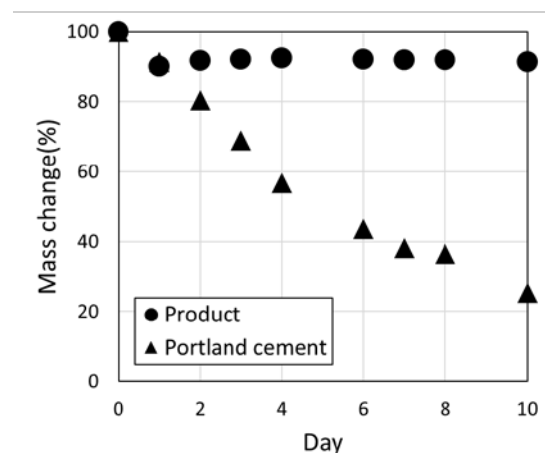


Fig. 10 Mass change of the product and Portland cement in sulfuric acid solution.

CONCLUSION

We tried to prepare geopolymer cement from crushed dust, water, fused dust and coal fly ash. A hardened geopolymer product was obtained by adding 3 g of coal ash to 7 g of the mixture with the ratio of crushed stone dust: water: fused dust = 1: 1: 2. It was found that curing in water after heating at 80 °C was effective for producing stable geopolymer. From the acid resistance test, it was found that the prepared geopolymer cement has higher acid resistance than Portland cement.

REFERENCES

- [1] Chugoku Bureau of Economy, Trade and Industry, Market and business environment survey for promoting new business · recycling using rock resources and by-products, report, 2007, pp. 1-81.
- [2] S. Onishi, T. Wajima, T. Imai, S. Susumu, Alkali Fusion Process of Waste Stone Dust to Synthesize Faujasite Using Rotaky Kiln, Mechanics, Materials Science & Engineering Journal, Vol. 9, No. 1, 2017, pp. 287-292.
- [3] T. Wajima, Alkali Fusion Synthesis of Zeolitic Materials from Waste Dehydrated Cake Discharged from Recycling of Construction Waste Soil, Natural Resources, Vol. 8, 2017, pp. 300-305.
- [4] T. Wajima, Synthesis of zeolite from blast furnace slag using alkali fusion with addition of EDTA, Advanced Materials Research, pp. 1044-1045, p.p. 124-127.
- [5] T. Wajima, K. Munakata, Material conversion from waste sandstone cake into cation exchanger using alkali fusion, Ceramics International, Vol. 38, No. 2, 2012, pp. 1741-1744.
- [6] T. Wajima, K. Munakata, Y. Ikegami, Conversion of Waste Sandstone Cake into Crystalline Zeolite X Using Alkali Fusion, Materials Transactions, Vol. 51, No. 5, 2010, pp. 849-854.
- [7] T. Wajima, K. Yoshizuka, T. Hirai, Y. Ikegami, Synthesis of Zeolite X from Waste Sandstone Cake Using Alkali Fusion Method, Materials Transactions, Vol. 49, No. 3, 2008, pp. 612-618.
- [8] Lijalem A., Joaquín P.P., Yonas C., Isabel D., Conventional versus alkali fusion synthesis of zeolite A from low grade kaolin, Applied Clay Science 132-133, 2016, pp. 485-490.
- [9] Jintang L., Xue Z., Xiaobing Y., Chaonan W., Xuetao L., Synthesis of pure sodalite with wool ball morphology from alkali fusion kaolin, Materials Letters 161, 2015, pp. 157-159.
- [10] Liew Y.M., Heah C.Y., Long-yuan L., Nur A.J., Mohd M.A.B.A., Tan S.J., Kamarudin H., Characteristics of geopolymer and case examples of construction, Construction and Building Materials 156, 2017, pp. 9-18.
- [11] Hammad R. K., N.K. Lee, S.M. Park, N. Abba, H.K. Lee, Synthesis of geopolymer-supported zeolites via robust one-step method and their adsorption potential, Journal of Hazardous Materials 353, 2018, pp. 522-533.
- [12] S. Moukannaa, M. Loutou, M. Benzaazoua, L. Vitola, J. Alami and R. Hakkou, Recycling of phosphate mine tailings for the production of Geopolymers, Journal of Cleaner Production 185, 2018, pp. 891-903.
- [13] N.B. Singh, Foamed geopolymer concrete, Materials Today, Proceedings 5, 2018, pp. 15243-15252.
- [14] Part W. K., Mahyuddin R., Cheah C. B., An overview on the influence of various factors on the properties of geopolymer concrete derived from industrial by-products, Construction and Building Materials 77, 2015, pp. 370-395.
- [15] Peng M.X., Wang Z.H., Shen S.H., Xiao Q.G., Li L.J., Tang Y.C., Hu L.L., Alkali fusion of bentonite to synthesize one-part geopolymeric cementscured at elevated temperature by comparison with two-part ones, Construction and Building Materials 130, 2017, pp. 103-112.
- [16] Piotr R., Magdalena K. and Włodzimierz M., Spectroscopic studies of fly ash-based geopolymers, Spectrochimica Acta Part A: Molecular and Biomolecular Spectroscopy 198 2018, pp. 283-289.
- [17] Ankur M., Rafat S., Sulfuric acid resistance of fly ash based geopolymer concrete, Construction and Building Materials 146, 2017, pp. 136-143.
- [18] Melkon T., Gunther M., Stefan K. H., Relation of water adsorption capacities of zeolites with their structural properties, Microporous and Mesoporous Materials 264, 2018, pp. 70-75.
- [19] Habbib G., Oliver S., Yvan M., Philippe K., The Reconstruction of Natural Zeolites, book, pp. 1-5.

DESALINATION OF SEAWATER USING NATURAL ZEOLITE FOR AGRICULTURAL UTILIZATION

Takaaki Wajima¹

¹Graduate School of Engineering, Chiba University, Japan

ABSTRACT

We attempted to make agricultural cultivation solution from seawater with a simple process using natural zeolite. In 21st century, the demand for food is increasing due to the global population growth, and securing farmland is one of the most important factors in food production. Approximately 20 % of farmland in the world is salt-damaged soil with unsuitable properties for agriculture by high salinity water, and simple desalination methods of high salinity water to improve salt-damaged soil is desired. Natural zeolite has a cation exchange ability, and is available in large quantities at low cost. In this study, desalination of seawater, as high salinity water, using Japanese clinoptilolite zeolites with typical exchangeable cation, Na⁺, K⁺, NH₄⁺, Mg²⁺ and Ca²⁺, were examined. Ca²⁺-type zeolite indicates the highest reduction of NaCl from seawater among these ion-exchanged natural zeolites. The column experiment using Ca²⁺-type natural zeolite shows that pH can be controlled to neutral and salinity can be reduced by the reaction between Ca²⁺ in zeolite and other ions in seawater. Although Radish sprouts did not grow in seawater, they could be grown in the solution treated with column process of Ca²⁺-type natural zeolite.

Keywords: Seawater Desalination, Natural zeolite, Radish sprout growth, Ca-ion exchange

INTRODUCTION

In the 21st century, global environmental issues are very serious and effective utilization of energy and mineral resource and securing food and water are urgent problems. Production of a stable supply of food is essential to sustain human life. Securing agricultural water is one of the most important factors in food production. Due to the global population growth, the demand for water is increasing. Many countries of the Middle East and Africa are in a chronic shortage of water, and it is expected that half of the countries in the world will get into a water shortage in 2025 [1].

One of the ways to supply water resources is seawater desalination because seawater is the most abundant water resources on earth. The multi stage flash (MSF) method and the reverse osmosis membrane method (RO) are well known desalination technologies [2], but these technologies are expensive for agricultural use because they are producing high-quality fresh water for domestic or industrial use. However, the highest utilization of the fresh water in the world is irrigation, and the percentage of irrigation utilization is 70% of the total freshwater utilization [3]. Agricultural water should contain elements for crops rather than be highly purified. Seawater contains the essential elements needed for plant growth, but its high concentration of NaCl causes salt damage that precludes its direct use. Irrigation water has no need to be high-quality fresh water and can be obtained by reducing high content of NaCl in

seawater.

The securing farmland is also one of the most important factors in food production. Approximately 20 % of farmland in the world is salt-damaged soil with unsuitable properties for agriculture by high salinity water. Furthermore, the cultivated lands in northeast Japan were damaged by tsunami, and became salted soil not to use for agriculture. Therefore, simple and inexpensive technique is desirable for agricultural use to decrease salinity of saline water or salted soil.

Natural zeolite occurs in natural deposits, generally associated with grassy volcanic rock, and is available in large quantities at low cost [4], especially Japan is volcanic country with abundant natural zeolite deposits, such as clinoptilolite, mordenite and so on. Based on their high ion-exchange capacity, absorptivity, water retention and low cost, natural zeolites have been used in agronomy, horticulture and industry [5]. Therefore, natural zeolite has possibility to be used to reduce NaCl in saline water at low cost. There are some papers for seawater desalination using natural zeolites [6-8]. Little information is available, however, on the treatment of saline water with natural zeolite.

In this study, we investigated the ability of ion-exchanged Japanese natural zeolite for seawater desalination. Reduction of NaCl from seawater using Japanese clinoptilolite-type zeolites with typical exchangeable cation, Na⁺, K⁺, NH₄⁺, Mg²⁺ and Ca²⁺, were examined, and column test using ion-exchanged natural zeolite was performed to produce the solution

for agricultural utilization from seawater.

MATERIALS AND METHOD

Samples

Seawater used in this study was collected from the surface layer in Imari Bay, Saga Prefecture, Japan. Japanese clinoptilolite-type natural zeolite, which was obtained from the deposit of Koriyama, Kagoshima prefecture, Japan, was used in zeolite treatment.

Ion-exchanged Natural Zeolite Treatment

Five different ion-exchanged natural zeolites, Na^+ , K^+ , NH_4^+ , Mg^{2+} and Ca^{2+} -zeolite, were prepared, and the NaCl reductions in seawater by these ion-exchanged zeolites were compared. Before the experiment, natural zeolites used in this experiment was grounded by mill, sieved under 500 μm , and dried in drying oven at 80 °C overnight.

Na^+ and NH_4^+ -zeolites were prepared using the method reported in [9], and K^+ , Mg^{2+} and Ca^{2+} -zeolites were prepared as follows. Na^+ -zeolite (100 g) was put into 4 M KCl, 2 M MgCl_2 or 2 M CaCl_2 solution (500 mL) in 1 L vessel, and set in drying oven at 80 °C overnight. Then, the slurry was filtrated, and the solid was put into each fresh solution (500 mL) again. This procedure was repeated 3 times, then the obtained solid was washed with 80 % EtOH, and dried at 80 °C overnight to obtain K^+ , Mg^{2+} and Ca^{2+} -zeolite. It is noted that all exchangeable cation sites in natural zeolite was completely occupied by the objective cations.

The reduction of NaCl in seawater using ion-exchanged natural zeolites was examined as follows. 1.5 g of natural zeolite was added to 15 mL of seawater, and stirred for 2 hours with a magnetic stirrer. After stirring, the slurry was filtered, and then fresh natural zeolite was added to the filtrate. This procedure was repeated 5 times. The concentrations of Na^+ , K^+ , Mg^{2+} , Ca^{2+} , Cl^- and SO_4^{2-} in seawater and the filtrate after each times of zeolite treatments were determined using ion chromatograph (DX-120, Dionex).

Column Test using Ion-exchanged Natural Zeolite

Before the column test, Ca-exchanged natural zeolite packed column was prepared. Natural zeolite particles with the diameter of 1.0 mm (40 g) was packed into the glass column tube (inner diameter: 14 mm, height: 30 cm) sandwiched between layers of quartz wool, 1 M $\text{Ca}(\text{NO}_3)_2$ solution (100 mL) was then fed to the column from bottom to top at a flow

rate of 10 mL/min using a ceramic pump, and the effluent was circulated to the column again for 2 hours. After circulation, distilled water (800 mL) was passed through the column to remove the excess $\text{Ca}(\text{NO}_3)_2$ in the column to prepare the Ca-exchanged natural zeolite column. Four these columns were prepared.

Seawater desalination experiment was done using Ca-exchanged natural zeolite column. Seawater (40 mL) was fed to the Ca-exchanged column from bottom to top at a flow rate of 4 mL/min using a ceramic pump, and the effluent was circulated to the column again for 2 hours. After circulation, the solution was completely passed through the column to collect the column treated seawater. This column treated seawater was fed to the fresh Ca-exchanged column, and done as the same procedure. This operation was repeated 4 times.

The pH, salinity and the concentrations of main elements, Na^+ , K^+ , Mg^{2+} , Ca^{2+} , Cl^- and SO_4^{2-} , in the solution after passing through the column was measured using pH meter (Horiba, F-72), salt meter (MK, YK-31SA) and ion chromatograph (Tosho, IC-2010), respectively. The changes of each element on each step represent as the ratio of measured concentrations to the original concentrations in seawater (R) as follows;

$$R_M = \frac{C_M}{C_0} \quad (M: \text{Na}^+, \text{K}^+, \text{Mg}^{2+}, \text{Ca}^{2+}, \text{Cl}^-, \text{SO}_4^{2-}) \quad (1)$$

where C_0 and C_M are the initial concentration in original seawater and the measured concentration in the treated solution, respectively.

Growth Test

The solution after 4 times column treatment, tap water and seawater were applied to growth test using radish sprouts (*Raphanus sativus*). During this test, cultivation was conducted for 10 days at room temperature to investigate the possibility of using the obtained solutions for cultivation.

RESULTS AND DISCUSSION

Desalination Ability of Ion-exchanged Natural Zeolite

Figure 1 shows the change of (a) Na^+ and (b) Cl^- concentrations in seawater as a function of the number of zeolite treatment. Although Na^+ content is almost constant using Na^+ -type zeolite, other types zeolites can decrease Na^+ content in seawater. The order of Na^+ reduction is $\text{NH}_4^+ \rightleftharpoons \text{K}^+ \rightleftharpoons \text{Ca}^{2+} > \text{Mg}^{2+} > \text{Na}^+ \rightleftharpoons 0$, which is good accordance with adsorption affinity of clinoptilolite for cations [10]. On the other

hands, Mg^{2+} - and Ca^{2+} -type zeolites, including divalent cations, can decrease Cl^- contents in seawater, while Cl^- contents are almost constant using Na^+ -, NH_4^+ - and K^+ -type zeolites, including monovalent cations.

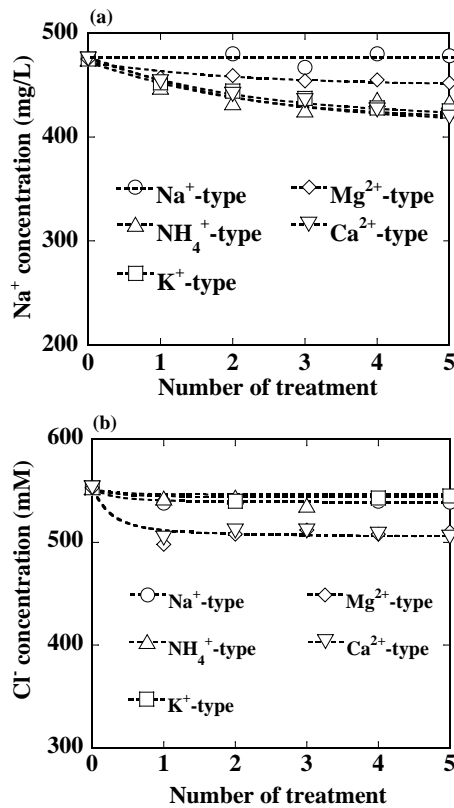


Fig. 1 Change of (a) Na^+ and (b) Cl^- concentrations in seawater as a function of the number of zeolite treatment.

Table 1 shows the chemical compositions of seawater and the solution after 5-times treatment with ion-exchanged natural zeolites. It is noted that original seawater indicates typical chemical compositions of seawater [2], [11]. The cation including in each type-zeolite is high content in each solution, and the contents of K^+ and Ca^{2+} , which are the cations with high adsorption affinity of clinoptilolite, decrease, except the solutions treated with K^+ - and Ca^{2+} -type zeolite, respectively. It is considered that the exchangeable cations with high mobility (high affinity) can be exchanged with high content of Na^+ in seawater. SO_4^{2-} content is almost constant using all types zeolites. It is unclear why divalent-type zeolite can reduce only Cl^- content in seawater. Anion removal using zeolite may depend on surface adsorption because zeolite is cation exchanger. One of the reasons may be that the surface properties of divalent-type zeolite are different to monovalent-type, which indicates higher affinity for Cl^- than SO_4^{2-} .

These results suggest that Ca^{2+} -type natural zeolite is the best for NaCl reduction from seawater.

Table 1 Chemical compositions of seawater (SW) and the solution after 5-times treatment with ion-exchanged natural zeolites (NZ).

	SW	Na^+ -NZ	NH_4^+ -NZ	K^+ -NZ	Mg^{2+} -NZ	Ca^{2+} -NZ
Na^+	475	477	402	415	450	406
NH_4^+	0.0	0.0	66.5	0.0	0.0	0.0
K^+	10.3	0.3	0.9	59.8	5.7	3.1
Mg^{2+}	56.0	51.2	51.9	52.4	73.7	57.3
Ca^{2+}	11.7	6.8	9.3	10.1	10.4	51.1
Cl^-	553	541	562	548	507	506
SO_4^{2-}	27.8	28.0	27.6	27.5	27.2	27.1

Unit: mmol/L

Desalination using Column

The pH and salinity of the solution after natural zeolite column treatment on each step are shown in Fig. 2. The pH of seawater is 7.76, and those of the solution after zeolite treatment are neutral (pH 6.5 - 7.5), which indicates the solution pH after natural zeolite treatment is neutral to be used for cultivation. The salinity of seawater is 3.40 %, and with increasing the number of treatment to four times, that of the solution gradually decreases to 0.66%, which is approximately one-fifth of the original salinity of seawater.

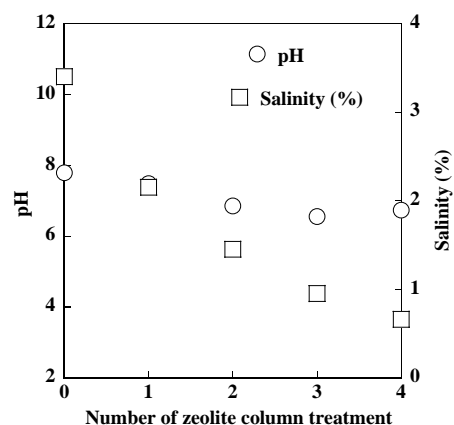


Fig. 2 pH and salinity of the solution treated with Ca-exchanged natural zeolite columns.

Changes of each element in the solution during the zeolite treatment are shown in Fig. 3. The contents of Na^+ , K^+ , Mg^{2+} , Cl^- and SO_4^{2-} drastically decreases on first zeolite treatment and then gradually decrease after second zeolite treatment, which is approximately below one-fifth of the original contents of seawater, while that of Ca^{2+} drastically increases and then be almost constant after second zeolite treatment.

Therefore, the decrease of salinity mainly depends on the decreases of all elements, except Ca^{2+} .

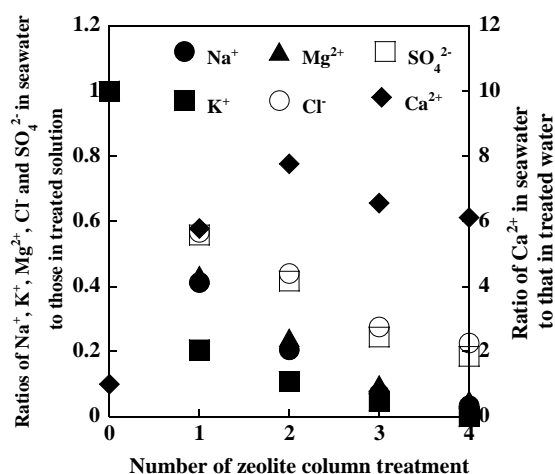


Fig. 3 Ratios of Na^+ , K^+ , Mg^{2+} , Ca^{2+} , Cl^- and SO_4^{2-} in seawater to those in the solution treated with Ca-exchanged natural zeolite column.

Table 2 shows the chemical composition, salinity, and pH of seawater and the solutions after various times of natural zeolite treatment. Although seawater contains high amounts of Na^+ (12191 mg/L), Cl^- (21891 mg/L) and other elements and indicates high salinity (3.4 %) The solutions after zeolite treatment contain lower amounts of Na^+ , Cl^- , K^+ , Mg^{2+} and SO_4^{2-} than seawater, except Ca^{2+} , and indicates lower salinity than seawater. It is noted that pH of the solution is neutral to be used for cultivation. The contents of Na^+ , Cl^- , K^+ , Mg^{2+} , SO_4^{2-} and Ca^{2+} in the solution after 4-times natural zeolite column treatments are 405 mg/L, 4959 mg/L, 0 mg/L, 70 mg/L, 504 mg/L and 2466 mg/L, respectively, which indicates that the solution contains low NaCl and minerals, Mg^{2+} and Ca^{2+} , and indicates low salinity (0.66 %) for plant growth.

Table 2 Chemical compositions, salinity and pH of seawater (SW) and the solution after 1-4 times treatment with Ca-exchanged natural zeolite columns.

	SW	1- times	2- times	3- times	4- times
Contents (mg/L)					
Na^+	12191	5027	2501	857	405
K^+	682	140	74	33	0
Mg^{2+}	1360	592	330	135	70
Ca^{2+}	403	2330	3132	2644	2466
Cl^-	21891	12409	9643	6036	4959
SO_4^{2-}	2724	1520	1136	667	504
Salinity (%)	3.40	2.15	1.45	0.95	0.66
pH	7.79	7.48	6.85	6.55	6.73

Figure 4 shows the growth test of radish sprouts for 10 days at room temperature. Although we could not observe the germination of radish sprouts using seawater, we could confirm the growth of radish sprouts using the treated solution like using distilled water. These results suggested that it is possible to prepare the solution for agricultural cultivation from seawater using Ca-type natural zeolite treatment.

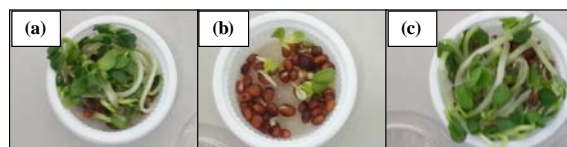


Fig. 4 Observation of *Raphanus sativus* after 10-days growing using (a) tap water, (b) seawater, and (c) the solution after 4 times zeolite treatment of seawater.

CONCLUSION

We investigated desalination behaviors from seawater using Japanese clinoptilolite-type natural zeolite in order to be used as desalination agent for producing irrigation water from salty water. The ability of ion-exchanged clinoptilolite zeolite for NaCl reduction from seawater was examined. Among typical ion-exchanged zeolite, such as Na^+ -, K^+ -, NH_4^+ -, Mg^{2+} - and Ca^{2+} -type natural zeolites, Ca^{2+} -type zeolite is the best for reduction of NaCl from seawater. We could decrease the salinity of seawater using a simple Ca-exchanged natural zeolite column, and can obtain the solution with neutral pH and low salinity to be used for cultivation. Although radish sprouts did not grow in seawater, they could be grown in the solution after zeolite treatment. These results suggested that it is possible to prepare a solution for

agricultural cultivation from seawater using a simple Ca-exchanged natural zeolite treatment. I found that Ca-natural zeolite can be desalinate seawater by removing both cations and anions. In future, Ca-exchanged natural zeolite will be applied to improve salted soil to cultivate crops.

ACKNOWLEDGEMENTS

This study was performed under Cooperative Research Program of Institute of Ocean Energy, Saga University (11002A).

REFERENCES

- [1] World Water Council (WWC), World Water Vision. Making Water Everybody's Bus. Earthscan, 2002.
- [2] Sea Water Society Japan and Salt Science Foundation, Sea Water, its Property and Technology. Tokai Daigaku Shuppan, 1994.
- [3] Tilizer M.M., Conference Proceedings, in Proc. the 2nd Autoanalyzer symposium in Osaka, 2006, pp. 4-15.
- [4] Tominaga H., Zeolite no Kagaku to Ouyou, Kodansha, 2001.
- [5] Barrer R.M., Zeolites and Clay minerals as Sorbents and Molecular Sieves, Academic Press, 1978.
- [6] Wajima T., Ion exchange properties of Japanese natural zeolites in seawater, Anal. Sci., Vol. 29, 2013, pp. 139-141.
- [7] Wibowo E., Rokhmat M., Sutisna, Khairurrijal and Abdullah M., Reduction of seawater salinity by natural zeolite (Clinoptilolite): Adsorption isotherms, thermodynamics and kinetics, Desalination, Vol. 409, 2017, pp. 146-156.
- [8] Okawa Y. and Wajima T., Desalination of seawater using Ca-A zeolite for agricultural utilization, Conference Proceedings, in Proc. 5th Int. Symp. Exhib. Aqua Sci. Water Resour., 2017, pp.252-257.
- [9] Ohmori Y. and Hosoi Y., The simple design method for regeneration condition of ammonium ion exchanged natural zeolite by saturated sodium chloride solution, J. Jpn. Soc. Water Environ., Vol. 23, 2000, pp. 795-802.
- [10] Akgü M., Karabakan A., Acar O. and Yürüm Y., Removal of silver (I) from aqueous solutions with clinoptilolite, Microporous and Mesoporous Mater., Vol. 94, 2006, pp. 99-104.
- [11] Nakajima T., Deep Seawater Utilization, Midori Shobou, 2002.

COMPARISON OF COD AND TSS REMOVALS FROM ARTIFICIAL RIVER WATER BY MUDBALLS MADE WITH ACTIVATED EM1 AND EM4 SOLUTIONS

Fadjari Lucia Nugroho, Deni Rusmaya and Muthia Damayanti
Department of Environmental Engineering, Faculty of Engineering, Universitas Pasundan, Indonesia

ABSTRACT

In Indonesia surface waters are often polluted by domestic waste. The use of Effective Microorganisms (EM) mixed with rice bran and clay soil then shaped into mudballs has been suggested as a means to directly improve water quality of polluted rivers. This study examined the removal of COD and TSS by 2.5 cm ϕ mudballs made with two different kinds of activated EM solutions, i.e. EM1 and EM4. Batch experiments at 30°C were conducted where artificial river water was treated with mudballs made from rice bran, and clay soil, which were mixed with either activated EM1 or EM4 solutions. Removal efficiencies of 120 mg/L COD by the mudballs were respectively 60.3% with EM1 and 59.4% with EM4. Removal efficiencies of 100 mg/L TSS were respectively 100% with EM1 and 97.9% with EM4. Statistical hypothetical testing of the experimental data suggests that at $\alpha=0.05$, there is no difference in removal efficiencies of COD and TSS by mudballs made with either EM1 or EM4. COD and TSS removal efficiencies are correlated with mudballs' diameter; where increasing diameter results in better removal efficiencies. pH values of artificial river water after 5 days treatment by mudballs mixed with EM1 and EM4 were respectively 6.2 and 4.8. TSS isotherm sorption by mudballs with EM1 better fits the BET model, with $q_m=32.4$ mg/g, whereas that with EM4 better fits the Langmuir model, with $Q_m=7.52$ mg/g; $K_L=0.0168$ L/mg and $R_L=0.373$. It appears that EM1 would be the preferred EM solution for direct treatment of polluted surface waters.

Keywords: Adsorption isotherms, Effective Microorganisms, Mudballs, River Water

INTRODUCTION

Urban rivers are major assets to communities as they provide numerous benefits, including fresh water, recreation, landscape amenity, habitat provision and flood control [1]. However in Indonesia, surface waters are often polluted by both domestic as well as industrial waste. For instance, the average COD and TSS levels of Cikapundung River, Bandung City, Indonesia in 2013 were 120 mg/L and 100 mg/L respectively; with maximum levels at times reaching as high as 400 mg/L COD and 350 mg/L TSS [2].

Although conventional physical-biological treatment methods can be applied to treat polluted surface waters, they are often costly and not eco-friendly. Hence the use of Effective Microorganisms (EM) that are mixed with clay soil and shaped into balls, - known as "EM mudballs", - has been proposed as an alternative means to directly improve water quality of polluted rivers [3]. These so-called "EM-mudballs" are capable of reducing suspended solids, turbidity, as well as COD content of the polluted river; which would also improve the river's DO content.

The concept of EM, which is a mixed culture of naturally occurring effective, beneficial, non-pathogenic microorganisms was first promulgated

by Professor Dr. Teruo Higa of the University of Ryukus, Okinawa, Japan and have been applied for amongst others the treatment of water and wastewater, improvement of recycled water and solving sanitary problems [4].

Nugroho et al. [2] reported that the removal efficiencies of 120 mg/L COD and 100 mg/L TSS from artificial river water by 2.5 cm ϕ mudballs made from rice bran, clay soil and EM4 activated solution at 30°C were 59.4% COD and 99.7% TSS respectively.

However, the pH of artificial river water treated by EM4 mudballs becomes acidic even when the pH value of the artificial river water solution was initially alkaline [5]. pH values in the acidic range could potentially harm aquatic organisms, and in fact based on statutory Indonesian regulations, pH of Indonesian surface waterways must range between 6-9. EM4 is manufactured locally in Indonesia, and consists of a mixed culture of Gram negative and Gram positive rod-shaped bacteria, some of which are spore-forming, as well as *Mucor sp.* and *Penicillium sp.* fungi and actinomycetes [5].

In Malaysia, mudballs made from EM1 activated solution (EMS) have been used to clean up rivers, including Sungai Kelian in the state of Perak where EM-mudballs improved river water quality from Class IV (suitable for irrigation) to Class III

(suitable for water supply with extensive treatment) [3]. EM1 is the original Effective Microorganisms solution developed by Dr. Higa in the 1980s, made up of a mixed culture of microorganisms including lactic acid bacteria, photosynthetic bacteria, actinomycetes, yeasts and fermenting fungi.

As artificial river water treated with EM4 mudballs produces an acidic pH value [5], the objective of this current study was therefore to discern whether EM1 mudballs also produce similar results. The removal efficiencies of COD and TSS in artificial river water by mudballs made with either EM1 or EM4 solutions were therefore compared. Parameters analyzed included COD and TSS removal efficiencies, change in pH values of the treated artificial river water, correlation between removal efficiencies and mudballs' diameter as well as TSS isotherm adsorption model.

METHODS

All experiments were conducted as batch experiments. COD was measured by close reflux titrimetry, TSS was measured by gravimetry methods and pH was measured using Lutron pH-208 pH-meter.

Materials

EM1 solution used in the experiments is a registered trademark of EMRO and was procured from Seikatsu, Japan. Whereas, the EM4 solution used in the experiments was manufactured by Songgo Langit Persada and procured locally in Bandung, Indonesia. The EM solutions are sold in a dormant state and hence had to be activated. Activation of the dormant EM solutions was performed by diluting 5% EM solution with distilled water and leaving the mixture to ferment for a day at room temperature [5].

The mudballs (MB) were prepared by mixing 20% rice bran and 80% dry clay soil with 40% activated EM solutions (v/w), shaped into 2.5 cm ϕ balls, which were then left to ferment in covered baskets for 7 days at room temperature.

Artificial river water with a COD content of 120 mg/L and TSS content of 100 mg/L was prepared by adding glucose and 60 mesh sieved kaolin powder into tap water [5].

Experiments

Batch experiments with artificial river water

The batch experiments were carried out in 250 mL Erlenmeyer flasks. Mudballs (MB) made with either EM1 (EM1-MB) or EM4 (EM4-MB) activated solutions were mixed with 200 mL artificial river water. The flasks were then incubated

in a shaker water bath at 30°C. The COD, TSS and pH values of the treated river water solutions were measured daily.

TSS adsorption experiments

The TSS adsorption experiments were carried out in 250 mL Erlenmeyer flasks containing 200 mL tap water mixed with kaolin powder producing a TSS concentration of 100 mg/L. Varying quantities of EM1-MB or EM4-MB (1 - 10 g) were then added into the TSS solution and the flasks placed in a shaker water bath adjusted to 30°C. The TSS was measured after 3 days of shaking.

Calculation of adsorption isotherms

Adsorption isotherms describe the equilibrium relationships between adsorbent and adsorbate [6]. The isotherm equations used to determine the TSS adsorption model were the Freundlich, Langmuir and Brunauer-Emmett-Teller (BET) isotherm equations. The Freundlich isotherm is an exponential equation that assumes that as the adsorbate concentration increases so too does the concentration of the adsorbate on the adsorbent surface [7]. This isotherm can be used for non-ideal sorption that involves heterogeneous surface energy systems, hence not restricted to the formation of a monolayer. The mathematical expression of the Freundlich isotherm is as follows:

$$\frac{x}{M} = K_F C_e^{\frac{1}{n}} \quad (1)$$

where $\frac{x}{M}$ is the amount of adsorbate adsorbed by the adsorbent (mg/g), K_F is a rough indicator of the adsorption capacity (mg/g), $1/n$ is the adsorption intensity and C_e is the equilibrium liquid-phase concentration of the adsorbate (mg/L).

The Langmuir isotherm equation is based on the assumption of monolayer coverage (the layer is one molecule thick) of adsorbate over a homogenous adsorbent and that when equilibrium is attained no further adsorption can take place. Adsorption is assumed to take place at specific homogenous sites in the adsorbent and the adsorption of each molecule has equal adsorption energy [8]. The theoretical Langmuir isotherm equation is as follows:

$$\frac{x}{M} = \frac{Q_m K_L C_e}{1 + K_L C_e} \quad (2)$$

where Q_m is the maximum amount of adsorption corresponding to complete monolayer coverage on the surface (mg/g); and K_L is the Langmuir constant related to the energy of adsorption (L/mg).

The Brunauer-Emmett-Teller (BET) adsorption isotherm is a theoretical equation that was developed in order to describe multilayer adsorption systems

[9]. The model assumes that a number of layers of adsorbate accumulate at the surface and each layer follows the Langmuir isotherm model. As such, the the BET isotherm equation is as follows:

$$\frac{q}{q_m} = \frac{bc}{(C_s - 1)[1 + (b - 1)C/C_s]} \quad (3)$$

where C is the aqueous concentration of adsorbate (mg/L), C_s is the saturation concentrations for adsorbate in solution and q_m is maximum capacity of adsorbent for adsorbate (mg/g)

RESULTS AND DISCUSSIONS

COD and TSS Removal Efficiency

Figure 1 show the results obtained regarding COD and TSS removal efficiencies by 2.5 cm ϕ MB made with either EM1 or EM4 activated solutions (EM1-MB and EM4-MB). Whereas, Table 1 shows the changes in pH, COD and TSS values over time in artificial river water treated with EM1-MB and EM4-MB.

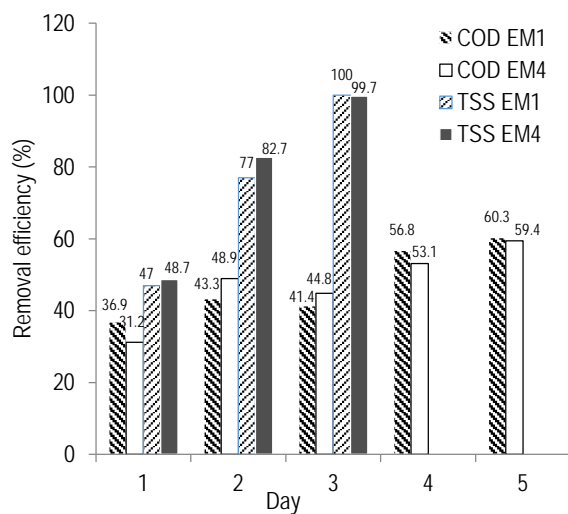


Fig. 1 COD and TSS removal efficiencies (%) of artificial river water by EM1-MB and EM4-MB at 30°C

The results presented in both Fig. 1 and Table 1 show that maximum COD and TSS removals were attained after 5 and 3 days incubation respectively at 30°C. COD removal efficiencies by EM1-MB and EM4-MB were respectively 60.3% and 59.4%; hence it initially appeared that slightly better COD removal was obtained with EM1-MB. Likewise slightly better TSS removal efficiency was obtained with EM1-MB as TSS removal efficiency with EM1-MB was 100%, while that of EM4-MB was 99.7%. Accordingly, to confirm whether COD and TSS removal efficiencies by EM1-MB and EM4-

MB are different, statistical hypothetical testing against the COD and TSS experimental data was performed. The results are presented in Table 2

Table 1 Changes in pH, COD and TSS values of artificial river water treated with EM1-MB and EM4-MB at 30°C

Day	pH		COD(mg/L)		TSS (mg/L)	
	EM1	EM4	EM1	EM4	EM1	EM4
0	5.1	4.1	120	120	100	100
1	5.5	4.65	75.7	82.6	53.3	51.3
2	5.5	4.48	68.1	61.3	22.3	17.3
3	5.7	4.6	70.3	66.2	0	0.67
4	6	4.76	51.9	56.3	0	0.67
5	6.2	4.82	47.6	48.7		
6	6.2	4.82	47.6	48.7		

Table 2 Statistical hypothetical testing of COD and TSS removal efficiencies by EM1 and EM4 Mudballs

	% COD removal	% TSS removal
α	0.05	0.05
Hypothesis	$H_0: \mu_{EM1} = \mu_{EM4}$ $H_1: \mu_{EM1} > \mu_{EM4}$	$H_0: \mu_{EM1} = \mu_{EM4}$ $H_1: \mu_{EM1} > \mu_{EM4}$
Results of t testing	$t_{calculated} < t_{table}$	$t_{calculated} < t_{table}$
Conclusion	% COD removal by EM ₁ = COD removal by EM ₄	% TSS removal by EM ₁ = TSS removal by EM ₄

The results presented in Table 2 show that at $\alpha = 0.05$, COD and TSS removal efficiencies by mudballs made with either EM1 or EM4 activated solutions are the same. COD removal is attributed to both physical (sorption) and biodegradation processes, whereas TSS removal is attributed to physico-sorption processes alone [2].

With regard to changes in pH values (Table 1), after 5 days the pH value of artificial river water treated with EM4-MB was pH<5, whereas that treated with EM1-MB was pH>6. Accordingly, the pH of artificial river water treated with EM1-MB meets Indonesian statutory regulations, while that treated with EM4-MB does not meet statutory Indonesian regulations. The differences in pH values are attributed to differences in the types of microorganisms present in EM1-MB and EM4-MB. EM4 solution includes mixed cultures of Gram negative and Gram positive rod-shaped bacteria, some of which are spore-forming, as well as actinomycetes and fungi of the *Mucor* and *Penicillium* genera [5], whilst the EM1 used in this study contains amongst others *Bacillus sp.* as well as

Gram negative rod shaped non-spore forming bacteria, as well as fungi such as *Mucor sp.* and *Bipolaris sp.* [10]. Both *Bacillus sp.* and Gram negative rod-shaped non-spore forming bacteria are not categorized as lactic acid bacteria given that by definition lactic acid bacteria are Gram-positive, non-sporeforming cocci, coccobacilli or rods that ferment glucose to lactic acid or to lactic acid, CO₂ and ethanol. Therefore different types of microbial consortia present in the EM solutions would attribute to differences in the abilities of the EM1 and EM4 microorganisms to produce organic acids that in turn would affect the pH values. In comparison, Namsivayam et al. [11] reported that after 5 days domestic sewage treated with EM solution composed of *Lactobacillus planetarium* (lactic acid bacteria), *Candida utilis* (yeast), *Streptomyces albus* (actinomycetes) and *Aspergillus oryzae* (fungi) had a pH of 8.4 and 14% reduction in COD. The SS, DO, COD, BOD and pH values of Kelian River, Malaysia improved after being treated with mudballs made from EM1 activated solution [3]. On the other hand, after 12 days of incubation at room temperature the pH of produced water treated with EM solution composed of *Lactobacillus plantarum*, *Aspergillus sp.* and *Penicillium italicum* decreased from 8.03 to 3.71 and had a COD reduction of 60% [12].

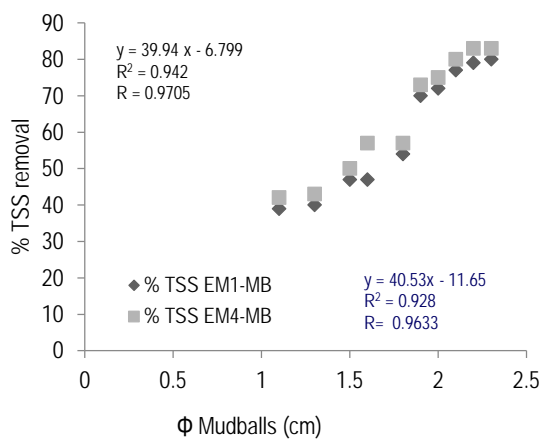


Fig. 2 Correlation between TSS removal efficiency and mudballs' diameter

Figures 2 and 3 respectively depict correlation between removal efficiencies of TSS and COD with mudballs' diameter. As shown in Fig. 2 and Fig. 3 the determination coefficient (R^2) and the correlation coefficient (R) indicate a high correlation between TSS as well as COD removal efficiencies against mudballs' diameter, whether this is with EM1 or EM4. The correlation coefficient (R) for TSS removal efficiency against mudball diameter is

0.9633 and 0.9705 for EM1-MB and EM4-MB respectively. Whereas, the correlation coefficient (R) for COD removal efficiency versus mudballs' diameter is 0.9549 and 0.9675 for EM1-MB and EM4-MB respectively. These values indicate a significant correlation between TSS as well as COD removals against mudballs' diameter, where increasing mudball diameter results in better removal efficiencies of COD and TSS. This is understandable as COD removal is attributed to both physical (sorption) and biodegradation processes, whereas TSS removal is attributed to physico-sorption processes alone [2]. Hence larger mudball diameters would provide more sorption sites that adsorbed the organic material and suspended solids contained in the artificial river water, resulting in better removal efficiencies.

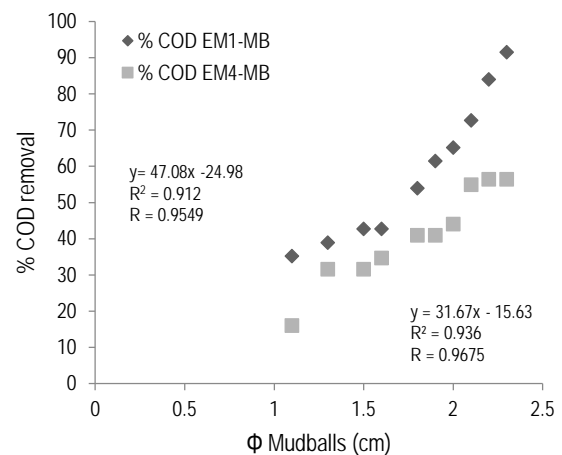


Fig. 3 Correlation between COD removal efficiency and mudballs' diameter

Adsorption of TSS

Figure 4 depicts the TSS adsorption (mg/g) by different quantities of EM1-MB and EM4-MB after 3 days of incubation at 30°C.

As shown in Fig. 4, TSS adsorptions by both EM1-MB and EM4-MB are higher at lower quantities of mudballs. Given that adsorption of the TSS involves migration by pore diffusion of the TSS from the surface into the interior of the porous adsorbent, it is understandable that more TSS can move into the smaller sized less compacted mudballs in comparison to the larger sized, dense and heavier mudballs [2]. However, as indicated in Fig. 2 removal efficiency is greater with larger sized mudballs, given that the adsorption mechanism for TSS removal by the mudballs entails a surface phenomenon and larger diameters will provide more sorption sites.

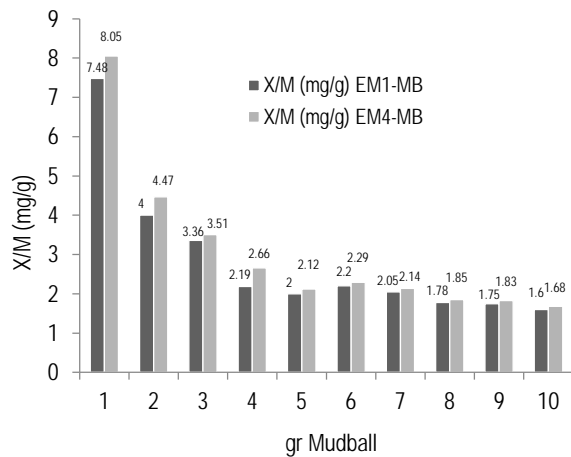


Fig. 4 Adsorption of TSS (mg/g) by different quantities of EM1-MB and EM4-MB at 30°C, $C_0 = 100$ mg/L

The experimental data were plotted against the Freundlich, Langmuir and BET isotherm models in order to describe TSS adsorption by the mudballs. Table 3 presents the results obtained from this exercise.

Table 3 Calculated isotherm parameters and regression coefficients (R) for TSS adsorption by EM1-MB and EM4-MB

Isotherm	EM1-MB	EM4-MB
Freundlich	$n = 1.373$	$n = 1.212$
	$K_F = 18.509$	$K_F = 14.26$
	$R = 0.7714$	$R = 0.8240$
Langmuir	$Q_m = 0.1041$	$Q_m = 7.52$
	$K_L = 67.32$	$K_L = 0.0168$
	$R = 0.8231$	$R = 0.8619$
		$R_L = 0.373$
BET	$q_m = 32.42$	$q_m = 2.19$
	$R = 0.8394$	$R = 0.7211$

The regression coefficients (R) presented in Table 3 suggest that TSS adsorption by EM1 mudballs better fits the BET isotherm adsorption model, with $q_m = 32.42$ mg/g. Whereas, that with EM4 mudballs better fits the Langmuir isotherm adsorption model, with $Q_m = 7.52$ mg/g and $K_L = 0.0168$ L/mg. The BET isotherm is an extension of the Langmuir isotherm that accounts for adsorption by multiple layers of adsorbate, which appears to be the case of EM1 mudballs as the mudballs themselves consisted of a mixture of rice bran and clay soil. The Langmuir isotherm accordingly applies to each layer of adsorbate. In the case of the Langmuir isotherm, its' essential feature is a dimensionless parameter known as the separation factor or equilibrium parameter, R_L , defined as

follows [13]:

$$R_L = \frac{1}{1 + K_L C_0} \quad (4)$$

where K_L is the Langmuir constant (L/mg) and C_0 is the initial concentration of the adsorbate (mg/L). Lower R_L values indicate that the adsorption is favorable, with the shape of the isotherm being either irreversible ($R_L = 0$), favourable ($0 < R_L < 1$), linear ($R_L = 1$), or unfavourable ($R_L > 1$) [13]. Hence the $R_L = 0.373$ indicates that adsorption of TSS by EM4-MB is indeed favorable.

CONCLUSION

Batch experiments were conducted at 30°C to study differences in removal efficiencies of 120 mg/L COD and 100 mg/L TSS in artificial river water by 2.5 cm Φ mudballs made from rice bran and clay soil that were inoculated with two different types of activated effective microorganisms (EM) solutions, these being either EM1 which is the original EM solution developed by Dr. Higa in the 1980s or EM4 solution, which is a local EM solution fabricated in Indonesia. Statistical hypothetical testing at $\alpha = 0.05$ indicates that there is no difference in removal efficiencies of COD and TSS by mudballs made with either EM1 or EM4 activated solutions. However measurements of pH values show that whereas the final pH value of EM4-MB treated artificial river water is in the acidic range (i.e. pH = 4.8), that treated with EM1-MB has a pH value of 6.2 which is within the pH range required by statutory Indonesian regulations for surface water, this being 6-9. The differences in pH values produced by EM1-MB and EM4-MB are attributed to differences in microbial consortia present in EM1 and EM4 solutions. The adsorption mechanism of TSS by EM1-MB is better described by the BET isotherm, which is an extension of the Langmuir isotherm that indicates adsorption by multiple layers of adsorbate, with the Langmuir isotherm applying to each layer of adsorbate. The q_m value of TSS adsorbed by EM1-MB is 32.42 mg/g. With regards to EM4-MB, the results indicate that adsorption mechanism of TSS by EM4-MB appear to better fit the Langmuir isotherm, which is based on monolayer coverage on a homogenous material. The Langmuir parameters obtained for EM4-MB were $Q_m = 7.52$ mg/g; $K_L = 0.0168$ L/mg and $R_L = 0.373$. This latter R_L value indicates favorable adsorption. The results of this study also show that mudball diameter affects removal efficiencies of COD and TSS where increasing diameters produce better removal efficiencies. The correlation coefficient (R) for COD removal efficiency against mudball diameter was 0.9548 and 0.9675 for EM1-MB and EM4-MB respectively. The correlation coefficient (R) for TSS removal efficiency against

mudball diameter was 0.9633 and 0.9705 for EM1-MB and EM4-MB respectively. Based on the above results, it can be surmised that EM1 activated solution would be the preferred EM solution for the direct treatment of polluted surface water, as pH value of the treated surface water would still meet statutory Indonesian regulations. The mudballs' diameter should also be adjusted to obtain optimum results.

ACKNOWLEDGEMENTS

The works were financially supported by the Indonesian Ministry of Technological Research and Higher Education.

REFERENCES

- [1] Covarrubia JC, Rayburg S, Neave M, The Influence of Local Land use on the Water Quality of Urban Rivers, *International Journal of GEOMATE*, Vol. 11, Issue 23, 2016, pp. 2155-2161.
- [2] Nugroho FL, Rusmaya D, Yustiani YM, Hafiz FI, and Putri RBT, Effect of Temperature on Removal of COD and TSS From Artificial River Water by Mudballs Made From EM4, Rice Bran and Clay, *International Journal of GEOMATE*, Vol. 12, Issue 33, 2017, pp. 91-95.
- [3] Zakaria Z, Gairola S, Shariff N, Effective Microorganisms (EM) Technology for Water Quality Restoration and Potential for Sustainable Water Resources and Management, Conference proceedings, in Proc. International Congress on Environmental Modelling and Software Modelling for Environment's Sake, Fifth Biennial Meeting, Ottawa, Canada, 2010, p. S.0.04.
- [4] Higa T, Parr JF, Beneficial and Effective Microorganisms For A Sustainable Agriculture and Environment, *International Nature Farming Research Center*, Atami Japan, 1994, p. 4
- [5] Rusmaya D, Nugroho FL, Yustiani YM, Hafiz FI, Putri RBT, Improving Artificial River Water Quality Using Mudballs Made From EM4, Rice Bran and Clay Soil, Conference proceedings, in Proc. 5th Environmental and Management Conf. on Green Technology Towards Sustainable Environment, 2015, pp. OP/AE/002-1 - OP/AE/002-8.
- [6] Hossain MA, Ngo HH, Guo WS, Nguyen TV, Removal Copper from Water by Adsorption onto Banana Peel as Bioadsorbent, *International Journal of GEOMATE*, Vol. 2, No. 2, (SI. No. 4), 2012. pp. 227-234.
- [7] Freundlich H, Adsorption in Solution, *Chemie*, 57, 1906, pp. 384-410.
- [8] Langmuir I, Adsorption of Gases on Plane Surfaces of Glass, Mica and Platinum, *J. Am. Chem. Soc.* 40, 1918, pp. 1361-1403.
- [9] Foo KY, Hameed BH, Insights Into the Modeling of Adsorption Isotherm Systems, *Chem. Eng. J.* 156, 2010, pp. 2-10.
- [10] Nugroho FL, Rusmaya D, Damayanti M, Identifikasi Mikroorganisme Pada EM1 dan Mudball (Dedak Padi, Tanah Liat dan EM1) Yang Digunakan Dalam Penjernihan Air Sungai Buatan, *Infomatek*, Vol. 19, No. 2, 2017, pp 91-100.
- [11] Namsivayam SKR, Narendrakumar G, Kumar JA, Evaluation of Effective Microorganism (EM) for treatment of domestic sewage, *Journal of Experimental Sciences*, Vol. 2, Issue 7, 2011, pp. 30-32.
- [12] Stanley HO, Ekoh PE, Impact of Effective Microorganisms on the Microbiological and Physicochemical Parameters of Produced Water, *International Annals of Science*, Vol.3, Issue 1, 2017, pp. 6-12.
- [13] Hall KR, Eagleton LC, Acrivos A, Vermeulen T, Pore and Solid Diffusion Kinetics in Fixed Bed Adsorption Under Constant Pattern Conditions, *Ind. Eng. Chem. Fundamentals*, Vol. 5, No. 2, 1966, pp. 212-223.

THE ESTIMATION OF THE LAKE COLAC WATER BALANCE USING ISOTOPIC RATIO OF WATER, AMOUNT OF PRECIPITATION AND EVAPORATION VALUES IN VICTORIA, AUSTRALIA

Hiroki Kitagawa¹, Peter G Dahlhaus² Hiroyuki Ii³

¹Graduate School of Systems Engineering, Wakayama University, Japan

²Principal Research Fellow Centre for eResearch and Digital Innovation, Federation University, Australia

³Faculty of Systems Engineering, Wakayama University, Japan

ABSTRACT

The Lake Colac and creek waters were sampled in both winter and summer, August 2017 to April 2018 and pH, ORP, EC, temperature, dissolved ions and oxygen isotopic ratios for sampled waters were measured. Water level of the Lake Colac and pan water level beside the Lake Colac were also measured. There was much precipitation in winter and surface water flowed into the lake, therefore, the lake and pan water levels increased. The creek water with low soluble substances was connected with south of the Lake Colac. EC value in the north of lake decreased gradually after precipitation because creek water did not flow into the lake. There was little precipitation in summer and pan water level was only dropped and pan water dried up, however, the lake water was not dried up because creek water flowed into the lake sufficiently even in summer. Groundwater was believed to be a main water source at the north of Lake Colac, however groundwater did not flow into the Lake Colac because HCO_3^- values of lake waters were lower than those of groundwater and close to those of creek water. As the result of EC record from March 2006, EC value did not increase even after the lake dried up. It was revealed that the lake water flowed out underground because there is no flowing-out from the lake to creek. Evaporation rate in the Lake Colac in sampling period was estimated 37.9% (approximately 9028500m³) by using oxygen isotopic ratio.

Keywords: Precipitation, Evaporation, stable isotopic ratio, dissolved ions

INTRODUCTION

The Lake Colac is one of the biggest fresh water lakes in Victoria. Many farmers use groundwater for agriculture and dairy farming, however, excess pumping up groundwater for agriculture and dairy farming changes supply of surface water and under groundwater flows into lakes [1], [2]. and then for protecting water quality and quantity of the lake, it's important to understand relation between groundwater and surface water for the Lake Colac, therefore the purpose of this research reveals that the amount of groundwater and evaporation in the Lake Colac to assess groundwater and surface water interaction. The Lake Colac has been studied for many years [1][2], however these studies have no frequency for sampling and it is difficult to reveal the impact from groundwater, precipitation and evaporation in the Lake Colac. This research has much more data than previous ones and it can be revealed that hydrological cycle as groundwater, surface water and evaporation in the Lake Colac.

STUDY AREA

Fig.1 shows the location map showing the Lake



Fig.1 The location map showing the Lake Colac in Corangamite in Victoria.

Colac in Corangamite region in Victoria. There are a lot of lakes or wetlands in Corangamite area and those lakes including the Lake Colac are recognized as being of international ecological value and registered as Ramsar Convention.

The Lake Colac is in Western plains between

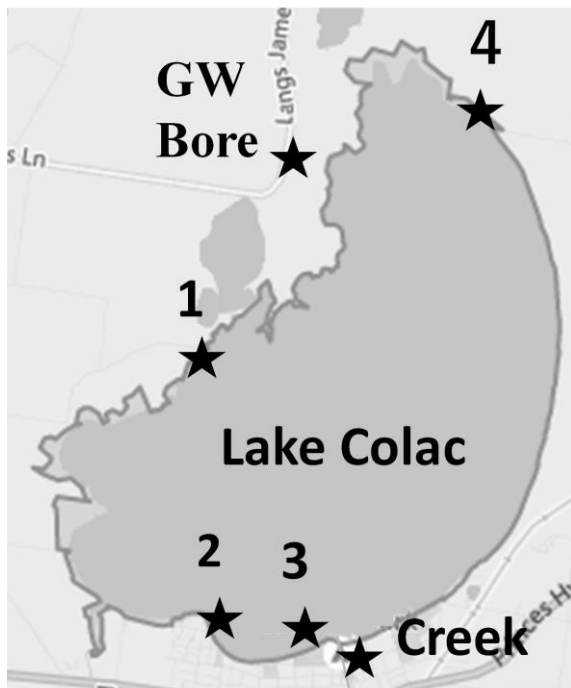


Fig.2 Sampling points for the Lake Colac.

and Otway Ranges [3]. The Lake Colac is connected with Barrongarock Creek and the creek water always flows into the Lake Colac. The amount of annual rainfall is 600mm~700mm and there is no precipitation in summer.

METHOD

Fig.2 shows sampling points for the Lake Colac. Sampling of the lake and creek waters were performed from August to September 2017 and from February to April 2018. EC, pH, ORP and temperature were measured by using a calibrated field kit. Sampled waters were measured main dissolved ions and oxygen stable isotopic ratios.

Fig.3 shows the way of measuring water level for the Lake Colac. An iron stick with a brick was put at No.1 sampling point shown in Fig.2 in the Lake Colac and the length from the top of brick to water level was measured. For estimating of evaporation pan was also put at the garden without shade near No.2 sampling point in the Lake Colac and both the lake and pan waters were compared.

Stable oxygen isotopic ratios were measured by mass spectrometer (Sercon Geo Wet System) with dual inlet and equilibrium with CO_2 and H_2 gas method. This isotope ratio is useful tracer for clarifying the origin for groundwater or evaporation rate. Oxygen isotope ratio is generally expressed $\delta^{18}\text{O}$. It is presented as per mil (‰) of the standard average seawater (SMOW: Standard Mean Ocean Water). The formulas are shown in equation (1). $\delta^{18}\text{O}$ of

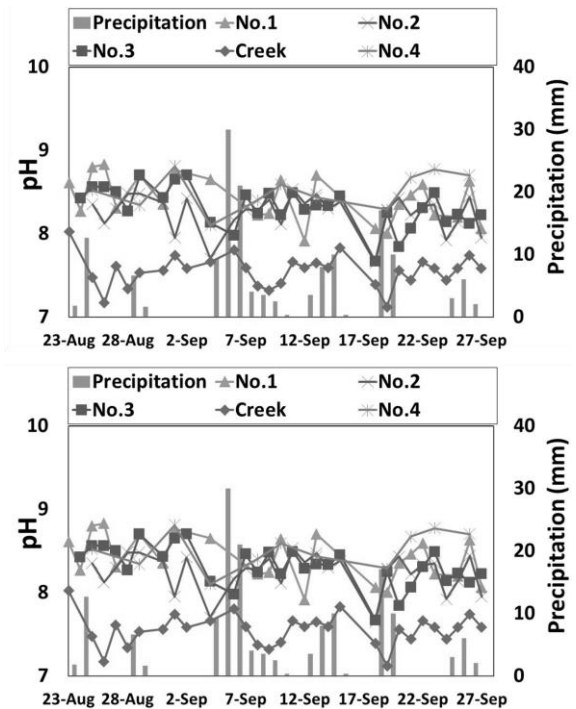


Fig.3 pH values and amount of precipitation for the Lake Colac in both winter and summer.

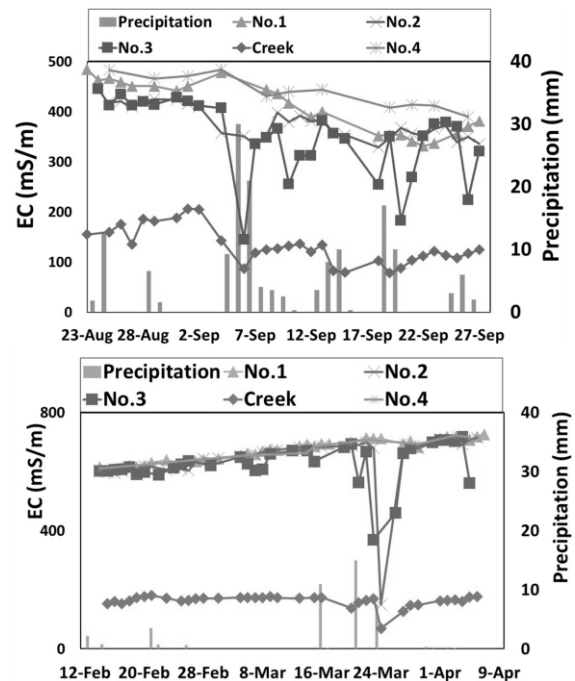


Fig.4 EC values and precipitation for the Lake Colac in both winter and summer.

SMOW is denoted as $(\text{D}/\text{H}) \text{ SMOW}$, $(^{18}\text{O}/^{16}\text{O}) \text{ SMOW}$ and $\delta^{18}\text{O}$ of the sample is denoted as $(\text{D}/\text{H}) \text{ Sample}$, $(^{18}\text{O}/^{16}\text{O})$. Measurement error of $\delta^{18}\text{O}$ is $\pm 0.2\text{‰}$.

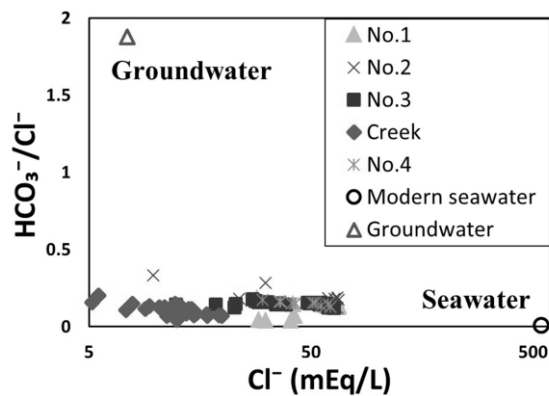


Fig.5 Relationship between $\text{HCO}_3^-/\text{Cl}^-$ and Cl^- for the Lake Colac and Creek waters, groundwater and seawater.

$$\delta^{18}\text{O} = [({}^{18}\text{O}/{}^{16}\text{O})_{\text{Sample}}/({}^{18}\text{O}/{}^{16}\text{O})_{\text{SMOW}} - 1] \times 1000: \quad (1)$$

Water level of the Lake Colac and pan water level beside the Lake Colac were also measured. The level of pan water is measured close to No.2 on the map. A stick and block are set up on No.1 and water level was measured from the top of block in the lake water.

RESULT

Fig.3 shows that pH values for the Lake Colac in both winter and summer. The pH value for the lake water ranged from 8 to 9 and its for creek water were from 7 to 8 in winter. Both the Lake Colac and creek water reacts with rocks such as limestone, pH values will become higher. Therefore, both waters did not react with limestone. On the other hand, pH values for the Lake Colac are from 8.5 to 9 because there is less precipitation in summer. pH values for the Lake Colac and creek waters in winter are lower than those in summer

Fig.3 shows EC values for the Lake Colac and creek water in both winter and summer. No.3 sampling point is close to creek and water at No.3 is mixed with creek water, therefore EC values for No.3 sampling point were lower than any other sampling points when it rained. No.1 and No.4 sampling points are far from creek and water for these sampling points are hardly mixed with creek water. EC values for the Lake Colac and creek water are increasing constantly in summer, however those for creek water shifted constantly without precipitation.

Main dissolved ions

Fig.5 shows relationship between $\text{HCO}_3^-/\text{Cl}^-$ and Cl^- for the Lake Colac and creek waters and groundwater in both winter and summer. The values of HCO_3^- for groundwater are generally higher than those for surface water because generally groundwater reacts

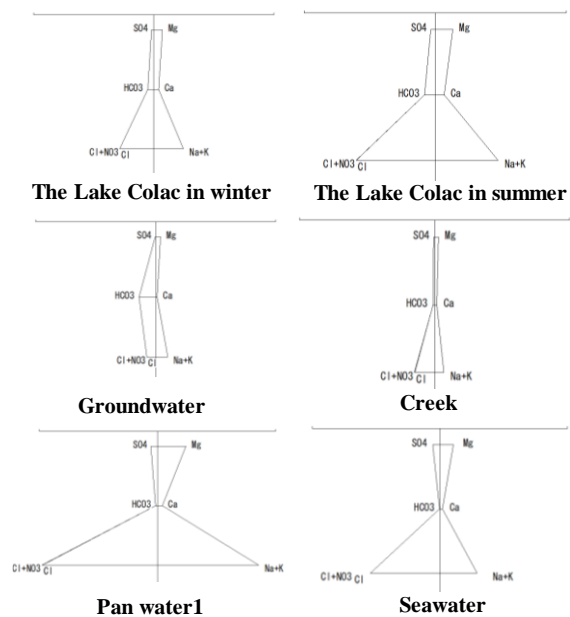


Fig.6 Hexa Diagram for the Lake Colac and creek waters in both winter and summer, groundwater, pan water and seawater.

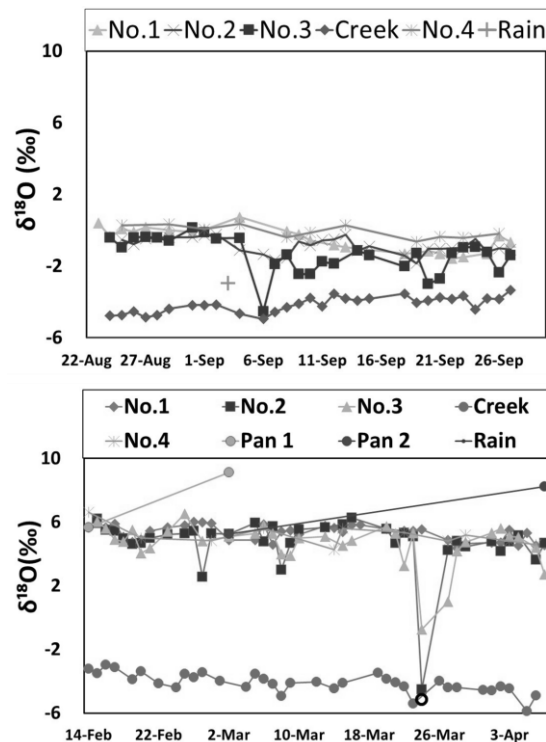


Fig.7 $\delta^{18}\text{O}$ values for the Lake Colac and creek waters in both winter and summer, pan water, groundwater and seawater.

with carbonate rocks for long term. If groundwater flows into the Lake Colac, the values of $\text{HCO}_3^-/\text{Cl}^-$ for the Lake Colac are changed, however the values of

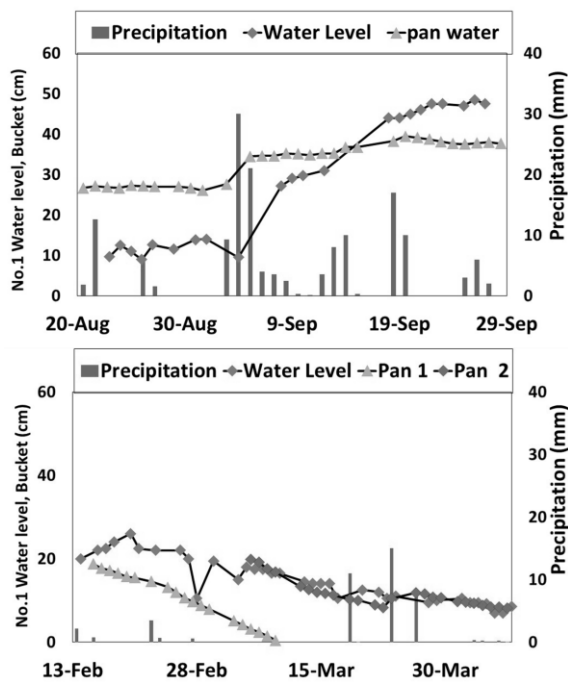


Fig.8 Water level for the Lake Colac and pan waters in both winter and summer and amount of precipitation.

$\text{HCO}_3^-/\text{Cl}^-$ for the Lake Colac were uniformed, therefore it is thought that groundwater did not flow into the Lake Colac.

Fig.6 show Hexa diagram of lake water, groundwater and creek water for the Lake Colac area in both winter and summer. The lake water in winter was sampled 21st September and that in summer was sampled 24th March.

Chemical compositions for the Lake Colac waters in both winter and summer and creek water, pan water were similar to that for modern seawater and Na^+ and Cl^- are higher than any other dissolved ions because aerosol such as Na^+ or Cl^- in precipitation from the sea has been concentrated as evaporation in summer. Chemical composition for groundwater is different from other water because groundwater is reacted with rocks or soil underground. Ions composition for Pan water 1 is the same as seawater. Pan water was water taken at No.1 sampling point in the Lake Colac 16th February and only evaporated in pan. The value of HCO_3^- for pan water was relatively lower than that for the Lake Colac and creek. The lake and creek waters are contacted with soil included carbonated minerals, however pan water is contacted without soil and HCO_3^- is decomposed in pan therefore the value of HCO_3^- for pan water was relatively lower. It is thought that only surface water flows into the Lake Colac and evaporated in summer

Isotopic Ratio

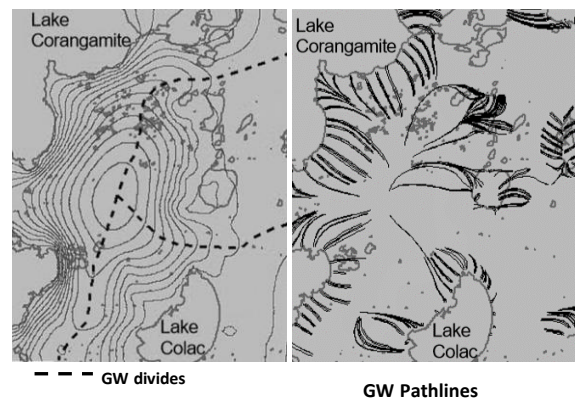


Fig.9 Groundwater path lines around the Lake Colac.

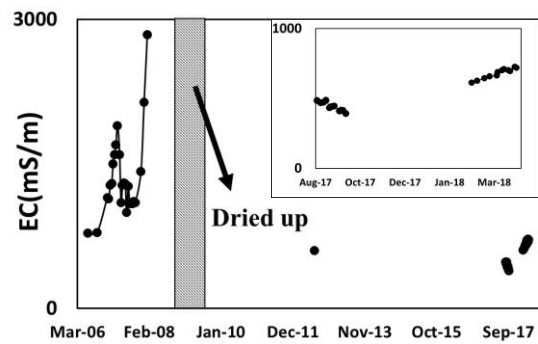


Fig.10 EC values for the Lake Colac between March 2006 and April 2018.

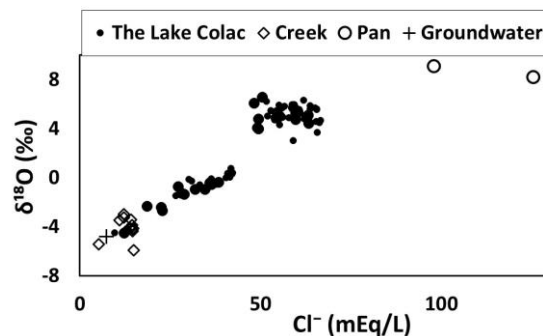


Fig.11 Relationship between Cl^- and $\delta^{18}\text{O}$ for the Lake Colac and creek waters, pan water and groundwater.

Fig.7 shows the values of $\delta^{18}\text{O}$ for the Lake Colac and creek water, precipitation, groundwater. Those for Pan water 1 and 2 were also measured. $\delta^{18}\text{O}$ values for creek water and precipitation ranged from -3‰ to -6‰ and those for groundwater were -4‰. It is thought that creek water and groundwater derived from precipitation and those water was not evaporated. Those for the Lake Colac in winter

ranged from 0‰ to -2‰ and those in summer ranged from +3‰ to +5‰.

$\delta^{18}\text{O}$ values for Pan 1 water were taken from No.1 sampling point in the Lake (then +5.6 ‰) and increased to +9.1‰ and those for Pan 2 water were also taken from No.1 sampling point in the Lake (then +5.2‰) and were increased to +8.2‰.

The Lake Colac water is thought to be much evaporated, however creek water flows into the lake, therefore $\delta^{18}\text{O}$ values for the Lake Colac are not higher than those for pan water.

Water Level

Fig.8 shows water level for the Lake Colac and pan waters, the amount of precipitation in both winter and summer. There is much precipitation in winter, therefore water level for both the Lake Colac and creek waters increased. Although water level for the Lake Colac increased after 19th September, that for pan water decreased. It is thought that it took a time that surface water flowed into the lake and water level for the Lake Colac still increased.

There is less precipitation in summer, therefore water level for both the Lake Colac and creek water decreased. Pan water 1 was almost dried out 9th March, therefore another pan (pan water 2) was set close the Lake Colac.

In summer water level for the Lake Colac changed much in a few days. It is thought that depth of the Lake Colac is shallow and then the water level is easy to be affected by wind speed and direction.

CONSIDERATION

Fig.9 shows groundwater path lines around the Lake Colac. It was thought that groundwater came from Wallion Hill to the Lake Colac [3], however, as shown in Fig.5, HCO_3^- values for the lake were not smaller than those for groundwater but creek water, therefore groundwater doesn't flow into the Lake Colac in both winter and summer and the Lake Colac is dominated only surface water.

Fig.10 shows EC values for the Lake Colac between March 2006 and April 2018. EC values of the lake water between March 2006 and February 2008 were measured by Tweed [3]. EC values of the lake between August 2017 and April 2018 were measured in this study. In the summer of 2008 to 2009 the Lake Colac water dried up completely, however the lake partially refilled for only one year. Before dried up EC values ranged 1000 mS/m to 3000 mS/m and After dried out those values were under 1000 mS/m in this study, therefore it is revealed that the lake water has been flowing out to underground. Because if the Lake Colac is only destination for the creek, dissolved ions especially Na^+ or Cl^- were precipitated in the lake and even precipitation and creek water flow into the lake, EC values for the lake water

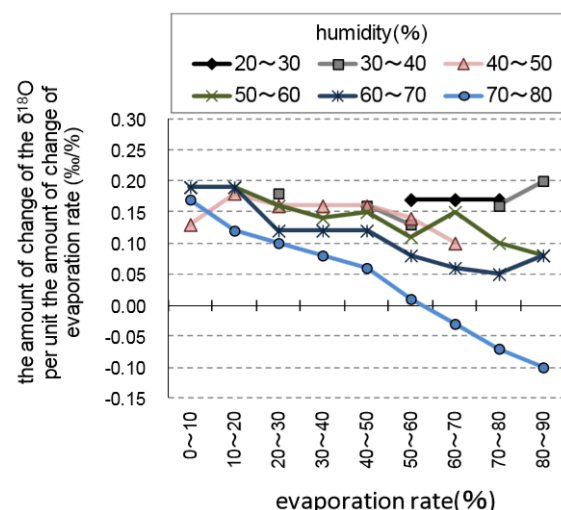


Fig.12 Relationship between the amount of change the $\delta^{18}\text{O}$ per unit the amount of change of evaporation (‰/‰) and evaporation (%).

		Average in winter	Average in summer
Lake Colac No.4	Cl^- (mEq/L)	37.43	55.85
	$\delta^{18}\text{O}$ (‰)	-0.08	5.15
Creek	Cl^-	12.69	12.89
	$\delta^{18}\text{O}$	-4.15	-4.10

Table 1 Average of $\delta^{18}\text{O}$ and Cl^- values for the Lake Colac and creek waters both winter and summer.

increase, however those values decreased after dried up.

Fig.11 shows relationship between Cl^- and $\delta^{18}\text{O}$ for the Lake Colac and creek water, pan water, groundwater and precipitation. Those for the lake and creek water are in a proportion. Cl^- ion is generally stable in environment, therefore the value is not easy to be changed and used as index for evaporation. This result also reveals that the lake water was evaporated, therefore evaporation rate for the Lake Colac can be estimated.

Miyahara and Ii estimated evaporation rates of water for the Lake Inawashiro in Japan by using oxygen isotopic ratio [4]. Fig.12 shows variation of the amount of change of the $\delta^{18}\text{O}$ per unit the amount of change of evaporation rate about humidity from 20% to 80%. Table1 shows the change of $\delta^{18}\text{O}$ for the Lake Colac and creek waters. No.4 in the Lake Colac is far from creek, therefore it is most reliable value in the lake. The average humidity in Colac from September 2017 to March 2018 is approximately 60%. The amount of change of $\delta^{18}\text{O}$ and 0.14‰/‰, the amount of change of the $\delta^{18}\text{O}$ per unit the amount of change of evaporation rate shown in expression (2).

$$5.3 (\text{‰}) / 0.14 (\text{‰}/\text{‰}) \doteq 37.9 (\%) \quad (2)$$

Area of the Lake Colac is 2778hec (27,780,000 m³) and the depth is 2.5m and then the volume of the lake is estimated 23,150,000 m³. Therefore, amount of evaporation in the Lake Colac from September 2017 to March 2018 was estimated 9,000,000 m³.

CONCLUSION

It was thought that the Lake Colac was composed by groundwater and surface water, however this study revealed that groundwater does not flow into the Lake Colac in August 2017 to April 2018 because groundwater level is lower than the Lake Colac in summer and even its level increases in winter, water level for the Lake Colac is high in winter, therefore groundwater does not flow into the lake as pressure of the lake water.

Moreover, the lake water is thought to flow out to underground because if the Lake Colac is destination for creek without flow-out, dissolved ions (especially Cl⁻) increase every year, however EC value did not increase even after the lake had dried out.

It was revealed that 37.9% (approximately 9,000,000 m³) of the Lake Colac water was evaporated in September 2017 to March 2018 by using oxygen isotopic ratio.

REFERENCES

- [1] Annette B.Barton., Andrew L. Herczeg., Peter G. Dahlhaus. And Lames W. Cox., A geochemical approach to determining the hydrological regime of wetlands in a volcanic plain, south-eastern Australia, Groundwater and Ecosystems, Chapter 7, 2013, pp. 69-79.
- [2] Sarah. Tweed., Marc. Leblanc. and Ian. Cartwright., Groundwater-surface water interaction and the impact of a multi-year drought on lakes conditions in South-East Australia, Journal of hydrology, 379, 2009, pp. 41-53.
- [3] Russell. Crosbie., Andy. Herczeg., Jim. Cox., Peter. Dahlhaus., Phil Davies and John. Dighton., Defining Groundwater Flow Systems on the Volcanic Plains to Accurately Assess the Risks of Salinity and Impacts of Changed Landuse, 2007, pp. 1-55.
- [4] Sarah. Tweed., Mike. Grace., Marc. Leblanc., Ian Cartwright and Donna. Smithyman., The individual response of saline lakes to a severe drought, Science of the total environment, 409, 2011, pp. 3919-3933.
- [5] Miyahara S and Ii H., Proposal of simple Measurement Method for Evaporation Rate by Using Oxygen Isotopic Ratio, International Journal of GEOMATE, Vol. 3, No.1, 2012, pp. 318-324.

EFFECT OF 17 α -METHYLTESTOSTERONE ON SEX REVERSAL OF RED TILAPIA (*OREOCHROMIS NILOTICUS* X *OREOCHROMIS* *MOSSAMBICUS*) IN FREE-SWIMMING STAGE

Supamas Sriwongpuk¹

¹Faculty of Agricultural Technology, Rajamangala University of Technology Thanyaburi, Thailand

ABSTRACT

The effect of 17 α -Methyltestosterone (MT) on sex reversal of Red tilapia (*Oreochromis niloticus* x *Oreochromis mossambicus*) in free-swimming stage by immersion and feeding technique were carried out at Department of fisheries, Faculty of Agricultural Technology, Rajamangala University of Technology Thanyaburi, Pathumthani Province during April to July 2017. The experimental design was a factorial experiment in CRD studied on two factors: 1) sex reversal by immersion treatment of 17 α -MT (0, 150 and 300 μ g/l) for 3 hours (T₁, T₂ and T₃) and 2) sex reversal by feeding treatment of 17 α -MT (40, 60 and 80 mg/kg) for 28 days (F₁, F₂ and F₃). Results from these studies indicated that free-swimming stage that undergone immersion treatment of 17 α -MT in 300 μ g/l for 3 hours (T₃) was the highest in growth rate about weight, total length (28 days), ADG, FCR and survival rate (0.731 g, 3.340 cm, 0.024 g/d, 0.627 and 95.443 % respectively). The immersion treatment of 17 α -MT in 150 μ g/l for 3 hours (T₂) was medial growth rate among other factors. The immersion treatment of 17 α -MT in 0 μ g/l for 3 hours (T₁) was the minimal growth rate but had the highest sex ratio of male (83.889 %). Sex reversal by feeding treatment of 17 α -MT in 60 mg/kg for 28 days (F₂) was the highest in growth rate about weight, ADG and FCR (0.644 g, 0.022 g/d and 0.714 respectively). Sex reversal by feeding treatment of 17 α -MT in 80 mg/kg for 28 days (F₃) was a medial growth rate and the highest of survival rate (95.037 %) and sex ratio of male (85.667 %). Sex reversal by feeding treatment of 17 α -MT in 40 mg/kg for 28 days (F₁) has a good growth rate but the other factors were minimal.

Keywords: 17 α -Methyltestosterone, sex reversal, Red tilapia (*Oreochromis niloticus* x *Oreochromis mossambicus*), free-swimming stage

INTRODUCTION

Tilapia are freshwater fish belonging to the family Cichlidae. They are native to Africa, but were introduced into many tropical, subtropical and temperate regions of the world during the second half of the 20th century [1]. Tilapia is a worldwide fish of great commercial importance and it is recognized as one of the most important aquaculture species of the 21st century. Tilapia is currently ranked second only to carps in global production [2]. The world's total tilapia production in 2012 was 4.2 million tones. Tilapia aquaculture is rapidly expanding with a global production of about 2.8 million metric tons in 2008 [3] and estimated to increase to 8.89 million metric tonnes by the year 2020 [4].

This rapid global production of tilapia is due to the introduction of improved strains of Nile tilapia (*Oreochromis niloticus*) which is the major farmed tilapia species. The important aquaculture species are the Nile tilapia (*O. niloticus*), blue tilapia (*O. aureus*), Java tilapia (*O. mossambicus*) and Zanzibar tilapia (*O. hornorum*). The red tilapia (*O. hybrids*) developed from crosses of the main *Oreochromis* culture species also has become popular in recent years. Other tilapia species are cultured only by small-scale farmers in Africa [5]. Nile tilapia was

then introduced in different countries during the 1970s but problems including inbreeding, insufficient fish seed supply, stagnant production and poor fish growth hindered small scale aquaculture production. Large scale genetic improvement programs have been established for *O. niloticus* in Asia [6] and genetic methodologies to control sex have now resulted in the reliable production of all male fry to help overcome the problem associated with excessive fry production in culture ponds [7].

The Genetic Improvement in Farmed Tilapia (GIFT) project in the Philippines created strains of *O. niloticus* that grew up to 60% faster than their relatives [8]. The benefits of the GIFT strain include significantly faster growth rates than other farmed strains, improved survival in polluted waters and that they can be raised in extensive systems without the need for commercial feeds. The development of hormonal sex-reversal techniques in the 1970s represented a major breakthrough that allowed male monosex populations to be raised to uniform, marketable sizes. Although several species of tilapia are cultured commercially, research on nutrition and culture systems, along with market development and processing including value addition in Nile tilapia made the species as the predominant cultured species worldwide. The species matures at a larger size and is

less fecund and thus less prone to overpopulation. Today, tilapia are often farmed with multiple species in the same pond, such as shrimp and milkfish. This not only optimizes the financial return if space is limited, but also helps to prevent the growth of harmful bacteria and serves to remove excess organic matter in the water [9].

Initially, GIFT trials were conducted in Bangladesh, China, Thailand and Vietnam, as well as in the Philippines. Today, 13 countries in Asia have received GIFT to develop national breeding and dissemination programmes and GIFT's fast growth and high yield have encouraged many rural families to take up environmentally friendly aquaculture across the region. As many new fish farmers are women, this empowers them as it improves local supplies of high-quality, affordable protein and benefits the nutrition of the household. The "GIFT Fish" was the result of this carefully conducted genetic selection and improvement programme based on broodfish collected from four African countries (Egypt, Ghana, Kenya and Senegal) and four commercial *O. niloticus* strains (from Israel, Singapore, Taiwan, Province of China and Thailand) used in the Philippines [10]. In the initial phase of the research, it was evident that the gain in growth and survival through crossbreeding were less than expected. This was followed by a pure breeding strategy among the best performing purebred and crossbred groups that led to the build-up of a genetically-mixed base population. This population formed the basis for the final selection program through a combined family and within family selection strategy [11]. Subsequent selection resulted in the emergence of the GIFT strain, which is purported to have an 85 percent cumulative genetic gain compared to the base population [6].

Hormonal sex reversal has been extensively used for sex determination and producing monosex fish for aquaculture purposes. Steroid hormones or hormone analogues as well as non-steroid compounds are commonly used for producing monosex tilapia. The hormones are generally incorporated into larval feeds and administered to undifferentiated larvae at very early larval stages (preferably at first feeding) for sufficient time to enable sex reversal. The use of hormones has been under increasing public criticism due to their possible health and environmental impacts. As a result, the use of hormones for sex reversal of tilapia is either licensed (in USA) or banned (in Europe) [12]. Androgens are steroid hormones derived from cholesterol synthesized naturally by the adrenal cortex. Steroids are group of lipids with several unique properties affecting growth and development. Steroids are called androgens, if they are able to induce male characteristics and estrogens, if they induce female characteristics. The hormone testosterone is ineffective as an androgen when given orally and has a short duration of action

when administered parenterally because of rapid hepatic metabolism [13].

"Aquatic Animals" is a healthy diet that rich in protein, high quality fat and many types of fatty acids. Especially tilapia (*O. niloticus*), which is considered good protein and cheap. All people around the world can be accessed. Tilapia is a good source of fat contains all kinds of essential fatty acids and lower cholesterol when compared to other meat or aquatic animals together. In addition, the texture of tilapia meat is white when cooked to make a colorful appetizing and very delicious. It can be cooked in a variety of menus. For this reason, Tilapia is popular among consumers both in Thailand and abroad. Sex reversal by immersion and feeding may lessen the duration of treatment and lower the cost of hormone used. The present study aims to investigate the potentiality different doses of 17 α -MT with respect to the determination of the optimum dose.

METHODOLOGY

The experiment was conducted at the laboratory of Tilapia Hatchery, Division of Fisheries, Faculty of Agricultural technology, Rajamangala University of Technology Thanyaburi (RMUTT).

1. Experimental Design

This study was designed as a factorial experiment in CRD. The experiment was divided into 9 treatments with 3 replications per trail and carried out in a 50 liters glass cabinet filled with 30 liters volume of water (total of 27 experimental units) for 28 days. The experiments in this study was conducted to investigate two factors: immersion and feeding. There are 3 concentration levels of 17 α -Methyltestosterone (MT): 0, 150 and 300 micrograms per liter (T₁, T₂ and T₃) in the first factor (immersion) and 3 concentrations levels of 17 α -MT of 40, 60 and 80 milligrams per kilogram feed (F₁, F₂ and F₃) in the secondary factor (feeding).

2. Preparing of 17 α -MT for immersion

Free-swimming stage or fry (3 days old) whose yolk sac have been absorbed were collected from the hatchery between 1,600-1,700 hours and were transferred to the laboratory. Four thousand and fifty free-swimming stages were immersed in different concentrations of 17 α -MT hormone concentrations of 0, 150 and 300 $\mu\text{g l}^{-1}$ for three hours. Immersion was done using plastic containers (1.5 liter capacity each) which were suspended in aquarium measuring 24 cm x 50 cm x 30 cm. Aerators were provided in each container to facilitate the continuous movement of Free-swimming stage in the water column.

3. Preparing of 17 α -MT for feeding

Hormone treated feed was prepared as described [14]. The 17 α -MT was the hormone used. A stock solution was made by dissolving hormone in 50 ml of 95% ethanol. Treatments were made by taking the accurate amount of the hormone from the stock solution and different doses were prepared viz. 60 mg and 80 mg 17 α -MT kg⁻¹. This solution was evenly sprayed over 500 g of shrimp starter feed containing 40% protein and mixed thoroughly. The feed-alcohol-hormone mixture was mixed again and again to ensure an equal distribution of the 17 α -MT throughout the feed. Treated diets were dried at room temperature for 24 hours and then kept in airtight containers since androgens will breakdown when exposed to sunlight or high temperature. The prepared diets were stored at 4°C in refrigerator before fed to fry of red tilapia. The diets containing 17 α -MT were characterized as follows:

T₁: diet + 40 mg 17 α -MT kg⁻¹ of diet

T₂: diet + 60 mg 17 α -MT kg⁻¹ of diet

T₃: diet + 80 mg 17 α -MT kg⁻¹ of diet

4. Rearing

Sex reversal of tilapia free-swimming stage or fry whose yolk sac have been absorbed was done by oral administration of 17 α -MT through feed. After three days of hatching, the fry was shifted to nine glass aquaria. Three replicates for each treatments having 30 liters of water each, containing 300 nos of fry for sex reversal treatment. Free swimming stage was administrated orally 17 α -MT mixed feed containing 40% crude protein at three different dose rates viz. 40 (T₁); 60 (T₂) and 80 (T₃) mg 17 α -MT kg⁻¹ of feed. The feeding was supplied to 6 times (7.00 9.00 11.00 13.00 15.00 and 17.00 am) daily during the day light hours for 28 days.

During the rearing period, water quality parameters (temperature, pH, dissolved oxygen (DO), Total Ammonia and Nitrite) in the net enclosures were measured weekly up to the end of the experiment. Temperature and DO concentration were measured by YSI DO meter Model 55 while pH by a pen-type HANNA pH meter. Total Ammonia and Nitrite by titration. The mean length, weight and survival rate of the fish in each treatment were recorded. After twenty eight days, the percentage of male and females were recorded.

5. Specifying of sex rates

To find out how sexual development after twenty eight days of treatment, the sex was determined depending on the secondary sexual characters. All surviving fish were placed in iced box and immediately dissected for sex differentiation. Sexes

of fingerlings (male female, intersex) were identified by gonad squash technique [15].

6. Statistical analysis

In order to calculate the statistical significance between the growth of the groups treated with different doses of 17 α -MT, a comparison of the different parameters were described according to [16]. T-test was used to find out the statistical significance in term of growth parameter, survival rates and sex ratio.

RESULTS AND DISCUSSION

Effect of dietary 17 α -Methyltestosterone on sex reversal of red tilapia (*O. niloticus* x *O. mossambicus*) in free-swimming stage by immersion and feeding technique. The experimental design was a factorial experiment in CRD studied on two factors: 1) sex reversal by immersion treatment of 17 α -MT (0, 150 and 300 μ g/l) for 3 hours (T₁, T₂ and T₃) and 2) sex reversal by feeding treatment of 17 α -MT (40, 60 and 80 mg kg⁻¹) for 28 days (F₁, F₂ and F₃). The two factors are not combined. The results are as follows (Table 1).

1. Growth parameters and survival rate

1.1 average weight and length

After twenty eighty days of 17 α -MT treatment with three concentration of 0, 150, 300 mg l⁻¹ in free-swimming stage of red tilapia by immersion technique. The experiment was carried out in a laboratory at 30 fish density per liter with average weight of 0.482, 0.698 and 0.731 grams, respectively and with average length of 3,156, 3,331 and 3,340 centimeters respectively. The results show that the immersion of 17 α -MT with a concentration of 300 mg l⁻¹ were the heaviest weight and length and followed by concentration of 150 and 0 mg l⁻¹. Feeding of 40, 60 and 80 mg kg⁻¹: the average weight was 0.624, 0.644 and 0.642 grams, respectively, and an average length of 3.292, 3.282 and 3.252 centimeters, respectively. It was found that feeding hormone of 60 mg kg⁻¹ was the highest weight and followed by 80 and 40 mg kg⁻¹. And length by feeding of 40 mg kg⁻¹ was the longest and followed by 60 and 80 mg kg⁻¹ (Table 1). This was better than the results of [17] that was conducted to produce sex reversal tilapia (*O. niloticus*) seed in fiberglass tanks in recirculating systems with different densities for 21 days. He found that 10 densities l⁻¹: the final weight was 0.066 \pm 0.03 grams and the mean length was 1.00 \pm 0.36 centimeters. This may be in this experiment fed the fish by ad-libitum technique. This method will feed little by little until the fish filled. Each time it takes

about 30 minutes for the fish to get food fully then the weight and length are considered in good standing.

Table 1 Effect of 17 α -MT on sex reversal of red tilapia (*O. niloticus* x *O. mossambicus*) in free-swimming stage by immersion and feeding technique.

Factor	Weight on 28 day (g)	Weight gain (g)	Length on 28 day (cm)	Increased length (cm)	ADG (g d ⁻¹)	FCR	Survival rate (%)	Male ratio (%)
Hormone Concentration (immersion)								
T ₁	0.428 ^b	0.472 ^b	3.156 ^b	3.066 ^b	0.018 ^b	0.928 ^a	94.852 ^{ab}	83.889 ^a
T ₂	0.698 ^a	0.688 ^a	3.331 ^a	3.241 ^a	0.021 ^{ab}	0.646 ^b	93.222 ^b	82.111 ^a
T ₃	0.731 ^a	0.721 ^a	3.340 ^a	3.243 ^a	0.024 ^a	0.627 ^b	95.443 ^a	82.222 ^a
Hormone Concentration (feeding)								
F ₁	0.624 ^a	0.614 ^a	3.292 ^a	3.22 ^a	0.022 ^a	0.742 ^a	94.110 ^a	80.667 ^a
F ₂	0.644 ^a	0.634 ^a	3.282 ^a	3.315 ^a	0.022 ^a	0.714 ^a	94.370 ^a	81.889 ^a
F ₃	0.642 ^a	0.632 ^a	3.252 ^a	3.192 ^a	0.019 ^a	0.743 ^a	95.037 ^a	85.667 ^a

Note: Different English letters in the vertical mean significantly different (P < 0.05).

T₁ = Hormone concentration 0 μ g l⁻¹ used for immersion

T₂ = Hormone concentration 150 μ g l⁻¹ used for immersion

T₃ = Hormone concentration 300 μ g l⁻¹ used for immersion

F₁ = Hormone concentration 40 mg 17 α -MT kg⁻¹ used for feeding

F₂ = Hormone concentration 40 mg 17 α -MT kg⁻¹ used for feeding

F₃ = Hormone concentration 40 mg 17 α -MT kg⁻¹ used for feeding

Table 2 Water quality parameters observed in the glass tank of red tilapia

Water Quality Parameters	Man-Max	Standard value*
pH	8.38 \pm 0.00-9.31 \pm 0.59	6.59-.0
DO (mg l ⁻¹)	3.38 \pm 0.01-5.91 \pm 0.02	\geq 3
Temperature (°C)	27.00 \pm 0.00-29.00 \pm 0.10	32.00-25.00
Total Ammonia (mg l ⁻¹)	0.01 \pm 0.01-0.36 \pm 0.04	\leq 0.5
Nitrite (mg l ⁻¹)	0.00 \pm 0.00-0.02 \pm 0.02	\leq 0.1

Note: *The standard of water quality for fish farming

1.2 Average Daily Grain (ADG)

The ADG of the free-swimming stage at 3 concentrations (0, 150 and 300 μ g l⁻¹) by immersion were 0.018, 0.021 and 0.024 g d⁻¹, respectively. It was found that at 300 μ g l⁻¹ was the best growth rate and followed by 150 and 0 μ g l⁻¹. The ADG by feeding at 3 concentrations (40, 60 and 80 mg kg⁻¹) were 0.022, 0.022 and 0.019 g d⁻¹, respectively. It was found that feeding at 40 and 60 mg kg⁻¹ were the best growth rate and followed by 80 mg kg⁻¹. There is the experiment about the level of 17 α -MT concentration on sex reversal of three strain of Nile Tilapia in Thailand. It found that the growth rate of Red Tilapia was 0.023 g d⁻¹. Which is close to the present experiment and show that red tilapia have the best daily growth rate. [18].

1.3 Feed Conversion Ratio ((FCR)

The FCR of the free-swimming stage at 3 concentrations (0, 150 and 300 μ g l⁻¹) by immersion were 0.928, 0.646 and 0.627, respectively. It was found that at 300 μ g l⁻¹ was the best FCR and followed by 150 and 0 μ g l⁻¹. The FCR by feeding at

3 concentrations (40, 60 and 80 mg kg⁻¹) were 0.742, 0.714 and 0.743, respectively. It was found that feeding at 60 mg kg⁻¹ were the best FCR and followed by 40 and 80 mg kg⁻¹. This was better than the results of [17] that was conducted to produce sex reversal tilapia (*O. niloticus*) seed in fiberglass tanks in recirculating systems with different densities for 21 days. He found that FCR of Red Tilapia was 2.860. This may be due to feeding by ad-libitum technique has less food loss than other methods, resulting in lower FCR values.

1.4 Survival rate

The survival rate of the free-swimming stage at 3 concentrations (0, 150 and 300 μ g l⁻¹) by immersion were 94.852, 93.222 and 95.443 %, respectively. It was found that at 300 μ g l⁻¹ was the best survival rate and followed by 0 and 150 μ g l⁻¹. The survival rate by feeding at 3 concentrations (40, 60 and 80 mg kg⁻¹) were 94.110, 94.370 and 95.037 %, respectively. It was found that feeding at 80 mg kg⁻¹ were the best survival rate and followed by 60 and 40 mg kg⁻¹. This was better than the results of the experimental of 17 α -

MT on sex reversal of Nile Tilapia (*O. nilotica*) by immersion of 300 $\mu\text{g l}^{-1}$ and feeding of 60 mg kg^{-1} . The result of the survival rate were 83.8 ± 7.1 , 77.3 ± 13.1 , 78.0 ± 5.7 , 74.4 ± 5.1 , 79.9 ± 12.5 and 66.1 ± 10.9 %, respectively. This may be due to this present study, the factors were controlled in all experiments, especially water quality and the environment. The fish do not stress, feeding regularly making good health and good growth. It has a higher survival rate [19].

2. Sex ratio

The sex ratio of the free-swimming stage at 3 concentrations (0, 150 and 300 $\mu\text{g l}^{-1}$) by immersion were 83.889, 82.111 and 82.222 %, respectively. It was found that at 0 $\mu\text{g l}^{-1}$ was the best male ratio and followed by 300 and 150 $\mu\text{g l}^{-1}$. The sex ratio by feeding at 3 concentrations (40, 60 and 80 mg kg^{-1}) were 80.6667, 81.889 and 85.667 %, respectively. It was found that feeding at 80 mg kg^{-1} were the best male ratio and followed by 60 and 40 mg kg^{-1} . The experimental of 17 α -MT on sex reversal of Nile Tilapia (*O. nilotica*) by immersion of 300 $\mu\text{g l}^{-1}$ and feeding of 60 mg kg^{-1} for 45 days. The result of the sex ratio was 100 % and higher than this present study. This may be due to the longer duration of hormone exposure. The third level headings [19].

3. Water quality

Hormonal feeding of red tilapia with different methods and concentrations for a period of 28 days. Daily water quality check every day throughout the trial period. It was found that pH were 8.38 ± 0.00 - 9.31 ± 0.59 , Dissolved Oxygen (DO) were 3.38 ± 0.01 - 5.91 ± 0.02 mg l^{-1} , Water temperature were 27.00 ± 0.00 - 29.00 ± 0.10 °C, Total Ammonia were 0.01 ± 0.01 - 0.36 ± 0.04 mg l^{-1} and Nitrites were 0.00 ± 0.00 - 0.02 ± 0.02 mg l^{-1} . (Table 2) Found that the water quality in this present study were satisfactory manner [20]. Due to the quality control of the water throughout the duration of the experiment. The fish do not stress and has a higher survival rate.

CONCLUSION

According to study the effect of 17 α -MT on sex reversal in free-swimming stage of Red Tilapia (*O. niloticus* x *O. mossambicus*) by immersion (0, 150 and 300 $\mu\text{g/l}$) for 3 hours and feeding (40, 60 and 80 mg/kg) for 28 days. It has been found that free-swimming stage that undergone immersion treatment of 17 α -MT in 300 $\mu\text{g l}^{-1}$ (T_3) was the highest in growth rate about weight, total length (28 days), ADG, FCR and survival rate. The immersion treatment of 17 α -MT in 150 $\mu\text{g l}^{-1}$ (T_2) was medial growth rate among other factors. The immersion

treatment of 17 α -MT in 0 $\mu\text{g l}^{-1}$ (T_1) was the minimal growth rate but had the highest sex ratio of male. Sex reversal by feeding treatment of 17 α -MT in 60 mg kg^{-1} (F_2) was the highest in growth rate about weight, ADG and FCR. Sex reversal by feeding treatment of 17 α -MT in 80 mg kg^{-1} (F_3) was a medial growth rate and the highest of survival rate and sex ratio of male. Sex reversal by feeding treatment of 17 α -MT in 40 mg kg^{-1} for 28 days (F_1) has a good growth rate but the other factors were minimal.

ACKNOWLEDGEMENTS

The author would like to express sincere appreciation to the Faculty of Agricultural Technology and the Institute of Research and Development, Rajamangala University of Technology Thanyaburi (RMUTT), for their financial support.

REFERENCES

- [1] Pillay T.V.R., Aquaculture: Principle and Practices, Fishing Book News, London, 1990, pp. 1-575 pp.
- [2] Ridha M.T., Comparative study of growth performance of three strains of Nile tilapia, (*Oreochromis niloticus* L.) at two stocking densities, Aquaculture Research, Vol. 37, 2006, pp. 172-179.
- [3] FAO, FAOSTAT. Food and Agriculture Organization of the United Nations, 2010.
- [4] Tacon, A.G.J., Metian M., Global overview on the use of fish meal and fish oil in industrially compounded aquafeeds: Trends and future prospects, Aquaculture, Vol. 285, 2008, pp. 146-158.
- [5] Teichert-Coddington, D.R., Green B., Boyd C.E., Harvin J.L., Rodriguez R., Martinez D., and Ramirez E., Effect of diet protein on food conversion and nitrogen discharge during semi-intensive production of *Penaeus vannamei* during the wet season. In: D. Burke, B. Goetze, D. Clair, and H. Egna (Editors), Fourteenth Annual Technical Report, Pond Dynamics/Aquaculture CRSP, Office of International Research and Development, Oregon State University, Corvallis, Oregon, 1997, pp. 71-77.
- [6] Eknath, A.E., Tayamen M.M., Palada de Vera M.S., Danting J.C., Reyes R.A., Dionisio E.E., Gjedrem J.B. and Pullin R.S.V., Genetic improvement of farmed tilapias: the growth performance of eight strains of *Oreochromis niloticus* tested in eleven different environments. Aquaculture, Vol. 111, 1993, pp. 171-188.
- [7] Mair, G.C., Abucay, J.S., Beardmore, J.A. and Skibinski, D.O.F., Growth performance trails of genetically male tilapia (GMT) derived from

- YY-males in *Oreochromis niloticus* L.: on station comparisons and mixed-sex and sex reversed male populations, *Aquaculture*, Vol. 137, 1995, pp. 313-322.
- [8] Eknath A.E. and Acosta B.O., Genetic Improvement of Farmed Tilapias (GIFT) Project Final Report, March 1998 to December 1997. ICLARM, Makati City, Philippines, 1998, pp. 21-22.
- [9] Troell M., Joyce A., Chopin, T., Neori, A., Buschmann, A. H., Fang, J-G., Ecological engineering in aquaculture-Potential for integrated multi-trophic aquaculture (IMTA) in marine offshore systems. *Aquaculture*, Vol. 297(1-4), 2009, pp.1-9.
- [10] Day, M.M. and Gupta, M.V., Socio-economic aspects of disseminating improved tilapia in Asia: an introduction. *Aquacult. Econ. And Manage*, Vol. 4(1&2), 2000, pp. 5-12.
- [11] Eknath, A.E., Managing aquatic genetic resources. Management Example 4: The Nile Tilapia, in Thorpe J (ed.), *Conservation of Fish and Shellfish Resources: Managings Diversity*, London, Academic Press, 1995, pp. 176-94.
- [12] Penman, D.J. and B.J. McAndrew, Genetics for the management and improvement of cultured tilapias. In: M.C.M. Beveridge and B.J. McAndrew (Editors), *Tilapia: Biology and Exploitation*. Kluwer Academic Publishers, The Netherlands, 2000, pp. 227-266.
- [13] Brueggemeier, R.W, Androgens, anabolics and antiandrogens. In: M.Verderame, (Ed.). *Handbook of Hormones, Vitamins, and Radiopaques*. CRC Press, Inc., Boca Raton, FL, USA, 1986. pp. 1-49.
- [14] Killian H. S. and Kohler C.C., Influence of 17 α -methyltestosterone on red tilapia under two thermal regimes. *J. World Aqua. Soc.*, Vol. 22, 1991, pp. 83-94.
- [15] Guerrero R.D. and W.L. Shelton, An acetocarmine squash method for sexing juvenile fishes. *Progressive Fish Culturist*, Vol. 35, 1974, p. 56.
- [16] Fisher R.A., *Statistical Methods for research, Workers*, 11th ed. Oliver and Boyd, London, 1950, pp. 1-354.
- [17] Thongchai Y., Tharaphand W., Juthamas C. and Soontorn K., Seed Production of Sex Reversal of Nile Tilapia, *Oreochromis niloticus* (Linnaeus, 1758), in Fiberglass Tanks Using Water Circulation System at Different Stocking Densities. Technical Paper No. 21, 2011.
- [18] Kriangsak M.A., Arnuparp W., Rogelio C. and Yuthana S., The Concentration Level of 17 α -Methyltestosterone Hormone for Three Stained of Tilapia Sex Reversal, *Fisheries Conference* 2006, pp 306-315.
- [19] Nuanmani P., Saifon S. and Chintana N., Effects of androgens on sex reversal of nile tilapia, *Thai Fisheries Gazette (Thailand)*, Vol.57, No.3,2004 pp. 251-259.
- [20] Boyd C.E., *Water Quality in Warm water Fish Ponds*, Auburn University, 1979, pp. 1-39.

SEASONAL VARIATION AND SOURCE ANALYSIS OF MONITORING PM10 DATA IN NORTHERN THAILAND

Pantitcha Outapa* and Katiya Ivanovitch
Faculty of Public Health, Thammasat University, Lampang, Thailand

ABSTRACT

This study examines emission sources and meteorological data affecting ambient concentrations of pollution haze in Northern Thailand on the basis of particulate matter (PM10) concentrations monitored and collected by Thailand's Pollution Control Department over a three-year period at thirteen stations in eight provinces. Increasing pollution and its major emission sources have been analyzed to reflect the seasonal variation of meteorological data over the periods of dry and rainy seasons. The results show that daily PM10 concentrations were at their highest levels during the dry season from January to April. In the course of a three-year time span, from 2015 to 2017, almost all monitoring stations recorded average PM10 concentration levels that were approximately 1 to 3 times higher than the Thailand's daily ambient air quality standard ($120 \mu\text{g}/\text{m}^3$). It was also observed that the average PM10 concentrations in areas under study were significantly higher than the average air quality recorded during the rainy season. The meteorological data, including temperature and winds blowing from the southerly and southeasterly directions, were significantly related to the increase of average PM10 concentrations. By contrast, the relative humidity and the wind speed were significantly related with the decrease of average PM10 concentrations. Forest fires and agricultural waste burning have been identified as the major sources of PM10 concentration in each site.

Keywords: Particulate matter, Haze, Seasonal variation, Thailand

INTRODUCTION

For more than fifteen years, the haze pollution has been a serious problem during dry seasons in Northern Thailand [1], [7]. Emission sources are forest fires, biomass burning, motor vehicles, solid waste burning and some industries [2]. The haze pollution has adverse effects on transportation by causing visibility problems for air travel. More importantly, the haze pollution also damages the human respiratory systems by high concentrations of airborne particulates below 10 microns (PM10) [3], [8]. Likewise, a significantly negative impact of PM10 depositions is observed on fruits, vegetables and vegetation in general [3].

In 2016, Thailand's pollution reports showed that the 24-hour average of respirable suspended particulate matter (RSPM or PM10) in Northern Thailand exceeded on many days the country's ambient air quality standard of 120 micrograms per cubic meter ($\mu\text{g}/\text{m}^3$), reaching the peak concentration at $317 \mu\text{g}/\text{m}^3$ during the dry season from January to April [9]. Forest fires alone accounted for 70% of observed PM10 concentrations [10]. Other factors affecting PM10 concentrations included geography, seasonal weather variations and meteorological conditions [1], [2], [4], [8].

In this study, average PM10 concentrations and

emission sources are analyzed on the basis of the meteorological data and haze pollution during dry and rainy seasons in Thailand's 8 Northern provinces. The relationship between average PM10 concentrations and the meteorological data has been investigated at 13 monitoring stations, located in 8 Northern provinces and operated by Thailand's Pollution Control Department (PCD).

MATERIALS AND METHODS

Description of the study area and monitoring stations

The area selected for this study covered the following provinces in Northern Thailand: Chiang Mai ($20,107 \text{ km}^2$), Mae Hong Son ($12,681 \text{ km}^2$), Lampang ($12,534 \text{ km}^2$), Chiang Rai ($11,678 \text{ km}^2$), Nan ($11,472 \text{ km}^2$), Phrae ($6,539 \text{ km}^2$) Phayao ($6,335 \text{ km}^2$) and Lamphun ($4,506 \text{ km}^2$). Most of the study area is located in valleys surrounded by mountain ranges. The area has thirteen air monitoring stations managed by Thailand's Pollution Control Department (PCD). The map of the geographical position of the sites within the study areas is shown in Fig. 1. The coordinates and the description of monitoring stations are presented in Table 1.



Fig. 1 Study area and monitoring stations.

Table1. Coordinates of study sites and monitoring stations.

Province	Monitoring Station (Code)	Latitude	Longitude	Characteristics
Chiang Rai	Wiang Muang (WM)	19° 54' 33" N	99° 49' 24" E	Suburban, 5 m distance to the road.
	Wiang Phang Kham (WPK)	20° 25' 38" N	99° 53' 2" E	Suburban, 5 m distance to the main road.
Chiang Mai	Chang Phueak (CP)	18° 50' 26" N	98° 58' 11" E	Suburban, 150 m distance to the road.
	Si Phum (S)	18° 47' 27" N	98° 59' 24" E	Urban, close to a busy road.
Lampang	Phra Bat (PB)	18° 16' 42" N	99° 30' 24" E	Suburban, 300 m distance to the road, close to the airport.
	Sop Pat (SP)	18° 15' 3" N	99° 45' 50" E	Rural, 5 m distance to the quiet road, a park surrounding.
	Ban Dong (BD)	18° 25' 37" N	99° 45' 27" E	Rural, a park surrounding.
	Mae Mo (MM)	18° 16' 57" N	99° 39' 35" E	Rural, a park surrounding.
Lamphun	Nai Muang (NM)	18° 34' 3" N	99° 0' 29" E	Suburban, 100 m distance to the road.
Mae Hong Son	Chong Kham (CK)	19° 18' 16" N	97° 58' 18" E	Suburban, a park surrounding, close to the airport.
Nan	Nai Wiang (NW)	99° 0' 29" N	100° 46' 35" E	Suburban, 100 m distance to the road.
Phrea	Na Chak (NC)	18° 7' 42" N	100° 9' 45" E	Suburban, 100 m distance to the road, a park surrounding.
Phayao	Wiang (W)	19° 10' 0" N	99° 53' 49" E	Suburban, 100 m distance to the road.

PM10 concentration and meteorological data analysis

Hourly PM10 concentrations at the 13 monitoring stations were obtained from the PCD monitoring system during the January-April dry season and the June-September rainy season from 2015 to 2017. Methods of Beta Ray attenuation and Tapered Element Oscillating Microbalance (TEOM) were used for measuring PM10 concentrations at the monitoring stations. That has made it possible to obtain differences of average PM10 concentrations during dry and rainy seasons.

The daily meteorological data, including wind speed, wind direction, temperature and relative humidity, were obtained from the PCD's air monitoring stations.

Source analysis

Data on burnt areas were obtained from the Geo-Informatics and Space Technology Development Agency (Public Organization), or GISTDA, of Thailand's Ministry of Natural Resources and Environment. A linear regression analysis is used to investigate the relationship between average PM10 concentrations and burnt areas. That relationship is also examined on the basis of fire hotspots data, obtained from Thailand's Forest Fire Control Division.

RESULTS

Concentration and seasonal variation of PM10

Figure 2 shows average annual PM10 concentrations during dry and rainy seasons in Thailand's 8 Northern provinces from 2015 to 2017. That evidence indicates that the Thai ambient PM10 annual standard of 50 micrograms per cubic meter ($\mu\text{g}/\text{m}^3$) was not exceeded. However, during those three years, the annual averages of PM10 concentrations were higher in dry seasons than in rainy seasons. In addition, Figure 3 shows that the proportion of days (%) when PM10 concentrations (in 24-hour averages) exceeded the Thai ambient PM10 24-hour average standard ($<120 \mu\text{g}/\text{m}^3$) in each monitoring station was approximately in the range of 8-19% for 2015, 6-30% for 2016 and 0-19% for 2017.

The PM10 concentration averages in dry and rainy seasons are presented in Figure 4. A three-year peak of the average PM10 concentration is shown at the CK monitoring station ($210 \mu\text{g}/\text{m}^3$).

According to the selected areas of the study, Lampang province showed the highest of 30% exceed the average standard of Thai ambient PM 10 24-hour, follow by Chiang Rai (23%), Mae Hong Son (18%), Prae (12%), Chiangmai (9%), Phayao (6%) and Nan province (2%), respectively.

In terms of seasonal variations, average PM10 concentrations during the dry season were significantly higher than during the rainy season ($P<0.001$, *t*-test). The standard deviations (SD) of average PM10 concentrations during dry and rainy seasons were 73.38 ± 13.05 and 20.05 ± 5.32 , respectively. Results of the test are shown in Table 1.

Relationships between average PM10 concentrations and meteorological data, including wind speed, wind direction, temperature and relative humidity, were examined using datasets of the BD monitoring station in the Lampang Province. That is where the highest average of PM10 concentrations was found. The correlation coefficients of PM10 concentrations and meteorological data were the highest for relative humidity ($P<0.001$), followed by wind speed ($P=0.048$), temperature ($P=0.034$) and wind direction from south ($P=0.001$) and southeast ($P=0.01$). The linear equation model of these relationships is shown as Eq. (1).

$$Y_{PM10con.} = 159.457 - 1.723X_{RH} - 13.644X_{ws} + 0.868X_{Temp} + 9.538X_{wd5} + 6.861X_{wd4} \quad (1)$$

Where $Y_{PM10con.}$ is PM10 concentration in $\mu\text{g}/\text{m}^3$; X_{RH} is relative humidity (%); X_{ws} is wind speed in m/s ; X_{Temp} is temperature in Celsius degrees; X_{wd5} is wind direction from the south; X_{wd4} is wind direction from the southeast. The values of *y*-intercepts in above equations could be interpreted as a relationship between average PM10 concentrations and meteorological data. The relative humidity and wind speed show a significantly inverse relationship with average PM10 concentrations ($P<0.05$), while the average PM10 concentrations are positively related to changes in temperature and southerly and south-easterly winds ($P<0.05$).

Table 1. Results of *t*-test comparing average PM10 concentrations in dry and rainy seasons.

Parameter	Mean	Std. Deviation	t	df	p-value
PM10 in Dry season	73.3829	13.05008	24.522	38	0.001
PM 10 in Rainy season	20.0520	5.31829			

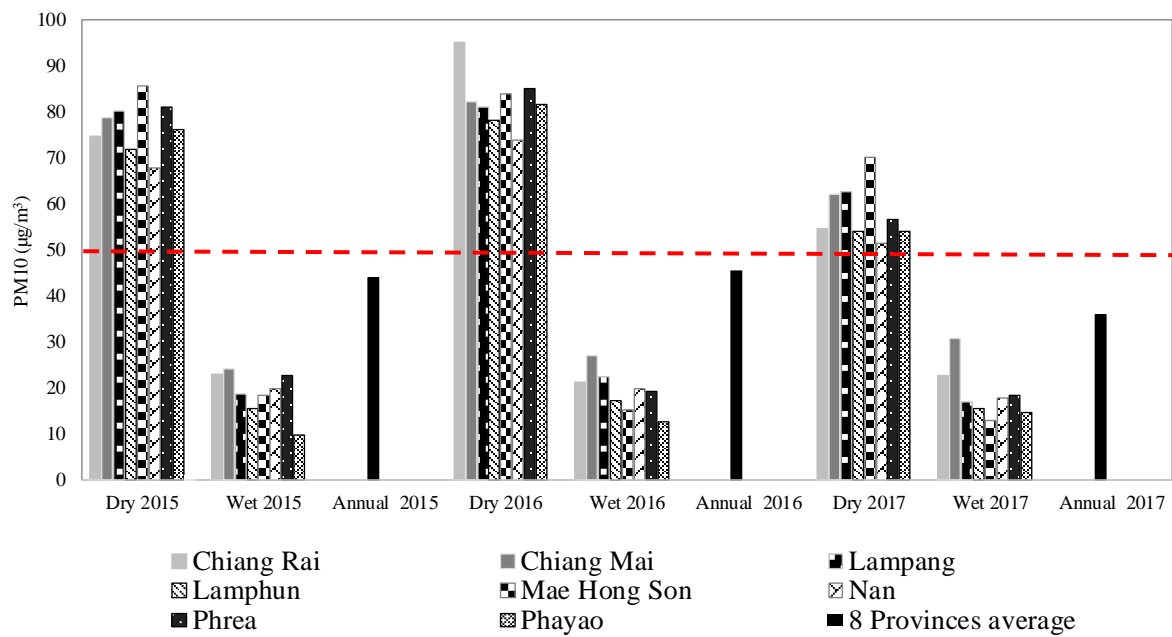


Fig. 2 Average annual PM10 concentrations in Northern Thailand.

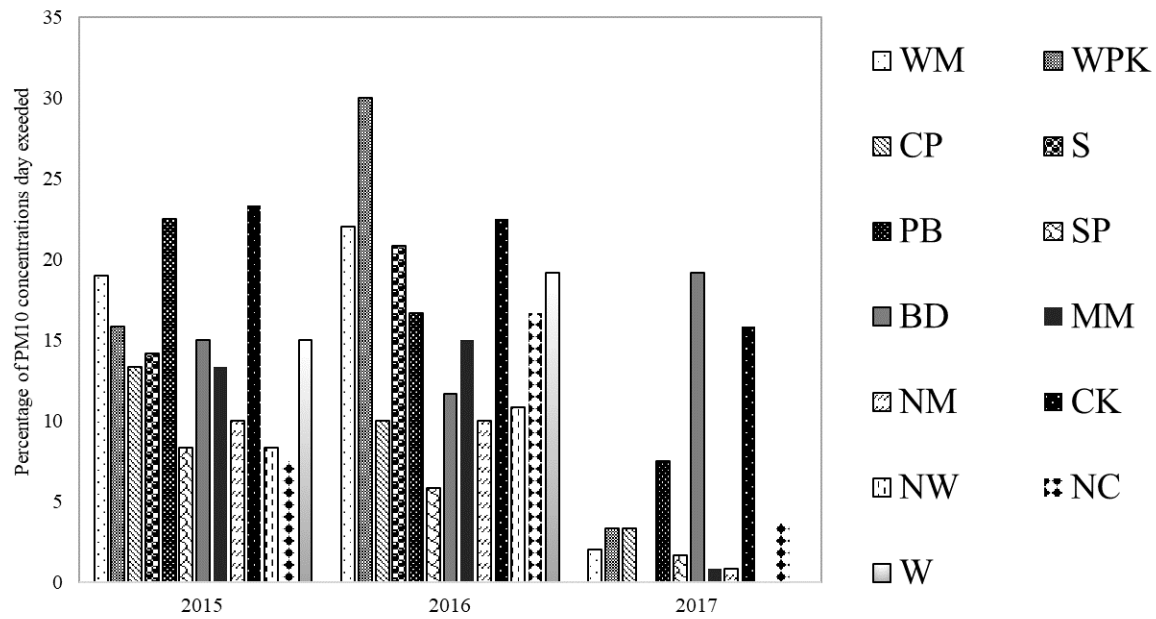


Fig. 3 Percentage by which daily average PM10 concentration exceeded standard in 13 monitoring stations.

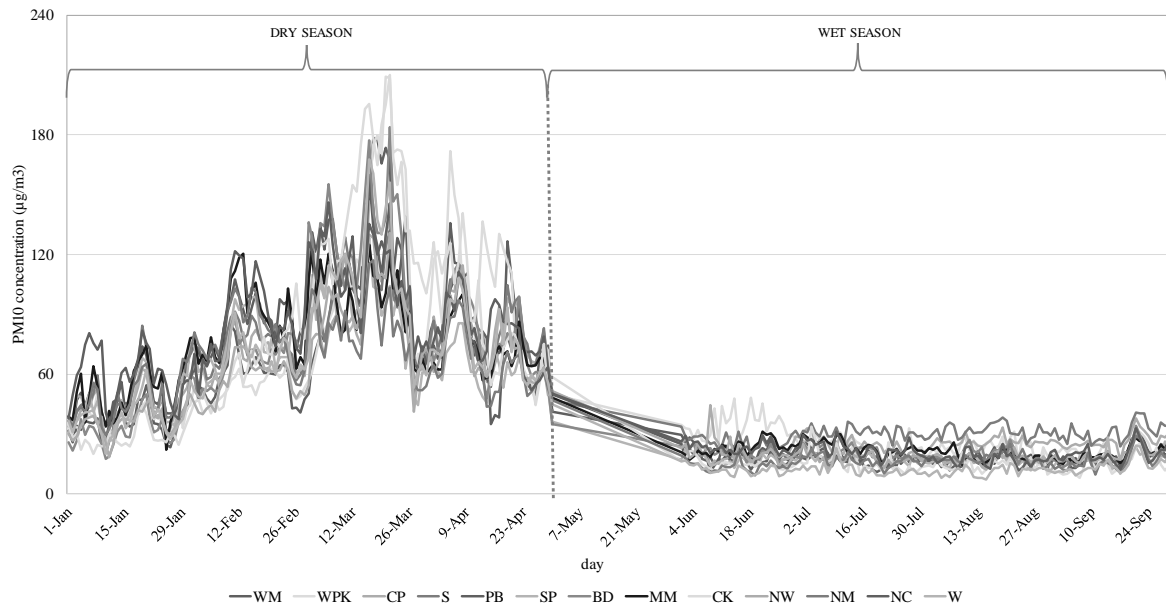


Fig. 4 Daily average of PM10 concentration during dry and rainy seasons at 13 monitoring stations in Northern Thailand

Source analysis of PM10 concentration

Most forest fires in Northern Thailand are observed during the dry season. The data collected by the Department of Forestry in 2017 showed that the major emission sources of haze pollution were forest fires during the harvesting of non-timber products (75.21%), followed by hunting (7.76%) and agricultural burning (4.04%). Other factors accounted for 12.99% of haze pollution.

Table 2. Amount of fire hotspots in Northern Thailand (unit: point).

Year	Study area	Agricultural	Forest	Total
2015	Chiang Rai	74	714	8,236
	Chiang Mai	178	1,833	
	Lampang	192	606	
	Lamphun	57	309	
	Mae Hong Son	168	2,142	
	Nan	120	1,201	
	Phrea	110	319	
	Phayao	36	177	
2016	Chiang Rai	127	1,235	6,812
	Chiang Mai	134	758	
	Lampang	155	660	
	Lamphun	39	204	
	Mae Hong Son	87	1,252	
	Nan	66	977	
	Phrea	118	606	

Year	Study area	Agricultural	Forest	Total
2017	Phayao	82	312	5,200
	Chiang Rai	38	115	
	Chiang Mai	186	1,782	
	Lampang	189	465	
	Lamphun	49	276	
	Mae Hong Son	48	1,114	
	Nan	60	478	
	Phrea	55	244	
	Phayao	19	82	

In addition, the information of the burnt areas, detected by the Landsat 8 satellite images and presented by the GISTDA, showed increasing PM10 concentrations during the dry season. The Pearson correlation analysis found a significant relationship between average PM10 concentrations and burnt areas in 8 provinces over the period from 2015 to 2017 ($P < 0.05$). That was confirmed by the linear regression analysis showing that burnt areas were significantly and positively related to PM10 concentrations ($P < 0.001$). The equation estimating that relationships is shown as Eq. (2).

$$Y_{PM10con.} = 0.04X_{area} + 65.108 \quad (2)$$

Where $Y_{PM10con.}$ is PM10 concentration in $\mu\text{g}/\text{m}^3$ and X_{area} is burnt area in km^2 . The values of y-intercept in the equation above could be taken to represent the PM10 concentration in burnt areas.

The data in Table 2, obtained from Thailand's Forest Fire Control Division, show fire hotspots (in points) in the study area from 2015 to 2017, indicating that forest fires and the agricultural waste burning remain the major sources of pollution. In particular, as Eq. 3 shows, increasing average PM10 concentrations are significantly and positively related to fire hotspots in each area ($P < 0.05$).

$$Y_{PM10con.} = 0.049X_H + 62.289 \quad (3)$$

Where $Y_{PM10con.}$ is PM10 concentration in $\mu\text{g}/\text{m}^3$ and X_H is the amount (in points) of fire hotspots.

CONCLUSION

This study is based on a 3-year dataset from 2015 to 2017, collected at 13 monitoring stations in Northern Thailand, to evaluate the sources and the seasonal variation of average PM10 concentrations. The results show that the average PM10 concentrations are significantly and positively related to burnt areas and the amount of fire hotspots in each location covered by this analysis. The highest level of PM10 concentration -- at $210 \mu\text{g}/\text{m}^3$ -- during those three years was found in the period of dry season. Average dry season PM10 concentrations were significantly higher than those observed during the rainy season ($P < 0.001$, t-test).

The increasing average PM10 concentrations were significantly related to meteorological data, such as temperature, southerly and southeasterly winds. On the other hand, relative humidity and wind speed were found to have a significantly inverse relationship with average PM10 concentrations. Average PM10 concentrations were significantly and positively related to increasing fire hotspots ($P < 0.05$). The main sources of PM10 concentrations in the areas covered by this study were forest fires and agricultural waste burning.

The meteorological data indicate that seasonal changes and PM10 emission sources have to be taken together to investigate major causes of haze pollution.

ACKNOWLEDGEMENTS

The authors sincerely thank the Pollution Control Department and the Forest Fire Control Division of Thailand's Ministry of Natural Resources and Environment for providing the data used in this analysis. This study was partially supported for publication by Thammasat University, Thailand.

REFERENCES

- [1] Pengchai P., Chantara S., Sopajaree K., Wangkarn S., Tengcharoenkul U., Rayanakorn Environ M. Seasonal variation, risk assessment and source estimation of PM 10 and PM10-bound PAHs in the ambient air of Chiang Mai and Lamphun, Thailand. *Environmental Monitoring and Assessment*. Vol. 154, 2009, pp. 197-218.
- [2] Oanh N.T.K., Leelasakultum K. Analysis of meteorology and emission in haze episode prevalence over mountain-bounded region for early warning. *Science of the Total Environment* Vol. 409, 2011, pp. 2261-2271.
- [3] Sooktawee S., Humphries U., Patpai A., Kongsong R., Boonyapitak S., Piemyai N. Visualization and Interpretation of PM10 Monitoring Data Related to Causes of Haze Episodes in Northern Thailand. Vol. 37, Issue 2, 2015, pp. 33-48
- [4] Pimonsree S. Seasonal variation of PM10 Concentrations in Northern Technology and Innovation for Sustainable Development. International Conference (TISD2010) Faculty of Engineering, Khon Kaen University, Thailand, 4-6 March 2010
- [5] Pardthaisong L., Sin-ampol P., Suwanprasit C., Charoenpanyanet A. Haze Pollution in Chiang Mai, Thailand: A Road to Resilience. *Procedia Engineering* Vol. 212, 2018, pp. 85-92.
- [6] Pongpiachan S., Choochuay C., Chalachol J., Kanchai P., Phonpiboon T., Wongsuesat S., Chomkhae K., Kittikoon I., Hiranyatrakul P., Cao J., Thamrongthanyawong S. Chemical characterisation of organic functional group compositions in PM2.5 collected at nine administrative provinces in northern Thailand during the Haze Episode in 2013. *Asian Pacific Journal of Cancer Prevention* Vol. 14, Issue 6, 2013, pp. 3653-3661.
- [7] Sirimongkonlertkul N., Upayokhin P., Phonekeo V. Multi-Temporal Analysis of Haze Problem in Northern Thailand: A Case Study in Chiang Rai Province. *Kasetsart Journal (Natural Science)* Vol. 47, Issue 5, pp. 768-780.
- [8] Li M., Zhang L. Haze in China: Current and future challenges *Environmental Pollution*. Vol. 189, 2014, pp. 85-86.
- [9] Pollution Control Department (PCD). Thailand state pollution 2017. Bangkok, Thailand, 2018. ISBN 978-616-316-391-2.
- [10] Kreasuwun J., Chotamornsak C., Ratchiranukul P., Wiranvejayan O. Weather analysis and air pollution warning. The Thailand Research Fund. Bangkok, Thailand, 2008.

- [1] Pengchai P., Chantara S., Sopajaree K.,

SPATIAL ANALYSIS OF COMMUNITY'S ACCEPTANCE FOR SUDS APPLICATIONS IN NHIEU LOC – THI NGHE SUB-BASIN, HO CHI MINH CITY, VIETNAM

Nguyen Hoang My Lan^{1,2}, Vo Le Phu² and Le Van Trung²

¹ Faculty of Urban Studies, Ho Chi Minh City University of Social Sciences and Humanities, VNU-HCM, Viet Nam; ² Faculty of Environment and Natural Resources, Ho Chi Minh City University of Technology, VNU-HCM, Viet Nam

ABSTRACT

With the purpose of imitating the nature drainage process at the site before development, Sustainable Urban Drainage System (SUDS) – a widely recognized solution to urban drainage and flood mitigation – is one of the most sustainable approaches to reduce the effect on the quality and quantity of run-off from urban development areas. Moreover, SUDS can improve the conditions of living environment for the communities, which defines the community amenity and social benefit. The concept of community's acceptance was used in this study to identify the social benefit of SUDS techniques in Nhieu Loc – Thi Nghe sub-basin where flooded areas have increased in quantity, frequency and level of severity. The purpose of this paper, firstly, is to examine the relationship between variables and the community's acceptance of proposed SUDS techniques in Nhieu Loc – Thi Nghe sub-basin, Ho Chi Minh City, including Rainwater Harvesting, Green Roof, Green Open Space, Pervious Pavement, and Pervious Parking Lot. Then, the public acceptance data obtained from the survey from November 2016 to March 2017 was adjusted and converted into GIS data layer. By correlation test in SPSS, there is a statistically significant relationship between the community's acceptance of SUDS techniques and both the understanding of SUDS techniques and the living places of respondents in Nhieu Loc – Thi Nghe sub-basin. Through Hot Spot Analysis in GIS, most of the acceptability hot-spots located in the extent of standard deviation ellipse of floods from 2007 to 2017 which lied entirely in the lowest elevation of the sub-basin. Therefore, the City government should increase the community perception of SUDS as well as its benefits in flooding management before planning to improve current drainage system.

Keywords: Sustainable Urban Drainage System, Spatial statistics, Community's acceptance, Urban flooding

INTRODUCTION

The conventional drainage systems are designed to collect and transport stormwater run-off from urban areas as quickly as possible via sewer networks and water treatment facilities to nearby receiving water bodies [11]. Also, these systems are not planned for either water quality improvement or amenity making. On the contrary, Sustainable Urban Drainage System – SUDS, introduced in the 1990s and commonly applied in developed countries, is considered as one of the sustainable approaches to deal with urban flooding. According to The Construction Industry Research and Information Association – CIRIA (2007), SUDS is designed to minimize the impacts from the development on the quantity and quality of the runoff and maximize amenity and biodiversity opportunities [22]. These objectives should all have equal standing, and the ideal solution will achieve benefits in all three categories, although the extent to which this is possible will depend on site characteristics and constraints.

A perfect SUDS scheme or treatment train should have a series of drainage techniques ranging from prevention, source control, site control and regional management, respectively. Through the SUDS scheme, wherever possible, storm-water and run-off should be managed and infiltrated into the ground by landscape features, such as rain garden, swale, pond, rather than being conveyed to and stored in large conventional pipelines and treatment stations. Building an ideal treatment train with a full range of SUDS components is more practical for new development than existing dense urban areas due to the limitation of available spaces for complete installation [33]. Hence, retrofitting existing storm-water management measures and turn them into sustainable infrastructures are the most satisfactory approach for flooding control in rapidly urbanized areas, like Ho Chi Minh City where the built-up area has increased over time. In SUDS treatment train or management train, techniques in prevention and source control stage should be preferred to others in site and regional control, which can be feasible and cost-effective in developed areas. According to

Lamond et. al (2014), the most appropriate SUDS features for retrofit within dense central business district (CBD) are green roofs, pervious paving, rainwater gardens and small treatment trains [44].

In term of social benefits, the most common notion used to assess SUDS sustainability is the community's acceptability or acceptance [55, 6]. Chui and Ngai (2016) found that despite not having a strong understanding of SUDS or SUDS benefits, the city dwellers in Hongkong were willing to pay for SUDS retrofitting in public places and private properties equal to 8.8% of the current government spending on storm-water management and 1.8% of the property price, respectively [55]. Also, the residents in Dundee, Scotland, UK were willing to pay more for their properties near the green spaces provided by SUDS features; and the more they knew about SUDS functions, the more they paid for retrofitting SUDS [66].

Therefore, the objective of this paper is to answer the question "Is there any significant relationship between the community's acceptance to SUDS techniques and other variables, including the demographic information, the knowledge of SUDS, the places of living, and the spatial distribution of inundations in Nhieu Loc – Thi Nghe sub-basin?".

STUDY AREA AND METHODOLOGY

Study area and data collection

Ho Chi Minh City, Vietnam is one of the Top 20 coastal cities with the greatest rate of the population exposed to flooding in the 2070s (including both climate change and socioeconomic change) [77]. In recent years, flooding has become the most significant issue to affect the city's growth and create the economic loss, as well. Ho Chi Minh City (HCMC) has considerably been flooded, especially during the rainy season from June to November and during flood-tide between September and December. According to the Ministry of Natural Resources and Environment [88], with the worst case scenario of climate change, the average temperature and precipitation in HCMC up to 2100 are projected to increase 1 – 3.5°C and 14.7 – 23.4%, respectively. Moreover, 17.8% of the city area will be flooded when the sea level rises 100cm, in which Binh Thanh is the most inundated district with more than 80% of its area.

Based on the Master Plan of Drainage System in HCMC to 2020 issued in 2001, Nhieu Loc – Thi Nghe (NL-TN) sub-basin with the area of 33.2km² is one of the central drainage catchments in HCMC and comprises whole or part of seven districts including 1, 3, 10, Phu Nhuan, Tan Binh, Go Vap, and Binh Thanh. Land elevation in NL-TN sub-basin ranges from 0.5m to 10.6m and ascends from the NL-TN canal toward the Northern and the Southern. The Eastern of NL-

TN sub-basin has the lowest elevation which creates the most frequently and seriously flooded routes.

From 2010-2017, this sub-basin has challenged the annual average of twenty inundated locations including the deepest and the most spreading in the whole city. In this study, after collected from Ho Chi Minh City's Steering Center for Flood Control, flooding data were analyzed and converted into GIS layer for spatial pattern and trend analysis.

A face-to-face interview by questionnaire was conducted from November 2016 to March 2017 with 238 households which distributed randomly in the NL-TN sub-basin extend. Over 60% of the respondents located around the NL-TN canal and in the Eastern of the sub-basin where flooding has occurred more frequently (Fig. 1). The number of interviewees in the Western was otherwise the lowest because of limited accessibility. The 5-Likert scale was used to quantify the answer to whether the residents were willing to accept to install proposed SUDS techniques in their properties or surrounding areas. 1 in 5-Likert scale represents for *Strongly disagree* and 5 represents for *Strongly agree*. Moreover, the coordinate of households was collected and then geocoded in ArcMap for further spatial analysis.

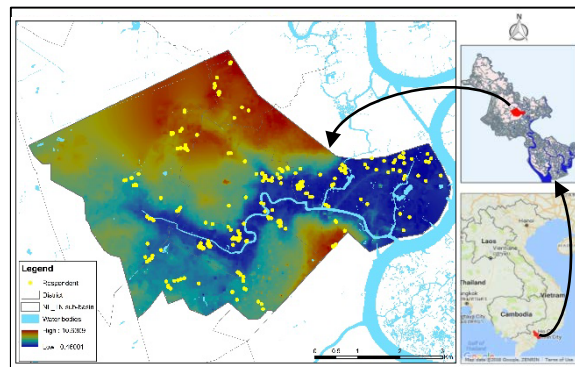


Fig. 1 Respondents' distribution in Nhieu Loc – Thi Nghe sub-basin

The Statistical Package for the Social Sciences (SPSS) software (Version 23) was used for statistical analysis, including descriptive statistics and correlation tests between observed variables. In this study, the Chi-square test and Kendall correlation test were used to examine the relationship between acceptability and other observed variables. The null hypothesis was that the two or more than two sets of measures were similar, used in Chi-square test and that there was no correlation between two variables, used in Kendall correlation test. The significant value (*p-value*) of 0.05 or 95 percent confident was used to retain or reject the null hypothesis. Phi and Spearman rank (Spearman's rho) correlation coefficient were then used to measure the strength of the relationship between two variables after claiming that the relationship existed significantly. Both Phi and

Spearman's rho vary from -1 to 1 where positive value indicates a direct relationship and negative denotes an inverse correlation. The higher coefficient is, the stronger relationship exists between tested variables.

Geotis-Ord Spatial Statistic

Hot Spot Analysis – one of the spatial statistic tools in ArcMap (Version 10.4) is used to create a map of statistically significant hot and cold spots based on *Getis-Ord Gi** or G_i^* statistic. This statistic measures the degree of association that results from the concentration of points and all other points included within a certain radius of distance from the original point [99].

$$G_i^* = \frac{\sum_{j=1}^n w_{ij} x_j - \bar{X} \sum_{j=1}^n w_{ij}}{s \sqrt{n \sum_{j=1}^n w_{ij}^2 - (\sum_{j=1}^n w_{ij})^2}} \quad (1)$$

Where x_j is the attribute value for feature j , w_{ij} is the spatial weight between feature i and j , and n is equal to the total number of features. \bar{X} – the mean of attribute x and S are calculated by the following equations.

$$\bar{X} = \frac{\sum_{j=1}^n x_j}{n} \quad (2)$$

$$S = \sqrt{\frac{\sum_{j=1}^n x_j^2}{n} - (\bar{X})^2} \quad (3)$$

The G_i^* returned for each feature in the dataset is a z -score which, together with p -value, tells whether the null hypothesis of the spatial concentration can be rejected or not. A close-to-zero G_i^* value implies random distribution of the observed spatial events. Conversely, positive and negative G_i^* statistics with high absolute values correspond to the clusters of high- and low-valued events, respectively [1010].

Hot Spot Analysis tool creates a new feature class with a z -score, p -value and confidence level bin (Gi_Bin) for each feature in the input dataset. The Gi_Bin field identifies statistically significant hot (high value) and cold (low value) spots, assigned values of +/- 1, +/-2, and +/-3 reflecting the 99%, 95%, and 90% of confidence level, respectively. While features with 0 for Gi_Bin field are not statistically significant clustering.

Standard Deviation Ellipse

The Standard Deviation Ellipse (SDE) tool is commonly used to measure the trend for a set of features. The output ellipse is shaped by the x - and y -directions from the mean center of the input dataset. The SDE is given as:

$$SDE_x = \sqrt{\frac{\sum_{i=1}^n (x_i - \bar{X})^2}{n}} \quad (4)$$

$$SDE_y = \sqrt{\frac{\sum_{i=1}^n (y_i - \bar{Y})^2}{n}} \quad (5)$$

Where x_i and y_i are the coordinates for feature i , $\{\bar{X}, \bar{Y}\}$ represents the Mean Center for the features, and n is equal to the total number of features.

The rotation of the long axis measured clockwise from noon is calculated as:

$$\tan \theta = \frac{A+B}{C} \quad (6)$$

$$A = (\sum_{i=1}^n \tilde{x}_i^2 - \sum_{i=1}^n \tilde{y}_i^2)$$

$$B = \sqrt{(\sum_{i=1}^n \tilde{x}_i^2 - \sum_{i=1}^n \tilde{y}_i^2)^2 + 4(\sum_{i=1}^n \tilde{x}_i \tilde{y}_i)^2}$$

$$C = 2 \sum_{i=1}^n \tilde{x}_i \tilde{y}_i$$

Where \tilde{x}_i and \tilde{y}_i are the deviations of the xy -coordinates from the Mean Center. When the features have a spatially normal distribution in which they are densest in the center and become increasingly less dense toward the periphery, one standard deviation is created to encompass approximately 68% of the input features centroids.

In this study, two SDEs were created from the data of flooding in 2017 and 2010-2017. The SDE of 2017 was calculated based on the hypothesis that experiences with flooding in the most recent year would affect the community's acceptability to proposed SUDS techniques. After that, these SDEs could be used to observe the spatial relationship of the community's acceptance to SUDS techniques and flooding situation or trend.

RESULTS AND DISCUSSIONS

The result of flooding data analysis shows that flood occurred 167 times from 2007 to 2017 and concentrated on roads in NL-TN sub-basin, with the total flooded route over 65,000 km. Submerged sites mostly located in Binh Thanh district where is NL-TN canal and Sai Gon river intersection and has the lowest elevation in sub-basin. Therefore, the Standard Deviation Ellipse of floods in 2007-2017 (SDE-1) lied mostly in Binh Thanh district with the long axes doubled the short one and the rotation was more than 87 degrees. Particularly, based on directional trend analysis, the SDE of floods in 2017 (SDE-2) covered the NL-TN canal entirely as well as below 5m land (Fig. 2) and had the area of 20km², twice as much as SDE-1. The trend of both SDE-1 and SDE-2 had the same direction which was along the NL-TN canal and mostly parallel with the east-west axis of sub-basin.

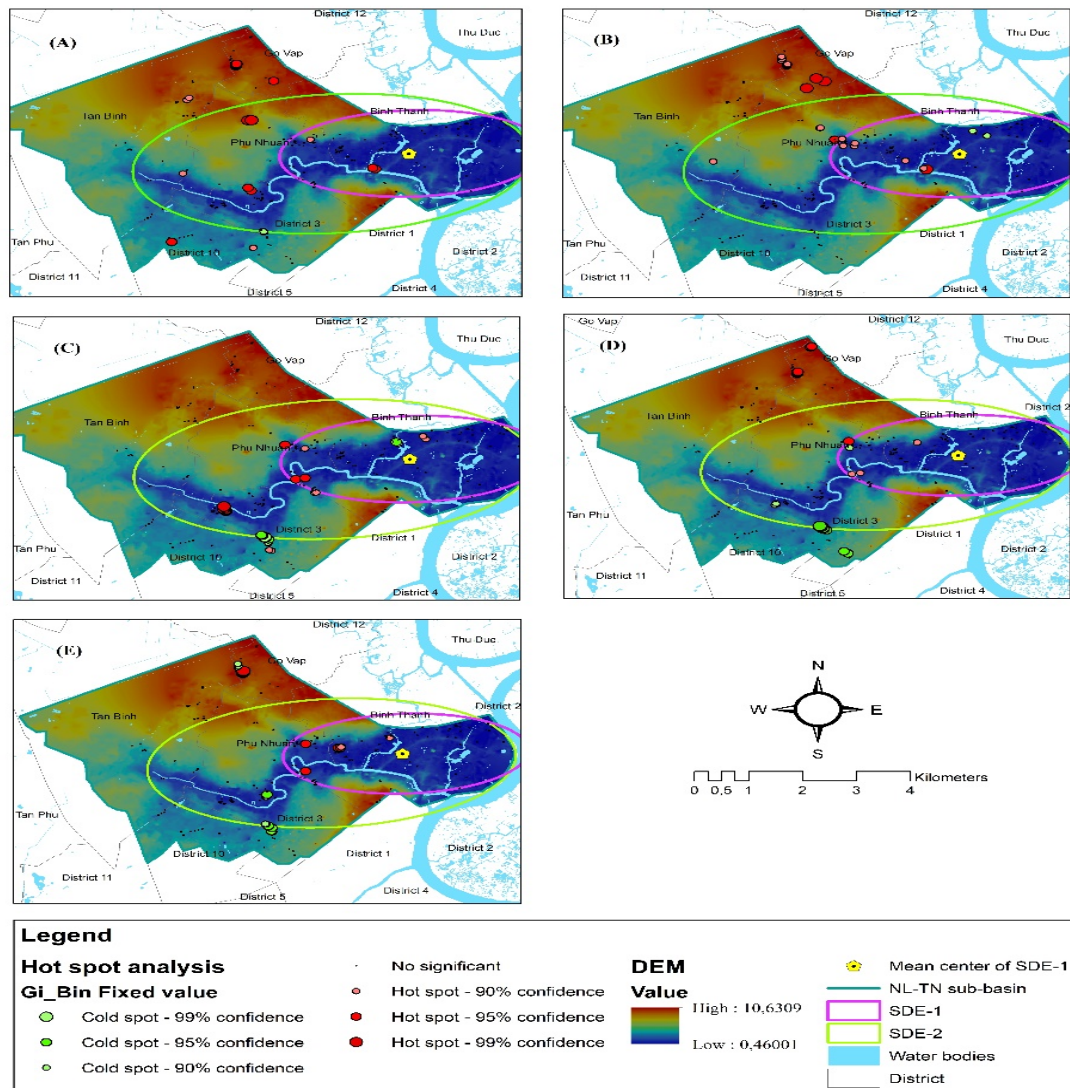


Fig. 2 Statistically significant Cold and Hot spots location of the community acceptance of SUDS techniques in NL-TN sub-basin: (A) Rainwater Harvesting, (B) Green Roof, (C) Green Open Space, (D) Pervious Pavement, and (E) Pervious Parking Lot

Table 1 Correlation efficient between acceptability to SUDS techniques and other observed variables

Acceptability to SUDS techniques	Age ^a	Sex ^a	Income ^b	Knowledge of corresponding techniques ^a	District ^a	Flood frequency ^b
Rainwater Harvesting	-0.104	0.221*	-0.067	0.428**	0.475**	0.099
Green Roof	-0.021	0.131	0.052	0.464**	0.454**	-0.024
Green Open Space	0.156*	0.061	0.046	0.530**	0.325	0.137*
Pervious Pavement	-0.068	0.083	-0.032	0.479**	0.408*	0.158*
Pervious Parking Lot	-0.096	0.162	-0.106	0.388**	0.455**	0.133*

^aPhi correlation efficient

^bSpearman's rho efficient

* $p = 0.05$, ** $p = 0.01$

Rainwater Harvesting refers to the collection of water from surfaces on which rain falls and subsequently storing this water for later use [111]. Furthermore, domestic household rainwater harvesting has the potential to groundwater recharge, resulting reduction in the rate of land subsidence. There is, however, still much concern about the quality of rooftop, stored rainwater, including chemical and microbiological factors [111], and available spaces for storage installation.

Green Roofs are the systems which cover a building's roof with vegetation and designed to increase localized infiltration, attenuation and/or detention of storm-water [1212]. GR is one of the SUDS components which can meet all the three goals of sustainability: water quality, water quantity, and amenity [1313]. Most of the respondents showed their anxieties for these two techniques because of their difficulties in both operation and maintenance.

Generally, pervious surfaces, such as *Pervious Pavement*, *Green Open Space* and *Pervious Parking Lot*, allow rainwater to infiltrate through the surface into an underlying storage layer, where water is stored before infiltration to the ground, reuse or release into surface water [22]. Permeable pavements could be the promising performance of the SUDS to provide storage capacity for extreme rainfall and water quality control to meet the good status required by environmental agencies [11]. However, that the operation and maintenance of pervious surface may be costly and need new skills [1414] is the reason for those who totally disagree to install these methods (63 of 124 comments).

In NL-TN sub-basin, the proposed SUDS techniques are accepted more in Binh Thanh and Go Vap, where inundation occurred more frequently and severely than in district 1, 3 and 10 because of the limitation of available spaces for construction. Based on the results of correlation tests (**Table 1**), these differences of acceptability by places are statistically significant, except for GOS, and these associations are from moderate to strong relationships ($0.3 < \text{Phi coefficient} < 0.4$). Besides, the understanding of SUDS technique is the factor to make strong positive relationships with SUDS acceptability, thus the City government should increase the community perception of SUDS as well as its benefits in flooding management before planning to improve current drainage system.

Figure 3 shows that NL-TN sub-basin has experienced the annual average of twenty inundated locations from 2010 to October 2017. In NL-TN sub-basin, Nguyen Huu Canh street, passing the mean center of SDE-1 (Fig. 2), possesses the deepest and the most spreading flooded points in the whole city. It is easily found that almost the hot spots of the community's acceptance of five SUDS techniques

concentrated in the extent of SDE-1 and SDE-2. It indicates that experiences with floods in recent years have prompted respondents to adopt new and more sustainable drainage techniques. Moreover, these hot spots also appeared in the North of sub-basin with higher elevation and fewer flooded locations, except for GOS. Respondents living along NL-TN canal preferred to GOS because they wanted to not only improve aesthetics but also manage floods for their better living conditions.

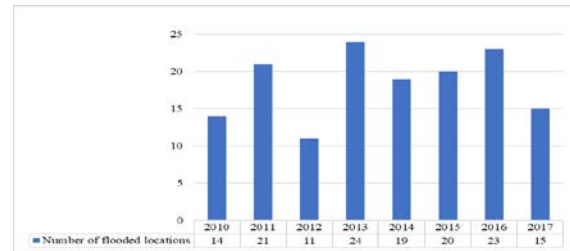


Fig. 3 Number of flooded locations in Nhieu Loc – Thi Nghe sub-basin from 2010 to October 2017

CONCLUSIONS

In this study, the characteristics of the community's acceptance of five proposed SUDS techniques were explored by collecting survey data, statistical analysis, and correlation tests. Interestingly, most of the respondents would be willing to adopt the new and sustainable drainage techniques for better living conditions. Among the significant influent factors to the acceptability, how the respondents know SUDS techniques and where they live are the most strongly positive ones. The research result showed that, however, the residents in NL-TN sub-basin favored the drainage techniques which are constructed in public or surrounding areas rather than those retrofitted with their properties.

Regarding spatial pattern, spatial analysis and statistics were used to only detect the community's acceptance in the relationship to directional trend of floods in NL-TN sub-basin. Most of the acceptability hot-spots located in the extent of standard deviation ellipse of floods from 2007 to 2017 which lied entirely in the lowest part of the sub-basin. For further improvement, there is a need to increase the observed samples to represent the whole sub-basin significantly and explore the spatial characteristics in correlation to land-use data, especially the impervious surface data.

REFERENCES

- [1] Zhou, Q., A Review of Sustainable Urban Drainage Systems Considering the Climate

- Change and Urbanization Impacts, *Water*, 6 (4) (2014) pp. 976-992.
- [2] Woods-Ballard, B., Kellagher, R., Martin, P., Jefferies, C., Bray, R., and Shaffer, P., *The SUDS manual*. Vol. 697. CIRIA, London, 2007.
 - [3] Mguni, P., Herslund, L. and Jensen, M. B., Sustainable urban drainage systems: examining the potential for green infrastructure-based stormwater management for Sub-Saharan cities, *Natural Hazards*, 82 (2) (2016) pp. 241-257.
 - [4] Lamond, J., Wilkinson, S., Rose, C., and Proverbs, D., Sustainable urban drainage: retrofitting for improved flood mitigation in city centres. 2014.
 - [5] Chui, T. F. M. and Ngai, W. Y., Willingness to pay for sustainable drainage systems in a highly urbanised city: a contingent valuation study in Hong Kong, *Water and Environment Journal*, 30 (1-2) (2016) pp. 62-69.
 - [6] Jose, R., Wade, R. and Jefferies, C., Smart SUDS: recognising the multiple-benefit potential of sustainable surface water management systems, *Water Science and Technology*, 71 (2) (2015) pp. 245-251.
 - [7] Hanson, S., Nicholls, R., Ranger, N., Hallegatte, S., Corfee-Morlot, J., Herweijer, C., and Chateau, J., A global ranking of port cities with high exposure to climate extremes, *Climatic change*, 104 (1) (2011) pp. 89-111.
 - [8] Ministry of Natural Resources & Environment - MONRE, Climate change and sea level rise scenarios for Vietnam: summary for policymakers. Ha Noi, 2016.
 - [9] Getis, A., Spatial filtering in a regression framework: examples using data on urban crime, regional inequality, and government expenditures, in *Perspectives on spatial data analysis*. 2010, Springer. p. 191-202.
 - [10] Songchitruksa, P. and Zeng, X., Getis-Ord spatial statistics to identify hot spots by using incident management data, *Transportation Research Record: Journal of the Transportation Research Board*, (2165) (2010) pp. 42-51.
 - [11] Vo Le Phu and Bui, T. D., Rainwater harvesting: the new direction for Ho Chi Minh City, Vietnam, *Journal of Science & Technology*, 50 (1C) (2012) pp. 188-198.
 - [12] Ossa-Moreno, J., Smith, K. M. and Mijic, A., Economic analysis of wider benefits to facilitate SuDS uptake in London, UK, *Sustainable Cities and Society*, 28 (2017) pp. 411-419.
 - [13] Uzomah, V., Rapid decision support tool based on novel ecosystem service variables for retrofitting sustainable drainage systems in the presence of trees. University of Salford, 2016.
 - [14] Malulu, I. C., Opportunities for integrating sustainable urban drainage systems (SuDS) in informal settlements as part of stormwater management. Stellenbosch: Stellenbosch University, 2016.

DEVELOPING FINE PARTICLE FILTERING SYSTEM FOR MOTORCYCLE EXHAUST USING COCO FIBERS

Arinto Y.P. Wardoyo¹, Firdy Yuana¹, and Selly Y. A. Elbasari¹

¹Faculty of Mathematics and Natural Science, Brawijaya University, Indonesia

ABSTRACT

Fine particles from motor vehicle exhaust emissions become a major problem for the environment and human health. This burden requires a new technology of filtering system with a high efficiency. However, the filtering system for motorcycle exhaust is still limited. Thus, we developed a new filtration system using coco fibers mixed to tapioca glues with the variation ratio such as 50:50 (Filter 1); 60:40 (Filter 2); 70:30 (Filter 3); and 80:20 (Filter 4). The efficiency is calculated by the ratio of the fine particle concentration in the exhaust emission before and after passing through the filter. The fine particle concentration was measured using a Digital Dust Monitor (Kanamax, Model 3443) when the motorcycle was operating in the idle condition. The fine particle concentration was measured for twenty sampling time. The filter efficiency was tested using three different motorcycles (M1, M2, and M3). The result showed that the filter efficiency was found between 12% and 33% depending on the filter thickness, density, and composition of the coco fiber and the glue.

Keywords: Fine particles, Coco fiber filter, Motorcycle, Exhaust emission, Efficiency

INTRODUCTION

The population of a motor vehicle in the world has been increasing from year to year. Some factors that influence the growth rate of the motor vehicles are the increased population and the economic growth [1]. The growth rate of motor vehicles was also related to the urbanization [2]. From many kinds of motor vehicles, the motorcycle is widely used as the common vehicle due to its high efficiency, low fuel consumption, long durability, and easy of use. Thus, the motor vehicle population growth can be linked to the emission of motor vehicles (particulate matter and gaseous emissions) that influence the air quality level.

Particulate matter (PM) is a key component of air pollution in which motorcycle is one of the source. Thus, PMs become a major problem for the environment. The size of PMs ranges from nanometers (submicron) to microns in the diameter size. Generally, they are classified into PM_{0.1} (ultrafine particles), PM_{2.5} (fine particles), and PM₁₀ (coarse particles).

Especially for the particulate matters with the diameter less than 2.5 μm , PM_{2.5} consists of major and minor elements, inorganic ions, elemental carbons, and some organic compounds [3]. The accumulation concentrations of PM_{2.5} in the ambient air, whether the indoor or outdoor environment, may affect ecological balance and does have an impact on human health. In an indoor environment, fine particle toxicity was influenced by its deposition velocity onto human body surfaces [4]. A long-term exposure to fine particles was associated with the

blood pressure alteration [5]. Many epidemiologic studies have been conducted to investigate the pulmonary responses to the exposure to fine particles in a mice model [6]. The previous studies have confirmed that fine particles have an association with coronary artery disease [7]. They are able to induce oxidative stress and to cause inflammatory cytokines gene expression and secretion [8].

Several studies have been conducted to improve the filtration technology in the motor vehicle exhaust system. A diesel particulate filter (DPF) of the heavy-duty diesel trucks has been investigated recently [9]. The previous study confirmed the latest filtration technology using an electrostatic force to reduce the concentrations of ionic ultrafine particles [10]. Even, the thermal energy generated from the motorcycle muffler has been utilized to reduce the concentration of fine particles [11].

In other sides, the data about a porosity-based filter developed from the coconut fiber has not been available. Meanwhile, the reference of the biomass particulate filter for the motorcycle exhaust system is still limited. In this study, four variations of biomass fine particle filters were tested in a laboratory test bench. The study included three motorcycle samples in different manufacturers and engine types that selected randomly. The aim of this research was to provide the detail information about the performance of the particulate filter in reducing the concentrations of fine particles emitted by motorcycle, including the factors that related to the filter efficiency.

MATERIALS AND METHODS

Motorcycle Samples

The study included three different motorcycle samples preferred randomly in Malang, Indonesia. The description of the vehicle samples is presented in Table 1. The names of the motorcycle samples are replaced by the letter code of M1-M3.

Table 1 Motorcycle samples classification

Motor Samples	Engine Capacity (cm ³)	Model Years
M1	150	2013
M2	150	2013
M3	150	2013

Note: Each motorcycle sample was purchased from random user in a standard engine condition (4-stroke engine, manual transmission) with the same gasoline type and octane number.

Fine Particle Filters

The coco fibers were purchased from the local market around Brawijaya University, Malang, Indonesia. The coco fibers were chopped up and naturally air-dried in order to reduce the moisture content. When the fibers were dry (moisture content < 15%), the coconut fibers were grinded to become the fine-grained powder. The powder was mixed with the tapioca glue in four different variation ratios in order to generate four different filters: F1, F2, F3, and F4. The filter cake was mixed with the dilution water. When it came blended, it was pressed on a metal screen with a constant pressure in order to generate a filter sheet with the specific thickness (Table 2). The filter sheet was naturally air-dried.

Table 2 Specifications of the fine particle filters

Parameter	F1	F2	F3	F4
Coco Fiber : Glue (Ratio)	50:50	60:40	70:30	80:20
Diameter [cm]	7.620	7.620	7.620	7.620
Thickness [cm]	0.154	0.178	0.205	0.241
Density [g/cm ³]	0.232	0.215	0.201	0.195
Dilution Water [cm ³]	500	500	500	500

Particle Measurement

Particle measurement was conducted at the Laboratory of Air Quality and Astro Imaging Physics Department, Brawijaya University, Malang, Indonesia. The measurement was conducted in an indoor room (laboratory test bench), with a constant

room temperature and fine particle concentration during ambient monitoring ($T_{ambient} = 27 - 28^{\circ}\text{C}$). The location of the measurement was also greater than 1000 m from the nearest public roadway. The particle measurement set-up (filter test bench) is represented in Fig. 1.

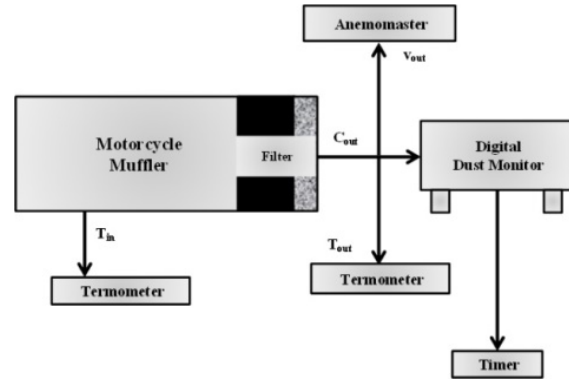


Fig. 1 Schematic of the bench-scale fine particle filters test system.

Each filter was installed individually on the outlet of the motorcycle muffler using a filter converter kit (diameter: 76.2 mm). The motorcycle engine was turned on for 1 minute for a warming up process, with a constant condition (idling state at 1000 RPM). A Digital Dust Monitor (Kanomax Inc., Model 3443) was used to measure the fine particles concentration. The pressure drop of the exhaust flow rate after treatment (v_{out}) was monitored by an Anemomaster (Kanomax Inc., Model A031). The inlet (T_{in}) and outlet temperatures (T_d) were measured with digital thermometers. The ambient temperature ($T_{ambient}$), relative humidity, and gaseous emissions (CO and CO₂) were reported from a Q-Trak (TSI, Model 8554). These measurements were conducted before (C_{in}) and after (C_{out}) applying the filter to the motorcycle muffler in every 10 seconds as the interval time of the measurement. All measurements were repeated three times.

Statistical Analysis

The recorded fine particle concentrations were analyzed using Eq. (1) in order to determine the filter efficiency (E_f) [10].

$$E_f = [(C_{in} - C_{out}) / (C_{in})] \times 100\% \quad (1)$$

The filter efficiency was interpreted as the mean \pm SD from all motorcycle samples. The difference between filter was determined using a Student's t -test, in which the p -values of less than 0.05 were considered to be statistically significant [6]. The statistical analysis was carried out using Microsoft Excel 2016.

RESULTS

Fine Particles Concentration

In order to understand the filtration behavior on the fine particles reduction, the concentrations of fine particles were measured before and after applying the filter. Fig. 2 shows the effects of the installed filters with a constant condition. Compared to the C_{in} , all filters could decrease the concentrations of fine particle emissions ($p < 0.05$).

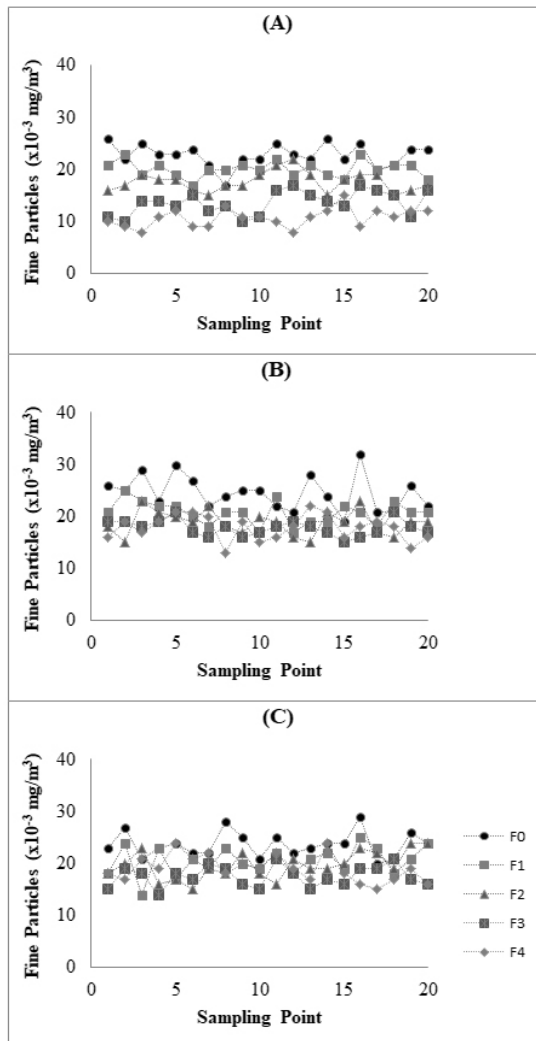


Fig. 2 Fine particle concentrations of F0 (C_{in}) and C_{out} from Filter 1 (F1) - Filter 4 (F4) for all motorcycle samples: (A) M1; (B) M2; and (C) M3.

Filter Efficiency

Filtration test was conducted to determine the filter efficiency in reducing fine particles. Figure 3 below represents the filter performances (mean \pm SD, for all motorcycle samples, $n = 3$), as calculated using Eq. (1).

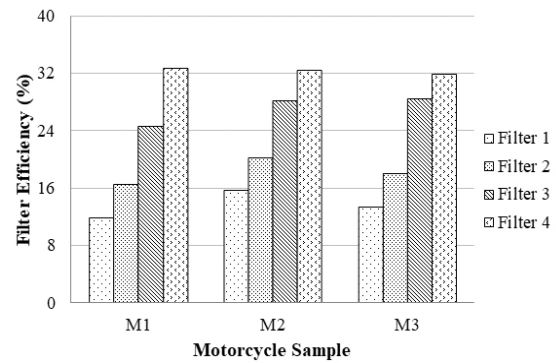


Fig. 3 Filter performance on fine particle concentrations, $p < 0.05$ (mean \pm SD from three repeated measurements in three different motorcycle samples).

Figure 3 shows the efficiency of the four different filters with the different thickness level. Based on the filter thickness, F4 had the highest efficiency when applied in M1 (33%), whereas the lowest efficiency was obtained at F1 applied in M1 (12%). The similar results were found in M2 and M3. In the sample of M2, F1, F2, F3, and F4 generated 16%, 20%, 28%, and 32% of the filter efficiencies, respectively. Similarly, F1 and F2 generated 13% and 18% of the filter efficiencies when applied in M3. On the other hands, the efficiencies of the filters F3 and F4 in M3 were 28% and 32%, whereas the F4 generated the highest efficiency. The value was significantly higher than the efficiency of F1 (up to 19% higher). Among three different motorcycle samples, F4 has the highest efficiency. This result was consistent with the result obtained from the previous study [12].

DISCUSSION

Figure 3 depicts the mean efficiency, in which the filter efficiency is influenced by the thicknesses of the filters. This tendency is proven in this study, as the thickness variation of the filter was investigated to determine the efficiency. According to the results, the increase in the filter thickness has better ability in reducing fine particles showing to the higher efficiency. In order to get a better understanding, Fig. 4 below interprets the correlation between the filter thickness and the filter efficiency.

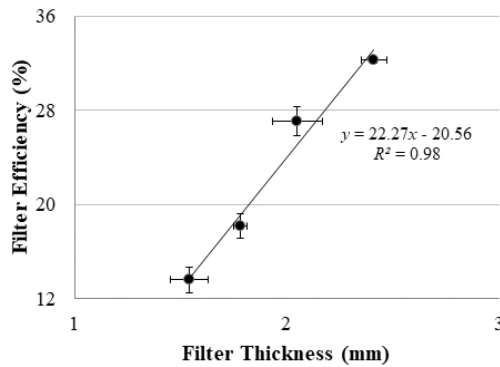


Fig. 4 The correlation between filter thickness and filter efficiency.

Based on Fig. 4, the linear regression analysis shows an extreme positive correlation between the filter thickness and the filter efficiency, since the R^2 value is 0.98 (≈ 1). The correlation is interpreted as a linear function with the approximation equation $y = 22.27x - 20.56$. This trendline indicates that there is a strong correlation between the filter thickness and the filter efficiency.

The different efficiency level E_f of the filters might be related to the filter porosity. In this state, the porosities across the substrate of the coconut fibers might influence the filter efficiency. As confirmed in the previous study, the porosity distribution of the filter, including the pore size distribution, can represent the performance of a particulate filter [13]. The porosity level of a filter has a correlation with the filter thickness and density.

According to the results, F4 had the highest filter efficiency. Interestingly, the thickness of F4 was the highest, 0.24 cm. In contrast, the density of the filter F4 was only 0.195 g/cm³. Although F4 was the thickest filter, F4 had the lowest density level. These results indicated that F4 had the most porosity level due to their lowest density level.

As shown in Table 2, F4 is the thickest filter (0.36 – 0.87 mm thicker than other filters) with the lowest porosity level. Thus, as expected F4 has the highest efficiency level, related to the filter thickness. As the thickest filter, F4 might have more fibroin content due to its high coco fiber ratio (80%). The coco fiber ratio of F4 was up to 10% higher than F3, F2, and F1. These different coco fiber ratio might influence the porosity of the filters since the fluid flow through porous media is related to the media porosity [14]. Since the filter density is not only the influencer factor, the filter efficiency is much more influenced by the filter thickness.

The density and porosity might indicate the existence of pressure drop that reflected filter performance [15]. As interpreted below (Fig. 5), we

had measured the level of pressure drop related to the flow rate of the emission. The results showed that F1 had the most pressure drop (58%). Meanwhile, the lowest pressure drop level was referred to F4, as the most porous filter (22%). Based on the flow rate measurements of the outlet, the values of v_{out} was 0.09 m/s, 0.10 m/s, 0.11 m/s, and 0.16 m/s for F1, F2, F3, and F4 respectively. In other sides, the v_{in} was 0.21 m/s. There was no difference between T_{in} and T_d .

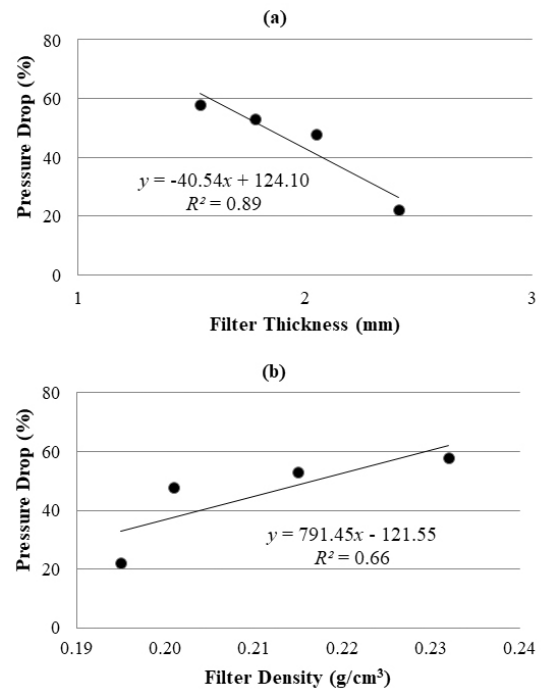


Fig. 5 a). Filter thickness vs pressure drop, $R^2 = 0.89$; b). Filter density vs pressure drop, $R^2 = 0.66$.

These results reflect the correlation (linear regression functions) between the filter density – filter thickness and pressure drop, together with the filter performance E_f . The thickness of the fibrous media structures influences the permeability and the airflow [16]. The more porous filter had more tapioca glue. The more concentration of coco fiber increased the filter efficiency, together with the decreasing amount of the pressure drop. These results indicated that the thickest filter F4, with the highest coco fiber ratio, could decrease the most fine particles concentration though it had the lowest density level.

CONCLUSION

We have developed the filter using coco fibers for motorcycle fine particles with the efficiency in the range of 12 to 33% depending on the filter thickness,

density, and the composition ratio between coco fibers and tapioca glue.

ACKNOWLEDGEMENTS

The authors wish to acknowledge Arif Budianto, Mia A. Pawestri., Ayu Wenda I. Putri., Rudi Andika, and Renado Anggara for their excellent technical assistance.

REFERENCES

- [1] Dayal Sharma R., Jain S., and Singh K., Growth rate of Motor Vehicles in India - Impact of Demographic and Economic Development, *J. Econ. Soc. Stud.*, Vol. 1, No. 2, 2011, pp. 137–154.
- [2] Riley K., Motor Vehicles in China: The Impact of Demographic and Economic Changes, *Popul. Environ.*, Vol. 23, Issue 5, 2002, pp. 479–494.
- [3] Minguillón M. C., Rivas I., Moreno T., Alastuey A., Font O., Córdoba P., Álvarez-Pedrerol M., Sunyer J., and Querol X., Road traffic and sandy playground influence on ambient pollutants in schools, *Atmos. Environ.*, Vol. 111, 2015, pp. 94–102.
- [4] Shi S., Li Y., and Zhao B., Deposition velocity of fine and ultrafine particles onto manikin surfaces in indoor environment of different facial air speeds, *Build. Environ.*, Vol. 81, 2014, pp. 388–395.
- [5] Chan S. H., Van Hee V. C., Bergen S., Szpiro A. A., DeRoo L. A., London S. J., Marshall J. D., Kaufman J. D., and Sandler D. P., Long-term air pollution exposure and blood pressure in the sister study, *Environ. Health Perspect.*, Vol. 123, No.10, 2015, pp. 951–958.
- [6] Bai R., Zhang L., Liu Y., Meng L., Wang L., Wu Y., Li W., Ge C., Le Guyader L., and Chen C., Pulmonary responses to printer toner particles in mice after intratracheal instillation, *Toxicol. Lett.*, Vol. 199, 2010, pp. 288–300.
- [7] McGuinn L. A., Ward-Caviness C., Neas L. M., Schneider A., Di Q., Chudnovsky A., Schwartz J., Koutrakis P., Russell A. G., Garcia V., Kraus W. E., Hauser E. R., Cascio W., Diaz-Sanchez D., and Devlin R. B., Fine particulate matter and cardiovascular disease: Comparison of assessment methods for long-term exposure, *Environ. Res.*, Vol. 159, 2017, pp. 16–23.
- [8] Cachon B. F., Firmin S., Verdin A., Ayi-fanou L., Billet S., Cazier F., Martin P. J., Aissi F., Courcot D., Sanni A., and Shirali P., Proinflammatory effects and oxidative stress within human bronchial epithelial cells exposed to atmospheric particulate matter (PM_{2.5} and PM_{>2.5}) collected from Cotonou, Benin, *Environ. Pollut.*, Vol. 185, 2014, pp. 340–351.
- [9] Quiros D. C., Yoon S., Dwyer H. A., Collins J. F., Zhu Y., and Huai T., Measuring particulate matter emissions during parked active diesel particulate filter regeneration of heavy-duty diesel trucks, *J. Aerosol Sci.*, Vol. 73, 2014, pp. 48–62.
- [10] Wardoyo A. Y. P., Budianto A., and Abdurrouf, Filtration of submicron particles from motorcycle emission using a DC low electrostatic filter, *Int. J. Appl. Eng. Res.*, Vol. 12, No.8, 2017, pp. 1725–1728.
- [11] Wardoyo A. Y. P., Nuriyah L., and Darmawan H. A., Developing Reheated Filter of Motorcycle Exhaust for Reducing PM_{2.5} Emissions, in *Proc. Int. Semin. Sensor, Instrumentation, Meas. Metrol.*, 2017, pp. 42–45.
- [12] Wardoyo A. Y. P., Juswono U. P., and Riyanto S., Developing particulate thin filter using coconut fiber for motor vehicle emission, in *Proc. AIP Conf. Proc.* 1719, 2016, pp. 030043-1-030043-4.
- [13] Gong J., Stewart M. L., Zelenyuk A., Strzelec A., Viswanathan S., Rothamer D. A., Foster D. E., and Rutland C. J., Importance of filter's microstructure in dynamic filtration modeling of gasoline particulate filters (GPFs): Inhomogeneous porosity and pore size distribution, *Chem. Eng. J.*, Vol. 338, 2018, pp. 15–26.
- [14] Tien C. and Ramarao B. V., Can filter cake porosity be estimated based on the Kozeny-Carman equation?, *Powder Technol.*, Vol. 237, 2013, pp. 233–240.
- [15] Rapagnà S., Gallucci K., and Foscolo P. U., Olivine, dolomite and ceramic filters in one vessel to produce clean gas from biomass, *Waste Manag.*, Vol. 71, 2018, pp. 792–800.
- [16] Gervais P., Bémer D., Bourrous S., and Ricciardi L., Airflow and particle transport simulations for predicting permeability and aerosol filtration efficiency in fibrous media, *Chem. Eng. Sci.*, Vol. 165, 2017, pp. 154–164.

POLYETHYLENETEREPHTHALATE-BASED ACTIVATED CARBON PRODUCTION: PRELIMINARY STUDY ON KOH ACTIVATION WITH MICROWAVE ASSIST

Sirasit Meesiri¹, Nattawut Seayang¹, Weeraphong Homnan¹, Navadol Laosiripojana², and Anusorn Boonpoke¹

¹School of Energy and Environment, University of Phayao, Thailand

²The Joint Graduate School of Energy and Environment,
King Mongkut's University of Technology Thonburi, Thailand

ABSTRACT

Since the beginning of the plastic age, drinking bottle waste has been increasing worldwide. Petroleum plastic waste is composed mainly of Polyethyleneterephthalate (PET), which is durable and can remain in the environment for a long period, thereby causing significant harm to humans, flora, and fauna. Waste recycling is one of the promising mitigation strategies being used to reduce the amount of final disposal. This research, a preliminary investigation of activated carbon production conditions from PET bottle waste, was carried out using fractional factorial design (FFD) with 95% confidence level. Starter material PET waste was obtained from a local recycling factory. Crusted and sieved PET was carbonized at 700 °C for 1 h., then impregnated with potassium hydroxide (KOH) and heated in a microwave. The production factors included char:KOH ratio (1 to 3 by weight), microwave power (540 to 900 watt), and microwave heating time (10 to 30 min). PET-based activated carbon (PET-AC) showed high iodine adsorption capacity ranging from 759.38–1,125.34 mg/g. It was found that all production factors were significant contributors to the characteristics of PET-AC. The highest iodine adsorption capacity was found at the condition of 3 by weight, 900 watt, and 30 min for ratio, microwave power, and heating time, respectively. This research confirmed that PET bottle waste could be converted to a highly valuable nanoporous adsorbent. However, the optimum production conditions for PET-AC will be carried out using a more detailed describable design of experiment (DOE).

Keywords: Activated carbon, Polyethyleneterephthalate, Design of experiment, Microwave

INTRODUCTION

Activated carbon (AC) is a black material with high surface area and high porosity. It have been widely used in various applications such as separation/purification of gas and liquids, removal of color and toxic substances in water [1-4]. The activated carbon could be made from various raw materials that contain low ash content, high fixed carbon, and low cost [5], such as coal [6], coconut and palm shell [7], wood [8], agricultural residual [9], pipe (PVC) [10], and PET bottle waste [11, 12]. PET is one of the most abundant municipal, industrial, and ocean wastes. It takes approximately 180 years to degrade. To lessen the problem of PET waste, it could be used as the starter material for activated carbon production due to its low organic content and a high percent of carbon yield post the carbonization process [13].

Activated carbon preparation can be made by two different methods: physical activation using CO₂ and steam for increased surface area and porosity, and chemical activation by chemical agents such as KOH [14], ZnCl₂ [15], HNO₃, and NaOH [16, 17]. Typically, the surface area in chemical activation is higher than in physical activation. Physical activation

using CO₂ and steam provided a surface area of 1,000 m²/g [11, 18, 19] while chemical activation gave 1,000–3,200 m²/g [6, 14, 16]. Convection furnace has been used as activation reactor at high temperature in the activation process with a long time period and high energy consumption, with the resulting non-uniform porosity and surface of activated carbon [4, 20]. Recently, microwave irradiation has been performed because it has a shorter activation time and reduces the non-uniform problem. The microwave heating is different from convection or conduction heating; it heating within the molecular level by dipole rotation and ionic conduction [21, 22]. Microwave heating consumes less energy than electrical furnace heating [23].

This research aimed to investigate the optimum production condition of PET-based activated carbon using chemical activation and microwave heating.

METHODOLOGY

PET-char Preparation

The PET bottle waste was washed and crushed to 1–3 mm. and dried at 80°C for 24 h. PET was converted to char to remove volatile matter and

increase carbon content before activation. Twenty grams of sieved PET was carbonized at 700°C with a 10°C/min heating rate under nitrogen atmospheres for 1 h., and then it was cooled at room temperature. The remaining black solid material was called char.

PET-AC Preparation

The mixture of char and KOH at designed ratios (1:1 and 1:3 by wt.) were placed in a quartz tube container with 32 mm diameter and heated in a microwave oven (Samsung model ME711K) under a nitrogen flow rate of 200 ml/min at given power (540 and 900 watt) and time (10 and 30 min). Then, the activated char was rinsed with 10% hydrochloric acid and washed with hot distilled water until the pH reached neutral. The solid adsorbent was dried at 105°C overnight. The resulting activated char was then called PET-based activated carbon (PET-AC).

PET-AC Characterization

Iodine number was determined using Standard Detection Method (ASTM Designation: D4607-86). The surface area, pore volume and pore size distribution of PET-AC were analyzed by using N₂ adsorption/desorption isotherms at 77 K (Micro Active for ASAP 2460, Norcross, USA). The surface area was calculated with the Brunauer Emmett Teller (BET) theory. Pore volume and pore size distribution were calculated by non-negative regularization. The surface morphology of PET-AC was taken by scanning electron microscopy (SU8030, Hitachi, Tokyo, Japan). The carbon, hydrogen, nitrogen, and sulfur contents were determined by elemental analyzer (LECO CHN628 Series Sulfur, USA) and approximate analysis was used to determine the moisture. Volatile organic carbon, fixed carbon, and ash was carried out according to the ASTM D 7582-10.

Experimental Design

This is the design of the experiment using fractional factorial design (FFD) to determine the optimum conditions for the preparation of PET-AC. The investigation factors char:KOH ratio (by wt.), microwave power (watt), and microwave heating time (min) were selected in the model. The FFD was done for three factors, two levels, and three replicates, with a total of 12 experiments.

RESULTS AND DISCUSSION

PET Activated Carbon Characteristics

The N₂ adsorption isotherms of the produced PET-AC indicated type IV with hysteresis loop (Fig. 1) based on the classification isotherm of IUPAC classification [24, 25]. It was indicated that PET-AC was composed mainly of mesoporous materials [11, 24, 25].

The pore size distribution of PET-AC was shown in Fig. 2. The number of pores in microporous and mesoporous rang with an average pore size of 2.03 nm. The BET surface area for the PET-AC was 1,345 m²/g with a total pore volume of 0.68 cm³/g. The obtained PET-AC had a relatively high surface area compared to previous reports, as shown in Table 1.

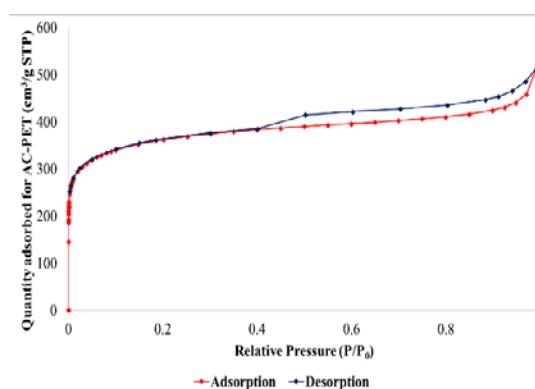


Fig. 1 N₂ adsorption/desorption isotherm of PET-AC obtained from the optimum production condition

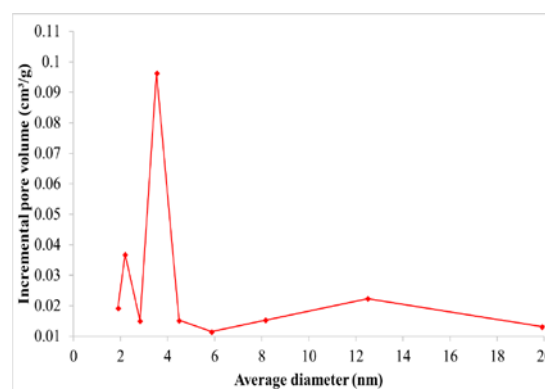


Fig. 2 Pore size distributions of PET-AC

Table 1 Comparison of the pore structure of activated carbon from different method

Raw material	Activating agent	Heating method	S _{BET} (m ² /g)	V _T (cm ³ /g)	Ref.
PET	KOH	Microwave	1,345	0.68	This work
PET	CO ₂	furnace	1,117	0.44	[18]
PET	CO ₂	furnace	790	0.43	[11]
PET	CO ₂	furnace	1,110	0.39	[26]
PET	Steam	furnace	1,170	0.63	[19]

Scanning Electron Microscopy (SEM)

The SEM morphologies of the PET-char and PET-AC are showed in Fig. 4. From the SEM images, it was observed that PET-AC exhibits a higher pores distribution than PET-char after being carbonized by chemical activation and microwave heating process.

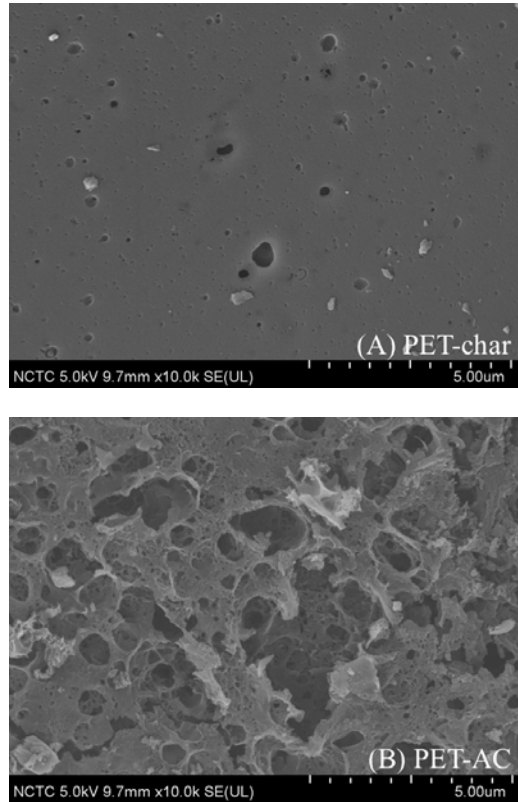


Fig. 4 SEM images of PET-char and PET-AC

Elemental Analysis

The elemental analyses of PET-char and PET-AC are showed in Table 2. It was found that the PET-AC shows a higher carbon content than the PET-char due to the elimination of some oxygen from the carbon surface [27]. If we compare the surface areas and total

Table 2 Elemental analyses of PET-char and PET-AC

Sample	Ultimate analysis (%) ¹					S_{BET} (m ² /g)	V_T (cm ³ /g)	Ref.
	C	H	O	N	S			
PET-Char	55.76	1.43	42.55	0.26	-	-	-	This work
PET-AC	80.08	1.45	17.94	0.52	-	1,345	0.680	This work
PET-50S ²	96.49	0.42	2.97	0.08	-	1,524	0.607	[18]
PET-50C ³	97.31	0.42	2.21	0.02	-	1,850	0.743	[18]

¹dry basis

²PET-based activated carbon steam activation

³PET-based activated carbon CO₂ activation

pore volumes of the high and low carbon content activated carbon, it can be seen that the activated carbon with high carbon content has surface area and pore volume higher than activated carbon with low carbon content.

Optimum PET-AC Production Conditions

The predicted optimal values for the independent factor were as follows: 3 by weight, 900 watt, and 30 min for ratio, microwave power, and heating time, respectively. This work, the preparation conditions of PET-AC using FFD are generated by Design Expert software. The various conditions and levels are given in Table 3. The analysis of variance (ANOVA) of iodine adsorption capacity are shown in Table 4. It was indicated that all observed factors, A (char:KOH ratio), B (microwave power), and C (microwave heating time) are significant (p-value less than 0.05). A regression equation is developed by FFD for iodine adsorption are shown in Eq. (1).

$$\text{Iodine adsorption} = +888.06 + 52.66A + 105.41B + 71.67C \quad (1)$$

Table 3 Factors and levels

Factors	Code	Level	
		-1	+1
Char:KOH ratio	A	1	3
Microwave power (watt)	B	540	900
Microwave heating time (min)	C	10	30

The suitability of the model equation was evaluated by 0.9918 and 0.9866 of adjusted R² and predicted R², respectively. The fact that the adjusted R² and the predicted R² are high indicates that there is a good equation in this model between the experiment data and the model prediction [5, 9, 22, 28]

Table 4 Analysis of variance (ANOVA) for fractional factorial design

Source	Sum of squares	Df	Mean square	F-value	P-value
Model	2.282E+05	3	76082.71	445.33	< 0.0001
A	33271.64	1	33271.64	194.74	< 0.0001
B	1.333E+05	1	1.333E+05	780.42	< 0.0001
C	61643.37	1	61643.37	360.81	< 0.0001
Pure error	1366.78	8	170.85		
Cor total	2.296E+05	11			

The predicted versus actual plots for iodine adsorption capacity are shown in Fig. 5. The actual iodine adsorption capacity was the real experimental data while the predicted iodine adsorption capacity represented adsorption capacity by using optimization (Eq. (1)). It was shown that the predicted values agreed well with the actual indicating high model ability [22, 29].

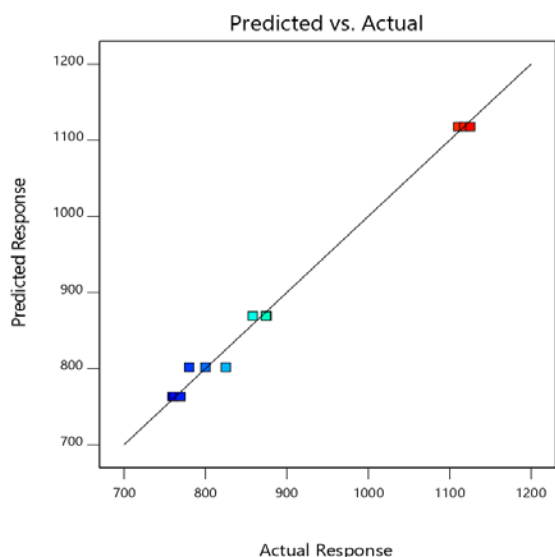


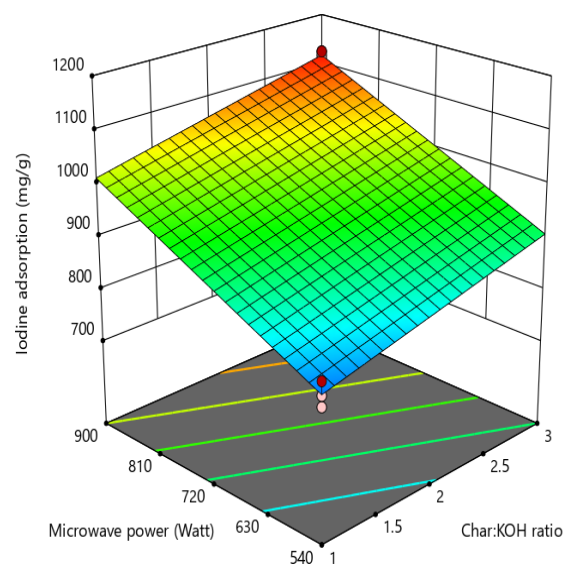
Fig. 5 Plot of actual response versus predicted response for iodine adsorption capacity

The response surface of combined effect of overall factors in this work (char:KOH ratio, microwave power and microwave heating time) are shown in Fig. 6. The iodine adsorption capacity of PET-AC increases with the increase in all factors due to the improvement in the porosity of the activated carbon.

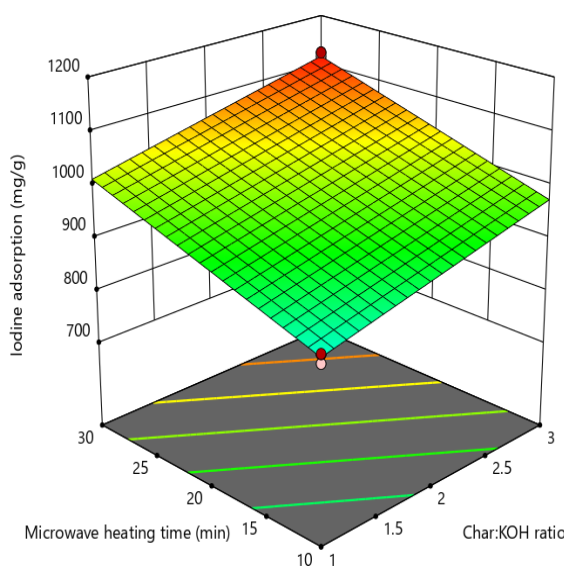
CONCLUSION

The PET-based activated carbon was successfully produced by KOH activation heating by microwave radiation. The optimum condition for the preparation of PET-based activated carbon were 3 by weight, 900

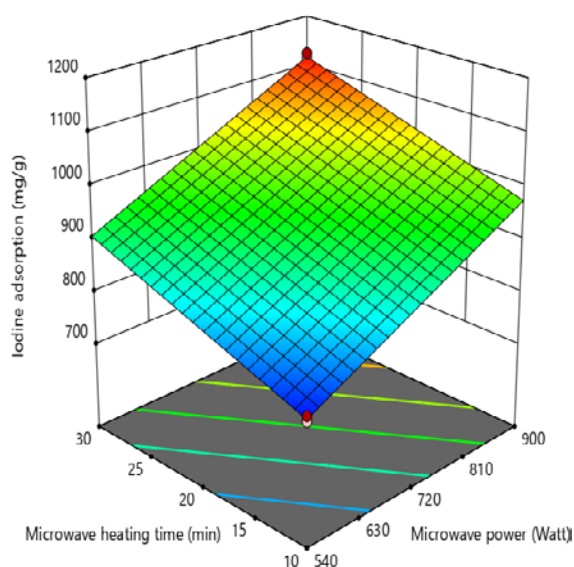
watt, and 30 min for ratio, microwave power, and heating time, respectively. The highest iodine adsorption capacity was 1,117.8 mg/g. The BET surface area for PET-AC was 1,345 m²/g.



(A) Microwave power versus char:KOH ratio



(B) Microwave heating time versus char:KOH



(C) Microwave heating time versus microwave power

Fig. 6 3D response surface graph for Iodine adsorption capacity.

Acknowledgements

This study was financially supported by the National Research Council of Thailand (NRCT), University of Phayao (RD60054) and the Thailand Graduate Institute of Science and Technology (TGIST: SCA-CO-2560-4588-TH).

REFERENCES

- [1] Xu, J., et al., Preparation and characterization of activated carbon from reedy grass leaves by chemical activation with H_3PO_4 . Vol. 320. 2014. 674-680.
- [2] Wigmans, T., Industrial aspects of production and use of activated carbons. Carbon, 1989. 27(1): p. 13-22.
- [3] Lu, P.-J., et al., Chemical regeneration of activated carbon used for dye adsorption. Journal of the Taiwan Institute of Chemical Engineers, 2011. 42(2): p. 305-311.
- [4] Ji, Y., et al., Preparation of activated carbons by microwave heating KOH activation. Applied Surface Science, 2007. 254(2): p. 506-512.
- [5] Gottipati, R. and S. Mishra, Process optimization of adsorption of Cr(VI) on activated carbons prepared from plant precursors by a two-level full factorial design. Chemical Engineering Journal, 2010. 160(1): p. 99-107.
- [6] Yang, S., H. Hu, and G. Chen, Preparation of carbon adsorbents with high surface area and a model for calculating surface area. Carbon, 2002. 40(3): p. 277-284.
- [7] Su, W., L. Zhou, and Y. Zhou, Preparation of Microporous Activated Carbon from Raw Coconut Shell by Two-step Procedure1 Supported by the National Natural Science Foundation of China (No.20336020). Chinese Journal of Chemical Engineering, 2006. 14(2): p. 266-269.
- [8] Wang, T., S. Tan, and C. Liang, Preparation and characterization of activated carbon from wood via microwave-induced $ZnCl_2$ activation. Carbon, 2009. 47(7): p. 1880-1883.
- [9] Xin-hui, D., et al., Regeneration of microwave assisted spent activated carbon: Process optimization, adsorption isotherms and kinetics. Chemical Engineering and Processing: Process Intensification, 2012. 53: p. 53-62.
- [10] Qiao, W.M., et al., Preparation of activated carbon fibers from polyvinyl chloride. Carbon, 2004. 42(7): p. 1327-1331.
- [11] Esfandiari, A., T. Kaghazchi, and M. Soleimani, Preparation and evaluation of activated carbons obtained by physical activation of polyethyleneterephthalate (PET) wastes. Journal of the Taiwan Institute of Chemical Engineers, 2012. 43(4): p. 631-637.
- [12] Mendoza-Carrasco, R., et al., Preparation of high-quality activated carbon from polyethyleneterephthalate (PET) bottle waste. Its use in the removal of pollutants in aqueous solution. Journal of Environmental Management, 2016. 181: p. 522-535.
- [13] László, K., Adsorption from aqueous phenol and aniline solutions on activated carbons with different surface chemistry. Colloids and Surfaces A: Physicochemical and Engineering Aspects, 2005. 265(1): p. 32-39.
- [14] Otowa, T., Y. Nojima, and T. Miyazaki, Development of KOH activated high surface area carbon and its application to drinking water purification. Carbon, 1997. 35(9): p. 1315-1319.
- [15] Xiao, X., et al., Preparation of activated carbon from Xinjiang region coal by microwave activation and its application in naphthalene, phenanthrene, and pyrene adsorption. Journal of the Taiwan Institute of Chemical Engineers, 2015. 53: p. 160-167.
- [16] Shim, J.-W., S.-J. Park, and S.-K. Ryu, Effect of modification with HNO_3 and NaOH on metal adsorption by pitch-based activated carbon fibers. Carbon, 2001. 39(11): p. 1635-1642.
- [17] Wu, F.-C. and R.-L. Tseng, High adsorption capacity NaOH-activated carbon for dye removal from aqueous solution. Journal of Hazardous Materials, 2008. 152(3): p. 1256-1267.
- [18] Lorenc-Grabowska, E., M.A. Diez, and G. Gryglewicz, Influence of pore size distribution on the adsorption of phenol on PET-based activated carbons. Journal of Colloid and Interface Science, 2016. 469: p. 205-212.

- [19] László, K. and A. Szűcs, Surface characterization of polyethyleneterephthalate (PET) based activated carbon and the effect of pH on its adsorption capacity from aqueous phenol and 2,3,4-trichlorophenol solutions. *Carbon*, 2001. 39(13): p. 1945-1953.
- [20] Zhong, Z.-Y., et al., Preparation of peanut hull-based activated carbon by microwave-induced phosphoric acid activation and its application in Remazol Brilliant Blue R adsorption. *Industrial Crops and Products*, 2012. 37(1): p. 178-185.
- [21] Liu, Q.-S., et al., Modification of bamboo-based activated carbon using microwave radiation and its effects on the adsorption of methylene blue. *Applied Surface Science*, 2010. 256(10): p. 3309-3315.
- [22] Xin-hui, D., et al., Preparation of activated carbon from *Jatropha* hull with microwave heating: Optimization using response surface methodology. *Fuel Processing Technology*, 2011. 92(3): p. 394-400.
- [23] Yuen, F.K. and B.H. Hameed, Recent developments in the preparation and regeneration of activated carbons by microwaves. *Advances in Colloid and Interface Science*, 2009. 149(1): p. 19-27.
- [24] Bansal, R.C. and M. Goyal, *Activated carbon adsorption*. 2005: CRC press.
- [25] Sing, K.S.W., Reporting physisorption data for gas/solid systems with special reference to the determination of surface area and porosity (Recommendations 1984), in *Pure and Applied Chemistry*. 1985. p. 603.
- [26] Bratek, W., et al., Characteristics of activated carbon prepared from waste PET by carbon dioxide activation. *Journal of Analytical and Applied Pyrolysis*, 2013. 100: p. 192-198.
- [27] Liu, Q.-S., et al., Preparation and characterization of activated carbon from bamboo by microwave-induced phosphoric acid activation. *Industrial Crops and Products*, 2010. 31(2): p. 233-238.
- [28] Hoseinzadeh Hesas, R., et al., Preparation of granular activated carbon from oil palm shell by microwave-induced chemical activation: Optimisation using surface response methodology. *Chemical Engineering Research and Design*, 2013. 91(12): p. 2447-2456.
- [29] Danish, M., et al., Application of optimized large surface areadate stone (*Phoenix dactylifera*) activated carbon for rhodamin B removal from aqueous solution: Box-Behnken design approach. *Ecotoxicology and Environmental Safety*, 2017. 139: p. 280-290.

EFFECT OF SUSPENDING TRAFFIC ON A HIGHWAY IN A MOUNTAINOUS REGION IN CENTRAL JAPAN ON THE SUCCESSION OF SLOPE VEGETATION

Teruo Arase¹, Akane Nishio¹, Tetsuo Okano¹ and Taizo Uchida²

¹Faculty of Agriculture, Shinshu University, Japan;

² Faculty of Engineering, Kyushu Sangyo University, Japan

ABSTRACT

Gonbei Highway, a winding road in a mountainous region in central Japan, was damaged by typhoons in the autumn of 2004, and a 9-km stretch of the highway has remained closed (without being restored). We established 11 survey sites to examine slope vegetation along Gonbei Highway in the summer of 2004 (just before the area was damaged by typhoons), and we conducted surveys again in 2016 (12 years after the damage), including at 5 survey sites along the closed section of the road. At each survey site, a quadrat (2 m × 5 m) was established on the mountain side and the valley side of the road. The deterioration of the road surface was also observed. Here, we examine the effects of suspending traffic on roadside vegetation and road surface deterioration. Our results showed that succession to arboreal vegetation was not observed at the roadside sites along the closed section of the road: vegetation coverage increased significantly along the closed section with increasing coverage of shrubs (mainly bamboo grass). In contrast, tree seedlings increased in the passable sections. Thus, the suspension of traffic and the subsequent long-term absence of roadside vegetation management allowed bamboo grass to increase, and the community of bamboo grass prevented invasion and growth of tree seedlings. Obvious deterioration of the road surface was not observed, excepting sparse cracks and weed invasion. Consequently, the dominance of bamboo grass may be one of the criteria by which to judge the necessity of vegetation management along roads closed to traffic.

Keywords: Roadside Slope, Road surface, Vegetational succession, Suspension of traffic, Gonbei Highway

INTRODUCTION

Recently, fewer winding roads with tunnels or elevated bridges have been newly built as highway construction has focused on roads with higher traffic volume and improved safety. While the necessity of maintaining old highways is reduced in this strategy, abandoning these highways may lead to disasters such as landslides: since roads placed on hillsides can disrupt the natural flows of surface water and ground water unless they are properly engineered [1], lack of maintenance will spoil the road and roadside slopes by uncontrolled water and sediment flows.

Plant growth prevents erosion on roadside slopes [2]: leaves mitigate the direct impact of raindrops on the soil surface, roots retain soil, and transpiration reduces excessive soil water in the ground. To maintain these functions, it is necessary to monitor and manage the roadside slope vegetation. Inadequate management leads to undesirable vegetation on roadside slopes, narrowed fields of view, and even damage to the road by fallen trees or landslides [3]. There are few reports on the vegetation succession along old or closed roads to date. Since the lifespan of asphalted road is usually planned to be around 10 years in Japan [4], vegetation succession on roadside slopes should also

be surveyed 10 to 12 years after traffic is suspended.

Gonbei Highway, an asphalt mountain road in Nagano Prefecture in central Japan, has fulfilled an important role in joining the two regions (Kami-ina and Kiso regions) on either side of the Kiso Mountains. This highway is a winding mountain road that crosses the Gonbei Pass at an elevation of 1550 m and was designated as a national highway (Route 361). In the autumn of 2004, rainfall and winds from several typhoons passing over the area (Fig. 1) damaged the highway, and a 9 km section located on Mt. Kyogatake was closed [6]. In 2006, a new and less winding highway (bypass of Route 361) traversing the newly constructed ‘Gonbei tunnel’ was opened to traffic [6]. This road construction was undertaken in order to improve access to medical services for residents in the Kiso region, where there are no general hospitals. Subsequently, Old Route 361 was closed without being restored following the disaster in 2004 and the designation as a national highway was removed (Fig. 2). Despite the change in designation, this road remains important: the area along this road is a Japanese larch (*Larix kaempferi*) forest, and some radio facilities are located there. Further, if traffic on the new Route 361 is suspended, the Old Gonbei Highway will be the only road joining these two

regions. Due to infrequent access, it is difficult to monitor and maintain this road and the surrounding roadside slopes.

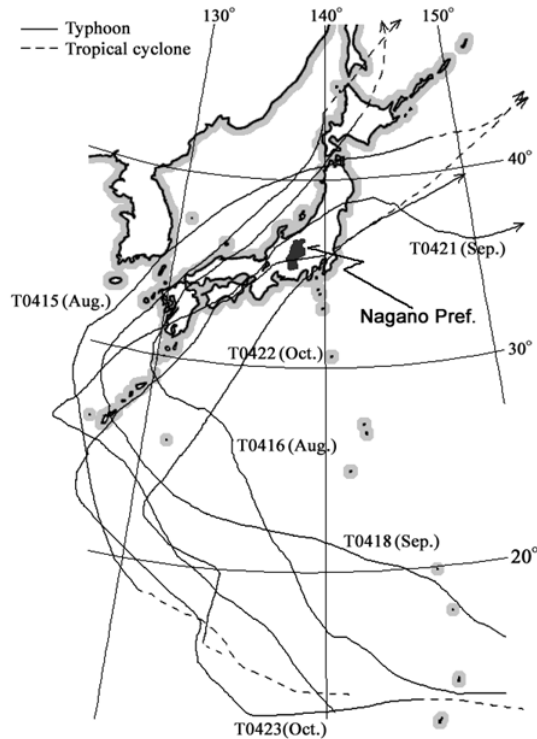


Fig. 1 Paths of typhoons that produced heavy rains and strong winds in the research area in 2004. Figure is based on original data and graphs reported in [5].

In the present study, we surveyed roadside slope vegetation in the summer of 2004 (just before the area was damaged by typhoons) and again in 2016 (12 years after the damage) to examine the effect of suspending traffic on roadside vegetation. The original survey was designed to evaluate wild herbaceous plants for utilization in vegetation technology [7], but the sites were damaged by the passing typhoons soon after the vegetation survey in 2004, and the subsequent follow-up study described here was planned. Based on analyses of the changes in vegetation based on coverage percentage and species composition, we discussed how and when to manage roadside slope vegetation along closed roads.

METHODS

Vegetation Survey

The research area is the roadside area along Old Gonbei Highway in Nagano Prefecture, central Japan. This winding highway joined Ina City (Kaminina region) and Shiojiri City (Kiso region), but a 9 km length of this highway has been closed since the autumn of 2004.

In July 2004, eleven sites (labeled A to K) were established at approximately regular intervals along the road for a vegetation survey. Each site is comprised of two plots of roadside slopes (2 m × 5 m per plot, mountain side and valley side). The section of road closed in autumn 2004 included 5 sites (labeled E to I) out of the 11 sites. The elevation and slope direction at each site are described in Table 1.

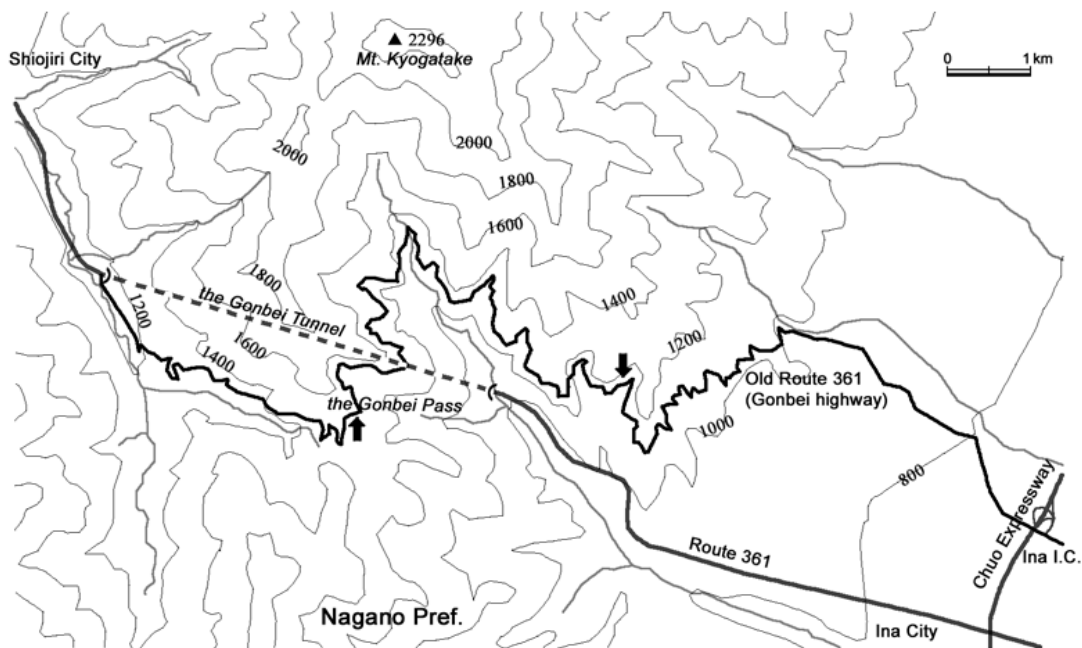


Fig. 2 Old Route 361 (Gonbei Highway) and newly constructed Route 361. Arrows indicate the placement of gates for closing the road to traffic.

Table 1 Vegetation survey sites

No.	Elevation (m)	Slope direction	Condition	Location
A	955	SW	Passable	Ina City
B	1150	SW		↑
C	1110	SW		
D	1180	E		
E	1260	SE	Closed	
F	1330	S		
G	1419	S		
H	1530	E		
I	1550	S	Passable	↓
J	1390	SW		Shiojiri
K	1235	S		City

In 2004 (just before the area was damaged by typhoons) and in 2016 (after the damage), coverage of each plant species in each plot was measured in each of the tree, shrub and herb layers. Plant coverage was ranked using the classes of the Braun-Blanquet scale as follows:

- +, sparse vegetation with coverage by area of less than 1% over the total plot area;
- 1, vegetation coverage between 1% and 10% of total plot area;
- 2, vegetation coverage between 10% and 25% of total plot area;
- 3, vegetation coverage between 25% and 50% of total plot area;
- 4, vegetation coverage between 50% and 75% of total plot area;
- 5, vegetation coverage of more than 75% of total plot area.

Observation of Road Surface

To conduct the 2016 vegetation survey, we accessed sites in the closed section of the road by walking in from the gate closing the road. Consequently, we explored the entire closed section of Gonbei Highway while conducting the vegetation survey.

Since there was no current information regarding the condition of the road in the closed section, we observed the road surface for parameters including the presence or absence of cracks, dips, accumulation of fallen branches or leaves, and invasion of weeds to gather preliminary information in the investigation of the deterioration of the road surface in the survey area.

Data Analysis

To compare the total vegetation coverage percentage, each coverage class was reported as a single medium percentage (e.g., class 5, which had coverage percentages ranging between 75% and

100%, was reported as being 87.5%). The change in coverage percentage (Δ = coverage percentage in 2016 - coverage percentage in 2014) was calculated for each slope and was considered for combinations of two factors (section: passable or closed, slope: mountain side or valley side). Significant differences among coverage percentages were detected by analyses of variance and Tukey's HSD test.

Because of the large dominance in the herb layer in 2016, we additionally noted of the dormancy form [8] for each plant species. Each plant species was categorized into a corresponding dormancy form, and the total coverage percentage by form was calculated. The composition differences of dormancy forms were analyzed by the analysis of variance (F-test). Dormancy forms were categorized in the present study as follows:

A, annual or biennial herb;

P, perennial herb with dormant bud close to the ground;

N, shrub with dormant bud 0.3 to 2 m above the ground (includes bamboo grass);

M, tree with dormant bud 2 to 8 m above the ground; and

MM, large tree with dormant bud over 8 m above the ground.

In this analysis, if a small seedling of an MM species was detected in the herb layer, the coverage data of the species was categorized as 'MM'. Therefore, the composition of the dormancy form can be used to evaluate the potential progression of vegetation succession.

RESULTS

Roadside Slope Vegetation

Table 2 shows the changes in vegetation coverage percentage (Δ) in each layer after 12 years. In the tree layer, the effect of section (passable road or closed road), slope direction, and their interaction were not significant, and the change trend was not apparent (ranged from -15% to +20%). In the shrub layer, the effect of section was significant (F-test, $p < 0.05$). The coverage percentage increased by around +50% in the passable section, and it increased by less than +20% in the closed section. In the herb layer, the effect of section was also significant (F-test, $p < 0.02$); coverage percentage decreased in the passable section, with a notable decrease of around -40% on the valley side, whereas it increased by around +30% in the closed section.

Fig. 3 shows the change of the composition of dormancy forms of plants in the herb layer. The effects of year (2004 or 2016), section (passable or closed) and slope (mountain side or valley side) were significant (F-test, $p < 0.0001$, 0.02, 0.005, respectively). The effect of interaction of year \times section was also significant (F-test, $p < 0.005$),

Table 2 Change in vegetation coverage percentage in each layer

Section	Slope	year	Layer				
			Tree		Shrub		Herb
Passable (n=6)	Mountain side	2004	31.8		8.8		52.3
		2016	10.4		54.9		48.2
		Δ	-21.3	a	46.2	ab	-4.2
	Valley side	2004	38.1		19.1		54.3
		2016	23.4		70.3		16.6
		Δ	-14.7	a	51.2	a	-37.8
Closed (n=5)	Mountain Side	2004	12.5		23.6		52.9
		2016	7.5		32.5		81.9
		Δ	-5.0	a	8.9	c	29.0
	Valley side	2004	23.6		16.7		29.3
		2016	37.5		35.8		55.4
		Δ	13.9	a	19.1	bc	26.1

Each value denotes the average percentage obtained from plots.

Different letters in columns denote significantly different means as determined by Tukey's HSD test ($p < 0.05$).

indicating that the change in composition of dormancy forms after 12 years differed between the passable and closed sections.

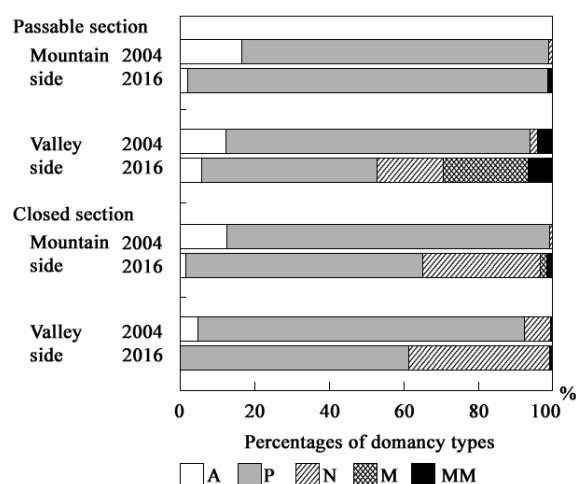


Fig. 3 Changes of composition of dormancy forms of plants as the total coverage percentage in the herb layer

In 2004, each slope was primarily dominated by P (perennial herbs) and around 5% to 15% of A (annual or biennial herbs). At 12 years later, A (annual or biennial herbs) decreased on each slope, and M or MM (tree seedlings) markedly increased in the passable section. In contrast, the dominance of N (shrub) became obvious in the closed section. The following representative plant species were categorized into each dormancy form in the survey plots:

A, *Amphicarpaea bracteata* ssp. *edgeworthii* (Fabaceae), *Oplismenus undulatifolius* (Poaceae);
P, *Artemisia indica* var. *maximowiczii* (Asteraceae), *Miscanthus sinensis* (Poaceae);

N, *Sasa* spp. (Poaceae), *Rubus* spp. (Rosaceae);
M, *Lindera praecox* (Lauraceae), *Deutzia crenata* (Hydrangeaceae); and

MM, *Quercus* spp. (Fagaceae), *Alnus hirsuta* (Betulaceae).

Of the N (shrub) in the herb layer, bamboo grass (*Sasa* spp.: *S. borealis*, *S. sikokiana* and *S. senanensis*) comprised the majority of the species. Although the coverage percentage was sparse in 2004, it increased to rank 4 (50% to 75%) or 5 (75% to 100%) in 2016 in some plots in the closed section of the highway.

To examine the relationship between the shrub layer and herb layer, the correlation of coverage percentages between these layers was determined. As a result, the correlation coefficient was not significant in the passable section ($r = 0.223$; F-test, ns), but it was significant ($r = -0.542$; F-test, $p < 0.02$) in the closed section.

Road Surface

In the section of closed road, obvious dips or differences in level were not observed. However, mash-like or linear cracks were sparsely observed (Fig. 4). The former is caused by deterioration of asphalt and the latter seems to occur where paving different construction was conducted.

Accumulation of fallen branches and leaves was especially observed on the shoulder of the road, and fine fallen leaves (e.g., needle-like leaves of Japanese larch) accumulated on linear cracks (Fig. 4).

Weeds growing in the road surface were scattered and were concentrated where fine leaves accumulated in cracks in the road. The number of weed species was as small as 0 to 5 per site, and no tree seedlings were observed. Representative species were *Plantago asiatica* (Plantaginaceae), *Erigeron*

annuus (Asteraceae) and *Juncus tenuis* (Juncaceae). Most of the species growing in the road surface were not present in the adjacent roadside slope vegetation: in the road surface, on average only 0.6 (0 to 2) species per site were observed out of 13.4 (6 to 20) species growing on the adjacent roadside slope vegetation.



Fig. 4 Deterioration of road surface in the closed section of Gonbei Highway
Cracks, accumulated fallen leaves, and scattered invading weeds can be observed. Length of the red and white striped pole = 2 m.

DISCUSSION

In the closed section of Gonbei Highway, we found that tree and shrub layer coverage percentages did not increase markedly (Table 2), despite the long-term suspension of traffic creating a disturbance-free environment. In other words, the composition of tree seedlings (M and MM) occupying the herb layer was larger in the passable section than in closed section (Fig. 3), suggesting the advanced progression of vegetation succession occurred in the passable section. These unexpected results are due to the presence or absence of N (especially bamboo grass) in the herb layer, since there is a negative correlation between the coverage percentages of shrub layer and herb layer in the closed section.

Colonization of bamboo grass has been reported to suppress the establishment of tree seedlings (e.g., [9] [10]). In the present study, it is considered that the disturbance due to vegetation management in the passable section prevented colonization of bamboo grass, allowing tree seedlings to grow. However, in the disturbance-free environment of the closed section, the colonization of bamboo grass was accelerated, suppressing the recruitment and growth of tree seedlings. It is generally considered that the growth of bamboo grass should be controlled in forestry practice, but it can also be useful for

preventing the growth of trees in the management of roadside slope vegetation. The colonization of a sedge (*Carex oxyandra*: Cyperaceae) has also been reported to suppress tree seedlings [9] [10] and might be preferable over bamboo grass in the management of roadside slope vegetation.

The road surface of Gonbei Highway in the closed section was not deteriorated or heavily invaded by weeds, probably due to the asphalt coverage and its location in a cool climate at high elevation. In contrast, there is a report of an unpaved working path for forestry becoming almost covered with plants, including tree seedlings, after only 3 years [11]. In that case, the road surface is not usually paved, and the rapid development of vegetation is desirable to reduce the risk of erosion [12]. Compared to unpaved working paths, the road surface of Gonbei Highway seems to be well maintained, even in the closed section after 12 years. The weeds on the road surface included a small number of species that had little relation to the species found in the slope vegetation, suggesting that unique vegetation, though in an early stage, was extending along the closed highway. This vegetation succession, even in a mountain area, shows similarities to vegetation growing in cracks in roads in urban areas [13]. The seeds of weeds might have been gradually introduced in the area by water, wind or wild animals and birds from outside the area since there has been little automobile or human traffic after the suspension.

CONCLUSION

In the present study, we surveyed Gonbei Highway, a winding road in a mountainous region in central Japan. It was damaged by typhoons in the autumn of 2004, and a 9 km stretch of the highway has remained closed. We established 11 survey sites to examine slope vegetation along Gonbei Highway in the summer of 2004 (just before the area was damaged by typhoons), and we conducted surveys again in 2016 (12 years after the damage), including at 5 survey sites along the closed section of the road. Our results were as follows:

- (1) On the roadside slopes, succession to arboreal vegetation was not observed at the sites along the closed section of the road. In herb layer, vegetation coverage increased significantly along the closed section with increasing coverage of shrub species (mainly bamboo grass). In contrast, tree seedlings increased in the passable sections.
- (2) On the road surface in the section of closed road, obvious deterioration was not observed, excepting mash-like or linear cracks. The road surface vegetation was seemed to be just in the early stage of succession: weeds growing in the road surface were scattered and were concentrated where fine leaves accumulated in cracks in the road. No tree

seedlings were observed, and most of the species growing in the road surface were not present in the adjacent roadside slope vegetation.

The suspension of traffic and the subsequent long-term absence of roadside vegetation management allowed bamboo grass to increase, and the community of bamboo grass prevented invasion and growth of tree seedlings. Bamboo grass might also be useful to prevent the invasion of weeds, especially non-native species, through the road into roadside slope vegetation. Consequently, the dominance of bamboo grass in roadside slope vegetation may be one of the criteria by which to judge the necessity of vegetation management along roads closed to traffic.

REFERENCES

- [1] Jones, J.A., Swanson, F.J., Wenple, B.C. and Snyder, K.U., Effects of Roads on hydrology, Geomorphology, and Disturbance Patches in Stream Networks, *Conservation Biology*, Vol. 14, 2000, pp. 76-85.
- [2] Togari, A., A Guide to Vegetation Construction –Fundamental Knowledge of Vegetation, The Journal of Japan Railway Civil Engineering Association, Vol. 36, Issue 10, 1998, pp.798-801. (in Japanese)
- [3] Kawanishi, Y., Ozaka, K., Kobayashi, T., Ueshima, K. and Sudou, S., The Ideal State of the Vegetation on the Expressway Slopes, and Its Management Plan, *Journal of the Japanese Society of Revegetation Technology*, Vol. 42, Issue 1, 2016, pp.208-211 (in Japanese)
- [4] Road conservation technology Center ed., Road Management Technology Handbook, Kajima Publishing Co., 2010, pp. 1-111 (In Japanese)
- [5] Japan Meteorological Agency, Various Kinds of Data and Report HP, <www.jma.go.jp/jma/menu/menureport.html>, referred in Feb. 2nd, 2017
- [6] Ina Construction Office of Nagano Prefecture, Traffic Restrictions Information HP <<http://yassy.asystem-a.org/xdoboku/inakenn/index.htm>>, referred in Feb. 2nd, 2017
- [7] Fujii, M., Studies on the Revegetation using Wild Fabaceae Species Growing on the Roadside Slopes along Gonbei Highway, Graduation Thesis of Shinshu University, 2004, pp. 1-21 (in Japanese)
- [8] Numata, M and Yoshizawa, M. eds., *Weed Flora of Japan –Illustrated by Colour (a New Publication)*, Zenkoku Noson Kyouiku Kyokai Publishing Co. Ltd., 1978, pp. 8-22.
- [9] Arase, T., Okano, T. and Shirota, T., Colonization and Morphological Changes of a Sedge Restricting Regeneration after Wind Damage in a Natural Forest, *International Journal of GEOMATE*, Vol. 12, Issue 31, 2017, pp. 100-104.
- [10] Arase, T., Okano, T. and Shirota, T., Methods of Suppressing Colonizing Sedge to Help to Establish Tree Seedlings in a Natural Forest, *International Journal of GEOMATE*, Vol. 12, Issue 32, 2017, pp. 19-24
- [11] Ogura, A., Suzuki, H., Usuda, T., Yamaguchi, T., Tanaka, Y. and Umeda, S., A Case of vegetation Recovery on a Working Path, *Bulletin of the Ishikawa Agriculture and Forestry Research Center Forestry Experimental Station*, Vol. 44, 2012, pp. 42-43. (in Japanese)
- [12] Sato, H., Effective Forest Management to Reduce Fine Sediment Production and Delivery, *The Journal of the Japanese Forest Society*, Vol. 88, Issue 1, 2006, pp. 50-59.
- [13] Uchida, T., Xue, J.H., Hayasaka, D., Arase, T., Haller, W.T. and Gettys, L.A., The Relation between Road Crack Vegetation and Plant Biodiversity in Urban landscape, *International Journal of GEOMATE*, Vol. 6, Issue 12, 2014, pp. 885-891

ISOTOPIC RATIOS AND CHEMICAL COMPOSITION OF PRECIPITATION BETWEEN FOOT OF THE BUILDING AND TOP OF THE BUILDING IN OSAKA CITY AND WAKAYAMA CITY, JAPAN

Toshiki Ueda¹ and Hiroyuki Ii²

¹Graduate School of Systems Engineering, Wakayama University, Japan

²Faculty of Systems Engineering, Wakayama University, Japan

ABSTRACT

Amount of precipitation and soluble substances may depend on altitude because raindrop evaporates and condensates during the falling process from cloud to ground and then to clarify altitude effect is important. To compare mountain areas with plain areas does not only contain altitude effect but also the distance effect from the sea or the other mountain. Therefore, in this study, comparing precipitation sampled at the top of the high building with precipitation sampled at the foot of the high building, influence of difference of altitude on isotope or soluble substances was clarified. The high altitude sampling point at the Abenoharukasu building in Osaka City is 295m tall. Another high sampling point at Systems Engineering Building in Wakayama University is 112m tall. Precipitation on the ground at both buildings was sampled. As a result of comparing these precipitations, isotope values of precipitation sampled at high altitude were lower than those sampled at low altitude for the same case and both values were the same for the other cases. The difference was thought to be caused by evaporation because stable isotope values change with evaporation and then the humidity of air before precipitation is thought to be important. Low altitude precipitation contained high Ca^{2+} and HCO_3^- and high altitude precipitation contained high Cl^- .

Keywords: altitude effect, precipitation, soluble substances, stable isotope, humidity

INTRODUCTION

It is important to clarify evaporation and reaction of raindrop until raindrop reaches the ground for estimating chemical composition and isotope values of precipitation. Stable isotopic ratios of precipitation are influenced by regional characteristics due to meteorological and spatial conditions such as the amount of precipitation, temperature and altitude. For example, Waseda, Nakai, 1983[1]; Asai, Tsujimura, Wilson Yetoh FANTONG, 2014[2] have been reported that isotope ratios at low altitudes are higher than high altitudes in the mountain. This feature is called the altitude effect, and there are two main factors that cause the altitude effect. The first factor is the difference in the amount of evaporation during precipitation falling. Precipitation arrived at low altitude point travelled longer distance relative to precipitation at high altitude point. Amount of evaporation relates to travelling distance. Then, the amount of evaporation of precipitation arrived at low altitude was high. In particular, under the low humid condition, the evaporation rate is high and then the isotope difference is large [3]. The second factor is that isotopic ratios of early precipitation often includes heavier than that of late precipitation due to the condensation process of Rayleigh during a

precipitation event[4]. However, it has not been clarified how much these factors contribute to altitude effect.

Regarding the chemical composition, it was reported that acid rain affected the decline of forest and acidification of lakes in Europe and North America from the 1960s to the 1970s, and the cause of acid rain has been investigated worldwide [5][6]. However, change of soluble substances of precipitation with altitude has not been clarified.

In this study, we assumed that the altitude effect was a phenomenon peculiar to the mountains. And precipitation was collected at high buildings where updraft was unlikely to occur and the straight distance between water sampling points was short. The purpose of this study is to clarify the relation of oxygen stable isotopic ratios or soluble substances with altitude for precipitation using the high building.

METHOD

Sampling and Analysis

Fig.1 shows survey points. Precipitation sampling in this study was performed in Tennoji-ku, Osaka City and Sakaedani, Wakayama City. Fig.2 shows the sampling points of Tennoji-ku, Osaka City. One

precipitation sampling point is near the roof of Abenoharukasu (= OH«Osaka high») whose altitude is about 306m, and another point is Tenshiba (= OL«Osaka Low») whose altitude is about 11 m. The difference in altitude and the straight distance between both points is about 295 m and about 410 m. Fig.3 shows the sampling points of Sakaedani, Wakayama City. One precipitation sampling point is rooftop of building B, Wakayama University whose altitude is about 112 m and another point is Green Planet House Parking whose altitude is about 70 m. The difference in altitude and the straight distance between both points at Wakayama is about 42 m and about 650 m.

Sampling was performed from September to December 2017 in Osaka City and from June to December 2017 in Wakayama City. The stable isotopic ratios were expressed as δ values ‰, and an isotope mass analyzer (Geo Wet System, Sercon Co.) was used for analysis. δ values ‰ represented by following equation.

$$\delta = (R_{\text{sample}} / (R_v - \text{smow}) - 1) \times 1000 \text{ ‰} \quad (1)$$

R; $^{18}\text{O}/^{16}\text{O}$, V-SMOW: Vienna-Standard Mean Ocean Water.

Measurement error of $\delta^{18}\text{O}$ was within $\pm 0.1\text{‰}$.

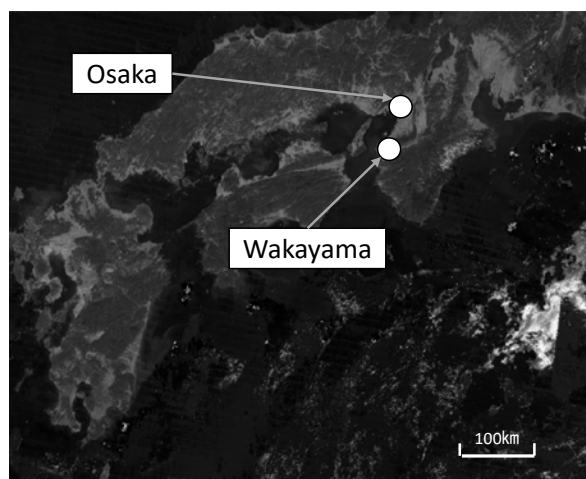


Fig.1 Survey points in this study

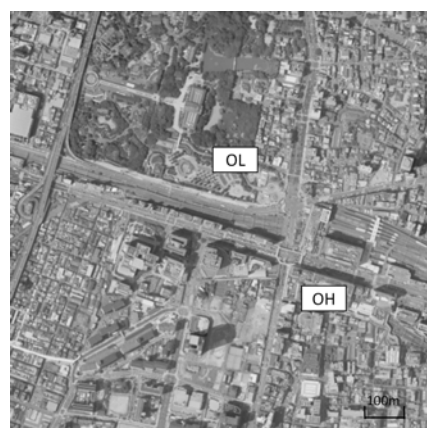


Fig.2 Sampling points of Tennoji-ku, Osaka city.

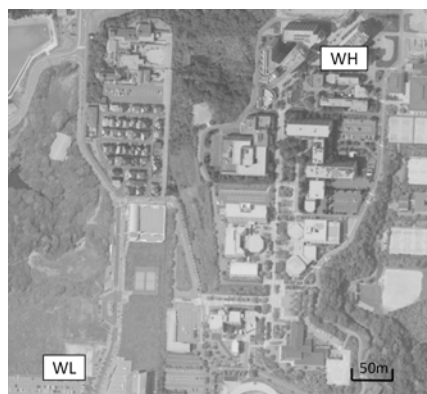


Fig.3 Sampling points of Sakaedani, Wakayama city

RESULT AND DISCUSSION

$\delta^{18}\text{O}$ value in each event

Fig.4 shows time series of $\delta^{18}\text{O}$ values of precipitation sampled at both high and low altitudes in Osaka and Wakayama Cities. From this result, in Osaka city, $\delta^{18}\text{O}$ values of OL sampling point were -3 to -14 ‰ and $\delta^{18}\text{O}$ values of OH sampling point were -3 to -13 ‰. In Wakayama City, $\delta^{18}\text{O}$ values of WL sampling point were -2 to -12 ‰ and $\delta^{18}\text{O}$ values of WH sampling point were -2 to -12 ‰. $\delta^{18}\text{O}$ values of each precipitation at all points changed with each rainfall event. In Osaka City, the $\delta^{18}\text{O}$ values at OL and OH were almost the same until October 18th and after October 24th the difference of $\delta^{18}\text{O}$ value at between OH and OL sampling points were -1.04 to -1.47 ‰.

On the other hand, in Wakayama City, the altitude difference of $\delta^{18}\text{O}$ values at both points was hardly found, and then the values of WL and WH were almost the same. When precipitation evaporation occurs, light isotope selectively evaporates rather than heavy isotope by Rayleigh process, as a result,

$\delta^{18}\text{O}$ value of precipitation at the low altitude becomes high.

The altitude effect of the oxygen isotopic ratios of precipitation is from -0.2 to -0.3 ‰ / 100 m in various places in Japan according to [7]. The oxygen isotopic ratios per altitude in Osaka City were -0.35 to -0.49 ‰ / 100 m which were in agreement with previous results. In Wakayama City, the $\delta^{18}\text{O}$ values of WL and WH were about the same, then precipitation does not evaporate during fall and isotope values keep uniform values.

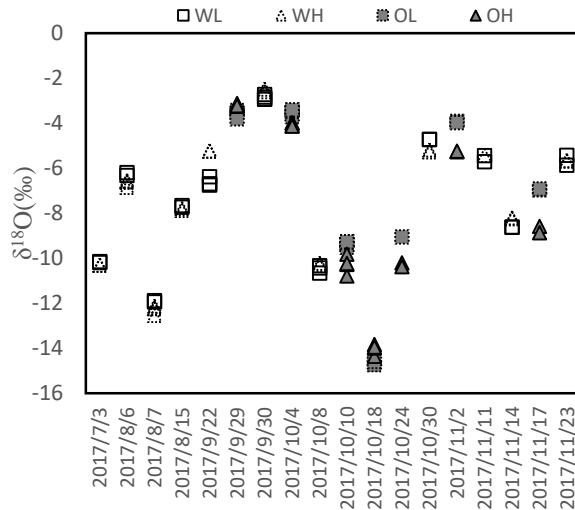


Fig.4. Time series of $\delta^{18}\text{O}$ values of precipitation sampled at both high and low altitudes in Osaka and Wakayama Cities

Characteristics of the large difference of $\delta^{18}\text{O}$ values between the foot of the building and top of the building

Fig.5 shows the relationship of the difference (OL – OH) of the $\delta^{18}\text{O}$ values between high and low sampling points and the humidity in Osaka City. The humidity values for each precipitation event in Fig.5 show the beginning of precipitation. When humidity was low, about 70 %, the difference of isotope values for precipitation between low and high sampling points was plus and altitude effect was recognized. Therefore, under low humidity condition, isotope values easily increase during precipitation falling because water is eager to evaporate.

Fig.6 shows the relationship of the difference (WL – WH) of the $\delta^{18}\text{O}$ values between high and low sampling points and the humidity in Wakayama City. In Wakayama City the difference for $\delta^{18}\text{O}$ of precipitation increased with the decrease of humidity.

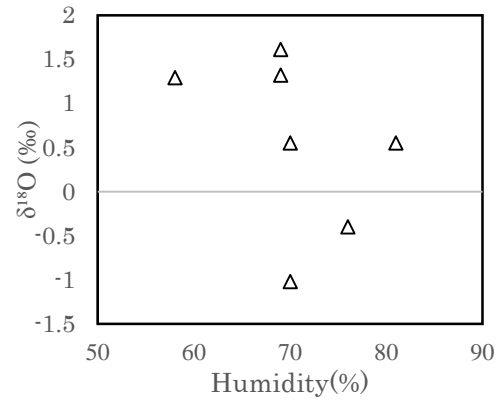


Fig.5 The relationship of the difference (OL – OH) of the $\delta^{18}\text{O}$ values at between high and low sampling points and the humidity in Osaka City

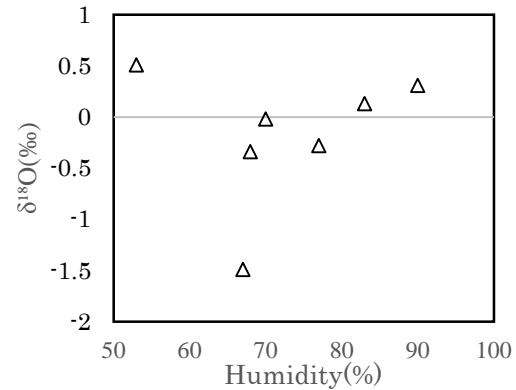


Fig.6 The relationship of the difference (WL – WH) of the $\delta^{18}\text{O}$ values at between high and low sampling points and the humidity in Wakayama City

As unsaturated air rises adiabatically, atmospheric pressure does not only decrease but also temperature, water vapor pressure, and dew point. Finally unsaturated air reaches the dew point altitude where the air is saturated with water.

$$H = 125 \times (T_0 - \tau_0) \quad (2)$$

H ; Altitude at dew point, T_0 ; Surface temperature, τ_0 ; Dew point. Surface temperature and vapor pressure are used from Japan Meteorological Agency at Osaka and Wakayama.

From a dew point altitude it is possible to estimate an altitude for bottom of cloud bottom altitude and then a dew point altitude, and indicate the distance between the cloud and the ground. Therefore, it is important to estimate changes of the dew point altitude for calculating falling distance. And then, we focused on relationship between $\delta^{18}\text{O}$ values difference and dew point altitude. Fig.7 shows the relationship of the difference (OL - OH) of the $\delta^{18}\text{O}$

values at between high and low sampling points and the dew point altitude in Osaka City. The dew point altitude increased with the difference of isotope values for precipitation at between low and high sampling points.

Fig.8 shows the relationship of the difference (WL – WH) of the $\delta^{18}\text{O}$ values at between high and low sampling points and the dew point altitude in Wakayama City. In Wakayama City the difference for $\delta^{18}\text{O}$ of precipitation increased with the increase of dew point altitude.

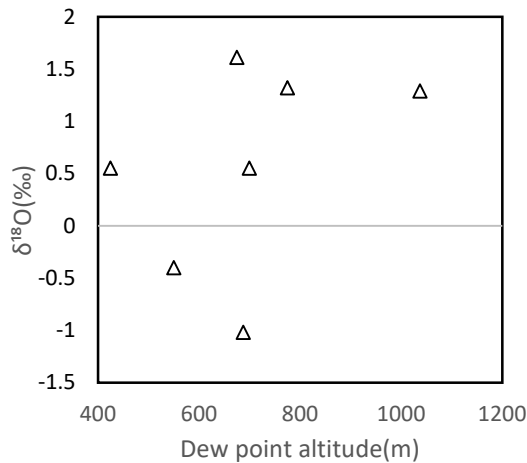


Fig.7 The relationship of the difference (OL – OH) of the $\delta^{18}\text{O}$ values at between high and low sampling points and the dew point altitude in Osaka City.

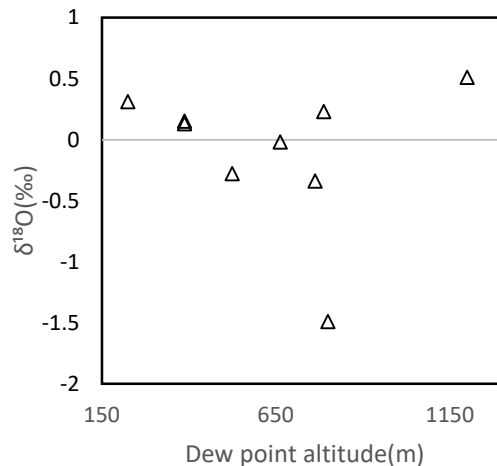


Fig.8 The relationship of the difference (WL – WH) of the $\delta^{18}\text{O}$ values at between high and low sampling points and the dew point altitude in Wakayama City.

Characteristics of chemical composition between foot of the building and top of the building

Fig.9 shows the change in the average content of chemical components for precipitation at between high and low sampling points in Osaka City. In Osaka City, Ca^{2+} and HCO_3^- concentrations at low sampling points were high, however, Cl^- and NO_3^- concentrations of precipitation at high sampling points were high.

Fig.10 shows the change in the average content of chemical components for precipitation at between high and low sampling points in Wakayama City. In Wakayama City, Ca^{2+} and HCO_3^- concentrations of precipitation at low altitude sampling points were high, however, Cl^- and SO_4^{2-} concentrations of precipitation at high altitude sampling points were high.

From these results, Cl^- concentrations at high altitude in both Osaka City and Wakayama City were high, however, Ca^{2+} and HCO_3^- concentrations of precipitation at high altitude sampling points were high.

At the low altitude sampling point, high Ca^{2+} and HCO_3^- was thought to be caused by asphalt dust contained CaCO_3 [8].

As generally Cl^- source in precipitation was sea salt, the difference between both altitudes was not high. Then, little high Cl^- concentration at high sampling points in both cities was thought to be influenced sea salt because both cities are near the sea and rising sea salt from sea surface directly is mixed precipitation.

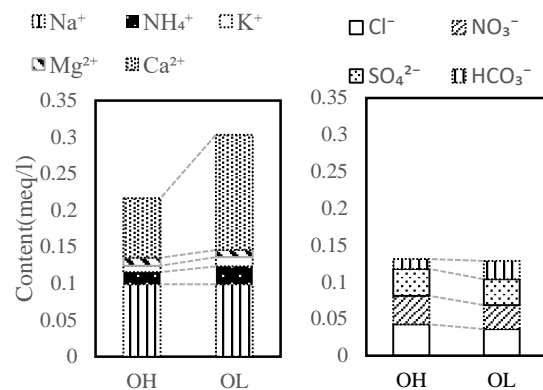


Fig.9 The change in the average content of chemical components for precipitation at between high and low sampling points in Osaka City

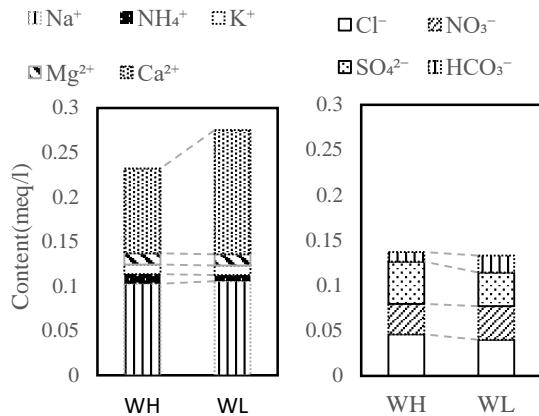


Fig.10 The change in the average content of chemical components for precipitation at between high and low sampling points in Wakayama City

Relationship between Cl^- and evaporation

During precipitation falling, when raindrop evaporates, soluble substances such as Cl^- of precipitation increase. Then, Fig.11 shows the relationship between the difference (OL-OH) of Cl^- and the difference (OL-OH) of $\delta^{18}\text{O}$ values in Osaka City. Cl^- concentration differences between low and high sampling points increased with $\delta^{18}\text{O}$ value differences (0 to 1.5‰). Then evaporation was thought to occur during precipitation falling process from top of the building to ground in Osaka City.

Fig.12 shows the relationship between the difference (WL-WH) of Cl^- and the difference (WL-WH) of $\delta^{18}\text{O}$ values in Wakayama City. Cl^- concentrations at both low and high sampling points were the about same excluding one data under various differences (-0.4 to 0.4 ‰) of $\delta^{18}\text{O}$ values between the top of building and ground in Wakayama City. In Wakayama City, the difference of $\delta^{18}\text{O}$ values between the top of the building and ground was not always plus and evaporation was not clear. Therefore Cl^- concentration was thought to be uniform at both high and low altitude points.

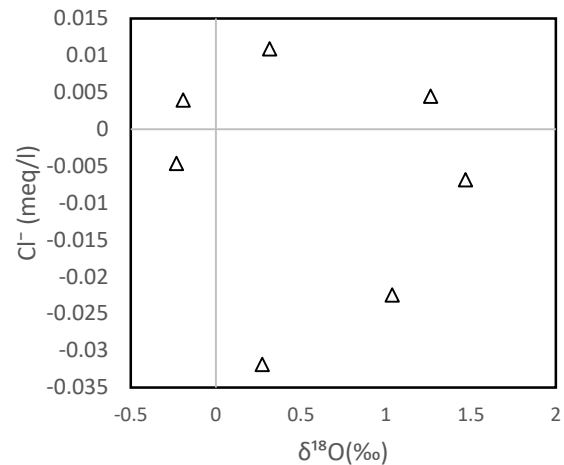


Fig.11 The relationship between the difference (OL-OH) of Cl^- and the difference (OL-OH) of $\delta^{18}\text{O}$ values in Osaka city

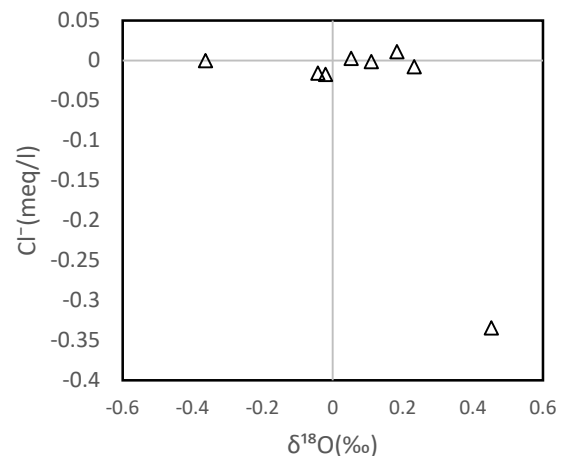


Fig.12 The relationship between the difference (WL-WH) of Cl^- and the difference (WL-WH) of $\delta^{18}\text{O}$ values in Wakayama city

CONCLUSION

Amount of precipitation and soluble substances may depend on altitude because raindrop evaporates and condensates during the falling process from cloud to ground and then to clarify altitude effect is important.

Then the purpose of this study is to clarify the relation of oxygen stable isotopic ratios or soluble substances with altitude for precipitation using the high building.

The $\delta^{18}\text{O}$ values at ground and top of the building were almost the same until October 18th and after October 24th the difference of $\delta^{18}\text{O}$ value at between ground and top of the building were -1.04 to -1.47 ‰.

On the other hand, in Wakayama City, the altitude

difference of $\delta^{18}\text{O}$ values at both points was hardly found, and then the values of ground and top of the building were almost the same.

And then, differences of isotope and humidity between the high altitude point and the low altitude point in Osaka City and Wakayama City were studied. When humidity was low in the precipitation event, the difference of isotope was large. Therefore, humidity was thought to be largely influenced by precipitation evaporation due to difference in altitude. The dew point altitude increased with the difference of isotope values for precipitation at between low and high sampling points.

Regarding chemical composition, in Osaka City, low altitude precipitation contained high Ca^{2+} and HCO_3^- and high altitude precipitation contained high Cl^- and NO_3^- . On the other hand, in Wakayama City, low altitude precipitation contained high Ca^{2+} and HCO_3^- , and high altitude precipitation contained high Cl^- and SO_4^{2-} . From these results, Cl^- concentrations at high altitude in both Osaka City and Wakayama City were high, however, Ca^{2+} and HCO_3^- concentrations of precipitation at high altitude sampling points were high. At the low altitude sampling point, high Ca^{2+} and HCO_3^- was thought to be caused by asphalt dust contained CaCO_3 .

Cl^- concentration differences between low and high sampling points in Osaka City increased with $\delta^{18}\text{O}$ value differences (0 to 1.5 ‰). Then evaporation was thought to occur during precipitation falling process from top of the building to ground in Osaka City.

In Wakayama City, the difference of $\delta^{18}\text{O}$ values between top of the building and ground was not always plus and evaporation was not clear. Therefore Cl^- concentration was thought to be uniform at both high and low altitude points.

REFERENCES

- [1] Amane WASEDA, Nobuyuki NAKAI "Isotopic compositions of meteoric and surface waters in Central and Northeast Japan" *Earth science* 17, 83-91 1983
- [2] Kazuyoshi ASAI, Maki TSUJIMURA, Wilson Yetoh FANTONG "Temporal variation of stable isotope ratios in precipitation on Chubu-mountainous areas : a case study of Mt.Ontake, Japan" *Journal of Japan Hydroculture* Vol.44, No.2, 67-77 2014
- [3] Satoshi Miyahara, Hiroyuki Ii "Proposal of Measurement for Evaporation Rate by Using Oxygen Isotopic Ratio" *Int. j. of GEOMATE*, Sept, 2012, Vol. 3, No.1(Sl.No.5), pp.318-324
- [4] YABUSAKI Shiho "Characteristics of Stable Isotopes in Precipitation at Kumagaya City, Saitama Prefecture" *Global environment research*, Vol.12 (2010)
- [5] Hisao Sakai, Takeshi Morisawa, Tetsuya Sengoku "Characteristics of pH, EC values and ionic components in rain and snow for 7 years at Mt. Ontake, Central Japan" *Jpn. J. For. Environment* 45 [1], 21-27 2003
- [6] Hiroshi HARA "Precipitation Chemistry in Japan" The Chemical Society of Japan 1997, No.11
- [7] Shiho YABUSAKI, Norio TASE, Maki TSUJIMURA and HAYASHI "Characteristics of Stable Isotopes in precipitation at South Slope of Mt. Tsukuba" Tsukuba University Terrestrial Environment Research Center Report No.9, 15-23, 2008
- [8] Norio Fukusaki "Chemical characteristics of constituents in precipitation collected on Mt. Tanigawa" Niigata Prefecture Sanitary and Eco Institute Annual Report vol.9 1993

REGENERATION FOR SOCIO ECOLOGICAL PRODUCTION LANDSCAPE IN SERIOUSLY ENVIRONMENTAL DAMAGED RURAL AREA

Takato Azegami¹, Hirokazu Abe², Noriko Otsuka³ and Tomoko Miyagawa⁴

¹ Graduate School of Engineering, Osaka University, Japan; ² Cyber Media Centre, Osaka University, Japan;

³ ILS Institut für Landes- und Stadtentwicklungsforschung gGmbH, Germany; ⁴ Faculty of Systems Engineering, Wakayama University, Japan

ABSTRACT

This research aims to explore the regeneration for socio ecological production landscape in seriously environmental damaged rural area through the field survey of prior efforts around the area. In Fukushima, six years have passed since the nuclear accident, and evacuation orders for about 32,000 people living in Namie, Iitate, Tomioka and Yamakiya District of Kawamata, have been lifted by April 2017. However, since the socio ecological production landscape has lost, the lifting of this evacuation order will not lead directly to the return home of residents. The challenge is how to restore people's former life which was based on agriculture and forestry and this research looks into the ways of regenerating the socio ecological production landscape, using interview with local community representatives and field observation. The case study has revealed that the decontamination of forest is still in a trial stage and the key obstacle is the fact that there are still a few people who wish to return because the future concrete outlook is still not visible. However, a new community has been gradually generating by the approach which a part of farmers resume farming with external researchers and volunteers with interest. It seems to lead to the potential for regeneration of the socio-ecological production landscape.

Keywords: Socio-ecological Production Landscape; Serious Environmental Damage; Fukushima; Community Participation

INTRODUCTION

Background of This Research

Recently a number of mountainous rural areas are facing the difficulty in maintaining villages due to the rapid depopulation and aging society. In these areas, it is also difficult to maintain the functions of the village community and the socio ecological production landscape which have been managed by the villagers. Some villages have been undertaking regeneration of socio ecological production landscape affected by serious environmental damage which requires a strict risk management against various stigmas as well as the burden of restoring the environment. Especially in Fukushima, six years have passed since the nuclear accident, and evacuation orders for about 32,000 people living in Namie, Iitate, Tomioka and Yamakiya District of Kawamata, have been lifted by April 2017. However, since the socio ecological production landscape has lost, the lifting of this evacuation order will not lead directly to the return home of residents. The challenge is how to restore people's former life that was based on

agriculture and forestry and this research looks into the ways of regenerating the socio ecological production landscape, using interview with local community representatives and field observation. The case study has revealed that the decontamination of forest is still in a trial stage and the key obstacle is the fact that there are still a few people who wish to return because the future concrete outlook is still not visible. However, a new community has been gradually generating through an approach which some farmers resume farming with external researchers and volunteers who are interested in the regeneration. It seems to lead to the potential for regeneration of the socio-ecological production landscape.

This research will explore the regeneration for socio ecological production landscape in seriously environmental damaged rural area of Fukushima through the field survey of prior efforts around the area.

Fukushima Daiichi Accident and Residency Restriction

The Great East Japan earthquake had occurred on March 11, 2011. Tsunami hit the Fukushima Daiichi Nuclear Power Plant (FDNPP) and it exploded. The radioactive pollutant from FDNPP had diffused widely in the surrounding area. 332,691 residents were forced to evacuate.

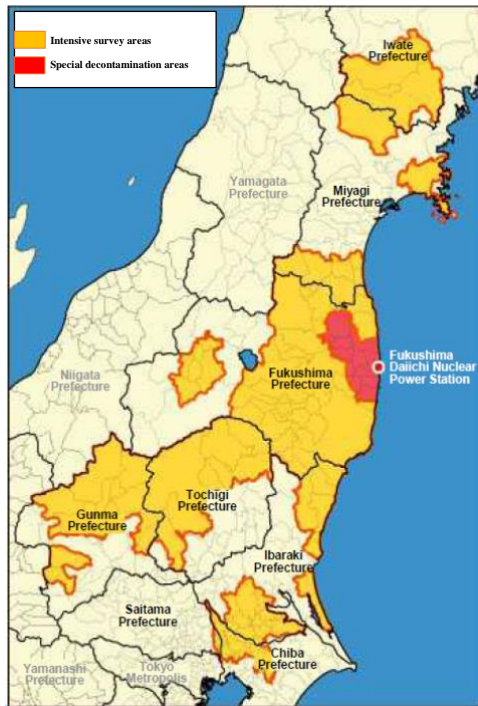


Fig.1 Designated areas in Special Measure Act for Radioactive Pollution in 2012 [1] (Courtesy Ministry of Environment)

To tackle this catastrophic event, the Special Measure Act for Radioactive Pollution came into force 2012. Two types of areas were designated in the Act which are Intensive Contamination Survey Areas (ISA) and Special Decontamination Areas (SDA). Figure.1 shows a part of map of ISA and SDA. ISA (under 20 mSv/y) shows yellow color in the map, in which municipalities were obliged to implement decontamination. SDA (over 20 mSv/y) shows red color in the map, in which the national government carries out decontamination. Left side map of Fig.2 shows the SDA, within Red dot line, where residency is restricted or prohibited by the national government in 2012. Red color shows the zones (over 50mSv/y) where residency is prohibited for an extended period. Yellow color shows the zones (from more than 20mSv/y to less than 50mSv/y) where residency is restricted. Green color shows the zones (20mSv/y) where residents will be allowed to return after decontamination

After six years from the disaster, decontamination work has progressed. On April 2017, residency restriction of 12 areas was lifted. They are shown as green color areas in Right side map of Fig.2. The range of residency prohibit area (within Red dot line) has decreased to one-third of the initial area. Also, the decontamination of the living area of human being (areas within only 20 meter from the settlements) had been completed, and the residents of these areas could return to home. From now on, it is necessary to resume farming and to ensure security against radioactive contamination.

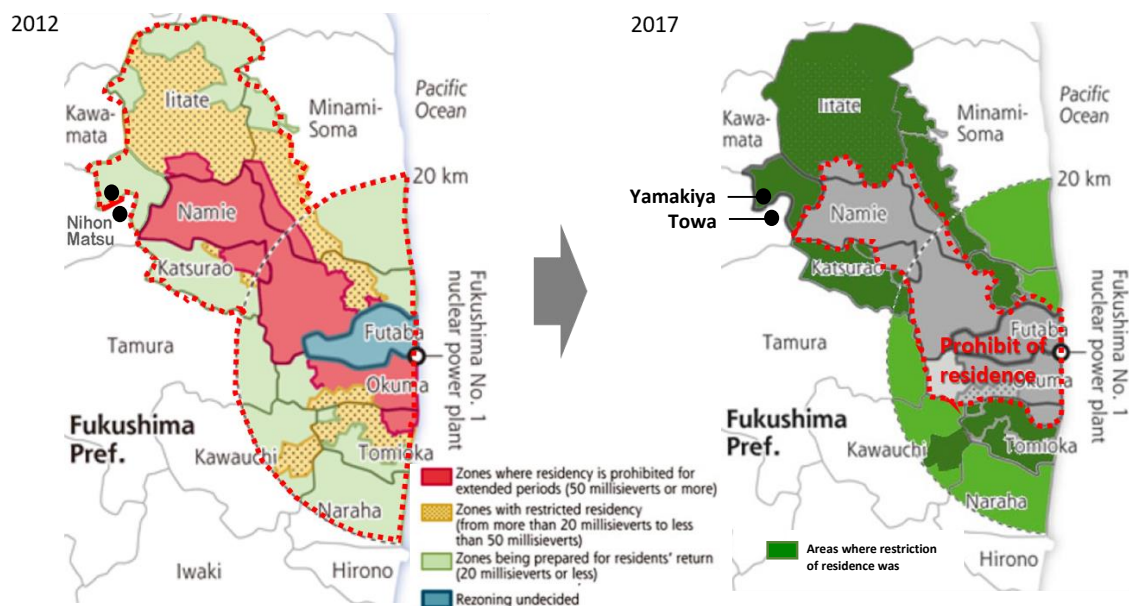


Fig.2 Changes of SDA /left: Jan. 2012/ right: April 2017 (author edited the SDA map Ministry of environment [2])

This paper aims to explore the regeneration for socio ecological production landscape in seriously environmentally damaged rural area of Fukushima through the field survey of prior efforts around the area.

It will focus on two areas; the Yamakiya area and the Towa areas which are neighbouring villages (See Fig.2). Yamakiya Area was located within the SDA. On the other hand, the Towa Area was located outside the SDA. Then, residents in Towa Area were allowed to return home and restarted agriculture soon after the nuclear disaster.

This paper will investigate leading activities in the Towa Area that have taken countermeasures against various social problems aiming for reconstruction which was located outside SDA despite the actual damage of radioactive contamination. We also aim to obtain knowledge for the regeneration of socio-ecological production landscapes in other rural areas. Study methods used in this research are literature reviews and field survey regarding on current condition of the two villages and interviews with five representatives and young farmers of Towa area and Yamakiya area.

RESULTS AND DISCUSSIONS

This research investigated prior attempts in contaminated areas. We conducted an interview survey on representative people in the both Areas. In fact, it appeared to be a gap of in their reconstruction in the two areas. Here, we show some noteworthy activities and initiatives in the Yamakiya area and the Towa area.

Towa Area

Current Condition

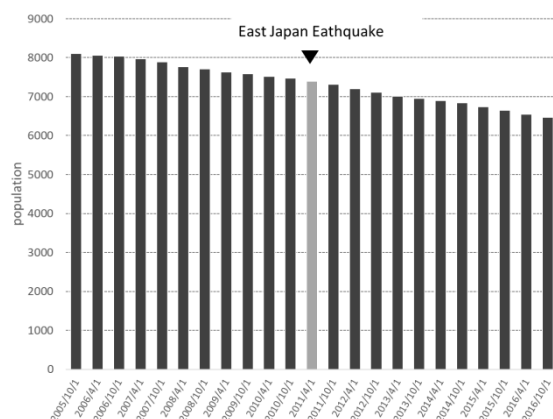


Fig.6 Changes in Population of the Towa in Nihonmatsu City/ 2000-2017 (Data of Nihonmatsu City [3])

The changes in the population of Towa in

Nihonmatsu City from 2000 to 2016 are shown in Fig.6. It was maintaining a gradual rate of descent from before the earthquake in Towa area. This is a common phenomenon in many mountainous areas in Japan. It can be seen that no significant population decline has occurred before and after the disaster. Also, because Towa area was out of the evacuation instruction area, it can be inferred that the community maintenance of the agricultural field were achieved in spite of the contamination. In the following results from the four interviews are presented.

Interview of a Young Farmer; Representative of Kibounotane Company

Interviewee M is the representative of Kibounotane Company. She is also one of the young farmers who decided to return to the TOWA area to continue parents' farming by organic cultivation. When she graduated from a university in Tokyo, the Great East Japan Earthquake occurred. She said that the Towa area was in a difficult situation, there were harmful rumour damage, and the workers were aging.

It is necessary to increase the number of people involved in the town, and to continue to increase the people who can work in the community maintenance of the town, by conveying the current situation to many people. And I believe that it is important what to produce a diversity of the number of people.



Fig.7 Agricultural Experience and Farmer Tour (Courtesy Kibounotane Company [4])

Therefore, she established the Kibounotane Company. This company aims to get many people to be informed the current situation of Fukushima through engaging in agricultural experience and farmer tour around the Towa area. Also this company promotes organic cultivation of rice and vegetables, and web sales etc.

She talked about the green tourism of the post

disaster;

I would like to focus on not only agriculture but also career building and education in the area. And, I would like to not only engage in the framework of disaster reconstruction but also expand activities with people outside the region from now on.

Also, she talked about agriculture,

Although general agriculture has resumed, there are still harmful rumours regarding the radioactive contamination. The number of farmers resumed is very small. Moreover they are almost over 65 years old. Then, they can only last ten to twenty years if young farmers don't return.

Furthermore, she said about the future of the Towa area

Even now, there is no change in the severe situation, but increasing the number of people involved in the town and communicating the situation of the town will be a solution to the problem. How many key person can connect local person and the person who wish to immigrate here?

And I want to increase the number of people who can be active and create diversity.

Interview of Representative of Fukushima Organic Agricultural Network

Interviewee S is the representative of Fukushima Organic Agricultural Network and Director of NPO Yuuki no Sato Towa Association (YSTA). He is also a person who is familiar with the process of reconstruction and promotion for agriculture in Towa Area



Fig.8 NPO Yuuki no Sato Towa Association [5]

NPO YSTA was established in 2005 which has members of approximately 250 households, including

local farmers who felt a sense of crisis when being marginalized during the 'Municipal Merger' by government Policy. After the disaster, the group was entrusted to the operation of the road station 'Michino-Eki' from the city and acted as a base of activities on reconstruction. Local residents of this group have comprehensively undertaken various activities such as branding of local agricultural products, sixth industrialization (agricultural diversification), support of new farmers, and exchange with cities and green tourism etc.

The interview respondent talked about the road station Fukushima Towa in his book published in 2012 [6].

We are positioning the station of road as a base for local production and local consumption by small-quantity multipurpose agriculture centring mainly on vegetables and upland field creation.

We also open a variety of events, and the office of NPO YSTA is also installed.

It is not only a function to sell products but also a place for joint activities in the area and a place to tackle the issue of community development..

'Satoyama Rebuilding Project' started from 2009 with the goal of regenerating local communities, farmlands and forests.

As an extension of the project, in August 2011 after the earthquake, 'Yuuki no Sato Towa Satoyama Rebirth Plan / Disaster Reconstruction Program' started. It was notable that the efforts of such a framework after the earthquake disaster and the restoration with a long-term perspective were carried out at an early stage.

He talked about the difference between the Towa area and the Yamakiya area.

There is a big difference between the Yamakiya area and the Towa area. One of them is a neighbouring town guarantee system-being responsibility by Tokyo Electric Power Company. There was compensation of 100,000 yen per person in the Yamakiya area what is located inside the SDA, but no compensation was offered in the Towa area since it was outside of SDA.

The famers in Towa had to start soon after the disaster without the compensation after the disaster in spite of under decontamination process.

Summary of the Towa Area

The findings in this section are summarised as follows.

1. It is necessary for the regeneration of environmentally damaged rural area to increase the number of people involved in the town, and to continue to increase the people who can work in the community maintenance of the town, by conveying the current situation to many people.
2. In the Towa area there is a framework called NPO YSTA, this organization played a great role in comprehensively connecting people and towns.
3. It was notable that the efforts of such a framework after the earthquake disaster and the restoration with a long-term perspective by utilizing the government measures such as "Reconstruction Plan / Disaster Recovery Plan", were carried out at an early stage.

Yamakiya Area

Current Condition

The changes in population of Yamakiya district in Kawamaya Town from 1995 to 2018 are shown in Fig.9. It was maintaining a gradual rate of descent from before the earthquake in the Yamakiya area. This is the same as Towa.

However, from 2011 (after the disaster) to 2017 (until the lifting of the evacuation order), there were no resident.

Even after the evacuation direction was cancelled the number of residents were 100 in 2017, 300 in 2018, and only about 20% of the total residents had returned, and the number of evacuees still remains high in Yamakiya.

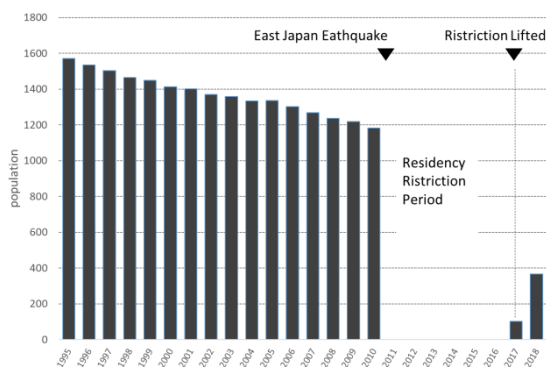


Fig.9 Changes in Population of Yamakiya/ 2000-2017 (Data of Town Council of Kawamata [6])

Interview of Young Farmer, member of Abukuma Cut Flower Group

Interviewee H is also one of the few young farmers who decided to return to the Yamakiya area. He would like to keep the community of Yamakiya by cultivating Turkey bellflower. And he is devoted to continuing the Abukuma Cut Flower Group. People in the Yamakiya area were forced to evacuate due to the disaster, cultivation was cancelled in 2011 and 2012.

After that, by utilizing the 'Fukushima Prefecture Farming Resumption Support Project' in 2013, we tried to demonstrate a good example of the cultivation of Turkey bellflower in the evacuation area, decontaminated agricultural land beforehand and carried out test cultivation.

After completing the trail of cultivation, they planted seedlings in 2014, and 9450 bottles of flowers shipped.

Overcoming the blank for three years, they are shipping high quality Turkish bellflower



Fig.10 Abukuma Cut Flower Group [7]

The interview respondent talked about the Community development.

First of all, it is important that you can make a stable living as a farmer in the Yamakiya area. And I think that we can increase the number of members of this group.

In addition, he suggested about a matter of the Yamakiya Area.

I heard that the number of people who are thinking of returning to Yamakiya will increase little by little.

However, the Yamakiya area originally had many elderly people, and from now on, it is predicted that

the population of the town will decrease more, so the survival of local community maintenance like the association of neighbourhood is a problem. Also, I think that it is better to encourage revitalization as a commercial facility for "Tonya no Sato" as a reconstruction base facility.



Fig. 11 Tonya no Sato (Author's photo)

Tonya no Sato, one of the 'Michi-no-Eki', is to be developed as a symbolic facility of reconstruction based on 'Plan for promoting commercialization of the Yamakiya area restoration base (March 2015)'. It has been planned to contribute to the living support of people who returned home from evacuation, as a facility for people to gather and create bustling, and to revitalize local communities scattered by evacuation.

He talked about the decontamination

Radioactive contamination in Yamakiya area is not worrying too much, since there are some higher points of air dose rate in the Towa area outside of SDA higher than Yamakiya inside of SDA.

The grace of the mountains such as wild vegetables and mushrooms was familiar to people in the Yamakiya area long ago, but decontamination of Satoyama is a serious task, so I think that I do not have to force it.

Interview of Young Musician, Chairperson of the performance group 'Yamakiya Taiko'

Interviewee E is the leader of the performance group called Yamakiya taiko. This group was formed in 2001 to raise reputation of the region with traditional drums that have been played for a long time at the summer festival in the Yamakiya Area.

He suggested about a matter of Yamakiya Area.

The Yamakiya area is rich in nature, but the climate in winter is severe. Many people from

Yamakiya work in Kawamata Town and Fukushima City.

Six years have passed since we evacuated, but many people still do not come back to the Yamakiya area. I hope that Yamakiya will become a place where they can come back any time, even if I do not live in the Yamakiya area,

And, unless the Great East Japan Earthquake happens, there is a connection that was not born.

Many people have supported me, so I believe that I can give back them.

Interview of Chairperson of the Neighbourhood Community Association of Yamakiya

Interviewee G is Vice Chairman of the Yamakiya Farm Association. He is a person who participated widely in activities, such as events, dialogues, etc. as a face of the town, in various situations as well as agriculture since the disaster.

He talked about the community.

There was a place point of time I was almost giving up as it is a disaster, but with the cancellation of the evacuation order in the Yamakiya area, I had to think about what to do in the town. I tried to resume the living of the old Yamakiya area, but I could not see anything of the future vision. And I noticed that there was no human connection in this current area.

Furthermore, he raised a concern about the Yamakiya Area.

Although there is strong belief among the people who have returned to the Yamakiya area now, there are many elderly people who do not have physical strength or energy and the problem is that the young generation does not return. There is a system of the central government that supports agriculture, but it is necessary to plan things ahead for years and there is anxiety as to whether or not to continue.

I think that it is good to create places other than agriculture where we can do what we can do

Summary of the Yamakiya area

The findings in this section are summarized as follows.

1. Various activities and efforts at Yamakiya have a big role for reconstruction. Each activity contains a strong intention for the revitalization of the town. However, in the current Yamakiya area, there is no organizational structure that strongly connects

residents, each of which remains independent activities.

2. The current situation of Yamakiya and the Towa areas which are neighbouring towns presented a big difference by the division caused by administrative boundary of inside or outside SDA. This contrasting recovery process was a negative effect on community revitalization because this is a typical administrative division caused by the central government's policy. It seems that a more flexible approach to designating SDA is needed.

CONCLUSIONS

In this research we examined the activities in two contrasting areas in Fukushima. Results are as follows.

1. Various activities and efforts at Yamakiya played a critical role in reconstruction. Each activity contains a strong intention for revitalization of the town. However, In the Yamakiya area, there is no public organization system that strongly connects residents, and each follows currently an independent activity. On the other hand, in the Towa area there is a framework called NPO YSTA which gives a framework for comprehensively connecting people and towns.

2. The current situation of the Yamakiya and the neighboring Towa area had a big difference caused by administrative division by the government's policy on evacuation order. This contrasting recovery process was a negative effect on the community redevelopment. It seems that a more flexible approach for designating SDA is needed.

3. It is necessary for the Yamakiya Area to increase the number of people involved in the rebuilding of the town, and to continue to support the people who can work in the community maintenance of the town, by disseminating the current situation to many people. The role of rural tourism is important as in the Towa Area important.

4. It should be noted that the efforts in anticipation of such a framework after the earthquake disaster and the restoration with a long-term perspective by utilizing the government measures such as "Reconstruction Plan / Disaster Recovery Plan", were carried out at an early stage in the Towa Area.

ACKNOWLEDGEMENTS

We would like to thank the interviewees for this paper for their helpful comments.

Our thanks are also owed to Dr Tetsuo Yasutaka of AIST for his helpful supports on this research. Also our thanks go to Grants-in-Aid for Scientific Research of Japan Society for the Promotion of Science (18k18602) and the Obayashi Foundation.

REFERENCES

- [1] Framework of Decontamination, Ministry of the Environment Government of Japan, Jan, 2012 (<http://josen.env.go.jp/en/>)
- [2] Special decontamination Area, Ministry of the Environment Government of Japan, Jan, 2012
- [3] Resident population by district (census) of Nihonmatsu City, Fukushima (<http://www.city.nihonmatsu.lg.jp/page/dir002602.html>) in Japanese
- [4] Kibounotane Company (<http://kibounotane.jp/aboutus/index.html>) in Japanese
- [5] Masatoshi Sugeno, Hiroshi Hasegawa, 'Agricultural activity overcome radioactivity', Commons Publishing, 2012 in Japanese
- [6] Resident population by district (census) of Kawamata Town, Fukushima, (<http://www.town.kawamata.lg.jp/site/sinsai-saigai/Yamakiyatikukyojyuujoyoukyou.html>) in Japanese
- [7] Fukushima Prefectural Government, Agriculture, Forestry and Fishery Case Studies (<https://www.pref.fukushima.lg.jp/site/fff-syoku-furusato/jireisyu.html>) in Japanese

HOLISTIC LANDSCAPE PLANNING'S VALUE FOR NATURAL DISASTER RECONSTRUCTION: WILLINGNESS TO PAY FOR NEW RESIDENCE IN DIFFERENT RECONSTRUCTION PLANNING APPROACHES

¹Misato Uehara

¹Graduate School of Science and Technology, Shinshu University, Japan

ABSTRACT

Practical evidence demonstrating the effectiveness of holistic landscape planning is limited, because comprehensive decision-making is misunderstood as depriving individual sectors' authority and budgets. Author compared the difference of recovery speed from disaster and the quality of relocation housing in the two municipalities in contrasting planning process from the Japan Earthquake and Tsunami (2011) disaster. Shinch town has recovered by bottom up planning process and author's site-analysis which based on 1969's McHarg's landscape planning principle and 1980's Japan Land Agency's environmental database. Whereas, Soma city has recovered by top-down planning process, which was the same method as other municipalities affected by tsunami. In this test, 263 students evaluated relocation houses' prices. Author analyzed subjects' attribute data that could potentially affect their evaluation: evaluator's sex, environment in childhood, and demand for future environment. T-test and multiple regression analysis were performed to analyze the concurrent effects of holistic planning process. Welch's t-test found that the mean of relocation residential WTP price (\$). Shinch town's house (mean=\$185400) was significantly higher than that of Soma city (mean=\$157680. $t=15.9$, $p<2.2e-16$ (two-tailed), $d.f.=3622.1$), $\$1=\text{¥}100$). A multiple linear regression was calculated to predict [WTP], based on [USP : Under Shinch town planning process] and [VDD : Volunteer or donation to a disaster area]. (Predicted WTP is equal to $[150200] + [+27700] ([USP]) + [+8176] ([VDD])$. [USP] is coded as [Shinch:1 or Soma:0], and [VDD] is coded as [Yes:1, No:0].). These findings could help us in recovery planning from disasters.

Keywords: Land use planning process, 2011 Tohoku disaster, Reconstruction. Cost-benefit, Climate-change

INTRODUCTION

Amendola [1] indicated that between 1984 and 2003, more than 4 billion people were affected by extreme natural events, and that between 1990 and 1999, the cost of natural disasters was more than 15 times higher than during 1950-1959 [2]. The research noticed that the standard planning approaches to disasters were too reactive, although there had been some progress toward integrated and proactive risk management for disasters in many countries. Moreover, in most countries there has been little integration among the relevant responsibilities. For example, disaster prevention generally has nothing to do with land use planning. Formerly, many Japanese people believed that modern technology could prevent damage from any natural disasters, but this belief is proved to be a fault, by the 2011 Earthquake and Tsunami Disaster in Japan. Thus, we should change the fragmentary approach to a new holistic approach with citizen's participation. In fact, the disasters which attack our society are becoming more and more frequent and unpredictable.

Unfortunately, many relocation sites after the disasters are still based on fragmentary approaches.

On the other hand, in 1969 Ian L. McHarg [3] compared the cost effectiveness of uncontrolled growth and controlled growth with comprehensive land use planning in Baltimore County, Maryland. On that basis, he showed that it is possible to increase development income by comprehensive land use plan. George Hundt Jr [4] analyzed the actual Baltimore's regional development. He indicated that although McHarg's master plan was extremely effective for the restriction development, it did not achieved housing development. Melissa Wagner [5] and Yang, B. [6] pointed out that McHarg's original analysis for land suitability in New York Staten Island and The Woodlands, Texas were effective to avoid disasters respectively.

In such circumstances the following has not been clarified. Can the comprehensive planning process contribute to not only the avoidance of disasters but also the development of the housing which has higher value? This present study aimed to evaluation of the real value of reconstructed housing with holistic land use planning approach in 2011 Tohoku earthquake and tsunami disaster area.

METHOD

Study Area Selection

In this research, we focused on the two municipalities' redeveloped houses for the tsunami damage area, which were planned by contrasting process in Fukushima prefecture. Shinchu town provided the residents with many reconstruction sites by bottom up planning process and our site suitability analysis using the Ian McHarg's landscape principle and 1980's Japan Land Agency's historic data [3], [7]. Shinchu town's process involved citizen and public co-determination, whereas Soma city only determined a quick-fix solution without renewed planning. Unfortunately, most areas which are affected by this disaster carried out their reconstruction, using the method which is similar to Soma city's one.

The land evaluation of the Shinchu town's planning process is important for the following reasons. Ryuzo Eda operated the Shinchu town's reconstruction planning. He was a graduate of the Hokkaido University's Dr. Hidetsugu Kobayashi laboratory, which had incorporated McHarg's theory into education early.

In addition, this town utilized author's land suitability analysis for bottom-up planning with Tadayoshi Inoue 's support, which was the results of Land suitability analysis with McHarg's land evaluation process and historical environmental data of the Japan Land Agency in author's laboratory. This 1980's data was a historically important achievement that has been saved miraculously in the author's university's laboratory. This is the first application of Ian McHarg's ecological planning for Asian country. While the database was being constructed, there was cooperation among landscape architects, politicians, architects and bureaucrats in Japan and the United States. This non-digitized paper data (maps and index tables) were digitized by the author. After that, the disaster risks at Shinchu town's relocated residential site and the place being considered for a new factory were verified by this data and ecological planning process in 2012,2015.

. However, the other tsunami disaster areas which are bigger than Shinchu town have difficulty in making a holistic relocation planning with victims without the author's land suitability analysis and McHarg's planning approach.

Monitoring Until the Housing Relocation Is Completed

The author analyzed the two towns' reconstruction process until the completion of housing; this section compares each town's development achievement rate, from the candidate site selection (2012) to close -out of recovery and reconstruction (2015).

Reconstruction Housing Evaluation by WTP

Based on the photographs of each reconstruction residential area taken in 2015, author conducted a questionnaire survey of CVM to 263 students. Its purpose was to investigate how much we would like to pay for 14 site houses (Shinchu town's 7 sites, Soma city's 7 site). The hedonic approach deals with actual sales volume. It is difficult to obtain appropriate price data, because the rebuild relocation housing construction used subsidies. Therefore, the author decided to carry out a CVM (WTP) approach, using the virtual evaluation method instead of the houses' actual prices. The author also considered a web questionnaire which surveyed actual victims, but there is a bias to evaluate their own housing and region samples highly. Furthermore, in actual disaster areas, the young generation's outflow to the other big city is a serious problem. So the author used university's students as subjects. In the CVM virtual evaluation method, generally a two-step selection method is selected, to avoid a decrease of the number of samples due to an answer of 0 yen. However, in order to have 14 sites of reconstruction houses evaluated, this research required to present the average sales price (20 million yen) of the reconstructed housing at coastal region of Fukushima and required to have students answer the evaluation price by free description (Open -end method).

Photographing and Processing Completed Reconstruction Houses

Photos of each relocation houses were taken to reflect each types of houses and the surrounding environment. In addition, each photo was processed to minimize temporal effects such as sky's brightness. Regarding actual price evaluation of CVM, in order to eliminate the influence of the evaluation order, this CVM test showed the subjects the photos of Shinchu town and of Soma city mutually.

Statistical Processing

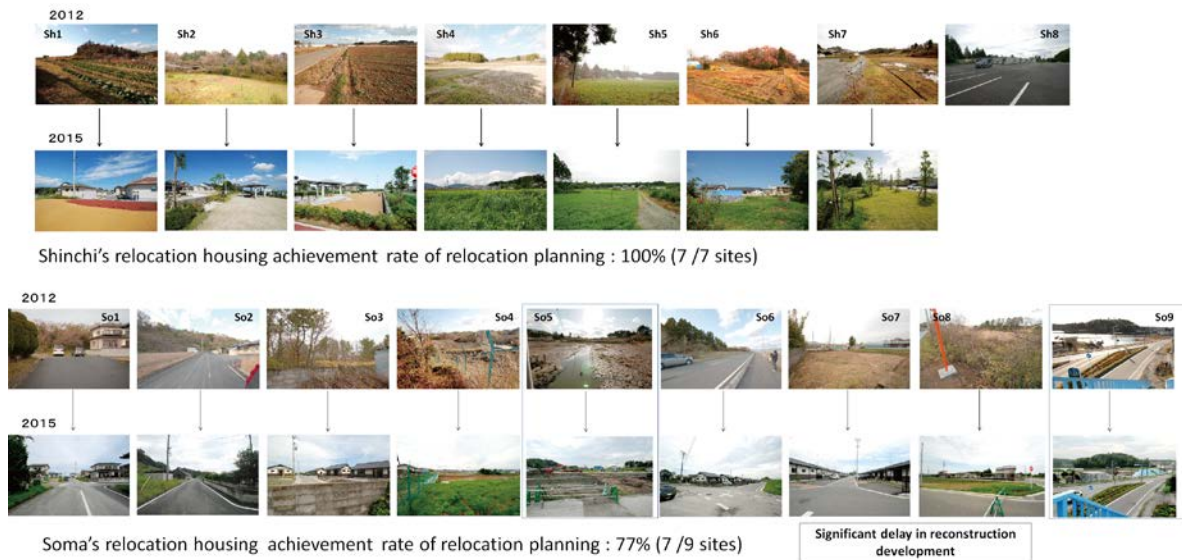


Photo 1 Difference in progress of housing relocation between Shinchi town and Soma city

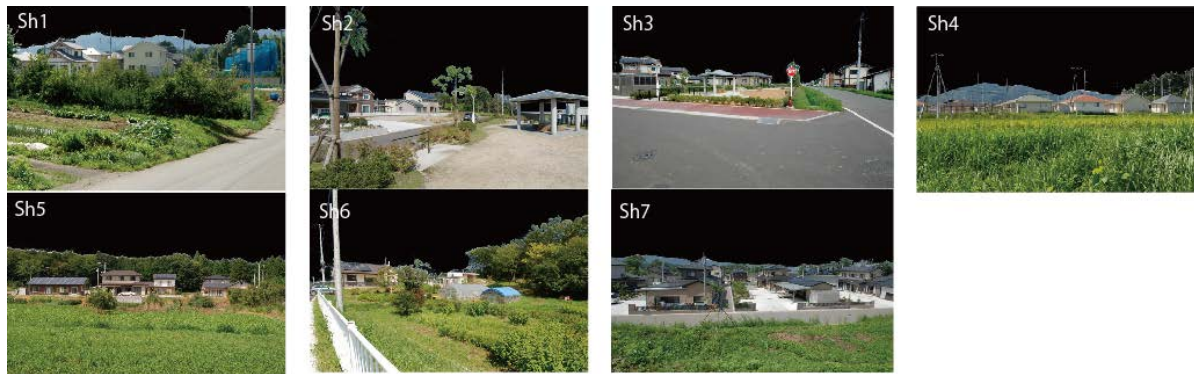


Photo 2 Shinchi town's real relocation houses in 7 sites

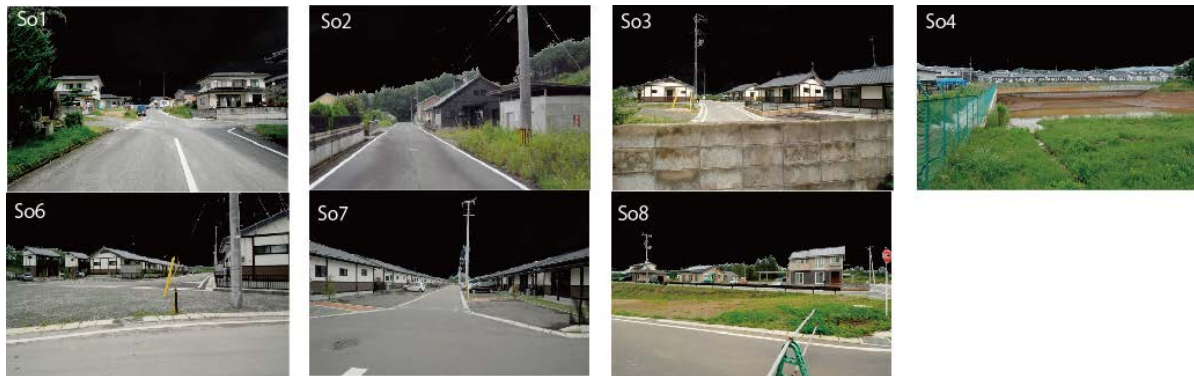


Photo 3 Soma city's real relocation houses in 7 sites

Wilcoxon's t-test and multiple regression analysis were performed to analyze the concurrent effects of holistic environmental planning process. A logit model including both planning style (Shinchi or Soma) tested the significance of the related variable. Underlying the results is the contribution of adding each variable stepwise procedure.

RESULT

Study Area Selection

Shinichi town decided the policy to purchase the tsunami inundation residential area by consultation with government, which is decided fastest in the disaster areas. Tadayoshi Inoue helped the initial direct negotiation between Shinchi town and government, but the other municipalities had not tried contact with the government. Shinichi town could start to decide the suitable site to rebuild houses by consultation with its residents from the whole town smoothly. On the other hand, Soma City and many other municipalities basically used the remaining place of the residential zone, which had

been planned already as the relocation's destination. These site planning was determined before the disaster in 2011. Shinchichi town's reconstruction process with residents' participation required a lot of time and effort, but the Soma city's process did not. But Soma city's victims might have to build houses in the areas which is not suitable for development, because the planned residential zone had already been taken up in proper land [8].

The author evaluated a natural disaster's risk of relocation housing candidate site of Shinchichi town and Soma city, using Japan Land Agency's data in 1980 and McHarg's land suitability analysis in 2011. Shinchichi town's housing candidate sites were decided by many workshops with its residents and the administer. Interestingly, these sites coincide with the areas which judged to be safe by author's comprehensive land suitability analysis. On the other hand, Soma city's sites were evaluated danger than Shinchichi's sites.

On the other hand, Soma city's sites were evaluated more dangerous than Shinchichi town's sites.

The result of disaster risk assessment by the author was also referred by Shinchichi town, and they decided the 7 relocation places in 2012. Since 2011, 700 billion dollars was used as the reconstruction budget in the tsunami disaster areas. But 100 thousand victims moved to another big city from the affected area until 2015, although building infrastructure and housing was promoted. In such circumstances Shinchichi town is a successful model that restored the population, except for big cities. The other big cities whose population has recovered are Minami-Soma and Iwaki, which had temporary workers at Fukushima nuclear power plant and radioactive decontamination work, and Sendai, where is the biggest city in the Tohoku region.

Monitoring Until the Housing Relocation Is Completed

Photo 1 shows the difference of two municipalities' development achievement rate. The Shinchichi town's completion rate of relocation houses has been 100% (7/7 sites) until 2015. On the other hand, that of Soma city has been 77% (7/9 sites) until 2015. Moreover, the occupancy rate of Soma city's completed relocated houses is also low.

Relocated Housing Evaluation by WTP

Shinchichi town's and Soma city's relocation houses in each 7 sites

Photo 2,3 show each relocation houses' types and surrounding environments. Comparing the completed reconstruction houses of the two municipalities, Shinchichi town's process involved citizen and public co-determination, whereas Soma city only determined a quick-fix solution without

Table 1 Willingness-to-pay estimates (\$1=¥100)

willingness-to-pay estimate	(1\$ = ¥100)	
	Shinchichi town's new house	Soma city's new house
(Ecological Planning)		
the mean	185400.3	157680.4
standard deviation	56314.2	49591.4
95% confidence intervals	88165.4 282635.2	47263.9 268096.9
	Test statistics	probability
Welch t-test	15.85	p < 2.2e-16

Table 2 Evaluation result of relocation house's WTP by multiple regression analysis

	All data		
	Model1		
Variable	Estimate	t value	Pr(> t)
Intercept	154330	30.038	< 2e-16 ***
ME: Major of Education	5035	-1.779	0.075247 .
MF: Major of Fiber Science	7046	1.764	0.077752 .
MLE: Major of law and economy	6200	2.066	0.038928 *
ML: Major of literature	6484	2.224	0.026180 *
MM: Major of Medical	-2342	-0.311	0.756
MS: Major of Science	9236	2.403	0.016322 *
ME: Major of Engineering	-4937	-1.588	0.112
USP: Under Shinchichi town planning process	27720	16.157	< 2e-16 ***
GUS: Grow up in the suburbs	-786	-0.301	0.764
GUU: Grow up in the urban	-8956	-2.357	0.018454 *
GUC: Grow up in the countryside	2678	0.844	0.399
GUA: Grow up in the apartment	3503	0.802	0.423
GUD: Grow up in the detached house	-5975	-1.979	0.047883 *
DSL: Desire of suburb living	-3595	-1.370	0.171
DUL: Desire of urban living	-25314	-6.660	3.16e-11 ***
DCL: Desire of countryside living	11544	0.387	0.699
DAL: Desire of apartment living	13253	2.478	0.013248 *
DDL: Desire of detached house living	8176	2.309	0.020986 *
TTD: Traveling to a disaster area	-8980	-2.863	0.004216 **
VDD: Volunteer or donation to a disaster area	6346	3.339	0.000849 ***

built in paddy field, wetland and so on, which is not suitable for development, because the land which is proper for residential zone had already been used.

Evaluation of two municipalities' WTP differences by t-test

The difference between the mean WTP of the Shinchichi town and Soma city was 27720 \$ / house (Table 1). In addition to using Welch t-tests, we compared the two municipalities' average of relocation house price. As a result, it was cleared that Shinchichi town's WTP is higher than that of Soma city.

Evaluation of relocation house's WTP by multiple regression analysis

This section examines the relationship among the evaluation (WTP) to the relocation housing after 2011 Tohoku earthquake disaster, the difference of planning process (Shinchichi's way or Soma's way), and the respondent attribute by multiple regression analysis (Table2).

Since the obtained WTP scores follows a normal distribution, analysis using that value was carried out. 269 individuals were interviewed and 263 of that were valid responses. Table 2 shows the

analysis result of the contribution of adding each variable falling a stepwise procedure. The author did not inform the subjects of the difference of two towns' planning process and these photos' location. This table shows the largest positive contribution to explaining variation in WTP is USP (Under Shinchichi town's planning process). The VDD (Volunteer or donation to a disaster area) also has positive contribution to explaining variation in WTP.

CONCLUSION

Prior works documented the existence of farmland and green space's value [9] [11]; for example, Mbolatiana Rambonilaza [10] reports that most of visitors were willing to pay for the use of wooded recreation areas. Furthermore, approximate half of the respondents were willing to pay to prevent the conversion of forested parks to another land use for quality of their housing environment.

Yan Song [12], Fanhua Kong [13], Hee Jin Yang [14], Shabana, Ghaffar Ali [15] and value, planning process and time change from the plan announcement. For example, Fanhua Kong [13] reported that proximate urban green space (the size-distance index of forest park, accessibility to parks and green spaces) has a positive impact on houses' prices.

In addition, Ian L. McHarg [3] compared the cost effectiveness of an uncontrolled land use development with that of a comprehensively controlled land use development, in Baltimore County, Maryland. This simulation showed the possibility to increase development revenue. George Hundt Jr [4] indicated that McHarg's Baltimore master plan did not achieve houses' development, although it was effective for the controlled development.

Melissa Wagner [5], and Yang, B. [6] proved the usability of the original McHarg's land use plan for natural disasters. But, actual development deviated from original McHarg's land use planning. Then, the purpose of this present study is to clarify that the comprehensive planning process contributes to not only avoidance of disaster impact but also development of higher value housing."

As a result, the author found that in this virtual case, the candidate sites selected by Shinchichi town's careful bottom-up planning process correspond with the safer sites (low natural disaster risk) which was judged by author's evaluation with 1980's Japan Land Agency's data and McHarg's land analysis / planning process. This result indicates that there is a possibility that larger municipalities also can select suitable land for relocation site easily using the 1980's environmental assessment data and McHarg's planning process. If large municipalities could use them, they could select the proper relocation sites in shorter time. Shinchichi town needed a lot of time to

accomplish the relocation, but the author's method can help save time. The realization of this process might be difficult without the planning supports above because the selection of residence areas requires detailed discussion between the town and its residents.

Next, the author found that Shinchichi town's relocation house's WTP is higher than Soma city's WTP statistically. In addition, multiple linear regression analysis indicates that USP (Under Shinchichi town's planning process) and VDD (Volunteer or donation to a disaster area) are positive contribution. This result means Shinchichi town's process increased value of relocation houses' value (27,719 \$ / house).

These findings extend research result of McHarg[3], George Hundt Jr. [4], Wagner [5], and Yang, B. [6]. ; The analysis of holistic land suitability and planning process are useful for selection of reconstruction site and development of valuable new residence for victims in 2011 Tohoku earthquake and Tsunami disaster field.

In other words, this WTP comparison indicates the comprehensive planning process contribute to not only avoidance of disasters but also development of reconstructed housing with higher value after disaster.

Most notably, this is the first study on the knowledge to investigate the effectiveness of holistic land suitability analysis and planning process for reconstruction housing from natural disaster.

Tohoku Earthquake and Tsunami disaster had serious social damage: Magnitude-9 earthquake, Tsunami disaster area 561km², Dead 15,894 people, missing 2,500 people, Destroyed buildings 120,000, Half-destroyed buildings 278,000. This disaster's direct financial damage is \$199 billion dollars. The damage due to the radiation effect is estimated to cost approximately 641 million dollars in Fukushima prefecture [16]. In addition, although 700 billion dollars of reconstruction expenses had been used, 100 thousand victims moved to other big cities from restoring home towns. So it is very important that the houses which based on holistic land use planning get higher evaluation than the house by top-down planning process in Tohoku disaster areas.

However, although our hypotheses were supported statistically, there is limitation that the sample were students, not actual victims. Therefore, the work in the future should include follow-up work designed to evaluate by actual young victims who leaved home town.

ACKNOWLEDGEMENTS

This work was supported by JSPS KAKENHI Grant Number 15K21039 and Research Institute for Humanity and Nature (RIHN: a constituent member of NIHU) Project No 14200103. The author

gratefully acknowledges the help of Makoto Fujii and Yuka Utsugi.

REFERENCES

- [1] Aniello Amendola, Joanne Linnerooth-Bayer, Norio Okada, Peijun Shi, Towards integrated disaster risk management: case studies and trends from Asia- Natural Hazards, Natural Hazards, Vol.44(2), 2008, pp.163-168.
- [2] Parker, Ronald Steven, Hazards of nature, risks to development: an IEG evaluation of World Bank assistance for natural disasters, The World Bank, Washington, DC. Vol.1, 2006
- [3] Ian L. McHarg, Design with Nature., Garden City: American Museum of Natural History, 1969, pp.1- 197
- [4] George Hundt Jr, Thomas L. Daniels, The Plan for the Valleys Assessing the Vision of Ian McHarg and David Wallace, Journal of Planning History, Vol 17, Issue 1, 2018, pp3-19
- [5] Melissa Wagner, Joanna Merson, Elizabeth A. Wentz, Design with Nature: Key lessons from McHarg's intrinsic suitability in the wake of Hurricane Sandy, Landscape and Urban Planning, Vol.155, 2016, pp33-46
- [6] Yang, B., & Li, M. H. Assessing planning approaches by watershed streamflow modeling: Case study of The Woodlands; Texas. Landscape and Urban Planning, Vol.99 (1), 2011., pp 9-22.
- [7] Japan land agency, Evaluation method of land use suitability by ecological planning - Survey report, 1980, Regional planning team, in Japanese
- [8] Misato Uehara, Tadayoshi Inoue, Gen Shintaku, The Favorable Settlement Relocation Process After the 2011 Earthquake and Tsunami Disaster in Japan by Evaluating Site Environments and Accessibility, International Review for Spatial Planning and Sustainable Development, Vol.3, Issue1, 2015, pp119-130
- [9] John M. Halstead, M.S., Measuring the Nonmarket Value of Massachusetts Agricultural Land: A Case Study, Journal of the Northeastern Agricultural Land Economics Council, Vol.13, Issue1, 1984, pp. 12-19
- [10] Mbolatiana Rambonilaza, Jeanne Dachary-Bernard, Land-use planning and public preferences: What can we learn from choice experiment method?, Landscape and Urban Planning, Vol.83, Issue 4, 2007, p318-326
- [11] Liisa Tyrväinen, Hannu Väänänen, The economic value of urban forest amenities: an application of the contingent valuation method, Landscape and Urban Planning, Vol.43, 1998 pp. 105-118
- [12] Yan Song, Gerrit-Jan Knaap, New urbanism and housing values: a disaggregate assessment, Journal of Urban Economics, Vol.54, Issue 2, 2003, pp218-238
- [13] Fanhua Kong, Haiwei Yin, Nobukazu Nakagoshi, Using GIS and landscape metrics in the hedonic price modeling of the amenity value of urban green space: A case study in Jinan City, China, Landscape and Urban Planning, Vol.79, 2007, pp.240-252
- [14] Hee Jin Yang, Jihoon Song, Mack Joong Choi, Measuring the Externality Effects of Commercial Land Use on Residential Land Value: A Case Study of Seoul, Sustainability, MDPI, Open Access Journal, vol. 8(5), 2016, pp1-15
- [15] Shabana, Ghaffar Ali, Muhammad Khalid Bashir, Hassan Ali, Housing valuation of different towns using the hedonic model: A case of Faisalabad city, Pakistan, Habitat International Vol.50, 2015, pp240-249
- [16] Kenta Tanaka, Shunshuke Managi, Impact of a Disaster on Land Price: Evidence from Fukushima Nuclear Power Plant Accident, The Singapore Economic Review, Vol.61(1), 2016, pp.1-15

THE ADSORPTION OF HEAVY METALS FROM INDUSTRIAL WASTEWATER USING SARGASSUM CRASSIFOLIUM

Lily Surayya Eka Putri¹ and Eka Syafiq¹

¹Faculty of Science and Technology, State Islamic University Syarif Hidayatullah Jakarta, Indonesia

ABSTRACT

Sargassum crassifolium is the origin strains of macroalgae from Indonesia which was the most effectively adsorb heavy metals from liquid solution and it was investigated the adsorptive capability of heavy metals in industrial wastewater. The macroalgae were collected at Kotok Besar Island, Seribu Island, North Jakarta, Indonesia and were treated with the variety of pH 2, 3, 4, 5 and 9 for 60 minutes oscillation, in duplicate assessment. The macroalgae was selectively effective for removal of Cd, Hg, and Pb compared with other heavy metals, achieving 75-99.05% adsorption efficiency, mostly in acidic condition for 60 minutes oscillation, except Hg. The selectivity order for other metal ion uptake by *S. crassifolium* was Cu>Fe>Co>Ni>Cr with percentage removal below 56%. Due to the low cost, availability and significantly high adsorption capability, the brown macroalgae *S. crassifolium* is able to be used for selective removal of heavy metals from industrial wastewater effectively in acidic pH range.

Keywords: Adsorption, Heavy metals, Industrial wastewater, *Sargassum crassifolium*

INTRODUCTION

An increase in human population leads to a significant enhancement in waste production. Nowadays, the most notable wastes are the heavy metals because of the high toxicity to living creatures [1]. Along with the development of science and technology, the use of heavy metals, especially in industries is increasing and causing many environmental problems [2]. Heavy metals wastes are discharged into the environment from various industries working on electroplating, leather tanning, water cooling, pulp, and ore and petroleum processing industries that are suspected to be highly toxic to ecology and human health [3], and can also contaminate the environment persistently [4, 5]. In Indonesia, Government Regulation of Republic of Indonesia No. 82/2001 on Water Quality Treatment and Water Pollution Control [6] is used to monitor the heavy metals concentrations commonly generated by industries.

The removal of heavy metals from the environment is the urgent action to conserve nature in a sustainable and further to protect human health. The biological agent is one of the most efficient methods used to reduce the pollution of heavy metals in water including macroalgae [7, 8, 9], microalgae [10, 11, 12], mushroom [13], and agriculture waste [14]. The ion exchange and the formation of complex compounds are the heavy metal adsorption schemes that occur within the walls of algal cells. The structure of the cell wall produces a high seaweed binding capacity because

it has the various functional groups involved including: (1) alginic acid, with carboxyl groups and sulfated polysaccharides, as well as sulfonic acid, in brown algae matrix [15, 16, 17]; (2) sulfated galactans in red algae [15, 18, 19]; and (3) an external capsule composed of proteins and/or polysaccharides in green algae [20].

Algal materials have been broadly observed for heavy metal adsorption, particularly the potential of marine algae, including macroalgae which has been widely investigated. Non-living seaweed or dried seaweed can be used as an alternative to the low-cost adsorbents [14] compared to other methods such as more expensive physicochemical processes. In Indonesia, the studies of macroalgae as heavy metal adsorbents are limited in an aqueous solution, such as the study of adsorption of Cu(II) on *Sargassum crassifolium* [21], Cr(III) on *Euchema spinosum* [22] and Pb(II) on *Sargassum duplicatum* [23], *S. crassifolium*, *Euchema spinosum* and *Padina minor* [24]. The study of heavy metals removal from industrial wastewater, however, has not been widely conducted.

An inexpensive material such as marine macroalgae is suitable for removing the heavy metals from industrial wastewater [15, 16, 18-20, 25]. In the present study, the industrial wastewater was used as a medium to test the ability of *S. crassifolium* to adsorb the heavy metals and as a continuation of the previous study that conducted testing with an aqueous solution. *Sargassum crassifolium* is a genuine strain of Indonesian seaweed that grows abundantly in Indonesian

waters. Therefore, it is appropriate to use *S. crassifolium* as an adsorbent in this study which aims to analyze its efficiency to adsorb the heavy metals from the industrial wastewater. The results of this study can be applied in the industrial wastewater treatment and subsequently contribute to reducing the pollution in the aquatic environment.

MATERIALS AND METHODS

This study was conducted in the Integrated Laboratory Center of the Faculty of Science and Technology, State Islamic University Syarif Hidayatullah Jakarta, including preparation of the samples. The biomass samples of macroalgae *S. crassifolium* were collected from the water surrounding Kotok Besar Island, Seribu Islands, North Jakarta, Indonesia. The samples were used in the dried form. For wastewater sample, it was obtained from the company of hazardous wastes treatment located in Cileungsi region, Indonesia.

Preparation of Adsorbent

All sediments or small organisms which were trapped in the macroalgae samples were washed with the seawater and put in the zipped plastic bag, then brought to the laboratory. In the laboratory, all samples were washed and rinsed again using distilled water and then dried in an oven at 50 C for 24 hours to get the stable weight. The dried samples were pounded with a mortar and pestle and sieved to the size 250-500 µm. The powder of adsorbent was ready to use and kept it at room temperature.

Adsorption Test

The experimental design used was Completely Randomized Design with two (2) replications. The eight heavy metals, including Cd, Co, Cr, Cu, Fe, Hg, Ni, and Pb, and 5 variations of pH, namely 2, 3, 4, 5, and 9 which were oscillated for 60 minutes (refer the result from the previous study). The correlation between pH and adsorption efficiency was analyzed using one-way ANOVA.

The characteristic of Industrial wastewater obtained from the company was measured using ICP (Inductively Coupled Plasma), including pH, chemical oxygen demand (COD), Total Dissolved Solids (TSS), NH₃, and initial concentration of heavy metals. Furthermore, 0.5 g of dried *S. crassifolium* was put into 50 mL wastewater and stirred for 60 minutes using a magnetic stirrer at 200 rpm. The solution pH was adjusted to 2, 3, 4, 5 and 9 with HCl (0.1 M) and NaOH (0.1 M). Then, the solution were filtered with Whatman paper BF/C code and the filtrate was analyzed using ICP

to determine the metals concentration at 543 nm wavelength.

Metals uptake and removal were calculated as the difference in the metal concentration(s) before and after sorption [26], according to Eq. (1).

$$q = (C_i - C_f) \times \frac{V}{M} \quad (1)$$

$$R = \frac{C_i - C_f}{C_i} \times 100\% \quad (2)$$

Where q =metal adsorption (mg/g); M = dry biomass (g); V= volume of the initial lead solution (L); C_i= initial concentration of lead in aquatic solution (mg/L); C_f = final concentration of lead in the aquatic solution (mg/L) at given time (t; min); R = removal percentage (%).

RESULT AND DISCUSSION

The preliminary research of the present study had been conducted in an aqueous solution on various types of macroalgae, *Euchema spinosum*, *Padina minor* and *Sargassum crassifolium* on Pb and Cr adsorption using various initial concentrations of 200, 300, 400, 500, 750, and 1000 mg/L and 7 variations of contact time, namely 10, 20, 30, 45, 60, 90, and 120 minutes [24] at pH 5 [9]. Based on the study, *S. crassifolium* achieved 97-98% (Fig. 1) as the highest adsorption of Pb at 60 minutes contact time (Fig. 2). This was higher and relatively faster than the study of Sweetly et al [9] which achieved 89.75% removal. This is due to the high availability of active sites to bind adsorbent such as -COOH, -OH and -NH₂ [27]. The ability of heavy metal adsorption by *S. crassifolium* tends to decrease after 60 minutes oscillation because the metal binding on the active site has already saturated.

The highest Cr adsorption by *S. crassifolium* was 99% achieved at 30 minutes contact time.

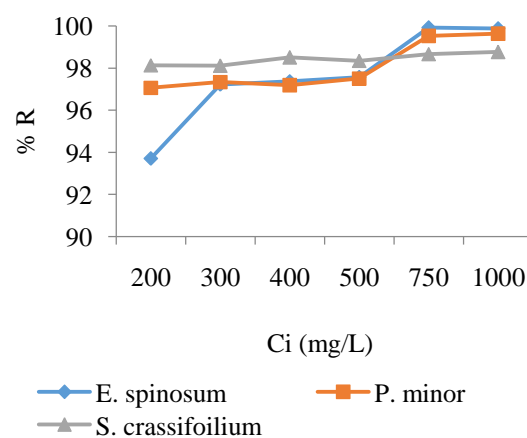


Fig. 1 Adsorption percentage of heavy metal in an aqueous solution at different initial concentration [24]

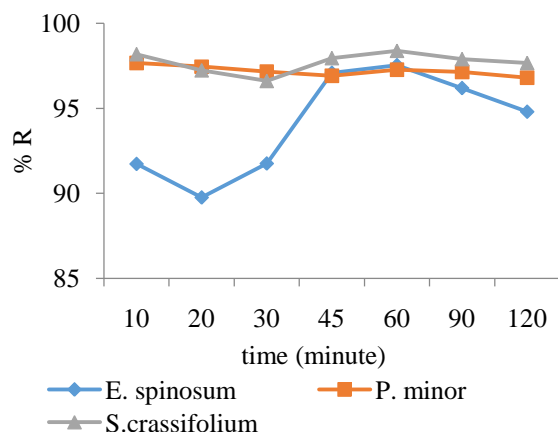


Fig. 2 Adsorption percentage of heavy metal in aqueous solution at various contact time [24]

Sargassum crassifolium showed the fastest time to reach the highest adsorption percentage than *E. spinosum* and *P. minor*, due to the high number of active sites (carboxyl, amine, and hydroxyl) on the surface of the *S. crassifolium*'s epidermis.

Therefore, of the previous study' results, *S. crassifolium* belonging to *Phaeophyta* division could be claimed as the most suitable adsorbent for lead supported by a stronger form of the cell wall, predominantly alginic acid or alginate, compared to *E. spinosum* (*Rhodophyta*) and *P. minor*. Macroalgae *S. crassifolium* was able to adsorb 97-98% of lead (Fig. 1) and capacity of adsorption 55.56 mg/g fit Freundlich model (Tabel 1). This was assumed *S. crassifolium* had high adsorption capacity on heavy metal. Other studies have also supported by these findings [8, 9, 15,17, 21, 23, 25].

The observation was continued using industrial wastewater to analyze the capability of macroalgae *S. crassifolium* on heavy metals adsorption, in various pH, 2, 3, 4, 5 and 9 for 60 minutes oscillation as the optimal contact time refer to the previous study.

Table 1 Constant Value of Langmuir & Freundlich Isotherm

Adsorbent	Langmuir		
	a	b	R ²
<i>E. spinosum</i>	32.26	0.0046	0.984
<i>P. minor</i>	40.00	0.0026	0.934
<i>S. crassifolium</i>	55.56	0.0008	0.882
	Freundlich		
	k	n	R ²
<i>E. spinosum</i>	3.322	2.841	0.892
<i>P. minor</i>	4.846	1.390	0.862
<i>S. crassifolium</i>	2.453	1.379	0.976

Source: [24]

The pH value is one of the most important parameters in an experiment on a biosorption. Various studies have been conducted but using different biomass, such as Sweetly et al [9] using *Sargassum*, while Vimala and Das [13] using mushrooms as an adsorbent. The concentration of hydrogen ions in adsorption is one of the important parameters affecting the ionization rate of the adsorbent during the reaction and the replacement of positive ions in the active site [22].

The industrial wastewater used was assumed containing a high concentration of heavy metals as end-product of the industrial process. The wastewater samples obtained from the company of hazardous wastes treatment in Indonesia is a mixture of wastewater solution from various industrial companies. Thus, it absolutely contains a lot of heavy metals which have specific biochemistry characteristics and should be given serious attention from all stakeholders.

The types of heavy metals contained in the industrial wastewater were Cd, Co, Cr, Cu, Fe, Hg, Ni, and Pb with initial pH 7.91. Several parameters, including pH, COD, TDS, NH₃, and heavy metals from the industrial wastewater were also analyzed using standard methods (APHA-AWWA) [28]. The initial concentration of the various parameters for the untreated industrial wastewater is exhibited in Table 2. The untreated concentration was then compared to the treated industrial wastewater with *S. crassifolium* is presented in Table 3. In order to determine the safe limit of wastewater discharged into the environment, the Government Regulation of the Republic of Indonesia No. 82/2001 [6] is used as a guideline.

Based on the regulation, most of the concentration of the heavy metals from the sample of industrial wastewater in various pH were above the threshold limit, but not too far away, except Cd,

Table 2 Characterization of the untreated industrial wastewater

Parameter	Initial Concentration (mg/L)
pH	7.91
COD	8160
TDS	18890
NH ₃	656
Heavy metals:	
Cd	0.10
Co	0.0505
Cr	0.41
Cu	0.102
Fe	2.69
Hg	0.27
Ni	1.1125
Pb	0.04

Table 3 Concentration of heavy metals after treated by *S. crassifolium*

Met.	TH (mg/L)	Cf (mg/L)				
		pH 2	pH 3	pH 4	pH 5	pH 9
Cd	0.01	0.001	0.001	0.001	0.001	0.01
Co	0.2	0.026	0.027	0.031	0.036	0.043
Cr	0.05	0.252	0.269	0.35	0.412	0.403
Cu	0.02	0.044	0.045	0.088	0.481	0.058
Fe	0.3	2.608	1.546	1.3	1.186	1.169
Hg	0.001	0.008	0.0072	0.006	0.0065	0.002
Ni	0.003	0.62	0.619	0.69	0.805	0.916
Pb	0.03	0.033	0.01	0.026	0.031	0.046

Note: TH: threshold limit based on Government Regulation of Republic Indonesia no 82/2001

Co, Hg, and Pb were safely to be discharged to the environment (Table 3). Although the final concentration on those metals was still above the regulated threshold limit, the adsorption efficiency of those metals was quite good reaching 37.78-56.86% removal ($\text{Cu} > \text{Fe} > \text{Ni} > \text{Cr}$). However, in terms of environment quality, this condition is not good and needs a serious attention especially on treatment process, including pH, type of adsorbent, and contact time to get an optimum heavy metals adsorption by the adsorbent.

Regarding the adsorption capability of heavy metals by *S. crassifolium*, the percentage removal of Cd, Hg, and Pb from industrial wastewater was the highest, reaching 75-99.05%, mostly in acidic pH range, except Hg were in alkaline pH, as shown in Fig. 3. It further was followed by $\text{Cu} > \text{Fe} > \text{Co} > \text{Ni} > \text{Cr}$ was found 37.78-56.86% removal in acidic pH range, as similar as reported by Davis et al [15]. It is was assumed due to the dissolution of some cytoplasmic components or ions, such as carbonates released into the solution and anion types, similar to the study by Latinwo et al [29] for chromium uptake.

The carboxylic groups in the brown algae are generally the most abundant acidic functional group, such as in *S. crassifolium*. They constitute the highest percentage of binding sites (more than

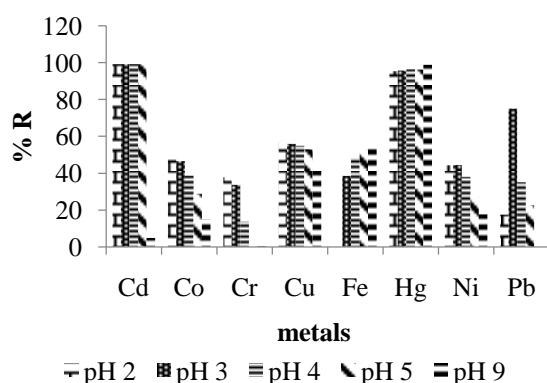


Fig. 3 Removal percentage of heavy metal on industrial wastewater

70%), especially in dried brown algal biomass [30]. Thus, the adsorption efficiency of the brown algae displays at pHs near the apparent dissociation constant of carboxylic acids as the majority of metals of interest (i.e. Cd, Co, Cu, Fe, Ni, Pb) [15], which is similar to this study result.

The optimum removal of those metals from the industrial wastewater was completely achieved at 60 minutes contact time which was contrary to the review by Davis et al [15] in red and brown macroalgae which were achieved in 180 minutes, although the adsorption efficiency was almost the same. The contact time did not show significantly correlated, as reported by Putri [24], however, it has a very significant effect on the cost of the industry for the processing of waste, including electricity and tools use. Besides, the metal hydrolysis constants, the ion size (ionic radius) and electronegativity have to be considered for the affinity of the adsorbent for adsorbing heavy metals [31].

Each type of heavy metal has the ability to bind with the cationic group on different macroalgae active sites depending on the chemical properties of the heavy metal and is highly dependent on the acidity (pH) conditions. The highest adsorption capability of *S. crassifolium* was achieved at range pH 2-5 for Cd, Co, Cr, Cu, Ni, and Pb, which similar to Sudiarta and Diantariani [22] and Susanti [32], except for Hg and Fe which was removed as much as 98.81% and 53.48 from the solution at pH 9. This is similar to the study reported by Cossich et al [33] for Cr, Latinwo [29] for Cr and Fe, and Davis et al [15] for Cd, Pb, Ni, and Cu. However, the affinity of the adsorbent for adsorbing Hg from industrial wastewater is quite rare studied. Huang and Lin [8] studied Hg adsorption by *Sargassum* in an aqueous solution which found pH 8-10 was the optimum adsorption capability with 70% removal of heavy metals. Another study was reported for red algae which could adsorb 99% Hg at pH 7-10 [34]. Similar to this study, the adsorption efficiency of Hg by *S. crassifolium* had almost reached 98% removal from industrial wastewater at pH 9.

The studies reported above were tested in the aqueous solution which was differed from this study trialed in industrial wastewater. In this study, several heavy metals were removed from industrial wastewater below 56.86%, only Cd, Co, Hg, and Pb with 75-99.05% removal. Nevertheless, all the heavy metals were safely discharged to the environment because the concentrations were still below the threshold limit in accordance with the regulation [6]. The different adsorption capacity was due to the affinity of adsorbent to adsorb heavy metal which was related to the cationic binding system. At acidic pH ($\text{pH} < 5$), it had positive surface charge and electrostatic repulsion from a number of

H⁺ ions and cationic species caused a lower attachment of metal ions. On the contrary, the adsorbent's sites carried negative charges at alkaline pH (pH>5) which favoring metal cationic complexes attachment.

Thus, it can be confirmed that this experiment considers selective removal of heavy metals from industrial wastewater, in suitable pH (p<0.05) and contact time, in order to reach the optimum removal percentage. The safe concentration of heavy metals discharged into the environment, especially into the waters, is an important point because it can interfere with the life of living organisms and ultimately lead to death. That is why the international institutions develop standardization for food consumption that could expose through food to human through the food chain in nature. Those international institutions are the World Health Organization (WHO), Food and Agriculture Organization (FAO), European Medicine Agency (EMA) and Joint Expert Committee on Food Additives (JECFA) providing the guidelines of tolerable daily intake on exposure of heavy metals for the human being based on body weight (Table 4).

Table 4 Tolerable Daily Intake (TDI) for heavy metals

Metals	TDI (mg/50-60kg bw)		
	WHO/FAO [35]	EMA [36]	JECFA [37]
Cd	0.06	-	1
Co	-	-	-
Cr	0.05-0.2	0.3	-
Cu	3	0.05	-
Fe	0.8	0.26	0.8
Hg	0.005	-	1
Ni	1.4	0.3	-
Pb	0.214	-	2

The concentration of heavy metals in food is the important information that has to be obeyed by all stakeholders in the industries. Foods from the fishery products are mostly exposed to pollutants in the waters, which are mainly derived from industrial wastewater. Many studies reported contamination of heavy metals in the organism [38, 39, 40], in sediments and waters [40, 41]. They reported that industrial wastes contribute to the water pollution and is responsible for solving that problem.

In connection with the results of this study, the final concentration of heavy metals in the wastewater after the treatment by *S. crassifolium* was relatively safe for Cd, Cu, Hg, Ni, and Pb in accordance with TDI guideline, except for Cr and Fe. Therefore, the treatment of the industrial wastewater is the important process to conserve the

aquatic ecosystem which further has a serious impact on human health. The regulations set by the government have to be obeyed by all industry stakeholders and prioritize law enforcement for those who violate.

CONCLUSION

Sargassum crassifolium from the Phaeophyta division showed the best ability to selectively adsorb 37.78-99.05% of heavy metals from industrial wastewater at pH 2-3 or 9 and contact time of 60 minutes. The highest adsorption capability was 75-99.05% for Cd, Hg, and Pb. Most of the heavy metals are still above the standard, both by the Government Regulation of the Republic of Indonesia No. 82/2001 and TDI standard, however, it exhibits high adsorption efficiency.

This finding is useful for the industries which produce hazardous wastewater in the production process. This study is able to reduce the cost and time of wastewater treatment efficiently, although the selectivity of the heavy metals adsorption is one of the limitations of this study. However, the slightest reduction of a pollutant from industrial wastewater is very influential on environment condition and will give a significant contribution to the conservation of living organisms in the ecosystem sustainably.

ACKNOWLEDGEMENTS

Authors would like to thank State Islamic University (UIN) Syarif Hidayatullah Jakarta which had given financial support for this research. We thank the hazardous waste treatment company for the technical support in research material and data assessment. We also thank students and laboratory staffs of Biology Department, Faculty of Science and Technology UIN Syarif Hidayatullah Jakarta for field and laboratory work's support.

REFERENCES

- [1] Conti ME and Cecchetti G, "A biomonitoring study: trace metals in algae and mollusks from Tyrrhenian coastal areas", Environmental Research, Vol. 93, 2003, pp.99-112.
- [2] Lu FC, Basic Toxicology Principle: Target Organ and Risk Assessment, 2nd Edition, Translator Nugroho, E., Universitas Indonesia, Jakarta, 2000.
- [3] Sudarmaji, "Mercury Level (Hg) in Kupang and Its Relation to Mercury Level (Hg) in Consumers Blood Consuming at Kenjeran Beach Surabaya" (thesis). Airlangga University, Surabaya, Indonesia, 2001.

- [4] Gerke TL, Scheckel KG, Maynard JB, "Speciation and distribution of vanadium in drinking water iron pipe corrosion by-products", The Science of the total environment, Vol. 408, No. 34, 2010, pp. 5845–5853.
- [5] Liber K, Doig LE, White-Sobey SL, "Toxicity of uranium, molybdenum, nickel, and arsenic to *Hyalella azteca* and *Chironomus dilutus* in water-only and spiked-sediment toxicity tests", Ecotoxicology and Environmental Safety, Vol. 74, 2011, pp. 1171–1179.
- [6] Government Regulation of Republic of Indonesia No. 82/2001 on Water Quality Management & Water Pollution Control.
- [7] Al-Homaidan AA, Al-Ghanayem AA and Al-Khalifa AH, "Green algae as bioindicator of heavy metal pollution in Wadi Hanifah Stream, Riyadh, Saudi Arabia", Int. J. Water Resour. Arid Environ., Vol. 1, No.1, 2011, pp. 10-15.
- [8] Huang S and Lin G, "Biosorption of Hg(II) and Cu(II) by biomass of dried *Sargassum fusiforme* in aquatic Solution", J. Environ. Health Sci. Eng., Vol. 13, No. 21, 2015, pp. 1-8.
- [9] Sweetly DJ, Sangeetha K and Suganthi B, "Biosorption of heavy metal lead from aqueous solution by non-living biomass *Sargassum myricostum*", IJAIEM., Vol. 3 No. 4, 2014, pp. 39-45.
- [10] Putri LSE, Fauziah and Dasumiati, "Biosorption ability of microalgae *Scenedesmus dimorphus* for Cr (VI) and Cd in aqueous solution", Adv. Sci. Lett., Vol. 21, 2015, pp. 196-198.
- [11] Putri LSE, Dewi PS and Dasumiati, "Adsorption of Cd and Pb using biomass of microalgae *Spirulina platensis*", International Journal of GEOMATE, Vol. 13, Issue 37, 2017, pp.121-126.
- [12] Rinanti A, Fachrul MF, Hadisoebroto R, and Silalahi M, "Improving biosorption of Cu(II)-ion on artificial wastewater by immobilized biosorbent of tropical microalgae", International Journal of GEOMATE, Vol. 13, issue 36, 2017. pp. 06-10.
- [13] Vimala R and Das N, "Biosorption cadmium (II) and lead (II) from aqueous solutions using mushrooms: A comparative study", J. Hazard. Mater., Vol. 168, 2009, pp. 376-382.
- [14] Ashraf MA, Mahmood K, and Wajid A, "Study of low cost for biosorption of heavy metals", In Proceeding of International Conference on Food Engineering and Biotechnology IPCBEE 9, Singapore, 2011, pp. 60-68.
- [15] Davis TA, Volesky B, Mucci A, "A review of the biochemistry of heavy metal biosorption by brown algae", Water Research, Vol. 37, 2003, pp. 4311–4330.
- [16] Pennesi C, Totti C, Romagnoli T, Bianco B, De Michelis I, et al., "Marine Macrophytes as Effective Lead Adsorbents", Water Environment Research, Vol. 84, No. 12, 2012, pp. 1–8.
- [17] Sheng PX, Ting YP, Chen JP, Hong L, "Sorption of lead, copper, cadmium, zinc, and nickel by marine algal biomass: characterization of biosorptive capacity and investigation of mechanisms", Journal of Colloid and Interface Science, Vol. 275, 2004, pp. 131–141.
- [18] Pennesi C, Veglio F, Totti C, Romagnoli T, Beolchini F, "Nonliving biomass of marine macrophytes as arsenic(V) adsorbents", Journal of Applied Phycology, Vol. 24, 2012, pp. 1495–1502.
- [19] Sari A, Tuzen M, "Biosorption of total chromium from aqueous solution by red algae (*Ceramium virgatum*): equilibrium, kinetic and thermodynamic studies", Journal of hazardous materials, Vol. 160, 2008, pp. 349–355.
- [20] Bulgariu D and Bulgariu L, "Equilibrium and kinetics studies of heavy metal ions biosorption on green algae waste biomass", Bioresource technology, Vol. 103, 2012, pp. 489–493.
- [21] Ronaldo IH, Silalahi N, Wahyuni, "Adsorption of Cu (II) ion using brown algae biomass encapsulated aqua-silica gel", JKK, Vo. 2, No. 3, 2013, pp. 148-152.
- [22] Sudiarta IW and Diantariani NP, "Biosorption of Cr (III) on adsorbent of seaweed *Eucheuma spinosum*", Indo. J. Chem., Vol. 8, No. 1, 2008, pp. 78-82.
- [23] Buhani, Suharso and Sembiring Z, "Biosorption of Pb (II), Cu (II) and Cd (II) ions on *Sargassum duplicatum* immobilized silica gel matrix", Indo. J. Chem., Vol. 6, No. 3, 2006, pp. 245-250.
- [24] Putri LSE, Biosorption of Lead using Macroalgae *Eucheuma spinosum*, *Padina minor* and *Sargassum crassifolium* in Aqueous Solution. Journal of Applied Sciences, Volume 04, Issue 2, 2016, pp. 520-525
- [25] Montazer-Rahmati MM, Rabbani P, Abdolali A, Keshtkar AR, "Kinetics and equilibrium studies on biosorption of cadmium, lead, and nickel ions from aqueous solutions by intact and chemically modified brown algae", Journal of Hazardous Materials, Vol. 185, 2011, pp. 401–407.

- [26] Ok YS, Yang JE, Zhang YS, Kim SJ, and Chung DY, "Heavy metals adsorption by a formulated zeolite-portland cement mixture", *J. Hazard. Mater.*, Vol. 147, 2007, pp. 91-96.
- [27] Wang J and Chen C., "Adsorbents for heavy metals removal and their future", *Biotechnol. Adv.*, 27, 2009, pp.195-226..
- [28] APHA-AWWA, "Standard Methods for The Examination of Waste and Wastewater", 16th ed. American Public Health Association, Washington, DC, 1985.
- [29] Latinwo GK, Jimoda LA, Agarry SE, and Adeniran JA, "Biosorption of some heavy metals from Textile Wastewater by Green Seaweed Biomass", *Universal Journal of Environmental Research and Technology*, Vol. 4, Issue 4, 2015, pp. 210-219.
- [30] Percival EGV and McDowell RH, "Chemistry and Enzymology of Marine Algal Polysaccharides", Academic Press, London, UK, 1967.
- [31] Agarry, S. E., Ogunleye, O. O. and Ajani, O. A. (2015). Biosorptive removal of cadmium (II) ions from aqueous solution by chemically modified onion skin: batch equilibrium, kinetic and thermodynamic studies. *Chemical Engineering Communications* 202, 655-673.
- [32] Susanti, T, 'Study of the biosorption of Cr (VI) metal ions by green algae biomass immobilized with calcium alginate" (thesis). University of Indonesia, Depok, 2009.
- [33] Cossich ES, Tavares CRG, and Ravagnani TMK, "Biosorption of chromium(III) by *Sargassum* sp. biomass", *Journal of Biotechnology*, Vol. 5, No. 2, 2002, pp. 133-140.
- [34] Zaib M, Athar MM, Saeed A, Farooq U, Salman M, and Makshoof MN, "Equilibrium, kinetic and thermodynamic biosorption studies of Hg(II) on red algal biomass of *Porphyridium cruentum*", *Green Chemistry Letters and Reviews*, Vol. 9, No. 4, 2016, pp. 179-189.
- [35] WHO/FAO, "Joint WHO/FAO Food Standards Program Code Alimentarius Commission 13th Session," Report of the Thirty Eight Session of the Codex Committee on Food Hygiene, Houston, Texas, USA, ALINORM 07/30/13, 2007.
- [36] European Medicines Agency," Guideline on the specification limits for residues of metal catalysts', London, January 2007.
- [37] WHO/FAO-JECFA, "Joint Expert Committee on food additives (JECFA): Limit test for heavy metals in food additive specifications", FAO joint secretary, September 2002.
- [38] Putri LSE, Prasetyo AD, and Arifin Z, "Green Mussel (*Perna viridis* L.) as bioindicator of heavy metals pollution at Kamal Estuary, Jakarta Bay, Indonesia", *Journal of Environmental Research and Development*, Vol. 6 , No. 3, 2012, pp. 1-8.
- [39] Rabaoui L, Balti R, "Assessment of heavy metal pollution in the gulf of Gabes (Tunisia) using four mollusc species", *Medit. Mar. Sci*, Vol. 15, No. 1, 2014, pp. 45-58.
- [40] Begum A, Hari KS, and Khan I, "Analysis of heavy metals in water, sediments and fish samples of Madivala Lakes of Bangalore, Karnataka, *International Journal of ChemTech Research* Vol.1, No. 2, 2009, pp. 245-249.
- [41] Hejabi AT, Basavarajappa HT, And Q, and Saeed AM, "Heavy Metal Pollution in Kabini River Sediments", *International Journal of Environmental Research*, Vol. 4, No. 4, 2010, pp.629-636.

MEDICAL WASTE MANAGEMENT IN PRIVATE CLINICS IN SURABAYA AND FACTORS AFFECTING IT

Susi A Wilujeng¹, Enri Damanhuri² and Mochammad Chaerul²

¹Environmental Engineering Department, Institut Teknologi Sepuluh Nopember, Surabaya, Indonesia

²Environmental Engineering Department, Institut Teknologi Bandung, Bandung, Indonesia

ABSTRACT

Health care services generate solid wastes that impose environmental risk if not properly managed, especially the one categorized as hazardous. The compliance of those facilities to the regulation regarding waste management—from the source by waste reduction, segregation, storage, transportation, treatment, and burial—is important to be investigated to identified whether it has been conducted properly. This study was conducted in 17 representative clinics by sampling their solid waste for five consecutive days, observing whether the operation of their solid waste management is conforming the related regulations, and performing logistic regression analysis to develop the correlation between independent variables (sanitary officer that specifically responsible for managing waste; routine budget allocated for waste management; standard operational procedure (SOP) for waste management; and waste management training for staffs) and dependent variables (color-coded waste containment; symbol assignment on waste container; and waste storage location). The results show that the medical waste generation rate was 0.070 kg/patient/day. Composition of the waste from clinics comprised of 21% sharps, 42% infectious, and 37% general waste. The process of solid waste segregation, collection, and storage has not complied with the standard regulated by the government. Logistic regression analysis shows that for implementation of color-coded container the affecting factors are budget and SOP; for the availability of waste storage is staff training; while for symbol assignment there seem to be no significant factors affecting it.

Keywords: binary logistics regression, health care clinics, medical waste, solid waste management, Surabaya City

INTRODUCTION

Healthcare solid waste is waste generated from activities in healthcare facilities such as hospitals, clinics, research centres, and laboratories related to medical procedures. Of this waste, 75–95% consists of non-hazardous, domestic-like waste that poses no health or environmental risks, and 10–25% is composed of hazardous waste that poses health and environmental risks [1]. Due to its infectious nature, this waste must be well managed to prevent it from spreading diseases [2,3]. Infectious diseases such as cholera, dysentery, skin infections and hepatitis can be epidemically spread by improper medical solid waste management [4]. Inadequate waste treatment and disposal can also cause indirect health risks. Waste landfill, when not properly managed, may release pathogens, toxic pollutants, and odours to the environment. It can also expedite the growth of insects, rodents, and worms that lead to the spread of diseases. Improperly operated waste incineration may emit dangerous gases to the environment [1].

The difficulties faced by developing countries in managing their medical solid waste is caused by a lack of financial investment, awareness on the part of administrators, trained staff, and appropriate technologies. Furthermore, the absence of national-

level standards and regulations leads to ineffective control and an inability to impose legal penalties on those who neglect their waste management duties [5]. Several developing countries, including Jordan, Iran, Brazil, India, Cameroon, Botswana, Vietnam, and Nepal, to name a few, have already implemented ministerial-level medical waste management regulations [6]. Indonesia also has comparable regulations. Environment and Forestry Ministry Regulation number 56, regulate the management of hazardous waste from health care facilities. This regulation has been adopted by Ministry of Health to regulate and monitor clinics by issuing Ministry of Health Regulation no 27 2017, Guidelines for Infection Prevention and Control at Health Service Facilities. This regulation standardises the management of hazardous waste at the point of origin by regulating waste reduction, segregation, containment, transportation outside the facility of origin, treatment and burial [7].

Unfortunately, many healthcare facilities fail to comply with these regulations, continuing to improperly dispose of their waste without punishment [8]. These facilities dispose of their untreated medical waste mixed with general waste in open areas [9]. The limited availability of waste

collection facilities, including the use of unsafe containers and the absence of colour-coding for medical waste, also posed obstacles to proper waste segregation [8]. The segregation of waste in accordance with its type, waste containment, as well as storage that complies with standards, is key to the control of risk at the origin of waste. The owners or operators of healthcare clinics play a crucial role in this process. Segregation is the key to minimizing waste. It can reduced the amount of medical waste to be treated up to 70.1% thus reduce significant amount of cost [10]. Mistakes in segregating waste at the source or placing the waste in the wrong container occurred in small hospitals and clinics [11]. The well-executed waste segregation at the source by providing good containers is the early steps of a good waste management that are important to do.

Logistic regression model is one of regression methods used to find out the correlation of categorized response variable with one or more independent variable as category or continue. The research objectives were to investigate the management of medical solid waste in clinics in Surabaya, and to determine the factors that influence the implementation of waste containment and storage using logistics regression.

METHODS

This research is a descriptive study of solid waste management in clinics in Surabaya City that took place in 2017. Out of 285 clinics, the study was conducted in 17 clinics, spread across the city, that were willing to issue a formal permit. Waste generation sampling was performed over five consecutive working days by weighing the waste and recording the number of outpatients. To investigate the clinics' compliance with the waste management regulations set out in Ministry of Environment and Forestry Regulation No. 56, 2015, observation and survey questionnaires were also conducted.

The clinics' waste management practices were analysed using binary logistics regression. Four independent variables were determined for this analysis: a sanitary officer specifically responsible for managing waste (X_1), routine budget allocated for waste management (X_2), standard operating procedure (SOP) for waste management displayed in the clinic (X_3), and waste management training for staff (X_4). The dependent variables being observed were: colour-coded waste containment (Y_1), symbol assignment on waste containers (Y_2), and waste storage location (Y_3). The absence of any of these variables was coded '0' and its presence was coded '1' [12]. The complete set of variables used for the logistic regression model is presented in Table 1.

Table 1. Variables used for logistic regression model

No	Variable Independent	Coding
1	Sanitary officer (X_1)	1 = Present 0 = Absent
2	Waste management routine budget (X_2)	1 = Present 0 = Absent
3	Waste management SOP (X_3)	1 = Present 0 = Absent
4	Waste management training (X_4)	1 = Present 0 = Absent
Dependent		
1	Colour-coded container (Y_1)	1 = Present 0 = Absent
2	Symbol assignment on container (Y_2)	1 = Present 0 = Absent
3	Waste storage location (Y_3)	1 = Present 0 = Absent

Modelling analysis was conducted using IBM SPSS 20 software. Three models resulted: colour-coded container model, symbol assignment model, and waste storage model. The logistic regression model follows equation (1).

$$p(Y) = \frac{\exp(\beta_0 + \beta_1 x_1 + \dots + \beta_k x_k)}{1 + \exp(\beta_0 + \beta_1 x_1 + \dots + \beta_k x_k)} \quad (1)$$

where β_0 is constant, β_j is the regression coefficient and j is the number of predictor (independent) variables.

The logistic regression model requires predictor variables to have no multicollinearity. By calculating VIF, the multicollinearity can be determined. If VIF is less than 10 or the tolerance is more than 0.1, then the variables are free of multicollinearity. Table 2 presents the results of the multicollinearity test, which shows that the dependent variables used in this study fit the requirement.

Table 2. Multicollinearity test

Variables	Tolerance	VIF
Sanitary officer (X_1)	0.362	2.765
Waste management routine budget (X_2)	0.881	1.135
Waste management SOP (X_3)	0.283	3.532
Waste management training (X_4)	0.178	5.603

RESULT AND DISCUSSION

Surabaya City is the capital city of East Java Province, a metropolis with 2,95 million inhabitants covering an area of 33.306 Ha. Healthcare facilities in the city comprise 61 hospitals offering various classes and types of services, 63 community health centres, and 285 clinics [13].

The clinics observed in this study are privately

owned. The establishment of a clinic is subject to government permission and the clinic owner must obtain an operational permit. Subsequently, the government will guide and supervise its operation. Clinics must comply with regulatory requirements governing their location, buildings, rooms, infrastructure, equipment and staffing. One of these requirements is to have waste management facilities [14].

Waste management in clinics

All clinics studied already separate their medical and non-medical (domestic-like) waste. Medical waste is further separated into sharps and infectious waste, which are contained in different containers. Government-owned community health centres in Surabaya separate their waste in a similar manner [15].

According to the regulations, medical waste containers must be equipped with lids or covers made of a puncture- and leak-resistant material. They must be lined with yellow plastic bags and must feature a proper identifying symbol according to the nature of the waste they contain. The survey results show that the containers in use are equipped with hard plastic lids, but only 41.2% of clinics use yellow containers, and only 29.4% of clinics have affixed infectious symbols on containers. The sharps symbol has been used because sharps are contained in special containers made of thick cardboard. Figure 1 shows the typical containers used to contain medical waste in clinics.

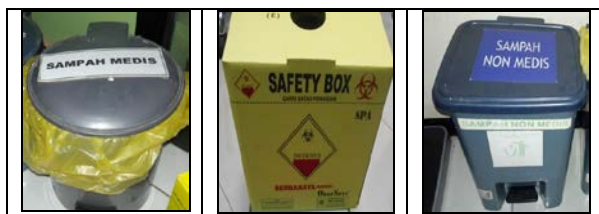


Fig. 1 Containment of medical waste, sharps and non-medical waste

The five-day waste generation sampling shows that the waste generated by clinics consisted of 21% sharps, 42% infectious waste, and 37% general waste. This composition differs from the composition of hospital solid waste in other developing countries. In Tripoli, Libya, the composition of sharps, infectious waste and general waste is 4%, 21%, and 74%, respectively. In Dhaka, Bangladesh, the composition is 2.8%, 18.4% and 78.7%, respectively, while in Gujranwala, Pakistan, the composition is 0.87%, 25.8% and 73.8%, respectively [6]. This discrepancy arises because clinics only provide outpatient services; as a result, the waste generation from patients and staff

activities are limited.

The waste generation survey results show the generation of 0.07 kg/patient/day of medical waste and 0.040 kg/patient/day of non-medical waste. The patients visiting clinics are solely to get treatment and no other activities, therefore the generation of non medical waste is low. The rate at which clinics in this study generated medical waste is similar to the rates in Pakistan (0.06 kg/patient/day), South Africa (0.07 kg/patient/day) and Tanzania (0.01 kg/patient/day) [1]. Surabaya City Health Department recorded 256,143 patients per day, giving a waste generation figure of approximately 18 tonnes/year—a sizeable number that must be given serious attention.

Non-medical waste does not require special treatment; thus, it is directly transferred to the nearest temporary waste storage site to await transportation to the government-owned landfill in Benowo. In contrast, medical waste requires special treatment. None of the clinics studied treat their own waste. They must therefore subcontract this activity to another party who has permission to transport and treat hazardous waste. Unfortunately, not all clinics were able to produce a manifest to prove that their subcontractors had the proper permits. The small volume of waste generated by the clinics means that daily transportation by the third party is impractical. Therefore, clinics must provide a waste storage area. This area must be protected with an impermeable floor and must be free of rodents and other animals. The maximum storage time is two days; if storage exceeds this timeframe, the waste must be kept at or below 0° Celsius. The survey shows that only 41.2% of clinics provide a special safe room, without a cooler, for storing their medical waste. The rest of the clinics keep their medical waste in a standard storage area or other unspecified space within the clinic, without posting any signs.

The success of solid waste management depends on the organisational capabilities of the clinic's management, such as the presence of operations staff, operational guidance and adequate budget, as well as the clinic's staff's knowledge regarding how to properly manage the waste. The survey shows that only 11.8% of clinics have a dedicated sanitary manager, while the rest allocate responsibility for waste management to administrative staff. Only 47.1% of clinics allocate a routine budget for waste management. Moreover, only 23.5% of clinics have standard operating procedures for waste management, while a mere 17.6% of clinics have staff that have been trained in waste management. These low numbers show the lack of awareness of clinic management of the importance of medical waste management. On the other hand, the absence of routine government control mechanisms to enforce clinics' compliance with regulations worsens the situation. For better medical waste

management, Surabaya Government needs to make an effort to increase awareness, provide readily applied guidance or SOPs, and—if needed—stimulant funding for clinics to manage their medical waste. Provision of a good waste management facility as an example for clinics may also be useful.

The correlation between the presence of dedicated sanitary staff, operational procedures, budget and training, on the one hand, and colour-coded containment, symbol assignment and storage area provision, on the other, is analysed using logistic regression.

Logistic regression model for colour-coded waste container

The first step in creating a logistic regression model is to perform a univariate test model between the dependent variables with each independent variable. The test on β_j will show whether a predictor variable can feasibly fit into the model. Each feasible variable will be modelled for the colour-coded container. The hypothesis is as follows:

$$\begin{aligned} H_0 : \beta_j &= 0 \text{ (no partial effect)} \\ H_1 : \beta_j &\neq 0, \text{ (has partial effect)} \\ \text{where } j &= 1, 2, 3, 4 \end{aligned}$$

Table 3. Univariate logistic regression test on colour-coded container

Independent Variable	B	Wald	Sig.
Var Dep.: colour-coded container (present vs absent)			
Sanitarian (X ₁)	21.89	0.00	0.99
Routine Budget (X ₂)	1.76	2.64	0.10*
SOP (X ₃)	1.91	2.15	0.14*
Training (X ₄)	1.28	0.91	0.34

Note: $\alpha = 15\%$

Based on Table 3, when $\alpha = 15\%$, the independent variables routine budget and SOP significantly affect the implementation of a colour-coded container for medical waste, showed by a sig. value of less than $\alpha = 15\%$; therefore, H_0 is rejected. A value of $\alpha = 15\%$ was applied because of this study's small sample size ($n = 17$), giving a very small error tolerance. Subsequently, a parameter significance test was performed with the multivariate model, as shown in Table 4.

Table 4. Multivariate logistic regression test on colour-coded container

Independent Variable	B	Wald	Sig.
Var Dep.: colour coded container (vs absent)			
Constant	-1.99	3.36	0.07*
Routine Budget (X ₂)	2.10	2.64	0.10*
SOP (X ₃)	2.32	2.15	0.14*

Note: $\alpha = 15\%$; $R^2 = 0.387$

Based on Table 4, it can be concluded that budget and SOP significantly affect the implementation of colour-coded containers, as shown by sig. being smaller than $\alpha = 15\%$, which means that H_0 is rejected. The resulting simulant logistic model is expressed as equation (2):

$$g(x) = -1.99 + 2.10 \text{ Routine_budget}_{(1)} + 2.32 \text{ SOP}_{(1)} + e \quad (2)$$

with a probability function fit expressed by equation (3):

$$\pi(x) = \frac{\exp(-1.99 + 2.10 \text{ Routine_Budget}(1) + 2.32 \text{ SOP}_{(1)})}{1 + \exp(-1.99 + 2.10 \text{ Routine_Budget}(1) + 2.32 \text{ SOP}_{(1)})} \quad (3)$$

Logistic regression model for symbol assignment on the waste container

Table 5 shows that the independent variables with a sig. of less than $\alpha = 15\%$ are budget and SOP, which means that both variables significantly affect symbol assignment. Subsequent multivariate analysis, as shown in Table 6, demonstrates that those variables did not simultaneously affect the implementation of symbol assignment on the waste container, as indicated by the sig. value exceeding $\alpha = 15\%$. Therefore, for this model, only a univariate model results; we were unable to produce simultaneous probability using a multivariate model.

Table 5. Univariate logistic regression test on symbol assignment on waste container

Independent Variable	B	Wald	Sig.
Var Dep.: symbol assignment (vs absent)			
Sanitarian (X ₁)	1.01	0.44	0.51
Routine Budget (X ₂)	2.08	2.66	0.10*
SOP (X ₃)	2.80	4.08	0.04*
Training (X ₄)	1.99	2.06	0.15

Note : $\alpha = 15\%$

Table 6. Multivariate logistic regression test on symbol assignment on waste container

Independent Variable	B	Wald	Sig.
Var Dep.: symbol assignment (vs absent)			
Routine Budget (X ₂)	-0.29	0.15	0.70
SOP (X ₃)	1.25	1.04	0.31

Note : $\alpha = 15\%$; $R^2 = 0.642$

Logistic regression model for waste storage area

The third model generated is a logistic regression with waste storage area as the dependent variable. Table 7 shows that the independent variables with a sig. of less than $\alpha = 15\%$ are SOP and training. This means that both of these variables significantly affect whether clinics provide storage for their

medical waste or not.

Table 7. Univariate logistic regression test on waste storage area

Independent Variable	B	Wald	Sig.
Var Dep.: storage area (vs absent)			
Sanitarian (X ₁)	-0.69	1.60	0.21
Routine Budget (X ₂)	-0.69	0.96	0.33
SOP (X ₃)	-1.20	3.34	0.07*
Training (X ₄)	-0.92	2.39	0.12*

Note : $\alpha = 15\%$

The subsequent multivariate logistic regression test (Table 8) on independent variables found to have an effect in the univariate modelling (X₃ and X₄) resulted in the emergence of one significant independent variable: training. The sig. of variable X₄ which is staff training, is less than $\alpha = 15\%$; thus, H₀ is rejected. Therefore, the only variable that has a significant effect on the clinic's provision of a waste storage area is whether or not any training is provided for their staff. The resulting model is expressed as equation (4):

$$g(x) = -1,204 \text{ Training}_{(1)} + e \quad (4)$$

with the probability function expressed as equation (5):

$$\pi(x) = \frac{\exp(-1,204 \text{ Training}_{(1)})}{1 + \exp(-1,204 \text{ Training}_{(1)})} \quad (5)$$

Table 8. Multivariate logistic regression test on waste storage area

Independent Variable	B	Wald	Sig.
Var Dep.: storage area (vs absent)			
SOP (X ₃)	21.61	0.00	0.99
Training (X ₄)	-1.20	3.34	0.07*

Note : $\alpha = 15\%$; $R^2 = 0.642$

The R^2 of the model was 57.2% indicating that two independent variables, SOP and trianing, can partially explain Y3 variable which is medical waste storage. While the remaining 42.8% is described by other variables outside the model.

Based on the probability function developed, clinics that arrange medical waste training (X₄ = 1) has the probability to provide medical waste storage of 0.230.

CONCLUSION

This study successfully obtained data on the generation and composition of solid waste from clinics in Surabaya. Composition of waste from clinics comprised of 21% sharps, 42% infectious,

and 37% general waste. Waste generation survey results show that medical waste generation was 0.070 kg/patient/day, and non-medical was 0.040 kg/patient/day.

The segregation of solid waste into non-hazardous and hazardous categories is being undertaken by all clinics. Nevertheless, waste containment is not compliant with the regulations governing the proper management of hazardous medical waste. Clinics subcontract the treatment of their medical waste to third parties; therefore, they require temporary storage for their waste prior to its transportation to treatment facilities. Not all clinics have an appropriate storage area. Moreover, not all clinic operators have special sanitary staff, routine budgets, SOPs, and training for their staff.

The performance of a logistic regression analysis demonstrated that the factors that significantly affect the implementation of colour-coded waste containers in clinics are the presence of a routine budget and SOPs for medical waste management. A multivariate logistic analysis modelling the assignment of the symbol on waste containers yielded no significant variable. Thus, the model is based only on a univariate analysis. As for appropriate waste storage areas, the most significant factor affecting their presence is the waste management training provided to the clinic's staff.

This results show that assistance and supervision to clinics by Ministry of Health as the one who issue the operational permit must be improved. This is to ensure that the solid waste generated does not harm environment and health. Future research need to be conducted to further study the routine budget provided by clinics, as well as how good the staffs in charge knowledge of medical waste management.

REFERENCES

- [1] Chartier, Y., Emmanuel, J., Pieper, U., Rushbrook, P., Stringer, R., Townend, W., Wilburn, S., Zghondi, R., Safe management of wastes from health-care activities, World Health Organization, 2014, pp. 3-21.
- [2] El-Salam, M.M. A, Hospital waste management in El-Beheira Governorate, Egypt, Journal Environmental Management, Volume 91, Issue 3, 2010, pp. 618–629.
- [3] Al-Khatib, I.A., Sato, C., Solid health care waste management status at health care centers in the West Bank-Palestinian Territory, Waste Management, Volume 29, Issue 8, 2009, pp. 2398–403.
- [4] Coker, A., Sangodoyin, A., Sridhar, M., Booth, C., Olomolaiye, P., Hammond, F., Medical waste management in Ibadan, Nigeria: obstacles and prospects, Waste Management, Volume 29, Issue 2, 2009, pp. 804–11.

- [5] Liu, H.C., You, J.X., Lu, C., Shan, M.M., Application of interval 2-tuple linguistic MULTIMOORA method for health-care waste treatment technology evaluation and selection, *Waste Management*, Volume 34, Issue 11, 2014, pp 2355–2364.
- [6] Ali, M., Wang, W., Chaudhry, N., Geng, Y., Hospital Waste Management in Developing Countries: A Mini Review, *Waste Management Research*, Volume 35, Issue 6, 2017, pp.1-12
- [7] Ministry of Environment and Forestry Indonesia, No. 56 The Year 2015, Technical Procedures and Requirements Management of Hazardous and Toxic Waste Material from Health Care Service Facilities.
- [8] Irianti, S., Heart, S., Prasetyoputra, P., Determinant of Hospital Waste Management in Indonesia: Focusing on the importance of Segregation at Source and Color Coded Collection System, *Journal of Applied Science in Environmental Sanitation*, Volume 8, Issue 2, 2013, pp. 135-144.
- [9] Chaerul, M., Tanaka, M., Shekdar, A.V., A system dynamics approach for hospital waste management, *Waste Management*, Volume 8, Issue 2, 2008, pp. 442–449.
- [10] Taghipour, H., Mosaferi, M., 2009. Characterization of medical waste from hospitals in Tabriz, Iran, *Science Total Environment*, Issue 407, 2009, pp. 1527–1535.
- [11] Zhang, H.J., Zhang, Y.H., Wang, Y., Yang, Y.H., Zhang, J., Wang, Y.L., Wang, J.L., 2013. Investigation of medical waste management in Gansu Province, China, *Waste Management & Research*, Volume 31, Issue 6, 2013, pp. 655–659.
- [12] Agresti, A. An Introduction to Categorical Data Analysis, John Wiley and Son, Second Edition, 2007, pp. 99-121.
- [13] Wilujeng, S., Damanhuri, E., Distribution Pattern of Solid Health Care Waste in Surabaya, Conference Proceedings, in *Proceeding International Seminar on Environmental Health and Sustainable Tourism*, Udayana University, Bali Indonesia, 2016, pp.242-254.
- [14] Wilujeng, S., Damanhuri, E., Chaerul, M., Management of Solid Waste from Community Health care Facility in Surabaya City, Conference Proceedings, in *Proceeding International Conference on Green Agro Industri and Bioeconomy*, Universitas Brawijaya, Malang Indonesia, 2017, pp.115-119.

PUBLIC HEARING WITHIN THE ENVIRONMENTAL AND HEALTH IMPACT ASSESSMENT SYSTEM: A CASE STUDY FORM THAILAND

Chutarat Chompunth

National Institute of Development Administration, THAILAND

ABSTRACT

The integration of public participation in Environmental and Health Impact Assessment (EHIA) is very significant in terms of its implication for sound decision-making and the sustainability of development activities. In this regard, the Thai EHIA system provides for a participation of stakeholders in an implementation of mega development projects. This is carried out through a number of techniques, particularly the holding of public hearings. In public hearings within the Thai EHIA context, shareholders are brought together in a forum to express their ideas and offer recommendations on a proposed project in order to guidance the decision-making process. Frequently, this forum leads to violent conflict among stakeholders. This study is aimed to state the importance of public participation in the Thai EHIA system and to evaluate the current practice of public hearing in development of a coal-fired power station. The case study, the Krabi coal-fired power plant project was premeditated and examined. The study revealed that the requirements for public hearing in the EHIA system have been promoted remarkably by both the 2007 and 2017 Constitutions. It concludes that public participation, in form of public hearing, in the EHIA process is essential and could bring gigantic benefits to all stakeholders including project owner, local communities, project proponent, and the nation as a whole. Thus, Thai citizens request greater participation in the decision-making processes concerning controversial matters. Where public participation is disregarded, environmental conflicts and difficulties may be created for project development execution and sustainability.

Keywords: public hearing, public participation, environmental and health impact assessment, stakeholders

INTRODUCTION

The Thailand was one of the very first countries in Southeast Asia that implemented EIA [1]. The first institutionalization of the EIA process in Thailand began with the proclamation of the ENQA 1975. Section 17 of this act authorized the ministers, with the approval of the NEB, to specify notification for the type and size of projects or activities requiring EIA. In July 1981, the first notification specifying types and sizes of projects and activities requiring an EIA was announced. This notification applied to either public or private projects. In the early stages of implementation, the contribution from political and economic institutions to the promotion of environmental impact assessment was low, and environmental institutions usually had less power than economic agencies. The ONEB was perceived as not having sufficient authority. The EIA process was also criticized as being a closed process, it was primarily conducted by the project proponent, and was not available for the public unless the project proponent was willing to involve them [2].

Until present, a mass of environmental problems and conflicts has occurred throughout Thailand. These controversies have dramatically increased public awareness of the deteriorating state of the environment and also the lack of an approach to deal with the country's natural resources. Thus, the

government formulated a new Enhancement and Conservation of National Environmental Quality Act B.E. 2535 (1992) [3].

The EIA is a systematic process which aims to predict, determine, and evaluate the significant environmental impacts of development projects in advance. It is also regarded as a useful analytical mechanism by providing this useful information to the decision maker to manage the decision process more systematically, timely and effectively [4]. Currently, in Thailand there are both the EIA and EHIA system, which concerns health impact, processes are compulsory system of procedural control mechanisms under the NEQA 1992 and the 2017 Thai Constitution. Regarding the NEQA 1992, the EIA procedures are described in sections 46 to 48 that the projects or activities that might cause significant impacts to the environment must have an assessment of environmental impacts before the projects or activities are implemented. The projects or activities that are obligated by law to obtain permission prior to construction or operation are required to prepare an EIA report and submit it to the permitting authority [[2], [3]].

In practice, the Thai EIA/EHIA process is largely controlled by the government. An expert review committee has been established for the EIA/EHIA system. The expert review committee comprises of expert members who are qualified and specialized in

various fields of related disciplines and the legal authority competent to grant permission for the project including: the secretariat of the OEPP as a chair, the head of the licensing agency, the head of involved governmental agencies, a maximum of seven environmental experts who are appointed by the ONEB, and an OEPP officer as a secretary [5].

Between the years 2007-2017, more than 100 EHIA were conducted in Thailand and all of these were the subject of public hearing. This paper attempts to explore where many development projects were subjected to public hearings, what are the objectives and purposes, form and outcomes of public hearings. In practically, the problems concerning to the public hearing practice are investigate in order to find out alternative approach to improve the practice.

PUBLIC HEARING PRACTICE IN THE EHIA SYSTEM IN THAILAND

Public hearing is a form of participation in which stakeholders and proponents are brought together in a forum to express their opinions and offer suggestions on a proposed undertaking in order to influence the decision-making process. The purpose of this activity is to collect useful information from stakeholders for government decision-making so that a decision can be made on the foundation of objective facts. Moreover, it is a significant provision prescribing the detailed procedure on how the citizen can be involved in an administrative decision-making process. Thai law provides that citizens have the right to object to a project, and to participate in the hearing to articulate their views and evidence [5]. Since 1992, many public hearing activities have been arranged; many of them relating to huge development projects with potential effects on the quality of people's lives and the environment. In practice, however, the procedures have still been obstructed by some difficulties, for example, an unclear authority of the administrators; limitations on the project that can have a public hearing; and, unsystematic procedures [[2], [5]]. In practice, most public hearings last for a period of about three to five hours and are well attended. In a particular case, as many as 100-500 people attended the meeting. These included community's leaders, community representatives, government officials, the project proponents and the project opponents.

In Thai experience, many public hearings were carried out, and most of these hearings were carried out because of strong requests and pressure from the public. They did not take place on the initiative of the government. In addition, they were organized after the decisions about the development project or activities were already made. As a result, the public hearing in Thailand is perceived as a process that

cannot stop the unrest, and was always too late to solve conflicts [6]. The important cases of public hearings in Thailand, which were perceived as unsuccessful, include the Yadana gas pipeline project, the Kao Hin Son Coal-fired power plant project and, particularly, the Krabi power plant project [3].

The principles and processes for conducting public hearings are still unsystematic and complicated [[5], [6]]. There must be publicity processes concerning this activity. All basic information, such as, the appointment of committees, topics for the public hearing, summary of proposals by all related organizations, time of activity and registration period, venues for registration, how to provide information to the committees, and the characteristics of people that can register to join the activity has to be officially announced and widely notified to ensure that all related persons and parties are informed. Moreover, during the hearing process all relevant information, evidence and opinions from stakeholders and interested parties must be heard and be open to the public in order to avoid any influence or bias [7].

Because of these weak points of the directive, some have argued that the public hearing regulation should be reviewed, and reenacted as a parliamentary act.

RESEARCH METHODOLOGY

Qualitative research was conducted utilizing a case study strategy of inquiry. A case study methodology is chosen as a key strategy to explain and conduct an in-depth study of a public hearing practice.

The data collection methods included semi-structured interviews, non-participant observation, and documental review. A total of 29 semi-structured interviews were conducted with 17 community members, including community leaders and members, who participated in public hearing of the case study and 12 government officials, NGOs and EHIA practitioners who were key players in the public participation processes. Community participants were sought out using a snowball sampling approach starting with community leaders identified in EHIA reports and meetings with practitioners. The interviews took place in the participants' hometown and workplace.

All interviews and field notes were transcribed and coded into thematic categories. The data collected is often represented by quotes in the text below. These have been selected to highlight the intent and voice of our participants.

RESULT AND DISCUSSION

BACKGROUD INFORMATION OF THE CASE STUDY: The Krabi coal-fired power plant

The Krabi coal-fired power plant project is one of a large-scale project in the south of Thailand which having significant environmental problems, in particular air pollutions. The project is located in Krabi province. According to the 2007 Thai Constitution, power plant projects that have a production capacity exceeding 100 megawatts per day, must conduct an Environmental and Health Impact Assessment (EHIA) study and submit this EHIA report before getting an approval from the Authority. Thus, the Krabi power plant project was required by law to conduct an EHIA study. Accordingly, the Krabi coal-fired power plant is suitable to be examined how public participation process through public hearing practice in managing environmental pollution control did not succeed since the project is having conflicts with a high level of controversy among stakeholders.

RATIONALS FOR PUBLIC HEARINGS IN THAILAND

Typically, the Thai EHIA Procedure requires the project developer to hold a public hearing as public participation practice in EHIA system where:

- the expected environmental and health impacts are considered extensive and far reaching;
- there is great adverse public reaction to a proposal; and
- there will be relocation or dislocation of communities.

In practice, the Thai regulations have accounted for the holding of public hearings on 35 types of development projects for EIA and on 12 types of mage-development projects. This can be attributed to the need to relocate or resettle affected communities as well as the strong public concerns expressed about the overall impacts of these projects.

OBJECTIVES AND PURPOSE OF PUBLIC HEARING

The main objectives for organizing these public hearings as part of the EHIA review process are:

- to provide a forum for the proponent to inform the entire community of the outcome of the Environmental Assessment of proposed undertakings;
- to verify the accuracy of the EHIA findings in relation to the situation on the ground;
- to confirm that all the affected parties and stakeholders have been adequately consulted and have been part of the various decision-making processes;

- to offer the affected and interested parties, as well as other stakeholders, the opportunity to express their opinions on any issues considered outstanding; and
- to promote effective public participation and ensure confidence in the Thai EHIA process as well as support for the proposed undertaking.

RESEARCH FININGS

Noticeably, public participation techniques employed in this case study were varied and could range from traditional public participation methods on an education and information provision level, to a more interactive approach such as public meetings. However, the majority of participation techniques were traditional. Thus, the public did not have more opportunities to discuss the issue and there was no appropriate means to manipulate the decision. Many affected villagers were frustrated with the participation process and their government because they felt that the process was not a participation process in which they could make any change to the decision or create appropriate dialogue. It seemed to be just a public relations activity to convince them to accept the project already approved. Clearly, in this case, traditional participation techniques had been unsuccessful in developing collaboration between stakeholders.

This tallies with other finding [8] that traditional methods, in particular public hearings or meetings, was always held in a fixed place or location and at a fixed time, often during office hours. Thus, many people were not available to attend. These activities could be dominated by minority groups and are often difficult for the lay people to understand since the whole process often involves highly technical information. Importantly, these meetings could lead to confrontation among stakeholders.

Although there were many arguments expressing dissatisfaction with the implementation of participation methods, many participants enjoyed the developer's activities such as seminars, site tour and sports activities. One local villager highlighted that:

"I liked the multiple types of their participation approaches. They provided more benefits to us. I like their creative activities in particular the social activity. They made people share ideas, do more activities together. It benefits the whole society. Whenever we wanted to make input or learn more information about the power plant, we had a variety of ways to do that. They set up an open exhibition at their site for more than a month, and they also provided staff to answer our questions. They invited students and teachers to our communities to run their seminars. They did give us the information we wanted

to know” (Villager 6).

Frequently, traditional public participation techniques have been criticized as ineffective approaches to engage the public, Daniels and Walker [9] pointed out that, although traditional methods were being widely applied to provide the public with an opportunity to communicate their concerns with the authority and receiving feedback, they focused one-way transmission of information from the developer or the authority to the public and the public had less opportunity to input into an early stage of the decision-making processes. Importantly, a meaningful public input is not guaranteed. The citizens do not know how their input will be used and whether it will influence the decision.

Although, there were many participation activities, in particular meetings or seminars, conducted by both sides [7], only supporters for each group attended these events. The project supporters joined in the forums conducted by the developers, while the project opponents always refused to participate in the activities organized by the project proponent or even the government. At the same time the local villagers set up their own activities to educate themselves on the issues. They conducted regular meetings in their location every week and most of them were supplied with information by NGOs and academics. One villager stated that: “In fact, we wanted to discuss or debate with the project owners; but when we set up the seminar with NGOs or other academics, they did not come. We wanted them to be in the forum to clarify our enquiries” (Villager 11). Another villager argued that:

“Although I did join in some of their programs, most of the participants were their supporters. The developers invited only their supporters. Most of the impacted villagers did not participate. We did not believe what they tried to convince us. Their information was not correct” (Villager 4).

In the Krabi case, at the beginning of the conflict escalation process, the protestors called for a public hearing to make their voice heard. However, the government paid no attention to their requests. Finally, the public hearing was conducted later but it could not solve the problem since it was too late and the conflict was too complicated to solve. Although the public hearing was not the only technique employed to solve the problem, it seemed to be the most recognized mechanism to engage the public and solve the conflicts. There were a great number of the research interviewees who experienced this event. Some of them gave their perspectives on the positive side of the public hearing as follows.

“From my point of view, it was a useful

mechanism because it is a method for all stakeholders and interested parties to meet with one another and discuss together to find out agreements and disagreements. In the public hearing, there were a great number of the representatives from different stakeholders for instance; central government officers, local government officers, the developers, and local villagers. Different opinions were presented appropriately. I thought that was a pretty good mix of opinions. Although this vehicle did not work for this case, I think this was a good approach that had to happen” (Local government officer 4).

On the other hand, many participants felt that the public hearing was not effectively arranged and, importantly, caused more conflicts. One academic researcher pointed out one weak point associated with large public hearings whereby too many participants in the hearing made it impractical for the organizers to allow every participant to present their ideas, so the organizers could not accurately ascertain the representative public views (Academic 1). Obviously, in this case, the public hearing seemed not to be an effective technique to engage the public, or to solve the conflict among stakeholders.

“Basically, the public hearing aimed to bring everybody’s input into one forum. However, you could have too many difficulties if the participants did not sit down together, discuss based on reason, listen to other voices, and try to accept the views of everybody. Many different ideas were raised. How to manage this complex issue was still problematic. Moreover, how to make everyone pleased and accept the forum was more difficult” (Academic 1).

A public hearing is a classic example of a participation technique grounded in a traditional approach, and perhaps it is the oldest and most widely used technique for citizens to participate in governmental decision making at the local, national, and international level. Frequently, the public hearing is the only main approach in the public participation program. In the Thai experience, a public hearing was a common technique which the government usually adopted to solve conflict problems in construction projects in a non-violent way [10]. However, it was clear that frequently this technique was not successful in solving the conflict in Thai society [11].

On the equality issue, a public hearing hardly ever allows people to participate equally in the process with government officers and experts. This is because, normally, in the hearing, the authorities define the agenda, set up the format, and provide the information and analytical resources. Petts and Halvorsen [12] stated that the structure of the public hearing process could lead to expert bias and by nature of the public hearing, participants may not

truly the representatives of the public. In the public hearing of the Krabi power plant, a number of villagers claimed that the hearing committees were not neutral enough since some of them worked for, and had a close relationship with, the project proponent. Many participants agreed that public hearing committees should be neutral and allocate time fairly and give an opportunity for all participants to express their ideas, both negative and positives (Academic 1 and Local leader 2).

Moreover, more than two-thirds of the participants from local villages claimed that the seats and the presentation time were distributed unequally between the participants. They explained that almost all of the participants in the hearing event were supporters. This made the villagers who wanted to be involved in the process feel that the hearing process was unequal and unfair. Thus, they boycotted the forum. The protestors sent only their representatives into the hearing. As one villager explained:

“It was unacceptable from the beginning of the hearing process. The stage could carry less than two-hundred participants. The number of impacted villagers who wanted to participate in the forum was vast and they could not all be registered. Only the members of central and local governments, the project owner, academia, and the villagers who supported the project were booked on the stage. On that day, we went there but we were excluded. We could not get in. We were all around the hall. The seats were limited and not enough for us. Furthermore, the process was not neutral, we did not want join them. We sent our representatives to present our concerns” (Local leader 5).

One leader of the protestors, who joined in the hearing process, stated that there were limitations of presentation time for the protestors in the hearing and that the participants from the supporters and the developer had more chances to speak. She said that:

“We wanted to express our perspectives, our concerns but we had very limited time. The representatives from the project owners and their supporters spent a lot of time talking. They had more opportunities to speak. I thought the process was offensive” (Local leader 2).

OUTCOMES OF PUBLIC HEARINGS

At the end of any public hearing the panel submits a report making its findings and recommendations to the decision-maker or the authorities as an input to the EIA/EHIA review process. The authorities, to make a final decision, will determine all these concerns and recommendations. When the final decision is made on the project EIS, the Agency notifies the proponent,

the Minister of Environment, Science and Technology, the appropriate sector Minister, the appropriate District Authority, and relevant government departments.

It is important to the government that the findings of public hearings have had considerable influence on the EHIA study. In some cases certain aspects of the project proposal had to be altered, additional mitigation proposals and commitments were made and final decision on projects delayed until substantive issues were addressed. For instance in this case study, the public hearing showed that an important group was not represented on the community and therefore were creating problems for the power plant in its concerns.

CONCLUSION

Evidently, in the Thai EHIA's system, public hearings are mandated by law; however, they can lead to troublesome rather than productive participation. It allows not only for the diffusion of antagonism, but also the assuaging of public opinions. This is especially the case if hearings are held late in the planning process, and there were no, or few, previous attempts to engage the public. As clearly presented in this case study, when the public hearing was held too late, it could not resolve conflict among stakeholders, and the situation became more controversial. This statement was supported by one key informant from educational section that:

“In the Thai's experience, we hardly found a successful public hearing. Indeed, Thai citizen ordinarily preferred to avoid controversy. However, in this case when people's voices were not heard, they started to oppose the project. Public hearings could easily lead to confrontation among stakeholders. Importantly, the lay people were more likely not to listen to others' concerns. Confrontation might work in a strong democratic country but not in Thailand. We were different. In my opinion, the public hearing was not suitable with the Thai context”.

In summary, it could be argued that development projects, either initiated by the government or private sector which may cause significant impacts to the environment, must conduct a public participation process in form of public hearing in Thailand. In accordance with this finding, as stated by many academic and researchers [[7], [12], [13]], although the public hearing is a forum for discussions, it is often superficial and causes conflict over the exploration of the common ground. Evidently, had public hearings has earlier distinguished as a weak mechanism for public involvement in many context. It could be said that the hearing could intimidate and

be prone to adversarial confrontation. In many development project in Thailand, a public hearing is not the most appropriate means of engaging the public. Thus, there is a keen need to find out the most appropriate participation technique to engage the public in the decision-making process. The key lesson is that public participation in EHIA study is essential and may lead to substantial benefits for both the project's proponent and affected community. Where it is ignored it leads to conflicts and problems for every development project implementation, acceptability and sustainability.

REFERENCES

- [1] Chesoh, S., Environmental Impact Assessment of Power Development Project: Lessons from Thailand Experiences, *Asian Social Science*, 7(9), pp 119-123, 2011.
- [2] Chompunth, C., Public Participation in Environmental Management in Constitutional and Legal Frameworks, *American Journal of Applied Science*, 10 (1), pp. 73-80, 2013.
- [3] Ogunlana, S. O., T. Yotsinsak and S. Yisa, An Assessment of People's Satisfaction with the Public Hearing on the Yadana Natural Gas Pipeline Project, *Environmental Monitoring and Assessment*, 72(2), pp. 207-225, 2001.
- [4] Creighton, J. L., *The Public Participation Handbook: Making Better Decisions Through Citizen Involvement*, San Francisco, Jossey Bass, 2005.
- [5] Manowong, E. and S. O. Ogunlana (2006). "Public Hearings in Thailand's Infrastructure Projects: Effective Participations?" *Engineering, Construction and Architectural Management* 13(4): 343-363.
- [6] Chaisomphob, T., J. Sanguanmanasak and K. Swangjang, Role of Public Participation in Planning Power Plant Project in Thailand, *Thammasat International* 9(1), pp. 67-73, 2004.
- [7] Chutarat Chompunth (2017). "Role of Public Participation in Environmental Impact Assessment in Thailand." *International Journal of GEOMATE*. Vol. 12(33): 109-113.
- [8] Vantanen, A. and M. Marttunen, Public Involvement in Multi-Objective Water Level Regulation Development Projects-Evaluating the Applicability of Public Involvement Methods, *Environmental Impact Assessment Review*, 25(3), pp. 281-304, 2005.
- [9] Daniels, S. E. and G. B. Walker (2001). *Working Through Environmental Conflict: The Collaborative Learning Approach*. Westport, Praeger Publishers.
- [10] Petts, J. (2003). "Barriers to Deliberative Participation in EIA." *Journal of Environmental Assessment Policy and Management* 5(3): 269-293.
- [11] Gunes, Y. and A. A. Coskun (2005). "Legal Structure of Public Participation in Environmental Issues in Turkey." *Journal of Environmental Assessment Policy and Management* 7(3): 543-568.
- [12] Halvorsen, K. E. (2001). "Assessing Public Participation Techniques for Comfort, Convenience, Satisfaction, and Deliberation." *Environmental Management* 28(2): 179-186.
- [13] Almer, H. L. and T. M. Koontz (2004). "Public Hearings for EIAs in Post-Communist Bulgaria: Do They Work?" *Environmental Impact Assessment Review* 24(5): 473-493,

SEMI-ARTIFICIAL SLUDGE PRODUCTION BY UTILIZING INORGANIC MATTERS OBTAINED FROM NATURAL "HEDORO"

Hirosuke Hirano^{1,*}, Davin H. E. Setiamarga^{2,3,4}

¹ Department of Civil Engineering, National Institute of Technology, Wakayama College, Japan

² Department of Applied Chemistry and Biochemistry, National Institute of Technology, Wakayama College, Japan

³ Department of Ecosystem Engineering, Faculty of Advance Engineering, National Institute of Technology, Wakayama College, Japan

⁴ The University Museum, The University of Tokyo, Japan

* Corresponding Authors; email: hirano@wakayama-nct.ac.jp

ABSTRACT

Studies focusing on the utilization of physical and chemical properties of sludge have been hampered by the difficulties of sample preservation while maintaining the desirable original physical and chemical properties. Meanwhile, re-obtaining samples with similar characteristics from nature is almost impossible. Previously, we reported the creation of an artificial sludge mimicking the general properties of the natural sea floor sludge of the Funabashi in Chiba. However, although useful for recreating sludge with high organic content (Funabashi = 23.61%), the method was not useful for recreating sludge with low organic content (e.g. Hidaka in Wakayama = 5.58%), because one of the ingredients, zeolite, has a high organic content (7.79%). In this study, we focused on the creation of a semi-artificial sludge using inorganic matters obtained from natural sea sludge. Sludge from Hidaka Port was cryopreserved in 4°C, 0°C, and -20°C for a week, and changes in properties such as water content, of the 0°C and -20°C samples, were confirmed. We then recollected sludge samples from Hidaka, and removed their organic content by burning at 600°C. Artificial organic materials were then added to the obtained inorganic matters, following the method described in our previous study. The resulting semi-artificial sludge mimics the properties of original. Thus in this study, we are successful in adjusting our previously proposed method, by recreating low organic content sludge by utilizing inorganic matters collected from natural samples. Future studies involving changing production and preservation conditions will be conducted to increase the robustness of our result reported here.

Keywords: Artificial Sludge, Sea Sludge, Inorganic Content, Cryopreservation, Hidaka Port

1. INTRODUCTION

1.1 Report of our previous studies

Hedoro, which is a Japanese word for sludge collected from aquatic environment floor, is known to bring unwanted environmental effect in closed water environment (e.g. is lake, pond, and harbor). In a previous study, hedoro is composed of inorganic matter such as mud or sand, organic matter from nutrient salt or protein, and sulfide as the cause of the "rotten egg" smell [1]. Hedoro is also known to bring malicious environmental effects such as eutrophication causing bacterial and other organismic blooms, bad smell caused by hydrogen sulfide, and captured radioactive cesium. Accordingly, in order to purify water environment, methods have been devised to clean the hedoro from the aquatic environment, such as decontamination. Some decontamination methods have been reported by previous studies, for example decomposing

hydrogen sulfide by oxygen [2], and decontamination by decomposing organic matter [3].

However, in such studies, it is crucial to obtain and to collect hedoro every time for the clean sludge research, because hedoro is only available in nature. However, the condition of the natural environment (e.g. weather and seasonal changes) during sampling affects the characteristics of the hedoro. It is impossible to set all environmental conditions to be the same for all samples. For example, we have shown that the organic contents in Hidaka Port in Wakayama in Japan changes each month, [4].

We proposed the production of an artificial sludge useful for research requiring sludge with its early values constant. By hedoro's chemical analysis, we found that we were able to produce artificial sludge by using dry yeast as the source of organic matter, zeolite for inorganic matter, and sodium sulfide nonahydrate ($\text{Na}_2\text{S} \cdot 9\text{H}_2\text{O}$) to recreate sulfide content. In this experiment, we succeeded to reproduce hedoro collected from the Funabashi port

in Chiba, Japan [5]. We also showed that dry yeast, as the source of organic matter in artificial sludge, has the ability of capturing cesium, and thus similar to natural hedoro [6] [7].

1.2 Artificial sludge weaknesses

During our previous experiment to produce the artificial sludge, we first made the “artificial sludge base” by mixing dry yeast and $\text{Na}_2\text{S} \cdot 9\text{H}_2\text{O}$. Next, we added zeolite with the sludge base: base composition equals to 0:100, 41.7:58.3, and 83.3:16.7. We calculated the calibration curve of the heat-weight loss analysis (TG; Thermo-Gravity analysis) (Fig. 1) by primary equation and quadratic equation, and use average value as best addition rate of the sludge base to produce the artificial sludge. However, when we measure the 0:100 sample, despite the lack of organic content addition, we found out that it has the organic contents of 7.79%. The main ingredient zeolite, being made of only inorganic matter (silicon and aluminium), is supposed to content no organic material. We considered that the ingredient zeolite probably captured microorganisms and water in the air, and thus obtained its organic content.

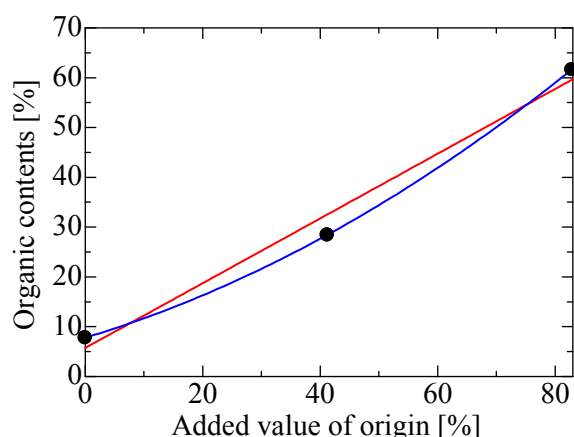


Fig. 1: Calibration curve in artificial sludge

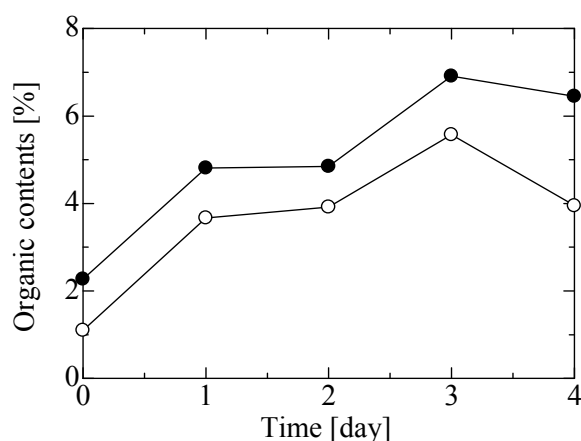


Fig. 2: Change of zeolite by time series

To test the possibility that zeolite capture organic matter from the air, we then burned the zeolite in 600 °C to get rid all of possibly contained organic matter (the incinerating temperature of organic matter), and put the obtained sample in the open air in the lab. The organic content was then measured by TG once a day, and we found the organic content 6.91% as the maximum value after putting the samples for four days (Fig. 2). From this result, we can conclude that zeolite has the possibility to obtain organic matter during preservation. Accordingly, when such preserved zeolite was used to produce an artificial sludge, it is impossible to reproduce an artificial sludge with the organic content lower than the organic content of the zeolite itself.

2. CHANGES OF HEDORO PROPERTIES DURING STORAGE

In this study, we proposed one way of long-term storage of natural hedoro, because it is difficult to reproduce low organic content by our present artificial sludge. Some have suggested to store the samples at low temperature: freezing at -20 °C to -18 °C, cold storage at 0 °C, and refrigeration at 2 °C to 6 °C. For this experiment, we put our samples in a freezer for the -20 °C treatment, ice pack for the 0 °C treatment (Fig. 3), and in a fridge for the 2 °C–6 °C treatment. Change of the hedoro samples' organic contents and moisture contents were measured daily after one week. Samples were collected in Hidaka port in 22th February 2018 and 30th March 2018. The organic contents of the samples were 2.00% in February and 1.16% in March.

We measured the organic contents twice for each sample. Both measurement results showed only slight differences as shown in Table 1 (-0.01%/day to 0.00%/day). We also checked the possibility of the same slight differences in other hedoro samples collected from a channel in Gobo city at Wakayama,. The organic contents of the channel's hedoro samples were 16.40% and 4.69%. Interestingly, our organic content measurement showed that both



Fig. 3: Ice petri dish

samples had an organic content increase of +1.93% to +2.30% daily (Table 2). Standard deviation, it was shown results as Table 3. Values were under 3.8% (n=3) in all, so we understood that has no problem in present results of organic contents. On the other hands, in our present study, we are unable to

Table 1: Change of organic contents in storage (1)

Time [days]	Organic contents [%]	Original organic contents [%]	Change [%]	Change of average by time [%/day]	Way of save
7	1.75	2.00	-0.25	0.00	Free zing
7	1.38	1.16	0.22		
7	1.70	2.00	-0.30	-0.01	Save in ice
7	1.35	1.16	0.19		
7	1.64	2.00	-0.36	-0.01	Refrigeration
7	1.41	1.16	0.25		

Table 2: Change of organic contents in storage (2)

Time [days]	Organic contents [%]	Original organic contents [%]	Change [%]	Change of average by time [%/day]	Way of save
7	31.09	16.40	14.69	2.30	Free zing
8	24.69	4.69	20.00		
7	27.14	16.40	10.75	2.28	Save in ice
8	28.83	4.69	24.14		
8	21.31	16.40	14.31	1.93	Refrigeration
8	20.82	4.69	16.62		

Table 3: Results of standard deviation to change organic contents in storage

	n	Standard deviation in organic contents		
		Free zing [%]	Save in ice [%]	Refrigeration [%]
Natural hedoro in Hidaka port	3	0.22	0.47	0.32
	3	0.21	0.18	0.20
Channel's hedoro in Gobo city	3	1.13	3.73	1.47
	3	1.16	1.89	3.46

pinpoint with confidence the reason of the daily increase, because the samples were put in airtight ziplock bags to prevent outside contamination. Some possibilities could be related to temperature changes [8] - [13] and possible microbial contaminations and proliferations [4] [14] [15].

Based on this observation, although refrigeration (2 °C to 6 °C) seemed to be probably the better way of storage (as shown by the slight increase; Table 2), it still could not prevent the changes of organic content.

In the previous sections, we have discussed that it is almost impossible to store natural hedoro with its original physical and chemical conditions kept unchanged. The organic content of a hedoro sample changes, even only days after sample collection. For example, hedoro in Hidaka port collected in April 30 was measured on the next day to have an organic content of 12.54%, but after 11 days, the value changed to 1.38%, and after 13 days, 1.61%, all samples kept at room temperature.

We also measured the changes of the moisture content in the sludge during preservation. We have previously mentioned that when a hedoro was frozen, its moisture content expanded during the ice crystal formations, causing component materials of hedoro to be broken. The structure and physical properties of such samples, when thawed, changed to be like those of tundra soil thawed samples; materials became spongy, with increased but leaky moisture content. We measured the changes of moisture contents of our samples by TG analysis. First, we heated the samples at 100°C for five minutes to sterilize possible contaminations. After that, we start our first measurement, and subsequently repeat measurements every five minutes, while continuously heating the samples at 100°C. Our samples were the hedoro collected from the Hidaka port (organic contents: 2.00% and 1.16%), hedoro from a channel in Gobo City (organic contents: 16.40% and 4.69%), and artificial sludge samples (organic contents: 20.64% and 28.01%). The results are shown in Fig. 4 to Fig. 9 (●: Refrigeration, ▲: Freezing, □: cold storage in ice).

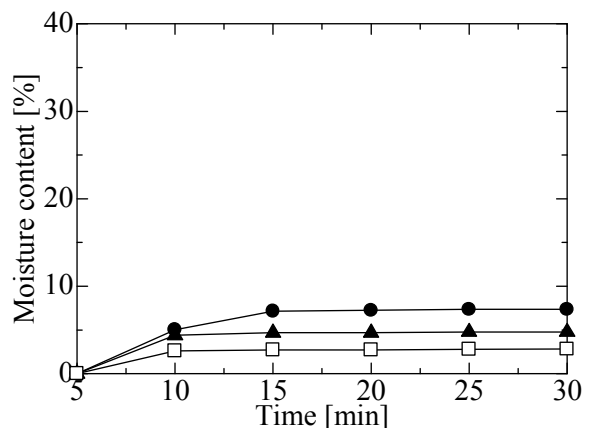


Fig. 4: Change of moisture content in hedoro (1)

Our result indicates that for the hedoro collected from Hidaka port, the lowest values of released moisture content were 2.81% (first sample; organic content: 2.00%; preservation method: cold storage in ice; Fig. 4) and 8.28% (second sample; organic content: 1.16%; preservation method: cold storage in ice; Fig. 5). For hedoro samples from the Gobo City channel, the values were 17.51% (first sample; organic content: 16.40%; preservation method: cold storage in ice; Fig. 6) and 13.24% (second sample; organic content: 4.69%; preservation method:

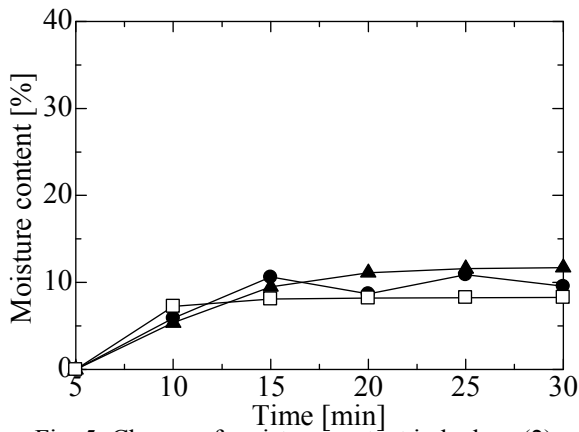


Fig. 5: Change of moisture content in hedoro (2)

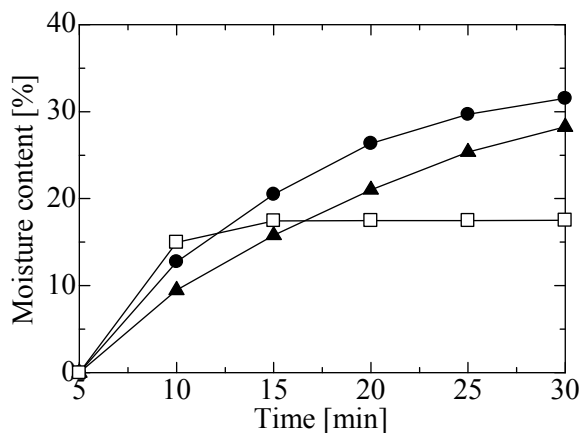


Fig. 6: Change of moisture content in channels (1)

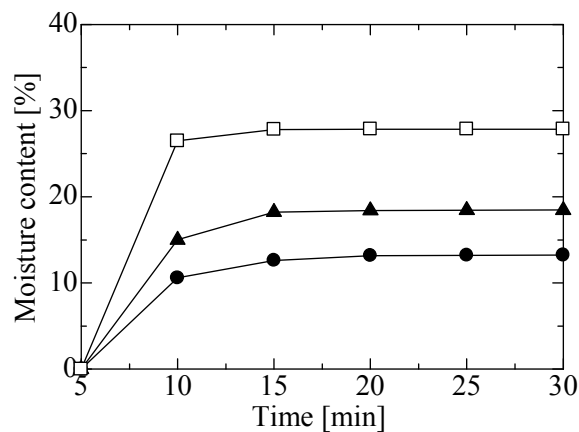


Fig. 7: Change of moisture content in channels (2)

refrigeration; Fig. 7).

Our result for the artificial sludge were inconclusive (Fig. 8 and 9; organic contents were set to 20.64% for the first sample, and 28.01% for the second sample). This result, however, emphasize the difficulties of maintaining both the moisture and organic content of samples during preservations,

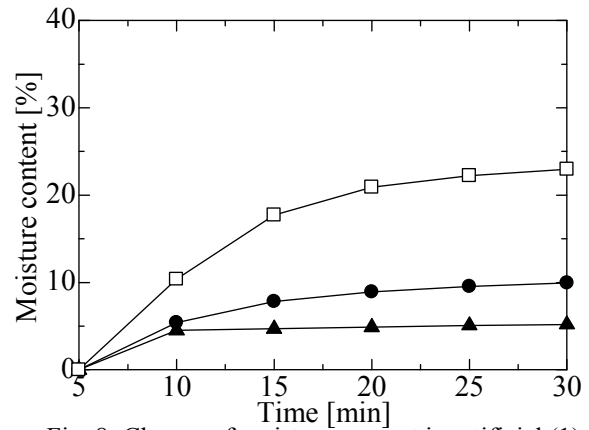


Fig. 8: Change of moisture content in artificial (1)

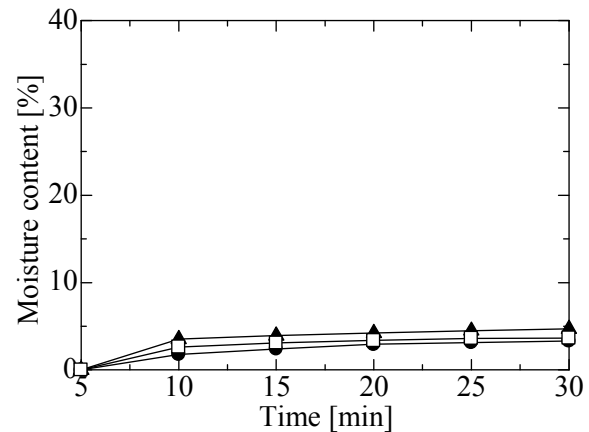


Fig. 9: Change of moisture content in artificial (2)

Table 4: Significant difference in moisture content

	n	Significant difference		
		● and ▲	▲ and □	● and □
Natural hedoro (1)	3	p = 0.495	p = 0.498	p = 0.497
Natural hedoro (2)	3	p = 0.367	p = 0.446	p = 0.421
Channel's hedoro (1)	3	p = 0.498	p = 0.363	p = 0.469
Channel's hedoro (2)	3	p = 0.498	p = 0.498	p = 0.498
Artificial sludge (1)	3	p = 0.498	p = 0.498	p = 0.496
Artificial sludge (2)	3	p = 0.494	p = 0.496	p = 0.496

regardless of the method utilized, and we can show this difficulties from results that is no significant difference (Table 4). Without doubt, such changes also will affect the physical and chemical properties of the samples. The artificial sludge production method follows our previous report [5].

Then, we considered relation with organic

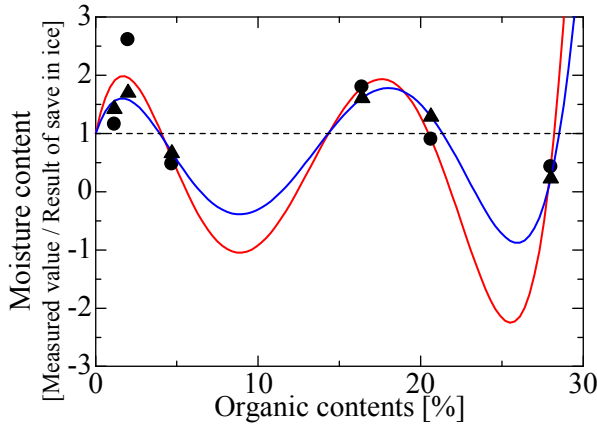


Fig. 10: Relation with organic matter and water (1)

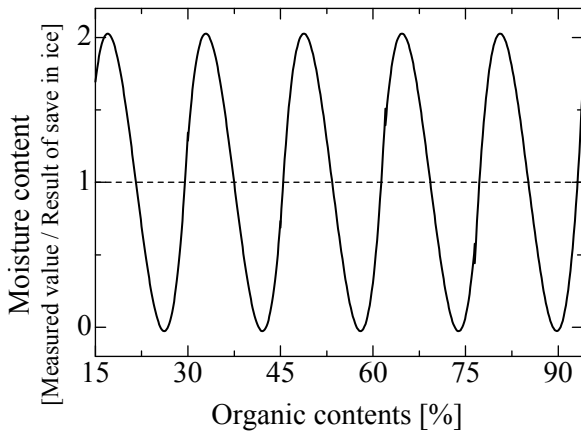


Fig. 11: Relation with organic matter and water (2)

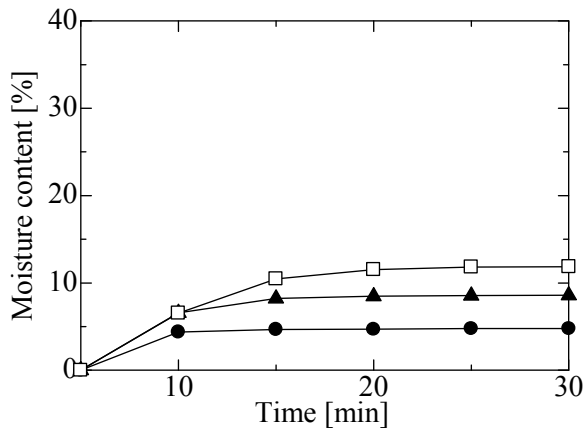


Fig. 12: Change of moisture contents by times
(●:7 days, ▲:15 days, □: 30 days)

contents and moisture content; we thought result of freezing is standard as 1, and changed values in others than freezing. Result was Fig. 10, it was shown relationship. But it was wrong that shown values under 0, so we regulated two conditions in relationship; maximum value was nearly 2, and minimum value was over 0. As a result, we guessed formulas in relation with organic contents (X) and moisture content (Y) (Fig. 11).

$$Y = 0.0053X^3 - 0.3435X^2 + 7.0758X - 45.062 \quad (13.65 \leq X < 29.53) \quad (1)$$

$$Y = 0.0053X^3 - 0.5967X^2 + 22.0250X - 265.740 \quad (29.53 \leq X < 45.43) \quad (2)$$

$$Y = 0.0053X^3 - 0.8498X^2 + 45.0240X - 788.110 \quad (45.43 \leq X < 61.33) \quad (3)$$

$$Y = 0.0053X^3 - 1.1030X^2 + 76.0730X - 1740.200 \quad (61.33 \leq X < 77.23) \quad (4)$$

$$Y = 0.0053X^3 - 1.3561X^2 + 115.1700X - 3249.900 \quad (77.23 \leq X < 93.13) \quad (5)$$

$$X = 1.7 + 7.95 * n \quad (n: \text{Constant}) \quad (6)$$

methods follow our previous report of artificial sludge [5].

3. SEMI-ARTIFICIAL SLUDGE

3.1 The production of semi-artificial sludge using inorganic matter extracted from natural hedoro

In our present study, inorganic matter from two hedoro samples collected from the Hidaka port (February 2018 and May 2018) were extracted by combustion at 600 °C to completely burn organic materials from the samples. Then, we made three types of artificial sludge with differing organic contents, by using the leftover inorganic matters from the burnt samples. The organic content were calibrated using the previously mentioned "artificial sludge base" (= sludge base). The three types of samples are as follow: sludge base/natural sludge inorganic matter = 0/100, 41.7/58.3, and 83.3/16.7. We then created a calibration curve to analyze the organic/inorganic ratio. These compositional ratios enabled us to recreate samples mimicking the natural hedoro collected in February (organic content = 1.30%; Fig. 13), and in May (organic content = 1.50%; Fig. 14). Based on or analysis using the hedoro were 3.10% to recreate February sample, and calibration curve, the best value of sludge base powder addition/inorganic material from the natural 0.73% for May sample. We were successful in following the recipe, with the margin error during addition between 0.13% – 0.14%.

3.2 Results

The resulting semi-artificial hedoro, interestingly, showed different organic content ratio than what was predicted by the calibration curve. For the February sample recreation, the expected organic content was 1.22%, and for May was 1.58%. However, the actual observation value we obtained were 1.31% (Table 4) and 2.86% (Table 5), respectively. Therefore, the February sample-mimicking semi-artificial hedoro had +0.09% than the expected value, while the May one showed +1.28% than expected value.

The result indicated that we were unable to recreate the May sample, because the margin of error was bigger than 1.0%. This is probably because it is difficult to add the sludge base powder less 1.0% of the total organic/inorganic mix, since in this experiment we only made ca. 1 gram of semi-artificial sludge.

When we looked at the calibration curve, some inorganic content values were too high (more than 98.94% = organic content values were under 1.06%), causing the ideal values of sludge base needed in the mix, in effort to reproduce such samples, to be less than 0.0%. This indicates also that there are some places we still need to improve in the present

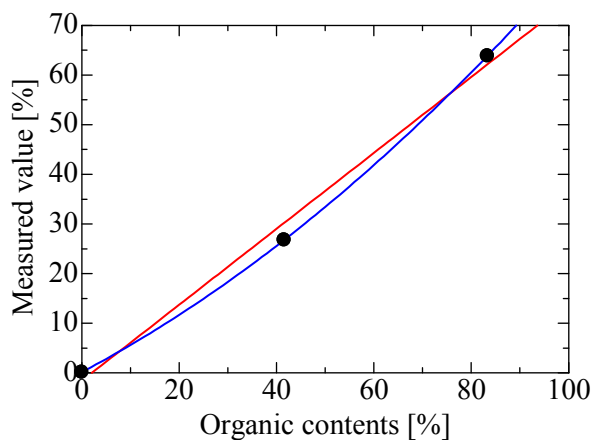


Fig. 13: Calibration curve (1)

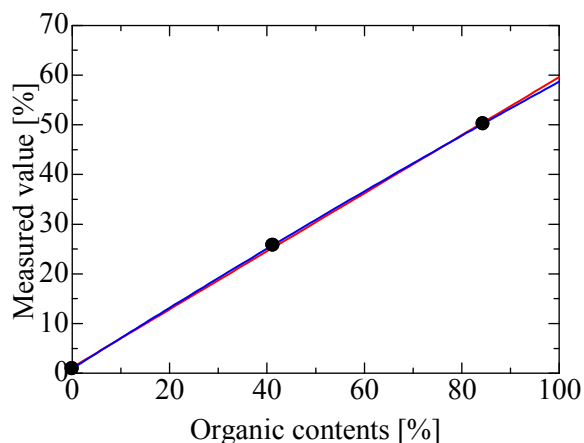


Fig. 14: Calibration curve (2)

method presented here.

However, despite some weaknesses, we were successful in further improving the weaknesses of our artificial sludge production methods reported previously [5]. For example, in a previous section (2.1), we mentioned that it was impossible to recreate natural hedoro with low organic contents (less than 6.91%). However with our method presented here, although future research for improvement is still needed, we were successful - with certain limitations- to recreate low organic contents hedoro, such as those from the Hidaka port, and we need to resolve reproducibility, consider from p value in significant difference (Table 6). As these results, we understood that higher reproducibility in first experiment (Table 4) by 0.181 than second experiment (Table 5) by 0.499. But we couldn't show p value under 0.05 in this study.

4. CONCLUSION

In our present study, we were successful in improving our previously reported method to recreate natural hedoro with low organic content (high inorganic content) by utilizing inorganic matter extracted from the original natural hedoro. Inorganic matter storage is much easier and more

Table 4: Result of reproduction (1)

22th Feb., 2018		Organic contents [%]
Natural	Average as 1.30	0.92
		1.43
		1.53
Semi-artificial (Added 2.96% of A. S. powder)	Average as 1.31	1.09
		1.37
		1.47

Table 5: Result of reproduction (2)

25th May, 2018		Organic contents [%]
Natural	Average as 1.50	1.40
		1.77
		1.33
Semi-artificial (Added 0.86% of A. S. powder)	Average as 2.86	2.80
		3.17
		2.61

Table 6: Standard deviation and significant difference in semi-artificial hedoro

	Standard deviation	significant difference
Natural (1)	0.268	p = 0.181
Semi-artificial (1)	0.161	
Natural (2)	0.196	p = 0.499
Semi-artificial (2)	0.232	

reliable, since organic matters changes drastically during storage, causing changes to the properties of the hedoro samples. Therefore, the recreation of a semi-artificial sludge using preserved inorganic materials extracted from the original natural samples would allow successful recreations of the original natural hedoro.

To summarize:

- (1) If use zeolite in artificial sludge like previous study, it is difficult to mimic under 6.91% by conditions.
- (2) About to storage hedoro for experiment, organic contents were changed under freezing. So it is important to keep under refrigeration when storage organic matter.
- (3) Moisture contents were changed by many elements; way of storage, time of storage, and organic contents.
- (4) It is impossible to keep hedoro same as natural conditions.

In the future, we will try to improve our method to recreate natural hedoro with low organic content, or high inorganic content. We will also consider and test other possible source of organic matter besides yeast extract, and inorganic matter besides zeolite.

REFERENCES

- [1] Yoshida T., About generation and the removal of the sludge - In bottom sampler examination of the Gulf of Minamata, HEDORO, No. 1, 1974, pp.11–27.
- [2] Okamoto K., Toyama T., and Komoriya T., Ocean Decontamination: High Ability Removal Method to Radioactive Cesium from Ocean Sludge by Using Micro Bubbles and Activating Microorganisms. *International Journal of GEOMATE*, Vol. 12, Issue 32, 2017, pp.57–62.
- [3] Hirano H., Toyama T., Nishimiya N., and Okamoto K., Removal of Cesium from Sea Sludge through Decomposition of Organic Matter with Aqueous Hydrogen Peroxide. *International Journal of GEOMATE*, Vol. 8, Issue 1, 2015, pp.1203–1206.
- [4] Hirano H., Semura D., Sakamoto K., Toyama T., and D. H. E. Setiamarga, A Dynamic changes of organic content over time in the sea sludge collected from the Gobo/Hidaka coastal area in Wakayama, southwest Japan. *IOP Conference Series: Earth and Environmental Science*, (Accepted).
- [5] Hirano H., Toyama T., Nishimiya N., D. H. E. Setiamarga., Morita S., Uragaki Y., and Okamoto K., Artificial Sludge Based on Compositional Information of a Natural Sea Sludge. *International Journal of GEOMATE*, Vol. 12, Issue 31, 2017, pp.95–99.
- [6] Uragaki Y., Morita S., Hirano H., Ability of adsorbed cesium by organic matter from sea sludge. 50th Annual Conference of Japan Society on Water Environment, 2016, pp. 622.
- [7] Hirano H., Sakamoto K., and Semura D., Comparison of adsorbed ability for cesium, by inorganic matter and sea sludge Part2: changing decontaminate ability by values of Cs in sample. 51th Annual Conference of Japan Society on Water Environment, 2017, pp. 404.
- [8] Tamamura S., Sakai T., Shimizu S., Ishijima Y., Igarashi T., Variation in inorganic nitrogen and organic carbon concentrations in groundwater samples stored under cold and frozen conditions. *Journal of Groundwater Hydrology*, Vol. 54, Issue 2, 2012, pp.107–116.
- [9] Ide T., Kawasaki K., Yamashiro H., and Matsuda A., Conditioning of excess activated sludge by freezing and thawing process - the change of physical chemical properties of sludge with half-freezing and extended freezing -. *Suishitsuodakukenkkyu*, Vol. 10, No. 10, 1987, pp. 618–623. (in Japanese)
- [10] Kawasaki K., Matsuda A., and Ide T., Conditioning of excess activated sludge by freezing and thawing process - the change of settling characteristics of sludge floc -. *Kagakukogakuronbunshu*, Vol. 16, No. 1, 1990, pp. 16–22. (Japanese)
- [11] Fujita M., Sludge dewatering by freezing. *Japanese Journal of Freezing and Drying*, Vol. 36, 1990, pp. 10–13. (in Japanese)
- [12] F. D. Sanin, P. A. Vesilind, and C. J. Martel, Pathogen reduction capabilities of freeze-thaw sludge conditioning. *Water Research*, Vol. 28, No. 11, 1994, pp. 2392–2398.
- [13] B., Örmeci, Freeze-thaw conditioning of activated sludge: effect of monovalent, divalent, and trivalent cations. *Journal of Rediduals Science & Technology*, Vol. 1, No. 3, 2004, pp. 143–150.
- [14] K. Hua, J. Q. Jiang, Q. L. Zhao, D. J. Lee, K. Wanga, and W. Qiu, Conditioning of wastewater sludge using freezing and thawing: Role of curing. *Water Research*, Vol. 45, issue 18, 2011, pp. 5969–5976.
- [15] Noda S., Koyama K., Takakuwa T., and Akutsu T., Experimental studies on dewatering of digested sludge by freezing thawing and filtration method. *Eiseseikougaku*, Vol. 9, 1964, pp. 41–53. (in Japanese)
- [16] Sato A., Nakamura D., Suzuki T., and Nishimoto S., Change of moisture content of unsuitable soil through freezing and thawing process appeared in natural cold climate. *Japanese Goetechnical Journal*, Vol. 4, No. 2, 2009, pp. 205–214. (in Japanese)

EFFECTIVENESS OF USING CICADA SHELL AND RIVER BRYOPHYTE AS AN INDEX OF AVAILABLE CU, ZN, PB, AS, NI AND CR CONTAMINATION

Hiroyuki Ii¹

¹Faculty of Systems Engineering, Wakayama University, Japan

ABSTRACT

Cicada shells, mainly Black Cicada, were analyzed in metropolitan parks in Wakayama and Osaka prefectures. Cu, Pb, Cr, Zn, and Ni concentrations of black cicada shell at parks which were developed on former factory land were 10 to 100 times or 10 times higher than those at normal metropolitan parks. Therefore, high Pb, Cr, Zn, and Ni concentrations of black cicada shells were thought to have been caused by soil metal concentration. Cu, Pb, Zn and As concentrations of large brown, small and evening cicada and anotogaster sieboldii shells at metal mines were high and their high concentration was influenced by soil contamination caused by tailings. Cr and Ni concentrations of small, evening and robust cicada shells at serpentinite areas were 10 times higher than those of other normal cicada shells. Therefore, high Cr and Ni concentration was also thought to be caused by serpentinite soil metal concentration. As a result, metal concentration of cicada shell was thought to be influenced by soil metal condition. For Pb Zn, Cu Cr, Ni, and As, metal concentrations of adult cicada were lower than those of cicada shell. Metal concentration of river bryophyte was influenced by mine activity such as waste water from tailings and geological condition. The maximum differences for Pb Zn, Cu Cr, Ni, and As concentrations between contaminated areas and non-contaminated areas were very high, 80,000, 1,000, 20,000, 5,000, 2,000, and 2,000 times. Therefore, river bryophyte was influenced by river metal contamination and was also clarified to be an index of river contamination. .

Keywords: Cicada shell, Metal, Bryophyte, Contamination

INTRODUCTION

Heavy metal concentration for soil is not uniform and it is difficult to measure available heavy metal concentration for terrestrial organisms because available heavy metal for terrestrial organisms depends on chemical form. Cicada shell and bryophyte are studied as an index of available heavy metal concentration for terrestrial organisms. Cicada larva lives in soil over several years and gets nutrition from the roots of trees. Heavy metal is accumulated in cicada larva through a bio-concentration process. Some kinds of heavy metal for cicada shell are concentrated from cicada comparing concentrations between cicada and cicada shell. As cicada shell can be sampled on tree and leaves, cicada shell is easier than adult cicada to determine living place. Therefore the metal concentration of cicada shell is thought to indicate the available metal concentration of soil around the living place [1], [2].

Heavy metal concentration for river water is very changeable and river metal contamination is thought to be cause by river water and river sediments. Consequently, it is difficult to measure the available heavy metal of river water. River bryophyte grows slowly and heavy metal concentration is relatively high in normal plants by a high bio-concentration process. Therefore, bryophyte heavy metal

concentration along streams is useful for estimating river metal contamination, geological condition and metal waste water in river catchment around living place [3], [4]. The purpose of this study was therefore to clarify the effectiveness of using cicada shell as an index of soil metal contamination and river bryophyte as an index of river metal contamination.

METHOD

Cicada shells and river bryophytes were sampled from 2015 to 2017 and 2015 to 2018 respectively. Sampling points were widely selected for covering metal contaminated and non-contaminated places. In particular, the Adelaide mine area with a large production of crocoite (CrPbO₄) was selected for bryophyte sampling expecting Pb and Cr contamination [5]. The Waidani, Ikuno and Tada mines were also selected as Pb, As, Cu and Zn contamination places [6], [7].

The sampling points of black cicada shell were Nishikino metal wire factory (NMF) in the south of Osaka prefecture, Wakayama University (WUI) on the Mesozoic sedimentary rock (Izumi Formation) at the north of Kinokawa River, Akiba mountain (AMG) and Wakayama Castle (WCG) on

Sanbagawa Green schist, Wakaura and Saigasaki park (WSP) on Sanbagawa pelitic schist at the south of Kinokawa River in Wakayama Prefecture [8], Shirasagi Park (SIA), Suminoe Park (SuNA), Sumiyoshi Park (SuYA), and Sumiyoshitaisya (SuTA) on alluvial sediment in the Osaka plain, Nagai Park (NPP) on the plateau sediment, and Osaka Castle Park (OCF) which was developed after closing a military factory in Osaka prefecture. Other kinds of cicada shell were sampled at Ikuno polymetal mines (IKM), Tada Ginzan silver and copper mine (TGM), Tada housing site (THS) near Tada mine, south of Nakase mine (NSS), north of Nakase mine (NNS) on serpentinite in Hyogo prefecture [7]. Shell of anotogaster sieboldii was sampled at Waidani polymetal mine (WVM) in Okayama prefecture.

The sampling points of Australian bryophyte were the Adelaide mine shaft and entrance (ADM), Adelaide mine tailing (ADO) and creek near Adelaide mine (ADC), Dundas Extended mine pond (DEP) and tailing (DET), Stichtite Hill (SHS) on serpentinite [5], Queen River from copper mine waste (QER) in the west of Tasmania Island and Costerfield mine Sb mine (CFA) and Dayslesford gold mine (DFG) in Victoria state [9]. Dundas extended mine and Adelaide mine produce a lot of Pb and Cr mineral. The sampling points of Canadian bryophyte were the Vermilion copper and nickel mine (VMP) and Crown reserve cobalt and silver mine (CCR) in Ontario Province. The sampling points of bryophyte of Japan were IKM, TGM, Nishinomaki arsenic mine (NSA), WVM, Mineoka serpentinite (MNS), Kongo granite mountain (KGG), Yoshino granite plateau, Ningyotouge granite mountain (NGG), and Okayama granite area (OKG).

Sampled cicada shell and bryophyte were dried after ultrasonic cleaning then dissolved with concentrated nitric acid solution. The solution after filtration with 0.45 micrometer and stream water sample were analyzed for metal concentration by ICP-AES (Inductively Coupled Plasma Atomic Emission Spectroscopy, SPS1700HVR ; Seiko Instruments Inc.).

RESULTS

Metal Concentration of Cicada Shell

Fig.1 shows Pb concentration of cicada shell. The Pb concentration of black cicada varied less than 0.01 to 600 ppm. NMF reached 600 ppm. Although the distance between SuNA, SuYA and SuTA is less than several km and under same geological condition, Pb concentration of SuTA shrine is, several tens ppm, 10 times higher than those of SuNA and SuYA parks. Pb concentration of

black cicada at OCF is also little high, 10 ppm. Excluding NMF, OCF and SuTA, Pb concentration of black cicada were 1 to 10 ppm. As NMF is metal wire factory, SuTA is shrine and OCF is past closed factory, therefore these soils were thought to be contaminated. Pb concentration of the evening and small cicada at IKM was high, 10 to 200 ppm and those of large brown at TGM were several tens ppm, over 10 times higher than those at THS although distance between both places was 10 km. Pb concentration of anotogaster shell at WVM was over 10 ppm.

Fig.2 shows Zn concentration of cicada shell. The Zn concentration of black cicada varied less than 10 to 1,000 ppm. Those at WUI and AMG were low, 10 to 100 ppm and at the other places 100 to 1,000 ppm. Zn concentrations of small cicada at IKM were high, 100 to 10,000 ppm. Zn concentrations of evening and large brown cicada were 10 to 100 ppm. Zn concentration of small cicada at IKM was high, 10 to 200 ppm and those of large brown at TGM were over 10 times higher than those at THS although distance between both places was 10 km. Zn concentration at WVM was 500 to 700 ppm.

Fig.3 shows Cu concentration of cicada shell. The Cu concentrations of black cicada were uniform, several to several tens ppm and difference between locations was less than 10 times. Cu concentration of small cicada at IKM was high, several tens to 2,000

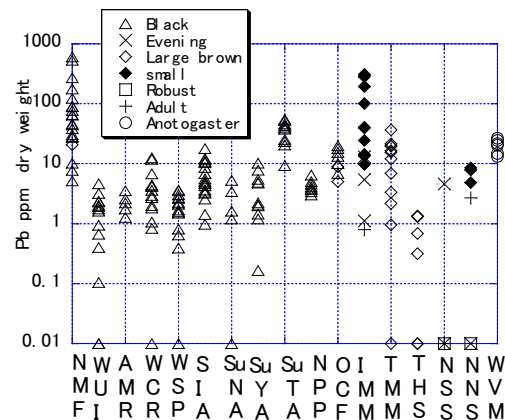


Fig.1 Pb concentration of cicada shell

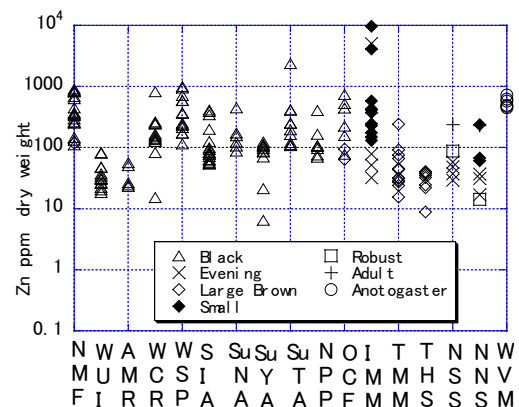


Fig.2 Zn concentration of cicada shell

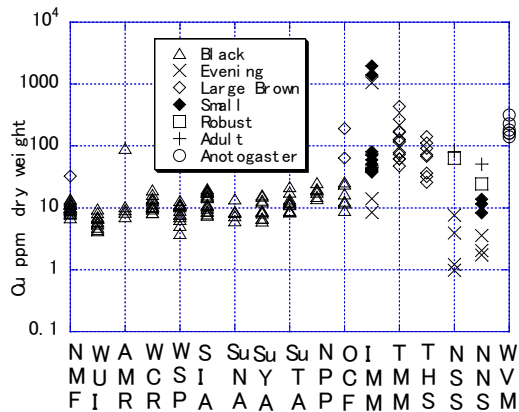


Fig.3 Cu concentration of cicada shell

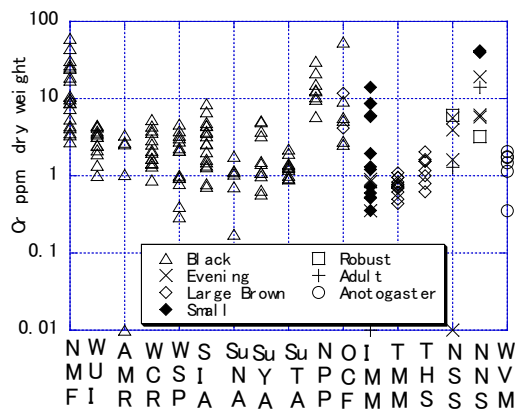


Fig.4 Cr concentration of cicada shell

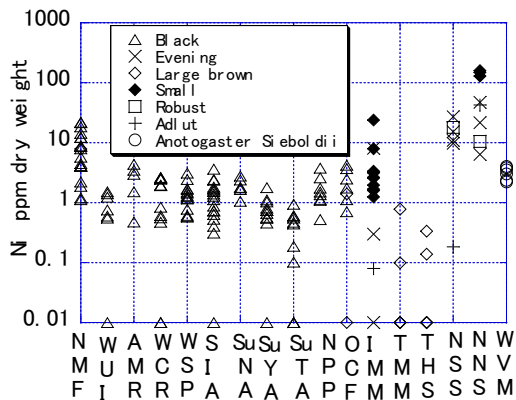


Fig.5 Ni concentration of cicada shell

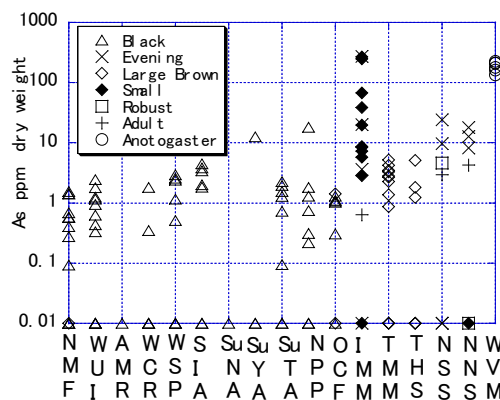


Fig.6 As concentration of cicada shell

ppm and those of large brown at TGM reached 700 ppm, over 10 times higher than those at THS although distance between both places was 10 km. Cu concentration at WVM was over 100 ppm. Cu concentrations of evening cicada were very low, 1 to 10 ppm at Nakase areas (NSS and NNS).

Fig.4 shows the Cr concentration of cicada shell. The Cr concentration of black cicada varied less than 1 to 60 ppm. NMF reached 60 ppm. Cr concentrations of black cicada at NPP were also a little high, 10 ppm. Excluding NMF and NPP, Cr concentration of black cicada were 1 to 10 ppm. Cr concentration of small cicada at IKM was variable, several 0.1 to 10 ppm and those of large brown at TGM were less than 1 ppm. Cr concentration at WVM was less than several ppm. Cr concentrations of evening cicada at NSS and NNS were several to several tens ppm.

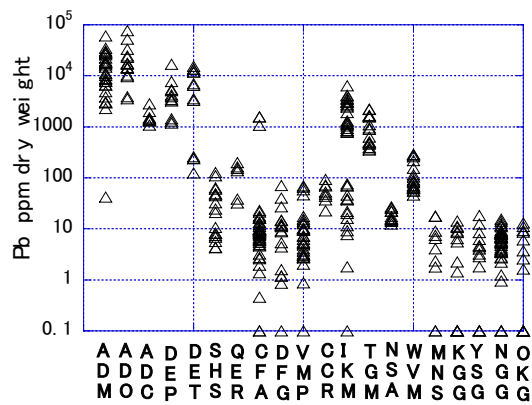
Fig.5 shows Ni concentration of cicada shell. The Ni concentration of black cicada varied less than 0.1 to 20 ppm. NMF were high and reached 20 ppm. Ni concentrations of black cicada at SuTA are little low, less than 1 ppm. Excluding NMF and SuTA, Ni concentration of black cicada were about 1 ppm. Ni concentration of small cicada at IKM was 1 to 10 ppm and those of large brown at TGM were less than 1 ppm. Ni concentration at WVM was several ppm. On the other, Ni concentrations of small and evening cicada at NNS were also 10 to 100 ppm.

Fig.6 shows the As concentration of cicada shell. The As concentration of black cicada varied 0.1 to 10 ppm. NMF were low 0.1 to 1 ppm although other metal was relative to high. As concentrations of evening and small cicada at IKM were high, 1 to 200 ppm. As concentration of anotogaster shell at WVM was high, 200 ppm. As concentrations of large brown cicada were 1 to 10 ppm.

Adults at IKM are small cicada and adults at NNS and NSS are robust cicada. Comparing cicada shell with adults, Pb, As, Cr and Ni concentrations of small and robust cicada adults were smaller than those of shells excluding Ni concentrations at NNS. For Ni concentrations robust cicada at NNS, cicada shell is lower than those of adult. Zn and Cu concentrations of robust cicada adult were higher than those of shells however those of small cicada shells and adults were the same. Totally, adult metal concentrations were lower than those of shell.

Metal Concentration of Bryophyte

Fig.7 shows Pb concentration for river bryophyte. Pb concentrations at the Adelaide mine area (ADM, ADO, ADC, DEP, DET) were extremely high, over 1,000 ppm and reached 80,000 ppm and reached also over 3,000 ppm at Japanese metal mines (IKM and TGM). Those at WVM were about 100. Those at non-contaminated area (MNS,



KGG, YSG, NGG

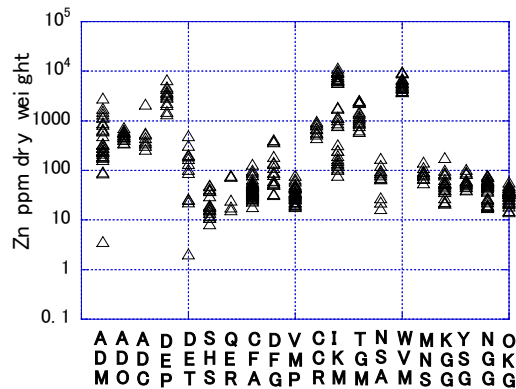


Fig.7 Pb concentration for river bryophyte.

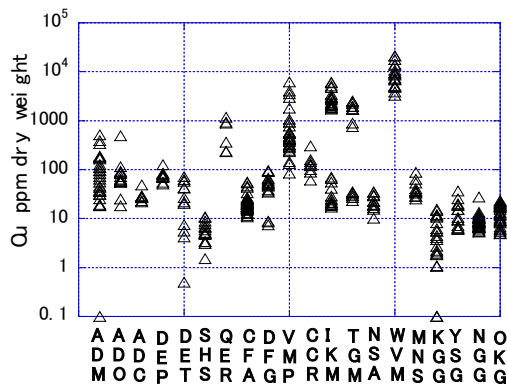


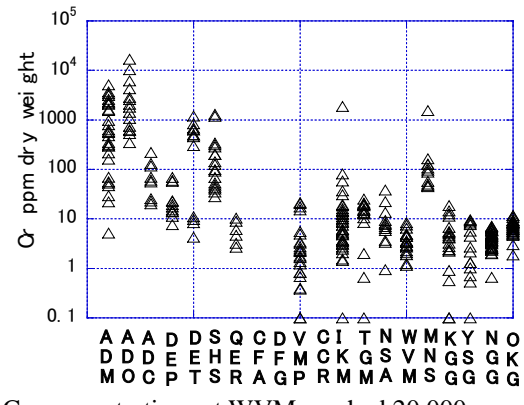
Fig.8 Zn concentration for river bryophyte.

Fig.9 Cu concentration for river bryophyte.

and OKG) were 1 to 10 ppm. Those at the other areas (SHS, QER, CFA, DFG, VMP and CCR) were 1 to 100 ppm.

Fig.8 shows Zn concentration for river bryophyte. Zn concentrations at Adelaide mine area (ADM, ADO, ADC, DEP, DET) were high, 100 to several 1,000 ppm and reached 7,000 ppm and reached also over 10,000 ppm at Japanese metal mines (IKM and WVM). Those at TGM were about 1000 ppm. Those at non-contaminated area (MNS, KGG, YSG, NGG and OKG) were 10 to 100 ppm. Those at the other areas (SHS, QER, CFA, VMP and NSA) were 10 to 100 ppm.

Fig.9 shows Cu concentration for river bryophyte.



Cu concentrations at WVM reached 20,000 ppm

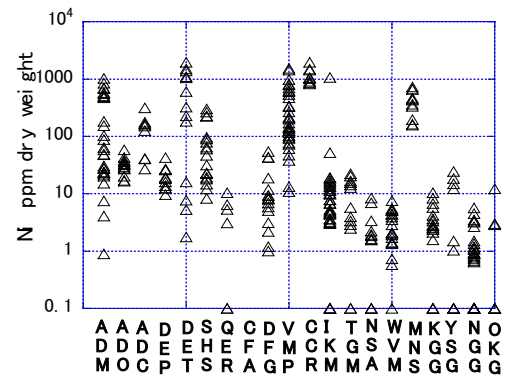


Fig.10 Cr concentration for river bryophyte.

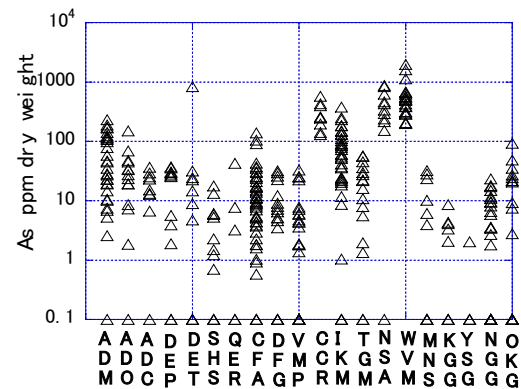


Fig.11 Ni concentration for river bryophyte.

Fig.12 As concentration for river bryophyte.

those at VMP, IKM and TGM were also high values, several 1,000 ppm. Those at Adelaide mine area (ADM, ADO, ADC, DEP, DET) were 10 to 1,000 ppm. Those at non-contaminated area (MNS, KGG, YSG, NGG and OKG) were 1 to several tens ppm. Those at the other areas were 10 to 100 ppm.

Fig.10 shows Cr concentration for river bryophyte. Cr concentrations at Adelaide mine area (ADM, ADO and DET) were extremely high, 10 ppm to 5,000 ppm. Those at serpentinite (SHS and MNS) were high, 100 ppm. Those at non-contaminated area (KGG, YSG, NGG and OKG) were 1 to 10 ppm. Cr concentration at high Cu sampling points, QER, VMP and WVM were less

than 10 ppm.

Fig.11 shows Ni concentration for river bryophyte. Ni concentrations at Adelaide mine area (ADM, DET), Vermilion mine (VMP), Cobalt (CCR) in Canada and serpentinite area (SHS and MNS) reached extremely high, 2,000 ppm. Those at non-contaminated area (KGG, YSG, NGG and OKG) were less than 1 to several tens ppm. Ni concentration at high Cu sampling points, IKM, TGM, QER, and WVM were less than several tens ppm.

Fig.12 shows As concentration for river bryophyte. As concentrations at WVM reached extremely high, 2,000 ppm and those at ADM, CCR, IKM and NSA also reached 500 ppm. Those at non-contaminated area (KGG, YSG, NGG and OKG) were less than 1 to several tens ppm. As concentration at high Cu sampling points, TGM, QER, and VMP were less than several tens ppm as same as Non-contaminated area.

DISCUSSION

Mainly, black cicada shells were analyzed in metropolitan parks in Wakayama and Osaka Prefecture because large amounts of cicada shell samples were easily obtained in metropolitan parks. On the other hand, in forests, cicada shells are scattered and it is difficult to get a lot of cicada shells in a narrow area. Cicada shell was very limited in forests and it is important to find trees concentrated with cicada shells. Then, if the contaminated area located in the forest, sampled cicada is not always expected species in the forest and cicada shell is not always found in contaminated areas. In the forest, large brown, evening, small or robust cicada shells were found in Kansai district.

NMF is a steel wire factory and Pb, Cr, Zn, and Ni concentrations of black cicada shell at NMF were 10 to 100 times or 10times higher than those at other points. In particular, the factory uses stainless (Ni and Cr alloy) and Ni and Cr contamination for soil is estimated and Pb or Zn was also thought to be used for producing steal wire. Therefore, high Pb, Cr, Zn, and Ni concentrations of black cicada shells were thought to be caused by soil metal concentration.

OCF is a metropolitan park but was a military factory in former times. Cr, Pb, and Cu concentrations of black cicada shell were relatively high, 10 times higher than those of black cicada. Cr, Pb, and Cu concentrations of Cicada shell were thought to be influenced by soil metal concentration after the military factory.

IKM and WVM are closed polymetal mines and their tailing contains Zn(sphalerite ZnS), Cu(chalcopyrite CuFeS₂), As(arsenopyrite FeAsS), and Pb(galena PbS) minerals and TGM is a silver

and copper mine those tailing contains Zn(sphalerite ZnS), Cu(chalcopyrite CuFeS₂), and Pb(galena PbS) minerals [7]. Although shell specie were different, Cu, Pb, Zn and As concentrations of small and evening cicada and anotogaster shells at IKM and WVM were high and their high concentration was influenced on soil contamination caused by tailings as well as high Pb, Cu and Zn concentration for large brown at TGM mine.

Cr and Ni concentrations of small, evening and robust cicada shells at NSS and NNS were 10 times higher than those of other normal cicada shells. Generally Ni and Cr concentration of serpentinite such as ultrabasic rock is high relative to other rocks. Therefore, high Cr and Ni concentration was also thought to be caused by soil metal concentration.

As a result, metal concentration of cicada shell was thought to be influenced by soil metal condition. The maximum values of each metal for black, evening, small and large brown cicada shell were 600, 200, 200 and several tens ppm for Pb, 1,000, 100, 10,000, and 100 ppm for Zn, 60, 10, 2,000 and 700 for Cu, 60, several tens, 10 and several ppm for Cr, 20, 100, 100 and 1 ppm for Ni, and 10, 200, 200 and 10 ppm for As.

High Pb concentration river bryophyte was found at metal mine areas (ADM, ADO, ADC, DEP, DET, IKM, TGM and WVM) and the maximum value was 80,000 ppm. On the other hand, those at non-contaminated area were 1 to several ppm and then Pb concentration of river bryophyte was influenced by mine activity such as waste water from tailings. The maximum difference between contaminated area and non-contaminated area was 80,000 times. High Zn concentration river bryophyte was found at metal mine areas (ADM, ADO, ADC, DEP, DET, IKM, TGM and WVM) and the maximum value was 10,000 ppm. On the other hand, those in non-contaminated areas were 10 to 100 ppm so the Zn concentration of river bryophyte was deemed influenced by mine activity such as waste water from tailings. The maximum difference between contaminated area and non-contaminated area was 1,000 times. High Cu concentration river bryophyte was found at metal mine areas (ADM, ADO, ADC, DEP, DET, IKM, TGM and WVM) and the maximum value was 20,000 ppm. On the other hand, those at non-contaminated area were 1 to several tens ppm and then Cu concentration of river bryophyte was influenced by mine activity such as waste water from tailings. The maximum difference between contaminated area and non-contaminated area was 20,000 times. High Cr concentration river bryophyte was found at Adelaide mine areas (ADM, ADO, and DET) and serpentinite areas (SHS and MNS) and the maximum value was 5,000 ppm. The

Adelaide mine area is accompanied with serpentinite.

On the other hand, those at non-contaminated area excluding serpentinite area were 1 to 10 ppm so the Cr concentration of river bryophyte was deemed influenced by mine activity such as waste water from tailings and geological condition. The maximum difference between contaminated areas and non-contaminated areas was 5,000 times. High Ni concentration river bryophyte was found at Adelaide mine area (ADM, DET), Vermilion mine (VMP), Cobalt (CCR) in Canada and serpentinite area (SHS and MNS) and the maximum value was 2,000 ppm. On the other hand, those at non-contaminated area excluding serpentinite area were 1 to several tens ppm and then Ni concentration of river bryophyte was influenced by mine activity such as waste water from tailings and geological condition. The maximum difference between contaminated area and non-contaminated area was 2,000 times. High As concentration river bryophyte was found at WVM, ADM, CCR, IKM and NSA and the maximum value was 2,000 ppm. Ore mineral at CCR and NSA was arsenic cobalt mineral and arsenic Sulphur mineral. On the other hand, those in the non-contaminated area were 1 to several tens ppm therefore As concentration of river bryophyte was influenced by mine activity such as waste water from tailings. The maximum difference between contaminated area and non-contaminated area was 2,000 times.

CONCLUSION

Mainly, black cicada shells were analyzed in metropolitan parks in Wakayama and Osaka prefecture. In forests, large brown, evening, small or robust were found in the Kansai district. Pb, Cr, Zn, and Ni concentrations of black cicada shell at steel wire factory were 10 to 100 times or 10 times higher than those at other points. Cr, Pb, and Cu concentrations of black cicada shell at a metropolitan park after military factory were relatively high, 10 times higher than those of black cicada. Therefore, high Pb, Cr, Zn, and Ni concentrations of black cicada shells were thought to have been caused by soil metal concentration.

Cu, Pb, Zn and As concentrations of small and evening cicada and anotogaster shells at polymetal mines were over 10 times higher than those at non-metal mine area and then their high concentration was influenced on soil contamination caused by tailings. Cr and Ni concentrations of small, evening and robust cicada shells at serpentinite areas were 10 times higher than those of other normal cicada shells. Generally Ni and Cr concentration of serpentinite such as ultrabasic rock is high relative to other rocks. Therefore, high Cr and Ni concentration was also

thought to be caused by soil metal concentration. For Pb Zn, Cu Cr, Ni, and As, metal concentrations of adult cicada were lower than those of cicada shell.

Metal concentration of river bryophyte was influenced by mine activity such as waste water from tailings and geological condition. The maximum differences for Pb Zn, Cu Cr, Ni, and As concentrations between contaminated area and non-contaminated area were very high, 80,000, 1,000, 20,000, 5,000, 2,000, and 2,000 times. Therefore, river bryophyte was influenced by river metal contamination and was also clarified to be an index of river contamination.

REFERENCES

- [1] Robinson G.R. Jr. Sibrell P.L. Boughton C.J. and Yang L.H., Influence of soil chemistry on metal and bioessential element concentrations in nymphal and adult periodical cicadas, *JScience of the Total Environment*, Vol. 374, 2007, pp. 367-378.
- [2] Clark Jr D.R., Organochlorines and heavy metals in 17-years cicada pose no apparent dietary threat to birds, *Environ. Monit. Assess.*, Vol.20, 1992, pp47-54.
- [3] Debéna S., Aboala J.R., Carballeira A., Cesab M. and Fernández J.A., Monitoring river water quality with transplanted bryophytes, A methodological review, *Ecological Indicators* Vol.81, 2017, pp.461-470.
- [4] Kubohara T and H. Ii, "Evaluation of metal contamination for river using bryophyte in the Kinokawa River catchment", *International Journal of GEOMATE*, Vol. 13, Issue 37, Sep., 2017, pp. 108-115.
- [5] Bottrill R.S., Williams P.A., Dohnt S., Sorrell S. and Kemp N.R., Crocoite and associated minerals from Tasmania, *Australian Journal of Mineralogy*, Vol.12, No.2, Dec., 2006, pp.59-90.
- [6] Ii H. and Nishida A., Effectiveness of using river insect larvae as index of Cu, Zn, and As contaminations in rivers, Japan, *International Journal of GEOMATE*, Vol. 12, Issue 33, May, 2017, pp. 153-159.
- [7] Nakamura T. and Sakiyama T., Mineral Resources in Hyogo Prefecture, *Humans and Nature*, No. 6, September 1995, pp.197- 243.
- [8] Wakayama City Children's Science Museum, <http://www.city.wakayama.wakayama.jp/kodomo/sassi/ganseki/chizu/wakayama.htm>
- [9] Department of Energy and Minerals, Government of Victoria, Australia, *Minerals of Victoria* (1:1,000,000), 1992.

STUDY ON REMOVAL OF CONTAMINATED SOIL ON FOREST SLOPE FOCUSING ON DIFFERENCE IN DENSITY OF SUBSURFACE GROUND

Keiichiro Shibata¹, Hidenori Yoshida², Daisuke Matsumori³, Matsumoto Naomichi⁴ and Kazushi Moriki⁵
^{1,5} Graduate school of engineering, Kagawa university, ² Faculty of engineering and design, Kagawa
university, Japan; ³ Penta-ocean construction, Japan; ⁴ Technical staff, Kagawa university, Japan

ABSTRACT

A large amount of radioactive cesium was released from the Fukushima Daiichi nuclear power station. Decontamination in living area has been almost completed for seven years. However, decontamination has not progressed much in forests where people do not enter. The decontamination of soil on forest slope cannot be done using heavy machinery unlike that on flatland. The effective decontamination method for the forest slope is desired. Therefore, in this study, the collecting method of slope surface soil through flushing water and the soil separation method focusing on difference in density of minerals were proposed and examined. In the proposed method, it is expected to reduce the volume of contaminated soil through the separation of contaminated part and non-contaminated one. In this study, the laboratory test is conducted to evaluate the usefulness of the proposed method. In the test, a device of simulating the slope and a device to flush the soil by flowing water are produced. When an actual soil is utilized for experiment, it is difficult to ensure the experimental repeatability due to soil variability. Therefore, simulated soil is consisted of Toyoura standard sand and vermiculite. To simulate soil contaminated with cesium, cesium standard solution is added into the simulated soil. The soil is set on the slope, and the test is conducted to flush and collect the soil by running water from upside to downside. As a result, it is clarified that only the soil containing cesium can be removed by separating the soil after flushing.

Keywords: Radioactive cesium, Forest slope, Vermiculite, Contaminated soil

INTRODUCTION

The Great East Japan Earthquake, which is the most powerful earthquake on record, occurred in Sanriku offshore on March 11, 2011. The Fukushima Daiichi nuclear energy plant of the Tokyo Electric Power Company (1F) was hit by the great Tsunami several times after an hour of the earthquake. The power facilities were widely destroyed, and the basement room and the shaft were inundated with the Tsunami. Major quantity of radioactive materials were discharged from the 1F. The radioactive materials is spread to atmosphere, which is fallen down mountain, river and marine by rain breeze. Also, the radioactive materials that have fallen into the mountains are firmly bonded to the clay minerals in the soil. Especially, the cesium-137 has been extensively detected in Fukushima prefecture because the cesium-137 has been vigorously discharged and long half period. The radioactive cesium has been decontaminated by removing the top soil because it has settled in the surface layer of the soil after being absorbed by atmospheric dust as in [1]. The decontamination around the living environment of the resident is almost completed due to a hard decontamination work since the accident. On the other hand, there are places where the decontamination is completed and decontamination is

uncompleted in forests away from the living environment of residents. The completion ratio of decontamination of forests in the area where the country implements the decontamination is shown in Table 1. Also, from this table, there is a difference in the completion ratio of the decontamination depending on geographical features. Some forests in the area such as Iitate village and Kawamata town are scarcely decontaminated. Although the air dose rate of forest decreases year by year due to the decontamination work and half-life, it is still higher than that in living area. The decontamination in forests is difficult because it is hard to enter heavy machinery to remove the top soil. The decontamination of contaminated soils on flat grounds is primarily done by removing the top soil. Furthermore, on forest slopes, careful decontamination work is required as excessive removal of top soil can cause landslides.

For radioactive cesium in the forest soil, a removal method using wood chips is devised by Kaneko et al. at Yokohama National University as in [2]. The method utilizes the property that fungi absorb radioactive cesium. The wood chip is placed in the bag and radioactive cesium is adsorbed into the cellulose body contained in the wood chip. After that, the decontamination is completed by collecting the bag. This method is inexpensive. However, it takes

time because it can be removed only by the power of fungi. Alternatively, the previous studies are conducted by the faculty of engineering, Ibaraki University in order to control the moving of cesium on the forestry slope, and it has two features as in [3]. One is that the bentonite is spread onto the leaf mold in the forest so as to control the resorption of the radioactive cesium to plants. The other is that the moving of the bentonite including the radioactive cesium is controlled by polyion-complex (PIC) of excess positive charge and negative charge. The radioactive cesium in the air and solution is adsorbed into the bentonite. The resorption to the plant is controlled by the absorption performance of the bentonite. Alternatively, the forest ecosystem is not destroyed because the elements such as the flow of rainwater are used in this method. Furthermore, the PIC is harmless because the raw material of PIC is commonly used as the thickener of ice-creams as in [4]. The moving of cesium is controlled, but the contaminated soil is not reduced in this method. Besides, it takes time to complete the work due to the use of rainfall. Based on these points, in previous study, the simple decontamination method is proposed in order to decontaminate the contaminated soil on the slope by flowing water as in [5]. From this study, it was clarified that it was possible to remove about 50% of cesium by running water from simulated contaminated soil and stirring after recovery of running water. On the other hand, it was mentioned as a problem that the variability occurred in the flowing water time and the flowing water amount in the produced equipment. Thus, in this study, the reproducibility of the test is improved by improving the equipment. Then, the method of recovering only soil containing cesium is proposed by using the difference in the specific gravity of the soil after collection. In this method, only clay mineral that specifically adsorbs cesium such as vermiculite is recovered from mixed sand and separated. Furthermore, other cesium is recovered by washing thorough stirring, which leads to volume reduction of contaminated soil.

Table 1 Decontaminated situation of forest in town and village

Cities	Decontamination completion ratio (%)
Tamura city	100
Kawauchi village	74
Iitate village	3
Kawamata town	12
Katsurao village	67
Okuma town	44

CESIUM IN THE SOIL

A large number of radioactive materials was

released by the accident in the 1F. The radioactive cesium has harmful long-term effects due to its long half-life. The volume of spreading strontium-90 is comparatively small, despite its long half-life. The cesium exists as the monovalent cation in the soil, and it is absorbed into the soil particle having a negative charge. Especially, the cesium is selectively absorbed into the small clay particle. The cesium is adhered to the soil due to the 2:1 types of lamellar silicate. When the part of silicon or aluminum substitute for another element having a few positive charges in the silicon tetrahedron sheet or aluminum octahedron sheet, the negative charge is expressed with the shortage of positive charge in the sheet. Moreover, the cation is absorbed in order to neutralize the intercalation. The charge in this intercalation shows a high selectivity for the cesium ion. That is because the six-membered ring is nearly equal to the ion radius of the cesium ion in the basal seat of the silicon tetrahedron sheet. Alternatively, the bonding strength with the six-membered ring becomes larger as the hydration energy is smaller, and the bonding strength of cesium ion is the highest. Generally, the six-membered ring is occupied by the potassium ion because the abundance of potassium ion predominantly is major in the soil (see Fig. 1 of top part). The terminal of the layer in the clay mineral is swelled by the disintegration, and the potassium ion is discharged. Thus, the empty space that another cation gains entry is formed. This space is called the frayed edge (see Fig. 1 of bottom part), and the extraction of cesium ion from the frayed edge is very difficult. It is almost impossible to extract the cesium in the frayed edge only by flowing water. Thus, in this study, it is considered that the contaminated surface soil can be collected with the flowing water by utilizing the strong fixation.

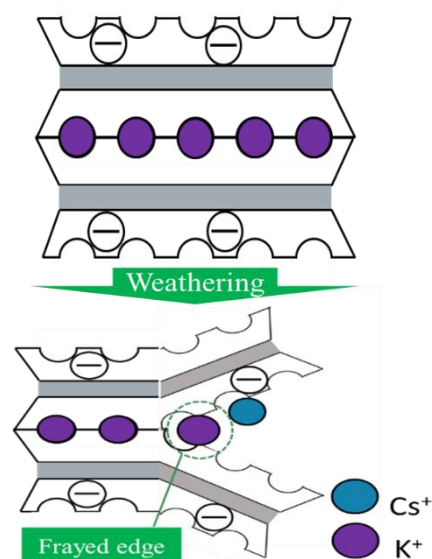


Fig. 1 Top part of 2:1 types of lamellar silicate and bottom part of Frayed edge

METHOD

The simulated soil used in the test and the test method are explained, respectively. Alternatively, in this study, all of the tests are conducted three times under the same conditions to ensure the repeatability of the tests.

Assumed contaminated soil

In this study, the Toyoura standard sand, vermiculite or their mixed sand is used as the assumed contaminated soil to which the cesium is added. The Toyoura standard sand consists of uniform grain size. The vermiculite contains the silicate mineral that mainly consists of the oxidized silicon, magnesia and aluminum oxide. The vermiculite has a high adsorption performance for cesium as in [6], and the mechanism of absorption has been clarified as in [7]. The vermiculite is widely distributed to Fukushima soil, and the vermiculite constitutes barriers to the decontamination of cesium in a soil. Based on the past study as in [5], 9.5 g of the standard sand and 0.5 g of vermiculite is mixed in order to make the assumed contaminated soil.

Test and analysis method

In order to imitate the real behavior of cesium in the soil slope, the slope device is produced (see Fig. 2). The slope device consists of two equipment: one is the slope section and another is the flowing water section. A 3D making device is used to produce the slope section (20.0 cm x 20.0 cm x 6.5 cm). The slit is set at the bottom of slope section in order to collect the water and soil which contain cesium. Although details will be described below, the assumed soil falls into this slit by flushing water from the upper part of the slope of the equipment. Also, the slope angle is set to about 9 degrees to avoid the flow disruption. The flowing water section is made by the polyvinyl chloride (PVC) pipe having the spiral holes. The rotating shaft is set on the top of the slope, and the PVC pipe and the rotating shaft are connected. The PVC pipe is rolled at 10 rpm, and the water is evenly flowed out from each hole by rolling the PVC pipe.

The test is divided into two steps. In the first step, the mixed sand containing cesium on the slope is recovered by running water, and the cesium is separated from soil by stirring. Specifically, 1 ml of a cesium chloride solution (about 3.3 ppm of initial concentration) is added to the mixed sand and the curing of mixed sand is conducted. It is known that the time required for adsorption of cesium to clay minerals is long. Also, a long period has elapsed since radioactive cesium deposited in the soil of Fukushima. Based on these points, a curing period is established to investigate the influence of passage of time on the absorption of cesium in the soil. The curing period is

0, 7, 14 and 28 days. After curing, the mixed sand is set on the slope of the equipment. The assumed soil is collected by flushing water from the rolling pipe at the upper part of the slope. The water and assumed contaminated soil are collected from the slit by flushing water. The cesium concentration in the supernatant of the solution is analyzed by an AAS (Atomic Absorption Spectrometer). In the second step, the recovered the assumed contaminated soil is classified by sieving. From some trials of sieving at an early stage, it is found that the sieving of the sand is difficult under the moisture condition of the sand. Therefore, the assumed contaminated soil is dried for 24 hours in an oven dryer set at 110 °C. The using sieve size is 425, 250 and 106 µm. After classification, the assumed contaminated soil remaining in each sieve is stirred, and the cesium concentration is analyzed by the AAS (Atomic Absorption Spectrometer) to calculate the extraction ratio for soil that remained in each sieve. As the screwing method, 200.0 mL of pure water is poured into the collected soil, and the sample is screwed with 300 rpm for 10 minutes by the stirrer. The calculation formula of the extraction ratio is shown below.

$$\text{Extraction ratio (\%)} = \frac{\text{extracted amount (mg)}}{\text{added amount (mg)}} \times 100 \quad (1)$$

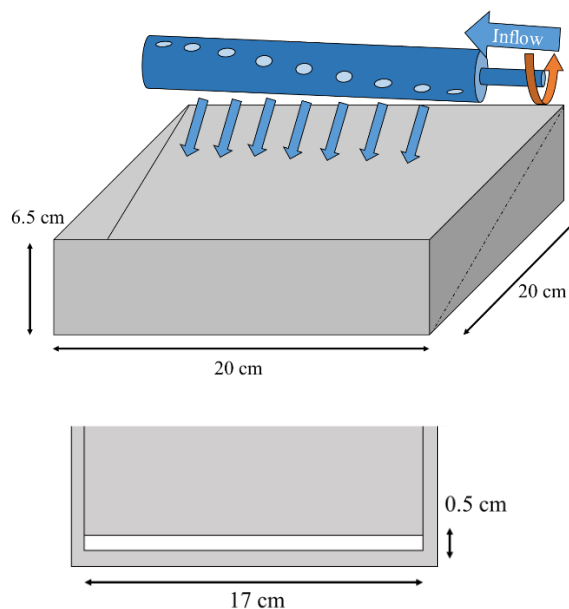


Fig. 2 Slope device

TEST RESULTS

The results of test in the each step are shown and discussed, respectively. The each result is shown thorough the graph. The value in the graph is the

average one of the test of the three times.

Test result of first step

In the first step, the assumed contaminated soil is recovered by flushing water, and the concentration of cesium in the supernatant of the recovered sample is analyzed by AAS. The results are shown in Fig. 3. The extraction ratio of cesium and the curing period of cesium are shown in the vertical and horizontal axes, respectively. In the specimens without the curing period, the extraction ratio of cesium is about 7%, and over 90% of cesium remained in the assumed mixed soil. The extraction ratio of cesium is low in the case of setting on curing period of cesium compared to case of the specimen without curing period. The extraction ratio hardly change even if the curing period is prolonged. It is found that the extracting of cesium from contaminated soil in a real situation is difficult by only flushing water regardless of the length of curing period.

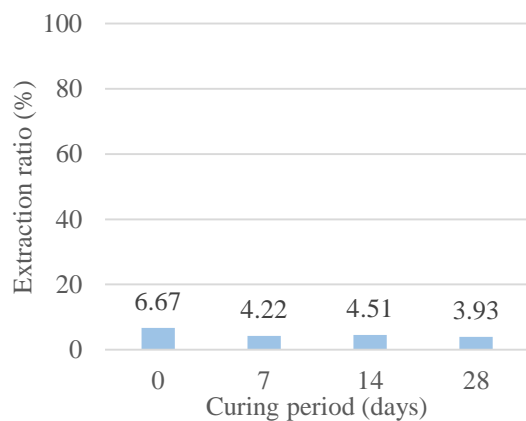


Fig. 3 Extraction ratio of cesium after flushing water

Test result of second step

In the second step, the recovered soil in the first step is dried, and classified by sieving. The amount of recovered soil is measured. After measuring, the sieved soil is washed out by stirring, and the concentration of cesium in the solution which is used during the stirring is analyzed by the AAS.

First, the mass of the assumed soil remaining in each sieve is shown in Table 2. The mass of the assumed soil before the test is 10 g, which means that almost all assumed soil is recovered by flushing water. It is suggested that the flushing water is effective for collecting of the contaminated soil on the slope. Alternatively, all of the soil remaining in 425 μm of the sieve are the vermiculite because all standard sand pass through 425 μm of the sieve.

Secondly, the extraction ratio of cesium extracted

by stirring is shown in Fig. 4. The extraction ratio of cesium and the curing period of cesium are shown in the vertical and horizontal axes, respectively. The lower the extraction ratio is, the longer the curing period is getting. It is considered that the cesium is adsorbed into the frayed edge in vermiculite by curing as the reason. Moreover, the cesium tend to be extracted easily from the soil that remained in 106 μm of the sieve. As this reason, it is presumed that most of the soil remaining in 106 μm of the sieve is the standard sand. From these facts, it is suggested that the concentration of cesium can be reduced by screwing the soil except frayed edges such as the standard sand. Also, the amount of contaminated soil may be reduced by separating the vermiculite containing a lot of cesium from the soil.

Table 2 Mass of soil remaining in each sieve

Sieve mesh (μm)	Curing period (days)			
	0	7	14	28
425	0.46	0.45	0.44	0.48
250	1.09	1.35	1.38	1.93
106	8.40	8.13	8.13	7.53
Bottom	0.03	0.03	0.03	0.02
Total	9.99	9.97	9.98	9.96

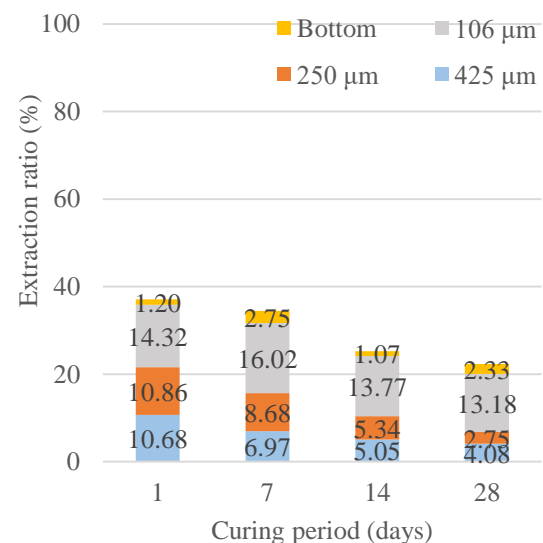


Fig. 4 Extraction ratio of cesium after sieving and screwing

CONCLUSIONS

In this study, the test equipment assuming the forest slope is made and the recovering test of the assumed contaminated soil by flushing water is conducted in order to establish a new decontamination method for the soil of the forest slope where the decontamination work is hard. The standard sand and the vermiculite are mixed to model

the assumed contaminated soil. The contaminated part of the soil can be reduced by separating and recovering the soil because the their adsorption property of minerals involved in the soil for cesium is greatly difference. Therefore, the recovered contaminated soil is classified according to the minerals by the mesh control with sieve. After classification, washing out by stirring is attempted to reduce the concentration of cesium in the assumed contaminated soil by separating the main part in which cesium is mainly involved. As a result of the test, the assumed soil is recovered with only flushing water. Furthermore, the standard sand and the vermiculite are separated by the mesh control with sieve. In other words, it is suggested that only vermiculite adsorbing cesium strongly should be recovered to reduce the contaminated soil. The extracting cesium from the separated standard sand with stirring may also lead to the reduction of the concentration of cesium in the contaminated soil. From the above results, it is considered that the proposed method has usefulness for removing the contaminated soil on the forest slope and for the reduction of the contaminated soil by separating the soil part in which cesium is mainly involved. On the other hand, the assumed contaminated soil in this test is different from actual complicated soil. Therefore, the universal knowledge is not necessarily obtained only by this experiment. For example, the soil such as the decomposed granite soil has the complicated soil structure and contains a large amount of clay. The clay may have a frayed edge, and a lot of cesium may be adsorbed into the frayed edge. In near future, it is necessary to examine whether the decontamination and the volume reduction by the proposed method are possible for the soil such as the decomposed granite soil.

ACKNOWLEDGEMENT

The part of this work was supported by Japan Society for the Promotion of Science, the Grants-in-Aid for Scientific Research (C) (Grant number: 18J12343).

REFERENCES

- [1] Ministry of Agriculture, Forestry and Fisheries, Technical document on measures against decontamination of agricultural land, part 2 of construction, 2013, pp. 31-33.
- [2] B. Rafferty, et al., Decomposition in two pine forest: The mobilisation of ^{137}Cs and K from forest litter, *Soil Biol. Biochem.*, Vol. 29, No. 11/12, 1997, pp. 1673-1681.
- [3] Ibaraki University, KUMAGAI GUMI CO., LTD. and Japan Atomic energy Agency, "New technology to control the removal of radioactive cesium from forest to living area", May 2016, pp. 1-4.
- [4] Naganawa H, Kumazawa N, Saitoh H, Yanase N, Mitamura H, Nagano T, Kashima K, Fukuda T, Yoshida Z and Tanaka S, Removal of Radioactive Cesium from Surface Soils Solidified Using Polyion Complex Rapid Communication for Decontamination Test at Iitate-mura in Fukushima Prefecture, *Transactions of the Atomic Energy Society of Japan*, Vol. 10, 2011, No. 4, pp. 227-234.
- [5] Awal A.S.M.A, Hosseini H. and Hossain M.Z., Strength, Modulus of Elasticity and Shrinkage Behaviour of Concrete Containing Waste Carpet Fiber, *International Journal of GEOMATE*, Vol. 9, Issue 17, 2015, pp. 1441-1446.
- [6] Shibata K, Yoshida H and Matsumoto N, Study on removal method of cesium from slope soil using simple slusher, *International Journal of GEOMATE*, Vol. 14, Issue. 45, 2018, pp. 136-143.
- [7] Suzuki N, Amano Y, Ochi K and Toshiyuki C, "Cesium uptake with the natural raw vermiculite. ~Concerning the grain size to adsorbability, and its application to the column method~", *Journal of Ion Exchange*, Vol. 26, 2015, Issue. 3, pp. 29-33.
- [8] Motokawa R, Endo H, Yokoyama S, Nishitsuji S, Kobayashi T, Suzuki S and Yaita T, "Collective Structural Changes in Vermiculite Clay Suspensions Induced by Cesium Ions", *Scientific Reports (online)*, Vol. 4, Jun 2014, article number 6585 (online)

MAPPING STABLE ISOTOPIC RATIOS OF STREAM WATER AND CU, ZN, PB AND AS CONCENTRATIONS OF BRYOPHYTE ALONG STREAMS IN THE EAST OF OKAYAMA AND TOTTORI PREFECTURES, JAPAN

Hiroyuki Ii¹ and Masahito Yoshimura²

¹Faculty of Systems Engineering, Wakayama University, Japan; ²DOWA Holdings Co., Ltd., Japan

ABSTRACT

The stable isotopic ratio of precipitation is useful for estimating both the recharge area and resource of groundwater as well as for mapping of precipitation. Stream water is representative of precipitation for small river catchment so stream water was sampled and analyzed. A distribution map of oxygen and hydrogen stable isotopic stream water values along the Yoshiikawa and Tenjinkawa rivers show that isotope values decreased with distance from the Inland Sea implying that southward wind or cloud was mainly controlled isotope values and that the influence of the Japan Sea on isotope of precipitation was low.

Bryophyte grows slowly and accumulates heavy metals relative to other life by a high bio-concentration process. Therefore, bryophyte heavy metal concentration along streams is deemed useful for estimating river metal contamination, geological condition and metal waste water in the river catchment. Bryophyte along streams was also sampled at the same time of stream water sampling. A map for Zn, Cu, As, and Pb concentrations of bryophyte shows that metal concentrations of stream bryophyte around the watershed area were low whereas metal concentrations around Tsuyama Basin and Yanahara mine, were medium relative to those of the other areas excluding the Waidani mine area. In the Waidani mine area, Zn, Cu, As, and Pb concentrations of bryophyte were extremely high as well as high Zn, Cu, As, and Pb concentrations of stream water and high bio-concentration factor for bryophyte was maintained.

Keywords: Oxygen isotope, hydrogen isotope, bryophyte, river water

INTRODUCTION

Oxygen and hydrogen stable isotopic ratios of precipitation change with their distance from the sea, altitude, latitude, amount of precipitation and temperature [1], [2], [3]. The stable isotopic ratio of precipitation is useful for estimating recharge area and groundwater resources such as spring water and geothermal water and is important to the mapping of precipitation. Although the stable isotopic ratios of precipitation change with each precipitation event, stable isotopic ratios of river water are uniform values relative to those of precipitation because of the homogenization for precipitation. Stream water is a representative of precipitation for small river catchment [4], [5].

Bryophyte grows slowly and accumulates heavy metals relative to other life by a high bio-concentration process. Therefore, bryophyte heavy metal concentration along streams is deemed useful for estimating river metal contamination, geological condition and metal waste water in river catchment [6], [7], [8].

Streams are upper catchment and are generally not influenced by human activity. Therefore, neither sewage water nor agricultural seepage flows into streams. Then, in this study, using stream water or

bryophyte along streams which excluded sewage and agricultural seepage, data for metal contaminations of bryophyte and stable isotope values of precipitation were accumulated and mapped. In particular, in the eastern part of Okayama and Tottori Prefectures connecting the Japan Sea with the Inland Sea, it is possible to analyze the influence of the Japan Sea on isotope of precipitation [2], [3]. The area also includes the Ningyotouge uranium mine [9], the Yanahara pyrite mine [10] and the Waidani copper mine [11] so it was selected as a study area shown in Fig.1.

METHOD

Stream water and bryophyte along streams were sampled from 2012 to 2016. Measurement of δD and $\delta^{18}O$ for sampled water was carried out using an isotopic ratio measurement system (Sercon Geo Wet System). δD and $\delta^{18}O$ are presented in per mil (‰) of the standard average seawater (SMOW: Standard Mean Ocean Water). The formulas are shown in equation (1) and (2). δD and $\delta^{18}O$ of SMOW are denoted as (D/H) SMOW, ($^{18}O/^{16}O$) SMOW and δD and $\delta^{18}O$ of sample are denoted as (D/H) Sample,

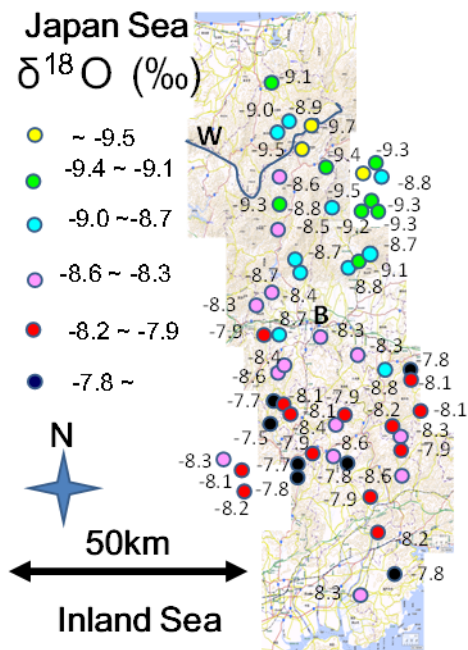


Fig.1 distributions of hydrogen stable isotopic values of stream water

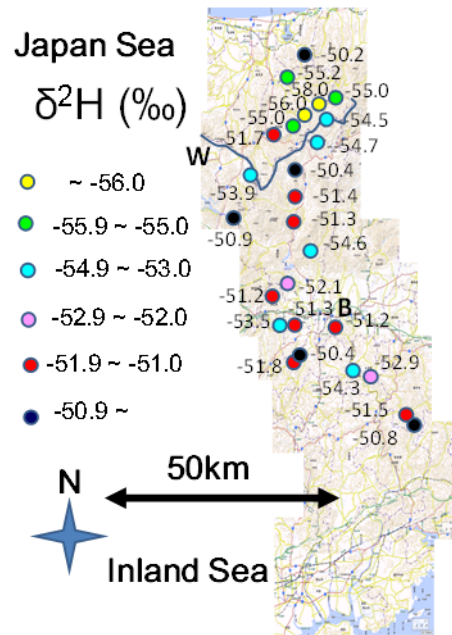


Fig.2 distributions of oxygen stable isotopic values of stream water.

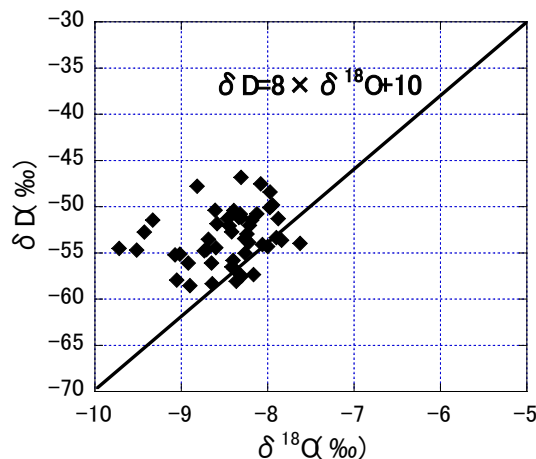


Fig.3 Relation between oxygen and hydrogen isotopic ratios

($^{18}\text{O}/^{16}\text{O}$) Sample. Measurement error of δD is ± 1.0 ‰ and measurement error of $\delta^{18}\text{O}$ is ± 0.1 ‰.

$$\delta\text{D} = [(\text{D}/\text{H}) \text{ Sample} / (\text{D}/\text{H}) \text{ SMOW} - 1] \times 1000: (1)$$

$$\delta^{18}\text{O} = [(^{18}\text{O}/^{16}\text{O}) \text{ Sample} / (^{18}\text{O}/^{16}\text{O}) \text{ SMOW} - 1] \times 1000: (2)$$

Sampled bryophyte were dried then dissolved with concentrated nitric acid solution. The solution, after filtration with 0.45 micrometer and stream water sample, were analyzed for metal concentration by ICP-AES (Inductively Coupled Plasma Atomic Emission Spectroscopy, SPS1700HVR ; Seiko Instruments Inc.).

RESULTS AND DISCUSSION

Isotope

Fig.2 and 3 show the distributions of oxygen and hydrogen stable isotopic values of stream waters along the Yoshiikawa and Tenjinkawa rivers. Both results show the minimum values around the watershed (W line as shown in Fig 2 and 3), between the Yoshiikawa River and Tenjinkawa River in the north of map, were found and isotope values increased gradually, apart from the mountain peak. In particular, maximum values were found around the Inland Sea. There are many small mountains between the Inland Sea and the watershed as well as very complicated topographic features. Point B was Tsuyama Basin and its altitude was low relative to the areas. Fig.4 shows the relation between oxygen and hydrogen isotopic ratios. From Fig.4, isotopic values were distributed between the meteoric line ($\delta\text{D} = 8 \times \delta^{18}\text{O} + 10$) and $\delta\text{D} = 8 \times \delta^{18}\text{O} + 20$ and the distribution had common values [2], [3].

Generally, the oxygen and hydrogen stable isotopic ratios of precipitation changes with their distance from the sea and altitude [1], [2], [3], [5]. Although complicated features and a basin were found, both isotope values decreased with distance from the Inland Sea. Southward wind or cloud was mainly thought to control isotope values and as a result, the influence of the Japan Sea on isotopes of precipitation was low. Southward wind or cloud must pass across Shikoku Island before it passes across the study area, therefore isotopic values were thought to be low relative to Wakayama and the same as Nara area [4].

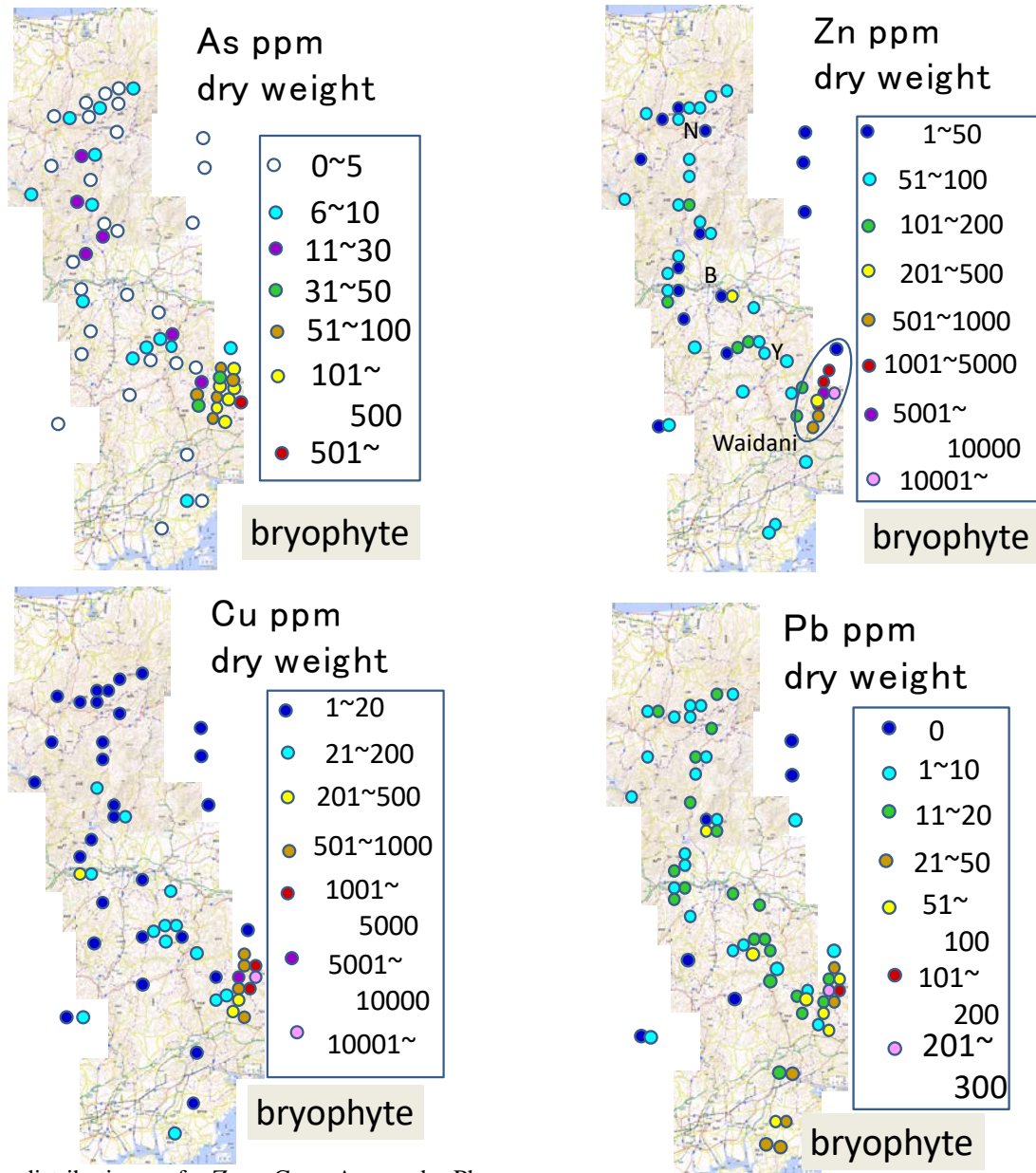


Fig.4 distribution of Zn, Cu, As and Pb concentrations for river f bryophyte

Metal concentration of bryophyte

Fig.4 shows distributions of Zn, Cu, As and Pb concentration for river bryophyte. Excluding the Waidani mine area in the southeast of the study area, Zn concentrations were 1 to 200 ppm. In particular, Zn concentrations of river bryophyte around the watershed area (Ningyotouge uranium mine, N) were low, less than 100 ppm. Around the Tsuyama Basin (B) and the Yanahara mine (Y), Zn concentrations were 200 to 500 ppm. On the other hand, Zn concentrations of river bryophyte around the Waidani mine area were over 500 ppm and the maximum value reached over 10,000 ppm.

Excluding the Waidani mine area, Cu concentrations were 1 to 200 ppm. In particular, Cu

concentrations of river bryophyte around the watershed area were low, less than 20 ppm. Around the Tsuyama Basin and the Yanahara mine, Zn concentrations were 20 to 500 ppm. In contrast, Cu concentrations of river bryophyte around the Waidani mine area were over 500 ppm and the maximum value reached over 10,000 ppm.

As concentrations of river bryophyte around the watershed area (Ningyotouge uranium mine) were low, less than 10 ppm and less than 30 ppm around the Tsuyama Basin and the Yanahara mine excluding the Waidani mine area. However, As concentrations of river bryophyte around the Waidani mine area were over 50 ppm and the maximum value reached over 500 ppm.

Pb concentrations of river bryophyte around the watershed area were low, less than 20 ppm and found to be from 20 to 100 ppm around the Tsuyama

Basin, the Yanahara mine and the Inland Sea excluding the Waidani mine area. However, Pb concentrations of river bryophyte around the Waidani mine area were over 59 ppm and the maximum value reached 300 ppm.

Waidani mine area

There are some small scale closed copper mines in the Waidani Valley at the northeast of Wake which were operated until 70 years ago. Tailings containing ores and slag which were disposed of along the top of a local valley with no protection. Pyrite FeS_2 , sphalerite ZnS , chalcopyrite CuFeS_2 and arsenopyrite FeAsS and galena PbS were found in the tailings and Zn, Cu, Pb, and As contamination was suspected. River water originated from the tailings seepage [11].

At the top of the valley, there are large tailing places from which the south and north rivers originated. The upstream, middle and downstream of the south river are WSU, WSM and WSD and the length was 4 km. The sampling points from the upstream to downstream of the north river are WNT, WNH, WNU, WNM and WND and the length was 3 km. WNT is spring from the tailing. WNH is head of river with no tailing and WNU is a stream after

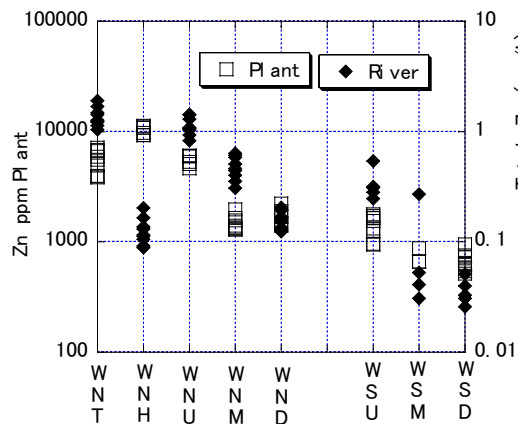


Fig.5 Zn concentration for bryophyte and river water

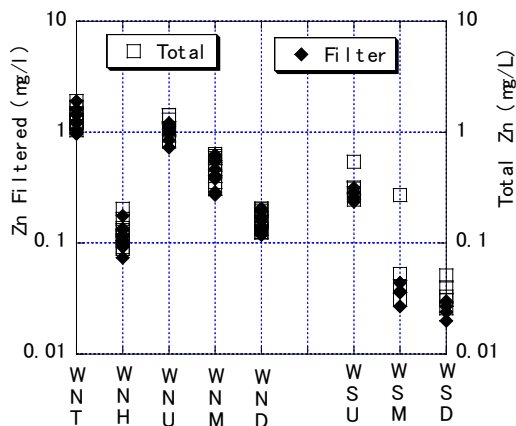


Fig.6 total and soluble Zn concentration of river

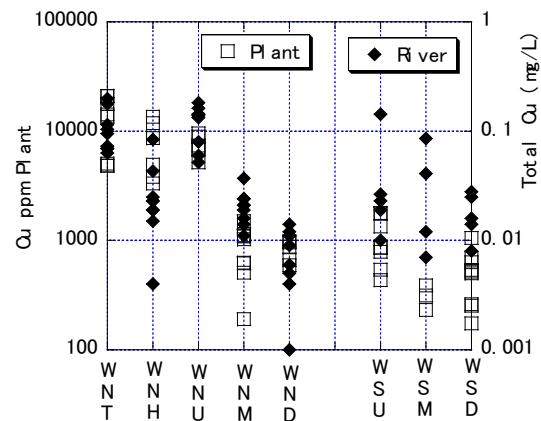


Fig.7 Cu concentration for bryophyte and river water

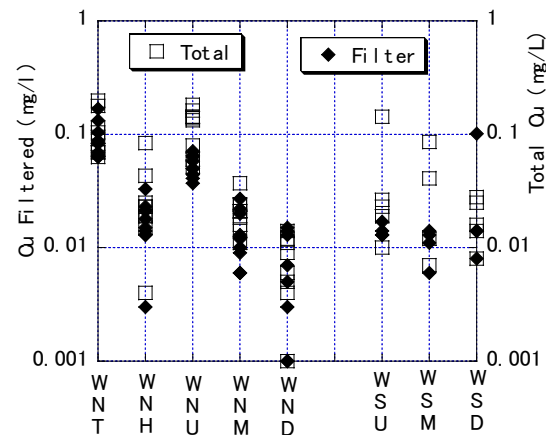


Fig.8 total and soluble Cu concentration of river

river with no tailing and WNU is a stream after WNT and WNH streams join [11].

Fig.5 shows Zn concentration for river bryophyte and river water at the the Waidani area. Zn concentration for river bryophyte was over 500 ppm and in particular reached 10,000 ppm beside tailings. Zn concentration for river bryophyte decreased with downstream and 1,000 ppm at 3 km and 900 ppm at 4 km from the tailing. Total Zn concentration of river water also decreased from about 2 mg/l to 0.03 mg/l with down the stream which exceeded the Japanese Environment Standard for rivers (0.03 mg/l) [11]. Therefore, Zn concentration for river bryophyte changed with total Zn concentration of river water.

Fig.6 shows total and soluble Zn concentrations of river water at the Waidani area. Soluble concentration was filtered with a 0.45 micrometer. Both concentrations were almost the same so Zn migrated in soluble style while river bryophyte directly is thought to have absorbed Zn from river water. Therefore, the Zn concentration of river bryophyte changed with the Zn concentration of river water. The bio-concentration factor for Zn is 10,000 from Zn concentration of river bryophyte and river water at the Waidani area assuming 1 L = 1kg.

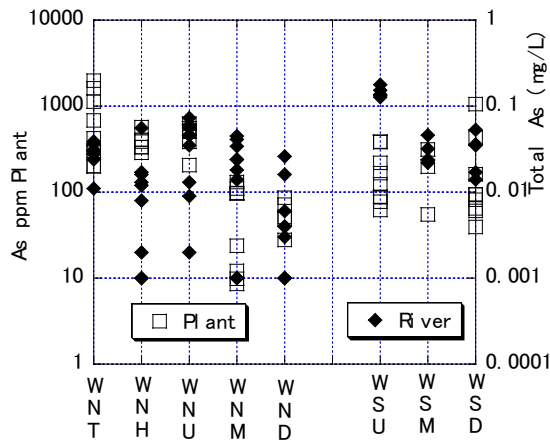


Fig.9 As concentration for bryophyte and river water

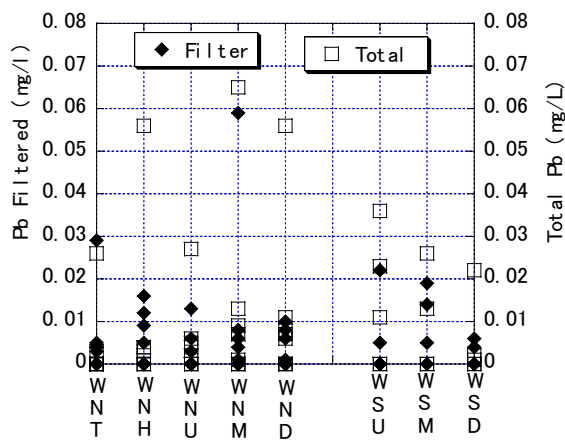


Fig.10 total and soluble As concentration of river

Excluding the Waidani area, the Zn concentration of river water was very low, less than 0.005 mg/l and Zn concentration of river bryophyte were 1 to 200 ppm. The bio-concentration factor for Zn excluding the Waidani area ranges from 200 to 40,000 however almost it coincided with the calculated values at the Waidani area.

Fig.7 shows Cu concentration for river bryophyte and river water at the Waidani area. Cu concentration for river bryophyte was over several hundred ppm and in particular reached 10,000 ppm beside tailings. Cu concentration for river bryophyte decreased with downstream and 600 to 1,000 ppm at 3 km and 200 to 800 ppm at 4 km from the tailing. Total Cu concentration of river water also decreased from about 0.2 mg/l to less than 0.01 mg/l down the stream. Although these values were less than the Japanese Effluent Standard (3 mg/l) [11], Cu concentration for river bryophyte changed with total Cu concentration of river water.

Fig.8 shows total and soluble Cu concentrations of river water at the Waidani area. Both concentrations were not always the same and total Cu concentration was often higher than soluble Cu concentration. Cu migrated by soluble and particle style down the steam. Therefore, Cu concentration

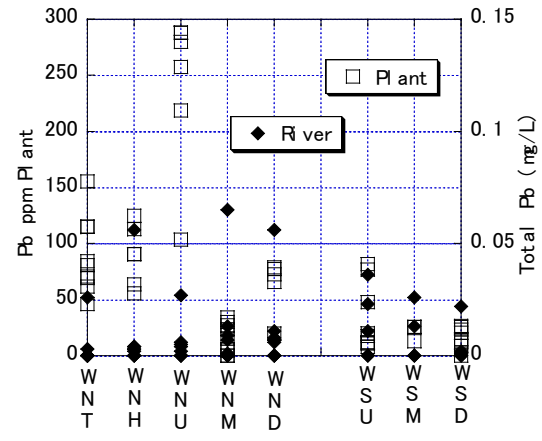


Fig.11 Pb concentration for bryophyte and river water

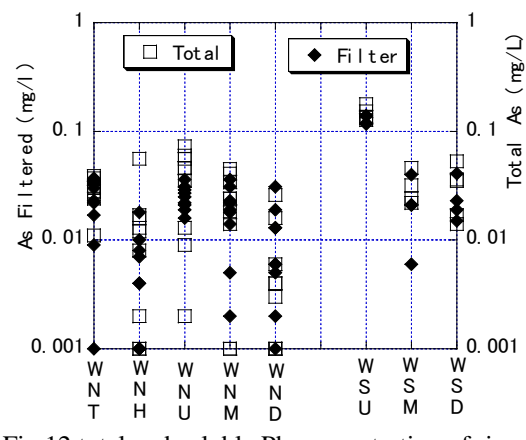


Fig.12 total and soluble Pb concentration of river

of river bryophyte changed with total or soluble Cu concentration. The bio-concentration factor for Cu is 10,000 from Cu concentration of river bryophyte and river water at the Waidani area assuming 1 L = 1kg [7]. Excluding the Waidani area, Cu concentration of river water was very low, less than detection limit, 0.001 mg/l and then the bio-concentration factor for Cu excluding the Waidani area could not be calculated.

Fig.9 shows As concentration for river bryophyte and river water at the Waidani area. As concentration for river bryophyte was over several tens ppm and in particular reached 1,000 ppm beside tailings. As concentrations for river bryophyte decreased going downstream from 1,000 ppm to 10 ppm at 3 km and 4 km from the tailing. Total As concentration of river water did not clearly decrease going downstream and ranged from 0.001 to 0.2 mg/l which was over the Japanese Effluent Standard for river (0.1 mg/l) [11].

Fig.10 shows total and soluble As concentrations of river water at Waidani area. Both concentrations were almost the same, so it is thought that As migrated in soluble style and river bryophyte is thought to have directly absorbed As from river water. Therefore, As concentration of river bryophyte changed with As concentration of river

water. The bio-concentration factor for As is 1,000 to 10,000 from As concentration of river bryophyte and river water at the Waidani area assuming 1 L = 1kg. Excluding the Waidani area, the As concentration of river water was very low, less than the detection limit, 0.001 mg/l and then the bio-concentration factor for As excluding the Waidani area could not be calculated.

Fig.11 shows Pb concentration for river bryophyte and river water at the Waidani area. Pb concentration for river bryophyte was over several tens ppm and in particular reached 50 to 300 ppm around tailings. Pb concentration for river bryophyte decreased going downstream to 50 ppm ~ 100 ppm at 3 km and less than 50 ppm at 4 km from the tailing. Total Pb concentration of river water did not clearly decrease going downstream and ranged from less than 0.001, detection limit to 0.07 mg/l which was less than the Japanese Effluent Standard for river (0.1 mg/l).

Fig.12 shows total and soluble Pb concentrations of river water at the Waidani area. Both concentrations were not always the same and total Pb concentration was often higher than soluble Pb concentration. Pb migrated in soluble and particle style down the stream. Therefore, Pb concentration of river bryophyte changed with total or soluble Pb concentration. The bio-concentration factor for Pb is variable, 20,000 to 40,000 at the Waidani area assuming 1 L = 1kg [7]. Excluding the Waidani area, Pb concentration of river water was very low, less than the detection limit, 0.001 mg/l therefore the bio-concentration factor for Pb excluding Waidani area could not be calculated.

CONCLUSION

Stream water is representative of precipitation for small river catchment so stream water was sampled and analyzed. A distribution map of oxygen and hydrogen stable isotopic stream water values along the Yoshiikawa and Tenjinkawa rivers show that isotope values decreased with distance from the Inland Sea implying that southward wind or cloud was mainly controlled isotope values and that the influence of the Japan Sea on isotope of precipitation was low.

Bryophyte along streams was also sampled at the same time of stream water sampling. A map for Zn, Cu, As, and Pb concentrations of bryophyte shows that metal concentrations of stream bryophyte around the watershed area (Ningyotouge uranium mine, N) were low and around the Tsuyama Basin, (B) and the Yanahara mine (Y), metal concentrations were medium relative to those of the other areas excluding the Waidani mine area. In the Waidani mine area, Zn, Cu, As and Pb

concentrations of bryophyte were extremely high as well as high Zn, Cu, As, and Pb concentrations of stream water and high bio-concentration factor for bryophyte was maintained [7].

REFERENCES

- [1] Sakai H. and Matsihisa Y., Stable Isotope Geochemistry, University of Tokyo Press. 1996. PP. 93-100.
- [2] Mizota C. and Kusakabe M., Spatial distribution of δD - $\delta^{18}O$ values of surface and shallow groundwaters from Japan, south Korea and east China, *Geochemical Journal*, Vol.28, 1994, pp.387-410.
- [3] Machida I. and Kondo A., Stable Isotope Ratios of Natural Water in Japan, *J. Japan Soc. Hydrol. & Water Resour.* Vol. 16 No.5, 2003, pp.556-569.
- [4] Ishizuka M., Sone Y., Ii H. and Hirata T., Effect of enriched early dropped rainwater on mesoscale isotopic distribution in surface water on the Kii Peninsula, Japan, *Water Resources Research*, Vol.42, W12410, 2006, pp.1-16.
- [5] Clark I. and Fritz P., *Environmental Isotopes in Hydrogeology*. New York: Lewis Publisher, 1999, ch. 1, 2, 3 and 4.
- [6] Debéna S., Aboala J.R., Carballeira A., Cesab M. and Fernández J.A., Monitoring river water quality with transplanted bryophytes: A methodological review, *Ecological Indicators* 81 (2017) 461–470.
- [7] Kubohara T and H. Ii, "Evaluation of metal contamination for river using bryophyte in the Kinokawa River catchment", *International Journal of GEOMATE*, Vol. 13, Issue 37, Sep., 2017, pp. 108-115..
- [8] Satake K., Shibata K. and et al., "Copper accumulation and location in the moss *Scopelophila cataractae*", *Journal of Bryology*, Vol.15, Issue 2, 1988, pp.353-376.
- [9] The Geological Survey of Japan and Atomic Fuel Corporation, Prospecting and development of Uranium Deposits of Ningyo-touge Uranium Field in Japan, *Mining Geology*, Vol.14, No.63, 1964, pp.1-10.
- [10] Mitsuno C. Nureki T. Sugita M. and Asami M., *Geology and Modes of Occurrence of Iron Sulfide Deposits in the Yanahara Mining District*, *Mining Geology*, Vol.25, No.5, 1975, pp.331-345.
- [11] Ii H. and Nishida A., Effectiveness of using river insect larvae as index of Cu, Zn, and As contaminations in rivers, Japan, *International Journal of GEOMATE*, Vol. 12, Issue 33, May, 2017, pp. 153-159.

REDUCTION OF NUTRIENTS IN PUBLIC MARKET WASTEWATER BY PHYCOREMEDIATION

Radin Maya Saphira Radin Mohamed^{1*}, Alfituri Ibrahim Abdullah Abuala², Najeeha Mohd. Apandi³, Adel Al-Gheethi⁴, Aisha A. Amhimmid Alqantosh⁵ and Amir Hashim Mohd. Kassim⁶

^{1,2,3,4,5,6}Micro-pollutant Research Centre (MPRC), Department of Water and Environmental Engineering, Faculty of Civil & Environmental Engineering, Universiti Tun Hussein Onn Malaysia, 86400 Parit Raja, Batu Pahat, Johor, Malaysia.

ABSTRACT

Phycoremediation using microalgae has high potential for reducing nutrient load in public market wastewater (PMW). However, the reduction efficiency depends on the initial concentrations of microalgae and PMW. In the present study, the reduction of total nitrogen (TN), total phosphorus (TP), and total organic carbon (TOC) in PMW using *Scenedesmus* sp., was investigated as a function of different PMW concentrations. *Scenedesmus* sp. was inoculated with 10^6 cell/mL into 500 ml of PMW and incubated outdoors under full sunlight for 19 days. The results revealed that higher microalgae growth was recorded in PMW than in Bold's basal medium (BBM). The maximum reduction values of nutrients were 91.51% for TN, 92.67% for TP, and 90.2% for TOC were achieved by 50% of PMW. The findings indicated that phycoremediation with *Scenedesmus* sp. can successfully reduce the nutrient load of PMW.

Keywords: Public Market Wastewater, *Scenedesmus* sp., Phycoremediation,

INTRODUCTION

Wastewater is a general term that refers to various types of liquid wastes generated through activities that utilize massive volumes of water [1]. The source of wastewater determines the final characteristics of wastewater [2]. For instance, public market wastewater (PMW) contains high levels of organic matter (> 600 mg/L of biochemical oxygen demand [BOD]) and solids derived from fish, meat, poultry, vegetable, and fruit residues; PMW is thus classified as highly polluted wastewater [3]. Fresh foodstuff, poultry waste scraps, and fish entrails contain high concentrations of total nitrogen (TN), total organic carbon (TOC), and total phosphorus (TP) which contribute effectively to the contamination of PMW [4]. TP and TN concentrations in PMW reached up to 25 mg/L and 61 mg/L, respectively, as a result of contamination with blood residues from meat, fish, and poultry processing [5]. Therefore, the direct discharge of PMW into natural water bodies contributes in the water pollution and promotes eutrophication [5]. Hence, PMW must be treated for the removal of organic matter, nutrients, pathogens, and heavy metals prior to its final discharge into the environment.

Among several wastewater treatment technologies, phycoremediation is one of the most efficient techniques for PMW because the high nutrient load of PMW supports microalga growth rates and thus improve nutrient uptake [6], [7].

Besides, the microalgae biomass generated during the phycoremediation process has several applications as biofuel, biodiesel, fish feed, fertilizer, pharmaceuticals, and cosmetic ingredients [8]. Furthermore, phycoremediation with mass-cultured microalgae is cheaper than conventional aerobic wastewater treatment systems because of its low energy input, initial capital cost, and operational cost [9]. Wastewater from the dairy industry and municipal waste, and industrial wastewater have been previously used as a microalgae production medium [7], [10], [11]. In this research, the growth of *Scenedesmus* sp. and nutrient reduction in different concentrations of PMW were investigated.

MATERIALS AND METHODS

PMW Collection

PMW was collected at Pasar Awam Rengit, Jalan Kampung Rengit Laut, Rengit, 83100 Rengit, Johor, Malaysia (1.67757, 103.14563). The pH, BOD, chemical oxygen demand (COD), total soluble solids (TSS) TN, TP, and TOC of the PMW samples were determined according to APHA (2005).

Scenedesmus sp. Culturing

Scenedesmus sp. was refreshed by sub-culturing in autoclaved Bold's Basal Medium (BMM), (Bischoff and Bold, 2003). The culture medium was

incubated at room temperature for 8 days prior for use in phycoremediation.

Experimental Setup

The experiment was set up in a 1 L Erlenmeyer flask containing 500 mL of PMW. BBM was used as the control medium. PMW samples were filtered and diluted with distilled water to produce five different concentrations (10%, 25%, 50%, 75%, and 100%). *Scenedesmus* sp. was inoculated with 10^6 cell/mL. The phycoremediation process was conducted outdoors under full sunlight for 19 days. Each flask was shaken twice a day to prevent sedimentation.

Scenedesmus sp. Growth

The growth of *Scenedesmus* sp. was estimated by the harvesting of cell biomass from the culture medium using centrifugation at 4000 rpm for 5 minutes. The supernatant was discarded while the algal pellets were suspended in 45 mL of autoclaved and filter-sterilized Gillard's F/2 solution. A fixed volume of 10 mL aliquots was taken from the suspended solution and transferred to cuvettes. The optical density of the *Scenedesmus* sp. growth was estimated at 650 nm (OD₆₅₀) in a DR 6000 spectrophotometer (Janway, USA). Gillard's F/2 solution was used as the blank [15], [16].

Nutrient Removal

The reduction of TP, TN, and TOC was determined according to Eq. 1 [12,13,14].

$$\begin{aligned} \text{Removal Efficiency (\%)} &= \left(\frac{C_0 - C_t}{C_0} \right) \times 100\% \quad (1) \end{aligned}$$

RESULTS AND DISCUSSION

PMW Characteristics

Seven parameters were tested to characterize PMW samples. These parameters were selected according to the Environmental Quality Act (1974), Regulation 2009). The characterization data of PMW are shown in Table 1.

Table 1: Characteristics of public market wastewater (PMW) in comparison with effluent standards and previously reported values.

Parameter	PMW conc.	Effluent standard (Environmental Quality Act, 1974)	
		Standard A	Standard B
pH	7.5	6.0–9.0	5.5–9.0
BOD	1208	20	50

COD	3432	50	100
TN	968	-	-
TP	178	5	10
TOC	1798	-	-

Note: (–) Not detectable. All parameters, except for pH, are expressed in mg/L.

It can be noted that raw PMW with 10%, 25%, 50%, 75% and 100% dilutions have high BOD and COD levels of 222–1208 and 443–3432 mg/L, respectively, while TN and TP were 968 and 178 mg/L, respectively. These values are higher than BOD levels of 85.39–92.62 and 71–122 mg/L reported by previous studies [17], [18]. The high concentrations of COD and BOD might be related to the presence of organic materials in PMW which differ seasonally and geographically [19].

Growth of Scenedesmus sp.

The growth of *Scenedesmus* sp. in different concentrations (10%, 25%, 50%, 75% and 100%) of PMW is depicted in Fig. 1.

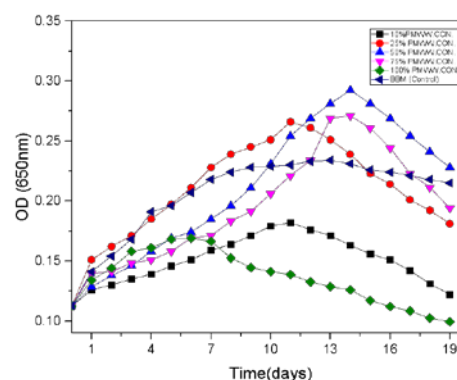


Fig. 1: Growth of *Scenedesmus* sp. in PMW during phycoremediation

The highest growth rate was recorded in 50% PMW on day 14 of phycoremediation. OD₆₅₀ increased from 0.112 to 0.2923 from day 1 day to day 14 and decreased to 0.228 on the 19th day of phycoremediation. The results of the present research corresponded with those reported by Chen [3], who indicated that optimum *Chlorella* growth was observed in 50% piggy wastewater.

Meanwhile, the microalga growth in 25% and 75% PMW reached the maximum values of 0.266 and 0.271 on day 11 and day 14 of phytoremediation, respectively, and decreased thereafter. In contrast, microalga growth rates in 10% and 100% PMW were 0.182 and 0.169, respectively, and decreased after day 11 and day 6 of phycoremediation, respectively. This behavior may be attributed to the low nutrient content of 10% PMW or to the excessive nutrient content of 100% PMW, as shown in Table 1. These results indicate

that the PMW had high nutrient loads and should be subjected to the dilution process before the phycoremediation process. Furthermore, microalga growth rates in BMM, the control medium, were 0.112 and 0.228 on day 0 and day 19 of cultivation. The maximum value of microalga growth in BBM was 0.234 which was observed on day 13 of cultivation. Therefore, microalga can be successfully cultured in different concentrations of PMW.

Nutrient Removal Efficiency of *Scenedesmus* sp.

In this study, the removal rates of TN, TOC, and TP were used as indices of nutrient removal by *Scenedesmus* sp.. Table 2 shows that in 50% PMW, TN levels decreased by 91.51% after phycoremediation with *Scenedesmus* sp. Accordingly, TN levels dropped from 613 mg/L to 52 mg/L in 50% PMW. By contrast, TN levels in the control decreased by 14.68% from 613 mg/L to 523.01 mg/L in the control samples. TN removal rates in 10%, 25%, and 75% PMW were 85.3%, 88.6% and 70.7% respectively. The lowest TN removal rate was 57.49% which was observed in 100% PMW. This result may be attributed to the negative growth rate of the alga. However, TP removal rates in 50% PMW was 92.67%. Specifically, TP levels decreased from 111.84 mg/L to 8.19 mg/L after phycoremediation. TP removal rates in the control, 10%, 25%, 75%, and 100% PMW were approximately 22.01%, 75.6%, 91.16%, 79.34%, and 62.92% respectively. In 50% PMW, TOC decreased from 1022.03 mg/L to 100.08 mg/L. This decrement is equivalent to a reduction of 90.2% ($11.14 \pm 0.96\%$ in the control). Meanwhile, TOC removal rates in 10%, 25%, and 75% PMW were 80.97%, 86.51%, and 77.91% respectively. The lowest TOC removal rate was observed in 100% PMW, in which TOC levels decreased from 1798.22 mg/L to 897.23 mg/L (50.10%). These phenomena may be attributed to the different nutrient loads associated with different PMW concentrations.

Overall, phycoremediation using *Scenedesmus* sp. successfully removed TN, TP, and TOC from PMW. In a previous study, Jais [17] found that *Scenedesmus* sp. was able to remove TN, TP, and TOC from PMW at the rates of 73.01%, 76.77%, and 71.73%, respectively

Table 2: Nutrient removal efficiency as a function of PMW concentration

PMW Concentration	Int. conc. (mg/L)	F. conc. (mg/L)	Removal percentage (%)	Control (%)
TN				
10 %	223	32.76	85.30	14.14
25 %	396	45.13	88.60	19.69
50 %	613	52	91.51	14.68
75 %	758	222.07	70.703	15.39
100 %	968	411.43	57.49	12.39

TP				
10 %	33.08	8.07	75.60	21.58
25 %	58.96	5.20	91.169	17.65
50 %	111.84	8.19	92.67	22.01
75 %	158.03	32.64	79.34	22.70
100 %	178	66	62.92	11.59
TOC				
10 %	389	74	80.97	23.33
25 %	697	94.02	86.51	15.50
50 %	1022.03	100.08	90.20	11.14
75 %	1458	322.01	77.91	24.48
100 %	1798.22	897.23	50.10	20.92

Note: Int. conc.: initial concentration and F. conc.: final concentration.

CONCLUSION

The present study demonstrated that different PMW concentrations affect the efficacy of nutrient removal from wastewater using phycoremediation with *Scenedesmus* sp. The highest nutrient removal rates were observed in 50% PMW. Therefore, the PMW concentration must not exceed 50% to facilitate phycoremediation effectively. Furthermore TN, TOC, and TP removal rates in 50% PMW were 91.51%, 90.20%, and 92.67%, respectively. To conclude, phycoremediation with microalgae represents the best biological wastewater treatment process given its low cost.

ACKNOWLEDGEMENTS

The authors wish to thank the Ministry of Science, Technology and Innovation (MOSTI) for funded this research through the E-Science Fund S029 (02-01-13-SF0135). They are also immensely grateful to the Research Management Centre (RMC), UTHM through the IGSP U682 grant.

REFERENCES

- [1] Pahazri, Nor Fadzilah, R. M. S. R. Mohamed, A. A. Al-Gheethi, and Amir Hashim Mohd Kassim., Production and harvesting of microalgae biomass from wastewater, *Environmental Technology Reviews*, Vol. 5, Issue 1, 2016, pp. 39-56.
- [2] Eriksson, Eva, Karina Auffarth, Mogens Henze, and Anna Ledin., Characteristics of grey wastewater. *Urban water*, Vol. 4, Issue 1, 2002, pp. 85-104.
- [3] Chen, Zhuo, Huu Hao Ngo, and Wenshan Guo., A critical review on the end uses of recycled water. *Critical reviews in environmental science and technology*, Vol. 43, Issue 14, 2013, pp. 1446-1516.
- [4] Apandi, Wan Mohamad, Wan Asma, and Hazel Monica Matias Peralta., Removal of nutrients and selected heavy metals in wet market wastewater by using microalgae *scenedesmus* sp. In *Applied Mechanics and Materials*, vol. 773,

- Trans Tech Publications, Vol. 773-774, 2015, pp. 1210-1214.
- [5] Jais, Noor Maisara, R. M. S. R. Mohamed, A. A. Al-Gheethi, and MK Amir Hashim., The dual roles of phycoremediation of wet market wastewater for nutrients and heavy metals removal and microalgae biomass production. *Clean Technologies and Environmental Policy*, Vol. 19, Issue 1, 2017, pp.37-52.
 - [6] Rawat, I., R. Ranjith Kumar, T. Mutanda, and F. Bux., Dual role of microalgae: phycoremediation of domestic wastewater and biomass production for sustainable biofuels production. *Applied Energy* Vol. 88, Issue 10, 2011, pp. 3411-3424.
 - [7] Gani, Paran, N. M. Sunar, H. Matias-Peralta, Abdul AA Latiff, and A. R. A. Razak., Influence of initial cell concentrations on the growth rate and biomass productivity of microalgae in domestic wastewater. *Appl. Ecol. Environ. Res* Vol. 14, Issue 2, 2016, pp. 399-409.
 - [8] Eloka-Eboka, Andrew C., and Freddie L. Inambao., Effects of CO₂ sequestration on lipid and biomass productivity in microalgal biomass production. *Applied Energy*, Vol. 195, 2017, pp.1100-1111.
 - [9] Zhou, Wenguang, Paul Chen, Min Min, Xiaochen Ma, Jinghan Wang, Richard Griffith, Fida Hussain., Environment-enhancing algal biofuel production using wastewaters. *Renewable and sustainable energy reviews*, Vol. 36, 2014, pp. 256-269.
 - [10] Chokshi, Kaumeel, Imran Pancha, Arup Ghosh, and Sandhya Mishra., Microalgal biomass generation by phycoremediation of dairy industry wastewater: an integrated approach towards sustainable biofuel production. *Bioresource technology*, Vol. 221, 2016, pp. 455-460.
 - [11] Umamaheswari, J., and S. Shanthakumar., Efficacy of microalgae for industrial wastewater treatment: a review on operating conditions, treatment efficiency and biomass productivity. *Reviews in Environmental Science and Bio/Technology*, Vol. 15, Issue 2, 2016, pp. 265-284.
 - [12] Malla, Fayaz A., Shakeel A. Khan, Gulshan K. Sharma, Navindu Gupta, and G. Abraham., Phycoremediation potential of *Chlorella minutissima* on primary and tertiary treated wastewater for nutrient removal and biodiesel production. *Ecological Engineering*, Vol. 75, 2015, pp. 343-349.
 - [13] Hena, S., S. Fatimah, and S. Tabassum. Cultivation of algae consortium in a dairy farm wastewater for biodiesel production." *Water Resources and Industry*, Vol. 10, 2015, pp. 1-14.
 - [14] Chiu, Sheng-Yi, Chien-Ya Kao, Tsai-Yu Chen, Yu-Bin Chang, Chiu-Mei Kuo, and Chih-Sheng Lin., Cultivation of microalgal *Chlorella* for biomass and lipid production using wastewater as nutrient resource. *Bioresource technology*, Vol. 184, 2015, pp. 179-189.
 - [15] Cuaresma, María, Marcel Janssen, Evert Jan Van den End, Carlos Vílchez, and René H. Wijffels., Luminostat operation: A tool to maximize microalgae photosynthetic efficiency in photobioreactors during the daily light cycle? *Bioresource technology*, Vol. 102, Issue 17, 2011, pp. 7871-7878.
 - [16] Doan, Thi Thai Yen, Balasubramanian Sivaloganathan, and Jeffrey Philip Obbard., Screening of marine microalgae for biodiesel feedstock. *Biomass and Bioenergy*, Vol. 35, Issue 7, 2011, pp. 2534-2544.
 - [17] Jais, Noor Maisara & Apandi, W. M., Asma, W., Removal of nutrients and selected heavy metals in wet market wastewater by using microalgae *scenedesmus* sp. In *Applied Mechanics and Materials*, Vol. 773-774, 2015, pp. 1210-1214.
 - [18] Zulkifli A. R, Roshadah, H. & Tunku Khalkausar T. F., Control of water pollution from non-industrial premises. Department of Environment, Malaysia 2011.
 - [19] Hann, Simon, Chris Sherrington, Olly Jamieson, Molly Hickman, Peter Kershaw, Ayesha Bapasola, and George Cole., Investigating options for reducing releases in the aquatic environment of microplastics emitted by (but not intentionally added in) products, 2017.

AMOUNT OF PRECIPITATION ON TOPOGRAPHY FROM OSAKA PLAIN TO NARA BASIN ACROSS IKOMA MOUNTAINS, JAPAN

Hiroki Nishiwaki¹ and Hiroyuki Ii²

¹Graduate School of Systems Engineering, Wakayama University, Japan

²Faculty of Systems Engineering, Wakayama University, Japan

ABSTRACT

Water vapor content is important parameter for high precipitation phenomenon in around mountain and mountain shadow area. When rain cloud with rich vapor or wet air met the mountain, new rain cloud occurs and grows around the mountain. Grown rain cloud cross mountain and goes to mountain shadow area. Grown cloud did not disappear quickly and dropped a lot of rain to mountain shadow. As a result, in the mountain and mountain shadow area, amount of precipitation is higher than that around the area. Therefore, amount of precipitation in the slope of Ikoma Mountains increased with topography that collected a lot of water vapor where high slope of mountain or recessed to the east side. When rain cloud or air comes from western where clouds do not meet another mountain before the Ikoma Mountains during from April to June, amount of precipitation increased from the Ikoma Mountains to Nara Basin because rain cloud or air was wet.

Keywords: Precipitation, Water vapor content, Mountain, Mountain shadow area.

INTRODUCTION

It is known that amount of precipitation increased with altitude in mountain [1]. Increase in precipitation is different for each mountain. In Nagano and Yamanashi prefecture, Japan, amount of precipitation every event increased from 5 to 10 per cent with 100 m in higher [2] and in Yamagata and Fukushima prefecture, Japan, increased from several per cent to 20 per cent with 100 m in higher [3]. When air or cloud crosses mountains in land, updraft brings out at the mountain and new cloud occurs and rain cloud grows. Grown rain cloud drops lot of rain around mountain. In other hand, amount of precipitation in the Owase, Japan didn't increase in mountain [4]. Thus, relationship topography and precipitation has not been clarified because topography of mountain is complicated. Grown cloud drops to region far from the mountain. On 15th October, 1998, Liner rain band

occurred around the Rokko Mountain and there localized heavy rain in Kyoto City, 50 km from the Rokko Mountain [5]. Such localized heavy rain occurs most of region in Japan [6]. Then, it is necessary to clearly influence of cloud grown around the mountain that amount of precipitation behind the mountain. Therefore, in this study, the purpose is to clarify the relation between amount of precipitation and topography and then rain sample was sampled from the Osaka Plain to the Nara Basin across the Ikoma Mountains covering big topography change.

METHOD

Topography of Osaka Plain, Ikoma Mountains and Nara Basin and Analysis

Fig. 1 shows location of study area. This study area was between from the Osaka Plain to the Nara Basin cross the Ikoma Mountains in Osaka prefecture and Nara prefecture, Japan. The Osaka Plain is the topography among sea and three mountains. The Ikoma Mountains is located in the north-south direction on the border of Osaka and Nara prefecture and the altitude of many mountain peaks is 300 m to 400 m. The Nara Basin is located at the east of the Ikoma Mountains and is surrounded by mountains all direction. Fig.2 shows location of sampling point and observation stations for Japan Weather Association. In this study, two types of data were used for amount of precipitation. First type of data was sampling data and there were 25 rain gauged points from the eastern Osaka to the Nara Basin cross the Ikoma Mountains. There were 4 sampling points north of 34° 41'

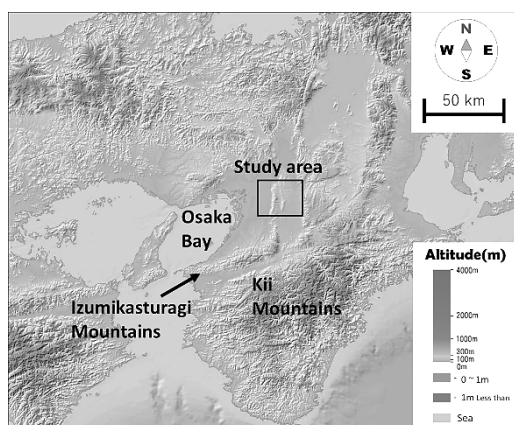


Fig. 1 Location of study area

north longitudes are called North-1 to North-4 in order from west. There were 11 sampling points from $34^{\circ} 39'$ to $34^{\circ} 41'$ north longitudes are called Center-1 to Center-11 in order from west. There were 10 sampling points south of $34^{\circ} 39'$ north longitudes are South-1 to South-10 in order from west. Rain sampling was performed 24 times by every precipitation from January to June in 2018. Sampler was 500 ml bottle. Wide mouth of sampler, 61.0 mm in diameter. Amount of precipitation was measured by the following equation.

$$P = (W/\rho)/((C/2)^2 \times \pi)$$

P: Amount of precipitation (mm), W: Weight (g), ρ : Density of water (10^{-3} g/mm³), C: Caliber of Sampler (61.0 mm). Second type was data observed by JMA (Japan Weather Association) and data of Ikoma, Nara and Yao observation stations were also used for analysis. There 4 points North-1 to North-4 were called North Line. There 13 points Center-1 to Center-11, Ikoma and Nara were called Center Line.

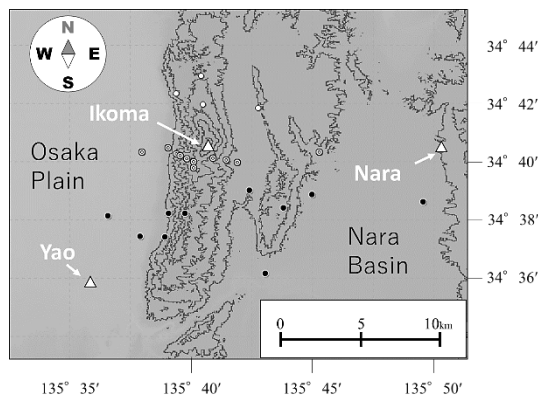


Fig. 2 Location of sampling point. Open triangles are points observed by JMA. Open circles are North Line. Double circles are Center Line. Closed circles are South Line.

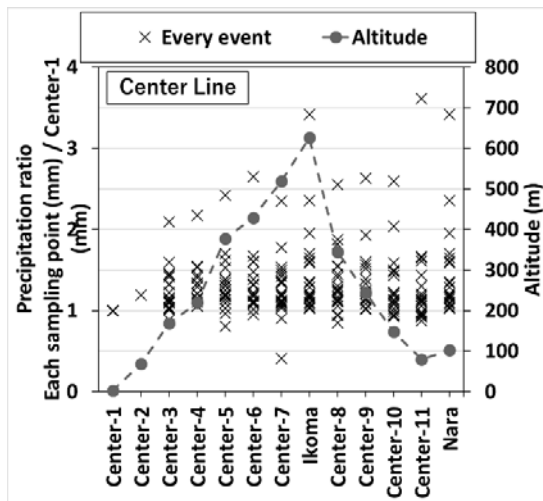


Fig. 3b Precipitation ratios for Center Line

There 10 points South-1 to South-10 were called South Line.

Data of wind direction and wind speed were obtained from JMA at Ikoma. Wind direction of each event was obtained and was shown as 8 directions. Cloud direction was estimate by weather chart. Cloud direction was shown as 8 directions. Weather chart was announced by JMA.

RESULTS AND DISCUSSION

Precipitation ratio for each sampling area

In this study, precipitation ratio was used to compare topography change. Precipitation ratio is amount of precipitation on each sampling point divided by amount of precipitation on base point in the Osaka Plain for comparing amounts of precipitation between the Osaka Plain to Nara basin.

Fig. 3 shows precipitation ratios and altitude in North, Center and South Line. In North and Center Line, base point was assumed Center-1. In South

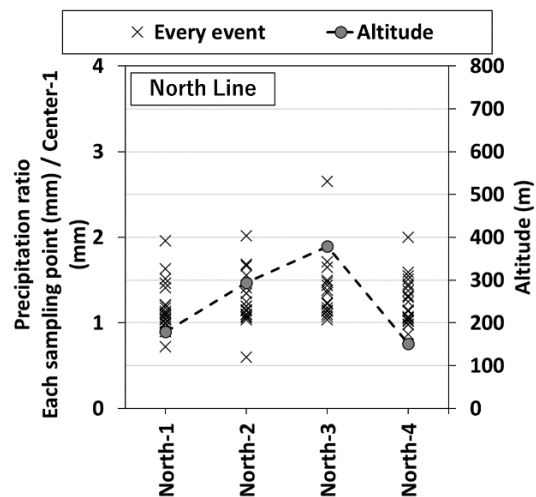


Fig. 3a Precipitation ratios for North Line

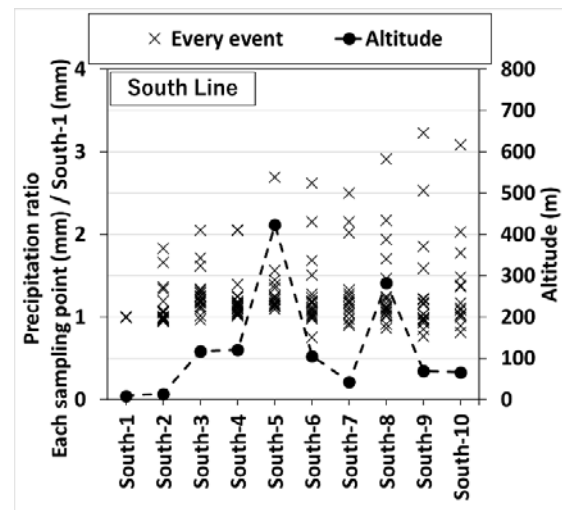


Fig. 3c Precipitation ratios for South Line

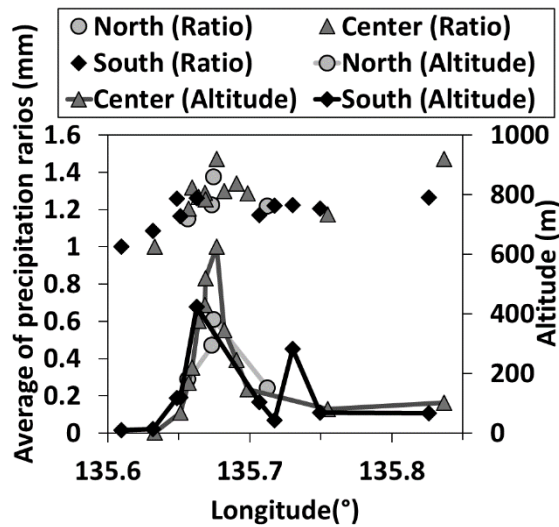


Fig. 4 Average of precipitation ratios for each sampling points and altitude of topography

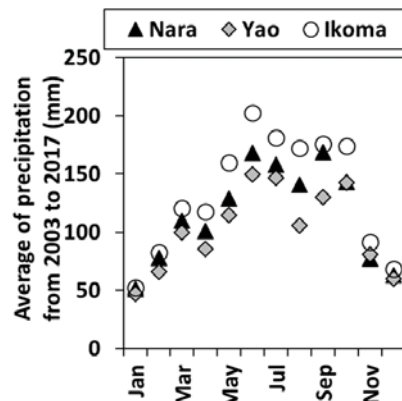


Fig. 5 Average of precipitation observation by JMA every month from 2003 to 2017

Line, base point was assumed South-1. Fig. 4 shows average precipitation ratio for each sampling points. Average precipitation ratios were calculated by the data of 95% of confidence interval. Center-1 and South-1 points are located in flat area of the east Osaka plain and their precipitation ratios were assumed 1.0. There are 3 points North-3, Ikoma, South-5 was mountain peak. Precipitation ratio in mountain peak were always 1.0 or more and average were the highest ratio on those Line. 11 points from North-1 to North-2 in North Line, from Center-2 to Center-7 in Center Line and from South-2 to South-4 in South Line are called west slope of the Ikoma Mountains. In the west slope of the Ikoma Mountains, most of precipitation ratios showed 1.0 or more and average showed from 1.1 to 1.4. Amount of precipitation in west slope increased with altitude. Three points from Center-8 to Center-10 are located in east slope of the Ikoma Mountains. In the east slope, most of precipitation ratios showed 0.9 or more and average about 1.3. Precipitation ratios for the east slope were less than those of mountain peak. Amount

of precipitation in east slope of the Ikoma Mountains decreased with distance from peak of mountain. Six points North-4, Center-11 and from South-6 to South-9 are located in the west side of Nara basin. In west side of the Nara Basin, most of precipitation ratios showed 0.8 or more and average showed 1.2. Amount of precipitation on the east side of the Nara Basin were about the same and higher than amount of precipitation on flat area of the Osaka Plain.

There 2 points Nara and South-10 are located in the east side of Nara basin. In west side of the Nara Basin, most of precipitation ratios for each sampling points showed 1.0 or more and average showed 1.3 and 1.5. Amount of precipitation on east side of the Nara Basin were higher than amount of precipitation on west side of the Nara Basin and flat area of the east Osaka Plain. In general, amount of precipitation decreases with increase of distance from the sea because vapor is not supplied to clouds from land.

Fig. 5 shows monthly precipitation from JMA data from 2003 to 2017. Monthly precipitation on Ikoma was the largest precipitation on other two points and amount of precipitation on Nara were higher than Yao where are located on the east Osaka Plain. These results are in agreement with results of Fig. 3 and Fig. 4. Thus, from both observation and sampling data it found that amount of precipitation on the Nara Basin were concluded to be large than those of the east Osaka Plain.

Relationship between precipitation ratios from Osaka Plain to west slope of the Ikoma Mountains and altitude

From Fig.3 and Fig.4, amount of precipitation in the west slope of Ikoma Mountains increased with altitude and amount of precipitation in the Nara Basin was higher than the Osaka Plain. Thus, first, high precipitation phenomenon in the west slope of Ikoma Mountains was examined.

Fig.6 shows relationship between precipitation ratio for flat area and west slope every event and altitude. In Fig. 6, Base point was assumed to be Center-1. Most of precipitation ratio for each point were varied from $Y = 5.7 \times 10^{-4}x + 0.6$ to $Y = 5.7 \times 10^{-4}x + 1.2$ (Y: precipitation ratio, x: Altitude) and range of precipitation ratios was 0.6, large variety. Amount of precipitation on the west slope of Ikoma Mountains increased with 5.7 % per 100 m in height. Amount of precipitation increased with altitude because high altitude slope collects a lot of water vapor.

On South-3 & South-4, precipitation ratios varied from 0.9 to 1.4 and amount of precipitation were as large as those at the sampling points on about 400 m in height. When air meets slope, air rises along slope. Air temperature decreases with elevation by adiabatic expansion and then saturated vapor pressure decreases. When air vapor pressure is over the

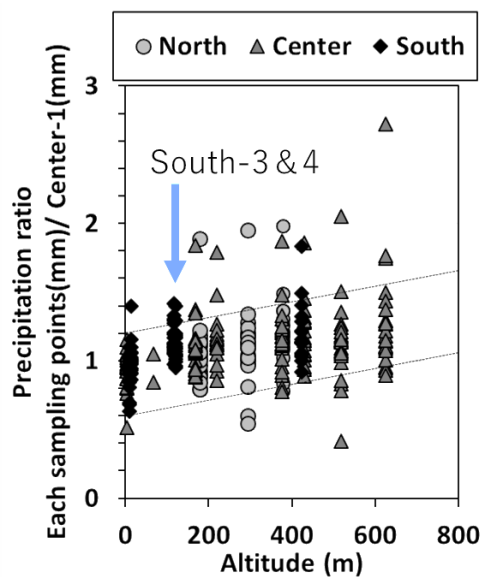


Fig. 6 Relationship between precipitation ratio for flat area and west slope every event and altitude. Upper broken line is $Y = 5.7 \times 10^{-4}x + 1.2$ and Lower broken line is $Y = 5.7 \times 10^{-4}x + 1.2$.

saturated vapor pressure, raindrops occur and make rain cloud. Topography around South-3 and South-4 are recessed to the east side. When air meets recessed topography, a lot of air vapor is gathered to center and rise along slope. A lot of air vapor makes a lot of rain cloud. Thus, topography that collects a lot of water vapor is important for high precipitation phenomenon.

Relationship between high precipitation on peak of mountain and cloud direction

From Fig.6, amount of precipitation on the west slope of Ikoma Mountains increased with altitude. However, amount of precipitation always did not increase because precipitation ratios had large variety. Weather conditions of events was examined when precipitation ratio for peak of mountains was high. Therefore, in detail weather condition was analyzed for clarifying variety of precipitation ratios. Table 1 shows weather conditions when precipitation ratio on Ikoma observation station was 1.5 or more. When precipitation ratio on South-5 was high, precipitation ratio on Ikoma observation station was also high and season of high precipitation ratio was only from April to June. From Fig.6, differences of monthly precipitation between Yao and Ikoma observation stations from March to July were higher than those from January to March. In Japan, temperature from March to July is higher than those from January to March. High temperature air has a lot of vapor and many rain drops and clouds occur on the slope of Ikoma Mountains. Seasonal condition is one important parameter for high precipitation phenomenon because determine whether the cloud or

air is dry or wet.

Table. 1 Weather conditions of events when precipitation ratio based on Center-1 for Ikoma was 1.5 or more

Date	Amount of precipitation (mm)	Precipitation ratio on peak	Air temperature (°C)	Wind Direction	Wind speed (m/s)	Cloud Direction
	Center-1	Ikoma	Ikoma	Ikoma	Ikoma	
Apr 6th	13.0	2.0	10.7	W	4.1	W
May 2nd	7.6	1.6	16.8	W	3.5	SW & W
May 18th	8.4	1.6	18.1	W	5.2	W
May 23th	8.5	1.7	14.8	NE	1.9	W
Jun 5th	44.6	1.7	15.5	E	3.0	W
Jun 6th	10.6	2.4	18.5	W	3.6	W
Jun 14th	1.8	3.4	15.8	E	2.7	SW

Many winds for high precipitation ratio event were west and some wind directions were east and northeast. Then, wind direction is not absolute parameter to determine whether high or low precipitation ratios. However, western wind can easily come up the Ikoma Mountains slope because the mountain direction is south to north and most of events was thought to depend on wind direction.

On May 5th, cloud direction varied west and southwest because low pressure was near the study area. For 14 events between April and June excluding May 2nd, 6 cloud directions were southwest and 8 cloud directions were west. Most cloud directions were west. If rain clouds come from west, rain clouds move from the Osaka Bay to the Ikoma Mountains across the Osaka Plain. Rain clouds go up along the slope and amount of precipitation increases around the mountain area. If rain clouds come from southwest, rain clouds cross the Izumikasturagi Mountains or the Kii Mountains before the Osaka Plain. When rain clouds cross the Izumikasturagi Mountains and the Kii Mountains, amounts of precipitation increase around those mountains. After passing through those mountains, some clouds disappear and wet air is dried. Then, cloud direction is one important parameter because decide whether the cloud or air is dry or wet.

Topography that collects a lot of water vapor is important for high precipitation phenomenon. Seasonal condition and cloud direction were parameter decide whether the cloud or air is dry or wet. Wet air makes new cloud in the slope. Therefore, high precipitation phenomenon in slope of mountain was concluded to be caused by water vapor content.

Relationship between high precipitation on Nara Basin and mountain

High precipitation phenomenon in the slope of Ikoma Mountains was concluded to be caused by water vapor content. Second, high precipitation phenomenon in the Nara Basin was examined.

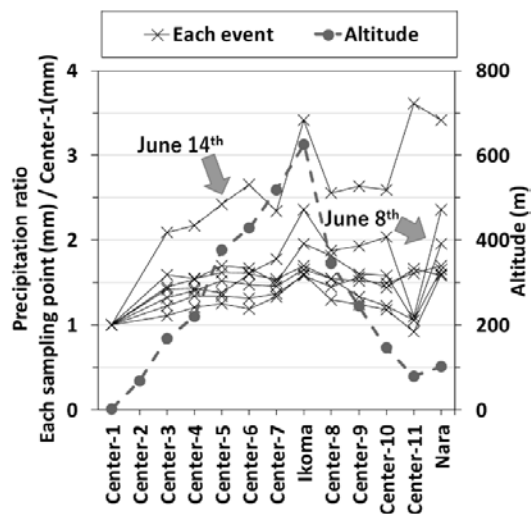


Fig. 7 Precipitation ratios of events when precipitation ratio for Center Line based on Center-1 for Nara was 1.5 or more.

Fig. 7 shows precipitation ratios in the Center Line when precipitation ratio on Nara observation station was 1.5 or more. Precipitation ratios on Nara observation station were 1.5 or more and precipitation ratios on Ikoma observation station were 1.5 or more were the same day. When precipitation ratio on Ikoma observation station was high, precipitation ratio on Nara observation station was also high. Especially, precipitation ratio on Nara observation station on June 9th and June 14th was very high. Then, relationship between cloud direction and high precipitation phenomenon for Nara Basin was examined. Fig. 8 shows move of rain cloud on June 14th and June 9th. High precipitation phenomenon for the Nara Basin had two types. First type was that rain cloud grew around mountains located on the western of Nara and grown cloud made rain in the Nara Basin like June 9th.

On June 9th, small size rain cloud came from west to Nara cross the Ikoma Mountains. From 2:10 to 2:20, rain cloud met the Ikoma Mountains and rain

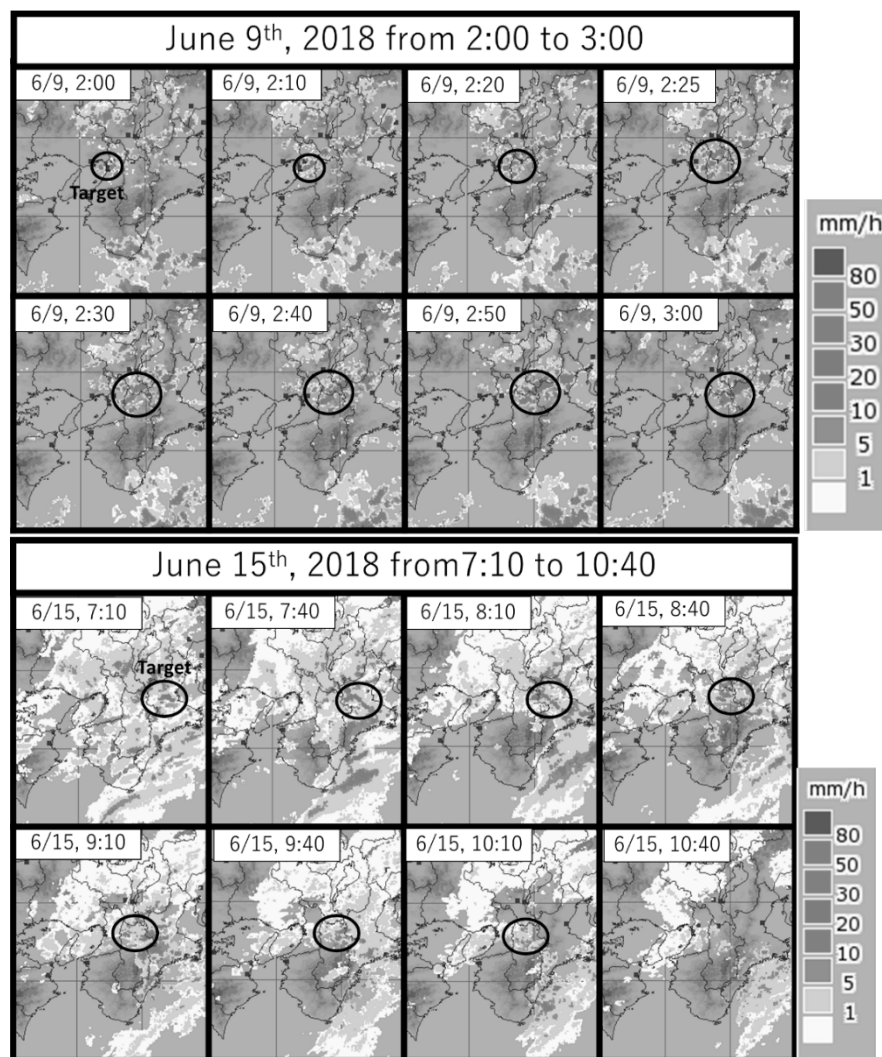


Fig. 8 Move of rain cloud on June 14th and June 9th. High precipitation phenomenon for the Nara Basin had Two types

cloud grew. Grown cloud passed through Nara from 2:25 to 3:00.

Second type was that strong rain cloud come from the eastern Nara Basin like a June 15th. On June 15th, many big rain clouds moved from southwest to northwest and some small size and strong rain cloud came from east to west. At 7:10, small size cloud grew around the Kasatori Mountain located in the eastern Nara basin and moved to the Nara Basin. From 8:10 to 10:10, rain cloud made a lot of rain in the Nara Basin. After passing through the Nara Basin, rain cloud become weak and made rain to the Ikoma Mountains and the Osaka Plain from 10:10 to 10:40. Both first and second type, the Nara Basin was located as a mountain shadow. When air with rich vapor met the mountain, rain cloud grew around the mountain and cross mountain. Grown cloud did not disappear quickly and made a lot of rain behind mountain shadow. Then, water vapor content was important parameter of high precipitation phenomenon for mountain and mountain shadow area.

CONCLUSION

The purpose of study is to clarify the relation between amount of precipitation and topography. Then rain sample was sampled from the Osaka Plain to Nara Basin cross the Ikoma Mountains covering big topography change.

Amount of precipitation for the Nara Basin were higher than Osaka Plain. amount of precipitation in the west slope of Ikoma Mountains increased with altitude and amount of precipitation in the Nara Basin was higher than the Osaka Plain. Thus, first, high precipitation phenomenon in the west slope of Ikoma Mountains was examined. Amount of precipitation on the west slope of Ikoma Mountains increased with 5.7 % per 100 m in height. Especially, amount of precipitation in topography recessed to the east side were very high. High altitude slope collects a lot of water vapor. When air meets recessed topography, a lot of air vapor is gathered to center and rise along slope. Thus, Topography that collects a lot of water vapor is important for high precipitation phenomenon.

Amount of precipitation always did not increase because precipitation ratios had large variety. Weather conditions were examined when precipitation ratio for peak of mountains was high. Deference of monthly precipitation between flat area and mountain peak from March to July were high. In Japan, temperature from March to July is high and High temperature air has a lot of vapor and many rain drops and clouds occur on the slope of Ikoma Mountains. Seasonal condition is important one parameter for high precipitation phenomenon because determine whether the cloud or air is dry or

wet. Most cloud directions were west. when precipitation was high for mountain peak. If rain clouds come from northwest or west, rain clouds move from the Osaka Bay to the Ikoma Mountains across the Osaka Plain. Amount of precipitation increases around the mountain area. If rain clouds come from southwest, rain clouds cross the Izumikasturagi Mountains and the Kii Mountains before the Osaka Plain. After passing through the Izumikasturagi Mountains and the Kii Mountains, some clouds disappear and wet air is dried because of rain around those mountains. Then, cloud direction is one important parameter because decide whether the cloud or air is dry or wet. Topography that collects a lot of water vapor is important for high precipitation phenomenon. Seasonal condition and cloud direction were parameter decide whether the cloud or air is dry or wet. Wet air makes new cloud in the slope. Therefore, high precipitation phenomenon in slope of mountain was concluded to be caused by water vapor content.

Second, high precipitation phenomenon in the Nara Basin was examined. When precipitation ratio for Ikoma was high, precipitation ratio for Nara was high. Then, relationship between cloud direction and high precipitation phenomenon for Nara Basin was examined. The Nara Basin was located mountain shadow. When rain cloud with rich vapor met the mountain, rain cloud grew around the mountain and cross mountain. Grown cloud did not disappear quickly and dropped a lot of rain to mountain shadow. Then, water vapor content was important parameter of high precipitation phenomenon for mountain and mountain shadow area.

REFERENCES

- [1] Yabusaki S., Kono T., "Characteristics of stable isotopes in precipitation at Kyoto basin", Bulletin of geo-environmental science, Vol. 14, 2010, pp. 23-30.
- [2] Suzuki H., Nakakita E., "Analysis of Dependence of Heavy Rainfall on Elevation Using Data Observed at Railway Stations and Meteorological Stations", Annual journal of Hydraulic Engineering, Vol.51, 2007, pp. 283-288.
- [3] Suzuki H., Nakakita, E., "Dependence of Heavy Rainfall on Elevation Along Railroad in Mountainous Area", Annual journal of Hydraulic Engineering, Vol.54, 2010, pp .337-342.
- [4] Yamada T, Hibino T, Araki T, "Statistical Characteristics of Rainfall in Mountainous Basins" Journal of Japan Society of Civil Engineers, No. 527, 1995, pp 1-13.
- [5] Higashi K. and Fuji T., A Case Study on Local Heavy Rainfall Observed in Kyoto City on 15 October 1998, Kyoto Sangyo University essays. Social science series, Vol.33, 2004, pp.86-103.
- [6] Tsuguti H. and Kato T., Objective Extraction of Heavy Rainfall Events and Statistical Analysis on their Characteristic Features, Tenki, Vol.61, No.6, 2014, pp.455-469.

STUDY ON ADSORPTION PERFORMANCE OF FOOD WASTES FOR VARIOUS HEAVY METALS

Keiichiro Shibata¹, Hidenori Yoshida², Tsumugi Inoue³, Matsumoto Naomichi² and Yoshihiro Suenaga²

¹Graduate school of engineering, Kagawa university, Japan; ²Kagawa university, Japan; ³Okayama city, Japan

ABSTRACT

The harmful materials are came to a head through the redevelopment in empty lots in recent years. The soil and groundwater contaminations are often caused by the heavy metals and the volatile organic compounds. The cleaning treatment water for the excavated soil and the contaminated water pumping is generated by digging and washing the contaminated soil. The adsorption disposal by the activated carbon is conducted as the disposal method for both contaminated water and pumped groundwater after the aeration disposal. However, the activated carbon has a low adsorption performance for inorganic substances such as the heavy metals. Thus, in this study, the rice husk and fish bones which are an industrial waste are focused on. The material cost is saved by using the industrial waste. The product process of the fish bone is only burning and the rice husk is not manufactured. It is examined whether both materials can be used as the adsorbent for the heavy metals. As the results of examinations, it is clarified that some heavy metals such as Zn^{2+} and Cd^{2+} are well adsorbed into both materials and both materials are useful as the recycling materials.

Keywords: Soil and groundwater contamination, Fish bone absorber, Rice husk, Heavy metals

INTRODUCTION

In recent years, the soil contamination and groundwater contamination because harmful materials are came to a head through the redevelopment in empty lots. According to the reports of each prefecture's soil pollution case and groundwater pollution case released by the Ministry of the Environment as in [1], [2], the number of bath cases has increased since 1991, when the soil environmental standards were enacted. In particular, the number of both cases has rapidly increased in 2002 by executing the Soil Contamination Countermeasures Act, and the cases have increased again in 2010 when executing the revision Soil Contamination Countermeasures Act. The researched cumulative number of cases is 19,927, and the cumulative number of cases that exceeds the environmental standard value is among 9,733 in the case of soil contamination cases grasped by prefectures by the end of 2014. The soil and groundwater contaminations are often caused by the heavy metals and the volatile organic compounds (VOC). The VOC has the characteristics that it is difficult to dissolve in water and its viscosity is low. Thus, the VOC moves in the soil and easily reaches the groundwater surface. On the other hand, the soil pollution by heavy metals is difficult to spread deeply because most of heavy metals are easily adsorbed by minerals in soil. However, the certain heavy metals such as hexavalent chromium and arsenic are highly soluble in groundwater, and have high mobility in soil.

Therefore, there are many cases of groundwater contamination by hexavalent chromium and arsenic among heavy metals.

The cleaning treatment water for the excavated soil and the contaminated water pumping is generated by digging and washing the contaminated soil. The adsorption disposal by the activated carbon is conducted as the disposal method for both contaminated water and pumped groundwater after the aeration disposal. The activated carbon is most frequently used as an adsorbent, it is inexpensive compared to other adsorbents, and has an advantage of having a high specific surface area. Especially, it is known that the activated carbon has a high adsorption performance for organic substances such as a VOC. However, the activated carbon has a low adsorption performance for inorganic substances such as the heavy metals. For this reason, adsorbents such as the zeolite and the silica are used for inorganic substances, but they have the disadvantage that the manufacturing cost is higher than that of activated carbon. It is predicted that the number of soil and groundwater contamination increases with redevelopment etc. in the future. Therefore, the adsorbent which can be manufactured at low cost is required. Thus, in this study, the rice husk and fish bones which are an industrial waste are focused on. The material cost is saved by using the industrial waste. The unprocessed rice husk and only burned fish bone are used as an adsorbent in order to reduce the manufacturing cost. Also, the adsorption performance of the rice husk and fish bone for heavy metals are examined whether both

materials can be used as a new adsorbent.

MATERIALS AND METHODS

In this study, the rice husk and fish bone, food waste, are adopted as an adsorbent for the heavy metals as has noted above. Their material properties are explained below.

Rice husk

The rice husk is the shell of berry taken from the spike of rice. The rice husk is covered with a wax component which protects the surface of the organism called the cuticle. The rice husk is hard to decompose since the wax component shed the water. The rice husk is shown in Fig. 1, and has the feature that about 20 percent of silica is contained. Bamboo is also said to have a lot of silica, but even it is less than 0.1% in the case of raw bamboo. The silica is the silicon dioxide or the generic name of substances which constituted by silicon dioxide. The rice husk is very hard and difficult to process due to the properties of silicic acid which is the raw material of glass contained in chaff. The amount of rice husk emissions is about 2 million tons annually nationwide, and most of them are discarded as the industrial waste since the usage of unprocessed rice husk is limited. The unprocessed rice husk has been used for packing or seedling cover materials, but the usage as plastics material has been increasing in recent years. Although it is considered that the optimum processing and utilization method of unprocessed rice husk are few, the rice husk ash made by burning rice husk has been studied for many uses. In Thailand, the rice husk is used as a heat source to generate steam and power. The rice husk ash given off from these generation is used for material of cement. As a similar technology, the researches for making building materials for houses from rice husk, which were developed by the National Institute of Advanced Industrial Science and Technology Kyushu Industrial Technology Laboratory (now Kyushu Center for Industrial Science and Technology) is conducted. After using rice husk as a heat source, the rice husk ash, caustic lime and glass fiber are mixed and solidified to produce boards that can be widely used as lightweight building materials for general houses such as insulation materials. Furthermore, a study that the rice husk ash is mixed in concrete are also conducted as in [3]. In addition, it is confirmed by the studies of Nakanoku University of Chukyo University that rice husk ash has high adsorption rate for radioactive materials such as the cesium and strontium.

As noted above, various usage methods are studied for the rice husk ash, but it is necessary to control the temperature at 400 ~ 600 °C and burn in order to produce the high quality rice husk ash as in [4]. Crystallized silicic acid and dioxin may be

generated when the burning temperature falls below 400 °C. Practical realization has not progressed much due to the difficulty of such processing. In order to propose a new method of utilizing raw rice husk and to reduce the cost of processing, in this study, an adsorption performance of dried rice husk for heavy metals without processing is examined (see Fig. 1).



Fig. 1 Dried rice husk

FbA (Fishbone Absorber)

Hydroxyapatite is the basic calcium phosphate, and its chemical formula is $\text{Ca}_{10}(\text{PO}_4)_6(\text{OH})_2$. Hydroxyapatite is excellent in biocompatibility and used for materials such as artificial bone and implants because it is a major constituent of teeth and bones. In addition, hydroxyapatite has many functions such as high adsorptive property (especially amino acids, proteins, lipids, sugars, etc.), ion exchange properties, catalytic properties, and ionic conduction properties as in [5], [6], [7]. It is artificially synthesized by many methods and it is used in various fields including the biomaterials. According to study of Nishiyama et al., it is already known that hydroxyapatite has adsorption properties not only for heavy metals but also for strontium as in [8]. Some hydroxyapatite is derived from cattle bones and pig bones, but in this study, the adsorbent based on hydroxyapatite derived from fish bones (Fishbone Absorber, hereinafter referred to as FbA and, see Fig. 2) is used for various tests. The size of the piece is approximately 1 cm square and its weight is approximately 0.6 g. The FbA is produced by burning fish bone discarded at a fishing port.



Fig. 2 FbA

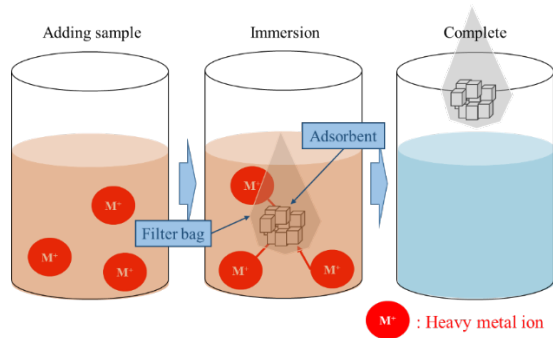


Fig. 3 Removal method for heavy metals ion in the solution

RESULTS AND DISCUSSION

Among various materials which are harmful to the environment and the human body, and in this study, 9 types of Cr^{6+} , Cr^{3+} , Mn^{2+} , Ni^{2+} , Zn^{2+} , As^{3+} , Se^{4+} , Cd^{2+} , Hg^{2+} are selected. The materials section is based on the harmful substances specified by the uniform effluent standards of the Ministry of the Environment. Se^{4+} is the cation in the solution though Se^{4+} is a nonmetallic element. Furthermore, Se^{4+} is targeted in the test because Se^{4+} is comprehended in the harmful material and the cation in the solution. For chromium, trivalent and hexavalent samples are prepared because their waste water standards are different depending on the valence. The test conditions are set and adsorption tests for each heavy metal are conducted in order to examine the basic adsorption performance of the rice husk and the FbA for heavy metals. First, 300 mL of pure water is put in a cylindrical container, and a standard solution of each heavy metal (analytical reagent adjusted to 1000 mg / L) is added. The standard solution of 1 mL and 5 mL (about 3.3 and 16.4 ppm of initial concentration, respectively) is added in order to ascertain the adsorption amount per unit mass of the adsorbent for each heavy metal ion. Secondly, the adsorbent is put in the filter bag and it is immersed in the solution assuming collection of adsorbent after the end of the test. The adsorbent is taken out after immersing in a thermostat set at 25 °C for 168 hours, and the concentration of each heavy metal ion in the solution is analyzed by an ICPS emission spectrometer. The adsorption performance of each adsorbent is evaluated by the adsorption ratio derived from the residual concentration of each ion in the solution to the initial concentration at the time of addition of standard solutions. All tests are conducted

three times in order to ensure reproducibility, and the test results are shown by their average values.

Test results

The test results using the rice husk and the FbA as the adsorbent are shown graphically. The adsorption ratio of heavy metal and heavy metal are shown in the vertical and horizontal axes, respectively. The numerical value written on the top of the bar graph is the pH value which is measured immediately after taking out the adsorbent. Table 1 shows the pH values of each test specimen before adding the adsorbent. The pH of all test specimens indicates from weak acid to strong acid before adding adsorbent because the standard solution is an acidic solution.

Adsorption test of rice husk

First, the results of the adsorption test using the rice husk as an adsorbent for each heavy metal are shown in Figs. 4 and 5, which correspond to the adsorption tests to 1 mL (initial concentration is about 3.3 ppm) and 5 mL (initial concentration is about 16.4 ppm) additions of heavy metal standard solution, respectively. The mass of rice husk is 0.6 g, and this mass is almost equal to the mass of FbA single piece.

As shown in Fig. 4, 80 percent or more of Zn^{2+} , Cd^{2+} , and Hg^{2+} are adsorbed to rice husk when 1 mL of the sample was added. On the other hand, Cr^{6+} and As^{3+} are not adsorbed at all. All three types of ions with high adsorption ratio are group 12 elements. The Group 12 elements are also called zinc group elements. They are metal elements, and classified as typical elements. The Group 12 elements are considered to be closer to the adsorption mechanism of alkaline earth metal than other heavy metals classified as transition elements because the zinc group elements are divalent cation. According to Shannon's ionic radius table, the ionic radius of the three zinc group elements are relatively close (see Table 2). The high adsorption rate for ions whose ionic radii are close suggests that rice husk may adsorb the ions by physical adsorption rather than chemically adsorbed. It is necessary to clarify adsorption mechanism in near future. Alternatively, Mn^{2+} and Ni^{2+} is the divalent cations in solution similarly to Zn^{2+} , Cd^{2+} , and Hg^{2+} with high adsorption ratio to the adsorbent. However, the adsorption ratio remains around 50 percent. From these facts, it is considered that not only the ion valence but also the

Table 1 pH value before adding adsorbent

	Cr^{3+}	Cr^{6+}	Mn^{2+}	Ni^{2+}	Zn^{2+}	As^{3+}	Se^{4+}	Cd^{2+}	Hg^{2+}
1 mL	3.4	4.6	3.5	3.5	3.4	5.8	3.6	3.4	3.5
5 mL	2.8	3.5	2.8	2.7	2.8	4.8	2.6	2.8	2.8

ionic radius are related to the adsorption performance. On the other hand, there are exceptions such as Cr^{3+} , and other factors also need to be examined in near future. Focusing on pH, the pH value of Cr^{6+} and As^{3+} are higher than that of the other specimens and show neutrality. It is a possibility that the adsorption ratio may be improved by adjusting the pH value of the solution to a low value and making an acidic environment.

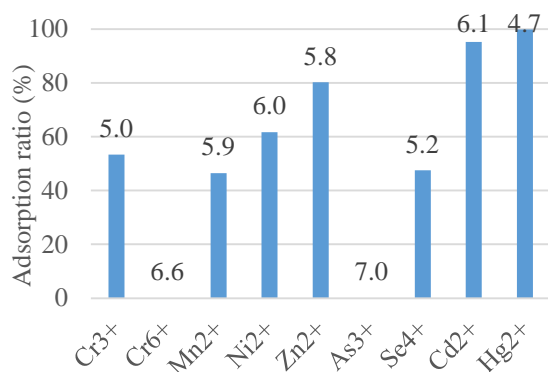


Fig. 4 Adsorption performance of rice husk (adding amount of 1 mL)

As shown in Fig. 5, the adsorption ratio decreases in most of the specimens to compare with using 1 mL of sample when 5 mL of the sample is added. It is considered that the amount capacity of adsorbing each ion of 0.6 g of rice husk may be clarified by increasing the amount of sample added. Although the adsorption ratio decreases as the most of samples, the divalent cations, Mn^{2+} , Ni^{2+} , Zn^{2+} , Cd^{2+} , and Hg^{2+} tend to be relatively adsorbed. Especially, the rice husk for Hg^{2+} has a relatively high adsorption ratio even if the addition amount is increased five times. The fact that 50% of the added amount is adsorbed suggests the adsorption amount increases. Almost all of Hg^{2+} is adsorbed in the 1 mL of addition amount and about half adsorption in 5 mL, and there is a possibility that the adsorption limit amount for Hg^{2+} is between 1 and 5 mL. These results shows that the adsorption limit amount for Hg^{2+} may be between 1 and 5 mL. The reason why the adsorption ratio decreases in most samples is considered to depend on the difference in the initial pH value (see Table 1). The heavy metal ion is easily adsorbed in the lower initial pH value. On the other hand, among all specimens, the adsorption ratio in the only specimen of As^{3+} is high and the pH values after the test is almost the same regardless of the amount of addition. In near future, the test should be conducted by

adjusting the pH value in order to clarify the influence of the pH value on the adsorption of each heavy metal ion, and the test in which the addition amount is minutely set is conducted in order to ascertain the adsorption limit amount of rice husk.

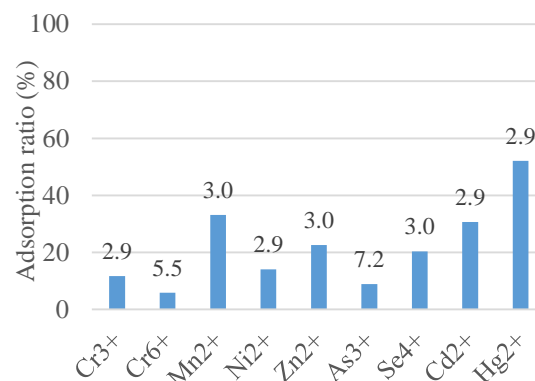


Fig. 5 Adsorption performance of rice husk (adding amount of 5 mL)

Adsorption test of FbA

First, the results of the adsorption test using the FbA as an adsorbent for each heavy metal are shown in Figs. 6 and 7 which correspond to the adsorption test to 1 mL (initial concentration is about 3.3 ppm) and 5 mL (initial concentration is about 16.4 ppm) additions of heavy metal standard solution, respectively. The 1 piece of FbA (about 0.6 g) is used in the test.

As shown in Fig. 6, the adsorption ratio for Hg^{2+} is the highest all of samples and 90% or more of Hg^{2+} is adsorbed to the FbA when 1 mL of the sample is added. Subsequently, the adsorption ratio of Zn^{2+} and Cd^{2+} is high, and the results are similar to those of the test using rice husk. On the other hand, the adsorption ratio to Cr^{6+} and As^{3+} is low, and the result is also similar to the case using the rice husk, while the adsorption ratio for Mn^{2+} is higher than that of the case using rice husk. The adsorption ratio of Mn^{2+} is about 50% when the rice husk is used. However, it exceeded 70% in the case using the FbA. It is considered that Mn^{2+} has a property to promote the calcification of bone in increasing the adsorption ratio of the FbA to Mn^{2+} . Mn^{2+} is a necessary mineral for the calcification of bone and is more easily absorbed into bone than other ions. It is presumed that Mn^{2+} is adsorbed to the FbA rather than rice husk because the FbA is derived from fish bone. Additionally, the adsorption ratio of Cr^{3+} is slightly higher than that of the case using the rice husk. A slight precipitate is confirmed when the specimen of Cr^{3+} using the FbA

Table2 Ionic radius (Å) (Shannon)

Cr^{3+}	Cr^{6+}	Mn^{2+}	Ni^{2+}	Zn^{2+}	As^{3+}	Se^{4+}	Cd^{2+}	Hg^{2+}	Si^{4+}	Ca^{2+}
0.62	0.44	0.67	0.69	0.74	0.58	0.50	0.95	1.02	0.40	1.00

is observed. It is widely known that heavy metal ions might precipitate hydroxides by increasing the pH value as in [9], [10]. The value varies depending on the heavy metal ion and the element coexisting in the solution, and the specimen of Cr^{3+} generates a precipitate due to this property. As a result, the adsorption ratio increases by decreasing the ion concentration in the solution. Even in the specimens except the test specimen to which Cr^{3+} is added, the pH value is changed from weak acid to neutral in the case of using the rice husk. On the other hand, it increased to weak alkalinity in some specimen when the FbA is used. The adsorption performance of rice husk and FbA are very similar, but their effects on pH value in solution are different. As this reason, the FbA is fired while the rice husk is not burned. The rice husk ash is often used as a conditioner for soil to neutralize acidic soils as in [11]. It is clarified that the rice husk and FbA can be used not only as an adsorbent for heavy metals but also as a pH value adjustment material by controlling the used amount in the case of using both materials as contaminated water on site.

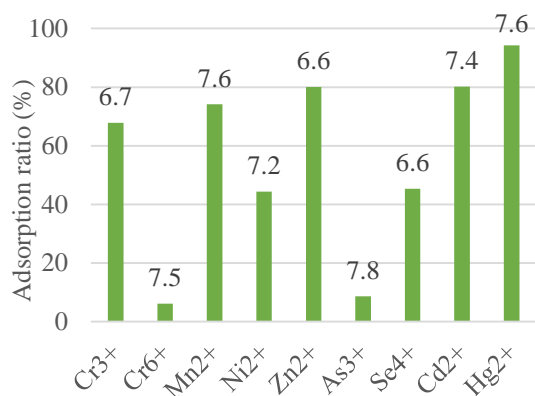


Fig. 6 Adsorption performance of FbA (adding amount of 1 mL)

As shown in Fig. 7, the adsorption ratio for Cd^{2+} and Hg^{2+} is relatively high when 5 mL of the sample is added, and the values exceed 60%. For Hg^{2+} , it is presumed that the adsorption limit amount is between 1 and 5 mL as in the case of adding the rice husk. The amount of adsorption for Cd^{2+} increases as the added amount increases. The solution is acidic because the pH value is low when 5 mL is added. It is considered that the pH value is low and the solution is acidic in the case of adding 5 mL. It is necessary to adjust the pH and conduct additional tests in order to clarify the consideration. The adsorption ratio for other samples is lower than that of adding 1 mL, and the results show a similar tendency of those of 1 mL addition of heavy metals. Some samples increase the amounts of adsorption such as Hg^{2+} and Mn^{2+} , and it is needed to investigate each sample of adsorption limit amount in detail. It is revealed that adsorption ability is higher

for divalent cations, in particular, Group 12 elements, in both cases of addition amount of 1 mL and 5 mL. As shown in Table 2, the ionic radius of the three kinds of ions which belong to group 12, are close to the ionic radius of Ca^{2+} . This result suggests that the FbA may remove heavy metal ions from solution by physical adsorption. The heavy metal ions are adsorbed to the FbA and Ca^{2+} is released instead, so that the adsorption performance may be higher for heavy metal ions with a close ionic radius. If the adsorption mechanism of FbA is physical adsorption, heavy metals adsorbed to the FbA can be taken out. In addition, both the FbA and heavy metals can be reused. Therefore, the adsorption mechanism may be examined in near future.

The adsorption performance of FbA is higher than that of rice husk in the case of adding 5 mL of most sample through all the test results. The rice husk has a high adsorption performance when additive amount is as small as 1 mL. On the other hand, the FbA is more useful than the rice husk when the content of heavy metal ion in the solution exceeds a certain amount. Additionally, the adsorption performance of FbA is higher than that of rice husk in the case of adding 5 mL of sample. It is assumed that the FbA has more marginal adsorption than rice husk.

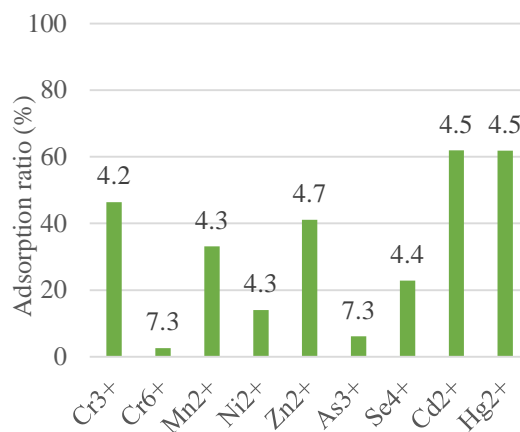


Fig. 7 Adsorption performance of FbA (adding amount of 5 mL)

CONCLUSIONS

In this study, the hydroxyapatite (FbA) derived from fish bones and rice husk which are known as industrial waste were focused. The possibility as a new adsorbent was investigated by elucidating the fundamental adsorption performance for harmful substances and the principle of these materials. In the tests, the adsorption effect of rice husk and FbA on nine kinds of heavy metals which have harmful effects to the ecosystem was examined. The test was conducted preparing the addition amount of the heavy metals to 1 mL, 5 mL in order to ascertain the adsorption amount per unit mass of the adsorbent. As

a result, it is confirmed that more than 40% of additive amount of all metals except As^{3+} and Cr^{6+} can be absorbed by the both adsorbents. In particular, both adsorbents had high adsorption ratio for Group 12 elements such as Hg^{2+} , Cd^{2+} , Zn^{2+} . The rice husk and FbA have similar property of adsorption for 9 metals, and both adsorbents had powerful adsorption effect on divalent cations. Alternatively, it is presumed that other factors such as ionization tendency, ionic radius and specific gravity are related to ion adsorption as well as ionic valence. As shown in Table 1, in case of the FbA, the ionic radius of well adsorbed heavy metal ions is close to the ionic radius of the main component Ca^{2+} of the FbA. It is necessary to examine the influence of these factors on adsorption and the reason why the rice hulls and FbA have similar adsorption performance to heavy metals should be discussed in more detail.

For the pH, the FbA tends to change the pH of solution to alkaline more than the rice husk. It is considered to be caused by whether or not the calcination process is carried out. Depending on the firing temperature, organic acids is thermally decomposed or released as carbon dioxide in the process of burning substances including organic substances. Therefore, alkali metals and alkaline earth metals such as sodium, potassium and calcium remain on the surface of the material as oxides, carbonates and hydroxides. The pH value rises in the solution because these pyrolysis residue elutes. As a result, it is necessary to consider the influence of the pH value when the FbA is adopted as the adsorbent. For As^{3+} and Cr^{6+} , the adsorption ratio may also change by adjusting the pH value. Therefore, it is necessary to adjust the pH value and conduct the same test. The each limit amount of adsorption for FbA and rice husk were different for heavy metal ion to compare the adsorption ratio according to the additive amount of sample. The adsorption ratio of rice husk is high in the case of using 1mL, and that of FbA is high in the case of using 5 mL. It is suggested that the FbA has a higher adsorption limit than the rice husk. Additionally, the adsorption performance of rice husk may be improved by adjusting low concentration of heavy metal ion, and that of FbA by adjusting high concentration. In near future, it is necessary to examine the adsorption performance by drastically decreasing or increasing the additive amount of heavy metal ion and widening the range of concentration.

ACKNOWLEDGEMENTS

This work was supported by Japan Society for the Promotion of Science, the Grants-in-Aid for Scientific Research (C) (Grant number: 18J12343). Also, in carrying out this study, Nihon Kogyo Co.,

Ltd. provided FbA. We express our gratitude here.

REFERENCES

- [1] Ministry of the Environment, Ministry of Water and Atmospheric Environment, Research results on the construction situation of the soil contamination countermeasure law and the case of soil pollution surveys and measures in 2014, 2016, pp. 1-33.
- [2] Ministry of the Environment, Ministry of Water and Atmospheric Environment, Measurement results of groundwater in 2014, 2015, pp. 2-55.
- [3] Norihiro K, Takumi U and Kazuhide S, Fundamental study of fresh and hardening property of concrete with non-crushed rice husk ash, Concrete Research and Technology, Vol. 28, 2017, pp. 1-13.
- [4] Kozo I and Naomichi H, Thermal treatment and characteristics of rice husk ash, The Society of Inorganic Materials, Vol. 3, No. 263, 1996, pp. 312-318.
- [5] Moritsugu H and Takeshi N, Inorganic components of bones of fish and their advanced utilization, The Journal of Shimonoseki University of Fisheries, Vol. 43, No. 4, 1995, pp. 185-194.
- [6] Aoki H, Tatsuhiko Y and Toshiyuki K, Apatite as a marvelous biomaterial and the surface technology, Surface Technology, Vol. 58. No. 12, 2007, pp. 744- 750.
- [7] Hironori S, Toshiyuki E and Tatsuya S, Development of a medical grinding tool considering material properties of wet bone for minimally invasive surgery, The Japan Society of Mechanical Engineers, Vol. 79, No. 804, 2013, pp. 254-265.
- [8] Yuichi N, Tadashi H, Jun Y, Yoko Y and Toshiro O, Adsorption and removal of strontium in aqueous solution by synthetic hydroxyapatite, Journal of Radioanalytical and Nuclear Chemistry, Vol. 307, Issue. 2, 2016, pp. 1279-1285.
- [9] Konen Y and Masakatsu S, Heavy metal contamination and its new countermeasure method, Society of Environmental Conservation Engineering, Vol. 3, No. 4, 1974, pp. 235-242.
- [10] Naoki K, The relationship between pH and the concentration of heavy metal ions, The Chemical Society of Japan, Vol. 46, No. 12, 1998, pp. 806-807
- [11] Yaren b, Kazuo H, Makoto H, Shizuko I, Shohei A and Motoyasu K, Processing and utilization of rice husk charcoal, Journal of the Japanese Society of Agricultural Machinery, Vol. 62, No. Supplement, 2000, pp. 185-186.

THE ACUTE EFFECT OF TRADITIONAL THAI MASSAGE ON RECOVERY FROM FATIGUE IN BASKETBALL PLAYERS

Nopparak Kaesaman^{1,3} and Wichai Eungpinichpong^{2,3}

¹Graduate School, Khon Kaen University, Thailand

²Faculty of Associated Medical Sciences, Khon Kaen University, Thailand

³Research and Training Center for Enhancing Quality of Life of Working-Age People,
Khon Kaen University, Thailand

ABSTRACT

Massage has been used as an alternative treatment for professional athletes for decades. However, it has hardly been used for rapid recovery on the sport field that always needs rapid recovery during half-time break of competition such as basketball. This study aims to investigate the acute effects of Traditional Thai Massage on recovery in basketball players as indicated by heart rate variability (HRV) and physical fitness. A cross-over design was administered. Sixteen basketball players were randomly allocated into two groups: intervened with Traditional Thai Massage (TTM) and Control (C). Each period, the participants underwent 20 minutes of basketball-playing simulation after which they were assessed on HRV and physical fitness. Then they received either 10-minute TTM intervention or 10-minute rest, and were assessed again immediately after the interventions with 3 days washout period. The results showed that HRV and physical fitness were significantly increased ($P < 0.05$) in both groups after the interventions. There was no significant difference of LF/HF ratio (LF/HF ratio) in the control group. Mean changes in Grip strength test (GST) and High Frequency (HF) were found to be higher in the TTM than the control on between-group comparison ($P < 0.05$). Both TTM and passive rest could enhance recovery after strenuous basketball playing. However, the TTM showed superior improvement from fatigue than passive rest as indicated by HRV and GST.

Keywords: Traditional Thai Massage (TTM), Heart Rate Variability (HRV), Basketball Players, Fatigue, Recovery

INTRODUCTION

Recovery is one of the basic principles in athletic training methodology [1]. Fast recovery from muscle fatigue is vital in sport events especially when athletes require maximum energy for better performance during competition. Frequently, an interval between matches in each competition could be varied depends on the local competition rules. Thus, it is crucial for athletes to be provided with a sufficient treatment that has an immediate effect on the muscle recovery after the highly vigorous muscle activities. The appropriate muscle recovery process must quickly reduce the fatigue. If the improper muscle treatment is applied to the athletes, it may lead to reduced physical performance, increased risk of injury, or even emotional stress during competition.

Several methods of muscle recovery have been suggested for professional athletes, including the use of hot/cold therapies, stretching techniques, and sport massage. Among various muscle recovery strategies, manual massage is considered as the most natural technique that be gently and directly applied to the injured areas to enhance the elasticity of muscle and joints while relaxing the tendons [2].

Furthermore, manual massage could provide an increase of skin temperature which helps stimulating the blood flow [3]-[5], and reduces the muscle soreness [6]. In most cases, massage are used to recover the fatigued muscle, stretch the affected muscle, and improve the mood states during and after the competition [7].

Traditional Thai Massage (TTM) is a deep-tissue type of manual massage which mainly use for promote relaxation and wellbeing. In addition, it has been modified to use with athletes to facilitate recovery of fatigued muscles after the competitions such as Thai boxing, and football. The applied Thai massage used for athletes' muscle recovery consists of the massage techniques of rubbing, rolling, pressing, squeezing with fingers and palm, gently chopping with hand to stretch the joints throughout the body, including all major muscle bundles of arms, legs, and abdomen. The applied massage also focuses on stretching the ten nerve lines of Thai massage. Previous studies have shown the empirical evidence that massage arouses the temperature on the skin that can increase the blood flow [3]-[5]. In addition, massage can minimize soreness [2] [8], enhance flexibility [2], reduce sympathetic nervous system while increasing parasympathetic nervous

system [2], [9], [10].

Basketball is one of the most popular sports in the world. It requires the players' use of strenuous energy as well as ultimate strength of the muscle and mobility skills throughout the game. In general, basketball players move approximately 4,500-5,000 meters in 40 minutes [11]. Every two minute, the players run, walk, spin, jump, slide, etc [12]. Fifteen percent of each game is considered as highly intense exercise [13]. Due to the heavy physical movement, the injuries often occur [14]. However, the basketball players are given with limited time off to obtain the recovery during the intervals. Thus, it is essential for the basketball players to meet these needs in order to compete at full strength and recover quickly during and after the competition.

Yet, no studies have reported the effect of traditional Thai massage on the recovery by using HRV or other parameters to determine its efficiency in the context of intense sport, particularly Basketball. Hence, it is important to examine the acute effect of traditional Thai massage on the recovery of basketball players. The results of the study are expected to provide evidence for further sport performance improvement, and enhance the understanding in the extent of sport and sport science.

The purposes of this study are to examine the acute effects of traditional Thai Massage on recovery in basketball players during the competition, and compare the acute effects of traditional Thai Massage and passive rest on recovery in basketball players during the competition.

METHODS

Study design and participants

This study was a crossover randomized controlled trial, approved by the ethics committee of Khon Kaen University, Thailand (HE602113). The included participants were 16 males (mean age 20.13 ± 1.31 years), with a mean age of 20.13 ± 1.31 years, average of 72.69 ± 11.25 kilograms, average body mass index of 177 ± 6.68 cm, and average body mass index of 24.05 ± 5.79 kg/m². They were 3-year experienced basketball players with no history of serious disease. Before participating in this study, the participants were advised to refrain from eating, drinking alcohol, smoking, and consuming caffeine for at least 2 hours.

Procedure and protocol

The participants were basketball players of Sakon Nakhon Rajabhat University. They were provided with orientation to understand the criteria of the research and consent to participate in the

study. The participants will divide into two groups. The first group was intervened by traditional Thai massage (TTM), receiving massage for ten minutes. The second group is controlled group (C), allowed to gain passive rest for ten minutes. This research is a crossover randomized controlled trial. All participants were examined for two times. That is, an individual participant would receive traditional Thai massage; then passive rest.



Figure 1 Diagram of study protocol and variable measured. TTM and C group: 10 minute for each protocols, 1 trial per protocol, wash out 3 day. TTM: Traditional Thai Massage.

Heart Rate Variability (HRV)

The participants sat on a comfortable chair with a backrest, with eyes opened. HRV parameters were measured three minutes by using the device, called Ubio macpa, Korean version. The values of HR, RMSSD, SDNN, HF, LF, and LF / HF ratio were used to evaluate HRV.

Physical Fitness

Sit and reach test (SRT) was measured as described by [15]. Subjects sit with the soles of their feet against the box, and with their hips flexed to about 90° to assume an upright sitting position. And then subjects flex their hip joints and vertebral column (with possible contributions from shoulder joint flexion and scapular elevation) to reach forward as far as possible. A centimeter scale is printed on the top surface of the box.

Grip strength test (GST) was measured using a Grip dynamometer (TKK 5401, Japan). The participants griped the dynamometer with four fingers, except the thumb, and controlled the width of the handle. The arms were naturally lowered. Maximum strength was applied to the dynamometer without touching the body. [16].

Back strength test (BST) back strength of the participants was measured using a Back-leg-chest dynamometer. The participant was positioned with body erect and knees bent so that the grasping hand rests at proper height. Then, by straightening the knees and lifting the chain of the dynamometer, pulling force was applied on the handle. The body would be inclined forward at an angle of 60 degrees for the measurement of back strength [17].

Leg strength test (LST) leg strength was also measured using a back-leg-chest dynamometer. The

participant was asked to stand erect with knees bent so that the grasping hand rests at proper height. The individual then lifted the handle of the dynamometer, bending his legs, and then straightened the legs [17].

Traditional Thai massage (TTM) and Passive rest

The participants in Traditional Thai Massage group are given 10 minutes of massage whereas the controlled group are given 10 minutes to rest. In the room, the temperature is controlled at 25-26 °C. In the TTM group, Thai traditional and Effleurage massage techniques are applied throughout the body of the participants including biceps and triceps (arms), deltoid (shoulders), latissimus dorsi, thoracolumbar fascia, trapezius (back), and stretching muscles which consist of hamstrings, rectus femoris, arms, and back. In the C group, the participants are provided with a regular passive rest (half time).

Statistical analysis

The data were presented as mean \pm SD. Shapiro-Wilk test was used to verify normality of data. Crossover study design analysis was employed. The paired t-test statistic was used to compare the mean between the groups. The independent sample t-test statistic was used to compare mean between groups. Statistical significance value was set at $p < 0.05$.

RESULT

Table 1 shows the comparison of the statistic values in each group. The results of RMSSD, SDNN, HF, LF, SRT, GST, BST, and LST, were significantly increased ($P < 0.05$). whereas HR, was significantly decreased ($p < 0.05$) in two group.

However, the LF/HF ratio increased significantly ($P < 0.05$) only in the TTM group. HF values were significantly different ($P < 0.05$) and no significant differences in the comparison of results between groups is presented in Table 2.

DISCUSSION

The result showed that Thai traditional massage has acute effect on recovery from fatigue in basketball players in both groups. According to the HRV and physical fitness results, the average recovery level in the Thai traditional massage group was higher than in the non-Thai traditional massage group that received only passive rest. The positive result on recovery in the group treated by Thai traditional massage was considered as the process that body systematically reacts to the massage, including the biochemical processes in cellular, tissue and organ level.

It was found that body relaxation contributes to lower blood pressure because the stimulation of parasympathetic from the massage [18]. In this study, the basketball players significantly noticed the mental and muscle tension, refreshment and power boost to play more effectively in another half of the game. This result was consistent with the previous studies that stated that massage can increase HRV [2], reduce sympathetic activity, and increase parasympathetic activity [19], [20]. Even with the different types of massage, the result showed the decrease of HR and increase of SDNN, RMSSD, LF, HF, and LF-HF Ratio. Thus, the results indicated that Thai traditional massage can reduce sympathetic activity and increase parasympathetic activity which contribute to the greater recovery rate in basketball

Table 1 Comparison of the results in each group

Results	TTM group (n=16)		Controlled group (n=16)	
	Before	After	Before	After
RMSSD(ms)	12.08 \pm 3.2	21.49 \pm 3.63*	12.23 \pm 2.65	18.46 \pm 4.02*
SDNN (ms)	38.83 \pm 13.15	46.43 \pm 13*	41.56 \pm 9.47	46.08 \pm 11.44*
HR (bpm)	130.53 \pm 10.54	98.86 \pm 6.95*	134.74 \pm 8.12	104.6 \pm 8.04*
HF (ms ²)	6.56 \pm 0.76	7.95 \pm 0.77*	6.34 \pm 0.84	7.57 \pm 0.67*
LF (ms ²)	7.86 \pm 0.9	8.84 \pm 0.78*	7.86 \pm 1	9.2 \pm 0.86*
LF-HF ratio	1.18 \pm 0.04	1.25 \pm 0.08*	1.17 \pm 0.05	1.19 \pm 0.11
SRT (cm)	11.56 \pm 5.05	13.13 \pm 5.06*	12.19 \pm 5.02	12.13 \pm 5.03*
GST (kg)	39.66 \pm 4.96	40.6 \pm 5.46*	39.28 \pm 6.58	38.74 \pm 6.25*
BST (kg)	127.94 \pm 18.65	143.47 \pm 20.12*	131.72 \pm 25.06	138.42 \pm 22.21*
LST (kg)	150.41 \pm 26.97	162.63 \pm 27.22*	154.59 \pm 34.33	161.36 \pm 31.71*

Data are expressed as mean \pm SD. TTM – traditional Thai massage; RMSSD – the square root of the mean squared differences of successive normal R-R intervals; SDNN – the standard deviation of the normal-to-normal intervals; HR – heart rate; HF – high frequency; LF – low frequency; LF/HF ratio – low frequency per high frequency ratio; SRT - Sit and reach test; GST - Grip strength test; BST - Back strength test; LST - Leg strength test. Significant change within group, * $p < 0.05$

Table 2 Comparison of the results between two groups

Results	Compared before		Compared after	
	TTM –Traditional Thai massage (n=16)	Passive rest (n=16)	TTM –Traditional Thai massage (n=16)	Passive rest (n=16)
RMSSD (ms)	12.08±3.2	12.23±2.65	21.49±3.63	18.46±4.02
SDNN (ms)	38.83±13.15	45.31±12.32	30.24±8.78	25.58±8.86
HR – heart rate (bpm)	130.53±10.54	134.74±8.12	98.86±6.95	104.6±8.04
HF – high frequency (ms ²)	6.56±0.76	6.34±0.84	7.95±0.77*	7.57±0.67
LF – low frequency (ms ²)	7.86±0.9	7.86±1	8.84±0.78	9.2±0.86
LF/HF ratio – low frequency per high frequency ratio	1.18±0.04	1.17±0.05	1.25±0.08	1.19±0.11
SRT - Sit and reach test (cm)	11.56±5.05	12.19±5.02	13.13±5.06	12.13±5.03
GST - Grip strength test (kg)	39.66±4.96	39.28±6.58	40.6±5.46	38.74±6.25
BST - Back strength test (kg)	127.94±18.65	131.72±25.06	143.47±20.12	138.42±22.21
LST - Leg strength test (kg)	150.4±26.97	154.59±34.33	162.63±27.22	161.36±31.73

Table 3 Comparison of the mean change scores (pre–post) of HRV and physical fitness tests between the (TTM) and control groups

Results	TTM – Traditional Thai massage (n=16)	Passive rest (n=16)	Different (95% CI)
RMSSD (ms)	9.41±2.74	6.23±2.69	-3.18(-5.56 to -0.80)
SDNN (ms)	7.61±5.87	4.51±5.87	3.1(-1.14 to 7.33)
HR – heart rate (bpm)	-31.68±8.05	-30.14±5.79	-1.54(-3.53 to 6.60)
HF – high frequency (ms ²)	1.39±0.95	1.23±0.77	-0.16(-0.79 to 0.45)
LF – low frequency (ms ²)	0.98±1.06	1.34±1.22	-0.36(-1.18 to 0.47)
LF/HF ratio – low frequency per high frequency ratio	0.08±0.1	0.03±0.1	0.05(-0.02 to 0.12)
SRT - Sit and reach test (cm)	1.56±0.96	-0.06±1.61	1.62(0.67 to 2.58)
GST - Grip strength test (kg)	0.94±2.07	-0.54±4.44	1.48(-1.01 to 3.99) *
BST - Back strength test (kg)	15.53±16.79	6.7±13.04	8.83(-2.02 to 19.69)
LST - Leg strength test (kg)	12.22±10.32	6.76±13.21	5.46(-3.10 to 14.02)

players.

Thai traditional massage dilates the blood vessels [4], [5], [21], which helps remove oxygenated blood and waste from the muscle e.g. lactic acid; as a consequence, the acidity in muscles is diminished. This leads phosphofructokinase - an enzyme that controls process of glycolysis - to generate the energy to the muscles, and improves the binding of protein myosin and actin in muscle contraction; as a result, the muscles work effectively [22]. Moreover, Thai traditional massage helps the blood vessels to transport oxygen to the muscles so that the muscles can perform better. In additional, Thai traditional massage at the arms, legs, and back helps tissues around these organs improve flexibility, especially when they contract [23]. All these effects of massage may contribute to improve overall performance of the basketball players.

For Thai traditional massage, the mechanical pressure is used by pressing on the muscle tissues to increase muscle flexibility for several benefits: to reduce the tension at the joints and muscle, and increase the degree of movement and elasticity [24]. The mechanism of massage has an effect on autonomic nervous system resulting in better mental relaxation because the massage can reduce the process of sympathetic activity while increasing parasympathetic activity [25]. This reduces the cortisol level, which in turn, lowers anxiety, eventually leading to relaxation [24], [26]. This result was in accordance with the previous studies of [2] and [27] indicating that massage helps reduce the anxiety. Likewise, [5] revealed that massage alleviates muscle tightness and heals the sore muscle after intense exercise.

CONCLUSION

The results of this study showed that Thai traditional massage has more acute effect on the recovery of basketball players than the passive rest. Hence, Thai traditional massage is an effective approach for muscle recovery since it improves the performance of basketball players during the competition. This method of Thai traditional massage could be applied to the basketball players during the breaks of the game, or even to other types of sports that are held with the breaks during the competition e.g. football, Sepak takraw, volleyball, etc. Therefore, sport massage as an alternative recovery method for athletes, trainers or interested parties could be applied in sports for greater performance and success.

ACKNOWLEDGMENTS

The authors would like to thank the volunteers who participated in this study. The study was supported by the Research and Training Center for Enhancing Quality of Life of Working-Age People at Khon Kaen University, and we would like to thank the Sakon Nakhon Rajabhat University for data collection.

REFERENCES

- [1] Rushall, B. S., & Pyke, F. S. (1990). Training for sports and fitness. Melbourne, Australia: Macmillan Educational.
- [2] Buttagat, V., Eungpinichpong, W., Chatchawan, U. & Kharmwan, S. (2011). The immediate effects of traditional Thai massage on heart rate variability and stress-related parameters in patients with back pain associated with myofascial trigger points. *Journal of Bodywork and Movement Therapies*, 15(1), 15-23.
- [3] Zhang, W., Takahashi, S., Miki, T., Fujieda, H., & Ishida, T. (2010). A pilot study exploring the effects of reflexology on cold intolerance. *Journal of Acupuncture and Meridian Studies*, 3(1), 43-48.
- [4] Hinds, T., McEwan, I., Perkes, J., Dawson, E., Ball, D., & George, K. (2004). Effects of massage on limb and skin blood flow after quadriceps exercise. *Medicine and science*.
- [5] Mori, H., Ohsawa, H., Tanaka, T. H., Taniwaki, E., Leisman, G., & Nishijo, K. (2004). Effect of massage on blood flow and muscle fatigue following isometric lumbar exercise. *Medical Science Monitor*, 10(5), CR173-178.
- [6] Corrie A Mancinelli, D. Scott Davis, Leila Aboulhosn, Misty Brady, Justin Eisenhofer, Stephanie Foutty. (2006). The effects of massage on delayed onset muscle soreness and physical performance in female collegiate athletes. *Physical Therapy in Sport*.
- [7] Cafarelli, E., F. Flint. (1992). The role of massage in preparation for and recovery from exercise. An overview. *Sport Med*, 14,1-9.
- [8] Corrie A. Mancinelli, D. Scott Davis, Leila Aboulhosn, Misty Brady, Justin Eisenhofer, Stephanie Foutty. (2006). The effects of massage on delayed onset muscle soreness and physical performance in female collegiate athletes. *Physical Therapy in Sport*, 7, 5-13.
- [9] Lindgren, L., Rundgren, S., Winsö, O., Lehtipalo, S., Wiklund, U., & Karlsson, M. et al. (2010). Physiological responses to touch massage in healthy volunteers. *Autonomic Neuroscience: Basic and Clinical*, 158(1-2), 105-110.
- [10] Pishbin, T., Firoozabadi, S.M.P., Jafarnia Dabanloo, N., Mohammadi, F. & Koozehgari, S. (2010) Effect of physical contact (hand-holding) on heart rate variability. *International Journal of Advanced Computer Science*, 2(12), 452-456.
- [11] Goran Vučković, Brane Dežman, Nic James, Frane Erčul, (2010). Analysis of the movement intensity of national level basketball guards and centres in defence and offence- A case study. *Kinesiologia Slovenica*, 16(3), 66-76.
- [12] Crisafulli A, Melis F, Tocco F, Laconi P, Lai C, Concu A. (2002). External mechanical work versus oxidative energy consumption ratio during a basketball field test. *J Sports Med Phys Fitness*, 42, 409-417.
- [13] McInnes, S.E., Carlson, J.S., Jones, C.J., & McKenna, M.J. (1995). The physiological load imposed on basketball players during competition. *Journal of Sports Sciences*, 13, 387-397.
- [14] Lakomy, J. and D.T. Hayton. (2004). The effect of enforce, rapid deceleration on performance in a multiple sprint test. *J Strength Con Res*, 18,579-583.
- [15] Wells, K. F., & Dillon, E. K. (1952). The Sit and Reach—A Test of Back and Leg Flexibility. *Research Quarterly. American Association for Health, Physical Education and Recreation*, 23(1), 115-118.
- [16] You Sun Ko, Sung Eun You (2015). Comparisons of physical fitness and body composition among Sasang types with and without body mass index as a covariate, *Integrative Medicine Research*, 4, 41-47.
- [17] Shyamal Koley, Aseem Khajuria, and Sheri Melton. (2010). The correlation between back strength and leg strength among indian inter-university male cricketers. *Physical Education and Sport*, 8(2), 125 – 132.
- [18] Wichai Eungpinichpong. *Therapeutic Thai Massage*. Bangkok. Suweriyasarn publishing, 2008; 54-8.
- [19] Lindgren, L., Rundgren, S., Winsö, O., Lehtipalo, S., Wiklund, U., & Karlsson, M. et al.

- (2010). Physiological responses to touch massage in healthy volunteers. *Autonomic Neuroscience: Basic and Clinical*, 158(1-2), 105–110.
- [20] Pishbin, T., Firoozabadi, S.M.P., Jafarnia Dabanloo, N., Mohammadi, F. & Koozehgari, S. (2010) Effect of physical contact (hand-holding) on heart rate variability. *International Journal of Advanced Computer Science*, 2(12), 452-456.
- [21] Monedero J, Donne B. Effect of recovery interventions on lactate removal and subsequent performance. *Int J Sports Med* 2000; 21: 593-7.
- [22] Frayn KN. Metabolic regulation. A human perspective. Portland Press, London 1996; p.182.
- [23] Wilmore JH, Costill DL. Physiology of sport and exercise. Human Kinetics. Champaign, IL 1994; 524-5.
- [24] Weerapong, P., Hume, P.A., & Kolt, G.S. (2005). The mechanisms of massage and effects on performance, muscle recovery and injury prevention. *Sports Medicine*, 35(3), 235-256.
- [25] Lee, Y.H., Park, B.N., & Kim, S.H. (2011). The effects of heat and massage application on autonomic nervous system. *Yonsei Medical Journal*, 52(6), 982-989.
- [26] Sripongngam Thanarat, (2015). Immediate Effects of Traditional Thai Massage on Psychological Stress as Indicated by Salivary Alpha-Amylase Levels in Healthy Persons. *Medicine and science*, 21: 216-221.
- [27] Kunikata, H., Watanabe, K., Miyoshi, M., & Tanioka, T. (2012). The effects measurement of hand massage by the autonomic activity and psychological indicators. *The Journal of Medical Investigation*, 59(1-2), 206-212.

THE POTENTIAL OF TROPICAL MICROALGAE AS FLOCCULANT IN HARVESTING PROCESS

Astri Rinanti^{1*}, Ronny Purwadi²

¹Environmental Engineering Department, Faculty of Landscape Architecture and Environmental Technology,
Universitas Trisakti, Jakarta, Indonesia

²Chemical Engineering Department, Faculty of Industrial Technology, Institut Teknologi Bandung, Bandung,
Indonesia

ABSTRACT

This environmental biotechnology research aims to obtain a diversity of freshwater tropical microalgae which has the ability to form a floc naturally to be utilized as bioflocculants in the process of harvesting other tropical microalgae biomass that does not have such ability. The microalgae *Chlorella vulgaris*, *Chlorella sorokiniana*, *Chlorococcum* sp., *Closterium* sp., *Oscillatoria* sp., *Monoraphidium* sp, *Ankistrodesmus* sp and *Scenedesmus obliquus* are cultivated in batch culture and their environmental condition are controlled at 25°C, fed with 5% pure CO₂ with flow rate of 5 L/min. To determine the ability of microalgae strain as microalgae flocculant or not, it is necessary to calculate recovery efficiency. The addition of *Scenedesmus obliquus* and *Ankistrodesmus* sp as flocculant microalgae followed by slow mixing allows better interaction between flocculant microalgae and non-flocculant microalgae, so the floc size increases. *Scenedesmus obliquus* and *Ankistrodesmus* sp can be used as flocculant species because the value of settling for both types of microalgae is more than 50% for 60 minutes while other microalgae species can be categorized as non-flocculant microalgae since within 60 minutes settles less than 50%. The study also proved that no greenhouse gas was formed during the bioflocculation process. Thus the method of bioflocculation with *Scenedesmus obliquus* and *Ankistrodesmus* sp is feasible to be applied to harvest microalgae biomass on an industrial scale.

Keywords: Bioflocculation, Tropical microalgae, Flocs, Harvesting, Diversity

INTRODUCTION

In a series of microalgae biomass production systems, the harvesting stage must be through first before entering any processing stage of the microalgae, such as to be bioenergy raw materials, foodstuffs, raw materials of drugs and cosmetics. In order to obtain high biomass production, it is necessary to do research on harvesting with the right method without causing new problems. Since microalgae biomass concentrations are often very low with size only a few micrometers (1 to 30 µm), then harvesting of microalgae becomes difficult [1] and expensive [2]. The cost of harvesting can be reduced significantly by choosing a more efficient and economical harvesting technique. Although some harvesting techniques have currently known, the main disadvantage of such of them is requiring expensive operational costs due to high energy dependence and less environmentally friendly.

Centrifugation is one of the most commonly used harvesting techniques because its ability to produce 80-90% harvested biomass from cultivation results in only one stage thus increasing efficiency in the harvesting stage [3], [4]. Harvested microalgae can

reach up to 20% of total solids when using centrifugation [1]. However, centrifugation is a technique with high capital, energy and operational costs [5].

In addition, this process allows the components in the cell to be damaged [3], [6]. Another technique that is commonly used is sedimentation, but this technique is inefficient with time and requires space to build a storage pond. Harvesting of microalgae using filtration techniques can only be done to harvest microalgae which larger than 100 µm and have filamentous or colonized cell shape, such as *Spirulina* sp. and *Micractinium* sp [7].

Harvesting of microalgae biomass using chemical flocculants and bioflocs has been done by previous researchers. mentions that flocculation is ideal for harvesting microalgae smaller than 100 µm and not colonizing. Flocculation using chemicals can also lead to nutrient degradation, changes in temperature and dissolved O₂ [8]. Chemical flocculants may contaminate the water used as microalgae culture medium. Water remaining after harvesting when disposed directly into the environment must be processed first to meet the required quality standards. The process requires a lot of money and energy. The

addition of chemical compounds can also cause changes in the composition of microalgae cells [9], [10].

Bioflocculation is a technique of harvesting microalgae whose principle is similar to flocculation, which is the difference is the flocculant material used. Bioflocculation uses living things such as bacteria, fungi, or microalgae as flocculants. Flocculation using bacteria [11] and fungi [12] are alternatives to replace chemical flocculants, so the effects of chemical pollution on culture media can be reduced. However, the use of fungi and bacteria as flocculants requires additional special media as a source of energy for its growth. In addition, bacteria and fungi can contaminate microalgae [11], [13].

The use of microalgae as flocculants does not require different growth media so it reduces additional costs. In addition, it will prevent bacterial contamination of the microalgae to be harvested [13]. Most importantly, bioflocculation by utilizing microalgae is more environmentally friendly because residual water harvesting that not contain chemicals can be reused or can be disposed of without require special treats with high cost.

In addition, microalgae flocculants can reduce dependence on energy used in the harvesting process until microalgae processing becomes a useful product. Thus, the problems to be studied include the fastest and most stable microalgae floc formulation test by taking into account the gradient criteria of floc forming speed. In addition, optimal flocculant microalgae ratios of non-flocculant microalgae need to be determined to obtain maximum yield. To find out how far the bioflocculation technique gives an effect of efficiency in harvesting, it will be extracted to obtain by products, such as lipids and starch.

By studying the floc forming speed gradient, it is particularly expected to provide information on the diversity of microalgae as the flocculant agent that gives the highest biomass yield. In general, this research is expected to provide scientific contribution to the development of microalgae biomass production technology that is more economical, efficient and environmentally friendly.

RESEARCH METHODOLOGY

Cultivation of Flocculant and Non Flocculant Microalgae

Microalgae were cultivated using an artificial growth medium of Provasoli Haematococcus Media (PHM). Microalgae that grow in light and climate are controlled 25 °C in temperature, fed with 5% pure CO₂ with a flow rate of 5 L · min⁻¹, illuminated by fluorescent lamps (4000 lux)) with 16/8 hour light/dark cycle [14]. All microalgas were tested on its ability to improve the recovery efficiency.

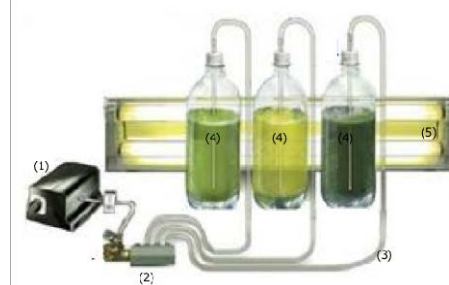


Fig. 1 Scheme of Microalgae Cultivation in Batch Culture, not to scale

(1) aerator, (2) regulator to regulate aeration rate, (3) silicone hose for aeration channel, (4) bottle of culture, (5) fluorescent lamps

The Study of Flocculation (%) of Microalgae by Flocculants and Fioflocculants

The precipitation of non flocculating microalgae with bioflocculant is obtained from the calculation of OD₇₅₀ (Optical Density) data using equation 1 [13].

$$recovery (\%) = \frac{OD_{750}(t_0) - OD_{750}(t)}{OD_{750}(t_0)} \cdot 100 \quad (1)$$

OD₇₅₀(t₀) is the turbidity of sample taken at time zero and OD_{a750} (t) is the turbidity of the sample taken at time t.

To determine the ability of microalgae strain as microalgae flocculant or non-flocculant microalgae, it is necessary to calculate recovery efficiency, i.e. recovery by non-flocculant microalgae to flocculating microalgae divided by non-flocculant microalgae recovery without presence of flocculant microalgae [13].

$$recovery\ efficiency (\%) = \left[1 - \frac{\frac{OD_{a750}(t)}{OD_{a750}(t_0)}}{\frac{OD_{b750}(t)}{OD_{b750}(t_0)}} \right] \cdot 100 \quad (2)$$

OD_{a750}(t₀) and OD_{a750}(t) are the turbidities of samples of non-flocculating microalga with flocculating microalga taken at time zero and at time t, respectively. OD_{b750}(t₀) is the turbidity of sample of non-flocculating microalga taken at time zero and OD_{b750} (t) is the turbidity of the same sample taken at time t (Fig. 2)

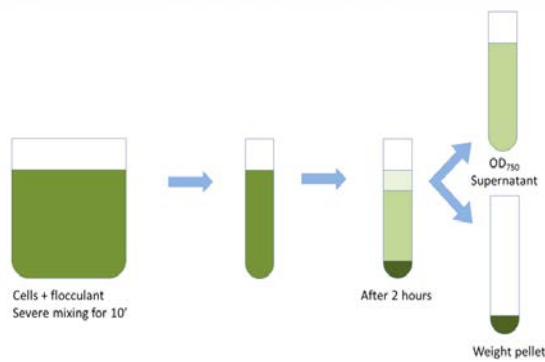


Fig. 2 Determination of Recovery Efficiency

RESULT AND DISSCUSION

Flocculation tests have been performed on 8 types of microalgae identified morphologically, as shown in Figure 3. The 6 of 8 microalgae were *Chlorella vulgaris*, *Chlorella sorokiniana*, *Chlorococcum* sp., *Closterium* sp., *Oscillatoria* sp., and *Monoraphidium* sp. (Fig. 3 a, b, c, d, e, f) in the first 1 to 6 hours visual observation remained unflocculated and sedimentated, while the other 2 species were *Scenedesmus obliquus*, *Ankistrodesmus* sp. (Fig. 3g, h) experienced floc formation followed by a settling time of less than 60 minutes of observation.

The experimental results have shown that the addition of *Scenedesmus obliquus* and *Ankistrodesmus* sp as flocculant microalgae followed by slow mixing allows better interaction between flocculant microalgae and non-flocculant microalgae, so the floc size increases.

Settling time depends greatly on flock size. The larger the size of the floc that is formed, the faster settling time. Flocculation efficiencies is influenced by several factors, i.e pH [14], dosage of biofloccurrent [11], [15] and proper mixing [12]. Initial pH values of culture can be adjusted to improve flocculation efficiency [14]. Incorrect doses may decrease flocculation efficiency. Mixing is necessary to increase the contact between microalgae cells so as to facilitate the formation of large flocs in a shorter time than without adequate mixing [12].

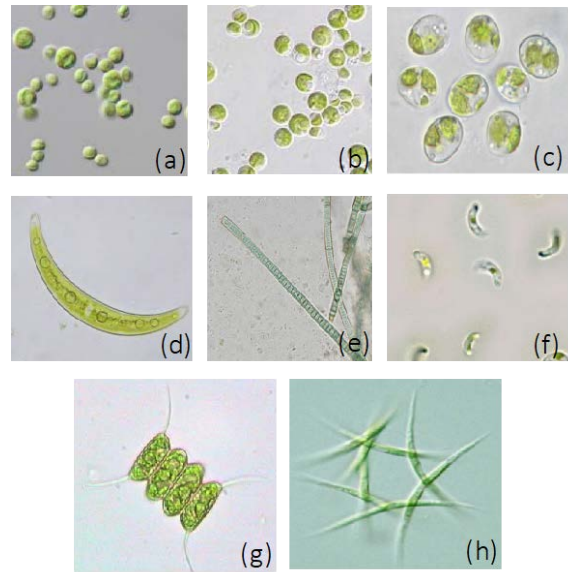


Fig. 3 Non flocculant microalgae: a) *Chlorella vulgaris*, b) *Chlorella sorokiniana*, c) *Chlorococcum* sp., d) *Closterium* sp., e) *Oscillatoria* sp., f) *Monoraphidium* sp. Flocculant microalgae: g) *Scenedesmus obliquus*, h) *Ankistrodesmus* sp.

Flocculant formation occurring in the flocculant microalgae can be seen in Fig. 4, while the microalgae flocculation capability and ability within 60 minutes of observation can be seen in Fig. 5. Figure 5 shows that the addition of *Scenedesmus obliquus* into culture followed by slow mixing allows increasing interaction between the flocculant microalgae cells and the non-flocculant microalgae so that the flocculation performance is efficient.

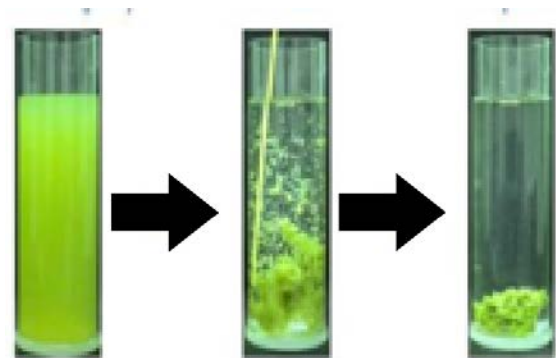


Fig. 4 The formation of floc on *Scenedesmus obliquus* within 60 minutes of observation

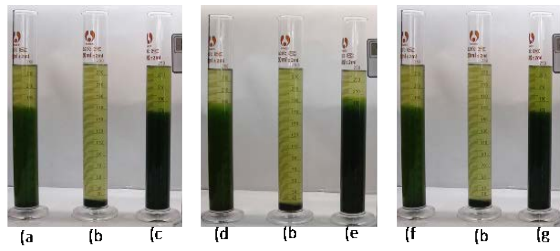


Fig. 5. The ability of microalgae flocculation within 60 minutes of observation: a) *Chlorella vulgaris*, b) *Scenedesmus obliquus* c) *Chlorella sorokiniana*, d) *Chlorococcum* sp., e) *Closterium* sp., f) *Oscillatoria* sp., g) *Monoraphidium* sp.

On a laboratory scale, the effectiveness of dewatering technology in relation to the process of harvesting of many microalgae biomass has been reported to have achieved significant efficiencies, but increasing to a larger scale still make problems, i.e less economically viable if harvesting implemented to produce products such as biofuel [5], [16]. In contrary, bioflocculation harvesting is an environmentally friendly method, consuming less energy, can take place relatively quickly (within minutes).

The flocculant and non-flocculant microalgae species were determined from the settling percentage (%) calculated on the basis of the OD_{750nm} value of each microalgae (Eq. 1). The value of OD_{750nm} for *S.obliquus* and *Ankistrodesmus* sp. initially $0.20 \pm 7.16 \times 10^{-3}$ and $0.18 \pm 9.17 \times 10^{-3}$ respectively and subsequently decreased rapidly after the first hour to $0.09 \pm 4.13 \times 10^{-3}$ and $0.095 \pm 3.89 \times 10^{-3}$, then decreased slowly until the 12th hour became $0.04 \pm 6.16 \times 10^{-3}$ and $0.05 \pm 3.38 \times 10^{-3}$. Salim et al. [13] states that species potentially made as microalgae flocculants are microalgae with a settling value (%) of 50 or more within 60 minutes.

Table 1. Percentage of the settling value in the first 60 minutes

Tropical microalgae	Settling value
Flocculant microalgae	
1. <i>Scenedesmus obliquus</i>	$55.1\% \pm 1.24$
2. <i>Ankistrodesmus</i> sp	$52.3\% \pm 3.71$
Non flocculant microalgae	
1. <i>Chlorella vulgaris</i>	$17.3\% \pm 0.88$
2. <i>Chlorella sorokiniana</i>	$16.7\% \pm 1.13$
3. <i>Chlorococcum</i> sp.	$21.5\% \pm 1.19$
4. <i>Closterium</i> sp.	$25.1\% \pm 1.36$
5. <i>Oscillatoria</i> sp.	$27.3\% \pm 2.11$
6. <i>Monoraphidium</i> sp.	$17.8\% \pm 1.89$

This indicates that *Scenedesmus obliquus* and *Ankistrodesmus* sp can be used as flocculant species because the value of settling for both types of microalgae is more than 50% for 60 minutes while other microalgae species can be categorized as non-flocculant microalgae since within 60 minutes settles less than 50% (Table 1). The fastest of settling occurs in the ratio of flocculant and non-flocculant microalgae is 4: 4 compared to 1: 4, 2: 4 and 3: 4 ratios. This suggests that the addition of more flocculant species may increase the precipitation percentage. Salim et al. [13] suggest that the addition of flocculant species with higher concentrations in harvesting will increase the settling percentage.

The results of this study also show that the difference of settling rate (%) among non-flocculant microalgae species is affected by the size of each kind of microalgae. The size of non-flocculant microalgae of *Chlorella* sp. is measuring 2.0-10.0 μm , *Monoraphidium* sp. is 2-11 μm , *Chlorococcum* sp. is 5.0-12.0 μm , *Closterium* sp. is 10-15 μm , *Oscillatoria* sp. is 10-150 μm with filament 2-20 μm while *Scenedesmus* and *Ankistrodesmus* have sizes of 15-20 μm and 12-14 μm respectively. According to [10] the rate of particle precipitation is influenced by the size of the particle, the larger the size of a particle the easier the settling.

Sathe [19] mentions that bioflocculation is a spontaneous flocculation of microalgae cells occurring as a result of extracellular polymeric substances (EPS) secretion when the microalgae are under stress conditions. Lack of nutrients is a major factor causing microalgae cells to overexpress the substance of the extracellular polymer [20]. The substance of the extracellular polymer produced by the microalgae will trigger the formation of cell clumps, which then will form a precipitated biomass

The results of bioflocculation observations under a microscope with 10x magnification showed microalgae forming large networks connected to each other. At the beginning of mixing ($t=0$) visible cells flocculant and non-flocculant microalgae are still separated and not bounded at all. Gradually the binding process begins to occur as the cells begin to experience stress due to decreased nutrition and trigger the microalgae to secrete the extracellular polymer. The resulting extracellular polymer creates bonds between microalgae cells. The bond between the flocculant and non-flocculant microalgae cells at 5th hour has begun to appear with the bond formation between the microalgae species. More microscopically bonds begin to appear at 12th hours, when non-flocculant species are bound to flocculant species and form larger batches of biomass, causing the flocs cells to settle.

The study also proved that no greenhouse gas was formed during the bioflocculation process. Thus the method of bioflocculation with *Scenedesmus obliquus* and *Ankistrodesmus* sp is feasible to be applied to harvest microalgae biomass on an industrial scale.

Conclusion

It is work examined the flocculation performance of the 6 freshwater microalgae i.e *Chlorella vulgaris*, *Chlorella sorokiniana*, *Chlorococcum* sp., *Closterium* sp., *Oscillatoria* sp., *Monorapidium* sp induced by the bioflocculant *Ankistrodesmus* sp and *Scenedesmus obliquus*. This research is an advanced research as an effort to obtain the technique of cheap harvesting and environmentally friendly, so that economic feasibility in microalgae biomass production can be improved. Thus bioflocculation can be industrialized. Furthermore, further research is needed to analyze the biochemical composition of microalgae harvested by bioflocculation to produce biofuel. Further information on energy consumption and process costs should also be further investigated for the development of commercialization of microalgae based products

ACKNOWLEDGEMENTS

The authors would like to thank Directorate for Research and Community Services as well as Directorate General for Strengthening Research and Development at the Ministry of Research, Technology, and Higher Education of Indonesia for funding this study through the scheme of “*Hibah Penelitian Pasca Doktor* (Post-Doctoral Research Grant) 2018”.

REFERENCES

- [1] Sim T. S., Goh A., Becker E.W.,1988. Comparison of Centrifugation, Dissolved Air Flotation and Filtration Technique for Harvesting Sewage-grown Algae, Biomass, Vol.16, 1988, pp. 51-62, doi:0144-4565/88/\$03.50
- [2] Lee A.K., Lewis D.M., Ashman P.J., Microbial Flocculation, A Potentially Low-Cost Harvesting Technique For Marine Microalgae for The Production of Biodiesel, J Apply Phycol, Vol. 21, pp. 559–56, 2009, doi 10.1007/s10811-008-9391-8
- [3] Thompson R. W., D’Elia L., Keyser A., Young C., Algae Biodiesel. Faculty Worcester Polytechnic Institute. An Interactive Qualifying Project Report, 47, 2010.
- [4] Chen, C., Yeh, K., Aisyah, R., Lee, D., Chang, J., Cultivation, Photobioreactor Design and Harvesting of Microalgae for Biodiesel Production: A Critical Review, Bioresource Technology, Vol.102, No.1, 2011, pp. 71-81, ISSN 0960-8524
- [5] Wijffels, R.H., Barbosa, M., An Outlook on Microalgal Biofuels, J Science, 2010, doi:10.1126/science. 1189003
- [6] Li, Y., Wan, C., Algae for Biofuel, Departement of Food, Agricultural and Biological Engineering, The Ohio State University. 3, 2011.
- [7] Gouveia, L. and Oliveira, A. N., Microalgae as A Raw Material for Biofuels Production, J. Ind Microbiol Biotechnol, Vol. 36, 2009, pp. 269–274.
- [8] Mata, T. M., Martins, A. A., Caetano, N.S., Microalgae for Biodiesel Production and Other Applications: A Review, Renewable and Sustainable Energy Reviews, Vol. 14, 2010, pp. 217-232.
- [9] Papazi A., Makridis P., Divanach P., Harvesting *Chlorella minutissima* Using Cell Coagulants, J Appl Phycol. Vol. 22, 2010, pp. 349–355.
- [10] Pillai J, Flocculants and Coagulants: The Keys to Water and Waste Management in Aggregate Production: Nalco Company, 1997.
- [11] Ndikubwimana T., Zeng X., Liu Y., Chang J.S., Lu Y., Harvesting of Microalgae *Desmodesmus* sp. F51 by Bioflocculation with Bacterial Bioflocculant, Algal Res, Vol. 6, 2014, pp. 186–93.
- [12] Li X. Y., Yang S.F., Influence of Loosely Bound Extracellular Polymeric Substances (EPS) on The Flocculation, Sedimentation and Dewaterability of Activated Sludge, Water Reserch, Vol. 41, 2007, pp. 1022-10340. doi:10.1016/j.watres.2006.06.037.
- [13] Salim S., Bosman R., Vermue M.H., Wijffels R.H., Harvesting of Microalgae by Bio-flocculation, J Appl Phycol, Vol. 23, 2011, pp. 849-855. doi: 10.1007/s10811- 010-9591-x.
- [14] Rinanti, A., Dewi, K., Astuti, D.I., Kardena, E., Improvement of Carbon dioxide Removal through Artificial Light Intensity and Temperature by Constructed Green Microalgae Consortium in A Vertical Bubble Column Photobioreactor, Malaysian Journal of Microbiology, Vol.10, No.1, 2014, pp. 29-37.
- [15] Rinanti, A., Purwadi, R., Bioflocculation Activity in Harvesting System: A Biotechnology Approach for Microalgae Biomass, Aceh International Journal of Science and Technology, Aceh International Journal of Science and Technology, Vol.7, No.1, 2018, pp.

- 111-121.
- [16] Zheng H., Gao Z., Yin J., Tang X., Ji X., Huang H., Harvesting of Microalgae by Flocculation with Poly (γ -Glutamic Acid), *Bioresour Technol*, Vol. 112, 2012, pp. 212–20.
 - [17] Coward T., Lee J.G., Caldwell G.S., Development of A Foam Flotation System for Harvesting Microalgae Biomass, *Algal Res*, Vol. 2, No. 2, 2013, pp. 135–44.
 - [18] Barsanti L., Gualtieri P., *Algae: Anatomy, Biochemistry, and Biotechnology*, Taylor & Francis, Boca Raton, 2006.
 - [19] Sathe S., Culturing and Harvesting Microalgae for The Large-scale Production of Biodiesel, *Microbial Engineerring Research Group*. 97, 2010.
 - [20] Lee A.K., Lewis D.M., Ashman P.J., Microbial Flocculation: A Potentially Low-Cost Harvesting Technique for Marine Microalgae for The Production of Biodiesel, *J Apply Phycol*. Vol. 21, 2009, pp. 559–567, doi 10.1007/s10811-008-9391-8

UTILIZATION OF WATER QUALITY MODELING TO DETERMINE MAXIMUM BOD LOAD OF UPSTREAM CITARUM RIVER

Yonik Meilawati Yustiani*, Sri Wahyuni and Syarifah Nur Fitria Dewi
Faculty of Engineering, Universitas Pasundan, Indonesia

ABSTRACT

Citarum River as the largest river in West Java gives an important role for the life of the community either directly or indirectly. However the pollution that occurs on the Citarum River is very high that its tributary water cannot be used properly. One of the efforts to rehabilitate the quality of the Citarum River is by utilizing the water quality modeling. The purpose of this study was to obtain the maximum BOD values that can be accepted by the Citarum River for the rehabilitation purpose. The modeling prepared in this research was using Streeter-Phelps equation. The data analyzed in this study is derived from the West Java Province Government monitoring sampling in 2013, 2014 and 2015. Sampling area covers Dayeuhkolot area to Nanjung. The calculation result using Streeter Phelps equation provides the concentration value of deficit oxygen and BOD load. The deficit oxygen calculated by the model show its concentration was ranging between 3.20 mg/L and 3.68 mg/L, while the maximum BOD load concentration is ranging between 8.06 mg/L and 23.83 mg/L. Using this value, the government can create a strategy for managing the Citarum River so that its water quality can be returned in accordance with its designation.

Keywords: Deficit oxygen, BOD, Upstream Citarum River, Water quality modeling

INTRODUCTION

Citarum River is the main river and one of the largest river in West Java with a length of ± 297 km, and the watershed area of 6.614 km². Citarum River at Wayang Mountain located in District Kertasari Bandung Regency at an altitude of 2182 m above sea level and empties into the Java Sea. Citarum River crosses 7 districts and 2 cities of Bandung, Sumedang, Cianjur, Bogor, Purwakarta, Karawang, Bekasi, Bandung and Cimahi. The Citarum rivers amount to ± 36 tributaries. The Citarum River and its tributaries are utilized for various needs such as agricultural irrigation, industrial activities, raw water sources [1a], water sources for fisheries and as hydroelectric power plants.

Environmental damage in the upper part of the Citarum river can be seen from the community's behavior such as dumping garbage directly into the river, resulting in the accumulation of garbage, the decrease of land conservation areas, the density of population settlements, river pollution by domestic and industrial waste, and others causing floods, drought, and landslides often occur in the upper reaches of the Citarum River. This indicates that the quality decline has already begun in the upstream area of Citarum [2].

Monitoring is the important aspect that needs to be conducted properly in stakeholder's responsibilities, authorities and resources [3]. One effort to monitor and control river water pollution is to analyze the water quality data of the river using

the modeling. Modeling is a more time-saving effort, effort and cost compared to direct measurement. The purpose of this research is to analyze the water quality of Upper Citarum River by modeling dissolved oxygen (DO) and biochemical oxygen demand (BOD) with Streeter Phelps method as the effort to determine the maximum organic pollutant load that can be discharged to water body. The maximum load will contribute to regulate wastewater discharge of industries and other activities along upstream region of Citarum River.

METHODOLOGY

Research Location

This location the research takes place on the upper region of Citarum River with segments from Dayeuhkolot to Nanjung. Some of the problems of the Upper Citarum Watershed especially for the Dayeuhkolot area to Nanjung are the development of settlements around river banks. The housing were developed without good planning. There are many daily activities of people who throw garbage directly into the river, the remnants of fertilizers or pesticides from agricultural areas, hospital waste, and cattle manure waste. There are also development of the textile industry and dispose of its waste into the river, so that the river becomes the final disposal without first processing. Figure 1 shows the Citarum watershed as well as the research sites on the upstream. The figure also gives information of

watershed performance of Citarum River, where the light brown shaded indicates a rather poor performance area and the yellow shaded indicates poor performance area, considering the environmental quality.

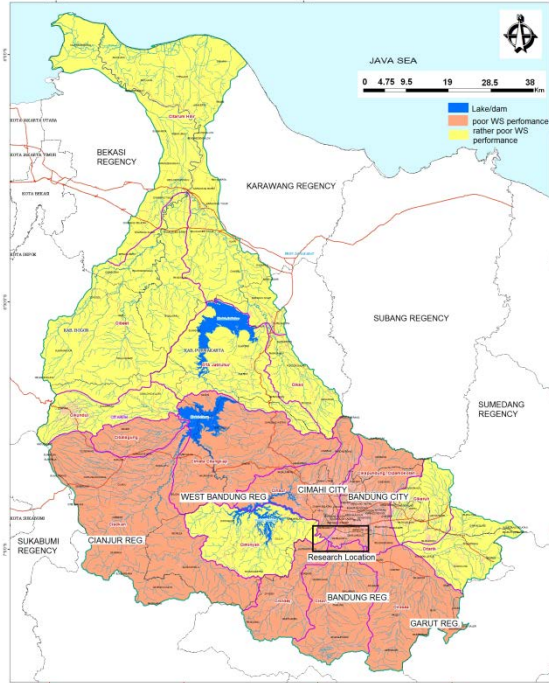


Figure 1. Citarum Watershed [4] and research location.

Figure 2 shows the location of the sampling station on the upstream Citarum River.



Figure 2. Sampling station points.

There are 5 points along the upper Citarum River sampled. The sampling points have the following coordinates: 6°59'29.8"S 107°37'47.5"E, 6°59'21.3"S 107°37'28.7"E, 6°59'07.3"S 107°33'46.7"E, 6°58'41.5"S 107°33'06.3"E, 6°56'50.8"S 107°32'05.1"E respectively for Stations 1, 2, 3, 4 and 5. While along the segment is divided into sub-segment as the area of pollution load calculation. Determination of sampling point is with the consideration that the point can represent the water quality condition of Upper Citarum River, can

represent the level of pollution caused by activity of industry, agriculture and domestic and can represent condition of incoming creek discharge. Figure 3 shows the schematic diagram of the research segment for the purposes of calculating water quality and pollutant load. Samplings were conducted during dry season.

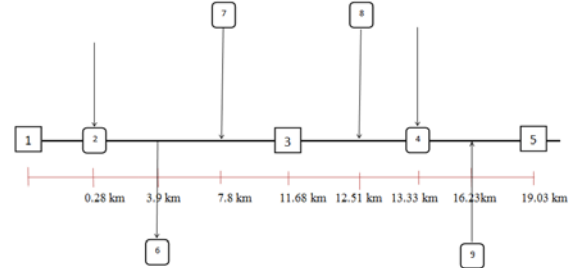


Figure 3. Diagram of domain segmentation.

Laboratory Analysis

Laboratory analysis was conducted using Standard Methods [5]. The BOD measurements consist of sample dilution, incubation for 5 days at 20°C and dissolved oxygen measurements before and after incubation. Dissolved oxygen concentration was measured using electrochemical method. The method of determining dissolved oxygen by electrochemical method is a direct way to determine dissolved oxygen by means of DO meter.

Equations

Some of the equations used in the calculation of water quality and pollutant load in this study are equations for calculating ultimate BOD (Eq. 1)[6], [7], Streeter Phelps' oxygen deficit (Eq. 2)[7] and maximum pollutant load (Eq. 3). The maximum pollutant load equation was modification of classic Streeter Phelps equation which focusing in the remaining capacity of river water in receiving pollutant.

$$L_a = L_0 e^{-\frac{k_d}{u}x} \quad (1)$$

Where:

L_a = concentration of BOD ultimate (mg/L)

L_0 = concentration of BOD₅ at initial position (mg/L)

K_d = deoxygenation rate coefficient (1/day)

x = distance from initial position (m)

u = flowrate (m/s)

$$D = D_0 e^{-\frac{k_a}{u}x} + \frac{K_d \cdot L_a}{K_a - K_d} \left(e^{-\frac{k_d}{u}x} - e^{-\frac{k_a}{u}x} \right) \quad (2)$$

Where:

D = deficit oxygen concentration (mg/L)

k_a = reaeration rate coefficient (1/day)

L_a = concentration of BOD ultimate (mg/L)

D_0 = concentration dissolved oxygen in $x=0$ (mg/L)

$$\log L_a = \log D_{all} + \left(1 + \frac{k_d}{k_a - k_d} \left(1 - \frac{D_0}{D_{all}} \right)^{0.418} \right) \log \frac{k_a}{k_d} \quad (3)$$

Where:

D_{all} : allowed oxygen deficit (mg/L)

RESULT AND DISCUSSION

According to the water quality monitoring, the DO concentrations measured were under the government standard. Figure 4 shows the concentration of DO in the upstream Citarum River of the year 2013, 2014 and 2015. Figure 5 display the concentration of BOD of Citarum River in the year of 2013, 2014 and 2015.

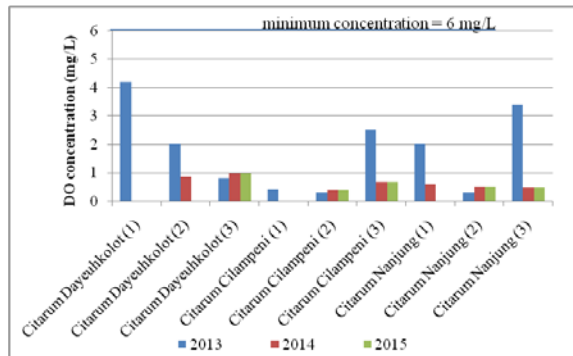


Figure 4. DO concentration in the upstream Citarum River.

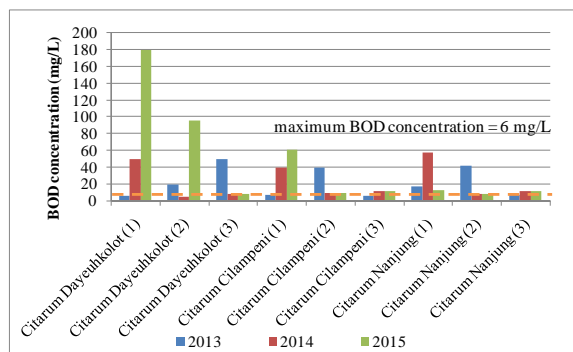


Figure 5. BOD concentration in the upstream Citarum River.

The monitoring of BOD concentrations were also indicated that pollution has been occurred in the recent year. Almost all BOD concentration were recorded above the maximum allowed standard. High concentration of BOD can be indicated as the pollution activities from the domestic and agricultural area.

Based on the monitoring results, primary samplings were conducted in the more detail

segmentation between Dayeuhkolot and Nanjung area.

Table 1 shows the result of sample river water analysis for the parameter of temperature, pH, DO and BOD.

Table 1. Laboratory analysis result

Parameter	Unit	Standard*	Sampling Location (Station No.)				
			1	2	3	4	5
Temperature	°C	normal	23.8	24.9	26.5	25.3	24.1
pH	-	5-9	6.61	6.15	6.51	6.41	6.41
DO	mg/L	≥6	3.2	4.6	3.3	6.1	3.4
BOD	mg/L	6	0.5	10.5	5.5	16	2.5

*) Standard of West Java Province, Governor Decree no.39, year 2000

DO concentrations of almost all sampling points do not meet the B class standard. 39 of 2000 except only point 4 that meets the predetermined quality standard of 6.1 mg/L. B class of the standard that regulate the water quality for the purpose of raw water for drinking water. BOD concentrations that meet the quality standard of Group B of Governor's Decree no. 39 of 2000 are at point 1, 3 and 5. At that point, there is already a pollutant input from domestic and non domestic waste, but still within the standard limit. Calculations using the Streeter Phelps model use DO and BOD data as the basis for determining pollution profiles. The Phelps Streeter model links the rate of change in oxygen deficit with distance to deoxygenation rate (oxygen depletion) and deoxygenation or reaeration (addition of oxygen in water).

In order to calculate the oxygen deficit and actual DO, the value of saturated DO is necessary. The saturated DO concentrations were obtained based on actual temperature of river water. Table 2 displays the saturated dissolved oxygen in the sampling stations.

Table 2. Saturated DO

Sampling Station	Temp (°C)	Saturated DO (mg/L)
1	23.8	8.47
2	24.9	8.30
3	26.5	8.06
4	25.3	8.24
5	24.1	8.43

In every tributary point, the concentration of DO, BOD and temperature after mixing were calculated using the mass balance equation considering each water discharge, then Eq. 1 was used to calculate the ultimate BOD. The deoxygenation constant used is the range k_d for the Cikapundung River flow between 0.10 - 0.37 [8], where Cikapundung River

is one of the tributaries Citarum. This value is similar and in the range of urban rivers in Indonesia deoxygenation rate coefficient, i.e Citepus River, Rangkui River, Cimanuk River [9]-[11]. The ultimate BOD value can be seen in Figure 6.

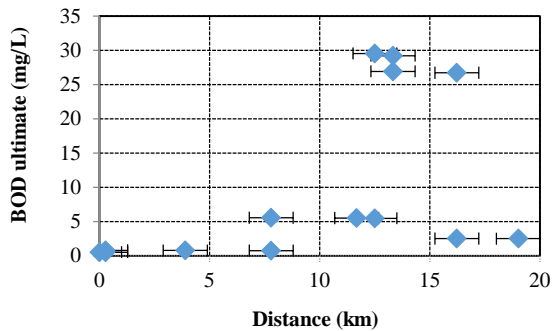


Figure 6. BOD ultimate

At km 0 to km 12.51 before mixing the BOD value still meet the quality standard that is less than 6 mg/L. At km 12.51 after mixing up to km 16.23 before mixing the BOD value increases and exceeds the quality standard that is more than 6 mg/L due to the influent of domestic waste into the river. High concentrations of BOD occurred due to influent of waste from plastic factories and other industries entering the river and densely populated areas. At km 16.23 after mixing up to km 19.03 BOD decreases which is usually due to the occurrence of dilution by rain water.

The value of dissolved oxygen concentration can be seen in Figure 7.

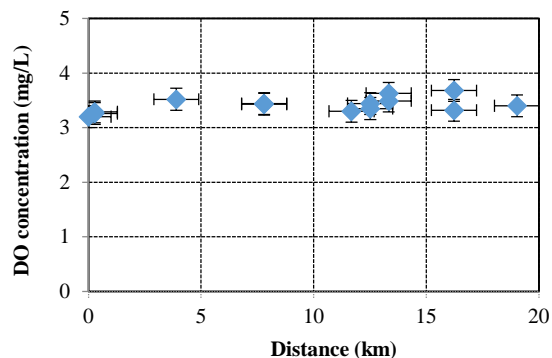


Figure 7. Concentration of Dissolved Oxygen (mg/L)

For DO concentrations ranging from km 0 to km 19.03 up and down and did not meet the quality standard of Group B Governor's Decree no. 39 of 2000 is less than 6 mg/L, due to the large number of domestic waste due to the density of the population and industrial waste due to the existence of some industries around the location of observation and dispose of its waste directly to the river and processing first.

The calculation of maximum load of BOD is used Eq. 3. The maximum load is affected by the actual BOD load and the deoxygenation rate. Maximum load values can be viewed in Figure 8.

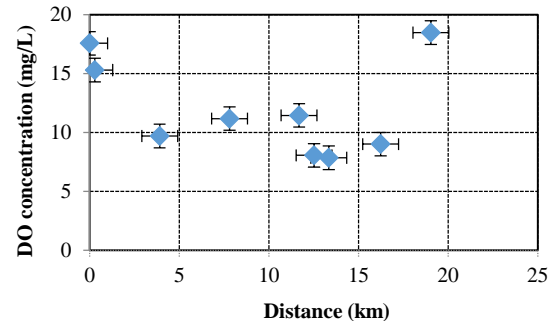


Figure 8. Maximum BOD load.

The modeling results show that the maximum pollutant loads in the middle part of the research segment are low. The lowest BOD load is 8.06 mg/L located at km 12.51, whereas the highest BOD load is 18.47 mg/L at km 19.03. In the middle section, the pollution has already high and the river capacity to perform self purification restricts any additional pollutant to enter the water body.

CONCLUSION

Several important findings can be summarized from this research, i.e.:

- The pollutant source for Upstream Citarum River comes from domestic waste, agricultural waste and industrial waste.
- The sample measurement data shows for DO parameters that almost all points did not meet the quality standard of Group B of Governor's Decree No. 39 Year 2000.
- BOD concentration of the sample water also show pollution in several points.
- The calculation result with Streeter Phelps method shows that the DO concentration range is as low as 3.20 mg/L to 3.68 mg/L. BOD maximum load value of 8.06 mg/L to 23.83 mg/L.
- Based on the research results, the water quality of the Upper Citarum River shows that they do not meet the quality standard.

Based on the results, it is recommended a major rehabilitation on the river water quality of Citarum River, both in the pollution sources and in the river.

REFERENCES

- [1] Afiatun E., Notodarmodjo, S., Effendi, A.J., Sidarto, K.A. Cost minimization of raw water sources by integrated water supply systems (A case study for Bandung, Indonesia). International Journal of Geomate, June, 2018, Vol. 14, Issue

- 46, pp. 32-39. DOI: 10.21660/2018.46.9 813
- [2] Fulazzaky M.A. Water quality evaluation system to assess the status and the suitability of the Citarum river water to different uses. *Environ. Monit. Assess.*, 168, 2010, pp. 669-684.
- [3] Ginkel, C.H. Water Quality in Upper Citarum River Basin: towards a better understanding of a heavily polluted catchment. *Student Undergraduate Research e-Journal*, Vol 2, 2016, pp.
- [4] Ministry of Environment and Forestry. Citarum Watershed (Map). <http://sipdas.menlhk.go.id/documents/170>, access June 8, 2018.
- [5] American Public Health Association-APHA; American Water Works Association-AWWA; Water Environment Federation-WEF. *Standard Methods for the Examination of Water and Wastewater*. 22nd edition. Washington. 2012.
- [6] Ajayi, A.A., Peter-Albert, C.F., Ajojesu, T.P., Bishop, S.A., Olasehinde, G.I., Siyanbola, T.O. Biochemical Oxygen Demand and Carbonaceous Oxygen Demand of the Covenant University Sewage Oxidation Pond. *Covenant Journal of Physical and Life Sciences (CJPL)*, Vol 4 no. 1, 2016, pp. 11-19.
- [7] Chapra, S.C. *Surface Water – Quality Modeling*. McGraw-Hill International Editions, 1997, p.391
- [8] Yustiani, Y.M., Nurkanti, M., Suliasih, N., Novantri, A. Influencing Parameter of Self Purification Processes in the Urban Area of Cikapundung River, Indonesia. *International Journal of Geomate*, Vol. 14, Issue 43, 2018, pp. 50-54. DOI:10.21660/2018.43.3546
- [9] Yustiani, Y.M., Mulyatna, L., Pranata, F. The Deoxygenation Rate Determination Based on Physical Condition of River Body, Case Study of Citepus River. *Padjadjaran International Physics Symposium 2013, AIP Conf. Proc.* 1554, pp. 281-284. DOI: 10.1063/1.4820340
- [10] Yustiani, Y.M., Pradiko, H., Amrullah, R.H. The study of deoxygenation rate of Rangkui River water during dry season. *International Journal of Geomate*, Vol. 15, Issue 47, 2018, pp. 164-169. DOI: 10.21660/2018.47.28822
- [11] Yustiani, Y.M., Wahyuni, S., Alfian, M.R. Investigation on the deoxygenation rate of water of Cimanuk River, Indamayu, Indonesia. *Rasayan J.Chem*, vol. 11, no. 2, 2018, pp. 475-481. DOI: 10.7324/RJC.2018.1121892

TURBIDITY REDUCTION OF THE RAW DRINKING WATER FOR PILOT SCALE ELECTROCOAGULATION DEVELOPMENT

*E. Afiatun¹, H. Pradiko¹ and E. Fabian¹

¹Faculty of Engineering, Universitas Pasundan, Indonesia

*Corresponding author

Abstract

A preliminary study to reduce the turbidity of drinking water by electrocoagulation method has been previously investigated. Subsequent studies were then conducted with various turbidity and initial precipitation treatments. Cikapundung River and Cisangkuy River are the main drinking water sources in Bandung with very fluctuating turbidity. In the water supply system, turbidity is one of the important factors to be observed due to several reasons such as aesthetic, consideration of load to filtration, and disinfection process. This study aims to applying the electrocoagulation process to reduce turbidity as an alternative to conventional coagulation system by utilizing Poly Aluminum Chloride (PAC). Electrocoagulation is one method of water treatment by combining the process of coagulation, flotation and electrochemistry. In this work, the electrocoagulation experiments were set up by varying the current density from 10-30 volts with 5-30 minutes detention time so that the turbidity variation could be created in a range of 25 Nephelometric Turbidity Unit (NTU) up to 400 NTU. In addition, the experiments were carried out by a precipitation process prior to the electrocoagulation process. The optimum conditions of the electrocoagulation process with both initial and non-precipitated depositions occurred at an initial turbidity of 400 NTU with electrocoagulation time and with a 100 RPM fast stirring for 10 minutes to have a turbidity reduction of 99.52% and 98.28 %. The optimum current density for non-precipitating conditions was 21.33 A / m², whereas it is with precipitating of 46.22 A / m². This optimum condition is useful for a pilot scale development.

Keywords: electrocoagulation, optimum conditions, precipitation, raw water, turbidity

INTRODUCTION

Drinking water sources of Bandung City come from surface water that are Cikapundung River and Cisangkuy River [1] – [3]. These raw water sources are affected by upstream conditions, pollution along the stream, as well as the climate and weather that result in this surface water quality changing over time. Water quality in Cikapundung river also influenced by hydrological and land cover factors [4]. Such conditions lead to the need for raw water treatment before being utilized. Turbidity is one of pollutant parameters that is of primary concern as it often exceeds the quality standard. According Sawyer (2003) in the system of drinking water supply turbidity is one important factor for several reasons including aesthetic factors, filterability, the number of harmful organisms that affect the disinfection process [5].

Raw water treatment process of Bandung City generally use Poly Aluminum Chloride (PAC) as coagulant to bind turbidity. The use of PAC increasingly large due to the condition of the quality of raw water is getting more and more decreased [6]. The large use of PAC leads to a large and dangerous sludge of processing waste. In this regard, more efficient raw water treatment alternatives are needed and produce less sludge.

Electrocoagulation is one method of water treatment by combining the process of coagulation, flotation and electrochemistry. The electrocoagulation mechanism follows the basic principle used in the electrolysis cell system, where the anode and cathode are the site of the reduction oxidation reaction. The electrical energy applied to the anode dissolves the aluminum into the solution which then reacts with the hydroxy ion from the cathode to form aluminum hydroxy. Hydroxy coagulates and flocculates suspended particles resulting in a removal of solids from treated water [7]

The research that has been done on 100 NTU turbidity concentration, obtain optimal condition of removal process under conditions with stirring, optimum detention time 10 minutes, optimum voltage 10 Volt, and optimal current density 21.33 A / m² [8]. In this research, the raw water treatment process by electrocoagulation method is used to set aside the variation of turbidity concentration at the optimum condition of previous research. In this study also tested the initial precipitation process before the electrocoagulation process, as an effort to eliminate suspended particles.

The aim of this research is to analyze the efficiency of the electrocoagulation process using

aluminum plate electrode to decrease the concentration of turbidity parameters in Cisangkuy River and Cikapundung River, which further become the reference in pilot scale research.

RESEARCH METHODS

Tools and Materials

The tool components consist of: batch scale reactor made of glass with dimensions of 12 cm x 9 cm x 12 cm with a working volume of 1 liter equipped with 100 RPM magnetic stirrer, and flocculator with a speed of 60 RPM. The dimension of the submerged aluminum plate is 7.5 cm x 7.5 cm x 0.15 cm. The dc power supply used is with an output voltage of 0 - 30 volts. Artificial turbidity is made from mud samples originating from Cikapundung and Cisangkuy Rivers.

Methods

The research was conducted on each current density at each variation of turbidity with the influence of the initial deposition process and without the influence of the initial deposition process.

The research flow diagram can be seen in Figure 1

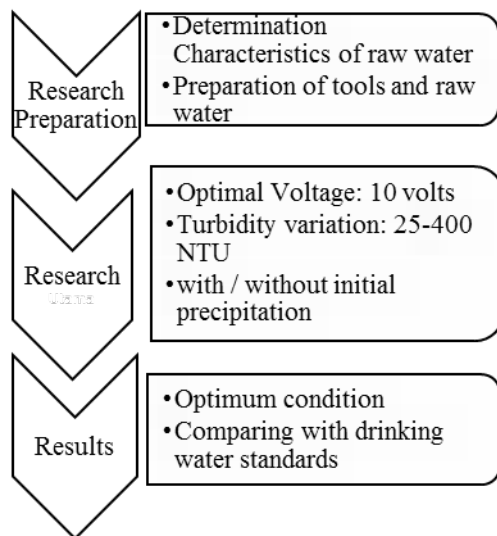


Fig. 1 Flow Chart of Research

Reactor Design

The sketch of electrocoagulation reactor design can be seen at Figure 2.

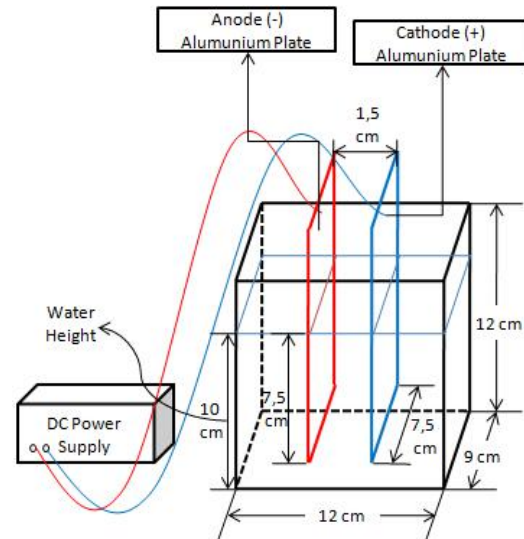


Fig 2. Electrocoagulation reactor design [8].

Overall, the reactor design to be operated is as follows:

Table 1. Reactor operation

Electrode Type	Aluminum Plate
Distance between Electrodes	1,5 cm
Optimal Voltage	10 Volts
Optimal Detention Time	10 minutes
Number of Electrodes	One pair
The submerged plate area	7,5 cm x 7,5 cm
Rapid mixing	100 rpm, during electrocoagulation process
Slow mixing	10 minutes 60 rpm
Variety of turbidity	25, 50, 100, 200, 300, and 400 NTU
Time of precipitation after electrocoagulation process	15 minutes
The height of the plate from the bottom of the reactor	2,5 cm

Data Collection

Samplig

Samples are taken at a height of $\frac{1}{2}$ - $\frac{2}{3}$ from the bottom of the reactor and approximately 5 cm from the edge of the reactor using a pipette.

Sample Turbidity Test

Testing of sample turbidity by using Lutron turbidimeter model TU-2016.

Electrical Conductivity Test (DHL)

The sample was tested for conductivity by using conductivity / TDS meter of Lutron model Yk-22Ct model.

Data Analysis

Turbidity of samples that have been treated with electrocoagulation method then compared with initial turbidity. Electrocoagulation performance can be known from the efficiency percentage in reducing the turbidity level to meet the drinking water quality standard of Indonesian Ministry of Health Regulation No. 492 / MENKES / PER / IV / 2010. Meanwhile, the effectiveness of pollutant removal can be calculated by the formula [9].

$$R\% = (C_{in} - C_{ef}) / C_{in} \times 100\% \quad (1)$$

Where :

R = Removal efficiency (%)

C_{in} = Influent concentrations (NTU)

C_{ef} = Effluent concentrations (NTU)

RESULT AND DISCUSSION

The research was conducted based on optimum condition of preliminary research that has been done. The research was conducted using electrocoagulation process which was equipped with fast stirring using magnetic stirrer at 100 RPM for 10 minutes, followed by slow stirring using flocculator with speed 60 RPM for 10 minutes. Precipitation is done for 15 minutes.

The research was conducted on several variations of turbidity, ie 25 NTU - 400 NTU. In addition, a study was conducted by combining the electrocoagulation process with the initial precipitation process to see how much the effect of the initial precipitation on turbidity removal.

Electrocoagulation Process in Each Variation of Turbidity

The turbidity variations used in the study were 25, 50, 100, 200, 300, and 400 NTU. Each turbidity variation was treated using any variation of current density resulting from 10, 20, and 30 Volt voltages with a detention time of 10 minutes. The results were then compared with drinking water quality standards. The results were obtained as follows:

Table 2. Electrocoagulation efficiency for each variation turbidity

No	Initial Turbidity (NTU)	Detention Time (minutes)	Current Density (A/m ²)	Turbidity after Processing (NTU)	Efficiency (%)
1	25	10	21.33	2.07	91.72
2			46.22	1.92	92.32
3			67.56	1.57	93.72
4	50	10	21.33	3.38	93.24
5			46.22	2.56	94.88

No	Initial Turbidity (NTU)	Detention Time (minutes)	Current Density (A/m ²)	Turbidity after Processing (NTU)	Efficiency (%)
6	100	10	67.56	1.79	96.42
7			21.33	1.74	98.26
8			46.22	0.94	99.06
9			67.56	0.42	99.58
10	200	10	21.33	0.37	99.82
11			46.22	0.00	100.00
12			67.56	0.00	100.00
13	300	10	21.33	0.90	99.70
14			46.22	0.49	99.84
15			67.56	0.00	100.00
16	400	10	21.33	0.66	99.84
17			46.22	0.21	99.95
18			67.56	0.00	100.00

Turbidity value through electrocoagulation process on each variation of turbidity and current density already meet the applicable quality standard. Graphically, the turbidity removal on each variation of turbidity and current density can be seen in the Fig. 3

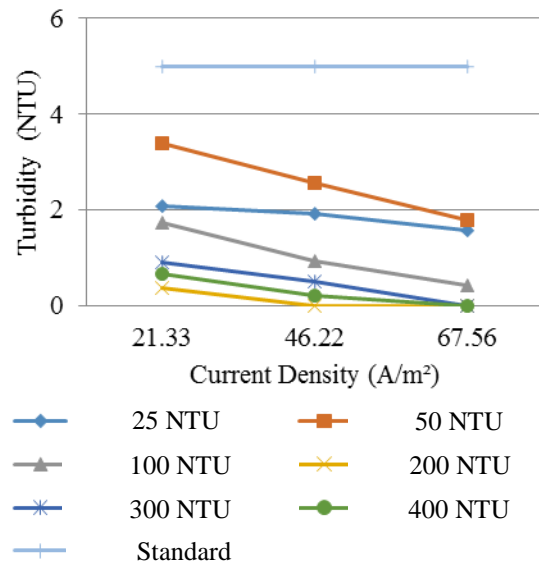


Fig.3 Turbidity removal at each variety of Current Density

Based on Fig. 3, it can be seen that the final turbidity value of the processing result is better along with the increasing of current density used. The higher the initial turbidity value the higher the effluent value produced by the treatment, although there is no significant difference.

Processing using the lowest current density to the highest, all of which already meet the applicable drinking water quality standards. Percentage of

processing efficiency can be seen in Fig.4.

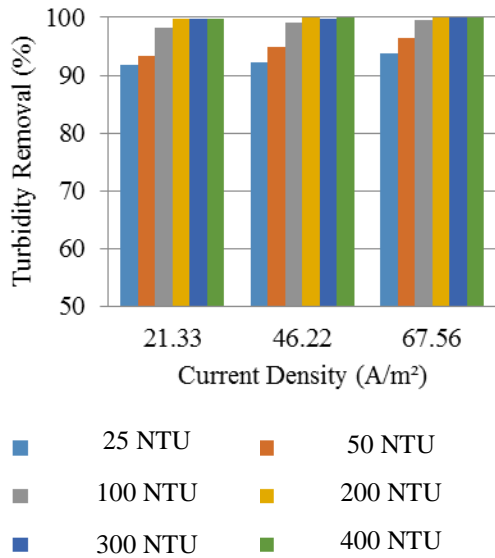


Fig 4. Processing efficiency at any variety of turbidity

From Fig. 4 it can be seen that the processing efficiency has been very high, up to exceed 91% although using the lowest current density. The higher the current density given the higher the processing efficiency.

Electrocoagulation Process with Initial Precipitation

Further experiments were carried out by combining the initial precipitation process with electrocoagulation. The turbidity variations used in this experiments were 25, 50, 100, 200, 300, and 400 NTU. Turbidity is then processed by using the current density generated by a voltage of 10 and 20 volts. After the experiments, the results obtained as follows :

Table 3. Efficiency of turbidity removal with initial precipitation and electrocoagulation

No	Initial Turbidity (NTU)	Turbidity after Initial Precipitation (NTU)	Current Density (A/m ²)	Turbidity After Processing (NTU)	Efficiency (%)
1	25	19,27	21,33	5,23	72,86
2	50	26,27		5,62	78,60
3	100	34,96		5,66	83,80
4	200	41,06		5,55	86,49
5	300	55,00		7,05	87,19
6	400	62,67		6,90	88,99
7	25	19,27	46,22	3,57	81,47
8	50	26,27		3,29	87,48

No	Initial Turbidity (NTU)	Turbidity after Initial Precipitation (NTU)	Current Density (A/m ²)	Turbidity After Processing (NTU)	Efficiency (%)
9	100	34,96	21,33	2,98	91,47
10	200	41,06		2,79	93,20
11	300	55,00		2,23	95,95
12	400	62,67		1,93	96,92

At a current density of 21.33 A / m², the turbidity value after the initial precipitation and electrocoagulation on each turbidity variation has not been able to meet the applicable quality standards, while at the current density of 46.22 A / m² the effluent obtained is able to meet the applicable quality standards. The turbidity removal by electrocoagulation and the initial precipitation in each turbidity variation can be seen in Fig. 5.

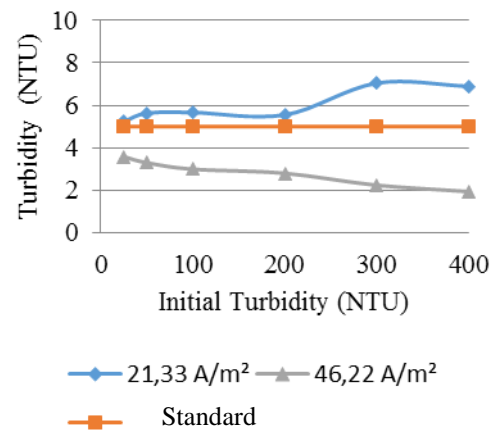


Fig. 5 Decrease of turbidity with initial precipitation and electrocoagulation

Based on Fig. 5 it can be seen that at a current density of 21.33 A / m² the final turbidity value increases with increasing initial turbidity of the sample. However, at a current density of 46.22 A / m² the value of the final turbidity decreases with the increasing initial turbidity. The processing efficiency can be seen in Fig. 6.

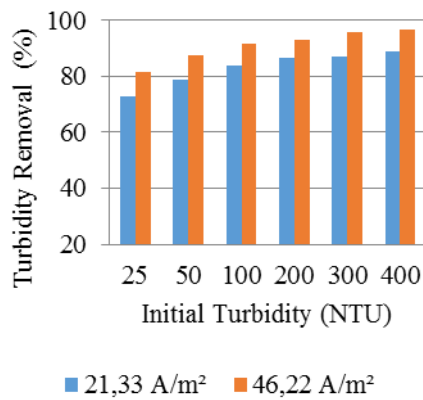


Fig. 6. Efficiency of turbidity removal with initial precipitation and electrocoagulation

From Fig. 6 it can be seen that the efficiency of the turbidity removal at the initial precipitation followed by the electrocoagulation process gives better results at a current density of 46.22 A / m².

Comparison of Electrocoagulation With and Without Initial Precipitation

Turbidity removal with electrocoagulation and with or without initial precipitation at current density of 21.33 A / m² can be seen in Fig. 7.

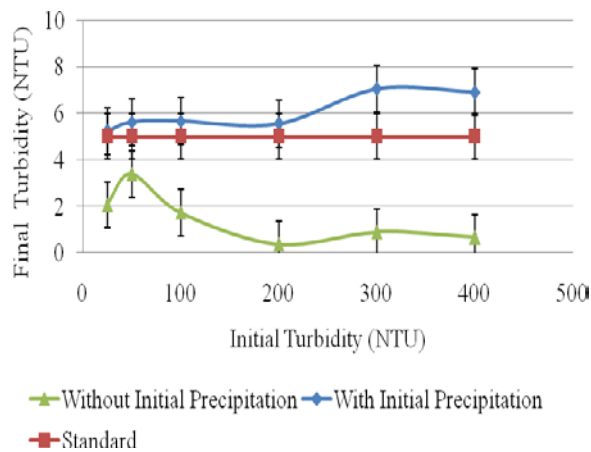


Fig. 7 Decrease of turbidity at current density 21.33 A / m²

Based on Fig. 7, it can be seen that the final turbidity value of the processing with the initial precipitation still can not meet the quality standard, while for the processing without the initial precipitation can meet the quality standard. The removal of turbidity with electrocoagulation with and without precipitation at a current density of 46.22 A / m² can be seen in Fig. 8.

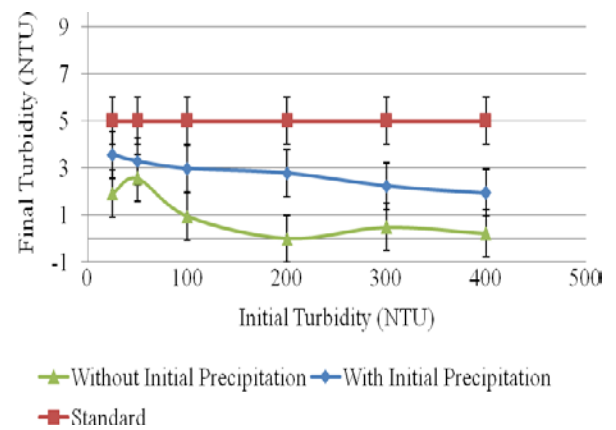


Fig. 8 Decrease of turbidity at current density 46.22 A / m²

Based on Fig. 8, it can be seen that the final turbidity value of the processing with and without the initial precipitation already meet the quality standard. The processing efficiency with and without initial precipitation at a current density 21.33 A / m² can be seen in Fig. 9.

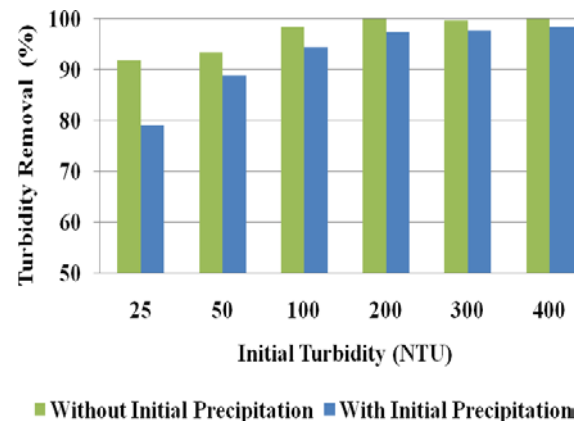


Fig. 9 Efficiency of turbidity removal at current density 21.33 A / m²

From Fig. 9 it can be seen that the efficiency of electrocoagulation process without initial precipitation gives higher yield than using the initial precipitation. In each variation of turbidity there is a significant difference in efficiency when using current density 21.33 A / m². The processing efficiency with and without initial deposition at a current density 46.22 A / m² can be seen in Fig. 10.

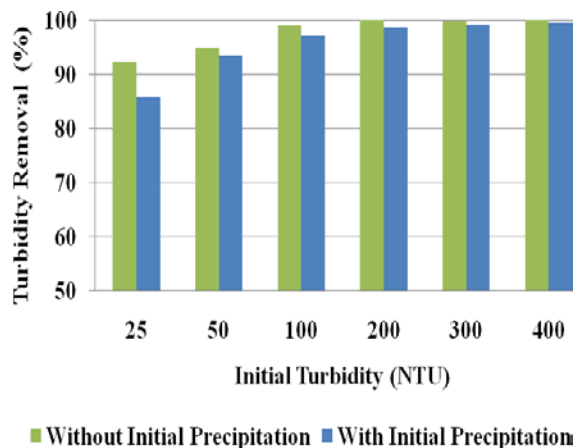


Fig. 10 Efficiency of turbidity removal at current density 46.22 A / m²

From Fig. 10 it can be seen that the efficiency of electrocoagulation process without initial precipitation gives higher yield than using the initial precipitation. At initial turbidity of 25 NTU there is significantly difference in efficiency, whereas for other initial turbidity variation there is no significantly difference. The large number of particles causes the distance between the particles closer, resulting in faster flocculation, larger floc size and more particle bonding. While at the time of initial deposition, large particles have precipitated in advance so that floc is more difficult to form

CONCLUSION

- At the current density 21.33 A/m² the final turbidity value of the electrocoagulation process with the initial precipitation still can not meet the quality standard, while for the processing without the initial precipitation can meet the quality standard.
- At the current density 46.22 A/m² the final turbidity value of the electrocoagulation process with and without the initial precipitation already meet the quality standard.
- The results in this study became the basis of subsequent research on a pilot scale

REFERENCES

- [1] Afiatun, E., Notodarmojo, S., Effendi., A.J., Sidarto, K.A., Cost Minimization of Raw Water Source by Integrated Water Supply Systems (a Case Study for Bandung, Indonesia), *International Journal of GEOMATE*, Vol. 14 Issue 46, 2018, pp. 32-39.
- [2] Yustiani Y.M., Lidya L., Towards an Information System of Modeling and Monitoring of Cikapundung River, Bandung, Indonesia, *Procedia Engineering* 154, 2016, pp. 353-360.
- [3] Yustiani, Y.M., Lidya, L., Matsumoto, T., Rachman, I., Komariah, I. Formulation of the Information System of River Water Quality in the Cikapundung River, Bandung, Indonesia. *International Journal of Engineering and Technology*. 2017, Vol 9 No. 1, pp: 137-142. DOI: 10.21817/ijet/2017/v9i1/170901416
- [4] Pradiko, H., Arwin, Soewondo, P., Suryadi, Y., The Change of Hydrological Regime in Upper Cikapundung Watershed, West Java Indonesia, *Procedia Engineering* 125, 2015, pp.229-235
- [5] Sawyer, C.N., McCarty, P.L., *Chemistry for Environmental Engineering*, 4th ed., McGraw-Hill, New York, 2003
- [6] Afiatun, E., Pradiko, H., Prayoga, H., A Turbidity Removal Strategy From The Water Resources of Bandung City, Indonesia, *International Journal of GEOMATE*, Vol. 12 Issue 34, 2017, pp. 57-61.
- [7] Kuokkanen, V. Kuokkanen, T. Rämö, J. & Lassi, U. 2013. Recent Applications of Electrocoagulation Treatment of Water and Wastewater. *Green and sustainable Chemistry*. 89-121.
- [8] Pradiko, H., Afiatun, E., Fabian, E., Influence of Mixing and Detention Time in Electro Coagulation Process to Treat Raw Water at Badak Singa Water Treatment Plant, *Indonesian Journal of Urban and Environmental Technology*, Vol 1, Number 2, 2018, pp. 137-150.
- [9] Nasrullah, M. Singh, L. & Wahid, Z.A. , Treatment of Sewage by Electro Coagulation and the Effect of High Current Density. *Energy and Environmental Journal*. Vol. 1, 2012.

GEOSPATIAL MODEL OF PHYSICAL AND SOCIAL VULNERABILITY FOR TSUNAMI RISK ANALYSIS

Abu Bakar Sambah^{1,2}, F. Miura³, Guntur¹, Sunardi¹, and A. F. Febriana¹

¹Faculty of Fisheries and Marine Science, University of Brawijaya, Indonesia; ²Marine Resources
Exploration and Management Research Group, University of Brawijaya, Indonesia, ³Faculty of Engineering,
Yamaguchi University, Japan

ABSTRACT

Tsunami risk assessment is required to support preparedness activities and effective disaster reduction. In this study, the analysis of physical and social vulnerability for tsunami risk assessment was applied for tsunami mitigation activities in coastal areas. The analysis was applied in the southern coastal area of East Java, Indonesia. The application of Geographical Information System (GIS) was used to capture, store, manipulate, analyze, manage, and visualize geographic data that used for tsunami risk analysis. GIS make possible in integrating a complex layer of geographic phenomenon and the parameter of tsunami vulnerability. In this case, the spatial overlay of physical and social vulnerability was done using spatial multi-criteria approach. Physical vulnerability parameters analyzed in this study were elevation, slope, land use, and distance from the coast. While the social vulnerability parameters include number of population, age distribution, number of women, and people with disabilities. The results described the visualization of possible damage and loss areas that may result from tsunami attack. The analysis illustrated that the most vulnerable areas of the tsunami were areas with low elevation, very sloping slopes, areas that close enough to the coastline and the land use type of residential class. The areas with high vulnerability class also illustrated by social vulnerability parameters especially population density. The estimates of affected areas due to tsunamis can help the decision-makers in mitigating the possible consequences of tsunamis, managing the emergency response related to tsunami disaster, and developing plans for recovery and reconstruction after the tsunami event.

Keywords: Geospatial, Tsunami, Vulnerability, Risk

INTRODUCTION

The tsunami disaster has been considered a major disaster such that many researches have been done to assess both its vulnerability and risk for coastal areas. Tsunami risk assessment has been done to quantify the potential damage and losses area due to tsunami [1]–[2]. Tsunami risk assessment needs an integrated analysis of geospatial data related to the tsunami hazard and the element of risk [3]. In order to assess tsunami risk, the assessment of vulnerability is necessary. In common, risk assessment implies two dimensions; the assessment of hazard (external part), and the assessment of vulnerability (internal) [4]. Tsunami vulnerability is analyzed after the evaluation of tsunami potential and probability. It depends on how close the communities are to the hazard source, and their social and economic characteristics [5]. Vulnerability also defines as “*The conditions determined by physical, social, economic, and environmental factors or processes, which increase the susceptibility of a community to the impact of hazards*” [6]. Vulnerability is trans-disciplinary and multi-dimensional, which covers social, economic, physical, political, engineering and ecological

aspects and dimensions [7].

The negative impact of tsunami occurrence in coastal areas is not a recent phenomenon, but model of study for assessing the impact damage, vulnerability, and risk is a relatively new trend [8]. The project of Coastal Risk Analysis for Tsunamis and Environmental Remediation (CRATER) has been applied for assessing tsunami vulnerability in coastal area using the parameters of infrastructural, geomorphological, and ecological features, elevation, coastal proximity, and parameters of land use [9]. Moreover, the PPATHOMA Tsunami Vulnerability Assessment (PTVA) model has been applied also for providing initial assessments of building vulnerability [10]–[11]–[12].

Indian Ocean includes South area of East Java Indonesia is located at one of the most active geological subduction zones. During December 2004 and July 2006 most recent seaquakes followed by huge tsunamis and it is expected to occur also in the near future [7]. Highly destructive tsunamis have been recorded at a number of locations in South Java, Indonesia (East Java in June 1994, Cilacap and Pangandaran in July 2006) [13]–[14]. It affected almost every sector of economy, including agriculture, fishery, tourism, transportation, housing,

and health [15].

In order to construct better disaster mitigation due to tsunami, appropriate analysis related to the tsunami vulnerability and risk assessment is necessary. The application of geospatial analysis for tsunami vulnerability and risk assessment has also applied using remote sensed dataset [12]–[16]–[17]–[18]–[19]. Another geospatial approaches has also applied soil type, urban form and social dataset for assessing potential natural hazard [20] and has determined the tsunami-vulnerable area by comparing the map tsunami-affected area and the topography data, which is related to land elevation, land use class, and the distance from the coast [21]. This study tried to assess the potential of affected area as the impact of tsunami, in which tsunami vulnerability areas will be calculated using both physical and social vulnerability parameters.

METHODS

Research Area

Tsunami vulnerability mapping using physical and social vulnerability parameter was applied in the coastal area of Blitar district, East Java, Indonesia (Fig. 1). This area is bordered by District of Malang, East Java on the East part. It also directly faces the Indian Ocean on south part.

Geographically, Blitar district is located at the southern of East Java with a height of 167 meters above sea level, at coordinates of $111^{\circ} 40' - 112^{\circ} 10'$ East longitude and $7^{\circ} 58' - 8^{\circ} 9' 51''$ South latitude. Blitar district has a 45 km-long coastline with 26,100 hectares of 4 nautical miles areas, and 63,330 hectares of 12 nautical miles.

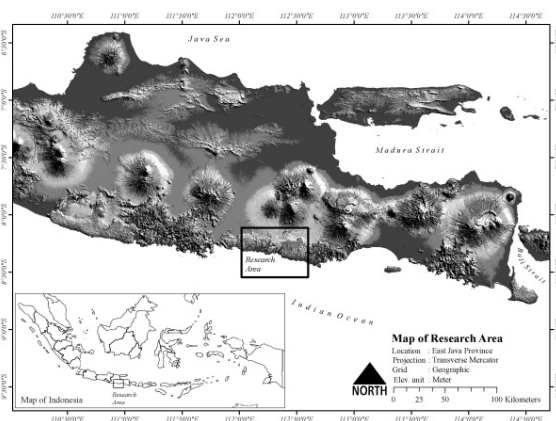


Fig. 1 Research area.

Dataset

In order to create tsunami vulnerability map of research area, the parameter of both physical and social vulnerability was collected. Physical vulnerability parameter includes elevation, slope, land use, and coastal proximity. Moreover, social vulnerability parameter consists of population density, gender, age, and disabilities. The elevation and slope data was created from The ASTER Global Digital Elevation Model (ASTER GDEM) version 2. ASTER GDEM was collected from <https://gdex.cr.usgs.gov/gdex/>. The analysis of Landsat 8 OLI satellite image was applied to create land use map. Landsat image was collected from <https://earthexplorer.usgs.gov/>. In addition to prepare coastal proximity, digital vector map of the research area was applied. Social vulnerability data was collected from Indonesia Central Bureau of Statistics.

GEOSPATIAL ANALYSIS

Data analysis was done through geospatial analysis. The analysis consists of four steps (Fig. 2). It starts with data acquisition, pre-processing, geospatial analysis, and result. Data consist of two data type, raster and vector dataset. ASTER GDEM was applied for elevation and slope data as one of physical vulnerability data. Moreover, Landsat 8 OLI satellite image as raster data was applied in order to create land use map.

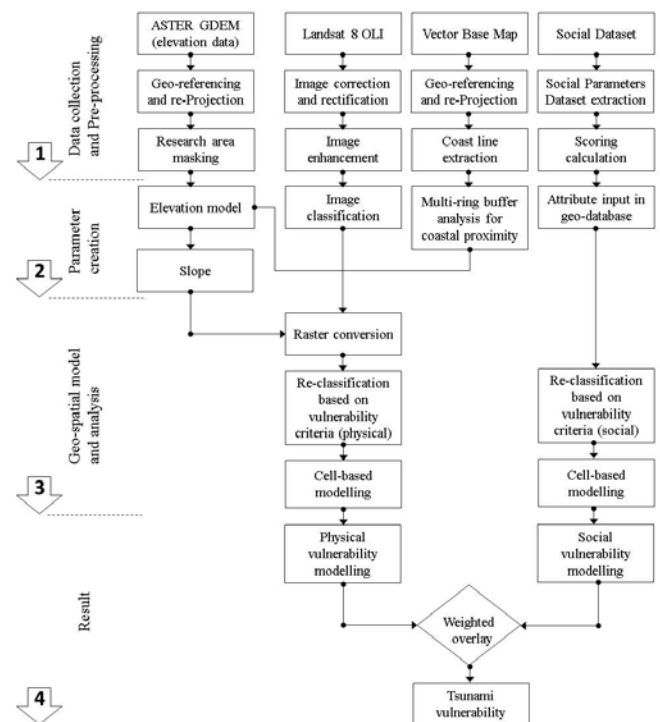


Fig. 2 Research step.

Vector data includes base map of research area, and it was applied for creating costal proximity, the distance from coast line to the hinterland. All parameters were classified in five classes based on the physical tsunami vulnerability. Social vulnerability data was taken from Indonesia Central Bureau of Statistics. Data were classified and scored based on the criteria of social tsunami vulnerability. It consists of population density, gender, age, and disabilities.

Data analysis for creating tsunami vulnerability map, as a combination of physical and social tsunami vulnerability, was done using cell-based modelling in the term of geographical information system. All parameter applied in the model were converted to raster dataset. This data consist of a matrix of cell and were classified in different weight. Weighted overlay is a type of suitability analysis that helps in analyzing geographic data based on multiple criteria. Weighted overlay allows the user to combine weight of several different types of information and visualize it, in which multiple factors can be evaluated at once [22]–[23]. The illustration as described in Fig. 3.

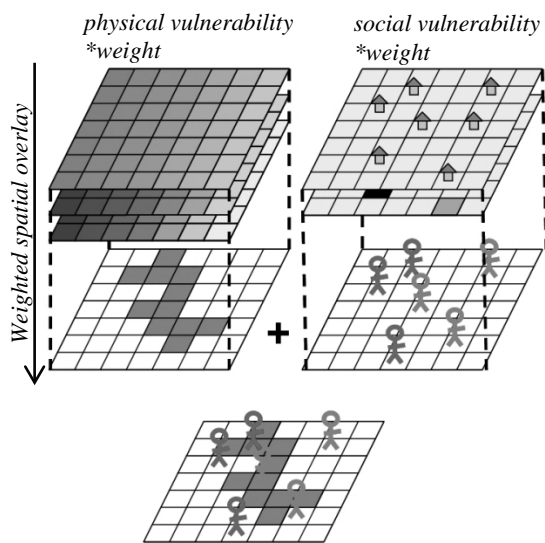


Fig. 3 Illustration of weighted overlay through cell-based modelling.

Physical Vulnerability

Four physical vulnerability parameters were converted to raster cell type and analyzed using weighted overlay to create map of tsunami vulnerability. Raster cells of all parameters were classified based on its value to five classes of vulnerabilities represent low, slightly low, medium, slightly high and high vulnerability. The vulnerability classes and its weight as described in Table 1, and tsunami vulnerability map as described in Fig. 4.

Table 1 Physical vulnerability classes and weight [12]–[24]–[25]–[26]

Parameters	Weight (%)	Vulnerability Classes				
		5	4	3	2	1
Elevation (m)	45.94	<5	5-10	10-15	15-20	>20
Slope (%)	25.53	0-2	2-6	6-13	13-20	>20
Land use	11.81	Urban area	Agriculture	Bare soil	Water	Forest
Coastal proximity (m)	16.71	0-293	293-514	514-762	762-1032	>1032

1=low, 2=slightly low, 3=medium, 4=slightly high and 5=high vulnerability

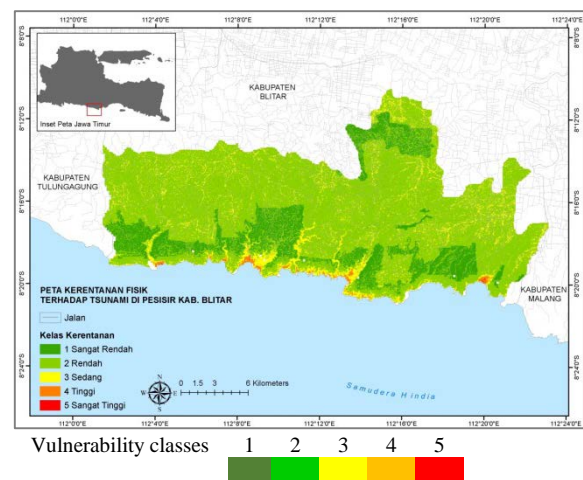


Fig. 4 Tsunami vulnerability map based on physical parameter

Figure 4 describes tsunami vulnerability map in coastal area of Blitar district based on physical parameters. Diverse elevation of research area causes the different level of vulnerability. In some coastal areas close to the ocean covered by high cliffs and it described low class of tsunami vulnerability. The area of high vulnerability is found only in areas with elevations close to 0 or less than 5 meters. This area identified as bay area with some settlement

Social Vulnerability

Social vulnerability can be defined as the exposure of groups or individuals to unexpected changes and disruption to livelihoods [27]. Social vulnerability also can be measured as a result of social and place inequalities [28].

Moreover, it defined also as the limitation of a community to the impact of natural disasters that influence its ability or resilience in order to mitigate, recover, and preparedness from the impacts. [29]. Social vulnerability map was created using four

parameters and weighted equally. The calculation was based on the criteria as described in Table 2. Social vulnerability map as described in Fig. 5.

Table 2 Social vulnerability criteria and weight [3]

Parameters [a]	Σ [b]	Proportion* [c]	Score** [d]	Weight [e]
Population density	P	[b]/total population	[c]/maximum proportion	25
Gender	G	[b]/total woman	[c]/maximum proportion	25
Age***	A	[b]/total age	[c]/maximum proportion	25
Disabilities	D	[b]/total disabilities	[c]/maximum proportion	25

* determine the factor of each village divided by number per sub-district

** the same value for all places on all the social variables

*** number of elderly and children

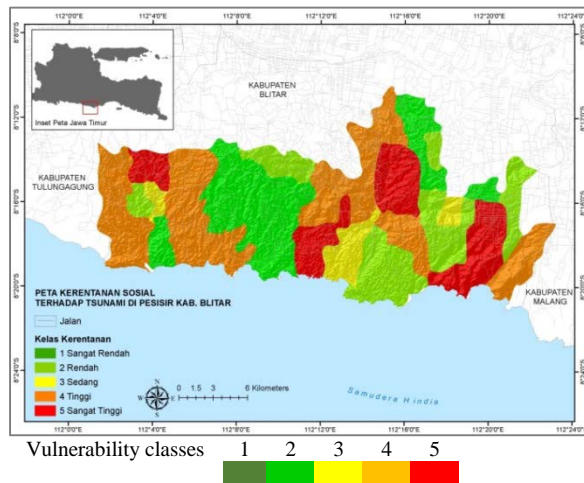


Fig. 5 Tsunami vulnerability map based on social parameter

DISCUSSION

Vulnerability represents the susceptibility of a given population to damaging effects from exposure to hazardous events [30]–[31]. The combination of physical and social parameters for assessing tsunami vulnerability area using cell-based modelling is one of the approaches in order to support risk analysis. Cell-based modelling calculated every single pixel of the parameter based on its score and weight. The analysis follows arithmetic logic as below.

$$\text{Vulnerability} = \sum W_i X_i \quad (1)$$

$$\text{Total vulnerability} = \sum (\text{physical vulnerability} \times \text{weight}) + (\text{social vulnerability} \times \text{weight}) \quad (2)$$

Total vulnerability illustrated the vulnerability area due to tsunami in which four parameters of physical vulnerability and four parameter of social vulnerability were combined (spatial overlay) as described in Fig. 6.

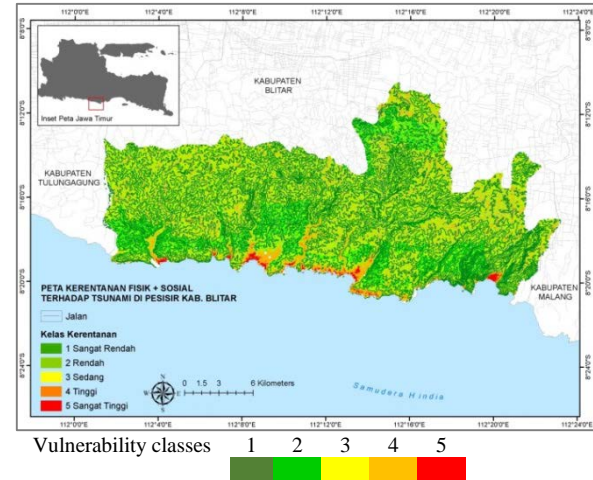


Fig. 6 Tsunami vulnerability map

Table 3 Total vulnerability area

No	Vulnerability classes	Area (Ha)
1	low	50,3204
2	slightly low	176,5883
3	medium	824,6320
4	slightly high	383,9447
5	high	4,2357

Vulnerability maps as described in Fig. 6 includes the information of total area per vulnerability classes (Table 3) may be good for communication tool for disaster preparedness [32]. The information of the map also plays an important role for effective early warning system. People often do not understand their risk; the social vulnerability map provides information on village or sub-districts with relatively high vulnerability. By integrating the physical and social vulnerability in the early warning system, coastal communities will be aware of their risks. As consequent, it will enhance community's preparedness for tsunami.

CONCLUSION

Geospatial model followed by the weighted cell-based processing described good result in assessing tsunami vulnerability area. The combination of physical and social vulnerability parameters in model also described good approaches in order to create tsunami vulnerability map. The map is important in determining the possibility area that could be affected by tsunami wave. The result illustrated important information in many

applications to support disaster risk management and mitigation strategies. Furthermore, in order to obtain an accurate tsunami vulnerability map and inundation map, this method can be applied by adding other vulnerability parameter such as coastal ecology (coral reef), barrier island, coastal type, and also tsunami direction.

ACKNOWLEDGEMENTS

The research is a part of tsunami risk mapping project in coastal area of East Java funding by Ministry of Research, Technology and Higher Education Republic of Indonesia. Authors are thankful too to METI and NASA for the ASTER GDEM products, USGS for Landsat 8 OLI image, and Geospatial Information Agency of Indonesia (BIG) for providing the basic map of the study area. We also thank to Laboratory of Disaster Prevention System, Yamaguchi University, Japan and Laboratory of Marine Resources Exploration, Brawijaya University Indonesia.

REFERENCES

- [1] Tinti, S., Assessment of Tsunami Hazard in The Italian Seas, *Natural Hazards*, Vol.4, 1991, pp. 267-283.
- [2] Clague, J. J., Munro, A. & Murty, T., Tsunami Hazard and Risk in Canada, *Natural Hazards*, Vol. 28, 2003, pp. 433-461.
- [3] Eddy, GIS in disaster management: a case study of tsunami risk mapping in Bali, Indonesia", Masters (Research) Thesis, 2006, James Cook University, Australia.
- [4] Chambers, R., Vulnerability, Coping and Policy, *IDS Bulletin*, Vol. 20, 1989, pp.1-7.
- [5] Cutter, S.L., Mitchell, J. T. and Scott, M.S., Revealing the Vulnerability of People and Places: a Case Study of Georgetown Country, South Carolina. *Annals of the Association of American Geographers*, Vol. 90, 2000, pp. 713-737.
- [6] ISDR, Living with Risk: A Global Review of Disaster Reduction Initiatives UNISDR, Geneva, 2004.
- [7] Post J., Zosseder K., Strunz G., Birkmann J., Gebert N., Setiadi N., Anwar H. Z., Harjono H, Nur M., Siagian T., Risk and Vulnerability Assessment to Tsunami and Coastal Hazards in Indonesia: Conceptual Framework and Indicator Development. In: *Proceedings of the International Symposium on Disaster in Indonesia: Problems and Solutions*, Padang, July 2007.
- [8] Dwyer, A., Zoppou, C., Nielsen, O., Day, S. and Roberts, S., Quantifying Social Vulnerability: A Methodology for Identifying Those at Risk to Natural Hazards. *Geoscience Australia*, 2004.
- [9] Dall'Osso, F., Bovio, L., Cavalletti, A., Immordino, F., Gonella, M. and Gabbianelli, G., A Novel Approach (The CRATER Method) for Assessing Tsunami Vulnerability at The Regional Scale Using ASTER Imagery, *Italian Journal of Remote Sensing*, Vol. 42 No. 2, 2010, pp. 55-74.
- [10] Papathoma, M. and Dominey-Howes, D., Tsunami Vulnerability Assessment And Its Implications For Coastal Hazard Analysis And Disaster Management Planning, *Gulf of Corinth, Greece, Natural Hazards and Earth System Sciences*, Vol. 3 No. 6, 2003, pp. 733-747.
- [11] Papathoma, M., Dominey-Howes, D., Zong, Y. and Smith, D. Assessing Tsunami Vulnerability, An Example from Herakleio, Crete", *Nat. Hazards Earth Syst. Sci.*, Vol. 3 No. 5, 2003, pp. 377-389.
- [12] Abu Bakar Sambah Fusanori Miura, Remote Sensing and Spatial Multi-Criteria Analysis for Tsunami Vulnerability Assessment, *Disaster Prevention and Management*, Vol. 23 Issue 3, 2014, pp. 271 – 295.
- [13] Synolakis C., Imamura F., Tsuji Y., Matsutomi H., Tinti S., Cook B., Chandram Y.P., and Usman M., Damage, Condition of East Java Tsunami of 1994 Analyzed. *Eos, Transactions, American Geophysical Union*, Vol. 76, No. 26, June 27, 1995, pp. 257, 261-262.
- [14] Reese, S., Cousins, W.J., Power, W.L., Palmer, N. G., Tejakusuma, I. G. and Nugrahadi, S., Tsunami Vulnerability of Buildings and People In South Java–Field Observation After the July 2006 Java Tsunami. *Natural Hazards and Earth System Science*, Vol. 7, 2007, pp. 573-589.
- [15] Levy, J.K. and Gopalakrishnan, C., Promoting Disaster-Resilient Communities: The Great Sumatra-Andaman Earthquake of 26 December 2004 And The Resulting Indian Ocean Tsunami. *Water Resources Development*, Vol. 21, 2005, pp. 543-559.
- [16] Sinaga, T.P., Adhi, N., Yang-Won, L. and Yongcheol, S., GIS Mapping of Tsunami Vulnerability: Case Study of the Jembrana Regency in Bali, Indonesia, *KSCE Journal of Civil Engineering*, Vol. 15, No. 3, 2011, pp. 537-543.
- [17] Karen, E., K. C. Joyce, S. Wright, V. Samsonov, and V. G. Ambrosia, Remote Sensing and the Disaster Management Cycle, In *Advances in Geoscience and Remote Sensing*, edited by G. Jedlovec. Croatia: InTech, 2009.
- [18] Yamazaki, F., K. Kouchi, and M. Matsuoka, Tsunami Damage Detection Using Moderate-Resolution Satellite Imagery, *Proceeding of the*

- 8th U.S. National Conference on Earthquake Engineering, San Francisco, CA, April 18–22, 2006.
- [19] Sambah A.B. and Miura F., Spatial Data Analysis and Remote Sensing for Observing Tsunami-Inundated Areas, *International Journal of Remote Sensing*, Vol. 37, Issue 9, 2016, pp. 2047-2065.
 - [20] Hsien, L.C. and Sheng, C.H., The Use of Spatial Analysis Techniques In Mapping Potential Natural Hazard Areas: A Case Study of Taiwan”, *Procedia Environmental Sciences*, Vol. 10, No. Part B, 2011, pp. 1092-1097.
 - [21] Gokon, H. and Koshimura, S., Mapping of Building Damage of The 2011 Tohoku Earthquake Tsunami in Miyagi Prefecture, *Coastal Engineering Journal*, Vol. 54, No. 1, 2012, pp. 126-138.
 - [22] ESRI, Environmental Systems Research Institute, Inc. Analyze Site Conditions Using Weighted Overlay, 2015, ESRI.
 - [23] Guntur, Abu Bakar Sambah, Fusanori Miura, Fuad, and Defrian Marza Arisandi. Assessing Tsunami Vulnerability Areas Using Satellite Imagery and Weighted Cell-Based Analysis. *International Journal of Geomate*, June, 2017, Vol.12, Issue 34, Pp. 115-122.
 - [24] Van Zuidam R.A., Guide To Geomorphologic-Aerial Photographic Interpretation and Mapping, International Institute for Geo-Information Science and Earth Observation, Enschede, 1983, The Netherlands.
 - [25] Sengaji E., and Nababan B., Tsunami Risk Level Mapping in Sikka, East Nusa Tenggara, *Journal of Tropical Marine Science and Technology*, Vo. 1, No. 1, June 2009, pp 48-61, (Indonesia edition).
 - [26] Iida K., Magnitude, Energy And Generation Mechanisms of Tsunamis and A Catalogue of Earthquakes Associated With Tsunamis, *Proceeding of Tsunami Meeting at the 10th Pacific Science Congress*, 1963, pp. 7-18.
 - [27] Adger W.N., Social Vulnerability to Climate Change and Extremes In Coastal Vietnam. *World Dev*, 27(2), 1999, pp. 249–269.
 - [28] Cutter S.L., Boruff B.J., Shirley W.L., Social Vulnerability To Environmental Hazards. *Soc Sci Q* 84(2), 2003, pp. 242–261.
 - [29] Cutter S.L., Emrich C.T., Moral Hazard, Social Catastrophe: The Changing Face of Vulnerability Along The Hurricane Coast. *Ann Am Acad Polit* 604, 2006, pp.102–112.
 - [30] Blaikie P., Cannon T., Davis I., and Wisner B., *At Risk: Natural Hazards, People's Vulnerability, and Disasters*, London: Routledge, 2004.
 - [31] Du Y., Yibo D., Zixiong L., and Guangwen C., The Role of Hazard Vulnerability Assessments in Disaster Preparedness and Prevention in China”, *Mil Med Res*, Vol. 2:27, 2015.
 - [32] Fekete, A., Spatial Disaster Vulnerability and Risk Assessments: Challenges in Their Quality and Acceptance. *Natural Hazards*, Vol. 61, Issue 3, 2012, pp. 1161–1178.

HYDROLOGICAL AND NITRATE LOADING MODELING IN LAM TAKLONG WATERSHED, THAILAND

Chau Ngoc Tran^{1,2}, *Chatpet Yossapol¹

¹School of Environmental Engineering, Institute of Engineering, Suranaree University of Technology,
Thailand

²Faculty of Engineering-Technology-Environment, An Giang University, Vietnam

ABSTRACT

Water pollution is largely associated with the growth of agriculture, urbanization, and industrialization. By the year 2016, the quality of significant surface water sources in Thailand has been evaluated and categorized as 34% good quality, 46% fair quality and 20% poor quality. According to the Pollution Control Department of Thailand, the lower Lam Taklong river, one of the critical watersheds of Thailand, is considered to have a poor water quality. In Lam Taklong watershed, non-point sources area approximately covered 89% of the total area, those sources became the significant contributors of water pollutants, particularly nutrients to the Lam Taklong watershed. Plus, water quality researches of the watershed were carried out with many different watershed models, but SWAT model has not been applied to allot the pollutant loading from diffuse sources. Therefore, the main objective of this study is to apply the SWAT model to simulate flow and nitrate from 2007 to 2013, and allocate NO₃⁻ loading in upstream is lower than downstream of the Lam Taklong watershed. The results of the study can be a useful tool for the management of surface water resources in the Lam Taklong watershed.

Keywords: SWAT, Lam Taklong watershed, Nitrate, Diffuse source

1. INTRODUCTION

Lam Taklong watershed (LTW) is one of the critical watersheds of Thailand. It is a part of the Mun river watershed, in the Northeastern region of Thailand. In addition, it has a role of drainage, recreation, and environmental conservations. LTW was covered with extended large forests in the past. At the present, most areas have been invaded, deforested and converted into communities, farmland, orchards and deserted areas and others to keep up with local progress.

Lam Taklong watershed has a high economic growth rate but is still facing water scarcity. Wijitkosum [1] analyzed the water situation in the Watershed which was subject to the economic plan of the government. LTW was on the brink of a water shortage and this problem was at the peak during the maximum water usage and minimum water asset. As result of the economic value, it is necessary to conduct a hydrological and water quality modeling research in Lam Taklong watershed. The results show the accuracy of the flow simulation, helping planners to come up with a reasonable flow and water quality management.

Netnapa [2] applied Soil and Water Assessment Tool (SWAT) model for evaluations streamflow, sediment, nutrient loading simulations in Lam Takong River basin. That author demonstrated that

SWAT model could be a useful tool for water resources managements in Lam Takong River basin.

The water flow change at the outlet of Kosynthos river watershed affected the nutrient loads [3]. Previous studies in Lam Taklong basin have not estimated relationship between flow and nitrate in LTW.

In this study, ArcGIS integrated with the SWAT model, which can realistically represent the spatial variability of watershed characteristics, will be used to study upstream and downstream areas in Lam Taklong River basin. SWAT model is selected for this study because it is included channel degradation routine with detail appropriate for watershed management [4]. The results could be a useful tool for water resources planning in LTW.

2. MATERIALS AND METHODOLOGY

2.1. Study Area

Lam Taklong River basin is a part of the Mun watershed in Northeastern region of Thailand, is also a sub-basin of the great Mekong river. The length of the river is 220 km, originated from Khao Yai National Park, has an area of 3,518 km² covering six districts in Nakhon Ratchasima province and more 880,000 population reside [5] (Fig. 1).

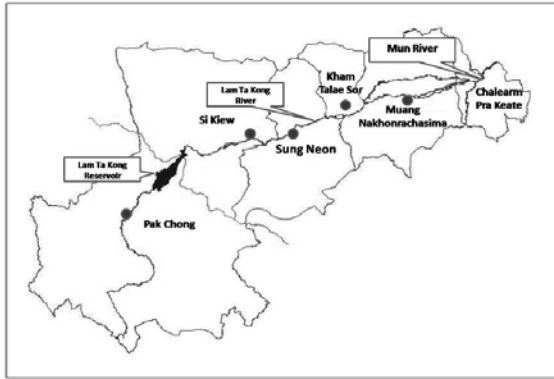


Fig. 1 Lam Taklong watershed.
(Wijitkosum, 2010)

LTW is under the influence of southwest and northeast monsoon. From May to October, the southwest monsoon brings moisture from the Indian Ocean causing rain, peaking in August and September. The average amount of rainfall is 1,454 mm (2010).

2.2 Model Description

ArcGIS 10.1 software is integrated the SWAT2012 (Soil and Water Assessment Tool) model to calculate the flow in Lam Taklong watershed. SWAT model was selected for this study due to a wide variety and with proper testing [6].

The subwatershed discretization of SWAT divides the watershed into 29 subbasins. Then, subbasins continue to be partitioned into 309 multiple hydrologic response units (HRUs) based on soil and land use distribution of the watershed. For each HRU, the land phase of the hydrological cycle is modeled, and flow from each HRU are calculated. Then flow from HRUs within a subbasin are summed to get flow from this subbasin.

For a subbasin located downstream of another subbasin, flow from land phase are added at the outlet of the upstream subbasin and then continue to be routed through the channel.

The necessary data is collected for simulation of flow in the Lam Taklong river. The main input data for simulating the hydrological processes in Arc SWAT are the base map data, meteorological data and observed flow data.

The ArcSWAT2012 interface is used to delineate the Lam Taklong basin based on an automatic procedure using Digital Elevation Model (DEM) data. A DEM grid map with a 30m spatial resolution was available. Moreover, a mask map which identifies the focused area for delineation to reduce the processing time and a burn-in river map which helps to accurately predict the location of the stream network was also input.

Calibration is used autocalibration tools in

SWAT-CUP. Automatic calibration and uncertainty analysis capability is directly incorporated in SWAT2012 via the SWAT-CUP software developed by Swiss Federal Institute of Aquatic Science and Technology [7] and R^2 [8] will be selected as the efficiency criterion. SWAT-CUP includes automated as well as the semi-automated program SUFI2 for model calibration.

The sensitive parameters from the sensitivity analysis results will be considered in the calibration process. The following parameters will be included in the calibration CN2, ALPHA_BF, GW_DELAY, GWQMN.

2.3 Input Data

The main input data for simulating the hydrological processes in ArcSWAT are the base map data, meteorological data and observed data. The necessary data is showed in Table 1.

Table 1 Model input data sources for the Lam Taklong watershed

Data type	Source	Detail
Topography (DEM) 30mx30m	Land Development Department	Elevation, slope
Soil	Land Development Department	Spatial soil variability Soil types and properties
Land use	Land Development Department	Land cover classification and spatial representation
Weather stations	Thai Meteorological Department	Daily precipitation Temperature Relative humidity Wind speed Solar radiation
Flow of water	Lam TaKlong Water Supply & Maintenance Project	M89 and M164 stations ($m^3 day^{-1}$)
Water quality	Regional Environment Office 11	Sediment ($mg l^{-1}$) Nitrate nitrogen ($mg l^{-1}$)

The base map data is overlaid by land use and soil data. Climate data input consists of temperature, relative humidity, wind speed, solar radiation; the weather data and the rainfall data. Observed data consists of concentration of sediment and nitrate nitrogen.

3. RESULT AND DISCUSSION

The Lam Taklong watershed is delineated into sub-basins using the digital elevation map (30m) and it is divided in 29 subbasins outlet of Lam Taklong River (Fig 2).

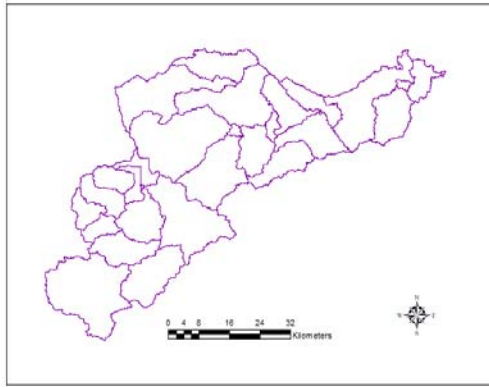


Fig. 2 Subbasins of lam taklong watershed.

Land use data are required for pollution assessment because of activities that we do on land can affect on generate the pollutants. The digital land use data were obtained from Land Development Department (LDD) in the year 2011.

The U.S. Natural Resource Conservation Service (NRCS) classifies soils into 4 hydrologic groups based on infiltration characteristics of the soils including group A (high infiltration rate), group B (moderate infiltration rate), group C (slow infiltration rate) and group D (very slow infiltration rate). Soil data was obtained from LDD including fourteen soil series with soil texture class and quantitative particle size distribution analysis by LDD were transformed to hydrologic soil group.

The delineated sub-basin map, land use, and soil map will be overlaid. SWAT simulate different land use in each sub-basin. Lam Taklong River watershed's DEM, land use and soil data are integrated to accumulate flow direction, and stream network in Lam Taklong River (Fig 3).

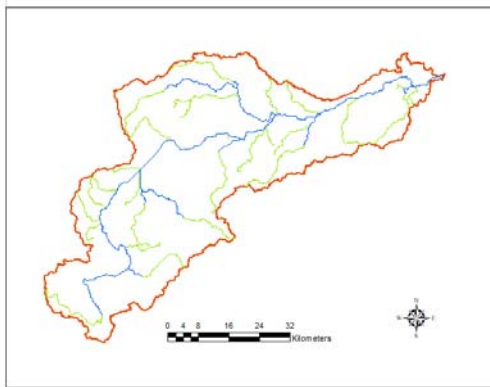


Fig. 3 Stream network of Lam Taklong watershed

3.1 Simulated monthly flow in Lam Taklong Watershed

Calibration is conducted in lower LTW by adjusting input four parameter values CN2 (-0.1516),

ALPHA_BF (0.287), GW_DELAY (51.42), GWQMN (1.89) from initial default conditions.

The sensitive parameters were replace SWAT model to simulate flow and nitrate loading. The simulated flow was compared to observed flow in upstream LTW.

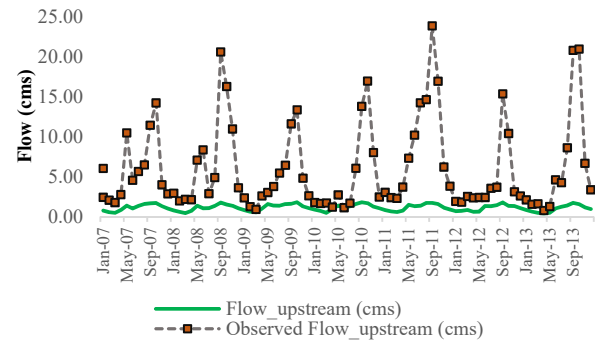


Fig. 4 Simulated monthly flow and observed monthly flow at upstream of LTW

The simulated flow values are compatible with minimum observed flow values in lower LTW from 0.4 to 1.8 m³/s (Fig. 4). Similarly, simulated flow values in upper LTW from 1.6 to 2.7 m³/s is close to the average observed flow value. The simulated flow at subbasin outlet of LTK is shown Fig. 5 during 7 years.

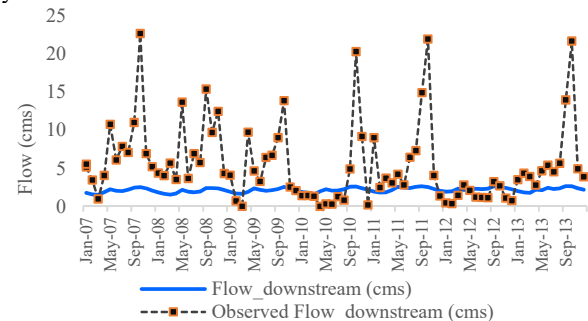


Fig. 5 Simulated monthly flow and observed monthly flow at downstream of LTW

The average monthly observed and simulated flow from 2007 to 2014 for an outlet of LTW is presented in Fig. 5. SWAT has simulated during a time period when the average daily precipitation is input date. The model was validated for an average time period from January 2007 to July 2014. Test results show that with the modified values for the model SWAT, the Nash-Sutcliffe R² for monthly total flows was 0.66.

Results obtained by using the model's modified values for simulating flow accentuate the critical need for model calibration in order to ensure that hydrologic processes are well represented on a watershed.

3.2 Nitrate loading simulation in Lam Taklong Watershed

Sediment and nitrate was calibrated after flow calibration. Simulated nitrate values in downstream is higher upstream.

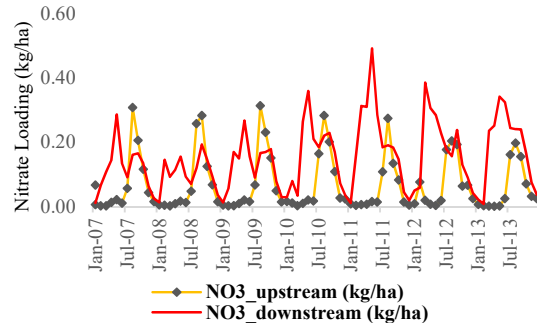


Fig. 6 Simulated nitrate loading in upstream and downstream of LTW.

However, the upper area has the high nitrate loading from July to September and from March to June in the lower area. In contrast, both of two areas had the low nitrate loading is from december to January. This result is consistent with Netnapa's study [2] that September was the month with the highest $\text{NO}_3\text{-N}$ while January and December were the lowest months.

3.3 The influence of the flow on nitrate nitrogen loading

3.3.1 Upstream area

The simulated results of flow and nitrate loading in upstream of LTW showed that they have a proportional relationship (Fig. 7).

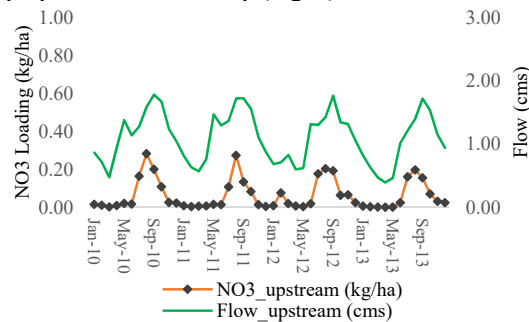


Fig. 7 Relationship of flow and nitrate loading in upstream of LTW

Both of flow and nitrate loading value in LTW upstream have the lowest value in January and the highest in September.

3.3.2 Downstream area

In contrast to upstream, downstream flow values are inversely proportional to nitrate loading values. They are showed in Fig. 8.

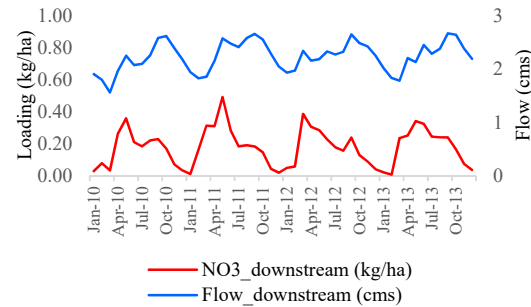


Fig. 8 Relationship of flow and nitrate loading in downstream of LTW.

As the flow rate increases, nitrate loading values tend to decrease from May to October. However, from November to January flow and nitrate loading value have the same downtrend.

4. CONCLUSION

For this study, calibration process was conducted with four parameters CN_2 , ALPHA_BF , GW_DELAY , GWQMN . The R^2 value 0.66 is compared to the results from Zhao et al [9] the regression coefficient of measured value and simulation value was 0.63 and it shows that the correlation between observed and simulated monthly runoff is good. This means that the SWAT model is suitable for fluid flow and nitrate. Determination of accurate parameters in calibration when modeling watersheds are vital for simulating streamflow data corresponding to measured values.

The simulated flow and nitrate loading values in LTW upstream have a proportional relationship, oppositely in downstream they have inverse ratio from May to October.

ACKNOWLEDGEMENTS

The author thanks anonymous reviews for their comments and suggestions; Dr. Chatpet for his huge contribution in improving the paper; the Land Development Department, Regional Environmental Office 11, the Royal Irrigation Department, the Thai Meteorology Department, Lam Ta Klong Water Supply and Maintenance Project for providing data and results from SWAT model; and the SUT-PhD scholarship for ASEAN countries for financial support in Suranaree University of Technology in Thailand.

REFERENCES

- [1] S. Wijitkosum and T. Sriburi, "Evaluation of Water Resource Management In Lam Ta Kong Watershed: The Water Scarcity Area of Thailand," vol. 4, no. 4, pp. 1047–1057, 2010.
- [2] N. Pongpetch, P. Suwanwaree, C. Yossapol, S. Dasananda, and T. Kongjun, "Using SWAT to assess the critical areas and nonpoint source pollution reduction best management practices in Lam Takong river basin, Thailand," *EnvironmentAsia*, 2015.
- [3] V. Pisinaras, C. Petalas, G. D. Gikas, A. Gemitzi, and V. A. Tsihrantzis, "Hydrological and water quality modeling in a medium-sized basin using the Soil and Water Assessment Tool (SWAT)," *Desalination*, vol. 250, no. 1, pp. 274–286, 2010.
- [4] N. A. Staley, T. Wynn, D. Ph, B. Benham, G. Yagow, and V. Tech, "Modeling Channel Erosion at the Watershed Scale : Model Review and Case Study," no. March, 2006.
- [5] N. Pongpetch, P. Suwanwaree, C. Yossapol, S. Dasananda, and T. Kongjun, "Sediment and Nutrient Load Environmental Factors of Lam Takong River Basin, Thailand," *Adv. Mater. Res.*, vol. 1030–1032, pp. 594–597, 2014.
- [6] J. G. Arnold, J. R. Kiniry, R. Srinivasan, J. R. Williams, E. B. Haney, and S. L. Neitsch, "Soil & Water Assessment Tool: Input/output documentation. version 2012," *Texas Water Resour. Institute, TR-439*, pp. 207–208, 2013.
- [7] Swiss Federal Institute of Aquatic Science and Technology (Eawag), *Usermanual SWATCUP*. 2015.
- [8] P. Krause, D. P. Boyle, and F. Bäse, "Comparison of different efficiency criteria for hydrological model assessment," *Adv. Geosci.*, vol. 5, pp. 89–97, 2005.
- [9] W. J. Zhao, W. Sun, Z. L. Li, Y. W. Fan, J. S. Song, and L. R. Wang, "A Review on SWAT Model for Stream Flow Simulation," *Adv. Mater. Res.*, vol. 726–731, pp. 3792–3798, 2013.

WATER QUALITY ASSESSMENT BASED ON THE WATER QUALITY INDEX (WQI) APPROACH USING GEOSPATIAL ANALYSIS

Rina Febrina¹ and Abu Bakar Sambah^{2,3}

¹Faculty of Engineering, Malahayati University, Indonesia, ²Faculty of Fisheries and Marine Science, University of Brawijaya, Indonesia; ³Marine Resources Exploration and Management Research Group, University of Brawijaya, Indonesia.

ABSTRACT

Water quality refers to the chemical, physical, or biological characteristics of water, in which assessing the condition of water relative to the requirements of biotic species or to any human purposes. The aim of this study was to analyze the water quality of the Way Kuripan River based on the Water Quality Index (WQI) calculation method. Water samples were taken from five different areas (WK01, WK02, WK03, WK04 and WK05). WQI was calculated on the basis of six parameters; dissolved oxygen (DO), biochemical oxygen demand (BOD), chemical oxygen demand (COD), pH, total suspended solid (TSS) and ammoniac-nitrogen (NH₃-N). The calculation started by identifying the equation of the Sub-Index (SI) based on the parameter value, calculating the Sub-Index (SI) of each parameter, and calculating the Water Quality Index. The results show that WK01 and WK04 have WQI values of 70.3 and 70.11. Those values show that water quality of the Way Kuripan River was in class III or slightly polluted. WK02 (WQI = 55.8) and WK03 (WQI=53.8) were highly polluted. The lowest WQI of the Way Kuripan River was in WK05 = 38.3, and classified as Class V (highly polluted). Moreover, Geospatial analysis was done to identify the distribution of water quality geographically. It shows that home industry and human activities, were spread along the river flow, and it caused the fluctuation of water quality. The results of this study can be used as a reference by the local government for water resources management.

Keywords: Water quality index, Way Kuripan River, Chemical, physical, and biological characteristics

INTRODUCTION

Water pollution increases day by day in many places in the world. On the other hand the availability of water supply decreases continuously. Based on the circumstance, water quality in many parts in the world is dropped continuously. Water quality is always an important and interesting topic to discuss.

Water quality is one of the most important factors that must be considered when evaluating the sustainable development of region [1]. The most useful tool to monitor and assess the water quality is by using the water Quality Index (WQI) which is a single number like a grade explains the total water quality at a certain area and time based on several water quality parameters [2]. It also assesses the suitability of the quality of the water for a variety uses such as agriculture, aquaculture, and domestic use [3]. WQI was first proposed by Horton 1965, later, numerous of indices have been developed all over the world such as Weight Arithmetic (WA), National Sanitation Foundation (NSF), Canadian Council of Ministers of the Environment (CCME), British Columbia, Oregon etc [4]-[5]-[6]-[7]. Over the years, many researchers have been conducted to monitor and study water quality [8]-[9]-[10]-[11]-[12]-[13]-[14].

In Southeast Asia regions, the most recognized WQI is DOE WQI. The WQI was developed by the Department of Environment of Malaysia [15]. DOE WQI calculation has been used as standard calculation for water quality in Water Quality Monitoring Program in Malaysia [7].

In this study, DOE-WQI method [9] was applied to analyze the water quality of Way Kuripan River. Way Kuripan River is one of the largest rivers in Bandar Lampung city, Indonesia. Along the river, there are landfill, industrial, residential and agriculture. The water body of the river practically receives, industrial waste, liquid waste from landfill, domestic wastes and drainage water from the residential area. The river were utilize for some purposes such as cleaning and sanitizing by the people living in surrounding areas. To identify the distribution of water quality in the Way Kuripan River some approach is needed. The integrated analysis of geospatial and water quality index calculation will describe the distribution of water quality along the river and determine the class of polluted water.

METHOD

Study Area

The analysis applied in the area of Way Kuripan River, Bandar Lampung city. In general, Lampung can be described as hilly to mountainous terrain, and characteristic of steep slopes with a slope of more than 25% and an average altitude of 300 meters above sea level. Way Kuripan River was created by the confluence of Way Simpang Kiri River and Way Simpang Kanan River. The length and the catchment area of the Way Kuripan River were 9.6 km and 60.81 km². Research location as described on Fig. 1.

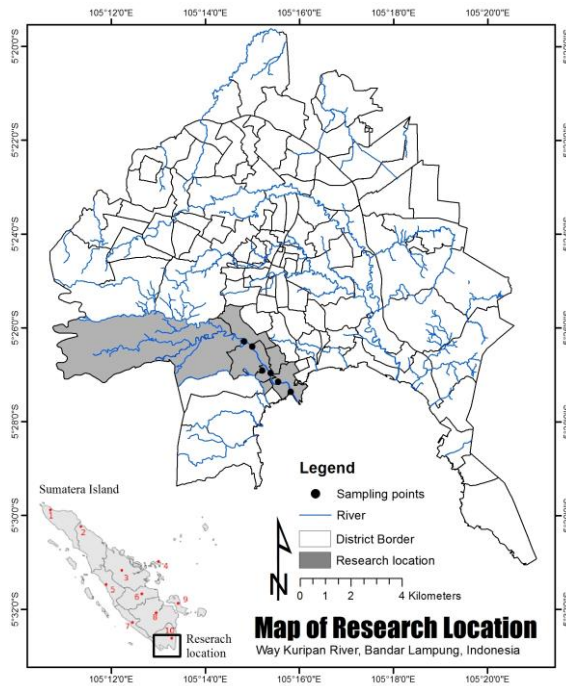


Fig.1 Research location

Data Collection

The water samples consist of 5 points and were taken during January 2017. Each sampling site was positioned by Global Positioning System (GPS), as illustrated in Table 1 and Fig. 2.

Table 1 Sampling point coordinate

ID	Latitude (S)	Longitude (E)
WK01	05°26.458'	105°15.026'
WK02	05°26.712'	105°15.169'
WK03	05°26.910'	105°15.387'
WK04	05°26.194'	105°15.461'
WK05	05°26.212'	105°15.778'

The surface water sample was collected about a half of the river depth due to the velocity of water flow less than 5m³/s [16]. Water samples from each station were stored in one liter polyethylene bottles for analysis of selected parameters included: pH,

Biological Oxygen Demand (BOD), Chemical Oxygen Demand (COD), Dissolve Oxygen (DO), Ammoniac Nitrogen (NH₃-N), Total Suspended Solid (TSS).

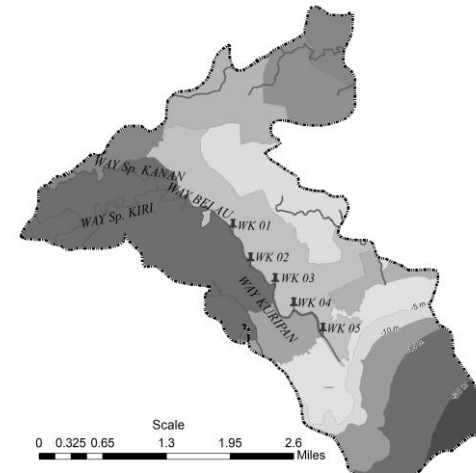


Fig.2 Sampling point

The surface water sample was collected about a half of the river depth due to the velocity of water flow less than 5m³/s [16]. Water samples from each station were stored in one liter polyethylene bottles for analysis of selected parameters included: pH, Biological Oxygen Demand (BOD), Chemical Oxygen Demand (COD), Dissolve Oxygen (DO), Ammoniac Nitrogen (NH₃-N), Total Suspended Solid (TSS).

Data Analysis

The algorithm applied for calculating WQI was developed by the Department of Environment of Malaysia. The algorithm was described as follows:

$$WQI = (0.22SIDO) + (0.19SIBOD) + (0.16SICOD) + (0.15SIAN) + (0.12SIpH) \quad (1)$$

Where, *WQI* = Water Quality Index, *SIDO* = Sub-index *DO*, *SIBOD* = Sub-index *BOD*, *SICOD* = Sub-index *COD*, *SIAN* = Sub-index *AN*, *SISS* = Sub-index *TSS*, *SIpH* = Sub-index *pH*.

Every sub-index was calculated based on the equation in certain condition which is:

$$SIDO; SIDO = 0 \text{ for } x \leq 8; SIDO = 100 \text{ for } x \geq 92; SIDO = -0.395 + 0.030x^2 - 0.00020x^3 \text{ for } 8 < x < 92.$$

$$SIBOD; SIBOD = 100.4 - 4.23x \text{ for } x \leq 5; SIBOD = 108 * \exp(-0.055x) - 0.1x \text{ for } x > 5. SICOD; SICOD = -1.33x + 99.1 \text{ for } x \leq 20; SICOD = 103 * \exp(-0.0157x) - 0.04x \text{ for } x > 20. SIAN; SIAN = 100.5 - 105x \text{ for } x \leq 0.3; SIAN = 94 * \exp(-0.573x) - 5 * |x - 2| \text{ for } 0.3 < x < 4; SIAN = 0 \text{ for } x \geq 4. SISS; SISS = 97.5 * \exp(-0.00676x) + 0.05x \text{ for } x \leq 100; SISS =$$

$71 \cdot \exp(-0.0061x) - 0.015$ for $x < 1000$; $SISS = 0$ for $x \geq 1000$. $SIpH$; $SIpH = 17.2 - 17.2x + 5.02x^2$ for $x < 5.5$; $SIpH = -242 + 95.5x - 6.67x^2$ for $5.5 \leq x < 7$; $SIpH = -181 + 82.4x - 6.05x^2$ for $7 \leq x < 8.75$; $SIpH = 536 - 77x + 2.76x^2$ for $x \geq 8.75$. (2)

General rating scale for the DOE WQI was between 0 and 100. The interpretation of the value applied in some water resources development purposes is described below:

- **For general use of water:** $0 \leq x < 60$ = high polluted water; $60 \leq x < 80$ = slightly polluted water; $x > 80$ = clean water. For classification of water: $0 \leq x < 40$ = Class V; $40 \leq x < 50$ = Class IV; $60 \leq x < 80$ = Class III; $80 \leq x < 90$ = Class II; $x > 90$ = Class I.
- **For public water supply:** $0 \leq x < 40$ = not acceptable for public water supply; $40 \leq x < 50$ = doubtful for public water supply; $60 \leq x < 80$ = needs expensive treatment for public water supply; $80 \leq x < 90$ = needs minor purification for public water supply; $x > 90$ = no need treatment for public water supply.
- **For recreation water:** $0 \leq x < 20$ = not acceptable for recreation; $20 \leq x < 30$ = obvious pollution appearing, still not acceptable for all recreation; $30 \leq x < 40$ = only for boating; $40 \leq x < 50$ = doubtful for water contact; $50 \leq x < 70$ = acceptable for water contact but needs bacteria count; $x > 70$ = acceptable for all water sport.
- **For fisheries:** $0 \leq x < 30$ = not acceptable for fisheries; $30 \leq x < 40$ = only for coarse fish; $40 \leq x < 50$ = only for handy fish; $50 \leq x < 60$ = doubtful for sensitive fish; $60 \leq x < 70$ = marginal for trout; $x > 70$ = acceptable for all fish.
- **For navigation:** $0 \leq x < 30$ = not acceptable for navigation; $30 \leq x < 40$ = obvious pollution appearing; $x > 50$ = acceptable for all navigation.
- **For water transportation:** $0 \leq x < 10$ = not acceptable for water transportation; $x > 10$ = acceptable for water transportation.

RESULT AND DISCUSSION

Water Sample Analysis

Water samples were analysis at Health Laboratory of UPTD/Local technical implementation unit includes five parameters; Dissolved Oxygen (DO), Biological Oxygen Demand (BOD), Chemical Oxygen Demand (COD), Ammonia (AN), Suspended Solid (SS) and Degree of Acidity (pH). The result of analysis as described in Table 2.

The value as shown in Table 2 were compared with the water quality standard in accordance with Government Regulation of the Republic of Indonesia No. 82, year of 2001 (Table 3) on the

Management of Water Quality and Control of Water Pollution [17].

Table 2 Analysis result

No	Para Meters (mg/l)	Analysis Result				
		WK 01	WK 02	WK 03	WK 04	WK 05
1	DO	3.69	3.56	4.04	1.45	3.05
2	BOD	2	30	29	4	131
3	COD	6	9	32	6	468
4	AN	0.03	0.03	0.12	0.16	0.03
5	SS	1	1	1	1	1
6	pH	7.56	7.36	7.20	7.47	7.61

Table 3 Government regulation of the Republic of Indonesia No. 82, year of 2001

Quality Standard			
Class I (mg/l)	Class II (mg/l)	Class III (mg/l)	Class IV (mg/l)
6	4	3	0
2	3	6	12
10	25	50	100
0.5	-	-	-
50	400	400	400
6-9	6-9	6-9	5-9

Table 2 shows the value of Dissolved Oxygen (DO) at sample points of WK01, WK02, WK05 were 3.69 mg/l; 3.56 mg/l and 3.05 mg/l, and it included in water quality standard of class III [17]. While at the sample points WK03 and WK04 have DO value of 4.04 mg/l (Class II) and 1.45 mg/l (almost close to Class IV). DO is one of the important parameters in water quality analysis. The DO value indicates the amount of oxygen available in a body of water. The greater the DO value on water, indicating the water has good quality. Conversely, if DO value is low, it can be seen that the water has been contaminated. The value of DO also shows the extent to which the water body is able to accommodate water biota such as fish and microorganisms. The results shows that the value of DO increasingly smaller the downstream. As for the BOD value there was an increase from upstream to downstream. The increasing of BOD value was above the standard of the class IV water quality, and this occurred at sample points of WK02, WK03 and WK05; 30 mg/l, 29 mg/l and 131 mg/l, respectively.

The highest BOD value occurred in the downstream area (WK05=131mg/l) while the upstream of the river had a low BOD value of 2 mg/l, and included in class I. The BOD value indicates the amount of oxygen required by microorganisms to decompose dissolved organic substance and some of the organic substances suspended in water. The greater the value of BOD

means the process of decomposition of organic substance occurs in large quantities and will absorb oxygen in water thereby reducing the amount of dissolved oxygen (DO). The increase in BOD value from upstream to downstream indicates the quality of river water has decreased. This is because the source of pollutants is not only from the previous water flow but also from the surrounding settlements that dispose of domestic waste directly into the river. In addition, the activities of ships entering the estuary by disposing of waste from ships such as engine oil and others also increase the source of pollutant to downstream areas.

In addition, COD value at sample point of WK01, WK02, WK04 were 6 mg/l, 9 mg/l and 6 mg/l, and included in the standard of water quality class I. COD value at sample point of WK03 was 32 mg/l, and it almost close to the standard of water quality class III. While the COD value for the downstream area (WK05) was very high, equal to 468 mg/l, far exceeds the water quality standard required by the government.

The downstream region requires the greatest amount of oxygen compared to other regions for chemical reaction processes to decompose the contaminants. Level of ammonia (AN) at sample point of WK 02 to WK 04 has increased with highest AN concentration occurring at sample point of WK 04 (0.16 mg/l). It did not exceeding recommended quality standard based on Government regulation No. 82, 2001 (equal to 0.5 mg/l). In this area the dominant activity is the settlements whose effluents are directly discharged into river bodies and poor sanitation of the people. This is in accordance with the statement of Effendi (2003) which states that high ammonia level is an indication of the contamination of organic materials derived from domestic waste, industries and run-off agricultural fertilizers [16].

SS (Suspended Solid) parameter of Way Kuripan River at sample point of WK01 up to WK05 has the same value (1 mg/l). Concentrations of SS from upstream to downstream described the water quality standard of class I and Class II based on Government Regulation, so that SS content of river water of Way Kuripan did not affect to the allocation of raw water, facilities/infrastructure of recreational water, animal husbandry and fishery interests. Although SS was not a toxic but with the increasing value of SS means increasingly penetration of light obstructed into the river.

Moreover, pH was classified as normal, and it indicated that life of aquatic biota still in good enough condition. The overall analysis of water quality of Way River Kuripan illustrated that some the result did not meet the criteria of quality standard according to Government Regulation of Republic of Indonesia No. 82, year of 2001 on the Management

of Water Quality and Control of Water Pollution [17].

Analysis of DOE - Water Quality Index (DOE-WQI)

Based on the analysis of Way Kuripan River water samples (Table 2), it can be calculated the sub-index value of each parameter. The analysis of water quality used DOE-WQI method applying the equation (1). The results of DOE-WQI calculations are presented in Table 4.

Table 4 WQI Value of Way Kuripan River

No.	Sample Location	WQI	Class
1	WK01	70.3	III (Slightly Polluted)
2	WK02	55.8	IV (Polluted)
3	WK03	53.8	IV (Polluted)
4	WK04	70.11	III (Slightly Polluted)
5	WK05	38.3	V (Highly Polluted)

The analysis of WQI described the decreasing value of water quality from upstream to downstream; it is related to the contamination level. At the sample point of WK01 the WQI value was 70.3, it means that the water quality in upper river area is slightly polluted. Based on the investigation of pollution source in upstream area occurred due to erosion of vacant land and residential area. Upstream water can be used for drinking water needs, although it requires processing first. It also safe for fisheries activities and suitable for all types of water sports, shipping and water transportation. The areas between upstream and downstream at the sample points of WK02, WK03, WK04 have WQI values of 55.8, 53.8 and 70.11. The source of pollution was dominated by domestic and household wastes generated from the contribution of Karang City urban village with dense population Village (see land use map on Fig 3).

The water quality at the sample points of WK02 and WK03 were worse compared to WK04, due to the existence of SABO DAM between sample points WK03 and WK04. The high concentration of contaminants from the previous water flow (WK02 and WK03) became lower when through SABO DAM due to an increase in water discharge. Water discharge gives a significant influence on the improvement of water quality level. Water quality on WK02 and WK03 were doubtful for drinking water use because the pollution level was higher than WK01. The class category of this area was Class IV (polluted). It needs routine bacterial control if apply for sport in contact with water. While for fisheries only allowed for fish that are cultivated but still doubtful for more sensitive fish but permitted for shipping and water transportation.

WK04 has a value approaching WK01. While the downstream of Way Kuripan River (WK05) has a WQI value of 38.3, including in the highly polluted category (Class V). The source of pollution was caused by market or shops (Purwata and Karang City urban village), home industry, temporary shelter which is widely located along the river flow, the flow of in and out of traditional fishing boats and from dense settlements in Purwata. River water in the downstream area can not be used for drinking water, whereas for fisheries only fish can live in permissible dirty water. Sailing and water transportation were permitted even though there was still polluted. Overall the Way Kuripan River condition from upstream to downstream has been contaminated with varying levels of pollution.

Geospatial Analysis

Spatial analysis describes an approach which study entities using geographic properties. It also defined as an approach to applying statistical analysis and other analytic techniques to geo-reference dataset [18]. All sampling points and result of measurement were plotted based on its geographical information on thematic map. The maps showed not only the information of water quality value, but also illustrated the relationship between water quality distribution and surrounding land use.

Sampling point of Way Kuripan River spatially spread from coastal line to the hinterland in around 2.8 km of length. The land use surrounding sampling point illustrated urban or settlement area (Fig. 3), in which the forest area found at north and west part of the area.

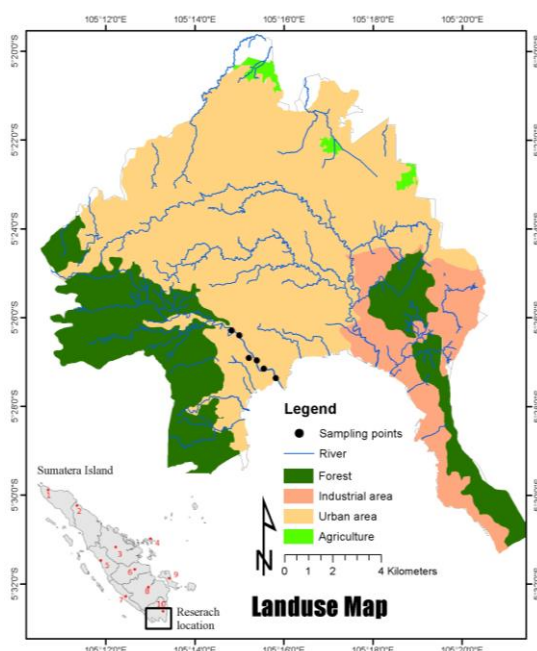


Fig.3 Land use map

As described in laboratory test of water quality, the sampling point of WK02 and WK03 illustrated highly polluted water. This area consist of two different sub-district in both side of the river, in which mostly covered by urban area.

Mapping the water quality parameters using spatial analysis, a Geographical Information System approach, can be useful for taking quick decisions as graphical representation. It would be easy to facilitate government or policy maker in taking a decision especially in water resources management. The analysis specially designed for handling a geographical data. The advantage of using a geospatial analysis is handling attribute data in conjunction with spatial features.

CONCLUSION

In general, the water quality of Way Kuripan River is in contaminated status with varying level of pollution. The results of the analysis show that WK01 and WK04 have WQI values of 70.3 and 70.11, with the category of river water quality of class III (slightly contaminated). At the sample points of WK02 and WK03 have WQI values of 55.8 and 53.8. The water quality at the sample points is included in polluted category (Class IV). The value of WQI at the sample point of WK05 is 38.3 with the status of highly polluted water quality (Class V). The results of this study can be used as a reference by the local government to overcome the contamination of Way Kuripan River water with water pollution control strategy, utilization, monitoring and maintenance of water resources in Way Kuripan watershed.

REFERENCES

- [1] Cordoba E. B., Martinez A. C., and Ferrer E. V., Water quality indicators: comparison of a probabilistic index and a general quality index. The case of the Confederacion Hidrografica del Jucar (Spain). *Ecological Indicators*, vol 10, pp 1049–1054, 2010.
- [2] Al-Obaidy A. M. J. and Mouloud B. K. J., Evaluating raw and treated water Quality of Tigris River within Baghdad by index analysis. *Journal of Water Resource and Protection*, Vol. 2, pp. 629 – 635, 2010.
- [3] Cude C., Oregon Water Quality Index: a tool for evaluating water quality management effectiveness, *Journal of American Water Resource Association*, Vol.37, No.1. 2001.
- [4] Brown R. M., Clelland N. I. Mc., Deininger R. A. and Tozer R. G., A water quality index - do we dare. *Water and Sewage Works*, vol. 2, pp. 339-343, 1970.

- [5] CCME (Canadian Council of Ministers of the Environment). Canadian Water Quality Guidelines for the Protection of Aquatic Life: CCME Canadian Council of Ministers of the Environment, Winnipeg, Manitoba. 2001.
- [6] Kannel P. R., Lee S., Lee Y. S., Kannel S. R. and Khan S. P., Application of water quality indices and dissolved oxygen as indicators for river water classification and urban impact assessment. *Environmental Monitoring and Assessment*, Vol. 132, pp.93-110, 2007.
- [7] Rahman Z. A., Water Quality Management in Malaysia. Department of Environment Malaysia. Article retrieved in 2002 from internet website: <http://www.iges.or.jp/jp/ltp/pdf/fr2.pdf>.
- [8] Al-Shujairi S. H., Develop and apply water quality index to evaluate water quality of Tigris and Euphrates Rivers in Iraq., *International Journal of Modern Engineering Research*, 3 (4), 2119, 2013.
- [9] DOE (Department of Environment Malaysia). Malaysia Environmental Quality Report 2000. Department of Environment, Ministry of Science, Technology and Environment Malaysia, pg 86. Maskha Sdn. Bhd: Kuala Lumpur. 2001.
- [10] Kim A.G and Cardone C. R., Scatterscore a reconnaissance method to evaluate changes in water quality. *Environmental Monitoring and Assessment*, Vol. 111, pp.207-295, 2005.
- [11] Liou S.M., Lo S. L. and Wang S. H., A generalized water quality index for Taiwan. *Environmental Monitoring and Assessment*, vol 96, pp. 35-32, 2004.
- [12] Meher P.K., Sharma P., Gautam Y. P., Kumar A. and Misha K. P., Evaluation of water quality of Ganges River using water quality index tool. *Environment Asia*, 8 (1), 124, 2015.
- [13] Sargaonkar A. and Deshpande V. Development of an overall index of pollution for surface water based on a general classification scheme in Indian context. *Environmental Monitoring and Assessment*, Vol. 89, pp. 43-67, 2003.
- [14] Tsegaye T., Sheppard D., Islam K. R, Johnson A. W., Tadesse, Atalay A. and Marzen L. Development of chemical index as a measure of in-stream water quality in response to land use and land cover changes. *Water, Air, and Soil Pollution*, Vol.174, pp. 161-179, 2006.
- [15] Sari I. and Omar W. M. M., Assessing The Water Quality Index of Air Itam Dam, Penang, Malaysia, *Proceeding of International Conference on Environmental Research and Technology (ICERT)*, pp. 601-605, 2008.
- [16] Effendi H., Telaah Kualitas Air: Bagi pengelolaan sumber daya dan lingkungan perairan, pp. 19, 2003.
- [17] Republik Indonesia. Peraturan Pemerintah Nomor 82 Tahun 2001. *Tentang Pengelolaan Kualitas Air dan Pengendalian Pencemaran Air*. Jakarta; Sekretaris Negara. 2001.
- [18] Hemakumara, GPTS, and Rainis, Ruslan. Geo-statistical modeling to evaluate the socio-economic impacts of households in the context of low-lying areas conversion in Colombo metropolitan region-Sri Lanka. Paper presented at the AIP Conference Proceedings. 2015.

THE AWARENESS OF ENVIRONMENT CONSERVATION BASED ON OPINION DATA MINING FROM SOCIAL MEDIA

Kunyanuth Kularbphetong¹

¹Faculty of Science and Technology, Suan Sunandha Rajabhat University, Thailand

ABSTRACT

Social media have become an important role in society and people widely use social media platforms to express and criticize their opinion. With the previous studies, there is much of research to develop and harvest information and knowledge from social media data for decision making and prediction. The awareness of environment conservation has become a significant issue nowadays and building and raising environment awareness is to conserve and protect the nature for the benefits of humans. Opinion mining is one of text mining approaches to assess the attitude in a given subject and the attitude may be positive or negative opinion. The paper proposes to conduct social media opinion mining in case of the awareness of environment conservation of Thai people. This study shows that social media effects to build and raise the awareness of environment protection and furthermore this research can apply to other fields and industries aspects as well. .

Keywords: Sentiment analysis, opinion mining, awareness, environment conservation, social media

INTRODUCTION

Urban growth in all regions of the world is undeniable, especially in capital cities or economy cities, and the growth of the city means the movement of a large group of people who come together to pursue a career and live. This situation causes enormous consumption and environmental degradation. Environmental crisis is one of the major problems in the world that affects the viability of the most biological systems in the future. Therefore, the requirement to quickly resolve environmental degradation problem is an essential to cultivate good moral traits in environmental awareness. The Environment awareness is the foundation of the psychology to acknowledge the human actions that cause to deteriorate environment and the result will get back to destroy human life.

Nowadays, social media are increasingly used to disseminate information and express everyone's opinion to an online society where users can communicate and convey their attitude through social network. Social media has become a new digital medium that has played a significant role in the rapidly changing society in terms of being part of the current news media process. When the internet technology is growing by leaps and bounds, social media takes an action to be a channel for news media and affects to the digital economy of the country. There are many kinds of social media platforms according to the purpose of using as following [1]: social networking (Facebook, LinkedIn, Google+), microblogging (Twitter, Tumblr), photo sharing (Instagram, Snapchat, Pinterest), and video sharing (YouTube, Facebook

Live, Periscope, Vimeo). Social media becomes a vital part of everyday life and the number of social users has rapidly increased to reach 3.196 billion, up 13 percent year-on-year [2]. Therefore, the use of social media to disseminate information is a new phenomenon of Thai social life and it has an influence in people's behavior and decision making in various fields.

Also, the trend of using online media is likely at a rapid pace and the influence of user generate content plays an increasingly important role to impact on people's behavior because user generate content is more reliable and generates faster and stronger streams. The power of social movement through online media acts as the communication mechanisms to interact and integrate online community for driving the purpose of social issues in Thai society.

Opinion mining is one of text mining approaches to assess the attitude in a given subject and the attitude may be positive or negative opinion and sentiment analysis is the analysis of emotions and feelings from the text to express the feelings of people such as positive feelings or negative feeling. The information of people think has always been a crucial part to influence on decision making. Social media sentiment helps to understand the perceived positive or negative mood what people post on social media This research proposes to conduct social media opinion mining in case of the awareness of environment conservation of Thai people to understand and perceive the feeling of the awareness of environment conservation of Thai people.

RELATED WORKS

A literature reviews of relevant researches for exploration and adaptation information shows that sentiment analysis is the instrument to understand what people think and what feeling they are. It amalgamates with many other fields like natural language processing, statistics, and text analysis to extract the emotional feeling from text. According to M. Baykara and U. Gürtürk [3], tweets from twitter were analyzed to classify users' categorization in news, politics, and culture. Bollen et al. [4] investigated the tweets posted on Dow Jones Industrial Average (DJIA) to measure positive vs. negative mood and Google-Profile of Mood States (GPOMS) by using Self-Organizing and Fuzzy Neural Network and the result shown that the mood states will directly affect investment decisions and stock market. Facebook posts were performed on sentiment analysis to measure data available to public domain [5]. The comments of fan page Facebook and tweet of Twitter were classified into some categories, positive, negative, and neutral sentiment by using TF-IDF in Indonesia; Gojek, Grab, and Uber and the results indicates that the comments on social media are evaluated the performance of these business transport online [6]. Barbosa et al. [7] propose a method to identify sentiments from tweets and the data sources was provided by labels to solve different bias. The social media analytics engine, by employed fuzzy similarity-based classification method, was proposed to automatically classify text into sentiment categories (positive, negative, neutral and mixed) and it is able to collect, filter, classify, and analyze social media text data and describes and predicts analytic information on dashboard [8]. Also, explained extends six emotions on new smart services over mobile devices, the approach is used emotional dictionaries and considers linguistic parameters to identify results [9].

There are several approaches proposed to extract information from social media and it can be classified to 2 main techniques as follows: statistical technique and machine learning technique. Linear discriminant analysis (LDA), one of the statistical technique, was applied to explore relationship between Facebook fan pages and visitor engagements of the exhibitions [11] and logistic regression was used to analyze textual data from social [12]. Machine Learning was applied to extract information from text data and for example, Gurkhe et al. [10] implemented the machine extracted the polarity (positive, negative or neutral) of social media data set by using naive Bayesian technique. With the advance technologies, the enhancement of this research is continually move forward to widespread in various other fields.

RESEARCH METHODOLOGIES

This section describes how to conduct this research and the methodologies applied in this project as follows: Data preparation; Feature extraction; Model Building and Testing and Evaluation.

Data Preparation

In the first stage, data were collected form social media and internet web sites and it was posted to express the opinion about environment conservation. Tweepy API [13] is used to retrieve the tweets and data, like twitterID, hashtag, date of created tweet, tweet text, and retweet count, was stored in the database. Some selected Thai hashtags were presented in Table 1. The second type of data source is news and related web sites related to the concept of environment conservation. Data is the text format that requires to be preprocessing to clean and manage data before analyzing text mining. Preprocessing step of the data set is following: removing URLs, hashtags, username, and symbols; replacing the emotion icons and correcting the spelling words.

Table 1 Example of selected Thai hashtags

#รักโลก #รักษ์โลก #โลกร้อน #ประหยัดไฟ #พกถุงผ้า #ปลูกต้นไม้ #ใช้จักรยาน #ประหยัดน้ำ #คัดแยกขยะ #งดถุงพลาสติก #รักษาสีสิ่งแวดล้อม #ขยะรีไซเคิล #ขยะย่อยสลาย #อนุรักษ์พลังงาน #ลดเลิกเพื่อช่วยโลก #ปลูกป่าช่วยชาติ #รักษาป่าไม้ #ลดมลพิษ #อนุรักษ์สิ่งแวดล้อมและป่าไม้ #วันรักต้นไม้ #พื้นที่สีเขียว #รักษาผืนป่า #ปลูกต้นไม้ #ลด ค เมิ อ ง ร ้อ น ด ั ว ย มี อ ร ะ #ปลูกฝังจิตสำนึกรักษ์โลก #การจัดการขยะ #ป ล ู ก ป ่า เ ท ศ พ ร ะ ก ี ย ร ติ #ประหยัดพลังงานไฟฟ้า #จิตอาสา #ทดแทนคุณแผ่นดิน #ปลูกเพื่อให้

However, Thai language is different from English because it's no marks or symbols to indicate the scope of each word or sentence.

The figure 1 was shown the system overview and data was collected from tweeter and related web sites. LEXiTRON Corpus was used to analyze words and meaning of words [14]. This research was specified related domains collected from similar related information.

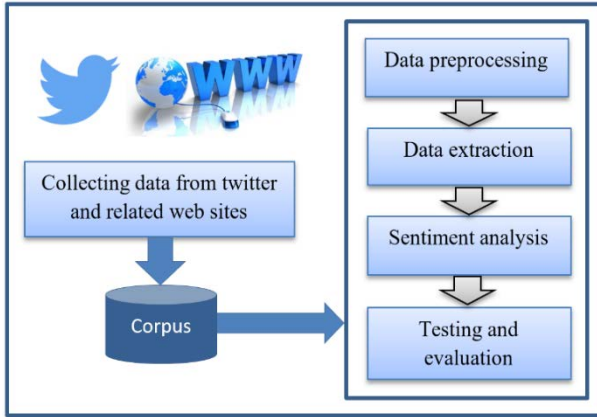


Fig. 1 The System Overview.

Feature Selection

Feature Selection is the reduction of data size by reducing the original data size and losing key features using the selection technique. This process of extracting comments is to pull out the feature of the comment to determine what features use this project. Thai stop word is removed the insignificant words without meaning change. For example, the sentence is “ร้าน กาแฟ หลายร้าน ถ้า พก แก้ว ได้ ส่วนลด ด้วยค่ะ ช่วยลดโลกร้อนและประหยัดตั้ง” and the result was presented in figure 2.

ร้าน|กาแฟ |หลาย |ร้าน| ถ้า |พก| แก้ว| ได้| ส่วนลด
|ด้วย|ค่ะ| ช่วย |ลดโลกร้อน| และ| ประหยัด| ตั้ง

Fig. 2. Example Sentence.

For instance, the word “ค่ะ” is a non-significant word and in the feature selection process, the feature will be cut off. Thai segmentation technique is applied to extract data and data extraction stage is the process to extract data and labels the training set, annotated positive, negative or neutral, to identify the category of text by hand. The data consists of 2,964 sets and assigned weight each set as a positive, negative and neutral review. Labels were used as 1 for a positive review, 0 for a neutral review and -1 for a negative review. TF-IDF (Term Frequency-Inverse Document Frequency) was applied to determine indexing for using for training process.

$$W_{(f,d)} = TF_{(f,d)} \times IDF_{(f)} \quad (1)$$

$$IDF_{(f)} = \log \frac{|D|}{|DF_{(f)}|} \quad (2)$$

Where $TF_{(f,d)}$ presents the frequency of the feature (f) in documents (d) and $W_{(f,d)}$ shows the weight of a feature (f) in (d). $|D|$ explains the number of

documents in the training data set (Training Set) and $|DF_{(f)}|$ is the number of documents that feature (f) appears. $IDF_{(f)}$ is inverse document frequency used to identify positive, negative or neutral. Unlike TFIDF mentioned above, this study divides data into two parts, one for positive data, and one for negative. Furthermore, according to K. Ghag, K. Shah [15], SentiTFIDF was applied to this project to classify the positive, negative and neutral emotional mood and then the set of emotional words were stored in database to be further next process.

Model Building

To build model, Naïve Bayes and Support Vector Machine (SVM) were used to build a sentiment classifier. The data were divided to be 2 sets: training and testing sets with the ratio 70:30.

Naive Bayes classifier, based on Bayes' theorem, is one of the crucial techniques in machine learning used to many fields like customer segmentation or sentiment analysis.

$$P(c|x) = \frac{P(x|c)P(c)}{P(x)} \quad (3)$$

$P(c|x)$ is the posterior probability of the attribute X that has set the label of class C. $P(x|c)$ is the likelihood that the data in class C contains attribute X. $P(c)$ is prior probability of class C. $P(x)$ is the predictor prior probability.

Support Vector Machine is the significant supervised algorithm that can solve a classification problem and the concept of SVM is to define data in the feature space and create hyperplane to separate different class labels.

Testing and Evaluation

Accuracy, recall, precision and F-measure were used to evaluate the performance of text models.

$$precision = \frac{TP}{TP+FP} \quad (4)$$

$$recall = \frac{TP}{TP+FN} \quad (5)$$

$$Accuracy = \frac{TP+TN}{TP+FP+FN+TN} \quad (6)$$

$$F - measure = \frac{2 \times precision \times Recall}{precision + Recall} \quad (7)$$

Where TP represents the number of correctly classified documents (True Positive), FP is all documents retrieved (False Positive) and accuracy is the percentage of documents correctly classified, recall is the percentage of relevant documents correctly retrieved (TP) with respect to all relevant documents (TP + FN) and F-Measure is consisted of a single measure Precision (P) and Recall (R).

EXPERIMENTAL RESULTS

After preprocessing data, to label data with polarity words from the comments were applied to set train data of extracted words. Then, sentiment analysis was used to label each comment to three groups of similar comments: positive, negative and neutral based on their polarity scores. The result gained from the experiment by using Naïve Bayes classification and SVM algorithms as shown in table 2. The data from this project was collected from social network and accuracy, precision and F-measure was used to evaluate the effective of classification models.

Table 2 classification performance

	Accuracy	Precision	Recall	F-score
SVM	80.5	82.5	85.7	83
Naïve bay	72.6	79.7	76.8	74.2

The SVM classification model is better than Naïve bay with accuracy of 80.5, precision of 82.5, recall of 85.7 and f-measure of 83 as displayed in fig 3. The result when using the model shows that the model can use to detect the concept of environment conservation and the positive awareness is more the other awareness in the number of words and the average length of Tweet's on data set.

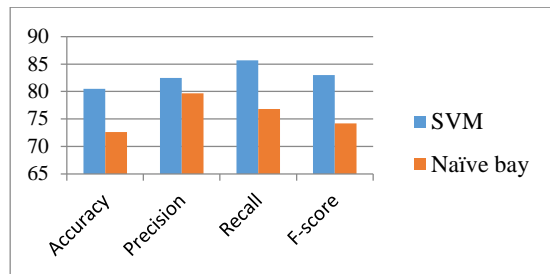


Fig. 3. The Results of Classification Performance.

CONCLUSION

The awareness of environment conservation has currently become an important topic and to educate and implant environment awareness social media has influenced in society and people. Therefore, the sentiment analysis is the powerful approach to identify opinion, to extract opinion's feature, to classify sentiment, and to display the results in visualization and summarization. This research describes the methods to conduct social media opinion mining in case of the awareness of environment conservation of Thai people. This approach collected data from twitter and related web sites and then it shows how to preprocess and extraction the results. The results show that social media effects to build and raise the awareness of environmental protection and furthermore this

research can apply to other fields and industries aspects as well. However, there are some errors with word wrapping and comment extraction because of the typing error and occurring of new social words.

ACKNOWLEDGEMENTS

The authors gratefully acknowledge the financial subsidy provided by Suan Sunandha Rajabhat University.

REFERENCES

- [1] Warren Jolly. (2018). "The 6 Most Effective Types of Social Media Advertising in 2018", ECOMMERCE MARKETING. Available: <http://www.bigcommerce.com/blog/social-media-advertising/>
- [2] Dave Chaffey. (Mar, 2018). "Global social media research summary 2018", Available : <https://www.smartinsights.com/social-media-marketing/social-media-strategy/new-global-social-media-research/>
- [3] Muhammet Baykara and Uğur Gürtürk, "Classification of social media shares using sentiment analysis", proceeding of International Conference on Computer Science and Engineering (UBMK, 2017) DOI: 10.1109/UBMK.2017.8093536
- [4] Bollen, J., Mao, H., and Zeng, X.-J., "Twitter mood predicts the stock market", Journal of Computational Science vol. 2(1):1–8, 2010.
- [5] Federico Neri, Carlo Aliprandi, Federico Capeci, Monsterrat Cuadros, Tomas, "Sentiment Analysis on social media", IEEE/ACM International conference on Advances in Social Networks analysis and mining, pp. 919-926, 2012.
- [6] M. H. Saragih and A. S. Girsang, "Sentiment Analysis of Customer Engagement on Social Media in Transport Online," in International Conference on Sustainable Information Engineering and Technology (SIET), pp. 24–29, 2017.
- [7] L. Barbosa, J. Feng. "Robust Sentiment Detection on Twitter from Biased and Noisy Data". COLING 2010 Poster vol, pp. 36-44.2010.
- [8] Wang, Z., Chong, C. S., Lan, L., Yang, Y., Ho, S. B., & Tong, J. C., "Fine-grained sentiment analysis of social media with emotion sensing", Presented at the Future Technologies Conference, San Francisco, CA, USA. Dec. 2016, doi:10.1109/FTC.2016.7821783

- [9] Athena Vakali, Despoina Chatzakou, Vassiliki Koutsonikola and Georgios Andreadis, "Social data sentiment analysis in smart environments extending dual polarities for crowd pulse capturing", 2013, Available: <https://pdfs.semanticscholar.org/1b2c/374cae2e5c57965211bb5b715b4b45d31c3.pdf>
- [10] Lee, T., Shia, B., & Huh, C., "Social Media Sentimental Analysis in Exhibition's Visitor Engagement Prediction", American Journal of Industrial and Business Management, 06(03), pp. 392-400, 2016.
- [11] Virgile Landeiro , Aron Culotta, "Robust text classification in the presence of confounding bias", Proceedings of the Thirtieth AAAI Conference on Artificial Intelligence, , Phoenix, Arizona, Feb 2016.
- [12] Dhiraj Gurkhe, Niraj Pal and Rishit Bhatia, "Effective Sentiment Analysis of Social Media Datasets using Naive Bayesian Classification", International Journal of Computer Applications (0975 8887) vol. 99 - No. 13, August 2014
- [13] Tweepy API, Available : <http://www.tweepy.org/>
- [14] LEXITRON, Available: <https://www.nstda.or.th/th/nstda-knowledge/11180-lexitron>
- [15] K. Ghag, K. Shah, "SentiTFIDF-Sentiment classification using relative Term Frequency Inverse Document Frequency", International Journal of Advanced Computer Science and Applications, vol. 05, no. 02, pp. 36-43, 2014.

LIFE CYCLE IMPACT ASSESSMENT OF NEW GROUND MATERIAL AND EMBANKMENT CONSTRUCTION METHODS CONSIDERING RECYCLING

Hideyuki Ito¹, Kento Aimon² and Takahiro Fujii³

^{1,3}College of Science and Technology, Nihon University, Japan; ²Taisei Corporation, Japan

ABSTRACT

In Japan, the conventional cut-and-fill method is often used in banking construction methods. However, this construction method is pointed out that it causes land subsidence and/or landslide in soft ground. For solving these problems, various new construction methods using the ground materials such as EPS (styrofoam), recycled foamed waste glass and expanded polystyrene beads have been developed as new lightweight and workable composite geomaterials. These new construction methods are believed to be effective for construction on soft ground and landslide-prone areas. In existing researches of this field, they aimed to identify areas for improvement and the problems associated with the use of these new ground materials. However, there are few researches that focused on negative impacts to land use, by exhausting air pollution and GHGs (Green House Gases) with recycling from the perspective of environmental economics field. Thus, in this research, we compared conventional cut-and-fill method and some new ground materials such as the expanded polystyrol construction method using the new EPS geomaterial, the lightweight embankment construction method with EPS beads and the foamed waste glass construction method using embankment material with recycled waste by analyzing the negative impacts to land use considered ecosystem services and life cycle cost (LCC) including external cost by emissions of GHGs and air pollutants such as SO_x and NO_x using life cycle impact assessment analysis.

Keywords: Life Cycle Assessment, Life Cycle Impact Assessment, Life Cycle Cost, New Ground Material

INTRODUCTION

In Japan, social assets including roads that were constructed from the postwar period to the high-growth period are facing a renewal period. In this context, it will be important from now on for establishing a circulation-type society that include the reuse of materials recycled from wastes and the selection of environmentally friendly construction methods. Currently, the conventional cut-and-fill method is most widely used among embankment construction methods. The conventional cut-and-fill method is considered to have a chance of causing ground sinking and/or landslide at soft grounds and the areas likely to experience landslide, construction methods that take advantage of new ground materials like expanded polystyrene (EPS) are believed to be effective for the construction on soft grounds and the areas likely to experience landslide because of their lightweight properties and construction properties, etc.

While there are previous researches such as a comparative analysis done by Ito et al. [1] on the influences and costs caused to environments by the various construction methods and a study performed by Ochiai et al. [2] in which the potential of mixed ground materials made from wastes is discussed.

However, no research has ever been conducted where the impacts made by new recycling-friendly

ground materials on land use including air-pollution substances, global greenhouse gas (GHGs) and ecosystem services are comprehensively assessed as external costs.

Thus, the purpose of this research is to do a comparative analysis by life cycle impact assessment (LCIA) for each kind of embankment construction methods using new ground materials. Specifically, this research performs, while taking account of the presence or absence of the recycling of wastes, a comprehensive assessment of external costs converted to a currency for the respective embankment construction methods including the external costs attributable to the emission of air-pollution substances and GHGs and those resulting from the land use at every lifecycle stage.

LITERATURE REVIEW

In the previous researches about the lifecycle assessment (LCA) that pay attention to new ground materials and the presence or absence of the recycling of wastes, Ito et al. [1] revealed that environmental burdens and lifecycle costs could be reduced in each kind of embankment construction methods utilizing new ground materials (EPS) and wastes (expanded beads and expanded waste glass) if recycling would be done while considering lifecycle stages. However,

any external cost was not considered in this research.

Ochiai et al. [2] organized additional values, physical natures and the grouping of constitutional materials of various mixed ground materials in their previous researches regarding the materials constituting mixed ground materials, which reported more than one research result on mixed ground materials. In addition, they assessed environmental burdens and the recycling efficiency of mixed ground materials made from wastes. However, since these researches figured out environmental burdens only from the production process of embankment materials, environmental burdens were not analyzed through the entire lifecycle.

Amano et al. [3] visualized the potential of recycled materials in paving roads. More specifically, they revealed that environmental burdens could be reduced to a maximum by around 40% with the use of recycled materials at both the stages of construction and maintenance/repair, by totaling the environmental burdens and costs associated with the construction of paved roads and their maintenance/repair for respective stages of initial construction and maintenance/repair and by evaluating the lifecycle of paved roads from both the sides of environmental burdens and costs. Both of the environmental burdens and costs for asphaltic pavement at the stage of its maintenance/repair accounted for 40 to 50% of those at its entire stages. This research, however, didn't deal with an impact on road structures and surrounding environments in the entire lifecycle.

In their previous research that employed LCA and environmental economy assessment methods, Ito et al. [4] performed an LCIA of biodiversity and ecosystem services based on the extinction risk of living things while focusing on the construction of wooden residences and steel residences. Then, this research assessed an impact on biological ecosystems and ecosystem services that would disappear due to the alteration and occupation of land occurring in the entire lifecycle. However, this research only made an assessment of residence construction, not new ground materials.

Inazumi et al. [5] previously conducted an assessment research of social and environmental efficiency regarding the recycling of construction polluted mud as a ground material. Specifically, they discussed an evaluation method of social and environmental efficiency assessing the recycling of wastes from a social perspective by internalizing environmental burdens as an environmental cost, in

addition to environmental assessments, LCAs using environmental accounting methods, social and environmental efficiency and cost calculation utilizing the Monte Carlo simulation. However, this research dealt with construction polluted mud and its impact assessment of land use was not enough.

Kamemura et al. [6] implemented a research with regard to the lifecycle cost assessment of civil engineering structures with considering the risk. Specifically, it showed the size and characteristics of risks as well as the effects of objects by optimizing cost statistics regarding the construction costs for structures and their operation/maintenance costs while they are in use. However, this research only made an assessment on the lifecycle cost.

Omine et al. [7], after organizing the additional values, physical natures and the grouping of constitutional materials of various mixed ground materials, estimated the CO₂ emission at the production stage of cement stabilization soil, bubble mixed lightweight soil, fluidization disposal soil, clay mixed calcination fixation agent and tire chip mixed soil, although they didn't assess impacts resulting from polluted substances other than CO₂.

While Minegishi et al. [8] explained about the strength and impacts of repeated stress ratios made on the deformational characteristics of EPS mixed lightweight soil, Kagawa [9] analyzed the characteristics and physical strengths as earth fill of the EPS civil engineering method as well as the durability, weather resistance, environment in soil and drug resistance of EPS. Such previous research analyzed the strength, etc. of EPS but didn't make its lifecycle assessment.

Onitsuka et al. [10] demonstrated the potential of expanded waste glass materials as new materials by doing an experiment for improving the engineer characteristics of expanded waste glass materials and fundamental road bases, although they didn't implement an environmental assessment with the LCA method.

It is concluded from the above that no research has ever, while focusing attention on respective construction methods using new ground materials, conducted a comprehensive assessment in terms of external costs resulting from the emission of air-pollution substances and GHGs as well as those due to the land use including ecosystem services.

METHOD AND SYSTEM DETAILS

In this research, the Mineoka area in mountainous roads located in the southern part of Chiba prefecture

was selected as case study area as well as in the previous research [1], and then compared above 4 construction methods. The summary of each embankment construction method using new ground materials is shown in Table 1.

We also set a same functional unit that provides a logical basis for comparing the environmental performance of alternatives for applying LCA to these four construction methods based on the previous research [1]. We defined the target road condition (2 lanes, 7 m wide and 1m long) as a functional unit and then, it was hypothesized that the inclined a the angle between the mountain and the road is 35°.

Setting of Recycle Method in Each Construction Method

For the purpose of analyzing recycled embankment materials and environmental burdens, this research conducted a survey on how to recycle embankment materials by doing a questionnaire survey and an interview survey with ten construction companies and then set a recycling method based on the results of such surveys. In order to take account of recycling, this research based on the presumption established from the results of the research by Ito et al. [1] that roads would be reconstructed in 100 years from the start of their service, assumed that embankment construction work would be done four times in total as well as the system boundary.

In addition, since the interview survey had found that recycling was difficult in the EPS construction method, it was assumed that roads would be reconstructed every 100 years with virgin materials. This research aims to identify future tasks and improvement plans through the calculation of the total environmental burdens and costs generated depending on the presence or absence of recycling.

Estimation Method for External Costs Attributable to Air Pollution and GHGs

The impacts made including on environments, human health and social assets by air-pollution substances and GHGs that are emitted in road construction throughout the overall lifecycle are integrated in terms of a currency. In this research, a LCIA was performed utilizing the values representing the emission amounts of air-pollution substances and GHGs estimated in the research by Ito et al. [1] External costs were estimated in a way to integrate them by multiplying the total amounts of air-pollution substances and GHGs that are emitted in all lifecycle stages by the original unit for external costs per unit emission amount in respective environmental impact fields used in the Life-cycle Impact assessment Method based on Endpoint modeling (LIME2) environmental impact integration software [11].

Estimation Method for External Costs Caused by Influences on Land Use

The impacts made on land use by the alteration and occupation of land in the entire lifecycle are substantial. In this respect, the impacts given on ecosystem services from the perspective of land use are assessed in term of a currency with classifying land use into four categories such as forests, tidelands, waters and desserts. Regarding the analysis method, the influenced area is calculated by land use classification for respective construction methods and then the external costs resulting from the loss of ecosystem services are estimated.

First, the recycling methods and the utilization amounts of materials per unit area for respective construction methods that were set in the previous researches are shown in Table 2 and Table 3. Then, the setting of land use classification is illustrated in

Table 1 Summary of each embankment construction method using new ground materials

Expanded Polystyrol Construction Method	EPS blocks are stacked as embankment materials and are integrated by dedicated clamps. When stacked, these ultra-lightweight embankments have advantages of their compressive resistance, durability, and independent stack design.
Lightweight EPS Bead Mixture Method	Lighter soil is used, comprising EPS beads mixed with soil and sand. This method is effective for use in soil fills on soft ground and in landslide-prone areas due to its capability of reducing the applied load on the ground more effectively than ordinary soil and sand.
Foamed Waste Glass Method	Foamed waste glass is a porous embankment material manufactured by pulverizing, burning, and foaming recycled waste glass. The specific gravity and degree of water absorption can be controlled during manufacturing according to the requirements of specific applications. Hence, foamed waste glass is used in a wide range of applications including civil engineering, greening of slopes and rooftops, agriculture, water purification, and heat insulation. This material is lightweight, water permeable, water retentive, fire resistant, and a good thermal insulator.

Table 4 and the conversion factors for calculating impacted area by fuel/energy consumption in each lifecycle based on JEMAI-LCA database [12], existing research [4] and the hearing survey to construction companies are shown in Table 5.

The estimated results of influenced land area per unit amount are obtained by figuring out the influenced area per functional unit based on the ultimate recoverable reserves of materials used in respective construction methods and such area. Table 6 shows the estimated/calculated results of impacted area by land use classification for respective construction methods.

Table 2 Recycling methods

Construction method	Recycle (first time)	Recycle (from second time)
Cut & Fill (R)	Virgin material is used for first time	Used banking material mixed with cement is reused from second time
EPS (V)	No recycle because EPS block cannot be recycled	
Lightweight EPS bead mixture method (V)	Virgin material is used for first time	Used banking material mixed with cement is reused from second time
Lightweight EPS bead mixture method (R)	After used styrofoam was blasted, it is used by mixing soil and cement	EPS beads is removed from demolished banking material and then recycle the styrofoam
Foamed waste glass method (R)	Virgin material is used for first time	Demolished banking material is recycled

Table 3 Utilization amounts of materials per unit area for respective construction methods

	Soil	Cement	EPS Block	Aluminum	Zinc	EPS beads	Foamed waste glass	Clamping materials
Unit	kg/m ²	kg/m ²	m ³ /m ²	kg/m ²	kg/m ²	kg/m ²	kg/m ²	kg/m ²
Cut & Fill (R)	15,750	645	-	-	-	-	-	-
EPS (V)	-	-	367.08	2.15	1.70	-	-	734.17
Lightweight EPS bead mixture method (V)	19,250	1,790	-	-	-	161.22	-	-
Lightweight EPS bead mixture method (R)	19,250	1,790	-	-	-	161.22	-	-
Foamed waste glass method (V)	-	-	-	-	-	-	5,250	-
Foamed waste glass method (R)	-	-	-	-	-	-	5,250	-

Table 4 Land use classification of impacted area

Energy	Crude Oil	Electricity	Natural Gas	Coal
Country	Saudi Arabia	Japan	Australia	Australia
Type of Land Use	Oil field Desert area	Tideland	Sea area	Mine
Impact	Impact by oil field development	Impact to tideland by reclamation for constructing thermal power station	Impact by developing natural gas field	Impact by coal mine development

RESULTS AND DISCUSSION

Estimated Results of External Costs Due to Emission of Air-Pollution Substances and GHGs

The estimated result of external costs attributable to the emission of polluted air substances and GHGs demonstrated that the external costs for the EPS

Table 5 Conversion factors for calculating impacted area by fuel/energy consumption

Estimation Item		Conversion Factor	
Impacted area by obtaining construction materials	Impacted area by obtaining aggregate	4.00E-04	m ² /kg
	Impacted area by obtaining lime	1.10E-03	m ² /kg
	Impacted area by obtaining aluminum	6.88E-05	m ² /kg
	Impacted area by obtaining zinc	3.63E-03	m ² /kg
Impacted area at production phase	Impacted area by constructing and operating refinery	4.02E-03	m ² /kg
	Impacted area by constructing and operating zinc refinery	3.57E-02	m ² /kg
	Impacted area by constructing and operating cement works	7.90E-07	m ² /kg
	Impacted area by constructing and operating manufacturing plant of EPS block	2.92E-05	m ² /kg
	Impacted area by manufacturing clamping materials	4.0E-05	m ² /kg
	Impacted area by manufacturing expandable beads	2.92E-05	m ² /kg
	Impacted area by constructing and operating recycling factory of waste glass	1.10E-02	m ² /kg
Impacted area by recycle facility	Impacted area by constructing and operating recycling factory of styrofoam	1.54E-04	m ² /kg
	Impacted area by constructing and operating recycling factory of steel	6.20E-02	m ² /kg
	Impacted area by reclaiming waste material	1.39E-01	m ² /m ³
	Impacted area by extracting crude oil	2.00E-04	m ² /kg
Impacted area by extracting energy	Impacted area by generating electric power	2.60E-07	m ² /kWh
	Impacted area by extracting natural gas	4.70E-01	m ² /kg
	Impacted area by mining coal	7.50E-04	m ² /kg

construction method were the smallest as shown in Figure 1. Also, it was found that the emission of SO_x being a cause for air pollution would make substantial impacts on the increase in external costs, that the biggest external costs were those for the expanded waste glass materials construction method, and that the said external costs would be in the same range as those for the expanded beads lightweight soil construction method if taking account of recycling.

Table 6 Impacted area by land use classification for each construction method

Construction Method	Total Impacted Area of each Land Use for 300 Years							
	Total Impacted Area (m ²)	Material	Impact to Land		Energy		Total	
		Forest	Forest	Tideland	Tideland	Sea area	Forest	Tideland
Cut & Fill ①V②-④R		36.8	1.0	2189.3	3.8.E-05	0	37.8	2189.3
EPS ①-④V		0	1.0	1.4	1.5.E-04	0.4	1.0	1.4
Lightweight EPS bead mixture ①-④V		38.7	1.0	10703.1	1.8.E-04	0	39.7	10703.1
Lightweight EPS bead mixture ①-④R		38.7	1.0	2675.9	1.1.E-04	0	39.7	2675.9
Foamed waste glass ①-④V		0	1.0	3150.0	1.3.E-03	178.1	1.0	3150.0
Foamed waste glass ①V②-④R		0	1.0	787.5	3.4.E-04	44.5	1.0	787.5

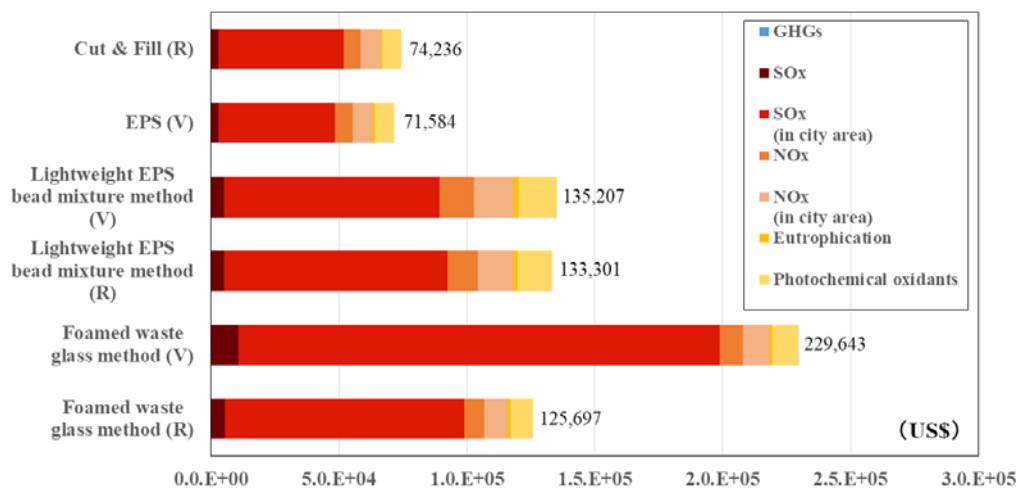


Figure 1 Estimated results of external costs of emission of air-pollution substances and GHGs

Estimated Results of External Costs Caused by Impacts on Land Use

The impacts made on land use by the alteration and occupation of land in the entire lifecycle are substantial and therefore there is a need to assess the impacts on ecological services from the perspectives of land use such as forests, tidelands and waters. In this context, the influenced area was calculated by land use classification for respective construction methods and then the external costs resulting from the loss of ecology services were estimated.

First, the total amounts of fuels and energies per functional unit were estimated according to the JLCA-LCA database [12] and also the interview survey and the total amounts of all raw materials to be used in respective database were calculated. Then, the influenced area by each land use was figured out by multiplying such amounts by respective influenced areas per estimated unit amount. Also, the areas influenced by the collection of construction materials and respective fuels/energies as well as by each land use such as the occupation of factories, etc.

were calculated, then by summing up which influenced areas the influenced areas by land use classification for respective construction methods were figured out. Lastly, external costs were estimated by multiplying the estimated influenced areas by land use classification for respective construction methods by the economic value of ecological services per unit area which was estimated in the previous research.

Consequently, the external costs for the EPS construction method were found to be the smallest as shown in Figure 2 because the estimation was made on the presumption that crude oil being the raw material for EPS blocks would be produced in the desert areas of Saudi Arabia and therefore its impact on ecological services was considered to be small. The external costs for the expanded waste glass materials construction method V which causes a considerable impact on tidelands by occupying the land were estimated to be the biggest. Further, it was shown that external costs would be substantially influenced depending on the presence or absence of recycling.

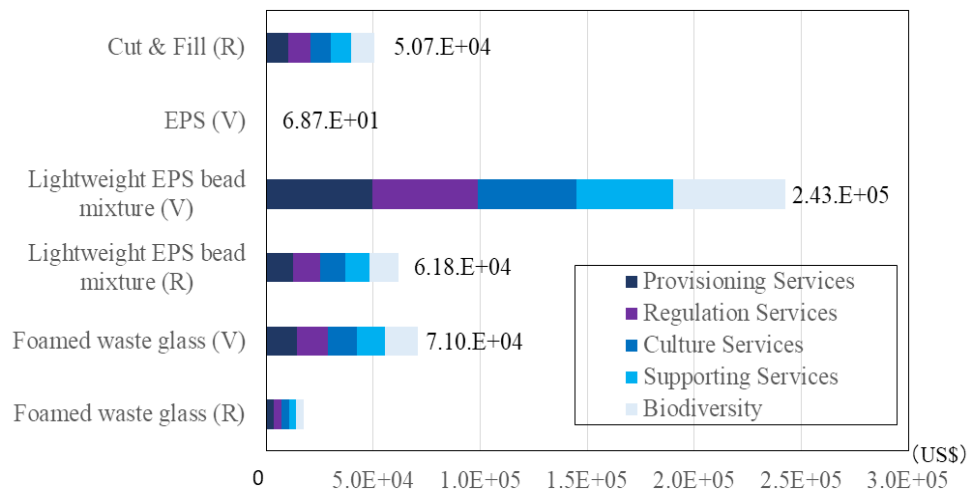


Figure 2 External costs caused by impacts on land use

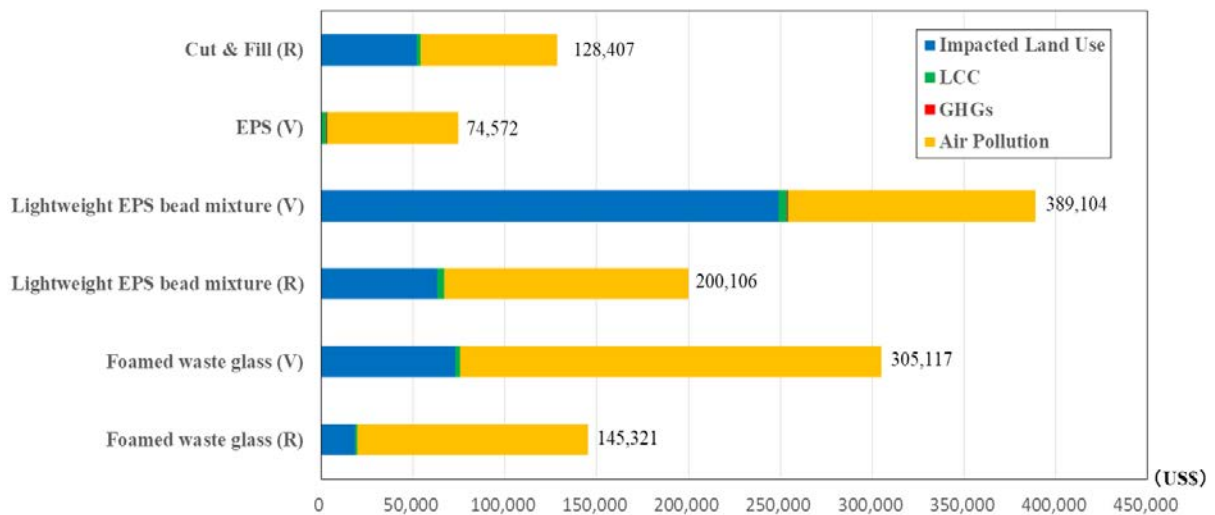


Figure 3 Total external costs of each construction method

Estimated Results of Total External Costs

Figure 3 shows the total external costs by summing up the life cycle cost estimated by existing research [1] and all external costs by emission of GHGs, air-pollution and impacts on land use.

As the result, the total external costs were increased in the order of EPS, cut & fill, foamed waste glass method (R), lightweight EPS bead mixture method (R), lightweight EPS bead mixture method (V) and foamed waste glass method (V).

In addition, it was shown that total external costs would be substantially influenced depending on the presence or absence of recycling. In terms of foamed waste glass method (V), since the external cost of GHGs and air pollution at extraction of raw materials phase was very big, the technical improvement for reducing those emissions is necessary.

CONCLUSION

This research, while paying attention to the presence or absence of recycling, made a comprehensive LCIA including of external costs generated by land use as well as by air-pollution substances and GHGs in addition to market prices. External costs by life stage for respective construction methods were clarified through such effort and accordingly future tasks for reducing the external costs were presented.

From now on, there is a need to identify future tasks including the elaboration of original units for external costs with considering regional characteristics.

REFERENCES

- [1] H. Ito, K. Yamanaka, H. Noguchi, T. Fujii and K. Minegishi, Comparative Analysis of New Geomaterials and Embankment Construction

- Methods Considering Recycling, International Journal of GEOMATE, Vol.13(35), 2017, pp.114-119.
- [2] H. Ochiai and K. Omine, Evaluation of environmental impact and development of mixed composite materials with new additional value. The Foundation Engineering & Equipment, Vol. 32, Aug. 2004, pp. 9-11.
 - [3] K. Amano and K. Makita, Life Cycle Evaluation of the Environmental Loading and Construction Cost in Paving Process, Journal of Japan Society of Civil Engineers, Vol.657, 2000, pp. 57-64.
 - [4] H. Ito and K. Hayashi, Assessment of Biodiversity and Ecosystem Services Utilized Life-Cycle Assessment and Environmental Economic Valuation -Case Study of Wooden and Steel Framed House, Sociotechnica, Vol.12, 2015, pp. 34-42.
 - [5] S. Inazumi, H. Otsu, T. Isoda, and Y. Shigematsu, "Evaluation of social environmental efficiency on recycling of construction sludges as ground materials", Journal of Geological Engineering, Vol. 68, March 2012, pp. 163-174.
 - [6] K. Kamemura, M. Hori, K. Murata and S. Konishi, Life Cycle Cost of Civil Structures Considering Risks, Soil mechanics and foundation engineering, Vol.51(10), 2004, pp. 30-32.
 - [7] K. Omine and H. Ochiai, Evaluation of Environmental Impact and Recycling Efficiency for Composite Geomaterials Using Wastes, Symposium of Environmental Geotechnical Engineering, Vol.6 2005, pp. 203-208.
 - [8] K. Minegishi, K. Makiuchi and R. Takahashi, Strength and Deformation Properties of Lightweight Geomaterials Mixed with EPS Beads, 2001 Annual Meeting of Japan Society of Civil Engineering, 2001, pp. 426-427.
 - [9] M. Kagawa, Lecture. New Materials for Soil Improvement. 4. Method with Expanded-Polystyrene, Material, Vol.40 (449), pp. 242-248.
 - [10] Onitsuka K, Yokoo M, Hara Y, and Yoshitake S, Engineering Properties of Foaming Waste-glass Material and an Example of its Utilization, Journal of Soils & Foundations, Vol. 47 (4), 1999, pp. 19-22.
 - [11] N. Itsubo and A. Inaba, Environmental Impact Assessment Method for Supporting Decision Making, Japan Environmental Management Association for Industry, 700pp, 2010.
 - [12] Japan Environmental Management Association for Industry, Option Data Pack for JEMAI-LCA PRO, Database for JLCA-LCA provided by Japan Environmental Management Association for Industry, 2009.

TRACE ELEMENTS CONCENTRATIONS OF SEAWEED BESIDE MANY CLOSED COPPER MINES IN SADAMISAKI PENINSULA

Erika Ueno¹ and Hiroyuki Ii²

¹ Graduate School of Systems Engineering, Wakayama University, Japan;

² Faculty of Systems Engineering, Wakayama University, Japan

ABSTRACT

About 66 copper mines operated in Sadamisaki Peninsula from middle Meiji to Taisho era although at present all the mines closed. From the previous study, seaweed metal concentration sampled around the Takaura mine was clarified to be high. Metal concentrations of seaweed are generally high compared to metal concentrations of seawater because of bio-concentration process and depend on long term living under surrounding condition. Then, seaweeds were sampled at both copper mine area and non-copper mine area. The mine area is around Sadamisaki Peninsula and the surrounding non copper mine areas are Yashiro Island in Yamaguchi prefecture and Kada in Wakayama prefecture. Copper, iron, manganese, lead, zinc, calcium, magnesium and arsenic concentrations of seaweeds were measured and their concentrations were studied with sampling location, seaweed type and sampling season. As a result, copper, iron and manganese concentrations of green seaweed were 334, 8195 and 1109 mg/kg high, high, arsenic concentration of brown seaweed was 0.6 to 196 mg/kg, high and magnesium concentration in *Ulva* was higher than *Sargassum fusiforme*. Iron and magnesium concentrations in Oshima were high. Oshima is a geology that contains a lot of iron and magnesium. It was found that the concentration of trace elements in seaweed was greatly affected by the surrounding environment and the geology of the growing place.

Keywords: Trace element, Mine, seaweed, *Ulva*, Geology

INTRODUCTION

Seaweed contains many kinds of trace elements, because sea water contains various kinds of elements. The elements are indispensable for human beings and marine creatures [1]. Seaweed gets nutrition and heavy metal by taken in seawater. Then, seaweed stores nutrition and the heavy metals such as arsenic in the body for long term. This characteristic is bioconcentration. It is clear that heavy metal concentration in seaweed is higher than that in seawater by bioconcentration. In previous studies, characteristics of trace element concentration in each region were studied [2]-[6].

The one of the study area is the Sadamisaki Peninsula located in the western part of Ehime prefecture and the area is famous for many closed copper mines operated in Taisho to beginning of Showa era [7]. And development of mines was actively carried out in Taisho era.

Figure.1 shows points of mining trace in the Sadamisaki Peninsula. There were 66 mine traces operated during the heyday. Although at present all mines closed, waste water from some closed mines and from tailings of mines still flows into sea. As the most area of the Sadamisaki Peninsula is mountainous and its coast is steep slope and cliff, waste water directly flows into sea.

Therefore, seaweed sampled around the

Sadamisaki Peninsula can be assumed as seaweed in metal contamination sea. Then, seaweed in the Sadamisaki Peninsula and the other areas of the Seto Inland Sea are sampled and their trace element concentrations are measured and the influence from the surrounding environment is evaluated.

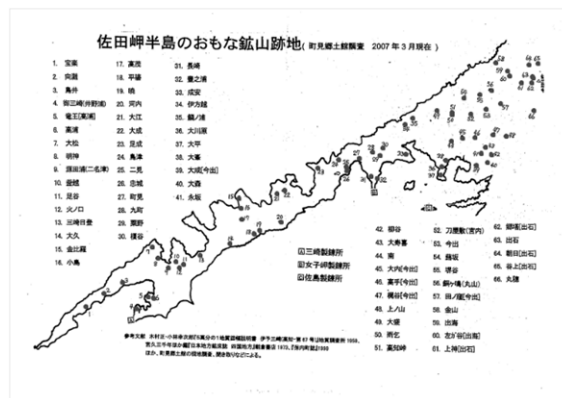


Fig.1 Points of mining trace at the Sadamisaki Peninsula

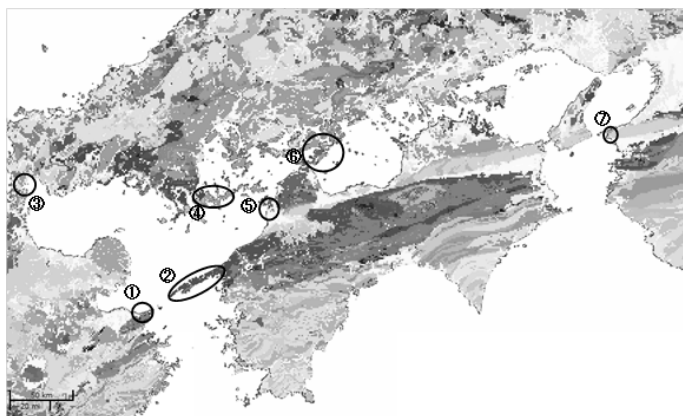


Fig.2 Study area

Table 1: Study area name and geology

Number	Study area	Prefectures	Geology
①	Saganoseki	Oita	Pelitic schist
②	Sadamisaki Peninsula	Ehime	Sanbagawa metamorphic belt
③	Shimonoseki	Yamaguchi	Granite
④	Yashiro Island	Yamaguchi	Felsic plutonic rocks
⑤	Baishinji Shiraishi	Ehime	Felsic plutonic rocks
⑥	Ooshima Innoshima	Hiroshima Ehime	Mixed rock Granodiorite
⑦	Kada	Wakayama	Marine sedimentary rock

METHOD AND STUDY AREA

Fig.2 shows study area, and Table 1 shows study area name and geology. Sanbagawa metamorphic belt mainly composed of green rocks (basaltic rocks metamorphosed) and granodiorite are rich for iron and magnesium.

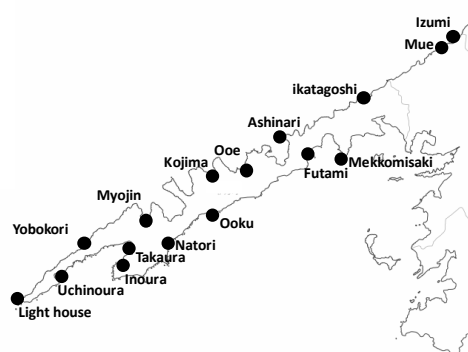


Fig.3 Sampling points at Sadamisaki Peninsula

Fig.3 shows sampling points at Sadamisaki Peninsula.

8 sampling points along the Seto Inland Sea are Lighthouse, Yobokori, Myoujin, Kojima, Ooe, Ikatagoshi, Mue and Izumi. 7 sampling points along the Seto Inland Sea are Uchinoura, Takaura, Inoura, Natori, Ooku, Futami, Mekkomisaki.

The seaweeds for survey have been collected at the time of the ebb tide. The collected seaweeds were dried after water washing and the dried samples were dissolved with concentrated nitric acid. Heavy metal concentration of solution after filtration with 0.45 micro meter filter was measured by ICP-AES. Trace element concentration in seaweed was calculated according to equation (1)

$$\frac{\text{concentration in dry weight (mg/kg)} = \frac{\text{concentration in liquid (mg/kg)} \times \text{Weight of nitric acid (g)}}{\text{Dry weight of sample (g)}} \dots (1)$$

RESULTS

The trace element concentrations in seaweed at the 7 study areas

In the previous study, heavy metal concentration in seaweed at the Kii Peninsula was measured and heavy metal concentration pattern for each seaweed species was also clarified. It's known that Cu and Fe concentrations in green seaweed were higher than those in brown and red seaweed and that there was no clear difference of Pb and Zn concentrations among green, brown and red seaweeds and that As concentration in brown seaweed was higher than those in green and red seaweed. In this research, to clarify the tendency for study area.

First, to compare elements such as copper, lead and arsenic that will adversely affect the human body.

Cu concentrations in seaweed

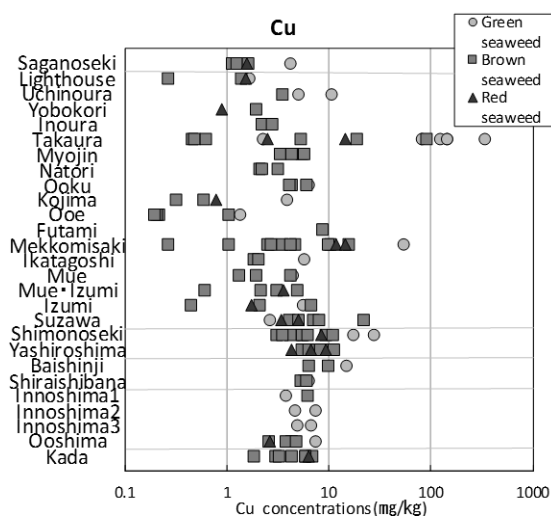


Fig.4.1 Cu concentrations in seaweed

Fig.4.1 shows Cu concentration in seaweed for study area. Green seaweed, brown seaweed, and red

seaweed are shown as circle, square and triangle. Cu concentrations in green seaweed were plotted at 1 to 334 mg/kg, and among them, those in *Ulva* at Takaura was high. Cu concentrations in brown seaweed, it was plotted at 0.2 to 89 mg/kg, and among them, those in *Scytosiphon lomentaria* at Takaura was high. Cu concentration in red seaweed were plotted at 0.8 to 14 mg/kg, and among them, those in *Gloiopeltis furcata* at Takaura was high. In most study points, Cu concentrations in green seaweed were higher than those in brown and red seaweed.

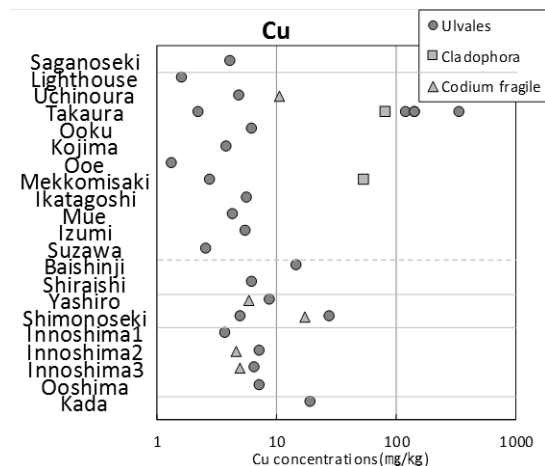


Fig.4.2 Cu concentrations in green seaweed

Fig.4.2 shows Cu concentrations in green seaweed. Cu concentration in *Ulva* at Takaura was 121 to 334 mg/kg, and Cu concentrations in *Ulva* at the other study points were 1 to 27 mg/kg. Therefore, Cu concentrations in *Ulva* at Takaura were higher than those at the other area.

Mn concentrations in seaweed

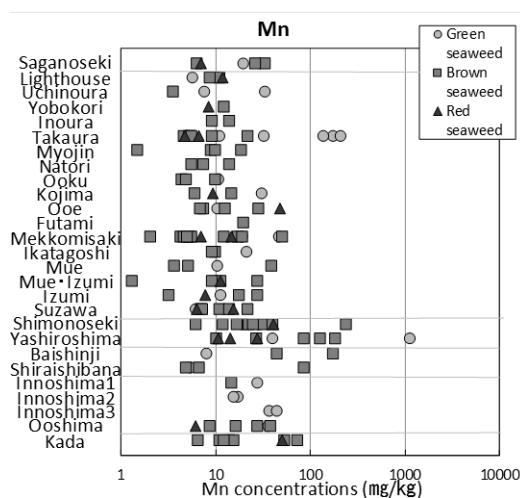


Fig.5 Mn concentrations in seaweed

Fig.5 shows Mn concentrations in seaweed. Mn concentrations in green seaweed were plotted at 5 to 1109 mg/kg, and among them, those in *Ulva* at Yashiro Island was high. Mn concentrations in brown seaweed were plotted at 1 to 239 mg/kg, and among them, those in *Sargassum siliquastrum* at Shimonoseki was high. Mn concentrations in red seaweed were plotted at 4 to 50 mg/kg, and among them, those in *Chondrus ocellatus* Holmes at Kada was high. There is no difference in Mn concentration for each seaweed. And regardless of the study points, there were no difference.

Pb concentrations in seaweed

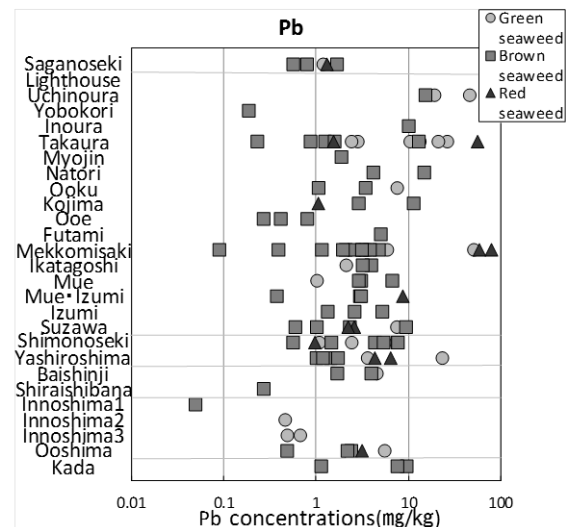


Fig.6 Pb concentrations in seaweed

Fig.6 shows Pb concentrations in seaweed. Pb concentrations in green seaweed were plotted at 0.4 to 50 mg/kg, and among them, those in *Cladophora* at Mekkomisaki was high. Pb concentrations in brown seaweed were plotted at 0.05 to 15 mg/kg, and among them, those in *Sargassum muticum* at Uchinoura was high. Pb concentrations in red seaweed were plotted at 0.9 to 78 mg/kg, and among them, those in *Gloiopeltis furcata* at Mekkomisaki was high. Therefore, there was no difference in Pb concentration for each seaweed. Comparing the sampling site, Pb concentrations at Uchinoura, Takaura and Mekkomisaki were higher than those at the other study points.

As concentrations in seaweed

Fig.7.1 shows As concentrations in seaweed. As concentrations in green seaweed were plotted at 0.4 to 19 mg/kg, and among them, those in *Codium fragile* at Shimonoseki were high. As concentrations in brown seaweed were plotted at 0.6 to 196 mg/kg, and among them, those in *Sargassum macrocarpum* at Yashiro Island were high. As concentrations in

red seaweed were plotted at 0.8 to 19 mg/kg, and among them, those in *Grateloupia turuturu* at Kojima were high. As concentrations in brown seaweed were higher than those in green and red seaweed. But there was no difference by region.

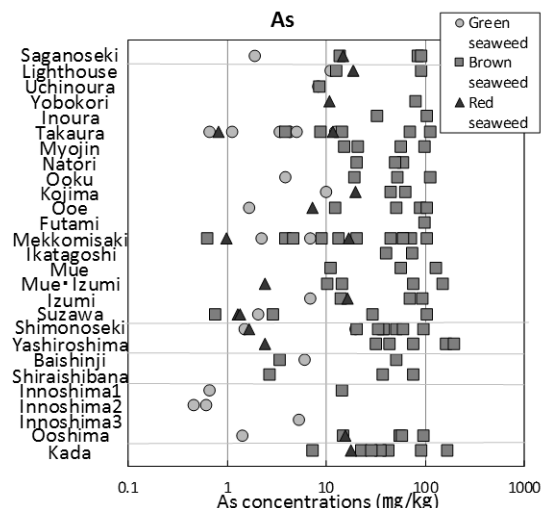


Fig.7.1 As concentrations in seaweed

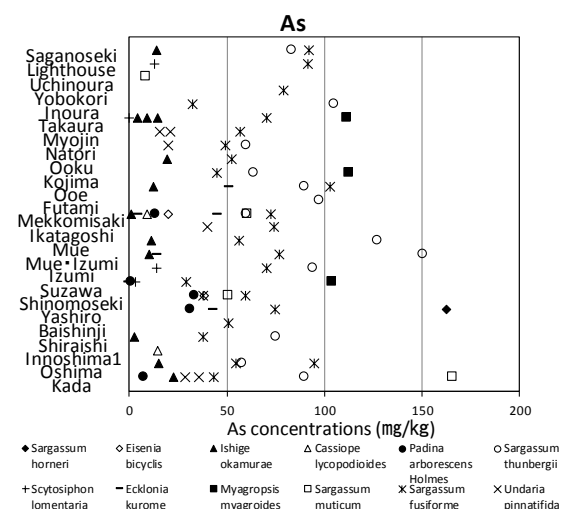


Fig.7.2 As concentrations in brown seaweed

Fig.7.2 shows As concentrations in brown seaweed. It separates symbols for each kind of brown seaweed. *Sargassum fusiforme* and *Sargassum thunbergii* could be collected at most points. As concentrations in *Sargassum fusiforme* were plotted at 29 to 103 mg/kg. As concentrations in *Sargassum thunbergii* were plotted at 57 to 150 mg/kg. Because it can be sampled easily and there are differences in concentrations, it is considered that these two seaweeds are suitable for comparison of As concentration.

Next, to compare elements such as iron, zinc, calcium and magnesium that will be nourishing for

the human body

Fe concentrations in seaweed

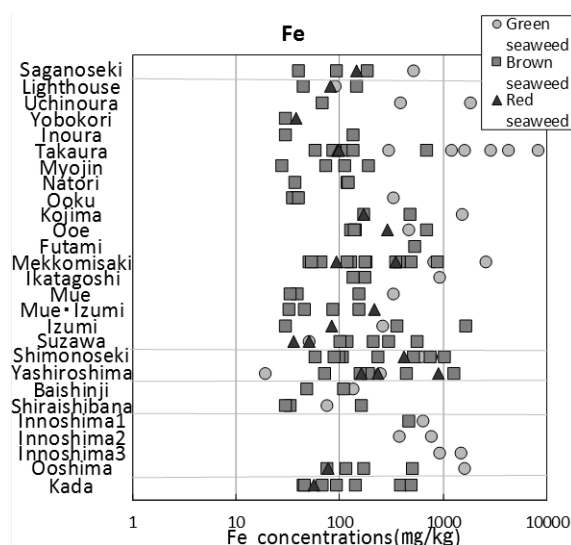


Fig.8.1 Fe concentrations in seaweed

Fig.8.1 shows Fe concentrations in seaweed. At most points, Fe concentrations in green seaweed are higher than those in brown and red seaweed.

Fe concentrations in green seaweed were plotted at 19 to 8195 mg/kg, among them, those in *Ulvaes* at Takaura was high. Fe concentrations in brown seaweed were plotted at 27 to 1675 mg/kg, among them, those in *Scytosiphon lomentaria* at Izumi was high. Fe concentrations in red seaweed were plotted 36 to 905 mg/kg, among them, those in *Lomentaria catenata* at Yashiro Island was high. Therefore, green seaweed is considered suitable for comparison of Fe concentration.

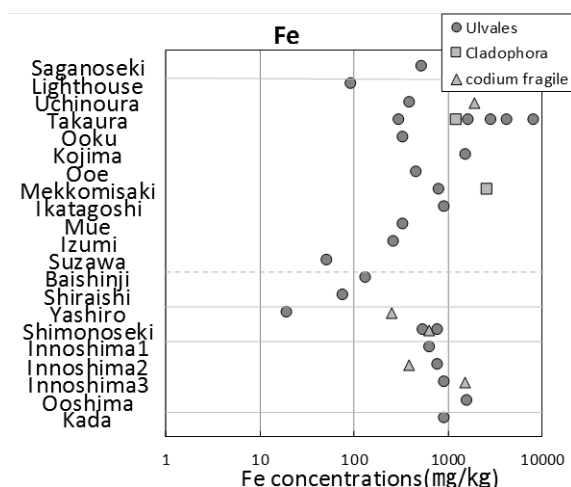


Fig.8.2 Fe concentrations in green seaweed

Fig 8.2 shows Fe concentrations in green seaweed. Fe concentrations in *Ulvaes* were plotted

at 19 to 8195 mg/kg, those in other green seaweed were plotted at 250 to 2580 mg/kg. Therefore, Fe concentrations in Ulvales were higher than those in the other green seaweed.

Zn concentrations in seaweed

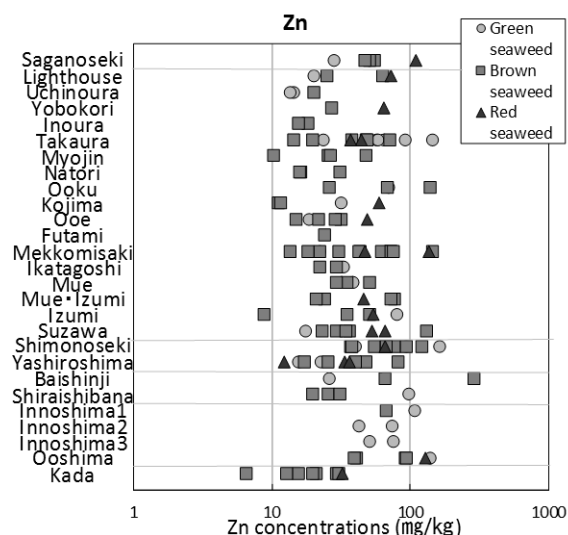


Fig.9 Zn concentrations in seaweed

Fig.9 shows Zn concentrations in seaweed. Zn concentrations in most seaweed were plotted 10 to 100 mg/kg at most sampling points. Therefore, there is no difference in Zn concentration for each seaweed, and there was no difference for each region.

Ca and Mg concentrations in the two seaweeds

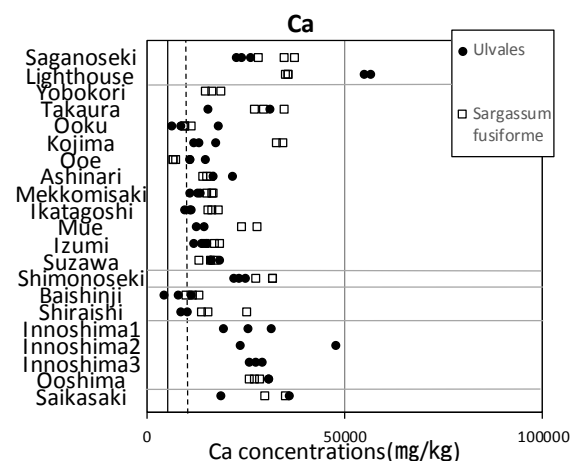


Fig.10 Ca concentrations in the two seaweeds

Fig.10 shows Ca concentrations in Ulvales and Sargassum fusiforme. A solid filled circle indicates Ulvales, and a square outline indicates Sargassum fusiforme. The solid line is the standard component

concentration of Ulvales, and the dotted line is the standard component concentration of Sargassum fusiforme. This standard component concentration was quoted from the Ministry of Education, Culture, Sports, Science and Technology [8].

Ca concentrations in Ulvales were plotted 4300 to 93000 mg/kg, and standard component concentration was 4900 mg/kg. Ca concentrations in Sargassum fusiforme were distributed 6500 to 37000 mg/kg, and standard component concentration was 10000 mg/kg.

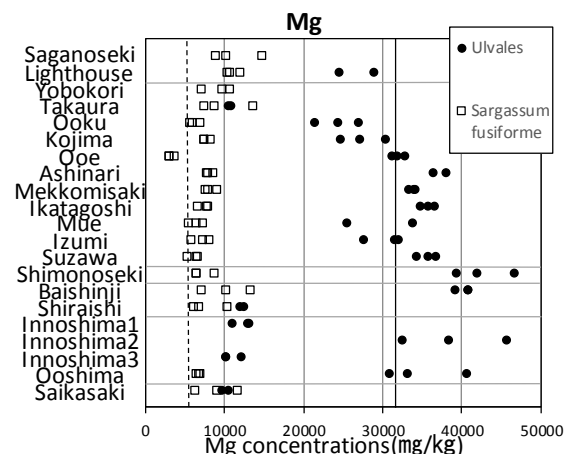


Fig.11 Mg concentrations in the two seaweeds

Fig 11 shows Mg concentrations in Ulvales and Sargassum fusiforme. Mg concentrations in Ulvales were distributed 9700 to 47000 mg/kg, and standard component concentration was 32000 mg/kg. Mg concentrations in Sargassum fusiforme were distributed 2900 to 15000 mg/kg, and standard component concentration was 6400 mg/kg.

Ca and Mg concentrations in Sargassum fusiforme were no clear difference for each study point. But these concentrations in Ulvales were difference in each study points. Especially, Ca concentrations in Ulvales at Lighthouse and Innoshima2 were higher than those at the other study points.

DISCUSSION

At Takaura there is a large copper mine trace, and there is a drainage groove continuing from the mine trace. So, at Takaura it seems that the influence from the mining site extends to seaweed.

When comparing study points, Fe concentrations in Ulvales at Sadamisaki Peninsula, innoshima and Ooshima were higher than those at the other study area. As a factor, it is conceivable that the geology of the three points contains a lot of iron.

The Sadamisaki Peninsula is a peninsula made of cupriferous iron sulfide deposit. Therefore, about 66 copper mines operated in Sadamisaki Peninsula

from middle Meiji to Taisho era although at present all the mines closed. The mine is composed of FeS_2 and CuFeS_2 , and waste water contains copper and iron. Among them, the Takaura mine becomes a large scale mine trace in the Sadamisaki Peninsula. Takaura faces Takaura Bay, and there is little influence from ocean current.

At Oshima which is similar to Sadamisaki Peninsula, Fe and Mg concentrations in Ulvales were higher than those at the other study area. As a factor, the influence from geology is considered. The main geological features of the Sadamisaki Peninsula and Oshima with high Fe and Mg concentrations are composed of mafic rocks containing a lot of Fe and Mg minerals.

As a factor that Fe and Mg concentrations in Ulvales were higher than those in the other seaweeds, it is thought that Chloroplasts in the body of the Ulvales are involved. The chloroplast contains chlorophyll. Mg is a core element for chlorophyll.

Takaura is considered to be the possibility of copper contamination comparing normal area such as the Kada and Yashiro Island areas. In addition, seaweed growing in a part of Sadamisaki Peninsula including Takaura and Oshima is considered to be rich in Fe and Mg concentrations due to geological influences.

CONCLUSION

Cu concentration in Ulvales at Takaura was higher than those at the other study area. Pb concentration in seaweed at Uchinoura, Takaura and Mekkomisaki were higher than those at the other study area. As concentrations in brown seaweed were higher than those in the other seaweed. Especially, As concentrations in *Sargassum muticum* and *Sargassum fusiforme* were higher than those in the other brown seaweed. Fe concentrations in Ulvales at Takaura, Kojima and Oshima were higher than those at the other study area. Zn concentrations of seaweed at all sampling points were uniform and Zn concentration deference between each species was not found. Mg concentrations in Ulvales were 3 times higher than those in *Sargassum fusiforme*.

Ulvales can be collected easily at each point, and Cu, Fe and Mg concentration range is wide. Therefore, it is considered that Ulvales is suitable for concentration comparison. Takaura is considered to be the possibility of copper contamination comparing normal area such as the Kada and Yashiro Island areas. In addition, seaweed growing in a part of Sadamisaki Peninsula including Takaura and Oshima is considered to be rich in Fe and Mg concentrations due to geological influences

REFERENCE

- [1] Oishi K, Science of seaweed: Asakura Bookstore, 1933.
- [2] Abe N, Sudo S, Sera K, Saitou Y, Yoshida N and Kudo T, "PIXE analysis of trace heavy metal elements concentrated in seaweed" Report on NMCC Collaborative Research Results 11, 2003, pp.70-77.
- [3] Ii H, "AS, SR, ZN, FE, MN, PB AND CU CONCENTRATIONS OF SEAWEED AT THE KII PENINSULA, JAPAN" International Journal of GEOMATE, June, 2016, Vol. 10, Issue 22, pp. 2036-2042.
- [4] Ii H, "CU, ZN AND AS CONTAMINATION OF SEAWEED BESIDE SHIZUKI AND KANAYAMA METAL MINES IN JAPAN" Int. J. of GEOMATE, Sept., 2015, Vol. 9, No. 1 (Sl. No. 17), pp. 1411-1417.
- [5] Yamamoto T, and Ishibasi M, "The Content of Trace Elements in Seaweeds", in Proc. 7th Int. Seaweed Symposium, 1971, pp. 511-514.
- [6] Yamamoto T, "Chemical Studies on the Seaweeds (27) The relations between Concentration Factor in Seaweeds and Residence Time of Some Elements in Sea Water", Records of Oceanographic Works in Japan., Vol. 11, No.2, March. 1972, pp. 65-72.
- [7] Fujioka K, Human geography of the Cape Peninsula - Ehime Prefecture Sadamisaki Peninsula Scientific Research Report -: Taimeido, 1966.
- [8] MINISTAY OF EDUCATION, CULTURE, SPORTS, SCIENCE AND TECHNOLOGY JAPAN, "Japan Food Standards Ingredients Table", 2015.
- [9] Kimura T and Kobayashi K, "Report on copper sulfide iron ore floor survey in the western part of Ehime prefecture" Geological Surveyor Monthly Report, 1954, 5(10) pp.505-528.
- [10] Ken'ichi Hanaoka, Shinnji Miyamoto and masakatsu Usui, "Effect of hot water washing and soaking on the arsenic content of the brown alga *Akamoku*, *Sargassum horneri*" Journal of National Fisheries University 61(1) 23-26(2012).
- [11] Masayuki KATAYAMA, Motohiro KASAMA and Yohko SUGAWA-KATAYAMA "Accumulation of iron and magnesium in growing Hijiki(*Sargassum fusiforme*) plants." Trace Nutrients Research, 2012, 29:100-105.
- [12] JL Smith, G Summers & R Wong, "Nutrient and heavy metal content of edible seaweeds in New Zealand" new Zealand Journal of Crop and Horticultural science, 38:1, 19-28.
- [13] G. N. Saenko, M. D. koryakova, V. F. Makienko and I. G. Dobrosmyslova, "Concentration of Polyvalent Metals by Seaweeds in Vostok Bay, Sea of Japan", Marine Biology 1976, 34, 169-176.

HEATING VALUE ENHANCEMENT BY BIOGAS PURIFICATION USING NATURAL ZEOLITE AND RICE STRAW-BASED BIOCHAR

Ambar Pertiwinigrum^{1,2}, Margaretha Arnita Wuri³, Andang Widi Harto⁴, Rachmawan Budiarto⁴ and Misri Gozan⁴

¹Faculty of Animal Science, Universitas Gadjah Mada, Indonesia; ²Agrotechnology Innovation Center, Universitas Gadjah Mada, Indonesia; ³Faculty of Engineering, Christian University of Surakarta, Indonesia;

⁴Faculty of Engineering, Universitas Gadjah Mada, Indonesia; ⁵Faculty of Engineering, Universitas Indonesia, Indonesia

ABSTRACT

Biogas has many incentives to replace firewood and crop straw for cooking in rural area. However, to access sustained adoption of clean, carbon neutral and eco-friendly household fuels, raw biogas needs to be purified before used. Beside methane (CH₄), raw biogas contains trace components adversely affecting appliances or end-user. For example, carbon dioxide (CO₂), the greatest impurities in biogas, affect the decrease of heating value. In some literature, the adsorption for CO₂ was claimed to be cheap, simple and adoptable for CO₂ removal. This study aims to investigate utilization rice straw-based biochar as partial substitute adsorbent for CO₂ removal. Carbon dioxide removal using rice straw-based biochar combined with natural zeolite (Z-RB) at room temperature and gas pressure range of 5-7 bar. Carbon dioxide removal using Z-RB increased the theoretical and empirical heating value of biogas from 1214.48 kJ to 1766.34 kJ and from 276 kJ to 288.55 kJ respectively. From this observation, the blue flame that appeared from the combustion of purified biogas using Z-RB went out for longer than using natural zeolite only (Z-Z).

Keywords: Heating value, Biogas purification, CO₂ removal, Rice straw-based biochar, Methane

INTRODUCTION

In Indonesia, 96% of national energy needs are supplied from fossil fuels based energy such as petroleum, natural gas and coal [1]. The constantly increasing demand for energy led to a long-term dependency on coal and other fossil fuels [2]. Nevertheless, the traditional biomass energy such as crop straw and firewood are still dominant in rural area [3]. The traditional biomass energy is burnt directly for domestic utilization such as cooking, heating and lighting. Unfortunately, combustion of these fuels leads to high level of health damaging air pollution from particulate matter (PM), carbon monoxide (CO), nitrous oxide (NO₂) and poly aromatic hydrocarbons (PAHs) [4]. People in rural areas waste too much of their time to collect crop straw or firewood for cooking, moreover, they breath polluted air from the traditional biomass energy combustion that can threatens their life.

Whereas the availability of clean, low cost and high efficient fuel could significantly improve the living quality, economic sector [5] and public health in rural area. Biogas is a clean and smokeless fuel, which can be an excellent substitute for these traditional biomass energies. H Pathak [6] and Amanda [7] claimed that biogas technology is an attempt of greenhouse gases (GHGs) mitigation. The multiple benefits of biogas technology should

encourage government to promote biogas technology as a way to combat global warming and health hazards from the traditional biomass energy combustion. In some developing countries, biogas dissemination has some obstacle, such as Indonesian's policy, public lack of skill and lack of biogas related research [8]. On the other hand, in Indonesia the existence of raw material of biogas, the natural resources of biomass-based livestock and agriculture sector, is abundant [9]. Biogas contains methane (CH₄), a flammable gas with a heating value of 21-24 MJ/m³ [10]-[11]. A lower heating value of biogas is due to the considerable carbon dioxide (CO₂) composition in the biogas content, so to increase the biogas heating value the removal of carbon dioxide (CO₂) by biogas purification technology is required [10]-[13].

According to some references, adsorption is a cheap, simple and adoptable method for CO₂ removal [14]-[15]. Carbon dioxide removal using the biomass waste-based adsorbent, such as biochar and activated carbon, has been developed [14], [16]-[18]. However, the application of rice straw based biochar for CO₂ removal in biogas purification is rare. This study aims to investigate the influence of rice straw-based biochar application as a natural zeolite partial substitute as adsorbent in biogas purification system. Because it is known that natural zeolite has the best ability to eliminate CO₂ [15].

METHODOLOGY

Materials

Rice straws were prepared to produce biochar as partial substitute of natural zeolite for CO₂ removal. Agrotechnology Innovation Center of Universitas Gadjah Mada provided the biogas that will be purified. Biogas was generated from anaerobic digestion of cow manure. Aquadest, thermometer and biogas stove were prepared to calculate the heating value needed for boiling water.

Experimental

Rice straw-based biochar production

Rice straws were collected from rice fields and chopped into 10-15 cm size. Rice straw-based biochar was produced through pyrolysis process. Before converted to biochar, rice straws were dried under direct sunlight to evaporate the water content. Pyrolysis was carried out at 500°C and was then held for 4 hours straight when a temperature was reached. The biochar-based rice straw was then characterized using infrared (IR) spectroscopy instruments to identify the surface functional groups.

Biogas purification through removing CO₂

Carbon dioxide removal in biogas purification aims was to increase the biogas heating value. Stainless steel was used to make the adsorption column with 40 mm diameter and 200 mm length. The detailed scheme of biogas purification unit was illustrated in Fig. 1 and the adsorbents formulations were formulated in Table 1. CO₂ adsorption was carried out at room temperature and gas pressure ranged between 5-7 bar. The CH₄ contents of before and after adsorption biogas samples then analyzed with gas chromatography (GC) instrument.

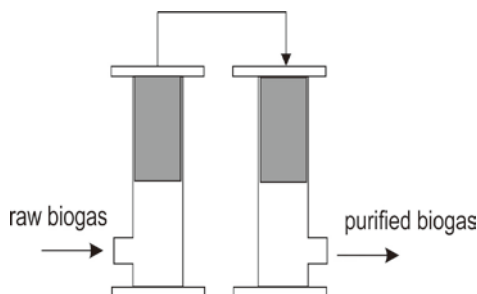


Fig. 1 Details scheme of CO₂ adsorption unit

Table 1. Adsorbents for CO₂ adsorption in biogas

Code	Column 1 (40:40 grams)	Column 2 (40:40 grams)
Z-Z	Natural zeolite : natural zeolite	Natural zeolite : natural zeolite
Z-RB	Natural zeolite : rice straw-based biochar	Natural zeolite : rice straw-based biochar

Calculation the heating value of biogas

The heating value of the purified biogas samples was then calculated. Amanda stated that the heating value of biogas is correlated linearly with the content of CH₄ dissolved therein [7]. The calculation of the biogas heating value was derived from the percentage of CH₄ content, so theoretically heating value calculation can be written as follows:

$$E_{\text{biogas}} = LHV \times {}_n\text{CH}_4 \quad (1)$$

Equation (1), E_{biogas} shows the heating value in biogas tank (kJ). LHV represents the lower heating value of CH₄ (kJ/mol) and ${}_n\text{CH}_4$ represent the CH₄ content in biogas (mol). The heating value of raw biogas and purified biogas were then compared to investigate the CO₂ removal effect on the heating value enhancement.

Calculation the heating value needed to boil water

The purified biogas then packed into a four bar pressure tank. In this study, the purified biogas then used to boiling water using a biogas stove. Each 1000 ml is prepared and boiled with a biogas stove. The temperature rises and boiling time were recorded every 30 seconds until the water boiled. The needed heating value for boiling water was calculated with the formulation in Equation (2):

$$Q = m \times c \times \Delta T \quad (2)$$

Q represents the needed heating value for boiling water (kJ), m is mass of water (kg), c is specific heat of water (kJ/kg K) and ΔT is the difference between initial and final water temperature (K).

RESULTS AND DISCUSSION

Characteristic functional groups of rice straw-based biochar

Rice straw-based biochar characterized using IR spectroscopy to determine functional group on biochar surface. IR spectroscopy sample was prepared using KBr pellets and analyzed with wave number ranges in between 400-4000 cm⁻¹. The result

of IR spectroscopy analysis showed in Fig. 2. The IR spectra in Fig. 2 confirmed the typical bands of biochar's functional groups were similar to the previous studies. The bands at 3503 cm^{-1} corresponds to the hydroxyl groups vibration of the biochar [17]-[18]. The absorption at 1110 cm^{-1} also confirmed the C-O bonds vibration of phenol, alcohol or carboxylic group on biochar's surface [17], [19]. The C=C aromatic carbons was confirmed from the absorption at 1609 cm^{-1} [17]-[19] justified.

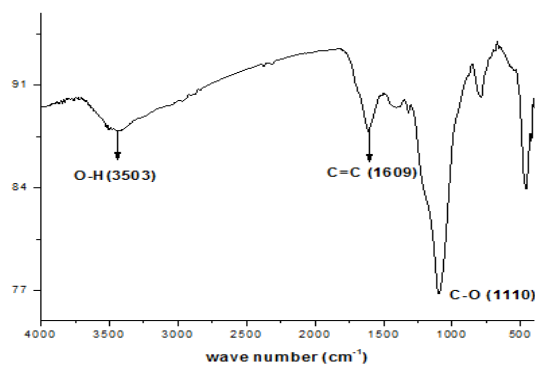


Fig. 2 IR spectra of rice straw-biochar

The Biogas Heating Value Enhancement after CO_2 Removal

Carbon dioxide removal process using adsorbents aims to enhance the biogas heating value through the increase in CH_4 content. Methane played an important role in generating energy by biogas combustion [10]-[11]. The linear relationship between CH_4 content and the biogas heating value was investigated in this paper. The comparison of CH_4 content in raw and purified biogas after CO_2 removal using adsorbents according to Table 1. is shown in Fig. 3. Fig. 3 showed that raw biogas (biogas before the CO_2 removal) has a lower CH_4 content compared with purified biogas. This means the biogas purification using CO_2 removal has been done successfully. Natural zeolite and rice straw-based biochar are able to capture and trap CO_2 molecules on their cavities [15]-[16].

The greatest increase of CH_4 content is shown by purified biogas with Z-RB adsorbent of 44.85% compared to Z-Z adsorbent of only 1.4%. It can be concluded that CO_2 adsorption by rice-based biochar is greater than natural zeolite. Yu-Fong et al. [17] reported that the higher specific surface area of rice straw-based biochar play an important role in capturing CO_2 molecules, well compared to Z-Z. Ambar et al. [18] and Margaretha et al. [19] also reported that the higher CO_2 removal performed by combination of natural zeolite and livestock waste based-biochar compared to natural zeolite only.

Natural zeolite used in this study is similar to natural zeolite used by Margaretha et al. [19] with specific surface area of $27.9\text{ m}^2/\text{g}$. And biochar, according to , has specific surface area about $200\text{--}300\text{ m}^2/\text{g}$ [20]. It means that biochar has better capability of CO_2 removal than natural zeolite.

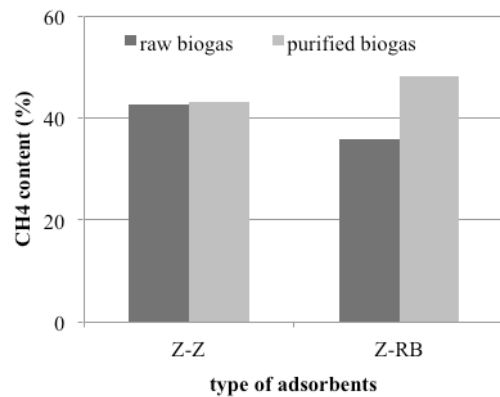


Fig. 3 Methane content of raw and purified biogas

The linear relationship between CH_4 content and the biogas heating value was also shown in this Fig. 4. The increase of biogas CH_4 content was represented by the increase of the heating value. Before the CO_2 removal using Z-Z, raw biogas had 1513.65 kJ heating value per tank. There was an increase of 1534.31 kJ per tank in heating value after the CO_2 removal. The higher increase in CH_4 content was performed by Z-RB from 1214.48 to 1766.34 kJ per tank. The results support that the higher heating value depend on the CH_4 content in the biogas. The same phenomenon of the heating value increased after biogas purification has also been reported by previous researcher [10]-[13]. Adalberto [10] reported that the raw biogas heating value is 50 MJ/kg has increased to 45 MJ/kg (90% CH_4 content) after purifying.

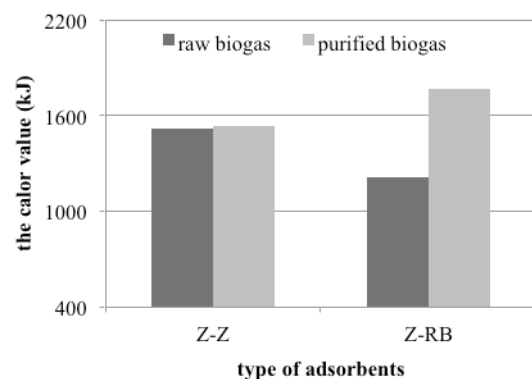


Fig. 4 The heating value of raw and purified biogas

Since purified biogas were prepared for domestic

utilization as combustion energy for cooking, combustion test are also necessary. Biogas combustion test was conducted by observation of boiling water with biogas. The biogas heating value was calculated from the energy it needed to boiled water. The empirical biogas heating value was then compared with the theoretical biogas heating value. The results of the needed energy to boiled water showed in Table 2. It was concluded that biogas purification using Z-RB were greater compared to Z-Z. From the observation, the blue flame rose from the purified biogas combustion using Z-RB arise longer than the purified biogas combustion using Z-Z. This is because the purified biogas using Z-RB adsorbent has a greater CH₄ content that act as a fuel. The difference between empirical and theoretical heating values on the results of this study is due to the correction energy factors lost due to the use of biogas stoves (biogas stoves have an efficiency of 15-25%).

Table 2. The empirical heating value of raw and purified biogas

Code	Raw biogas (kJ)	end-point time of blue flame (seconds)	Purified biogas (kJ)	end-point time of blue flame (seconds)
Z-Z	239.44	140	249.44	270
Z-RB	276	540	288.55	600

From the findings showed that there was association between CO₂ removal for enhancing heating value of biogas. The increase in heating value after biogas purification through CO₂ removal using natural zeolite and biochar would encourage rural communities to use biogas energy for cooking. The higher efficiency energy of biogas has impact on the increasing types of cooking fuel that would be selected by rural communities. Although the use of biogas not fully replaces other fuels for cooking, it can be used as an environmentally friendly and clean alternative fuel for cooking in rural area. Cahyono *et al.* [21] also claimed that biogas purification is a good approach to sustainable bio-energy.

CONCLUSION

From this study result, concluded that rice straw-based biochar can be used as alternative adsorbent for CO₂ removal in biogas purification process. In addition, the use of natural zeolite combined with rice straw-based biochar gave greatest impact of increasing the biogas heating value. The theoretical

and empirical biogas heating value after CO₂ removal increased from 1214.48 to 1766.34 kJ and from 276 to 288.55 kJ respectively. In other words, the CO₂ removal in biogas could enhance the biogas heating value. Based on results in this study, the effort on quality upgrading by biogas purification through CO₂ removal would encourage biogas technology adoption in rural areas.

ACKNOWLEDGEMENTS

This research was supported by Grant Program from Universitas Gadjah Mada, Indonesia (Number 1849/UN1/DITLIT/DIT-LIT/LT/2018). The authors also would like to thank Universitas Gadjah Mada and USAID through Sustainable Higher Education Research Alliances (SHERA) program for helpful.

REFERENCES

- [1] National Energy Council, Outlook Energy 2014, Indonesia, Ministry of Energy and Mineral Resources, 2014.
- [2] Qiu C. and Tianbiao, Biogas System in Rural China: Upgrading from Decentralized to Centralized?, Renewable and Sustainable Energy Reviews, Vol. 78, 2017, pp.933-944.
- [3] International Energy Agency, World Energy Outlook 2006, Paris, International Energy Agency, 2006.
- [4] The World Bank, Household Cookstoves, Environment, Health, and Climate Change: A New at An Old Problem, Washington, The World Bank, 2011.
- [5] Zhang P., Yang Y., Tian Y., Yang X., Zhang Y., Zheng Y. and Wang L., Bioenergy Industries Development In China: Dilemma and Solution, Renewable and Sustainable Energy Reviews, Vol. 13, Issue 9, 2009, pp.571-2579.
- [6] H. Pathak, N. Jain, A. Bhatia, S. Mohanty and Navindu G., Global Warming Mitigation Potential of Biogas Plants in India, Environmental Monitoring and Assessment, Vol. 157, 2009, pp.407-418.
- [7] Amanda D.C. and Michael E.W, Cow Power: The Energy and Emissions Benefits of Converting Manure to Biogas, Environmental Research Letters, Vol. 3, 2008, pp.1-8.
- [8] Agabu S., Shabbir H.G. and Seveliano P., Rural Domestic Biogas Supply Model for Zambia, Renewable and Sustainable Energy Reviews, Vol. 78, 2017, pp.683-697.
- [9] Chandra, W.P. and Ambar P., Novel Design of Tunnel Type Biodigester, in Proceeding 14th ISSAT International Conference on Reliability and Quality in Design, 2008, pp. 289-292.
- [10] Adalberto N, Juan M.M. and Jorge E.L., Treatment of Biogas Produced in Anaerobic Reactors for Domestic Wastewater: Odor Control and Energy/Resource Recovery,

- Reviews in Environmental Science and Bio/Technology, Vol. 5, 2006, pp.93-114.
- [11] Olumide W.A., Yaqian Z., Ange N., Doan P.M. and Nathalie L., A review of Biogas Utilisation, Purification and Upgrading Technologies, Waste Biomass Valorization, Vol. 8, 2017, pp.267-283.
- [12] Qie S., Hailong L., Jinying Y., Longcheng L., Zhixin Y. and Xinhai Y., Selection of Appropriate Biogas Upgrading Technology – A Review of Biogas Cleaning, Upgrading and Utilisation, Renewable and Sustainable Energy Reviews, Vol. 51, 2015, pp.521-532.
- [13] Wojciech M.B., A Review of Potential Innovations for Production, Conditioning and Utilization of Biogas with Multiple-criteria Assessment, Renewable and Sustainable Energy Reviews, Vol. 54, 2016, pp.476-481.
- [14] Muhammad R.A.M., Mohammad R.K., Mohammed M.R., Abdullah M.A. and Shuichi T., Methane Enrichment of Biogas by Carbon Dioxide Fixation with Calcium Hydroxide and Activated Carbon, Journal of the Taiwan Institute of Chemical Engineers, Vol. 58, 2016, pp. 476-481.
- [15] A. Alonso-Vicaro, Jose R.O., S. Gill-Rio, O. Gomez-Jimenez-Aberasturi, C.A. Ramirez-Lopez, J. Torrecilla-Soria and A. Dominguez, Purification and Upgrading of Biogas by Pressure Swing Adsorption on Synthetic and Natural Zeolites, Microporous and Mesoporous Materials, Vol. 134, 2010, pp.100-107.
- [16] Anne E.C., Bin G. and Ming Z., Carbon Dioxide Capture using Biochar Produced from Sugarcane Bagasse and Hickory Wood, Chemical Engineering Journal, Vol. 249, 2014, pp.174-179.
- [17] Yu-Fong H., Pei-Te C., Chun-Hao S., Shang-Lien L., Liping S., Yuan Z., and Chungsheng Q., Microwave Pyrolysis of Rice Straw to Produce Biochar as An Adsorbents for CO₂ Capture, Energy, Vol. 84, 2015, pp.75-82.
- [18] Ambar P., Margaretha A.W. and Rachmawan B. Evaluation The Calorific Value of Biogas After Carbon Dioxide Adsorption using Natural Zeolite and Biochar, Unpublished Work but Accepted, 2018.
- [19] Margaretha A.W., Ambar P. and Rachmawan B., Methane Enrichment by Carbon Dioxide Adsorption on Natural Zeolite and Biochar Derived from Chicken Manure, in Proc. The 9th International Graduate Students and Scholars' Conf. in Indonesia, 2017, pp.911-918.
- [20] Zhang Z., Zhang S., Yang H., Shi T. and Chen Y., Influence of NH₃/CO₂ Modification on The Characteristic of Biochar and The CO₂ Capture, Bioenergy, Vol. 6(4), 2003, pp. 1147-1153.
- [21] Cahyono, A., Bambang H.S., Bambang S., Ambar P., Wiranti, Iwan S. and Dibyo P., Integrated Bio-cycles Farming System for Production of Bio-gas through GAMA DIGESTER, GAMA PURIFICATION and GAMA COMPRESSING, Journal of the Japan Institute of Energy, Vol. 90, 2011, pp. 1085-1089.

THE POTENTIAL IMPROVEMENT OF PUBLIC TRANSPORT IN MINIMIZING AIR POLLUTION

Lasmini Ambarwati¹, and Amelia K. Indriastuti²

¹Faculty of Engineering, Brawijaya University, Malang, Indonesia; ²Faculty of Engineering, Diponegoro University, Semarang, Indonesia

ABSTRACT

Improvement of public transport is an essential effort to encourage mobility. Declining mobility occurs due to increasing travel length for most people in big cities as consequence from urban development. Urban development with the phenomenon of urban sprawl has been a big issue since the beginning of 20th century which has effects on increasing traffic congestion, demand for mobility and air pollution. Research has addressed improvement of public transport, monorail system in minimizing air pollution cost due to urban sprawl. Air pollution cost is imposed on road users. Current research is insufficient to reveal the effects of urban sprawl on cost build-up caused by emission of air pollution. This paper examines the extent to which the improvement of monorail system is able to increase accessibility, reduce air pollution as well air pollution cost due to housing development in the suburbs. Comparative analysis was conducted to assess the influences of design of monorail system and existing public transport on differences of air pollution cost. The results show that design of monorail system has significant effect on the reduction of air pollution concentration and cost compared to the existing condition. The reduction of light vehicles due to the design of monorail shows a better accessibility and air quality of residents in the western regions of Surabaya City as case study area in the morning peak hour.

Keywords: Air pollution, Monorail system, Urban sprawl, Emission parameter, Mode choice

INTRODUCTION

Urban development with the phenomenon of urban sprawl occurs in many cities the world-wide. The phenomenon of urban sprawl influences living condition due to the change of complex pattern of land use, transportation pattern, and socio economic development. Urban sprawl is a pattern of land use in urban area that illustrates low levels of some dimensions such as density, continuity, concentration, compactness, centrality, diversity and proximity [1]. Urban sprawl represents a rapid expansion of residential area at the outskirt of the town, causing a spatial mismatch of jobs and residential dwellings, further causing imbalance in transport with high dependence on automobile [2]. Some consequences of this phenomenon are the increase of personal mobility and automobile dependence, and associated with health hazards such as air pollution, vehicles accidents, and pedestrian injuries and fatalities [3].

Improvement of public transport were held in Georgia in order to capture transport issues [4]. Costabile and Allegrini [5] explained that the impacts of improvement of transport technology in the reduction of vehicles pollution could be integrated with “intelligent” transport management system. The integrated system

was designed for the real case of Beijing in assessing the real-time traffic-related air pollution. They recommended further research to understand the mechanisms leading to air pollution impacts from transport emissions, to reduce the uncertainty in our ability to quantify the relationships between all emissions and all impacts, especially for NO₂ and particles.

The vehicle fleet is the largest single source of global air pollution. The fastest growing source of carbon dioxide emissions is exhausted from road traffic, having huge environmental problems with US\$93 billion worth of damage to health and environmental quality each year in the US [6].

The phenomenon of urban sprawl has been identified in most Indonesian cities since the beginning of the 20th century. A pattern of urban development with increasing settlement growth in the suburbs was reflected this phenomenon. The phenomenon occurs in the city of Surabaya as case study area, are characterized by an estimated 38% of the population lives in the suburbs [7]; most of them commute every day to work in the central urban area. This condition has significant consequences for mobility, increasing traffic congestion. It has strongly increased since the late 1990s; predominantly due to increasing numbers of

motorcycles and private cars. Current mode choice by residents in the city of Surabaya: private car (30%), motorcycle (62%), and other vehicle types (8%, mostly minibuses). This situation results in significant increase of time, cost and productivity losses, and an increase in air pollution. Improvement of public transport is expected to change modal split from private vehicles to

public transport, to reduce the amount of air pollution from motorized vehicles, and to lessen air pollution cost imposed to road users, as well to decrease travel time and distance. Currently, a substantial source of environmental pollution and traffic congestion in urban areas due to private road transports.

Numerous studies in transport strategies have been conducted such as transport demand management (TDM) with the aims of reducing the air pollution from motor vehicles. Mitchell [8] explained that there was a significant level of environmental inequality in Leeds, in the UK. Briefly, environmental inequality was reduced by an analysis of transport strategies with natural fleet renewal and road-user charges. Another transport strategy has been conducted by two demand management measures, i.e. road pricing and the vehicle quota scheme (VQS), revealed as effective instrumental in controlling both congestion and automobile ownership [9]. These studies on transport strategies, such as TDM and the promotion of technology to control emission, found that those strategies were insufficient to control the phenomenon of urban sprawl.

An insufficient number of studies have considered improvement public transport related to minimize the impacts of the phenomenon of urban sprawl and opportunity to reduce air pollution concentration and cost. Here with, this research focuses on improvement of public transport, i.e. monorail system related to impact assessment, particularly air pollution concentration in the existing condition and the condition with a design of monorail system. This study will assess air pollution cost imposed to road users with expansion of housing development in western region of the city of Surabaya.

An extensive survey was conducted to estimate the mode choice of residents due to the design of monorail system. The results of this study are expected to inform an effectiveness of design of monorail system in order to minimize the phenomenon of urban sprawl and to assist in policy making with regard to addressing air pollution as part of the control of urban sprawl.

This paper is structured as follows: data collection and methodology are elaborated in Section “Methods” consisting of background information on the existing public transport and improvement of public transport in the city of Surabaya. Section “Results” details a simulation analysis of transport, measurement of air pollution values, procedure to assess change of transport modal split and air pollution cost and concentration. This section discusses the estimation of emission parameters and compares the impacts of each emission parameter as well air pollution cost for each parameter. Section “Conclusions and recommendations” presents conclusions and recommendations for further research.

METHODS

The city of Surabaya is a case study area, the second biggest city in Indonesia. Surabaya City, the capital city of East Java Province, comprises 31 districts and 163 villages (Fig.1), the total area of 327 km², and is located at an altitude of 3-6 m above mean sea level.

The city has a population of 2,765,908 [7]. The population density in 2011 was estimated more than 11,000 people per km². A major problem related to settlement development occurs in the city. In the central urban area, several informal settlement areas are built, having a high density (45% built-up area). This situation is contrary to suburban, low density. Data was collected for each village (called *desa*) within the urbanized area of Surabaya City.

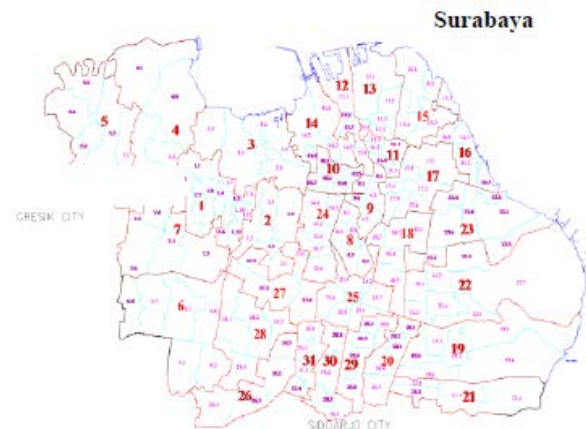


Fig.1 The study area (Surabaya City), located in East Java Province, Indonesia

Currently, Surabaya public transport network comprises minibus/paratransit and busses. There are 68 available paratransit routes, and 22 bus routes. The Local Government has planned to improve transport infrastructures such as monorail and tram system as seen in Fig.2.

The data was collected by 2010 Census data, secondary data from the Department of the Environment. Primary data was collected by distributing questionnaires to 163 villages (approximately 554 respondents). The questions consisted of three parts: socio-economic background, trip characteristic, transport mode choice. Traffic counting, speed study

and road geometric inventory were investigated on the several road-sections of Surabaya City (31 roads). Vehicle emission values were determined based on traffic volume and speed.



Fig. 2 The monorail routes

Monorail accommodates the passengers in the western and eastern regions, as seen in Fig. 2. The assessment of the effect of monorail operation on the decrease of air pollution concentration and cost is conducted.

The research framework consists of the background condition of public transport system and further plan of public transport development. The result is expected to

reduce the use of private vehicles and air pollution, to increase the beneficial received from improvement of public transport as illustrated in Fig. 3.

Improvement of Public Transport (PT) Systems

The existing public transport consists of minibusses (paratransits) with 68 routes and busses in 22 available routes (minibus accommodates 8–12 passengers, while bus has 50–55 seats). The frequency of minibusses and busses are approximately 20–25 veh/h and 5–6 veh/h respectively. An on-board survey for bus andminibus/paratransit was conducted in order to understand the current performance ofpublic transport and monorail systems planned, such as capacity, quality, and efficiency. Each region of the city is served by approximately 26 minibus routes, except the southern region of the city, which is accommodated by 10 minibus routes.

The Government of Surabaya City plans a monorail system in order to decrease the amount of traffic congestion, to provide alternative options of public transport that are safe, comfortable and scheduled [10]. The properties of the proposed monorail system are: a ticketprice of approximately \$0.82, stop spacing of 0.5–2 km, seat capacity of 177 seats. The improvements to public transport are expected to encourage the users of cars and motorcycles to shift their transport mode.

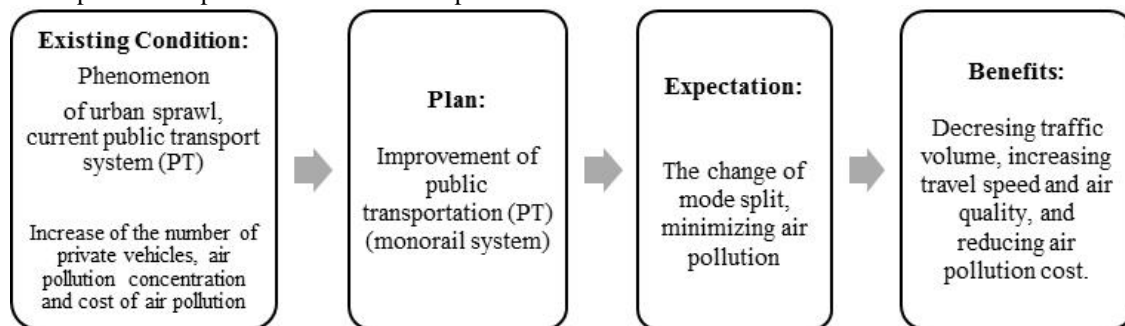


Fig. 3 The research framework

Assessment of Emission Load

The assessment was conducted in two analysis, i.e. the current public transport condition and the design of monorail system.

The analysis of the motorized vehicle emissions were classified based on vehicle types and air pollutant substances. Subsequently, the values of pollutant can be calculated based on traffic volume and traffic composition [11], as follows:

Air pollutant (gr) = traffic flow of each vehicle class (veh) x emission value for each parameter for each type of vehicles (g/veh.mile) x road length mile (l)

Unit emission loads (g/veh km) are vary for different modes and different speeds. Relevant emission substances are CO, CO₂, NO_x, SO_x, and HC. The number of passengers was based on the average vehicle occupancy, i.e. automobiles/private cars, minibuses, medium buses, large buses, trucks and motorcycles accommodate 3 passengers, 8 passengers, 30 passengers, 55 passengers, 2 passengers, and 2 passengers respectively. The standard value of motorized vehicle emissions based on traffic volume and traffic composition is shown in Table 1.

Table 1. The standard value of motorized vehicle emissions in Peak Hours (gr/pas-mile)

Mode	HC	CO	NO _x	SO _x
Automobile	2.42	18.13	1.47	0.05
Car Pool	0.88	6.55	0.53	0.02
Diesel Bus (medium or large bus, truck)	0.06	0.81	0.36	0.05

Source:[11] .

Calculation of Air Pollution Cost

The comparative analysis is conducted based on the existing condition and design of monorail system condition. According to [12], air pollution cost for urban road is calculated by using the following:

$$\text{Air pollution cost (\$)} = \text{air pollution cost constant (\$/veh-mile)} \times \text{peak hour traffic volume (veh)} \times \text{road length (mile)} \quad (2)$$

The air pollution cost constant is shown in Table 2.

Table 2. Air pollution cost content (\\$/veh-mile)

HC	CO	NO _x	SO _x
7.20	12	0.60 – 8.40	0.01 – 0.36

Source: [11].

Note : the value will convert from USD into IDR

RESULTS

This section explains the assessment of modal split on existing condition and improvement of public transport situation, emission parameter concentration and cost imposed to road users.

Modal Split

The comparative analysis is conducted in order to know the change of modal split for each vehicle class based on the existing condition and design of monorail system condition. Three cases are simulated by OmniTRANS model, consisting of estimation of transport model parameters for each condition and emission parameters. Simulation model has been done in previous research [13].

The following the results of previous research as follows:

- The design of monorail systems (C3) encourages the use of public transport up to 37% from the current trend.
- The number of cyclists in C3 also increases six times compared to the current trend 2030. This finding means that this case can influence the load of traffic flow and air quality on the road corridors.

Briefly, provision of sufficient PT is necessary to

take over from users other modes. The increase of passengers in the monorail system reduces the use of private motorized vehicles, is expected to decline emission parameters.

Value of Air Pollution Parameter

Three cases are proposed in order to understand reduction of traffic volume because some private vehicle users change to use the monorail system.

The loads of emissions based on specific weighted emission parameters regarding air quality for the city of Surabaya roads are required. The weighted emission parameters refer to air quality data containing the weighted emission values per vehicle kilometer (gr/veh-km) and depend on average speed standard of each vehicle class for each road type (motorway, urban, and rural). The weighted parameters, such as CO, NO_x, SO_x, and HC are estimated. The values were analyzed for the current base 2010 according to [12], the procedure for determining air pollutants at micro level due to traffic, as explained as follows:

$$qCO = 867.92 \cdot U_v^{-0.8648} \quad (3)$$

$$qNO_x = 0.0005 \cdot U_v^2 - 0.0656 \cdot U_v + 3.6586 \quad (4)$$

where U_v is average speed standard for each vehicle class for each road type in km/hr.

The emission load for each parameter has been computed by simulation of the OmniTRANS model, based on the simulated flows on the transport network, for various cases; the results are presented in Table 4. Improvement of the PT system with the design of monorail system (C3) has an effect on decreasing the load of private vehicles (cars and motorcycles), as reflected in 30% (cars) and 50% (motorcycles) reducing CO emission compared to C2 as explained in Table 3.

Table 3 Weight emission for CO for each case

Transport mode	Concentration of CO		
	Case		
	(C1) Current Base	(C2) Current trend	(C3) Monorail system
Cars	22.8	65.3	21.2
Motorcycles	53.4	124	60.3
PT	84.3	45.1	20
Total (all vehicles)	160.5	234.4	101.5

Comparative analysis of emission parameter for different road corridor

The operation of monorail in western part of Surabaya areas can reduce the air pollutant concentration. A great benefit for the community due to an increase of air quality and air pollution cost is

obtained. A significant difference of emission concentration and cost occurs on Lontar St. and Sungkono St. as described in Table 4.

Reducing CO concentration is amounted 71% by assumption of ticket price of monorail 2,500 IDR more than the price of existing public transport (minibus and bus). It can be concluded that monorail operation can reduce the amount of CO pollutant, because of the decrease of user of motorized vehicle on the roads and increase of monorail user.

The air pollution costs on each street can be calculated after the value of air pollutant on Lontar St. and Sungkono St. were identified, using the Equation (2, and converted into IDR (1 USD = 13,500 IDR).

Table 4 The value of emission parameter on Lontar St.(gr) and Sungkono St

Vehicle Type	Traf. Vol. (veh/h)	HC	CO	NO _x	SO ₂
Automobile	929	9,639	72,213	5,855	199
Car Pool	22	332	2,471	200	8
Diesel Bus ^{*)}		9	125	56	8
Motorcycle	3,319	47,434	113,841		
Total		57,414	188,650	6,111	215
Private car	4,108	410,451,825	684,086,376	256,532,391	10,831,368
Public transit	78	7,793,389	12,988,982	4,870,868	205,659
Bus	1	99,915	166,525	62,447	2,637
Truck	17	1,698,559	2,830,932	1,061,599	44,823
Motorcycle	9,607	959,885,756	1,599,809,594	599,928,598	25,330,319
Total					4,578,682,562

Table 5 Prediction of vehicle emissions on Lontar St. and Sungkono St. with Monorail Operation (gr)

Sce.	Mode	Peak Hour (Average of Morning, Noon and Afternoon)							
		Lontar St.				Sungkono St.			
		HC	CO	NO _x	SO _x	HC	CO	NO _x	SO _x
I	Automobile	1,570	11,763	954	33	8007	59,983	4,864	165
	Car Pool	42	311	25	1	221	1,659	134	4
	Diesel Bus	221	1,658	134	5	266	1,995	162	6
	Motorcycle	7,191	53,877	4,369	149	21,524	161,25	13,074	445
	Total	4,628	34,668	2,811	95	23,581	176,66	14,324	487
II	Automobile	194	1,451	118	4	983	7,359	597	20
	Diesel Bus	230	1,727	140	5	355	2,660	215	7
	Motorcycle	10,247	76,765	6,224	212	30,673	229,79	18,632	634
	Total	6,637	49,722	4,032	137	33,814	253,33	20,540	699
III	Automobile	443	3,317	269	9	2,380	17,827	1,445	49
	Diesel Bus	248	1857	150	5	522	3,912	317	11
	Motorcycle	13,124	98,322	7,972	271	39,282	294,29	23,862	812
	Total								

From the results of change of mode split, the traffic volume reduction can be obtained as shown before, thus the air pollutant reduction can be calculated using Equation 1, as seen in Table 5. Three scenarios of monorail systems with the change of ticket price are set in order to know the different concentration of air pollution parameter for each vehicle type. First scenario is condition with monorail ticket 2,5000 IDR less cheap than the existing public transport. Second scenario is condition which is monorail ticket similar to the existing public transport. The third scenario is done by monorail ticket 2,5000 IDR more expensive than the existing public transport.

Table 5 explains that CO is the major component of the motorized vehicle emission. Thus, motorcycle gives the largest contribution in air pollution, followed by automobile. As amount of air pollution is influenced by the characteristics of vehicle engine.

Scenario 1 is the condition with monorail ticket is cheaper than the existing modes, the monorail passengers increase, thus the amount of emission is the lowest concentration. Meanwhile, scenario 3 is the highest emission concentration for each parameter due to less reduction of use of private vehicles. Scenario 3 has the effect on reduction of 26% HC, 23% CO, and 24% NO_x. Scenario 2 has impacts on reduction of HC and CO up to 44% and NO_x up to 47%. Meanwhile, scenario 1 has significant decreasing HC up to 66%, CO up to 71%, and NO_x up to 82%.

The difference of cost due to CO emission between road with business places and with residential areas in road corridors is approximately 3 billion IDR as seen in Table 6.

Table 6. Prediction of Air Pollution on Lontar St. and Sungkono St. with Monorail Operation (IDR)

Vehicle Type	Peak Hour (Average of Morning, Noon and Afternoon)			
	CO	Total	CO	Total
Private car	106.520.753	855.111.763	542.706.304	
Public transit	1.776.271		9.547.457	
Bus	-		388.559	2.994.659.300
Truck	5.273.305		5.883.898	
Motorcycle	315.954.207		945.697.792	

There were a significant reduction between existing condition of air pollution cost (with no monorail) and the condition with monorail. By applying Scenario 3, the community can save about 26% of the air pollution cost, while applying Scenario 2 can save 44%. Scenario 1 can reduce air pollution cost from 5.19 trillion IDR to 1.71 trillion, or save about 67%. So, it can be concluded

that the investment of monorail will delivered a significant benefit in the savings of air pollution cost as illustrated in Fig. 4.

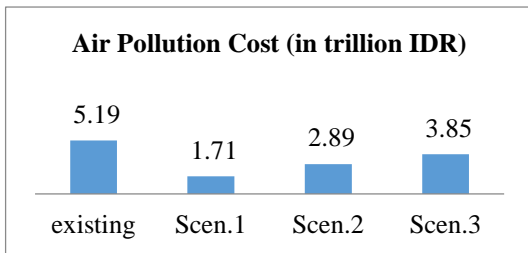


Fig. 4 Total of Air Pollution Cost on Lontar St. and Sungkono St. due to Monorail Operation

CONCLUSIONS AND RECOMMENDATIONS

Conclusions

This study demonstrated that improvement of public transport with the design of monorail system is necessary to address the mobility and emission problems in fast growing urban areas and the associated effects of urban sprawl. Consideration on air quality, i.e. i.e. HC, CO, NO_x, SO_x concentration is an important factor in urban transport planning with analysis of three cases.

The case (C3) with improved PT systems such as monorail system was characterized by the smallest emissions rates of each parameter. This case (C3) also can reduce the use of private vehicles (cars and motorcycles) and decrease 30-50% of emission parameter compared to the existing public transport.

Scenario 1 of monorail operation will decline HC up to 66%, CO up to 71%, and NO_x up to 82% total on both streets. Thus the air pollution cost will decline up to 67%. Scenario 2 can reduce HC and CO up to 44% and NO_x up to 47%, and the total air pollution of both streets on peak time is reduced about 44%. Scenario 3 only lessened 26% HC, 23% CO, and 24% NO_x, and the total air pollution of both streets on peak is saved 26%.

The highest air pollutant cost occur on road corridors as business places. The difference cost of CO emission between road corridor with business places and with residential areas is high cost about 3 billion IDR.

Recommendations

An integration of spatial-transport strategies as well an environmental assessment would provide more sophisticated and long-term advantages when designing improvements of public transport systems related to housing planning. The integrated approach should also be based on residents' preferences as regards the impact of such new developments.

The further research for air pollutant cost assessment should be conducted in order to estimate the air pollutant suitable with the Indonesian road environment and the change of monorail tariff.

REFERENCES

- [1] Bekele, H., Urbanization and urban sprawl. Master of Science Thesis-Department of Infrastructure Section of Building and Real Estate Economics Kungliga Tekniska Högskolan, 2005.
- [2] Duncan, J. E., Frank, J., The search for efficient urban growth patterns. Tallahassee, FL: Florida Department of Community Affairs, 1989.
- [3] Frumkin, H., Urban Sprawl and Public Health. Public Health Reports 117, 201, 2002.
- [4] Karanadze, L., The Main Aspects of Sustainable and Healthy Urban Transport Development in Georgia, Ministry of Environment of Georgia, 2006.
- [5] Costabile, F., Allegrini, I., A new approach to link transport emissions and air quality: an intelligent transport system based on the control of traffic air pollution. Environ. Model. Software. 23, 2008, pp.258–267.
- [6] Carley, M., & Christie, I., Managing sustainable development. Routledge, 2017.
- [7] Statistic Bureau of Surabaya, The Figures of Surabaya City in 2010 (in Indonesian).
- [8] Mitchell, G., Forecasting environmental equity: air quality responses to road user charging in Leeds, UK. J. Environ. Manage. 77, 2005, pp. 212–226.
- [9] Chin, A.T., Containing air pollution and traffic congestion: transport policy and the environment in Singapore. Atmos. Environ. 30, 1996, pp. 787–801.
- [10] Department of Transport of Surabaya City, Surabaya MRT: Surabaya Mass Rapid Transportation (SMART). Technical Report. Surabaya, Indonesia, 2013.
- [11] Litman, T., Transportation Cost Analysis. Victoria, 1995.
- [12] The Ministry of General Works, Law no. 017/T/BM/1999, Procedure for prediction of air pollution in micro scale from traffic (in Indonesian), Jakarta, 1999.
- [13] Ambarwati, L., Verhaeghe, R.J., Pel, A.J., Arem, B. van, The influence of integrated space-transport development strategies on air pollution in urban areas, Transportation Research Part D 44, 2016, pp. 134–146

PURIFICATION EXPERIMENTS ON THE PASIG RIVER, PHILIPPINES USING A CIRCULATION-TYPE PURIFICATION SYSTEM

Okamoto Kyoichi¹, Komoriya Tomoe², Toyama Takeshi¹, Hirano Hirosuke³,
Garcia, Teodinis⁴, Baccay, Melito⁴, Macasilhig Marjun⁴, Fortaleza Benedicto⁴

¹Professor, CST, Nihon University, Japan; ²CIT, Nihon University, Japan; ³National College of Technology, Wakayama College, Japan; ⁴Technological University of the Philippines, Philippines

ABSTRACT

Polluted sludge from the Pasig River, which connects Laguna de Bay to Manila Bay in the Philippines, exerts a very large environmental load on the surrounding area. The river used to be a good route for transportation and an important source of water for the old Spanish Manila. However, the river is now very polluted due to human negligence and industrial development, and biologists consider it unable to sustain aquatic life. Many researchers have investigated the purification of the Pasig River, without satisfactory results. Here, we investigate fine-bubble technology for purification of polluted sludge. The critical point in this technique is the activation of bacteria existing in the area using fine bubbles. Sludge is decomposed and purified by activating aerobic bacteria after creating an aerobic state. In this study, our objective is to test the performance of the purification system on the sludge and water in the Pasig River by comparing the results to a case study in Funabashi Port, Japan. We achieved good results, with a significant decrease in total nitrogen in both the Pasig River and Funabashi Port samples. The system is an effective purification system for treating sludge from the Pasig.

Keywords: Fine bubbles, Purification of Sludge, Circulation-Type Purification System, Pasig River, Aerobic Bacteria

INTRODUCTION

The Pasig River in the Philippines connects Laguna Lake to Manila Bay and divides the Philippine capital Manila into a northern and southern part. The Pasig River is a tidal estuary and the flow direction depends on the difference in water level between Manila Bay and Laguna Lake. The Pasig River was historically used as a very important transportation route and water source. The river is now very polluted due to a human negligence and industrial development, as in [1]. There are many research papers as in [2], [3] investigating the river, but no study has made considerable progress from the point of view of purification. One author investigated the COD (chemical oxygen demand) at about 15 points along the river [2]. We measured the current COD in the river and found that the value has almost doubled since the year 2000.

In general, polluted matter in solid form elutes in water and polluted matter in water settles to the riverbed when pollution is severe. It is best to treat both pollution sources without a distinction between solids and water. In addition, the treatment must be effective for both freshwater and seawater, since the river flows into the sea and is tidally influenced.

Here, it is considered that the best treatment method is a decomposition purification system using the circulation of fine bubbles to activate naturally occurring aerobic bacteria. The system was

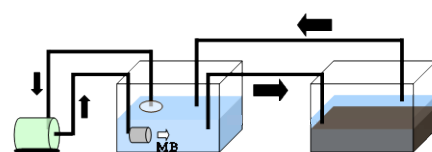
developed by one of the authors of this paper to treat ocean sludge, as described in [3]. This system has already been shown to be efficient for purification [3].

In this study, our objective is to demonstrate the effectiveness and efficiency of the circulation-type purification system for treatment of the Pasig River.

EXPERIMENTAL SYSTEM

Experimental Devices

The experimental device consisted of two parts, shown in Fig. 1. The water circulates through two tanks. In one tank, fine bubbles are generated, using a system based on [5]. The fine bubbles have micro-size diameters and high solubility. This means that water with a high concentration of dissolved oxygen (DO) circulates through the tanks.



Fine-Bubble Generator Experimental Tank

Fig. 1 Schematic Representation of the Experimental Apparatus

The second part of the device is the experimental tank. Here, sample water and sludge are treated. This apparatus was set up in one of the laboratories of the Integrated Research and Training Center (IRTC) of the Technological University of the Philippines (TUP), Manila.



Fig. 2 Picture of the Experimental Apparatus

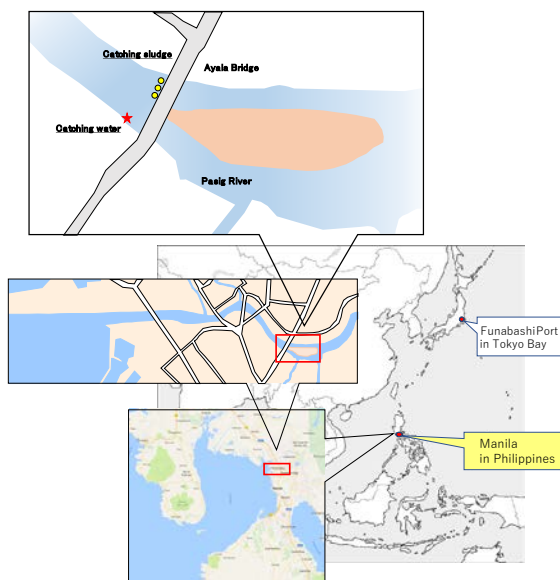


Fig.3 Sludge (Circle) and Water (Star) Sampling Points at the Ayala Bridge on the Pasig River, Manila



Fig.4 Sampling Sludge and Water in the Pasig River

Sampling Points for Sludge and Water

Sedimentary sludge samples were collected using an Ekman-Berge bottom sampler at the Ayala Bridge on the Pasig River as shown in Fig. 3 and Fig. 4. Water samples were collected at wharf near sludge sampling point in [3].

Samples from Funabashi Port, Japan shown in Fig. 5 were used to compare the efficiency and effectiveness of the purification system for the Pasig.

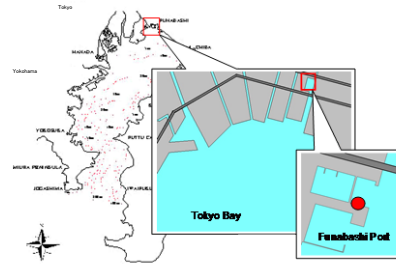


Fig.5 Sampling Point at Funabashi Port in Japan

Experimental Procedure

The dimensions of the experimental device are shown in Table 1. A sedimentary sludge sample of 0.417 (kg) and 25(L) of river water were collected. The samples were then put in the experimental tanks. The quality of the samples was measured from the moment the fine bubble generator started. After six hours of fine bubble generation, a microorganism activator was added in liquid form. The main component of the activator was help with some nutrients and enzymes. The microbial activator was added in a 100 (mg/L) concentration. The measured sample quality parameters were water temperature, pH, DO, ammonia nitrogen ($\text{NH}_4\text{-N}$), nitrite nitrogen ($\text{NO}_2\text{-N}$), nitrate nitrogen ($\text{NO}_3\text{-N}$), total nitrogen (T-N), and COD. Measurement of these parameters was conducted 24, 48, 60, and 72 hours from the time the fine-bubble generator started. Water temperature and DO were measured using a multi-parameter water quality meter (portable fluorescent dissolved oxygen meter). A digital water analyzer; Digital Pack Test (Kyoritsu Chemical-Check Lab., Corp.) was used to measure $\text{NH}_4\text{-N}$, $\text{NO}_2\text{-N}$, $\text{NO}_3\text{-N}$, and T-N.

Table 1 Dimension of the Experimental Devices

Water = 25 L, Sludge= 0.417 kg
Size of Water Tank = 200x270x370 mm
Flow Rate for Fine Bubble Generator = 43 L/min
Flow Rate for Circulation Water Pump = 10 L/min
Microbial Activator = 100 mg/L

RESULTS AND CONSIDERATIONS

Water Temperature, pH and Dissolved Oxygen

Measured results of water temperature, pH, and DO are shown in Fig. 6. The water temperature stabilized at 30 degree Celsius, pH was constant at around 8.0, and the DO stabilized around 6.0 mg/L.

The water temperature, pH, and DO are the basic environmental conditions of the experiment and should be kept constant as much as possible for proper interpretation of the other measured parameters.

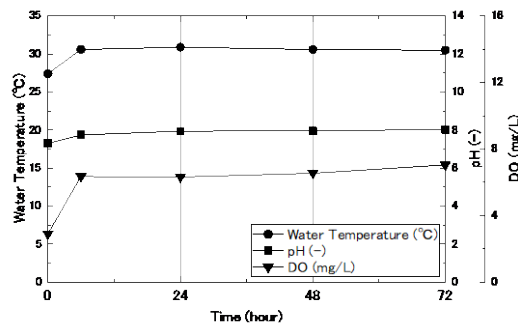


Fig. 6 Changes in Water Temperature, pH, and Dissolved Oxygen during the Experiment

Results of DIN (Dissolved Inorganic Nitrogen) and T-N in the Pasig River

The DIN is the totality of $\text{NH}_4\text{-N}$, $\text{NO}_2\text{-N}$, and $\text{NO}_3\text{-N}$. Figure 7 shows the results of measured DIN and T-N. There was a significant decrease in DIN from hour after 24 to until 72. DIN decreased a little at about 6 hours, but decrease rapidly after 24 hours. Therefore, it seems that bacterial denitrification occurred in the system.

The measured T-N showed that the quality of the sample improved. The temporary increase in T-N at about six hours may have been due to a slight delay in the inclusion of the microbial activator. After inclusion of the activator, T-N decreased significantly to 72 hours. The purification system performed very well since the concentration of T-N after 72 hours was about 50% of the starting value.

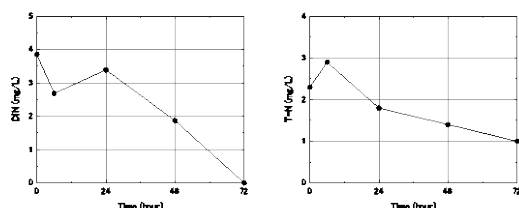


Fig. 7 Changes in DIN and T-N in the Pasig River

Comparison of the Purification Results for T-N with Funabashi Port in Japan

To compare the results of Funabashi Port and the Pasig River, we carried out experiments to understand the effect of the ratio of sludge and water. The experimental conditions, with variable amounts of water and sludge, are shown in Table 2. The usual parameters used at Funabashi Port in Japan are 1 kg of sludge and 30 L of water and the total experimental time is 120 hours. Case 1 was treated as the standard ratio of sludge, Case 2 was half the standard sludge ratio, and Case 3 tested a lower volume of water. These sludge and water are from Funabashi Port.

Figure 8 shows the results of T-N for the three cases. We estimated that purification of the samples in Case 2 in Fig.8 is completed in half the time of Case 1 according to the ratio of sludge. However, there was no change in the performance due to the difference in water volume between Case 2 and 3.

According to the above, Fig. 9 presents the results of Case 1 in half the run time, i.e. 60 hours instead of 120 hours. Therefore we can get assuming linear relation. Here, the y-axis shows the normalized expression.

Figure 10 shows a comparison of the results of T-N between Funabashi Port and the Pasig River. From the results, the circulation-type purification system indicates the same tendency and good purification performance. The tendency of the purification results is almost the same.

Table 2 Experimental Condition for Comparison of the Sludge Ratio

Case1: Water = 25L, Sludge = 0.84kg ; Standard
Case2: Water = 25L, Sludge = 0.42kg ; 1/2
Case3: Water = 20L, Sludge = 0.42kg ; 1/2

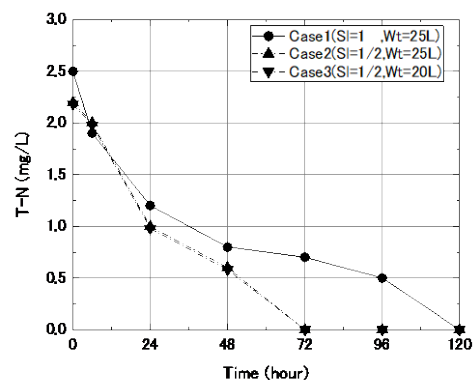


Fig.8 Comparison of T-N with Different Sludge Ratios

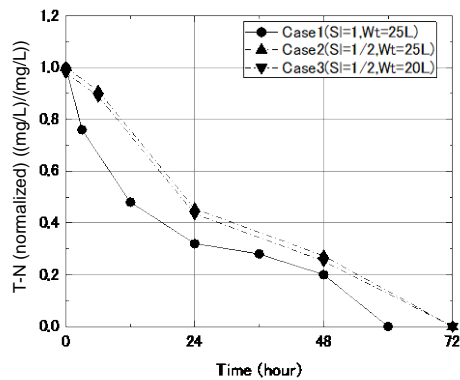


Fig. 9 Normalized T-N in Samples with Different Sludge Ratio

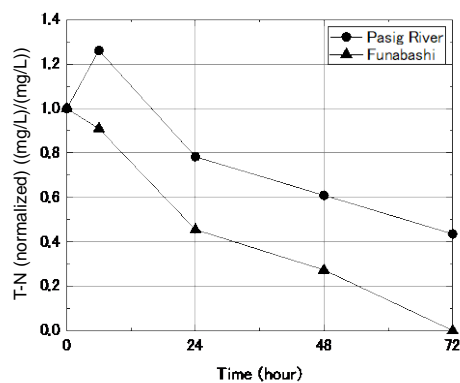


Fig. 10 Comparison of T-N in the Pasig River with Funabashi Port

Visualization of Results

Figure 11 shows the experimental visual scene at 0, 24, 48, and 72 hours. Changes to the water color in the tank can be clearly seen, which demonstrates the purification effects.

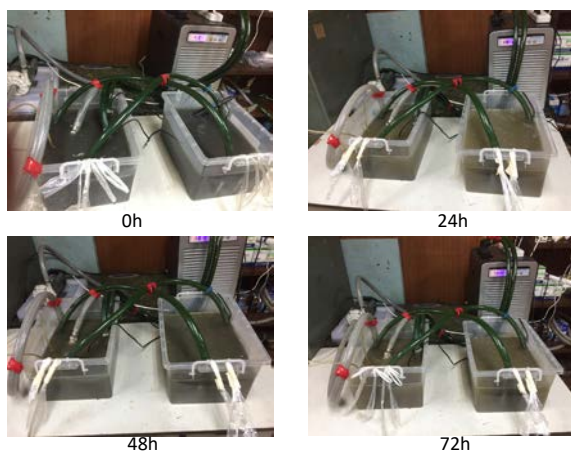


Fig. 11 Photos of the Experimental Tank with Time

Comparison of the Solid Results for the Pasig River and Funabashi Port

Comparison of EDX (Energy Dispersion Type X-ray Analysis Device) Results between the Pasig River and Funabashi Port

Figure 12 shows a comparison of the EDX results from the Pasig River and Funabashi Port. Comparing the beginning and the end of the experiments, S (sulfur) decreased but Na (sodium) increased slightly. The change in Si (silica) differed between the two locations; no change was observed in the Pasig River sample however the proportion of Si in the Funabashi Port sample decreased. It seems the Si (silica) ratio in Funabashi Port sample decreased a little by the relatively increase of Al and Fe. The other results showed the same tendency for both locations.

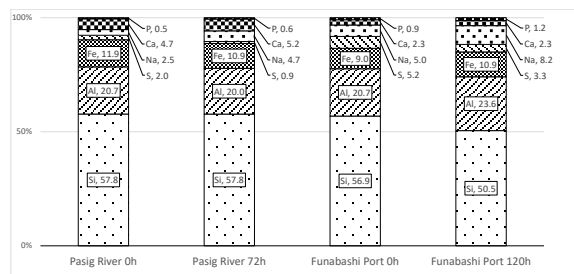


Fig. 12 EDX Results from the Pasig River and Funabashi Port

Comparison of SEM (Scanning Electron Microscope) Results for the Pasig River and Funabashi Port

Figure 13 shows a comparison of the SEM results from the Pasig River and Funabashi Port, at a magnification of 1000 times. Comparing the beginning and the end of the experiments, no change was observed for the Pasig River samples.

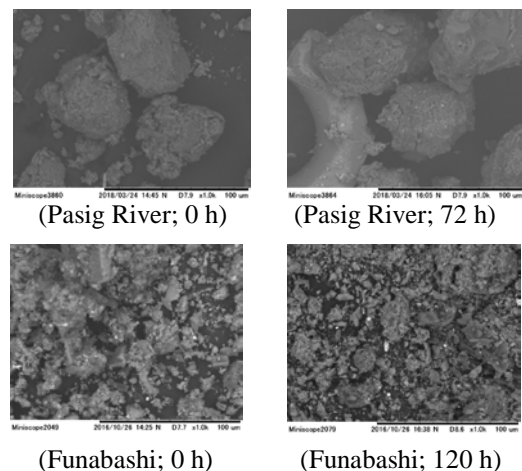


Fig. 13 SEM Results from the Pasig River and Funabashi Port

The diameter of the sludge particles from the Pasig River is relatively large so they are resistant to abrasion. On the other hand, the diameter of the sludge particles from the Funabashi Port is relatively small, so that the diameter decreased after treatment.

CONCLUSION

The effectiveness and efficiency of treatment of the Pasig River using the circulation-type purification system were determined.

1) The purification efficiency was good as demonstrated by the decrease in DIN and T-N concentrations.

We carried out three experiments to determine the effect of a variable ratio of sludge and water. From the results, an interpolation factor was determined. By changing the time axis using the factor, we compared T-N in the Pasig River and Funabashi Port and a very good purification tendency was obtained for both locations. From the results:

2) The purification performance was very good, as shown by the decrease in T-N in both the Pasig River and Funabashi Port samples.

3) The water color in the tanks over time also visually demonstrated very good purification results. From the results of EDX, the weight ratio of the matter in the solid dry sludge was calculated.

From the results of SEM, the change in diameter of the sludge particles was identified.

4) From all the above, it appears this system can treat both polluted sludge and water which is very useful in application to the Pasig River.

ACKNOWLEDGEMENTS

The authors would like to express sincere thanks for executing the experiments to Mr. Nogawa, Daisuke, a graduate student, Mr. Tateishi, Shotaro, a student of Nihon University, Prof. Reynaldo, Baarde, Head of Construction Engineering and management Department of TUP, and also help for writing paper to Ogawa, Ma.Richie C., a staff of Nihon University.

This work was supported by a KAKENHI (Grant-in-Aid for Scientific Research (C-17K06969)).

REFERENCES

- [1] Gorme et al, The Water Quality of the Pasig River in the City of Manila, Philippines: Current Status, Management and Future Recovery, 2010.
- [2] Urase T., Nadaoka K., Yagi H., Iwasai T., Suzuki T., Siringan F., Garcia T.P. and Thao T. T., Effect of urban emissions on the horizontal distribution of metal concentration in sediments in the vicinity of Asian large cities, *Journal of Water and Environment Technology*, Vol.4, No.1, 2006.
- [3] Okamoto K., Hotta K., Toyama T. and Kohno H., Purification System of Ocean Sludge by Activating Microorganisms, *International Journal of GEOMATE (Geotec, Const. Mat. & Env.)*, Vol.6, No.1, March, 2014, pp.791-795.
- [4] Matsuo K., Maeda K., Ohnari H., Tsunami Y. and Ohnari H., Water Purification of a Dam Lake Using Micro Bubble Technology, *Progress in Multiphase Flow Research I*, 2006, pp.279-286.
- [5] Okamoto K. and Hotta K., Purification System of Ocean Sludge by Using Coagulants and Activating Microorganisms, *International Journal of GEOMATE (Geotec, Const. Mat. & Env.)*, Vol.4, No.2, June, 2013, pp.574-579.
- [6] Sone T, Yamashita K and Okamoto K, Identification of Microorganism in Purification Process for Ocean Sludge by using Purification System with Circulation Type, *Japan Association for Coastal Zone Studies*, July 2014.
- [7] Okamoto K and Toyama T, Ocean Decontamination: High Efficiency Removal Method of Radioactive Cesium from Ocean Sludge by Using Microbubbles and Activating Microorganisms, *The Japan Society of Naval Architects and Ocean Engineers*, May, 2016.
- [8] Okamoto K. and Toyama T., Ocean Decontamination: Removal Efficiency of Radioactive Cesium from Ocean Sludge by using Microbubbles and Activating Microorganisms, *International Journal of GEOMATE (Geotec., Const. Mat. & Env)*, Vol. 10, Issue 21, May, 2016, pp. 1924-1928.
- [9] Komoriya T., Okamoto K. and Toyama, T., Removal of Radioactive cesium from Ocean sludge by the bacterium using Purification System of Circulation Type, *International Journal of GEOMATE*, Vol.15, Issue 47, July, 2018, pp.53-57.

PERFORMANCE OF A CIRCULATION TYPE PURIFICATION SYSTEM DURING THE TREATMENT OF SLUDGE FROM MANILA BAY AND TWO PORTS IN JAPAN

Komoriya Tomoe¹, Okamoto Kyoichi², Toyama Takeshi², Hirano Hirotsuke³,
Garcia, Teodinis⁴, Baccay, Melito⁴, Macasilhig Marjun⁴, Fortaleza Benedicto⁴

¹CIT, Nihon University, Japan; ²CST, Nihon University, Japan; ³National College of Technology, Wakayama College, Japan; ⁴Technological University of the Philippines, Philippines

ABSTRACT

Ocean sludge can have negative effects on local marine ecosystems. Here, the use of fine-bubble technology was investigated for applications involving the purification of sludge. The principle of this technology is that bacteria that can degrade sludge are activated by the aerobic conditions induced by the fine-bubbles. One of the authors has developed a fine-bubble decomposition system for ocean sludge that is of the circulation type. Here, we tested the performance of this system during the treatment of sludge from Manila Bay and two ports in Japan. The results showed that the system performed well when treating the sludge. Potentially beneficial bacteria isolated from the Manila Bay sludge experiments were identified by 16S rRNA gene sequence analyses.

Keywords: Fine-bubbles, Purification of Sludge, Circulation Type Purification System, Manila Bay

INTRODUCTION

It is very important to reduce the amount of sedimentary sludge in the ocean. Plans to reduce such sludge are usually based on dredging or sand covers. Dredging is a simple method whereby the sludge is physically removed. However, the dredged sludge needs to be treated after removal, which takes time and money. Sand covers, in general, reduce contamination from ocean sludge, but they too can stress living organisms and ecological systems and are not ideal in places where navigation is a concern. Hence, better sludge management options are needed.

Here, we explore the use of fine-bubble technology to promote sludge degradation. Fine-bubbles can change conditions from an anaerobic state into an aerobic state. One of the authors has developed a method for decomposing sludge by using microorganisms activated by the aerobic state induced by micro-bubbles. Subsequently, very good results were achieved with this method [1–3]; for example, the method enabled the treatment time to be reduced to 5 days. Here, the purification system was used to treat sludge from the following three areas: Funabashi Port in Tokyo Bay, Japan, Hidaka Port in Wakayama Prefecture, Japan, and Manila Bay, Philippines. The main objective of this study was to assess the performance of the purification system.

The ports of Funabashi and Hidaka are important ports in Japan. Manila Bay is a natural harbor that is located in the capital city of the Philippines. It has served as a key area for socio-economic development in the country and has helped to facilitate commerce and trade between the Philippines and nearby

countries. Because of the high levels of human activity and industrialization around Manila Bay, the water quality within the bay is degraded [4].

EXPERIMENTAL SYSTEM

Experimental Devices

The experimental devices consisted of two parts, as shown in Fig. 1. Specifically, the water circulates through two tanks in the purification system. In one tank, fine-bubbles are generated. These fine-bubbles have a micro-sized diameter and high solubility. This allows water with high concentrations of dissolved oxygen to circulate readily through the tanks. The fine-bubble generator was based on earlier work [5–6]. The other tank is the experimental tank. In this tank, sea water and sludge were combined.

This apparatus was set up in one of the laboratories of the Integrated Research and Training Center (IRTC) of the Technological University of the Philippines (TUP), Manila, Philippines.

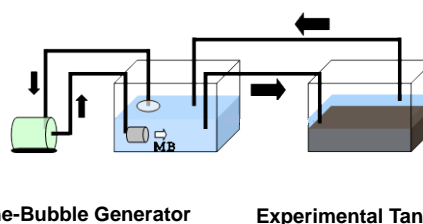


Fig. 1 Purification System of the Circulation Type

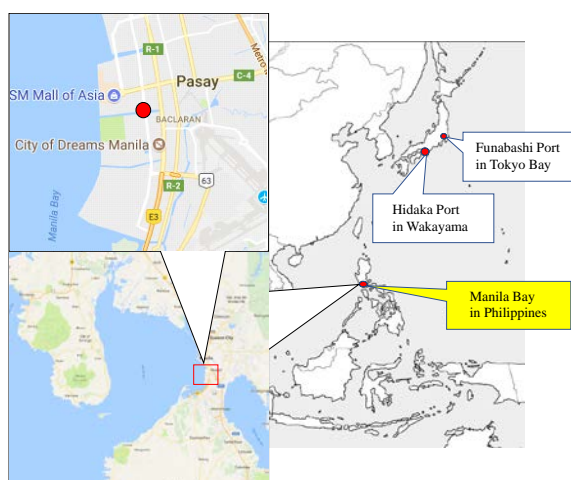


Fig 2. Locations of the study sites in Manila Bay, Philippines, and Funabashi and Hidaka, Japan

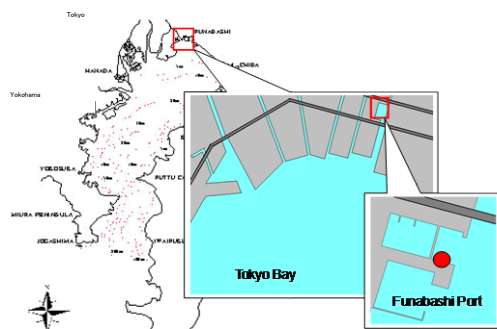


Fig.3 Sampling Point at Funabashi Port in Japan



Fig.4 Sampling Point at Hidaka Port in Japan



Fig. 5 Sediment Sampler

Collection Points for Sludge and Sea Water

To investigate the efficiency of the purification system, sea water and sedimentary sludge samples were collected from Manila Bay in the Philippines at the site indicated by the red circle in Fig. 2. Other samples were collected from the ports of Funabashi and Hidaka at the sites indicated by the red circles in Figs. 3 and 4, respectively.

Experimental Procedure

Sedimentary sludge was collected by using the sediment sampler, shown in Fig. 5. The collected samples were then placed into the tanks (Fig. 6). The time that the fine-bubble generator was started was used as the start time for sample measurements. After 6 hours of generating fine-bubbles, a microbial activator was added, which consisted of kelp with some nutrients and enzymes; it was in liquid form. The amount of microbial activator added was 100 mg/L. The water quality was assessed by taking measurements of the water temperature, chemical oxygen demand (COD), and concentrations of dissolved oxygen (DO), ammonia nitrogen ($\text{NH}_4\text{-N}$), nitrite nitrogen ($\text{NO}_2\text{-N}$), nitrate nitrogen ($\text{NO}_3\text{-N}$), and total nitrogen (T-N). Measurements were conducted after 24, 48, 60, and 72 hours from the start time, i.e., the time that the micro-bubble generator was started. Dissolved oxygen and water temperature were measured with a multi-parameter water quality meter (portable fluorescent dissolved oxygen meter). Ammonia nitrogen, nitrite nitrogen, nitrite nitrogen, and total nitrogen concentrations were measured by using a Digital Pack Test (Kyoritsu Chemical-Check Lab, Corp.). Additional specifications of the experimental devices are given in Table 1.



Fig. 6 Photograph of the Actual Experiment

Table 1 Specifications of the Experimental Devices

Water = 25 L, Sludge= 0.1875 kg
Size of Water Tank = 200x270x370 mm
Flow Rate for Fine Bubble Generator = 43 L/min
Flow Rate for Circulation Water Pump = 10 L/min
Microbial Activator = 100 mg/L

EXPERIMENTAL RESULTS

Water Temperature and Dissolved Oxygen

The measured water temperature and dissolved oxygen results are shown in Fig. 7. The water temperature stabilized at 30 degrees C, and the DO stabilized at around 7.5 mg/L. The stable water temperatures and DO concentrations were desirable because this facilitated proper interpretation of the results for the other parameters that were measured. The above data also demonstrate that aerobic conditions were present in the experiments.

Dissolved Inorganic Nitrogen, Total Nitrogen and Chemical Oxygen Demand

The level of dissolved inorganic nitrogen (DIN) represents the total amount of ammonia nitrogen ($\text{NH}_4\text{-N}$), nitrite nitrogen ($\text{NO}_2\text{-N}$), and nitrate nitrogen ($\text{NO}_3\text{-N}$). Figure 8 shows the results for the DIN. The DIN concentrations abruptly decreased within 24 hours and thereafter remained at almost undetectable levels for the 48 hour and 72 hour time points. These data indicate that denitrifying bacteria were present in the system.

The T-N results are shown in Fig. 9. The T-N concentrations first decreased and then slightly increased by about 20% within the first 48 hours. However, after 72 hours, T-N was not detected in the system, which implies that the purification system performed well. The temporary increase of T-N between 24 hours and 48 hours may have been due to delayed effects from the addition of the microbial activator.

The results for the COD are shown in Fig. 10. The COD remained constant at 20 mg/L for 24 hours and then increased to 25 mg/L at 48 hours possibly because of the microbial activator. Then, the COD returned to 20 mg/L at 72 hours. These results confirm the efficiency of the system.

Comparison of the Purification Results for Total Nitrogen in Manila Bay Samples with Those from the Ports of Funabashi and Hidaka in Japan

Figure 11 shows the results for the T-N concentrations versus time for the three experiments conducted with sludge from three places, namely, Manila Bay and the ports of Funabashi and Hidaka. The T-N concentrations decreased dramatically in all three experiments. The T-N concentrations reached undetectable levels within 72 hours for the samples from Manila Bay and Hidaka, whereas the T-N concentrations only reached undetectable levels after 120 hours for the samples from Funabashi. According to these results, the purification system of the circulation type showed good purification performance.

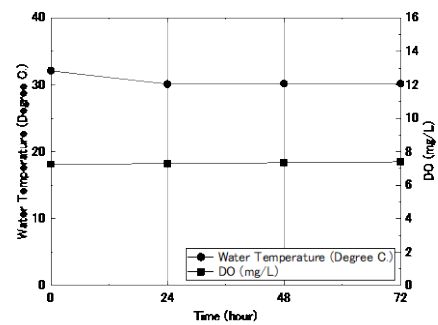


Fig.7 Changes in Water Temperature and Dissolved Oxygen (DO)

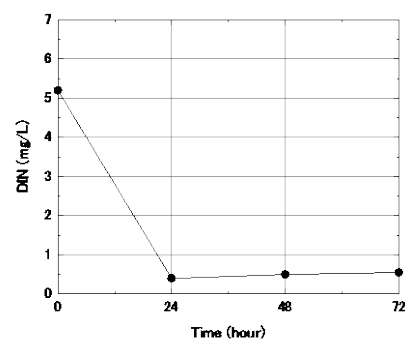


Fig.8 Changes in Dissolved Inorganic Nitrogen (DIN)

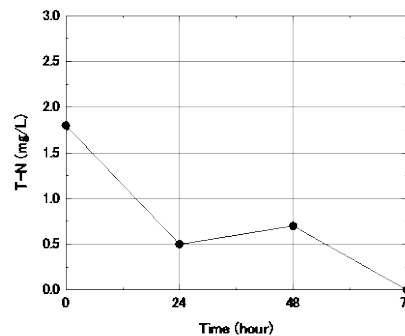


Fig.9 Changes in Total Nitrogen (T-N)

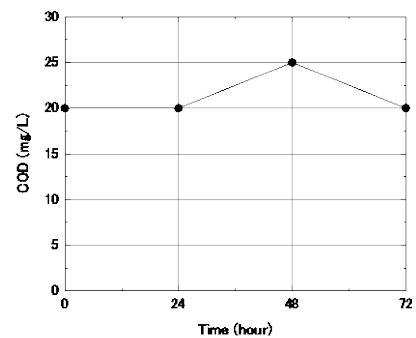


Fig.10 Changes in the Chemical Oxygen Demand (COD)

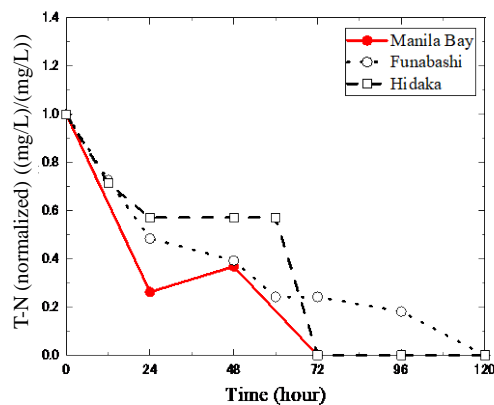


Fig. 11 Comparison of the Total Nitrogen (T-N) Results for Manila Bay Samples with Those from the Ports of Funabashi and Hidaka

Comparison of the Purification Results for Elemental Compositions in Manila Bay Samples with Those for Funabashi and Hidaka Port in Japan

Figure 12 shows comparisons of the EDX (Energy Dispersion type X-ray analysis device) results for samples from Manila Bay and the ports of Hidaka and Funabashi.

Compared with the beginning and the end of the experiments, S (sulfur) decreased in each treatment. Interestingly, Na (sodium) increased by a small amount only at Funabashi. The other components showed similar tendencies. The largest decrease in Si (silica) occurred in the Funabashi samples.

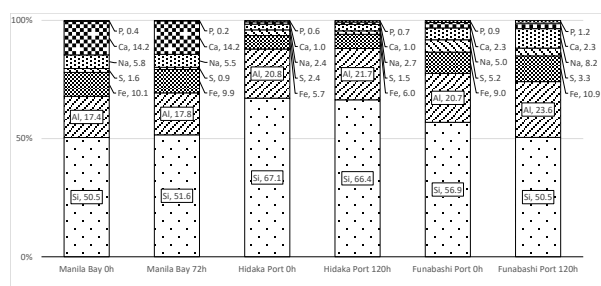


Fig. 12 Results from the EDX (Energy Dispersion Type X-ray Analysis Device) for Manila Bay and the Ports of Hidaka and Funabashi

Microbial Analyses

Microbial analyses were performed to identify the useful bacteria in the fine-bubble treatment of Manila Bay sludge. Bacteria were isolated from the sludge experiments and identified by 16S rRNA gene sequence analyses according to methods described in earlier work [7].

The following six species of bacteria were identified from sludge at 0 and 24 h: *Rhodococcus* sp., *Bacillus* sp., *Exiguobacterium* sp., *Serratia* sp., *Pseudomonas* sp., and *Marinobacter* sp. (Table 3).

We concluded that *Rhodococcus* sp., *Exiguobacterium* sp., and *Marinobacter* sp. were uniquely valuable for breaking down the sludge. Previous studies have shown that *Rhodococcus* sp. have the ability to participate in fossil fuel biodesulfurization reactions, and *Exiguobacterium* sp. have been detected in unique environments with temperatures ranging from -12 to 55 degrees C [8]. *Marinobacter* sp. can degrade hydrocarbons, as discussed in [9].

Table 3 Sequence Analysis Results for the Six Isolated Stains

Strain No.	Length (bp)	% similarity
1	1624	98 % <i>Rhodococcus</i> sp.
2	1005	95 % <i>Bacillus</i> sp.
3	1075	92 % <i>Exiguobacterium</i> sp.
4	593	93 % <i>Serratia</i> sp.
5	453	79 % <i>Pseudomonas</i> sp.
6	1509	97 % <i>Marinobacter</i> sp.

CONCLUSION

Experiments were carried out to assess the performance of a circulation type purification system during the degradation of sludge samples from Manila Bay in the Philippines and the ports of Funabashi and Hidaka in Japan. According to the results for several measured parameters, namely, water temperature, dissolved oxygen, dissolved inorganic nitrogen (DIN), total nitrogen (TN), and chemical oxygen demand (COD), the performance of the purification system was very good. In particular, DIN and TN concentrations decreased markedly during the treatments within a short period of time, which were reflective of improvements in the water quality of the samples. Six species of bacteria were isolated from the sludge from Manila Bay. *Pseudomonas* sp. was identified as the same bacteria found in [7].

ACKNOWLEDGEMENTS

The authors would like to express sincere thanks to Mr. Nogawa, Daisuke, a graduate student, Mr. Tateishi, Shotaro, a student of Nihon University, and Prof. Reynaldo, Baarde, Head of the Construction Engineering and Management Department of TUP

for executing the experiments; we are also grateful to Ogawa, Ma.Richie C., staff of Nihon University, for assistance with writing the paper.

This work was supported by a KAKENHI Grant-in-Aid for Scientific Research (C-17K06969).

REFERENCES

- [1] Okamoto, K., Komoriya, T., and Toyama, T., Comparison of Purification Performance against Ocean Sludge in Two Sea-Area by Using Purification System of Circulation Type, Proceedings of the 6th International Conference on Civil Engineering, 2017.
- [2] Okamoto, K., and Hotta, K., Purification Experiments on Sedimentary Sludge by Microorganism Activation, Recent Advances in Marine Science and Technology 2010 – PACON International, 2010, pp. 151–166.
- [3] Okamoto, K., Hotta, K., Toyama, T., and Kohno, H., Experiments on Purification of Ocean Sludge by Activating Microorganisms, The International Offshore (Ocean) and Polar Engineering Conference, 2011.
- [4] Jacinto, G.S., Azanza, R.V., Velasquez, I.B., and Siringan, F.P., Manila Bay: Environmental Challenges and Opportunities, In Wolanski, E. (Ed.), The Environment in Asia Pacific Harbors, 2006, Springer, pp. 309–328.
- [5] Matsuo, K., Maeda, K., Ohnari, H., Tsunami, Y., and Ohnari, H., Water Purification of a Dam Lake Using Micro Bubble Technology, Progress in Multiphase Flow Research, Vol. 1, 2006, pp. 279–286.
- [6] Okamoto, K., Hotta, K., Toyama, T., and Kohno, H., Purification System of Ocean Sludge by Activating Microorganisms, International Journal of GEOMATE (Geotechnique, Construction Materials and Environment), Vol. 6, No. 1, 2014, pp. 791–795.
- [7] Komoriya, T., Okamoto, K., and Toyama, T., Effect of Adding of Bacteria on the Removal of Radioactive Cesium from Ocean Sludge in a Circulation Type Purification System, International Journal of GEOMATE (Geotechnique, Construction Materials and Environment), Vol. 12, 2017, pp. 121–126.
- [8] Vishnivetskaya, T.A., Kathariou, S., and Tiedje, J.M., The Exiguobacterium Genus: Biodiversity and Biogeography, Extremophiles, Vol. 13, 2009, pp. 514–555.
- [9] Brito, E.M.S., Guyoneaud, R., Goñi-Urriza, M., Ranchou-Peyruse, A., Verbaere, A., Crapez, M.A.C., Wasserman, J.C.A., and Duran, R., Characterization of Hydrocarbonoclastic Bacterial Communities from Mangrove Sediments in Guanabara Bay, Brazil, Research in Microbiology, Vol. 157, 2006, pp. 752–762.

ESTIMATION OF GROUNDWATER RECHARGE AND SALINIZATION IN A COASTAL ALLUVIAL PLAIN AND OSAKA MEGACITY, JAPAN, USING $\delta^{18}\text{O}$, δD , AND Cl^-

Yusuke Tomozawa¹, Shin-ichi Onodera¹, Mitsuyo Saito²

¹ Graduate School of Integrated Arts and Sciences, Hiroshima University;

² Graduate School of Environmental and Life Science, Okayama University

ABSTRACT

Seawater intrusion and salinization are the most common problems of water pollution in coastal groundwater. To clarify the process of groundwater salinization in a coastal alluvial plain, we estimated the groundwater recharge and salinization process in Osaka coastal groundwater using $\delta^{18}\text{O}$, δD , and Cl^- . Water samples were collected at 14 boreholes of 9 plots with depth of -5 to -60 m amsl in March 2015. The $\delta^{18}\text{O}$ values and Cl^- concentrations of the groundwater varied spatially from -6.4 ‰ to -4.7 ‰ and 17 mg/L to 5193 mg/L, respectively. Based on Cl^- concentrations, the maximum mixing ratio of seawater with the concentration of 1800 mg/L into groundwater was estimated to be 29% about 3 km inland from the shoreline at the depth of about -40 m. The relationship between $\delta^{18}\text{O}$ and Cl^- of groundwater and seawater indicated three types of end members: seawater with high Cl^- and $\delta^{18}\text{O}$, a groundwater source with lower Cl^- and lower $\delta^{18}\text{O}$ (-5.6 ‰), and a groundwater source with lower Cl^- and the lowest $\delta^{18}\text{O}$ (-7.2 ‰). According to the relationship between the altitude of groundwater recharge and $\delta^{18}\text{O}$ established by previous research, two types of groundwater recharge and source areas were estimated to be coastal lowland and upland with altitudes <10 m amsl and surrounding hill 18 km inland from the shoreline with altitudes of 100 m amsl.

Keywords: Coastal groundwater, Stable isotope, Chloride, Seawater intrusion

1. INTRODUCTION

The resource value of groundwater has been recognized again in recent years and considered widely, such as for water use in an emergency and heat for renewable energy. Within the Big Movement in Japan, the "Basic Law on the Water Cycle" was established in March 2014. It requires efforts to understand water circulation throughout the basins of Japan, including the groundwater recharge zone.

For the use of groundwater as a sustainable water resource, water quality is important from the viewpoint of safety, and it is necessary to maintain and manage water quality [1-3].

Seawater intrusion is the most common water quality problem for coastal groundwater. The main factors of seawater intrusion are disturbance of the water balance in an aquifer caused by excess pumping (a human factor) and influences such as topography, geology, sediment, etc. (natural factors). It is important to understand the degree of influence of each of these factors to manage seawater intrusion.

Since 1940, ground settlement has been a problem in the Osaka Plain because seawater intrusion has occurred correspondingly. However, groundwater intake restrictions have been strengthened to recover the groundwater level, so the level has been almost stable in recent years. Although several studies concerning water quality [4-11] have been conducted, this research was not sufficient to elucidate in detail

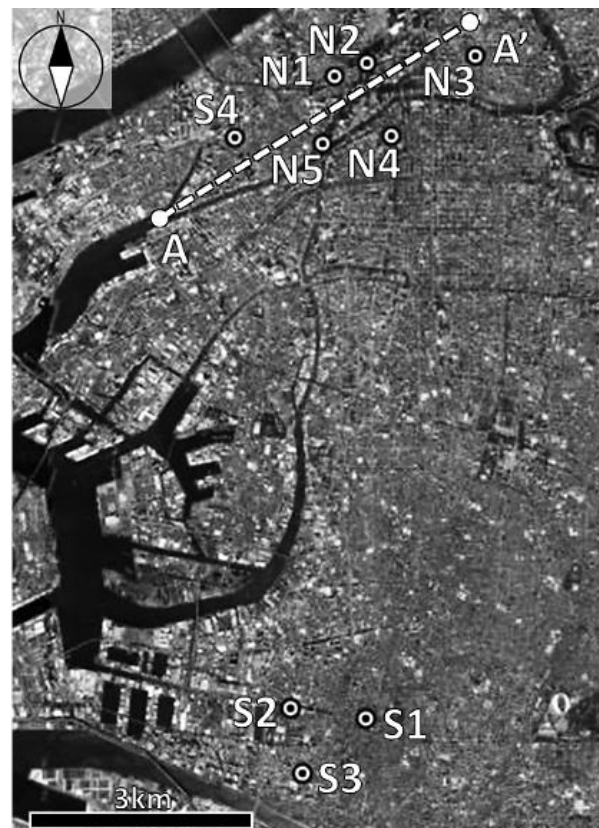


Fig. 1 Study area

the groundwater recharge/flow in the entire Osaka Plain. Therefore, the aims of this study were to

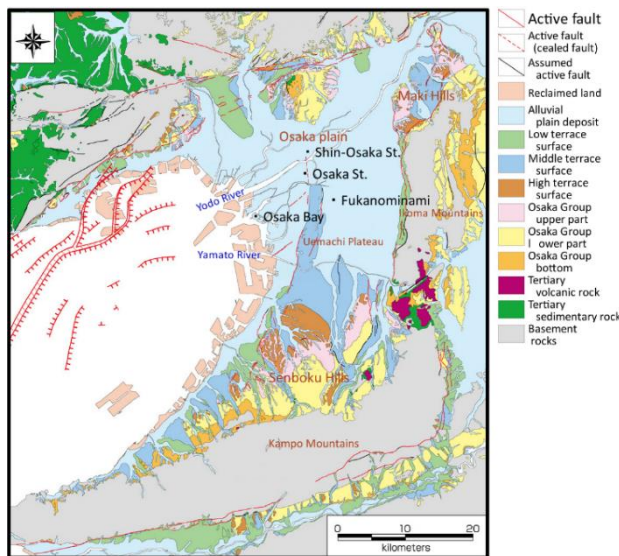


Fig. 2 Topography / Geology
(Modified after KG-NET, Kansai Area Ground Work Meeting (2007) [13])

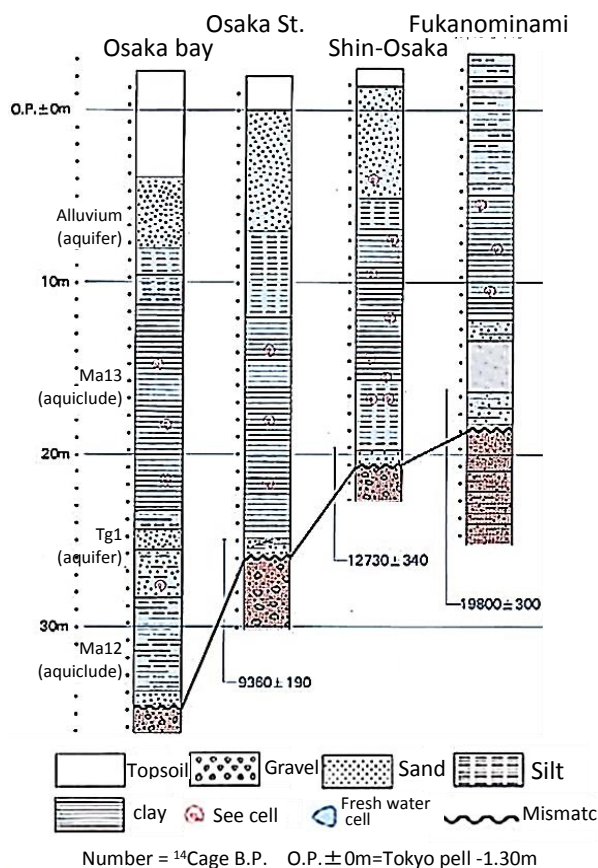


Fig. 3 Geologic columnar section
(modified after Ichihara et al. [12])

confirm the situation of seawater intrusion into the coastal groundwater and estimate the recharge process of the water by measuring the concentrations of chloride ion (Cl^-) and stable hydrogen and oxygen isotopes as well as analyzing the isotopic ratios ($\delta^{18}\text{O}$, δD) and comparing them with the existing values in the literature.

2. STUDY AREA AND METHOD

The research was conducted in the Osaka Plain. The locations of observation wells are shown in Fig. 1, and the geological features of the region are shown in Fig. 2 and Fig. 3 [12][13].

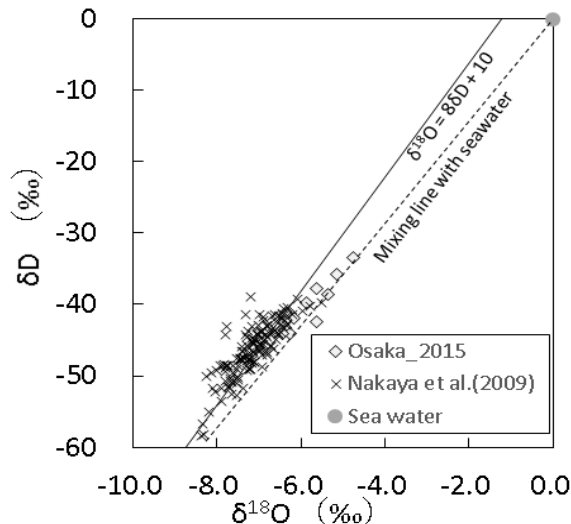
The flat area is covered with alluvial deposits. The geological column from soil surface can be summarized as (example from Osaka Bay) top soil (a), sand (b), silt (c), clay (d), sand and mixed silt (e), silt (f), sand (g), and gravel (h). Aquifers are assumed to be located in sand layer (b), gravel layer (h), alluvium, the 1st Hongan laminated gravel layer (Tg1), and the 2nd volcanic gravel layer (Tg2) near the deeper G.L-60m aquiclude (Ma13–Ma11), which is located between each aquifer [9][14].

Nine observation wells on the coast of Osaka Bay were the target of our research. Five observation wells (N1 to N5) were under the jurisdiction of the Research Council of Groundwater Environment. Two observation wells (S3 and S4) were under the jurisdiction of the Ministry of Land, Infrastructure and Transport, and the other two wells (S1 and S2) were under the authority of Osaka Prefecture (Fig. 1).

The assumed aquifer and depth (G.L-m) of each observation well follow:

- Alluvium: S1/6.70 m, S3/10.50 m, S4/10.20 m, N3-AS/22.00 m.
- The 1st Hongu laminated gravel layer (Tg1): S2/25.00 m, N1-Tg1/37.50 m, N2-Tg1/31.60 m, N3-Tg1/40.50 m, N4-Tg1/40.20 m, N5-Tg1/ 39.30 m.
- The 2nd Huang layered gravel layer (Tg2): N1-Tg2/56.25 m, N2-Tg2/56.80 m, N4-Tg2/61.70 m, N5-Tg2/59.75 m

The strainer length of N1 to N5 is 4.0 m, and those of S1 to S4 are 3.7 m, 3.0 m, 7.6 m, and 8.0 m, respectively. The groundwater level measurement and sample collection were carried out in March 2015. The observation wells were drained before sampling. The electrical conductivity, pH, and dissolved oxygen concentration of the sample water were measured on site. Cl^- concentration and stable hydrogen and oxygen isotopes were analyzed in the laboratory. The Cl^- concentration was analyzed by ion chromatography (Shimadzu Corporation, CL-VP), and the stable isotope ratios (δD , $\delta^{18}\text{O}$) were calculated with the WS-CRDS method (Picarro Company, L2120-i).

Fig. 4 δ diagram

(\times refers to analysis values by Nakaya et al. [14], the same below)

3. SITUATION OF SEAWATER INTRUSION

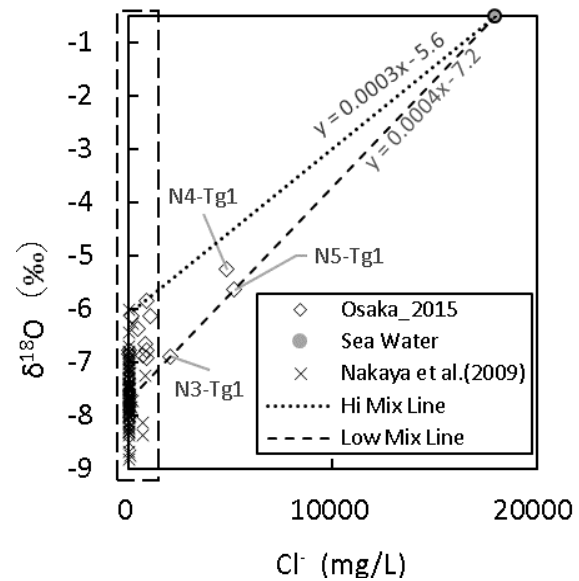
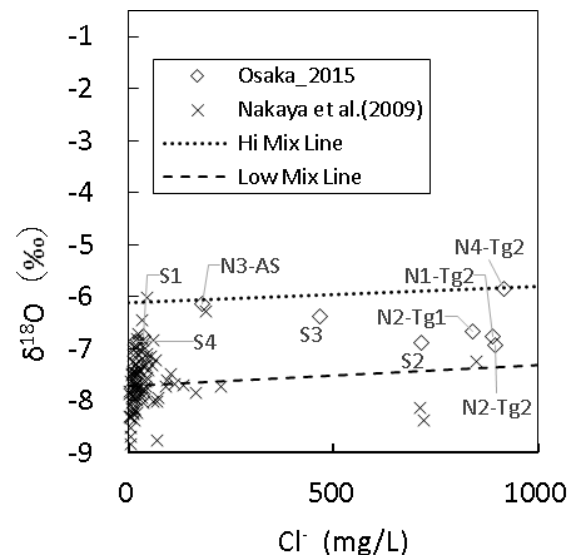
Fig. 4 shows a δ diagram with data of the groundwater and the meteoric water line ($\delta D = 8\delta^{18}O + 10$) around the Osaka Plain by Nakaya et al. [14] for comparison. The data plotted along the meteoric water line with a slope of roughly 8, indicating that the water was derived from rainwater. Some data plotted near the mixing line of modern sea water (δD : 0‰, $\delta^{18}O$: 0.0‰) and the lower limit of groundwater. It is suggested that the mixing of groundwater and sea water shifted isotopic values to heavier ones.

Fig. 5 and Fig. 6 show the correlation between $\delta^{18}O$ and Cl^- . The concentrations of Cl^- at N5-Tg1 and N4-Tg1 were 5193 mg/L and 4813 mg/L, respectively. These concentrations were particularly high, indicating saltification. Given the values of modern seawater of $\delta^{18}O$: 0.0 ‰, Cl^- : 18000 mg/L, seawater intrusion occurs when the mixing ratio of sea water is 0.1 to 28.9 %. At the other points, Cl^- concentration was 500 to 1000 mg/L, which confirmed the occurrence of seawater intrusion. Intrusion of seawater is stronger in the Yodo River Basin (N1–N5, S4) than in the Yamato River Basin (S1–S3).

The intersection of the vertical line with the high mixing line and the low mixing line was -7.2 to -5.6 ‰ (Fig. 5). These values were included in the freshwater side data. We assume that groundwater and modern seawater are mixed in the aquifer.

4. $\delta^{18}O$ AND Cl^- DISTRIBUTION CHARACTERISTICS IN CROSS SECTION AA'

Fig. 7 shows the distribution of (a) Cl^- and (b)

Fig. 5 $\delta^{18}O-Cl^-$ Fig. 6 $\delta^{18}O-Cl^-$

(Inside the dotted rectangle in Fig. 5)

$\delta^{18}O$ at cross section AA'. N5-Tg1 and N4-Tg1 occur in the vicinity of about -40 m at the center in the figure and have especially high seawater intrusion.

The cross-sectional distribution of Cl^- shows that N4-Tg1 and N5-Tg1 have high concentrations of Cl^- . Wells N4 and N5 have low groundwater level, and groundwater samples were collected from the surroundings. We assume that seawater intrusion had already occurred at the sampling period. The Tg2 layer has moderate depth compared to the Tg1 layer.

The upper layers of S4 and N3-AS show a contrasting condition with N5-Tg1 and N4-Tg1. The Cl^- concentrations are low and there is fresh water on top of salt water.

The distributions of $\delta^{18}O$ show heavy values (-4.8 ‰, -5.1 ‰) at the points where Cl^- concentrations are high (N4-Tg1, N5-Tg1). Other points have values ranging from -5.4 ‰ to -6.4 ‰

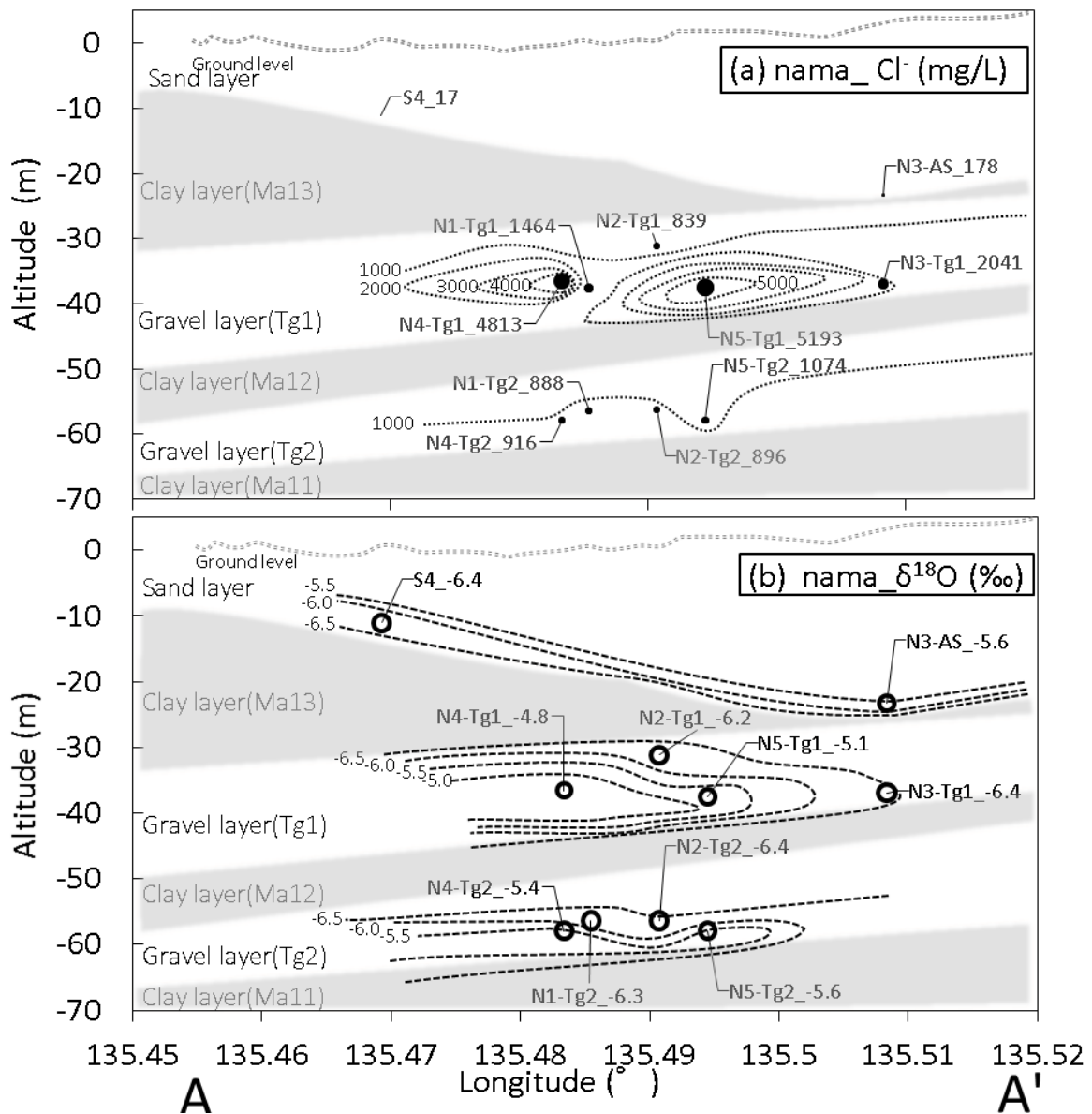


Fig. 7 Distribution of (a) Cl^- and (b) $\delta^{18}\text{O}$ in cross section A-A' in Fig. 1

and show an ambiguous distribution feature. Therefore, each value is considered to be a value generated by mixing with modern seawater.

Freshwater $\delta^{18}\text{O}$ before mixing corresponds to the intersection of the mixing line (the line connecting the plot of each value and the plot of the value of modern seawater) in Figs. 5 and 6 with the ordinate. Also, the mixing ratio of sea water was calculated with the Cl^- concentration of modern seawater as 100%. As a result, the $\delta^{18}\text{O}$ of fresh water before mixing with the heaviest point (N5-Tg1) was -7.2‰ , and the salt water mixing ratio was 29%.

In addition, the rough altitude of the study of Nakaya et al. [14] was obtained from the $\delta^{18}\text{O}$ results of surface water in the recharge zone of the Osaka Plain groundwater. The altitude effect characteristic is a decrease of the $\delta^{18}\text{O}$ of precipitation from low-

altitude areas to high-altitude areas. This feature can be used to obtain the groundwater recharge elevation. In the Osaka Plain, a $\delta^{18}\text{O}$ of water value of -7.2‰ corresponds to water recharged at 100 m altitude. The light water is considered to be recharged in the mountainous area, while the heavy water is presumed to be recharged on the hill/plateau area at less than 100 m elevation.

The calculation result for $\delta^{18}\text{O}$ at N5-Tg1 and N3-Tg1 was -7.2‰ . These points are located in the 1st volcanic gravel layer. This location can be inferred as representing water recharged in the mountainous areas. Shallow groundwater on the sea side of point N5 cannot reach light water from the mountains and is considered to be heavy water ($\delta^{18}\text{O}$: -7.1‰ or more) recharged on the plateaus and flat ground.

Particularly, there was some heavy water at N3-

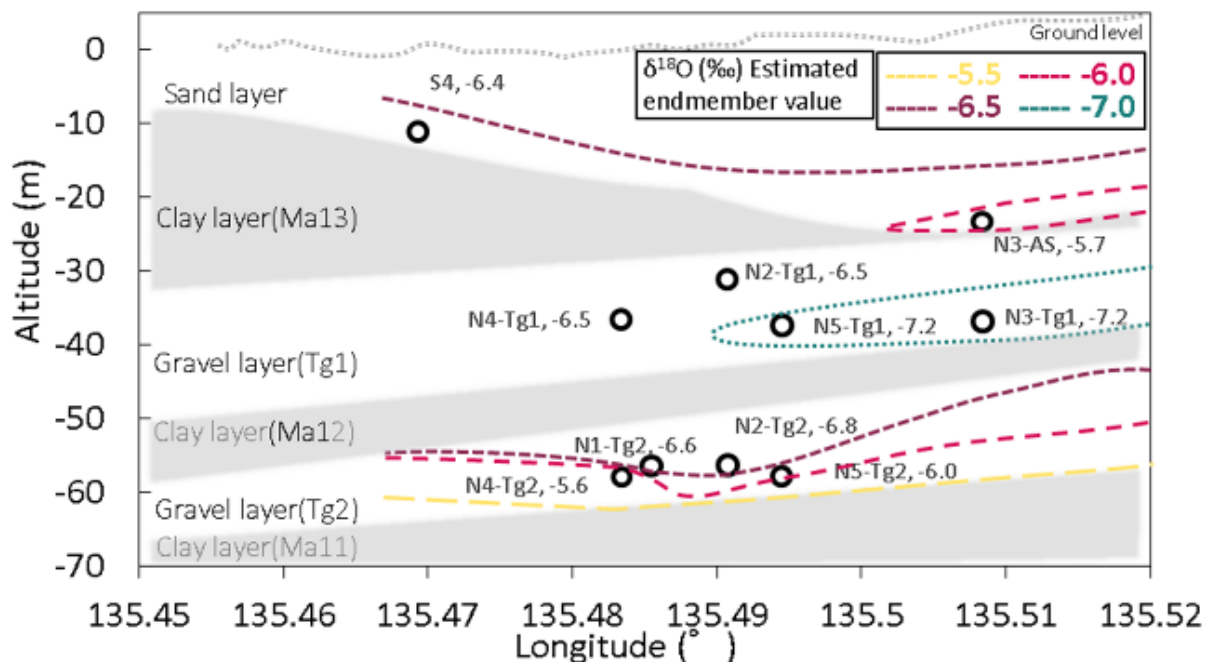


Fig. 8 Distribution of freshwater $\delta^{18}\text{O}$ before mixing in cross section A-A' in Fig. 1

AS (-5.7‰) and N4-Tg2 (-5.6‰). These locations have a different type of aquifer. The water recharged at the 0 m altitude area estimated from the altitude effect is $\delta^{18}\text{O}$: -6.9‰ . Thus, these heavy waters cannot be explained by the altitude effect. One possible reason for the heavy water is that precipitation accumulates in reservoirs, rice fields, waterways, etc., evaporates, and isotopic fractionation occurs. Other unknown factors such as contamination of sewer water into groundwater, influences from underground structures, and some others are also conceivable. However, data explaining these waters are currently lacking.

Discussion of the constant altitude effect used in this case is necessary. For example, $\delta^{18}\text{O}$ of precipitation is known to change seasonally [15], and there is the possibility that one-time sampling is not sufficient.

Even if heavy water factors are revealed, the process of heavy water invading each aquifer is still difficult to explain. Therefore, various approaches using other tracers are considerably necessary.

5. CONCLUSION

In this study, Cl^- concentration was measured to trace seawater intrusion, and $\delta^{18}\text{O}$ and δD were measured to estimate the water recharge process.

The results showed that seawater intrusion with a maximum mixing rate of seawater of 29 % was confirmed in groundwater collected in 2015. The groundwater is considered to be derived from precipitation.

We suggested that the groundwater is formed from three sources: (i) recharge in mountainous areas

with altitudes of 100 m or more, (ii) recharge in hilly areas and plateaus with altitudes less than 100, and (iii) modern seawater.

However, some heavy water cannot be explained by the altitude effect. Therefore, it is necessary to clarify the factors causing the generation of this water. The restoration process from seawater intrusion may be captured in the future by sampling water regularly.

6. ACKNOWLEDGEMENTS

This research was partially supported by the Research Council on the Groundwater Ground Environment FY2008. We thank the Kinki Regional Development Bureau, Ministry of Land, Infrastructure and Transport, Osaka Prefectural Environmental Agriculture, Forestry and Fisheries Department, and Osaka City Environment Bureau for their cooperation during this investigation. We also thank our colleagues Ms. Hiroko Ito and Mr. Yutaka Maruyama (former graduate student of Hiroshima University) from the Geo-Research Institute for their great help in collecting the samples.

REFERENCES

- [1] Masuda H., The Future of Urban Water Resources and Groundwater, Kyoto University Academic Press, 2010, p 249.
- [2] Taniguchi M., Importance of groundwater as security, Journal of Groundwater Hydrology, Vol. 55, 2013, pp 5-11.
- [3] Taniguchi M., Asia's Underground Environment—Remaining Global Environmental Issues, Gakuhosha, 2010.
- [4] Tsurumaki M., Summary of groundwater quality

- water research committee activities, Symposium on groundwater ground environment 2003 released papers, 2003, pp 81-90.
- [5] Tsukamoto T. and Tsurumaki M., About abnormal water quality, found in "Chronology of groundwater quality water quality", Symposium on groundwater ground environment 2003 released papers, 2003, pp 99-106.
 - [6] Aoki K., Tsurumaki M. and Nishida M., Salt water phenomenon in southern part of Sennan area and optimum water volume, Symposium on groundwater ground environment 2003 released papers, 2003, pp 91-98.
 - [7] Tsukamoto T., Characteristics of water quality of groundwater observation well in Osaka area, Symposium on groundwater ground environment 2010 released papers, 2010, pp 87-94.
 - [8] Onodera S., Shimizu Y., Ito H., Tsukamoto T., Oki T. and Aoki K., Influence of nitrogen changes on Osaka Plain and its groundwater quality, Kansai Geo-Symposium 2013 Paper Collection, 2013, pp 27-30.
 - [9] Ito H., Onodera S., Saito M., Maruyama Y., Jin K. and Katsumi T., About the inclusion status of heavy metals etc. in groundwater in Osaka plain and its surrounding area, Kansai Geo-Symposium 2015 Paper collection, 2015, pp 91-96.
 - [10] Saito M., Onodera S., Ito H., Maruyama Y., Taniguchi M., Jin K. and Katsumi T., On the interaction between groundwater and sewerage along the coast of Osaka Bay—Looking at nutrient salts, Kansai Geo-Symposium 2015 Paper Collection, 2015, pp 87-90.
 - [11] Onodera S., Saito M. and Shimizu Y., On the tendency of water quality contamination of groundwater in coastal giant cities, Kansai Geo-Symposium 2016 Paper Collection, 2016, pp 3-4.
 - [12] Ichihara M., Fujino Y., Mori K., Nakakose K., Kusaka M. and Murota A., Osaka Group and Osaka Plain, URBAN KUBOTA, NO.16, 1975, pp 2-11.
 - [13] KG-NET and Kansai Geo-informatics Research Committee, Osaka Bay from Osaka Plain of Shin-Kansai Earthquake, KG-NET and Kansai Geo-informatics Research Committee, 2007, p 354.
 - [14] Nakaya S., Mitamura M., Masuda H., Uesugi K., Motodatge Y., Kusakabe M., Iida T., and Muraoka K., Recharge sources and flow system of groundwaters in Osaka Basin, estimated from environmental isotopes and water chemistry, Journal of Groundwater Hydrogy, Vol. 51-1, 2009, pp 15-41,
 - [15] Tanoue M., Ichiyanagi K. and Shimada J., Seasonal variation and spatial distribution of stable isotopes in precipitation over Japan, Journal of Japanese Association of Hydrological Sciences, Vol. 43-3, 2013, pp 73-91.

ANALYSIS OF STATISTICAL METHODS FOR WATER-LEVEL FORECASTS OF NIGER INNER DELTA IN MALI

*Barry Kassambara¹, Homayoon Ganji¹ and Takamitsu Kajisa¹

¹Graduate School of Bioresources, Mie University, Japan

ABSTRACT

The Niger Inner Delta (NID), a wetland that was selected as an International Important Wetland under the Ramsar Convention (on February 1st, 2004) still can be considered a hotspot of biodiversity in the Sahel. The Niger River as the main source of water for the NID is also used for urban life and irrigation. Therefore, the sustainable use of water to ensure the environmental flow in the NID is under discussion. In this paper, we evaluate the performance of different models established with empirical (Artificial Neural Network and Regressions) or Conceptual Variable Source Area (Water Balance Method WBM) approaches. The result of evaluation and validation based on determination coefficient (R^2), Root Mean Squared Error (RMSE) and Nash-Sutcliffe Efficiency (NSE) show that all the models have good results however the Levenberg Marquardt Artificial Neural Network has the best fitting for validation and testing periods.

Key words: Niger Inner Delta, water-level, wetland, simulation model

INTRODUCTION

For many decades, water shortage has been a dire problem for millions of people living along the southern fringe of the Sahara Desert [1]

The Niger river has its source in the Fouta Djallon Mountains in the South of Guinea (West Africa), it flows northeast through the Upper Niger basin and enters the Niger Inland Delta (NID) in Mali with a large floodplain ranging from 30,000 to 40,000 km² along the Niger River in Mali [2] (See Fig 1). The annual flooding of large alluvial plains is a vital resource for many ecosystem services, including agriculture, livestock, groundwater recharge, and biodiversity (see Fig 2). The rapid expansion of irrigation upstream, by the diversion dams on the Niger river and its subsidiary (Bani), have a significant impact on the Water-Level (WL) in the NID downstream [3].

The main objective of this study is to develop

Statistical/stochastic and Conceptual/Physical models for Niger Inner Delta water level forecasting and make a comparison between these different models. The evaluation and forecasting of water-level fluctuation (WLF) is increasingly important for the NID owing to its close relation to human living and production, and socio-economically and environmentally sustainable development.

STUDY AREA AND DATA SOURCES

Beyond the town of Ségou, the Niger River forms a vast inland delta with an area of 41,800 km² (Fig. 1 & 2); it joins with its main tributary, the Bani, at Mopti and then forms several lakes. The watershed area of this Inner Delta covers 130,000 km² [3]. The NID is extremely flat and contains many lakes and streams of varying morphology. The altitude of the river bed decreases by only approximately 10 m over the 350

km between the entry and exit of the delta [4]. For this study the data are from different sources (Table 1): The Niger river flow at Mopti and the Water Level at

Akka are from the Malian Government Hydraulic Service, the meteorological data are from Mali-Meteo & Atmospheric Science Data Center (NASA)

Table 1: Data type and data sources

No	Station	Source	Date	Data Type
1	Mopti Station	Malian Government Hydraulic Service	1960-2015	Water flow
2		Malian Meteorological Service		Rainfall
3		Atmospheric Science Data Center (NASA)		Temperature, wind velocity, Solar Insolation
4	Akka Station	Malian Government Hydraulic Service		NID Water-Level

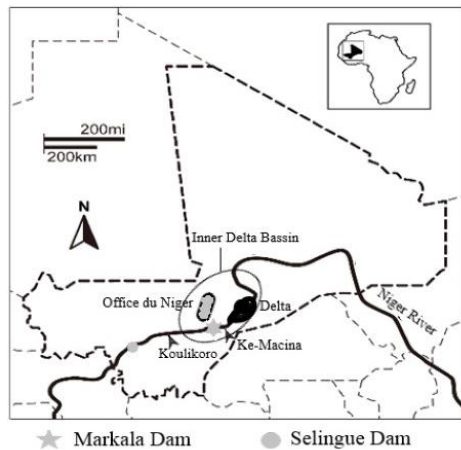


Fig. 1 The Niger Inner Delta in Mali



Fig. 2 NID during dry season (Source Google)

METHODS

The most common methods for river flow and WL forecasting are physical, conceptual and/or statistical rainfall-rainoff methods [5], [4], [6]. In recent years Artificial Intelligence (AI) as a modern approach for data series analysis has received a great deal of attention for hydrology modeling, including Artificial Neural Network (ANN), and Adaptive Neuro-Fuzzy Inference System (ANFIS) [5], [7], [8], [9], [10], [11], [12], [13]. For our study we have implemented six (06) different models based on empirical and stochastic approaches.

Artificial Neural Network (ANN)

An artificial neural network (ANN) is a non-linear black box statistical/stochastic approach [11]; the main objective is to find the optimum architecture of an ANN that can model the relationship between input and output variables. In this study we use the Matlab Neural Network tool to train the different models. For each of the following ANN algorithms, the monthly rainfall, evapotranspiration and the river discharge at Mopti station were designated as predictors and the water level at Akka station as the predictant.

The most commonly used ANN structure is the feed-forward multilayer perceptron (MLP). It is a network formed by simple neurons called perceptron. The perceptron computes a single output from multiple real-valued inputs by forming combinations of linear relationships according to input weights and even nonlinear transfer functions [5].

Mathematically, the MLP can be express as:

$$\mathbf{y} = \mathbf{f}(\sum_{i=1}^n \mathbf{w}_i \mathbf{p}_i + \mathbf{b}) \quad (1)$$

Previous studies indicated that the Levenberg-Marquardt algorithm produces reasonable results for most ANN applications [14], [5]. For the present study we considered the three algorithms available in Matlab: Levenberg-Marquardt (LM), Bayesian Regularization (BR) and Scaled Conjugate Gradient (SCG) algorithms.

Levenberg-Marquardt Algorithm

Levenberg-Marquardt (LM) is the most popular alternative to Gauss-Newton method for finding the minimum of the function $\mathbf{F}(\mathbf{x})$ that is a sum of:

$$F(\mathbf{x}) = \frac{1}{2} \sum_{i=1}^m [f_i(\mathbf{x})]^2 \quad [15] \quad (2)$$

Let the Jacobian of $f_i(\mathbf{x})$ be denoted $J_i(\mathbf{x})$, then the LM method searches in the direction given by the solution \mathbf{p} of the equation $(J_k^T J_k + \lambda_k I) \mathbf{p}_k = -J_k^T f_k$ (2)

Where λ_k are nonnegative scalars and I is the identity matrix.

Bayesian Regularization Algorithm

This algorithm uses David MacKay's Bayesian techniques to optimize regularization which requires the computation of the Hessian matrix [16]. Typically,

training aims to reduce the sum of squared errors E_D and the regularization adds an additional term E_W [17]. The objective term becomes $F = \beta E_D + \alpha E_W$

$$(3)$$

where β and α are the objective function parameters.

Scaled Conjugate Gradient Algorithm

The Scaled Conjugate Gradient (SCG) method, as most of the feedforward neural networks, is based on the gradient descent algorithm well known in optimization theory [18]. The SCG avoids the line search per learning iteration by using a LM approach in order to scale the step size.

Gaussian Process Regression (GPR) Model with Matlab Regression Learner

Gaussian process regression (GPR) models are kernel-based probabilistic models [19].

A linear regression model is of the form:

$$\mathbf{y} = \mathbf{x}^T \boldsymbol{\beta} + \boldsymbol{\varepsilon} \quad (4)$$

Where $\boldsymbol{\varepsilon} \sim N(0, \sigma^2)$. The error variance σ^2 and the coefficient $\boldsymbol{\beta}$ are estimated from the data. A GPR model explains the response by introducing the latent variable, $f(x_i)$, $i = 1, 2, \dots, n$, from a Gaussian Process (GP), and explicit basis functions, \mathbf{h}

Water Balance Model (WBM)

The water depth in the NID may be obtained using the Variable Source Area (VSA) model as follows:

$$\mathbf{H}_{i+1} = \mathbf{Max}(\mathbf{H}_i + (\mathbf{Q}_{i+1} - \mathbf{Q}_{out}) \frac{\mathbf{D}}{\mathbf{A}_1} + (\mathbf{R}_{i+1} -$$

$$ET_{0i+1}D)^{\frac{(A_1+A_2)}{A_1}}, \gamma)$$

(5)

The outflow Q_{out} is $Q_{out} = \beta \text{Max}(H_i, 0)^\alpha$

(6)

The wet soil area is given as $A_2 = \delta \sqrt{A_1}$

(7)

Time, monthly maximum inflow from Mopti station upstream (Q_i), monthly rainfall (R) the daily potential Evapotranspiration (ET_0), the number day of each month (D), and pond water surface (A_1) data were fed into the spreadsheet. To estimate the maximum water level (H_i) at various time steps using the equation 6 based on the parameters α , β , γ and δ . The Generalized Reduced Gradient (GRG) nonlinear solving method was used.

Multiple Linear Regression (MLR)

As opposed to simple linear regression models, which describe the linear functional relationship between a single explanatory variable X (inflow, Rainfall, ET_0) and the response variable Y (NID Water-Level), multiple linear regression models comprise the use of a collection of explanatory variables for describing the behavior of Y [20]. In formal terms $y = \beta_0 + \sum_{j=1}^k \beta_j x_{ij}$ (8)

Parameter estimation in multiple linear regression is based on the least squares methods. The equation to

estimate the monthly maximum water level of the NID will be as:

$$H_{max} = \beta_0 + \beta_1 ET_0 + \beta_2 Rain + \beta_3 Q_{max}$$

(9)

RESULTS

The monthly data from 1960 to 2010 were used for the model validations, and the monthly data from 2011 to 2015 for testing. To validate and evaluate the models, Correlation Coefficient (CC), squared R (R^2), Root Mean Squared Error (RMSE) and Nash-Sutcliffe Efficiency (NSE) were used (Table 2). The plots of the monthly maximum WL (Hmax) variation for different models are shown in Fig 3.

The Nash-Sutcliffe Efficiency (NSE) is a normalized statistic that determines the relative magnitude of the residual variance (“noise”) compared with the measured data variance (“information”). The NSE indicates how well the plots of observed versus simulated data fit [21].

The NSE is computed as shown below:

$$NSE = 1 - \left[\frac{\sum_{i=1}^n (Y_i^{obs} - Y_i^{sim})^2}{\sum_{i=1}^n (Y_i^{obs} - Y^{mean})^2} \right] \quad (10)$$

Where Y_i^{obs} is the i^{th} observation WL, Y_i^{sim} is the i^{th} simulated value of WL, Y^{mean} is the mean of observed WL, and n is the total number of observations.

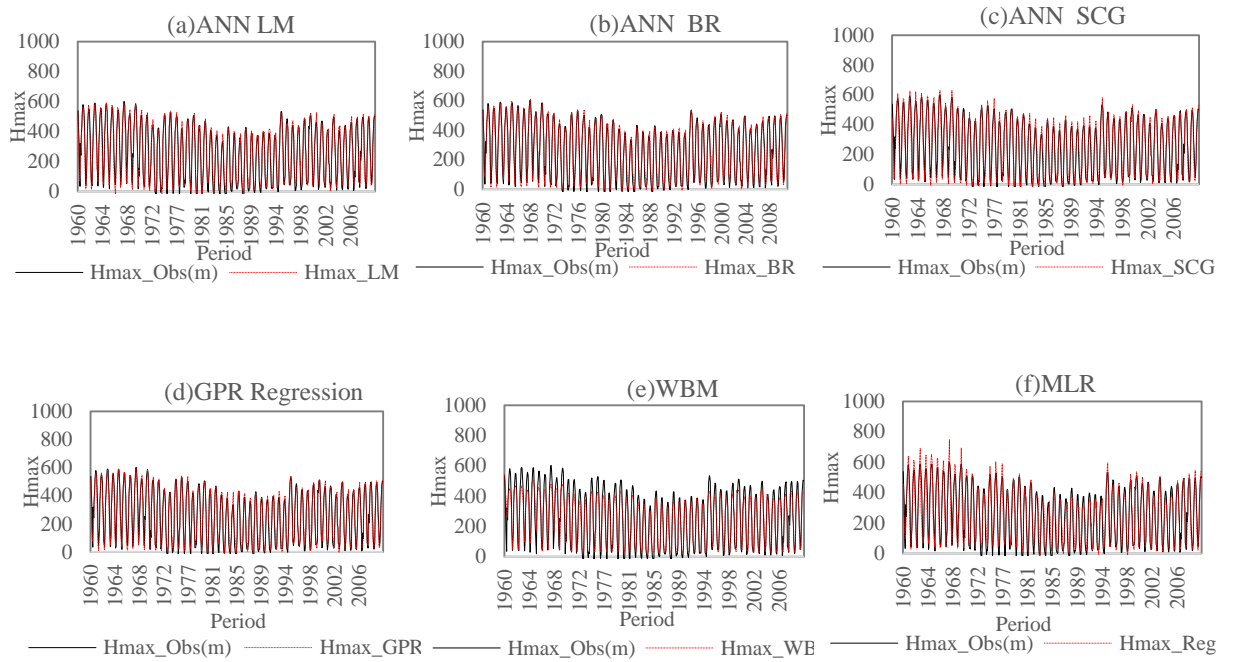


Fig. 3 Validation scatter plots of observed versus modelled water level. (a) Levenberg-Marquardt ANN, (b) Bayesian Regularization ANN (c) Scaled Conjugated ANN, (d) Gaussian Process Regression, (e) Water Balance Model (WBM), (f) Multilinear Regression model.

Table 2: Model validation and Evaluation statistics

N	Model	Validation (1960-2010)				Evaluation (2011-2015)			Parameters
		CC	R^2	RMSE(cm)	NSE	CC	R2	RMSE(cm)	Algorithm
a	Hmax_LM	0.97	0.94	41.47	0.9477	0.97	0.95	38.36	Algorithm
b	Hmax_BR	0.97	0.89	59.00	0.9450	0.97	0.95	38.20	Algorithm
c	Hmax_SCG	0.96	0.92	52.05	0.9141	0.96	0.92	46.99	Algorithm
d	Hmax_Mat_GPR	0.97	0.93	46.88	0.9141	0.97	0.95	37.51	
e	Hmax_WBM	0.95	0.91	60.00	0.8415	0.96	0.93	39.88	$\alpha=1.29, \beta=228.73, \delta=59.19, \gamma=0.32$ $\beta_0 = 1070.2, \beta_1 = -156.65, \beta_2 = -1.14, \beta_3 = 0.12$
f	Hmax_MLR(excel)	0.93	0.87	65.02	0.8532	0.96	0.92	46.68	

DISCUSSION

The models' performance from R^2 , RMSE and NS are given in table 2 and fig 4. It can be seen from the results of validation that the ANN (LM, BR and SCG)

perform much better for each of the algorithms, followed by Gaussian Process Regression; the Water Balance Model and the Multilinear Regression Model have the worst

performance. For all the models the NSE values of validation are close to 1, which is in the range of acceptable levels (between 0 and 1 where 1 is the optimal value) according to Moriasi et al. [21],

however ANN Levenberg-Marquardt algorithm has the best result for each performance index.

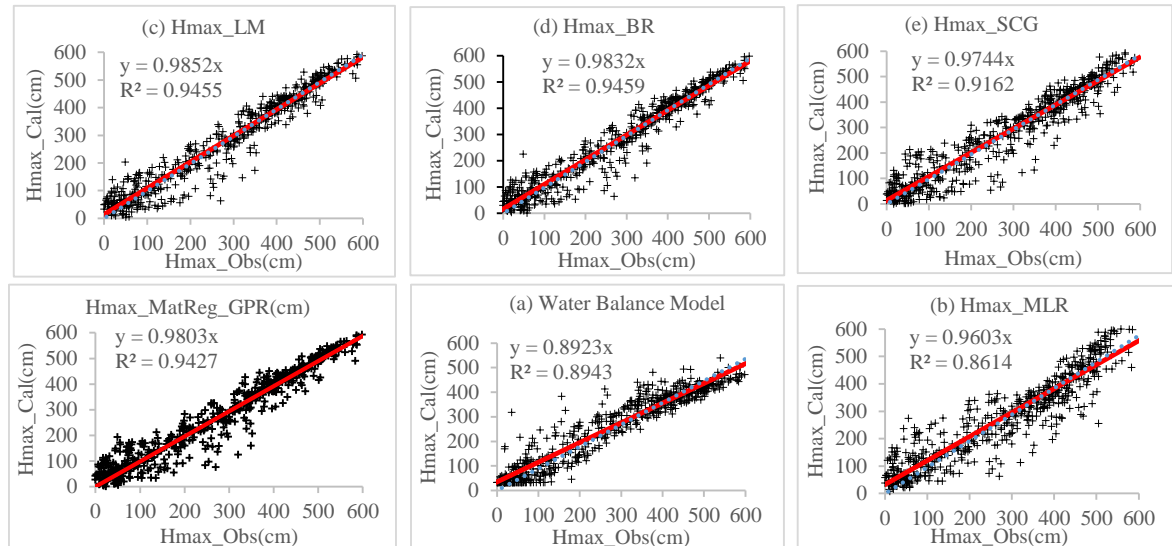


Fig. 4 (a) Levenberg-Marquardt ANN, (b) Bayesian Regularization ANN (c) Scaled Conjugated ANN, (d) Gaussian Process Regression, (e) Water Balance Model (WBM), (f) Multilinear Regression model (MLR).

CONCLUSION

The accuracy of different models for forecasting the maximum monthly water level of the Niger River Inner Delta was investigated using different statistical/stochastic methods with the input data of water inflow discharge in Mopti station, the rainfall and the ET_0 . From the results, the Artificial Neural Network Levenberg-Marquardt is the best model to predict the water level of the Inner Niger River Delta. However, the ANN Bayesian Regularization, the ANN Scaled Conjugate Gradient and the Gaussian Process Regression can be applied with minimal error.

ACKNOWLEDGMENT

Our warm thanks Mali's National Direction of Hydraulic for their support in terms of providing some

data. Thanks to the Laboratory of Water Resources Engineering of Mie University for their help.

REFERENCES

- [1] L. Zwart, P. v. Beukering, B. Kone and E. Wymenga, The Niger, a Lifeline. Effective Water Management in the Upper Niger Basin, Leo Zwarts (RIZA), Pieter van Beukering (IVM), Bakary Kone (Wetlands International) and Eddy Wymenga (A&W), Eds., Sevare (Mali), Amsterdam (Netherlands): Wetlands International/Institute for Environmental Studies (IVM)/A&W Ecological, 2005, p. 169.
- [2] A. Mariko, G. Mahe, D. Orange, A. Royer, A. Nonguierma, A. Amani and E. Servat, "Suivi des zones d'inondation du Delta Interieur du Niger, Perspective avec les donnees de basse resolution NOAA/AVHRR," *Gestion Integree en zones inondables tropicales*, pp. 231-244, 2002.

- [3] B. Kassambara, H. Ganji and T. Kajisa, "Impact of Agricultural Water Allocation on the Ecosystems in the Inner Niger River Delta," *GEOMATE*, vol. 14, no. 42, pp. 164-170, 2018.
- [4] M. Ibrahim, D. Wisser, A. Ali, B. Diekkrüger, O. Saidou, A. Mariko and A. Alfouda, "Water Balance Analysis over the Niger Inland Delta-Mali: Spatio-temporal Dynamics of the Flood Area Water Losses," *MDPI-HYDROLOGY*, vol. 4, no. 40, pp. 1-23, 2017.
- [5] M. Rezaeianzadeh, H. Tabari, A. Arabi Yazdi, S. Isik and L. Kalin, "Flood flow forecasting using ANN, ANFIS and regression models," *Springer*, vol. 25, no. 1, pp. 25-37, 2014.
- [6] E. A. Rosenberg, A. W. WOOD and A. C. STEINEMANN, "Statistical applications of physically based hydrologic models to seasonal streamflow forecasts," *WATER RESOURCES RESEARCH*, vol. 47, no. W00H14, pp. 1-19, 2011.
- [7] J. C. Risley, M. W. Gannett, J. K. LEA and E. A. Roehl Jr, An Analysis of Statistical Methods for Seasonal Flow Forecasting in the Upper Klamath River Basin of Oregon and California, Reston, Virginia: U.S. Geological Survey (USGS), 2005.
- [8] C. Dawson and R. Wilby, "Hydrological modelling using Artificial Neural Networks," *Progress in Physical Geography*, vol. 25, no. 1, pp. 80-108, 2001.
- [9] M. Rezaeianzadeh, H. Tabari and A. Arabi Yazdi, "Flood flow forecasting using ANN, ANFIS and regression models," *Springer-Verlag*, vol. 25, no. 1, pp. 25-37, 2014.
- [10] L. Xiong, K. M. O'Connor and S. Guo, "Comparison of three Updating Schemes Using Artificial Neural Network in Flow Forecasting," *Hydrology and Earth System Sciences*, vol. 8, no. 2, pp. 247-255, 2004.
- [11] A. MohammadKaltch, "Monthly riverflow forecasting using artificial neural network and support vector regression models coupled with wavelet transform," *ELSEVIER*, vol. 54, pp. 1-8, 2013.
- [12] C. W. Dawson and R. Wilby, "An artificial neural network approach to rainfall-runoff modelling," *Hydrological Sciences Journal*, vol. 43, no. 1, pp. 47-66, 2009.
- [13] M. S. Khan and P. Coulibaly, "Application of Support Vector Machine in Lake Water Level Prediction," *Journal of Hydrologic Engineering*, vol. 11, no. 3, pp. 199-205, 2006.
- [14] K. Özgür, "Streamflow Forecasting Using Different Artificial Neural Network Algorithms," *JOURNAL OF HYDROLOGIC ENGINEERING*, vol. 12, no. 5, pp. 532-539, 2007.
- [15] D. W. Marquardt, "An Algorithm for Least-Squares Estimation of Nonlinear Parameters," *J. Soc. INDUST. APPL. MATH.*, vol. 11, no. 2, pp. 431-441, 1963.
- [16] D. J. C. MacKay, "Bayesian Interpolation," *Computation and Neural Systems*, vol. 4, pp. 415-447, 1992.
- [17] F. D. Foresee and M. T. Hagan, "GAUSS-NEWTON APPROXIMATION TO BAYESIAN LEARNING," in *International Conference on Neural Network*, Houston, TX, USA, 1997.
- [18] M. D. Moller, "A Scaled Conjugate Gradient Algorithm for Fast Supervised Learning," *Neural Networks*, vol. 6, pp. 525-533, 1993.
- [19] C. E. Rasmussen and C. K. I. Williams, Gaussian Processes for Machine Learning, Cambridge, Massachusetts: The MIT Press, 2006.
- [20] M. Naghettini, Fundamentals of Statistical Hydrology, Belo Horizonte, Brazil: Springer, 2016.
- [21] D. N. Moriasi, J. G. Arnold, M. W. Vanliew, R. L. Binger, D. R. Harmel and T. L. Veith, "Model Evaluation Guidelines for Systematic Quantification of accuracy in Watershed Simulations," *ASABE Soil & Water Division*, vol. 50, no. 3, pp. 885-900, 2007.
- [22] Z. Yu, G. Lei, Z. Jiang and F. Liu, "ARIMA Modelling and Forecasting of Water Level in the Middle Reach of the Yangtze River," in *ICTIS*, Banff(CANADA), 2017.

ENHANCEMENT OF BIOMETHANE PRODUCTION POTENTIAL FROM THE ALKALINE PRETREATED POLY (LACTIC ACID) WASTE BY THE CO-DIGESTION PROCESS

Sutisa Samitthiwetcharong^{1,2} and Orathai Chavalparit^{1,2,3}

¹Department of Environmental Engineering, Chulalongkorn University, Bangkok 10330, Thailand

²Research Unit of Environmental Management and Sustainable Industry, Faculty of Engineering,
Chulalongkorn University, Bangkok 10330, Thailand

³Research Program: Sustainable management of industrial and agricultural wastes for transitioning to a circular economy, Center of Excellence on Hazardous Substance Management (HSM), Bangkok 10330, Thailand

ABSTRACT

The objective of this research was to evaluate the yield of biomethane production from anaerobic co-digestion process and biodegradation potential of post-consumer Polylactic acid (PLA) plastic waste. PLA waste was pretreated with sodium hydroxide (NaOH) and then utilized as co-digestion substrate along with organic waste. The potential of alkaline pretreatment and co-digestion of PLA on food waste and market waste for methane production was investigated. The CSTR batch carried out different samples in laboratory scale. Results from the CSTR tests showed that the utilization of pretreated PLA as a single substrate was able to produce 148 L/kgVS_{added} of biomethane. The co-digestion of pretreated PLA and market waste was able to enhance the yield of biomethane production as much as 282.7 L/kgVS_{added}. Whilst biomethane produced by co-digestion of pretreated PLA and food waste was 211.6 L/kgVS_{added}, which was 1.6 times more than that produced by utilizing only food waste.

Keywords: Polylactic acid (PLA), Thermal-alkaline pretreatment, Co-digestion, Methane production

INTRODUCTION

Bioplastics are eco-friendly biodegradable plastics which can degrade under appropriate environmental conditions. Nowadays, bioplastics are widely used in many countries in order to reduce the consumption of petroleum-based plastics [1]. It is expected that the growth of biopolymers and bioplastics worldwide could increase as high as 12% annually. In 2018, the global production capacity of bioplastics is 6.6 million tons. Among the various types of bioplastics, Polylactic acid (PLA) is the second most consumed bioplastics [2]. Generally, PLA is derived from renewable resources such as corn starch, tapioca roots, chips, starch and sugarcane. PLA is available commercially for various applications, including films, bags, packaging, electronic parts, and medical plastics. However, the most common use of PLA as biodegradable polymer is in medical and food packaging. Despite PLA's utility for various applications, there are some limitation, e.g. PLA's slow degradation rate, and its low affinity to the cells whose degradation process depends on pH and temperature [3]. As a result, finding an appropriate method for PLA recycling/recovery can be a challenging task.

Generally, landfilling is considered the best

option for PLA waste disposal. Theoretically, PLA is produced by polymerization reaction of lactic acid. Accordingly, landfilling could disrupt biological and chemical degradation mechanism significantly. As a result, PLA might be unable to be broken down and consumed directly by cells as effectively as lactic acid could be. Moreover, PLA has highly crystalline structures which are not easy to degrade under aerobic and anaerobic mesophilic conditions [4]. Sin [5] stated that the degradation of PLA was initiated through hydrolysis process, followed by enzymatic or microorganism digestion. Such degradation leads to PLA fragmentation and ultimately transforms PLA into harmless substances. Massardier-Nageotte [4] reported that PLA showed some mass loss when aerobic conditions were applied. However, the mass loss was insignificant in anaerobic conditions. The explanation is that the biodegradation of PLA is very slow, because of a lack of microorganism colonization on the sample's surface. Kale [6] reported that PLA under composting plant disappeared within 30 days, while landfill required 6 months for a major fragmentation to occur, and 15 months for significant amount of mass loss. For bi-digester condition, the fermentation of PLA under anaerobic biodegradation at 37 °C took 100 days to complete the degradation process [7]. Furthermore,

thermophilic condition can increase the efficiency of PLA biodegradation as well. The experiment proved that using 1.5 L reactor at 55 °C was able to result in 91% degradation of PLA within 75 days, along with 53.8% production of methane [8].

Currently, there are a few researches that focus on methane production by anaerobic fermentation as source of renewable energy. Samitthiwetcharong [9] observed that biogas production from pretreated PLA with 0.5 M NaOH at 60 °C could obtain 215 ml/gVS_{added}, which was 3.7 times higher than that obtained from non-pretreated PLA. Vasmara [10] also stated that biogas production from biochemical methane potential (BMP) at 55°C from PLA could obtain biogas for 282 mL CH₄ g⁻¹ VS. When PLA was utilized along with pig slurry in co-digestion process, M_{max} was achieved at 12% which was higher than in theory. Methane ratio during PLA degradation at 35°C and 55°C ranges from 50% to 60% [8]. As for this research, the main focus was the precursor of PLA for biogas production. The aim of this study was to enhance biogas yield achieved from anaerobic co-digestion process of organic food waste/market waste and alkaline pretreated PLA, whose pretreatment process was done by soaking PLA in NaOH.

MATERIALS AND METHODS

Substrate and Raw Materials

A commercial PLA film with 80 µm thickness was used in this experiment. The PLA film was cut into 1-2 mm pieces using grinder. The alkaline pretreatment condition was done by soaking the cut PLA film in 0.5 M sodium hydroxide solution (w/v) in the ratio of 1 g of PLA to 10 ml of NaOH, for 2.5 days at ambient temperature. Biochemical methane potential (BMP) experiments were used to determine an optimum pretreatment condition of PLA [9].

Food waste and market waste were collected from Chulalongkorn University's cafeteria and fresh markets in Bangkok. Major components of the food waste were rice and vegetables, while most of the markets' organic waste components were various kinds of vegetables such as Chinese cabbage, cauliflower, cabbage, Chinese kale, and lettuce. The vegetable waste was grinded to be used for the experiment.

Inocula used in CSTR reactor were obtained from mesophilic anaerobic digester from a biogas production plant of a soft drink company. The inocula were analyzed by using the standard methods to determine the total solids (TS) and volatile solids (VS) as shown in Table 1.

Experimental Procedure

Four reactors were used in this study. Each reactor

contained 2% of the VS and a different variation of conditions as shown in Table 2. Different batches of biomass mixtures and fractions were prepared in order to investigate biogas production and performance of co-digestion process. For each reactor, the ratio of substrate to inocula was maintained at 3 L: 2 L, that is preparing 3 L of the 2% VS substrate and 2 L of the 2.5% inocula. Flowchart of biomethane production experiment is shown in Fig. 1.

Operation Scheme

The amount of substrate fractions with an initial 3 L of 2% VS was added to CSTR. 3 g/L of NaHCO₃ was added to the reactor to provide buffer capacity. The ratio of substrate and its chemical characteristics in each reactor is shown in Table 2. The volume of biogas production in each reactor was recorded on a daily basis. The experimental batches were incubated until no further gas was produced (60 days). For 3 times a week, a 50 ml sample from each reactor was taken and analyzed for TS, VS, and sCOD. A methane gas composition analyzer was used to measure methane content by using Gas Chromatography and Thermal Conductivity Detector (TCD).

Table 1 Characteristics of substrates and inocula

Substrate	TS (%)	VS (%)	COD (mg/L)	pH	C/N ratio
Food waste	35.29	33.83	148,732	4.95	31.15
Market waste	49.38	45.85	41,239	5.68	11.01
PLA	99.78	99.78	-	-	-
Inocula	-	2.5%	-	-	8.51

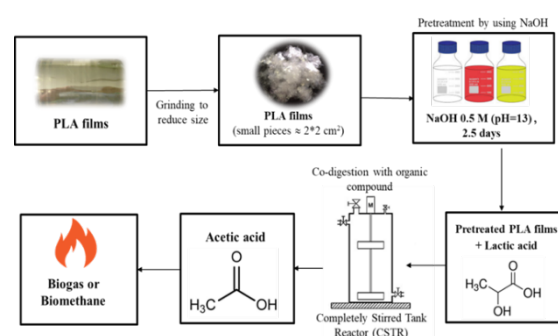


Fig. 1 Flowchart of biomethane production from alkali pretreatment PLA with food waste.

RESULTS AND DISCUSSION

Effect of NaOH Pretreatment on PLA

The PLA was pretreated by soaking in 0.5 M NaOH solution (w/v) for 60 hours prior to its use as feedstock for anaerobic digestion in CSTR.

Table 2 Experimental setup: number of substrates in each batch reactor and chemical characteristics

Reactor	Substrate	TVS(%)	TVS (%)	%C	%N	C/N ratio
1	PLA	2	2.0	33.56	-	-
2	PLA pretreated with 5 M NaOH for 48 h (pretreated PLA)	2	2.56	39.98	-	-
3	Co-digestion of pretreat PLA and food waste with ratio 1:1 (pretreated PLA: FW = 1:1)	2	2.65	36.77	1.08	34.13
4	Co-digestion of pretreat PLA and market waste with ratio 1:1 (pretreated PLA:MW= 1:1)	2	2.54	30.01	1.43	21.02

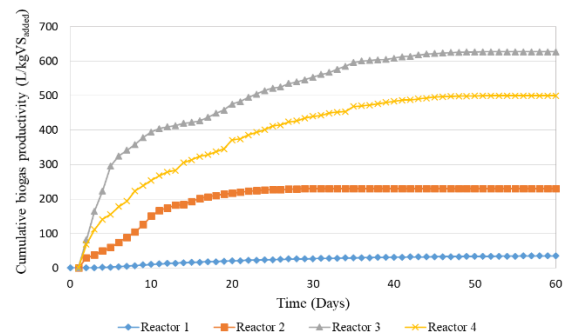
The NaOH solution used for PLA pretreatment was analyzed for lactic acid. The result showed that the concentration of lactic acid was 18,200 mg/l. Gorrasi [11] reported that hydroxide ion (OH^-) from NaOH could increase reaction rate of hydrolysis by minimizing PLA's structures in which the PLA was degraded into lactic acid form. The detection of Lactic acid might confirm that the hydrolyzed PLA was transformed into lactic acid, which would convert into acetic acid whose methanogens could enable biogas production [3], [12]-[13]. As a result, pretreatment with alkaline solution proved to be effective for PLA to be utilized along with organic food waste or other biomass for anaerobic digestion or co-digestion process for biomethane recovery.

Biomethane Production

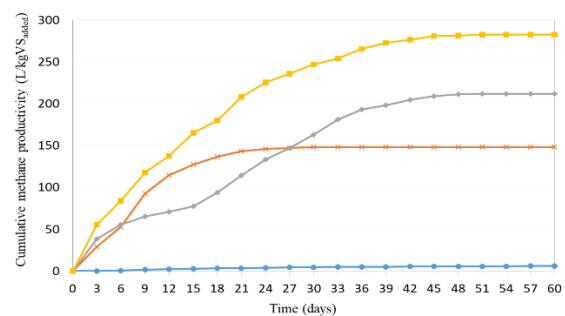
Co-digestion of alkaline pretreated PLA and organic waste could increase methane content in the obtained biogas. The biogas and methane yielded from the pretreated PLA film substrate were 230 and 148.3 L/kgV_{Sadded}, respectively (Fig. 2). It was observed that the percentage of methane in biogas was as high as 64.5%. This resulted from hydrolysis and defragmentation of the PLA into lactic acid according to the pretreatment process. Consequently, the microorganism that produced acid could directly transform the lactic acid into acetic acid in which methanogens could transform the acetic acid into methane. However, the methane generation since the starting of the system operation until the biological reaction was completed in 27 days.

The results from co-digestion experiment showed higher amount of biogas and methane yield than the yield from the reactor which utilized only pretreated

PLA. In co-digestion process, it was observed that the ratio of 1 pretreated PLA to 1 food waste could achieve the highest biogas production, i.e., 627.4 L/kgV_{Sadded}.



(a) Biogas yield



(b) Methane yield

Fig. 2 Cumulative biogas and methane productivity of pretreated PLA and co-digestion of pretreated PLA with organic waste.

Table 3 pH, temperature and VFA/ALK ratio from co-digestion of pretreated PLA and organic waste

Reactor	substrate	pH	Temp (°C)	VFA/ALK ratio	SCOD remove (%)
1	PLA	6.50 – 7.95	29.9 – 34.9	-	-
2	Pretreated PLA	6.65 – 7.94	30.7 – 34.6	0.07-0.33	88.37
3	Pretreated PLA: FW = 1:1	6.78 – 7.82	29.7 – 34.7	0.07-0.39	94.32
4	Pretreated PLA: MW =1:1	6.90 – 7.96	30.7 – 34.9	0.05-0.37	90.51

The reactor that utilized the ratio of 1 pretreated PLA to 1 market waste was the second highest biogas production, which was approximately 500.4 L/kgVS_{added}. However, methane content in the biogas obtained from pretreated PLA and market waste was significantly higher than that obtained from pretreated PLA and food waste. As a result, the co-digestion of pretreated PLA and food waste achieved the highest methane yield at 282.7 L/kgVS_{added}, while the methane yield achieved from co-digestion of pretreated PLA and food waste was 211.6 L/kgVS_{added}. Theoretically, lactic acid is the primary reactant for biogas production process. This might explain why biogas production increased. Furthermore, co-digestion of bioplastic and organic waste could increase biomethane production. Wang [12] found that organic waste could increase degradation rate of PLA in an anaerobic condition with proper temperature, pressure and ammonia content derived from protein in food waste.

In addition, the co-digestion of pretreated PLA and market waste obtained 1.9 times higher amount of methane than that obtained from using pretreated PLA as a single substrate as shown in Fig. 3. Also, the experiment of the co-digestion of pretreated PLA and food waste could increase methane production capacity for 1.43 times higher than that of the reactor which utilized only pretreated PLA. Drawing from the results, it might be concluded that co-digestion of pretreated PLA and organic waste could enhance methane production in co-digestion anaerobic process.

Digester Performance

Table 3 shows pH and alkalinity ratios (VFA/ALK) of the effluents during the 60-day incubation period of various substrates. The results showed that all of the CSTR experimental batches had VFA/ALK ratio within the range of 0.05-0.39 (Fig 4). Alkalinity result of each batch also accounted for higher than 2,500 mg as CaCO₃/l which showed great buffer capacity of the overall systems. These results might indicate a high stability of the system in which the VFA/ALK should be below 0.4.

Result from soluble COD removal efficiency (Table 3) showed that normal, non-pretreated, PLA could not be biologically degraded within 65 days in an anaerobic condition, while alkaline pretreated PLA could be biologically degraded by anaerobic bacteria. Consequently, alkaline pretreatment could help promote the degradation of PLA and turn it into lactic acid by increasing the rate of hydrolysis. Lactic acid can be transformed into biogas later on [9]. The results also showed that the COD removal efficiency of the pretreated PLA was at the same rate as the market waste.

Scanning Electron Microscopy (SEM) Study

Topological study of the pretreated PLA films was done by using the Scanning Electron Microscopy (SEM) with magnification of 2000 times (as shown in Fig. 5-8). Four sets of PLA films and pretreated PLA films were used for the topological studies, i.e., 1) PLA film obtained from non-pretreated PLA digestion, 2) pretreated PLA digestion, 3) Co-digestion of pretreated PLA: FW, and 4) Co-digestion of pretreated PLA: MW. For the pretreated PLA films, high density of pores was observed for only 15 days of operation. The density of pores was further increased after 60 days of operation.

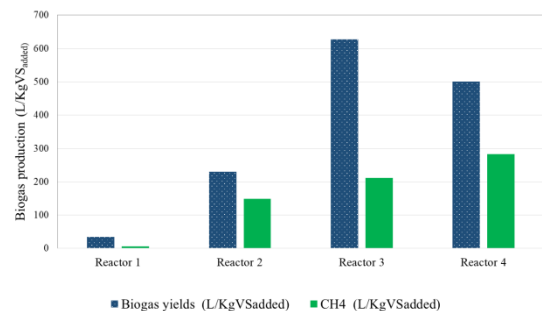
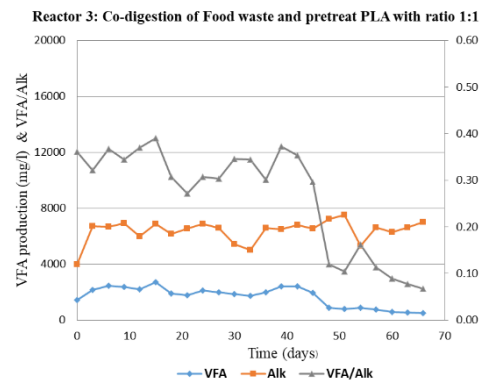
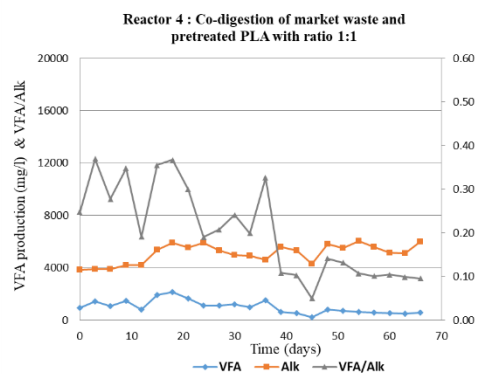


Fig. 3 Biogas and methane productivity of pretreated PLA and co-digestion of pretreated PLA with organic waste.



(a) pretreated PLA:FW = 1:1



(b) pretreated PLA:MW = 1:1

Fig. 4 The performance of an anaerobic digester of co-digestion.

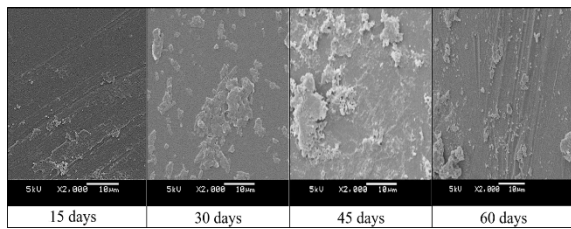


Fig. 5 Surface of non-pretreated PLA films from single substrate digestion

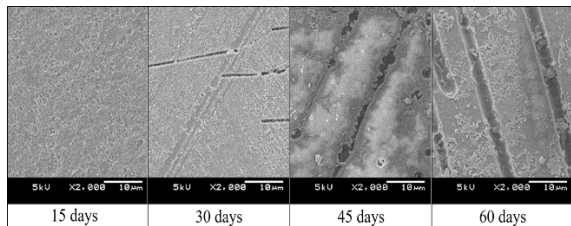


Fig. 6 Surface of alkaline pretreated PLA films

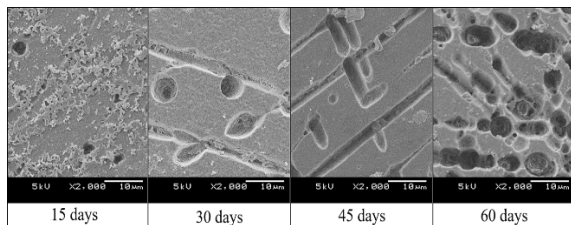


Fig. 7 Surface of pretreated PLA films from co-digestion with food waste.

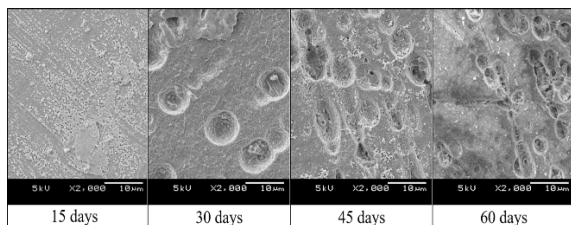


Fig. 8 Surface of pretreated PLA films from co-digestion with market waste.

This result indicates that NaOH could enhance porosity of PLA film which would increase biodegradation process and bioavailability for microorganism and enzyme to function more effectively. Results from fig. 6 and 7 emphasized the enhancement of biogas production due to co-digestion of pretreated PLA. It was shown that using pretreated PLA with organic waste, from single substrate digestion, could promote biogas production, which is a result of PLA's high porosity.

CONCLUSION

Pretreatment of PLA film with NaOH at pH 13 (NaOH 0.5 M) for 60 hours could promote PLA degradation, which would turn PLA into lactic acid and the lactic acid would further transform into acetic acid which is the primary substrate of biogas

production. Furthermore, co-digestion of alkaline pretreated PLA with market waste and food waste could achieve more biomethane yield than that achieved by utilizing only PLA. As a result, PLA waste could be used as a substrate for anaerobic co-digestion process. In addition, alkaline pretreatment of PLA could help promote biomethane yield as well.

ACKNOWLEDGEMENTS

This research was financially supported by the authors thank the Office of Higher Education Commission (OHEC) and the S&T Postgraduate Education and Research Development Office (PERDO) for the financial support of the Research Program and the 90th Anniversary of Chulalongkorn University Fund (Ratchadapiseksomphot Endowment Fund).

REFERENCES

- [1] Borrisuttanakul S., Thai Bioplastics Industry Association (TBIA), International Business Directory for Innovative Bio-based Plastics and Composites, 2012, pp. 119.
- [2] Chaisu K., Bioplastic Industry from Agricultural Waste in Thailand. *Journal of Advanced Agricultural Technologies*, Vol. 3, No. 4, 2016.
- [3] Elsayy M.A., Kim K.H., Park J.W. and Deep A., Hydrolytic Degradation of Polylactic Acid (PLA) and Its Composites. *Renewable and Sustainable Energy Reviews*, Vol. 79, 2017, pp. 1346-1352.
- [4] Massardier-Nageotte V., Pestre C., Cruard-Pradet T. and Bayard R., Aerobic and Anaerobic Biodegradability of Polymer Films and Physico-chemical Characterization. *Polymer Degradation and Stability*, Vol. 91, Issue 3, 2006, pp. 620-627.
- [5] Sin L.T., Rahmat A.R. and Rahman W.A.W.A., Degradation and Stability of Poly (lactic Acid). *Polylactic Acid*, 2013, pp. 247-299.
- [6] Kale G., Auras R., Singh S.P. and Narayan R., Biodegradability of Polylactide Bottles in Real and Simulated Composting Conditions. *Polymer Testing*, Vol. 26, Issue 8, 2007, pp. 1049-1061.
- [7] Itävaara M., Karjomaa S. and Selin J.F., Biodegradation of Polylactide in Aerobic and Anaerobic Thermophilic Conditions. *Chemosphere*, Vol. 46, Issue 6, 2002, pp. 879-885.
- [8] Yagi H., Ninomiya F., Funabashi M. and Kunioka M., Anaerobic Biodegradation Tests of Poly (lactic acid) and Polycaprolactone Using New Evaluation System for Methane Fermentation in Anaerobic Sludge. *Polymer Degradation and Stability*, Vol. 94, Issue 9, 2009, pp. 1397-1404.
- [9] Samitthiwetcharong S., Kullavanijaya P. and Chavalparit O., Anaerobic Biodegradation of

- Poly (lactic acid) Under Mesophilic Condition Using Thermal-alkaline pretreatment. IOP Conference Series: Materials Science and Engineering, Vol. 222, 2017.
- [10] Vasmara C. and Marchetti R., Biogas Production from Biodegradable Bioplastics. Environmental Engineering and Management Journal, Vol. 15, No. 9, 2016, pp. 2041-2048.
- [11] Gorrasi G. and Pantani R., Effect of PLA Grades and Morphologies on Hydrolytic Degradation at Composting Temperature: Assessment of Structural Modification and Kinetic Parameters. Polymer Degradation and Stability, Vol. 98, Issue 5, 2013, pp. 1006-1014.
- [12] Wang F., Hidaka T., Tsuno H. and Tsubota J., Co-digestion of Polylactide and Kitchen Garbage in Hyperthermophilic and Thermophilic Continuous Anaerobic Process. Bioresource Technology, Vol. 112, 2012, pp. 67-74.
- [13] Kim M.S., Na J.G., Lee M.K., Ryu H., Chang Y.K., Triolo J.M., Yun Y.M. and Kim D.H., More Value from Food Waste: Lactic Acid and Biogas Recovery. Water Research, Vol. 96, 2016, pp. 208-216.

PERFORMANCE OF AIR CONDITIONING SYSTEM IN EDUCATIONAL BUILDING FOR ENERGY CONSERVATION

Nantamol Limphitakphong¹, Nuttasate Chaikatetham², Therdtchai Khaimook², and Orathai Chavalparit^{1,2}

¹Research Unit of Environmental Management and Sustainable Industry, Faculty of Engineering,
Chulalongkorn University, Bangkok, 10330, Thailand

²Department of Environmental Engineering, Faculty of Engineering, Chulalongkorn University,
Bangkok, 10330, Thailand

ABSTRACT

Building sector plays an important role in energy consumption globally. In tropical countries like Thailand, more than half of all energy is usually supplied for cooling systems. The objective of this study, therefore, is to investigate the environmental performance of an air-conditioning (AC) system for an educational building and to propose strategies for mitigating GHG through energy efficiency measures toward a campus-wide sustainable energy policy. According to data collected, the results demonstrate that the existing AC system consumes about 70% of total energy consumption. The existing system's low energy efficiency caused the whole building's performance to fall below the building energy code standard stipulated by the Thailand's Ministry of Energy. To improve the building's performance, replacement of the current AC system with a highly efficient AC system is needed. This, however, would be costly. Alternative energy conservation measures, including changing window panes, walls, and roof tile materials and installing thermal insulation were proposed to quantify the amount of energy savings as well as GHG emissions reductions. The findings will be useful for building owners, architects and policy makers as a guide about whether to use existing materials or new materials when planning to for a building's energy-efficiency.

Keywords: Environmental performance, Energy efficiency measure, Air-conditioning system, Educational building

INTRODUCTION

Due to increasing global concern about climate change, energy efficiency and environmental remediation have broadly become main areas of research. One of the main issues concerning the effort to limit global temperature rise to only 2 degrees Celsius above pre-industrial levels is the building sector, since it consumes a huge amount of energy and resources and emits a large amount of greenhouse gas (GHG) [1]-[2]. In tropical countries, increased use of air conditioning to maintain thermal comfort in buildings is a main factor causing an increasing of energy demand whereas increased use of heater is a key pressure for the temperate countries [3]-[5]. Accordingly, it could be implied that high potentials of either energy saving or GHG emission reduction can be achieved through energy improvement options for Heating, Ventilating, and Air Conditioning (HVAC) system of buildings. Recently, numerous studies have validated that advanced cleaner technologies and higher energy efficiency equipment coupled with changing occupant habits will save about 30-50% of total energy consumption for both new and existing buildings [6]-[9].

In Thailand, the final energy consumption of the domestic building sector accounted for 22% of the

total national consumption and its consumption has increased rapidly with growth rate of 82% over the last two decades [10]. To cope with a concern of supplying energy for such a huge demand sufficiently, the Thailand's Ministry of Energy has issued Ministerial Regulation stipulating the type and size of buildings and standards criteria and methods of designing energy conservation building, B.E. 2552 (2009) and provided for the monitoring of designated commercial buildings which consume more than twenty-million megajoules of power energy equivalent annually [11]. Among the six categories of designated commercial building, data obtained from Department of Alternative Energy Department and Efficiency (DEDE) demonstrated that the educational institution building stock accounted for 9% and consumed around 15% of total energy demand for buildings [12]. Consequently, research on ways to improve the energy efficiency of this type of building would definitely contribute significant positive impacts on energy security. Chavalparit and Limphitakphong [13] have evaluated the energy efficiency and environmental performance of buildings in Bangkok and emphasized that most of the energy use in educational building was attributed to electricity consumption for HVAC system, resulting in the greatest portion of GHG emission as

a consequence. Thaipradit [14] has provided evidence demonstrating that building insulation materials have a significant impact on the energy and environmental performance of educational buildings in Thailand. Chaayat [15] has applied the concept of using phase change material for improving the cooling efficiency of an air conditioner and found that the modified air-conditioner could decrease the annual electrical consumption by about 1.13 MWh while having a payback period for modifying equipment of 4.15 years.

In addition, since the Thai Ministry of Energy has pledged to reduce around GHG emissions by 20-25% by 2030 in the 21st conference of the parties, commercial buildings have become a major contributor in reducing such number of reductions through energy efficiency measures [16]. This study, therefore, was aimed at investigating the environmental performance of existing air-conditioning (AC) system for educational building and to propose strategies for mitigating GHG through energy efficiency measures toward a campus-wide sustainable energy policy. Besides applying advanced technology and higher energy efficiency equipment replacement, changing building envelopes were also evaluated to identify alternative options for improving existing buildings, based on either an environmental or economic performances perspective. The information provided from the findings of this study can be useful for policy makers and building planners in determining strategies for either reducing energy demand and GHG emission or saving expenditures of educational institutions in tropical countries like Thailand.

MATERIALS AND METHODS

Building Description

This research was performed using a 5-storey educational building at Chulalongkorn University as a case study. The case study building, as described in Table 1, is located in the heart of Bangkok at 13.92 latitude and 100.6 longitude with a range of dry-bulb temperature of 19.0 – 37.2°C and humidity ratio of 11.2 – 28.7 g_w/kg_{da} throughout the year [17].

Evaluation of the Energy Efficiency of the Air Conditioning System

To evaluate the efficiency of electrical consumption in air conditioning (AC) system, three parameters involving cooling performance (CP), coefficient of performance (COP), and energy efficiency ratio (EER) were investigated following Eq. (1) – (4).

Table 1 The basic parameters of case study educational building

Building parameters	Specifications
Floors	5 floors above ground
Gross floor area	1,862.28 m ²
Air-conditioned area	1,195.43 m ²
Structure	Concrete
Envelope	Brick and curtain wall combination
Glass	Clear flat glass
Roof	Flat roof, concrete slab

CP is used for validating results of actual cooling performance with the idle to assure its accuracy. Whereas the results of COP and EER were testified in accordance with Thai industrial standard of AC system (TIS2134:2553).

$$CP = WI/CL \quad (1)$$

$$CL = 5.707 \times 10^{-3} \times A \times V \times 60 \times (H_r - H_s) \quad (2)$$

$$COP = \Delta h_{out}/\Delta h_{in} \quad (3)$$

$$EER = COP \times 3.412 \quad (4)$$

WI = Watt input (kW), inspecting at condensing unit by power meter

CL = Cooling load (TR), inspecting at fan coil unit

A = Cross-sectional area (m²)

V = Velocity (m/s)

H_r = Enthalpy Return (kJ/kg dry air), referring to psychometric chart

H_s = Enthalpy Supply (kJ/kg dry air), referring to psychometric chart

Δh_{out} = Difference of enthalpy at fan coil unit (kJ/kg)

Δh_{in} = Difference of enthalpy at condensing unit (kJ/kg)

Energy Simulation

To identify the potential of alternative options for improving building's energy efficiency, Building Energy Code (BEC) software version 1.0.6 developed by DEDE in accordance with the Ministerial Regulation on type or size of buildings and standards criteria and methods of designing energy conservation buildings B.E. 2552 (2009), was used in this study to estimate the amount of energy savings compared with the current consumption. Data input in the program are classified into 6 categories, including building envelope, lighting system, AC system, photovoltaic (PV) system, hot water (HW) system, and other equipment. However, since there

are no PV and HW systems in this building case study and lighting system and others equipment share a little portion of energy consumption, this study therefore only focused on the AC system and envelope materials that are related to heat transfer through building envelope and building's energy demand. Furthermore, four options for improving energy efficiency of the building were examined to signify a key building material resulting in better building performance as presented its properties in Table 2 - 3.

Environmental Performance Analysis

Due to global concern about climate change, the environmental impact of energy consumption was demonstrated in terms of CO₂ emission through the following equation (Eq. 5);

$$ER = (BE_{EC} - PE_{EC}) \times EF_{GRID} \quad (5)$$

Where ER is mission reduction of each measures (kgCO₂/yr). BE_{EC} refers baseline energy consumption (kWh/yr) and PE_{EC} represents project energy consumption (kWh/yr). EF_{GRID} stands for emission factor of electricity production, which is approximately 0.6093 kgCO₂/kWh for Thai grid production [18].

Economic Performance Assessment

A payback period (PB) analysis was used in this

study as demonstrated in Eq. (6) to assess the economic performance of each energy efficiency improvement measure. A trade-off between investment cost and energy expenditure savings will help signify and prioritize the possible measures for implementation. When the total investment cost is paid by the saving of energy cost, it is a point of break-even, which thereafter entails no monetary loss from implementation.

$$PB (yr) = \frac{\text{Investment cost (USD)}}{\text{Energy cost saving } (\frac{\text{USD}}{\text{yr}})} \quad (6)$$

RESULTS AND DISCUSSIONS

Energy Consumption of Educational Building: A Case Study

Through 12 months of data collection, the case study building consumed about 127,489 kW of electricity, approximately 71% of this total power consumption was attributed to the AC system. Such a portion is quite high compared with the average energy consumption proportion of educational buildings (59%) presented by Phupadthong [9]. This indicates that the efficiency of AC system in this case study is probably low, resulting in consuming higher amount of energy than the typical case. An energy efficiency evaluation of AC system also emphasized that among all the AC equipment, only two of them comply with the Thai industrial standards as presented in Table 4.

Table 2 Properties of opaque materials

Type		Thermal Conductivity (W/m·K)	Density (kg/m ³)	Specific Heat (kJ/kg·K)
Ceiling Insulation Materials	PVC Gypsum	0.211	684	1.09
	Aluminum Foil Gypsum	0.322	745	1.09
	Polyurethane	0.023	24	1.59
	Glass Wool (Stay Cool)	0.039	12	0.96
Wall Materials	Autoclaved Aerated Concrete	0.476	1,280	0.84
	Concrete Block	0.546	2,210	0.92
Roof Tile Materials	Concrete Profile Tiles	0.993	2,400	0.79
	Asbestos Cement Corrugated	0.395	2,000	1.00

Table 3 Properties of transparent materials

Glass Type	Thickness m	Visible Ray		Solar Energy			U-value w/m ²	SH GC
		Reflectance	Transmittance	Reflectance	Transmittance	Absorption		
Tinted Glass	0.006	7.0	0.760	5.0	49.0	46.0	5.74	0.6
Solartag (TS560)	0.006	5.2	0.361	4.8	21.9	73.3	5.35	0.4

In addition, DEDE building regulations define a suitable level of overall thermal transfer value (OTTV) and residential thermal transfer value (RTTV) at 50 and 15 watt/m² for an educational building. The low energy efficiency of the existing AC system in this study, apparently, lead the whole building performance to fall below the standard of this regulation.

High Efficiency of Air Conditioning System Replacement

Because the current AC system plays such an important role in the building's energy demands and seemingly caused the building to fall below standard a high efficiency AC replacement. Based on the assumption that every AC equipment that have has become obsolete or declines in performance will be replaced with a high efficiency AC at the same capacity, the result demonstrated that such implementation requires an investment of 39,224 USD. This investment will reduce energy

consumption by about 25,886 kWh a year, or if converted to GHG emissions, it equates to a reduction of 15,772 kgCO₂e/yr. The break-even point of each AC capacity types, as illustrated in Fig.1, will be 6.3, 6.6, 21.1 and 30 yrs. for 12000 Btu, 18,000 Btu, 30,000 Btu and 36,000 Btu, respectively.

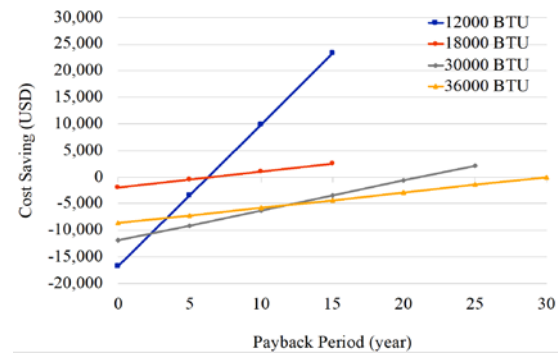


Fig 1 Economic assessment for air conditioning system replacement

Table 4 Energy performance of air conditioning system in building case study

No.	Capacity (Btu)	Ideal Performance* (kW/TR)	Actual AC Efficiency			Comply with TIS**
			CP	COP	EER	
1	12000	1.17	1.66	2.13	7.25	FAIL
2	36000	1.13	2.89	1.22	4.15	FAIL
3	12000	1.17	1.70	2.07	7.05	FAIL
4	48000	1.13	1.23	2.86	9.76	PASS
5	30000	1.16	5.44	0.65	2.20	FAIL
6	12000	1.20	3.94	0.89	3.05	FAIL
7	36000	1.13	2.77	1.27	4.33	FAIL
8	38000	1.14	1.22	2.90	9.87	PASS
9	30000	1.16	9.15	0.38	1.31	FAIL
10	18000	1.25	2.14	1.65	5.62	FAIL
11	30000	1.16	1.62	2.18	7.42	FAIL
12	36000	1.13	2.05	1.72	5.87	FAIL
13	12000	1.10	2.07	1.70	5.78	FAIL
14	12000	1.17	6.00	0.59	2.00	FAIL

*To validate the measurement, CP value of actual AC efficiency shall higher than ideal performance.

**COP and EER should not less than 2.82 and 9.60 respectively to pass the Thai industrial standard [19].

Table 5 Performance of improving existing building through envelope materials

Material Type	Investment	Energy Saving		Payback Period (yr.)	GHG reduction (kgCO ₂ e/yr.)
	Cost (USD)	Quantity (kWh/yr.)	Expenditure (USD/yr.)		
Tinted Glass	801.74	5,138.6	688.22	1.1	3,131
Polyurethane	3,607.41	11,108.2	743.87	2.2	6,768
Autoclaved Aerated Concrete	2,934.87	9,951.6	733.06	2.0	6,064
Concrete Profile Tile	1,665.75	2,125.2	59.07	5.3	1,295
Total	6,845.32	22,762.2	1,676.72	2.0	13,869

Note: Electricity charge is about 0.147 USD/kWh

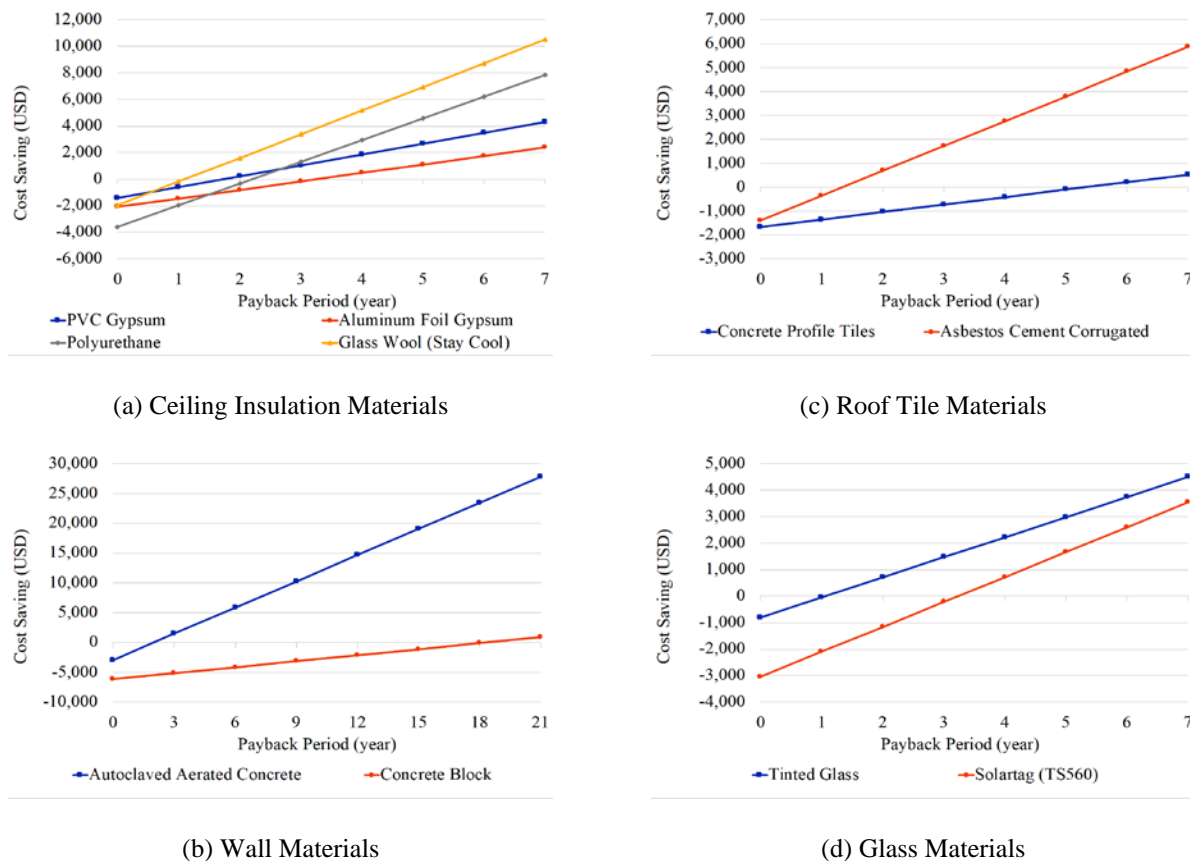


Fig 2 Economic assessment for improving building envelope materials

Options for Improving the Energy Efficiency of Buildings

Besides changing the AC system, which requires a payback period of more than 6 years, alternative options for improving energy efficiency of a building should be examined. Figure 2 illustrated the payback period for implementing each measure of the four energy efficiency improvement options described in Table 2-3. It was found that the option with the shortest payback period consists of installing polyurethane insulation above the ceiling, using autoclaved aerated concrete instead of bricks, roofing with concrete profile tiles, and installing tinted glass. The best 4 measures, therefore, were integrated to re-investigate the maximum level of energy demand reduction as well as GHG reduction through envelope materials improvement. The result as presented in Table 5 revealed that more than 22 MW/yr. of electricity will be saved and about 13,869 kgCO₂e/yr. will be reduced if these four measures are implemented together. Moreover, it will help increase the building's performance to meet the code of designated building regulation eventually.

CONCLUSION

A large portion of final energy is attributed to the building sector and its demand is going to increase in the near future abruptly. Audits to monitor and help manage buildings' energy performance is vital. The performance of the case building at Chulalongkorn University was investigated to identify hotspots and to propose strategies for mitigating GHG. The findings revealed that the efficiency of the air conditioning system was poor as most equipment failed to meet the Thai industrial standards. Either a highly efficient air conditioner replacement or improving building envelope should be implemented to amend this. The initiatives on considering performance-based energy efficiency measures can contribute to a campus-wide sustainable energy policy. Further actions on monitoring energy performance and its improvement and future research on other factors influencing energy consumption and GHG emission from this and other buildings are needed, otherwise this small-scale energy assessment will have little positive effect on Thailand's environmental sustainability.

ACKNOWLEDGEMENTS

This research was funded by the Ratchadapisek Sompoch Endowment Fund (2016), Chulalongkorn University (CU-59-002-IC).

REFERENCES

- [1] Intergovernmental Panel on Climate Change (IPCC), Climate Change 2014: Synthesis Report, Contribution of Working Groups I, II and III to the Fifth Assessment Report of the Intergovernmental Panel on Climate Change, Geneva, Switzerland, 2014, 151 pp.
- [2] United Nations Framework Convention on Climate Change (UNFCCC), Decision 1/CP.21: Adoption of the Paris Agreement, Paris Climate Change Conference, 2015.
- [3] Agdas D., Srinivasan R.S., Frost K. and Masters F.J., Energy use assessment of educational buildings: Toward a campus-wide sustainable energy policy, *Sustainable Cities and Society*, Vol. 17, 2015, pp. 15-21.
- [4] Zanni D., Righi A., Mora T.D., Peron F. and Romagnoni P., The energy improvement of school buildings: analysis and proposals for action, *Energy procedia*, Vol. 82, 2015, pp. 526-532.
- [5] Varun, Sharma A., Shree V. and Nautiyal H., Life cycle environmental assessment of an educational building in Northern India: a case study, *Sustainable Cities and Society*, 2012, Vol. 4, pp. 22-28.
- [6] Salvalai G., Malighetti L.E., Luchini L. and Girola S., Analysis of different energy conservation strategies on existing school buildings in a Pre-Alpine Region, *Energy and building*, Vol. 145, 2017, pp. 92-106.
- [7] Rospi G., Cardinale N., Intini F. and Negro E., Analysis of the energy performance strategies of school buildings site in the Mediterranean climate: A case study the schools of Matera city, *Energy and building*, Vol. 152, 2017, pp. 52-60.
- [8] Chaichaloempreecha A., Winyuchakrit P. and Limmeechokchai B., Long-term energy savings and GHG mitigations in Thailand's building sector: impacts of energy efficiency plan, *Energy procedia*, Vol. 138, 2017, pp. 847-852.
- [9] Phupadtong A., Limphitakphong N., Kanchanapiya P., Tantisattayakul T. and Chavalparit O., The assessment of the environmental and economic performances for improving existing educational building: a case study of Bangkok, Thailand, *International Journal of Sustainable Energy Development*, 2018, In press.
- [10] Department of Alternative Energy Department and Efficiency (DEDE), Thailand, Final energy consumption by economic sectors, 2018
- [11] Ministry of energy (MoE), The ministerial regulation type or size of buildings and standards criteria and methods of designing energy conservation building B.E. 2552, 2009
- [12] Department of Alternative Energy Development and Efficiency (DEDE), Thailand, Lists of designated buildings, 2018.
- [13] Chavalparit O. and Limphitakphong N., Pathways to level up net zero carbon building towards smart cities. *Unisearch Journal*, Vol. 5, Issue 1, 2018, pp. 16-22.
- [14] Thaipradit P., Limphitakphong N., Kanchanapiya P., Tantisattayakul T. and Chavalparit O., The influence of building envelop materials on its life cycle performance: a case study of educational building in Thailand, *Key Engineering Materials*, 2018, In press.
- [15] Chaayat N., Energy and economic analysis of a building air-conditioner with a phase change material (PCM), *Energy Conversion and Management*, 2015, Vol. 94, pp. 150-158.
- [16] Limphitakphong N. and Chavalparit O., Potential of greenhouse gas emissions reduction in Thailand, Thailand's Second Assessment Report on Climate Change 2016, Thailand Research Fund. Bangkok, 2016, pp. 456-497.
- [17] EnergyPlus, Weather data, 2018, <https://www.energyplus.net/weather>
- [18] Electricity Generating Authority of Thailand (EGAT), Thailand, Thailand grid mix electricity life cycle inventory database, 2009.
- [19] Thai Industrial Standards Institute (TISI), Room air conditioners: energy efficiency, 2013

WILLINGNESS TO PAY (WTP) BY CONTINGENT VALUATION METHOD(CASE STUDY: WASTE MANAGEMENT SERVICES)

¹Marselina, ²Ria Virsa

^{1,2}Economic and Business Faculty, Lampung University, Indonesia

ABSTRACT

This study aims to estimate the household WTP on the tariff of waste management service with the Contingent Valuation Method and to investigate the relationship between respondent characteristics with their WTP. Questioners are designed with 8 options of waste management services with some more reasonable tariff. The sample consists of 200 households selected randomly in Bandar Lampung city, Indonesia. The result indicates that household's WTP for waste management services is 200% higher than before, if services are upgraded. Other results indicate that the level of education, number of family, job, income, knowledge and satisfaction of respondents to waste management services are positively correlated with WTP. Government has to review the tariff policy to obtain a more awareness tariff that encourage the sense of responsibility of the community to protect the environment.

Keyword: *Willingness to pay, Waste management services, Tariff, Contingent valuation method*

1. INTRODUCTION

Waste issues are becoming an important issue of the environment in Indonesia. This problem is getting worse along with the population growth and the bad attitude of households disposing their rubbish without being responsible. This habit is driven by the low cost of waste management service which is set by government. As a public good, waste management services is non market because no one can express their preference, so the tariff of its cannot be determined by market mechanism. So that way, this tariff does not reflect the actual cost, includes environment damaging.

Based on local regulation in Bandar Lampung city, one of Indonesia provinces, the average of tariff of waste management service is between is 20,000 IDR to 30.000 IDR per month. This tariff is only operational costs such as fuel prices for waste transport vehicle, labor, and vehicle maintenance and has not taken into consideration of environmental damage. According to Hagos (2012), the tariff must also be includes the cost of recycling and composting. This low tariff encourage people to easily dispose of waste regardless environment damage and this attitude will undermine environmental conditions.

Based on this background, it is needed to have a technique for estimating of tariff that encourage environmental awareness. One of methods to estimate it, is Willingness To Pay (WTP). WTP is a technique to know the willingness of individuals to pay for public goods benefit in which the price of its can not be determined by market mechanism. WTP is an individual valuation technique on natural resources in order to improve the quality of the environment.

Banga, M (2011) also suggested to used WTP to avoid the problem of free-riders in the determination of tariffs for public goods services.

WTP is based on the user's perception of s of the public service. To get user perception, it can be used Contingent Valuation Method (CVM). CVM is a method of measuring someone's preference (FontaWM, 2008). CVM is measuring WTP by eliciting stated user preferences through direct surveys. User are directly asked about their WTP by using open-ended questions (Makkonen.M,et all, 2011). In this surveys, user are offered some alternative services or condition with varying attributes. WTP is inferred indirectly from their ranking or ratings of these alternative services. CVM is can be used to determine the price of tourism services, apartment tariffs, utilizing wildlife, environmental quality.

In Indonesia, there is still miss interpretation, in which all the public service and procurement services including waste management services are government duties and it should be free of charge. In order to have a common point in determining the tariff, it should involve the participation of the household. Afroz (2011) found the same point, in which households do not care about waste management. According to Tansatrisna (2014), the participation of households in waste management services can be indirect participation, namely the involvement of households in financial matters. This participation in waste management is reflected by making payment of user tariff for garbage. According Manurung (2008), one form of participation on waste management can be seen from the willingness to pay for the improvement of

waste management facilities so that cleanliness and environmental quality can be maintained.

Public participation is essential and may lead to enormous benefits for sustainability development (Chutarat C: 2017). Teddy (2017) also agree that waste management services are facilitated by the government but managed by the community which requires active community involvement. Involvement, participation and some characteristic of household determines their choices in WTP. Brahim, Djemaci (2015) and James, K Boyce (2003) found that some characteristics of household such as education level, gender, age, lines of class, race, ethnicity, house type, house distance, income and service quality, awareness, perception and household satisfaction level toward the benefits of public goods in correlating with WTP. Effects on WTP is high when they are interactions each others. Age tends to increase income and higher income has higher opportunities to get high education and high education tends to increase their awareness of environment (Makonenn,2011). The more aged, the more knowledge and experience of environmental benefits and the more concern for the environment. This relationship increase the WTP. Family members will add family members' information about environmental issues because in Indonesia, environmental issues become the curriculum taught in schools.

Community awareness of the environment is influenced by the level of education and knowledge about environment (Finger,1994). According to Mustafa.U (2014), household concerning will affect WTP and it increase along with improving the quality of services. Survey conducted by Gregory O. Thomas, et al (2018) also found that having children may change people's individual environmental attitudes and behaviour, and the results indicate that having a new child is associated with a small decrease in the frequency of a few environmental behaviour. According to James, K Boyce (2003) income inequalities can influence environmental degradation. Inequalities may affect the overall extent of environmental quality, so that the higher income the higher WTP. High level of awareness and knowledge and positive attitude will increases the environmental protection(Aminrad,Z:2013).

2.OBJECTIVE

This study aims (1) to calculate the willingness to pay of household to waste management service in order to get the tariff which is resulting which can arouse the awareness of households to be more responsible, (2) to investigate the relationship between respondent's characteristic with their WTP. This study is expected to provide inputs to the government's

policy of setting, in particular the of waste management services.

3.CITATION AND REFERENCE LIST

WTP is an individual valuation technique on natural resources in order to improve the quality of the environment. Some experts also define WTP is the maximum price a benefiter willing to pay for a given quantity of product or services (Wartenbroch and Skiera,2002). WTP as a way of calculating the ability of each individual on an aggregate basis to pay in order to improve environmental conditions to conform to desired standards. Economic valuation is an attempt to provide quantitative value to goods and services produced by natural resources and environment regardless of whether market value is available or not (Susilowati, 2002). CVM is done by asking directly to benefiter about the value of benefits of public goods includes resources and environment.

Indramawan (2014) asks to 120 respondents in Semarang Barat and he found that almost 85% of respondents are willing to pay higher tariff. He also found that the level of education and family income has a positive effect on the size of WTP. Huntari (2015) found that the average WTP of consumers on waste treatment services is higher than the tariffs paid. Yunis (2012) found the average of household WTP in Tampan Pekanbaru is IDR 10.330 per month. Banga et al (2011) in Uganda, found that WTP can be increased by improving the service quality.

Contingent Valuation Method (CVM) is a method for valuing natural resources and the environment. This approach is done to measure the economic value of goods that cannot be determined because non market price. According to Fonta WM (2008), CVM is a technique to analyze the valuation function that can provide qualitative information that is difficult to identify using other conventional valuation techniques. CVM is done because household is unable to express its preference for economic . CVM is also practiced by Fried (1995) to find out WTP hunters for tourism hunting services Cervus Elaphus in Oregon National Park - Latin America, obtained WTP for \$1,063 for each hunt. Afroz (2010) saw household WTP for garbage dumping tariffs in Kuala Lumpur. Ragens (1991) conducted a study of household WTP to control pollution through counter measures against water pollution in coastal areas of Kristians and Fjord - Norway. Fried (1998) used CVM to research hunting tourism services. Brahim, D (2015), Nasir (2009)

4.RESEARCH METHODOLOGY

This research is field study with survey technique. Data were obtained from questionnaires

given to households located in densely populated housing with the highest volume of waste. Determination 200 household respondent used judgment random sampling technique. in Sukabumi district whose waste is managed by city waste management service of Bandar Lampung, Indonesia value of waste management service. One way to know benefit from public goods is to use CVM s by asking the ability of household pay for waste management service.

It begins by designing a questionnaire that describes some of the preferred bids from the improved conditions of waste management services at a reasonable tariff that follows. The initial conditions of service and of management services at the study sites are taken as start points. Start point condition of waste management service is managed 3 times a week in the afternoon, with garbage cart, with tariff IDR 20.000 / bulan. The average waste per day disposed of every household in the study site was 3 plastics or 90 plastic/ month. It means the value of waste management during this per pack of garbage IDR 222.22 / plastic. Then 7 scenarios of waste management services were created by raising the per stage of service IDR 10.000/stage, in which IDR 10.000 is considered on household ability. Designed questioner asked to respondent. If most respondents answer one scenario selected, then this scenario is the actual WTP desired

Table 1: Scenarios, Services and Tariff

Scenario	Services	Tariff
Scenario A	Garbage is managed 2x a week, in the afternoon with a garbage car	166
Starting Point	Garbage is managed 3x a week, in the afternoon with a garbage car	222
Scenario B	Garbage is managed 3x a week, in the morning, with garbage cart	277
Scenario C	Garbage is managed 4x a week, late afternoon, by truck	333
Scenario D	Garbage is managed 4x a week. morning with garbage truck	388
Scenario E	Garbage is managed 5x a week, early morning with garbage truck	444
Scenario F	Garbage is managed 6x a week, morning with garbage truck	500
Scenario G	Garbage is managed 7x a week, morning with garbage truck	555

Hypothesis Development

Meanwhile, to obtain the second objective of the relationship between the characteristics of the respondent with the WTP he selected, the correlation and crosstab analysis techniques are used. The respondent's characteristic consists of 6

elements, namely the number of family members, the level of education, the type of work, the level of income, the level of service satisfaction and the level of knowledge of the dangers of unmanaged solid waste. The hypothesis developed as follows:

Ha (1): Numbers of Family is a significant and positive correlation with WTP.

Ha (2): Level of education has positive correlation with WTP.

Ha (3): The type of work of respondents has positive relationship with WTP.

Ha (4): Level of income level has positive relationship with WTP.

Ha (5): The level of satisfaction of respondents has positive relationship with WTP.

Ha (6): The level of knowledge has positive relationship with the WTP.

5.RESULT

The starting point if this study is based on tariff paid by household of IDR 222/plastic or IDR 20.000/month with 3 times a week it collected and transported in the afternoon. Garbage is managed with slower waggle wagon and taking 3 times a week caused smell is not good.

Based on the survey results, most of respondents are dominantly choose scenario G, by 37% . They desired the waste management services working every day or 7 times a week, managed in the morning by garbage truck and they agree to pay normal tariff as IDR 555/ plastic or IDR 50.000 /month. This WTP increase 200% if compare to they paid before. 20% of respondents choose the same condition, 19% of respondents are willing to pay IDR 388,00 /plastic or scenario D that is garbage managed four times a week, managed in the morning by garbage truck. The rest or 36% of respondents chose to spread among scenarios A, B, C, E, F. The result of the respondent's choice is shown in Table 2 below.

Table 2. WTP of Waste Management Services Per Plastic

	WTP	Percent
Valid	166	3.0
	222	10.0
	277	13.0
	333	7.0
	388	19.0
	444	2.0
	500	9.0
	555	37.0

The result indicates that most of household's WTP of waste management service is IDR 555/plastic or IDR 50.000/month if the services is upgraded. The desired services is garbage collected and transported everyday, in the morning so

garbage is not decomposed yet and make air pollution in the afternoon. It's mean, WTP of the community can be pushed to increase if their satisfaction of public services is increased.

Correlation Between the Characteristics Of Respondents with Their WTP

Relationship of some characteristics of respondents with WTP used Pearson Product Moment Test. Characteristics of respondents consists of 6 elements, namely the number of family members, the amount of income, the level of education, the type of work, the level of satisfaction on waste management services and the level of knowledge of respondents about the importance of processing waste and maintaining the environment. Of the six characteristics of the household respondents, only the type of work has no correlation with WTP, while five characteristics have a positive correlation. Their effects on WTP when they are interactions each others (Makkonenn,2011). The result of the test as follows.

Table 3. Correlation Between Characteristics of Respondents with Their WTP

Characteristic Respondent	coefficient	Sign
The of family member	0,593	0,000*
Level Education	0,786	0,000*
Type of Work	0,155	0,125
Level of Income	0,733	0.000*
Level of Satisfaction	0,740	0.000*
Level of Knowledge	0,568	0.000*

*) sign on 95%

There is a positive correlation between the number of family member and WTP, with coefficient correlation of 59.3%. The more family number,, the more increase WTP. The effects on WTP when they are interactions each others. While family members become bigger, it will add family members' information about environmental issues because in Indonesia,environmental issues is one of the curriculum taught in schools. This awareness will encourage their WTP.

Age tends to increase income and higher income has higher opportunities to get high education and high education tends to increase their awareness of environment (Makkonenn,2011). It means the awareness is also supported by education. The result find that there is positive correlation between level of education with WTP, with coefficient

correlation equal to 78,6%. The higher level of education that has been taken has influenced the respondents' mindset of environmental quality so that their WTP increases. With higher levels of education respondents tend to better understand about the effect of waste on environment. Higher knowledge raises awareness for a healthy environment. Level of income is also correlate with WTP with 73,3%. It means that if the household has more income, they have higher paying capacity. By adding WTP to IDR 555/plastic, it doesn't matter. This finding is supported by Feitosa et al (2017), that the respondents' income, age and duration of school determine WTP of waste management service. He recommend that communities be encouraged to participate in waste management to safeguard the environment, economics, institutions and social sustainability. Type of work is not significant correlation with WTP. This finding is also supported by consumption theory by Keynes, in which the current consumption depends on the disposable income of household. Consumer income will affect consumer decisions in consuming certain goods or services. The higher the income, the higher the ability to buy goods or services. The higher income will increase demand for better environmental quality. Others finding, that there is positive correlation between the satisfaction level of waste management services with WTP. Level of satisfaction of respondents to waste management services in Sukabumi, Bandar Lampung with WTP for example, provision of public goods and services will provide benefits for households. Guritno (2003) states theoretically, the provision of public goods and services will be optimal if the satisfaction obtained by households is similar to the dissatisfaction that households get by taxes/s. The increase in the services provided is expected to have an impact on the satisfaction of households in Sukabumi households will increaseWTP. The satisfaction of the household increase due to the increasing of the quality of waste management service. Household will pay higher for the services. According to Hagos (2012) more services that should be provided and enhanced by the government include collection services, waste is disposed of properly, and recycling and composting features are added, more WTP increase. Banga et al (2011) also supports this finding that WTP for waste management service in Kampala City, Uganda can be improved by improving the quality of waste services.

The knowledge level of the respondents about the impact on the environment is correlated with the WTP with coefficient correlation of 56.8%. The more knowledge about environmental, the higher their WTP. According to Ladiyance et al (2014), respondents who have good knowledge about the benefits and damage of environment,

they will tend to be more likely to be willing to pay. Finger (1994) also find that environment experience is positively correlated with environmental awareness. People who have environmental experiences are willing to pay higher. Respondents have more knowledge respondents will do activities that are not environmentally damaging and are likely to be willing to make conservation efforts environment.

5.CONCLUSION

WTP of households for waste management services can be increased up to 200 % if the service is upgraded. There is a positive correlation between characteristic of respondents such as, the level of education, the level of satisfaction, income, level of satisfaction, and knowledge of respondents to their WTP except type of work,. Local government needs to review the local regulation concerning WTP and better services. It is necessary for government of Indonesia to review local regulation of waste services by paying attention to WTP . Government should be upgraded the public services and training for household to processing rubbish by sorting, selecting, utilizing and dispose waste wisely.

REFERENCES

- [1] Afroz,R.2011.Using a Contingent Valuation Approach for Improved Solid Waste Management Facility.Journal Elsevier Waste Management, Vol.31.800-808.
- [1] Aminrad,Z, Sharifah ZB, Sayed ZASH, MahyarSakari.2013. Relationship Between Awareness, Knowledge and Attitudes Towards Environmental Education Among Secondary School Students in Malaysia. World Applied Sciences Journal 22 (9): 1326-1333.
- [2] Banga, Margaret. 2011. Households Willingness to Pay for Improved Solid Waste Collection Services in Kampala City, Uganda. The Journal of Environment and Development.
- [3] Brahim, Djemaci. 2015. Using a Contingent Valuation Approach for Improved Household Solid Waste Management in Algeria. Munich Personal.
- [4] Chutarat Chompunth. 2017. Role of Public Participationin Environemnetal Impact Assasement in Thailand. International Jurnal of GEOMATE. Volume 12. Issue 33.
- [5] Feitosa, Anny K.2017. Economic Valuation of Urban Solid Waste: A Review. Revista Spacious.Vol 38 No14.pp1
- [6] Finger, M. 1994. From Knowledge to Action? Exploring The Relationship Between Environmental Eperiences, Learning, and Behavior. Journal of Social Issues 50 (3),141-160.
- [7] Fonta.W.Metall .2008.Using A Contingent Valuation Approach for Improved Solid Waste Management Facility:Evidence from Enugu State Nigeria.Journal of African Economics.
- [8] Ghanem Samar Khairy. 2018.The Relationship Between Population and The Environment and Its Impact on Sustainable Development in Egypt Using a Multi Equation Model Environment, Development and Sustainability, Volume 20, Issue 1, pp 305-340
- [9] Gregory O. Thomas, Rose Fisher, Lorraine Whitmarsh, Taciano L. Milfont, Wouter Poortinga.2018. The impact of parenthood on environmental attitudes and behaviour a longitudinal investigation of the legacy hypothesis. Population and Environment. Volume 39, Issue 3, pp 261-276
- [10] Hagos et all. 2012.Households Willingness To Pay for Improved Urban Waste Management in Mekelle City,Ethiopia. Discussion Paper Series.nEfDDP 12-06
- [11] Huntari,D. 2015. Willingness to Pay of Household Analysis On Waste Management Case Study:Rajabasa Raya, City, Indonesia. Paper. Lampung University.
- [12] Indramawan, Dandy P. 2014. WTP Analysis Integrate tariffd Waste Management at Kecamatan West Smarang. Diponegoro University.Paper.
- [13] James K. Boyce, 2003.Inequality and Environmental Protection. Paper. Political Economy Research Institute. MIT.
- [14] Ladiyance,S danYuliana, L. 2014.Variable Effected Willingness To Pay Household at Bidaracina Jatinegara, East Jakarta.Widya Journal.Vol 2.No 2.
- [15] Manurung R. 2008. Persepsi dan partisipasi siswa sekolah dasar dalam pengelolaan sampah di lingkungan sekolah. Jurnal Pendidikan Penabur.
- [16] Makkonen. M, Halttunen. V, Frank L.2011.The Effects of Gender, Age, and Income on the Willingness to Pay for Music Downloads. BLED Proceedings. AIS Electronic Library (AISeL)
- [17] Muniarti,Eindah.2017.Willingness To Pay (WTP) Analysis For The Rent of Subsidied Apartment at Keteguhan West Teluk Betung Barat, Bandar Lampung City Of Indonesia. Paper.
- [18] Mustafa,U.et all. 2014.Capturing WTP dan Its Determinant for Improved Solid Waste Managemen. Pide working Paper. No 110, Pakistan.
- [19] Tansatrisna, D. 2014. Persepsi dan Partisipasi Rumah tangga dalam Pengelolaan Sampah Rumah Tangga.
- [20] Yunis,M, 2012. WTP Analisisi of Houishold on Cleanness in Tampan Pekanbaru, Riau, Universitas Riau

BIOETHANOL PRODUCTION FROM AGRICULTURAL PRODUCTS AND FRUITS OF BANGLADESH

Md. Abul Kalam Azad^{*1} and Nilufa Yesmin²

^{1,2}Institute of Environmental Science, University of Rajshahi, Rajshahi-6205, Bangladesh

ABSTRACT

Bangladesh is an energy deficient country. Petroleum is the main energy source of Bangladesh imported from the Middle East spending a huge amount of foreign currency. However, the sub-tropical climate of Bangladesh is favorable for cultivation of different agricultural products and fruits. This research was carried out to find out the potentiality of bioethanol production from different agricultural products and fruits of Bangladesh. In 100 gm of agri-products (boiled) and fruits (ripen), 300 ml of distilled water was added and blended and then sterilized. Alpha-amylase enzyme (1750 unit) was added to degrade the starch into simple sugar compound. For alcoholic fermentation, 200 ml yeast (*Saccharomyces cerevisiae* CCD) was added to make the total volume 500 ml and incubated at 31°C for 6-days. From the fermentation of agri-products (potato, sweet potato, corn, pumpkin and carrot), a highest bioethanol production was observed in sweet potato. Bioethanol production capacity of four fruits (orange, banana, papaya and sofeda) was also assessed. A high yield of bioethanol was found from a local variety of banana called *Sagor Kola*. The purity of bioethanol in single distillation for banana and sweet potato was 40% and 35%, respectively. This research proved that Bangladesh has a good prospect of bioethanol production from banana and sweet potato.

Key words: Bioethanol, Agricultural products, Fruits and Fermentation

INTRODUCTION

Bioethanol is considered to be the most optimistic biofuel. Ethanol fermented from renewable sources for fuel or fuel additives is known as bioethanol. Bioethanol, unlike petroleum, is a form of renewable energy source that can be produced from agricultural feedstocks [1]. The first generation of ethanol production used corn as a substrate, later corn was considered as a feedstock lead to the second generation of production of ethanol which used microorganisms and different wastes as a substrates [2]. The cheapest and easily available source for the production of bioethanol is fruit wastes. It is a potential energy source, from which ethanol can be obtained. Fruit waste which is thrown away has very good antimicrobial and antioxidant potential.

Rapid increase of population and exponential growth on industrialization load on fossil fuel resources and the resources are being depleted very fast. Therefore, it is required to discover alternative cheaper sources of fuel for fulfillment of worldwide demand. The main task is to develop easier techniques by using cheaper source for the production of bioethanol so that the common people can also produce it by themselves. For this purpose fruit wastes were taken as a substrate for the ethanol production with use of yeast *Saccharomyces cerevisiae* [3]. In this study, comparison of bioethanol production from different

agri-products and ripen fruits such as bananas, papaya, orange and sofeda were studied.

The objective of this study is to determine the production efficiency of bioethanol from different agri-products and ripen fruits of Bangladesh.

MATERIALS AND METHODS

Raw Material Collection

The agri-products (potato, sweet potato, corn, pumpkin and carrot) and fruits (orange, banana, papaya and sofeda) were collected from the local market of Rajshahi city, Bangladesh.

Yeast Strain and Culture Media

Yeast strain (*Saccharomyces cerevisiae* CCD) was collected from the Spirit Section of Carew and Co., Darsana, Bangladesh. For yeast culture, modified YMPD (Yeast-Malt-Peptone-Dextrose) broth culture media was used. The YMPD media was prepared with yeast extract (3.0 g), malt extract (3.0 g), peptone (5.0 g) and dextrose (10.0 g). All of these ingredients were dissolved in 1000 ml of water and adjusted to pH 6.0.

Production of Bioethanol from different Agri-Products

About 100g of agri-products (potato, sweet potato, corn, pumpkin and carrot) was boiled blended in 300 ml distilled water. About 1750 unit of α -amylase enzyme and 200 ml of 2-days old yeast were added to each treatment and adjusted to pH 6.0, and incubated at 31°C for 6-days. After incubation period, turbidity of solution and produced ethanol were measured.

Bioethanol Production from different Ripen Fruits

Different ripen fruits like banana, orange, papaya and sofeda pulps were extracted by blending with blender machine. The fruits fresh or blanched were mashed. Then it was used as raw materials for bioethanol production. For optimum bioethanol production 200 ml of 2-days old yeast was added in 300 ml fruit pulp solution (20%), adjusted to pH 6.0, and incubated at 31°C. After 6 days of fermentation the crude fermented fruit solution was first centrifuged at 12,000 rpm to remove the unused starch and yeast cell. Then, the clear solution was taken into rotary evaporator for separation of ethanol at 78.5°C for five minutes.

Estimation of Total Sugar before and after Fermentation

Total sugar content was determined by sugar measurement machine named "On Call Plus". Sugar concentration before and after fermentation were measured.

Distillation Process

Distillation was carried out using a distillation apparatus. Heating of fermented materials was carried out at 78.5°C.

Measurement of Purity of Produced Alcohol

The percent of purity of produced bioethanol from agri-products and fruits was measured by using an alcohol meter (Jiujiangnongduji, China). This meter can measure the alcohol purity from 0-100%.

RESULTS AND DISCUSSION

Production of Bioethanol from different Agri-Products

Bioethanol production from five different agri-products (potato, sweet potato, corn, pumpkin, carrot) were assessed. It was found that sugar content in sweet potato (14.9 mmol/L) is higher than other four agri-products. Sweet potato produces a

large amount (95 ml) of bioethanol with 35 % (v/v) purity and after fermentation the sugar concentration was reduced to 5.9 mmol/L from 14.9 mmol/L. The lowest amount of bioethanol was produced from pumpkin with purity of 6% (Table 1).

Table 1 Bioethanol production from different agri-products

Name of Agri-products	Volume after fermentation (ml)	Volume after distillation (ml)	Purity of Bioethanol % (v/v)
Potato	465	67	18
Sweet Potato	487	95	35
Corn	449	82	15
Pumpkin	466	64	6
Carrot	459	70	10

Ethanol production from spoiled starch rich vegetables by sequential batch fermentation was studied by Satish [4], Kumar *et al.* [5] used sweet potato as raw material for the production of ethanol and the production was only 0.15%. This vast variation may due to the larger amounts of fermentable sugars are present in agri-products.

Bioethanol Production from different Ripen Fruits

The study of bioethanol production from ripen fruits like orange, banana, papaya and sofeda has not been done widely, so the present investigation was carried out for the production of ethanol with ripen fruits. The productions of bioethanol from four different ripen fruit pulps (orange, banana, papaya, sofeda) were assessed during this study. Sugar content in banana (27.9 mmol/L) was higher than other three fruits and it produces a large amount (97 ml) of bioethanol with 40 % (v/v) purity and after fermentation, sugar concentration is reduced to 12.8 mmol/L from 27.9 mmol/L. The lowest amount of ethanol was produced from sofeda (Table 2).

Table 2 Bioethanol production from different ripen fruits

Name of Fruits	Volume after fermentation (ml)	Volume after distillation (ml)	Purity of Bioethanol % (v/v)
Orange	482	87	30
Banana	493	97	40
Papaya	460	83	20
Sofeda	445	81	18

This result is quite similar with some studies of banana waste [6]. The amount of produced ethanol in present study is higher compare to the studies of Hossain *et al.* [7] and Kumar *et al.* [5]. Hossain *et al.* [7] reported that rotten pineapple produces 8.7% ethanol.

Bioethanol Production from different Varieties of Banana

The bioethanol production from four different varieties of banana (sagor, sabri, chinichampa and bitchi kola) was assessed. It was shown that the sugar content in sagor kola (27.9 mmol/L) is higher than other three varieties of banana and it produces a large amount (97 ml) of bioethanol with 40 % (v/v) purity and after fermentation the amount of total sugar was reduced to 13.8 mmol/L from 27.9 mmol/L. The lowest amount (81 ml) of ethanol was produced from bitchi kola with purity of 20% (Table 3).

According to Hossain *et al.* [7], 900g of rotten banana with 35% distilled water adding 3g/L yeast and adjusted pH at 5.8 was incubated at 35°C for 3 days and found the bioethanol purity only 7.1% (v/v).

Janani *et al.* [8] observed the rate of ethanol production through fermentation of apple, grapes, papaya and banana waste by *Saccharomyces cerevisiae* at pH 5.4 and temperature 30°C, bioethanol and observed the yields 4.73%, 6.21%, 4.19% and 5.4%, respectively.

Kumoro *et al.* [9] used jackfruit juice and the ethanol production was 12.13%. Ethanol yield in fruit pulps varied significantly between the fruit samples and the highest yield was 35.86% in the mixed fruit pulps sample, followed by 28.45% in banana pulp and the lowest yield was 26.5% in mango pulp. The fermentation of enzymatic hydrolysis of acid pretreated mixed fruit pulps (banana and mango) by yeast showed an incubation period of 48 h as optimum for maximum ethanol of 35.86% corresponding to a fermentation efficiency of 70.33%. In peels samples, the maximum yield was 13.84% in banana and 9.68% in mango at 42 h of incubation. The results of present ethanol yield are similar to the observations of Sirkar *et al.* [10] in the case of banana. This observation is consistent with the report of Akin-Osanaiye *et al.* [11], which indicated that the amount of yeast influenced ethanol production in agro wastes. The current observations are in good agreement with similar results reported by Pramanik and Rao [12] for grape waste.

Table 3 Bioethanol production from different varieties of banana

Banana Varieties	Volume after fermentation (ml)	Volume after distillation (ml)	Purity of Bioethanol % (v/v)
Sagor	493	97	40
Sabri	486	87	30
Chini-champa	460	83	35
Bichikola	445	81	20

CONCLUSIONS

From this study we conclude that sweet potato and banana are the good and cheaper sources for bioethanol production. These sources can be used for small and large scale production of bioethanol because sweet potato and banana are available everywhere in Bangladesh.

The production of ethanol from the agri-products and fruits can be improved further by using genetically engineered yeast strains that are capable of converting multiple sugars in to ethanol and using of proper distillation process for increasing the percentage of purity of produced bioethanol.

REFERENCES

- [1] Singh, A., and Jain, V.K., Batch fermentation of cane molasses for ethanol production by *Zymomonas mobilis*. Journal of Indian Chemical Engineering, Vol. 37, 1995, pp.80-94.
- [2] Grassi, M., Modern Bioenergy in the European Union. Renewable Energy, Vol. 16, 1999, pp.985-990.
- G [3] Gohel, H.R., Ghosh, S.K. and Braganza, V.J., Yeast as viable and prolonged feedstock for biodiesel production. International Journal of Renewable Energy Research, Vol. 3(1), 2013, pp. 126-131.
- [4] Satish, B., Ethanol production from spoiled starch rich vegetables by sequential batch fermentation. International Journal of Biotechnology & Biochemistry, Vol. 3, 2010, p. 351.
- [5] Kumar, A., Kumar, N., Baredar, P. and Sukla, A., A review on biomass energy resources, potential, conversion and policy in India Renew. Sustain. Energy Rev. Vol. 45, 2015, pp. 530-539.

- [6] Snehal R. Patil and Gaurav A. Zope., Production of Biofuel from Banana waste. *International Journal of Innovative Research in Science, Engineering and Technology*, Vol. 6, 2017, pp. 551-554.
- [7] Hossain, A.B.M.S. and Fazliny A.R., Creation of alternative energy by bioethanol production from pineapple waste and the usage of its properties for engine), *Afr. J. Microbial. Res.* Vol. 4(9), 2010, pp.813-819.
- [8] Janani, K., Ketzi, M., Megavathi, S., Vinothkumar, D. and Ramesh, B.N.G., Comparative studies of ethanol production from different fruit wastes using *Sacchromyces cerevisiae*. *International Journal of Innovative Research in Science, Engineering and Technology*, Vol. 2, 2013, pp. 7161-7167.
- [9] Kumoro A.C., Rianasari D., Pinandita A.P.P., Retnowati, D.S. and Budiya, C.S., Preparation of Wine from Jackfruit (*Artocarpus heterophyllus lam*) Juice using beaker yeast: Effect of yeast and initial sugar concentrations. *World Applied Sciences Journal*, Vol. 16, 2012, pp. 1262-1268.
- [10] Sirkar, A., Das, R., Chowdhury, S. and Sahu, S.J., An experimental study and mathematical modeling of ethanol production from banana peels by hydrolysis and fermentation. *International Journal of Science and Research*, Vol. 88, 2008, pp. 4-10.
- [11] Akin-Osanaiye, B.C., Nzelibe, H.C. and Agbaji, A.S., Production of ethanol from (papaw) agro waste: effect of saccharification and different treatments on ethanol yield. *African Journal of Biotechnology*, Vol. 4 (7), 2005, pp.657-659.
- [12] Pramanik, K. and Rao, D.E., Kinetic study on ethanol fermentation of grape waste using *Saccharomyces cerevisiae* yeast isolated from toddy. *IE (I) Journal*, Vol. 85, 2005, pp.53-58.

ISOLATION OF STRESS TOLERANCE YEAST STRAIN FROM PAPAYA WASTES

Gemilang Lara Utama^{1,2}, Dwi Wahyudha Wira³ and Roostita L. Balia³

¹Faculty of Agro-Industrial Technology, Universitas Padjadjaran, Indonesia;

²Center for Environment and Sustainability Science, Universitas Padjadjaran, Indonesia;

³Faculty of Veterinary Medicine, Universitas Padjadjaran, Indonesia

ABSTRACT

Papaya wastes is naturally fermented and potentially overgrown by microorganisms such yeasts. The research aims to determine the presence of ethanol-fermenting yeasts on papaya wastes which has the ability to tolerate high glucose and ethanol contents. Yeasts isolated from papaya wastes with using Potato Dextrose Agar/PDA which modified with 3% yeast extract/YE and 10 ppm Amoxicillin, then incubated for 48h at room temperature. The isolates were identified macroscopic and microscopically then the yeast-like isolates cultured on Nutrient Broth/NB with the addition of 3% YE, 10 ppm Amoxicillin and 30% glucose or alcohol to be tested for the tolerance ability towards high glucose and alcohol. Yeasts presence on high glucose and alcohol media was determine by UV-Vis spectrophotometer by measuring optical density (OD) for UV absorbance at $\lambda=600\text{nm}$. The isolate with highest OD at glucose and alcohol media grown at papaya wastes for 72h and the ethanol contents measured by chromium dichromate oxidation methods every 24h. Species identification performed using sequence analysis of the rRNA gene internal transcribed spacer (ITS) region with using primers ITS1 (5'-TCCGTAGGTGAACCTGCGG-3') and ITS4 (5'-TCCTCCGCTTATTGATATGC-3'), the sequences compared with the GenBank database using Basic Local Alignment Search Tools/BLAST algorithm. The results showed that three yeast-like isolates found from papaya wastes, with Y1 isolate identified as best isolate with the OD of 0.4699 at 30% glucose media and OD of 0.0960 at 30% alcohol media, with the highest ethanol fermented at 48h was 4.34%. The rate of isolate identification by sequence analysis resulted 96.20% (531/552) identical with *Pichia sp.* strain AQGWD 7.

Keywords: *Papaya, Wastes, Yeasts, Stress, Tolerance*

INTRODUCTION

Papaya (*Carica papaya*) waste is the second highest fruit wastes found in wet market particularly in West Java, Indonesia. As one of the featured product of West Java, papaya is constantly available in every season. However, the number of underutilized papaya wastes had demonstrated the potential usage or unsettling influence that can be come about.

The plenitude of papaya waste has been raising an approach to increase its economic value. Papaya waste commonly utilized for livestock feed or crude material of compost [1] [2]. Others started to create papaya as a biomass of crude materials for the making of sustainable power sources such biogas [3] [4]. Other sustainable power source that can be created from papaya biomass is ethanol [5] [6].

Papaya wastes contain high complex saccharide in a form of lignocelluloses which could be hydrolyzed into D-glucose and D-xylose then converted furthermore into ethanol by microorganism [7]. However, papaya wastes potential in ethanol fermentation is not just resulted from its complex-cellulose compound yet in addition from the biological aspect that represented by the existence of indigenous microorganisms which naturally fermenting ethanol when the putrefaction occurs [8].

The potential of indigenous microorganisms

isolated from papaya wastes is still rarely revealed especially for the ability in ethanol production. Kowser, et al. [8] has been isolated the potential acetic acid bacteria from rotten papaya that potential in utilizing ethanol for producing acetic acid. The latest research has been isolated yeast from various agriculture wastes including papaya that has xylose-utilizing ability in producing ethanol [9].

Yeasts has been known as the best microorganisms for ethanol producing activity, however yeasts with the ability in tolerating stress when the ethanol production occurs still hard to find [10] [11].

High sugar and ethanol stress was the common inhibitor when the ethanol fermentation occurs [12] [13] [14]. Both conditions could influence the osmotic pressure or membrane fluidity which disturbs yeasts growth and ethanol fermentation process [15]. Thusly, indigenous yeasts with the ability to tolerate high sugar and ethanol in ethanol fermentation still need to discover.

MATERIALS AND METHODS

Indigenous Yeasts Isolation from Papaya Waste

Papaya waste was randomly collected from the local market in Bandung City, Indonesia, blended aseptically then transferred into containers and stored in the refrigerator. Using Potato Dextrose Agar/PDA

(Oxoid Ltd.) which modified with 3% yeast extract/YE (Kraft Inc.) and 10 ppm Amoxicillin, indigenous yeasts isolated from papaya wastes then incubated at room temperature for 48h. The morphological characteristics of indigenous yeasts was identified macroscopic and microscopically [15] [16].

Stress Tolerance Tests

To determine indigenous yeasts tolerance ability towards stress caused by high glucose and ethanol contents, 30% glucose or alcohol added into Nutrient Broth/NB (Oxoid Ltd.) modified with 3% yeast extract/YE (Kraft Inc.), 10 ppm Amoxicillin. Spectrophotometer UV-Vis used for measuring optical density (OD) at $\lambda=600\text{nm}$ to determine yeasts presence on high glucose and alcohol media [15].

Ethanol Fermentation

Papaya waste weighed and blended aseptically with the dilution ratio of 1:1.5. Indigenous yeast with stress tolerance, cultured at papaya wastes in room temperature for 72h. The ethanol that resulted was measured by chromium dichromate oxidation methods every 24h [15] [16].

Indigenous Yeast Species Identification

rRNA gene internal transcribed spacer (ITS) region was used to identify indigenous yeast species, using sequence analysis of the with using primers ITS1 (5'-TCCGTAGGTGAACCTGCGG-3') and ITS4 (5'-TCCTCCGCTTATTGATATGC-3'). The gene sequencing has been done by Macrogen Inc., the sequence results then compared with the database of GenBank using BLAST algorithm (<https://blast.ncbi.nlm.nih.gov/Blast.cgi>) [17].

RESULTS AND DISCUSSIONS

Morphological Characteristic of Papaya Indigenous Yeasts

Indigenous yeasts isolation results showed that three yeast-like colonies have been identified from papaya wastes (Fig. 1). According to morphological characteristics, the three isolates could be categorized as yeast. The isolates has cell length of 1-5 μm up to 20-50 μm , width of 1-10 μm also has unicellular colonies, round, ouval, long shaped with the establishment of pseudomycelium [18]. The results also in accordance with the characteristic of yeasts strain that isolated from papaya which has smooth surface, spherical or ouval shape, creamy white color and presence of pseudomycelium [16].

Yeasts Tolerance towards High Glucose

High glucose tolerance test results (Fig. 2) showed that all of the indigenous yeasts can be survived at 30% of glucose content media with Y1 and Y2 as the

best isolates that shown OD of 0.4699 and 0.4656 respectively while Y3 reach OD of 0.4034.

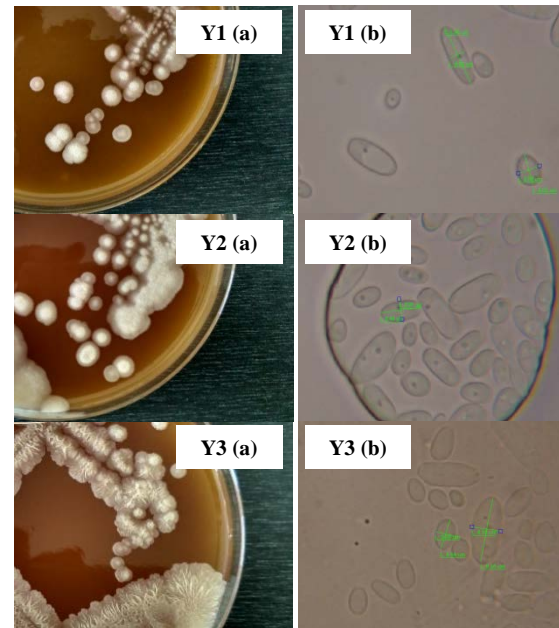


Fig. 1 (a) macro and (b) microscopic (1000x magnification) morphology of indigenous yeasts colony (Y1, Y2, Y3)

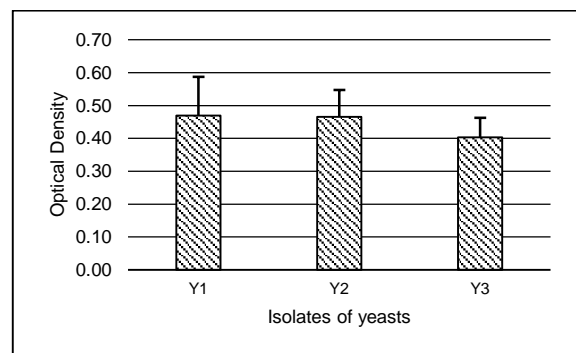


Fig. 2 Yeast optical density on high glucose media

Determination of glucose-tolerance was done to decide the capability of indigenous yeast isolated from papaya waste in generating ethanol on high osmotic pressure condition [19]. Mostly yeast growth was inhibited by the osmotic pressure that resulted from high contents of sugar up to 30 % [20] [16].

However, higher ethanol also could be resulted from high sugar available because ethanol generated from sugar fermentation by microorganism [21]. The rate of ethanol generation was also influenced by sugar concentration [19]. Therefore, the ability in tolerating high glucose contents was important in resulting high ethanol.

At the beginning of fermentation, yeasts with the ability to tolerate osmotic pressure could consume glucose, doing glycerol synthesis and producing low

acid [22]. High glucose osmotic stress can be combated by efficient glycerol transport into inside the yeasts cell [23]. Assimilation succinic and acetic acid by several *non-Saccharomyces* yeasts could help in surviving the osmotic stress condition [22] [24].

Yeasts Tolerance towards High Ethanol

Figure 3 has been shown all the indigenous yeast isolates had tolerance ability towards high ethanol up to 30% which determined by optical density of isolates Y1 (0.096), Y2 (0.075), and Y3 (0.070). The yeast presence on high ethanol environment due to normally papaya waste contains high sugar and the ethanol was accidentally generated when the putrefaction occurs.

High ethanol contents could delay the growth of yeasts [25]. Ethanol interrupt the permeability of yeast cell wall then the sorting and signaling function will be disturbed so that the growth, fermentation and viability of yeasts cell also decrease [26]. Therefore, ethanol tolerance test was performed to find out the indigenous yeast capability in tolerating stress resulting from high ethanol.



Fig. 3 Yeast optical density on high ethanol media

Ethanol fermentation

Indigenous yeast isolate of Y1 chosen as best isolate with the ability in tolerating glucose and ethanol up to 30% then used to ferment the papaya waste for resulting ethanol. The results (Fig. 4) showed that the ethanol contents tend to increase until 48h with the contents of $4.34 \pm 0.086\%$, then decrease at 72h ($1.28 \pm 0.001\%$).

Natural ethanolic fermentation usually occurs and dominated by non-*Saccharomyces* yeasts at the early stages of fermentation [27]. The dominance will last for 2-3 days and affect the ethanol contents until 5% then decrease [28].

Early fermentation has shown the high rate of yeasts growth by utilizing amino acids and vitamins for continuing the ethanol fermentation [29]. Organic acids, esters, and ethanol dominated the early stage fermentation which resulted from β -glucosidase, β -xylosidase and some proteases enzyme [20].

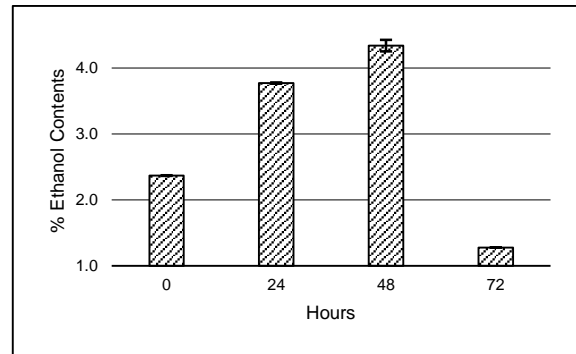


Fig. 4 Ethanol fermentation

After the growth end, non-*Saccharomyces* yeasts have respiro-fermentative regulatory mechanism that can decrease ethanol contents [31]. Carbon source available is consumed for respiration so that the ethanol decreases [32] [33].

Yeast Identification

Gene sequencing results (Table 1) showed that the ITS1 primer gained 725 of 756 (95.90%) sequences identical with *Pichia sp.* stains QAUPK01 (KT987926.1) and the nearest phylogenetic relatives which shown by the tree (Fig. 6). Meanwhile, the results of ITS 4 primer had shown higher identical sequences with 531 of 552 (96.20%) identical with *Pichia sp.* stains AQQWD7 (KP721590.1) with the nearest phylogenetic relatives shown by Fig. 7. The indigenous yeast isolate has close relatives with *Pichia kudriavzevii*, *Candida xylopsoci*, and *Issatchenkia sp.*

Table 1 Results of Yeast Identification

Primer	ITS1	ITS4
Identities	725/756	531/552
Percent Identities	95.90	96.20
Nearest phylogenic relative	<i>Pichia sp.</i>	<i>Pichia sp.</i>
Strain	QAUPK01	AQQWD 7
Accession number	KT987926.1	KP721590.1

Pichia kudriavzevii previously known as *Issatchenkia orientalis* has been isolated from various natural sources and used for ethanol production. Some other strain of *Pichia kudriavzevii* also shown tolerance towards acid, ethanol, thermal and salt stress with higher thermotolerant activity than conventionally used ethanol-fermenting yeasts i.e. *S.cerevisiae* [34]. *Pichia kudriavzevii* is acidophilic yeasts which grow better under acidic conditions (pH of 4-6) that could lead the intracellular enzymes for optimal sugar conversion to ethanol and the other study mentioned that the yeast presenting ethanol tolerance ability[35] [36].

The ability of indigenous non-*Saccharomyces* yeasts in naturally grown and producing ethanol at room temperature has been escalated since the

ethanol-tolerance ability characterized [37]. Gidado, et al. [36] found that indigenous yeast species with identical sequence of 97-98% to *Pichia kudriavzevii* has the ability to grow and ferment ethanol up to 20%

v/v. *Pichia kudriavzevii* strains GY1 was the most adaptive, efficient and effective in various sugars (fructose, galactose, glucose, lactose and sucrose) utilization for ethanol production [38].

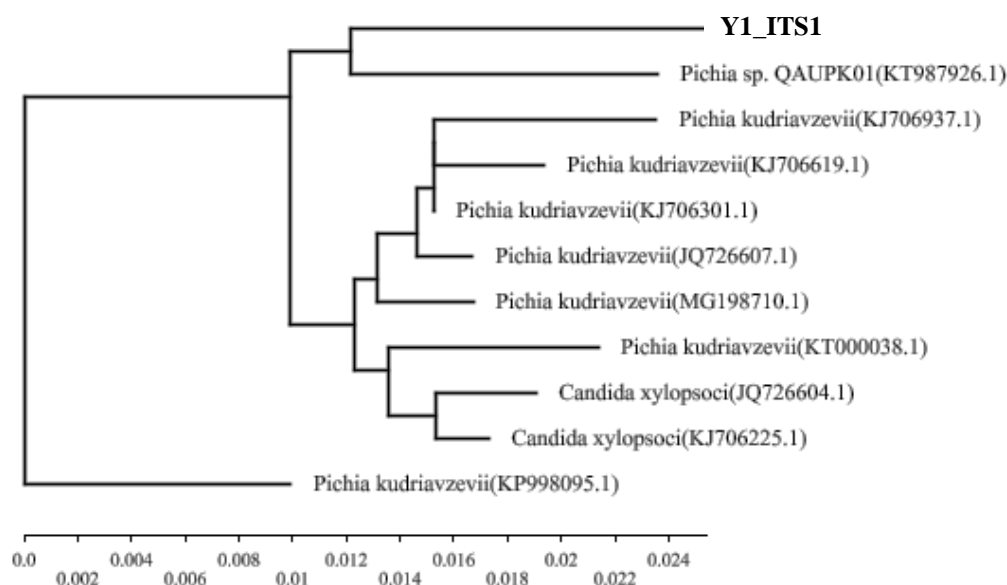


Fig. 6 ITS1 Phylogenetic Tree

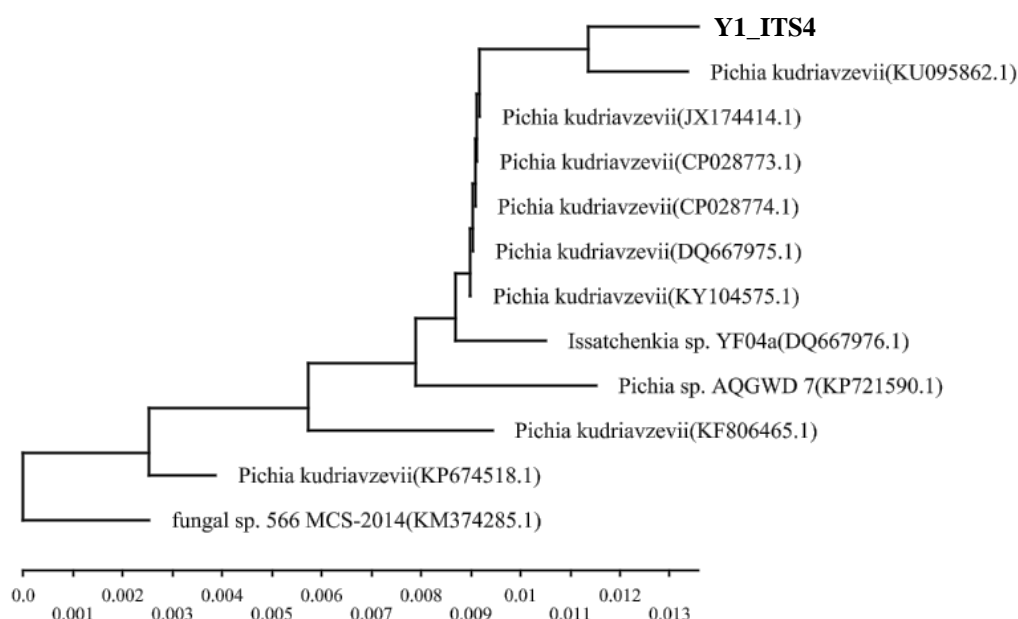


Fig. 7 ITS4 Phylogenetic Tree

CONCLUSION

Three yeast-like colonies isolated from papaya wastes. Isolate Y1 chosen as best isolate in tolerating stress from glucose and ethanol contents up to 30% with the OD of 0.4699 and 0.0960 respectively. The chosen indigenous yeast isolates fermenting $4.34 \pm 0.086\%$ v/v ethanol from papaya waste for 48h. Gene identification gained 96.20% (531/552) sequence identical with *Pichia* sp. strain AQGWD 7.

ACKNOWLEDGEMENTS

Author would like to thank Rector of Universitas Padjadjaran for the Research Fundamental Grant of Hibah Internal Unpad and Travel Award 2018. Also thanked the Student Research Group, Vivi Fadila Sari, Isfari Dinika and Syarah Virginia who helped in the laboratory.

REFERENCES

- [1] Jara-Samaniego J., Pérez-Murcia M. D., Bustamante M. A., Paredes C., Pérez-Espinoza A., Gavilanes-Terán I., et al., Development of organic fertilizers from food market waste and urban gardening by composting in Ecuador. PLoS ONE, Vol. 12 Issue 7, 2017: e0181621. <https://doi.org/10.1371/journal.pone.0181621>
- [2] Sadh P. K., Duhan S., and Duhan J. S., Agro-industrial wastes and their utilization using solid state fermentation: a review. Bioresources and Bioprocessing, Vol. 5 Issue 1, 2018, pp.1-15.
- [3] Onthong U., and Juntarachat N., Evaluation of biogas production potential from raw and processed agricultural wastes. Energy Procedia, Vol. 138, 2017, pp.205-210.
- [4] Budiyo, Manthia F., Amalia N., Matin H. W. A., and Sumardiono S., Production of biogas from organic fruit waste in anaerobic digester using ruminant as the inoculums. MATEC Web of Conferences, Vol. 156 Issue 3, 2018, pp.1-5.
- [5] Jayaprakashvel M., Akila S., Venkatramani M., Vinothini S., Bhagat J., and Hussain J. A., Production of bioethanol from papaya and pineapple waste using marine associated microorganisms. Biosciences Biotechnology Research Asia, Vol. 11 (SE), 2014, pp.193-199.
- [6] Jahid M., Gupta A., and Sharma D. K., Production of bioethanol from fruit wastes (banana, papaya, pineapple and mango peels) under milder conditions. J. Bioprocess Biotech, Vol. 8 Issue 3, 2018, pp. 1-11.
- [7] Promon, S. K., Studies on isolation of yeast from natural sources for bioethanol production from vegetable peels and the role of cellulose degrading bacteria (*Bacillus subtilis*) on ethanol production. Bangladesh: BRAC University, 2015.
- [8] Kowser J., Aziz M. G., and Uddin M. B., Isolation and characterization of *Acetobacter aceti* from rotten papaya. J. Bangladesh Agril. Univ., Vol. 13 Issue 2, 2015, pp. 299-306.
- [9] Htet N. N. W., Hlaing T. S., Yu S. Z., and Yu S. S. Isolation and characterization of xylose-utilizing yeasts for ethanol production. J. Bacteriol. Mycol. Open Access, Vol. 6 Issue 2, 2018, pp. 109-114.
- [10] Utama G. L., Kurnani T. B. A., Sunardi, Cahyandito M. F., and Roostita, L. B. Joint cost allocation of cheese-making wastes bioconversions into ethanol and organic liquid fertilizer. Bulgarian Journal of Agricultural Science, Vol. 23 Issue 6, 2017, pp. 1016-1020.
- [11] Utama G. L., Kurnani T. B. A., Sunardi and Roostita, L. B. Reducing cheese-making by-product disposal through ethanol fermentation and the utilization of distillery waste for fertilizer. International Journal of GEOMATE, Vol. 13 Issue 37, 2017, pp. 103-107.
- [12] Indah H., Putri F., and Utama G.L. Preliminary studies of halophilic yeasts antimicrobial activities isolated from cocoa bean pulp towards *E. coli* and *Salmonella spp.* International Journal on Advance Science, Engineering and Information Technology, Vol. 5 Issue 2, 2015, pp. 107-109.
- [13] Putri F., Indah H., and Utama G.L. Preliminary Identification of Potential Halophilic Bacteria Isolated from 'Asam Sunti'–Indonesian Traditional Herbs, in Inhibiting the Growth of *E. coli* and *Salmonella spp.* International Journal on Advance Science, Engineering and Information Technology, Vol. 5 Issue 3, 2015, pp. 152-154.
- [14] Utama G. L., Putri F., Indah H., and Balia R. L. Preliminary identification of inhibition activities towards *Eschericia Coli* and *Salmonella spp.* by pickle's indigenous halotolerant bacteria. International Journal on Advance Science, Engineering and Information Technology, Vol. 5 Issue 2, 2015, pp. 123-125.
- [15] Utama G. L., Kurnani T. B. A., Sunardi, and Balia R. L. The isolation and identification of stress tolerance ethanol-fermenting yeast from mozzarella cheese whey. International Journal on Advance Science, Engineering and Information Technology, Vol. 6 Issue 2, 2016, pp. 252-257.
- [16] Parameswari K., Hemalatha M., Priyanka K., and Kishori B. Isolation of yeast and ethanol production from papaya (*Carica papaya*) and grape (*Vitis vinifera*) fruits. International Journal of Scientific and Engineering Research, Vol. 6 Issue 2, 2015, pp. 100-104.
- [17] Utama G. L., Sugandi W. K., Lembong E., and Suryadi E. Isolation and identification of ethanol and glucose tolerance yeasts strain from *Tacca leontopetaloides*. Microbiology Indonesia, Vol. 11 Issue 4, 2017, pp. 129-136.
- [18] Utba F., Balia R. L., and Utama G. L. The presence of indigenous yeasts with proteolytic activity isolated from homemade-mozzarella whey. Scientific Papers Series-Management, Economic Engineering in Agriculture and Rural Development, Vol. 18 Issue 1, 2018, pp. 507-513.
- [19] Thancharoen, K. Rotten banana waste management for bioethanol producing ethanologenic yeast. Conference Proceedings, in Proc. Int. Conf. on Biologica, Civil and

- Environmental Engineering, 2015.
- [20] D'Amato D., Corbo M. R., Del Nobile M. A., and Sinigaglia M. Effects of temperature, ammonium and glucose concentrations on yeast growth in a model wine system. *International Journal of Food Science and Technology*, Vol. 41, 2006, pp. 1152-1157.
- [21] Jaiswal A., Tomer D., and Bhatnagar T. Bioethanol production by novel indigenous yeast strains from lignocellulosic waste. *J. Microb. Biochem. Technol.*, Vol. 8, 2016, pp. 474-477.
- [22] Rantsiou K., Dolci P., Giacosa S., Torchio F., Tofalo R., Torriani S., et al. *Candida zemplinina* can reduce acetic acid produced by *Saccharomyces cerevisiae* in sweet sine fermentations. *Applied and Environmental Microbiology*, Vol. 78 Issue 6, 2012, pp. 1987-1994.
- [23] Mukherjee V., Redeka D., Aerts G., Verstrepen K. J., Lievens B. and Thevelien J. M. Phenotypic landscape of non-conventional yeast species from different stress tolerance traits desirable in bioethanol fermentation. *Biotechnology for Biofuels*, Vol. 10 Issue 216, 2017, pp. 1-19.
- [24] Nakayama S., Morita T., Negishi H., Ikegami T., Sakaku K., and Kitamoto D. *Candida krusei* produces ethanol without producing succinic acid a potential advantage for ethanol recovery by pervaporation membrane separation. *FEMS Yeast Research*, Vol. 8, 2008, pp. 706-714.
- [25] Ali M., Chernova T. A., Newnam G. P., Yin L., Shanks J., Karpova T. S., et al. Stress-dependent proteolytic processing of the actin assembly protein Lsb1 modulates a yeast prion. *Biol. Chem.*, Vol. 289 Issue 40, 2014, pp. 27625-39.
- [26] Navarro-Tapia E., Nana R., Querol A. and Pérez-Torrado R., Ethanol cellular defense induce unfolded protein response in yeast. *Front. Microbiol.*, Vol. 7 Issue 189, 2016, pp. 1-12.
- [27] Wang C., Mas A., and Esteve-Zarzoso B., 2016. The interaction between *Saccharomyces cerevisiae* and non-*Saccharomyces* yeast during alcoholic fermentation is species and strain specific. *Front. Microbiol.*, Vol. 7 Issue 502, 2016, pp. 1-11.
- [28] Romano P., Fiore C., Paraggio M., Caruso M., and Capece A., Function of yeast species and strains in wine flavour. *Int. J. Food Microbiol.*, Vol. 86 Issue 1-2, 2003, pp. 169-80.
- [29] Ciani M., Capece A., Comitini F., Canonico L., Siesto G. and Romano P. Yeast interactions in inoculated wine fermentation. *Front. Microbiol.*, Vol. 7 Issue 555, 2016, pp. 1-7.
- [30] Lopez S., Mateo J. J. and Maicas S. Screening of *Hanseniaspora* strains for the production of enzymes with potential interest for winemaking. *Fermentation*, Vol. 2 Issue 1, 2015, pp. 1-16.
- [31] Ciani, M. and Comitini, F., Yeast interaction in multi-starter wine fermentation. *Curr. Opin. Food Sci.*, Vol. 1, 2015, pp. 1-6.
- [32] Quirós M., Rojas V., Gonzalez R., and Morales, P., Selection of Non-*Saccharomyces* yeast strains for reducing alcohol levels in wine by sugar respiration. *Int. J. Food Microbiol.*, Vol. 181, 2014, pp. 85-91.
- [33] Gobbi M., De Vero L., Solieri L., Comitini F., Oro L., Giudici P., and Ciani M., Fermentative aptitude of non-*Saccharomyces* wine yeast for reduction in the ethanol content in wine. *Eur. Food Res. Technol.*, Vol. 239, 2014, pp. 41-48.
- [34] Chamnipa N., Thanonkeo S., Klanrit P., and Thanonkeo P. The potential of the newly isolated thermotolerant yeast *Pichia kudriavzevii* RZ8-1 for high temperature ethanol production. *Biotechnol. Ind. Microbiol.*, Vol. 49 Issue 2, 2018, pp. 378-391.
- [35] Ruyters S., Mukherjee V., Verstrepen K. J., Thevelein J. M., Willems K. A., and Lievens B. Assessing the potential of wild yeasts for bioethanol production. *J. Ind. Microbiol. Biotechnol.*, Vol. 42 Issue 1, 2015, pp. 39-48.
- [36] Maxwell, G. R. S., Archibong, E. V., Ogechi, N., Chibuzor, I. A., Nennaya, I. R., and Ogbe, S. B. Isolation and identification of local ethanol tolerant yeast populating distillation and milling sites in Nigeria. *American J. of BioScience*, Vol. 4 Issue 5, 2016, pp. 58-63.
- [37] Maxwell G. R. S., Anna O. O., Akpan E. G., Chidoize O. P., Nennaya I. R., and Josiah H. Isolation and characterization of yeast inhabiting alcohol processing environment in Bayelsa State, Nigeria. *Adv. in Appl. Sci.*, Vol. 1 issue 3, 2016, pp. 78-85.
- [38] Maxwell G. R. S., Anna O. O., Akpan E. G., Nennaya I. R., and Ogbe S. B.. Ethanol production by alcohol tolerant yeasts using different carbohydrate sources. *Adv. in Appl. Sci.*, Vol. 2 issue 5, 2017, pp. 69-74.

MOBILE DEVICES: ITS IMPACT TO ACADEMIC PERFORMANCE

Charito G. Ong¹, Cipriana P. Flores²

¹ University Registrar, University of Science and Technology of Southern Philippines, Cagayan De Oro City

²Senior Faculty, San Isidro College, Malaybalay City

ABSTRACT

Notwithstanding the step up in educational indicators like college attendees, noteworthy challenges linger concerning the delivery of quality education in both public and private institutions. To ably find feasible resolutions to these challenges, a large amount of hope is placed in new information and communication technologies (ICTs), mobile phones being one example (Ramos, 2008). This paper evaluated the crucial role of mobile phone-facilitated learning to enhance educational outcomes in Capitol University by investigating the results of mobile learning intervention. Specifically, this research examined the impact of mobile phones to College English performance in two specific ways: 1) its influence to *language ratings*, and 2) in promoting *communicative competence*. Analysis of the language classrooms through classroom observation indicated that there is relevant evidence of mobile phones facilitating students' communicative competence in their English language classes. Mobile learning, or mLearning, in this paper takes advantage of opportunities offered by portable technologies. The term covers: *learning with portable technologies*, where the focus is on the technology which could be in a fixed location, such as a classroom; *learning across contexts*, where the focus is on the mobility of the learner, interacting with portable or fixed technology; and *learning in a mobile society*, with a focus on how society and its institutions can accommodate and support the learning of an increasingly mobile population (Atkinson, 2007). The concept of mobile learning understood as learning facilitated by mobile devices in this paper gains toehold in the academic society. Findings of the rising number of mLearning associated by the development of students' communicative competence earned focus here as well. With the escalating interest now being given to the function of mobiles in the educational sector of the academe, there is a need at this point in time to take stock of the available evidence of the educational benefits that mobile phones provide towards students' language competencies. Thus, this paper explores the results of observing mLearning-abled-students that took place in Capitol University in relation to their Language performance in their English classes. In exploring how mobile phone-facilitated mLearning contributes to improved language competencies, this paper earned two specific issue-results: 1) the influence of mobiles in English Language performance was declared highly significant based on findings, and 2) the role of mobiles in promoting students' communicative competence was rated highly exceptional. Of note, the classes observed mostly used mobile phones in their language classes. The formation of this paper flows as follows. After the introduction, the paper slots in with the literature that discusses how mobile technology can address interrelationship with communicative competencies. The paper then examines college English classes that involved the use of mobile phones as a teaching methodology. The paper wraps up with a discussion of the potential of mobile phone-facilitated mLearning in improving language skills as well as with indications for possible future areas of research.

Keywords: Mobile phones, mobile learning, communicative competence, information and communication technologies, language ratings

INTRODUCTION

Mobile learning is considered special compared to other types of learning activity. An essential case in point is that learners are continually on the move; hence a proof. A study by Vavoula (2005) of everyday adult learning found that 51% of the reported learning episodes took place at home or in the learner's own office at the workplace, i.e. at the learner's usual environment. The rest occurred in

the workplace outside the office (21%), outdoors (5%), in a friend's house (2%), or at places of leisure (6%). Other locations reported (14%) included places of worship, the doctor's.

In the context of language education, this reality exists outside the formal learning environment. The history of simulations in language education goes back to the time when language learning was formulated as "communicative competence".

Language education operationalized this insight in the concept of "task" (Prahbu, 1987). Where tasks, so to speak, involved simple hypotheses about communicative functions, simulations represented a more sophisticated way to "orchestrate" the quest for communicative competence. A wide range of exciting simulations were invented and tested through role play, reflecting real authentic linguistic situations.

From a recent review in *languages, technology and learning* (Milton 2006) posited that learning a language is different from any other subject in the curriculum. It combines explicit learning of vocabulary and language rules with unconscious skills development in the fluent application of both these things. For language learners, this implies that they should be able to master both grammatical knowledge and fluency, the latter being often difficult to provide in classrooms where a couple of lessons a week may fail to provide the meaningful exposure to the foreign language required for learning. Games and simulations have been part of second and foreign language education for decades (Crookall 2007, Li & Topolewski 2002). Simulation/gaming techniques proved to be an extremely powerful

means of helping people to acquire foreign or second language skills (Crookall & Oxford 1990, Baltra 1990, Li & Topolewski 2002, Garcia-Carbonell, Rising, Montero and Watts 2001).

In the recent years until today, learning comes in coexistence with mobile devices used by the millennial-learners. Though educators have recently voiced concern about the detrimental effect that text messaging is having on teenagers' vocabulary; it is still mostly utilized in extending students' vocabulary.

Figure 1 below illustrates in schematic form the theoretical components of this research showing the relationship between the different elements of the study model.

The students' language performance takes the main role in the model. In the academe, the students are considered as the core in the process. To meet the objectives for them to learn, different strategies are employed. Teachers make use of simulations, games, language guides, mobile phones, and web-chat. The end all specifically contribute to the development of students' language competence and academic rating.

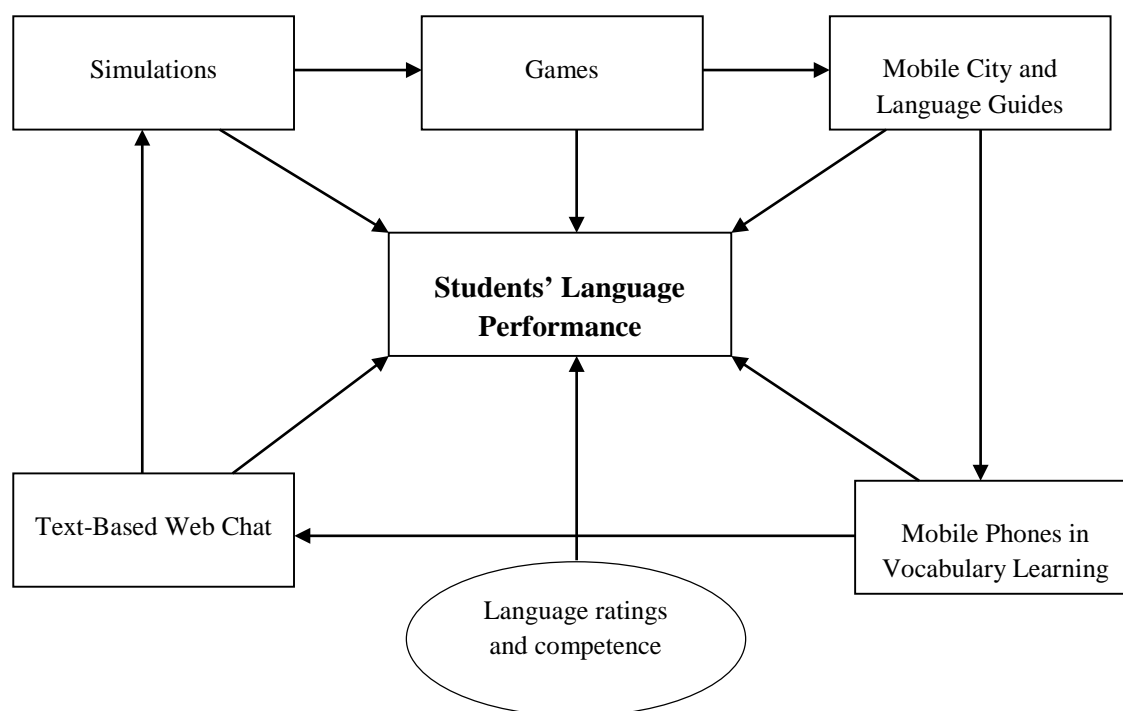


Fig.1 The theoretical framework of the research

METHODOLOGY

This research was done using teacher and student questionnaires, students' reflective diaries, impromptu feedback from students and teachers which were gathered in the school through a focus group discussion. Observation of classes was likewise employed for two weeks with an hour daily session.

The questionnaire content focused on how students fair in their classes with the aid of mobile phones. Similar topic was sought for in the students' reflective diary, impromptu feedback and focus group discussion. Moreover, in the classroom observation, the researchers took notes of the students' speaking engagement time.

FINDINGS

The following findings were found out in the conduct of the study:

1. Both students and teachers stated that students had made progress in speaking English as a result of being immersed with the learning. Students remarked on progress made in comprehension, competence, grammar and vocabulary. Students regarded the integrated technologies as a positive move from more traditional methods of learning English. They embraced the 'new age' technology and it proved to break down barriers to students' learning and speaking of English. 95% of respondents reported that they had 'enjoyed' using the technology for teaching and learning English.
2. Students also reported a reduced amount of pressure in communicating through English using the integrated technologies than they usually experienced in face-to-face settings in the classroom. Students' abilities to learn autonomously were enhanced – the technologies facilitated learning at any time, in any place and at the students' own pace. 93% of students recommended that other students should also be given the opportunity to use the technologies for learning and practicing English.
3. In the reflective notes, 35 respondents commented that they, as mobile learners began to expect and demand the ability to seamlessly manage and synchronize assignment access, delivery, review and completion between their desktop PC and

their mobile devices. The students identified challenges related to the workings of the mlearning system.

4. In the focus group discussion, students made suggestions for improvements to the system should the mlearning be extended. They wanted more experiences of it in their other classes; not only in English subject. Moreover, teachers commented positively on the shift from more teacher-led learning to student-led learning that mlearning allowed. Teachers noticed increased motivation and student interest for using English. They stated that students found using the technologies more interesting and fun compared with the traditional learning methods.
5. Teachers also observed as manifested in the questionnaire answer that students learned certain topics faster when using the technologies. Teachers' perspectives on the technology impact were also positive. They reported enjoying the shift from providing feedback in a traditional manner using 'a red pen' to more modern ways via feedback sheet. They also commented favorably on their increased ability to hear more from those students who are usually shy in the classroom thereby promoting students' communicative competencies. Teachers commented on the success of the text-message delivery of English vocabulary – to such an extent that students requested that they could receive vocabulary during their summer break to their personal mobile phones. Likewise, teachers commented that for the entire term, students' language ratings improved.
6. Though some students switched phones and others dropped out without advising their teachers, it was observed in the classroom observation done by the researchers that students were given enough time to communicate. They were excited to share their experiences using the mobile phone as a tool. Most of the students were confident and revealed communicative competence as they phased on with the activities.

CONCLUSIONS

The subsequent conclusions were drawn from the findings of this study:

1. Keegan (2003) says mobile learning will provide the future of learning. This statement was proven true for this research and has provided an insight into the role mobile learning could play in the future of the English language. The ability of teachers and students alike to embrace the change is vital. The students' self-esteem were boosted through the use of mobile phone as a tool for learning. Learning was fun for them, not a chore.
2. The respondents that followed the SMS modules indicated that the modules enabled them to pursue their school work according to their own schedule. Obviously, the mobile learning system enabled these students to have higher ratings and communicate effectively in English. Some students even pointed to the added benefit of being able to do their lessons during breaks.
3. Overall, the students' expressed interest in following modules covering their English subject areas was an amazing edge. They likewise expressed excitement regarding the use of mobiles for learning. Hence, mobile learning must be considered as a must for use in the tertiary level in the Philippine school system.

RECOMMENDATIONS

As a result of the aforesaid findings and conclusions, the following items are recommended:

1. Another study can be done in this same topic covering other subject areas such as Filipino and Mathematics. These are considered difficult subjects in the Philippines as more exposure of students are English based.
2. Communicative teaching coupled with mobile learning should be tried out in the tertiary level. After all, this is but the goal of teaching, for students to be able to communicate.
3. Maintaining the student-centered approach among classes is further recommended as a possible avenue for research. This is to be tied up with modules that promote student competence.

REFERENCES

- [1] Atkinson, D. (2007) Toward a Sociocognitive approach to second Language acquisition, *The Modern Language Journal*, Volume 86, Issue 4, Date: December 2002, Pages: 525-545
- [2] Baltra, A. (1990) *Language Learning Through Computer Adventure Games*. Simulation & Gaming 21, 4.
- [3] Bo-Kristensen, M., Ankerstjerne, N., Neutsky-Wulff, C. & Schelde H. (2008) *Mobile City and Language Guides: New Links Between Formal and Informal Learning Environments*, in: Remenyi, D. (ed.) *Proceedings of the 7th European Conference on eLearning*. Reading, UK: Academic Conferences Limited
- [4] Crookall, D. & Oxford, R.L. (1990) *Simulation, Gaming, and Language Learning*. Newbury House Publishers
- [5] Crookall, D., Oxford, R.L. & Saunders, D. (1987) *Towards a Reconceptualisation of simulation: From representation to reality*. Simulation/Games for learning, 17
- [6] Garcia-Carbonell, A., Rising, B., Montero, B., Watts, F. (2001) *Simulation/gaming and the acquisition of communicative competence in another language*. Simulation and gaming 32,4
- [7] Hymes, D. 1972. *On Communicative Competence*. In: Pride P.A. & J. Holmes (eds.) *Sociolinguistics*. Harmondsworth: Penguin Books, s. 269-293
- [8] Keegan, Desmond. (2003). *Learning in a Mobile Age*. Academia.edu.follow research.
- [9] Kukulska-Hulme, A. & Shield, L. (2007) *Overview of Mobile Assisted Language Learning: Can mobile devices support collaborative practice in speaking and listening?* (Paper retrieved at <http://vsportal2007.googlepages.com/>, last accessed January 26, 2009)
- [10] Li, R-C, Topolewski, D. (2002) *ZIP & TERRY: a new attempt at designing language learning simulation*. Simulation and gaming 33, 2.
- [11] Milton, J. (2006) *Literature review in languages, technology and learning*. Futurelab Series. Can be downloaded from www.futurelab.org.uk/research/lit_review.htm
- [12] Vavoula, P. M Sharples (2005) *Report 11: Literature Review in Mobile Technologies and Learning*. Nesta Future Lab
- [13] Prahbu, N.S. 1987. *Second language Pedagogy*. Oxford University Press.
- [14] Ramos (2008). *Using Mobile Phones to Improved Educational Outcomes*. IRRODL.
- [15] Vetter, Jeannot, L., and A. Chanier, T. (2006) *Cambridge Journals Online - Abstract*. Copyright © 2006 Cambridge University Press.

GEOPOLYMER BEADS FROM COAL FLY ASH AND WASTE PEN SHELLS

Kimmie Dela Cerna¹, Jose Isagani Janairo² Roy Alvin Malenab³ and Michael Angelo Promentilla

¹Chemical Engineering Department, Gokongwei College of Engineering, De La Salle University;

² Biology Department, College of Science, De La Salle University

ABSTRACT

This paper presents our exploratory study on the development of a nanomaterial-enhanced inorganic polymer-based composite that can be used for environmental application. Geopolymer, also known as a kind of alkali-activated material, is an inorganic polymer binder formed from chemical reactions of alumino-silicate oxides or alkaline activation of reactive alumino-silicate materials resulting in two- or three-dimensional polymeric network of Si-O-Al bond. This material has been recently gaining attention as an alternative binder for Ordinary Portland cement (OPC) due to its waste valorization opportunities, lower embodied energy and CO₂ footprint. However, the geopolymer technology is not the “cure-all” for material selection problem. Geopolymers would have a wide range of properties depending on the raw materials and process conditions. This paper thus present the recent results from our experimental studies in the Philippines using coal fly ash and waste pen shell to produce geopolymer beads, wherein the porous matrix are functionalized and enhanced with nanomaterials such as nanosilver.

Keywords: fly ash, geopolymer, alkali-activated material, nanomaterial, waste pen shells

INTRODUCTION

The term geopolymer was first coined by Joseph Davidovits back in the 1970's, pertaining to a class of material whose molecular structure consists of an amorphous to semi-crystalline inorganic network of mineral molecules [1]. The mechanical properties of geopolymers, such as its compressive strength and density, are generally comparable to that of Ordinary Portland Cement (OPC). They are also reportedly more resistant to chemical attacks, such as exposure to acidic environments, as well as fire damage. Because of these specific properties, plenty of researches today focus on the use of geopolymers as a more environmentally-friendly construction material.

Recent studies on geopolymers have started to investigate its applications for other industries, particularly in refractory materials [2,3], in solidification/stabilization of heavy metals lining for cement pipes to increase their durability [6], and in treating contaminated water [7].

In this study, a new potential application of geopolymers will be explored. They will be formed into bead shapes about 4-5mm in diameter and used as matrices for nanosilver attachment. Foaming agents were also used to increase the porosity of the beads. These beads were then coated with nanosilver

and tested for its antimicrobial activity against *E. coli* in water.

MATERIALS AND METHOD

Materials

Coal Fly Ash (CFA) from Central Luzon, Philippines and waste pen shells from the southernmost part of Luzon were used as the solid raw materials. On the other hand, NaOH micropearls and water glass solution were used as activating solution. Hydrogen peroxide (50% solution) and Sodium Lauryl Sulfate (SLS) were used to adjust the density of the geopolymer paste and provide added porosity to the beads. AgNO₃ and NaBH₄ was used for the nanosilver coating of the beads.

Synthesis of Geopolymer Beads

Geopolymer beads were synthesized using a modified method described in [8,9]. The waste pen shells were first washed, dried, and crushed to small pieces. Then, they were calcined in a furnace for two hours at 700°C. The calcined shells were finally crushed with a mortar and pestle, and sieved to mesh #200. Figure 1 shows the waste pen shells before and after calcination.



Fig. 1 Waste Pen Shells Before and After Calcination

The fly ash and the calcined shells were first combined at a total weight of 80g to form the solid precursor. An amount of 7.47g of a 12M NaOH solution was added with 29.87g of WGS to form the alkali activator solution. The solid precursor was then added to the alkali activator and stirred by hand for 1 minute. 1.7mL of water was also added, then hand-stirring was done for another 2 minutes. Finally, varying masses of a 50% H_2O_2 solution was dropped in, ranging from 0.15% to 0.35% of the mass of the geopolymer. This was stirred thoroughly for another 2 minutes. The resulting paste was brown and had a thick consistency.

The geopolymer paste was then loaded into a syringe and dropped into a hot PEG-600 solution at 90°C. The dropwise addition of the paste, coupled with the high temperature of the medium, allows the paste to rapidly solidify into 4-5mm beads shown in Fig. 2. The formed beads were left in the PEG for about 20 minutes in order to fully harden, then transferred, rinsed thoroughly, and left to cure in a laboratory oven at 90°C for 24 hours.



Fig. 2 Geopolymer Beads

Nanosilver Coating of the Geopolymer Beads

An in-situ reduction process of AgNO_3 into nanosilver was done with the beads. Exactly 20mL of AgNO_3 with a concentration of ranging from 0.1M to 0.5M was introduced to a beaker containing 20 geopolymer beads. This allows the silver ions in the AgNO_3 to be attached to the geopolymer. The beads in AgNO_3 solution was left for 2 hours. After, the AgNO_3 was decanted off, and another 20mL of

fresh AgNO_3 of the same concentration was added. This ensures the entire surface of the geopolymer, including all accessible pores, have been covered with the silver ions. This was left for another 2 hours, then decanted off. Lastly, 20mL of 1M NaBH_4 was added into the silver-ion-coated geopolymer. This rapidly reduced the attached silver ions on the geopolymer surface into nanosilver. The NaBH_4 was left for two hours, then again decanted off. The resulting nanosilver-coated geopolymer was then allowed to dry in a laboratory oven at 60°C before storing for future use.

Antimicrobial Activity Test of Geopolymer Beads

A 10^5 cfu/mL inoculum was first prepared using a culture of *E. coli* made 24 hours prior to the experiment. The 30mL of this inoculum was placed in a beaker containing 20 nanosilver-coated beads. The beaker was then agitated in an orbital shaker set at 300rpm. Exactly 1.5mL of 5% (wt) solution of sodium thiosulfate was added 30 minutes after. This immediately halts the antimicrobial activity of the silver ions. Then, 1mL of the liquid from each sample and their serial dilutions (up to 10^{-3}) were plated in agar and left to incubate at 37°C for 24 hours.

RESULTS AND DISCUSSION

Surface Morphology

SEM-EDX analysis was done on the uncoated beads to examine their surface morphology. Figure 3 shows the SEM images of the geopolymer bead. The porous surface of the geopolymer is evident from these images.

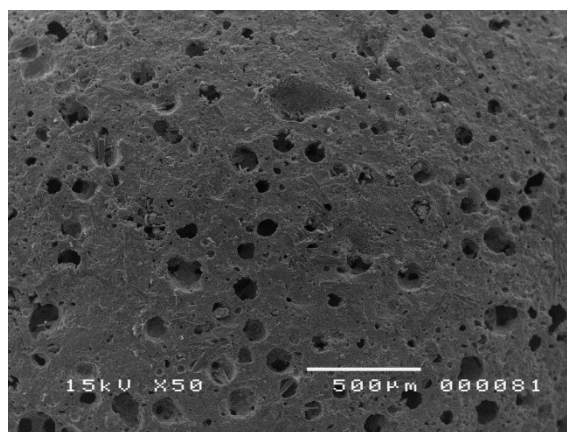


Fig. 3 SEM Image of Porous Uncoated Beads

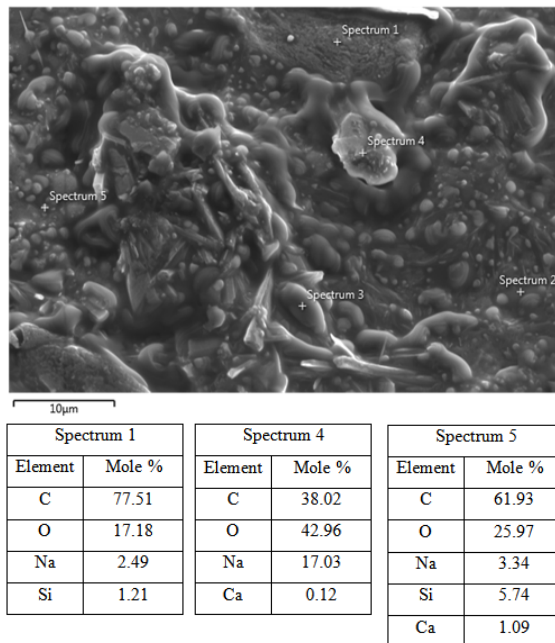


Fig. 4 SEM-EDX of Uncoated Beads

On the other hand, Fig. 4 shows the EDX analysis. It can be seen from the elemental analysis that C and O are the main constituents on the geopolymer surface. This is attributed to the formation of Na_2CO_3 and CaCO_3 , from the carbonation of NaOH and Ca(OH)_2 , respectively [10]. FTIR analysis was also done on the beads before and after washing them. It is expected that washing will remove some of the carbonate species from the geopolymer, particularly Na_2CO_3 . Figure 5 shows the FTIR spectrum.

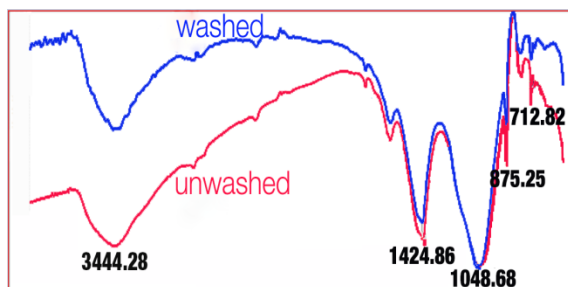


Fig. 5 FTIR Spectrum of Washed and Unwashed Beads

The broad peak between 3400cm^{-1} and 3500cm^{-1} correspond to the OH stretching vibrations and in the hydration products of the geopolymer. On the other hand, the sharp peak at $\sim 1400\text{cm}^{-1}$ is attributed to the asymmetric stretching vibrations from the O-C-O bonds in the carbonate groups. This is present in both of the samples. A peak at $\sim 880\text{cm}^{-1}$ is also indicative of the presence of calcite species [10]. For both of these peaks, a difference in intensity was observed for the washed samples, an indication that indeed some of the carbonates have been removed from washing. On the other hand, the peaks at ~ 1050

cm^{-1} are attributed to the asymmetric vibrations of the Si-O/Al-O bonds in the SiO_4 and AlO_4 groups [11], while the peak at $\sim 700\text{cm}^{-1}$ may be from bending vibrations from the Si-O-Si and Si-O-Al gel [10].

Nanosilver-coated geopolymer

Figure 6 shows the surface morphology of the nanosilver-coated beads. It can be seen that a fine, powdery substance is predominant on the surface. EDX analysis shows this substance is mostly silver, with smaller amounts of oxygen and carbon.

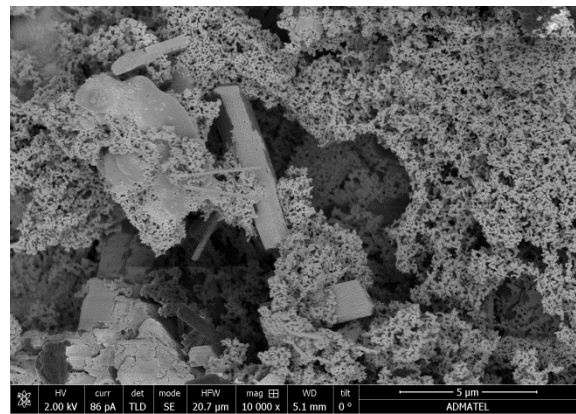


Figure 6. SEM Image of Nanosilver-Coated Beads

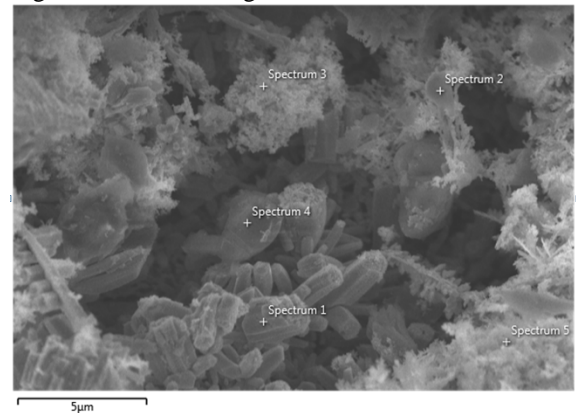


Figure 7. SEM-EDX of Nanosilver-Coated Beads

Antimicrobial activity of the geopolymer beads

Equation 1 was used to compute for the antimicrobial efficiency, AE.

$$AE = \frac{\text{initial count} - \text{final count}}{\text{initial count}} \times 100\% \quad (1)$$

Table 1 summarizes the results from the antimicrobial test of the beads. Using statistical analysis

via ANOVA, it was inferred that the amount of H_2O_2 , the concentration of $AgNO_3$, and the interaction between these two factors are significant. The resulting regression model is also shown in Eq. 2. It is evident from the results that majority of the trials were successful in eliminating at least 95% of the *E. coli* in the water sample.

Table 1 Antimicrobial Efficiencies

% H_2O_2	$AgNO_3$ (M)	AE (%)
0.25	0.3	95.46
0.15	0.3	93.58
0.25	0.3	97.97
0.25	0.5	95.94
0.35	0.1	99.56
0.15	0.1	98.7
0.35	0.5	97.61
0.35	0.3	98.88
0.25	0.3	97.79
0.15	0.5	87.68
0.25	0.3	98.65
0.25	0.3	99.94
0.25	0.1	99.94

$$AE = 103.1 - 7.2H_2O_2 - 42.5AgNO_3 + 113.4H_2O_2 * AgNO_3 \quad (2)$$

From the interaction plot (between the amount of H_2O_2 added and the concentration of $AgNO_3$ used) shown in Fig. 8, it is evident that overall, increased H_2O_2 had a positive effect on the antimicrobial efficiency. This was as expected, as increasing H_2O_2 amounts increases the porosity of the geopolymer beads, and thus increases the available space for nanosilver attachment. However, notable from the interaction plot is that the positive effect of H_2O_2 is magnified at high levels of $AgNO_3$ (0.5M). This may be an indication that at low concentration of $AgNO_3$, majority of the silver ions have already attached to the pore spaces; thus, increase in available space (brought about by introducing more H_2O_2) no longer increases antimicrobial efficiency.

Figure 9 above shows the contour plot for antimicrobial efficiency. It is evident that generally, lower concentrations of $AgNO_3$ produced the most antimicrobial beads. This may be because the use of higher concentrations of $AgNO_3$ produces coarser nanosilver particles, thus having reduced contact surface with the water sample. Similar results have been obtained by [13], where they found that increasing $AgNO_3$ concentration from 1mM to 4mM led to increase in particle size and decrease in sedimentation activation energy.

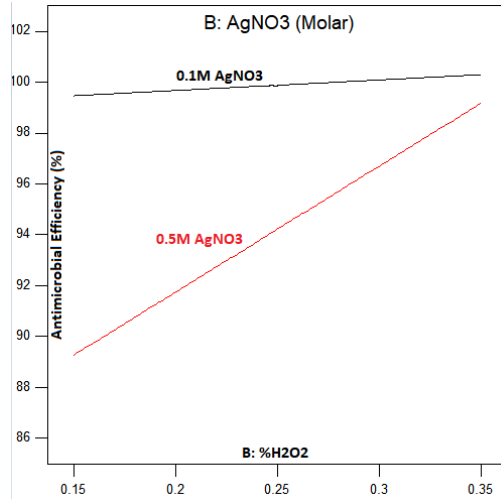


Figure 8. Interaction Plot between % H_2O_2 and $AgNO_3$ Concentration

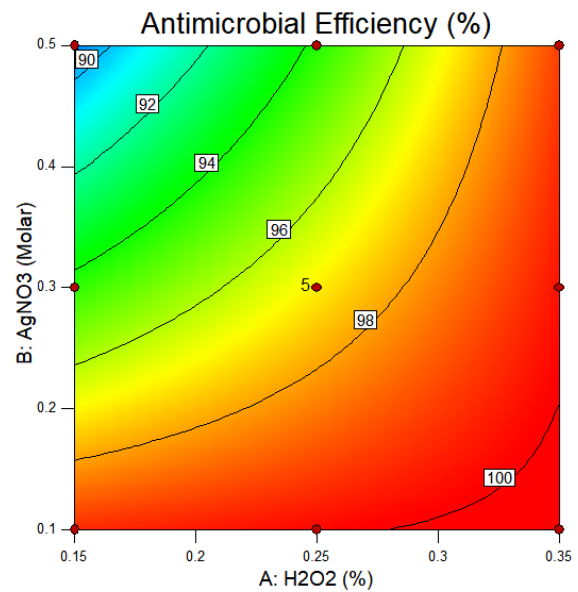


Figure 9. Contour Plot for AE

CONCLUSION

This study demonstrates the potential of producing porous geopolymer beads from fly ash and waste pen shells. Indication also suggests that nanosilver-coated geopolymer beads were effective in killing *E. coli* in a water sample, with results as high as 99.9% removal. Increased porosity of the geopolymer beads and lower concentrations of $AgNO_3$ thus enhanced antimicrobial activity of the beads. Future work will investigate further the amount of silver loading and leachability in the beads.

ACKNOWLEDGEMENTS

The authors would like to acknowledge the financial support from Engineering Research and Development for Technology (ERDT), PCIEERD-ADMATEL grant, and URCO Research Project.

REFERENCES

- [1] Davidovits, J. (1991). Geopolymers. *Journal of Thermal Analysis*, 37(8), 1633–1656.
- [2] Temuujin, J., Rickard, W., Lee, M., & van Riessen, A. (2011). Preparation and thermal properties of fire resistant metakaolin-based geopolymer-type coatings. *Journal of Non-Crystalline Solids*, 357(5), 1399–1404.
- [3] Villaquirán-Caicedo, M. A., de Gutiérrez, R. M., Sulekar, S., Davis, C., & Nino, J. C. (2015). Thermal properties of novel binary geopolymers based on metakaolin and alternative silica sources. *Applied Clay Science*, 118, 276–282.
- [4] Dermatas, D., & Meng, X. (2003). Utilization of fly ash for stabilization/solidification of heavy metal contaminated soils. *Engineering Geology*, 70(3-4), 377–394.
- [5] Van Jaarsveld, J. G. S., Van Deventer, J. S. J., & Lorenzen, L. (1997). The potential use of geopolymeric materials to immobilise toxic metals: Part I. Theory and applications. *Minerals Engineering*, 10(7), 659–669.
- [6] Chindaprasirt, P., & Rattanasak, U. (2016). Improvement of durability of cement pipe with high calcium fly ash geopolymer covering. *Construction and Building Materials*, 112, 956–961. doi:10.1016/j.conbuildmat.2016.03.023
- [7] Catauro, M., Bollino, F., Papale, F., & Lamanna, G. (2014). Investigation of the sample preparation and curing treatment effects on mechanical properties and bioactivity of silica rich metakaolin geopolymer. *Materials Science & Engineering. C, Materials for Biological Applications*, 36, 20–24.
- [8] Tang, Q., Ge, Y.-Y., Wang, K.-T., He, Y., & Cui, X.-M. (2015). Preparation of porous P-type zeolite spheres with suspension solidification method. *Materials Letters*, 161, 558–560.
- [9] Xia, Y., Jiang, X., Zhang, J., Lin, M., Tang, X., Zhang, J., & Liu, H. (2017). Synthesis and characterization of antimicrobial nanosilver/diatomite nanocomposites and its water treatment application. *Applied Surface Science*, 396, 1760–1764.
- [10] Pasupathy, K., Berndt, M., Castel, A., Sanjayan, J., & Pathmanathan, R. (2016). Carbonation of a blended slag-fly ash geopolymer concrete in field conditions after 8years. *Construction and Building Materials*, 125, 661–669. doi:10.1016/j.conbuildmat.2016.08.078
- [11] Ahmari, S., & Zhang, L. (2013). Utilization of cement kiln dust (CKD) to enhance mine tailings-based geopolymer bricks. *Construction and Building Materials*, 40, 1002–1011. doi:10.1016/j.conbuildmat.2012.11.069
- [12] Zhang, X., & Shi, B. (2015). Preparation of a nanosilver composite plant medium with antimicrobial capability through a nontoxic method. *Nanomaterials and Nanotechnology*, 5, 21. doi:10.5772/60913

DIFFUSION OF MERCURY FROM ARTISANAL SMALL-SCALE GOLD MINING (ASGM) SITES IN MYANMAR

Tomonori Kawakami¹, Misa Konishi¹, Yuki Imai¹ and Pyae Sone Soe²

¹ Faculty of Engineering, Toyama Prefectural University, Japan; ² Graduate School of Agriculture Kyoto University, Japan

ABSTRACT

In some developing countries, such as Myanmar, mercury used for gold refining in artisanal small-scale gold mining (ASGM) is emitted into the atmosphere and water, causing environmental pollution. In this study, the diffusion of mercury from ASGM in Thabeikkyin Township, Mandalay Division, Myanmar was investigated. Air samples, water samples and hair were collected from the ASGM sites. The mercury concentration in the atmosphere in the gold mining area reached 74,000 ng/m³ at the maximum concentration, which exceeded WHO guideline of 1,000 ng/m³. The mercury concentration in the Ayeyarwady River and the groundwater pumped from the gold mining tunnel was 4.6 ng/l and 29-35 ng/l, respectively. The limit of mercury in hair is considered to be 50 µg/g, at which concentration nervous symptoms may appear, while 11 µg/g is the concentration at which adverse effects on fetuses could take place. The average mercury concentration in hair was 1.5 µg/g for ASGM workers, while it was 1.1 µg/g for nonworkers. An analysis of hair indicated that the mercury was not at a level that would adversely affect human health, so far.

Keywords: Mercury, Myanmar, Hair, Water, Atmosphere

INTRODUCTION

Minamata Disease

Organic mercury compounds, such as methylmercury (Me-Hg), which is more intensely toxic than inorganic compounds, could cause neurological symptoms when they are taken into the human body. Minamata disease, a mercury-related disease, occurred in 1950-1960 in Japan. A bioaccumulation took place in the fish and shellfish in Minamata Bay, where industrial effluent contaminated with Me-Hg was discharged. People who ingested such polluted fish and shellfish developed Minamata disease, resulting in loss of consciousness and even, sometimes, death [1].

The Minamata Convention

The Minamata Convention is a multilateral environmental agreement that obligates parties to reduce or control sources of mercury pollution in order to protect human health and the environment. Since mercury is easily transported across national boundaries [2], international cooperation was required for its control. The Minamata Convention on Mercury, adopted on October 10, 2013, and signed by 128 countries, is a legally binding international agreement that was designed specifically to address global mercury pollution [3]. The objective of the Convention is “to protect human health and the environment from

anthropogenic emissions and releases of mercury and mercury compounds.”

The importance of artisanal and small-scale gold mining (ASGM) on rural development has caused debate among policy makers. However, the Minamata Convention includes a mix of provisions to control and reduce the major sources of mercury, including mercury use in ASGM. For example, the development of national action plans (NAPs) for ASGM is an obligation under Article 7. The best available technology and best environmental practices (BAT/BEP) must be utilized to protect against the sources of air pollution as organized by the convention. The NAP for ASGM is required to regulate the informal sector of ASGM and intends to accomplish this through requirements for countries. Key to such an NAP is the development of mercury inventories and baselines of the ASGM sector in order to monitor improvements and to establish regulatory standards for reduction [3].

On September 24 - 29, 2017, the first Conference of the Parties (COP1) was held in Geneva, Switzerland, to initiate enforcement of the convention.

ASGM in Myanmar

The government of Myanmar, had not yet signed the Minamata Convention when it was closed to signatures on October 9, 2014. However, the government of Myanmar is preparing to ratify the Convention, as stated in a letter addressed to UN

Environment and the Global Environment Facility (GEF) on June 30, 2015. During that period, Myanmar participated in the Asia and the Pacific Regional Workshop to support the ratification and effective implementation of the Minamata Convention on Mercury from March 17 to 18, 2015, in Jakarta, Indonesia [4].

The GEF and the government of Myanmar have initiated the collaboration project titled “Development of Minamata Initial Assessment and National Action Plan for Artisanal and Small Scale Gold Mining in Myanmar.” The project aims at the ratification and early implementation of the Minamata Convention by providing key national stakeholders in Myanmar with the scientific and technical knowledge and tools needed for that purpose [4].

Implementation of the Minamata Convention will require a series of international obligations on the part of the government of Myanmar to reduce the use of mercury and to control the transport and import/export of mercury. These requirements should give the ASGM sector and responsive policy makers a better understanding as to how to improve their environment.

Mercury Use in ASGM

The mercury in the atmosphere includes both natural and anthropogenic emissions. According to the United Nations Environment Program (UNEP), 1960 tons of the mercury emitted in 2010 came from anthropogenic activities such as ASGM, the burning of fossil fuels, and the production of cement. ASGM is the largest source of mercury emissions. In ASGM, mercury is used to produce a gold-mercury amalgam to extract gold from gold ore. Mercury is vaporized by burning the gold-mercury amalgam to separate gold from the amalgam. This process has been adopted in many developing countries such as Myanmar and Indonesia, since it is an easy and cheap process for purifying gold [6]. It is reported that in the watershed of the Amazon river in Brazil, inorganic mercury turns into organic mercury to bioaccumulate through the food chain after a large amount of mercury has been used for ASGM and released into the environment [5]. The number of workers engaged in ASGM is estimated to be 20 million in more than 50 developing countries. Among them are 650,000 females and 1-1.5 million children [7]. It is concerning that the workers, including children, aspirate gaseous mercury, and the residents around ASGM eat polluted fish.

Mercury Emissions from ASGM in Myanmar

ASGM is operating in the Thabeikkyin Township, Mandalay Division of Myanmar. Gold

ore is mined underground 20-30 m below the surface by digging a level after making a vertical tunnel (Fig. 1). A large amount of groundwater comes out of the tunnel and is pumped to the residential house in the village near the ASGM for daily life (Fig. 2).

The purification process in ASGM is as follows: Gold ore taken from the mine underground is first dried up and crushed by a powdering machine (Fig. 3). The powder is then put in a pan with water to separate gold particles by gravity. In the bottom of the pan, gold particles are collected with some sand. Mercury is added to the pan to extract mercury by the formation of a gold-mercury amalgam. The gold-mercury amalgam is squeezed through a cloth to remove liquid mercury, which remains without reacting to the gold (Fig. 4). Finally, an operator vaporizes the mercury in the gold-mercury amalgam using a burner to obtain purified gold. The vaporized mercury is emitted into the atmosphere without any treatment, not only polluting the environment but harming human health, especially the health of workers.

In this study, the diffusion of mercury from ASGM in the Thabeikkyin Township, Mandalay Division of Myanmar was investigated to better understand the environment as related to mercury emissions from ASGM.



Fig. 1 Vertical gold mine tunnel



Fig. 2 Groundwater leaked form the tunnel



Fig. 3 Machine that powders gold ore



Fig. 4 Squeezing the gold-mercury amalgam

MATERIALS AND METHODS

Site Descriptions

In this study, the diffusion of mercury from ASGM in the Thabeikkyin Township, Mandalay Division of Myanmar was investigated to evaluate the effect of ASGM on the environment. Figures 5 and 6 show Mandalay of Myanmar and the site where ASGM is operating heavily. At the ASGM site, five ASGMs were operating (Sites 1-5 in Fig. 6). The atmospheric mercury concentration was measured at Site 5 to elucidate the spatial distribution. At Site 5, the mercury concentration of the groundwater leaked from the gold mining tunnel, which was pumped to residents, was measured. The groundwater from Sites 1-4 was sampled. The mercury content in human hair was measured for both ASGM workers and nonworkers at Sites 1-5. In addition, the mercury concentrations of the Ayeyarwady River, which flows through Mandalay, were measured.

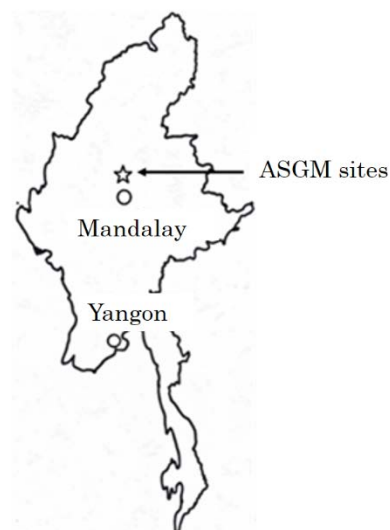


Fig. 5 ASGM sites in Mandalay Division of Myanmar

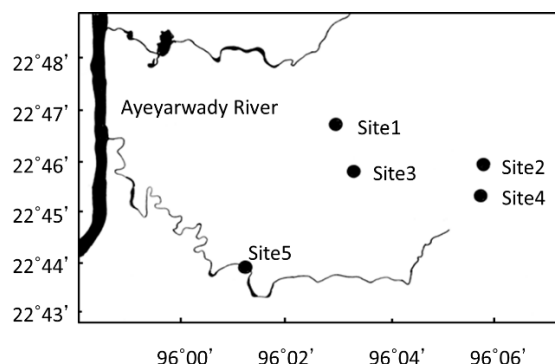


Fig. 6 Enlarged map of ASGM sites

Measurement of the Mercury Concentration in the Atmosphere

Mercury exists in the atmosphere as gaseous mercury and particulate mercury. The total mercury is the sum of the gaseous and particulate mercury. The major forms of mercury in the atmosphere are gaseous elemental mercury (GEM, $\text{Hg}(0)$), reactive gaseous mercury (RGM, $\text{Hg}(\text{II})$), and total particulate mercury (TPM, $\text{Hg}(\text{p})$) [8]. Since $\text{Hg}(0)$ is hard to dissolve in water, it has a long retention time in the atmosphere, and it contributes 95% of the total mercury in the atmosphere. $\text{Hg}(\text{p})$, which adheres to particle matter suspended in the atmosphere contributes several percentage points in general, except near the emission source [9]. Accordingly, the total mercury in the atmosphere can be estimated by measuring the gaseous mercury.

Atmospheric samples were collected by passive samplers and active samplers at the same time. An active sampler system, which collects gaseous and particulate mercury separately, is shown in Fig. 7

[10]. GEM was collected in a tube (M-160, Nippon Instruments Corp., Ltd.) with an air pump (MP-Σ30, Shibata Science). To capture Hg(p), a quartz fiber filter with a pore size of $0.3\ \mu\text{m}$ was attached at the intake nozzle. The air was aspirated at a rate of $0.5\ \text{L min}^{-1}$. The total volume of aspirated air was recorded in the pump system, and the atmospheric mercury concentrations were then calculated from the air volume and the amount of mercury absorbed.

Passive samplers were also used to measure the spatial distribution of mercury [11]. The passive sampler had the same dimensions as the Ogawa passive sampler for sulfur dioxide, which is cylindrical with a diameter of 2 cm and a length of 3 cm. Diffuse plates with a thickness of 2 mm and 22 holes were placed at both ends of the cylinder. As an absorber, a quartz fiber filter coated with gold was set inside the diffuse plate (Fig. 8). The main body and the diffuse plates were made of fluorine resin, which allows the sampler to be cleaned in acidic solution. The mercury absorbed on the quartz fiber filters was converted proportionally to the atmospheric concentrations by using the atmospheric concentrations obtained by the active sampler system.

Two and three active samplers and 13 and 17 passive samplers were placed at various locations around the ASGM for the first survey from March 2 to 3, 2017, and for the second survey from October 19 to 20, respectively. The passive sampler was set under the roof of ASGM facilities and residential houses and attached to trees. It was covered with a cup so as not to get wet from rain when it is attached to trees. Active and passive sampling continued for 24 hours. Gaseous and particulate mercury collected by the active and passive samplers was measured using a heat-vaporizing atomic absorption method (MA-2, Nippon Instruments) after taking them to Japan. The instrument has a detection limit of 0.03 ng. When a passive sampler is used, the absorbed mercury on the quartz fiber filters cannot be converted directly into the mercury concentration in the atmosphere. To obtain the ratio between the atmospheric mercury concentration and the amount of mercury adsorbed into the filter, both active and passive samplers were operated simultaneously at two or three points in the same location. Assuming that the amount of mercury measured by a passive sampler is proportional to the atmospheric mercury concentration measured by an active sampler, the amount of mercury obtained by a passive sampler was converted into the atmospheric mercury concentration based on the proportion [11].

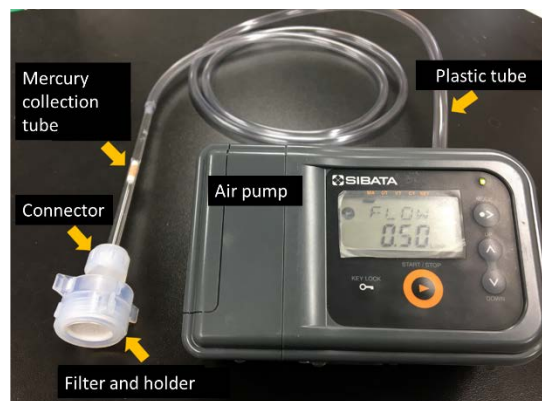


Fig. 7 Active sampler system operated with a dry battery

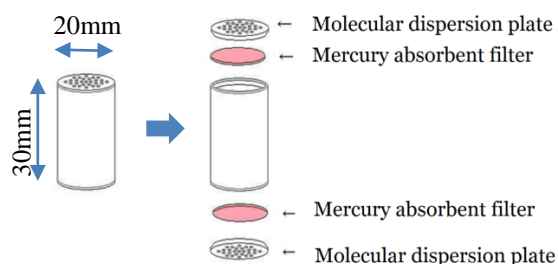


Fig. 8 Passive sampler. Quartz fiber filters coated with gold are placed inside the diffuse plates.

Measurement of Mercury in Water Samples

Bromine chloride solution, prepared by mixing 1.08 g of KBr and 1.52 g of KBrO_3 into 100 mL of hydrochloric acid, was used for cleaning the sampling bottles and the degradation of the organic matter in the sample water. Samples collected in Myanmar were kept in Teflon bottles washed by a bromine chloride solution and pure water. Ten mL of 0.1% L-cysteine solution was added to every 1 L of sample solution to prevent the vaporization of mercury and the adherence of mercury to the walls of bottles. After adding L-cysteine solution, samples were taken to Japan for analyses. The reduction vaporization method was applied for analysis. Five mL of bromine chloride solution was added to every 1 L of the water samples one day before analysis to degrade organic matter. On the following day, 200 mL of the samples and 2 w/v% of hydroxylammonium chloride solution were mixed in a reduction bottle to deactivate the bromine chloride. After 10 mL of 50 v/v% sulfuric acid solution and 10 mL of 10 w/v% tin(II) chloride were added, mercury vaporized by bubbling was analyzed by a gold amalgam method using a mercury analyzer (MA-2, Nippon instruments) [12].

Two well water samples were collected at each site shown in Fig. 6: Site1 (Kapani village), Site2

(Khwin Village), Site3 (Latpanpyant village), Site4 (Wattay village and Phatshae village), and Site5 (Chaungyi village). Groundwater leaked from the gold mine tunnel was collected at Site 5. Ayeyarwady River water was collected at the center flow of the river in the city of Mandalay, which is located downstream of the ASGM sites. Ayeyarwady River water upstream of the ASGM sites was also collected.

Measurement of Mercury in Human Hair

The mercury content in hair samples taken from 39 ASGM workers and 11 nonworkers (age:18-57) from Sites 1-5 was measured by the heat-vaporization method with the mercury analyzer (MA-2, Nippon instruments). Hair samples were taken in accordance with the protocol permitted by the ethics committee of Toyama Prefectural University, permission number H29-6 on the effect of the use of mercury in ASGM in Myanmar on human health.

RESULTS AND DISCUSSION

Atmospheric Mercury around the ASGM in Myanmar

In Fig. 9, the distribution of the gaseous mercury concentration from the first survey is shown as bars. The highest concentration of 10,900 ng/m³ was observed near a small house where the burning process took place at the ASGM site. It was more than ten times of the WHO guidelines of 1,000 ng/m³ [13]. Even in the residential area outside the ASGM, the lowest concentration measured 130 ng/m³ which is a much higher level than the 0.9 -1.5 ng/m³ in non-polluted areas [14,15].

In Fig. 10, the distribution of the gaseous mercury concentration from the second survey is shown as bars. The highest concentration of 74,000 ng/m³ was observed in the same place where the highest concentration was observed in the first survey, even though there was no burning during the 24-hour sampling. ASGM workers should aspirate higher concentrations of mercury during the vaporization of mercury at the small house. In the main office of ASGM, 5,300 ng/m³ of mercury concentration was measured. Even in the residential area outside the ASGM, generally higher concentrations, with a maximum concentration of 1,600 ng/m³, were observed. The highest concentration was observed in front of the so-called gold shop, where the gold-mercury amalgam brought by the village people was burnt, and the gold shop bought the resultant purified gold. The gold shop sold mercury and goods needed for ASGM, such as pans. The highest concentration of

mercury indicated that the burning process was also taking place in the gold shop outside the ASGM. In fact, residents of the village dug tunnels in their backyards to obtain gold ore, and they do gold-mercury amalgamation in their house as part of their everyday activities. This is the reason for the high concentration of mercury that prevailed throughout the entire village. The high concentrations of gaseous mercury of 10-1461 ng/m³ were reported outside the ASGM area in Central Sulawesi, Indonesia which was one of the largest ASGM sites in Indonesia with 760 ASGM plants [16]. The usage of mercury outside the ASGM may be the reason why higher level of gaseous mercury was observed in Myanmar than that in Central Sulawesi.

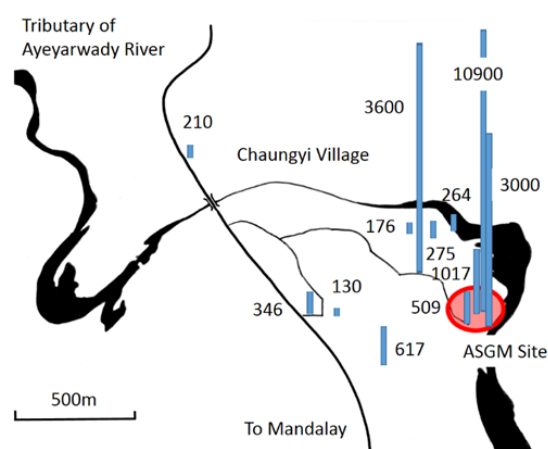


Fig. 9 Spatial distribution of Hg(0) observed in the first survey (unit: ng/m³)

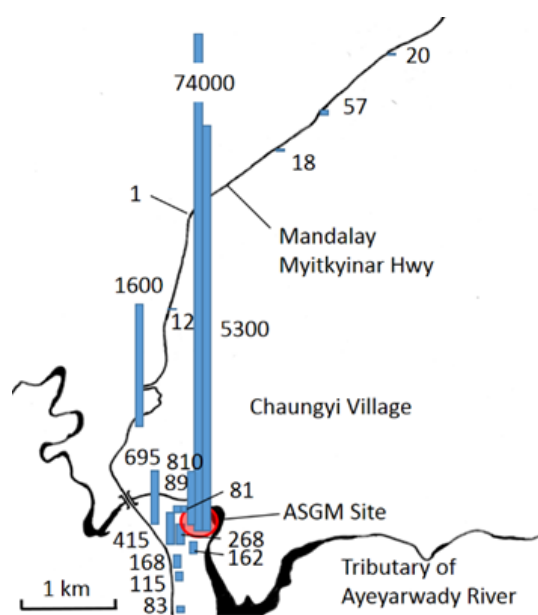


Fig. 10 Spatial distribution of Hg(0) observed in the

second survey (unit: ng/m³)

Table 1 Mercury concentration in water samples collected in Myanmar

Site	Type	Hg (ng/L)
Site 1	Ground water	20.9
	Ground water	12.1
Site 2	Ground water	0.0
	Ground water	2.0
Site 3	Ground water	1.2
	Ground water	0.0
Site 4	Ground water	20.1
	River water	12.9
Site 5	Leaked water	29.3
	Leaked water	34.5
	Water to the village	27.1
Ayeyarwady river	Upper	3.8
	Lower	4.6

Mercury Concentration in Water

Table 1 shows the mercury concentration in water samples. The sample taken at the center of the Ayeyarwady River in Mandalay located downflow of the ASGM showed 4.6 ng/L. Even the sample taken from upper flow of the Ayeyarwady River showed 3.8 ng/L. Comparing these concentrations with the typical mercury concentration in lakes and rivers, 1-3 ng/L [17], the mercury concentration in the Ayeyarwady River was slightly higher but not exceptionally so.

Groundwater leaked from the ASGM tunnel was 29.3 ng/L and 34.5 ng/L in the first and second surveys, respectively. The groundwater at Site1 and Site 4 also had concentrations higher than 20 ng/L. Although none of the samples exceeded WHO guidelines for drinking water, 500 ng/L [18], the use of mercury in ASGM could affect the mercury concentration in groundwater, since most of the mercury in groundwater is derived from atmospheric sources [19].

Mercury Content in Hair

Hair mercury is a biomarker for Me-Hg, and is often used to characterize Me-Hg exposures [20]. The lowest limits of mercury considered to pose risks of neurosis and health concerns to unborn babies are 50 µg/g and 11 µg/g, respectively [21]. Figure 11 shows the mercury content in the hair of ASGM workers and nonworkers. The maximum levels of the ASGM workers and the nonworkers were 5.7 µg/g and 2.9 µg/g, respectively. The average levels of mercury content in the ASGM workers and the nonworkers, 1.5 µg/g and 1.1 µg/g, respectively, were within the normal level of 1-2

µg/g [18]. Nonworkers seemed to have lower levels; however, based on to t-test, there were no significant differences between the two groups. The lower mercury level in hair may be due to less indexicality of hair for mercury vapor [18].

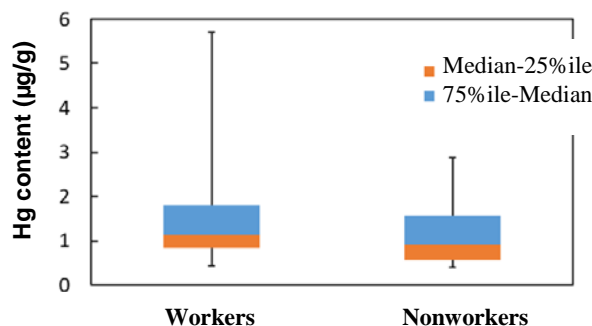


Fig. 11 Mercury content in the hair of ASGM workers and nonworkers

CONCLUSION

The government of Myanmar has initiated a collaborative project called “Development of Minamata Initial Assessment and National Action Plan for Artisanal and Small Scale Gold Mining in Myanmar”. The project’s goal was the ratification and early implementation of the Minamata Convention by providing key national stakeholders in Myanmar with scientific and technical knowledge and tools needed for that purpose.

In this study, mercury concentrations in the atmosphere, water, and human hair were measured in two surveys in ASGM areas in the Thabeikkyin Township, Mandalay Division of Myanmar performed in March and October, 2017.

The first and second surveys revealed that the highest concentrations of mercury in the atmosphere of ASGM sites reached 10,900 ng/m³ and 74,000 ng/m³, respectively. Even in the village outside the ASGM, concentrations higher than the WHO guidelines of 1,000 ng/m³ were observed. This was caused by the use of mercury for gold mining in village households and by the burning process taking place at the gold shop.

In the ASGM site, groundwater, especially the groundwater leaked from the gold mining tunnel, had elevated concentrations of mercury, indicating that ASGM had contaminated the groundwater with mercury. Although the mercury concentration was much lower than the WHO guidelines, the mercury concentration in the Ayeyarwady River could be affected by ASGM as well.

An analysis of hair indicated that the average levels of mercury content in the ASGM workers and the nonworkers, 1.5 µg/g and 1.1 µg/g, respectively, were within the normal level of 1-2 µg/g. Based on

to t-test, there were no significant differences between the two groups. To this point, the mercury is not at a level that would adversely affect human health.

REFERENCES

- [1] Harada, M., Minamata disease: methylmercury poisoning in Japan caused by environmental pollution, *Critical Reviews in Toxicology*, 25(1), 1995, pp.1-24.
- [2] David C. Evers, Susan Egan Keane, Niladri Basu, David Buck, Evaluating the effectiveness of the Minamata Convention on Mercury: Principles and recommendations for next steps, *Science of the Total Environment*, 888-903, 2016, pp.569-570.
- [3] United Nations Environment Programme, Minamata Convention on Mercury, 2013.
- [4] Global Environmental Facility, Request for Chemicals and Wastes Enabling Activity, Development of Minamata Initial Assessment and National Action Plan for Artisanal and Small Scale Gold Mining in Myanmar, GEF Project ID-9805, 2017, <https://www.thegef.org/project/development-minamata-initial-assessment-and-national-action-plan-artisanal-and-small-scale-4>.
- [5] United Nations Environment Programme, Global Mercury Assessment 2013 Sources, Emissions, Releases and Environmental Transport, 2013.
- [6] Minoru Yoshida and Hirokatsu Akagi, Environmental pollution of mercury use in gold mining in developing countries, *Environmental Science*, 17(3), 2004, pp.181-189.
- [7] The World Bank, CASM's holistic approach to small-scale mining aims to transform this activity from a source of conflict and poverty into a catalyst for economic growth and sustainable development, *Communities, Artisanal and Small-Scale Mining (CASM)*, 2008, pp.1-4.
- [8] Munthe J., I. Wängberg, N. Pirrone, Å. Iverfeldt, R. Ferrara, R. Ebinghaus, X. Feng, K. Gårdfeldt, G. Keeler, E. Lanzillotta, S. E. Lindberg, J. Lu, Y. Mamane, E. Prestbo, S. Schmolke, W. H. Schroeder, J. Sommar, F. Sprovieri, R. K. Stevens, W. Stratton, G. Tuncel, A.U rba, Intercomparison of methods for sampling and analysis of atmospheric mercury species, *Atmospheric Environment*, 35, 2001, pp.3007-3017.
- [9] Kouji Marumoto and Masahiro Sakata, Review of recent studies on mercury in the atmosphere, *Chikyukagaku(Geochemistry)* 34, 2000, pp.59-75.
- [10] Kagaya, S., Amatani, M., Nagai, T., Tohda, K. and Kawakami, T., A Simple Method for Determination of Gaseous and Particulate Mercury in Atmosphere, *Journal of Ecotechnology Research*, 13, 2007, pp.241.
- [11] Kuniki, R., Kawakami, T., Kagaya, S., Inoue, T., Rosana, E. and Nagafuchi, O.; Measurement of gaseous mercury concentration in the atmosphere - Development of a passive sampler -, *Environmental Engineering Research*, 46, 2009, pp.355-359.
- [12] EPA, Method 1631, Revision E:Mercury in Water by Oxidation, Purge and Trap, and Cold Vapor Atomic Fluorescence Spectrometry, <http://www.caslab.com/EPA-Methods/PDF/EPA-Method-1631.pdf>.
- [13] WHO/Europe, Chapter 6.9 Mercury http://www.euro.who.int/__data/assets/pdf_file/0004/123079/AQG2ndEd_6_9Mercury.PDF.
- [14] Lin C-J., S. O. Pehkonen, The chemistry of atmospheric mercury: a review, *Atmospheric Environment*, 33, 1999, pp.2067-2079.
- [15] Shannon J. D., E. C. Voldner, Modeling atmospheric concentrations of mercury and deposition to the great lakes, *Atmospheric Environment*, 29, 1995, pp.1649-1661.
- [16] Yuka Serikawa, Tomonori Kawakami, Basir Cyio, Isrun Nur, Rosana Elvince and Takanobu Inoue, Emission and dispersion of gaseous mercury from Artisanal Small Scale Gold Mining plants in Palu City, Central Sulawesi, Indonesia, *Environmental Science*, 24(4), 2011, pp.269-274.
- [17] Fan, Anna M.. "Mercury." In Lawrence Fishbein, Arthur Furst, and Myron A. Mehlman, eds., *Genotoxic and Carcinogenic Metals: Environmental and Occupational Occurrence and Exposure*. Advances in Modern Environmental Toxicology, Vol. 11. Princeton, N. J., Princeton Scientific Publishing, 1987.
- [18] WHO, Guidelines for drinking-water quality, fourth edition, 2011.
- [19] Grace M. Vandal, Robert P. Mason, William F. Fitzgerald, Cycling of volatile mercury in temperate lakes. *Water, Air, and Soil Pollution*, 56, 1991, pp.791-803.
- [20] WHO/UNEP DTIE Chemicals Branch, Guidance for Identifying Populations at Risk from Mercury Exposure, 2008.
- [21] National Institute of Minamata Disease, Mercury and health, http://www.nimd.go.jp/english/kenkyu/docs/Mercury_and_health.pdf.

REMOVING ARSENIC AND FLUORIDE FROM HOT SPRING WATER BY ELECTROLYSIS

Yuki Imai¹, Misa Konishi¹, and Tomonori Kawakami¹

¹Faculty of Engineering, Toyama Prefectural University, Japan

ABSTRACT

Currently in Japan, there are many hot springs containing fluoride and arsenic with high concentration. Although the national minimum effluent standard for arsenic and fluoride is 100 µg/L and 8 mg/L, respectively, they are not applied to the hotels with hot spring since no appropriate treatment techniques are available. The objective of this research is to reduce fluoride and arsenic in hot spring wastewater by using electrolysis technique to meet the national minimum effluent standards.

The electrolysis system with an anode bath and a cathode bath separated by a diaphragm was adopted. Fluoride and arsenic co-precipitate with magnesium hydroxide formed in the cathode bath in which pH value increases as the electrolysis progresses. The Gero hot spring containing fluoride and arsenic as 17 mg/L and 120 µg/L, respectively, was used as a model effluent.

Since Gero hot spring water contains almost no magnesium, magnesium chloride was added as a magnesium source. The addition of 100-200 mg/L could reduce the fluoride concentration to less than 8 mg/L. The arsenic concentration decreased to less than 10 µg/L. 1040 C/L of electricity was required for the operation. The electrolysis system successfully reduce the fluoride and arsenic concentrations below the national minimum effluent standards.

Keywords: hot spring waste water, arsenic, fluoride, electrolysis, national minimum effluent standard

INTRODUCTION

Intake of drinking water containing high concentrations of fluoride for a long term could cause fluorosis, such as dental fluorosis and skeletal fluorosis. In order to prevent human health from fluorosis, the standard for drinking water and the national minimum standards were set as 0.8 mg/L and 8 mg/L, respectively. Currently in Japan, however, there are many hot springs containing fluoride in excess of the national minimum effluent standards. A temporal standard is applied to hotels with hot springs since no appropriate treatment techniques are available. Adsorption, ion exchange and reverse osmosis (RO) techniques can be used for removing fluoride from drinking water, however, co-existing contaminants in hot springs degrade their effectiveness [1,2]. In addition, RO is not available for wastewater treatment due to rejected water with concentrated contaminants [3]. Even though the Japanese Ministry of Environment invited private companies to compete for the treatment technique for the wastewater, no effective technology has been developed yet [4]. Accordingly, the ministry decided to extend the term of validity of the temporal provisional standard for 2001 after reviewing the regulation in 2016 [5].

On the other hand, long-term exposure to arsenic from drinking water and food could cause cancer and skin lesions. Arsenic is naturally present at high levels in the groundwater of a number of

countries, and it is highly toxic in its inorganic form. The national minimum effluent standards of arsenic have been set at 100 µg/L. In Japan, many hot springs contain arsenic exceeding the national minimum effluent standard such as Kusatsu hot spring (250–1260 µg/L) [6], Gero hot spring (140 µg/L) [7], and Yudanaka hot spring (1240 µg/L) [8]. Hot spring inns are exempted from arsenic regulations. This is also due to the lack of effective technologies to remove arsenic.

The authors have been developing technologies to remove fluoride from drinking water in developing countries. In developing countries, inexpensive and easy-to-operate equipment is required. Fluoride removal by an electrolysis system is one of the technologies applicable to hot spring waste water. The electrolysis system consists of electrolysis baths separated by a diaphragm. When electrolysis progresses, magnesium contained in well water in a cathode bath precipitates as a form of magnesium hydroxide as the pH increases, and fluoride co-precipitates with magnesium hydroxide [9,10]. Moreover, arsenic was found to be removed efficiently by this electrolysis method. With this electrolysis method, fluoride and arsenic can be removed simultaneously. In drinking water, it is rare that fluorine and arsenic exist at the same time in high concentrations; however, the waters of both Kusatsu and Gero hot springs have higher concentrations of fluoride and arsenic than the minimum effluent standards. It is

preferable that they should be treated and removed.

The objective of this research was to remove fluoride and arsenic simultaneously from hot spring wastewater using an electrolysis system to meet the national minimum effluent standards.

MATERIALS AND METHODS

For the simultaneous removal of fluoride and arsenic, an electrolysis system was used. The electrolysis system consists of an anode bath and a cathode bath separated by a diaphragm. When water containing magnesium is electrolyzed in the electrolysis system, magnesium precipitates as a form of magnesium hydroxide by increasing the pH value of the cathode bath. Fluoride and arsenic coprecipitate with magnesium hydroxide when the electrolysis progresses.

Experiments were carried out in a continuous flow system. Fig.1 (a) shows the flow diagram of the continuous electrolysis system, and Fig.1 (b) shows a photo of the electrolysis system used in the experiment. The diaphragm of the electrolysis system shown in Fig.1 (b) is made of an uncalcined plate. An aeration bath is added to the electrolysis system. The sizes of the anode and cathode baths were 7 cm (H) × 40 cm (L) × 1 cm (W) and 7 cm (H) × 40 cm (L) × 2 cm (W), respectively. The volumes of the anode and cathode baths were 280 mL and 560 mL, respectively. As shown in Fig.1 (a), a constriction plate to restrict the mixing of the solution before and after was provided in the flow in the anode and cathode tanks. A plastic (PVC) plate 0.5 mm thick was used as the constriction plate. The constriction plate provided an open area 1 cm deep from the bottom. In this study, the compartments in the anode bath were named the “+1 cell” and the “+2 cell” from upstream to downstream. The compartments in the cathode bath were named the “-1 cell” and the “-2 cell” from upstream to downstream. A platinum wire (purity 99.99%, diameter 0.6 mmφ, length 1 m) was used as the electrode for the anode, and a stainless steel wire (SUS 304, diameter 1.0 mmφ, length 1 m) was used for the cathode.

Table 1 shows the water quality of the Gero hot spring. The Gero hot spring, which contains fluoride and arsenic, was used as a model effluent. Since Gero hot spring water contains almost no magnesium, magnesium chloride was added as a magnesium source when electrolysis was carried out.

In the laboratory, the water taken from the Gero hot spring was put in a bucket, and magnesium chloride was added to adjust the magnesium concentration. The hot spring water (Mg added) was introduced into the anode bath and the aeration bath of the electrolysis cell. Carbonate and bicarbonate, which interfere with the formation of magnesium hydroxide, were removed from the raw water by introducing the effluent water from the anode bath with low pH into the aeration bath. The size of the aeration bath was 6.5 cm (H) × 6.5 cm (L) × 6.5 cm (W), and the volume was 275 mL. The generated carbon dioxide was expelled to the atmosphere by aeration. As the operating condition, the treatment capacity was 10 L/day. The residence time in the cathode bath was 80 minutes. Electrolysis was carried out at a constant current by using a constant current power supply (TAKASAGO ZX-400 M).

We investigated the effect of the flow rate ratio, which is the ratio of the flow rate to the anode bath (a):aeration bath (b), magnesium concentration, and current on the removal of fluoride and arsenic.

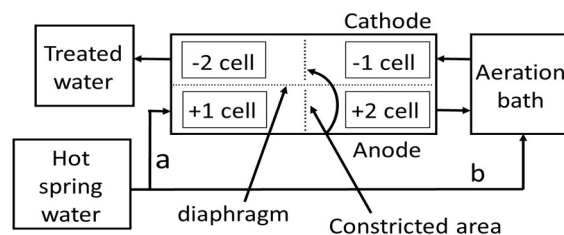


Fig.1 (a) Schematic diagram of the sequential flow reactor

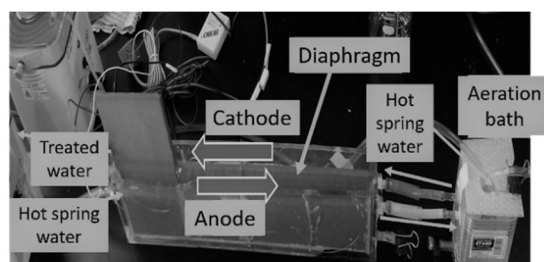


Fig.1 (b) The electrolytic equipment used for the experiment

Table 1 Water quality of the Gero hot spring

	pH	Na ⁺ (mg/l)	K ⁺ (mg/l)	Mg ²⁺ (mg/l)	Ca ²⁺ (mg/l)	F ⁻ (mg/l)	Cl ⁻ (mg/l)	SO ₄ ²⁻ (mg/l)	As (mg/l)	Alkalinity (μeq/l)
Literature[11]	9.5	108.9	1.2	0	1.9	16.5	75	10.9	140	-
Measured value	9.2	105.2	0.6	0	0	16.9	75	11.4	114	1329

Effect of The Flow Rate Ratio

The flow rate ratio of the hot spring water supplied to the anode bath (a) and the aeration bath (b) was varied—a:b=10:0, 5:5, 2:8, or 0.6:9.4—under conditions in which the magnesium concentration and the current were set at 100 mg/L and 120 mA, respectively.

Effect of The Magnesium Concentration

The magnesium concentration was varied—0, 50, 100, or 200 mg/L—under conditions in which the flow rate ratio and the current were set at a:b=0.6:9.4 and 120 mA, respectively.

Effect of The Electrolysis Current

The current was varied—80, 120, or 200 mA—under conditions in which the flow rate ratio and the magnesium concentration were set at a:b=0.6:9.4 and 100 mg/L, respectively.

Analyses

Sampling was conducted at the raw water exit, +1 cell, +2 cell, aeration bath, -1 cell, and -2 cell after continuing to operate for 24 hours or more for stabilizing.

The concentration of As was analyzed by ICP-MS (Agilent 7700 Series).

The ionic component concentrations of F⁻, Cl⁻, NO₃⁻, SO₄²⁻, PO₄³⁻, Na⁺, K⁺, NH₄⁺, Mg²⁺, and Ca²⁺ were analyzed by ion chromatographs.

(Cation: Thermo ICS 1500, separation column IonPac CS 12A, eluent methanesulfonic acid 30 mmol/L, suppressor CERS 500)

(Anion: Thermo ICS 2000, separation column IonPac AS 18, eluent KOH 23–40 mmol/L (gradient), suppressor AERS 500)

The pH was measured by a glass electrode method with a BECKMAN Ø 32 pH Meter (electrode: BECKMAN 511070).

RESULTS AND DISCUSSION

Effect of The Flow Rate Ratio

Fig.3.1 (a) shows the effect of the flow ratio on the removal rate of fluorine and arsenic. When the anode side had a small flow rate, a higher removal rate was observed. The fluoride concentrations in each cell with various flow rate ratios are shown in Fig.3.1 (b), and the arsenic concentrations are shown in Fig.3.1 (c). When the flow rate ratio was a:b=10:0, the entire amount of raw water was supplied to the anode. On the other hand, when a:b=0.6:9.4, the majority was supplied to the mixed aeration tank.

When the flow rate ratio a:b=10:0, no significant change in fluorine concentration was observed in each cell. On the other hand, in the case of a:b=0.6:9.4, the fluoride concentration increased slightly due to the Coulomb force in the +1 cell and the +2 cell; however, the fluoride concentration was close to that of the raw water in the aeration bath to which the majority of the raw water was supplied. Thereafter, the fluoride concentration rapidly decreased in -1 and -2 cells. For arsenic, even when the flow rate ratio was a:b=10:0, the arsenic concentration decreased in the -1 and -2 cells. The highest removal ratio of arsenic was also recorded when the flow rate ratio was a:b=0.6:9.4.

The pH and magnesium concentrations in each cell at various flow rate ratios are shown in Fig.3.1 (d) and Fig.3.1 (e), respectively. The pH in the aeration bath was less than 4 irrespective of the flow rate ratio, indicating that carbonate and bicarbonate had been removed. When the flow rate ratio was a:b=10:0 and a:b=0.6:9.4, there was a difference in pH in the -1 and -2 cells. In the former case, the pH in the -2 cell was 8.10, while in the latter case, it was 10.05. When taking the solubility of magnesium as 16.6×10^{-5} mol/L [12], the solubility product is calculated to be $K_{sp}=[Mg^{2+}][OH^{-}]^2 = [16.6 \times 10^{-5}][33.2 \times 10^{-5}]^2 = 1.83 \times 10^{-11}$. When the same solubility product is assumed, a magnesium concentration of 35 mg/L in the solution is obtained at pH=10.01, which almost coincides with the measured value of 34 mg/L. At pH 8.10, if the same solubility product of magnesium hydroxide is assumed, the solubility is $(10^{(10.05-8.10)})^2=7900$ times higher than that at pH=10.05, indicating that theoretically no

precipitation occurs. In fact, slight precipitation was found only in the vicinity of the electrode. Consequently, the magnesium concentration did not decrease greatly, as shown in Fig.3.1 (e). The difference in the pH value in the -2 cell affects the formation of $\text{Mg}(\text{OH})_2$ and the removal of arsenic and fluoride.

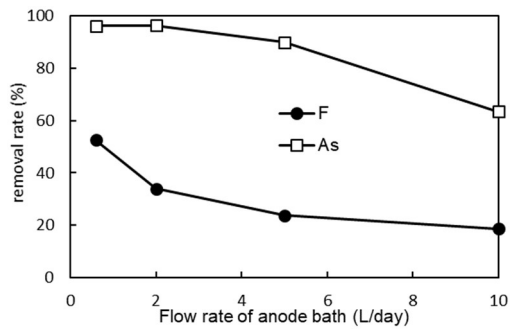


Fig.3.1 (a) Effect of the flow rate ratio on the removal rates of fluoride and arsenic

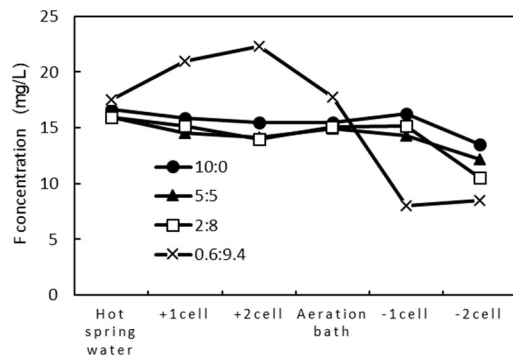


Fig.3.1 (b) Change in the fluoride concentration in each cell

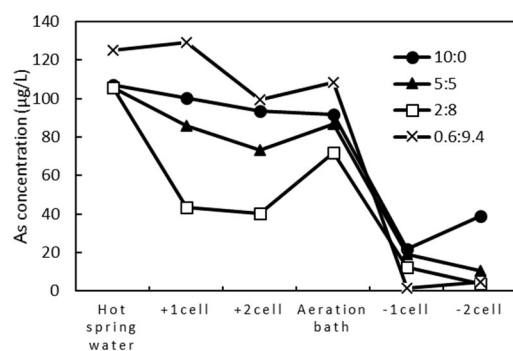


Fig.3.1 (c) Change in the arsenic concentration in each cell

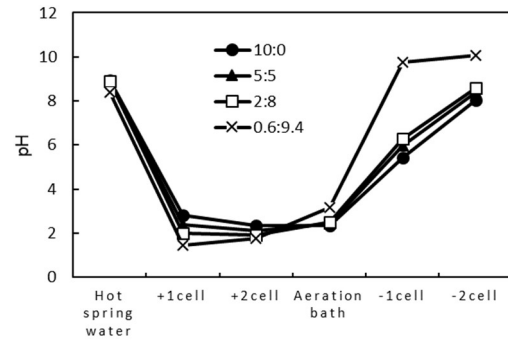


Fig.3.1 (d) Change in the pH in each cell

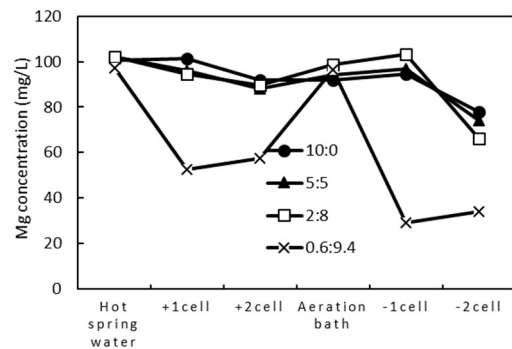


Fig.3.1 (e) Change in the Mg concentration in each cell

Effect of The Magnesium Concentration

Fig.3.2 (a) shows the influence of fluoride and arsenic on the removal rate when the magnesium concentration in the raw water was varied. The higher the magnesium concentration, the higher the removal rate of fluoride and arsenic. However, when the magnesium concentration was 50 mg/L or more, the removal rate of arsenic stayed within 90 to 100%.

Fig.3.2 (b) and (c) show the fluoride concentration and the arsenic concentration, respectively, in each cell when the magnesium concentration was varied. In the legend of the figures, Mg 0, Mg 50, Mg 100, and Mg 200 indicate when the magnesium concentration in the raw water was 0 mg/L, 50 mg/L, 100 mg/L, and 200 mg/L, respectively. When the magnesium concentration was varied between 100 and 200 mg/L, 8 mg/L (removal rate 53%) of the fluoride concentration in the treated water (-2 cell) was obtained. The arsenic concentration in treated water (-2 cell) was less than 10 $\mu\text{g/L}$ when the magnesium concentration was 50 mg/L or more.

Fig.3.2 (d) and (e) show the pH and the magnesium concentration, respectively, in each cell when the magnesium concentration was varied. When 200 mg/L of magnesium was added, about 100 mg/L of magnesium remained in the treated water (-2 cell). The reason is that the pH did not increase sufficiently. However, the magnesium reduction from the raw water in treated water (-2 cell) was largest when 200 mg/L of magnesium was added, leading to the highest removal of fluoride.

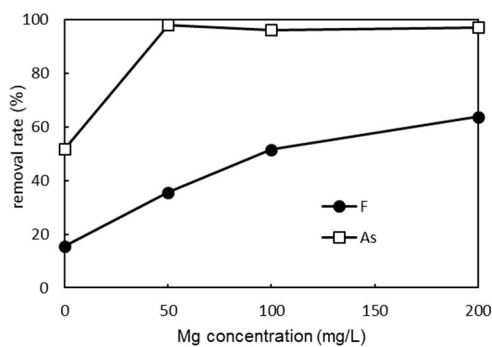


Fig.3.2 (a) Effect of the magnesium concentration on the removal rates of fluoride and arsenic

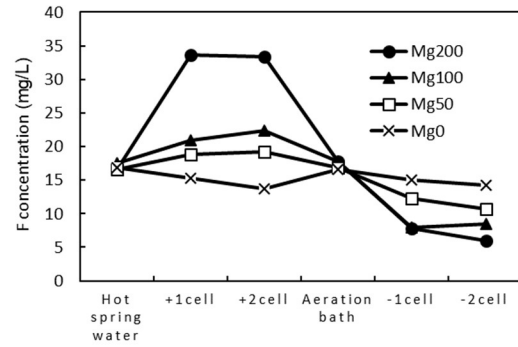


Fig.3.2 (b) Fluoride concentration for different Mg concentrations

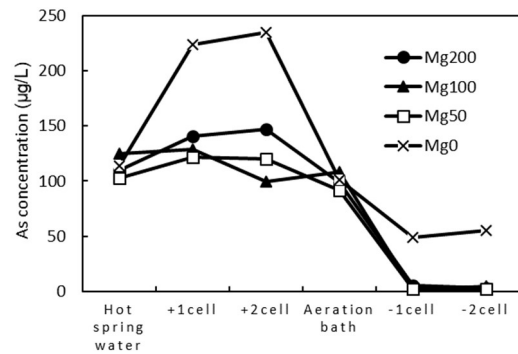


Fig.3.2 (c) Arsenic concentration for different Mg concentrations

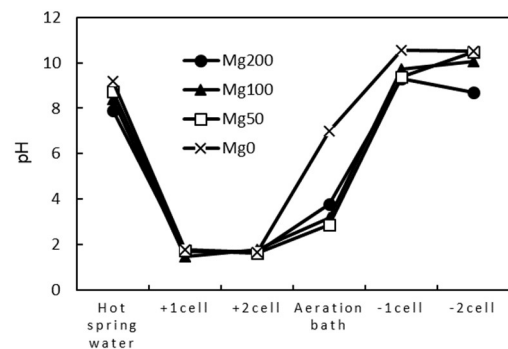


Fig.3.2 (d) pH for different Mg concentrations

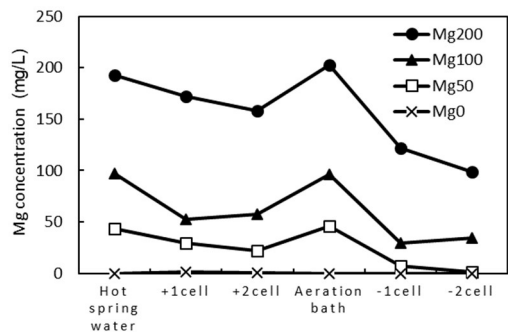


Fig.3.2 (e) Magnesium concentration for different Mg concentrations

Effect of The Electrolysis Current

Fig.3.3 (a) shows the influence of the current on the removal rates of fluoride and arsenic. Fig.3.3 (b) and (c) show the fluorine concentration and the arsenic concentration, respectively, when the electrolysis currents were varied. Electrolysis currents larger than 120 mA did not increase fluoride removal but did increase arsenic removal. As shown in Fig.3.3 (c), when the current was 120 mA or more, an arsenic concentration of less than 10 $\mu\text{g/L}$ was obtained. The pH and magnesium of each cell are shown in Fig.3.3 (d) and Fig.3.3 (e), respectively. Changes in pH due to different currents were hardly observed; however, differences in magnesium concentrations were observed in each cell. With a current of 80 mA, magnesium was not sufficiently precipitated, which could be the cause of the low removal rates of fluorine and arsenic.

When the current was 120 mA, the fluoride removal rate was the highest, and the fluoride concentration met the national minimum effluent standard. The arsenic concentration was also less than 10 $\mu\text{g/L}$.

The amount of electricity per day with a current of 120 mA was calculated to be 10400 C/day. Since the flow rate was 10 L/day, the electricity required per 1 L was 1040 C/L.

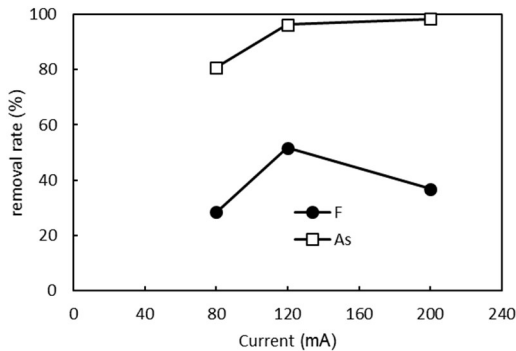


Fig.3.3 (a) Effect of the current on removal rates of fluoride and arsenic

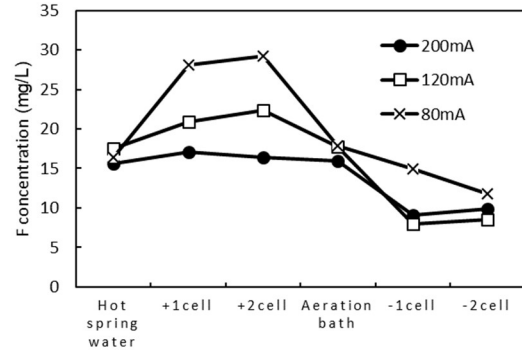


Fig.3.3 (b) Fluoride concentrations in different currents

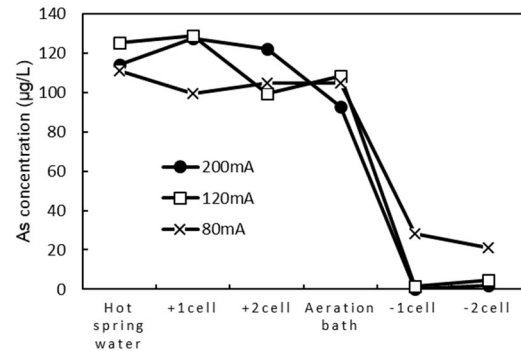


Fig.3.3 (c) Arsenic concentrations in different currents

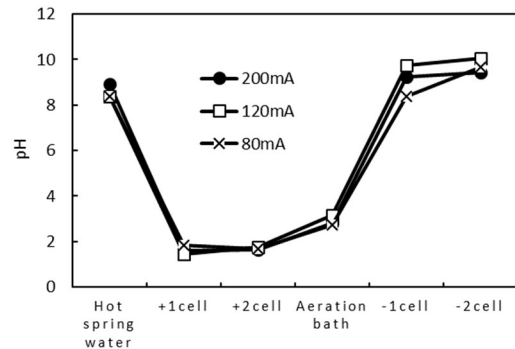


Fig.3.3 (d) pH in different currents

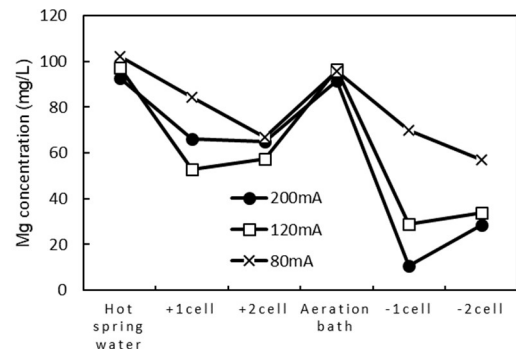


Fig.3.3 (e) Magnesium concentrations in different currents

CONCLUSION

An electrolysis system was operated with the aim of simultaneously removing fluorine and arsenic from hot spring wastewater. The electrolysis system consisted of electrolytic cells separated by a diaphragm made of an uncalcined plate. The electrolysis system was used to remove arsenic and fluoride by the co-precipitation of magnesium hydroxide on the cathode side with fluoride or arsenic.

The wastewater of the Gero hot spring was used as a model. Since the Gero hot spring did not contain magnesium, magnesium was added externally. The addition of 100–200 mg/L could reduce the fluorine concentration in raw water from 16.9 mg/L to 8 mg/L or less. Simultaneously, the arsenic concentration could be reduced from 114 µg/L to 10 µg/L or less.

ACKNOWLEDGEMENTS

This research was partly supported by JSPS KAKENHI Grant Number 17K18910.

REFERENCES

- [1] Maurice S. Onyango and Hitoki Matsuda, Fluoride Removal from Water Using Adsorption Technique Fluoride and the environment, Vol. 2, 2006.
- [2] Paripurnanda Loganathan, Saravanamuthu Vigneswaran, Jaya Kandasamy, Ravi Naidu, Defluoridation of drinking water using adsorption processes, Journal of Hazardous Materials, Vol. 248-249, 2013, pp. 1-19.
- [3] Stéphane Nicolas, Laurence Guihard, Alain Marchand, Bernard Bariou, Abdeltif Amrane, Ali Mazighi, Nabil Mameri, Azzeddine El Midaoui, Defluoridation of brackish northern Sahara groundwater - Activity product calculations in order to optimize pretreatment before reverse osmosis, Desalination, Vol. 256, Issue 1-3, 2010, pp. 9-15.
- [4] Ministry of the Environment Government of Japan, Exploration into development and dissemination of technology for wastewater treatment from hot spring, <http://www.env.go.jp/water/onsen-haisui/tech.html>, 2018.6.9.
- [5] Ministry of the Environment Government of Japan, Notification, No.1606161, Review of the temporal minimum effluent standard for boron, fluoride, ammonium, nitrite and nitrate, 2016.
- [6] Yukiko Sakai and Tsuneo Takishima, Arsenic Content in the Hot Spring Waters in Gunma Prefecture, Hot Spring Sciences, Vol. 26, No. 1, 1975, pp. 13-25.
- [7] Gifu Research Center for Public Health, Hot spring analysis data, 2013.
- [8] Kimio Noguchi, Chemical Components of the Hot Spring Waters in Nagano Prefecture, Hot Spring Sciences, Vol. 18, No. 2, 1967, pp. 47-64.
- [9] Tomonori Kawakami, Hikaru Miyazaki, Yuki Imai, Misa Konishi, Fluoride Removal from Groundwater by an Electrolysis System, Journal of Arid Land Studies, Vol. 27, Issue 1, 2017, pp. 41-47.
- [10] Yuki Imai, Shiori Yanagawa, Misa Konishi, and Tomonori Kawakami, Removing Fluoride from a Hot Spring Using an Electrolysis System, International Journal of GEOMATE, Vol. 12, Issue 32, 2017, pp. 101-106.
- [11] Gifu Research Center for Public Health, Hot spring analysis data, 13B04774, No. 125, 2013.
- [12] Kagaku Binran Basic edition II, rev. 5, The chemical society of Japan, 2004.

A DEVELOPMENT OF WASTE MANAGEMENT MODEL: A CASE STUDY OF SI MUM MUANG MARKET IN THAILAND

Anucha Jaisai and Chutarat Chompunth*
School of Environmental Development Administration,
National Institution of Development Administration, Thailand

ABSTRACT

The objectives of this research are to 1) study waste management in Si Mum Muang Market, PathumThani Province, Thailand, 2) to study factors affecting waste management and 3) to find out a developmental guideline in waste management. According to waste problem of the case study, there are 240 tons of wastes per day, waste disposal fee is 30 million baht per year, and landfill site may not enough in the future. This problem also causes pollution and environmental impact to local communities. This study employed qualitative research methodology. Data were collected through in-depth interviews and participatory observation, and action research was conducted. SWOT Analysis was conducted to analyze data. The study showed that Waste management of the Si Mum Muang Market is under control of Donmuang Pattana Co., Ltd. The company encourages its supervisory staffs to invent waste management's innovation namely "One to Three innovation". This technique contributes value benefits as follows, reducing waste disposal fee, increasing value, create an organic waste product and lead to sustainable environmental business. Internal factors affecting success in waste management include vision of management executives, systemic thinking, empirical practice, and high level of having experience and proficient on waste management. External factors are public awareness on environment, government sector and environmental organization in supporting the development of waste management at Si Mum Muang Market. Finally, for effective waste administration, the organization should provide more opportunities for the public to participate in waste management activities and determine carefully on any impact to public health and environment.

Keywords: Waste Management, SWOT Analysis, One to Three Innovation, Environmental Business

INTRODUCTION

The pollution problems of Thailand are numerous including a variety of aspects from the industry, the agriculture, community, tourist attractions and the market that produces environmental impacts to the environment. The environmental pollution that is the priority issues including, water pollution, air pollution, noise pollution and waste pollution and waste. The cause of the increasing the environmental pollution problems are 2 mains reasons. The first one is that the average population increase of the global population tend much higher even if campaign about family planning succeed but the amount of increase of population growth is still like exponential population which is a multiplier increasing, when more people want to consume more resources on all sides, food, housing, energy and others, Secondly, the expansion of economic and technological progress resulting in an economic expansion makes a high living standard. The consumption of natural resources is over the basic necessities of life [1]. So, it is necessary to use more energy as well. At the same time, the technological progress is supported to bring the natural resources to use easier and more.

RESEARH RATIONAL

One problem that important to all sector such as industry, agricultural community, tourist attraction places and the market is the pollution problems caused by community waste and solid waste. Accumulated solid waste may result in dirtiness and environmental nuisances including odors, flies, and blowing litter that directly causes an aesthetic problem. In the long-term effects, solid waste can also contaminate the environment by solid waste disposal that transfers harmful substances to the air, water and soil, which may destroy the environment and pose human health problems. The situation of waste from 2010 to 2017 is massive, there was the volume of waste up to 26.77 million tons and it was appropriately managed only 7.2 million tons. The rest is under inappropriate managed and from the academic research, in Thailand, community waste can be recycled only 5.1 million tons, this problem causes environmental problems and affect to people's health [2]. Thailand

has an increasing production of municipal solid waste that, allied to the current un-effective waste management system, makes the search for alternatives of waste management essential.

Market

Market is the exchange of goods as a center of community in life along in the Thai culture for a long time. The main product is all kind of food especially fresh food and according to its position as a gathering source of food. Frequently, it was found that the market is the source of wide spread diseases causing from food infective disease. These problems are caused by the environmental un-sanitation of the market such as waterlogged, waste residues, smelly *etc.* In order to control the market to be complied with hygiene standard, the market is necessary to segregation their waste and properly manage them. The developer must improve the market hygiene by following guidelines under the Public Health Act 2535. Moreover, there are many authorities controlling and supporting the whole sale market to comply with Thai laws and regulations including, Local governments, Provincial Health Office, Department of Health and so on. Thus, it is important for the developer to search for appropriately alternatives of manage municipal solid waste from the hole sale market. *One to Three Innovation* as an innovative waste management of Si Mum Muang market is investigated and suggested as a practice to other wholesale market in Thailand.

Si Mum Muang wholesale market

Si Mum Muang is a wholesale market which is known as leader for wholesale fruits and vegetables in Thailand. The market is operated in the north part of Bangkok more than 33 years. The market's vision is as "the market is clean, convenient, and peace which are a basic structure together with the participation in the management chain, product quality, efficiency and social responsibility". Although consumer's demand is continued to be increased by the circumstances of the economic expansion, Si Mum Muang Market still committed to be an honest trader in order to maintain leadership of the fruit and vegetable trade center by planning the future to be market in new era. The market focuses on building good relationships and engages in improving the quality of life of the society. The market also focus on the customer's convenient from sellers to customers by developing the trade area and a project for a lot of cars to come in the area of the market, Manage Transportation, Transfer goods services both product release and effective delivery. The waste management from activities with a daily average of 200 tons by managing waste from the source, also, the campaign for the seller, worker, customer and

people in the community to cooperate effectively and with the health care of the cleanliness follow the sanitation principles, provided to the sellers in the market. It is an approach working of a successful organization and should be taken as an example of an effective environmental management.

Research methodology and Data analysis

This research is an action research with the invention of innovative waste management of Si Mum Muang Market, KhuKhot subdistrict, Lam LukKa District, Pathum Thani province. The researcher used the questionnaire to collect data and descriptive data analysis by using the technical environment analysis (SWOT Analysis) to analyze in order to understand the operations of all waste management of Si Mum Muang Market with One to three innovation and factors in the operation of Si Mum Muang Market. Collect data by interviewing someone that involved in waste management of Si Mum Muang Market. More details, step by step are as follows:

1. Explore the basics information about waste management of Si Mum Muang Market, Pathum Thani Province by seeking information from literature sources. Use documentary research that related to waste management, reducing the amount of waste, waste management in community, factors that makes accomplish and case studies in various areas as well as other documents related to the objectives of the study.

2. The study of waste management of Si Mum Muang Market to understand the guideline of waste management as policy and study the successful in implementing the waste management in the market.

3. Data were collected by interview the executive of the market and the traders involved which are important people up to 29 key informants. The details are as follows: 5 of the executive of the market, 1 of the environmental manager who is responsible for waste recycle and management of Si Mum Muang Market, 5 of the waste management staff workers of Si Mum Muang Market, 2 waste collector, 9 of merchants, 4 of the office environment in Pathum Thani province, 3 authorities from department of environmental policy.

4. The data collected by observation method such as, observing the work of the officers involved. Practice of traders and the participation of customers in the market.

5. Processing, summarize and presentation of the results of the study by bring the data from the study in the target area, the process of exchange, brainstorming of study group, analyze format and find the factors leading to the success along with guidelines to add more in order to expand the result of the waste management that appropriate with Si

Mum Muang Market to achieve the most effective environmental management and report the results.

Results and Discussion

Case study background

This study was undertaken in Si Mum Muang Market, Thailand. It is located in Pathum Thani province, which is about thirty kilometers from the north of Bangkok, Thailand. It is one of the largest wholesale agricultural products markets in Thailand, and a trading point for farmers, sellers and buyers of the large quantities of both locally produced and imported food products. There are more than 30,000 customers daily and approximately 10,000 metric tons of goods are traded daily. The primary product categories traded at this market were fruits, vegetables, meat and fish, rice and crops, flowers, pet supplies, and plants.

The study concluded that affecting factors to Si Mum Muang Market of effective waste management is an innovative “One to three” which leads to business sustainable environment.

In this study, proposed solid waste management options for Si Mum Muang Market, Thailand were designed to minimize the initial generation of community waste through source reduction, then through reuse and recycle to further reduce the volume of material being sent to dispose of at landfills or being disposed of by other alternatives. Options development of solid waste management for the market is focused on (1) solid waste generation, (2) solid waste handling and separation and storage, and (3) solid waste collection. Solid waste in this case study can be classified into many groups including organic waste, plastic, food waste, wood, paper, glass, clothes, metal, and miscellaneous.

In-depth interviews were conducted in this study to interview the environmental manager and stakeholders regarding solid waste management. The results showed that Si Mum Muang Market officers who work in the solid waste management department mentioned that solid waste management in the market is efficient in terms of solid waste disposal. They can transform the organic waste to make useful products, they can still handle the collection of a large amount of solid waste well, as they can collect the solid waste from the market space properly and provide coverage to all zones of the market. Execution of a solid waste management system is crucial to deal with the solid waste generation as economically and safely as possible. It is vital that all solid waste are professionally as possible collected from all sources, and disposed of in controlled disposal facilities. All collected waste are stored separately in three types of garbage bins including; green, yellow and blue. Green garbage bins are used to store organic waste, yellow garbage bins are used to store recyclable waste and blue garbage bins are used to stock general waste. Green

and blue bins are placed at every stall and shop. Yellow garbage bins are set near every block of the commercial zone.

Since 2012, the principals of the Market have been implementing and developing customized recycling programs of all types and sizes of solid waste in the market. Si Mum Muang Market provides Sustainability Reports for each of its customers to demonstrate its site by site what type of wastes are being recycled and the quantity of the waste, allowing its stakeholders to see the impact/success of their recycling efforts in a more quantifiable manner. Benefits of recycling are as follows; to reduce waste to landfills which spares the land and reduces pollution/contamination; and, to reduce waste removal costs as recyclables are removed from solid waste procedures. Most importantly, Si Muang Market is now effectively connected to all local, and municipal governments to ensure that its operations and practices meet all laws and regulations.

In this market, composting is gaining a substantial amount of push. As composting is the process of recycling organic material which typically includes food production scraps and crop growing waste. Its practices are environmentally sensitive and lower their garbage collection costs by removing food waste from the garbage stream which routinely be transferred to landfills.

The results also showed that the merchants who are better informed about solid waste management information likely have better solid waste management behavior. The reason could also be because merchants who are regularly informed about appropriate solid waste management may understand the method to minimize the solid waste generation rate and the ways to separate solid waste into recyclable and non-recyclable items to reuse or recycle solid waste again. Regularly provided information is a key factor that can give the information to the merchants, and better information might increase the participation in solid waste management. With regard to the sources of information, a survey study done in many place [5] mentioned that most recyclers are more likely to have one or more sources of information, for example newspapers and television. Various sources of recycling knowledge coming from public education and information through public campaigns showed a positive correlation with recycling rates.

The case study analysis by technique environment analysis (SWOT Analysis are presented as follows.

Within the business organization has two dimensions including, the dimension of the strengths that leaders are visionaries, work in a systematic approach by encourages staff to develop their potential in the field of waste management. So, staff try to invent new innovations in waste management

as 1 of waste management will get 3 benefits and it was called innovative "One to three" to reduce waste from source in order to save the cost of waste disposal, adding value to solid waste and create products from organic waste this concept leads the organization to achieve environmentally sustainable business. This is consistent with the results of a study of Poboorn, *etc.* [3] studied the local authorities practice to overcome the global warming crisis: A case study of municipal district Klang city. It was found that a municipal district Klang city focus on a development of personnel skill and people awareness in all sectors. It also improved the workflows, applies applicable technologies, and implement many activities to reduce global warming in the municipality. The Municipal also giving priorities on development of staffs skill and it will boost staff's knowledgeable and competence on the field of waste management even more and more. The staff can use their knowledge and expertise to develop and improve the organization's operations practices more efficient.

For weakness dimension, it was found that Si Mum Muang Market was a wholesale market of vegetables, fruits and raw materials. There are large amounts of merchants and affect to amount of waste of 240 tons per day. Thus, there is a large amount of waste and the budget of waste disposal is quite high. The market still has no unblemished guidelines for planning waste management and no clear guideline for the operators to perform the operation practice effectively.

The external business organization has two dimensions including the dimension of a chance which is a chance to discover that there is a Government and environmental organizations in supporting the development of waste management's Si Mum Muang Market to be effective. From the interviews of Si Mum Muang market executives said that "In the past had the local authorities and the education authorities that gave priority and support to Si Mum Muang Market such as KhuKhot Municipal supported and educated about waste management to the market staff of waste management department. Kasetsart University came in to support staff on controlling and training procedures how to make the biological fermentation as well as support staff for biological fermentation. While Khonkean University do many research on bringing the fruits and vegetables in Si Mum Muang market for cattle feeding and supported the information on fruit and vegetable scrap to make efficiently cattle feeding product" (Personal interview, May 15, 2561), This finding corresponds to many research [4], [5] that participation is beneficial to an implementation of waste management policies and a development for various projects which concerning an conservation of natural resources and the environment. This might because

all stakeholder can monitor for surveillance and warning particularly any projects or activities that affect public health, social and environmental quality. Importantly, waste management programs of Si Mum Muang market focus on public participation practice which strongly benefit to the public, surrounding communities and the public as a whole. However, for the threat dimension, it was found that Si Mum Muang market as a large-scale market, so there are communities living around the market a lot, causes many complaints from people surrounding areas, as presented in the interviews of market staffs that "In the past, there were a lot of complaints from people around the market. They were mainly about the environmental problems because of Si Mum Muang market is so large and has a lot of solid waste which may cause environmental and health impact to the community as well as disturbing people living surrounding the markets. That is why Si Mum Muang market need to find approaches and means to deal with these significant issues" which corresponds to many researches [2], [6], [7] that the organization should be accountable and open to the communities. There must be a good criterion or terms include the success of the mission together with the efficiency of operation and cost-effective use of resources in the environmental management of local government agencies that need to use the local resources is critical to reducing operational costs. So it can be concluded that Si Mum Muang market has a social responsibility in environmental management and solution of environmental issues from the complaints of the people living around the project site.

Conclusion and recommendations from the study

To be successful in waste management practice as a case study, it should be an integration between the educational program and the providing of appropriate solid waste management. In accordance with the educational program, it aims to increase the awareness of merchants by educating them in terms of proper solid waste management. A solid waste management system is also important to deal with the solid waste generation to ensure that all solid waste are appropriately transferred and disposal [8].

To make the operation of waste management more broadly effective, business organization should spread the innovation of waste management to other function in order to expand broader efficiency and sustainability approaches by suggestions as follows:

- 1) Recruiting enough workers with direct knowledge in waste management
- 2) Increase public relations to the right knowledge to the traders in the area such as posters, pamphlets and etc.
- 3) In order to prevent waste from outside to inside the market. There should be a point of waste disposal so that the person can be drop properly.

4) Bio-compost should be more introduced, in order to help the communities in wastewater treatment. The market should be encouraged to build on or sold to third parties in order to increase revenue to the market.

5) Add more channel in order to promote the market for the customers to be more environmental friendly practice.

Finally, it could be summed that people's participation is the one of significant factor to achieve the successful solid waste management of this case study. The recommendation is that a knowledge and information project is needed to educate the customers. The motivating broadcasts might help people to understand more and have better environmental friendly behavior. As a study found that better information can make separation and recycling behavior easier.

REFERENCES

- [1] Chesoh, S. 2011. Environmental Impact Assessment of Power Development Project: Lessons from Thailand Experiences, Asian Social Science, Vol. 7, Issues 9, pp 119-123.
- [2] Chompunth, C. 2017, Role of Public Participation in Environmental Impact Assessment in Thailand. International Journal of GEOMATE, May, Vol.12, Issue 33, pp.109-113.
- [3] Peeraya. V, Chamlong. P, and Chutarat. C. 2014. Local Authority's Solid Waste Management: A Case Study of Muangklang Municipality, Rayong Province. Journal of Environmental Management. Vol. 10, Issues 2, 71-81.
- [4] Lamboglia R., Raffaele F., Mancini D. and S. Garzella, 2018. From a waste crisis to sustainability strategies: The case study of Naples' waste collection firm, Journal of Cleaner Production, Vol. 186, Issue 10, pp. 726-735.
- [5] Lee W. H. and J. Morris Chang, 2004, A waste collection policy based on empirical behavior, Information Sciences, Vol. 167, Issue 1-4, pp. 129-146.
- [6] Kinnaman T. C. and D. Fullerton, 2000. Waste and Recycling with Endogenous Local Policy, Journal of Urban Economics, Vol. 48, Issue 3, pp. 419-442.
- [7] Fujita S. and H. Tamura, 2004. Life Cycle Management for Selecting the Way of Disposing Domestic Kitchen Waste, IFAC Proceedings Volumes, Vol. 37, Issue 11, pp. 109-114.
- [8] Putters K., 2005, HIA, The next step: Defining models and roles, Environmental Impact Assessment Review, Vol. 25, Issues 7-8, 2005, pp. 693-701.

MECHANICAL PERFORMANCE OF ABACA-GEOPOLYMER COMPOSITE EXPOSED TO ELEVATED TEMPERATURES

Roy Alvin J. Malenab¹ and Michael Angelo B. Promentilla^{1,2}

¹Gokongwei College of Engineering, De La Salle University, Philippines; ²National Research Council of the Philippines, Philippines

ABSTRACT

Geopolymer binders are the most promising green alternative to ordinary Portland cement due to their demonstrated “good to superior” mechanical and thermal properties, chemical and fire resistance, among others. However, the use of geopolymer in several applications is being limited because of its brittle nature. In this study, samples of fly ash based geopolymer reinforced with fixed dose of chemically modified waste abaca fibers cured at different temperatures were synthesized and characterized in terms of compressive and flexural strengths. Then experimental short-term thermal endurance of select composites was employed. Composites gained compressive strength after exposure to 200°C while retained its room-temperature compressive strength when exposed further up to 600°C. Furthermore, results indicated that flexural strength decreases with increasing exposure temperature. Scanning electron microscopy analyses were also performed to examine the microstructure of the geopolymer matrix and to investigate the failure mechanism in the fiber-geopolymer composite before and after exposure to elevated temperatures.

Keywords: Geopolymer, Natural fiber, composite

INTRODUCTION

Geopolymer is a new class of ceramic-like inorganic polymer material composed primarily of tetrahedral silica and alumina which are formed through the reaction of aluminosilicate ions under the presence of an alkali activator resulting into hardened 3-D molecule networks [1]. These materials are more ecologically friendly compared to ordinary Portland cement (OPC) since geopolymerization of precursors from natural source or industrial solid residues does not release carbon dioxide during the low temperature reaction [2]. In addition, geopolymer binders exhibit rapid development of good to excellent mechanical strength and superior resistance to heat, fire and acid [3],[4],[5],[6]. Furthermore, the abundance of aluminosilicate raw materials makes geopolymer a low cost option as main component of many building materials [7].

Similar to conventional OPC-based construction materials, however, geopolymer exhibits brittle behavior with low tensile strength and is sensitive to cracking that impose constraints in structural design and affects the long-term durability of structures [8],[9]. To overcome these limitations, different fibers have been used to reinforce geopolymer cementitious materials [10] ranging from high cost, high strength metal oxide or silicon carbide fibers to low cost, abundant and renewable natural fibers [7]. Recently, plant or cellulosic fibers are becoming more attractive reinforcement than synthetic fibers because of their natural abundance, low cost, low

density, good mechanical properties, nontoxicity, etc. [11],[12],[12],[13].

In general, geopolymers are known to perform better than the conventional concretes made with OPC in fire, due to their ceramic-like properties [14],[15] that led to its applications as fire resistance, refractory in the glass industry, thermal insulation and other uses requiring good performance at high temperatures [16]. Although geopolymer as binder and its composites have been well studied, there are limited published research assessing the effect of design parameters on the performance of these materials in terms of its fire resistance and responses to elevated temperatures [16],[17].

In this study, mechanical performance of geopolymer reinforced with untreated abaca fiber was assessed after exposure to different elevated temperatures. Structural and morphological changes in the composites were also studied.

MATERIALS AND METHODOLOGY

Materials

For the preparation of geopolymer matrix, fly ash from a coal-fired power plant in Bataan, Philippines was used as aluminosilicate source. Chemical composition of the fly ash, as determined by X-ray fluorescence (XRF) analysis, is given in Table 1. Based on ASTM specification, the coal fly ash is a class F fly ash or low-calcium fly ash having a total SiO₂, Al₂O₃, and Fe₂O₃ of 89.2% (more than 70%).

As-received sodium hydroxide (NaOH) micropearls to prepare 12M NaOH solution and commercial water glass solution (modulus = 2.5, 34.1% SiO₂, 14.7% Na₂O and 51.2% water by weight) were used to prepare the alkaline activator.

Residual abaca fibers used in this study were collected from abaca farms in Dumaguete City, Philippines. These were by-products of fiber extraction from plant source followed by segregation into commercial grades based on color and texture. Residual fibers are usually disposed as waste.

Table 1 Chemical composition of fly ash

Components	wt %
Fe ₂ O ₃	20.8
SiO ₂	43.2
CaO	4.5
Al ₂ O ₃	25.2
Others	5.8
Loss on ignition	2.5

Synthesis of Abaca Fiber Reinforced Geopolymer Composite Materials

First, fly ash and abaca fibers (99:1 by weight) was dry-mixed to ensure uniform fiber distribution. For every 1kg of fly ash-fiber mixture, 400g of alkaline activator, well-mixed 80g of water glass solution and 320g of 12 M NaOH solution [18], was required. The overall mass ratio of solids (fly ash and fiber) to activator was based from a previous study [19] to achieve a mixture with considerable compressive strength and good workability.

To prepare the composite, alkaline activator was poured into a bucket then fly ash and fibers were gradually added with mixing in between using a laboratory motorized hand-held mixer. Mixing was continued for about 15 minutes or until the mixture become homogenous. Water was added to attain the desired consistency. Then, the mixture was poured into 5 cm × 5 cm × 5 cm cube molds (for compressive strength test) and 5 cm × 5 cm × 18 cm bar molds (for flexural strength test). After 24 hours, samples were demolded and cured in the oven at 75°C for 46 hours. Then, samples were cured at ambient conditions in resealable plastic bags for 28 days before subjecting to various testing. Pristine geopolymer samples, i.e., with no abaca fiber reinforcement were prepared to serve as the reference material.

Exposure to Elevated Temperature

Specimens at age of 28 days at ambient conditions were exposed to different temperatures (200°C, 400°C and 600°C). The specimens were placed in a furnace and heated at constant heating rate of 10°C/min up to a desired temperature for two hours.

After that, the furnace was turned off while the specimens were allowed to cool down inside the furnace to room temperature.

Characterization

Compressive and flexural strengths of control specimen and those exposed to elevated temperatures were determined. For compressive strength testing, cured cubic samples were subjected to a constant stress rate of 0.25 MPa/s until failure. Flexural strengths or modulus of rupture of samples were obtained by three-point bending test at a constant stress rate of 0.25 MPa/s.

Fourier transform infrared (FTIR) spectroscopy and Scanning electron microscopy (SEM) analyses were also performed to examine the changes in structural and morphological characteristics of samples before and after exposure to high temperatures.

RESULTS AND DISCUSSION

Mechanical Properties

Compressive and flexural strength results before and after temperature exposure of pristine and fiber-reinforced geopolymer specimens are summarized in Fig. 1 and Fig. 2, respectively. Figure 1 shows the similarity in compressive strength progression between the pristine and fiber-reinforced geopolymers. Prior to thermal exposure, compressive strength of pristine geopolymer (45.2 ± 7.6 MPa) is higher than that of fiber-reinforced (28.0 ± 2.9 MPa). After exposure to 200°C, both pristine and reinforced samples gained up to 23 MPa and 15 MPa increase in compressive strength, respectively. However, both samples decreased in compressive strength after exposure to 400°C while almost no further strength losses when exposed at 800°C were observed for both samples.

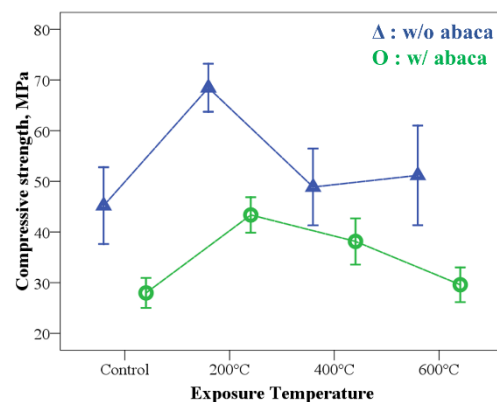


Fig. 1 Compressive strength of pristine and abaca fiber reinforced geopolymer.

As presented in Fig. 2, pristine and fiber-

reinforced geopolymer samples showed slightly different tendency in flexural strength evolution after exposure to elevated temperatures. Room-temperature flexural strength of fiber-reinforced geopolymer (3.7 ± 0.4 MPa) is higher when compared to unreinforced samples (2.0 ± 0.2 MPa). After exposure to 200°C , flexural strength of fiber-reinforced geopolymer decreased to 2.1 ± 0.4 MPa. Further flexural strength loss (1.1 ± 0.6 MPa) was observed after exposure to 400°C while less pronounced decrease (0.5 ± 0.3 MPa) was detected after thermal exposure to 600°C .

Flexural strength of pristine geopolymer also decreased from 2.1 ± 0.2 MPa to 0.9 ± 0.4 MPa after exposure to 200°C . No changes in flexural strength were detected after subjecting the samples to higher temperatures up to 600°C . It can be observed that flexural strength of pristine and fiber reinforced geopolymers are almost the same after exposure to 400°C and 600°C .

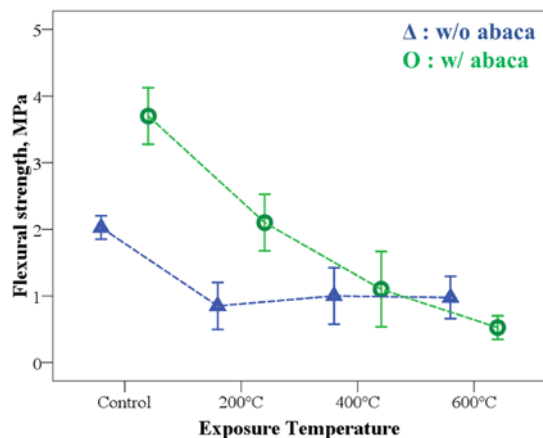


Fig. 2 Flexural strength of pristine and abaca fiber reinforced geopolymer.

Strength losses can be associated to the degradation of the geopolymer matrix. Similar to OPC-based materials, geopolymer degradation mechanism can be categorized into three: 1) thermal incompatibility, 2) pore pressure effect and 3) phase transformation [20]. These could explain the decrease in compressive strength of pristine and fiber-reinforced geopolymers when exposure temperature from 200°C to 400°C and decrease in flexural strength after exposure to 200°C . Degradation of the fiber in the geopolymer composite could also contributed to the observed strength losses within the temperature range of exposure. Based on thermogravimetric studies, thermal degradations of the different components of plant fiber such as abaca range from 160°C to 500°C [18],[21],[22].

Increase in strength of geopolymers after thermal exposure are reported in literature [20],[23]. In this study, pristine and fiber-reinforced geopolymer gained compressive strength after exposure to 200°C .

This could be explained by further geopolymerization of unreacted fly ashes and/or sintering process [20].

FTIR analysis can provide important information on the geopolymerization from solid precursors involving complicated chemical processes. Figure 3 shows the spectra of fly ash and geopolymer samples exposed to elevated temperatures. The major IR characteristic bands of geopolymeric specimens from various systematic investigations are given in Table 2. The spectrum of fly ash shows broad peaks ($1,100$ and $1,015\text{ cm}^{-1}$) due to glassy or amorphous nature and heterogeneity of fly ash [24]. Significant spectral differences can be observed between the fly ash and geopolymer samples. The Si-O-T (T is either Si or Al) at $1,100\text{ cm}^{-1}$ of the fly ash shifted to a lower wavenumber ($1,070\text{ cm}^{-1}$) in the different geopolymer samples indicating alkali activation or reaction products of fly ash and alkali activator were formed. Reduction in shoulder due to increasing intensity of this peak was also observed and most noticeable for geopolymer exposed at 400°C (inset of Fig. 3) while became flatter at 600°C . For the other peak at $1,015\text{ cm}^{-1}$, shifting to a lower wavenumber was not observed however compared to fly ash, the peak becomes sharper in the control or unexposed to high temperature sample. Its intensity decreased with exposure temperature. New peaks at 795 cm^{-1} , 690 cm^{-1} and 615 cm^{-1} appeared corresponding to other Si-O, Al-O and ring vibrations.

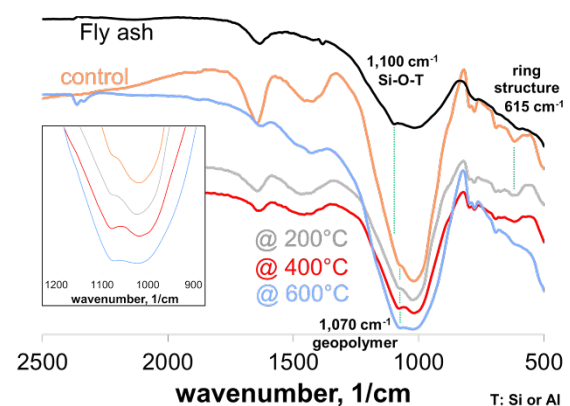


Fig. 3 FTIR spectra of unexposed (control) and after exposure to elevated temperature geopolymer samples.

The good to excellent compressive strength of geopolymer is due to its 3D aluminosilicate structure as already pointed in numerous studies [25],[26],[27]. The observed gain in compressive strength of samples exposed at a certain temperature (200°C) can be explained by further geopolymerization of partially polymerized aluminosilicate species [28]. It is also possible that as water molecules were evaporated from the geopolymer matrix, dissolved species exceeded its solubility limit, thus further precipitation

happened that resulted to increase in strength [29]. These are supported by the changes in IR spectra from $1,070\text{ cm}^{-1}$ to $1,015\text{ cm}^{-1}$ wavenumber for further geopolymerization and at around $1,640\text{ cm}^{-1}$ wavenumber for the water evaporation. In addition, sintering of geopolymer at elevated could also contributed to strength gain [20]. In contrary, exposure to higher temperature could destroy geopolymer backbone due to thermal incompatibility resulting to decline in strength. The overall compressive strength progression observed in this study could be due to combined effects of the these processes [20].

Table 2 IR characteristic band of geopolymers.

Wavenumber cm^{-1}	Assignment	References
1,640	water	[30]
1,425	sodium carbonate	[31],[32]
1,070-1,015	Si-O-T asymmetric stretching vibration	[24],[29],[32]
795	Si-O-Si vibration	[29]
	AlO_4 stretching	[30]
690	3-unit ring vibration	[33]
615	6-unit ring vibration	[33]

Scanning electron images of fractured control (not exposed to elevated temperature) and exposed to 400°C are shown in Fig. 4. The enhancement of flexural strength of fiber reinforced geopolymer composite is due to good interaction between the matrix and fiber as shown in the SEM image (Fig. 4a). In fact, some geopolymeric particles were deposited on the fiber surface. Fiber pullout and fiber fracture possibly control the failure mechanism of the composite. Compared to the fiber in the control sample, after exposure to 400°C , damages to fibers were observed as shown in Fig. 4b. This could explain the decrease in flexural strength of the fiber reinforced geopolymers exposed up 600°C . In fact at 400°C and 600°C exposure, flexural strength of pristine and fiber reinforced specimens are almost the same, thus, fibers are no longer functioning as reinforcements.

CONCLUSION

This study evaluated the compressive and flexural strengths of fiber reinforced geopolymer composites before and after exposure to elevated temperature up to 600°C . The pristine and fiber reinforced samples gained compressive strength after exposure to 200°C and eventually returned to its original strength when exposed up to 600°C . This was due to combined effect of further geopolymerization

followed by degradation as result of the thermal contact experienced by the matrix based on FTIR analysis. The observed improvement in flexural strength between control pristine and reinforced geopolymers was associated to good adhesion between the fibers and geopolymer matrix. However due to excessive removal of water from the composite and thermal degradation of fiber, flexural strength declined continuously after exposure from 200°C to 600°C . Chemical treatment of matrix and/or fiber may delay or prevent this phenomenon to sustain the reinforcing objective of the synthesized composite.

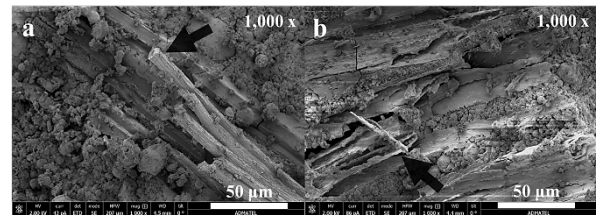


Fig. 4 SEM images of a) control and b) exposed to 400°C fiber reinforced geopolymer composites.

ACKNOWLEDGEMENTS

This research was financially supported by the National Research Council of the Philippines (NRCP), Philippine Council for Industry, Energy and Emerging Technology Research and Development (PCIEERD), Advanced Device and Materials Testing Laboratory (ADMATEL) and Electronics Product Development Center (EPDC). The authors would like to acknowledge the following for their contribution to this study: Ms. Patricia Isabel K. Bravo, Antonio L. Kalaw, Bernardo B. Bernardo, Zachary Cole L. Ang, Don Angelo V. Joson I, Gian Dominic C. Mercado, Ramon Tirso Manuel A. Santillan and Jedwig Siegfried S. Tan.

REFERENCES

- [1] Davidovits, J. Geopolymer Chemistry and Applications. Vol. 171, 2008
- [2] Turner, L. K. and Collins, F. G. Carbon Dioxide Equivalent ($\text{CO}_2\text{-e}$) Emissions: A Comparison between Geopolymer and OPC Cement Concrete. Construction and Building Materials Vol. 43, 2013, pp. 125–130.
- [3] Jaarsveld, J. G. S. Van, Deventer, J. S. J. Van, and Lorenzen, L. The Potential Use of Geopolymeric Materials to Immobilise Toxic Metals: Part I. Theory and Applications. Minerals Engineering Vol. 10, Issue 7, 1997, pp. 659–669.
- [4] Zhang, T., Gao, P., Gao, P., Wei, J., and Yu, Q. Effectiveness of Novel and Traditional Methods to Incorporate Industrial Wastes in Cementitious

- Materials - An Overview. Resources, Conservation and Recycling Vol. 74, 2013, pp. 134–143.
- [5] Rios, S. , Ramos, C. , Fonseca, A. V. Da , Cruz, N. , and Rodrigues, C. Colombian Soil Stabilized with Geopolymers for Low Cost Roads. *Procedia Engineering* Vol. 143, Issue 1ctg, 2016, pp. 1392–1400.
- [6] Yankwa Djobo, J. N. , Elimbi, A. , Kouamo Tchakouté, H. , and Kumar, S. Mechanical Properties and Durability of Volcanic Ash Based Geopolymer Mortars. *Construction and Building Materials* Vol. 124, 2016, pp. 606–614.
- [7] Musil, S. S. , Keane, P. F. , and Kriven, W. M. Green Composite: Sodium-Based Geopolymer Reinforced with Chemically Extracted Corn Husk Fibers. *Developments in Strategic Materials and Computational Design IV* 2013, pp. 123–133.
- [8] Sakulich, A. R. Reinforced Geopolymer Composites for Enhanced Material Greenness and Durability. *Sustainable Cities and Society* Vol. 1, Issue 4, 2011, pp. 195–210.
- [9] Yang, T. , Han, E. , Wang, X. , and Wu, D. Surface Decoration of Polyimide Fiber with Carbon Nanotubes and Its Application for Mechanical Enhancement of Phosphoric Acid-Based Geopolymers. *Applied Surface Science* Vol. 416, 2017, pp. 200–212.
- [10] Chen, H. *Biotechnology of lignocellulose: Theory and practice*. 2014.
- [11] Mohammed, L. , Ansari, M. N. M. , Pua, G. , Jawaid, M. , and Islam, M. S. A Review on Natural Fiber Reinforced Polymer Composite and Its Applications. *International Journal of Polymer Science* Vol. 2015, 2015, pp. 1–15.
- [12] Yan, L. , Kasal, B. , and Huang, L. A Review of Recent Research on the Use of Cellulosic Fibres, Their Fibre Fabric Reinforced Cementitious, Geo-Polymer and Polymer Composites in Civil Engineering. *Composites Part B: Engineering* Vol. 92, 2016, pp. 94–132.
- [13] Reinforced Geopolymer Composites: A critical review.
- [14] Bakharev, T. Geopolymeric Materials Prepared Using Class F Fly Ash and Elevated Temperature Curing. *Cement and Concrete Research* Vol. 35, Issue 6, 2005, pp. 1224–1232.
- [15] Ahmed, S. F. U. *Fibre-reinforced geopolymer composites (FRGCs) for structural applications*. Woodhead Publishing Limited: 2014.
- [16] Bernal, S. A. , Bejarano, J. , Garzón, C. , Gutiérrez, R. M. De , Delvasto, S. , and Rodríguez, E. D. Composites: Part B Performance of Refractory Aluminosilicate Particle / Fiber-Reinforced Geopolymer Composites. *Composites Part B* Vol. 43, Issue 4, 2012, pp. 1919–1928.
- [17] Kong, D. L. Y. and Sanjayan, J. G. Damage Behavior of Geopolymer Composites Exposed to Elevated Temperatures. *Cement and Concrete Composites* Vol. 30, Issue 10, 2008, pp. 986–991.
- [18] Malenab, R. , Ngo, J. , and Promentilla, M. Chemical Treatment of Waste Abaca for Natural Fiber-Reinforced Geopolymer Composite. *Materials* Vol. 10, Issue 6, 2017, pp. 579.
- [19] Kalaw, M. E. , Culaba, A. , Hinode, H. , Kurniawan, W. , Gallardo, S. , and Promentilla, M. A. Optimizing and Characterizing Geopolymers from Ternary Blend of Philippine Coal Fly Ash, Coal Bottom Ash and Rice Hull Ash. *Materials* Vol. 9, Issue 7, 2016.
- [20] Pan, Z. , Sanjayan, J. G. , and Rangan, B. V. An Investigation of the Mechanisms for Strength Gain or Loss of Geopolymer Mortar after Exposure to Elevated Temperature. *Journal of Materials Science* Vol. 44, Issue 7, 2009, pp. 1873–1880.
- [21] Jabbar, A. , Militký, J. , Wiener, J. , Javaid, M. U. , and Rwawiire, S. Tensile, Surface and Thermal Characterization of Jute Fibres after Novel Treatments. *Indian Journal of Fibre and Textile Research* Vol. 41, Issue 3, 2016, pp. 249–254.
- [22] Zhang, J. , Feng, L. , Wang, D. , Zhang, R. , Liu, G. , and Cheng, G. Thermogravimetric Analysis of Lignocellulosic Biomass with Ionic Liquid Pretreatment. *Bioresource Technology* Vol. 153, 2014, pp. 379–382.
- [23] Kong, D. L. Y. and Sanjayan, J. G. Effect of Elevated Temperatures on Geopolymer Paste, Mortar and Concrete. *Cement and Concrete Research* Vol. 40, Issue 2, 2010, pp. 334–339.
- [24] Rees, C. A. , Provis, J. L. , Lukey, G. C. , and Deventer, J. S. J. Van In Situ ATR-FTIR Study of the Early Stages of Fly Ash Geopolymer Gel Formation. *Langmuir* Vol. 23, Issue 17, 2007, pp. 9076–9082.
- [25] Davidovits, P. J. 30 Years of Successes and Failures in Geopolymer Applications . *Market Trends and Potential Breakthroughs . Geopolymer 2002 Conference* 2002, pp. 1–16.
- [26] Duxson, P. , Fernández-Jiménez, A. , Provis, J. L. , Lukey, G. C. , Palomo, A. , and Deventer, J. S. J. Van Geopolymer Technology: The Current State of the Art. *Journal of Materials Science* Vol. 42, Issue 9, 2007, pp. 2917–2933.
- [27] Provis, J. L. and Deventer, J. S. J. *van Alkali Activated Materials*. 2014.
- [28] Pan, Z. and Sanjayan, J. G. An Investigation of the Mechanisms for Strength Gain or Loss of Geopolymer Mortar after Exposure to Elevated Temperature. 2009, pp. 1873–1880.
- [29] Lee, W. K. W. and Deventer, J. S. J. Van Use of Infrared Spectroscopy to Study Geopolymerization of Heterogeneous Amorphous Aluminosilicates. *Langmuir* Vol. 19,

- Issue 21, 2003, pp. 8726–8734.
- [30] Palomo, A. , Grutzeck, M. W. , and Blanco, M. T. Alkali-Activated Fly Ashes: A Cement for the Future. *Cement and Concrete Research* Vol. 29, Issue 8, 1999, pp. 1323–1329.
- [31] Barbosa, V. F. F. , MacKenzie, K. J. D. , and Thaumaturgo, C. Synthesis and Characterisation of Materials Based on Inorganic Polymers of Alumina and Silica: Sodium Polysialate Polymers. *International Journal of Inorganic Materials* Vol. 2, Issue 4, 2000, pp. 309–317.
- [32] Fernández-Jiménez, A. , Palomo, A. , and Criado, M. Microstructure Development of Alkali-Activated Fly Ash Cement: A Descriptive Model. *Cement and Concrete Research* Vol. 35, Issue 6, 2005, pp. 1204–1209.
- [33] Criado, M. , Fernández-Jiménez, A. , Palomo, A. , Sobrados, I. , and Sanz, J. Effect of the SiO₂/Na₂O Ratio on the Alkali Activation of Fly Ash. Part II: ²⁹Si MAS-NMR Survey. *Microporous and Mesoporous Materials* Vol. 109, Issue 1–3, 2008, pp. 525–534.

ON THE IMAGE BASED ON SMART PHONE USERS IN PUBLIC SPACE

¹Yuki Ogimoto and ²Kazunari Tanaka

¹Engineering, Osaka Institute of Technology, Japan; ²Engineering, Osaka Institute of Technology, Japan

ABSTRACT

The purpose of this study is to find the relationship between the characteristics of space and pedestrian features, grasp the relationship between the place of daily, everyday actions, including mobile phone usage action and the image of the surrounding space. It is ultimately to design by taking human behavior into consideration human behavior. The authors extract external factors that appear to be affecting people. Furthermore, the authors will calculate specific figures and analysis them. Analysis is made on the relationship between the elements of the spatial shape extracted by the physical survey, by the image analysis as well as human attributes. The survey was conducted in the open space around Osaka station. The author found that the mobile phone operation position is different depending on the state at the time of usage. Currently, we chose a place where smartphones are easy to use. And it is the where people are trying to capture the future visually. Future developments will capture changes in the field of vision. From there, is to select a place where there is a high necessity for maintenance.

Keywords: mobile phone, pavement, open space, public space

INTRODUCTION

The purpose of this research is to design pavement taking pedestrians into consideration, especially the elderly, which is the fastest growing age group. In recent years, It is considered that the walking path of people is changing due to the design of sidewalks and the walking environment. By analyzing the elements of the spatial shape, The authors believe that the authors can utilize this for urban planning, by clarifying the route according to individual's age. In previous studies, walkability tests and analysis were performed for each type of pavement. There are few studies on public spaces. If it is possible to grasp the respective walking route by attributes such as age group, then this can lead to improve functional design universally. Designers are trying to create space that various people can use easily. However, there are actually various aspects to consider for design.

PURPOSE AND METHOD OF RESEARCH

The authors find the relationship between the characteristics of space shape and pedestrian features, grasp the relationship with the place of each action and the shape of the surrounding space. It is ultimately best to propose a design taking into consideration human behavior.

In this research, the authors will quantitatively find the influence of invisible design, utilizing physical and pedestrian behavior data obtained from a field survey.

Ultimately, the authors will refine it to detailed

analysis that finds how space design affects pedestrian influence, while acquiring a large amount of pedestrian behavior data. In order to grasp and express the influence of the spatial shape and the influence range. The authors extract external factors that are appear to be affecting people. Furthermore, the authors will specific figures and analyze them, Analysis is made on the relationship between the elements of the spatial shape extracted by the survey and human attributes.

POINT OF INTEREST

In conducting this research, the author focuses on mobile phones and public spaces. Currently, mobile phones are spreading globally. With the advent of smartphones from 2010, it became indispensable to our daily lives. The graph shows the penetration rate of communication terminals in Japan (Figure 1).

However, due to mobile phones accidents are also occurring.

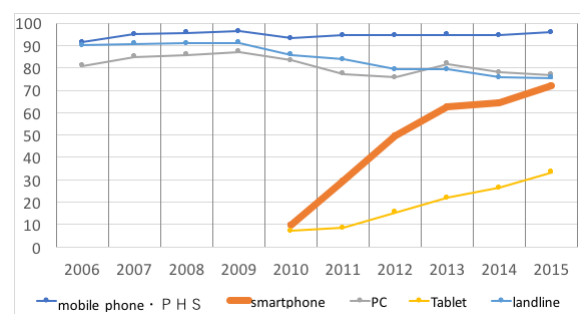


Fig. 1 Japanese communication terminal of Penetration
TARGET AREA

For the target area, the authors wanted to use a space that had various features common in public places such as; pillars, walls, stairs, monuments etc.

Osaka is one of the central urban areas in Japan. The number of tourists is the highest every year, centered on Osaka, many tourist attractions are adjacent. Therefore, it was targeted around Umeda, which is considered to be one of the center areas in Osaka (Figure 2,3).

In this research, the authors will cover a space used mainly by pedestrians. A preliminary survey was conducted in the open space around Osaka station, and a place considered to be similar was set as the target site. In addition, this survey is a place with many railway stations.



Fig. 2 People flow at the osaka station

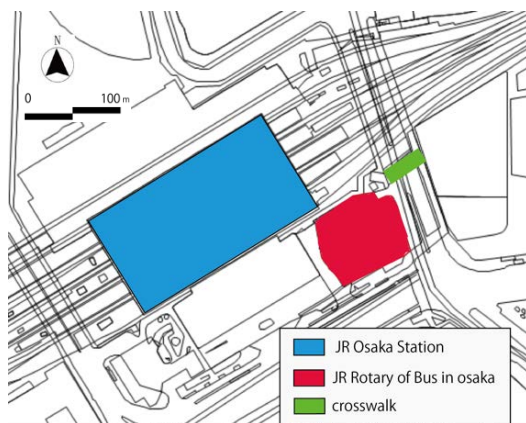


Fig. 3 Target Area

INVESTIGATION AND ANALYSIS

In this research, I can know the usage situation by find places where mobile phones are used. For that

purpose, we photo shooting at the target location.

INVESTIGATION (1)

First, the authors took the photos to capture the location and constituent elements of the people standing around, then plotted this on GIS (Figure 4,5).

The one shown in the figure shows the operator of the smartphone and the non-operator of the smartphone. The shooting point is indicated by a 60 degree cone. The survey summary is shown in the table (Table 1).

Table 1 Survey summary

Schedule	2017 August 30 (Wednesday), September 1 (Friday)
Time frame	8: 20 - 9: 00
weather	Cloudy weather
Target area	osaka station around in osaka
Method	photo shooting

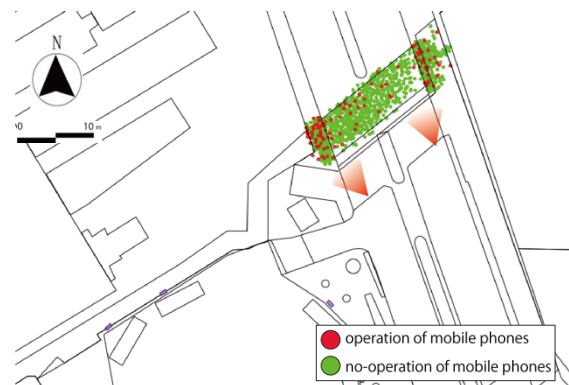


Fig. 4 Position of people focusing on the operation of mobile phones (crosswalk)



Fig. 5 Position of people focusing on the operation of mobile phones (Bus Rotary)

RESULT (1)

Next, from the obtained results, we calculated where people concentrate (Figure 6). The method of analysis was done by density estimation. The red part shows a high numerical value. This method can reduce the error in the case of representing the concentrated part of the person. This has been proved by a previous study [3].

In addition, there were two types of behavior for people who operate mobile phones. The first one is operates without walking the mobile phone. The second is operating a mobile phone while walking .

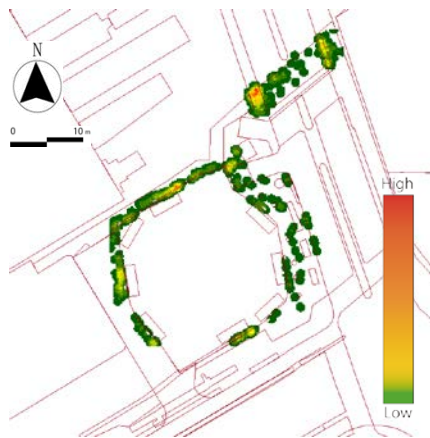


Fig. 6 This is the example for figure formatting

ANALYSIS (1)

Based on the above result, we analyzed the two kinds of behavior of the person who operates the mobile phone separately. The method was carried out at the same point density as before.

The place which shows the high numerical value of the first graph is in front of the pedestrian crossing (Figure 7). Also, the place which shows the high numerical value of the second graph is also the pedestrian crossing (Figure 8).



Fig. 7 operates without walking the mobile phone

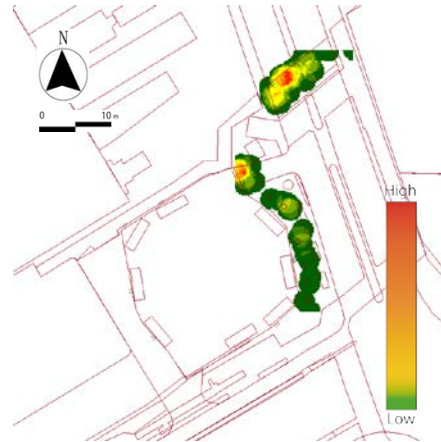


Fig. 8 operating a mobile phone while walking

CONSIDERATION

The results commonly showed that the place of the pedestrian crossing was high. Therefore, the author considers it necessary to investigate the location of the pedestrian crossing in detail.

INVESTIGATION (2)

The purpose of this survey is for detailed analysis of pedestrian crossings.

The outline of the survey is shown in the table (Table 2). The survey method is movie shooting at people. The shooting time was 1 minute and 40 seconds. It is 1 minute 30 seconds between the red signal and 10 seconds of the blue signal.

Also, the author did this survey three times.

Table 2 Survey summary

Schedule	2017 August 23 (Wednesday)
Time frame	8: 30 - 9: 00
weather	Cloudy weather
Target area	crosswalk
Method	Movie shooting

RESULTS (2)

The results are shown in the figure. In this figure, the authors pointed to the person who operates the mobile phone and the person who does not operate the mobile phone (Figure 9)[2].

The author will compile those results.



Fig. 9 People flow at the osaka station

Table 3 Operators of mobile phones in crosswalks

Contents	Number of people
Operator of mobile phone	145
Non-operator of mobile phone	370
Total number of two	515

ANALYSIS (2)

From the calculated result, the proportion of people who operate mobile phones while walking was calculated (Table 4). All proportions were calculated based on the number of pedestrians caught in the vicinity of the pedestrian crossings. The purpose of this analysis is to clarify, as manipulation of mobile phones while walking is becoming a social problem.

Table 4 Percentage of operators of mobile phones at pedestrian crossings

Contents	Proportion(%)
Operator of mobile phone (515)	28.2
People who start to operate mobile phones while walking(515)	13.0
Percentage of mobile phone operators walking smashing (145)	46.2

DISCUSSION

The place to operate the smartphone is a place to forcibly stop walking.

Therefore, it is considered to be a place where pedestrians make time to operate mobile phones.

At the present stage, I studied weekday. However, the attributes of people change on holidays. Therefore, if you investigate holidays as well, you can design suitable for the city.

CONCLUSION

In this research, the authors focused attention on pedestrians in public spaces in the city and observed and analyzed them. From the survey, we were able to grasp those who used cell phones in public spaces.

In addition, analysis clarified where it concentrates. When touching a mobile phone at a pedestrian crossing, 46.2% of the people found that they used the mobile phone while walking. The above results were discussed.

REFERENCES

- [1] Maeda K., Higa K., Tanaka K. and Yosikawa S Civil Engineering Association Kansai Branch Annual Scientific Lecture Summary IV-19 2015
- [2] Yanobe T., Tanaka K and Yoshikawa S, STUDY DOWNTOWN STVANGER TO THE PEDESTRIAN SPACE 25.A-3-3(CD)
- [3] Sato T. and Maruyama T., Analyzing Visitors' Activity Area in Downtown Kumamoto using Smartphone-based Travel-Survey Date Journal of the City Planning Institute of Japan, Vol.50 No.3 2015 October .
- [4] Yogo Y., Hayashida K. and Watanabe H., Spatial usage behavior by age in station concourse 2012 pp651 ~ pp652
- [5] E.FUNABIKI N.MATUMOTO I.KATAYAMA elationship between visitor behaviour at“Eki Naka Squares” and spatial composition. — Comparison of JR Tokyo Station Marunouchi North Exit Concourse and JR Sapporo Station West Concourse—
- [6] Kabata A., Oonishi R. and Yamaguchi K., Migration characteristics of rental cycle in Kyoto city sightseeing using GPS log data - For foreign tourists – Proceeding of city planning No16 2018 p37-40
- [7] AIHARA K., Grasping dynamism of tourist behavior and thoughts through big data analysis JOHO KANRI Vol.59 No11 February 2017

IMAGE ANALYSIS ON NIGHT SEQUENTIAL IMAGES

Hiroki Komai¹ and Kazunari Tanaka²

¹Engineering, Osaka Institute of Technology, Japan; ²

ABSTRACT

Night scape has a beauty that attracts people. In recent years, due to the spread of cameras and SNS, there are many new trends and new popular spots. As a byproduct, this seems to attract tourist. In this research, the characteristics of the night scape were analyzed using the photos and post contents from SNS. As a result, by the analysis to evaluate a part of the values, the examples: the perseverance, the painfulness and the merriment are appeared of the night scape.

Keywords: Image analysis, Night scape, SNS

INTRODUCTION

N Night scape attracts a lot of people regardless of race, gender, generation. It is a visual stimulus that brings healing to modern people who have various stresses in modern society. The night scape has an ability to allow one to collect themselves. In recent years, popularization of smartphones and digitization of cameras has progressed, giving many people easy access to cameras that are now high performance. At the same time, information exchange platforms of SNS (social network service) have become popular. It became possible to “share” one’s information or “moments” with unspecified numbers of people. SNS leads trends and when people shoot a night scape with their camera and post it to SNS the post receives a lot of attention and that location becomes a popular night scenic spot. That popular night scenic spot is then sought after by tourists which leads to increased regional revitalization. It is indispensable to focus attention on people’s consciousness to find a characteristic night scape.



Fig. 1 Night scape

PURPOSE AND METHOD

In this research, we aim to grasp what kind of emotion people feel from a night view. This insight into emotion should become a clue for the characteristics of an optimal night view.

For the research method, we collected lyrics from songs related to nightscape photos and night scenes.

After that, analyze classification and characteristics of nightscape photograph and analyze the lyrics.

Next, we retrieve words obtained by analysis of collected lyrics and classify them.

Finally, from the relationship between the analysis result of the night scape photograph and the words obtained by the lyrics analysis, we analyze the image of the nightscape picture and make conclusions.

HOW TO COLLECT PICTURES

Flickr is a photo posting site from overseas boasting the most photos posted in the world. In Flickr, registered users can freely classify photos in Flickr with keywords called “tags”. In addition, each user has a function to create a “set” in which thumbnails of a plurality of photos are arranged in the same title on their respective top page. The sets here are more flexible than the traditional file sorting method, it is possible to put one picture in multiple sets or not in any set. In this way, it is easy to classify and search pictures, as the relationship between pictures and words has an SNS-like aspect.

Furthermore, Flickr has released its own API (Application Programming Interface), allowing applications to “mash up” with SNS.

In this research, we selected Flickr as a photo collection site.

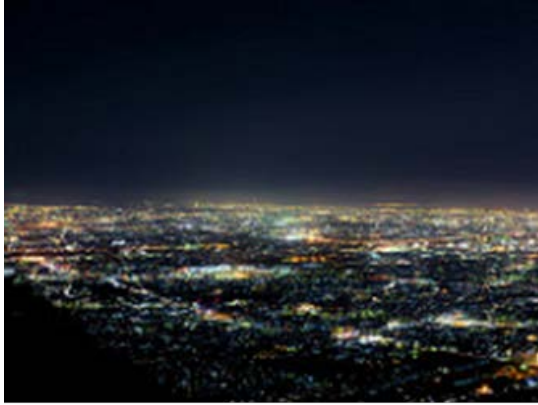


Fig. 2 Examples of pictures collected using Flickr

COLLECTING NIGHT SCAPES PICTURES

In this research, we analyzed images of night scenery searching photos with “night view” tags. However, there are enormous amounts of photographs taken from countless nightscape spots making it difficult to analyze all of them. Therefore, in this research, we selected nightscape spots and targeted nightscape photographs taken within them.

Night scene spots were targeted at 26 places with reference to the website. After that, we collected photographs of the target night scenic spots and sorted out pictures other than night scenes. Then, six target night spot spots where the ratio of the total number of searches and night view photos exceeded 30% were taken as the target of this study.

Table 1 Percentage of target spot and night view photo

place	percentage(%)
Mount Hiei driveway	7.6
Mount OIwa view place	0.0
Mount Mandoro observatory	100.0
Abeno harukasu	13.8
Seaside cosmos	23.1
Umeda sky building	11.2
Orix Honmachi building	15.2
Mount Satsuki driveway	-
Izumotsu parking area	56.1
Jusou Pass observatory	-
Kanku outlook hall	7.6
Hannan sky town	50.0
Mount Maya	33.6
Rokkou garden terrace	6.5
Mount Rokkou observatory	-
Mount Nadamaru park	27.3
Maiko park	6.5
Kobe port tower	7.8
Venus village	37.8
Port Island north park	66.0
Itami sky park	4.1
Yamatedai north park	0.4
Awaji service area	5.9
Mount Wakakusa	2.2
Shigi Ikoma sky line	25.0
Saisyogamine view place	-

COLLECTION OF LYRICS

In this research, we use lyrics to analyze nightscape pictures. The lyrics to be used were for songs in which words related to night were included in lyrics out of a total of 280 songs by the ranking of sales each year from 1989 to 2016.

ANALYSIS OF LYRICS

In this research, text mining was used for lyrics analysis. Text mining is a method for discovering useful information from sentences.

It uses a method of natural language processing to extract bits from sentences by dividing sentences into words and phrases and statistically analyzing the occurrence frequency of words and the relationship between words. Therefore, text mining is considered to be an effective means for realizing the objective of analyzing a large amount of text data efficiently and objectively.

It can be divided into parts that categorize sentences by natural language processing and statistical analysis of categorized data. Therefore, in order to implement it, software that executes natural language analysis to separate sentences into words and software to perform statistical analysis are required. In the case of text mining software, there is software capable of performing both of these functions, and software only capable of categorizing the former sentences.

In this research, we analyzed lyrics using "IBM SPSS Text Analytics for Surveys" which categorizes sentences.

For lyrics of extracted songs, we extracted words expressing night scenes and adjectives and adverbs that psychologically evaluate them. Examples are shown in Table 1 and Table 2.

Table 2 Extraction of night scenery and psychology

Night scape word	Psychological words
city	get over(norikoeru),miracle(kiseki),Painful(tsurai),etc...
light	To watch over(mimamoru),To succeed(setsunaku),etc...
sky	happiness(siwase),break down(kowasu),To die(kareru),etc...
night sky	Important thing(taisetsunamono),Goodbye(sayonara)

Table 3 Extraction of night scenery and psychology

Night scape word	Psychological words
street light	severely
light	To watch over(mimamoru),To succeed(setsunaku),etc...
sky	happiness(siwase),break down(kowasu),To die(kareru),etc...
night sky	Important thing(taisetsunamono),Goodbye(sayonara)
bridge	To be sunny(harenu),My chest hurts(munegaitamu)
sea	break down(kowasu),to hug(dakisimeru),To die(kareru)etc...

EVALUATION OF NIGHT SCAPE PHOTOS THROUGH LYRICS

In this study, we have grasped the image of the night view photograph from the relationship between the constituent elements and lyrics expressing the psychology associated with the extracted night view photo. Here, the constituent elements of night scenes are taken out, and words of psychology evaluation are arranged in parallel for each.

RESULTS AND DISCUSSION

Analysis of nightscape photos and lyrics revealed that various emotions can be obtained from the night view. The results found that night scenery attracts people with its beauty, but also that a possibility that simply feeling that it is beautiful is only part of the surface layer. Table 2 and Fig. 3, and Table 3 and Fig. 4 correspond to each other. Starting with Table 2 and Fig. 3, it can be expressed that "a hardship must be overcome". With Table 3 and Fig. 4, it can be expressed as "I hope to focus on important things". From these analyzes and considerations, it turned out that people have various emotions, regardless of their consciousness, when looking at night views. There was also a tendency that positive and negative emotions coexisted with the photographs targeted this time. These provide suggestions on how to draw out the charm of the night view attracting people.

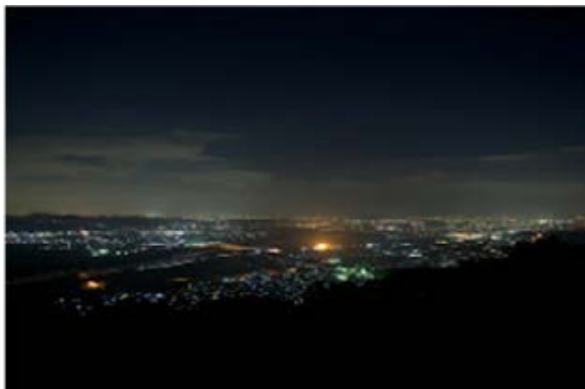


Fig. 3 Example 1 of analysis and consideration



Fig. 4 Example 2 of analysis and consideration

CONCLUSION

In this research, we tried grasping emotions and images obtained from night scenes using night view photos and lyrics. As a result, we think that we found one evaluation method of a characteristic night time landscape. Moreover, it was revealed that various emotions are obtained from the space constituent elements of night views. From this result, I think that we could grasp a part of the charm of the night view.

I think that discovering the attractiveness of night views using new indicators and methods will be significant in the future nightscape analysis. Moreover, we think that this could lead to the possibility of contributing to the creation of a characteristic night view.

REFERENCES

- [1] Hiroki T, Kazunari T, Shin Y , Boundary focusing on light environment in urban space , Civil Engineering Association Kansai Branch Annual Scientific Lecture Concert Summary, IV-14, 2013.
- [2] Yuji O, Kazunari T, Shin Y , Analysis and Evaluation of Landscape Based on Tourist Behavior, Geographical Information System Conference Presentation Proceedings, Vol. 26, 2017,C-1-2(CD).

ON THE SPATIAL ELEMENTS FROM A BIRD'S-EYE VIEW SCAPE

Nobuaki Tanaka¹, Kazunari Tanaka²

¹ Osaka Institute of Technology, University; ² Japan

ABSTRACT

When it comes to landscapes, beautiful landscapes are formed from local climates such as history and customs by elements such as varying nature and demographic structures. A feature that creates these beautiful landscapes is the linear landscape element. This linear element is characterized as being beautiful because landscape elements that can be continuously viewed form a beautiful landscape such as a building that looks continuous due to the shape and color, in addition to linear landscape elements such as rivers and roads. Hypotheses concerning continuity and image are present not only in urban landscapes, but also in the landscape of rural areas and mountainous regions. Therefore, in this research, focusing on a bird's eye view from high vantage points, we aim to examine urban landscapes by analyzing their elements, shape, view and area. As for the examination method, we analyzed and expressed the continuity of streets, rivers, green roads, etc., using image analysis and GIS. From the results, we extract and consider the relationship between the position and shape of elements with regards to continuity and the beauty of urban landscapes.

Keywords: High-rise building, Bird's eye view, Landscape, Continuity, Visibility analysis

INTRODUCTION

In Japan, there are various climates. There are places to enjoy beautiful scenery, such as views from a natural observation point such as a mountain, or a view from man-made point such as a bridge. The view from a mountain or high-rise building etc., provides a majestic landscape that people cannot see much in everyday life. The landscape from this altitude is called an "overhead view", which is important when viewing landscapes (Fig. 1).

Meanwhile, in recent years, various techniques have been used to capture attractive urban landscapes. A combination of elements such as arrangement and shape of buildings and trees etc., that is continuous is what forms a beautiful landscape. Sexuality is also one of the elements that directs the appeal of the landscape, for example, a sprawling grassland, the scenery of a city from the top of a mountain or the roof of a building, the continuous light in a night view, etc., all feel beautiful. Such continuity is important in forming a beautiful landscape because it is possible to view from various places and angles. We believe that future landscape design can be done by grasping the relationship between the continuity of the city, and the overlooking landscape.



Fig. 1 Picture of bird's eye view

PURPOSE

There are many places where we can see the urban landscape, for this research we focused on high-rise buildings. In Japan there are more than 500 buildings over 100m tall. Offices and condominiums are becoming taller, and it is becoming more common for people to view the urban landscape from a bird's eye view.

Also, beautiful urban landscapes are related to shapes and colors that are continuous. Hypotheses about continuity and image are established not only in the city, but also in the landscape of rural areas and mountainous areas. However, in general high-rise buildings are concentrated in big cities, and therefore, in some cases the buildings obstruct the view. Therefore, for this research it is crucial to be able to observe the unobstructed urban landscape from a bird's-eye view from a high-rise building in Osaka city, and subsequently examining the urban landscape by analyzing elements and shapes, view and areas.

METHOD

First of all, a questionnaire survey was conducted to grasp the relationship between the overhead view and the landscape elements in a linear direction. From the results, when looking at the city from a bird's-eye view, it was more attractive when the roads, rivers, and greens were linear as landscape elements. Taking this into account, we will discover where we can see many elements when looking at a target area. By analyzing the depression angle from the test building, we grasp how much we can see continuously from a

bird's-eye view.

INVESTIGATION

A questionnaire survey was conducted using the paired comparison method for the influence of continuity from an overhead view (Table 1). This investigation is a method of choosing which one is perceived as more attractive by showing two images. This time, we collected 10 pictures randomly taken from a high-rise building. From these images, we altered them by removing linear roads, rivers, and greens (Fig. 2~3). We had 20 of these images randomly arranged. The questionnaire date and time and target number of people are as shown in Table 1. The average of the questionnaire results was graphed (Fig. 2). Results showed that overall the landscape was considered more attractive when the linear elements exist. However, in the case of 1 and 8, the image without the linear landscape elements was more attractive. The reason for this is that in the case of 1, we believe that shadows affected the outcome. In the original image, the difference between light and dark is small, and in the created image, the created image is better because the light and dark areas are clear. In the case of 8, we thought that the miscellaneous townscape looked beautiful, thus making the created image more attractive.

Table 1 Outline of questionnaire survey

Target	Osaka Institute of Technology students 78 people
Date and time	9-May-18
Method	Questionnaire survey by pair comparison



Fig. 2 Original image

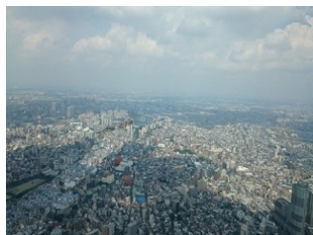


Fig. 3 Create image

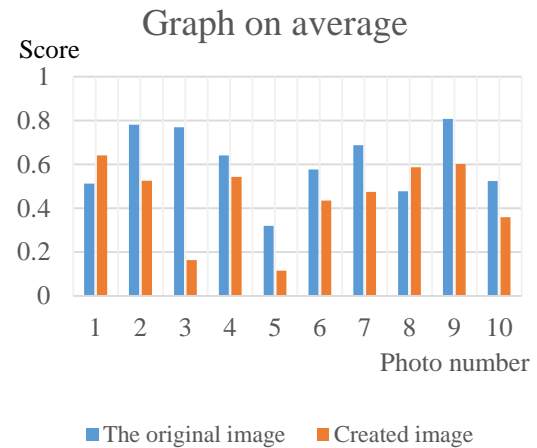


Fig. 4 Average value of the questionnaire result

In order to ascertain the validity of this result, a t-test was performed (Table 2). By conducting this test, it can be confirmed as to whether or not the given results were by chance. Since the absolute value of the t value is larger than the absolute value of the boundary value of the t value from the table, and the value of the p value is smaller than 0.05 even from the p value, there is some statistically significance between the two variables. This means that the difference between the average values cannot be said to be 0. Therefore, from this result it can be said that the more continuous the road, river, greenery etc., the more statistically significant and attractive the landscape. However, there were some results that did not have significance.

Table 2 Result of t test of 1 and 11

name	1	11
Average	0.51282051	0.64102564
Variance	0.25308025	0.23310023
Observed number	78	78
Pearson correlation	0.76777190	
Difference from hypothesized average	0	
degree of freedom	77	
t-ratio	-3.36504523	
P(T<=t) One side	0.00059788	
t Boundary value One side	1.66488454	
P(T<=t) both sides	0.00119575	
t Boundary value on both sides	1.99125440	

INVESTIGATION

The target area of this research is Osaka city. Osaka city has rivers that are wide and winding with rich greenery and parks along the banks, along with numerous buildings and structures. In addition, large-scale roads are stretched in a lattice pattern, and the landscape is formed taking into consideration the continuity of buildings and harmony between the roads and buildings (Fig. 3).



Fig. 5 Target area

SELECTION OF VIEWPOINT

We selected high-rise buildings as viewpoints. To do the selection, we use skyline possibility analysis from existing research[1]. The reason for using this analysis is that this analysis identifies the areas where you can see the skyline from various places. The area where the frequency of occurrence of skyline possibility is high is a boundary line that separates the ground from the sky, which can be said to be an obstacle or a noticeable object. On the contrary, when viewed from the building, you can see a wide range of landscapes. From this relationship you can see the area where urban space is regarded as a wide area landscape. To do this analysis, we created a 250m mesh DSM (Digital Surface Model) from existing research; Osaka city, which is the target area, has a generation range of about 20km square. Using this DSM, we identified a place where you can see a wide area overlooking the city of Osaka. The darker the blue color, the easier it is to view the skyline. As a result, it came out that the Osaka station neighborhood and Tennoji station would be high visibility. Narrowed further, Ebuchi Harukasu, a place with public nature was selected as an optimal location.

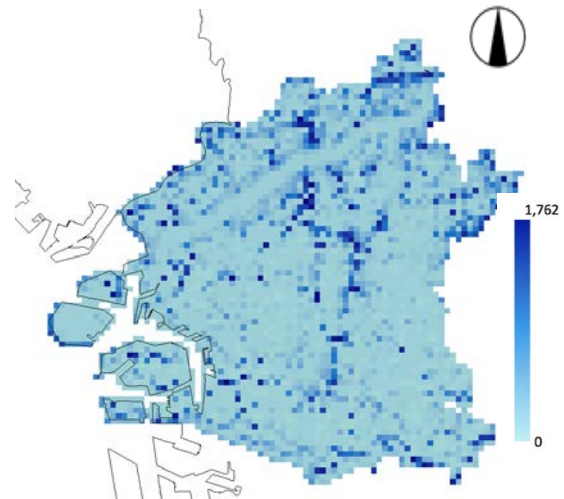


Fig. 5 Skyline possibility appearance distribution [1]

DEPRESSION ANALYSIS

Depression angle analysis was conducted in order to grasp the area that would be visible from a bird's-eye view from the selected building. The depression angle analysis was carried out using the DSM to grasp the overhead view that can be seen from each viewpoint, and the position of the point was set at a height of the observation platform (at 1.5m). As for the depression angle, we also verified the bird's-eye view from existing research and obtained quantitative analysis results (Figure 3). From this result it is possible to analyze at the lower limit of the depression angle of 30 ° or more.

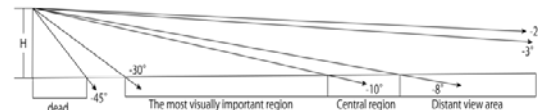


Fig. 6 Hypothetical number of Bird's eye view scape[2]

Table 3 Hypothetical number of Bird's eye view scape[2]

Viewpoint height (H)	Angle	Distance (D)
Visual axis (Central vision)	- 8 ~ -10°	5.7H~7.1H
Depression general lower limit	-30°	1.7H
Minimum depression angle lower limit	-45°	H
Hypersurface general upper limit	-2 ~ -3°	19H~29H

The analysis results from the observatory of Abeno Harukasu is shown in Figure 6. From the results, it was possible to grasp the area that can be viewed from a bird's eye view from the viewpoint. Specifically, there were many areas in the southern part of Osaka city which are in the good visible region. However, the scope of view in Umeda is limited because there are many high-rise buildings.

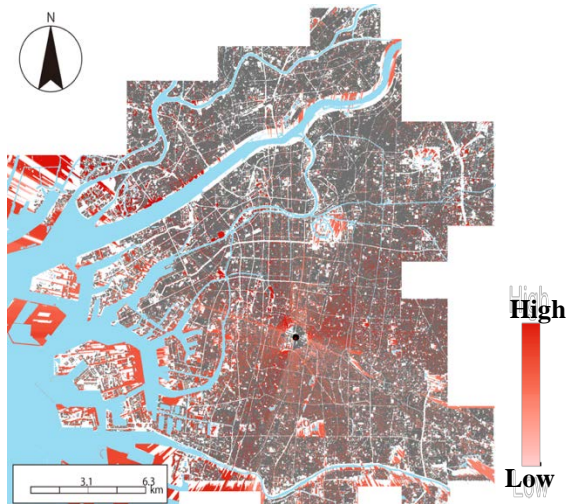


Fig. 6 Result of declination analysis

RESULTS AND DISCUSSION SECTION

We grasp the area where we can see the target area from the result. Also, I can see various things such as roads and buildings. However, in this analysis, we have not been able to grasp areas with continuity. Therefore, we think that it is necessary to classify it as buildings, roads, etc. and find continuity as an overlooking landscape.

CONCLUSION

In this research, we analyzed the overhead view and continuity. At first, when looking at the bird's-eye view, we investigated whether it is more attractive to have linear landscape elements such as roads and rivers. As a result, it was concluded that it is better to have linear elements. From this, we analyzed Osaka city. From the perspective of the skyline appearance, we found a viewpoint with a nice view which one can see the various landscape components in Osaka city such as concrete, declination analysis, continuously as an overlooking landscape.

As a future prospect, we analyzed the depression angle only from a close-up view, but since the viewable display area changes according to the height, analysis including the distant view area is necessary. Moreover, by visualizing the boundary between the

color difference, we also want to represent the continuity of the landscape component quantitatively.

REFERENCES

- [1] Okabe Y, Yoshikawa S and Tanaka K., Landscape Analysis of Skyline in Building Group and Mountains, Conference of Geographical Information Systems Conference Presentation Papers, Vol. 25, D-4-4.
- [2] Shinohara O, Higuchi D., Natural terrain and landscape, Civil Society year Science Lecture IV, 1971.
- [3] Sato T, Yoshikawa S and Tanaka K., Modeling of Nightscape, Conference of Geographical Information Systems Conference Presentation Papers, Vol. 18, pp.275-278.
- [4] Masuno T, Yoshikawa S and Tanaka K., The Quantitative Description of the Continuity on Cityscape, Conference of Geographical Information Systems Conference Presentation Papers, Vol. 17, pp. 583- 586.

THE EFFICIENCY OF FLY ASH AND CEMENT SLAG TO DEVELOPMENT BUILDING

Ranti Hidayawanti¹, Supriadi Legino², Iriansyah Sangadji³, Rony Panca Adi Widodo⁴
^{1,2,3}Sekolah Tinggi Teknik PLN, ⁴Adhimix Precast Indonesia

ABSTRACT

In the world of construction, concrete is the most important element in which in the concrete there is a collection of natural mineral aggregates or granules that can be separated by mechanical means if the aggregate is stirred in water. A large amount of raw material is used in the manufacture of concrete, it is commonly known that Fly ash and cement slag can be used as cement replacement materials.. This is due to the difficulty of the availability of cement in the market and the impact of rising prices for cement which continues to soar up, so that waste can be recycled for making concrete. This paper investigates the ratio of fly ash and 50% cement slag and waste management used. To produce lightweight concrete with environmentally friendly structure utilized coal waste in Suralaya such as fly ash, cement slag as a good soil stabilization material in the construction of high rise buildings. This research has analytical compressive strength at the age of 1,3,7 and 28 days, the need for water for the same workability. From experimental data obtained the same quality using Cement Slag using a smaller number of average 70 kg / m³ and Initial setting time of Cement Slag 50% on average 36 minutes faster than FA 50%. Besides that the utilization of fly ash and cement slag can minimize waste and with the use of the mixture can reduce production costs. From a financial standpoint, the application of this system can prevent companies from potentially losing billions / year.

Keywords: Fly ash, cement slag, concrete, compressive strength, production cost.

I. INTRODUCTION

The construction of high-rise buildings currently demands good quality materials, almost 70% of the use of materials from the building is concrete so that to meet the construction of high-rise buildings will be demanded high-quality concrete[1]. It has been commonly known that the use of fly ash can be used for mixed use of concrete but what about the slag concrete in which both components are hazardous waste?. The results show that significantly improved workability and strength development are obtained at an increased admixture content [2]. Many research has been done to review the effect of added ingredients on improving the quality of concrete. One of the added ingredients that is often to be used in mixed concrete mix is fly ash and cement slag. Due to their good performance and environmental friendliness, fly ash-based construction materials have great [3]. Fly-ash which is the remnants of coal combustion, flowed from the combustion chamber through the kettle in the form of smoke bursts, which is formed of fine particles and is an inorganic material formed from the change of mineral materials due to the combustion process of the coal combustion process on the generating unit steam (boiler) will form two kinds of ash that is fly ash (fly ash) and bottom ash (bottom ash). In Indonesia, the use of toxic hazardous waste such as cement slag, Fly Ash, bottom ash cannot be used directly but there must be

a waste management. Fly Ash-Bottom Ash is classified as hazardous waste so that any management in storage, transport, collection, utilization, management and stockpiling must be recorded and traceable as evidenced by the manifest document and each of the actors shall have a valid license and appropriate with designated it. Disposal of fly ash from coal-fired power plants causes economic and environmental problems. Violations of the provisions of hazardous waste management regulations result in administrative sanctions up to criminal sanctions in the form of prison confinement 1-5 years and a fine of 1-5 billion as stipulated in the Law of Indonesia No. 32 of 2009 on the management and protection of the environment. The purpose and objectives of this paper Innovation are as follows :

- Making Effective Management System which facilitate the process of data collection of coal ash in and out every day (First In First Out).
- Knowing the quality of Fly Ash and Cement Slag
- Determine standard of cement use for concrete mix when using fly ash and cement slag with comparison 50%
- Knowing the level of efficiency of using fly ash waste and cement slag waste.

II. LITERATURE REVIEW

The production process of electricity of Coal Steam Power Plant produced side products which are

Fly ash and bottom ash. Fly ash is a solid waste produced from coal-fired power plants[4]. The product is kept in big stack with size of particles grains smooth[5]. From the waste can be used as mixture of cement replacement for high rise building. According [6] to form an economical aggregate sand substitute to be used as a concrete filler product. Fly ash can be used for concrete mixed.. In utilization of waste can be compared to the other waste such as cement slag. Cement slag is a chemical reaction as one of popular activation method which is considered to fix hydrolic characteristic of the slag [7]. This work presents chemical activation of blast-furnace slag-blended Portland cement. According to [8] a partial replacement of Portland cement (PC) by ground granulated blast furnace slag (GGBFS) is an effective method to improve the durability of concrete due to its lower diffusivity and higher chemical resistance compared to PC. Both media will react to decrease production cost because the usage of cement is relatively increase in every years. The production of cement, the primary ingredient in concrete [9]. The production cost pressed in order to get the highest advantage but still considered the quality without relieve the ingredients which cause bad quality in the development of high rise building.

For concrete calculations in finding correlation graph w/c (cement water factor) to compressive strength used exponential regression formula and in the calculation used MS Excell program.

$$Y = ae^{bx} \dots\dots\dots 1)$$

a = compressive strength (kg/cm²)
b = w/c
e = exponential (2,718)
R = Coefficient (if close to 1 then the value is good)

As for determining the water requirement against w/c used the formula :

$$Y = a + bx \dots\dots\dots 2)$$

a = water requirement (litr/m³)
b = w/c

III. RESEARCH METHODOLOGY

In this research the methodology is used as follows :

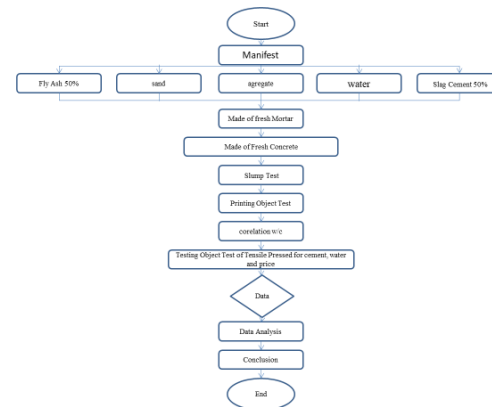


Fig.1 Flowchart Methodology

Starting from the management waste, it will be check through the manifest. During the experiment, it get observed and test such as workability (slump), the need of water for the same workability to seek the correlation graph of w/c toward tensile pressed at the age of 1,3,7 and 28 days and determined the need of cement, water and price for concrete which is using fly ash and cement slag.

IV. EXPERIMENTAL SETUP

The experiments performed on a laboratory scale include mortar cube experiments and concrete experiments using a small mixer.

Materials used in this experiment are as follow :

- Cement : Type I (OPC) Ex. PT. Indocement Tunggal Perkasa
- Fly Ash 50% : Ex. Pelabuhan Ratu
- Source Fly ash taken from this research including Fly ash ex. Suralaya Factory, Fly ash ex. Pindodeli and Fly ash ex. Indhobarat, Fly ash ex. Pelabuhan Ratu. Most of the usage of fly ash using fly ash ex. Suralaya 96%, the use of fly ash ex. Pindodeli 2% while Fly ash Indobarat 1%, therefore it is needed another source as alternative pozzolan as mineral add material in order to get appropriate quality and cost. Other fly ash alternatives are obtained from various sources that produce Fly ash, for example the Jakarta cement slag.
- Cement Slag 50% : Ex. Semen Jakarta
- Split : Split Ex. BCA Suplier Bangun Jaya
- Sand : Natural Sand Ex. Belitung
- Water : Well Plant Precast Cibitung

V. RESULT AND DISCUSSION

5.1 Transportation of Hazardous waste

Fly ash and bottom ash are the dominant hazardous waste generated from Power Generation activities in PLTU Suralaya. Not all waste can be used for concrete mixes for construction buildings, but for coal waste can be used as well. The amount of ash produced depends on ash content in coal. Here is the hazardous Waste Distribution Flow.

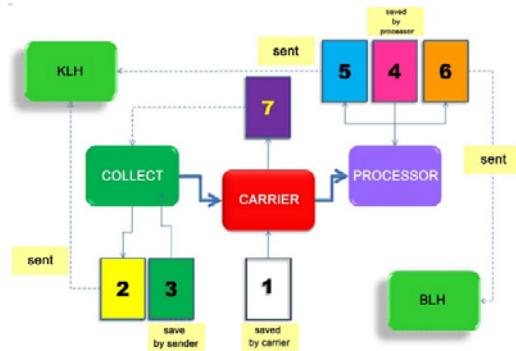


Fig.2 Process Flow of Hazardous Waste Manifest Distribution

The Manifest document consists of 7 sheets, with the final holder of the manifest for the 3rd and 7th sheets hold by the sender (producer), sheet 1 is hold by the carrier, the 2nd and 5th sheets are hold by the Ministry of the Environment, the 4th sheet is hold by the recipient, the 6th sheet is hold by the governor which is delivered by the carrier.

5.2 Mortar Experiment Result

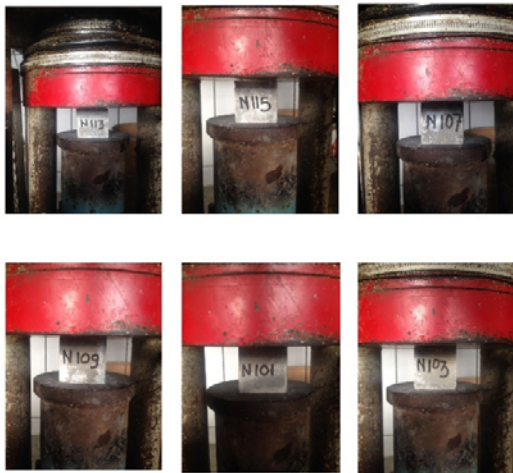


Fig.3 Laboratory Test Result on Mortar Fly Ash Comparison with Cement Slag

Fly ash and slag cement have been treated sustainable materials for the use of cement products for wastewater infrastructure due to their capabilities of corrosion resistance[10] .

5.3 Concrete Experimental Result

Concrete experiments were performed with the composition of Fly Ash 50% and 50% cement slag are as follows :

Table 1. Test Result Data of Fly Ash Test with Cement Slag

Compressive Strength (kg/cm ²) a age	w/c 0,5 FA 50	w/c 0,5 SJ 50
1 day	104	101
3 day	219	229
7 day	330	353
Percentage of comparison		
1 day	1,00	0,97
3 day	1,00	1,05
7 day	1,00	1,07
28 day	1,00	1,07
Realitation Trial Mix		
Realitation w/c	0,500	0,500
	1,000	1,000
Change of water (ltr/m ³)	0	0
change of water (%)	1,000	1,000
Initial seting time		
hours:minutes	05.40	05.04
Delta		00.36
Slump (cm)		
Slump Plain	10	5
Slump After 30'	-	-
Developing Compressive strength		
Age of day	% Compressive Strength after 28 days	
1	0,45	0,41
3	0,95	0,94
7	1,44	1,44
28	1,00	1,00

In order to know the quality of Fly Ash and Cement Slag, and viewed from Mortar and concrete experiment then it is got the combination as follows:

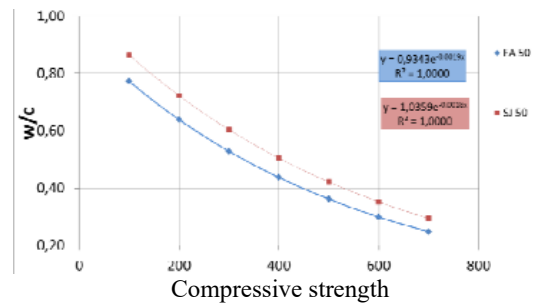


Fig.4 The relation of compressive strength against W/C.

The above graph shows a compressive strength relationship to w / c, where the compressive strength of cement slag is relatively the same as that of fly ash. From the analysis of the exponential linear regression graph above can be seen near the scatter point or coefficient value R = 1.

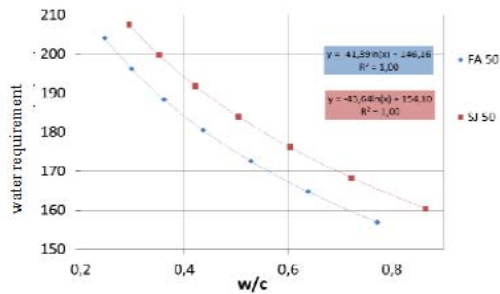


Fig.5 The relation of water requirement with w/c
From the above linear regression graph analysis can be seen the value of $R = 1$ means good and can be used.



Fig.6 Distribution of Molen Truck for High Rise Building foundry with Fly Ash and Cement Slag

Nowadays, concrete is a material widely used to make high-rise buildings. Thus to meet the construction of high-rise buildings will be demanded high-grade concrete. But along with the increasing human need for better infrastructure, then the concrete with high quality is much needed, for example for high rise buildings.



Fig.7 Floor and column concrete with concrete containing FA and cement slag

The development of construction in Indonesia occurred so fast, this research has been done to

develop construction technology ranging from construction materials to technology used in the construction itself. The development of these construction materials can be seen from the many types of added materials used as additives in the normal concrete mortar. These added ingredients aim to improve the quality of concrete to be better and environmentally friendly. Alkali-activated fly ash-slag (AAFS) concrete is a new blended alkali-activated concrete that has been increasingly studied over the past decades because of its environmental benefits and superior engineering properties. [10] To know the quality of cement against fly ash, and evaluated from mortar and concrete experiment, it is got combination as follows :

Table 2 Comparison of composition for efficiency

Quality K	Goal kg/m ³	w/c		water (litr/m ³)		Cementius		Price (IDR)	
		FA 50	Slag cement 50	FA 50	Slag Cement 50	FA 50	Slag cement 50	FA 50	Slag Cement 50
100	149	0.670	0.754	163	166	243	221	395.940	400.190
200	249	0.554	0.630	171	174	308	277	413.879	417.701
300	349	0.458	0.526	178	182	389	346	438.197	441.215
400	449	0.379	0.439	186	190	492	432	470.279	471.946
500	549	0.313	0.367	194	198	620	539	511.874	511.418
600	649	0.259	0.307	202	206	780	671	565.181	561.524
700	749	0.214	0.256	210	214	979	834	632.950	624.607

From the table above with the comparison of the composition between Fly Ash and Cement Slag 50% for high rise building, for example taken K300 with FA 438.197 (IDR) and cement slag 441.215 (IDR) whereas for normal production cost without the use both materials with the same quality is about 470 million, so the diffence is about 30 million (IDR). If the production cost per year, for example 1 billion/m³ than the efficiency can be generated is 1 billion x 30 million = 30 billion, so with utilization of fly as and cement slag it can avoid the company from potential loss of billions/ year. The cost of production is the amount of costs incurred by an industry to process raw materials into finished goods. By optimizing the available production factors optimally in order to produce optimal output.

IV. CONCLUSION

With the implementation of Innovation the use of Fly Ash and Cement Slag and by experimental method, it can be concluded that :

1. The use of Fly Ash and cement Slag semen is needed to replace the role of cement and sand.
2. With the same w/c of compressive strength cement slag 50% bigger than Fly Ash that is equal to 23%.
3. In order to get the same workability the water usage of cement slag 50% is larger with averages 4 liters / m³
4. The bigger usage of fly ash and cement slag materials made smaller production cost which can help the need of the development in the future.

ACKNOWLEDGEMENTS

The authors acknowledge to Leaders of STT PLN who have provided good support morale material and concrete laboratory civil engineering of adhimix also committee of Science, Engineering & Environment.

REFERENCES

- [1] R. Hidayawanti, S. Legino, and D. Harjanto, "OPTIMIZING THE UTILIZATION CEMENT SLAG AND FLY ASH OF," no. March, pp. 14–18, 2018.
- [2] A. Keulen, Q. L. Yu, S. Zhang, and S. Grünewald, "Effect of admixture on the pore structure refinement and enhanced performance of alkali-activated fly ash-slag concrete," *Constr. Build. Mater.*, vol. 162, pp. 27–36, 2018.
- [3] G. Xu and X. Shi, "Characteristics and applications of fly ash as a sustainable construction material: A state-of-the-art review," *Resour. Conserv. Recycl.*, vol. 136, no. August 2017, pp. 95–109, 2018.
- [4] X. Tan, F. Han, and F. Zhao, "Preparation of Autoclaved Foamed Concrete Block from Fly Ash and Carbide Slag," vol. 02006, pp. 1–6, 2018.
- [5] L. Nguyen, A. J. Moseson, Y. Farnam, and S. Spatari, "Effects of composition and transportation logistics on environmental, energy and cost metrics for the production of alternative cementitious binders.," *J. Clean. Prod.*, vol. 185, pp. 628–645, 2018.
- [6] R. N. Lieberman *et al.*, "Environmental impact and potential use of coal fly ash and sub-economical quarry fine aggregates in concrete," *J. Hazard. Mater.*, vol. 344, pp. 1043–1056, 2018.
- [7] A. Allahverdi, A. Maleki, and M. Mahinroosta, "Chemical activation of slag-blended Portland cement," *J. Build. Eng.*, vol. 18, pp. 76–83, 2018.
- [8] E. Yogarajah, T. Nawa, and T. Igarashi, "Physical, chemical, and mineralogical characteristics of blast furnace slag on durability of concrete," *MATEC Web Conf.*, vol. 147, p. 01007, 2018.
- [9] L. C. Chao and C. P. Kuo, "Ternary Blends of High Aluminate Cement, Fly ash and Blast-furnace slag for Sewerage Lining Mortar," *IOP Conf. Ser. Mater. Sci. Eng.*, vol. 303, no. 1, 2018.
- [10] G. Fang, W. K. Ho, W. Tu, and M. Zhang, "Workability and mechanical properties of alkali-activated fly ash-slag concrete cured at ambient temperature," *Constr. Build. Mater.*, vol. 172, pp. 476–487, 2018.

GEOSPATIAL PREDICTION OF SOIL EROSION USING MODIFIED BIVARIATE FREQUENCY RATIO TECHNIQUE

Abdulkadir Taofeeq Sholagberu¹, Muhammad Raza Ul Mustafa^{1,2}, Khamaruzaman Wan Yusof¹, Ahmad Mustafa Hashim¹, Muhammad Waris A. Khan³

¹Department of Civil and Environmental Engineering, Universiti Teknologi PETRONAS, 32610 Seri Iskandar, Perak, Malaysia

²Centre for Urban Resource Sustainability, Institute of Self-Sustainable Building, Universiti Teknologi PETRONAS, 32610 Seri Iskandar, Perak, Malaysia

³Faculty of Industrial Management, Universiti Malaysia Pahang, 26300 Gambang, Pahang, Malaysia

ABSTRACT

Erosion is one of the most serious environmental problems with adverse effects on agricultural productivity and hydrological systems. Prediction of erodible locations is very crucial for sustainable watershed management. This study is aimed at predicting geospatial distribution of erosion under the influence of causative factors (CFs) using modified bivariate frequency ratio, GIS and remote sensing techniques. The study considered dynamic CFs which often ignored in previous studies together with static CFs for erosion susceptibility analysis. Essential factors such as drainage density, lineament density (LD) and length-slope (LS) were selected as static factors, and land surface temperature (LST), soil moisture index (SMI), normalized difference vegetation index (NDVI) and rainfall erosivity as dynamic factors. Spatial correlations between classes of each CFs and occurrence of erosion were evaluated. The results showed that most erosion occurred in the class of 150.81 - 282.75, 0.337 - 0.369 km/km², 1.174 - 1.255, 24.20 - 32.64 °C and 1.250 - 1.358 for LS-factor, LD, NDVI, LST and SMI respectively. Analysis of prediction rates for each CFs indicates that LS-factor, SMI and LST were the most prominent factors triggering erosion in Cameron Highlands. The accuracy of developed susceptibility map from CFs' prediction rates was 68.6%. This suggests that the map was acceptable for watershed management, optimal land-use planning and prevention of erosion.

Keywords: Soil erosion, dynamic causative factors, susceptibility, frequency ratio

INTRODUCTION

Erosion is one of the most serious environmental problems that degrade land and threatens agricultural productivity and hydrologic systems in a watershed [1]. Human activities in the watershed such as increasing agricultural practice, massive land clearing for development, deforestation, etc cause drastic changes in land-use and land-cover patterns which enhances erosion phenomenon. Soil erosion process is modified basically by some biophysical factors of the watershed such as soil, climate, terrain characteristics and land-cover [2]. Hence, area specific studies are often applied for erosion assessment. These factors interact in a complex manner that makes erosion prediction or measurement difficult. Vijith, et al. [3] reported that Asia, Africa and South America have very high erosion rate with average value of 30-40 ton/ha/year. The ecological related issues of soil erosion have necessitated the development of sustainable erosion control measures. Substantial efforts have been spent on the development of soil erosion models [4]. Soil loss estimation and identification of critical zones are very crucial for the implementation of best management practice [2].

Susceptibility analysis is used for the assessment

of relative probability of occurrence of soil erosion in a particular location within watershed under the influence of causative factors (CFs). This predicts geospatial distribution of occurrence of soil erosion within the watershed and classifies areas into zones of different degrees of susceptibility to erosion [5]. The analysis could be accomplished by using two approaches: qualitative or quantitative approach. The former is subjective as the analysis rest largely on the experts' opinion and less accurate while the latter is objective and more accurate because it is statistical and probabilistic in nature [6]. The quantitative approach is categorized into bivariate and multivariate techniques to analyze numerical data and statistics in order to express the relationship between erosion and its CFs [7]. These two techniques analyze the historical linkage between CFs of a given erosive process and the distribution of the erosional landforms [8]. The target of this analysis is to establish, evaluate and visualize susceptibility, hazard and risk associated with natural events [5]. In bivariate technique, CFs maps are combined with erosional distribution map based on weighting values estimated for each factor. Some examples of bivariate techniques reported in literatures are frequency ratio (FR), statistical index and weight of evidence.

In the analysis of erosion susceptibility, selection

of appropriate CFs is the starting point [9]. Previous studies showed that majority of CFs considered were static factors such as slope angle, length-slope, plan curvature, stream power index, slope aspect and topographic wetness index, normalized difference vegetation index (NDVI), landuse/landcover, lithology, lineament, soil erodibility (k-factor), etc. These factors remain unchanged for a relatively long period of time. Furthermore, many of these are redundant that should not be simultaneously used as it often lead to overweighting of the results [9]. However, there are some important dynamic CFs such as land surface temperature (LST), soil moisture index (SMI) and rainfall erosivity (R-factor) whose impacts on erosion susceptibility results have not been investigated. Some literatures have indicated that these factors are crucial in triggering erosion but often neglected in many susceptibility analyses due to data unavailability [9-11]. Therefore, the aim of this study is to predict geospatial distribution of soil erosion in Cameron Highlands, Malaysia using modified bivariate FR technique. The study considers both non-redundant static and dynamic CFs for erosion susceptibility analysis of complex watershed where there is increasing rate of erosion due to the increased human-environment interactions.

MATERIALS AND METHODS

Soil erosion susceptibility analysis start with the identification of erosion affected spots in the area under study. In Cameron Highlands, a total of 159 erosion affected spots were identified as shown in Figure 1a. Based on this, erosion CFs required for the analysis were prepared and evaluated (see Figures 1b-1h) using ArcGIS 10.1, ENVI 5.0 and Geomatica 2016 software. These factors were extracted from various sources having different scales and generalization. The non-redundant static factors: drainage density (DD), LS-factor, lineament density (LD) were extracted from digital elevation model (DEM 5m spatial resolution) and dynamic CFs: NDVI, SMI and LST were derived from Landsat-8 image obtained from USGS database. R-factor was derived from monthly rainfall data (2006-2016) obtained from Malaysian Department of Irrigation and Drainage. The detailed procedures for the extraction of LST and SMI described by Abdulkadir, et al. [12] were used. All these CFs were considered due to their roles in triggering erosion and their previous implementation by many earliest researchers in erosion susceptibility analysis. For instance, some of non-redundant static CFs considered are DD [3, 6, 13], length-slope [14, 15], LD [1, 3] whose detailed descriptions could be found in the aforementioned literatures. Similarly, dynamic (multi-temporal) CFs such as R-factor [9, 16], LST [10], SMI [17] have been highlighted by researchers to influence erosion. Hence, they were introduced to

assess their significance in erosion susceptibility analysis.

After preparation of all the CFs, modified bivariate frequency ratio (FR) technique was adopted to estimate the probabilistic relationship between response (i.e., erosion) and predictor variables (i.e., erosion CFs) [18]. This method was chosen owing to its simplicity in application and understanding of the results. It evaluates the ratio of area of erosion occurred pixels to the total study area and the ratio of erosion occurrence probability to the non-occurrence for a given attribute [19]. FR application for susceptibility analysis commenced by reclassifying all the CFs into ten (10) classes and the number of training points (erosion occurred points) within each class were evaluated. FR for each causative factor were evaluated by finding the ratio of percentage target occurrence in each subcategory to percentage category of CFs in question as given in Equation 1. The relative frequency (RF), prediction rate (PR) and susceptibility index (SI) respectively defined as shown in Equations 2, 3, and 4 were evaluated. The PR and SI are used to define the mutual relationship among the CFs and occurrence of soil erosion. The expressions were applied and the results of the analyses are presented.

$$FR = \frac{\% \text{ target occurrence in each subcategory}}{\% \text{ category of an independent factor}} \quad (1)$$

$$RF = \frac{\text{factor class FR}}{\sum \text{factor classes FR}} \quad (2)$$

$$PR = \frac{(RF_{\max} - RF_{\min})}{\text{MIN. total of } (RF_{\max} - RF_{\min})} \quad (3)$$

$$SI = \frac{\sum(RF \cdot PR)}{\text{MAX.}(RF \cdot PR)} * 100 \quad (4)$$

RESULTS AND DISCUSSION

This section discusses the results obtained for the susceptibility analysis for geospatial prediction of soil erosion in Cameron Highlands watershed. The results are presented in Tables 1(a-g) for each factor. These Tables showed the correlations between classes of each CFs and occurrence of soil erosion in the watershed. In the case of correlation between soil erosion and SMI, erosion mostly occurred in the SMI classes of 0.852-1.032 and 1.152-1.358 because their respective ratios were greater than 1.0. The SMI class of 1.250-1.358 had the highest frequency ratio value as shown in Table 1a. Locations within the watershed with very low SMI were relatively dried compared to other locations. The results of SMI analysis with respect to soil erosion suggest that the drier locations were more prone to erosion than wet locations [17]. This is because drier soils are loose and could easily be detached and moved by runoff in the event of rainfall. The LST range of values where most of soil erosion took place was 24.20-32.64 °C as shown in

Table 1b. The locations with these highest LST values are the hottest regions in the study area. These locations have relatively low SMI values [11, 20] because solar radiations reduce the soil moisture content. Thus, erosion occurrence was prominent in those locations. Regions with NDVI values ranges between 1.174-1.494 and 1.623-1.759 are locations

where most erosion occurred with highest experienced at NDVI range of 1.174-1.255 as shown in Table 1c. This region with relatively low NDVI indicates lesser vegetation abundance. Therefore, there is very high tendency to have erosion occurring in such locations as experienced in the study [21].

Tables 1(a-h). Frequency ratio and prediction rates for soil erosion CFs

a) Factor classes (SMI)			b) Factor classes (LST)			c) Factor classes (NDVI)		
	Ratio	RF		Ratio	RF		Ratio	RF
0.852 - 0.993	4.153	0.095	15.95 - 19.87	22.105	0.437	0.984 - 1.173	0.000	0.000
0.994 - 1.032	1.730	0.040	19.88 - 21.80	0.766	0.015	1.174 - 1.255	6.882	0.285
1.033 - 1.060	0.962	0.022	21.81 - 22.23	0.597	0.012	1.256 - 1.327	4.965	0.205
1.061 - 1.082	0.988	0.023	22.34 - 22.88	0.200	0.004	1.328 - 1.391	5.778	0.239
1.083 - 1.104	0.751	0.017	22.89 - 23.47	0.202	0.004	1.392 - 1.449	3.616	0.150
1.105 - 1.126	0.395	0.009	23.48 - 24.19	0.378	0.007	1.450 - 1.494	1.114	0.046
1.127 - 1.151	0.523	0.012	24.20 - 25.04	1.114	0.022	1.495 - 1.534	0.079	0.003
1.152 - 1.189	1.041	0.024	25.04 - 26.09	3.572	0.071	1.535 - 1.573	0.172	0.007
1.190 - 1.249	3.004	0.069	27.60 - 27.60	7.826	0.155	1.574 - 1.622	0.157	0.006
1.250 - 1.358	30.210	0.690	27.61 - 32.64	13.843	0.274	1.623 - 1.759	1.405	0.058
d) Factor classes (LS)			e) Factor classes (LD)			f) Factor classes (DD)		
	Ratio	RF		Ratio	RF		Ratio	RF
0 - 2.22	0.000	0.000	0.09 - 0.134	0.116	0.012	13 - 18279	0.037	0.003
2.23 - 7.76	0.000	0.000	0.135 - 0.170	0.447	0.048	18280 - 40203	0.520	0.045
7.77 - 14.42	0.000	0.000	0.171 - 0.207	0.772	0.083	40204 - 62789	1.614	0.141
14.43 - 21.07	0.000	0.000	0.208 - 0.242	1.180	0.127	62790 - 86690	1.033	0.090
21.08 - 28.83	0.000	0.000	0.243 - 0.275	0.946	0.102	86691 - 110931	1.313	0.114
28.84 - 38.81	3.356	0.001	0.276 - 0.307	1.206	0.129	110932 - 138357	0.864	0.075
38.82 - 53.22	264.315	0.064	0.308 - 0.336	0.987	0.106	138358 - 170221	1.386	0.121
53.23 - 80.94	596.648	0.144	0.337 - 0.369	1.593	0.171	170222 - 205077	2.644	0.230
80.95 - 150.80	808.169	0.195	0.370 - 0.407	1.892	0.203	205078 - 244898	2.064	0.180
150.81 - 282.75	878.384	0.597	0.408 - 0.477	0.298	0.032	244899 - 319504	0.000	0.000
g) Factor classes R-factor			(h) Model prediction rates					
	Ratio	RF	CFs	Min	Max	[Max-Min]	Min tot.	PR
2015.22 - 2086.83	1.309	0.136	SMI	0.009	0.690	0.681	0.191	3.576
2086.84 - 2146.89	1.959	0.203	NDVI	0.000	0.285	0.285		1.494
2146.90 - 2200.02	0.933	0.097	LST	0.004	0.437	0.433		2.272
2200.03 - 2248.54	0.000	0.000	DD	0.000	0.230	0.230		1.209
2248.55 - 2292.43	0.190	0.020	LS-Factor	0.000	0.597	0.597		3.133
2292.44 - 2334.01	1.087	0.113	LD	0.012	0.203	0.191		1.000
2334.02 - 2382.52	0.906	0.094	R-Factor	0.000	0.203	0.203		1.066
2382.53 - 2440.27	1.336	0.139						
2440.28 - 2500.34	1.923	0.199						
2500.35 - 2604.29	0.000	0.000						

The results for LS-factor in Table 1d showed that the highest ratio occurred in the region with highest value (i.e., 150.81-282.75). This underscores the influence of slope-length on occurrence of soil erosion as highlighted by many researchers [22]. Higher LD regions suggest high geological faults (i.e., presence of fractured and weathered terrain) in the watershed that could enhance soil erosion. This was experienced in the study area as depicted in Table

1e and conformed to description made by Barrow, et al. [23]. The results for the remaining CFs such as DD and R-factor are presented in Tables 1f and 1g respectively. The prediction rates were evaluated for each factor by finding the minimum RF, maximum RF and the differences between both as shown in Table 1h. The obtained values were used to evaluate contribution of each factor. The analysis showed that all the CFs contributed significantly to the occurrence

of erosion. SMI had the highest impact on soil erosion followed by LS-factor and the least was LD as shown in Table 1h. The prediction rate values for each factor was then applied in ArcGIS 10.1 for the development

of erosion susceptibility maps as shown in Figure 2. This predicts the potential locations where erosion could occur based on the CFs.

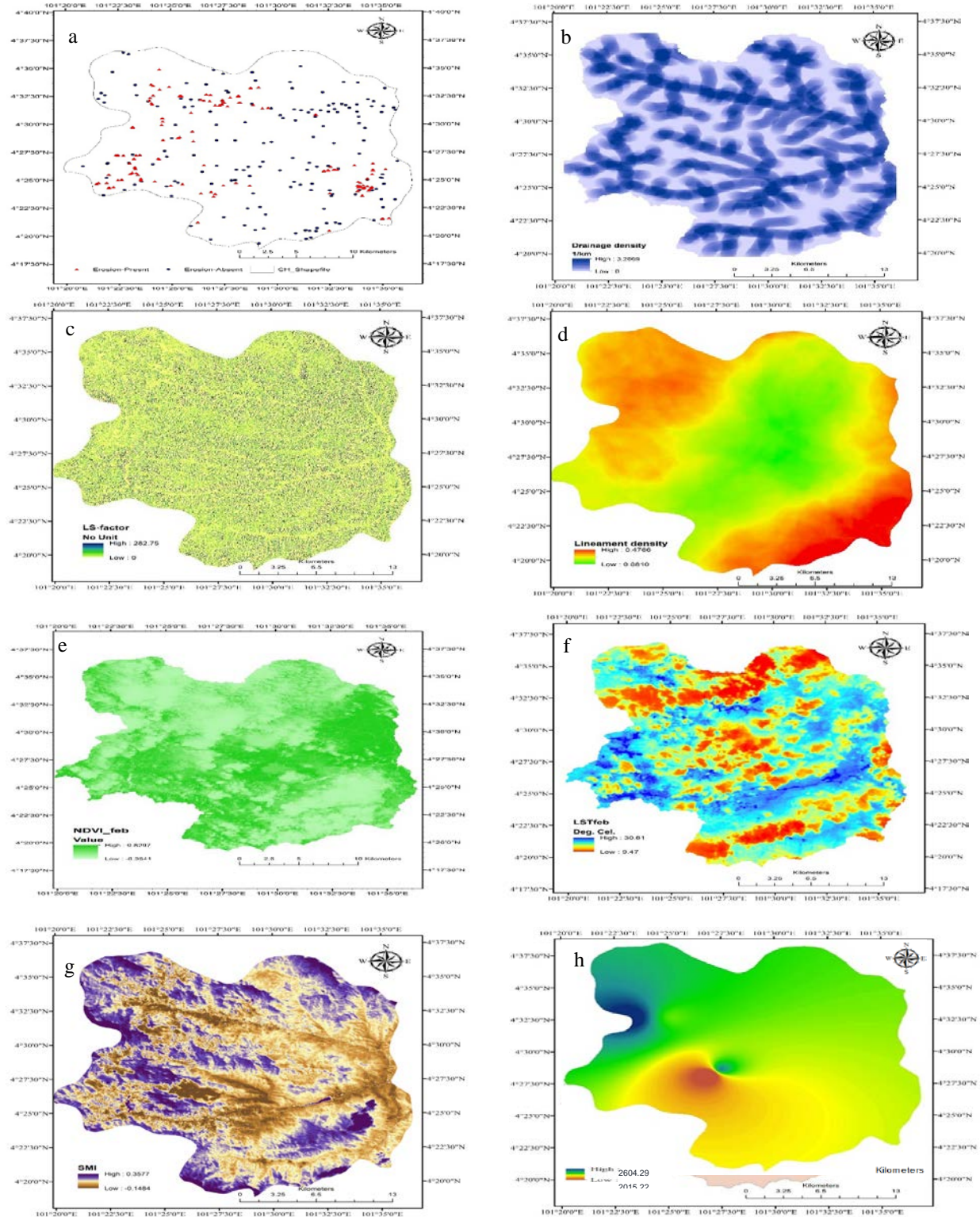


Figure 1. Maps for erosion locations and CFs (a) Training points (b) DD (c) LS-factor (d) LD (e) NDVI (f) LST (g) SMI (h) R-factor

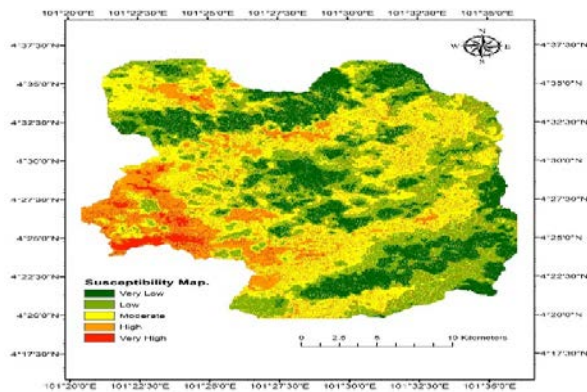


Figure 2. Erosion susceptibility map

Accuracy of the soil erosion susceptibility map obtained was evaluated by using area-under-curve (AUC) technique. An AUC “measures the quality of probabilistic model describing its ability to reliably predict the occurrence or non-occurrence of events” [24]. Its values often range between 0 and 1 in which closer to 1 indicate perfect prediction and close to 0.5 indicates that the model is inaccurate [25]. It is widely accepted and adopted by researchers for evaluation of susceptibility mapping accuracy [26]. The AUC value was estimated to be 68.6%. This indicates that FR method performed fairly well in erosion susceptibility assessment and the map could be used for sustainable management of the watershed. Susceptibility map produced was classified into five classes using natural break approach as in Figure 2. Most northeast and central regions of the study area were mostly identified as “very low” susceptible zones while “high” susceptible zones are distributed across the western region. The percentage area occupied by regions with very low, low, moderate, high and very high susceptible zones to soil erosion are 42.3, 36.9, 16.4, 3.8 and 0.5% respectively.

CONCLUSION

This present study applied modified bivariate FR technique for geospatial prediction of soil erosion in Cameron Highlands. The study considered some important CFs which often neglected in many susceptibility analyses along with other non-redundant CFs. As a result, DD, LD and LS were selected as static factors, and LST, SMI, NDVI and R-factor as dynamic factors. Correlations between subclasses of each CFs and occurrence of soil erosion were evaluated. The results showed that most erosion took place in the subclasses of 150.81 - 282.75, 0.337 - 0.369 km², 1.174 - 1.255, and 1.250 - 1.358 for LS, LD, NDVI, and SMI respectively. The analysis of prediction rates for all the factors showed that contributed significantly to the occurrence of erosion with the SMI having the highest value followed by LS. The results of prediction rates for the CFs were applied for the development of erosion susceptibility

map. The accuracy of model was assessed using area-under-curve method and was estimated to be 68.6% accurate. This suggests that the map is valid for geospatial erosion prediction and acceptable for optimal land-use and sustainable management of the watershed against erosion and it related hazards.

ACKNOWLEDGEMENTS

This study was supported by the Universiti Teknologi PETRONAS Malaysia under University Research Internal Fund-URIF 2016 Grant (0153AA-G04) and Graduate Assistance Scheme. Authors also acknowledged Malaysian Department of Irrigation and Drainage for the provision of rainfall data.

REFERENCES

- [1] G. S. Pradeep, M. N. Krishnan, and H. Vijith, "Identification of critical soil erosion prone areas and annual average soil loss in an upland agricultural watershed of Western Ghats, using analytical hierarchy process (AHP) and RUSLE techniques," *Arabian Journal of Geosciences*, vol. 8, pp. 3697-3711, 2015.
- [2] B. Ganasri and H. Ramesh, "Assessment of soil erosion by RUSLE model using remote sensing and GIS-A case study of Nethravathi Basin," *Geoscience Frontiers*, vol. 7, pp. 953-961, 2016.
- [3] H. Vijith, M. Suma, V. Rekha, C. Shiju, and P. Rejith, "An assessment of soil erosion probability and erosion rate in a tropical mountainous watershed using remote sensing and GIS," *Arabian Journal of Geosciences*, vol. 5, pp. 797-805, 2012.
- [4] M. Nearing, V. Jetten, C. Baffaut, O. Cerdan, A. Couturier, M. Hernandez, *et al.*, "Modeling response of soil erosion and runoff to changes in precipitation and cover," *Catena*, vol. 61, pp. 131-154, 2005.
- [5] P. Magliulo, "Assessing the susceptibility to water-induced soil erosion using a geomorphological, bivariate statistics-based approach," *Environmental Earth Sciences*, vol. 67, pp. 1801-1820, 2012.
- [6] T. Kavzoglu, E. K. Sahin, and I. Colkesen, "Selecting optimal conditioning factors in shallow translational landslide susceptibility mapping using genetic algorithm," *Engineering Geology*, vol. 192, pp. 101-112, 2015.
- [7] D. T. Bui, O. Lofman, I. Revhaug, and O. Dick, "Landslide susceptibility analysis in the Hoa Binh province of Vietnam using statistical index and logistic regression," *Natural hazards*, vol. 59, p. 1413, 2011.
- [8] F. Guzzetti, A. Carrara, M. Cardinali, and P. Reichenbach, "Landslide hazard evaluation: a review of current techniques and their

- application in a multi-scale study, Central Italy," *Geomorphology*, vol. 31, pp. 181-216, 1999.
- [9] P. Magliulo, A. Di Lisio, and F. Russo, "Comparison of GIS-based methodologies for the landslide susceptibility assessment," *Geoinformatica*, vol. 13, pp. 253-265, 2009.
- [10] X. Xue, Y. Luo, X. Zhou, R. Sherry, and X. Jia, "Climate warming increases soil erosion, carbon and nitrogen loss with biofuel feedstock harvest in tallgrass prairie," *Gcb Bioenergy*, vol. 3, pp. 198-207, 2011.
- [11] T. S. Abdulkadir, M. R. Muhammad, W. Y. Khamaruzaman, and H. M. Ahmad, "Geostatistical based susceptibility mapping of soil erosion and optimization of its causative factors: A conceptual framework," *Journal of Engineering Science and Technology*, vol. 12, pp. 2880-2895, 2017.
- [12] T. S. Abdulkadir, M. R. Muhammad, W. Y. Khamaruzaman, and H. M. Ahmad, "Assessing the influence of terrain characteristics on spatial distribution of satellite derived land surface parameters in mountainous areas," in *37th IAHR World Congress*, Kuala Lumpur Malaysia, 2017, pp. 2897-2906.
- [13] S. Pal, "Identification of soil erosion vulnerable areas in Chandrabhaga river basin: a multi-criteria decision approach," *Modeling Earth Systems and Environment*, vol. 2, p. 5, 2016.
- [14] S. Fernández, J. Marquínez, and R. Menéndez-Duarte, "A sapping erosion susceptibility model for the southern Cantabrian Range, North Spain," *Geomorphology*, vol. 95, pp. 145-157, 2008.
- [15] F. Lucà, M. Conforti, and G. Robustelli, "Comparison of GIS-based gully susceptibility mapping using bivariate and multivariate statistics: Northern Calabria, South Italy," *Geomorphology*, vol. 134, pp. 297-308, 2011.
- [16] T. S. Abdulkadir, M. R. Mustafa, Y. W. Khamaruzaman, and A. M. Hashim, "Evaluation of rainfall-runoff erosivity factor for Cameron Highlands, Pahang, Malaysia," *Journal of Ecological Engineering*, vol. 17, pp. 1-8, 2016.
- [17] J. Vahabi and D. Nikkami, "Assessing dominant factors affecting soil erosion using a portable rainfall simulator," *International Journal of Sediment Research*, vol. 23, pp. 376-386, 2008.
- [18] G. Demir, M. Aytekin, A. Akgun, S. B. Ikizler, and O. Tatar, "A comparison of landslide susceptibility mapping of the eastern part of the North Anatolian Fault Zone (Turkey) by likelihood-frequency ratio and analytic hierarchy process methods," *Nat Hazards* vol. 65, pp. 1481-1506, 2013.
- [19] A. Ozdemir and T. Altural, "A comparative study of frequency ratio, weights of evidence and logistic regression methods for landslide susceptibility mapping: Sultan Mountains, SW Turkey," *Journal of Asian Earth Sciences*, vol. 64, pp. 180-197, 2013.
- [20] I. Sandholt, K. Rasmussen, and J. Andersen, "A simple interpretation of the surface temperature/vegetation index space for assessment of surface moisture status," *Remote Sensing of environment*, vol. 79, pp. 213-224, 2002.
- [21] W. J. D. Van Leeuwen and G. Sammons, "Vegetation dynamics and erosion modeling using remotely sensed data (MODIS) and GIS," presented at the 10th Biennial USDA Forest service remote sensing applications, U.S., 2005.
- [22] B. Liu, M. Nearing, P. Shi, and Z. Jia, "Slope length effects on soil loss for steep slopes," *Soil Science Society of America Journal*, vol. 64, pp. 1759-1763, 2000.
- [23] C. Barrow, J. Clifton, N. Chan, and Y. Tan, "Sustainable development in Cameron highlands, Malaysia," *Malaysian Journal of Environmental Management*, vol. 6, pp. 41-57, 2005.
- [24] A. Nandi and A. Shakoor, "A GIS-based landslide susceptibility evaluation using bivariate and multivariate statistical analyses," *Engineering Geology*, vol. 110, pp. 11-20, 2010.
- [25] T. Fawcett, "An introduction to ROC analysis," *Pattern recognition letters*, vol. 27, pp. 861-874, 2006.
- [26] O. F. Althuwaynee, B. Pradhan, and S. Lee, "Application of an evidential belief function model in landslide susceptibility mapping," *Computers & Geosciences*, vol. 44, pp. 120-135, 2012.

NONLINEAR BEHAVIOR AND THERMAL DAMAGE OF THERMAL LAGGING IN CONCENTRIC LIVING TISSUES SUBJECTED TO GAUSSIAN DISTRIBUTION SOURCE

Hamdy M. Youssef^{1,2}, Najat A. Al-Ghamdi³

¹ Alexandria University, Dept. of Mathematics, Faculty of Education, Alexandria, Egypt

²Umm Al-Qura University, Dept. of Mechanics, Faculty of Engineering, Makkah, KSA

³ Umm Al-Qura University, Dept. of Mathematics, Faculty of Science, Makkah, KSA

ABSTRACT

The effects of thermal lagging with high-order became essential to describe non-equilibrium heating in tissues. Our paper studies the temperature rise behavior in living tissues theoretically during the treatment by magnetic tumor hyperthermia based on the non-linear form of the dual-phase-lag model. Experimentally, it was found that the concentration of magnetic particles is in Gaussian distribution through the radial direction when magnetic fluid is injected into the living tissue space. Hence, the governing partial differential equation in concentric spherical space is solved in the Laplace transform domain. Some comparisons between the non-linear and linear effects of phase-lag time's parameters on bio-heat transfer have been studied and discussed. The thermal damage quantity for the tumor has been calculated with different values of the phase-lag times. The results show that the non-linear and linear effects of phase-lag times on bio-heat transfer have significant effects on the tumor, the tissue, and the thermal damage quantity.

Keywords: Nonlinear Behavior; Thermal Lagging; Thermal Damage; Living Tissue; Gaussian distribution Source

INTRODUCTION

Hyperthermia (also called thermal therapy or thermotherapy) is a kind of medical treatment in cancer therapy; it is elevated body temperature to 40–44 C. Hyperthermia is used with radiation therapy and chemotherapy to treat cancer [1]. Cells in these areas are often cell cycle arrest and so most resistant to growth prohibiting drugs. It remains unclear whether these cells are sensitive to heat damage; moreover, heat can motivate vascularization and increase oxygenation of the tissue, thermotherapy make cancer cells more motivate to radiation or harm other cancer cells that radiation cannot damage [2, 3]. These studies have been certain in a number of clinical studies [4, 5] which indicate that elevation of the temperature within a tumor has a cytotoxic influence on radio resistant cells when heated to temperatures above 42 C. There is a variety of techniques [3, 6] to increase the temperature within the human body. Hyperthermia for the processing of cancer is under study, including all body hyperthermia, partial or regional hyperthermia, and local hyperthermia. In several biologists studying the behavior of bio-heat transfer in tissues during magnetic fluid hyperthermia management, the distribution of the magnetic particles was always regarded as homogenous in a limited spherical domain [7-11]. Furthermore, Salloum et al. [12] experimentally evaluated magnetic nan-ofluid

transport and heat distribution stimulated by commercially available magnetic nanoparticles injected into the extracellular area of biological tissue using agarose gel with porous structures alike to human tissue. Pennes model [13] described temperature distribution in the living biological tissues. The connection between [14] arterial blood and the heat transfer in a living tissue are taken. The model known as the bioheat equation remains used today. Pennes inserted a medium response term to the basic heat equation that accounts for the mitigating effect of blood flow. This convective term depicts heat transport by means other than propagation. Wissler [15] explicated the validity of Pennes' model connected to normal thermal distribution in living tissue. supposed mixed boundary conditions in resting tissue, Pennes' model strictly describes the decay of temperature from the core of the body to the surface [14]. The Pennes bio-heat transfer equation (PBT) is based on the classical Fourier's law, taken into account a blood perfusion term, which is proportionate to the volumetric rate of blood perfusion and the difference between the average arterial blood and tissue temperatures. Pennes bio-heat model is true only if when the venous blood flows from the capillary bed to the main supply vein, its temperature remains the same as the tissue temperature disregard the size of the vessel and the flow rate. Youssef modified the theory of heat conduction in deformable bodies which have been

investigated by Chen and Gurtin, which depends upon two distinct temperatures, the conductive temperature and the thermodynamic temperature [16]. For time-independent situations, the difference between these two temperatures is proportional to the heat supply, and in the absence of any heat supply, the two temperatures are identical. Youssef considered the non-Fourier's heat conduction based on one relaxation time. Youssef applies the two-temperature heat conduction in many applications [17-21]. In this work, two-temperature bio-heat transfer equations based on second-order effects in thermal lagging was introduced and used to discuss the variation of temperature in a laser-irradiated biological tissue.

FORMULATION OF THE PROBLEM

In a magnetic fluid hyperthermia, magnetic particles are injected into at the center of tumor surrounded by the normal tissue and radially diffuse from the injected point in Gaussian distribution [12]. For excitation of an alternating magnetic field, magnetic particles become the space-dependent heating sources in the tissue. For $t > 0$, the heat is transferring in the radius direction symmetrically. The small tumor is regarded as a solid sphere with the radius R [7-11]. The temperature distribution in the tumor $0 \leq r \leq R$ and normal $R \leq r < h$ tissues is the function of the distance r from the center of the sphere and time t .

Youssef proposed the two-temperature model to differentiate between the conductive temperature and the dynamical temperature as:

$$q_i(r, t + \tau_{qi}) = -K_i \nabla T_i^c(r, t + \tau_{Ti}), \quad i = 1, 2, \quad (1)$$

$$T_i^c(r, t) - T_i^D(r, t) = \beta_i \nabla^2 T_i^c(r, t), \quad i = 1, 2. \quad (2)$$

Where $i = 1$ for $0 \leq r \leq R$ and $i = 2$ for $R \leq r < h$,

β_i is a non-negative parameter which is called two-temperature parameter, T_i^c is the conductive temperature, T_i^D is the dynamical temperature, K the heat conductivity, q the heat flux, and t is the time, τ_q, τ_T are the phase-lag time parameters of the heat flux and the temperature gradient, respectively. In general, the relaxation times τ_q, τ_T take a minimal value, while in the biological materials this parameter is more significant.

The energy conservation equation of bio-heat transfer is described in the context of the two-temperature model as:

$$\rho_i C_i \frac{\partial T_i^D(r, t)}{\partial t} = -\nabla \cdot q_i(r, t) - w_{bi} C_b \rho_b (T_i^D(r, t) - T_0) + (q_{mi}(r, t) + q_{ni}(r, t)), \quad i = 1, 2 \quad (3)$$

The term $w_{bi} C_b (T_i^D(r, t) - T_0)$ expresses the heat caused by convection within the tissue per unit mass of the tissue and it is considered to be homogenous and $T_0 = 37^\circ C$ is the reference temperature of the tissue and the tumor.

The second order Taylor series of the DPL model can be rewritten as

$$\left(1 + \tau_{qi} \frac{\partial}{\partial t} + \frac{\tau_{qi}^2}{2} \frac{\partial^2}{\partial t^2}\right) q_i(r, t) = -K_i \left(1 + \tau_{Ti} \frac{\partial}{\partial t} + \frac{\tau_{Ti}^2}{2} \frac{\partial^2}{\partial t^2}\right) \nabla T_i^c(r, t), \quad i = 1, 2 \quad (4)$$

Consequently, it gives

$$\left(1 + \tau_{qi} \frac{\partial}{\partial t} + \frac{\tau_{qi}^2}{2} \frac{\partial^2}{\partial t^2}\right) \nabla \cdot q_i(r, t) = -K_i \left(1 + \tau_{Ti} \frac{\partial}{\partial t} + \frac{\tau_{Ti}^2}{2} \frac{\partial^2}{\partial t^2}\right) \nabla^2 T_i^c(r, t), \quad i = 1, 2 \quad (5)$$

A high order differential equation of bio-heat transfer is obtained from equation (3) as:

$$K_i \left(1 + \tau_{Ti} \frac{\partial}{\partial t} + A \frac{\tau_{Ti}^2}{2} \frac{\partial^2}{\partial t^2}\right) \frac{1}{r^2} \frac{\partial}{\partial r} \left(r^2 \frac{\partial T_i^c(r, t)}{\partial r}\right) = \left(\rho_i C_i \frac{\partial T_i^D(r, t)}{\partial t} - w_{bi} C_b \rho_b (T_0 - T_i^D(r, t)) - q_{mi}(r, t) - q_{ni}(r, t) \right) \left(1 + \tau_{qi} \frac{\partial}{\partial t} + B \frac{\tau_{qi}^2}{2} \frac{\partial^2}{\partial t^2}\right), \quad i = 1, 2. \quad (6)$$

where the values of the coefficients α_1 and α_2 are $\alpha_1 = \alpha_2 = 0.0$ for DPL type I equation, $\alpha_1 = 1.0, \alpha_2 = 0.0$ for DPL type II equation, and $\alpha_1 = \alpha_2 = 1.0$ for DPL type III equation.

Consider the following functions:

$$\theta_i(r, t) = r(T_i^c(r, t) - T_0), \quad i = 1, 2 \quad (7)$$

$$\varphi_i(r, t) = r(T_i^D(r, t) - T_0), \quad i = 1, 2.$$

Hence, we have from equations (6) and (7) that

$$K_i \left(1 + \tau_{Ti} \frac{\partial}{\partial t} + \alpha_i \frac{\tau_{Ti}^2}{2} \frac{\partial^2}{\partial t^2}\right) \left(\frac{\partial^2 \varphi_i(r, t)}{\partial r^2}\right) = \left(\rho_i C_i \frac{\partial \theta_i(r, t)}{\partial t} + w_{bi} C_b \rho_b \theta_i(r, t) - r q_{mi}(r, t) - r q_{ni}(r, t) \right) \left(1 + \tau_{qi} \frac{\partial}{\partial t} + \alpha_i \frac{\tau_{qi}^2}{2} \frac{\partial^2}{\partial t^2}\right), \quad i = 1, 2. \quad (8)$$

$$\theta_i(r, t) = \varphi_i(r, t) - \beta_i \frac{\partial^2 \varphi_i(r, t)}{\partial r^2}, \quad i = 1, 2. \quad (9)$$

Assume the following spatial heating source

$$q_{ri}(r, t) = q_0 H(t) e^{-(r^2/r_0)}, \quad (10)$$

where r_0 is a parameter which determines how far the diffusion of the injected magnetic particles occurs and q_0 determines the maximum strength of the spatial heating source at the injection site. The function $H(t)$ is Heaviside unit step function

Applying Laplace transform for equation (8) and (10) defined as:

$$\bar{f}(s) = \int_0^\infty f(t) e^{-st} dt, \quad (11)$$

where we will use the following initial conditions:

$$\varphi_i(r, t)|_{t=0} = \theta_i(r, t)|_{t=0} = \frac{\partial \varphi_i(r, t)}{\partial t} \bigg|_{t=0} = \frac{\partial \theta_i(r, t)}{\partial t} \bigg|_{t=0} = 0. \quad (12)$$

Thus, we get

$$\frac{\partial^2 \bar{\varphi}_i}{\partial r^2} - \lambda_i^2 \bar{\varphi}_i = -f_i, \quad i = 1, 2, \quad (13)$$

$$\text{where } \lambda_i^2 = \frac{h_{qi}(\rho_i C_i s + w_{bi} C_b \rho_p)}{K_i h_{Ti} + \beta_i h_{qi}(\rho_i C_i s + w_{bi} C_b \rho_p)},$$

$$f_i = \frac{\bar{q}_{mi} + h_{qi} \bar{q}_{ri}}{[K_i h_{Ti} + \beta_i h_{qi}(\rho_i C_i s + w_{bi} C_b \rho_p)]},$$

$$h_{Ti} = \left(1 + s\tau_{Ti} + \alpha_1 \frac{s^2 \tau_{Ti}^2}{2}\right), \quad h_{qi} = \left(1 + s\tau_{qi} + \alpha_2 \frac{s^2 \tau_{qi}^2}{2}\right),$$

$$\bar{q}_{ri}(r, s) = \frac{q_0}{s} e^{-(r^2/r_0)}, \quad \bar{q}_{mi} = \frac{q_{mi}}{s}.$$

The general solution of the differential equation (13) takes the form

$$\bar{\varphi}_1(r, s) = c_{11} e^{-\lambda_1 r} + c_{12} e^{\lambda_1 r} + \frac{f_1}{\lambda_1^2} r, \quad 0 \leq r \leq R, \quad (14)$$

and

$$\bar{\varphi}_2(r, s) = c_{21} e^{-\lambda_2 r} + c_{22} e^{\lambda_2 r} + \frac{f_2}{\lambda_2^2} r, \quad R \leq r < h. \quad (15)$$

Apply the boundary conditions

$$\bar{\varphi}_1(r, s)|_{r=0} = 0, \quad \bar{\varphi}_1(R, s) = \bar{\varphi}_2(R, s), \quad \frac{K_1}{r} \frac{\partial \bar{\varphi}_1(r, s)}{\partial r} \bigg|_{r=R} = \frac{K_2}{r} \frac{\partial \bar{\varphi}_2(r, s)}{\partial r} \bigg|_{r=R}, \quad \bar{\varphi}_2(r, s)|_{r=h} = 0. \quad (16)$$

We get the following system of linear equations:

$$c_{11} + c_{12} = 0, \quad (17)$$

$$e^{-\lambda_1 R} c_{11} + e^{\lambda_1 R} c_{12} - e^{-\lambda_2 R} c_{21} - e^{\lambda_2 R} c_{22} = \left(\frac{f_2}{\lambda_2^2} - \frac{f_1}{\lambda_1^2}\right) R, \quad (18)$$

$$\begin{aligned} & -\lambda_1 K_1 e^{-\lambda_1 R} c_{11} + \lambda_1 K_1 e^{\lambda_1 R} c_{12} + \lambda_2 K_2 e^{-\lambda_2 R} c_{21} \\ & - \lambda_2 K_2 e^{\lambda_2 R} c_{22} = \left(\frac{f_2}{\lambda_2^2} - \frac{f_1}{\lambda_1^2}\right) R, \end{aligned} \quad (19)$$

$$c_{21} e^{-\lambda_2 h} + c_{22} e^{\lambda_2 h} = -\frac{f_2}{\lambda_2^2} h. \quad (20)$$

We solve equations (17-20), we complete the solution in the Laplace transform domain.

THE THERMAL DAMAGE

The Arrhenius burn integration induced by Henriques and Moritz is widely used. Their results showed that progressively decreasing temperatures could produce a burn injury of standard threshold severity as the thermal insult period is logarithmically increased. They conducted two different experiments, which involved boundary conditions of constant temperature and constant heat flux in computing the time-temperature relationship at the dermal-epidermal junction. They worked out the solution of the Fourier heat conduction equation for a semi-infinite body to model the transfer of heat through the skin. Based on their observation, Moritz and Henriques proposed that skin damage could be represented as a chemical rate process, which is calculated by using a first order Arrhenius rate equation. Whereby damage is related to the rate of protein denaturation $\kappa(T)$ and exposure time t at a given absolute temperature T . The measure of thermal damage Ω was introduced, and its rate $\kappa(T)$ were postulated to satisfy:

$$\kappa(T) = \frac{d\Omega}{dt} = A \exp\left(-\frac{E_a/\eta}{T}\right), \quad (21)$$

which leads to

$$\Omega = A \int_0^t \exp\left(-\frac{E_a/\eta}{T}\right) dt, \quad (22)$$

where A is a material parameter (frequency factor); E_a is the activation energy; η is the universal gas constant. Equation (37) indicates that a reaction proceeds faster with larger values of T or A for the same E_a , or with smaller values of E_a for the same value of A . The constants A and E_a are usually obtained experimentally. After the pioneering work of Henriques and Moritz, many researchers have also proposed some other models, but most of them have a similar format. There are only differences in the coefficients used in the burn damage integral, which are mainly due to the different experimental databases used to define the models and the different emphasis

when analyzing the burn process where

$$T_i^c(^{\circ}C) = \frac{\varphi_i}{r} + T_0 + 237.$$

NUMERICAL INVERSION OF THE LAPLACE TRANSFORM

To determine the distribution $\varphi_i(r, t)$ of each layer, we will use a Riemann-sum approximation method to obtain the numerical results in which, any function in Laplace domain can be inverted to the time domain as:

$$Z(t) = \frac{e^{\kappa t}}{t} \left[\frac{1}{2} \bar{Z}(\varepsilon) + \operatorname{Re} \sum_{n=1}^N (-1)^n \bar{Z} \left(\varepsilon + \frac{in\pi}{t} \right) \right], \quad (23)$$

where Re is the real part and i is imaginary number unit. For faster convergence, numerous numerical experiments have shown that the value of ε satisfies

the relation $\varepsilon t \approx 4.7$ Tzou. The value of $\frac{\varphi_1(r, t)}{r}$ at $r = 0$ is undefined value and it must be replaced by its limit as $\lim_{r \rightarrow 0} \frac{\varphi_1(r, t)}{r}$ and by using L'Hôpital's rule as:

$$\left. \frac{\varphi_1(r, t)}{r} \right|_{r=0} = \lim_{r \rightarrow 0} \frac{\varphi_1(r, t)}{r} = \left. \frac{d\varphi_1(r, t)}{dr} \right|_{r=0}. \quad (24)$$

NUMERICAL RESULTS AND DISCUSSION

To simulate the thermal response within a small spherical tumor of radius $R = 0.005$ m and its surround tissue, the thermal material properties of the tumor and the tissue are provided in Table1. The volumetric heat capacity of blood is $\rho_b C_b = 4.18 \times 10^6$ J/m³/K and the spatial heating source is specified with $q_0 = 6.15 \times 10^6$ W/m³, $r_0 = 0.75 \times R$ and $h = 4.0 \times R$.

Table1: Properties of Tumor-Tissue Model

Parameter	Unit	Tumor	Tissue
K	W / m K	0.778	0.642
ρ	kg / m ³	1660	1000
C	J / kg K	2540	3720
w_b	m ³ / s / m ³	0.0064	0.0064
T_0	^o C	37	37
q_m	W / m ³	29000	450
x	m	0.005	0.02
β	m ⁻²	0.000001	0.000001

Figure 1 shows the heat conduction increment along the distance range of tumor $0.0 \leq r \leq R = 0.005$ and

of tissue $R = 0.005 \leq r \leq h = 0.02$ at the instant time $t = 20$ s and $\tau_r = 5.0$ s, $\tau_q = 15.0$ s. DPL type I, II, III for the one-temperature and two-temperature model, respectively, have been represented in this figure to discuss the effect of the two temperature parameter on the conductive temperature increment. The two-temperature parameter β has significant effect where the conductive temperature increment decreases in the context of the two-temperature model for the three DPL types. The non-linear effects of τ_r^2 , τ_q^2 are very significant. The heat conduction temperature increment is greater in the context of DPL type III than DPL type I and Type II. The non-linear term of τ_q^2 plays a vital role to increase the heat conduction temperature increment in the context of the one-temperature model and the two-temperature model. In the tumor space, the heat conduction temperature increment in the context of DPL type III is greater than DPL type I and DPL type I is greater than DPL type II. In the tissue space, the three types are much closed based on one-temperature parameter while they are coinciding based on the two-temperature model. The difference values of the heat conduction increment in the context of the one-temperature model and the two-temperature model are greater in the tumor space than its values in the tissue space because the positions $0 \leq r \leq R$ are in the range of the heating source. Figures 2-4 show the heat conduction increment of DPL type I, II, and III, respectively, in the context of the one-temperature model and two-temperature model, respectively. The non-linear effects of τ_r^2 , τ_q^2 are significant. The heat conduction temperature increment is greater in the context of the one-temperature model than the two-temperature model. The non-linear term of τ_q^2 plays a vital role to increase the heat conduction temperature increment in the context of the one-temperature model while it has a limited role in the context of the two-temperature model. In the tumor space, the heat conduction temperature increments when $\tau_r = 15.0$ s, $\tau_q = 30.0$ s is greater when $\tau_r = 10.0$ s, $\tau_q = 20.0$ s, and then $\tau_r = 5.0$ s, $\tau_q = 10.0$ s, while the three cases are coinciding in the context of the two-temperature model. In the tissue space, the three types are much closed based on one-temperature parameter while they are coinciding based on the two-temperature model. The difference values of the heat conduction increment in the context of the one-temperature model and the two-temperature model are greater in the tumor space than its values in the tissue space because the positions $0 \leq r \leq R$ are in

the range of the heating source. Figures 5-7 show the heat conduction increment of DPL type I, II, and III, respectively, in the context of the one-temperature model and two-temperature model, respectively. The non-linear effects of τ_T^2 , τ_q^2 are significant. The heat conduction temperature increment is greater in the context of the one-temperature model than the two-temperature model. The non-linear term of τ_q^2 and the time t are playing vital roles to increase the heat conduction temperature increment in the context of the two models. The difference values of the heat conduction increment in the context of the one-temperature model and the two-temperature model are greater in the tumor space than its values in the tissue space because the positions $0 \leq r \leq R$ are in the range of the heating source. Figures 8-10 shows the thermal damage of DPL type I, II, and III, respectively, in the context of the one-temperature model and two-temperature model, respectively. The line passing through the damage $\Omega = 1.0$ separates between the irreversible damage above and the reversible damage below. The non-linear effects of τ_T^2 , τ_q^2 are significant. The thermal damage is greater in the context of the one-temperature model than the two-temperature model. The non-linear term of τ_q^2 and the position r are playing vital roles to increase or decrease the heat thermal damage in the context of the two models. The only one case that has irreversible damage occurred when $\tau_q > \tau_T$ for the one-temperature model and the two-temperature model and all the other cases when $\tau_q < \tau_T$ and $\tau_q = \tau_T$ has reversible damage to the two models. The one-temperature model offers irreversible damage quantity more than the two-temperature parameter. The DPL type III offer irreversible damage quantity more than the DPL type I and then the DPL type II offers the smallest irreversible damage quantity.

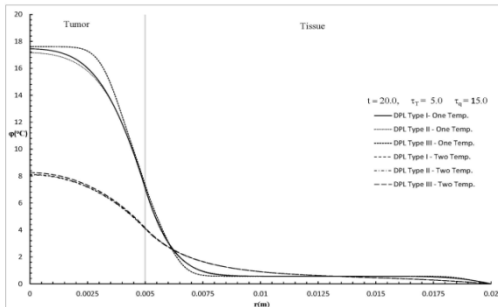


Figure 1: The heat conduction increment with different DPL types

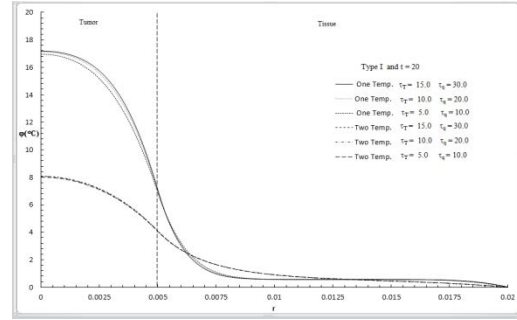


Figure 2: The heat conduction increment of DPL type I

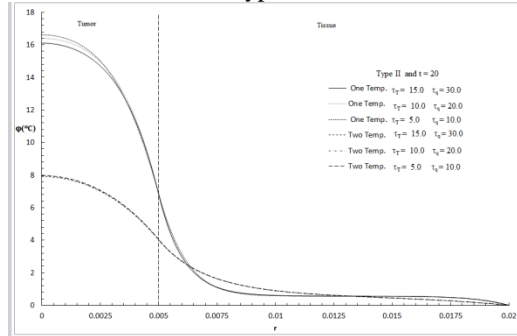


Figure 3: The heat conduction increment of DPL type II

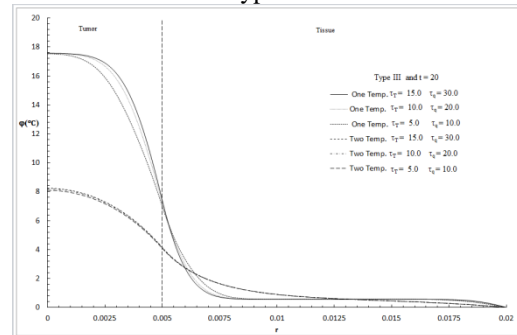


Figure 4: The heat conduction increment of DPL type III

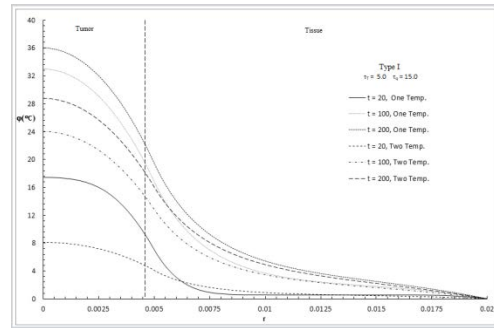


Figure 5: The heat conduction increment of DPL type I at a different time and various r

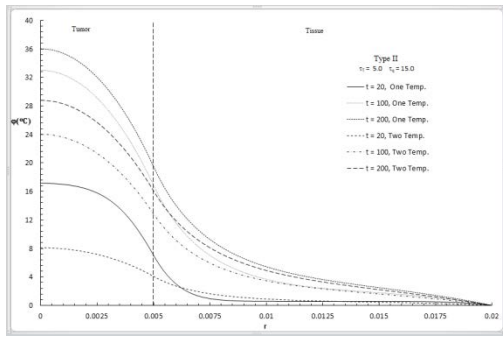


Figure 6: The heat conduction increment of DPL type II at a different time and various r

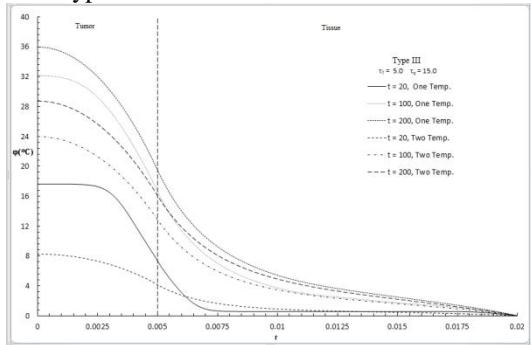


Figure 7: The heat conduction increment of DPL type III at a different time and various r

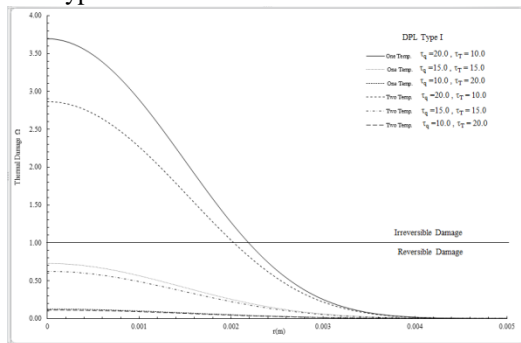


Figure 8: The thermal damage quantity of DPL type I of the tumor

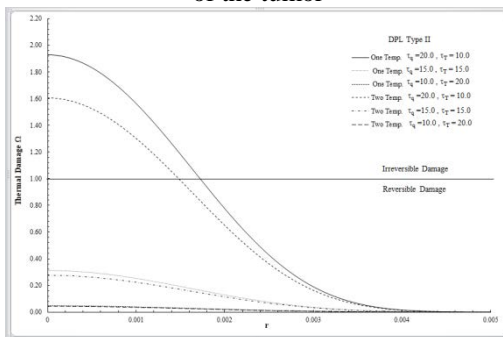


Figure 9: The thermal damage quantity of DPL type II of the tumor

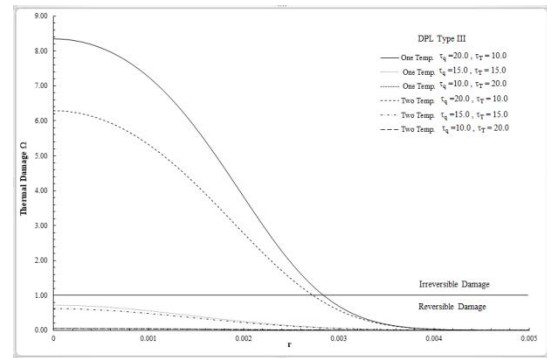


Figure 10: The thermal damage quantity of DPL type III of the tumor

REFERENCES

- [1] J. Otte, "Hyperthermia in cancer therapy," *European journal of pediatrics*, vol. 147, pp. 560-569, 1988.
- [2] J. Van der Zee, "Heating the patient: a promising approach?," *Annals of oncology*, vol. 13, pp. 1173-1184, 2002.
- [3] P. Wust, B. Hildebrandt, G. Sreenivasa, B. Rau, J. Gellermann, H. Riess, *et al.*, "Hyperthermia in combined treatment of cancer," *The lancet oncology*, vol. 3, pp. 487-497, 2002.
- [4] M. Johannsen, U. Gneveckow, K. Taymoorian, B. Thiesen, N. Waldöfner, R. Scholz, *et al.*, "Morbidity and quality of life during thermotherapy using magnetic nanoparticles in locally recurrent prostate cancer: results of a prospective phase I trial," *International Journal of Hyperthermia*, vol. 23, pp. 315-323, 2007.
- [5] B. Kozissnik, A. C. Bohorquez, J. Dobson, and C. Rinaldi, "Magnetic fluid hyperthermia: advances, challenges, and opportunity," *International Journal of Hyperthermia*, vol. 29, pp. 706-714, 2013.
- [6] K. Maier-Hauff, F. Ulrich, D. Nestler, H. Niehoff, P. Wust, B. Thiesen, *et al.*, "Efficacy and safety of intratumoral thermotherapy using magnetic iron-oxide nanoparticles combined with external beam radiotherapy on patients with recurrent glioblastoma multiforme," *Journal of neuro-oncology*, vol. 103, pp. 317-324, 2011.
- [7] W. Andrä, C. d'Ambly, R. Hergt, I. Hilger, and W. Kaiser, "Temperature distribution as function of time around a small spherical heat source of local magnetic hyperthermia," *Journal of Magnetism and Magnetic Materials*, vol. 194, pp. 197-203, 1999.
- [8] H. Bagaria and D. Johnson, "Transient solution to the bioheat equation and optimization for

- magnetic fluid hyperthermia treatment," *International Journal of Hyperthermia*, vol. 21, pp. 57-75, 2005.
- [9] K.-C. Liu and H.-T. Chen, "Analysis for the dual-phase-lag bio-heat transfer during magnetic hyperthermia treatment," *International Journal of Heat and Mass Transfer*, vol. 52, pp. 1185-1192, 2009.
- [10] S. Maenosono and S. Saita, "Theoretical assessment of FePt nanoparticles as heating elements for magnetic hyperthermia," *IEEE transactions on magnetics*, vol. 42, pp. 1638-1642, 2006.
- [11] N. Tsuda, K. Kuroda, and Y. Suzuki, "An inverse method to optimize heating conditions in RF-capacitive hyperthermia," *IEEE Transactions on Biomedical Engineering*, vol. 43, pp. 1029-1037, 1996.
- [12] M. Salloum, R. Ma, D. Weeks, and L. Zhu, "Controlling nanoparticle delivery in magnetic nanoparticle hyperthermia for cancer treatment: experimental study in agarose gel," *International Journal of Hyperthermia*, vol. 24, pp. 337-345, 2008.
- [13] H. H. Pennes, "Analysis of tissue and arterial blood temperatures in the resting human forearm," *Journal of applied physiology*, vol. 1, pp. 93-122, 1948.
- [14] L. X. Cundin, W. P. Roach, and N. Millenbaugh, "Empirical comparison of Pennes' bio-heat equation," in *Optical Interactions with Tissue and Cells XX*, 2009, p. 717516.
- [15] E. H. Wissler, "Pennes' 1948 paper revisited," *Journal of applied physiology*, vol. 85, pp. 35-41, 1998.
- [16] P. J. Chen, M. E. Gurtin, and W. O. Williams, "On the thermodynamics of non-simple elastic materials with two temperatures," *Zeitschrift für angewandte Mathematik und Physik ZAMP*, vol. 20, pp. 107-112, 1969.
- [17] H. Youssef, "Theory of two-temperature-generalized thermoelasticity," *IMA journal of applied mathematics*, vol. 71, pp. 383-390, 2006.
- [18] H. Youssef, "State-space approach to two-temperature generalized thermoelasticity without energy dissipation of medium subjected to moving heat source," *Applied Mathematics and Mechanics*, vol. 34, pp. 63-74, 2013.
- [19] H. M. Youssef, "State-space approach to fractional order two-temperature generalized thermoelastic medium subjected to moving heat source," *Mechanics of Advanced Materials and Structures*, vol. 20, pp. 47-60, 2013.
- [20] H. M. Youssef and N. Alghamdi, "Thermoelastic damping in nanomechanical resonators based on two-temperature generalized thermoelasticity theory," *Journal of Thermal Stresses*, vol. 38, pp. 1345-1359, 2015.
- [21] H. M. Youssef and A. El-Bary, "Two-temperature generalized thermo-elastic medium thermally excited by time exponentially decaying laser pulse," *International Journal of Structural Stability and Dynamics*, vol. 16, p. 1450102, 2016.

THE COMPLEX OF FIELD PILING STATIC LOADING TESTS ON AKSAI, NORTHWEST KAZAKHSTAN

Askar Zhussupbekov¹, Iwasaki Yoshinori², Abdulla Omarov³, Karlygash Borgekova⁴ and Sungat Akhazhanov⁵

^{1,3,4,5} Department of Civil Engineering, L.N. Gumilyov Eurasian National University, Kazakhstan;

²Geo-Research Institute, Japan

ABSTRACT

This paper presents the complex analysis of diverse field loading tests of ten large diameter deep bored piles in Aksai of the northwest Kazakhstan. Overall ten field tests on bored piles with diameter 600 mm, depth 15.51 m and 21.85 m were performed correspondingly. Two static lateral, four static tensions and four static compression pile loading tests were carried out on the construction site of KPC Gas Debottlenecking Project. Static loading tests applied load to a deep-foundation element gradually for measuring foundation settlement. Applied load and head movement are measured for static axial compression and tension load tests. Applied loads are determined using a load cell and hydraulic jack pressure. The foundation's head movement can be measured using digital or mechanical dial gages, a number of types of displacement transducers, string potentiometers, or a combination of these devices. The applied load and head movement is plotted and interpreted to define the foundation's geotechnical load. The static loading tests were performed on axial compression by ASTM D1143, axial tension by ASTM D3689 and lateral by ASTM D3966. The load-settlement and the load-displacement curves were obtained from field tests. These curves were analyzed to identify the bearing capacity. Comparison of bearing capacity of bored piles with different length in problematic soil conditions of West Kazakhstan were discussed in this paper. The analysis showed that the bearing capacity of bored piles with different lengths corresponds to the design requirements.

Keywords: *Pile test, PLT, STPLT, SCPLT, SLPLT*

INTRODUCTION

The Karachaganak field is one of the world's largest oil and gas condensate fields located in northwest Kazakhstan and covering an area of more than two hundred eighty square kilometers. The Karachaganak field is located in a remote and challenging working environment with the ambient temperature ranging from minus forty degrees Celsius in winter to plus forty degrees in summer. The field, the top of which is located at a depth of around three thousand five hundred meters, is some one thousand six hundred meter thick and very complex and unique. Karachaganak Field is a gas condensate field in Kazakhstan. It is located about twenty three kilometers east of Aksai (Aksai) in the northwest of Kazakhstan. The field was once a massive Permian and Carboniferous reef complex covering an area thirty by fifteen square kilometers.

ENGINEERING-GEOLOGICAL CONDITIONS OF THE CONSTRUCTION SITE AKSAI, IN NORTHWEST KAZAKHSTAN

The Karachaganak Field is one of the world's largest gas condensate fields. It is located in the Pre-Caspian Basin, which extends from the southeastern

margin of the Russian Platform down to the northern coast of the Caspian Sea. The North Caspian is a pericratonic depression of Late Proterozoic-Early Paleozoic age (see Figure 1).

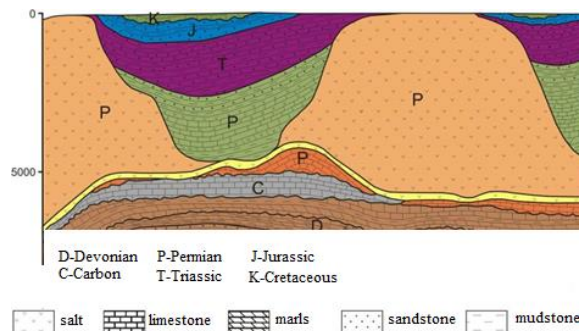


Fig.1 The geological structure of the Karachaganak field.

Sediments in the five hundred thousand square km basin are up to twenty two km thick in places. The basin is subdivided into numerous zones by large salt domes, and the primary salt layer, the Permian Kungurian salt, separates strata vertically into subsalt and suprasalt layers. The basin is bounded to the east by the Hercynian Ural

Mountains and to the southeast and south by other orogenic belts. In the north, the basin lies on the flank of the Voronezh Massif in the west and the Volga-Ural Platform in the north. Numerous oil and gas fields have been discovered in this region in addition to Karachaganak, such as Astrakhan, Tengiz and Zhanazhol Fields [1].

The depositional setting of the field is also varied. On the basis of core sample analysis and seismic studies the following depositional settings have been identified: limestone, talus, normal marine, shallow marine, inner reef lagoon, reef core, relatively deep water, slope, and anhydrite (see Figure 2).

In geological structures of a site of researches take part: EGE-1: Loam-heavy, dusty, yellowish-brown, brown color, lumpy, weakly wet, from solid to semisolid consistence, setting; EGE-2: Clay-light, brownish black, yellowish-brown and brown color, lumpy, weakly wet, from solid to semisolid plastic consistence, setting; EGE-4: Clay-light, dusty, brown and light brown color, lumpy, weakly wet, from solid to tough plastic consistence; EGE-5: Clay reddish-brown, dark brown color with black free designs, solid weakly wet, from solid to tough plastic consistence; EGE-6: Clay-light, dusty, greyish-brown, dun color with free designs of grey color, average density, weakly wet, wet, from semisolid to tough plastic; EGE-7: Clay-light, dusty, dun, grey, dark grey color, average density, wet, tough plastic.

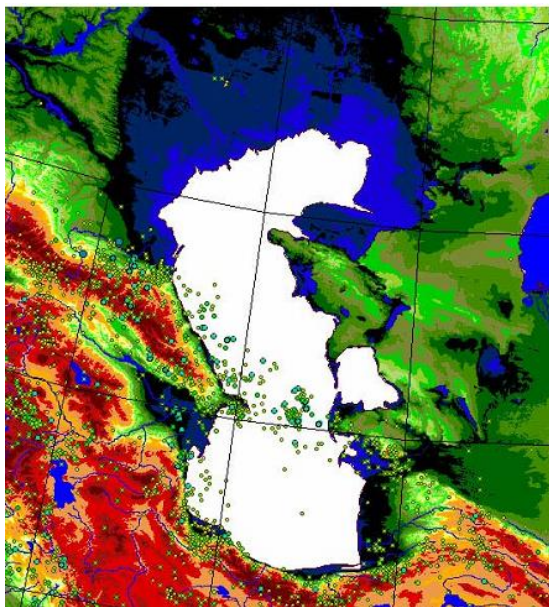


Fig. 2 Location of earthquake epicenters to the northern coast of the Caspian Sea.

Results of physic-mechanical properties of soil the bases of construction site are resulted from top to down in Table 1.

Table 1 Standard and design values of physical and mechanical characteristics of soils

N E G E	S O I L	Soil Consist ency g/cm ³	Speci fic cohe sion MPa	Ang le of inter nal fric tion, deg.	Mod ulus of defor ma tion	De sign resis tance kPa
		ρ	c	ϕ	E	R_0
1	L O A M	1.73	-	-	9.34	400
		1.96	0.006	20	4.4	200
2	C L A Y	1.77	-	-	7.39	400
		1.97	0.008	19	4.78	200
4	C L A Y	1.92	-	-	8.08	400
		2.03	0.015	19	7.10	250
5	C L A Y	1.94	0.029	17	7.59	250
		2.01	-	-	-	-
6	C L A Y	1.96	0.026	18	8.09	250
		2.01	-	-	-	-
7	C L A Y	1.98	0.020	19	8.33	250
		2.03	-	-	-	-

Field testing of soils by cone penetration test was executed for more detailed partition of soils and determination of bearing capacity of piles on soils.

Soil Field Tests PLT (Plate Load Test)

Plate Load Test is a field test for determining the ultimate bearing capacity of soil and the likely settlement under a given load. The Plate Load Test basically consists of loading a steel plate placed at the foundation level and recording the settlements corresponding to each load increment. The test load is gradually increased till the plate starts to sink at a rapid rate. The total value of load on the plate in such a stage divided by the area of the steel plate gives the value of the ultimate bearing capacity of soil. The ultimate bearing capacity of soil is divided by suitable factor of safety to arrive at the value of safe bearing capacity of soil. PLT tests by loading a plate with a diameter of 300 mm are made in accordance with requirement GOST20276 (1999) or ASTM D 1194. The plate loading test (further PLT)

was carried out in the workings at a depth of 1.2 m while maintaining the natural addition of soil, with a flat die 300 mm in diameter, to determine the elastic modulus of deformation (see Figure 4) [2-3].

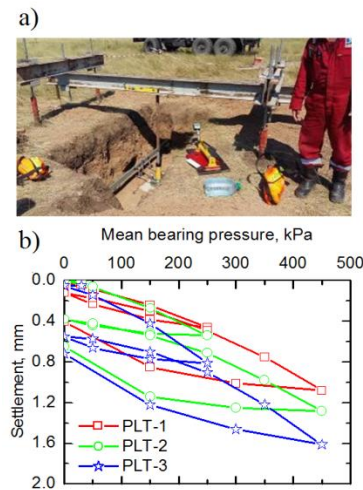


Fig. 4 Plate load test: (a) Photo field test and (b) nature of load-settlement curve (PLT-1, PLT-2 and PLT-3).

Testing with a flat stamp consisted in the fact that the stamp was placed on the bottom of the pit, on the previously cleaned and leveled surface of the ground, after which a step-by-step loading was performed on the stamp. The subsequent stage of loading was carried out after the decay of the deposit from the previous loading. As a support, beams fixed on both sides on the anchor piles were used. Totally three tests one test in Plate Load Test 1 (further PLT-1), second test in Plate Load Test 2 (further PLT-2) a depth of 1.2 m had been made. The load intensity and settlement observation of the plate load test are plotted. The figure shown below shows a set of typical load settlement curves. Figure 4 shown the results the pressure-settlement diagrams of Plate load tests of PLT-1, PLT-2 and PLT-3.

Modulus of deformation of soils in PLT-1 – 108.8 MPa, PLT-2 – 86.1 MPa and PLT-3 – 61.7 a depth of 1.2 m.

The pile installation through technology CFA

Modern geoenvironment face with engineers and designers modern requirements, therefore traditional technologies were replaced by recent economically, ecologically and energy-efficient technologies, including pile foundation. Pile foundation is a widespread type of foundations on construction sites of Kazakhstan. Expediency of pile foundation is explained by high value of bearing capacity of high-rise buildings. At the same time settled design Standards is not corresponding with new emerged technologies, because of absence any

recommendation for new pile design. CFA pile is a type of drilled foundation in which the pile is drilled to the final depth in one continuous process using a continuous flight auger. The use of the continuous flight auger rig avoids many of the problems of drilling and concreting piles experienced when using conventional power augers. The new CFA equipment can perform piles in most type of soils (including sand, gravel, silt, clay, chalk and weak weathered rock) with diameters up to 1200 mm and lengths down to 35-40 meters. So, with proper planning and design, performing equipment and skilled personnel, high production rates and high quality product can be achieved, Klosinski & Rychlewski (2003). Installation of CFA pile consist of following steps: placing the boring machine to the boring place; boring the pile hole to the design level; removing the screw with simultaneous concrete filling under the high pressure and replace the boring machine, installation of steel anchor into the pile body with preparation of pile head. In modern CFA technology the systematic employment of devices auto-recording the drilling data represent a real breakthrough considering that in the past the CFA method was not accurate, and relied on the operator's ability: now such devices guarantee the control and recording of the data during the whole construction process. The recorded working data are usually drilling/withdrawal speed, rotation speed, depth, concrete pressure and delivery rate per increment of auger lift during casting. The CFA construction sequence is comprised of five stages in Figure 5.

Stage 1. The digging tip of the auger is fitted with an expendable cap;

Stage 2. The auger is drilled into the ground to the required depth;

Stage 3. Concrete is pumped through the hollow stem, blowing off the expendable cap under pressure;

Stage 4. Maintaining positive concrete pressure, the auger is withdrawn all the way to the surface;

Stage 5. Reinforcement is placed into the pile up to the required depth.

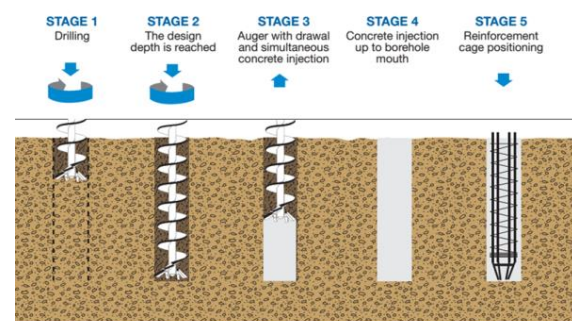


Fig. 5 The CFA construction sequence.

Static Pile Loading Test

Static Compression Pile Loading Test

In this article loading tests used for deep drilling piles in KPC Gas Debottlenecking Project near Aksai, Kazakhstan. Bored piles which have diameter 600 mm and from 15.53 to 21.85 m depths have been executed at the Caspian Sea for more shipments platforms construction site. Some of the requirements of the designer of piled foundations and to what extent the accessible testing methods comply with these requirements are considered. Finally, some recommendations are made for testing methods suitable for problematical ground conditions of Kazakhstan are introduced.

Static Compression Pile Loading Test (further SCPLT) one of the more reliable field tests in analyzing pile bearing capacity. SCPLTs carried out for four piles on the construction site (see Figure 6). The measured relationships between the pile head load, L , and the head settlement, S , of the test piles are shown in Figure 7.

It is seen from Figure 7 that the load-settlement curves of four piles SCPLT-1,-2, -3 and SCPLT-4 are almost identical, having an ultimate shaft capacity of 1050 kN (SCPLT-3 and SCPLT-4), 1310 kN (SCPLT-2) and 1975 kN (SCPLT-1).

Standard – SNiP RK 5.01-03-2002 – ultimate value of settlement of the tested pile is determined as and depending on category of construction is equal to 16 or 24 mm. The last argument shows conditional character of SLT method [4-6].

According to Kazakhstan Standard 1% of constructed piles on construction site must be tested by SCPLT, but at least 2 SCPLTs in a site must be done.

According to SCPLT results, the load-settlement diagrams were drawing (see Figure 7). The pressure in the jack was created with the help of manual electro-hydraulic pump station NER -1,6A40T1 with power distribution, the moving of concrete piles was fixed by caving in measurers MA100BU100, which were positioned on center of unmovable bearings with the benchmark system. For reference beams using two H-beams with $h=20$ cm and length 5.3 m which bolted with clamp to screw piles BAU 114*4*2000 drilled in soil with depth 1.5 m.

Testing platform presented itself system from steel, which consists of metallic beam and 2 platforms located on equidistant distances from the centre main beams (see Figure 6a). Most of the static pile load tests are performed using reaction systems (see Figure 6b). SCPLT is a highly accurate and robust system that enables you to monitor static pile tests whilst also ensuring the safety of site operatives.

This test is used to measure the axial deflection of a vertical deep foundation when loaded in static axial compression. This vertical compression pile

maintained load test is usually carried out to ensure the structural and geotechnical soundness of the pile and also to predict settlement of other piles.



Fig. 6 Field pile test by SCPLT method a) platform b) anchors pile.

The usual procedure is to increase the load in stages until the proposed working load and a certain factor of safety is reached and then to unload and to leave the load off until the rise or rebound substantially ceases, the test is standardized by ASTM D1143 [7]. Vertical static loading of piles using the SCPLT method is one of the most widely used field test methods for soil used to analyze pile bearing capacity. The pile may be tested in two standards cycles:

- The 1st cycle tests the pile to its 150% of the Design Load.
- The 2nd cycle tests the pile to its 200% of the Design Load.

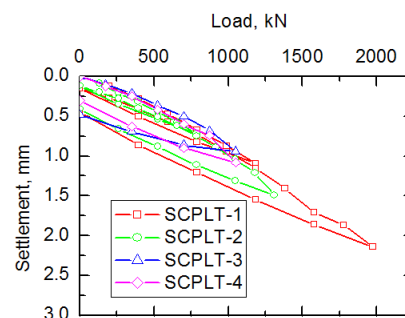


Fig. 7 Results of Static Compression Pile Load Test (piles SCPLT-1, -2, -3 and SCPLT-4).

Static compression pile loading tests were performed on bored piles No. SCPLT-1,-2, -3 and SCPLT-4, which are with depth from 15.53 and 21.85. In SCPLT testing, the test load on the pile is

specified for one and two cycles (one 1050 kN (SCPLT-3,-4) and two cycles from 786 kN to 1310 kN (SCPLT-2) and from 1185kN to1975kN (SCPLT-1), respectively). Loading and unloading was carried out in the following sequence (SCPLT-1): 0, 25, 50, 75, 100, 125, 150, 100, 50, 0, 25, 50, 100, 125, 150, 175, 200, 225, 250, 200, 150, 100, 50 and 0% of design. In the first cycle, the experimental pile was loaded to 150% of the design value (1185 kN); during the second cycle, to 200% (1975 kN). The hold time while loading was 60 min; while unloading –15 min. It took 300 min, respectively, to attain peak load [7].

Static Tensile Pile Loading Test

Static tensile loading test do not apply concrete and composite piles, prestressed reinforced concrete piles without transverse reinforcement bored piles with enlarged base and screw piles. It is allowed to use the piles with the help of which the soil test was tested with static top down load. The depth of the pile subsidence during test conducted for the purpose of determination of the negative friction in subsiding soils, apply equal to the distance from the surface of the soil to the depth where the soil additive from its own weight during soaking equal the maximum permissible draft for the planned building or structure. For the criterion of conditional stabilization deformation take the exit velocity of the pile from soil on each stage of the application tensile load must be no more than 0.1 mm in the last 1 hour of observation or pile foundations of buildings and structures (except bridges), and pile foundations for bridge piers - no more than 0.1 mm in the last hour of observation. Load at the control pile test with tensile load during construction should not exceed the design tensile load on pile indicated in calculation of the pile foundation.

In this paper static tensile loading tests used for deep CFA bored piles in construction site Aksai (see Figure 8). Bored piles which have diameter 600 mm and from 15.51 to 21.71 m depths have been executed at the Caspian Sea for more shipments platforms construction site.



Fig. 8 Static Tension Pile Loading Test.

Loading and unloading was carried out in the

following sequence (for STPLT): 0, 25, 50, 75, 100, 125, 150, 100, 50, 0, 25, 50, 100, 125, 150, 175, 200, 225, 250, 200, 150, 100, 50 and 0% of design. In the first cycle, the experimental pile was loaded to 360 kN of the design value; during the second cycle, to 600 kN. According to STPLT results, the load - settlement diagrams were drawing (see Figure 9) [7].

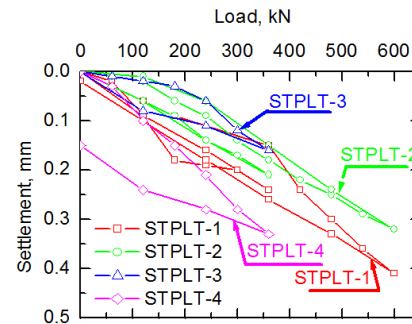


Fig. 9 Results of Static Tension Pile Load Test (piles SCPLT-1,-2,-3 and SCPLT-4).

Static Lateral Pile Loading Test

This test method covers procedures for testing vertical and batter piles either individually or in groups to determine the load-deflection relationship when subjected to lateral loading. It is applicable to all deep foundation units regardless of their size or method the actual lateral load capacity of the pile-soil system can best be determined by lateral testing. Such testing measures the response of the pile-soil system to lateral loads and may provide data for research and development, engineering design, quality control, and acceptance or rejection under specifications. Under the iterative elastic method of analysis that considers the nonlinear response of the soils, lateral testing combined with proper instrumentation can be used to determine soil properties necessary for the structural design of the pile to resist the lateral load to be applied.



Fig. 10 Static Lateral Pile Loading Test.

In this article static Lateral loading tests used for deep CFA bored piles in construction site Aksai (see Figure 10). Bored piles which have diameter 600 mm and from 15.51 to 20.50 m depths have been

executed at the Caspian Sea for more shipments platforms construction site.

Loading and unloading was carried out in the following sequence (for SLPLT): 0, 25, 50, 75, 100, 125, 150, 100, 50, 0, 25, 50, 100, 125, 150, 175, 200, 225, 250, 200, 150, 100, 50 and 0% of design. In the first cycle, the experimental pile was loaded to 150% of the design value (120 kN); during the second cycle, to 250% (200 kN) [7]. According to SLPLT result, the load - displacement diagrams were drawing (see Figure 11).

Table 2 presents a comparative analysis of the bearing capacity of piles, obtained by different methods in this research.

Table 2 Results of complex of field piling static loading tests

#	Pile #	L, m	D, mm	Load, kN	S, mm
Static Compression Pile Loading Test					
1	SCPLT-1	20.50	600	1975	2.14
2	SCPLT-2	15.53	600	1310	1.48
3	SCPLT-3	21.85	600	1050	0.94
4	SCPLT-4	21.72	600	1050	1.08
Static Tension Pile Loading Test					
1	STPLT-1	20.50	600	600	0.41
2	STPLT-2	15.51	600	600	0.32
3	STPLT-3	21.71	600	360	0.16
4	STPLT-4	21.69	600	360	0.33
Static Lateral Pile Load Test					
1	SLPLT-1	15.51	600	200	6.19
2	SLPLT-2	20.50	600	200	7.27

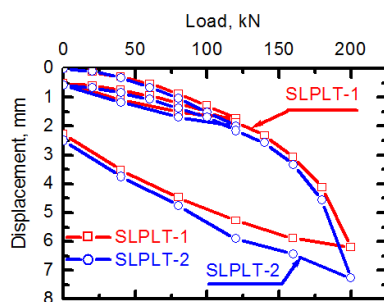


Fig. 11 Results of Static Lateral Pile Load Test (SLPLT-1 and SLPLT-2).

CONCLUSION

Existing pile foundation standards practiced in Kazakhstan are out-of-date and are in urgent need for modernization. This paper presented very short descriptions of coming changes to the concept of Kazakhstan pile foundation design.

The results of the axial compression and tension loading tests performed in soft to firm or stiff clays demonstrated the suitability of CFA bored pile foundations. The results of the loading testing program confirmed that the CFA bored pile is a viable deep foundation option for construction Oil and Gas in remote areas West Kazakhstan and demonstrated their advantages.

Static pile loading test is the most reliable method to obtain the load-settlement relation of piles. Most of the static pile load tests are performed using reaction systems. The number of pile load tests in construction site is limited to 2 piles in usual of construction site in Kazakhstan.

The results of the full-scale load tests are also used to validate the theoretical model used for CFA bored pile design installed in soft and problematical soils of northwest of Kazakhstan.

The bearing capacity of CFA boring piles according to the results of shown table 5 amounted to be maximal load 1975 kN, settlement from 0.94 mm to 2.14 mm. These investigations are important for understanding of behavior of piles on problematical soil ground of Aksai, northwest of Kazakhstan.

REFERENCES

- [1] Zhussupbekov, A., Omarov, A., Zhukenova, G., Tanyrbergenova, G. (2017). Pile Foundations of Mega Projects: New Railway Station and LRT in Problematical Soil Ground of Astana. *Procedia Engineering*, Vol. 189, Pages 511-518.
- [2] GOST 20276-99 (1999). Soils. Field methods for determining the strength and strain characteristics.
- [3] ASTM D 1194. Standard Test Method for Bearing Capacity of Soil for Static Load and Spread Footings.
- [4] Zhussupbekov A.Zh., Lukpanov R.E., Omarov A.R. (2016). Experience in Applying Pile Static Testing Methods at the Expo 2017 Construction Site. *Journal of Soil Mechanics and Foundation Engineering*. Volume 53, Issue 4, Pages 251-256.
- [5] Zhussupbekov A., Omarov A. (2016). Modern Advances in the Field Geotechnical Testing Investigations of Pile Foundations. *Procedia Engineering*, Vol. 165, Pages 88-95.
- [6] Zhussupbekov, A.Z., Lukpanov, R.E., Omarov, A.R. (2016). Bi-directional Static Load testing. *Fourth Geo-China International Conference (Geotechnical Special Publication)*. Shandong, China. Pages 35-42.
- [7] ASTM D1143 / D1143M - 07(2013) Standard Test Methods for Deep Foundations Under Static Axial Compressive Load.

SEE 2019

Bangkok, Thailand

Invitation to participate

- The "International Journal of GEOMATE" is a Scientific Journal of the GEOMATE International Society that encompasses a broad area in Geotechnique, Construction Materials and Environment.
- The key objective of this journal is to promote interdisciplinary research from various regions of the globe.
- The editorial board of the journal is comprised of extensively qualified researchers, academicians, scientists from Japan and other countries of the world.
- It is peer-reviewed Journal that is published quarterly till 2015 and now bimonthly. All articles published in this journal are available on line.
- Contributors may download the manuscript preparation template for submitting paper or contact to the Editors-in-Chief

editor@geomatejournal.com

ISSN: 2186-2990

DOI: <http://dx.doi.org/10.21660/geomate>



Scopus

EBSCO

CENGAGE Learning

U

GIF

doi

crossref

VOLUME 00

Issue 00

Month, Year

International Journal of GEOMATE

(Geotechnique, Construction Materials and Environment)



THE GEOMATE INTERNATIONAL SOCIETY

<http://www.geomatejournal.com/>